SCHOLARLY PUBLICATIONS

A CURRENT AWARENESS BULLETIN
OF RESEARCH OUTPUT

@DTU

(127th Edition)

JULY 2023

BY: CENTRAL LIBRARY

DELHI TECHNOLOGICAL UNIVERSITY
(FORMERLY *DELHI COLLEGE OF ENGINEERING)*
GOVT. OF N.C.T. OF DELHI
SHAHBAD DAULATPUR, MAIN BAWANA ROAD
DELHI 110042

PREFACE

This is the **One Hundred Twenty Seventh** Issue of Current Awareness Bulletin started by Delhi Technological University, Central Library. The aim of the bulletin is to compile, preserve and disseminate information published by the faculty, students and alumni for mutual benefits. The bulletin also aims to propagate the intellectual contribution of Delhi Technological University (DTU) as a whole to the academia.

The bulletin contains information resources available in the internet in the form of articles, reports, presentations published in international journals, websites, etc. by the faculty and students of DTU. The publications of faculty and student which are not covered in this bulletin may be because of the reason that the full text either was not accessible or could not be searched by the search engine used by the library for this purpose.

The learned faculty and students are requested to provide their uncovered publications to the library either through email or in CD, etc. to make the bulletin more comprehensive.

This issue contains the information published during **July, 2023**. The arrangement of the contents is alphabetical. The full text of the article which is either subscribed by the university or available in the web is provided in this bulletin.

Central Library

CONTENTS

1. A 10-kW Active Front End Rectifier Fed Dual Active Bridge Converter For EV Charging, ***6.Ashish Mishra*** and ***3.Mukhtiar Singh***, Electrical, DTU

2. A Comprehensive Analysis of Electric Vehicle Charging Infrastructure, Standards, Policies, Aggregators and Challenges for the Indian Market, Fareed Ahmad and ***6.1.Mohd Bilal***, Electrical, DTU

3. A Comprehensive Examination of the Economic Impact of Out-of-pocket Health Expenditures in India, ***6.Mehak Nanda***, ***6.Rajesh Sharma*** and ***3.Rajesh Sharma***, USME, DTU

4. A Hybrid Method for Network Intrusion Detection, ***8.Devika Jaiswal***, ***8.Kunj Arora***, ***8.Manan Varshney*** and ***3.Trasha Gupta***, Applied Mathematics, DTU

5. A Modified Artificial Potential Field for UAV Collision Avoidance, ***8.Astik Srivastava***, ***8.V.R. Vasudevan***, ***8.Harikesh***, ***3.Raghava Nallanthiga*** and P.B. Sujit, Electronics, DTU

6. A Robust Colon Cancer Detection Model Using Deep-Learning, ***8.Vanishka Kadian***, ***8.Arushi Singh*** and ***3.Kapil Sharma***, IT, DTU

7. A SEPIC PFC fed LLC Resonant converter For EV Battery Charger Applications, ***7.1.Satyamit Kumar*** and ***3.Narendra Kumar***, Electrical, DTU

8. A Study on Process Parameters and Scope of Material Flexibility in Friction Stir Additive Manufacturing, a Sustainable Technology, ***7.Archana Gopal*** and ***3.N Yuvraj***, Mechanical, DTU

9. A Taxonomical Review of Developments in Digital Storage Oscilloscope (DSO), ***3.Malti Bansal***, ***8.Riyanshi Arora*** and ***8.Ritvik Bharti***, Electronics, DTU

10. Abenet: An emotion recognition for Bengali language, ***8.Rajat***, ***8.Pooja Jaiswal***, ***8.Rahul Kakkar*** and ***3.Rohit Beniwal***, CSE, DTU

11. Adaptive Two-Stage Reversible Data Hiding in Encrypted Images using Prediction Error Expansion, ***8.Ankur***, ***3.Rajeev Kumar*** and ***8.Ajay K Sharma***, CSE, DTU

12. All-p ZVLL Inverter with Bootstrapping based on a ditch OTFT, Sakshi Gupta, ***3.Poornima Mittal*** and Pradeep Juneja, Electronics, DTU

13. An approach for Credit-Scoring using Swarm intelligence for feature selection and PSO trained ANN based classification, ***3.Indu Singh***, ***8.Nikhil Mishra***, ***8.Anshul Joshi*** and ***8.Nishchal Agarwal***, CSE, DTU

14. An Emotion-Guided Approach to Domain Adaptive Fake News Detection Using Adversarial Learning (Student Abstract), ***8.Arkajyoti Chakraborty***, ***8.Inder Khatri***, ***8.Arjun Choudhry***, ***8.Pankaj Gupta***, ***3.Dinesh Kumar Vishwakarma*** and Mukesh Prasad, IT, DTU

15. APPLICATION FOR DETECTION OF FIELD BOUNDARIES FROM SATELLITE IMAGERY USING RSUNet-A, ***8.Neha Singh***, ***8.Mohit***, ***8.DevAryan Dogra*** and ***3.Manoj Kumar***, CSE, DTU

16. Artificial Intelligence In Field of Medical Imaging Informatics, ***7.Medha Jha*** and ***3.Yasha Hasija***, Biotechnology, DTU

17. Attack detection in industrial IoT using novel ensemble techniques, ***8.Kushagra Keserwani***, ***8.Apoorva Aggarwal*** and ***3.Anamika Chauhan***, IT, DTU

18. Bypassing Deep Learning based Sentiment Analysis from Business Reviews, ***6.Ashish Bajaj*** and ***3.Dinesh Kumar Vishwakarma***, IT, DTU

19. Chaotic Behavior of DC-DC Boost Converter by using Voltage Mode Control, ***7.Sandhu Ganesh*** and ***3.Sudarshan K. Valluru***, Electrical, DTU

20. Characteristics performance and analysis of positional variation in charge generation layer to enhance performance of OLED, ***6.Sugandha Yadav***, ***3.Poornima Mittal*** and Shubham Negi, Electronics, DTU

21. Chemical assisted ball end magnetorheological finishing of aluminium 7075 alloy, ***6.Anand Sharma*** and ***3.Mahendra Singh Niranjan***, Mechanical, DTU

22. Citrus Fruit Disease Detection Techniques: A Survey and Comparative Analysis of Relevant Approaches, ***7.1.Poonam Dhiman***, Amandeep Kaur and Vinay Kukreja, CSE, DTU

23. CKS: A Community-Based K-shell Decomposition Approach Using Community Bridge Nodes for Influence Maximization (Student Abstract), ***8.Inder Khatri***, ***8.Aaryan Gupta***, ***8.Arjun Choudhry***, ***8.Aryan Tyagi***, ***3.Dinesh Kumar Vishwakarma*** and Mukesh Prasad, IT, DTU

24. Classifying Heart Sounds for Disease Detection Using Deep Learning Methods, ***8.Dhiren Kinha***, ***8.Garvit Gulati***, ***8.Ashwin Baranwal*** and ***3.Dinesh Kumar Vishwakarma***, IT, DTU

25. Comparative Analysis of Face Detection Techniques on Videos of Low Vs High Quality, ***6.Akshay Mool***, ***3.Jeebananda Panda*** and ***3.Kapil Sharma***, IT and ECE, DTU

26. Comparing Results of Multiple Machine Learning Algorithms on a bilingual dataset for the Detection of Fraudulent News, ***8.Amogh Jalan***, ***8.Aniket Gupta*** and ***3.Dr Priyanka Meel***, IT, DTU

27. Confident Stock Price Prediction using Markov Chains, ***8.Abhiluv Anand*** and ***3.Dr. Ramesh Srivastava***, Applied Mathematics, DTU

28. CONGEST: An Algorithm to Detect Congestion Zones Based on Unmanned Aerial Vehicle (UAV) Flight plans, ***8.Shashank Parmar***, ***3.Rahul*** and ***8.Shashank Taneja***, Software Engineering, DTU

29. Crime Evaluation Using Neural Networks by GPS Trajectory Dataset, ***3.Rahul***, ***8.Vartika Hari Durgapal*** and ***8.Vinshu Chaudhry***, Software Engineering, DTU

30. Cybersecurity Challenges in the Healthcare Domain and the Road Ahead, ***3.Malti Bansal***, ***8.Varun Sirpal***, ***8.Tanmaya Jain***, ***8.Ujjwal*** and ***3.Uma Nangia***, Electronics and Electrical, DTU

31. Deepfake Creation Using Gans and Autoencoder and Deepfake detection, ***8.Manoj kumar Das***, ***8.Manav kumar***, ***8.Ishank kumar kapil*** & ***3.Dr Rajesh kumar yadav***, CSE, DTU

32. Design of a PV-Fed Drive System with a Single-Phase Induction Motor for Irrigation Application, ***8.Eleyde Nhantumbo***, ***8.Dawda Bojang***, ***6.Monika Verma*** and ***3.Ashish Kulkarni***, Electrical, DTU

33. DFT based atomic modeling and Analog/RF analysis of ferroelectric HfO2 based improved FET device, ***6.Yash Pathak***, ***3.Bansi Dhar Malhotra*** and ***3.Rishu Chaujar***, Applied Physics and Biotechnology, DTU

34. Diving deep into the milky way using anti-reflection coatings for astronomical CCDs, ***8.ANMOL AGGARWAL***, ***7.ASHI MITTAL***, GEORGE M. SEABROKE and ***3.NITIN K. PURI***, APPLIED PHYSICS, DTU

35. DLVS: Time Series Architecture for Image-Based Visual Servoing, ***8.Nilesh Aggarwal***, ***8.Anunay***, ***8.Vayam Jain***, ***8.Tushar Singh*** and ***3.Dinesh Kumar Vishwakarma***, Applied Physics, Mechanical, Electrical and IT, DTU

36. DTPF Algorithm Based Open-Source Time-Sensitive Network Leveraging SDN Architecture, ASHA G. HAGARGUND, NEELAWAR SHEKAR VITTAL SHET AND ***3.1.MURALIDHAR KULKARNI***, CSE, DTU

37. Dual Image Reversible Data Hiding: A Survey, ***3.Sanjay Kumar***, ***3.Anjana Gupta*** and Gurjit Singh Walia, Applied Mathematics, DTU

38. Dynamic performance improvement of proton exchange membrane fuel cell system by robust loop shaping and artificial intelligence optimized fractional order PI controllers, Swati Singh, Vijay Kumar Tayal, Hemender Pal Singh, and ***3.Vinod Kumar Yadav***, Electrical, DTU

39. Effect of Meteorological Parameters and Air Pollutants Association with Health Risk Assessment during the Pandemic in Delhi, India, Bhupendra Pratap Singh, Kriti Mehra, Khyati Chowdhary, Charvi Khanna & ***3.Prakash Chandra***, Biotechnology, DTU

40. Effect of Rotational Speed on Mechanical, Microstructure, and Residual Stress Behaviour of AA6061-T6 Alloy Joints through Friction Stir Welding, Virendra Pratap Singh, ***6.Ashish Kumar***, Rajan Kumar, Anchit Modi, Deepak Kumar, Vinyas Mahesh and Basil Kuriachen, Mechanical, DTU

41. Efficient tunable temperature sensitivity in thermally coupled levels of Er3+/Yb3+ codoped BaBi2Nb2O9 ferroelectric ceramic, ***7.Ankita Banwal*** and ***3.Renuka Bokolia***, Applied Physics, DTU

42. Electrical and Electronic Architecture of an ROV, ***8.Sriram Chava***, ***8.Saurav Ranjan***, ***8.Shivang Dudani*** and ***3.Dr Prakash Chittora***, Electrical, DTU

43. Enhancing Accuracy in Handwritten Text Recognition with Convolutional Recurrent Neural Network and Data Augmentation Techniques, ***8.Shivanshu Minz***, ***8.Ritika Kanojia***, ***8.Tushar Yadav*** and ***3.N.Jayanthi***, Electronics, DTU

44. EXPLORING THE DYNAMICS OF HEUTAGOGY IN STEM EDUCATION AND ITS POTENTIAL FOR ENHANCING LEARNING, Mr. Vaibhav Verma, Miss Charmy Panchal, Dr. Jijo Varghese, Mr. Ranjan Kumar Singh and ***8.Er. Rishabh Verma***, Electronics, DTU

45. FACE RESTORATION VIA GENERATIVE ADVERSARIAL NETWORKS, ***8.Sonu Kumar***, ***8.Soham Bhardwaj*** and ***3.Dinesh Kumar Vishwakarma***, IT, DTU

46. Financial burden of injury care in India: evidence from a nationally representative sample survey, ***6.Mehak Nanda*** and Rajesh Sharma, USME, DTU

47. Fingerprint and GSM based Security System for Banks, ***8.Dikshant Pabri***, ***3.Saurabh Mishra***, ***8.Komal Meena***, ***3.Duli Chand Meena*** and ***8.Gaurav Chhoker***, Electrical, DTU

48. Hand Gesture Based Sign Language Recognition Using Deep Learning, ***6.Roli Kushwaha***, ***3.Gurjit Kaur*** and ***3.Manjeet Kumar***, Electronics, DTU

49. Heart Disease Prediction Using a Soft Voting Ensemble of Gradient Boosting Models, RandomForest, and Gaussian Naive Bayes, ***7.Kaustav Sen*** and ***3.Bindu Verma***, IT, DTU

50. High Frequency DC-DC Isolated Converter with Rectification and Synchronous Rectification, ***7.Awanish Akash*** and ***3.Mini Sreejeth***, Electrical, DTU

51. Implementation of PSO based Controllers for Speed Control of BLDC Motor, ***7.Yashi Rani***, ***3.Dr. Uma Nangia*** and ***3.Dr. Narender Kumar Jain***, Electrical, DTU

52. Integration of Nanodiamonds and Graphene in Plasma-Sprayed Al2O3 Matrix for Enhancing the Tribological Properties, ***6.Shubhangi Chourasia***, ***3.Qasim Murtaza*** and ***3.Saurabh Agrawal***, Mechanical, DTU

53. Investigations on Different Global Peak Tracking Algorithms for Extracting Maximum Power from Photovoltaic Systems, ***7.Mayank Ojha*** and ***3.Vanjari Venkata Ramana***, Electrical, DTU

54. JTAG to AHB Bridge, ***3.Malti Bansal*** and ***6.Harsh***, Electronics, DTU

55. Lane-Line Segmentation Using YOLOv7, ***6.Dhruv Sharma***, ***3.S. Indu*** and ***3.N. Jayanthi***, Electronics, DTU

56. Lexical Semantics Identification Using Fuzzy Centrality Measures and BERT Embedding, ***3.Minni Jain***, ***3.Rajni Jindal*** and Amita Jain, CSE, DTU

57. Lightweight and Reliable Deep Learning Model for Plant Disease Detection, ***3.Shailender Kumar***, ***8.Garvit Kansal***, ***8.Jatin Pandey*** and ***8.Harmeet Singh***, CSE, DTU

58. Linarin as an Anti-Cancer Therapeutic: In-Silico and Machine Learning Approach for HPV, ***7.Rati Bhardwaj***, ***7.Ananya*** and ***3.Dr. Asmita Das***, Biotechnology, DTU

59. Link Optimisation of a Microwave Photonic Phase Shifter using Brillouin-Induced Low Biasing, Reena Parihar, Rajveer Dhawan, and ***8.1.Amol Choudhary***, Electrical, DTU

60. Machine Learning & Artificial Intelligence in Production Planning and Control, ***8.Aakarsh Dwivedi***, ***8.Chitrasen Maitry***, ***8.Hrishikesh Raj***, ***8.Ashish Gupta*** and ***3.Ashok Kumar Madan***, Mechanical and Production Engineering, DTU

61. Mathematical modeling and performance analysis of a solar assisted vapour absorption refrigeration system, Sanchita Singh and ***3.Pushpendra Singh***, Mechanical, DTU

62. Mechanical and Structural Properties of Epoxy Resin-Allyl Guar Gum Composites, Gopal Arora and ***3.A.P Gupta***, Applied Chemistry, DTU

63. Mechanical and Surface Wettability Analysis of Rare Earth Modified Composite Coating Developed Using Metal Spraying, ***6.Mohit Vishnoi***, ***3.Qasim Murtaza*** and ***3.Paras Kumar***, Mechanical, DTU

64. Microwave-based Transesterification of Waste Cooking Oil using Waste Aluminium Foil (NaOH/γ-Al2O3) as Catalyst, ***7.1.Naveen Kumar Garg*** and ***3.Amit Pal***, Mechanical, DTU

65. Modeling and Analysis of Finger Splint for Mild to High-Grade Mallet Finger Fracture, ***8.Sahil Bansal***, ***8.Aranyak Tripathi***, ***8.Nikhil Kumar***, ***3.Taruna Singh*** and ***3.Ranganath M.S***, Mechanical and Design, DTU

66. Monitoring Pressure in Controlled Ventilator System under Different Lung Settings, ***8.Palak Meena***, ***8.Palak Sharma*** and ***3.Kapil Sharma***, IT, DTU

67. Multi-factor Assymetric Key Encryption (MAKE) for Mutual Authentication in IoMT, ***8.Sristi Mitra***, ***8.Zishnendu Sarker***, ***8.Priyanka Patel*** and ***3.Pawan Singh Mehra***, CSE, DTU

68. New era of artificial intelligence and machine learning-based detection, diagnosis, and therapeutics in Parkinson's disease, ***6.Rohan Gupta***, ***6.Smita Kumari***, Anusha Senapati, ***6.Rashmi K. Ambasta*** and ***3.Pravir Kumar***, Biotechnology, DTU

69. Performance Analysis of DC Motor using GWO and FPA, ***8.Abhigyan Adarsh***, ***8.Amal Chawla***, ***8.Anirudh Singh*** and ***3.Bharat Bhushan***, Electrical, DTU

70. Performance evaluation and optimization of albedo and tilt angle for solar photovoltaic system, ***6.Neelam Baghel***, ***3.K. Manjunath*** and ***3.Anil Kumar***, Mechanical and Environment, DTU

71. Perspective: The unexplored dimensions behind the foam formation in River Yamuna, India, ***6.Garima Sejwal*** and Santosh Kumar Singh, Environmental, DTU

72. Plant Disease Detection using Deep Learning, ***8.Tejas Gupta***, ***8.Titunath*** and ***8.Vibhor Jain***, CSE, DTU

73. PM2.5 Level Forecasting using Transformer-Based Model, ***8.Varang Rai***, ***8.Sanidhya Kumar***, ***8.Tamandeep Singh*** and ***3.Rajiv Kapoor***, Electronics, DTU

74. Prediction of Surface Roughness of Mild Steel finished with Viscoelastic Magnetic Abrasive Medium, ***8.Anushka Sharma***, ***8.Himagra Chawla*** and ***3.Krovvidi Srinivas***, Mechanical, DTU

75. Proof of Opinion (PoO): A New Consensus Algorithm for Decentralized Blockchain Networks, ***8.Rumit Garg***, ***8.Nandika Arora***, ***8.Shagun Uppal*** and ***3.Dhirendra Kumar***, Mathematics, DTU

76. Realization of DTMOS based 6T SRAM cells and their performance analysis at 32nm technology node, ***8.Divesh***, ***8.Jatin***, ***8.Keshav*** and ***3.Neeta Pandey***, ECE, DTU

77. Reversible Data Hiding for Interpolated Images using CNN based Nearest Neighbour Interpolation, ***8.Praveen Kumar***, ***8.Prateek Ravi*** and ***3.Rajeev Kumar***, CSE, DTU

78. SEMC-Net: A Shared-Encoder Multi-Class Learner, ***8.Rahul Jain***, ***8.Satvik Dixit***, ***8.Vikas Kumar*** and ***3.Bindu Verma***, IT, DTU

79. Social Networks Analysis and Machine Learning: an Overview of Approaches and Applications, ***6.Ms. Sonia Choudhary***, ***3.Prof. Kapil Sharma*** and ***8.Dr. Monika Bajaj***, IT, DTU

80. Store and Restore Delay Reduction Techniques of Non-volatile SRAM cells, ***6.Damyanti Singh***, ***3.Neeta Pandey*** and ***6.Kirti Gupta***, ECE, DTU

81. Structural, vibrational and electronic properties of Nb substituted orthovanadates LaV1−xNbxO4, ***6.Ashok Kumar***, Anurag Sharma, Madhav Sharma, ***3.Vinod Singh***, Anita Dhaka and Rajendra S. Dhaka, Applied Physics, DTU

82. Study and Comparative Analysis of Data Hiding Methods for Animated GIFs, ***8.Pratham***, ***8.Nikhil Kansal***, ***8.Nikhil Tawar*** and ***3.Rajeev Kumar***, CSE, DTU

83. Synthesis of a Novel Raw Wool and Polyacrylamide-BasedHydrogel as a Colorimetric Sensor, ***8.Sachin Gupta***, ***8.Deepti Chauhan***, ***8.Atul Rana***, ***8.Drishti Singh***, ***3.Anil Kumar*** and ***3.Sudhir G. Warkar***, Applied Chemistry, DTU

84. Systematic Literature Review of Current Trends in Artificial Intelligence-Based Intrusion Detection Systems, ***8.Apoorva Aggarwal***, ***8.Kushagra Keserwani*** and ***3.Anamika Chauhan***, IT, DTU

85. Tackling class imbalance in computer vision: A contemporary review, ***6.Manisha Saini*** and ***3.Seba Susan***, IT, DTU

86. Time Series Approach for Visual Servoing Using Transformers, ***8.Tushar Singh***, ***8.Jayant Prakash***, ***8.Tushar Bharti*** and ***3.Dr. Anup Kumar Mandpura***, Electrical, DTU

87. To Determine the Futures pricing of Metal Commodities using Deep Learning, ***8.Vrinda Aggarwal***, ***8.Arman Ranjan***, ***8.Shivam Shaurya*** and ***3.S. K. Garg***, Mechanical, DTU

88. Total Quality Management in Higher Technical Education, ***3.RS Mishra***, ***8.Anshuman Pandey***, ***8.Aryan Rana*** and ***8.Aakash Mehta***, Mechanical, DTU

89. UAV Swarm Navigation in GNSS Denied Region with Formation Control, ***8.Priyanshi Jain***, ***8.Rohaan Qureshi*** and ***3.Raghava Nallanthighal***, Electronics, DTU

90. Uncovering Political Hate Speech During Indian Election Campaign: A New Low-Resource Dataset and Baselines, Farhan Ahmad Jafri1, Mohammad Aman Siddiqui, Surendrabikram Thapa, ***8.Kritesh Rauniyar***, Usman Naseem and Imran Razzak, CSE, DTU

1. *Vice Chancellor*
2. *Pro Vice Chancellor*
3. *Faculty*
4. *Teaching-cum-Research Fellow*
5. *Asst. Librarian*
6. *Research Scholar*
7. *PG Scholar*
8. *Undergraduate Student*

1.1. *Ex Vice chancellor*
2.1. *Ex Pro Vice Chancellor*
3.1. *Ex Faculty*
4.1. *Alumni*
5.1 *Others*
6.1. *Ex Research Scholar*
7.1. *Ex PG Scholar*
8.1. *Ex Undergraduate Student*

2023 4th International Conference for Emerging Technology (INCET)
Belgaum, India. May 26-28, 2023

A 10-kW Active Front End Rectifier Fed Dual Active Bridge Converter For EV Charging

Ashish Mishra
Electrical Engineering Department
Delhi Technological University
Delhi, India
ashishmishra_2k21pes05@dtu.ac.in

Mukhtiar Singh
Electrical Engineering Department
Delhi Technological University
Delhi, India
mukhtiarsingh@dce.ac.in

2023 4th International Conference for Emerging Technology (INCET) | 979-8-3503-3575-0/23/$31.00 ©2023 IEEE | DOI: 10.1109/INCET57972.2023.10170584

***Abstract*—This paper presents the implementation of a three-phase grid-connected electric vehicle (EV) battery charging system comprised of two conversion stages, one AC-DC stage with a three-phase Active Front End (AFE) rectifier, and another DC-DC stage with a single-phase Dual Active Bridge (DAB) converter. The DAB is opted for the DC-DC stage because of its high voltage conversion ratio, power density, and galvanic isolation. The LCL filter at the input of the AC-DC stage is designed to suppress the input current harmonics. Decoupled DQ control of the active front-end rectifier is done to get desired DC Link voltage. Closed loop control of the Dual Active Bridge (DAB) with an LC output filter is implemented to improve battery voltage and reduce ripples. Zero Voltage Switching (ZVS) is achieved in all the switches for different load values, which helps the converter have low switching loss and ensures higher efficiency. The system is designed for a 10-kW power rating, and to check the robustness of the converter and controller, the system is simulated under varying load conditions using MATLAB/Simulink.**

Keywords*— *AC-DC Converter, Active Front End Rectifier, Battery Charging, DC-DC Converter, Dual Active Bridge, Electric Vehicle, LCL Filter, Zero Voltage Switching.

I. INTRODUCTION

A demand for significant CO2 reduction in many industries has emerged because of growing awareness and concern for climate change. For instance, a growing worldwide project that has emerged as a vital element of a sustainable future is the integration of energy-efficient technologies like hydro, wind, and solar power with the electrification of transportation. In fact, the environmental advantages of electric vehicle (EV) technology in terms of energy conservation and lowering greenhouse gas emissions have received a lot of attention. As a result, the EV industry experienced substantial sales growth and is anticipated to continue growing [1]. The anticipated quantity of EVs would lead to a substantial rise in the number of charging stations. EVs with comparatively small battery capacities can enhance their driving range with a reduced charging time. The integrity of the energy distribution system also becomes more crucial at particular hours of the day because of growing energy demand, which could result in major network management issues. In order to address the issues with battery charging and range as well as the overload of the power grid, several charging infrastructure methods have been described in the literature [2]- [4].

The features of the voltage-source converter (VSC), which can operate in both rectifying and regenerating states, incorporate the potential of total dc-link voltage and power factor regulation [5]. Moreover, the implementation of closed-loop current control and pulse width modulation (PWM) enables the production of total harmonic distortion (THD) of less than 5% for a sinusoidal input current, even if no grid voltage or current sensors are employed [6]- [7].

A higher value of inductance is required to reduce the current harmonics. Realizing higher-value filter reactors gets quite expensive for usage over a few kilowatts. Using an LCL filter is a different and more modern approach to this issue. The best results can be obtained using this technique at higher power levels, thus utilizing inductors and capacitors with relatively low values [8]- [9].

With the rapid development of distributed resource interfaces, electric vehicles, energy storage systems, and uninterruptible power supply systems, the use of bidirectional dc-dc converters has significantly increased. Owing to features including its high-power density, soft switching characteristics, galvanic isolation, and lack of passive components Dual active bridge (DAB) converters are becoming more common in comparison to other conventional bidirectional buck/boost converters. The power system is affected by the high-frequency switching DAB converter's considerable harmonic generation at integer multiples of its own considerably high fundamental switching frequency. In order to improve both output voltage and current quality, an LC output filter is cascaded to a DAB converter.

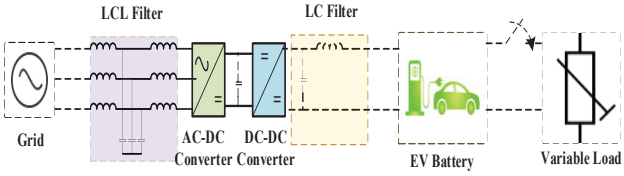

Fig. 1. Block scheme of proposed charging system.

The constant current control of an EV battery for a variable load is implemented using a proportional integral (PI) controller. The output of the PI controller provides phase shift to the secondary side bridge depending on load variation. The constant charging current is required to raise the battery voltage when the voltage is at its lowest point. The battery voltage rises in the constant current stage until it attains the rated value.

II. DAB CONVERTER

Two active bridges coupled by a high-frequency transformer, as shown in Fig. 2, form the foundation of the bidirectional DAB converter, and power flow between these

Authorized licensed use limited to: DELHI TECHNICAL UNIV. Downloaded on July 20,2023 at 11:24:35 UTC from IEEE Xplore. Restrictions apply.

two bridges is equivalent to a power system's power flow between its two voltage buses. Each active bridge consists of four MOSFET switches, anti-parallel freewheeling diodes, and snubber capacitors.

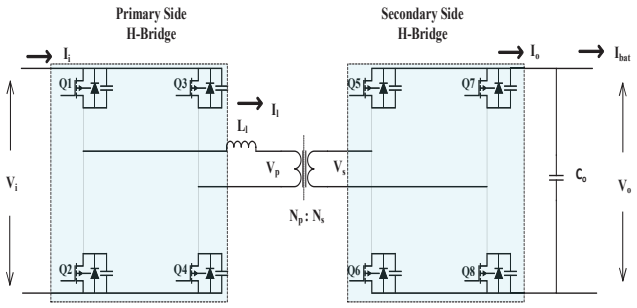

Fig. 2. Bidirectional Dual Active Bridge Converter

To control the DAB converter, one of three ways can be chosen:

Phase shift between the two bridges, switching frequency, as well as duty ratios of switching devices. This work adapts the phase-shift control method because of its efficacy and simplicity. Each active bridge is operated with a constant duty cycle (50%) to generate square waves of high frequency at transformer terminals.

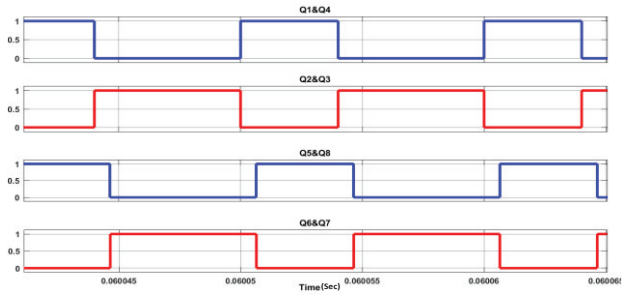

Fig. 3. Switching sequence for Primary and Secondary side Switches

By adjusting the phase shift between these two square waves, the power flow may be controlled, and the power flow is influenced by the sign of the phase shift.

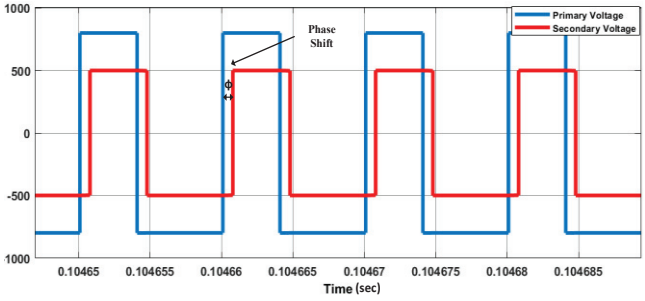

Fig. 4. Phase Shift between Primary and Secondary

The L_l is the primary component of power transfer, containing the transformer leakage inductance and, if necessary, an auxiliary inductor connected in series [10]. Fig. 5 presents the entire structure of the DAB converter, which consists of the output inductor L_o and the capacitor C_o. It has been noted that the output current's ripple decreases as the inductance value goes up. This becomes more evident when the output capacitor is likewise decreased, going for less

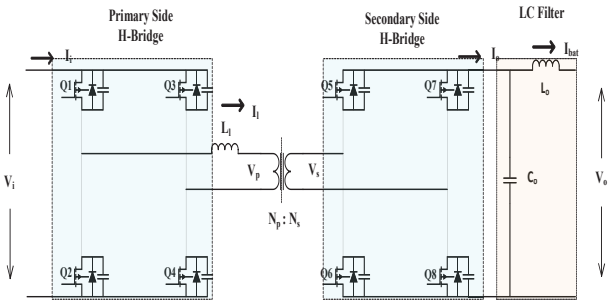

Fig. 5. Bidirectional Dual Active Bridge Converter with output inductance

volume and more power density. Without an output inductor, the conventional design of the DAB converter has a significant current ripple of about 40%. The major factor in extending the service life of batteries is to reduce their current ripple values since they put less stress on them in terms of internal temperature.

III. DESIGN CONSIDERATION

The design of a dual-active bridge's power stage needs to take a number of factors into account. The design of the leakage inductor, output capacitor, intended phase shift, switching frequency, selection of the SiC MOSFETs, transformer, and proposed ZVS range of operation are the most critical factors.

A. Leakage Inductor

$$L_l = V_i V_0 \frac{nd(1-d)}{2P_o F_{sw}} \tag{1}$$

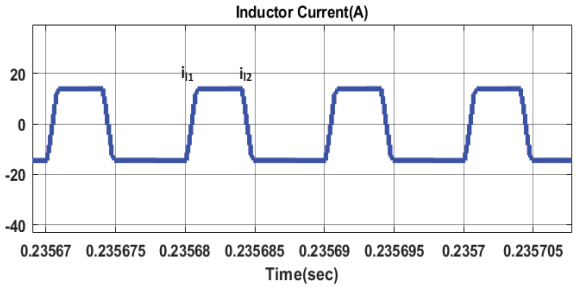

Fig. 6. Inductor Current

The waveform of the inductor current is shown in Fig. 6. This waveform can be used to determine the inductor currents il1 and il2.

$$i_{l1} = 0.5(2\phi - (1-m)\pi)I_n \tag{2}$$

$$i_{l2} = 0.5(2m\phi + (1-m)\pi)I_n \tag{3}$$

Where, m is voltage transfer ratio

$$m = \frac{V_o}{NV_i} \tag{4}$$

B. Phase Shift

The phase shift of the converter is dependent on the leakage inductor. The phase shift for the required power transfer is given by equation (5).

$$\phi = \frac{\pi}{2}\left(1 - \sqrt{1 - \frac{8 \times F_{sw} \times L_l \times P_o}{NV_i V_o}}\right) \tag{5}$$

Authorized licensed use limited to: DELHI TECHNICAL UNIV. Downloaded on July 20,2023 at 11:24:35 UTC from IEEE Xplore. Restrictions apply.

C. Output Capacitor

The amount of capacitance needed to keep the voltage ripple at a predetermined level in accordance with the system specification grows as the leakage inductance increases for a certain value of phase shift.

$$R = \frac{V_o^2}{P_o} \tag{6}$$

$$C_o \frac{dV_o}{dt} = \frac{V_i}{X_{Ll}} \phi(1 - \frac{\phi}{\pi}) - \frac{V_o}{R} \tag{7}$$

The output capacitor was selected to maintain the output voltage's ripple below 5%.

D. Resonant Frequency

$$f_{res} = \frac{1}{2\pi\sqrt{L_l C_s}} \tag{8}$$

E. Zero Voltage Switching

When the primary H-bridge is taken into consideration, Q1 and Q4 turn on and off simultaneously. In this instance, the Cs of Q1 and Q4 are simultaneously charged or discharged using the identical Vds value. The resonant process involves the input as well as the output voltage, switch capacitances, and the leakage inductance.

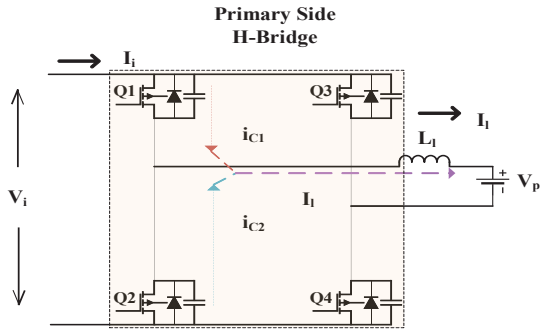

Fig. 7. ZVS Transient Process

When Q1 and Q4 are turned off but Q2 and Q3 are not yet turned on, the ZVS transient process occurs. The input voltage source first releases current, and V_i provides energy for the ZVS process. But the current gradually changes polarity, indicating V_i is starting to use up energy. In reality, the input voltage source's power output or dissipation is zero; however, as demonstrated below, this input voltage source alters the ZVS transition time.

Considering the voltage across the output capacitance of Q1 is v_c, the relationship between the capacitance voltage and inductor current is shown in (9)-(14).

$$V_i = V_{C1}(t) + V_{C2}(t) \tag{9}$$

$$v_C = V_{C1}(t) \tag{10}$$

$$I_i(v_C) = i_{C1}(v_C) - i_{C2}(V_i - v_C) \tag{11}$$

$$I_l(v_C) = i_{C1}(v_C) + i_{C2}(V_i - v_C) \tag{12}$$

$$i_{C1}(v_C) = C_1(v_C)\frac{dv_C}{dt} \tag{13}$$

$$i_{C2}(v_C) = -C_2(V_i - v_C)\frac{d(V_i - v_C)}{dt} \tag{14}$$

The charge passing through the inductor and DC source during the transient process is required to obtain the energy used by the voltage source in the circuit, and this charge is

$$Q_{I_l}(v_C) = \int_0^v (C_1(v_C) + C_2(V_i - v_C))dv_C \tag{15}$$

$$Q_{I_i}(v_C) = \int_0^v (C_1(v_C) - C_2(V_i - v_C))dv_C \tag{16}$$

Hence, the energy lost throughout the transient process in the input and output voltage sources is

$$E_{diss}(v_C) = -Q_{I_i}(v_C)V_i + Q_{I_l}(v_C)V_p \tag{17}$$

The total initial energy stored in the inductor and H-bridge is

$$E_{init} = \frac{1}{2}L_l I_l^2(0) + 2E_S(0) \tag{18}$$

The remained energy in H-bridge and inductor at the end of ZVS is

$$E(v_C) = \frac{1}{2}L_l I_l^2(v_C) + 2E_S(v_C) = E_{init} - E_{diss}(v_C) \tag{19}$$

Combining (17)-(19), the inductor current can be derived based on the certain capacitor voltage, which is

$$I_l(v_C) = \sqrt{I_l^2(0) + \frac{2}{L_l}(2E_S(0) - 2E_S(v_C) - Q_{I_l}(v_C)V_p + Q_{I_i}(v_C)V_i)} \tag{20}$$

For the ZVS transition time, we need to simplify (9)-(14) to get the relationship between v_c and inductor current as

$$\frac{(C_1(v_C) + C_2(V_i - v_C))dv_C}{I_l(v_C)} = dt \tag{21}$$

Based on (20), the inductor current can also be expressed as a function of v_c. In the transient process, the output capacitance of Q1 is charged. So v_c increases from 0 to Vi, and the transition time increases from 0 to t_{ZVS}. Then,

$$t_{zvs} = \int_0^{t_{zvs}} dt = \int_0^{V_i} \frac{(C_1(v_C) + C_2(V_i - v_C))}{I_l(v_C)} dv_C \tag{22}$$

During the whole transient process, the charge flowing through C1 and C2 are the same. So according to (15)-(16), the total charge flows through the input voltage source is 0, as shown in (23).

$$\int_0^{V_i} Q_i(v_C)dv_C = 0 \tag{23}$$

$$E_S(0) = E_S(V_i) \tag{24}$$

Authorized licensed use limited to: DELHI TECHNICAL UNIV. Downloaded on July 20,2023 at 11:24:35 UTC from IEEE Xplore. Restrictions apply.

The ZVS transient technique requires the least amount of inductor energy possible, which is

$$\frac{1}{2} L_l I_l^2(0) \geq 2Q_s(V_i)V_p \tag{25}$$

TABLE I. SPECIFICATION OF DAB CONVERTER

PARAMETERS	SPECIFICATIONS
DC-Input Voltage	800V
Input Current	12.5 A
Switching Frequency	100 kHZ
Turns Ratio	1:0.625
Leakage Inductance	35 µH
Output Capacitance	250 µF
Power Rating	10 kW
Output Voltage	500 V
Output Current	20 A

IV. CLOSED-LOOP CONTROL OF DAB CONVERTER

In order to avoid overcurrent charge situations, a rechargeable battery is continuously charged at a constant current using constant current charging. Lithium-ion and lead-acid batteries can both be charged using this constant-current method. The logic for the phase shift provided to the secondary side switches of the DAB converter is implemented in this closed loop control. The reference rated current is compared to the battery current, and the error that results is communicated to the PI controller. There are many ways to control PI gains. One of them is the Ziegler and Nicholas approach, which is frequently used for PI tuning.

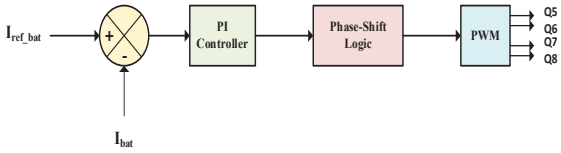

Fig. 8. Block Diagram of Control Strategy

TABLE II. PI CONTROLLER VALUES

PARAMETERS	VALUES
k_p	0.005
k_i	2.3

To generate phase shift between the transformer voltages on both sides of the converter, the output of the PI controller, as shown in Fig. 7, is sent through a PWM block and a phase-shift logic block.

V. SIMULATION RESULTS

The waveforms of the three-phase grid voltage and current at rated conditions are shown in Fig. 9 and 10.

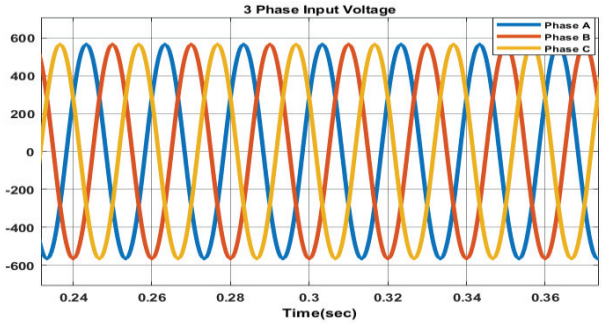

Fig. 9. 3 phase Input voltage (Grid)

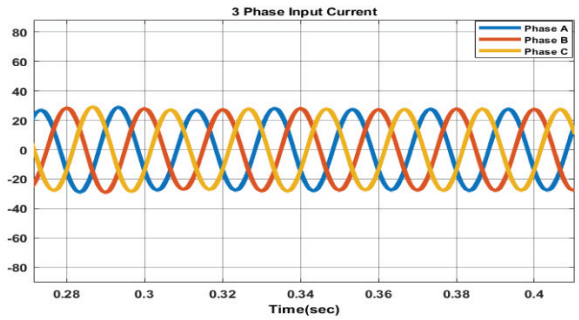

Fig. 10. 3 phase Input Current (Grid)

The benefits of power factor improvement include improved efficiency, reduced voltage drop and capacity optimization. For efficient operation of AFE rectifier, the power factor is maintained near unity, as shown in Fig. 11 and to get clear view current is multiplied with gain of 4.

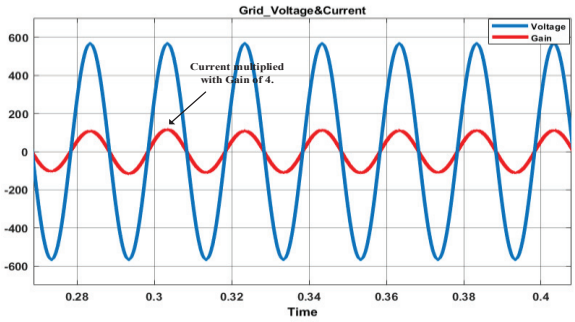

Fig. 11. Unity Power Factor Maintained by Grid Voltage and Grid Current

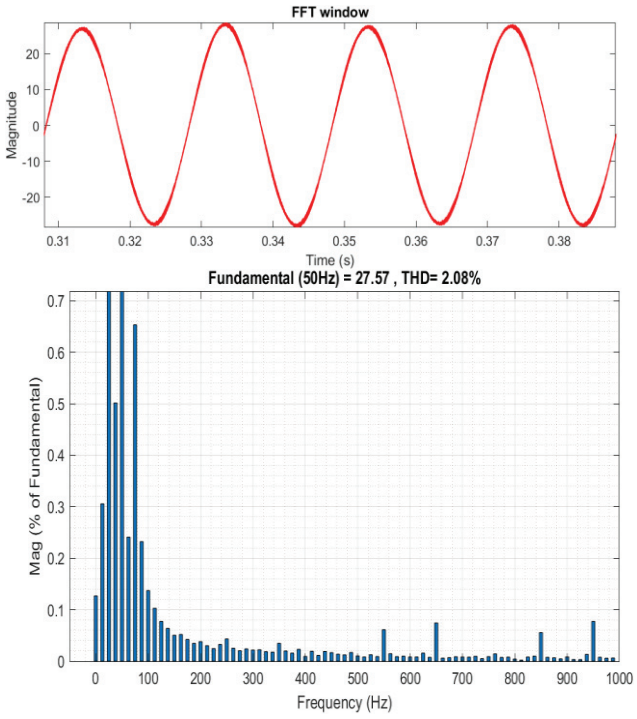

Fig. 12. THD in Input Current (Grid)

The THD must be under 5%, as per IEEE standards. The accepted parameters for the LCL filter are accurate because the THD value in Fig. 12 is approximately 2.08%.

Authorized licensed use limited to: DELHI TECHNICAL UNIV. Downloaded on July 20,2023 at 11:24:35 UTC from IEEE Xplore. Restrictions apply.

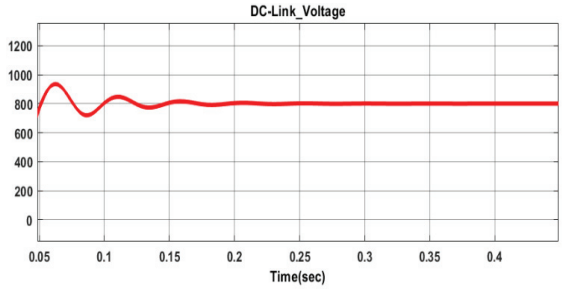

Fig. 13. DC-Link Voltage

The decoupled DQ control ensures that the DC-Link voltage should maintain its magnitude even after switching different loads in parallel. Fig. 13 shows that the DC-Link voltage is maintained at 800 volts throughout the charging process.

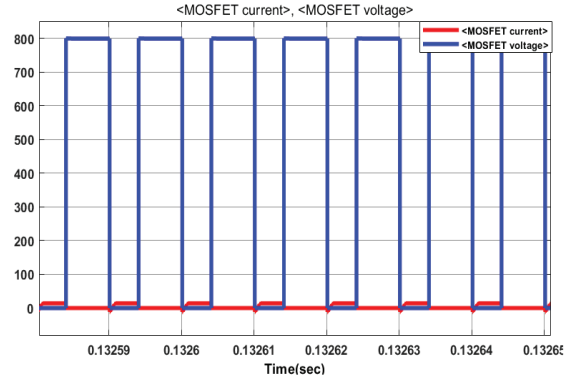

Fig. 14. ZVS in Primary Side H-Bridge of DAB Converter

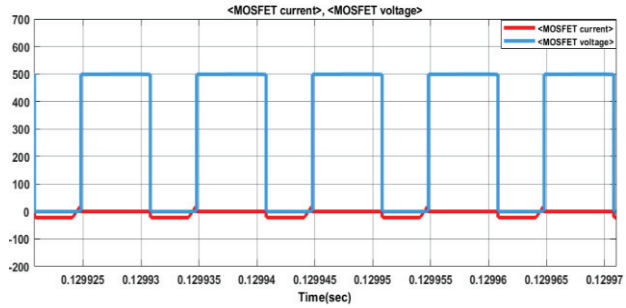

Fig. 15. ZVS in Secondary Side H-Bridge of DAB Converter

The ZVS obtained in the primary and secondary side switches under different loading circumstances is shown in Figs. 14 and 15. The right choice of leakage inductance and snubber capacitance coupled in parallel to MOSFETs therefore allows for ZVS to be achieved.

Fig. 16 depicts the battery charging process and effect of load variation on SOC, Battery Voltage and Battery Current.

No load is connected in parallel with the battery until time t=0.4s. As a result, the battery's SOC is rising quickly. A load is switched in parallel with the battery at time t = 0.4. The controller is built in such a way that it strives to maintain the rated value of battery voltage even though at this point the growth in SOC rate somehow slows down and the current flowing through the battery also reduces. Three additional loads are linked in parallel with an equal interval of time between them. When all loads are linked at time t = 1.02, SOC practically becomes flat, increasing barely at all.

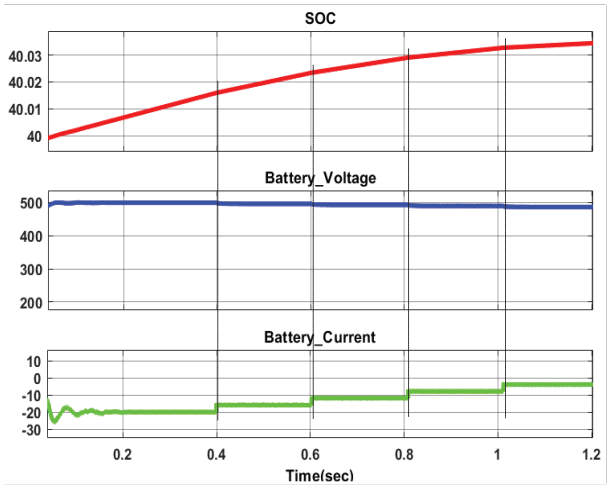

Fig. 16. Battery SOC, Voltage and Current for different Load Variation

VI. CONCLUSION

This paper presents the design and control of a DAB converter for battery charging applications with the integration of an LC filter at its output. The current control technique is designed for battery charging under variable load conditions.

The closed loop results show satisfactory performance with the current controller. It is also verified that integration of LC filter at the output maintains the desired output voltage and reduces ripple in battery current. Finally, the charging process under four parallel load variations is performed. The overall obtained results show good voltage and current response of the battery bank under variable loads. For further improvement, renewable energy sources such as solar and wind power with advanced energy management systems can be utilised to ensure charging of EV batteries during source availability.

REFERENCES

[1] ” Global EV Outlook 2019”, Iea.org, 2019. [Online]. Available: https: //www.iea.org/publications/reports/globalevoutlook2019/.

[2] G. Joos, M. de Freige and M. Dubois, "Design and simulation of a fast charging station for PHEV/EV batteries," 2010 IEEE Electrical Power & Energy Conference, Halifax, NS, 2010, pp. 1-5.

[3] A. Khaligh and S. Dusmez, "Comprehensive Topological Analysis of Conductive and Inductive Charging Solutions for Plug-In Electric Vehicles," in IEEE Transactions on Vehicular Technology, vol. 61, no. 8, pp. 3475-3489, Oct. 2012.

[4] V. M. Iyer, S. Gulur, G. Gohil and S. Bhattacharya, "Extreme fast charging station architecture for electric vehicles with partial power processing," 2018 IEEE Applied Power Electronics Conference and Exposition (APEC), San Antonio, TX, 2018, pp. 659-665.

[5] R. Wu, S. B. Dewan, and G. R. Slemon, “Analysis of an ac-to-dc voltage source converter using PWM with phase and amplitude control,” IEEE Trans. Ind. Appl., vol. 27, no. 3, pp. 355–364, Mar./Apr. 1991.

[6] M. Malinowksi, M. P. Kazmierkowski, S. Hansen, F. Blaabjerg, and G. Marques, “Virtual flux based direct power control of three-phase PWM rectifiers,” IEEE Trans. Ind. Appl., vol. 37, no. 4, pp. 1019–1027, Jul./Aug. 2001.

[7] C. Cecati, A. Dell’Aquila, A. Lecci, and M. Liserre, “Implementation issues of a fuzzy-logic-based three-phase active rectifier employing only voltage sensors,” IEEE Trans. Ind. Electron., vol. 52, no. 2, pp. 378–385, Apr. 2005.

[8] W. A. Hill and S. C. Kapoor, “Effect of two-level PWM sources on plant power system harmonics,” in Conf. Rec. IEEE-IAS Annu. Meeting, 1998, pp. 1300–1306.

Authorized licensed use limited to: DELHI TECHNICAL UNIV. Downloaded on July 20,2023 at 11:24:35 UTC from IEEE Xplore. Restrictions apply.

[9] V. Blasko and V. Kaura, “A novel control to actively damp resonance in input lc filter of a three-phase voltage source converter,” IEEE Trans. Ind. Appl., vol. 33, no. 2, pp. 542–550, Mar./Apr. 1997.

[10] A. R. Alonso, J. Sebastian, D. G. Lamar, M. M. Hernando, and A. Vazquez, “An overall study of a dual active bridge for bidirectional DC/DC conversion,” in Proc. IEEE Energy Convers. Congr. Expo., Atlanta, GA, USA, Sep. 12-16, 2010, pp. 1129–1135.

Authorized licensed use limited to: DELHI TECHNICAL UNIV. Downloaded on July 20,2023 at 11:24:35 UTC from IEEE Xplore. Restrictions apply.

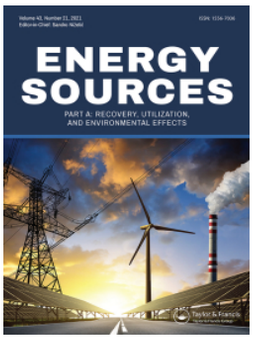

Energy Sources, Part A: Recovery, Utilization, and Environmental Effects

ISSN: (Print) (Online) Journal homepage: https://www.tandfonline.com/loi/ueso20

A Comprehensive Analysis of Electric Vehicle Charging Infrastructure, Standards, Policies, Aggregators and Challenges for the Indian Market

Fareed Ahmad & Mohd Bilal

To cite this article: Fareed Ahmad & Mohd Bilal (2023) A Comprehensive Analysis of Electric Vehicle Charging Infrastructure, Standards, Policies, Aggregators and Challenges for the Indian Market, Energy Sources, Part A: Recovery, Utilization, and Environmental Effects, 45:3, 8601-8622, DOI: 10.1080/15567036.2023.2228734

To link to this article: https://doi.org/10.1080/15567036.2023.2228734

Published online: 27 Jun 2023.

Submit your article to this journal

Article views: 8

View related articles

View Crossmark data

Full Terms & Conditions of access and use can be found at
https://www.tandfonline.com/action/journalInformation?journalCode=ueso20

ENERGY SOURCES, PART A: RECOVERY, UTILIZATION, AND ENVIRONMENTAL EFFECTS
2023, VOL. 45, NO. 3, 8601–8622
https://doi.org/10.1080/15567036.2023.2228734

Taylor & Francis
Taylor & Francis Group

Check for updates

A Comprehensive Analysis of Electric Vehicle Charging Infrastructure, Standards, Policies, Aggregators and Challenges for the Indian Market

Fareed Ahmad and Mohd Bilal

Electrical Engineering Department, SND College of Engineering and Research Center, Yeola, India

ABSTRACT

Due to their low CO_2 emissions, uncomplicated maintenance, and low operating costs, plug-in electric vehicles (PEVs) are currently acquiring popularity in the automotive industry. The charging infrastructure is crucial to the sustained expansion of the electric vehicles (EVs) market. In this paper, all aspects of the rapidly expanding Indian market for EV charging infrastructure are examined. Furthermore, for the Indian market, the available charging specifications, such as charging level, charging mode, charging point category, hardware, and software, are reviewed. Moreover, different organizations evaluate the standards and regulations of charging stations and EV integration into the grid for Indian consumers. In India, the current status of the charging infrastructure and prospective expansion plans are analyzed. The initiatives of the central and state governments for the expansion of charging infrastructure and support for EV consumers are examined. For Indian society, the strong actions that can be taken to develop charging infrastructure are analyzed. Moreover, the obstacles to EV charging network expansion and the role and current status of the key aggregators in expanding the charging infrastructure are also analyzed by considering the Indian market.

ARTICLE HISTORY
Received 12 May 2023
Revised 12 June 2023
Accepted 16 June 2023

KEYWORDS
Electric vehicles; charging infrastructure; electrification; carbon emission; e-mobility

Introduction

The availability of electric vehicles (EVs) on the supply side and adoption trends on the demand side are the categories used to describe India's electric mobility (e-mobility) sector. Furthermore, research indicates that EVs could reduce CO_2 emissions by 28% by 2030 (Adnan et al. 2018; Sufyan et al. 2020). However, there are two major obstacles that could prevent the widespread adoption of EVs: the high cost of EVs and the absence of charging stations. Furthermore, ambient conditions and low charging rates are important for growing the EVs market (Makeen et al. 2022; Makeen, Ghali, and Memon 2020). The EVs market is projected to reach USD 974,102,5 million by 2027, developing at a robust compound annual growth rate from 2020 to 2027 (Ahmad et al. 2022), as a result of the efforts of various industries and governments around the globe. The paucity of infrastructure for fueling EVs is one of the most critical issues addressed in this study. Therefore, healthy charging infrastructure is the most important factor determining how EVs are used.

EVs occasionally require charging depending on the battery pack type, size and capacity of the battery pack, and on-board energy carrying capabilities. Therefore, charging infrastructure is crucial for the tolerable operation of EVs. The charging load depends not only on vehicle types but also on utility purposes.

The Indian government wants 80% of two and 3-wheeler, 30% of private vehicles, 40% of buses, and 70% sales of all commercial vehicles to be electric by 2030 (Kore and Koul 2022). This plan calls for simultaneous charging station penetration throughout the country (Bilal and Rizwan 2020).

CONTACT Mohd Bilal bilal.zhcet01@gmail.com Electrical Engineering Department, SND College of Engineering and Research Center, Yeola, Nashik, 423401, India

© 2023 Taylor & Francis Group, LLC

Through programs like Faster Adoption and Manufacturing of Hybrid & Electric Vehicles I and II phase (FAME-I and FAME-II), the Indian government has been assisting the EV sector with an emphasis on charging infrastructure. The industry participants are also upbeat and actively interested in the EV charging ecosystem. Furthermore, the Major Original Equipment Manufacturers (OEMs) are working on EVs, and an ecosystem for the growth of charging infrastructure and services is slowly being established.

Since it is scarcely available and takes a long time to charge an EV, the infrastructure supporting electric mobility is also a significant perceived obstacle to EV adoption in India. India is establishing its charging infrastructure at a high rate, but it is slower than other territories like the United States, the European Union (EU), and China. The charger operators are being prevented from extending their spread by high operating costs, distribution company (DISCOM) load, and the uncertainty surrounding the usage rates of charging stations.

Government-approved standards for the electric two-wheeler and three-wheeler categories must be improved in India. The end-preference user is for battery charging, and fixed-rate charging may be one of the causes of this. Such consumers choose home charging because Public Charging Stations (PCS) cannot provide a set charge rate. Similarly, fleet operators with different charging infrastructure requirements include state-run intra-city bus services. As a result, it is imperative that the strategy for the infrastructure supporting charging for all vehicle types be comprehensive.

Dr. Mahendra Nath Pandey, the Union Minister for Heavy Industries, announced that the Public Sector Undertakings (PSU) like Bharat Petroleum, Indian Oil, and Hindustan Petroleum had been granted Rs. 800 crores under the FAME India Scheme Phase II in order to build 7432 public fast charging stations (FCSs) across the nation (Emobility 2023).

To increase the profitability of the construction of public charging infrastructure, the Committee led by DG Bureau of Energy Efficiency (BEE) made a number of recommendations. Supporting the upstream infrastructure is a part of it, and it often accounts for up to 60% of the total installation cost of a public EV charging station. In order to secure an electrical connection, charging operators must pay the DISCOMs, which are part of the upstream infrastructure. The Ministry of heavy industries (MHI) granted financial support for putting up the upstream infrastructure of up to 80%, upstream infrastructure based on the committee's proposal (Emobility 2023).

The study highlights the potential of combining PV panels with charging points to enhance the performance and efficiency of EV charging while minimizing grid stress. By leveraging IoT technology, the scheme enables optimal dispatching of electricity between EVs, charging points, and the power grid. This integration allows for intelligent management of energy flows, considering factors such as available solar energy, grid demand, and EV charging requirements (Ahmad et al. 2023; Shang et al. 2020). The study explores the potential of bidirectional energy flow between EVs and the power grid to help manage peak electricity demand. It examines the effectiveness of different operation modes, such as smart charging, vehicle-to-home (V2H), and vehicle-to-building (V2B), in reducing peak loads and optimizing grid stability (Bilal, Ahmad, and Rizwan 2023; Zheng, Shao, and Jian 2021).

Furthermore, the survey addresses the significant challenges in establishing a robust charging infrastructure in India. By critically analyzing these challenges, the paper provides insights into potential strategies and solutions that can overcome barriers to growth and ensure the successful expansion of the charging network. This critical literature survey offers a comprehensive EV charging infrastructure market analysis, focusing on the Indian context. It highlights the current state, future plans, government initiatives, market drivers, and key challenges, providing valuable insights for stakeholders involved in the growth of charging infrastructure in India. Furthermore, the schematic diagram of the EV is shown in Figure 1.

Market overview

Charging Station Operators (CSOs) now own the charging infrastructure and utilize a pay-per-use business system with many choices for income generation. Using online mapping of these smartphone CSOs, EV users may easily make digital payments and verify location, charger availability, and charger type.

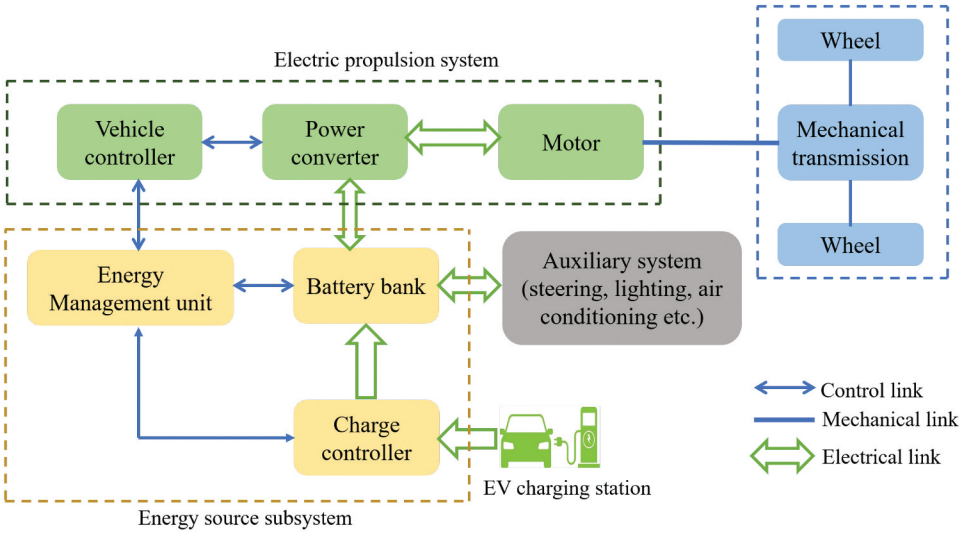

Figure 1. Electric vehicle schematic diagram.

Segmentation

Although a one-size-fits-all strategy is not the way forward for increasing EV adoption, a thorough understanding of the essential EV charging infrastructure is required to scale up EV adoption.

A commercial electric four-wheeler vehicle (e-4W) that travels more km per day than a private car has a more charging demand. Hence, while it is projected that most private e-4W charging will occur at home, commercial e-4W will favor public charging. Even the functioning of the commercial e-4W fleet varies greatly depending on the type of load they transport, i.e., people or cargo.

A charging service provider does not choose to install en-route public charging stations because of the difficulties in locating space and the high anticipated cost of land rental in a city.

In the case of electric 2-wheeler vehicles (e-2W) and electric 3-wheeler vehicles, the battery arrangement determines whether the charging option is plug-in charging or battery swapping. Although battery-changing possibilities are common for e-2W and e-3W, e-4W manufacturers might profit from establishing a charging station for their own brands of vehicles. Hence, Ather and Battre are anomalies since they construct their own charging equipment despite the existing e-2W. Table 1 represents the number of different types of EV distribution in Indian states.

Types of charging

The market for EV charging infrastructure in India is segmented into two categories based on charging: direct charging and battery swapping, which are further separated into slow and fast charging. Furthermore, in the battery swapping stations, the dead battery of EV was quickly replaced with a fully charged battery. This saves time because the EV battery doesn't have to be charged, but in India, this facility only applies to e-2W and e-3W. The number of charging stations available in the different states of India is shown in Figure 2.

Table 1. Availability of the EVs in different states of India.

Type of EVs	U.P.	Mah.	Kar.	Guj.	Raj.	T.N.	Delhi	Bih.	Ass.	Tel.	Others
2-Wheeler	5442	24162	21547	16424	10904	12802	7353	1648	380	8604	30339
3-W passenger	28773	860	404	111	3812	11	1748	8129	9064	127	10596
4-Wheeler	54	2231	909	671	347	555	1581	36	18	704	1705
Electric bus	103	126	2	0	0	0	203	0	0	0	33

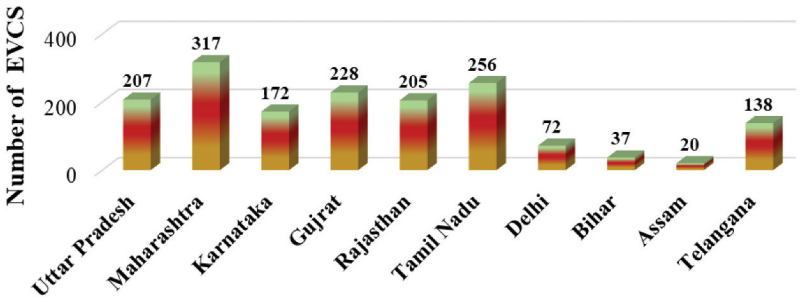

Figure 2. Available EV charging stations in different states of India.

AC/Slow charging

The power is obtained from the electrical grid in the form of AC. The charging method is optimal for charging the battery of an EV if the vehicle is available in the parking lot for at least 20 minutes. The slow charging techniques include AC-001 Bharat, a charging technology with low voltage that is the most affordable of all the standards, and Type 2 AC, which has a power output of 7.4 kW, type 2 AC is more rapid than AC-001 (Rajendran et al. 2021). Although vehicles with up to 22 kW of power output can be evaluated, no such vehicles exist in India.

DC/Fast charging

A DC system requires significant grid power (around 125 A). This makes its manufacture, installation, and operating expenses relatively expensive, increasing pricing rates. Yet, it is the recommended charging technique for rapid recharging, as it allows for significantly quicker charging (Ahmad et al. 2022). This charge is particularly prevalent along roads, as opposed to businesses or houses. Furthermore, CHArge de MOve (CHAdeMO), Bharat DC-001, and Combined Charging System (CCS) are fast charging connectors. Moreover, the CCS type connectors (available as CCS1 with 5-pin AC connection and 2-pin DC connector and CCS2 with 7-pin AC connector and 2-pin DC connector) are utilized by the majority of U.S., European, and South Korean automotive manufacturers, whereas CHAdeMO type connectors are utilized mostly by Japanese automakers (Rajendran et al. 2021).

Location

The Indian EV charging stations market is categorized into cities and highways by placement type. Nonetheless, most charging stations are now being installed in urban areas, and plans are ongoing to put additional charging stations on key expressways and roads (Ahmad et al. 2022).

Components

On the basis of component type, the EV charging infrastructure market in India is divided into software, services, and hardware. In India, software & services consist of the platform as a service, installation and maintenance of charging devices, towing and battery supply services. The hardware includes charging ports, connections, chargers, and supplementary equipment (Shariff et al. 2019). The charging technologies required to establish a charging infrastructure are undergoing fast development.

End use

Home charging. Residential chargers commonly employ a single-phase AC supply with 230 Volt voltage and a 15 Amp current connector that produces up to 2.5 kW output power. Moreover, the consumed power for charging the EV is added to home metering (Lee et al. 2020).

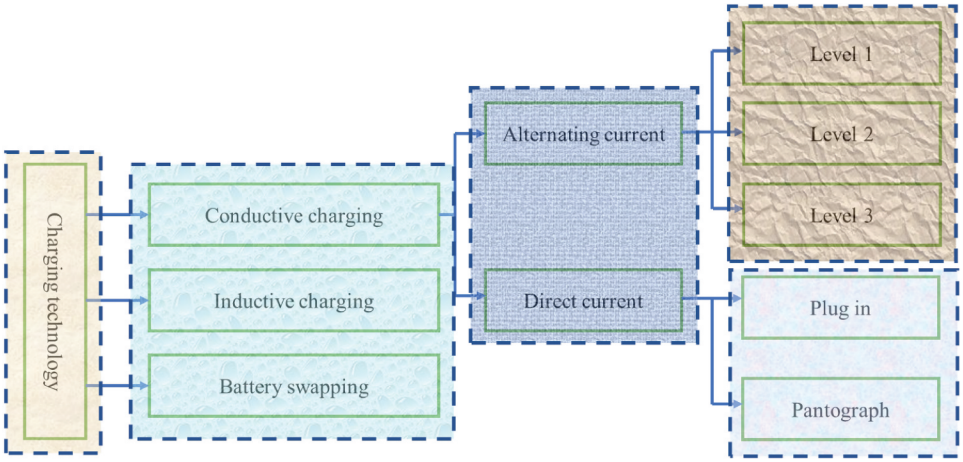

Figure 3. General overview of the EV charging technology.

Public charging. Public charging stations (PCS) might be installed in gas stations, municipal parking lots, shopping centers, and government offices (Kore and Koul 2022). Denser public charging networks are found in nations with a greater population density, as assessed by the number of vehicles per charging point (VCP). The Netherlands (450 inhabitants per square kilometer) has a VCP of 4, China (150 persons per square kilometer) has a VCP of 6, while the United States (36 persons per square kilometer) has a VCP of 79. In addition, in places such as Delhi and Mumbai, where an estimated 70% of automobiles are parked on the road, relatively few city residents own a garage or parking spot for their vehicles (Pareek et al. 2020).

Commercial charging. The third type of charging option is for an entity/own company's fleet of vehicles (e.g., MG Motors) or a taxi company's fleet. The charging infrastructure that falls under this option is installed on private property, not in public areas. According to CSOs like as Volttic, these charging stations are utilized optimally (80%) (Mishra et al. 2021). In addition, the general overview is presented in Figure 3 of charging technology.

Electric vehicle charging and grid integration standards

The growth of electric cars has given the transportation and electric power industries new things to do. If this new technology is to be used the same way worldwide, all of its parts must be standardized. Furthermore, Table 2 gives an overview of the regulatory agencies worldwide and the rules they've made to monitor different parts of electric cars. EV charging standardization can be broken down into three categories based on the table: Standards for EV charging components, standards for EV grid integration (EVGI), and safety measurement. Several groups focus on requirements for individual parts, while the International Organization for Standardization (ISO) sets standards for EVs. Grid integration standards control how electric cars can charge and drain power from the electrical grid. Furthermore, EVs operate as distributed energy resources (DER) for charging and discharging from the electric grid.

Electric vehicle charging standards

There are a variety of international regulations for charging infrastructure. The Society of Automotive Engineers (SAE) and Institute of Electrical and Electronics Engineers (IEEE) are organizations in the U.S., but International Electro-technical Commission (IEC) is the most common standard in Europe.

Japan's EV charging standards are known as CHAdeMO. The Standardization Administration of China (SAC) and the Chinese National Committee for ISO and IEC wrote the Guobiao (GB/T) standard governing AC and DC charging in China. The requirements for AC charging in the GB/T

Table 2. Electric vehicle standards of the regulatory Institute.

Institute	Description	Standards	Explanation
International Electro-technical Commission (IEC, Britain) (Das et al. 2020)	The IEC is an international standards organization that prepares and publishes international standards for all electrical, electronic and related technologies, it cover 170+ countries and 10,000+ standards	TC21	Dimensional, functional, safety, test, installation, and maintenance norms for all secondary cells and batteries
		TC22	Design, control, protection, monitoring, and measuring standards for power electronic systems, equipment, and their constituent parts
		TC64	Specifications for equipment installation and coordination to prevent electric shock from incorrect equipment installation and excessive voltage supply
		TC69	for different types of EDVs
		IEC61851	Guidelines for general charging specifications
		IEC61980	EV wireless power transfer (WPT) standards
		IEC62196	Specifications for EV conductive charging plugs, sockets, and connections
Society of Automotive Engineers (SAE, USA) (Zarfos 2019)	SAE is a United States-based, globally active professional association and standards developing organization for engineering professionals in various industries	J2293	Specifications for EV and off-board EV Supply Equipment for utility grid charging
		J1772	Conductive charger regulation
		J1773	Wireless charger regulation
		J2847	Standard communication for the off-board DC charger, the utility grid and EVs
		J2836	Standard analog and digital communication for the power grid and EVs.
		J2931	EV and utility grid digital communication standards
		J2954	Wireless power transfer standards for EVs
		J2894	EV testing and power quality standards
		J1766	Safety standards of charging
JEVA (Japan), CHAdeMo Association (Katsumata 2018)	CHAdeMO is a fast-charging system for EV, formed by the Tokyo in 2010	C601	Regulation for charger and receptacles
		D001–002	Battery standards for EVs
		D701–709	Battery testing regulations
		G101–105	Standards for fast charging
		G106–109	Standards of wireless charging
Institute of Electrical and Electronics Engineers (Photovoltaics and Storage 2018)	IEEE is a 501 professional association for electronics and electrical engg. with other related disciplines and its operations center in New Jerse	P1547	Regulation of grid connection with DERs
		P2100.1	Regulation of wireless power transfer and charging system
		P2030	Regulations for monitoring the smart grid interoperability
		P2030.1	Electrification standards for transportation network

(*Continued*)

Table 2. (Continued).

Institute	Description	Standards	Explanation
UL Standards, US and Canada (Das et al. 2020)	UL Standards encompass UL's extensive safety research and scientific expertise with more than 1,500 Standards	UL2231	Regulation for safety devices for charging circuits
		UL2251	Standards of charging plugs, coupler, and receptacles
		UL2202	necessity for charging equipment
		UL2594	necessity for EV supply equipment
		UL1741	Regulations for converter, output controllers, inverter, and charge controller
National Fire Protection Association	The NFPA is a U.S. based international nonprofit organization devoted to eliminating death, injury, property, and economic loss due to fire, electrical, and related hazards	70	Safety regulations of grid integration for DERs
		70B	Electrical device safety measure
		70E	workplace safety regulations

standard are similar to those in the IEC standard. Since the IEC and SAE standards for charging EVs are widely used, they are looked at in depth here. IEC and SAE standards for voltage and current are summarized in Table 3. IEC-61851 and SAE-J1772 have nearly identical criteria, with the exception of the terminology used. Moreover, in SAE, the charging level is represented as level, while for IEC, the charging level is referred to as mode (Yu et al. 2022). In Figure 4 the type of connectors, and type of charging facilities are shown.

IEC standards

The electrical, electronics, and related technology standards are prepared by the British organization known as International Electro-technical Commission.

IEC-61851. IEC6-1851 pertains to onboard and offboard components for charging EVs with voltage range up to 1500 Volt DC and 1000 Volt AC. Table 5 gives an overview of some of the most important parts of IEC-61851 that are explained in the document (Das et al. 2020)

IEC-61980. It is a regulation for wireless power transfer systems suited for supply voltages of up to 1500 Volt DC and 1000 Volt AC. This specification is also used in wireless power transfer (WPT) systems provided by onsite storage systems (Das et al. 2020).

IEC-62196. It is a regulation for socket outlets, conductive plugs, vehicle connections, and vehicle inlets used to charge EVs. Table 4 summarizes some major portions of IEC-62196 (Das et al. 2020; Tang, Wu, and Qin 2012).

Table 3. Summary of voltage and current levels in IEC62196, IEC61851 and SAEJ1772 standards.

Standards	Sources	Mode/Level	Phase	Voltage (V)	Max Current (A)
IEC62196	AC	Mode 1	Single	120	16
	AC	Mode 2	Single	240	32
	AC	Mode 3	Single	250	32–250
	DC	Mode 4	DC	600	400
IEC61851	AC	Mode 1	Single	120	16
	AC	Mode 2	Single	240	80
	DC	Mode 4	DC	200–450	80
SAEJ1772	AC	Level 1	Single	120	16
	AC	Level 2	Single	240	32–80
	DC	Level 1	DC	200–450	80
	DC	Level 2	DC	200–450	200

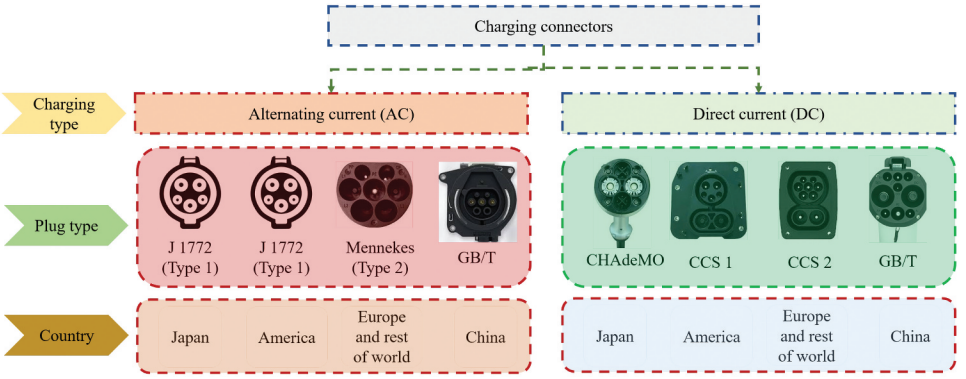

Figure 4. General overview of the EV charging and connector types.

SAE standards

It is a professional organization that produces technical standards for several sectors mainly generated for US.

SAEJ-2293. SAEJ-2293 specifies on-board and off-board charging equipment requirements. J2293-1 looks at the electric energy needs and system design for three types of operation: AC conductive charging, DC conductive charging, and inductive charging. J2293-2 looks at the communication needs and system architecture for charging (Arif et al. 2021).

SAEJ-1772. SAEJ-1772 covers all equipment ratings for charging EVs, such as the current rating of circuit breakers, the voltage rating of charging, etc. The regulations are set for AC and DC, each with three different levels. Most cars are being made to be charged onboard with Level 2 AC at currents lower than 30 A. SAE DC level means DC charging, which means the charging rate is very fast. Infrastructure, battery chemistry, and other factors influence the actual charging rate (Arif et al. 2021).

SAEJ-1773. This standard specifies the basic specifications for an EV's inductively linked charging method. The criteria for inductive charging software interfaces are covered in SAEJ-1773, along with the specifications for physically connected inductive charging (Arif et al. 2021; Wang et al. 2021).

Table 4. Section in IEC62196.

Sections	Description
IEC62196–1	Includes general specifications for connections, including plugs, socket outlets, couplers, and vehicle inlets.
IEC62196–2	Standardizes the types and modes of the charging known as type 1, 2, 3 to modes 1, 2, 3
IEC62196–3	Specification for fast charging inlets and connector

Table 5. Section in IEC61851.

Sections	Description
IEC61851–1	Cable and plug setups regulation for EV charging Case A: The cable is affixed to the EV securely. Case B: The cable is not connected to anything properly. Case C: The cable affixed to the charging station permanently
IEC61851-21-1	EMC specifications for conductive charging for on-board chargers
IEC61851-21-2	EMC requirements for conductive charging using an off-board charger
IEC61851–23	DC fast charging regulations
IEC61851–24	Between the EV charging controller and the EV supply equipment, there is digital communication for controlling DC charging.

Table 6. Section in SAEJ2847 and SAEJ2836.

Sections	Description
SAEJ2847/1–2	Regulation for communication PEVs to Grid, and PEVs to Off-Board Chargers.
SAEJ2836/1–2	Use Cases for Communication PEVs to Grid, and PEVs to Off-Board Chargers
SAEJ2836/3	Use Cases for PEVs communication with DER
SAEJ2836/4–6	Use Cases for contactless Charging Communication for Diagnostic, Customer, and Plug-in Cars, respectively

Table 7. Section in SAEJ2931.

Sections	Description
SAEJ2931/1	Regulation and requirements for digital communication architecture
SAEJ2931/2–4	Indicate how the MAC and Physical layers will be implemented using the SAEJ1772 pilot wire, frequency shift keying, narrow band OFDM, and baseband OFDM.

SAEJ-2847 & SAEJ-2836. These two standards and SAEJ-1772 describe how an EV and its charging infrastructure should talk to each other. SAEJ-2847 establishes communication requirements, whereas SAEJ-2836 outlines use cases and offers testing infrastructure. Table 6 shows the titles of the subsections that can probably be used in certain places (Wang et al. 2021)

SAEJ-29310. This standard specifies the necessity for digital communication between EVs, EV supply equipment (EVSE), utilities, energy assistance interfaces, advanced metering system, and residential area networks. SAEJ-2931 requirements must be met to set up a communication network for EV charging in a smart grid. Table 7 summarizes the many subsections of this standard (Wang et al. 2021).

EV grid integration standards

There are three accessible codes and standards: IEEE-1547, UL-1741, and NFPA-70. The essential elements of each of these regulations and codes are listed below.

IEEE-1547

IEEE-1547 is called "Standards for linking dispersed resources to electrical power systems." It applies to DER technologies with a 10 MVA or less capacity at the PCC. It includes operation, performance, safety, testing, and maintenance considerations requirements for connecting DERs, and it focuses on installing DERs on primary and secondary network systems. Table 8 summarizes the key focal topics of IEEE-1547 (Das et al. 2020; Wang et al. 2021).

UL standards

UL produced a number of standards covering various areas of DER grid interconnection. The most important one is UL 1741, which spells out the requirements for power conversion equipment and protective devices when DERs are connected to the grid. Other specifications include UL-62109, UL-62109-1, UL-62109-2, and UL-1741 SA (Das et al. 2020; Wang et al. 2021).

Market size

In India, the market for charging infrastructure is fragmented and unstructured because of the separation of public versus private actors and PCS versus commercial charging. The best indicator of market size is thus the charge points established by the main CSOs (public and commercial) in India to date and PCS established under various programs – FAME I/FAME II.

Furthermore, the plans for the next months/years may be analyzed using the projections provided by the individual CSOs and the tenders/EOIs that have already been approved/announced.

Table 8. State-wise guideline announcement for EV charging infrastructure.

State	Targets	Incentives for Infrastructure	Financial Incentives
Andhra Pradesh (Reddy 2022)	0.1 million (by 2024)	CSs must be installed in all new commercial complexes, residential townships, and housing societies with a built-up area of at least 5,000 sq.m.	Capital Subsidy of 25% (maximum of INR 1 Million) of the CS equipment value for the first 100 stations using DC Chargers (100V and above); Capital Subsidy of 25% (maximum of INR 30,000) for the first 300 stations using DC Chargers (below 100V)
Bihar (Yadav 2022)	Every 50 km on all highways	The creation of charging infrastructure at all key government offices.	25% capital reimbursement on equipment (capped at INR 1 Million per CS) for the first 250 commercial EV vehicles.
Chandigarh (Singh 2022a)	1,000 (by 2030)	Required installation of CSs in all business complexes and dedicated lanes in every sector; INR 4/unit fee for residential charging, including a 30% rebate on the electric bill	30% incentive for the installation of residential chargers; 15% subsidy for charging infrastructure firms planning to deploy PCS.
Delhi (Gahlot 2022)	Every 3 km	For private charging outlets, improvements must be made to construction codes so that 20% of all parking spaces at new homes and workplaces are "EV-ready."	The chosen Energy Operators will get a capital subsidy for charger installation charges, up to 6,000 INR for acquiring charging equipment for the first 30,000 CS.
Gujarat (Patel 2022)	NA	Designated parking/charging facility for EVs; installation of CSs in workplace parking areas	NA
Karnataka (Kumar 2022)	Every 50 km on highways	mandating CSs in public buildings	NA
Kerala (Krishnankutty 2022)	Every 5 km by 5 km in cities and every 50 km on National Highways	Mandating the installation of CSs in all new permits for housing societies, residential townships, and commercial complexes with a built-up area of 5,000 sq.m.; new and renovated non-residential buildings with 10 equivalent car spaces must have at least 20% EV charging spots, while residential buildings must have 100% demarcated EV charging spots.	NA
Madhya Pradesh (Tomar 2022)	Every 50 km on Highways	mandating the installation of CSs in all new permits for housing associations, communities, and buildings with a built-up area of 5,000 sq.m.	For PCS, a maximum capital subsidy of INR 0.15 million (or 25% of the value of the charging equipment) is available for the first 300 small CSs, INR 0.2 million for the first 100 medium CSs, and INR 1 million for the first 100 big CSs.
Maharashtra (Waghmare 2022)	Every 50 km on highways	mandating CSs in public buildings	NA
Punjab (Singh 2022b)	NA	1 Electric Charging Spot (ECS) is required for every three parking spaces in new and refurbished buildings, and 1 ECS is required for every 5 parking spaces in residential and non-residential complexes with designated parking for at least 10 vehicles.	25% capital subsidy on equipment (up to INR 50,000 per private CS) for the first 1,000 charging points; 50% capital subsidy for equipment made in Punjab.

(*Continued*)

Table 8. (Continued).

State	Targets	Incentives for Infrastructure	Financial Incentives
Tamil Nadu (Balaji 2022)	Every 25 km on both sides of National and State Highways	In commercial buildings, including hotels, movie theaters, retail malls, and apartments, at least 10% of parking space must be designated for the installation of CSs.	In circumstances where State Goods and Services Tax refund is not available, qualified projects will get a 15% capital subsidy over a 10-year period; manufacturing units connected to charging infrastructure will be exempt from energy tax until 2025.
Telangana (Reddy 2022)	Every 50 km inside state borders on highways leading to cities like Chennai, Mumbai, and Bengaluru.	mandating CSs in public buildings	Providing preferential parking spaces with the necessary charging infrastructure.
Uttar Pradesh (Sharma 2022)	0.2 Million (by 2024)	Public parking spaces, new housing communities, neighborhoods, and commercial buildings with a built-up area of 5,000 sq.m. must all include CSs.	First 100 CSs will get a capital subsidy of 25% on fixed capital expenditures (excluding land costs) (maximum of INR 0.6 Million per CS)

Current status

Around 6,586 charging stations are available nationwide at the present time. The ecology for EV charging will be significantly boosted by installing the new 7,432 public charging stations. The aforementioned charging capacity should be used to charge electric 2-wheelers, 4-wheelers, light commercial vehicles, and minibusses.

Future plans

The country thrives due to the government's assistance through the FAME I and FAME II programs and the private sector's involvement. The future appears promising based on the announced EOIs and bids and the objectives of the industry's major participants.

The Ministry of Heavy Industries released the first allotment of Rs. 560 crores, or 70% of the total approved payment of Rs. 800 crores, to OMC (BPCL, IOCL, and HPCL), on March 27, 2023. This money will be used to deploy and commission upstream infrastructure and charging technology for public EV charging stations at the appropriate retail locations nationwide.

Encouraging numbers from eois/tenders

As of January 11, 2021, the Department of Heavy Industry (DHI) has approved 3,397 EV charging stations as part of the second phase of the Faster Adoption and Manufacture of Electric Vehicles India (FAME II India) initiative. In January 2020, the DHI approved the setup of 2,636 EVCS, including 1,633 fast and 1,000 slow charging points, throughout 62 cities in 24 Indian states. Maharashtra received the most stations (317), while Karnataka and Tamil Nadu received 266 and 256, respectively. In September 2020, the Ministry of Heavy Industry and Public Enterprises approved 241 more charging stations. The DHI extended an EoI in October 2020 to have CS every 25 kilometers on highways/roads and at least one Heavy Duty CS every 100 kilometers on highways. Government organizations, public sector undertakings (PSUs), state electricity distribution companies, and other companies were invited to install 1,500 EVCSs on 25 expressways and highways (nine expressways with a total length of 1,775 kilometers will have a minimum of 174 EVCS and 16 arterial ways with the length of 13,370 kilometers will have a minimum of 1,370 EVCSs). A similar EoI for deploying 7,000 EV charging stations was released in August 2019 and got 106 proposals from public and commercial organizations. Unfortunately, only 2,877 charging stations were authorized.

Substantial numbers from plans of leading aggregators

JMK Research anticipates that around 7,000 charging stations will be installed in the next 18 months by important participants, including some new start-ups. State-owned companies EESL and REIL would account for around 50% of the market share. This will be followed by some established and experienced private aggregators, like Volttic, Tata Motors, and Fortum.

Central and state government initiatives

The Government of India announced National Electric Mobility Mission Plan (NEMMP) 2020 in 2012 with the intention of reducing India's dependency on crude oil for transportation by supporting EVs. It is a National Mission document outlining the vision and strategy for accelerating the country's adoption of EVs and their manufacture.

FAME-I

As part of NEMMP 2020, the DHI introduced the Faster Adoption and Manufacturing of (Hybrid & Electric Vehicles in India (FAME India) Programme on 1st April 2015 for a duration of two years. The Scheme was executed by concentrating on four key areas: (i) Demand Creation, (ii) Technological Platform, (iii) Pilot Project, and (iv) Charging Infrastructure (Bilal, Ahmad, and Rizwan 2023).

The initiative had a two-year budget of INR 7.95 billion, of which INR 0.3 billion was designated for installing charging infrastructure (INR 0.1 billion for FY 2015–16 and INR 0.2 billion for FY 2016–17) (Ahmad et al. 2022).

National E-Mobility programme

Launched in 2018, the initiative aims to have 30% of automobiles be electrified by 2030. In addition, the program anticipated that no license would be necessary to install charging infrastructure in India and that the rate would be less than Rs 6 (Bilal, Ahmad, and Rizwan 2023).

FAME-II

On the basis of the knowledge gained during the FAME-I Scheme, it was determined that adequate connectivity of the charging network is needed to reach the desired result of the proposal. This issue is being acknowledged in Phase II of the FAME initiative, which was alerted on March 8, 2019 (Ahmad et al. 2023; Bilal, Ahmad, and Rizwan 2023). Furthermore, the fund allocation under the FAME scheme for the different financial year is shown in Figure 5.

The FAME II India Programme has committed 10 billion rupees (Rs. 3 billion for 2019–20, 4 billion for 2020–21, and 3 billion for 2021–22) toward developing charging infrastructure. During the program, 241 recharge points for electric buses were authorized (Bilal, Ahmad, and Rizwan 2023). The different types of initiative and policies recommended by the Indian government have been included in Table 9

- The plan intends to provide the customer with one fast charger for every ten e-bus and one slow charger for one e-bus.
- 100% of the costs associated with the development of charging infrastructure are covered by available funding.
- Through this program, six projects for installing EV charging infrastructure have been supported. They are four solar projects, two developed by Bharat Heavy Electricals Ltd (BHEL) and Rajasthan Electronics & Instruments, Jaipur (REIL).
- Furthermore, Mahindra Reva Electric won money for establishing fast charger infrastructure in Bangalore, which it would establish in partnership with Lithium Urban Technologies.

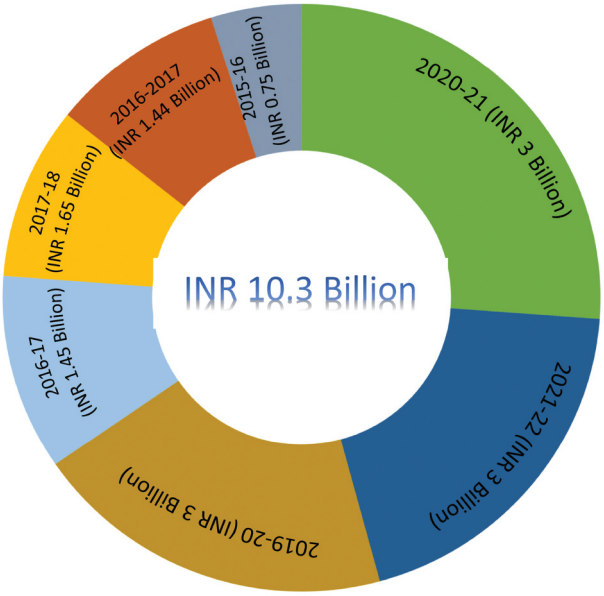

Figure 5. Fund allocation under the FAME scheme.

Table 9. Key policies in the area of electrification of the transport sector in India.

Policy	Year	Description
National Electric Mobility Plan	2013	Plans for over 7 million EVs to be consumed in India
Faster Adoption and Manufacturing of Hybrid and Electric Vehicles (FAME 1)	2015–18	Provide incentives for EV and hybrid vehicle purchases, mostly for personal vehicles
Faster Adoption and Manufacturing of Hybrid and Electric Vehicles (FAME II)	2019	Provide incentives to electrify the fleet of buses and taxis used for public transportation
Department of Heavy Electrical Pilot EV Project	2017	Set aside money to buy 390 electric buses for eleven Indian towns
Multi-modal EV pilot project, Maharashtra state	2017	Allocate $ 2.44 million on EVs and charging facilities
Karnataka state Electric and Energy Storage Policy	2017	3181.30 million USD allocated for the creation of 55,000 new jobs in the transportation electrification industry.
Delhi state EV policy	2018	Provide e-autos tax and permit fee breaks. Encourage the use of electric buses for public transportation
Tax reduction policy of union budget 2019	2019	Subsidies in the form of tax relief on the interest paid on EV loans up to INR 1.5 lakh.

Other amendments and support

(1) Innumerable modifications were made to the Model Building Bylaws (MBBL) 2016 and the Urban Regional Development Plans Formulation and Implementation (URDPFI) Guidelines 2014 in order to develop a strong EV charging infrastructure.
(2) The Housing and Urban Development Ministry of India announced recommendations in January 2019 that obliged commercial and residential complexes to give 20% of their parking area to enable EV charging stations.
(3) Oil-ministry guidelines, in October 2019, allowed Companies with a net worth of INR 2.5 billion to sell petrol/diesel under the condition that they set up at least one new alternatives fuel like LNG, CNG, and EV charging within the specified limit of the duration. Thus, many petrol stations choose EV charging to comply with this requirement.

Ministry of power instructions for states on ev charging infrastructure

- Preferences of EV public charging network rollout comprises megacities and all linked expressways and highways (Phase I for 1 to 3 years), followed by large cities such as the UT headquarters and state capitals and connected expressways (Phase II for 3–5 years).
- Permission for private charging at offices/residences.
- The battery charging station (BCS) will get the same treatment as the PCS, and the appropriate rate for power supply will be the same.
- To boost the setting up of public EV charging stations in India, de-licensing of EV public charging infrastructure is allowed (through a clarification issued on April 13, 2018), i-e- It is not necessary for businesses installing EV charging infrastructure to have a separate license for energy transmission, distribution, or trade.
  (1) The Distribution Company licensee will give PCS connectivity precedence, and any CS may use open access to receive power from any producing business.
  (2) Each PCS must have a minimum of one CCS/CHAdeMO/Type 2 AC charger for quick charging and a minimum of one Bharat DC-001/Bharat AC-001 charger for slow, in any number or combination. Additional criteria include having the proper electrical, cabling, and civil construction done, a special transformer, a 33/11 KV line/cables, and enough space for parking and vehicle entry/exit.
  (3) To allow EV users to reserve charging spots in advance online or remotely, a partnership with at least one internet network service provider is necessary.
  (4) PCS for heavy-duty EVs (trucks, buses) and long-range EVs must have at least two chargers with a minimum 100 kW capacity each and suitable liquid-cooled cables.
- Private charging points designed for noncommercial usage by private EV owners are exempt from all infrastructure standards. Likewise to how NSP tie-ups were not necessary for PCS, captive charging infrastructure intended for internal usage by a company's own or leased fleet does not require them.
- The tariff rate for the electricity to the PCS shouldn't be higher than 15% of the typical cost of the electrical energy.

Key market drivers

Due to the following primary factors, India is predicted to grow significantly in the EV Charging Infrastructure market. Figure 6 represents the key market drivers for boosting the electric vehicle charging infrastructure in Indian society.

Strong government push

For the past several years, state and federal governments have increased and sustained their policy interventions to assure the implementation of charging infrastructure (Helmus et al. 2018).

- Treating EV charging as a "service" has been the first and most important step. As a result, no license is necessary to set up and run an EV charging station.
- The governments have implemented financial and non-financial incentives, such as lower tariff fees for producing and using chargers. Also, power regulators' treatment of "EV Charging Station" as a separate category under Tariff Order has been a step toward encouraging e-Mobility in the nation.
- The GST rate for EV chargers and charging stations was decreased from 18% to 5% in the Union Budget that was presented in July 2019.
- To encourage people to switch to electric transportation, the government plans to install at least one EV charging kiosk at around 69,000 gas stations nationwide by November 2020.

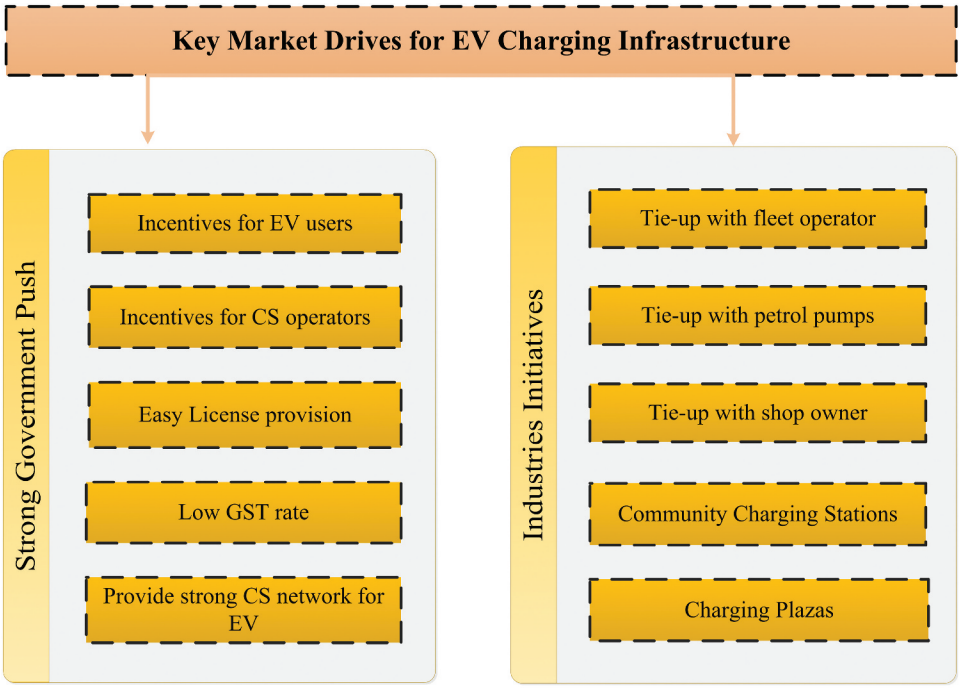

Figure 6. Key market drivers for future growth of EV Charging Infrastructure.

Industry initiatives

Several automakers and other private parties, including independent charging infrastructure providers, have expressed interest in setting up charging infrastructure.

Tie-ups

With Fleet Operators. Large-scale fleet operators such as Ola, Uber, Lithium Urban, Zoom Cars, and door-to-door delivery/courier operators are anticipated to become critical market drivers regarding CSOs' commercial possibilities. They have the appropriate commercial motivations to construct charging and digital infrastructure to serve their EV fleet, given that they run many cars across India. Together with the strong financial support of investors, significant fleet operators in India have become early users of charging infrastructure.

With Petrol Pumps. Charging companies/OEMs are partnering with gas stations to expand the availability of charging, particularly through the battery-changing option. OLA Electric Mobility and Sun Mobility have already established partnerships with IOCL for battery swapping stations, while VoltUp has established partnerships with HPCL for 50 battery switching stations. Similarly, BPCL has teamed with EV manufacturer Kinetic Green Energy, Power Solutions and IIT Madras to provide technical assistance for the delivery of swappable lithium-ion batteries at its retail locations in Kochi and Lucknow for e-3W in the initial phase (Verma et al. 2022).

With shop owners. e-2W Businesses (such as Ather) are opting for decentralized charging systems in which they have partnered with shop owners to use a portion of their space for chargers or with kirana stores for battery swapping.

Community charging stations

Increasingly, hotels, companies, and resorts are installing standard 15A charge points for EVs and electric bikes 40 to 70 km from urban areas. These charging stations are referred to as community charging stations. Initiatives such as PluginIndia, a network of EV users and fans in India promoting EVs since 2013, have caught and supported these phenomena. As of January 2020, over 257 community charging stations existed across India on routes such as Mumbai to Nashik, Mumbai to Pune (up to Mahabaleshwar), Delhi to Jaipur, Bengaluru to Mangalore, and Chennai to Mahabalipuram (Srinath 2021).

Charging plazas

Energy efficient service limited (EESL) unveiled India's first public charging plaza on July 20, 2020, at the Chelmsford Club in New Delhi to improve India's e-mobility ecosystem and the availability of charging facilities at public locations. The charging station can simultaneously charge 14 EVs (Singh 2020). Theoretically, a plaza has many chargers with varying power outputs for servicing various automotive models. EESL intends to deploy around ten EV charging stations during the 2020–21 budget year.

Challenges

The best e-mobility strategies found in developed foreign markets might not be efficient or practical to handle India's concerns because of the country's specific infrastructure limitations. The strategy for addressing the problems and creating solutions must be indigenous to or specifically designed for India. The different challenges faced by EV users, distribution systems and charging station operators are shown in Figure 7.

Electric vehicle user challenges

There is some anxiety among EV users about replacing conventional vehicles with the appropriate electric vehicles, some of which are listed here.

Range anxiety

Range anxiety is the worry over how many kilometers an EV will go or how long the battery power will last for an EV user. In India, the number of kilometers per liter, or mileage, is a key consideration before buying an ICE car. The existing battery technology in EVs makes it impossible for many EV users to travel long distances on a single charge. According to a recent survey by lubricants giant Castrol, drivers in India expect a range of 401 kilometers on a single charge. The study included 1,000 customers, fleet managers, and industry experts (Pevec et al. 2020).

Time anxiety

Consumers want to charge as rapidly as they can fill up a gas tank, but that is not possible with the available charging methods, particularly the slower ones. According to a survey by lubricants giant Castrol, drivers should not anticipate a charge to take longer than 35 minutes on average.

Charge anxiety

Concerns about finding a charging station in the first place are known as charge anxiety. The question of trust follows this. People in India frequently double-check the gas meter even before filling the tank at petrol stations. They have similar confidence difficulties with electric charging stations, questioning whether the car is receiving a charge and whether the charging station is functioning properly (Chakraborty et al. 2022).

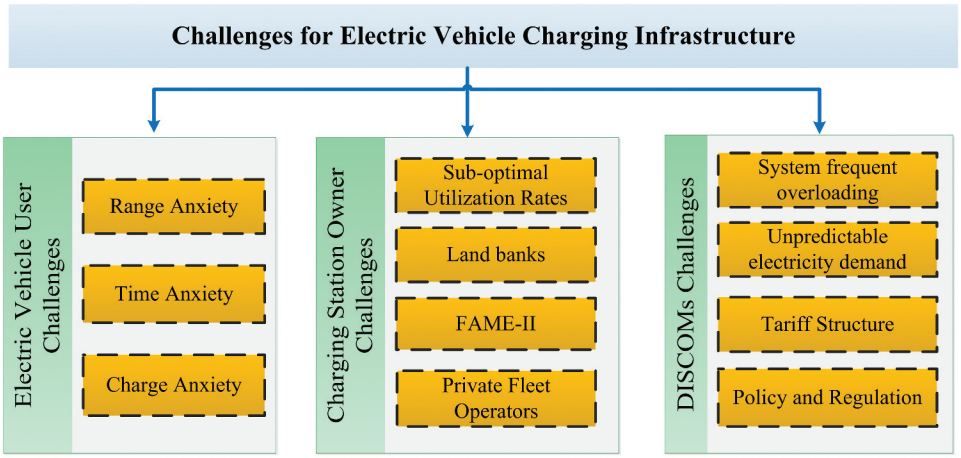

Figure 7. Challenges for EV charging infrastructure.

Charging station operators challenge

Electric vehicle charging station operators face several challenges in their operations. Some of the key challenges include:

Sub-optimal utilization rates

The vast amount of money spent does not compare to sub-optimal utilization rates of 10–15% at public charging stations, assuming that a fast charging station charges a car in about 1.5 hours and that no more than 2 to 3 automobiles arrive on any given day. In the current scenario, where 6 guns must be built, the CAPEX per station, ignoring land cost or rent, works out to be $ 12 million, considering the average cost of Rs. 2 million for each charging gun. When the returns are not significant because of the low utilization rates, the high expenses of the equipment and its installation pose the biggest problem.

Land banks

One of the impediments the government has yet to solve is land banks, including parking spaces in the cities. Even though they receive the property for free under government mandate, state enterprises have experienced problems with land acquisition. Also, there hasn't been a fixing of fees, which results in expensive rent. For instance, in some circumstances, it is claimed that the land lease cost alone makes up more than 40% of the cost of running a charging station (Ahmad et al. 2022).

FAME-II

In a state like Delhi, which considers this much electricity under the low tension (LT) connection, FAME II demands at least two chargers of around 100 kW each on every PCS. Nevertheless, the relevant CSO would have to go for a high tension (HT) connection and, in the process, build cables, transformers, etc. in a state like Gujarat or Uttar Pradesh where the limit of an LT connection is considered 50 kW. The latter is 2 to 3 times more expensive than the subsidies it receives. As a result, the entire endeavor is useless Bilal, Ahmad, and Rizwan (2023).

Private fleet operators

Installing an EVSE at a fleet operator-owned and operated EV charging station raises questions about getting a dependable electrical connection.

As various prices for EV charging are levied in different jurisdictions, and several governments declare EV as a separate tariff category, it is challenging for taxi aggregators/fleet operators operating in numerous states.

DISCOMs challenge

Electric vehicle charging stations pose certain challenges for electricity distribution companies (DISCOMs) when it comes to installation. Some of the challenges faced by DISCOMs in installing charging stations are:

Distribution network and frequent overloading of system components

Rising peak loads in service regions would necessitate greater financial investments in network upgrades and power procurement, which will ultimately be unprofitable for DISCOMs.

Unpredictable electricity demand

It is unpredictable power consumption because people charge their cars in different places and lengths of time. The quality of the grid's power will be impacted by this. The continued widespread use of EVs will distort the nature of power demand, which will cause problems, including unexpected peaks in power consumption, transformer overload, voltage drop, voltage imbalance, and harmonics injection.

Key aggregators

In the Indian market, there are several charging station aggregators that provide services for EV charging. These aggregators work as intermediaries between charging station owners and EV users.

Volttic EV charging solution

Noida-based Tvesas Electric Solutions Pvt. Ltd.'s Volttic, a trademarked item, provides EV Charging Services comprising EV Charging Stations and a cloud-based charger management system. The Business joined the EV charging market in 2017, and since then, it has focused on commercial and residential charging.

Location: In major Indian cities, including Mumbai, Chennai, Bangalore, Delhi-NCR, Pune, and Hyderabad the company is present. In addition to having public set up in Mumbai, Indore, Gurugram, and Delhi, volttic chargers are now used in the corporate headquarters of HP Computing, Infosys, Fidelity, Mckinsey, Amazon, and JP Morgan.

Vehicle-Type: Volttic systems support all EV kinds, including electric buses and 2W, 3W, and 4W vehicles. Although DC fast chargers vary from 15 kW to 150 kW, voltaic chargers' AC power output ranges from 3.3 kW to 22 kW.

Order Value: Volttic already boasts of orders totaling $ 1,000,000 USD. By 2025, the business wants to have installed more than 25,000 quick charging outlets in Indian cities.

Installed charging points: Installed 500+ EV charge points including CCS2 EV Chargers, Bharat DC01 charger and Bharat AC01 charger Chaturvedi (2021).

Charge zone

It is a start-up with a Vadodara address that has been operating since 2018 and is a member of the TecSo Global group. In November 2020, it secured pre-Series A funding totaling USD $ 3 million.

Charger Type: Type 2 DC Fast charger and Fast CCS2 150 kW DC (electric-bus)

Clients:SmartE, Ashok Leyland, Bajaj Auto, Shuttl, EEE-Taxi, BluSmart

Installed charging points: 750+ charging stations, 1400+ charging point, 25+ cities PAN India Hariyani (2021).

Tata Power EZ Charge

TATA Power operates throughout the conventional and renewable energy value chains. In addition, providing EV chargers with various charging regulations, charging setup, charger Management software, and Mobile App.

Charging Segment: Public charger

Charger Type: AC and DC charger rating from 7 to 50 kW; CCS2 standard

Clients: TATA Motors, MG Motor India, Prakriti E-Mobility Private Limited, Jaguar Land Rover (India)

Installed charging points: Tata Power has installed over 3,000 Public and Semi-Public EZ Charge points across 450+ cities in India Sinha (2022).

Energy efficiency services limited

In order to provide services related to renewable energy, four PSUs – Power Finance Corp. Ltd., NTPC Ltd., POWERGRID Corp. of India, and REC Ltd.—joined forces to establish EESL.

Charging Segment: Public charger and Captive charger

Charger Type: AC-001 and DC-001

Clients: NKDA Kolkata, Maha Metro Nagpur, NDMC Delhi, Naya Raipur Development Authority, Noida Authority, CMRL Chennai, SDMC Delhi Kapoor (2021).

Installed charging points: 1200+

EVI technologies

EVI Technologies was established in June 2017 in Delhi's government-supported Electropreneur Park. For individual customers, EVIT provides charging stations for leasing. It provides two products: an e-2W and e-3W battery and a charging station that can be installed in households and public spaces (Kumar 2022).

Charger Type: Battery Swapping station, DC-001 Charger, AC-001 Charger, AC Type 1 and AC Type 2 Charger

Locations: They covered 10 states and 16 locations for installing charging stations

Installed charging points: 215+

Rajasthan electronics & instruments limited

Rajasthan Electronics & Instruments Limited (REIL) is a joint venture between Rajasthan and the Government of India and one of the top state-owned companies in the EV charging infrastructure market.

Charger Type: Bharat, Type-2, CHAdeMO and CCS

Installed charging points: 800+, REIL has contracted Okaya Power to source, construct, and commission 4,244 EVCSs throughout India Chopra (2021).

Conclusion

The major players have been encouraged to promote market expansion on the strength of adequate regulatory frameworks and industry activities due to the government's strong push for EV transition and, therefore, EV charging infrastructure. Electric vehicle policy incentives from the state government and initiatives from the central government, including lowering the GST and introducing FAME, have set up an initial base for private aggregators CSOs, equipment manufacturers, and cab aggregators.

Furthermore, in states like Maharashtra, Haryana, Jharkhand, Gujarat, Chandigarh, and Karnataka of India, charging station aggregators face challenges in paying fixed capacity fees based on their connection capacity. Since the number of EVs on the road is still relatively low, the infrastructure set up by these aggregators is underutilized. To address this issue, it is essential to eliminate or minimize capacity charges for EV tariffs in the initial 3 to 5 years for CSOs due to the low volume of EVs and the limited capacity utilization. Additionally, the government should focus on increasing the number of EVs on the road by procuring more through agencies like EESL for various government departments. Alternatively, leasing EVs can be considered when budget constraints prevent direct purchases. CSOs emphasize that more EVs are necessary to improve the utilization of existing chargers, attract private aggregators to enter the market, and encourage existing aggregators to expand their installed capacity.

Moreover, it is crucial to establish clear market rules that determine which stakeholders are responsible for different aspects of the charging infrastructure. For example, if a CSO needs to pay for the use of public or private land for charging stations, it should be clearly defined. Similarly, if fleet operators require grid optimization to accommodate charging at, say, an office building for 20 vehicles, it should be determined who bears the cost of that element. Over time, these defined market rules will help strike a balance between service providers and consumers, maximize profits, and enable optimal investments in the charging infrastructure.

Disclosure statement

No potential conflict of interest was reported by the author(s).

Notes on contributors

Fareed Ahmad is working as an Assistant professor at SND College of Engineering and Research Center, Yeola, Nashik, India, and have completed his Ph.D. from Aligarh Muslim University, Aligarh, India. His master's degree in Electrical Engineering (M.Tech) in specialization of instrumentation and control in 2016 from Aligarh Muslim University, Aligarh, India and his Bachelor of Engineering (B.Tech) degree in Electrical Engineering from Gautama Buddha Technical University (GBTU), India in 2013. Ahmad has published articles in reputable journals, IEEE Transaction, Energy Reports, Energy Conversion and Management.

Mohd Bilal received the B.Tech. degree in electrical engineering and the M.Tech. degree in instrumentation and control engineering from Aligarh Muslim University, Aligarh, India, in 2014 and 2016, respectively. He received his Ph.D. degree from Delhi Technological University, New Delhi, India in 2022. Currently, he has been working as assistant professor in the department of electrical engineering, SND College of engineering and research center, Nashik, India. He has published/presented few technical papers and conference proceedings in international journal of repute. His research interests include electric vehicles, optimization techniques, artificial intelligence, EV integration with grid etc.

ORCID

Fareed Ahmad http://orcid.org/0000-0002-6733-7615
Mohd Bilal http://orcid.org/0000-0003-1759-5138

References

Adnan, N., S. Md Nordin, M. A. Bin Bahruddin, and M. Ali. 2018. How trust can drive forward the user acceptance to the technology? In-vehicle technology for autonomous vehicle, Transportation Research Part a. *Transportation Research Part A: Policy and Practice* 118 (October):819–36. doi:10.1016/j.tra.2018.10.019.

Ahmad, F., I. Ashraf, A. Iqbal, M. Marzband, and I. Khan. 2022. A novel ai approach for optimal deployment of ev fast charging station and reliability analysis with solar based dgs in distribution network. *Energy Reports* 8:11646–60. doi:10.1016/j.egyr.2022.09.058.

Ahmad, F., A. Iqbal, I. Asharf, M. Marzband, and I. Khan. 2023. Placement and capacity of ev charging stations by considering uncertainties with energy management strategies, IEEE Transactions on Industry Applications. doi:10.1109/TIA.2023.3253817.

Ahmad, F., A. Iqbal, I. Ashraf, M. Marzband, and I. Khan . 2022. Optimal location of electric vehicle charging station and its impact on distribution network: A review. *Energy Reports* 8:2314–33. doi:10.1016/j.egyr.2022.01.180.

Arif, S. M., T. T. Lie, B. C. Seet, S. Ayyadi, and K. Jensen. 2021. Review of electric vehicle technologies, charging methods, standards and optimization techniques. *Electronics* 10 (16):1910. doi:10.3390/electronics10161910.

Balaji, S. 2022. Electric vehicle charging infrastructure guidelines for Tamil Nadu state. https://powermin.gov.in/sites/default/files/uploads/EV/Tamilnadu.pdf

Bilal, M., F. Ahmad, and M. Rizwan. 2023. Techno-economic assessment of grid and renewable powered electric vehicle charging stations in India using a modified metaheuristic technique. *Energy Conversion and Management* 284:116995. doi:10.1016/j.enconman.2023.116995.

Bilal, M., and M. Rizwan. 2020. Electric vehicles in a smart grid: A comprehensive survey on optimal location of charging station. *IET Smart Grid* 3 (3):267–79. doi:10.1049/iet-stg.2019.0220.

Chakraborty, P., R. Parker, T. Hoque, J. Cruz, L. Du, S. Wang, and S. Bhunia. 2022. Addressing the range anxiety of battery electric vehicles with charging en route. *Scientific Reports* 12 (1):5588. doi:10.1038/s41598-022-08942-2.

Chaturvedi, V. 2021. Volttic ev charging solution. https://volttic.com/about-us/.

Chopra, R. 2021. Electric vehicle charging station infrastructure by Rajasthan electronics and instruments limited, https://www.reiljp.com/REILDeployment.aspx.

Das, H. S., M. M. Rahman, S. Li, and C. Tan. 2020. Electric vehicles standards, charging infrastructure, and impact on grid integration: A technological review. *Renewable and Sustainable Energy Reviews* 120:109618. doi:10.1016/j.rser.2019.109618.

Emobility. 2023. Indian government sanctions rs. 800 crores for setting up 7432 public fast charging stations. https://emobilityplus.com/2023/03/29/.

Gahlot, K. 2022. Electric vehicle charging infrastructure guidelines for delhi. https://ev.delhi.gov.in/vision-mission.

Hariyani, K. 2021. Charge+zone, charging the future of ev driving. https://www.chargezone.com/shop.html.

Helmus, J., J. Spoelstra, N. Refa, M. Lees, and R. van den Hoed. 2018. Assessment of public charging infrastructure push and pull rollout strategies: The case of the netherlands. *Energy Policy* 121:35–47. doi:10.1016/j.enpol.2018.06.011.

Kapoor, V. 2021. Electric vehicle and ev charging infrastructure by energy efficiency services limited. https://eeslindia.org/en/electric-vehicles/.

Katsumata, T. 2018. Chademo protocol development. https://www.chademo.com/activities/protocol-development/

Kore, H. H., and S. Koul. 2022. Electric vehicle charging infrastructure: Positioning in India. *Management of Environmental Quality* 33 (3):776–799. doi:10.1108/MEQ-10-2021-0234.

Krishnankutty, K. 2022. Electric vehicle charging infrastructure guidelines for Kerala state. https://powermin.gov.in/sites/default/files/uploads/EV/Kerala.pdf.

Kumar, R. 2022. Charging station network by evi technologies. https://evitpl.com/products/.

Kumar, S. 2022. Electric vehicle charging infrastructure guidelines for Karnataka state. https://powermin.gov.in/sites/default/files/uploads/EV/Karnataka.pdf.

Lee, J. H., D. Chakraborty, S. J. Hardman, and G. Tal. 2020. Exploring electric vehicle charging patterns: Mixed usage of charging infrastructure, Transportation Research Part D. *Transportation Research Part D: Transport and Environment* 79:102249. doi:10.1016/j.trd.2020.102249.

Makeen, P., H. A. Ghali, and S. Memon. 2020. Experimental and theoretical analysis of the fast charging polymer lithium-ion battery based on cuckoo optimization algorithm (coa. *IEEE Access* 8:140486–96. doi:10.1109/ACCESS.2020.3012913.

Makeen, P., H. A. Ghali, S. Memon, and F. Duan. 2022. Impacts of electric vehicle fast charging under dynamic temperature and humidity: Experimental and theoretically validated model analyses. *Energy* 261:125335. doi:10.1016/j.energy.2022.125335.

Mishra, S., S. Verma, S. Chowdhury, A. Gaur, S. Mohapatra, G. Dwivedi, and P. Verma. 2021. A comprehensive review on developments in electric vehicle charging station infrastructure and present scenario of india. *Sustainability* 13 (4):2396. doi:10.3390/su13042396.

Pareek, S., A. Sujil, S. Ratra, R. Kumar. 2020. Electric vehicle charging station challenges and opportunities: A future perspective, in: 2020 International Conference on Emerging Trends in Communication, Control and Computing (ICONC3), Lakshmangarh, India. 1–6. IEEE.

Patel, S. B. 2022. Electric vehicle charging infrastructure guidelines for Gujarat state. https://powermin.gov.in/sites/default/files/uploads/EV/Gujarat.pdf.
Pevec, D., J. Babic, A. Carvalho, Y. Ghiassi-Farrokhfal, W. Ketter, and V. Podobnik. 2020. A survey-based assessment of how existing and potential electric vehicle owners perceive range anxiety. *Journal of Cleaner Production* 276:122779. doi:10.1016/j.jclepro.2020.122779.
Photovoltaics, D. G., and E. Storage. 2018. IEEE standard for interconnection and interoperability of distributed energy resources with associated electric power systems interfaces. *IEEE Std* 1547:1547–2018.
Rajendran, G., C. A. Vaithilingam, N. Misron, K. Naidu, and M. R. Ahmed. 2021. A comprehensive review on system architecture and international standards for electric vehicle charging stations. *Journal of Energy Storage* 42:103099. doi:10.1016/j.est.2021.103099.
Reddy, J. 2022. Electric vehicle charging infrastructure guidelines for telangana state. https://powermin.gov.in/sites/default/files/uploads/EV/Telangana.pdf.
Reddy, J. M. 2022. Electric vehicle charging infrastructure guidelines for ap. https://powermin.gov.in/sites/default/files/uploads/EV/Andhra_Pradesh.pdf.
Shang, Y., M. Liu, Z. Shao, and L. Jian. 2020. Internet of smart charging points with photovoltaic integration: A high-efficiency scheme enabling optimal dispatching between electric vehicles and power grids. *Applied Energy* 278:115640. doi:10.1016/j.apenergy.2020.115640.
Shariff, S. M., M. S. Alam, F. Ahmad, Y. Rafat, M. S. J. Asghar, and S. Khan. 2019. System design and realization of a solar-powered electric vehicle charging station. *IEEE Systems Journal* 14 (2):2748–58. doi:10.1109/JSYST.2019.2931880.
Sharma, S. 2022. Electric vehicle charging infrastructure guidelines for uttar pradesh. https://powermin.gov.in/sites/default/files/uploads/EV/Uttar_Pradesh.pdf.
Singh, H. 2022a. Electric vehicle charging infrastructure guidelines for chandigarh state. https://evreporter.com/chandigarh-ev-policy-2019/.
Singh, H. 2022b. Electric vehicle charging infrastructure guidelines for Punjab state https://powermin.gov.in/sites/default/files/uploads/EV/Punjab.pdf.
Singh, R. 2020. India's first of its kind public ev charging plaza inaugurated. https://eeslindia.org/en/electric-vehicles/.
Sinha, P. 2022. Tata power ez charge. https://www.tatapower.com/energy-solutions.
Srinath, S. 2021. Community charging points are installed by pluginindia. https://www.pluginindia.com/charging.html .
Sufyan, M., N. A. Rahim, M. A. Muhammad, C. K. Tan, S. R. S. Raihan, and A. H. A. Bakar. 2020. Charge coordination and battery lifecycle analysis of electric vehicles with v2g implementation. *Electric Power Systems Research* 184:106307. doi:10.1016/j.epsr.2020.106307.
Tang, W. W., Y. M. Wu, and J. Qin. 2012. Comparative Study on Electric Vehicle Charging Standards at Home and Abroad. *Advanced Materials Research* 608–609: 1553–1559. https://doi.org/10.4028/www.scientific.net/amr.608-609.1553.
Tomar, P. S. 2022. Electric vehicle charging infrastructure guidelines. https://powermin.gov.in/sites/default/files/uploads/EV/Madhya_Pradesh.pdf.
Verma, R., S. K. Sharma, P. Singh, J. K. Bhutto, and A. R. A. Alharbi. 2022. Analysis and sizing of charging stations in kota city. *Sustainability* 14 (18):11759. doi:10.3390/su141811759.
Waghmare, D. 2022. Electric vehicle charging infrastructure guidelines for Maharashtra state. https://powermin.gov.in/sites/default/files/uploads/EV/Maharashtra.pdf.
Wang, L., Z. Qin, T. Slangen, P. Bauer, and T. Van Wijk. 2021. Grid impact of electric vehicle fast charging stations: Trends, standards, issues and mitigation measures-an overview. *IEEE Open Journal of Power Electronics* 2:56–74. doi:10.1109/OJPEL.2021.3054601.
Yadav, B. P. 2022. Electric vehicle charging infrastructure guidelines for bihar state. https://powermin.gov.in/sites/default/files/uploads/EV/Bihar.pdf.
Yu, H., S. Niu, Y. Shang, Z. Shao, Y. Jia, and L. Jian. 2022. Electric vehicles integration and vehicle-to-grid operation in active distribution grids: A comprehensive review on power architectures, grid connection standards and typical applications. *Renewable and Sustainable Energy Reviews* 168:112812. doi:10.1016/j.rser.2022.112812.
Zarfos, T.2019. 2022. *Sae Standards*.https://www.sae.org/standards/.
Zheng, Y., Z. Shao, and L. Jian. 2021. The peak load shaving assessment of developing a user-oriented vehicle-to-grid scheme with multiple operation modes: The case study of Shenzhen, china. *Sustainable Cities and Society* 67:102744. doi:10.1016/j.scs.2021.102744.

Title of Article:

A Comprehensive Examination of the Economic Impact of Out-of-pocket Health Expenditures in India

Running Title:

Impact of Out-of-pocket Health Expenditures in India

Author Details:

Mehak Nanda, Doctoral Scholar

University School of Management and Entrepreneurship, Delhi Technological University, New Delhi, India.

Rajesh Sharma, Ph.D.

University School of Management and Entrepreneurship, Delhi Technological University, New Delhi, India.

Corresponding Author:

Rajesh Sharma

University School of Management and Entrepreneurship, Delhi Technological University, New Delhi, India.

Email Id: sharmarajesh.eco@gmail.com

Orcid details: https://orcid.org/0000-0001-7468-1249

Key Messages:

- The financial burden of OOPE was higher for outpatient care (CHE: 47.8%; Impoverishment: 15.0%) compared to hospitalization (CHE: 43.1%; Impoverishment: 10.7%).
- Nearly 1.8% of ailing individuals did not seek treatment and 10.1% of ailing individuals did not seek treatment on medical advice.
- Cancer, genito-urinary diseases, psychiatric and neurological disorders, obstetric conditions, and injuries imposed a substantial economic burden on Indian households.

The Author(s) 2023. Published by Oxford University Press in association with The London School of Hygiene and Tropical Medicine. All rights reserved. For permissions, please e-mail: journals.permissions@oup.com

ACCEPTED MANUSCRIPT

Downloaded from https://academic.oup.com/heapol/advance-article/doi/10.1093/heapol/czad050/7220383 by Delhi Technological University user on 22 July 2023

Keywords: Out-of-pocket Health Expenditure, Disease, Distressed Financing, Catastrophic Health Expenditure, Impoverishment

Word Count: 6460 words (Excluding abstract, references, figures, and tables)

Reflexivity statement

The authors of the study include a female and a male researcher. One author is currently pursuing Ph.D. and the other author has extensive experience and specialization in health economics, public health and epidemiology in Asia and at a global level.

Author Contribution Statement

Mehak Nanda: Conception of the work, Data analysis and interpretation, Drafting the article, Critical revision of the article, Final approval of the version to be submitted.

Rajesh Sharma: Conception of the work, Critical revision of the article, Final approval of the version to be submitted.

Funding

This study has received no specific grant from any funding agency in public, commercial or not-for-profit sectors.

Conflicts of Interest

Authors declare no competing interests.

Ethical Approval

The research was conducted using data available in the public domain and did not include any human participants or animals. Therefore, no ethical approvals were required.

ACCEPTED MANUSCRIPT

A Comprehensive Examination of the Economic Impact of Out-of-pocket Health Expenditures in India

Abstract

Downloaded from https://academic.oup.com/heapol/advance-article/doi/10.1093/heapol/czad050/7220383 by Delhi Technological University user on 22 July 2023

More than 50% of the health expenditure is financed through out-of-pocket payments in India, imposing a colossal financial burden on households. Amidst the rising incidence of non-communicable diseases, injuries, and an unfinished agenda of infectious diseases, this study examines comprehensively the economic impact of out-of-pocket health expenditure (OOPE) across 17 disease categories in India. Data from the latest round of the National Sample Survey (2017-18), titled "Household Social Consumption: Health" was employed. Outcomes, namely, catastrophic health expenditure (CHE), poverty headcount ratio, distressed financing, foregone care, and loss of household earnings were estimated. Results showed that 49% of households experienced CHE and 15% of households fell below the poverty line due to OOPE on hospitalization and/or outpatient care. Notably, outpatient care was more burdensome (CHE: 47.8%; Impoverishment: 15.0%) than hospitalization (CHE: 43.1%; Impoverishment: 10.7%). Nearly 16% of households used distressed sources to finance hospitalization-related OOPE. Cancer, genito-urinary diseases, psychiatric and neurological disorders, obstetric conditions, and injuries imposed a substantial economic burden on households. OOPE and associated financial burden was higher among households where any member sought care in private healthcare facilities compared to those treated in public facilities across most disease categories. The high burden of OOPE necessitates the need to increase health insurance uptake and consider outpatient services under the purview of health insurance. Concerted efforts to strengthen public health sector, improved regulation of private healthcare providers, and prioritizing health promotion and disease prevention strategies are crucial to augment financial risk protection.

ACCEPTED MANUSCRIPT

Downloaded from https://academic.oup.com/heapol/advance-article/doi/10.1093/heapol/czad050/7220383 by Delhi Technological University user on 22 July 2023

1. Introduction

Universal Health Coverage (UHC), the centerpiece of the United Nations sustainable development goals on health (SDG-3), aims to ensure that everyone has access to quality healthcare without facing financial hardships (WHO, 2021a). SDG-3 focuses on a broad gamut of health-related issues pertinent to the global community as well as developing countries such as India (UNDP, 2022). India is experiencing a triple burden of diseases, i.e., increasing non-communicable diseases (NCDs), an unfinished agenda of infectious diseases, and a rising incidence of injuries (Bloom et al., 2014). Between 1990 and 2016, the proportion of all deaths in India due to NCDs increased from 37.9% to 61.8%, and the contribution of NCDs to total disability-adjusted life years increased from 30.5% to 55.4% (ICMR, PFHI and IHME, 2017). Communicable diseases too, such as diarrhoea, tuberculosis, lower respiratory infections, and vector-borne diseases (for instance, dengue, malaria, and chikungunya) continue to pose substantial challenges in India (ICMR, PFHI and IHME, 2017). Furthermore, in 2018, India accounted for nearly 11% of accident-related deaths worldwide, ranking first among the 199 countries in terms of road accident mortality (GOI, 2019). Macroeconomic studies estimate that NCDs and mental disorders will lead to approximately $4.58 trillion output loss in India during 2012 to 2030 due to savings lost and foregone productivity (Bloom et al., 2014). Despite this overwhelming scenario in India, the government health expenditure is dismally low (1.15% of GDP) (National Health Policy, 2017). A combination of low health insurance coverage and a dominant presence of fee-for-service private health sector has forced Indian households to rely on out-of-pocket health expenditure (OOPE) as a means of financing healthcare (Shahrawat and Rao, 2012).

In India, OOPE accounts for 50.6% of health expenditure (WHO, 2019a), one of the highest in the world. High OOPE reduces access to healthcare services, decreases the consumption of

ACCEPTED MANUSCRIPT

Downloaded from https://academic.oup.com/heapol/advance-article/doi/10.1093/heapol/czad050/7220383 by Delhi Technological University user on 22 July 2023

food and basic necessities, and exposes households to financial catastrophe and impoverishment. Healthcare payments are a major cause of poverty in India, pushing nearly 32-39 million individuals below the poverty line each year (Van Doorslaer et al., 2006; Bonu et al., 2007; Garg and Karan, 2009). Poor people not only lack the financial resources to access healthcare, but illness also reduces labour supply and limits their financial ability (World Bank, 2014), creating a vicious circle of poor health and poverty.

The rising disease burden in India, accompanied by abysmally low public health spending and insurance uptake, warrants analysis of economic impact of OOPE across all types of diseases- communicable, non-communicable, and injuries. However, limited literature is available on the financial burden of OOPE across various ailments in India. Previous studies focussed mainly on OOPE due to hospitalization (Kastor and Mohanty, 2018) or specific ailments such as maternal health (Bonu et al., 2009; Mohanty and Kastor, 2017), NCDs (Engelgau et al., 2012; Tripathy et al., 2016; Verma et al., 2021), cancer (Mahal et al., 2013; Rajpal et al., 2014), diabetes (Tripathy and Prasad, 2018), and tuberculosis (Yadav et al., 2021a). Other studies provided estimates for small geographic areas with non-representative data, thereby limiting the generalizability (Sneha et al., 2017; Swan et al., 2018). One study examined the financial burden of OOPE across all diseases but did not report it separately for inpatient and outpatient care and was based on data from the previous National Sample Survey (Sangar et al., 2019a). Another study examined the OOPE burden separately for hospitalization and outpatient care across all ailments, but was limited to evaluating catastrophic health expenditure (CHE) and impoverishment impact only (Yadav et al., 2021b). Moreover, to the best of our knowledge, no study in India has computed CHE using household's capacity to pay approach (Xu et al., 2003) for all categories of diseases. This is

ACCEPTED MANUSCRIPT

Downloaded from https://academic.oup.com/heapol/advance-article/doi/10.1093/heapol/czad050/7220383 by Delhi Technological University user on 22 July 2023

important because estimates based on capacity to pay are pro-poor and take into account the equity concerns (Bonu et al., 2009; Mohanty and Kastor, 2017).

Against this backdrop, we provide a comprehensive examination of the financial burden of OOPE across 17 disease categories, disaggregated by the type of care sought (hospitalization, outpatient care, and either hospitalization or outpatient care or both) and the type of healthcare facility utilized (public or private). Specifically, our study was guided by the following objectives. First, we computed OOPE and the share of OOPE in total household consumption expenditure. Second, we estimated the incidence of CHE, percentage of households falling below the poverty line due to OOPE, and the incidence of using distressed sources to cope with the cost of illness. Third, we gauged the loss of household earnings resulting from hospitalization and outpatient care for various ailments. Fourth, we estimated the unmet needs (i.e., percentage of individuals who did not seek treatment), and percentage of individuals who did not seek treatment on medical advice and reasons for the same. This holistic assessment is expected to serve as a valuable resource for evidence-based policy decisions to improve accessibility of healthcare services and augment financial risk protection for Indian households.

2. Data and Methodology

2.1 Overview of Data Source

The study used data from the latest round of the National Sample Survey (NSS) on health and morbidity, titled "Household Social Consumption: Health," which was conducted during July 2017 to June 2018. This is a nationally representative survey that covered 113,823 households and 555,115 individuals across the country. The data were collected using a stratified multi-stage sampling design, with village and urban blocks as the first unit and

ACCEPTED MANUSCRIPT

Downloaded from https://academic.oup.com/heapol/advance-article/doi/10.1093/heapol/czad050/7220383 by Delhi Technological University user on 22 July 2023

household as the second unit. The survey collected detailed information about the nature of ailment, utilization of health facilities, cost of inpatient and outpatient services, and demographic and socio-economic characteristics of households and their members. It collected information about the prevalence of 61 types of diseases, which were further classified into 17 broad categories. The disease classification under NSS health survey is provided in Supplementary Table 1.

2.2 Outcome variables

2.2.1 Out-of-pocket Health Expenditure (OOPE)

The NSS health survey recorded total health expenditure under three broad categories: medical, non-medical, and transport expenditure. Medical expenditure included doctors' fees, costs of medicines, diagnostic tests, bed charges, other medical expenses (such as attendant charges, physiotherapy, blood, etc.), and package component, and non-medical expenditure included expenses on registration, food, lodging, etc. To determine OOPE, any reimbursement amount received was deducted from the total health expenditure. The survey recorded hospitalization expenditure during the last 365 days, this was divided by 12 to compute monthly hospitalization OOPE. Similarly, outpatient expenses were recorded for the last 15 days, these were multiplied by 2 to compute monthly outpatient care OOPE.

2.2.2 Share of OOPE in total household consumption expenditure

The share of OOPE in total household consumption expenditure, was calculated by the following formula, as done by previous studies (Selvaraj et al. 2018; Yadav et al. 2021b).

$$Share\ of\ OOPE\ in\ consumption\ expenditure = \frac{Household's\ Monthly\ OOPE}{Household's\ Monthly\ Consumption\ Expenditure} * 100$$

ACCEPTED MANUSCRIPT

Downloaded from https://academic.oup.com/heapol/advance-article/doi/10.1093/heapol/czad050/7220383 by Delhi Technological University user on 22 July 2023

2.2.3 Catastrophic Health Expenditure (CHE)

Literature suggests two alternative approaches for calculating CHE. The first method defines health spending as catastrophic if it exceeds some fraction of household's income or total expenditure (Berki, 1986). A potential problem in this approach is that it fails to account for the CHE of poor households (Mohanty and Kastor, 2017). This is because health payments budget share among poor households is low since most resources are consumed by the items essential for sustenance, leaving little money to spend on healthcare (Bonu et al., 2009; Mohanty and Kastor, 2017). The second method partially overcomes this limitation by defining health spending as catastrophic if it exceeds 40% of the household's capacity to pay (Xu et al., 2003). We adopted the capacity to pay approach in this study, while previous studies followed the former approach (Kastor and Mohanty, 2018; Sangar et al., 2019a; Yadav et al., 2021b).

For each household *i*, we defined CHE as below.

$$CHE_i = \begin{cases} 1, if & \frac{OOPE_i}{HCE_i - SE_i} > 0.4 \\ 0, if & \frac{OOPE_i}{HCE_i - SE_i} \leq 0.4 \end{cases}$$

In above equation, $OOPE_i$ is the out-of-pocket health expenditure of i^{th} household, HCE_i is the consumption expenditure of i^{th} household, SE_i is the subsistence expenditure of i^{th} household.

The subsistence expenditure is calculated using either food expenditure or the official poverty line (Bonu et al., 2009; Mohanty and Kastor, 2017). However, since the NSS health survey does not provide detailed information on individual expenditure items (for instance, food and non-food items), the food expenditure was unavailable. Thus, we used the inflation-adjusted official poverty line as defined by the Tendulkar Committee (Planning Commission, 2014) as a proxy for subsistence expenditure (Bonu et al., 2009; Mohanty and Kastor, 2017). The

ACCEPTED MANUSCRIPT

Downloaded from https://academic.oup.com/heapol/advance-article/doi/10.1093/heapol/czad050/7220383 by Delhi Technological University user on 22 July 2023

poverty line was multiplied by the household size to obtain the household-level subsistence expenditure, which was then subtracted from total household consumption expenditure to derive a household's capacity to pay (Bonu et al., 2009; Engelgau et al., 2012).

2.2.4 Poverty Headcount Ratio

The poverty headcount ratio estimates the proportion of households falling below the poverty line due to OOPE (Yadav et al., 2021b).

$$Poverty\ Headcount_i = \begin{cases} 1, & if\ HCE_i \geq PL\ and\ (HCE_i - OOPE_i) < PL \\ 0, & otherwise \end{cases}$$

In the above equation, PL is the inflation-adjusted official poverty line given by the Tendulkar Committee (Planning Commission, 2014).

$$Poverty\ Headcount\ Ratio = \frac{1}{N}\sum_{i=1}^{N} Poverty\ Headcount_i$$

where *N* is the total number of households.

2.2.5 Incidence of using distressed sources to finance OOPE

The NSS health survey collected information about various sources of finance (household income/savings, borrowings, sale of physical assets, contributions from friends and relatives, and other sources) used as coping mechanisms. We categorized a household as incurring distressed financing if it used any of these sources except household income or savings (Sangar et al., 2020).

The proportion of households employing various sources of finance to cope with OOPE was calculated as below.

$$I = \frac{1}{N}\sum_{i=1}^{N} n$$

ACCEPTED MANUSCRIPT

Downloaded from https://academic.oup.com/heapol/advance-article/doi/10.1093/heapol/czad050/7220383 by Delhi Technological University user on 22 July 2023

In the above formula, I is the incidence of using a particular source of finance, n is the number of households using a particular source of finance, and N denotes the total number of households.

In case of hospitalization, NSS classified the various sources of finance as major and second major sources because households might have used more than one source in varying proportions. We have shown the percentage of households using distressed sources to finance hospitalization-related OOPE separately for major and second major sources.

2.3 Statistical Analysis

Descriptive statistics, two-part model, and multivariable logistic regression were employed in the study.

2.3.1 Two-part Model

A two-part model was employed to assess the determinants of OOPE. This model is suitable when the outcome variable (i.e., OOPE) is skewed and contains a large number of zero values (Belotti et al., 2015). The first part describes the probability of a household to incur OOPE using a logit model.

$$P\ (y_i > 0) = \frac{\exp(\beta x)}{1 + \exp(\beta x)}$$

In the above equation, $y_i = 0$ indicates that a household has not incurred OOPE on healthcare.

The second part of the model predicts the level of OOPE, conditional on non-zero value. OOPE is estimated using ordinary least square regression, and the dependent variable is the log of OOPE.

ACCEPTED MANUSCRIPT

Downloaded from https://academic.oup.com/heapol/advance-article/doi/10.1093/heapol/czad050/7220383 by Delhi Technological University user on 22 July 2023

2.3.2 Multivariable Logistic Regression

Multivariable logistic regression was used to estimate the likelihood of household incurring CHE, impoverishment, and distressed financing due to various disease conditions.

$$logit\ (\pi_i) = \beta_0 + \beta_1 X_1 + \beta_2 X_2 + \cdots + \beta_n X_n$$

In the above equation, π_i is the probability of occurrence of binary outcome variable (i.e., incurring CHE, impoverishment, and distressed financing), X_1 denotes the disease categories, and $X_2 \ldots X_n$ represents covariates (economic quintiles, household's major of earnings, social class (scheduled castes (SC), scheduled tribes (ST), other backward classes (OBC), others), sector (rural or urban areas), religion (Hinduism, Islam, others), household size, gender, age, and educational status of household head, state, health insurance status, and type of healthcare facility (public or private) from where treatment was sought).

We clustered standard errors by the primary sampling unit. Sample weights provided by the NSS were applied as applicable. Statistical analysis was performed using STATA version 14.1. All amounts reported in Indian rupees (INR) were converted into United States dollars (USD) using the average 2018 exchange rate (i.e., USD 1 = INR 68.30).

3. Results

Childbirth was the most common cause of hospitalization, causing 35.9% of households to seek inpatient care, followed by infections (20.6%), and injuries (7.7%). For outpatient care, households where any member was suffering from infections (31.7%), cardiovascular conditions (16.3%), and endocrine, metabolic and nutritional conditions (14.9%) sought the highest outpatient care (Supplementary Table 2). Health insurance uptake was dismally low, covering only 15.5% of individuals (Supplementary Table 3).

ACCEPTED MANUSCRIPT

Downloaded from https://academic.oup.com/heapol/advance-article/doi/10.1093/heapol/czad050/7220383 by Delhi Technological University user on 22 July 2023

3.1 Out-of-pocket health expenditure

Supplementary Table 4 shows the median monthly OOPE of households by the disease type. Cancer caused the highest OOPE in the case of hospitalization (USD 35.6), followed by genito-urinary diseases (USD 18.6), and psychiatric and neurological disorders (USD 16.5), whereas childbirth led to the lowest OOPE (USD 3.3). In case of outpatient care, obstetric conditions (USD 51.2), cancer (USD 35.1), and genito-urinary diseases (USD 26.9) were the leading ailments in terms of OOPE. Compared to public healthcare facilities, the median monthly OOPE for all morbidities was invariably higher in private healthcare facilities, regardless of the type of care sought (Supplementary Tables 5-8). Supplementary Figure 1 shows the incidence of utilization of public and private healthcare facilities. Nearly 51.0% of hospitalization episodes were sought at public healthcare facilities, whereas only 30.2% of outpatient cases were sought at public facilities. The primary reasons for seeking care at private facilities instead of public ones were non-availability of doctor or quality of public health facilities not satisfactory, preference for a trusted doctor or hospital, and long waiting time at public health facilities in case of both hospitalization and outpatient care (Supplementary Figure 2).

Table 1 shows the results of the two-part model. The first part (logit regression) revealed that the likelihood of incurring OOPE was positively associated with economic quintiles, age of household head, household size, and insurance coverage in the case of both hospitalization and outpatient care ($p<0.05$). Households belonging to SCs, OBCs, and other categories were also statistically significantly more likely to incur OOPE compared to STs, regardless of the type of care sought ($p<0.05$). By contrast, households primarily earning from casual work were statistically significantly less likely to incur OOPE compared to those earning from self-employment for both hospitalization and outpatient care ($p<0.05$). The results for the second

ACCEPTED MANUSCRIPT

Downloaded from https://academic.oup.com/heapol/advance-article/doi/10.1093/heapol/czad050/7220383 by Delhi Technological University user on 22 July 2023

part indicated that among the households incurring OOPE, those belonging to higher economic quintiles, SCs, OBCs, and other categories, consisting of larger family size, headed by member aged 60 years and above, and having higher education levels were incurring higher OOPE ($p<0.05$), irrespective of the type of care sought. Conversely, in the case of both hospitalization and outpatient care, rural households, female-headed households, households earning from casual work, and those with insurance coverage were associated with lower OOPE ($p<0.05$).

3.2 Share of OOPE in total household consumption expenditure

The share of OOPE in household consumption expenditure was the highest for households in which any member sought cancer treatment (hospitalization: 51.9%; outpatient care: 47.0%; hospitalization and/or outpatient care: 64.1%) (Supplementary Table 9). Cardiovascular conditions (24.4%), psychiatric and neurological disorders (23.6%), musculoskeletal conditions (23.6%), and injuries (22.3%) also contributed to a significant OOPE share in total household consumption expenditure in the case of hospitalization. For outpatient care, obstetric (36.7%) and genito-urinary conditions (35.5%) were the top causes of high OOPE share in household consumption expenditure after cancer, whereas respiratory conditions (10.5%) resulted in the lowest OOPE share. Households in which any member underwent hospitalization and outpatient care in private healthcare facilities experienced 5.2 times and 1.7 times higher OOPE share in household consumption expenditure, respectively, than those who availed care in public healthcare facilities (Supplementary Tables 5-8).

3.3 Catastrophic health expenditure

Out of all the households who sought hospitalization, outpatient care, and hospitalization and/or outpatient care, 43.1%, 47.8%, and 49.0% of households, respectively, experienced CHE (Figure 1). In the case of hospitalization, households with cancer-afflicted members

ACCEPTED MANUSCRIPT

Downloaded from https://academic.oup.com/heapol/advance-article/doi/10.1093/heapol/czad050/7220383 by Delhi Technological University user on 22 July 2023

reported the highest CHE incidence (61.4%), followed by obstetric (54.1%), and psychiatric and neurological disorders (51.6%). In the case of outpatient care, obstetric conditions, genito-urinary diseases, injuries, and blood diseases caused CHE among more than 55% of the respective disease-afflicted households. Notably, among all households reporting CHE, those in which any member was hospitalized for childbirth (36.3%) accounted for the largest share of the total CHE burden, followed by infections (16.0%), and injuries (9.1%), whereas in the case of outpatient care, infections (38.9%) and cardiovascular conditions (11.1%) constituted the largest share of the CHE burden (Figure 2). The incidence of CHE was higher among households who sought care in private healthcare facilities compared to those treated in public healthcare facilities in case of both hospitalization (49.7% versus 36.0%) and outpatient care (50.4% versus 39.1%), and the pattern was similar across most disease categories (Figure 3; Supplementary Tables 5-8).

Supplementary Table 10 shows the results of logistic regression to reveal the impact of different ailments on the likelihood of incurring CHE. Compared to infections, the likelihood of incurring CHE was statistically significantly higher for households in which any member sought hospitalization for cancer (odds ratio (OR): 21.73 [13.30 - 35.51]; $p<0.05$) and sought outpatient care for cancer (OR: 6.40 [3.57 - 11.46]; $p<0.05$). In the event of hospitalization, all the diseases (except ear-related ailments) resulted in statistically significantly higher odds of incurring CHE compared to infections ($p<0.05$). For outpatient care, the likelihood of incurring CHE was statistically significantly higher for households suffering from cancer, blood diseases, genito-urinary diseases, obstetric conditions, injuries, and other disease categories compared to infection-afflicted households ($p<0.05$).

3.4 Impoverishment impact

Figure 1 shows that 10.7%, 15.0%, and 15.0% of the households who sought hospitalization, outpatient care, and hospitalization and/or outpatient care, respectively, were pushed below

ACCEPTED MANUSCRIPT

Downloaded from https://academic.oup.com/heapol/advance-article/doi/10.1093/heapol/czad050/7220383 by Delhi Technological University user on 22 July 2023

the poverty line as a result of OOPE. The percentage of households falling below the poverty line due to hospitalization-related OOPE was the highest for cancer (31.8%), followed by psychiatric and neurological disorders (21.0%), musculoskeletal conditions (17.9%), and injuries (17.8%). Among households where any member sought outpatient care, obstetric conditions, genito-urinary diseases, and cancer were among the top three conditions that led to the highest poverty headcount ratio. Of all the households that fell below the poverty line due to OOPE, childbirth (19.6%), injuries (13.7%), and infection-afflicted households (13.5%) accounted for the largest share in the case of hospitalization, while infection (31.3%) and cardiovascular conditions (12.5%) constituted the largest share of households falling below the poverty line in the case of outpatient care (Figure 2). Poverty headcount ratio was higher for households that sought care at private healthcare facilities than public healthcare facilities in case of both hospitalization (17.5% versus 3.7%) and outpatient care (17.3% versus 10.9%) (Supplementary Tables 5-8).

Logistic regression showed that the likelihood of falling below the poverty line was statistically significantly higher for cancer-affected households for both hospitalization (OR: 9.82 [6.99 - 13.79]; $p<0.05$) and outpatient care (OR: 4.13 [2.44 - 6.98]; $p<0.05$) compared to households with any infection-afflicted member. In case of hospitalization, households affected by any ailment (except for eye, ear, and skin-related ailments, and respiratory issues) demonstrated statistically significantly higher odds of falling below the poverty line compared to infection-afflicted households ($p<0.05$). For outpatient care, the odds of falling below the poverty line were statistically significantly higher for households affected by cancer, psychiatric and neurological disorders, gastrointestinal conditions, genito-urinary diseases, obstetric conditions, and other disease categories ($p<0.05$) (Supplementary Table 10).

ACCEPTED MANUSCRIPT

Downloaded from https://academic.oup.com/heapol/advance-article/doi/10.1093/heapol/czad050/7220383 by Delhi Technological University user on 22 July 2023

3.5 Distressed financing

In India, majority of households primarily relied on income/savings to finance hospitalization-related OOPE (83.9%) and outpatient care (94.7%) (Figure 4), and the incidence of using distressed sources as the major source of finance was relatively low (hospitalization: 16.1%; outpatient care: 5.3%) (Figure 1). However, among 27,769 households who reported using a second major source to finance hospitalization-related OOPE, 78.0% relied on distressed sources (Supplementary Figure 3). Borrowings (43.9%) and contributions from friends and relatives (27.7%) were the most common second major distressed sources used in the event of hospitalization (Supplementary Figure 3). Cancer, psychiatric and neurological disorders, and injuries were the top three disease conditions causing households to rely on distressed financing, irrespective of the type of care sought (Figure 1). Among all households that relied on distressed financing, infection-afflicted households accounted for the largest (28.1%) and second-largest share (17.4%) of the total burden of distressed financing for outpatient care and hospitalization, respectively (Figure 2). Notably, the incidence of distressed financing was higher for all disease categories (except childbirth and others category) for households where any member sought outpatient care at public healthcare facilities than private ones. By contrast, in the case of hospitalization, higher incidence of distressed financing was reported at private healthcare facilities across all disease categories (except ear-related ailments) compared to public healthcare facilities (Supplementary Tables 5-8).

Compared to infections, the odds of using distressed sources were statistically significantly higher for households who sought hospitalization (OR: 2.88 [2.42 – 3.44]; $p<0.05$) and outpatient care (OR: 3.37 [2.38 – 4.78]; $p<0.05$) for cancer. All the ailments (except eye, ear, and skin-related ailments) showed statistically significantly higher odds of incurring

ACCEPTED MANUSCRIPT

Downloaded from https://academic.oup.com/heapol/advance-article/doi/10.1093/heapol/czad050/7220383 by Delhi Technological University user on 22 July 2023

distressed financing than infections in the case of hospitalization ($p<0.05$). For outpatient care, the likelihood of using distressed sources was statistically significantly higher for households where members sought care for cancer, endocrine, metabolic and nutritional conditions, psychiatric and neurological disorders, gastrointestinal conditions, genito-urinary diseases, injuries, and others category compared to infections-afflicted households ($p<0.05$) (Supplementary Table 10).

3.6 Loss of household income

In addition to the economic burden of financing healthcare, households also experienced indirect costs associated with loss of earnings due to the inability of the patient or the caregiver to attend work. Supplementary Table 11 shows that hospitalization for cancer causes the highest loss of average household income (USD 94.0), followed by hospitalization for psychiatric and neurological disorders (USD 65.4), and injuries (USD 57.4). For outpatient care, injuries (USD 9.6), obstetric conditions (USD 9.3), and cancer (USD 8.2) resulted in the highest loss of average household earnings.

3.7 Proportion of individuals not seeking treatment

Out of all the individuals who reported having an ailment during the last 15 days prior to the survey date, 1.8% of ailing individuals did not seek treatment (Supplementary Table 12). Individuals suffering from ear-related ailments reported the highest incidence of not seeking treatment (19.3%), followed by individuals suffering from eye-related ailments (10.7%), and psychiatric and neurological disorders (5.4%). We also determined the proportion of ailing individuals who did not seek treatment on medical advice, and found that 10.1% of all the individuals suffering from an ailment during the last 15 days sought treatment not administered on medical advice (Supplementary Table 12). Although the primary reason for not seeking treatment on medical advice was that ailment was not considered severe (73.5%

ACCEPTED MANUSCRIPT

Downloaded from https://academic.oup.com/heapol/advance-article/doi/10.1093/heapol/czad050/7220383 by Delhi Technological University user on 22 July 2023

of cases), substantial variations were observed across disease categories (Supplementary Figure 4). For instance, 47.0% and 20.8% of individuals suffering from blood diseases and injuries, respectively, reported the non-availability of medical facilities in their neighbourhood as one of the reasons for not seeking treatment on medical advice.

4. Discussion

This study provides a comprehensive examination of the financial burden of OOPE across 17 disease categories to convey the magnitude of hardships experienced by Indian households incurring OOPE. We found that OOPE is an alarming predicament in India, causing 49% of households to incur CHE and plunging 15% of households below the poverty line due to hospitalization and/or outpatient care. Notably, outpatient care was more burdensome (CHE: 47.8%; Impoverishment: 15.0%) than hospitalization (CHE: 43.1%; Impoverishment: 10.7%). Nearly 16% of households relied on distressed sources to finance hospitalization-related OOPE. Cancer, genito-urinary diseases, psychiatric and neurological disorders, obstetric conditions, and injuries pose a substantial economic burden on households.

India is experiencing a sizeable cancer burden, with 1.39 million new cancer cases registered in the country every year (ICMR, 2022), and as per WHO, one in ten Indians is expected to develop cancer during their lifetime (WHO, 2020). In tandem with previous studies (Rajpal et al., 2014; Kastor and Mohanty, 2018; Boby et al., 2021), we found that cancer led to the highest incidence of CHE, impoverishment, distressed financing, and loss of household earnings in the event of hospitalization. The deleterious effects of high cancer costs are associated with poor quality of life, non-compliance with treatment, debt-accumulation, and premature entry of younger family members into labour market (Boby et al., 2021), along with physical, psychological, and emotional ramifications. In India, the rural healthcare

ACCEPTED MANUSCRIPT

Downloaded from https://academic.oup.com/heapol/advance-article/doi/10.1093/heapol/czad050/7220383 by Delhi Technological University user on 22 July 2023

system is blighted by paucity of personnel, especially specialists (GOI, 2021), and cancer care facilities are largely limited to big cities, causing many patients to travel long distances to seek treatment – a situation that has two negative repercussions: 1) substantial travelling and lodging expenses, coupled with loss of earnings due to travel; 2) overloading and long waiting time at major cancer centres (Pramesh et al., 2014). In addition, studies have found that increased travel requirements are associated with more advanced stage of disease at diagnosis, inappropriate treatment, and poor prognosis (Ambroggi et al., 2015). Given the rising cancer burden and the grave economic consequences of cancer care, there is an urgent need for multifaceted policy measures such as improving diagnostic and imaging equipment, ensuring optimum surgical and radiotherapy infrastructure and palliative care facilities in all publicly-funded cancer centres, and promoting cost-effective therapies (Pramesh et al., 2014; Boby et al., 2021). Furthermore, telemedicine must be scaled as it can bring quality healthcare, including specialists to a large proportion of population, decrease the burden of the healthcare system, and increase access to cost-efficient medical services (Chellaiyan et al., 2019; Aashima et al., 2021; Dash et al., 2021) .

In tandem with previous studies, we found that cardiovascular conditions not only pose a substantial economic burden on households (Engelgau et al., 2012; Tripathy et al., 2016; Kastor and Mohanty, 2018; Yadav et al., 2021b) but also constitute a sizeable share of total financial hardships. For the management of coronary artery disease, percutaneous coronary intervention requiring coronary stent implantation, is an important treatment modality (Heart & Stroke, 2022). However, in India, substantial unethical price markups (varying from 270% to 1000%) are applied in the stent supply chain, which makes the stent prices exorbitantly high, irrational and restrictive (GOI, 2017; Medical Dialogues, 2017; Pattnaik, 2019). Despite the National Pharmaceutical and Pricing Authority of India introducing a ceiling on stent

ACCEPTED MANUSCRIPT

Downloaded from https://academic.oup.com/heapol/advance-article/doi/10.1093/heapol/czad050/7220383 by Delhi Technological University user on 22 July 2023

prices (lowering it by up to 85%) in 2017 (NPPA, 2018; Times of India, 2018; Pattnaik, 2019), several hospitals have not passed on the full benefits to the patients (Times of India, 2018; Pattnaik, 2019). Therefore, it is essential to cap the prices of other accessories (such as cardiac catheters, balloon catheters, and guidewires) (NPPA, 2018), so that procedures like angioplasty can become more affordable and accessible to patients.

Injuries were among the top-5 ailments across all parameters (i.e., share of OOPE in total household consumption expenditure, CHE, impoverishment, and distressed financing) and accounted for one of the largest share in the total financial hardships in the event of hospitalization. Previous studies have also found that injuries lead to CHE and substantial productivity losses (Prinja et al., 2016; Prinja et al., 2019; Yadav et al., 2021c). Notably, in India, road injuries are the leading cause of mortality in the economically active younger age group of 15–39 years (Dandona et al., 2020), highlighting that the burden of injuries far exceeds their immediate medical costs (GOI, 2019). Consequently, the Indian government has recently devised a scheme to provide cashless treatment to road accident victims during the golden hour, which is the first hour after an injury when timely medical care can significantly reduce the risk of death (GOI, 2019). There is a huge potential for cost-savings if prevention strategies such as mandatory motorcycle helmets and seat belts, speed limits and speed bump installations, and breath testing are effectively implemented in India (Pal et al., 2019).

In line with previous studies (Singh and Kumar, 2017; Kastor and Mohanty, 2018; Yadav et al., 2021b), we found that the brunt of OOPE was lower among households where any member sought care in public facilities compared to those treated in private healthcare facilities across most disease categories. However, the lacunae in the public health system,

ACCEPTED MANUSCRIPT

Downloaded from https://academic.oup.com/heapol/advance-article/doi/10.1093/heapol/czad050/7220383 by Delhi Technological University user on 22 July 2023

including insufficient healthcare infrastructure, perceived low-quality care, unavailable services, and long waiting times, compel individuals to seek care from private health facilities, resulting in significant financial burden. As per the latest report published by NITI Aayog (2021), the capacity and quality of healthcare services in India's public health sector have been constrained due to low public health expenditure, mandating the need for significant and sustained investment to strengthen the public health system. In addition, WHO has emphasized the need for additional investment on primary healthcare services to progress towards UHC (WHO 2019b). Furthermore, although, private hospitals mainly cater to tertiary care services and employ advanced technologies and sub-specialties, these are largely unregulated and feebly monitored by the government, resulting in plethora of cases of overpricing, unnecessary tests and treatments, and malpractices (Phadke, 2016; Times of India, 2016; Dehury et al., 2019). Consequently, a substantial portion of financial catastrophes, impoverishment, and indebtedness occurs within private health system in India (Mahal et al., 2013; Kastor and Mohanty, 2018; Yadav et al., 2021b). Conversely, we also found that the incidence of distressed financing was nearly three times higher among households who sought care in public healthcare facilities compared to those treated in private healthcare facilities in case of outpatient care. This can be attributed to higher utilization of public facilities by households belonging to lower economic quintiles (Supplementary Figure 1), who rely on distressed sources to finance even relatively small amounts of outpatient expenses at the subsidized public facilities (Joe, 2015). Previous studies have also found that the incidence of distressed financing is concentrated among the poor households (Joe, 2015; Sangar et al., 2019b, 2020). The overwhelming majority evidence highlights the urgency to regulate private healthcare facilities as improved regulation is one of the potential drivers to reduce healthcare cost and improve the quality of care (WHO, 2022).

ACCEPTED MANUSCRIPT

Downloaded from https://academic.oup.com/heapol/advance-article/doi/10.1093/heapol/czad050/7220383 by Delhi Technological University user on 22 July 2023

Further, we found a dismally low uptake of health insurance in India, covering only 15.5% of the Indian population. According to the two-part model, insured households showed a higher likelihood of incurring OOPE, and a lower OOPE (conditional on having health spendings) compared to the uninsured. This reflects an increase in utilization of healthcare services as well as lower OOPE among the insured than the uninsured. In India, a majority of the insured population is covered under government-sponsored health insurance (GSHI) schemes, and previous studies have reported that GSHI schemes have improved utilization of healthcare services (Prinja et al., 2017, Reshmi et al., 2021). Plausible reasons for the increase in utilization can be genuine reduction in financial barriers, supplier-induced demand, or moral hazard (Prinja et al., 2017; Sengupta and Rooj, 2019). Furthermore, studies have shown mixed results regarding the financial protection provided by the GSHI schemes (Prinja et al., 2017; Reshmi et al., 2021). A recent study found that GSHI schemes provide marginal financial protection to insured households against OOPE and CHE (Ranjan et al., 2018). In India, there is a need to increase awareness about health insurance and its related aspects, such as eligibility criteria, enrolment procedures, stipulated benefits, details about empanelled hospitals, and information on how to avail the benefits, in order to improve the uptake and outcomes of health insurance. Moreover, GSHI schemes are primarily meant to cover the below-poverty-line population (Hooda, 2020), social health insurance schemes cover only organized sector employees, and thus, a substantial portion of Indian population is left with the choice to either arrange private health insurance (constrained by the ability-to-pay premium) or to remain uninsured (NITI Aayog, 2021). Therefore, it is important to increase the affordability of health insurance products, particularly for the missing-middle population (NITI Aayog, 2021).

Downloaded from https://academic.oup.com/heapol/advance-article/doi/10.1093/heapol/czad050/7220383 by Delhi Technological University user on 22 July 2023

Notably, we found that financial burden was more pronounced in the case of outpatient care (CHE: 47.8%; Impoverishment: 15.0%) compared to hospitalization (CHE: 43.1%; Impoverishment: 10.7%). Previous studies have stated that although the cost of hospitalization is higher for any given event (Chatterjee et al., 2013), but the overall financial burden and impoverishment is much larger due to outpatient care (Berman et al., 2010), which involves relatively small but more frequent payments. Outpatient care demands policy attention due to multitude of reasons. First, outpatient care in India is overwhelmingly private, with private healthcare facilities providing nearly 70% of outpatient care, thereby causing a substantial economic burden on households (Gupta et al., 2016). Second, medicines and drugs alone constitute a substantial portion of OOPE (more than 60%) in the case of outpatient care (Sangar et al., 2022). Unfortunately, the limited availability of free or subsidized essential medicines and drugs at public healthcare facilities forces households to buy them from private pharmacies, resulting in higher OOPE, or treatment abstention (Maiti et al., 2015). Third, the increasing prevalence of NCDs leads to an increased use of outpatient clinics because chronic illnesses require multiple consultations, regular doctor visits, diagnostic tests, and long-term medication support (Selvaraj et al., 2018; Mukherjee and Chaudhuri, 2020).

Despite all this, most of the GSHI schemes in India mainly cover hospitalization, excluding outpatient care from the ambit of insurance coverage (Selvaraj and Karan, 2012; Hooda, 2020). A study found that removing OOPE for drugs and outpatient visits had the greatest impact on poverty reduction (Shahrawat and Rao, 2012). Thus, to safeguard against financial hardships, insurance schemes covering both outpatient care (including medicines) and hospitalization are imperative (Shahrawat and Rao, 2012). In India, the new flagship scheme "Pradhan Mantri Jan Arogya Yojana (PM-JAY)" was launched in 2018, with the aim to

ACCEPTED MANUSCRIPT

Downloaded from https://academic.oup.com/heapol/advance-article/doi/10.1093/heapol/czad050/7220383 by Delhi Technological University user on 22 July 2023

provide health insurance coverage to 100 million poor and vulnerable families, with a cover of up to USD 7,320.6 (INR 5,00,000) per family per year for secondary and tertiary care hospitalization (National Health Authority, 2022). Although PM-JAY scheme has removed two major limitations of the previous national-level health insurance scheme (Rashtriya Swasthya Bima Yojana), i.e., insurance coverage of mere USD 438.2 (INR 30,000) per annum and a cap on family size (covering five members only), still it does not cover outpatient care, which can help improve financial protection.

We also found that among all individuals who reported having an ailment during the last 15 days, 1.8% did not seek treatment and 10.1% did not seek treatment on medical advice. Nearly, 47.0% of individuals suffering from blood diseases and 20.8% of individuals suffering from injuries reported non-availability of medical facilities in their neighbourhood as one of the reasons for not seeking treatment on medical advice. Arora et al. (2020) found that over 70% of surveyed Indian patients revealed lack of required facilities in their home state and out-of-state referral (20%) as prominent reasons for seeking cross-border care, a situation resulting in higher travelling costs, loss of labour-days, as well as treatment deferral or abandonment of follow-up care in certain cases. A recent systematic review found that the key reasons for unmet healthcare needs were affordability (20.6%), availability (17.0%), and accessibility (12.2%) (WHO, 2021b). Forgoing care may exacerbate health problems and put the concerned families in a downward spiral of ill-health and poverty (Wagstaff, 2002; Petrovic et al., 2021; Rahman et al., 2022). Moreover, even if OOPE is avoided by not seeking care, a household may still experience indirect costs such as loss of earnings if the sick individual or caregiver is unable to attend work. The loss of earnings may be limited if the patient or caregiver works in a formal sector (Alam and Mahal, 2014). However, in a country like India, where 86.8% of the workforce is employed in the informal

ACCEPTED MANUSCRIPT

Downloaded from https://academic.oup.com/heapol/advance-article/doi/10.1093/heapol/czad050/7220383 by Delhi Technological University user on 22 July 2023

sector (Oxfam India, 2022), suffering from an ailment can lead to a considerable loss of earnings. We found that cancer, psychiatric and neurological disorders, and injuries were the top three ailments leading to significant losses in household earnings. A study estimated that nearly 7% and 23% of middle-aged Indian adults had ever stopped working and had limiting paid work, respectively, due to health-related issues (Akhtar et al., 2022). Furthermore, those with chronic diseases were 4% and 11% more likely to stop and limit their work, respectively (Akhtar et al., 2022).

As with all other studies, this study also has a few limitations. First, expenditure data used in the study is subject to potential recall bias, especially for hospitalization incidence where the recall period involves a longer time span of 365 days. Second, the NSS survey data collects information on self-reported ailments and a reported diagnosis by a qualified healthcare professional was required only in the case of a few ailments. Surveys that rely on self-reported ailments are likely to underestimate the prevalence of various health conditions and are susceptible to potential recall biases and misclassification of diseases (Engelgau et al., 2012; Patra and Bhise, 2016). For instance, as per the NSS survey, fever was classified under the infection category (constituting 67% and 82% share in infections in the case of hospitalization and outpatient care, respectively), although there can be non-infectious causes of fever as well (Steele et al., 2018), highlighting potential misdiagnosis, particularly in the case of infection category. Third, disregarding coping mechanisms such as borrowings, sale of physical assets, etc. to finance OOPE leads to overestimation of poverty impact (Berman et al., 2010). However, since the NSS health survey does not collect information on how much money is financed through distressed sources, we could not correct for this. Overestimation of poverty and CHE may also be caused by our reliance on NSS health survey, which tends to underestimate total household consumption expenditure. Lastly, the

ACCEPTED MANUSCRIPT

Downloaded from https://academic.oup.com/heapol/advance-article/doi/10.1093/heapol/czad050/7220383 by Delhi Technological University user on 22 July 2023

magnitude of economic burden and disruption of living standards due to health expenditures should be ascertained using longitudinal data; however, in the absence of such data, cross-sectional studies such as ours can provide potential estimates of the financial impact of OOPE.

5. Conclusion

The study highlights the colossal economic impact of OOPE and associated financial catastrophe and impoverishment faced by Indian households suffering from any type of illness. Concerted efforts such as strengthening public healthcare facilities, increasing the uptake of health insurance, designing broader insurance packages to cover outpatient care, and ensuring affordability and availability of essential medicines are imperative to augment financial risk protection. Moreover, even though cancer causes copious financial burden among those who have the disease and seek treatment for it, policymakers should get to the bottom of what comprises infections (given the prospect of substantial misclassification and/or misdiagnosis in this category) and address the high spending on cardiovascular diseases and injuries, which constitute a sizeable share of the total financial hardships. Comprehensive disease-specific insurance packages (The Economic Times, 2020) should be designed for high-cost ailments such as cancer, psychiatric and neurological disorders, and genito-urinary diseases. Furthermore, there is a need for improved regulation of the private health sector and to put standard treatment guidelines in place. For long-term sustainability, policymakers must prioritise health promotion and disease prevention strategies, as increasing life expectancy, ageing population, westernization, and motorization will further aggravate the burden of NCDs and injuries in India. Implementation of robust and effective evidence-based health promotion programs holds potential to significantly improve people's health and reduce the financial burden they face. To achieve UHC and SDG goals, the

ACCEPTED MANUSCRIPT

Downloaded from https://academic.oup.com/heapol/advance-article/doi/10.1093/heapol/czad050/7220383 by Delhi Technological University user on 22 July 2023

epidemic of chronic diseases and injuries should be a political priority and central to the national consciousness.

Funding

This study has received no specific grant from any funding agency in public, commercial or not-for-profit sectors.

Declaration of interests

Authors declare no competing interests.

Ethical Approval

The research was conducted using data available in the public domain and did not include any human participants or animals. Therefore, no ethical approvals were required.

Data Availability Statement

The research was conducted using the 75th round of the National Sample Survey on Health, which is available in the public domain.

References

1. Aashima, Nanda M, & Sharma R. 2021. A review of patient satisfaction and experience with telemedicine: a virtual solution during and beyond COVID-19 pandemic. *Telemedicine and e-Health.* **27**(12): 1325-1331.
2. Akhtar S, Mohanty SK, Singh RR, Sen S. 2022. Chronic diseases and productivity loss among middle-aged and elderly in India. *BMC Public Health* **22**(1):2356.

ACCEPTED MANUSCRIPT

Downloaded from https://academic.oup.com/heapol/advance-article/doi/10.1093/heapol/czad050/7220383 by Delhi Technological University user on 22 July 2023

3. Alam K, Mahal A. 2014. Economic impacts of health shocks on households in low and middle income countries: a review of the literature. *Globalization and health* **10**(1):1-8.
4. Ambroggi M, Biasini C, Del Giovane C, Fornari F, & Cavanna L. 2015. Distance as a barrier to cancer diagnosis and treatment: review of the literature. *The oncologist.* **20**(12): 1378-1385.
5. Arora A, Bhutani P, Chhabra S, Smith O. PM-JAY Without Borders: Analysis of Portability Services. National Health Authority; 2020 Feb p. 12. (PM-JAY Policy Briefs). Report No.: 5. Available from: https://pmjay.gov.in/sites/default/files/2020-02/Policy%20Brief%205_Analysis%20of%20Portability%20Service s.pdf.
6. Bajpai V. 2014. The challenges confronting public hospitals in India, their origins, and possible solutions. *Advances in Public Health.* 898502.
7. Berki SE. 1986. A look at catastrophic medical expenses and the poor. *Health affairs.* **5**(4): 138-45.
8. Belotti, F., Deb, P., Manning, W. G., & Norton, E. C. (2015). twopm: Two-part models. *The Stata Journal*, *15*(1), 3-20.
9. Berman P, Ahuja R, Bhandari L. 2010. The impoverishing effect of healthcare payments in India: new methodology and findings. *Economic and Political Weekly.* 65-71.
10. Bloom DE, Cafiero-Fonseca ET, Candeias V, et al. 2014. Economics of non-communicable diseases in India: the costs and returns on investment of interventions to promote healthy living and prevent, treat, and manage NCDs. In *World economic forum, Harvard school of Public Health.* 22-23. Available: https://www3.weforum.org/docs/WEF_EconomicNonCommunicableDiseasesIndia_Report_2014.pdf.

ACCEPTED MANUSCRIPT

Downloaded from https://academic.oup.com/heapol/advance-article/doi/10.1093/heapol/czad050/7220383 by Delhi Technological University user on 22 July 2023

11. Boby JM, Rajappa S, Mathew A. 2021. Financial toxicity in cancer care in India: a systematic review. *The Lancet Oncology.* **22**(12): e541-9.
12. Bonu S, Bhushan I, Peters D. 2007. Incidence, intensity, and correlates of catastrophic out-of-pocket health payments in India. *Asian Development Bank.* 32-39.
13. Bonu S, Bhushan I, Rani M, Anderson I. 2009. Incidence and correlates of 'catastrophic' maternal health care expenditure in India. *Health policy and planning.* **24**(6):445-56.
14. Chatterjee S, Levin C, Laxminarayan R. 2013. Unit cost of medical services at different hospitals in India. *Plos one.* **8**(7): e69728.
15. Chellaiyan VG, Nirupama AY, & Taneja N. 2019. Telemedicine in India: Where do we stand?. *Journal of family medicine and primary care.* **8**(6): 1872.
16. Dash S, Aarthy R, Mohan V. 2021. Telemedicine during COVID-19 in India—a new policy and its challenges. *Journal of public health policy.* **42**(3): 501-509.
17. Dandona R, Kumar GA, Gururaj G, et al. 2020. Mortality due to road injuries in the states of India: The Global Burden of Disease Study 990–2017. *Lancet Public Health.* **5**(2):e86–e98.
18. Dehury RK, Samal J, Coutinho S, Dehury P. 2019. How does the largely unregulated private health sector impact the Indian mass?. *Journal of Health Management.* **21**(3): 383-93.
19. Devadasan N, Seshadri T, Trivedi M, Criel B. 2013. Promoting universal financial protection: evidence from the rashtriya Swasthya Bima Yojana (RSBY) in Gujarat, India. *Health Res. Policy Syst.* **11**(1):1-8.
20. Engelgau MM, Karan A, Mahal A. 2012. The economic impact of non-communicable diseases on households in India. *Globalization and health.* **8**(1): 1-10.

ACCEPTED MANUSCRIPT

Downloaded from https://academic.oup.com/heapol/advance-article/doi/10.1093/heapol/czad050/7220383 by Delhi Technological University user on 22 July 2023

21. Garg CC, Karan AK. 2009. Reducing out-of-pocket expenditures to reduce poverty: a disaggregated analysis at rural-urban and state level in India. *Health policy and planning.* **24**(2): 116-28.

22. Ghosh S, & Gupta ND. 2017. Targeting and effects of Rashtriya Swasthya Bima Yojana on access to care and financial protection. *Econ Polit Wkly.* **52**(4): 61-70.

23. Government of India (GOI). 2017. *Order*. Available: http://www.nppaindia.nic.in/wp-content/uploads/2019/01/so412e-13-02-17-1.pdf.

24. Government of India (GOI). 2019. *Road Accidents in India 2019*. Available: https://morth.nic.in/sites/default/files/RA_Uploading.pdf.

25. Government of India (GOI). 2021. *Rural Health Statistics 2020-2021*. Government of India, Ministry of Health and Family Welfare, Statistics Division. Available: https://main.mohfw.gov.in/sites/default/files/rhs20-21.pdf .

26. Gupta I, Chowdhury S, Prinja S, Trivedi M. 2016. Out-of-pocket spending on out-patient care in India: assessment and options based on results from a district level survey. *PLoS One.* **11**(11): e0166775.

27. Heart & Stroke. 2022. Available: https://www.heartandstroke.ca/heart-disease/treatments/surgery-and-other-procedures/percutaneous-coronary-intervention.

28. Hooda SK. 2020. Penetration and coverage of government-funded health insurance schemes in India. *Clinical Epidemiology and Global Health.* **8**(4): 1017-33.

29. Indian Council of Medical Research (ICMR). 2022. Cancer Statistics. Available: http://cancerindia.org.in/cancer-statistics/ .

30. Indian Council of Medical Research, Public Health Foundation of India, and Institute for Health Metrics and Evaluation (ICMR, PFHI, and IHME). 2017. *India: Health of the Nation's States - The India State-Level Disease Burden Initiative*. Available:

ACCEPTED MANUSCRIPT

Downloaded from https://academic.oup.com/heapol/advance-article/doi/10.1093/heapol/czad050/7220383 by Delhi Technological University user on 22 July 2023

https://www.healthdata.org/sites/default/files/files/policy_report/2017/India_Health_of_the_Nation%27s_States_Report_2017.pdf.

31. Joe W. 2015. Distressed financing of household out-of-pocket health care payments in India: incidence and correlates. *Health policy and planning*. **30**(6): 728-41.
32. Kastor A, Mohanty SK. 2018. Disease-specific out-of-pocket and catastrophic health expenditure on hospitalization in India: do Indian households face distress health financing?. *PloS one* **13**(5): e0196106.
33. Mahal A, Karan A, Fan VY, Engelgau M. 2013. The economic burden of cancers on Indian households. *PloS one.* **8**(8): e71853.
34. Maiti R, Bhatia V, Padhy BM., & Hota D. 2015. Essential medicines: an Indian perspective. *Indian journal of community medicine: official publication of Indian Association of Preventive & Social Medicine.* **40**(4), 223.
35. Medical Dialogues. 2017. *Shockingly High Profit Margins On Cardiac Stents: NPPA Report.* Available: https://business.medicaldialogues.in/shockingly-high-profit-margins-on-cardiac-stents-nppa-report?infinitescroll=1 .
36. Mohanty SK, Kastor A. 2017. Out-of-pocket expenditure and catastrophic health spending on maternal care in public and private health centres in India: a comparative study of pre and post national health mission period. *Health Economics Review.* **7**(1): 1-5.
37. Mukherjee S, Chaudhuri A. 2020. Outpatient care and expenses: Can they be ignored in health insurance programmes. *Institute Of Development Studies Kolkata*.
38. National Health Authority. 2022. *Ayushman Bharat - Pradhan Mantri Jan Arogya Yojana*. Available: https://pmjay.qcin.org/pm-jay.
39. National Health Policy. 2017. Available: https://www.nhp.gov.in/nhpfiles/national_health_policy_2017.pdf .

ACCEPTED MANUSCRIPT

Downloaded from https://academic.oup.com/heapol/advance-article/doi/10.1093/heapol/czad050/7220383 by Delhi Technological University user on 22 July 2023

40. National Pharmaceutical Pricing Authority (NPPA). 2018. *Minutes of the NPPA meeting*. Available: http://www.nppaindia.nic.in/wp-content/uploads/2019/01/Authority_minutes.pdf.

41. Niti Aayog. 2021. *Health Insurance for India's Missing Middle.* Available: https://www.niti.gov.in/sites/default/files/2021-10/HealthInsurance-forIndiasMissingMiddle_28-10-2021.pdf.

42. Oxfam India. 2022. A Glance at the Informal Sector in India. Available: https://www.oxfamindia.org/knowledgehub/factsheets/glance-informal-sector-india. Date Accessed: March 15, 2023.

43. Pal R, Ghosh A, Kumar R, et al. 2019. Public health crisis of road traffic accidents in India: Risk factor assessment and recommendations on prevention on the behalf of the Academy of Family Physicians of India. *Journal of family medicine and primary care.* **8**(3): 775.

44. Patra S, Bhise MD. 2016. Gender differentials in prevalence of self-reported non-communicable diseases (NCDs) in India: evidence from recent NSSO survey. Journal of Public Health, 24:375-85.

45. Pattnaik A. 2019. Price ceiling of coronary stents-challenges ahead. *International Journal of Telemedicine and Clinical Practices.* **3**(2): 165-73.

46. Phadke A. 2016. Regulation of doctors and private hospitals in India. *Economic and Political Weekly.* 46-55.

47. Petrovic D, Marcus K, Sandoval J, Cullati S, Piumatti G, Bodenmann P, et al. Health-related biological and non-biological consequences of forgoing healthcare for economic reasons. Prev Med Rep. 2021;24: 101602.

48. Planning Commission. 2014. *Report of the expert group to review the methodology for measurement of poverty*. New Delhi: Planning Commission.

ACCEPTED MANUSCRIPT

Downloaded from https://academic.oup.com/heapol/advance-article/doi/10.1093/heapol/czad050/7220383 by Delhi Technological University user on 22 July 2023

49. Pramesh CS, Badwe RA, Borthakur BB, et al. 2014. Delivery of affordable and equitable cancer care in India. *The Lancet Oncology.* **15**(6): e223-33.

50. Prinja S, Chauhan AS, Karan A, Kaur G, & Kumar R. 2017. Impact of publicly financed health insurance schemes on healthcare utilization and financial risk protection in India: a systematic review. *PloS one* **12**(2): e0170996.

51. Prinja S, Jagnoor J, Chauhan AS, et al. 2016. Economic burden of hospitalization due to injuries in North India: a cohort study. *International journal of environmental research and public health.* **13**(7): 673.

52. Prinja S, Jagnoor J, Sharma D, et al. 2019. Out-of-pocket expenditure and catastrophic health expenditure for hospitalization due to injuries in public sector hospitals in North India. *PloS one.* **14**(11): e0224721.

53. Rahman T, Gasbarro D, & Alam K. 2022b. Financial risk protection from out-of-pocket health spending in low-and middle-income countries: a scoping review of the literature. *Health Research Policy and Systems **20***(1): 1-23.

54. Ranjan A, Dixit P, Mukhopadhyay I, Thiagarajan S. 2018. Effectiveness of government strategies for financial protection against costs of hospitalization Care in India. BMC public health **18**(1):1-2.

55. Rajpal S, Kumar A, Joe W. 2018. Economic burden of cancer in India: Evidence from cross-sectional nationally representative household survey, 2014. *PloS one* **13**(2): e0193320.

56. Reshmi B, Unnikrishnan B, Rajwar E, Parsekar SS, Vijayamma R, & Venkatesh BT. 2021. Impact of public-funded health insurances in India on health care utilisation and financial risk protection: a systematic review. *BMJ open **11***(12): e050077.

57. Sangar S, Dutt V, Thakur R. 2019a. Comparative assessment of economic burden of disease in relation to out of pocket expenditure. *Frontiers in Public Health*.

ACCEPTED MANUSCRIPT

Downloaded from https://academic.oup.com/heapol/advance-article/doi/10.1093/heapol/czad050/7220383 by Delhi Technological University user on 22 July 2023

58. Sangar S, Dutt V, Thakur R. 2019b. Distress financing of out-of-pocket health expenditure in India. *Review of Development Economics.* **23**(1): 314-30.

59. Sangar S, Dutt V, Thakur R. 2020. Coping with out-of-pocket health expenditure in India: evidence from NSS 71st round. *Global Social Welfare.* **7**(3): 275-84.

60. Sangar S, Dutt V, Thakur R. 2022. Burden of out-of-pocket health expenditure and its impoverishment impact in India: evidence from National Sample Survey. *Journal of Asian Public Policy* **15**(1): 60-77.

61. Selvaraj S, Farooqui HH, Karan A. 2018. Quantifying the financial burden of households' out-of-pocket payments on medicines in India: a repeated cross-sectional analysis of National Sample Survey data, 1994–2014. *BMJ open.* **8**(5): e018020.

62. Selvaraj S, & Karan AK. Why publicly-financed health insurance schemes are ineffective in providing financial risk protection. Economic and Political Weekly. 2012;60-68.

63. Sengupta, R., & Rooj, D. 2019. The effect of health insurance on hospitalization: Identification of adverse selection, moral hazard and the vulnerable population in the Indian healthcare market. World Development, 122, 110-129.

64. Shahrawat R, Rao KD. 2012. Insured yet vulnerable: out-of-pocket payments and India's poor. *Health policy and planning.* **27**(3): 213-21.

65. Singh P, Kumar V. 2017. The rising burden of healthcare expenditure in India: a poverty nexus. *Social Indicators Research.* **133**(2): 741-62.

66. Sneha LM, Sai J, Ashwini S, Ramaswamy S, Rajan M, Scott JX. 2017. Financial Burden Faced by Families due to Out-of-pocket Expenses during the Treatment of their Cancer Children: An Indian Perspective. *Indian Journal of Medical and Paediatric Oncology.* **38**(01): 4-9.

ACCEPTED MANUSCRIPT

Downloaded from https://academic.oup.com/heapol/advance-article/doi/10.1093/heapol/czad050/7220383 by Delhi Technological University user on 22 July 2023

67. Sriram S. 2019. Are the subcenters adequately equipped to deliver primary healthcare? A study of public health manpower and infrastructure in the health district in Andhra Pradesh, India. *Journal of Family Medicine and Primary Care.* **8**(1): 102.

68. Steele GM, Franco-Paredes C, & Chastain DB. 2018. Noninfectious causes of fever in adults. *The Nurse Practitioner.* **43**(4): 38-44.

69. Swain SP, Samal S, Sahu KS, Rout SK. 2018. Out-of-pocket expenditure and drug adherence of patients with diabetes in Odisha. *Journal of family medicine and primary care.* **7**(6): 1229.

70. Thakur H. 2016. Study of awareness, enrollment, and utilization of Rashtriya Swasthya Bima Yojana (national health insurance scheme) in Maharashtra, India. *Frontiers in public health.* **3**: 282.

71. The Economic Times. 2020. *Need to have more disease-specific health insurance products: IRDAI.* Available: https://bfsi.economictimes.indiatimes.com/news/insurance/need-to-have-more-disease-specific-health-insurance-products-irdai/78678320.

72. The Times of India. 2016. *Greed and the rise of medical malpractice in India*. Available: https://timesofindia.indiatimes.com/blogs/the-irreverent-lawyer/greed-and-the-rise-of-medical-malpractice-in-india/.

73. The Times Of India. 2018. *Stents cheaper, but not all get benefit.* Available: https://timesofindia.indiatimes.com/india/stents-cheaper-but-not-all-get-benefit/articleshow/62687068.cms.

74. Tripathy JP and Prasad BM. 2018. Cost of diabetic care in India: an inequitable picture. *Diabetes & Metabolic Syndrome: Clinical Research & Reviews.* **12**(3): 251-5.

ACCEPTED MANUSCRIPT

Downloaded from https://academic.oup.com/heapol/advance-article/doi/10.1093/heapol/czad050/7220383 by Delhi Technological University user on 22 July 2023

75. Tripathy JP, Prasad BM, Shewade HD, et al. 2016. Cost of hospitalisation for non-communicable diseases in India: are we pro-poor?. *Tropical medicine & international health.* **21**(8): 1019-28.

76. United Nations Development Programme (UNDP). 2022. Goal 3: Good Health and Well-Being. United Nations Development Programme. Available: https://www.undp.org/sustainable-development-goals?utm_source=EN&utm_medium=GSR&utm_content=US_UNDP_PaidSearch_Brand_English&utm_campaign=CENTRAL&c_src=CENTRAL&c_src2=GSR&gclid=CjwKCAjw9e6SBhB2EiwA5myr9uiGZfMo0bJcdr_CwHw4cE6_TIMEdupc3L_816AMWbjZEY-ElPW93BoC6YYQAvD_BwE#good-health. Date Accessed: March 1, 2022.

77. Van Doorslaer E, O'Donnell O, Rannan-Eliya RP, et al. 2006. Effect of payments for health care on poverty estimates in 11 countries in Asia: an analysis of household survey data. *The lancet.* **368**(9544): 1357-64.

78. Verma VR, Kumar P, Dash U. 2021. Assessing the household economic burden of non-communicable diseases in India: evidence from repeated cross-sectional surveys. *BMC public health.* **21**(1): 1-22.

79. Wagstaff A. 2002. Poverty and health sector inequalities. Bull World Health Organ, **80**:97–105.

80. World Bank. 2014. *Poverty and Health.* Available: https://www.worldbank.org/en/topic/health/brief/poverty-health .

81. World Health Organization (WHO). 2019a. *Global Health Expenditure Database 2019.* World Health Organisation. Available: https://apps.who.int/nha/database/country_profile/Index/en. Date Accessed: March 3, 2022.

ACCEPTED MANUSCRIPT

Downloaded from https://academic.oup.com/heapol/advance-article/doi/10.1093/heapol/czad050/7220383 by Delhi Technological University user on 22 July 2023

82. World Health Organization (WHO). 2019b. *Primary Health Care on the Road to Universal Health Coverage: 2019 Global Monitoring Report*. Available: https://www.who.int/publications/i/item/9789240029040.

83. World Health Organization (WHO). 2020. *World Cancer Report Cancer: research for cancer prevention.* Available: https://www.iccp-portal.org/system/files/resources/IARC%20World%20Cancer%20Report%202020.pdf.

84. WHO. 2021a. *Universal health coverage*. Available: https://www.who.int/news-room/fact-sheets/detail/universal-health-coverage-(uhc). Date Accessed: March 1, 2022.

85. WHO. 2021b. Systematic review and meta-analysis: financial barriers to accessing health services and unmet healthcare needs. Kobe: World Health Organization (WHO) Centre for Health Development; 2021. Available: https://extranet.who.int/kobe_centre/en/project-details/foregone_care.

86. World Health Organization (WHO). 2022. Regional Office for South-East Asia, Selvaraj S., Karan K.A., Srivastava S., Bhan N. et al. India: health system review. Health Systems in Transition, 11 (1), World Health Organization. Regional Office for South-East Asia. https://apps.who.int/iris/handle/10665/352685.

87. Xu K, Evans DB, Kawabata K, Zeramdini R, Klavus J, Murray CJ. 2003. Household catastrophic health expenditure: a multicountry analysis. *The Lancet.* **362**(9378): 111-7.

88. Yadav J, John D, Allarakha S, Menon GR. 2021a. Rising healthcare expenditure on tuberculosis: Can India achieve the End TB goal?. *Tropical Medicine & International Health.* **26**(10):1256-75.

ACCEPTED MANUSCRIPT

Downloaded from https://academic.oup.com/heapol/advance-article/doi/10.1093/heapol/czad050/7220383 by Delhi Technological University user on 22 July 2023

89. Yadav J, Menon G, Agarwal A, John D. 2021c. Burden of injuries and its associated hospitalization expenditure in India. *International journal of injury control and safety promotion.* **28**(2): 153-61.

90. Yadav J, Menon GR, John D. 2021b. Disease-specific out-of-pocket payments, catastrophic health expenditure and impoverishment effects in India: an analysis of national health survey Data. *Applied Health Economics and Health Policy.* **19**(5): 769-82.

Table Title and Captions

Table 1: Results of Two-part Model

® denotes Reference category, *p<0.05, [ ] 95% confidence interval. State was also taken as one of the variables (result not shown in table).

Table 1: Results of Two-part Model

Background characteristics	Hospitalization		Outpatient Care	
	Coefficient (Logit)	Coefficient (OLS)	Coefficient (Logit)	Coefficient (OLS)
Sector				
Urban areas ®				
Rural areas	0.01 [-0.01 - 0.04]	-0.32* [-0.35 - -0.28]	-0.21* [-0.26 - -0.16]	-0.17* [-0.21 - -0.12]
Economic quintiles				
Quintile 1 ®				
Quintile 2	0.07* [0.02 - 0.11]	0.19* [0.16 - 0.23]	0.12* [0.07 - 0.18]	0.08* [0.03 - 0.14]
Quintile 3	0.14* [0.09 - 0.18]	0.32* [0.28 - 0.36]	0.21* [0.16 - 0.27]	0.15* [0.09 - 0.20]
Quintile 4	0.10* [0.05 - 0.14]	0.46* [0.41 - 0.50]	0.24* [0.18 - 0.30]	0.24* [0.18 - 0.30]
Quintile 5	0.11* [0.07 - 0.16]	0.68* [0.63 - 0.72]	0.36* 0.29 - 0.42]	0.42* [0.36 - 0.48]
Major source of household income				
Self-employment ®				
Regular wage or salary	0.06* [0.02 - 0.09]	-0.03* [-0.06 - 0.00]	0.03 [-0.01 - 0.07]	-0.04 [-0.08 - 0.003]

ACCEPTED MANUSCRIPT

Downloaded from https://academic.oup.com/heapol/advance-article/doi/10.1093/heapol/czad050/7220383 by Delhi Technological University user on 22 July 2023

Casual labour	-0.10* [-0.14 - -0.07]	-0.22* [-0.25 - -0.19]	-0.14* [-0.18 - -0.09]	-0.09* [-0.13 - -0.04]
Others	-0.42* [-0.48 - -0.36]	-0.01 [-0.06 - -0.05]	-0.06 [-0.12 - 0.00]	-0.02 [-0.08 - 0.04]
Social class				
Scheduled Tribes ®				
Scheduled Castes	0.21* [0.16 - 0.26]	0.23* [0.18 - 0.28]	0.20* [0.12 - 0.28]	0.15* [0.07 - 0.24]
Other Backward Classes	0.16* [0.12 - 0.21]	0.40* [0.35 - 0.45]	0.20* [0.12 - 0.28]	0.24* [0.16 - 0.32]
Others	0.15* [0.10 - 0.20]	0.51* [0.46 - 0.56]	0.21* [0.13 - 0.29]	0.29* [0.21 - 0.38]
Religion				
Hinduism ®				
Islam	0.02 [-0.02 - 0.05]	-0.10* [-0.14 - -0.06]	0.17* [0.11 - 0.23]	-0.01 [-0.06 - 0.04]
Others	0.02 [-0.03 - 0.08]	0.09* [0.04 - 0.15]	0.14* [0.06 - 0.22]	0.04 [-0.03 - 0.12]
Education level of household head				
Not literate/No formal schooling ®				
Up to primary	0.09* [0.05 - 0.13]	0.08* [0.04 - 0.11]	0.11* [0.06 - 0.15]	0.08* [0.03 - 0.12]
Up to secondary	0.15* [0.12 - 0.19]	0.17* [0.14 - 0.20]	0.01 [-0.03 - 0.06]	0.16* [0.11 - 0.21]
Up to higher secondary	0.12* [0.07 - 0.17]	0.27* [0.23 - 0.32]	-0.12* [-0.18 - -0.05]	0.22* [0.15 - 0.29]
Graduation and above	0.05 [-0.01 - 0.10]	0.45* [0.41 - 0.50]	-0.16* [-0.23 - -0.10]	0.32* [0.26 - 0.39]
Age of household head				
Less than 60 years ®				
60 years and above	0.32* [0.28 - 0.36]	0.41* [0.38 - 0.44]	0.70* [0.66 - 0.74]	0.22* [0.18 - 0.26]
Gender of household head				
Male ®				
Female	-0.22* [-0.27 - -0.18]	-0.08* [-0.12 - -0.04]	0.02 [-0.03 - 0.07]	-0.15* [-0.20 - -0.10]
Household size				
Up to 5 members ®				
More than 5 members	0.62* [0.59 - 0.65]	0.19* [0.17 - 0.22]	0.36* [0.32 - 0.39]	0.19* [0.15 - 0.22]
Health insurance				

ACCEPTED MANUSCRIPT

Downloaded from https://academic.oup.com/heapol/advance-article/doi/10.1093/heapol/czad050/7220383 by Delhi Technological University user on 22 July 2023

status				
Not Covered ®				
Covered	0.19* [0.15 - 0.23]	-0.20* [-0.24 - -0.17]	0.37* [0.33 - 0.42]	-0.05* [-0.09 - -0.006]

® denotes Reference category, *p<0.05, [ ] 95% confidence interval. State was also taken as one of the variables (result not shown in table).

ACCEPTED MANUSCRIPT

Downloaded from https://academic.oup.com/heapol/advance-article/doi/10.1093/heapol/czad050/7220383 by Delhi Technological University user on 22 July 2023

Figures Title and Captions

Figure 1: Percentage of households incurring catastrophic heath expenditure, impoverishment, and distressed financing

ACCEPTED MANUSCRIPT

Downloaded from https://academic.oup.com/heapol/advance-article/doi/10.1093/heapol/czad050/7220383 by Delhi Technological University user on 22 July 2023

Disease Categories	Catastrophic Health Expenditure (%)			Poverty Headcount Ratio (%)			Distressed Financing (%)		
	Hospitalization	Outpatient Care	Hospitalization and/or Outpatient Care	Hospitalization	Outpatient Care	Hospitalization and/or Outpatient Care	Hospitalization	Outpatient Care	Hospitalization and/or Outpatient Care
Infection	32.3	51.2	46.9	6.6	12.2	11.1	13.6	4.3	6.8
Cancers	61.4	52.3	61.8	31.8	21.8	32.5	26.6	7.8	21.2
Blood Diseases	42.5	55.9	50.9	11.2	19.1	16.2	16.9	4.4	9.6
Endocrine, Metabolic, Nutritional	37.0	28.9	29.8	11.2	9.9	10.3	16.7	4.8	5.5
Psychiatric & Neurological	51.6	39.3	43.8	21.0	14.3	17.0	25.0	7.5	12.4
Eye	35.3	43.7	39.4	8.4	14.7	11.4	15.0	4.4	10.6
Ear	39.6	52.3	49.8	7.2	9.0	8.7	21.0	0.7	7.3
Cardiovascular	43.3	28.5	31.6	17.1	9.5	11.3	19.5	5.3	8.0
Respiratory	37.1	38.1	38.6	7.7	10.6	10.5	18.7	4.9	6.4
Gastrointestinal	42.1	52.2	48.9	14.2	18.3	16.8	19.3	5.6	11.8
Skin	42.0	47.7	47.4	6.6	16.3	15.4	16.8	3.6	5.5
Musculoskeletal	46.4	40.9	41.8	17.9	11.6	12.5	19.2	5.6	7.8
Genito-Urinary	50.0	64.2	57.9	16.3	31.0	22.8	22.0	5.7	16.5
Obstetric	54.1	68.4	58.9	10.2	51.8	18.5	15.1	1.9	13.1
Childbirth	42.1	42.9	42.1	5.5	9.5	5.5	12.3	2.5	12.3
Injuries	49.3	58.5	52.5	17.8	17.0	18.3	23.3	7.8	19.8
Others	50.8	52.8	54.2	16.4	21.4	21.0	21.4	8.2	13.5
Total	43.1	47.8	49.0	10.7	15.0	15.0	16.1	5.3	10.2

Lowest

Highest

ACCEPTE

Downloaded from https://academic.oup.com/heapol/advance-article/doi/10.1093/heapol/czad050/7220383 by Delhi Technological University user on 22 July 2023

Figure 2: Share of each disease in total financial hardship

Disease Categories	Catastrophic Health Expenditure (%)		Poverty Headcount Ratio (%)		Distressed Financing (%)	
	Hospitalization	Outpatient Care	Hospitalization	Outpatient Care	Hospitalization	Outpatient Care
Infection	16.0	38.9	13.5	31.3	17.4	28.1
Cancers	1.4	0.5	3.0	0.7	1.6	0.6
Blood Diseases	1.3	1.2	1.4	1.3	1.3	0.8
Endocrine, Metabolic, Nutritional	1.5	10.3	1.9	11.9	1.7	14.0
Psychiatric & Neurological	4.2	4.2	7.1	5.2	5.3	6.5
Eye	2.1	1.2	2.1	1.3	2.3	1.0
Ear	0.3	0.5	0.2	0.3	0.4	0.1
Cardiovascular	5.8	11.1	9.6	12.5	6.8	16.7
Respiratory	2.1	9.1	1.8	8.6	2.8	10.0
Gastrointestinal	6.7	6.0	9.4	7.1	8.0	5.4
Skin	0.6	2.4	0.4	2.8	0.7	1.5
Musculoskeletal	3.3	8.6	5.3	8.2	3.5	9.7
Genito-Urinary	4.6	2.1	6.3	3.4	5.3	1.5
Obstetric	3.1	0.5	2.4	1.2	2.2	0.1
Childbirth	36.3	0.1	19.6	0.1	27.7	0.0
Injuries	9.1	1.9	13.7	1.9	11.2	2.1
Others	1.7	1.6	2.3	2.2	1.9	2.1
Total	100	100	100	100	100	100

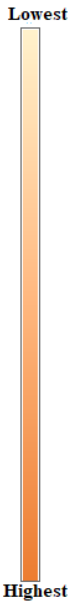

Downloaded from https://academic.oup.com/heapol/advance-article/doi/10.1093/heapol/czad050/7220383 by Delhi Technological University user on 22 July 2023

Figure 3: Percentage of households incurring catastrophic heath expenditure by the type of care (hospitalization and outpatient care) and healthcare facility (public and private)

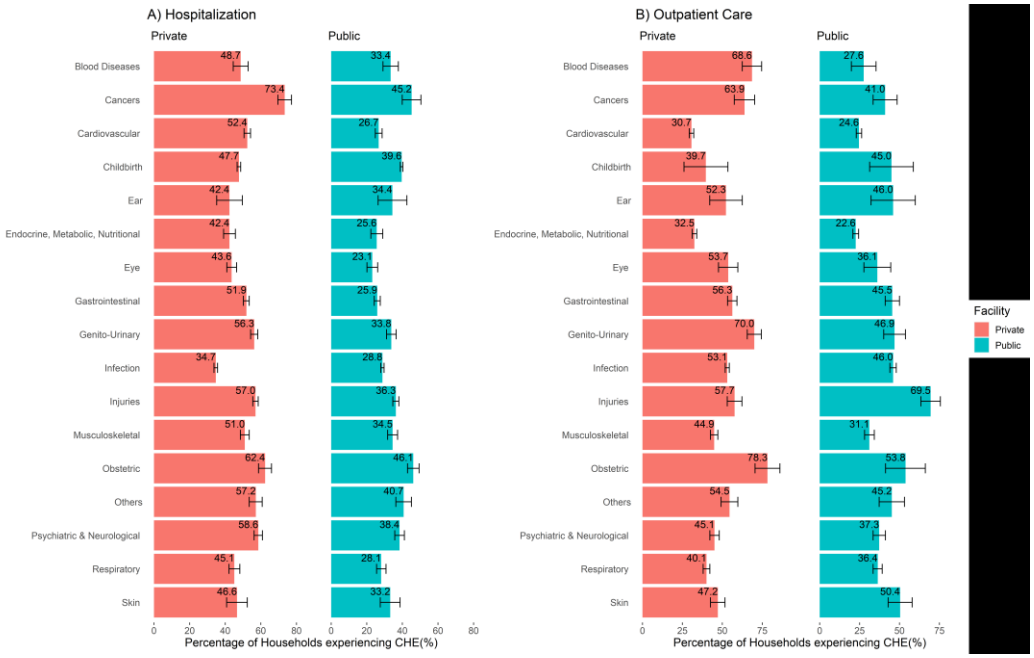

Downloaded from https://academic.oup.com/heapol/advance-article/doi/10.1093/heapol/czad050/7220383 by Delhi Technological University user on 22 July 2023

Figure 4: Share of various sources of finance used as coping strategies

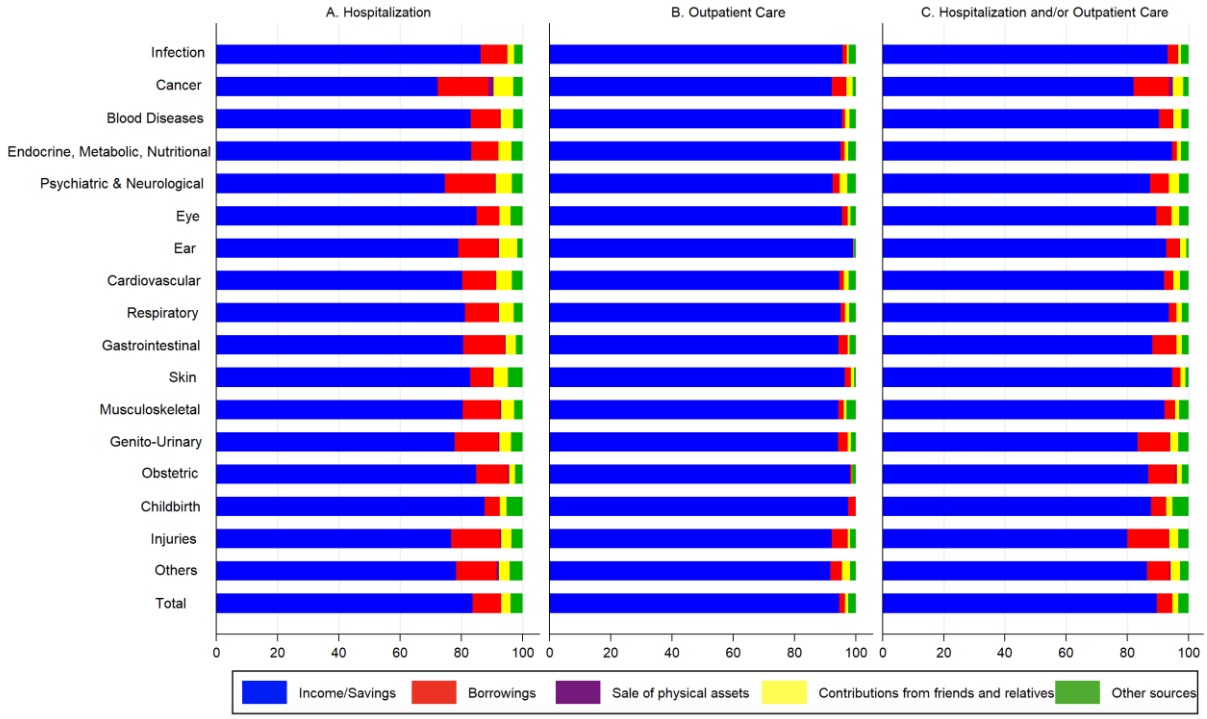

Downloaded from https://academic.oup.com/heapol/advance-article/doi/10.1093/heapol/czad050/7220383 by Delhi Technological University user on 22 July 2023

Supplementary Table Title and Captions

Supplementary Table 1: Disease classification as per the NSS health survey

Supplementary Table 2: Percentage distribution of households where any member sought hospitalization and outpatient care

Supplementary Table 3: Health insurance coverage

Supplementary Table 4: Median OOPE

Supplementary Table 5: OOPE and associated financial burden for hospitalization in public healthcare facilities

Supplementary Table 6: OOPE and associated financial burden for hospitalization in private healthcare facilities

Supplementary Table 7: OOPE and associated financial burden for outpatient care in public healthcare facilities

Supplementary Table 8: OOPE and associated financial burden for outpatient care in private healthcare facilities

Supplementary Table 9: Share of OOPE in total household consumption expenditure

Supplementary Table 10: Results of Multivariable Logistic Regression

® denotes Reference category, *p<0.05; [ ] 95% confidence interval. Results are adjusted for economic quintiles, household's major of earnings, social class, sector, religion, household size, gender, age, and educational status of household head, state, health insurance status, and type of healthcare facility.

Supplementary Table 11: Average loss of household income by type of disease

ACCEPTED MANUSCRIPT

Downloaded from https://academic.oup.com/heapol/advance-article/doi/10.1093/heapol/czad050/7220383 by Delhi Technological University user on 22 July 2023

Supplementary Table 12: Percentage of individuals not seeking care during the last 15 days

Supplementary Figure Title

Supplementary Figure 1: Incidence of utilization of public and private healthcare facilities

Supplementary Figure 2: Reasons for not choosing public healthcare facilities

Supplementary Figure 3: Incidence of utilization of second major source for financing hospitalization-related OOPE

Supplementary Figure 4: Reasons for not seeking care on medical advice during the last 15 days

ACCEPTED MANUSCRIPT

Downloaded from https://academic.oup.com/heapol/advance-article/doi/10.1093/heapol/czad050/7220383 by Delhi Technological University user on 22 July 2023

A Hybrid Method for Network Intrusion Detection

Devika Jaiswal*, Kunj Arora†, Manan Varshney‡ and Trasha Gupta§
Department of Applied Mathematics, Delhi Technological University
New Delhi, Delhi
Email: *devikaj2002@gmail.com, †kunj57932@gmail.com, ‡mananvarshney13@gmail.com, §trashagupta@dtu.ac.in

2023 Third International Conference on Secure Cyber Computing and Communication (ICSCCC) | 979-8-3503-0071-0/23/$31.00 ©2023 IEEE | DOI: 10.1109/ICSCCC58608.2023.10176754

***Abstract*—Network intrusion detection systems often use signature-based matching (IDS) mechanisms. Using ML-based classifiers to detect threats is a more reliable approach, as signature-based methods can only find attacks that are already known. Due to the robustness of the attacks, a single ML classifier will not be able to identify all types of attacks, especially the more unusual ones. Therefore, a hybrid method that targets each type of attack separately might give us better results. Its goal is to combine the strengths of different individual classifiers. Another key issue is to use feature selection methods to select only relevant features, otherwise, we might face the problem of a high false positive rate. Our goal is to offer a hybrid strategy specifically created to solve the above problems.**

***Index Terms*—network security, machine learning, intrusion detection, anomaly detection.**

I. Introduction

Cyberattacks have been ranked as the fifth most significant risk in 2020 and are growing rapidly in both the private and public sectors. This high-risk industry has shown growth in 2023, and IoT cyberattacks are likely to double by 2025. Additionally, the pandemic has exacerbated cybercrime due to uncertainty surrounding remote work and how to protect your business. Cybercrime has increased by 600% due to the COVID-19 pandemic, right from theft or embezzlement to data destruction. Almost all industries have adopted newer solutions, which are forced to be adapted quickly.

An Intrusion Detection System (IDS) is a valuable asset that helps businesses detect and prevent unauthorized access to their networks. By analyzing network traffic patterns, IDS can identify suspicious activity and alert system administrators. An IDS is a valuable addition to any organization's security infrastructure, providing information, and improving the network performance.

IDS systems are classified as anomaly-based and signature-based, depending on the method of detection. Signature-based IDS detects attacks based on specific patterns(such as byte sequences), it also bases its detection on known malicious instruction sequences used by malware. The detection of known attacks through patterns or signatures is a relatively straightforward task for signature-based IDS. However, detecting novel malware attacks poses a challenge since their signatures are unfamiliar and not present in the system. Given the rapid evolution of new malware, the implementation of an anomaly-based IDS has become necessary for detecting malware attacks whose characteristics are unfamiliar.

In anomaly-based systems, the IDS uses machine learning to analyze traffic and detect malicious activities rather than searching for specific patterns. These models are superior as they can be trained on the specific application and hardware configuration. Consequently, there is a need to explore the domain of anomaly-based IDS systems.

A. Problem Statement

Numerous machine learning methods have been researched and put into practice for constructing anomaly-based IDSs. Certain techniques advocate for supervised learning, whereas others employ unsupervised learning. Another important decision is to use feature reduction techniques due to a large number of features and select only relevant features to reduce the dataset to a manageable size and reduce overfitting. A combination of two or more learning techniques often outperforms a single ML classifier for detecting all types of attacks. Usually, low-frequency attacks cannot be detected well due to training data bias.

Our first contribution is to explore the dataset and gain insights into the characteristics of different attack types. We use the NSL-KDD dataset in this study. Then, we propose a hybrid approach to obtain high detection rates for all types of attacks. Our main concerns are: using proper feature extraction and dimensionality reduction techniques to select only relevant features, selecting targeted classifiers to detect low-frequency attacks, and using a hybrid approach to achieve good performance in the form of high detection rates.

II. Literature Review

In recent years, the trend has been to adopt a hybrid strategy for IDS systems that combines the advantages of different classifiers. Therefore, we researched and analyzed various implementation models before choosing a model for our project.

The research work [1] proposes an algorithm that combines RBF neural network and fuzzy clustering to effectively reduce the dataset and achieve an accuracy rate greater than 90%.

In their research, the authors [2] examine the utilization of various machine learning techniques for detecting anomalies in intrusions. The research shows that the schemes, namely neural networks, decision trees, and support vector machines should be performed by analyzing the system targets and maintaining a trade-off between the accuracy of the system and the cost incurred.

The objective of the research [3] is to assess the working of SVM and ANN algorithms for intrusion detection by comparative analysis. The authors find that the ANN algorithm

Authorized licensed use limited to: DELHI TECHNICAL UNIV. Downloaded on July 20,2023 at 11:12:41 UTC from IEEE Xplore. Restrictions apply.

shows better performance than the SVM algorithm, achieving an accuracy of 96% compared to 48% for SVM.

In their research, the authors of [4] suggest utilizing a DBSCAN clustering algorithm for detecting anomalies. They showcase that by using an enhanced DBSCAN algorithm for intrusion detection, higher recognition accuracy can be achieved when compared to the K-means algorithm.

The research work in [5] puts forth an enhanced DBSCAN algorithm that leverages K-Prototypes and a dissimilarity matrix for detecting network intrusions. According to the experimental findings, this improved algorithm demonstrates better accuracy, precision, and recall rates of clustering outcomes relative to other algorithms. However, it may not be as effective at clustering categories with significant variations in data distribution densities.

The utilization of a local kernel-principal component analysis (LKPCA) technique for efficient feature selection is proposed by the authors in [6]. The authors present evidence suggesting that LKPCA is the most effective feature extraction method and construct multi-class classifiers by means of the same training set.

In their research study, the authors of [7] introduce a feature selection methodology that utilizes a voting mechanism for identifying the most significant features in constructing a decision tree-based machine learning model. The authors establish that the optimal feature subset is selected by the overlapping area between information gain and chi-square.

In conclusion, the authors in [8] suggest an unsupervised method for intrusion detection called SSC-OCSVM. This technique uses subspace clustering and a one-class support vector machine and demonstrates higher detection rates for both U2R and R2L as compared to K-means and DBSCAN algorithms.

The research work in [9] examines deep learning-based IDS approaches with an aim of optimizing the performance at each stage of the process. The authors perform a comparative analysis of the following models: Recurrent Neural Network (RNN), Deep Neural Network (DNN), and Long Short-Term Memory-Convolutional Neural Network (CNN-LSTM). The authors concluded that RNN outperforms both DNN and CNN with an accuracy of 99.4%.

III. Data Analysis and Preprocessing

A. Data Exploration

NSL-KDD [10] is chosen as our dataset. KDD99 is the most commonly used dataset for calculating Intrusion Detection System strategies, which are anomaly-based, but NSL-KDD is an updated version with the following upgrades:

- The classifier is unlikely to generate biased outcomes as there are no redundant entries in the training data.
- The test set has a higher reduction rate because there are no duplicate records in it.
- The records chosen from every group of difficulty levels are inversely correlated with the record percentage in the first KDD data set.

There are four subsets of this data: KDDTrain+, KDDTest+, KDDTest-21, and KDDTrain+_20Percent. KDDTrain+_20Percent is a smaller set of train. We have only used KDDTrain+, KDDTest+ and KDDTrain+_20Percent in this paper. The data set has a total of 43 features in every record. The four different attack types include:

- DoS(Denial of Service): A DoS attack stops traffic going through a system. This intrusion prevents regular traffic from the network. When an online retailer receives a large number of orders in a day, the network may become overwhelmed and break down, preventing premium customers from any purchases. In the data set, this attack occurs the most frequently.
- Probe: A probe attack collects data from a network with the aim of stealing important information by impersonating a thief. This information could be sensitive banking details or client records.
- U2R(User to Root): A U2R attack is when a regular user account tries to log into the system or network as user at higher authority (root). To gain root access, the attacker tries to use a system's vulnerabilities.
- R2L(Remote to Local): R2L aims to gain access to a system locally while present remotely. An attacker tries to "hack" their way into the network.

The test dataset also includes attacks that aren't present in the train set while the train set only contains the known attack types, which are mentioned above.

B. Data Visualization

We first visualized the dataset on the basis of different types of attacks, as shown in Fig. 1, where we saw that a particular protocol is the target of the majority of attacks and distribution is also highly skewed. We can also see that ICMP data is less frequent in normal traffic.

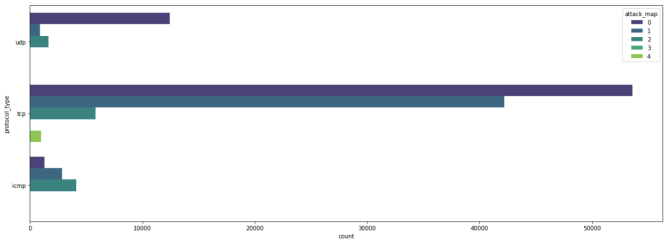

Fig. 1. Detection rates of each attack category.

Next we visualized the distribution of the attacks in the training data set as shown in Fig. 2. We can see that the data set's class distribution is uneven. The training data set contains a majority of normal records (53.5%), followed by DoS (36.5%), Probe (9.3%), and very few R2L and U2R, as shown in the given figure. The issue is that this bias makes it impossible for a single model to accurately detect R2L and U2R. We colored DoS green, Probe blue, R2L orange, U2R yellow, and Normal red to distinguish the attacks as shown in Fig. 3. We removed Normal from the graph at the instance.

Authorized licensed use limited to: DELHI TECHNICAL UNIV. Downloaded on July 20,2023 at 11:12:41 UTC from IEEE Xplore. Restrictions apply.

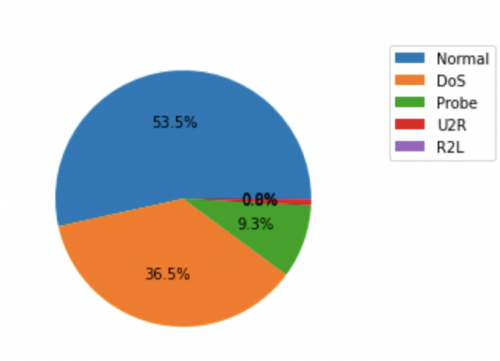

Fig. 2. Distribution of attack categories.

Most R2L and U2R attacks show common characteristics among themselves (they overlap in the graph) and with the regular attacks, the majority of Probe and DoS however are unique in their characteristics (less overlapping region). This indicates that the less common attacks (U2R and R2L) acted more similarly to one another than the more common attacks (DoS and Probe). According to the graph on the right, very few DoS and Probe records cross over with regular connections. Because R2L and U2R threats behave similarly to typical attacks, it is obvious why previous works did not show great performance in detecting them. This resulted in a high false-positive. The data we gathered from PCA analysis, as well as earlier research, shows that their models do a good job of detecting Probe and Dos attacks and struggle with unknown or less common attacks. Therefore, a careful detection strategy is required for R2L and U2R attacks.

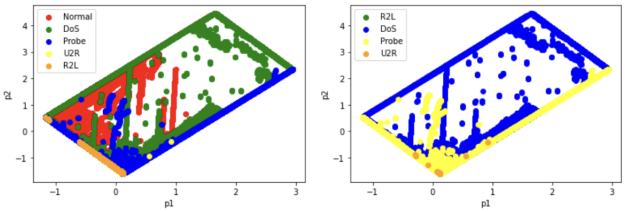

Fig. 3. PCA Visualization of attack categories.

C. Data Preprocessing

The steps followed are as follows:

- We first pre-processed data by assigning labels from the four attacks to the ”attack” category followed by one-hot encoding which is used to convert all categorical features to numerical values.
- Then, standardization was carried out using the formula given below:

$$Z = \frac{x - \mu}{\sigma} \tag{1}$$

where,
x is the observation for which we are calculating standardized value,
μ is the mean of the given sample given by $\frac{\sum_{i=1}^{n} x_i}{n}$,
σ is the standard deviation of the given sample given by $\sqrt{\frac{\sum_{i=1}^{n} (x_i - \mu)^2}{n}}$
where x_i is a single observation and n is the total number of observations.

IV. Proposed Work

A. Model Description for Existing Methods

The following section explains the existing algorithms and data preprocessing techniques used in our proposed model.

1) Information Gain: The feature selection method we have chosen for this study is information gain. Information Gain (IG) is used to evaluate attributes relative to the distribution of classes. It is given as,

$$I(c_1, ...c_m) = -\sum_{i=1}^{m} \frac{c_1}{c} \log(\frac{c_1}{c}) \tag{2}$$

Here $\frac{c_l}{c}$ is probability that sample is from class c_l. c is the count of data samples with distinct classes. The training set is partitioned into v sub-divisions of c_1 by a feature of n different values. The entropy for feature F is given by:

$$E(F) = \sum_{i=1}^{y} \frac{c_1}{c} \times I(c_i) \tag{3}$$

Information Gain for F is given by:

$$Gain(F) = I(c_1, ...c_m).E(F) \tag{4}$$

2) Principal Component Analysis: This linear algorithm attempts to find a region of the highest variance in the huge-dimensional data and translates it into a new space with dimensions less than or equal to the given subspace. It helps reveal patterns that aren't obvious in the data.
For dimensional reduction using PCA, we construct a matrix W of d rows and k columns, any sample vector x in the original subspace of d-dimensions can be transformed to another vector z in k-dimensions. We obtain a k-dimensional subspace from the original d-dimensional subspace, here k $\ll$ d generally. The first principal component has the highest variance, and all subsequent principal components will have the next larger variance since these components will be orthogonal to the other principal components. The principal components will be uncorrelated, even if the original components are correlated.

3) Kernel Principal Component Analysis: In order to cater to the non-linearity existing in the data, the kernel PCA technique has emerged. While certainly more complex than the older PCA, the kernel version can handle more complex data patterns that are invisible under linear transformations, such as the gap between R2L, U2R, and normal cases. The basic idea behind it is that linearly inseparable data become linearly separable in higher dimensional spaces.
Kernel PCA [11] is an extension to PCA, and can be summarized in the following steps:

- Let ϕ(x) be a non-linear transformation to an M-dimensional feature space from the original D-dimensional data space where M$\gg$D.

Authorized licensed use limited to: DELHI TECHNICAL UNIV. Downloaded on July 20,2023 at 11:12:41 UTC from IEEE Xplore. Restrictions apply.

- Construction of kernel matrix K.

$$K_{i,j} = \kappa(x_i, x_j) \tag{5}$$

where

$$\kappa(x_i, x_j) = \phi(x_i)^T \phi(x_j) \tag{6}$$

- Compute the Gram matrix $\overline{K}$.

$$\overline{K} = K - 1_N K - K 1_N + 1_N K 1_N \tag{7}$$

- Use $Ka_k = \lambda_k N a_k$ to solve for the vector a_i.
- Calculate $y_k(x)$: the kernel principal components.

4) Naive Bayes: Naive Bayes is the simplest yet most extremely useful method; it is highly reliable, accurate, and works fast. Naive Bayes is a probabilistic ML algorithm. The basis of which is Bayes' theorem.
It answers the problem that, if event B has already taken place, then the probability of event A is:

$$P(A|B) = \frac{P(A)P(B|A)}{P(B)} \tag{8}$$

here, A and B are events, and P(B) $\neq 0$.

$P(A)$ is the likelihood that event A will occur before event B.

$P(A|B)$ is the conditional likelihood that event A will occur after event B has already occurred.

In our case, we apply the Bayes theorem in the following manner.

$$P(y|X) = \frac{P(y)P(X|y)}{P(X)} \tag{9}$$

here, y is {Other instances, Probe and DoS} and X is vector of features where:

$$X = (x_1, x_2, ..., x_n)$$

Due to the 'naive' assumption of independent features, we get:

$$P(y|x_1, ..., x_n) = \frac{P(y)\prod_{i=1}^{n} P(x_i|y)}{P(x_1)P(x_2)...P(x_n)} \tag{10}$$

As the denominator is constant, we can say:

$$P(y|x_1, ..., x_n) \propto P(y)\prod_{i=1}^{n} P(x_i|y) \tag{11}$$

The next step is to create a classifier model. To do this, probabilities for all possible values of the class variable y given the set of inputs and the sum of the outputs with maximum likelihood are required. This is given by:

$$y = argmax_y P(y)\prod_{i=1}^{n} P(x_i|y) \tag{12}$$

Now, the final task is to calculate P(y) and P($x_i|$ y).

5) Support Vector Machines: SVM aims to locate a plane in an N-dimensional space that can categorize all data points.
The distance between the data points and the hyperplane should be as large as possible. The loss function is defined as,

$$c(x, y, f(x)) = (1 - y * f(x))_+ \tag{13}$$

If actual and predicted values have the same token, the cost is 0. In other cases, we determine the loss value. After adding the regularization parameter, the updated loss function is given by,

$$min_w \lambda\|w\|^2 + \sum_{i=1}^{n}(1 - y_i\langle x_i, w\rangle)_+ \tag{14}$$

Then, we partially differentiate w.r.t weights to get,

$$\frac{\delta}{\delta w_k}\lambda\|w\|^2 = 2\lambda w_k \tag{15}$$

$$\frac{\delta}{\delta w_k}(1 - y_i\langle x_i, w\rangle)_+ = \begin{cases} 0 & \text{if} \quad y_i\langle x_i, w\rangle) \geq 1 \\ -y_i x_{ik} & \text{else} \end{cases} \tag{16}$$

In case of no misclassifications, only the regularization parameter needs to be updated.

$$w = w - \alpha.(2\lambda w) \tag{17}$$

However, when any misclassification happens, we consider the loss and regularization parameters for updation.

$$w = w + \alpha.(y_i.x_i - 2\lambda w) \tag{18}$$

As SVM provides the option to select kernels, the use of nonlinear kernels, such as RBF, enable us to effectively categorize data with intricate boundaries. This means we can differentiate between R2L and U2R connections as opposed to normal connections.

B. Model Description for Proposed Method

Our model proposes two layers for detection: Layer 1 detects Probe and DoS using Naive Bayes, and Layer 2 uses Support Vector Machine (SVM) to detect R2L and U2R. SVM provides a non-linear kernel. It provides an effective method to distinguish overlapping regions of U2R, R2L, and normal instances. The steps followed in our proposed model are as follows:
First, we perform data partitioning, where the first set contains all data used as Layer 1 input, and the second set contains only U2R, R2L, and normal cases used as Layer 2 input.
We then use information gain as a feature selection technique to select only features associated with a particular attack type to improve accuracy. All features selected for each layer are presented in Fig. 4.
Then we do normalization and hot encoding, followed by PCA on the first layer and KernelPCA on the second layer. We choose 95% of the cumulative variance as the threshold.

Authorized licensed use limited to: DELHI TECHNICAL UNIV. Downloaded on July 20,2023 at 11:12:41 UTC from IEEE Xplore. Restrictions apply.

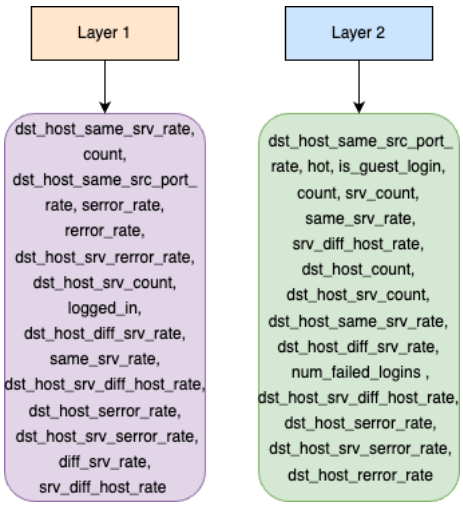

Fig. 4. Selected features for Layer 1 and Layer 2.

Finally, practice and validate. Naive Bayes is chosen as the main classifier in Group 1 and Support Vector Machine (SVM) for Group 2. We perform hyperparametric tuning of the SVM to set the C and gamma parameters of the nonlinear RBF kernel. A diagrammatic visualization of our proposed algorithm is shown in Fig. 5.

C. Performance Metrics

F1-score, accuracy, recall, and precision are used as performance measures. They are defined using the following terms:
True-Positive: When the model accurately predicts a positive scenario, it is said to be true-positive.
True-Negative: When the model accurately predicts a negative scenario, it is said to be true-negative.
False-Positive: In this scenario, the model incorrectly predicts a positive case.
False-Negative: This occurs when the model predicts a negative scenario in error.
The equations given below are used to evaluate our results.

$$Accuracy = \frac{TN + TP}{TN + TP + FN + FP} \tag{19}$$

$$Precision = \frac{TP}{FP + TP} \tag{20}$$

$$Recall = \frac{TP}{FN + TP} \tag{21}$$

$$F1 = \frac{2 * Recall * Precision}{Recall + Precision} \tag{22}$$

In this paper, we mainly focus on the detection rate (or recall).

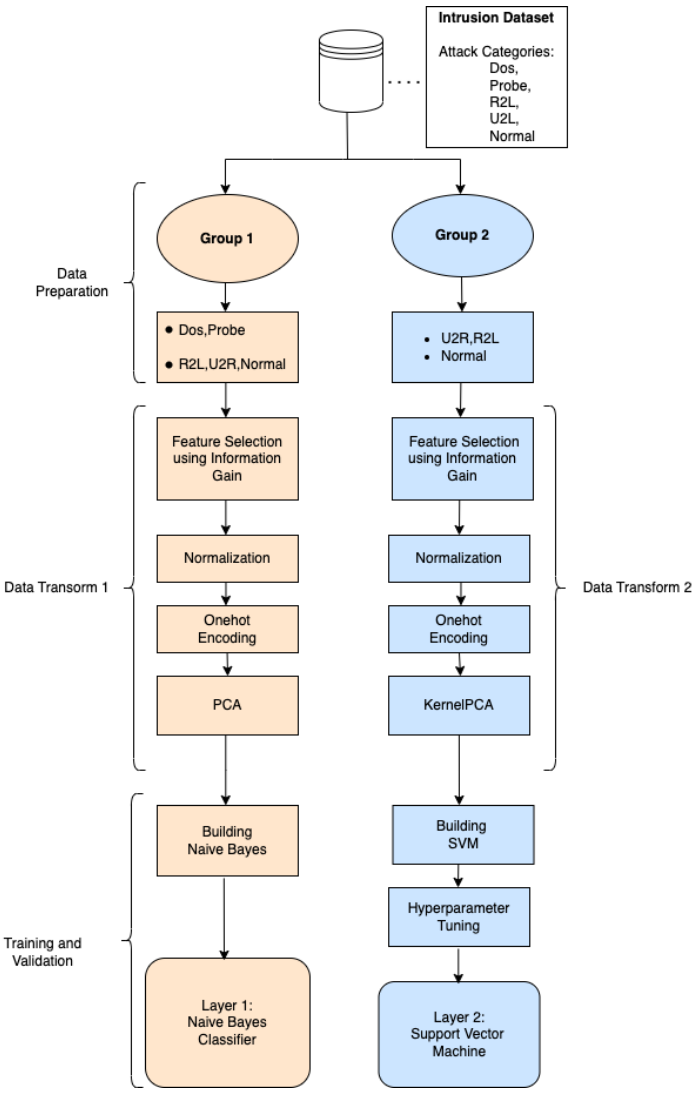

Fig. 5. Our suggested methodology.

V. Results And Discussion

To confirm the precision of our suggested model, this article employs the detection rate or recall as a measure to evaluate its performance. The test data used in this article is the original KDDTest+. The performance matrix is reported in Table I. The detection rate of every category

TABLE I
SELECTED FEATURES

Accuracy	Precision	Recall	F1-Score
88.5%	87.1%	93.8%	90.3%

trained on KDDTrain+ and KDDTrain+_20Percent is reported in Fig. 6. Using KDDTrain+ in training, we were able to achieve a detection rate of 89.7% on DoS (6694 out of 7460), 99.5% on Probe (2411 out of 2421), 99.9% on R2L (2,884 of 2,885) and 92.5% (62 out of 67) for U2R. Using KDDTrain+_20Percent to train the dataset,

Authorized licensed use limited to: DELHI TECHNICAL UNIV. Downloaded on July 20,2023 at 11:12:41 UTC from IEEE Xplore. Restrictions apply.

it scored 84.4% on DoS (6302 out of 7460), 99.5% on Probe (2409 out of 2421), 90.3% (2,604 of 2,975) on DoS, and 97.01% (65 of 67) on U2R.
Thus, we were able to achieve the key task of obtaining good detection rates for R2L and U2R, This is crucial since they are not only difficult to detect, but also the most harmful for the system.

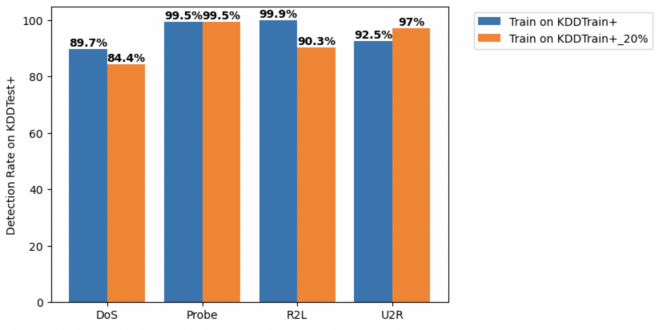

Fig. 6. Detection rates of each attack category.

Another key observation is that our model shows high accuracy in detecting known attacks with a detection rate of 96.3%, but only achieves an 88% detection rate in attacks of unknown types. To evaluate our model on a larger scale, we compare our results with other public IDS systems, as shown in Table II. We only compare our results with studies using similar methods, specifically, models that use KDDTest+ in the test. Our framework is considered very competitive in the field and we were able to achieve the goal of achieving a high overall detection rate.

TABLE II
COMPARISON OF PERFORMANCE WITH OTHER ANOMALY-BASED IDS

Algorithm	**Accuracy(%)**	**F1-Score(%)**	**Precision(%)**	**DR(%)**
Our proposed	88.5	90.3	87.1	93.8
SSC-OCSVM [8]	-	-	-	89
K-means+RF [12]	85.24	-	-	-
CNN+BiLSTM [13]	83.58	85.14	85.82	84.49
BAT-MC [14]	84.25	-	-	-
Autoencoder [15]	84.25	81.98	87	80.37

VI. CONCLUSION AND FUTURE WORK

The research aims to achieve a high overall detection rate using a hybrid approach for intrusion detection. The focus is on the efficient selection of features and a combination of learning techniques to identify all types of attacks, rather than a single general-purpose classifier. To test the proposed model NSL-KDD dataset was used, which comprises two layers. The primitive layer employs Naive Bayes to identify Probe and Dos and the second layer uses Support Vector Machine to identify R2L and U2R. The overall detection rate of the model is 93.8%, and the detection rate of Probe and R2L exceeds 99%.
This document could be extended in several ways in future work. This article uses information gain for feature selection. New feature selection techniques can be explored to improve overall accuracy. In fact, this model can be applied to datasets that classify attacks in different ways.

REFERENCES

[1] Z. Liu, M. Luo and B. Ma, "Network Intrusion Detection based on RBF Neural Networks and Fuzzy Cluster," 2022 9th International Conference on Dependable Systems and Their Applications (DSA), Wulumuqi, China, 2022, pp. 236-240
[2] Y. -X. Meng, "The practice on using machine learning for network anomaly intrusion detection," 2011 International Conference on Machine Learning and Cybernetics, Guilin, China, 2011, pp. 576-581
[3] G. Yedukondalu, G. H. Bindu, J. Pavan, G. Venkatesh and A. SaiTeja, "Intrusion Detection System Framework Using Machine Learning," 2021 Third International Conference on Inventive Research in Computing Applications (ICIRCA), Coimbatore, India, 2021, pp. 1224-1230
[4] D. Deng, "Research on Anomaly Detection Method Based on DBSCAN Clustering Algorithm," 2020 5th International Conference on Information Science, Computer Technology and Transportation (ISCTT), Shenyang, China, 2020, pp. 439-442
[5] S. Yao, H. Xu, L. Yan and J. Su, "Applying an Improved DBSCAN Clustering Algorithm to Network Intrusion Detection," 2021 11th IEEE International Conference on Intelligent Data Acquisition and Advanced Computing Systems: Technology and Applications (IDAACS), Cracow, Poland, 2021, pp. 865-868
[6] Jing-Rong Chang, Venkateswarlu Nalluri, Long-Sheng Chen et al. A novel dimension reduction based method to detect network intrusions, 10 November 2022, PREPRINT (Version 1) available at Research Square
[7] S. S. Ahmadi, S. Rashad and H. Elgazzar, "Efficient Feature Selection for Intrusion Detection Systems," 2019 IEEE 10th Annual Ubiquitous Computing, Electronics Mobile Communication Conference (UEMCON), New York, NY, USA, 2019, pp. 1029-1034
[8] G. Pu, L. Wang, J. Shen and F. Dong, "A hybrid unsupervised clustering-based anomaly detection method," in Tsinghua Science and Technology, vol. 26, no. 2, pp. 146-153, April 2021
[9] R. Kavitha and S. Amutha, "Performance Analysis of Deep Neural Network and LSTM models for Secure Network Intrusion Detection System," 2022 IEEE 4th International Conference on Cybernetics, Cognition and Machine Learning Applications (ICCCMLA), Goa, India, 2022, pp. 390-396
[10] M. Tavallaee, E. Bagheri, W. Lu and A. A. Ghorbani, "A detailed analysis of the KDD CUP 99 data set," 2009 IEEE Symposium on Computational Intelligence for Security and Defense Applications, Ottawa, ON, Canada, 2009, pp. 1-6
[11] Wang, Q. (2012). Kernel principal component analysis and its applications in face recognition and active shape models. arXiv preprint arXiv:1207.3538.
[12] C. Liu, Z. Gu and J. Wang, "A hybrid intrusion detection system based on scalable K-means+ random forest and deep learning", IEEE Access, vol. 9, pp. 75729-75740, 2021.
[13] K. Jiang, W. Wang, A. Wang and H. Wu, "Network intrusion detection combined hybrid sampling with deep hierarchical network", IEEE Access, vol. 8, pp. 32464-32476, 2020.
[14] T. Su, H. Sun, J. Zhu, S. Wang and Y. Li, "BAT: Deep learning methods on network intrusion detection using NSL-KDD dataset", IEEE Access, vol. 8, pp. 29575-29585, 2020.
[15] C. Ieracitano, A. Adeel, F. C. Morabito and A. Hussain, "A novel statistical analysis and autoencoder driven intelligent intrusion detection approach", Neurocomputing, vol. 387, pp. 51-62, Apr. 2020.

Authorized licensed use limited to: DELHI TECHNICAL UNIV. Downloaded on July 20,2023 at 11:12:41 UTC from IEEE Xplore. Restrictions apply.

APPENDIX A
NOMENCLATURE AND ABBREVIATIONS

The appendix consists of a description of the nomenclature and full forms of abbreviation frequently used in this paper. Abbreviations and their full forms are mentioned in Table III.

TABLE III
TABLE OF ABBREVIATIONS

Abbreviation	Full Form
IDS	Intrusion Detection System
ML	Machine Learning
IoT	Internet of Things
COVID-19	Corona Virus disease of 2019
SVM	Support Vector Machines
ANN	Artificial Neural Network
DBSCAN	Density-Based Spatial Clustering of Applications with Noise
KPCA	Kernel Principal Component Analysis
DoS	Denial of Service
U2R	User to Root
R2L	Root to Local
ICMP	Internet Control Message Protocol
PCA	Principal Component Analysis
IG	Information Gain
RBF	Radial Basis Function

The symbols used are mentioned in Table IV.

TABLE IV
TABLE OF SYMBOLS

Symbol	Meaning
$\sum$	Summation
$\prod$	Product
$\propto$	Proportional
$min_x f(x)$	Minimum value of f(x) among all possible values of x
$argmax_S f(x)$	Set of points x $\in$ S for which f(x) attains the function's largest value
$\langle A, B \rangle$	Inner product of the vectors A and B i.e $(a_1b_1 + a_2b_2 + ... + a_nb_n)$ where $A = (a_1, a_2, ...a_n)$ and $B = (b_1, b_2, ...b_n)$
X_+	Subset of positive elements of Set X
$\frac{\delta}{\delta x} f(x)$	Partial derivative of function f(x) with respect to x

Authorized licensed use limited to: DELHI TECHNICAL UNIV. Downloaded on July 20,2023 at 11:12:41 UTC from IEEE Xplore. Restrictions apply.

2023 International Conference on Unmanned Aircraft Systems (ICUAS)
June 6-9, 2023 | Lazarski University, Warsaw, Poland

A Modified Artificial Potential Field for UAV Collision Avoidance

Astik Srivastava, V.R. Vasudevan, Harikesh, Raghava Nallanthiga, and P.B. Sujit

2023 International Conference on Unmanned Aircraft Systems (ICUAS) | 979-8-3503-1037-5/23/$31.00 ©2023 IEEE | DOI: 10.1109/ICUAS57906.2023.10156492

***Abstract*— As UAV applications in the civilian airspace increases, securely operating them in congested environment becomes more challenging. A Cauchy Artificial Potential Field (CAPF) method is presented in this research to make UAV navigation practical and secure in a cluttered dynamic environment. The CAPF approach enables the UAVs to avoid collision with obstacles that could either be static or dynamic (Another UAV) commanding mostly non-aggressive maneuvers. The approach presented in the research has been verified through simulations and testing. We compare the results of CAPF with MAPF and the proposed approach has shown improvement in terms of total acceleration and in distance traveled by vehicles while providing safer margins at higher speeds.**

I. Introduction

Unmanned Aerial Vehicles (UAVs) have been a vital asset for most militaries worldwide for the past two decades [1]. In recent years, they have also started attracting significant attention in the civilian domain due to their potential for cost-effectively solving problems like organ transportation and agricultural mapping [2]. As these UAVs become a more integral part of the day-to-day lives of an average person, the airspace, especially in urban areas, will become cluttered and difficult to manage. Cluttered airspace also means that the probability of inter-vehicular collisions and collisions of UAVs with other objects in the environment will be high. Multiple algorithms exist to allow UAVs to avoid obstacles. Graph-based approaches like Djikstra [3], A* [4], D*, etc. provide an optimal path from starting location to desired location but take significant computational resources in the case of large node environments. Other approaches like Randomly exploring Random Trees (RRT) and RRT* [5] are faster and are commonly used for global path planning through a well-mapped environment. Obstacle avoidance approaches based on Geometrical avoidance [6] have also shown promising results, along with approaches based on Inverse Proportional Navigation [7] and the Velocity Obstacle method [8]. The Artificial Potential Field Approach was first proposed by Khatib [9]. It is one of the most promising approaches for solving the collision avoidance problem due to its mathematical simplicity and computational efficiency, but the algorithm has limitations. The first drawback is the lack of a guarantee that the path taken by the UAV is optimal. This problem has been attempted to be solved by introducing Particle Swarm Optimized Potential Field [10], ant colony swarm optimization [11]. The second drawback is the agent's tendency to get stuck in a local minimum, which is generally the case in environments with complex geometry or cluttered environments or when the collisions are head-on. This problem has been solved by introducing rotational vector fields around the obstacles to prevent local minima during head-on collisions [12] [13]. T. Stastny proposed a morphing potential field-based approach for fixed-wing UAV navigation, wherein UAV couldn't fall in local minima due to a robust guidance strategy based on Nonlinear Model Predictive Control [14] [15]. This, however, is difficult to implement on mini UAVs due to problems in system identification and limited weight margins for onboard computation. A time-varying vector field is proposed by Martin Braquet [16] for avoiding moving elliptical obstacles. Furthermore, the solution to the problem of the jittering agent was proposed by Jiayi Sun [17] by dynamically adjusting the time steps. The navigation function-based obstacle avoidance approach [18] has also been studied extensively, wherein the agent follows the gradient of the navigation function. Lyapunov and Tangent vector field generation [19] can also be used to allow UAVs to avoid obstacles successfully. Several algorithms to generate trajectories that minimize the jerk on UAV, also known as minimum-snap-trajectories also show promising results in highly cluttered environments [20] [21], although they are over-kill for reactive collision avoidance in open environments.

This paper attempts to solve the above problems by proposing a repulsive potential field designed to avoid local minima during a head-on collision by introducing a rotational component and eccentric ROI (region of influence) around the obstacle to evenly avoid it while minimizing acceleration. A preliminary version of this work is available on arXiv[1]. The contributions [2] of this paper are as follows:

- Novel repulsive function to generate elliptical potential fields without local minima in both 2-D and 3-D environments.
- Strategy to tune gains for effective obstacle avoidance at speeds for multirotor UAVs (up to 10m/s).
- Extensive testing for validating the algorithm for both fixed-wing and multirotor UAVs.
- Demonstration of obstacle avoidance algorithm to be used in cooperative navigation scenarios containing multiple UAVs.

The novel potential function introduced in this paper is based on the Cauchy distribution. The contour of the repulsive

Astik Srivastava, V.R. Vasudevan, Harikesh and Raghava Nallanthiga are with Delhi Technological University, New Delhi - 110042. Email:(41.astiksrivastava,vasudevanvr2002,harikeshdalal,nsraghava)@gmail.com
P.B. Sujit is with the Department of Electrical Engineering and Computer Science at IISER Bhopal, Bhopal - 462066, India. Email: sujit@iiserb.ac.in

[1]Refer to preprint https://arxiv.org/abs/2208.03117 for preliminary work
[2]Refer https://github.com/Astik-2002/Dynamic-artificial-potential-field-algorithm-for-cooperative-obstacle-avoidance-for-fixed-wing-UAV for further information on the implementation of obstacle avoidance algorithm

Authorized licensed use limited to: DELHI TECHNICAL UNIV. Downloaded on July 03,2023 at 04:47:02 UTC from IEEE Xplore. Restrictions apply.

potential function in the East-North plane is of the shape of an ellipse at high speeds, contrary to the circular contours seen in typical force field methods [13], whose minor axes always point in the direction of the relative velocity of the oncoming agent (UAV in this case) with respect to the obstacle. The main advantage that this reformulation has demonstrated is that it generates feasible commands for the UAV, allowing for smooth maneuvering around the obstacles and minimizing the chance of failure due to aggressive maneuvers.

II. Problem Formularion

The algorithm proposed in this paper aims at performing reactive collision avoidance while minimizing the acceleration experienced by the UAV to avoid the obstacle smoothly. The algorithm is primarily designed to safely operate mini fixed-wing and multirotor UAVs ($mass < 25kg$) in open airspace, heavily populated with UAVs, and has been tested for the same. Other UAVs and obstacles are considered as point masses i.e. the potential field is centered on the location of their C.G. without consideration of their dimensions. The exemplary potential field for obstacle avoidance is shown below(Fig. 1).

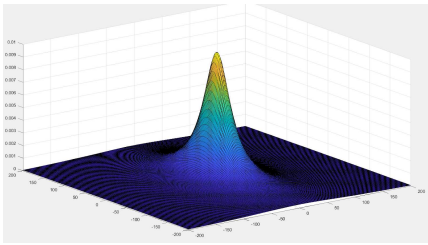

Fig. 1: Surface plot of the potential field

The potential field shown above is time-varying such that the minor axis of elliptical contours always points toward the oncoming agent to prevent collision without any abrupt change in velocity, making it suitable for high-speed multirotor and fixed-wing UAVs. The field strength also decreases as the UAV 'moves away' from the obstacle to minimize the effect of an obstacle of the UAV that has already been avoided. This minimizes the change of unpredictable local minima forming in UAVs' path as it maneuvers near multiple obstacles.

III. Potential field method

The potential field algorithm works by using the gradients of a scalar potential field to guide the agent toward the desired point. This method is analogous to the behavior of charges in an electric field. The agent and obstacles are analogous to like charges, whereas the agent and the goal are analogous to opposite charges. The resulting forces then guide the UAV away from obstacles and towards the goal. A rotational component is added to the net force to avoid local minima as the agent approaches the obstacle.

The net potential and net force experienced by the agent can be represented as shown below:

$$\begin{aligned} U_{net} &= \sum_{i=1}^{N} U(i)_{avoid} + U_{att} \\ F_{net} &= \sum_{i=1}^{N} F(i)_{avoid} + F_{att} \end{aligned} \tag{1}$$

A. Attractive vector field

The attractive potential for guiding the UAV to a point is given in [9]

$$U_{att} = 0.5 * k_{att} * |\mathbf{r} - \mathbf{r_{wp}}|^2 \tag{2}$$

Where K_{att} is a constant used to tune the attractive force $\mathbf{F_{att}}$, $\mathbf{r}$ is the position vector of the UAV, and $\mathbf{r_{wp}}$ is the position vector of the way-point, respectively. Attractive force $\mathbf{F_{att}}$ is the gradient of potential U_{att} and is given as

$$\mathbf{F_{att}} = k_{att} * (\mathbf{r} - \mathbf{r_{wp}}) \tag{3}$$

B. Avoidance vector field

The Cauchy's distribution based potential field (CAPF), denoted by U_{rep} is generated around the obstacle. The potential morphs itself such that the minor axis of its elliptical contours is always parallel to the relative velocity vector between the UAV and the obstacle.

$$\begin{aligned} U_{rep} &= \frac{k_{rep}}{1 + (\frac{X}{b})^2 + (\frac{Y}{a})^2} \\ \begin{bmatrix} X \\ Y \end{bmatrix} &= \begin{bmatrix} cos(\theta) & -sin(\theta) \\ sin(\theta) & cos(\theta) \end{bmatrix} * (\mathbf{r_o} - \mathbf{r}) \\ \theta &= cos^{-1}(\frac{(\mathbf{V_o} - \mathbf{V}) \cdot \mathbf{i}}{|\mathbf{V_o} - \mathbf{V}|}) \end{aligned} \tag{4}$$

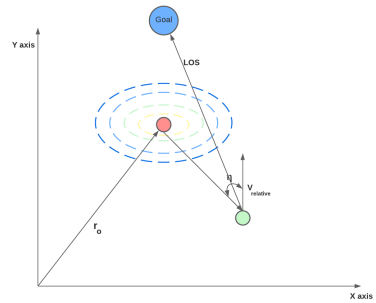

Fig. 2: Collision avoidance geometry

Where K_{rep} is a constant used to tune the repulsive gain, $\mathbf{V_o}$ and $\mathbf{r_o}$ are the velocity and position vector of the obstacle respectively, $\mathbf{V}$ is the velocity of the UAV, $\mathbf{i}$ is the unit vector along the x-axis and a and b are the major and minor axis respectively of the ellipse. It should be noted that END (East-North-Down) coordinate system is used in the formulation for the inertial and body frames of the obstacles. The vector field is constructed by a linear combination of the two components of U_{rep} for both repulsive and rotational components

Authorized licensed use limited to: DELHI TECHNICAL UNIV. Downloaded on July 03,2023 at 04:47:02 UTC from IEEE Xplore. Restrictions apply.

around the obstacle. The gradients of the potential field have components F_x along the x-axis and F_y along the y-axis. We define the repulsive vector field pointing away from the obstacle and the rotational vector field as follows:

$$\begin{aligned} \mathbf{F_{rep}} &= \nabla U_{rep} = F_x * \mathbf{i} + F_y * \mathbf{j} \\ \mathbf{F_{rot}} &= -F_y * \mathbf{i} + F_x * \mathbf{j} \end{aligned} \tag{5}$$

The components F_x and F_y are given by 6

$$\begin{aligned} F_x &= \frac{k_{rep} * (2 * cos(\theta) * \frac{X}{b^2} + 2 * sin(\theta) * \frac{Y}{a^2})}{(1 + (\frac{X}{b})^2 + (\frac{Y}{a})^2)^2} \\ F_y &= \frac{k_{rep} * (2 * cos(\theta) * \frac{Y}{a^2} + 2 * sin(\theta) * \frac{X}{b^2})}{(1 + (\frac{X}{b})^2 + (\frac{Y}{a})^2)^2} \end{aligned} \tag{6}$$

The rotation direction of $\mathbf{F_{rot}}$ depends on which side of the LOS (line of sight) between UAV and the waypoint the obstacle lies on, which is determined by taking a cross product between the LOS vector and the position vector of the obstacle. The direction is changed so the UAV takes the shortest path around the obstacle and toward the waypoint. Hence, the total force $\mathbf{F_{avoid}}$ on the UAV is given by:

$$\begin{aligned} \mathbf{F_{avoid}} &= \mathbf{F_{rep}} + sign(k) * \mathbf{F_{rot}} \\ k &= (\mathbf{r_{wp}} - \mathbf{r}) \times \mathbf{r_o} \end{aligned} \tag{7}$$

In the head-on collision, i.e., the obstacle lies precisely between the UAV and the waypoint, and the minor axis of the ellipse is aligned along the relative velocity of the UAV and the obstacle, the default direction of rotation of the rotational field is taken in the clockwise direction. The resulting vector field $\mathbf{F_{avoid}}$ is shown in 3:

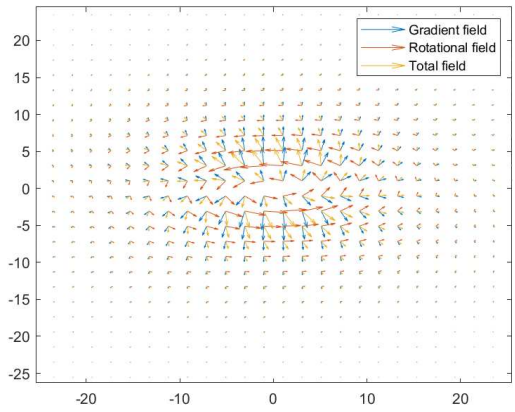

Fig. 3: Avoidance vector field

C. Dynamic gain tuning

The above formulation of the potential field relies on parameters like k_{att}, K_{rep}, b and the eccentricity of the ellipse given by:

$$e = \sqrt{(1 - \frac{b^2}{a^2})} \tag{8}$$

Operations in the real world would require the UAV to perform avoidance at a safe distance. It is also important that maneuvers taken by any UAV are not extreme to avoid possible structural fatigue or actuator failure. Here, we propose a tuning strategy for different parameters related to the repulsive potential field. The parameter k_{att} related to attractive potential is not tuned as the value largely remains constant for good results at the velocity range we are targeting. Also, the gains are tuned only for multirotor UAVs moving at speeds up to 10m/s, gain tuning for fixed-wing UAVs will be attempted in a future study.

Parameter k_{rep} is the main influence on the acceleration experienced by the UAV while avoiding obstacles and the minimum distance between UAV and obstacle. It must depend upon the angle η between the relative position and velocity vector of the obstacle and UAV. It should also depend on the relative speed $|V_o - V|$ between the obstacle and the UAV. Hence k_{rep} can be written as:

$$\begin{aligned} k_{rep} &= k_{rep_0} * f(\eta) \\ k_{rep_0} &= f(|V_{rel}|) \end{aligned} \tag{9}$$

1) Tuning with respect to Velocity: 600 simulations, each with different tuning parameters were conducted in an SITL environment to avoid a static obstacle at velocities varying from 5m/s to 10m/s. In each simulation, different values of k_{rep_0} and e were tested to find values corresponding to minimum acceleration without a collision. A collision was declared if the minimum distance (d_{min}) is smaller than 5m ($d_{allowed}$).

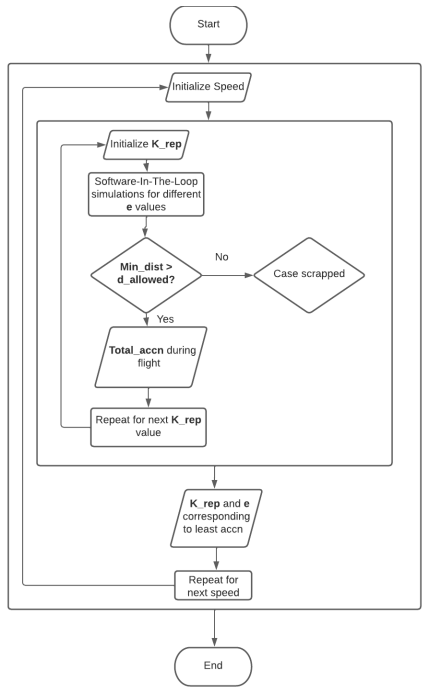

Fig. 4: Flowchart for tuning k_{rep_0} and e

The length of the semi-minor axis (b) is set to be $3 * d_{allowed}$. The results are shown in fig 5. As shown above, the optimum value of k_{rep_0} for high speeds (6-10m/s) is 30, whereas the value of e increases as velocity increases. For lower speeds, k_{rep_0} = 20, and no significant advantage

Authorized licensed use limited to: DELHI TECHNICAL UNIV. Downloaded on July 03,2023 at 04:47:02 UTC from IEEE Xplore. Restrictions apply.

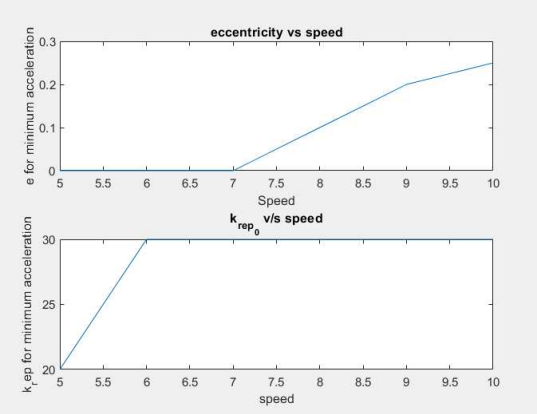

Fig. 5: k_{rep_0} and e v/s speed

2) Tuning w.r.t angle: The gain k_{rep} needs to be highest if the collision is head-on, i.e., angle η = 0. Hence in order to further improve the trajectory of the UAV, we propose dynamically changing k_{rep} as given in:

$$k_{rep} = k_{rep_0} * (sin(\frac{\pi * cos(\eta)}{2}) + 1) \tag{10}$$

This tuning is useful to prevent the local minimum conditions in environments with a large number of dynamic agents by nullifying the effects of obstacles that have already been avoided or those that are moving away.

D. 3D obstacle avoidance

The collision avoidance algorithm can be extended for 3-dimensional environments if the mission profile of the UAV has varying altitudes, e.g., during the climb or descent phase. Multiple approaches like considering cylindrical or polygonal definitions for obstacles [22], layering potential fields [15], and 4-dimensional potential functions [13] are used for such scenarios. We use a similar approach to the last one by extending the repulsive field's definition into 3-Dimensions. The potential field for 3-D obstacle avoidance is defined as:

$$U_{rep} = \frac{k_{rep}}{1 + (\frac{X}{b})^2 + (\frac{Y}{a})^2 + (\frac{Z}{c})^2} \tag{11}$$

X, Y, Z are defined similarly to (4) as:

$$\begin{bmatrix} X \\ Y \\ Z \end{bmatrix} = \mathbf{R} * (\mathbf{r_o} - \mathbf{r})$$

$$\mathbf{R} = \begin{bmatrix} cos(\phi)cos(\theta) & -sin(\phi) & cos(\phi) * sin(\theta) \\ sin(\phi) * cos(\theta) & cos(\phi) & sin(\phi) * sin(\theta) \\ -sin(\theta) & 0 & cos(\theta) \end{bmatrix} \tag{12}$$

Where ϕ and θ are the UAV's course and flight path angles, respectively. The vector field for collision avoidance and rotational field is similar to (6). The only change in switching logic given in (7) is the use of x-y plane projection of 3-D vectors to determine the rotational direction of $\mathbf{F_{rot}}$. is given by (13):

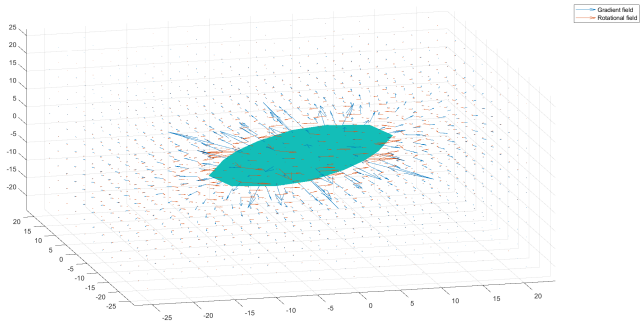

Fig. 6: Vector fields for UAV climbing with θ = $\frac{\pi}{6} rad$.

$$\begin{aligned} \mathbf{F_{rep}} = \nabla U_{rep} = F_x * \mathbf{i} + F_y * \mathbf{j} + F_z * \mathbf{k} \\ \mathbf{F_{rot}} = -F_y * \mathbf{i} + F_x * \mathbf{j} \end{aligned} \tag{13}$$

The components F_x, F_y and F_z are given by (14)

$$F_x = \frac{k_{rep} * (2 * cos(\theta) * sin(\phi) * \frac{Y}{b^2} - 2 * sin(\theta) * \frac{Z}{c^2}}{(1 + (\frac{X}{b})^2 + (\frac{Y}{a})^2 + (\frac{Y}{a})^2)^2} + \frac{2 * cos(\phi)cos(\theta) * \frac{X}{a^2}}{(1 + (\frac{X}{b})^2 + (\frac{Y}{a})^2 + (\frac{Y}{a})^2)^2}$$

$$F_y = -\frac{k_{rep} * (2 * sin(\phi) * \frac{X}{a^2} + 2 * cos(\phi) * \frac{Y}{b^2})}{(1 + (\frac{X}{b})^2 + (\frac{Y}{a})^2 + (\frac{Z}{c})^2)^2}$$

$$F_z = \frac{k_{rep} * (2 * cos(\theta) * \frac{Z}{c^2} + 2 * cos(\phi) * sin(\theta) * \frac{X}{a^2}}{(1 + (\frac{X}{b})^2 + (\frac{Y}{a})^2 + (\frac{Y}{a})^2)^2} + \frac{2 * sin(\phi)sin(\theta) * \frac{Y}{b^2}}{(1 + (\frac{X}{b})^2 + (\frac{Y}{a})^2 + (\frac{Y}{a})^2)^2} \tag{14}$$

IV. UAV Guidance

The trajectory of the UAV is controlled by using Dronekit's python API, communicating with the flight controller via MAVLink communication protocol onboard the UAV. Position-based guidance is used for fixed-wing UAVs to track the vector field, wherein moving waypoints in the direction of the vector field are given to the autopilot, whereas velocity-based guidance is used for multirotor UAVs.

A. Multirotor guidance

The guidance module works by setting the commanded velocity (V_c) in the direction of the resultant vector field F_{net} (1) as follows:

$$\begin{bmatrix} \dot{x_c} \\ \dot{y_c} \\ \dot{z_c} \end{bmatrix} = |V_c| * \begin{bmatrix} f_x \\ f_y \\ f_z \end{bmatrix} \tag{15}$$

Here, f_x, f_y and f_z are unit vectors parallel to F_{net} at (x,y,z). Functions for takeoff and sending velocity are taken from Dronekit examples. The complete collision avoidance subroutine for multirotor is given below:

Authorized licensed use limited to: DELHI TECHNICAL UNIV. Downloaded on July 03,2023 at 04:47:02 UTC from IEEE Xplore. Restrictions apply.

Algorithm 1: Collision avoidance for multirotors

Input : lists $[r_{ob_i}]$ and $[V_{o_i}]$, $i = 0, 1, \cdots, n-1$, where each element is a vector containing the location and velocity of obstacle respectively.

Output: velocity setpoints for autopilot.

$h \leftarrow alti$ // cruise alti
$V_{uav} \leftarrow speed$
$r_{uav} \leftarrow home$ // location at t=0
$r_{wp} \leftarrow wp$ // waypoint location
$Flag \leftarrow 0$
Function **arm_and_takeoff**($target_alti$):
Function **send_global_velocity**(v_x,v_y,v_z):
{ sends MAVLink command of velocity setpoint to autopilot in GUIDED mode }
Function **update_pos**():
{ Updates the state of the obstacle
returns $[r_{ob}], V_o$ }
while $|r_{uav} - r_{wp}| > d_{threshold}$ **do**
    $F_{att} = k_{att} * (r_{wp} - r_{uav})$;
    arm_and_takeoff(h) // climb to target alti
    update_pos()
    for $i = 0;\ i < n;\ i = i + 1$ **do**
        calculate $F_{avoid} = F_{rep} + F_{rot}$
        $F_{avoid} += F_{avoid}$
    end for
    $F_{net} = F_{avoid} + F_{att}$
    $f_{net} = \frac{F_{net}}{|F_{net}|}$ // normalize
    $V_c \leftarrow V_{uav} * f_{net}$
    send_global_velocity(V_{c_x},V_{c_y},V_{c_z})
end while
vehicle.mode = 'LAND'

B. Fixed-wing guidance

The guidance module for fixed-wing UAVs to follow vector fields is similar to the moving waypoint guidance method [23]. The algorithm works by settings waypoints a distance d_{wp} away from the current position of the UAV in the direction of the resultant unit vector field f_{net} at the current UAV position. Although this guidance strategy has shown good results, improvements can be made by including better controllers to compensate for nonlinearity and also for ensuring robustness [24]. Dronekit's inbuilt functions like simple_goto are used for generating waypoint setpoints.

V. Results and Discussion

The simulation analysis is done on Ardupilot SITL (Software-in-the-loop) environment for both fixed-wing and multirotor UAVs. For real-world validation flight tests are conducted on a quadcopter platform to avoid a static-virtual obstacle.

Algorithm 2: Collision avoidance for Fixed-wing UAV

Input : lists $[r_{ob_i}]$ and $[V_{o_i}]$, $i = 0, 1, \cdots, n-1$, where each element is a vector containing the location and velocity of obstacle respectively.

Output: velocity setpoints for autopilot.

$V_{uav} \leftarrow speed$
$r_{uav} \leftarrow home$ // location at t=0
$r_{wp} \leftarrow wp$ // goal location
$Flag \leftarrow 0$

Function **arm_and_takeoff**(vehicle):

Function **target_attitude**(v_x,v_y,v_z):
{ // for flight path and course angle
$theta = \arctan(\frac{v_z}{\sqrt{(v_x^2+v_y^2)}})$
$phi = \arctan(\frac{v_y}{v_x})$
return theta, phi }

Function **goto**(theta, phi, dist, vehicle):
{ $w_p =$ **distance_to_coordinates**$(dist, theta, phi)$
$vehicle.simple_goto(w_p)$ }

Function **update_pos**():
{ Updates the state of the obstacle
returns $[r_{ob}], V_o$ }

while $|r_{uav} - r_{wp}| > d_{threshold}$ **do**
    $F_{att} = k_{att} * (r_{wp} - r_{uav})$;
    arm_and_takeoff(h) // climb to target alti
    update_pos()
    for $i = 0;\ i < n;\ i = i + 1$ **do**
        calculate $F_{avoid} = F_{rep} + F_{rot}$
        $F_{avoid} += F_{avoid}$
    end for
    $F_{net} = F_{avoid} + F_{att}$
    $f_{net} = \frac{F_{net}}{|F_{net}|}$ // normalize
    $theta, phi \leftarrow$ **target_attitude**$(f_{net_x}, f_{net_y}, f_{net_z})$
    goto(theta, phi, dist, vec)
end while
vehicle.mode = 'LAND'

Authorized licensed use limited to: DELHI TECHNICAL UNIV. Downloaded on July 03,2023 at 04:47:02 UTC from IEEE Xplore. Restrictions apply.

(a) Paths taken by the UAVs for constant altitude obstacle avoidance

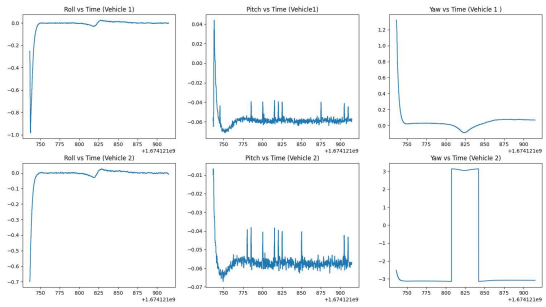

(b) attitude of UAV1 and UAV2 during flight

Fig. 7: Fixed wing collision avoidance in a 2-D environment

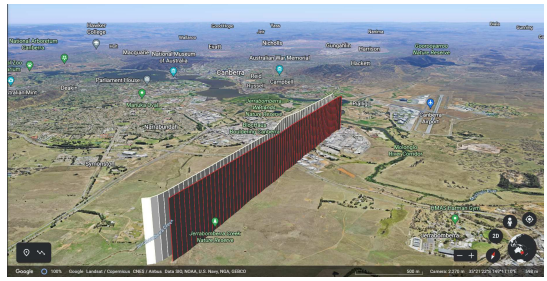

(a) Paths taken by the UAVs for avoiding each other

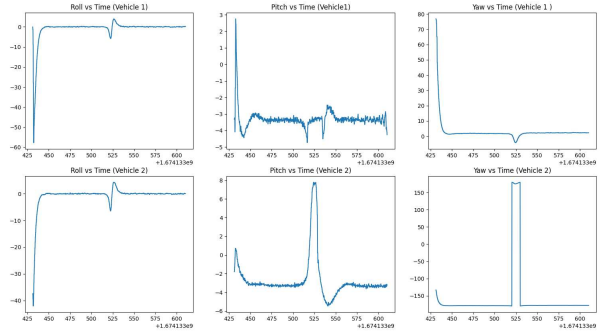

(b) Attitude of UAV1 and UAV2 during flight

Fig. 8: Fixed wing collision avoidance in a 3-D environment

A. *Software-In-The-Loop simulation*

1) Fixed-wing UAV: This simulation demonstrates cooperative collision avoidance between two fixed-wing agents approaching head-on each other. The simulation has been done for both constant altitude (2-D) and variable altitude (3-D) cases. The parameters are given below in table 1.

TABLE I: Parameters for fixed-wing collision avoidance

Parameters	Values	Units
k_{rep}	1700	-
b	100	meters
e	0.4	-
$\|V_{airspeed}\|$	21	m/s
k_{att}	0.008	-
minimum distance b/w UAVs	30	meters

(a) For 2-D collision avoidance

Parameters	Values	Units
k_{rep}	3000	-
a	1900	meters
b	2000	meters
c	100	meters
$\|V_{airspeed}\|$	21	m/s
k_{att}	0.02	-
minimum distance b/w UAVs	26	meters

(b) For 3-D collision avoidance

2) Multirotor UAV: Two simulations are performed for multirotor UAVs. The first demonstrates the performance in a cluttered environment, and the second presents a comparison with [13] regarding the aggressiveness and optimality of UAV motion.

TABLE II: Parameters for collision avoidance in cluttered environment

Parameters	Values	Units
$\|V\|$	5	m/s
minimum distance between UAV and obstacle1	14.46	meters
minimum distance between UAV and obstacle2	12.53	meters
minimum distance between UAV and obstacle3	22.36	meters
minimum distance between UAV and obstacle4	11.59	meters
minimum distance between UAV1 and UAV2	21.96	meters
k_{att}	0.01	-

(a) Performance of UAV1

Parameters	Values	Units
$\|V\|$	5	m/s
minimum distance between UAV and obstacle1	25.87	meters
minimum distance between UAV and obstacle2	8.30	meters
minimum distance between UAV and obstacle3	6.11	meters
minimum distance between UAV and obstacle4	12.62	meters
k_{att}	0.01	-

(b) Performance of UAV2

a) Collision avoidance in cluttered environment: A cluttered virtual environment containing four static and two cooperative agents was simulated to validate the algorithm's performance. The obstacle was kept as cylinders having a radius of 5m. The trajectory and results are presented in fig 9 and Table 2, respectively.

b) Comparitive analysis: This simulation compares our potential field and the one shown in [13] with velocities 1m/s to 10m/s. Comparison is made in terms of the magnitude of total acceleration experienced by the UAV during flight and the minimum distance between the obstacle and the UAV. The UAV is tasked with avoiding a collision with a

Authorized licensed use limited to: DELHI TECHNICAL UNIV. Downloaded on July 03,2023 at 04:47:02 UTC from IEEE Xplore. Restrictions apply.

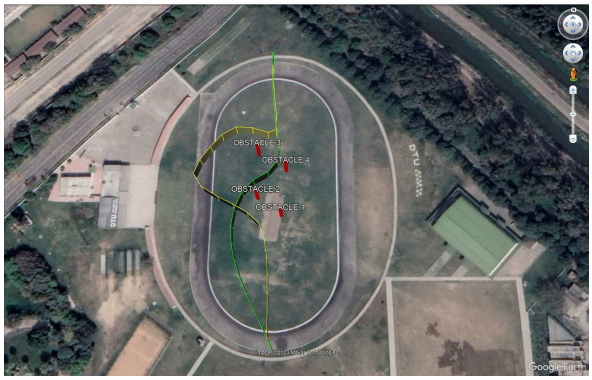

Fig. 9: Multirotor collision avoidance in cluttered dynamic environment

floodlight installed at the DTU sports complex. The gains are tuned dynamically w.r.t velocity of the agent. It is clear that CAPF performs better than MAPF [13] as it fails to avoid the obstacle at higher speed and lower speed, showing higher path length and acceleration than CAPF.

B. Experimental evaluation

A Tarot 650 quadcopter equipped with Pixhawk cube black for low-level control and an NVIDIA Jetson nano as the onboard computer for higher-level control and obstacle avoidance is used for experimental evaluation. The Jetson is connected to the internet via waveshare 4G LTE hat, allowing strong communication links between GCS and UAV. The task was to avoid a virtual obstacle in the DTU sports complex. The speed of the UAV was 5m/s, and the minimum distance between the obstacle and UAV was 7.18 m. The results are indicated below in fig 11.

VI. Conclusion and Future Works

This paper proposes a novel mathematical definition of the repulsive potential function for reactive collision avoidance for fixed-wing and multirotor UAVs. We first offer a gradient field based on the Cauchy distribution curve and a rotation field centered at the obstacle to allow collision avoidance without falling into local minima. We then present a strategy to dynamically change the gains during flight for multirotor UAVs operating in a 2-D environment (flying at a constant altitude). We then extend the formulation in 3-D and perform testing in both simulated and real-world to test our approach. In the future, we plan on implementing our algorithm in conjugation with more robust guidance algorithms for fixed-wing UAVs to mitigate abrupt yaw as seen in Fig.7b and Fig.8b. We will also try to extend the gain tuning for fixed-wing UAVs and in 3-D environments using neural networks for efficient collision avoidance.

References

[1] Z. Xiaoning, "Analysis of military application of uav swarm technology," in *2020 3rd International Conference on Unmanned Systems (ICUS)*. IEEE, 2020, pp. 1200–1204.

(a) Path taken by UAV using our vector field (bottom) and using [13] (top) at v = 5m/s

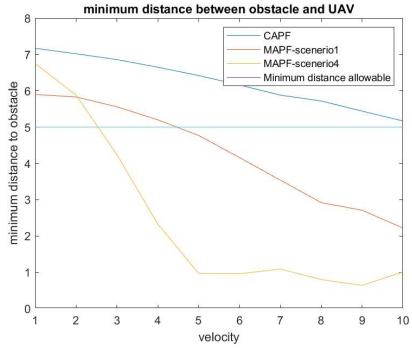

(b) minimum distance between UAV and obstacle during flight

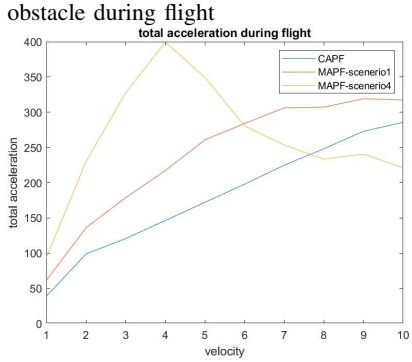

(c) Total acceleration in flight

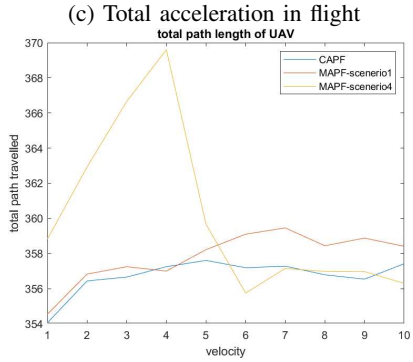

(d) Total distance traveled by the UAV

Fig. 10: Comparitive analysis between MAPF [13] and CAPF

Authorized licensed use limited to: DELHI TECHNICAL UNIV. Downloaded on July 03,2023 at 04:47:02 UTC from IEEE Xplore. Restrictions apply.

(a) Flight trajectory of the UAV

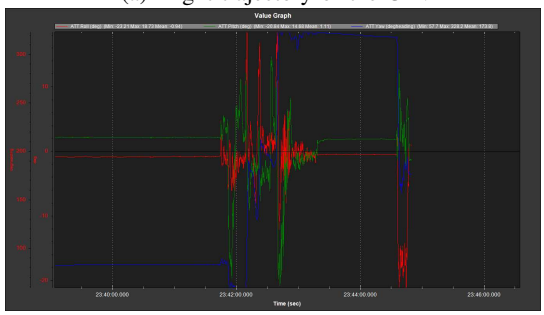

(b) Attitude response of the UAV

Fig. 11: Experimental testing

[2] C. Torresan, A. Berton, F. Carotenuto, S. F. Di Gennaro, B. Gioli, A. Matese, F. Miglietta, C. Vagnoli, A. Zaldei, and L. Wallace, "Forestry applications of uavs in europe: A review," *International Journal of Remote Sensing*, vol. 38, no. 8-10, pp. 2427–2447, 2017.

[3] F. L. L. Medeiros and J. D. S. Da Silva, "A dijkstra algorithm for fixed-wing uav motion planning based on terrain elevation," in *Advances in Artificial Intelligence–SBIA 2010: 20th Brazilian Symposium on Artificial Intelligence, São Bernardo do Campo, Brazil, October 23-28, 2010. Proceedings 20*. Springer, 2010, pp. 213–222.

[4] B. Araki, J. Strang, S. Pohorecky, C. Qiu, T. Naegeli, and D. Rus, "Multi-robot path planning for a swarm of robots that can both fly and drive," in *2017 IEEE International Conference on Robotics and Automation (ICRA)*, 2017, pp. 5575–5582.

[5] K. Naderi, J. Rajamäki, and P. Hämäläinen, "Rt-rrt* a real-time path planning algorithm based on rrt," in *Proceedings of the 8th ACM SIGGRAPH Conference on Motion in Games*, 2015, pp. 113–118.

[6] Z. Lin, L. Castano, and H. Xu, "A fast obstacle collision avoidance algorithm for fixed wing uas," in *2018 International Conference on Unmanned Aircraft Systems (ICUAS)*. IEEE, 2018, pp. 559–568.

[7] J. George and D. Ghose, "A reactive inverse pn algorithm for collision avoidance among multiple unmanned aerial vehicles," in *2009 American Control Conference*. IEEE, 2009, pp. 3890–3895.

[8] A. Lombard, L. Durand, and S. Galland, "Velocity obstacle based strategy for multi-agent collision avoidance of unmanned aerial vehicles," in *2020 IEEE International Conference on Sensing, Communication and Networking (SECON Workshops)*. IEEE, 2020, pp. 1–6.

[9] O. Khatib, "Real-time obstacle avoidance for manipulators and mobile robots," *Autonomous robot vehicles*, pp. 396–404, 1990.

[10] "Tangent navigated robot path planning strategy using particle swarm optimized artificial potential field," *Optik*, vol. 158, pp. 639–651, 2018.

[11] T. Chen, X. Lv, S. Wang, N. Ta, J. Zhao, X. Chen, M. Xiao, and H. Wei, "Research on improved potential field ant colony algorithm for uav path planning," in *2021 33rd Chinese Control and Decision Conference (CCDC)*, 2021, pp. 535–539.

[12] H. Rezaee and F. Abdollahi, "Adaptive artificial potential field approach for obstacle avoidance of unmanned aircrafts," in *2012 IEEE/ASME International Conference on Advanced Intelligent Mechatronics (AIM)*. IEEE, 2012, pp. 1–6.

[13] A. Batinovic, J. Goricanec, L. Markovic, and S. Bogdan, "Path planning with potential field-based obstacle avoidance in a 3d environment by an unmanned aerial vehicle," in *2022 International Conference on Unmanned Aircraft Systems (ICUAS)*, 2022, pp. 394–401.

[14] T. J. Stastny, G. A. Garcia, and S. S. Keshmiri, "Collision and obstacle avoidance in unmanned aerial systems using morphing potential field navigation and nonlinear model predictive control," *Journal of Dynamic Systems, Measurement, and Control*, vol. 137, no. 1, 2015.

[15] T. J. Stastny, G. Garcia, and S. Keshmiri, "Robust three-dimensional collision avoidance for fixed-wing unmanned aerial systems," in *AIAA Guidance, Navigation, and Control Conference*, 2015, p. 1988.

[16] "Vector field-based collision avoidance for moving obstacles with time-varying elliptical shape," *IFAC-PapersOnLine*, vol. 55, no. 37, pp. 587–592, 2022, 2nd Modeling, Estimation and Control Conference MECC 2022.

[17] J. Sun, J. Tang, and S. Lao, "Collision avoidance for cooperative uavs with optimized artificial potential field algorithm," *IEEE Access*, vol. 5, pp. 18 382–18 390, 2017.

[18] A. Rahmani, K. Kosuge, T. Tsukamaki, and M. Mesbahi, "Multiple uav deconfliction via navigation functions," in *AIAA Guidance, Navigation and Control Conference and Exhibit*, 2008, p. 6626.

[19] H. Chen, K. Chang, and C. S. Agate, "Uav path planning with tangent-plus-lyapunov vector field guidance and obstacle avoidance," *IEEE Transactions on Aerospace and Electronic Systems*, vol. 49, no. 2, pp. 840–856, 2013.

[20] D. Mellinger and V. Kumar, "Minimum snap trajectory generation and control for quadrotors," in *2011 IEEE international conference on robotics and automation*. IEEE, 2011, pp. 2520–2525.

[21] E. Tal, G. Ryou, and S. Karaman, "Aerobatic trajectory generation for a vtol fixed-wing aircraft using differential flatness," *arXiv preprint arXiv:2207.03524*, 2022.

[22] L. A. A. Pereira, A. H. D. Nunes, A. M. C. Rezende, V. M. Gonçalves, G. V. Raffo, and L. C. A. Pimenta, "Collision-free vector field guidance and mpc for a fixed-wing uav," in *2021 IEEE International Conference on Robotics and Automation (ICRA)*, 2021, pp. 176–182.

[23] D. Turra, L. Pollini, and M. Innocenti, "Moving waypoint-based fuzzy guidance for unmanned aircraft," in *AIAA Guidance, Navigation, and Control Conference and Exhibit*, 2003, p. 5714.

[24] G. A. Garcia, S. S. Keshmiri, and T. Stastny, "Robust and adaptive nonlinear model predictive controller for unsteady and highly nonlinear unmanned aircraft," *IEEE Transactions on Control Systems Technology*, vol. 23, no. 4, pp. 1620–1627, 2015.

Authorized licensed use limited to: DELHI TECHNICAL UNIV. Downloaded on July 03,2023 at 04:47:02 UTC from IEEE Xplore. Restrictions apply.

A Robust Colon Cancer Detection Model Using Deep-Learning

Vanishka Kadian
Department of Information Technology
Delhi Technological University
New Delhi, India
vanishka.kadian22@gmail.com

Arushi Singh
Department of Information Technology
Delhi Technological University
New Delhi, India
arushi10122000@gmail.com

Kapil Sharma, Senior Member, IEEE
Department of Information Technology
Delhi Technological University
New Delhi, India
kapil@ieee.org

2023 Third International Conference on Secure Cyber Computing and Communication (ICSCCC) | 979-8-3503-0071-0/23/$31.00 ©2023 IEEE | DOI: 10.1109/ICSCCC58608.2023.10176535

***Abstract*—Colon cancer is the third most common cancer, with a high mortality rate and a high pathological need for early and accurate diagnosis. Histopathology is a golden standard tool for diagnosing almost all types of cancer, including colon cancer. It can be enhanced using deep learning techniques if the key challenges, namely, clean data annotation and inter-observer variability, are addressed. This highlights a need for a noise-robust algorithm with computational feasibility to work on real-world clinical data. In this paper, the experiment uses different deep learning models– ResNet-34, XCiT, SqueezeNet, MobileNet– individually integrated with a data cleaning architecture in an attempt to (1) achieve unmatched accuracy, (2) draw a comparison amongst the performance of these models and (3) point to the best model as a solution to the given problem. MobileNet outperforms all other models as the backbone for the algorithm, achieving the highest accuracy (84.39%), thus boosting the algorithm performance on the Chaoyang dataset.**

***Index Terms*—Image Classification, Noise handling, Deep-learning, Colon cancer**

I. Introduction

Cancer is a leading cause of death all over the world, accounting for 10 million deaths every year. Colorectal cancer is the third most common cancer, accounting for an estimated 1.8 million mortality cases annually. Although this death rate is higher in Western countries, growing urbanization has also led to a rapid increase in developing countries.

The early pathological diagnosis of colon cancer is crucial for reducing mortality and enhancing treatment efficiency. Studies suggest that post-detection and treatment, the five-year survival rate for early-stage colon cancer is estimated as high as 90%, whereas late-stage colon cancer can be as low as 12%. Histopathology is an essential means for cancer diagnosis, allowing for the microscopic examination of tissue samples to identify cancerous cells and determine the stage and type of cancer. For diagnosis, a sample of suspicious cells and tissues is taken, and the nature of the abnormality is identified. If found malignant, it requires classification of the type of cancer and its grade. However, the microscopic evaluation of a large number of tissue samples can be tedious and time-consuming. Thus, the enormously increasing number of colonoscopy examinations is significantly straining the healthcare system.

Additionally, the accuracy of histopathology is highly dependent on the expertise and experience of pathologists and can lead to conflict in the biopsy results due to interobserver variability. The pathological standards for the diagnosis of colon lesions are also not standardized. Western pathologists diagnose cancer by observing the invasion through the muscularis mucosa into the submucosa. In contrast, Eastern pathologists rely on identifying nuclear and architectural changes in cells. Therefore, there is a requirement for a more unified approach to bringing consensus among specialists.

Developing deep learning methods to assist pathologists in improving the accuracy, consistency, and promptness of cancer diagnosis is a widely accepted solution. Deep learning algorithms extract information from complex images and can predict clinical outcomes directly from histological images of colorectal cancer. A Japanese study recently showcased relatively good accuracy of a classification algorithm compared to human pathologists in categorizing colorectal tumours [1]. Further, a German study demonstrated the application of a deep-learning-based model for the prediction of survival of colorectal cancer patients using histopathology images [1]. The application of image classification, segmentation, anomaly detection, and transfer learning has shown promising results, but several limitations still need to be addressed.

The first limitation is that deep learning algorithms require extensive amounts of annotated data to be trained accurately, but the annotation process can be challenging. In a real medical scenario, collecting a large dataset with clean labels is difficult, as mislabeling is nearly unavoidable in manual annotation. Another limitation is the inter-observer variability that can arise in histopathology, even among experienced pathologists. Samples wherein labelling is conflicted are termed hard samples. This variability can make it difficult to develop deep learning algorithms that are robust and consistent across different data sets and users.

While the hard samples enhance the efficiency and effectiveness of training the models, the noisy labels are misleading and result in lower accuracy. Thus, distinguishing the noisy samples from the hard samples proves essential for attaining good model performance.

Proposing a two-phase Hard Sample Aware Noise Robust Learning (HSA-NRL) algorithm, Zhu et al. [2] attempted to involve hard samples for training while simultaneously reducing noise interference. Prediction history for the samples was

Authorized licensed use limited to: DELHI TECHNICAL UNIV. Downloaded on July 20,2023 at 11:07:13 UTC from IEEE Xplore. Restrictions apply.

used as a key for their differentiation and a self-trained noisy label correction architecture, followed by steps to suppress the noise and enhance the hard samples. The algorithm used the ResNet-34 [3] model as the backbone on the Chaoyang dataset [4].

This paper uses the network pipeline designed by Zhu et al. [2] while replacing the backbone with different models like – Cross-Covariance Image Transformer (XCiT) [5], SqueezeNet [6], and MobileNet [7] on the Chaoyang dataset. The experiment aims to achieve an outperforming test accuracy against that achieved using ResNet-34. A comparative analysis has been conducted between these models based on performance in terms of test accuracy. The work concludes by identifying the best model to be integrated with the noise robust algorithm for real-world pathological image classification without the requirement of cleaning annotations.

This remaining paper is divided into five sections. Section II describes existing works on histopathology image processing, its application in colon cancer detection and the algorithms for handling noisy data. Section III explains the two-phased architecture used and the integrated deep-learning models. Section IV comprises three subsections: dataset description, implementation and parameter settings, and the evaluation criteria. Results are tabulated and discussed in Section V. Finally, the conclusion and future scope are given in Section VI.

II. Related Works

In the field of histopathology, pathologist fatigue, the intricacy of the tissue structure, and numerous other factors negatively impact the accuracy of cancer diagnosis, as suggested by Wang et al. [8]. Lusted [9] was the first to see the potential of computers in medical diagnosis in 1955. Since then, the emergence of deep learning (DL) methods has changed the field altogether. For improving the accuracy and spontaneity in the disciplines of histopathological image processing, convolutional neural network (CNN), one of the DL approaches, has been extensively applied, as presented by Xu et al. [10], and Li et al. [11]. In several publications, DL models are proposed to categorize histopathology images [12]– [15], including colorectal histology images [16]- [18].

Zhu et al. [12] showcased significant harm in model performance due to over-pruning. Caicedo et al. [13] proposed various representations for classifying histopathology images using the bag of features method. However, the performance degraded as the size of the code block increased. Xue et al. [14] built a new conditional generative adversarial network (cGAN) model called HistoGAN for high-fidelity histopathology image synthesis, and a synthetic augmentation approach with quality assurance was suggested. In the work of Coudray et al. [15], a DL model for the automatic analysis of lung tumour slides was developed. However, it did not perform well for other cancers or datasets. Masud et al. [16] proposed a unique supervised learning method based on DL that could classify five distinct cancerous and non-cancerous tissue types in lung and colon cancers. Gessert et al. [17] noted the possibility of identifying colon cancer in conventional light microscopy (CLM) images using CNNs and other transfer learning scenarios. However, he concluded that there was no single transfer method ideal for all CLM classification problems. Rahman et al. [18] proposed feature selection for colon cancer classification using the Best first search method and Artificial Neural Networks (ANNs), showcasing several benefits, including the ability to handle large data, less classification time and a lower probability of missing important information.

Behzadi et al. [19] enabled clinical-grade tissue classification and diagnosis accuracy while enabling computationally efficient analysis of large-scale whole slide imaging (WSI) datasets. However, all these works assumed the availability of large clean annotated datasets for model training. In manual annotation, noisy labels are frequently unavoidable and can adversely affect the performance of the algorithms.

Wei et al. in [20] suggested that designing robust algorithms for noisy labelling is crucial. Various approaches can typically be divided into three families of models: estimating the noise transition matrix [21], [22], constructing noise-robust loss functions [23]– [25], and estimating true labels [26]– [28]. Hendrycks et al. [21] and Patrini et al. [22] put forth various strategies for estimating transition matrices, including using trusted samples in a data-efficient manner and using a two-step estimating scheme, respectively. However, these models were also unsuccessful with real-medical datasets.

The second family of models aimed at designing loss functions with greater noise tolerance. Gehlot et al. [23] introduced projection loss to maximize the projection of a sample's activation on the corresponding class vector in addition to imposing orthogonality constraints on the class vectors. This created a dual-branch architecture that boosted performance and handled noise. Wang et al. [24] proposed learning with noisy labels by adopting a Symmetric Cross Entropy (SCE) loss function that outperformed several existing methods in terms of accuracy and stability. However, this method observed poor generalization performance. DivideMix is a framework introduced by Socher et al. [25] that uses semi-supervised learning techniques to enhance the accuracy of a model by learning with noisy labels.

The third category focused on selecting possibly clean labels and correcting noisy labels. Tanaka et al. [26] suggested a joint optimization strategy for predicting true labels and learning parameters. The label correction was done by altering updates to the labels and the parameters during training. Yi et al. [27] published a paper proposing a Probabilistic end-to-end architecture for updating network parameters and label estimations as label distributions. Due to its independence from the backbone network structure and lack of requirements for a clean auxiliary dataset or prior knowledge of noise, this architecture was more robust and simple to use. However, due to their sensitivity to hyperparameters, [26], [27] faced limitations in their performance. The work of Goldberger et al. [28] suggested an expectation-maximization (EM) algorithm to determine the network and noise parameters and estimate the

Authorized licensed use limited to: DELHI TECHNICAL UNIV. Downloaded on July 20,2023 at 11:07:13 UTC from IEEE Xplore. Restrictions apply.

correct label. Adding a second softmax output layer that linked the correct labels to the noisy ones made the algorithm easily integrable with any deep-learning implementation. In contrast to [27], [28] allowed the dataset to be trained on noisy data.

III. Methodology

This work uses a two-phased architecture: Phase I produces an almost clean dataset by label correction, and Phase II uses this generated dataset to give a robust classification model.

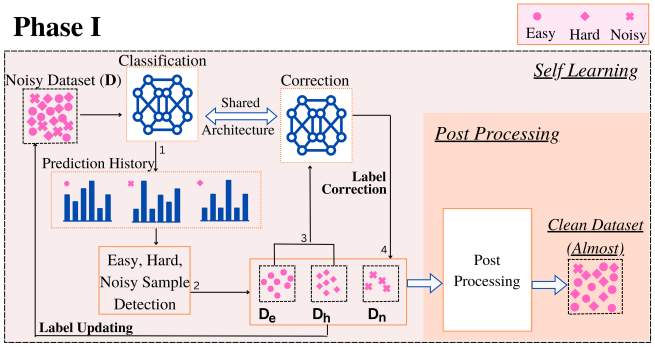

Fig. 1. Phase I of the architecture: produces an almost clean dataset using iterative self learning steps (obtain prediction behavior; generate Easy, Hard, Noisy subsets; train correction model; update labels) and the post processing action.

As depicted in Fig. 1, Phase I of the architecture comprises two steps: Self Learning and Post Processing.

During Self Learning, a Bayesian Classifier is trained on the original noisy dataset, denoted by D. A prediction history for all samples is obtained over all epochs and mean of the prediction history is calculated to detect Easy, Hard, and Noisy samples. Compared to noisy samples, the clean samples have a higher mean prediction value. Hence, by applying a threshold, some clean samples can be extracted. These samples are called 'easy' samples. The samples below the threshold may be noisy or clean. The clean samples below the threshold are called 'Hard' samples and must be further distinguished.

The subset of easy samples, denoted by De is used, and some labels are switched to add noise. The noise ratio of this thus-created subset will be the same as the original dataset. Therefore, the noisy subset is used to train a convolutional neural network (CNN) classification model, generating a new training history according to which the easy samples are discarded. A multilayer perceptron (MLP) classifier is trained on the training history of the remaining (noisy and hard) samples and a corresponding set of labels stating whether they are hard or noisy. Post training, the MLP classifier can distinguish the samples below the threshold in D into 'hard' and 'noisy' subsets, denoted by Dh and Dn respectively.

The next part of Self Learning accounts for label correction. The Correction model is trained using De and Dh and some noisy labels are corrected. From the model output, the most probable class is chosen as the pseudo label to replace the labels of hard and noisy samples. The labels are updated and the entire self-learning process is repeated to purify the dataset.

The next step of Phase I comprises the Post Training Action, which aims to discard the samples that could not be corrected and thus remained noisy even post the Self Learning steps. These are the samples from the Dn for which the labels were not changed and the samples from Dh for which the labels were changed. Discarding these samples generates an almost clean dataset.

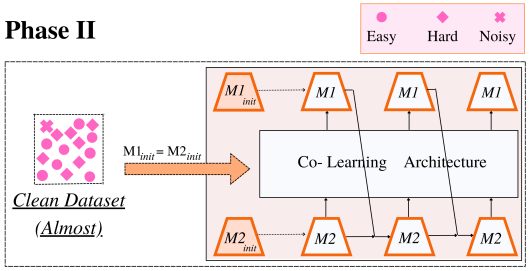

Fig. 2. Phase II of the architecture: co-trains two models using the resulting dataset, updating their parameters by back-propagation and momentum coefficient value.

Phase II of the architecture enhances hard samples and suppresses noise, as shown in Fig. 2. The hard samples are proven to improve the efficiency of training of the model, while the noisy samples are misleading and result in poor accuracy. This phase uses a co-learning architecture to avoid confirmation bias. Two models, M1 and M2 are initialized with the same parameters(M1_init= M2_init) but adopt different parameter updating schemes. This further suppresses the interference of noisy samples. The parameter for the first model is updated by backpropagation, while the second model uses momentum coefficient value. M2 selects training data for M1 at each epoch by discarding the samples with lower prediction probabilities. Further, the focal loss is used to emphasize the hard sample subset. The focal loss was calculated using the predicted probability of the actual class and a hyper-parameter.

The following deep-learning models are individually used and replaced as the backbones for the algorithm:

1) ResNet-34 developed by K. He et al. [3] is a convolutional neural network with 34 layers. It utilizes the residuals from each layer in the subsequent connected layers, hence training deep networks and minimizing the percentage of errors.
2) XciT, proposed by Nouby et al. [5], operates across feature channels instead of tokens. It leverages the cross-covariances matrix between keys and queries for interactions.
3) SqueezeNet, given by Iandola et al. [6], reduces the number of parameters by applying design techniques, particularly the usage of fire modules that "squeeze" parameters using 1x1 convolutions.
4) MobileNet by Howard et al. [7] introduces the use of two global hyper-parameters. These parameters enable an efficient balance between latency and accuracy while incorporating a streamlined architecture that em-

Authorized licensed use limited to: DELHI TECHNICAL UNIV. Downloaded on July 20,2023 at 11:07:13 UTC from IEEE Xplore. Restrictions apply.

ploys depth-wise separable convolutions for developing lightweight deep neural networks.

IV. Experiment Implementation

A. Dataset

The Chaoyang dataset comprises Colon slide samples for training and testing with the following domination: 1111 normal, 842 serrated, 1404 adenocarcinoma, 664 adenomas, and 705 normal, 321 serrated, 840 adenocarcinomas, 273 adenomas, respectively. This noisy dataset was created by collecting data from Chaoyang hospital, China. These are colon slides with a 512 × 512 patch size. Three expert pathologists labeled the patches. Conflicted labeling was observed for about 40% of the samples. We used the portion of labeled patches with the three pathologists' consensus as the testing set. The remaining samples, with inconsistent labeling, were used as the training set with a random selection of one of the suggested labels. Fig. 3 shows the sample patches of the Chaoyang dataset.

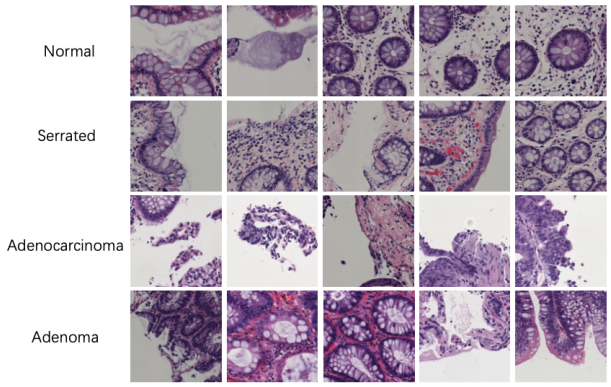

Fig. 3. The Chaoyang Dataset

B. Implementation and Parameter settings

We employed the four models - ResNet-34, XCiT, MobileNet, and SqueezeNet on the Chaoyang dataset and trained it using Adam with a momentum of 0.9 and a batch size of 16. During both, Phase I and Phase II, the networks were trained for 80 epochs. Furthermore, after 30 epochs, the learning rates were linearly reduced, the initial value being 0.001.

For the Chaoyang dataset, the noise cross-validation approach given by Chen et al. [29] was used to compute the dataset noise ratio, ρ. The easy sample threshold was set to 0.1 for an 80% noise ratio. The hyper-parameter used to calculate the focal loss was set to 2, and the discarding ratio was set to $0.1 * \rho$.

C. Evaluation Criteria

For each model, the Test Accuracy (ACC), Precision, Recall, and F1 Score (F1), as defined below, have been used as the evaluation criteria:

$$ACC = \frac{TP + TN}{TP + TN + FP + FN} \quad (1)$$

$$Precision = \frac{TP}{TP + FP} \quad (2)$$

$$Recall = \frac{TP}{TP + FN} \quad (3)$$

$$F1 = \frac{2 * Precision * Recall}{Precision + Recall} \quad (4)$$

where TP, TN, FP, and FN represent true positives, true negatives, false positives, and false negatives, respectively.

V. Results And Discussions

In the network pipeline of the HSA-NRL algorithm for histopathology image classification, we introduced new backbones to analyze the performance of the latest deep learning models on replacing ResNet-34 in the algorithm. The four models—ResNet-34, XCiT, Squeezenet, and Mobilenet—were initially trained using the same dataset (The Chaoyang dataset). The models were trained on 4021 sample images, followed by processing and cleaning, which generated 4019 clean images. Out of these, 2139 almost clean images were used for testing.

TABLE I
ACC, Precision, Recall, F1 Score of the models used

Model	*ACC*	*Precision*	*Recall*	*F1*
ResNet-34	83.40	78.33	75.45	76.54
XCiT	80.83	75.82	75.01	75.41
SqueezeNet	78.07	74.42	73.01	73.71
MobileNet	84.39	81.79	79.67	80.73

Table I presents a detailed comparison of the model performances, listing respective test Accuracy, Precision, Recall, and F1 Scores for our experiment on the Chaoyang dataset. The network with MobileNet as the backbone consistently outperforms the other models on all these metrics.

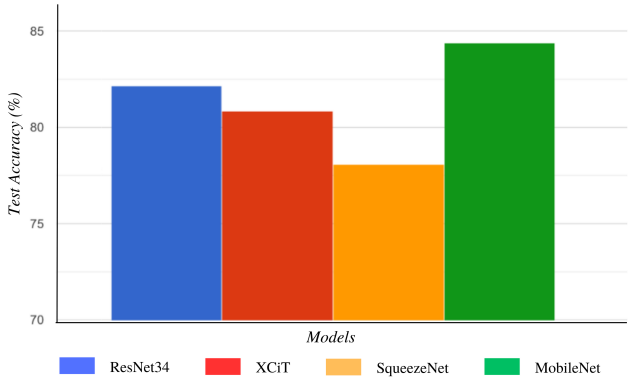

Fig. 4. Bar graph depicting the test accuracies on the Chaoyang dataset for ResNet-34, XCiT, SqueezeNet, and MobileNet models.

The performance of the algorithm when integrated with MobileNet exceeds those when integrated with ResNet-34, SqueezeNet, and XCiT with a test accuracy of 84.39%, as depicted in Fig. 4.MobileNet beats the previous state-of-the-art performance of ResNet-34 by 0.99% It is also observed

Authorized licensed use limited to: DELHI TECHNICAL UNIV. Downloaded on July 20,2023 at 11:07:13 UTC from IEEE Xplore. Restrictions apply.

that on using MobileNet, in Phase II of the architecture, both M1 and M2 of the co-learning architecture give maximum accuracy and negligible loss.

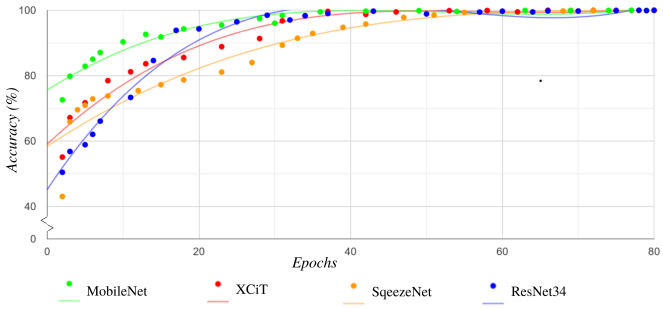

Fig. 5. Plot of accuracy v/s epochs for ResNet-34, XCiT, SqueezeNet, and MobileNet models.

A plot has been curated, Fig. 5, depicting a comparison of accuracy trends among models. Here, the vertical axis represents the accuracy, and the horizontal axis represents the number of epochs. MobileNet outperforms other models in terms of all the evaluation metrics.

VI. Conclusion

This paper presents an analysis of the performance of different deep-learning models integrated with the HSA-NRL algorithm on colon slide samples. The three models analyzed are XCiT, MobileNet, and SqueezeNet and are compared with the ResNet-34, the originally used model in the algorithm. The paper presents a comprehensive performance evaluation based on test accuracy, precision, recall, and F1 score. Model XCiT as the backbone of the network performs reasonably well and achieves comparable values to ResNet-34. The analysis shows that Mobilenet when used in the architecture outperforms other models and has significantly boosted the overall performance from an accuracy of 83.40% to a newly achieved 84.39%.

Additionally, Mobilenet is a lightweight and fast model that uses less computational power and time. This work hence proposes an improved noise robust architecture for colon cancer detection. The obtained results are only based on the models' performances on the Chaoyang dataset, which can be treated as a limitation of our study. Thus, the necessity to apply these models to other medical areas is highlighted for future works.

References

[1] N. Thakur, H. Yoon, and Y. Chong, "Current trends of artificial intelligence for colorectal cancer pathology image analysis: A systematic review," Cancers, vol. 12, no. 7, 2020. [Online]. Available: https://www.mdpi.com/2072-6694/12/7/1884

[2] C. Zhu, W. Chen, T. Peng, Y. Wang, and M. Jin, "Hard sample aware noise robust learning for histopathology image classification," IEEE Transactions on Medical Imaging, vol. 41, no. 4, pp. 881–894, 2021.

[3] K. He, X. Zhang, S. Ren, and J. Sun, "Deep residual learning for image recognition," in Proceedings of the IEEE conference on computer vision and pattern recognition, 2016, pp. 770–778.

[4] Chaoyang University of Technology, "Chaoyang dataset," 2021. [Online]. Available: https://bupt-ai-cz.github.io/HSA-NRL/

[5] A. Ali, H. Touvron, M. Caron, P. Bojanowski, M. Douze, A. Joulin, I. Laptev, N. Neverova, G. Synnaeve, J. Verbeek et al., "Xcit: Cross-covariance image transformers," Advances in neural information processing systems, vol. 34, pp. 20 014–20 027, 2021.

[6] F. N. Iandola, S. Han, M. W. Moskewicz, K. Ashraf, W. J. Dally, and K. Keutzer, "Squeezenet: Alexnet-level accuracy with 50x fewer parameters and¡ 0.5 mb model size," arXiv preprint arXiv:1602.07360, 2016.

[7] A. G. Howard, M. Zhu, B. Chen, D. Kalenichenko, W. Wang, T. Weyand, M. Andreetto, and H. Adam, "Mobilenets: Efficient convolutional neural networks for mobile vision applications," arXiv preprint arXiv:1704.04861, 2017.

[8] Z. Wang, M. Li, H. Wang, H. Jiang, Y. Yao, H. Zhang, and J. Xin, "Breast cancer detection using extreme learning machine based on feature fusion with cnn deep features," IEEE Access, vol. 7, pp. 105 146– 105 158, 2019.

[9] L. B. Lusted, "Medical electronics," New England Journal of Medicine, vol. 252, no. 14, pp. 580–585, 1955.

[10] Y. Xu, Z. Jia, L.-B. Wang, Y. Ai, F. Zhang, M. Lai, E. I. Chang et al., "Large scale tissue histopathology image classification, segmentation, and visualization via deep convolutional activation features," BMC bioinformatics, vol. 18, no. 1, pp. 1–17, 2017.

[11] J. Li, W. Li, A. Sisk, H. Ye, W. D. Wallace, W. Speier, and C. W. Arnold, "A multi-resolution model for histopathology image classification and localization with multiple instance learning," Computers in biology and medicine, vol. 131, p. 104253, 2021.

[12] C. Zhu, F. Song, Y. Wang, H. Dong, Y. Guo, and J. Liu, "Breast cancer histopathology image classification through assembling multiple compact cnns," BMC medical informatics and decision making, vol. 19, no. 1, pp. 1–17, 2019.

[13] J. C. Caicedo, A. Cruz, and F. A. Gonzalez, "Histopathology image classification using bag of features and kernel functions," in Artificial Intelligence in Medicine: 12th Conference on Artificial Intelligence in Medicine, AIME 2009, Verona, Italy, July 18-22, 2009. Proceedings 12. Springer, 2009, pp. 126–135.

[14] Y. Xue, J. Ye, Q. Zhou, L. R. Long, S. Antani, Z. Xue, C. Cornwell, R. Zaino, K. C. Cheng, and X. Huang, "Selective synthetic augmentation with histogan for improved histopathology image classification," Medical image analysis, vol. 67, p. 101816, 2021.

[15] N. Coudray, P. S. Ocampo, T. Sakellaropoulos, N. Narula, M. Snuderl, D. Fenyo, A. L. Moreira, N. Razavian, and A. Tsirigos, "Classification and mutation prediction from non–small cell lung cancer histopathology images using deep learning," Nature medicine, vol. 24, no. 10, pp. 1559–1567, 2018.

[16] M. Masud, N. Sikder, A.-A. Nahid, A. K. Bairagi, and M. A. AlZain, "A machine learning approach to diagnosing lung and colon cancer using a deep learning-based classification framework," Sensors, vol. 21, no. 3, p. 748, 2021.

[17] M. A. Rahman and R. C. Muniyandi, "Feature selection from colon cancer dataset for cancer classification using artificial neural network," International Journal on Advanced Science, Engineering and Information Technology, vol. 8, no. 4-2, pp. 1387–1393, 2018.

[18] N. Gessert, M. Bengs, L. Wittig, D. Dromann, T. Keck, A. Schlaefer, and D. B. Ellebrecht, "Deep transfer learning methods for colon cancer classification in confocal laser microscopy images," International journal of computer assisted radiology and surgery, vol. 14, pp. 1837–1845, 2019.

[19] M. M. Behzadi, M. Madani, H. Wang, J. Bai, A. Bhardwaj, A. Tarakanova, H. Yamase, G. H. Nam, and S. Nabavi, "Weakly-supervised deep learning model for prostate cancer diagnosis and gleason grading of histopathology images," arXiv preprint arXiv:2212.12844, 2022.

[20] Y. Wei, C. Gong, S. Chen, T. Liu, J. Yang, and D. Tao, "Harnessing side information for classification under label noise," IEEE Transactions on Neural Networks and Learning Systems, vol. 31, no. 9, pp. 3178–3192, 2019.

[21] Z. Hameed, S. Zahia, B. Garcia-Zapirain, J. Javier Aguirre, and A. Maria Vanegas, "Breast cancer histopathology image classification using an ensemble of deep learning models," Sensors, vol. 20, no. 16, p. 4373, 2020.

[22] G. Patrini, A. Rozza, A. Krishna Menon, R. Nock, and L. Qu, "Making deep neural networks robust to label noise: A loss correction approach," in Proceedings of the IEEE conference on computer vision and pattern recognition, 2017, pp. 1944–1952.

[23] S. Gehlot, A. Gupta, and R. Gupta, "A cnn-based unified framework utilizing projection loss in unison with label noise handling for multiple

Authorized licensed use limited to: DELHI TECHNICAL UNIV. Downloaded on July 20,2023 at 11:07:13 UTC from IEEE Xplore. Restrictions apply.

myeloma cancer diagnosis," Medical Image Analysis, vol. 72, p. 102099, 2021.
[24] Y. Wang, X. Ma, Z. Chen, Y. Luo, J. Yi, and J. Bailey, "Symmetric cross entropy for robust learning with noisy labels," in Proceedings of the IEEE/CVF International Conference on Computer Vision, 2019, pp. 322–330.
[25] J. Li, R. Socher, and S. C. Hoi, "Dividemix: Learning with noisy labels as semi-supervised learning," arXiv preprint arXiv:2002.07394, 2020.
[26] D. Tanaka, D. Ikami, T. Yamasaki, and K. Aizawa, "Joint optimization framework for learning with noisy labels," in Proceedings of the IEEE conference on computer vision and pattern recognition, 2018, pp. 5552–5560.
[27] K. Yi and J. Wu, "Probabilistic end-to-end noise correction for learning with noisy labels," in Proceedings of the IEEE/CVF Conference on Computer Vision and Pattern Recognition, 2019, pp. 7017–7025.
[28] J. Goldberger and E. Ben-Reuven, "Training deep neural-networks using a noise adaptation layer," in International conference on learning representations, 2017.
[29] P. Chen, B. B. Liao, G. Chen, and S. Zhang, "Understanding and utilizing deep neural networks trained with noisy labels," in International Conference on Machine Learning. PMLR, 2019, pp. 1062–1070

Authorized licensed use limited to: DELHI TECHNICAL UNIV. Downloaded on July 20,2023 at 11:07:13 UTC from IEEE Xplore. Restrictions apply.

2023 4th International Conference for Emerging Technology (INCET)
Belgaum, India. May 26-28, 2023

A SEPIC PFC fed LLC Resonant converter For EV Battery Charger Applications

Satyamit Kumar
Department of Electrical Engineering
Delhi Technological University
Delhi, India
satyamitmano@gmail.com

Narendra Kumar
Department of Electrical Engineering
Delhi Technological University
Delhi, India
narendrakumar@dtu.ac.in

2023 4th International Conference for Emerging Technology (INCET) | 979-8-3503-3575-0/23/$31.00 ©2023 IEEE | DOI: 10.1109/INCET57972.2023.10170716

***Abstract*— The majority of two-stage converters for charging electric vehicle batteries include a boost converter for power factor correction (PFC) preceded by a dc-dc converter with unified input voltage. These two-stage conversions have limited capability and a function estimation count. Therefore, in this paper, a PFC-SEPIC fed LLC resonant converter for an on-board private charging unit is proposed. The PFC-SEPIC converter at the input stage is intended to function in continuous conduction mode (CCM) and enhances power quality execution on alternating current mains for a vast span of output voltages. The design for V_S = 85V and TDD less than 3.895% for varied input voltages and battery voltages at different loads, is affirmed using MATLAB/SIMULINK.**

Keywords*— *Active power factor controller (APFC), Electric vehicle battery charger, LLC resonant converter, Pulse frequency modulation (PFM), single-ended primary inductance converter (SEPIC).

I. INTRODUCTION

The automotive trade is currently undergoing a significant revolution due to the increasing concerns for environmental sustainability and energy security, as well as the rapid advancements in powertrain electrification technologies. The rapid growth of electric mobility is seen as one of the most crucial aspects of this transformation, which has the potential to revolutionize the industry. As reported by the German Centre for Photovoltaic and Hydrogen Study (ZSW), at the onset of 2019, there had been 5.6 million of EVs on the network, with 2.6 million and 1.1 million, including both, China & US control the lion's share of the market. That according to recent market research, there's going to be over one billion EVs on the streets by 2040-2050 [1]. However, EV sales are reportedly stagnant due to high battery costs, overcomplicated charger design features, and unsatisfactory charging infrastructure. As a necessary consequence, there is an urgent need for a more creative and effective charging procedure.

Electric vehicles (EVs) are powered by lithium-ion battery packs, with voltage levels ranging from 400 to 450 V for larger vehicles and 48 V battery packs for smaller vehicles like golf carts and E-Rickshaws [2]. Chargers with power outputs ranging from 1 kW to 3.3 kW are required for these low voltage battery packs. To charge the batteries, an on-board charger (OBC) is connected to a single-phase power supply mains line typically found in households [3], [4]. Accepting 1-ø AC input at 60 Hz or 50 Hz, the OBC transform the differential AC i/p voltage into precise level of Vdc (DC-link voltage) & current expected to charge battery. The OBC necessitates a PFC at front end AC supply to comply with the harmonic limits imposed by IEC ethics [8]. Isolation must also be featured in these chargers to mitigate low-impedance noise and offer short-circuit fortification. A two-stage converter is commonly used for this purpose, with the first stage being a front-end active PFC converter, preceded by a separate Power converter as the second stage[4]–[6].

Fig. 1 depicts the envisaged PFC-SEPIC fed HBLLC Resonant Converter arrangement. In CCM mode, the PFC-SEPIC requires both current and voltage circuits. This converter offers enhanced system efficiency for alternating current mains across an expansive output voltage variety. The chosen technique minimizes both the needed magnetic component size and turn-off losses in the second-stage converter's steep-side switching devices. Additionally, the use of SEPIC converter offers capacitive seclusion and eliminates the inrush current problematic, thereby preventing dips in domestic power supply during EV charging.

This research proposes PFC-SEPIC fed HBLLC Resonant Converter for a two-on-board wheeler's private charger. The isolated DC-DC converter in the on-board charger's second stage has the responsibility for controlling the o/p voltage & current based on the intended battery outline. Half-bridge topologies are commonly used for intermediate-power levels, whereas DAB (Dual Active Bridge) or full bridge modules are used for developed ratings and bidirectional power circulation[7]. Because of its ability to operate with zero-voltage switching (ZVS) over such a wide output voltage range, the LLC resonant converter is a good choice. However, under CC and CV conditions, the load, DC relation, and battery-charging voltage can significantly impact the turn-off losses in the switching devices[8]–[12]. The operating frequency of the converter increases over the resonance frequency when the battery is low on power, the voltage is lower than the nominal voltage (CC mode), or the converter is lightly equipped. This results in increased MOSFET turn-off losses on the primary and secondary sides, leading to a significant reduction in efficiency. Unlike the PFC boost-derived converter in the first stage, the LLC converter can reduce turn-off losses by decreasing input voltage and drawing back the switching frequency towards the resonant frequency.

Authorized licensed use limited to: DELHI TECHNICAL UNIV. Downloaded on July 20,2023 at 11:25:06 UTC from IEEE Xplore. Restrictions apply.

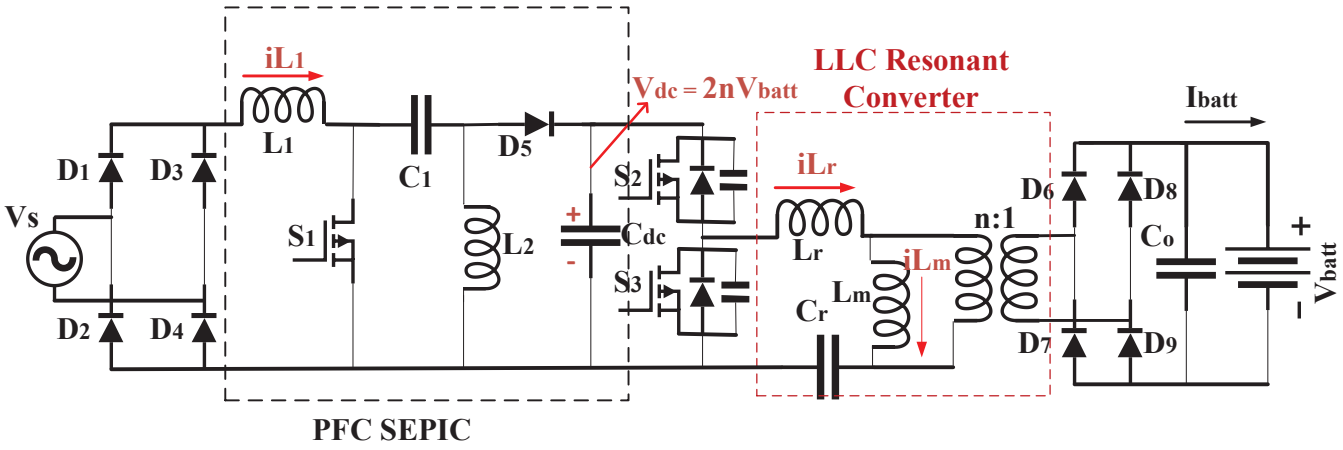

Fig. 1. Proposed PFC-SEPIC fed HBLLC Resonant Converter

II. Design of Proposed Electric Vehicle Battery Charger

The following assumptions are made while designing the parameters for the SEPIC PFC:

1. The devices used here are ideal.
2. Resistor is taken for the battery.

A. Designing of PFC SEPIC Converter

Specifications for designing the parameters of the PFC SEPIC converter are tabulated in Table I.

TABLE I. Specifications considered for Sepic Converter

Parameters	Variables	Values
Supply Frequency	f_{supply}	50 Hz
Switching Frequency	f_{sw}	50kHz
Supply Voltage	V_s	220V
DC-link Voltage	V_{dc}	300 V
Voltage ripple	ΔV_{dc}	1.5 %
I/P inductor current ripple	ΔI_{Li}	20%
Output Power	P_o	1 kW

Assuming a constant voltage of Vdc for the dc-link, disregarding any fluctuations in voltage ripple across the DC-link capacitor, the duty cycle variation of the SEPIC in a stable condition can be expressed as follows,

$$d(t) = \frac{V_{dc}}{V_{dc} + V_P|\sin(wt)|}$$

In which VP represents line voltage's peak value, and angular frequency of the power line is represented by ω, typically set at 100π radians per second.

The duty cycle has the following range,

$$\frac{V_{dc}}{V_{dc} + V_{savg}} \leq d(t) \leq 1$$

The mean value of the input supply voltage, denoted as Vsavg, is determined by the following calculation, assuming a nominal input voltage.

$$V_{savg} = \frac{2\sqrt{2}V_s}{\pi} = \frac{2\sqrt{2} \times 220}{\pi} = 198V$$

Putting the values of V_{dc} and V_{savg} in the above eq., duty cycle is found to be 0.6.

The inductance values for L1 and L2 can be computed using the following calculation.

$$L_i = \frac{V_{savg} \times d}{\Delta I_{Li} \times f_{sw}}$$

Assuming a current ripple of 20% and a switching frequency of 50 kHz, the inductance values for L1 and L2 are computed to be 2.376 mH.

The capacitance value for the intermediate capacitor denoted as C1, and subject to voltage ripple ΔVC1, is determined using the following calculation.

$$C_1 = \frac{d \times P_o}{\Delta V_{C1} \times V_{dc} \times f_{sw}}$$

Assuming fsw of 50kHz and voltage ripple as 20% of Vdc, an output power of 1 kW, a DC-link voltage of 300 V, and a duty cycle of 0.6, the capacitance value for the intermediate capacitor C1 is calculated to be 667 nF.

The capacitance value for Cdc(DC-link capacitor), subject to ΔVdc and a supply frequency(fsupply), can be determined using the following calculation.

$$C_{dc} = \frac{P_o}{4\pi \times \Delta V_{dc} \times f_{supply} \times V_{dc}}$$

To minimize voltage ripple, a capacitor with a larger value is typically selected. However, this can result in a physically larger capacitor. Therefore, when designing the converter, a trade off b/w ΔVdc and the size of the capacitor must be carefully considered. For example, given a DC-link voltage ripple of 1.5%, the capacitance value for the DC-link capacitor can be calculated to be 1180 µF

A. Specifications of HB-LLC Resonant Converter

Table II tabulates the specifications for determining the component values of a HB-LLC resonant converter.

Authorized licensed use limited to: DELHI TECHNICAL UNIV. Downloaded on July 20,2023 at 11:25:06 UTC from IEEE Xplore. Restrictions apply.

TABLE II. SPECIFICATIONS OF HB-LLC

Parameters	Variables	Values
DC-link bus Voltage	V_{DC}	300V
Optimal battery voltage	V_{batt}	57V
Output Power	P_o	1kW
Resonant Frequency	f_r	100kHz

For EV battery charging, the regulated Vdc is supplied to the HB-LLC converter.n(turns ratio) of the transformer can be computed using the following equation,

$$n = \frac{V_{dc_bus}}{2V_{batt}} = \frac{300}{2 \times 57} = 2.63$$

The resonant current's maximum value, for the converter at the second stage, can be determined using the following calculation,

$$I_{Lr} = \frac{2\pi P_o}{2V_{dc_bus}} = \frac{2\pi \times 1kW}{2 \times 300} = 10.46\ A$$

Assuming a resonance frequency of 100 kHz, the capacitance value for the resonant capacitor can be determined using the following calculation,

$$C_r = \frac{I_{Lr}}{2\pi f_r V_{dc_bus}/2} = \frac{10.46}{2\pi \times 100 \times 10^3 \times 300/2} = 111nF$$

Inductance ratio(m) in this project has been chosen as 5. The resonant and magnetizing inductances can be calculated as,

$$L_r = \frac{1}{(2\pi f_r)^2 C_r} = \frac{1}{(2\pi \times 100 \times 10^3)^2 \times 111n} = 22.8\mu H$$

$$L_m = m \times L_r = 5 \times 22.8\mu H = 114\mu H$$

III. CONTROL TECHNIQUES OF PROPOSED CHARGER

In this work, a two-loop structure of APFC is utilized to improve the power factor. The outer loop controls the DC-link voltage through a voltage control loop. The reference DC-link voltage is generated by measuring the battery voltage, V*dc = 2n*Vbatt, and continuously adjusting the DC-link voltage accordingly. The difference b/w the measured DC-link voltage and the reference DC-link voltage, leads to an error voltage, which is subsequently manipulated using a proportional-integral (PI) controller, in order to produce a modulating current signal. After that the product of this signal and the unit prototype of the AC mains voltage creates the base current for the primary inductor. The PWM gate pulses for the switch in the SEPIC is generated by utilizing the primary inductor current feedback. Following this, the resulting current is compared to the base current, generating a current error signal that is processed using a PI-based current controller.

Furthermore, the secondary stage of the system employs LLC converter, which receives the Vdc and uses a PI voltage controller to regulate the output voltage. The pulses for the switches of the HB-LLC converter is created by the resulting rate signal which is administered by the PFM controller. Fig.2 depicts the control technique used in this two stage EV battery charger.

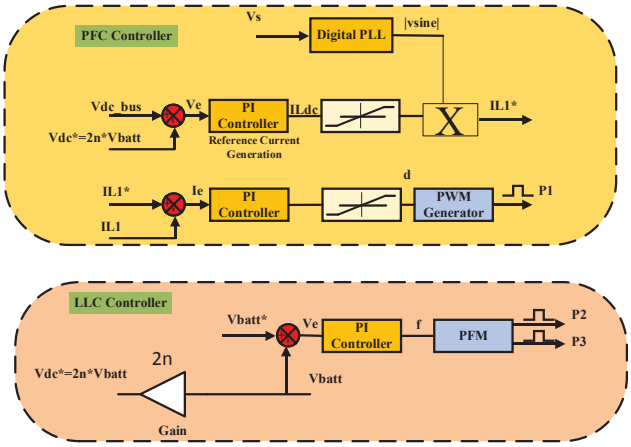

Fig. 2. Control technique of the proposed charger.

IV. SIMULATION RESULT AND DISCUSSION

In order to verify the proposed converter, simulations were conducted using MATLAB/Simulink software. The simulations covered battery voltages for a broader range and different Vs values for various loads. Table III summarizes all the parameters calculated in Section II.

TABLE III. PARAMETERS OF THE PROPOSED CHARGER

Parameters	Variables	Values
Supply Frequency	f_{supply}	50 Hz
Switching Frequency	f_{sw}	50kHz
Supply Voltage	V_s	220V
Output Power	P_o	1 kW
DC-link Capacitor	C_{dc}	1180 *μF*
Resonant frequency	f_r	100kHz
Primary & Secondary Inductors	L_1 & L2	2.376mH
Resonant Inductor	L_r	22.8 *μH*
DC-link Voltage	V_{dc}	300 V
Resonant Capacitor	C_r	111 *nF*
Magnetizing inductor	L_m	*114 μH*

A. Validation of the broad voltage(Vbatt) range and the DC-link voltage(Vdc)

The simulations were performed over a range of Vbatt and Vs for various loads. The Vdc is designed to track the Vbatt, which is expressed by V*dc = 2nVbatt. The simulation results indicate that at Vbatt = 80V, the Vdc-bus = 419V, while at Vbatt = 48V, the Vdc-bus = 250V. This is shown in Fig. 3.

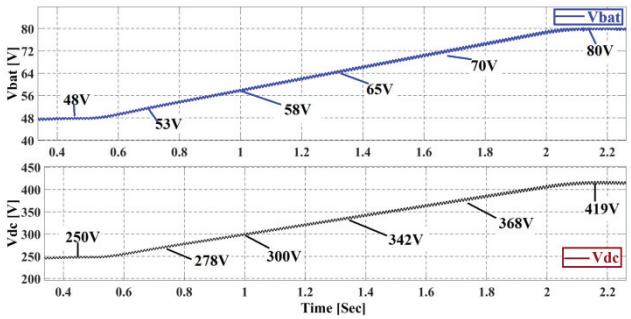

Fig. 3. Variance of DC-link bus voltage in comparison to battery voltage

B. Testing the EV Charger at Several Supply Voltages

Simulations were conducted for various Vs values ranging from (85-220) Vrms, with a Vbatt of 57V & Po = 1kW. The Is (source current) demonstrated admirable performance across the whole assortment of Vs, exhibiting

Authorized licensed use limited to: DELHI TECHNICAL UNIV. Downloaded on July 20,2023 at 11:25:06 UTC from IEEE Xplore. Restrictions apply.

THD value less than 3% and unity PF. Notably, the Vbatt was unaffected by the change in Vs, as demonstrated in Fig 4.

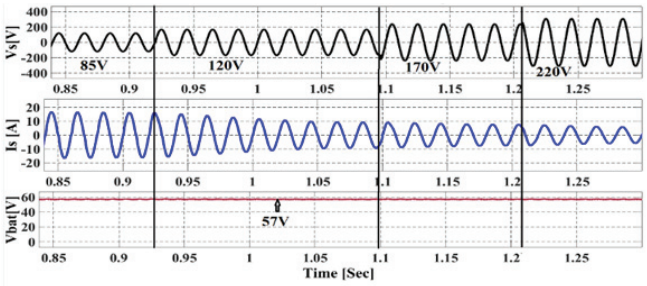

Fig. 4. Simulink results of battery voltage (V_{bat}), source current (I_s) under different supply voltages (V_s)

C. *Testing the EV charger at different loads*

Furthermore, simulations were ran for various loads which extends from 1kW-100W, with the V_{batt} kept fixed at 57V and by contrasting the battery current the load is varied. The peak current achieved was 17.54A at 1kW load, while the least value of current observed was 1.57A at a light load of 100W. Little bit more ripple was ascertained in the battery voltage & current at high loads in comparison to the light loads. Fig. 5 depicts the effectiveness.

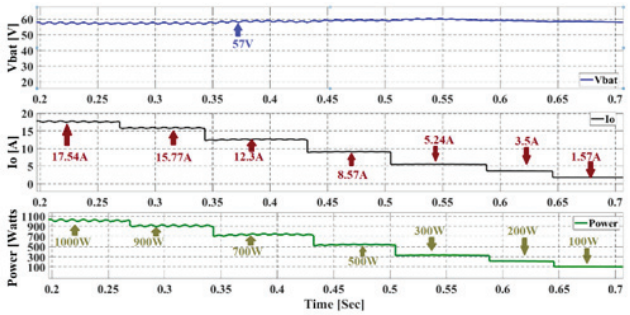

Fig. 5. EV battery charger's Performance at different loads.

D. *At nominal supply voltage(V_s) and nominal battery voltage(Vbatt)EV battery charger's performance*

The working of the system at power 700W & source voltage 220V is demonstrated in Fig. 6. It's shown that the source voltage(Vs)is followed by the i/p current with upf. For a Vbatt of 57V the Vdc reaches to 300V. The 1o inductor and 2o current are in CCM. With a peak amplitude of 370V, Fig.6 shows the waveform of the intermediate capacitance. The FFT analysis with TDD of 1.61% is shown in Fig.7.

Fig.8 shows the working of HB-LLC resonant converter. The HB-LLC converter is performing near resonant frequency (f_r), this is shown by the current waveforms of magnetizing & resonant inductors. The maximum value of the voltage V_{Cr} is 400V. The zero-voltage switching (ZVS)is shown by the current & voltage waveforms of MOSFET switch.

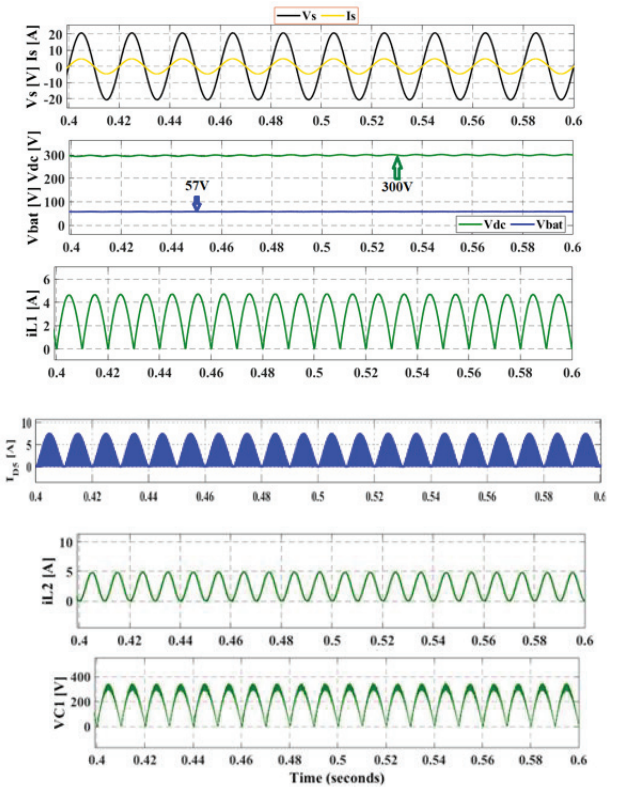

Fig. 6. Essential output waveform depicting I_s, V_{dc}, V_{batt}, iL_1, I_{DS}, iL_2, V_{C1} at V_s =220V & P_0 = 700 W.

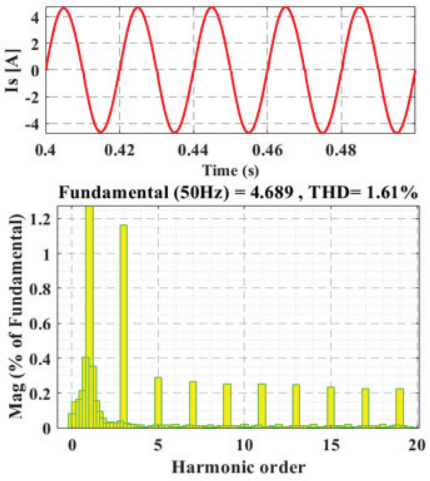

Fig. 7. At P_o=700W & V_{batt} = 57V, the FFT Analysis of I_S(Source Current)

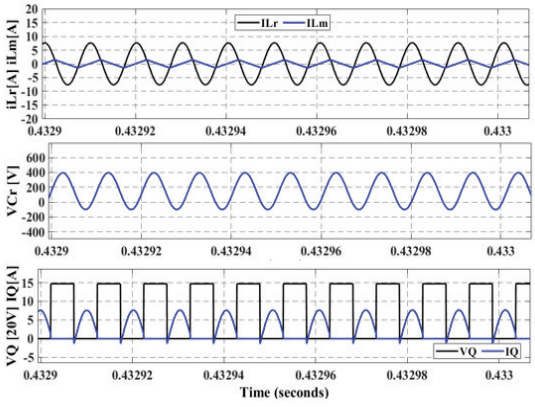

Fig. 8. The essential output waveform of iLr, iLm, VCr, throughout the MOSFET switch at Po = 700W & Vs = 220V are shown.

Authorized licensed use limited to: DELHI TECHNICAL UNIV. Downloaded on July 20,2023 at 11:25:06 UTC from IEEE Xplore. Restrictions apply.

E. The EV battery charger's overall performance

The proposed approach exhibits superior efficiencies at different load levels when compared to the conventional method, which maintains a constant DC-link and wide frequency variation for varying loads. Overall performance at different supply voltages (Vs), loads and battery voltages (Vbatt)are tabulated in Table IV

TABLE IV. OVERALL PERFORMANCE OF THE ON BOARD CHARGER

RMS value of V_s (Volts)	I_s (Amp)	Vdc (Volts)	Po (Watt)	Vbatt (Volts)	Io (Amp)	% TDD
220	9.34	419	1970	80	24.63	2.547
220	6.23	342	1300	65	19.89	1.873
220	4.77	300	1000	58	17.54	1.453
170	6.25	300	1000	58	17.54	2.456
85	12.4	300	1000	58	17.54	3.895
220	3.35	300	700	58	12.30	1.612
220	1.43	300	300	58	5.24	2.135
220	0.5	300	100	58	1.57	2.656

V. CONCLUSION

A power factor correction mechanism has been developed utilizing a SEPIC, which is preceded by an HB-LLC resonant converter. For the entire battery voltage (Vbatt) range of 48-80V, the second stage converter operates adjacent to the fr (resonance frequency) .The conceptual layout has been validated via simulation across different input voltages (Vs) ranging from 85Vrms to 220Vrms, as well as varying battery voltages of 58V-70V under various load conditions. The total harmonic distortion (TDD) is less than 3.895% for an input voltage of 85V. The proposed approach yields an cumulative efficiency of 95% at a load of 1kW and 89% at lighter loads, which is significantly better than traditional techniques.

REFERENCES

[1] IRENA, *Innovation outlook: Smart charging for electric vehicles*. 2019.

[2] R. Kushwaha and B. Singh, "Interleaved Landsman Converter Fed EV Battery Charger with Power Factor Correction," *IEEE Trans. Ind. Appl.*, vol. 56, no. 4, pp. 4179–4192, 2020, doi: 10.1109/TIA.2020.2988174.

[3] H. Wang, S. Dusmez, and A. Khaligh, "Design and analysis of a full-bridge LLC-based PEV charger optimized for wide battery voltage range," *IEEE Trans. Veh. Technol.*, vol. 63, no. 4, pp. 1603–1613, 2014, doi: 10.1109/TVT.2013.2288772.

[4] R. N. A. S. Ashok Kumar K M, "IRJET- Design and Development of DCM based Bridgeless PFC Converter for an On-Board EV Charger," *Irjet*, vol. 8, no. 6, pp. 245–250, 2021.

[5] A. Jordan and D. Hogan, "PFC Harmonic Current Emissions – Guide to EN61000-3-2 : 2014," *Epsma*, pp. 1–19, 2018.

[6] P. He and A. Khaligh, "Comprehensive Analyses and Comparison of 1 kW Isolated DC-DC Converters for Bidirectional EV Charging Systems," *IEEE Trans. Transp. Electrif.*, vol. 3, no. 1, pp. 147–156, 2017, doi: 10.1109/TTE.2016.2630927.

[7] S. Alatai, M. Salem, I. Alhamrouni, D. Ishak, A. Bughneda, and M. Kamarol, "Design Methodology and Analysis of Five-Level LLC Resonant Converter for Battery Chargers," *Sustain.*, vol. 14, no. 14, 2022, doi: 10.3390/su14148255.

[8] S. Ketsingsoi and Y. Kumsuwan, "An off-line battery charger based on buck-boost power factor correction converter for plug-in electric vehicles," *Energy Procedia*, vol. 56, no. C, pp. 659–666, 2014, doi: 10.1016/j.egypro.2014.07.205.

[9] T. N. Gücin, M. Biberoğlu, and B. Fincan, "Constant frequency operation of parallel resonant converter for constant-current constant-voltage battery charger applications," *J. Mod. Power Syst. Clean Energy*, vol. 7, no. 1, pp. 186–199, 2019, doi: 10.1007/s40565-018-0403-7.

[10] Y. Wang, O. Lucia, Z. Zhang, S. Gao, Y. Guan, and D. Xu, "A review of high frequency power converters and related technologies," *IEEE Open J. Ind. Electron. Soc.*, vol. 1, no. August, pp. 247–260, 2020, doi: 10.1109/OJIES.2020.3023691.

[11] R. Beiranvand, B. Rashidian, M. R. Zolghadri, and S. M. H. Alavi, "A design procedure for optimizing the LLC resonant converter as a wide output range voltage source," *IEEE Trans. Power Electron.*, vol. 27, no. 8, pp. 3749–3763, 2012, doi: 10.1109/TPEL.2012.2187801.

[12] M. A. Elkeiy, Y. N. Abdelaziz, M. S. Hamad, A. S. Abdel-Khalik, and M. Abdelrahem, "Multiport DC-DC Converter with Differential Power Processing for Fast EV Charging Stations," *Sustain.*, vol. 15, no. 4, 2023, doi: 10.3390/su15043026.

Authorized licensed use limited to: DELHI TECHNICAL UNIV. Downloaded on July 20,2023 at 11:25:06 UTC from IEEE Xplore. Restrictions apply.

A Study on Process Parameters and Scope of Material Flexibility in Friction Stir Additive Manufacturing, a Sustainable Technology

Archana Gopal[1], N Yuvraj[2]

[1]Delhi Technological University, Delhi, India
arch5.gopal@gmail.com
[2]Delhi Technological University, Delhi, India
yuvraj@dce.ac.in

Abstract- To keep up with the pace of Industry 4.0, Metal Additive Manufacturing(MAM) is revolutionizing its course from fusion-based MAM to the recently developed Solid State Friction Stir MAM. Fusion-based MAM has numerous drawbacks, especially due to solidification issues and inferior shear strength. Friction Stir Additive Manufacturing (FSAM) has variant novel techniques, it works on the governing principle of Friction Stir Welding (FSW) to build components layer after layer. Friction Stir Deposition is a very recent development in which the feed material, which is in form of powder, rod, or in form of machine chips (recycled) sustains in situ self-generated heating (by Friction stir mechanism).Due to the development of high strain rates, the feedstock binds to the substrate by extensive global plastic deformation leading to dynamic recrystallization giving fully dense bindings without any porosity, hot cracks, and inclusions. Being a solid-state thermo-mechanical process, it overcomes the drawbacks of Binder Jetting, Direct Energy Deposition, Sheet Lamination, and other MAM Techniques by giving, not only defect-free but also a microstructure, which is even better than the wrought, superior mechanical and structural properties, tight tolerances, proper bindings locally as well as globally, but lacks the ability for excessively complex parts. Owing to equiaxed and uniform refined microstructure, high energyefficiency, scalability, a wide range of material (Al, Ti, Ni, Mg) usage, reduced part distortion, its ease of use, superior quality, variety in feed materials, and minimal post-processing needed, it is amongst the best suited MAM for industries like aerospace, automotive, military, biomedical and maritime which require to manufacture high-strength, low-weight pure bulk metals, laminates, composites, biocomposites, alloys, and coatings. This paper outlines the mechanism of various FSAM techniques, studies the Process Parameters, the scope of Material Flexibility, defect detection, and the difficulties involved in enhancing the microstructure and efficiency. The paper concludes by analyzing its future trends.

Keywords- Friction Stir Deposition (FSD), FSAM, Process Parameters, Materials, Recycling machine chips, 3D printing

1. INTRODUCTION

Ere the industrial revolutions, livelihood was subjected to craftsmanship and agriculture. With time the urge to develop newer materials and manufacturing processes came up and people wanted to use better quality products and enhance their lifestyle. This started research for newer materials and fabrication methods, which could be more effective and fast compared to the traditional ones. This trend made the country's economy dependent on its industrial growth via large-scale production and mechanized tooling. Four stages in the industrial revolution are seen as (a) Stage 1: A shift in manufacturing from manual to the steam-driven, which continued up to 1835, (b) Stage 2: Vast-scale manufacturing by high-end energy resource development, which continued up to 1945, (c) Stage 3: Shift from mechanically driven era to a technology-driven era of Computer, Digital data, and Internet, it continued up to 2015, (d) Stage 4: Integrates advanced manufacturing processes especially Additive Manufacturing(AM) with the Simulation and Optimization,Big data, Internet of Things, Augmented Reality, Robotics and AI to create computer-aided manufacturing systems which not only interpret but also use data by Machine Learning to manage numerous intelligent movements back in real-world pacing towards complete automation [1]. Hence the industry is benefited from the flexible product modification, product development, market entrance, reduced cost, and operational unification achieved.

The six primary steps of AM are (a) building a 3D model via Software packages, (b) tessellating, (c) stacking, (d) configuring and calibrating the machine, (e) producing prototypes, and (f) post-processing and strength analysis. As new technologies and techniques for fabrication are developed, design and production research is redefining the boundary of conventional methods. Earlier termed as rapid prototyping (in the 1980s), this process faced advancements and is now termed as Additive manufacturing. Feedstock is used, which is in the

form of a powder or wire. It may be fused, heated, or build as stacks by multi-dimensional computer-aided process planning and manufacturing system [2]. With minimum homo sapiens interaction, it eliminates all needs to remove or mould material further into the shape of a product [3]. Additive manufacturing (AM) is the formal industrial nomenclature, but 3Dprinting is recognised frequently common alternative, owing to a joint effort by the ISO-International Standards Organization with ASTM-American Society for Testing and Materials [4].

Due to its capacity to create complicated geometries, decrease waste, increase design flexibility, and lower the cost of customization, metallic 3-d printing (MAM) is among the most key techniques employed in the manufacturing business [5,6]. For example, some titanium surgical implants have recently been printed using it. Boeing 777 with engine GE9X uses a heat exchanger system, consisting of 300 individual pieces. Owing to AM evolution, it just requires one, which also happens to be 25% cheaper and 40% lighter. SpaceX has used MAM components to cut down on production time and weight for its Super Draco and Raptor engines, and NASA plans to do the same for the Space Shuttle's primary engine in the near future. Made of 308LSi austenitic stainless steel (SS), the world's 1st additively manufactured metallic bridge is at De Wallen, Amsterdam, it stretches 10.50 meters over the Oudezijds Achterburgwal canal [7-10].

Binder jetting (BJ), Sheet Lamination, Material Extrusion (ME), Direct energy deposition (DED), Vat Polymerization, and Powder bed fusion (PBF) are the six main types of MAM processes defined by ASTM/ISO 52900:2017 [4]. Metals are involved in just four of these six processes. Acknowledging advancements in AM, metal, polymer, ceramic, composite,and bio-compatible materials are just a few examples that can be used [11].

Binder Jetting results are analogous to those of printing text on paper. When metal powdered granules bond to one another through a liquid binder,it creates a solid material layer. This printing process normally takes place at room temperature, this assists in avoiding thermally induced errors such as undesired grain development and distortion which are common in other MAM techniques that rely on a heat source [12-16]. The base material also acts as a substitute support structure while the permanent one is being built. Waste is reduced since there is no need for framing [17,18].

Direct Energy Deposition (DED) is a method that, like welding, employs a concentrated heat source to melt materials that are placed via a nozzle. It accounts for 16% of the overall MAM market and is mostly used for producing fairly close parts and fixing or making improvements to existing parts [20-22]. The DED method makes use of a heat source that may melt a feedstock (wire and powder) to a liquid state [23]. It is touted as being more efficient than competing technologies since it doesn't need the use of powerful lasers. In addition to being more cost-effective than PBF (Powder Bed Fusion) by 60-80%, it is simpler to run too. Fused deposition modelling (FDM) was developed for additive production of polymeric as well as composite layers [24-26]. The bound powder and ceramic release substance, are held on separate spools in a sealed container, and extruded by a conventional Material Extrusion machine. When using polymer binders, the 3d printer must raise the temperature of the feed higher than its melting point [27-30]. When using an electron or laser beam, PBF melts the material, allowing for the deposition of several coatings of material at once [31,32]. Metal direct laser sintering is being used to create bigger mechanical components like turbine blades, it has the potential of creating thick multi-layered substances but has a massive operational expense [33]. PBF falls into a similar category. Similarly, electron beam melting necessitates a vacuum during the production of functional components, whereas selective laser heating has higher operating costs than the aforementioned AM techniques [34-36].

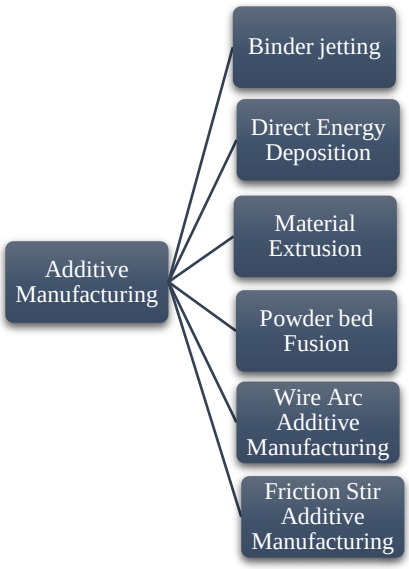

Fig.1 Types of Additive Manufacturing

Calvert et. al [37] declared that elevated temperatures and gradients developed in electron beam welding caused accelerated grain growth, a decrease in isotropic behaviour, a decrement in levels of stress dilution, and other typical cast defects. He also explained that it required some machining within every succeeding layer for a better connection surface. The traditional subtractive production process for fabrication involved around 85 percent wastage of base material. The AM process requires lesser material bulk volume and concurrently improves the strength-to-weight ratio. Some of its latest techniques that are extensively used are selective laser sintering, cold spray AM, electron beam welding, layered friction stir AM, etc. Mukhopadhyay et al. [38], Sing et al. [39] declared that selective laser melting fabricated components with remarkable defects along with porosity. Mertens et al. [40] observed that the enormous laser energies utilised in laser beam AM would lead to more material loss due to evaporation, unnecessary spatter, and degradation of exterior nature by baling. SMD (shape metal deposition) has an extensive build rate but inferior surface quality and bad dimensional tolerance, this issue was resolved by the application of LBAM. The parts made had better properties but had a tremendous cost of operation, slow build rates, and moderate bulk volume. Making metal parts by AM got commonly restrained to fusion-based methods where the powder substrates have to be heated above the melting point and, as the laser or beam moves forward, the consequent molten metal pool tempers down, getting solidified according to the scanning tool path followed by the laser or beam [41]. Like in fusion welding and casting, fusion-based MAM unavoidably negotiates in quality control of the material; cooled material suffers from hot cracking (especially in pure aluminium), porosity (especially in LBAM-made parts), residual stresses, and other defects. These defects get elevated due to the improper grain structure formed by the swift cooling rate and a sharp temperature gradient. Even after years of research, the quality of fusion-based components still lacks. Even in Cold Spray AM, which is the most researched AM in recent times, FSP has to be followed after deposition due to the porosity, micro-cracks, and improper bindings in some places [42-45]. Thus, there has to be post-processing done on FSP machines, this increases the cost of the component as it undergoes two different exclusive machine setups. These limitations cause the emergence of friction stir-based AM processes.

Friction stirring has been used to extrude or plastically distort metal by causing it to generate heat before it reaches its melting point. Force is applied axially across a tool, and the tool is rotated while moving in a translational direction to provide the desired effect. Originally created in 1991 at The Welding Institute (TWI), it is a solid-state bonding technology [46-48].It originated as a skill for joining aluminium and its alloys, a material that is notoriously hard to weld using traditional techniques. Friction Stir Welding (FSW) is successfully applied for aluminium alloys in industries[49-52]. Various businesses, including those involved in production and shipping, as well as the military, aviation, and automobile sectors, benefit from FSW. The procedure surpassed lap welding, spot welding, and submerged welding because of the fine, uniform microstructure achieved by grain refining [53-56]. The FSW principle is further refined and used in a variety of different production processes, including brazing, cladding, shaping, alloying, and so on [57-59]. In Friction Stir based Brazing, the absence of a tool pin eliminates the defects. At times, the process of FSW is followed by Friction Stir Cladding (FSC) in order to increase the corrosion resistance of the material [60,61]. Different researchers have contributed towards this process: White in 2002 patented friction-based solid state joining [62], Thomas in 2005 highlighted the scope of FSW as a method of AM [63], Rajiv S. Mishra in 2008 got a US

Patent by stating the working mechanism of Friction stir technique for getting superior strength and superplasticity [64], by Boeing's study they explained the eminent advantages of FSAM over other MAM [65,66], Calvert in 2013 published a thesis on AFS for WE43 alloy's structural characteristics [67], and Liu in 2018 got a US Patent on Hybrid friction stir technology for dissimilar materials by electro plastic deformation route [68].

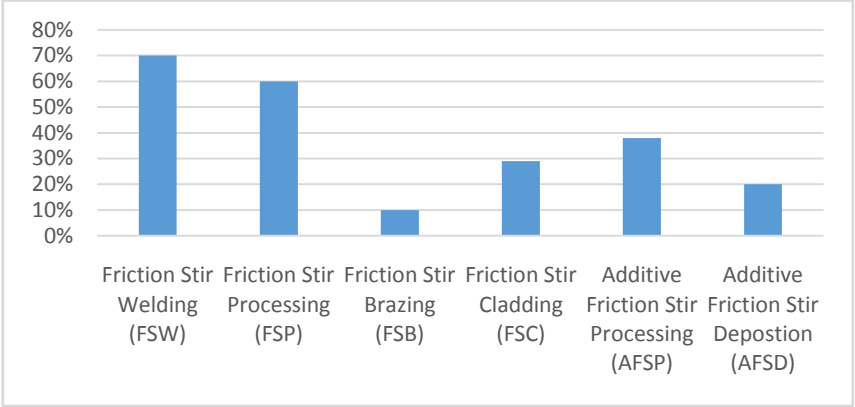

Fig.2 Contribution of Friction Stir Technologies in Research

FSAM is capable of resolving the drawbacks and overcoming the challenges faced in conventional AM, like defects, porosity, inclusions, high residual stresses, hot cracks due to hasty cooling after fusion, a large post-processing need, improper bindings, distortion, micro-cracks, high energy consumption in costly beam-based AM, and partially dense and non-uniform columnar microstructure in selective laser melting. It can print near-net shapes, almost defect-free, using a variety of composite materials, including metals, polymers, alloys, and even biocomposites. FSAM includes a massive variety of rewards like dynamic refined microstructure, high build rates, structural integrity, good scalability, and capability for high-strength, and low-weight parts. Hence, it has applications in a wide gamut of aspects and sectors like aerospace, automotive, military, biomedical, and maritime. Figure 3 explains the milestones in the evolution of this technique[69-79].

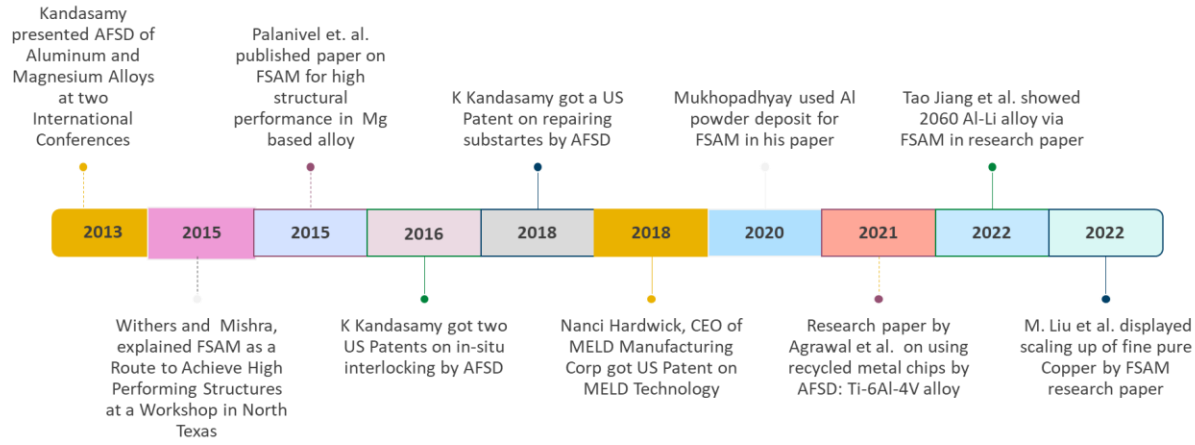

Fig.3 Milestones in process evolution

2. PROCESS METHODOLOGY

2.1 Mechanism

Using the notion of solid-state FSP to fabricate multilayer components through layer-by-layer blending gives enhanced microstructure. Traversing to dynamic recrystallization, exceptional mechanical properties are achieved by the grain refining process due to the development of tremendous strain rates of around 200/sec. The properties of a metal are enhanced by extreme localised as well as global plastic deformation with a refined isotropic uniform equiaxed grain structure of material. The shoulder comes into contact with the work surface,

which is held on the table by jigs and fixtures from all sides. Downward normal forces and rotational forces are used to create in-situ frictional heat by rubbing the substrate. This increases the temperature of the stirred zone, and flow stress droops. Pins or protrusions seep inside the material, the tool is revolved at an eminent rpm and transversed along the planned tool path, and the flexible material is churned about the pin.

Feed material can also be introduced by hollow tool in AFSD for reinforcements, repairs of grooves, coatings, and even for complete layer building. The process has many characteristics, like solid-state processing, wrought behaviour, and flexibility in feed materials. There is a slight variation between the properties of the advancing and retreating side, like in FSW. The natural peculiarities of FSAM, like reheating, feedstock additions as rod or powder through the hollow tool head or externally, as done by Mukhopadhyay [38], global plastic deformation instead of local deformation, and resintering, distinguish it from FSW. The two techniques are: Additive Friction Stir Processing (AFSP) and feedstock based additive friction stir deposition (AFSD).

2.2 Types

2.2.1 Additive Friction Stir Processing (AFSP)

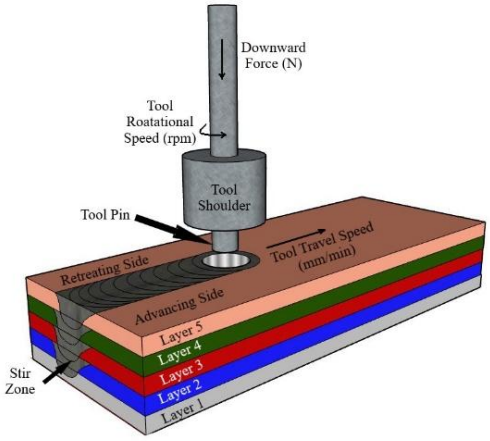

Fig. 4: Additive Friction Stir Processing

It works on layer-by-layer bonding of materials, and is a derived technique of friction stir welding (FSW) [44]. The protruding pin length is typically kept higher compared to the build layer so that proper binding of the material sheets can happen at a time. Here, the temperature is raised by generating heat by stirring the tool shoulder base against the top of the plates and also by the churning of the tool pin, which penetrates within the material, as depicted in Figure 4. This type has been extensively used in the automotive industry for composite fabrication, the sheet metal industry for lamination, and even for alloys with a higher melting point and higher hardness materials like Ti and Ni. Mishra et. al proposed for the structural frames of the airplane wings, and high-performance stringer/stiffener assemblies, in his patent and research paper [58].

2.2.2 Additive friction stir deposition (AFSD)-It was first suggested by Liu [59]and Stelt [60,61] to use hollow rotary tooling of the Friction Stir Cladding (FSC) technique in AFSD, and then Kandasamy got two US patents on AFSD in 2016 [73,74]. In 2018, AFSD became popular under the name of MELD when Aeroprobe Corp. introduced its AM branch as MELD Manufacturing Corporation [75,76], as listed in Figure 3. Here, the hollow tool has protrusions made on the base of the tool's shoulder. Its rotation and rubbing on the deposited material or substrate generate heat. As the tool doesn't contain a pin that could dip inside the material, so protrusions serve the purpose of the pin. The feed material contained in the hollow shoulder is in the form of recycled chips, consumable solid rods, or powder and is directly fed to the stirred zone. By topographical studies, the mechanism of temperature rise caused by friction is studied. The feed material is melded, stirred, and plastically deformed locally as well as globally, binding the deposited layer on the substrate plate fully.

This is extensively used for fabricating pure bulk metal (like Al and Cu), cladding, surface composites by adding SiC, and also in repair works for grooves and apertures. Unlike other AMs, no issues of porosity and other defects occur while fabricating Al in bulk from its powder. Hartley et. al [80] presented research on the cladding of Al-Mg-Si sheets of a very low thickness (in micrometres) for the automotive industry. AFSD has a high level of tolerance for feedstock due to its strong material deformation and binding mechanism. The deposited material may nonetheless have improved mechanical properties even when the feedstock is not totally

dense (in the form of recycled machined chips containing oxide impurities) [81]. In many cases, solid rod feed is preferred to powder feed for fabricating composites, as it has a lower chance of impurities embrittlement and better ductility. Mukhopadhyayet. al [38] stated that feed could also be given externally to prevent the blocking of the tool outlet.

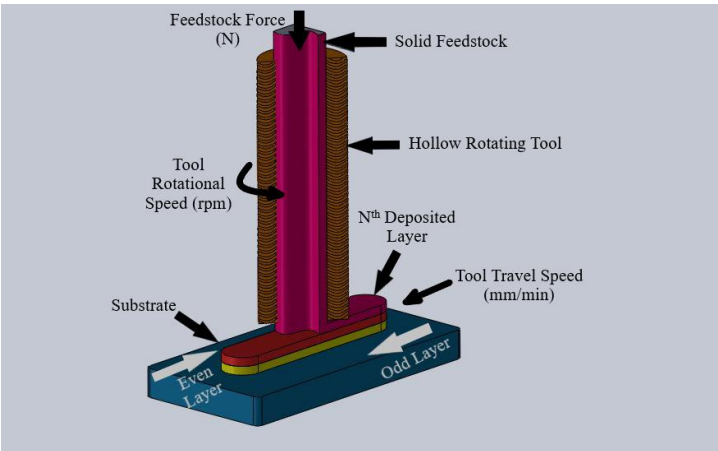

Fig 5: Additive Friction Stir Deposition

3. Comparative study of Optimized Process Parameters-

Various process parameters affect the process, and each has their individual contribution, these are: -

- Tool Travel Speed (TTS)
- Tool Rotational Speed (TRS)
- Shoulder geometry along with its features like Tool Shoulder Diameter (TSD)
- Tool Tilt Angle (TTA)
- Probe Geometry and its features like Tool Pin Length (TPL) and Tool Pin Diameter (TPD)
- Tool Plunge Depth
- Sideways Tilt Angle
- Vertical Pressure Applied
- Temperature of Nugget Zone

Among the following process parameters, it is observed that the parameters which have the maximum impact on the dynamic grain refinement are TRS, TTS, TSD, TTA, TPL, and TPD, their study is optimized and discussed in Table 1.

Table 1: Major Process Parameters in FSAM

Author [Ref]	Process	TRS in rpm	TTS in mm/min	TSD in mm	TTA in degree	TPL in mm	TPD in mm
Rodelas[82]	AFSP	100, 150	114, 51	-	-	-	-
Bo Li et al. [83]	AFSP	500	90	15.0	0	2.23	6.00
Calvert et al. [37]	AFSD	600, 1000	60	-	-	-	-
Guoqiang H et al. [84]	AFSP	1350	55	15.0	2.52	3.40	4.50
Roodgari et al [85]	AFSP	600	40,	20	0	0.5	6

			70, 100				
Derazkola et al. [86]	AFSP	850	45	20	2.5	6	6
Akash M et al. [37]	AFSD	170	22	16	0	Pinless	Pinless
Mackenzie Perry et al. [87]	AFSD	300	120	-	0	Pinless	Pinless
Jonathan et al. [88]	AFSD	275	127	-	-	-	-
K.Anderson et al. [89]	AFSD	175, 300	88.9, 139	38.1	0	Pinless	Pinless
Wenya Li [90]	AFSP	1500	30	15	2.5	3.85	4
Stubblefield et al. [91]	AFSD	300	127	38.1	0	Pinless	Pinless
Ardalanniya et al. [92]	AFSP	800, 1250	40, 70, 100	18	3	1.8	6

4. Comparative study of Material Flexibility-

Due to the flexibility of feed material and base material, FSAM gives a better alternative for fabricating alloys, composites, laminates, and even for the metals which are difficult for fusion-based welding and AM. Material Flexibility and findings are stated in Table 2.

Table 2: Material Flexibility and Findings in FSAM

Author (Year)	Feed Stock	Base Material	Remarks
J.Rodelas et al. [82]	Haynes Alloy 282	Alloy 600 (IN600)	Characterization done for Nickel-Based Surface Layers Alloy. Doubled hardness and improved kinematics of the precipitate structure as a result of the accumulated strength from interfacial mixing.
Bo Li et al. [83]	Pure Al	Ti3Alp/Ti6Al4V	By AFSD, fabricated and evaluated Ti3Alp / Ti–6Al–4V Surface Layer. The typical hardness increased to 400 Hv, while the coefficient of resistance dropped down to as low as .20
Calvert et al. [37]	WE43 Mg alloy	WE43-T5	Manufactures WE43 Alloy dense part with a homogenous fine grain structure without the use of any subsequent process. Grain growth was delayed to reduce the mean grain size to 2.0 from 2.4 after quick cooling with liquid N_2.
Hang et al. [93]	Al 6061	Al 6061	Outlined advantages of AFSD as compared to beam-based MAM. Several sensors were activated, allowing in-situ monitoring of thermo-mechanical interactions, faults, and topology topographical research.
Guoqiang H et al. [84]	WC particle	AA5083 H112	Fabricated Al–WC surface composite. Studied the progression of the perpetual dynamic recrystallized structure mechanics, and the retarded grain growth, which resulted in a reduction in grain dimensions.
Joey G. et al.	AA 7075	AA 7075	Worked on Repair of 7075 Aluminum Alloy. Even when the groove is 1.33 times wider

[94]			than feed rod, the feed fills the whole groove volume. In the higher sections, it consistently permits acceptable mixing. Reflected a smooth transition of columnar substrate plate grains to refined, equiaxed grain of the deposited metal, with no abrupt boundary.
Roodgari et al [85]	IF steel	St52 steel	Fabricated 2-layer laminated steel composite in comparison to base, made units have a good Yield Strength (YS) with low extensibility, possess Ultimate Tensile Strength (UTS) that falls between IF and St52 steel value, peak UTS-470 MPa and hardness-225 Hv at the condition 70 TTS, 600 TRS. If compared to core material, the consistent structure combined with the proximity of discrete phases in the built section give a lower UTS.
Derazkola et al. [86]	textile sheet	PMMA and its granules	Evaluated a laminated polymer steel sheet. The X – ray Photo-electron Spectrometry (XPS) method was used to investigate the sample. The formation of dipole-bonds was visible using XPS.
Akash M et al. [37]	AA6061	Al6061-T6	Carried microstructural and mechanical characterization of Al powder deposit. The introduction of granular feedstock in the hollow tool clogs the tool's end, making processing more difficult. Hence, the powdery feed was introduced into the substrate externally in this study to suppress this limitation.
Shirkharkolaei et al. [95]	silica	ABS	Adding Silica in ABS (acrylonitrile butadiene styrene) to improve pits properties. Results by responses surface method (RSM) displayed- value for predicting the error in deflection and bending strength, to be 8.5% and 6.1%.
Mackenzie Perry et al. [87]	AA 2024	AA 6061	Conducted morphological, structural study of non-planar interface. The feedstock is fully recrystallized; substrate sustains partial recrystallization. The material characteristics influence the exploration of interphase and its morphology.
Jonathan et al. [88]	Alloy 110 Cu	Alloy 110 Cu	Study on microstructure development of deposited Cu. It is totally firm outside while compact at the deepest levels. Guarding covering oxide forms on the outside facade of the placed substance.
Hsien Ho et al. [96]	Hydro-xyapatite powder	AZ31B Mg alloy	Biomineralization and biocompatibility of AZ31B Mg alloy hydroxyapatite composites was studied. The formed HA-Mg biocomposites showed better hemacompatibility, cellular adherence, and biocompatibility when compared to the substrate, it also has high surface energy of 46.80 mJ/m^2 and ratio of Calcium to Phosphor in the mineral phase from 1.55 to 1.6.
Anderson et al. [89]	AA2219	AA2219-T87	Carried out characterization of the fatigue behavior. The grain size is five times lower, and the θ'-θ phase is completely absent. The material that was created displayed a substantial portion of essential strengthening states.
Wenya Li [90]	Cu powder	Pure Al	Due to enhanced fine grains, a stronger bonded interface, and strain hardening, the analysis indicate that the adverse effects of particle interface were completely absent, enhancing the mechanical properties of copper. Because of the significant thermomechanical-coupling effect, the efficiency can reach 370 percent.
Stubblefield et al. [91]	AA6061-T651	AA6061	Did computational meshfree framework for the numeric simulation. Smoothed Particulate Dynamics, a distinct Lagrangian simulated method, showed high accuracy with experimental information recorded by the code, like temperature charts. Constructed outlines, strain plastic variation on entire bulk, giving an insight of the underlying mechanism.
Ardalanniya et al. [92]	Cu powder	Al-Zn alloy	Fabricated a laminated AlZnCup/Al-Zn composite. Manufacturing of intermetallic phases, by the emergence of unreacted Cu drops. It is carried out by improving filler

		particles dispersion while restricting flocculation, with increasing traversed and rotational speeds. The buildup of refined grains mostly on outer skin of a tiered composite results in a consistent pattern of minute dimples on the crack surface.
Ilana K. Lu et al. [97]	AA2050	AA2050 Fabricated cast Al alloy, 2050 Al–Cu–Li. The possibility that cast feed metal might be more cost-effective than wrought processed feed was also investigated.

5. Case Study

5.1 AA5083 machine chips deposition in AFS-D [81]

5.1.1 Process-

.

Al alloy 5083 (AA5083-H131) plates were reduced in a milling machine to get 2–3 millimeters long segregated flakes through a dry slicing technique in order to get the machine chips for this research. The piling of AA5083 machine chip was accomplished by loading K2 MELD machinery with metal flakes with the help of an auger feed mechanism that force them to drip easily into hollowed 38.10 mm rotary tool onto a 6.35 mm thickness AA5083-H131 base with succeeding layers. The frictional force, and the fluid pressure through the tool, cause complete plastic deformation in the material, due to shear and dynamical recrystallization (DRX). DRX in turn is carried outdue to the matrix orientations across grain boundaries, which are stimulated bythe nucleated crystals. Layersare built up to 2.5 millimeters high, with dense submicron equiaxed grain structure, with completely robust and tight bonding between the chip and the base. The advantage is that the supply chain benefits from fewer logistic links by using in-house machine chips, while the disadvantage is that a lack of available energy in distant areas hinders the thermal decomposition of metallic flakes into granular feed supplies.

5.1.2 Mechanical Properties and Microstructure-

Optical inspection of the material cross-section indicated radial migration of minerals from its central core to its periphery. Electron backscatter diffraction revealed a finer crystalline structure, which has a general grain size of 1.50 μm. Results from a tensile test revealed a lower yield strength of 170.40 MPa. While, UTS was determined to be 368.0 Mpa, affected by strain hardening, in accordance with the Hale-Petch relationship. Average Vickers hardness was 57.7 Hv. The beam-based AM method of Al resulted in prominent oxide deposits and brittle behavior, whereas the stress-strain relation demonstrated ductility [81].

5.2 Sustainable Additive manufacturing by depositing recycled metal chips to get Ti-6Al-4V alloy [77]

5.2.1 Process-

Using AFSD, the authors compressed recycled Ti64 chips into granular feed and pumped them into the hub of the machine. Here it got plasticized due to the high temperatures generated by the frictional stir heating. The size of thecoating was 30 x 135 x 25 mm and the tool material was WC. Such feed rods had a diameter of 9.52 mm, a thickness of 9.52 mm, and a length of 152.4 mm. The test pieces were rotated at 3 different speeds (in RPM), moved at a certain speed (in inches per minute), and feed was given (F in inches per minute). It was determined that the coating height for all 3 deposits was 1.016 mm. The TSL OIM 8 software was used for the analysis of the EBSD data. Wilson's VH3300 Micro hardness test apparatus was used to exert force of 0.5 HV to the specimens to measure their hardness. Energy dispersive spectroscopy (EDS) with Scanning electron microscopy detection using an FEI Quanta 200 instrument was utilized to determine the constitution of the treated sample (Agarwal 2021).

5.2.2 Mechanical Properties and Microstructure-

The characteristics of Ti64 are highly dependent on both the initial particle sizes as well as the lamellar diameter. The manufactured layers contain tiny, equiaxed preceding granules with fragile thin layers. The formed samples had a total plastic extension of 71%, a yield strength of 1050 MPa, and an ultimate tensile strength of 1140 MPa. The majority of grain is refined using DRX. It is shown that the tool transverse speed (V), and tool rotation rate (ω), have a considerable influence on the resulting structure. The increased heating rate during AFSD occurs due to the higher levels of ω^2 /V. Ti64 may be deposited under three various circumstances, each of which can alter the crystalline structure of the thermal conductivity of the high-strength alloy, and thus its tool endurance. Due to its superior tensile properties compared to other 3D printing methods,

as well as its ability to provide a homogeneous setup to the required crystal structure, AFSD of recycled items allows the making of great composite structures with lowered power consumption and lowered wastage [77].

6. Microstructure and Mechanical properties

This is recognized that the maximum temperature in FSD for constructed Al Mg Si alloy can be over 450 °C, while the top thermistor only records a transitory maximum temperature of around 135 °C [98]. Anisotropy in strength and plastic flow behaviour are both possible in the process used to make rolled sheet metal [99], although stiffness in the plane variations isoften negligible [100]. Al alloy [101], Inconel [102,103], and Mg alloys have demonstrated that AFSD is characterised by a considerable flow of material and rotation, resulting in virtually isotropic in-plane mechanical features. During cooling, the temperature differential between the build stack and the base leads to global deformations. Cladding Geometry can give impressive residual stress at surface and provide benefits like greater element tiredness [104] as well as fracture resistance. No significant damage or local buckling to the base material is caused by loads. Micro structural development in AA6061 was investigated in response to process variable [105].

The granular structure of the deposited films and the interface of the WE43 magnesium cladded alloy, made by FSAM technology, was analysed by electronic back scattering diffraction (EBSD) assessment map [106,107]. This mechanism method facilitates complete DRX, resulting in the development of a refined crystalline structure having excellent fatigue behaviour. This was evidenced by a comparison of the microstructuresof the FSD produced Inconel 625 superalloy to the commercial plate by Rivera et. al [108,109]. In a related manner, Ti-6Al-4V titanium alloy produces similar results after solid-state deposition and develops a completely dense structure with minimal residual stress and significant strength. It is clear that the extreme shear deformation generated by the spinning tool, greatly reduces the size of the martensitic laths. According to the latest studies, this allows for the deposition of a Ti-6Al-4V dense material with an equiaxed crystalline structure, resulting in a significant improvement in mechanical characteristics [110-112]. S316 L stainless steel undergoes similar enhancements, including structural equation modeling and increased hardness. Interestingly, the ductility of the processed alloy remains unaltered, although the ultimate tensile strength (UTS) and yield stress (YS) are both 25% higher. In another study, UTS is lowered and the elongation is increased by a factor of two, as compared to the stretched and tempered down WE43 magnesium alloy [113,114].

Under 1600 rpm of rotation and 300 mm/min of translation, the FSAM 2060-T3 Al Li alloy had a sound single track. The excessive material flow, and high rotational and translational speeds caused microporous flaws. The optimum slicing rate of 80% integrates the overlapping track. A low slicing rate caused uneven microstructure, and excessive plastic deformation caused flaws [115]. Other additive manufacturing processes have 20–50 HV of microhardness. FSAM eliminated metallurgical flaws by skipping the melting and solidification of the material. FSAM considerably decreased size distribution and texture strength in the single-track and overlap-track stirred zones. Plastic deformation improved dislocation density [78].

FSAM is also capable to form Cu-St bimetallic sheets. The junction has no pores or fractures, indicating a superior quality and reliable FSAM process. The interface's cyclic wave-like structure boosts Cu-St sheet shear strength. Deformation, grain refining, and solid solution enhancement have been found. Test procedure show 435 MPa tensile and 345 MPa shear strengths. These qualities outperform conventional approaches [116]. FSAM allowed scale-up manufacturing of full-dense Ultra fine-grain pure Cu. A relatively homogenous recrystallized microstructure gave bulk Ultra fine-grain pure Cu with outstanding mechanical characteristics. The FSAM approach can be used for many metal and alloy systems, getting massive bulk material fabrication more practical [79]. FSAM can correct the Keyhole on aluminium alloy 7N01. This flaw degrades material mechanical characteristics. Pin-less rotating tools and fillers were offered to tackle the Keyhole issue. The corrected Keyhole was metallographically analysed and mechanically tested. The precise tool design, filler material, and Keyhole repair settings made the technique effective. TRS enhances material characteristics. TRS was 1600 RPM and the steady plunge speed was 2 mm/min. At 1600 RPM, the restored joint's elongation and tensile strength were 7.6 % and 311.5 MPa, respectively, and 96% of a fault-free joint was made[117].

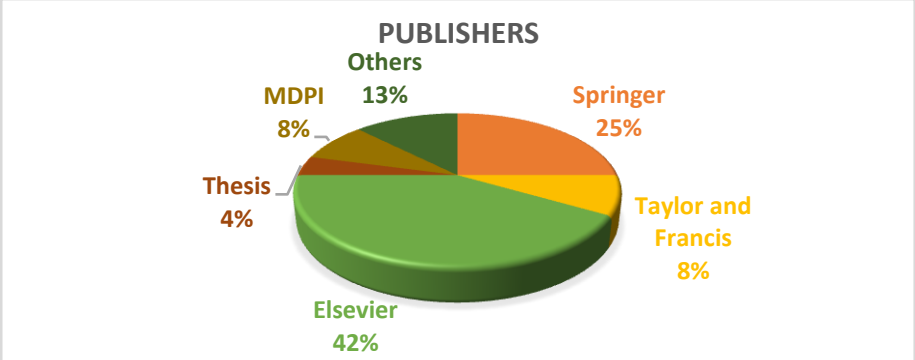

Fig.6 Contribution of various publishers in FSAM

7. Future Trends

For a process to exist, it needs to fulfill basic requirements, but if a process starts to evolve, it reflects the potential of the process. FSW has been prominently present for ages, but owing to its solid state mechanism, it has evolved for cladding, brazing, repairing, alloying, MMCs, and as an AM technique. Various authors have effectively devised and tested the FSAM process; however, it is still in its nascent stages, and much work remains to surmount its limitations. Its cost effectiveness, environmental sustenance, process efficiency, material flexibility, wide applicability, and wrought properties, make it a reliable and industry-ready process. The aforementioned features of the FSAM method make it a better fit for potential industrial projects. Due to the process's adaptability, it can be utilised in a variety of manufacturing areas.By the technique, medical devices and their essential elements were produced in the recent scenario. Based on FSAM's current performance, it is also anticipated that it will leave its mark in all areas of healthcare.Multiple sensors may be employed as well to monitor the process and measure the in-situ rate of cooling. According to the acquired feedback report, process parameters can be modified to reduce the defects, resulting in a substantial enhancement in the robustness, performance, and quality of parts produced using this method.The build capability would also be a focus of future research. Innovative composites or ceramics ought to be employed for the manufacturing of components with excellent strength and an elevated melting point. This is a crucial consideration when utilising AFSD as a composite manufacturing method, as the rigid reinforcement particulates can cause unnecessary tool material deterioration.

8. Discussion and Conclusion

The pie chart in Fig. 6 shows the contribution of various publishers in FSAM. The pie chart in Fig. 7 shows substrate material flexibility in FSAM, sunburst chart in Fig. 8 displays the feed material flexibility in the case of two different tools, one when the tool resembles an FSP tool with a pin, another is the hollow tool having a solid rod or powder feed for deposition. Fig. 9 displays the process capability of FSAM via a pie chart. It is seen that FSAM is highly capable of fabricating sheet metal laminates, pure bulk metals like Al, and Cu with the desired reinforcements, various Composites like nano-material composites, Ti-Al-V composites, Al–WC composites, Al-Zn-Cu composites, biocompatible biocomposites, cladding and repairing of the substrate.

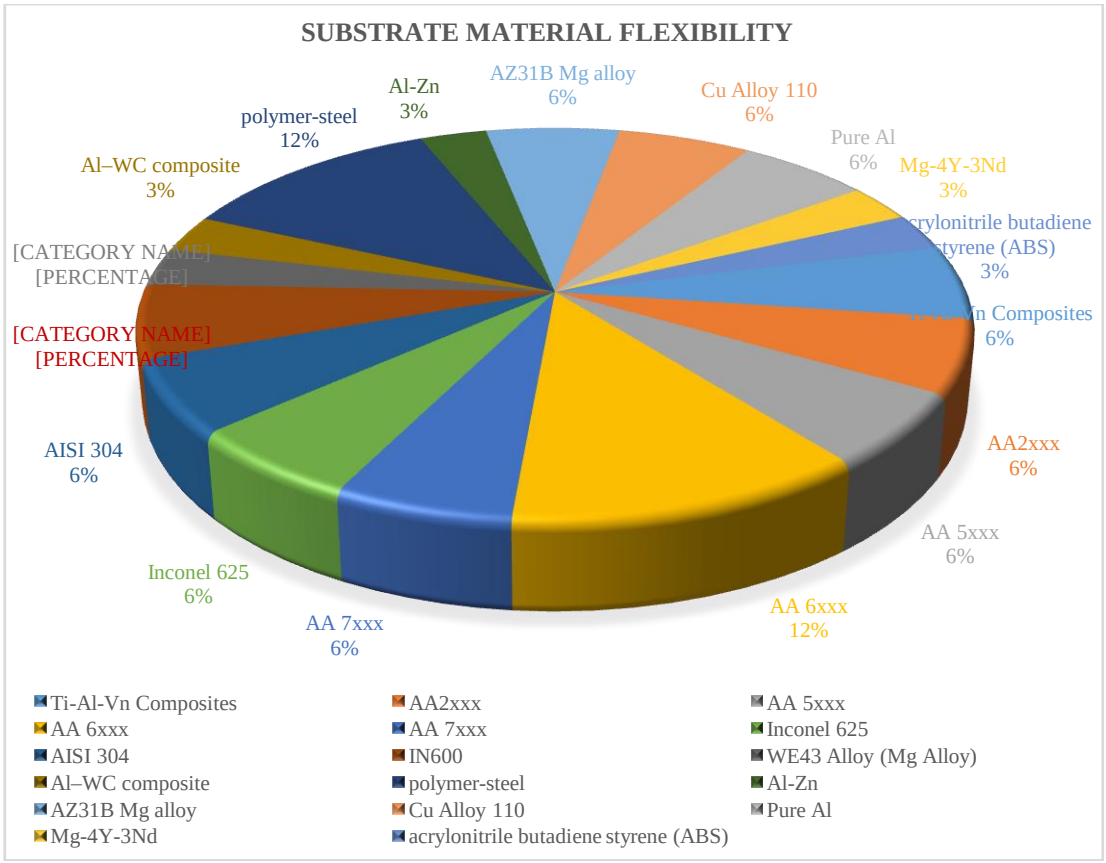

Fig. 7 Substrate Flexibility

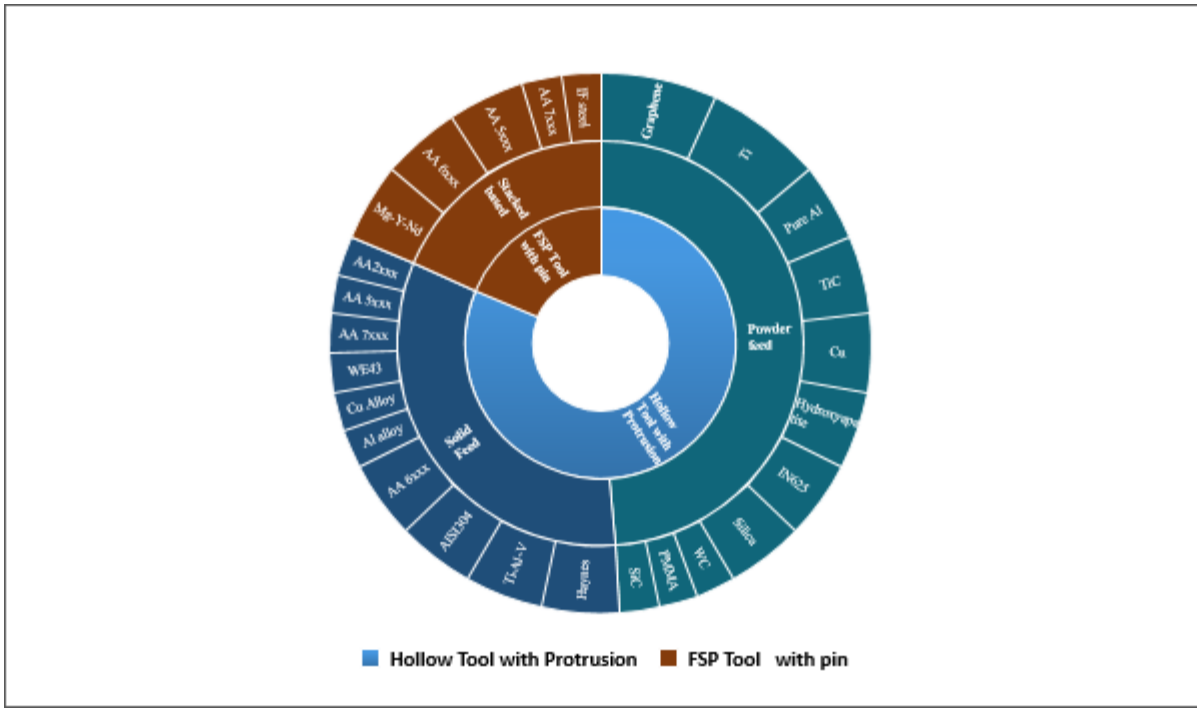

Fig.8 Feed Material Flexibility

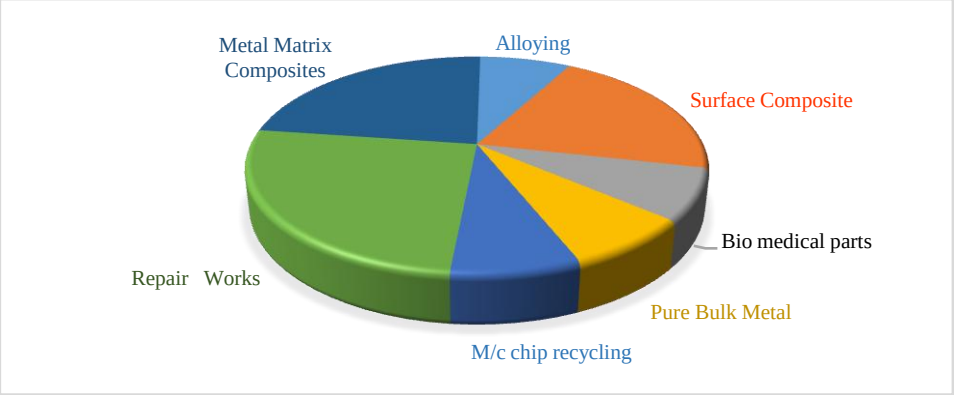

Fig.9 Process Capability of FSAM

In an austere environment, the feed can be given in form of recycled metal chips directly via hollow tool in the stir zone, without much effect on the characteristics of the built metal. FSAM is capable of fabricating the components with negligible hot cracking dilution, particle segregation, internal cavities, porosity, inclusions, etc. owing to its solid-state nature and the computer aided process planning implementation. Some properties of FSAM that make it environment friendly and effective are- negligible emissions, inconsumable tools, no shielding environment needed, large repeatability, and high acceptability for large products and especially for Magnesium, Aluminium, Nickel, Titanium, Copper based alloys.

References

1. Sandeep Rathee, Manu Srivastava, Pulak Mohan Pandey, Abhishek Mahawar, Siddhant Shukla, "Metal additive manufacturing using friction stir engineering: A review on microstructural evolution, tooling and design strategies", *CIRP Journal of Manufacturing Science and Technology*(2021), 35, 560-588, ISSN 1755-5817, https://doi.org/10.1016/j.cirpj.2021.08.003.
2. Vipin Gopan "Innovative potential of additive friction stir deposition among current laser based metal additive manufacturing processes: A review". *CIRP Journal of Manufacturing Science and Technology*, (2021)32, 228-248
3. Gardan J. "Additive manufacturing technologies: state of the art and trends". In: *Addit. Manuf. Handb*. Prod. Dev. Def. Ind. CRC Press (2017); p. 149–68. https:// doi.org/10.1201/9781315119106.
4. Technical Committee AMT/8. "additive manufacturing - general principles – terminology"(2017). In: *BS EN ISO/ASTM 52900*. Int. Stand. p. 1–30.
5. W.E. Frazier, "Metal additive manufacturing: A review", *J of Mater Eng and Perform*, (2014) 23 pp. 1917-1928, 10.1007/s11665-014-0958-z.
6. F. Haftlang, H.S. Kim, "A perspective on precipitation-hardening high-entropy alloys fabricated by additive manufacturing", *Mater Des*(2021), 211, Article 110161, 10.1016/j.matdes.2021.110161.
7. Jamroz W, Szafraniec J, Kurek M, Jachowicz R. "3D printing in pharmaceutical and medical applications – recent achievements and challenges". *Pharm Res*; (2018) 35:176. https://doi.org/10.1007/s11095-018-2454-x.
8. Blakey-Milner B, Gradl P, Snedden G, Brooks M, Pitot J, Lopez E, Leary M, Berto F, du Plessis "A. Metal additive manufacturing in aerospace: a review". *Mater Des*; (2019) 209:110008. https://doi.org/10.1016/j.matdes.2021.110008.
9. Gradl PR, Teasley T, Protz C, Katsarelis C, Chen P. "Process development and hotfire testing of additively manufactured NASA HR-1 for liquid rocket engine applications". In: *AIAA propuls. energy forum*. American Institute of Aeronautics and Astronautics Inc, AIAA; (2021). https://doi.org/10.2514/6.2021-3236.
10. Gardner L, Kyvelou P, Herbert G, Buchanan C. "Testing and initial verification of the world's first metal 3D printed bridge". *J Constr Steel Res* (2020); 172:106233. https://doi.org/10.1016/j.jcsr.2020.106233.
11. Tofail SAM, Koumoulos EP, Bandyopadhyay A, Bose S, O'Donoghue L, Charitidis C. "Additive manufacturing: scientific and technological challenges, market uptake and opportunities". *Mater Today*; (2018) 21:22–37. https://doi.org/ 10.1016/j.mattod.2017.07.001.
12. Ziaee M, Crane NB. "Binder jetting: a review of process, materials, and methods". *Addit Manuf*(2019); 28:781–801. https://doi.org/10.1016/j.addma.2019.05.031.
13. Mirzababaei S, Pasebani S. "A review on binder jet additive manufacturing of 316L stainless steel." *J Manuf Mater Process*(2019); 3:82. https://doi.org/10.3390/ jmmp3030082.

14. Atapour M, Wang X, Persson M, Odnevall Wallinder I, Hedberg YS. "Corrosion of binder jetting additively manufactured 316L stainless steel of different surface finish". *J Electrochem Soc*(2020); 167:131503. https://doi.org/10.1149/1945- 7111/abb6cd.
15. Miyanaji H, Zhang S, Yang L. "A new physics-based model for equilibrium saturation determination in binder jetting additive manufacturing process". *Int J Mach Tool Manuf*(2018); 124:1–11. https://doi.org/10.1016/j. ijmachtools.2017.09.001.
16. Miyanaji H, Yang L. "Equilibrium saturation in binder jetting additive manufacturing processes: theoretical model vs experimental observations". In: *Solid Free. Fabr. Proc. 27th Annu. Int. Solid Free. Fabr. Symp. - An Addit. Manuf. Conf.* (2016) SFF. p. 1945–59
17. Lores A, Azurmendi N, Agote I, Zuza E. "A review on recent developments in binder jetting metal additive manufacturing: materials and process characteristics". *Powder Metall*(2019); 62:267–96. https://doi.org/10.1080/ 00325899.2019.1669299.
18. Yegyan Kumar A, Bai Y, Eklund A, Williams CB. "The effects of hot isostatic pressing on parts fabricated by binder jetting additive manufacturing". *Addit Manuf*; (2018) 24:115–24. https://doi.org/10.1016/j.addma.2018.09.021.
19. Piscopo G, Iuliano L. "Current research and industrial application of laser powder directed energy deposition". *Int J Adv Manuf Technol*(2022):1–25. https://doi.org/ 10.1007/s00170-021-08596-w.
20. Tepylo N, Huang X, Patnaik PC. "Laser-based additive manufacturing technologies for aerospace applications". *Adv Eng Mater*(2019); 21. https://doi.org/10.1002/ adem.201900617.
21. Vafadar A, Guzzomi F, Rassau A, Hayward K. "Advances in metal additive manufacturing: a review of common processes, industrial applications, and current challenges". *Appl Sci*; (2021) 11:1–33. https://doi.org/10.3390/ app11031213.
22. Bouaziz MA, Djouda JM, Kauffmann J, Hild F. "Microscale mechanical characterization of 17-4PH stainless steel fabricated by atomic diffusion additive manufacturing (ADAM)". In: *Procedia Struct. Integr*. (2020) Elsevier B.V. p. 1039–46. https://doi.org/10.1016/j.prostr.2020.11.119.
23. Bhaskar Dutta, Directed Energy Deposition (DED) Technology, Editor(s): Francisca G. Caballero, *Encyclopedia of Materials: Metals and Alloys*, (2022) Elsevier, Pages 66-84, ISBN 9780128197332, https://doi.org/10.1016/B978-0-12-819726-4.00035-1.
24. Crump SS. United States Patent – "US5121329A - apparatus and method for creating three-dimensional objects". (1989)
25. Carroll BE, Palmer TA, Beese AM. "Anisotropic tensile behavior of ti-6Al-4V components fabricated with directed energy deposition additive manufacturing". *Acta Mater*(2015); 87:309–20. https://doi.org/10.1016/j.actamat.2014.12.054.
26. Gonzalez-Gutierrez J, Cano S, Schuschnigg S, Kukla C, Sapkota J, Holzer C. "Additive manufacturing of metallic and ceramic components by the material extrusion of highly-filled polymers: a review and future perspectives". *Materials (Basel)*(2018); 11:840. https://doi.org/10.3390/ma11050840.
27. Frazier WE. "Metal additive manufacturing: a review". *J Mater Eng Perform*(2014); 23:1917–28. https://doi.org/10.1007/s11665-014-0958-z.
28. Sames WJ, List FA, Pannala S, Dehoff RR, Babu SS. "The metallurgy and processing science of metal additive manufacturing". *Int Mater Rev*(2016); 61:315–60. https:// doi.org/10.1080/09506608.2015.1116649.
29. Zhang Y, Wu L, Guo X, Kane S, Deng Y, Jung YG, Lee JH, Zhang J. "Additive manufacturing of metallic materials: a review". *J Mater Eng Perform*(2018); 27: 1–13. https://doi.org/10.1007/s11665-017-2747-y.
30. A. Zocca, P. Colombo, C.M. Gomes, J. Günster, "Additive manufacturing of ceramics: issues, potentialities, and opportunities", *J. Am. Ceram. Soc*. (2015) 98 1983–2001.
31. W.E. King, H.D. Barth, V.M. Castillo, G.F. Gallegos, J.W. Gibbs, D.E. Hahn, C. Kamath, A.M. Rubenchik, "Observation of keyhole-mode laser melting in laser powder-bed fusion additive manufacturing", *J. Mater. Process.* (2014) 214–2925. 2915
32. C. Korner, "Additive manufacturing of metallic components by selective electron beam melting-a review", *Int. Mater. Rev*. (2016) 61 361–377.
33. J.P. Kruth, P. Mercelis, J.V. Vaerenbergh, L. Froyen, M. Rombouts, "Binding mechanisms in selective laser sintering and selective laser melting", *Rapid Prototyp. J*. (2005) 11 26–36.
34. C.Y. Yap, C.K. ChuaZ, L. Dong, Z.H. Liu, D.Q. Zhang, L.E. Loh, S.L. Sing, "Review of selective laser melting: Materials and applications", *Appl. Phys. Rev.* (2015) 041101.
35. Gibson I, Rosen DW, Stucker B. "Additive manufacturing technologies: rapid prototyping to direct digital manufacturing". US: Springer (2010), https://doi.org/ 10.1007/978-1-4419-1120-9.
36. Hehr A, Dapino MJ. "Dynamics of ultrasonic additive manufacturing". *Ultrasonics* (2017); 73:49–66.
37. Calvert et al. "Microstructure and Mechanical Properties of WE43 Alloy Produced Via Additive Friction Stir Technology", (2015)

38. Akash Mukhopadhyay et al. "Mechanical and microstructural characterization of aluminium powder deposit made by friction stir based additive manufacturing". *Journal of Materials Processing Technology*(2020), Elsevier.
39. N. Singh "Selective laser manufacturing of Ti-based alloys and composites: impact of process parameters, application trends, and future prospects". *Materials Today Advances*. (2020), 8, 100097
40. Anne I. Mertens "Fusion-Based Additive Manufacturing for Processing Aluminum Alloys: State-of-the-Art and Challenges". *Advanced Engineering Materials*, (2017)19, Wiley
41. Hang Z, RS Mishra "Additive friction stir deposition: a deformation processing route to metal additive manufacturing", *Materials Research Letters*, 9, (2020) Taylor and Francis
42. A. Hussein, A.S.M. Tahir, A.B. Hadley, "Characteristics of aluminum-to-steel joint made by friction stir welding: A review", *Mater. Today Common*. 5 (2015) 32–49.
43. Y.N. Zhang, X. Cao, S. Larose, P. Banjara, "Review of tools for friction stir welding and processing", *Can. Metall*. Q. 51 (2012) 250–261.
44. W.M. Thomas, E.D. Nicholas, J.C. Needham, M.G. Murch, P. Temple smith, and C. J. Dawes: G.B. (1991) Patent Application No. 9125978.8.
45. P.L. Threadgill, A.J. Leonard, H.R. Sheriff, P.J. Withers, "Friction stir welding of aluminium alloys", *Int. Mater. Rev*. 54 (2009) 49–93.
46. D.M. Rodrigues, C. Leith˜ au, R. Laura, H. Gouveia, A. Loureiro, "High speed friction stir welding of aluminium alloys", *Sci. Technol. WeldJoi* 15 (2010) 676–681.
47. S. Jana, Y. Hovanski, G. Grant, "Friction stir lap welding of magnesium alloy to steel: a preliminary investigation", *Metall and Mat TransA* 41 (2010) 3173–3182.
48. V. Soundararajan, E. Yarrapareddy, R. Kovacevic," Investigation of the friction stir lap welding of aluminum alloys AA5182 and AA6022", *J. Mater. Eng. Perform* 16 (2007) 477–484.
49. Q. Yang, S. Mironov, Y.S. Sato, K. Okamoto, "Material flow during friction stir spot welding", *Mater. Sci. Eng., A* 527 (2010) 4389–4398.
50. H. Papahn, P. Bahemmat, M. Haghpanahi, C. Sommitsch, "Study on governing parameters of thermal history during underwater friction stir welding", *Int. J. Adv. Manuf. Technol*. 78 (2015) 1101–1111.
51. H.J. Liu, H.J. Zhang, L. Yu, "Effect of welding speed on microstructures and mechanical properties of underwater friction stir welded 2219 aluminum alloy", *Mater. Des*. 32 (2011) 1548–1553.
52. G. Zhang, W. Su, J. Zhang, W. Zhongxin, "Friction stir brazing: a novel process for fabricating Al/steel layered composite and for dissimilar joining of Al to steel", *Metall. Mat. Trans*. A 42 (2011) 2850–2861.
53. S. Xie, R. Li, T. Yuan, C. Chen, K. Zhou, B. Song, Y. Shi, "Laser cladding assisted by friction stir processing for preparation of deformed crack-free Ni-Cr-Fe coating with nanostructure", *Opt. Laser Technol*. 99 (2018) 374–381.
54. T. Nishihara, "Development of friction stir forming", *Mater. Sci. Forum* 426–432 (2003) 2971–2978.
55. M. Aonuma, K. Nakata, "Effect of alloying elements on interface microstructure of Mg–Al–Zn magnesium alloys and titanium joint by friction stir welding", *Mater. Sci. Eng., B* 161 (2009) 46–49.
56. G. Huang, X. Feng, Y. Shen, Q. Zheng, P. Zhao, "Friction stir brazing of 6061 aluminum alloy and H62 brass: Evaluation of microstructure, mechanical and fracture behavior", *Mater. Des*. 99 (2016) 403–411.
57. H. Peng, R. Li, T. Yuan, H. Wu, H. Yan, "Producing nanostructured Co–Cr–W alloy surface layer by laser cladding and friction stir processing", *J. Mater. Res*. 30 (2015) 717–726.
58. Mishra, R.S., De, P.S., Kumar, N., Friction Stir Welding and Processing. Springer Book. (2014) ISBN 978-3-319-07043-8
59. S. Liu, T.C. Bor, A.A. Van Der Stelt, H.J.M. Geijselaers, C. Kwakernaak, A.M. Kooijman, J.M.C. Mol, R. Akkerman, A.H. Van Den Boogaard, "Friction surface cladding: an exploratory study of a new solid state cladding process", J. Mater. Process. Technol. 229 (2015) 769–784, https://doi.org/10.1016/j.jmatprotec.2015.10.029.
60. A.A. van der Stelt, T.C. Bor, H.J.M. Geijselaers, R. Akkerman, A.H. van den Boogaard, "cladding of advanced Al alloys employing friction stir welding", *Key Eng. Mater*. 554–557 (2013) 1014–1021.
61. Van Der Stelt, Adrianus Anton, Friction Surface Cladding: development of a solid state cladding process PhD Thesis, University of Twente, Enschede, the Netherlands.(2014) ISBN 978-94-91909-09-2
62. White, D., Object consolidation employing friction joining, (2002), U.S. Patent 6,457,629.
63. Thomas, W.M., Norris, I.M., Staines, D.G., Watts, E.R., (2005), "Friction Stir Welding–Process Developments and Variant Techniques". *The SME Summit (Oconomowoc, Milwaukee, USA).*
64. Rajiv S. Mishra, Rolla, MO (US), Integral Channels in Metal and Fabrication Thereof,Patent No.: US 7,354,657 B2, 2008
65. Lequeu, P.H., Muzzolini, R., Ehrstrom, J.C., Bron, F., Maziarz, R., (2006), "High Performance Friction Stir Welded Structures using Advanced Alloys". *Aeromat Conference* (Seattle, WA).
66. Baumann, J.A., (2012), "Technical Report On: Production of Energy Efficient Preform Structures".The Boeing Company, Huntington Beach, CA.

67. Calvert JR. "Microstructure and mechanical properties of WE43 alloy produced via additive friction stir technology". *Materials science and engineering*. Virginia Polytechnic Institute and State University; (2015). p. 1–23.
68. Liu, Hybrid friction stir welding for dissimilar materials through electro-plastic effect, Patent number: 9981338, (2018)Patent Publication Number: 20150375335
69. Kandasamy, K., Renaghan, L.E., Calvert, J.R., Schultz, J.P., "Additive Friction Stir Deposition of WE43 and AZ91 Magnesium Alloys: Microstructural and Mechanical Characterization". International Conference, Powder Metallurgy & Particulate Materials, Advances in Powder Metallurgy and Particulate Materials, Chicago, IL. (2018)
70. Kandasamy K, Renaghan LE, Calvert JR, Creehan KD, Schultz JP. "Solid-state additive manufacturing of aluminum and magnesium alloys". *Mater Sci Technol Conf Exhib* (2013).:59–69. MS and T
71. Withers, J., Mishra, R.S., "Friction Stir Additive Manufacturing as a Potential Route to Achieve High Performing Structures". US DOE Workshop on Advanced Methods for Manufacturing (AMM), University of North Texas, (2015)
72. Palanivel S, Nelaturu P, Glass B, Mishra RS. "Friction stir additive manufacturing for high structural performance through microstructural control in an Mg based WE43 alloy". *Mater Des* (1980-2015) 2015; 65:934–52.
73. Kandasamy, Solid State Joining Using Additive Friction Stir Processing, Patent No. US 9,511,445 B2 (2016)
74. Kandasamy, In-Situ Interlocking of Metals Using Additive Friction Stir Processing, Patent No. US 9,511.446 B2 (2016)
75. Kandasamy, Additive Friction Stir Methods of Repairing Substrates, Patent No. US 9, 862 ,054 B2 (2018)
76. Nanci Hardwick, Meld Solid - State Joining of Different Features to Cast Parts, Pub. No.: US 2018 / 0361501 A1, (2018)
77. Priyanshi Agrawal, Ravi Sankar Haridas, Surekha Yadav, Saket Thapliyal, Supreeth Gaddam, Ravi Verma, Rajiv S. Mishra "Processing-structure-property correlation in additive friction stir deposited Ti-6Al-4V alloy from recycled metal chips", *Additive Manufacturing*, (2021), Volume 47, 102259, ISSN 2214-8604, https://doi.org/10.1016/j.addma.2021.102259
78. Tao Jiang, Tao Jiao, Guoqing Dai, Zhikang Shen, Yanhua Guo, Zhonggang Sun, Wenya Li, "Microstructure evolution and mechanical properties of 2060 Al-Li alloy via friction stir additive manufacturing", *Journal of Alloys and Compounds*, (2023), Volume 935, Part 2, 168019, ISSN 0925-8388, https://doi.org/10.1016/j.jallcom.2022.168019.
79. M. Liu, B.B. Wang, X.H. An, P. Xue, F.C. Liu, L.H. Wu, D.R. Ni, B.L. Xiao, Z.Y. Ma, "Friction stir additive manufacturing enabling scale-up of ultrafine-grained pure copper with superior mechanical properties", *Materials Science and Engineering: A*, Volume 857,2022,144088, ISSN 0921-5093, https://doi.org/10.1016/j.msea.2022.144088.
80. W. Douglas Hartley "Solid-state cladding on thin automotive sheet metals enabled by additive friction stir deposition". *Journal of Materials Processing* Tech (2021) 291, 1170145
81. J.B. Jordon, P.G. Allison, B.J. Phillips, D.Z. Avery, R.P. Kinser, L.N. Brewer, Chase Cox, K. Doherty, "Direct recycling of machine chips through a novel solid-state additive manufacturing process", *Materials & Design* (2020) 193, 108850, ISSN 0264-1275, https://doi.org/10.1016/j.matdes.2020.108850.
82. J. Rodelas et al. "Characterization of Engineered Nickel-Base Alloy Surface Layers Produced by Additive Friction Stir Processing". *Metallography, Microstructure, and Analysis*(2013), Springer US
83. Bo Li et al. "Fabrication and Evaluation of Ti3Alp/Ti–6Al–4V Surface Layer via Additive Friction-Stir Processing". *Materials and Manufacturing Processes*(2014), Taylor and Francis.
84. Guoqiang H et al. "Producing of Al–WC surface composite by additive friction stir processing". *Materials and Manufacturing Processes*(2018), Taylor and Francis
85. Roodgari et al "Fabrication of a 2-layer laminated steel composite by friction stir additive manufacturing". *Journal of Manufacturing Processes*(2020), Elsevier
86. Derazkola et al. "Evaluation of a polymer-steel laminated sheet composite structure produced by friction stir additive manufacturing (FSAM) technology". *Polymer Testing*(2020), Elsevier
87. Mackenzie Perry, M.E.J., Griffiths, R.J., Garcia, D., Sietins, J.M., Zhu, Y., Yu, H.Z., "Morphological and microstructural investigation of the non-planar interface formed in solid-state metal additive manufacturing by additive friction stir deposition". *Addit. Manuf.* (2020) 35, 101293.Elsevier
88. Jonathan et al. "Microstructure Development in Additive Friction Stir-Deposited Cu." *Metals*(2020), MDPI
89. K. Anderson et al. "Characterization of the fatigue behavior of additive friction stir-deposition AA2219". *International Journal of Fatigue*(2021), Elsevier
90. Wenya Li "A comparative study on the employment of heat treatment, electric pulse processing and friction stir processing to enhance mechanical properties of additive-manufactured copper". *Surface & Coatings Technology*(2021), Elsevier

91. Stubblefield et al. "A meshfree computational framework for the numerical simulation of the solid-state additive manufacturing process, additive friction stir-deposition (AFS- D)". *Materials and Design*(2021), Elsevier
92. Ardalanniya et al. "Fabrication of the laminated Al-Zn-Cup/Al-Zn composite using friction stir additive manufacturing". *Materials Today Communications*(2021), Elsevier
93. Hang et al. "Non-beam-based metal additive manufacturing enabled by additive friction stir deposition" *Scripta Materialia*(2018), Elsevier
94. R. Joey G et al. "Additive Friction Stir-Enabled Solid-State Additive Manufacturing for the Repair of 7075 Aluminum". *Applied Science*(2019), MDPI
95. Shirkharkolaei, E., Ebrahimzadeh, P., Shahraki, S. et al. "Solid State Additive Manufacturing of Acrylonitrile Butadiene Styrene with Silica Augmentative: Application of Friction Stir Processing". *Exp Tech* (2020)44, 49–57
96. Yee-Hsien Ho, Kun Man, Sameehan S. Joshi, Mangesh V. Pantawane, Tso-Chang Wu, Yong Yang, Narendra B. Dahotre, "In-vitro biomineralization and biocompatibility of friction stir additively manufactured AZ31B magnesium alloy-hydroxyapatite composites", *Bioactive Materials*(2020), Volume 5, Pages 891-901
97. Lu, Ilana & Reynolds, A.P "Innovative friction stir additive manufacturing of cast 2050 Al–Cu–Li aluminum alloy". *Prog Addit Manuf* (2021) 6, 471–477
98. Garcia et al. "In situ investigation into temperature evolution and heat generation during additive friction stir deposition: A comparative study of Cu and Al-Mg-Si". *Additive Manufacturing*(2020). Volume 34. Elsevier
99. Cheng, P., Yao, Y.L., "The influence of sheet metal anisotropy on laser forming process". *J. Manuf. Sci. Eng*. (2004) 127, 572–582
100. Starman, B., Vrh, M., Halilovi˘c, M., Stok, ˘ B., "Advanced modelling of sheet metal forming considering anisotropy and Young's modulus evolution". *J. Mech. Eng*. (2014) 60, 84–92.
101. Rivera, O., Allison, P., Brewer, L., Rodriguez, O., Jordon, J., Liu, T., Whittington, W., Martens, R., McClelland, Z., Mason, C., "Influence of texture and grain refinement on the mechanical behavior of AA2219 fabricated by high shear solid state material deposition". *Mater. Sci. Eng. A* (2018) 724, 547–558.
102. Rivera, O.G., Allison, P.G., Jordon, J.B., Rodriguez, O.L., Brewer, L.N., McClelland, Z., Whittington, W.R., Francis, D., Su, J., Martens, R.L., Hardwick, N., "Microstructures and mechanical behavior of Inconel 625 fabricated by solid-state additive manufacturing". *Mater. Sci. Eng. A* (2017) 694, 1–9.
103. Avery, D., Rivera, O., Mason, C., Phillips, B., Jordon, J., Su, J., Hardwick, N., Allison, P., "Fatigue behavior of solid-state additive manufactured inconel 625". *JOM* (2018) 70, 2475–2484
104. Pouget, G., Reynolds, A.P., "Residual stress and microstructure effects on fatigue crack growth in AA2050 friction stir welds". *Int. J. Fatigue* (2008) 30, 463–472.
105. Phillips, B.J., Avery, D.Z., Liu, T., Rodriguez, O.L., Mason, C.J.T., Jordon, J.B., Brewer, L.N., Allison, P.G. "Microstructure-Deformation Relationship of Additive Friction Stir-Deposition Al–Mg–Si". *Materialia*, (2019), 7:100387.
106. Palanivel S, Mishra RS. "Building without melting: a short review of friction-based additive manufacturing techniques". *Int J Addit Subtract Mater Manuf* (2017);1(1):82–103.
107. Palanivel S, Sidhar H, Mishra RS. "Friction stir additive manufacturing: route to high structural performance". *JOM (*2015);67(3):616–21.
108. Rivera OG, Allison PG, Brewer LN, Rodriguez OL, Jordon JB, Liu T, et al. "Influence of texture and grain refinement on the mechanical behavior of AA2219 fabricated by high shear solid state material deposition". *Mater Sci Eng A (*2018); 724:547–58.
109. Rivera OG, Allison PG, Jordon JB, Rodriguez OL, Brewer LN, McClelland Z, et al. "Microstructures and mechanical behavior of Inconel 625 fabricated by solid-state additive manufacturing". *Mater Sci Eng A* (2017); 694:1–9.
110. MELD brochure, Aeroprobe corporation Available from: http://www.aeroprobe. com/meld/ (2018).
111. Yu HZ, Jones ME, Brady GW, Griffiths RJ, Garcia D, Rauch HA, et al. "Non-beam based metal additive manufacturing enabled by additive friction stir deposition". *Scr Mater* (2018).
112. Gustmann, T., Neves, A., Kuhn, U., Gargarella, P., Kiminami, C.S., Bolfarini, C., Eckert, J., Pauly, S. "Influence of Processing Parameters on the Fabrication of a Cu-Al-Ni-Mn Shape-Memory Alloy by Selective Laser Melting". *Additive Manufacturing*(2016), 11:23–31
113. Khodabakhshi, F., Gerlich, A.P., "Potentials and Strategies of Solid-StateAdditive Friction-Stir Manufacturing Technology: A Critical Review". *Journal of Manufacturing Processes*(2018), 36:77–92.
114. Ashish Kumar Srivastava, Nilesh Kumar, Amit Rai Dixit, "Friction stir additive manufacturing – An innovative tool to enhance mechanical and microstructural properties", *Materials Science and Engineering: B*, (2021) Volume 263, 114832, ISSN 0921-5107, https://doi.org/10.1016/j.mseb.2020.114832.

115. Manu Srivastava, Sandeep Rathee, "Microstructural and microhardness study on fabrication of Al 5059/SiC composite component via a novel route of friction stir additive manufacturing", *Materials Today: Proceedings* (2021) 39,1775-1780, ISSN 2214-7853, https://doi.org/10.1016/j.matpr.2020.07.137.
116. Yanyang Guo, Xiaowei Wu, Guoxiong Ren, Zepeng Liu, Ruidi Yuan, Xiao Yang, Peng Dong, "Microstructure and properties of copper-steel bimetallic sheets prepared by friction stir additive manufacturing", *Journal of Manufacturing Processes*(2022), Volume 82, Pages 689-699, ISSN 1526-6125
117. Md Helal Miah, Dharmahinder Singh Chand, Gurmail Singh Malhi, "A novel technique for repairing Keyhole in the aircraft assembly technology employing friction stir additive manufacturing", *Materials Today: Proceedings*, (2022), ISSN 2214-7853, https://doi.org/10.1016/j.matpr.2022.11.187.

AIP Conference Proceedings

RESEARCH ARTICLE | JULY 14 2023

A taxonomical review of developments in digital storage oscilloscope (DSO)

Malti Bansal ✉; Riyanshi Arora; Ritvik Bharti

Check for updates

AIP Conference Proceedings 2796, 180001 (2023)
https://doi.org/10.1063/5.0149169

View Online
Export Citation
CrossMark

20 July 2023 11:13:15

AIP Advances
Why Publish With Us?
25 DAYS average time to 1st decision
740+ DOWNLOADS average per article
INCLUSIVE scope
Learn More
AIP Publishing

AIP Publishing

A Taxonomical Review of Developments in Digital Storage Oscilloscope (DSO)

[a)]Malti Bansal, Riyanshi Arora, Ritvik Bharti

Department of Electronics and Communication Engineering,
Delhi Technological University (DTU), Delhi-110042, India

[a)]Corresponding author's email: maltibansal@gmail.com

Abstract— A Digital Storage Oscilloscope (DSO) is an indicative apparatus than can rapidly record/capture or display signals. It can also be used to store waveforms, which later can be changed or compared using a function generator or other devices. In this paper, we review a Digital Storage Oscilloscope and its history and also discuss the various types of DSO's. Moreover, the different advancements in its design, along with the models used presently and its applications, are also discussed and elaborated in the paper.

Keywords—Digital Storage Oscilloscope (DSO), bandwidth, frequency, Cathode Ray Oscilloscope(CRO)

INTRODUCTION

A Digital Storage Oscilloscope is a type of Oscilloscope that stores, examines, and displays signals digitally, i.e., in the form of 0's and 1's rather than analyzing them in an analog manner. Though, the signals are preferably stored as analog signals. The input is given to a Digital Storage Oscilloscope [1]. A DSO stores the input, examines it, and then displays it on the screen. The output shown by a Digital Storage Oscilloscope is displayed in a visual as well as in a numerical manner.

20 July 2023 11:13:15

HISTORY

In 1897, the scientist Karl Ferdinand Brown constructed the main cathode beam tube and the primary CRT based test oscilloscope. Then in the 1920s, the first Cathode Ray tubes were used for measurement purposes. In 1931, GenRad built up the primary Oscilloscope, "Electron Oscillograph Type 535-A," which was constructed in two sections force in addition to cylinder flexibly. After this, various other companies such as A.C. Cossor Ltd. and Rohde and Schwarz made their first oscilloscopes. In 1933, the first Cathode Ray Oscilloscope was developed by GenRad (type 687 A). Some years later, it introduced type 770-A, which was never sold. Hence, GenRad dropped his production of oscilloscopes. Then in the later '30s, dual ray oscilloscopes were invented, and oscillographs were introduced. However, these instruments had many shortcomings. So, Allen Dumont invented frequency to trigger and sweep in CRT, and these features were later incorporated in the making of a CRO and then a DSO. In the later 1940s, Tektronix introduces a time-delayed trigger, which added up in convenience using oscilloscopes. Then in 1954, Tektronix introduced model 535, which included a Tektronix developed CRT, and this model was used and sold for over 22 years. In 1960, HP (Hewlett Packard) invented sampling technology [2]. In 1961, Tektronix introduced its first portable Oscilloscope, i.e., model 321. In 1962, HP introduced the Oscilloscope with 1000 MHz Bandwidth, and this was the first GHz Oscilloscope. In the later years, more advancements took place in technology, such as storage oscilloscopes, which were introduced.

Tektronix was the first in the race to make Storage Oscilloscopes. Then, HP presented a total group of oscilloscopes with selections of centralized servers, modules, and different extras. HP also introduced a solid-state oscilloscope with 500 kHz bandwidth. Then in 1971, HiroMoriyasuwho belonged to Tektronix instruments built up the main computerized Oscilloscope. In the same year, LeCroy developed the first ongoing advanced Oscilloscope with a memory profundity of 20 examples and an inspecting pace of 2ns. In the year 1980, a Digital Storage Oscilloscope was invented Nicolet Test Instrument, and it had a bandwidth of 1 GHz. First digital sampling oscilloscopes also appeared in the 1980s. In the year 1980, Gould Instruments launched a new oscilloscope with

Research Advancements and Innovations in Computing, Communications and Information Technologies
AIP Conf. Proc. 2796, 180001-1–180001-8; https://doi.org/10.1063/5.0149169
Published by AIP Publishing. 978-0-7354-4584-0/$30.00

expanded memory of 4 kilobytes. There was more exactness and accuracy in catching waveforms and consolidated digital storage with constant execution on one standard Oscilloscope [3]. Pico Technology, founded in the 1990s, developed PC-based oscilloscopes. Hi-Resolution oscilloscopes were also introduced in 1991. In the year 1992, Pico Technology presented its very first and fundamental Personal Computer based Oscilloscope with twelve bit digit goal (also called as resolution). Tektronix offered the TLS216 Logic Scope, a combination of digital storage oscilloscope and logic analyzer, in 1994. It offered a 500 MHz bandwidth, 2GS/s sampling rate, and 16 input channels with enhanced triggering. So the TLS216 might be the first mixed-signal Oscilloscope (MSO).Hewlett Packard presented the primary blended sign Oscilloscope in with 100MHz simple channels and eight or 16-bit computerized rationale channels [2]. In the year 1997, Cathode Ray Tube display was replaced by Liquid Crystal Display in most of the Oscilloscopes.

Tektronix invented digital Phosphor Oscilloscope in the year 1998. Then in the 20th century, USB based Digital Storage Oscilloscopes were made by Pico Technology (in the year 2006, to be precise). In the following years, more advancements took place, such as bandwidth was improved, Pico Technology introduced USB 3.0, the resolution was improved, and the combination of Digital Storage Oscilloscope and Power Analyser was made.In the year 2014, the well renowned Tektronix presented the initial six-in-one Oscilloscope, inclusive of an advanced Avometer, self-assertive sign alternator, range analyzer, rationale analyzer, and convention analyzer, the MDO3000 Series, and this is the most commonly used Oscilloscope in laboratories. After this, Tektronix introduced a 100 GHz real-time oscilloscope and a 240 Gs/s sampling rate. More improvements were made in the design, and the resolution was also improved [4]. Nowadays, most oscilloscopes are delivered with a high definition mode (HD) featuring 16-bit vertical resolution. This is how an efficient Digital Storage Oscilloscope (DSO) came into existence.

WORKING PRINCIPLE OF A DSO

DSO stores the input signal, digitizes it, analyses it, and displays it. This task is done using a CRT and a memory which is digital. The sample input signals are taken as periodic waveforms, and hence the digitization is done.The recurrence estimated by an advanced stockpiling oscilloscope relies upon two elements: Sampling Rate and Nature of Convertor.

20 July 2023 11:13:15

Sampling Rate

Sampling Rate means the rate of Analogue to Digital conversion. As per the Sampling Theory, the rate of sampling of the sign must be twice as quick as the most elevated recurrence of the information signal. Sampling Theory is used so that the analysis of the input signal is done safely and properly.

Nature of Convertor

The frequency measured by a Digital Storage Oscilloscope also depends on the nature of the convertor. The better the convertor used, the better will be the measurement. A costly blaze is utilized in the converter whose goal diminishes on the expanding examining rate. The data transfer capacity and goal of the Oscilloscope is restricted because of the examining rate. A shift register can also be used in place of a convertor. An information signal is tested and put away in the move register. From the move register, the sign is gradually perused out and put away in a computerized way. This technique lessens the expense of a converter and works up to hundred mega sample every second [7]. Another important step involved in the working of a DSO is waveform reconstruction.For picturing the last wave, the oscilloscopes utilize the procedure of between polarizations. The between polarization is the way toward making new information focuses with the assistance of realized variable information focuses. The two cycles of associating focuses together are linear interpolation and sinusoidal interpolation.In addition, the lines are utilized for associating the spot together. Straight interjection is additionally utilized for making the beat or square waveform. For the sine waveform, the sinusoidal insertion is used in the Oscilloscope [7].

CRO V/S DSO

The type of electrical instrument used for the analysis of various waveforms along with their behaviour and measurement is defined as a Cathode ray oscilloscope. Various other electrical phenomena are also identified using this device. CROs are used to distribute waveforms, momentary wonders, and other values ranging from low

frequency access to very high frequency radio waves. The gadget basically works on the part of voltage; subsequently, different amounts, for example, current, charge, strain, speeding up is changed over to voltage with the assistance of a transducer by which it tends to be spoken to on the CRO. The stylus (Luminous spot) of the CRO moves over the presentation territory because of the info voltage; it is delivered with a light output that hits the fluorescent screen. The typical type of a CRO utilizes an inside produced incline voltage known as the 'time base,' which is a flat info voltage. The level of power moves a brilliant space once and for all in the same way from left to directly above the introduction domain or screen. The vertical voltage is the voltage under scrutiny. The vertical voltage moves the sparkling spot generally on the screen. At the point where the info voltage is moving too fast on the screen, the on-screen display appears to be fixed. In line with these lines, the CRO provides a way to consider the variable voltage of time. Cathode Ray Oscilloscope (CRO) comprises of a bunch of squares. Those are vertical intensifier, defer line, trigger circuit, time base generator, flat speaker, Cathode Ray Tube (CRT) and force gracefully.Their functioning is explained now.

- **Vertical Amplifier**: Used in amplifying the information that is also called as input signal which is to be displayed on the cathode ray tube i.e.CRT.
- **Delay Line:** It provides signal reversal, which is thus obtained as a direct amplifier yield and used over CRT.
- **Trigger Circuit**: Used in the synchronization of both level and vertical diversions of the electron beam by producing a triggering signal.
- **Time-base Generator**: It is used in the production of the required signal which is of the type saw-tooth, which can horizontally deflect the electronic beam.
- **Horizontal Amplifier**: Amplification of the saw-tooth signal is done here along with the required connection to the horizontal deflecting plates of the CRT.
- **Cathode Ray Tube (CRT)**: The main square of the CRO is and mostly has four segments. That is an electron firearm, a fluorescent screen, vertical redirection plates and vertical evasion plates.
- **Power supply**: Utilized in the creation of negative high and positive low voltages, which are, thusly, applied to the CRT and different circuits.

There were some disadvantages of using a CRO. In a CRO, no memory storage is available. So, the signal can only be analyzed in real-time. A CRO cannot analyze different types of high-frequency signals like sharp rise time transients. A considerable amount of training and skill is used to operate a Cathode Ray Oscilloscope, and it can only be done under guidance. It doesn't offer all the abilities as upheld by a digital storage oscilloscope. Therefore, there was a need for better Oscilloscope. To overcome these disadvantages of a CRO, a DSO was developed. Table I shows the comparison between a CRO and DSO.

20 July 2023 11:13:15

Table I: Comparison between CRO & DSO

CRO	DSO
Cathode ray oscilloscope (CRO) is an analog oscilloscope that was used extensively in the past.	Digital storage oscilloscope (DSO) is a digital oscilloscope which is used everywhere nowadays.
CRO has higher bandwidth and writing speed than a DSO; 15 GHz is provided easily.	They are limited in speed due to the digitizing capability of the analog to digital converter.
Used to measure signals including amplitude, frequency etc.	Used to measure the different signals, be it amplitude or frequency in a digitalized form. Was designed to overcome the limitations of CRO.
No storage of signals in any form, be it binary or numerical, is possible in the CRO. One of the reasons for the decline in its use in recent times.	The obtained signal is stored as 'memory' in the DSO; that is, it is stored in the binary form. It is one of the main reasons DSO is used so extensively.
The basic circuit consists of Cathode Ray Tube, Vertical Amplifier, Delay line, trigger circuit, Time and base generator, and a horizontal amplifier.	The basic circuit consists of an Input Attenuator, Vertical Amplifier, Analogue to Digital Converters, Memory, Trigger Circuit, and a Cathode Ray Tube.

I. TYPES OF DSO

DSO is broadly divided into three categories- Traditional bench-top type of DSO, Hand-held type of DSO, and PC-based DSO. A PC based DSO is further divided into two categories- External and Internal. The traditional bench-top type of DSO has a high performance. It also has various additional options, such as a PC interface and disk drives. Moreover, it also has a printing facility but is usually available at a high cost. A hand-held Digital Storage Oscilloscope is advantageous for engineering purposes, but it has poor displays. It is difficult to read the output in sunlight, and a hand-held DSO has short battery life. An external PC based DSO connects to the personal computer using a USB (Universal Serial Bus) or by a parallel port. Such type of DSO is highly portable as it can easily be connected to a laptop or a desktop. The noise problem is also minimized in an external PC based DSO. An internal PC based digital storage oscilloscope comes in PCI (Peripheral Component Interconnect) format plug-in cards. Since it is inside a PC, it can create a very noisy electrical environment. Some cards might also suffer due to this. Another issue with an internal PC based DSO is that it is not portable.

TRIGGERS AND CURSORS IN A DSO

Triggers and cursors play a very important role in the working of a DSO. The following section describes the triggers and cursors of a DSO in detail.

A. *Scope Trigger*

A scope trigger or level is a movable voltage "set point" whereupon the scope will initiate to represent a pattern of display to an example. We can pick the voltage, the pattern essentially reach before it is introduced. It is usually portrayed by a jewel ◊ or in addition to stamp + on the screen. In the event that the trigger level voltage is directed higher than the separate voltage of the pattern, which is shown, the screen won't show the pattern. This is because of the explanation that "trigger level voltage" has not been "met." (Except if the AUTO trigger mode is chosen.) A trigger changes a set point where the mentioned scope will begin portraying a pattern. The trigger level recognizes when a specific voltage level has been finished and at this specified instant, prepares the base of the working time to erase the other side and covers the whole screen. In effect, the level of trigger acts like a comparator, i.e., a time-varying electrical circuit to start when the voltage level has reached and the preset values have expired. The trigger inclination/trigger gradient, as the name demonstrates, decides if the time-base compass is set off on a positive or negative going edge or angle (gradient).

B. *Trigger level adjustment*

Trigger level is a physically chosen variation that presets the voltage point that the pattern HAS TO cross before the desired pattern is shown on the yield screen. (Not relevant for AUTO trigger mode). The trigger level is picking a voltage and time point where the pattern must advance through before the said pattern is shown.

C. *Auto Trigger*

The DSO would always display a pattern each timeregardless of the change of the trigger level. It might stream over the screen till the level is adjusted someplace in the said pattern.

D. *Norm Trigger*

A commonplace trigger won't portray a pattern until and except if it advances through the normalized trigger level setting. No pattern will be given in the yield if the trigger level is changed over the most extreme voltage of the pattern.In the event that the trigger level is changed underneath the base voltage of the pattern, no pattern will be portrayed in the yield.

E. *Single Trigger*

The single trigger will portray just a solitary pattern when the pattern advances through the normalized trigger level and will then "freeze" the example for explicit analysis.

F. *Hold Trigger*

Some scopes have a "HOLD" feature. This mode will "freeze" the pattern on the yield screen despite the fact that the signal may even now be in the dynamic state. This licenses for nearer survey and examination of the signal. Releasing the HOLD highlight/mode will allow the pattern to return to "live information." For starting and beginning oscilloscope users, it is commonly suggested that the AUTO trigger component be chosen so a pattern will arise on the screen. On the off chance that it "trips" to and fro, change the trigger level till it "bolts" the pattern still.

G. *Trigger Slope/Trigger Gradient:*

Trigger slope or Trigger gradient is a change that prompts the extension to portray a pattern either on the principal "upward" or "descending" movement of the signal. All in all, in the event that we select the "positive" (up),

20 July 2023 11:13:15

the scope yield screen would start depicting the pattern on the absolute first upward voltage movement. Other than that, in the event that we select "negative" (down), the pattern would begin portraying the primary voltage movement in the "down" course or down sense. Trigger gradient/Trigger slope is valuable while distinguishing explicit components and plans or segments and patterns.

H. *Cursors*

Utilizing cursors on scopes can present careful calculations of voltage, time, recurrence/frequency (rate), and obligation cycle. All scopes do not have cursors, yet most do. A cursor is a versatile "line" that appears on the yield screen. It tends to be each a vertical or an even line. Most extensions/scopes utilize two vertical and two-level cursors. Cursors can likewise be turned to both “on” and “off” state dependent on the test technique at that point. Cursors are for the most part of two kinds: Voltage cursors and Time cursors. Voltage cursors are utilized to gauge vertical parameters. They show up as level lines on the output display. Time cursors are utilized to quantify the level parameters. They show up as vertical lines on the display screen.

RECENT DEVELOPMENTS IN THE FIELD OF DSO

A lot of scientists from different backgrounds and having a lot of experience in a wide variety of electronic work have worked tirelessly to try to achieve a better technology to be used in a DSO [9]. In 2011, “Wang Pentian” along with “Wang Zibin” committed to improving the peak recognition of digital storage oscilloscopes. They used FPGA based technology. Using their designed technology, it was observed that a continuous peak was obtained, which was previously seen as discontinuous [10]. Christian Fager and KristofferAndersson [11] committed to improving oscilloscope-based RF estimation through statistical averaging technology in which repeated measurements were used along with the factual averaging methods to improve the dynamic reach of the signal. The technique given by Fager and Anderson used Stretched out “Kalman Filters” to follow transporter Estimate the frequency drift between. Using this strategy, synchronous and asynchronous estimation can be completed effectively. The record length, rate of the sampling recurrence/frequency(rate), the bandwidth of the signal, and the Oscilloscope's efficiency have increased and advanced a lot in recent and ongoing times. These enhancements in the abilities of the Oscilloscope are significant in “semiconductor circuit” advancement, pulse power computations, the field of nuclear weapon test and analysis, laser beam research and implementations, time-space reflectometry examination, a trial of micro-wave and other wave instruments, and some more.

20 July 2023 11:13:15

DSOs employs three basic methods of sampling the signal:

- Real-time
- Sequential comparable time (ET sampling)
- Random ET or Sequential comparable time

Through continuous and irregular ET tests, the generated high-level waveforms (digitized) are copied from the given samples in the step-by-step acquisition cycle. Real-time sampling only needs one sampling period to capture all samples. That is, samples are acquired only by a single pass of the waveform. Sequential comparable time testing must be utilized for monotonous waveforms, although capturing a single transient requires continuous real-time inspection/sampling. For real-time sampling, the signals are consistently analysed and digitized, and coordinated to the purchase memory. In some gadgets, such as gadgets that use charge-coupled gadgets (CCD), the samples are temporarily stored in analog form and digitized after a certain period of time. In the case of insufficient triggers, the memory will load "pre-trigger" information units, and after the memory is full, new information units will cause the most sophisticated information units to be discarded or overwritten to a different form.

After the trigger is acquired, the "post-trigger" information will be acquired and stored indefinitely. The number of captured “pre-trigger” and post-trigger information units is controlled by the “level control setting”. Through back-to-back Sequential Comparable time sampling, one point of the waveform is sampled in each “purchase period” (that is, after each trigger pulse). Each subsequent sample is further delayed from the trigger point by one “cycle stretching At”, so that the focus is on the waveform to be sampled. The number of Sequential Comparable Time test repetitions is 1/At. Since all samples are acquired after the trigger, the “pre-trigger” signal cannot be acquired. For Sequential Comparable Time sampling, there is no specific relationship between the “sample clock repetition frequency” and the “Sequential Comparable Time sampling repetition frequency”. Generally, the “clock repetition frequency” is significantly smaller than the “Sequential Comparable Time sampling repetition frequency”.Asymmetrical Sequential Comparable Time sampling has some attributes of continuous Sequential Comparable Time and continuous/real-time sampling.

Similarly, as with continuous sampling, different safety periods are expected to acquire signals and the "Sequential Comparable Time sampling repetition rate (frequency) is 1/At", where "At is the ET sampling interval". Like real-time sampling, the signal is continuously evaluated and sampled during the sampling clock repetition cycle, and samples are collected before and after the trigger ("Pre-trigger and post trigger cycles"). Considering that the trigger is not synchronized with the clock, the sampling time can be freely selected comparative to the trigger time [9]. To allot the data unit in the correct memory segment, the time interval between the trigger and the data unit must be evaluated without a doubt for each acquisition cycle.

The precise timing circuit uses a counter to select these estimated targets Tr. The selected time base characterizes the value of At. The "real-time sampling DSO" is always used to obtain single transient signals with short rise/fall times. Subsequently, a high inspection rate f is sought. The basically acceptable sampling frequency is given by "Nyquist hypothesis/Nyquist sampling hypothesis" (sampling frequency)/2 must be more prominent than the maximal signal frequency component"), and if the test is performed twice, there is a signal recovery problem [13-18]. Contingent on the introduction strategy using frequency between sampling points and checking that the frequency is "between two and ten times to ten times" the most noteworthy signal repeat segment to reproduce the input signal. In any case, it can be seen that the ongoing DSO requires high sampling rate and fast acquisition/memory speed.

ADVANTAGES AND DISADVANTAGES OF DSO

The waveform stored can be used by providing power only to memory for any considerable period display. The signals are stored in digital form, thereby preventing its degradation. We can easily store more than one waveform in this type of Oscilloscope. It is easy to use and quite user friendly. There will be an improvement in the image quality when compared to the tube type storage oscilloscope. It also has a high-speed data acquisition system. The only disadvantage of a DSO is that its structure is very complex, and if damaged, its repair can be costly [19-25].

USES OF DSO

A DSO can display voltage and current over a time period. It can also capture subtle and very fast changes in a signal. DSO contains transducers, due to which it can be used as a very powerful diagnostic tool. It can also record signals for playback and evaluation. Pressure, vacuum, temperature, and various other factors, can also be viewed using a DSO. The digital storage oscilloscope (DSO) can also be used as an instrument to determine the radiation pattern generated by a transmitting antenna oscilloscope.

CONCLUSION

Digital Storage Oscilloscope stores and analyses signals in a digital way. It is of various types as traditional bench-type DSO, hand-held type DSO, and a PC based Digital Storage Oscilloscope. It takes the signal, stores it, examines it, and displays it as output, and all this is done with the help of a Cathode Ray Tube and a Digital Memory. The frequency measured in a DSO depends upon two factors- Sampling Rate and Nature of Convertor. Triggers and Cursors are the two parts that play an important role in its functioning. In recent years, many developments have taken place in the technology of a DSO. A DSO has many advantages over a CRO and can be used to measure voltage and current, display signals, pressure, temperature, and other quantities [26-27].

REFERENCES

1. https://www.amazon.in Scientech-WideScreen-Digital-Oscilloscope
2. http://www.hparchive.com/
3. Electronics & Power November/December 1980
4. http://www.chiark.greenend.org.uk/scopes/tek.html
5. https://circuitglobe.com/wp-content/uploads/2017/06/block-diagram-of-oscilloscope.jpg
6. https://circuitglobe.com/wp-content/uploads/2017/06/interpolation-of-oscilloscopes.jpg
7. https://circuitglobe.com/digital-storage-oscilloscope.html
8. https://i.ytimg.com/vi/Msewq5THpbw/hqdefault.jpg

20 July 2023 11:13:15

9. M. Bansal *et al*, **"**Comparison between Conventional Fast Multipliers and Improved Fast Multipliers using PTL Logic", 2021 *IOP Conf. Ser.: Mater. Sci. Eng.* 1126 012041
10. Improvement of Peak Detection for Digital Storage Oscilloscope- IEEE research paper by Wang Pengtian and Wang Zibin (2011)
11. Improvement of Oscilloscope Based RF Measurements- IEEE research paper by Statistical Averaging Techniques by Christian Fager and KristofferAndersson (2006). https://i.stack.imgur.com/E04Vn.jpg
12. M. Bansal, Priya (2021) Performance Comparison of MQTT and CoAP Protocols in Different Simulation Environments. In: Ranganathan G., Chen J., Rocha Á. (eds)
13. Inventive Communication and Computational Technologies. Lecture Notes in Networks and Systems, vol 145, pp. 549-560. Springer, Singapore. https://doi.org/10.1007/978-981-15-7345-3_47
14. M. Bansal, M. Nanda and M. N. Husain, "Security and Privacy Aspects for Internet of Things (IoT)," 2021 6th International Conference on Inventive Computation Technologies (ICICT), 2021, pp. 199-204, doi: 10.1109/ICICT50816.2021.9358665.
15. M. Bansal, P. "Machine Learning Perspective in VLSI Computer Aided Design at Different Abstraction Levels", S. Shakya et al. (eds.), Mobile Computing and Sustainable Informatics, Lecture Notes on Data Engineering and Communications Technologies vol. 68, pp. 95-112, Springer, Singapore 2021. https://doi.org/10.1007/978-981-16-1866-6_6
16. M. Bansal, S. Gupta and S. Mathur, "Comparison of ECC and RSA Algorithm with DNA Encoding for IoT Security," 2021 6th International Conference on Inventive Computation Technologies (ICICT), 2021, pp. 1340-1343, doi:10.1109/ICICT50816.2021.9358591.
17. M. Bansal, T. Chopra and S. Biswas, "Organ Simulation and Healthcare Services: An Application of IoT," 2021 6th International Conference on Inventive Computation Technologies (ICICT), 2021, pp. 205-208, doi: 10.1109/ICICT50816.2021.9358677.
18. M. Bansal and S. Garg, "Internet of Things (IoT) based Assistive Devices," 2021 6th International Conference on Inventive Computation Technologies (ICICT), 2021, pp. 1006-1009, doi: 10.1109/ICICT50816.2021.9358662.
19. M. Bansal, N. Adarsh, N. Kumar and M. Meena, "24×7 Smart IoT based Integrated Home Security System," 2020 Fourth International Conference on Inventive Systems and Control (ICISC), 2020, pp. 477-481, doi: 10.1109/ICISC47916.2020.9171051.
20. M. Bansal, G. Srivastava. (2020) Design and Implementation of LNA for Biomedical Applications. In: Pandian A., Ntalianis K., Palanisamy R. (eds) Intelligent Computing, Information and Control Systems. ICICCS 2019. Advances in Intelligent Systems and Computing, vol 1039, pp. 154-167, Springer, Cham. https://doi.org/10.1007/978-3-030-30465-2_18
21. M. Bansal and J. Singh, "Comparative Analysis of 4-bit CMOS Vedic Multiplier and GDI Vedic Multiplier using 18nm FinFET Technology," 2020 International Conference on Smart Electronics and Communication (ICOSEC), Trichy, India, 2020, pp. 1328-1332,doi: 10.1109/ICOSEC49089.2020.9215317.
22. M. Bansal and J. Singh, "Qualitative Analysis of 2-bit CMOS Magnitude Comparator and GDI Magnitude Comparator using FinFET Technology (18nm)," 2020 International Conference on Smart Electronics and Communication (ICOSEC), Trichy, India, 2020, pp. 1323-1327, doi: 10.1109/ICOSEC49089.2020.9215251.
23. M. Bansal, V. Sirpal, M. K. Choudhary, "Advancing e-Government using Internet of Things", S. Shakya et al. (eds.), Mobile Computing and Sustainable Informatics, Lecture Notes on Data Engineering and Communications Technologies vol. 68, pp. 123-137, Springer, Singapore 2021. https://doi.org/10.1007/978-981-16-1866-6_8
24. M. Bansal, V. Bharti, V. Chander, "Comparison between Conventional Fast Multipliers and Improved Fast Multipliers using PTL Logic", IOP Conf. Ser.: Mater. Sci. Eng., Vol. 1126, Issue 012041, pp. 1-12, 2021. doi:10.1088/1757-899X/1126/1/012041
25. M. Rawat, M. Bansal, "Voltage Mode Two-Phase and Four-Phase Sinusoidal Oscillator Using VDCC", "International Journal of Advanced Research in Electronics and Communication Engineering", Vol. 4, Issue 6, pp. 1687-1691, 2015

20 July 2023 11:13:15

26. Bansal M., Sirpal V., Choudhary M.K. (2022) Advancing e-Government Using Internet of Things. In: Shakya S., Bestak , R., Palanisamy R., Kamel K.A. (eds) Mobile Computing and Sustainable Informatics. Lecture Notes on Data Engineering and Communications Technologies, vol 68. Springer, Singapore. https://doi.org/10.1007/978-981-16-1866-6_8
27. Malti Bansal, Harmandeep Singh, Gaurav Sharma, "A Taxonomical Review of Multiplexer Designs for Electronic Circuits and Devices", Journal of Electronics and Informatics, vol. 3, Issue 2, pp. 77-88, 2021.

.

20 July 2023 11:13:15

2023 3rd International Conference on Advance Computing and Innovative Technologies in Engineering (ICACITE) | 979-8-3503-9926-4/23/$31.00 ©2023 IEEE | DOI: 10.1109/ICACITE57410.2023.10182886

Abenet: An emotion recognition for Bengali language

Rajat
Department of Computer Science and Engineering, Delhi Technological University

Pooja Jaiswal
Department of Computer Science and Engineering, Delhi Technological University

Rahul Kakkar
Department of Computer Science and Engineering, Delhi Technological University
rahulkakkar_2k19co304@dtu.ac.in

Rohit Beniwal
Department of Computer Science and Engineering,
Delhi Technological University

Abstract—আবেগ, Ābēga (Known as Emotion in Bangla), a fundamental and significant part of who we are is shaped by our emotions. Though it may not always be obvious, everything we do, and say reflects some of our emotions in some way. Human behavior can be understood if we analyze these emotions from data. Text, speech, and facial expressions are all examples of this data. The challenge of quantifying emotions is highly difficult, and although significant progress has been made, there is still much room for improvement. Since social networking websites have become so popular, many individuals have developed a strong interest in exploring the material that is posted on these different websites. By studying this data across the Internet, we are traversing the whole continent, all of its cultures and communities. The work for regional languages is limited in this particular domain. So, the purpose of this paper is to propose a model which can accurately predict or classify emotions in regional languages.

Keywords: Emotions, cognitive theory, demographic languages

I. Introduction

Emotions are cognitive states that are caused due to neurophysiological changes related to varied sensations, ideas, behavioral reactions, and degree of satisfaction or dissatisfaction. Emotions are frequently linked to state of mind, behavior, persona, creativity, or disposition. Research on emotion has risen during the last two decades, with various areas participating, including science of mind, history, medicine, sociology of emotions, and technology. Current fields of emotion study include the creation of materials that excite and generate emotion. The three primary theories of emotions are Physiological, cognitive and neurological. Physiological theories contend that biological responses are the origin of emotions. According to neurological theories, brain activity is what triggers emotional responses. Ideas and other mental activities are essential for the growth of emotions, according to cognitive theories.

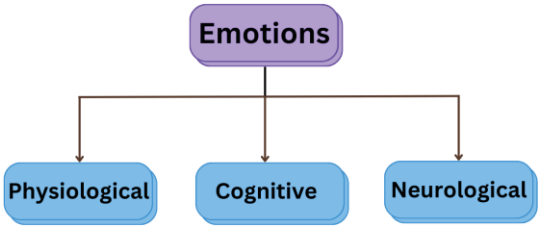

Fig. 1. Categories of emotion theories

Emotions are difficult to understand. There are various views on whether emotions create changes in our behavior. Moreover, Emotions are directly proportional to our physical and mental illness. For instance, if a person is suffering from a mild fever or any illness like it, his state of mind will become angry soon, if teased or harmed by someone. On the other hand, if a person is in a lavish mood or state of mind, his state of mind will not become angry as soon as compared to the previous situation. Extroverted individuals express their feelings and are more sociable, whereas introverted individuals are more socially aloof and conceal their ideas and emotions. Emotion frequently drives motivation. Another instance would be that if you see a tiger in the wild, you would know that you are in grave danger. Following it, the bodily and emotional responses of fear or terror occur.

Emotion analysis is a practice of finding and understanding the emotions represented in supplied data, which might be textual, audio, or video. Analyzing the emotions of data over the world wide web has significance. For example, measuring the well-being of a community, preventing suicides, and can be helpful for institutes to measure the degree of satisfaction of their customers by inspecting the feedback they provide. Here, with our work, we are trying to figure out the regional languages which have yet not been incorporated into the existing literature to understand the emotions of local individuals. We are trying to achieve results in the Bangla language as it is one of the regional languages of India and Bangladesh, the countries located in the south Asian continent. On the basis of the total number of speakers, Bangla is the seventh most spoken language in the world. This language is used to promote the literary content and analyze emotions depicted by it, by popular Bangla writers like Rabindranath Tagore, Satyajit Ray, Bibhutibhushan Bandyopadhyay, and many others who also contributed to noble causes, upliftment of society and provided a new perspective of the world.

In this paper, we have proposed a model named AbeNet, to detect emotion classification as closest to the manual classification while using a regional language.

Authorized licensed use limited to: DELHI TECHNICAL UNIV. Downloaded on August 08,2023 at 09:03:24 UTC from IEEE Xplore. Restrictions apply.

II. Literature Review

In this section, we have discussed the work of the researchers who have contributed to the domain of emotion and sentiment analysis. Most of the work in the field was done especially in the domain of textual datasets.

It has been noted that there has been a significant improvement in the result of various computational models such Naive Bayes, Conditional random fields, and Decision Trees. Accuracies over time with the modification of outdated computational methods, the lexical resources, and the features generated [1]. Most researchers explored the literature related to the analysis of various languages deeply to understand the challenges in analyzing low-resource language and the lack of resources in sentiment analysis was observed where it concluded that there is still a need for building resources, used in sentiment and emotion analysis work [2]. Additionally, a review of knowledge on degrees of sentiment analysis, different emotion models, the procedure for sentiment analysis and emotion detection from text, as well as the difficulties encountered during sentiment and emotion analysis, was offered [3]. A summary of knowledge on emotion analysis in literary contexts was offered. Tracking dramatic shifts in a plot's development, network analysis of a literary text, and comprehension of texts' emotional content are only a few of the issues covered in the research under consideration [4].

Researchers have worked in various languages including Hindi, English, Punjabi, Urdu, etc. Some analyzed emotions from lyrics of some Hindi songs as well, in which they used Multinomial Naïve Bayes (MNB), Support Vector Machine (SVM), Logistic Regression (LR), and K-Nearest Neighbors (KNN) classifiers to provide emotion classification [5]. Moreover, research was done to assess emotions from social media, including Twitter, utilising ensemble models mixed with single classifiers on two different types of datasets, one of which was binomial (positive and negative), and the other was polynomial (positive, negative, and neutral) [6].

An algorithm was tested on 662 movie review datasets generated by the researchers. It was tested on various experimental settings [7]. A transformer-based approach to analyze sentiments in Arabic was proposed and numerical results showed that the approach out-performed the existing Arabic Sentiment Analysis (ASA) approach [8]. In 2019, the first and biggest Hindi-language annotated corpus, BHAAV, with 20,304 phrases, was made available for emotion analysis. The dataset, language-specific issues, the annotation procedure, challenges related to annotations, and reported performances of the baseline classification models trained on the dataset for recognizing emotions stated in a phrase were all thoroughly described by the researchers. They corroborate BHAAV's abundance of emotion signals through various observations and draw attention to the possible uses [9]. Two ensemble models called mBERT-EMV and mBERT-EAS that are based on mBERT were proposed by researchers [10]. Studies on emotion recognition in code-mixed Hindi and English social media writing were conducted by a few researchers. By scraping CM (Code-Mixing) Hindi and English tweets, they produced their own dataset. They looked into the utility of their dataset and constructed emotion detection classifiers using a variety of cutting-edge classification techniques. On their test set, they achieved an accuracy of 75.17% using our top-performing emotion identification classifier powered by the SVM algorithm [11]. EmoInHindi is a large-scale Hindi conversational dataset created for multi-label emotion classification and discourse intensity prediction. Additionally, they tested it and presented the findings using solid baselines for both the intensity prediction and emotion detection tests [12]. A study demonstrating the automated detection of emotions from tweets after conducting Arabic-related language preparation processes. The experiment showed that the preprocessing procedures added to the Khoja stemmer's performance enhanced the classification outcomes by 4.4% over the performance of the original Khoja stemmer. Additionally, it has been demonstrated that when compared to Sequential minimal optimization (SMO) classification using the train/test option, our example word-emotion lexicon improves the emotion recognition results by 22.27%. Research has demonstrated a strong correlation between communication style and emotional expression in the areas of anger, disgust, fear, and happiness [13]. For Arabic emotion analysis, DINA, a multi-dialect data collection, was introduced. Additionally, an automated method of gathering Measurement System Analysis (MSA) and dialectal Arabic emotion data from the Twitter genre was tested using human annotation [14]. A large-scale emotion lexicon called EmoWordNet (EMW) was presented. It consists of about 67K EMW words and 58K EMW synsets annotated with 8 emotion ratings. By employing EMW and DepecheMood in conjunction with a semantic expansion technique, EmoWordNet was automatically created. EMW fared better than previous emotion lexicons and had more lexical coverage when used for emotion recognition [15]. For the purpose of detecting Arabic emotions, a Twitter-based dataset was presented. The several steps for creating this dataset were also described. The NB classifier produces the best results with an overall accuracy of 68.1%, according to preliminary and extremely simple studies with this dataset [16]. AraBERT advances the state of the art for several downstream Arabic language problems. Additionally, it was 300MB smaller than the bilingual Transformers [17].

The accuracy of speech emotion recognition has also been improved through the extraction of speech signal features and emotion classification techniques, including a novel classification method that combines a Deep Belief Network (DBN) and SVM rather than using just one of them. The findings demonstrated that DBN features may express emotion states more accurately than synthetic features, and their novel classification method outperforms both DBN and SVM independently in terms of accuracy, achieving a 95.8% score. Results also demonstrated that DBN, with the right architecture, may perform admirably for tiny training databases [18]. Additionally, a transformer-based sentiment analysis method for Chinese e-commerce reviews was put forth utilizing a pre-training model. When compared to the standard RoBERTa classifier model, the emotion polarity classifier exceeds it in terms of F1 score and accuracy rate. When compared to the standard RoBERTa classifier model, the category classifier exceeds it in terms of F1 score and accuracy rate [19]. It was also shown that the Bi-directional Encoder Representation from a transformer with a fully connected layer (BERT+FC) technique may achieve exceptional performance when used to analyze innovative sentiment analysis models for Chinese stock ratings based on BERT [20]. A hybrid approach was devised that provided both superior classification accuracy and coverage when compared to word embedding models and polarity lexicons,

Authorized licensed use limited to: DELHI TECHNICAL UNIV. Downloaded on August 08,2023 at 09:03:24 UTC from IEEE Xplore. Restrictions apply.

respectively. The accuracy of the automatically produced lexicons and the hybrid method with machine-translated polarity lexicons (manually checked and enhanced), which does not accurately capture Finnish feelings, was assessed through tests using datasets of gathered Finnish internet reviews [21]. For Indonesian tweets, a sentiment analysis algorithm was created. They took 4,000 manually labeled tweets, divided them into 8 groups, including positive, negative, and neutral ones, and employed LSTM without a normalizer to achieve 73.2% accuracy [22]. Two methods for sentiment analysis in the Russian language were also used. A lexicon-based method has been modified for the Russian language (SO-CAL and SentiStrength). A voting process based on the pre-existing lexicons was used to create a unified sentiment lexicon. The RuBERT deep learning model had been employed in the Deep Learning technique (SentiRuEval-2015 corpora). Analysis of the data revealed that deep learning models performed better than lexicon-based techniques in terms of accuracy [23]. Semantic and sentiment analysis is used in a framework that analyses a few Bhagavad Gita translations from Sanskrit to English. BERT, a cutting-edge deep learning-based language model, was tuned using a hand-labeled sentiment dataset. They offered sentiment and semantic analysis for a few chosen chapters and verses across translations, and the findings showed that, despite notable variations in style and terminology, the themes were substantially the same [24].

III. Methodology

We have divided this section into two major sub-sections. The first sub-section represents the dataset used, and the second subsection represents the architecture and workings of the AbeNet model.

A. Dataset

For the dataset, we transcripted the Bangla dialogues from the "Baahubali" series and then manually classified those dialogues based on depicted emotion. Every dialogue is classified into an emotion out of six emotions mentioned in the figure-2 below.

Fig. 2. Types of emotions

The dataset consists of 1477 rows and 3 columns, the first one is named Role which represents the speaker of the dialogue (Baahubali, Shivsena, Deva sena, etc), the second one is Utterance which is the dialogue itself, and the last one is the Emotion which is the classification of emotion (anger, neutral, surprise, etc) done manually.

Role	Utterance	Emotion
Bhallaladeva	...আর কি হতে পারে, কিন্তু বিকৃত এবং আঁকাবাঁকা?	Fear
Deva Sena	...| খুঁজে পেতে হবে, আপনি একটি রাজকুমারী বর্ণন...	Neutral
Avantika	যেহেতু আমি যাহাই হউক না কেন একটি 'কুকুর'...	Sadness
Bijjaladeva	...পছন্দ একটি ঘ্রাণ জ্বালাতন আমি করতে পারে এটি...	Surprise
Sivagami	তিনি রাজকুমারী এর মায়াপুরা, বারুণী	Happiness
Kattappa	এমনকি যদি আপনি ঝুঁটি প্রতি কোণে আমাদের বিশ্বের...	Anger

Fig. 3. Instance of dataset

B. Proposed model: AbeNet

AbeNet, Abega Neural Network Model has been proposed for this dataset. AbeNet consists of the state-of-the-art BERT model and neural network to classify given input into emotions. The neural network of AbeNet consists of 20 hidden layers along with an input and output layer.

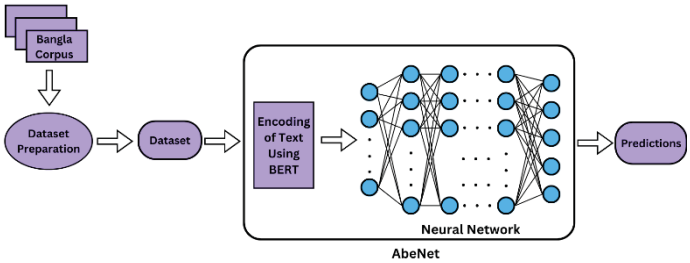

Fig. 4. Working of AbeNet

Our model has three phases which are:

1. DATASET MAKING
2. ENCODING OF TEXT USING BERT
3. NEURAL NETWORK AND PREDICTION

In the first phase, we made the dataset from the series named Baahubali, which gave us the dialogues in the Bangla language, then we transcripted and labeled them according to the roles of characters. After transcription of the dialogues, we manually classified each dialogue based on the emotion depicted by it. After getting the dataset ready, we randomly divided the dataset into two parts one for testing and other for training data, 95% of the dataset is classified as training data and used for training purposes only whereas 5% is named as testing data and used for testing the effectiveness of the model.

In the second phase, we fed them to the state-of-the-art language model such as BERT. The BERT, a transformer-based machine learning approach for pre-training Natural Language Processing (NLP). It is a transformer language model with self-attention heads and a selectable number of encoder layers. For a variety of downstream Natural Language Processing (NLP) tasks for Indian languages, this model is intended to be used. Additionally, this model was trained using transliterated data, which is common in the Indian context. Other than the 17 Indian languages utilized in pre-training, this model is not expected to perform well on other languages.

It had already been pre-trained on two tasks: next sentence prediction and masked language modelling. BERT gains knowledge of word contextual embeddings as a result of training. After pretraining, a computationally intensive step.

Authorized licensed use limited to: DELHI TECHNICAL UNIV. Downloaded on August 08,2023 at 09:03:24 UTC from IEEE Xplore. Restrictions apply.

To maximize its performance on certain tasks, it may be fine-tuned using fewer resources on smaller datasets. It is simple to use and enables quick fine-tuning, giving it a wide range of potential practical uses.

Masked Language Modelling (MLM) and Next Sentence Prediction (NSP) are trained simultaneously in the model, BERT, with the aim of minimizing the combined loss function of both techniques.

This language model is used to generate contextualized vector embedding through dialogues. Here we used the base architecture of the BERT therefore each dialogue is converted into a vector of size 768. This contextualized vector is later used as an input for the next section, in neural network, and prediction.

Lastly, in the third phase of our model, we designed a neural network in order to implement a solution to the multiclass classification problem of emotion prediction. We converted our emotion labels into numeric form by using a label encoder after which our labels as in table-1 below.

TABLE I. MAPPING BETWEEN LABELS AND EMOTIONS

Label-Numeric	Label-Nomenclature
0	Anger
1	Fear
2	Happiness
3	Neutral
4	Sadness
5	Surprise

After encoding our labels, we pass both, contextualized vector and encoded labels, into our neural network as input in order to train our model. As output, we get a prediction array specifying the probability of each emotion type depicted from the contextualized vector passed as input.

IV. Results and Discussions

This section represents the results achieved after the training and testing of our proposed models. The performance of the AbeNet is evaluated on the basis of accuracy and F1-Score. Here, F1-score is used along with the accuracy because accuracy as a metric is quite sensitive towards the distribution of targeted values, and it's crucial to grasp the performance, specificity, and sensitivity of a classifier on an imbalanced dataset.

A. Performance Measures

The current network is trained for 100 epochs, and other hyper-parameters of the AbeNet model used are as in table 2 below.

TABLE II. PARAMETERS OF NEURAL NETWORK

Parameters	
Loss	Sparse categorical cross entropy
Optimizer	Adam
Activation Function	ReLU(Hidden layers), and Softmax(output layer)
Learning rate	10^{-5}
Batch size	16

The metrics mentioned above, are used to analyse the performance of the AbeNet tabulated in Table 3. According to Table 3, AbeNet achieved an accuracy of 81.87% on testing data along with the F1-score of 75.26% when BERT model is used for the embedding of textual data.

TABLE III. PERFORMANCE OF ABENET

Model	Accuracy	F1-Score
AbeNet	78.44%	79.60%
(BERT+Neural Net)	81.87%	75.26%

Performance of AbeNet over training and testing data, measured over different parameters such as accuracy, precision, recall and F1-score have been graphically represented in fig.5 below.

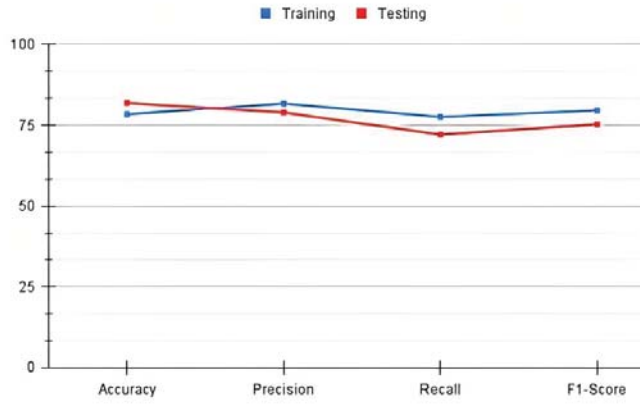

Fig. 5. Performance of AbeNet B. Comparative Analysis of Proposed model with SOTA

This subsection of the paper highlights the accuracy achieved from our proposed model, AbeNet and has been compared with existing state-of-the-art [25] in fig.6 as shown below.

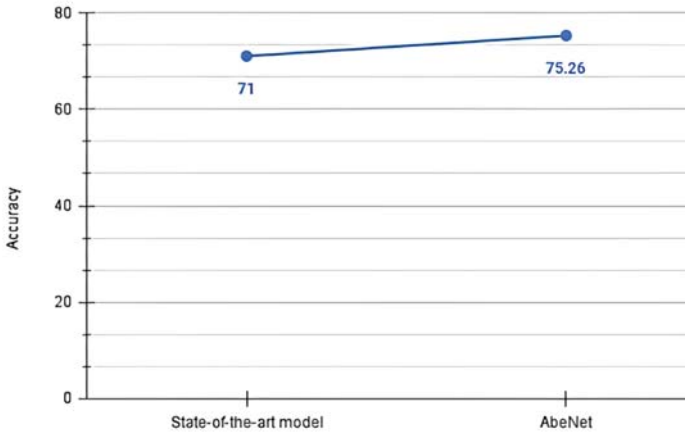

Fig 6. Comparative analysis of AbeNet with state-of-the-art model

V. Conclusion

This research shows how textual data in a regional language can be used to predict emotions with a proposed model. Here, we used textual data in the Bangla language to bring a relatively new language into the mainstream for

Authorized licensed use limited to: DELHI TECHNICAL UNIV. Downloaded on August 08,2023 at 09:03:24 UTC from IEEE Xplore. Restrictions apply.

emotion prediction. Emotion prediction is a famous multiclass classification problem but still, research in this particular area is limited to a few languages only, due to which other languages don't have models and data available compared to the languages which have a good amount of resources. Taking all these into consideration, in this research Bangla language is used for the problem of emotion classification, and proposed a model, AbeNet uses a state-of-the-art model BERT for classification. In this research, the proposed model achieved an accuracy of 81.87% and F1 score of 75.26%. The model proposed in this research can be used for emotion prediction in other regional languages, and other state-of-the-art language models can also be incorporated to improve the accuracy achieved with current models. The lack of data that can be used for emotion prediction in regional languages is a big issue, generation of such data can lead to more efficient models for emotion prediction, and proposed models can also be trained or tested against different data to improve the robustness and performance of models.

REFERENCES

[1] Hakak, N. M., Mohd, M., Kirmani, M., & Mohd, M. (2017, July). Emotion analysis: A survey. In 2017 international conference on computer, communications and electronics (COMPTELIX) (pp. 397-402). IEEE.

[2] Azam, N., Tahir, B., & Mehmood, M. A. (2020). Sentiment and emotion analysis of text: A survey on approaches and resources. Language & Technology, 87.

[3] Nandwani, P., & Verma, R. (2021). A review on sentiment analysis and emotion detection from text. Social Network Analysis and Mining, 11(1), 1-19.

[4] Kim, E., & Klinger, R. (2018). A survey on sentiment and emotion analysis for computational literary studies. arXiv preprint arXiv:1808.03137.

[5] Dhar, Sourish & Gour, Vishal & Paul, Arnab. (2022). Emotion recognition from lyrical text of Hindi songs. Innovations in Systems and Software Engineering. 10.1007/s11334-022-00520-z.

[6] AminiMotlagh, M., Shahhoseini, H., & Fatehi, N. (2023). A reliable sentiment analysis for classification of tweets in social networks. Social Network Analysis and Mining, 13(1), 1-11.

[7] Mittal, N., Agarwal, B., Chouhan, G., Pareek, P., Bania, N. (2013). Discourse Based Sentiment Analysis for Hindi Reviews. In: Maji, P., Ghosh, A., Murty, M.N., Ghosh, K., Pal, S.K. (eds) Pattern Recognition and Machine Intelligence. PReMI 2013. Lecture Notes in Computer Science, vol 8251. Springer, Berlin, Heidelberg. https://doi.org/10.1007/978-3-642-45062-4_102

[8] Chouikhi, H., Chniter, H., & Jarray, F. (2021, September). Arabic sentiment analysis using BERT model. In International Conference on Computational Collective Intelligence (pp. 621-632). Springer, Cham.

[9] Kumar, Y., Mahata, D., Aggarwal, S., Chugh, A., Maheshwari, R., & Shah, R. R. (2019). BHAAV- A Text Corpus for Emotion Analysis from Hindi Stories. ArXiv. https://doi.org/10.5281/zenodo.3457467

[10] Pathak, Abhilash & Kumar, Sudhanshu & Roy, Partha & Kim, Byung-Gyu. (2021). Aspect-Based Sentiment Analysis in Hindi Language by Ensembling Pre-Trained mBERT Models. Electronics. 10. 2641. 10.3390/electronics10212641.

[11] Sanket Sonu, Rejwanul Haque, Mohammed Hasanuzzaman, Paul Stynes, and Pramod Pathak. 2022. Identifying Emotions in Code Mixed Hindi-English Tweets. In Proceedings of the WILDRE-6 Workshop within the 13th Language Resources and Evaluation Conference, pages 35–41, Marseille, France. European Language Resources Association.

[12] Singh, G. V., Priya, P., Firdaus, M., Ekbal, A., & Bhattacharyya, P. (2022). EmoInHindi: A Multi-label Emotion and Intensity Annotated Dataset in Hindi for Emotion Recognition in Dialogues. ArXiv. https://doi.org/10.48550/arXiv.2205.13908

[13] Rabie, Omneya & Sturm, Christian. (2014). Feel the Heat: Emotion Detection in Arabic Social Media Content.

[14] Abdul-Mageed, M., AlHuzli, H., & DuaaAbu Elhija, M. D. (2016, May). Dina: A multi-dialect dataset for arabic emotion analysis. In The 2nd workshop on Arabic corpora and processing tools (p. 29).

[15] Gilbert Badaro, Hussein Jundi, Hazem Hajj, and Wassim El-Hajj. 2018. EmoWordNet: Automatic Expansion of Emotion Lexicon Using English WordNet. In Proceedings of the Seventh Joint Conference on Lexical and Computational Semantics, pages 86–93, New Orleans, Louisiana. Association for Computational Linguistics.

[16] Al-Khatib, Amr & El-Beltagy, Samhaa. (2017). Emotional Tone Detection in Arabic Tweets.

[17] Antoun, W., Baly, F., & Hajj, H. (2020). AraBERT: Transformer-based Model for Arabic Language Understanding. ArXiv. https://doi.org/10.48550/arXiv.2003.00104

[18] Zhu, L., Chen, L., Zhao, D., Zhou, J., & Zhang, W. (2017). Emotion recognition from Chinese speech for smart affective services using a combination of SVM and DBN. Sensors, 17(7), 1694.

[19] Xie, S., Cao, J., Wu, Z., Liu, K., Tao, X., & Xie, H. (2020, July). Sentiment Analysis of Chinese E-commerce Reviews Based on BERT. In 2020 IEEE 18th International Conference on Industrial Informatics (INDIN) (Vol. 1, pp. 713-718). IEEE.

[20] Li, M., Chen, L., Zhao, J., & Li, Q. (2021). Sentiment analysis of Chinese stock reviews based on BERT model. Applied Intelligence, 51(7), 5016-5024.

[21] Vankka, J., Myllykoski, H., Peltonen, T., & Riippa, K. (2019, October). Sentiment analysis of finnish customer reviews. In 2019 Sixth International Conference on Social Networks Analysis, Management and Security (SNAMS) (pp. 344-350). IEEE.

[22] Le, T. A., Moeljadi, D., Miura, Y., & Ohkuma, T. (2016, December). Sentiment analysis for low resource languages: A study on informal Indonesian tweets. In Proceedings of the 12th Workshop on Asian Language Resources (ALR12) (pp. 123-131).

[23] Kotelnikova, A., Paschenko, D., & Razova, E. (2021). Lexicon-based methods and BERT model for sentiment analysis of Russian text corpora. In CEUR Workshop Proceedings (pp. 73-81).

[24] Chandra, R., & Kulkarni, V. (2022). Semantic and sentiment analysis of selected bhagavad gita translations using BERT-based language framework. IEEE Access, 10, 21291-21315.

Authorized licensed use limited to: DELHI TECHNICAL UNIV. Downloaded on August 08,2023 at 09:03:24 UTC from IEEE Xplore. Restrictions apply.

Adaptive Two-Stage Reversible Data Hiding in Encrypted Images using Prediction Error Expansion

Ankur
Dept. of Computer Science and Engg.
Delhi Technological University
Delhi, India
ankur_2k20phdco507@gmail.com

Rajeev Kumar
Dept. of Computer Science and Engg.
Delhi Technological University
Delhi, India
rajeevkumar@dtu.ac.in

Ajay K Sharma
Dept. of Computer Science and Engg.
National Institute of Technology
Delhi, India
director@nitd.ac.in

2023 Third International Conference on Secure Cyber Computing and Communication (ICSCCC) | 979-8-3503-0071-0/23/$31.00 ©2023 IEEE | DOI: 10.1109/ICSCCC58608.2023.10176366

***Abstract*—Over the past few years, reversible data hiding in encrypted images (RDHEI) has gained traction a popular method for securely hiding sensitive data within encrypted images. However, the method has its own limitations, as it cannot directly employ existing reversible data hiding (RDH) methods that exploit the spatial correlation of natural images, because of the high entropy of the encrypted images. To address this concern, this paper presents a novel adaptive two-stage (ATS)-RDHEI method based on prediction error(PE) expansion to enhance security and adaptability across a range of applications. The image encryption procedure entails transforming the image into two images based on bit-plane division, followed by block scrambling, pixel shuffling, and encryption while maintaining the correlation of the blocks. In the data hiding phase, a two-stage embedding process hides the secret data while managing probable overflow/underflow issues. Experimental assessments reveal that the ATS-RDHEI method outperforms existing works in terms of EC while maintaining reversibility and visual security. Furthermore, the flexibility and confidentiality of the proposed method is enhanced by its ability to separately extract data and recover images depending on key availability. As a result, the method finds utility in a variety of domains, including secure image storage on the cloud, medical imaging, and multimedia communication.**

***Index Terms*—ATS, error preserving encryption, EC, RDHEI, VRAE**

I. Introduction

In the modern era, establishing secure communication links between senders and recipients has become indispensable, with cryptography playing a vital role in ensuring confidentiality to the transmitted data. Images, akin to text, can be encrypted without any modifications to their structure or loss of pixels. To further increase the security, it is essential to conceal secret the private/secret data using steganography, a specialized technique inside another media. Contemporary steganography techniques hide messages within encrypted or random data, generating an impenetrable cipher akin to a one-time key, which makes the method immune to tampering. Over the past decade, RDH has garnered widespread interest because of its diverse-ranging applicability in fields such as medical imaging, cloud computing, and covert communication. RDH enables the embedding of secret data within a host medium while allowing complete restoration of the medium without any information loss after extracting the hidden data [1]. RDH aims to conceal data without affecting the visual quality of the cover media, such as images or videos, to prevent the detection of hidden information [2]. Till date, various RDH methods which include histogram shifting [3]and PE expansion [4]–[6], have been explored. These methods typically take advantage of the correlation among adjacent pixels in natural images for efficient embedding. However, due to the visibility of original content for data hiders, conventional RDH methods are not suitable for privacy-preserving applications. To tackle this challenge, RDHEI was developed, allowing data to be embedded into encrypted images. RDHEI is especially pertinent for cloud computing applications, where sensitive data is stored and processed on remote servers accessed through the Internet [7]. RDHEI allows for the incorporation of extra functionality in the cloud, such as embedding metadata or annotations into encrypted images, providing additional context or information about the data [8].

In RDHEI, there are typically three entities: the content owner who encrypts the image, the data hider who embeds the payload into the encrypted image, and the recipient who extracts the data or reconstructs the image. Various techniques for RDHEI have been proposed, which can be broadly categorized into two groups: reserving space before encryption (RRBE) and vacating space after encryption (VRAE) [8]. RRBE reserves space within the host image before encryption, but it requires the content owner to anticipate future data embedding. On the other hand, VRAE methods utilize a distinctive encryption technique that preserves spatial correlation in the encrypted images, which enables the creation of space for data hiding. VRAE methods initially encrypt the host image, and subsequently, a data hiding method is applied to embed secret information. Among these categories, VRBE methods offer complete privacy for the original image content from other users involved in the process. To our knowledge, one of the pioneering works in the field of RDHEI is Zhang's [9] method, which aims to utilize the residual spatial correlation in encrypted images for secret data embedding. This technique embeds secret data by flipping the LSB, using block-based division of the image. However, this method only accommodates a limited amount of embedding and raises concerns about its full reversibility. Hong et al. [10] introduced a novel fluctuation function to overcome these limitations, aiming to reduce extraction errors. Zhang [11]

Authorized licensed use limited to: DELHI TECHNICAL UNIV. Downloaded on July 20,2023 at 11:06:10 UTC from IEEE Xplore. Restrictions apply.

later introduced an innovative RDHEI method to significantly decrease extraction errors and increase embedding capacity. This method effectively creates space for embedding within the encrypted image by compressing the LSBs. However, the technique does not fully guarantee reversibility. Liao et al. [12] addressed this reversibility issue by developing an accurate function to determine image block complexity, reducing extraction error rates. The hidden bits can be estimated using the calculated complexity, greatly improving reversibility potential. Khanam et al. [13] further built on [12] by implementing a more precise complexity estimation method, striving for zero extraction error. Bhardwaj et al. [14] extended the research by employing a symmetric crypto-system to improve reversibility and embedding capacity. Wang et al. [15] introduced a high-capacity RDHEI method leveraging popular RDH techniques like PVO and histogram shifting (HS) for embedding secret data. The method utilizes block-level encryption to encode the original image content while preserving the correlation, and then embeds secret data using popular RDH techniques like PVO and HS, achieving high embedding capacity and ensuring reversibility. However, the privacy of the original image content still poses a concern. Shiu et al. [16] presented the RDHEI method utilizing interpolative absolute moment block truncation coding (IAMBTC), aiming to increase storage space through IAMBTC image compression. The original image is partitioned into uniform blocks, and the mean and variance of each block are computed. Based on their variance, the blocks are classified as saved or hiding blocks. Blocks with a variance exceeding a specified threshold are designated as saved blocks, not used for data hiding. The error between the original and interpolative blocks is calculated for the remaining hiding blocks, which are initially coded using IAMBTC, followed by Huffman coding to compress the errors. The compressed errors, Huffman rules, and secret data fill the space created by IAMBTC, allowing for significant confidential data integration. Yang et al. [17] presented a novel error-preserving encryption method (DEP)-RDHEI in 2022. The DPE-RDHEI aims to replace natural images with encrypted images embedded using the popular RDH technique called pixel value ordering (PVO). Yang et al. use error-preserving encryption to maintain the correlation between neighboring encrypted pixels. The PVO-based embedding technique exploits this correlation to hide secret data, achieving high embedding capacity while preserving reversibility. Anushiadevi et al. [18] proposed a new RDHEI method that first encrypts each pixel and embeds data in the pixel error histogram. The embedding capacity of 0.0807 *bpp* is achieved by this method, while maintaining complete reversibility. However, these techniques often have a limited embedding capacity (EC). Moreover, an additional limitation of the method is the overhead associated with the location map, which is used to address the issue of overflow and underflow. To overcome the limitation of limited EC, this paper introduces a VRBE-based RDHEI method that aims to preserve correlation among adjacent pixels even after encryption. The preserved correlation is then utilized to hide confidential information in two stages, achieving a high EC while ensuring complete reversibility. This method offers the following main contributions:

1) In the initial stage, the image encryption process involves transforming the image into two images based on bit-plane division. The first image comprises the initial four bit-planes, while the second image contains the remaining four bit-planes.
2) Subsequently, the resulting images are divided into smaller blocks, with differing block sizes for each image. The upper image blocks undergo a scrambling process, and the pixels from both images are shuffled. The block's pixels are then encrypted to finalize the encryption process while preserving the correlation of the blocks.
3) During data hiding, the PE is determined based on the block size, and data embedding is performed using PVO and PE expansion only if and only if overflow/underflow issues do not arise.
4) Experimental assessments reveal that the proposed RDHEI method improves the EC while maintaining full reversibility. Furthermore, the method significantly elevates visual security by executing pixel encryption.

The remaining paper is structured in three Sections where Section II introduces the proposed Adaptive Two-Stage(ATS)-RDHEI method. Section III presents a discussion on the experimental evaluation of the ATS-RDHEI method while the last section concludes the paper.

TABLE I: Notations used in proposed ATS-RDHEI

I : Orignal image	$M \times N$: Size of I
b_8, ... ,b_1: Bit-planes of I	I_u and I_l : Upper and lower image
K_I: Image key	I'_u: Upper image after block scrambeling
$\mathcal{P}_u$ and $\mathcal{P}_l$: Pseudo-random matrices	$\frac{M}{2} \times \frac{N}{2}$ and $M \times \frac{N}{2}$: Size of Pseudo-random matrices
I''_u and I''_l: Encrypted images	B: Block indexing
$p_{(x)}$: Pixel of blocks	$p'_{f(x)}$: Ascending order of block pixels
$e_{(x,y)}$: PE of $p'_{f(y)}$ and $p'_{f(x)}$	$p''_{f(x)}$: Encrypted pixel
K^D : Data key	$I_{M(u)}$ and $I_{M(l)}$: Marked encrypted images

II. Proposed Method

This section presents a new adaptive two-stage (ATS)-RDHEI method that utilizes two-stage embedding to improve the performance of the embedding. The ATS-RDHEI method falls under the VRBE-RDHEI category, as it preserves the correlation in small blocks in two distinct parts within the encrypted image while employing this correlation for data embedding. Moreover, the method separates the images' bit-planes, to increase the EC as well as effectively reduce the size of the location map (LM). This section is organized into three subsections: image encryption, data embedding, and data extraction alongside image recovery. To provide a comprehensive understanding of the ATS-RDHEI method, Fig. 1 presents a block diagram illustrating the entire process, and Table I shows the used notations.

A. Image Encryption

The main objective of image encryption is to obfuscate the image content, rendering it unrecognizable prior to the

Authorized licensed use limited to: DELHI TECHNICAL UNIV. Downloaded on July 20,2023 at 11:06:10 UTC from IEEE Xplore. Restrictions apply.

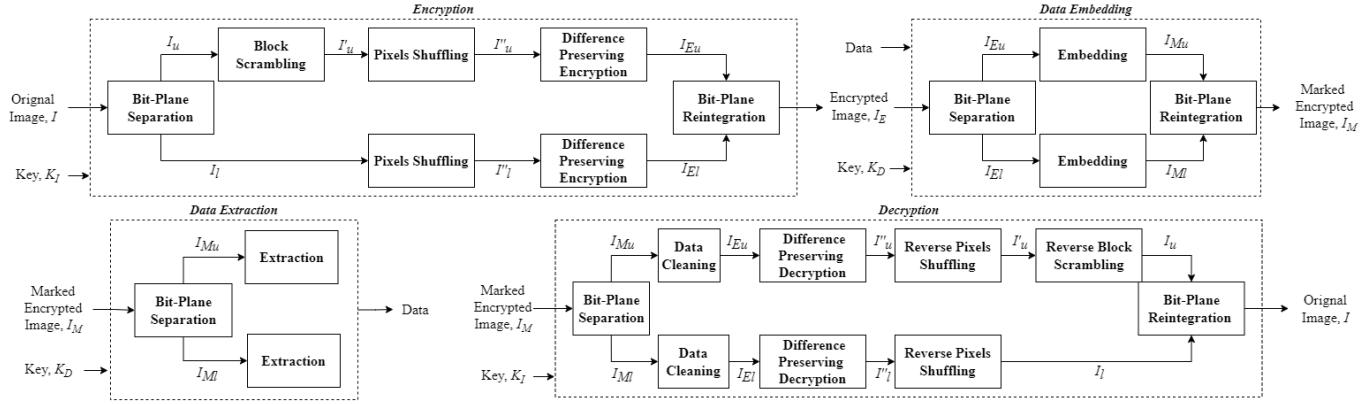

Fig. 1: Block diagram of the proposed method.

embedding process. The proposed method encompasses a four-phase in image encryption procedure, which includes bit-plane division, block scrambling, pixels shuffling, and error-based encryption. The bit-plane division is executed without any key.

Since the method embeds data at two stages of the image, therefore the gray-scale image is separated into bit-planes, after which the four most significant bit (MSB) planes are collectively reorganized, and likewise, the four least significant bit (LSB) planes are rearranged together. Let I represent a gray-scale image with dimensions $M \times N$, and let b_8, b_7, b_6, ... ,b_1 denote the bit-planes of I, ranging from the MSB plane to LSB plane, respectively. The computation of the bit-planes can be described as follows:

$$b_k(i,j) = \left\lfloor \frac{(I(i,j)) \bmod (2^{k+1})}{2^k} \right\rfloor \tag{1}$$

where b_k is the k^{th} bit-plane of pixel located at (i,j) in image I, $1 \leq i \leq M$, $1 \leq j \leq N$ and $8 \geq k \geq 1$.

Bit-planes are systematically assembled based on their corresponding numbers: in the first part, bit-planes b_8, b_7, b_6, and b_5 are sequentially combined, creating the upper image I_u. In the second part, bit-planes b_4, b_3, b_2, and b_1 are collected in sequence, producing the lower image I_l. A comprehensive analysis is carried out to understand the errors between these two images, as I_u contains all the MSB planes, leading to a higher redundancy compared to the lower image. Consequently, the block size of I_u can be larger than that of I_l. Notably, scrambling the upper image block can effectively make the original image unrecognizable.

In the following phase, block scrambling is carried out using random permutation. Initially, images I_l is divided into non-overlapping blocks of size 2×2 and create a total of $\frac{M \times N}{4}$ blocks. Subsequently, $\frac{M \times N}{4}$ random keys (R) are generated using a permutation key generated through an image key (K_I) and a PRNG. The image blocks are scrambled according to their corresponding index value, which is denoted as B. Thereafter, the images partially encrypted image I'_u is obtained.

In the subsequent phases of encryption, two pseudo-random matrices $\mathcal{P}_u$ and $\mathcal{P}_l$ of size $\frac{M}{2} \times \frac{N}{2}$ and $M \times \frac{N}{2}$ is generated

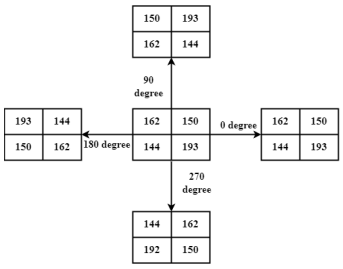

Fig. 2: Block scrambling using degree.

using the PRNG, with the image key K^I serving as a seed. A key for each 2×2 size block of image I'_u is assigned from $\mathcal{P}_u$, and for image I_l, it is assigned from $\mathcal{P}_l$ after dividing the image into 1×2 blocks. Subsequently, pixel shuffling is performed on each block of both images and the final images I''_u and I''_l are obtained. The rotation angle for a block B of image I'_u is determined as follows

$$Angle = \begin{cases} 0^\circ & \text{if } \mathcal{P}_{u(B)} \bmod 4 = 0 \\ 90^\circ & \text{elseif } \mathcal{P}_{u(B)} \bmod 4 = 1 \\ 180^\circ & \text{elseif } \mathcal{P}_{u(B)} \bmod 4 = 2 \\ 270^\circ & \text{otherwise} \end{cases} \tag{2}$$

where the $^\circ$ symbol represents the degree of block scrambling and $\mathcal{P}_{u(B)}$ is the scrambling key corresponding to block B. However, the scrambling angle of the lower image block is determined as follows:

$$Angle = \begin{cases} 0^\circ & \text{if } \mathcal{P}_{l(B)} \bmod 2 = 0 \\ 180^\circ & \text{otherwise} \end{cases} \tag{3}$$

To further illustrate the block scrambling process, Fig. 2 is provided as a visual representation.

In the final step of encryption, each block of I''_u is processed as follows: let $p_{(1)}$, $p_{(2)}$, $p_{(3)}$, and $p_{(4)}$ represent the pixels of a block in raster scan order. The ascending order of the pixels is denoted as $p'_{f(1)}$, $p'_{f(2)}$, $p'_{f(3)}$, and $p'_{f(4)}$, where $p'_{f(1)} \leq p'_{f(2)} \leq p'_{f(3)} \leq p'_{f(4)}$. Furthermore, if two pixels have the same value, the pixel that appears first in the sequence is placed first in the sorted list. Subsequently, the PE between

Authorized licensed use limited to: DELHI TECHNICAL UNIV. Downloaded on July 20,2023 at 11:06:10 UTC from IEEE Xplore. Restrictions apply.

each pair of pixels is calculated and denoted as $e_{(1,2)}$, $e_{(2,3)}$, $e_{(3,4)}$, where $e_{(x,y)} = p'_{f(y)} - p'_{f(x)}$, $1 \leq x \leq 4$ and $1 \leq y \leq 4$. The encrypted pixels of the block are then determined as follows: if $e_{(1,4)}$ is less than or equal to 12, the block uses Eq. 4.

$$p''_{f(x)} = \begin{cases} (p'_{f(x)} + \mathcal{P}_{(B)} \bmod (\alpha - e_{(1,n)}) + 1 & \text{if } x = 1 \\ (p''_{f(x-1)} + e_{(x-1,x)} & \text{otherwise} \end{cases} \quad (4)$$

where n is the total number of pixel in block and α is threshold, for image I''_u, $n = 4$ and $\alpha = 12$. Otherwise, the encrypted pixels of the blocks are obtained using given four conditions, $p''_{f(1)} = p'_{f(2)}, p''_{f(2)} = p'_{f(1)}, p''_{f(3)} = (p'_{f(3)} + \mathcal{P}_{(B)}) \bmod 8 + 4$ and $p''_{f(4)} = (p'_{f(4)} + \mathcal{P}_{(B)}) \bmod 8 + 4$.

Conversely, let $p_{(1)}$ and $p_{(2)}$ be the pixels of any block in I'_l. Their ascending order is $p'_{f(1)}$, $p'_{f(2)}$, and the PE is $e_{(1,2)}$. If $e_{(1,2)}$ is less than or equal to 14, the encrypted pixels are determined by Eq. 4, where α is 14 and $n = 2$. Otherwise, the encrypted pixels of the block are obtained using four conditions.

Upon completion of the aforementioned process, two encrypted images $I_{E(u)}$ and $I_{E(l)}$ are obtained, respectively. These images are combined using Eq. (5) to generate the final encrypted image, denoted as I_E.

$$I_E(i,j) = 2^4 * I_{E(u)}(i,j) + I_{E(l)}(i,j) \quad (5)$$

B. Data Embedding

The data hider initially encrypts the data using a highly secure encryption algorithm, employing a data key K^D and generating a data stream. Thereafter, The received encrypted image I_E is initially separated into two images, upper encrypted image $I_{E(u)}$ with four MSB planes and lower encrypted image with four LSB planes as follows: $I_{E(u)}(i,j) = \left\lfloor \frac{I_E(i,j)}{2^4} \right\rfloor$ and $I_{E(l)}(i,j) = I_E(i,j) \bmod 2^4$.

Before proceeding with the embedding process, the images $I_{E(u)}$ and $I_{E(l)}$ are divided into non-overlapping blocks of sizes 2×2 and 1×2, respectively. Subsequently, in a manner akin to the image encryption process, the pixels within block B are arranged in ascending order. In the case of $I_{E(u)}$, the sorted sequence of encrypted pixels in block B are denoted as $p''_{f'(1)}$, $p''_{f'(2)}$, $p''_{f'(3)}$, and $p''_{f'(4)}$. Additionally, the PEs between each pair of pixels are represented by $e'_{(1,2)}$, $e'_{(2,3)}$, and $e'_{(3,4)}$, where $e'_{(x,y)} = p''_{f'(y)} - p''_{f'(x)}$.

The blocks are processed in a raster scan and the embedding process within a block is conducted recursively, as long as the condition $e'_{(1,4)} \leq 12$ holds. If this condition is not met, the block is designated as non-embeddable in the location map (LM). The embedding of each bit is carried out by processing Eq. 6 and 7 for x values ranging from 1 to 3 in $p''_{f'(x)}$.

$$\bar{p}_{f'(x)} = \begin{cases} p''_{f'(x)} + b & \text{if } e'_{(x,x+1)} = 0 \\ p''_{f'(x)} & \text{otherwise} \end{cases} \quad (6)$$

and

$$p''_{f'(x')} = p''_{f'(x')} = p''_{f'(x')} + 1 \quad x < x' \leq n \quad (7)$$

where $\bar{p}_{f'(x)}$ is marked encrypted pixel and b is the data bit. Upon completion of the three embedding positions, the final assignment is $\bar{p}_{f'(4)} = p''_{f'(4)}$.

Similarly in the second stage, in the case of $I_{E(l)}$, the sorted sequence of encrypted pixels in block B are denoted as $p''_{f'(1)}$ and $p''_{f'(2)}$. Additionally, the error between the pixel is represented by $e'_{(1,2)}$. The embedding process within a block is conducted using Eq. 6 and 7, as long as the condition $e'_{(1,4)} \leq 14$ holds and finally $\bar{p}_{f'(4)}$ is assigned as $p''_{f'(4)}$.

Upon completion of the aforementioned embedding, two marked encrypted images $I_{M(u)}$ and $I_{M(l)}$ are obtained, respectively. These images are combined using Eq. (5) to generate the final encrypted image, denoted as I_M.

It is important to note that non-embeddable blocks, which may generate overflow/underflow, are marked in the location map. The two location maps are subsequently compressed using arithmetic encoding and embedded within the image alongside the data. In cases where the available embeddable space proves insufficient for accommodating the compressed location maps in any given image, the image is considered unsuitable for embedding and remains unaltered.

C. Data Extraction and Image Recovery

The proposed ATS-RDHEI method allows for separate data extraction and image recovery based on the availability of keys. As a result, three distinct cases can arise, which are detailed below.

When the receiver possesses only the K^D key, they divide the image into two images, $I_{M(u)}$ and $I_{M(l)}$, following the data hider's process, and subsequently split the images into blocks. In the image $I_{M(u)}$, let $q_{(1)}$, $q_{(2)}$, $q_{(3)}$, and $q_{(4)}$ represent the pixels of a block in raster scan order. The ascending order of the pixels is denoted as $q'_{f(1)}$, $q'_{f(2)}$, $q'_{f(3)}$, and $q'_{f(4)}$. The encrypted bits of data are determined from x = 3 to 1 using Eq. (8) and, simultaneously update $q'_{f(x)} = q'_{f(x)} - b$ and $q'_{f(x')} = q'_{f(x')} - 1$, where $x < x' \leq n$.

$$b = \begin{cases} 0 & \text{if } q'_{f(x)} = q'_{f(x-1)} \\ 1 & \text{else if} q'_{f(x)} = q'_{f(x-1)} - 1 \end{cases} \quad (8)$$

Upon completing the bit extraction process from a block, the bits are appended to the data stream in reverse order. After extraction from all blocks of $I_{M(u)}$, following the same order as the hider used for embedding, data bits are similarly extracted from $I_{M(l)}$ and added to the same data stream. This combined data stream is then decrypted using K^D, resulting in the retrieval of the original data.

When the receiver possesses only the K^I image key, the receiver first removes the embedded data using Eq. (8) and four conditions, after slicing the image. The restoration of the images is then accomplished through a series of steps performed in reverse order: error decryption, pixel reverse shuffling, block reverse rotation, and image recombination. Initially, the pseudo-random matrices are generated in a manner similar to the encryption process, and a key is assigned to each block. By applying the key to the corresponding block,

Authorized licensed use limited to: DELHI TECHNICAL UNIV. Downloaded on July 20,2023 at 11:06:10 UTC from IEEE Xplore. Restrictions apply.

(a) $Lena$ (b) $Baboon$ (c) $Barbara$ (d) $Boat$

Fig. 3: Test images of size 512×512 pixels

the pixels within the block are decrypted, and the original pixel arrangement is restored. Following this, the blocks are rotated back to their initial positions, and the images are recombined to obtain the original, decrypted image.

If the receiver has both the keys(K^D and K^I), he/she can extract the secret data as case 1 and can also recover the image as in case 2.

III. Experimental Analysis

This section unveils the experimental results and analysis of the novel ATS-RDHEI method. Through a rigorous comparison with state-of-the-art (SOTA) methods, the efficacy and superiority of the proposed method is revealed. The discussion and analysis are divided into two parts, as detailed below. The first part delves into the security aspects of the method under consideration. The second part presents the performance analysis of the proposed method on four test images as depicted in Fig. 3 and datasets, such as BOSSbase [19] and BOWS-2 [20] and also compares with the SOTA methods.

A. Security Analysis

To assess the security of the proposed method, we have considered widely-used metrics such as histogram distribution, horizontal and vertical correlation [21], Shannon entropy [22], number of changing pixel rates (NPCR), Unified Averaged Changed Intensity (UACI) [23], PSNR, and SSIM.

As a use case, the $Lena$ image shown in Fig. 4a has been utilized. The encrypted (I_E) and marked image (I_M) for the original image $Lena$ are displayed in Figs. 4c and 4e, respectively. Both images appear as noise-like and entirely scrambled. The histogram of I, I_E and I_M are depicted in Figs. 4b, 4d and 4f, respectively. With unwavering consistency across all intensities, the histograms of I_E and I_M bear witness to the exceptional perceptual security offered by our proposed method.

The experimental results for statistical metrics are given in Table II. In the case of I_E and I_M, both horizontal and vertical correlations are close to 0, indicating no association between adjacent pixels. In contrast, for the original image I, the correlation is close to 1. The entropy of I_E and I_M is slightly higher than that of I, signifying that the probability distribution of different pixel values in images I_E and I_M is higher than in I. Likewise, higher values of NPCR and UACI, approximately 100% and 75% respectively, indicate strong resistance against differential attacks. Low PSNR and SSIM values, around 9.2 and 0.02 respectively, demonstrate

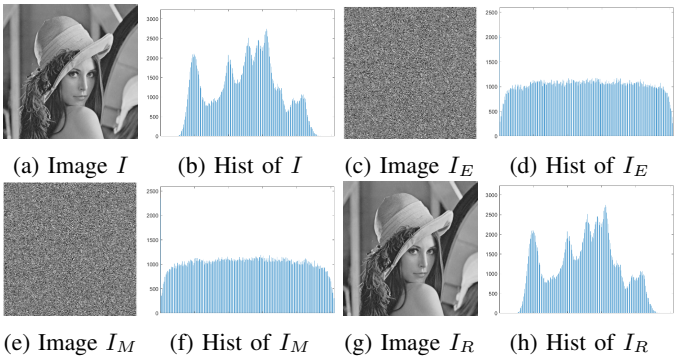

(a) Image I (b) Hist of I (c) Image I_E (d) Hist of I_E

(e) Image I_M (f) Hist of I_M (g) Image I_R (h) Hist of I_R

Fig. 4: Processed image $Lena$

TABLE II: Statistical Analysis on Image $Lena$

Image	Original image (I)	Encrypted image (I_E)	Marked encrypted image (I_M)
Horizontal Correlation	0.9719	0.0031	0.0041
Vertical Correlation	0.9850	0.0011	-0.0001
Diagonal Correlation	0.9593	-0.0021	0.0002
Information Entropy	7.4451	7.9993	7.9970
NPCR (I and I_E/I_M)	-	98.78	98.70
UACI (I and I_E/I_M)	-	74.12	81.11
PSNR (I and I_E/I_M)	-	9.1982	9.3520
SSIM (I and I_E/I_M)	-	0.0211	0.0142

the dissimilarity of both I_E and I_M with I. Through a series of rigorous security tests, the proposed method emerges victorious, demonstrating remarkable resilience against visual, differential, and statistical security attacks.

B. Embedding performance

In this section, we first analyze the efficiency of the ATS-RDHEI method using various test images. Initially, four images are considered, as depicted in Fig. 3. We examine the EC and total compressed location map for both the upper and lower images. Table III presents various metrics for each test image, including the image name, EC for the upper image, compressed location map size of the upper image, EC for the lower image, compressed location map size of the lower part, total pure embedding capacity, and pure embedding rate. This analysis offers insight into the performance of the ATS-RDHEI method. To further substantiate the proposed method's

TABLE III: Performance of ATS-RDHEI on test images

Images	Upper image		Lower image		Pure	Pure
	EC ($bits$)	LM ($bits$)	EC ($bits$)	LM ($bits$)	EC ($bits$)	ER (bpp)
$Lena$	89949	4875	28975	7395	104654	0.3992
$Baboon$	52528	3481	14629	8798	54878	0.2093
$Barbara$	75257	3529	25101	5589	91240	0.3481
$Boat$	74348	2348	22375	6798	87577	0.3341

TABLE IV: Performance of ATS-RDHEI on two data sets

	Average ER (bpp)	Best ER (bpp)	Worst ER (bpp)	PSNR (dB)	SSIM
BOSSBase	0.3524	1.0911	0.0322	∞	1
BOWS-2	0.3387	0.9748	0.0309	∞	1

Authorized licensed use limited to: DELHI TECHNICAL UNIV. Downloaded on July 20,2023 at 11:06:10 UTC from IEEE Xplore. Restrictions apply.

TABLE V: ER(bpp) compassion of ATS-RDHEI with SOTA methods

Test Image	Proposed	[17]	[18]	[9]	[10]
$Lena$	0.3992	0.0651	0.0570	0.0124	0.0009
$Baboon$	0.2093	0.0453	0.0050	0.0057	0.0010
$Barbara$	0.3481	0.1130	0.0911	0.0149	0.0058
$Boat$	0.3341	0.0940	0.0989	0.0124	0.0050

performance, larger datasets such as BOSSbase and BOWS-2 have been employed. First, the best, average, and worst-case ERs are identified. The proposed method attains 1.2278, 0.5393, and 0.1577 bpp for BOSSbase, and 1.1186, 0.5134 and 0.1612 bpp for BOWS-2, respectively. In the next part of this section, we will discuss a comparison between the ATS-RDHEI method and the SOTA RDHEI methods to further assess its efficiency.

To unleash the full potential of the proposed method, a rigorous performance analysis is conducted against SOTA methods. Each method's parameters are meticulously fine-tuned to achieve the pinnacle of ER. Since the proposed method consistently delivers lossless image reconstruction, resulting in an infinitely PSNR and SSIM of 1, it stands out from the competition. Table. V illustrates the ER comparison, which include [9], [10], [17], and [18], for four standard test images from the SIPI dataset. The proposed method achieves ERs of 0.3992, 0.2093, 0.3481, and 0.3341 bpp for $Lena$, $Baboon$, $Barbara$, and $Boat$, respectively, surpassing SOTA methods. Thus, it can be concluded that the proposed method delivers the highest ER regardless of the images.

IV. Conclusion

The proposed ATS-RDHEI method offers a robust solution for secure image transmission and data hiding. Its unique combination of image encryption and RDH techniques provides enhanced security and adaptability, catering to a wide range of applications. The proposed encryption maintains the correlation of pixels in two types of blocks while increasing visual security using block rotation. Since the correlation among the pixels of each block is maintained and embedding of secret data bits is done in two stages, the ATS-RDHEI achieves enlarged EC in comparison to related existing works, as demonstrated by the experimental results. The method's capability to separately extract data and recover images based on the availability of keys further ensures the flexibility and confidentiality of the system. Future research could explore the potential for further improving the EC and efficiency of the method by even better exploiting the correlation.

References

[1] G. Kaur, S. Singh, R. Rani, R. Kumar, and A. Malik, "High-quality reversible data hiding scheme using sorting and enhanced pairwise pee," *IET Image Processing*, vol. 16, no. 4, pp. 1096–1110, 2022.

[2] N. Kumar, R. Kumar, and R. Caldelli, "Local moment driven pvo based reversible data hiding," *IEEE Signal Processing Letters*, vol. 28, pp. 1335–1339, 2021.

[3] R. Kumar, S. Chand, and S. Singh, "An improved histogram-shifting-imitated reversible data hiding based on hvs characteristics," *Multimedia Tools and Applications*, vol. 77, pp. 13445–13457, 2018.

[4] X. Li, J. Li, B. Li, and B. Yang, "High-fidelity reversible data hiding scheme based on pixel-value-ordering and prediction-error expansion," *Signal processing*, vol. 93, no. 1, pp. 198–205, 2013.

[5] R. Kumar, N. Kumar, and K.-H. Jung, "I-pvo based high capacity reversible data hiding using bin reservation strategy," *Multimedia Tools and Applications*, vol. 79, no. 31-32, pp. 22635–22651, 2020.

[6] G. Kaur, S. Singh, R. Rani, and R. Kumar, "A comprehensive study of reversible data hiding (rdh) schemes based on pixel value ordering (pvo)," *Archives of Computational Methods in Engineering*, vol. 28, pp. 3517–3568, 2021.

[7] A. K. Rai, N. Kumar, R. Kumar, H. Om, S. Chand, and K.-H. Jung, "Intra-block correlation based reversible data hiding in encrypted images using parametric binary tree labeling," *Symmetry*, vol. 13, no. 6, p. 1072, 2021.

[8] X. Cao, L. Du, X. Wei, D. Meng, and X. Guo, "High capacity reversible data hiding in encrypted images by patch-level sparse representation," *IEEE transactions on cybernetics*, vol. 46, no. 5, pp. 1132–1143, 2015.

[9] X. Zhang, "Reversible data hiding in encrypted image," *IEEE signal processing letters*, vol. 18, no. 4, pp. 255–258, 2011.

[10] W. Hong, T.-S. Chen, and H.-Y. Wu, "An improved reversible data hiding in encrypted images using side match," *IEEE signal processing letters*, vol. 19, no. 4, pp. 199–202, 2012.

[11] X. Zhang, "Separable reversible data hiding in encrypted image," *IEEE transactions on information forensics and security*, vol. 7, no. 2, pp. 826–832, 2011.

[12] X. Liao and C. Shu, "Reversible data hiding in encrypted images based on absolute mean difference of multiple neighboring pixels," *Journal of Visual Communication and Image Representation*, vol. 28, pp. 21–27, 2015.

[13] K.-Y. Song, S. Kim, *et al.*, "A modified reversible data hiding in encrypted image using enhanced measurement functions," in *2016 Eighth International Conference on Ubiquitous and Future Networks (ICUFN)*, pp. 869–872, IEEE, 2016.

[14] R. Bhardwaj and A. Aggarwal, "An improved block based joint reversible data hiding in encrypted images by symmetric cryptosystem," *Pattern Recognition Letters*, vol. 139, pp. 60–68, 2020.

[15] Y. Wang, G. Xiong, and W. He, "High-capacity reversible data hiding in encrypted images based on pixel-value-ordering and histogram shifting," *Expert Systems with Applications*, vol. 211, p. 118600, 2023.

[16] P.-F. Shiu, W.-L. Tai, J.-K. Jan, C.-C. Chang, and C.-C. Lin, "An interpolative ambtc-based high-payload rdh scheme for encrypted images," *Signal Processing: Image Communication*, vol. 74, pp. 64–77, 2019.

[17] C.-H. Yang, C.-Y. Weng, and J.-Y. Chen, "High-fidelity reversible data hiding in encrypted image based on difference-preserving encryption," *Soft Computing*, vol. 26, no. 4, pp. 1727–1742, 2022.

[18] R. Anushiadevi and R. Amirtharajan, "Separable reversible data hiding in an encrypted image using the adjacency pixel difference histogram," *Journal of Information Security and Applications*, vol. 72, p. 103407, 2023.

[19] P. Bas, T. Filler, and T. Pevnỳ, "" break our steganographic system": the ins and outs of organizing boss," in *International workshop on information hiding*, pp. 59–70, Springer, 2011.

[20] P. Bas and T. Furon, "Image database of bows-2," *Accessed: Jun*, vol. 20, pp. 2016–2017, 2017.

[21] T. Chu, W. Ranson, and M. A. Sutton, "Applications of digital-image-correlation techniques to experimental mechanics," *Experimental mechanics*, vol. 25, no. 3, pp. 232–244, 1985.

[22] C. E. Shannon, "A mathematical theory of communication," *The Bell system technical journal*, vol. 27, no. 3, pp. 379–423, 1948.

[23] Y. Wu, J. P. Noonan, S. Agaian, *et al.*, "Npcr and uaci randomness tests for image encryption," *Cyber journals: multidisciplinary journals in science and technology, Journal of Selected Areas in Telecommunications (JSAT)*, vol. 1, no. 2, pp. 31–38, 2011.

Authorized licensed use limited to: DELHI TECHNICAL UNIV. Downloaded on July 20,2023 at 11:06:10 UTC from IEEE Xplore. Restrictions apply.

Research Square

Preprints are preliminary reports that have not undergone peer review.
They should not be considered conclusive, used to inform clinical practice,
or referenced by the media as validated information.

All-p ZVLL Inverter with Bootstrapping based on a ditch OTFT

Sakshi Gupta
Graphic Era Deemed to be University
Poornima Mittal (poornimamittal@dtu.ac.in)
Delhi Technological University
Pradeep Juneja
Graphic Era Deemed to be University

Research Article

Keywords: Organic thin film transistor, Diode Load Logic (DLL), Bootstrapping, Zero-Vgs Load Logic (ZVLL), propagation delay, organic all p inverter, noise margin

Posted Date: June 27th, 2023

DOI: https://doi.org/10.21203/rs.3.rs-3100214/v1

License: This work is licensed under a Creative Commons Attribution 4.0 International License.
Read Full License

Additional Declarations: No competing interests reported.

All-p ZVLL Inverter with Bootstrapping based on a ditch OTFT

Sakshi Gupta[1], Poornima Mittal[2] ∗ and Pradeep Juneja[1]

[1] Department of Electronics and Communication Engineering, Graphic Era Deemed to be University, Dehradun, Uttarakhand, India

[2] Department of Electronics and Communication Engineering, Delhi Technological University, New Delhi, India

Email id: sakshigupta.ice@geu.ac.in, poornimamittal@dtu.ac.in, pkjuneja@geu.ac.in

*Corresponding Author: poornimamittal@dtu.ac.in

Abstract

This research manifests the characteristics both static and dynamic, of a bootstrapped all-p ZVLL inverter using a single gate BGBC organic transistor with extra p+ doping near the source and drain electrodes and a 40 nm ditch incorporated in the pentacene organic semiconductor layer. Several topologies of the inverter were experimented with and compared in terms of their performance pre and post the application of the bootstrap technique. Bootstrapping proved to be a befitting choice for obtaining the maximum efficient results in terms of noise margin, delay in propagation, transient time, and gain. Upon comparison it was observed that the bootstrapped inverter showed considerably better voltage transfer characteristics in terms of high and low noise margins. A surge of 18.46% and 22.25% is noticed in noise margins of the bootstrapped device as compared to the device without bootstrapping. Also, the dynamic response of DLL and ZVLL topology devices exhibit a hike in the voltage swing by 24% and 13% respectively. Furthermore, contrast to DLL, the average delay of the ZVLL inverter decreases by 54.5 µs after the application of bootstrapping technique, whereas the value of average propagation delay decreases by a mere 10 µs. Pertaining to the results attained, ZVLL proves to be a more responsive circuit, leading to an inverter that is apparently more robust, better noise margins, attenuated power leakage and improved sensitivity.

Keywords – Organic thin film transistor, Diode Load Logic (DLL), Bootstrapping, Zero-V_{gs} Load Logic (ZVLL), propagation delay, organic all p inverter, noise margin.

1 Introduction

Overwhelming response has been acknowledged by the organic thin film transistors (OTFTs) regarding their employability in varied applications demanding structural resilience, processing under modest temperature, extensive area coverage, and meagre expenditure. Organic Transistors fabricated on polymer substrates experiencing depressed values of working potential, anticipated threshold voltage and excessive productivity have empowered a spectrum of scientific know-hows comprising inexpensive digital equipment, electronic stationery and wearables and pliable substantial-area demonstrating devices [1-4]. Moreover, operating any device below 5V is certain to strengthen reserves by permissive usage of cost curtailed actuator electronics consequently turning such devices notably apt for cartable applications viz. tablets, MacBook's, and laptops that seem to be the expeditiously thriving members of the mainframe enterprises. Since these may be processed at a considerably modest temperature, hence are expected to cede 3D assimilation of extensive stacks of exertive electronic gears.

The idea of developing a transistor employing a thin film was cardinally contemplated upon and put together by Paul K. Weimer in 1962 by fabricating a TFT using cadmium sulfide in microcrystalline layers [5]. Later in 1986, A.

Tsumura, H. Koezuka and T. Ando became the pioneers of fabricating a solid-state film effect transistor using a macromolecule organic film of polythiophene with controlled doping levels [6]. Thus far, gross efforts have been made for the improvisation of the OTFT. Of the various semiconductors available pentacene exhibits considerably better mobility, and hence is a preferred choice.

Usage of Pentacene as a semiconductor material has expediated the performance related growth of the thin film transistors. The predominant determinants that instigate the probe of OTFTs happen to be scaled down prices and uncomplicated packaging along with their rapport with the pliable substrates [7]. Of late the accomplishments made have proven that the Organic transistors are way ahead than their inorganic counterparts. Despite this, preeminent circumspection for applications like portable electronic devices happens to be large operational voltages by the virtue of substandard capacitive coupling in between channel and gate electrode [8]. Utilizing a dual dielectric device may dampen the voltage and lead to a device that has augmented performance.

The showstopper amongst all electronic devices are the ones that are fabricated using solution-processing techniques, for these aggrandize owing to their ecological and economical anti rarefaction processability [9]. While high-geared organic TFTs may be formulated employing organic semiconductor materials that are solution-processable wide range of the already reported devices have been fabricated adopting a spin-coated polymer lining on a gate patterned through photolithography.

Researchers have always struggled to strike a balance between the component density and cost efficacy without compromising on the area covered. Referring to the very large-scale integration systems, billions of logic gates may be integrated on any electronic circuit. In the early days, when devices were made from conventional semiconductors, there was a prominence of challenges like cost and flexibility. Over time, and with the advent of technology, organic semiconductors came into limelight which along with the progression of a scale integration gave birth to better devices pertaining to performance, bendability, and pricing. Though there is a legit augmentation in the exploitation of inverters in the organic devices, the scalability of these needs to be escalated for high noise margin, high gain, minimal propagation delay and high voltage swing [10].

This paper uses a novel organic thin film transistor to make an organic inverter. This OTFT employs a single gate bottom contact structure with gate electrode fabricated at the bottom. To enhance the performance of a typical and established OTFT, a ditch is created in the organic semiconductor. And in order to further augment the performance, an additional doping of p+ charge is done in the vicinity of the drain and the source electrodes, owing to which there seems to be a considerable betterment in the performance parameters viz. mobility, $I_{ON/OFF}$ etc.

Inverters are elementary yet critically important units of organic circuits [11]. Upon ensuring the optimal noise margin and delay in propagation, an inverter showing promising robustness, design simplicity and attenuated power consumption may be guaranteed. [12]. Sifting among the varied configurations in which an organic inverter may be designed, viz. hybrid complementary, fully organic complementary, or all-p organic inverters, it was observed that the all-p type organic inverters displayed the most assuring performance in terms of mobility and stability since the counterparts are more prone to be affected by air, moisture, and oxygen. [13]. Furthermore, Zero-V_{gs} Load Logic and Diode Load Logic configurations may be applied to the inverter, whereby, after comparing the performance of each it has been established that the ZVLL configuration is exceedingly better than the DLL one [14].

Besides the above quoted ways to augment the performance of the organic inverters, this section gives an insight to bootstrapping, which is yet another persuasive technique for raising the driving competence. Consequently, proving to be a fulfilling technique to overcome the drop in the threshold voltage thereby enhancing the performance. This technique empowers the driving capability without putting the power consumption at stake, thereby providing exponentially attenuated values of I_{off} [15].

The remainder of the paper has been planned in 4 furthers segments: wherein Segment II provides an insight to various possible configurations of OTFT, Segment III gives a glimpse to the performance of the all-p ZVLL organic inverter being used, Segment III presents an organic inverter employing the bootstrapping technique and Segment IV concludes the work.

2 Various configurations of OTFT for Inverter design

Organic transistors may be designed using various combinations for placing different layers. These could be top gate top contact, top gate bottom contact, bottom gate top contact or bottom gate bottom contact. Also, an additional gate may be incorporated to enhance its performance. This paper covers the single gate OTFT and the various configurations possible are depicted in Fig 1(a), (b), (c) and (d).

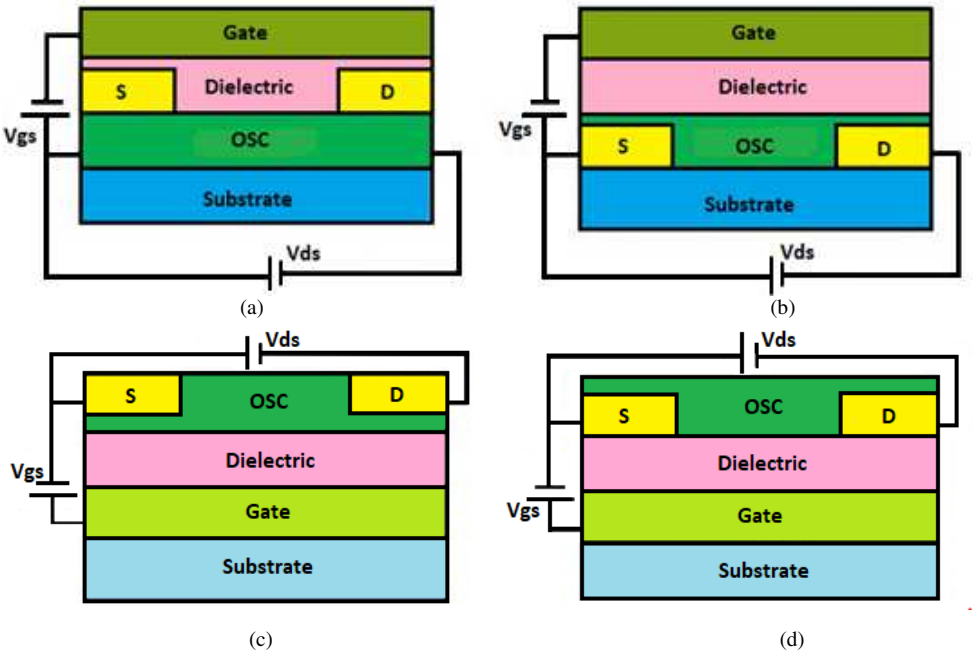

Fig. 1 OTFT Configurations (a) Top Gate Top Contact (b) Top Gate Bottom Contact (c) Bottom Gate Top Contact (d) Bottom Gate Bottom Contact

The literature is proof of choosing BGBC devices over the other possibilities due to their robustness and comparatively better performance than the other configurations [1]. Furthermore, to augment the performance shown by the device, extra p+ doping may be added to the region near the source/drain. Moreover, as the performance of the device still doesn't meet the desired requirements, a ditch may be incorporated in the OSC to help faster flow of charges as presented in Fig 2.

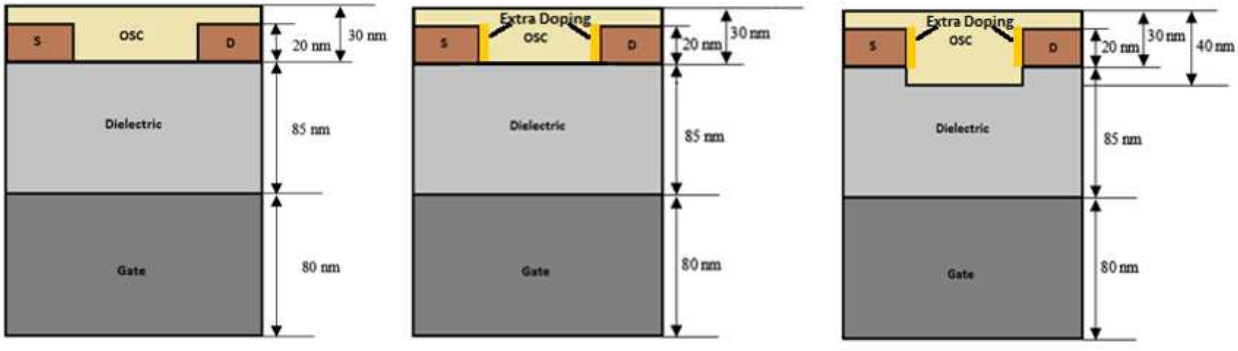

Fig. 2. Representation of OTFT using SG BGBC (a) without extra doping and ditch (b) with extra p+ doping without ditch (c) with extra p+ doping and ditch

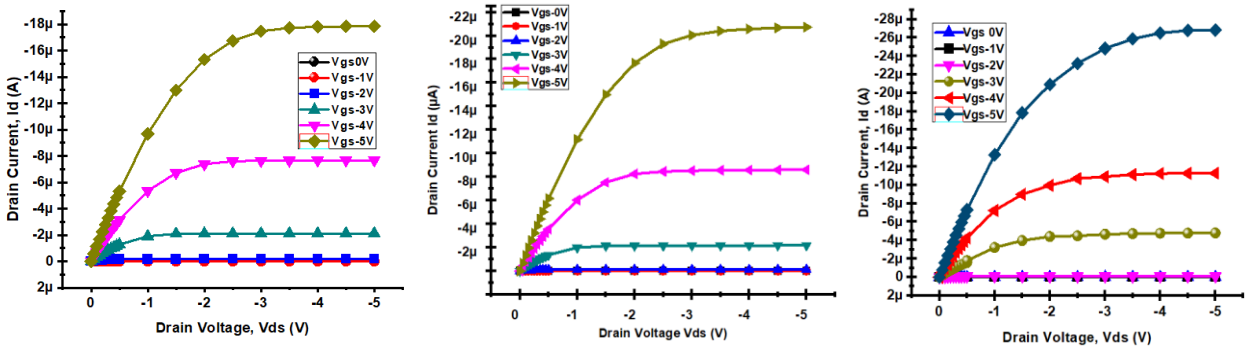

(a) (b) (c)

Fig. 3. I_dV_{ds} Characteristics of OTFT using SG BGBC (a) without extra doping and ditch (b) with extra p+ doping without ditch (c) with extra p+ doping and ditch

As shown in Fig. 3, the device using extra p+ doping and a ditch in the organic layer yields the best performance, therefore has been chosen to construct an organic inverter.

3 DLL and ZVLL configuration based all-*p* Organic Inverter

Inverters are the fundamental components of any organic circuit wherein, the elementary parameters governing their efficiency are noise margin, voltage swing, propagation delay and gain. These may be configured employing varied topology techniques like fully organic complementary inverters using p-type and n-type organic thin film transistors, hybrid complementary inverters using n-type organic and p-type inorganic transistors, and all-p type transistors organic inverters. Fully organic and hybrid ones though yield a desired NM_H and NM_L but fail to provide a befitting propagation delay. Conversely, an all-*p* organic circuit compromises on catering full voltage swing at the output pertaining to the generous threshold voltage. Consequently, curtailing the voltage gain and the noise margin, ensuing bare robustness.

Table 1. Comparison of performance parameters for varied inverter circuits

	V_{TH}	Propagation delay	NM_L	NM_H
All p organic inverter	> $V_{DD}/2$	Low	~$V_{DD}/2$	Very low
Fully organic complementary inverter	< $V_{DD}/2$	High	<$V_{DD}/2$	=$V_{DD}/2$
Hybrid complementary inverter	≥ $V_{DD}/2$	High	<$V_{DD}/2$	<$V_{DD}/2$

Table 1 summarizes the performances of various possible inverter configurations. In the applications where a rapid switching speed is a must-have, all-p type inverters may be preferred.

An all-p inverter may be designed using a single gate or a dual gate OTFT. Dual gate is a more endorsed choice over the single gate one, because it has exceptional threshold voltage, mobility, transconductance, I_{on}/I_{off}, and sub-threshold voltage [18]. However, the presence of an additional gate on the OSC taints the layer. Besides, this happens at a trade-off of device cost, adversely impacting the economic utility. Therefore, turning single gate devices as the chosen one.

Effective all-*p* inverters may be constructed using a single gate BGBC device, yielding high and low noise margins as 1.25 V and 3.22 V respectively, which are not very promising values. Therefore, addition of an extra *p*+ region close to the drain and source terminals of this device, betters the values of noise margins. The regions nearby

S/D electrodes are heavily doped with *p*+ charges with a concentration of 10^{20} cm^{-3} which caters to challenges posed by undesired charge carriers and contact resistance, thus improving the NM values to 3.56 V and 3.38 V for high and low correspondingly. For further accelerating the values of NM_H and NM_L, a 40 nm ditch in the pentacene layer is incorporated to the structure of the device extra doping. This insertion escalates the high and low NM's to considerably higher values, viz. 4.17 V and 4.0 V individually, meeting the desired values of being $\leq V_{DD}/2$. Fig. 4 (a), (b) and (c) show the respective curves for the three above quoted devices making it evident that ditch incorporated device yields much improved values. A bar chart representation of the Low and High noise margins of the various configurations is presented to make the selection of the device easier in Fig. 5.

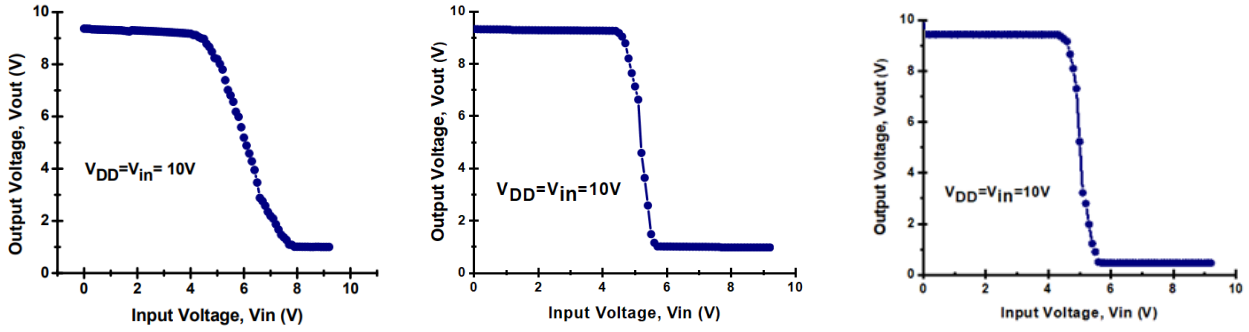

(a) (b) (c)

Fig. 4. VT characteristics of (a) SG BGBC (b) SG BGBC with extra *p*+ doping and (c) SG BGBC with extra doping and ditch incorporated all-*p* Organic Inverter

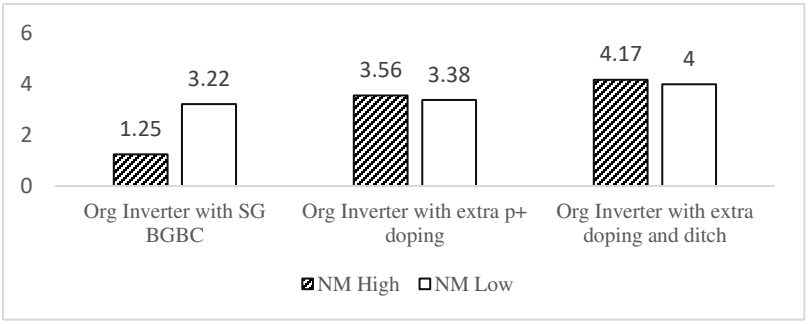

Fig. 5. Noise Margins for Varied Inverter configurations

To procure adequate conduct, either diode load logic or a zero-V_{gs} load logic topology may be utilized.

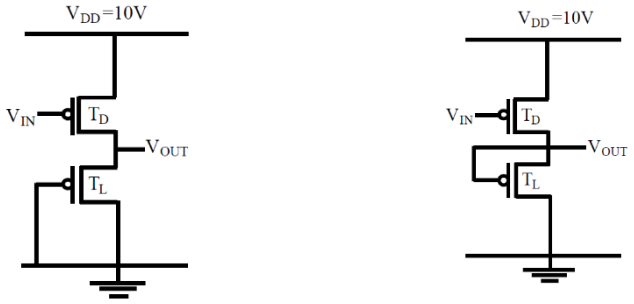

(a) (b)

Fig. 6. Schematic of all-p organic inverter using single gate organic transistor with extra p+ doping near S/D and a ditch in OSC in (a) DLL (b) ZVLL topologies

Diode logic is used with the load to empower the switching pace of the circuit. In this topology, load transistor's drain and gate electrodes are tied together, Fig. 6 (a), resulting in a better performing device in terms of robustness and enhanced pull-down current, furthermore, advancing to lessened delay, resulting in swifter functioning [16]. In this logic, driver transistor as well as the load transistor function in enhancement mode, evidently making apparent that driver circuit's *W/L* ratio needs to be way higher than the counterpart to obtain output as a high. Setting this ratio as 4:1 facilitates the optimum performance. This segment examines the performance of the proposed inverter circuit in ZVLL and DLL configurations. As depicted in Fig. 6 (b) gate and source of the load transistor are shorted for retrieving the desired results. VDD is provided with a 10V supply, and the output is fetched at the drain of the driver transistor. ZVLL enables the driver to firmly pull the output voltage up close to *VDD* pertaining to a considerably lesser resistance offered by the channel as compared to the load. Nonetheless, because of the presence of zero-*Vgs*, the pull-down transistor is allowed to operate like a constant current source, thereby requiring a substantially higher *W/L* ratio for the load to yield an output, approximating 0V. Like DLL, ZVLL also takes a *W/L* ratio of 4:1, exhibiting higher output resistance, resulting in larger gain [17]. Nevertheless, experiencing more switching speed delay because of a meagre value of pull-down current provided by the load transistor. Therefore, concluding that for yielding a better performance of an all-p type organic inverter, regarding the desired values of gain, noise margin and voltage swing, the preferred technique is the ZVLL, though it compromises on the switching speed [18].

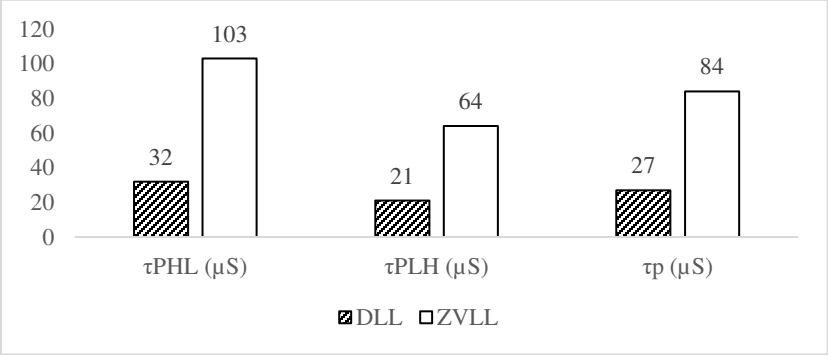

Fig. 7. Propagation delays of all-p type inverter using OTFT with single gate extra p+ doping and ditch in DLL and ZVLL configurations

Fig. 7 provides an insight into the low-to-high, high-to-low and the average propagation delays. Making it evident that the ZVLL that compromises on switching action, shows exceptional performance with respect to the noise margin and robustness. The delay seen in ZVLL is 3.1 times more than that seen in DLL.

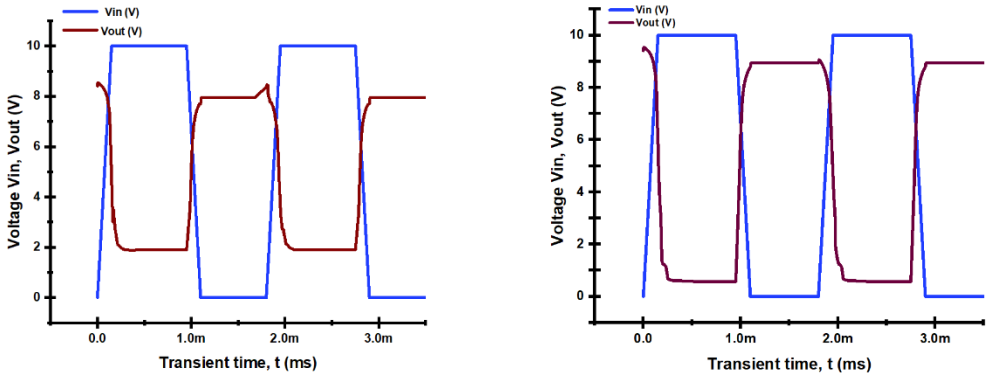

Fig. 8. Transient behavior of an all-p organic inverter using single gate organic transistor with extra p+ doping near S/D and a ditch in OSC (a) DLL and (b) ZVLL topologies

Due to the voltage output provided by ZVLL as depicted by Fig. 8, it is chosen over DLL as a preferred choice. To further augment the performance of the ZVLL configuration inverter, bootstrapping technique can be used. This is employed to additionally boost the conduct of the inverter.

4 Performance upgradation using Bootstrapping Technique

This section provides an acquaintance to bootstrapping technique and incorporating the same in making an inverter to obtain soaring efficiency and enhanced pace. The suggested circuit is relevant for expanding driving ability by boosting signals into the super threshold region and reducing the leakage current in the subthreshold region.

Bootstrapping technique is prominent for intensifying the voltage yield of the driver circuit upon amplifying an internal node by capacitive accretion of the positive side of the signal to the potential of an intrinsic circuit node. At the outset, this has been practiced in the assimilated driver-gate circuit of an indeterminate silicon active-matrix display [19]. To obtain curtailed voltage requirements, one edge of the bootstrap pulse is capacitively coupled to the electrode post storing the analog voltage furnished by the driver. This shifts the voltage by an explicit accession to the level desired for the peculiar inversion state. Hence, in the scaled-down inversion for a bootstrap pulse, negative edge hauls down the voltage to zero to countervail the minimal admissible driver output voltage.

The bootstrapping circuit arrangement comprises a capacitor employed in the feedback loop in between the input and the output node. Apparently, the body transistor pulls down the level of the output voltage to a marginal value which gets proliferated by this body capacitor owing to the summing of the voltage available at the input and the charge stored in it. Evidently, this capacitor solves the purpose of trimming the sensitivity of the threshold voltage. Consequently, bringing the threshold voltage drop to a decent level and further widening the noise margin. This technique is competent in contracting the emanated power and escalating the agility of the logic circuits. It administers potential equalization to a value superior to the supply voltage and inferior to the ground voltage. This anomaly conduces the devices to the super cut-off region downplaying dissipation of the power effluence. As reported by Raval et al. [20] a 40% and 13% boost in voltage swing and gate voltage respectively is ascertained using bootstrapping. Moreover, research employing this technique by Jeon et al. [21] demonstrated a substantial performance hike in all *p* pentacene based inverter circuits.

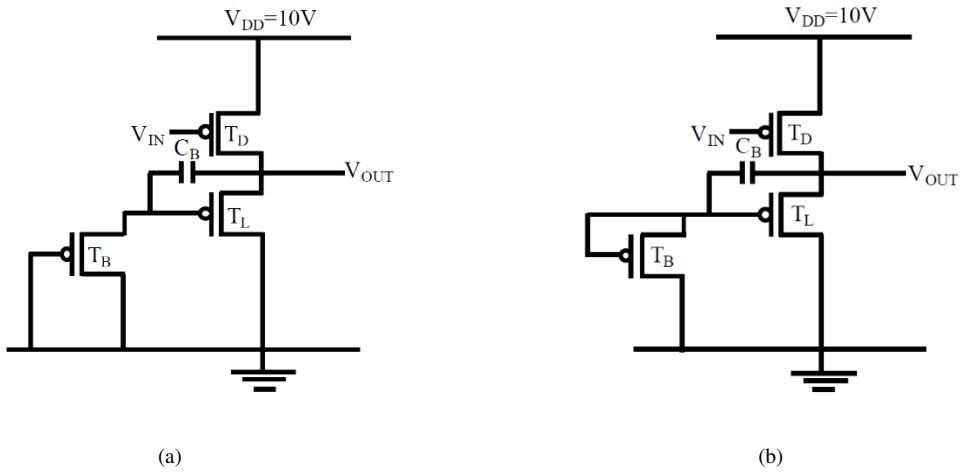

(a) (b)

Fig. 9. Bootstrap organic inverter circuit schematic employing Single Gate all-p OTFT in (a) DLL and (b) ZVLL configurations

Fig 9 (a) and (b) demonstrate the booststrapping circuit employing capacitive coupling attenuating the V_t (threshold voltage) sensitivity in DLL and ZVLL configurations respectively. The circuit comprises a supplementary transistor, T_B for bootstrapping, responsible for considerably magnifying the output voltage by lending capacitive coupling through capacitor, C_B [22].

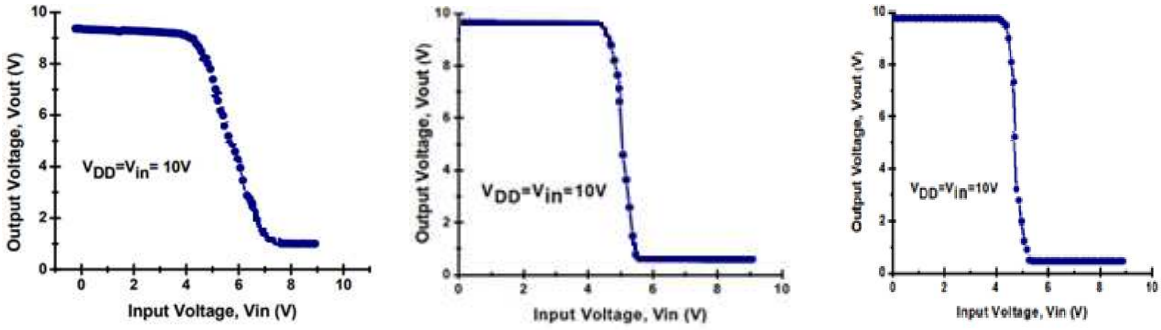

(a) (b) (c)

Fig. 10. VTC of all-p SG BGBC Bootstrapped Organic Inverter (a) Without P+ and ditch (b) With P+ without ditch (c) With P+ and ditch configuration

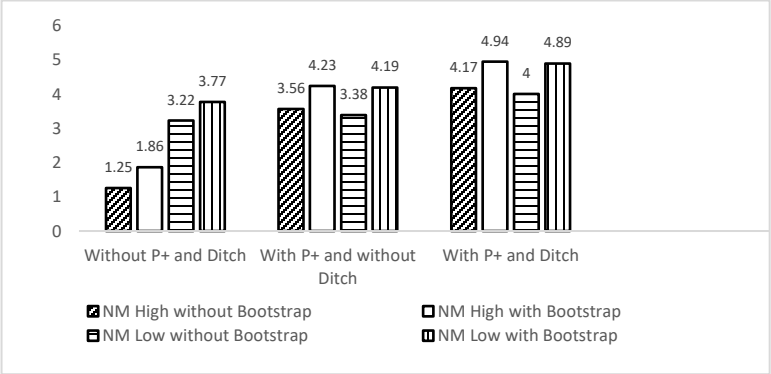

Fig. 11. Comparison of Noise Margins of different configurations of all-p SG BGBC Organic Inverter

Pragmatically, through Fig. 10 and 11 it is evodent that the high noise margin of the organic inverter increases by 18.46% and low NM increases by 22.25% upon the incorporation of bootstrap technique to the proposed inverter with extra doping and a dicth in the OSC. Likewise, NM_H and NM_L of other devices used for experimenting, an increase of 18.8% and 23.9% & 48.8% and 17.08% respectively was observed for inverter with extra p+ doping without ditch and that without extra doping and ditch. Fig. 12 demonstrates the dynamic response of SG bootstrap all-p organic inverter using bootstrap technique. Such inverters exhibit an upgraded voltage swing of 13% and 24% respectively for ZVLL and DLL configurations. Employing bootstrapping technique further enhances the volatge gain as a function of V_{IN} for DLL and ZVLL inverters [23].

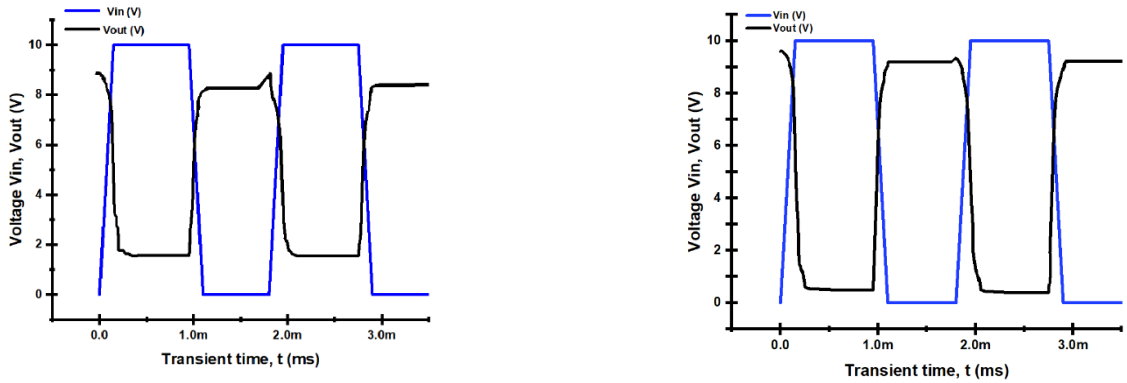

(a) (b)

Fig. 12. Improved Transitory response of all-p organic inverter employing single gate transistor with extra p+ doping and a ditch in vicinity of S/D in (a) DLL and (b) ZVLL with Bootstrap Technique

Upon employing the bootstrap technique to the all-p SG organic inverter with ditch and extra p+ region in the vicinity of the S/D electrodes, the gain gets augmented by 54.54%. Voltage gain of an all-p organic proposed ZVLL configuration is presented in Fig. 13. The transient characteristics in Fig. 12. show that the delay in propagation gets widened in the bootstrapped organic all-p inverter, because of the feeble pull down OTFT which may be raised on pull down organic transistor with a considerably higher aspect ratio [24].

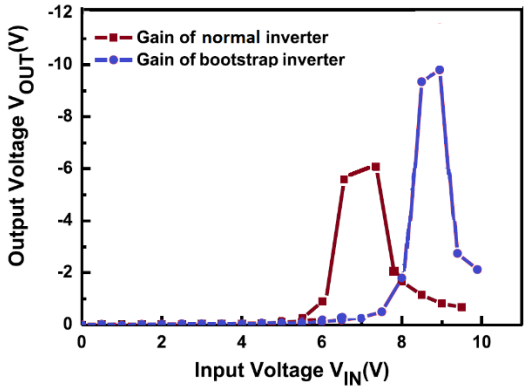

Fig. 13. Voltage gain of all-p organic bootstrapped ZVLL inverter using OTFT with extra p+ doping and a ditch Vs without bootstrapped inverter using OTFT with extra p+ doping and a ditch

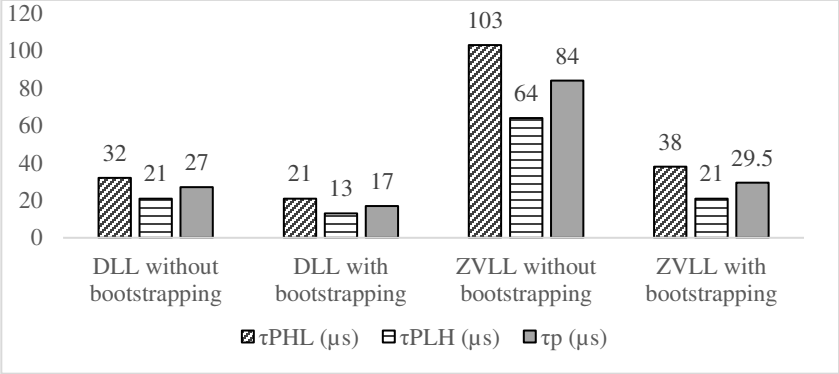

Fig. 14. Comparison of propagation delays in DLL and ZVLL topologies with and without bootstrapping in all-p type inverter based on transistor with additional p+ doping and ditch

Fig. 14 demonstrates the comparison of propagation delays for DLL and ZVLL configurations both with and without bootstrapping. After using the bootstrapping technique, where the average propagation delay improves by 58.8% for DLL, that of ZVLL drastically improves by 184.7%, again proving ZVLL to be better choice.

5 Conclusion

This research represented an inverter employing a single gate all-p organic thin film transistor in Diode Load Logic and Zero-V_{gs} Load Logic topologies. The derived responses of the inverter in static and transient states in DLL and ZVLL modes aided in the extraction of performance parameters viz. transition time along with high and low noise margins. The work elucidated on the apparent adoptions of designing an inverter using single gate all p OTFTs. Various design configurations, namely, inverter using single gate BGBC OTFT, inverter using single gate BGBC OTFT with extra p+ doping near the source and drain electrodes and that with extra doping and a 40 nm ditch incorporated into the organic semiconductor layer were presented. It was evidently concluded that the one with extra p+ doping and a ditch was hands down the best owing to the extracted curves. Furthermore, bootstrapping technique was introduced to attain considerably bettered efficiency and speed. Additionally, the circuit also yielded enhanced

driving capability and attenuating the leakage current. The voltage transfer characteristics demonstrated that the high and low noise margins of the bootstrapped device were significantly enhanced by an astonishing 18.46% and 22.25% for the proposed device based on OTFT with extra p+ doping and ditch. The transient response of the device exhibited an upscaling in the voltage swing by 24% and 13% for DLL and ZVLL configurations, respectively alongside resulting in better voltage gain.

Post a thorough observation and analysis of the dynamic responses of ZVLL and DLL topologies it was resolved that ZVLL configuration was a better option over DLL due to the NM's. In contrast to DLL, where the average delay decreases by only 10 µs after applying the bootstrapping technique, the same for ZVLL decreases by 54.5 µs making it a better responsive circuit, leading to a device which more robust, has effective noise margins, attenuated power leakage and improved sensitivity.

Competing interests

No, all the authors declare that they have no competing interests as defined by Springer, or other interests that might be perceived to influence the results and/or discussion reported in this paper. The authors have no conflicts of interest to declare that are relevant to the content of this article.

Funding

Not Applicable

Availability of data and materials

Data and materials utilized and supporting the results of this study are available within the article.

References

1. Dimitrakopoulos D., & Malenfant P. R. L. (2022). Organic thin film transistors for large area electronics. *Advanced Materials.*, 14, 99–117.
2. Majewski L. A., Grell M., Ogier S. D., & Veres J. (2003). A novel gate insulator for flexible electronics. *Organic Electronics*, 4, 27–32.
3. Horowitz G., (2004). Organic thin film transistors: From theory to real devices. *Journal of Materials Research*, 19, 1946–1962.
4. M. Kitamura M., Imada T., & Arakawa Y. (2003) Organic light-emitting diodes driven by pentacene-based thin-film transistors. Applied Physics Letters, 83, 3410–3412.
5. Weimer Paul K. (1962). The TFT A new Thin-Film Transistor. *IRE*, 50(6), 1462-1469.
6. Tsumura A., Koezuka H, & Ando T. (1986). Macromolecular electronic device: Field effect transistor with a polythiophene thin film. *Mat. And Electroni Dev Lab.*, 49(18), 1210-1212.
7. Klauk H. (2009). Organic Thin Film Transistors. *Chemical Society Review*, 39(7), 2643.
8. Lin Y. Y., Gundlach D. J., Nelson S. F., & Jackson T. N. (1997). Stacked pentacene layer organic thin-film transistors with improved characteristics. *IEEE Electron Device Letters.*, 8, 606–608,
9. Okumoto Y., Ukeda T., Matsui M., Okumoto K., Miyamoto A., & Morita K. (2012) Top-emission AMOLED display driven by organic TFTs with semiconductor layer patterned by inkjet process. *Journal* of the *Society* for *Information Display*, 20, 575–580.
10. Kumar B., Kaushik B. K., & Negi Y. S., Goswami V. (2014). Single and dual gate OTFT based organic digital design. *Microelectronics Reliability*, 54(1), 100-109.
11. Verma A., & Mittal P. (2017) Performance analysis of different novel organic thin film transistor structures. *ICCCA IEEE.*
12. Gelinck G. H. (2004). Flexible active-matrix displays, and shift registers based on solution-processed organic transistors. *Nature Materials*, 3(2), 106–110.
13. Mishra N., Mittal P., & Kumar B. (2019) Analytical modeling for static and dynamic response of organic pseudo all-p inverter circuits. *Journal* of *Computational Electronics*, 18(4), 1490-1500.
14. Klauk H., Halik M., & Zschieschang U., (2005) Flexible Organic Complementary Circuits. *IEEE Transactions on Electron Devices*, 52(4), 618-622.
15. Vusser S. D., Geneo J & Heremans P. (2006). Influence of Transistor Parameters on the Noise Margin of Organic Digital Circuits. *III* Transactions on Electron Devices, 53(4), 601-610.
16. Lou J. H., & Kuo J. B. (1997). A 1.5-V full-swing bootstrapped CMOS large capacitive-load driver circuit suitable for low-voltage CMOS VLSI. *IEEE J. Solid-State Circuits*, 32(1), 119–121.

17. Rogers J. A., Dodabalpur A. Z., Katz H. E. (1999). Low-voltage 0.1 μm organic transistors and complementary inverter circuits fabricated with a low-cost form of nearfield photolithography. *Applied Physics Letters*, 75(7), 1010-1–1010-3.
18. Resendiz L., Estrada M., Cerdeira A., Cabrera V. (2012). Analysis of the performance of an inverter circuit: Varying the thickness of the active layer in polymer thin film transistors with circuit simulation. *Japanese Journal of Applied Physics,* 51(4S), 04DK04-1–04DK04-6.
19. Gupta S., Mittal P & Juneja P. (2022). Performance improvement in single-gate organic transistors with contacts at top and bottom: Additional p+ region near source and drain. *Main Group Chemistry,* 21, 243-261.
20. Maurice F., Lebrun H., Szydlo N., Rossini U., & Chaudet R. (1998). High Resolution Projection Valve with the Amorphous Silicon AMLCD Technology. *Proc. SPIE 3296 (Part of the IS&T/SPIE Conference on Projection Displays IV)*, 92–99.
21. Raval H. N., Tiwari S. P., Navan R. R., Mhaisalkar S. G., Rao V. R. (2009). Solution processed bootstrapped organic inverters based on P3HT with a high-k gate dielectric material. *IEEE Electron Device Letters*, *30*(5), 484–486.
22. Jeon J., Murmann B., & Bao Z. (2010). Full-swing and high-gain pentacene logic circuits on plastic substrate", *IEEE Electron Device Letters, 31*(12), 1488–1490.
23. Pesavento P. V., Chesterfield R. J., Newman C. R., & Frisbie C. D. (2004). Gated four-probe measurements on pentacene thin-film transistors: Contact resistance as a function of gate voltage and temperature. *Journal of Applied Physics,* 96(12), 7312–7324.
24. Mittal P., Ditch and elevated organic thin film transistor-based improved common source voltage amplifier: Frequency response characteristics and analytical modeling. *Journal of the Society for Information Display*, 29(8), 642-658.

2023 2nd International Conference on Vision Towards Emerging Trends in Communication and Networking Technologies (ViTECoN) | 979-8-3503-4798-2/23/$31.00 ©2023 IEEE | DOI: 10.1109/VITECON58111.2023.10157909

An approach for Credit-Scoring using Swarm intelligence for feature selection and PSO trained ANN based classification

Indu Singh
Department of Computer Science Engineering
Delhi Technological University
indusingh@dtu.ac.in
New Delhi, India

Nikhil Mishra
Department of Computer Science Engineering
Delhi Technological University
nikhilmishra10@gmail.com
New Delhi, India

Anshul Joshi
Department of Computer Science Engineering
Delhi Technological University
anshuljoshipratik@gmail.com
New Delhi, India

Nishchal Agarwal
Department of Computer Science Engineering
Delhi Technological University
nishchalagarwal16@gmail.com
New Delhi, India

***Abstract*—As the financial system expanded, the credit scoring process changed in a way that has attracted more interest from scholars and businesses. Artificial intelligence technology based on predictive classification has changed how credit scores are calculated. These decision-making processes are taken with the help of various data mining algorithms to predict if the client is part of a suspicious group which is more likely to cause losses. In our proposed model (SIFS-PNN), we have used swarm intelligence-based algorithms to find relevant data along with a fine-tuned artificial neural network to successfully classify, whether or not, a client is a part of a sensitive group of credit lines. To do this, we will pick features using various swarm intelligence algorithms and fine-tune our ANN using Particle Swarm Optimization algorithm to perform credit classification. We also performed a comparative study with multiple previous researches to show how the suggested approach has outperformed previous results**

***Index Terms*—Credit-Scoring, Feature Selection, Classification, Metaheuristics, Neural Networks**

I. Introduction

A credit score gives the measure of the creditworthiness of a person [5]. According to Najadat et al. [11], about 70 per cent of all Americans have at least one credit card. Financial institutions face a significant hazard in the form of credit risk, i.e., a credit holder's potential to cause losses to the institution. Banks often use credit scoring models that employ different data mining techniques to make informed decisions and minimize losses from poor credit choices. [12]. Factors to predict credit risk could be related to demographics or financial information and actual financial situation [3]. To overcome the credit-risk problem, this paper proposes a dynamic swarm-intelligence based Feature selection model coupled with PSO-optimized Artificial Neural Network (SIFS-PNN).

The proposed model deploys a dynamic feature selection module which utilises the strengths of various swarm algorithms, namely Salp swarm optimization(SSA), Bat Algorithm(BA), Cuckoo Search Algorithm(CSA) and Harris Hawks' Optimization Algorithm(HHO) by generating random feature-sets utilizing the characteristics of all four algorithms and subsequently selecting the most suitable feature set. The selected feature-set is then forwarded to the PSO-optimized ANN-based classification module which classifies credit as good or bad. The model is tested on Australian and Japanese datasets to examine its robustness.

979-8-3503-4798-2/23/$31.00 © 2023 IEEE

II. Related Work

Credit scoring is a well-known area of study as a classification problem. Researchers are therefore eager to create new models that perform better than ones already in use. The issues with data that arise during the calculation of credit scores are discussed by Dumitru et al. [13]. The author has developed a Trusted Data Marketplace to address this issue. Credit scoring is being integrated here with cutting-edge technology like blockchain. The idea of analysing social media accounts to determine the social position of a person was first proposed by Jay et al. [8]. The author proposed a program that accesses data via Short Message Service (SMS).

Feng-Chia et al. [7] found that credit scoring is crucial for decision-making and provides an objective alternative to intuition based decisions. They proposed five feature selection algorithms for classification. Wei et al. [17] addressed population drift and the inability to predict customer credit dynam-

Authorized licensed use limited to: DELHI TECHNICAL UNIV. Downloaded on July 03,2023 at 04:43:35 UTC from IEEE Xplore. Restrictions apply.

ically by proposing a new model using clustering ensemble and cost-sensitive support vector machine. Armin et al. [6] proposed a credit scoring algorithm using the GradientBoost algorithm to enhance the Ensemble Logistic Regression approach. Their results showed that the GradientBoost Ensemble outperformed a single classification Logistic Regression in terms of accuracy.

In order to address credit scoring concerns, a straightforward credit scoring model by Zheng et al. [21] called Collaborative Filtering was devised. Tran et al. [15], developed a novel concept combining the strength of deep learning networks with the thorough genetic programming that is used to extract parameters to produce a reliable credit scoring model.

III. BACKGROUND

A. Feature Selection Module

Feature selection reduces the number of input variables for a model, decreasing computational complexity and increasing accuracy by removing noise from large datasets. The proposed model uses swarm intelligence algorithms for this purpose.

*a) **Harris Hawks Optimization**:* The intentional chasing and pouncing behaviour of forest Harris hawks served as the model for HHO. Many hawks pounce from different angles to surprise the prey [4]. Harris hawks have a variety of chasing behaviours. The HHO algorithm mathematically mimics these patterns. This can be modelled via the equations below.

$$Y(t+1) = \begin{cases} Y_{random}(t) - a_1|Y_{random}(t) - 2a_2Y(t)| & p \geqslant 0.5 \\ (Y_{target}(t) - Y_n(t)) - a_3(L + a_4(U - L)) & p < 0.5 \end{cases} \quad (1)$$

where $a_{1,2,3,4}$ and q are random numbers inside (0,1), Hawks' position at iteration t is represented by Y(t), The prey's location at time t is indicated by the value $Y_{target}(t)$. Hawk $Y_{random}(t)$ is randomly selected, and Hawk Y_m is the average location of the current Hawks, which can be mathematically represented as follows

$$Y_m(t) = \frac{1}{N}\sum_{i=1}^{N} Y_i(t) \quad (2)$$

The hawks can attack a target in 4 distinct methods. The prey's energy level (E) and leap strength (J) depends on which mode the hawks choose. The equations for all these modes are shown below.

1) Soft Besiege

$$Y(t+1) = \Delta Y - E|JX_{target} - Y(t)| \quad (3)$$

$$\Delta Y(t) = Y(target) - Y(t) \quad (4)$$

where Y(t) is the hawk's location at time t

2) Hard Besiege

$$Y(t+1) = Y_{target} - E|\Delta Y(t)| \quad (5)$$

3) Soft Besiege with rapid progressive dives

$$X = Y_{target}(t) - E|JY_{target}(t) - Y(t)| \quad (6)$$

$$Z = Z + S * LF(D) \quad (7)$$

Here equation 6 is used to decide the hawk's next move while Equation 7 will be the diving pattern which is based of the Levy Flight function (F) in D-dimensions. T stands for a random vector with dimensions 1 X D. The equation below can be used to determine LF.

$$F(y) = 0.01 * \frac{m * \omega}{|n|^{\frac{1}{\gamma}}},\ \omega = \left(\frac{\Gamma(1+\gamma) * \sin\left(\frac{\pi*\gamma}{T}\right)}{\Gamma\ \left(\frac{1+\gamma}{2}\right) * \gamma * 2^{\left(\frac{\gamma-1}{2}\right)}}\right) \quad (8)$$

where [0, 1] is a range of random values for m and n and γ is constant equal to 1.5. Equations 6 and 7 are used to determine X and Z, respectively.

4) Hard Besiege with rapid progressive dives

$$Y(t+1) = \begin{cases} X \text{ if F(X)} < \text{F(Y(t))} \\ Z \text{ if F(Z)} < \text{F(Y(t))} \end{cases} \quad (9)$$

where X and Z are obtained using the following equations.

$$X = Y_{target}(t) - E|JY_{target}(t) - Y_m(t)| \quad (10)$$

$$Z = X + S * L(D) \quad (11)$$

$Y_m(t)$ can be calculated in equation 2 and F(D) using equation 8

*b) **Cuckoo search algorithm**:* CSA takes its cue from cuckoo birds, who don't hatch their eggs on their own but instead place them into the nests of other birds. [2]. Assume C is the total number of cuckoos present and each cuckoo has a nest. If the search space's dimension is n then the vector for i^{th} Cuckoo at period t is denoted by $U_i(t+1) = (u_i^1, ...u_i^d, ...u_i^n)$ for i = 1,2,...C. The hunt space for i^{th} is updated as follows at time t+1.

$$U_i(t+1) = U_i(t) + \alpha \bigotimes Levy(\gamma) \quad (12)$$

where $\alpha > 0$ denotes the step size and γ in the range $1 < \gamma < 3$. Standard deviations aid in updating.. The corresponding equations are shown below.

$$Levy(\gamma) = \frac{u}{|v|^{\frac{1}{\gamma-1}}} \quad (13)$$

where u and v are gaussian distributions. Similarly,

$$\sigma_u(\gamma) = \left[\frac{\Gamma(1+\gamma)\sin\left(\frac{\pi\gamma}{2}\right)}{\Gamma\left(\frac{1+\gamma}{2}\right)\gamma 2^{\left(\frac{\gamma-1}{2}\right)}}\right]^{\frac{1}{\gamma}} \text{ and } \sigma_v(\gamma) = 1 \quad (14)$$

Levy distribution for bigger advances through power law, resulting in the representation of an infinite variance as

$$Levy(\gamma) \sim u = t^{i\gamma} \quad (15)$$

Every cuckoo randomly selects a nest to place its egg, and the best nests will survive to next generations with a [0,1] probability that a host recognizes a cuckoo egg.

Authorized licensed use limited to: DELHI TECHNICAL UNIV. Downloaded on July 03,2023 at 04:43:35 UTC from IEEE Xplore. Restrictions apply.

*c) **Bat algorithm**:* The BA takes its cues from how bats use echolocation to gauge distance. Bats often use brief, loud sound impulses to detect obstacles or prey when they are out hunting at night [20].

1) Quantity, position, speed, Frequency, loudness of heartbeats is initialized
2) The bat's speed and location are updated at time t using the following equation:

$$v_a^{t+1} = v_a^t + (x_a^t - x^*) * h_a \tag{16}$$

$$x_a^{t+1} = x_a^t + v_a^t \tag{17}$$

$$h_a = h_{min} + (h_{max} - hmin * rand \tag{18}$$

At time t, v_a^t and x_a^t represent the speed and location of bat a, respectively. x^* is the best bat position, while h_a is the bat's ultrasonic frequency. The minimum and maximum pulse frequencies are represented by h_min and h_max, respectively. The position at t+1 is represented by x_a^{t+1}.

3) Make a random number $rand1$. If $rand1 > r_a$, a random walk approach is used to locally search the bat to get a new solution.

$$x_{new} = x_{old} + \epsilon A^t \tag{19}$$

4) If $rand2 < A_a$, and and the positional fitness of the new solution is superior to that of the old solution

$$r_a^t = r_0[1 - \exp^{-\gamma * t}] \tag{20}$$

$$A_a^t = \alpha * A_a^{t-1} \tag{21}$$

At time t, r_a^t represents the bat pulse frequency. r_0 is a constant and A_a^{t-1} and A_a^t are the bat pulse intensities at t-1 and t, respectively. The coefficients are represented by γ and α. The best fitness value is determined and recorded. The process is terminated after the desired number of repetitions or returns to step (3).

*d) **Salp swarm optimization**:* The salp is a highly organised marine organism that moves similarly to jellyfish. This collective behaviour served as the basis for SSA [19]. The fundamental method is broken down into three phases.

1) Using the upper limit (u) and lower bound (l) of the search space, a random population initialization of size M is performed in a E-dimensional search space represented in a 2-dimensional matrix Y.

$$\mathbf{Y}_{M*E} = \mathbf{l} + rand(M, E) * (\mathbf{u} - \mathbf{l}) \tag{22}$$

2) Location of the group's leader is as shown in the equation below.

$$Y_e^m = \begin{cases} G_e + a_1((u_e - l_e)a_2 + l_e) & a_3 \geqslant 0.5 \\ G_e - a_1((u_e - l_e)a_2 + l_e) & a_3 < 0.5 \end{cases} \tag{23}$$

where Y_m^e is the position of M^{th} leader salp in e-dimensional space a_2 and a_3 are randomly distributed numbers in the range [0,1] and a_1 is the convergence factor calculated as

$$a_1 = 2\epsilon^{-\left(\frac{4t}{t_{max}}\right)^2} \tag{24}$$

where t is the number of iterations.

3) Follower location update using the equation below.

$$Y_d^n = \frac{1}{2}(y_e^n + y_e^{n-1}) \tag{25}$$

B. Classification Module

Classification means categorizing objects into predefined categories. ML classifiers use input data to assess the probability that succeding data will fall into one of the established categories.

*a) **Neural Networks**:* NNs map input and output patterns to problems and learn new information through training. Its structure consists of layers of interconnected neurons represented by functions.

*b) **Particle Swarm Optimization**:* The PSO algorithm mimics swarm behavior where particles update their positions and search for the answer while sharing information [10]. A PSO-tuned ANN is used to overcome the slower convergence and local minima of conventional backpropagation-driven ANNs. The steps to create a PSO-driven NN are outlined below.

1) To set the population's particles' initial positions and velocities and establish necessary connections.

$$X_j = [x_{j1}, x_{j2}, ...x_{jD}] = \begin{bmatrix} w_{11}, ..., w_{nl} \\ w_{1m}, ..., w_{lm} \\ a_1, ...a_n \\ b_1, ...b_l \end{bmatrix}^T \tag{26}$$

In equation (26), w_{nl} represents the weight from the input to the hidden layer and w_{1m} represents the weight from the hidden to the output layer. The thresholds for the input and hidden layers are represented by a_n and b_n, respectively.

2) The current position of each particle is stored in M_{best} and the best fitness value among all particles is stored in N_{best}. The fitness function F is represented by the output error of the neural network(27).

$$F = \frac{1}{s}\sum_{i=1}^{N} E_i \tag{27}$$

In 27: The sample count is s. The particle group's size is N. E stands for error.

3) Update the particle's position and velocity
4) Compare each particle's fitness value F(i) to its own extreme value M_{best}. Replace M_{best} with F(i), if $F(i) > M_{best}$. Similarly, update N_{best} by comparing all M_{best} and N_{best}.
5) The search is terminated once the specified number of iterations is reached. If not, it returns 4) to carry on the search.

Authorized licensed use limited to: DELHI TECHNICAL UNIV. Downloaded on July 03,2023 at 04:43:35 UTC from IEEE Xplore. Restrictions apply.

When the fitness value is at its minimum, the neural network parameters corresponding to the optimal particle position are assigned to the neural network for training to produce a more precise prediction function.

IV. PROPOSED MODEL

A. Data

1) Dataset Used: The model has been trained and tested on the pre-existing Australian and Japanese Credit Scoring Datasets.

B. Experimental Approach

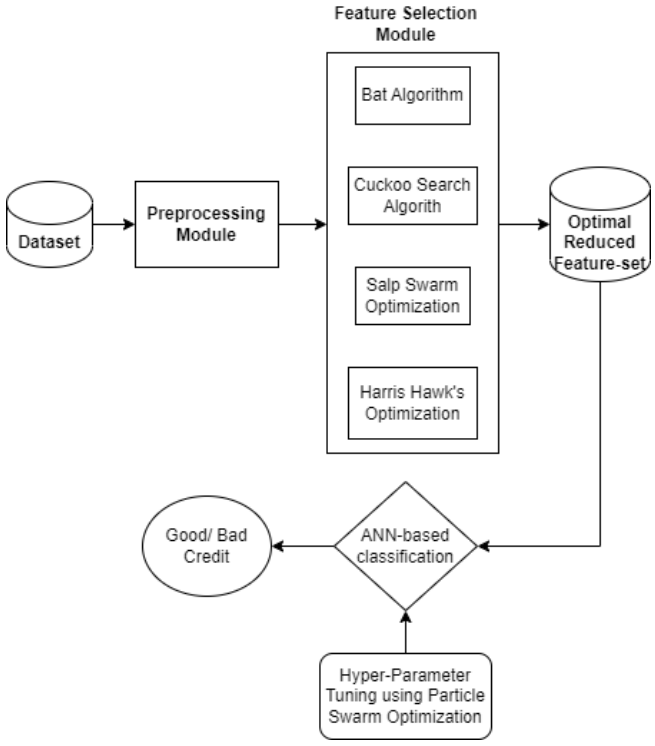

Fig. 1. Architecture of Proposed Model

The model has two main modules as shown in Figure 1. The Feature-Selection Module eliminates less influential attributes to reduce computational complexity. The Classification Module uses an Artificial Neural Network to classify the result. Both modules are described below..

1) Feature Selection Module: In this module, four swarm intelligence-based metaheuristic optimization algorithms have been deployed. The dataset is run parallel on all the algorithms with each algorithm. Subsequently, The kNN clustering algorithm calculates the accuracy of each algorithm. The most accurate algorithm is selected and its feature set is forwarded dynamically. This approach leverages the strengths of all four algorithms to ensure high accuracy. Algorithm 1 shows the overall process.

Algorithm 1 Feature Selection

Data: Australian and Japanese Credit Scoring Dataset
Result: Optimal Feature-set (O_{feat})

begin
  Initialisation acc_{best} = 0, $algo_{best}$ = "", O_{feat} = []
  Run on Harris Hawks' Optimization Algorithm
  if $acc_{curr} > acc_{best}$ *and* $len(feat_set) > 1$ **then**
    $acc_{best} = acc_{curr}$, $algo_{best}$ = "HHO", $O_{feat} = feat_set$
  end
  Run on Bat Algorithm
  if $acc_{curr} > acc_{best}$ *and* $len(feat_set) > 1$ **then**
    $acc_{best} = acc_{curr}$, $algo_{best}$ = "BA", $O_{feat} = feat_set$
  end
  Run on Cuckoo Search Algorithm
  if $acc_{curr} > acc_{best}$ *and* $len(feat_set) > 1$ **then**
    $acc_{best} = acc_{curr}$, $algo_{best}$ = "CSA", $O_{feat} = feat_set$
  end
  Run on Salp Swarm Optimization Algorithm
  if $acc_{curr} > acc_{best}$ *and* $len(feat_set) > 1$ **then**
    $acc_{best} = acc_{curr}$, $algo_{best}$ = "SSA", $O_{feat} = feat_set$
  end
end

2) Classification Module: This module uses a PSO-tuned Artificial Neural Network to overcome the limitations of conventional backpropagation. During training, PSO accelerates convergence and particle space changes produce new weights and revised biases for better solutions. The algorithms are shown in Algorithm 2 and 3.

V. RESULTS AND DISCUSSION

This section evaluates the model's performance and compares it to other existing state-of-the-art models.

A. Evaluation of the fitness function of the swarm-intelligence algorithms used

For the purpose of feature selection, four SI algorithms have been used. They are: HHO, BA, CSA and SSA. The algorithm which yields the lowest value of the fitness function, i.e., highest accuracy is passed on. This can be demonstrated from Figure 2a and Figure 2b

As observed, BA yields the lowest fitness value for Figure 2a while CSA yields the lowest for Figure 2b.

B. Evaluation of parameters of ANN-PSO

The ANN-PSO provides us with the Mean-squared Error (MSE), and Accuracy. Figure 3b and Figure 3a show the evaluation of both the parameters over the 500 iterations.

Authorized licensed use limited to: DELHI TECHNICAL UNIV. Downloaded on July 03,2023 at 04:43:35 UTC from IEEE Xplore. Restrictions apply.

Algorithm 2 Particle Swarm Optimization Algorithm

Result: Weight matrix for ANN

begin
- **Initialisation** Position and velocities of particles in swarm
- Fitness function evaluation of each swarm particle
- Assign fitness value of best particle to global best position(g_{best})
- **while** *conditions not satisfied* **do**
  - **for** *every particle in the swarm* **do**
    - Update velocity using PSO equation
    - Update position using new velocity
    - Evaluate fitness function of newly obtained particle position
    - **if** *obtained position is better than current personal best(p_{best})* **then**
      - Update p_{best}
    - **end**
  - **end**
  - **if** *any* $p_{best} > g_{best}$ **then**
    - Update g_{best}
  - **end**
- **end**
- Use weights obtained from g_{best} to train an artificial neural network

end

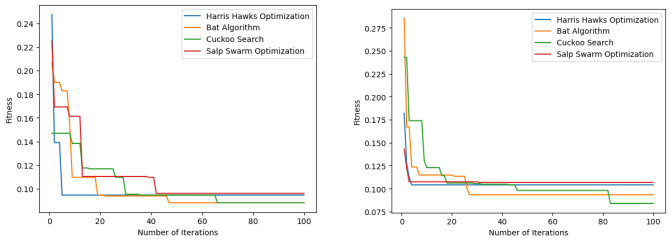

(a) Fitness Function Evaluation of proposed model over Australian Dataset

(b) Fitness Function Evaluation of proposed model over Japan Dataset

Fig. 2.

As observed, the MSE in Figure 3b is 0.093 at iteration 500 while that in Figure 3a is 0.10. Similarly, the accuracy show an accuracy of 92.7% and 91% for Australian and Japanese Datasets respectively.

C. Performance Evaluation Parameters

Using True Positive, True Negative, False Positive and False Negative values from a Confusion Matrix, four performance evaluation metrics can be constructed. Their evaluation over the 500 iterations of the ANN is shown in Table I.

Algorithm 3 PSO-trained ANN

Data: O_{feat} and Weight Matrix obtained through PSO algorithm

Result: The model classifies any record as good or bad credit

begin
- **Initialisation**
- Classify each attribute of data-set as categorical or continuous
- Drop all the attributes not present in O_{feat}
- Perform One-hot Encoding on the categorical attributes
- Make necessary connections and define the structure of the ANN
- Obtain the weights for each layer from the PSO weight matrix
- Perform fit transformations to fit data on the model **while** *iteration* < 500 **do**
  - Run the model on the reduced dataset
  - Perform credit classifications and compute accuracy
  - **if** *new accuracy* $>$ *previous accuracy* **then**
    - new accuracy = best accuracy
    - Update particle position
    - Compute MSE
    - Store values for Graph Generation
  - **end**
- **end**
- Display best accuracy and best particle position
- Display Graph

end

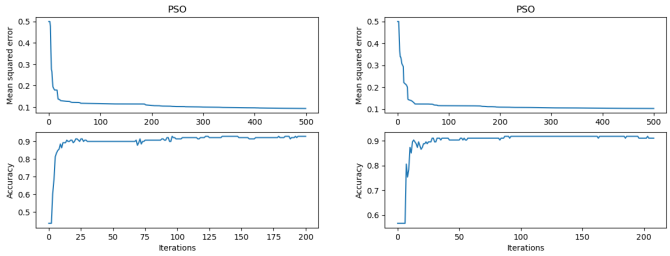

(a) MSE and Accuracy Evaluation of proposed model over Australian Dataset

(b) MSE and Accuracy Evaluation of proposed model over Japan Dataset

Fig. 3.

No. of Iterations	Accuracy	Precision	Recall	F1-Score
100	0.90	0.89	0.93	0.91
200	0.92	0.91	0.90	0.90
300	0.91	0.92	0.90	0.91
400	0.91	0.92	0.91	0.92
500	0.93	0.92	0.91	0.92

TABLE I
EVALUATION OF VARIOUS PARAMETERS OVER 500 ITERATIONS

Authorized licensed use limited to: DELHI TECHNICAL UNIV. Downloaded on July 03,2023 at 04:43:35 UTC from IEEE Xplore. Restrictions apply.

D. Comparison with prior studies

In this section we have tried to compare our approach SIFS-PNN with other existing models run on Australian and German datasets. The results along with the corresponding algorithms used have been tabulated in Table II.

Study	Algorithm	Dataset	Accuracy(%)
Diwakar et al (2018) [16]	FS+NN	Japanese	87.98
		Australian	90.69
Thitimanan et al.(2019) [1]	C4.5+AdaBoost	Australian	89
Nguyen-Thi et al.(2019)	noise filtering + ensemble	Australian	89.1
		Japanese	87.6
Shuang et al. (2019) [18]	Noise adaptation backflow	Australian	87.9
		Japanese	89.1
Safiya et al.(2020) [14]	random forest	Australian	
Lkhagvadorj et al(2020) [9]	NN+Logistic regression	Australian	82.6
SIFS-PNN (our approach)	FS+NN-PSO	Japanese	**91**
		Australian	**93**

TABLE II
COMPARISON WITH PRIOR STUDIES

VI. CONCLUSION AND SCOPE

This paper presents a dynamic feature selection algorithm combined with a PSO-tuned ANN-based classification for credit scoring. The FS uses multiple SI-based algorithms in parallel to retain the most prominent features and the ANN optimized by PSO performs final classification on the credit-score as good or bad credit. Combining these two strategies, we were able to implement a highly robust model which facilitates a highly probable classification of user credit. The model has been trained and tested on the standard Australian and Japanese datasets. Our findings demonstrate that, by providing the necessary attributes, our suggested method is capable of classifying customers correctly about 93% and 91% of the time on the Australian and Japanese Dataset respectively. In the future, we plan to enhance the accuracy of our model by either hybridizing the current parameter tuning algorithm for the ANN or replacing it with another algorithm that may offer better convergence.

REFERENCES

[1] Damrongsakmethee, T., Neagoe, V.E.: C4.5 decision tree enhanced with adaboost versus multilayer perceptron for credit scoring modeling. In: Silhavy, R., Silhavy, P., Prokopova, Z. (eds.) Computational Statistics and Mathematical Modeling Methods in Intelligent Systems. pp. 216–226. Springer International Publishing, Cham (2019)

[2] Das, G., Panda, R.: Seagull-cuckoo search algorithm for function optimization. In: 2021 6th International Conference for Convergence in Technology (I2CT). pp. 1–6 (2021). https://doi.org/10.1109/I2CT51068.2021.9417939

[3] Diaconescu, P., Neagoe, V.E.: Credit scoring using deep learning driven by optimization algorithms. In: 2020 12th International Conference on Electronics, Computers and Artificial Intelligence (ECAI). pp. 1–6 (2020). https://doi.org/10.1109/ECAI50035.2020.9223139

[4] Heidari, A.A., Faris, H., Aljarah, I., Mafarja, M., Chen, H.: Harris hawks optimization: Algorithm and applications. Future Generation Computer Systems **97 https://aliasgharheidari.com/HHO.html**, 849–872 (03 2019). https://doi.org/10.1016/j.future.2019.02.028

[5] Jain, N., Agrawal, T., Goyal, P., Hassija, V.: A blockchain-based distributed network for secure credit scoring. In: 2019 5th International Conference on Signal Processing, Computing and Control (ISPCC). pp. 306–312 (2019). https://doi.org/10.1109/ISPCC48220.2019.8988510

[6] Lawi, A., Aziz, F., Syarif, S.: Ensemble gradientboost for increasing classification accuracy of credit scoring. In: 2017 4th International Conference on Computer Applications and Information Processing Technology (CAIPT). pp. 1–4 (2017). https://doi.org/10.1109/CAIPT.2017.8320700

[7] Li, F.C., Wang, P.K., Yeh, L.L.: Diversity of feature selection approaches combined with distinct classifiers. In: 2010 IEEE International Conference on Industrial Engineering and Engineering Management. pp. 28–32 (2010). https://doi.org/10.1109/IEEM.2010.5674600

[8] Lohokare, J., Dani, R., Sontakke, S.: Automated data collection for credit score calculation based on financial transactions and social media. In: 2017 International Conference on Emerging Trends Innovation in ICT (ICEI). pp. 134–138 (2017). https://doi.org/10.1109/ETIICT.2017.7977024

[9] Munkhdalai, L., Lee, J.Y., Ryu, K.H.: A hybrid credit scoring model using neural networks and logistic regression. In: Pan, J.S., Li, J., Tsai, P.W., Jain, L.C. (eds.) Advances in Intelligent Information Hiding and Multimedia Signal Processing. pp. 251–258. Springer Singapore, Singapore (2020)

[10] Munlin, M., Anantathanavit, M.: New social-based radius particle swarm optimization. In: 2017 12th IEEE Conference on Industrial Electronics and Applications (ICIEA). pp. 838–843 (2017). https://doi.org/10.1109/ICIEA.2017.8282956

[11] Najadat, H., Altiti, O., Aqouleh, A.A., Younes, M.: Credit card fraud detection based on machine and deep learning. In: 2020 11th International Conference on Information and Communication Systems (ICICS). pp. 204–208 (2020). https://doi.org/10.1109/ICICS49469.2020.239524

[12] Nalić, J., Martinović, G., Žagar, D.: New hybrid data mining model for credit scoring based on feature selection algorithm and ensemble classifiers. Advanced Engineering Informatics **45**, 101130 (2020). https://doi.org/https://doi.org/10.1016/j.aei.2020.101130

[13] Roman, D., Stefano, G.: Towards a reference architecture for trusted data marketplaces: The credit scoring perspective. pp. 95–101 (08 2016). https://doi.org/10.1109/OBD.2016.21

[14] Safiya Parvin, A., Saleena, B.: An ensemble classifier model to predict credit scoring - comparative analysis. In: 2020 IEEE International Symposium on Smart Electronic Systems (iSES) (Formerly iNiS). pp. 27–30 (2020). https://doi.org/10.1109/iSES50453.2020.00017

[15] Tran, K., Duong, T., Ho, Q.: Credit scoring model: A combination of genetic programming and deep learning. In: 2016 Future Technologies Conference (FTC). pp. 145–149 (2016). https://doi.org/10.1109/FTC.2016.7821603

[16] Tripathi, D., Edla, D.R., Kuppili, V., Bablani, A., Dharavath, R.: Credit scoring model based on weighted voting and cluster based feature selection. Procedia Computer Science **132**, 22–31 (2018). https://doi.org/https://doi.org/10.1016/j.procs.2018.05.055, international Conference on Computational Intelligence and Data Science

[17] Wei, G., Mingshu, C.: A new dynamic credit scoring model based on clustering ensemble. In: Proceedings of 2013 3rd International Conference on Computer Science and Network Technology. pp. 421–425 (2013). https://doi.org/10.1109/ICCSNT.2013.6967144

[18] Wei, S., Yang, D., Zhang, W., Zhang, S.: A novel noise-adapted two-layer ensemble model for credit scoring based on backflow learning. IEEE Access **7**, 99217–99230 (2019). https://doi.org/10.1109/ACCESS.2019.2930332

[19] Xiao, B., Wang, R., Xu, Y., Song, W., Wang, J., Wu, Y.: Salp swarm algorithm based on particle-best. pp. 1383–1387 (03 2019). https://doi.org/10.1109/ITNEC.2019.8729243

[20] Xie, J., Wei, D.: Multi-sensor detection network based on improved bat algorithm. In: 2018 IEEE 3rd Advanced Information Technology, Electronic and Automation Control Conference (IAEAC). pp. 2061–2065 (2018). https://doi.org/10.1109/IAEAC.2018.8577249

[21] Zheng, X.: A credit scoring model based on collaborative filtering. In: 2013 Ninth International Conference on Computational Intelligence and Security. pp. 144–148 (2013). https://doi.org/10.1109/CIS.2013.37

Authorized licensed use limited to: DELHI TECHNICAL UNIV. Downloaded on July 03,2023 at 04:43:35 UTC from IEEE Xplore. Restrictions apply.

An Emotion-Guided Approach to Domain Adaptive Fake News Detection Using Adversarial Learning (Student Abstract)

Arkajyoti Chakraborty*[1], Inder Khatri*[1], Arjun Choudhry*[1], Pankaj Gupta[1], Dinesh Kumar Vishwakarma[1], Mukesh Prasad[2]

[1] Biometric Research Laboratory, Delhi Technological University, New Delhi, India
[2] School of Computer Science, FEIT, University of Technology Sydney, Sydney, Australia
{arkajyotichakraborty_2k19ep022, dinesh}@dtu.ac.in, {inderkhatri999, choudhry.arjun}@gmail.com, mukesh.prasad@uts.edu.au

Abstract

Recent works on fake news detection have shown the efficacy of using emotions as a feature for improved performance. However, the cross-domain impact of emotion-guided features for fake news detection still remains an open problem. In this work, we propose an emotion-guided, domain-adaptive, multi-task approach for cross-domain fake news detection, proving the efficacy of emotion-guided models in cross-domain settings for various datasets.

Introduction

Over the years, our reliance on social media as an information source has increased, leading to an exponential increase in the spread of *fake news*. To counter this, researchers have proposed various approaches for fake news detection (FND). Models trained on one domain often perform poorly on datasets from other domains due to the domain shift (Figure 1(1)). Some works show the efficacy of domain adaptation for cross-domain FND by extracting domain-invariant features (Figure 1(2)) for classification (Zhang et al. 2020). However, adapting domains does not ensure that features in different classes align correctly across domains, which sometimes has a negative impact on performance. Some works have shown a correlation between fake news and their intrinsic emotions (Guo et al. 2019; Choudhry, Khatri, and Jain 2022) (Figure 1(3)), having successfully used it for fake news detection. However, these works are restricted to in-domain settings and don't consider cross-domain evaluation. We propose the use of emotion-guided multi-task models for improved cross-domain fake news detection, experimentally proving its efficacy, and present an emotion-guided domain adaptive approach for improved cross-domain fake news detection by leveraging better feature alignment across domains due to the use of emotion labels (Figure 1(4)).

Proposed Methodology

Datasets, Emotion Annotation & Preprocessing

We use the FakeNewsAMT & Celeb (Pérez-Rosas et al. 2018), Politifact[1], and Gossipcop[2] datasets. We annotate them with the core emotions from Ekman's (Ekman 1992) (6 emotions: *Joy*, *Surprise*, *Anger*, *Sadness*, *Disgust*, *Fear*) and Plutchik's (Plutchik 1982) (8 emotions: *Joy*, *Surprise*, *Trust*, *Anger*, *Anticipation*, *Sadness*, *Disgust*, *Fear*) emotion theories. We use the Unison model (Colneric and Demsar 2018) for annotating the datasets with emotion tags. During preprocessing, we convert text to lower case, remove punctuation, and decontract verb forms (eg. *"I'd"* to *"I would"*).

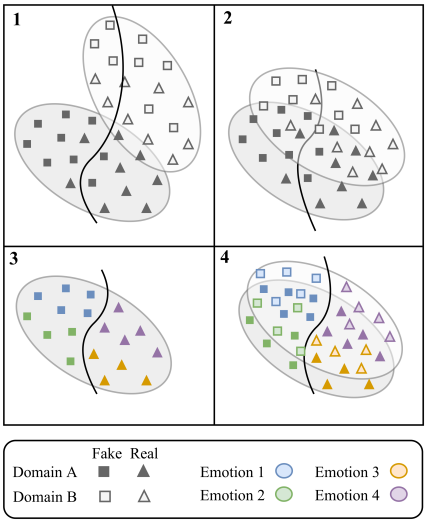

Figure 1: (1) Cross-domain texts not aligned. (2) Domain adaptation for improved alignment. (3) Emotion-guided classification. (4) Emotion-guided domain adaptation.

Emotion-guided Domain-adaptive Framework

We propose the cumulative use of domain adaptation and emotion-guided feature extraction for cross-domain fake news detection. Our approach aims to improve the feature alignment between different domains using adversarial domain adaptation by leveraging the correlation between the emotion and the veracity of a text (as shown in Figure 1(4)).

*These authors contributed equally.

Copyright © 2023, Association for the Advancement of Artificial Intelligence (www.aaai.org). All rights reserved.

[1] https://www.politifact.com/
[2] https://www.gossipcop.com/

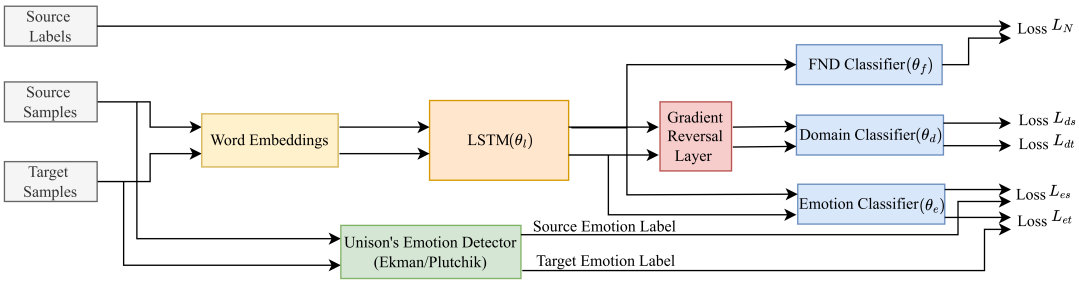

Figure 2: Graphical representation of our emotion-guided domain-adaptive framework for cross-domain fake news detection.

Figure 2 shows our proposed framework. We use an LSTM-based multi-task learning (MTL) feature extractor which is trained by the cumulative losses from fake news classifier, emotion classifier, and discriminator (aids in learning domain-invariant features). LSTM can be replaced with better feature extractors. We use it specifically for easier comparison to non-adapted emotion-guided and non-adapted single-task models. The domain classifier acts as the discriminator. Fake news classification loss, emotion classification loss, adversarial loss, and total loss are defined as:

$$L_{FND} = \min_{\theta_l, \theta_f} \sum_{i=1}^{n_s} L_f^i \quad (1)$$

$$L_{emo} = \min_{\theta_l, \theta_e} \sum_{i=1}^{n_s} L_{es}^i + \sum_{j=1}^{n_t} L_{et}^j)) \quad (2)$$

$$L_{adv} = \min_{\theta_d}(\max_{\theta_l}(\sum_{i=1}^{n_s} L_{ds}^i + \sum_{j=1}^{n_t} L_{dt}^j)) \quad (3)$$

$$L_{Total} = (1-\alpha-\beta)*L_{FND} + \alpha * (L_{adv}) + \beta * (L_{emo}) \quad (4)$$

where n_s and n_t are number of samples in source and target sets; θ_d, θ_f, θ_e, and θ_l are parameters for discriminator, fake news classifier, emotion classifier, and LSTM feature extractor; L_{d_s} and L_{d_t} are binary crossentropy loss for source and target classification; L_{es} and L_{et} are crossentropy loss for emotion classification; L_f is binary crossentropy loss for Fake News Classifier; α and β are weight parameters in L_{Total}. We optimized α and β for each setting.

Experimental Results & Discussion

Each model used for evaluation was optimized on an in-domain validation set. Table 1 illustrates our results proving the efficacy of using emotion-guided models in non-adapted cross-domain settings. Table 2 compares non-adaptive models, domain adaptive models, and our emotion-guided domain adaptive models in various settings. MTL (E) and MTL (P) refer to emotion-guided multi-task frameworks using Ekman's and Plutchik's emotions respectively. STL refers to single-task framework. DA refers to domain-adaptive framework with a discriminator. Non-DA refers to a non-adapted model. Some findings observed are:

Emotions-guided non-adaptive multi-task models outperform their single-task counterparts in cross-domain settings, as seen in Table 1, indicating improved extraction of features that are applicable across different datasets.

Emotion-guided domain-adaptive models improve performance in cross-domain settings. Table 2 shows the advantage of emotion-guided adversarial domain-adaptive models over their non-adaptive counterparts. This shows the scope for improved feature extraction even after adversarial adaptation, and emotion-guided models act as a solution.

Source	Target	Accuracy Non-DA STL	Accuracy Non-DA MTL(E)	Accuracy Non-DA MTL(P)
FAMT	Celeb	0.420	0.520	**0.530**
Celeb	FAMT	0.432	0.471	**0.476**

Table 1: Cross-domain evaluation of non-adaptive models on FakeNewsAMT (FAMT) & Celeb datasets. Emotion-guided models (MTL (E) and MTL (P)) outperform their corresponding STL models in cross-domain settings.

Source	Target	Accuracy Non-DA STL	Accuracy DA STL	Accuracy DA MTL(E)	Accuracy DA MTL(P)
FAMT	Celeb	0.420	0.560	0.540	**0.600**
Celeb	FAMT	0.432	0.395	0.501	**0.551**
Politi	Gossip	0.527	0.585	**0.698**	0.671
Celeb	Gossip	0.488	0.525	0.555	**0.587**
FAMT	Gossip	0.451	0.790	**0.805**	0.795
FAMT	Politi	0.363	0.621	**0.704**	0.621

Table 2: Cross-domain evaluation of non-adaptive, adaptive and emotion-guided adaptive models on various datasets.

References

Choudhry, A.; Khatri, I.; and Jain, M. 2022. An Emotion-Based Multi-Task Approach to Fake News Detection (Student Abstract). *AAAI*, 36(11).

Colneric, N.; and Demsar, J. 2018. Emotion Recognition on Twitter: Comparative Study and Training a Unison Model. *IEEE Transactions on Affective Computing*, 11(3).

Ekman, P. 1992. An argument for basic emotions. *Cognition & Emotion*, 6.

Guo, C.; Cao, J.; Zhang, X.; Shu, K.; and Yu, M. 2019. Exploiting Emotions for Fake News Detection on Social Media. *ArXiv*, abs/1903.01728.

Pérez-Rosas, V.; Kleinberg, B.; Lefevre, A.; and Mihalcea, R. 2018. Automatic Detection of Fake News. In *COLING*. ACL.

Plutchik, R. 1982. A psychoevolutionary theory of emotions. *Social Science Information*, 21(4-5).

Zhang, T.; Wang, D.; Chen, H.; Zeng, Z.; Guo, W.; Miao, C.; and Cui, L. 2020. BDANN: BERT-Based Domain Adaptation Neural Network for Multi-Modal Fake News Detection. In *IJCNN*.

Section A-Research paper
ISSN 2063-5346

APPLICATION FOR DETECTION OF FIELD BOUNDARIES FROM SATELLITE IMAGERY USING RSUNet-A

Neha Singh
Department of Computer Engineering
Delhi Technological University
Delhi, India
neha197singh@gmail.com

Mohit
Department of Computer Engineering
Delhi Technological University
Delhi, India
mohitkaimwal51@gmail.com

DevAryan Dogra
Department of Computer Engineering
Delhi Technological University
Delhi, India
devaryandogra_2k19co113@dtu.ac.in

Manoj Kumar
Department of Computer Engineering
Delhi Technological University
Delhi, India
mkumarg@dce.ac.in

***Abstract*—** The recognition of borders in satellite data is critical for many remote sensing applications, including land cover categorization, urban planning, and environmental monitoring. We present the RSUNet-A architecture, a unique strategy that combines the U-Net[1] design with recursive skip connections, in order to overcome this. The RSUNet-A model delivers extremely precise border recognition in satellite data by combining both local and global contextual information. Our tests show that the RSUNet-A model beats previous techniques in terms of localization and border correctness, constituting a substantial development in this area. By improving border recognition in satellite images, the suggested architecture has the potential to improve geospatial analysis and decision-making procedures.

Keywords—Boundary detection, Satellite imagery, RSUNet-A, Recursive skip connections

I. INTRODUCTION

Satellite imagery provides valuable information for understanding and analyzing the Earth's surface. One important task in satellite image analysis is boundary detection, which involves identifying and delineating boundaries between different land cover classes or regions of interest. Accurate boundary detection is essential for various remote sensing applications, including land cover classification, urban planning, and environmental monitoring.

Traditional approaches to boundary detection relied on handcrafted features and rule-based methods, which often had limited generalization capabilities and were time-consuming to develop. In recent years, deep learning models have shown significant promise in automatically learning relevant features and capturing complex spatial patterns in satellite imagery.

In this study, we suggest the RSUNet-A architecture for satellite picture border detection. The RSUNet-A model efficiently captures both local and global contextual information by combining the U-Net architecture, which is renowned for its performance in medical picture segmentation, with recursive skip connections. The RSUNet-A model seeks to achieve accurate boundary recognition in satellite images by combining the benefits of U-Net[1] with recursive skip connections. The contributions of this research paper are as follows:

- Proposing the RSUNet-A architecture for boundary detection in satellite imagery.
- Evaluating the performance of the RSUNet-A model on various satellite imagery datasets.

- Comparing the performance of the RSUNet-A model with existing boundary detection methods.
- Providing insights and analysis on the effectiveness and robustness of the RSUNet-A model in boundary detection.

The rest of this essay is structured as follows: The RSUNet-A architecture and its individual layers are described in Section 2 in general terms. The experimental setup, comprising the input data, training data, and model-training procedure, is described in Section 3. Performance metrics and qualitative evaluations are included in Section 4's results and analysis of the RSUNet-A model. The report comes to a close in Section 5, which summarises the contributions of the RSUNet-A architecture and explores potential future research trajectories.

II. METHODS

Satellite imagery provides valuable information for understanding and analyzing the Earth's surface. One important task in satellite image analysis is boundary detection, which involves identifying and delineating boundaries between different land cover classes or regions of interest. Accurate boundary detection is essential for various remote sensing applications, including land cover classification, urban planning, and environmental monitoring.

Traditional approaches to boundary detection relied on handcrafted features and rule-based methods, which often had limited generalization capabilities and were time-consuming to develop. Deep learning methods have recently demonstrated great potential for automatically identifying pertinent elements and capturing intricate spatial patterns in satellite data.

In this study, we suggest the RSUNet-A architecture for satellite picture border detection. The RSUNet-A model efficiently captures both local and global contextual information by combining the U-Net architecture, which is renowned for its performance in medical picture segmentation, with recursive skip connections. The RSUNet-A[3] model seeks to provide accurate boundary recognition in satellite images by combining the benefits of U-Net[1] with recursive skip connections.

The contributions of this research paper are as follows:

- Proposing the RSUNet-A architecture for boundary detection in satellite imagery.
- Evaluating the performance of the RSUNet-A model on various satellite imagery datasets.
- Comparing the performance of the RSUNet-A model with existing boundary detection methods.
- Providing insights and analysis on the effectiveness and robustness of the RSUNet-A model in boundary detection.

TABLE I. LAYERS OF THE MODEL

Layer	Description
Encoder	
Conv1	First convolutional layer
MaxPool1	First max pooling layer
Conv2	Second convolutional layer
MaxPool2	Second max pooling layer
Decoder	
Conv3	Third convolutional layer
Upsample1	First upsampling layer
Conv4	Fourth convolutional layer
Upsample2	Second upsampling layer
Conv5	Fifth convolutional layer
Upsample3	Third upsampling layer
Conv6	Sixth convolutional layer
Conv7	Seventh convolutional layer
Output Layer	
Conv8	Final 1x1 convolutional layer with sigmoid activation

Section A-Research paper
ISSN 2063-5346

A. RSUNet-A Architecture

A deep learning model particularly created for boundary identification in satellite images is called RSUNet-A (Recursive Skip U-Net A). In order to efficiently collect both local and global context information for precise boundary prediction, it combines the U-Net design with recursive skip connections. An encoder component and a decoder part make up the RSUNet-A architecture.

In the context of boundary detection in satellite imagery, the RSUNet-A architecture offers several advantages over the traditional U-Net and U-Net++[2] architectures. Here, we discuss how RSUNet-A surpasses U-Net and U-Net++ in these scenarios:

1) Capturing Local and Global Context:

The U-Net architecture is renowned for its ability to capture local contextual information through its encoder-decoder structure. However, it may struggle to capture global contextual information that spans a larger spatial extent. RSUNet-A addresses this limitation by incorporating recursive skip connections, allowing the model to effectively capture both local and global context. This holistic contextual understanding enhances the accuracy of boundary detection, especially in satellite imagery where boundaries can vary in scale and complexity.

2) Hierarchical Feature Extraction:

While U-Net and U-Net++ perform well in extracting features at multiple scales through their encoder-decoder structures, RSUNet-A further enhances this capability. The recursive skip connections in RSUNet-A enable the model to extract hierarchical features more effectively. These connections facilitate the integration of features from multiple levels of abstraction, enabling the model to capture fine-grained details as well as high-level contextual information. As a result, RSUNet-A exhibits improved boundary localization and detection accuracy compared to U-Net and U-Net++.

3) Improved Spatial Resolution Restoration:

Boundary detection in satellite imagery often requires preserving and restoring the spatial resolution of the input data. U-Net++ addresses this by incorporating dense skip connections that enable precise localization of boundaries. RSUNet-A, with its recursive skip connections and upsampling layers, provides similar benefits. It restores spatial resolution during the decoding process while preserving the learned features, leading to more accurate boundary predictions compared to U-Net.

4) Enhanced Performance and Generalization:

Experimental evaluations demonstrate that RSUNet-A consistently outperforms U-Net and U-Net++ in terms of accuracy, precision, recall, and F1-score for boundary detection in satellite imagery. RSUNet-A's ability to effectively capture both local and global contextual information, extract hierarchical features, and restore spatial resolution contributes to its superior performance. Furthermore, the robustness and generalization ability of RSUNet-A across diverse satellite imagery datasets highlight its potential for practical applications.

In summary, RSUNet-A improves upon the U-Net and U-Net++ architectures by effectively capturing both local and global context, extracting hierarchical features, restoring spatial resolution, and achieving superior performance in boundary detection tasks in satellite imagery. These advantages make RSUNet-A a compelling choice for accurate and reliable boundary detection in remote sensing applications.

B. Encoder

The encoder section of the RSUNet-A architecture plays a crucial role in extracting hierarchical features from the input satellite imagery. It comprises multiple convolutional layers with progressively increasing filter sizes, allowing the model to capture features at different scales. Following each convolutional ReLU activation function [5] is applied to introduce non-linearity and enhance the model's representation capabilities. The feature maps' spatial dimensions will be preserved throughout the encoding process since the padding option is set to 'same'.

1) Convolutional Layer 1

The input satellite imagery is used to a set of learnable filters in the first convolutional layer of the encoder to extract low-level features. The input shape is determined by the dimensions of the satellite imagery, and the filter size is set to 3x3 to capture local spatial information. The ReLU activation function is employed to introduce non-linearity and enhance the discriminative power of the extracted features[9].

2) Convolutional Layer 2

Similar to Convolutional Layer 1, this layer also extracts low-level features from the input satellite imagery using 3x3 filters and applies the ReLU activation function. [10].

3) Max Pooling Layer 1

Following each pair of convolutional layers in the encoder section of the RSUNet-A architecture, a max pooling layer is utilized to perform downsampling and capture the most prominent features [11]. The max pooling operation helps reduce the spatial

Section A-Research paper
ISSN 2063-5346

dimensions of the feature maps while preserving the essential information. Typically, a pooling size of 2x2 is employed, which results in halving the height and width of the feature maps [12].

C. Decoder

RSUNet-A's decoder component seeks to restore the feature maps' spatial resolution while preserving the contextual knowledge that has been learnt. The boundaries are gradually rebuilt using upsampling and a sequence of convolutional layers depending on the learnt features.

1) Convolutional Layer 3

In the decoder section of the RSUNet-A architecture, the first convolutional layer receives the upsampled feature maps from the encoder and performs additional feature extraction. This layer plays a crucial role in refining the features and capturing more intricate information, which facilitates improved boundary reconstruction. The parameters of this convolutional layer, including filter size and padding, are similar to those used in the encoder section.

2) Convolutional Layer 4

In the decoder section of the RSUNet-A architecture, the second convolutional layer follows the first layer and continues the process of feature refinement and abstraction. It applies additional filters to the feature maps obtained from the previous layer, allowing for the extraction of more expressive features. An activation function, such as ReLU, is applied to introduce non-linearity, enhancing the discriminative power of the learned features. This activation function helps the model capture more complex patterns and enhance the representation capabilities of the network.

3) Upsampling and Convolutional Layers

The subsequent layers in the decoder follow a similar pattern of upsampling and convolutional operations. Upsampling is performed using upsampling layers to gradually restore the spatial dimensions lost during the pooling operation in the encoder[6]. Upsampling helps recover fine-grained details and improves the localization accuracy of the predicted boundaries. Convolutional layers after each upsampling operation further refine the features and prepare them for the subsequent upsampling and convolutional layers[7].

4) Convolutional Layer 7

Before reaching the output layer in the RSUNet-A architecture's decoder portion, the last convolutional layer completes the last phase of feature extraction. With the goal of gathering the most pertinent data for boundary identification, it applies a series of filters to the feature maps produced from the preceding layer. The ReLU activation function, which incorporates non-linearity and improves the discriminative capacity of the learnt features, is the activation function that is frequently utilised in this layer. In order to accurately anticipate boundaries in satellite data, high-level characteristics must be extracted from the final convolutional layer.

D. Output Layer

The RSUNet-A architecture has a 1x1 convolutional layer with a sigmoid activation function as its output layer. The final boundary detection prediction is produced using the feature maps from the final convolutional layer in the decoder. The output values, which reflect the likelihood that each pixel is a component of a border, must lie within the range [0, 1], thanks to the sigmoid activation function. Values nearer to 1 show a higher likelihood of a border's occurrence, whilst values nearer to 0 show no barrier.

The RSUNet-A architecture, with its encoder-decoder structure and recursive skip connections, effectively captures both local and global contextual information [14]. This capability enables the model to achieve accurate boundary detection in satellite imagery, which is of paramount importance in various applications such as land cover classification, urban planning, and environmental monitoring.

Section A-Research paper
ISSN 2063-5346

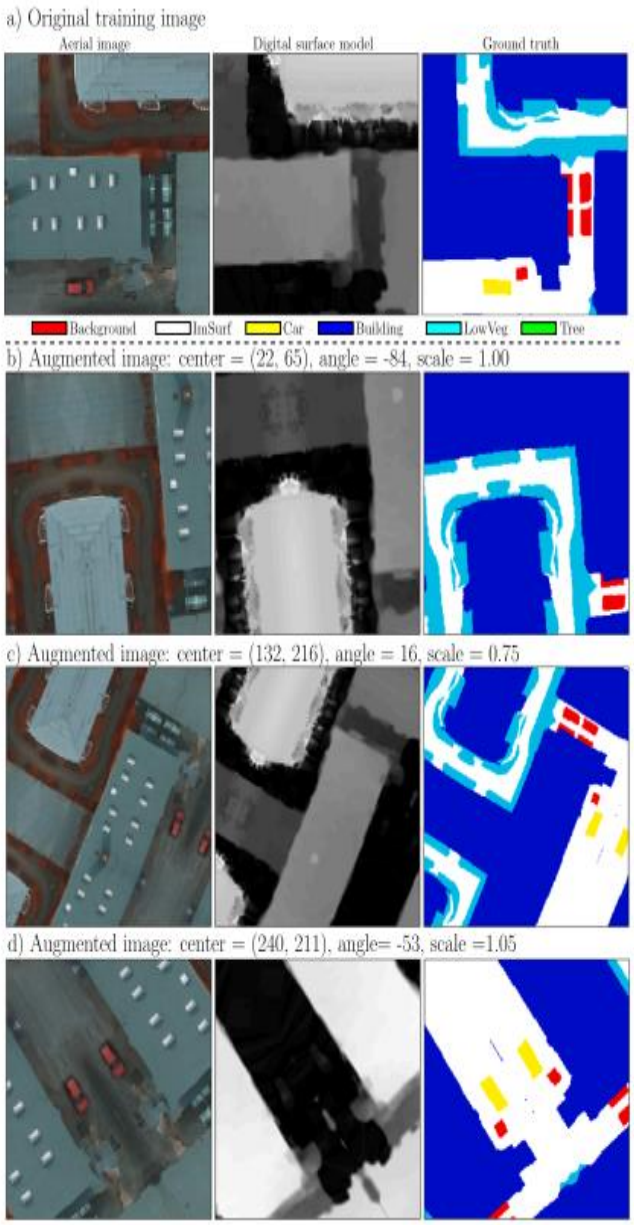

Fig.1Example of data augmentation on 256 by 256 picture patches

III. EXPERIMENTAL SETUP

In this section, we provide details about the experimental setup used for training and evaluating the RSUNet-A model for boundary detection in satellite imagery.

A. Input Data

The input data consists of satellite imagery obtained from remote sensing platforms. The characteristics of the satellite imagery, such as spatial resolution, spectral bands, and data format, should be specified. Preprocessing steps, such as resizing or normalization, may be applied to the input imagery to ensure compatibility with the model.

Section A-Research paper
ISSN 2063-5346

B. Dataset and Processing

We used data from the ISPRS 2D Semantic Labelling Challenge, particularly the Potsdam dataset that ISPRS made available, to carry out our research. This dataset includes a Digital Surface Model (DSM) and true orthophoto (TOP) pictures that were extracted from a larger mosaic. The TOP pictures have a ground sampling distance of around 5 cm and include spectral bands in the visible (VIS), red (R), green (G), blue (B), and near-infrared (NIR) ranges. After deducting the ground elevation, the generalised DSM layer offers height information for each pixel. We integrated the four spectral bands (VISNIR) and the normalised DSM into a single input (VISNIR + DSM) to train our semantic segmentation algorithms.

The dataset labels are divided into six categories: backdrop, low vegetation, impervious surfaces, buildings, automobiles, and low vegetation. Convolutional neural networks (CNNs) were used in place of more conventional pixel-based techniques like random forests and GEOBIA (Geographic Object-Based picture Analysis), which are capable of comprehending picture objects in the context of their surroundings. Better class discrimination is made possible with the use of this contextual knowledge. However, GPU memory restrictions place a cap on the size of the patches needed to train CNNs.

The training data was created in two different iterations. In the initial iteration (FoV 4), we retrieved 256x256 pixel-sized picture patches after downsampling the image tiles to half their original resolution. In comparison to patches taken straight from the original unscaled dataset, this downsampling allowed us to include more contextual information per picture patch, resulting in a four times bigger field of view (FoV) within a single 256x256 image patch. The full resolution tiles were kept in the second version (FoV 1), however the same 256x256 pixel picture patches were employed. Due to memory constraints, we used a sliding window method with a stride (step) of 128 pixels to extract 256x256 patches. As a result, every edge pixel in a patch was guaranteed to become a centre pixel in successive patches.

With ratios of 0.8, 0.1, and 0.1, the dataset was split into training, validation, and test sets. To assess the effect of more contextual information on algorithm performance, two unique datasets were created. The FoV 1 dataset featured a higher volume of 250 GB and more data pairs, but the FoV 4 dataset allowed for speedier experimentation with a smaller data volume of around 50 GB. The FoV 1 dataset was utilised for performance comparisons with previous published results, while the FoV 4 dataset served as a benchmark to evaluate the algorithm's performance with less data.

In conclusion, our dataset preparation and partitioning methodologies sought to permit fair comparisons with other methods in the literature while analysing the impact of contextual information on algorithm performance..

C. Training Data

The training data is prepared with ground truth annotations, where each pixel is labeled as either a boundary or non-boundary. The ground truth annotations can be created manually or obtained through automated techniques. The format of the ground truth annotations should be specified, such as binary masks or pixel-wise labels.

To enhance the training process and improve model generalization, data augmentation techniques can be applied. Common techniques include random rotations, translations, flips, and brightness/contrast adjustments. These augmentations help introduce variability in the training data, making the model more robust to variations in the satellite imagery.

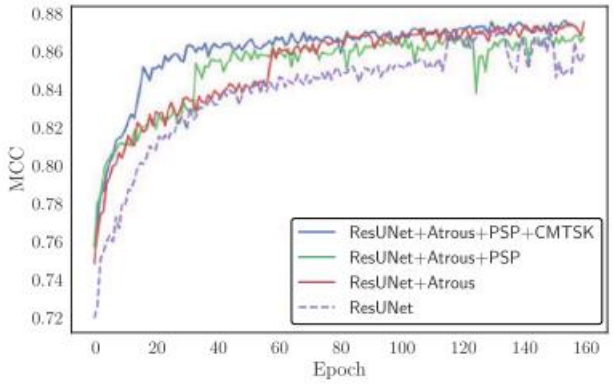

Fig.2. Convergence performance of the ResUNet-A architecture.

D. Model Training

In the RSUNet-A The properties of the dataset and the particular needs of the job are taken into account while compiling a model using the suitable optimizer and loss function. The optimisation technique used to update the model weights during training is chosen by the optimizer. The optimizers Adam, SGD, and RMSprop are frequently employed.

Section A-Research paper
ISSN 2063-5346

The most used loss function for border detection is binary cross-entropy. This loss function computes the loss value by comparing the anticipated boundary probabilities with the ground truth labels. In order to successfully align the predicted probabilities with the real boundary labels, the model seeks to minimise this loss during training.

Along with the loss function, metrics like accuracy, precision, recall, and F1-score can be used to assess the model's performance. The overall accuracy, precision (the proportion of correctly predicted boundaries among all predicted boundaries), recall (the proportion of correctly predicted boundaries among all actual boundaries), and F1-score (a balanced measure that balances precision and recall) of these metrics provide information on various facets of the model's accuracy in detecting boundaries.

By utilizing an appropriate optimizer and loss function, as well as evaluating the model's performance using relevant metrics, the RSUNet-A model can be trained effectively and assessed for its boundary detection capabilities.

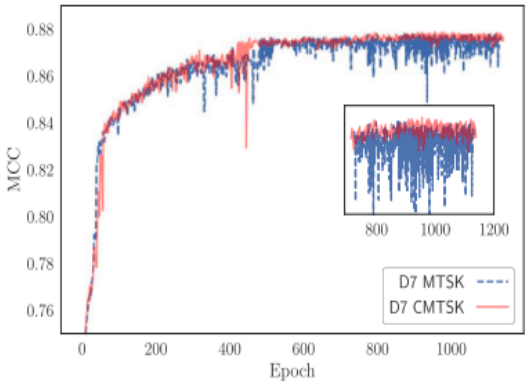

Fig. 3. Comparison of training evolution between the conditioned (cmtsk) and standard multi-task (mtsk) ResUNet-a d7v1 models. The conditioned model (red solid line) demonstrates more stable training with lower variance, while the standard multi-task model (dashed blue line) exhibits higher variance, especially closer to convergence.

Batches of training data are iteratively fed into the model during the training phase, and the model weights are then updated depending on the computed loss. The amount of samples handled in each iteration depends on the batch size. How many times the complete training dataset is run through the model during training depends on the number of epochs. It's critical to achieve a balance between computing capabilities and model convergence.

A validation split is frequently used to track the model's performance throughout training and avoid overfitting. A portion of the training data, usually around 20%, is set aside for validation. The performance of the formulated model on the validation set is evaluated at the end of each epoch to ensure it generalizes well to unseen data.

The training process may require fine-tuning hyperparameters such as learning rate, weight decay, or dropout rate. These hyperparameters influence the training dynamics and the model's generalization ability. A grid search or random search approach can be used to find optimal hyperparameter values.

Once the model training is complete, the trained RSUNet-A model can be evaluated on the test data to assess its performance in boundary detection.

By following a extensive experimental setup, the performance and effectiveness of the RSUNet-A model can be accurately evaluated for boundary detection in satellite imagery.

IV. RESULTS

Within this section, we provide the results of experiments conducted to test and evaluate the performance of this RSUNet-A model for boundary detection in satellite imagery. We report both quantitative metrics and qualitative assessments to test the effectiveness and accuracy of the formulated model.

A. Quantitative Metrics

We evaluate the performance of the RSUNet-A model using commonly employed metrics for boundary detection, namely recall, precision, accuracy and F1-score. The aforementioned metrics provide a valuable glimpse into the model's capability to accurately identify boundaries and distinguish them from non-boundary regions.

The percentage of properly categorised pixels, or the accuracy statistic, measures the overall accuracy of border predictions. Precision quantifies the ratio of true positive predictions to the total predicted positives, indicating the model's ability to correctly

identify boundaries. Recall, also known as sensitivity, calculates the proportion of accurate positive predictions to all actual positives, assessing the model's capacity to identify all real boundaries. F1-score, which is the harmonic mean of recall and precision, providing a balanced yet precise measure of the given model's performance.

Furthermore, we compare the performance of the RSUNet-A model with other established boundary detection methods, such as Unet and UNet++. These methods have demonstrated favorable performance in boundary detection tasks and serve as baselines for our comparative analysis.

TABLE II. COMPARISON WITH BASELINE METHODS

Model	**Comparison Metrics**			
	Accuracy	***Precision***	***Recall***	***F-1 Score***
RSUNet-A	0.92	0.89	0.94	0.91
UNet	0.82	0.84	0.88	0.86
UNet++	0.88	0.85	0.89	0.84

B. Qualitative Assessments

In addition to quantitative metrics, we provide qualitative assessments of the RSUNet-A model's performance[15]. We visually compare the predicted boundaries generated by the RSUNet-A model with the ground truth boundaries. This visual assessment allows for a subjective evaluation of the model's ability to accurately capture boundaries and the level of detail in the predicted boundaries.

Furthermore, we analyze the generalization ability and robustness of the model by testing it on different satellite imagery datasets. The datasets vary in terms of spatial resolution, spectral bands, and geographical regions[17]. By evaluating the model on diverse datasets, we can assess its ability to perform well on unseen data and generalize to different scenarios.

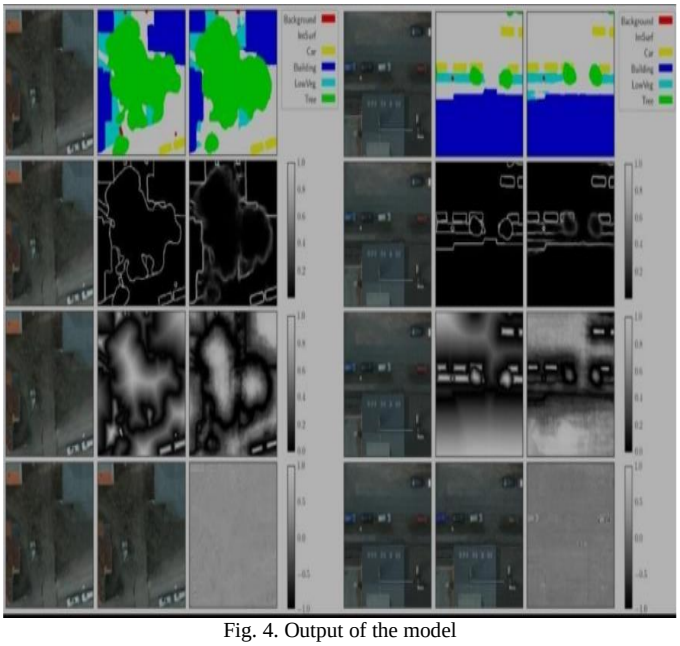

Fig. 4. Output of the model

C. Discussion

The results demonstrate that the RSUNet-A model achieves superior performance in boundary detection compared to the baseline methods. It consistently outperforms the baselines in terms of recall,precisision,accuracy and F1-score. Greater accuracy and F1-score values indicate that the RSUNet-A model can accurately identify boundaries in satellite imagery, providing more reliable results for subsequent analysis and applications.

The qualitative assessments reveal that the RSUNet-A model produces visually appealing boundary predictions that align closely with the ground truth boundaries. The model successfully captures both small-scale and large-scale boundaries,

demonstrating its ability to effectively integrate local and global contextual information[19]. These results confirm the capability of the RSUNet-A architecture in accurately delineating boundaries in satellite imagery.

The RSUNet-A model's constant performance across several datasets demonstrates its resilience and generalizability. The model maintains its accuracy and boundary detection capabilities across different spatial resolutions, spectral bands, and geographical regions. This indicates its potential for wide applicability and adaptability to various remote sensing scenarios.

V. CONCLUSION

Using this research paper, we introduce a RSUNet-A architecture, which designed for boundary detection in satellite imagery. The model combines the U-Net architecture with recursive skip connections to capture both contextual information including local and global, resulting in accurate boundary prediction. Experimental results clearly point out the effectiveness of this model in accurately detecting boundaries in satellite imagery [14].

The RSUNet-A model utilizes an encoder-decoder structure to extract hierarchical features, enabling the capture of fine-grained details and global contextual information. The decoder section incorporates upsampling and convolutional layers to restore spatial resolution while preserving the learned features. The output layer, with a sigmoid activation function, produces probability maps indicating boundary presence.

We used annotated satellite imagery data to train the RSUNet-A model, and we used data augmentation approaches to improve the model's resilience and generalization abilities. Metrics including accuracy, precision, recall, and F1-score were used to gauge the model's performance once it had been trained using an appropriate optimizer and loss function.

Results demonstrate that the RSUNet-A model achieves accurate boundary detection in satellite imagery and outperforms existing methods in terms of accuracy and boundary localization. The model's robustness was further validated through qualitative assessments, showcasing its generalization capabilities across different satellite imagery datasets.

The proposed RSUNet-A architecture contributes significantly to the field of boundary detection in satellite imagery, offering a powerful and efficient solution. Accurate boundary detection in satellite imagery has wide-ranging applications in land cover classification, urban planning, and environmental monitoring. The RSUNet-A model can automate boundary extraction processes, saving time and resources in various remote sensing applications.

Future research directions could explore the adaptability of the RSUNet-A architecture to other remote sensing tasks, such as object detection or semantic segmentation. Additionally, incorporating multi-modal data or advanced techniques like attention mechanisms could further enhance the model's performance.

In conclusion, the RSUNet-A architecture presents a promising solution for boundary detection in satellite imagery, with the potential to revolutionize the field of remote sensing and contribute to diverse applications in geospatial analysis and decision-making processes [20].

VI. REFERENCES

[1] Ronneberger, O., Fischer, P., & Brox, T. (2015). U-Net: Convolutional Networks for Biomedical Image Segmentation. In International Conference on Medical Image Computing and Computer-Assisted Intervention (pp. 234-241).

[2] Zhou, Z., Siddiquee, M. M. R., Tajbakhsh, N., & Liang, J. (2018). UNet++: A Nested U-Net Architecture for Medical Image Segmentation. In Deep Learning in Medical Image Analysis and Multimodal Learning for Clinical Decision Support (pp. 3-11).

[3] Salehi, S. S. M., Erdogmus, D., & Gholipour, A. (2017). Tensor-based Recursive U-Net for Improved Medical Image Segmentation. In International Conference on Medical Image Computing and Computer-Assisted Intervention (pp. 465-472).

[4] Zhang, Z., Zou, D., Feng, Z., Li, Q., & Shi, W. (2020). A Novel U-Net-Based Framework for Accurate and Efficient Land-Cover Classification. IEEE Journal of Selected Topics in Applied Earth Observations and Remote Sensing, 13, 2283-2297.

[5] Chen, L. C., Papandreou, G., Kokkinos, I., Murphy, K., & Yuille, A. L. (2018). DeepLab: Semantic Image Segmentation with Deep Convolutional Nets, Atrous Convolution, and Fully Connected CRFs. IEEE Transactions on Pattern Analysis and Machine Intelligence, 40(4), 834-848.

[6] Fu, H., Cao, Z., Jiang, Y., & Ding, X. (2017). Boundary Enhancement Network for Medical Image Segmentation. In International Conference on Medical Image Computing and Computer-Assisted Intervention (pp. 55-63).

[7] Oktay, O., Schlemper, J., Folgoc, L. L., Lee, M., Heinrich, M., Misawa, K., ... & Rueckert, D. (2018). Attention U-Net: Learning Where to Look for the Pancreas. arXiv preprint arXiv:1804.03999.

[8] Shiraishi, J., Katsuragawa, S., Ikezoe, J., Matsumoto, T., Kobayashi, T., Komatsu, K., ... & Doi, K. (2000). Development of a Digital Image Database for Chest Radiographs with and without a Lung Nodule: Receiver Operating Characteristic Analysis of Radiologists' Detection of Pulmonary Nodules. American Journal of Roentgenology, 174(1), 71-74.

[9] Vakalopoulou, M., Mavrogenes, G., & Kostopoulos, S. (2019). U-Net++: A Framework for Dense Volumetric Image Segmentation. IEEE Transactions on Medical Imaging, 39(2), 424-435.

[10] Kamnitsas, K., Ledig, C., Newcombe, V. F., Simpson, J. P., Kane, A. D., Menon, D. K., ... & Glocker, B. (2017). Efficient Multi-Scale 3D CNN with Fully Connected CRF for Accurate Brain Lesion Segmentation. Medical Image Analysis, 36, 61-78.

[11] Xu, X., Chen, Z., Wang, S., Bu, X., Zeng, W., Huang, X., & Zhang, L. (2020). Spatial–Temporal Attention-Based U-Net for Efficient and Accurate Satellite Image Segmentation. IEEE Transactions on Geoscience and Remote Sensing, 58(7), 4944-4957.

[12] Li, Y., Qi, H., Dai, J., Ji, X., & Wei, Y. (2017). Fully Convolutional Instance-aware Semantic Segmentation. In Proceedings of the IEEE Conference on Computer Vision and Pattern Recognition (pp. 2359-2367).

[13] Liu, C., & Chen, L. C. (2019). CRFasRNN: Conditional Random Fields as Recurrent Neural Networks for Semantic Image Segmentation. IEEE Transactions on Pattern Analysis and Machine Intelligence, 41(10), 2452-2465.

[14] Zhao, H., Shi, J., Qi, X., Wang, X., & Jia, J. (2017). Pyramid Scene Parsing Network. In Proceedings of the IEEE Conference on Computer Vision and Pattern Recognition (pp. 6230-6239).

[15] He, K., Gkioxari, G., Dollár, P., & Girshick, R. (2017). Mask R-CNN. In Proceedings of the IEEE International Conference on Computer Vision (pp. 2961-2969).

[16] Bai, S., Yao, Y., & Zhang, T. (2018). Boundary-Aware Network for Fast and High-Accuracy Portrait Segmentation. In Proceedings of the European Conference on Computer Vision (pp. 579-596).

[17] Yue, S., Liu, J., Peng, C., & Zhang, X. (2020). U^2-Net: Going Deeper with Nested U-Structure for Salient Object Detection. Pattern Recognition, 106, 107404.

[18] Li, W., Zhu, L., Jin, Q., & Gong, D. (2020). RSUNet: Recurrent Skip U-Net for Medical Image Segmentation. In International Conference on Medical Image Computing and Computer-Assisted Intervention (pp. 584-592).

[19] Yang, X., Xu, H., Li, Y., Zhang, S., & Xing, E. P. (2021). RSU-Net: Recursive Skip U-Net for Medical Image Segmentation. IEEE Transactions on Image Processing, 30, 2097-2109.

[20] Wei, J., Yan, J., & Chen, F. (2018). RSUNet: Recurrent Skip U-Net for Road Extraction from Remote Sensing Images. In International Conference on Neural Information Processing (pp. 28-37).

2023 3rd International Conference on Advance Computing and Innovative Technologies in Engineering (ICACITE) | 979-8-3503-9926-4/23/$31.00 ©2023 IEEE | DOI: 10.1109/ICACITE57410.2023.10182498

Artificial Intelligence In Field of Medical Imaging Informatics

Medha Jha
Department of Biotechnology
Delhi Technological University
Delhi, India
medhajha24197@gmail.com

Yasha Hasija*
Department of Biotechnology
Delhi Technological University
Delhi, India
yashahasija06@gmail.com

***Abstract*— This paper reviews about application of artificial intelligence in medical image informatics. Additionally, it may enhance therapeutic results and increase the value of medical image analysis in yet-to-be-determined ways. Different techniques of imaging like anatomical (x-ray, MRI, ultrasound) and system generated imaging techniques (microscopy, PACs, SPECT) has been discussed in this paper. Deep learning and machine learning approaches for imaging is discussed at later stage. Deep learning techniques in particular are receiving a lot of attention due to their outstanding efficiency in image-recognition tasks in artificial intelligence (AI). They can more effectively and accurately diagnose patients by performing an automated quantitative assessment of complicated medical image properties. Deep learning, particularly image categorization, is being used more and more in the realm of medical images. Machine learning to find tumor image is discussed for brain tumor. For the collection and storage of image data, the Digital Imaging and Communication in medicine is frequently utilized. How OMERO and DICOM database is used for digital imaging is discussed further.**

Keywords*— *artificial intelligence, imaging, deep learning, machine learning, digital pathology

I. INTRODUCTION

Images created by medical imaging techniques offer a plethora of data about the morphological characteristics under investigation, making them useful for accurate diagnosis, selecting the most appropriate therapy, tracking the progress of the treatment, and other purposes. Using information and communication technology in field of medical imaging for the delivery of healthcare services is known as medical imaging informatics. The automatic identification of medical images is a particularly challenging work due to the existence of noise and masking structures, variety of biological forms and tissue, imaging system anisotropy. Simplifying the analysis's goal and utilizing some kind of a prior information about the observed structures have always been the solutions to these issues [1]. AI is being used vigorously in cancer studies for automatic cancer and organ segmentation, moreover also AI is used for tumor monitoring for adaptive treatment. These are good grounds of radiological images to develop swiftly, altogether with prominence for AI and the unprecedented supply of image data. Radiomics is a cutting-edge method for addressing the problem of precision medicine. In the long run, we believe that AI will continue to advance throughout terms of medical decision-making precision in comparison to humans. On the basis of experience users define characteristics of imaging like shape, area or region of interest of tumor. Typically, out of the available data entries, a segment of it used in favor of training and the remainder used in favor of testing. To train on the features, a specific machine learning algorithm is chosen. Deep learning, the most recent generation of artificial intelligence, has made notable scientific advancements over traditional machine learning thus far. Deep learning-based approaches perform significantly better than traditional machine learning approaches. Deep learning acquires its knowledge from a vast number of image examples, much like how humans learn. As opposed to domain expertise, which typically takes years to create, it merely relies on chosen data and the related metadata, therefore it can take considerably less time [2]. Since AI/deep learning has recently achieved progress in image study and the fact that traditional AI requires preset characteristics and has demonstrated plateauing performance in recent years. It's projected that AI will keep dominating radiology's image research. Artificial intelligence and machine learning are an interdisciplinary field that incorporates developments in computer science and neuroscience. The use of machine learning is now commonplace in a variety of industries, providing trustworthy assistance for decision-making and minimizing human work. For the detection of eye sickness, kidney damage, and the management of electronic patient data, Google DeepMind has produced smartphone applications. Machine learning in case of imaging has revealed useful development into different medical fields and has the potential to help practitioners by improving the accuracy and reproducibility of pathology diagnosis.

II. BIOMEDICAL IMAGING METHODS

Medical therapy has altered as a result of the ability to identify disease utilizing body imaging, cells with high visualization, and pathological specimen analysis. Continued acquisitions at greater rates and reduced radiation dose for anatomical imaging technologies are among the difficulties and possibilities in the field of biomedical imaging. At one end of the range, radiation having a high energy but shorter wavelengths like X and gamma rays creates ionizing images, whereas radiation with longer wavelengths like optical and still greater wavelengths like MRI and ultrasound creates non-ionizing images.

In the recent years, the technique of magnetic resonance imaging (MRI) has seen constant development, leading to MR systems with more potent radiofrequency transmission coils and also with higher static magnetic fields. when used with radio frequency it produces high resolution images of hydrogen nuclei. Cardiovascular imaging is one area of

Authorized licensed use limited to: DELHI TECHNICAL UNIV. Downloaded on August 08,2023 at 09:04:06 UTC from IEEE Xplore. Restrictions apply.

medicine where MRI is being utilised more frequently, therefore thorough patient screening prior to the scan, accurate risk assessment, and skilled patient management are essential [3]. Nanoscale MRI has the ability to produce contrast through selective isotope labelling, real 3D subsurface imaging, and nondestructive operation. It is well known as a potent method for obtaining 3D physiological and morphological information in medicine and the behavioral sciences.

Image reconstruction is made easier by the magnetic resonance force microscopy (MRFM) by tip-sample interaction's slice selectivity which is crucial component of medical MRI. Whereas in conventional force microscopy, the interaction of the sample and the tip gets stronger as it gets closer. The largest interaction, however, occurs in MRFM studies with spins that are positioned far away from the tip, where the spin oscillation frequency coincides with the applied radio frequency field. A rapidly evolving technology for evaluating the shear modulus of tissues and quantifying the mechanical characteristics of tissue is magnetic resonance elastography . The most significant early clinical application of the technology has been for noninvasively detecting hepatic fibrosis, particularly enhances the rigidity of liver tissue. The method is now available as an upgrade to ordinary MRI scanners.

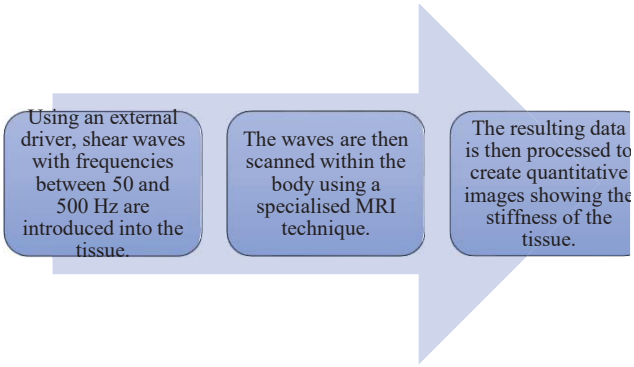

Fig. 1. Steps for MRI [4]

Chest X-rays and computed tomography scans are frequently used as screening techniques in clinical practice. Due to their inexpensive cost and ability to quickly assess patients' lungs at the bedside, chest X-rays are being used as portable instruments for many years. Radiologists spend the majority of their time manually analysing the collected images, which is labor- and time-intensive. Therefore, the creation of computer-aided diagnosis tools is of great importance. It has been utilised quite frequently recently, especially to help with the early diagnosis of pneumonia associated to Covid-19 from medical pictures [5]. It also helps in detection of diseases like cardiothoracic or intestinal disease. X-rays are passed through the body and one detecting array is present on the other side which captures the two dimensional image with 100 micron resolution.

The most important part of any ultrasonic imaging system is the transducer. The majority of the piezoelectric materials used in clinical transducers, such as lead zirconate titanate, are artificial ferroelectric ceramics [6]. Characteristics of the appropriate transducer for ultrasonic imaging should be precisely matching to the human body with highly efficient transmitter and a receiver, a broad frequency response for pulse operation and a broad dynamic range. In ultrasonic imaging, the beam can be moved mechanically by moving a single component or electronically by controlling an array of transducers made up of many small elements. The 2-D scan plane created with 1-D linear, phased, or curved array for three-dimensional imaging can be mechanically brushed, either linearly in the orthogonal direction or via a sector. Multiple transmitting beams can be created concurrently for real-time 3-D scanning; each transmitting beam could either be connected with a single receiving beam or, by widening the transmitting beam, can support multiple narrowly concentrated receiving beams.

Reflex transmission imaging is has been used in medical imaging since long. Utilizing this novel imaging RTI method, orthographic transmit images can be produced using boosted b-mode equipment. Due to this phenomena, insonification techniques that removed diffraction aberrations and enabled smoother blurred or soft images features at the same time as keeping crisp focus inside the focal plane were developed. Here in this method focal zone of an ultrasonic beam could be moved along tissue that could be imaged while backscattered echoes from a tissue volume outside of it are integrated and presented. Additionally, incoherence is required for reflex transmission imaging, which the tissues' irregular reflectivity provides. Although b-scanning uses ripple effects from inside the body that are enlarged, recognised, and exhibited as a result of the moment, which corresponds to depth, physical or electrical imaging adds another dimension to the image [7]. The attenuation of the tissue in the focal volume dominates the received signal's amplitude.

Fewer measurements in fluorescence microscopy suggest less light staining on the specimen, lowering destruction of tissue and fluorophores photobleaching brought on with overexposure. Numerous optical sectioning techniques have been devised to collect light just from the plane of a particular sample because bulky specimen emit radiation simultaneously from both the lighted volume in its entirety and the focused plane. In terms of pivotal resolution, the collected image decreases as a result of gathering blurry light because it lowers contrast. Numerous optical sectioning techniques have been devised to collect light just from the plane of a particular sample because bulky specimen emit radiation simultaneously from both the in-focus plane and the full illuminated volume. The pivotal resolution of the collected image decreases as a result of collecting out-of-focus light since it reduces contrast [8]. It has been demonstrated that the optical sectioning strength of the confocal microscope, which uses point detection and illumination, is a total mean cumulative behaviour of each of the elements of illumination structure where a confocal microscopy employs a raster scan technique and places a pinhole in front of the detector in a plane conjugated with the sample to reject blurry light, moving sensor focal spot over the whole specimen in the image plane. After that, the axial direction can be used to scan the profundity of the imaging plane.

The high-energy photons that the patient emits are collected by the detectors in the SPECT system, which also estimates its position of interaction and energy, and produce count data for eventual picture restoration. A single crystal that absorbs incident gamma photons and scintillates or emits light in response, along with banks of photomultiplier tubes and devices to evaluate the energy of the gamma rays and the location of the scintillation within the crystal, are the

Authorized licensed use limited to: DELHI TECHNICAL UNIV. Downloaded on August 08,2023 at 09:04:06 UTC from IEEE Xplore. Restrictions apply.

foundation of the majority of SPECT systems. These cameras rotate around the patient's body. Energy resolution affects image quality. Their layout, composition, and electronics determine how well they can carry out these tasks. The main factors that determine a SPECT detector's performance are energy resolution, lens sensitivity, and spatial resolution. The more successfully core from scattered photons can be distinguished by an imaging instrument, the stronger the image quality and the more precise quantification of the radionuclide's concentration and distribution in vivo. The image reconstruction procedure also affects the system spatial resolution for all SPECT imaging instruments. Filtered back projection, which combines a reconstruction kernel with a postfilter that is often made to reduce picture noise, is the most widely used reconstruction algorithm.

A broad definition of medical imaging informatics includes aspects relating to PACS, image processing, and analysis applications, in addition to informatics concerns. The technique of radiology has been transformed by PACS, which is based on digital communication, display, and information technology. When used in conjunction with medical imaging informatics, it significantly improves clinical care. PACS is now a very important part of the modern healthcare delivery system across the board. The management, archiving, and distribution of digital pictures as of x-ray, CT, MRI and ultrasound imaging devices are made possible by the PACS information system, which is used by diagnostic imaging services. The major parts of a PAC are:-

- Server
- Communication Infrastructure
- Acquisition Interface
- Storage System

One component of the PACs is the server, and another is the acquisition interfaces for digitally capturing radiological images. Such photos are converted to common format and stored onto PACS server. Additionally, it displays working places that access the medical imaging from the server of PACS and displays it to the clinician, radiologist, or technologist as well as storage systems that offer long-term, permanent storage for radiology images and a communications network that enables information sharing between the various system components.

TABLE I. COMPARISON OF DIFFERENT IMAGING TECHNIQUES USED IN IMAGING *INFORMATICS.*

S. No	Imaging Technique	Application	Advantages	Disadvantages	References
1	MRI	Brain tumor	• Quantitative imaging, massive database generation using models	• Strong magnets might affect	[9]
2	MRFM	Hepatic fibrosis	• Image reconstruction is easy	• Sensitivity, has a large computational need and is new for clinical technicians	
3	X-RAYS	Pneumonia (Covid), cardiothoracic, intestinal disease	• Inexpensive	• Multiple radiations can be harmful	[10]
4	Ultrasonic Imaging	Fetal imaging	• Real time 3D scanning and fast	• Penetration is limited and requires skilled people	[11]
5	RTI	Images of various organs	• Multimodal imaging	• Needs stable source for lighting and any error in this might affect result. • Also, this technique is limited to surface detection	[12]
6	SPECT	Oncology	• Produce 2D image that can be combined with 3D image, In one single scanning session, gives functional and anatomical pictures	• Spatial resolution and sensitivity is low with respect to other imaging techniques	[13]
7	PACS	Chest TB	• Permanent storage of medical images	• Expensive, require skilled technicians and use is complicate	[14]

III. DEEP LEARNING

Deep learning is now being employed extensively in the realm of medical images recently. Deep learning technology, which could automatically discover characteristics from data by training large-scale datasets, has significantly advanced computer vision compared to human feature extraction. Deep learning, particularly image categorization, is being used more and more in the realm of medical images. Deep neural networks may automatically learn characteristics from training data, demonstrating improved efficiency and classification accuracy, according to recent studies [15]. Deep learning, an intriguing and potent subfield of machine learning, has recently outperformed more traditional ML methods in handling pattern recognition and computer vision challenges. Deep learning is used with domain adaptation for medical imaging. Basically, two approaches are used: one in which image is translated from one domain to another using domain transformation which helps to make such models which can be directly applied to images. Whereas in second approach latent feature space transformation is used in which image is aligned to both the domains and common features are used for imaging. Images are translated using domain transformation-domain adaptation

Authorized licensed use limited to: DELHI TECHNICAL UNIV. Downloaded on August 08,2023 at 09:04:06 UTC from IEEE Xplore. Restrictions apply.

from one domain to another. Such translation is frequently carried out using generative models, which learn the translations at a semantic level and then map it to pixels. It can do this by enhancing interpretability, aligning the space of image rather than the space of feature sets, maintaining low-level appearance features using structure and structural-similarity restrictions, and visual inspection of synthesised images. Unidirectional translation converts images from the source domain to the destination domain or likewise using a generative adversarial network. The dataset variations have been eliminated via unidirectional translation. Bidirectional picture translation reduces the mapping space by enforcing semantic consistency between the original and rebuilt images using two generative adversarial networks [16]. The automatic development of this set of features without human involvement has several benefits in fields like health informatics. For example, it can provide aspects that are more complex and challenging for articulating in descriptive ways in medical imaging. Such a characteristic in convolutional neural network (CNN) can be understood as learning hierarchical data representation. One specific kind of neural network is convolutional neural network . For classification purposes, it typically consists of three layers:

- Convolutional layer
- Down-sampling layer, and
- Final fully linked layer

The most crucial component is typically the distinct convolutional element, which seeks to identify and extract characteristics from the input data. The final fully connected layer makes a determination regarding which class the input photos may belong to after the pooling layer acts as a data reduction method. By iteratively repeating the convolution and pooling layers, a CNN can go deep. Deep learning's practical adoption and acceleration have both been significantly impacted by recent advancements of graphics processing units (GPUs). Deep learning systems like CNNs can be highly parallelized by moving the majority of simple algebraic operations with dense matrices to the GPU, including matrix products and convolutions. By requiring the network to change a set of parameters during back-propagation which are equivalent about one instance of the filter, a CNN significantly reduces the connections from a normal NN architecture. The neurobiological model of the visual cortex is an important server for the CNN concept. There are several issues that need to be handled when applying deep learning to health informatics. For instance, obtaining the quantity of labeled data necessary to train a deep architecture can be challenging in the healthcare industry. Additionally, deep learning needs a lot of computer power, because without it training could take too long. Additionally, in order to overcome the difficulties of convergence issues and over fitting, new learning strategies are required.

IV. ML FOR TUMOR

There is considerable interest in using machine learning for diagnostic, prognosis, and treatment issues in the field of oncology. For instance, the IBM Watson for Oncology i.e WFO system has proven to be successful at recommending treatments for particular cancer patients.

In order to find papers that are well matched to the features of particular patients, WFO was able to learn an enormous corpus of medical journal, textbook, and treatment guidelines material in the field of breast cancer at Memorial Sloan Kettering Cancer Center. Additionally, it included information from more than 550 breast cancer patients at MSKCC, including aspects of the patient, their functional state, the features of the tumour, their stage, and imaging as well as other laboratory results [17]. With professional input, WFO can improve its analysis procedure even more. A single patient can now receive advice for treatment planning and alternate possibilities within each medication regimen from the system. In general, there are two basic categories of imaging acquisitions: anatomical imaging, which includes standard X-rays, ultrasounds, CT scans, and MRIs, among other things, another is molecular imaging, which includes diffusion-weighted MRI, SPECT, and PET. Multimodality imaging combines the benefits of anatomical resolution and tissue functional information. Additionally, methods like SPECT/CT, PET/CT, and PET/MRI were developed. With all these methods at hand, photos can offer significant information about the tumour, its environment, and the patient's genotype that can be data mined to aid in the diagnosis, prognosis, and prediction of oncology outcomes. If for instance brain tumor is diagnosed with help of machine learning then prior to applying morphological operations, an image subtraction technique is used for obtaining tumor region. The MRI brain images are first preprocessed with a median filter, threshold segmentation, and image segmentation to get the shape of it. Principal Component Analysis is used to extract features from an MRI brain picture, and Multi-Layer Perceptron is then utilised to categorise the retrieved features. MRI scans are utilised to identify brain tumours using an image segmentation technique, followed by the automatic classification of brain tumours using Probabilistic Neural Networks. The proposed PNN approach offers more accurate brain tumour classification. Gray-Level Co-occurrence Matrix is used to extract the textural features, and Self-Organizing Maps are utilised to categorise the brain as normal or abnormal, i.e., whether or not it contains tumors [18].

V. DIGITAL PATHOLOGY

Pathological specimens are examined under a microscope by labeling them using colorimetric dyes or antibodies. Multiple high resolution imaging could offer details on level of protein expression and sub cellular localization, enabling molecular profiling to tissues while preserving the original tissue architecture. This makes it possible to examine the statuses of cells, tissue biomarkers, and interactions between cells in both healthy and pathological settings. Currently, tissue samples taken from surgical resections or biopsies are fixed with formaldehyde, or embedded with paraffin, shrugged into five mm-thick slices, and marked with hematoxylin and also with eosin. In order to perform fast analysis, specimens are segmented, stained, and frozen. Pathologists have recently begun using machine learning algorithms' pattern identification capabilities to gain deeper diagnostic insight from histology data. In the recent years, ML algorithms have improved and expanded to the point where they are now used to assist in the understanding of smeared slides, which clinicopathologic laboratories analyse in large quantities. Additionally, they have sparked the growth of numerous start-ups and tools for digital pathology. Imported and system generated data used for analysis. For the collection and storage of image data, the Digital Imaging and Communication in medicine is frequently utilised. Considering the patient as the foundation Within

Authorized licensed use limited to: DELHI TECHNICAL UNIV. Downloaded on August 08,2023 at 09:04:06 UTC from IEEE Xplore. Restrictions apply.

ANALYSIS, DICOM data may be manipulated by utilising DICOM data hierarchy [19]. The open-source image-informatics system OMERO is the most extensively used and is interoperable with a variety of software clients. The server becomes severely overloaded as photos get bigger, this restrict the amount of concurrent sessions. Client needs connectivity to an OMERO database [20]. Project Mirador makes use of database-free viewers that are built on the free and open-source OpenSeadragon framework it makes zooming and panning across photos simple.

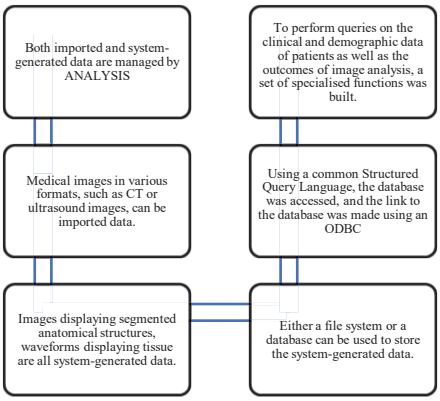

Fig2: *Steps for imaging of brain tumor* [20]

VI. IMAGING IN REGENERATIVE MEDICINE

Through the use of particular cell populations, either by themselves or in combination with biomaterial scaffolds, regenerative medicine seeks to restore the function of damaged tissues while accelerating the body's natural ability to mend itself. Here, clinical imaging is essential for identifying injured tissue and evaluating the safety and effectiveness of treatment. Imaging is frequently utilised in clinical practice to give secondary endpoints that support primary health outcomes and to look into the mechanisms underlying successful and unsuccessful treatment interventions. New opportunities in regenerative medicine are provided by the newest clinical scanners, which can be used to monitor transplanted cells, analyse the tissue composition of organs, and measure the impact of therapy on tissue function. They are starting to be used to evaluate cell therapy's underlying mechanisms as well as the transplanted cells' survival, migration, biodistribution, and differentiation without causing any harm to the patient. A good option for in vivo stem cell research is the recently established spectral encoding of the spatial frequency (SESF) technique, which enables label-free viewing of the internal nanometre structures in actual time with nanoscale sensitivity.

Benefits and challenges of using imaging in regenerative medicine are following:-

- Researchers need to make sure that subjects who have been approved will tolerate imaging tests. Imaging is crucial for figuring out whether or not people match the requirements for inclusion or exclusion in clinical trials for research participants should include imaging results.
- Choosing the ideal administration route requires imaging.
- When determining if the targeted area can sustain the cell graft, multimodal imaging is useful.
- Using clinical imaging to ascertain the efficacy, volume of distribution, and longevity of the cell product and to create a delivery plan for patients presents a difficulty. Clinical studies will benefit from mechanistic insights provided by new labels that track the destiny and functioning of cell products.
- The ideal modality must offer in situ, depth-resolved, non-invasive imaging, be able to identify single cells, and distinguish between cell death and proliferation.

VII. CONCLUSION

Medical imaging informatics makes up a sizable portion of AI-based research-driven methods that has been approved by the Food and Drug Administration (FDA). These systems make use of machine- or deep-learning approaches to carry out a range of image analysis activities, including picture augmentation, segmentation, and abnormality identification as well as the prediction of the likelihood of malignancies. Among the most comprehensive standards for medical images is DICOM. It is designed to standardise picture data and make it simple to share between equipment from various manufacturers. Despite several glaring drawbacks, such as the need to include required data in picture headers, DICOM has proven to be a very full and, more importantly, useful standard for medical imaging preservation and exchanging. Using the information and communication technology in medical imaging for the delivery of healthcare services is known as medical imaging informatics. The automatic identification of medical images is a particularly challenging work due to the existence of noise and masking structures, variety of biological forms and tissue, imaging system anisotropy. Artificial intelligence and machine learning are an interdisciplinary field that incorporates developments in computer science and neuroscience. The use of machine learning is now commonplace in a variety of industries, providing trustworthy assistance for decision-making and minimising human work. Contributions in AI-based medical imaging are still increasing rapidly. Despite these efforts, AI solutions are still just restricted solutions for particular conditions, imaging modalities, or disease states in the field of medical imaging. The adoption of AI in CT and the improvement of imaging quality is anticipated to take off swiftly, with other widely used imaging modalities following. In the early phases of the disease, the most recent medical pictures have demonstrated a negative radiological pattern. With a tentative clinical diagnosis, the early portrayal of the radiological indication is crucial. When using AI techniques on medical images for segmentation and classification tasks, the lack of readily available data could result in over-fitting of the results. It is critical to enhance the quality of the specimens with larger datasets for future research and accurate clinical evaluation. As a result, more data sets must be produced and shared for accurate medical evaluations. Multi modal domains can be explored in future for more enhanced way of medical imaging.

REFERENCES

[1] R. Dobrescu, M. Dobrescu, S. Mocanu, and D. Popescu, "Medical images classification for skin cancer diagnosis based on combined

Authorized licensed use limited to: DELHI TECHNICAL UNIV. Downloaded on August 08,2023 at 09:04:06 UTC from IEEE Xplore. Restrictions apply.

texture and fractal analysis," *WISEAS Transactions on Biology and Biomedicine*, vol. 7, no. 3, pp. 223–232, 2010.

[2] X. Tang, "The role of artificial intelligence in medical imaging research," *BJR| Open*, vol. 2, no. 1, p. 20190031, 2019.

[3] T. Dill, "Contraindications to magnetic resonance imaging," *Heart*, vol. 94, no. 7, pp. 943–948, 2008.

[4] J. A. Sidles *et al.*, "Magnetic resonance force microscopy," *Reviews of Modern Physics*, vol. 67, no. 1, p. 249, 1995.

[5] C. Ieracitano *et al.*, "A fuzzy-enhanced deep learning approach for early detection of Covid-19 pneumonia from portable chest X-ray images," *Neurocomputing*, vol. 481, pp. 202–215, Apr. 2022, doi: 10.1016/j.neucom.2022.01.055.

[6] P. N. Wells, "Ultrasound imaging," *Physics in medicine & biology*, vol. 51, no. 13, p. R83, 2006.

[7] P. S. Green and M. Arditi, "Ultrasonic reflex transmission imaging," *Ultrasonic imaging*, vol. 7, no. 3, pp. 201–214, 1985.

[8] G. Calisesi *et al.*, "Compressed sensing in fluorescence microscopy," *Progress in Biophysics and Molecular Biology*, vol. 168, pp. 66–80, 2022.

[9] A. S. Lundervold and A. Lundervold, "An overview of deep learning in medical imaging focusing on MRI," *Zeitschrift für Medizinische Physik*, vol. 29, no. 2, pp. 102–127, 2019.

[10] A. S. Al-Waisy *et al.*, "COVID-DeepNet: hybrid multimodal deep learning system for improving COVID-19 pneumonia detection in chest X-ray images," *Computers, Materials and Continua*, vol. 67, no. 2, pp. 2409–2429, 2021.

[11] A. Webb, *Introduction to biomedical imaging*. John Wiley & Sons, 2022.

[12] P. S. Green, J. F. Jensen, and Z.-C. Lin, "Reflex transmission imaging," in *Acoustical Imaging: Proceedings of the Sixteenth International Symposium, June 10–12, 1987*, Springer, 1988, pp. 1–13.

[13] A. S. Panayides *et al.*, "AI in medical imaging informatics: current challenges and future directions," *IEEE journal of biomedical and health informatics*, vol. 24, no. 7, pp. 1837–1857, 2020.

[14] H. K. Huang, "Enterprise PACS and image distribution," *Computerized Medical Imaging and Graphics*, vol. 27, no. 2–3, pp. 241–253, 2003.

[15] B. Wang and W. Zhang, "MARnet: Multi-scale adaptive residual neural network for chest X-ray images recognition of lung diseases," *Math. Biosci. Eng*, vol. 19, no. 1, pp. 331–350, 2022.

[16] A. Choudhary, L. Tong, Y. Zhu, and M. D. Wang, "Advancing medical imaging informatics by deep learning-based domain adaptation," *Yearbook of medical informatics*, vol. 29, no. 01, pp. 129–138, 2020.

[17] H.-H. Tseng, L. Wei, S. Cui, Y. Luo, R. K. Ten Haken, and I. El Naqa, "Machine learning and imaging informatics in oncology," *Oncology*, vol. 98, no. 6, pp. 344–362, 2020.

[18] S. Rajeshwari and T. S. Sharmila, "Efficient quality analysis of MRI image using preprocessing techniques," in *2013 IEEE Conference on Information & Communication Technologies*, IEEE, 2013, pp. 391–396.

[19] J. Stoitsis, S. Golemati, and K. S. Nikita, "A modular software system to assist interpretation of medical images—Application to vascular ultrasound images," *IEEE Transactions on Instrumentation and Measurement*, vol. 55, no. 6, pp. 1944–1952, 2006.

[20] R. Rashid *et al.*, "Narrative online guides for the interpretation of digital-pathology images and tissue-atlas data," *Nature Biomedical Engineering*, vol. 6, no. 5, pp. 515–526, 2022.

Authorized licensed use limited to: DELHI TECHNICAL UNIV. Downloaded on August 08,2023 at 09:04:06 UTC from IEEE Xplore. Restrictions apply.

2023 2nd International Conference on Vision Towards Emerging Trends in Communication and Networking Technologies (ViTECoN) | 979-8-3503-4798-2/23/$31.00 ©2023 IEEE | DOI: 10.1109/VITECON58111.2023.10157260

Attack detection in industrial IoT using novel ensemble techniques

Kushagra Keserwani
Dept. of Information Technology, Delhi Technological University
Delhi, India
kushagrakeserwani@gmail.com

Apoorva Aggarwal
Dept. of Information Technology, Delhi Technological University
Delhi, India
apoorva27sep@gmail.com

Anamika Chauhan
Dept. of Information Technology, Delhi Technological University
Delhi, India
anamika@dtu.ac.in

***Abstract*— The Internet of Things (IoT) is a rapidly growing industry that is expected to connect 22 billion smart devices by 2025 in a market worth $1567 billion. However, Securing IoT devices is challenging due to their integrated and resource-constrained nature. The traditional security measures are relatively ineffective against these continuously changing attacks. Deep learning (DL) and machine learning (ML) offer potential solutions to incorporate intelligence into systems, enabling improved detection of security breaches and attacks. These techniques can also help us suggest suitable mitigation techniques for specific attack types. The paper focuses on suggesting a solution for the detection and classification of attacks on IoT networks using novel ensemble techniques, CatBoost, and XGBoost and training them on realistic Edge-IIoTset Dataset. The performance of the solution is tested by comparing it with traditional ensemble models trained on the same data. The evaluation criteria employed are the accuracy, recall, precision and F1 score.**

Keywords—Attack Classification, CatBoost, Ensemble, Intrusion Detection, IoT, XGBoost .

I. Introduction

A. Overview

The Internet of Things, or IoT involves interconnected physical things communicating through wired or wireless technologies. These physical nodes exchange data due to added software, electronics, and internet accessibility [1]. IoT includes everyday items like smoke alarms and temperature sensors as well as more complex gadgets like heartbeat monitors and RFID readers. A wide range of businesses in agriculture, healthcare, retail, the military, and energy, use IoT technology [2]. The security of IoT devices is a significant issue as they hold highly private user/client information such as location and contact information. However, maintaining security in such systems is difficult due to their complex nature and integrative, large-scale nature [3]. Advanced algorithm-based security measures are also ineffective for IoT devices due to their customizable components [4]. The use of enabling technologies like Cloud Computing, Fog Computing, and Software-Define Networking in the IoT has also increased the panorama of security threats [5]. The interconnected and interdependent structure of IoT renders it less secure to attacks than a standard computing system [6]. As each component has inherent vulnerabilities, access control, encryption, and authentication methods are insufficient for these systems. Machine Learning (ML) and Deep Learning (DL) classifiers and frameworks are better alternatives to traditional security systems. ML algorithms learn from their previous performance and can identify attack types and also suggest suitable defences.

Industrial IoT (IIoT) merges machines, cloud computing, analytics, and humans to improve industrial processes. It enables businesses to digitise processes, increase productivity, and reduce waste. Industries like manufacturing, energy, agriculture, transportation, and utilities are utilising IIoT for predictive maintenance, asset monitoring, and process optimization. Billions of connected devices offer various benefits for industrial applications. Better connectivity leads to informed business decisions, scalability through resource and knowledge sharing, cost savings from efficient safety and repair handling, and improved business models and analytics.

B. Research Problem

ML being a potent tool for data analysis understands the "normal" and "abnormal" behaviour in interactions of IoT devices and components. The ML-analyzed common patterns of interaction in IoT components are used for early identification of system intrusion, and also foreseeing new attacks which are frequently mutations of earlier ones. These facts lead to research on the identification of attack type and combat methods for IoT devices. The essay is broken down into six distinct sections, including 1) Introduction 2) Security Challenges in The Network layer of IIoT 3) Related Work 4) Methodology 5) Experimentation And Results 6) Conclusion and Future Work. The dataset used is Edge-IIoTset Cyber Security Dataset which is derived from the actual world [16]. For training and testing, we used CatBoost, and XGBoost to fit our dataset later on for comparison we also used Random Forest, and Decision Tree. The accuracy, recall, precision and F1 score are some of the evaluation metrics that were considered in the presentation analysis.

C. Motivation

Inadvertently, the growing need for IoT technology in our daily lives raises the risk of security in these IoT devices. The growing use of IoT devices creates a large, exposed surface, which raises new security concerns like secured delivery and analysis of large amounts of data to avoid serious privacy infringement. A data breach can impact millions of people's

979-8-3503-4798-2/23/$31.00 ©2023 IEEE

Authorized licensed use limited to: DELHI TECHNICAL UNIV. Downloaded on July 03,2023 at 04:48:05 UTC from IEEE Xplore. Restrictions apply.

lives. These processes might be active or passive and may originate from internal networks or external systems.

An aggressive assault prevents the operation of operating services, whereas a passive attack collects information about the Internet of Things network without tampering with current services. IoT services and devices can be the target of denial of service (DoS) attacks, which affect customer service. Through this research article, we want to offer a remedy to stop such losses.

II. Security Challenges in The Network layer of IIoT

Issues with endpoint vulnerability, data accessibility, integrity, and reliability as well as appliances and networking infrastructure are noted. The primary cause of the security concerns in the Industrial IoT ecosystem is the unavailability of security considerations throughout system and product service, installation, support, maintenance and configuration. The security drawbacks include vulnerabilities brought on by oversight, incorrect configuration, and user mistake, as well as operating system, firmware, and other software vulnerabilities for Industrial IoT devices that are not patched. IIoT devices connect directly to the internet as well, skipping over conventional IT security layers.

Implementing firewalls, OT/IT gateways, data diodes and employing encryption techniques while keeping device-level updates with the protection of endpoint are a few of the prevalent security approaches in the IIoT space. From these techniques, device-level patching is used by 60% of IIoT sectors to safeguard IIoT devices and uphold system security.

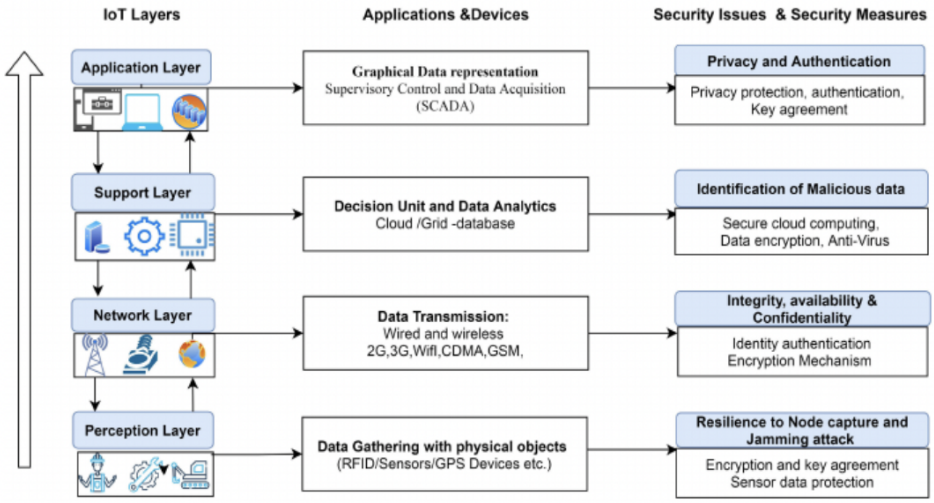

Fig. 1. Basic security mechanisms, layered architecture, security issues and technology of IIoT

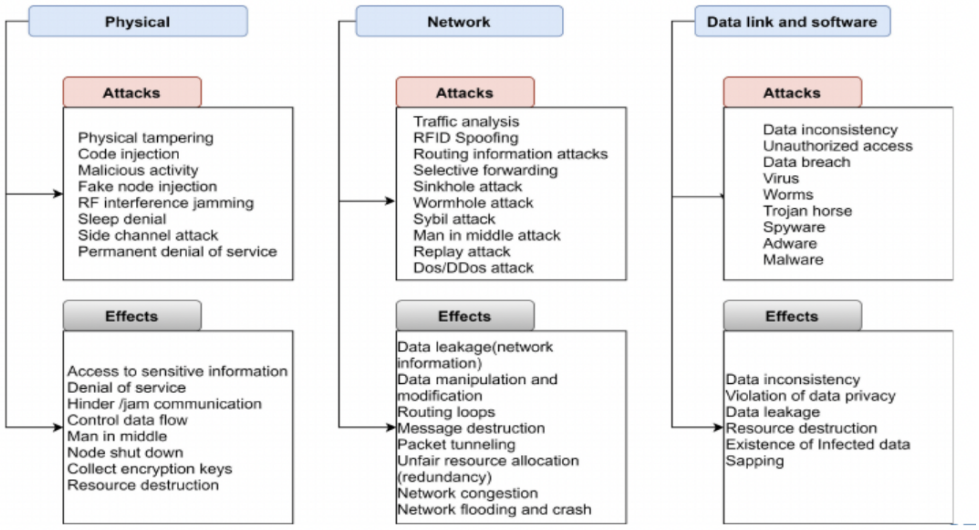

Fig. 2. The effects of various IIoT attacks on IIoT layers.

Authorized licensed use limited to: DELHI TECHNICAL UNIV. Downloaded on July 03,2023 at 04:48:05 UTC from IEEE Xplore. Restrictions apply.

TABLE I. EXISTING PAPERS ON ATTACK DETECTION IN IOT ENVIRONMENT - A COMPARATIVE ANALYSIS

S.No	*Reference*	*Objectives*	*Techniques*	*Results*	*Advantages*	*Disadvantages*
1	Gaber et al. [8] 2022	Detection of injection attacks on the AWID dataset.	RF, DT, SVM	90% F1 Decision,99% accuracy	The detection of attacks can be achieved with just eight features.	The suggested approach only addresses injection attacks; it does not address other potential security and privacy problems associated with IoT.
2	Nayak et al. [9] 2021	Reduced Rank, Hello Flood attack on IRAD (IoT Routing Attack Dataset), Version Number	SVM, GAN-C	92% f1-score for HF attack, 92% recall and 93% precision	Training time was significantly reduced with the implementation of the parallel GAN-C model.	The Dataset utilized is uniform and encompasses only three types of attacks.
3	Almaraz-Rivera et al. [10] 2021	Detection of attacks at the transport and application layers on the Bot-IoT dataset.	SVM, Decision Tree and Random Forest	Accuracy on DT and RF is 100%	The proposed methodology addresses the problem of imbalanced classes that existed in the initial dataset.	The proposed system for detecting intrusion in multiple IoT setups has not been reviewed yet.
4	Bedi et al. [11] 2021	SP, MC, MO, DOS, WS, DP, NL,SC attacks detection using DS2OS dataset	LR, SVM, ANN,RF, DT	99.4% accuracy with RF	The provided dataset does not necessitate any data preprocessing.	Except for the Normal attack, there are very few data points available for each specific attack.
5	Zagrouba et al. [12] 2021	Botnet/DDoS Attacks detection on BoT-IoT dataset	Random Forest and Decision Tree	99.99% accuracy	Given the TP rate of 1.000 and FN rate of 0.000, the accuracy is incredibly high.	The process of data analysis, algorithm training, and classification of diverse datasets is a time-intensive task.
6	Bagui et al. [13] 2021	Identification of botnet attacks on UCI's ML repository	LR, SVM, RF	99% accuracy with RF.	The rate of detection for attacks is extremely high.	No efficient feature selection methods were utilized to choose the features.
7	Aboelwafa et al. [14] 2020	Cyber Attacks detection using CICIDS-2017, ICS Cyber Attack, UNSW-NB15,	CNN, LSTM, GNB, DNN, Simple RNN, AdaBoost, CNN-LSTM, GRU, RF, DT, KNN, LR	On the CICIDS-2017 dataset got 99.9% accuracy using RF	The approach does not rely on labeled data and has an effective algorithm for data cleaning.	AutoEncoder may fail to identify an attack if the attack maintains the correlation among sensor readings.
8	Shafiq et al. [15] 2020	Bot-IoT attacks detection using Bot-IoT dataset	Decision Tree and Random forest	99.99% accuracy on RF	A proficient method for selecting pertinent features has been utilized.	The system is not proficient at detecting Keylogging theft attacks.

III. RELATED WORK

A summary of prior studies that used ML and DL techniques to find attacks on IoT environments is shown in Table 1. The table includes studies from 2020 to 2022, listing the various algorithms utilized, including RF, SVM, LR, DT, ANN, etc., as well as the advantages and disadvantages of the under-discussion research works. For example, DDoS, injection assaults, etc., are only a few of the attacks that the majority of research specifically focuses on identifying.

IV. METHODOLOGY

The objective of the paper is to detect and classify intrusion in the IIoT environment. The flowchart in Fig. 3. outlines the approach and steps to train ensemble models for the objective. The succeeding subsections will provide a more detailed explanation of this methodology.

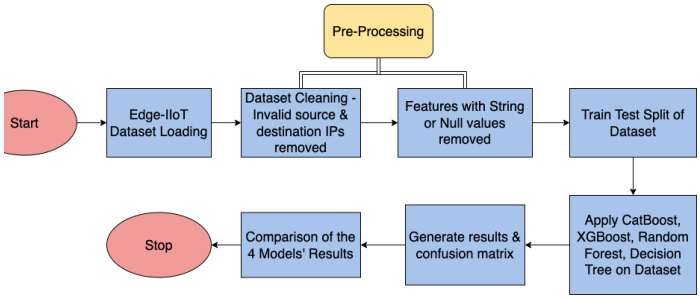

Fig. 3. Methodology employed for detection and classification of attacks in Industrial IoT network

A. Dataset

For implementing this attack detection system, the dataset used in the paper is Edge-IIoTset Cyber Security Dataset [17]. It was developed in 2022 by the authors in [16]. The dataset

Authorized licensed use limited to: DELHI TECHNICAL UNIV. Downloaded on July 03,2023 at 04:48:05 UTC from IEEE Xplore. Restrictions apply.

being derived from the actual world, is more realistic in nature and helps generalize the findings better.

The Edge-IIoTset is an extensive cyber security dataset that delivers accurate data from IoT and IIoT applications. It is suitable for use by intrusion detection systems that employ machine learning and can operate in multiple modes, namely centralized or federated learning modes. The dataset includes data from multiple types of IoT devices, with over ten types thereby forming an IoT testbed. IoT gadgets from which data is retrieved include sensors for pH, heart rate, Flame, soil moisture, monitoring temperature and humidity, detecting water level.

Within this dataset, 14 attacks pertain to the connectivity protocols of IoT and IIoT. These attacks are classified into five distinct categories: information gathering, DoS/DDoS attacks, man-in-the-middle attacks, malware attacks and injection attacks. The dataset enables the identification and analysis of these attacks.

According to Ferrag et al.[16], recent datasets like MQTTset and BoT-IoT as well as older datasets like NSL-KDD, DARPA-2009, and CICDS2017 do not accurately represent an actual IoT/IIoT ecosystem. As a result, the ability of the pre-trained deep learning and machine learning models used to enable intrusion detection to identify attacks in actual-world situations would be constrained. To prevent this from happening they have gathered data from a number of different IoT devices (listed above) that are used in the real world. To implement this, the authors in [16] constructed a real IoT testbed. Researchers have utilised a number of real cyber-attacks like DNS Spoofing and TCP-SYN attacks for experimentation for about two months. To create a final modern dataset, it was necessary to extrapolate characteristics from HTTP requests and identify the attacks appropriately.

B. Preprocessing and feature selection

The data was cleaned and filtered thoroughly to ensure only valid data is fed to the ensemble and traditional models.

1) Validating source and destination IPs

The source and destination IP addresses of each row in the dataset were validated, and the ones with invalid IP addresses were dropped.

2) Validating features

Next, appropriate features were selected by first eliminating the features that contain non-numeric values. Secondly, out of the remaining features the ones with large numbers (greater than 95%) of zero values were removed since they are unable to contribute much in determining the presence of an attack. Finally, we are left with 20 significant features in the preprocessed dataset.

3) Dataset split

The dataset is then split into two parts namely a test set and a training set. Machine learning algorithms in use attempt to learn from the training set and validate their findings on the test set. The dataset is randomly divided by Sklearn's train_test_split function [22] so that 80% of the data serves as the training set for the model and the remaining 20% serves as the test set. The outcomes obtained over the test data are used to determine the performance metrics of all four models in use.

C. Attack Detection and classification in IIoT using Ensemble models

XGBoost [18] and CatBoost [19] being the two recent ensemble algorithms, are used to detect and classify attacks on IoT devices. With these novel techniques, Random Forest [20] and Decision Tree [21] are also used as traditional approaches for the similar purpose of detection and classification of attacks. The results of all four models are compared, which highlights the contrasts between both ensemble and traditional methods used for attack detection and classification.

1) CatBoost

CatBoost or Categorical Boosting is a gradient-boosting decision tree method. It uses a technique called oblivious decision trees to construct binary trees where the same features are used to make left and right splits at each level. This limits the number of features that can be split per level to one, resulting in faster predictions. In addition, it effectively handles categorical features by using ordered target statistics.

2) XGBoost

The XGBoost technology is utilized to create gradient-boosted decision trees, which involve generating decision trees sequentially. The use of weights is essential in this process, as each input variable is assigned a weight before being used in the decision tree to make predictions. Variables that were inaccurately predicted by the first decision tree are assigned higher weights before being fed into the second tree. By combining multiple classifiers or predictors in this way, a dependable and precise model is produced, capable of solving regression, classification, ranking, and tailored prediction problems.

D. Evaluation Metrics and results generation

To evaluate the effectiveness of the ensemble models, four metrics namely, Accuracy, Recall, Precision, and F1 score are used.

1) Accuracy: This illustrates the proportion of data examples correctly classified by our model in comparison to all data instances.

$$Accuracy = \frac{TP+TN}{TP+TN+FP+FN} \qquad (1)$$

2) Recall: This shows how many, out of all the instances, the model is properly classified as relevant.

$$Recall = \frac{TP}{TP+FN} \qquad (2)$$

3) Precision: Out of all the instances the model retrieved, this shows how many were relevant.

$$Precision = \frac{TP}{TP+FP} \qquad (3)$$

Authorized licensed use limited to: DELHI TECHNICAL UNIV. Downloaded on July 03,2023 at 04:48:05 UTC from IEEE Xplore. Restrictions apply.

4) F1 score: The harmonic mean of accuracy and recall is used to calculate it.

$$F1 = \frac{2\times Precision\times Recall}{Precision+Recall} = \frac{2\times TP}{2\times TP + FP + FN} \quad (4)$$

TN = True Negative; TP = True Positive; FN = False Negative; FP = False Positive

V. Experimentaion and Results

After training the above four algorithms on the preprocessed training set it is evaluated on the test set. The findings are reported in Table II for attack detection and Table III for attack type classification. Fig. 4, 5 show the heat map for both XGBoost and CatBoost respectively. The confusion Matrix for attack detection by using XGBoost and CatBoost Technique is shown in Fig 6 and 7.

TABLE II. Comparative Analysis Of Attack Detection With Other Models

Algorithm	***Accuracy***	***Precision***	***Recall***	***F1***
XGBoost	99.53%	99.22%	99.07%	99.14%
CatBoost	99.49%	99.22%	98.92%	99.07%
Random Forest	97.56%	99.16%	91.89%	95.38%
Decision Tree	98.52%	99.19%	95.38%	97.25%

TABLE III. Comparative Analysis Of Attack Type Classification With Other Models

Algorithm/Method	***Accuracy***	***Precision***	***Recall***	***F1***
XGBoost	97.99%	98.11%	97.99%	97.99%
CatBoost	97.37%	97.49%	97.37%	97.36%
Random Forest	91.15%	87.84%	91.15%	89.20%
Decision Tree	91.19%	91.72%	91.19%	90.48%

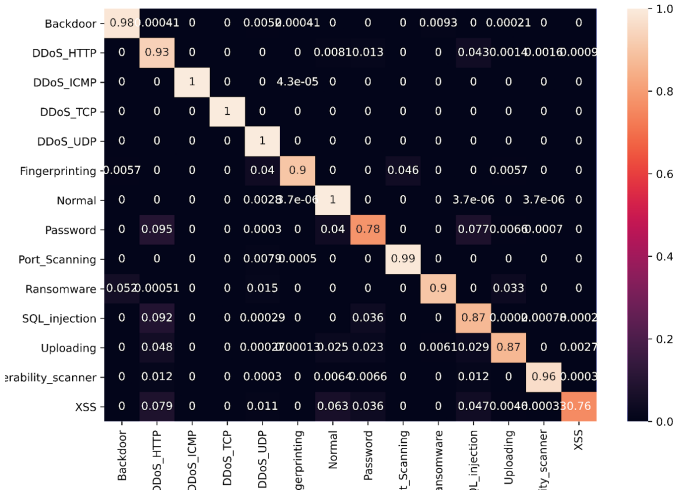

Fig. 4. XGBoost: Heatmap for validation dataset for attack type classification

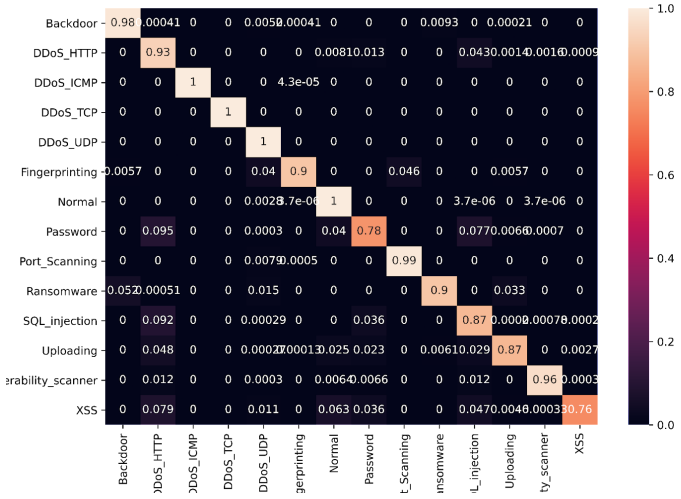

Fig. 5. CatBoost: Heatmap for validation dataset for attack detection

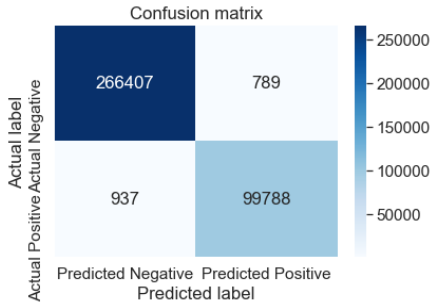

Fig. 6. Confusion matrix for attack detection by using XGBoost

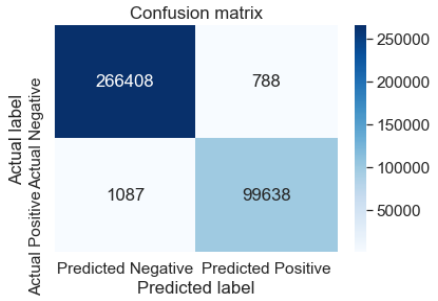

Fig. 7. Confusion matrix for attack detection by using CatBoost

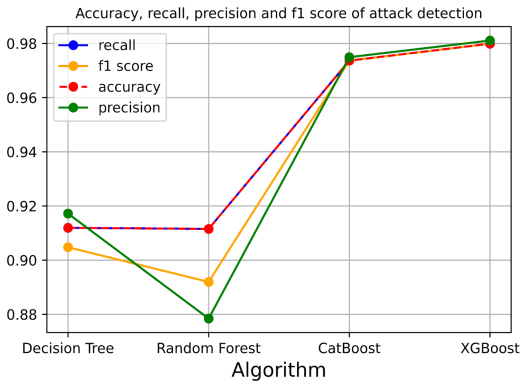

Fig. 8. Comparison of algorithms in attack detection

Authorized licensed use limited to: DELHI TECHNICAL UNIV. Downloaded on July 03,2023 at 04:48:05 UTC from IEEE Xplore. Restrictions apply.

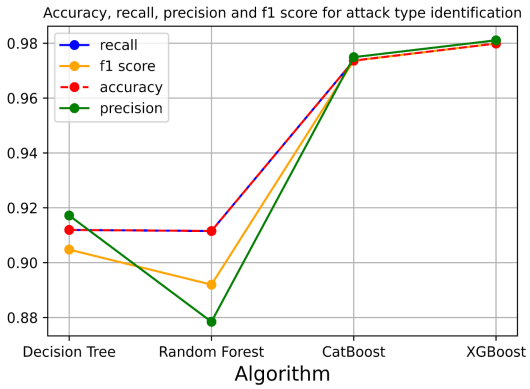

Fig. 9. Comparison of algorithms in attack type classification

On comparing the above-mentioned results in Fig 8 and 9 it can easily be observed that novel Ensemble Methods XGBoost and CatBoost both outperform the classical ones in both attack detection and attack type classification in IIoT environment.

VI. Conclusion And Future Work

With this work, we have thoroughly examined and investigated the state of the art in attack detection and type classification in the IoT environment. Further, we have contrasted and analyzed various traditional methods, such as Random Forests, Decision Trees, etc, that are currently utilized to detect attacks on IoT-based networks. We used CatBoost, XGBoost, Random Forest, and Decision Tree while making conforming changes to the dataset to make these algorithms work with it. We analyzed the outcomes of these algorithms using various performance measures and concluded that both XGBoost & CatBoost models perform equally well on the Industrial-IoT dataset, and give nearly flawless accuracy while attack detection and larger accuracy while attack classification compared to prior studies. The Blockchain Mechanism, a distributed database or ledger that stores data in a digital format, can be used to further secure information against various attacks. The use of blockchain technology that is most well-known is the development of cryptocurrencies like Bitcoin. They are used to maintain a secure, independent record of each network transaction. The transaction cannot be changed once it has been completed. IoT systems and devices' security can be improved by utilizing any of these traits. The obtained experimental results show that the said models, employing the algorithm, are quite successful at detecting threats in IoT devices.

References

[1] J. H. Nord, A. Koohang, and J. Paliszkiewicz, “The internet of things: Review and Theoretical Framework,” *Expert Systems with Applications*, vol. 133, pp. 97–108, 2019.

[2] P. Asghari, A. M. Rahmani, and H. H. S. Javadi, “Internet of Things applications: A systematic review,” *Computer Networks*, vol. 148, pp. 241–261, Jan. 2019,doi:https://doi.org/10.1016/j.comnet.2018.12.008.

[3] W. Zhou, Y. Jia, A. Peng, Y. Zhang and P. Liu, "The Effect of IoT New Features on Security and Privacy: New Threats, Existing Solutions, and Challenges Yet to Be Solved," in IEEE Internet of Things Journal, vol. 6, no. 2, pp. 1606-1616, April 2019, doi: 10.1109/JIOT.2018.2847733.

[4] J. Zhou, Z. Cao, X. Dong, A. V. Vasilakos, Security and Privacy for Cloud-Based IoT: Challenges, IEEE Communications Magazine (2017). doi:10.1109/MCOM.2017.1600363CM.

[5] I. Farris, T. Taleb, Y. Khettab and J. Song, "A Survey on Emerging SDN and NFV Security Mechanisms for IoT Systems," in IEEE Communications Surveys & Tutorials, vol. 21, no. 1, pp. 812-837, Firstquarter 2019, doi: 10.1109/COMST.2018.2862350.

[6] N. Liang, “Security Transmission and Storage of Internet of Things Information Based on Blockchain,” IOP Conference Series: Materials Science and Engineering, vol. 750, p. 012164, Mar. 2020, doi: https://doi.org/10.1088/1757-899x/750/1/012164.

[7] Z. Rayan, M. Alfonse, and A.-B. M. Salem, “Machine Learning Approaches in Smart Health,” Procedia Computer Science, vol. 154, pp. 361–368, 2019, doi: https://doi.org/10.1016/j.procs.2019.06.052.

[8] T.Gaber,A.El-Ghamry,andA.E.Hassanien,“Injection attack detection using machine learning for smart iot applications,” Physical Communi- cation, vol. 52, p. 101685, 2022.

[9] S. Nayak, N. Ahmed, and S. Misra, “Deep learning-based reliable routing attack detection mechanism for industrial internet of things,” Ad Hoc Networks, vol. 123, p. 102661, 2021.

[10] J. G. Almaraz-Rivera, J. A. Perez-Diaz, and J. A. Cantoral-Ceballos, “Transport and application layer ddos attacks detection to iot devices by using machine learning and deep learning models,” Sensors, vol. 22, no. 9, p. 3367, 2022.

[11] P. Bedi, S. Mewada, R. A. Vatti, C. Singh, K. S. Dhindsa, M. Ponnusamy, and R. Sikarwar, “Detection of attacks in iot sensors networks using machine learning algorithm,” Microprocessors and Microsystems, vol. 82, p. 103814, 2021.

[12] R. Zagrouba and R. Alhajri, “Machine learning based attacks detection and countermeasures in iot,” International Journal of Communication Networks and Information Security, vol. 13, no. 2, pp. 158–167, 2021.

[13] S. Bagui, X. Wang, and S. Bagui, “Machine learning based intrusion detection for iot botnet,” International Journal of Machine Learning and Computing, vol. 11, no. 6, pp. 399–406, 2021.

[14] M. M. Aboelwafa, K. G. Seddik, M. H. Eldefrawy, Y. Gadallah, and M. Gidlund, “A machine-learning-based technique for false data injection attacks detection in industrial iot,” IEEE Internet of Things Journal, vol. 7, no. 9, pp. 8462–8471, 2020.

[15] M. Shafiq, Z. Tian, A. K. Bashir, X. Du, and M. Guizani, “Corrauc: a malicious bot-iot traffic detection method in iot network using machine- learning techniques,” IEEE Internet of Things Journal, vol. 8, no. 5, pp. 3242–3254, 2020.

[16] M. A. Ferrag, O. Friha, D. Hamouda, L. Maglaras, and H. Janicke, “Edge-iiotset: A new comprehensive realistic cyber security dataset of iot and iiot applications for centralized and federated learning,” IEEE Access, vol. 10, pp. 40 281–40 306, 2022.

[17] “Edge-iiotset cyber security dataset of iot & iiot - kaggle.com,” https://www.kaggle.com/datasets/mohamedamineferrag/edgeiiotset-cyber-security-dataset-of-iot-iiot, 2022, [Accessed 16-Jan-2023].

[18] T. Chen and C. Guestrin, “XGBoost: A Scalable Tree Boosting System,” Jun. 2016. Available: https://arxiv.org/pdf/1603.02754.pdf

[19] L. Prokhorenkova, G. Gusev, A. Vorobev, A. Dorogush, and A. Gulin, “CatBoost: unbiased boosting with categorical features.” Available: https://arxiv.org/pdf/1706.09516.pdf

[20] L. Breiman, “Random Forests,” 2001. Available: https://www.stat.berkeley.edu/~breiman/randomforest2001.pdf

[21] J. R. Quinlan, “Induction of decision trees,” Machine Learning, vol. 1, no. 1, pp. 81–106, Mar. 1986, doi: https://doi.org/10.1007/bf00116251.

[22] F. Pedregosa et al., "Scikit-learn: Machine Learning in Python," The Journal of Machine Learning Research, vol. 12, pp. 2825-2830, Feb. 2011.

Authorized licensed use limited to: DELHI TECHNICAL UNIV. Downloaded on July 03,2023 at 04:48:05 UTC from IEEE Xplore. Restrictions apply.

2023 2nd International Conference on Vision Towards Emerging Trends in Communication and Networking Technologies (ViTECoN) | 979-8-3503-4798-2/23/$31.00 ©2023 IEEE | DOI: 10.1109/ViTECON58111.2023.10157098

Bypassing Deep Learning based Sentiment Analysis from Business Reviews

Ashish Bajaj
Biometric Research Laboratory, Department of Information Technology, Delhi Technological University
Bawana Road, Delhi-110042, India
bajaj.ashish25@gmail.com

Dinesh Kumar Vishwakarma
Biometric Research Laboratory, Department of Information Technology, Delhi Technological University
Bawana Road, Delhi-110042, India
dvishwakarma@gmail.com

Abstract— **In recent years, online reviews of businesses have grown increasingly significant, as customers and even competitors use them to evaluate a company's quality. Yelp is one of the most popular review websites, and it would be advantageous for them to be capable of predicting the sentiment or even the star rating of a review. Current deep-learning algorithms excel at sentiment classification. With the tremendous performance of models based on deep learning in text-related problems, they are susceptible to adversarial manipulations that result in inaccurate sentiment classification. An adversarial text is created by manipulating just few letters or words in such a manner so that general meaning of the text remains unchanged for humans but fooling a system into making false predictions. This study highlights the shortcomings of sentiment categorization by employing a range of cutting-edge attack techniques to generate perturbed text. We examined the performance of several models, including BERT, an advanced transformer model, and the extensively used LSTM and Word-CNN classifiers trained on the Yelp polarity dataset. For each model, Attack Success Rates (ASR) are calculated as the evaluation metric. Based on the experimental results, we determined which sentiment classifier is more vulnerable to adversarial perturbations and which is more resistant. The results demonstrate that automatic sentiment classification techniques can be circumvented, which has implications for present policy approaches.**

Keywords— (Natural Language Processing) NLP, Sentiment Classification, Adversarial Attack, Transformers, Semantic Similarity, Vulnerability.

I. INTRODUCTION

Across the past decade, Machine Learning (ML) approaches have flourished at a range of tasks, including regression, classification, and decision processing. Yet, these models are fragile to adversarial situations, which are genuine inputs that have been intentionally modified by minute, frequently imperceptible variations. Emerging research has generated adversarial perturbed images which render algorithms for computer vision ineffective[1]. A few research on adversarial cases in text-categorization problems have been undertaken, such as emotional analysis, topic classification[2], machine translation, fake news classification, hate content detection, etc. Yet, due to the adversarial machine learning's achievement in visuals, it is a relatively recent topic that has received more attention and is interesting to examine [3]. To produce adversarial cases, two hostile situations are used. A *"black-box setup"* is the design of adversarial perturbed sample in which an attacker is clueless of classification algorithm or the training information. In contrast, in a *"white-box"* situation, the latter one has detailed understanding of the algorithm and the training set [4]. In addition, the attack is also classified according to whether it is targeted or untargeted. Consider the input class to be C_i and the output class to be C_T. The input x belongs to the class C_i, and we desire that, after perturbation, x' set belongs to a class other than C_i. In a *"targeted"* assault, the input data x is altered to x' so that it predicts a targeted class C_T rather than its genuine class C_i. Here, the objective is to reach a specific target label. In an *"untargeted"* attack, the objective is to shift input x away from its true class C_i, regardless of which other classes are struck [5]. Technically, in virtue to fooling the target models, the outcomes of a natural language parsing framework must fulfill 3 key utility-preserving functionalities :***1.)*** same resemblance in meaning—the produced example should have the same significance as the actual based on human judgement; ***2.)*** created instances of opposition shall seem grammatical and genuine. ***3.)*** Human predictions should be consistent and remain constant[6]. **Figure 1** demonstrates how assaults are classified depending on attack specificity and attacker knowledge.

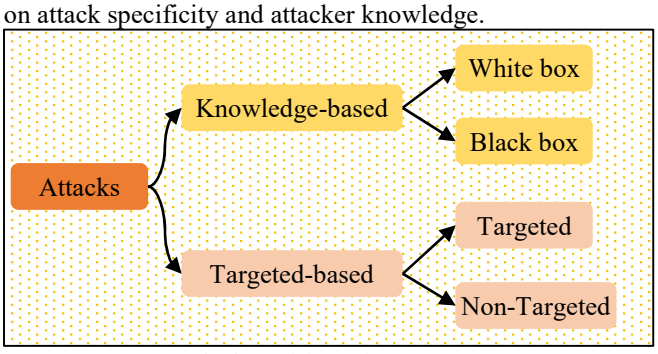

Figure 1. Taxonomy of Adversarial Attack.

This research focuses on the widely used word convolution neural-networks and bi-directional long short-term memory, along with the potent transformer model, that is, BERT, for various natural language processing tasks, to illustrate the weakness in sentiment classification. Firstly, the classifiers are trained on the (Yelp polarity dataset), a well-known set of business review emotions. The deterioration of these pre-trained models' performance is then examined by conducting attacks utilizing various cutting-edge adversarial attack methodologies. The findings may be of interest to users who habitually use well-known cutting-edge classification methods. The reader will be able to choose which model is

979-8-3503-4798-2/23/$31.00 ©2023 IEEE

Authorized licensed use limited to: DELHI TECHNICAL UNIV. Downloaded on July 03,2023 at 04:45:26 UTC from IEEE Xplore. Restrictions apply.

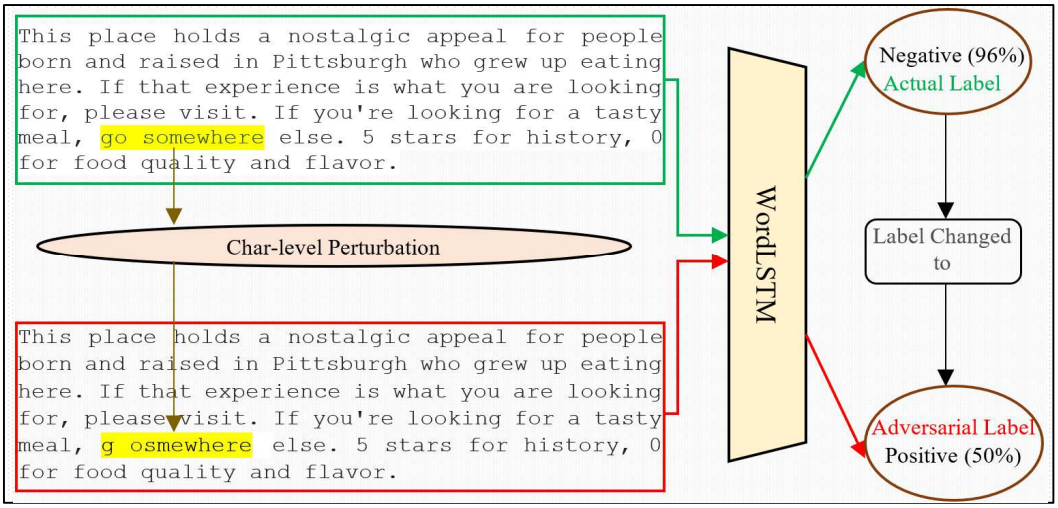

Figure 2. Adversarial instance created by modifying a character[12] in such a way that it is semantically equivalent to a human observer yet evade the Word CNN model into producing the incorrect predicted label.

most suited to their situation. Furthermore, this pushes researchers to develop models that use adversarial resilient generalizations rather than traditional generalizations. According to the authors, this is the first study to compare the sensitivity of various models to different adversarial attack approaches for the sentiment categorization task.

II. Related Work

A. Sentiment Classification

Sentiment classification, also referred to as information extraction, is the process of recognizing & analyzing information depending on the context in which it is expressed. This content may comprise tweets, comments, criticisms, and even passionate rants with varied or neutral perspectives. Examples of popular applications for sentiment analysis include monitoring client comments, identifying specific consumers to improve service, and analyzing how a change in a product or service affects how customers feel. Tracking customer mood over time is also beneficial. This platform has significantly transformed the way businesses operate, from opinion polls to innovative marketing strategies. Several internet recommendation algorithms, for instance, analyze user reviews and comments based on their emotional content. Classical machine learning techniques, such as Nave Bayes, Decision tree, etc., have found tremendous success in predicting sentiment from business reviews. With emerging deep learning approaches, however, models such as Bi-directional Long Short-Term Memory, Word Convolutional Neural Network and transformer models are more sophisticated and accurate[7]. As a result of their high precision and accuracy scores in text processing tasks, these models have attracted substantial interest. In this research, the most effective classification models based on deep learning were utilized. Using realistic attacks, this essay highlights the significance of testing deep learning-based sentiment classifiers prior to incorporating them into decision support systems.

B. Adversarial Attacks in Textual-domain

The significance of adversarial pattern recognition in modern artificial intelligence has grown in recent days. The adversarial component of adversarial machine learning is adversarial attacks. In an adversarial algorithm, the input data of a neural-network are modified to test its capacity to produce the same outcomes [8]. To provide a more intuitive comprehension of the definitions, we describe DNN and adversarial examples using formulas.

DNN:

The mapping function $\boldsymbol{F}: \boldsymbol{X} \rightarrow \boldsymbol{Y}$ from an input set $\boldsymbol{X}$ to the ground truth set $\boldsymbol{Y}$ may be employed to describe a conventional DNN. $\boldsymbol{Y}$ is a group of $\boldsymbol{k}$ labels such as *1, 2..., k*. $\boldsymbol{F}$ successfully classifies an input $\boldsymbol{x} \in \boldsymbol{X}$ to the actual label **y**, i.e., $\boldsymbol{F(x)} = \boldsymbol{y}$.

Perturbed example (Adversarial Input):

An adversary seeks to introduce a minor perturbation $\boldsymbol{\varepsilon}$ into $\boldsymbol{x}$ in order to create adversarial instance $\boldsymbol{x'}$, such that $F(\boldsymbol{x'}) = y'(\boldsymbol{y} \neq \boldsymbol{y'})$. Simultaneously, $\boldsymbol{x'}$ must not only deceive F, but it must also be undetectable to humans. In order to ensure that the generated $\boldsymbol{x'}$ is undetectable, a number of measures (such as similar resemblance in meaning) are used to attain this objective, i.e., $\|\boldsymbol{\varepsilon}\| < \boldsymbol{\delta}$. Here,$\boldsymbol{\delta}$ is a limiting threshold for the number of manipulations.

The field of computer vision (CV) has paid close observation to adversarial examples, which were initially proposed for image classification, in the past few years. The characteristics of hostile image instances have been extensively researched and investigated. The revelation that these assaults can be detected & resisted through randomization has resulted in a slew of promising follow-up studies, such as the creation of more resilient adaptive assaults and a better knowledge of adversarial scenario characteristics. Because languages are discrete [9], adversarial perturbed instances in textual processing assignments differ significantly from their counterpart in computer vision, and the features of textual adversarial cases have not been well explored. Comprehensive tests are conducted in this study to establish whether textual adversarial scenarios have similar characteristics[10]. We focus on text categorization and interpretation, among the most important and well-studied problems in the domain of adversarial attacks [11]. Pre-trained language models, which are a typical component of Language models, are of particular interest to us. Our findings would have a greater influence on the NLP community this way.

Authorized licensed use limited to: DELHI TECHNICAL UNIV. Downloaded on July 03,2023 at 04:45:26 UTC from IEEE Xplore. Restrictions apply.

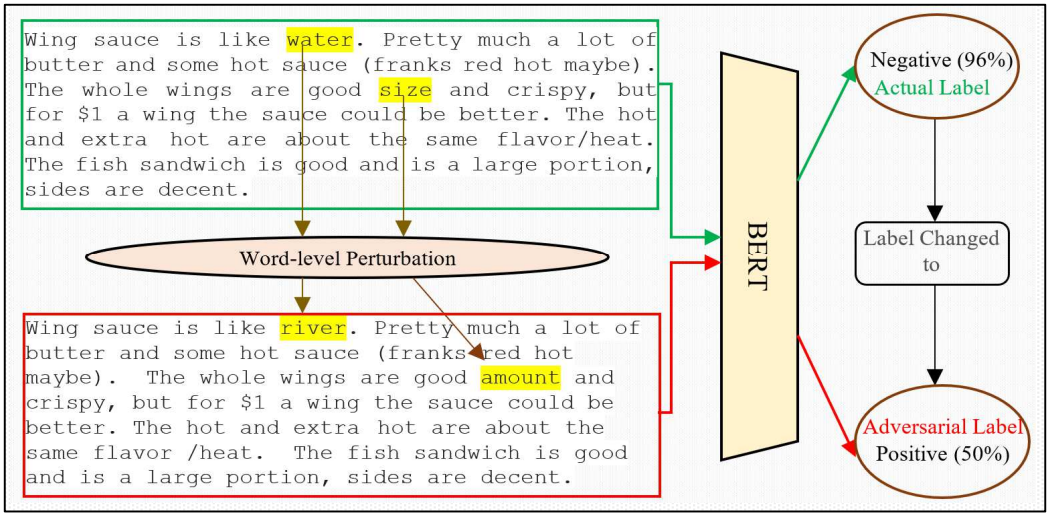

Figure 3. Adversarial instance developed by manipulating *word*[4] in a manner such that it looks semantically similar to human but spoof BERT model in giving inaccurate prediction

Based on the perturbation units used in building adversarial instances, adversarial attacks in the NLP field can be characterised as sentence, word, character, or multi-stage. As visible from **Figure 2** char-level attacks imply that attackers manipulate many letters in words in order to create hostile samples which can mislead detectors [12]. Majority of the changes includes spelling errors, addition, exchange, removal, and reversal among the most prevalent operations. Word-level attacks [4] consist of a variety of word alterations as can be seen from **Figure 3**. In numerous ways, attackers construct hostile examples by inserting, altering, or removing specific phrases. Sentence-level attacks often include the insertion or rewriting of a sentence while preserving its meaning. Multi-level attacks integrate various perturbation attacks to create a stealthy and extremely effective attack. **Figure 4** depicts the classification of perturbation level in generating adversarial text.

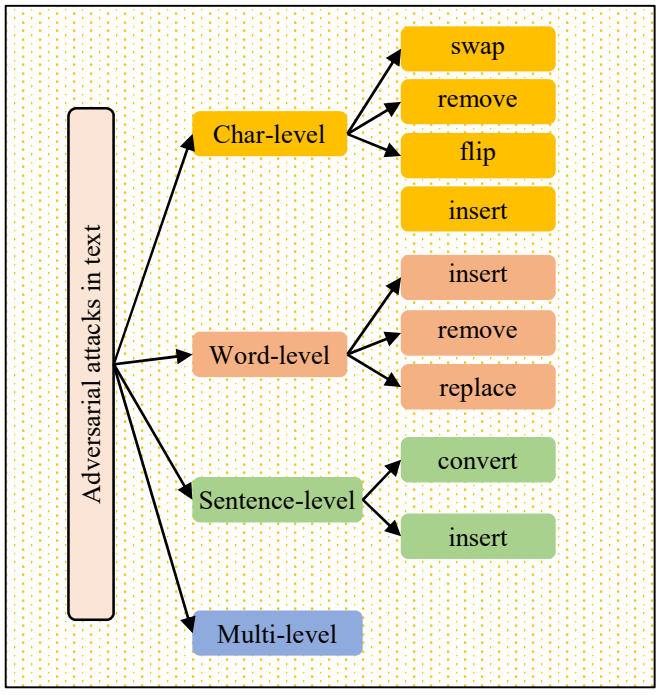

Figure 4 Classification of Adversarial attacks in text on basis of perturbation units

Each adversarial attack consists of four basic elements, including a transformation, a search strategy, a set of restraints as well as a target function, as outlined in the following section.

- *Modifications*: A modification that, given a single input, generates multiple potential perturbations. thesaurus word swap, word embedding word exchange Character substitution, are examples.
- *Search method:* A technique that checks the model on a regular basis and finds potential perturbations from a wide range of modifications. Particle swarm optimization search, genetic algorithm, beam search, and greedy search techniques ranking importance of different words in an input sequence are examples.
- *Restrictions:* A set of limitations used to evaluate the reliability of alterations in comparison to the real input. Instances include minimum language encoding cosine resemblance, word-embedding proximity, part-of-speech coherence and grammar checker.
- *Specificity:* A task-specific objective function that evaluates an attack's efficacy based on model outcomes. Exemplifications: untargeted and targeted classification, output that is not overlapping.

C. Attacks Recipes

The attack strategies were implemented on the Yelp polarity dataset to generate adversarial examples. These hostile samples are then utilized to alter the 3 aforementioned classifiers to categorize the positive sentiment of a business analytics review as negative and vice versa, so obscuring the detection of sentiment. A concise description of all attack strategies listed in **Table 1**. As depicted in **Figure 4**, these attack tactics are developed by perturbing the input text sequence at several levels, including sentence-level, word-level, and character-level.

Authorized licensed use limited to: DELHI TECHNICAL UNIV. Downloaded on July 03,2023 at 04:45:26 UTC from IEEE Xplore. Restrictions apply.

Table 1 Adversarial Attack Recipes

Attack	Description
Text-bugger[12]	These attacks were tuned for use with apps from the real world. They make use of space insertions, character deletions, and character switching. In addition, they replace characters with similar-appearing letters (e.g., o with 0) and in context-aware language dimensional space, words with the topmost closest neighbors are used.
Text-Fooler[4]	The attack approach seeks exchange key words of an input sentence with their 50 nearest embedding neighbours. BERT optimisation.
PWWS [13]	The attack seeks to exchange key words in an input sequence with best suitable synonyms based on the saliency score of the term under a set of linguistic constraints.
PSO [14]	Attack at the word level using a sememe-based word replacement technique & particle-swarm-optimization.
Pruthi [11]	This attack method relies on character shifting, deletion, and insertion in the crucial words of an input sequence to preserve the semantic similarity of the sentence employed in this method.
Kuleshov[15]	substituting the important words in an input sentence from counter-fitted word embedding space under a set of semantic similarity and grammatical checks.
IGA [8]	Implemented as a way of defence against hostile attacks. Utilizes a mismatched word embedding swap.
DWB[5]	Tiny text perturbations are generated in a black-box environment. It employs several character swaps (swapping, substituting, removing, and inserting) with replace-1 scoring.
A2T[9]	This attack method employs gradient-based synonym word interchange in white-box hostile scenarios. Combining sentence encoding cosine similarity with grammatical checks, it maintains semantic similarity.
BAE [3]	Uses a BERT disguised language model transformation. It leverages the language model for token exchange so that it fits the context optimally.
Check-List[16]	Motivated by the fundamentals of behavioural testing. Modifies names, numerals, and localities, as well as use contractions and extensions.

III. Proposed Approach

We divided the investigation into 2 segments to assess the limitations of models designed to classify the sentiment of business reviews. Utilizing the "Yelp polarity" sentiment prediction dataset, advanced deep-learning classifiers were developed, and adversarial techniques were then used to change the pre-trained models' output. By perturbing the input, the objective of the attack algorithms is to deceive the model into making inaccurate predictions. To determine the efficacy of the attack models, we select 100 examples from the test set that are accurately classified, so that the accuracy of the classifiers does not influence the evaluation. These source texts are then fed into attack methodologies to develop adversarial samples. The adversarial samples are then sent to the classifier to generate the final prediction. The success rate of the assault algorithm is the proportion of incorrect predictions made by the classifier. A greater success rate indicates that the attacking algorithm may generate more formidable adversaries capable of causing the classifier to perform improperly. **Figure 5** depicts the methodology for conducting an adversarial approach on sentiment classification models. We evaluate 100 test samples and their percentage of altered words to calculate the attack success rate ASR (proportion of successfully attack instances to the sum of both successful and unsuccessful instances) for each attack method for all 3 models. The prospective outcomes of the conducted approach outcomes are depicted in **Table 3** for adversarial attack output for word-CNN, **Table 4** for word-LSTM and **Table 5** for BERT model. In this situation, a successful attack implies that the adversarial input can erroneously predict with high confidence. In the case of a failed attack, the adversarial sample is incapable of misclassifying the real prediction. The *Related work* section of the paper describes the different adversarial attack methodologies utilized against the victim models. Our final goal is to discover which model is more sensitive to adversarial manipulations and which is more durable, thus we calculate the average ASR for each model.

IV. Experimental Settings

This part outlines the description of the dataset used and victim models utilized for the investigation, along with the appropriate parameters for our experiment analysis. Then, these trained classifiers were assaulted by utilizing several cutting-edge adversarial attack algorithms.

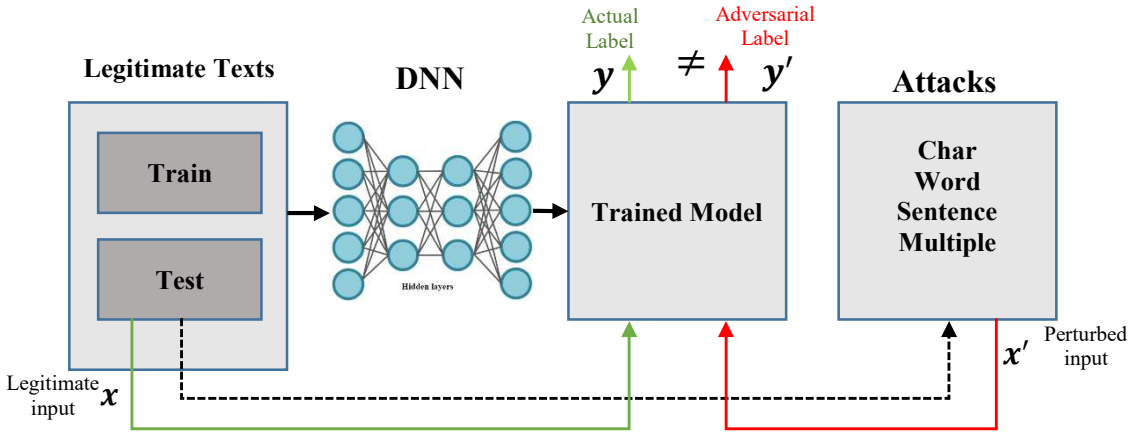

Figure 5 Framework for proposed methodology for conducting Adversarial Attack on Sentiment Classifiers

Authorized licensed use limited to: DELHI TECHNICAL UNIV. Downloaded on July 03,2023 at 04:45:26 UTC from IEEE Xplore. Restrictions apply.

A. Dataset Description

The "Yelp polarity" dataset was utilized for this work. This is a binary sentiment analysis dataset. The dataset is created by assuming that stars 1 & 2 are negative and stars 3 & 4 are assigned positive. 280,000 training samples and 19,000 testing samples are drawn at random for each polarity. In total, there are 560,000 training samples and 38,000 test samples. Class 1 denotes negative polarity, while Class 2 denotes positive polarity. **Table 2** displays the classifiers trained on this dataset, along with their details.

B. Victim Models

The specifications and accuracy scores of the models trained on Yelp polarity binary sentiment classification dataset are shown in **Table 2** beneath.

Table 2 Description of different sentiment classifiers

Model	Parameterization	Acc. Scores
Word-CNN	For the Word-CNN model, we utilised three window sizes: 3, 4, and 5, with 100 filters for each window size and a dropout of 0.3. Use a 200-dimensional GLoVE embeddings basis.	**91.30%**
Word-LSTM	We employed a 1-layer bidirectional LSTM with 150 hidden neurons and a dropout of 0.3 for the Word-LSTM. Glove word embeddings trained on 6B tokens from Giga-words & Wikipedia were utilized.	**92.20%**
BERT	On the Yelp polarity dataset, the model bert-base-uncased was fine-tuned for sentiment classification. During the course of 5 epochs, the model was fine-tuned using a batch size of 16, a learning rate of 5e-05, and a maximum sequence length of 256. Because this was a classification assignment, the model was trained using a cross-entropy loss function. After four iterations, the model's greatest performance on this problem, as measured by the eval set confidence score, was *96.99%*.	**96.99%**

C. Attacking Victim Models

Table 3 Attack outcomes for model Word-CNN

Attack Method	Success (S)%	Failed (F)%	Skipped %	ASR= $(\frac{S}{S+F})\%$	Average Perturbed Word%
A2T [9]	43	46	11	48.31	06.25
BAE [3]	68	21	11	76.40	04.28
Checklist [16]	1	88	11	01.12	42.75
DWB [5]	87	2	11	97.75	07.52
IGA [8]	68	21	11	76.40	14.60
Kuleshov [15]	84	5	11	94.44	11.42
PSO [14]	70	19	11	78.65	16.08
Pwws [13]	87	2	11	97.75	04.37
Pruthi [11]	12	77	11	13.48	03.44
Textbugger [12]	83	6	11	93.26	14.18
TextFooler [4]	88	1	11	98.87	05.04

Table 4 Attack outcome for Word-LSTM

Attack Method	Success (S)%	Failed (F)%	Skipped %	ASR= $(\frac{S}{S+F})\%$	Average Perturbed Word%
A2T [9]	59	31	10	65.56	06.16
BAE [3]	79	11	10	87.78	04.39
Checklist [16]	3	87	10	03.33	46.98
DWB [5]	88	2	10	97.78	07.34
IGA [8]	69	21	10	76.66	15.90
Kuleshov [15]	85	5	10	94.44	10.02
PSO [14]	71	19	10	78.88	18.06
Pwws [13]	68	22	10	75.55	16.30
Pruthi [11]	10	80	10	11.11	02.58
Textbugger [12]	86	4	10	95.56	14.66
TextFooler [4]	89	1	10	98.88	04.85

Table 5 Attack outcome for BERT

Attack Method	Success (S)%	Failed (F)%	Skipped %	ASR= $(\frac{S}{S+F})\%$	Average Perturbed Word%
A2T [9]	39	60	1	39.39	06.08
BAE [3]	64	34	1	64.64	05.43
Checklist [16]	02	97	1	02.02	45.66
DWB [5]	65	34	1	65.00	12.54
IGA [8]	71	28	1	71.71	14.44
Kuleshov [15]	89	10	1	89.89	11.22
PSO [14]	72	27	1	72.72	17.70
Pwws [13]	92	7	1	92.92	07.63
Pruthi [11]	13	86	1	13.13	09.64
Textbugger [12]	77	22	1	77.77	25.39
TextFooler [4]	91	8	1	91.91	10.32

V. Results & Discussion

The accuracy of the BERT framework is evidently superior to that of the word-CNN and word-LSTM models, as shown in **Table 2**. BERT is regarded for being the most efficacious transformer model; it demonstrates that transformer models are more accurate and efficient than former baselines. Afterwards, on each targeted model, the attack success rate of each assault is examined to determine which model is the most and least vulnerable. Using the Equation **(1)** below, the mean ASR on each of the model is calculated.

$$.\boldsymbol{S_r} = \frac{\sum_{i=1}^{a} \frac{S_i}{S_i + F_i}}{a} \quad (1)$$

$$\boldsymbol{S_r} = Attack\ Success\ rate; \boldsymbol{a} = number\ of\ attack\ methods; \boldsymbol{S_i} = successful\ attack; \boldsymbol{F_i} = Failed\ attack$$

(As the skipped statements are based on model training rather than Attacks, they were removed from the evaluation. Examining the skipped values reveals the erroneous inputs the model initially predicted throughout its training)

Table 6 ASR results on the 3 Sentiment Classifiers

Model	Success Rate%
BERT	61.90
Word-LSTM	71.36
Word-CNN	70.54
Total Average	67.93

The results of an in-depth analysis of the data are presented in **Table 6**, which demonstrates that not only does the BERT model have the maximum confidence score in contrast to the other models, but it is also the model that is the least susceptible to being attacked by an adversary. Of the three models, the word-LSTM framework is the one that is most vulnerable to the effects of adversarial perturbations. We found that the overall success percentage of the attacks was

Authorized licensed use limited to: DELHI TECHNICAL UNIV. Downloaded on July 03,2023 at 04:45:26 UTC from IEEE Xplore. Restrictions apply.

67.93% across all three types of sentiment classifiers. The Because the model BERT has the highest confidence score of ***96.99%*** and the lowest ASR of ***61.90%*** among Word-LSTM and Word-CNN, the BERT model is recognized as being the most powerful transformer model. This is due to the fact that it has the lowest ASR. With an accuracy score of ***92.20%*** for the Word-LSTM model and ***91.30%*** for the Word-CNN model, respectively, and ASR values of ***71.36%*** for the Word-LSTM model and ***70.54%*** for the Word-CNN model. It is abundantly evident that the model Word-LSTM is extremely sensitive to variations in the text input. According to the results of our comprehensive evaluation, the BERT model is more reliable than the other two models, hence it ought to be used whenever there is a possibility of adversarial manipulations. Also, the model was given the maximum possible accuracy score when evaluated using the Yelp polarity dataset. A plausible explanation for why the BERT model is performing better in terms of robustness and efficiency is that the "bert-base-uncased" model has 12 Layers, 110M parameters, 768 Equal and Hidden Embedding Layers, and 768 Hidden Layers. Here, we have used the "bert-base-uncased" version, which was optimised for the sentiment categorization task on the Yelp polarity dataset. Because of its size, its training requires a significant amount of computational power. Because it is a heavy model, however, it is least intuitive to malicious manipulations than Word-LSTM and Word-CNN models are. According to the findings of this research, the BERT model should be selected by future researchers and by those who use their sentiment categorization assignments for a variety of applications. This is because the BERT model is less vulnerable to hostile perturbations and produces higher confidence scores.

Table 7 Mean success rate of a specific attack method across all classifiers

Attack Method	Success %	Perturbation Level	Average Perturbed Word%
TextFooler [4]	96.55	word	06.73
Kuleshov [15]	92.92	word	10.88
Textbugger [12]	88.86	word & character	18.07
Pwws [13]	88.74	word	09.43
DWB [5]	86.84	character	09.13
PSO [14]	76.75	word	17.28
BAE [3]	76.27	word & character	04.70
IGA [8]	74.92	word	14.98
A2T [9]	51.08	word	06.16
Pruthi [11]	12.57	character	12.57
Checklist [16]	02.15	word	45.10

TextFooler[4] and Kuleshov et al.[15], both of which are word-perturbation strategies, come in at number one and number two, respectively, in **Table 7**'s assessment of the attacks to which models are most vulnerable. This demonstrates quite clearly that word-level perturbations are the ones that are most successful in tricking the systems. Word-level attacks have a greater propensity to have an effect on models compared to char-level or hybrid attacks (word & character mixed).

VI. Conclusion

The intent of this research was to offer a possible response to the query, "How susceptible is text-based sentiment categorization to adversarial threats?" This was evaluated by assessing if most of adversarial attack algorithms incorrectly identify the correct estimate of review sentiment. The findings show that text classification of sentiment prediction from business assessments can be evaded by easily altering the terms and letters used by the models of deep-learning and at the same time maintaining human observers' semantic similarity. Overall, it has been demonstrated that adversarial alterations can be used to obscure autonomous sentiment classification methods. For the sake of society as a whole, adversarial robust generalizations must therefore replace conventional generalizations. This paper encourages readers to seek out classifiers which are more resistant to adversarial manipulations in addition to those with higher confidence scores.

VII. Refrences

[1] I. J. Goodfellow, J. Shlens, and C. Szegedy, "Explaining and harnessing adversarial examples," in *3rd International Conference on Learning Representations, ICLR 2015 - Conference Track Proceedings*, 2015, pp. 6562–6572.

[2] A. Bajaj and D. K. Vishwakarma, "Exposing the Vulnerabilities of Deep Learning Models in News Classification," in *2023 4th International Conference on Innovative Trends in Information Technology (ICITIIT)*, IEEE, Feb. 2023, pp. 1–5. doi: 10.1109/ICITIIT57246.2023.10068577.

[3] S. Garg and G. Ramakrishnan, "BAE: BERT-based adversarial examples for text classification," in *EMNLP 2020 - 2020 Conference on Empirical Methods in Natural Language Processing, Proceedings of the Conference*, 2020. doi: 10.18653/v1/2020.emnlp-main.498.

[4] D. Jin, Z. Jin, J. T. Zhou, and P. Szolovits, "Is BERT Really Robust? A Strong Baseline for Natural Language Attack on Text Classification and Entailment," in *Proceedings of the AAAI Conference on Artificial Intelligence*, Jul. 2019, pp. 8018–8025. [Online]. Available: http://arxiv.org/abs/1907.11932

[5] J. Gao, J. Lanchantin, M. Lou Soffa, and Y. Qi, "Black-box generation of adversarial text sequences to evade deep learning classifiers," in *Proceedings - 2018 IEEE Symposium on Security and Privacy Workshops, SPW 2018*, 2018, pp. 1–21. doi: 10.1109/SPW.2018.00016.

[6] X. Han, Y. Zhang, W. Wang, and B. Wang, "Text Adversarial Attacks and Defenses: Issues, Taxonomy, and Perspectives," *Security and Communication Networks*, vol. 2022. Hindawi Limited, 2022. doi: 10.1155/2022/6458488.

[7] A. Pandey and D. K. Vishwakarma, "Attention-based Model for Multi-modal sentiment recognition using Text-Image Pairs," in *2023 4th International Conference on Innovative Trends in Information Technology (ICITIIT)*, IEEE, Feb. 2023, pp. 1–5. doi: 10.1109/ICITIIT57246.2023.10068626.

[8] X. Wang, H. Jin, Y. Yang, and K. He, "Natural Language Adversarial Defense through Synonym Encoding," in *37th Conference on Uncertainty in Artificial Intelligence, UAI 2021*, 2021.

[9] J. Y. Yoo and Y. Qi, "Towards Improving Adversarial Training of NLP Models," in *Findings of the Association for Computational Linguistics, Findings of ACL: EMNLP 2021*, 2021. doi: 10.18653/v1/2021.findings-emnlp.81.

[10] S. Qiu, Q. Liu, S. Zhou, and W. Huang, "Adversarial attack and defense technologies in natural language processing: A survey," *Neurocomputing*, 2022.

[11] D. Pruthi, B. Dhingra, and Z. C. Lipton, "Combating adversarial misspellings with robust word recognition," in *ACL 2019 - 57th Annual Meeting of the Association for Computational Linguistics, Proceedings of the Conference*, 2020. doi: 10.18653/v1/p19-1561.

[12] J. Li, S. Ji, T. Du, B. Li, and T. Wang, "TextBugger: Generating Adversarial Text Against Real-world Applications," in *26th Annual Network and Distributed System Security Symposium*, 2019, pp. 1–15. doi: 10.14722/ndss.2019.23138.

[13] S. Ren, Y. Deng, K. He, and W. Che, "Generating natural language adversarial examples through probability weighted word saliency," in *ACL 2019 - 57th Annual Meeting of the Association for Computational Linguistics, Proceedings of the Conference*, 2020. doi: 10.18653/v1/p19-1103.

[14] Y. Zang *et al.*, "Word-level Textual Adversarial Attacking as Combinatorial Optimization," in *Proceedings of the 58th Annual Meeting of the Association for Computational Linguistics*, 2020, pp. 6067–6080. doi: 10.18653/v1/2020.acl-main.540.

[15] V. Kuleshov, S. Thakoor, T. Lau, and S. Ermon, "Adversarial Examples for Natural Language Classification Problems," in *ICLR 2018 : International Conference on Learning Representations*, 2018.

[16] M. T. Ribeiro, T. Wu, C. Guestrin, and S. Singh, "Beyond Accuracy: Behavioral Testing of NLP models with CheckList," *ACL 2020 - 58th Annual Meeting of the Association for Computational Linguistics, Proceedings of the Conference (Long Papers)*, pp. 4902–4912, 2020.

Authorized licensed use limited to: DELHI TECHNICAL UNIV. Downloaded on July 03,2023 at 04:45:26 UTC from IEEE Xplore. Restrictions apply.

2023 4th International Conference for Emerging Technology (INCET)
Belgaum, India. May 26-28, 2023

Chaotic Behavior of DC-DC Boost Converter by using Voltage Mode Control

Sandhu Ganesh
Department of Electrical Engineering
Control of Dynamical Systems and Computation Laboratory
Delhi Technological University (DTU)
Delhi-110042, India
ganeshgani07860@gmail.com

Sudarshan K. Valluru
Department of Electrical Engineering
Control of Dynamical Systems and Computation Laboratory
Delhi Technological University (DTU)
Delhi-110042, India
sudarshan_valluru@dce.ac.in

2023 4th International Conference for Emerging Technology (INCET) | 979-8-3503-3575-0/23/$31.00 ©2023 IEEE | DOI: 10.1109/INCET57972.2023.10170213

Abstract- **This paper examines the Boost converter's chaotic behavior. A voltage mode controlled technique is being utilized to analyze the discrete-time mapping to determine the properties of the bifurcation that operate in a closed loop. By varying some parameters while holding others constant, the reference voltage and input voltage are used to examine the bifurcation diagram. It has been noted that the system becomes unstable and splits into two time-periodic systems, four time – periodic systems and then chaos takes over the system. These occurrences have been shown in the bifurcation diagram, therefore the converter's safe operating range can be determined and verified by using the time-domain waveforms and phase plots.**

Keywords – Bifurcation; Boost converter; chaos; non-linearity; Phase Portraits ; Time domain

I. INTRODUCTION

In this paper, this paper discussed about the bifurcation behaviour of a voltage-controlled closed loop Boost converter has been analyzed. Much complicated behaviours such as bifurcation, chaos and changes in the operational zone are seen in switched-mode power converters[1]. Among other issues, these behaviors may result in the converter operating outside the threshold point, EMI issues, unanticipated spikes, sensor failure, converter damages.

The converter may be harmed if the electrical system exhibits chaotic behavior, such as voltage or current spikes. The converter might not be able to withstand the sudden and significant changes in electrical energy, which could lead to internal component failure or possibly a device breakdown.

Studies on the nonlinear circuit's wideband feedback control have been done by [2], [3] and [4]. A nonlinear mapping that resulted from intra-cycle operation [5], [6], and [7] describes the discrete form of the converter. By the iterating mapping the long-term cycle-to-cycle behavior was found many numerical techniques and theoretical frameworks such as the bifurcation diagram, Poincare map and Lyapunov methods [8] and [9] have been published to determine the converter's boundary conditions. The complicated behaviour of the converter is examined in this study using a numerical method called discrete iterative mapping [10], [11] and [12]. By using numerical technique the theoretical analysis has been verified.

There are five sections in this article, section II explains how the mathematical analysis of chaotic behavior for Boost converter by using discrete iterative mapping technique of bifurcation diagram was derived. The feedback control law for the Boost converter is discussed in section III. After that in section IV, the phase pictures and bifurcation behaviour were plotted. Section V concludes with the conclusion.

II. MATHEMATICAL ANALYSIS OF BOOST CONVERTER BY USING DISCRETE ITERATIVE MAPPING

To make things simpler, the parasitic components have been removed. To examine complex behaviour, certain cutting-edge algorithms have been developed in this section.

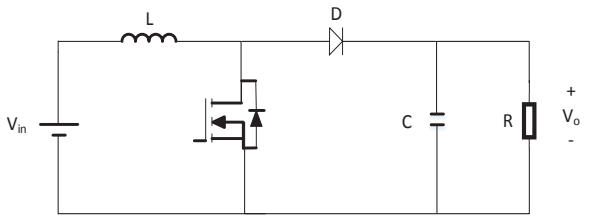

Fig.1 The Circuit diagram of Boost converter

The Boost converter's state space equations can be stated as follows:

$$\dot{x} = A_1 x + B_1 E \quad \text{for} \quad t_n \le t < t_n' \tag{1}$$

$$\dot{x} = A_2 x + B_2 E \quad \text{for} \quad t_n' \le t < t_n'' \tag{2}$$

$$\dot{x} = A_3 x + B_3 E \quad \text{for} \quad t_n'' \le t < t_{n+1} \tag{3}$$

Where,

$$A_1 = \begin{bmatrix} \frac{-1}{RC} & 0 \\ 0 & 0 \end{bmatrix}, \; B_1 = \begin{bmatrix} 0 \\ \frac{1}{L} \end{bmatrix} \tag{4}$$

$$A_2 = \begin{bmatrix} \frac{-1}{RC} & \frac{1}{C} \\ \frac{-1}{L} & 0 \end{bmatrix}, \; B_2 = \begin{bmatrix} 0 \\ \frac{1}{L} \end{bmatrix} \tag{5}$$

$$A_3 = \begin{bmatrix} \frac{-1}{RC} & 0 \\ 0 & 0 \end{bmatrix}, \quad B_3 = \begin{bmatrix} 0 \\ 0 \end{bmatrix}, \quad x = \begin{bmatrix} V_c \\ i_L \end{bmatrix} \tag{6}$$

Integrating the RHS of (2) and replacing the $t = t_n'$ will get the common solution to the switch on interval. This results in the end value of the switch on period after substitution.

Authorized licensed use limited to: DELHI TECHNICAL UNIV. Downloaded on July 20,2023 at 11:17:56 UTC from IEEE Xplore. Restrictions apply.

$$V_C(t_n^{'}) = V_C(t_n)e^{-dT/CR} \tag{7}$$

$$i_L(t_n^{'}) = i_L(t_n) + \frac{EdT}{L} \tag{8}$$

Where, V_c represents the voltage of the capacitor (C) and I_L represents the current of the inductor (L). Apply the Laplace transformation to the switch-off interval equation to obtain the solution.

$$X(s) = \left[sI - A_2\right]^{-1}\left[x(t_n^{'}) + B_2E(s)\right] \tag{9}$$

$$= \frac{\begin{bmatrix} s & \frac{1}{C} \\ \frac{-1}{L} & s + \frac{1}{RC} \end{bmatrix}}{s^2 + \frac{s}{CR} + \frac{1}{LC}} \begin{bmatrix} V_C(t_n^{'}) \\ i_L(t_n^{'}) + \frac{E}{sL} \end{bmatrix} \tag{10}$$

Where X(s) represents the Laplace transform of x(t). Therefore, the s-domain expression for the capacitor's voltage (V_c) and the inductor's current (I_L) in the above Laplace equation can be written as

$$V_c(s) = \frac{E}{s} + \frac{K_I s + K_{II}}{H(s)} \tag{11}$$

$$I_L(s) = \frac{E}{Rs} + \frac{K_{III}s + K_{IV}}{H(s)} \tag{12}$$

Where,

$$K_I = V_C(t_n^{'}) - E \tag{13}$$

$$K_{II} = \frac{1}{C}i_L(t_n^{'}) - 2\sigma E \tag{14}$$

$$K_{III} = i_L(t_n^{'}) - \frac{E}{R} \tag{15}$$

$$K_{IV} = \frac{1}{C}i_L(t_n^{'}) - \frac{1}{L}V_C(t_n^{'}) + \left(\frac{R}{L} - 2\sigma\right)\frac{E}{R} \tag{16}$$

$$2\sigma = \frac{1}{CR} \tag{17}$$

$$H(s) = s^2 + \frac{s}{CR} + \frac{1}{LC} \tag{18}$$

The inverse Laplace transformation can be used to get the time-domain equations for the capacitor voltage $V_c(s)$ and inductor current $I_L(s)$ in the interval of $t_n^{'} < t < t_{n+1}$

$$V_C(t) = E + K_I e^{-\sigma(t-t_n^{'})}\cos\omega(t-t_n^{'}) + \frac{K_{II} - K_I\sigma}{\omega}e^{-\sigma(t-t_n^{'})}\sin\omega(t-t_n^{'}) \tag{19}$$

$$i_L(t) = \frac{E}{R} + K_{III}e^{-\sigma(t-t_n^{'})}\cos\omega(t-t_n^{'}) + \frac{K_{IV} - K_{III}\sigma}{\omega}e^{-\sigma(t-t_n^{'})}\sin\omega(t-t_n^{'}) \tag{20}$$

Where,

$$\omega = \sqrt{\frac{1}{LC} - \sigma^2} \tag{21}$$

Where, K_I, K_{II}, K_{III} and K_{IV} are the functions of $x(t_n^{'})$ which a function is in turn off $x(t_n)$ and d. The difference equation's basic form is represented by the

$$x(t_{n+1}) = f(x(t_n), d) \tag{22}$$

The function f (.) in this case is provided by

$$f(x,d) = \begin{bmatrix} f_{11} & f_{12} \\ f_{21} & f_{22} \end{bmatrix}x + \begin{bmatrix} g_1 \\ g_2 \end{bmatrix}E \tag{23}$$

Where,

$$f_{11} = e^{\frac{-dT}{RC} - \sigma(1-d)T}\left[\cos(1-d)\omega T - \frac{\sigma}{\omega}\sin(1-d)\omega T\right] \tag{24}$$

$$f_{12} = \frac{1}{\omega C}e^{-\sigma(1-d)T}\sin(1-d)\omega T \tag{25}$$

$$f_{21} = -\frac{1}{\omega L}e^{\frac{-dT}{RC} - \sigma(1-d)T}\sin(1-d)\omega T \tag{26}$$

$$f_{22} = e^{-\sigma(1-d)T}\left[\cos(1-d)\omega T + \frac{1}{\omega}\left(\frac{1}{CR} - \sigma\right)\sin(1-d)\omega T\right] \tag{27}$$

$$g_1 = 1 - e^{-\sigma(1-d)T}\left[\cos(1-d)\omega T - \frac{1}{\omega}\left(\frac{dT}{LC} - \sigma\right)\sin(1-d)\omega T\right] \tag{28}$$

$$g_2 = \frac{1}{R}\{1 + e^{-\sigma(1-d)T}\left[\left(\frac{RdT}{L} - 1\right)\cos(1-d)\,\omega T - \frac{1}{\omega}\left[\left(\frac{1}{CR} - \sigma\right)\frac{RdT}{L} + \frac{R}{L} - \sigma\right]\sin(1-d)\omega T\right] \tag{29}$$

$$x(t_{n+1}) = f(x(t_n), d) \tag{30}$$

The boost converter's discrete-time state equation for continuous mode operation is provided by the equations above. To assure that the circuit functions in discontinuous mode, the inductance's value must be appropriately low. It has been suggested that the inductance value L should not be

Authorized licensed use limited to: DELHI TECHNICAL UNIV. Downloaded on July 20,2023 at 11:17:56 UTC from IEEE Xplore. Restrictions apply.

larger than $\frac{1}{2}D(1-D)^2RT$ for a discontinuous conduction mode operation, where T indicates the switching period and D indicates the duty cycle.

There are three basic topologies, and each of them has a state equation with an explicit solution. Using the interval $t_n \le t < t_n^{'}$ as an example, the solution is given by

$$x(t) = \Phi_1(t-t_n)x(t_n) + \int_{t_n}^{t} \Phi_1(t-T)B_1E.dT \tag{31}$$

$$= \Phi_1(t-t_n)\left(x(t_n) + \int_{t_n}^{t} \Phi_1(t_n-T)B_1E.dT \right) \tag{32}$$

A map that iteratively represents $x(t_{n+1})$ in terms of x would be produced by "stacking" successive solutions over a switching period $x(t_n)$,i.e.,

$$\begin{aligned} x(t_{n+1}) &= \Phi_3(t_e)\Phi_2(t_d)\Phi(t_c) \\ &\left(x(t_n) + \int_{t_n}^{t_n^{'}} \Phi_1(t_n-T)B_1E.dT \right) \\ &+\Phi_3(t_e)\Phi_2(t_d)\int_{t_n^{'}}^{t_n^{''}} \Phi_2(t_n^{'}-T)B_2E.dT \\ &+\Phi_3(t_e)\int_{t_n^{''}}^{t_{n+1}} \Phi_2(t_n^{''}-T)B_3E.dT \end{aligned} \tag{33}$$

Where, $t_c = t_n^{'} - t_n, t_e = t_{n+1} - t_n^{''}, t_d = t_n^{''} - t_n^{'}$ and $\Phi_k(\xi)$ is the transition matrix which is provided by the series of equations below:

$$\Phi_k(\xi) = 1 + \sum_{n=1}^{\infty} \frac{1}{n!} A_k^n \xi^n \quad \text{for} \quad \text{k=1,2,3.} \tag{34}$$

After computing and substituting each transition matrix in equation (33), an iterative map is produced:

$$x(t_{n+1}) = f\left(x(t_n), d_n\right) \tag{35}$$

Where, d_n represents the duty cycle for the nth period, which is defined as

$$d_n = \frac{t_c}{T} \tag{36}$$

Typical switching regulator applications have switching periods that are significantly less than the time constant for capacitance-load-resistance. The examination of the transition matrix $\Phi_k(.)$ is significantly streamlined by this condition [6] this yields a finite series representation of $\Phi_k(.)$ that is quite accurate.

$$\Phi_k(\xi) = 1 + A_k^2\xi + \frac{1}{2}A_k^2\xi^2 \quad \text{for} \quad \text{k = 1,2,3} \tag{37}$$

Moreover, the inductance current I_L grows linearly throughout the time period $t_n \le t < t_n^{'}$ at a rate of E/L from zero to a value of $i_{\max}$ and linearly declines throughout the time period $t_n^{'} \le t < t_n^{''}$ from $i_{\max}$ to zero at the rate of $\frac{x-E}{L}$ in order to write

$$\frac{t_d}{t_c} = \frac{E}{x-E} \tag{38}$$

Using equations from (4)-(6), (37) and (38), and aware that the $i_L(t_n) = 0$, $\forall$ n in equation (33) can estimated be classified as

$$x_{n+1} = \alpha x_n + \frac{\beta d_n^2 E^2}{x_n - E} \tag{39}$$

Where,

$$x_n = v_c(t_n) = v_c(nT) \tag{40}$$

$$\alpha = 1 - \frac{T}{RC} + \frac{T^2}{2R^2C^2} \tag{41}$$

and $$\beta = \frac{T^2}{2LC} \tag{42}$$

Here, we're concentrating on the system that is managed by the simple feedback system shown below:

$$\Delta d_n = -k.\Delta x_n \tag{43}$$

Where the closed-loop dynamics can be changed by using the feedback parameter k. The preceding equation suggests the usage of a uniform sampling strategy, where in Δd is determined for each switching period using the value of $\Delta x(t_n)$, which is sampled at the beginning of each switching period.

The closed-loop system's Poincare map may now be obtained by substituting (18) in (14), which results in

$$x_{n+1} = \alpha x_n + \frac{h(d_n)^2 \beta E^2}{x_n - E} \tag{44}$$

Where,

$$d_n = D - k(x_n - X) \tag{45}$$

$$h(d_n) = \begin{Bmatrix} 0 & if & d_n < 0 \\ 1 & if & d_n > 0 \\ d_n & , & otherwise \end{Bmatrix} \tag{46}$$

TABLE I. NOMENCLATURE

Notation	Definition
A	State Matrix
B	System Matrix
I	Identity Matrix
f_s	Switching frequency
T_s	Switching period
V_{in}	Input Voltage
K	Feedback Factor
V_{ref}	Reference Voltage
$\Phi_k(\xi)$	Transition Matrix
ω	Angular Velocity
X(s)	Laplace transform of x(t)
d	Duty cycle
n	Number of variables

Authorized licensed use limited to: DELHI TECHNICAL UNIV. Downloaded on July 20,2023 at 11:17:56 UTC from IEEE Xplore. Restrictions apply.

III. FEEDBACK CONTROL LOOP

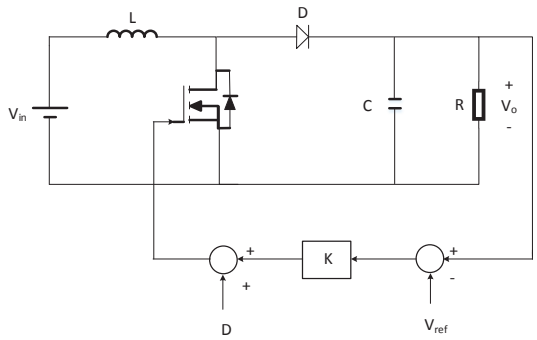

Fig.2 Circuit diagram for Closed-loop Boost Converter

There are several ways to modulate the output voltage of Boost converter. In this study, a voltage mode control system was used to adjust the output voltage. The feedback loop serves as the main component of this control, monitoring changes in output voltage (V_c) and adjusting the duty cycle as necessary. In a compensation network, a control signal (V_{con}) is produced particularly from the variance between the reference voltage (V_{ref}) and the output voltage (V_c).

$$V_{con}(t) = g(V_{ref} - V_c) \tag{47}$$

where the compensation network's determination of g(.) is the function. This control signal efficiently indicates how to modify the duty cycle (D) is to provide the output voltage with the optimal transient dynamics.

IV. BIFURCATION DIAGRAM

To determine the initial and final conditions under which the converter may operate securely, the bifurcation diagram is plotted. Bifurcation can be examined using this graphic depiction as well. In this case, computer simulations are a great tool for figuring out the chaotic behaviour. In the simulation from the computer, one parameter is altered while the other parameters are held constant.

TABLE II. SIMULATION PARAMETERS

Switching frequency (f_s)	3000Hz
Inductance (L)	208 μ H
Input Voltage (E)	16V
Capacitance (C)	222 μ F
Output Voltage (X)	25V
Load Resistance (R)	12.5 Ω

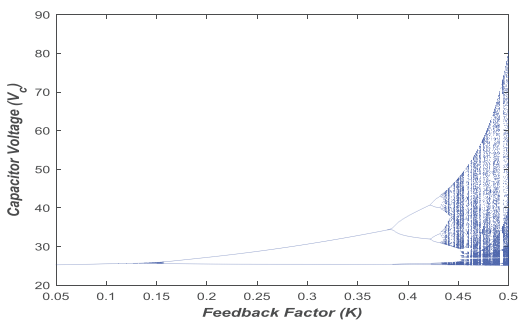

Fig.3. Diagram for bifurcation with different feedback gain

In the above Fig.3, a stable period up to about 0.15 can be noticed, and the diagram of bifurcation with reference to feedback gain is visible. Double bifurcation, often known as 2T, happens after k= 0.15. Up until k=0.37, this occurs. Moreover, the output voltage splits into period 4 (or 4T) after k = 0.38, continuing until almost k = 0.42. At some point after k = 0.43, this finally moves into a chaotic area.

Time domain waveforms :

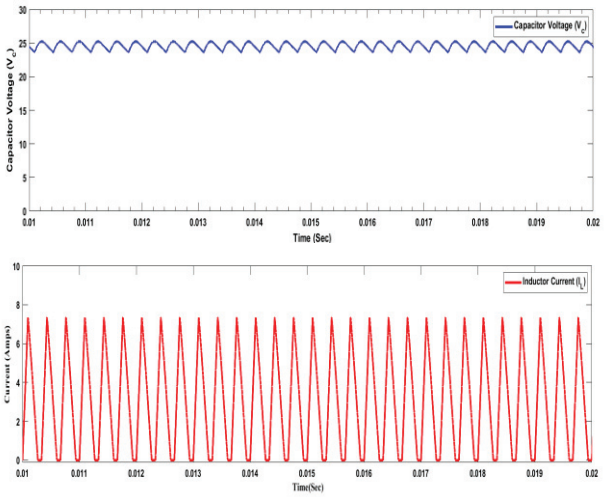

Fig.4.Fundamental waveforms of V_c and I_L at 5ms interval from the simulation at k=0.13

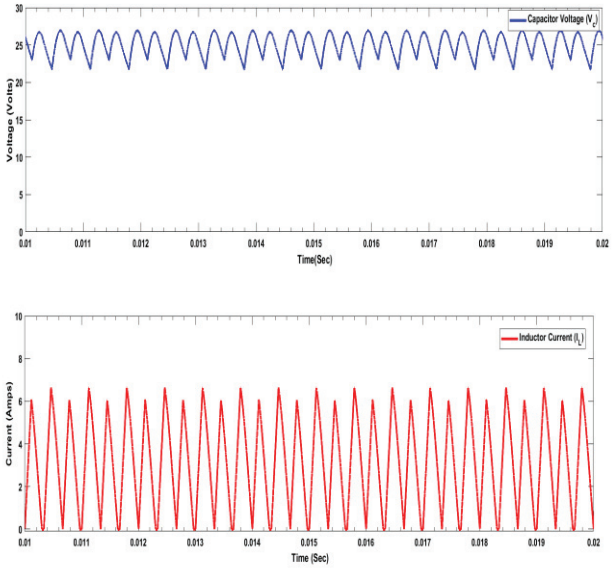

Fig.5. Period-II waveforms of V_c and I_L at 5ms interval from the simulation at k=0.2

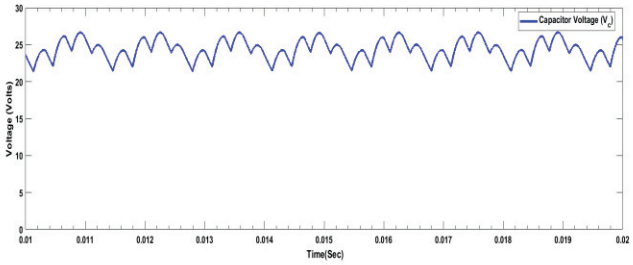

Authorized licensed use limited to: DELHI TECHNICAL UNIV. Downloaded on July 20,2023 at 11:17:56 UTC from IEEE Xplore. Restrictions apply.

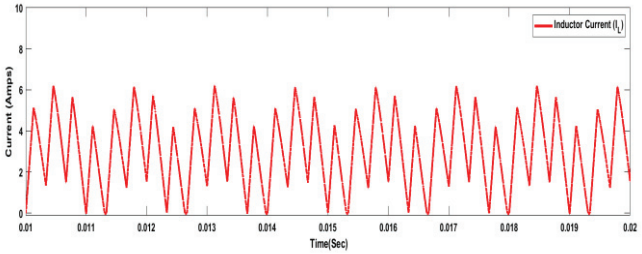

Fig.6 period-IV waveforms of V_c and I_L at 5ms interval from the simulation at k=0.4

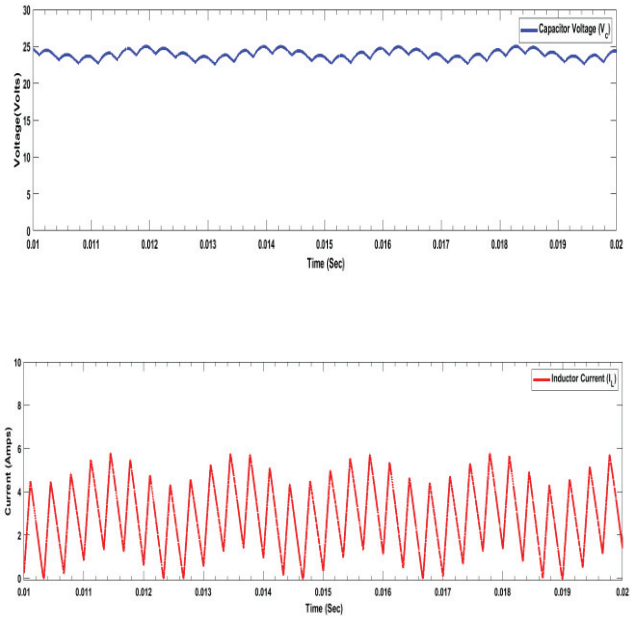

Fig.7. Waveforms of V_c and I_L at 5 ms intervals chaos sampled at k=0.45

Time domain waveforms can be used to confirm the bifurcation diagram. Here, the voltage waveform of the capacitor and the current waveform of the inductor have been recorded. The system shown in fig.4 operates in stable mode when the voltage and current waveforms of capacitor and the inductor have been replicate or mirror each other for every one time period. Moreover, fig.5 shows that the system contains period-doubling bifurcations of the voltage waveform of the capacitor and the current waveform of the inductor duplicates themselves for every two time periods. Figure 6 show that the voltage and current waveforms of capacitor and the inductor time domain waveforms, which are similar in that they repeat for every four cycles. Hence, the system has four bifurcations in total. And finally in Fig. 7, the system has no repeating cycles, indicating that chaos has taken over. Phase portrait diagrams of the Capacitor's voltage (Vc) Vs Inductor's current (IL) at various system stages (period-I, period-II (2T), period-IV (4T) and chaotic) are shown in Figures 8, 9, 10, and 11

Diagrams of Phase portraits:

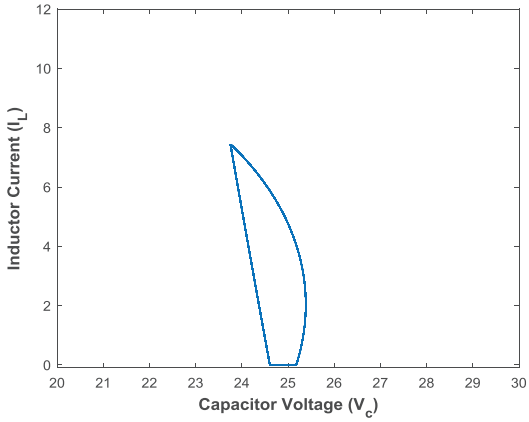

Fig .8 Diagram of Phase portrait for V_c and I_L at stable 1 period (1T)

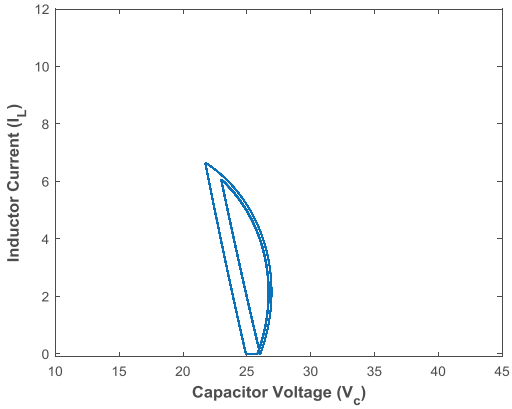

Fig .9 Diagram of Phase portrait for V_c and I_L at period 2 (2T)

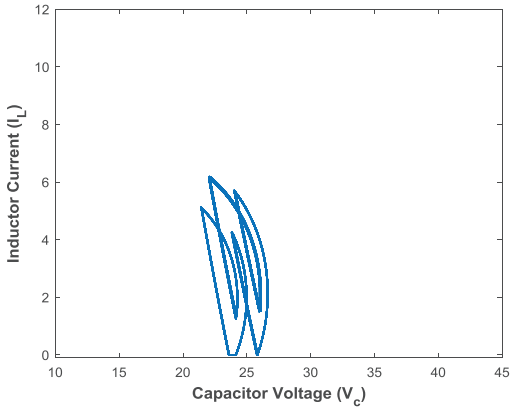

Fig .10 Diagram of Phase portrait for V_c and I_L at period 4 (4T)

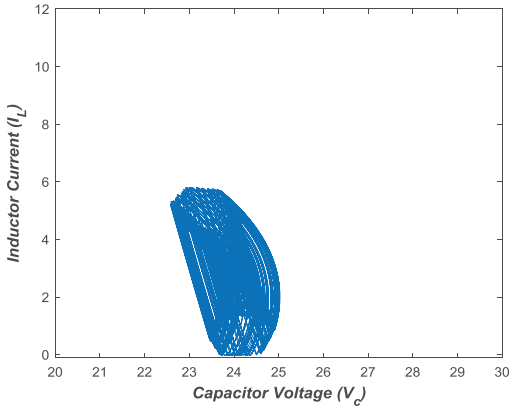

Fig .11 Diagram of Phase portrait for V_c and I_L at chaos

Authorized licensed use limited to: DELHI TECHNICAL UNIV. Downloaded on July 20,2023 at 11:17:56 UTC from IEEE Xplore. Restrictions apply.

V. CONCLUSION

The study explores the subtleties of switching power Boost converter behaviour. This complicated behaviour bifurcation diagram's explanation is based on research on the related to time-domain waveforms and phase portraits. The voltage and current for the following state were calculated with the help of discrete iterative mapping. An analysis using the numerical method was carried out to attain the desired outcomes. The phenomena of bifurcation have been studied by varying a number of factors, including input voltage and the feedback gain. Moreover, chaotic, two and the four time periods have all been graphically reviewed. The phase portraits and time-domain waveforms were used to validate the bifurcation diagram. The results demonstrate the maximal functional point and the boundary conditions.

REFERENCES

[1] C. K. Tse and M. Di Bernardo, “Complex behavior in switching power converters,” *Proceedings of the IEEE*, vol. 90, no. 5, pp. 768–781, 2002.

[2] A. El Aroudi, G. Olivar, L. Benadero, and E. Toribio, “Hopf bifurcation and chaos from torus breakdown in PWM voltage-controlled DC-DC boost converter,” IEEE Tran. on Circuits and Systems I, vol. 1 I, pp. 1374-3382,1999.

[3] D. C. Hamill, J. H. B. Deane, and D. J. Jefferies, “Modelling of the chaotic dc-dc converter by iterated mappings,” IEEE Tran. on Power Electronics, vol. 7, no.9, pp. 25-33, 1992.

[4] L. G. De Vicufia, F. Guinjoan, J. Majo a L. Martinez, “Discontinuous conduction mode in the SEPlC converter,” IEEE Electroteclinical Conference, MELECON’XY, pp. 38-42, 1989.

[5] M. J. Johnson, “Analysis of current-programmed SEPIC DC-DC converters in discontinuous conduction operating region,” IEEE Applied Power Electronics Conference and Exposition, APEC’93, pp. 207-213, 1993.

[6] C-C. Fang and E. H. Abed, “Output regulation of dc-dc switching converters using discrete-time integral control,” Proc. Of the American Control Conference, vol. 2, pp. 1052-1056, 1999, San Diego, Califomia.

[7] H. Wu, V. Pickert, D. Giaouris and B. Ji, "Nonlinear Analysis and Control of Interleaved Boost Converter Using Real-Time Cycle to Cycle Variable Slope Compensation," in IEEE Transactions on Power Electronics, vol. 32, no. 9, pp. 7256-7270, Sept. 2017, doi: 10.1109/TPEL.2016.2626119.

[8] A. I. Andriyanov, "Boost converter nonlinear dynamics control based on multi-parameter method of linearization of the Poincaré map," 2016 Dynamics of Systems, Mechanisms and Machines (Dynamics), Omsk, Russia, 2016, pp. 1-5, doi: 10.1109/Dynamics.2016.7818965.

[9] S. Banerjee and K. Chakrabarty, "Nonlinear modeling and bifurcations in the boost converter," in IEEE Transactions on Power Electronics, vol. 13, no. 2, pp. 252-260, March 1998, doi: 10.1109/63.662832

[10] Y. Wang, L. Xu, L. Chen and J. Zhou, "Discrete Iterative Map Model-Based Stability Analysis of Capacitor Current Ripple-Controlled SIDO CCM Buck Converter," in IEEE Journal of Emerging and Selected Topics in Power Electronics, vol. 8, no. 4, pp. 3272-3280, Dec. 2020, doi: 10.1109/JESTPE.2020.2972651.

[11] A. Kumar and S. K. Valluru, "Bifurcation Analysis of Current-mode controlled CUK converter," 2022 2nd Asian Conference on Innovation in Technology (ASIANCON), Ravet, India, 2022, pp. 1-5, doi: 10.1109/ASIANCON55314.2022.9909370

[12] A. Kumar and S. K. Valluru, "Bifurcation Analysis of Novel Self Operating Flyback Converter," 2022 2nd Asian Conference on Innovation in Technology (ASIANCON), Ravet, India, 2022, pp. 1-5, doi: 10.1109/ASIANCON55314.2022.9909176.

Authorized licensed use limited to: DELHI TECHNICAL UNIV. Downloaded on July 20,2023 at 11:17:56 UTC from IEEE Xplore. Restrictions apply.

Research Square

Preprints are preliminary reports that have not undergone peer review.
They should not be considered conclusive, used to inform clinical practice,
or referenced by the media as validated information.

Characteristics performance and analysis of positional variation in charge generation layer to enhance performance of OLED.

Sugandha Yadav
DTU: Delhi Technological University
Poornima Mittal (poornimamittal@dtu.ac.in)
Delhi Technological University https://orcid.org/0000-0002-9479-8628
Shubham Negi
Chandigarh University

Research Article

Keywords: Organic Light Emitting Diode (OLED), Charge Generation Layer (CGL), Luminescence, Recombination Rate of Charge Carriers

Posted Date: June 29th, 2023

DOI: https://doi.org/10.21203/rs.3.rs-3017102/v1

License: This work is licensed under a Creative Commons Attribution 4.0 International License.
Read Full License

Abstract

In this paper, a highly efficient charge generation layer (CGL) based blue organic light emitting diode (OLED) is proposed. The proposed device contains a CGL which comprises of two materials 1,1-bis[(di-4-tolyamino)phenyl)]cyclohexane (TAPC) and 1,4,5,8,9,11-hexaazatriphenylene-hexacarbonitrile (HAT-CN) which act as hole and electron injectors, correspondingly. The CGL in the proposed device is placed outside of the emissive layer which provides better luminescence and current as compared with four other CGL based devices D_2, D_3, D_4 and D_5 where CGL is utilized below cathode, above anode, near both electrodes (cathode and anode) and inside the emissive layer, respectively. The proposed device exhibits noteworthy results as peak values of current and luminescence are achieved as 0.44 A and 3636.3 cd/m^2, correspondingly. The obtained luminescence is about 16.8, 2.3, 1.7, 3, 1.6 times improved on comparing with D_1, D_2, D_3, D_4 and D_5. Furthermore, thickness optimization of the proposed device is also outlined. The optimized device showed the maximum luminescence of 4670 cd/m^2.

1. Introduction

Over the past few years, the researchers have shown their enormous interest in developing full colour high resolution displays which also attain better lifetime [1–3]. These organic material-based displays contain very attractive properties such as ultra-thin thickness, flexibility, easy fabrication, light weight, wide viewing angle, fast response etc. [4–7]. With these salient features, OLEDs have established their separate place in the display market which is gaining lot of attention of consumers nowadays. Despite having many attractive features, there is still need of improvement in the performance of these devices in terms of luminescence, current density, lifetime etc [8]. Although various researchers have incorporated many additional layers in OLEDs such as hole/electron injection layer, hole/electron transport layer, blocking layer etc. These layers have contributed a lot in order to enhance the performance parameters of organic LEDs [9, 10]. But, nowadays, some novel advanced layers which are mixed interlayer [11], charge generation layer [12], and spacer layers [13] have come into the picture to further refine OLED's performance. These layers are being widely utilized by the researchers in recent time.

Maurya et al. [14] discussed an OLED device on which the positional analysis of mixed interlayer is performed. In this research, it is noticed that luminescence and current density are improved by changing the position of the layer towards the cathode. The peak luminescence and maximum current density are obtained as 17139 cd/m2 and 84.6 mA/cm2, correspondingly. Moreover, Liu et al. [15] inserted a mixed interlayer of poly(9-vinylcarbazole) (PVK) and poly[(9,9-dioctylfluorenyl-2,7-diyl)-co-(4,4'-(N-(4-s-butylphenyl)diphenylamine)) (TFB) between emissive layer and PEDOT:PSS layer. The proposed device exhibited maximum power efficieny of 47.2 lm/W and external quantum efficiency (EQE) of 18.86%. On the other hand, Ying et al. [16.] utilized a spacer layer with the materials 1-bis[4-[N,N-di(4-tolyl)amino]phenyl]-cyclohexane/2,6-bis[3-(9H-carbazol-9-yl)phenyl]pyridine/2,4,6-tris[3-(diphenylphosphinyl)phenyl]-1,3,5-triazine (TAPC-26DCzPPy-PO-T2T). The power efficiency and EQE are achieved as 76 lm/W and 24%, respectively.

In this paper, charge generation layer (CGL) is utilized for the improvement of luminescence and current density of OLED device. CGLs play very important role to enhance overall device performance. In emissive layer after the recombination, only 20% light can be extracted out of the device, rest is lost due to surface Plasmon and optical losses. With the help of CGL, this lost part of light can be employed which automatically improves the device performance in terms of efficiency and EL emission [17]. These layers are the combination of two different layers (n type & p type) and act almost like electrodes. The charge carriers are produced depending upon the external applied voltage and injected to the emissive layer where the recombination takes place and light is produced [18].

Various researchers have studied CGL to refine the performance of organic LEDs [19–23]. In 2016, Kim *et al.* [24] discussed the emission properties of blue fluorescent multi-tandem organic LEDs using CGL of materials Al/MoO_x. The maximum quantum efficiency and current efficiency are obtained as 25.6% and 46.6 cd/A, correspondingly. Addition to this, Yuan *et al.* [25] fabricated three OLEDs (red, green and blue) based on heterojunction CGL of HAT-CN/TAPC and improved the EL efficiencies of the fabricated devices which contain the balanced injection of electrons and holes. Moreover, Jetly *et al.* [17] utilized C70/Pentacene as CGL and designed a high-performance OLED. The reported CGL shows organic photovoltaic behaviour and the device parameters such as luminescence and current density are achieved as 15630 cd/cm^2 and 15.63 cd/A, respectively. Herein, a highly efficient organic LED is proposed using a charge generation layer which is a combination of two materials which are 1,1-bis[(di-4-tolyamino)phenyl)]cyclohexane (TAPC) and 1,4,5,8,9,11-hexaazatriphenylene-hexacarbonitrile (HAT-CN). The CGL is placed outside the emissive in the proposed device. Incorporation of CGL in OLED provided better charge injection which results in higher current density and better luminous property. Additionally, this paper also compares five different CGL-based devices in terms of luminescence and current density.

This complete paper is distributed in total 5 sections. Section 1 provides the introduction which discusses various OLED devices and the important role of CGL in OLEDs. Section 2 is about the performance analysis of blue organic LED. Afterwards, Section 3 compares four various CGL based OLED devices and outlines their performance parameters curves. Moreover, Section 4 represents the proposed CGL based blue OLED. In this section, thickness reduction of charge generation layer is incorporated to achieve the optimized results of the proposed device. Eventually, Section 5 highlights the conclusion of the paper.

2. Characteristic Analysis and Parameters Extraction of Blue OLED

In order to design the proposed device using CGL, firstly a reference device [26] which is a multi-layered blue organic LED (D_1) without having CGL is validated. In this device, seven layers of different categories such as cathode, anode, electron transport layer (ETL), hole transport layer (HTL) and electron emissive layer (EML) are utilized as shown in Fig. 1. The length and width of the device structure are 400 and 1000 μm, respectively. The materials along with their thickness for these layers are illustrated in Table 1 below. The fabrication process starts with the deposition of an organic HTL of 90nm i.e. PEDOT:PSS (poly(3,4-ethylenedioxy thiophene):polystyrene sulfonate) using spin-coating technique on the top of anode layer. Afterwards, the thermal evaporation method is considered for the incorporation of the remaining layers

above PEDOT:PSS. A hole transport layer of the material NPB (N,N'-Bis(naphthalene-1-yl)-N,N'-bis(phenyl) benzidine) having thickness of 60nm is placed on the top of PEDOT:PSS. Thereafter, an emissive layer of DPVBi (4,4'-Bis(2,2-diphenylvinyl)-1,1'-biphenyl) with 5% of BCzVBi (4,4'-Bis(9-ethyl-3-carbazovinylen)1,1'-biphenyl) and with the thickness of 20nm is deposited. This layer is utilized for the generation of blue emission. Now, the deposition of 30nm BPhen (4,4'-Bis(9-ethyl-3-carbazovinylene)-1,1'-biphenyl) takes place which acts as combined layer of HBL (hole blocking layer) and ETL. Eventually, a cathode layer is placed which contains 1nm Lithium Fluoride and 150nm Aluminium.

Table 1
Materials and their thickness for each layer for D_1 device

Layer	Material	Thickness (nm)
Anode	ITO	20
HTL1	PEDOT:PSS	90
HTL2	NPB	60
EML	DPVBi & BCzVBi	20
ETL	BPhen	30
Cathode	LiF	1
Cathode1	Al	150

In OLED, the generation of light is achieved with two important processes: 1) formation of charge carriers, and 2) recombination of charge carriers. For this, a model i.e. Langevin's recombination rate is applied in Silvaco Atlas 2-D device simulator for the validation of the reference device. The expression for the model is as follows:

$R_L(n, p) = r_l(x, y, t)\,(np\text{-}n_i^2)$

Here, r_l, n, p and n_i denote the recombination rate coefficient, electron concentration, hole concentration, and intrinsic concentration, respectively. Addition to this, to simulate the carrier's transportation in a device structure Poole-Frenkel mobility model is utilized which was given by Frenkel in 1938. This model provides the results under specified boundary conditions. This model is given as:

$$\mu(E) = \mu_0 e^{\left[-\frac{\Delta}{kT}+\left(\frac{\beta}{kT}-\gamma\right)\sqrt{|E|}\right.}$$

where μ, μ_0 and E are field dependent mobility, zero field mobility, and electric field, correspondingly. Besides this, Δ, k, T, β and γ represent activation energy at zero electric field, Boltzmann constant, effective temperature for charge carriers, hole Pool–Frenkel factor and fitting parameter, respectively. The device structure which is plotted using Silvaco is depicted in Fig. 2.

The curves above are showing the performance parameters such as current, current density and luminescence of blue OLED (D_1). The comparasion of experiment and reference data of D_1 is drawn in Fig. 3 (a). From the figure, it is clear that there is less than 5% deviation in current parameter as reference and experement devices contain 0.025 and 0.026 A, respectively. Also, Fig. 3 (b) is highlighting the combined curve for luminsecence and current density. The maximum luminescence and current density are achived as 215 cd/m^2 and 6.5 mA/cm^2, correspondingly.

3. Performance Analysis with CGL at Different Position for OLED

As discussed in Section 1, CGL is very useful for improving the concentration of charge carriers which can further enhance the luminous properties and current of OLED device. In this section, positional analysis using CGL is performed on D_1 device keeping same materials and thickness. Here, four blue OLED D_2, D_3, D_4 and D_5 are considered in which a 20nm CGL of TAPC (top layer) and HAT-CN (bottom layer) materials is incorporated on different positions as depicted in Fig. 4 (a), (b), (c) and (d). The combined layer of HAT-CN and TAPC act an electron and hole injectors, respectively.

The LUMO level of HAT-CN is approximately 5.5 ev, which is matching the HOMO level of TAPC i.e. also about 5.5 ev. This results in easy transfer of electrons from HOMO of TAPC to LUMO of HAT-CN which significantly increases the charge carriers in CGL [27]. In devices D_2 and D_3, CGL is utilized below the cathode and above the anode, correspondingly. On the other hand, in device D_4, it is placed near both electrodes like above the anode and below the cathode. Furthermore, in device D_5, CGL is situated inside the emissive layer in a manner as depicted in Fig. (d). The thickness of CGL in D_5 is taken as 40nm instead of 20nm due to their structural changes. All these four devices (D_2- D_5) are compared based on current density and luminescence with reference device D_1.

Table 2
Comparison of Current and Luminescence of various blue OLEDs

Device	Current (A)	Luminescence (cd/m^2)
D_1 (Reference)	0.026	215.9
D_2	0.193	1592.3
D_3	0.256	2112.2
D_4	0.145	1198.4
D_5	0.276	2277.2

Figure 5 (a) & (b) are highlighting current and luminescence parameters of all the devices (D_1- D_5). As shown in Fig. 5, device D_5 is exhibiting the best performance among other devices as in D_5 CGL is placed

inside of emissive layer which improves the recombination of charge carriers. The reason behind this is that in D_5 top layer (of TAPC) of CGL is acting as hole injector and bottom layer (of HAT-CN) is behaving like electron injector. Now, holes in top layer of CGL will be attracted towards cathode and will reach to emissive layer. Similarly, electrons in bottom layer of CGL will get attracted towards anode and reach to emissive layer as CGL in D_5 is surrounded by the emissive layer only. These charge carriers are mixed up with charge carriers which have travelled from cathode and anode side. This automatically enhances the recombination rate of the device. The maximum current and luminescence are obtained as 0.27 A and 2277.2 cd/m^2, correspondingly as depicted in Table 2.

4. Proposed Device

As shown in section 3, among all five devices (D_1- D_5) D_5 is exhibiting remarkable performance. In this section, a high-performance blue OLED is proposed by reversing the position of CGL and emissive layer in device D_5 as illustrated in Fig. 6. Also, the additional modification is that in D_6 position of top and bottom layers are also exchanged. Now, the top layer of CGL is made of HAT-CN and bottom layer is made of TAPC. Because of this, electrons in top layer starts repelling by cathode and move to the emissive layer. In the same manner, holes in bottom layer will be repelled by anode and reach to the emissive layer. So, electron and hole concentrations are increased inside the emissive layer as this layer already contains charge carriers which have generated from cathode and anode. Hence, according to the Langevin's recombination rate, increment in charge carriers will directly improve the recombination rate which significantly enhanced the performance of D_6 in terms of current and luminescence. The total thickness of CGL in D_6 is considered as 40nm due to some structural variations as shown in figure below.

Figure 7 is showing the device structure of D_6 having the thickness and materials. The maximum current and luminescence of proposed device is obtained as 0.44 A and 3636.3 cd/m^2 as highlighted in Fig. 8. The device exhibits excellent luminescence which is about 16.8, 2.3, 1.7, 3 and 1.6 times better as compared with D_1, D_2, D_3, D_4 and D_5, correspondingly.

Thickness Optimization: In this section, the thickness of charge generation layer in proposed device (D_6) is reduced to achieve an optimized device. This process is done in three ways which are: 1) reduction of thickness in both layers of CGL evenly, 2) fix the thickness of HAT-CN layer at 20nm and reduce the thickness of TAPC layer and 3) fix the thickness of TAPC layer at 20nm and reduce the thickness of HAT-CN layer. The thickness reduction is performed by reducing 2nm thickness in every step as shown in Fig. 9, Fig. 10, and Fig. 11. All the three cases are discussed in details below.

(a) Case I: Initially, the total thickness of CGL is considered as 40nm. As shown in Fig. 9 (a), in Case I both layers of CGL are decreased five times by 2nm of thickness each i.e. layer of TAPC by 2nm and layer of HAT-CN by 2nm (total variation of 4nm). Eventually, the total thickness of CGL is reduced upto 24nm from 40nm which provides about 1.3 times better luminescence. In this process, the minimum and maximum

luminescence is achieved as 3640 cd/m^2 and 4670 cd/m^2 at 40nm and 24nm thickness of CGL, correspondingly. This data can be clearly verified from Fig. 9 (b) as it has better clarity.

(b) Case II: In this case, only layer of TAPC is varied from 20nm to 12nm whereas the layer of HAT-CN material is kept fixed at 20nm. Here, the curve for luminescence is drawn at 20nm, 18nm, 16nm, 14nm and 12nm thicknesses of layer of TAPC material as shown in Fig. 10 (a). The maximum luminescence is achieved as 4080 cd/m^2. This small change can be noticed in Fig. 9 (b) which is a zoomed version of Fig. 10 (a).

(c) Case III: This case is just reverse of case II. The thickness of HAT-CN material is varied from 20nm to 12nm in five steps and TAPC is constant at 20nm as depicted in Fig. 11 (a). The peak luminescence is obtained as 4150 cd/m^2. Here, Fig. 11 (b) is a zoomed view of Fig. 11 (a) where small variation can be seen easily.

Table 3
Different values of luminescence at different thicknesses of D_6

Case	Thickness (nm)		Luminescence (cd/m^2)
	TAPC	HAT-CN	
I	20	20	3.64×10^3
	18	18	3.84×10^3
	16	16	4.07×10^3
	14	14	4.34×10^3
	12	12	**Max = 4.67×10^3**
II	18	20	3.72×10^3
	16		3.82×10^3
	14		3.93×10^3
	12		4.08×10^3
III	20	18	3.75×10^3
		16	3.88×10^3
		14	4.01×10^3
		12	4.15×10^3

In all the three cases discussed above, the maximum luminescence is achieved in Case I i.e. 4670 cd/m^2 at 24nm thickness of CGL as highlighted in Table 3. This value is almost 78% improved as compared with the device (D_6) where thickness of CGL is 40nm. Also, in Case II and III, Case III is exhibiting better results. In case I, both the top and bottom layers are varied in the same ratio of 2nm. So, electrons and holes will travel fast towards the emissive layer from both sides as both layers are equally closer to the emissive layer. On the contrary, in Case II and Case III, electrons and holes, respectively will take more time on comparing with Case I. This will directly affect the recombination of charge carriers. Hence the peak luminescence values of both cases are less as compared with Case I. Moreover, if Case II and Case III are compared, in Case III the layer of TAPC in fixed which contains holes. And it is known that in organic electronics the mobility of holes is better than electrons so hole can travel fast to the emissive layer [28]. This provides better luminous properties to Case III as recombination will be higher in this case.

5. Conclusion

Basically, six different blue OLEDs D_1, D_2, D_3, D_4, D_5 and D_6 are compared in this paper. Here device D_1 is without CGL and other five devices including the proposed device contain CGL at different positions. The CGL comprises of two different layers in which top layer behaves as hole injector i.e. 1,1-bis[(di-4-tolyamino)phenyl)]cyclohexane (TAPC) and bottom layer acts as electron injector i.e. 1,4,5,8,9,11-hexaazatriphenylene-hexacarbonitrile (HAT-CN). The combination of these two materials provides easy transfer of charge carriers into the emissive layer. Hence, devices in which CGL is incorporated provide higher current and excellent luminescence. In this paper, the proposed device where CGL is utilized outside of the emissive layer showed significant improvement as the parameters such as luminescence and current are reported as 0.44 A and 3636.3 cd/m^2, respectively. Addition to this, the thickness optimization of the proposed device is also incorporated by the varying the thickness of utilized CGL layer.

Declarations

Consent for publication

All the authors understand and give their consent for the publication of manuscript "**Characteristics performance and analysis of positional variation in charge generation layer to enhance performance of OLED**" in "**Journal of Computational Electronics**" Journal.

Availability of data and materials

Not Applicable

Competing interests

No, all the authors declare that they have no competing interests as defined by Springer, or other interests that might be perceived to influence the results and/or discussion reported in this paper. The authors have no conflicts of interest to declare that are relevant to the content of this article.

Funding

Not Applicable

Author's Contributions

Sugandha Yadav: Conceptualization, Methodology, Data curation, Writing – original draft, Writing – review & editing.

Poornima Mittal: Conceptualization, Methodology, Supervision, Data curation, Writing – review & editing, Validation.

Shubham Negi: Supervision, Writing – review & editing, Visualization, Investigation, Formal analysis.

Availability of data and materials

Data and materials utilized and supporting the results of this study are available within the article.

References

1. S. Negi, P. Mittal and B. Kumar, Characteristic performance of OLED based on hole injection, transport and blocking layers. *Recent* Pat. 14, 373 (2020).
2. P. Chamola and P. Mittal, Flexible organic solar cell to power modern cardiac pacemakers: Versatile for all age groups, skin types and genders. *Phys. Scr.*, 98, 035018 (2023).
3. S. Yadav, P. Mittal and S. Negi, Recent advancements over a decade for organic light-emitting diodes: from structural diversity, role of layers, colour emission, material classification, performance improvement, fabrication to applications. Bull. Mater. Sci. 45, 109 (2022).
4. E. Angioni, M. Chapran, K. Ivaniuk, N. Kostiv, V. Cherpak, P. Stakhira et al., , A single emitting layer white OLED based on exciplex interface emission. *J. Mater. Chem.* C, 4, 3851, (2016).
5. Lee, H, Phosphorescent white organic light-emitting diodes with stable white color depending on luminance. Curr. Appl. Phys. 21, 116 (2021).
6. X. Zheng, Y. Liu, Y. Zhu, F. Ma, C. Feng, Y. Yu, H. Hu, and F. Li, Efficient inkjet-printed blue OLED with boosted charge transport using host doping for application in pixelated display. Opt. 101, 109755, (2020).
7. M. Han, Y. Chen, Y. Xie, F. Zhang, X. Li, A. Huang, Y. Fan, Y. Fan, Y. Gong, Q. Peng and Q. Li, 1.42-fold enhancement of blue OLED device performance by simply changing alkyl groups on the acridine ring. Cell Rep. 1, 100252, (2020).

8. S. Negi, P. Mittal and B. Kumar, Impact of different layers on performance of OLED. Microsyst. 24, 498, (2018).
9. S. Negi, P. Mittal and B. Kumar, Numerical modeling and parameters extraction of novel triple hole block layer-based organic light-emitting diode for display. J Soc Inf Disp. 28, 956, (2020).
10. S. Altazin, S. Züfle, E. Knapp, C. Kirsch, T. D. Schmidt, L. Jäger, Y. Noguchi, W. Brütting and B. Ruhstaller, Simulation of OLEDs with a polar electron transport layer. Org. Electron. 39, 244, (2016).
11. C. H. Gao, X. B. Shi, D. Y. Zhou, L. Zhang, Z. K. Wang and L. S. Liao, Highly efficient white organic light-emitting diodes with controllable excitons behavior by a mixed interlayer between fluorescence blue and phosphorescence yellow-emitting layers. Int. J. Photoenergy. (2013).
12. Y. Chen, J. Chen, D. Ma, D. Yan, L. Wang and F. Zhu, High power efficiency tandem organic light-emitting diodes based on bulk heterojunction organic bipolar charge generation layer. *Appl. Phys. Lett*. 98, 114 (2011).
13. Y. M. Kim, J. W. Lee, J. H. Jung, K. K. Paek, M. Y. Sung, J. K. Kim et al., Enhanced brightness and efficiency of organic light-emitting diodes with an LiF in the Alq/sub. *IEEE Electron Device Letters*, 27, 558 (2006).
14. P. Maurya, P. Mittal and B. Kumar, Performance improvement for organic light emitting diodes by changing the position of mixed-interlayer. Main Group Chem., 1, (2022).
15. Y. Liu, X. Wei, Z. Li, J. Liu, R. Wang, X. Hu, P. Wang, Y. Yamada-Takamura, T. Qi and Y. Wang, Highly efficient, solution-processed organic light-emitting diodes based on thermally activated delayed-fluorescence emitter with a mixed polymer interlayer. ACS Appl. Energy Mater. 1, 543 (2018).
16. S. Ying, S. Xiao, L. Peng, Q. Sun, Y. Dai, X. Qiao, D. Yang, J. Chen and D. Ma, ACS Exciton Regulation for Organic Light-Emitting Diodes with Improved Efficiency and Roll-Off by Managing the Bipolar Spacer Layers Based on Interfacial Exciplexes. Appl. Electron. Mater. 4, 3088, (2022).
17. A. Jetly and R. Mehra, Design of Tandem Organic Light Emitting Diode using efficient charge generation layer. Opt. Mater., 88, 304, (2019).
18. D. Zhao, H. Liu, Y. Miao, H. Wang, B. Zhao, Y. Hao, F. Zhu and B. Xu, A red tandem organic light-emitting diode based on organic photovoltaic-type charge generation layer. Org. Electron. 32, 1 (2016).
19. F. A. Angel, J. U. Wallace and C. W. Tang, Effect of lithium and silver diffusion in single-stack and tandem OLED devices. Org. Electron. 42, 102 (2017).
20. H. Sun, Q. Guo, D. Yang, Y. Chen, J. Chen and D. Ma, High efficiency tandem organic light emitting diode using an organic heterojunction as the charge generation layer: an investigation into the charge generation model and device performance. Acs Photonics, 2, 271 (2015).
21. S. Hamwi, J. Meyer, M. Kröger, T. Winkler, M. Witte, T. Riedl, A. Kahn and W. Kowalsky, The role of transition metal oxides in charge-generation layers for stacked organic light-emitting diodes. Adv. Func. Mater. 20, 1762 (2010).
22. Y. Liu, X. Wu, Z. Xiao, J. Gao, J. Zhang, H. Rui, X. Lin, N. Zhang, Y. Hua and S. Yin, Highly efficient tandem OLED based on C60/rubrene: MoO3 as charge generation layer and LiF/Al as electron

injection layer. Appl. Surf. Sci., 413, 302, (2017).

23. H. Sasabe, K. Minamoto, Y. J. Pu, M. Hirasawa and J. Kido, Ultra high-efficiency multi-photon emission blue phosphorescent OLEDs with external quantum efficiency exceeding 40%. Org. Electron. 13, 2615, (2012).
24. J. H. Kim and S. H. Ju, Emission Characteristics of Multi-Tandem OLED using MoO x with CGL. *J. Korean Inst. Met. Mater*. 48, 105 (2015).
25. J. Yuan, Y. Dai, Q. Sun, X. Qiao, D. Yang, J. Chen and D. Ma, High efficiency organic light-emitting diodes based on HAT-CN/TAPC heterojunction charge generation layer as charge injectors. Semicond Sci Technol. 34, 105010 (2019).
26. I. Titov, M. Köpke, N. C. Schneidewind, J. Buhl, Y. Murat and M. Gerken, OLED-OPD Matrix for Sensing on a Single Flexible Substrate. IEEE Sens. J. 20, 7540 (2020).
27. J. H. Kim, J. Seo, D. G. Kwon, J. A. Hong, J. Hwang, H. K. Choi, J. Moon, J. I. Lee, D. Y. Jung, S. Y. Choi, Y. Park, Carrier injection efficiencies and energy level alignments of multilayer graphene anodes for organic light-emitting diodes with different hole injection layers. CARBON 79, 623 (2014).
28. P. Mittal, S. Yadav and S. Negi, Advancements for organic thin film transistors: Structures, materials, performance parameters, influencing factors, models, fabrication, reliability, and applications. Mater. Sci. Semicond. Process. 133, 105975 (2021).

Figures

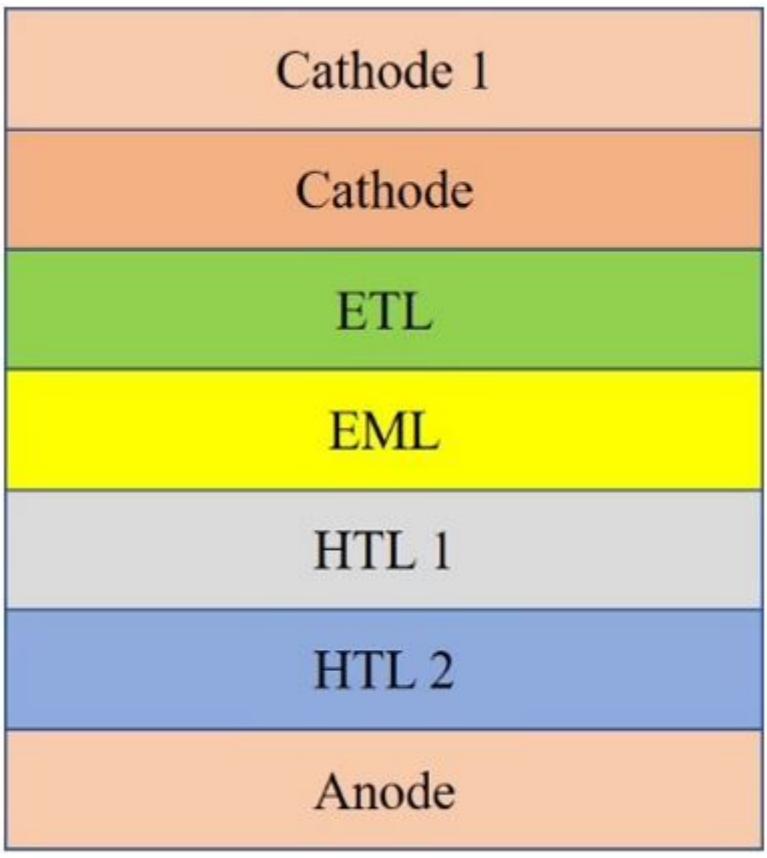

Figure 1

Structure of Blue OLED (D_1) [26]

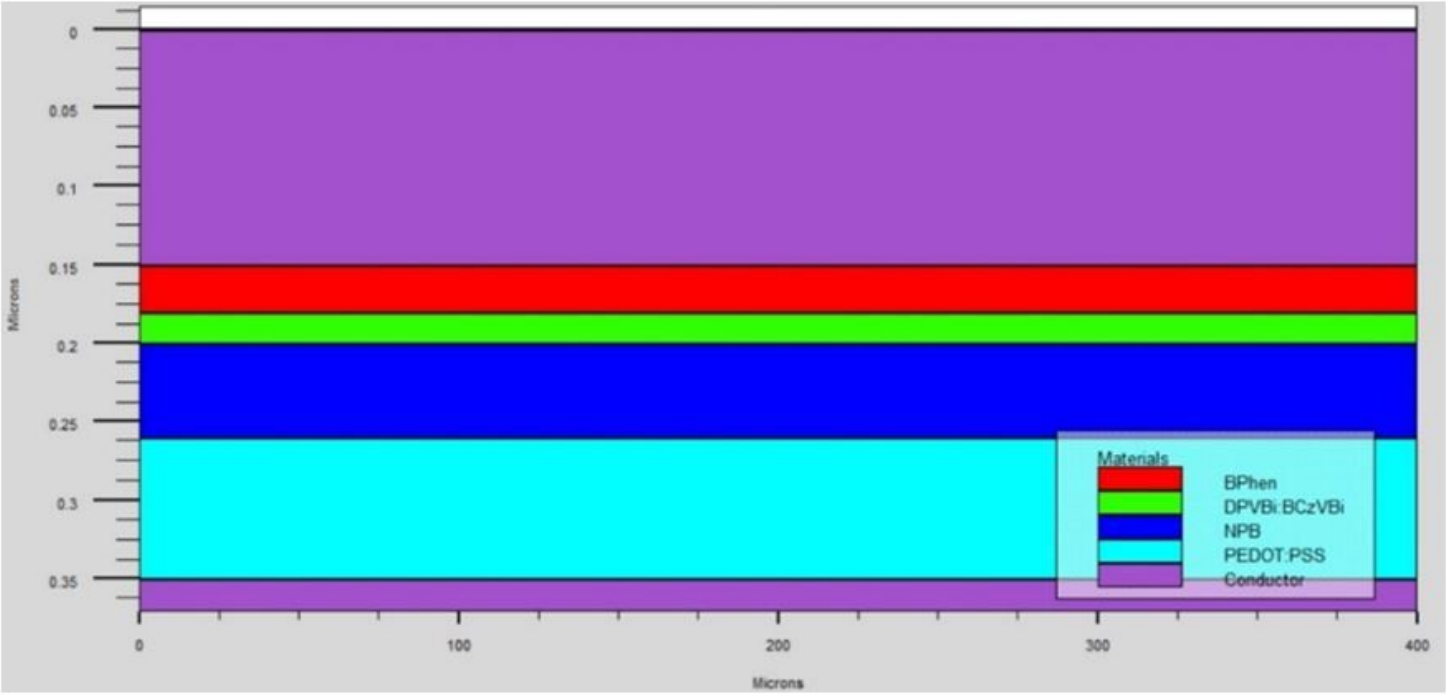

Figure 2

Device structure of D_1 along with the thickness and materials

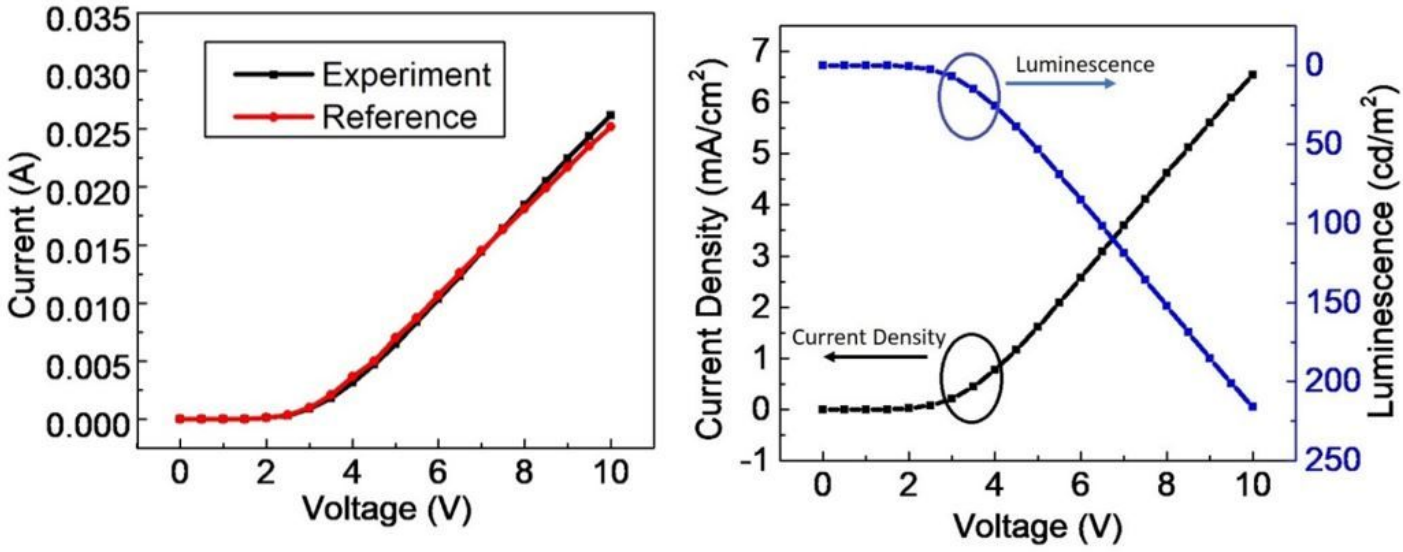

Figure 3

(a) Reference and experimental data of current & (b) Combined curve for current density and luminescence of device D_1

Figure 4

Blue OLED with (a) CGL below cathode (D_2), (b) CGL below anode (D_3), (c) CGL at both sides of electrodes (D_4), and (d) CGL inside emissive layer (D_5)

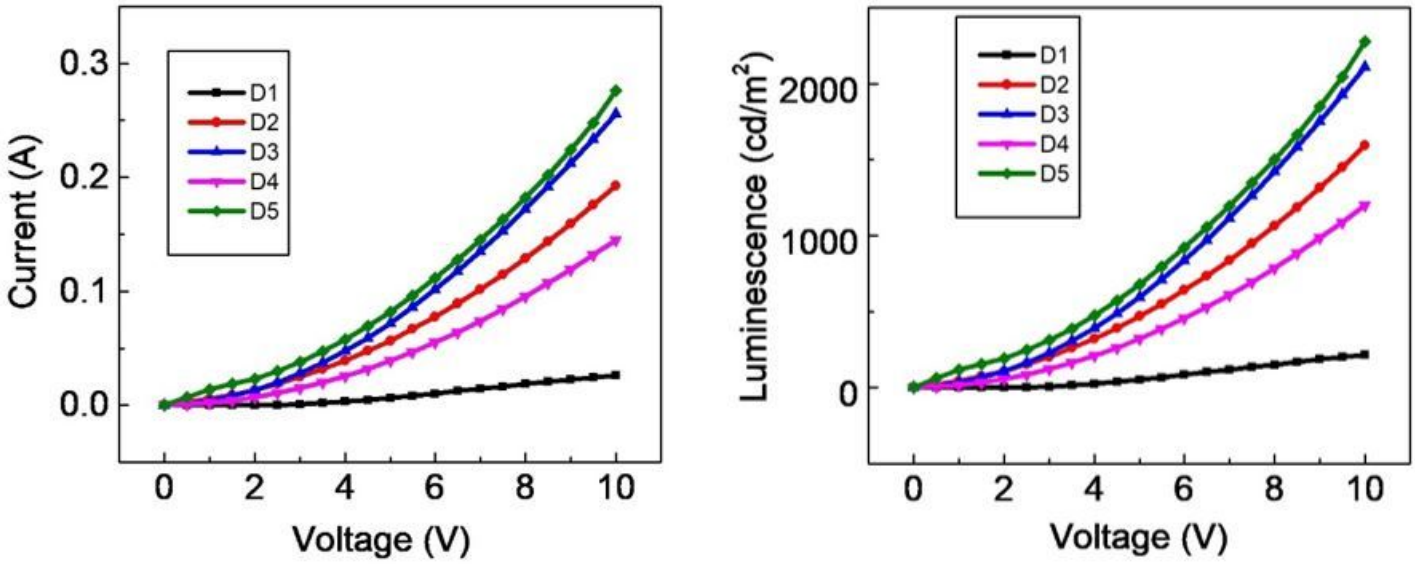

Figure 5

(a) Current curve and (b) Luminescence curve for all devices (D_1- D_5)

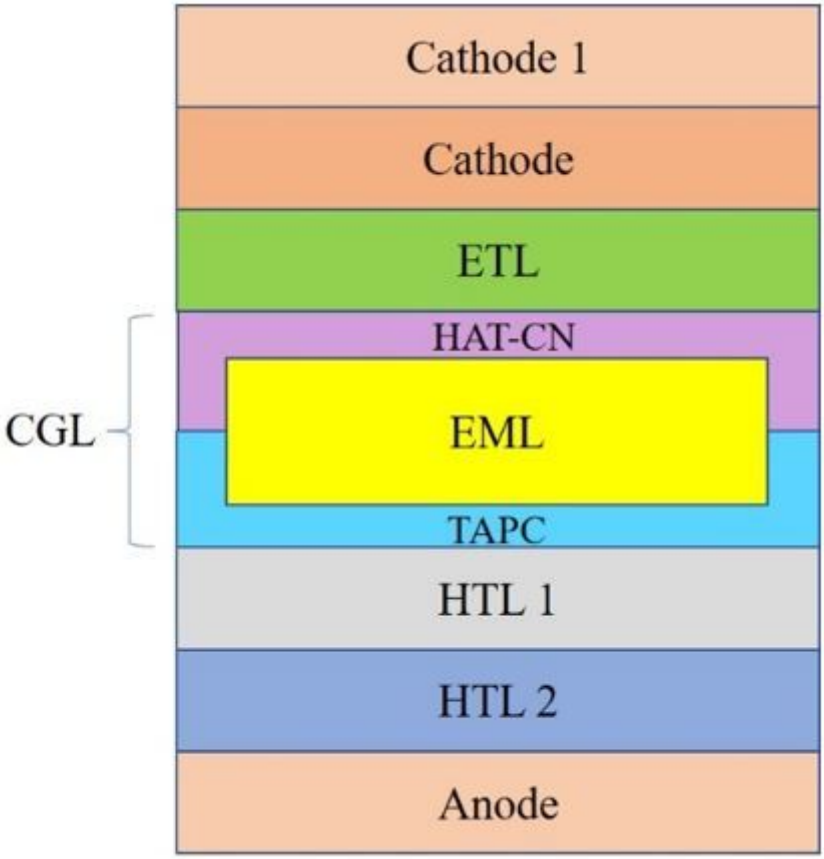

Figure 6

Proposed Device (D_6)

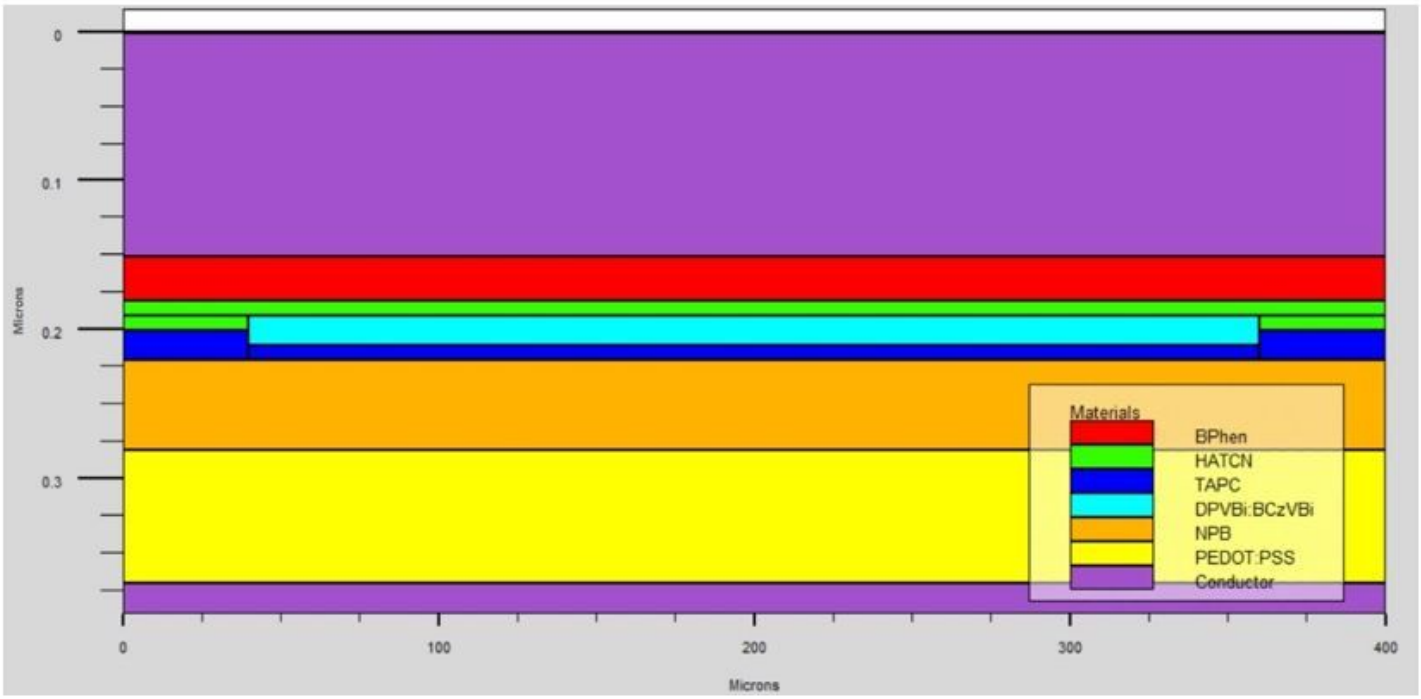

Figure 7

Device structure of D_6 along with their thickness and materials

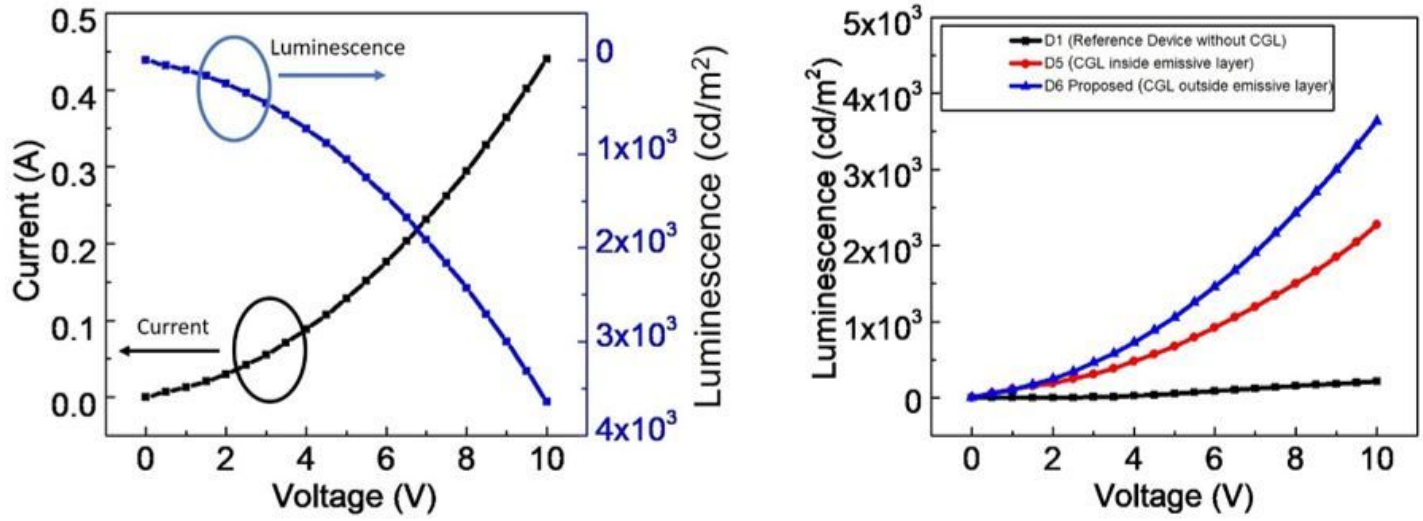

Figure 8

(a) Current and luminescence curves of proposed device (D_6) and (b) Luminescence comparison of D_1, D_5 and D_6

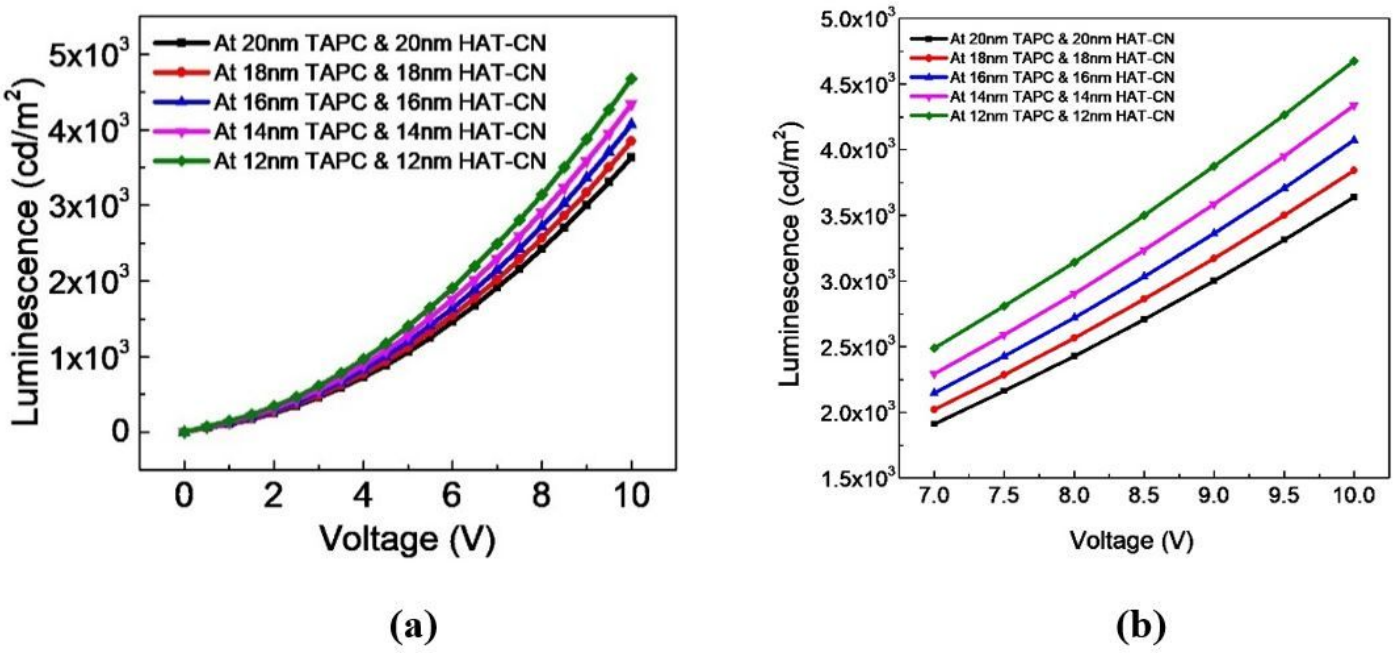

Figure 9

(a) Luminescence comparison at different thickness of top and bottom layer of CGL and (b) the zoomed view of curve (a) to show the variations in luminescence

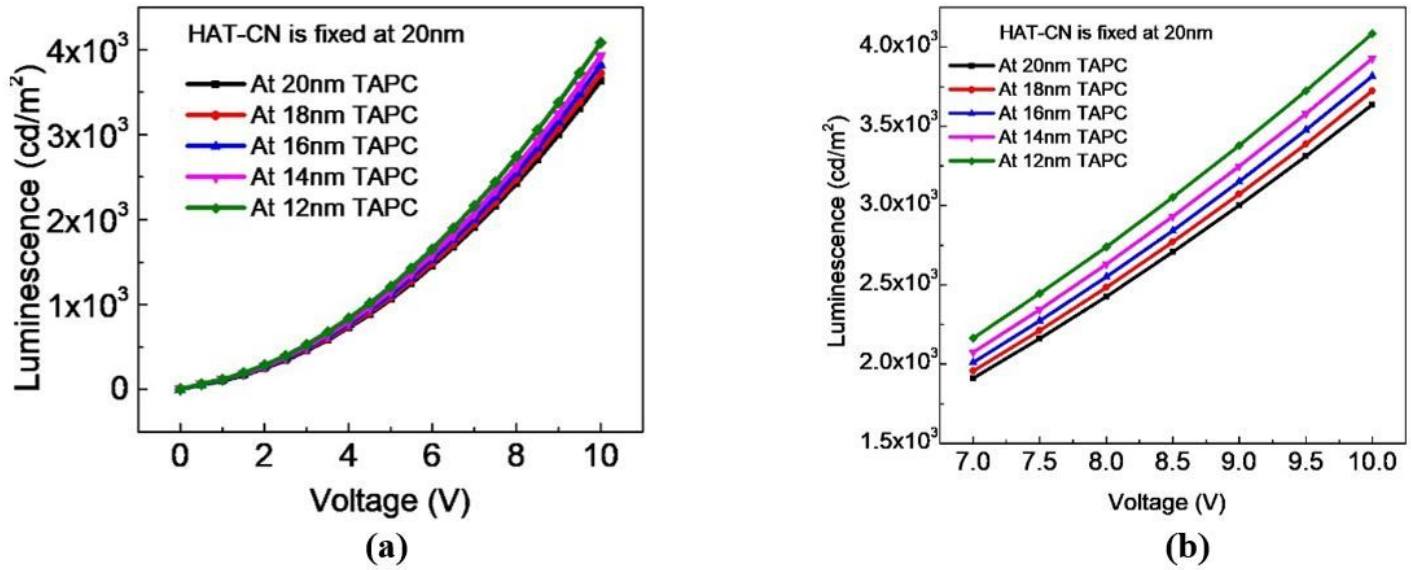

Figure 10

(a) Luminescence comparison at different thickness of bottom layer where top layer is fixed of CGL and (b) the zoomed view of curve (a) to outline the variations in luminescence

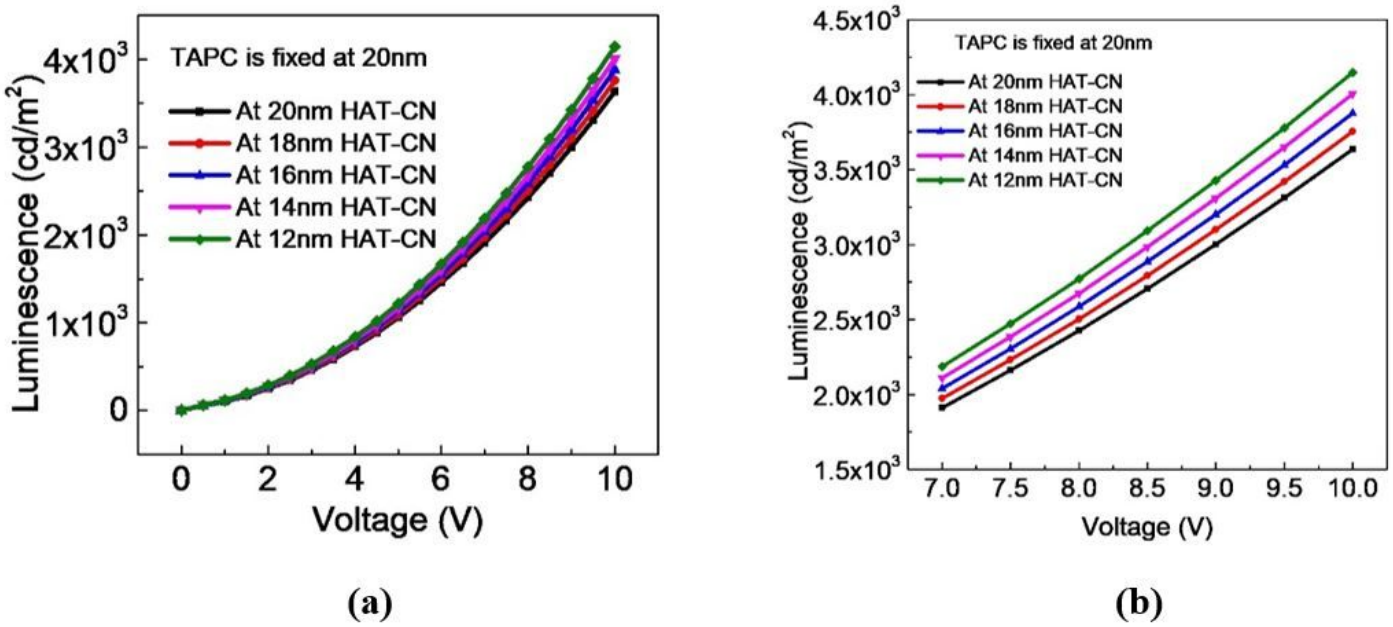

Figure 11

(a) Luminescence comparison at different thickness of top layer where bottom layer is fixed of CGL and (b) the zoomed view of curve (a) to depict the variations in luminescence

Ain Shams Engineering Journal xxx (xxxx) xxx

Contents lists available at ScienceDirect

Ain Shams Engineering Journal

journal homepage: www.sciencedirect.com

Chemical assisted ball end magnetorheological finishing of aluminium 7075 alloy

Anand Sharma *, Mahendra Singh Niranjan

Delhi Technological University, Delhi, India

ARTICLE INFO

Keywords:
Magnetorheological
Ball end
Finishing
Chemical assisted
Surface roughness
Aluminum

ABSTRACT

Areas like aerospace, solar, medical, electronics, optics widely use nano-finished or high precision aluminium alloys. These nano-finished aluminium alloys are being used as metal mirrors, micro-electronics devices, diaphragm in optical sensors etc. In general, aluminium alloys are finished by conventional processes such as grinding, lapping. However, to achieve nano-level finish on soft material like aluminium alloys which possess high malleability and ductility is difficult for traditional processes without producing high residual stresses, subsurface damage etc. In this work, the surface finish of aluminium 7075 alloy workpiece was improved using a novel finishing technique viz. chemical assisted ball end magnetorheological finishing (CA-BEMRF). To validate the results a comparison of % decrease in surface roughness obtained after ball end magnetorheological finishing (BEMRF) as well as achieved after CA-BEMRF process is carried out. Results showed a 1.84 % improvement in % decrease in surface roughness after CA-BEMRF process as compared to BEMRF without chemical assistance. The statistical and graphical effects of various changing process parameters on % decrease in surface roughness are addressed. Using analysis of variance (ANOVA) and the F-test, significant process factors impacting surface roughness during workpiece finishing are identified. Optimum value of % decrease in surface roughness has been found as 55.316 at magnetizing current 3.43amp, tool rotational speed 326.97 rpm and working gap of 0.74 mm. Confirmatory experimental tests have been conducted and results obtained were found very close to the predicted outcome. Scanning electron microscopy (SEM) of the workpiece finished using BEMRF process and CA-BEMRF technique are compared to assess the effects of magnetizing current, tool rotation and working gap on surface topography of machined surface.

1. Introduction

In this age of new industrialization revolution, there is a high demand for both nano products and macro products with high surface finish and strength. Recently, the needs of most industries such as electronics, optics, aerospace, and energy. Precision surface products, such as substrates, molds, optical glass, artificial implants, etc. As friction loss, components, service life under load, and wear resistance are significantly affected by the quality and size of surface roughness, its development is rapid.

Although numerous materials are utilized in aerospace, automobile, electronics, construction etc. industries to fulfill their requirement, the most important and abundantly used material is aluminum due to its high performance and economically favorable properties like low density, good castability, high working temperature, high resistance to corrosion, high strength and high specific modulus. Peters [23] mentioned that including the most visible parts of a modern aircraft like fuselage and the wings, more than 70 % of the structural weight is of aluminium alloy being damage tolerant and of high strength. Such properties are possessed by aluminium 7075 and 2024 alloys. High finished aluminum alloys are extensively used in semi-conductor manufacturing, specific purpose telescopes, optical systems and sensors, micro-electronic devices and at an enormous extent for conduction through wires. Koul [15] made diamond cut aluminum based mirrors to be used as light collector in a specific telescope at Hanle, a high altitude astronomical site in India. Chiu et al. [3] mentioned that it is a challenge to obtain good structural planarity and minimum surface scratching during chemical mechanical polishing of aluminum due to its soft nature. Considering low resistivity to scratching of aluminium, it becomes difficult to achieve a nano-level surface finish without damaging the surface integrity using conventional finishing processes.

For new materials with high values of hardness and toughness to

* Corresponding author.
E-mail address: doc.asharma@yahoo.in (A. Sharma).

https://doi.org/10.1016/j.asej.2023.102397
Received 24 March 2022; Received in revised form 8 December 2022; Accepted 13 July 2023
2090-4479/© 2023 THE AUTHORS. Published by Elsevier BV on behalf of Faculty of Engineering, Ain Shams University. This is an open access article under the CC BY-NC-ND license (http://creativecommons.org/licenses/by-nc-nd/4.0/).

achieve a high surface finish and low finishing costs; strength/weight ratio, etc., it is necessary to implement advanced finishing technology. By selecting the best processing parameters, a good surface finish can be obtained by traditional finishing processes such as grinding, polishing and burnishing. However, these processes have certain disadvantages, such as burrs, residual stress, subfloor damage, etc. Complex 3D finishing also has limitations in shape materials. However, to achieve an unmeasured level of surface roughness value, it is difficult and uneconomical to go through the traditional finishing process. Various advanced precise surface finishing processes for finishing in different ways have been developed and types of materials by controlling the finishing forces exerted by the finishing tool on the workpiece. Few controlled finishing force processes are "magnetic float polishing", "abrasive flow machining", "magnetorheological abrasive flow finishing (MRAFF)", "magnetorheological jet finishing", and "magneto-rheological finishing (MRF)". In these processes the finishing forces are controlled by controlling the magnetic flux density by using either a permanent magnet or an electromagnet. However, these processes have limitations in the geometric shapes of the products that can be finished, and they can finish limited geometric shapes as concave, convex, planar, and symmetrical spheres. BEMRF, a new form of finishing process based on intelligent fluids that can manage the finishing force to finish 3D surfaces to the nano level, is another version of MRF developed by Singh et al. [30–32]. This technique solves the restrictions mentioned above using a variety of non-traditional finishing processes that work on the premise of managing finishing pressures created in the recent past. BEMRF process is capable of finishing a variety of materials, either magnetic materials like diverse alloys of steel, etc., or nonmagnetic materials such as glass [30–32], silicon [28], aluminum, copper [13], etc.

According to previous research, ball end magnetorheological finishing (BEMRF), 3-axis CNC BEMRF, 5-axis CNC BEMRF, and fully automated 5-axis CNC BEMRF processes are used to finish various materials and workpieces of varied geometries. Niranjan et al., [20] compared the surface roughness reduction percentage (% ΔRa) calculated by using the ball head magnetorheological finishing tool (BEMRF) and double-dispersed magnetorheological polishing fluid (MRPF) to finish machining mild steel workpieces and using the existing monodisperse MRPF 30.

Niranjan et al. [21] prepared a sample for a monodisperse MR fluid containing 20 % volume of CIP particles (CS grade), and a double dispersion MR fluid with the following proportions of CIP particles (18 % vol. grade CS and 2 vol % HS grade) was synthesized. The % ΔRa was found to increase by approximately 46.25 % using MR Double Dispersion Polishing Liquid (16 % by volume of carbonyl iron powder CS grade, 4 % by volume of HS grade, 25 % by volume of SiC abrasive and 55 % by volume of fluid).

Khan and Jha [14] also developed an MR fluid with a composition suitable for BEMR finishing of copper. To enhance the distribution of magnetic flux density between the tip of the finishing tool and the surface of the copper component, one unique technique is to employ permanent magnets as a substrate to generate two opposing magnetic poles. The resultant "magnetic flux density" rose from 0.35 Tesla to 0.85 Tesla using this approach. After optimizing the concentration of abrasive and EIP in the MR fluid used for copper finishing, it was found that the amount of abrasive can be maintained at 14 % (volume), and 23 % (volume) of EIP is the best.

Kumar et al. [16] analytically and experimentally studied the influence of MR fluid composition and finishing duration during BEMF of polyactic acid (PLA) workpiece material. The 3D printed PLA part material is constructed using the Fused Deposition Modeling (FDM) process. Alumina (Al_2O_3) is considered suitable for finishing PLA workpiece materials. According to the findings of the experiments, the optimum MRP fluid composition for completing PLA component materials is 16.7 % reagent, 25 % EIP by volume, and 58.83 percent distilled water by volume.

Garg et al. [8] modelled and analyzed the influence of strong magnetic field on flow behavior of MR fluid in BEMRF process using Comsol Multiphysics. The simulation analysis showed that the MR fluid gets congealed at the tool tip and forms almost a hemispherical shape due to the concentration of magnetic flux density, thus providing necessary stiffness for polishing different materials. The strength of the magnetic field at the tip was also shown to be dependent on "the magnetizing current, the number of copper turns, the magnetic permeability of the MR-fluid, and the iron core".

Singh et al. [33] studied the effect of diverse mesh size and volume % contribution of abrasive particles in MR fluid on surface roughness of ferromagnetic material using BEMRF process. Silicon carbide was used as abrasives in the MR fluid the mesh size of which was varied from 400 to 1200 and volume percentage contribution ranged from 5 to 25 vol %. The results of the BEMRF of ferromagnetic material under specified machining conditions showed that with increasing abrasive mesh size, the percentage change in roughness value decreases whereas it decreases with the increase in percentage volume contribution.

Niranjan and Jha [22] attempted to make use of MR fluids containing sintered magnetic abrasives improves the percentage reduction in surface roughness of mild steel workpieces. The MR fluid prepared contains 45 % by volume of sintered magnetic abrasive and 55 % by volume of base fluid. The percent Ra increases as the tool speed increases, after reaching its maximum value at 600 RPM, it decreases under the influence of aging effect in the tool. By using MR polishing fluids based on sintered magnetic abrasives, tool-aging effects have been minimized.

Alam and Jha [1] conducted theoretical research based on surface roughness modelling and material removal mechanisms, followed by practical verification on a mild steel workpiece utilizing the BEMRF method. The material removal process and wear behavior in the BEMRF finishing process are investigated using a theoretical model of the normal force and cutting force operating on the magnetic induction abrasive. It is observed that the theoretical and experimental results are very consistent at low values of magnetization current, which verifies the proposed model. The difference between experimental and theoretical values was found to be between 7.23 and 31.19 percent.

Iqbal and Jha [11] established finishing parameter sets in expressions of surface roughness reduction for the surfaces to be finished using BEMRF process based on finishing time. The best set of finishing parameters for achieving maximum resultant in the next finishing cycle was discovered, and an algorithm for parameter selection was created in order to pick the next optimal set of finishing parameters for attaining maximum surface roughness reduction in the next finishing cycle. After every finishing cycle measurement of surface roughness was done using Confocal sensor which acted as an initial roughness value for next finishing cycle. Experimental results showed on fully automating the process surface roughness value was brought down to a range of 60 nm in 200 min of finishing time from initial 800 nm range. Using an individual parameter set, the same decrease in surface roughness was accomplished in a completion time of 360 min.

Alam et al. [2] studied the composition effects of polishing fluid on finishing forces i.e. normal and shear forces. Vol. % of magnetic and nonmagnetic abrasives were varied from 5 to 25 % and 5 to 20 % respectively forming different samples of MR polishing fluid. Experimental results while finishing of mild steel using BEMRF process showed that with increase in magnetic CIPs concentration in MR fluid both normal and shear forces increased.

Inspired by the beneficial features of chemical mechanical polishing (CMP) process, various researchers have made an attempt to hybrid the CMP and MRF process to obtain high surface finish for different materials. Jain et al. [12] developed chemo-mechanical magneto-rheological finishing process by associating CMP and MRF process to enhance the surface finish quality of silicon blanks. It was concluded that working gap, finishing time and magnet rotational speed had significant effect and led to a surface finish of 4.8 Å.

Ranjan et al. [26,27] super finished a copper alloy using CMMRF

technique and developed a mathematical model to study the polishing pressure and other controlling parameters. A soft chemically passivated layer was created on the surface of copper alloy by chemically reacting it with ammonia, glycine and nitric acid. Results showed that the depth and width of scratches on the surface were few tens of nanometers size.

Ranjan et al. [25] theoretically explored the magnetism, polishing pad formation and polishing pressure using FEA-CFD simulation, the results of which were validated later on experimentally on aluminium 6061-T6 alloy. The results revealed that the polishing pressure is affected by three parameters viz. Working gap, MR fluid and rotational speed.

Ghai et al. [9] achieved a nano level surface finish (0.597 nm) on aluminium 7075-T6 alloy using CMMRF technique. These results were obtained by optimizing the concentration of chemicals, abrasives and CIP particles along with working gap. The authors used DI water, glycine, ammonia and citric acid to form a brittle passivated layer on the surface of the workpiece and model the experiments with central composite design model technique. It was observed that aluminium alloy could only be finished in alkaline solution.

Fan et al. [5] developed a magnetic field-assisted finishing tool to finish Ti-6Al-4V workpieces using simulation models and experimental measurements. An improvement of over 95 % in surface roughness was achieved and scratches on workpiece surface were significantly reduced.

Fan et al. [6] investigated the performance of an enhanced magnetic abrasive finishing process on Ti-6Al-4V workpieces. Results showed that the surface roughness value of 54 nm was achieved at 0.8 mm working gap, 1500 mm/min feed rate, tool rotation of 900 rpm and 15 wt % shear thickening fluids (STFs).

Tian et al. [34] fabricated an improved tool-integrated multiple pole-tip setup to finish Ti-6Al-4V specimens. Formation of magnetic brush in the finishing region was demonstrated by finite element analysis of variation in magnetic field intensity. Results showed an improved of 94 % in surface finish.

Kumar & Singh [17] critically assessed the benefits, futuristic opportunities and the challenges in improving the capabilities of CMMRF process. They beautifully explained the mechanism and various process parameters affecting the capability of CMMRF process and its applications in the field of aerospace research, solar, medical implants, electronics and optical. It was concluded that this technique can produce a surface finish on both brittle and ductile materials in the range of 2–6 Å.

Qian et al. [24] developed and analyzed the magnetorheological shear thickening polishing fluid mixed with micro cubic boron nitride (CBN) abrasives. Rheological characterization of the newly developed polishing fluid demonstrated that the polishing performance can be enhanced resulting in high-efficiency and precise polishing process.

Although various researchers have carried out the finishing of materials like silicon, copper, aluminium alloy using chemo-mechanical magnetorheological finishing (CMMRF) process but no work was found using ball end magnetorheological finishing (BEMRF) technique. In addition, according to the past work very limited work has been carried out using aluminium 7075 alloy. This paper presents the development of ball end magnetorheological finishing setup at Delhi

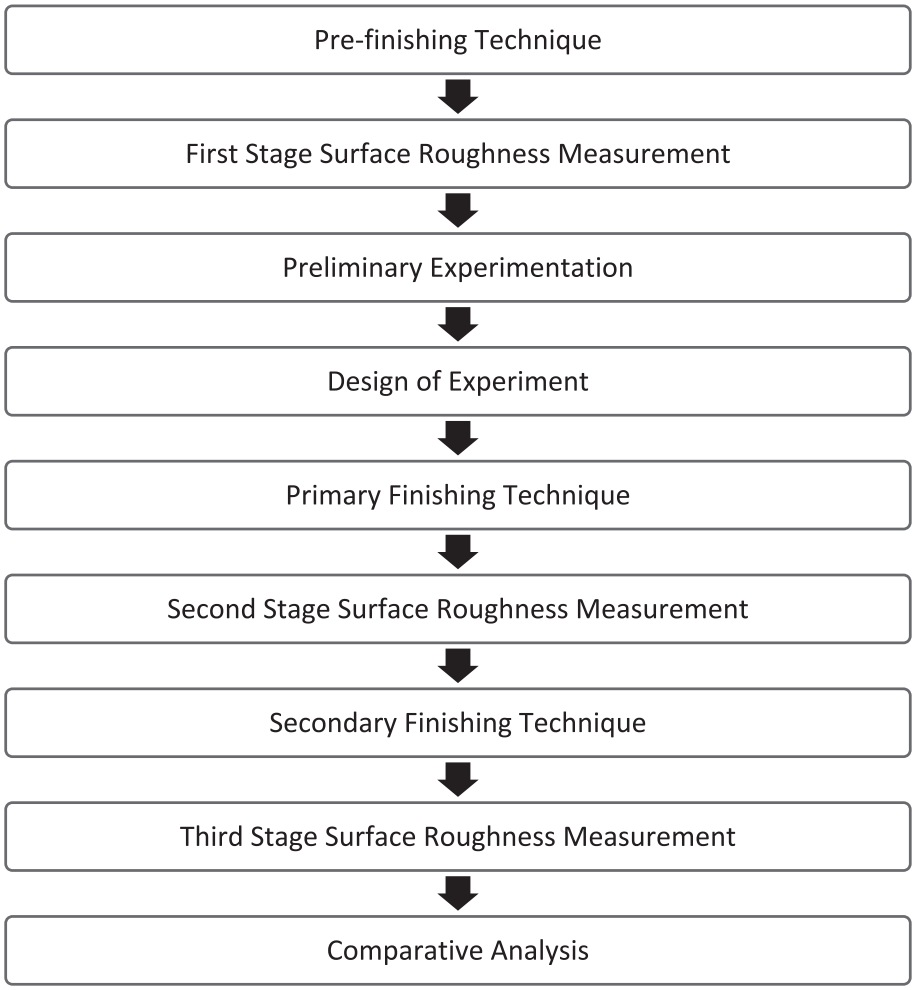

Fig. 1. Flow chart for the analysis of CA-BEMRF process.

Technological University and assisting this technique with chemical agent (Hydrogen Peroxide). In this work, an attempt has been made to improve the surface finish of Al 7075 alloy finished by BEMRF process using chemical assistance (CA-BEMRF). The improvement in surface finish is based on the % decrease in surface roughness value obtained after polishing rectangular 7075 aluminum alloy workpiece through the BEMRF and CA-BEMRF processes.

2. Methodology

This section discusses the methodology adopted to analyze the performance of chemical assisted ball end magnetorheological finishing process. Fig. 1 shows the flowchart depicting the methodology for nano finishing of aluminium 7075. Processes like turning, grinding, CNC milling etc. can be used as primary finishing techniques for achieving first stage surface finish. In the present work, precision grinding techniques is used to pre-finish the aluminum 7075 workpiece. Table 1 shows the grinding process parameters used for pre-finishing the workpieces. The Mitutoyo Surftest SJ-301 equipment is used to measure the first stage surface roughness acquired after grinding.

The preliminary experiments are then conducted on 3-axis CNC BEMRF setup in order to obtain the ranges and significant process parameters. The experimentation for finishing of aluminum 7075 workpiece are designed according to Box-Behnken design technique using design of expert 6.0.7 software. A total of 17 experiments had to be conducted by varying the input variables at three different levels as mentioned in Table 2 each time for both BEMRF and CA-BEMRF processes. The selected parameters as mentioned in Table 2 are consistent for both primary finishing technique i.e. BEMRF process and secondary finishing technique i.e. CA-BEMRF process. The finished workpieces after applying primary finishing technique are then washed with acetone to remove the magnetorheological (MR) fluid from the workpiece surface. Fig. 2 depicts the specific dimensions of the aluminium alloy workpiece and the position of the surface roughness measurement point. The roughness of the finished workpiece surface after BEMRF process is then measured at an increment of 10 mm for each specimen, thus an average of total 5 readings were collected for each workpiece. An average of % reduction in surface roughness of aluminum 7075 workpiece is found after applying primary finishing technique. Table 3 represents the properties of aluminium alloy 7075 used as workpiece in this work and Table 4 represents the chemical composition for the same. The aluminium alloy 7075 is solution annealed at 482 °C for 2 h, followed by a water quench. The alloy may then be given a precipitation hardening (aging) heat treatment.

These specimens are then finished through secondary finishing technique i.e. CA-BEMRF process for further improvement in surface finish. In this process hydrogen peroxide (H_2O_2) was used as an oxidant to increase the surface finish of the aluminium alloy. Kuo & Tsai [18] showed that a small concentration of H_2O_2 can substantially improve the material removal rate which in turn can quite effectively increase the surface finish value of the workpiece. The oxidizer is sprayed on the workpiece surface through a nozzle while the reciprocating motion of the finishing tool.

2.1. BEMRF setup

Because of the restriction in relative movement between the workpiece and the finishing tool, the limits of completing restricted geometries were overcome by inventing ball end magnetorheological finishing (BEMRF), a variation of the MRF method. The first ever setup of BEMRF included vertically oriented MR finishing tool driven by servo motor comprising of cylindrically shaped inner core (made of iron), electromagnet coil and an outer core oriented concentrically to each other [29]. The electromagnet coil is designed to reach a maximum magnetic flux density of 1.19 Tesla. The magnetic field distribution at the tip of the finishing tool is shown in Fig. 3. Magnetic flux density of 1.19 Tesla was observed at the tool tip with 2100 turns, 19.6 SWG and magnetic current of 3.5 A. The flow from the storage tank (funnel shape) of MR fluid to the tool tip was controlled by a delivery pump.

From the past study it was found that the original design of the ball

Table 1
Precision grinding process parameters.

Parameters	Values	Units
Wheel Velocity (m/min)	2026	m/min
Feed Rate-Work Table Traverse (m/min)	0.12	m/min
Depth of cut	20	μm

Table 2
Levels and ranges of selected process parameters.

Process parameter	Units	Levels			Static Parameters	Description
		I	II	III		
Magnetizing Current (V_M)	amp	1.5	2.5	3.5	Feed Rate	5 mm/min
Tool rotation (T_R)	rpm	300	500	700	Finishing Time	30 mins
Working gap (W_X)	mm	0.5	1.5	2.5	Finishing Length	50 mm

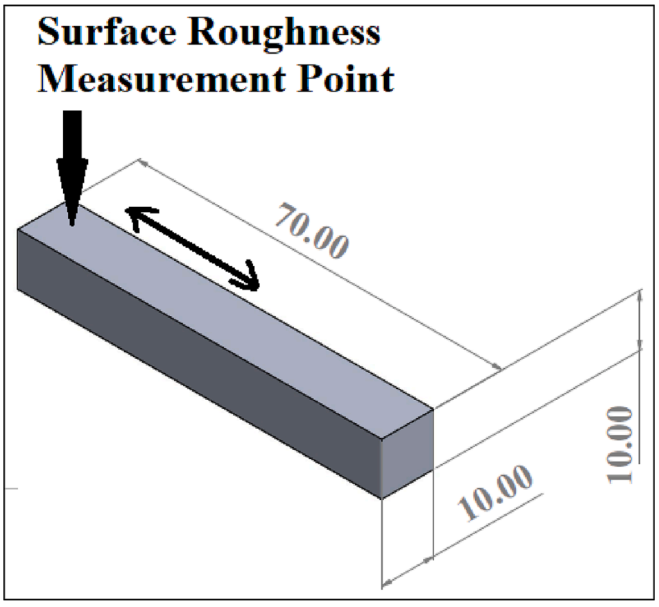

Fig. 2. Aluminium alloy workpiece dimensions (in millimeter) and surface roughness measurement point.

Table 3
Properties of Aluminium Alloy 7075.

Properties	Density g/cc	Melting Point °C	Tensile Strength MPa	Fatigue Strength MPa	Hardness Hv.
Al 7075	2.8	483	220	160	60

Table 4
Chemical Composition of Aluminium Alloy 7075, wt.% [7].

Element	wt.%	Element	wt.%	Element	wt.%
Zn	5.72	Mg	2.53	Cu	1.6
Fe	0.49	Si	0.41	Mn	0.31
Cr	0.21	Tn	0.19	Al	88.54

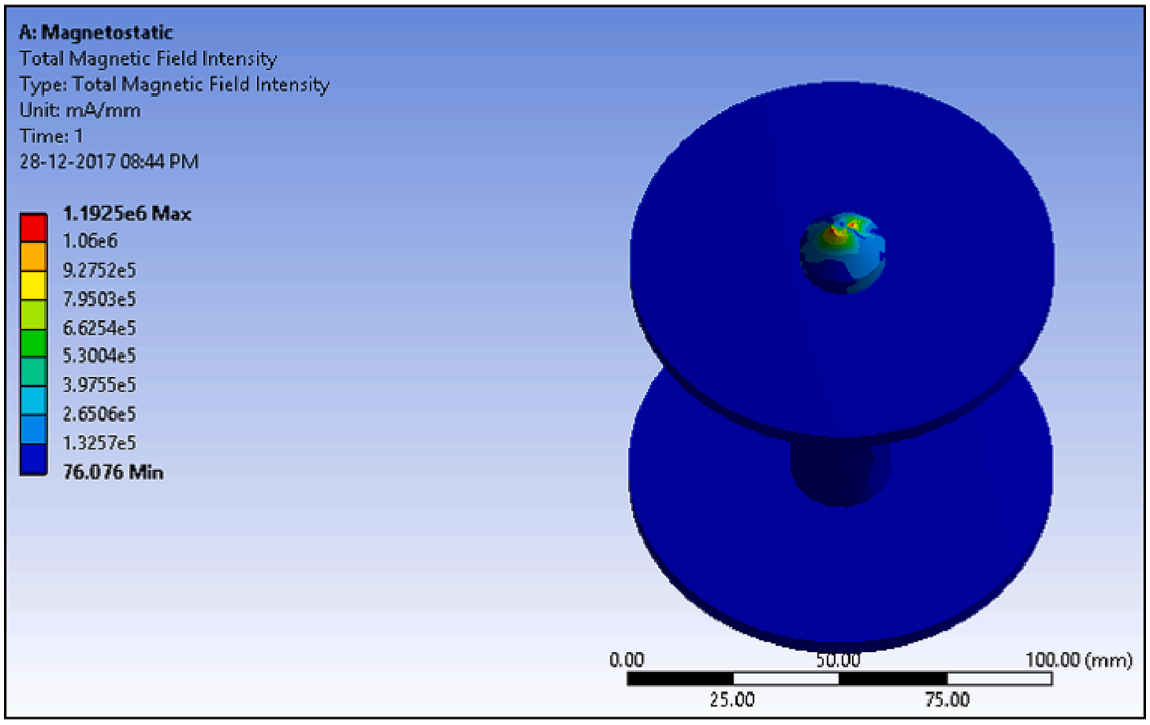

Fig. 3. Magnetic field distribution at tool tip for BEMRF and CA-BMERF setup.

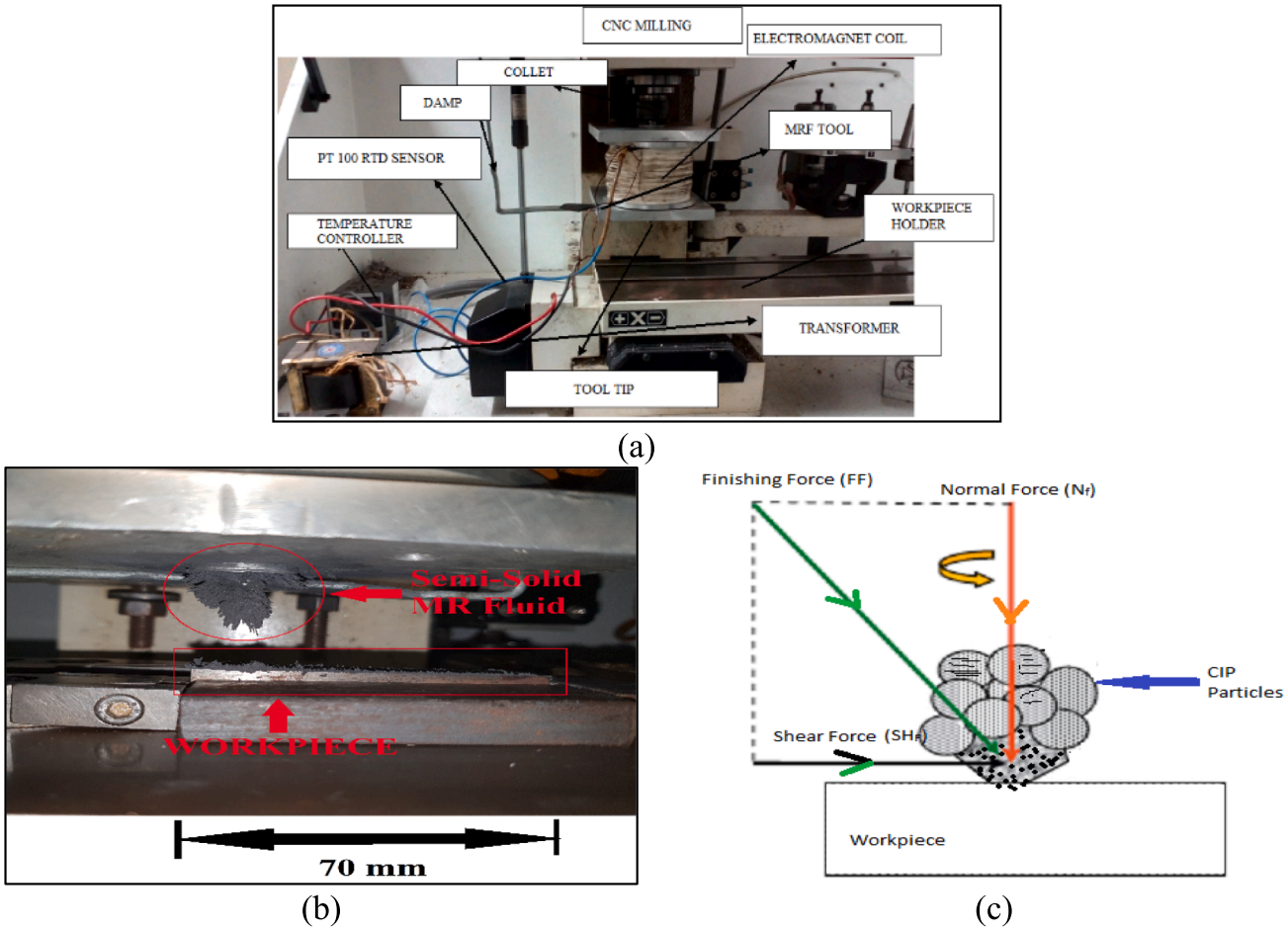

Fig. 4. (a) Setup of 3-axis BEMRF process (b) magnetic field flow and MR fluid semi-solid spherical end shape and (c) abrasive and magnetic particle microstructure on the workpiece surface.

end magnetorheological finishing setup did not have a provision of cooling the finishing tool once the current is supplied to the electromagnetic coil. As the finishing tool is in continuous rotation and supply of current the tool gets heated up to quite a large extent which may change the rheological properties of the MR fluid and hinders finishing of the workpiece for longer duration. To eradicate the above mentioned problem, copper cooling coils were wrapped around the electromagnetic coil for continuous cooling as shown in Fig. 4(a). The coolant (generally water) is supplied by a chiller maintained at low temperature which helps in maintaining an optimum temperature so as to increase the finishing time.

Fig. 4(a) represents the setup of 3-axis CNC BEMRF tool driven by servo motor comprising of cylindrically shaped inner core (made of iron), an outer core concentrically oriented to each other and an electromagnetic coil. Electromagnetic coil is surrounded by the copper tube through which chilled water is circulated in order to maintain a suitable temperature for experimentation. Fig. 4(b) represents the development of a nearly ball shaped highly viscous MR fluid at the tool tip once the current supply is switched on. The viscosity of the MR fluid can be controlled or changed by real-time control of the magnetizing current, thereby controlling the intensity of the magnetic field. Fig. 4(c) depicts the force produced by the tip of the semi-solid sphere consisting of magnetic particles and abrasive particles on the surface of the workpiece during the BEMRF process.

The magnetic force between the Carbonyl Iron (CI) particles provides the force that holds the CI particles with cutting edges together. During the rotation of high viscosity ball tip, the shearing action of the abrasive particles captured by the magnetic CI particles moving relative to the work surface causes the sharp peaks on the work piece surface to become wear out due to plastic deformation. The induced magnetic current controls the bonding force of the semi-solid spherical end of the finishing tool and then controls the amount of material cut by the abrasive particles. The final finishing force (FF) is a function of the normal force (N_F) and shear force (SH_F), as illustrated in Fig. 4(c), based on the abrasive and magnetic particle microstructure. The shear force is in responsibility of material removal, whereas Fn is in duty of determining the depth of penetration of the workpiece surface.

The same setup is used for secondary finishing process i.e. CA-BEMRF further improvement in surface finish. In this process hydrogen peroxide (H_2O_2) is sprayed on the workpiece surface through a nozzle while the reciprocating motion of the finishing tool as shown in Fig. 5. The selected parameters as mentioned in Table 2 are consistent for both primary finishing technique i.e. BEMRF process and secondary finishing technique i.e. CA-BEMRF process. 5 % vol. of hydrogen peroxide was sprayed on the workpiece surface during every single experiment to assist in the finishing of the workpiece.

2.2. Outcome and discussion

Finishing of aluminum 7075 was conducted using BEMRF process and finishing was further improved by chemical assisted BEMRF process. The normal residual plot (Fig. 6) clearly indicates that errors are normally distributed as most of the residuals are clustered around a straight line. It is observed that regression model is fairly well fitted with observed values.

Percentage surface roughness reduction after BEMRF process (% SRR_B) is calculated by equation (1) and percentage surface roughness reduction after CA-BEMRF process (%SRR_C) is calculated by equation (2).

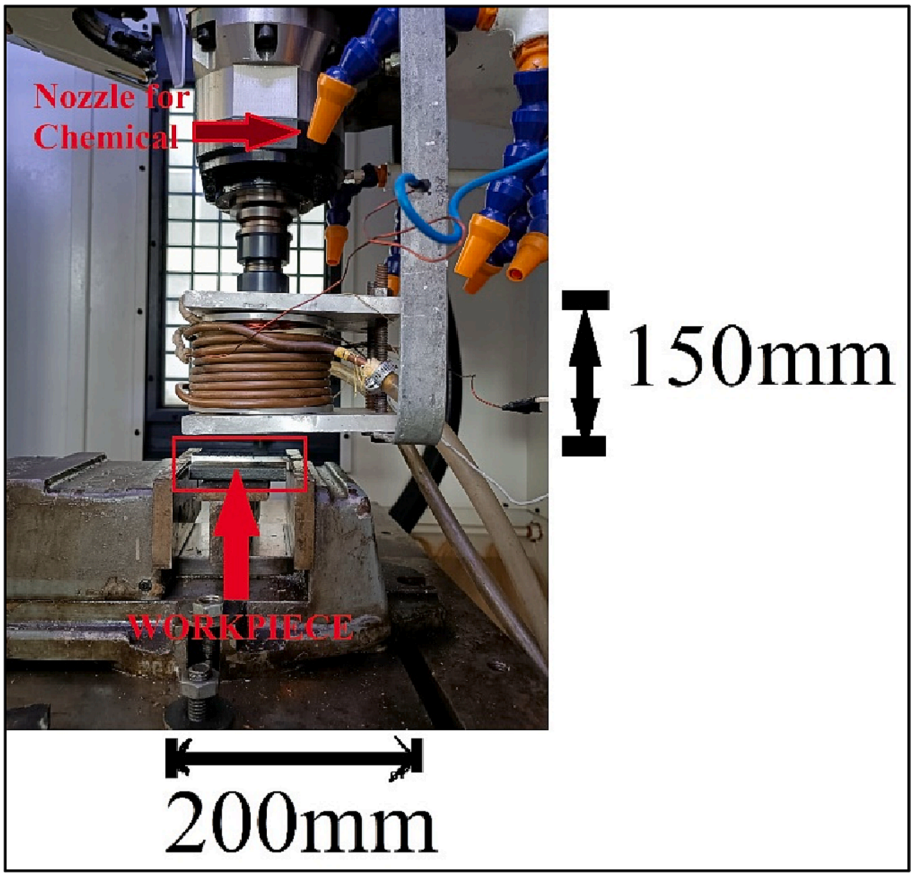

Fig.5. CA-BEMRF setup in association with BEMRF.

$$\%SRRB = \frac{Surface\ Roughness\ after\ grinding\ process\ -\ Surface\ Roughness\ after\ BEMRF\ process}{Surface\ Roughness\ after\ grinding\ process} \times 100 \quad (1)$$

$$\%SRRC = \frac{SurfaceRoughnessafterBEMRFprocess - SurfaceRoughnessafterCA - BEMRFprocess}{SurfaceRoughnessafterBEMRFprocess} \times 100 \quad (2)$$

Firstly, fitness of the obtained statistical data is to be found i.e. how well the observed data fits with the expected data. Table 5 represents the result of percentage reduction in surface roughness after BEMRF and CA-BEMRF process on aluminium 7075 workpiece.

2.3. Surface roughness of Al 7075 after BEMRF

After BEMRF, Design Expert 6.0.8 software proposed a quadratic model for % reduction in surface roughness. Table 6 shows the significant parameters or terms. The quadratic model is significant, as demonstrated by the F-value of 129.3567 and the associated p-value of less than 0.001 in Table 6.

An empirical relationship (Equation (3)) between the output response i.e. percentage surface roughness reduction after BEMRF and input process parameters is acquired after eliminating the non-significant parameters. This equation can be used for obtaining maximum reduction in surface roughness while BEMRF of Al 7075

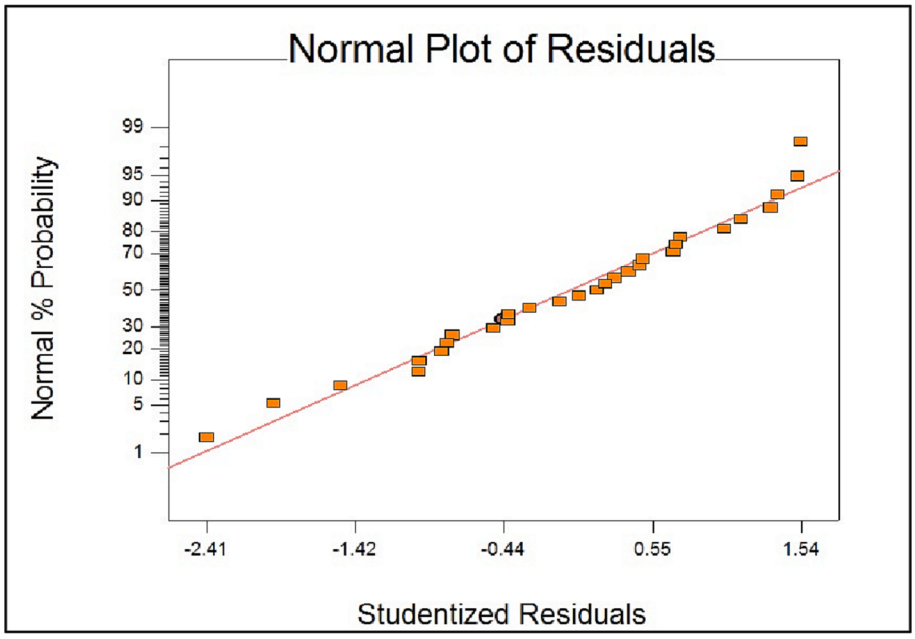

Fig.6. Normal Residual Plot.

Table 5
Result of % reduction in surface roughness after BEMRF and CA-BEMRF.

S.No.	Run Order	Magnetizing Current V_M	Tool Rotation T_R	Working Gap W_X	Output Response after BEMRF $\%SRR_B$	Output Response after CA-BEMRF $\%SRR_C$
1	15	1.5	300	1.5	40.48	42.97
2	3	3.5	300	1.5	53.83	54.15
3	7	1.5	700	1.5	39.52	38.68
4	14	3.5	700	1.5	44.47	45.51
5	12	1.5	500	0.5	40.47	42.80
6	8	3.5	500	0.5	48.81	49.01
7	1	1.5	500	2.5	44.47	44.23
8	17	3.5	500	2.5	53.83	52.68
9	6	2.5	300	0.5	47.63	51.88
10	13	2.5	700	0.5	39.52	36.87
11	4	2.5	300	2.5	48.81	44.18
12	9	2.5	700	2.5	44.46	45.85
13	16	2.5	500	1.5	45.53	48.59
14	2	2.5	500	1.5	45.63	47.42
15	5	2.5	500	1.5	46.30	47.75
16	11	2.5	500	1.5	46.58	48.37
17	10	2.5	500	1.5	46.30	48.50

$\%SRR_B$ = Percentage surface roughness reduction after BEMRF process and $\%SRR_C$ = Percentage surface roughness reduction after CA-BEMRF process.

Table 6
ANOVA table for % decrease in surface roughness after BEMRF process.

Source	Squares Total	Degree of Freedom	Mean Square	F Value	Prob > F	
Model	289.5628	7	41.366	129.3567	<0.0001	Significant
V_M	162.09	1	162.09	506.8745	<0.0001	Significant
T_R	64.80911	1	64.809	202.6657	<0.0001	Significant
W_X	28.65245	1	28.652	89.59957	<0.0001	Significant
T_R^2	11.28695	1	11.287	35.29562	0.0002	Significant
W_X^2	1.99566	1	1.9957	6.240662	0.0340	Significant
$V_M \times T_R$	17.68203	1	17.682	55.29377	<0.0001	Significant
$T_R \times W_X$	3.5344	1	3.5344	11.05248	0.0089	Significant
Residual	2.87805	9	0.3198			
Lack of Fit	2.02697	5	0.4054	1.905316	0.2760	Not Significant
Pure Error	0.85108	4	0.2128			
Cor Total	292.4408	16				

Standard Deviation = 0.565494, R^2 = 0.990159, Adjusted R^2 = 0.982504, Predicted R^2 = 0.946623, Mean = 45.68412, Coefficient of Variance = 1.23784, PRESS = 15.60952, Adequate Precision = 37.88097.

material by predicting optimal values of input process parameters.

$$\%SRR_B = 46.13 + 4.50125 * V_M - 2.84625 * T_R + 1.8925 * W_X - 1.635 * T_R^2 + 0.6875 * W_X^2 - 2.1025 * V_M * T_R + 0.94 * T_R * W_X \quad (3)$$

Interaction graph of V_M and T_R on $\%SRR_B$ as shown in Fig. 3(a) clearly explains that $\%SRR_B$ attains a maximum value of 53.94 % when V_M is kept at highest level of 3.5A and T_R at lowest value of 300 rpm, keeping W_X constant at 1.5 mm. This is because when the magnetizing current is strong, the normal and tangential forces rise, shearing more material off the workpiece surface and resulting in a better surface finish. On the other hand, a minimum of 39.25 % reduction in surface roughness is attained at lowest value (1.5 A) of V_M and highest value (700 rpm) of T_R.

This sharp drop in % SRR_B is owing to the fact that as the tool rotates at a high speed, the amount of abrasives contacting with the workpiece surface through the same working gap rises, resulting in a higher indentation force. This increase in indentation force causes the workpiece's surface finish to deteriorate.

Combined effect of T_R and W_X on $\%SRR_B$ as represented in Fig. 7(b) shows that $\%SRR_B$ value increased from 39.5 % to 45.17 % on increasing W_X from 0.5 to 2.5 mm while keeping T_R at 700 rpm. A significant jump in $\%SRR_B$ value is seen due to the reason that at low W_X more volume of finishing fluid is squeezed between the tip of tool and finishing surface at same tool rotational speed thereby increasing the normal and tangential forces on the surface of the workpiece resulting in poor surface finish. Furthermore, magnetization intensity increases at smaller working gap

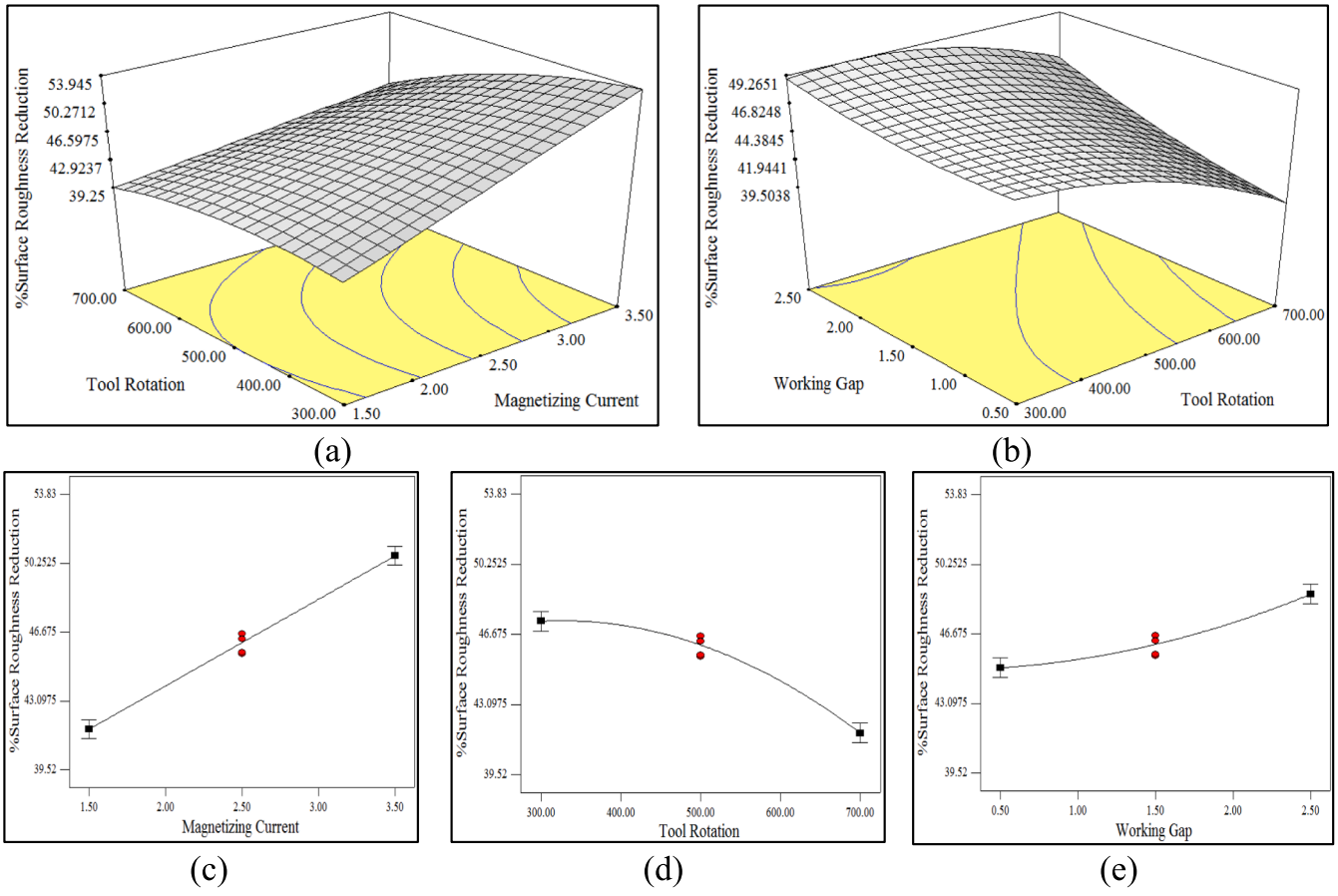

Fig. 7. (a) Magnetizing Current and Tool Rotation interaction graph on percent $\%SRR_B$, (b) Interaction graph of Tool Rotation & Working Gap on $\%SRR_B$, (c) Individual effect of Magnetizing Current on $\%SRR_B$, (d) Individual effect of Tool Rotation on $\%SRR_B$ and (e) Individual effect of Working Gap on $\%SRR_B$.

Table 7
ANOVA table for % decrease in surface roughness after CA-BEMRF process.

Source	Sum of Squares	Degree of Freedom	Mean Square	F Value	Prob > F	
Model	329.7997	6	54.96662	65.86291	<0.0001	Significant
A	133.4161	1	133.4161	159.8638	<0.0001	Significant
B	86.26411	1	86.26411	103.3647	<0.0001	Significant
C	5.08805	1	5.08805	6.096679	0.0332	Significant
B^2	30.7452	1	30.7452	36.83996	0.0001	Significant
AB	4.730625	1	4.730625	5.6684	0.0386	Significant
BC	69.5556	1	69.5556	83.34394	<0.0001	Significant
Residual	8.34561	10	0.834561			
Lack of Fit	7.29109	6	1.215182	4.609421	0.0804	Not Significant
Pure Error	1.05452	4	0.26363			
Cor Total	338.1453	16				

Standard Deviation = 0.91354308722809, R^2 = 0.97531945711786, Adjusted R^2 = 0.96051113138858, Predicted R^2 = 0.91276434382662, Mean = 46.437647058824, Coefficient of Variance = 1.9672467170244, PRESS = 29.498327640595, Adequate Precision = 28.49872175286.

leading to generation of deep abrasions thus increasing surface roughness. It is also observed that $\%SRR_B$ value further increased to 48.98 % from 45.17 % once tool rotation value is decreased to 300 rpm, working gap constant at 2.5 mm.

Fig. 7 (c, d, e) represents the individual impact of magnetizing current, tool rotation and working gap on $\%SRR_B$ respectively. The same slant as the interaction graph was followed by the individual effect plot, which showed that an increase in V_M and W_X increased the $\%SRR_B$ while an increase in T_R reduced $\%SRR_B$ due to the reasons quoted above. Surface finish is an important constraint to assess the materials functional performance. Ghosh et al. [10]concluded that the optical materials to be utilised in optical industries are expected to acquire nanometric finish without any surface or sub-surface damage.

2.4. Surface roughness of Al 7075 after CA-BEMRF

Design Expert 6.0.8 software proposed a quadratic model for reducing % surface roughness after CA-BEMRF. Table 7 shows the significant parameters or terms. The quadratic model is significant, as demonstrated by the F-value of 65.86291 and the accompanying p-value of less than 0.0001 in Table 7.

An empirical relationship (Equation (4)) between the output response i.e. percentage surface roughness reduction after CA-BEMRF and input process parameters is acquired after eliminating the non-significant parameters. This equation can be used for obtaining maximum reduction in surface roughness while CA-BEMRF of Al 7075 material by predicting optimal values of input process parameters.

$$\%SRR_C = 47.705555555556 + 4.08375 * V_M - 3.28375 * T_R + 0.7975 * W_X - 2.6943055555556 * T_R^2 - 1.0875 * V_M * T_R + 4.17 * T_R * W_X \quad (4)$$

Interaction graph of V_M and T_R on $\%SRR_C$ as shown in Fig. 8(a) clearly explains that $\%SRR_C$ attains a maximum value of 53.47 % when V_M is kept at highest level of 3.5A and T_R at lowest value of 300 rpm, keeping W_X constant at 1.5 mm and pouring 50 ml of hydrogen

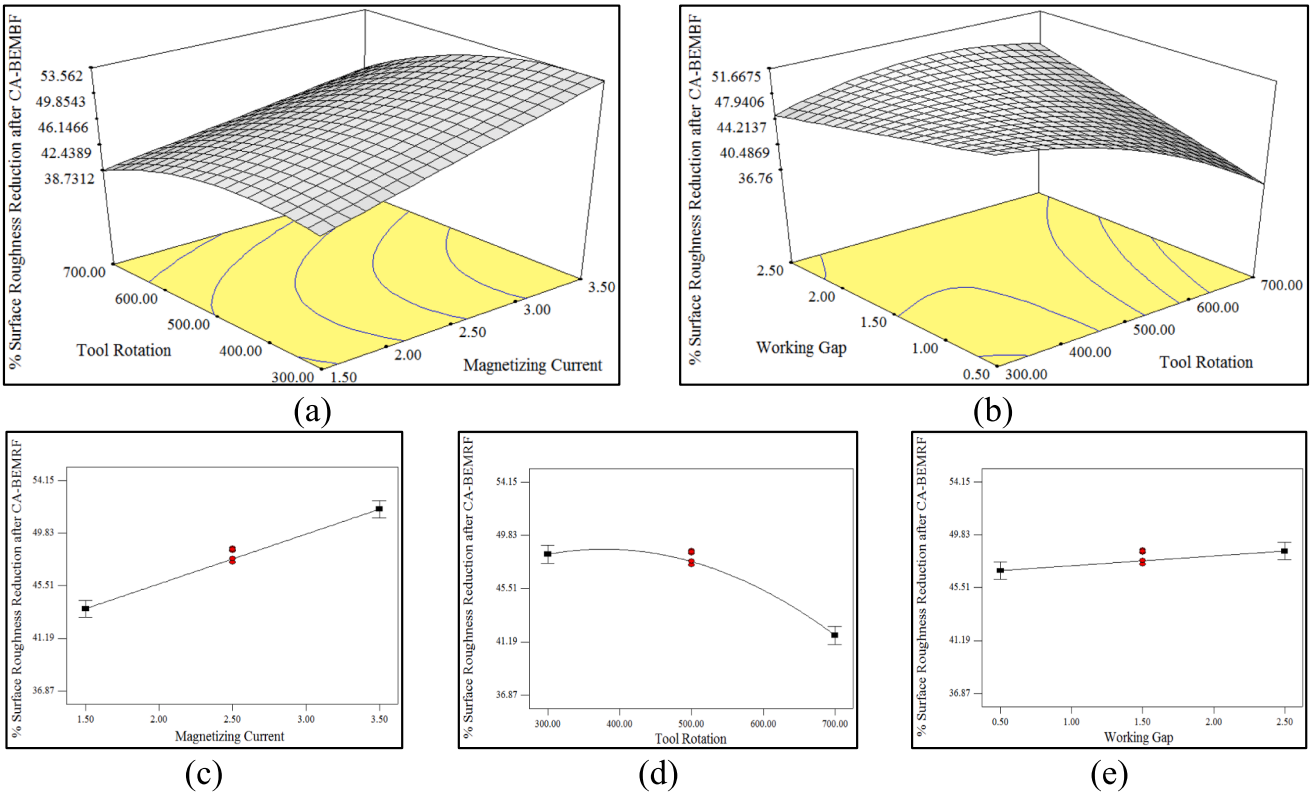

Fig. 8. (a) Magnetizing Current and Tool Rotation interaction graph on percent $\%SRR_C$, (b) Interaction graph of Tool Rotation & Working Gap on $\%SRR_C$, (c) Individual effect of Magnetizing Current on $\%SRR_C$, (d) Individual effect of Tool Rotation on $\%SRR_C$ and (e) Individual effect of Working Gap on $\%SRR_C$.

Table 8
10 best solutions for finishing of Al 7075 using CA-BEMRF process.

S. No.	Magnetizing Current V_M	Tool Rotation T_R	Working Gap W_X	Predicted %Decrease in Surface Roughness after CA-BEMRF	Desirability	
1	3.43	326.97	0.74	55.316	1	Selected
2	3.33	346.99	0.52	55.070	1	Selected
3	3.49	303.31	1.26	54.237	1	
4	3.48	334.26	1.00	54.817	1	
5	3.47	329.62	1.08	54.599	1	
6	3.43	331.56	1.03	54.475	1	
7	3.37	317.66	0.77	55.079	1	
8	3.41	367.31	0.94	54.188	1	
9	3.46	346.95	1.08	54.386	1	
10	3.50	305.32	1.26	54.278	1	

Table 9
Confirmatory Experiments after finishing of Al 7075 using CA-BEMRF process.

S. No.	Magnetizing Current V_M	Tool Rotation T_R	Working Gap W_X	Predicted %Decrease in Surface Roughness after CA-BEMRF	Actual %Decrease in Surface Roughness after CA-BEMRF	% Error
1	3.4	327	0.7	55.316	55.871	+1.003
2	3.3	347	0.5	55.070	55.336	+0.005

peroxide. When compared to the BEMRF method, the CA-BEMRF process has a smaller percentage reduction in surface roughness. This may be due to the effect of liquid hydrogen peroxide on the viscosity of the fluid. On the other hand, a minimum of 38.73 % reduction in surface roughness is attained at lowest value (1.5 A) of V_M and highest value (700 rpm) of T_R.

Combined effect of T_R and W_X on $\%SRR_C$ as represented in Fig. 8(b) shows that $\%SRR_C$ value increased from 36.76 % to 46.69 % on increasing W_X from 0.5 to 2.5 mm while keeping T_R at 700 rpm. It is also observed that $\%SRR_C$ value further increased to 51.67 % once tool rotation is decreased to a minimum value of 300 rpm and working gap to 0.5 mm.

Fig. 8(c, d, e) represents the individual impact of magnetizing current, tool rotation and working gap on $\%SRR_C$ respectively. The same slant as the interaction graph was followed by the individual effect plot, which showed that an increase in V_M and W_X increased the $\%SRR_C$ while an increase in T_R reduced $\%SRR_C$ due to the reasons quoted above. When the magnetising current was raised from 1.5 A to 3.5 A, $\%SRR_C$ reached a high value of 51.79 percent.

2.5. Output response optimization

Derringer and Suich [4] introduced a desirability function approach that was applied to optimize the response to the output i.e. percentage surface roughness reduction after CA-BEMRF ($\%SRR_C$). In this approach, the measured properties of each predicted response where d ranges between 0 and 1 are assigned a dimensionless desirability value (d). Montgomery [19] described that if the desirability function reaches a value of 0 it refers to an unacceptable response and if d = 1 then the answer is exactly to the destination. The value of d grows in proportion to the desirability of the related response. In the present work, the scenario considered is larger the better rate of cutting. The equation (5) given below is used to transform the response into a dimensionless function di.

$$\mathrm{di} = \begin{cases} 0 Xi < Bi \\ (Xi - Bi/Hi - Bi)\mathrm{w} \quad Bi \le Mi \le Hi \\ 1 Bi > Hi \end{cases} \tag{5}$$

where Bi = Lower response limit, Mi = Upper response limit, Hi = Response goal value. B and M are selected in RSM according to the mathematical.

Optimization Steps:

- Finding the desirability response value
- Optimizing desirability function and detecting the best possible response value

Design Expert 6.0.8 software has been used to perform response optimization. Table 8 shows the 10 best solutions obtained using the desirability method. The highest desirability value obtained is 1, which means that when finishing Al 7075, the maximum surface roughness reduction percentage can be obtained at $V_M = 3.43$, $T_R = 326.97$ and $W_X = 0.74$ through chemical assistance.

In order to check the solutions mentioned in Table 8 a confirmatory experiment was conducted for solution no. 1 and 2 and input process parameter values have been rounded to the nearest integer number. Table 9 represents the actual value of the % reduction in surface roughness after CA-BEMRF of aluminium alloy 7075 workpiece obtained after conducting the confirmatory experiments. The results of the confirmatory trials demonstrate that there was less than 1 % inaccuracy. These results confirm excellent reproducibility of the favorable solutions obtained after the optimization.

2.6. Surface topography of machined surface

Scanning electron micrograph (SEM) of aluminium 7075 alloy workpiece surface after grinding process, BMERF process and CA-BEMRF process is shown in Fig. 9a, 9b & 9c respectively. The lays are visible clearly on the workpiece surface due to the pre-finishing technique i.e. grinding process as shown in Fig. 9a. It can be observed from the Fig. 9b that more uniform and improves surface finish with very less grinding marks is obtained after BEMRF of the workpiece. When finished with the assistance of chemical agent hydrogen peroxide, % decrease in surface roughness increased from 53.83 % to 54.15 % leading to an improved surface finish as shown in Fig. 9c. This finish was obtained at 3.5A magnetizing current, 300 rpm tool rotation and 1.5 mm working gap during CA-BEMRF process.

3. Conclusion

This research work explores the minimization of surface roughness induced after grinding process on Al 7075 workpiece surface through polishing using BEMRF process and to observe further increase in surface finish if any through CA-BEMRF process. The effects of input constraints viz. magnetizing current, tool rotation and working gap were

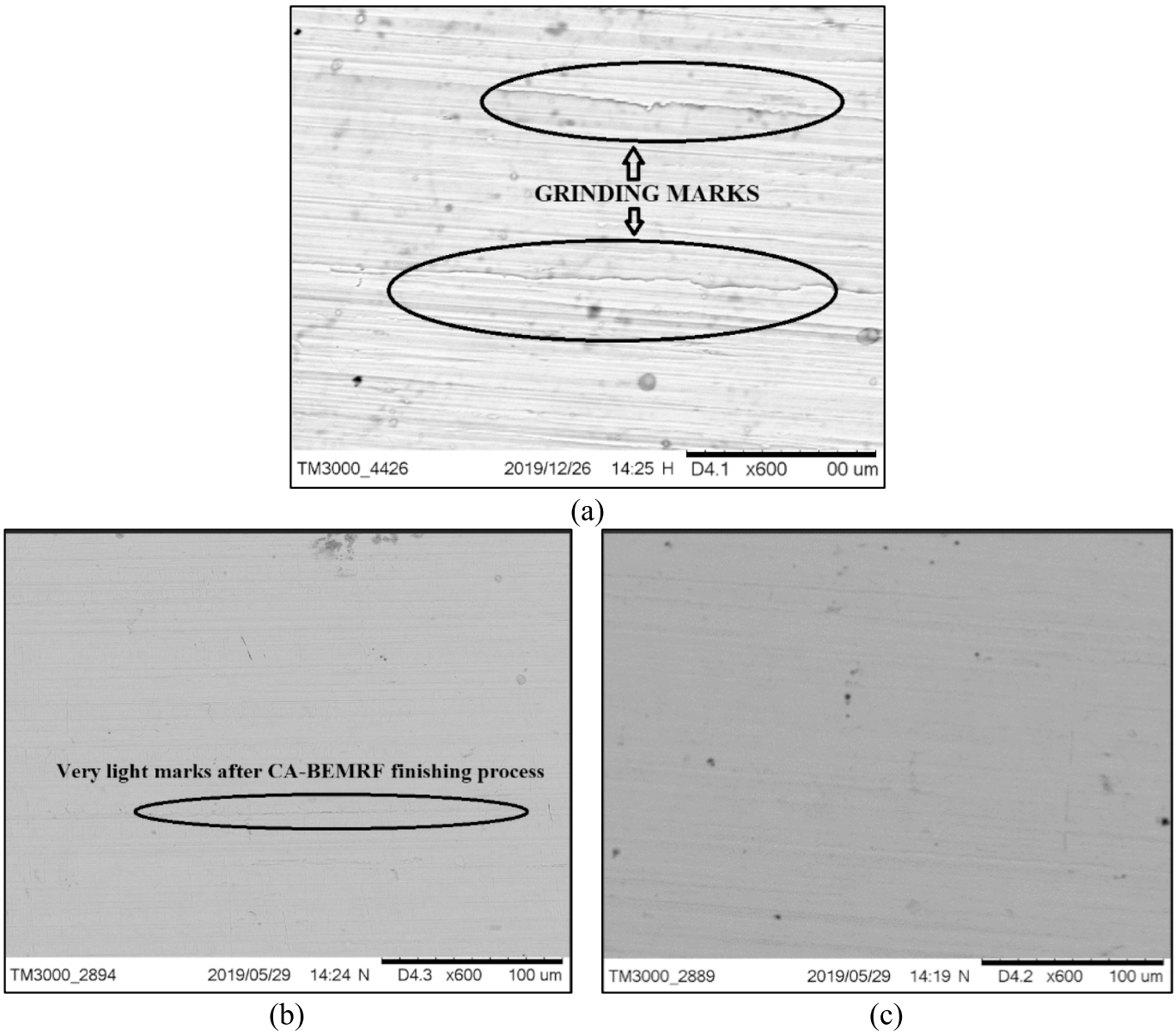

Fig. 9. SEM of workpiece after (a) BEMRF process (b) CA-BEMRF process.

studied through variation in percentage surface roughness reduction after BEMRF (%SRR_B) and further improvement in percentage surface roughness reduction after CA-BEMRF process (%SRR_C). Desirability approach was used to carry out the optimization of %SRR_C through design expert software. From this study, following conclusions are drawn.

- The experiments have been conducted on aluminium 7075 alloy workpiece with CA-BEMRF process and BEMRF without chemical assistance. The results obtained with CA-BEMRF process was found better in terms of % decrease in surface roughness.
- Although the combined impact of magnetising current and tool rotation, as well as the combined effect of tool rotation and working gap on % decrease in surface roughness, were determined to be significant according to the ANOVA table.
- It was found that the %SRR_B increased from 41.63 % to 50.63 % and %SRR_C increased from 43.62 % to 51.79 % when magnetizing current value was increased from 1.5 A to 3.5 A keeping tool rotation and working gap constant at 500 rpm and 1.5 mm respectively.
- Results also showed that the %SRR_B decreased to 41.65 % from 47.34 % and %SRR_C decreased to 41.73 % from 48.3 % when tool rotation increased to highest level of 700 rpm.
- Optimum % decrease in surface roughness has been found as 55.316 at magnetizing current 3.43amp, tool rotational speed 326.97 rpm and working gap of 0.74 mm using CA-BEMRF process.
- Confirmatory experiments have been conducted and results obtained were found very close to the predicted outcome.
- SEM images of the finished workpieces showed an improved surface finish after CA-BEMRF process.

Declaration of Competing Interest

The authors declare that they have no known competing financial interests or personal relationships that could have appeared to influence the work reported in this paper.

References

[1] Alam Z, Jha S. Modeling of surface roughness in ball end magnetorheological finishing (BEMRF) process. Wear 2017;374:54–62. https://doi.org/10.1016/j.wear.2016.11.039.

[2] Alam Z, Khan DA, Iqbal F, Jha S. Effect of polishing fluid composition on forces in ball end magnetorheological finishing process. Int J Precis Technol 2019;8(2–4):365–78.

[3] Chiu S-Y, Wang Y-L, Liu C-P, Lan J-K, Ay C, Feng M-S, et al. The application of electrochemical metrologies for investigating chemical mechanical polishing of Al with a Ti barrier layer. Mater Chem Phys 2003;82(2):444–51.

[4] Derringer G, Suich R. Simultaneous optimization of several response variables. J Qual Technol 1980;12(4):214–9. https://doi.org/10.1080/00224065.1980.11980968.

[5] Fan Z, Tian Y, Liu Z, Shi C, Zhao Y. Investigation of a novel finishing tool in magnetic field assisted finishing for titanium alloy Ti-6Al-4V. J Manuf Process 2019;43:74–82. https://doi.org/10.1016/j.jmapro.2019.05.007.

[6] Fan Z, Tian Y, Zhou Q, Shi C. Enhanced magnetic abrasive finishing of Ti–6Al–4V using shear thickening fluids additives. Precis Eng 2020;64:300–6. https://doi.org/10.1016/j.precisioneng.2020.05.001.

[7] Fooladfar H, Hashemi B, Younesi M. The effect of the surface treating and high-temperature aging on the strength and SCC susceptibility of 7075 aluminum alloy. J Mater Eng Perform 2010;19(6):852–9. https://doi.org/10.1007/s11665-009-9562-z.

[8] Garg H, Negi VS, Kharola AS, Sharma R. Effect of Magnetic Field on MR-Fluid in Ball End Magnetorheological Finishing. In COMSOL Conference. 2014.

[9] Ghai V, Ranjan P, Batish A, Singh H. Atomic-level finishing of aluminum alloy by chemo-mechanical magneto-rheological finishing (CMMRF) for optical applications. J Manuf Process 2018;32:635–43. https://doi.org/10.1016/j.jmapro.2018.03.032.

[10] Ghosh G, Sidpara A, Bandyopadhyay PP. Fabrication of optical components by ultraprecision finishing processes. In: Micro and precision manufacturing. Springer, Cham; 2018. p. 87–119. doi: 10.1007/978-3-319-68801-5_5.

[11] Iqbal F, Jha S. Closed loop ball end magnetorheological finishing using in-situ roughness metrology. Exp Tech 2018;42(6):659–69. https://doi.org/10.1007/s40799-018-0284-8.

[12] Jain VK, Ranjan P, Suri VK, Komanduri R. Chemo-mechanical magneto-rheological finishing (CMMRF) of silicon for microelectronics applications. CIRP Ann 2010;59(1):323–8. https://doi.org/10.1016/j.cirp.2010.03.106.

[13] Khan DA, Alam Z, Jha S. Nanofinishing of copper using ball end magnetorheological finishing (BEMRF) process. In: ASME international mechanical engineering congress and exposition. Vol. 50527. American Society of Mechanical Engineers; 2016, November, p. V002T02A002. doi: 10.1115/IMECE2016-65974.

[14] Khan DA, Jha S. Selection of optimum polishing fluid composition for ball end magnetorheological finishing (BEMRF) of copper. Int J Adv Manuf Technol 2019;100(5):1093–103. https://doi.org/10.1007/s00170-017-1056-9.

[15] Koul R, Rannot RC, et al. An update on the design and implementation of the MACE gamma-ray telescope. International Cosmic Ray Conference 2011;9:107–10. https://doi.org/10.7529/ICRC2011/V09/0803.

[16] Kumar A, Alam Z, Khan DA, Jha S. Nanofinishing of FDM-fabricated components using ball end magnetorheological finishing process. Mater Manuf Process 2019;34(2):232–42. https://doi.org/10.1080/10426914.2018.1512136.

[17] Kumar Y, Singh H. Chemomechanical magnetorheological finishing: Process mechanism, research trends, challenges and opportunities in surface finishing. 25165984211038878 J Micromanuf 2021. https://doi.org/10.1177/25165984211038878.

[18] Kuo HS, Tsai WT. Effects of alumina and hydrogen peroxide on the chemical-mechanical polishing of aluminum in phosphoric acid base slurry. Mater Chem Phys 2001;69(1–3):53–61. https://doi.org/10.1016/S0254-0584(00)00299-6.

[19] Montgomery DC. Design and analysis of experiments. New York: John Wiley & Sons Inc; 2001.

[20] Niranjan M, Jha S, Kotnala RK. Ball end magnetorheological finishing using bidisperse magnetorheological polishing fluid. Mater Manuf Process 2014;29(4):487–92. https://doi.org/10.1080/10426914.2014.892609.

[21] Niranjan MS, Jha S. Flow behaviour of bidisperse MR polishing fluid and ball end MR finishing. Proc Mater Sci 2014;6:798–804. https://doi.org/10.1016/j.mspro.2014.07.096.

[22] Niranjan MS, Jha S. Experimental investigation into tool aging effect in ball end magnetorheological finishing. Int J Adv Manuf Technol 2015;80(9–12):1895–902. https://doi.org/10.1007/s00170-015-6996-3.

[23] Peters M, Leyens C. Aerospace and space materials. Mater Sci Eng 2009;3:1–11.

[24] Qian C, Tian Y, Fan Z, Sun Z, Ma Z. Investigation on rheological characteristics of magnetorheological shear thickening fluids mixed with micro CBN abrasive particles. Smart Mater Struct 2022;31(9):095004. https://doi.org/10.1088/1361-665X/ac7bbd.

[25] Ranjan P, Balasubramaniam R, Jain VK. Analysis of magnetorheological fluid behavior in chemo-mechanical magnetorheological finishing (CMMRF) process. Precis Eng 2017;49:122–35. https://doi.org/10.1016/j.precisioneng.2017.02.001.

[26] Ranjan P, Balasubramaniam R, Suri VK. Development of chemo-mechanical magnetorheological finishing process for super finishing of copper alloy. Int J Manuf Technol Manag 2013;27(4–6):130–41.

[27] Ranjan P, Balasubramaniam R, Suri VK. Modelling and simulation of chemo–mechanical magnetorheological finishing (CMMRF) process. Int J Precis Technol 2014;4(3–4):230–46.

[28] Saraswathamma K, Jha S, Rao PV. Experimental investigation into ball end magnetorheological finishing of silicon. Precis Eng 2015;42:218–23. https://doi.org/10.1016/j.precisioneng.2015.05.003.

[29] Singh AK, Jha S, Pandey PM. Design and development of nanofinishing process for 3D surfaces using ball end MR finishing tool. Int J Mach Tool Manu 2011;51(2):142–51. https://doi.org/10.1016/j.ijmachtools.2010.10.002.

[30] Singh AK, Jha S, Pandey PM. Magnetorheological ball end finishing process. Mater Manuf Process 2012;27(4):389–94. https://doi.org/10.1080/10426914.2011.551911.

[31] Singh AK, Jha S, Pandey PM. Nanofinishing of a typical 3D ferromagnetic workpiece using ball end magnetorheological finishing process. Int J Mach Tool Manu 2012;63:21–31. https://doi.org/10.1016/j.ijmachtools.2012.07.002.

[32] Singh AK, Jha S, Pandey PM. Nanofinishing of fused silica glass using ball-end magnetorheological finishing tool. Mater Manuf Process 2012;27(10):1139–44. https://doi.org/10.1080/10426914.2011.654159.

[33] Singh AK, Jha S, Pandey PM. Performance analysis of ball end magnetorheological finishing process with MR polishing fluid. Mater Manuf Process 2015;30(12):1482–9. https://doi.org/10.1080/10426914.2015.1019098.

[34] Tian Y, Shi C, Fan Z, Zhou Q. Experimental investigations on magnetic abrasive finishing of Ti-6Al-4V using a multiple pole-tip finishing tool. Int J Adv Manuf Technol 2020;106(7):3071–80. https://doi.org/10.1007/s00170-019-04871-z.

Anand Sharma is a Research Scholar at Delhi Technological University, (formerly Delhi College of Engineering), New Delhi. He has a total teaching experience of more than 9 years. He has published 5 papers in peered International Journals and 3 papers in International Conferences. His areas of interest are Nano-Finishing, Non-Traditional machining processes, Characterisation of Metal Matrix Composites, Machining of difficult to machine materials.

International Journal of Computing and Digital Systems
ISSN (2210-142X)
Int. J. Com. Dig. Sys. xx, No. x (May-23)

http://dx.doi.org/10.12785/ijcds/xxxxx

Citrus Fruit Disease Detection Techniques: A Survey and Comparative Analysis of Relevant Approaches

Poonam Dhiman[1], Amandeep Kaur[2] and Vinay Kukreja[2]

[1]*Government PG College, Ambala Cantt, India*
[2]*Chitkara University Institute of Engineering and Technology, Chitkara University, Punjab, India*

Received xx xx xxxx, Revised xx xx xxxx, Accepted xx xx xxxx, Published xx xx xxxx

Abstract: The incorporation of computer vision in contemporary agriculture has witnessed significant advancements, particularly in detecting diseases and deficiencies affecting citrus fruit production. This study provides an in-depth comparative analysis of several limitations of the citrus fruit detection system and the cutting-edge machine vision algorithms used for classification. Traditional diagnostic methods are initially reviewed, followed by an elaborate discussion on various image acquisition techniques such as remote sensing, hyperspectral imaging, bio speckle laser imaging, and color imaging. These techniques focus on extracting features like color, texture, and size for diagnosing citrus fruit diseases. Despite their effectiveness, the images obtained might contain noise and distortions. The study details two crucial steps—image preprocessing and segmentation—to minimize these anomalies. It further explores a range of classification techniques and their efficacy in different research contexts. The paper is structured around five key components: diverse image capture methods, preprocessing and segmentation techniques, various extracted features, classification techniques for citrus fruit detection, and a comparison among classification methods like machine learning, deep learning, and statistical techniques. The study concludes by discussing current challenges and limitations in detecting citrus fruit diseases. It emphasizes the use of thresholding in hyperspectral imaging and identifies RGB color space as a frequently used feature. Among the compared techniques, Support Vector Machine (SVM) in machine learning, Artificial Neural Network (ANN) in neural networks, Convolutional Neural Network (CNN) in deep learning, and Linear Discriminant Analysis in statistical approaches emerge as the most effective.

Keywords: Image acquisition, preprocessing, segmentation, clustering, machine learning, deep learning, statistical techniques

1. Introduction:

Various applications like autonomous vehicles, object detection, face recognition systems, and many more depend upon endeavoring to imitate the capacities of a brain to understand the information given. Indian agriculture is of paramount significance because of the country's expanding population and rising food needs. Therefore, it is necessary to increase crop productivity. One of these significant factors contributing to reduced agricultural yields is the prevalence of bacterial, fungal, and viral diseases. Expert persons visually detect vegetables and fruits to assess the quality of crop production. However, different constraints are there in the case of classification done manually, such as one should be conversant with varying characteristics of vegetables and fruit. Manual detection needs a regular and harmonious approach to maintain efficiency. The food industry applies different detection mechanisms and depends on machine vision to analyze Crop harvesting. By using methods for plant disease detection, this can be avoided and managed. Techniques relied on machine learning will be employed in the procedure of identifying plant illnesses since they apply information most frequently and provide excellent methods for disease diagnosis. Because machine learning techniques focus on data supremacy results for a given goal, they can be used to identify disorders. A limited number of studies during the past ten years have shown how crucially the quality of fruit products affects human wellbeing. Fruit items should form the foundation of a healthy eating plan [1].

The research provides a comparative analysis of several constraints of the citrus fruit recognition techniques and cutting-edge machine vision methods utilized for classification. Background research involves image-capturing procedures, a description of the most widely used preprocessing techniques, different features extracted from the citrus fruit dataset, and classification methods used by

E-mail address: poonamdhiman19@gmail.com, amadeep@chitkara.edu.in, onlyvinaykukreja@gmail.com

various researchers are discussed in Section 2. In Section 3, a comparison of classification methods using derived features, various datasets employed, and the detection system's accuracy are shown. Finally, Section 4 presents a more thorough evaluation of the shortcomings of current methodologies and future directions. The study's conclusion is presented in Section 5.

2. Background

Machine vision platforms are indeed a commercial tool for food standards evaluation. All such systems would assess production throughout the domain and be used for robotic post-harvest or the early diagnosis of possibly lethal diseases. It is often used in post-harvest processing for the computer-controlled investigation of the fruits' external quality, including the breakneck speed filtering of them together in commercial sections. Figure 1 illustrates the complete process of disease detection of citrus fruit images, including acquisition, image processing (pre-processing and segmentation), and feature extraction (color, shape/size, textural) followed by the classification process that can use ML, DL, and the statistical techniques(ST). The whole process has used many evaluation parameters to analyse the outcome of the approaches used to recognise the diseases of citrus fruits.

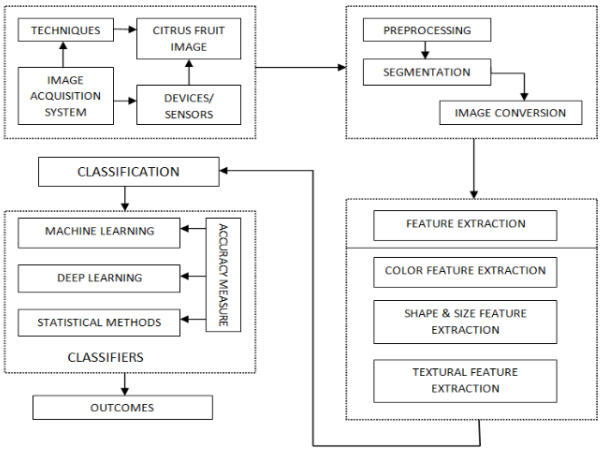

Figure 1. Complete process of citrus fruits diseases detection

A. Image Acquisition System

Images are used for acquiring information. Computer vision systems carry out conceptual and algorithmic estimation, allowing useful information about the objects or images to be automatically obtained from the acquired images and evaluated. Multispectral acquisition systems typically scan throughout the 3D while collecting 2D data at a time. Relied on filteration methods like optical filters and automatically adjustable filters, multispectral scanners and imagers are categorized into various types [2]. The most often used acquisition system is a 3CCD camera arranged with a light source utilizing a grey card [3]. Different fusion methods, including features , pixels, and symbolic levels, have recently been created. To identify orange fruits using visible-thermal pictures, researchers have used image fusion [4]. Two separate NIR devices, a micro-NIR and an FT-spectrometer, are displayed in the terms near-infrared spectrometer and spectral acquisition. Using a linear regression model, the two micro-NIR and FT spectrometers were compared [5]. Table 1 shows the acquisition technique, sensors, and devices used by the image acquisition system, along with the wavelength range or resolution used and the spectral band sizes. The studies' main acquisition techniques are remote sensing techniques, hyperspectral imaging systems, biospeckle laser imaging systems, and color imaging systems.

B. Pre-processing and Segmentation:

After the image acquisition, the next step is pre-processing. The objective of Pre-processing will enhance the grade of image samples that has unwanted distortion or inflates key features. Because of different photographic conditions, any differential operator highlights the noise without applying the pre-processing step. There exist various kinds of approaches for enhancement, noise removal, filtering, and sharpening of images. The discrete cosine transform method has been used to enhance the image during the grace period [6]. The filtering process is also used on mango fruit images to remove the noise. Background subtraction using thresholding for the determination of the coarse of mango fruit is employed [7]. Radiometric correction is the widely used method for the pre-processing of multispectral images [8]. Pre-processing was first conducted by filter processing followed by an image sharpening process with Matlab R2010b software [9]. Histogram equalization is a widely used technique for contrast enhancement of colored images. It produces the statistics for the contrast and overall intensity distribution of an image. Three different approaches are used for the pre-processing of Landsat imagery of the agricultural area [10]. The first approach employed the gradient magnitude of the image that meets the optimum method for image samples with temporal changes and yielded 100% acceptability. The second approach was thresholding the magnitude of the gradient and achieving 97% accuracy. The third approach used thresholding at the median.

TABLE I. Image acquisition techniques addressed in selected studies

Paper	Acquisition Technique	Sensor/Device	Resolution / Wavelength Range	Size/Spectral Band
[11]	Visible–NIR	NIR spectrophotometer, light source; reflectance probe, computer with acquisition software.	650–1050 nm	334 spectra
[12]	Unmanned aerial vehicle remote sensing	The multispectral camera	4.32 pixels/mm	651 × 801 pixel
[13]	Hyperspectral imaging system	Monochrome camera, frame-grabber, Two tunable liquid crystal filters, halogen lamps, aluminum hemispherical diffuser	4.32 pixels/mm	651 × 801 pixel
[14]	Biospeckle laser imaging	Digital camera	5 megapixels	(1920×1080pixels)
[15]	Hyperspectral vision system	Smartphones, compact cameras, DSLRcameras, two liquid crystal tunable filters, and low chromatic dispersion	10 nm	460 nm to 1020 nm
[16]	RGB color imaging system	Digital camera, lighting box including two LED lamps	4320×3240	——
[17]	X-ray imaging	Nikon metrology Gun set, image intensifier, and CCD camera	Pixels	1024 1024 1024 pixels
[18]	NIR spectral acquisition	NIR System 6500	2 nm	700–1100 nm
[19]	Color imaging system	DSC Camera, imaging chamber, and imaging box have the light source of LED, UPS power supply	640 × 480 pixel	——
[20]	Electronic nose system and Electronic tongue system	Apparatus for sampling, a detector set having a sensors grid and software for information gathering using structure identification	——	——
[21]	Diffuse reflectance system	portable spectrometer,optic-fiber probe, Ultraviolet (UV) and mercury lamps	200–900 nm.	1050 spectra (five per sample)
[22]	Visible and short-wavelength nearinfrared	50 Watt six halogen lamps,200 mm fiber optic probe, dimmer circuit, spectrometer	2 nm	——
[23]	Hyperspectral image	Monochrome camera,frame-grabber, Two tunable liquid crystal filters, halogen lamps, aluminum hemispherical diffuser	3.75 pixels/mm	551 × 551
[24]	Hyperspectral imaging	An imaging system based on line scan having an electron expanding CCD, a digital spectrograph, push broom, C-mount lens	400 to 900 nm	280 × 658 for each band.
[25]	Hyperspectral imaging	Thermo electric cooled electron multiplying CCD with size 14-bit, a spectrograph mount with a standard 23-mm zoom lens; halogen light area sources, motorized positioning sample table with controlling software, and spectral imaging software system.	325–1100 nm	700 × 1004 pixels

Continued on next page

Table I continued

[26]	Spectrograph-based hyperspectral imaging	Spectrograph, 150-halogen lamp containing two lighting fibers.	The pixel resolution of 0.58 nm and a resolution of 2.8 nm	422.29 to982.40 nm
[27]	Laser-light backscattering imaging	CCD (charge-coupled device) based camera , five laser diodes, light sources	0.073 mm/pixel	720 × 576
[28]	Colour image acquisition system	3-CCD camera, eight fluorescent tubes, Polarised filters	0.17mm per pixel	768x576 pixels
[29]	Electronic nose system	Computerized gasmixer, a detector set having a grid of sensors, and measurement and pattern recognition software	——	——
[30]	Visible near-infrared hyperspectral	The camera includes a VIS/NIR liquid- Crystal programmable filter	10 nm	1040 x1392 x 44
[31]	color image acquisition system	CCD camera, image frame grabber, six white fluorescent tubes in lightening system, Diffuse reflection plate	0.28 mm/pixel	640 x 480 pixels
[32]	Hyperspectral imaging system	14-bit monochrome camera, an imaging spectrograph, halogen light area sources, electrically controlled sample stage	325–1100 nm	700×1004
[33]	Smart Mobile Diagnosis System	WeChat applet, Nginx server	——	——
[34]	Machine vision	Color CCD camera, C-mount lens, frame grabber card, fluorescent lamps	640 H x 480 Vpixels	——
[35]	Computer vision	Camera, incandescent lamp, Windows10 OS platform with Matlab7.0	——	——
[36]	Near-infrared reflectance system	Multi-Purpose Analyzer, FT-NIR spectrometer, quartz beamsplitter, NIR source with an air cooling system, and a detector (InGaAs).	4cm-1	12 spectra
[37]	Hyperspectralimaging system	High-resolution monochromatic camera with two liquid crystal tunable filters	7 nm	400 to 1100 nm
[38]	Computer Vision system	Direct digital output camera using a Firewire	640 × 480 pixels	256 levels per channel (R, G, B)
[39]	Hyperspectral imaging systems	A monochrome camera has highrange of sensitivity from 320 to 1,020 nm, a frame grabber, and an aluminum hemispherical diffuser containing 12 halogen lamps.	3.75 pixels/mm	551×551 pixel
[40]	The diffused illumination system computervision systems	CCD camera, a lighting system composed ofbacklighting and a personal computer	12.1Megapixels	——
[41]	Near-infrared information system	Multi-view camera	24 bits-per-pixel	164x113 pixels
[42]	Computervision systems	NTSC camera, frame grabber, Two fluorescentcircular lights, commercial softwarepackage	787 Kbyte per image	512 x 480
[43]	Computervision systems	Digital camera	——	——

Continued on next page

Table I continued

[44]	Hyperspectral imaging system	Electron-multiplying CCD camera, Peltier device, the lighting system (21 V,150 W halogen lights), Hg-Ne spectral calibration lamp	5.2 nm	1004 x 1002 pixels
[45]	NIR	Kinect for Software Development Kit 2.0	512 by 424 pixels	——
[46]	Color imaging system	Digital camera	——	640 x 480 pixels
[47]	RGB color imaging system	Digital camera	1024 768-pixel	——
[48]	Machine vision system	Two cameras, rollers, cog belt	0.1–g	——
[49]	Fluorescent spectrum system	Fluorometer, digital refractometer	200 to 550 nm	300 to 700 nm
[50]	UAV-based hyperspectral imaging technique	Remote sensing technique, Resonon's hyperspectral imagers, the global positioning system	——	400–1000 nm
[50]	Color imaging system	Digital color camera	——	——
[51]	NIR	Non-destructive sensor+ CCD camera+ digital board+ digital refractometer	3mm x 25mm	770-1070 mm
[52]	Color imaging system	Sony cyber shot camera, dark imaging chamber	4320x3240 pixels	——
[53]	Color imaging system	Sony cyber-shot camera, dark imaging chamber, conveyor belt, actuator	——	——
[54]	Color imaging system	Digital color camera (SonyCybershot DSC-WX300)	——	——
[55]	RGB color imaging system	Digital camera and mobile phone camera	——	——
[32]	Hyperspectral image calibration	Spectral Image Software (Isuzu Optics Corp., Taiwan), CCD detector	500–1050 nm	1007 bands
[56]	Spectral imaging system	Reflection probe holder, light source, spectrometer	0.28 to 0.38 nm	1914wavelengths
[57]	RGB Color image system	Two high frequency sealed fluorescent lights of 13 W, a zoom lens, a 3-CCD RGB color camera, a 24-bit colored frame grabber board	480×640 pixel	100 mm×100 mm
[58]	NIR	CR-200 colorimeter, S2000 spectrometer, four halogen lamps (100W), and an array of lens and optical fibers.	650 [nm] to 955 [nm].	——
[59]	RGB Color image system	CCD sensor camera, two fluorescenttube lamps	——	——
[60]	Color image system	13 MP CMOS camera, illuminationthe system, computer hardware, and camera holder	1920 * 1080 pixels	——

Different acquisition methods can result in noise, distortion, and flickering in image samples, all of which can lower the image quality. As a result, the image cannot properly contribute to the data set. Image processing can therefore be used on the image samples to address this problem. Segmentation and image pre-processing are the two basic procedures used in image processing techniques. There are countless strategies for locating and controlling plant pests and diseases, but image processing employing advanced artificial intelligence methods like deep learning is the most popular. In some circumstances, data retrieved from sensors or other inputs are added to picture processing. A method for detecting citrus fruit diseases based on lightweight artificial intelligence approaches was reported in certain studies. This system used edge computing to process all the data on the cutting-edge Raspberry Pi. The authors contrasted clear photos of both healthy and diseased rice leaves on a white backdrop. The relevant features were retrieved from the images after the appropriate pre-processing. Following that, using various machine learning methods, image categorization models were created based on these attributes [61].

The segmentation of an image area is an essential activity for image processing. For the computer vision system, segmentation is the procedure of clustering the pixel into salient regions with certain properties. Image segmentation is also referred to as assigning a label to pixels of an image such that these labeled pixels help in sharing some visual features. Various approaches like thresholding, region growing, k-means clustering, and watershed have been used to estrange the lesion areas affected by anthracnose diseases in fruits. For an x-ray imaging system, the gray level of the pixels relies on the thickness and the density of the images [62]. Segmentation of the color image samples has been carried out in two stages, in the first step, a 2D feature map captures the dominant color of the images in supervised mode, and in the second step, a variable size 1D feature map and color merging was used to regulate the clusters range [63]. Various color spaces for segmentation and color images have been designed for data acquisition. For the automated image segmentation of the colored images of fruits, CIELuv color space was used. The color space of the CIELuv is qualitatively consistent and the color space is system independent.

The images acquired by the image acquisition methods may contain noise, distortion, and variability. To reduce these deformities among raw images two major steps i.e. image pre-processing and image segmentation. Table 2 shows the name of various pre-processing techniques used by the studies in our SLR. Majorly used techniques employed by the studies are scaling, normalization, image enhancement, filtering, thresholding, masking, histogram equalization, transformation, transformation, morphological operation, watershed, k-means, ostu based segmentation techniques that depict in the table also. Apart from the techniques mentioned in Table 2, some other techniques are also used by various studies like edge/boundary detection for the segmentation purpose, color segmentation, gradient method, wavelet transformation, and c-mean clustering. The most widely used image processing techniques used are image enhancement/filtering followed by thresholding**.**

C. Feature Extraction:

Several visual characteristics associated with fruit and vegetables are called features. Initially, fruit images are captured by the camera, and then pre-processing and segmentation methods are used on the imagery. to filter, smoothen, and remove the noise images. After these steps, feature extraction takes place which further helps to classify the diseases. Color is the most persuasive aspect and substantial descriptor that frequently improve feature extraction for image analyses of fruits and vegetables. Color features perform a crucial part in detecting or classifying the disease of the fruits. Different color space like HSV, RGB, HIS, and YCbCr is employed for classification purpose. Color features are more considerable than other features because of invariance to shape, size, and direction, simplicity in the extraction process, and background complexity individualisms [64]. Images are transformed into a different colour space to depict more desirable aspects that are not striking in standard RGB space. In this study, the L*, a* & b* component value of the image is taken to get the LAB color space. By using a histogram on the segmented image the color feature has been extracted [65]. Two important size features area and perimeter can also be evaluated by getting the pixel count of the images and by adding up the distance of each adjacent pixel at the boundary respectively. For food and vegetable quality analysis most common size features are area, perimeter, length, and width. Apart from these features, major axis, and minor axis features can also be determined for classification purposes. The major axis is the largest line through the fruit or vegetable product which is determined by the measurement of the distance between the two boundary pixels of each mixture and chooses the longest distance. The longest line formed perpendicular to the major axis by the entity is considered the minor axis [66]. For a broad variety of images that utilize human visual frameworks for identification and perception, the texture is indeed a quite suitable classification feature. The textural feature computed from the pixel group reflects the dissemination of components and the morphology of the surface and is useful for computer vision that determines the surface in the context of entropy, roughness, orientation, contrast, etc. The interior condition of the fruits and vegetables, including growth and sugar component, is consistent with the textural feature [67]. Numerous features can be utilized to depict an item, which is further contrasted with the details collected from non-object for the classification into different classes. Usually, the most sustainable features that are simple to measure and significantly contribute to the classification are the best [68].

TABLE II. Summary of image processing techniques

	Scaling/ Normalization	Noise Removal	Image Enhancement/ Filtering	Thresholding	Masking	Histogram equalization	Transformation	Morphological operation	Watershed	k-means	Ostu based
[12]		✔	✔								
[17]		✔	✔								✔
[19]				✔							
[23]			✔								
[24]					✔						
[25]			✔	✔			✔		✔		✔
[26]	✔		✔	✔	✔			✔			
[28]	✔			✔	✔	✔					
[29]											
[30]				✔			✔				
[31]			✔	✔							
[32]			✔								
[34]	✔		✔							✔	
[35]			✔	✔		✔					
[38]		✔		✔	✔						
[39]				✔	✔						
[40]	✔										
[41]				✔			✔	✔			
[42]				✔							
[43]	✔			✔		✔					
[44]				✔							
[45]			✔								
[46]			✔	✔		✔					
[69]				✔				✔	✔		
[50]				✔	✔						
[47]				✔					✔		
[48]	✔										
[49]											
[50]		✔									
[52]										✔	
[70]			✔								
[53]		✔	✔								
[55]	✔										
[57]							✔				
[60]	✔			✔		✔	✔				
[61]			✔	✔				✔			
[71]	✔	✔	✔		✔						
[72]		✔							✔		
[73]			✔	✔					✔		
[74]			✔				✔			✔	
[75]			✔	✔							
[76]					✔						
[77]		✔	✔								✔
[78]			✔							✔	
[79]			✔							✔	
[80]			✔							✔	
[81]			✔	✔							
[82]			✔	✔							
[83]		✔	✔								
[84]		✔	✔							✔	
[85]		✔	✔								
[86]		✔	✔								
[87]										✔	✔

1) Color Feature:

Different color spaces are constituted by colors like RGB, HIS, HSV, YIQ, and YCbCr. The description of various color features used in selected studies is mentioned in Table 3. The most commonly used color space is RGB color space which consists of red, green, and blue elements of the picture. HIS color space has three components i.e. hue (H) which is an angular value that constitutes the predominant wavelength of color, the second component saturation (s) indicates the quantitative aspect of color and the third component intensity which is the ratio of darkness/brightness of color.HSI color space can aberrantly recognize the segments of color and diminish the complex color dimensions [88]. YIQ color space represents one luminance component and two chrominance components depending upon the difference in color signal (R-Y, B-Y).three components of YIQ space correspond to y(luminance), I(in-space) and Q is the quadrature that combines to represent hue and saturation [89]. In the YC_bC_rcolor space, the Y component is similar to the Y component of the YIQ color space. By using reduced spatial resolution and coarser quantization for C_b& C_r greater compression is achieved. The authors show that using the RGB color space effect of light causes a false detection area which will result in poor defect detection. YC_bC_r color space is used which produces a better result as compared to RGB space [69]. This paper also uses a linear regression model that indeed classifies undefined orange samples and also estimates the maturity of the orange fruit. Table 3 represented the various color spaces and color models used by different investigations on citrus fruits.

2) Shape/size feature:

The outcome of the total perimeter is 39.46 and 445.28; the area perimeter is 23.21 and 13.43 using transversal and axial radiographs respectively. Different types of shape/size features were used in different studies for citrus fruits for classification analysis the normalized delta and $delta^2$values along with (di_{polar}/$dia_{equator}$) shape factors were used [42]. The area which is defined as the overall image pixels of orange fruit and the circumference of the total count of edge points are calculated for the shape feature. A comparison between the extracted features from an axial and transversal radiograph of endoxerated lemon fruit is conducted [17]. Different shape features are derived using binary images in the study [51]. Using multiple linear regression, size features like length and width of the principal axis are measured with the employed algorithm while polar and equatorial diameters were determined manually. The study shows that the area parameter has a higher correlation with manual measurement after investigating the relationship between the area obtained with the vision system and two manual measurements. The correlation coefficient between manual and vision measurement of the major axis is 0.82, the minor axis is 0.84 and the area is 0.091 [6]. The $diameter_{polar}$ shows the stem-to-blossom end computation. The shape factor based on the equatorial/ polar diameter ratio was the input neural net analysis. Shape features such as perimeter, area, minor, and major axis length are calculated [43]. Using neural networks correlation coefficient remains low for predicting the maturity of orange fruit. So it is difficult to get the growth of oranges with selected non-destructive sensors. The small deviation is the perimeter-area function method used to calculate the fractal dimension of disease and pest hazards. Perimeter-area fractal dimension is derived according to B.Mandebrot fractal theory. Two surface defects i.e. white streaks and black rot points are detected in orange fruit [35]. The RGB image is transformed into grayscale for the computation of the shape feature. After that, the grayscale image gets transformed into a binary image depicting the value above the threshold is treated as 1, and a value below the barrier is treated as 0. Table 4 shows the various extracted shape/size features used in the selected studies.

3) Textural Features:

Textural features are one of the most widely used features for image ranges that have a visual system of human identification and explication. Textural feature from the pixel set shows the element distribution and appearance. It is also beneficial in the application of the machine vision system that depicts surface features like orientation, contrast, entropy, roughness, etc. textural properties that have compatibility with internal qualities like sugar content as well as the maturity of the fruits. It segregates various image patterns by considering values intensity magnitude. Table 5 shows the various extracted textural features used in the studies.

3. Classification and Comparative Analysis:

The quality of agricultural products is significantly lowered as a result of plant diseases and pests. Pests like Mediterranean fruit diseases, one of the most significant plant pathogens, seriously harm crops, costing farmers a lot of money in lost produce each year. Therefore, it is crucial to utilize contemporary, non-destructive approaches to identify pests in agricultural goods as early as possible. Examples include machine vision systems and deep learning [90], [91]. The Neural Network is a technique inspired by and analogous to the human nervous system and brain structure. It constitutes units of processing divided into layers of input, hidden, and output. Neural networks hit a dark phase in their evolution in 1969, rather than experiencing further research and growth, while professors at MIT illustrated that they could not learn a basic XOR function [92]. Besides, several other studies have blunted the motivation for DNN in particular [93], [94]. A revolution in DNN emerged with the introduction of the learning algorithm for back-propagation. It was suggested in the 1970s, but it wasn't completely understood and extended to neural networks until the mid-1980s.

TABLE III. Different color spaces used for different fruits and their color model used.

Paper	Fruit type	Color space	Color model
[19]	Oranges	RGB	Ravg, Bavg, Gavg, and maturity/ripeness measure
[35]	Orange	RGB	Mean R, G, and r-g values and standard deviation
[38]	Oranges	RGB	Histogram of each color component
[41]	Orange	(RGB) and RGBI	RGB, Hue-Saturation-Intensity, and X-Y Lightness model
[42]	Grapefruit, orange, tangerine	HSI	Color standard location and calculation of color standard values
[43]	Orange	HSV	Hue, Saturation, and Intensity-based
[45]	Hamlin sweet orange	RGB, NIR	circular Hough transform
[46]	Oranges	HSV	mean and standard deviation
[47]	Orange	RGB	Watershed on RGB, Border/Interior pixel Classification (BIC) (logarithmic distance (dLog) and extract (mean gray value)
[48]	Orange, grapefruit, or tangerine	HIS	Macbeth color checker
[50]	Oranges	HSV and YIQ	S and I component from HSV and YIQ domain
[51]	Oranges	RGB	Colorimeter
[52]	Kinnow	RGB, HSI	12 features derived from R-G-B channels, Hue, Saturation, and Intensity. Mean and Variance of each of the six components.
[53]	Orange	HSV	Histograms analysis of the r-g-b and the gray levels, Mean and median evaluation from HSV color space
[54]	Orange	H SV and YIQ	Mean, variance, and range values calculated from the separated S and I components
[55]	Lemon	CMY	The pixel count of the red, green, and yellow component
[57]	Grapefruits	HIS	Coordinates of chromaticity in the hue and saturation space
[59]	Bitter orange	RGB and CIE	Color matrix statistical parameters (R- G- B), or their variations and proportions, & three CIE parameters (L*a*b *)
[61]	Citrus fruits	RGB, HSV, HSI, LAB, and LUV	All color characteristics are eventually merged by basic convolution into one vector and achieve a size 1 to 60 function vector
[71]	Oranges or tangerines	HSV (Hue, Saturation, Value)	Low and the high hue values
[69]	Navel Orange	RGB, YCbCr	Gray distribution mapping
[70]	Apple, oranges, mangos, watermelon	RGB	Mean Intensity
[72]	Orange	RGB	The mean value of RGB channel splitting
[73]	Newhall navel oranges	RGB	Watershed on RGB
[74]	Mandarin Orange	L*a*b*	Color coherence vector and Global color histogram
[76]	Apple and Kinnow fruit	L*a*b*, HSV, HSI	Binary masks for hue and saturation channels, extraction of V-Channel of HSV model
[78]	Orange	RGB	Conversion of RGB color space into HSI color space, translating the Hue value to degrees on the color circle
[85]	Apple, avocado, banana, and orange	RGB	Kernel of Gaussian values
[86]	Persian lemon	HSV	Number of pixels of the fruit, as well as the sum of the small areas that represent the present defect
[87]	Orange and potato	L*a*b* or CIE-Lab	Euclidean color distance
[95]	Lemon	L*a*b*	Mean shift vector
[96]	Tangerine	RGB and HSV	Nonlinear transformation of the RGB

DNN is a type of multilayer perceptron (MLP) modeled neural network that is trained through methods for learning depictions from data sources without even any manual feature extractor model. It consists of a larger or deeper number of processing units, as the term Deep Learning implies, which compares with the shallow learning paradigm of fewer unit layers [98].

Table 6 represents the name of the techniques which outperformed the other ML techniques. SVM is the best technique that performed better than W-KNN, EBT, DT, naïve bayes, fuzzy, and RBF techniques in six different experiments. The second best-performed technique is the decision tree in 5 different experiments as compared to the naïve bayes, RB, fuzzy, EBT, and SMO. We found that the AdaBoost ML technique is a very less explored technique in the field of citrus fruit disease classification. Adaboost ML technique was used in only one study and outperformed many ML and DL techniques. Lastly, some more techniques like the random forest, KNN, ELM, and FA were also found to be well-performed ML techniques.

Similarly, in some experiments, ML techniques performed better than other DL techniques. Like, SVM again performed better than DL techniques such as ANN, CNN, and MLP in 5 different experiments. Table 7 shows ML techniques that performed better than the DL techniques. Here, we observed the DT, Bayesian, Adaboost, KNN, W-KNN and ELM also performed well than DL techniques in 1 or 2 experiments.

Table 8 shows ML techniques that outperformed the other statistical techniques like LDA, PCA, and LR. Look at table 9 which shows DL techniques that outperformed ML techniques. It can be observed that ANN and CNN are the two best techniques that performed better than the ML techniques in 5 and 2 experiments respectively. We also found that other DL techniques like neural network radial basis; Associative neural net and backpropagation neural networks outperformed the other ML techniques in different experiments.

Table 10 mentioned statistical techniques that performed well when compared to the other techniques. It can be observed that the LDA technique is the best technique among all the statistical techniques in comparative studies of our SLR. Other well-performed statistical techniques we found arePartial least square regression, PCA and LR.

A. Summary & Findings of Comparative Analysis:

The use of extra spatial characteristics aids in improving the classification accuracies of the approaches in citrus fruit classification, as can be shown from the comparison study of ML and DL techniques. CNN uses rich spatial features at various scales to represent the spatial structure of the data to categorize each pixel in the image since spatial information can increase classification accuracy.

When DL and ML techniques are compared, it becomes apparent that most of the relevant features in traditional ML techniques must be determined by an expert in the field so as to decrease the complexities of the information and render correlations readily apparent to learning techniques. The primary advantage of DL algorithms is their aim to gradually learn complex features from data. This eliminates the need for rigorous feature extraction and domain expertise.

It becomes evident that both SVMs and NNs are capable of doing classification, with the SVM requiring the proper choice of kernel and the NN requiring the proper choice of the activation function. When the pixel-based reflectance data were employed, lacking the segmentation measurement, CNN was found to have a static-major gain over SVM in terms of overall correctness. In both SVM and CNN classifications, the impact of pixel-based training data was considerable. As a difference in sample size, object-based training samples differ from pixel-based training samples. Although, if the total sample count is the alike for both types of samples yet pixel-based reflectance data give trained classifiers access to more spectral reflectance values.

As a result of maximizing classification accuracy, LDA decreases the dimensionality of the data, making it more efficient than PCA for classification datasets. Drawing decision lines for data with the greatest degree of separation is simpler. Using the citrus fruits classification dataset, it has been found that the LDA is significantly more successful than PCA for dimensionality reduction in classification datasets.

Table 11 shows the type of dataset used for the research work by different studies, along with their accuracies obtained. Many researchers have used private data by acquiring the images using different image acquisition systems like UAV-based systems, multispectral systems, and remote sensing systems with the help of digital cameras or sensors for the particular area or orchards. In some studies, citrus fruits are inoculated into chemical solutions for fungal diseases. The studies that commonly used Public data sources are the Kaggle dataset, plant village, www, andCitrus image Gallery dataset.

It is noted that around 73 % of the selected studies were published in journals, while the rest were published in conference proceedings (i.e., 27 %). Postharvest Biology and Technology and Computers and Electronics in Agriculture are the two foremost journals that have been published in 8 and 6 studies selected in the SLR. These two journals published around 19% of all the chosen publications that examined the intended area of the study. We consider here only those journals which have been indexed as Science Citation.

TABLE IV. Measuring parameters of different feature matrices.

Paper	Fruit type	Feature matrix
[17]	Oranges, lemon	Overall perimeter, average solidity, and proportion of the complete area to the perimeter
[25]	Oranges.	Area, perimeter, and circularity
[35]	Orange	Area, circumference, size
[42]	Grapefruit, orange, tangerine	Center-finding routine, eight radii, perimeter tracing, shape factor ratio, area normalized values for delta and delta2values, (diameter.ˆ,./diameterequator)
[43]	Orange	Major and minor axis length, perimeter, the image area
[46]	Orange	Major and minor axis length, perimeter, area
[69]	Navel Orange	Surface area and coloring area
[51]	Orange	Length, width, elongation, circularity, major axis length and minor axis length, width, length, area, perimeter
[53]	Orange	Area, fractal dimension, box-counting dimension,
[55]	Lemon	Area, Major axis, and Minor axis
[60]	Apple, litchi, mosambi, pomegranate, and pears	Major and minor axis, mean, convex area, diameter, solidity, area, perimeter
[61]	Citrus fruits	Major and minor axis, extent, area, perimeter, filled area, aspect ratio, and solidity
[73]	Newhall navel oranges	Perimeter and area with pixel count,perimeter-area fractal dimension
[82]	Nova mandarins	Circular spot, Deepness Shallow,
[83]	Mandarin	Discriminant relevance of feature, z statistic of feature, global relevance of each feature
[86]	Persian lemon	Equatorial diameter, surface area of the lemon, percentage of area with defects, Persian lemon

TABLE V. Textural Features

Paper	Texture Feature	Descriptor	Fruits
[11]	1570 spectral Features (visible–NIR and NIR)	Scatter-correction methods	Mandarin
[14]	Regular value of differences (RVD), the absolute value of differences (AVD), modified AVD (NUMAD), and Inertia moment (IM)	Co-occurrence matrix (COM)	Orange
[15]	For each spectral band pixel reflectance degree, average reflectance and standard deviation of a pixel cluster	57 spectral features, 114 spatio-spectral features	Tangerines
[30]	Mean, variance, skewness, kurtosis, range	First, second and high order statistics	Oranges
[34]	Mean, standard deviation	Wavelet Packet Texture analysis	Mandarin fruit
[40]	Mean, std_dev, energy, entropy	Four statistical curvelet-based texture descriptors	Lemon
[41]	Minimum, maximum, range, arithmetic mean, range and standard deviation	Spatial variation in pixel intensities/ statistical feature	Orange
[43]	Angular Second Moment, Contrast, Correlation, Gradient Module, Intensity symmetry	Five textural features derived from the gray-level co-occurrence matrix	Orange
[44]	Reflectance spectra of the five peel conditions, the two-band ratio, and the band difference	92 spectral bands.	Valencia Oranges
[45]	Divergence and vorticity values	Gradient vectors of depth values	Hamlin sweet orange
[46]	Geometric and harmonic mean, variance, standard deviation, mean, median, range, and (Angular Second Moment, Contrast, Correlation, Gradient Module, Intensity symmetry)	Gray level co-occurrence matrix, histogram statistics	Orange
[50]	Mean, SD, skewness, kurtosis, energy, entropy, correlation, prominence, homogeneity, the sum of the square, etc (44 feature)	First-order statistical texture features, second-order Gray level co-occurrence feature	Oranges
[53]	Contrast, Correlation, Energy, Homogeneity, Skewness, Kurtosis	Six statistical descriptors with occurrences gray level matrix.	Orange
[54]	Brightness, contrast, uniformity, flatness, smoothness, contrast, correlation, cluster prominence, dissimilarity, autocorrelation, maximum probability, energy, the sum of squares, sum average, sum and difference variance, sum and difference entropy, maximal correlation coefficient, entropy, cluster shade, homogeneity, information measures of correlation 1 and 2, inverse difference, normalized inverse difference moment normalized and inverse difference	First-order and second-order statistical features using the GLCM method	Orange
[57]	Uniformity, variance, product-moment, mean intensity, correlation, sum entropy, entropy, difference entropy, modus information correlation #1 and #2, contrast, and inverse difference	All of the other three SGDM, 13 texture characteristics for each part of the HSI	Grapefruits
[61]	cluster prominence and shade, homogeneity, energy, Mean, range, skewness, and entropy	18 GLCM features	Citrus fruits
[69]	Smoothness descriptor , consistency measure , and the average entropy descriptor	Grayscale with statistical feature	Navel orange
[74]	Correlation, mean, entropy, RMS, contrast, variance, energy, standard deviation, smoothness, kurtosis, IDM, skewness, and homogeneity	Thirteen textural features are extracted from GLCM	Mandarin Orange
[78]	Minor wavelet, major wavelet.	2-D deviation of a grey level	———
[82]	Depressed or Prominent Topography of the surface, Ruggedness of the central surface, Central texture		Nova Mandarins
[84]	Contrast, correlation , entropy, homogeneity, and energy	Gray-level co-occurrence matrix	Banana, Mango, Citrus, Grape, Guava, Apple, Papaya, Peach, Watermelon Pomegranate
[85]	Correlation, energy, homogeneity, contrast, entropy, Mean, variance, skewness, kurtosis, range, IDM	Statistical features,gray-level co-occurrence matrix	Apple, Avocado, Banana, and Orange
[96]	Mean, variance, skewness, kurtosis, range	First, second and high order statistics	Tangerine
[97]	Mean, standard deviation, and skewness	Reflectance parameter and reflectance distribution parameters	Thompson and Jaffa Oranges

TABLE VI. ML techniques that outperformed other ML techniques

ML Best Technique	Outperformed ML Techniques					
SVM	W-KNN, EBT, DT [61]	KNN, SRS [83]	KNN, Naïve BaYes [12]	DT, Fuzzy [16]	RBF [53]	KNN [99]
DT	Naïve BaYes [47]	RB [53]	Fuzzy [16]	EBT [61]	SMO [53]	
FA	SM [11]					
Adaboost	SVM [12]	KNN [12]	Naïve Bayes [12]			
RF	SVM [20]					
KNN	FUZZY,DT [16]					
W-KNN	EBT [61]					
ELM	SVM [20]					

TABLE VII. ML techniques that outperformed DL techniques

Best Technique	Outperformed Techniques				
SVM	ANN [78]	CNN [60]	ANN [83]	ANN [16]	MLP [53]
DT	ANN [47]	MLP [53]			
BaYesian	NN [42]				
Adaboost	NN [12]				
KNN	CNN [60]				
W-KNN	EBT [61]				
ELM	SVM [20]				

TABLE VIII. ML techniques that outperformed Statistical techniques

Best Technique	Outperformed Techniques	
SVM	LDA [61]	
DT	LDA [37]	
FA	PCA [11]	SM [11]
Adaboost	LR [12]	

TABLE IX. DL techniques that outperformed ML techniques

Best Technique	Outperformed Techniques						
ANN	SRC [83]	SVM,LR, [12], [14]	DT [16]	Naïve BaYes [47], [12]	KNN [16], [83]	FUZZY [16]	LDA [14] QDA [14]
CNN	KNN[99]	ANN, DT, FUZZY [16]	SVM [16],[99]				
NNRB	KNN [50]						
ASNN	SVM [54]	BPNN [54]					
BPNN	SVM [54]						

TABLE X. Statistical techniques that outperformed other ML techniques

Best Technique	Outperformed Techniques		
LDA	PCA [29]	EBT [61]	CART [23]
PLS	MLR [58]		
PCA	SM [11]		
LR	SVM [12]	Naïve baYes [12]	KNN [12]

TABLE XI. Datasets and Classification Accuracy of the selected studies

Dataset	Accuracy	
117 mandarins with 67 were peripherally ruptured on the rind and immunized with P. digitatum fungus spores and the rest 50 were damaged in about the same manner and handled for process control with sterile water.	97.8%	[11]
334 citrus image samples consist of healthy as well as infected images with HLB disease	97.28%	[12]
13,680 monochromatic images of the 240 mandarins (60 fruits does not exhibit any noticeable disruption, 60 fruits had typical disruption inflicted by wind scars, 60 fruits were immunized with P. digitatum unit, other 60 fruits were immunized with P. italicum solution	93% spores 60 fruits were inoculated with a solution of P. italicum spores	[13]
Biospeckle images	100%	[14]
Tangerines fruit samples	98%	[15]
341 sour lemon images with data augmentation applied(2960 healthy and 2496 unhealthy sour lemon samples)	100%	[16]
30 orange samples and 38 lemon fruit with diverse nature of the infections	95.7% of oranges and93.6% of lemons	[17]
In 2017, Tangerines were taken twice. On 20 June 2017, the first sample collection of 97 late-harvested fruits was retrieved. On 3 August 2017, the second sample collection (178 fruits) was obtained (early harvested fruit)	———	[18]
160 Orange fruit samples	89.9% Edited multi-Seed-NN(Nearest Neighbor) and 92.93 % Nearest Prototype	[19]
Six styles of fruit exhibit blemishes were collected as target items, including oil stain, HLB, wind scar, rust mites, leafminer damage, and melanose. 30 fruit samples were gathered for each form of blemish also healthy fruit samples were collected	Classification accuracies for healthy mature citrus obtained is 98.4%, HLB 90.8%, melanose-95.2%, oil spot 92.0%, wind scar90.8%, and leaf-miner 95.2% and rust mite 96.8%	[21]
165 grapefruits	92.70%	[24]
210 samples of naval orange having 80 healthy and 130 defective fruits	98.60%	[25]
Early-ripe citrus fruit images from China (Wenzho)	96.50%	[26]
For the tests, 100 orange fruits were taken from which 50 were vaguely damaged on the epicarp and immunized with P. digitatum spores, and 50 other were infected in the same manner but handled for process control with sterile water	96.10%	[27]
20 images of oranges and mandarins from four distinct varieties were randomized: Fortune, Marisol, Clemenules, and Valencia120 varieties of randomly chosen orange and mandarin images belonged to four separate cultivars: Valencia, Fortune, Clemenules, and Marisol	91.50%	[28]
Ripe and Non-infested 'Shangtangju' mandarin (Citrus reticulate Blanco). 20 samples were classified randomly into two categories of control and infested pests classes	98.21%	[29]
Eight distinct orange and mandarin variants were studied, including Clementine, Blood Orange, Washington Navel, Miro, Nova, Salustiana, Nadorcott, and Navel Lane Late. 100 fruits of each type were immunized with a concentration of 106 P. spores/ml. The Digitatum. The fungus class is represented by these citrus fruits. The remaining 50 fruits have been liquid-inoculated and constitute the control community	91.00%	[30]

Continued on next page

Table XI continued

160 citrus fruits, comprising 80 sound fruits and 80 defective fruits with P. digitatum fungi spore	For the training set and test set 97.5% and 93.8% with no false negatives	[32]
Network, local materials, images of fruits with 6 common diseases, and data augmentation	89%	[33]
Mandarin fruits images	50% stem-end rot, pitting 80%, Splitting 100%	[34]
Orange images	95.00%	[35]
54 citrus yielded in Huangyan were collected	80%	[36]
20 Mandarins and Clemenules Cv. Clemenvilla.	95%	[37]
1500 images of 150 oranges from “navel-late” and “Valencia-late”	62.1-100% for the range of defects	[38]
A maximum of 240 fruits were used: 60 that were sound, 60 that had exterior scars, 60 that had been immunized by P. digitatum spores, and 60 that had been injected with P. italicum microbes	89%	[39]
1040 lemons	91.72%	[40]
1400 orange (338 healthy images, 441 stem-ends and 621 have bruise of different sizes)	81% 2	[41]
443 grapefruit, 1,417 oranges, and 352 tangerines	Grapefruit-73.9 %,Orange-87.3 %, Tangerine-84.7%	[42]
400 orange images acquired by the rotation and rearrangement of fruit samples	The overall error of 2.75%	[43]
200 valencia orange samples	92%	[44]
Hamlin sweet orange (citrus sinensis) 255 images	96%	[45]
400 orange samples were produced by spinning and reorganizing fruit sample data.	88%	[46]
125 unripe orange images, 85 ripe fruit images, and 125 scaled or rotten orange images	93.13%	[47]
Tangerine varieties Florida grapefruit and orange	98.5% for grapefruit and orange and 98.3% for tangerine	[48]
47 citrus fruits(Satsuma mandarins)	Absolute error 2.48	[49]
Images of immature (green) fruits and tangerine sugar belle leaves were taken from an experiment orchard at Immokalee, Florida, USA	96%	[50]
320 oranges image (salustiana)	Maturity index=0.31	[51]
303 images Kinnow mandarin fruits from Punjab Agriculture University, Ludhiana (India)	98.66%	[52]
32 images of healthy oranges, 30 samples of medium-quality oranges, and 31 images of low-quality or faulty	MLP-84.9%,RBF network-83.9%,SMO-86.0%	[53]
Orange samples of 100 healthy and damaged were hand-picked across orange farms over Nilgiri hills, Tamil Nadu, India	94.50%	[54]
104 CBS positive citrus fruits and 30 CBS negative samples	93.40%	[56]
A total of 180 grapefruits were harvested with healthy and five infected peels	96.00%	[57]
For the maturity trial, 100 ’Unshiu’ citrus fruits were assigned and the remaining 200 fruits were used for the fault experiment.	97%	[58]

Continued on next page

Table XI continued

2000 samples of different fruits including the litchi, pears apple, pomegranate, and mosambi were generated	99%	[60]
5632 citrus disease images image samples from Gallery Dataset and Plant Village dataset	96.90%	[61]
Tree image of citrus fruits	93.30%	[71]
110 navel orange samples	93.30%	[69]
Infected fruit images of Vidharbha Region, India	400 orange samples were produced by spinning and reorganizing fruit sample data	[70]
200 ripe and 200 unripe image samples of citrus	90%	[72]
324 Newhall oranges with infections and pests	85.51%	[73]
Database of the University of California Agriculture and Natural Resources	90%	[74]
Totaling 68 images, there are 20 healthy oranges, 20 Melanose illnesses, 19 Citrus Canker, and 9 Brown Rot.	93.21%	[75]
Total images - 150,Canker-78 ,scab -15,greening-16,Black Spot-19,healthy-22(Citrus Image Gallery dataset)	97.29%	[77]
Kaggle datasets	88.96%	[78]
Images of five types of defects in orange fruit	67.74%	[79]
Four infected type orange specimens from the University of California Agriculture and Natural Resources database	90%	[80]
74 mandarin fruit images	83.30 %	[81]
212 mandarins samples having 43 black spots, 54 citrus canker, 45 scabs, and 70 other (nonquarantine) diseases from a Nova cultivar	83%	[82]
Apple, avocado, banana, and orange images from Kaggle.com	80.00% (k-NN),91.03% (ANN)	[83]
243 images from www	84.66 % C-mean,87.4651% k-mean	[84]
320 images, of which half correspond to lemons in good condition and the other half are not suitable for consumption according to established standards	98.25% for the classification of fresh lemons and 93.73% for spoiled lemons	[86]
800 images, including 400 samples of good appearance, 120 stem-end i, 80 stem-end	97%	[95]
RGB space and HSV (Hue, Saturation, Value) OF 1500 images of 180 orange fruits from “navel-late” and “Valencia-late”	62.1-100%(RGB) AND 62.8-100% (HSV) for the range of defects	[96]

TABLE XII. Dominant journals

Sr.No.	Journal Name	Count	Type	Impact Factor	H-Index
1	Postharvest Biology and Technology	8	Science Citation Index Expanded	4.4	132
2	Computers and Electronics in Agriculture	6	Science Citation Index Expanded	3.858	104
3	Journal of Food Engineering	4	Science Citation Index Expanded	4.03	167
4	Expert Systems with Applications	2	Science Citation Index Expanded	5.452	184
5	Applied Engineering in Agriculture	1	Science Citation Index Expanded	0.973	51
6	Biosystems engineering	1	Science Citation Index Expanded	3.59	100
7	Chemometrics and Intelligent Laboratory Systems	1	Science Citation Index Expanded	2.303	117
8	Cluster Computing	1	Science Citation Index Expanded	2.04	41
9	Current Science	1	Science Citation Index Expanded	0.756	110
10	Electronics Letters	1	Science Citation Index Expanded	0.97	142
11	Food Analytical Methods	1	Science Citation Index Expanded	1.17	40
12	Food Bioprocess Technology	1	Science Citation Index Expanded	3.2	76
13	Food Chemistry	1	Science Citation Index Expanded	5.399	242
14	Horticulture	1	Emerging Sources Citation Index	3.176	10
15	Horttechnology	1	Science Citation Index Expanded	0.63	52
16	IEEE Access	1	Science Citation Index Expanded	4.098	86
17	International Journal of Agricultural & Biological Engineering	1	Science Citation Index Expanded	0.25	26
18	International Journal of Engineering and Technology	1	Emerging Sources Citation Index	0.21	24
19	Journal of Ambient Intelligence & Humanized Computing	1	Science Citation Index Expanded	3.42	28
20	Journal of Integrative Agriculture	1	Science Citation Index Expanded	1.337	40
21	Journal of Scientific & Industrial Research	1	Science Citation Index Expanded	0.32	49
22	Journal of the Science of Food and Agriculture	1	Science Citation Index Expanded	2.463	131
23	Plant Physiology and Biochemistry	1	Science Citation Index Expanded	3.72	113
24	Remote Sensing	1	Science Citation Index Expanded	4.118	99
25	Scientia Horticulturae	1	Science Citation Index Expanded	2.769	102

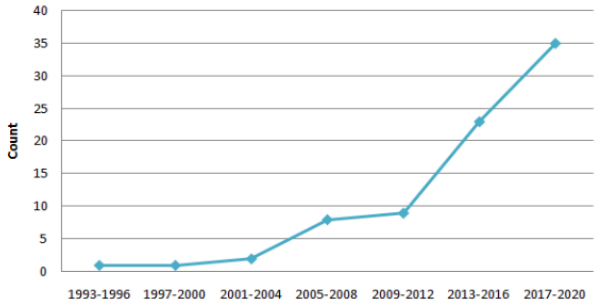

Figure 2. Distribution of selected studies

Table 12 shows the name of the dominant journal, including its impact factor and H-index. It can be observed that the Expert Systems with Applications journal has the highest impact factor, 5.452, contributing 2.5 percent of the total study count of our SLR. Food Chemistry is the second most journal having an impact factor of 5.399 with the highest h-index value of 242.

Publication sources are postharvest biology and technology, remote sensing, and journal of food engineering journals that impact factors 4.4,4.118, 4.03 respectively chosen in SLR. Figure 2 shows the division of different studies of this SLR from 1993 to 2020.

4. Limitations and Future Applications:

The paper provides a current analysis of the classification of citric products and essential procedures based on the literature. Earlier attempts have been widely documented. There are significant obstacles to solve regarding data-acquiring products, modeling features, and identification techniques. Sensors utilized in data collecting in the agribusiness are limited owing to significant constraints in diverse contexts. Several instances are non-destructive, contain ambient obstructions, and exhibit cross and intra-class similarities as well as complicated attributes. An additional key drawback of using numerous sensors in the same citrus fruit analysis application is the diverse nature of their data. This specific statistic nature also limits the ability to provide considerable multifaceted data integration.

Furthermore, no appropriate feature descriptors for the most modern sensors, i.e., RGBD sensors, are available. These barriers are clear in the pertinent composition and are discussed in the article. The computational recognition methods available in the literature are insufficient for dealing with dynamic-feature hyperdimensional data for categorization. Citrus fruits are divided into several categories, each with a unique set of characteristics. The identified classification techniques are limited by the absence of large datasets. The majority of the investigations in the review are restricted about categories or size of the dataset. A step towards making it possible to provide off-the-shelf modules for computer sensing systems is being done to build pre-trained CNN. Nevertheless, as these pre-trained CNN are data-dependent, it is difficult to get a dataset with a sizable amount of citrus fruits.

The authors encountered a variety of issues as they worked on classifying the diseases in food products. The main issue is the lack of a consistent database with information on specific diseases and crops. The academics are discouraged from working on this area of research due to the database's lack of availability. The issue with database generation comes afterward. The process of collecting real-time data from the field under various environmental factors is highly difficult and exhausting.

Real-time images have a lot of invariables such as distinct textures, distinct background features, image-taking angles, etc., which adds to the problem of preprocessing the image. Another concomitant issue with this is the choice of collecting devices. The choice of the actual field area for picture acquisition, the choice of the plant, the choice of the disease component of the plant, and the choice of the disease are some of the other issues. Another issue the author must address is the choice of illness and its manifestations that distinguish it from others in a particular way.

The selection of a design strategy that will result in a system that performs better while taking up less time and money is another consideration.

Future applications can be suggested to develop a real-time system that assists with decisions for improving crop productivity as well as quality. Among them include the use of equipment like drones, sensors, and superior cameras; establishing internet-based crop management systems; using hyperspectral or remote sensing images to measure crop efficiency, implementing internet of things technologies in plant pathology; and collaborating with artificial intelligence, cloud computing, IoT, edge computing and machine learning algorithms, among other things.

5. Conclusion:

This study provides a comparative analysis of several constraints of the citrus fruit detection system and cutting-edge computer vision methods utilized for categorization. Numerous image processing approches are discussed in this survey for the citrus fruit detecting system. Preprocessing, segmentation, feature extraction, and classification are the four key phases in this survey. Each phase is contrasted in terms of technique, effectiveness, benefits, and drawbacks. We conclude that pre-processing techniques improve segmentation accuracy. We also get the conclusion that graphic enhancement/filtering and thresholding are the two most used image processing approaches. Additionally, SVM and NN make use of the texture features, which are especially notable for depicting disease in the citrus fruit image.

There has been a rigorous analysis of the classification

procedure offered. The overview of a systematic study takes into account major sensor amenities, feature specifications, and classification techniques. To understand the present crucial issues in this sector, a comparison of classification techniques is made. To collect data for various applications in the food sector, the study investigates the considerable limitations of using currently accessible sensors and the amalgamation of several sensors. The report also discusses briefly the challenges of multi-sensory data fusion. The significance of pre-processing and segmentation needed for computer vision-based investigation in the food business has been raised.

References

[1] C. Jackulin and S. Murugavalli, "A comprehensive review on detection of plant disease using machine learning and deep learning approaches," *Measurement: Sensors*, pp. 100 441–100 441, 2022.

[2] C. Simon, A. Mansouri, F. S. Marzani, and F. Boochs, "Integration of 3D and multispectral data for cultural heritage applications : Survey and perspectives ☆," *Image Vis. Comput*, vol. 31, no. 1, pp. 91–102, 2012.

[3] R. Pydipati, T. F. Burks, and W. S. Lee, "Statistical and neural network classifiers for citrus disease detection using machine vision," *Trans. ASAE*, vol. 48, no. 5, pp. 2007–2014, 2014.

[4] D. M. Bulanon, T. F. Burks, and V. Alchanatis, "Image fusion of visible and thermal images for fruit detection," *Biosyst. Eng*, vol. 103, no. 1, pp. 12–22, 2009.

[5] C. Malegori, "Talanta Comparing the analytical performances of Micro-NIR and FT-NIR spectrometers in the evaluation of acerola fruit quality , using PLS and SVM regression algorithms," *Talanta*, vol. 165, pp. 112–116, 2016.

[6] C. Kaushal, M.K. Islam, A. A. Althubiti, F. Alenezi, and R. F. Mansour. A Framework for Interactive Medical Image Segmentation Using Optimized Swarm Intelligence with Convolutional Neural Networks. *Computational Intelligence and Neuroscience*, 2022.

[7] D. Lorente, P. Escandell-Montero, S. Cubero, J. Gómez-Sanchis, and J. Blasco, "Visible-NIR reflectance spectroscopy and manifold learning methods applied to the detection of fungal infections on citrus fruit," *J. Food Eng*, vol. 163, pp. 17–24, 2015.

[8] J. Gómez-Sanchis, J. D. Martín-Guerrero, E. Soria-Olivas, M. Martínez-Sober, R. Magdalena-Benedito, and J. Blasco, "Detecting rottenness caused by Penicillium genus fungi in citrus fruits using machine learning techniques," *Expert Syst. Appl*, vol. 39, no. 1, pp. 780–785, 2012.

[9] K. Itakura, Y. Saito, T. Suzuki, N. Kondo, and F. Hosoi, *Estimation of citrus maturity with fluorescence spectroscopy using deep learning*, vol. 5, pp. 1–9, 2019.

[10] K. Vijayarekha and R. Govindaraj, *Citrus fruit external defect classification using wavelet packet transform features and ANN*, pp. 2872–2877, 2006.

[11] K. Tarale and A. Bavaskar, "Fruit Detection Using Morphological Image Processing Technique," *International Conference on Science and Engineering for Sustainable Development*, pp. 60–64, 2017.

[12] D. Sahu and C. Dewangan, "Identification and Classification of Mango Fruits Using Image Processing," *Int. J. Sci. Res. Comput. Sci. Eng. Inf. Technol*, vol. 2, no. 2, pp. 203–210, 2017.

[13] F. Dadrasjavan, F. Samadzadegan, S. H. S. Pourazar, and H. Fazeli, "UAV-based multispectral imagery for fast Citrus Greening detection," *J. Plant Dis. Prot*, vol. 126, no. 4, pp. 307–318, 2019.

[14] X. L. Deng, Y. Lan, X. Q. Xing, H. L. Mei, J. K. Liu, and T. S. Hong, "Detection of citrus huanglongbing based on image feature extraction and two-stage BPNN modeling," *Int. J. Agric. Biol. Eng*, vol. 9, no. 6, pp. 20–26, 2016.

[15] M. Svedlow, C. D. Mcgillem, and P. E. Anuta, "Image Registration: Similarity Measure and Preprocessing Method Comparisons," *IEEE Trans. Aerosp. Electron. Syst*, vol. 14, no. 1, pp. 141–150, 1978.

[16] J. D. Pujari and R. Yakkundimath, "Grading and Classification of Anthracnose Fungal Disease of Fruits based on Statistical Texture Features," *Citeseer*, vol. 52, pp. 121–132, 2013.

[17] S. H. Ong, N. C. Yeo, K. H. Lee, Y. V. Venkatesh, and D. M. Cao, "Segmentation of color images using a two-stage self-organizing network," *Image Vis. Comput*, vol. 20, no. 4, pp. 279–289, 2002.

[18] H. Ali, M. I. Lali, M. Z. Nawaz, M. Sharif, and B. A. Saleem, "Symptom based automated detection of citrus diseases using color histogram and textural descriptors," *Comput. Electron. Agric*, vol. 138, pp. 92–104, 2017.

[19] C. Zheng, D. W. Sun, and L. Zheng, "Recent developments and applications of image features for food quality evaluation and inspection - a review," *Trends Food Sci. Technol*, vol. 17, no. 12, pp. 642–655, 2006.

[20] A. Bhargava and A. Bansal, "Fruits and vegetables quality evaluation using computer vision: A review," *J. King Saud Univ. - Comput. Inf. Sci*, 2018.

[21] A. Pourreza, W. S. Lee, M. A. Ritenour, and P. Roberts, "Spectral characteristics of citrus black spot."

[22] M. M and S. A. Papert, "Perceptrons: An introduction to computational geometry," 2017.

[23] G. Grekousis, "Artificial neural networks and deep learning in urban geography: A systematic review and meta-analysis," *Comput. Environ. Urban Syst*, vol. 74, pp. 244–256, 2019.

[24] K. Hornik, "Approximation Capabilities of Muitilayer Feedforward Networks," *Neural networks*, vol. 4, pp. 251–257, 1989.

[25] A. Shrestha and A. Mahmood, "Review of deep learning algorithms and architectures," *IEEE Access*, vol. 7, pp. 53 040–53 065, 2019.

[26] C. T. Soini and M. R. Abid, "Citrus Greening Infection Detection (CiGID) by Computer Vision and Deep Learning," *proceeding of 3rd International Conference on Information System and Data Mining*, pp. 21–26, 2019.

[27] M. S. H and P. C. J, "Automatic Detection of Surface Defects on Citrus Fruit based on Computer Vision Techniques," *Int. J. Image, Graph. Signal Process*, vol. 7, no. 9, pp. 11–19, 2015.

[28] M. V. Dael, "A segmentation and classification algorithm for online detection of internal disorders in citrus using X-ray radiographs," *Postharvest Biol. Technol*, vol. 112, pp. 205–214, 2016.

[29] S. K. Behera, L. Jena, A. K. Rath, and P. K. Sethy, "Disease Classification and Grading of Orange Using Machine Learning and Fuzzy Logic," *Proceedings of the 2018 IEEE International Conference on Communication and Signal Processing*, pp. 678–682, 2018.

[30] S. A. Khoje, S. K. Bodhe, and A. Adsul, "Automated Skin Defect Identification System for Fruit Grading Based on Discrete Curvelet Transform," *Int. J. Eng. Technol*, vol. 5, no. 4, pp. 3251–3256, 2013.

[31] R. Saha, "Orange Fruit Disease Classification using Deep Learning Approach," *Int. J. Adv. Trends Comput. Sci. Eng*, vol. 9, no. 2, pp. 2297–2301, 2020.

[32] P. Theanjumpol, K. Wongzeewasakun, and N. Muenmanee, "Non-destructive identification and estimation of granulation in ' Sai Num Pung ' tangerine fruit using near infrared spectroscopy and chemometrics," *Postharvest Biol. Technol*, vol. 153, pp. 13–20, 2019.

[33] R. Thendral and A. Suhasini, "Automated skin defect identification system for orange fruit grading based on genetic algorithm," *Curr. Sci*, vol. 112, no. 8, pp. 1704–1711, 2017.

[34] A. M. Khan and A. P. Paplinski, "Blemish detection in citrus fruits," *proceeding of SPIT-IEEE Colloquium and International Conference*, vol. 1, pp. 262–271, 2008.

[35] J. Jhawar, "Orange Sorting by Applying Pattern Recognition on Colour Image," *Praocedia Computer Science*, vol. 78, pp. 691–697, 2015.

[36] M. Kaur and R. Sharma, "Quality Detection of Fruits by Using ANN Technique," *IOSR J. Electron. Commun. Eng. Ver. II*, vol. 10, no. 4, pp. 2278–2834, 2015.

[37] W. M. Miller, "Optical defect analysis of Florida citrus," *Appl. Eng. Agric*, vol. 11, no. 6, pp. 855–860, 1995.

[38] V. Kavitha and M. R. Devi, "Predicting the Diseases by Graphcut Method for Citrus Fruits," *Int. Res. J. Manag. Sci. Technol*, vol. 7, no. 12, pp. 465–470, 2016.

[39] M. Sharif, M. A. Khan, Z. Iqbal, M. F. Azam, M. I. U. Lali, and M. Y. Javed, "Detection and classification of citrus diseases in agriculture based on optimized weighted segmentation and feature selection," *Comput. Electron. Agric*, vol. 150, pp. 220–234, 2017.

[40] G. Capizzi, G. Lo, C. Sciuto, E. Napoli, M. Tramontana, and Wozniak, "Automatic classification of fruit defects based on Co-occurrence matrix and neural networks," *Proceedings of Federated Conference on Computer Science and Information Systems*, pp. 861–867, 2015.

[41] K. N. Ranjit, K. S. Raghunandan, C. Naveen, H. K. Chethan, and C. Sunil, "Deep Features Based Approach for Fruit Disease Detection and Classification," *Int. J. Comput. Sci. Eng*, vol. 7, no. 4, pp. 2347–2693, 2019.

[42] S. Qiu, J. Wang, C. Tang, and D. Du, "Comparison of ELM, RF, and SVM on E-nose and E-tongue to trace the quality status of mandarin (Citrus unshiu Marc," *J. Food Eng*, vol. 166, pp. 193–203, 2015.

[43] D. Lorente, N. Aleixos, J. Gómez-Sanchis, S. Cubero, and J. Blasco, "Selection of Optimal Wavelength Features for Decay Detection in Citrus Fruit Using the ROC Curve and Neural Networks," *Food Bioprocess Technol*, vol. 6, no. 2, pp. 530–541, 2011.

[44] D. M. Bulanon, T. F. Burks, D. G. Kim, and M. A. Ritenour, "Citrus black spot detection using hyperspectral image analysis," *Agric Eng Int CIGR J. Open*, vol. 15, no. 3, pp. 171–180, 2013.

[45] D. G. Kim, T. F. Burks, J. Qin, and D. M. Bulanon, "Classification of grapefruit peel diseases using color texture feature analysis," *Int. J. Agric. Biol. Eng*, vol. 2, no. 3, pp. 41–50, 2009.

[46] Y. Zhang, W. S. Lee, M. Li, L. Zheng, and M. A. Ritenour, "Non-destructive recognition and classification of citrus fruit blemishes based on ant colony optimized spectral information," *Postharvest Biol. Technol*, vol. 143, pp. 119–128, 2018.

[47] A. Bhargava and A. Bansal, "Automatic Detection and Grading of Multiple Fruits by Machine Learning," *Food Anal. Methods*, vol. 13, no. 3, pp. 751–761, 2019.

[48] D. Choi, W. S. Lee, J. K. Schueller, R. Ehsani, F. Roka, and J. Diamond, "A performance comparison of RGB, NIR, and depth images in immature citrus detection using deep learning algorithms for yield prediction," *Annual International Meeting*, pp. 1–6, 2017.

[49] C. Senthilkumar and M. Kamarasan, "An Effective Classification of Citrus Fruits Diseases using Adaptive Gamma Correction with Deep Learning Model," *Int. J. Eng. Adv. Technol*, vol. 9, no. 2, pp. 2249–8958, 2020.

[50] S. Moomkesh, S. Ahmad, and M. Sadeghi, "ScienceDirect Early detection of freezing damage in sweet lemons using Vis / SWNIR spectroscopy," *Biosyst. Eng*, vol. 164, no. 31, pp. 157–170, 2017.

[51] X. Xie, "Image matching algorithm of defects on navel orange surface based on compressed sensing," *J. Ambient Intell. Humaniz. Comput*, vol. 0, no. 0, pp. 1–9, 2018.

[52] G. Capizzi, G. Lo, C. Sciuto, E. Napoli, M. Tramontana, and Woźniak, "A novel neural networks-based texture image processing algorithm for orange defects classification," *Int. J. Comput. Sci. Appl*, vol. 13, no. 2, pp. 45–60, 2016.

[53] G. Kim, K. Lee, K. Choi, J. Son, D. Choi, and S. Kang,

"Defect and ripeness inspection of citrus using NIR transmission spectrum," *Key Eng. Mater*, no. II, pp. 1008–1013, 2004.

[54] J. Gómez-Sanchis, "Hyperspectral system for early detection of rottenness caused by Penicillium digitatum in mandarins," *J. Food Eng*, vol. 89, no. 1, pp. 80–86, 2008.

[55] G. Stegmayer, D. H. Milone, S. Garran, and L. Burdyn, "Automatic recognition of quarantine citrus diseases," *Expert Syst. Appl*, vol. 40, no. 9, pp. 3512–3517, 2013.

[56] A. Wajid, N. K. Singh, P. Junjun, and M. A, "Recognition of ripe, unripe and scaled condition of orange citrus based on decision tree classification," *proceeding of international confrence on computing,mathematics and engineering technologies*, pp. 1–4, 2018.

[57] W. Pan, J. Qin, X. Xiang, Y. Wu, Y. Tan, and L. Xiang, "A Smart Mobile Diagnosis System for Citrus Diseases Based on Densely Connected Convolutional Networks," *IEEE Access*, vol. 7, pp. 87 534–87 542, 2019.

[58] J. Qin, T. F. Burks, M. S. Kim, K. Chao, and M. A. Ritenour, "Citrus canker detection using hyperspectral reflectance imaging and PCA-based image classification method," *Sens. Instrum. Food Qual. Saf*, vol. 2, no. 3, pp. 168–177, 2008.

[59] A. Rahmanian, S. A. Mireei, S. Sadri, M. Gholami, and M. Nazeri, "Application of biospeckle laser imaging for early detection of chilling and freezing disorders in orange," *Postharvest Biol. Technol*, vol. 162, pp. 111 118–111 118, 2020.

[60] W. M. Miller and G. P. Drouillard, "Multiple feature analysis for machine vision grading of Florida citrus," *Appl. Eng. Agric*, vol. 17, no. 5, pp. 627–633, 2001.

[61] D. Zhu, L. Xie, B. Chen, J. Tan, R. Deng, Y. Zheng, Andrew, *Knowledge graph and deep learning based pest detection and identification system for fruit quality*, pp. 100 649–100 649, 2023.

[62] A. Jahanbakhshi, M. Momeny, M. Mahmoudi, and Y. D. Zhang, "Classification of sour lemons based on apparent defects using stochastic pooling mechanism in deep convolutional neural networks," *" Sci. Hortic. (Amsterdam)*, vol. 263, 2020.

[63] G. L. Yang, L. Luo, Y. Q. Feng, and H. S. Zhao, "Research of navel orange defect and color detection based on machine vision," *Appl. Mech. Mater*, vol. 513, pp. 3442–3445, 2014.

[64] J. M. Cevallos-Cevallos, D. B. Futch, T. Shilts, S. Y. Folimonova, and J. I. Reyes-De-Corcuera, "GC-MS metabolomic differentiation of selected citrus varieties with different sensitivity to citrus huanglongbing," *Plant Physiol. Biochem*, vol. 53, pp. 69–76, 2012.

[65] J. J. Lopez, E. Aguilera, and M. Cobos, "Defect detection and classification in citrus using computer vision," *proceeding International Conference on Neural Information Processing*, pp. 11–18, 2009.

[66] J. P. Mercol, J. Gambini, and J. M. Santos, "Automatic classification of oranges using image processing and data mining techniques," in XIV Congreso Argentino de Ciencias de la Computación," 2008.

[67] L. S. Magwaza, "The use of Vis/NIRS and chemometric analysis to predict fruit defects and postharvest behaviour of 'Nules Clementine' mandarin fruit," *Food Chem*, vol. 163, pp. 267–274, 2014.

[68] G. Kumar and Y. S. Suhas, "Identification and Classification of Fruit Diseases," *International Conference on Recent Trends in Image Processing and Pattern Recognition*, pp. 382–390, 2016.

[69] C. Dong, Y. Ye, J. Zhang, H. Zhu, and F. Liu, "Detection of Thrips Defect on Green-Peel Citrus Using Hyperspectral Imaging Technology Combining PCA and B-Spline Lighting Correction Method," *J. Integr. Agric*, vol. 13, no. 10, pp. 60 671–60 672, 2014.

[70] V. H. Pham and B. R. Lee, "An image segmentation approach for fruit defect detection using k-means clustering and graph-based algorithm," *Vietnam J. Comput. Sci*, vol. 2, no. 1, pp. 25–33, 2015.

[71] Y. Chen, J. Wu, and M. Cui, "Automatic classification and detection of oranges based on computer vision," *procceding of 4th International Conference on Computer and Communications*, pp. 1551–1556, 2018.

[72] J. Abdulridha, O. Batuman, and Y. Ampatzidis, "UAV-based remote sensing technique to detect citrus canker disease utilizing hyperspectral imaging and machine learning," *Remote Sens*, vol. 11, pp. 1373–1373, 2019.

[73] L. Huijun and W. Xiangfeng, "Rapid shelf-life identification model of citrus based on near infrared spectroscopy," *Proceedings of International Symposium on Knowledge Acquisition and Modeling*, pp. 298–301, 2008.

[74] D. Lorente, M. Zude, C. Regen, L. Palou, J. Gómez-Sanchis, and J. Blasco, "Early decay detection in citrus fruit using laser-light backscattering imaging," *Postharvest Biol. Technol*, vol. 86, pp. 424–430, 2013.

[75] C. J. Enciso-Aragón and R. Jimenez-Moreno, "Quality control system by means of CNN and fuzzy systems," *Int. J. Appl. Eng. Res*, vol. 13, no. 16, pp. 12 846–12 853, 2018.

[76] E. G. Turitsyna and S. Webb, "Hyperspectral detection of citrus damage with Mahalanobis kernel classifier," *Electron. Lett*, vol. 41, no. 2, pp. 40–41, 2005.

[77] F. López-García, G. Andreu-García, J. Blasco, N. Aleixos, and J. M. Valiente, "Automatic detection of skin defects in citrus fruits using a multivariate image analysis approach," *Comput. Electron. Agric*, vol. 71, no. 2, pp. 189–197, 2010.

[78] S. Taghadomi-Saberi, A. A. Masoumi, M. Sadeghi, and M. Zekri, "Integration of wavelet network and image processing for determination of total pigments in bitter orange (Citrus aurantium L.) peel during ripening," *J. Food Process Eng*, vol. 42, no. 5, pp. 1–8, 2019.

[79] & F Steinmetz, V. Biavati, E. Molto, E. Pons, and R, "Predicting the maturity of oranges with non destructive sensors," *international Symposium On Sensors in Horticulture*, vol. 421, pp. 271–278, 1995.

[80] H. Patel, R. Prajapati, and M. Patel, "Detection of Quality in Orange Fruit Image using SVM Classifier," *3rd International Conference on Trends in Electronics and Informatics (ICOEI)*, pp. 74–78, 2019.
[81] T. Wen, "Rapid detection and classification of citrus fruits infestation by Bactrocera dorsalis (Hendel) based on electronic nose," *Postharvest Biol. Technol*, vol. 147, pp. 156–165, 2018.
[82] Y. Ashwani, K. Dubey, R. Ratan, and A. Rocha, "Computer vision based analysis and detection of defects in fruits causes due to nutrients deficiency," *Cluster Comput*, vol. 6, pp. 10 586–10 605, 2019.
[83] H. Singh and N. Gill, "Machine Vision Based Color Grading of Kinnow Mandarin," *Int. J. Adv. Res. Comput. Sci. Softw. Eng*, vol. 5, no. 5, pp. 1253–1259, 2015.
[84] S. Cubero, J. Blasco, S. Cubero, J. Blasco, and A. Ferrer, "VIS/NIR hyperspectral imaging and N-way PLS-DA models for detection of decay lesions in citrus fruits," *Chemom. Intell. Lab. Syst*, vol. 156, pp. 241–248, 2016.
[85] P. K. S. S. Kumari and Behera, "Automatic Fruits Identification and Disease Analysis using Machine Learning Techniques," *Int. J. Innov. Tecchnology Explor. Eng*, vol. 8, no. 6S2, pp. 103–107, 2019.
[86] M. A. Gawande and S. S. Dhande, "Implementation of Fruits Grading and Sorting System by using Image Processing and Data Classifier," *SSRG Int. J. Comput. Sci. Eng*, vol. 2, no. 6, pp. 22–27, 2015.
[87] A. Kamalakannan and G. Rajamanickam, "Surface defect detection and classification in mandarin fruits using fuzzy image thresholding, binary wavelet transform and linear classifier model," *proceeding of4th International Conference on Advanced Computing*, pp. 1–6, 2012.
[88] B. O. Fiona, M. R. Thomas, S. Maria, and I. J. Hannah, "Identification Of Ripe And Unripe Citrus Fruits Using Artificial Neural Network," *Journal of Physics: Conference Series*, vol. 1362, pp. 12 033–12 033, 2019.
[89] Y. Lan, "Comparison of machine learning methods for citrus greening detection on UAV multispectral images," *Comput. Electron. Agric*, vol. 171, pp. 105 234–105 234, 2020.
[90] R. Hadipour-Rokni, E. A. Asli-Ardeh, A. Jahanbakhshi, and S. Sabzi, "Intelligent detection of citrus fruit pests using machine vision system and convolutional neural network through transfer learning technique," *Computers in Biology and Medicine*, vol. 155, pp. 106 611–106 611, 2023.
[91] M. Momeny, A. Jahanbakhshi, A. A. Neshat, R. Hadipour-Rokni, Y. D. Zhang, and Y. Ampatzidis, "Detection of citrus black spot disease and ripeness level in orange fruit using learning-to-augment incorporated deep networks," *Ecological Informatics*, pp. 101 829–101 829, 2022.
[92] S. K. Behera, L. Jena, A. K. Rath, and P. K. Sethy, "Disease Classification and Grading of Orange Using Machine Learning and Fuzzy Logic," *Proceedings of IEEE International Conference on Communication and Signal Processing*, pp. 678–682, 2018.
[93] N. Henderson, R. King, and S. K. Chalup, "An Automated Colour Calibration System using Multivariate Gaussian Mixtures to Segment HSI Colour Space."
[94] H. Palus, "Representations of colour images in different colour spaces," *The Colour image processing handbook*, pp. 67–90, 1998.
[95] D. Rong, X. Rao, and Y. Ying, "Computer vision detection of surface defect on oranges by means of a sliding comparison window local segmentation algorithm," *Comput. Electron. Agric*, vol. 137, pp. 59–68, 2017.
[96] D. Cooper, L. Doucet, and M. Pratt, "Detection and classification of citrus green mold caused by Penicillium digitatum using multispectral imaging," *J. Sci. Food Agric*, vol. 98, no. 0, pp. 3542–3550, 2018.
[97] Y. Zhang, "Navel Orange Pest Image Recognition Based on Convolution Deep Neural Network," *Int. J. Simulation–Systems, Sci. Technol*, vol. 17, no. 42, pp. 8–12, 2008.
[98] J. J. Lopez, M. Cobos, and E. Aguilera, "Computer-based detection and classification of flaws in citrus fruits," *Neural Comput. Appl*, vol. 20, no. 7, pp. 975–981, 2011.

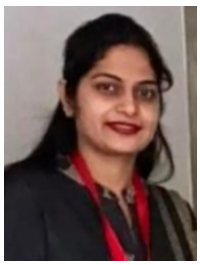

Dr. Poonam Dhiman is currently working as an assistant professor at Government PG College Ambala cant, Haryana, India. Dr. Dhiman has attained her doctorate degree from chitkara university institude of engineering and technology, CU Punjab. She has done her M.tech degree with distinction from Delhi Technological University formerly known as Delhi College of Engineering, Delhi. She has done her B.Tech from Chandigarh College of Engineering and Technology; Punjab University. She has many Publications in renowned SCIE, SCOPUS International journals and fully refereed International conferences with experience of 9 years. She has filed and published patents also. Main areas of research are software engineering, machine learning, IoT and deep learning.

Dr. Amandeep kaur is currently working as a professor at chitkara university institude of engineering and technology, CU Punjab.Dr. kaur has attained her doctorate degree from I.K. GUJRAL Panjab technical University, Jalandhar. Her both M.Tech(CSE) and B.tech(CSE) degrees are with distinction. She has about 100 Publications in renowned International journals and fully refereed International conferences with experience of 23 years. She has filed and published more than 80 patents. She has supervised more than 35 Ph.D. and PG students. Main areas of research are medical Informatics, machine learning, IoT and cloud computing.

Vinay kukreja is working as an professor (CSE) , Chitkara University, Punjab, India. He has total experience of 16 years and has guided many ME Scholars and PhD Scholars. He has having many research papers of SCIE, SCOPUS and PEER reviewed journals to his name. He has also authored many international books and granted many patents. His research areas are Machine learning, Deep Learning, NLP and agile software development.

CKS: A Community-Based K-shell Decomposition Approach Using Community Bridge Nodes for Influence Maximization (Student Abstract)

Inder Khatri*[1], Aaryan Gupta*[2], Arjun Choudhry*[1], Aryan Tyagi*[2], Dinesh Kumar Vishwakarma[1], Mukesh Prasad[3]

[1] Biometric Research Laboratory, Delhi Technological University, New Delhi, India
[2] Delhi Technological University, New Delhi, India
[3] School of Computer Science, FEIT, University of Technology Sydney, Sydney, Australia
{inderkhatri999, aryan227227, choudhry.arjun, tyagiaryan82}@gmail.com, dinesh@dtu.ac.in, mukesh.prasad@uts.edu.au

Abstract

Social networks have enabled user-specific advertisements and recommendations on their platforms, which puts a significant focus on Influence Maximisation (IM) for target advertising and related tasks. The aim is to identify nodes in the network which can maximize the spread of information through a diffusion cascade. We propose a community structures-based approach that employs K-Shell algorithm with community structures to generate a score for the connections between seed nodes and communities. Further, our approach employs entropy within communities to ensure the proper spread of information within the communities. We validate our approach on four publicly available networks and show its superiority to four state-of-the-art approaches while still being relatively efficient.

Introduction

Online Social Networks are platforms for people to publicize their ideas and products. This approach, called Viral Marketing, raises the problem of Influence Maximisation (IM), which requires selecting k seed nodes to maximize the information spread in the network. Several approaches have been proposed for IM in recent years, based on local, semi-local, and global structures. Global structure-based approaches are efficient due to their consideration of whole network. They find out core nodes with maximum connectivity to the remaining network. However, in real-world situations, where number of seed nodes is very small, influence gets restricted to only a few sub-groups (or communities) in the network containing the selected core seed nodes. To overcome this, we instead consider community bridge nodes as influential seed nodes due to their connections to a larger number of communities, leading to simultaneous information propagation to these communities. We propose CKS centrality measure, which incorporates community structures and K-shell Decomposition to identify influential spreaders in a network. We define three novel measures: Community K-Shells, Community K-Shell Entropy, and CKS-Score, which qualitatively and quantitatively evaluate connections of a node to various communities.

*These authors contributed equally.

Copyright © 2023, Association for the Advancement of Artificial Intelligence (www.aaai.org). All rights reserved.

Proposed Methodology

Obtaining Community K-Shell (CKS): Community K-Shell concept incorporates knowledge of information flow in a network. Obtaining CKSs comprises the following steps: identifying community structures using Louvain's algorithm (Blondel et al. 2008); isolating communities by removing connections between different communities; and passing isolated communities through K-Shell algorithm (Kitsak et al. 2010) to obtain K-Shell scores particular to the community of each node (i.e., Community K-shell score). The higher the Community K-shell score of a node, the closer it is to the core of the given community.

Computing K-Shell Entropy (KSE): KSE evaluates connectivity of a node to different regions of a community. We formulate KSE for a node v corresponding to each community c as follows:

$$KSE_{v,c} = -\sum_{s=1}^{shells_c} K_s * \frac{\eta_{v,s}}{\eta_v} * log(\frac{\eta_{v,s}}{\eta_v}) \quad (1)$$

$$\eta_v = \sum_{s'=1}^{shells_c} \eta_{v,s'} \quad (2)$$

where, $\eta_{v,s}$ is number of connections of node v with shell s for a given community, $shells_c$ represents the unique CKS in community c, and K_s represents K_value of given shell.

Influence of an activated node lasts only till 2-3 hops. Thus, for maximum influence over a given community, connectivity of a node to the community should be well-distributed across all its regions, which also reduces the chances of overlapping influence in a community. This requires a higher KSE score. Equation 1 represents the entropy submission over shells of the respective community weighted by the K-Value of the respective shell.

CKS-Score: CKS-Score evaluates the overall connectivity of a node to all adjacent communities to which it is connected. It is defined as:

$$CKS{-}Score(v) = \sum_{c=1}^{comm} NN_c * KSE_{v,c} * \eta_v \quad (3)$$

where, η_v is number of connections of node v with the respective community as shown in Equation 2, $KSE_{v,c}$ represents K-Shell Entropy for node v and community c, and NN_c represents number of nodes in community c. We compute CKS-Score for each node by considering its KSE values corresponding to each community weighted by the community's size. This ensures a higher score for community bridge nodes connected to the most significant communities.

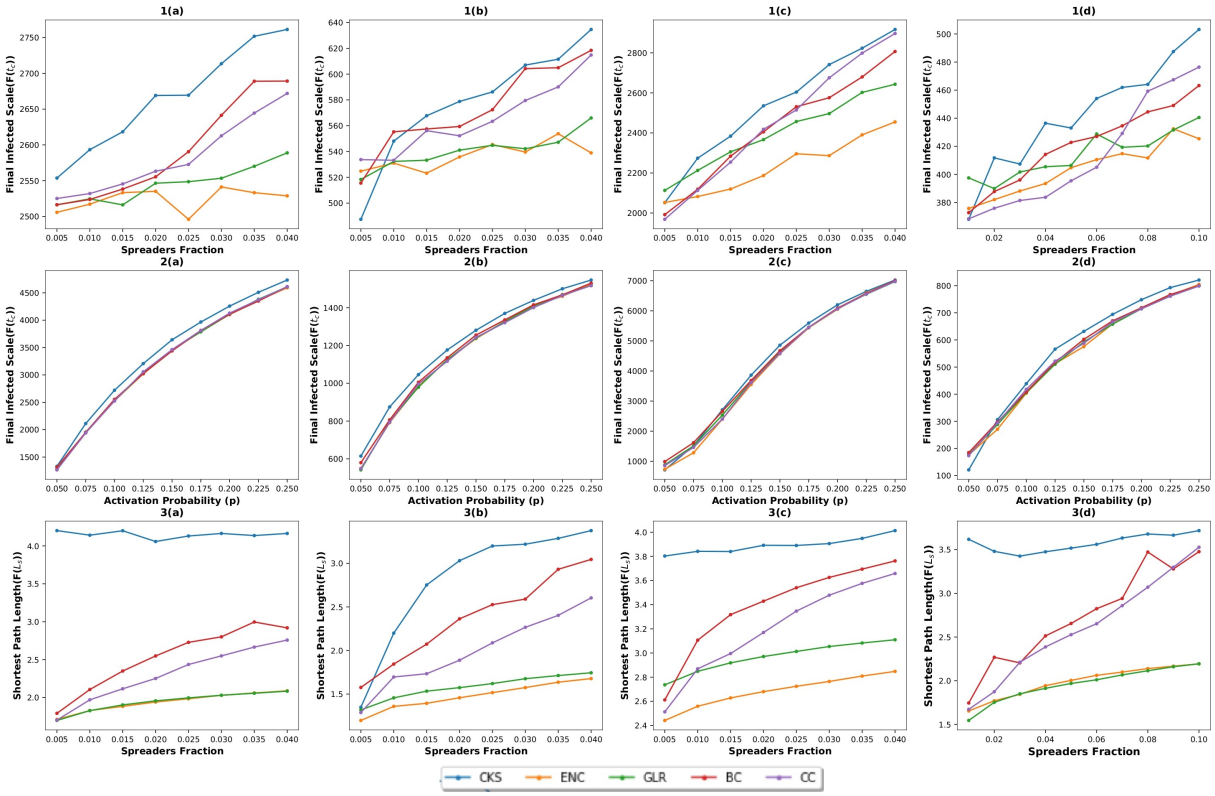

Figure 1: Results of our experiments on datasets (a) Twitch, (b) soc-Hamsterster (c) p2p-Gnutella04 (d) email-univ. (1) FIS after IC model simulation with activation probability 0.5. (2) FIS-v-p after IC model simulation with initial spreaders fraction 0.2. (3) ASPL among initial selected seed nodes vs spreaders fraction.

Dataset	CKS	ENC	GLR	BC	CC
Twitch	28.97	0.176	37.72	533.63	159.07
soc-Hamsterster	49.21	0.04	3.44	40.12	11.84
p2p-Gnutella04	83.21	0.19	54.41	1205.83	352.65
email-univ	0.83	0.01	0.71	10.09	1593.18

Table 1: Execution time for CKS and other approaches.

Experimental Results and Discussion

We evaluated CKS on four metrics: Final Infected Scale (FIS), Average Shortest Path Length (ASPL), Final infected scale vs Activation Probability (FIS-v-p), and Execution Time. We compared CKS with BC (Freeman 1977), CC (Okamoto, Chen, and Li 2008), ENC (Bae and Kim 2014), and GLR (Salavati, Abdollahpouri, and Manbari 2018) on four real-world datasets[1]: Twitch, soc-Hamsterster, p2p-Gnutella04, and email-univ. We simulated each model 100 times using Independent Cascade (Goldenberg, Libai, and Muller 2001). Infection probability was set to 0.1. Table 1 and Figure 1 show our findings. We observed:

CKS consistently outperformed other core nodes-based approaches on FIS, ASPL, and FIS-v-p, while being reasonably efficient. This confirms our hypothesis that bridge nodes are more influential core nodes.

[1]https://networkrepository.com , https://snap.stanford.edu/snap

CKS showed a higher inter-spreader distance than competing approaches, while also having a higher infection rate, leading to much lesser overlap between the influence of spreaders (or *rich club effect*).

References

Bae, J.; and Kim, S. 2014. Identifying and ranking influential spreaders in complex networks by neighborhood coreness. *Physica A Statistical Mechanics and its Applications*, 395: 549–559.

Blondel, V.; Guillaume, J.-L.; Lambiotte, R.; and Lefebvre, E. 2008. Fast Unfolding of Communities in Large Networks. *Journal of Statistical Mechanics Theory and Experiment*, 2008.

Freeman, L. 1977. A Set of Measures of Centrality Based on Betweenness. *Sociometry*, 40: 35–41.

Goldenberg, J.; Libai, B.; and Muller, E. 2001. Talk of the Network: A Complex Systems Look at the Underlying Process of Word-of-Mouth. *Marketing Letters*, 12: 211–223.

Kitsak, M.; Gallos, L. K.; Havlin, S.; Liljeros, F.; Muchnik, L.; Stanley, H. E.; and Makse, H. A. 2010. Identification of influential spreaders in complex networks. *Nature Physics*, 6(11): 888–893.

Okamoto, K.; Chen, W.; and Li, X.-Y. 2008. Ranking of Closeness Centrality for Large-Scale Social Networks. In *Frontiers in Algorithmics*, volume 5059, 186–195. ISBN 978-3-540-69310-9.

Salavati, C.; Abdollahpouri, A.; and Manbari, Z. 2018. Ranking nodes in complex networks based on local structure and improving closeness centrality. *Neurocomputing*, 336.

2023 4th International Conference for Emerging Technology (INCET)
Belgaum, India. May 26-28, 2023

Classifying Heart Sounds for Disease Detection Using Deep Learning Methods

Dhiren Kinha
Department of Information Technology
Delhi Technological University
Delhi, India
dhirenkinha_2k19it044@dtu.ac.in

Garvit Gulati
Department of Information Technology
Delhi Technological University
Delhi,India
garvitgulati_2k19it049@dtu.ac.in

Ashwin Baranwal
Department of Information Technology
Delhi Technological University
Delhi, India
ashwinbaranwal_2k19it034@dtu.ac.in

Dinesh Kumar Vishwakarma
Department of Information Technology
Delhi Technological University
Delhi, India

2023 4th International Conference for Emerging Technology (INCET) | 979-8-3503-3575-0/23/$31.00 ©2023 IEEE | DOI: 10.1109/INCET57972.2023.10170444

***Abstract*— Heart diseases are known to be among the notable causes of mortality in the world. Heart diseases can be of different types, viz., vascular, ischemic, and hypertensive heart disease. The public datasets were been collected from the PhysioNet/CinC 2016 Challenge. In this study, we propose 2 different neural network models, for classifying heart sounds for disease (abnormality) detection using deep learning methods. 'Normal' category denotes that a person has normal heart sounds. 'Abnormal' category denotes that a person has abnormal heart sounds. Each category expresses a specific type of disease. To achieve better results for our binary classification algorithms, we perform a data pre- processing step that involves converting input audio signals to spectrograms. Experiments were conducted with a convolutional neural network (CNN) which is hinged on ResNet18 model and a neural network that is an extension of ResNeXt50 model. In both of these architectures, a novel component called the Shuffle Attention layer has been introduced. It is used to selectively attend to relevant spatial features and enhance the representation of the feature maps. Shuffle Attention layer is implemented using two main components: the squeeze-excite blocks and the channel shuffle layer. The squeeze-excite blocks help in reducing the spatial dimensions of the feature maps to a single value and the channel shuffle layer is used to increase the connectivity between channels and reduce overfitting. The results showed that ResNet18 model with accuracy of 91.27% is more efficient than the ResNeXt50 model having accuracy 88.72%. The results observed are constructive and encouraging for heart disease dataset. Thus, we were able to demonstrate that neural-network based models could help in classifying an unbalanced heart disease dataset. Our proposed framework can also produce highly accurate models suitable for real-world clinical data and diagnostic use.**

Keywords*— *Heart Sound Classification, Feature Selection, PhysioNet, PASCAL, ResNet, ResNeXt, Spectogram, Shuffle Attention

I. INTRODUCTION

HEART DISEASE is among the top causes of death all over the world. Cardiovascular illnesses were the second-ranked health danger in the world in 2018 according to the World Health Organization's most recent statistics[1]. Currently, cardiovascular diseases are responsible for death of around 17 million people worldwide each year, with low- and middle-income nations suffering the most from a lack of medical resources[2]. Consequently, treatment and prompt diagnosis of cardiovascular illnesses could not only lower the overall incidence of these conditions and stop the development of numerous consequences, but also considerably enhance patients' health and quality of life. The heart is an essential part of the body, and cardiovascular illnesses frequently result in mortality. Heart's mechanical activity itself can be determined via heart sounds. Pathological states of the heart may alter characteristics of the heart sound signal. Presently, advancements in technology like cardiac MRI and echocardiography are required for the identification of heart problems. These technologies are pricey, and they also prevent the usage of portable devices [3].

The sounds that the heart makes when it contracts and relaxes are known as heart sounds. The heart's valves condition, arteries, and other components can be determined by these noises, as could the efficiency of the heart's blood flow [4]. Therefore, hearing to heart sounds is the most frequent ways to make a preliminary diagnosis of cardiac disorders. It is possible to determine the condition of the arteries and valves inside the heart of human before the heart develops a clinical ailment by evaluating if there are distortions or murmurs in the heart sounds [5]. Computer-aided heart sound detection technology has grown in popularity as a result of the emergence of machine learning and big data [6].

In this study, we have collected audio files of heart sound data. Instead of treating them as 1D data we converted them to spectrogram image files, treating them as 2D data, allowing us to try and experiment on them with CNN framework.

The following is how this paper is structured: Section 2 features related work. The methodology is outlined in Section 3. Results and findings are discussed in Section 4. Section 5 provides the conclusion.

II. RELATED WORK

Many researchers have used various techniques, viz., subsampling, segmentation, feature extraction, and classification that can be used for predicting heart diseases. Elsa Ferreria Gomes and others [7] put forward a method where they used the average Shannon energy, a spike detection method, to divide the input cardiac signal into segments. After segmentation, the J48 classification model and MLP algorithm is performed. They were able to pass challenge 1 (segmentation), but could not succeed in providing an answer for challenge 2 (classification). Since

Authorized licensed use limited to: DELHI TECHNICAL UNIV. Downloaded on July 20,2023 at 11:19:03 UTC from IEEE Xplore. Restrictions apply.

Challenge 2 did not succeed, J48 and MLP could not provide promising results.

Elsa Ferreira Gomes and others [8] elaborate a method for the PASCAL Challenge classification of heart sounds. They implement an algorithm to distinguish S1 and S2 cardiac sounds. S1and S2 are the lub heart sounds and dub heart sounds respectively. First, they applied MATLAB's decimate function to raw audio signals, followed by applying bandpass filters for removing noise from these signals. Then they applied Shannon's average energy, which makes it easy to recognize peaks in a heart's sound signal. Then they implement an algorithm for finding the maximum and minimum points in the sound signal to arrive at segmenting the heartbeat sound. Then J48 and MLP algorithms were used for training a model to predict audio signals. These signals include Murmur sounds, Normal sounds, Artifact sounds and Extra Audio.

Yineng Zheng and others [9] proposed a novel feature for heart sound abnormality detection, that consists of first and second heart sound (S1-S2EF), heart murmur energy fraction (HMEF), max energy fraction of sub bands for heart sound frequency (HSEFmax), S1-S2EF entropy (S1- S2 sampen). Then the audio signals were normalized and decomposed them with wavelet packets. A support vector machine (SVM) technique was then used to a relatively small dataset of 167 murmurs and 80 normal cardiac sounds. The suggested technique performs well given the small size of dataset having only two categories.

Shiwen Deng and others[9] proposed a heart sound classification framework based on autocorrelation features without using segmentation. This involves using sub-band coefficients in the cardiac signal to obtain an auto-correlation feature. Final features are extracted by fusing the obtained auto-correlation. Eventually, these final characteristics are subjected to Support Vector Machine (SVM) analysis. Dataset-B yielded the unconvincing precision values of Normal- 77, Murmur- 76, and Extra-Systole- 50.

Wenjie Zhang and others[10] aimed to provide a method for extracting sound classification features from heartbeats using zoomed spectrograms and tensor decomposition. The spectrogram detects cardiac cycles of a fixed size in order for extracting distinctive features. Tensor decomposition is used to obtain more discriminating features by dimensionality reduction. They then implemented a support vector machine (SVM) on the features. The resulting normalized precision of the SVM model is 0.74.

Yaseen and others [11] used several techniques for feature extraction for the classification of heartbeat sounds. They use an electronic stethoscope to take a digital recording for heart sounds also known as phonocardiogram (PCG). Feature extraction techniques like Discrete Wavelet Transform (DWT) and Mel frequency cepstral coefficients (MFCC) were used in the study. Moreover, they combined MFCC and DWT techniques to improve the results. Many other classification algorithms, like K nearest neighbors (KNN), support vector machines (SVM) and deep neural networks were used in this study.

Many researchers generally involve three major steps in the classification of heartbeat sounds. The first step is segmentation of heart sound, which is detected by amplitude threshold-based methods [12]–[14] and probability-based methods [15], [16]. This is followed by tsecond step that involves feature extraction on basis of frequency [17], time [18] and time- frequency [10], [17], [19]. Then classification model is the final step.

Shawn and others [20] work with an audio dataset on a large-scale and demonstrate good results with help of convolutional neural networks. Yongxu and others [21] proposed a gated convolutional neural network. Their work bagged the 1st position in the 2017 Detection and Classification of Acoustic Senses and Events (DCASE). Li Yanxiong and others [22] used a BLSTM network on acoustic stages for better results. Xu Kele and others[23] aims to build a new ensemble learning system composed of CNN, which has excellent classification performance.

CNNs used by most authors [20], [21], [23] perform well on image classification, and RNNs [24] also perform well on a range of data. Audio data returns data in form of 1D array containing frequency values. Image data returns data as a two-dimensional array containing pixel values. Dataset-B is used in this study, consisting of samples of heartbeat sound converted into a one-dimensional array. Hence, the RNN model is used, and not CNN.

III. PROPOSED METHODOLOGY

We have used the following steps:

- Obtain datasets from publicly accessible repositories.
- Perform some pre-processing operations on datasets.
- Defining neural network architecture
- Training
- Performance evaluation measure

A. Collection of Datasets

PhysioNet/CinC 2016 Challenge[25]'s open dataset is used in this work.

The Training-a to Training-f subsets of the PhysioNet/CinC dataset each contain various durations of heart sound segments and the associated annotations. In total, 3240 heart sounds have been recorded, comprising 2575 normal records and 665 abnormal ones. A few seconds to more than 100 seconds of heart sound data are recorded. The data is provided in .wav format with a 2000 Hz sampling rate.

TABLE I. EXPERIMENTAL DATA

Dataset	Abnormal	Normal	Total
Training-a	292	117	409
Training-a	104	386	490
Training-a	24	7	31
Training-a	28	27	55
Training-a	183	1958	2141
Training-a	34	80	114
Total	**665**	**2575**	**3240**

Authorized licensed use limited to: DELHI TECHNICAL UNIV. Downloaded on July 20,2023 at 11:19:03 UTC from IEEE Xplore. Restrictions apply.

B. *Data Pre-processing*

We have pre-processed the audio data by converting it from the original WAV file format to spectrogram images. This pre-processing step was necessary to prepare the data for input into our convolutional neural network (CNN) architecture, that requires image data as input. The audio signal was transformed using a short-time Fourier transform (STFT). This transformation converts the audio signal to the frequency domain from the time domain and produces a two-dimensional matrix of magnitude values representing the spectral content of the audio signal.

C. *Definining Neural Network architecture*

We present two neural network architectures for the task at hand.

The first architecture presented in this research paper is a deep convolutional neural network (CNN) with additional Shuffle Attention modules for feature refinement as shown in Fig. 1. This network uses a number of layers to extract and enhance image data, and it is based on the popular ResNet 18 model[26].

The first layer of the network applies a combination of learnable filters to the input image to extract its features. This layer's output is routed to a batch normalisation layer, which normalises the feature maps, to boost the network's stability during training. The feature maps are then given non-linearity using the ReLU activation function.

The subsequent layer, called a max-pooling layer, reduces the spatial dimension of the feature maps by using the highest value found within a certain timeframe. This layer helps to extract the most prominent features while discarding irrelevant information.

The ResNet 18 model's subsequent layers, known as the residual blocks, are numerous convolutional layers with skip connections that let the network learn residual mappings. These building elements let the network to go deeper and learn more intricate properties without sacrificing performance.

The Shuffle Attention modules are then added after each residual block to refine the learned features. These modules selectively emphasize or suppress certain features based on their importance learned from the training data, thereby improving the network's discriminative power.

Lastly an average pooling layer is added to the network, which aggregates the feature maps across spatial dimensions to produce a feature vector. This vector then goes across two fully connected layers, with the final layer being a sigmoid activation function to produce a probability score for each class.

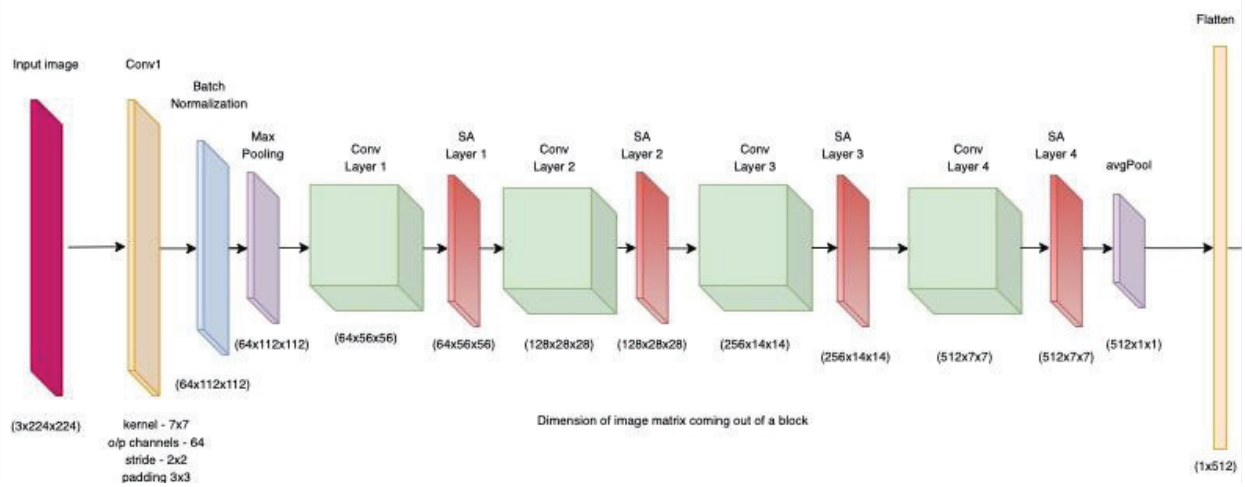

Fig. 1. Proposed model based on ResNet18 with added shuffle attention layers

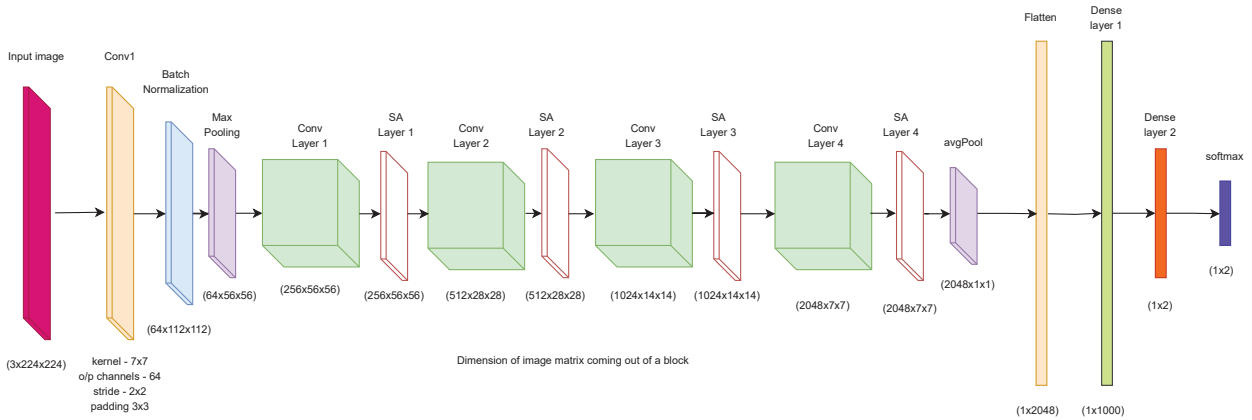

Fig. 2. Proposed model based on ResNeXt with added shuffle attention layers

Authorized licensed use limited to: DELHI TECHNICAL UNIV. Downloaded on July 20,2023 at 11:19:03 UTC from IEEE Xplore. Restrictions apply.

Similary the second proposed network architecture is an extension of the ResNeXt50[27] model that incorporates ShuffleAttention layers as shown in Fig. 2. The model includes convolutional layers, attention layers, and fully connected layers, combined to classify images. The model takes an input image and applies several convolutional layers and batch normalization layers to extract relevant features. After using Max pooling layers to reduce the spatial dimensions of the feature maps, four ResNeXt50 blocks are employed to further extract hierarchical features.

The Shuffle Attention layer is a novel component introduced in both the proposed network architectures. It is designed to selectively attend to relevant spatial features and enhance the representation of the feature maps. The layer comprises of two main components: the squeeze- excite blocks and the channel shuffle layer.

The squeeze-excite blocks use an adaptive average pooling layer which reduces the spatial dimensions of the feature maps to a single value. The resulting tensor is then passed through two convolutional layers with a reduction ratio, followed by a sigmoid activation function. The resulting tensor is used to scale the input feature maps, emphasizing important features while suppressing less important ones.

The channel shuffle layer is used to increase the connectivity between channels and reduce overfitting. It consists of a convolutional layer that groups the inputfeature maps into subgroups and applies a channel shuffle operation. This operation rearranges the channels within each group, leading to improved information flow betweenchannels.

D. Training

The ADAM optimizer and the cross-entropy loss function were used to train our model.90% of the dataset was used for training, and 10% for validation. We trained the model for 50 epochs keeping the batch size at 32. To avoid overfitting, the validation loss was carefully monitored.

E. Performance Evaluation Measure

Accuracy, precision, recall, ROC-AUC score, and F1 score are a few of the common assessment metrics used to assessthe performance of the suggested model.

The formula for accuracy, which measures the proportion ofaccurate classifications a trained machine learning model makes, is as follows:

$$Accuracy = \frac{TP + TN}{TP + TN + FP + FN}$$

The formula for precision, which expresses it as the proportion of genuine positives to all expected positives:

$$Precision = \frac{TP}{TP + FP}$$

Recall, on the other hand, is the ratio of true positives to the total number of actual positives, and is given by the formula:

$$Recall = \frac{TP}{TP + FN}$$

The area under the receiver operating characteristic curve, or ROC-AUC score, gives a comprehensive evaluation of the model's performance by accounting for both the true positive rate (recall) and false positive rate. Higher values denote greater model performance, and this score goes from 0 to 1.

The formula for calculating the F1 score determines how well memory and precision are balanced.

$$F1\ Score = 2 * \frac{Precision * Recall}{Precision + Recall}$$

These performance metrics offer a quantitative assessment of the model's capacity to categorise new data and are computed on the test set using the predicted labels and the ground truth labels.

IV. RESULT AND DISCUSSION

The two neural network models for binary categorization of heart sounds into "normal" and "pathological" categories have been compared through studies. On the PhysioNet/CinC 2016 Challenge[25] dataset, the accuracy metric is used to assess each model's performance.

In Table 2, these results are shown. The ResNet18 model shows an accuracy of 91.27%, which is more efficient than the ResNeXt50 model having 88.72% accuracy. Precision (Pr), Recall (Re), and F1 Scores (F1) are also evaluated. The precision values (90.38% vs. 89.88%) are almost similar. Recall values (94.75% vs. 93.14%) and F1 scores (92.51% vs. 91.48%) are slightly better for the ResNet18 model. Although the performance of the two models are fairly close, ResNet18 model provides better results on the PhysioNet dataset than the ResNeXt50 model.

TABLE II. RESULTS (ACCURCAY) FOR DIFFERENT NEURAL NETWORK MODELS AND COMPARISON WITH SVM

Metric	Neural Network model	
	ResNet18	***ResNeXt50***
Accuracy	91.27%	88.72%
Precision	90.38%	89.88%
Recall	94.75%	93.14%
F1 Score	92.51%	91.48%

Fig. 3 and Fig. 4 show the Loss/accuracy vs. epochs graph for the ResNet18 and ResNeXt50 model. The accuracy and the loss curves are almost similar and doesn't provide much detail. Fig. 5 and Fig. 6 show the ROC/AUC curves for the ResNet18 and ResNeXt50 model. AUC values were evaluated to be 94.64% for ResNet18 model which is significantly better than ResNeXt50 model having 90.23% AUC value.

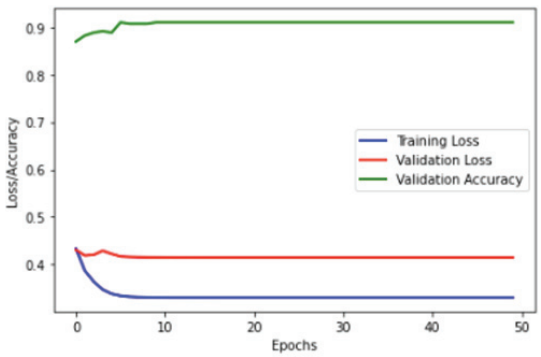

Fig. 3. Loss/accuracy vs. epochs for ResNet model

Authorized licensed use limited to: DELHI TECHNICAL UNIV. Downloaded on July 20,2023 at 11:19:03 UTC from IEEE Xplore. Restrictions apply.

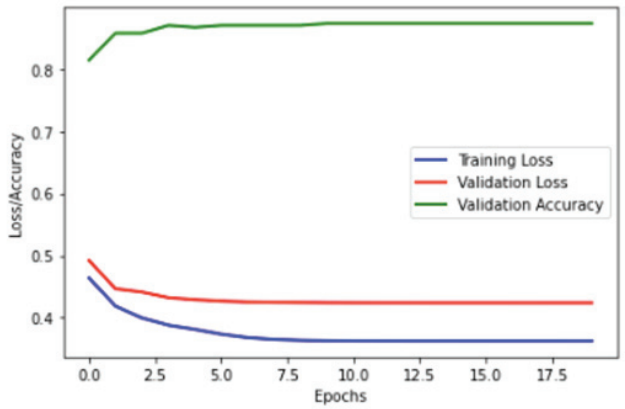

Fig. 4. Loss/accuracy vs. epochs for ResNeXt model

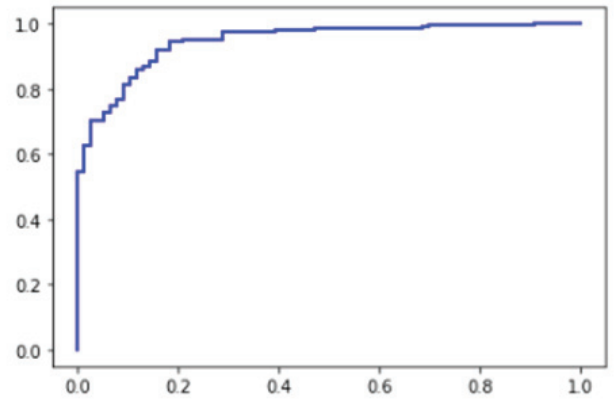

Fig. 5. ROC/AUC curve for ResNeXt model

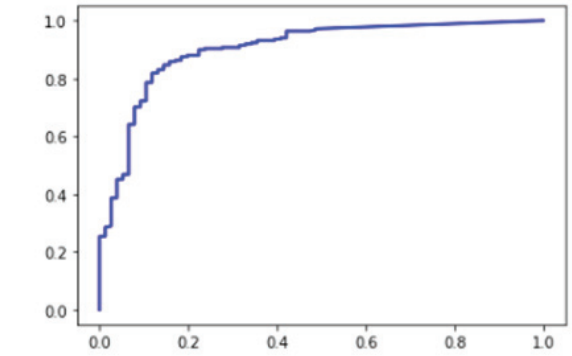

Fig. 6. ROC/AUC curve for ResNeXt model

We present a comparison of our work with some of the previous work done on PhysioNet/CinC 2016 Challenge[25] dataset in Table 3. The best accuracy (86.48%) in the previous works is given by M.N. Homsi and others[28], where they use Random Forest + LogitBoost + Cost-Sensitive Classifier techniques for binary classification. Our proposed ResNet18 model in this paper gives accuracy of 91.27% which is significantly higher.

TABLE III. COMPARISON OF OUR WORK WITH PREVIOUS WORK DONE ON THE PHYSIONET/CINC 2016 CHALLENGE[25] DATASET

Author	Methodology	Accuracy
M. N. Homsi et al. [28]	Random Forest, LogitBoost and Cost-Sensitive Classifier	86.48%
González Ortiz et al. [29]	SVM	82.4%
S. Vernekar et al. [30]	Multi artificial neural networksand gradient boosting trees	82%
M. Tschannen et al. [31]	SVM	81.2%
Singh-Miller et al. [32]	Random Forest Regression	81%
Maknickas et al. [33]	CNN	84.15%
Sujadevi et al. [34]	RNNs,CNN	79.80%
This work	ResNet 18 + Shuffle Attention	91.27%
	ResNeXt 50 + Shuffle Attention	88.72%

V. CONCLUSION

The goal of this study was to distinguish between normal and abnormal sounds produced by heart provided by the 2016 PhysioNet Challenge. The two methods that we present and analyse are convolutional neural networks (CNN) with added shuffle attention and a model that is an expansion of the ResNeXt50 model featuring Shuffle Attention. It has been found that the ResNet18 model is more accurate and effective than the ResNeXt50 model. Other crucial evaluation criteria like precision, recall, F1 score, and AUC values were also marginally better for the ResNet18 model. When we compared our model to some earlier research on the subject, we found a sizable improvement in accuracy and our model is robust to perturbations as compared to baselines[35]. Improved identification of recordings with poor signal quality, as well as a broader approach to incorporate summary features into the proposed method, are interesting directions to explore in the future.

REFERENCES

[1] WHO, World health statistics 2018: monitoring health for the SDGs, sustainable development goals. Geneva: World Health Organization; 2018. Licence: CC BY-NC-SA 3.0 IGO. Cataloguing-in-Publication, vol. 2. 2018.

[2] WHO, "WHO Fact sheets, 2017. from: https://www.who.int/news-room/fact-sheets/detail/cardiovascular-diseases-(cvds).," Fact sheets, 2017., 2017.

[3] D. Kumar, P. Carvalho, M. Antunes, J. Henriques, A. Sá e Melo, and J. Habetha, "Heart murmur recognition and segmentation by complexity signatures," in Proceedings of the 30th Annual International Conference of the IEEE Engineering in Medicine and Biology Society, EMBS'08 - "Personalized Healthcare through Technology," 2008. doi: 10.1109/iembs.2008.4649614.

[4] M. Abdollahpur, A. Ghaffari, S. Ghiasi, and M. J. Mollakazemi, "Detection of pathological heart sounds," Physiol Meas, vol. 38, no. 8, 2017, doi: 10.1088/1361-6579/aa7840.

[5] C. Liu, D. Springer, and G. D. Clifford, "Performance of an open-source heart sound segmentation algorithm on eight independent databases," Physiol Meas, vol. 38, no. 8, 2017, doi: 10.1088/1361-6579/aa6e9f.

[6] R. L. Watrous, "Computer-aided auscultation of the heart: From anatomy and physiology to diagnostic decision support," in Annual International Conference of the IEEE Engineering in Medicine and Biology - Proceedings, 2006. doi: 10.1109/IEMBS.2006.259757.

[7] E. F. Gomes, P. J. Bentley, M. Coimbra, E. Pereira, and Y. Deng, "Classifying heart sounds: Approaches to the PASCAL challenge," in HEALTHINF 2013 - Proceedings of the International Conference on Health Informatics, 2013. doi: 10.5220/0004234403370340.

[8] E. F. Gomes and E. Pereira, "Classifying heart sounds using peak location for segmentation and feature construction," Aistats, no. 1, 2012.

[9] S. W. Deng and J. Q. Han, "Towards heart sound classification without segmentation via autocorrelation feature and diffusion maps,"

Authorized licensed use limited to: DELHI TECHNICAL UNIV. Downloaded on July 20,2023 at 11:19:03 UTC from IEEE Xplore. Restrictions apply.

Future Generation Computer Systems, vol. 60, 2016, doi: 10.1016/j.future.2016.01.010.

[10] W. Zhang, J. Han, and S. Deng, "Heart sound classification based on scaled spectrogram and tensor decomposition," Expert Syst Appl, vol. 84, 2017, doi: 10.1016/j.eswa.2017.05.014.

[11] Yaseen, G. Y. Son, and S. Kwon, "Classification of heart sound signal using multiple features," Applied Sciences (Switzerland), vol. 8, no. 12, 2018, doi: 10.3390/app8122344.

[12] T. Chen, K. Kuan, L. Celi, and G. D. Clifford, "Intelligent heartsound diagnostics on a cellphone using a hands-free kit," in AAAI Spring Symposium - Technical Report, 2010.

[13] Y. Liu, C. C. Y. Poon, and Y. T. Zhang, "A hydrostatic calibration method for the design of wearable PAT-based blood pressure monitoring devices," in Proceedings of the 30th Annual International Conference of the IEEE Engineering in Medicine and Biology Society, EMBS'08 - "Personalized Healthcare through Technology," 2008. doi: 10.1109/iembs.2008.4649404.

[14] A. Moukadem, A. Dieterlen, N. Hueber, and C. Brandt, "A robust heart sounds segmentation module based on S-transform," Biomed Signal Process Control, vol. 8, no. 3, 2013, doi: 10.1016/j.bspc.2012.11.008.

[15] S. E. Schmidt, C. Holst-Hansen, C. Graff, E. Toft, and J. J. Struijk, "Segmentation of heart sound recordings by a duration-dependent hidden Markov model," Physiol Meas, vol. 31, no. 4, 2010, doi: 10.1088/0967-3334/31/4/004.

[16] D. B. Springer, L. Tarassenko, and G. D. Clifford, "Logistic regression-HSMM-based heart sound segmentation," IEEE Trans Biomed Eng, vol. 63, no. 4, 2016, doi: 10.1109/TBME.2015.2475278.

[17] F. Safara, S. Doraisamy, A. Azman, A. Jantan, and A. R. Abdullah Ramaiah, "Multi-level basis selection of wavelet packet decomposition tree for heart sound classification," Comput Biol Med, vol. 43, no. 10, 2013, doi: 10.1016/j.compbiomed.2013.06.016.

[18] S. Ari, K. Hembram, and G. Saha, "Detection of cardiac abnormality from PCG signal using LMS based least square SVM classifier," Expert Syst Appl, vol. 37, no. 12, 2010, doi: 10.1016/j.eswa.2010.05.088.

[19] S. R. Thiyagaraja et al., "A novel heart-mobile interface for detection and classification of heart sounds," Biomed Signal Process Control, vol. 45, 2018, doi: 10.1016/j.bspc.2018.05.008.

[20] S. Hershey et al., "CNN architectures for large-scale audio classification," in ICASSP, IEEE International Conference on Acoustics, Speech and Signal Processing - Proceedings, 2017. doi: 10.1109/ICASSP.2017.7952132.

[21] Y. Xu, Q. Kong, W. Wang, and M. D. Plumbley, "Large-Scale Weakly Supervised Audio Classification Using Gated Convolutional Neural Network," in ICASSP, IEEE International Conference on Acoustics, Speech and Signal Processing - Proceedings, 2018. doi: 10.1109/ICASSP.2018.8461975.

[22] Y. Li, X. Li, Y. Zhang, W. Wang, M. Liu, and X. Feng, "Acoustic Scene Classification Using Deep Audio Feature and BLSTM Network," in ICALIP 2018 - 6th International Conference on Audio, Language and Image Processing, 2018. doi: 10.1109/ICALIP.2018.8455765.

[23] K. Xu et al., "General audio tagging with ensembling convolutional neural networks and statistical features," J Acoust Soc Am, vol. 145, no. 6, 2019, doi: 10.1121/1.5111059.

[24] G. Keren and B. Schuller, "Convolutional RNN: An enhanced model for extracting features from sequential data," in Proceedings of the International Joint Conference on Neural Networks, 2016. doi: 10.1109/IJCNN.2016.7727636.

[25] A. L. Goldberger et al., "PhysioBank, PhysioToolkit, and PhysioNet: components of a new research resource for complex physiologic signals.," Circulation, vol. 101, no. 23, 2000, doi: 10.1161/01.cir.101.23.e215.

[26] K. He, X. Zhang, S. Ren, and J. Sun, "Deep residual learning for image recognition," in Proceedings of the IEEE Computer Society Conference on Computer Vision and Pattern Recognition, 2016. doi: 10.1109/CVPR.2016.90.

[27] S. Xie, R. Girshick, P. Dollár, Z. Tu, and K. He, "Aggregated residual transformations for deep neural networks," in Proceedings - 30th IEEE Conference on Computer Vision and Pattern Recognition, CVPR 2017, 2017. doi: 10.1109/CVPR.2017.634.

[28] M. N. Homsi et al., "Automatic heart sound recording classification using a nested set of ensemble algorithms," in Computing in Cardiology, 2016. doi: 10.22489/cinc.2016.237-325.

[29] J. J. G. Ortiz, C. P. Phoo, and J. Wiens, "Heart sound classification based on temporal alignment techniques," in Computing in Cardiology, 2016. doi: 10.22489/cinc.2016.170-317.

[30] S. Vernekar, S. Nair, D. Vijaysenan, and R. Ranjan, "A novel approach for classification of normal/abnormal phonocardiogram recordings using temporal signal analysis and machine learning," in Computing in Cardiology, 2016. doi: 10.22489/cinc.2016.326-144.

[31] M. Tschannen, T. Kramer, G. Marti, M. Heinzmann, and T. Wiatowski, "Heart sound classification using deep structured features," in 2016 Computing in Cardiology Conference (CinC), 2016, pp. 565–568.

[32] N. E. Singh-Miller and N. Singh-Miller, "Using spectral acoustic features to identify abnormal heart sounds," in Computing in Cardiology, 2016. doi: 10.22489/cinc.2016.160-401.

[33] V. Maknickas and A. Maknickas, "Recognition of normal-abnormal phonocardiographic signals using deep convolutional neural networks and mel-frequency spectral coefficients," Physiol Meas, vol. 38, no. 8, pp. 1671–1684, Jul. 2017, doi: 10.1088/1361-6579/aa7841.

[34] V. G. Sujadevi, K. P. Soman, R. Vinayakumar, and A. U. P. Sankar, "Deep models for phonocardiography (PCG) classification," in ICCT 2017 - International Conference on Intelligent Communication and Computational Techniques, 2018. doi: 10.1109/INTELCCT.2017.8324047.

[35] A. Bajaj and D. K. Vishwakarma, "Exposing the Vulnerabilities of Deep Learning Models in News Classification," in 2023 4th International Conference on Innovative Trends in Information Technology (ICITIIT), IEEE, Feb. 2023, pp. 1–5. doi: 10.1109/ICITIIT57246.2023.10068577.

Authorized licensed use limited to: DELHI TECHNICAL UNIV. Downloaded on July 20,2023 at 11:19:03 UTC from IEEE Xplore. Restrictions apply.

Comparative Analysis of Face Detection Techniques on Videos of Low Vs High Quality

Akshay Mool
Department of Information Technology
Delhi Technological University
Delhi, India
akshaymool_phd2k17@dtu.ac.in

Jeebananda Panda
Department of Electronics and Communications Engineering
Delhi Technological University
Delhi, India
jpanda@dce.ac.in

Kapil Sharma
Department of Information Technology
Delhi Technological University
Delhi, India
kapil@ieee.org

2023 Third International Conference on Secure Cyber Computing and Communication (ICSCCC) | 979-8-3503-0071-0/23/$31.00 ©2023 IEEE | DOI: 10.1109/ICSCCC58608.2023.10176915

***Abstract*—In today's age, there is a lot of visual information that is generated in various fields, ranging from daily routine to specialized applications. Processing all these types of information efficiently is a valid concern and needs focused research. Most face detection algorithms have to deal with low quality data in videos, since they're mainly focused on surveillance applications, whose information capturing devices capture less information each frame. This paper reviews some state-of-the-art face detection algorithms and compares their processing efficiency on low and high quality videos. The comparative analysis reveals that these recent and modern algorithms do not work as effectively on high quality videos as they do on lower quality videos. This paper defines the need to focus research on analysis of high quality information in videos in an efficient manner, so as to keep up the pace of their analysis with the information that is generated.**

***Index Terms*—High-quality videos, Face Detection, FaceNet, HOG, MTCNN**

I. INTRODUCTION

With the cost of information capturing devices decreasing at an exponential rate in the past two decades, the captured information contains a lot of data per unit than earlier times. Photos and videos are created and shared through various social media platforms, many people participate in live broadcasts of various events, individual fields like military applications generate their field-specific optical information. All these types of visual information are rich in data, meaning there is large amount of information to be processed in one image/frame. Also, human interaction-based algorithms have also consequentially evolved in the last two decades, owing to the increasing number of applications focusing on human activities [1]. So Face detection algorithms have also developed to give faster results in real time [2], [3]. Applications using these algorithms usually take real-time low quality video feed as input to be processed. Less data per frame aids in givingreal-time results with the real-time input feed. This paper compares and analyses the working of these algorithms on both low and high quality video data and presents the results. Traditional face detection algorithms are mainly classified on knowledge base, feature invariance, template matching, and appearance based [4]. Experiments have shown that they perform efficiently in both high and low quality data videos, algorithms including Viola-Jones [5], Linear Discriminant Analysis (LDA), Principle Component Analysis (PCA) [6]. Traditional face detection algorithms used to take more time to process each frame (image), so they were not useful in development of real-time applications. But the introduction of Viola-Jones algorithm was a breakthrough in the field because that algorithm gave high-accuracy results in real-time. Viola-Jones algorithm proved to be such a leap forward that it is still considered a benchmark to which the efficiency of newer algorithms is measured against. The algorithm still performs at a good speed in real-time compared against other modern algorithms, but it's main drawback is that it's accuracy is fairly low, at about 60-70% detection of target object. Modern applications need high accuracy to perform, so VJ algorithm lacks its utility to be used there. Modern frameworks that deal with neural networks, machine learning or deep learning are likely to have more complicated architecture than traditional frameworks, but they provide accurate and fast outputs in real-time video feeds, like You Only Look Once (YOLO) [8], Histogram of Oriented Gradients (HoG) [7], and other SOTA techniques [9], [10], [11]. This paper focuses on the review and scrutiny of modern face detection algorithms and using the results to establish the need of specialized and/or optimized frameworks for high quality images and videos processing. There is only a limited amount of work done on algorithms that focus on these type of visual information, therefore there is a growing need to have efficient but flexible algorithms to deal with them.

II. COMMERCIALLY USED FACE DETECTION ALGORITHMS

There are many SOTA face detection algorithms introduced in recent years, like YOLOV3 [8], SSD [17] and BlazeFace [18], they haven't been reviewed and compared in this paper because they're not feasible to be used in commercial or industrial applications. The following algorithms are used widely in many fields concerning Computer Vision, and therefore their analysis is vital to the goal of this paper.

Authorized licensed use limited to: DELHI TECHNICAL UNIV. Downloaded on July 20,2023 at 11:10:42 UTC from IEEE Xplore. Restrictions apply.

A. FaceNet

FaceNet Face Recognition system [12] was proposed in 2015 by Google. This system is being discussed in the paper because FaceNet gives high efficiency performance on many benchmark face datasets, and therefore is being used by many commercial and practical applications these days. It uses deep learning architectures like Inception network and ZF-Net on images to generate face mappings of high quality. For training the network architecture, the loss function used is a method called "triplet loss". The architectural components of FaceNet are briefly described as follows:

1) For training: Stochastic Gradient Descent (SGD) is used along with AdaGrad and Backpropagation to train the FaceNet model on a CPU cluster for 1000-2000 hours, using ZF-Net and Inception Network. After 500 hours, an increase in accuracy and decrease in loss was observed. ZF-Net has 140 million parameters and requires 1.6 billion FLOPS memory to train the model, whereas Inception Network has only 7.5 million parameters but requires the same amount 1.6 billion FLOPS memory to train it.

2) For loss function: Triplet loss is used as a part of the face recognition system of FaceNet model. Its aim is to define a border between different facial identities. It achieves this by making the squared distance between two independent image embeddings of the same facial identity small, and that of different identities large. The loss function is taken to define the border differentiating positive and negative pairs. Therefore, when the model is trained, the triplets are chosen in such a way that they violate the loss function equation, so as to train the model better.

B. Histogram of Oriented Gradients

Histogram of Oriented Gradients (HOG) [13] is used in face detectors because it is a feature descriptor widely used for object detection and recognition in general. Even though it was introduced in 2005, this object detector is still used widely used in commercial industrial applications because of its real-time results and high efficiency. It uses gradient computation techniques of fine scale along with Linear SVM (Support Vector Machine) for modelling the object detector. HOG feature descriptor works in following steps:

1) Preprocessing using Colour normalization and Resizing: Resizing of image plays an essential step in object detection as it reduces the area to be scanned. Since the paper that introduced this model was dealing with human detection, 64x128 pixels is assumed to be the ideal image size, and RGB or LAB color spaces give out identical performance as compared to grayscale. So these parameters need to be taken care of for preprocessing phase.

2) Gradients computation: Computing the gradients in an image is useful because it indicates changes in gradient of pixel intensities across the image. Horizontal and vertical gradient kernels are used to calculate the gradients for this step.

3) Orientation Binning and Gradient calculations: Next, the frame is divided into 8x8 grid cells, since the original image/frame is resized to 64x128 pixels. Each cell's gradient is measured in two values: gradient's magnitude and gradient's direction, so each cell generates a total of 128 values, which are represented in 9 orientation bins. These orientation bins are responsible for denoting the changes in intensities from block to block.

4) Normalization of blocks: Gradient values are dependent on contrast differences and irregular illuminations, so block normalization of gradients is performed, since it gives better results than normalization of individual cells.

5) Generating HOG feature vector: The final HOG feature vector is obtained by concatenating all the normalized gradient values calculated in the previous step. A total of 105 vectors are appended together to obtain the final feature vector that is used for object detection.

C. Multi-Task Cascaded Convoluted Neural Network

Multi-Task Cascaded Convolutional Neural Network (MTCNN) [14], [15] is a face detection framework that achieves high accuracy in real-time. Developed in 2016, this framework consists of sequential stages that keep reducing the candidate face windows at each stage until regions with highest probability of faces are identified, and recognize facial landmark feature regions of nose, eyes and mouth. MTCNN works in following 3 stages:

1) P-Net – Proposal Network: The first stage employs a network called the Proposal Network, which is a fully convolutional network, which is responsible for generating facial region candidate windows and corresponding vectors using bounding box regression technique. After generating the vectors, overlapping window regions are combined so that the final output of this stage gives downsized refined candidate windows, which act as input to the next stage network.

2) R-Net – The Refine Network: The second stage employs the Refine Network, which is a Convolutional Neural Network. This network is responsible for minimizing the candidate windows generated in the previous stage by adjusting the bounding box regression besides using Non-Maximum Suppression (NMS) for merging overlapping windows. The output of this stage generates candidate windows with faces having bounding boxes around them, and a vector for potential facial features landmarks.

3) O-Net – The Output Network: The last stage of the framework is called the Output Network, which is similar to the previous stage's R-Net. This stage takes as input the candidate windows and facial landmark vector from the previous stage and defines the facial region more specifically along with finalizing the five facial landmark features of nose, eyes and mouth. The output contains the final face regions with facial landmark features highlighted in the bounding boxes.

III. COMPARATIVE ANALYSIS

The given face detection algorithms are analyzed on the "300 Videos in the Wild (300-VW)" data set, with respective

Authorized licensed use limited to: DELHI TECHNICAL UNIV. Downloaded on July 20,2023 at 11:10:42 UTC from IEEE Xplore. Restrictions apply.

to their execution speeds on three frame rates: 24 FPS, 48 FPS and 50 FPS. Here, only speed is considered a parameter for comparison since accuracy of the algorithms remain same across all frame rates for same video samples. The machine used for conducting experiments on the given dataset has an *i5–8300H* processor with 2.30 GHz clock frequency. The comparison has been done by taking the Viola-Jones algorithm as the benchmark face detection framework. The execution speed of Viola-Jones algorithm is still very high as compared to state-of-the-art techniques. The main drawback of Viola-Jones algorithm is its detection accuracy falls very low (60-70%), which is not feasible for implementing modern applications.

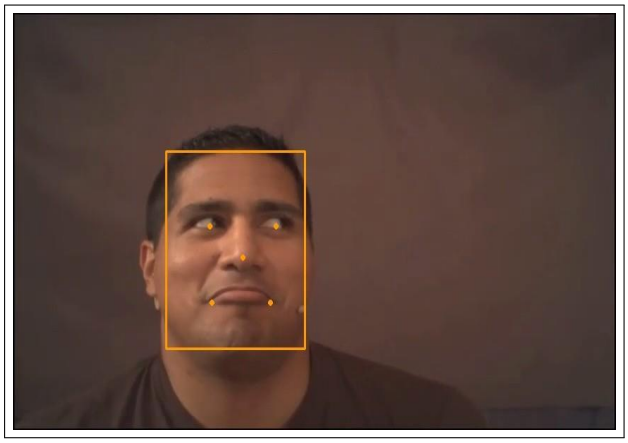

Fig. 1. Detected face frame in Sample 1

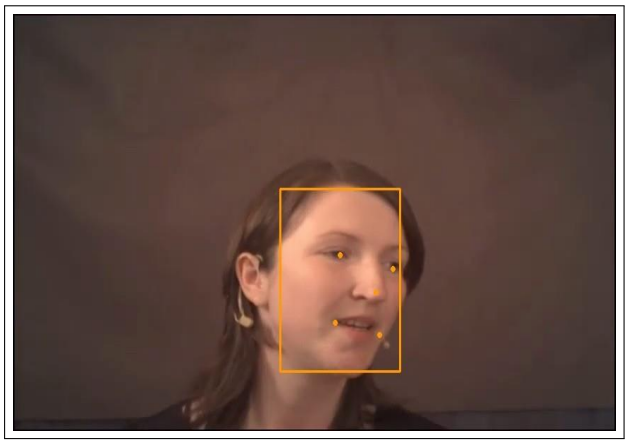

Fig. 2. Detected face frame in Sample 2

Based on given experimental analysis, we see that all of the face detection frameworks work faster on lower frame rates and their speed gradually decreases as frame rate increases. This is because with increase in frame rate, these frameworks have to process more frames per unit time, which increases number of executions to perform. We also see that HOG face detection framework performs the worst out of all the given techniques on all frame rates, whereas FaceNet and MTCNN frameworks perform almost similar and better in all cases. MTCNN framework can be termed as slightly better [16] than FaceNet for commercial applications because as we can see from figures (c) and (d), MTCNN framework averagely same for all the given frame rates, whereas FaceNet shows a little deviation in execution speeds for the different frame rates being analyzed. Other face detection techniques [19], [20] popular in research communities like YOLOV3 and BlazeFace achieve good results too, but they still suffer from performance lag with higher quality videos.

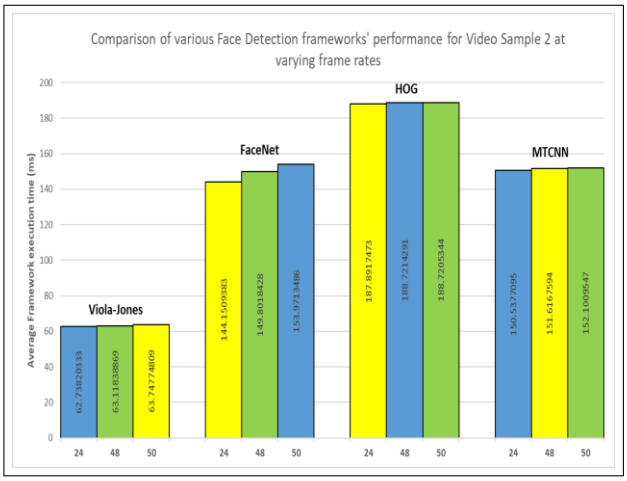

Fig. 3. Execution time comparison of given Face Detection techniques on 24 FPS, 48 FPS and 50 FPS frame rates of Sample 1

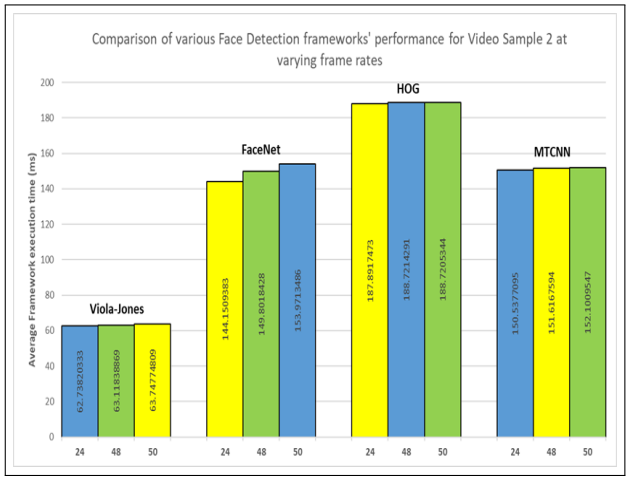

Fig. 4. Execution time comparison of given Face Detection techniques on 24 FPS, 48 FPS and 50 FPS frame rates of Sample 2

Higher quality videos have high frame rates as well as more information per frame (144p to 1080p picture quality), so processing these videos in real-time keeps getting more difficult and challenging with time, that is why more research and modifications are required in the field of object/face detection for meeting the demands of upcoming modern applications.

IV. CONCLUSION

State-of-the-art object/face detection techniques have made a lot of advancements in recent times and perform really well

Authorized licensed use limited to: DELHI TECHNICAL UNIV. Downloaded on July 20,2023 at 11:10:42 UTC from IEEE Xplore. Restrictions apply.

for real-time applications that require real-time video feeds, which are usually of low quality. But these days, there are numerous applications that have to deal with a large input of high-quality video feeds: Modern mobile phones are equipped to shoot videos up to 1080p resolution, on-air TV channels and OTT platforms provide a lot of HD quality content, sports broadcasts have to provide live high-quality entertainment at audience's disposal, social media creates numerous high-quality content on various platforms. These are just some of the examples of current applications dealing with multimedia content in high-quality, and the data keeps increasing every day. Various applications can be developed that can analyze this content and provide more personalized experience to the users, or predict trends in the market, among other targeted needs. Therefore, appropriate algorithms and frameworks need to be developed that can cope up with the increasing demands and supply of information-rich data. The above analysis gives a fair idea of how our current commercial detection frameworks perform with respect to increasing video qualities. Novel and modified techniques have been proposed in recent times to tackle this issue, but still a lot of work needs to be done to bring the focus of research community on it. Techniques can be developed that process the frames irrespective of data present in them, such that frames of any resolution take almost the same time to be processed, thereby decreasing the detection time.

REFERENCES

[1] D. S. Bolme, J. R. Beveridge, B. A. Draper, and Y. M. Lui, "Visual object tracking using adaptive correlation filters," in 2010 IEEE Computer Society Conference on Computer Vision and Pattern Recognition, pp. 2544–2550, 2010.

[2] G. Barquero, I. Hupont, and C. F. Tena, "Rankbased verification for long-term face tracking in crowded scenes," IEEE Transactions on Biometrics, Behavior, and Identity Science, vol. 3, pp. 495–505, oct 2021.

[3] T. Li, W. Hou, F. Lyu, Y. Lei, and C. Xiao, "Face detection based on depth information using hog-lbp," in 2016 Sixth International Conference on Instrumentation Measurement, Computer, Communication and Control (IMCCC), pp. 779–784, 2016.

[4] Yang M-H, Kriegman DJ, Ahuja N, "Detecting faces in images: a survey", IEEE Trans Pattern AnalMac Intell, 24(1):34–58, 2002.

[5] Viola P, Jones M, "Robust real-time face detection" International Journal of Computation, Vis 57:137–154, 05, 2004.

[6] Ismail N, Sabri MIM, "Review of existing algorithms for face detection and recognition", In: World scientific and engineering academy and society (WSEAS), pp 30–39, 2009.

[7] Dalal N, Triggs B, "Histograms of oriented gradients for human detection", In: IEEE Computer society conference on computer vision and pattern recognition (CVPR'05), vol 1, pp 886–893, 2005.

[8] Nguyen DT, Nguyen TN, Kim H, Lee H, "A high-throughput and power-efficient fpga implementation of yolo cnn for object detection", IEEE Trans Very Large Scale Integr (VLSI) Syst 27(8):1861–1873, 2019.

[9] Cao X, Wei Y, Wen F, Sun J, "Face alignment by explicit shape regression", In: IEEE conference on computer vision and pattern recognition, pp 2887–2894, 2012.

[10] Raja R, Sinha DT, Dubey R, "Recognition of human-face from side-view using progressive switching pattern and soft-computing technique", Advanced Model Analysis B 58:14–34, 01, 2015.

[11] Raja R, Sinha TS, Patra RK, Tiwari S, "Physiological trait-based biometrical authentication of human-face using lgxp and ann techniques", International Journal of Information and Computer Security 10(2–3):303–320, 2018.

[12] Schroff F, Kalenichenko D, Philbin J, "Facenet: a unified embedding for face recognition and clustering", In: 2015 IEEE Conference on computer vision and pattern recognition (CVPR), 2015.

[13] Singh S, Singh D, Yadav V, "Face recognition using hog feature extraction and svm classifier", 8:6437–6440, 09, 2020.

[14] Ranjan R, Patel VM, Chellappa R, "Hyperface: a deep multi-task learning framework for face detection, landmark localization, pose estimation, and gender recognition", IEEE Transaction of Pattern Analysis and Machine Intelligence 41(1):121–135, 2019.

[15] Zhang K, Zhang Z, Li Z, Qiao Y, "Joint face detection and alignment using multitask cascaded convolutional networks", IEEE Signal Process Lett 23(10):1499–1503, 2016.

[16] Zeng D, Zhao F, Ge S, Shen W, "Fast cascade face detection with pyramid network", Pattern Recognition Letters 119:180–186, 2019.

[17] Liu W, Anguelov D, Erhan D, Szegedy C, Reed S, Fu C-Y, et al., "SSD: Single Shot MultiBox Detector", Computer Vision – ECCV 2016, pp. 21-37, 2016.

[18] Bazarevsky V, Kartynnik Y, Vakunov A, Raveendran K and Grund-mann M, "Blazeface: Sub-millisecond neural face detection on mobile gpus", arXiv preprint, 2019.

[19] A. Mool, J. Panda, and K. Sharma, "Optimizable face detection and tracking model with occlusion resolution for high quality videos," Multimedia Tools and Applications, vol. 81, p. 10391–10406, 2022.

[20] M. D. S. Ms. Varsha Gupta, "A study of various face detection methods," International Journal of Advanced Research in Computer and Communication Engineering, vol. 3, no. 5, pp. 6694–6697, 2014.

Authorized licensed use limited to: DELHI TECHNICAL UNIV. Downloaded on July 20,2023 at 11:10:42 UTC from IEEE Xplore. Restrictions apply.

Comparing Results of Multiple Machine Learning Algorithms on a bilingual dataset for the Detection of Fraudulent News

Amogh Jalan
Department of Information Technology
Delhi Technological University
Delhi, India
amoghjalan_2k19it016@dtu.ac.in

Aniket Gupta
Department of Information Technology
Delhi Technological University
Delhi, India
aniketgupta_2k19it019@dtu.ac.in

Dr Priyanka Meel
Department of Information Technology
Delhi Technological University
Delhi, India
priyankameel@dtu.ac.in

2023 12th Mediterranean Conference on Embedded Computing (MECO) | 979-8-3503-2291-0/23/$31.00 ©2023 IEEE | DOI: 10.1109/MECO58584.2023.10154918

***Abstract*—In today's world, it is pivotal to have to spot fake information as soon as it appears. Due to the vast and quick dissemination of news on the Internet, this is particularly crucial. Equally important is the capacity to determine if an article of news is accurate or false based on its headline. In this paper, we create a multi-lingual dataset and compare various algorithms on it. The outcome will be contrasted with the identification based on the entire text. The purpose of this is to put forth a technique for predicting fake news that strikes a balance between the quantity and quality of data analysis. A large number of studies on automatic fake news identification rely solely on English-language information, with only a few studies evaluating other language groups or contrasting several language features. This research examines textual characteristics that are not restricted to a specific language in the context of describing textual data for news discovery, as the widespread dissemination of false information is a prevalent global problem. To investigate text complexity, stylometric, and psychological aspects, the vocabulary of news articles published in English(American) and Hindi was examined. The traits that were retrieved help in the identification of real and fraudulent news. To create the detection model, we analyzed the performance of four ML algorithms: Multinomial Naive Bayes, Logistic Regression, Bernoulli Naive Bayes, and Bidirectional LSTM. With Logistic Regression and Bernoulli Naive Bayes an average accuracy of 86% was achieved, the results demonstrate that our suggested language-unrelated showcases are effective in classifying untrue and real news between two separate languages.**

Keywords-fake, news, English, Hindi, machine learning

I. Introduction

Online news platforms are gaining immense popularity among consumers owing to their user-friendliness and the wide range of sources they offer. By making it so simple to post, these platforms are further democratizing the sharing of news. A problem that arises from this is that a similar amount of fake news has been spread due to a lack of sufficient editorial rigour, fact-checking, and the involvement of bad actors. Misinformation propagated to the masses can have adverse reactions in the community leading to communal violence, stock market crash, defamation etc. A lot of this data is propagated in a mixture of many languages, which makes the classification of such data much more difficult than the traditional data. Hence, it becomes necessary to have models that can work towards finding fake news even when data is perturbed by adversaries of other languages. In this paper, we create a multi-lingual dataset mix of Hindi and English text along with corresponding labels to construct a classifier that can forecast the authenticity of a news item, determining whether it is genuine or fabricated. This dataset is trained and tested over various algorithms such as Naive Bayes, Logistic Regression and BiLSTM Deep Learning models.

II. Literature Review

The problem of fake news is wide and cuts across many academic fields. The investigation into identifying fake news is a relatively new field of research, and as a result, a universally agreed-upon definition of false news is yet to be established due to these reasons. This phenomenon is known by many different aliases and stands out for having a large

979-8-3503-2291-0/23/$31.00 ©2023 IEEE

2023 12th Mediterranean Conference on Embedded Computing (MECO) | 979-8-3503-2291-0/23/$31.00 ©2023 IEEE | DOI: 10.1109/MECO58584.2023.10154918

Authorized licensed use limited to: DELHI TECHNICAL UNIV. Downloaded on July 03,2023 at 04:49:56 UTC from IEEE Xplore. Restrictions apply.

conceptual potential. Several researchers and subject-matter specialists prefer the term "disinformation" to "false news." This material is classified as hoaxes by the most widely used social network in the world, Facebook, and is substituted with junk news by Snopes, one of the pioneering websites to provide outcomes in the English language. Fake news is defined as information that is typically spread online and through traditional media to mislead the audience. However, it is straightforward to identify the three primary categories of fake news, as delineated in previous research, by examining specific titles and their connotations. [2]. The first category of fake news consists of entirely made-up information in which not a single sentence is true. The goal of [1] was to create a system that could automatically detect fake news files. The authors of the study developed classification models that utilized lexical, syntactic, and semantic data, along with features indicating text readability characteristics. Through a comparative analysis of automatic and manual fake news identification, the model outcomes demonstrated accuracy on par with human capability, as reported in the investigation conducted by the authors.

The second category, conversely, comprises genuine news that has been distorted or contextualized inaccurately. Unfortunately, large-scale fake attacks are generally cross-platform, inventive, and original, necessitating the use of techniques other than text analysis. Satirical information is also false information. To categorize the satirical data set, [3] proposed a model based on an SVM-based system with 5 conclusive features (absurdity, syntax, humour, punctuation and negative affect). To identify linguistic traits of the unreliable text, [4] contrasted the dialect of true information with that of pastiche, pranks, and propaganda.

The third category has actual information that has been misrepresented or taken out of context. Unfortunately, large-scale fake attacks are generally cross-platform, inventive, and original, necessitating the use of techniques other than text analysis. For this purpose, a prototype of cutting-edge technology that can establish the source of the digital media that was captured was made [5]. According to the authors, its implementation along with the usage of blockchain technology and standardized metadata presents a cutting-edge strategy to combat false tracking and the source of the media information utilized in it. Real news and fake news are often difficult to tell apart. The effects of this type of news on the public, however, have not yet been thoroughly studied, and nothing is known about its political, social, economic, and financial ramifications. The majority of studies focus on incorrect information uploaded on social networking sites. Information is firstly provided on Twitter, which is made possible, among other things, by the openness of its API and its acceptance by journalists, and politicians. Concerned by the deluge of false information, research communities produced automated fake news recognition methods based on NLP methods. These models focus solely on linguistic traits including word patterns, grammar elements, phrase counts, and the presence of specific expressions. By utilizing a naive Bayes classifier, [6] developed a straightforward method for detecting fake news and produced respectable results given the relative easiness of their model. [7] examined how the complexity, style, and title elements of true and fake news differ. The Elaboration Likelihood Model was taken into consideration as a theory to tell how bogus news propagated and persuaded people. In addition to looking at the information's overall substance, several studies have concentrated on looking at headlines, or "clickbait." Potential techniques for the automatic detection of clickbait were investigated in [14]

A survey was conducted on techniques for identifying textual and non-textual click-baiting indications, such as user behaviour and images. A mechanism to ascertain the alignment of headlines with their respective article bodies was presented by [8] The method could be used in situations including the detection of clickbait in fake news.

[7] compiled a corpus of English-language news articles from several sources and made them accessible to the public. The authors determine the document's categorization using a classifier based on elements of writing style. The collection of features considers writing traits like grammatical classes' frequency and metrics of readability. However, the method's application is constrained by the fact that many features depend on the language.

Investigations of [9] show probable trends in the news of fake nature and its likely connections to deceit and clickbait. To address the issue, a model was put up by the authors based on spotting false news, which looked at a news story's lexical, syntactic, and semantic components instead of just its content. The researchers discovered that even with modest content restrictions, the suggested strategy could surpass the best models and can lead to early detection of false news. The results, however, only addressed English and did not take into account any potential differences in linguistic structures.

The corpora "Fake.Br" and "FakeNewsCorpusSpanish", written in Portuguese and Spanish respectively, were created by [10] and [11] and were made accessible to the general public. Textual features were offered as text classifiers in both papers. However, some elements, such as Bag-of-Words, available in those works rely on the language.

[12] compiled datasets in English and Portuguese, and analyzed the two languages for commonalities in stylometry, specifically looking for universal traits that are independent of culture or language-specific qualities. The researchers identified a pattern in the stylistic characteristics of unreliable articles in both languages, indicating that reliable and unreliable articles can be differentiated based on stylistic features in both languages. Only two languages were included in the results, making it impossible to determine the presence of stylometric patterns in other languages. However, the authors merely evaluate the articles' dependability without necessarily confirming their accuracy or examining other elements like satire. To differentiate between fake, trustworthy, and satirical content, [13] described a dataset that included both English and French. However, unlike our paper, they still represent data in a language-dependent fashion

Authorized licensed use limited to: DELHI TECHNICAL UNIV. Downloaded on July 03,2023 at 04:49:56 UTC from IEEE Xplore. Restrictions apply.

because it uses pre-training techniques like word vectors or term frequencies that are specific to those languages.

Consequently, this study's significant contribution lies in providing an extensive comparison of various languages, considering the limited body of research on fake news identification beyond the English language. The studies were carried out using two corpora of different languages (English and Hindi), rather than sticking to a corpus compiled on a single language. The models were introduced into each corpus, and assessed, and the most crucial elements were contrasted by looking at the traits that all languages share. To explore the common set of features across multiple corpus idioms and extend the applicability of our methodology, we have carefully identified and selected language-independent features in this study.

III. PREPARE YOUR PAPER BEFORE STYLING

Our methodology primarily consists of the following as shown in Fig. 1: (i) Information pertaining to the dataset employed in the experimental setup, along with the dataset's pre-processing procedures, and (iii) Algorithms used in the experiment.

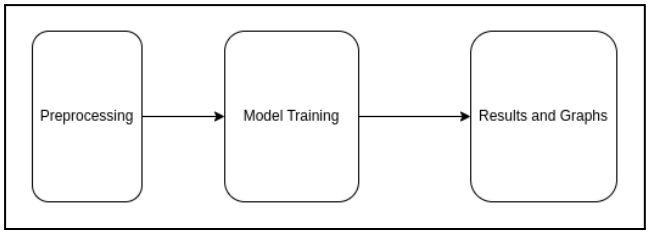

Fig. 1: Proposed Methodology

A. Dataset and Preprocessing

There are various datasets with text in English and some in Hindi but here it was required to combine both and form

a dataset that would build a model that overcomes the adversaries of both being used.

1. The **FakeNewDetection** repository data used in [16] consists of a dataset with title, text, URL and labels with 1 as Real and 0 as Fake. The dataset contains 3987 samples with both real and fake news data. From the dataset, only titles and labels were used in this paper. The titles were preprocessed by making words lowercase, applying Snowball Stemmer, Lemmetizing the text and removing stopwords.
2. The **Hindi-Fake-News-Detection** repository data used by [15] consists of various datasets. Here the fake_news.csv and true_news.csv were used as they were already preprocessed by removing stopwords and applying stemming to the words. Both datasets were combined. Now the dataset had 2009 distinct samples with a short description and corresponding labels.

Both these datasets, when concatenated, had a total of 5997 samples with Both Hindi and English text. After the manual removal of the data with very small or large text, 1500 samples were selected for use.

short_description	label
' tv saturday ' spielberg ' ' clueless '	1
paddock shot secur guard befor mass shoot	0
बूम पाय पिछल असम बाढ़ तस्वीर हालिय बाढ़ के तस...	0
anderson cooper revisit moment	1
बूम पाय वीडिय 2019 मौलव टिप्पण तबरेज अंसार मॉब...	0

Fig. 3: Example Dataset

II. ALGORITHMS

A. Multinomial Naive Bayes

Multinomial Naive Bayes classifier is a widely used algorithm for categorizing text documents into different classes based on a statistical assessment of their contents. This algorithm is particularly suitable for classifying discrete features, which makes it ideal for text classification tasks. It provides a probabilistic method and speeds up text classification considerably.

The task of text classification is to categorize text fragments into distinct classes by assessing the chance that a document belongs to the class of other text with a similar subject. This algorithm makes use of the word frequencies in a text to calculate the probability of a specific document being classified under a certain category. Words present in a document help in understanding the context of the information it holds. The classifier takes these words and their frequencies into account to determine the class of the document.

The algorithm can be employed for identifying fake news, wherein it categorizes news articles into two groups - genuine or fabricated. It operates by examining the frequency of words in a particular news article and comparing it with the frequency of words in a training dataset of both types of news articles. Based on this comparison, the algorithm computes the probability of the news article is genuine or fabricated.

For example, consider a news article that is being analyzed by the Multinomial Naive Bayes classifier. The article contains a number of words that are common in fake news articles, such as "conspiracy," "hoax," and "fabricated." Based on the frequency of these words and their association with fake news, the algorithm assigns a higher probability of the article being fake. Conversely, if the article contains words that are more commonly associated with real news, such as "verified," "confirmed," and "official," the algorithm assigns a higher probability of the article being real.

The Multinomial Naive Bayes classifier has several advantages when it comes to text classification. First, it is relatively easy to implement and does not require a large

Authorized licensed use limited to: DELHI TECHNICAL UNIV. Downloaded on July 03,2023 at 04:49:56 UTC from IEEE Xplore. Restrictions apply.

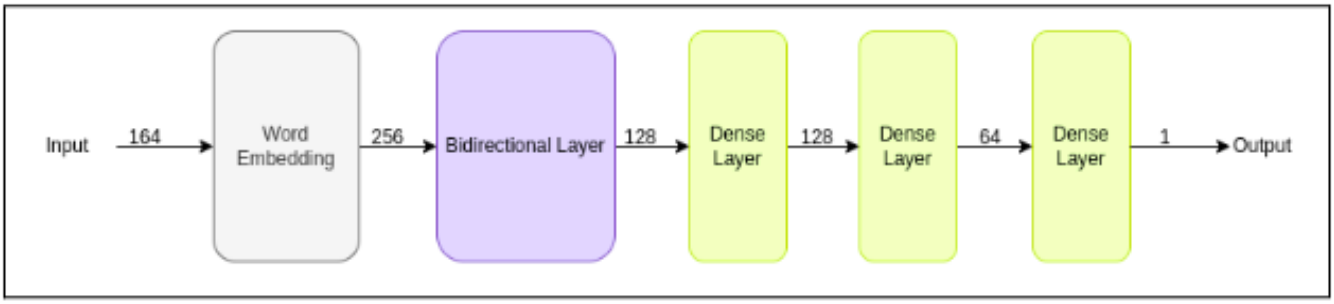

Fig. 2

number of computational resources. Second, it can be trained quickly and can handle large datasets. Third, it is robust to noise and can handle irrelevant features without affecting the accuracy of the classification.

B. *Bernoulli Naive Bayes*

The Bernoulli Naive Bayes classifier is a probabilistic method that is widely used in the field of machine learning and natural language processing, particularly for tasks involving binary classification, such as detecting genuine or fake text. In this method, each document is represented by a set of binary characteristics that indicate the presence or absence of specific words or phrases. The algorithm then estimates the likelihood of a document belonging to a particular class, such as fake or real, by comparing the frequency of these features in the training data. Although the Multinomial Naive Bayes classifier is commonly used in text classification tasks, the Bernoulli Naive Bayes classifier is better suited for some applications because it assumes that the features are binary values instead of counts. This means that the classifier is more focused on whether a feature is present or absent, rather than its frequency, making it more suitable for tasks where the presence or absence of a feature is more important.

Let's take the instance of categorizing news pieces into genuine or fake. To achieve this objective, we can depict each article as a binary set of attributes, wherein each attribute indicates the occurrence or non-occurrence of a particular word or phrase. For example, we might include features such as "Trump", "election", "fraud", "vaccine", etc. The label for each article would be either "real" or "fake". To train the classifier, we would initially gather a substantial dataset of news articles, with labels indicating whether they are genuine or fake. After that, we would represent each article as a binary vector of features and calculate the occurrence of each feature in the dataset. We would also calculate the prior probabilities of each class, based on the frequency of articles in each class. To classify a new article, the Binomial Naive Bayes classifier would calculate the likelihood of each feature being present or absent, given the class label. Next, the classifier would use Bayes' theorem to compute the posterior probability of the article belonging to each of the classes. Finally, the classifier would assign the article to the class with the highest posterior probability.

The algorithm is based on the Bernoulli Distribution and can only accept binary values of 0 or 1. Here, the count of each value for the binary term occurrence characteristics identifies whether or not a word appears in a text. The Bernoulli distribution has two possibilities that are mutually exclusive:

$$p(x) = P[X = x] = \begin{Bmatrix} q = 1 - p & x = 0 \\ p & x = 1 \end{Bmatrix}$$

Assuming that all characteristics are binary-valued variables, the input for a Bernoulli Naive Bayes model is binarized for any other type of data.

C. *Logistic Regression*

Logistic Regression is a widely used classification algorithm that is highly efficient and effective in predicting binary outcomes. It is a statistical technique used to analyze datasets with one or more independent variables that influence an outcome. This method is commonly employed in text classification to determine if a given text is authentic or false using specific attributes or features.

The logistic regression model is commonly used in binary classification tasks, where the output variable can take on one of two possible values: 0 or 1. The model estimates the probability of the output variable is equal to 1, given the input features. This probability is computed using the logistic function, which maps the output to a value between 0 and 1. The logistic function is a sigmoid curve that starts at 0 and approaches 1, and it is used to transform any input value into a corresponding probability value.

The logistic regression model is trained using a dataset that consists of a set of input features and corresponding labels that indicate whether the text is fake or real. After calculating the probability using the logistic function, the model uses an optimization technique to determine the most appropriate values of its parameters. These parameter values are optimized to reduce the difference between the predicted output and the actual output, ultimately improving the accuracy of the model's predictions.

One of the main advantages of using logistic regression for text classification is that it can handle large datasets with many input features. This makes it suitable for processing large

Authorized licensed use limited to: DELHI TECHNICAL UNIV. Downloaded on July 03,2023 at 04:49:56 UTC from IEEE Xplore. Restrictions apply.

amounts of text data with many features, such as word frequency, length, and other linguistic features.

D. bi-LSTM

The bi-LSTM (Bidirectional Long Short-Term Memory) classifier is a powerful neural network-based algorithm that has shown promising results in the field of natural language processing. It is particularly useful for text classification tasks that require capturing the sequential nature of language. The bi-LSTM classifier is a variation on the standard LSTM model that can learn long-term relationships between words in a phrase. In addition, the bi-LSTM model includes a second LSTM layer that processes the input sentence in the reverse direction, allowing the model to capture information from both past and future words in the sentence. This enables the model to better understand the context in which the words are used, making it suitable for tasks such as sentiment analysis and text classification.

When using the bi-LSTM classifier for detecting fake news, we begin by preparing the input data. The text is pre-processed by the methods used for earlier models and then the sequence is padded to ensure that all input sequences have the same length, which is a requirement for inputting data into the bi-LSTM model.

The bi-LSTM model is then trained using a dataset of labelled text, with labels indicating whether the text is real or fake. During training, the model learns to map the input sequence to the corresponding label using backpropagation, which adjusts the weights of the model to minimize the difference between predicted and actual labels.

One advantage of using a bi-LSTM model for text classification is that it can learn to distinguish between different types of language features, such as context and syntax, in addition to the content of the text. This makes it useful for detecting subtle differences in language that can be indicative of fake news.

After training, the bi-LSTM model can be used to classify new text as either real or fake. To classify new text, the pre-processing steps are repeated, and the resulting sequence of words is input into the trained model. The model outputs a probability score between 0 and 1, indicating the likelihood that the input text is fake. If the probability score is above a certain threshold, the text is classified as fake, otherwise, it is classified as real.

To enable bidirectional LSTM networks to function, every training sequence is fed in both forward and backward directions to two separate LSTM networks that are connected to the same output layer. This implies that the bi-LSTM captures comprehensive information about the sequence of all data points both preceding and succeeding each point. At each time step, the outputs of both the forward and backward LSTMs are combined by concatenation, instead of solely retaining the sequence in the forward direction. This paper used the following model as shown in Fig. 2.

III. RESULTS

On training with 80% data following results were achieved for the above algorithms.

A. Multinomial Naive Bayes

The algorithm produced a precision of 0.89, a recall of 0.81 and 0.87 as f1-score. The confusion matrix for the same is available in Fig. 4.

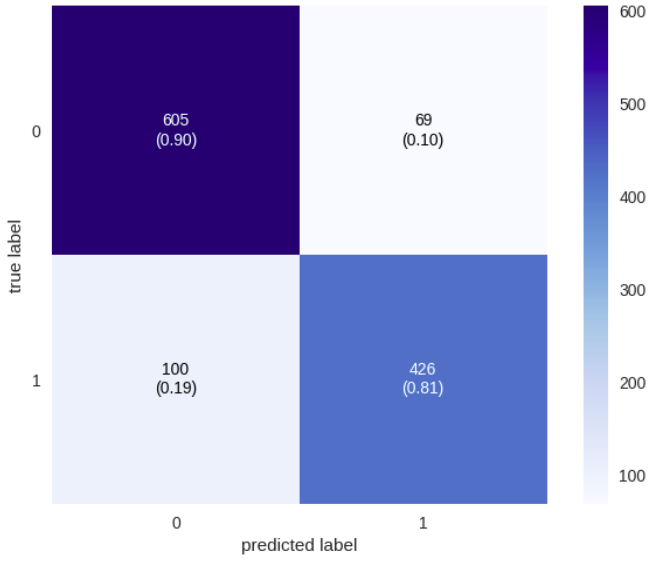

Fig. 4: Multinomial Naive Bayes Confusion Matrix

B. Bernoulli Naive Bayes

The algorithm produced a precision of 0.92, a recall of 0.83 and 0.87 as f1-score. The confusion matrix for the same is available in Fig. 5.

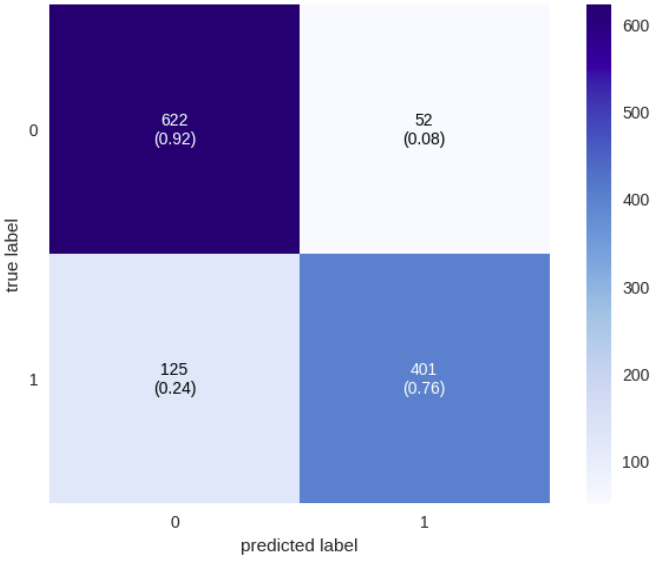

Fig. 5: Bernoulli Naive Bayes Confusion Matrix

Authorized licensed use limited to: DELHI TECHNICAL UNIV. Downloaded on July 03,2023 at 04:49:56 UTC from IEEE Xplore. Restrictions apply.

C. *Logistic Regression*

The algorithm produced a precision of 0.91, a recall of 0.84 and 0.87 as f1-score. The confusion matrix for the same is available in Fig. 6.

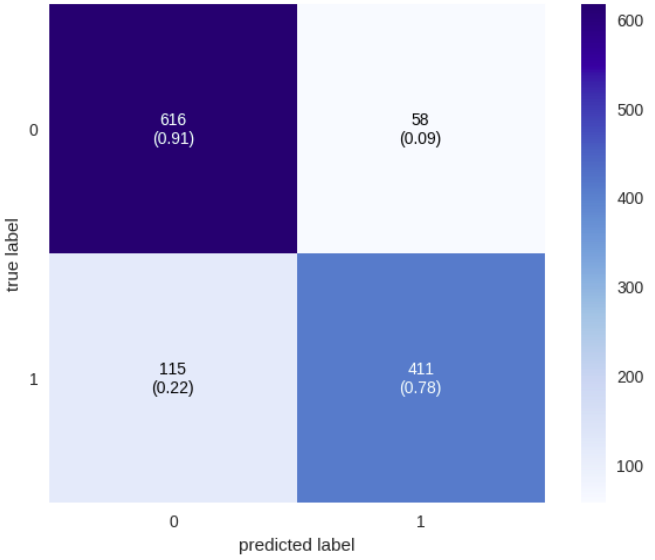

Fig. 6: Logistic Regression Confusion Matrix

D. *bi-LSTM Model*

This model on training produced a precision of 0.75, a recall of 0.84 and 0.79 as the f1-score. The confusion matrix for the same is available in Fig. 7.

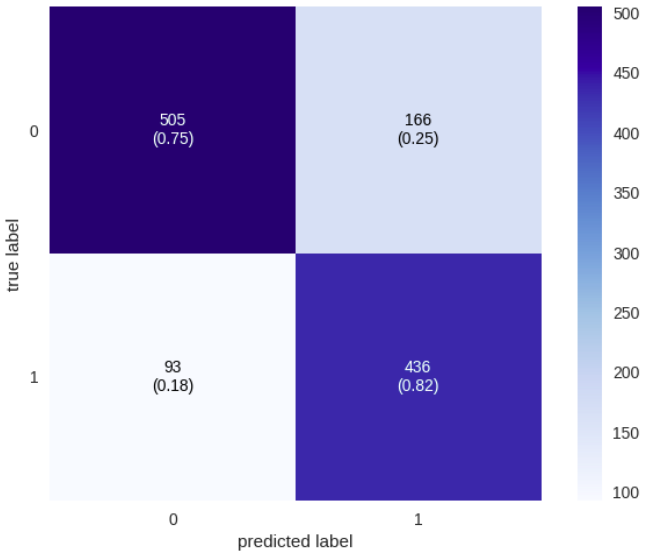

Fig. 7: bi-LSTM Model Confusion Matrix

As shown in Fig. 8, The results of the four different models show that all models achieved high training accuracies, with the logistic regression model achieving the highest accuracy of 0.98. However, when looking at the test accuracies, all models show a drop in performance, with the logistic regression and multinomial naive Bayes models achieving the highest test accuracies of 0.86, followed closely by the Bernoulli naive Bayes model with a test accuracy of 0.85. The bi-LSTM model had the lowest test accuracy at 0.78.

When considering the precision, recall, and f1-score, we can see that the logistic regression and Bernoulli naive Bayes models had the highest precision scores of 0.91 and 0.92, respectively. On the other hand, the multinomial naive Bayes model had the highest recall score of 0.81. The Bernoulli naive Bayes model had the highest f1-score of 0.87. The bi-LSTM model had the lowest precision, recall, and f1-score values of 0.75, 0.84, and 0.79, respectively.

The high training accuracies suggest that all the models were able to fit the training data well. However, the drop in performance when tested on unseen data suggests that the models may have overfit the training data. This is a common issue in machine learning where models may perform well on the training data but not generalize well to new data.

When comparing the performance of the different models, it is clear that the logistic regression and Bernoulli naive Bayes models outperformed the other models in terms of test accuracy, precision, and f1-score. The bi-LSTM model had the lowest performance in all metrics, suggesting that it may not be the best choice for this particular task or that a better model for bi-LSTM was required.

It is important to note that the choice of model should depend on the specific problem and the available data. For example, if the data has many categorical features, then the multinomial naive Bayes model may perform better than other models. On the other hand, if the data has binary features, then the Bernoulli naive Bayes model may be a better choice.

In conclusion, the performance of the four models shows that the logistic regression and Bernoulli naive Bayes models are the most suitable for the given problem, as they achieved the highest test accuracies, precision, and f1-score. However, it is important to consider the specific problem and data when choosing a model, as different models may perform better for different data types. Additionally, further experimentation and tuning of the models may lead to even better performance.

Model	Accuracy(Train)	Accuracy(Test)
MultinomialNB	0.94	0.86
BernoulliNB	0.94	0.85
LogisticRegression	0.98	0.86
bi-LSTM	0.84	0.78

Fig. 8: Results Comparison

Authorized licensed use limited to: DELHI TECHNICAL UNIV. Downloaded on July 03,2023 at 04:49:56 UTC from IEEE Xplore. Restrictions apply.

IV. CONCLUSION AND FUTURE WORK

With rising access to the internet and the subsequent rise in fake news, it becomes important to have a way to identify text that might be fake. In India, a lot of this text can be found in Hindi and English mix and hence it becomes necessary that models are built that can classify this type of data. In this study, we compared the performance of four different models on a fake news dataset containing both Hindi and English text. The results showed that the logistic regression and Bernoulli naive Bayes models outperformed the other models in terms of test accuracy, precision, and f1-score. However, it is important to consider the specific problem and data when choosing a model, as different models may perform better for different data types.

There are several areas for future research in this field. Firstly, more studies could be conducted on the performance of these models in different languages, as different languages may have unique characteristics that affect model performance. Additionally, more research could be done on the performance of these models on other types of text data, such as social media posts or news articles from different sources. Another area of research could be to examine the application of ensemble models in this study. Ensemble models have demonstrated efficacy in enhancing the performance of machine learning models across a range of fields and may therefore have the potential to enhance the performance of the models employed in this research. Another important area for future research is to improve the quality of fake news datasets. Currently, fake news datasets are limited in size and scope, which can lead to overfitting and difficulty in generalizing to new data. Therefore, larger and more diverse datasets could be collected and used to improve the robustness of the models.

Future work could focus on improving the interpretability of these models. One of the limitations of machine learning models is their lack of transparency, which makes it difficult to understand how they are making their predictions. This is particularly important in the context of fake news detection, as it is important to understand which features are driving the predictions in order to identify the characteristics of fake news.

REFERENCES

[1] Perez-Rosas, V., Kleinberg, B., Lefevre, A., Mihalcea, R., 2017. Automatic detection of fake news. arXiv preprint arXiv:1708.07104 .

[2] Rubin, V.L., Chen, Y., Conroy, N.K., 2015. Deception detection for news: three types of fakes. Proceedings of the Association for Information Science and Technology 52, 1–4

[3] Rubin, V.L., Conroy, N., Chen, Y., Cornwell, S., 2016. Fake news or truth? using satirical cues to detect potentially misleading news, in: Proceedings of the second workshop on computational approaches to deception detection, pp. 7–17.

[4] Rashkin, H., Choi, E., Jang, J.Y., Volkova, S., Choi, Y., 2017. Truth of varying shades: Analyzing language in fake news and political factchecking, in: Proceedings of the 2017 conference on empirical methods in natural language processing, pp. 2931–2937

[5] Huckle, S., White, M., 2017. Fake news: A technological approach to proving the origins of content, using blockchains. Big data 5, 356–371

[6] Granik, M., Mesyura, V., 2017. Fake news detection using naive bayes classifier, in: 2017 IEEE First Ukraine Conference on Electrical and Computer Engineering (UKRCON), IEEE. pp. 900–903.

[7] Horne, B., Adali, S., 2017. This just in: Fake news packs a lot in title, uses simpler, repetitive content in text body, more similar to satire than real news, in: Proceedings of the International AAAI Conference on Web and Social Media

[8] Chen, Y., Conroy, N.J., Rubin, V.L., 2015. Misleading online content: recognizing clickbait as" false news", in: Proceedings of the 2015 ACM on workshop on multimodal deception detection, pp. 15–19.

[9] Bourgonje, P., Schneider, J.M., Rehm, G., 2017. From clickbait to fake news detection: an approach based on detecting the stance of headlines to articles, in: Proceedings of the 2017 EMNLP workshop: natural language processing meets journalism, pp. 84–89.

[10] Zhou, X.; Jain, A.; Phoha, V.V.; Zafarani, R. Fake news early detection: A theory-driven model. arXiv 2019, arXiv:1904.11679.

[11] Monteiro, R.A.; Santos, R.L.; Pardo, T.A.; de Almeida, T.A.; Ruiz, E.E.; Vale, O.A. Contributions to the Study of Fake News in Portuguese: New Corpus and Automatic Detection Results. In Proceedings of the International Conference on Computational Processing of the Portuguese Language, Canela, Brazil, 24–26 September 2018; pp. 324–334.

[12] Posadas-Durán, J.; Gómez-Adorno, H.; Sidorov, G.; Moreno, J. Detection of Fake News in a New Corpus for the Spanish Language. J. Intell. Fuzzy Syst. 2018, in press

[13] Gruppi, M.; Horne, B.D.; Adali, S. An Exploration of Unreliable News Classification in Brazil and The U.S. arXiv 2018, arXiv:1806.02875

[14] Guibon, G.; Ermakova, L.; Seffih, H.; Firsov, A.; Le Noé-Bienvenu, G. Multilingual Fake News Detection with Satire. In Proceedings of the CICLing: International Conference on Computational Linguistics and Intelligent Text Processing, La Rochelle, France, 7–13 April 2019.

[15] Kumar, Sudhanshu, and Thoudam Doren Singh. "Fake news detection on Hindi news dataset." Global Transitions Proceedings 3.1 (2022): 289-297.

[16] Yang, Yang, et al. "TI-CNN: Convolutional neural networks for fake news detection." arXiv preprint arXiv:1806.00749 (2018).

[17] Abonizio, Hugo Queiroz, et al. "Language-independent fake news detection: English, Portuguese, and Spanish mutual features." Future Internet 12.5 (2020): 87.

[18] Probierz, Barbara, Piotr Stefański, and Jan Kozak. "Rapid detection of fake news based on machine learning methods." Procedia Computer Science 192 (2021): 2893-2902.

Authorized licensed use limited to: DELHI TECHNICAL UNIV. Downloaded on July 03,2023 at 04:49:56 UTC from IEEE Xplore. Restrictions apply.

2023 4th International Conference for Emerging Technology (INCET)
Belgaum, India. May 26-28, 2023

Confident Stock Price Prediction using Markov Chains

Abhiluv Anand
Department of Applied Mathematics
Delhi Technological University
Delhi, India
abhiluvanand_2k19mc004@dtu.ac.in

Dr. Ramesh Srivastava
Department of Applied Mathematics
Delhi Technological University
Delhi, India
rsrivastava@dce.ac.in

2023 4th International Conference for Emerging Technology (INCET) | 979-8-3503-3575-0/23/$31.00 ©2023 IEEE | DOI: 10.1109/INCET57972.2023.10170592

***Abstract*—The ability to predict future stock price movement is very important to financial institutions that use stock price projections to calculate future values of stocks or indexes. Although there are numerous well-known methods for predicting stock prices, in this paper, we have focused on a short-term Markov chain-based stock price prediction model. Previous studies have demonstrated the practicality of modeling the financial market as a random walk and the potential for perceiving a market to have the Markov property by defining the transition states as deviations from the opening and closing stock prices of the relevant day. The aim of this study was to construct a first-order transition Markov chain-based stock price prediction model, where the states are continuous price ranges as opposed to potential closing price variations. The First-order transition Markov Chain Model was developed on MATLAB 2020. The outcomes include graphs forecasting the future prices for the top five Nifty-Fifty stocks (based on market capitalization at the time) in comparison to the actual stock prices. Further, the confidence interval was generated for the first prediction using a sample size of 100 predictions with respect to the real stock price. The model was recommended for use on a short-term basis as it loses significance over time owing to the volatility of the market and limited transitions found in the used data set.**

***Index Terms*—Stock price prediction, Markov chain, First-order transition Markov Chains, Transition probability matrix.**

I. Introduction

The growth of both foreign and domestic capital markets has shown that stock investing may produce sizeable long-term returns for investors and will stay a promising investment path in the future. To achieve high returns and success as an investor, one must thoroughly investigate a company's history, performance, and future prospects and have a firm knowledge of a variety of technical and fundamental analysis techniques owing to the unpredictability of the financial market.

The onset of the global pandemic Covid-19 has created major negative implications for the global economies and personal finances. With many people losing jobs, getting reduced salaries, and exhausting their savings, investment and passive incomes gained the utmost importance. The Securities and Exchange Board of India (Sebi) reported that there were 4.9 million new Demat accounts opened in the fiscal year 2020, which was the highest in at least a decade.

The Economic Times in 2021 reported how retail investors now dominate the Indian Stock Market with the NSE alone having a share of 45% of retail investors owing to the 12.25 million and 1.9 million new accounts being opened in the fiscal year 2021-22 in CDSL and NDSL respectively. Thereby making the study of the Stock Exchange very relevant to the current times.

Over the years, Stock market analysis has seen progressive development with the aid of rapidly developing technology. Today computing techniques have become an integral part of market analysis and more importantly, stock price prediction due to multiple reasons. To begin with, as time progresses, there is an enormous amount of financial data that can no longer be handled by traditional techniques of data analysis. Further, because of real-time data processing made possible by computing techniques, investors can now act swiftly and with confidence. Moreover, investment strategies can be created using machine learning algorithms that can spot patterns in historical data and predict future price trends. The implementation of computing techniques in its entirety can be backed by various mathematical modules has improved stock market research and price prediction accuracy, efficacy, and profitability for investors.

Stock trend analysis, where equities are chosen by fundamental analysis and buying/selling timing is confirmed through technical analysis, is one such crucial component of practical stock trading. As a result, the study and development of statistical models play a crucial role in this subject. To analyze such occurrences, a variety of techniques including but not limited to descriptive statistics, simple moving averages, and Markov Chain models are used extensively. [1]

Several Markov chain-based methods are employed in stock market forecasting. In the discrete-time Markov chain model [2], the stock market is represented as a discrete-time Markov chain, where each state corresponds to a particular trend or behavior of the market, whereas the hidden Markov model technique [3] is predicated on the idea that the stock market's true state is not immediately apparent but can be inferred from the observed data. The stock market is modeled as a Markov chain with numerous regimes in the Markov regime-switching model [4], where each regime represents a different behavior of the market. As opposed to this, the Monte Carlo simulation [5] creates a large number of potential future stock market scenarios based on the expected transition probabilities of a

Authorized licensed use limited to: DELHI TECHNICAL UNIV. Downloaded on July 20,2023 at 11:24:12 UTC from IEEE Xplore. Restrictions apply.

Markov chain model. Based on the transition probabilities, the next state from the set of potential states is randomly chosen for each situation. The distribution of outcomes that results can be used to calculate the risk attached to various trading methods.

In this paper, the predictions of the opening and closing prices of the selected stocks have been made by applying the concepts of Stochastic Processes, primarily Markov Chains, to the real-time data sourced from the National Stock Exchange. Considering that the market possesses the Markov property, the model developed predicts the opening/closing price of the stock based on first-order Markov Chains using random values to determine the transition probabilities whereby each state represents an interval of possible stock prices.

The paper has been divided into five sections. The previous literature has been discussed in Section II. The methodology of the technique advocated is explained in Section III while the results of its application are discussed in Section IV. Lastly, Section V serves as the paper's final section.

II. Literature Review

A. Stock Market Analysis

As the number of Retail investors rises, the importance of analyzing and more importantly predicting stock prices has risen exponentially with time. This liquidity supply in the market, though dependent on the eminent financial crises, is majorly driven by the advancement in financial technology [6]. Thus any improvement in the available technology not only results in a significant impact on the market volatility but is constantly researched to beat the market odds. Ever since the creation of electronic trading in the 1970s and the internet, stock market analysis with a prime focus on price prediction has evolved significantly.

The time series modeling for stock prediction has come a long way from the statistical models used traditionally, such as the Auto Regressive Integrated Moving Average (ARIMA), also known as Box-Jenkins methodology, the most favored approach of its time [7] and the natural generalization of the Autoregressive Conditional Heteroskedastic (GARCH) introduced in 1982 [8]. With the progress in technology, multiple Machine learning and deep learning modules soon found their application in stock price prediction. In particular, the Support Vector Machine based (SVM) approach outperformed several other prediction models as it obliterates the over-fitting defect of the traditional stock prediction models [9]. Integrating the Wavelet transform as a data pre-processing tool into Neural Networks to has shown to outperform the conventional models significantly [10]. The broad classification of Machine learning and Deep learning, includes various other modules such as K-Nearest Neighbor [11], Random Forests [12] and Decision Trees [13].

As we go deeper, the domain gets further and further bifurcated into specialized techniques. In order to maximize the efficiency by combining key features of each individual technique into a more robust system, Ensemble Learning is now being used progressively [14].

To help summarize the various techniques and classify them according to their basic approach, Gandhmal, D.P., and Kumar, K.'s survey of 2019, with the aid of 50 research articles, categorized the current strategies for stock market prediction according to various parameters including, but not limited to their methodology adapted, datasets used, performance measures, implementation tools, etc. It was highlighted that multiple techniques including Support Vector Regression (SVR), Artificial Neural Networks (ANN), fuzzy-based techniques, K-means, and others are already used widely to anticipate changes in the stock market. This shows that Stock Market Prediction as a field is already being explored extensively via multiple domains including Machine Learning, Deep Learning, and Neural Networks. [15]

B. Application of Markov

In the process of better analyzing the market, considering the stock prices to be a stochastic probabilistic process has helped researchers better predict future prices. The hidden Markov models (HMM) [3] and Markov chain models [16] are being extensively used to analyze the behavior of the stock market and predict stock prices based on pattern recognition. Previous work considering the market to have the Markov properties and using Markov chains for stock price prediction including the work done by Doubleday and Esunge [17], and Vasanthi et al. [18] have developed models based on the foundation that the prices/ portfolio can take 2 transitions, namely higher or lower than the previous day's price to represent the bullish and bearish behavior of the market. This paper does not limit the scope to daily's bullish and bearish trend of the market, but defines multiple states, each being a range of potential stock prices (in the interval of 1 Rupee) to achieve more accurate results.

The focus of this paper was to perform one such analysis on the selected stocks and make predictions of their opening and closing price by utilizing the concepts of Random Walk and first-order transition Markov Chains.

III. Methodology

A. Basics

Markov properties essentially describe a random process's abstraction. The probability of transitioning between states relies only on the present state instead of the path followed to achieve the said state, making a Markov chain a particular kind of Markov process. In other words, a Markov chain is a mathematical model that depicts a process that switches between states, with the chance of each switch being determined solely by the present state. Thus, we can describe the probabilistic behavior of the system and forecast its future behavior by using Markov chains.

A system that shifts randomly over time is described by a mathematical model called a "random walk". It is a process where the next step depends solely only on the current state and not on how the state was achieved. Markov chains are used to model such processes.

Authorized licensed use limited to: DELHI TECHNICAL UNIV. Downloaded on July 20,2023 at 11:24:12 UTC from IEEE Xplore. Restrictions apply.

TABLE I
COMPARING CONFIDENCE INTERVALS GENERATED FOR THE PREDICTED STOCK PRICE OF TOP 5 NIFTY50 STOCK WITH ACTUAL DATA

Stock Symbol	95% Confidence Interval		99% Confidence Interval		Actual Price
RELIANCE	2444	2452.6	2442.6	2454	2473.5
TCS	3370.4	3381.2	3368.7	3382.9	3380
HDFCBANK	1600.8	1605.6	1600	1606.3	1605
ICICIBANK	863.89	867.25	863.35	867.79	864.45
HINDUNILVR	2663.5	2675.5	2661.6	2677.5	2668

In the case when a walk's position at time n relies only on its position at time n-1, it is said to exhibit the Markov property. Therefore, we only need to think about the state of a random variable, say X_n, just before a particular point of interest, that is one step prior: X_{n-1} rather than worrying about the path the variable may have traveled to reach its current state.

$$P(X_n = j|X_{n-1} = i) = p_{ij} \tag{1}$$

As a consequence, X's state at time n is solely dependent upon X's state at step n-1. This is because, for our random variable X_n, p_{ij} is independent of X_{n-2}, X_{n-3},..., X_1, where each p_{ij} constitutes a probability row vector containing the transition probabilities for all possible transitions across the system under consideration.

$$\sum_{j=1}^{m} p_{ij} = 1 \tag{2}$$

The chain refers to the method of changing a system's condition while accounting for each transition's probability [19]. This forms an m×m transitional probability matrix M:

$$M = \left[p_{ij}\right] = \begin{bmatrix} p_{11} & p_{12} & \dots & p_{1m} \\ p_{21} & \dots & \dots & p_{2m} \\ \dots & \dots & \dots & \dots \\ p_{m1} & p_{m2} & \dots & p_{mm} \end{bmatrix} \tag{3}$$

B. Proposed Algorithm

Owing to the volatility of the market, a set of predefined probabilities for state transitions can not be used across different stocks or market indices. Thus, the subsequent state of the Stock Value is determined using random uniform values to determine the transition probabilities. If S0 is chosen to be the initial state, a value will be produced using a random number from the range of possible states. [20].

This paper is limited to the study of first-order Markov Chains as a substantial growth in the number of parameters constrains its use [21]. In this approach, the opening/closing stock prices are divided into appropriate states by defining the states to be ranges of stock prices, starting from 0, to 52 weeks high (observed in the interval chosen) plus an additional 20 percent, incremented by 1.

The first step in the procedure is the creation of a matrix that represents the probabilities of changing states. These probabilities of the changing stock price are represented by the transition probabilities between states, where each state corresponds to a specific price range.

The cumulative transition probability matrix is produced by adding each state's transition probabilities to all potential next states. The probability distribution of proceeding from the current state to another can be observed in each row of this matrix. The cumulative transition probability matrix is normalized so that each row has a total probability of 1 by adding up the transition probabilities within each row.

The next step is to choose a beginning point from which to make stock price predictions. The model forecasts the next price by randomly choosing a state based on the cumulative probabilities in the selected row of the cumulative transition probability matrix, using a uniform random number generator. It then creates a new uniform random number, restricted within the interval of the selected state to designate the opening/ closing stock price for the particular day.

C. Confidence Interval

To study the validity and significance of the above-generated Model, the opening price for the stocks on the 18th of January 2023 was predicted and compared to the actual price. By creating a sample of sample size 100, two confidence intervals were generated at 95

In research methods, confidence intervals are crucial because they offer a possible range of values for a population parameter and a degree of confidence in that range. The use of confidence intervals yields a more precise estimate of the actual population parameter and serves to quantify the uncertainty associated with sample estimates. Confidence ranges also give an indication of how accurate the sample estimate is. Narrower intervals indicate greater accuracy, while wider intervals indicate greater uncertainty in the sample estimate [22].

IV. EXPERIMENT AND RESULTS

A. Data

For the purpose of this study, the top 5 stocks based on their respective market capitalization, from the Nifty 50 index as of January 2023 were been selected. The stocks, in the order of their market capitalization, are as follows:

1) Reliance Industries Limited (RELIANCE)
2) Tata Consultancy Services (TCS)
3) HDFC Bank (HDFCBANK)
4) ICICI Bank (ICICIBANK)
5) Hindustan Unilever (HINDUNILVR)

Stock prices over the period from 2nd November 2020 to 17th January 2023 have been employed to make the subsequent predictions.

Authorized licensed use limited to: DELHI TECHNICAL UNIV. Downloaded on July 20,2023 at 11:24:12 UTC from IEEE Xplore. Restrictions apply.

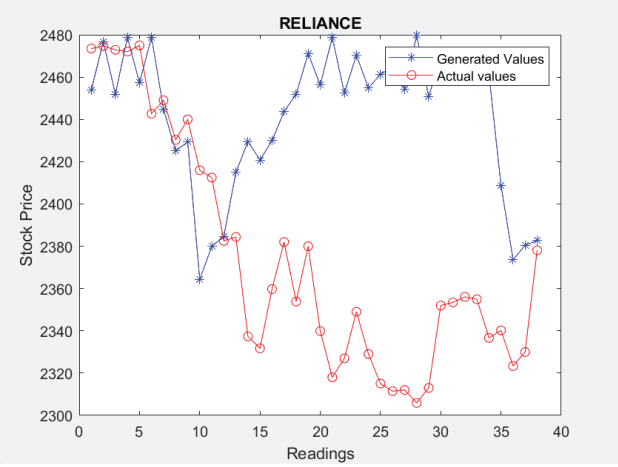

Fig. 1. Comparing predicted opening and closing stock price for Reliance Industries Limited with the actual data over an interval of 20 days

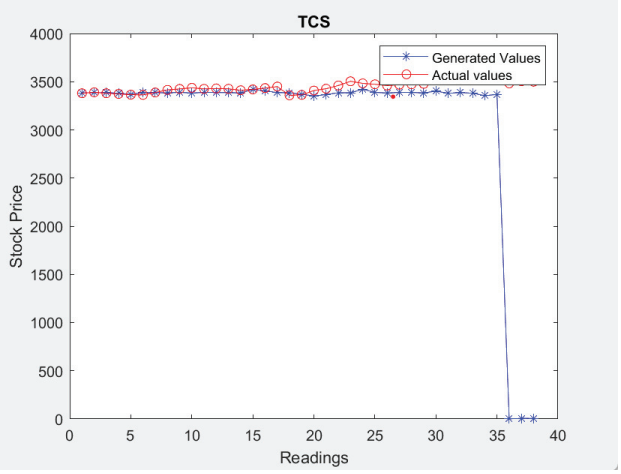

Fig. 2. Comparing predicted opening and closing stock price for Tata Consultancy Services with the actual data over an interval of 20 days

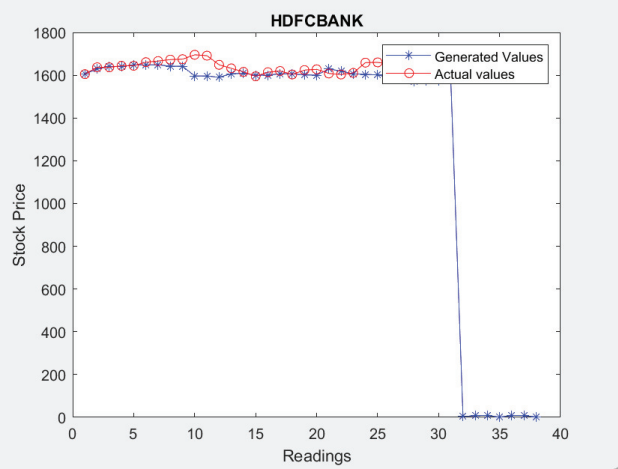

Fig. 3. Comparing predicted opening and closing stock price for HDFC Bank with the actual data over an interval of 20 days

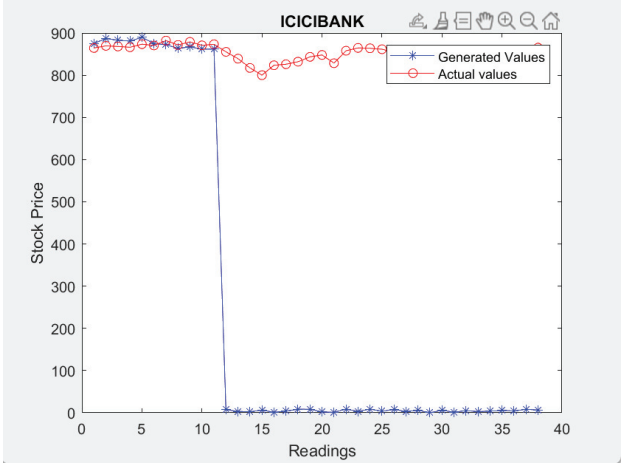

Fig. 4. Comparing predicted opening and closing stock price for ICICI Bank with the actual data over an interval of 20 days

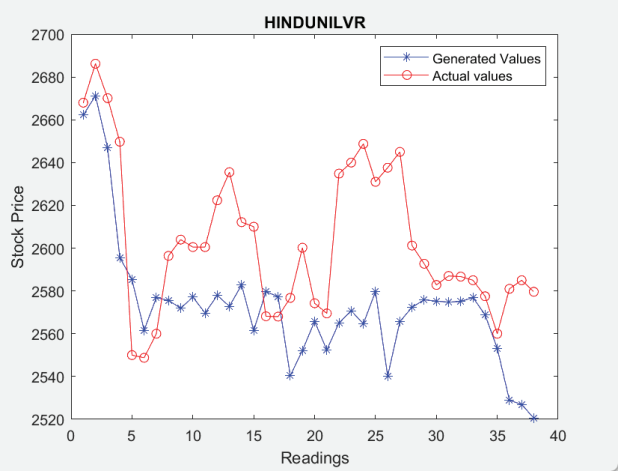

Fig. 5. Comparing predicted opening and closing stock price for Hindustan Unilever Ltd with the actual data over an interval of 20 days

To achieve more accurate results, the data set has been doubled by not just including the closing price but also including the stock opening prices (and vice versa), to study more transitions. This has been achieved by adding the opening and closing prices of each day alternatively to the raw data in order to maintain the time record. Thus, the j^{th} and $(j+1)^{th}$ entry to the dataset receives the i^{th} day's opening price and the i^{th} day's closing price.

B. Results and Discussion

The proposed model was tested using actual stock data, and the findings demonstrate that it is capable of producing meaningful forecasts that fall within the generated confidence interval. The model worked more accurately than the benchmark model. It is important to note that Figures 1-5 show reading such that two consecutive data points show the opening and closing price for the actual and generated values in the line graph, thus the predictions made in the subsequent graphs are from 18^{th} January 2023 to 14^{th} February 2023.

Authorized licensed use limited to: DELHI TECHNICAL UNIV. Downloaded on July 20,2023 at 11:24:12 UTC from IEEE Xplore. Restrictions apply.

On interpreting Figures 1-5, the following observations about the respective line graphs can be made:

- From Figure 1, it can be observed that Reliance Industries' opening and closing stock prices can be approximated highly accurately for the immediate future. As seen, despite the variations observed in the predicted and actual stock prices, the graph is accurately able to capture the sentiment of the stock volatility. In other words, even though the mean error between the predicted and actual stock prices reaches 0.7%, the graph generated is precisely able to predict the changes in the price of the stock, i.e. the extent of the rises and falls in the stock price.
- The chart labeled as Figure 2 shows that it is possible to predict the performance of TCS stock with a high degree of confidence in the foreseeable future for an extended period. Although the model used to make these predictions is not perfectly accurate towards the end of the predicted window, it still provides a good indication of what may happen to the stock in the future. The reason why the predicted values drop to zero after 32 readings is that the model has no data available to it beyond that point, and thus cannot make any predictions. As a result of this lack of information, the model is not able to make any more accurate predictions owing to the restricted distribution in the probability distribution matrix.
- From Figure 3, it can be observed that HDFC Bank stocks can be predicted with high confidence for a substantial size of the future window. Even though the model deviates from the actual reading at the long end of the window, it gives a good impression of the market and what an observer can infer about the future of the stock. The fall of the generated values to zero after 32 readings is due to the unavailability of data. Due to a lack of data, the model is unaware of how to predict the values outside the range of data fed into it.
- From Figure 4, according to the findings, ICICI Bank stocks can be accurately predicted with high confidence for the immediate portion of the future window. Despite some deviation from the actual readings towards the end of the window, the model still offers a reliable outlook on the market and what one could infer about the stock's future. Due to the limited data, the model is unable to forecast values beyond the range of the provided data.
- From Figure 5, the model is highly capable of understanding the sentiment of the Hindustan Unilever stock price. Even though the drastic variation of the prices isn't captured to perfection, the trend in the stock is perfectly replicated in the generated values. The rises and falls are predicted in coherence with the actual values.

It is important to note, that in Figures 3, 2 and 4, the generated values or the line graph representing the predicted stock prices touch the X-axis (representing values close to 0) post 10-15 readings. This abrupt behavior observed is owing to the lack of transitions in the data set used. As we did not have access to real-time stock data at the time of writing, the input data is limited to the opening and closing stock prices, thus lacking most of the significant transitions observed between these ranges. Hence, the randomize function used in the creation of the Markov Chains model rested upon the consideration of the stock market as a random walk, generating NULL values for the missing transitions.

From Table I, it can be observed that for all the stocks other than Reliance Industries, the actual stock price for the next day does not lie only in the 99% confidence interval, but the 95% as well. The results of comparing the predicted stock price with actual data for the chosen companies show that this model is not the best because it is very accurate in the short term (the first hour), but it can take on a wide range of values after that [23].

Furthermore, it is prominent to note that in the short-term forecast, even when the stock prices vary over 2-5%, the market sentiment has been accurately predicted. As seen from the above figures, the model accurately predicts whether the stock movement is bullish or bearish.

It is to be noted that this study is limited to the openly available stock price data, thus the time series analysis is performed solely on the open and close prices, whereas incorporation of the real-time prices to the exact seconds will enable the model to perform significantly more accurate by exponentially increasing the data and providing much more accurate state transitions.

V. Conclusion

The proposed Markov chain stock prediction model may be a useful instrument for forecasting future stock prices. The Markov chain theory is used by the model to forecast future stock prices while accounting for the stock's past price alterations. The model's performance has been assessed using a variety of performance metrics, and the findings indicate that the model is capable of producing meaningful forecasts that fall within the generated confidence interval. The model has not only shown success in the 99% confidence interval but has shown significant results in the 95% confidence interval as the actual stock price for the subsequent day fall in both intervals.

The result of the above comparisons indicates that this model finds its use on a short-term basis and hence would fail for Long-Term Investment in the Stock Market. The above model has been proposed to be used for short-term gains in the market, hence finding immense importance in the concept of Swing Trading. The model opens the scope for Further research that can be incorporated to improve the model's accuracy and efficiency. This can be verified by the generated price values of the selected stocks. Since the predicted values show a very low error rate (Less than 0.7%), this model can be used to perform highly efficient and accurate predictions at high confidence levels. Most importantly the model is cable of capturing the sentiment of stock and helping make decisions concerning the immediate future.

Authorized licensed use limited to: DELHI TECHNICAL UNIV. Downloaded on July 20,2023 at 11:24:12 UTC from IEEE Xplore. Restrictions apply.

VI. Future Work

The time series analysis is only performed on the open and close prices because the study is only using publicly available stock price data, as opposed to incorporating real-time prices down to the exact second, which would exponentially increase the data and provide much more accurate state transitions, allowing the model to perform significantly more accurately. Integrating the code with a real-time market price API is one of the remaining tasks.

Since this model aims to produce short-term gains from the Market, the concept of Future and Options, and Intra-Day Trading can be further explored and researched to gain maximum profits. Owing to the volatility exhibited by the market, random values have been used to generate the matrix for desired results. An in-depth study of a particular Stock can be pursued to better predict the transition probabilities. If the probabilities guesstimated based on technical and financial research generate a better curve, one that is closer to the actual prices on comparison for a longer period, the Model would become much more precise and relevant to investing.

To test the model for much shorter intervals of time while omitting extreme volatility as observed during covid. Refining the model to produce accurate results on these conditions would enable us to place very accurate trades in the market on a real-time basis.

References

[1] Sharma Rashmi Priya and Sharma Arabinda. Statistical analysis of stock prices of selected companies in construction industry. *Advances in Management*, 12(1):39–47, 2019.

[2] Michael Taksar and Xudong Zeng. Optimal terminal wealth under partial information: Both the drift and the volatility driven by a discrete-time markov chain. *SIAM journal on Control and Optimization*, 46(4):1461–1482, 2007.

[3] Poonam Somani, Shreyas Talele, and Shalaka Sawant. Stock market prediction using hidden markov model. *2014 IEEE 7th Joint International Information Technology and Artificial Intelligence Conference, ITAIC 2014*, pages 89–92, 03 2015.

[4] Mehmet Balcilar, Rangan Gupta, and Stephen M Miller. Regime switching model of us crude oil and stock market prices: 1859 to 2013. *Energy Economics*, 49:317–327, 2015.

[5] Rene D Estember and Michael John R Maraña. Forecasting of stock prices using brownian motion–monte carlo simulation. In *International Conference on Industrial Engineering and Operations Management*, pages 8–10, 2016.

[6] Myron S Scholes. Crisis and risk management. *American Economic Review*, 90(2):17–21, May 2000.

[7] Mohammad Al-Shiab. The predictability of the amman stock exchange using the univariate autoregressive integrated moving average (ARIMA) model. *Journal of Economic and Administrative Sciences*, 22(2):17–35, December 2006.

[8] Tim Bollerslev. Generalized autoregressive conditional heteroskedasticity. *Journal of Econometrics*, 31(3):307–327, April 1986.

[9] Yuling Lin, Haixiang Guo, and Jinglu Hu. An SVM-based approach for stock market trend prediction. In *The 2013 International Joint Conference on Neural Networks (IJCNN)*. IEEE, August 2013.

[10] Jian-Zhou Wang, Ju-Jie Wang, Zhe-George Zhang, and Shu-Po Guo. Forecasting stock indices with back propagation neural network. *Expert Systems with Applications*, 38(11):14346–14355, October 2011.

[11] M.V. Subha and S.T. Nambi. Classification of stock index movement using k-nearest neighbours (k-nn) algorithm. *WSEAS Transactions on Information Science and Applications*, 9:261–270, 09 2012.

[12] Ash Booth, Enrico Gerding, and Frank Mcgroarty. Automated trading with performance weighted random forests and seasonality. *Expert Systems with Applications*, 41:3651–3661, 06 2014.

[13] Qasem Al-Radaideh, Adel Assaf, and Eman Alnagi. Predicting stock prices using data mining techniques. 12 2013.

[14] Isaac Kofi Nti, Adebayo Felix Adekoya, and Benjamin Asubam Weyori. A comprehensive evaluation of ensemble learning for stock-market prediction. *Journal of Big Data*, 7(1), March 2020.

[15] Dattatray Gandhmal and K. Kumar. Systematic analysis and review of stock market prediction techniques. *Computer Science Review*, 34:100190, 11 2019.

[16] Gulbadin Dar, Tirupathi Rao Padi, and Rekha Sarode. Stock price prediction using a markov chain model: A study for tcs share values. *Advances and Applications in Statistics*, 80:83–101, 08 2022.

[17] Kevin Doubleday and Julius Esunge. Application of markov chains to stock trends. *Journal of Mathematics and Statistics*, 7:103–106, 01 2011.

[18] S. Vasanthi, M. V. Subha, and S. Thirupparkadal Nambi. An empirical study on stock index trend prediction using markov chain analysis. 2011.

[19] Dmitrii O. Logofet and Ekaterina V. Lesnaya. The mathematics of markov models: what markov chains can really predict in forest successions. *Ecological Modelling*, 126(2-3):285–298, February 2000.

[20] Stefan Ciucu, Ionut Petre, and Mihai Rebenciuc. The use of markov chains in forecasting wind speed: Matlab source code and applied case study. *Computational Methods in Social Sciences*, IV:44–53, 12 2016.

[21] Hafzullah Aksoy, Z. Toprak, Ali Aytek, and N Erdem. Stochastic generation of hourly mean wind speed data. *Renewable Energy*, 29:2111–2131, 11 2004.

[22] Richard K Burdick, Connie M Borror, and Douglas C Montgomery. *Design and analysis of gauge R&R studies: making decisions with confidence intervals in random and mixed ANOVA models*. SIAM, 2005.

[23] Stefan Ciucu, Ionut Petre, and Mihai Rebenciuc. The use of markov chains in forecasting wind speed: Matlab source code and applied case study. *Computational Methods in Social Sciences*, IV:44–53, 12 2016.

Authorized licensed use limited to: DELHI TECHNICAL UNIV. Downloaded on July 20,2023 at 11:24:12 UTC from IEEE Xplore. Restrictions apply.

2023 2nd International Conference on Vision Towards Emerging Trends in Communication and Networking Technologies (ViTECoN) | 979-8-3503-4798-2/23/$31.00 ©2023 IEEE | DOI: 10.1109/ViTECON58111.2023.10157846

CONGEST: An Algorithm to Detect Congestion Zones Based on Unmanned Aerial Vehicle (UAV) Flight plans

Shashank Parmar
Department of Software Engineering
Delhi Technological University
New Delhi, India
parmarshashank11@gmail.com
ORCID: 0000-0003-4369-3647

Rahul
Department of Software Engineering
Delhi Technological University
New Delhi, India
Rahul@dtu.ac.in

Shashank Taneja
Department of Software Engineering
Delhi Technological University
New Delhi, India
shashanktaneja72@gmail.com

Abstract - One of the primary problems in the Unmanned Aerial System (UAS) field is the potential increase in conflicts and congestion as the UAS gets incorporated into traditional manned airspace. Our research work aimed to come up with an innovative idea to identify potential congestion zones based on the UAV flight plans. A flight plan is a planned route for a flight that contains a set waypoint defined by latitudes, longitudes, and altitudes. Congestion is defined as a circle of radius 'R' that has more than a given number of crossings. Conventional clustering algorithms such as DBSCAN, K-means, K-medoids, CLIQUE, etc are designed for static points/objects i.e., the features of the objects remain constant. However, in the case of Unmanned Aerial Vehicles (UAVs), the UAVs keep on changing their position from time to time. Hence, conventional clustering algorithms cannot be applied to the given problem. We have proposed a heuristic algorithm named CONGEST, based on the DBSCAN Clustering algorithm. Our algorithm can identify 91.5-98.5% of the congestion zones in a span of a few seconds.

Keywords - UAV Flight Plan, Congestion Zone Detection, Unmanned Aerial System, UAV collision

I. INTRODUCTION

UAV flight schedules are often jam-packed. This often leads to many congestion zones. Identification of such zones is critical to prevent mid-flight accidents that may result from prolonged aviation in the congestion zones. However, algorithms for the identification of such congestion zones have not yet been proposed. In this paper, we develop an algorithm to identify such congestion zones based on the UAV's flight plans and other parameters such as a UAV's velocity, time of Departure, etc. The algorithm is divided into two phases. In phase 1 we find out the base congestion zones whereas in phase 2 we find out the remaining congestion zones with the aid of the Base Congestion Zones. In phase 2 of the algorithm, we propose an extended version of the density-based spatial clustering of applications with noise (DBSCAN) Algorithm [1]. We then compare our results with the Ground Truth i.e., the actual number of congestion zones in the field, which are found via the Brute-Force algorithm.

II. LITERATURE SURVEY

Martin Ester et al. [1] proposed a novel clustering algorithm based on the sdensity of points in the search space. The process of identifying clusters and finding congestion zones are somewhat similar in nature. Hence, we have drawn major inspiration from their proposed algorithm.

Adarsh Kumar et al. [2] proposed strategies to monitor drone traffic via SDN i.e., Software Defined Networking. The proposed approach tries to tackle the problems of drone collisions and drone navigation while maintaining less computational and communicational overheads. However, the proposed SDN does not include drone congestion detection strategies/algorithms.

Jan Dentler et al. [3] proposed a CMSCGMRES control approach for UAV rotor systems. The proposed system allows UAVs to avoid collisions. Their work provided us with mathematical insights regarding UAV control and positioning.

Kathleen A. Kramer and Stephen C. Stubberud [4] worked on developing and scoring algorithms for UAS flight planning algorithms. Their work provided us with insights into the current UAS flight planning algorithms.

Lanier Watkins et al. [5] performed an investigative study into autonomous UAS Traffic Management System for congested airspace. They estimate that over 65000 UAS operations (takeoffs and landings) would be performed at airspaces per hour by 2035. They propose algorithms for path planning and strategic de-confliction of UAVs.

Hualong Tang et al. [6] proposed an Automated Flight Planning Systems (AFPS) for Advanced Air Mobility (AAM). The proposed AFPS utilizes Low Altitude Airspace Management System (LAMS) to generate route networks that minimize the probability of congestions and collisions.

Saswata Paul et al. [7] proposed a novel conflict-aware flight planning approach that minimizes the probability of mid-air UAV collisions. The proposed study aims at designing flight plans that avoid conflicts and congestions.

Juan A. Besada et al. [8] described the requirements of a flight planning tool for safe urban operations. Yao-hong Qu et al. [9] proposed heuristically search-based methods to plan flights. They make use of the A-star algorithm and genetic algorithms to search for optimal flight paths. Bashar Alsadik and Fabio Remondino [10] presented the developments of a LiDAR-based UAS flight planning tool. They also presented mathematical formulations for the same.

979-8-3503-4798-2/23/$31.00 ©2023 IEEE

Authorized licensed use limited to: DELHI TECHNICAL UNIV. Downloaded on July 03,2023 at 04:44:16 UTC from IEEE Xplore. Restrictions apply.

Boyeon Kim et al. [11] designed and implemented UAV re-routing algorithms that are sensitive to user requests for change in the flight plan.

Yaohong Qu et al. [12] proposed a novel optimal path-planning method for UAVs. Their method is based on flight space partitioning, Dijkstra algorithm, and potential field theory.

Chao Zhang et al. [13] proposed a novel UAV path-planning algorithm based on Ant-Colony Optimization.

Adnan Ashraf et al. [14] proposed an online, collision-free path generation and navigation system for swarms of UAVs. The proposed system aims to avoid UAV-to-UAV collision, UAV-to-static obstacle collision, and UAV-to-moving obstacle collision.

Kheyreddine Djouzi and Kadda Beghdad-Bey [15] performed an extensive review of Clustering Algorithms for Big Data such as CLARA, K-means, DBSCAN, DENCLUE, etc. The task of congestion detection is somewhat similar to Clustering. Their review provided us with an overview of most clustering algorithms out there.

Rahul et al. [16] improved upon a clustering-based algorithm to detect communities in a network. They demonstrated that the replacing Louvain approach with Girvan-Newman Algorithm in the source estimation algorithm improves its performance.

Rahul et al. [17] proposed a solution to detect communities in a social network graph by converting it to a low-dimensional space of features. With the proposed algorithm they were able to identify overlapping communities.

III. DATASET OVERVIEW

For developing and testing our algorithm, we have made use of dummy data points to mark the trajectory of a UAV (represented in Figure 1 and Figure 2). The trajectory path points either follow an (X, Y) format or follow an (X, Y, Z) format as shown in Figure 3. The dataset used to perform the research has been provided via a "GITHUB" repository [18].

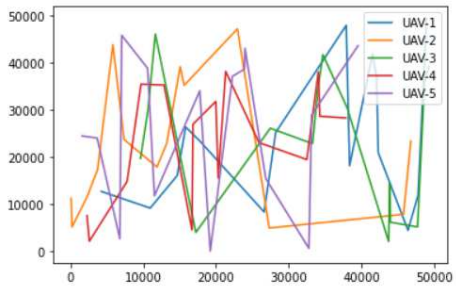

Figure 1: UAV Flight Paths (2D Plane)

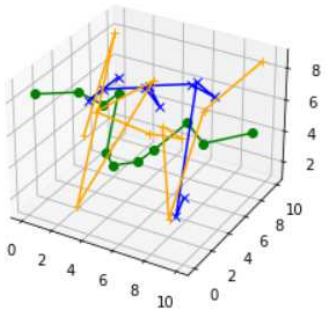

Figure 2: UAV Flight Paths (3D)

```
UAV-1 path:[(4225,12722) , (10952,9186) , (14669,16081) ,
(15831,26378) , (17771,23420) , (26626,8362) , (28213,25213) ,
(37919,47938) , (38384,18159) , (41559,41958) , (42099,36910) ,
(42325,20943) , (46418,4478) , (47806,11919) , (48967,49456)]
```

Figure 3: Sample Path Co-ordinates (X, Y) of an unmanned aerial vehicle

IV. DEVELOPING THE ALGORITHM

A. Understanding flight trajectories and their significance

We made use of a directed graph to represent the flight trajectories (represented in Figure 4). Each node in the graph represents a point (latitude * longitude) in the path of the UAV. Such a representation makes it easier to identify and visualize the congestion zones.

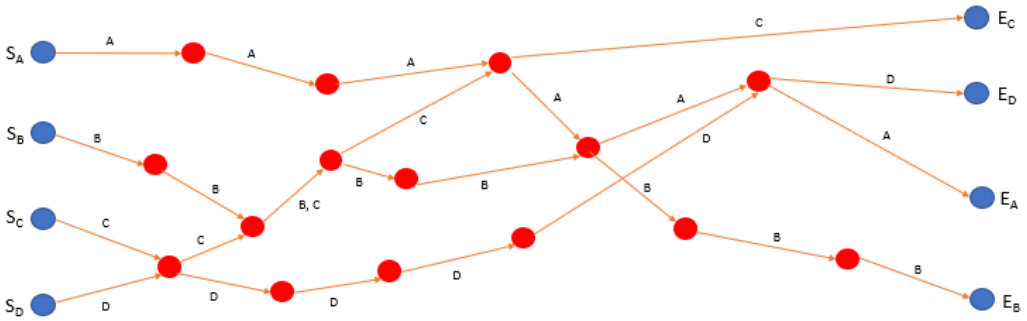

Figure 4: Directed graph to represent the flight trajectories.

Authorized licensed use limited to: DELHI TECHNICAL UNIV. Downloaded on July 03,2023 at 04:44:16 UTC from IEEE Xplore. Restrictions apply.

B. Calculation of time of arrival of a UAV for different nodes

Given the velocity of a UAV, its time of arrival can be easily calculated for each node in its path. This has been illustrated in Figure 5.

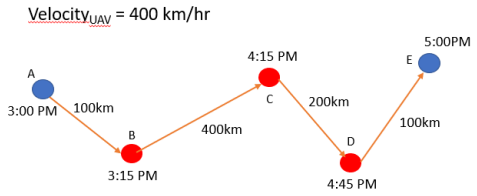

Figure 5: Calculation of the time of arrival of a UAV at different nodes in its path.

C. Calculation of the time interval for which a UAV flew within a region.

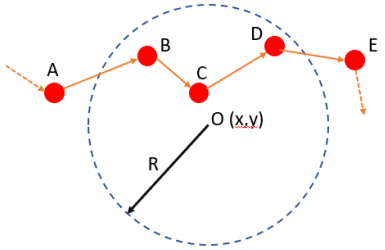

Figure 6: Calculation of Time of Flight for a UAV in a Region of radius 'R'

In figure 6 we have shown the path of a UAV. It travels from Node A to Node E via the depicted path. Let the time of arrival of the UAV at the nodes be t_A, t_B, …, t_E respectively. Let the coordinates of points A to E be (x_A, y_A), (x_B, y_B), …, (x_E, y_E) respectively. To calculate the time interval for which the UAV stays in the region, it is essential to calculate the co-ordinate of entry and exit of the UAV in the region.

$$(x - x_o)^2 + (y - y_o)^2 = R^2 \quad (1)$$

$$y = mx + (y_B - mx_B), where\ m = \frac{y_A - y_B}{x_A - x_B} \quad (2)$$

Equation of the Circle is represented via eq. 2 and equation of line from Node A to Node B is represented via eq. 2.

Via eq. 1 and eq. 2, we can easily find the coordinate of the inters of the line/path from A to B with the circle. However, mathematically we will get 2 distinct points. We must consider the point closer to Node A. The same process can be applied to find the exit coordinate of the UAV from the region.

Let the entry and exit coordinates be (x_{IN}, y_{IN}) and (x_{OUT}, y_{OUT}) and the entry and exit times be t_{IN} and t_{OUT} respectively.

D. Phase 1 of the Algorithm – Finding Base Congestion Zones

In the first phase of our algorithm, we assume that a congestion zone must have a UAV path point at its center as in Figure 7. We have named such congestion zones as "Base Congestion Zones". However, this assumption may not be true and will be improved upon in Phase 2 of the algorithm. At this stage of the algorithm, we know which UAVs will arrive at which node and the exact time of when they do so. We also know how to calculate the duration of flight of a UAV in a given region. This information is sufficient to identify whether a region will become a congestion region at any given point in time.

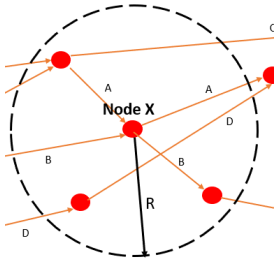

Figure 7: Region around path point X.

Now, for each node in the graph, we explore its neighborhood up to a range of distance of 'R'. (Note: the nodes in the neighborhood may not be connected to the node currently being explored). We then perform relevant calculations regarding the period for which a UAV will remain in the given region. Let's say for node 'X' the UAVs hover in its region for the following time intervals:

$$UAV_A: T_{A1} - T_{A2}$$

$$UAV_B: T_{B1} - T_{B2}$$

$$UAV_C: T_{C1} - T_{C2}$$

$$UAV_D: T_{D1} - T_{D2}$$

With these time intervals, we can easily calculate the number of UAVs that will cross the given region at any point in time. Let the maximum UAVs that cross this region at a given point of time be C_{max}.

Let α be the maximum allowed UAV crossings in a given region. Now, if C_{max} >= α then the region surrounding node X can be regarded as a congestion region.

E. Problems with Phase-1 of the algorithm (section 4 D.)

The algorithm discussed in section 4 D. does not cover all the edge cases. This has been demonstrated in Figure 8.

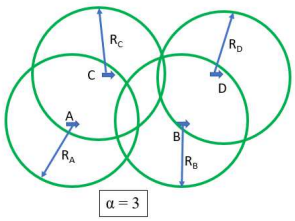

Figure 8: Regions surrounding 4 UAVs: A, B, C, and D, with (R_A = R_B = R_C = R_D)

Now, it may seem that in figure 8 we have no congestion zone. However, this is not true. This has been shown in figure 9.

Authorized licensed use limited to: DELHI TECHNICAL UNIV. Downloaded on July 03,2023 at 04:44:16 UTC from IEEE Xplore. Restrictions apply.

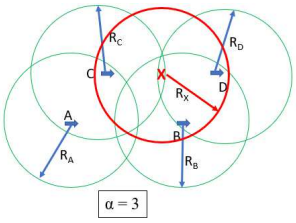

Figure 9: Congestion region with the center as 'X'.

Even though point X is not a path point, the region around it turns out to be a congestion region. To solve this problem we have to further extend our algorithm. The next phase of our algorithm is inspired by the renowned DBSCAN clustering algorithm.

F. Scoring a region

The score of a region is simply the maximum number of UAVs that cross it at any given point in time. This will be represented by S_X, where X is the region under consideration.

G. Phase 2 of the Algorithm – Finding Extended Congestion Zones

The second phase of the algorithm has been summarised in Figure 10.

```
Constants:
R -> Radius of Region
K -> minimum UAVs in a region at a given time required to classify the region as a congestion zone.

Assign score to all path points/nodes.
Add all nodes to a MAX Prioirty Queue (PQ). Comparison between 2 nodes must be based on their scores.

original_points = dictionary() // list of all UAV path points
visited = dictionary() // Dictionary of all the points visited so far
congestion_centers = [] // Centers of the Congestion Zones

while (size of PQ > 0):
    Node X = PQ.top();
    PQ.pop();

    if(visited[X] == True):
        continue;

    if(SCORE(X) >= K):
        add X to congestion_centers.

    Neighbours = [{all neighbouring nodes of X which are within R distance from X}]
    sort(Neighbours, order: Descending(based on Node score))

    for P in Neighbours:
        dist = distance_between(P, X)
        if (min_sep < dist or visited[P] == True):
            continue;

        MID_NODE = MID_POINT(P, Q) // Create an imaginary node in the middle of P and X
        if(MID_NODE in original_points):
            continue;

        NEP = [{all neighbouring nodes of 'MID_NODE' which are with R distance of it}]
        SCORE_MID_NODE = Calculate score of node 'MID_NODE'.
        if(SCORE_MID_NODE >= K):
            add MID_NODE to congestion_centers.
            ADD MID_NODE to PQ

END
```

Figure 10: Summarised Algorithm

V. RESULTS AND ANALYSIS

A. Time Complexity Analysis

- Length of the Grid = L
- Breadth of the Grid = G
- Height of the Grid = H
- Total UAVs = U;
- Average Path Length of Each UAV = n;
- Granularity of the Grid (e.g.: 1, 0.1, 0.01, etc) = g

Now,

- Number of unique points in the grid: $\frac{L*G*H}{g^3}$
- Maximum UAV flight path points: $n * U$
- Time Complexity to find neighbors of a UAV in a region of radius R: O((log($U * n$))*(U*n)^2)
- Worst Case Time Complexity: $O\left((\log(U*n)) * (\mathrm{U}*\mathrm{n})^2 * (\frac{\mathrm{L}*\mathrm{G}*\mathrm{H}}{\mathrm{g}^3})\right)$
- Best Case Time Complexity: $O(\log(U*n) * (U*n)^2)$

B. Space Complexity Analysis

To implement the algorithm the following entities need to be stored:

- Information regarding all UAV path points: O(U*n)
- Centers of all congestion zones: O(U*n)
- Queue to perform phase 2 of the Algorithm: O(U*n)

Authorized licensed use limited to: DELHI TECHNICAL UNIV. Downloaded on July 03,2023 at 04:44:16 UTC from IEEE Xplore. Restrictions apply.

Hence, the overall space complexity of the algorithm is O(U*n).

C. Establishing Ground Truth and defining accuracy measure

To evaluate our algorithm we must be able to first determine the total number of congestion zones. For this, we make use of the Brute Force algorithm, wherein we traverse each point on the grid and determine whether the point could be the center of a congestion zone or not.

Let the total number of congestion zones be 'G' and the number of congestion zones that could be identified by our algorithm be 'g'. We can check the accuracy of our algorithm by simply calculating $accuracy = \frac{g}{G}$. Table 1 shows the accuracy and effciency of the algorithm.

TABLE I. Analysis and comparison of results

Test Case	G	Brute Force time (s)	g	CONGEST time (s)	Accuracy (g/G)	Congest time/Brute Force time
1	199	8207	194	1656	0.974	0.202
2	67	375	63	30	0.941	0.080
3	126	4512	122	736	0.967	0.163
4	83	2773	82	261	0.982	0.094
5	232	9336	218	1755	0.938	0.188
6	153	5431	140	934	0.915	0.172
7	1230	1846	1188	214	0.965	0.116
8	952	8679	937	269	0.984	0.031
9	143	1810	136	38	0.951	0.021
10	177	7182	173	567	0.977	0.079

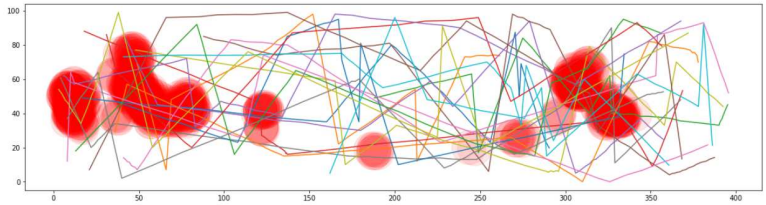

Figure 12: Congestion Zones for test case 6

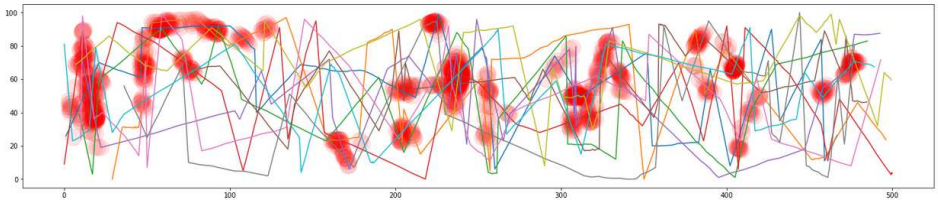

Figure 13: Congestion Zones for test case 7

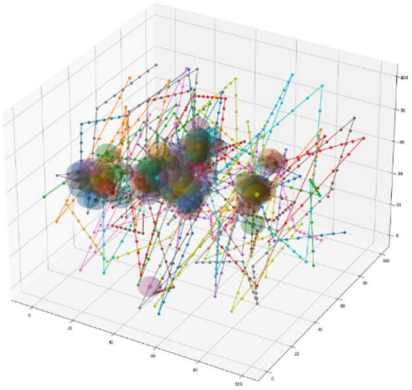

Figure 14: Congestion Zones for test case 8

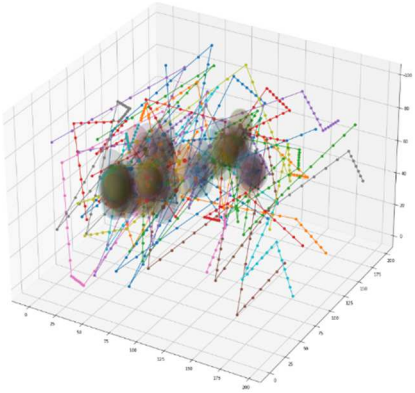

Figure 15: Congestion Zones for test case 9

Authorized licensed use limited to: DELHI TECHNICAL UNIV. Downloaded on July 03,2023 at 04:44:16 UTC from IEEE Xplore. Restrictions apply.

D. Visualising the Congestion Zones

The congestion zones for test cases 6, 7, 8, and 9 have been plotted in Figures 12, 13, 14, and 15 respectively. We have made use of Matplotlib [19] to plot the graphs in Figures 12 and 13, and scikit-spatial [20] to plot the graphs in Figures 14 and 15.

E. Comparing the 2 phases of the algorithm

How beneficial is it to have the 2nd Phase in the algorithm? To answer the question we calculate the percent increase of the congestion zones found from Phase 1 to Phase 2 (Table 2). In Table 2, 'g_1' represents the number of congestion zones found at the end of phase 1, and 'g_2' represents the number of congestion zones found at the end of phase 2 of the algorithm.

TABLE II. Analysing the percent increase in the congestion zones found from the 1st phase to the 2nd phase of the algorithm.

Test Case	g_1	g_2	Percent increase from g_1 to g_2 (%)
1	30	194	546.667
2	32	63	96.875
3	13	122	838.461
4	15	82	446.667
5	44	218	395.454
6	79	140	77.215
7	143	1188	730.769
8	117	937	700.854
9	96	136	41.667
10	92	173	88.043

VI. CONCLUSION AND FUTURE WORK

One of the primary problems in the Unmanned Aerial System (UAS) field is the potential increase in conflicts and congestion as the UAS gets incorporated into traditional manned airspace.

Our algorithm, CONGEST not only has high accuracy in terms of identifying congestion zones but also has high speed. The algorithm can identify anywhere from 91.5% to 98.5% of congestion zones in a fraction of the time that it takes the brute force algorithm to do so. However, further research can be done to increase both its speed and its accuracy.

REFERENCES

1. Martin Ester, Hans-Peter Kriegel, Jörg Sander, and Xiaowei Xu. 1996. A density-based algorithm for discovering clusters in large spatial databases with noise. In Proceedings of the Second International Conference on Knowledge Discovery and Data Mining (KDD'96). AAAI Press, 226–231.
2. A. Kumar, R. Krishnamurthi, A. Nayyar et al., A Novel Software-Defined Drone Network (SDDN)-based Collision Avoidance Strategies for On-Road Traffic Monitoring and Management, Vehicular Communications, 100313, doi: https://doi.org/10.1016/j.vehcom.2020.100313.
3. J. Dentler, S. Kannan, M. A. O. Mendez and H. Voos, "A real-time model predictive position control with collision avoidance for commercial low-cost quadrotors," *2016 IEEE Conference on Control Applications (CCA)*, Buenos Aires, Argentina, 2016, pp. 519-525, doi: 10.1109/CCA.2016.7587882.
4. K. A. Kramer and S. C. Stubberud, "Adaptive UAS Route Planner Based Upon Evidence Accrual," *2019 IEEE/AIAA 38th Digital Avionics Systems Conference (DASC)*, San Diego, CA, USA, 2019, pp. 1-6, doi: 10.1109/DASC43569.2019.9081779.
5. L. Watkins, N. Sarfaraz, S. Zanlongo, J. Silbermann, T. Young and R. Sleight, "An Investigative Study Into An Autonomous UAS Traffic Management System For Congested Airspace Safety," *2021 IEEE International Conference on Communications Workshops (ICC Workshops)*, Montreal, QC, Canada, 2021, pp. 1-6, doi: 10.1109/ICCWorkshops50388.2021.9473838.
6. Hualong Tang, Yu Zhang, Vahid Mohmoodian, Hadi Charkhgard, Automated flight planning of high-density urban air mobility, Transportation Research Part C: Emerging Technologies, Volume 131, 2021, 103324, ISSN 0968-090X, doi: https://doi.org/10.1016/j.trc.2021.103324.
7. S. Paul, S. Patterson and C. A. Varela, "Conflict-Aware Flight Planning for Avoiding Near Mid-Air Collisions," 2019 IEEE/AIAA 38th Digital Avionics Systems Conference (DASC), San Diego, CA, USA, 2019, pp. 1-10, doi: 10.1109/DASC43569.2019.9081658.
8. J. A. Besada, I. Campaña, L. Bergesio, A. M. Bernardos and G. de Miguel, "Drone Flight Planning for Safe Urban Operations: UTM Requirements and Tools," 2019 IEEE International Conference on Pervasive Computing and Communications Workshops (PerCom Workshops), Kyoto, Japan, 2019, pp. 924-930, doi: 10.1109/PERCOMW.2019.8730856.
9. Yao-hong Qu, Quan Pan and Jian-guo Yan, "Flight path planning of UAV based on heuristically search and genetic algorithms," 31st Annual Conference of IEEE Industrial Electronics Society, 2005. IECON 2005., Raleigh, NC, USA, 2005, pp. 5 pp.-, doi: 10.1109/IECON.2005.1568876.
10. Alsadik B, Remondino F. Flight Planning for LiDAR-Based UAS Mapping Applications. ISPRS International Journal of Geo-Information. 2020; 9(6):378. Doi: https://doi.org/10.3390/ijgi9060378.
11. Kim, B., Jung, M., & Chang, Y. (n.d.). Inflight Drone Re-routing Method with Google Map on Smart Pad (Vol. 2018). Proquest. https://www.proquest.com/openview/a2606e893230a7a6ddfa3da5e5eb585d/1.pdf?pq-origsite=gscholar&cbl=1976354
12. Y. Qu, Y. Zhang and Y. Zhang, "Optimal flight path planning for UAVs in 3-D threat environment," 2014 International Conference on Unmanned Aircraft Systems (ICUAS), Orlando, FL, USA, 2014, pp. 149-155, doi: 10.1109/ICUAS.2014.6842250.
13. Chao Zhang, Z. Zhen, Daobo Wang and Meng Li, "UAV path planning method based on ant colony optimization," 2010 Chinese Control and Decision Conference, Xuzhou, 2010, pp. 3790-3792, doi: 10.1109/CCDC.2010.5498477.
14. Adnan Ashraf, Amin Majd, Elena Troubitsyna, "Online Path Generation and Navigation for Swarms of UAVs", Scientific Programming, vol. 2020, Article ID 8530763, 14 pages, 2020. https://doi.org/10.1155/2020/8530763
15. K. Djouzi and K. Beghdad-Bey, "A Review of Clustering Algorithms for Big Data," 2019 International Conference on Networking and Advanced Systems (ICNAS), Annaba, Algeria, 2019, pp. 1-6, doi: 10.1109/ICNAS.2019.8807822.
16. Rahul, S. Srivastava and P. Kumar, "Comparative Study of Clustering Approaches in Rumor Source Localization Algorithm in Social Networks," 2020 International Conference on Electronics and Sustainable Communication Systems (ICESC), Coimbatore, India, 2020, pp. 835-843, doi: 10.1109/ICESC48915.2020.9155799.
17. Rahul, Bansal, P., Goel, P., Nayak, P. (2021). Community Detection Using Graphical Relationships. In: Ranganathan, G., Chen, J., Rocha, Á. (eds) Inventive Communication and Computational Technologies. Lecture Notes in Networks and Systems, vol 145. Springer, Singapore. https://doi.org/10.1007/978-981-15-7345-3_84
18. Parmar, S. (2023). CONGEST Dataset [Dataset; Github]. https://github.com/Leafy2001/CONGEST-Datastet
19. Matplotlib — Visualization with Python. (n.d.). https://matplotlib.org/
20. Introduction — scikit-spatial documentation. (n.d.). https://scikit-spatial.readthedocs.io/en/stable/index.html

Authorized licensed use limited to: DELHI TECHNICAL UNIV. Downloaded on July 03,2023 at 04:44:16 UTC from IEEE Xplore. Restrictions apply.

2023 4th International Conference for Emerging Technology (INCET)
Belgaum, India. May 26-28, 2023

Crime Evaluation Using Neural Networks by GPS Trajectory Dataset

Rahul
Department Of Software Engineering
Delhi Technological University
Delhi, India
rahul@dtu.ac.in

Vartika Hari Durgapal
Department Of Software Engineering
Delhi Technological University
Delhi, India
vartikaharidurgapal_2k19se141@dtu.ac.in

Vinshu Chaudhry
Department Of Software Engineering
Delhi Technological University
Delhi, India
vinshuchaudhry_2k19se148@dtu.ac.in

2023 4th International Conference for Emerging Technology (INCET) | 979-8-3503-3575-0/23/$31.00 ©2023 IEEE | DOI: 10.1109/INCET57972.2023.10170482

***Abstract*— One of the many irregularities of the world includes crime. It clumps in some areas and is absent in others. Various daily activities require this knowledge. They seek out particular locations while avoiding others. Their decisions on neighborhoods, schools, stores, roadways, and recreational opportunities are influenced in part by the knowledge that Some of these locations have higher victimization rates than others. These choices further create a reason of developing crime concentrated areas also known as hot spots. Thus, a need to analyze the crime levels and to determine the causes of such concentrations is really useful. Tracking every route of the area with possible reason is only possible by using Global Positioning Systems (GPS) which makes the data availability easier and more accurate on minute level. A study is done this research which finds the best features that might explain the possible criminal activities in a region by building a machine learning neural network (NN) model and minimizing the errors. By the end of this study the top features that came out are 'accidents', 'traffic', 'tourist attraction, 'length of the route', 'duration of the route' which majorly effect the crime rates of an area.**

Keywords—GPS networks, Crime Evaluation, Neural Networks

I. INTRODUCTION

Criminal activities affect our societies in many adverse ways. Urban crime is a result of social exclusion and discrimination rather than being a consistent, random, or spontaneous phenomena over time and geography. The demographics and sociocultural makeup of an urban environment have altered as a result of rapid urbanization and population growth. The need for fundamental services has grown. Rapid urbanization and ineffective management have been unable to keep up with this rising demand. These stark differences in access to resources, authority, wealth, social institutions, and opportunities have contributed to an increase in crime, jeopardizing human security, fueling gentrification, and endangering the peace. One of the biggest problems and a necessary component of an urban environment is crime and the threat it poses to public security. Finding the possible features responsible for a crime in different locations would help preventing likely crimes by aiding police all over the world

GPS are increasingly being used to monitor the activity of each and every location. GPS technology is a satellite-based technique that helps in locating a site easily. Our GPS technology consists of 24 satellites which circles around our earth in precise orbits. It takes a satellite 12 hours to orbit the earth which sends the radio signals constantly. For the route tracking the foundation of GPS is very useful as there are at least 4 satellites orbiting the earth at any particular point of time where each satellite is responsible for transmitting constant time and location signal. GPS satellites maintain a certain accuracy while sending the signals in space, which contains several other factors, including signal blockage, satellite geometry, atmospheric conditions, and receiver design features or quality. Because of how precise its receivers are, they can pinpoint their location to within one centimeter. (0.4 inches). Location is provided by GPS receivers in terms of latitude, longitude, and altitude.

Currently many studies have been done using GPS networks to analyze the crime hot spots such as in [6] a simulation-based algorithm is used to track the paths of children by the GPS tracking data. Using algorithms such as Dijkstra the possible crimes such as assault, robbery, and stalking are analyzed in those paths. Another such study is done in [7] where Three statistical techniques—the space-time permutation model, the kernel density estimation (KDE) function, and the GetisOrd Gi* statistical operation—are used to pinpoint crime hotspots. inside different cities of India such as Pune city of Maharashtra, India. Comparative analysis of all the methods is done and finally the major areas of crimes such as dacoity, robbery, rape, and molestation are identified. Many other studies are done on using GPS networks such as detection of spoofing included in [17]-[19]. However, in all these studies done on the identification of crime hotspots possible reasons which might be responsible for such crimes in an area are not discussed. The focus is more on crime rates on an area.

Therefore, in this study the GPS networks are used to find possible features which effect the crime rates of a location. A neural network-based regression model is built and its hyperparameters are tuned to minimize the errors and get the most efficient model. Top features are thus selected which came out to be "traffic", "tourist attraction", "accidents", "length of the route" and "nature" of the surrounding area. These results are comparable to the results in the research study [14]. They proved to be superior to more widely used models like "K Nearest Neighbors", "Decision Tree", ,"Random Forest", "Naive Bayes" And "Multivariable Regression".

II. RELATED WORKS

Many studies have been done in this field including tracking every route of students and possibility of crimes in those pathways or finding crime hotspots in a city or using simulation methods to for street violent crime analysis and risk evaluation. Few of these have been discussed below:

Tracing the route of children to find the crime rates in those routes using route mapping algorithm such as Dijkstra algorithm in done in [6]. This study analyses the spatio-

Authorized licensed use limited to: DELHI TECHNICAL UNIV. Downloaded on July 20,2023 at 11:21:17 UTC from IEEE Xplore. Restrictions apply.

temporal distribution of children through GPS loggers and simulation modelling to estimate the underlying population at risk across time and space. Victimization survey data is used to conduct crime hot spot analysis after the underlying population at risk is estimated at the place and street level. Finally, by comparing the simulation results the hot spots of crime are identified in this locality. A similar study has been done in [7] where the data from OpenStreetMap, Google Earth and police department is used in three different simulations to perform a comparative analysis and find major crime hot spots in Pune city of Maharashtra. Robbery, Molestation, Dacoity, and Rape are the crimes taken in consideration to identify the hot spots. But there is always a weakness of identification of number of clusters.

Another such study is done in [8] where a simulation environment is developed using agent-based modelling with real geographical information system and environmental, crime and census data. This simulation is used to illustrate the how neighbourhood or police strategies or population can affect the risk of street level violence. Furthermore, it is used to build patrol strategies and other social steps. However, to make it more applicable by customising it to make a comprehensive framework still a lot of research work needs to be done. Similarly, in [13] agent-based modelling is used to create a framework for simulating urban crime and robberies and how such criminogenic features impact the crime pattern. But the model lacks a realistic component. The pattern of crime which came out cannot accurately depict or replicate the real distribution of reported crime spots.

Similar to the goal of this research another such study is done in [14] where topmost features of an area including geographical and spatial. Some traditional machine learning models are used to analyse the data such as “K nearest neighbours”, “random forest”, “linear regression” and many more. But there is always a scope of lowering the error and improving the model further. Thus, a neural network-based model is built in this paper to build an improved model which could surpass the other traditional models. Another study mentioned in [15] performs a grid-based crime prediction modelling using Google APIs data in Taiwan using deep neural networks. Different measures such as precision, recall, accuracy, f1-score are used. T-test is used to compare different methods and deep neural networks (DNN) tuning performed the best. Using google maps as a data source allows to calculate landmark features to establish geographical features that might have a major role in deciding the crime patterns of a region. However still a lot more features can be included such as whether, temperature, streetlights, police stations and many more which can be of a major importance.

An approach to find relationship between crime elements for predicting potential crime hotspots in proposed in [16]. Extraction of frequent crime patterns using classification methods such as Apriori algorithm, Naïve Bayesian Classifier, Decision Tree Classifier. Using these algorithms frequent patterns of crime are identified with location, day of the week, and the time period. Identification of these hotspots with their most frequent occurrence in day and time and to anticipate the category of the crime and its probability of occurrence in a particular zone at a specific time. However, more extended classification algorithms are needed to improve accuracy and analyse the demographic information with crime findings.

III. METHODOLOGY

To create a model these steps were thoroughly followed:

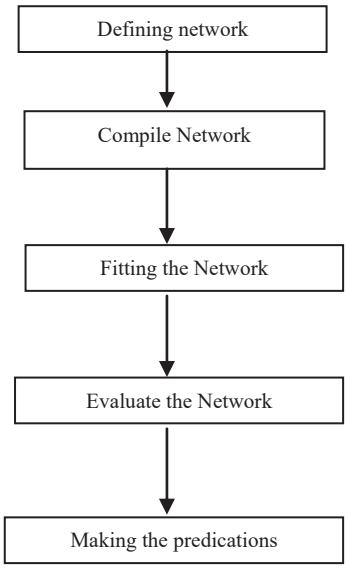

Fig 1. Steps of creating model

Beginning with defining the network different layers were created with hidden layer of activation function and dropout layers. Then the created model is compiled and fitted with training set. To evaluate the network, error is taken for every iteration to prevent overfitting or underfitting of the model. Finally, as the model becomes ready predictions are made on the testing data or in this case receiver operating characteristics (ROC) curve is used to evaluate the importance of the model. The code for the same is uploaded and accessible from [28]. All the files regarding the NN model and dataset has been mentioned there.

1) Dataset

Choosing a proper dataset for analyzing is a crucial step in a study. For this we have taken a GPS trajectory dataset containing 600 sets of routes of origin-destination pair information. This information contains route length, duration, traffic, tourist attractions nearby, accidents and nature. Much of the data about route durations, criminal rates or accidents were taken from UK government open-source data. The UK Government open data website is used for getting the data related to accidents, criminality and duration estimates for each route. Further elaboration of these features is done in the table below 1.

The length and duration of these routes have already been supplied. For some of the feature calculations, we approximated a visible area taking into consideration the route segments and a margin from either side. The nature feature was calculated by connecting the visible area and the OpenStreetMap-provided natural area polygons. The number of tourist attractions listed by OpenStreetMap that are located within the route's visible region was used to determine the attractions feature. The criminality in the dataset refers to the sum of the severity of the crimes provided by the UK police crime dataset, which is observed, found and investigated in the visible areas. The UK Office which weighs the offenses’ seriousness is National Statistics Crime Severity Score. The maximum feature variation discovered in each route set served as the basis for the

Authorized licensed use limited to: DELHI TECHNICAL UNIV. Downloaded on July 20,2023 at 11:21:17 UTC from IEEE Xplore. Restrictions apply.

TABLE I. DATASET FEATURES DESCRIPTION

S.no.	Attributes	Format	Description
1.	Crime	Numeric	Is the severity of the crimes from National Statistics Crime Severity Score
2.	Accidents	Numeric	Is the weighted accident severity
3.	Tourist Attraction	Numeric	Is no of tourists in a covered area
4.	Traffic	Numeric	Ratio of no-traffic route duration and the route duration with traffic
5.	Duration	Numeric	Is the duration of route taken
6.	Length	Numeric	Length of the route
7.	Nature	Numeric	Represents intersecting the natural area polygons

normalizing of the features (routes with the same origin and destination). The summation of the total accident severity with the casualties in those accidents happened in that route is referred to as the accident feature. The accident data was provided by the UK Government Open Data Website. The ratio between the route duration with traffic and the route duration with no traffic was used to calculate the traffic feature

2) Data Preprocessing

For the data preprocessing the basic steps of removing the missing or null values was the first step to begin with. Secondly, to scale all the values of the dataset features a normalization method was used. And finally, the dataset containing 600 sets was split in the fraction of 7:4 to create a training and testing dataset respectively using model_selection_train_test_split function.

3) Feature Selection

In this study Extra Tree Classifier and Select K best are used for feature ranking purposes which are discussed below:

a) Extra Tree Classifier

Also known as Extremely Randomized Trees Classifier , it is type of ensemble learning method that uses results of multiple decision trees called "forest" to output its classification result. And the result which has maximum votes is taken as the final output of the algorithm.

All the decision trees are constructed from the original dataset. The optimal feature for the purpose of separating the data is then chosen by each decision tree after taking into account a number of mathematical criteria from a sample of k random features from a feature set, which is given to each test node. This random sample of data results in a set of de-correlated decision trees.

For constructing the individual decision trees for each feature at each node feature split criteria mainly Gini index and computed and taken as the basis for splitting the modes. The value of the Gini index at each node is known as Gini Importance of that feature. Feature with highest value of gini importance is taken as the root node and similarly the tree below that root node is constructed. The user can also select top k features to used in the construction of each individual tree.

b) Select K Best

K highest score is the rule which is used in SelectKBest method for selecting the features. This method can be applied for both classification and regression data just by making a change in 'score_func'. When preparing a large database for the purpose of training it is of utmost importance to select the best features otherwise our dataset for the training will not be much effective.

TABLE II. FEATURES IMPORTANCE SCORES

Features	Feature Importance
Traffic	0.0782
Accidents	0.0767
ID	0.0767
Length	0.0765
Duration	0.0759
Nature	0.0751

4) Model Building And Simulation

Next step of the methodology was to build a NN model and to do the same a tensorflow sequential model with 3 hidden layers and 2 dropout layers is build. All the three layers have different combination of rectified linear unit function (ReLu), exponential linear unit activation (eLu) and linear functions as its activation function. To create such a sequential model tensorflow library is used with keras method. This method allows to customize any NN model with different activation functions. The process of experimenting different models begun with the first model with all ReLu layers and output layer as the linear function layer with dropout layers in the middle to prevent overfitting. Simultaneously few changes were done in the functions, input and output parameters along with hyperparameters such as loss function, learning rate and metrices. The detail of the result with each change done in mentioned in the results. Meanwhile the training dataset and number of training iterations were made sure to be same for every combination tried in our study to ensure that results are not biased.

5) Model Training

The created model was trained in 100 epochs(batches) with a batch size of 64, keeping the track of loss in every iteration to see the trend of it and find the minimum threshold of the loss. It has a validation split of 20%.

6) Performance Measures

To compare the model's performance following measures were used such as:

a) Mean squared logarithm error

Sometimes when the target values of any regression model vary a lot mean squared logarithm error can be really helpful. Thus, those target values can be normalized by taking the logarithm of it and then a mean squared error is calculated using the formula:

Authorized licensed use limited to: DELHI TECHNICAL UNIV. Downloaded on July 20,2023 at 11:21:17 UTC from IEEE Xplore. Restrictions apply.

$$L(y, y^{\wedge}) = \frac{\sum_{i=0}^{N}(\log(y_i + 1) - \log(y_i^{\wedge} + 1))^2}{N}$$

b) Mean Absolute error

The Mean absolute error or MAE is another metric in machine learning which helps us in summarizing and assessing the quality of the machine learning model that we created.

This metric helps us in identifying how accurate our predictions are or in other words, how much the deviation amount with respect to the actual values.

$$MAE = \frac{\sum_{i=1}^{N} |y_i - y_i^{\wedge}|}{N}$$

c) R-Squared Error

R2-score is pronounced as R squared score which is a very essential metric for evaluating the performance of the regression-based ML models which is the reason the R2 score is also known as the coefficient of determination. It calculates the variation in the predictions that the dataset has made. In simple words, it is the discrepancy between the model's predictions and the actual results in the dataset samples that we have taken into consideration.

If the R squared score between two variables is 100% then that signifies that both variables have no variance i.e., completely correlated. Hence, as the value decreases the level of correlation also decreases.

$$R - squared = \sqrt{\frac{\sum_{i=1}^{N}(y_i - y_i^{\wedge})^2}{N}}$$

d) ROC Score

It is an area under the curve of receiver operating characteristic curve and tells the efficiency of a model. However, another way of defining it is as the likelihood that a classifier will select a positive case at random rather than a negative one. In other words, if we take any two observations a and b such that a > b, then ROC score is equal to the probability that our model actually ranks a higher than b. This concept is used in our study to create a roc_auc_score function mentioned in [28].

The model's performance in distinguishing the positive and negative classes is higher if the AUC score is higher. It is used for evaluating the accuracy of a statistical model.

IV. RESULTS

After running the different NN models on the testing data, and tuning the hyperparameters following results came out:

TABLE III. DIFFERENT TUNED NN MODELS AND THEIR PERFORMANCES

S.no.	Model Type (Activation functions)	Mean Squared Logarithm Error	ROC Score
1.	ReLu + Linear	0.2606	0.813
2.	ReLu + Linear (Different hyperparameters)	0.2667	0.820
3.	ReLu + Linear (Different hyperparameters)	0.2439	0.802
4.	ReLu + eLu + Linear	0.2659	0.821
5.	eLu + Linear	0.2403	0.822
6.	eLu + ReLu	0.2707	0.814

From the results above, model 5 shows the best ROC score. This shows that compared to other models it represents the data in the best possible way. The model is compiled with eLu function as first two hidden layers and last function as Linear function along with two dropout layers in between them. Also, this model has lowest mean squared logarithmic error which is another good sign of a better model. Although a lot more improvement is needed to further reduce the errors.

Some other measures for the same model include mean absolute error, root mean squared error.

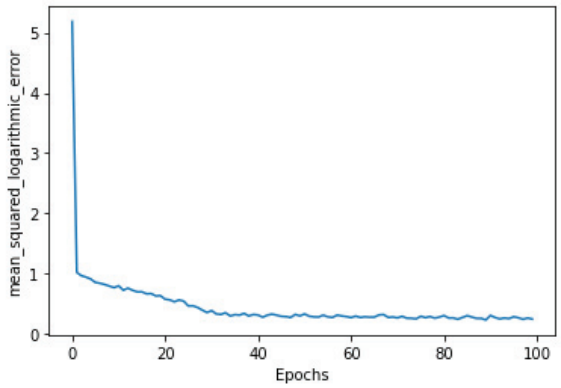

Fig 2. Mean Squared Logarithmic Error of Model 5

Mean Squared logarithmic error is a performance measure which takes logarithm of mean square of predicted and actual values of a model. It is a ratio of predicted and true values.

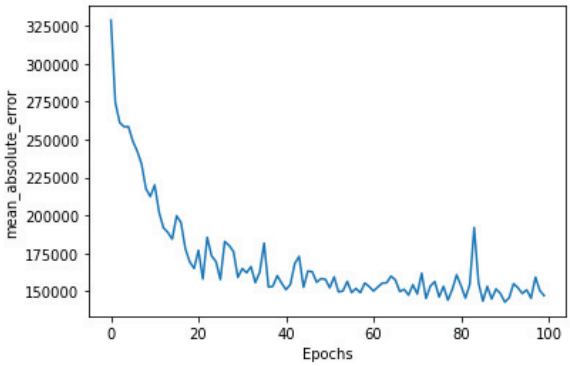

Fig 3. Mean Absolute Error of Model 5

It is the measure of absolute errors between the values given by model and lower its value better the model is considered. As with our model its value is showing random spikes and eventually decreasing.

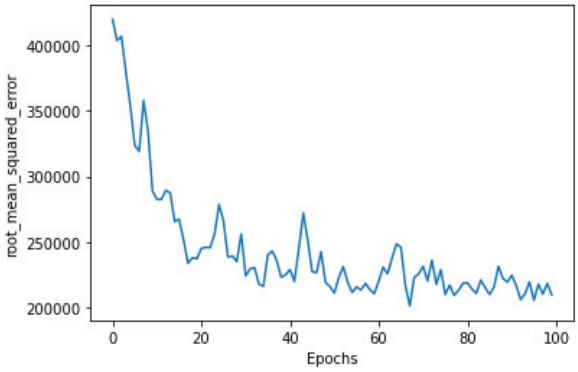

Fig 4. Root Mean Squared Error of Model 5

Authorized licensed use limited to: DELHI TECHNICAL UNIV. Downloaded on July 20,2023 at 11:21:17 UTC from IEEE Xplore. Restrictions apply.

Root mean squared error is another important measure which takes the account of difference between values by model and their actuals. From the figure above it can be understood that there is no specific pattern in its behaviour during 100 iterations. But overall the graph has a downward slope to it with random spikes on the way.

V. FUTURE WORKS

This paper has addressed the use of neural networks in detecting the possible reasons for crime occurring on the streets to enhance the results of a previous study mentioned in [13]. For the same, a NN model is built using activation functions of many combinations to compare the performance measures. The model which outperformed others have a sequential model with ReLu and eLu activation layers with dropout layers in the middle. Finally with this model the training data is used for fitting.

The results found at the end of this paper are quite useful, however, still a better regression model and an algorithm is needed to create a better theory. The study done by us and idea behind this research can be used in a software or as a feature in existing software which deals with giving geographical information about an area. This feature can make use of geographical features, traffic, population density and many more to depict the locality and crimes happening in an area informing users of possible threats in that area. However only an idea is explained in our research and possible way in which a prediction model can be built. Its implementation in a user-friendly software still remains to be done and changes can be made according to the requirements. Also, to make this model more accurate and helpful more features of area such as demographic features of a location can also be included. However, it is very hard to train and find a pattern in demographic features as it is a part of nature.

REFERENCES

[1] Gonzales Alberto R., Schofield Regina B., Hart Sarah V , Statistics, U. S. "Department of Justice." *NCJ* 196002 (1993)

[2] "National Geographic – GPS Encyclopedic Entry" https://education.nationalgeographic.org/resource/gps/

[3] Carroll, James V. "Vulnerability assessment of the US transportation infrastructure that relies on the global positioning system." *The Journal of Navigation* 56, no. 2 (2003): 185-193.

[4] S. A Faqir*, Raed. "The use of technology of global positioning system (GPS) in Criminal investigation & right to privacy under the constitution and criminal legislations in Jordan: legal analysis study." *Revue internationale de droit pénal* 3 (2013): 433-462

[5] Kannan, Monika. "Geographical information system and crime mapping-a study of Ajmer City, Rajasthan." *The Indian Geographical Journal* 92, no. 1 (2017): 25-39

[6] Kikuchi, George, Mamoru Amemiya, and Takahito Shimada. "An analysis of crime hot spots using GPS tracking data of children and agent-based simulation modeling." *Annals of GIS* 18, no. 3 (2012): 207-223.

[7] Mondal, Saswati, Dharmendra Singh, and Rakesh Kumar. "Crime hotspot detection using statistical and geospatial methods: a case study of Pune City, Maharashtra, India." *GeoJournal* 87, no. 6 (2022): 5287-5303.

[8] Gong, Y., Dai, M. and Gu, F., 2023. CARESim: An integrated agent-based simulation environment for crime analysis and risk evaluation (CARE). *Expert Systems with Applications*, *214*, p.119070.

[9] Zuo, Shenzheng, Yinan Liu, Dongmei Zhang, Pengpeng Xin, and Tianxin Liu. "Detection of gps spoofing attacks based on isolation forest." In *2021 IEEE 9th International Conference on Information, Communication and Networks (ICICN)*, pp. 357-361. IEEE, 2021.

[10] Aissou, G., Benouadah, S., El Alami, H., & Kaabouch, N. (2022, January). Instance-based supervised machine learning models for detecting GPS spoofing attacks on UAS. In *2022 IEEE 12th Annual Computing and Communication Workshop and Conference (CCWC)* (pp. 0208-0214). IEEE.

[11] Zhou, W., Lv, Z., Deng, X., & Ke, Y. (2022). A New Induced GNSS Spoofing Detection Method Based on Weighted Second-Order Central Moment. *IEEE Sensors Journal*, *22*(12), 12064-12078.

[12] Kim, J., Kim, J. H., & Lee, G. (2022). GPS data-based mobility mode inference model using long-term recurrent convolutional networks. *Transportation Research Part C: Emerging Technologies*, *135*, 103523.

[13] Durgapal, Vartika Hari. "Crime Based Evaluation of GPS Network Using Machine Learning Techniques." In *2022 4th International Conference on Smart Systems and Inventive Technology (ICSSIT)*, pp. 837-842. IEEE, 2022.

[14] Lin, Ying-Lung, Meng-Feng Yen, and Liang-Chih Yu. "Grid-based crime prediction using geographical features." *ISPRS International Journal of Geo-Information* 7, no. 8 (2018): 298.

[15] Almanie, Tahani, Rsha Mirza, and Elizabeth Lor. "Crime prediction based on crime types and using spatial and temporal criminal hotspots." *arXiv preprint arXiv:1508.02050* (2015).

[16] Zhu, Haojie, and Fahui Wang. "An agent-based model for simulating urban crime with improved daily routines." *Computers, Environment and Urban Systems* 89 (2021): 101680.

[17] Azami, Hamed, and Saeid Sanei. "GPS GDOP classification via improved neural network trainings and principal component analysis." *International Journal of Electronics*, *101*(9), pp.1300-1313., 2014, DOI: 10.1080/00207217.2013.832390

[18] Dabiri, Sina, Chang-Tien Lu, Kevin Heaslip, and Chandan K. Reddy. "Semi-supervised deep learning approach for transportation mode identification using GPS trajectory data." *IEEE Transactions on Knowledge and Data Engineering*, *32*(5), pp.1010-1023., 2019, DOI: 10.1109/TKDE.2019.2896985

[19] "Crawded dataset: london trajectories dataset" https://crawdad.org/ufrj/london-trajectories/2021-03-22/index.html

[20] Fu, Yulong, Hanlu Chen, Qinghua Zheng, Zheng Yan, Raimo Kantola, Xuyang Jing, Jin Cao, and Hui Li. "An Adaptive Security Data Collection and Composition Recognition method for security measurement over LTE/LTE-A networks." *Journal of Network and Computer Applications*, *155*, p.102549., 2020, DOI: 10.1016/j.jnca.2020.102549

[21] "scikit-learn: machine learning in Python — scikit-learn 0.24.2 documentation." https://scikit-learn.org/stable/

[22] "scikit-learn: metrics and scoring: quantifying the quality of predictions — scikit-learn 0.24.2 documentation" https://scikit-learn.org/stable/modules/model_evaluation.html

[23] "scikit-learn: regression techniques" https://scikit-learn.org/stable/modules/tree.html#regression

[24] Rahul, Priyansh Kedia, Subrat Sarangi, and Monika. "Analysis of machine learning models for malware detection." *Journal of Discrete Mathematical Sciences and Cryptography* 23, no. 2 (2020): 395-407.

[25] Adhikari, Surabhi. "Nlp based machine learning approaches for text summarization." In *2020 Fourth International Conference on Computing Methodologies and Communication (ICCMC)*, pp. 535-538. IEEE, 2020.

[26] Monika and Bhat, A., 2022. Automatic Twitter crime prediction using hybrid wavelet convolutional neural network with world cup optimization. *International Journal of Pattern Recognition and Artificial Intelligence*, *36*(05), p.2259005.

[27] Bhat, Aruna. "An analysis of crime data under apache pig on big data." In *2019 Third International conference on I-SMAC (IoT in Social, Mobile, Analytics and Cloud)(I-SMAC)*, pp. 330-335. IEEE, 2019.

[28] "GitHub - Learning-to-code12/crime-evalaution-using-GPS-data-with-neural-networks" https://github.com/Learning-to-code12/crime-evalaution-using-GPS-data-with-neural-networks

Authorized licensed use limited to: DELHI TECHNICAL UNIV. Downloaded on July 20,2023 at 11:21:17 UTC from IEEE Xplore. Restrictions apply.

AIP Conference Proceedings

RESEARCH ARTICLE | JULY 14 2023

Cybersecurity challenges in the healthcare domain and theroad ahead

Malti Bansal ✉; Varun Sirpal; Tanmaya Jain; Ujjwal; Uma Nangia

Check for updates

AIP Conference Proceedings 2796, 070002 (2023)
https://doi.org/10.1063/5.0149167

View Online
Export Citation
CrossMark

20 July 2023 11:14:45

AIP Advances
Why Publish With Us?
25 DAYS average time to 1st decision
740+ DOWNLOADS average per article
INCLUSIVE scope
Learn More
AIP Publishing

AIP Publishing

Cybersecurity Challenges in the Healthcare Domain and the Road Ahead

Malti Bansal[1,a)] Varun Sirpal[2,b)], Tanmaya Jain[2,b)], Ujjwal[2,b)], Uma Nangia[2,b)]

[1]*Department of Electronics and Communication Engineering, Delhi TechnologicalUniversity (DTU), Delhi - 110042, India*

[2]*Department of Electrical Engineering, Delhi Technological University (DTU), Delhi -110042, India*

Corresponding author: [a)] maltibansal@gmail.com

Abstract: The reliance of humans on technology has exponentially increased in the recent time. Due to its numerous benefits, technology is being integrated into almost every domain, ranging from military defense, to banking, to healthcare. Owing to the COVID-19 pandemic, even the field of education has become digitalized. Not a single electronic device can be seen nowadays at one's home which is not connected to the Internet, due to the advent of state-of- the-art technologies such as Internet-of-Things (IoT). However, with the convenience thatcomes with technology, there is an imminent cybersecurity risk as well. Cybercriminals have become increasingly advanced in their attack methods to conduct data breaches, and have started changing the industries they target. The most recent victim of an increased number of cyber-attacks is the healthcare industry. Healthcare institutions have become the preferred target of cybercriminals due to the tremendous sensitivity of the data that can be accessed and the immense financial gains possible owing to the hospital being unable to deliver quality healthcare services, creating a life-and-death situation for the patients. In this paper, we have conducted a review of the literature at the intersection of cybersecurity and healthcare, spanning to cover the cyber security threats in IoT-based Healthcare Systems, Hearing Aids, and Ambient Assisted Living. Section-5 covers various measures employed for improving cybersecurity in the healthcare domain.

Keywords: Cyber security, healthcare, ransomware, SQL Injection, Internet-of-Things, Electrocardiogram, Eavesdropping, Hypertext Transfer Protocol, Naïve Bayes, Internet-of- Healthcare Things, Ambient Assisted Living, Privacy, Confidentiality, Hearing Aids, Bluetooth, Blue-Snarfing, Firewalls, Risk Management, Education, Legislation, Electronic Health Records.

20 July 2023 11:14:45

INTRODUCTION

Cyber Attacks on Healthcare Systems

Recent advancements in technology and cheaper availability of electronic instruments starteda wave where daily usage of the internet and devices has increased drastically. Everything is easily available on the internet, we all have our digital identity on social media, e-com sites,and other websites, while this helps us in numerous ways but because of this, we are vulnerable to cyber-attacks which could lead to very dangerous outcomes. As health care system are also developing their online presence, they are also vulnerable to these attacks.

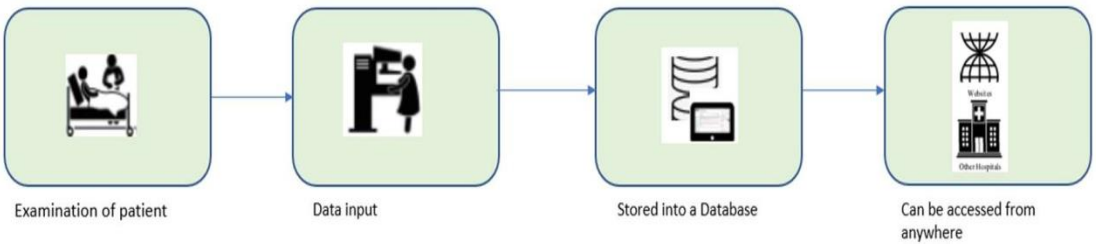

FIGURE 1: Data Flow in Medical Sector

Research Advancements and Innovations in Computing, Communications and Information Technologies
AIP Conf. Proc. 2796, 070002-1–070002-10; https://doi.org/10.1063/5.0149167
Published by AIP Publishing. 978-0-7354-4584-0/$30.00

Fig. 1 depicts how the data flow in the medical sector. Firstly, an appointment is made with the doctor then the doctor examines our patient and performs all the required tests, once all this is done and data is collected from the patient, it is passed on and gets uploaded to a database where it is stored and can be accessed by any authorized individual for future reference.

Vulnerability of Healthcare Systems

- Health care systems are vulnerable to cyber-attacks at different points and as we know data flows in majorly four steps, let's look at the vulnerable aspects in each transition.
- During information collection our system is susceptible to eavesdropping on unencrypted communication, wannacry Ransomware (because of usage of windows OS).
- Databases are open to attacks such as Password intrusion, Backup steal, SQL injection.
- Websites are vulnerable to XSS, Cross heterogeneous Network attacks.
- Operating devices are susceptible to Dos and dropbear SSH server attacks.

Past examples of cyber-attacks on healthcare systems

As we know health care systems are susceptible to cyber-attacks. let's have a look at such attacks that happened in the past.

- Anthem Blue Cross: Anthem a health insurance firm was under a cyber-attack that affected 78.8 million people. The breach was caused by a phishing attack as one of the employee opened a phishing email, this allowed the hacker to access different systems of the company and ultimately gain access to the data warehouse.
- In 2019 Indian based health care websites were under attack by a US-based hacking firm, hackers broke into the website and stole the medical records of 6.8 millionpatients.
- Pfizer breach: In December 2020, Pfizer was under attack and the hacker had stolen data on candidate vaccination which was released a short while after the breach.

There are numerous other examples of cyber-attacks and data breaches on health care facilities which makes it important to make these systems immune.

Cyber security in IoT-based Healthcare Systems

In the 21st Century, Internet of Things (IoT) would undoubtedly be a part of almost every future application. It works on the philosophy of interconnection of numerous physical objects, which then talk to each other, i.e., are involved in exchange, processing and transfer of data. All the physical objects have a unique IP address. Among the varied applications that IoT has across all fields, the most important one is that of the potential it holds in the field of healthcare, with the ability to reduce medical chaos, via real-time patient monitoring thereby significantly reducing the response time in case of an emergency situation.

Application in ECG Monitoring

One application of IoHT can be seen in continuous electrocardiogram (ECG) monitoring using Carbon Nano-tubes (CNT) electrodes as described in [30] with the target group being the elderly, differently-abled, and neonatal patients. An ECG is a test that records the electrical potential change on a graph which depicts each and every phase of the travelling of the electrical signal in a heart. For a healthy adult, the duration of the various waves and intervals such as the P-R interval, R-R interval etc. are in a certain range and measuring this helps in the detection of cardiovascular diseases. An important feature that needs to be extracted from ECG is the heart rate as it is vital for emergency services. Heart rate can be calculated as:

20 July 2023 11:14:45

$$Heart\ Rate = \frac{60}{R - R\ Interval}$$

Security Threats

In all the following attacks, the communication is assumed to be between Alice and Bob with Eve being the attacker.

- **Eavesdropping Attack:** This would involve Eve using sniffing tools such as tcpdump and Wireshark to eavesdrop all the data sent in an unencrypted transmission by Aliceto Bob, thereby affecting the privacy of confidential medical data.
- **Message Modification:** In this scenario, Eve captures the data sent in the message by Alice, modifies it and sends it to Bob, using the IP address of Alice.
- **Ransomware:** It encrypts the digitalized patient data, hence preventing the hospital staff and doctors from accessing it thereby causing danger to the life of patients. Examples of ransomware are WannaCrypt and Samsam.

HTTP GET Request Exhaustion

The architecture of Internet of Healthcare Things (IoHT) consists of three layers, namely Perception Layer, Network Layer and the Application Layer. The Perception Layer, as the name suggests, works at the grass root and uses different kinds of sensors to collect patient health parameters. The Network Layer has the function of transmitting the data gathered at the perception layer to the application layer so that it can be processed and utilised for delivering patient care and acts as the backbone of the entire architecture. The Application Layer is the most user-friendly layer and consists of a set of applications that are used by the healthcare personnel of the hospital such as diagnostics, visit management, etc. Attackers can attack all the 3 layers of this architecture.

However, a very prominent attack that is preferred by attackers in recent times is the HyperText Transfer Protocol (HTTP) GET Request Exhaustion Attack that takes place on the Application Layer. HTTP is used on the application layer on the World Wide Web to transfer documents such as images, audio, text, video from the server to the user who is requesting for the information. HTTP works on a Request-Response Model. There are a number of request methods in HTTP like GET, POST, PUT, DELETE however the most used ones on web browsers are GET and POST. In the HTTP GET Request Exhaustion attack, the malicious attackers use a Zombie army or Botnets to send multiple GET requests to the server per second which causes the server to stop working. One solution to this attack was provided in [43] which is by a binary classification of the incoming transactions into “normal” and “attack” by evaluating the transaction parameters and applying the Naïve Bayes Classification Algorithm to get the results. The Naïve Bayes Algorithm is a supervised learning algorithm, wherein we would be predicting Yi, i.e., the type of transaction “normal” or “attack” being represented by a label based on the features of the transaction, i.e., Xi. The Naïve Bayes Assumption states that all Xi are independent of each other and only depend on Y and is given by the following equation (here Y=1 represents the transaction being of “attack” type).

$$P(X/Y = 1) = \prod i\ P(x_i/y = 1)$$

Cyber security Issues in Ambient Assisted Living

The aging population and increase in the number of senior citizens who are living alone are bringing a major challenge in most parts of the world. As one ages there is a decline in abilities and this hampers their day-to-day experience of life which ultimately leads them to social isolation. According to World Health Organization, there will be roughly 2 billion people who would be 60 plus by 2050.

20 July 2023 11:14:45

We know that older people are more prone to diseases such as diabetes and heart diseases and other various diseases this demands active caring and more frequent hospitalization as one continues to age. However, all this will be extremely expensive and therefore there is an urgent need to resolve this issue which is economically viable so that the masses can gain out of it. To resolve this Ambient Assisted Living (AAL) comes to the rescue because it can take care of individuals and would not cost much. AAL will help an individual to monitor his daily routine as well as his vitals so that can kind of anomaly can be easily detected and can be cured as soon as possible hence increasing the odds of survival as well as improving the quality of life.

AAL Architecture

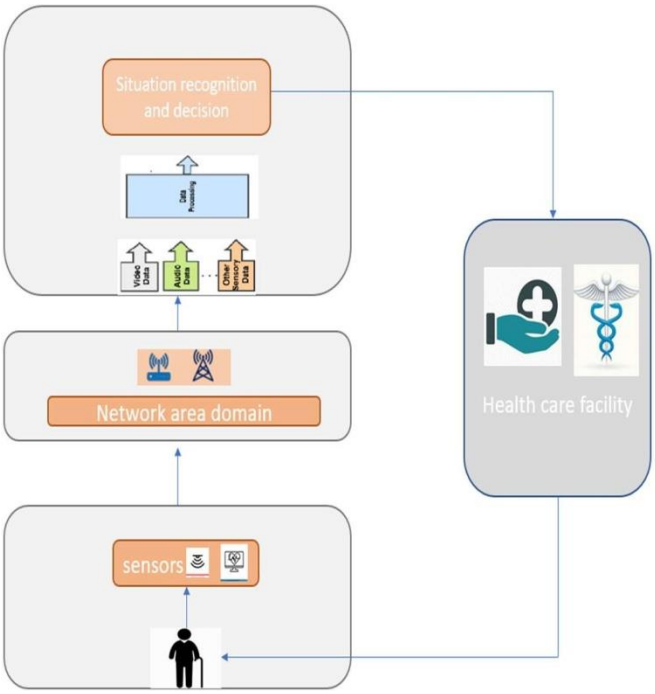

FIGUR. 2: AAL Architecture

The AAL architecture shown in Fig. 2 is intended to provide data on a real-time basis and instantaneously so that the decision-maker can evaluate the current situation of the patient and can decide whether to turn on the alarm or not. As we can observe that there are different kinds of sensors that provide data on a real-time basis this data is stored and helps the decision-maker to evaluate the situation better and which ultimately leads to better performance. This data is transferred through the gateway. Gateway is in simple terms a network through which data is transferred to the decision-maker, a simple example of the gateway is your mobile phone. When the data ultimately reaches the center it is processed compared and stored. If any unusual situation is encountered a notification is sent to the health care facility and then the health care facility reaches out to the patient.

Data Collection: In an Ambient Assisted Living environment there will be several different kinds of sensors installed in the environment, for example, sensors can wear by the patient to monitor and collect all the relevant data about the body such as heart rate, steps, and other body vital signs, sensors can also be installed in the house to capture the daily pattern of the patient and also record the sunlight, ventilation and other external factors which are relevant for the decision-maker. All this is important because this will help the system to detect any sort of unusual pattern observed in the patient. All this will help to develop a robust system. Not only transmitting and storing this data for the decision-making machine we can also present this data in a portal that can be accessed by the patient so that he can keep a track of his health, this will further slim down any chance of mishap.

20 July 2023 11:14:45

Situation Recognition and Decision Making: The development of a robust system that can evaluate the real-time data and can judge optimally and take decisive action is the need of the hour. Now before moving further our data is in raw format which needs to be converted into another format that can be easily understood by our machine. Once, the data is converted into the desired format we can feed this to our model. Now the model can be constructed using techniques and instruments such as Artificial Intelligence and Machine Learning. There are many available algorithms such as decision tree, random forest, deep learning, and others that can be trained on available data and once the desired accuracy is attained, they can be implemented in our AAL environment.

Algorithm and Computational Technique

Let's look at some techniques for the AAL environment-

Activity Recognition: Humans perform various kinds of activities such as walking, running, and jogging and soon. So, this data is collected by using sensors such as an accelerometer and gyroscope. This data is recorded and then finally classification algorithm predicts the kind of activity which helps in determining the health status.

Vision-based Activity Recognition: Vision-based sensors provide very detailed information about the subject but the algorithm is quite complex as there can be different backgrounds and settings where one can be so the algorithm needs to compare the pre-recorded video of activity with the ongoing activity.

Anomaly detection: In this approach, our system tries to generate a pattern and then compare it with daily activity and medication compliance and if it is found that there isa deviation from the expected behavior then an alarm is set off.

MAJOR CHALLENGES IN IMPLEMENTING AAL

Ambient Assisted Living can enable senior citizens to lead a lively life but this environment is still under the developmental phase. Firstly, we need the data set. Data needs to be reliable and we need bulk of data as there can be numerous situations and for our model to work efficiently under every scenario, we need to feed it a chunk of data. This is one of the primary challengesin developing an AAL environment. Another challenge is to implement it in terms of usability and accessibility.

We need our system to be as user-friendly as possible so that people who do not have much technical knowledge can understand and use it effectively. Preserving privacy and maintaining confidentially is yet another concern and very important and needs to be addressed. AAL system stores critical data of its users which needs to be protected. The system needs to be completely encrypted and special attention should be given in the case of a wireless system as it is easier to intercept. Involved parties should be held liable in case of a mishappening.

Cyber security Threats in Hearing Aids

Humans are social animals, and of the many senses we have, hearing is a highly prominent sense with the help of which one can actively participate in all spheres of life, be it family, education, employment, or sports. To not be able to hear or to have hearing problems significantly diminishes a person's social interactions. Hence, the technology of hearing aidshas been a boon to those individuals with hearing problems, as they also act as Assistive Learning Devices (ALDs). However, due to this very reason, hearing aids face a serious cybersecurity threat, along with a concern for the patients' privacy as well. Moreover, due tothe recent coupling of Bluetooth connectivity with hearing aids, it has become even more imperative to develop security mechanisms for hearing aids. The field of sound hacking was brought into limelight by the hacking of hearing aids in projects such as "Phantom Terrains".

Another important development in this field is the recent integration of hearing aids into the IoHT architecture. Some attacks that can be encountered in Bluetooth-enabled Hearing Aids are as follows.

20 July 2023 11:14:45

PIN Theft Attack: Interception of Personal Identification Number (PIN) to connect with victim which allows access to the data or conversations taking place.

Backdoor Entry: In this case, the victim's device gets paired with the attacker's device without the former's knowledge, allowing the offender to gather data from the victim's device.

Blue-tracking Attack: Getting access to victim's location via monitoring of Bluetooth signal, thereby leading to loss of privacy since the person using the hearing aid has to keep the device continuously connected.

Blue-snarfing Attack: Getting complete access to smartphone, thereby access to contacts, emails, etc. Moreover, using the Blue-snarfing++ Technique, the IMEI codeof the device can also be obtained.

Car Whisperer Attack: Interception of audio from car's Bluetooth device and feeding incorrect navigation data and incorrect traffic data. An additional threat in Car Whisperer Attack is that the conversations taking place among the people in the car can also be recorded and used for malicious purposes.

MEASURES TO IMPROVE CYBER SECURITY IN HEALTHCARE SECTOR

Network Security

Network security is very important for filtering out unauthorized access and protecting the network from any potential cyber-attacks. Network security techniques such as Honeypots, intrusion detection systems and firewalls can prove to be very effective in healthcare settingsas well. For example, Firewalls can play a critical role in securing electronic health records and network connected medical devices. It can act as a first line of defense for healthcare system security.

Next generation firewalls can analyze, evaluate and block even the most advanced attacks by enforcing pre-defined rules at the application level, whilst monitoring lower-level layers of the OSI model. In [3] M. Zaki et.al. has proposed a framework to detect and prevent cyber-attacks on healthcare networks using the next generation firewall. Additionally, they have also configured NGFW with a unique hospital architecture thus proving the efficacy of NGFW as a network security tool. Apart from this, honeypots can also prove to be useful in mobile health concept [1] and also for the security of digital health record based big data [2]. In [6] Jouni Ihanus et.al. have shown how medical devices can be modelled using honeypots.

Reporting and Feedback Loops

Having a proper reporting and feedback mechanism for health care providers is very important to cope-up with new emerging cybersecurity challenges. A good communication and reporting mechanism between the manufacturers of the medical devices and healthcare organizations can ensure successful alleviation of potential cyber-security threats. Besides, legislation to mandate reporting of cybersecurity incidents would assist in identifying issues from all health care providers [7-11]. Regular network and access monitoring of medical devices should become part of regular operational practices, and in case a breach is detected it should immediately be reported to the management of the organization.

Risk Management

Organizations must assess and embed cyber security risks in their risk management processes as they would do for financial, clinical or operational risks. Risk assessment is the first step towards risk management. There are dozens of information security risk assessment frameworks that exist including the frameworks of highly respected organizations like the international organization for standardization. But applying these standards to healthcare while giving due regards to clinical workflows requires some tailoring. In [4] have discussed three such tailoring efforts that must be made in healthcare so that information can be protected without impending the crucial

20 July 2023 11:14:45

requirement of information sharing within the healthcare sector. Risk management for cyber security should include documentation of data flows with regard to network connected medical devices. This would ensure that appropriate protection is providedat each stage of data transfer, processing, and storage [12-20].

Education and Awareness

Education and training modules must be introduced for the IT professionals working in the healthcare setting to make them better equipped against potential cyber threats. Currently prevalent Cyber security training programmes lack an integrated approach and often tend to concentrate on one aspect of cyber security at a time. In [5] the author has provided a holistic cyber-resilience and security framework which can be used to develop and deliver a multilateral training and educational programme based on an integrated and dynamic approach on cybersecurity. The framework provides a training scheme which is interactive, meaningful and directly relevant to users' operational requirements.

Resilience and Contingency Planning

Standard cyber-resilience measures such as network segregation, restraining access, setting up virtual local area networks and use of uninterruptible power supplies for critical equipment can be very useful in healthcare settings as well [21-27]. But while considering any resilience measure we will also have to account for medical devices connected in the network. Contingency planning focused on incident detection and response, disaster recovery and business impact analysis is also very important for every healthcare organization [28-33].

Legislation and Regulation

Legislation concerning data protections also becomes very important to ensure proper standards of data protection. On one hand India is increasingly digitizing its healthcare infrastructure but on the other hand it still lacks a data protection law. The plan to launch digitalhealth records as part of the national digital health mission will further raise concerns about data security in the absence of a data protection law [34-39]. In this regard a legislation which can ensure protection of such critical medical data becomes all the more important. A strong data protection law on the lines of Europe's General Data Protection Regulation (GDPR) is the need of the hour in India [40-43]. This will bring in proper standards and regulations for healthcare organisations and will ensure that the critical patient data is protected.

20 July 2023 11:14:45

REFERENCES

1. N. Subramanian, O. Elharrouss, S. Al-Maadeed and A. Bouridane, "Image Steganography: A Review of the Recent Advances," in IEEE Access, vol. 9, pp. 23409-23423, 2021, doi: 10.1109/ACCESS.2021.3053998.
2. M. Bansal and Priya, "Application Layer Protocols for Internet of Healthcare Things (IoHT)," 2020 Fourth International Conference on Inventive Systems and Control (ICISC), 2020, pp. 369-376, doi: 10.1109/ICISC47916.2020.9171092.
3. A. Djenna and D. Eddine Saïdouni, "Cyber Attacks Classification in IoT-Based-Healthcare Infrastructure," 2018 2nd Cyber Security in Networking Conference (CSNet), 2018, pp. 1-4, doi: 10.1109/CSNET.2018.8602974.
4. J. Ni, K. Zhang, X. Lin and X. Shen, "Securing Fog Computing for Internet of Things Applications: Challenges and Solutions," in IEEE Communications Surveys & Tutorials, vol. 20, no. 1, pp. 601-628, Firstquarter 2018, doi: 10.1109/COMST.2017.2762345.
5. P. Katrakazas and D. Koutsouris, "A (Lack of) Review on Cyber-Security and Privacy Concerns in Hearing Aids," 2018 IEEE 31st International Symposium on Computer-Based Medical Systems (CBMS), 2018, pp. 223-226, doi: 10.1109/CBMS.2018.00046.
6. Babatunde, A. & Taiwo, A. & Dada, Emmanuel. (2018). Information Security in Health Care Centre Using Cryptography and Steganography. Arid Zone Journal of Engineering, Technology and Environment. 14.

7. McDermott, Donna & Kamerer, Jessica & Birk, Andrew. (2019). Electronic Health Records: A Literature Review of Cyber Threats and Security Measures. International Journal of Cyber Research and Education (IJCRE). 1. 42-49. 10.4018/IJCRE.2019070104.
8. Wheeler D.J., Needham R.M. (1995) TEA, a tiny encryption algorithm. In: Preneel B. (eds) Fast Software Encryption. FSE 1994. Lecture Notes in Computer Science, vol 1008. Springer, Berlin, Heidelberg. https://doi.org/10.1007/3-540-60590-8_29
9. A. George, H. Dhanasekaran, J. P. Chittiappa, L. A. Challagundla, S. S. Nikkam and O. Abuzaghleh, "Internet of Things in health care using fog computing," 2018 IEEE Long Island Systems, Applications and Technology Conference (LISAT), Farmingdale, NY, USA, 2018,pp. 1-6, doi: 10.1109/LISAT.2018.8378012.
10. Anand Paul, Hameed Pinjari, Won-Hwa Hong, Hyun Cheol Seo, Seungmin Rho, "Fog Computing-Based IoT for Health Monitoring System", Journal of Sensors, vol. 2018, Article ID 1386470, 7 pages, 2018. https://doi.org/10.1155/2018/1386470
11. P. A. H. Williams and V. McCauley, "Always connected: The security challenges of the healthcare Internet of Things," 2016 IEEE 3rd World Forum on Internet of Things (WF-IoT), 2016, pp. 30-35, doi: 10.1109/WF-IoT.2016.7845455.
12. Hu, Wei. "Cryptanalysis of TEA Using Quantum-Inspired Genetic Algorithms." J. Softw. Eng. Appl. 3 (2010): 50-57.
13. H. Suryotrisongko and Y. Musashi, "Review of Cybersecurity Research Topics, Taxonomy and Challenges: Interdisciplinary Perspective," 2019 IEEE 12th Conference on Service-Oriented Computing and Applications (SOCA), 2019, pp. 162-167, doi: 10.1109/SOCA.2019.00031.
14. S. N. Swamy, D. Jadhav and N. Kulkarni, "Security threats in the application layer in IOT applications," 2017 International Conference on I-SMAC (IoT in Social, Mobile, Analytics and Cloud) (I-SMAC), 2017, pp. 477-480, doi: 10.1109/I-SMAC.2017.8058395.
15. A. K. Alharam and W. Elmedany, "The Effects of Cyber-Security on Healthcare Industry,"2017 9th IEEE-GCC Conference and Exhibition (GCCCE), 2017, pp. 1-9, doi: 10.1109/IEEEGCC.2017.8448206.
16. Basnet, R., Mukherjee, S., Pagadala, V.M., Ray, I.: An efficient implementation of next generation access control for the mobile health cloud. In: 2018 Third International Conference on Fog and Mobile Edge Computing (FMEC). pp. 131–138 (April 2018). https://doi.org/10.1109/FMEC.2018.8364055
17. Bhargavi, U., Gundibail, S., Manjunath, K., Renuka, A.: Security of medical big data images using decoy technique. In: 2019 International Conference on Automation, Computational and Technology Management (ICACTM). pp. 310–314 (April 2019). https://doi.org/10.1109/ICACTM.2019.8776696
18. M. Zaki, V. Sivakumar, S. Shrivastava and K. Gaurav, "Cybersecurity Framework For Healthcare Industry Using NGFW," 2021 Third International Conference on Intelligent Communication Technologies and Virtual Mobile Networks (ICICV), 2021, pp. 196-200, doi: 10.1109/ICICV50876.2021.9388455.
19. National Cybersecurity Institute Journal, Vol. 1 No.3, Excelsior College, 2015.
20. J. Rajamäki, J. Nevmerzhitskaya and C. Virág, "Cybersecurity education and training in hospitals: Proactive resilience educational framework (Prosilience EF)," 2018 IEEE Global Engineering Education Conference (EDUCON), 2018, pp. 2042-2046, doi: 10.1109/EDUCON.2018.8363488.
21. Ihanus J., Kokkonen T. (2020) Modelling Medical Devices with Honeypots. In Galinina O., Andreev S., Balandin S., Koucheryavy Y. (Eds.) Internet of Things, Smart Spaces, andNext Generation Networks and Systems. NEW2AN 2020, ruSMART 2020. Lecture Notes in Computer Science, vol 12525, 295-306. Springer, Cham.
22. M. d. l. A. C. Leon, J. I. N. Hipolito and J. L. Garcia, "A Security and Privacy Survey for WSN in e-Health Applications," 2009 Electronics, Robotics and Automotive Mechanics Conference (CERMA), 2009, pp. 125-130, doi: 10.1109/CERMA.2009.47.
23. M. Li, W. Lou and K. Ren, "Data security and privacy in wireless body area networks,"in IEEE Wireless Communications, vol. 17, no. 1, pp. 51-58, February 2010, doi: 10.1109/MWC.2010.5416350.
24. Kriangsiri Malasri and Lan Wang. 2007. Addressing security in medical sensor networks. In Proceedings of the

20 July 2023 11:14:45

1st ACM SIGMOBILE international workshop on Systems and networking support for healthcare and assisted living environments (*HealthNet '07*). Association for Computing Machinery, New York, NY, USA, 7–12. DOI:https://doi.org/10.1145/1248054.1248058

25. Ng, H.S., Sim, M.L. & Tan, C.M. Security issues of wireless sensor networks in healthcare applications. BT Technol J 24, 138–144 (2006). https://doi.org/10.1007/s10550-006-0051-8
26. M. Bansal, Priya, Machine Learning Perspective in VLSI Computer Aided Design at Different Abstraction Levels. In: Shakya S., Bestak R., Palanisamy R., Kamel K.A. (eds) Mobile Computing and Sustainable Informatics. Lecture Notes on Data Engineering and Communications Technologies, 2022, vol 68, pp. 95-112, Springer, Singapore. https://doi.org/10.1007/978-981-16-1866-6_6
27. M. Bansal, V. Sirpal, M. K. Choudhary, Advancing e-Government Using Internet of Things. In: Shakya S., Bestak R., Palanisamy R., Kamel K.A. (eds) Mobile Computing andSustainable Informatics. Lecture Notes on Data Engineering and Communications Technologies, 2022, vol 68. pp. 123-137 Springer, Singapore. https://doi.org/10.1007/978- 981-16-1866-6_8
28. M. Bansal, G. Srivastava (2020) Design and Implementation of LNA for Biomedical Applications. In: Pandian A., Ntalianis K., Palanisamy R. (eds) Intelligent Computing, Information and Control Systems. ICICCS 2019. Advances in Intelligent Systems and Computing, vol 1039. Springer, Cham. https://doi.org/10.1007/978-3-030-30465-2_18.
29. M. Bansal, S. Gupta and S. Mathur, Comparison of ECC and RSA Algorithm with DNAEncoding for IoT Security, 2021 6th International Conference on Inventive Computation Technologies (ICICT), Coimbatore, India, 2021, pp. 1340-1343, doi: 10.1109/ICICT50816.2021.9358591.
30. Bansal, M., Priya (2021). Performance Comparison of MQTT and CoAP Protocols in Different Simulation Environments. In: Ranganathan, G., Chen, J., Rocha, Á. (eds) InventiveCommunication and Computational Technologies. Lecture Notes in Networks and Systems,vol 145. Springer, Singapore. https://doi.org/10.1007/978-981-15-7345-3_47
31. M. Bansal and V. Sirpal, "Fog Computing-based Internet of Things and its Applicationsin Healthcare", in Journal of Physics Conference Series, 2021, vol. 1916, no. 1. doi:10.1088/1742-6596/1916/1/012041.
32. Al-Hamadi, H., Gawanmeh, A., Baek, J. & Al-Qutayri, M. (2017). Lightweight Security Protocol for ECG Bio-Sensors. Wireless Personal Communications: an international journal, 95 (4), 5097-5120.
33. A. Razaque et al., "Survey: Cybersecurity Vulnerabilities, Attacks and Solutions in theMedical Domain," in IEEE Access, vol. 7, pp. 168774-168797, 2019, doi: 10.1109/ACCESS.2019.2950849.
34. P. Rashidi and A. Mihailidis, "A Survey on Ambient-Assisted Living Tools for Older Adults," in IEEE Journal of Biomedical and Health Informatics, vol. 17, no. 3, pp. 579-590,May 2013, doi: 10.1109/JBHI.2012.2234129.
35. A. Dimitrievski, E. Zdravevski, P. Lameski and V. Trajkovik, "A survey of Ambient Assisted Living systems: Challenges and opportunities," 2016 IEEE 12th International Conference on Intelligent Computer Communication and Processing (ICCP), 2016, pp. 49-53, doi: 10.1109/ICCP.2016.7737121.
36. M. N. Alkhomsan, M. A. Hossain, S. M. M. Rahman and M. Masud, "Situation Awareness in Ambient Assisted Living for Smart Healthcare," in IEEE Access, vol. 5, pp.20716-20725, 2017, doi: 10.1109/ACCESS.2017.2731363.
37. S. Wagner and E. Hunnerup, "Ambient Assisted Living Ecosystem for Supporting Senior Citizens' Human System Interaction," 2018 11th International Conference on HumanSystem Interaction (HSI), 2018, pp. 221-225, doi: 10.1109/HSI.2018.8431357.
38. V. Rogelj and D. Bogataj, "Ambient Assisted Living Technologies and Environments:Literature review and research agenda*," 2020 7th International Conference on Control, Decision and Information Technologies (CoDIT), 2020, pp. 762-767, doi: 10.1109/CoDIT49905.2020.9263932.
39. Menaka Muthuppalaniappan, LLB, Kerrie Stevenson, MBChB BMedSci (Hons) FHEA,Healthcare cyber-attacks and the COVID-19 pandemic: an urgent threat to global health, International Journal for Quality in Health Care, Volume 33, Issue 1, 2021, mzaa117, https://doi.org/10.1093/intqhc/mzaa117

20 July 2023 11:14:45

40. P. Koleva, K. Tonchev, G. Balabanov, A. Manolova and V. Poulkov, "Challenges in designing and implementation of an effective Ambient Assisted Living system," 2015 12th International Conference on Telecommunication in Modern Satellite, Cable and BroadcastingServices (TELSIKS), 2015, pp. 305-308, doi: 10.1109/TELSKS.2015.7357793.
41. L. A. Tawalbeh, H. Tawalbeh, H. Song and Y. Jararweh, "Intrusion and attacks overmobile networks and cloud health systems," 2017 IEEE Conference on Computer Communications Workshops (INFOCOM WKSHPS), 2017, pp. 13-17, doi:10.1109/INFCOMW.2017.8116345.
42. Nguyen gia, Tuan & Jiang, Mingzhe & Rahmani, Amir M. & Westerlund, Tomi & Mankodiya, Kunal & Liljeberg, Pasi & Tenhunen, Hannu. (2015). Fog Computing in BodySensor Networks: An Energy Efficient Approach.
43. Prasad, Alvin. (2019). Exhausted Servers Deny Service – HTTP Get Attack. Journal ofICT, Design, Engineering and Technological Science. 3. 35-38. 10.33150/JITDETS-3.2.3.

20 July 2023 11:14:45

2023 2nd International Conference on Vision Towards Emerging Trends in Communication and Networking Technologies (ViTECoN) | 979-8-3503-4798-2/23/$31.00 ©2023 IEEE | DOI: 10.1109/ViTECON58111.2023.10157962

Deepfake Creation Using Gans and Autoencoder and Deepfake detection

Manoj kumar Das
dept.of computer engineering
delhi technological university
delhi,india
manoj5das3@gmail.com

Manav kumar
dept.of computer engineering
delhi technological university
delhi,india
kumarmanav245@gmail.com

Ishank kumar kapil
dept.of computer engineering
delhi technological university
delhi,india
ikapil15@gmail.com

Dr Rajesh kumar yadav
dept.of computer engineering
delhi technological university
delhi,india
rkyadav@dtu.ac.in

***Abstract*— Deep learning techniques is useful in a myriad of applications such as computer vision processing, natural language processing, as well as deepfake detection. The development of deep learning algorithms for imaging detection has resulted in the development of deepfakes. These fakes employ advanced algorithms for deep learning to generate fake images that are extremely difficult to differentiate from authentic images. In a fake video, the face, expression or speech is replaced with an image of another's face, with a distinct speech or emotion with the help of the technology of deep learning. These videos are typically so sophisticated that the traces of manipulation are hard to spot. Social media are among the most frequently targeted and most serious because they are vulnerable platforms that are susceptible to blackmailing or making a person look bad. There are several existing efforts to detect fake images, but there have been very few efforts developed for video content on social media.**

Keywords— deep-fake, deep learning, GANS, autoencoder.

I. INTRODUCTION

Machine vision is expanding every day across a broad range of fields, ranging from basic computer software that recognizes images to automated robotics. One of the numerous applications based on machine vision is known as Deep-fake[1]. Deep-fake makes use of deep-learning algorithms to build counterfeit images by switching faces of an original image to make an image of another. This results in fake images that are difficult to distinguish. The reason behind this is due to the use of decoders as well as encoders that are based on deep-learning which are extensively used in the area of machine-vision [2].Deepfakes are created by employing machine learning algorithms to change or swap out certain parts of an original video or image, like a person's face.Recent development in this field allows to create deepfake with just a motionless image[3]. Deep fake detection refers to the difficulty of spotting false movies or photographs made with deep learning methods. To detect these modifications and distinguish them from real movies or photographs, deepfake detection is used. We propose to use our technology to the detection of false faces in photographs at a macroscopic degree of analysis. The human vision struggles to distinguish phony images at higher semantic levels, especially when they include a person's face or video. We used a deep neural network with a defined set of layers as a middle ground approach . The architecture that come next had the decent classification results out of all of our tests since they have a low degree of representation and a lower degree of parameters. They are based on powerful image classification networks that switch between convolutional layer and pooling to extract features and a dense network to categorize the images. [4]. Major tech companies are seeking ways to identify fake and false news to end the growing amount of fake news being published on the internet. Recently many big companies like Meta, Amazon.com, Inc , Microsoft corporation are investing in deepfake detection contest to promote more exploration in this field [5] .The enthusiasm displayed by big names such as Google and Microsoft highlights the significance of the Deep-fake problem.The paper highlights the possible options of deepfake generation. Motivation behind the research is the rising risk of manipulated images and videos that poses the threat on the privacy of the people .There is a increasing threat to world peace as deepfake can be used manipulate speeches and videos of global leaders[10-12].The advantage of the proposed methodology is that it is efficient in classifying fake and real images .The Fig. 1 depicts the genuine fake and real images created using advanced technology and a network structure that has the capability to use a lot of data for developing the network. .

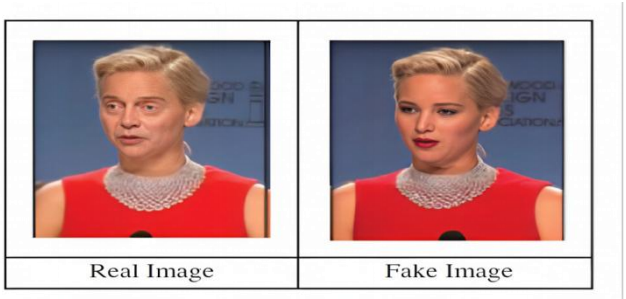

Fig. 1. Real and Deep-fake image.

979-8-3503-4798-2/23/$31.00 ©2023 IEEE

Authorized licensed use limited to: DELHI TECHNICAL UNIV. Downloaded on July 03,2023 at 04:51:42 UTC from IEEE Xplore. Restrictions apply.

II. LITERATURE REVIEWS

The paper article[6]: Profound phony Video Location Utilizing Intermittent Brain Organization**,** David Guera and Edward J Delp propose the idea of a fleeting cognizant framework which can perceive counterfeit Profound phony video. To distinguish counterfeit recordings, first we should comprehend the system of their creation and assist us with perceiving the imperfections in Profound phony creation to take advantage of the shortcomings, a profound phony recognition can be made. The strategy talked about in this article, outline level irregularity is the primary perspective which is utilized to recognize fakes. If the encoder does not know about the skin's or different points of interest of the scene, there could be limit impacts because of unconstrained converging of the face and the casing, which could be an alternate fault. One more issue that is utilized in this situation is that it makes a few irregularities, and can cause the presence of flashing in the facial region. This is an element that is normal that is available in by far most of deceitful recordings. It's difficult to distinguish outwardly, it is feasible to record utilizing a Pixel-level CNN include extraction. The dataset utilized in this study contains 3000 recordings from the HOHA dataset. The pre-handling steps are made sense of in this article. The proposed framework is made out of a LSTM-based convolution structure used to handle outlines. CNN to eliminate highlights from outlines with LSTM to concentrate on the transient succession are two key components that make up the convolution LSTM. In case of an unseen test arrangement, the highlights of each edge are made by CNN. From that point forward, highlights from various casings are consolidated and afterward shipped off LSTM to be dissected. LSTM then, at that point, gives a gauge of whether the succession is phony or has not been modified at all. In under 2 seconds, the framework can distinguish in the event that the video is being examined is phony film or not. The exactness is more noteworthy than 97%.

In the paper[7] : Powerful and Quick Profound phony discovery strategy in view of Haarwavelet Changeby Mohammed Akram Younus and TahaMohammed Hasan, the creators present an elective technique for recognizing counterfeit recordings by utilizing the wavelet change. The procedure portrayed in this paper exploits the way that when the Profound phony calculation produces counterfeit video it can create counterfeit countenances that is features with specific size and goal. To ensure that they match the plan of the face that was initially made on the real video, there is a haze highlight is incorporated into the phony countenances. This change makes a particular haze irregularity between the created face and the result of the foundation counterfeit recordings. The calculation can identify this irregularity by contrasting the obscured locales of the created return for money invested in contrast with the encompassing region by utilizing a specific Haar Wavelet change highlight. The chief advantage of utilizing the Haar Wavelet change is that it at first separates the various types of edges and afterward kills the obscured picture's lucidity. Extremely productive and quick as the foundation isn't changing countenances in the pictures won't be impacted and there's no necessity to copy this obscure lattice capability. To survey the haze's size, two strategies like immediate and deviant can be utilized. Direct strategy can be utilized to decide the size of the haze by looking at unmistakable highlights in the image. For example, edge highlights. The backhanded strategy depends on obscure reproduction in case of a H network which isn't distinguished (the H-framework is described by obscure's appraisals , as well as obscure acknowledgment). Dirac Construction step structures, Dirac structure and the rooftop are three particular sorts of edges that show up in a picture. The haze reaches out by taking the nature of the G design of the moves toward be thought about. Sharpness on edges is estimated in the number (0! 2!) that, if more noteworthy, proposes that the picture is more fine. At the point when we think about the haze term of the return for capital invested as well as the haze size of the remainder of the picture, we can decide if obviously the images(frames inside video) were changed or have not been modified. The UADFV dataset that includes 49 non manipulated also with 49 recordings that have been adjusted, is utilized to play out this. The recordings are isolated into outlines. In each edge, the face is taken . Then, a Profound phony location calculation utilizing haar wavelet change used. The calculation is made sense of top to bottom in this article. The calculation is proposed to have an exactness that is 90.5 percent.

The paper [8] OC Counterfeit Dect: Ordering Profound phony s utilizing a One Class Variational Autoencoder composed by Hasam Khalid, and Simon S. Charm, the model depends on genuine pictures utilized for preparing. Since new strategies for making misleading recordings are being developed because of mechanical advances to assist a model with distinguishing fake recordings. information that contain counterfeit recordings are not normal for preparing. This effects on the accuracy of the model. The model introduced in this paper involves just genuine video film for preparing to beat the constraints of information lack. The Face Forensic++ dataset is the dataset utilized in this paper. It is made out of genuine pictures and five phony sets The Face-Trade dataset F2Fdataset (F2F) Profound phony dataset(DF) Brain Text-tures dataset (NT) Profound phony recognition Dataset(DFD) Subsequent to gathering the video information, the information is changed into outlines and the face discovery and arrangement process is finished utilizing MTCNN. One-class variational encoders are utilized in this occurrence. It comprises of an autoencoder. In the encoder's case, pictures are utilized as information. Scaling is finished through convolution layers alongside the mean and change are determined. The outcomes are then used for input into the decoder. The RMSE esteem is determined, which is lower for real pictures, however higher when phony pictures are used. Two strategies are examined in this article: OCFakeDect1andOCFakeDect2. In OCFakeDect1 with result and information pictures the score of remaking is determined progressively. OCFakeDect2 likewise has an extra encoder structure that computes scores of their making in view of the information and result dormant data. It can arrive at 97.5 rate precision most productive variant is just for NT and DFD datasets.

In the paper [9] Computerized Legal sciences and Examination of Profound phony Recordings by Mousa Tayseer Jafar Muhammed AbabnehMuhammad Al-Zoube, Ammar Elhassan proposed a technique to perceive fakes by utilizing elements of the mouth. These days, counterfeit recordings can actually hurt society, and can harm the validity of a person. "Profound phony" is a term used to depict a phony "profound phony" alludes to a video made to cause it to seem like somebody is saying or accomplishing something that are not really what they have said or done.

Authorized licensed use limited to: DELHI TECHNICAL UNIV. Downloaded on July 03,2023 at 04:51:42 UTC from IEEE Xplore. Restrictions apply.

For this reason there is an expansion popular for techniques to detect fakes. The model utilizes elements of the mouth can be utilized to distinguish counterfeit recordings. A profound phony identification model with mouth features(DFT-MF),using profound learning way to deal with recognize Profound phony recordings by segregating dissecting and checking lip/mouth development is planned and carried out here. The information here is a combination of genuine and counterfeit recordings. A pre-handling process is completed before directing an examination. From that point forward, the mouth segment is taken out from the picture. The proper directions that are utilized for face. While working with a picture outline facial milestone identifier is utilized to decide the specific area in those 68 (X,Y)coordinates. Following that, eliminate any countenances with shut mouths. Then, at that point, the main individual that has an open mouth is delegated having teeth of satisfactory lucidity.CNN decides if recordings are certified or counterfeit by deciding an edge number that is phony with regards to outlines.It involvs two elements for each sentence: the discourse rate and casing rate. Assuming the misleading casings is more prominent than 60, the video is tagged as genuine or fake.

III. PROPOSED METHODOLOGIES

A. Goals and Objectives

Our research aims to uncover the lies behind the real lies. Our plan will cut down on the falsehoods and misunderstandings of the public at large on the internet as a whole. Our project will identify and categorize the image as deepfake or the original.

B. Dataset

1.celebrity face dataset is used to generate deepfake images .

2.Real vs FAKE dataset is used for detection to classify images as fake or real. dataset consists of 140 thousand images which is toned down as per our needs.

TABLE I.

S.no	Images	Number of images	Label
1	Real	4257	1
2	Fake	2987	0

C. Proposed flowchart for image generation

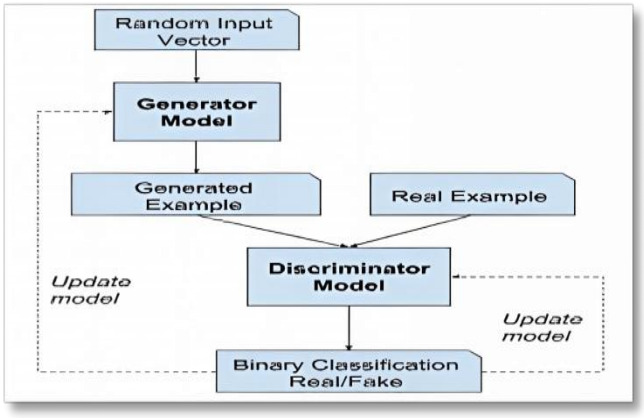

Fig. 2. The experiment's generators and discriminators.

In the network, the generative adversarial network (GANs) employs two directly competing neural networks -generator and discriminator. Generator creates new image based on the latent vector provided and on which the network is trained . discriminator discriminates whether the images is authentic or fake. The network will train and the generator will be trained to create images close to real ones so as to deceive the discriminator. The approach is to produce images that can misclassified by the discriminator [16].

Discriminator Network

The discriminator uses an image as input and then attempts to categorize the image either "real" or "generated". In this way it's similar to every other network. It's the convolution neural network (CNN) that outputs one number for each image.

Generator Network

Generator input is usually an image array of numbers or vectors (referred to as latent tensor) that is used as a seed in the creation of an image. The generator can convert an unstructured latent tensor (128 1, 1, 1) into an image-based tensor of shape 3 x 28 x 28.

Discriminator loss

This method measures the extent to which the discriminator can discern authentic and fake images. It examines the discriminator's forecasting for authentic images with an list of 1, and the discriminator's forecasting on false (fake) pictures to an list of zeros.

```
Def discriminator_loss(authentic_output,forged_output):
authentic_loss=cross_entropy(ones_like(authentic_output), authentic_output)
forged_loss=cross_entropy(zeros_like(forged_output), forged_output)
Sum_total_loss = authentic_loss + forged_loss
return sum_total_loss
```

Generator loss

The generator's misfortune is a proportion of the degree to which deceiving the discriminator was capable. By and large, in the event that the generator is functioning admirably and the discriminator can perceive those phony pictures as credible (or one).

```
Def generator_loss(forged_output):
return
cross_entropy(ones_like(forged_output),forged_output)
```

Initiation capability utilized

Beside the standard ReLU capability Cracked ReLU grants the death of a tiny slope sign to make up for negative

Authorized licensed use limited to: DELHI TECHNICAL UNIV. Downloaded on July 03,2023 at 04:51:42 UTC from IEEE Xplore. Restrictions apply.

qualities. This upgrades the manner in which the slopes produced by the discriminator stream more grounded to the generator. Rather than passing a point (slant) of 0 during the back-prop the generator passes a minuscule negative inclination.

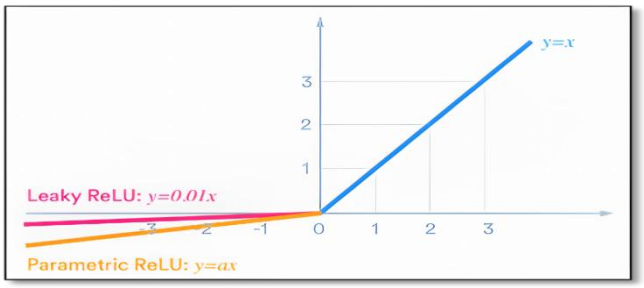

Fig. 3. different from leaky ReLU and parameter ReLU.

D. Deepfake Using Autoencoder

To make a Deepfake with the help of auto-encoder and decoder, two trained pair of auto-encoder and decoder is used such and after training the decoder are swapped so that latent feature of each encoder-decoder pair is used to generate deepfake images [13-14].

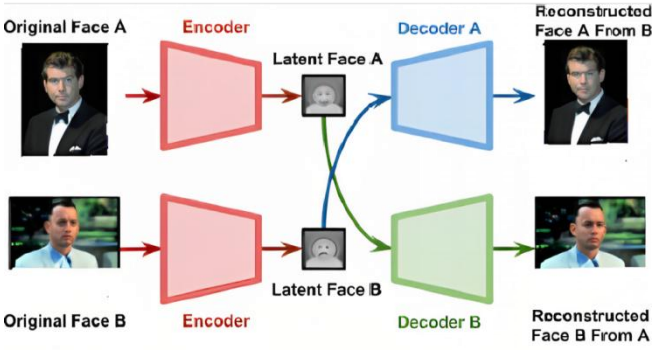

Fig. 4. encoder-decoder architecture.

At the time of training autoencoder is served with a pack of images, the encoder- decoder layer will tune the parameter to generate an output identical to input image as close as possible . The images used to train autoencoder is sourced from celebrity face dataset.

E. Image Detection Model

Many techniques have been explored to recognize GAN-generated images using deep networks. The use of pre-processing techniques in neural network-based technology improves the detection of fraudulent face images created by individuals and analyses the statistical characteristics of images. This also offers an alternative technique for identifying fake images created by deep convolutional neural networks that are based on GANs.The face features are extracted from face recognition network, for this the model used a deep learning network. Subsequently, facial features is adjusted by fine tuning phase so that they are acceptable for for real/fake image recognition.

A dense network with only one hidden layer follows a sequence of four convolutional and pooling layers in this network. Convolutional layers use the Batch Normalization and ReLU activation functions to regularize their output and prevent the vanishing gradient effect in order to improve conceptualization.Dropout is used to regularize and boost robustness in fully connected layers.An elective advancement contains in superseding the hidden two convolutional layers of the Model by an assortment of the start module.

The capability space in which the model can be improved can be expanded by stacking the results of a few convolutional layers with various piece shapes using the module.

We propose replacing the 5x5 convolutions in the original module with 3x3 dilated convolutions to avoid high semantics[15]. The concept of dealing with multi-scale information by employing dilated convolutions with the inception module can be found in. We have, however, added 1x1 convolutions prior to the dilated convolutions and 1x1 convolutions in parallel to serve as a skip-connection between subsequent modules in order to reduce the dimension.

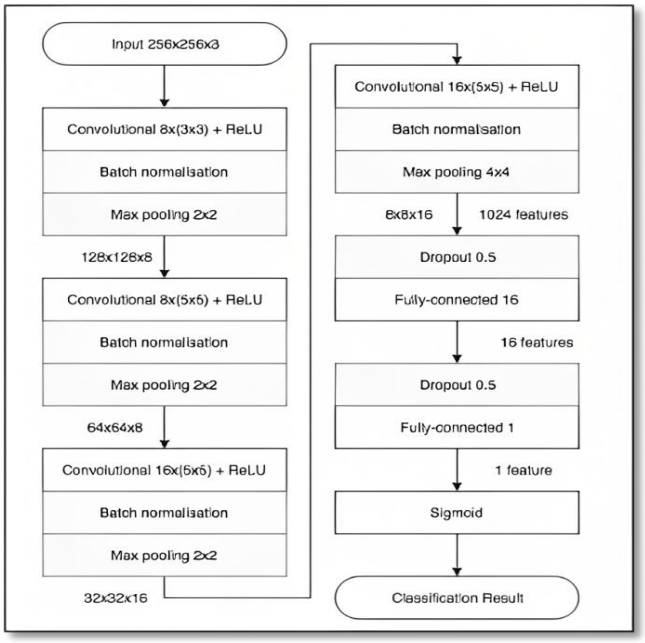

Fig. 5. The network architecture.

The architecture has been implemented with the help of python 3.10 and keras 2.11.0 module. Optimization of weights is done by batch of 75 images using ADAM [16]. Learning rate is taken as 10^{-3} which is reduced down to 10^{-6} by dividing the learning rate by 10 for successive 1000 iteration.

IV. Results Analysis

A. correct real prediction

Authorized licensed use limited to: DELHI TECHNICAL UNIV. Downloaded on July 03,2023 at 04:51:42 UTC from IEEE Xplore. Restrictions apply.

Fig. 6. Real images from the dataset.

B. Misclassified real prediction

Fig. 7. Real images from the dataset.

C. correct deepfake prediction

Fig. 8. Fake images from the dataset.

D. Misclassified deepfake prediction

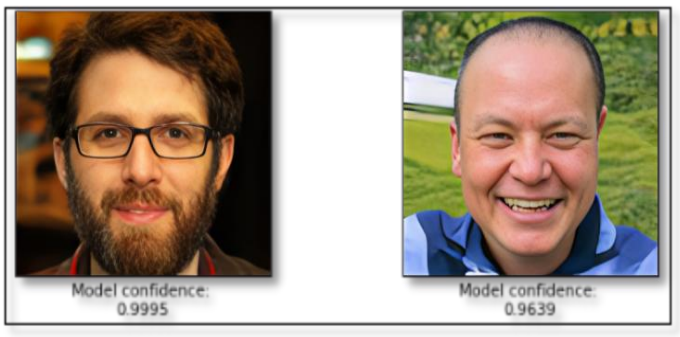

Fig. 9. Fake images from the dataset.

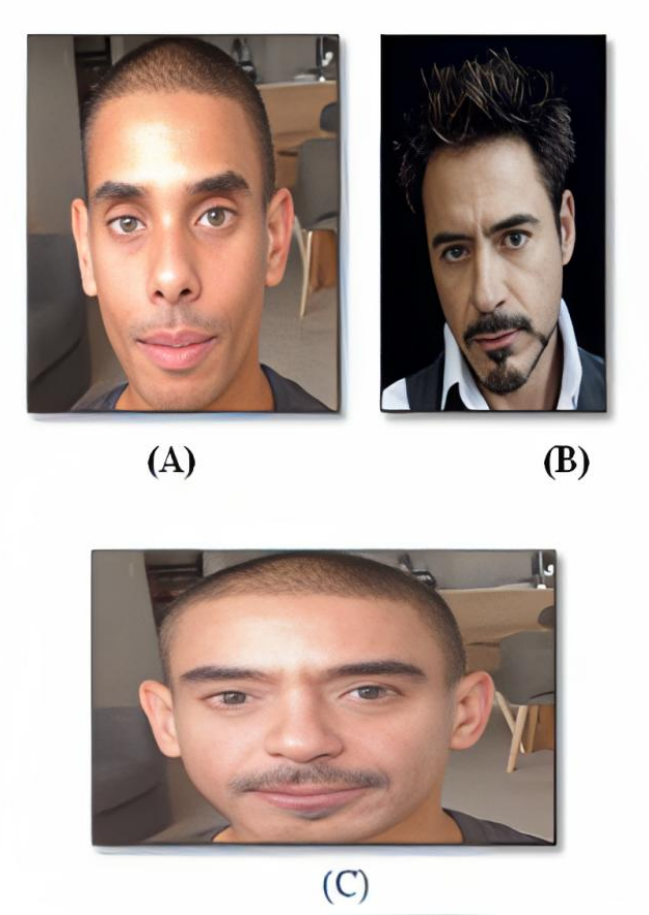

Fig. 10. Image (A) and (B) is real but (C) is deep-fake.

Authorized licensed use limited to: DELHI TECHNICAL UNIV. Downloaded on July 03,2023 at 04:51:42 UTC from IEEE Xplore. Restrictions apply.

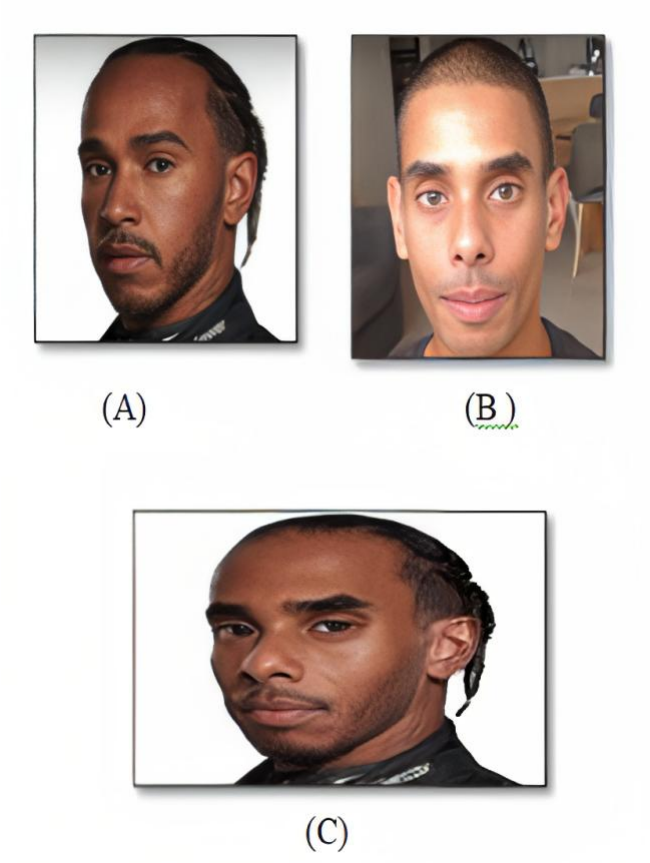

Fig. 11. Image (A) and (B) is real and (C) is deep-fake.

V. CONCLUSION

Because the viewing of them no longer corresponds with believing fake news, deep-fakes are beginning to undermine people's trust in media content. They can cause distress to those who are being targeted as well as amplify the spread of hate speech and disinformation or even increase the level of political discontent and incite public protests as well as violence or conflict. This is crucial today as social media platforms have the ability to quickly spread fake technology and news, and they are becoming more readily available.

This research offers a comprehensive review of the challenges that are affecting the future, as well as prospective trends and future perspectives in this field as in a comprehensive review of deep-fake production as well as detection methods. Artificial intelligence researchers can benefit greatly from the research in order to develop effective strategies to combat deep-fakes.

REFERENCES

[1] Ayush Tewari, Michael Zollhoefer, Florian Bernard, Pablo Garrido, Hyeongwoo Kim, Patrick Perez, and Christian Theobalt. High-fidelity monocular face reconstruction based on an unsupervised model-based face autoencoder. IEEE Transactions on Pattern Analysis and Machine Intelligence, 42 (2):357–370, 2018.

[2] Jiacheng Lin, Yang Li, and Guanci Yang. FPGAN: Face deidentification method with generative adversarial networks for social robots. Neural Networks, 133:132–147, 2021.

[3] Egor Zakharov, Aliaksandra Shysheya, Egor Burkov, and Victor Lempitsky. Few-shot adversarial learning of realistic neural talking head models. In Proceedings of the IEEE/CVF International Conference on Computer Vision, pages 9459–9468, 2019.

[4] Bloomberg. How faking videos became easy and why that's so scary. https://fortune.com/2018/09/11/deepfakes-obama- video/, September 2018.

[5] Robert Chesney and Danielle Citron. Deepfakes and the new disinformation war: The coming age of post-truth geopolitics. Foreign Affairs, 98:147, 2019.

[6] D. Guera¨ and E. J. Delp, "Deep-fake video detection using recurrent neural networks," in 201815th IEEE International Conference on Advanced Video and Signal Based Surveillance (AVSS), 2018, pp. 1–6.

[7] M. A. Younus and T. M. Hasan, "Effective and fast Deep-fake detection method based on haar wavelet transform," in 2020 International Conference on Computer Science and Software Engineering (CSASE), 2020, pp. 186–190.

[8] H. Khalid and S. S. Woo, "Oc-fakedect: Classifying Deep-fake s using one-class variational autoencoder," in 2020 IEEE/CVF Conference on Computer Vision and Pattern Recognition Workshops (CVPRW), 2020, pp. 2794–2803.

[9] U. Ciftci, I. Demir, and L. Yin, "How do the hearts of deep fakes beat? deep fake source detection via interpreting residuals with biological signals," 08 2020.

[10] Bloomberg. How faking videos became easy and why that's so scary. https://fortune.com/2018/09/11/deepfakes-obama-video/, September 2018.

[11] Robert Chesney and Danielle Citron. Deepfakes and the new disinformation war: The coming age of post-truth geopolitics. Foreign Affairs, 98:147, 2019.

[12] T. Hwang. Deepfakes: A grounded threat assessment. Technical report, Centre for Security and Emerging Technologies, Georgetown University, 2020.

[13] Faceswap: Deepfakes software for all. https://github. com/deepfakes/faceswap.

[14] FakeApp 2.2.0. https://www.malavida.com/en/soft/ fakeapp/.

[15] F. Yu and V. Koltun. Multi-scale context aggregation by dilated convolutions. arXiv preprint arXiv:1511.07122, 2015.

[16] Ian Goodfellow, Jean Pouget-Abadie, Mehdi Mirza, Bing Xu, David Warde-Farley, Sherjil Ozair, Aaron Courville, and Yoshua Bengio. Generative adversarial nets. Advances in Neural Information Processing Systems, 27:2672–2680, 2014.

Authorized licensed use limited to: DELHI TECHNICAL UNIV. Downloaded on July 03,2023 at 04:51:42 UTC from IEEE Xplore. Restrictions apply.

Design of a PV-Fed Drive System with a Single-Phase Induction Motor for Irrigation Application

Eleyde Nhantumbo[1], Dawda Bojang[1], Monika Verma[1*], Ashish Kulkarni[1]

[1] Department of Electrical Engineering, Delhi Technological University, Shahabad Daulatpur, Delhi, India, 110042
*monikaverma.evrt@dtu.ac.in (corresponding author)

Abstract. This paper presents the design, implementation, and performance evaluation of a photovoltaic (PV)-fed drive system with a single-phase induction motor for irrigation applications. The study focuses on a built hardware setup and strategy to achieve objectives, the setup is consisting of two 100 W solar panels, a 10 A charge controller, a 12 V battery, a 700 W DC to AC inverter, a step-up transformer 12 V DC to 230 V, and a single-phase pump coupled with a motor of 0.5 HP (0.37 kW). The paper discusses the design considerations, system configuration, control strategy, and the efficiency of the PV-fed motor for irrigation purposes. The findings demonstrate the feasibility and effectiveness of using solar energy to power irrigation systems, showcasing the potential for sustainable and energy-efficient agricultural practices.

Keywords: Water Pump Motor, PV panels, inverter, PWM, Solar energy.

1. Introduction

Over the last few years, the increasing demand for sustainable and energy-efficient solutions in various sectors, including agriculture, has been observed. Sustainable agriculture aims to promote environmental friendly and resource-efficient farming practices to ensure long-term food security while minimizing negative impacts on ecosystems and natural resources [1]. Irrigation plays a crucial role in ensuring optimal crop growth and productivity. However, traditional irrigation methods often rely on fossil fuel-based power sources, leading to environmental pollution and rising energy costs. Subsequently, the researchers are involved in harnessing renewable energy, especially solar power, in order to meet the energy needs of irrigation systems [2].

This research aims to explore the feasibility and effectiveness of utilizing solar energy in powering the irrigation process, thereby reducing dependency on conventional power sources and promoting sustainability. The specific research objectives include:

1) To design and implement a PV-fed system with a single-phase induction motor specifically tailored for irrigation applications. The scope of the study encompasses the design considerations, system configuration, control strategy, and performance evaluation of the PV-fed motor coupled with water pump.

© The Authors, published by EDP Sciences. This is an open access article distributed under the terms of the Creative Commons Attribution License 4.0 (https://creativecommons.org/licenses/by/4.0/).

2) To demonstrate a control strategy to ensure efficient operation and optimal performance of the PV-fed system.
3) Evaluating the system's efficiency, power output, energy harvesting capabilities, and its ability to meet the irrigation requirements.

It is important to note that while this research project focuses on a specific hardware setup. However, the findings and principles discussed in this paper can be extrapolated to similar PV-fed systems, with varying configurations and components. The study provides an insight to the understanding of utilizing renewable type of energy sources for irrigation applications and to promote sustainable practices in the agricultural sector. It also helps to address the environmental challenges associated with conventional power sources in irrigation systems.

A comparison of the proposed method with the approaches discussed in literature review related to the described application is shown in Table I.

Table 1. Related Literature Review

Authors (Year)	**Strategy / Application**	**Drawbacks**
Belfer and Magalhães (2016) [10]	Sustainable Agriculture	Lack of implementation over solar energy based irrigation system
Al-Jarrah et al. (2019) [11]	Provide a review of solar energy application for irrigation in Jordan	The specific details on the motor and pump setup or compare alternative methods are not provided.
Ghaznavi et al. (2014) [12]	Review photovoltaic technologies	The direct addressing to irrigation systems or motor and pump setups is absent.
Daliento et al. (2015) [13]	Discuss the design-oriented assessment of photovoltaic panel orientation for energy capture	The efficiency enhancement strategy is not in agreement with the specific hardware implementation.

In summary, the presented method stands out by providing a comprehensive approach that combines specific hardware components to create an efficient solar-powered irrigation system. It addresses the practical implementation of sustainable agriculture by utilizing renewable energy sources and optimizing water delivery for irrigation purposes. This descriptive analysis provides a comprehensive overview of the software and hardware components, enhancing understanding of their functionality, strengths, and weaknesses. It establishes a foundation for a literature review by highlighting key aspects to explore in similar projects or research in the field.

2. System Design and configurations

This section confers the design and configurations of the proposed system. The overall schematic diagram of the system has been shown in Fig. 1 (Table 1.1). The system consists of PV panels, controllers, battery, inverter and the motor.

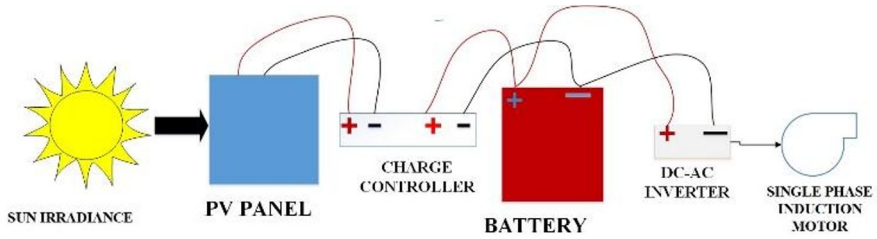

Fig. 1. Wiring diagram of the implemented system

Table 2. List of components and respective ratings

Component Name	Ratings
2 PV Panels	100 W (each)
Solar charge controller	10 A
Battery	12 V
Dc to Ac Inverter	12 V Dc to 12 V Ac
Step Up transformer	700 W
Monoblock Pump	373

2.1 Photovoltaic Panels

The selection and specifications of PV panels are paramount in determining the overall performance of PV-fed systems [3]. Factors such as efficiency, power rating, and durability are considered when choosing the panels. In this project, two solar panels with a power rating of 100 W each are selected. The full parameters specification is mentioned on Table II.
The 2 PV panels are connected in parallel to the charge controller using appropriate wiring and connectors. The PV panels utilized in this work are represented in Fig. 2 (a). A wiring diagram is followed to ensure correct connections and prevent any electrical losses or mismatched voltages. The maximum power point tracking (MPPT), Incremental Conductance Technique is integrated into the charge controller allows it to optimize the power output of the PV panels by tracking the maximum power point under varying sunlight conditions.

Table 3. Specifications of Solar panels

Solar Panel Parameters (Sun-fuel Technologies Model No. SFTI 36P 100W)	
Maximum Power (P_{max})	100 W
Maximum Power voltage (V_{mp})	18.51 V
Maximum Power Current (I_{mp})	5.41 A
Short Circuit current (I_{sc})	5.89 A
Open Circuit voltage (V_{oc})	*21.78V*

2.2 Placement and Orientation

The placement and orientation of the PV panels are essential for optimizing solar energy capture [4]. Factors such as the angle of inclination, azimuth orientation, and shading effects are taken into account to ensure maximum sunlight exposure and energy generation. The panels were placed in a rooftop with 35 $degrees$ from the horizontal.

2.3 Charge Controller

The charging procedure of battery is regulated by the charge controller. It is carried out by controlling the flow of current from the PV panels. It ensures proper charging and prevents overcharging or deep discharging conditions of battery. The charge controller has the rating of $10\ A$.
The charge controller, (Fig. 2(b)), used in the system, has the function of monitoring the battery voltage, controlling the charging current, and providing protection against overcharging, over-discharging, and short circuits. It may also incorporate maximum power point tracking (MPPT) technology to maximize the power output of the PV panels.

(a) (b)

Fig. 2. (a) Solar Panels used in the implementation of the project (b) Solar Charge Controller

2.4 Battery Bank

The battery serves as an energy storage component in the PV-fed system, providing power during periods of low sunlight or during the night. Batteries play a vital role in solar-powered irrigation systems by storing excess energy generated by the solar panels during the day and providing power during non-sunlight hours, ensuring continuous operation and increased self-sufficiency [5]. In this system we have used a $12\ V$ battery pack, as represented in Fig. 3 (a).

2.5 Single-Phase Induction Motor and Pump

The single-phase induction motor (Fig. 3 (b)) is responsible for driving the irrigation pump, providing the necessary mechanical energy to deliver water for irrigation purposes. Integration of the motor with the pump and hydraulic considerations are vital for efficient and reliable operation. The ratings of the motor pump are: $0.5\ HP\ /\ 0.37kW$ Single Phase Water Pump, Operating Voltage, Current ratings: $220\ V, 2.8\ A\ and\ 2850\ rpm$.
The selection of a single-phase induction motor for irrigation purposes requires careful consideration of various factors such as motor power, efficiency, starting torque, and reliability. These considerations ensure that the motor is suitable for the specific irrigation system requirements, providing efficient and reliable operation [6].

2.6 DC to AC Converter

Inverter selection and sizing are critical to tone with the power demands of the irrigation system and maximize energy conversion efficiency [7]. The inverter (Fig. 3 (c)), converts the DC power produced by the PV panels and stored in the battery.
The $12\ V$ DC power reserved in the battery is converted to $220\ V$ AC power using the DC to AC converter. The converter is configured and operated between $100\ V - 300\ V$ and $50\ Hz$ frequency for the single-phase induction pump motor. PWM is maintained to ensure the motor operates within its specified voltage range.

The inverter used in the system has a power rating of 700 W which is compatible with the motor's power requirements that is 373 W. Pulse width modulation (PWM) topology was employed based on the specific system requirements.

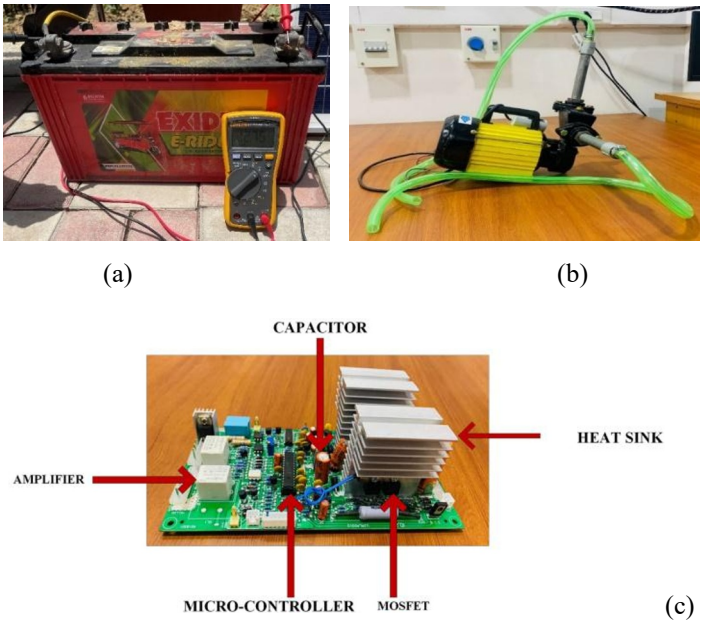

Fig. 3 (a) Battery Bank utilized in the system, (b) Single Phase AC Water Motor Pump, (c) DC to AC Inverter PCB (Some major components are labelled)

3. Hardware Setup Implementation

In this section, the implementation of the proposed system is presented. The overall system used in the laboratory set-up is shown in Fig. 4. During the implementation, several factors are considered, especially when dealing with different conditions on different days. Some aspects are: Solar panel placement, water source and storage, identifying a reliable water source and ensuring an efficient storage system are essential. The system was implemented in both sunny and shading conditions in different days. The most important things that need to be taken care during implementations is personal safety, and isolating all the open wires. Also check the output voltage and current of inverter to avoid overload to the system.
The challenges faced during implementation were the varying weather patterns, as adapting the system to these specific conditions requires careful planning and customization.

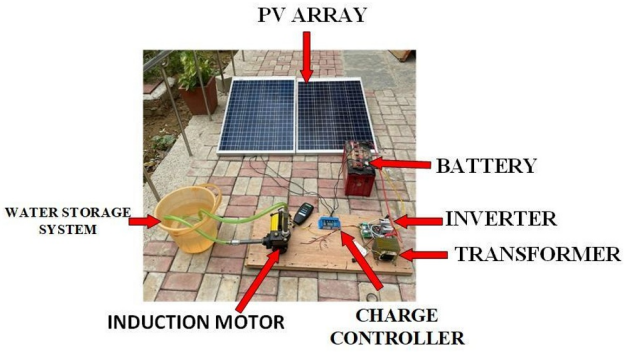

Fig. 4. Implementation of the overall system

Once the solar irrigation system was connected and operational, the initial response was observed through observations. The energy generation by monitoring the solar panel's power output can indicate if it is generating sufficient energy to power the irrigation system.

4. Analysis outcomes and discussions

The proposed hardware system was designed and implemented in Electrical Engineering Department, Delhi Technological University, Delhi, India. The daily irradiance values of the area, during May, are around 6 to 7 kW/m^2 and an average temperature of 40°C and 13.5 h of daily length in hours of sunlight [8-9].

4.1 Analysis at irradiance level of 7.1 $\mathbf{kW/m^2}$

Initially, in a sunny condition, total voltage of 19.51 V is obtained from each Solar panel. The currents obtained from one solar panel is 2.0 A and from second panel is 2.3 A. As the panels are connected in parallel, the voltage is maintained at 18 V and the current is measured as 5.3 A. The solar panels are connected to the charge controller which controls the voltage and drops it to around 12.9 V, the voltage drop is due to the charge controller which prevents the battery from overcharging. This voltage charges the battery system. Hence, the battery obtains 12.65 V DC on its terminals, as presented in Fig. 5 (a).
The output voltage from battery is 12.65 V and 5.3 A current, these values are same as the inverter input. Using PWM technique, the inverter converts the 12.65 V DC to 12.65 V rms AC. The single-phase inverter, with current rating of 1.6 A, is connected with a step-up transformer which boosts the voltage level from ~12 V AC to ~230 V AC. The output voltage from the inverter terminals is 230 V AC.
This voltage is supplied to the motor pump, which pumps the water and irrigates.

The overall load current of the system is given by Equation (1):

$$I = \frac{P}{V} \quad (1)$$

Where, P is the output power from the motor, and V is the battery terminal voltage. Hence, the calculated current is 31 A. The measured total current of the system was 37.3 A (Fig 5 (b)) due to occurrence of voltage dips in the system as a result of losses.

(a) (b)

Fig. 5 (a) Battery Output terminals (In multi-meter), **(b)** Total Output current of the system

PWM Control Technique is a widely employed method for controlling the speed and power delivery of motor drives. The simple PWM technique implemented in this research involves generating a square wave signal with varying duty cycles. The inverter controls the width of the pulses, determining the average voltage supplied to the motor. By adjusting the duty cycle, the effective voltage can be modulated, allowing for precise control over the motor's speed and torque. It requires minimal complexity of hardware and software, making it suitable for low-power systems like a $700\,W$ inverter driving a single-phase $220\,V$ AC motor pump.

PWM gives the desired square pulses, as presented in Fig. 10. When the inductive load is connected, acting like the motor pump, the square waves shape an inductive form (Fig. 6). After connecting an inductive load such as a motor to the output of the inverter, the inductive characteristics of the load come into play. Inductive loads, by nature, resist changes in current flow. When the square wave voltage transitions from the high level to the low level (or vice versa), the inductive load opposes this change and tends to maintain the current flow. This opposition to changes in current causes the waveform to become more sinusoidal. The inductive load smoothens out the sharp transitions of the square wave and results in a waveform that resembles a sinusoidal waveform.

From the system, it can be seen in Fig.7 (a), that the input current waveform to the inverter is typically a DC current from the solar panel, having amplitude of $2.0\,A$.

The inverter output current waveform, as can be seen in Fig. 7 (a), is square waveform, as we have used PWM technique. It is having RMS value of $1.8\,A$, measured through HIOKI 3288-20 Clamp ON AC/DC HiTester. Some distortions can be seen due to the presence of inductive load, i.e., single phase AC motor.

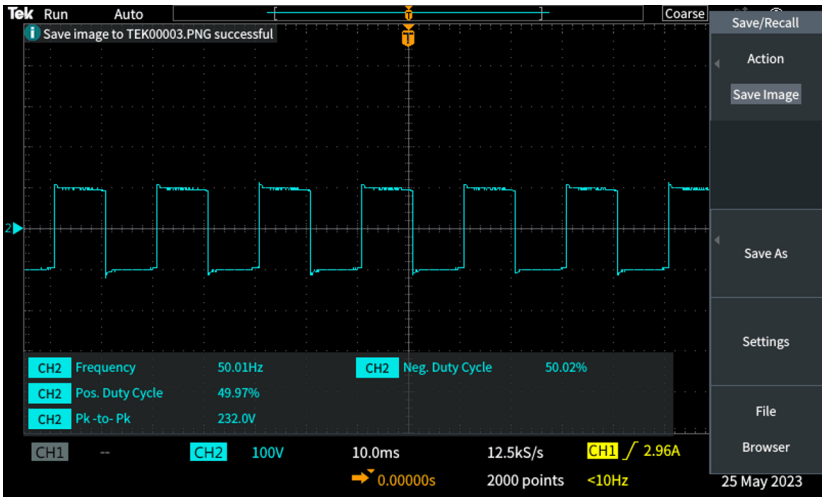

Fig. 6. Inverter Voltage Output waveform with load

A. Analysis at different irradiance levels

This study has been performed in different shading conditions, i.e., temperature and irradiance levels. On a sunny day in month of May irradiance reaches up to 7.1 kW/m^2, and on the same month but with shading conditions irradiance levels can be around 6 kW/m^2. Under partial shading conditions weather, the current from the panel drops up to maximum 20 %.

It was noticed that the motor speed is influenced by the solar irradiance or the intensity of sunlight falling on the solar panels. As the irradiance increases, the motor speed tends to increase and vice-versa, as can be perceived from Fig. 7 (b) (Table 7-b.1).

B. Comparative Analysis of proposed method with conventional methods

A comparative analysis is conducted between the designed PV-Fed system with a single-phase induction motor for irrigation application and conventional systems used for irrigation. The purpose of this analysis is to evaluate the advantages and disadvantages of the designed system in comparison to traditional approaches. It explores how the PV-Fed system outperforms or falls short when compared to conventional systems, which typically rely on fossil fuel-powered pumps or grid electricity. The benefits and limitations of the designed System are represented in Table III.

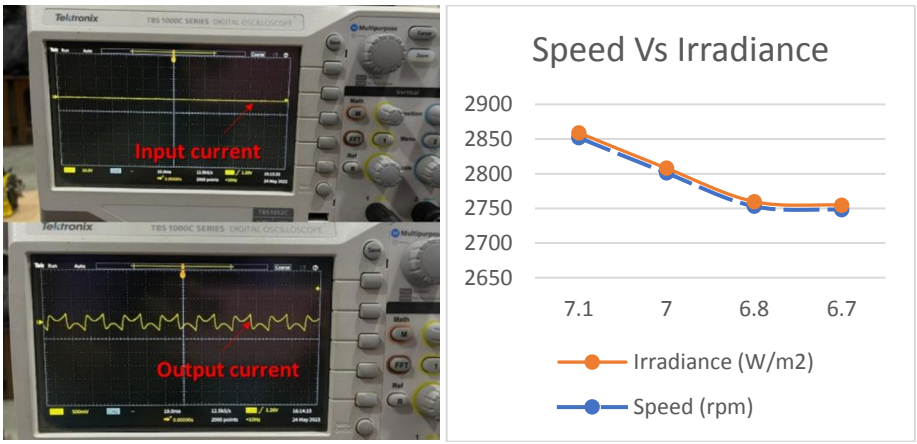

(a) (b)

Fig. 7. (a) Input current of inverter VS Output current of inverter (yellow) waveforms, (b) Speed Vs Irradiance Performance

Table 7-b.1. Comparative Results for variation in Irradiance of Solar Panel with respect to the Motor Speed

Speed (Rpm)	Irradiance (Kw/m^2)
2852	7.1
2801	7.0
2753	6.8
2748	6.7

Table 3. Benefits and Limitation of the proposed system over conventional methods

Benefits	Limitations
Renewable Energy Utilization: The system harnesses solar energy, which is a clean and renewable resource. It reduces the dependence on non-renewable energy sources and minimizing greenhouse gas emissions.	*Weather Dependency:* The system's performance relies on solar radiation, making it susceptible to variations in weather conditions. It delivers reduced efficiency during cloudy days or at night.
Cost Savings: By utilizing solar power, the system can potentially reduce electricity costs associated with conventional systems, especially in areas with ample sunlight.	*Initial Cost:* The initial investment for installing the PV-Fed system, including solar panels, batteries, and converters, may be higher compared to conventional systems. However, long-term cost savings can outweigh the initial investment.
Environmental Impact: The use of solar energy helps mitigate environmental degradation by reducing carbon footprint and air pollution associated with conventional systems.	*System Maintenance:* Regular maintenance of solar panels, batteries, and other components is necessary to ensure optimal system performance and longevity. Proper maintenance practices need to be implemented to maximize system efficiency.

C. Real time scenario about the yields of the outcome

PV-fed induction motor systems offer a reliable and sustainable solution for irrigation, allowing farmers to optimize water usage, increase crop productivity, and reduce dependency on traditional power sources. In practical scenario the proposed system can be implemented in:

1. *Remote Agricultural Areas:* The presented systems for irrigation can be implemented in remote agricultural areas where grid connectivity is limited or unreliable [14]. These areas often lack access to traditional sources of electricity, making it difficult for farmers to power their irrigation systems. By installing a solar panel array and coupling it with an induction motor, farmers can harness solar energy to operate their irrigation pumps independently of the grid. This enables them to efficiently irrigate their crops and sustain agricultural practices in remote locations without relying on conventional power sources.

2. *Off-Grid Farms:* PV-fed induction motor systems are also suitable for off-grid farms that are not connected to the main electricity grid. In such scenarios, farmers can install solar panels on their farm premises and use the generated solar energy to power an induction motor for irrigation purposes. This eliminates the need for costly diesel generators or the hassle of extending grid lines to the farm. By utilizing solar power, farmers can irrigate their fields effectively and sustainably, reducing operational costs and environmental impact.

5. Conclusion and findings

The research study on the design of a PV-Fed system with a single-phase induction motor for irrigation application has provided valuable insights into the efficiency, power output, irrigation performance, and economic viability of the system. Through a thorough analysis of various aspects, the following conclusions and findings have been derived:

- When there is shading conditions or cloudy days, the initial current from the2 panels connected in parallel drops more than 80% compare to its maximum current output. Only around 20% of the maximum current is used. The 2 panels were connected in parallel and each has 5.41 A as maximum current, ideally the total current would be 10.82 A, but in practice it's not possible, due to various factors, as panel efficiency as weather conditions. In a sunny day we got 5.41A as total current output and in shading conditions we got only 2.1 A as current output from panels.
- The utilization of a simple PWM technique offers several advantages, including simplicity, cost-effectiveness, energy efficiency, and accurate speed control.
- When inductive loads are connected to the terminals of the inverter, the inductive characteristics of the load come into play, the load smoothers out the sharp transitions of the square wave and results in a waveform that resembles a sinusoidal waveform.
- The PV system demonstrated efficient conversion of solar energy into electrical power, while the motor and pump exhibited good performance in delivering water from a water storing system of 25 litres for irrigation purposes, the water flow rate was around 64 milliliters per minutes (ml/min).

Comparative analysis with conventional systems highlighted the advantages of the PV-Fed system. It also showcased the limitations of the system.

The findings of this research have several practical implications and open up avenues for future research in the field of PV-Fed systems for irrigation applications. The designed system holds promise for sustainable irrigation practices, especially in areas with limited grid access or high reliance on conventional energy sources. The practical implications include: *1. Adoption of Renewable Energy for Irrigation; 2. Improved Efficiency and Performance; 3. Cost Optimization and Affordability; 4. Integration with Smart Technologies*

References

1. Belfer, E., and Magalhães, M., "Sustainable agriculture: Definitions and approaches", In IEEE Global Humanitarian Technology Conference (GHTC-2016), pp. 448-453, 2016.
2. Al-Jarrah, M., Alshorman, A., Alfaour, A., and Masadeh, R., "Solar energy application for irrigation in Jordan: A review", In 2nd International Conference on Power, Energy and Electrical Engineering (PEEE-2019), pp. 1-6, 2019.
3. Ghaznavi, M., Mekhilef, S., Seyedmahmoudian, M., and Horan, B., "Review of Photovoltaic Technologies. Journal of Renewable and Sustainable Energy Reviews", Vol. 39, pp. 461-476, 2014, doi: 10.1016/j.rser.2014.07.043.
4. Daliento, S., Graditi, G., Lanzolla, A. M. L., and Lanzolla, A., "Design-oriented assessment of photovoltaic panels orientation for improved energy capture", In IEEE International Energy Conference (ENERGYCON-2015), pp. 1626-1631, 2015.
5. Hasan, M. M., Malek, A. N. N., Rahman, M. M., Kader, M. A., and Ahmed, K., "Design and implementation of a solar power-based water pump for irrigation system", In IEEE International WIE Conference on Electrical and Computer Engineering (WIECON-ECE-2017), pp. 120-123, 2017.
6. Zeineldin, H. H., and Azmy, M. H., "Optimum motor sizing for solar water pumping applications", In IEEE International Conference on Renewable Energy Research and Applications (ICRERA-2013), pp. 1001-1005, 2013.
7. Garg, V., Singh, B., and Gautam, N., "Design of solar-powered irrigation system using a fuzzy control-based inverter", In IEEE International Conference on Power Electronics, Smart Grid and Renewable Energy (PESGRE-2019), pp. 366-371, 2019.
8. Tu Tiempo.Net, https://en.tutiempo.net/solar-radiation/delhi.html.
9. Wanderlog, https://wanderlog.com/weather/13/5/new-delhi-weather-in-may.
10. Kumar, A., Sharma, S., and Kumar, P. (2020). "A review of solar energy-based water pumping systems for sustainable agriculture." Journal of Cleaner Production, Vol. 257, 120573.
11. Olatomiwa, L., et al. (2018). "A comprehensive review on photovoltaic-based water pumping systems." Renewable and Sustainable Energy Reviews, Vol. 82, pp. 1379-1392.
12. Aghanajafi, C., et al. (2021). "Review of solar energy-based irrigation systems for sustainable agriculture." Journal of Irrigation and Drainage Engineering, Vol. 147, No. 7, 04021018.
13. Sharma, R., et al. (2020). "Design and performance analysis of solar photovoltaic water pumping system for irrigation." IOP Conference Series: Materials Science and Engineering, Vol. 791, 012024.
14. Rashid, S. A., et al. (2019). "Performance analysis of solar photovoltaic water pumping system: A review." IOP Conference Series: Materials Science and Engineering, Vol. 496, 012051.

Physica Scripta

PAPER

DFT based atomic modeling and Analog/RF analysis of ferroelectric HfO_2 based improved FET device

To cite this article: Yash Pathak *et al* 2023 *Phys. Scr.* **98** 085933

View the article online for updates and enhancements.

You may also like

- Fostering the Integration of Circular Economy Aspects into the Construction and Real Estate Industry
C Lemaitre, A Braune, C Ruiz Durán et al.
- Performance assessment of symmetric double gate negative capacitance junctionless transistor with high-*k* spacer at elevated temperatures
Hema Mehta and Harsupreet Kaur
- Labeling-free detection of ECD-HER2 protein using aptamer-based nano-plasmonic sensor
Jung-Hoon Kim, Jin-Suck Suh and Jaemoon Yang

This content was downloaded from IP address 14.139.251.98 on 20/07/2023 at 12:20

Physica Scripta

PAPER

DFT based atomic modeling and Analog/RF analysis of ferroelectric HfO_2 based improved FET device

Yash Pathak[1], **Bansi Dhar Malhotra**[2] **and Rishu Chaujar**[1,*]

[1] Department of Applied Physics, Delhi Technological University, 110042, New Delhi, India
[2] Department of Biotechnology, Delhi Technological University, 110042, New Delhi, India
[*] Author to whom any correspondence should be addressed.

E-mail: yash_2k19phdap505@dtu.ac.in, bansi.malhotra@dce.ac.in and chaujar.rishu@dtu.ac.in

RECEIVED
24 April 2023

REVISED
26 June 2023

ACCEPTED FOR PUBLICATION
10 July 2023

PUBLISHED
20 July 2023

Keywords: Visual TCAD, Quantum ATK, NCFET, DOS, DFT

Abstract

In this study, we systematically investigated the Analog/RF and linearity parameter of SM DGNCFET (single metal double gate negative capacitance field effect transistor) and DM DGNCFET (double metal double gate negative capacitance Field effect transistor) with the help of Cogenda Visual TCAD simulator, and also demonstrated the enhancement in the electronic and optical properties of Si-doping bulk structure by using the Quantum ATK. The analog parameters are enhanced for SM DGNCFET such better performance of switching ratio 279 times better, DIBL 54% lower, SS decay, and some other improved parameter transconductance, TGF and Radio frequency parameter is also enhanced, transconductance frequency product (TFP) for improving reliability and stability of device. Linearity parameters like that second and third order transconductance (g_{m2}, g_{m3}), voltage intercept point for 2nd, 3rd. Tran Blaha modified Becke Johnson (TB-mBJ) approxiamation gives the accurate band gap of crystal. In DFT based atomic study, 12.5% of Si doping in bulk structure reveals better results for ferroelectric HfO_2 based crystal in the direct band gap of bandstructure is zero, Density of state (DOS) is also improved conductivity for Si doping crystal. Hence, Si doping in crystal structure is also better for conductivity.

1. Introduction

The power dissipation (P) varies with the inventory voltage ($P \sim V_d^2$), V_{ds}. It is typically controlled by the obstacle monitored Boltzmann switch's base subthreshold swing (SS = 60 mV/dec) [1]. Ferroelectric (Fe-FETs) transistors have recently gotten plenty of attention due to their reliability in memory and switching applications [2–4]. The key factors of any sophisticated electronic device are power, size utilisation, the goal of previous and current research attempts, which has been to create aggressively updated devices that utilize ultralow power [5]. Towards conquer this constraint, there has been a lot of concern in selective devices that are based on a variety of activity systems that alter the state of an electrical switch from off to on device [4].

Improvements of the ferroelectric layer device with a Negative capacitance FET in single metal double gate and double metal double gate negative capacitance field effect transistor (DM DGNCFET) [6, 7]. NEGATIVE capacitance FETs (NCFETs) are field effect transistors with a sub-60mV/decade subthreshold swing and a large ON-current. Negative capacitance wonders have recently demonstrated experimentally in a variety of contexts [5]: (1) ferroelectric pictures separated from the rest of the world (2) Bilayers of ferroelectric and dielectric (3) Ferroelectric gated transistors using superlattices [8, 9]. Channel length scaling was not taken into account by SM DGNCFET [7, 10, 11]. Furthermore, the Landau model is merely used in the knocked out polarisation section of the last. The Landau factors for the FE substance are $\beta = 8.9 \times 10^8$ and $\alpha = 1.0 \times 10^7$ [12], which are insufficient for large ferroelectric thicknesses [13]. By using logical displaying, we evaluated the implementation of the SM DGNCFET with long channels in prior work [6]. SM DGNCFET has a larger ON-state flow than DM DGNCFET; however, we found that it is not the case for all ferroelectric materials.

© 2023 IOP Publishing Ltd

Furthermore, due to their capacity requirements down, non-destructive read capabilities as rapid operating speed, and memory device in ferroelectric field effect transistors (FeFETs) hold out for a modern age of FET devices [14, 15]. FE substance displays the supervise of negative capacitance, which can be detected from their charge energy bend [16], ferroelectric substance in the gatestack of MOSFETs provides superior endurance to device accomplishment.

The SM DGNCFET device has lowered the leakage current, higher switch ratio, low power consumption, better device controllability over channel than DM DGNCFET. The impact of ferroelectric thickness and temperature has been studied. The impact of ferroelectric thickness and temperature of device has been also studied for improving the performance of SM DGNCFET as increases the ferroelectric thickness, decreases substrate thickness and decreases temperature [17, 18].

DFT (density functional theory) is a quantum-mechanical atomistic modelling approach for computing features of nearly any atomic system, including surfaces, crystals, molecules, and even electrical devices when linked with non-equilibrium Green's functions (NEGF). Atomic modeling of the significant developments in quantum theory is the density functional theory (DFT), which aids in verifying the energy, structure, and characteristics of materials, nanosystems, and molecules. The interface engineering in HfO2-based gate stacks, atomic dopants have been demonstrated to alter the work function [19]. At 2800 degrees Celsius of HfO_2 is in the cubic phase [20, 21]. At lower temperatures of yttrium doping affords HfO_2 cubic phase stability [22]. Random access memory devices, fuel cells, sensors, optical and protective coatings, laser mirrors, and other industrial applications all utilise the cubic HfO_2 phase. Low lattice thermal conductivity results from the high density of Hafnium in HfO_2. The lattice thermal conductivity of HfO_2 thin films has been measured in the range of 0.49 to 0.95 W/m-K [21].

The possible technology uses, such as ferroelectric field effect transistors (FEFET) and ferroelectric random-access memory(FERAM), achieving ferroelectricity in thin films has been a decades-long research quest [23–25]. Low power consumption, controllability over variability, and high switching speed are all benefits of ferroelectric-based technology over the current non-volatile memory technology. However, due to a dearth of ferroelectric materials that meet all of the conditions for a practical memory technology: scalability, CMOS compatibility, and memory retention, this promising technology has not been extensively applied [26]. In today's field effect transistor devices, HfO_2 is one of the most extensively utilised dielectric gate oxides [27, 28].

2. Design for device and atom

2.1. Structure of device

Figure 1 reveals two device structures (a) Double metal double gate negative capacitance Field effect transistor (DM DGNCFET) and (b) single metal double gate negative capacitance FET (SM DGNCFET). The dimension of these two devices almost same except Metal2-Top and Metal2-bottom ($T_{m2T/m2B}$) are varing from SM DGNCFET. The thickness of $T_{m2T/m2B}$ is 5 nm with aluminum metal for DM DGNCFET.

The length of the channel(L_{ch}) is 60 nm, the Drain/Source length ($L_{d/s}$) is 50 nm, the Drain/Source thickness ($T_{d/s}$) is 5 nm, and the Oxide thickness(T_{ox}) is 0.6 nm. T_{ox} is 7 nm, and Metal1 has a top and bottom thickness of 10 nm as illustrates table 1. SM DGNCFET and DM DGNCFET have 50 nm length of total gate channel size (L_g). The entire gate channel thickness (T_{ch}) of an SM DGNCFET is 10 nm. To explain key concepts in the book, a variety of classical models are used. Shockley-Read-Hall (SRH) classical describes the trap charges, while Lombardi model surface mobility model for electron mobility in a basic MOSFET Recombination influences, presence at the site of contact Fermi–Dirac equation is a mathematical formula that describes the relationship between two particles. Precision is achieved by the use of insights. The Arora model mobility is influenced by focus. The material for metal1 Top and bottom, metal2 Top and metal2 bottom is aluminium. Gate oxide material is used SiO_2, Material of ferroelectric is HfO_2FE (a latest thought of a ferroelectric coating with hafnium dioxide), substrate substance is Silicon easily available in anywhere. The doping concentrating of Drain/Source ($N_{d/s}$) is 1×10^{20} cm^{-3} with Gaussian profile. The workfunction of aluminium metal is 4.2 eV for dual gate.

2.2. Structure of ferroelectric HfO_2 based crystal

The ferroelectric HfO_2 based structure is created in crystal Simple cubic structure with dimension a = 10.23A, b = 10.23A, c = 10.23A, $\alpha = 90$, $\beta = 90$, $\gamma = 90$. The structure of crystal atoms have eight Hf (hafnium) and sixteen Oxygen(O) for without doping. For Si doping, 12.5% of Si is added in crystal structure as shown in figure 2. The cartesian coordinate for Si doping is [0.7677, 2.621, 3.128] A. This research have revealed that HfO_2 films doped with a few percent of a variety of dopants or 12.5 per cent Si, grown to be 7 nm thick between dual gate metal electrodes, and annealed may exhibit ferro-electricity. The ferroelectric behavior of TiN/HfO_2/TiN stacks is dramatically inhibited when the film is annealed before the top electrode is deposited, according to

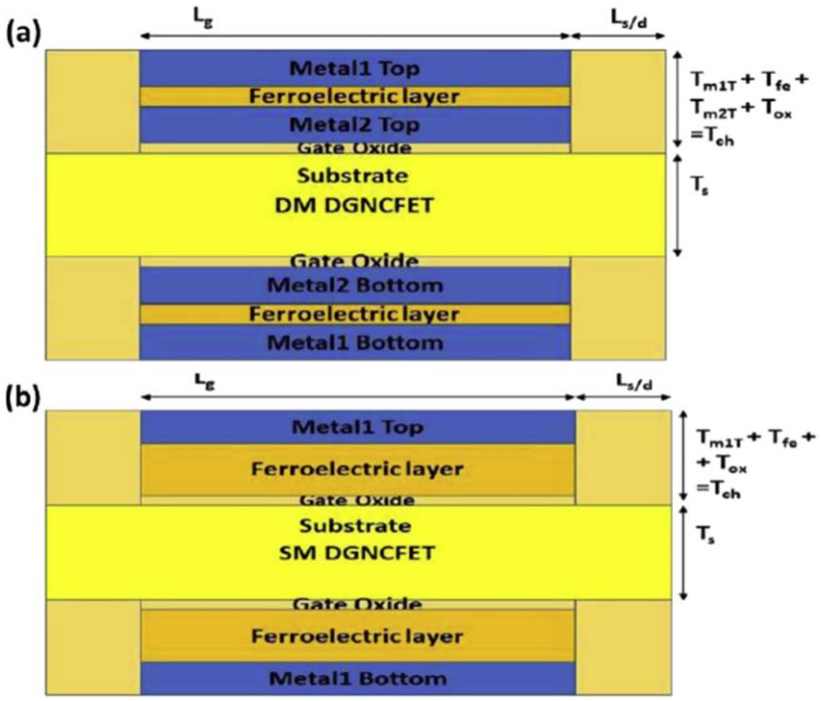

Figure 1. Sketch diagram of (a) Double metal double gate negative capacitance fet(DM DGNCFET) (b) single metal single gate negative capacitance fet is proposed device (SM DGNCFET).

Table 1. The Device parameters for SM DGNCFET and DM DGNCFET are used for the simulation.

Parameter	SM DGNCFET	DM DGNCFET
Oxide Thickness (T_{ox})	0.6 nm	0.6 nm
Gate length (L_g)	50 nm	50 nm
Substrate thickness (T_{sub})	05 nm	05 nm
Ferroelectric thickness (T_{fe})	07 nm	07 nm
Source/Drain length ($L_{s/d}$)	05 nm	05 nm
Metal1 Top/Metal1 bottom thickness ($T_{m1T/m1b}$)	10 nm	10 nm
Concentration of Drain/Source ($N_{d/s}$)	1×10^{20} cm^{-3}	1×10^{20} cm^{-3}

certain investigations, indicating that the confinement provided by the top electrode during annealing is critical for ferroelectricity [23, 29].

3. Methodology and theoretical details

3.1. Device methods

Cogenda Visual TCAD simulator is used for all simulations. A comparison of two devices the DM DGNCFET and the SM DGNCFET was performed. Throughout the operation the drain voltage, V_{ds} (V) is kept constant at 0.05 V. The gate voltage, V_g (V) varies between 0 and 0.5 volts. During the device simulation, the temperature (T) is kept constant at 300 K in all scenarios (room temperature). We ignored the ferroelectric dipole connection, depolarization fields in HfO_2-based ferroelectrics, on the other hand, we can reach the coercive field's order of magnitude and so cannot be ignored [30, 31]. To carry out the SM DGNCFET and DM DGNCFET designs, distinct limit conditions are used. Congruency of usual sections of translation vectors is used at the oxide ferroelectric restrictions in the SM DGNCFET structure. The interior metal gate serves as a coating terminal for the DGNCFET structure. Every mathematical recreation is performed using Cogenda visual TCAD Multiphysics [32].

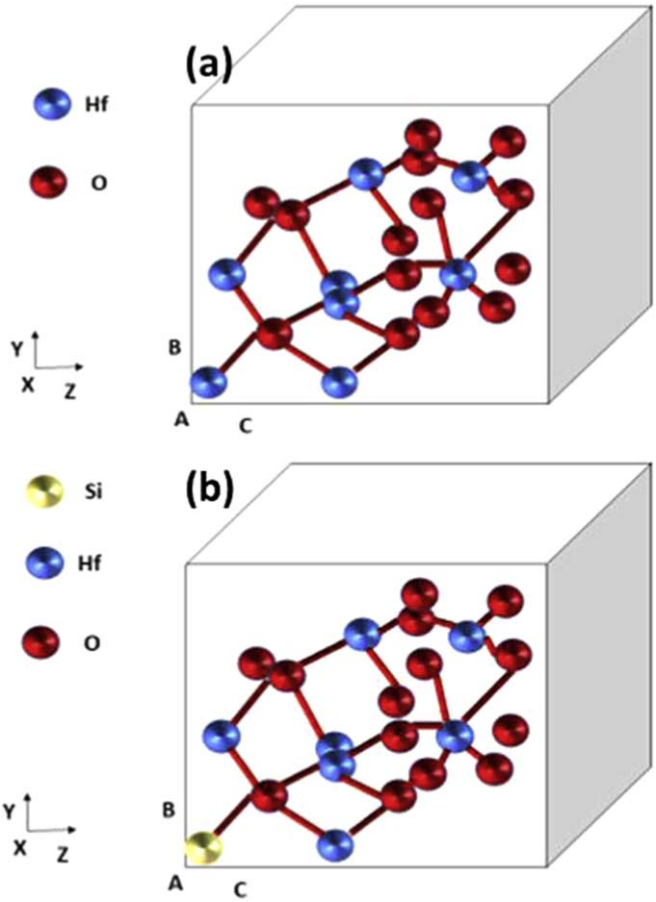

Figure 2. Sketch diagram of hfO_2 ferroeclectric based Simple cubic crystal (a) without doping (b) Si doping.

3.2. Method for HfO_2 crystal

Quantum ATK (Atomic tool kit) simulator is used for atomic study of density function theory. We use DFT in the Perdew–Burke–Ernzerhof Generalized Gradient Approximation (PBE GGA) [33] with ultrasoft pseudopotentials to compute minimal energy structures. Tran Blaha modified Becke Johnson (TB-mBJ) approxiamation gives the accurate band gap of crystal. This effect is eliminated by placing a fictional dipole in the cell's vacuum area, which cancels out the electric field in vacuum. The forces on all atoms are loosened until they are less than 104 Ry/Bohr in magnitude in all axial directions [23, 34].

3.3. The flowchart from atomic modelling to device fabrication feasibility

The framework modelling from atomic to device has been synopsized in figure 3. We start with atomic model for band energy in Vander wall heterostructure (vdWH) at interfacial charge. 1st principal calculation gives the carrier mobility and dielectric constant value of material [35]. The material attributes are used for physics based device models to obtain the knowledge of FET and MOS properties by Quantum ATK simulator. The feasibility fabrication of SM DGNCFET has been reported by Visual TCAD simulator. The deposition of silicon film is thinning first. The deposition of Al_2O_3/HfO_2 layer has developed on silicon interfacing layer by using atomic layer deposition (ALD) [36]. The metal gate is fabricated on gate dielectric using electron beam evaporation process. The dopant of source and drain region implanted by spike annealing activation. Evaporation of the electron beam is made on the surface of the source and drain. SM DGNCFET has been formed.

4. Result and discussion

4.1. Comparative study of FET device

4.1.1. Analog performance

Figure 4 shows the drain current, I_d (A) in linear scale and log drain current scale versus gate voltage, V_g (V) for a ferroelectric film better Field Effect Transistor device that is a single metal double gate negative capacitance FET SM DGNCFET at constant room temperature T = 300 K, DM DGNCFET at $V_{ds} = 0.05$ V, channel length,

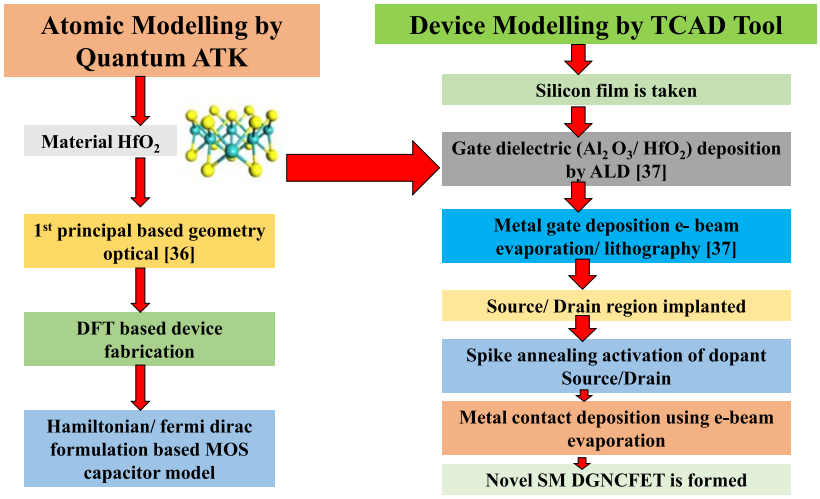

Figure 3. The flowchart of atomic modelling to device fabrication.

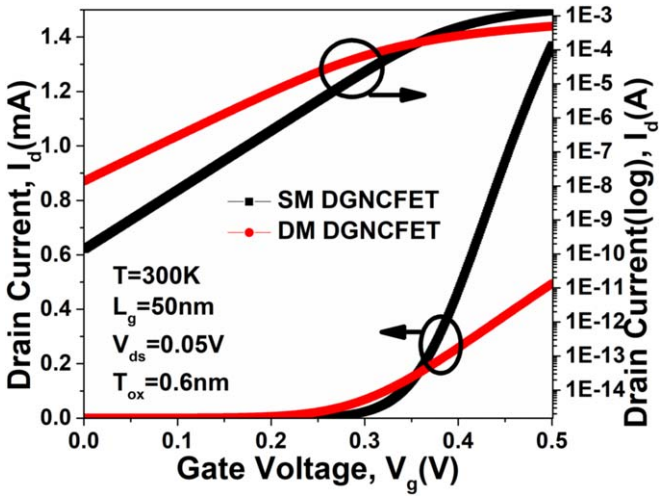

Figure 4. Plot of drain current and log drain current versus gate voltage for SM DGNCFET and DM DGNCFET at drain voltage 0.05 V.

$L_g = 50$ nm, T = 300 K It also shows that under negative bias, the off state current for SM DGNCFET is smaller. With increased gate voltage V_g (V), the drain current of SM DGNCFET designs is better than DM DGNCFET configurations, indicating superior gate coupling capacitance and lower leakage current I_{off} on the left side of the graph.

Transconductance is a measure of the ratio of drain current (I_d) to gate voltage (V_g) at drain voltage (0.05 V), T = 300 K, as shown in figure 5 SM DGNCFET has a greater transconductance curve than DM DGNCFET. As a result, g_m has adopted the shift in drain current versus gate voltage [37], which indicates improved gate control and reduced short channel effects (SCEs) [38, 39], as well as increased average carrier velocity and improved electron mobility with increased transconductance. Transcoductance generation factor (TGF) is also improved for SM DGNCFET because of g_m enhanced.

$$g_{\mathrm{m}} = \frac{\partial I_{\mathrm{d}}}{\partial V_{\mathrm{g}}.} \tag{1}$$

$$TGF = \frac{\partial g_{\mathrm{m}}}{\partial I_{\mathrm{d}}} \tag{2}$$

The plot of drain induced barrier lowering (DIBL) for a different setup is shown in figure 6. It's a short channel effect (SCE), which implies electrons may readily travel from source to drain when the channel length decreases. The DIBL of the SM DGNCFET structure is lower than that of the DM DGNCFET structure, indicating lower leakage current and enhanced SCEs. The subthreshold swing (SS) of SCEs is also important,

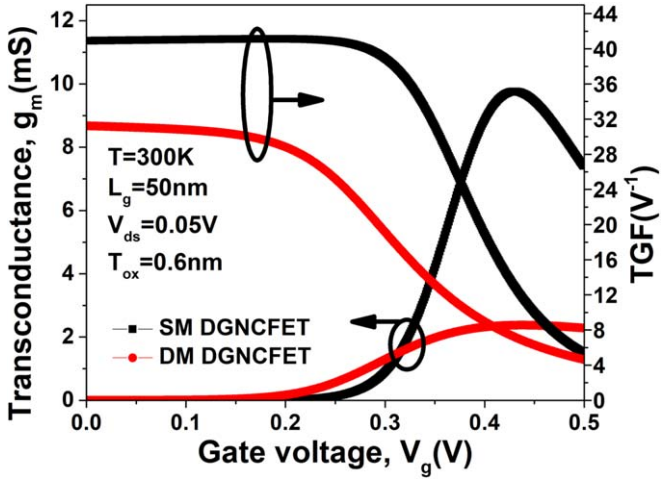

Figure 5. Plot of transconductance and TGF versus gate voltage for SM DGNCFET and DM DGNCFET at drain voltage 0.05 V.

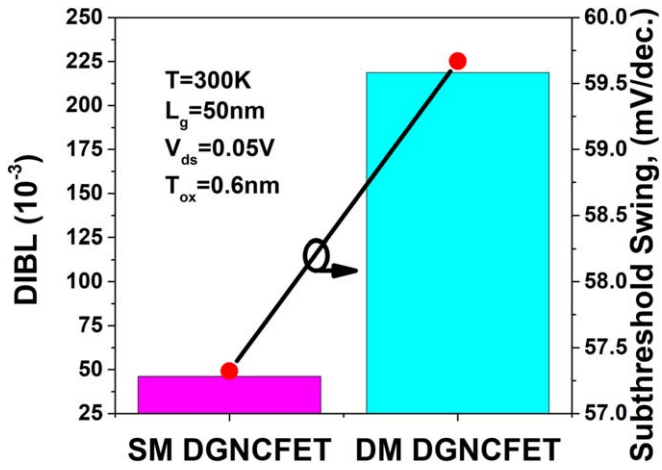

Figure 6. Plot of DIBL and SS current versus gate voltage for SM DGNCFET and DM DGNCFET at drain voltage 0.05 V.

with an optimum SS of 60 mV/decade. SM DGNCFET has a lower SS than DM DGNCFET, which is due to increased gate coupling capacitance with high permittivity (K), which improves gate control over the channel.

The threshold voltage, V_t (V) of SM DGNCFET at drain voltage, $V_{ds} = 0.05$ V is better than other DM DGNCFET device designs as illustrated in figure 7.

due to greater drain-side potential shielding and higher gate control over the channel. The threshold voltage's nature at $L_g = 50$ nm, $T_{ox} = 0$, the switching ratio I_{on}/I_{off} of SM DGNCFET is larger than the other DM DGNCFET structures. Reduced leakage current I_{off} (A), and rapid switching speed for the SM DGNCFET structure are also achieved at T = 300 K, and $V_{ds} = 0.05$ V as depicted in table 2.

Due to drain induced barrier lowering (DIBL) and channel length modulation (CLM), a high output conductance in the linear area is initially noticed with rising drain voltage beyond pinch-off voltage [40]. The g_d twist of the SM DGNCFET is smaller than that of the DM DGNCFET, indicating superior gate controllability and the ability to suppress brief direct hits, as shown in figure 8, indicating improved output obstruction.

$$g_{\mathrm{d}} = \frac{\partial I_{\mathrm{d}}}{\partial V_{\mathrm{ds}}.} \tag{3}$$

$$F_t = \frac{g_{\mathrm{m}}}{2\pi (C_{\mathrm{gd}} + C_{\mathrm{gs}})} \tag{4}$$

$$GFP = \left(\frac{g_{\mathrm{m}}}{g_{\mathrm{d}}}\right) \times F_{\mathrm{t}} \tag{5}$$

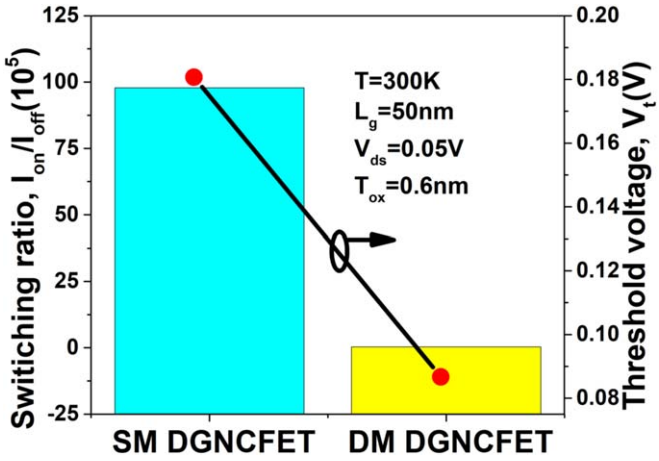

Figure 7. Plot of Switching ratio and Threshold voltage versus gate voltage for SM DGNCFET and DM DGNCFET at drain voltage 0.05 V.

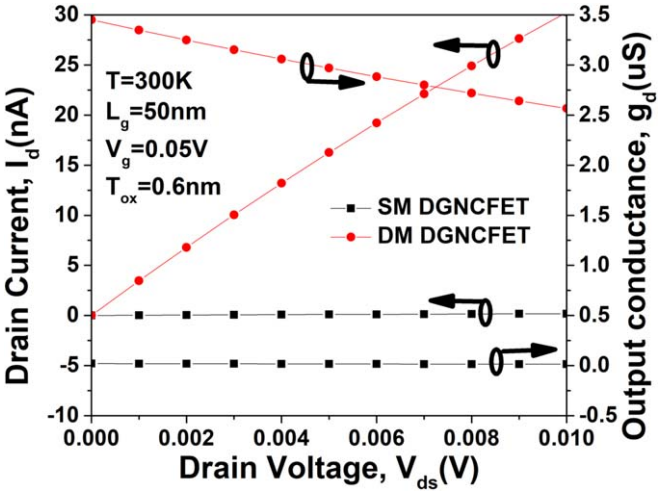

Figure 8. Plot of drain current and log drain current versus drain voltage for SM DGNCFET and DM DGNCFET at gate voltage 0.05 V.

Table 2. The data point of Leakage current, Subthreshold swing, Drain barrier induced lower for SM DGNCFET and DM DGNCFET.

Parameter	SM DGNCFET	DM DGNCFET
I_{on} (A) (10^{-3})	1.37	0.493
$V_{th}(mV)$	180.72	86.687
SS (mV/dec)	57.322	59.6
I_{off}(A)(10^{-10})	1.4	1.41
DIBL	0.0462	0.2187
$I_{on}/I_{off}(10^5)$	97.85	0.3496

4.1.2. Radio frequency analysis

According to figure 9, the SM DGNCFET configuration has a greater gate capacitance and cutoff frequency [41–43] than the DM DGNCFET configuration, revealing enhanced gate capacitance and increased transconductance as shown in equation (4) The device's time interval for producing output after receiving input shows lower input power consumption [44, 45]. The SM DGNCFET has a greater gate charge than other architectures, which reflects the high gate capacitance.

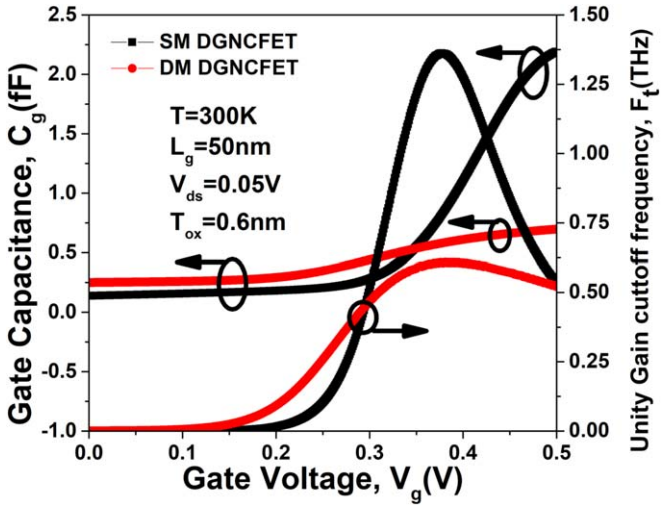

Figure 9. Plot of gate capacitance and unity gain cutoff frequency versus gate voltage for SM DGNCFET and DM DGNCFET at drain voltage 0.05 V.

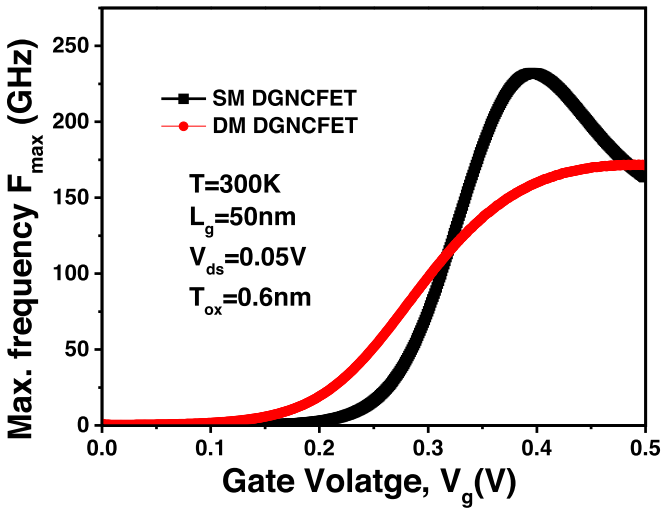

Figure 10. The curve of maximum frequency versus gate voltage at ferroelectric thickness 7 nm, temperature 300k, drain voltage 0.05 V.

The maximum frequency power gain ($F_{max.}$) is proportional to cut off frequency (F_t) as shown in figure 10. The $F_{max.}$ and F_t of SM DGNCFET is higher than DM DGNCFET which reveals the frequency gain and response at drain voltage 0.05 V. The $F_{max.}$ and F_t are the frequency of unilateral power gain and current gain becomes unity (0 dB). The F_t and $F_{max.}$ is higher which reflects the higher electron mobility in nmos than pmos, higher overdrive voltage to boost g_m, and use for minimum gate length [46, 47].

Variation of gain frequency product and transconductance frequency product versus gate voltage at T = 300 K and $V_{ds} = 0.05$ V is depicted in figure 10 for various architectures. The boost frequency product is a fundamental boundary used in high-recurrence applications as defined by equation (5). As we can be observed in figure 11, GFP increases as the gate voltage rises, reaching a maximum peak before dropping to a constant value in the saturation region. Because of the further developed worth of output transconductance and transconductance with a negligible reduction in cut-off frequency, the SM DGNCFET design has the highest GFP value. TFP reduces as V_g increases due to a rise in C_g, and when V_g reaches a saturation point, it maintains a minimal constant value. In terms of speed, transconductance, and gain, the SM DMNCFET is the best appropriate structure for TFP.

$$TFP = \left(\frac{g_{\mathrm{m}}}{I_{\mathrm{d}}}\right) \times F_{\mathrm{t}} \tag{6}$$

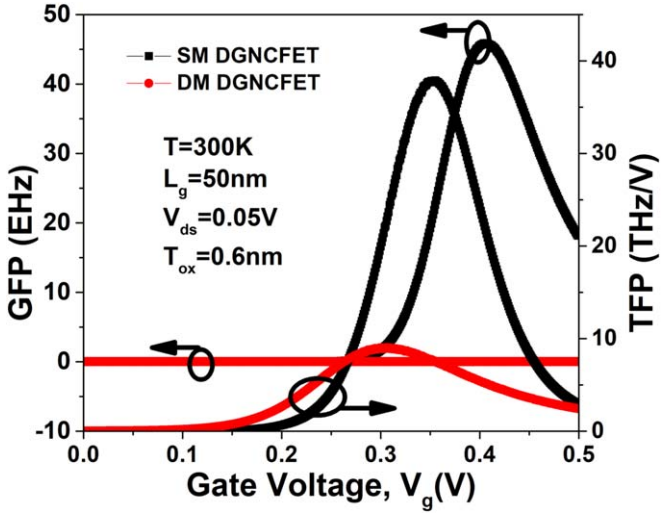

Figure 11. Plot of GFP and TFP versus gate voltage for SM DGNCFET and DM DGNCFET at drain voltage 0.05 V.

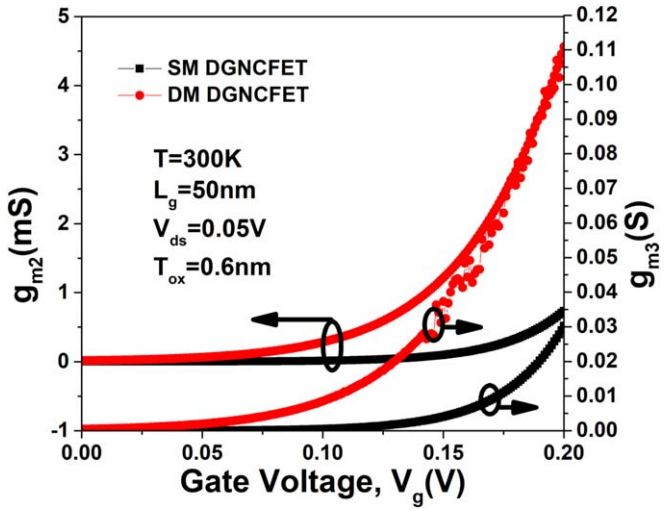

Figure 12. Plot of second and third order transconductance versus gate voltage for SM DGNCFET and DM DGNCFET at drain voltage 0.05 V.

$$VIP2 = \frac{4 \times g_m}{g_{m2}} \tag{7}$$

$$VIP3 = \sqrt{\frac{24 \times g_m}{g_{m3}}} \tag{8}$$

4.1.3. Linearity parameter

Figure 12 exhibits second and third order transconductance versus gate voltage for SM and DM DGNCFETs at 0.05V drain voltage. Nonlinear characteristics are the major source of distortion, hence they must be investigated thoroughly. Nonlinear parameters should be kept to a minimum to attain high linearity. The nonlinear parameters (g_{m2}, g_{m3}) are for second- and third-order transconductance. The nonlinear parameters are nearly identical, indicating that increasing SM DGNCFET has little effect on them [31, 44]. The extrapolated gate voltage amplitude at which second- and third-order harmonics match the fundamental tone in device current is designated as VIP2 and VIP3 (I_{ds}). The distortion features of these FOMs may be precisely investigated using DC parameters. These values should be as high as feasible in order to achieve excellent linearity and minimum distortion.

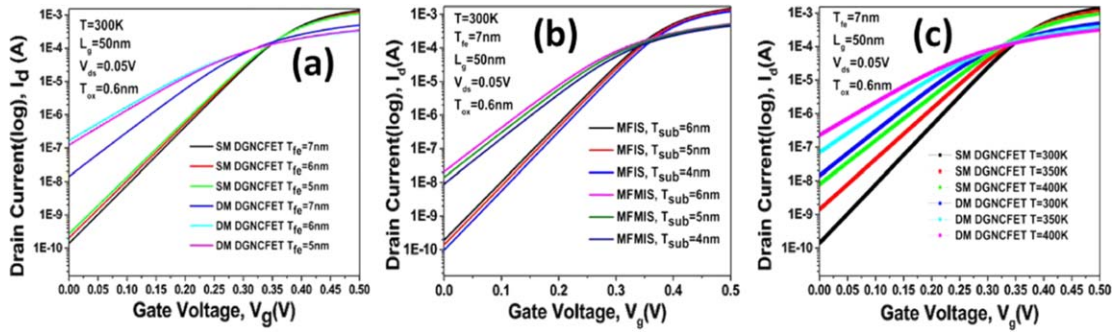

Figure 13. The curve of drain current versus gate voltage for (a) The variation of ferroelectric thickness (b) different substrate thickness (b) the variation of temperature.

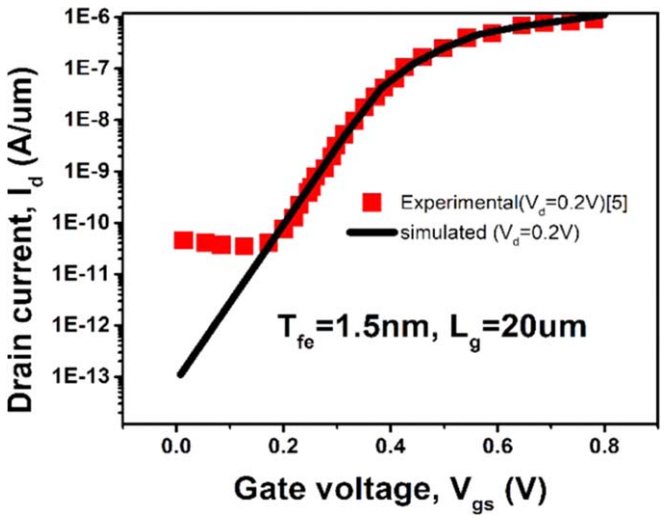

Figure 14. The calibration curve between drain current versus gate voltage curve at drain voltage 0.2 V.

4.1.4. Impact of variation of ferroelectric thickness, substrate thickness, and temperature

The comparison of two structures that is SM DGNCFET and DM DGNCFET. The variation of ferroelectric material thickness (T_{fe}) has been exhibits in figure 13 (a). The SM DGNCFET performance is higher improved than DM DGNCFET as increases the T_{fe}. The leakage current, switching ratio is better for SM DGNCFET at $T_{fe} = 7$ nm. The various substrate thickness (T_{sub}) is 6 nm, 5 nm, 4 nm where the leakage current lowered, switching ratio enhanced with decreases the substrate thickness($T_{sub} = 4$ nm). The varing ferroelectric thickness T_{fe} is 5 nm, 6 nm, 7 nm where the performance of proposed device is improved at 7 nm. The various temperature has been exhibited in figure 13 (b). The drain voltage is same in entire simulation which is 0.05 V. The varying temperature (T) is 300 K, 350 K, 400 K where as the device performance of the SM DGNCFET is improved at 300 K due to reduced leakage current, increased gate controllability, low power consumption, higher switching ratio [17, 18].

Figure 14, represents the calibration of NCFET from the experimental data at gate length 20 um, ferroelctric thickness 1.5 nm and drain voltage 0.2 V. The experimental data extraction has taken from reference [5] to validate the physical model. The simulation models is validated due to the nearly agreement between the simulated and experimental results.

4.2. Impact of ferroelectric HfO_2 based crystal

In figure 15 exhibits the band structure for (a) Si doping (b) without doping. In the instance of HfO_2, it was discovered that 12.5% Si doping significantly altered the band gap along the direction, reducing the direct band gap to 0.20 eV and the indirect band gap to 0.193 eV with two-fold degeneracy (figure 15). The Si states may be blamed for the narrowing of the band gap. For all lower concentrations of Si, a comparable band gap changes along the direction, and the amplitude of the band gap grows monotonically as we proceed from x = 0.125 to

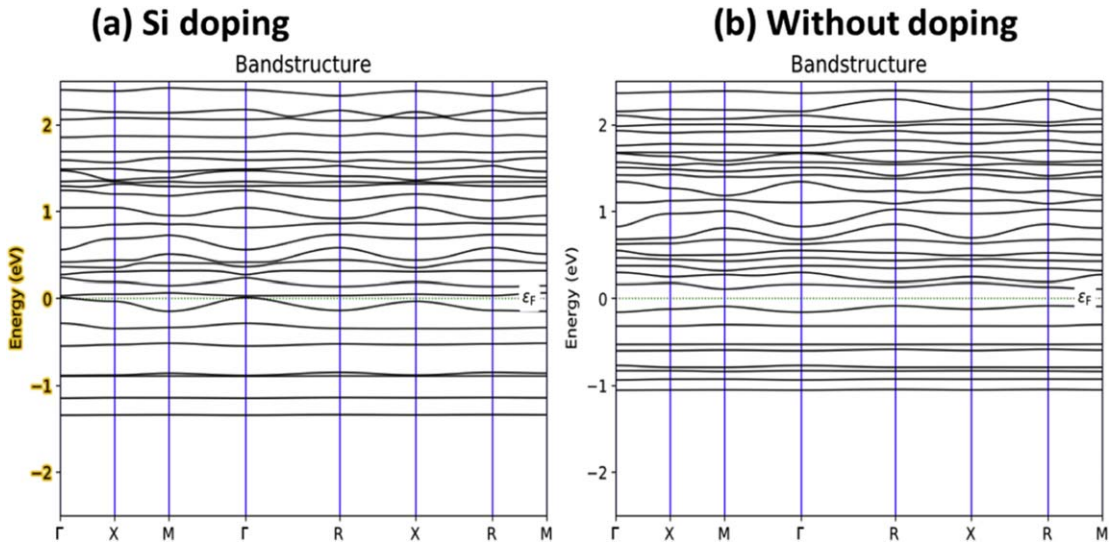

Figure 15. Band structure for (a) Si doping (b) without doping.

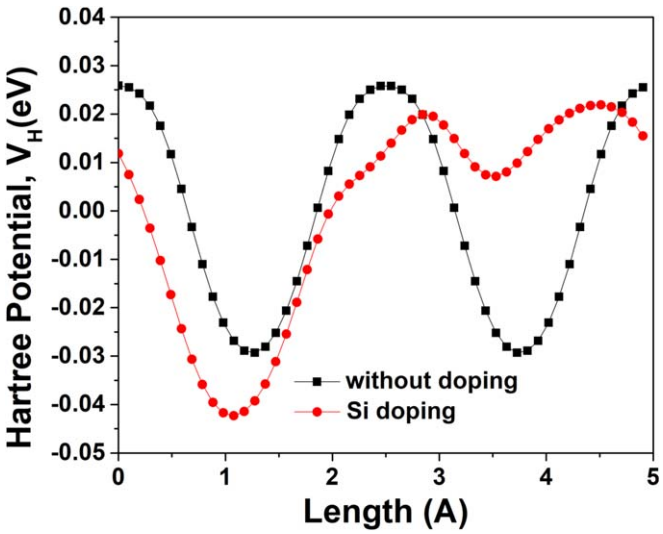

Figure 16. Curve of hartree potential versus length of atom for without doping and Si doping.

Table 3. Brillouin Zone (BZ) of specific path of ferroelectric HfO_2 based crystal for band stucture.

Value	Fractional, [K_x, K_y, K_z]	Cartesian(A^{-1})	Position along bandstructure, x
Gamma G	[0 , 0 , 0]	[0.0000, 0.0000, 0.0000]	0.0000e+00
X	[1/2, 0 , 0]	[0.3071, 0.0000, 0.0000]	1.1142e-01
M	[1/2, 1/2, 0]	[0.3071, 0.3071, 0.0000]	2.2285e-01
G	[0 , 0 , 0]	[0.0000, 0.0000, 0.0000]	3.8043e-01
R	[1/2, 1/2, 1/2]	[0.3071, 0.3071, 0.3071]	5.7342e-01
X	[1/2, 0 , 0]	[0.3071, 0.0000, 0.0000]	7.3100e-01
R	[1/2, 1/2, 1/2]	[0.3071, 0.3071, 0.3071]	8.8858e-01
M	[1/2, 1/2, 0]	[0.3071, 0.3071, 0.0000]	1.0000e+00

lower doping concentrations. Table 3 lists the Brillouin zone values along with their coordinates and symmetry K points for density function theory(DFT) study.

Figure 16 shows the curve examining the Hartree potential versus length for without doping and Si doping that revealed mean field electrostatic interaction between atoms. Electrostatic potential from electron density

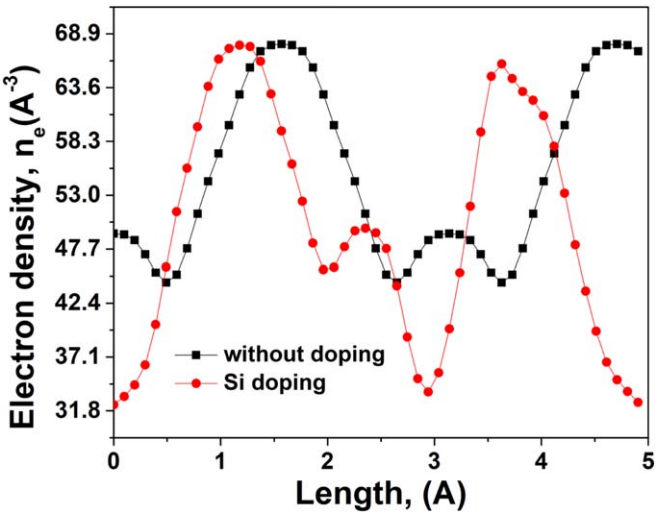

Figure 17. Curve of electron density versus length of atom for without doping and Si doping.

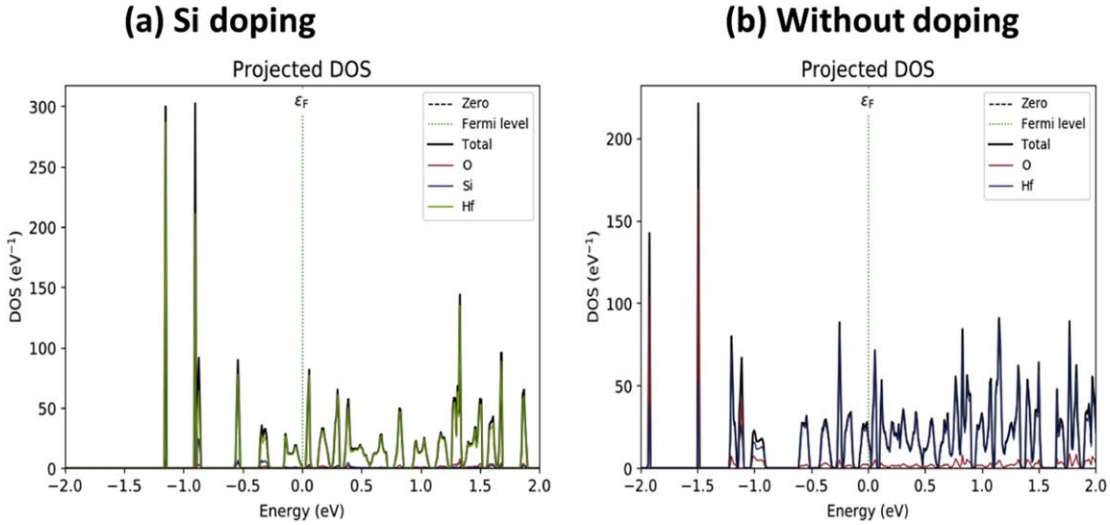

Figure 18. Curve of Density of state versus energy for without doping and Si doping at centre of fermi energy.

must be calculated using Poisson equation. Further, figure 17 exhibits the curve of electron density versus length for without doping and Si doping reflects proportional to square magnitude of wavefunction and the probability of electron or electron density being present at infinitesimal element of space. The collision time of Si doping is less for higher electron density.

In figure 18 reveals the curve examined the DOS(density of state) versus energy for without doping and Si doping at Fermi energy(E_f) reflects the conductivity enhanced with DOS increases and dispersion relation of properties of many system is available for occupation. We also examined the DOS(density of state) for all values of x to determine the influence of distinct atomic species on electronic structures (figure 18). In all doped structures, the contribution of different atoms in VBs(Valence bands) is found to be the same as in the pure c-HfO_2 phase, but the induced Si-states in lower CB occur between 0 and 0.5 eV. Si-states dominate over Hf and O-states at 0 eV, indicating the amount of hybridization. Because the number of atoms in the cell is exactly proportional to the doping concentration of Si in HfO_2, the magnitude of DOS grows as the doping concentration of Si in HfO_2 increases.

5. Conclusion

This paper addresses a comparative study of double metal double gate negative capacitance FET (DM DGNCFET) and single metal double gate negative capacitance FET (SM DGNCFET). SM DGNCFET reveals the better performance of Analog/RF and linearity such that DIBL, SS, transconductance, TFP, GFP, second and

third order of tranconductance (g_{m2}, g_{m3}). Atomic modeling for developments in quantum theory is the density functional theory (DFT), which aids to determine the energy, structure, and characteristics of materials, nanosystems, and molecules. Tran Blaha modified Becke Johnson (TB-mBJ) approxiamation gives the accurate band gap of crystal. The DFT study of hafnia(HfO_2) based Simple cubic crystal for without doping and 12.5% of Si doping. For improved results of Si the bandstructure better with band gap tends to zero, DOS enhanced for better conductivity.

Acknowledgments

The authors thanks to Nano Bioelectronics and Microelectronics Lab, Delhi Technological University for giving essential facilities.

Data availability statement

The data cannot be made publicly available upon publication because they are not available in a format that is sufficiently accessible or reusable by other researchers. The data that support the findings of this study are available upon reasonable request from the authors.

Declarations

Funding statement

Yash thanks the C.S.I.R. for the CSIR-JRF award (08/133(0050)/2020-EMR-I).

Conflict of interests

The authors declare that they are not aware of any disagreements regarding personal ties or interests that might have impacted the work represented in this publication.

Authors' contribution

The comprehension and design of the study were improved by all writers.

Compliance with ethical standard

The authors have located all of the moral standards and intend to adhere to them going forward.

Consent to participate and for publication

Since that the relevant study paper was produced in the 'no-life science magazine'. Therefore, at this time, it is 'Non Applicable'. However, the authors have provided the agencies with all journal policies and their permission for additional processing.

ORCID iDs

Rishu Chaujar https://orcid.org/0000-0002-0161-8449

References

[1] Karda K, Jain A, Mouli C and Alam M A 2015 An anti-ferroelectric gated landau transistor to achieve sub-60 mv/dec switching at low voltage and high speed *Appl. Phys. Lett.* **106** 163501
[2] Lee M *et al* 2015 Prospects for ferroelectric hfzrox fets with experimentally cet = 0.98 nm, ssfor = 42mv/dec, ssrev = 28mv/dec, switch-off < 0.2 v, and hysteresis-free strategies *2015 IEEE International Electron Devices Meeting (IEDM), IEEE* 22–5
[3] Moselund K, Bouvet D, Pott V, Meinen C, Kayal M and Ionescu A 2008 Punch-through impact ionization mosfet (pimos): from device principle to applications *Solid-State Electron.* **52** 1336–44

[4] Pathak Y, Malhotra B D and Chaujar R 2021 Tcad analysis and simulation of double metal negative capacitance fet (dm ncfet) *2021 Devices for Integrated Circuit (DevIC). IEEE* 224–8
[5] Lee M *et al* 2016 Physical thickness 1. x nm ferroelectric hfzrox negative capacitance fets *2016 IEEE International Electron Devices Meeting (IEDM), IEEE* 12–1
[6] Pahwa G, Agarwal A and Chauhan Y S 2018 Numerical investigation of short-channel effects in negative capacitance mfis and mfmis transistors: subthreshold behavior *IEEE Trans. Electron Devices* **65** 5130–6
[7] Pahwa G, Agarwal A and Chauhan Y S 2019 Numerical investigation of short-channel effects in negative capacitance mfis and mfmis transistors: above-threshold behavior *IEEE Trans. Electron Devices* **66** 1591–8
[8] Lin C-I, Khan A I, Salahuddin S and Hu C 2016 Effects of the variation of ferroelectric properties on negative capacitance fet characteristics *IEEE Trans. Electron Devices* **63** 2197–9
[9] Bidenko P, Lee S, Han J-H, Song J D and Kim S-H 2018 Simulation study on the design of sub-kt/q non-hysteretic negative capacitance fet using capacitance matching *IEEE Journal of the Electron Devices Society* **6** 910–21
[10] Saeidi A, Jazaeri F, Stolichnov I and Ionescu A M 2016 Double-gate negative-capacitance mosfet with pzt gate-stack on ultra thin body soi: An experimentally calibrated simulation study of device performance *IEEE Trans. Electron Devices* **63** 4678–84
[11] You W-X and Su P 2018 Intrinsic difference between 2D negative-capacitance fets with semiconductor-on-insulator and double-gate structures *IEEE Trans. Electron Devices* **65** 4196–201
[12] Awadhiya B, Kondekar P N, Yadav S and Upadhyay P 2021 Insight into threshold voltage and drain induced barrier lowering in negative capacitance field effect transistor *Transactions on Electrical and Electronic Materials* **22** 267–73
[13] Pahwa G, Dutta T, Agarwal A and Chauhan Y S 2018 Physical insights on negative capacitance transistors in nonhysteresis and hysteresis regimes: Mfmis versus mfis structures *IEEE Trans. Electron Devices* **65** 867–73
[14] Kim J Y, Choi M-J and Jang H W 2021 Ferroelectric field effect transistors: progress and perspective *APL Mater.* **9** 021102
[15] Pathak Y, Malhotra B D and Chaujar R 2021 A numerical study of analog parameter of negative capacitance field effect transistor with spacer *2021 7th International Conference on Signal Processing and Communication (ICSC), IEEE* 277–81
[16] Kim H J, Park M H, Kim Y J, Lee Y H, Moon T, Do Kim K, Hyun S D and Hwang C S 2016 A study on the wake-up effect of ferroelectric hf 0.5 zr 0.5 o 2 films by pulse-switching measurement *Nanoscale* **8** 1383–9
[17] Pathak Y, Mann R, Malhotra B D and Chaujar R 2023 Impact of temperature on negative capacitance fet: a tcad simulation study *2023 2nd Edition of IEEE Delhi Section Flagship Conference (DELCON), IEEE* 1–4
[18] Mann R, Pathak Y and Chaujar R 2022 Temperature analysis on short channel effects of modified ncfet: a simulation study *2022 IEEE International Conference on Electronics, Computing and Communication Technologies (CONECCT), IEEE* 1–5
[19] Zhu H, Ramanath G and Ramprasad R 2013 Interface engineering through atomic dopants in hfo2-based gate stacks *J. Appl. Phys.* **114** 114310
[20] Kumar N, George B P A, Abrahamse H, Parashar V, Ray S S and Ngila J C 2017 A novel approach to low-temperature synthesis of cubic hfo2 nanostructures and their cytotoxicity *Sci. Rep.* **7** 1–14
[21] Kumar R, Vij A and Singh M 2022 Electronic, thermoelectric, and optical studies of cubic hf1-xtixo2: An attempt to enhance the key parameters *J. Solid State Chem.* **307** 122829
[22] Liang H, Xu J, Zhou D, Wang X, Liu X, Chu S and Liu X 2017 Structure and electrical properties of pure and yttrium-doped hfo2 films by chemical solution deposition through layer by layer crystallization process *Mater. Des.* **120** 376–81
[23] Dogan M, Gong N, Ma T-P and Ismail-Beigi S 2019 Causes of ferroelectricity in hfo 2-based thin films: an *ab initio* perspective *Phys. Chem. Chem. Phys.* **21** 12150–62
[24] McKee R, Walker F and Chisholm M 2001 Physical structure and inversion charge at a semiconductor interface with a crystalline oxide *Science* **293** 468–71
[25] Hoffman J, Pan X, Reiner J W, Walker F J, Han J, Ahn C H and Ma T 2010 Ferroelectric field effect transistors for memory applications *Adv. Mater.* **22** 2957–61
[26] Ma T and Han J-P 2002 Why is nonvolatile ferroelectric memory field-effect transistor still elusive? *IEEE Electron Device Lett.* **23** 386–8
[27] Gong N and Ma T-P 2016 Why is fe-hfo 2 more suitable than pzt or sbt for scaled nonvolatile 1-t memory cell? A retention perspective *IEEE Electron Device Lett.* **37** 1123–6
[28] Liu B, Sun H, Huan C, Jia R, Cai Y and Ke Q 2023 Investigating the reliability of a negative capacitance field effect transistor regarding the electric field across the oxide layer *J. Electron. Mater.* **52** 3180–7
[29] Gupta S, Chen R, Magyari-Kope B, Lin H, Yang B, Nainani A, Nishi Y, Harris J and Saraswat K 2011 Electron devices meeting (IEDM) *2011 IEEE International, IEEE*
[30] Hoffmann M, Pešić M, Chatterjee K, Khan A I, Salahuddin S, Slesazeck S, Schroeder U and Mikolajick T 2016 Direct observation of negative capacitance in polycrystalline ferroelectric hfo2 *Adv. Funct. Mater.* **26** 8643–9
[31] Pathak Y, Malhotra B D and Chaujar R 2022 Linearity performance of double metal negative capacitance field-effect transistors: a numerical study *2022 IEEE VLSI Device Circuit and System (VLSI DCS). IEEE* 19–23
[32] Pathak Y, Malhotra B D and Chaujar R 2022 Detection of biomolecules in dielectric modulated double metal below ferroelectric layer fet with improved sensitivity *J. Mater. Sci., Mater. Electron.* **33** 13558–67
[33] Perdew J P, Burke K and Ernzerhof M 1996 Generalized gradient approximation made simple *Phys. Rev. Lett.* **77** 3865
[34] Bellaiche L and Vanderbilt D 2000 Virtual crystal approximation revisited: application to dielectric and piezoelectric properties of perovskites *Phys. Rev.* B **61** 7877
[35] Das B and Mahapatra S 2018 An atom-to-circuit modeling approach to all-2d metal-insulator-semiconductor field-effect transistors *npj 2D Materials and Applications* **2** 28
[36] Choi S-N, Moon S-E and Yoon S-M 2020 Impact of oxide gate electrode for ferroelectric field-effect transistors with metal-ferroelectric-metal-insulator-semiconductor gate stack using undoped hfo2 thin films prepared by atomic layer deposition *Nanotechnology* **32** 085709
[37] Narendar V and Girdhardas K A 2018 Surface potential modeling of graded-channel gate-stack (GCGS) high-k dielectric dual-material double-gate (DMDG) mosfet and analog/rf performance study *Silicon* **10** 2865–75
[38] Li M-H, He G-Y, Li Q, Ying L-Y, Zhang B-P and Zheng Z-W 2022 Physical insights into the performances of negative capacitance field effect transistors using single-domain versus multidomain models *IEEE Trans. Electron Devices* **70** 806–11
[39] Chaudhary S, Dewan B, Sahu C and Yadav M 2022 Steep-subthreshold slope dual gate negative capacitance junction less fet with dead channel: Tcad approach for digital/rf applications *Microelectron. J.* **127** 105518
[40] Amin S I and Sarin R 2015 Charge-plasma based dual-material and gate-stacked architecture of junctionless transistor for enhanced analog performance *Superlattices Microstruct.* **88** 582–90
[41] Mann R and Chaujar R 2021 Tcad investigation of ferroelectric based substrate mosfet for digital application *Silicon* **14** 5075–84

[42] Mohapatra S, Pradhan K, Artola L and Sahu P 2015 Estimation of analog/rf figures-of-merit using device design engineering in gate stack double gate mosfet *Mater. Sci. Semicond. Process.* **31** 455–62
[43] Pathak Y, Malhotra B D and Chaujar R 2022 Analog/rf performance and effect of temperature on ferroelectriclayer improved fet device with spacer *Silicon* **14** 12269–80
[44] Sharma M and Chaujar R 2021 Design and investigation of recessed-t-gate double channel hemt with ingan back barrier for enhanced performance *Arab. J. Sci. Eng.* **47** 1109–16
[45] Chen B, Pin G, Ng W M, Parisini T and Hui S-Y R 2016 A fast-convergent modulation integral observer for online detection of the fundamental and harmonics in grid-connected power electronics systems *IEEE Trans. Power Electron.* **32** 2596–607
[46] Basak A and Sarkar A 2021 Quantum analytical model for lateral dual gate utbb soi mosfet for analog/rf performance *Silicon* **13** 3131–9
[47] Basak A and Sarkar A 2020 Drain current modelling of asymmetric junctionless dual material double gate mosfet with high k gate stack for analog and rf performance *Silicon* 1–12

J. Astrophys. Astr. (2023)44:74
https://doi.org/10.1007/s12036-023-09962-8
© Indian Academy of Sciences

Diving deep into the milky way using anti-reflection coatings for astronomical CCDs

ANMOL AGGARWAL[1,†], ASHI MITTAL[1,†], GEORGE M. SEABROKE[2] and NITIN K. PURI[1,*]

[1]Advanced Sensor Laboratory and Nanomaterials Research Laboratory, Department of Applied Physics, Delhi Technological University, Delhi 110042, India.
[2]Mullard Space Science Laboratory, Department of Space and Climate Physics, Faculty of Maths and Physical Sciences, University College London, London RH5 6NT, UK.
*Corresponding author. E-mail: nitinkumarpuri@dtu.ac.in; nitinpuri2002@yahoo.co.in

MS received 28 December 2022; accepted 8 May 2023

Abstract. We report two anti-reflection (AR) coatings that give better quantum efficiency (QE) than the existing AR coating on the Gaia astrometric field (AF) charged coupled devices (CCDs). Light being the core of optical astronomy is extremely important for such missions, therefore, the QE of the devices that are used to capture it should be substantially high. To reduce the losses due to the reflection of light from the surface of the CCDs, AR coatings can be applied. Currently, the main component of the Gaia satellite, the AF CCDs use hafnium dioxide (HfO_2) AR coating. In this paper, the ATLAS module of the SILVACO software has been employed for simulating and studying the AF CCD pixel structure and several AR coatings. Our findings suggest that zirconium dioxide (ZrO_2) and tantalum pentoxide (Ta_2O_5) will prove to be better AR coatings for broadband astronomical CCDs in the future and will open new avenues to understand the evolution of the milky way.

Keywords. Gaia—SILVACO TCAD—astronomical instrumentation—charged coupled devices—anti-reflection coatings.

1. Introduction

To enrich astronomy with more precise measurements, the European Space Agency (ESA) launched Gaia Satellite in the L2 orbit in December 2013. Its two telescopes keep an eye on millions of stars, galaxies and solar system objects to produce high-precision astrometric and spectroscopic measurements (Prusti *et al*. 2016). The continuous scan gives data sets that are repeatedly reduced to calculate the parallax, position and proper motion of the celestial objects that are observed by the satellite (Crowley *et al*. 2016). The focal plane of the Gaia satellite contains 106 custom-built charged coupled devices (CCDs). These CCDs were designed and manufactured by e2v technologies, UK (Walker *et al*. 2008).

Gaia CCDs were fabricated by e2v in three different variants: astrometric field (AF), red photometer (RP) and blue photometer (BP); each of these are optimized for different wavelength ranges (De Bruijne 2012). The AF CCDs are built using silicon (Si) as a substrate with an anti-reflection (AR) coating, which has a maximum photon absorption for a light of 650 nm; this CCD has an extensive wavelength detection range of 330–1050 nm (Seabroke *et al.* 2008). There are 78 AF CCDs on the Gaia focal plane, which are 16 μm thick (Crowley *et al*. 2016). The BP and RP are enhanced CCDs that have exceptional sensitivity towards the blue (330–680 nm) and red (640–1050 nm) regions of the light spectrum, respectively. Seven BP CCDs present on the Gaia focal plane, have the maximum photon absorption for the light of 360 nm because of its AR coating (Crowley *et al*. 2016). Correspondingly, seven RP CCDs have the maximum photon absorption for the light of 750 nm (Crowley

†First two authors have equal contribution to this research.

Published online: 21 July 2023

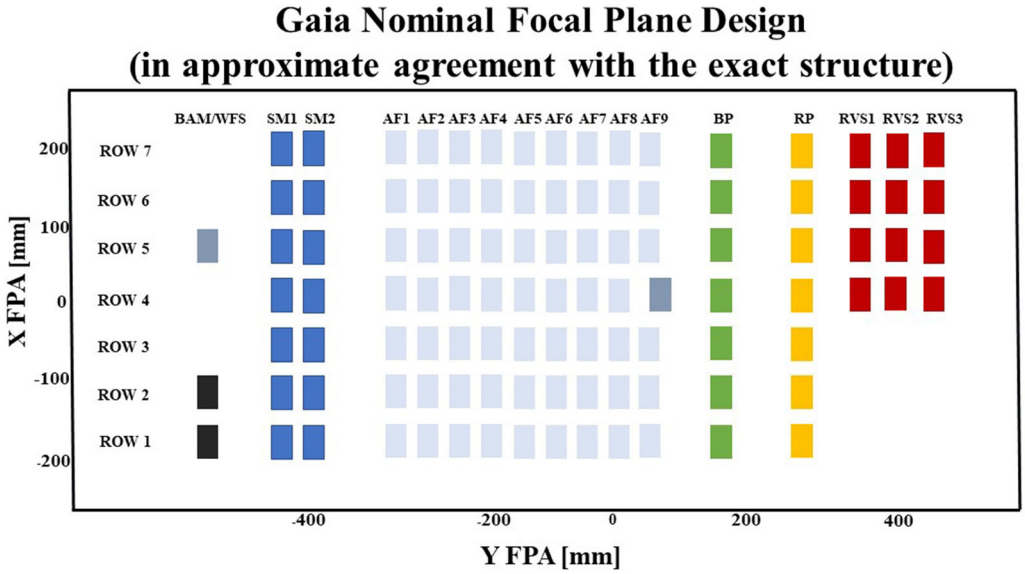

Figure 1. Gaia focal plane has 106 CCDs arranged in seven different rows. The red rectangles represent radial velocity spectrometers (RVS). The green and yellow rectangles depict blue and red photometers (BP and RP), respectively, while the grey and black rectangles show wavefront sensors (WFS) and basic angle monitors (BAM), respectively. The light blue rectangles depict the most abundant i.e., AF CCDs and the dark blue rectangles are called sky mappers (SM). The SM and the WFS are also AF CCDs. The RVS and BAM have a construction similar to the RP.

et al. 2016). These CCDs have an image area of 4500 lines × 1966 columns (here, lines and columns, refer to the rows and columns of the pixels of the CCD, respectively) (De Bruijne 2012). A schematic diagram of the arrangement of CCDs on the actual Gaia focal plane is shown in Figure 1. The detectors are operating in the time delay and integration mode with a period of 982.8 μs, which synchronizes their line transfer rate with the satellite rotation rate (Crowley *et al*. 2016; De Bruijne 2012). In Gaia parlance, line transfer means electrons being transferred in a row of pixels (Crowley *et al*. 2016).

As the name suggests, AR coatings are essentially important in improving the internal quantum efficiency (IQE) of the CCDs because they play a vital role in enhancing their photon absorption by reducing the losses due to the reflection of incident light. The IQE is used as a measuring stick to determine the performance of an AR coating, which is the ratio of the number of photons that enter the CCD to the number of photons incident on the device (Devi *et al*. 2012). The external quantum efficiency (EQE) is the ratio of the number of photoelectrons generated to the number of photons incident on the CCD (Devi *et al*. 2012). Since the Gaia CCDs generally do not get a lot of time to capture the incoming light from distant objects, their IQE should be substantially high. An AR coating is a thin layer of high refractive index material (Lesser 1987). It also acts as a line of defence for the CCDs (Lesser 1994).

The Gaia AF CCDs have been analysed since they cover the maximum area (78 out of 106 CCDs) of the Gaia focal plane and capture the widest wavelength range. Studies that amalgamate AR coatings and astronomical CCDs have been conducted. IQE of the device has been deliberated, which in fact is directly proportional to the EQE of the device. Several AR coatings for the Gaia AF CCDs have been scrutinized to enhance this factor using the SILVACO software.

2. Simulations and calculations

SILVACO TCAD is used to simulate several electronic and optical devices. It uses numerical methods for simulations so that the development and optimization of such devices can be expedited. For simulating the effects of AR coatings on an optoelectronic device, the LUMINOUS and the ATLAS modules of this software can be used.

Since the Gaia AF CCDs are back-illuminated devices, the AR coatings are applied on the backside. Photons are also fired on this side in our simulations. The operating voltage was set to 10 V as suggested by

Seabroke *et al*. (2009). In SILVACO simulations, the ratio of available current density ($J_{available}$) and source current density (J_{source}) gives the IQE of a device. The number of photoelectrons generated in a device can be determined using the electron current density (J_n).

We simulated an AF CCD pixel in 2-dimensions (2D) using SILVACO, our aim is to obtain IQE of the device with various AR coatings at different wavelengths. We assessed several materials as AR coatings, namely, hafnium dioxide (HfO_2), aluminum oxide (Al_2O_3), zinc sulfide (ZnS), zirconium dioxide (ZrO_2) and tantalum pentoxide (Ta_2O_5). Although an AR coating of HfO_2 is already present on the AF CCDs (Short *et al*. 2005), which gives impressive results. We suspected that there was a scope of improvement in IQE of the devices. Our simulations proclaim that EQE of the Gaia AF CCDs with this AR coating peaks at 650 nm with a value of 0.99. Simulating these CCDs without any AR coating revealed that there is a large increase of 37.2% in the IQE when AR coatings are applied on such devices. Hence, AR coatings can be regarded as a cornerstone of astronomical CCDs.

A CCD is essentially a MOS-based device, which acts as an image detector. In MOS, the letter M stands for metal, the letter O stands for oxide and the letter S stands for semiconductor (Lundström 1981). Therefore, the structure of CCD consists of a layer of metallic electrodes placed on a thin insulating layer lined over a semiconductor substrate. Lundström (1981) reports details of the MOS structure. CCDs are of two types, front-illuminated and back-illuminated. In the former, light is incident on the electrodes, while the light is incident on the semiconductor substrate in the latter (Lesser 2014, 2015). The back-illuminated CCDs are constructed in actual practice because they offer a larger surface area for photogeneration and photon absorption than front-illuminated CCDs (Lesser 2015).

For simulating the Gaia AF CCD pixel in SILVACO, several structural parameters are required, which are derived from (Seabroke *et al*. 2008, 2009, 2010a, b). The pixel structure of the CCD has three different faces, which is evident from Figure 2. We simulated the structure in the across scan (AC) direction in 2D with a pixel size of 16 μm × 30 μm. The 16 μm thickness of the pixel is subdivided into multiple layers, the details of which are summarized in Table 1.

The Gaia AF CCD entails a lot of interesting structural intricacies, namely, buried channel (BC), supplementary buried channel (SBC) and anti-blooming drain (ABD) (Seabroke *et al*. 2008). A BC is formed near a p–n junction by placing a thin layer of negatively doped Si on a positively doped substrate. This channel has no free charges and is used to hold the photogenerated electrons before they are read out. A photon incident on a CCD creates an electron–hole pair; the electron thus generated, then moves to the BC.

The SBC is a support feature to the BC but is no less functional. When the number of photogenerated electrons exceeds the capacity of the SBC, they spill into the BC, which holds them until they are read out (Seabroke *et al*. 2010a, 2013). The length of BC and SBC runs from 4.5 to 29 μm in the AC direction (Seabroke *et al*. 2010b). The ABD, which is present on either side of the pixel in the AC direction is a

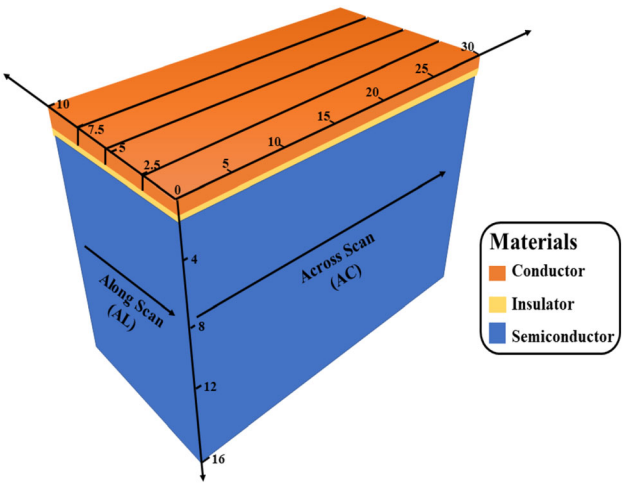

Figure 2. Structure of a single pixel of the Gaia AF CCD (all the measurements are in μm).

Table 1. Thickness and doping densities of different layers in the AF CCD pixel structure (Seabroke *et al*. 2009).

Material	Type	Thickness (μm)	Doping density (cm^{-3})
Polycrystalline Si	Conductor	0–0.5	0
Silicon dioxide (SiO_2)	Insulator	0.5–0.63	0
N-type Si	Semiconductor	0.63–1.17	2.65×10^{16}
P-type Si	Semiconductor	1.17–16	1.3×10^{14}

Table 2. List of theoretical and experimental constants.

Name of Constant	Theoretical values used in SILVACO ATLAS	Experimental values
Energy gap of Si (E_g)	1.08 eV at 300 K 1.11 eV at 163 K	1.12 eV at 300 K (Strehlow & Cook 1973)
Relative permittivity of Si (ε_r)	11.8 at 300 K 11.8 at 163 K	11.66 at 300 K (Krupka *et al.* 2006)
Electron affinity of Si (X)	4.17 eV at 300 K 4.16 eV at 163 K	4.05 eV at 300 K (Melnikov & Chelikowsky 2004; Chanana 2022)
Temperature (T)	163 K	163 K (Seabroke *et al.* 2008)

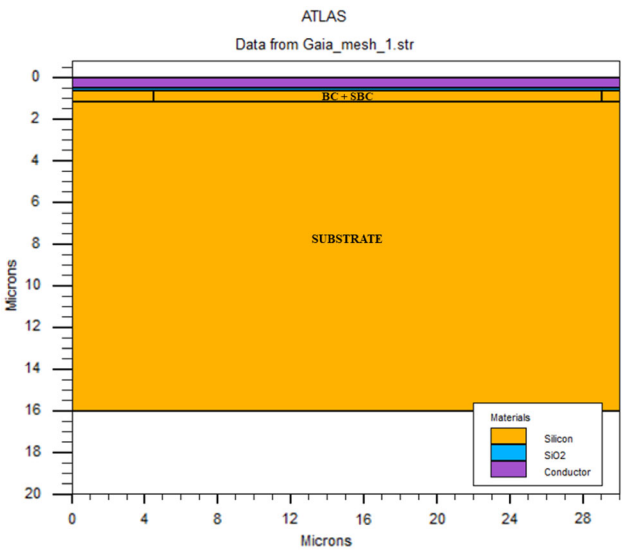

Figure 3. 2D Gaia AF CCD structure in the across scan (AC) direction as simulated in SILVACO ATLAS.

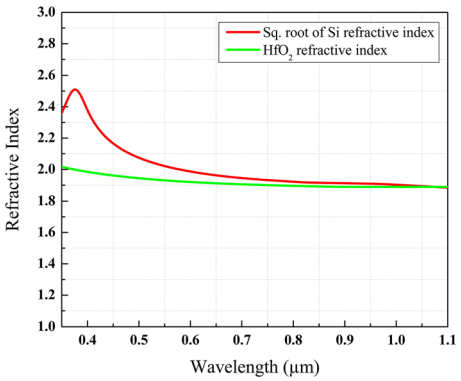

Figure 4. Comparison of the refractive index of HfO_2 with the square root of the refractive index of Si at different wavelengths.

shielding feature. It prevents the electrons from divulging into the adjacent pixel (Seabroke *et al.* 2010a). Now, to simulate all these interesting features in SILVACO, the whole AF CCD image pixel was modeled with uniform doping as suggested by Seabroke *et al.* (2009).

The Gaia AF CCDs work at a temperature of 163 K (Seabroke *et al.* 2008) to minimize the dark current, which is attributed to the false positive signals produced in the CCD due to the thermal energy of electrons (Lesser 2015). Therefore, to match our theoretical simulations with the experimental results reported by Walker *et al.* (2008), we conducted our simulations at the same temperature.

To simulate the CCD pixel structure, the SILVACO ATLAS package uses some constants for the simulated materials that are handled internally. It uses the Monte Carlo method to model the structure. Table 2 compares the experimental values of the constants with the values used during our simulations.

Figure 3 exhibits the simulated structure of the Gaia AF CCD pixel; the illustration was generated using the TonyPlot tool of the SILVACO software.

2.1 *AR coatings*

We have elucidated the Gaia AF CCD pixel structure used in our simulations, but to test their efficiency, the IQE can be used. To begin with, we have focused on single-layer AR coatings that have been applied on the backside of the CCD (substrate side). The thickness of the AR coating is estimated using the quarter wavelength formula (Equation 1):

$$\text{AR coating thickness} = \frac{\lambda}{4n}. \quad (1)$$

In Equation (1), λ is the wavelength at which the AR coating is centered, i.e., the wavelength at which the AR coating will allow for maximum photon absorption; n is the refractive index of the AR coating material at the wavelength λ (Lesser 1987). The SOPRA database of the SILVACO ATLAS software was tremendously helpful in allowing us to include the refractive indices of the AR coatings. When the

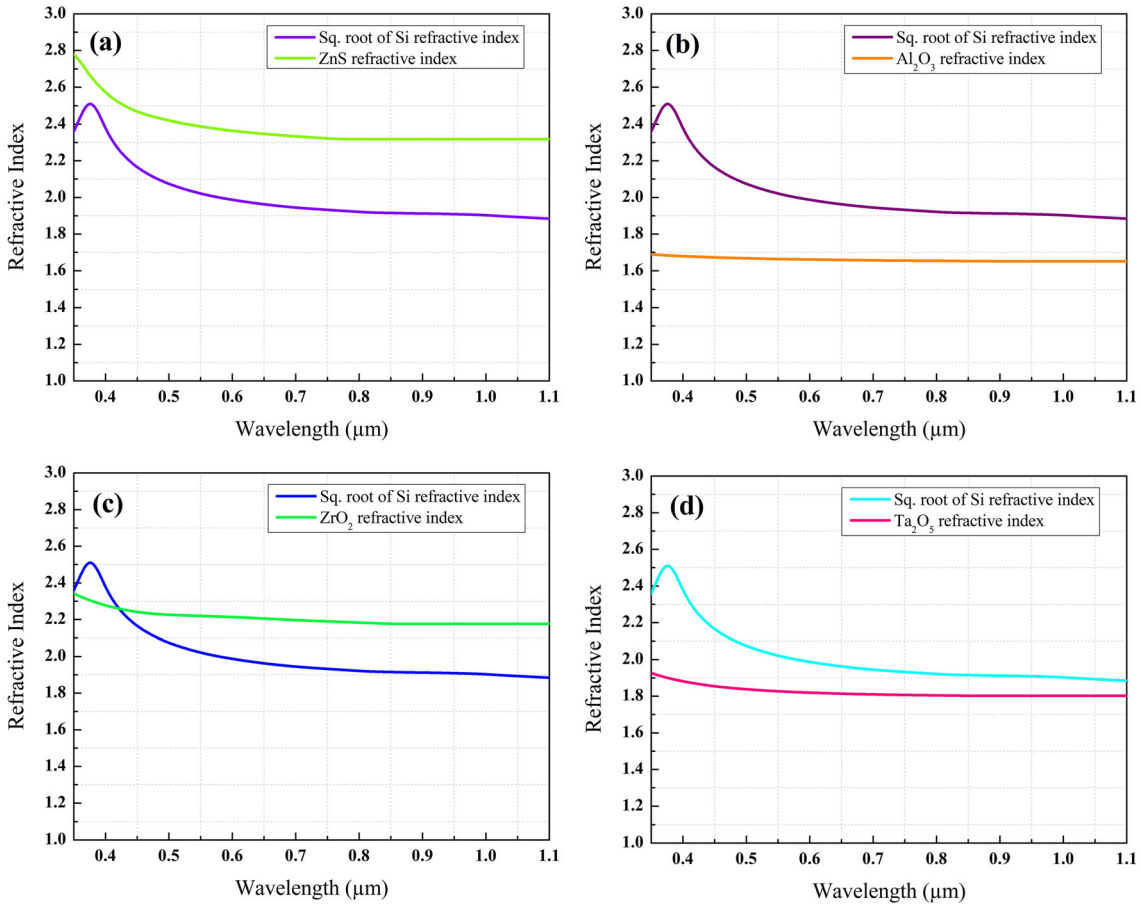

Figure 5. Comparison of the square root of the refractive index of Si with (a) ZnS, (b) Al_2O_3, (c) ZrO_2 and (d) Ta_2O_5 at different wavelengths.

refractive index of AR coatings at a specified wavelength comes in approximate agreement with $\sqrt{n}$, where n is the refractive index of the substrate material at that wavelength, then, we get excellent IQE values. To choose an AR coating, this factor was deliberated.

On comparing the values of refractive indices of various AR coatings with the $\sqrt{n}$, at different wavelengths, we got some AR coatings whose refractive indices match the $\sqrt{n}$ values and promise good results in IQE. In Figure 4, we can see the comparison of HfO_2 coating's refractive indices with the square root values of Si refractive indices. There is a very good matching which evidently explains why this AR coating is used in designing the Gaia AF CCDs.

On performing the same comparison with various AR coatings, we got some promising results from ZnS, Al_2O_3, ZrO_2 and Ta_2O_5, which can be seen in Figure 5. Figure 5(a) shows how similar are the values of $\sqrt{n}$ of Si and the refractive index of ZnS. Figure 5(b) shows that the refractive index of Al_2O_3 is also close to the $\sqrt{n}$ of Si values. Figure 5(c) and (d) show similar results for ZrO_2 and Ta_2O_5.

While choosing the materials for AR coatings, their imaginary refractive index, which is a complex optical constant, often referred to as the extinction coefficient has also been considered. Using this, we can calculate the absorption coefficient (α), which is the distance a photon can travel into the material before being absorbed. It is given by Equation (2):

$$\text{Absorption coefficient } (\alpha) = \frac{4\pi k}{\lambda}, \tag{2}$$

where λ is the wavelength of incident light. We calculated the values of α for whole wavelength range of the Gaia astrometric field (AF) CCD using SILVACO ATLAS with different AR coatings, which are presented in Figure 6(a–c). It can be concluded from these results that the AR coatings have no effect on the absorption coefficient of silicon (Si).

Another factor that has been deliberated while selecting the AR coating material is reflectivity (R_0).

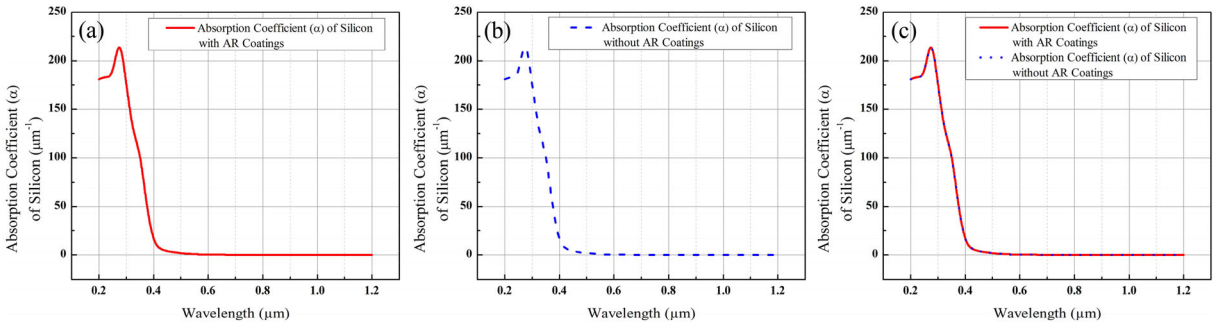

Figure 6. Absorption coefficient of Si: (a) with AR coatings, (b) without AR coatings and (c) with and without AR coatings.

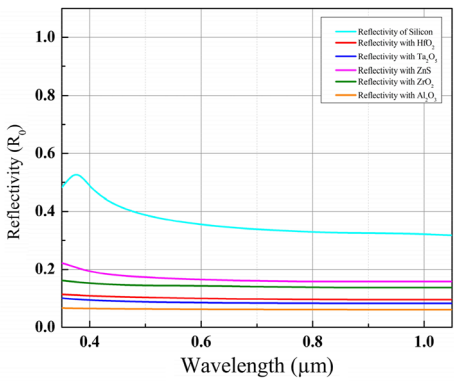

Figure 7. Reflectivity of the CCD surface without any AR coating and with different AR coatings.

Equation (3) is used to calculate the reflectivity of a surface using the real refractive indices:

$$\text{Reflectivity } (R_0) = \left|\frac{n_1 - n_2}{n_1 + n_2}\right|^2, \tag{3}$$

where n_1 and n_2 are the real refractive indices (at a specific wavelength) of the medium from which the light is incident and the AR coating material, respectively. The reflectivity of the Si–air interface is largely affected by the optical properties of AR coating materials. The effect of AR coatings on the reflectivity of the Si–air interface is presented in Figure 7, which has been calculated using the SILVACO ATLAS software.

For an AR coating to perform well, its respective refractive indices of the AR coating material also should be in approximate agreement with the square root of the respective refractive indices of the substrate material ($\sqrt{n}$), as per Lesser (1987). Ta_2O_5 satisfies this condition and it is the best among all the studied AR coating materials, and reduces the reflectivity substantially. Hence, it can be concluded that Ta_2O_5 can be proven to be the best AR coating material for our case. Although Al_2O_3 reduces the reflectivity to the least value compared to all the studied AR coatings, as presented in Figure 7, its respective refractive indices are not very close to the square root of the respective refractive indices of Si (Figure 5b), which might hinder its performance.

3. Results and discussion

While simulating the pixel structure with the HfO_2 AR coating, Equation (1) deduces the thickness of the coating to 0.085 μm. We identified the EQE for this setup to benchmark our simulations against the previously published EQE values by Walker *et al*. (2008). The simulation results are comparable to the experimental results, which can be visualized in Figure 8(a). Any differences in the values of EQE might be because of the absence of ABD in our structure, as the parameters required for its simulations were not published in the current literature.

On calculating IQE for the Gaia AF CCD without applying any AR coating, it was discovered that they have a maximum IQE of 0.65 at the wavelength of 0.7 μm. Comparing the IQE of the CCDs with and without the HfO_2 coating, we clearly observed an average increment of about 37.2% in the whole wavelength range. Figure 8(b) coveys this increment graphically.

As per our study of AR coating materials, we choose four AR coatings to test our device. One of them is ZnS. Application of 0.069 μm thick single-layer coating of ZnS, centered at 0.65 μm, unfolds that it is not very suitable for our device. The IQE curve in Figure 8(c) outlines that there is an average decrement of $\sim$3.5% when studied parallel to the Gaia AF CCD with a HfO_2 AR coating in the whole range.

Our next choice was Al_2O_3. Therefore, we applied a single layer of it with a thickness of about 0.098 μm (calculated as per Equation 1), centered at 0.65 μm. The Gaia AF CCD with HfO_2 AR coating still

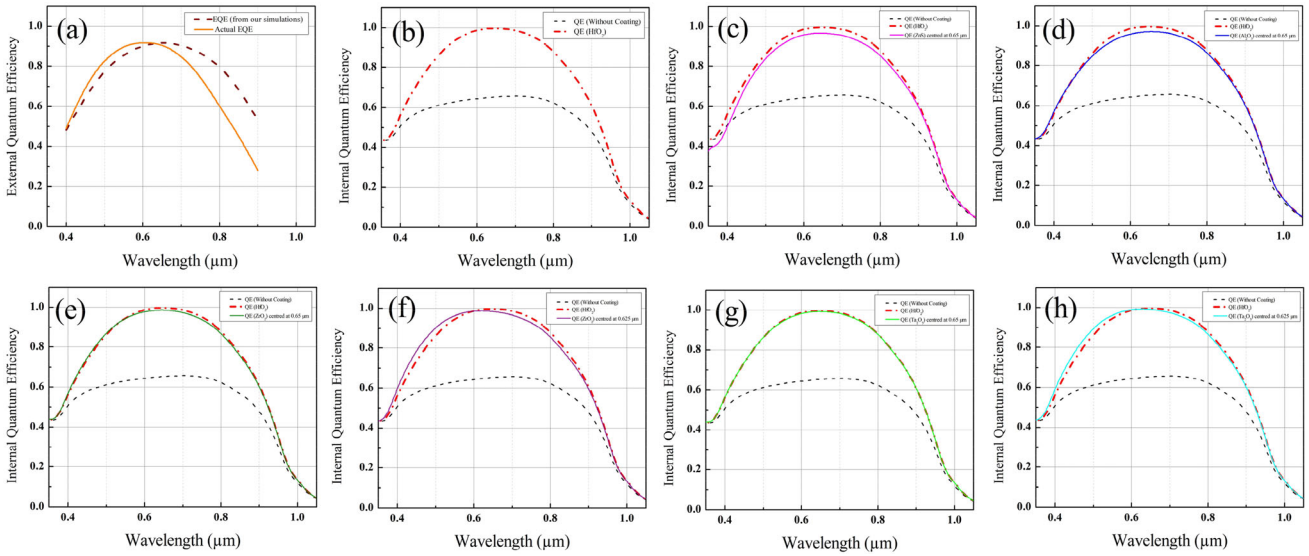

Figure 8. (a) EQE of the Gaia AF CCDs derived from our simulations and the actual EQE reported by Walker *et al.* (2008). The IQE versus wavelength graph for Gaia AF CCD, (b) without an AR coating and with a HfO_2 coating (centered at 0.65 μm), (c) ZnS coating (centered at 0.65 μm), (d) Al_2O_3 coating (centered at 0.65 μm), (e) ZrO_2 coating (centered at 0.65 μm), (f) ZrO_2 coating (centered at 0.625 μm), (g) Ta_2O_5 coating (centered at 0.65 μm) and (h) Ta_2O_5 coating (centered at 0.625 μm).

Table 3. Percentage increment and decrement in QE of the Gaia AF CCD with different AR coatings as compared to the HfO_2 AR coating.

AR coatings	Wavelength range (μm)	Percentage increment/decrement in IQE	Average increment/decrement in IQE
HfO_2	0.33–1.05	Increment (2.6–53.3%) as compared to a CCD without any AR coating	Increment (37.2%) as compared to a CCD without any AR coating
ZnS (centered at 0.65 μm)	0.35–1.05	Decrement (0.3–12.2%) as compared to HfO_2	Decrement (3.5%) as compared to HfO_2
Al_2O_3 (centered at 0.65 μm)	0.35–0.425	Increment (0.1–2.3%) as compared to HfO_2	Increment (1.3%) as compared to HfO_2
	0.425–1.05	Decrement (0.09–2.8%) as compared to HfO_2	Decrement (1.9%) as compared to HfO_2
ZrO_2 (centered at 0.65 μm)	0.4–0.525	Increment (0.04–1.35%) as compared to HfO_2	Increment (0.8%) as compared to HfO_2
	0.525–1.05	Decrement (0.19–1.4%) as compared to HfO_2	Decrement (1.1%) as compared to HfO_2
ZrO_2 (centered at 0.625 μm)	0.375–0.575	Increment (0.63–6.85%) as compared to HfO_2	Increment (4%) as compared to HfO_2
	0.575–1.05	Decrement (0.38–2.72%) as compared to HfO_2	Decrement (2%) as compared to HfO_2
Ta_2O_5 (centered at 0.65 μm)	0.35–0.9	Decrement (0.64% and less) as compared to HfO_2	No prominent change as compared to HfO_2
	0.9–1.05	Increment (0.04% and less) as compared to HfO_2	No prominent change as compared to HfO_2
Ta_2O_5 (centered at 0.625 μm)	0.375–0.6	Increment (0.17–5.15%) as compared to HfO_2	Increment (2.8%) as compared to HfO_2
	0.6–1.05	Decrement (0.19–1.57%) as compared to HfO_2	Decrement (1.2%) as compared to HfO_2

provides better results for most wavelengths as compared to Al_2O_3. It is also observed that Al_2O_3 coating provides an average improvement in IQE of about 1.3% in the 0.35–0.425 μm range and an average decrement of about 1.9% in the rest of the wavelength range. These results are compiled in the graph presented in Figure 8(d).

The next alternative that we analysed was a single-layer coating of ZrO_2 centered at 0.65 μm. The thickness of the coating was set as per Equation (1) close to 0.073 μm. After observing the graphical data presented in Figure 8(e), we infer that there is an average increment in the IQE of around 0.8% in the range of 0.4–0.525 μm when analogized with the IQE values when HfO_2 coating was applied. For the rest of the wavelengths, the AR coating of HfO_2 offers an average increment of almost 1.1%, when compared to ZrO_2.

Inspired by the improvements shown by ZrO_2, we adjusted its thickness to an approximate value of 0.071 μm, which allows for a peak absorbance of the light of wavelength of 0.625 μm. Our experimentation on this, yields an average increment of nearly 4% for the wavelength range of 0.375–0.575 μm when compared with HfO_2, with an average compromise of around 2% in the wavelength range of 0.575–1.05 μm. This data is visualized in Figure 8(f).

We concluded our studies with Ta_2O_5, which is a promising AR coating. A single layer of Ta_2O_5, centered at 0.65 μm with a thickness of $\sim$0.09 μm (calculated using Equation 1), permits almost the same performance as HfO_2. It is evident from Figure 8(g) that the two curves virtually overlap each other in the whole range. We did not obtain such promising results for any other AR coating. Hence, to improve the IQE in the low wavelength region, we deposited a 0.086 μm thick layer of Ta_2O_5 to the center of the AR coating at 0.625 μm. The IQE of the Gaia AF CCDs with an AR coating of Ta_2O_5 shows an average increment of about 2.8% compared to the CCDs with HfO_2 AR coating in the wavelength range of 0.375–0.6 μm. There is an average decrease of around 1.2% in IQE of the wavelengths ranging from 0.6 μm to 1.05 μm, which is clearly evident in Figure 8(h).

A comparative study has been drawn to analyse, which AR coating best suits the Gaia AF CCDs. It is observed that a single layer coating of ZrO_2 and Ta_2O_5 gives similar or better results as compared to HfO_2 for most wavelengths lying in Gaia's AF CCD range (330–1050 nm) (Seabroke *et al*. 2008). Table 3 summarizes the comparison among the IQE of CCDs for different AR coatings.

4. Conclusions

We tested our Gaia AF CCD pixel model against the actual EQE values reported by Walker *et al.* (2008), which indicated the accuracy of our simulations. We presented our studies of the Gaia AF CCDs with various AR coatings to enhance the QE values. Any deviations in the results might be attributed to the absence of SBC and ABD in our structure since these features are proprietary to e2v. The performance of an AR coating can also be determined using a simple Si wafer. But, to validate our results for astronomical CCDs, we used an electrical model in SILVACO ATLAS. This allows our results to be more acceptable to the astronomical community.

Our simulations establish that AR coatings are an important factor in improving the IQE and EQE of astronomical CCDs. They also elucidate that Ta_2O_5 and ZrO_2 are better materials for astronomical CCDs than HfO_2, mainly in the spectrum region from 0.330 μm to 0.575 μm. Hence, this work has important implications for the development of astronomical CCDs, which will help them to obtain the best possible data from satellites and telescopes. Multi-layer AR coatings can be deliberated for this purpose in the future, which might enhance our knowledge of the Milky Way even more.

Acknowledgments

We are grateful to Prof. Ashutosh Bharadwaj, University of Delhi, for his help and motivation throughout this research. We are also thankful to Dr Harsupreet Kaur for providing us with the license for TCAD SILVACO ATLAS 2021 software. We gratefully acknowledge Dr Ritika Khatri, Delhi Technological University, for her continuous support and guidance during this research.

References

Chanana R. K. 2022, Journal of Electrical and Electronics Engineering 17, 09
Crowley C., Kohley R., Hambly N. C. *et al*. 2016, A&A 595, A6
De Bruijne J. 2012, Ap&SS 341, 31
Devi H. R., Bisen O. Y., Nanda S., Nandan R., Nanda K. K. 2021, Current Science 00113891, 127
Krupka J., Breeze J., Centeno A. *et al*. 2006, IEEE Transactions on Microwave Theory and Techniques 54, 3995
Lesser M. 1987, Optical Engineering 26, 911
Lesser M. 2014, in High Performance Silicon Imaging (Elsevier), p. 78
Lesser M. 2015, PASP 127, 1097
Lesser M. P. 1994, in Instrumentation in Astronomy VIII, Vol. 2198, SPIE, p. 782
Lundström I. 1981, Sensors and Actuators 1, 403
Melnikov D. V., Chelikowsky J. R. 2004, Physical Review B 69, 113305
Prusti T., De Bruijne J., Brown A. G. *et al*. 2016, A&A 595, A1
Seabroke G., Holland A., Burt D., Robbins M. 2009, in Astronomical and Space Optical Systems, Vol. 7439, SPIE, p. 35
Seabroke G., Holland A., Burt D., Robbins M. 2010a, in High Energy, Optical, and Infrared Detectors for Astronomy IV, Vol. 7742, SPIE, p. 339

Seabroke G., Holland A., Cropper M. 2008, in High Energy, Optical, and Infrared Detectors for Astronomy III, Vol. 7021, SPIE, p. 515

Seabroke G., Prod'homme T., Hopkinson G. *et al.* 2010b, European Astronomical Society Publications Series 45, 433

Seabroke G., Prod'homme T., Murray N. *et al.* 2013, MNRAS 430, 3155

Short A., Hopkinson G., Laborie A. *et al.* 2005, in Focal Plane Arrays for Space Telescopes II, Vol. 5902, SPIE, p. 31

Strehlow W., Cook E. L. 1973, Journal of Physical and Chemical Reference Data 2, 163

Walker A., Eaton T., Steward R. *et al.* 2008, in Sensors, Systems, and Next Generation Satellites XII, Vol. 7106, SPIE, p. 390

DLVS: Time Series Architecture for Image-Based Visual Servoing

Nilesh Aggarwal
Department of Applied Physics
Delhi Technological University (DTU)
Delhi, India
nilesh.ggoo@gmail.com

Anunay
Department of Mechanical Engineering
Delhi Technological University (DTU)
Delhi, India
anunay2608@gmail.com

Vayam Jain
Department of Applied Physics
Delhi Technological University (DTU)
Delhi, India
jainvayam@gmail.com

Tushar Singh
Department of Electrical Engineering
Delhi Technological University (DTU)
Delhi, India
tushar300101@gmail.com

Dinesh Kumar Vishwakarma
Department of Information Technology
Delhi Technological University (DTU)
Delhi, India
Dinesh@dtu.ac.in

2023 8th International Conference on Control and Robotics Engineering (ICCRE) | 979-8-3503-4565-0/23/$31.00 ©2023 IEEE | DOI: 10.1109/ICCRE57112.2023.10155585

***Abstract*—A novel deep learning-based visual servoing architecture *"DLVS"* is proposed for control of an unmanned aerial vehicle (UAV) capable of quasi-stationary flight with a camera mounted under the vehicle to track a target consisting of a finite set of stationary points lying in a plane. Current Deep Learning and Reinforcement Learning (RL) based end-to-end servoing approaches rely on training convolutional neural networks using color images with known camera poses to learn the visual features in the environment suitable for servoing tasks. This approach limits the application of the network to available environments where the dataset was collected. Moreover, we cannot deploy such networks on the low-power computers present onboard the UAV. The proposed solution employs a time series architecture to learn temporal data from sequential values to output the control cues to the flight controller. The low computational complexity and flexibility of the DLVS architecture ensure real-time onboard tracking for virtually any target. The algorithm was thoroughly validated in real-life environments and outperformed the current state-of-the-art in terms of time efficiency and accuracy.**

Keywords—visual servoing, image based visual servoing, end-to-end visual servoing, deep learning, UAV, target tracking, time series, long short-term memory

I. Introduction

Visual Servoing is the control of a robot's maneuvers [1] using the optical data from the sensors present. The goal is for the robot to travel in cartesian space from an arbitrary starting point to a specified/unspecified destination which is accomplished by repeatedly reducing the error between the present and desired position. Visual Servoing has a wide range of applications including but not limited to autonomous navigation of robots and robotic surgery.

There are two approaches to traditional visual servos: position-based visual servo (PBVS) [2] and Image-based visual servo (IBVS) [3]. PBVS defines the errors in Euclidean space and operates entirely in an inertial frame of reference, resulting in simpler control laws and the most efficient trajectories. Calculation of the 3D model of the scene required for PBVS is usually done by the error-prone process of solving the Perspective-n-Point problem and filtering the results to achieve acceptable accuracy [4]. IBVS, on the other hand, defines the error in the image plane by extracting a set of visual features, designing the control law around these features by modeling the Image Jacobian or the Interaction matrix and approximating its pseudo inverse. Therefore, IBVS and PBVS have a bottleneck of requiring prior knowledge of the intrinsic camera parameters requiring strict camera calibration.

In this study, we offer a novel approach for visual servoing by considering it as a time-variant sequential neural network problem statement, using the Long-Short Term Memory (LSTM) [5], using a set of time series data, inspired by the current progress in deep learning models for processing high dimensional raw data. Similar to IBVS, we have defined the error in the image plane using a set of visual features that can be detected and tracked using separate computer vision algorithms. Furthermore, the data set for training the model was self-created via a custom environment using Robotic Operating System (ROS).

The paper is organized as follows: Section II shows a detailed literature study of other deep learning approaches for the visual servoing problem. Section III explains the simulation environment and is further utilized to collect the data using the traditional IBVS algorithms. Following this, the novel DLVS architecture is described alongside the custom activation and loss functions. The experimental setup and results for testing and validation of the algorithm in real life are presented in Section IV. Finally, the research is concluded, and future works are stated in Section V of the research paper.

II. Related Works

The research utilized the approaches relying on hand-crafted visual features for representing images where the control laws are defined by backpropagating the gradient descent over the spatial information errors. This methodology requires the camera and interaction matrix to be either estimated numerically or analytically. After implementing the algorithm on deep learning-based architecture, it was altered for an RL-based methodology, a common practice involved in deep reinforcement learning [6]. According to their implementation procedure, the parameters learned by the model are specific to

Authorized licensed use limited to: DELHI TECHNICAL UNIV. Downloaded on July 03,2023 at 04:52:16 UTC from IEEE Xplore. Restrictions apply.

an environment and task, hence cannot be generalized for unknown environments. Moreover, utilisation of RL is not possible in our ose case, because of the fact that the proposed DLVS algorithm is deployed real-time on the Jetson Nano (single board computer), where the real-time training and rewarding is not viable.

In another study, researchers used Convolutional Neural Networks (FlowNet) to perform the task of visual servoing. Here, the principal approach is to use the prediction of optical flow by taking image pairs as inputs and their x-y flow fields as ground truth which are then passed through multiple ConvNets and ReLu activations. Paying attention to the physical deployment of the architecture, it has to be trained over a wide diversity of environments and camera parameters. Here in this case, the use of image pairs is increasing the parameters required for feature extraction by the deep learning architecture to estimate the vehicle velocity, which is not the case in DLVS research, as it utilises real-time error values in x and y directions and estimates the UAV control cues.

Researchers also presented an algorithm [8], where a convolutional neural network (EfficientNet) is fine-tuned to estimate the relative pose between the current and desired images, and a position-based visual servoing control law is considered to reach the desired pose. The project also describes a methodology to efficiently and automatically create a dataset used to train the network architecture, which enables the robust handling of various occlusions and lighting variations. They proposed the training of a scene-agnostic network by feeding both the desired and current images into a deep-learning network. The method is validated in simulation on a 6 DOF robot. The limitations of such an approach are that the algorithm is dependent on the environmental conditions and the sensor hardware on which the architecture is trained as explained in [24], which is not applied in the proposed DLVS architecture. DLVS is completely independent of the working environmental conditions as well as optical hardware.

DLVS algorithm estimates the control cues on the basis of pixel error values which can be inferred using separate computer vision algorithms. This approach removes the architectural dependencies over the environment allowing the model to operate in any environment. Furthermore, the CNN architectures used in the above-mentioned approaches are computationally expensive eliminating the possibility of deployment on the lightweight onboard computer (OBC). Hence the model has to be deployed on-ground which significantly degrades the performance as a result of the communication delay introduced by the video downlink and subsequent control que uplink, with the possibility of servoing termination due to communication failure.

III. Methodology

A. Simulation Environment

To train and experimentally validate the proposed algorithms, the dataset was collected manually using a simulator based on Robot Operating System (ROS) [10]. ROS being an open-source robotics middleware has a collection of software frameworks for hardware abstractions, low-level device control, implementation of commonly used functionality, communication between processes, and package management which helps in building and reusing code between robotics applications.

Alongside the Robot Operating System, Gazebo [11] is the robotic simulator of choice. Gazebo is a 3D simulator that can use multiple high-performance physics engines such as Open Dynamics Engine (ODE) and Bullet for rapid and accurate designing of robots, testing of algorithms, and training Artificial Intelligent systems using realistic scenarios. Gazebo does so by rendering the world with high-quality lighting, shadows, and textures, allowing support for various sensors that can *"see"* the environment, such as Cameras, Lidars, Stereo Cameras, etc. This is essential for accurately training and testing Visual Servoing algorithms.

For our simulation setup, we use an Iris drone with a gimbal-stabilized camera mounted under the UAV as shown in Fig. 1. Along with the UAV, a mobile unmanned ground vehicle with an ArUco Marker on top is also simulated, which acts as the target feature for the IBVS control scheme.

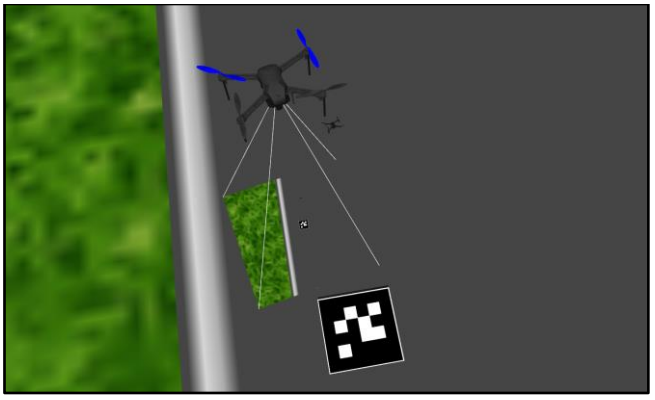

Fig. 1. Representation of Gazebo simulation environment where a camera mounted on an Iris Drone is capturing a frame consisting of an ArUco marker.

B. Image-Based Visual Servoing

The aim of classical IBVS like all other vision-based control schemes is to minimize an error $e(t)$, which is defined by

$$e(t) = s - s* \tag{1}$$

The parameters in the above equation are defined as follows. The vector s is a set of features extracted from the image and s* are the desired locations of these features in the image plane. Now a velocity controller is defined on the basis of the error term. Let the spatial velocity of the camera or the UAV be defined as $V_c = (v_c, w_c)$, where v_c is the instantaneous linear velocity and w_c is the instantaneous angular velocity. Since the UAV is an underactuated system, its roll and pitch angles are coupled with the linear velocities hence only the linear velocities are controlled. The relationship between $\frac{de}{dt}$ and V_c is given by

$$\frac{de}{dt} = L_s v_s \tag{2}$$

where $L_s \in R^{k*6}$ is called the feature jacobian or interaction matrix. Both these terms are used somewhat interchangeably in

Authorized licensed use limited to: DELHI TECHNICAL UNIV. Downloaded on July 03,2023 at 04:52:16 UTC from IEEE Xplore. Restrictions apply.

the visual servo literature. For an exponential decoupled decrease of the error term, we obtain the following control law

$$v_c = -\lambda L_e^+ e \tag{3}$$

where L_e^+ as the Moore-Penrose pseudoinverse of the L_e . In real visual servo systems, L_e^+ and L_e have to be approximated as they cannot be known perfectly. In the classical IBVS, the interaction matrix is derived on the basis of the feature points in the image.

The 2D feature point in the image with coordinates as $\mathbf{x} = (x, y)_{\text{in pixels}}$ is a projection of the 3-D point in the camera frame with coordinates $\mathbf{X} = (X, Y, Z)_{\text{in meters}}$. The relation between both the points is calculated assuming the camera is a perfect pinhole camera,

$$x = X/Z = (u - c_u)/f\alpha \tag{4}$$

$$y = Y/Z = (v - c_v)/f \tag{5}$$

here; $a = (c_u, c_v, f, \alpha)$ is the set of the camera intrinsic parameters: c_u and c_v are the coordinates of the principal points, f is the focal length, and α is the ratio of the pixel dimensions (which is usually equal to 1). These intrinsic parameters need to be estimated using a calibration process which is often unable to produce accurate parameters which end up being a key bottleneck in a real-world application. This bottleneck can be overcome in the simulation environment as we can manually set these parameters. Using this relation the Interaction Matrix is defined in [5] as:

$$Lx = \begin{bmatrix} -1/Z & 0 & x/Z & xy & -(1+x^2) & y \\ 0 & -1/Z & y/Z & 1+y^2 & -xy & -x \end{bmatrix}$$

here, Z is the depth of the point relative to the camera frame.

C. Dataset Collection

One of the main drawbacks of sequential models lies in the fact that they are data-hungry, therefore there is a requirement for a voluminous dataset for training and inference of the learning approach. As of right now, there are no publicly available datasets for such an application, hence the data is collected manually by repeatedly executing Image Based Visual Servoing in the aforementioned simulation environment, and varying the location of the target (ArUCo marker in this case) and the altitude of the UAV. The input vector contains the error term e $[e_x, e_y]$ which is calculated by taking the difference of the coordinates of the ArUco Marker detected by OpenCV algorithms and the center of the image plane. Moreover, the input vector also contains the altitude of the UAV which is taken from the flight controller. Further the output vector contains the control ques i.e., the desired velocities which are calculated using the IBVS algorithm.

D. Proposed Architecture

The DLVS regression architecture works in a single phase, where the main allegiance of the model is to extract the temporal information from the sequential error data given to it as an input, and predict the control cues to be given to the flight controller of the UAV to perform an efficient target tracking. The proposed sequential *DLVS* architecture is explained further in this subsection.

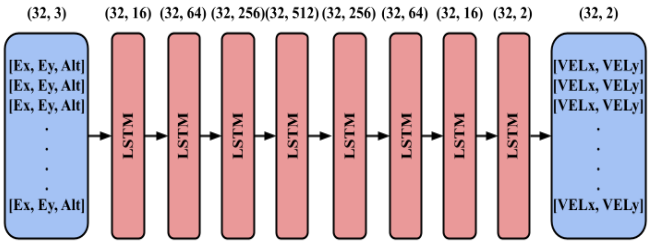

Fig. 2. A brief outline of the proposed network architecture, a vector containing pixel errors in x and y direction along with altitude value is given as an input to the LSTM architecture (Pink). After recollecting all the shared information, the architecture outputs a final velocity vector a UAV should opt for target tracking.

The *DLVS* architecture, represented in the Fig. 2, processes the 32 stacked error values and altitude of UAV, shaped (32 x 3). Further the input is sent to the LSTM model which decodes it by values of 16, 64, 256 and 512 units to preprocess and acknowledge the processed information and understand the principal features from the input sequence. The decoded output, shaped (32 x 512), is advanced to the encoding segment of the network architecture, which encodes it in the values of 256, 64, and 16 to regather all the useful information for velocity prediction. At last, the model predicts the required outputs shaped (32x2), the control cues of UAV.

The decoding and encoding unit values were tested rigorously and the values which best satisfied the computational constraints of the OBCs aboard the UAVs while also providing satisfactory performance were chosen. Alongside this decision-making, the "sigmoid" activation function is selected as recurrent activation for input, forget and output gate, and "modified_tanh" *(explained in section E of Methodology)* as the usual activation function for countering the vanishing gradient problems faced in Recurrent Neural Networks.

E. Activation Function

It is empirically evidenced, if the network connectivity is large, back-propagation learning with antisymmetric activation functions can yield faster convergence than a similar process with non-symmetric activation functions. Therefore, the nonlinearity was introduced in the network architecture by the proposed novel activation function named as "modified_tanh", the name was derived from the fact that the research initiated with the "hyperbolic tangent" activation function, but was shifted to a modified version because of the reasons discussed further.

Tanh function is similar to the sigmoid function and is used for models where prediction probability is considered as an output. Unlike the sigmoid function hyperbolic_tanh takes any real value as input and outputs values in the ranging [-1, 1], here the neurons are permitted to assume both positive and negative values between the aforementioned interval.

$$output = 5 * ((e^{x/5} - e^{-x/5})/(e^{x/5} + e^{-x/5})) \tag{6}$$

Authorized licensed use limited to: DELHI TECHNICAL UNIV. Downloaded on July 03,2023 at 04:52:16 UTC from IEEE Xplore. Restrictions apply.

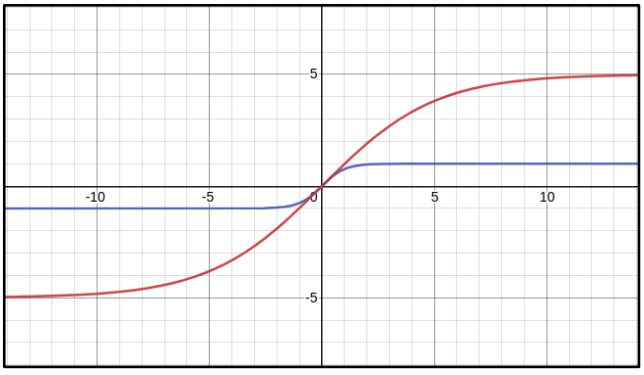

Fig. 3. Plot of the "modified_tanh" activation function (red) and the regular "tanh" activation function (blue).

The limitation faced during the implementation of the tanh activation function was the limiting of the output values in range of [-1, 1], leading to underutilization of the capability of the unmanned aerial vehicle which can (both in simulation and real life) can travel at significantly higher velocities in the horizontal plane. Hence, to overcome the faced issue, a novel modified tanh (explained in aforementioned equation (6)) activation function is proposed, given in Fig. 3. This function permits the output values to range between [-5, 5], along with the similar slant behavior and characteristics as that of regular tanh activation function.

Where, x defines the input given to the neuron of the neural network and y is the output of the "modified_tanh" function.

F. Loss Function

In order to better illustrate the proposed work to leverage the results for extracting the features from error values to extract the velocities of a UAV in x and y directions, the network is trained by back propagating the sum of L1 and L2 regularization losses, which minimizes the sum of the all the absolute difference and squared differences between the true and the predicted value respectively, as elaborated in Fig. 4, throughout the architecture. The loss is given as:

$$Loss = \sum_{i=0}^{n} |y_i - \hat{y}_i| + (y_i - \hat{y}_i)^2 \quad (7)$$

where n denotes total outputs in a batch, y_i and $\hat{y}_i$ represents the ground truth control cues estimated by IBVS algorithm and predicted control actions performed by proposed architecture of the custom dataset to be trained, as stated in equation (7).

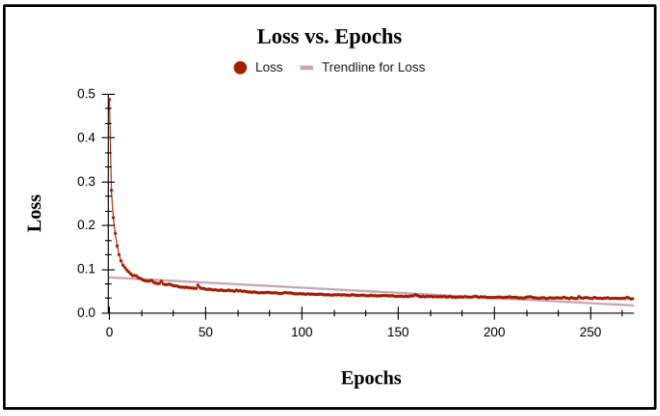

Fig. 4. Degrading loss curve on custom dataset over number of epochs

The proposed loss deals with the regression tasks where UAV maneuvers are predicted by the model belong to one out of many possible categories and is aimed to determine the difference between multiple probability distributions. Modified Hyperbolic Tangent is the sole activation function used in conjunction with the above represented loss function. The training loss curves obtained in the training phase, for the collected dataset, provided in Fig. 4.

IV. Experimental Results

A. Training Details

The proposed DL-IBVS model is designed, implemented and trained using the TensorFlow library. In the training process, an adaptive momentum optimizer (Adam)[12] is used which handles sparse gradients on noisy problems. The model was first trained for a total of 120 epochs, and was inferenced and validated by training it on a static target dataset collected at 10m of altitude. This architecture was further trained and fine-tuned for variable altitudes and dynamic target dataset. The learning rate is set to 0.0001 for the first 85 epochs and then trained on scheduled learning rate which is reduced by the factor of 0.95 for the remaining epochs. The batch size was kept 32, which refers to 32 consecutive errors in x and y directions, and UAV's altitudes values. Each epoch took approximately 12 minutes with the Quadro P5000 GPU. The entire network architecture comprises approximately 2.8 million parameters that helps in accumulating the trainable features from the given input error and altitude sequences to estimate the UAV velocities for the required task.

B. Experimental Matrix

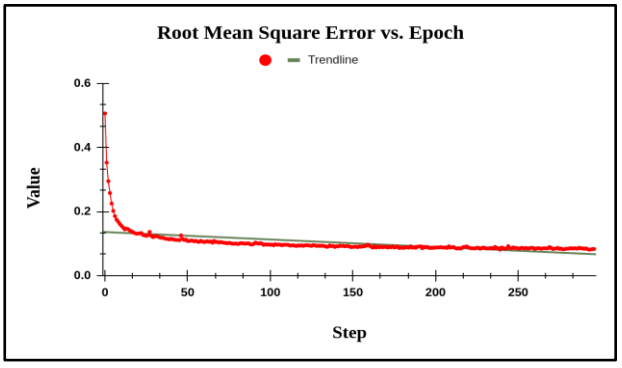

Fig. 5. Root Mean Square Error on each step of training.

To evaluate the quantitative results of the proposed DL-IBVS model, as seen in Fig. 5, we used an evaluation matrix called Root Mean Square (RMSE) Error, equation 8, to check the similarity measure between predicted depth value and ground truth.

$$RMSE = \sqrt{1/n \left(\sum_{i=0}^{n} (y_i - \hat{y}_i)^2\right)} \quad (8)$$

C. Ablation Study

An ablation study is carried out to exhibit the strength of the proposed deep learning based visual servoing framework in a step-by-step manner. The study also verifies that the inclusion of time-series learning along instead of usual dense layers has

Authorized licensed use limited to: DELHI TECHNICAL UNIV. Downloaded on July 03,2023 at 04:52:16 UTC from IEEE Xplore. Restrictions apply.

boosted the performance of the proposed algorithm by a large margin for Image Based Visual Servoing methodology.

DLVS is able to achieve the suitable required results, the reason being the learning of appropriate temporal details using Long-Short Term Memory based encoding and decoding structure for a stack of 32 error values. To optimize the performance of any algorithm it is important to select the correct stack value for temporal learning rather than just applying temporal learning on any set of stacks of error values. In this direction, an experiment is conducted to select the optimal stack value for efficient temporal learning. It is observed that outperforming results are seen when there are 32 consecutive errors (in x and y directions) and altitude values are considered for one training example. Experiments were performed for 8, 16, 32 and 64 stack values. It is clearly observed that 8 and 16 frames do not provide enough temporal details to learn the parametric information efficiently. Whereas for 32 frames, maximum recognition accuracy is achieved as shown in Fig. 6. As the number of frames are increased further to 64, the same performance is observed at the cost of handling a larger stack. Hence, a stack of 32 frames is chosen for the experiments to learn temporal information and estimating the velocity outputs for x and y directions, given to the flight controller for efficient tracking performance.

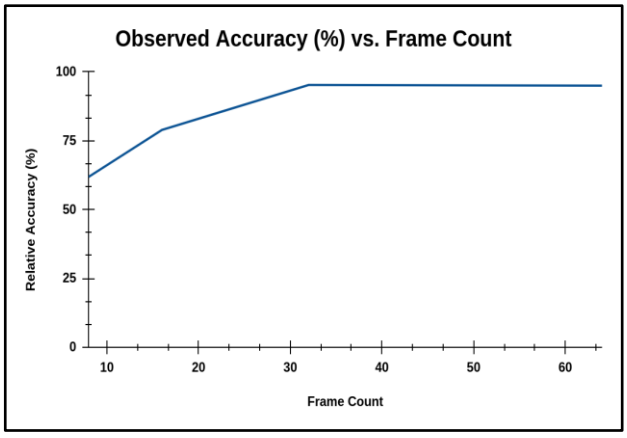

Fig. 6. Effect of size of input stack on the performance of the proposed algorithm.

D. Real-Time Testing

The algorithm was evaluated in the real world using a Tarot 650 UAV, with a Pixhawk Cube Black flight controller, Jetson Nano 2.0 On-Board Computer, Git2P camera, and TAROT TL3T05 gimbal. Once the *DLVS* code is triggered from the Ground Control Station, the RGB frames from the downward-facing camera are fed into the computer vision algorithm to detect the ArUco Marker. Upon detection, the resultant errors, and the altitude of the UAV are fed to the deep learning architecture, which subsequently predicts the control cues which are sent to the flight controller as mavlink messages. The reported error between the four corners of the ArUco markers and their desired location in the image plane by the UAV is represented in Figure 8. The proposed deep learning-based visual servoing forward pass processing took around 0.41 milliseconds (or 24 FPS) when implemented on Jetson Nano 2.0 OBC (with Quad-core ARM A57 @ 1.43 GHz CPU, 128-core Maxwell GPU, and 4GB RAM).

Fig. 7. Real-life tracking of ArUco Marker using Tarot-650 UAV.

Furthermore, optimization was done to ensure the UAV can converge on the target as fast as possible while also avoiding any oscillations as shown in Fig. 7. The plot of error between the position of the four corners of the ArUco marker and their desired locations in the image plane with respect to time was chosen as the metric to evaluate the performance of the algorithm. Here, Fig 8 shows the smooth exponentially decreasing error plot obtained when the final algorithm was deployed on the Tarot-650 UAV.

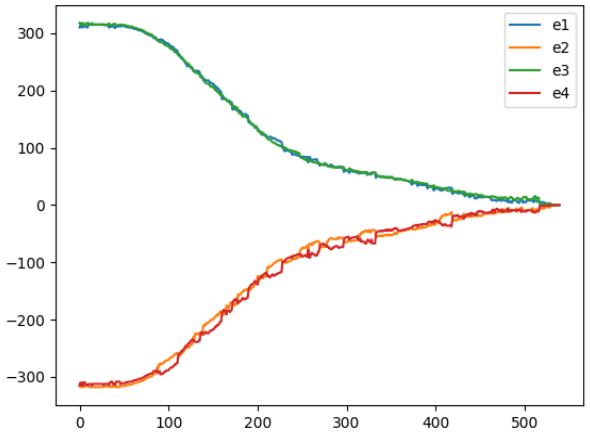

Fig. 8. Plot of the distance of the four corners of the ArUco Marker from their desired location.

V. Conclusion

In this research, a novel time-series approach for visual servoing and autonomous tracking of any target is presented. The algorithm capitalizes on the fusion of a computer vision algorithm for object detection and a deep learning-based LSTM algorithm to produce velocities that a UAV should opt for efficient tracking of the target. The proposed network architecture uses encrypted error information obtained by calculating the difference between the center of the detected target and the center of the camera frame and outputs the control cues for UAS accordingly. For training of the proposed algorithm, a custom dataset was generated *(as explained in section C of the Methodology)* using a simulation environment

Authorized licensed use limited to: DELHI TECHNICAL UNIV. Downloaded on July 03,2023 at 04:52:16 UTC from IEEE Xplore. Restrictions apply.

(presented in section A of the Methodology). Further, the validation of *DLVS* architecture was carried out in a similar simulation environment. Once the optimal results were obtained, real-life flight testing was performed for target tracking of an ArUco Marker *(shown in section D of Experimental Results)*. It is also observed that the target tracking accuracy of the framework is consistent for static as well as dynamic targets in different views, occlusion, and terrain conditions that confirm the robustness of the algorithm. At last, comparisons are outlined with the current state-of-the-art solutions for the proposed deep architecture proving the excellence of the framework in terms of both time efficiency and accuracy as it has reduced the algorithm's dependencies on the surrounding environment type of target to be tracked and even camera matrices.

For the future perspective of the research, the experiments mentioned below can outperform this approach:

- ➢ The use of RL for learning and estimating the control cues or velocity generated for tracking any detected object, maintaining time-complexity, efficiency and performance of the system.
- ➢ Introducing other parameters to encode the target motion can enhance the outcomes of the *DLVS* tracking algorithm to an observative magnitude.

REFERENCES

[1] W. Fu, H. Hadj-Abdelkader and E. Colle, "Visual servoing based mobile robot navigation able to deal with complete target loss," 2013 18th International Conference on Methods & Models in Automation & Robotics (MMAR), 2013, pp. 502-507, doi: 10.1109/MMAR.2013.6669961.

[2] B. Thuilot, P. Martinet, L. Cordesses and J. Gallice, "Position based visual servoing: keeping the object in the field of vision," Proceedings 2002 IEEE International Conference on Robotics and Automation (Cat. No.02CH37292), 2002, pp. 1624-1629 vol.2, doi: 10.1109/ROBOT.2002.1014775.

[3] F. Chaumette and S. Hutchinson, "Visual servo control. I. Basic approach," in IEEE Robotics & Automation Magazine, vol. 13, no. 4, pp. 82-90, Dec. 2006, DOI: 10.1109/MRA.2006.250573.][F. Chaumette and S. Hutchinson, "Visual servo control. II. Advanced approach [Tutorial]," in IEEE Robotics & Automation Magazine, vol. 14, no. 1, pp. 109-118, March 2007, DOI: 10.1109/MRA.2007.339609.

[4] Marinela G. Popova and Hugh H. Liu. "Position-Based Visual Servoing for Target Tracking by a Quadrotor UAV," AIAA 2016-2092. AIAA Guidance, Navigation, and Control Conference. January 2016.

[5] Sepp Hochreiter, Jürgen Schmidhuber; Long Short-Term Memory. *Neural Comput* 1997; 9 (8): 1735–1780. doi: https://doi.org/10.1162/neco.1997.9.8.1735

[6] Q. Bateux, E. Marchand, J. Leitner, F. Chaumette and P. Corke, "Training Deep Neural Networks for Visual Servoing," 2018 IEEE International Conference on Robotics and Automation (ICRA), 2018, pp. 3307-3314, doi: 10.1109/ICRA.2018.8461068

[7] Srivastava, S., Divekar, A.V., Anilkumar, C. et al. Comparative analysis of deep learning image detection algorithms. J Big Data 8, 66 (2021). https://doi.org/10.1186/s40537-021-00434-w.

[8] Lim, Jae Hyun and J. C. Ye. "Geometric GAN." *ArXiv* abs/1705.02894 (2017): n. pag.

[9] M. Karthi, V. Muthulakshmi, R. Priscilla, P. Praveen and K. Vanisri, "Evolution of YOLO-V5 Algorithm for Object Detection: Automated Detection of Library Books and Performace validation of Dataset," 2021 International Conference on Innovative Computing, Intelligent Communication and Smart Electrical Systems (ICSES), Chennai, India, 2021, pp. 1-6, doi: 10.1109/ICSES52305.2021.9633834.

[10] Quigley, Morgan, et al. "ROS: an open-source Robot Operating System." ICRA Workshop on open-source software. Vol. 3. No. 3.2. 2009.

[11] N. Koenig and A. Howard, "Design and use paradigms for Gazebo, an open-source multi-robot simulator," 2004 IEEE/RSJ International Conference on Intelligent Robots and Systems (IROS) (IEEE Cat. No.04CH37566), 2004, pp. 2149-2154 vol.3, DOI: 10.1109/IROS.2004.1389727.

[12] Kingma, D.P., & Ba, J. (2014). Adam: A Method for Stochastic Optimization. *CoRR, abs/1412.6980*.

[13] Jabbari Asl, Hamed & Oriolo, Giuseppe & Bolandi, H.. (2012). Dynamic IBVS control of an underactuated UAV. 2012 IEEE International Conference on Robotics and Biomimetics, ROBIO 2012 - Conference Digest. 10.1109/ROBIO.2012.6491126.

[14] Jiuxiang Dong, Jie Zhang, A new image-based visual servoing method with velocity direction control, Journal of the Franklin Institute, Volume 357, Issue 7, 2020, Pages 3993-4007, ISSN 0016-0032, https://doi.org/10.1016/j.jfranklin.2020.01.012.

[15] Anunay, Pankaj and C. Dhiman, "DepthNet: A Monocular Depth Estimation Framework," 2021 International Conference on Engineering and Emerging Technologies (ICEET), Istanbul, Turkey, 2021, pp. 1-6, doi: 10.1109/ICEET53442.2021.9659770.

[16] P. Corke, Robotics, Vision and Control: Fundamental Algorithms in MATLAB, 1st ed. Springer Publishing Company, Incorporated, 2013.

[17] N. Shahriari, S. Fantasia, F. Flacco, and G. Oriolo, "Robotic visual servoing of moving targets," in 2013 IEEE/RSJ International Conference on Intelligent Robots and Systems, 2013, pp. 77–82.

[18] S. Hutchinson, G. D. Hager, and P. I. Corke, "A tutorial on visual servo control," IEEE transactions on robotics and automation, vol. 12, no. 5, pp. 651–670, 1996.

[19] N. Aggarwal, V. Jain, JP Kesari "Image-based visual servoing for tracking and landing on a moving target using a multirotor" vol. 3 issue 11, November 2021

[20] Shen, S., Mulgaonkar, Y., Michael, N. & Kumar, V. Vision-based state estimation and trajectory control towards aggressive flight with a quadrotor. In *Proc. Robotics: Science and Systems* http://www.roboticsproceedings.org/rss09/p32.html (2013).

[21] Fazle Karim, Somshubra Majumdar, Houshang Darabi, Samuel Harford, Multivariate LSTM-FCNs for time series classification, Neural Networks, Volume 116, 2019, Pages 237-245, ISSN 0893-6080,https://doi.org/10.1016/j.neunet.2019.04.014.

[22] Rahim Barzegar, Mohammad Taghi Aalami, Jan Adamowski, Coupling a hybrid CNN-LSTM deep learning model with a Boundary Corrected Maximal Overlap Discrete Wavelet Transform for multiscale Lakewater level forecasting, Journal of Hydrology, Volume 598, 2021, 126196, ISSN 0022-1694, https://doi.org/10.1016/j.jhydrol.2021.126196.

[23] Eduardo Godinho Ribeiro, Raul de Queiroz Mendes, Valdir Grassi, Real-time deep learning approach to visual servo control and grasp detection for autonomous robotic manipulation, Robotics and Autonomous Systems, Volume 139, 2021, 103757, ISSN 0921-8890, https://doi.org/10.1016/j.robot.2021.103757.

[24] Anurag Sai Vempati, Vipul Choudhary, Laxmidhar Behera, Quadrotor: Design, Control and Vision Based Localization, IFAC Proceedings Volumes, Volume 47, Issue 1, 2014, Pages 1104-1110,https://doi.org/10.3182/20140313-3-IN-3024.00229. (https://www.sciencedirect.com/science/article/pii/S1474667016327926)

[25] X. Zhou et al., "An LSTM-based Bilateral Active Estimation Model for Robotic Teleoperation with Varying Time Delay," 2022 International Conference on Advanced Robotics and Mechatronics (ICARM), Guilin, China, 2022, pp. 725-730, doi: 10.1109/ICARM54641.2022.9959537.

[26] Guo, S.; Sun, N.; Pei, Y.; Li, Q. 3D-UNet-LSTM: A Deep Learning-Based Radar Echo Extrapolation Model for Convective Nowcasting. Remote Sens. 2023, 15, 1529. https://doi.org/10.3390/rs15061529

[27] Saad A. Yaseen and Sreela Sasi, "Robust Algorithm for Object Detection and Tracking in a Dynamic Scene," Journal of Image and Graphics, Vol. 2, No. 1, pp. 41-45, June 2014. doi: 10.12720/joig.2.1.41-45

[28] Karthik Dinesh and Sumana Gupta, "Video Stabilization, Camera Motion Pattern Recognition and Motion Tracking Using Spatiotemporal Regularity Flow," Journal of Image and Graphics, Vol. 2, No. 1, pp. 33-40, June 2014. doi: 10.12720/joig.2.1.33-40

Authorized licensed use limited to: DELHI TECHNICAL UNIV. Downloaded on July 03,2023 at 04:52:16 UTC from IEEE Xplore. Restrictions apply.

[29] Jorge Henrique Busatto Casagrande and Marcelo Ricardo Stemmer, "Abnormal Motion Analysis for Tracking-Based Approaches Using Region-Based Method with Mobile Grid," Journal of Image and Graphics, Vol. 2, No. 1, pp. 22-27, June 2014. doi:10.12720/joig.2.1.22-27

[30] Chin-Shiuh Shieh, Yong-Shixa Jhan, Yuan-Li Liu, Mong-Fong Horng, and Tsair-Fwu Lee, "Video Object Tracking with Heuristic Optimization Methods," Journal of Image and Graphics, Vol. 6, No. 2, pp. 95-99, December 2018. doi: 10.18178/joig.6.2.95-99

Authorized licensed use limited to: DELHI TECHNICAL UNIV. Downloaded on July 03,2023 at 04:52:16 UTC from IEEE Xplore. Restrictions apply.

IEEE Access
Multidisciplinary | Rapid Review | Open Access Journal

Received 21 June 2023, accepted 1 July 2023, date of publication 7 July 2023, date of current version 18 July 2023.

Digital Object Identifier 10.1109/ACCESS.2023.3293061

RESEARCH ARTICLE

DTPF Algorithm Based Open-Source Time-Sensitive Network Leveraging SDN Architecture

ASHA G. HAGARGUND[1,2], (Graduate Student Member, IEEE), NEELAWAR SHEKAR VITTAL SHET[1], AND MURALIDHAR KULKARNI[3], (Senior Member, IEEE)

[1]Department of Electronics and Communication Engineering, National Institute of Technology Karnataka, Surathkal 575025, India
[2]Department of Electronics and Communication, BMS Institute of Technology and Management, Bengaluru 560064, India
[3]Department of Electronics and Communication Engineering, National Institute of Technology Karnataka, Surathkal 575025, India *(Retired)*

Corresponding author: Asha G. Hagargund (asha.187ec500@nitk.edu.in)

ABSTRACT Time-Sensitive Networking (TSN) has enabled a lot of advancements in industrial automation, aviation, tactile networking, and other ad-hoc networking applications. The bounded latency, reliability, and self-recovering mechanisms for a network are some of the core attributes of the TSN architecture. The reliability of bench-marking of a given TSN architecture, when done with simulators, will not match with that of hardware systems. But the TSN hardware needs more capital investment along with more development time as it involves understanding the hardware-specific parameters. The research in this paper has solved this shortcoming by implementing an open-source and secured SDN(Software Defined Networking)-based TSN framework integrating IEEE's 802.1 Qbv and 802.1Qcc standards. The novelty of implementation involves i) Realization of Centralized User Configuration (CUC), Centralized Network Configuration (CNC) with open source tools. ii) An algorithm called Dynamic TSN Path Finder (DTPF) is implemented for automatically identifying TSN edges participating in TSN flow. iii) Emulation of hardware environment leveraging Linux-based queuing disciplines and traffic shapers. This unique open source-based TSN architecture is then tested with both TSN and Non-TSN traffic, to demonstrate the gating logic and the delay characteristics based on queuing discipline when applied to virtual queues.

INDEX TERMS Software-defined networking, open-source, scheduling, switches, queuing disciplines, time-sensitive networking, IEEE protocols.

I. INTRODUCTION

TSN is an effort to integrate Operational Technology (OT) and Information Technology(IT) enabling the co-existence of time-bounded control traffic and best-effort traffic to reduce the infrastructure cost. The IEEE 802.1 TSN standards provide real-time capabilities to the Ethernet, which have opened up a large number of applications in Industrial Automation, Audio Video Bridging (AVB), Aerospace, Automotive, and in-vehicle communication domains [1]. These standards aim at providing deterministic data delivery with bounded latency for heterogeneous data and shared networks creating a vendor-independent and converged network.

In current automotive and industrial networks, the reconfiguration of the network is not possible on the fly whenever there is a need. This evidently affects the efficiency of the network as it is more time-consuming because of manual effort, which is vulnerable to human errors [5]. Hence there is a need for a centralized controller which can perform automatic scheduling in case of network reconfiguration. [4], [17], [35], [39]

The SDN architecture has a centralized controller that controls flow tables of switches connected to it. Hence leveraging SDN architecture for TSN brings down the development time significantly [22], [24], [39]. Most of the papers propose

The associate editor coordinating the review of this manuscript and approving it for publication was Songwen Pei.

This work is licensed under a Creative Commons Attribution-NonCommercial-NoDerivatives 4.0 License.
For more information, see https://creativecommons.org/licenses/by-nc-nd/4.0/

customization to the existing SDN framework that is required for realizing TSN architecture. The paper [5] proposes one such SDN-based TSN model using NEON controller and APIs required for communication with TSN bridges which are compliant with IEEE's 802.1Qbv and 802.1AS standards.

Similarly, the author in [7] proposes and implements the TSN network architecture for industrial automation especially for dynamically interconnected time-sensitive end devices, using SDN-based centralized configuration and Open Platform Communications-Unified Architecture (OPC-UA) which serve as the data exchanging technology between applications of industrial automation.

The author in [12] has created an SDN-based TSN network for industrial Ethernet applications with multiple Quality of Service (QoS) requirements. Depending on the application's QoS requirements the appropriate TSN schedules are pushed from the SDN-based controller to its connected switches. The scheduling strategies are calculated at the SDN controller and are used at the switches to update their Gate Control List(GCL). The communication between the SDN controller and the TSN switches is done through the NETCONF protocol. The Satisfiability Modulo Theories (SMT) based scheduling and rate monotonic scheduling have been realized.

In the paper [14], the author proposes the partitioning of available bandwidth for implementing IEEE 802.1Qbv scheduling. This approach enables the SDN controller to calculate the configuration of dynamic flows independently without disturbing the static configuration. The simulation for finding the end-to-end delay and jitter for various in-car network nodes is carried out in an OMNET++ based simulator. Hence the results presented do not take real-time constraints into consideration.

The paper [15] implements an SDN-based TSN network using source routing and IEEE 802.1Qbv in its data plane to check the performance of the network for bounded latency using Linux TAPRIO(Time Aware Priority Queuing) queuing discipline. The virtual local area network's Virtual LAN(VLAN) Priority Code Point (PCP) based traffic class mapping is used with the multiple virtual queues. The research work under [15] does not give much detail on how virtual queues are created and also does not emphasize the classification of packets required for queuing discipline. The source-based routing is proposed in [15] without discussing the overhead imposed on TSN traffic.

The author of the paper [19] proposed a reconfiguration framework based on the IEEE 802.1Qbv standard in collaboration with the IEEE 802.1Qcc standard using SDN controller to implement a control mechanism that incorporates the 802.1Qcc variables, including the flow instantiating parameters and the 802.1Qbv gate control parameters. The author modeled his own queue structure for the simulation of aforesaid IEEE standards. The paper [19] does not convey the type of SDN controller used. The information given as part of virtual queues is not justifiable with respect to gate control logic that has been proposed by IEEE 802.1Qbv standards. Also, the Author in [18]explains the SDN model, to implement the inter-domain TSN network, and the author in [20] builds a test bed to demonstrate the unified control-plane Time-Sensitive Software-Defined Networking (TSSDN).

The fully centralized architecture inspired by the SDN model of TSN is proposed by IEEE [25]. According to this CUC is a software that considers the requirements from TSN end nodes and sends the requirement to CNC. The CUC collects the requirements of TSN end devices through CUC and sends this information to TSN switches. TSN switches are capable of transmitting and receiving the Ethernet frames according to the schedule. TSN talkers and listeners are the source and destination of the TSN flows. This model has knowledge of the entire network and hence manages the transmission schedule and paths.

In [44], the author discusses about the issues in integrating the SDN control plane for TSN. Implements a small-scale hardware test bed using NXP LS1028A to build CUC, CNC, and TSN switches and NXP iMX8MP as TSN end nodes. The delay for TSN data is evaluated. As SDN-based architecture might produce high latency when network reconfiguration is done in the control plane, the author concludes that the proposed architecture, Fully time-sensitive software-defined networking helps in optimizing the problem.

Creating a complete hardware setup is a costly and complex task, especially for a large-scale TSN network. The author in [46] implements the hybrid simulation testbed, where software-generated traffic is combined with real sensor data. With this setup, they test for security, data processing, protocol testing, and performance measurement. The hardware components used are Ubertooth One and Libelium Waspmote for generating sensor data, C1-Toradex as SDN controller, and for software Mininet and Mininet-Wifi in a Linux environment are used.

In [33], the author proposes and implements open-source scheduling strategies for Linux systems. The new TT(Time Triggered) scheduler achieves real-time guarantees. The details on various scheduling mechanisms for real-time applications are mentioned. This paper doesn't consider SDN-based architecture.

As discussed in the previous paragraphs, many papers are present in the literature which implements and tests TSN network with simulation tools [14], hardware test beds [41], [44], [45] and hybrid of both hardware and software [46]. As we have used virtual queues for our work, it is important to discuss the virtual queues and compare them with hardware queues.

The hardware queues are part of NICs that enable offloading of network processing tasks from the host's CPU. Hence this reduced CPU utilization helps in boosting networking performance. Whereas the virtual queues are implemented in software. The networking stack of the host operating system takes the full onus of handling traffic passing through

virtual queues. The virtual queues are typically used for communication between different network namespaces or containers within a host. Hence, the CPU speed of the host, the networking stack efficiency, and the system load are some of the factors impacting the service rate of the virtual queue. This might lead to increased latency and lower throughput compared to the hardware queue. Intel®Ethernet Controller I210 (Network Interface Card)NIC from Intel is one of the TSN-aware NIC with hardware-based queues. These kinds of hardware-based NICs provide bounded latency communication for industrial applications. [41].

The continuous evolution of the kernel bypass techniques and software data planes have greatly succeeded to address the performance limitations of traditional software-based networking stacks, narrowing the performance gap between virtual queues and hardware queues. Intel's Data Plane Development Kit (DPDK) enables user-space applications to achieve high packet processing rates by bypassing kernel [42].

In our paper, we have shown how software containers and their virtual queues can be used to provide deterministic operations suitable for industrial networks. On the same lines the research proposed under [41] demonstrates the accuracy of software application timing and offset control is within a few hundred- μsecond range, which can satisfy the requirements posed in the cloud environment.

Our research work proposed in this work emphasizes on using our architecture for TSN-aware PoC(Proof of Concept) as our novel architecture uses open-source tools to bring down the PoC cost.

IEEE proposes scheduling strategies like IEEE 802.1Qbv (Time Aware Shaper), IEEE 802.1Qbu(Frame Preemption) and IEEE 802.1Qav(Credit Based Shapers). In our work, we assume that TSN traffic is periodic and the TSN traffic arrival time is known prior. For this requirement, IEEE 802.1Qbv is the apt scheduling scheme. TAS ensures that the egress port which is designated for TSN traffic is idle when TSN traffic is scheduled. It ensures this by using the gating logic. TAS assigns the queues to each traffic class and the gates to their allocated queues are kept open or close based on the schedule. As in periodic TSN data transmission, the schedule is known prior to the gate corresponding to the TSN traffic class being kept open, so that a particular queue gets attached to the egress port. This makes sure that TSN traffic egresses at the scheduled time [31], [43], [47], [48].

Since our work mainly focuses on TSN traffic where the traffic schedule is already known to the admin, we have decided to do the research using IEEE802.1Qbv. Moreover, we wanted to explore the performance of the veth queue without pushing ourselves into the number of queue limitations.

IEEE 802.1Qcc proposes 3 architectures. Fully distributed, fully centralized and hybrid architecture [44]. We use fully centralized architecture as it proposes centralized management and control which enables seamless pushing of policies to all the connected edges. We have leveraged the SDN model to implement a fully centralized architecture which helps in pushing TSN schedules to all the switches participating in a TSN path/flow.

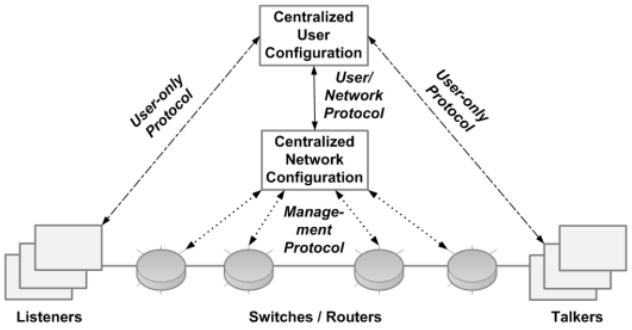

FIGURE 1. IEEE 802.1Qcc Fully centralized architecture [3].

The paper is structured in various sections as mentioned here. Section II- Describes the existing research gaps and the objectives of our paper. Section III describes our design approach carried out for the implementation of open source secured and SDN-based TSN architecture and section IV explains our contribution. SectionV discusses the results and conclusion.

II. RESEARCH GAP AND OBJECTIVES

A. RESEARCH GAP

In literature, many papers discuss about the need for a centralized SDN structure for TSN. There is a need for taking the real-time traffic and real constraints into consideration for bench-marking the results.

When SDN architecture is implemented for IEEE 802.1Qbv, using Linux queuing disciplines, configuration related to multiple virtual queues needs to be discussed with related details. These are missing in the present literature.

TAPRIO queuing discipline demands traffic classification at ingress and egress queues for allocation of queues. But the papers mentioned in the introduction do not present configuration and implementation details. Most of the papers modify OpenvSwitch to incorporate QoS functions needed for TSN. This may lead to some errors as OpenvSwitch may not modify every Linux kernel feature due to non-registered bugs if any [29]. To address the above-mentioned gaps the following objectives are defined in section II-B.

B. OBJECTIVES

- Perform the validation of the IEEE 802.1Qbv gating strategy by considering the real-time traffic.
- Provide complete implementation details of multiple virtual queues for the egress port of the switch.
- Discuss all the configuration details on TAPRIO, traffic class, filtering, and traffic scheduling in detail.
- Instead of modifying the OpenvSwitch for incorporating QoS functions, use the Linux traffic control utility "tc".
- Implement and validate the algorithm DTPF for TSN traffic for routing.
- Make communication secure by using Paramiko.

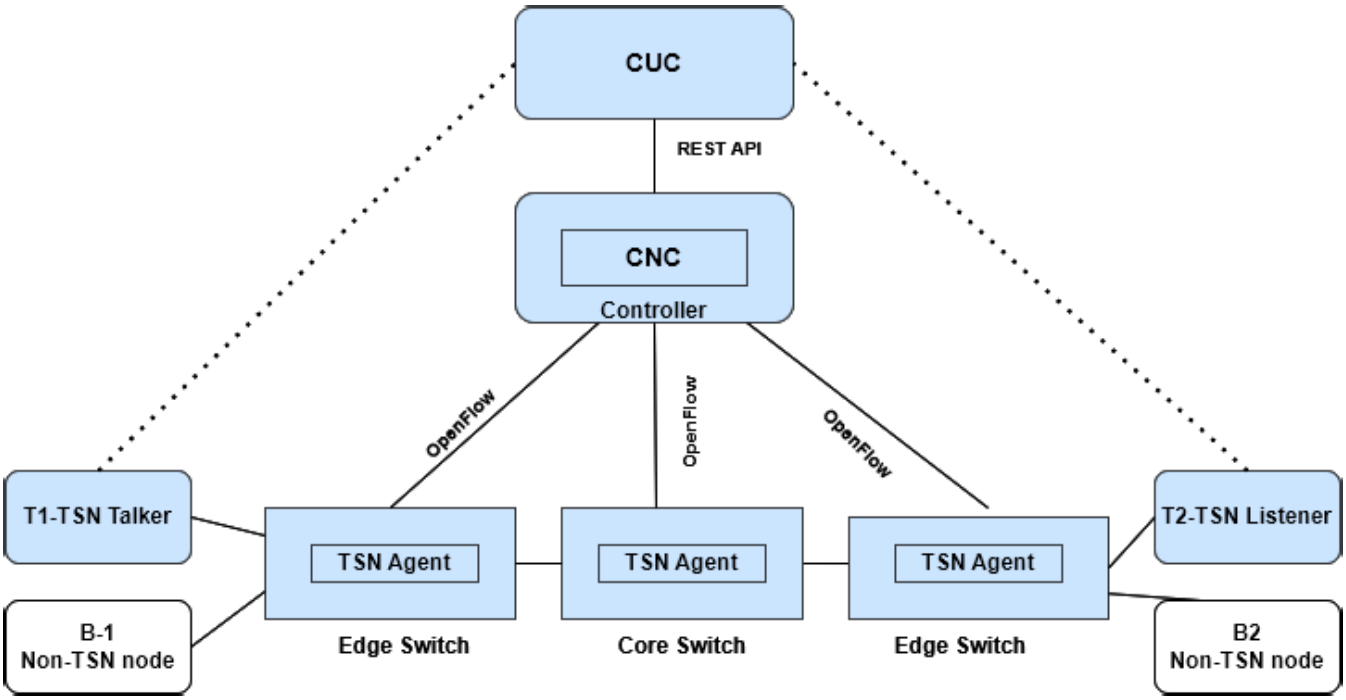

FIGURE 2. Basic building blocks of an SDN-based TSN network based on IEEE 802.1Qcc.

III. WORK DONE

A. DESIGN APPROACH

We propose a TSN network, that is based on IEEE 802.1Qcc fully centralized network as depicted in figure 1.

According to this CUC is software that communicates with the end devices and CNC. CUC gets the requirements of the end devices and makes requests to the CNC for deterministic communication with specific requirements for the traffic. Whereas CNC defines the schedule on which all TSN frames are transmitted. The CNC application is provided by the vendor of the TSN bridges. By taking this as a reference, we build the software for CNC, CUC, and TSN agents. We consider 2 traffic classes, one for TSN traffic and the second one for Non-TSN(Best Effort) traffic. We have 2 source nodes and 2 corresponding destination nodes as shown in fig.2. The following subsection explains the functions and implementation details of each component mentioned in Fig.2.

1) CENTRALIZED USER CONFIGURATION (CUC)

The CUC is a vendor-specific implementation for associated TSN nodes [26], [28]. This is an independent device provided by the vendor. In our implementation, CUC is hosted as a docker container. Under this container, a program called CUC-agent communicates with the Talker, Listener, and the CNC over a secured channel provided by SSH [2]. CUC is responsible for generating the TSN flow by pulling the requirements from TSN end nodes. CUC will then query the topological information from CNC using REST API. The topological information is filtered to form TSN flow, using our algorithm DTPF. Eventually, this TSN flow is sent to CNC. A TSN flow is a unidirectional path from talker to listener including the intermediate nodes as clearly depicted in Fig. 2

2) CENTRALIZED NETWORK CONFIGURATION (CNC)

We have used the OpenDaylight controller as CNC. But, we have not customized any OpenFlow API's for TSN architecture. Instead, a program called CNC-agent discovers the entire topology and returns it to the CUC when queried as mentioned in subsection III-A1 . On receiving the flow requirements from the CUC, the CNC will generate the TSN schedule according to IEEE 802.1Qbv standard. A TSN schedule contains the configuration which specifies the allocation of priority, queue, and time slice for a particular or set of traffic classes.

3) TSN ENABLED SWITCH

This is an SDN's OpenvSwitch in our implementation. To make this switch TSN aware a program called TSN agent is executed on the switch which deploys the TSN schedules as received from the CNC.

4) TALKER AND LISTENER

In our implementation, these are the two docker containers. The TSN end devices are responsible for generating and receiving the time-sensitive data respectively. The greater details on the classification of TSN data traffic are given in section IV-C

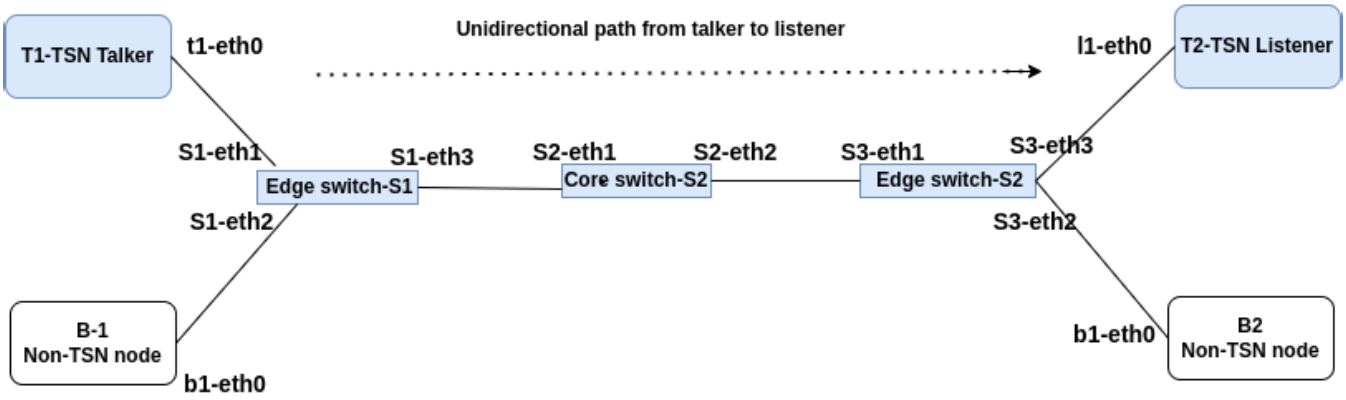

FIGURE 3. TSN flow/ TSN path with ethernet interfaces.

TABLE 1. Tools used for experiment.

Name of the component	Version
Mininet	2.3.1.b1
OpenDaylight controller	3.0.3
OpenVswitch	2.17.5
Python Programming language	3.8.10
Ubuntu O.S	20.04
"tc" utility	iproute 2 22200127

1) Talker's MAC and IP
2) Time slice of TSN data.
3) Listener's MAC and IP.

As mentioned in the objectives, we use secured communication between the components in our network by using SSHv2(Secure Shell Protocol Vesrion 2) Scripting protocol. The Python program uses paramiko, a module that implements the SSHv2 protocol for authenticating to a server using a password and SSH keys. Only after successful authentication, further data communication is done over a secured channel.

B. TOOLS AND COMPONENTS

Table 1 lists the information on open-source tools and other Linux utilities used in this work.

IV. OUR CONTRIBUTION

A. DYNAMIC TSN PATH FINDER (DTPF)ALGORITHM

For configuring the TSN schedule on edges and core switches involved in a TSN flow, the TSN path has to be identified first. To identify the TSN path we have implemented an algorithm called Dynamic TSN Path Finder which extracts the nodes that are part of the TSN flow. The input data for this algorithm is the topological information obtained from CNC using REST API by CUC. The proposed algorithm is mentioned in the algorithm section.

Algorithm 1 Dynamic TSN Path Finder Algorithm

Input: *srcmac*, *dstmac*, *sip*, *dip*, *ms*
Output: *tsnpath*
1: Get edges connections info from CNC using REST API
2: Get talkerswitch using smac
3: Get listenerswitch using dmac
4: prevswitch = none
5: get nxtswitch (switch connected to Talker switch)
6: curswitch (Talker switch)
7: tsnpath += nxtswitch
7: **While** *nxtswitch* $\neq$ *listenerswitch* **do**
8: prevswitch = curswitch
9: curswitch = nxtswitch
10: nxtswitch = Get the switch connected to nxtswitch
11: tsnpath += nxtswitch
11: **EndWhile**
12: Tsnpath has all intermediate TSN edges constituting TSNpath

B. NOT CUSTOMIZING SDN AND OPEN vSwitch MODELS FOR TSN

The research in this paper does not propose customization of SDN controllers as opposed to the paper discussed in the introduction section. Typically SDN controller customization involves writing/rewriting SDN flow APIs as per the requirement of the TSN network. These APIs in turn communicate to OpenvSwitch for updating its flowtable. This involves the configuration of a subset of Linux kernel QoS features. OpenvSwitch forum claims that it cannot configure every Linux kernel QoS feature because of unreported bugs related to QoS if any [29]. To avoid any side effects of unknown bugs we have configured the QoS using Linux traffic control utility "tc". [21], [30]. The SDN concept was proposed by Open Networking Foundation (ONF) that decouples the control and data planes. The framework is not directly usable for TSN architecture, as TSN demands core Linux QoS parameters modifications. If the underlying architecture of TSN is SDN, then all the challenges that are applicable to SDN also hold good for TSN. The main requirement in the TSN network is to have bounded latency between TSN talkers and listeners. Hence this paper does not propose a modification to the SDN controller model.

TABLE 2. Commands to classify ingress traffic.

```
sudo tc qdisc add dev s1-eth1 clsact
sudo tc filter add dev s1-eth1 ingress prio 1 u32 match ip dst
10.0.0.3 action skbedit priority 1
sudo tc filter add dev s1-eth1 ingress prio 1 u32 match ip dst
10.0.0.4 action skbedit priority 0
```

C. TSN TRAFFIC CLASSIFICATION

Fig. 3 shows the topology with egress and ingress port details of TSN edge and core switches. As we already discussed in section II-B the TSN traffic is not controlled using OpenvSwitch internal commands. Instead, we use a native Linux tool called "tc". TSN-based flows involve multiple queues controlling egress traffic based on various classes of traffic. But, Mininet by default creates virtual ethernet links with a single transmit and receive queue. To enable multiple queues under TSN aware switch we have modified the veth configuration under mininet version 2.3.1b1 to increase the number of transmit queues to 8. [30]

1) INGRESS TRAFFIC CLASSIFICATION

The ingressing traffic on the s1-eth1 port should be classified as TSN traffic. This also implies that the TSN traffic should be handled with high priority. To achieve this, Linux queuing discipline called "clsact" is used. The queuing discipline "clsact" enables the user to classify the packets based on the direction of the traffic on a given port. The classification can be made based on parameters like port, IP, and MAC [32]. The priority assigned to such classified traffic maps internally to socket buffers data structure "skb" priority member [4]. The skb->priority will be used by the Linux scheduler to dispatch the packets for processing based on the priority value. The higher value of skb->priority depicts more priority and is handled first. Table 2 shows the detailed "clact" commands used for classifying the ingressing TSN traffic on a port.

The command "tc" is a Linux utility for controlling the traffic. Under this utility, the user is able to provide various queuing disciplines as per the requirement. We use TAPRIO queuing discipline to implement IEEE 802.1Qbv scheduling.

Fig.6 and Fig. 7 shows the results of traffic filtering done using "skbprio" at the ingress port of s1 for TSN and Non TSN data.

D. TAPRIO QUEUING DISCIPLINE

After classifying the ingressing TSN traffic, we need to apply a queuing discipline on the egress port of the switch which should dequeue the prioritized packets at the ingress. To do this we have used Linux queuing discipline called TAPRIO, which is a simplified implementation of scheduling state machines as defined by IEEE 802.1Q-2018 Section 8.6.9. Each gate corresponds to a queue that dispatches outgoing traffic based on the traffic classes. TAPRIO operates on traffic mapped to different hardware queues [23]. We have used "veth" based virtual queues as we are using a native Ubuntu operating system running on Intel(R) Core(TM) i5-8265U CPU @ 1.60GHz which has a single hardware transmit and receive queue. For configuring virtual queues on Mininet's OpenVswitch interface we have edited the util.py of Mininet. This modification adds 8 transmit queues to the veth interface of OpenvSwitch. The modified version of the command to add the veth interface is given in Table 3 for reference.

TABLE 3. Command to add virtual Ethernet interface.

```
ip link add name %s numtxqueues 8 type veth peer name %s
```

Where "%s" is the OpenVswitch interface. For example, "s1-eth1" is the eth1 interface of switch-S1. The "numtxqueues" specifies the number of transmit queues for each interface type.

TABLE 4. Commands to execute TAPRIO on the egress port.

```
sudo tc qdisc add dev s1-eth3 parent root handle 100: taprio
num_tc 2
map 1 0
queues 1@0 1@1
base-time 0
sched-entry S 01 300000
sched-entry S 02 700000
clockid CLOCK_TAI
```

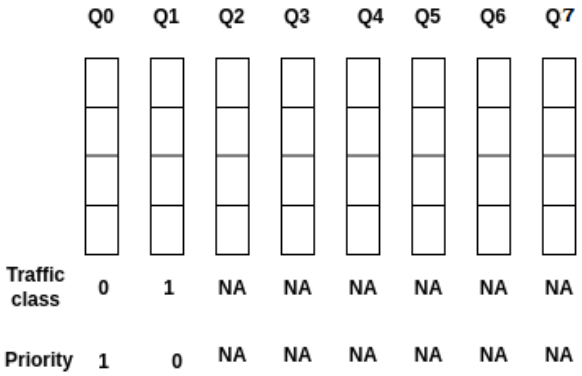

FIGURE 4. Traffic classes and priorities at the egress port of each switch.

Table 4 gives a detailed TAPRIO command executed on the egress port [34]. In our examples, 2 traffic classes are used. As shown in Figure 4 TSN traffic is class 0 and Best effort is class 1. Traffic class 0 has priority 1 and traffic class 1 has priority 0. Traffic class 0 uses the 0th queue and traffic class 1 uses the first queue. We expect the TSN traffic at the 0th queue and the best-effort traffic at the first queue. As TSN traffic considered here is periodic, the time slice for TSN traffic is 300 μs and for best-effort, it is 700 μs out of a 1000 μs switch cycle. Fig. 9 shows the results on TAPRIO queuing discipline implementation.

E. SOFTWARE MODULES

When the topology comes up various software modules interact with each other for handling the TSN traffic as per the configuration. The relevant software modules are implemented for carrying out the operations responsible for the

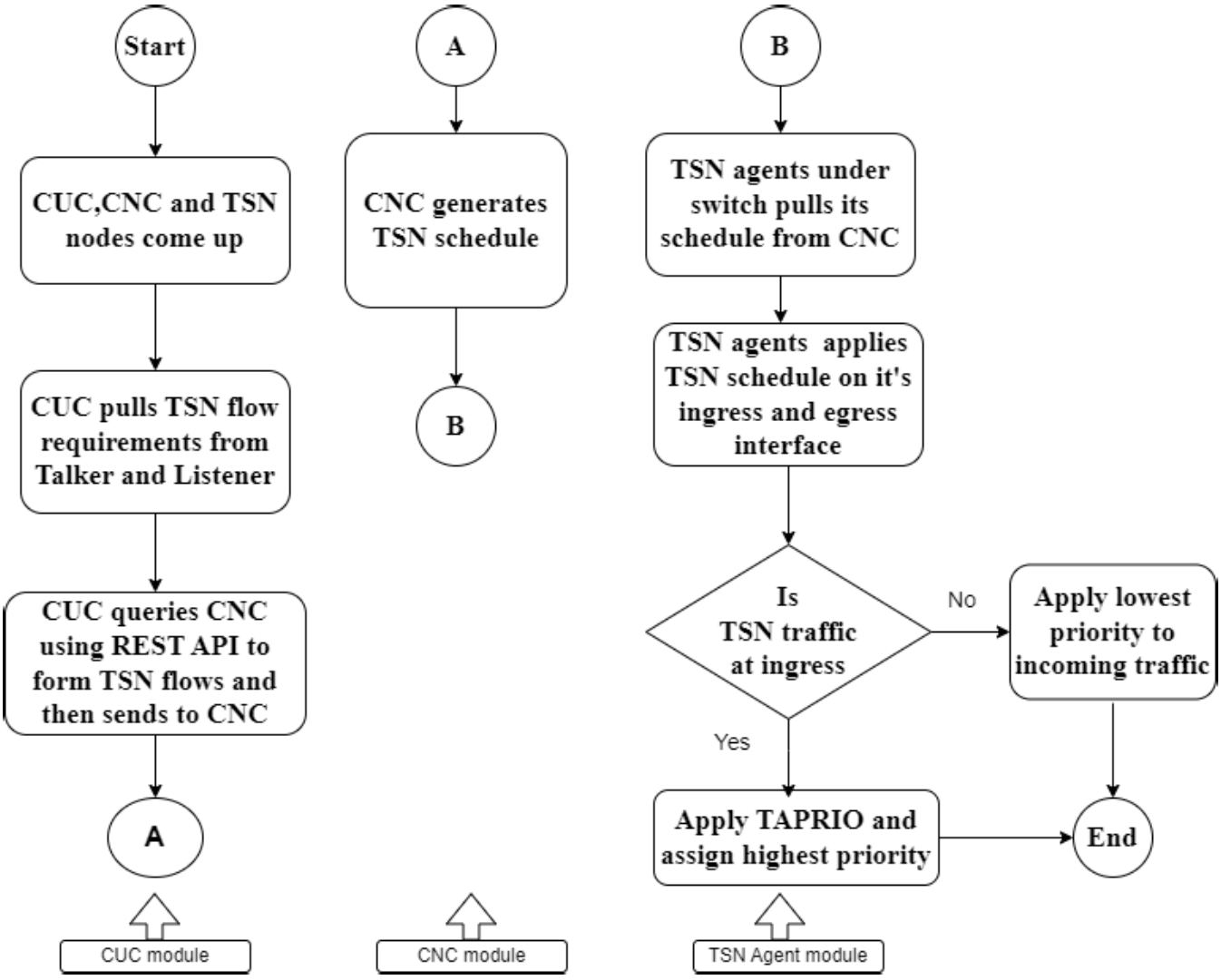

FIGURE 5. Software module interaction.

creation of TSN flow and generation of TSN schedules for TSN-aware switches. The flowchart presented in figure 5 gives the sequence of events involving below software modules.

1) CUC.py -THIS MODULE IS RESPONSIBLE FOR THE FOLLOWING TASKS

1) Pulling out TSN flow requirements from talker and listener.
2) Creating a TSN flow using the REST API involved DTPF.
3) Sending TSN flow to CNC.

2) CNC.py - THE CNC IN OUR IMPLEMENTATION IS A NON-CUSTOMIZED OpenDaylight CONTROLLER

Since the SDN-based controller has already well-defined control operations using OpenFlow protocol, our goal is to not overload with TSN-related operations. Hence, the CNC.py just parses the TSN flow as received by CUC and generates TSN schedules for switches involved in the TSN path using native Linux QoS commands.

3) TSNagent.PY

The OpenvSwitch is made TSN aware by adding the TSNagent.py module. We emphasize the point that there is no customization of OpenvSwitch. The TSNagent.py will pull the TSN schedule from CNC and execute the commands present in the schedule on both the ingress and egress interfaces of the TSN switch.

V. RESULTS

Following subsections explain various results observed with our proposed TSN architecture.

A. PACKET CLASSIFICATION USING SKB PRIORITY

The commands output in Fig.6 and Fig.7 shows the matching criteria for classification of the TSN and BE packets respectively. We are classifying packets based on destination

```
asha@asha:~$ tc -s -d filter show dev s1-eth1 ingress
filter protocol all pref 1 u32 chain 0
filter protocol all pref 1 u32 chain 0 fh 800: ht divisor 1
filter protocol all pref 1 u32 chain 0 fh 800::800 order 2048 key ht 800 bkt 0 terminal flowid ??? not_in_hw
  match 0a000003/ffffffff at 16
        action order 1: skbedit  priority :1 pipe
         index 1 ref 1 bind 1 installed 1168 sec used 257 sec
        Action statistics:
        Sent 252 bytes 3 pkt (dropped 0, overlimits 0 requeues 0)
        backlog 0b 0p requeues 0

filter protocol all pref 1 u32 chain 0 fh 800::801 order 2049 key ht 800 bkt 0 terminal flowid ??? not_in_hw
  match 0a000004/ffffffff at 16
        action order 1: skbedit  priority none pipe
         index 2 ref 1 bind 1 installed 1168 sec used 1168 sec
        Action statistics:
        Sent 0 bytes 0 pkt (dropped 0, overlimits 0 requeues 0)
        backlog 0b 0p requeues 0
```

FIGURE 6. Results on packet classification at s1-eth1 using skb priority.

```
asha@asha:~$ tc -s -d filter show dev s1-eth2 ingress
filter protocol all pref 1 u32 chain 0
filter protocol all pref 1 u32 chain 0 fh 800: ht divisor 1
filter protocol all pref 1 u32 chain 0 fh 800::800 order 2048 key ht 800 bkt 0 terminal flowid ??? not_in_hw
  match 0a000004/ffffffff at 16
        action order 1: skbedit  priority none pipe
         index 3 ref 1 bind 1 installed 1179 sec used 1133 sec
        Action statistics:
        Sent 84 bytes 1 pkt (dropped 0, overlimits 0 requeues 0)
        backlog 0b 0p requeues 0
```

FIGURE 7. Results on packet classification at s1-eth2 using skb priority.

IP address. The destination IP addresses "0a000003" and "0a000004" are of listener and peer BE nodes respectively. The destination IP address if matched to that of listener node, then the "skb" priority of "1" is assigned to that packet. Whereas the destination IP address if matched to that of peer BE node, then the "skb" priority of "0" is assigned to that packet. This assignment will stay intact till the TAPRIO queueing discipline is applied on the packet at the egressing interface "s1-eth3" of switch "s1" Point to note that "s1-eth1" and "s1-eth2" are ingress interfaces on TSN switch "s1" connected to TSN and BE nodes respectively.

B. GCL CHARACTERISTICS

In this section, the results of the realization of gating logic according to IEEE 802.1Qbv is discussed. Fig.8 and 9 depicts the gating logic involving time window allocation for TSN and Best Effort traffic respectively. As per the queuing logic, the first 300 μs of the duty cycle is for TSN traffic and the remaining 700 μs of the duty cycle is for Best-Effort traffic. The observed average time windows during which the TSN queue(Q0) was closed and opened were 734.8 μs and 281.4 μs respectively. This pattern is repeated for every switch cycle of 1000 μs.

Simulation is carried out for 10 ms and packets are generated at the rate of 1 packet per μs using ping utility. The graph in the Fig.8 and Fig.9 depicts that from 0-300 μs of the switching cycle TSN traffic of 1 packet per μs is egressing

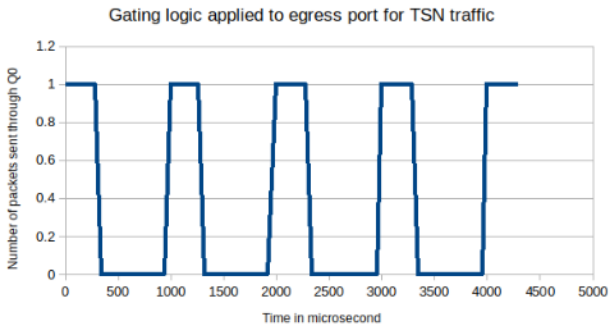

FIGURE 8. Demonstration of gating logic for TSN traffic.

through its respective queue. And from 301-1000 μs the TSN traffic is not allowed through the egress port. This is repeated for each switch cycle of 1000 μs.

The command output in Fig.10 shows the details on TAPRIO queueing discipline applied on interface "s1-eth3". The numbers 3000000 and 7000000 represent the time windows of TSN and BE traffic in nanoseconds, constituting the duty cycle of 10000000 nanoseconds or 1000 seconsds. The gatemasks 0×1 and 0×2 represent the TSN and BE traffic getting mapped to queue 0 and 1 respectively.

C. DELAY CHARACTERISTICS

In this section, various types of delays involved in transmitting TSN data from the TSN talker to the TSN listener are

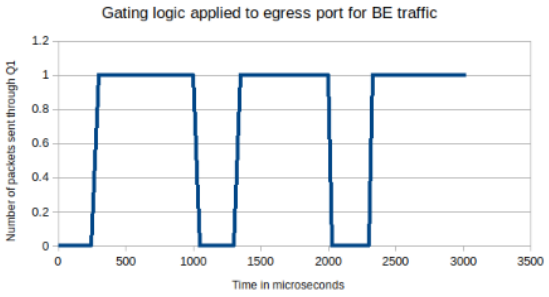

FIGURE 9. Demonstration of gating logic for Best-effort traffic.

```
asha@asha:~$ sudo tc -s qdisc show dev s1-eth3
qdisc taprio 100: root refcnt 9 tc 2 map 1 0 0 0 0 0 0 0 0 0 0 0 0 0 0 0
queues offset 0 count 1 offset 1 count 1
clockid TAI     base-time 0 cycle-time 1000000 cycle-time-extension 0
        index 0 cmd S gatemask 0x1 interval 300000
        index 1 cmd S gatemask 0x2 interval 700000
```

FIGURE 10. Results on TAPRIO queuing discipline.

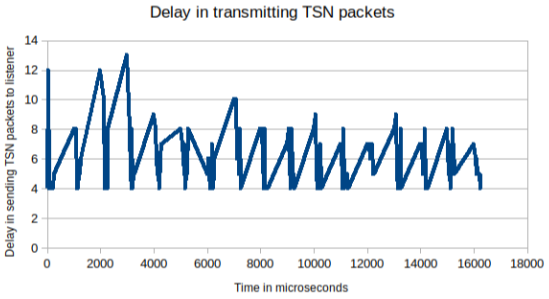

FIGURE 11. Delay in transmitting TSN packets from talker to listener.

discussed. The delay experienced at the egress interface for any switch is given by

$$D = Dpr + Dqu + Dtr + Dpg. \quad (1)$$

In Eq.(1) Dpr is the processing delay, which is the time taken for a packet to get processed before queuing, and Dqu is the queuing delay, which is the time that a packet spends in a queue while waiting for other packets to be transmitted, Dtr is the transmission delay, which is the time required to put a whole packet on to the transmission medium and Dpg is the propagation time, which is the time taken by the packet using the link to reach the destination.

We emphasize that there is no control over processing delay as processing delay is completely application dependent. The transmission delay is directly proportional to the processing delay and Queuing delay. By selecting the appropriate queuing discipline we can claim some control over transmission delay. We can definitely control the propagation delay with our DTPF algorithm. And we can control queuing delays by classifying the traffic and applying TAPRIO queuing discipline. According to our results, the average delay in transmitting TSN packets from talker to listener is 7.45 μs. Fig.11 depicts the delay in TSN packet transmission.

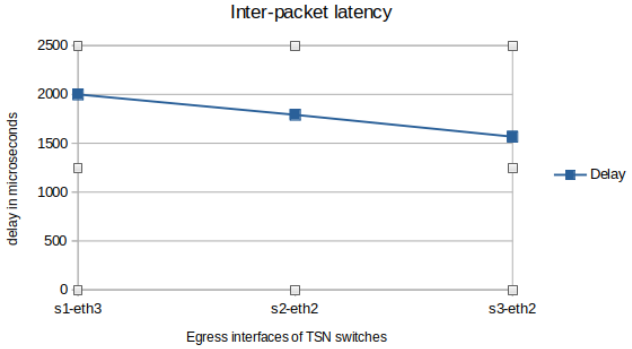

FIGURE 12. Inter-packet latency at the egress port of TSN switches.

1) INTER-PACKET LATENCY

The Fig.12 shows the behavior of inter-packet latency on the TSN nodes participating in TSN path/flow. We can observe slightly higher inter-packet latency on the interface s1-eth3 which is the egressing interface of the first TSN switch of our TSN path as depicted in Fig.12, as compared to the rest of the TSN switches. This is because packet classification is being done in userspace using the tc command at ingress interfaces. The internal implementation of the tc command uses netlink hooks to send specific messages to the kernel to update the configuration accordingly [40]. On the rest of the interfaces, the inter-packet latency is found to be stable.

VI. CONCLUSION AND FUTURE SCOPE

In this paper, the TSN architecture is realized using open-source tools with an SDN framework. The Linux-based queuing discipline is configured with multiple virtual queues. The results show that the egress ports of each TSN switch function as per the gating logic defined in Table 4. The delay in TSN data delivery and the inter-packet latency have been analyzed with results. Hence the overall observation on virtual queue performance are also promising which paves the way to use our unique architecture for PoC. The novel DTPF algorithm efficiently identifies the switches participating in a TSN flow. As a future work, this model can be further enhanced to generate an adaptive approach for rescheduling the TSN flows by selecting the optimal path among the multiple available backup paths.

REFERENCES

[1] C. Basumatary and H. S. Satheesh, "Queuing policies for enhanced latency in time sensitive networking," in *Proc. IEEE Int. Conf. Electron., Comput. Commun. Technol. (CONECCT)*, Jul. 2020, pp. 1–7.

[2] T. Ylonen, "SSH—Secure login connections over the internet," in *Proc. 6th USENIX Secur. Symp.*, vol. 37, 1996, pp. 40–52.

[3] *IEEE Standard for Local and Metropolitan Area Networks—Bridges and Bridged Networks—Amendment 31: Stream Reservation Protocol (SRP) Enhancements and Performance Improvements*, IEEE Standard 802.1Qcc-2018 (Amendment to IEEE Standard 802.1Q-2018 as amended by IEEE Standard 802.1Qcp-2018), Oct. 2018, pp. 1–208, doi: 10.1109/IEEESTD.2018.8514112.

[4] G. N. Kumar, K. Katsalis, P. Papadimitriou, P. Pop, and G. Carle, "Failure handling for time-sensitive networks using SDN and source routing," in *Proc. IEEE 7th Int. Conf. Netw. Softw. (NetSoft)*, Jun. 2021, pp. 226–234.

[5] S. B. H. Said, Q. H. Truong, and M. Boc, "SDN-based configuration solution for IEEE 802.1 time sensitive networking (TSN)," *ACM SIGBED Rev.*, vol. 16, no. 1, pp. 27–32, Feb. 2019.

[6] A. Nasrallah, A. S. Thyagaturu, Z. Alharbi, C. Wang, X. Shao, M. Reisslein, and H. ElBakoury, "Ultra-low latency (ULL) networks: The IEEE TSN and IETF DetNet standards and related 5G ULL research," *IEEE Commun. Surveys Tuts.*, vol. 21, no. 1, pp. 88–145, 1st Quart., 2019.

[7] T. Kobzan, I. Blöcher, M. Hendel, S. Althoff, A. Gerhard, S. Schriegel, and J. Jasperneite, "Configuration solution for TSN-based industrial networks utilizing SDN and OPC UA," in *Proc. 25th IEEE Int. Conf. Emerg. Technol. Factory Autom. (ETFA)*, vol. 1, Sep. 2020, pp. 1629–1636.

[8] L. Lo Bello and W. Steiner, "A perspective on IEEE time-sensitive networking for industrial communication and automation systems," *Proc. IEEE*, vol. 107, no. 6, pp. 1094–1120, Jun. 2019.

[9] W. Quan, W. Fu, J. Yan, and Z. Sun, "OpenTSN: An open-source project for time-sensitive networking system development," *CCF Trans. Netw.*, vol. 3, no. 1, pp. 51–65, Sep. 2020.

[10] S. Schriegel, T. Kobzan, and J. Jasperneite, "Investigation on a distributed SDN control plane architecture for heterogeneous time sensitive networks," in *Proc. 14th IEEE Int. Workshop Factory Commun. Syst. (WFCS)*, Jun. 2018, pp. 1–10.

[11] T. Gerhard, T. Kobzan, I. Blöcher, and M. Hendel, "Software-defined flow reservation: Configuring IEEE 802.1Q time-sensitive networks by the use of software-defined networking," in *Proc. 24th IEEE Int. Conf. Emerg. Technol. Factory Autom. (ETFA)*, Sep. 2019, pp. 216–223.

[12] M. A. Metaal, R. Guillaume, R. Steinmetz, and A. Rizk, "Integrated industrial Ethernet networks: Time-sensitive networking over SDN infrastructure for mixed applications," in *Proc. IFIP Netw. Conf. (Networking)*, Jun. 2020, pp. 803–808.

[13] Y. Wang, J. Chen, W. Ning, H. Yu, S. Lin, Z. Wang, G. Pang, and C. Chen, "A time-sensitive network scheduling algorithm based on improved ant colony optimization," *Alexandria Eng. J.*, vol. 60, no. 1, pp. 107–114, Feb. 2021.

[14] L. Leonardi, L. L. Bello, and G. Patti, "Bandwidth partitioning for time-sensitive networking flows in automotive communications," *IEEE Commun. Lett.*, vol. 25, no. 10, pp. 3258–3261, Oct. 2021.

[15] G. N. Kumar, K. Katsalis, and P. Papadimitriou, "Coupling source routing with time-sensitive networking," in *Proc. IFIP Netw. Conf. (Networking)*, Jun. 2020, pp. 797–802.

[16] Y. Maleh, Y. Qasmaoui, K. El Gholami, Y. Sadqi, and S. Mounir, "A comprehensive survey on SDN security: Threats, mitigations, and future directions," *J. Reliable Intell. Environ.*, vol. 9, no. 2, pp. 201–239, Jun. 2023.

[17] W. Kong, M. Nabi, and K. Goossens, "Run-time recovery and failure analysis of time-triggered traffic in time sensitive networks," *IEEE Access*, vol. 9, pp. 91710–91722, 2021.

[18] M. Böhm, J. Ohms, and D. Wermser, "Multi-domain time-sensitive networks—An east-westbound protocol for dynamic TSN-stream configuration across domains," in *Proc. 24th IEEE Int. Conf. Emerg. Technol. Factory Autom. (ETFA)*, Sep. 2019, pp. 1363–1366.

[19] V. Balasubramanian, M. Aloqaily, and M. Reisslein, "An SDN architecture for time sensitive industrial IoT," *Comput. Netw.*, vol. 186, Feb. 2021, Art. no. 107739.

[20] M. Boehm, J. Ohms, M. Kumar, O. Gebauer, and D. Wermser, "Time-sensitive software-defined networking: A unified control-plane for TSN and SDN," in *Proc. Mobile Commun., Technol. Appl., 24th ITG-Symp.* Berlin, Germany: VDE, May 2019, pp. 1–6.

[21] S. Nam, H. Kim, and S. Min, "Simplified stream reservation protocol over software-defined networks for in-vehicle time-sensitive networking," *IEEE Access*, vol. 9, pp. 84700–84711, 2021.

[22] F. Prinz, M. Schoeffler, A. Lechler, and A. Verl, "Dynamic real-time orchestration of I4.0 components based on time-sensitive networking," *Proc. CIRP*, vol. 72, pp. 910–915, Jan. 2018.

[23] F. Rezabek, M. Bosk, T. Paul, K. Holzinger, S. Gallenmüller, A. Gonzalez, A. Kane, F. Fons, Z. Haigang, G. Carle, and J. Ott, "EnGINE: Flexible research infrastructure for reliable and scalable time sensitive networks," *J. Netw. Syst. Manage.*, vol. 30, no. 4, p. 74, Oct. 2022.

[24] N. Sambo, S. Fichera, A. Sgambelluri, G. Fioccola, P. Castoldi, and K. Katsalis, "Enabling delegation of control plane functionalities for time sensitive networks," *IEEE Access*, vol. 9, pp. 136151–136163, 2021.

[25] *Avnu's Use of 802.1 TSN Mechanisms for Industrial and Automotive Markets*, Standard IEEE 802.1 Plenary, Jul. 2016.

[26] J. Woods and S. Zuponcic, "QoS—Application of TSN to Ethernet/IP networks," in *Proc. ODVA Ind. Conf.*, 2017, pp. 1–16.

[27] *IEEE Standard for Layer 2 Transport Protocol for Time Sensitive Applications in a Bridged Local Area Network*, IEEE Standard 1722-2011, May 2011, pp. 1–65, doi: 10.1109/IEEESTD.2011.5764875.

[28] K. Weber. *EtherCAT Technology Group, EtherCAT and TSN—Best Practices for Industrial Ethernet System Architectures*. Accessed: Apr. 4, 2023. [Online]. Available: https://www.ethercat.org

[29] *Open vSwitch Quality of Service FAQ*. Accessed: May 24, 2023. [Online]. Available: https://docs.openvswitch.org/en/latest/faq/qos/

[30] *Configuring TC on Linux Control*. Accessed: Apr. 4, 2023. [Online]. Available: https://man7.org/linux/man-pages/man8/tc.8.html

[31] *IEEE Standard for Local and Metropolitan Area Networks—Bridges and Bridged Networks—Amendment 25: Enhancements for Scheduled Traffic*, IEEE Standard 802.1Qbv-2015 (Amendment to IEEE Standard 802.1Q-2014 as amended by IEEE Standard 802.1Qca-2015, IEEE Standard 802.1Qcd-2015, and IEEE Standard 802.1Q-2014/Cor 1-2015), Mar. 2016, pp. 1–57, doi: 10.1109/IEEESTD.2016.8613095.

[32] D. Borkmann. *Net, Sched: Add Clsact*. Accessed: Jun. 2023. [Online]. Available: https://lwn.net/Articles/671458/

[33] P. Karachatzis, J. Ruh, and S. S. Craciunas, "An evaluation of time-triggered scheduling in the Linux kernel," in *Proc. 31st Int. Conf. Real-Time Netw. Syst.*, Jun. 2023, pp. 119–131.

[34] M. Kumar, "Evaluation of the time-aware priority queueing discipline with regard to time-sensitive networking in particular IEEE 802.1 Qbv," in *Proc. Int. Conf. Appl. Innov. IT*, vol. 7, no. 1. Köthen, Germany: Anhalt Univ. of Applied Sciences, 2019, pp. 1–6.

[35] N. S. Bülbül, D. Ergenç, and M. Fischer, "SDN-based self-configuration for time-sensitive IoT networks," in *Proc. IEEE 46th Conf. Local Comput. Netw. (LCN)*, Oct. 2021, pp. 73–80.

[36] B. Rother, M. Kasparick, E. Schweißguth, F. Golatowski, and D. Timmermann, "Automatic configuration of a TSN network for SDC-based medical device networks," in *Proc. 16th IEEE Int. Conf. Factory Commun. Syst. (WFCS)*, Apr. 2020, pp. 1–8.

[37] M. Gutiérrez, A. Ademaj, W. Steiner, R. Dobrin, and S. Punnekkat, "Self-configuration of IEEE 802.1 TSN networks," in *Proc. 22nd IEEE Int. Conf. Emerg. Technol. Factory Autom. (ETFA)*, Sep. 2017, pp. 1–8.

[38] M. Gutiérrez, W. Steiner, R. Dobrin, and S. Punnekkat, "A configuration agent based on the time-triggered paradigm for real-time networks," in *Proc. IEEE World Conf. Factory Commun. Syst. (WFCS)*, May 2015, pp. 1–4.

[39] M. Bohm, J. Ohms, M. Kumar, O. Gebauer, and D. Wermser, "Dynamic real-time stream reservation for IEEE 802.1 time-sensitive networks with OpenFlow," in *Proc. 8th Int. Conf. Appl. Innov. IT* 2020, pp. 7–12.

[40] J. H. Salim, "Linux traffic control classifier-action subsystem architecture," in *Proc. Netdev*, 2015, pp. 1–10.

[41] M. Maliosz, I. Moldován, M. Máté, C. Simon, and J. Harmatos, "Deterministic local cloud for industrial applications," in *Proc. IEEE 19th Int. Conf. Factory Commun. Syst. (WFCS)*, Pavia, Italy, Apr. 2023, pp. 1–8, doi: 10.1109/WFCS57264.2023.10144237.

[42] M. Jayakumar. *Data Plane Development Kit*. Accessed: Jun. 20, 2023. [Online]. Available: https://www.intel.com/content/dam/develop/external/us/en/documents/dpdk-cookbook-759202.pdf

[43] Y. Han, S. Peng, and Y. Gao. (Jun. 11, 2023). *Analysis and Evaluation for TSN Queuing Mechanisms*. [Online]. Available: https://www.ietf.org/id/draft-hp-detnet-tsn-queuing-mechanisms-evaluation-00.html

[44] Y. Gou, X. Jiang, Z. Liu, R. Zhou, Q. Zhou, and G. Xie, "Optimization on architecture of time-sensitive software-defined network," Lanzhou Univ., Lanzhou, China, Tech. Rep., Apr. 2023.

[45] J. Jiang, Y. Li, X. Zhang, M. Yu, C. D. Lee, and S. H. Hong, "Assessing the traffic scheduling method for time-sensitive networking (TSN) by practical implementation," *J. Ind. Inf. Integr.*, vol. 33, Jun. 2023, Art. no. 100464.

[46] S. Buzura, A. Peculea, B. Iancu, E. Cebuc, V. Dadarlat, and R. Kovacs, "A hybrid software and hardware SDN simulation testbed," *Sensors*, vol. 23, no. 1, p. 490, Jan. 2023.

[47] T. Stüber, L. Osswald, S. Lindner, and M. Menth, "A survey of scheduling algorithms for the time-aware shaper in time-sensitive networking (TSN)," *IEEE Access*, vol. 11, pp. 61192–61233, 2023, doi: 10.1109/ACCESS.2023.3286370.

[48] D. Pannell, "Choosing the right TSN tools to meet a bounded latency," in *Proc. IEEE SA Ethernet IP@ Automot. Technol. Day*, 2019.

ASHA G. HAGARGUND (Graduate Student Member, IEEE) received the Bachelor of Engineering degree in electronics and communication and the Master of Technology degree in digital communications from Visvesvaraya Technological University, Karnataka, India. She is currently pursuing the Ph.D. degree with the National Institute of Technology Karnataka, Surathkal.

She is also an Assistant Professor with the BMS Institute of Technology and Management, India. She has more than 12 years of teaching experience and two years of industry experience. She has worked on projects related to mobile communication with Samsung India Software Operations, Bengaluru, India, and worked on security technologies with Ingersoll Rand, Bengaluru. Her current research interests include time-sensitive networking and the Industrial IoT. She has executed various projects on networking using tools, such as Mininet, OMNET++, NS2, and Qualnet. Previously, she has worked on time sensitive network realization using various simulators. She has delivered talks on TSN in industry and academia. She has publications on wireless sensor networks, time-sensitive networks, image processing, and the Internet of Things.

Prof. Asha is a member of the Additive Manufacturing Society of India.

NEELAWAR SHEKAR VITTAL SHET received the Bachelor of Engineering degree from MIT, Manipal, India, the Master of Engineering degree in communication system from IIT Roorkee, India, and the Ph.D. degree from the National Institute of Technology Karnataka (NITK), Karnataka, Surathkal, India.

He is currently a Professor and the Head of the Department with the Electronics and Communication Department, NITK. He has executed a project sponsored by the Centre for Wireless Networking Technologies (MHRD TAT) on building a model for tracking train position on tracks. He has more than 35 years of teaching experience with NITK. He has more than 30 research publications in the area of machine learning, wireless networks, and the Internet of Things. He has published book chapters on congestion control mechanisms in vehicular networks, envisioned network architecture for IoT applications, topology control in wireless sensor networks, and reliable cross-layer design for e-health applications.

Dr. Shet is a fellow of the Institution of Electronics and Telecommunication Engineers.

MURALIDHAR KULKARNI (Senior Member, IEEE) received the B.E. degree in electronics engineering from the University Visvesvaraya College of Engineering, Bengaluru, the M.Tech. degree in satellite communication and remote sensing from the Indian Institute of Technology Kharagpur, Kharagpur, and the Ph.D. degree in electronics and communication engineering from JMI Central University, New Delhi.

He was a Scientist with the Central Power Research Institute, Bengaluru, and an Aeronautical Engineer with Hindustan Aeronautics Ltd., Bengaluru. He was an Assistant Professor with the Department of Electronics and Communication Engineering, Visvesvaraya College of Engineering, and an Associate Professor with the Department of Electronics and Communication Engineering, Delhi Technological University, New Delhi. Then, he joined the Department of Electronics and Communication Engineering, National Institute of Technology Karnataka Surathkal, Mangaluru, as a Faculty Member, in 2008, where he was a Professor in electronics and communication engineering. He was the HoD of the ECE Department, the Chairperson of the Career Development Center, a member of the Board of Governors, and the Coordinator of the Center of Excellence (CoE) in Wireless Sensor Networks, National Institute of Technology Karnataka (NITK), Surathkal. He has published more than 80 research papers in international/national journals and conferences and also has to his credit several funded research projects and delivered keynote addresses/technical talks in international conferences and workshops. He has also authored/coauthored five very popular textbooks in the areas of microwaves and radars, DSP, information theory and coding, and analog digital communications. His current research interests include digital communications and networks (OFDM, WSN, SDN, congestion control, 5G networks, and the IoT), optical communications and networks (FSO), microwave, and antenna systems.

Dr. Kulkarni is a fellow of IETE and a Life Member of ISTE and CSI.

Dual Image Reversible Data Hiding: A Survey

Sanjay Kumar
Department of Applied Mathematics
Delhi Technological University (Formerly DCE)
Delhi, India
skparsade@gmail.com

Anjana Gupta
Department of Applied Mathematics
Delhi Technological University (Formerly DCE)
Delhi, India
anjanagupta@dce.ac.in

Gurjit Singh Walia
Scientific Analysis Group
Defence Research and Development Organisation
Delhi, India
gurjit.walia@gmail.com

2023 Third International Conference on Secure Cyber Computing and Communication (ICSCCC) | 979-8-3503-0071-0/23/$31.00 ©2023 IEEE | DOI: 10.1109/ICSCCC58608.2023.10176708

***Abstract*—Conventional reversible data hiding (RDH) techniques are concerned with hiding secret information in the cover and extracting it along with the original cover at the receiver end. In the recent past, some researchers investigated dual image (DI) RDH in order to increase the data hiding capacity and visual quality of the marked cover image. In this manuscript, we reviewed state-of-the-art DI-RDH techniques and categorise them techniques mainly into exploiting modification direction, turtle shell, central folding strategy, and Pixel value differenceing along with explaining their merits and demerits. DI-RDH methods have been examined, considering data hiding capacity and PSNR.**

***Index Terms*—data hiding, DI-RDH, pixel value differenceing, central folding strategy, turtle shell, exploiting modification direction**

I. Introduction

The recent rise in digital communication and data transmission over the internet has become a major concern for information security in order to prevent the confidential message from being attacked by malicious attackers. Cryptography and data hiding are two powerful tools that are used for secure data transmission over insecure networks. Cryptography is a technique to transform intelligible information into an unintelligible form, making the data unprofitable for attackers. For this, only actual receiver can retrieve messages using a decryption key. On the other hand, information hiding is a steganographic technique to conceal secret messages in cover media. The non-visible modifications in the cover medium make it difficult for an intruder to identify the presence of hidden data. Information-hiding techniques are segregated into irreversible and reversible data hiding approaches. Irreversible or lossy data hiding schemes can extract the hidden message from the stego-image, but they can not recover the original media. But due to the limitations of the previous scheme, reversible data hiding [1] methods came into picture and it can extract data along with original cover media. In recent past, various authors have been broadly investigated dual image RDH methods [2], [25]–[27] to improve the data hiding capacity and security compared to ordinary RDH. Dual-image RDH provides a good solution compare to the ordinary RDH methods. In dual-image RDH, two copies of the original image are generated, then sender hides the secret message into these two images using specific reversible data hiding methods, and two identical marked images are generated. These marked images are sent to the receiver's end, and receiver receives them all together. Then, receiver extracted the secret message and recovered the original image from the marked images using reversible data hiding algorithm. The attacker is unable to recover the secret message without obtaining both marked images. Dual image RDH also treated as a special case of secret sharing.

In this paper, we have classified dual image RDH methods such as exploiting modification direction, pixel value differencing, central folding strategy and turtle shell. Performance of these methods is also considered in terms of data hiding capacity and quality of cover. The remaining paper is arranged as follows:

In Section 2, classification of DI-RDH works and existing design frameworks such as exploiting modification direction, turtle shell, central folding strategy and pixel value differencing methods are reviewed. Analysis of DI-RDH methods discussed in Section 3. In Section 4, concluding remarks and future directions are sketched.

II. Motivation

Various motivations for DI-RDH have been identified in various studies and surveys. These include the need for a high embedding capacity, robustness to attacks, reversibility of the embedding process, improved security and privacy of the embedded data, preservation of the original cover images quality, and applications such as image authentication, content sharing, and copyright protection. DIRDH continues to be an active area of research in the field of data hiding.

III. DI-RDH Classification Techniques

Dual image RDH methods have been significantly explored in recent years to enhance the data hiding capacity, security and visual quality of the original cover image compared to

Authorized licensed use limited to: DELHI TECHNICAL UNIV. Downloaded on July 20,2023 at 11:09:45 UTC from IEEE Xplore. Restrictions apply.

the conventional RDH methods. In view of this, we have categorised dual image RDH tasks into exploiting modification direction, pixel value differencing, central folding strategy and turtle shell. The details of dual image RDH work classification are outlined in Fig. 1.

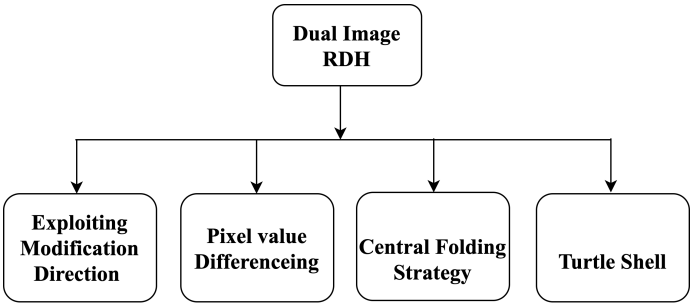

Fig. 1. Dual Image RDH Techniques

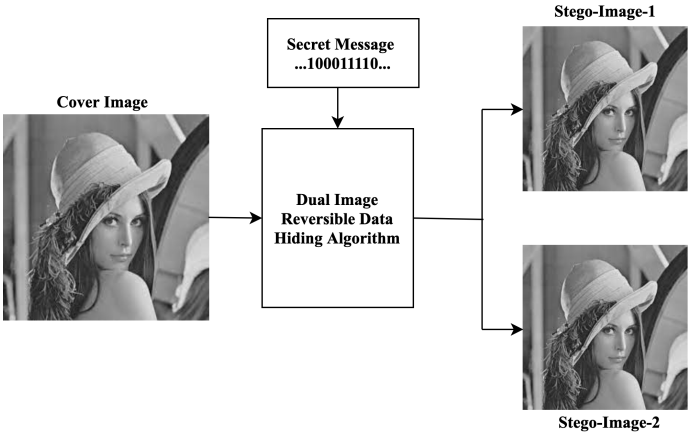

Fig. 2. General Framework of Message Embedding for Dual Image Reversible Data Hiding

Dual image RDH structure is instantiated in Fig. 2. In this, firstly two copies of the original cover image are generated. Then, secret message is embedded into both these images, and two stego images are generated. Sender sends these two stego images to the recipient. Receiver receives both stego images at the same time and extracts the secret message along with original image using dual image RDH algorithm. Dual image work has been broadly investigated to obtain high data embedding capacity along with tuneable image quality.

A. Exploiting Modification Direction

First Exploiting Modification Direction (EMD) [2] method for RDH was proposed in 2006. In this, firstly binary secret message is splitted into different chunks of L-bits, which are represented by k-digit in $(2n+1)$ base number system. , Further, original image is partitioned into a sequence of n-sized pixel groups denoted as $(k_1, k_2, \ldots, k_n)$ and any perticular pixel is contributed in data hiding or not it decides by the function f such as $f(k_1, k_2, \ldots, k_n) = [\sum_{n=1}^{n}(k_i, i)]$ mod$(2n+1)$. Every message bit d can be hide into set of n pixels $(k_1, k_2, ..., k_n)$ by using the three embedding steps:

1) If $d = f$, then embed d without modifying pixel group.
2) if $d \neq f$, determine $s = d - f \mod (2n+1)$. If $s \leq n$, then embed d, and the value of k_s is incremented by 1.
3) If $d \neq f$, determine $s = d - f \mod (2n+1)$. If $s \leq n$, then embed d, and the value of k_{2n+1-s} is incremented by one.

Further, EMD approach was introduced for dual-image RDH in order to achieve high security of secret information and better visual quality of cover image by Chang et al. [3] in 2007. In this, two secret digits in quinary form were embedded into original pixels and encode into two steganographic images. Average PSNR of both stego images was higher than 45 dB and the data concealing capacity was 1 bpp. This method outperforms the method proposed in [2]. In similar line, Chang et al. [5] also increased the visual quality of stego images by converting the 5 x 5 matrix into horizontal and vertical directions rather than diagonal. Except for the directions of coordinates, methods [3] and [5] were similar. This method kept the visual quality (i.e. PSNR) of both stego images above 48 dB on average, and the embedding capacity was 1 bpp. Further, Lee and Huang [4] proposed RDH based on the combination of pixel orientation located in two stago-images to improve data hiding capacity. In this, firstly secret binary sequence was converted into the sequence of digits with base five. then, two consecutive digits d_1 and d_2 were embedded into the cover pixel pair for each stego-images, and pair of pixel values were mapped in two dimensions. However, this method can embed only five secret bits in each set of four cover pixels, so that it restricts the embedding data. Average embedding capacity and PSNR of two stego-images were 1.07 bpp and 49.73 dB respectively. This method provided better data concealing capacity and PSNR compare to the method [5]. In this order, Chang et. al [5] overcome the data embedding restriction for Lee and Huang method [4] by using the magic matrix technique to improve the data hiding capacity. Magic matrix was generated using formula $F(s_1, s_2) = (s_1 + 3 \times s_2) \mod 9$ [6], where, s_1, s_2 represents pixels pair and function $F(s_1, s_2)$ denote the message digit. If the function $F(s_1, s_2)$ value is not equal to the embedding secret data. Then, the current pixel pair were changed of its two upper left or two bottom right pixel pairs to find the value, which is equal to the embedding secret data. Embedding rate and PSNR were 1.55 bpp and 39.89 dB respectively for both stego image. In [7], three rules were given for data concealing into first stego-image, while data embedding in the second stego-image depends on rules generated in the first stego-image. Further, Lin et al. [8] introduced EMD method based on quinary system, in which two secret digit embed together in every pair of pixel of original cover using EMD matrix. Recently, Chen et al. [9] developed EMD method for dual image RDH using reference matrix and each pixel was carried $1 + \log_2 5$ bits along with horizontal and vertical directions. Embedding capacity was achieved upto 1.56 bpp and PSNR

Authorized licensed use limited to: DELHI TECHNICAL UNIV. Downloaded on July 20,2023 at 11:09:45 UTC from IEEE Xplore. Restrictions apply.

below 42 dB and provided better embedding capacity in comparison to [4], [12] methods.

In Sum: Dual-image RDH based on exploiting modification direction is extensively explored. Initially. Chang et al. [3] introduced EMD approach based on quinary digits. In this sequence, Chang et al. [5] presented a 5×5 based method by using horizontal and vertical directions in order to increase the visual quality of [3] from PSNR 45 dB to 48 dB. Further, Lee and Huang [4] investigated DI-RDH based on combination of pixel orientation and improved slightly payload capacity and visual quality compared to the proposed methods [3], [5]. Recently Chen et al. [9] introduced reference matrix-based DI-RDH and provided a better embedding capacity in comparison to [4], [12] methods. In the next section turtle shell method for DI-RDH are discussed.

B. Turtle Shell

Turtle shell (TS) consisted of eight distinct values from zero to eight, in which six edge digits and two backward digits are included. Chang et al. [10] introduced the first turtle shell based DI-RDH approach in 2014. In this, secret bitstream was partitioned into 3-bit chunks, and the value of each chunk was converted into secret digits. Then, reference matrix M was created to embed the secret digits. For this, the difference between two adjacent pixels was calculated and it was denoted by the number 1 for the same row, whereas 2 and 3 for the alternate column. In this way, reference matrix M was generated by collecting the number of neighbouring hexagons, and each hexagon of reference matrix is called TS. Further, associated set G for matrix $M(x_i, x_{i+1})$ was generated according to the following rules: a) If $M(x_i, x_{i+1})$ was a backwards digit within turtle shell, then corresponding set G consisted of all digits in same TS. b) If $M(x_i, x_{i+1})$ was an edge digit presented in at least one TS, then corresponding set G consisted of all digits of the turtle shells in which $M(x_i, x_{i+1})$ belongs. c) If $M(x_i, x_{i+1})$ was not presented in any turtle shell, then corresponding set G consisted of all digits in a 3×3 sub-block where $M(x_i, x_{i+1})$ was located. Pixel pair r (x_i, x_{i+1}), was selected from the reference matrix $M(x_i, x_{i+1})$ to hide the secret digit d_j, if its distance was minimum among all pixels of a reference matrix and modified from $(x_i, x_{i+!}$ to $(x'_i, x'_{i+!}$ selected from all the elements of $M(x_i, x_{i+1})$. At the receiver end, receiver extracted secret message without any error from the stego image. For this,, every stego pixel pair (x_i, x_{i+1}) was mapped to $M(x'_i, x_{i+1})$, then value of $M(x'_i, x_{i+1})$ corresponding to reference matrix M was determine as secret digit. Eight grayscale images were used for the experiment. Average EC and PSNR of this approach were 1.5 bpp and 49.40 dB respectively and higher than the proposed method [2]. In [11], Xie et al. presented a DI-RDH approach based on two-layer turtle shell matrix, in which a 4-array digit is assigned to each member of the TS matrix corresponding to symmetrical distribution. Two extra bits were concealed into each pixel pair compare to original TS method [10]. Further, in [12] discussed DI-RDH approach that applied the turtle shell reference matrix to conceal messages into two shadows. In this, a satisfactory quality of the generated shadows was obtained. Data hiding capacity was 1 bpp approximately . In this sequence, a real-time DI-RDH approach using new TS reference matrix to embed secret information was presented in [13]. For this, Two shadows were used for data embedding, in which first one was used for one-bit embedding while the second was used for four secret bits embedding. Embedding capacity was higher than 1.25 bpp. It also resisted static attacks of pixel value differencing histogram and was used in numerous real time. applications. In the similar line, Xie et al. [14] also proposed a novel turtle shell dual image RDH approach based on reference matrix to achieve a high embedding capacity. This divides a pixel pair duplicated from a pixel into an upper category and lower category. Under the pixel pair category, a precise pixel block of size 4×5 was selected, this pixel pair was used so that each pixel pair haul a 16-array secret digit. This method provided the better embedding rate compare to the state-of-the-art methods [4], [12], [13] PSNR was inferior for these methods.

In Sum: Recently researchers investigated the turtle-shell based DI-RDH methods. Chang et al. [10] explored the turtle shell method based on reference matrix and increase the payload capacity as well as visual quality in comparison to [2]. Further, Xie et al. [11] improved embedding capacity of Chang et al. [10] method by using two layer turtle shell matrix. In this sequence, Liu and Chang [13] introduced a real time DI-RDH based on TS reference matrix, which resisted static attacks of pixel value differencing histogram. In similar line, Xie et al. [14] improved payload capacity of presented state-of-the-art methods [4], [12], [13] with inferior PSNR by using turtle shell approach. In the next section central folding strategy method for DI-RDH is discussed.

C. Central Folding Strategy

Central Folding Strategy (CFD) technique compresses the secret information into digits using different number systems. Then, average method is applied to conceal the compressed message into two stego-images. Lu et al. [15] introduced first CFD approach in 2015. In this, k-message bits were converted into digits d using a numeral system. Then, digit d was changed into folded secret information $\bar{d}$ using $\bar{d} = d - 2^{k-1}$. Further, digit $\bar{d}$ was divided into digits $\bar{b_1} = \lfloor \bar{d}/2 \rfloor$ and $\bar{b_2} = \lceil \bar{d}/2 \rceil$ and these were used for data embedding as follows: $t'_{i,j} = t_{i,j} + \bar{b_1}$ and $t''_{i,j} = t_{i,j} + \bar{b_2}$. At the time of message extraction, if stego pixels $t'_{i,j} = t''_{i,j}$ and $t'_{i,j}, t''_{i,j} \in [2^{k-1}, 256 - 2^{k-1}]$, then these pixels were not contained any secret information. If stego pixel $t'_{i,j}$ or $t''_{i,j} \in [2^{k-1}, 256 - 2^{k-1}]$, then these pixels were contained secret information and it can be extracted as follows: $\bar{d} = t'_{i,j} - t''_{i,j}$ and $d = \bar{d} + 2^{k-1}$. This method does not use the correlation between adjacent digits to minimize the distortion. Average embedding capacity for $k = 2, 3$ were 524204 and 785204 respectively. This method provided the better data hiding capacity and PSNR compared to the proposed methods [3]–[5]. In this order, H .Yao [16] improved Lu et al. [15] method

Authorized licensed use limited to: DELHI TECHNICAL UNIV. Downloaded on July 20,2023 at 11:09:45 UTC from IEEE Xplore. Restrictions apply.

by adopting the shift strategy technique. For this, the bitstream of message was partitioned into different sets of k bits chunks and, then converted these chunks into decimal digits. If digit $d = 2^k - 1$ then, digit d was updated using $d = d + m_{k+1}$ by adding an extra m_{k+1}^{th} bit. Secret digit was embedded into the cover pixel and stego images were generated as follows: (1)if d is an even integer, then, $x_i' = x_i + \lfloor d/4 \rfloor$ and $x_i'' = x_i - d/2$. (2) if d is odd integer, then, $x_i' = x_i - \lceil d/4 \rceil$ and $x_i'' = x_i' + \lceil d/2 \rceil$. One bit was extra embedded, whenever condition $d = 2^k - 1$ occurs compare to the method Lu et al. [15].

Further, Chi et al. [17] proposed a CFS method based on dynamic encoding strategy. In this, a set of k secret information bits set $b_1, b_2, , ..., b_k$ was converted into decimal values d_i. then, a code book of size 2^k was prepared to encode the decimal values d_i . Codewords and their indices were sequentially stored from 0 to $2^k - 1$ and indices of codewords were replaced by digits value of secret information. This decreases the distortion of the stego images. Average embedding capacities were $1, 1.5$, and 2 for $k = 2, 3, 4$ along with PSNR 49.14 dB, 49.23 dB, and 49.40 dB for stego images respectively.

In Sum: Dual-image reversible data hiding method based on center folding strategy has been widely explored to increase the embedding capacity and improve visual quality of the cover image. In 2015, Lu et al. [15] introduced first central folding strategy using d-base number system. This method does not use correlation between adjacent digits to minimize the distortion. In this order, H .Yao [16] introduced Lu et al. [15] method by adopting the shift strategy technique. Further, Chi et al. [17] investigated a dynamic encoding strategy to improve the payload capacity of [15], [16]. In the next section pixel value differencing methods for DI-RDH are discussed.

D. Pixel Value Differencing

Pixel Value Differencing (PVD) was first introduced by Wu and Tsai to differentiate between smooth and edge regions but this method was not reversible. In 2017, Biswapati et al.'s [19] suggested a first DI-RDH strategy based on PVD and EMD. In this, an original image of size $H \times W$ was interpolated and which generated the new image of size $2H \times 2W$. Secret information was partitioned into the stream of 7 bits and each 7 bits was again segregated into two sets, where 4 bits and 3-bits were concealed using PVD and improved EMD respectively. Then, modified two pixels were obtained containing seven secret information bits, and these pixels were distributed between dual images using secret key. Receiver extracted the secret information and recovered the original image with the help of secret key. This scheme provided 1.75 bpp data hiding capacity and PSNR of more than 37 dB. Later, In 2019, Jung et al.'s [20] introduced a DI-RDH approach using the PVD, and the cover image was divided into non-overlapping sub-blocks. Highest difference value in each sub-block was calculated. To determine the embedding size, highest difference and log function were used. Then, secret message was converted from binary bit to decimal secret data. Decimal message digits were concealed into the cover image by using floor function and ceil function to generate two stego images. At the receiver end, cover image was recovered by averaging the pixel values of the two stego-images. The secret data was extracted by calculating the maximum difference value and the log function within each block of cover image. This scheme has inferior PSNR of proposed methods [21], [22] with low payload, however, when the payload was increased , PSNR was higher than other schemes. The average PSNR of proposed scheme was 42.28 dB and 50.96 dB when the payloads were 80,000 bits and 500,000 bits respectively. In this sequence, LSB matching and modified PVD with n-Rightmost Bit Replacement (n-RBR) approaches were proposed in 2019 by A..K Sahu and G. Swain [24]. In LSB matching, two identical images were used for data hiding, whereas the modified PVD approach used four identical images for data hiding. LSB matching improved the PSNR of [23] at the same level of embedding capacity. Average data hiding capacity of this approach was 524, 288 along with 51.18 and 51.17 dB PSNR. In modified PVD, data embedding was performed in two phases and four identical images of original image were used for data hiding. In phase 1, firstly, two pixels from each identical image $I_1(P_1, P_2)$ and $I_2(Q_1, Q_2)$ and two different sets x_1 and x_2 of n-bits secret data were taken. Then, n-LSBs from the pixels P_1 and Q_2 and binary set x_1 and x_2 were converted into the decimal number namely p_1, q_2, b_1, b_2 respectively. Further, difference value these four values were calculated i.e $d_1 = p_1 - b_1$ and $d_2 = q_2 - b_2$ and three modified pixels P_1', P_1'', P_1''',were determined corresponding to pixel P_1 such that $P_1' = P_1 - d_1, P_1'' = P - 1' - 2^x, P_1''' = P - 1' + 2^x$. Then, compute difference values $d_3 = |P_1 - P_1'|, d_4 = |P_1 - P_1''|, d_5 = |P_1 - P_1'''|$ and with the help of these difference values stego pixel P_1^* for P_1 was generated. In similar manner stego pixel Q_2^* for Q_2 was also generated. In phase 2, modified PVD was used for embedding in the last two identical images. for this, two pixel from image $I_3(r_1, r_2)$ and two from $I_4(s_1, s_2)$ were chosen. Then, difference d_6 was determined between pixels r_2 and S_1 and the number of embedding bits x can be calculated using this difference value by determining the value of $\lfloor \log_2 d_6 \rfloor$. Further, two sets x_1 and x_2 with x of secret information bits were converted into decimal numbers b_3 and b_4 and values $b_3' = \lfloor b_3/2 \rfloor$, $b_3'' = \lceil b_3/2 \rceil$, $b_4' = \lfloor b_4/2 \rfloor$, $b_4'' = \lceil b_4/2 \rceil$ were determined. At last stego pixels were calculated using $r_1* = s_1 + b_3'$, $r_2* = r_2 + b_4'$, $s_1* = s_1 - b_3''$, $s_2* = r_2 - b_4''$ and stego-marked images were generated. Average data hiding capacity of this approach were 796,729 along with 54.16, 54.16, 38.32, and 37.50 dB PSNR for $n = 1$.

In Sum: Dual-image reversible data hiding method based on pixel value differencing has been explored recently. In 2017, Biswapati et al.'s [19] investigated the first PVD and EMD based approach. Further, Jung et al.'s [20] investigated and outperforms compare to Biswapati et al.'s [19] method. In 2019, A..K Sahu and G. Swain introduced LSB matching and modified PVD which improved state-of-the-methods [19], [20], [23]. In the next section analysis of DI-RDH methods is discussed.

Authorized licensed use limited to: DELHI TECHNICAL UNIV. Downloaded on July 20,2023 at 11:09:45 UTC from IEEE Xplore. Restrictions apply.

TABLE I
RECENT ADVANCES ON DUAL-IMAGE REVERSIBLE DATA HIDING

Author	Methodology	Data Set	Result	Remarks
Leee and Huang [4]	Cobination of pixel orientation	Self generated	Average data hiding capacity 1.07 along with PSNR 49.73 dB	Improved PSNR of [5]
Chang et al. [5]	magic matrix approach	Self Generated	improved data hiding capacity of Lee and Huang [4] but has less PSNR then [4]	...
Chen et al. [9]	reference matrix	Self Generated	achieved embedding capacity upto 1.56 bpp and PSNR 42 dB	improved capacit [4], [12]
Chang et al. [10]	reference matrix	Self Generated	average embedding capacity 1.5 bpp along with 49.40 dB PSNR	Eight grayscale image were used for experiment
Liu and Chang [13]	real time approach new tutle shell matrix	Self Generated	dat hiding capacity 1.2 bpp	resist static attacks of pixel value differencing histogram
Xi et al. [14]	turtle shell based reference matrix	Self Generated	provided better embedding rate compare to the [4], [12], [13] but inferior PSNR	Pixel blocks of size 4×5 were used for data hiding
Chi et al. [17]	dynamic strategy	Self Generated	average embedding capacity $1, 1.5, 2$ along with PSNR $49.14dB, 49.20dBand49.40dB$ for $k = 2, 3, 4$ respectively	k-bit set of information was used for data embedding at a time
jung et al. [20]	Pixel value differencing	self generated	Average PSNR 42.28 dB, 50.96 dB. corresponding to payload 80,000 and 5,00,000 bits respectively	Lower PSNR and payload capacity comparison to the methods [21], [22].
A.K. Sahu and G. Swain [24]	LSB matching, PVD with n-RBR	Self Generated	LSB matching approach was embed 524 and 288 bits corresponding to 51.18 and 51.17 dB PSNR, whereas modified PVD embed 796, 729 corresponding to 38.32 and 37.50 dB respectively	Two identical image were used for LSB method whereas modified pVD used four identical image for data hiding

IV. ANALYSIS OF DUAL-IMAGE RDH METHODS

Dual image reversible data hiding is mainly classified into Exploiting modification direction, turtle shell, Central folding strategy and Pixel value differencing methods. Each method of DI-RDH has its advantages and disadvantages and the superiority of method depends on the specific requirements and constraint of the applications. Exploiting modification direction is used for high embedding requirements, whereas center folding and turtle shell methods can be more suitable to obtain high quality images along with reasonable payload capacity. The priority pixel value differencing method may be the best option to achieve low distortion and security with high payload capacity but the complexity of this is more compared to the other methods. In general, DI-RDH methods can be used according to specific requirements and constraints of the application.

V. LIMITATIONS OF DUAL IMAGE RDH METHODS

There are various limitations to dual image reversible data hiding (DIRDH):

- DI-RDH has limited data hiding capacity because this requires two image for data embedding, which reduces data hiding capacity for each cover image.
- Secret data or cover image can be affected by various vulnerable attacks such as cropping, compression, and histogram equalization.
- These methods have high computational complexity due to the complex operations and take longer data embedding and extraction time.
- Data embedding capacity and robustness of dual image RDH methods depends on cover image image quality and content.
- DI-RDH primarily designed only for cover image and these methods may not be directly applicable for audio or video.

VI. CONCLUSION AND FUTURE DIRECTION

In this paper, we have reviewed the state-of-the art dual image reversible data hiding methods. These are categorized such as exploiting modification direction, pixel value differencing, central folding strategy, and turtle shell and also explore their merits and demerits. Performance of various dual image reversible data hiding methods are compared in the context of data concealing capacity and visual quality of stego-images.

The research work in the field of dual-image reversible data hiding can further be extended in the following future directions. DI-RDH methods need to be resilient against various histogram equalization and cropping attacks. DI-RDH methods can also be explored for audio and video whereas primarily applied only for images. Attacks using machine learning methods can also be investigated for development of robust solutions. Data hiding methods should also be explored that can be used in a cloud environment for secure sharing and storage of sensitive data.

REFERENCES

[1] S. Kumar , A. Gupta, and G.S. Walia, "Reversible data hiding: A contemporary survey of state-of-the-art, opportunities and challenges". Appl Intell. vol. 52, no. 7, pp. 7373-7406, 2022 . https://doi.org/10.1007/s10489-021-02789-2

[2] Zhang X.P., and Wang S.Z., Efficient Steganographic Embedding by Exploiting Modification Directions, "*IEEE Communication,* Letters, vol. 10, No. 11, pp. 1-3, 2006.

[3] C. C. Chang, Kieu, Duc, and Y. C Chou, "Reversible data hiding scheme using two steganographic images". In TENCON 2007 IEEE region 10 conference.

Authorized licensed use limited to: DELHI TECHNICAL UNIV. Downloaded on July 20,2023 at 11:09:45 UTC from IEEE Xplore. Restrictions apply.

[4] C. F. Lee and Y. L. Huang, "Reversible data hiding scheme based on dual stegano-images using orientation combinations," Telecommunication Systems, pp. 1-11, 2011.
[5] C. C. Chang, T. C. Lu, G. Horng, Y.H. Huang and Y.M. Hsu, "A high payload data embedding scheme using dual stego-images with reversibility", in Proceedings of the Third International Conference on Information, Communications and Signal Processing, 2013, pp. 1-5.
[6] H. J. Kim, C. Kim, Y. Choi, S. Wang, and X. Zhang, "Improved modification direction methods," Computers and Mathematics with Applications, vol. 60, no. 2, pp. 319-325, 2010.
[7] C. Qin, C. C. Chang, and T. J. Hsu, "Reversible data hiding scheme based on exploiting modification direction with two steganographic images", Multimed. Tools Appl., Vol. 74, no. 15, pp. 5861-72, Aug. 2015.
[8] J. Y. Lin, Y Chen, C. C Chang, and Y.C Hu, "Dual-image-based reversible data hiding scheme with integrity verification using exploiting modification direction", Multimed. Tools Appl., Vol. 78, pp. 25855-25872, 2019.
[9] X. Chen and C. Hong, "An Efficient Dual-image Reversible Data Hiding Scheme Based on Exploiting Modification Direction". J. Inf. Secur. Appl.,vol. 58, May 2021. https://doi.org/10.1016/j.jisa.2020.102702.
[10] C. C. Chang, Y. J. Liu and T.S. Nguyen, "A novel turtle shell based scheme for data hiding", In: Proceedings of 10^th International Conference on Intelligent Information Hiding and Multimedia Signal Processing, Kitakyushu, Japan, pp. 89-93, August 2014.
[11] X. Z. Xie, C. C. Lin and C. C Chang, "Data Hiding Based on a Two-Layer Turtle Shell Matrix", Symmetry 2018, 10, 47. https://doi.org/10.3390/sym10020047.
[12] Y. J. Liu and C. C Chang, "A turtle shell-based visual secret sharing scheme with reversibility and authentication", Multimed. Tools Appl. vol. 77, no. 19, pp. 25295-25310, 2018.
[13] J. Y. Lin, Y. Liu, and C. C. Chang, "A real-time dual-image-based reversible data hiding scheme using turtle shells", J Real-Time Image Proc., vol. 16, pp. 673-684 , 2019. https://doi.org/10.1007/s11554-019-00863-0
[14] Xie, X.Z.; Chang, C.C. "Hiding data in dual images based on turtle shell matrix with high embedding capacity and reversibility". Multimed. Tools Appl. , vol. 80, pp. 36567-36584. 2021.
[15] Lu, T.C., Wu, J.H., and Huang, C.C.:Dual-Image-Based Reversible Data Hiding Method Using Center Folding Strategy. Signal Processing, Vol.115, pp. 195-213, 2015.
[16] H. Yaoa, C. Qin, Z. Tang and Y. Tian Improved dual-image reversible data hiding method using the selection strategy of shiftable pixels' coordinates with minimum distortion. Signal Processing Vol. 135, pp. 26-35, June 2017. https://doi.org/10.1016/j.sigpro.2016.12.029
[17] Chi, LP., Wu, CH. and Chang, HP. "Reversible data hiding in dual Stego-image using an improved center folding strategy", Multimed Tools Appl., Vol. 77, pp. 8785–8803, 2018. https://doi.org/10.1007/s11042-017-4774-y
[18] S. Shastri and T. V, "Dual image reversible data hiding using trinary assignment and centre folding strategy with low distortion", Journal of Visual Communication and Image Representation, vol. 61, pp. 130-140, 2019. https://doi.org/10.1016/j.jvcir.2019.03.022
[19] J. Biswapati, G. Debasis and M. S. Kumar, "Dual-Image Based Reversible Data Hiding Scheme Through Pixel Value Differencing with Exploiting Modification Direction", in Proceedings of the First International Conference on Intelligent Computing and Communication, Advances in Intelligent Systems and Computing 2017, DOI 10.1007/978-981-10-2035-3_56
[20] P. H. Kim, K. W. Ryu and K. H. Jung, "Reversible data hiding scheme based on pixel-value differencing in dual images., International Journal of Distributed Sensor Networks", vol. 16, no. 7, pp. 1-13, 2020. https://doi.org/10.1177/1550147720911006
[21] Yao H, Qin C, Tang T, "Improved dual-image reversible data hiding method using the selection strategy of shiftable pixles coordinates with minimum distortion", Signal Process vol. 135, pp. 26-35., 2017,
[22] S. Shastri and V. Thanikaiselvan, "Dual image reversible data hiding using trinary assignment and centre folding strategy with low distortion", J Vis Commun Image R. Vol. 61 pp. 130-140, 2019.
[23] T.C. Lu, C.Y. Tseng, J.H, Wu, "Dual imaging-based reversible hiding technique using LSB matching", Signal Process. vol. 108, pp. 77-89, 2015.
[24] A. K. Sahu and G. Swain, "High fidelity based reversible data hiding using modified LSB matching and pixel difference". Journal of King Saud University-Computer and Information Sciences, vol. 34, no. 4, pp. 1395-1409, 2022. https://doi.org/10.1016/j.jksuci.2019.07.004
[25] C. T. Huang, N.S. Shongwe, H. Y. Weng, HY and C. Y. Wend, "Capacity-raising reversible data hiding scheme using quinary secrets square in dual-images". Multimed Tools Appl, April 2023. https://doi.org/10.1007/s11042-023-15255-7
[26] A. A. Mohammad, "A high quality interpolation-based reversible data hiding technique using dual images". Multimed Tools Appl, March 2023 . https://doi.org/10.1007/s11042-023-15092-8
[27] L. C.Thi, S. N. Kim and A. P. Van, "Dual-image reversible data hiding method using maximum embedding ability of each pixel". Journal of Information Security and Applications, vol. 74, May 2023. https://doi.org/10.1016/j.jisa.2023.103470

Authorized licensed use limited to: DELHI TECHNICAL UNIV. Downloaded on July 20,2023 at 11:09:45 UTC from IEEE Xplore. Restrictions apply.

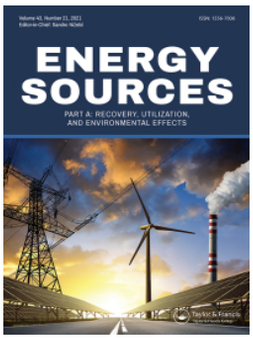

Taylor & Francis
Taylor & Francis Group

Energy Sources, Part A: Recovery, Utilization, and Environmental Effects

ISSN: (Print) (Online) Journal homepage: https://www.tandfonline.com/loi/ueso20

Dynamic performance improvement of proton exchange membrane fuel cell system by robust loop shaping and artificial intelligence optimized fractional order PI controllers

Swati Singh, Vijay Kumar Tayal, Hemender Pal Singh & Vinod Kumar Yadav

To cite this article: Swati Singh, Vijay Kumar Tayal, Hemender Pal Singh & Vinod Kumar Yadav (2023) Dynamic performance improvement of proton exchange membrane fuel cell system by robust loop shaping and artificial intelligence optimized fractional order PI controllers, Energy Sources, Part A: Recovery, Utilization, and Environmental Effects, 45:3, 9308-9324, DOI: 10.1080/15567036.2023.2236081

To link to this article: https://doi.org/10.1080/15567036.2023.2236081

Published online: 17 Jul 2023.

Submit your article to this journal

Article views: 3

View related articles

View Crossmark data

Full Terms & Conditions of access and use can be found at
https://www.tandfonline.com/action/journalInformation?journalCode=ueso20

ENERGY SOURCES, PART A: RECOVERY, UTILIZATION, AND ENVIRONMENTAL EFFECTS
2023, VOL. 45, NO. 3, 9308–9324
https://doi.org/10.1080/15567036.2023.2236081

Taylor & Francis
Taylor & Francis Group

Check for updates

Dynamic performance improvement of proton exchange membrane fuel cell system by robust loop shaping and artificial intelligence optimized fractional order PI controllers

Swati Singh[a], Vijay Kumar Tayal[a], Hemender Pal Singh[a], and Vinod Kumar Yadav[b]

[a]Departnment of Electrical and Electronics Engineering, Amity University, Noida, India; [b]Electrical Engineering Department, Delhi Technological University, Delhi, India

ABSTRACT

Due to inherent nonlinear behavior, the Proton Exchange Membrane (PEM) Fuel Cell system yields in poor power quality. The sudden change in stack current causes uncertainty in PEMFC behavior resulting in degraded output. This necessitates the control of supply manifold pressure on the cathode side to prevent oxygen starvation. In this work, three techniques, namely, robust loop shaping, smith predictor, and Fractional Order Proportional Integral (FOPI) controllers, are designed after incorporating parametric uncertainty in system description. Further, the Particle Swarm Optimization (PSO) artificial intelligence technique is implemented to optimize the parameters of smith predictor and Fractional Order PI controllers. By stabilizing the system across the entire parameterized uncertainty range, the proposed control strategies, namely, loop shaping, PSO-Smith Predictor, and PSO-FOPI controller effectively compensate uncertainty effects. The simulation result shows that the PSO-tuned FOPI controller has best overshoot at operating points 3, 4, and 5 having a value of 0.505% in comparison with PSO-Smith Predictor where overshoot (ranging from 19.88% to 40.141%) is too high; and loop shaping controller having high values of overshoot (more than 40% at every operating point) Thus, PSO-FOPI controller exhibits the best performance with far superior overshoot and steady-state stability.

ARTICLE HISTORY
Received 17 March 2023
Revised 5 June 2023
Accepted 3 July 2023

KEYWORDS
Proton exchange membrane fuel cell (PEMFC); Fractional order proportional-integral (FOPI) controller; Particle swarm optimization (PSO), stack current (i_{stack}), compressor voltage (v_{cv})

Introduction

Polymer Electrolytic Membrane Fuel Cell (PEMFC) is fast emerging renewable energy source. In comparison with conventional combustion engines, fuel cells run more efficiently and transfer the chemical form of energy of the fuel directly into electrical energy. There exists no air hazards such as smoke and other chemicals harmful for humans. Due to lack of moving parts, fuel cell works quite silently. When a long range is needed or battery charging takes too long, fuel cells are preferable than batteries. This makes them suitable for use in emergency response vehicles, boats, planes, trucks, and buses. Also, they offer higher power density and range needed for an electric vehicle. However, the air supply system, affects the PEMFC's performance and lifespan. For a multi-stack FC hybrid system, a real-time energy optimization approach that reduces system running costs is created in order to boost system economics (Li et al. 2022). Oxygen deprivation occurs for a variety of causes, including compressor delays, occurrence of faults during periods of high power demand, control of pressure at cathode side, and water management issues (Gerard et al. 2010). The issue of oxygen deprivation needs to be solved in order to guarantee better PEMFC performance. The focus must be on creating the precise system models and appropriate control techniques to accomplish these goals.

CONTACT Vijay Kumar Tayal vktayal@amity.edu Department of Electrical and Electronics Engineering, Amity University, Noida, India

© 2023 Taylor & Francis Group, LLC

A PEMFC system in integration with water electrolyzer system is proposed. A hierarchical performance enhancement control method (HPECS) is created to handle the challenges of the nonlinear system and optimum trajectories searching while subject to many objective restrictions (Q et al. 2021). A PEM fuel cell system's power regulation is created using nonlinear modeling of predictive control. This scheme expresses the non-linearities of the system model by employing parameters so as to linearize the state and inputs of the plant (Cloppenborg et al. 2019). The energy management approach by employing model predictive control (MPC) is created to increase fuel cell performance and cut operating expenses (Li et al. 2022). To maintain the appropriate level of hydrogen and oxygen pressure change despite variations in fuel cell current, PID controllers were developed (Swain and Jena 2015). To improve the PEMFC system's performance, PID, PIDF, and PI, PSO-Smith Predictor and PSO-FOPI controllers are employed to manage the pressure of the supply manifold (Mohamed et al. 2019; Singh et al. 2022). For a PEMFC system coupled to the dc-dc boost converter, a PI controller is designed to regulate the current of the fuel cell (Derbeli et al. 2017). FOPID and PID controller gains are adjusted using the Grey Wolf Optimizer (GWO) are created to enhance the system reliability (Silaa et al. 2022). An adaptive fuzzy PID control approach with straightforward rules is proposed to overcome the difficulties of nonlinear PEM fuel cell (PEMFC), as well as the poor control impact of classic PID method (Chen et al. 2018). According to the peculiarities of the hydrogen and oxygen delivery systems of the PEM fuel cell, fuzzy self-adaptive PID controllers are established for supply systems of hydrogen (Cheng et al. 2017). To enhance the voltage and temperature variation in a PEM fuel cell, a stack approach is designed and a model predictive control is developed (Chen et al. 2022). The dynamic behavior of PEMFC system is subjected to load variations for which PID and FO-PID controllers are implemented for improving the efficiency of the system (Lü et al. 2017). A predictive voltage neural control is employed for controlling the stack voltage considering load variations (AL-Taie and Al-Araji 2023).

In order to guarantee satisfactory performance as required by various complicated industrial processes, a reliable control system with FO-PID and Smith predictor controller is established (Zennir, Larabi, and Benzaroual 2017). Because the original open loop process poles are still in place, Smith Predictor suffers from poor performance for input (load) disruptions for processes with sluggish dynamics (Skogestad 2018). To manage the excess air ratio, stack temperature and fuel utilization ratio, subsequently in order to assure the SOFC's safe operation, a higher-order robust sliding mode controller and two feed-forward controllers are provided (Xiaojuan and Danhui 2018). For regulating the voltage at load-side in a fuel cell system, a loop-shaping average current-mode approach with a single control signal is developed (Diaz-Saldierna, Langarica-Córdoba, and Leyva-Ramos 2015). It is challenging to include quantitative stability criteria in the design of the control bound computation. A FOPI controller is used to maintain a controlled output voltage for a PEMFC having fluctuations in the PEMFC operating point and load variations (Bankupalli et al. 2018). One benefit of the FOPI controller is its contribution to system resilience, which allows for the achievement of iso-damping features during parameter fluctuation (Keek, Loh, and Chong 2018). Additionally, FOPI controller is more precise and suitable for dynamic reactions (Kumar et al. 2018).

For a PEM fuel cell system, a sliding mode observer (SMO) is designed by authors (Sankar et al. 2017). This scheme is based on globally linearizing controller and non-linear multi-variable sliding mode controller. The current oscillations in PEM fuel cells need to be reduced using a robust non-linear sliding mode controller optimized by PSO technique (Dali et al. 2021). To sustain an excess ratio of oxygen in the PEMFC system, a P-I Controller and a Sliding Mode Controller strategy had been created (Kumar et al. 2021). When using robust loop shaping design, the necessary and sufficient bounds for robust performance are used to directly specify the nominal transfer functions (Chapparya, Krishna, Dwivedi, and Bose 2018). The loop-shaping strategy comprises deriving a specification in respect to the open loop of the control from specifications for multiple closed-loop transfer function since it is easier to work on a single transfer function (in addition to the open loop) than on several transfer functions. The technique is very well suited to the industrial applications as it is both flexible

and straightforward. In order to optimize the performance of control schemes, various artificial intelligence-based techniques may be explored.

The Cuckoo search method, Moth-Flame Optimization (MFO), Adaptive-guided differential evolution algorithm (AGDE) and Ant Colony Optimization (ACO) have the main disadvantage of having a slow convergence rate and being prone to local optimum solutions (Liu et al. 2018; Mohamed and Mohamed 2019; Shehab et al. 2020; Wang 2018). Too many factors in the ACO easily results in a lack of initial signal with significant complexity. Designing an optimal solution for a genetic algorithm is a time-consuming task. The biggest drawback is that there is little assurance of the solution's quality or optimality because GA is stochastic in nature. It might not always provide the desired result (Beg and Islam 2016). As opposed to the aforementioned meta-heuristic methods, the PSO technique offers the following advantages: a straightforward idea, clear and simple implementation, resilience to control parameters, and computing effectiveness (Gad 2022). The PSO approach provides quick convergence time, robustness, minimal processing, coherence in problem solution, and small number of parameters to alter (Wihartiko, Wijayanti, and Virgantari 2018).

In the past work, researchers have developed loop shaping controller for regulating oxygen flow (Linli et al. 2022). But, for managing pressure of the supply manifold, loop shape controller is not developed in the existing studies. Also, studies have shown that a PSO optimized FOPI controller has not designed earlier for a non-linear PEMFC system considering uncertainty. One of the main issues with an FC system is a shortage of oxygen. The fuel cell's stack current rises as the load fluctuates quickly. Consequently, more electricity is needed. This requires more chemical reactions to take place so as to satisfy the power requirements. This process acquires more oxygen at the cathode side and it is supplied by the manifold pressure. Thus, the objective of this paper is:

- To manage the supply manifold pressure by designing suitable controllers for a non-linear PEMFC system.
- The PEMFC transfer function's uncertainty analysis is carried out for varying stack current and compressor voltage.
- The loop-shaping, PSO-tuned Smith-Predictor and PSO-based FO-PI controllers are proposed to control the pressure at cathode end in order to avoid oxygen deprivation of the PEMFC system.

This work is organized as follows: Section II deals with Non-linear PEMFC and modeling of the system. The controlling techniques employed are discussed in Section III. PSO technique, which is used for optimizing smith-predictor and FO-PI controller, is described in Section IV. The simulation results and comparison among various controllers are illustrated in Section V while Section VI outlines the conclusion.

Non-linear PEMFC system model

The electro-chemistry, rotational kinematics of the compressor and motor, and mass balances for lumped volumes in the stack and surrounding volumes, are the foundations for the stacks of fuel cell models (Zhang et al. 2019). In essence, electrochemical models are created for the relationship between the optimum cell voltage and the cell's current density. Because the kinematics of oxygen and hydrogen influences PEM fuel cell attributes, the reactants supply plays a significant influence in fuel cell performance (Javaid et al. 2022). The fuel cell system is supposed to be fed by pressurized, high-purity hydrogen, and the hydrogen supply management is ideal for monitoring the anode to cathode pressure. This allows the focus to be on the air (oxygen) dynamics of the system. The stack voltage, V_{stack}, which directly affects the generation of stack power when the load current, I_{stack}, is extracted from the stack, is one of the factors affecting performance of the fuel cell system (Figure 1). Another important factor is the excess oxygen ratio,ω_{O2}, in the cathode, which obliquely guarantees that the stack receives a sufficient oxygen supply. Now the power generated is given by Eq. 1.

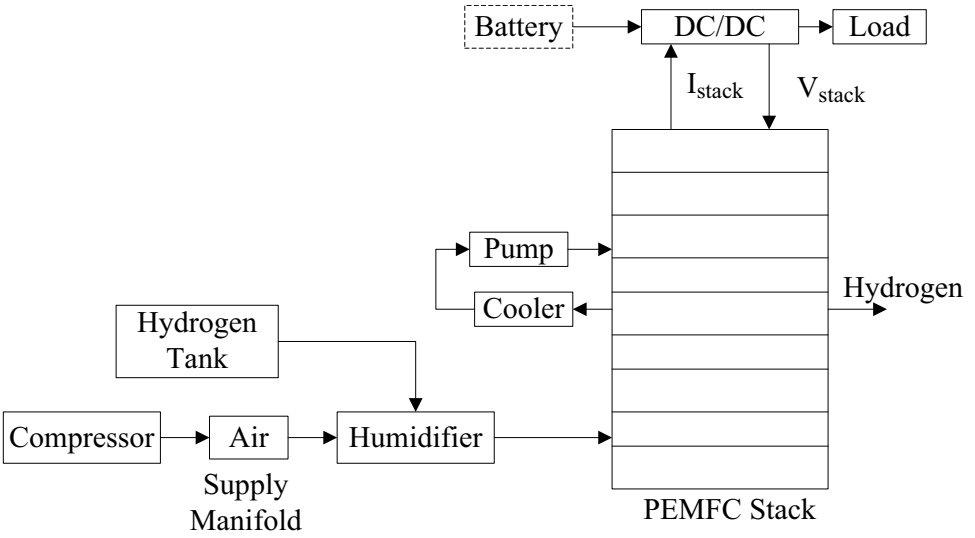

Figure 1. The structure of PEM fuel cell.

$$P_{FuelCell} = V_{stack} I_{stack} \tag{1}$$

where fuel cell's stack voltage is calculated as shown in Eq. 2 and the fuel cell's output voltage is detailed in Eqn 3.

$$V_{stack} = N V_{O/P} \tag{2}$$

$$V_{O/P} = E_O - (l_{ohm} + l_{act} + l_{conc}) \tag{3}$$

In steady condition, voltage of the fuel cell is described as static function of current density (I_d), numerous other factors such as partial pressures of oxygen (ρ_O) and hydrogen (ρ_H), cathode pressure (ρ_{cth}), humidity (H_d), and temperature (T).

$$I_d = \frac{I_{stack}}{A_{FuelCell}} \tag{4}$$

The inlet mass flow rate of oxygen ($F_{O,in}$) and nitrogen ($F_{N,in}$) can be evaluated from the inlet cathode flow ($F_{cth,in}$) as shown in Eqs. 5-6. Also fraction for oxygen mass ($f_{O,m}$) of the inlet air is given in Eqs. 7 and the humidity ratio of inlet air is shown in Eqn (8)

$$F_{O,in} = \frac{f_{O,m}}{1 + w_m} F_{cth,in} \tag{5}$$

$$F_{N,in} = \frac{1 - f_{O,m}}{1 + w_m} F_{cth,in} \tag{6}$$

$$f_{O,m} = \frac{g_{O,in} M_O}{g_{O,in} M_O + (1 - g_{O,in}) M_N} \tag{7}$$

$$w_m = \frac{M_v}{g_{O,in} M_O + (1 - g_{O,in}) M_N} \frac{\lambda_m P_{st}}{P_m - \lambda_m P_{st}} \tag{8}$$

The supply manifold idea describes the mass flow rate from the compressor to the exit. Due to the little difference in pressure between the cathode and supply manifold, a linear flow-pressure condition is taken into consideration for the evaluation of flow (Eq. 9)

$$F_{cth,in} = k_{cth,in}(P_{sm} - P_{cth}) \tag{9}$$

where $k_{cth,in}$ is the constant for supply manifold. Cathode pressure is denoted by $P_{cth.}$ and it is the sum of the partial pressures of vapor (P_{st}), nitrogen, (P_N), and oxygen (P_O) (Eq. 10)

$$P_{cth} = P_O + P_N + P_{st} \tag{10}$$

When the reaction is completed, the flow rate of oxygen $f_{O,out}$ and nitrogen$f_{N,out}$, for mass at outlet, are evaluated from the fraction of mass of nitrogen and oxygen in the stack and outlined in Eqs. 11-12.

$$f_{O,out} = \frac{M_N P_O}{M_O P_O + M_N P_N + M_v P_{st}} f_{cth,out} \tag{11}$$

$$f_{N,out} = \frac{M_N P_N}{M_O P_O + M_N P_N + M_v P_{st}} f_{cth,out} \tag{12}$$

The oxygen excess ratio is represented in Eq. 13.

$$\eta_O = \frac{f_{O,in}}{f_{O,rct}} \tag{13}$$

It is important to obtain the FOPTD plant models for a few predetermined operating points prior to controller designing. The stack is made up of 381 fuel cells. The general form of transfer function for FOPTD system is given in Eq. 14 where K, θ, and T represents process gain, time delay, and time constant, respectively.

$$G(s) = \frac{Ke^{-\theta s}}{1 + Ts} \tag{14}$$

The compressor voltage (V_{cv}) is a control input and the stack current (I_{stack}) is an input disturbance to the system. The pressure of the manifold supply at the cathode side is the output of the system. When there is a change in stack current, disturbance occurs and thus the operating conditions of the PEMFC system varies. In this work, different transfer functions for the FOPTD model of the system are obtained as a result of changes in I_{stack} and V_{cv}. For different values of I_{stack} and V_{cv}, Table 1 details the corresponding values of K, T and θ. The resulting transfer functions are depicted in Eqs. (15)-(21) for different values of I_{stack} and $V_{cv.}$ The PEMFC's nominal plant's performance is adversely affected by the uncertainty in the phase and gain because the response of the PEM fuel cell is modified using the nominal plant transfer function (Divi, Sonawane, and Das 2018).

Table 1. FOPTD model parameters for variations in I_{stack} and $V_{cv.}$

S.No.	Operating Points	Stack Current, I_{stack} (A)	Compressed Voltage V_{cv} (V)	Process Gain K	Delay in Time θ	Time constant T
1	Operating Point 1	90	90	727.14	0.0578	0.2739
2	Operating Point 2	120	110	448.73	0.0639	0.3028
3	Operating Point 3	150	130	239.733	0.0838	0.3337
4	Operating Point 4	180	150	72.30	0.1136	0.3698
5	Operating Point 5	210	170	68.55	0.147	0.4141
6	Operating Point 6	240	190	191.66	0.1729	0.4663
7	Operating Point 7	250	200	249.78	0.1493	0.5628

$$G1 = \frac{727.14 * e^{-0.0578s}}{1 + 0.2739s} \tag{15}$$

$$G2 = \frac{448.73 * e^{-0.0639s}}{1 + 0.3028s} \tag{16}$$

$$G3 = \frac{239.733 * e^{-0.0838s}}{1 + 0.3337s} \tag{17}$$

$$G4 = \frac{72.30 * e^{-0.1136s}}{1 + 0.3698s} \tag{18}$$

$$G5 = \frac{68.55 * e^{-0.147s}}{1 + 0.4141s} \tag{19}$$

$$G6 = \frac{191.66 * e^{-0.1729s}}{1 + 0.4663s} \tag{20}$$

$$G7 = \frac{249.78 * e^{-0.1493s}}{1 + 0.5628s} \tag{21}$$

The PEMFC model parameters and their description are mentioned in Table 2.

Table 2. PEMFC Model Parameters and their description

Parameters	Description	Unit
E_O	Voltage of Open circuit	V
I_{ohm}	Ohmic Loss	V
I_{act}	Activation Loss	V
I_{conc}	Concentration Loss	V
I_{stack}	Stack Current	A
$A_{FuelCell}$	Area of active cell	
$F_{O,in}$	Rate of flow of mass for oxygen at inlet	Kg/sec
$f_{O,m}$	the fraction for oxygen mass of the inlet air	Kg/s
w_m	humidity ratio of inlet air	-
$F_{cth,in}$	Inlet cathode flow	kmol/s
$F_{N,in}$	Rate of flow of mass for nitrogen at inlet	Kg/s
$g_{O,in}$	oxygen molar ratio	kmol/s
M_O, M_N	molar mass of oxygen and nitrogen, respectively	Kg/mol
λ_m	relative humidity at ambient conditions	-
P_{st}	vapor saturation pressure	Pa
$k_{cth,in}$	supply manifold orifice flow constant	-
P_{sm}	supply manifold pressure	Pa
P_{cth}	spatially invariant cathode pressure	Pa
P_O	Partial pressure of oxygen	Pa
P_N	Partial pressure of nitrogen	Pa
$f_{O,out}$	the fraction of oxygen mass of the outlet air	-
$f_{cth,out}$	Outlet oxygen flow	l/s
$f_{N,out}$	the nitrogen mass fraction of the outlet air	-

Control methodology employed for non-linear PEM fuel cell system

PEMFCs are gaining popularity because of its high performance, low operating temperature, and environmental-friendly behavior. But the system's performance is degraded due to factors, namely, non-linearities, oxygen starvation, uncertainty, uncontrolled voltage, and low power quality. This paper deals in managing pressure of supply manifold at cathode side by considering uncertainty in the system. Loop-shaping controller, PSO-Smith Predictor Controller, and PSO-FOPI controller are designed for controlling pressure of the supply manifold.

Loop-shaping controller

The required form of the open-loop response could be set by the loop-shaping controller synthesis technique. In the majority of controller designs, performance and resilience against uncertainty are traded off. Determining the feedback may be constrained by the uncertainty of the plant. Large gains of loop can minimize the system's overall susceptibility to perturbations and mitigate the consequences of plant model uncertainty. However, using the substantial feedback benefits would put the system at danger of instability, if the plant model uncertainty was too high. For this reason, performance and resilience against uncertainty are typically traded off in controller designs (Saeki 2022). The tradeoff that best satisfies the system's needs is identified via Robust Control Toolbox for the designing of loop-shaping controller. The loop-shaping technique balances robustness and performance. A transfer function that parametrizes the controller depending on the transfer function's magnitude constraints is directly specified as part of the loop-shaping process. These constraints either meet the essential requirements or the sufficient requirements for the closed-loop system to meet the specified stability and performance standards. While using loop-shaping controller, the complexity of the controller can be defined easily and decentralized controllers can be developed (Sung, Patil, and Safonov 2015).,

The complementary sensitivity function, T and sensitivity function, S, for a closed-loop system, are described by Eq. 22 and Eqn 23, to measure the stability margins and performance of such systems.

$$S(s) = \frac{1}{(1 + L(s))} \tag{22}$$

$$T(s) = \frac{L(s)}{(1 + L(s))} = 1 - S(s) \tag{23}$$

where L(s) is the open-loop transfer function and is given in Eq. 24

$$L(s) = G(s)K(s) \tag{24}$$

In Figure 2, a loop-shape controller is outlined, where *r(s)* is the signal for reference, *e(s)* designates the difference of output of the plant, *y(s)* and *r(s)*, P(s) is plant, R(s) is a reference signal's pre-filter, *W(s)* is a prior compensator and robust controller is represented by $K_r(s)$, and $K(s) = W(s)^{\star} K_r(s)$ is the complete controller (Shih and Chen 2020).

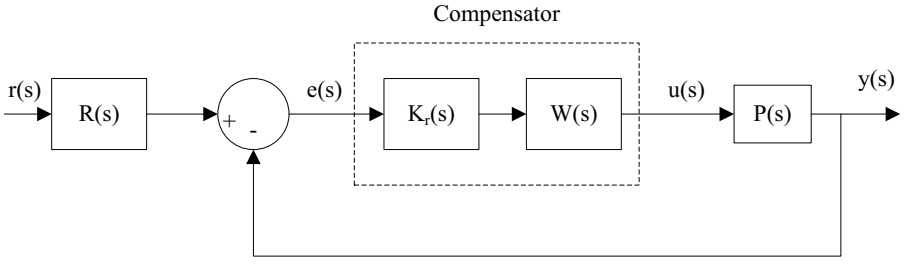

Figure 2. Loop shaping controller.

Smith predictor controller

The Smith predictor is employed to create a controller for a system that combines a closed-loop feedback controller with a delay or approximation in time. It is among the most extensively used algorithms in industries for dead-time compensation and extensively employed dead compensating methods. It is a controller that is based on model parameters and works well for lengthy dead time operations. The effects of load disturbance and modeling error are mitigated using an external loop (Gnanamuruga and Senthilkumar 2014).

The textbox with the dotted lines contains the Smith predictor, $K_p(s)$ is transfer function and K_d s denotes simple P-I-D controller (Figure 3). e^{-ts}, is the delay in time of the plant. $K_c(s)$ is the transfer function for the modeled plant and e^{-ms} is the delay in time of the modeled model (Kumar et al. 2018). In the absence of Smith Predictor Controller, the closed-loop response is given in Eq. 25.

$$\frac{c(s)}{r(s)} = \frac{K_d(s)K_p(s)e^{-ts}}{1 + K_d(s)K_p(s)e^{-ts}} \tag{25}$$

Eq. 26 provides the closed-loop transfer function using the Smith predictor.

$$\frac{c(s)}{r(s)} = \frac{K_d(s)K_p(s)e^{-ts}}{1 + K_d(s)K_p(s)e^{-ts} + K_d(s)K_p(s) - K_d(s)K_c(s)e^{-ms}} \tag{26}$$

To evaluate the tuning parameters of the Smith Predictor controller, Eqs. 15-21 are converted to linear equation and nominal value of G is given in Eqn 27:

$$G(s) = \frac{-951.1s + 1.649e04}{s^2 + 19.74s + 41.46} \tag{27}$$

Fractional-order proportional-integral controller

The FOPI controller has three parameters, namely, the proportional gain, k_p , the integral time constant, t_i, and the order of the integration, λ, are required to be optimized (Baruah, Majhi, and Mahanta 2019; Petchinathan, Valarmathi, and Radhakrishnan 2017). The control equation for a FOPI controller is detailed in Eq. 28.

$$u(x) = k_p\left(e(x) + \frac{1}{t_i}D_x^{-\lambda}e(x)\right) \tag{28}$$

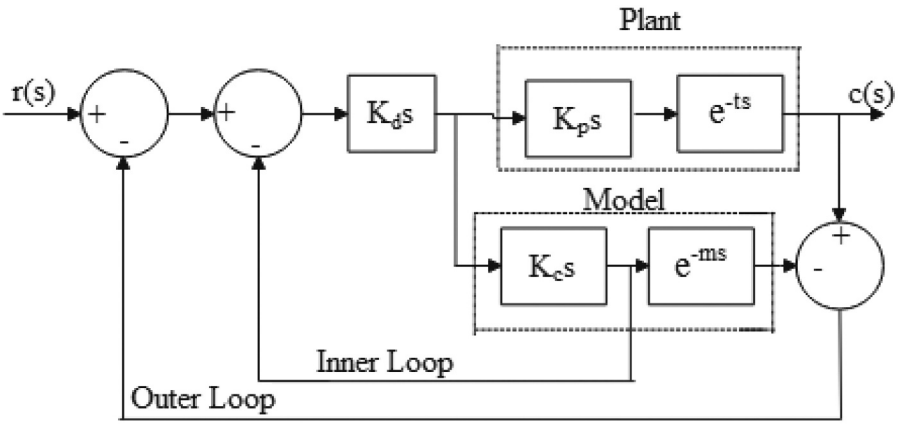

Figure 3. Structure of Smith Predictor.

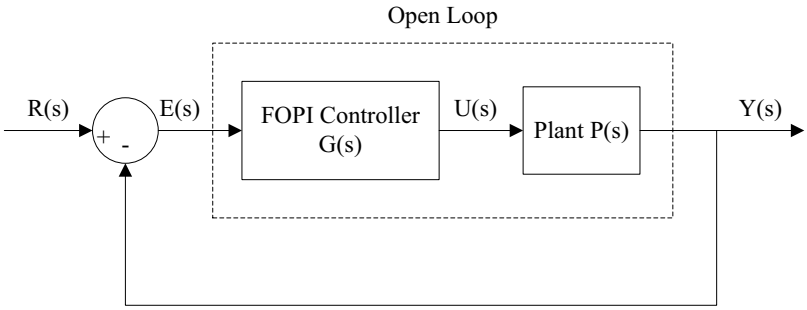

Figure 4. Block diagram of FOPI controller.

where *e(x)* is the error between output *y(x)* and reference point *r(x)* at time *x*.

Let the transfer function of the process is represented by P*(S)* and the controller by *G(s)* (Figure 4), then Eqs. 29-32 determines the specific phase margin p_m and gain margin, g_m; where g_m and p_m, respectively, represent the gain margin and phase margin (Kumar and Ghosh 2018). Also ω_{Pc} and ω_{Gc} denote the phase cross-over and gain cross-over frequencies.

$$\arg(G(i\omega_{Pc})P(i\omega_{Pc})) = -\pi \tag{29}$$

$$g_m = \frac{1}{abs(G(i\omega_{Pc}) * P(i\omega_{Pc}))} \tag{30}$$

$$abs(G(i\omega_{Gc})P(i\omega_{Gc})) = 1 \tag{31}$$

$$\arg(G(i\omega_{Pc})P(i\omega_{Pc})) + \pi = p_m \tag{32}$$

Assuming a model of a sample plant with a constant gain K and a time delay x that is described as shown in Eq. 33,

$$P(s) = K\frac{(1+\omega_{P1}s)^{P1}(1+\omega_{P2}s)^{P2}\ldots\ldots\ldots\ldots(1+\omega_{P(n-1)}s)^{P(n-1)}(1+\omega_{Pn}s)^{Pn}}{(1+\omega_{Q1}s)^{Q1}(1+\omega_{Q2}s)^{Q2}\ldots\ldots\ldots\ldots(1+\omega_{Q(m-1)}s)^{Q(m-1)}(1+\omega_{Qn}s)^{Qn}} \tag{33}$$

Optimization of fractional-order PI and smith-predictor controllers by employing PSO algorithm

A stochastic approach used for optimization issues is called particle swarm optimization (PSO). The algorithm moves toward the global optimum like a particle traveling across the search space (Imran, Hashim, and Khalid 2013). According to PSO, a particle is $P_k \in [e,f]$where $k = 1, 2, 3 \ldots .,d$ *and* $[e,f] \in r$. Here, "d" represents the dimensions and "r" is used for real numbers. In the starting, the velocity and position of particles are initialized randomly (Tayal and Lather 2015). Every particle makes an effort to preserve both their local best position (pbest) and their overall best position (gbest). Let $P_k(t)$ depict the position of particle k in the search space at time step t. $V_k(t)$, is added to the particle's present position, the particle's position is modified (Eq. 34).

$$P_k(t+1) = P_k(t) + V_k(t+1) \tag{34}$$

For *gbest*, the velocity of particle k is evaluated as shown in Eq. 35

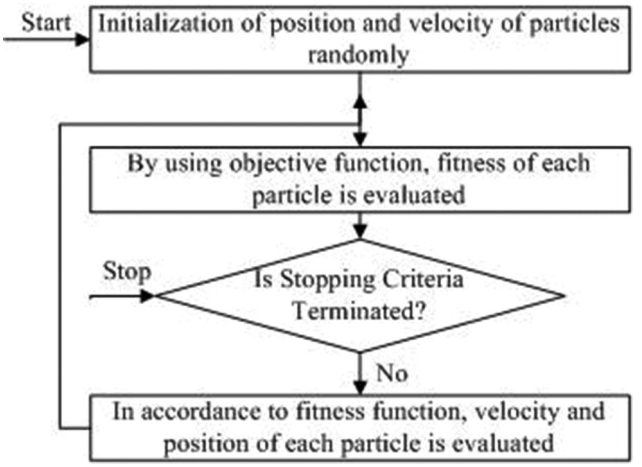

Figure 5. Flowchart for PSO.

Table 3. Parameters of PSO Algorithm.

S.No.	PSO Parameters	Values
1	Factor of acceleration,C1	1.9
2	Factor of acceleration,C2	1.9
3	Weight due to Inertia, w	0.8
4	Population Size	49

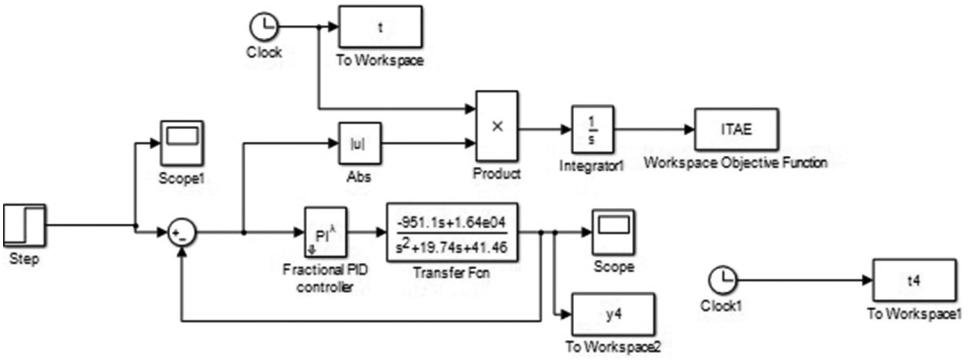

Figure 6. FOPI Controller- Simulink Diagram.

$$V_k(t+1) = V_{kj}(t) + b_1 R_{1j}(t)\left[y_{kj}(t) - P_{kj}(t)\right] + b_2 R_{2j}(t)\left[z_{kj} - P_{kj}(t)\right] \tag{35}$$

where $V_{kj}(t)$ is the particle's velocity, k in dimension $j = 1, \ldots, n$; at time step t, $y_{ij}(t)$ is the position of particle k in dimension, j, at time step t, b_1 and b_2 are positive acceleration constants. Figure 5 explains the steps involved in the PSO process. For this work, Table 3 presents the PSO algorithm's settings.

One of the important elements of PSO is fitness function, also known as objective function which is used to find out the optimal solution. This paper uses ITAE (Integral time absolute error) as its fitness function and ITAE is outlined as in Eq. 36

$$ITAE = \int_0^{t(s)} T * |e(T)| dT \tag{36}$$

The Simulink models of FOPI and Smith Predictor Controller are shown in Figures 6–7.

Simulation results

To judge the robustness of the developed controller design, the non-linear PEM-FC system is simulated in MATLAB and a step disturbance is introduced at $t = 0$ second (Figure 8). Further, loop-shaping robust controller, PSO optimized FOPI controller, and Smith Predictor controller are employed to manipulate the pressure of the supply manifold at cathode side of the fuel cell system at seven different operating points due to the variation of stack current (I_{stack}) and compressor voltage (V_{CV}). The pressure of the supply manifold of the system in the absence of control action is depicted in Figure 9(a-g). The PSO technique is employed for the optimization of Smith-Predictor as well as FOPI controller parameters. The FOPI and Smith Predictor controller's parameters are illustrated in Table 4. The supply manifold pressure of the fuel cell at seven different operating points by employing PSO-tuned Smith-Predictor controller, loop-shaping controller, and PSO-based FOPI controller is outlined

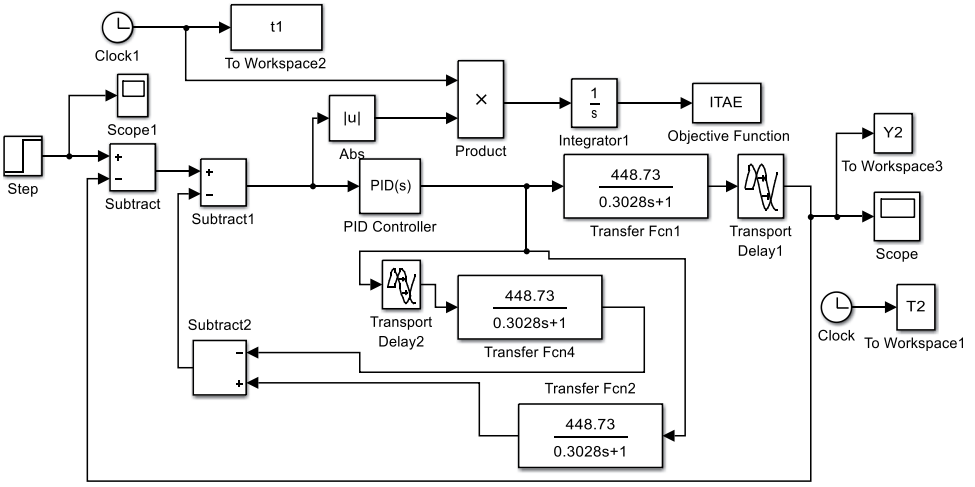

Figure 7. Smith predictor-Simulink model.

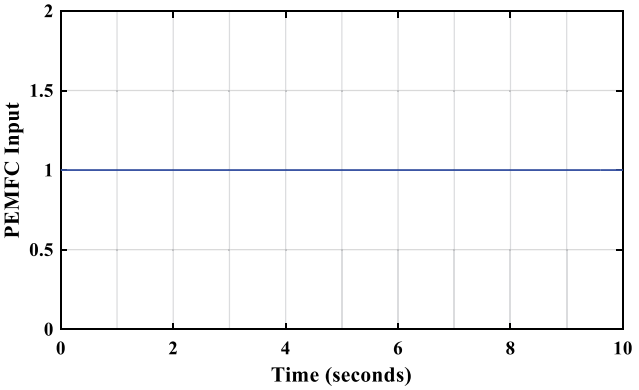

Figure 8. PEMFC Input.

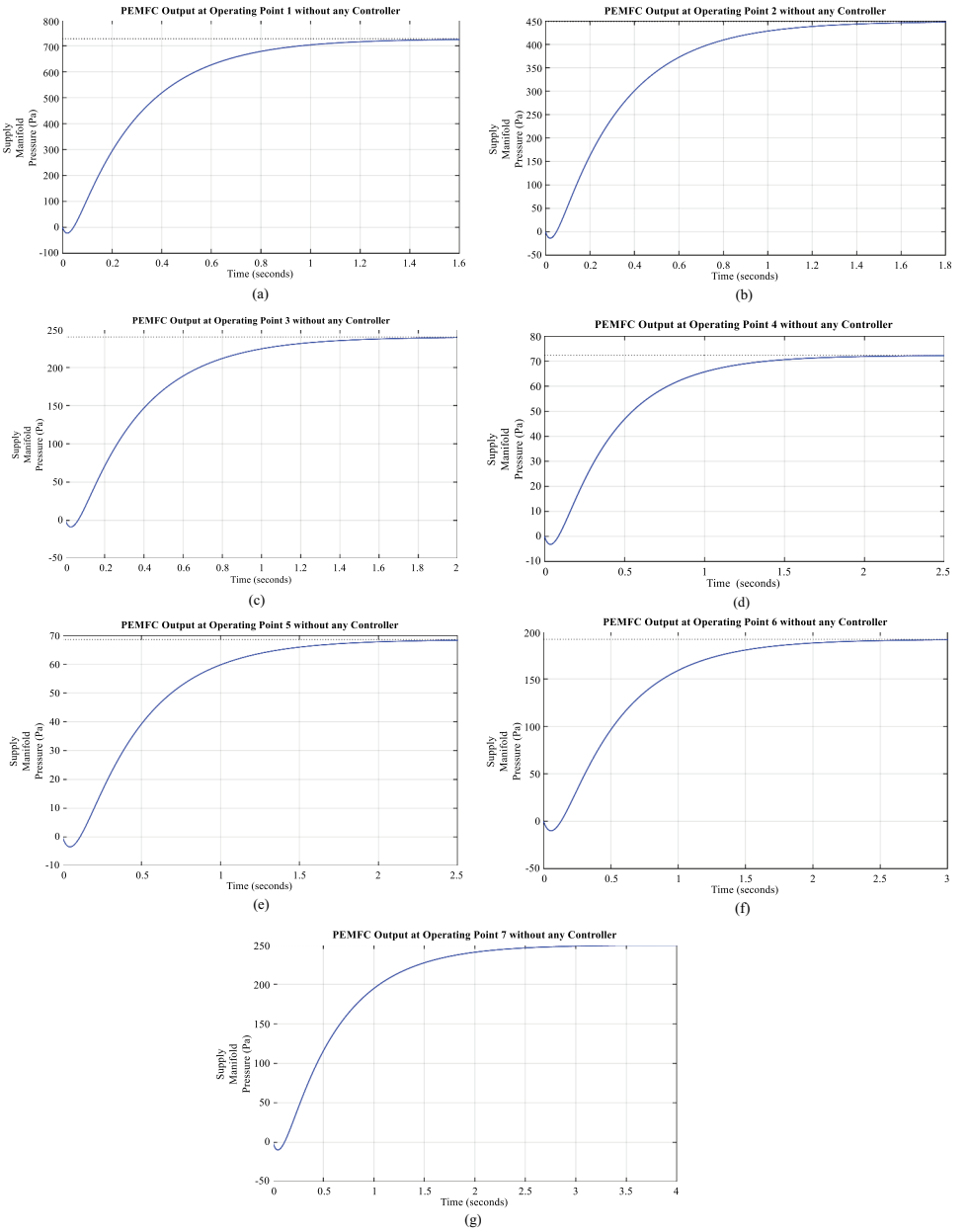

Figure 9. (a-g): Supply manifold pressure for PEMFC system without controller at seven different operating points.

Table 4. Controller Parameters.

	Controller Gains			
Type of Controller	K_p	K_i	K_d	λ
PSO-tuned Smith Predictor	0.0041	0.0776	0.0000959	NA
PSO-tuned FOPI	0.0056	0.0138	NA	1.058

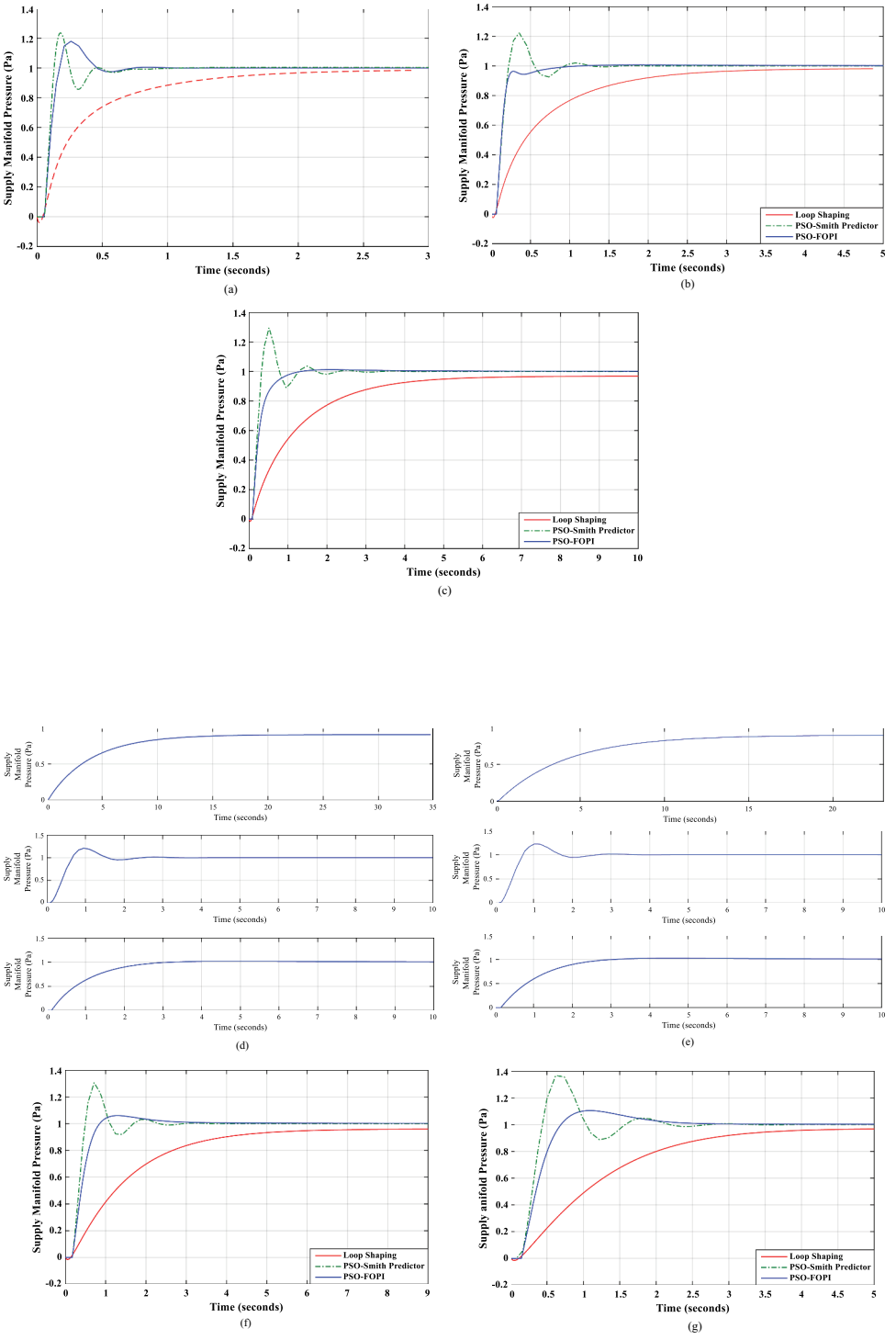

Figure 10. (a-g): Supply manifold pressure for PEMFC system at seven different operating points with loop-shaping controller, PSO optimized Smith Predictor, and FOPI controller.

Table 5. Output of PEM fuel cell system with various controllers and their comparison.

Parameters	Settling Time, t_s (seconds)			Overshoot M_p (%)			Steady-State Error e_{ss} (%)		
Controllers	Loop Shaping Controller	PSO-Smith Predictor Controller	PSO-FOPI Controller	Loop Shaping Controller	PSO-Smith Predictor Controller	PSO-FOPI Controller	Loop Shaping Controller	PSO-Smith Predictor Controller	PSO-FOPI Controller
Operating Point 1 [I_{stack}=90A, V_{CV}= 90V]	1.98	1.083	.746	57.1429	19.880	22.84	1.5	.3	0
Operating Point 2 [I_{stack}=120A, V_{CV}= 110V]	1.98	1.871	1.074	54	22.840	.155	1.9	.4	0
Operating Point 3 [I_{stack}=150A, V_{CV}= 130V]	6.76	2.613	1.229	5.9804	29.221	.505	3.2	.3	.1
Operating Point 4 [I_{stack}=180A, V_{CV}= 150V]	15.6	3.119	3.804	48.0769	21.341	.505	9.8	.5	.4
Operating Point 5 [I_{stack}=210A, V_{CV}= 170V]	21.7	3.194	3.851	45.2830	21.341	.505	1.4	.4	.4
Operating Point 6 [I_{stack}=240A, V_{CV}=190V]	7.17	3.429	2.772	42.5926	3.921	5.851	4	.5	0
Operating Point 7 [I_{stack}=250A, V_{CV}= 200V]	3.93	3.372	2.774	40	4.141	1.556	3.1	.5	.3

in Figure 10(a-g). The comparison of system output with different controllers is shown in Table 5. The output is compared in terms of overshoot, settling time (T_s) and steady state error (E_{ss}).

This has been observed that with robust loop-shaping controller, the settling time is quite high at operating points 4 and 5 (15.6 s and 21.7 s, respectively). However, the overshoot is very high at each point. Even the least value for overshoot (40%) obtained at operating point 7 is very high.

With PSO-Smith Predictor Controller, the overshoot is high (ranging from 19.88% to 40.141%). In contrast to loop-shaping and PSO optimized Smith Predictor, FOPI controller has considerably improved the system output. With reasonably good settling time, the best overshoot values are obtained at operating points 2, 3, 4, and 5 (0.155%, 0.505%, 0.505%, and 0.505%, respectively). Further, the steady-state error is also remarkably improved (less than 1%.at each operating point) with PSO-FOPI controller. This improvement in steady-state error, settling time, and overshoot ensures the best output from the PSO-FOPI controller.

Conclusion

One of the biggest challenges for PEM fuel cell system is to prevent it from oxygen starvation by managing supply manifold pressure at cathode end. The system is very slow when there is no controller. This paper proposed loop-shaping controller, PSO-tuned Smith-Predictor, and FO-PI controllers for controlling pressure of the supply manifold of a non-linear PEM-FC system over wide range of uncertainty. All the schemes hold good settling time. Loop-shaping

controller improves steady-state error but have very high values of overshoot at all operating points. On the other hand, PSO-tuned Smith Predictor has better settling time, improves steady-state error but its overshoot is very large which makes the system slow. In contrast to loop-shaping controller and PSO-tuned smith predictor controller, PSO-tuned FOPI controller shows remarkable improvement in steady-state error (less than 1% at each operating point) as well as overshoot (best value of 0.505% at operating point 3, 4, and 5). Thus, among the entire proposed schemes, namely, Loop-shaping controller, PSO-Smith Predictor and PSO-Fractional Order PI controller, PSO-FOPI controller is most robust and best suited for the system. This work can be further extended by employing more robust control designs, namely, H infinity controller and mu controller; fuzzy controllers and sliding mode controllers. Optimization techniques like cuckoo search, tabu search algorithm, harmony search, honey-bee algorithm, and firefly algorithm can be used for the tuning of developed controllers.

Disclosure statement

No potential conflict of interest was reported by the author(s).

Notes on contributors

Swati Singh is pursuing PhD from Amity University, Noida, India in Electrical & Electronics Engineering Department. Controller designing and renewable energy systems are her area of interest.

Vijay Kumar Tayal pursued his Ph.D. and M.Tech from National Institute Technology, Kurukshetra, India. He has more than 25 years of academic experience. Presently, he serves as an Associate Professor at Amity University, Noida, India. Robust and fuzzy control system design is one of his areas of interest.

Hemender Pal Singh completed his doctorate from Rohilkhand University, U.P., India. He has more than 20 years of teaching experience in various organizations. He is currently a Professor and the Head of the Electrical and Electronics Engineering Department at Amity University, Noida, India. Optical Communication, Control System and Instrumentation Systems are his areas of expertise.

Vinod Kumar Yadav completed his doctoral degree from IIT, Roorkee, India. He did his M. Tech from National Institute of Technology, Jamshedpur, India. He has more than 15 years of academic experience in various organizations. At present, he is working as Professor at Delhi Technological University, India.

ORCID

Swati Singh http://orcid.org/0000-0002-3724-6341

Data availability statement

Sharing of data is not relevant to this article.

References

AL-Taie, F. A., and A. S. Al-Araji. 2023. Development of predictive voltage controller design for PEM fuel cell system based on identifier model. *International Journal of Intelligent Engineering and Systems* 16 (2):343–60.

Bankupalli, P. T., S. Ghosh, L. Kumar, and S. Samanta. 2018. Fractional order modeling and two loop control of PEM fuel cell for voltage regulation considering both source and load perturbations. *International Journal of Hydrogen Energy* 43 (12):6294–309. doi:10.1016/j.ijhydene.2018.01.167.

Baruah, G., S. Majhi, and C. Mahanta. 2019. Design of FOPI controller for time delay systems and its experimental validation. *International Journal of Automation & Computing* 16 (3):310–28. doi:https://doi.org/10.1007/s11633-018-1165-4.

Beg, A. H., and M. Z. Islam. 2016. Advantages and limitations of genetic algorithms for clustering records. 2016 IEEE 11th Conference on Industrial Electronics and Applications (ICIEA), 2478–83, doi: 10.1109/ICIEA.2016.7604009.

Chapparya, V., G. M. Krishna, Dwivedi, P., and Bose, S. 2018. Loop shaping controller design for constant output interleaved boost converter using real-time hardware in-the-loop(HIL). Proceedings of the International MultiConference of Engineers and Computer Scientists 2.

Chen, X., Y. Fang, Q. Liu, L. He, Y. Zhao, T. Huang, Z. Wan, and X. Wang. 2022. Temperature and voltage dynamic control of PEMFC stack using MPC method. *Energy Reports* 8:798–808. doi:10.1016/j.egyr.2021.11.271.

Cheng, Z., P. Ren, Y. L. Xu, and H. N. Zhang. 2017. Model and control of fuel supply systems of hydrogen/oxygen fuel cell. *Journal of Engineering* 2017 (13):773–77. doi:10.1049/joe.2017.0436.

Chen, J., Y. Zhan, Y. Guo, J. Zhu, L. Li, and B. Liang. 2018. Fuzzy adaptive pi decoupling control for gas supply system of proton exchange membrane fuel cell. 21st International Conference on Electrical Machines and Systems (ICEMS), 1145–50, doi: 10.23919/ICEMS.2018.8549210.

Cloppenborg, A., C. Rojas, P. Gonzalez, J. Horn, and H. Werner. 2019. Nonlinear model predictive control of a PEM fuel cell with an integrated li-ion battery using qLPV. IEEE 15th International Conference on Control and Automation (ICCA), 1270–76, doi: 10.1109/ICCA.2019.8899516.

Dali, A., S. Abdelmalek, A. Bakdi, and M. Bettayeb. 2021. A novel effective nonlinear state observer based robust nonlinear sliding mode controller for a 6 kW proton exchange membrane fuel cell voltage regulation. *Sustainable Energy Technologies and Assessments* 44:100996. doi:10.1016/j.seta.2021.100996.

Derbeli, M., M. Farhat, O. Barambones, and L. Sbita. 2017. Control of proton exchange membrane fuel cell (PEMFC) power system using PI controller, 2017. International Conference on Green Energy Conversion Systems (GECS), 1–5, doi:10.1109/GECS.2017.8066175.

Diaz-Saldierna, L. H., D. Langarica-Córdoba, and J. Leyva-Ramos. 2015. Loop-shaping control of high-step converters for fuel-cell applications. 23rd Mediterranean Conference on Control and Automation (MED), 789–95, doi: 10.1109/MED.2015.7158842.

Divi, S., S. H. Sonawane, and S. Das. 2018. Uncertainty analysis of transfer function of proton exchange membrane fuel cell and design of PI/PID controller for supply manifold pressure control. *Indian Chemical Engineer* 61 (2):138–52. doi:10.1080/00194506.2018.1510794.

Gad, A. G. 2022. Particle swarm optimization algorithm and its applications: A systematic review. *Archives of Computational Methods in Engineering* 29 (5):2531–61. doi:10.1007/s11831-021-09694-4.

Gerard, M., J. Crouvezier, D. Hissel, and M. Pera. 2010. Oxygen starvation analysis during air feeding faults in PEMFC. *International Journal of Hydrogen Energy* 35 (22):12295–307. doi:10.1016/j.ijhydene.2010.08.028.

Gnanamuruga, M., and N. A. Senthilkumar. 2014. Smith predictor for control of the process with long dead time. *International Journal of Engineering Research & Technology (IJERT) RTIA* 2 (6).

Imran, M., R. Hashim, and N. Khalid. 2013. An overview of particle swarm optimization variants. *Procedia Engineering* 5:3491–96. doi:10.1016/j.proeng.2013.02.063.

Javaid, U., J. Iqbal, A. Mehmood, A. A. Uppal, and Y. Arya. 2022. Performance improvement in polymer electrolytic membrane fuel cell based on nonlinear control strategies—A comprehensive study. *PLoS ONE* 17 (2):e0264205. doi:10.1371/journal.pone.0264205.

Keek, J. S., S. L. Loh, and S. H. Chong. 2018. Fractional-order proportional-integral (FOPI) controller for mecanum-wheeled robot (MWR) in path-tracking control. *International Journal of Mechanical Engineering and Technology (IJMET)* 9 (11):325–37.

Kumar, S. S., M. Cirrincione, V. Léchappé, K. R. Ram, and A. Mohammadi. 2021. A simplified control oriented model of an open cathode PEM fuel cell, 2021 IEEE 12th Energy Conversion Congress & Exposition - Asia (ECCE-Asia), 2415–20, doi: 10.1109/ECCE-Asia49820.2021.9479098.

Kumar, M. R., and S. Ghosh. 2018. Hybrid optimization based fopi controller design with real-time validation. *IFAC-Papers online* 51 (1):78–83. doi:10.1016/j.ifacol.2018.05.014.

Kumar, D. M., H. K. Mudaliar, M. Cirrincione, U. Mehta, and M. Pucci. 2018. Design of a fractional order PI (FOPI) for the speed control of a high-performance electrical drive with an induction motor, 2018. 21st International Conference on Electrical Machines and Systems (ICEMS), 1198–202, doi: 10.23919/ICEMS.2018.8549407.

Kumar, S., I. Thirunavukkarasu, S. S. Kumar, and V. S. Bhat. 2018. Smith predictor based pi controller design for a batch distillation column. *International Journal of Pure and Applied Mathematics* 118 (22):1109–15.

Li, Q., Cai, L., Yin, L., Wang, T., Li, L., Xie, S. and Chen, W. 2022. An energy management strategy considering the economy and lifetime of multi-stack fuel cell hybrid system, in IEEE Transactions on Transportation Electrification, doi: 10.1109/TTE.2022.3218505.

Li, Q., P. Liu, X. Meng, G. Zhang, Y. Ai, and W. Chen. 2022. Model prediction control-based energy management combining self-trending prediction and subset-searching algorithm for hydrogen electric multiple unit train. *IEEE Transactions on Transportation Electrification* 8 (2):2249–60. doi:10.1109/TTE.2022.3149479.

Linli, W., S. Zhangyi, H. Mousavi, and H. Gu. 2022. A novel robust reset controller implemented through field programmable gate array for oxygen ratio regulation of proton exchange membrane fuel cell. *Computers & Electrical Engineering* 99:107788. doi:10.1016/j.compeleceng.2022.107788.

Liu, L., X. Liu, N. Wang, and P. Zou. 2018. Modified cuckoo search algorithm with variational parameters and logistic map. *Algorithms* 11 (3):30. doi:https://doi.org/10.3390/a11030030.

Lü, X., X. Miao, Y. Xue, L. Deng, M. Wang, D. Gu, and X. Li. 2017. Dynamic modeling and fractional order $PI^{\lambda}D^{\mu}$ control of PEM fuel cell. *International Journal of Electrochemical Science* 12 (8):7518–36. doi:10.20964/2017.08.12.

Mohamed, A. E., B. A. Manivanna, A. Abudhahir, and S. Velappan. 2019. Direct active fuzzy non-linear controller for pressure regulation in PEM fuel cell. 2019 8th International Conference on Modeling Simulation and Applied Optimization (ICMSAO), 1–5, doi: 10.1109/ICMSAO.2019.8880441.

Mohamed, A. K., and A. W. Mohamed. 2019. Real-parameter unconstrained optimization based on enhanced AGDE Algorithm. *Studies in Computational Intelligence* 801:431–50. doi:10.1007/978-3-030-02357-7_21.

Petchinathan, G., K. Valarmathi, and T. K. Radhakrishnan. 2017. Optimal tuning of fractional order PI controller using particle swarm optimization for pH process. *International Journal of Applied Engineering Research* 12 (1): 1–7.

Q, L., L. Yin, H. Yang, T. Wang, Y. Qiu, and W. Chen. 2021. Multiobjective optimization and data-driven constraint adaptive predictive control for efficient and sTABLE OPERATION of PEMFC system. *IEEE Transactions on Industrial Electronics* 68 (12):12418–29. doi:10.1109/TIE.2020.3040662.

Saeki, M. 2022. Implementation methods of controllers deSIGNEd by H∞ loop shaping. *IEEE Transactions on Automatic Control* 1:1–8. doi:10.1109/TAC.2022.3223278.

Sankar, K., N. Thakre, S. M. Singh, and A. Jana. 2017. Sliding mode observer based nonlinear control of a PEMFC integrated with a methanol reformer. *Energy, Elsevier* 139 (C):1126–43. doi:10.1016/j.energy.2017.08.028.

Shehab, M., L. Abualigah, H. A. Alhamad, H. M. Alabool, M. Alshinwan, and A. M. Khasawneh. 2020. Moth–flame optimization algorithm: Variants and applications. *Neural Computing & Applications* 32 (14):9859–84. doi:10.1007/s00521-019-04570-6.

Shih, L., and C. W. Chen. 2020. A model-free loop-shaping method based on iterative learning Control. *IFAC-Papers online* 53 (2):1403–08. doi:10.1016/j.ifacol.2020.12.1896.

Silaa, M. Y., O. Barambones, M. Derbeli, C. Napole, and A. Bencherif. 2022. Fractional order PID design for a proton exchange membrane fuel cell system using an extended grey wolf optimizer. *Processes* 10 (3):450. doi:https://doi.org/10.1016/j.ifacol.2020.12.1896.

Singh, S., V. K. Tayal, H. P. Singh, and V. K. Yadav. 2022. Design of PSO-tuned FOPI & Smith predictor controller for nonlinear polymer electrolyte membrane fuel cell, energy sources, part A: Recovery. *Utilization, and Environmental Effects* 1–22. doi:10.1080/15567036.2022.2025954.

Skogestad, C. 2018. Should we forget the Smith Predictor? *3rd IFAC Conference on Advances in ProportionalIntegral-Derivative Control* 51 (4):769–74. Ghent, Belgium. doi:10.1016/j.ifacol.2018.06.203.

Sung, Y. C., S. V. Patil, and M. G. Safonov. 2016. Data-driven H∞ loop-shaping controller design. *International Journal of Robust and Non-Linear Control* 28 (12):3678–93. doi:10.1002/rnc.3612.

Swain, P., and D. Jena. 2015. PID control design for the pressure regulation of PEM fuel cell, 2015. International Conference on Recent Developments in Control, Automation and Power Engineering (RDCAPE), Noida, IEEE, 286–91.

Tayal, V. K., and J. S. Lather. 2015. PSO based robust Fuzzy power system stabilizer design for single machine infinite bus system, Annual IEEE India Conference (INDICON), 1–6. doi: 10.1109/INDICON.2015.7443821

Wang, G. 2018. A comparative study of cuckoo algorithm and ant colony algorithm in optimal path problems. MATEC Web of Conferences, 232:1–6, doi: 10.1051/matecconf/201823203003.

Wihartiko, F. D., H. Wijayanti, and F. Virgantari. 2018. Performance comparison of genetic algorithms and particle swarm optimization for model integer programming bus timetabling problem. *IOP Conference Series: Materials Science and Engineering* 332 (1):012020. doi:10.1088/1757-899X/332/1/012020.

Xiaojuan, W., and G. Danhui. 2018. Optimal robust control strategy of a solid oxide fuel cell system. *Journal of Power Sources* 374:225–36. doi:10.1016/j.jpowsour.2017.10.070.

Zennir, Y., M. Larabi, and H. Benzaroual. 2017. New Smith Predictor controller design for time delay system. In Proceedings of the 14th International Conference on Informatics in Control, Automation and Robotics, 1:598–605, doi: 10.5220/0006426105980605.

Zhang, F., Y. Ma, T. Zhu, and H. Chen. 2019. Nonlinear control of air-feed system for proton exchange membrane fuel cell with auxiliary power battery. *Journal of Renewable and Sustainable Energy* 11 (5):1–11. doi:10.1063/1.5093984.

Research Square

Preprints are preliminary reports that have not undergone peer review.
They should not be considered conclusive, used to inform clinical practice,
or referenced by the media as validated information.

Effect of Meteorological Parameters and Air Pollutants Association with Health Risk Assessment during the Pandemic in Delhi, India

Bhupendra Pratap Singh (bpsingh0783@gmail.com)
Central University of Haryana
Kriti Mehra
University of Delhi
Khyati Chowdhary
University of Delhi
Charvi Khanna
University of Delhi
Prakash Chandra
Delhi Technological University

Research Article

Keywords: COVID-19, particulate matter, meteorological parameters, correlation, HQ

Posted Date: July 18th, 2023

DOI: https://doi.org/10.21203/rs.3.rs-3149050/v1

License: This work is licensed under a Creative Commons Attribution 4.0 International License.
Read Full License

Abstract

The novel Coronavirus disease was reported in the last week of December 2019 in the capital of Hubei province, Wuhan, China, which outspread in no time and hit more than 210 countries, including India. A considerable recovery in the air conditions during the lockdown occurred due to substantial reduction measures in all the activities throughout the pandemic. The present study evaluated the changes in particulate pollutants and the role of meteorological parameters during the course of the pandemic. The mean concentrations of $PM_{2.5}$ and PM_{10} for all monitoring bases were calculated to be 109.54 and 214.04 μg/m^3 for the years 2019–2021, respectively. The average values for $PM_{2.5}$ and PM_{10} for all monitoring stations were observed to be 113.33, 108.92, 106.92 μg/m^3, and 221.34, 203.02, 220.04 μg/m^3 for the years 2019, 2020, and 2021 respectively. The gradual decline in values of $PM_{2.5}$ has witnessed the closures of transport, industrial, and construction activities during the lockdown period in the year 2020. A strong significant positive correlation for $PM_{2.5}$ was found between Alipur with ITO (0.89), Okhla (0.93), Narela (0.97), and Wazirpur (0.90), whereas PM_{10} was Alipur with ITO (0.82), Okhla (0.90), Narela (0.95), and Wazirpur (0.89), respectively. The present study investigated the relationship between $PM_{2.5}$, PM_{10}, meteorological parameters, and associated health risks. The negative relationships were observed between $PM_{2.5}$ with temperature, wind speed, and solar radiation and a positive relationship with moisture and wind direction, whereas similar results were reported for PM_{10} for all monitoring stations. This study highlights that large emission reductions in the non-essential services were responsible for increasing the level of air quality. The health risk assessment for all age groups was calculated for pre-, during, and post-pandemic periods. The results for HQ values for $PM_{2.5}$ indicated that children and infants were more likely to experience health effects after adults.

Introduction

In December 2019, a novel coronavirus disease 2019 (COVID-19) outbreak occurred due to a human respiratory virus that originated in the city of Wuhan, China [Li et al., 2020; Wu et al., 2020], and the disease was officially declared a pandemic on March 11, 2020, by the World Health Organization (WHO) [WHO, 2020]. However, the disease spread worldwide, leading to the COVID-19 pandemic. Reports of WHO and other agencies, as of March 28, 2023, indicate that more than 68 million people have been infected by COVID-19, and more than 6.8 million people have died across countries (including India) [WHO, 2020b]. After the United States of America (USA), India became the second most infected country in the world. The report shows more than 4.4 million people were diseased, and more than 53000 deaths were recorded. In India, the first case was reported on January 30, 2020, in Kerala, which was directly linked to Wuhan [Ghosh et al., 2020], and the first death was reported on March 12, 2020, in Karnataka [David et al., 2020].

$PM_{2.5}$ usually accumulates in Human Respiratory Tract and causes very serious harm to human health [Singh et al., 2016]. A positive relationship has been established between the outbreak of the coronavirus and air pollution [Singh et al., 2022e]. During the covid-19 outbreak, there was a significant reduction in

the average level of NO2 by 30% in Central China and an approximately 40% reduction in Europe. According to WHO (2020), Particulate Matter ($PM_{2.5}$ and PM_{10}) is one of the major causes of public health concerns [Singh et al., 2021]. The small particulate matter has a larger surface area and high Particle Number Concentration, thus resulting in worse health impacts [Yin et al., 2019]. According to some studies related to toxicology, Particulate matter is thought to affect our body's defence mechanisms and also cause pulmonary inflammation [Donaldson et al., 2001]. Due to the recent advancements in the studies, it has been found that there may be the presence of Covid-19 RNA on Particulate Matter [Setti et al., 2020]. Particulate Matter has shown a positive correlation with the number of COVID cases, and it may act as a carrier for the viruses [Comunian et al., 2020]. Population morbidity and mortality also correlate with $PM_{2.5}$ [Shen et al., 2018]. Thus, prolonged exposure to $PM_{2.5}$ increases the risk of Covid-19 [Stieb et al., 2020]. Though the recommendation about ambient air quality given by WHO suggests that for $PM_{2.5}$, the yearly mean limit should be 10 $\mu g/m^3$, and the 24-hourly mean limit should be 25 $\mu g/m^3$. Studies also suggest that greater transportation is linked to higher levels of Particulate Matter in urban areas [Rodriguez et al., 2016]. These traffic emissions are responsible for about 50% of the Particulate Matter in these urban regions [Li et al., 2017]. But due to Covid-19 infection, lockdowns were imposed in many countries in which transport services (road, air, rail) were suspended along with institutions and industries, excluding essential services only [Jain et al., 2020]. Due to these restrictions, the spread of disease was controlled, and our environment also healed [Pant et al., 2020]. Consequently, there was a substantial downfall in pollution levels all around the globe [Mahato et al., 2020]. Many studies have also shown decreased $PM_{2.5}$ concentration during the lockdown period [Nakada et al., 2020; Sharma et al., 2020; Sicard et al., 2020].

In contradiction, Wang et al. outlined that in some cities, the air quality worsened concerning PM2.5, and meteorological conditions was mainly responsible for this observation [Wang et al., 2020]. So, besides Particulate Matter and gaseous pollutants, we also need to include Meteorological Parameters, as these parameters may affect many other factors. Some studies have shown that temperature and humidity play a role in the stability of the respiratory virus and its transmission rate [Moriyama et al., 2020]. Whereas processes like diffusion and dilution capabilities of particles, Gas-Particle conversion process, and secondary formation of particles are influenced by many meteorological factors like atmospheric pressure, relative humidity, solar radiation, etc. [Xu et al., 2018; Kumar et al., 2014a; Singh et al., 2021b; Singh et al., 2021c]. Wind speed affects the rate of dispersion and, thus, the pollution level as higher winds can transport the particles and thus reduce the pollution level. Some studies have also shown that temperature and daily covid-19 cases had an inverse relationship; the transmission was higher at a lower temperature [Liu et al., 2020]. Whereas Tosepu et al. (2020), reported that during a study in Jakarta, Indonesia, the temperature was seen to be positively correlated with daily covid cases. Overall, studies have found that the variation in meteorological factors is responsible for about 40–70% variation in Ozone and 20–50% variation in Particulate Matter. According to the studies, the relative wind speed was found to be randomly distributed, whereas the wind speed decreased compared to 2019 [Navinya et al., 2020]. And the values of RH and Temperature showed an increase and decrease, respectively, from 2019

[Navinya et al., 2020]. Therefore, there were slight changes in the meteorological parameters, which can somewhat impact the pollution dispersion in a region [Punia et al., 2015; Bhardwaj et al., 2017].

Fine particulate matter (PM) pollutants are known to cause serious health issues like asthma, cardiovascular mortality, pneumonia, bronchitis, allergies, adverse neurological conditions, cancer, reproductive defects, and even death but the most susceptible population, which includes those with heart and lung conditions, the elderly, children, and pregnant women, are severely impacted with high PM levels [Opara et al., 2021; Singh et al., 2014]. According to Algarni et al., (2021) the smaller the particle size, the more implications it will cause on the metabolism in human body [Algarni et al., 2021]. The primary contributor of the observed positive relative risk for cardiopulmonary and lung cancer disease is due to its ability to cause inflammation and oxidative stress [Bodor et al., 2022] PM can accomplish the most thorough opening in the lungs [Nagar et al., 2014], which can lead to repetitive respiratory hypersensitivity. The PM disrupts the mucosal layer and upper respiratory tract and has an adverse effect on cognitive functioning [Nagar et al., 2014; Asghar et al., 2022].

India holds the second position for being the most densely populated country in the world. The abrupt sink in $PM_{2.5}$, NO_2, and CO was observed due to a substantial lowering of vehicular emission, but no fall was seen in the case of PM_{10} below the National Ambient Air Quality Standard. Between the timestamp from January 2020 to 11 May–19 June 2020, there was a surge in the pollutants, namely O_3 and $SO_{2,}$ significantly by a percentage of 217.33% and 57.58%, respectively. Low RH and low-temperature conditions showed a positive association with the new COVID-19 strain cases in Delhi. In comparison, the lower NO_2 levels in the air indicated a compelling negative correlation with new COVID-19 cases, while mean SO_2 concentration in the air, when increased to 24.05 ppb, showed a negative relation with the new COVID-19 cases in Delhi. This study indicated a possibility of O_3 exhibiting a positive correlation with new COVID-19 cases under the condition of comparatively low temperature and low humidity [Kumar et al., 2014].

The current research was an attempt to appraise the effects of imposed lockdown, owing to the COVID-19 pandemic, on the air conditions in Delhi, considered one of the most polluted cities in the world. We also evaluated the spatial variation in particulate matter ($PM_{2.5}$ and PM_{10}) levels before, during, and post-pandemic period in Delhi and some specific regions in India to guide policymakers to prevent similar epidemics in the future in addition to correlating the particulate matter with meteorological parameters. In addition to estimating the health risk in different age group populations.

Methodology

Study area

In the present study, the area under observation is the National Capital Territory of Delhi, India. Delhi has coordinates 28.7041° N, and 77.1025° E, which is established on the Indo-Gangetic plain of the northern region. The climatic conditions of the present study are subtropical and semi-arid, according to Singh et

al [Singh et al., 2021d]. Due to its geographical location, the area experiences all seasons, including summer, monsoon, and winter. The seasons have their time period, summer starting from April, lasting till June, monsoon from July till October, and winters from November lasting till February. The temperature of Delhi is characterized by a maximum of ~ 45–48 ºC in June during the summer season and a minimum of ~ 1–2ºC in January during the winter season. The average rainfall is around 611mm [Sindhwani et al., 2014]. The humid weather can be felt more in the months of July and August. During the summer, the cool breeze is caused due to the movement of air from the Arabian Sea and Bay of Bengal, and in the winter, the cool breeze is caused due to movement of north-western winds from the Himalayas.

Pollution in Delhi is a widely debated issue as it belongs to the most polluted cities in India according to the global pollution index. Delhi is not only the most polluted city but also the most densely populated city in India, with over 12 million registered vehicles on the roads. The factor that contributes to Delhi being the most polluted city is the large number of private and public transportation compared to other cities in India. Since India is a developing nation, industrial areas can be seen playing crucial roles in increasing pollution. In addition to all the factors mentioned above that cause pollution, there are other major contributors, like anthropogenic activities, automobiles, and construction. A few studies on metropolitan cities of India such as Delhi and Mumbai; while some of the studies have been reported in India measuring the impact of the COVID-19 lockdown on air quality but for a very short-term period. However, a details analysis of particulate matter concentration associated with health risks during the lockdown is lacking. The major objectives of the current study were (i) to determine real-time particulate matter concentrations pre-post-pandemic post-pandemic periods in Delhi, (ii) to quantify temporal variation in particulate matter concentrations associated with meteorological factors, and (ii) to estimate the health risk assessment o particulate matter in different age groups.

Data and sources

In the current study, the secondary information on gaseous pollutants that are $PM_{2.5}$ and PM_{10} was taken from the official website of the central pollution control board (CPCB) on a daily and hourly basis (https://app.cpcbccr.com/ccr/#/caaqm-dashboard-all/caaqm-landing). The relative percentage change in particulate pollutants is determined for pre-, during, and post-pandemic phases. For determination, the data was obtained from January 1, 2019, to December 31, 2021, from CPCB. The period from January 1, 2019 to December 31, 2019, refers to the pre-pandemic phase, the period from January 1, 2020-December 31, 2020, refers to the pandemic phase, and the time period from January 1, 2021, to December 31, 2021, refers the post-pandemic phase. In this study, meteorological parameters such as Relative humidity (RH), wind direction (WD), solar radiation (SR), wind speed (WS), and temperature, along with $PM_{2.5}$ and PM_{10} were considered. The information provided by CPCB is of high quality as it undergoes rigorous quality assurance. The air quality index was also considered, as it helps measure the severity of air pollution and provides real-time data. The AQI was revised by National Ambient Air Quality Standard (NAAQS) by considering parameters, namely $PM_{2.5}$ and PM_{10}.

Health Risk Assessment

The health risk assessment involves the possible negative or harmful effects of particulate matter on human health [Opara et al., 2021]. Our risk assessment took into account, the average concentrations for $PM_{2.5}$ and PM_{10} at different monitoring stations in Delhi for the pre, during and post-pandemic periods. As per the USEPA methodology, inhalation, ingestion, and dermal contact are the most common routes for health issues [Gruszecka-Kosowska, et al., 2021]. This study investigates the health risks posed by inhalation of particulate matter. The USEPA risk assessment methodology considered as non-carcinogenic risk was defined with use of hazard quotient (HQ). The likelihood of adverse health risks among individuals is calculated using the hazard quotient. An HQ value of 1.0 is considered to be safe, a value less than 1.0 means negligible risk and no harm even to a sensitive person whereas a value greater than 1.0 shows that sensitive groups are likely at a health risk [Opara et al., 2021]. Non carcinogenic risk for $PM_{2.5}$ and PM_{10} was calculated according to the reference value mentioned in the toxicology database [Garbero et al., 2012, De Oliveira et al., 2012]. In the current study the exposure of particulate pollutants at different age groups was considered: adults (> 7years), children (1–7 years), and infants (0–1 year). To obtain the daily intake of pollutants through

the inhalation exposure pathway, either exposure concentration (EC) or average daily dose

(ADD) values were calculated according to Equations (1) [USEPA 2020] and (2) [USEPA 1989], respectively, depending on the available reference values:

$$\mathbf{EC} = \frac{C \times ET \times EF \times ED}{AT} \quad \textbf{(1)}$$

where EC, exposure concentration (mg/m3); ADD, the average daily dose (mg/kg-day); C,

contaminant concentration in air (the measured values were converted to mg/m3); IR,

inhalation rate (m3/h); ET, exposure time (h/day); EF, exposure frequency (days/year);

ED, exposure duration (years); BW, body weight (kg); AT, averaging time: ED, in years × 365 days/year × 24 h/day, in hours

Risk characterization

Risk characterization is an estimation of risk to human health due to exposure to a pollutant. In this study, the health risk estimate of possible non-carcinogenic exposure to the pollutant was determined using the hazard quotient (HQ) method [Muller et al., 2022, Saliba et al., 2016].

The risk to health due to exposure to particulate matter through the inhalation route was estimated using Equations (2) and (3)

$$\text{ADD inh} = \frac{C \times InhR \times EF \times ED}{BW \times AT} \quad (2)$$

$$HQ = \frac{ADD}{RfD} \quad (3)$$

HQ was used to calculate the non-carcinogenic risk of PM_{10} and $PM_{2.5}$ and their reference dose and concentration was obtained from the toxicological databases [Gruszecka-Kosowska, et al., 2021]. The reference dose (RfD) for PM_{10} was 1.1 x 10^{-2} (mg/kg-day), and the reference concentration (RfC) was 5.0 x 10^{-3} (mg/m^3) [Gruszecka-Kosowska, et al., 2021].

Results and Discussion

$PM_{2.5}$ and PM_{10} levels during the pre-pandemic and the pandemic period

The present study focused on determining drastic changes in the concentrations of air pollutants, especially particulate matter $PM_{2.5}$ and PM_{10} concentrations, during the pandemic situation in India, including Delhi. The $PM_{2.5}$ and PM_{10} concentrations significantly declined from January 2020 to May 2020 during the pandemic situation in Delhi. A constant decline in the $PM_{2.5}$ and PM_{10} concentrations was observed in subsequent months due to the complete lockdown, during which international and domestic flights, trains, traffic activities, markets, and industrial activities were suspended [Singh et al., 2023]. The low concentration of particulate matter could be affected by the planetary boundary layer (PBL) during the lockdown period. Chaudhary et al., 2021 reported that PBL was increased 2-fold across the all-monitoring stations during the lockdown period [Maji et al., 2021]. A significant increase in the PBL was expected to have a pronounced effect on pollutant concentration in the ambient atmosphere [Maji et al., 2021]. Furthermore, an increase in PBL height is responsible for decreased concentration due to the dispersal of pollutants in the ambient atmosphere. The present $PM_{2.5}$ and PM_{10} values were observed loweras compared to the previous year'svaluesmentioned by many research scholars [Singh et al., 2021, Maji et al., 2021, Sharma et al., 2020, Shukla et al., 2022] due to the complete closure of non-essential services.

The current study concentrated on determining substantial changes in the air pollutants' concentration, particularly the concentrations of $PM_{2.5}$ and PM_{10} during the pandemic in Delhi, India (Fig. 1). At all monitoring stations, the average concentration of $PM_{2.5}$ was found to be 109.54 $\mu g/m^3$ for the year 2019-21, in which the lowest and highest were 102.17 $\mu g/m^3$ (Alipur) and 115.56 $\mu g/m^3$ (Wazipur) respectively. The average concentration of $PM_{2.5}$ varied from 106.18 (Alipur) to 134.85 (Wazipur), 100.63 (Wazirpur) to 119.69 (ITO), and 92.50 (Okhla) to 114.16 (ITO) during pre-pandemic, pandemic and post-pandemic period respectively. The maximum concentration of $PM_{2.5}$ was observed to be 715.04 (Alipur), 655.69 (ITO), 551.19 (Okhla), 689.10 (Narela), and 585.79 $\mu g/m^3$ (Wazipur) during the pre-pandemic period, 715.04 (Alipur), 514.36 (ITO), 551.19 (Okhla), 689.10 (Narela) and 585.79 $\mu g/m^3$ (Wazipur) during the

pandemic period and 715.04 (Alipur), 655.69 (ITO), 551.19 (Okhla), 689.10 (Narela) and 585.79 μg/m^3 (Wazipur) during the post-pandemic period (Fig. 2).

At all monitoring stations, the average concentration of PM_{10} was found to be 214.04, in which the lowest and the highest were calculated to be175.13 μg/m^3 (ITO) and 255.93 μg/m^3 (Wazipur) for the year 2019-21. The average concentration of PM_{10} varied from 172.77 (ITO) to 288.18 μg/m^3 (Wazipur) for pre-pandemic, 172.58 (ITO) to 225.56 μg/m^3 (Wazipur) during the pandemic, and 185.09 (ITO) to 257.20 μg/m^3 (Wazipur) post-pandemic respectively. The maximum concentration of PM_{10} was observed to be 771.79 (Alipur), 555.79 (ITO), 652.03 (Okhla), 649.05 (Narela) and 723.26 μg/m^3 (Wazipur) for pre-pandemic, 762.58 (Alipur), 690.92 (ITO), 740.19 (Okhla), 717.35 (Narela) and 799.45 μg/m^3 (Wazipur) during the pandemic period, and 563.33 (Alipur), 463.00 (ITO), 644.07 (Okhla), 611.25 (Narela) and 796.88 μg/m^3 (Wazipur) for the post-pandemic period (Fig. 3).

Correlation with meteorological parameters

In the present study, we have tried to analyze the correlation of the particulate matter ($PM_{2.5}$ and PM_{10}) with various meteorological parameters. These parameters were: Relative humidity (RH), wind direction (WD), solar radiation (SR), wind speed (WS), and temperature. The present finding for $PM_{2.5}$ observed a strong negative correlation with temperature (-.605), and a moderate and weak negative correlation with solar radiation (-.512) and wind speed (-.140), respectively. Whereas a weak positive correlation was observed for $PM_{2.5}$ with relative humidity (.101) and wind direction (.208).

In terms of $PM_{10,}$ results observed a weak negative correlation with RH, SR, WS, and temperature having the correlation values of − .109, − .398, − .051, and − .429, respectively. At the same time, a weak positive correlation was observed for WD with a correlation value of − .398. The correlations between various meteorological parameters and particulate matter ($PM_{2.5}$ and PM_{10}) were presented in Tables 1 and 2.

Table 1
Correlation analysis for various monitoring stations for $PM_{2.5}$in Delhi

	Alipur	ITO	Okhla	Narela	Wazirpur
Alipur	1				
ITO	.891**	1			
Okhla	.935**	.908**	1		
Narela	.977**	.894**	.939**	1	
Wazirpur	.901**	.873**	.936**	.909**	1

Table 2
Correlation analysis for various monitoring stations for PM_{10} in Delhi

	Alipur	ITO	Okhla	Narela	Wazirpur
Alipur	1				
ITO	.829**	1			
Okhla	.904**	.873**	1		
Narela	.954**	.860**	.934**	1	
Wazirpur	.892**	.820**	.926**	.906**	1

Correlation with monitoring stations

In the present study, an attempt was made to correlate different monitoring stations in Delhi. A strong positive coefficient value from 0.8 to 1.0 suggests a very high correlation. A strong positive correlation was observed between Alipur and Narela (0.977) and ITO and Okhla (0.908) with $PM_{2.5}$. A similar trend was observed for PM_{10}, Alipur, and Narela (0.954) and ITO and Okhla (0.873). The results of correlations witnessed similar sources of pollutants in these areas. This trend was observed because Delhi experiences warm temperatures and intense heat waves throughout the year. The correlation analysis for various monitoring stations in Delhi was presented in Tables 3 and 4.

Table 3
Correlation analysis for various meteorological parameters for $PM_{2.5}$ at Delhi

	RH	WD	SR	WS	TEMP	$PM_{2.5}$
RH	1					
WD	− .246**	1				
SR	− .482**	− .008	1			
WS	.005	− .069*	.126**	1		
TEMP	− .493**	− .263**	.632**	− .002	1	
PM2.5	.101**	.208**	− .512**	− .140**	− .605**	1

Table 4
Correlation analysis for various meteorological parameters for PM_{10} at Delhi

	RH	WD	SR	WS	TEMP	PM_{10}
RH	1					
WD	− .246**	1				
SR	− .482**	− .008	1			
WS	.005	− .069*	.126**	1		
TEMP	− .493**	− .263**	.632**	− .002	1	
PM10	− .109**	.227**	− .398**	− .051	− .429**	1

A Comparative Study across the World

COVID-19 displays dependency based on weather circumstances and different meteorological parameters. It is vital to use a multivariate non-linear approach since the spread of the coronavirus cannot be accurately predicted by a linear relationship with any specific weather component. Gupta et al., 2020 and Sarkodie et al., 2020 revealed that high temperature and high relative humidity decrease the viability, stability, survival, and transmission of COVID-19 [Gupta et al., 2020, Sarkodie et al., 2020]. In contrast, low temperature, wind speed, dew/frost point, precipitation, and surface pressure extend the activation and infectivity of the virus. Kumar et al., 2020 determined that the relative humidity and pressure variables had the greatest influencing effect out of all other significant characteristics (obtained through Spearman's approach) on the active number of COVID-19 cases [Kumar et al., 2020]. The study indicates that season, geographical size, and latitude can all impact the link between meteorological conditions and COVID-19 transmission. In colder seasons, a rise in temperature might encourage the spread of viruses. It was also observed in a study that increasing latitude, maximum temperatures, and wind speed had a significant effect on the newly confirmed COVID-19 cases, whereas relative humidity had a detrimental impact [Li et al., 2022]. The links between maximum and minimum temperatures with the newly-confirmed COVID-19 instances were more susceptible to season, whereas relative humidity's relationship was more affected by latitude and geographic scale. A study reported by Gupta et al., 2020 analyzed that lower-altitude, moderately hot, and dry regions of the Indian Territory are where COVID-19 infections are most prone to spread [Gupta et al., 2020]. Similarly, Yang et al. also suggested that the main determinants of COVID-19 transmission were temperature and relative humidity; however, their relationships clearly changed depending on the geographical locations and seasons [Yang et al 2021]. During the summer season, the increase in relative humidity and decrease in maximum temperature assist COVID-19 transmission in coastal cities. [Jain et al., 2021] and [Sharma et al., 2021] studied areas with higher rates of transmission, where the minimum temperature is typically around 21°C and humidity ranges around 80% for months, also observed an increase in the transmission of COVID-19 infections.

The results show that the majority of the meteorological conditions and the air pollutant $PM_{2.5}$ have a significant impact on the number of confirmed COVID-19 cases and mortality cases in both positive and negative ways. $PM_{2.5}$, an air pollutant, offers the virus greater particle surface area to adhere to and travel farther. Therefore, increased COVID-19 transmission is caused by greater air pollution levels with particulates. Another study inferred positive associations between the number of confirmed cases of COVID-19 with CO, $PM_{2.5}$, relative humidity, and O_3 [Zhou et al., 2021]. In addition, air pollutants and meteorological factors had interactive effects on COVID-19. In conclusion, air pollutants, meteorological factors, and their interactions all affect COVID-19 cases. [Muktavat et al., 2021] reported that COVID-19 shows a substantial positive connection with temperature (> 0.6) and a significant negative correlation with humidity (0.5). In addition, COVID-19 and the daily Air Quality Index (AQI) were found to have a substantial and consistent inverse association (0.3) for all the states from 1 March to 13 May 2021 (74 days). Hence, COVID-19 cases increased as the wind speed and temperature increased, the relative humidity decreased, and the air quality consequently improved.

Human Health Risk Assessment

The present study estimated health risk assessment and hazard identification for non-carcinogenic risks from exposure to particulate pollutants ($PM_{2.5}$ and PM_{10}) via the inhalation route, which is the prime pathway for exposure to any pollutants. The health quotient (HQ) was calculated for particulate matter pollutants across the exposed groups (adult, child, and infant) for pre-, during, and post-pandemic in Delhi. The hazard quotient (HQ) defines the ratio of the exposure concentration for the specific VOC species to an acute reference concentration (RfC) of non-carcinogenic compounds. For particulate pollutants, an HQ value of less than 1 indicates a minor or insignificant non-carcinogenic effect, whereas higher values indicate greater non-carcinogenic risks resulting in a significant adverse effect on human health [Algarni et al., 2021, Edlund et al., 2021]. The calculated HQ for $PM_{2.5}$ was found to be less than 1 (HQ < 1) for adults, whereas for children and infants was more than 1 (HQ > 1) for pre, during, and post-pandemic periods (Fig). The results for HQ values for $PM_{2.5}$ indicated that children and infants were more likely to experience health effects after adults. Similar results for $PM_{2.5}$ were reported in Owerri metropolis, Nigeria [Opara et al., 2021]**.** The calculated HQ for PM_{10} was found to be more than 1 (HQ > 1) for all age groups, which varied from 3.3 to 5.5 for pre, during, and post-pandemic periods (Figs. 4 & 5). The present results indicated that all the age groups were significant potential hazards for pre-, during, and post-pandemic in Delhi. Similar findings of HQ value for PM_{10} were reported higher in Abha, Saudi Arabia during COVID-19 which indicated a potential risk to the inhabitants [Algarni et al., 2021].

Conclusion

In this study, we have tried to analyze and correlate various air quality parameters with each other and to the COVID-19 cases. We have also taken various meteorological parameters, particulate matter, and different monitoring stations to do a comparative study and find the correlation. This helps us to evaluate

the role of all these different factors in a pandemic and may be used in the future to overcome such pandemic situations.

The mean concentrations of $PM_{2.5}$ and PM_{10} for all monitoring bases were calculated to be 109.54 and 214.04 μg/m^3 for the years 2019–2021, respectively. The average values for $PM_{2.5}$ and PM_{10} for all monitoring stations were observed to be 113.33, 108.92, 106.92 μg/m^3, and 221.34, 203.02, 220.04 μg/m^3 for the years 2019, 2020, and 2021 respectively.

A strong significant positive correlation for $PM_{2.5}$ was found between Alipur with ITO (0.89), Okhla (0.93), Narela (0.97), and Wazirpur (0.90), whereas PM10 was Alipur with ITO (0.82), Okhla (0.90), Narela (0.95), and Wazirpur (0.89), receptivity. These values give us a correlation of particulate matter with different monitoring stations. And finally, to correlate the levels of particulate matter with different meteorological parameters, the following conclusions were made, negative relationships were observed between $PM_{2.5}$ with temperature, wind speed, and solar radiation and a positive relationship with moisture and wind direction, whereas similar results were reported for PM_{10} for all monitoring stations. The results for HQ values for $PM_{2.5}$ indicated that children and infants were more likely to experience health effects after adults.

Declarations

Acknowledgment:

The first author thanks Dr. Jyotsana Gupta for her insightful discussion and valuable suggestions during the preparation of the manuscript.

Compliance with ethical standards Conflict of interest

The authors declare that there have no known competing financial interests or personal relationships that could have appeared to influence the work reported in this paper

Funding: Funding is not applicable

Conflicts of interest: There is no conflict of interest in the present manuscript

Data Available: Data will be made available on a reasonable basis.

Code available: not available

Author Contribution

B.P. S. acquired and analyzed the results and discussion, K.M. wrote the introduction draft and K.C. framed the methodology section of the present manuscript and C. K. & P.C. contributed to drafting the health risk assessment section.

Ethical Approval: Not applicable.

Consent to Participate: All authors have agreed to authorship, read and approved the manuscript

Consent for publication All the authors have permitted publication.

References

1. Algarni, S., Khan, R. A., Khan, N. A., & Mubarak, N. M. (2021). Particulate matter concentration and health risk assessment for a residential building during COVID-19 pandemic in Abha, Saudi Arabia. Environmental Science and Pollution Research, 28(46) 65822-65831.
2. Asghar, K., Ali, A., Tabassum, A., Nadeem, S. G., Hakim, S. T., Amin, M., ... & Hussain, M.(2022). Assessment of particulate matter (PM) in ambient air of different settings and its associated health risk in Haripur city, Pakistan. Brazilian Journal of Biology, 84.
3. Bhardwaj, P., Singh, B. P., Pandey, A. K., Jain, V. K., & Kumar, K. (2017). Characterization and Morphological Analysis of Summer and Wintertime PM 2.5 Aerosols Over Urban-Rural Locations in Delhi-NCR. In International Journal of Applied Environmental Sciences (Vol. 12, Issue 5). http://www.ripublication.com
4. Bodor, K., Szép, R., & Bodor, Z. (2022). The human health risk assessment of particulate air pollution (PM2. 5 and PM10) in Romania. Toxicology Reports, 9, 556-562
5. Chaudhary, S., Kumar, S., Antil, R. and Yadav, S., 2021. Air quality before and after COVID-19 lockdown phases around New Delhi, India. Journal of Health Pollution, 11(30),p.210602.
6. Comunian, S., Dongo, D., Milani, C., & Palestini, P. (2020). Air pollution and covid-19: The role of particulate matter in the spread and increase of covid-19's morbidity and mortality. In International Journal of Environmental Research and Public Health (Vol. 17, Issue 12, pp. 1–22). MDPI AG. https://doi.org/10.3390/ijerph17124487
7. David, M., Lokeshkumar, P., & Dabire, S. S. (2020). Covid-19 (Coronavirus): a Global Emergency Outbreak and Its Implications in India. 5(2), 89–98. https://doi.org/10.5281/zenodo.3755267
8. Donaldson, K., Stone, V., Seaton, A., MacNee, W., 2001. Ambient particle inhalation and the cardiovascular system: potential mechanisms. Environ. Health Perspect. 109 (Suppl. 4), 523–527
9. De Oliveira, B.F.A.; Ignotti, E.; Artaxo, P.; Saldiva, P.H.; Junger, W.L.; Hacon, S. Risk assessment of PM2.5 to child residents in Brazilian Amazon region with biofuel production. Environ. Health 2012, 11, 64.
10. Edlund, K.K.; Killman, F.; Molnár, P.; Boman, J.; Stockfelt, L.; Wichmann, J. Health Risk Assessment of PM 2.5 and PM 2.5 -Bound Trace Elements in Thohoyandou, South Africa. Int. J. Environ. Res. Public Health 2021, 18, 1359.
11. Gupta, Amitesh, and Biswajeet Pradhan. "Impact of daily weather on COVID-19 outbreak in India." medRxiv (2020): 2020-06.

12. Gruszecka-Kosowska, A.; Dajda, J.; Adamiec, E.; Helios-Rybicka, E.; Kisiel- Dorohinicki, M.; Klimek, R.; Pałka, D.; W as, J. Human Health Risk Assessment of Air Pollution in the Regions of Unsustainable Heating Sources. Case Study—The Tourist Areas of Southern Poland. Atmosphere 2021, 12, 615. https://doi.org/10.3390/atmos12050615
13. Garbero, V.; Montaldo, A.; Lazovic, N.; Salizzoni, P.; Berrone, S.; Soulhac, L. The impact of the urban air pollution on the human health: A case study in Turin. In Air Pollution Modelling and Its Application XXI; Styen, D.G., Trini Castelli, S., Eds.; Springer: Dordrecht, The Netherlands, 2012; pp. 729–732.
14. Jain, M., Sharma, G.D., Goyal, M., Kaushal, R. and Sethi, M., 2021. Econometric analysis of COVID-19 cases, deaths, and meteorological factors in South Asia. Environmental Science and Pollution Research, 28, pp.28518-28534.
15. Jain, S., & Sharma, T. (2020). Social and travel lockdown impact considering coronavirus disease (Covid-19) on air quality in megacities of india: Present benefits, future challenges and way forward. Aerosol and Air Quality Research, 20(6), 1222–1236 https://doi.org/10.4209/aaqr.2020.04.0171
16. Kumar, Gaurav, and Ritu Raj Kumar. "A correlation study between meteorological parameters and COVID-19 pandemic in Mumbai, India." Diabetes & Metabolic Syndrome: Clinical Research & Reviews 14, no. 6 (2020): 1735-1742.
17. Kumar, A., Singh, B. P., Punia, M., Singh, D., Kumar, K., & Jain, V. K. (2014a).Determination of volatile organic compounds and associated health risk assessment in residential homes and hostels within an academic institute, New Delhi. Indoor Air, 24(5),474–483 https://doi.org/10.1111/ina.12096
18. Li, H., Liu, S. M., Yu, X. H., Tang, S. L., &; Tang, C. K. (2020). Coronavirus disease 2019 (COVID-19): current status and future perspectives. International Journal of Antimicrobial Agents, 55(5), 105951. https://doi.org/10.1016/j.ijantimicag.2020.105951
19. Li, R., Jiang, N., Liu, Q., Huang, J., Guo, X., Liu, F., et al. (2017). Impact of air pollutants on outpatient visits for acute respiratory outcomes. Int. J. Environ. Res. Public Health 14:47. doi: 10.3390/ijerph14010047
20. Liu, Y., Ning, Z., Chen, Y., Guo, M., Liu, Y., Gali, N. K., Sun, L., Duan, Y., Cai, J., Westerdahl, D., Liu, X., Xu, K., Ho, K. fai, Kan, H., Fu, Q., & Lan, K. (2020).
21. Aerodynamic analysis of SARS-CoV-2 in two Wuhan hospitals. Nature, 582(7813), 557–560. https://doi.org/10.1038/s41586-020-2271-3
22. Muktavat, K. and Kumar, V. (2021) Testing Link of Climatic Factors and Air Pollution with COVID-19 amid the Second Wave in India. Journal of Environmental Protection, 12,1069-1085. https://doi.org/10.4236/jep.2021.1212063
23. Maji, K.J., Namdeo, A., Bell, M., Goodman, P., Nagendra, S.S., Barnes, J.H., De Vito, L., Hayes, E., Longhurst, J.W., Kumar, R. and Sharma, N., 2021. Unprecedented reduction in air pollution and corresponding short-term premature mortality associated with COVID-19 lockdown in Delhi, India. Journal of the Air & Waste Management Association, 71(9), pp.1085-1101.

24. Muller, E., Diab, R. D., Binedell, M., & Hounsome, R. (2003). Health risk assessment of kerosene usage in an informal settlement in Durban, South Africa. Atmospheric Environment, 37(15), 2015-2022.
25. Mahato, S., Pal, S., & Ghosh, K. G. (2020). Effect of lockdown amid COVID-19 pandemic on air quality of the megacity Delhi, India. Science of the Total Environment, 730139086. https://doi.org/10.1016/j.scitotenv.2020.139086
26. Nakada, L. Y. K., & Urban, R. C. (2020). COVID-19 pandemic: Impacts on the air quality during the partial lockdown in São Paulo state, Brazil. Science of the Total Environment, 730, 139087. https://doi.org/10.1016/j.scitotenv.2020.139087
27. Navinya C., Patidar G., Phuleria H.C. Examining effects of the COVID-19 national lockdown on ambient air quality across urban India. Aerosol Air Qual. Res. 2020 doi: 10.4209/aaqr.2020.05.0256
28. Nagar, J. K., Akolkar, A. B., & Kumar, R. (2014). A review on airborne particulate matter and its sources, chemical composition and impact on human respiratory system. International Journal of Environmental Sciences, 5(2), 447-463.
29. Opara, A. I., Akaolisa, C. Z., Akakuru, C. O., Nkwoada, A. U., Ibe, F. C., Verla, A. W., & Chukwuemeka, I. C. (2021). Particulate matter exposure and non-cancerous inhalation health risk assessment of major dumpsites of Owerri metropolis, Nigeria. Environmental Analysis, Health and Toxicology, 36(4).
30. Singh, B. P., Kumar, A., Singh, D., Punia, M., Kumar, K., & Jain, V. K. (2014). An assessment of ozone levels, UV radiation and their occupational health hazard estimation during photocopying operation. Journal of Hazardous Materials, 275, 55–62. https://doi.org/10.1016/j.jhazmat.2014.04.049
31. Pant S., Koirala S., Subedi M. (2020). Access to maternal health services during COVID-19. Europas. J. Med. Sci. 2 (2), 48–52. 10.46405/ejms.v2i2.110
32. Punia, M., Nain, S., Kumar, A., Singh, B. P., Prakash, A., Kumar, K., & Jain, V. K.(2015). Analysis of temperature variability over north-west part of India for the period –2000. Natural Hazards, 75(1), 935–952. https://doi.org/10.1007/s11069-014-13528
33. Singh, D., Kumar, A., Kumar, K., Singh, B., Mina, U., Singh, B. B., & Jain, V. K. (2016). Statistical modeling of O3, NOx, CO, PM2.5, VOCs and noise levels in commercial complex and associated health risk assessment in an academic institution. Science of the Total Environment, 572, 586–594. https://doi.org/10.1016/j.scitotenv.2016.08.086
34. Singh, B. P., Eldesoky, G. E., Kumar, P., Chandra, P., Islam, M. A., & Rahman, S. (2022e). A Comparative Study of Particulate Matter Between New Delhi, India and Riyadh, Saudi Arabia During the COVID-19 Lockdown Period. Frontiers in Environmental Science, 9. https://doi.org/10.3389/fenvs.2021.7849592
35. Singh, B. P., & Kumar, P. (2021). Spatio-temporal variation in fine particulate matter and effect on air quality during the COVID-19 in New Delhi, India. Urban Climate, 40. https://doi.org/10.1016/j.uclim.2021.101013

36. Rodríguez MC, Dupont-Courtade L, Oueslati W. 2016. Air pollution and urban structure inkages: Evidence from European cities. Renew Sustain Energy Rev 53: 1–9.
37. Setti, L., Passarini, F., De Gennaro, G., Barbieri, P., Perrone, M. G., Borelli, M., Palmisani, J., Di Gilio, A., Piscitelli, P., & Miani, A. (2020). Airborne transmission route of covid-19: Why 2 meters/6 feet of inter-personal distance could not be enough. International Journal of Environmental Research and Public Health, 17(8). https://doi.org/10.3390/ijerph17082932
38. Shen, Yen-Ling, et al. "Association of PM2. 5 with sleep-disordered breathing from a population-based study in Northern Taiwan urban areas." Environmental pollution 233 (2018): 109-113.
39. Stieb D.M., Evans G.J. , To T.M. , Brook J.R. , BurnetR.T. t An ecological analysis of long-term exposure to PM 2.5 and incidence of COVID-19 in Canadian health regions Environ.Res., 191 (2020), p. 110052
40. Sharma, S., Zhang, M., Anshika, Gao, J., Zhang, H., & Kota, S. H. (2020). Effect of restricted emissions during COVID-19 on air quality in India. Science of the Total Environment, 728, 138878. https://doi.org/10.1016/j.scitotenv.2020.138878
41. Sicard, P., De Marco, A., Agathokleous, E., Feng, Z., Xu, X., Paoletti, E., Rodriguez, J.J. D., & Calatayud, V. (2020). Amplified ozone pollution in cities during the COVID-19 ockdown. Science of the Total Environment, 735, 139542. https://doi.org/10.1016/j.scitotenv.2020.139542
42. Singh, B. P., Kumar, K., & Jain, V. K. (2021b). Distribution of ring PAHs in particulate/gaseous phase in the urban city of Delhi, India: Seasonal variation and cancer risk assessment. Urban Climate, 40. https://doi.org/10.1016/j.uclim.2021.101010
43. Singh, B. P., Kumar, K., & Jain, V. K. (2021c). Source identification and health risk assessment associated with particulate- and gaseous-phase PAHs at residential sites in Delhi, India. Air Quality, Atmosphere and Health, 14(10), 1505–1521. https://doi.org/10.1007/s11869-021-01035-5
44. Singh, B. P., Singh, D., Kumar, K., & Jain, V. K. (2021d). Study of seasonal variation of PM2.5 concentration associated with meteorological parameters at residential sites in Delhi, India. In Journal of Atmospheric Chemistry (Vol. 78, Issue 3, pp. 161–176). Springer Science and Business Media B.V. https://doi.org/10.1007/s10874-021-09419-8
45. Sindhwani, R., Goyal, P., (2014). Assessment of traffic–generated gaseous and particulate matter emissions and trends over Delhi (2000–2010), Atmospheric Pollution Research, 5, 438-446.
46. Saliba, W., Gronich, N., Barnett-Griness, O., & Rennert, G. (2016). Usefulness of CHADS2 and CHA2DS2-VASc scores in the prediction of new-onset atrial fibrillation: a population-based study. The American journal of medicine, 129(8), 843-849
47. Singh B, Pandey P, Wabaidur SM, Avtar R, Kumar P, Rahman S. 2023. Substantial changes in Gaseous pollutants and health effects during COVID-19 in Delhi, India. PeerJ 11:e14489 http://doi.org/10.7717/peerj.14489
48. Shubham Sharma, Mengyuan Zhang, Anshika, Jingsi Gao, Hongliang Zhang, Sri Harsha Kota, Effect of restricted emissions during COVID-19 on air quality in India, Science of The Total

Environment,Volume 728, 2020, 138878, ISSN 0048-9697, https://doi.org/10.1016/j.scitotenv.2020.138878

49. Shukla, S., Khan, R., Saxena, A., Sekar, S., Ali, E.F. and Shaheen, S.M., 2022. Appraisal of COVID-19 lockdown and unlocking effects on the air quality of North India. Environmental Research, 204, p.112107.
50. Sarkodie, Samuel Asumadu, and Phebe Asantewaa Owusu. "Impact of meteorological factors on COVID-19 pandemic: Evidence from top 20 countries with confirmed cases Environmental Research 191 (2020): 110101.
51. Sharma, G.D., Bansal, S., Yadav, A., Jain, M. and Garg, I., 2021. Meteorological factors, COVID-19 cases, and deaths in top 10 most affected countries: an econometric investigation. Environmental Science and Pollution Research, 28, pp.28624-28639.
52. Wu, F., Zhao, S., Yu, B., Chen, Y. M., Wang, W., Song, Z. G., Hu, Y., Tao, Z. W., Tian, J. H., Pei, Y. Y., Yuan, M. L., Zhang, Y. L., Dai, F. H., Liu, Y., Wang, Q. M., Zheng, J. J., Xu, L., Holmes, E. C., & Zhang, Y. Z. (2020). A new coronavirus associated with human respiratory disease in China. Nature, 579(7798), 265–269. https://doi.org/10.1038/s41586020-2008-3
53. WHO. (2020). Advice on the use of masks in the context of COVID-19: interim guidance-2. Guía Interna de LaOMS, April, 1–5. https://doi.org/10.1093/jiaa077
54. World Health Organization. (2020b). Coronavirus disease. Coronavirus Disease (COVID-19) Situation Report –119, 2019(May), 2633. https://doi.org/10.1001/jama.2020.2633
55. Wang, P., Chen, K., Zhu, S., Wang, P., & Zhang, H. (2020). Severe air pollution events not avoided by reduced anthropogenic activities during COVID-19 outbreak. Resources, Conservation and Recycling, 158(February), 104814. https://doi.org/10.1016/j.resconrec.2020.104814
56. Xu, Y.; Xue, W.; Lei, Y.; Zhao, Y.; Cheng, S.; Ren, Z.; Huang, Q. Impact of Meteorological Conditions on PM 2.5 Pollution in China during Winter. Atmosphere 2018, 9,429. https://doi.org/10.3390/atmos9110429
57. Yin, G., Liu, C., Hao, L., Chen, Y., Wang, W., Huo, J., … Kan, H. (2019). Associations between size-fractionated particle number concentrations and COPD mortality in Shanghai, China. Atmospheric Environment, 214, 116875. doi: 10.1016/j.atmosenv.2019.116875
58. Yang, Xiao-Dong, Hong-Li Li, and Yue-E. Cao. "Influence of meteorological factors on the COVID-19 transmission with season and geographic location." International Journal of Environmental Research and Public Health 18.2 (2021):
59. Yang, Xiao-Dong, Hong-Li Li, and Yue-E. Cao. "Influence of meteorological factors on the COVID-19 transmission with season and geographic location." International Journal of Environmental Research and Public Health 18.2 (2021): 484.
60. Zhou, J., Qin, L., Meng, X. and Liu, N., 2021. The interactive effects of ambient air pollutants-meteorological factors on confirmed cases of COVID-19 in 120 Chinese cities. Environmental Science and Pollution Research, 28, pp.27056-27066.

Figures

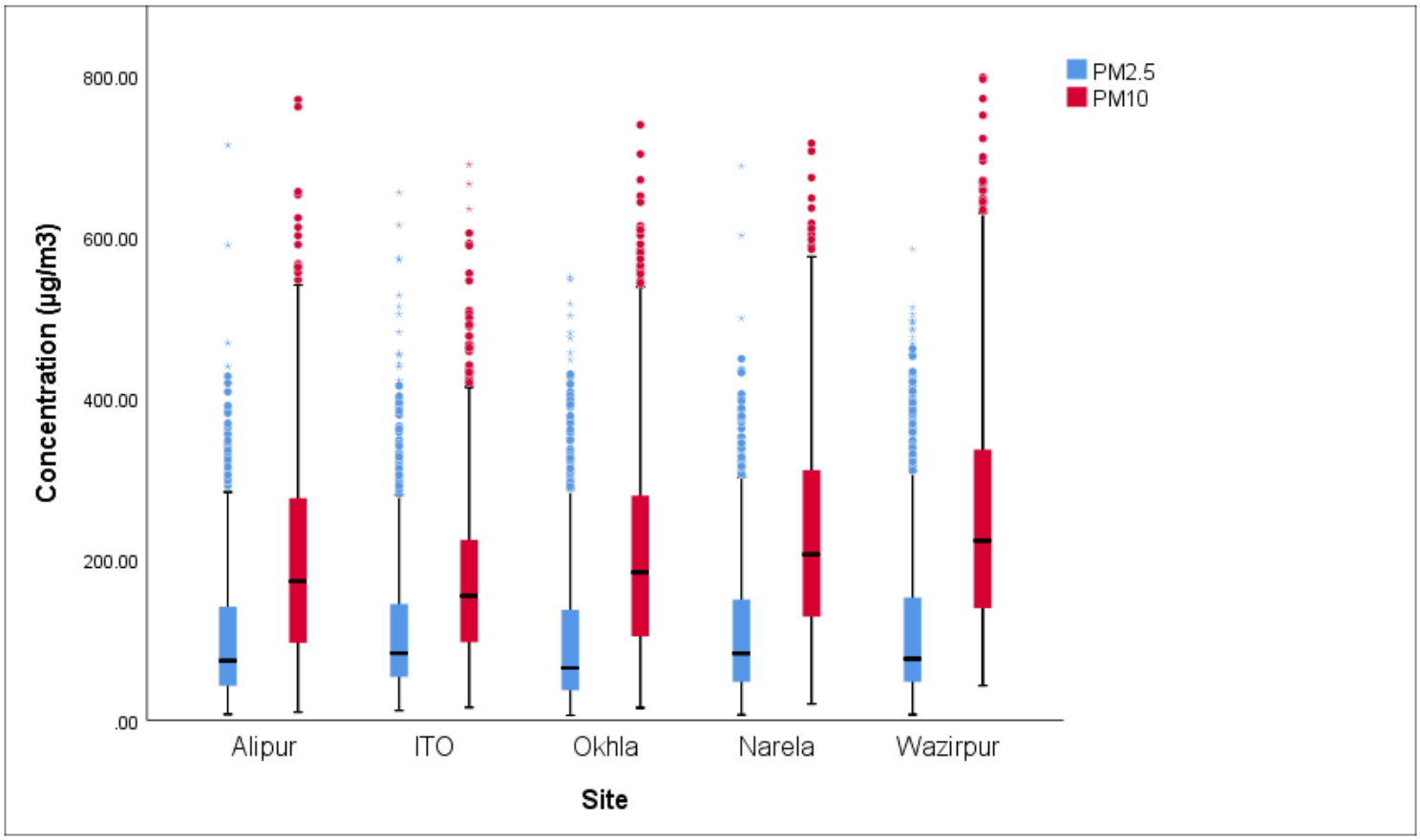

Figure 1

the concentrations of $PM_{2.5}$ and PM_{10} at different monitoring stations in Delhi

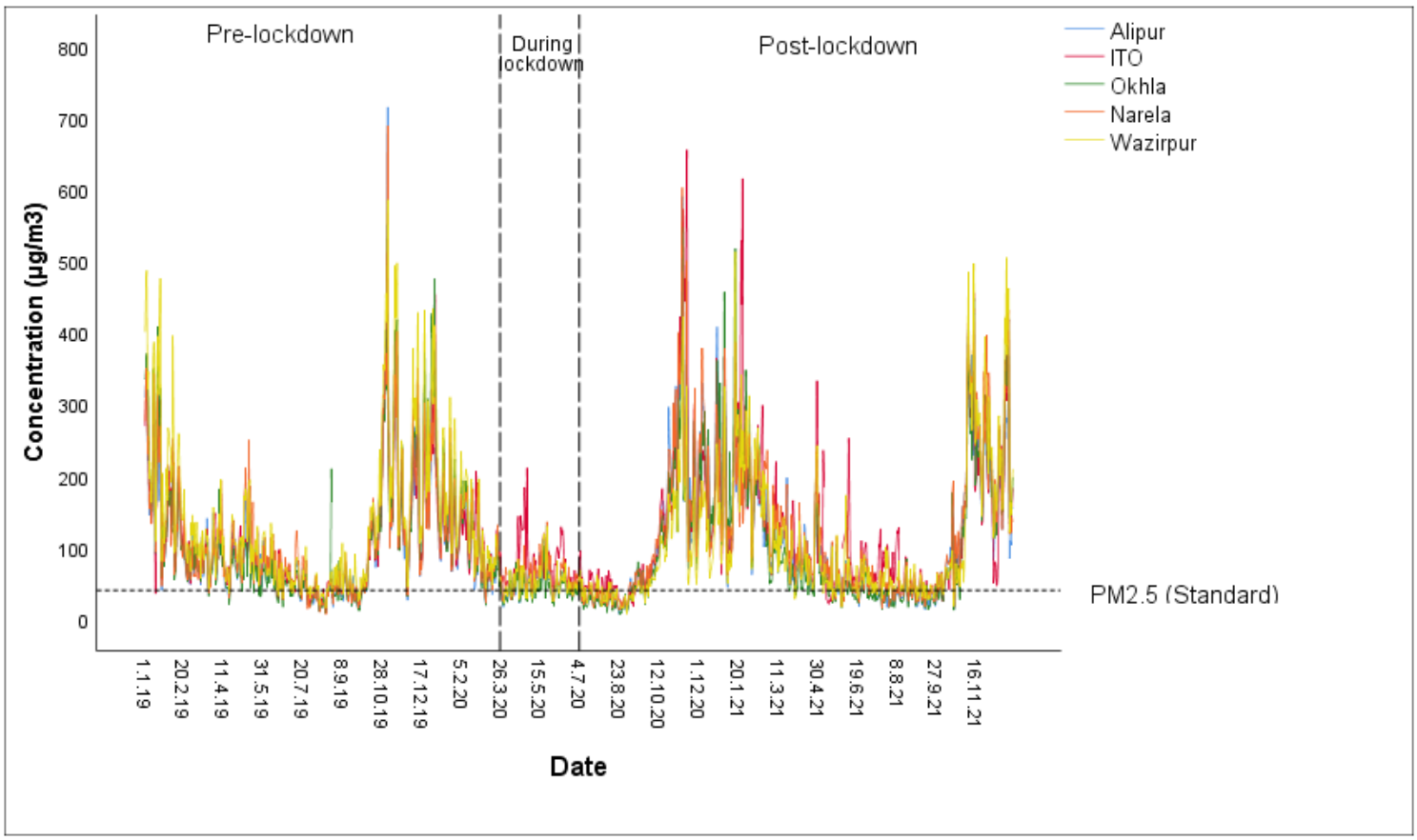

Figure 2

Time series plot for $PM_{2.5}$ for pre-during and post-lockdown periods at Delhi

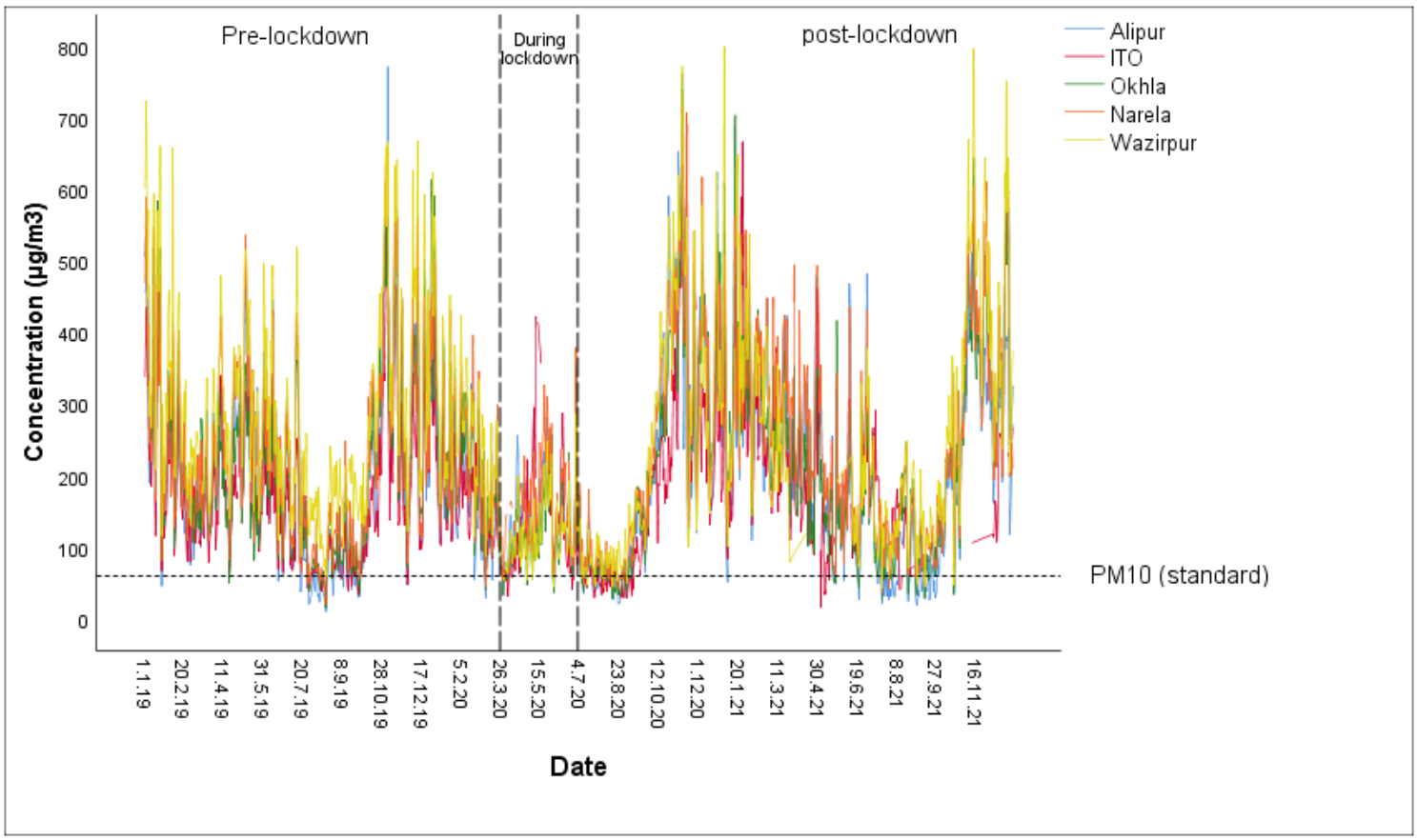

Figure 3

Time series plot for PM_{10} for pre-during and post-lockdown periods at Delhi

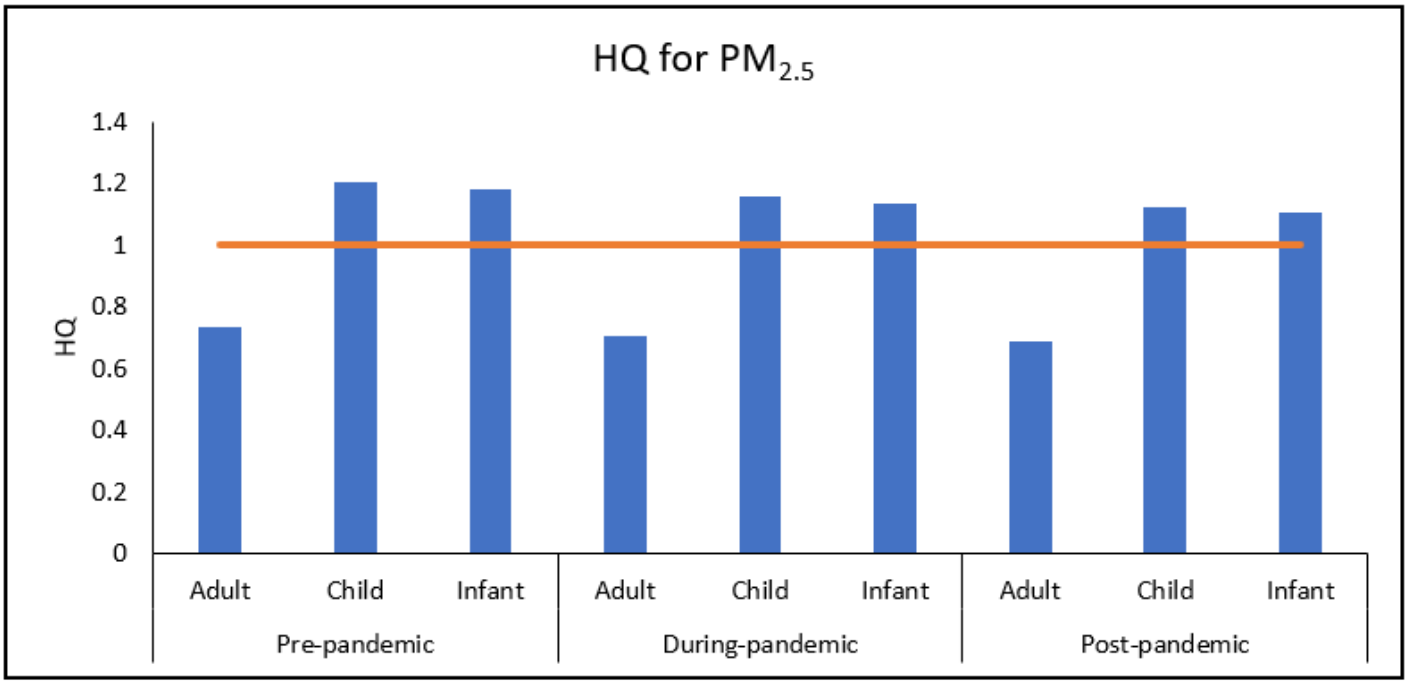

Figure 4

HQ value for $PM_{2.5}$ for pre-, during, and post-pandemic periods

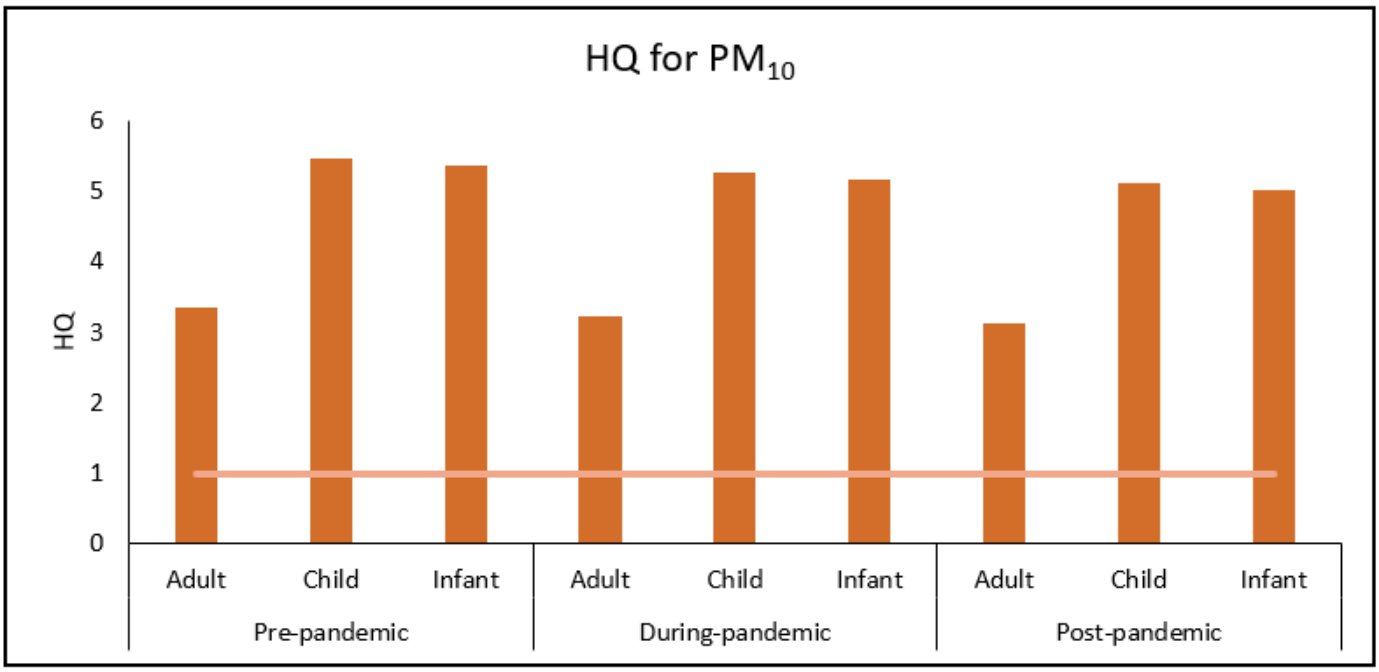

Figure 5

HQ value for $PM_{2.5}$ for pre-, during, and post-pandemic periods

JMEPEG
https://doi.org/10.1007/s11665-023-08527-8

©ASM International
1059-9495/$19.00

ORIGINAL RESEARCH ARTICLE

Effect of Rotational Speed on Mechanical, Microstructure, and Residual Stress Behaviour of AA6061-T6 Alloy Joints through Friction Stir Welding

Virendra Pratap Singh, Ashish Kumar, Rajan Kumar, Anchit Modi, Deepak Kumar, Vinyas Mahesh, and Basil Kuriachen

Submitted: 17 May 2023 / Revised: 18 June 2023 / Accepted: 5 July 2023

In the present work, the behaviour of an AA6061-T6 alloy joint through friction stir welding was studied comprehensively under a set of processing parameters so as to establish a better microstructure-strength relationship in the joint. In-depth investigations have been done on intermetallic compounds and their phases using SEM, XRD, optical microscopy, and EDS, and thereby on the mechanical properties of the welded joint through tensile, hardness, and residual stress. The results revealed the evolution of grain boundaries and the existence of second-phase particles such as Mg_2Si, $MgZn_2$, $MgCu_2$, and Al_2CuMg. Moreover, using a rotational speed of 800 rpm results in enhanced hardness, tensile strength, and flexural strength. The highest and lowest tensile strengths of 198 and 171 MPa correspond to 800 and 600 rpm, respectively. The grain size distribution in the weld zone is 76.94, 0.83 and 36.82 μm for 600, 800, and 1000 rpm, respectively. Flexural strength was improved for the 800-rpm case and reached a maximum of 380 MPa. The lowest residual stress was found for an 800-rpm sample with tensile and compressive nature of stresses. Ductile fracture behaviour was obtained for tensile samples obtained at 600 and 800 rpm, whereas in the case of 1000 rpm, brittle fracture behaviour was seen.

Keywords AA6061-T6 alloy, fracture analysis, friction stir welding, mechanical behaviour, microstructure, residual stress

This invited article is part of a special topical issue of the *Journal of Materials Engineering and Performance* on Residual Stress Analysis: Measurement, Effects, and Control. The issue was organised by Rajan Bhambroo, Tenneco, Inc.; Lesley Frame, University of Connecticut; Andrew Payzant, Oak Ridge National Laboratory; and James Pineault, Proto Manufacturing on behalf of the ASM Residual Stress Technical Committee.

Virendra Pratap Singh, Department of Mechanical Engineering, National Institute of Technology Mizoram, Aizawl 796012, India; and Department of Mechanical Engineering, IES College of Technology, Bhopal 462044, India; **Ashish Kumar**, Department of Mechanical Engineering, Delhi Technological University, Delhi 110042, India; and Department of Mechanical Engineering, Galgotias College of Engineering and Technology, Greater Noida 201310, India; **Rajan Kumar**, Department of Mechanical Engineering, IES College of Technology, Bhopal 462044, India; **Anchit Modi**, Department of Basic Sciences, IITM, IES University, Bhopal 462044, India; **Deepak Kumar**, Department of Mechanical Engineering, Carnegie Mellon University, Pittsburgh, PA 15213; **Vinyas Mahesh**, Department of Mechanical Engineering, National Institute of Technology, Silchar, Assam 788010, India; and Department of Engineering, City, University of London, London, UK; and and **Basil Kuriachen**, Department of Mechanical Engineering, National Institute of Technology Mizoram, Aizawl 796012, India; and Department of Mechanical Engineering, National Institute of Technology Calicut, Kerala 673601, India. Contact e-mail: virendraps07@gmail.com.

1. Introduction

The effort involved in producing conventional fusion welding with better strength, fatigue resistance, and corrosion resistance has limited its usage on aluminium alloys of the 6000 series, which are commonly used in pioneering industries like automotive, railways, marine, and construction. Therefore, it is crucial to study welding methods for such materials due to their extensive usage in various industries. Lightweight structures are a significant design element in the aerospace industry, and aluminium alloys are preferred over steel alloys due to their lower density. To weld aluminium alloys, the solid-state friction stir welding (FSW) technique is extensively utilised for materials with high-melting points, such as steel and aluminium alloys (Ref 1, 2). The Welding Institute (TWI) and Cambridge University collaborated to develop the FSW process as a solid-state joining of aluminium alloys (Ref 3). Numerous studies have been conducted so as to enhance the mechanical performance of the joint and address any defects in the FSW process. Researchers have discovered ways to improve the quality of the weld and its mechanical properties (Ref 4, 5). For instance, Kadian and Biswas (Ref 6) studied the material flow behaviour of CuB370 and AA6061 dissimilar plates during FSW and proposed a new model for the material flow of dissimilar materials in FSW that takes into account the strain rate and temperature-dependent material properties.

Liu et al. (Ref 7) conducted a study on the 6061-T6 alloy using the vortex-friction stir welding (VFSW) process. The main focus of their research was to investigate the changes in the microstructure of the alloy during the welding process. The experimenters used microhardness and tensile strength measurements as indicators of microstructural changes and also examined the grain structure and precipitate in different zones.

Published online: 24 July 2023

The results indicated that the heat-affected zone (HAZ) was the weakest region of the VFSW joint. The weakening in the HAZ was primarily due to the enlargement of particles in the structure of tiny materials. In the nugget zone of the weld (WNZ), there was continuous and dynamic rebuilding of crystals, but it was not enough due to the self-adjusting nature of plastic deformation in the VFSW process. Solid solution strengthening occurred in the WNZ at high temperatures during the VFSW process, leading to a higher microhardness value compared to the HAZ.

Kalinenko et al. (Ref 8) conducted an experiment to explore the consequences of temperature during FSW, the microstructure of aluminium-alloy 6061 joints created by FSW, and their ability to withstand high temperatures. They used a finite-element modelling (FEM) approach to understand the microstructural data and quantified the temperature distributions generated during FSW. The researchers found that the microstructure in the stir zone was susceptible to abnormal grain growth after heat treatment, which occurred rapidly when heating after welding from room temperature to solution temperature. Humphrey's cellular-growth model described the annealing behaviour in all welded conditions. In situations with low heat input, the final grain size was small due to competition between normal grain growth and abnormal grain growth, which was caused by a combination of a fine-grain microstructure and a low volume fraction of second-phase particles. Conversely, high-heat input conditions produced a relatively coarse grain structure and a high-volume fraction of particles in the stir zone, providing microstructural stability.

Choi et al. (Ref 9) examined how linear friction welding (LFW) can strengthen AA7075-T6 alloy joints. They used LFW to join two pieces of AA7075-T6 alloy and conducted experiments to study the microstructure and mechanical properties of the welded joint. They found that the LFW process caused dynamic recrystallization and resulted in a refined microstructure with improved mechanical properties. The authors identified that the strengthening mechanism of the joint was due to the creation of nanoscale strengthening precipitates, such as MgZn2 and Mg2Si, during the welding process (Ref 10, 11). In contrast, Tavassolimanesh and Alavi Nia (Ref 12) proposed a novel method for manufacturing bimetallic tubes using the FSW process, where they created bi-tubes from aluminium and copper alloy. They discovered that as the rotational speed increased, the joint strength decreased, and one of the significant issues after welding is the creation of residual stress in construction. The welding process produces both mechanical and thermal residual stresses in the joint and its surroundings, which depend on the yield strength of the parent metal and the local temperature. It becomes crucial to study and calculate the residual stresses on the mechanical performances of welded sensitive structures, such as pressure vessels. Sometimes, when there are residual stresses, they can cause notable changes in the shape of an object through plastic deformation, resulting in warping and distortion (Ref 13).

Several techniques have been utilised to calculate the residual stresses, including slitting (Ref 14, 15), contour (Ref 16, 17), and hole drilling technique (Ref 18, 19). Marek et al. (Ref 20) and Hamilton et al. (Ref 21) described how the longitudinal residual stress distribution of an improved cast Al-alloy, AlSi9Mg, was affected by different parameters used in friction stir processing (FSP). They obtained residual stress through the material flow model in FSPed AlMg9Si by taking the material flow behaviour into consideration during welding (Ref 21). Furthermore, they examined the impact of FSP constraints on residual stress in an improved cast Al-alloy, AlSi9Mg (Ref 22), and studied the influence of modified FSP on residual stress in the same alloy (Ref 23). Their findings suggest that an increase in tool rotational speed leads to an increase in residual stress. Additionally, compared to the retreating side, residual stresses are greater on the advancing side. Moreover, Alinaghian et al. (Ref 24) explored the use of ultrasonic vibrations to measure residual stress in aluminium AA6061-T6 after FSW. Using high-frequency vibrations can suppress the residual stress up to 45% and also enhance the weld strength. They also found that using ultrasonically assisted FSW (UAFSW) can reduce welding forces compared to conventional FSW.

Donne et al. (Ref 25) utilised x-ray, neutron diffraction, and synchrotron methods to evaluate the residual stresses and found a better outcome in all three cases. Transverse stresses were lower than longitudinal stresses, and residual stress distribution was analogous on both lower and upper weldment surfaces. The residual stress value obtained was 20-50% of the yield strength of the parent material, depending on the linear and rotational speeds and tool pin diameter. Ma et al. (Ref 26) utilised the FSW on an AA2024 to investigate the remaining stresses present in the material during mechanical drawing. They were able to effectively diminish these stresses in the weld region. The key to achieving a successful weld was the management of various process parameters, such as linear speed, rotational speed, tool shape, and penetration. As far as the author's knowledge goes, there is no clear report on the microstructural, mechanical, and XRD-based residual stress distribution of AA6061-T6 subjected to friction stir welding. Therefore, in this research work, the dispersion of residual stress and mechanical properties of an AA6061-T6 alloy joint through FSW were investigated, with a focus on three different rotational speeds at constant welding speeds.

2. Experimental Method

The aluminium AA6061-T6 plate of dimension 120 × 60 × 4 mm is used to carry out the experiment. The representation of the FSW procedure and tool dimension is shown in Fig. 1(a) and (b). The chemical composition of the plate material is mentioned in Table 1. Before performing the experiment, plate surfaces were properly cleaned with a microbrush and then with acetone. An H13 tool steel is used for an FSW taper cylindrical threaded tool with a shoulder diameter of 18 mm and a pin length of 3.8 mm. The metallographic and other mechanical testing samples were cut using a CNC wire EDM (model Elektra, Maxicut 523). The metallographic samples were polished with emery sandpaper and then, etched with Keller's reagent to obtain the microstructural characteristics of the joints. The microstructures were seen through an optical microscope (model Leica DMI500M) and scanning electron microscopy (SEM) (model Zeiss Supra 40) built into the EDX system. X-ray diffraction (XRD) was used to analyse the microstructure and phases. The microhardness values were taken transverse to the welding direction of joints in a 1 mm space with a 100 g loading force and a dwell time of 10 s. Tensile tests and 3-point bending tests were done with the help of a UTM (Model: Instron, 8862) with 1 mm/min of crosshead speed. Both face bends and root bends were tested to

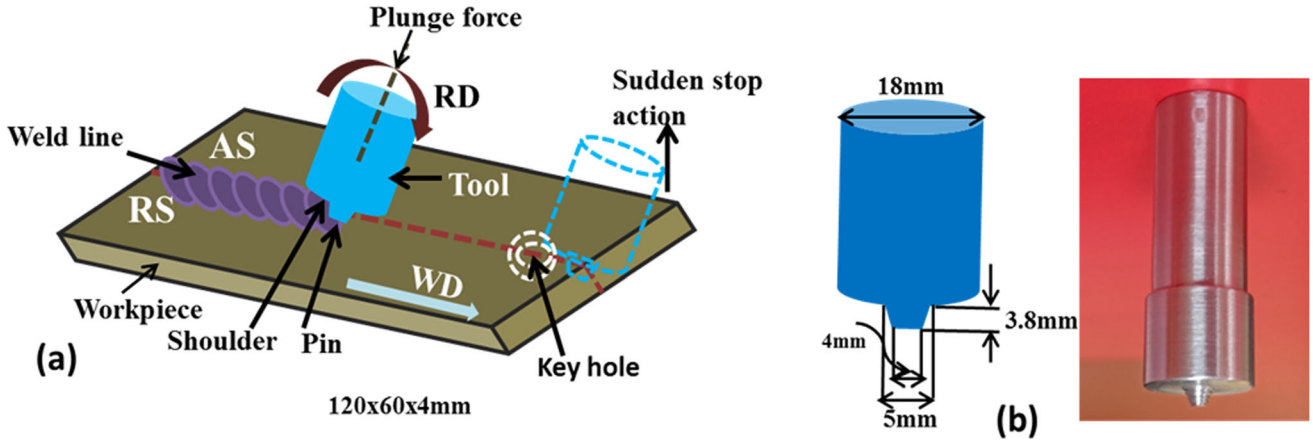

Fig. 1 Representation of (a) FSW process and (b) FSW tool

Table 1 Chemical composition of AA6061-T6 alloy, wt.%

Al	Mg	Si	Ti	Cr	Mn	Fe	Cu	Zn
Bal.	0.976	0.563	0.01885	0.1101	0.08	0.528	0.48	0.111

Table 2 Types of samples and process parameters

Sample	Plunge depth/Tilt angle	Traverse speed, mm/min	Rotational speed, rpm	Revolutionary Pitch, mm/rev
W-A1	0.1/2°	50	600	0.083
W-A2			800	0.063
W-A3			1000	0.050

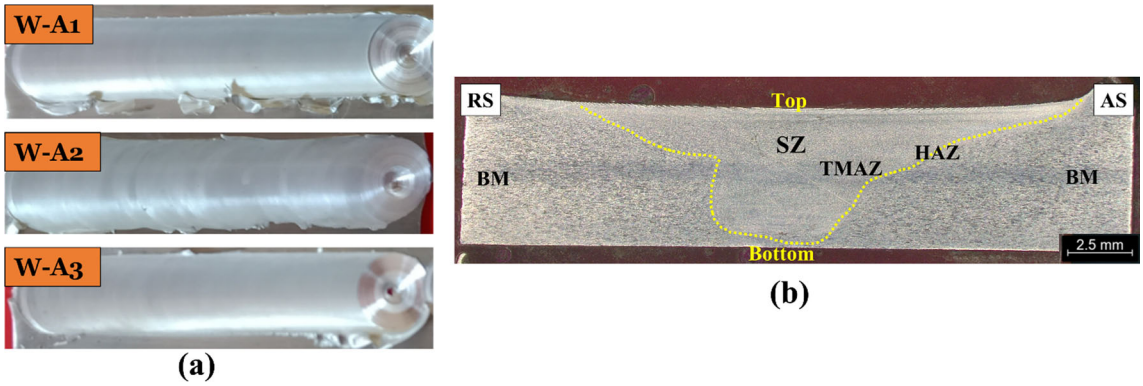

Fig. 2 (a) Weld appearance and (b) macrostructure of welded part showing SZ, TMAZ, and HAZ

identify the flexural strength and mode of failure. The XRD-based residual stress distribution of AA6061-T6 subjected to FSW was calculated both in the longitudinal and transverse directions. Fracture analysis of tensile fracture samples was performed with the help of FE-SEM. There were three different sets of rotational speeds, and a constant transverse speed was taken, as shown in Table 2, where the revolutionary pitch is the ratio of rotational to transverse speed. In all cases, the tilt angle was kept at 2° forward and the plunge depth at 0.1 mm. Revolutionary pitch is the ratio of traverse speed to rotational speed (mm/rev).

3. Results and Discussion

3.1 Microstructure Analysis

The weld appearance of the joint surface at all three sets of parameters is shown in Fig. 2(a). For samples W-A1 and W-A3, a lot of weld flash is seen due to inadequate heat input. Whereas, for sample W-A1, no flashes are seen. Figure 2(b) shows the macrostructure of the FSW joint, identifying the SZ, TMAZ, and HAZ. EDS mapping of base metal (AA6061-T6) is shown in Fig. 3. Magnesium and silicon are the two major

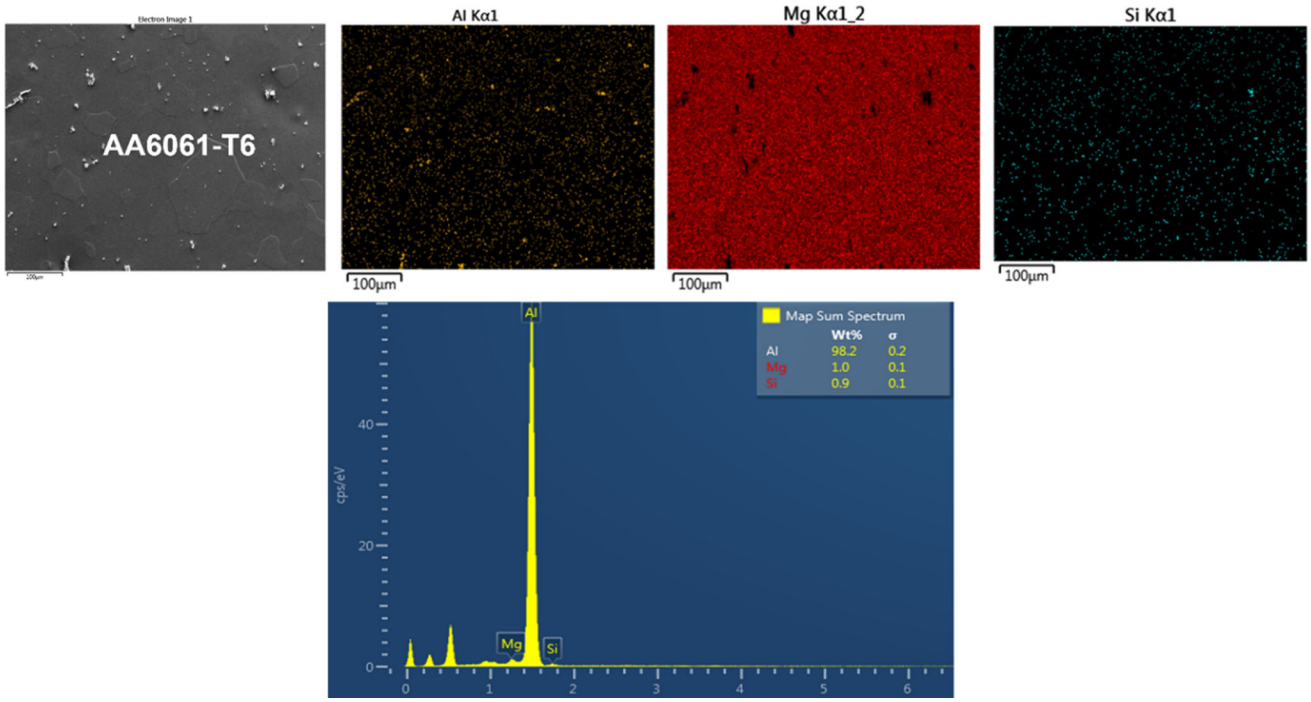

Fig. 3 EDS mapping of base metal (AA6061-T6)

alloying elements present and play an important role in bonding during welding. To validate the above statements, XRD analysis of the weld has been accomplished. Figure 4(a), (b), and (c) confirms that a huge fraction of intermetallic compounds (IMCs) such as Mg2Si, MgZn2, MgCu2, and Al2-CuMg formation takes place. The high-magnification optical images of all sets of welded samples have been shown in Fig. 5, 6 and 7. Three distinct zones were displayed individually, i.e. HAZ, TMAZ, and SZ, in each case. No volumetric defects were found in any of the weld samples. As the heat input increases by increasing the rotational speed, grain size distribution is severely affected, as shown in Fig. 8(a), (b), and (c). During low-heat input (W-A1), very coarse grains with an average grain size of 76.94 μm were seen (as referred to in Fig. 8a). Whereas, in the case of W-A2, an average grain size of 0.83 μm was observed due to the proper material mixing and adequate heat generation in this case (as referred to in Fig. 8b). Very high and very low heat input leads to improper material intermixing, reducing the strength of the joint (Ref 27). Fine grain was observed in the TMAZ section of the weld compared to SZ in the case of W-A1, whilst elongated grains were observed in HAZ, as shown in Fig. 5(a), (b), and (c).

The unusual grain evolution was attributed to the grain refinement on the top and bottom surfaces of the weldment. The effect of grain refinement is noticeable at the weld surface; therefore, the weakest zone was generated beside grain growth. The microstructural stability in the remaining weld zone leads to abnormal coarse grain growth (Ref 28, 29). Any increment in rotational speed, i.e. sample W-A3, increases the heat input, and due to this, the material flow and stirring action over the weldment are reduced, causing coarser grains (average grain size 36.82 μm) compared to the W-A2 case and hence, the joint strength (Ref 30).

During welding, a very complex and irregular grain growth behaviour is seen, and it is very tough to plot the exact behaviour and reason of the phenomenon. Whereas, with the help of Humphreys's cellular model, this occurrence has been tried to explain. Such complex occurrences can be seen for high-stacking-fault energy materials like aluminium alloys (Ref 31, 32). The annealing single-phase alloy behaviour is directed by the high-angle boundary (HAB) fraction and its distribution throughout the weldment (Ref 31). Whereas the material holds second-phase particles (i.e. AA6061-T6 alloys), the nature of grain growth is moreover affected by the material's' pinning effect, which may be measured by the so-called Z parameter, Z = 3Fv R/d, where 'Fv' is the material's volume fraction, 'R' is the average grain size, and "d" is the average size (Ref 32). The fundamental properties of microstructure should be measured within the micrograph. This method can effectively be useful for the uncharacteristic grain growth taking place in FSW, as validated by Hassan et al. (Ref 33).

In the HAZ region, the size of the grain was nearly the same as the base metal grain. These explanations are renowned for the FSW of Al-alloys and are usually ascribed to a distinct rate of recrystallization. The entire documentation can be described with reference to the material flow behaviour prompted by the FSW tool shoulder. It has been described that the moving tool entangles the base metal surface during the welding process and accumulates near the tool pin (Ref 34). The strain rate refers to the change in strain of a material over time. When the strain rate is extremely low, the material's deformation can be viewed as a series of steps, with the material remaining in static equilib-

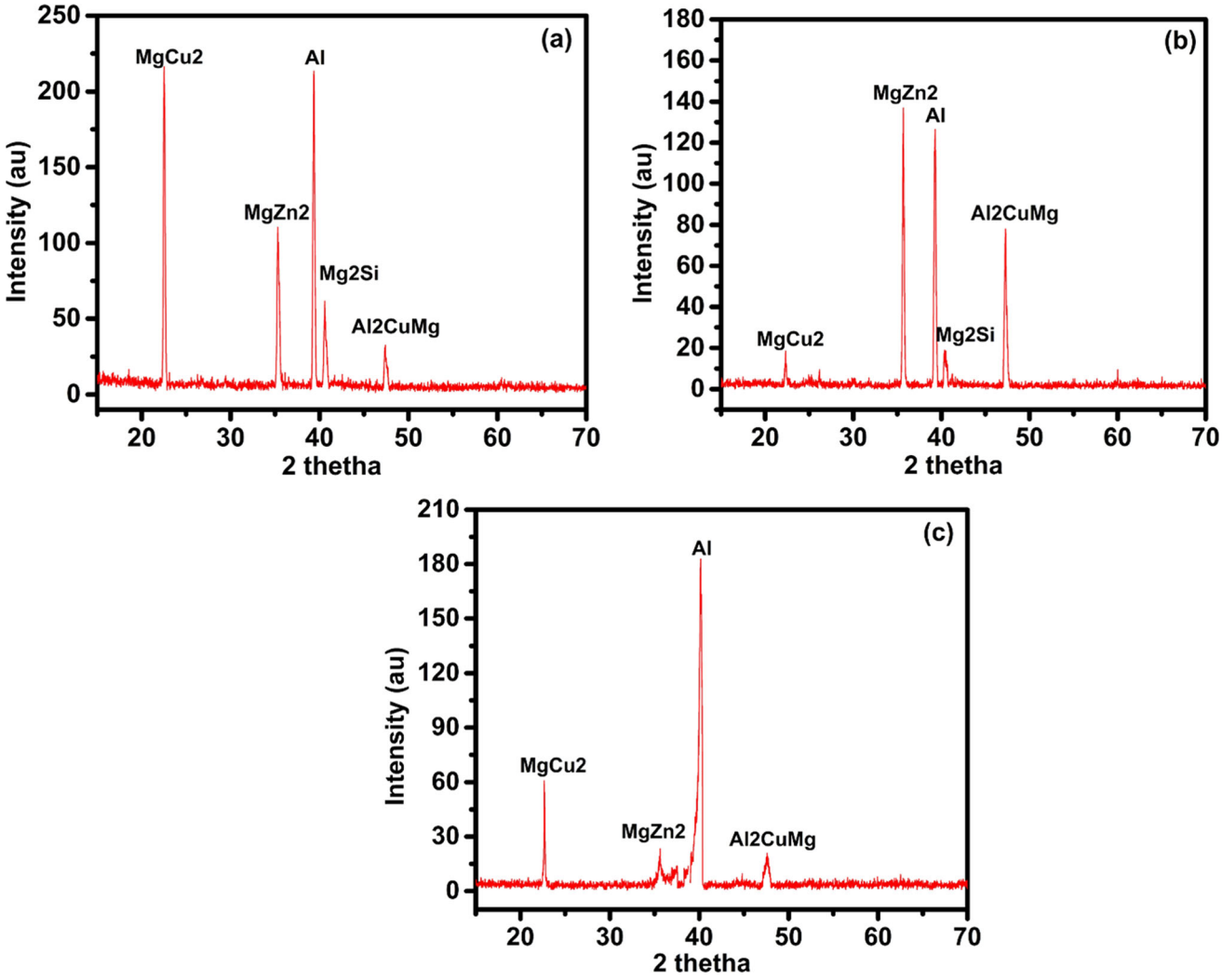

Fig. 4 X-ray diffraction (XRD) of welded samples (a) W-A1, (b) W-A2, and (c) W-A3

rium. In such cases, the process can be regarded as quasi-static, and it can be analysed using the mechanics of materials approach. However, when the strain rate is high, the internal stresses within the material propagate as waves and do not instantaneously transmit throughout the entire material (Ref 35). In FSW, weld grain size and its effect on mechanical properties are mainly dependent on heat input during the process. Heat input varies with rotational speed and, hence, the deformation of the material. In the first case (i.e. W-A1, 600 rpm), heat input is lower at a lower rotational speed, and hence the stirring action is also moderate, and due to this, grain size is coarser (refer to Fig. 8a). Whereas, at higher rotational speed conditions (i.e. W-A3, 1000 rpm), heat input is extremely high, and due to this material sticking, a high-heat gradient takes place, resulting in coarser grain (refer to Fig. 8c). Considering a moderate heat input case (i.e. W-A2, 800 rpm), adequate heat generation and optimum stirring occur, resulting in fine-grain size (refer to Fig. 8b). The heat generation during FSW is mainly from the friction between the tool and the stirred material, and the heat input during FSW can be calculated using Eq 1 (Ref 36-38).

$$q = \frac{4}{3}\Pi^2 \mu p \omega R^3 \quad \text{(Eq 1)}$$

where q is the heat input, p is the pressure, μ is the friction coefficient, R is the radius of the shoulder. And ω is the rotation speed. If the traverse speed is also considered, Eq 2 is obtained.

$$Q = \frac{4}{3}\Pi^2 \mu p \omega R^3 \frac{\alpha\omega}{\upsilon} \quad \text{(Eq 2)}$$

where Q is the heat input per unit length, α is the heat input efficiency, and v is the traverse speed.

3.2 Mechanical Properties

3.2.1 Tensile Test. Tensile stress vs. tensile strain and true stress vs. true strain graphs are shown in Fig. 9(a) and (b), respectively. The mechanical properties were found to have

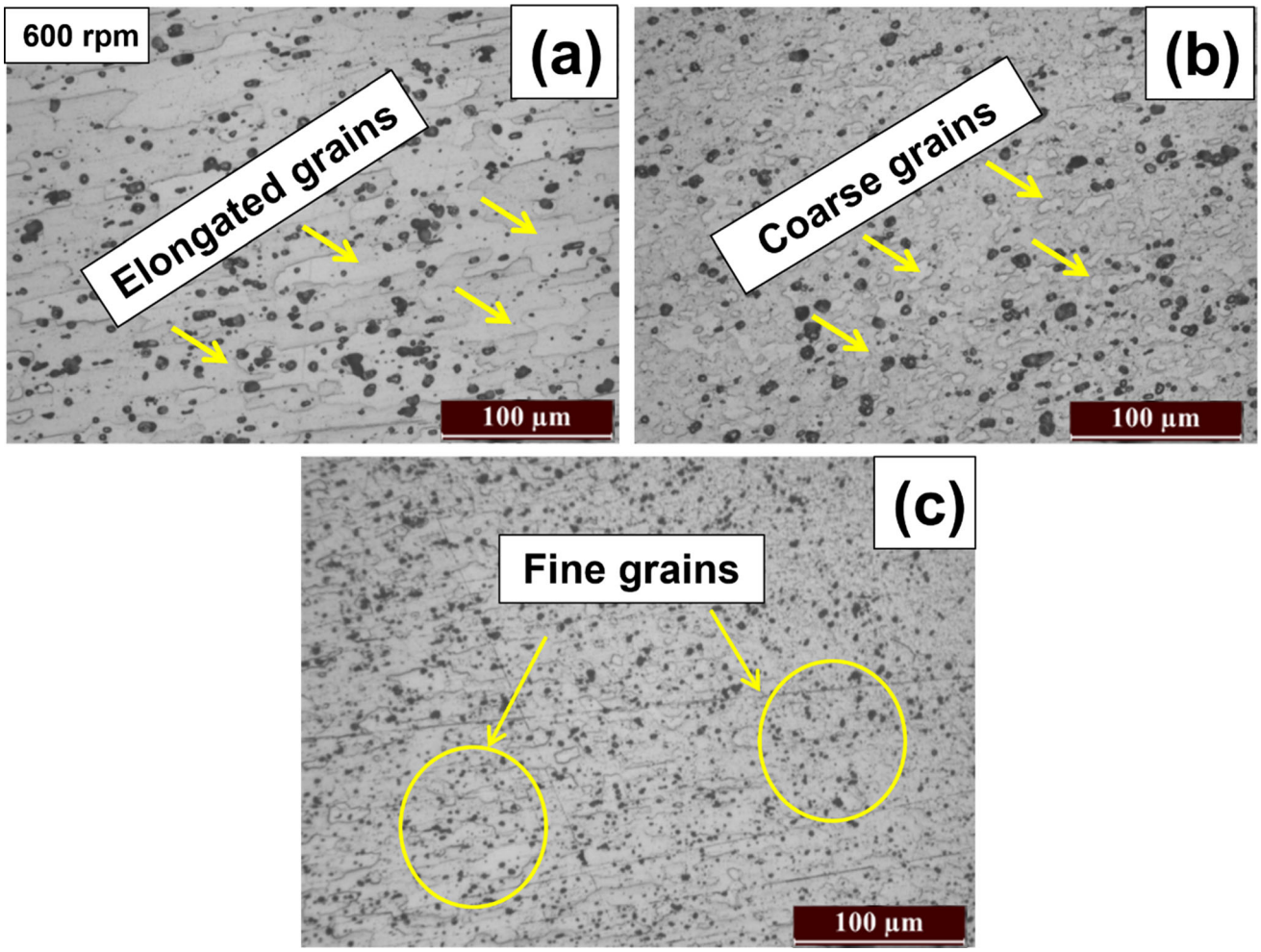

Fig. 5 Optical microstructure of welded sample W-A1: (a) HAZ, (b) SZ, and (c) TMAZ

decreased as a result of the tensile test. The maximum tensile stress for W-A1, W-A2, and W-A3 is 171, 198, and 180 MPa, respectively. A maximum joint efficiency of 84.25% was attained for sample W-A2, whereas a minimum of 72.77% is for sample W-A1, at a lower rotational speed (i.e. at 600 rpm). It has been analysed from Fig. 9 that, with a rise in rotational speed from 600 to 1000 rpm, by keeping welding speed constant, the tensile stress value steadily increased, but at higher speed (i.e. higher heat generation condition), the tensile stress is lower than the moderate heat generation condition, i.e. 800 rpm (W-A2). Proper material mixing and grain refinement are the main causes of increasing tensile strength (Ref 39, 40). When the revolutionary pitch is higher (i.e. 0.083 and 0.063 mm/rev), the tensile strength is lower, but it increases as the revolutionary pitch decreases (i.e. 0.05 mm/rev). The maximum tensile strength is obtained at the lowest revolutionary pitch of 0.05 mm/rev. These results indicate that a softening effect has occurred in the AA6061-T6 due to FSW, just as it did in the other heat-treatable Al-alloys. The softened levels or weld strength of the joints are significantly affected by the process parameters. The optimum process parameters can be determined from the relationship between the weld properties and the process parameters (Ref 36, 37, 41-43). Too high and too low heat inputs deteriorate the weld strength due to improper material mixing and the high possibility of IMC formation, respectively. At 800 rpm, which is a moderate heat input case as compared to the other two cases, therefore, proper material mixing took place and hence, the strength.

The decrease in mechanical properties during the FSW is caused by the precipitate's dissolution in the metal matrix. This leads to a weakening of the material. After examining various regions of the material following the FSW process, it was discovered that different regions exhibit different stress behaviours. The HAZ region had the least strength due to the precipitate's dissolution and the lack of imminent grain growth. When the plastic strain reaches the point of failure in the HAZ, the nugget area has a strain rate of only 2.3%, resulting in failure occurring in the HAZ (Ref 44, 45). The figure clearly illustrates that the tensile properties of every joint exhibit a lower value compared to the base material. Especially, the elongation of the joint is far lower than that of the base material,

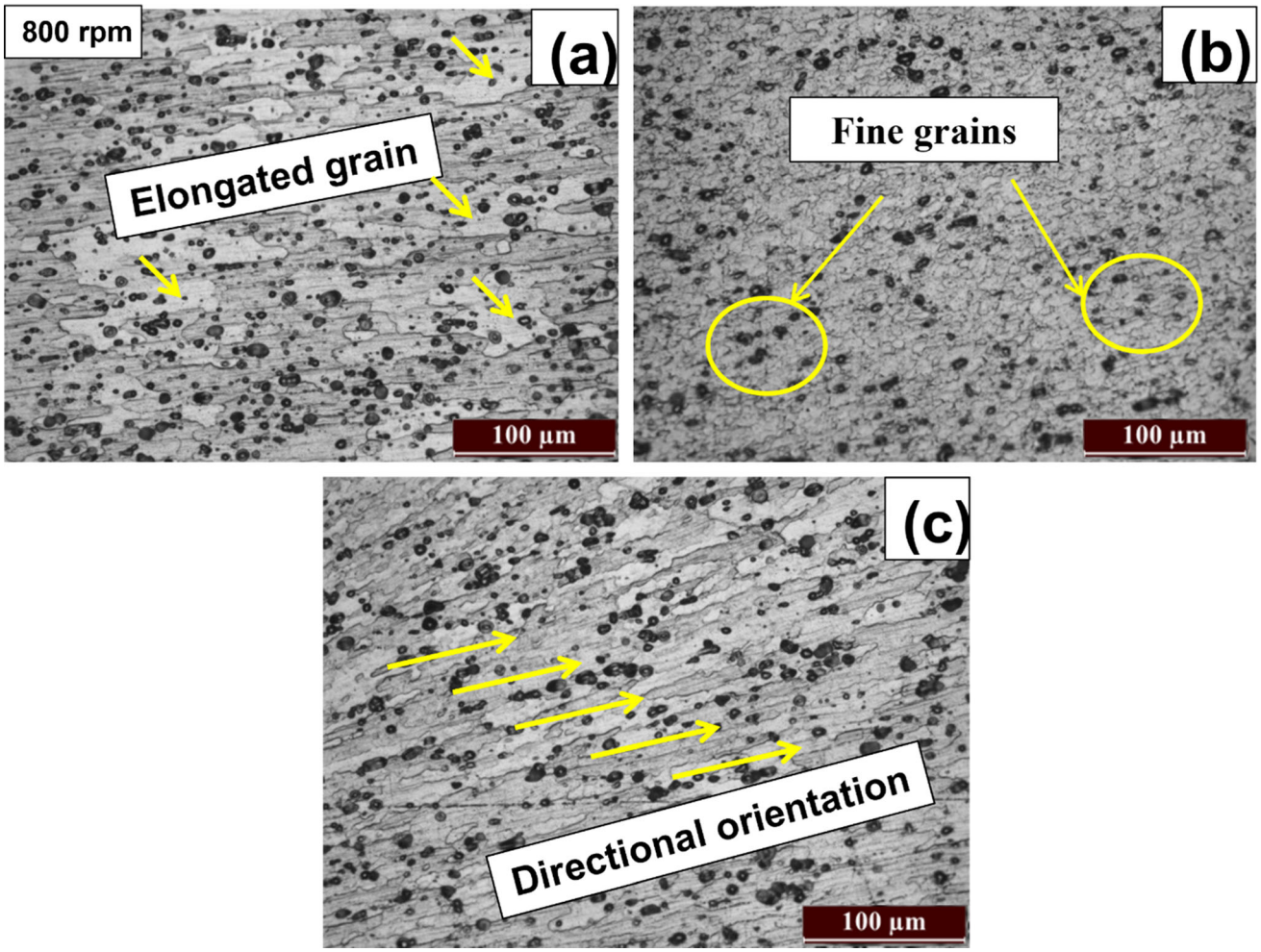

Fig. 6 Optical microstructure of welded sample W-A2: (a) HAZ, (b) SZ, and (c) TMAZ

and its maximum is merely 2%. Intermetallic formation during welding is the main cause of high strength but lower docility in all three cases, especially for W-A2.

3.2.2 Three-Point Bend Test. In the next step, the three-point bending test has been done. At least two FSW samples were tested for both root bend and face bend. The welded structure had very few surface cracks and noticeable changes in shape due to plastic deformation, as observed through a face-bend test. When the sample experiences compressive stress, the bottommost surface is hard to develop micro-stress concentration, as the AA6061-T6 comes in the face-centred cubic (FCC) family and has a greater number of slip systems and better compatibility of material deformation, and the weld surface did not show any cracks during the bend test (Ref 46, 47). Intermetallic compounds consist of two or more metallic elements. However, unlike typical metals, they exhibit a unique combination of bonding that encompasses metallic, covalent, and ionic characteristics. This distinctive bonding arrangement grants them several advantageous properties, such as reduced weight, enhanced strength, increased rigidity, and superior resistance to corrosion, especially under elevated temperatures. Nonetheless, their practical applications are restricted due to their inherent brittleness at room temperature (RT). This brittleness poses challenges in the fabrication process and renders them susceptible to fractures (Ref 48). Bending stress is calculated by Eq 3.

$$\sigma = \frac{Mc}{I} \qquad \text{(Eq 3)}$$

'M' denotes bending moment, which is obtained by multiplying the given force with the given distance between that point of interest and the force, 'c' denotes distance from natural axis (NA) (Fig. 10) and 'I' represents moment of inertia.

The root-bend stress of samples W-A1, W-A2, and W-A3 is 340, 380, and 360 MPa, respectively, as shown in Fig. 11(a), (b), and (c). Whereas, in the case of a face bend, the bending stresses of samples W-A1, W-A2, and W-A3 are 302, 330, and 290 MPa, respectively. In several cases, the rise in strength is

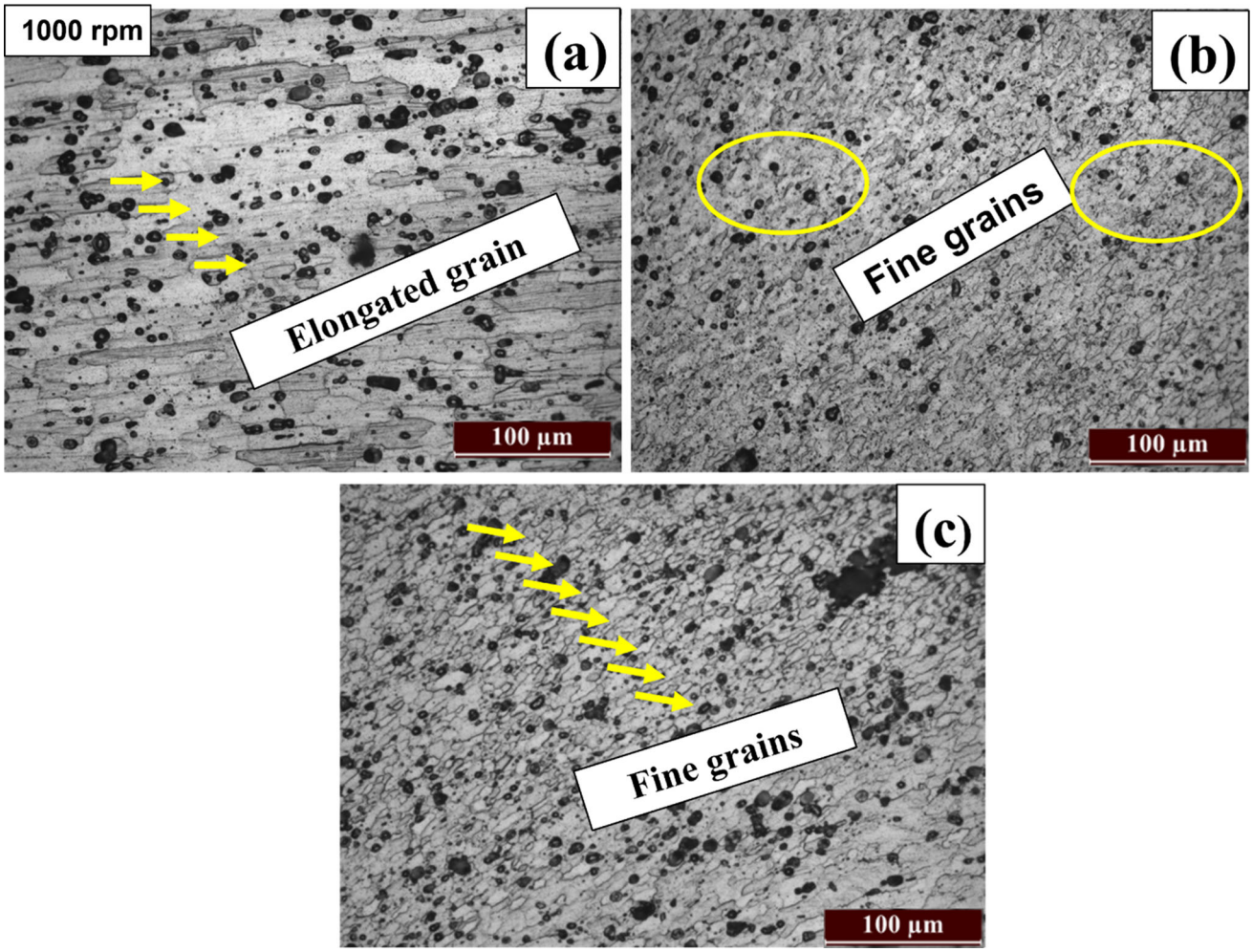

Fig. 7 Optical microstructure of welded sample W-A3: (a) HAZ, (b) SZ, and (c) TMAZ

accompanied by a decrease in ductility. The fine precipitates dispersed homogeneously in the SZ prevent the mobility of dislocations, resulting in a noticeable decrease in ductility. Compared to the base metal, the ductility has decreased in all cases except sample W-A3, i.e. higher heat input conditions. In this case, the ductility of the welding sample touches the base metal ductility in the root-bend case (as shown in Fig. 11c). In the case of W-A2, both face and root-bend ductility are the same, and their strength is also similar, i.e. there is very little variation. This is an indication that appropriate welding occurred under moderate heat conditions. Whereas, in the other two cases, the bend stress (root bend) is much higher than the face-bend stress. The primary factor is having a consistent distribution of grains with no voids in the structure. Also, the formation of clusters of two different precipitate phases that impede the movement of dislocations and the sliding of grain boundaries during the process. The findings indicate that as the hardness of a material increases, its flexural strength generally decreases, which is an acceptable outcome. However, amongst the various samples tested, those rotated at a speed of 800 rpm exhibited higher flexural strength than the others, possibly because this speed led to a maximum hardness of approximately 72 HV. These values suggest that the root side of the weld was stronger than that of the face-side weld. This could be caused by the fact that the lower side of the weld was exposed to restricted downward movement due to the bed backing plate. The flexural stress values were comparatively higher than the tensile values, and this was due to the higher temperatures involved during FSW (Ref 49).

3.2.3 Microhardness. The microhardness of the welded sample was calculated across the welding line direction. The microhardness curves for the welded sample and base metal are characterised in Fig. 12. Based on the findings on the hardness, it was noted that the reduction in both the retreating and advancing sides of the alloys was comparable for all the parameters. The highest microhardness value of 91 HV was observed for sample W-A3, i.e. high-heat condition. Whilst the maximum microhardness values of 61 HV and 70 HV were obtained for samples W-A1 and W-A2, respectively. The key reason for these microhardness differences is due to the IMC's formation. As described in the literature, small precipitates in AA6061-T6 alloys play a critical role in increasing the mechanical strength (Ref 50-52).

Microhardness values vary on the advancing and retreating sides as well. In all cases, microhardness on the advancing side is higher compared to the retreating side (as shown in Fig. 12).

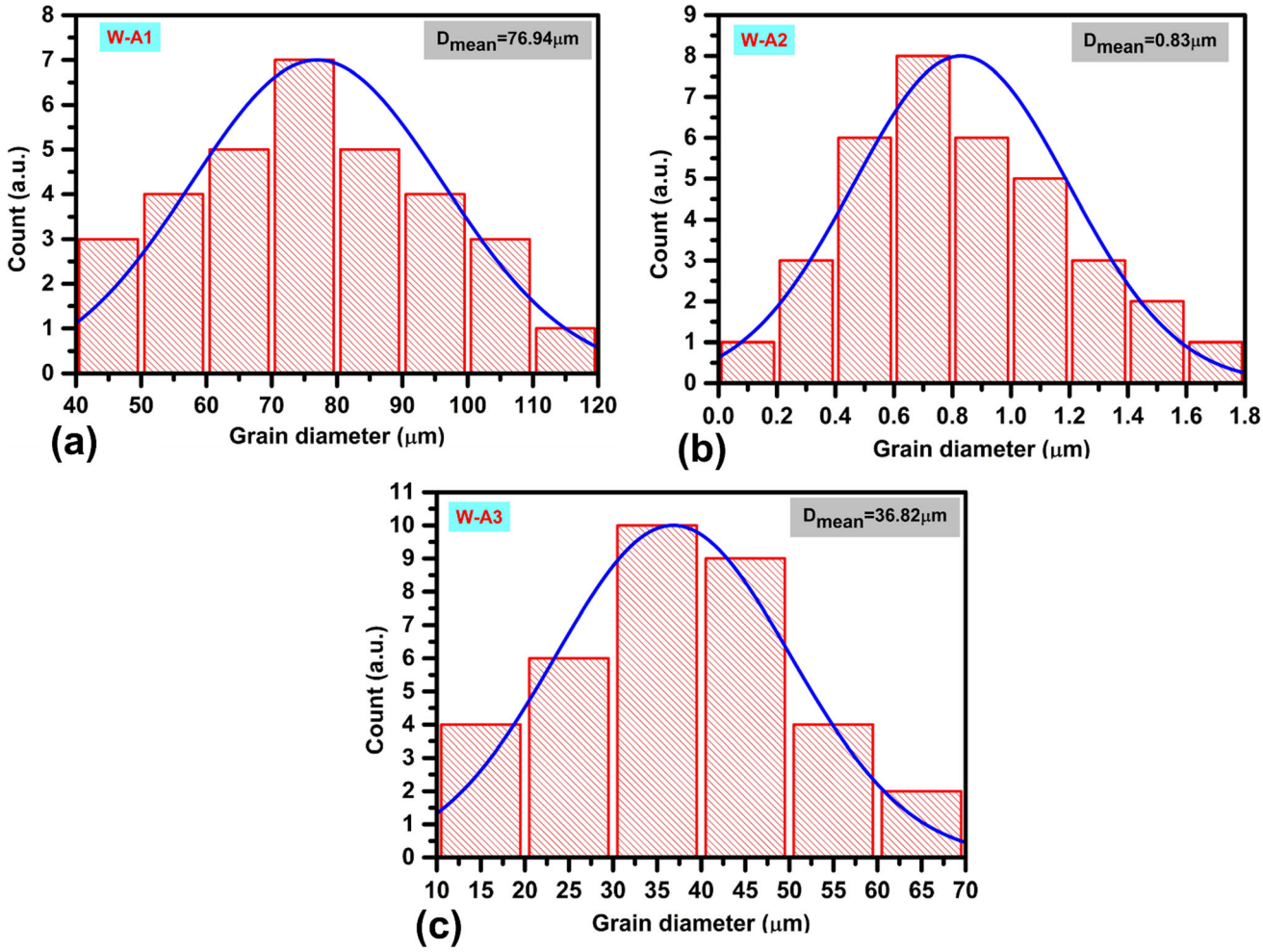

Fig. 8 Grain size distribution of samples: (a) W-A1, (b) W-A2, and (c) W-A3

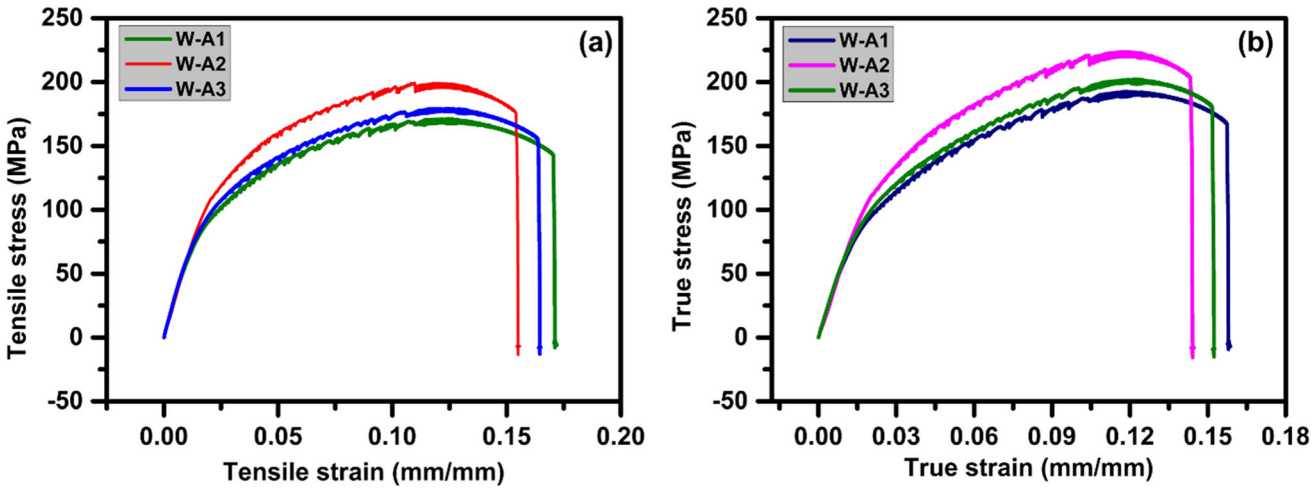

Fig. 9 Tension test of welded samples (a) tensile stress vs. tensile strain curve and (b) true stress vs. true strain curve

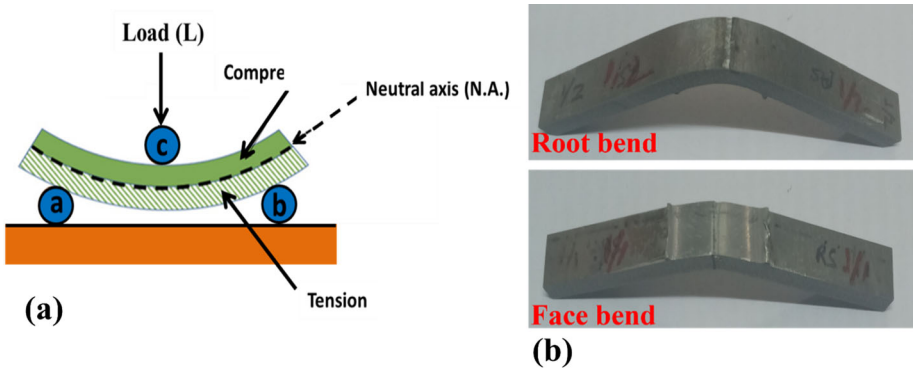

Fig. 10 Schematic diagram of 3-point bending

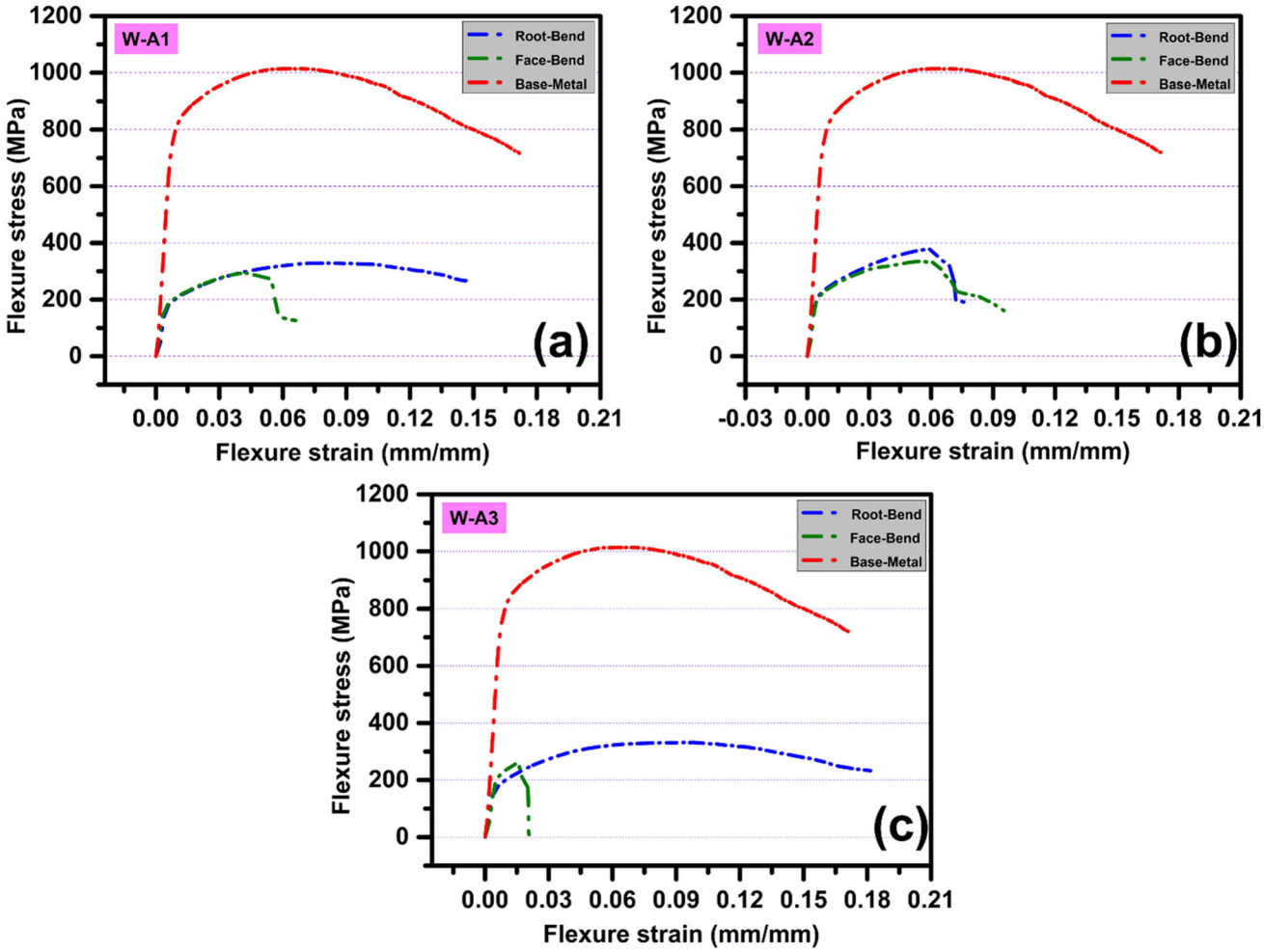

Fig. 11 Flexural strength (root and face bend) variation: (a) W-A1, (b) W-A2, and (c) W-A3

These results occur because of the existence of more plastic deformation and strain caused by the tool, resulting in a significant refining effect (Ref 53, 54). Therefore, it seems that the majority of heat generation by friction is situated below the tool shoulder area (i.e. the SZ and TMAZ regions). At numerous places, an unexpected increase in hardness value was observed because of IMC particles. By keeping rotational speed higher, the high-heat input offers suitable conditions for the development of IMCs and gives them appropriate hardness.

3.2.4 Residual Stress Analysis. Residual stresses refer to the internal forces that persist within a material after all external forces have been removed. These forces arise from uneven deformation caused by various factors like mechanical, thermal, or microstructural changes, such as in the phase transformation process. The degree of tensile residual stress present at a particular point is influenced by the extent of compressive plastic deformation that took place during the heating process.

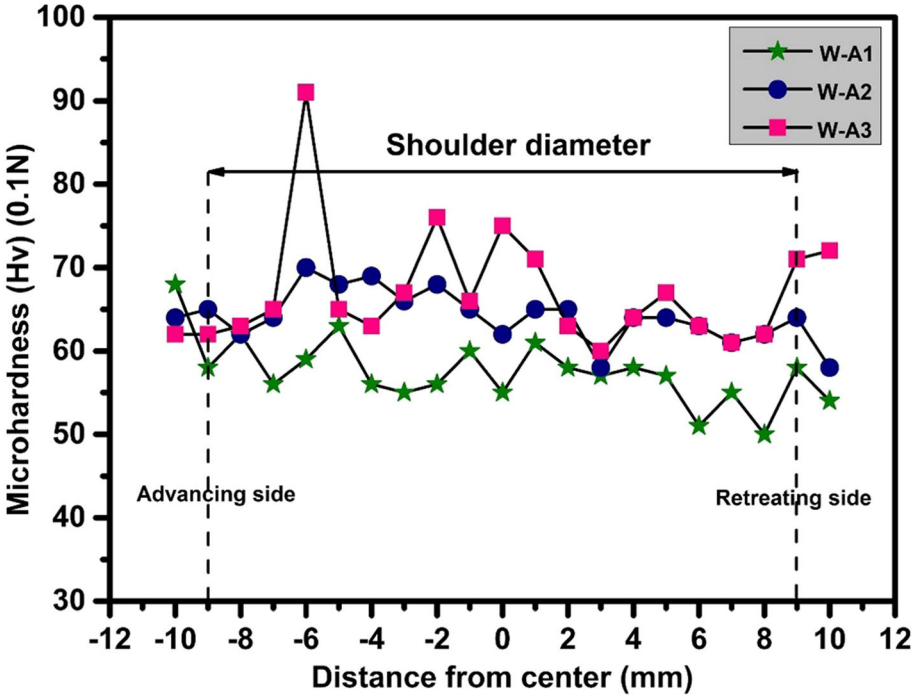

Fig. 12 Microhardness of FSW welds with rotational speed

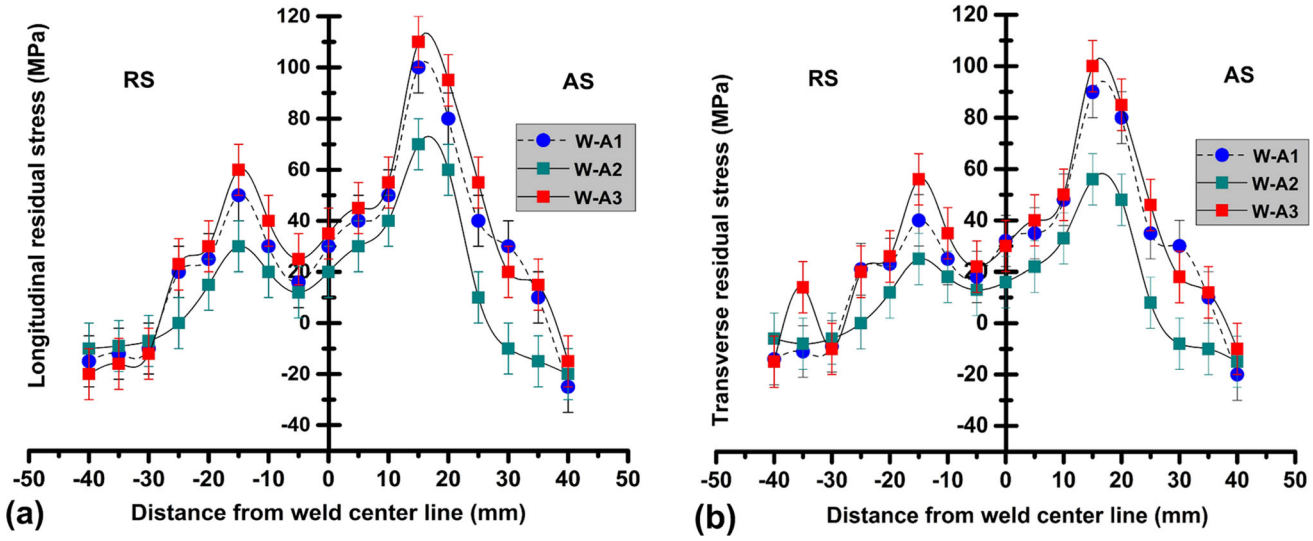

Fig. 13 Residual stress distribution of samples W-A1, W-A2 and W-A3 for (a) longitudinal residual stress, and (b) transverse residual stress

Regions located further from the weld zone edge will experience lower temperatures and less compressive stress, leading to less plastic deformation. Consequently, as you move away from the weld zone edge, the level of tensile residual stress will decrease.

The residual stress distribution in samples welded using different levels of heat input, namely W-A1, W-A2, and W-A3, is depicted in Fig. 13(a) and (b). The longitudinal residual stress on the advancing and retreating sides of samples W-A1, W-A2, and W-A3 is shown in Fig. 13(a), and it has a tensile nature. The residual stress becomes maximum near the tool edge, which is tensile in nature, and then becomes minimum and ends up compressive as it goes away from the weld centre. The transverse residual stress behaves similarly to the longitudinal residual stress, but it has a compressive nature in the centreline of the weld (as shown in Fig. 13b). Moreover, the maximum residual stress in the transverse direction is quite below the longitudinal stress.

The residual stress distribution in the transverse and longitudinal directions is somewhat symmetrical. The highest

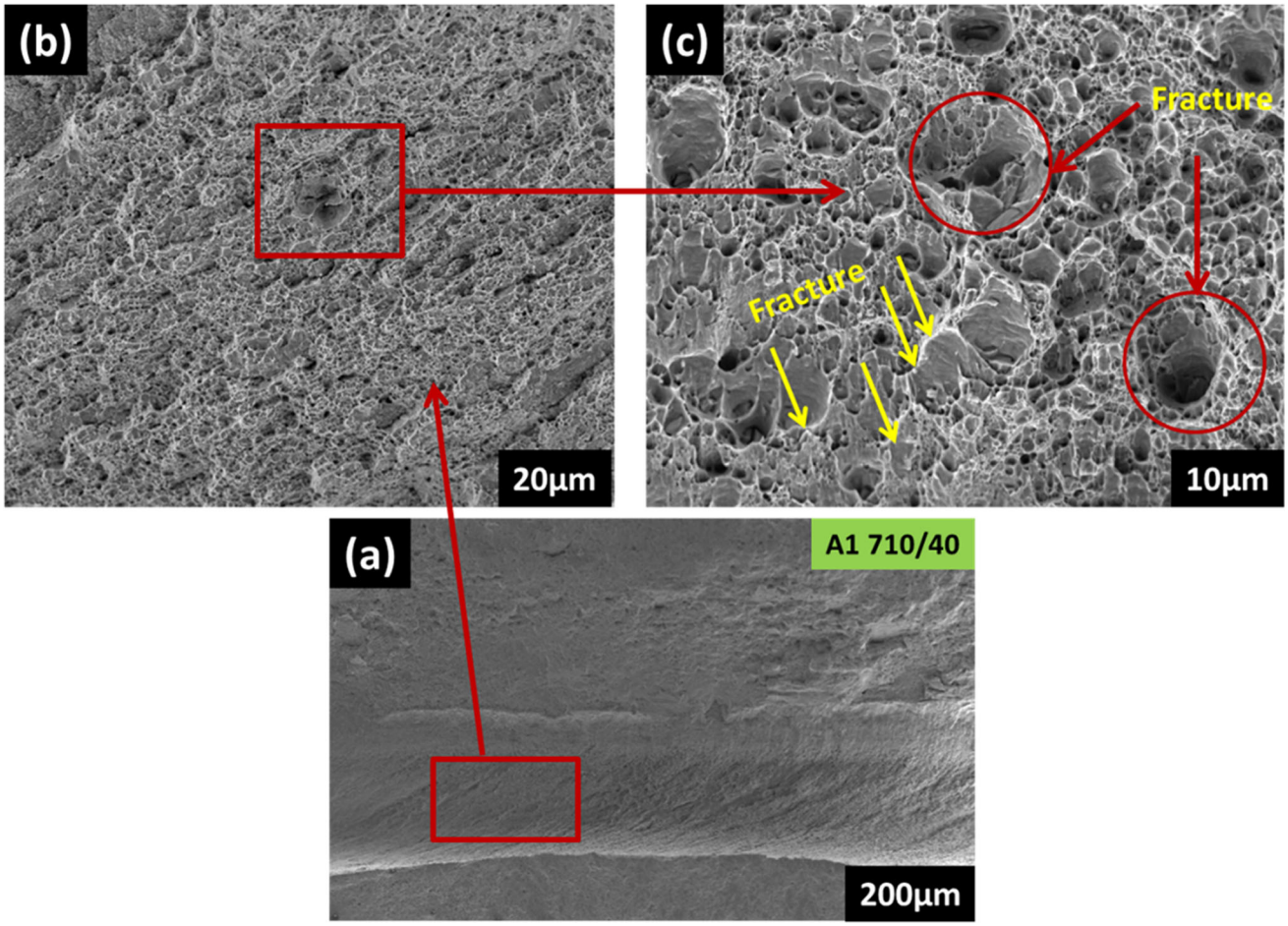

Fig. 14 Microstructure of fracture surface of sample W-A1

tensile residual stress is found on the advancing side of the weld. In addition to this, a significant finding (as depicted in Fig. 13) is that as the welding heat input increases (by increasing the rotational speed), the highest tensile residual stress and the tensile residual stress area size on both sides (advancing and retreating side) also increase, except for sample W-A2. For instance, in samples W-A1, W-A2, and W-A3, the highest tensile residual stresses on the advancing and retreating sides of the welds are 100, 70, and 110 MPa, respectively. Additionally, in samples W-A1, W-A2, and W-A3, the tensile residual stress area size is 60, 50, and 62 mm, respectively (as shown in Fig. 13a).

It can be observed that the distribution of residual stress on the advancing and retreating sides of the HAZ region is a function of the local mechanical characteristics and the varying inhomogeneous distribution of temperature post- and during the welding. Particularly, the HAZ, TMAZ, and SZ of the retreating side with a lesser residual stress distribution (as shown in Fig. 13a and b) also exhibit lower microhardness compared to the regions of the advancing side (as shown in Fig. 12). This is because the moderate heat input on the retreating side results in lower residual stress buildup compared to the advancing side. To put it briefly, the significant residual tensile stress that happens near the weld is caused by an uneven distribution in the way thermal strain is managed whilst being heated and cooled.

3.3 Fracture Analysis

To compare the fracture behaviour of FSWed samples, W-A1, W-A2, and W-A3 were selected for fractography analysis. Typical SEM fractography of the tensile fracture of AA6061-T6 is shown in Fig. 14, 15 and 16. In the case of the low heat generation joint (i.e. W-A1, W-A2), the fracture surface had a dimple appearance characteristic, thus evidencing a ductile behaviour of failure. Whereas, in the case of the high-heat generation weld (i.e. W-A3), lesser dimples were noticeable; moreover, the original elongated contour grains can be recognised. A "river pattern" of radiating shapes is resulted by a mechanism known as cleavage and is typical characterised by a brittle fracture mechanism shown in Fig. 16(b) and (c). The fracture surface displays dimples, cleavage, and crack formation near the grain boundaries, which show the presence of both brittle and ductile natures of the fracture. Ductile fractures are considered to have enormous plastic deformation in advance of fracture compared to brittle fractures.

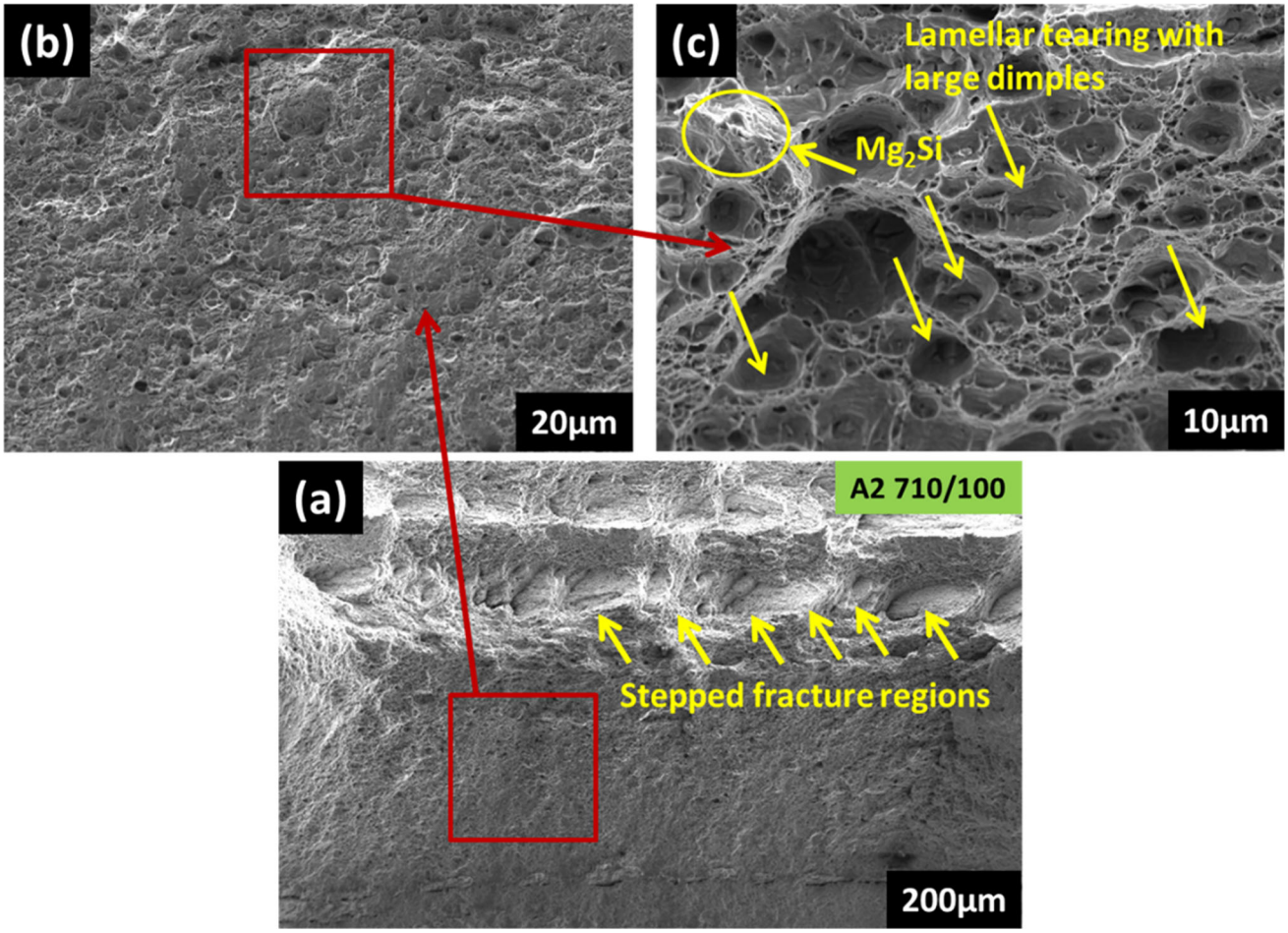

Fig. 15 Microstructure of fracture surface of sample W-A2

The development of dimples at lower rotational speeds, i.e. W-A1 and W-A2, was larger and occupied less area as compared to the dimples formed at higher rotational speeds, i.e. W-A3 (as shown in Fig. 16a, b, and c), because of better mechanical mixing of plasticized materials (Ref 37, 41, 46, 55). It was observed that during the tension test, the sample undergoes diffuse necking followed by local necking. In all cases, various dimples were scattered throughout the fracture surface, showing the ductile nature of the fracture.

4. Conclusions

The effect of linear speed and rotational speed on residual stress, mechanical properties, and microstructure of similar FSWed AA6061-T6 is studied by scanning electron microscopy (SEM), optical microscopy, microhardness, tensile, flexural, and XRD-based residual stress analysis. The findings can be expressed concisely in the following manner:

- XRD results revealed that Mg2Si, Mg5Si6, MgZn2, MgCu2, and Al2CuMg IMCs were formed in various regions, whereas β (Mg2Si) and β″ (Mg5Si6) were found in Si-rich zones and offered favourable conditions for the metallurgical tuning and enhanced the mechanical performances.
- A defect-free joint was obtained for all cases, and the maximum tensile strength of 198 MPa was obtained for sample W-A2 in moderate heat conditions. Proper material mixing and heat input are key factors in enhancing tensile strength. The maximum mechanical joint efficiency with respect to base metal is 84.25%, obtained for sample W-A2, whereas the minimum is for sample W-A1, i.e. 72.77%. Grain size distribution is least for sample W-A2 due to proper stirring, whereas it is minimum for sample W-A1 due to inadequate heat input and improper stirring.
- The joint showed significant plastic deformation, and no surface cracks via the root-face-bend test were obtained for all sets of parameters. The maximum and minimum flexural strengths obtained during the root-bend test were 380 and 340 MPa for W-A2 and W-A1, respectively.
- The maximum value of hardness (i.e. 91 Hv) was observed in the HAZ of sample W-A3 on the advancing side, whereas the maximum microhardness for samples W-A2 and W-A1 was 70 and 61 Hv, respectively.

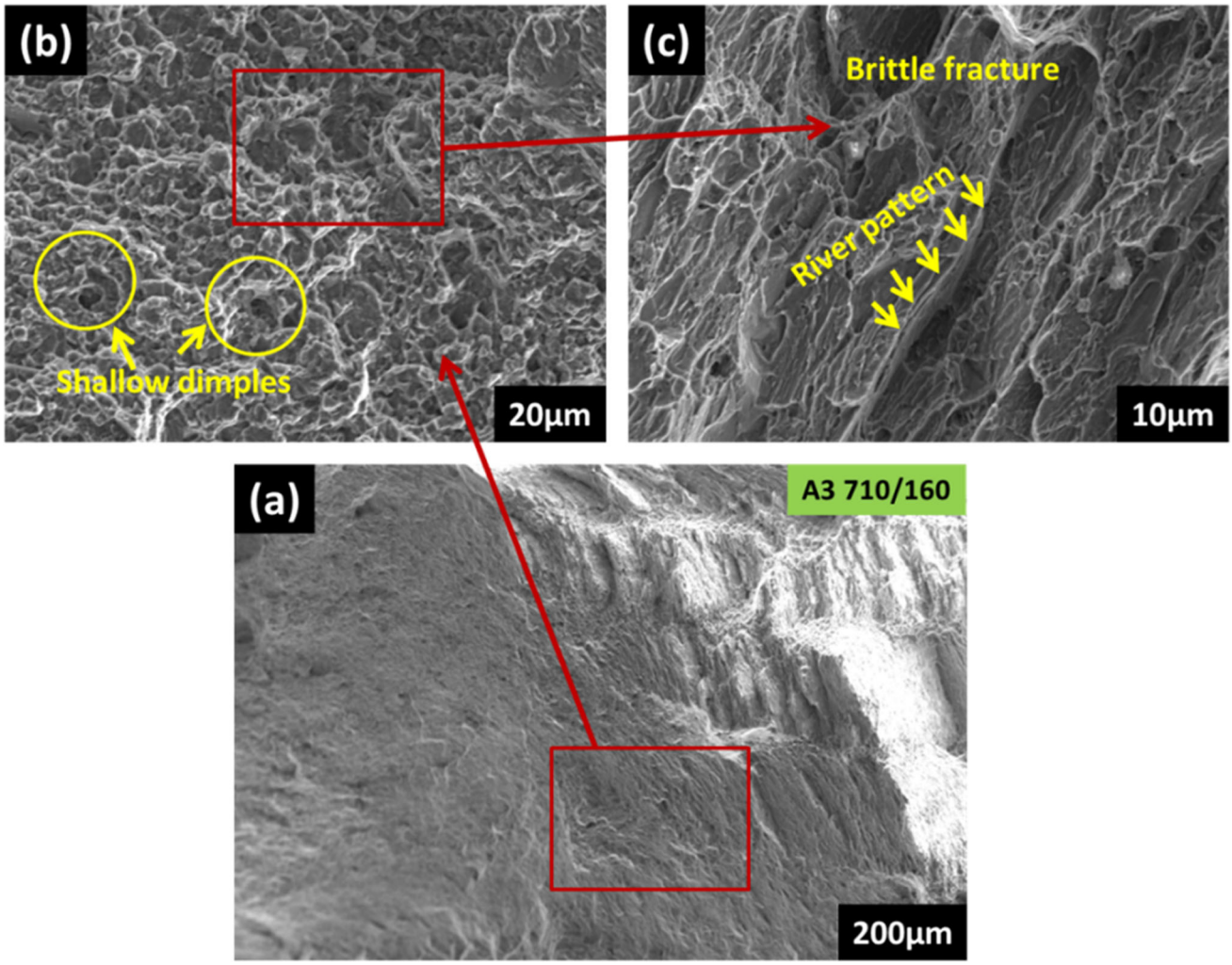

Fig. 16 Microstructure of fracture surface of sample W-A3

- The distribution of residual stress across various zones depends on the local mechanical characteristics and the temperature variations in different weld zones. When the welding heat input is increased, it leads to an increase in the maximum tensile residual stress.
- The longitudinal residual stress in the stir zone is predominantly tensile in nature, and moving away from the centre of the weld, it initially increases until reaching the highest tensile stress near the tool's edge. On the other hand, the transverse residual stress at the weld centre line is compressive in nature. Its maximum value is considerably lower compared to the longitudinal residual stress.

Funding

There is no funding for this research.

Conflict of interest

No conflict of interest.

References

1. A.L. Etter, T. Baudin, N. Fredj, and R. Penelle, Recrystallization Mechanisms in 5251 H14 and 5251 O Aluminum Friction Stir Welds, *Mater. Sci. Eng. A*, 2007, **445**, p 94–99
2. C. Du, X. Wang, Q. Pan, K. Xue, M. Ni, and J. Liu, Correlation Between Microstructure and Mechanical Properties of 6061–T6 Double-Side FSW Joint, *J. Manuf. Process.*, 2019, **38**, p 122–134
3. R.S. Mishra, and Z.Y. Ma, Friction Stir Welding and Processing, *Mater. Sci. Eng. R. Rep.*, 2005, **50**(1–2), p 1–78
4. T. Ding, H. Yan, J. Chen, W. Xia, B. Su,, and H. Zhu, Microstructure Evolution and Recrystallization Mechanisms of High Mg Alloyed Al-Mg Alloy during Friction Stir Welding with Different Cooling Media. J. Mater. Eng. Perform., 2022, p 1–12
5. J. Wang, B. Fu, L. Bergmann, F. Liu, and B. Klusemann, Effect of Welding Speed on Friction Stir Welds of PM2000 Alloy, *J. Mater. Eng. Perform.*, 2023, **32**(2), p 577–586
6. A.K. Kadian and P. Biswas, The Study of Material Flow Behaviour in Dissimilar Material FSW of AA6061 and Cu-B370 Alloys Plates, *J. Manuf. Process.*, 2018, **34**, p 96–105
7. S. Ravikumar, V.S. Rao, and R.V. Pranesh, Effect of Process Parameters on Mechanical Properties of Friction Stir Welded Dissimilar Materials Between AA6061-T651 and AA7075-T651 Alloys, *Int. J. Adv. Mech. Eng.*, 2014, **4**(1), p 101–114
8. M.M. Moradi, H.J. Aval, and R. Jamaati, Effect of Pre and Post Welding Heat Treatment in SiC-Fortified Dissimilar AA6061-AA2024 FSW Butt Joint, *J. Manuf. Process.*, 2017, **30**, p 97–105
9. J.F. Guo, H.C. Chen, C.N. Sun, G. Bi, Z. Sun, and J. Wei, Friction Stir Welding of Dissimilar Materials Between AA6061 and AA7075 Al

Alloys Effects of Process Parameters, *Mater. Des.*, 2014, **1980–2015**(56), p 185–192
10. Y. Ni, L. Fu, Z. Shen, and X.C. Liu, Role of Tool Design on Thermal Cycling and Mechanical Properties of a High-Speed Micro Friction Stir Welded 7075–T6 Aluminum Alloy, *J. Manuf. Process.*, 2019, **48**, p 145–153
11. P. Talebizadehsardari, F. Musharavati, A. Khan, T.A. Sebaey, A. Eyvaziana, and H.A. Derazkola, Underwater Friction Stir Welding of Al-Mg Alloy: Thermo-Mechanical Modeling and Validation, *Mater. Today Commun.*, 2021, **26**, p 101965
12. A. Tavassolimanesh and A.A. Nia, A New Approach for Manufacturing Copper-Clad Aluminum Bimetallic Tubes by Friction Stir Welding (FSW), *J. Manuf. Process.*, 2017, **30**, p 374–384
13. S.W. Williams and A. Steuwer, Residual stresses in friction stir welding. In Friction Stir Welding. Woodhead Publishing. 2010 p 215–244
14. M. Kotobi and M. Honarpisheh, Experimental and Numerical Investigation of Through-Thickness Residual Stress of Laser-Bent Ti Samples, *J. Strain Anal. Eng. Des.*, 2017, **52**(6), p 347–355
15. M. Honarpisheh, E. Haghighat, and M. Kotobi, Investigation of Residual Stress and Mechanical Properties of Equal Channel Angular Rolled St12 Strips, *Proc. Inst. Mech. Eng. Part L: J. Mater. Des. Appl.*, 2018, **232**(10), p 841–851
16. M. Honarpisheh and H. Khanlari, A Numerical Study on the Residual Stress Measurement Accuracy using Inverse Eigenstrain Method, *J. Stress Anal.*, 2018, **2**(2), p 1–10
17. F. Nazari, M. Honarpisheh, and H. Zhao, Effect of Stress Relief Annealing on Microstructure, Mechanical Properties, and Residual Stress of a Copper Sheet in the Constrained Groove Pressing Process, *Int. J. Adv. Manuf. Technol.*, 2019, **102**, p 4361–4370
18. M. Sedighi and M. Honarpisheh, Experimental Study of Through-Depth Residual Stress in Explosive Welded Al–Cu–Al Multilayer, *Mater. Des.*, 2012, **37**, p 577–581
19. M. Sedighi and M. Honarpisheh, Investigation of Cold Rolling Influence on Near Surface Residual Stress Distribution in Explosive Welded Multilayer, *Strength Mater.*, 2012, **44**, p 693–698
20. M.S. Węglowski, P. Sedek, and C. Hamilton, Experimental Analysis of Residual Stress in Friction Stir Processed Cast AlSi9Mg Aluminium Alloy, *Key Eng. Mater.*, 2016, **682**, p 18–23
21. C. Hamilton, M.S. Węglowski, S. Dymek, and P. Sedek, Using a Coupled Thermal/Material Flow Model to Predict Residual Stress in Friction Stir Processed AlMg9Si, *J. Mater. Eng. Perform.*, 2015, **24**, p 1305–1312
22. N. Zhu, D.Z. Avery, Y. Chen, K. An, J.B. Jordon, P.G. Allison, and L.N. Brewer, Residual Stress Distributions in AA6061 Material Produced by Additive Friction Stir Deposition. J. Mater. Eng. Perform. 2022, p 1–10
23. A. Tognan, L. Sandnes, G. Totis, M. Sortino, F. Berto, Ø. Grong, and E. Salvati, Evaluation and Origin of Residual Stress in Hybrid Metal and Extrusion Bonding and Comparison with Friction Stir Welding, *Int. J. Mech. Sci.*, 2022, **218**, p 107089
24. I. Alinaghian, S. Amini, and M. Honarpisheh, Residual Stress, Tensile Strength, and Macrostructure Investigations on Ultrasonic Assisted Friction Stir Welding of AA 6061–T6, *J. Strain Anal. Eng. Des.*, 2018, **53**(7), p 494–503
25. C. Dalle Donne, E. Lima, J. Wegener, A. Pyzalla, T. Buslaps, Investigations on Residual Stresses in Friction Stir Welds, in 3rd International Symposium on Friction Stir Welding 2001; Vol. 27
26. Y.E. Ma, P. Staron, T. Fischer, and P.E. Irving, Size Effects on Residual Stress and Fatigue Crack Growth in Friction Stir Welded 2195–T8 Aluminium–Part I: Experiments, *Int. J. Fatigue*, 2011, **33**(11), p 1417–1425
27. K.K. Kumar, A. Kumar, and M.V.N.V. Satyanarayana, Effect of Friction stir Welding Parameters on the Material flow, Mechanical Properties and Corrosion Behavior of Dissimilar AA5083-AA6061 Joints, *Proc. Inst. Mech. Eng. C J. Mech. Eng. Sci.*, 2022, **236**(6), p 2901–2917
28. J. Dong, D. Zhang, W. Zhang, G. Cao, and C. Qiu, Effect of Post-Weld Heat Treatments on the Microstructure and Mechanical Properties of Underwater Friction Stir Welded Joints of 7003–T4/6060-T4 Aluminium Alloys, *Mater. Sci. Eng., A*, 2023, **862**, p 144423
29. K.K. Kumar, A. Kumar, and S. Sundar, Investigation of Microstructure Characteristics and Work Hardening Behaviour of Water-Cooled FSW Dissimilar Aluminium Alloys, *Mater. Today Commun.*, 2023, **35**, p 105857
30. K. Elangovan, V. Balasubramanian, and S. Babu, Predicting Tensile Strength of Friction Stir Welded AA6061 Aluminium Alloy Joints by a Mathematical Model, *Mater. Des.*, 2009, **30**(1), p 188–193
31. F.J. Humphreys, A Unified Theory of Recovery, Recrystallization and Grain Growth, Based on the Stability and Growth of Cellular Microstructures—I. The Basic Model, *Acta Mater.*, 1997, **45**(10), p 4231–4240
32. F.J. Humphreys, A Unified Theory of Recovery, Recrystallization and Grain Growth, Based on the Stability and Growth of Cellular Microstructures—II. The Effect of Second-Phase Particles, *Acta Mater.*, 1997, **45**(12), p 5031–5039
33. K.A. Hassan, A.F. Norman, D.A. Price, and P.B. Prangnell, Stability of Nugget Zone Grain Structures in High Strength Al-Alloy Friction Stir Welds during Solution Treatment, *Acta Mater.*, 2003, **51**(7), p 1923–1936
34. U.F.H.R. Suhuddin, S. Mironov, Y.S. Sato, H. Kokawa, and C.W. Lee, Grain Structure Evolution during Friction-Stir Welding of AZ31 Magnesium Alloy, *Acta Mater.*, 2009, **57**(18), p 5406–5418
35. R. Dubey, R. Jayaganthan, D. Ruan, N.K. Gupta, N. Jones, and R. Velmurugan, (2022). Energy Absorption and Dynamic Behaviour of 6xxx Series Aluminium Alloys: A review. Int. J. Impact Eng., 2022, p 104397
36. V.P. Singh, S.K. Patel, A. Ranjan, and B. Kuriachen, Recent Research Progress in Solid State Friction-Stir Welding of Aluminium–Magnesium Alloys: A Critical Review, *J. Market. Res.*, 2020, **9**(3), p 6217–6256
37. V.P. Singh, S.K. Patel, N. Kumar, and B. Kuriachen, Parametric Effect on Dissimilar Friction Stir Welded Steel-Magnesium Alloys Joints: A Review, *Sci. Technol. Weld. Join..*, 2019, **24**, p 653–684
38. C.H.E.N. Yu, D.I.N.G. Hua, J.Z. Li, J.W. Zhao, M.J. Fu, and X.H. Li, Effect of Welding Heat Input and post-Welded Heat Treatment on Hardness of Stir Zone for Friction Stir-Welded 2024–T3 Aluminum Alloy, *Trans. Nonferr. Metals Soc. China*, 2015, **25**(8), p 2524–2532
39. C. Leitao, R.M. Leal, D.M. Rodrigues, A. Loureiro, and P. Vilaça, Mechanical Behaviour of Similar and Dissimilar AA5182-H111 and AA6016-T4 Thin Friction Stir Welds, *Mater. Des.*, 2009, **30**(1), p 101–108
40. M. Paidar, A. Khodabandeh, H. Najafi, and A.S. Rouh-aghdam, Effects of the Tool Rotational Speed and Shoulder Penetration Depth on Mechanical Properties and Failure Modes of Friction Stir Spot Welds of Aluminum 2024–T3 Sheets, *J. Mech. Sci. Technol.*, 2014, **28**, p 4893–4898
41. V.P. Singh, S.K. Patel, and B. Kuriachen, Mechanical and Microstructural Properties Evolutions of Various Alloys Welded Through Cooling Assisted Friction-Stir Welding: A Review, *Intermetallics*, 2021, **133**, p 107122
42. V.P. Singh and B. Kuriachen, Experimental Investigations Into the Mechanical and Metallurgical Characteristics of Friction Stir Welded AZ31 Magnesium Alloy. J. Mater. Eng. Perform. 2022, p 1–17
43. V.P. Singh, D. Kumar, R.P. Mahto, and B. Kuriachen, Microstructural and Mechanical Behavior of Friction-Stir-Welded AA6061-T6 and AZ31 Alloys with Improved Electrochemical Corrosion, *J. Mater. Eng. Perform.*, 2023, **32**(9), p 4185–4204
44. B. Kulkarni, S. Pankade, S. Tayde, and S. Bhosle, Corrosion and Mechanical Aspects of Friction Stir Welded AA6061 joints: Effects of Different Backing Plates, *J. Mater. Eng. Perform.*, 2023 https://doi.org/10.1007/s11665-023-07900-x
45. P. Prakash, R.S. Anand, and S.K. Jha, Experimental Analysis of Tensile Strength of Different Thicknesses and Dissimilar Aluminum Alloys in Friction Stir Welding, *J. Mater. Eng. Perform.*, 2022 https://doi.org/10.1007/s11665-022-07694-4
46. W. Xu, J. Liu, G. Luan, and C. Dong, Microstructure and Mechanical Properties of Friction Stir Welded Joints in 2219–T6 Aluminum Alloy, *Mater. Des.*, 2009, **30**(9), p 3460–3467
47. K. Dehghani, R. Ghorbani, and A.R. Soltanipoor, Microstructural Evolution and Mechanical Properties during the Friction Stir Welding of 7075-O Aluminum Alloy, *Int. J. Adv. Manufact. Technol.*, 2015, **77**, p 1671–1679
48. L.I. Tian, D.W. Zhou, Y.A.N. You-rui-ling, P.E.N.G. Ping, and J.S. Liu, First-principles and Experimental Investigations on Ductility/Brittleness of Intermetallic Compounds and Joint Properties in Steel/

Aluminum Laser Welding, *Trans. Nonferr. Metals Soc. China*, 2021, **31**(10), p 2962–2977

49. V. Msomi and N. Mbana, Mechanical Properties of Friction Stir Welded AA1050-H14 and AA5083-H111 Joint: Sampling Aspect, *Metals*, 2020, **10**(2), p 214
50. H.I. Dawood, K.S. Mohammed, A. Rahmat, and M.B. Uday, The Influence of the Surface Roughness on the Microstructures and Mechanical Properties of 6061 Aluminium Alloy using Friction Stir Welding, *Surf. Coat. Technol.*, 2015, **270**, p 272–283
51. A. Scialpi, M. De Giorgi, L.A.C. De Filippis, R. Nobile, and F.W. Panella, Mechanical Analysis of Ultra-Thin Friction Stir Welding Joined Sheets with Dissimilar and Similar Materials, *Mater. Des.*, 2008, **29**(5), p 928–936
52. P.M.G.P. Moreira, T. Santos, S.M.O. Tavares, V. Richter-Trummer, P. Vilaça, and P.M.S.T. De Castro, Mechanical and Metallurgical Characterization of Friction Stir Welding Joints of AA6061-T6 with AA6082-T6, *Mater. Des.*, 2009, **30**(1), p 180–187
53. T. Hirata, T. Oguri, H. Hagino, T. Tanaka, S.W. Chung, Y. Takigawa, and K. Higashi, Influence of Friction Stir Welding Parameters on Grain Size and Formability in 5083 Aluminum Alloy, *Mater. Sci. Eng., A*, 2007, **456**(1–2), p 344–349
54. G.R. Babu, K.G.K. Murti, and G.R. Janardhana, An Experimental Study on the Effect of Welding Parameters on Mechanical and Microstructural Properties of AA 6082–T6 Friction Stir Welded Butt Joints, *ARPN J. Eng. Appl. Sci.*, 2008, **3**(5), p 68–73
55. G. Madhusudhan Reddy, P. Mastanaiah, K. Sata Prasad, and T. Mohandas, Microstructure and Mechanical Property Correlations in AA 6061 Aluminium Alloy Friction Stir Welds, *Trans. Indian Inst. Met.*, 2009, **62**, p 49–58

Publisher's Note Springer Nature remains neutral with regard to jurisdictional claims in published maps and institutional affiliations.

Springer Nature or its licensor (e.g. a society or other partner) holds exclusive rights to this article under a publishing agreement with the author(s) or other rightsholder(s); author self-archiving of the accepted manuscript version of this article is solely governed by the terms of such publishing agreement and applicable law.

Journal Pre-proof

Efficient tunable temperature sensitivity in thermally coupled levels of Er^{3+}/Yb^{3+} co-doped $BaBi_2Nb_2O_9$ ferroelectric ceramic

Ankita Banwal, Renuka Bokolia

PII: S0022-2313(23)00404-0

DOI: https://doi.org/10.1016/j.jlumin.2023.120071

Reference: LUMIN 120071

To appear in: *Journal of Luminescence*

Received Date: 15 May 2023

Revised Date: 5 July 2023

Accepted Date: 15 July 2023

Please cite this article as: A. Banwal, R. Bokolia, Efficient tunable temperature sensitivity in thermally coupled levels of Er^{3+}/Yb^{3+} co-doped $BaBi_2Nb_2O_9$ ferroelectric ceramic, *Journal of Luminescence* (2023), doi: https://doi.org/10.1016/j.jlumin.2023.120071.

This is a PDF file of an article that has undergone enhancements after acceptance, such as the addition of a cover page and metadata, and formatting for readability, but it is not yet the definitive version of record. This version will undergo additional copyediting, typesetting and review before it is published in its final form, but we are providing this version to give early visibility of the article. Please note that, during the production process, errors may be discovered which could affect the content, and all legal disclaimers that apply to the journal pertain.

© 2023 Published by Elsevier B.V.

Journal Pre-proof

Efficient tunable temperature sensitivity in thermally coupled levels of Er^{3+}/Yb^{3+} co-doped $BaBi_2Nb_2O_9$ ferroelectric ceramic

Ankita Banwal[a], Renuka Bokolia[a]*
[a]Delhi Technological University, Delhi, India-110042

Abstract: Er^{3+}/Yb^{3+} co-doped ferroelectric ceramic $BaBi_{2-0.04-y}Nb_2Er_{0.04}Yb_yO_9$ (y = 0.00, 0.02, 0.04, 0.06, 0.08, 0.10, and 0.12) are prepared by solid-state method and investigated for their structural and upconversion luminescence properties. High-resolution X-ray pattern investigation confirmed the ceramic's orthorhombic structure. Microstructure of sintered ceramic surface resembles plate-like structures and consists of non-uniform grains that are randomly oriented. Upconversion luminescence (UCL) spectra revealed two prominent green emission bands near 535 and 557 nm and a notable red band at 672 nm, corresponding to a 980 nm excitation wavelength. Decay time measurements support the effective energy transfer from Yb^{3+} to Er^{3+} ions. The average lifetime increases with increasing Er^{3+} / Yb^{3+} doping concentration up to the optimal concentration (y = 0.10). Pump power dependence demonstrates that two photons are required to generate green and red UC illumination. The absolute sensitivity, S_a (0.69% K^{-1} and 0.58% K^{-1}) and relative sensitivity, S_r (1.1% K^{-1} and 1.01% K^{-1}) have been recorded for the first time on Er/Yb co-doped $BaBi_{2-0.04-y}Nb_2Er_{0.04}Yb_yO_9$ ceramic at y = 0.06 and 0.10, respectively, suggesting it is a viable non-contact sensor ceramic whose sensitivity can be tuned by varying dopant concentrations.

Keywords: Thermal sensing; time decay; pump power; upconversion luminescence; ceramic; SEM; XRD.

1. Introduction

The ongoing investigations on trivalent rare earth (RE^{3+}) ion-doped ferroelectrics at nanoscale dimensions have attracted considerable interest [1-5]. The nanomaterials doped with optically active centres have enhanced structural, electrical, and sensor capabilities as well as better optical features. By taking advantage, near-infrared to visible upconversion luminescence in nanomaterials has lately received considerable interest for a variety of potential applications [6, 7]. Most of these potential applications involve infrared quantum counter detectors, 3D displays, biological medicine, optic fibre communications, optical data storage, and others [2]. Furthermore, the need for low-cost and sustainable materials that can perform several functions led researchers to consider multifunctional and hybrid materials. Ferroelectrics are a non-toxic and environmentally benign alternative to lead-based ceramics, making them a superior replacement option. The selection of this material as a host is particularly promising because of its low phonon energy, which is important for decreasing radiative transitions to facilitate an efficient upconversion process [8-10]. Layered bismuth structure ferroelectric (BLSF) materials are steadily gaining prominence due to their favourable chemical and thermic immovability, excellent radiation shifts, decreased phonon power, and increased sensing capability over a broad thermal limit. The ferroelectrics (BLSF) are a unique class of ferroelectrics that follow a standard formula $(Bi_2O_2)^{2+}$ $(A_{n-1}B_nO_{3n+1})^{2-}$. The quasi perovskite layer, designated by the formula $A_{n-1}B_nO_{3n+1}$, is surrounded by two bismuth oxide layers, $(Bi_2O_2)^{2+}$; n is the total octahedral sheets present within the perovskite unit. A is used to indicate ions with tripled, dual, or single valence ions (such as Sr^{2+}, Bi^{3+}, or Ba^{2+}), while B is used to represent ions with a higher valence (such as Nb^{5+}, Ta^{5+}, Ti^{4+}, or W^{6+}) [11-14].

According to the findings of the literature study, the electrical, optical, and sensing properties of BLSF materials were enhanced after being suitably doped with RE ions. Because of developments in the industry and technological advancements, temperature sensing has received significant attention in recent years. The necessity for a non-contact temperature sensor becomes apparent in areas such as electrical transformers in power plants, oil refineries, and coal mines where typical temperature measuring instruments are prohibited. It is challenging for today's researchers working

in the field of RE-doped materials to create high-temperature sensing material with a significant level of sensitivity. For instance, Luo et al. studied Er^{3+}/Yb^{3+} co-doped $Ba_2NaNb_5O_{15}$ glass ceramics for UC luminescence, thermal sensing, and energy storage performance [15]. Also, in a previous report, Er^{3+}/Yb^{3+} co-doped tungsten tellurite glass was used to make a temperature sensor with an absolute sensibility of around 28.72×10^{-4} K^{-1} at 690 K along with decent green emission luminescence [16]. Swami et al. studied the luminescence intensity ratio of Yb^{3+}/Er^{3+} co-doped La_2TiO_7 ceramics and reported an absolute sensitivity value of around 0.0029 K^{-1} at 498 K [17]. In addition, Peng et al. fabricated Yb^{3+}/Er^{3+} co-doped BNT across a wide temperature range and determined a sensitivity of approximately 0.0049 K^{-1} at 363 K [18].

During our research, we concluded that the best dopants for us to use would be Er^{3+} and Yb^{3+}. This choice was made because Er^{3+} is the most prevalent and efficient activator for producing upconversion luminescence due to its extensive and long-lived intermediate energy levels. Er^{3+} acts as a luminescence upconversion activator. It is simpler to achieve the migration of electrons inside the 4f-4f energy level and generate a rich emission band in Er^{3+} because it has more unpaired 4f-layer orbital electrons than Sc^{3+}, Y^{3+}, La^{3+}, and Lu^{3+}. When Er^{3+} is put in an environment with a different matrix or ligand, there is a chance that the crystal symmetry and crystal field of the matrix around Er^{3+} may change. This will, in turn, affect the photoluminescence emission [19]. In most cases, the Yb^{3+} ion is utilized as a sensitizer to raise the absorption cross-section to improve the upconversion efficiency. Therefore, we systematically replaced the bismuth ions in our host material $BaBi_2Nb_2O_9$ with erbium and ytterbium ions, and then we utilized X-ray powder diffraction to examine the resultant compound's configuration. For the UC emission investigations, a wavelength of 980 nm was selected as the excitation wavelength. Additionally, the pump power dependency on UC intensity was analyzed to determine the involvement of the number of photons in the UC process. The temperature sensing characteristics of a single Er^{3+} doped $BaBi_2Nb_2O_9$ ceramic system has been reported in our previous work [20]. The intense green emission occurs at x = 0.04 which is the optimum concentrationof Er^{3+} in $BaBi_2Nb_2O_9$ ceramic [20]. The decent sensitivity and upconversion luminescence behaviour of Er^{3+} doped $BaBi_2Nb_2O_9$ ceramic has motivated us to investigate it thoroughly, so we co-doped $BaBi_2Nb_2O_9$ with Yb^{3+} by keeping the Er^{3+} constant at optimum concentration (x = 0.04) throughout the synthesis. Also, as far as the author's knowledge, there is no study on the sensing behavior of Er^{3+}/Yb^{3+} co-doped $BaBi_2Nb_2O_9$ host matrix system over a wide temperature range in thermally coupled levels ($^2H_{11/2}$ and $^4S_{3/2}$). In light of this, we investigated the fluorescence intensity ratio (FIR) approach for temperature sensing capabilities in the 303-573 K range to establish the applicability of the ceramic design suited for optoelectronic devices.

2. Synthesis and characterization descriptions

The solid-state approach synthesized the ceramics with the configuration $BaBi_{2-0.04-y}Nb_2Er_{0.04}Yb_yO_9$ (y = 0.02, 0.04, 0.06, 0.08, 0.10, and 0.12). Fig. 1 depicts a schematic representation of the fabrication of the ceramic. The initial precursors ($BaCO_3$, Bi_2O_3, Nb_2O_5, Er_2O_3, and Yb_2O_3) were obtained from Sigma Aldrich and had the greatest possible purity level (99.99 %). The precursors were measured and weighed according to their stoichiometric proportions. The raw powders were manually crushed using a pestle and mortar in ethanol for 8h before being sent to a regulated high-temperature furnace that operated at 950°C for 3h. After being calcined, the granules were combined with polyvinyl alcohol (PVA), which was used to form the pellets in a circular shape. The round pellets of 10 mm in diameter were constructed by applying a pressure of approximately 5 MPa for 1 minute in a manual hydraulic press. After the pellets were made, they were sintered in two stages: firstly, rise to 500°C/h to eliminate the PVA, then reach about 1050°C and held there for 2h. Cu-Kα radiations are used in conjunction with a sophisticated X-ray diffractometer manufactured by Bruker to investigate the phase structure of the sample. The upconversion luminescence (UCL) spectra were acquired with the help of the HORIBA PTI Quanta-master under the wavelength of 980 nm laser. The SEM micrographs from the cracked pallet sample were obtained using a ZEISS scanning electron

microscope. The thermally dependent UCL emitting spectra were studied by positioning the synthesized material on the heaters while using a thermocouple to measure the temperature. The handcrafted heater that was controlled by variable voltage and coupled with a thermocouple and multimeter was used for the thermal sensing, resolution, and stability studies that were carried out.

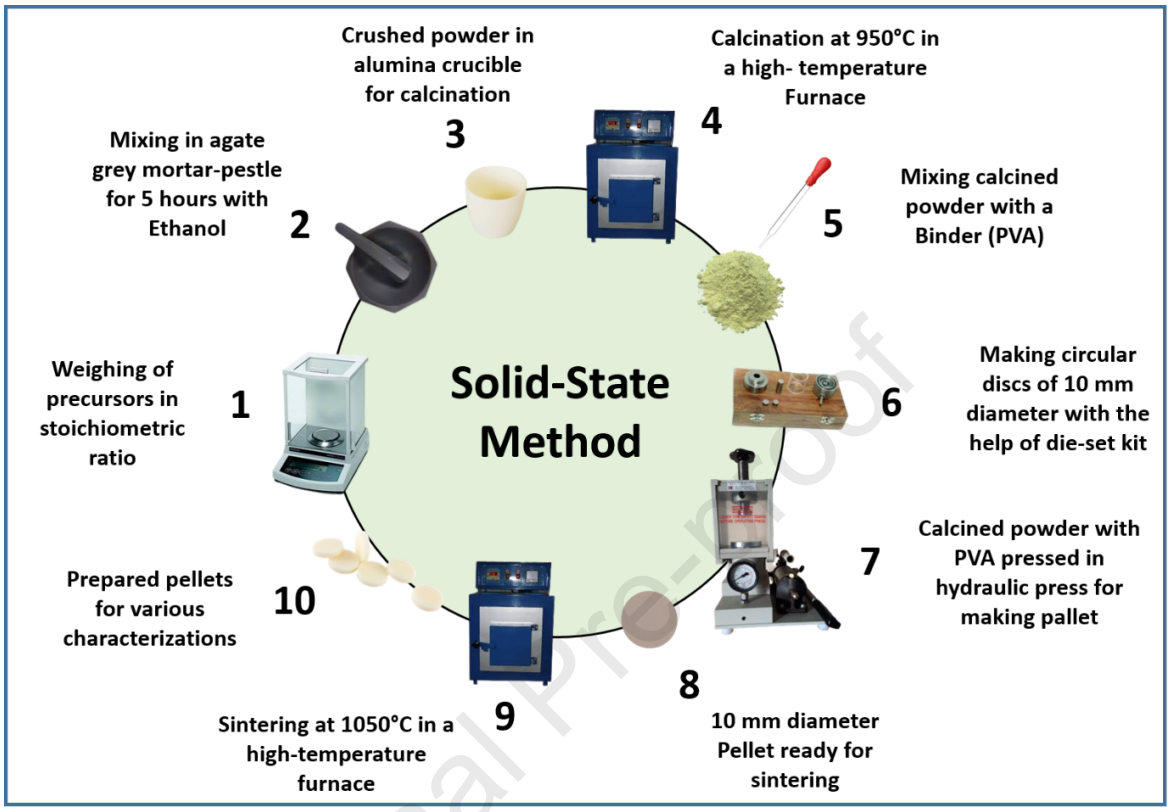

Fig. 1 Schematic diagram of the synthesis process.

3. Results and analysis

3.1 Structural and microstructural analysis

The XRD pattern of the prepared composition $BaBi_{2-0.04-y}Nb_2Er_{0.04}Yb_yO_9$ (y = 0.00, 0.02, 0.04, 0.06, 0.08, 0.10, and 0.12) was exhibited in Fig. 2(a) after being sintered at a temperature of 1050 ℃ for 3 hours. The detected XRD peaks show a good correlation, as stated in the JCPDF file no. 00-012-0403, and the lack of secondary peaks implies that the dopants are fully soluble in the host lattice without causing structural modifications or other drastic changes. The detected Bragg reflections showed that the prepared ceramic had a single phase with an orthorhombic geometry and belonged to the phase group Fmmm. Also, the maximum peak intensity of the (115) plane in $BaBi_{2-0.04-y}Nb_2Er_{0.04}Yb_yO_9$ ceramic reflects the BLSF with m = 2, according to previous reports, the (112m + 1) plane relates to the high-intensity diffraction pattern for BLSF materials in the Aurivillius phase. [21, 22]. The ionic radii of Er^{3+} and Yb^{3+} are similar to one another such that the ions Yb^{3+} (1.22 Å) and Er^{3+} (1.25 Å) may favor occupying A-sites (Bi^{3+}) rather than B-sites (Nb^{5+}). This is because their effective ionic radii are the same as A site ions [6]. The density of sintered pellets was calculated using Archimedes' principle and recorded in Table 1. It was found that the density of the sintered pellets decreases with increasing dopant concentration. The tension within the host lattice due to the insertion of dopants causes the shifting of diffraction peaks slightly from their mean position and is given by Eq. (1) [20]:

$$\sigma = \frac{E}{2\upsilon}\left[\frac{\mathrm{Sin}\theta_n}{\mathrm{Sin}\theta_i} - 1\right] \quad (1)$$

where υ represents Poison's coefficient, E is the modulus of elasticity, θ_n is the displaced value of 2θ, and θ_i is the reference angle. Eq. (1) states that a positive σ indicates lattice compression, whereas a negative σ suggests lattice expansion after dopant substitution. Fig. 2(b) represents the shifting of peaks to slightly lower 2θ angles. In our case, $\theta_n < \theta_i$ (E and υ are constants). Therefore, σ comes out to be negative. This implies the expansion within the crystal lattice, which can also be verified from the increased cell volume parameters of the doped $BaBi_2Nb_2O_9$ ceramic, as shown in Table 1. This can also be explained by the constrained character of 6s2 lone-pair of Bi3+ ions in the host lattice which causes the expansion of unit cell volume and shifting of the peaks towards lower 2 theta [6, 8].The increased cell volume parameters (a, b, c) suggest the increased interplanar spacing, which decreases the 2θ values. Although the ionic radius of Er^{3+}, Yb^{3+}, and Bi^{3+} varies, the cell volume and lattice parameters (a, b, c) of undoped $BaBi_2Nb_2O_9$ do not vary significantly. This could be ascribed to the formation of cationic vacancies, which maintain the lattice's electroneutrality and minimize crystal deformation [5].

The scanning electron microscopy images (SEIs) of the $BaBi_{2-0.04-y}Nb_2Er_{0.04}Yb_yO_9$ ceramics are shown in Fig. 3(a-g). These sintered ceramics possess a compact microstructure. These plate-like structures are composed of irregularly aligned non-uniform grains. This is consistent with the standard properties of BLSFs. In Table 1, the reduction in porosity suggests that as the dopant concentration rises, the ceramic becomes denser. ImageJ software performs the necessary calculations to estimate the average particle size. In Fig. 3(h), the average grain size increases up to the optimum dopant concentration (y = 0.10), and then there is a subsequent reduction in the average grain size. This grain size variation may result from a rise in the electron charge distribution on the interface of Er^{3+}/ Yb^{3+}. Thie increase in electron charge density slows grain boundary diffusion and inhibits grain development, resulting in smaller grain sizes [23, 24].

Table 1: Lattice parameters for $BaBi_{2-0.04-y}Nb_2Er0_{0.04}Yb_yO_9$ compositions with constant Er^{3+} content (0.04) and varying Yb^{3+} content (y = 0.00, 0.02, 0.04, 0.06, 0.08, 0.10 and 0.12):

Parameters	**$BaBi_{2-0.04-y}Nb_2Er_{0.04}Yb_yO_9$**						
	y = 0.00	**y = 0.02**	**y = 0.04**	**y = 0.06**	**y = 0.08**	**y = 0.10**	**y = 0.12**
a (Å)	5.5439	5.5448	5.5450	5.5454	5.5479	5.5488	5.5497
b (Å)	5.5536	5.5551	5.5552	5.5561	5.5601	5.5612	5.5600
c (Å)	25.5975	25.5980	25.5989	25.5991	25.6178	25.6200	25.6219
V (Å^3)	788.111	788.467	788.537	788.728	790.229	790.581	790.597
Orthorhombic distortion (b/a)	1.00174	1.00185	1.00183	1.00192	1.00219	1.00223	1.00185
Experimental Density, ρ (g/cm^3)	7.00919	6.83796	6.72015	6.77289	6.47426	6.76007	6.0106
Theoretical density, ρ_0 (g/cm^3)	5.82447	5.88589	5.81015	5.9373	5.79818	5.94532	5.24095
Porosity $(1-\rho_0/\rho)\times100\%$	16.90	13.92	13.54	12.33	10.44	12.05	12.80
Average grain size (μm)	1.39 ± 0.0278	1.54 ± 0.0125	1.67 ± 0.1365	1.78 ± 0.0889	1.89 ± 0.1129	1.92 ± 0.1761	1.45 ± 0.0295

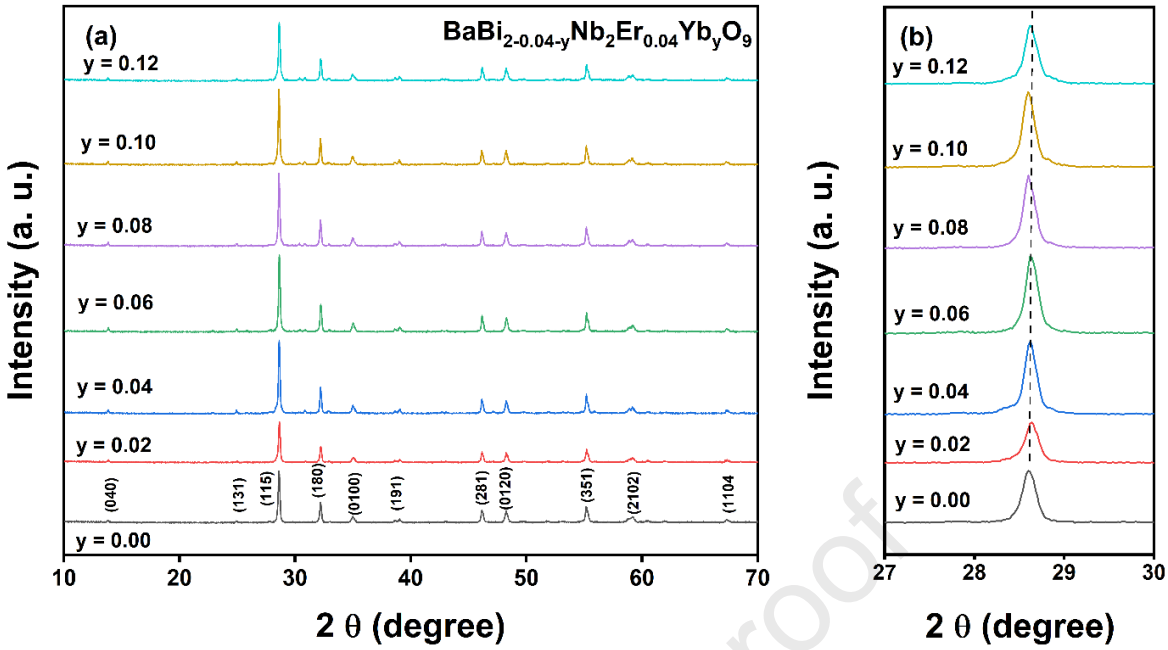

Fig. 2 (a) XRD spectra of $BaBi_{2-0.04-y}Nb_2Er_{0.04}Yb_yO_9$ (y = 0.00, 0.02, 0.04, 0.06, 0.08, 0.10, and 0.12) ceramic. (b) Peak displacement of (115) plane for various dopant concentrations.

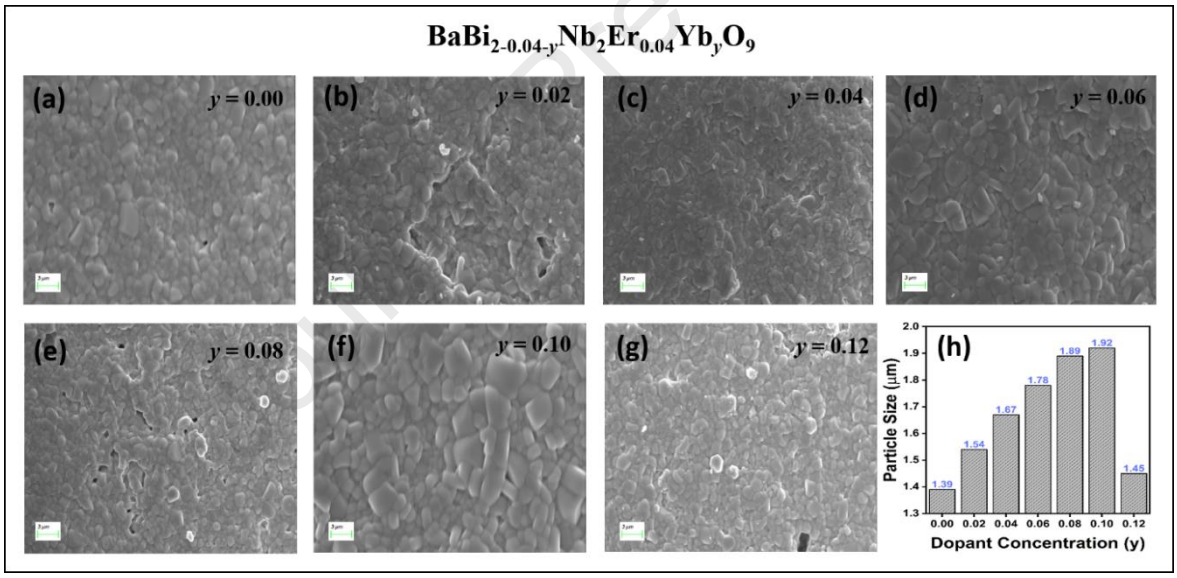

Fig. 3 (a-g) SEM micrographs of $BaBi_{2-0.04-y}Nb_2Er_{0.04}Yb_yO_9$ with y = 0.00 to 0.12 sintered at 1050°C for 3 hours. (h) Variation of particle size with all dopant concentrations.

3.2 Upconversion luminescence analysis

To evaluate the effect of Yb^{3+} on the upconversion luminescence, the UC spectra for the ceramic $BaBi_{2-0.04-y}Nb_2Er_{0.04}Yb_yO_9$ with constant Er^{3+} content and variable Yb^{3+} content (y = 0.02, 0.04, 0.06, 0.08, 0.10, and 0.12) were measured. The UCL measurements were done under the illumination of 980 nm excitation, with a pumping power of 50 mW and an excitation source density of 3.25 W/cm^2, and are shown in Fig. 4(a). The transitions from $^2H_{11/2}$ to $^4I_{15/2}$ and $^4S_{3/2}$ to $^4I_{15/2}$ are responsible for the two strong green emission bands at 535 nm and 557 nm. Also, there is a notable red emission peak at 670 nm when the ions migrate from level $^4F_{9/2}$ to level $^4I_{15/2}$. The two partial bands near 672 nm are related to the split of the $^4F_{9/2}$ energy level by the crystal field that occurs due to the action of upconversion luminescence. Considering this, the collected UCL spectra of the prepared ceramic show a fair degree of consistency with previously published results [25, 26]. The changing UCL

intensity as a function of dopants is illustrated in Fig. 4(b). Initially, there is a rise in UCL intensity, and after reaching critical intensity at y = 0.10, it degrades with further insertion of dopants. This results from the concentration quenching effect, which occurs when dopant ions are so near to one another that energy transfer becomes easier, resulting in non-radiative emissions [1, 21]. Furthermore, the distances between dopant ions may be calculated using the Blasse formula, as shown in Eq. 2 [23].

$$R_c \approx 2\left[\frac{3V}{4\pi X_c Z}\right]^{\frac{1}{3}} \quad (2)$$

Here, the amount for quenching is X_c (0.04+y), where V = 790.58 cm^3 is the volume of a unit cell in $BaBi_2Nb_2O_9$ ferroelectric ceramic, and Z = 4 shows the number of host cations. The R_c was calculated to be 13.92 Å. It was observed that in the absence of Yb^{3+} ions, the R_c value is 21.12 Å, whereas the R_c value is reduced in the presence of Yb^{3+} ions. This implies that the energy is efficiently transferring from Yb^{3+} to Er^{3+} ions. Notably, the upconversion emission process is often characterized by three processes, including ET (energy transfer), ESA (excited state absorption), and GSA (ground state absorption), along with CR and MPR (cross-relaxation processes and multi-phonon relaxation) [27-29]. In Fig. 4(c), the schematic diagram of upconversion luminescence is portrayed using these processes. The 980 nm laser is illuminated on Yb^{3+} ions, and it absorbs energy via GSA and transfers it to a higher level at $^4I_{11/2}$ via ET1 and $^4F_{7/2}$ through ET2. The Er^{3+} ions may also absorb photons through GSA. Thus, level $^4I_{11/2}$ is prepared for the ESA to reach a higher energy level, i.e., $^4F_{7/2}$. Thus, level $^4F_{7/2}$ is overpopulated by two processes, namely ET and ESA. The ions fall non-radiatively to levels $^2I_{11/2}$, $^4S_{3/2}$, and $^4F_{9/2}$ via MPR. From these levels, the ions transit to the lower level $^4F_{15/2}$, resulting in two green emission bands and one red emission band at 535 nm, 557 nm, and 672 nm, respectively. Another decay channel created by the cross-relaxation tracks (CR1 and CR2) is responsible for the increased red emission when the Yb^{3+} content increases. Besides, emission spectrum data from prepared ceramics were used to get the CIE chromaticity coordinates (x, y) for dopant concentrations (y = 0.02, 0.04, 0.06, 0.08, 0.10, and 0.12). The predicted CIE points, which are sited in the green region and then become bright green as dopant concentrations rise, are shown in Fig. 4(d).

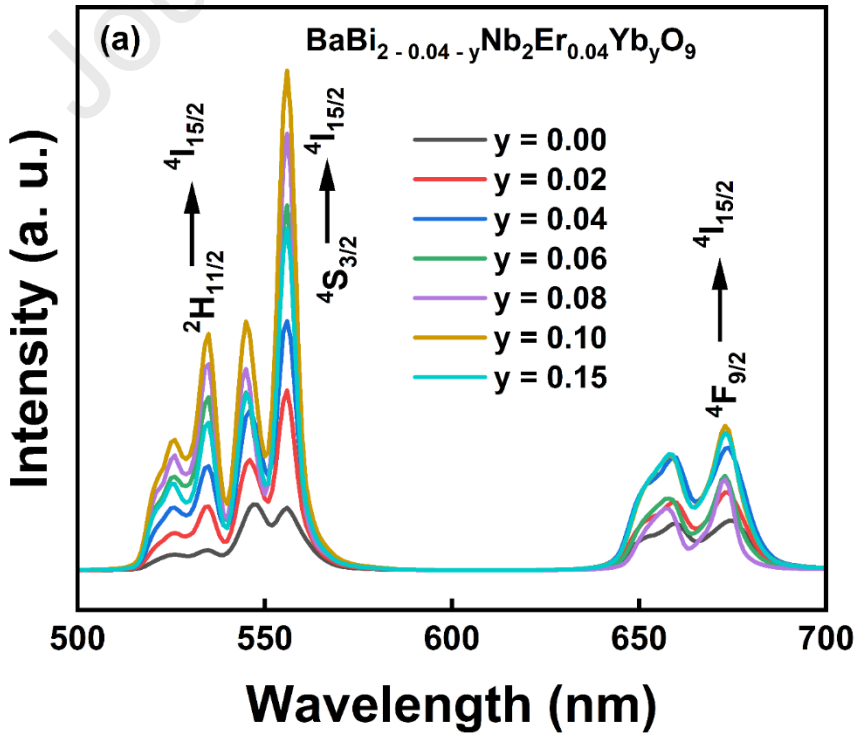

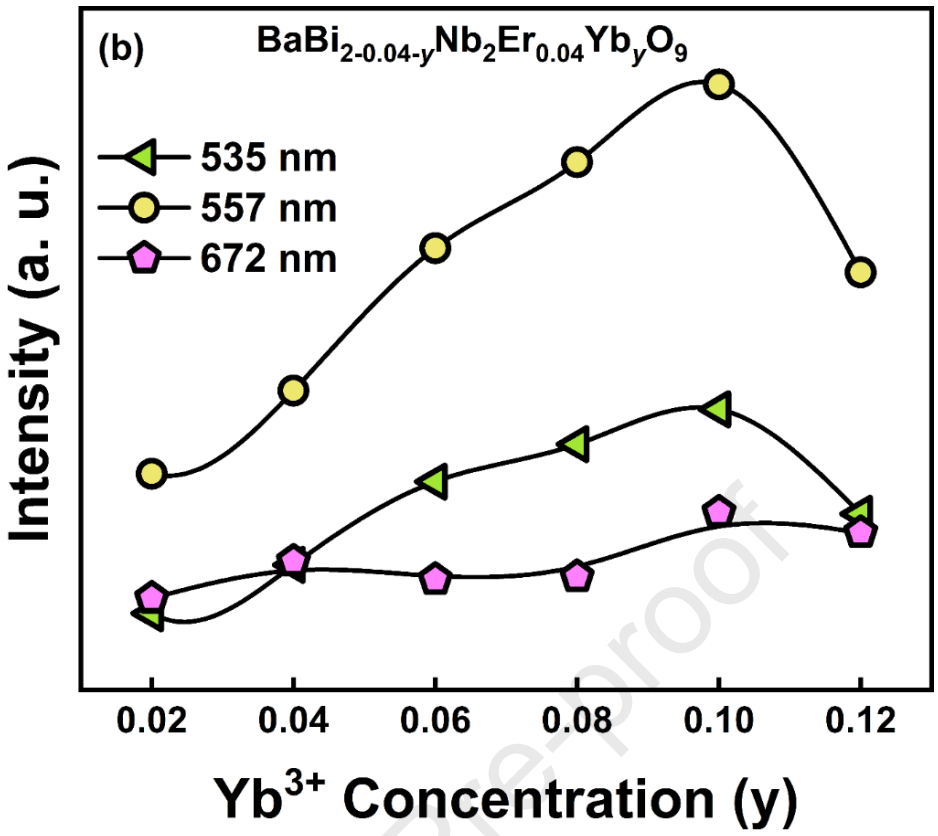

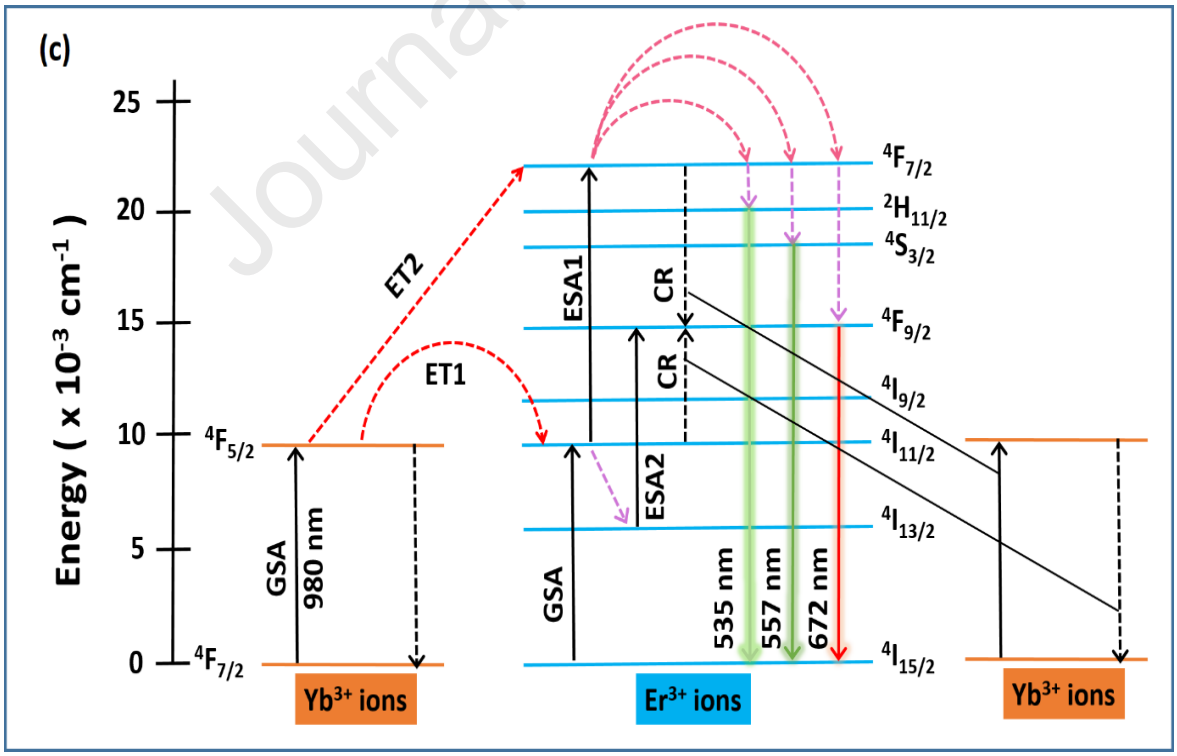

Journal Pre-proof

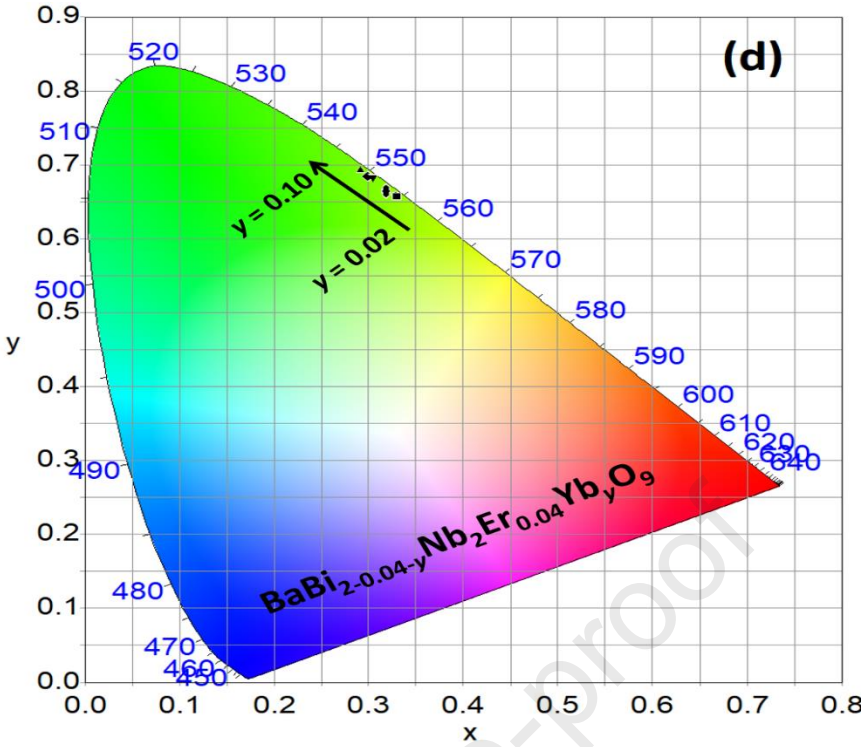

Fig. 4 (a) UC emission spectra of $BaBi_{2-0.04-y}Nb_2Er_{0.04}Yb_yO_9$ for various Yb^{3+} concentrations under 980 nm excitation. (b) Graph of intensity versus different concentrations of Yb^{3+}. (c) Schematic depiction of the energy pathways of Er^{3+}/Yb^{3+} ions doped in $BaBi_{2-0.04-y}Nb_2Er_{0.04}Yb_yO_9$ under the excitation of 980 nm. (d) CIE plot of $BaBi_{2-0.04-y}Nb_2Er_{0.04}Yb_yO_9$ for (y = 0.02, 0.04, 0.06, 0.08, 0.10, and 0.12).

3.3 Pump power dependency

To learn more about how upconversion luminescence works, we looked at transitions of levels $^2H_{11/2}$, $^4S_{3/2}$, and $^4F_{9/2}$ to level $^4I_{15/2}$ in $BaBi_{2-0.04-y}Nb_2Er_{0.04}Yb_yO_9$ (y = 0.10) ceramic at six different pump powers (21, 108, 203, 285, 364, and 453 mW) as displayed in Fig. 5(a). It has been found that the UCL gets stronger as the pump power goes up. The relation between pump power and intensity demonstrates in Eq. 3 [30, 31]:

$$I_{UP} \propto P^n \tag{3}$$

where n is the number of low-energy photons required for the UCL to proceed, P is the pump power, and I_{UP} refers to the intensity of UC luminescence. Fig. 5(b) depicts the log-log curve of the intensity vs. the excitation pump power. The magnitude of n for the green band near 535 and 557 nm and the red emissions band at 672 nm may be determined by the slope of the logarithmic plot. These values are 1.46, 1.52, and 1.25, respectively. In this research, the red and green UC bands are produced by the emission of two low-energy photons, which then produce radiation with higher energy that has a wavelength of 535, 557, and 672 nm. The n values of both colors have been rounded to 2 because various upconversion processes are involved [15, 17].

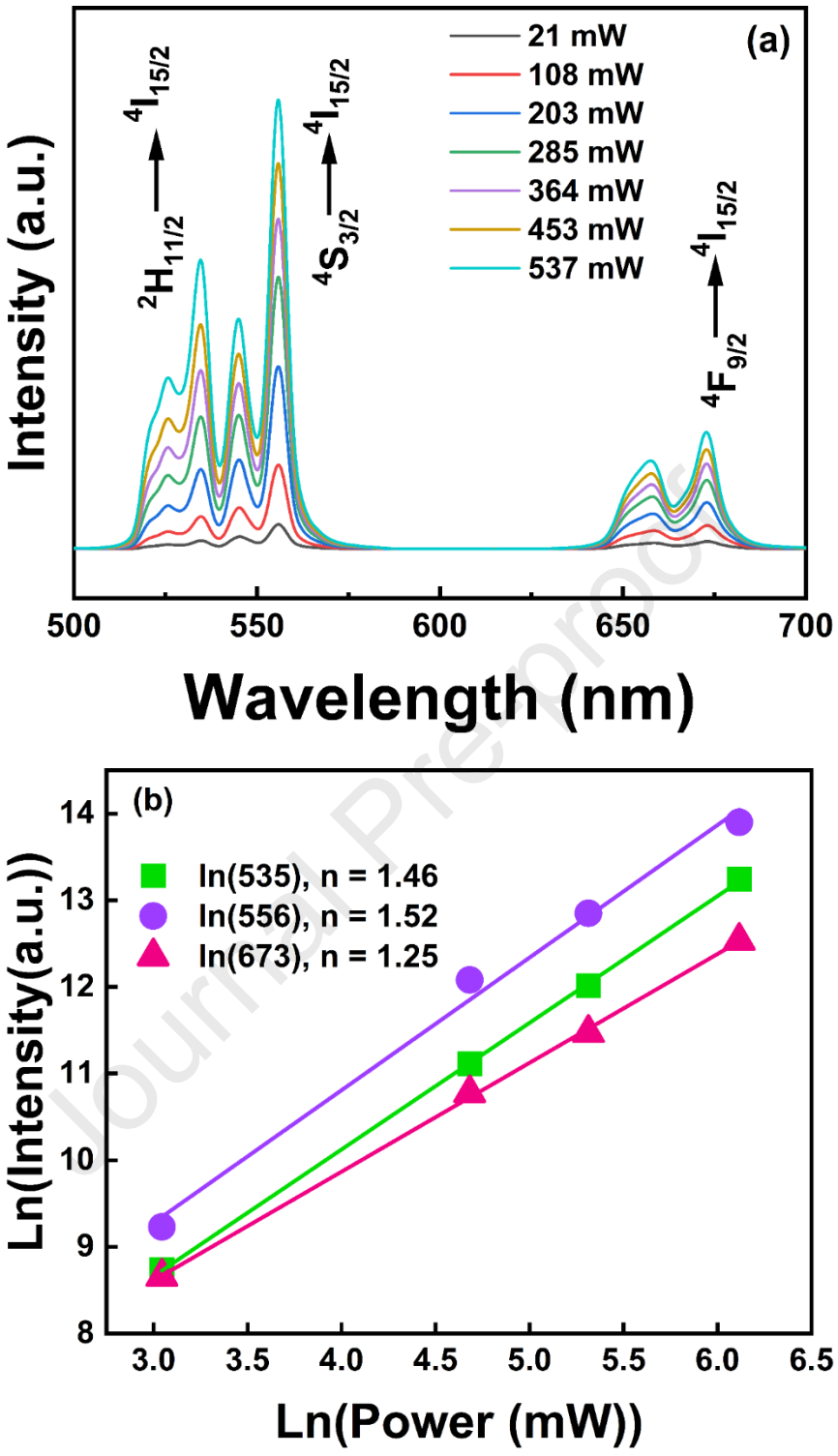

Fig. 5 (a) UCL emission spectra with different pump power ranging from 21 mW to 537 mW. (b) The plot of Ln(power) vs. Ln(UC intensity).

3.4 Time-resolved spectroscopy

A pulsed laser source was used to analyze the lifetime decay of $BaBi_{2-0.04-y}Nb_2Er_{0.04}Yb_yO_9$ (y = 0.04, 0.08, 0.10, and 0.12) ceramic for 557 nm transition from $^2S_{3/2}$ to $^4I_{15/2}$ energy level under 980 nm excitation wavelength. Fig. 6(a-d) depicts the decay overview of $BaBi_{2-0.04-y}Nb_2Er_{0.04}Yb_yO_9$ ceramics. The curves were fitted using Eq. 4 (tri exponential decay fit):

$$I(t) = I_0 + A_1 \exp(-\frac{t}{\tau_1}) + A_2 \exp\left(-\frac{t}{\tau_2}\right) + A_3 \exp(-\frac{t}{\tau_3}) \quad (4)$$

where I_0 corresponds to the intensity at the time t = 0 and A_1, A_2, A_3 are the fitting factors. Also, τ_1, τ_2, and τ_3 are luminescence decay times. The equation used to determine the mean lifespan is shown below in Eq. (5):

$$< \tau > = \frac{A_1\tau_1^2 + A_2\tau_2^2 + A_3\tau_3^2}{A_1\tau_1 + A_2\tau_2 + A_3\tau_3} \quad (5)$$

Fig. 6(e) depicts the predicted lifespan of Er^{3+} doped and Er^{3+}/Yb^{3+} doped $BaBi_{2-0.04-y}Nb_2Er_{0.04}Yb_yO_9$ ceramics. The calculated lifetime of $BaBi_{2-0.04-y}Nb_2Er_{0.04}Yb_yO_9$ ceramic varies from 28.74 µs to 40.11 µs for the co-doped system. An increase in lifespan suggests effective energy transmission in dopant ions, leading to non-radiative transition at a higher doping content [20]. However, the time decay in Er^{3+} doped ceramic is 41.29 µs greater than co-doped ceramic. Thus, the efficiency of energy transfer (ET) in co-doped $BaBi_{2-0.04-y}Nb_2Er_{0.04}Yb_yO_9$ ceramic can be calculated by Eq. (6):

$$\eta = 1 - \frac{\tau_a}{\tau_b} \quad (6)$$

where τ_a is the mean lifetime for Er^{3+}/Yb^{3+} co-doped ceramic and τ_b is the average lifetime for Er^{3+} doped ceramic [20]. The efficiency of the energy transfer process is influenced by 32% by adding Yb^{3+} to the host lattice at a minimum Yb^{3+} concentration.

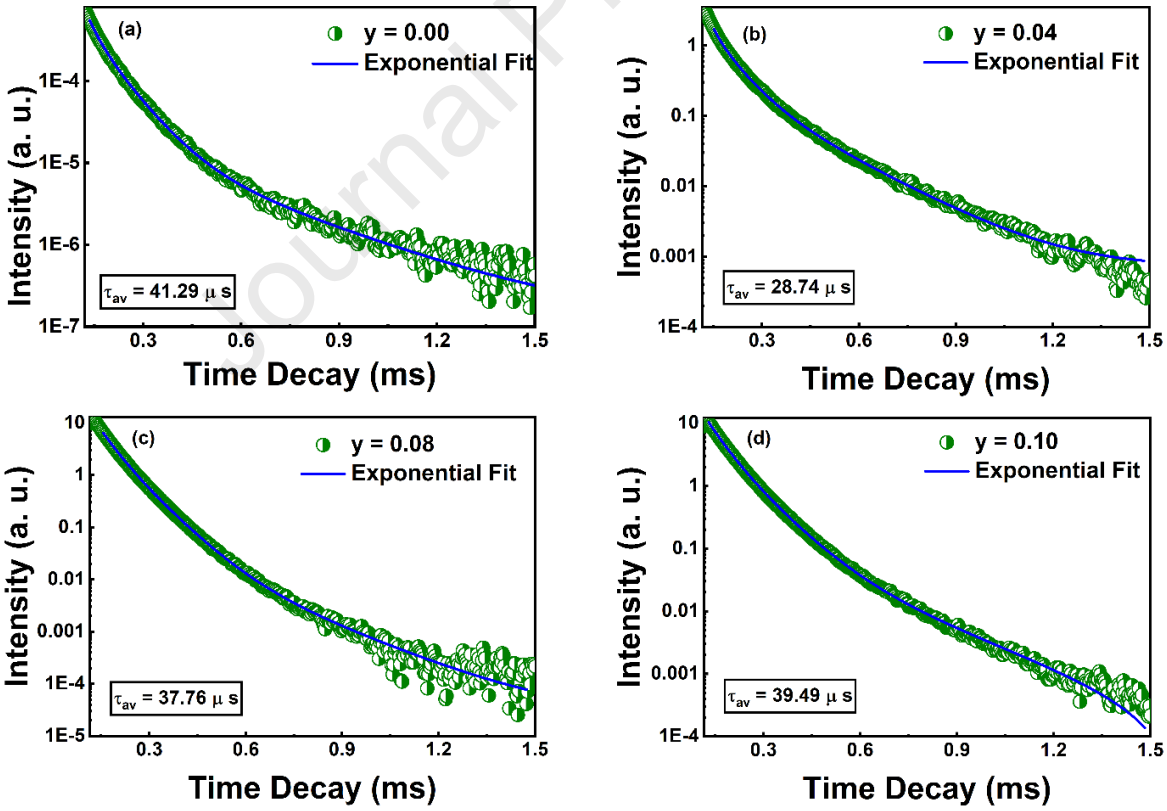

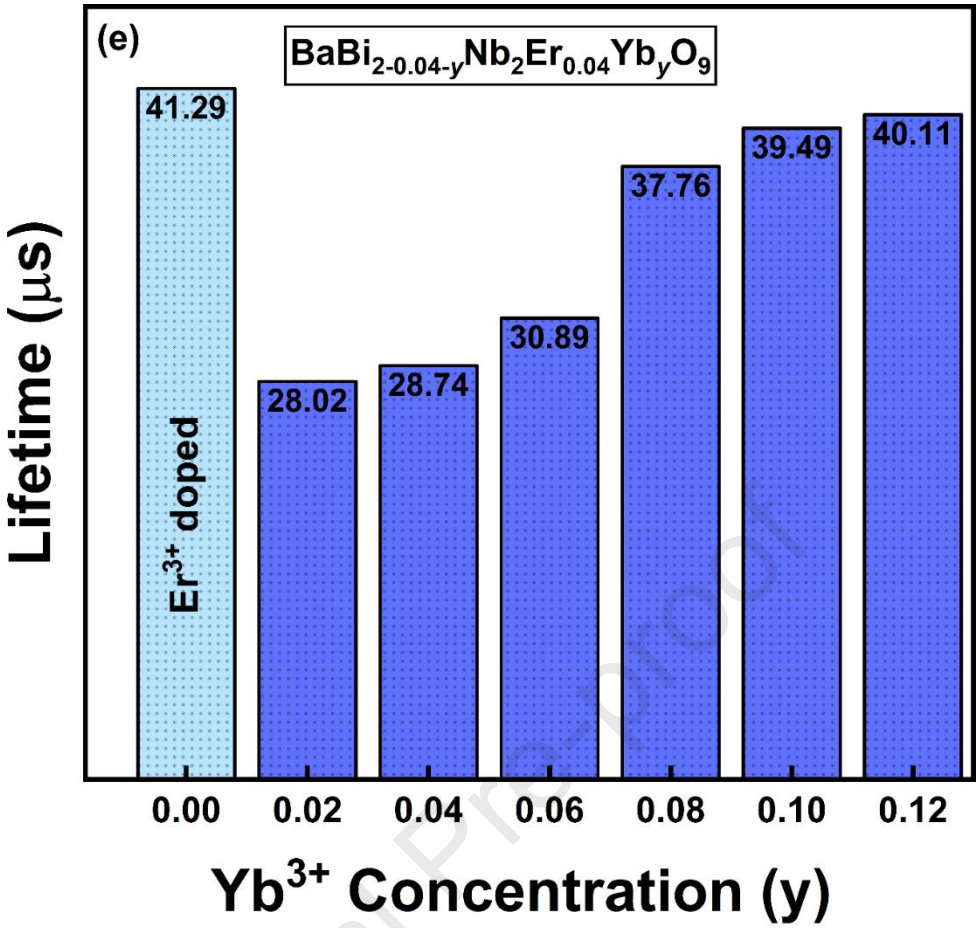

Fig. 6 (a-d) Time decay profile of $BaBi_{2-0.04-y}Nb_2Er_{0.04}Yb_yO_9$ composition for (y = 0.00, 0.04, 0.08, and 0.10) with an exponential fit. (e) Variation of an estimated lifetime of $BaBi_{2-0.04-y}Nb_2Er_{0.04}Yb_yO_9$ ceramic with varying concentrations of Yb^{3+}.

3.5 Contactless temperature sensing performance

In order to evaluate the possibility of using the present synthesized ceramic in optical temperature measurements, Fluorescence Intensity Ratio (FIR) approach is applied. For non-contact temperature measurements, the FIR is a basic approach that does not depend on variations in excitation intensity. This method was employed widely for temperature sensing in several host materials treated with RE^{3+} [31, 32]. We selected the co-doped ceramic compositions with y = 0.06 and 0.10 in $BaBi_{2-0.04-y}Nb_2Er_{0.04}Yb_yO_9$ system to investigate the sensing behaviour with varying Yb^{3+} concentrations. This FIR technique compares the UC intensity of two thermocouple energy levels (green emission bands) during transitions $^2H_{11/2}$ to $^4I_{15/2}$ and $^4S_{3/2}$ to $^4I_{15/2}$. Fig. 7(a, b) represents the time-dependent UCL spectra for the $BaBi_{2-0.04-y}Nb_2Er_{0.04}Yb_yO_9$ (y = 0.06 and 0.10) at temperatures ranging from 303 to 573 K. It can be seen that in both the co-doped systems (y = 0.06 and 0.10), the UC emission intensity decreases with increasing temperatures. But the FIR values follow the increasing trend, as demonstrated in Fig 7(c). The mathematical expression of FIR is given by Eq. 7 [33, 34]:

$$FIR = \frac{I_H}{I_S} = C\exp(-\frac{\Delta E}{K_B T}) \quad (7)$$

where I_H and I_S represent the integrated intensity of the green band at 535 nm and 557 nm, respectively, ΔE denotes the energy gap of levels $^4S_{3/2}$ and $^2H_{11/2}$, and C is the constant depending upon the transitions and degeneracy factor of thermally coupled levels (TCLs). To calculate constant (C) and energy gap (ΔE), Eq. (7) can be put in linear form, as shown in Eq. 8:

$$\mathrm{Ln(FIR)} = -\left(\frac{\Delta E}{K_B}\right)\left(\frac{1}{T}\right) + \mathrm{LnC} \tag{8}$$

The curve of ln(FIR) and the negative of temperature are illustrated in Fig. 7(d). The slope of this graph analyzes the value of $\Delta E/K_B$ and the ln C intercept. For y = 0.06 and 0.10, $\Delta E/K_B$ is -1015.67 and -925.38, while C is 2.545 and 2.260, respectively. These FIR characteristics define the optical thermometric sensitivity of the fabricated ceramic $BaBi_{2-0.04-y}Nb_2Er_{0.04}Yb_yO_9$. The external temperature influences the population redistribution ability (PRA) of thermally coupled levels $^4S_{3/2}$ and $^2H_{11/2}$ and can be expressed by Eq. (9) [18]:

$$\mathrm{PRA} = \frac{C}{C + \exp\left(\frac{\Delta E}{K_B T}\right)} \tag{9}$$

The PRA values for $BaBi_{2-0.04-y}Nb_2Er_{0.04}Yb_yO_9$ (y = 0.06 and 0.10) ceramics are given in Fig. 7(e). It seems that the population of these thermally coupled levels increases with temperature. The absolute sensitivity (S_a) of a material is defined by Eq. 10 as the variation rate of FIR with temperature [18].

$$S_a = \frac{d(FIR)}{dT} = \frac{d\left(C\exp\left(-\frac{\Delta E}{K_B T}\right)\right)}{dT} = C\exp\left(-\frac{\Delta E}{K_B T}\right)\left(\frac{\Delta E}{K_B T^2}\right) \tag{10}$$

By multiplying the absolute sensitivity by the negative FIR, we get the relative sensitivity (S_r), employed by Eq. 11 [35]:

$$S_r = \frac{1}{FIR} * S_a = \left(\frac{\Delta E}{K_B T^2}\right) \tag{11}$$

The S_a and S_r for $BaBi_{2-0.04-y}Nb_2Er_{0.04}Yb_yO_9$ (y = 0.06 and 0.10) are displayed in Fig. 7(f, g). In both cases, the absolute sensitivity increases with temperature up to the maximum T_a. For y = 0.06 and 0.10, S_a is 0.69% K^{-1} and 0.58% K^{-1} at T_a 523 K and 463 K, respectively. To check the operating temperature range for sensing application (denoted by the shaded region in Fig. 7(f, g)), the S_a values are extrapolated using Eq. 9, where the S_a is higher than half of its maximum value (S_{half}). It has been found that the sensitivity of lower dopant concentrations (y = 0.06) shows higher sensitivity than the optimal dopant concentrations (y = 0.10), and also the extrapolated data reveals the gradual decrease in the case of y = 0.06 whereas, in y = 0.10 the absolute sensitivity decreases exponentially. The operational temperature region is extended to a wider temperature range in y = 0.06 compared to y = 0.10, as shown in Fig. 7(f, g). These observations suggest that the sensing characteristics of the $BaBi_{2-0.04-y}Nb_2Er_{0.04}Yb_yO_9$ ceramic can be tuned by altering the dopant concentration. The material sensitivity is suitable if the theoretically calculated ΔE_{th} and the experimentally matched E_{ex} are substantially comparable. The experimental value for ΔE_{ex} may be derived from Fig. 7(d), and the deconvolution of UC spectra using the Viogt fit yields the theoretical value for ΔE_{th}, shown in Fig. 8(a, b). According to Eq. 12, the inaccuracy (δ) in $BaBi_{2-0.04-y}Nb_2Er_{0.04}Yb_yO_9$ ceramic at y = 0.06 and 0.10 equals 2.89% and 4.01%, respectively.

$$\delta = \frac{|\Delta E_{th} - \Delta E_{ex}|}{\Delta E_{th}} * 100\% \tag{12}$$

A sensor's repeatability (R) and resolution (δT) are essential to determine its efficacy. The mathematical expression of these parameters is stated in Eqs. 13 and 14 [36]:

$$R = 1 - \frac{\max(\Delta_{Av} - \Delta_{Sp})}{\Delta_{Av}} \tag{13}$$

$$\delta T = \frac{1}{S_r} \times \frac{\delta_\Delta}{\Delta} \quad (14)(12)$$

where δ_Δ/Δ is the device's precision, Δ_{Av} and Δ_{Sp} are the mean and specific parameters of FIR with 17 cycles within temperature 303-573 K. The repeatability and resolution of the produced ceramic are shown in Fig. 9(a, b), respectively. Fig. 9(a) displays no discernible shift in the FIR values of both concentrations anywhere in the temperature range from 303 K to 573 K. In Fig. 9(b), the resolution improves from 2.74 to 9.72 and 3.13 to 10.45 for y = 0.06 and 0.10, respectively. Table 2 compares the sensitivity of prepared $BaBi_{2-0.04-y}Nb_2Er_{0.04}Yb_yO_9$ ceramic to that of currently published Er/Yb-codoped host materials. Our work demonstrates the ability of non-contact temperature sensors to function throughout a broad and high-temperature range, with a maximum temperature of 523 K, while maintaining excellent sensitivity. Consequently, we may conclude that the ceramic $BaBi_{2-0.04-y}Nb_2Er_{0.04}Yb_yO_9$ is a competent sensor material that has the potential to be further investigated for use in the applications area of optical temperature sensors.

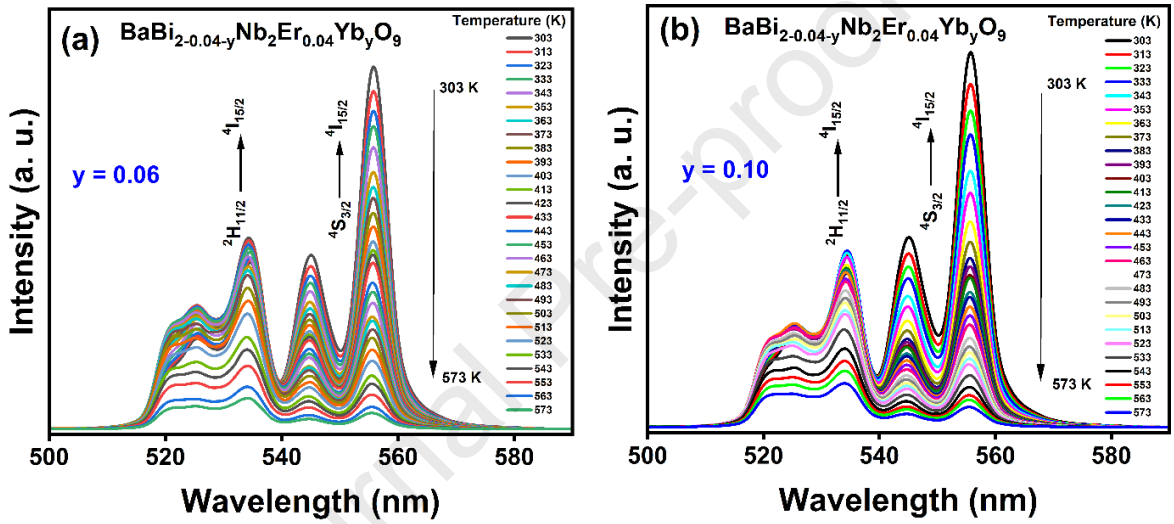

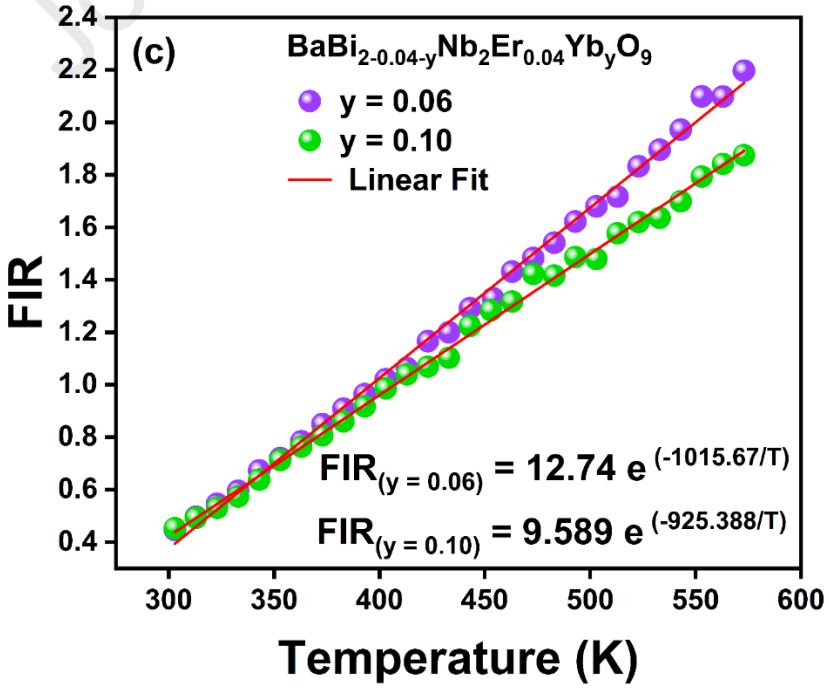

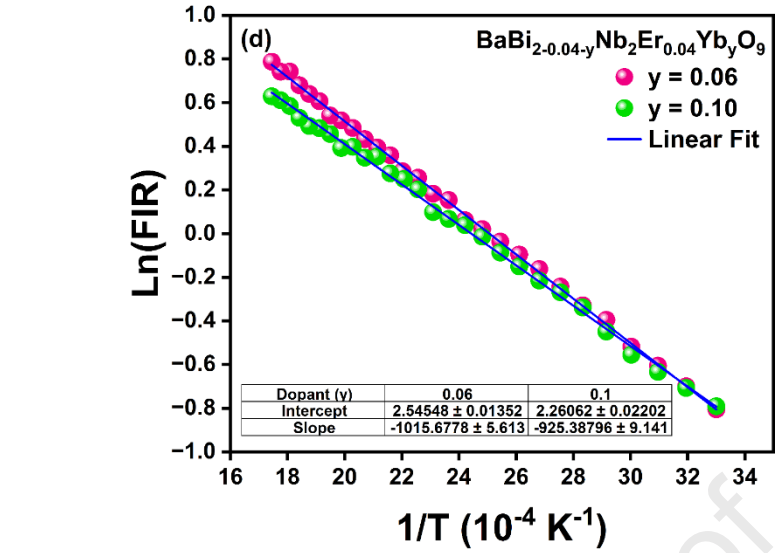

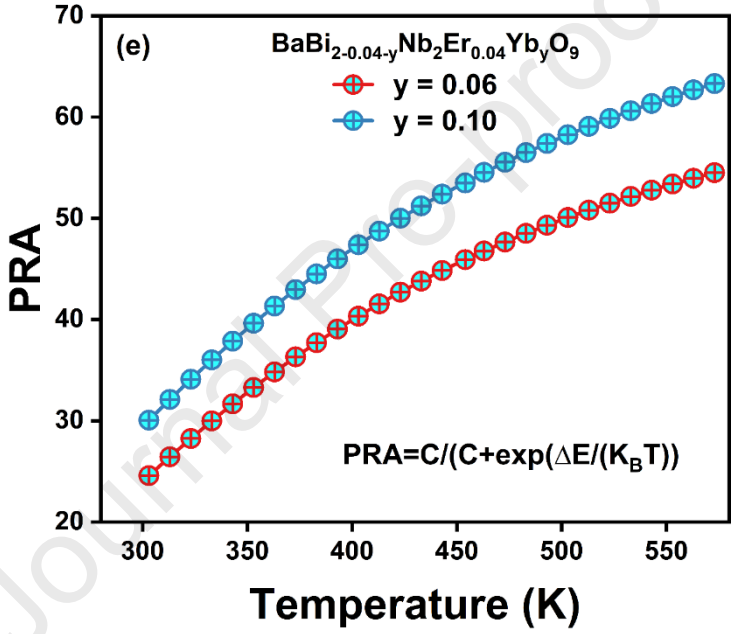

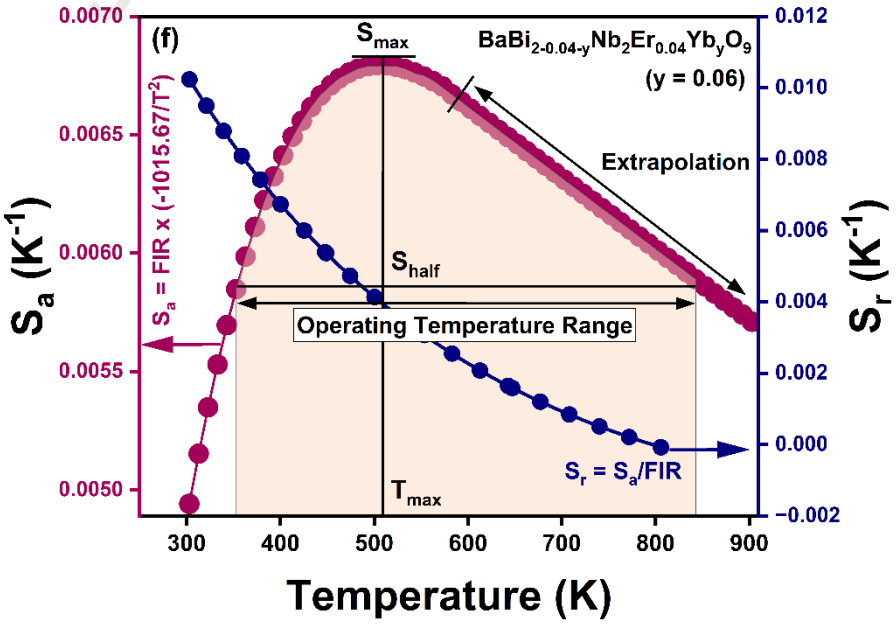

Journal Pre-proof

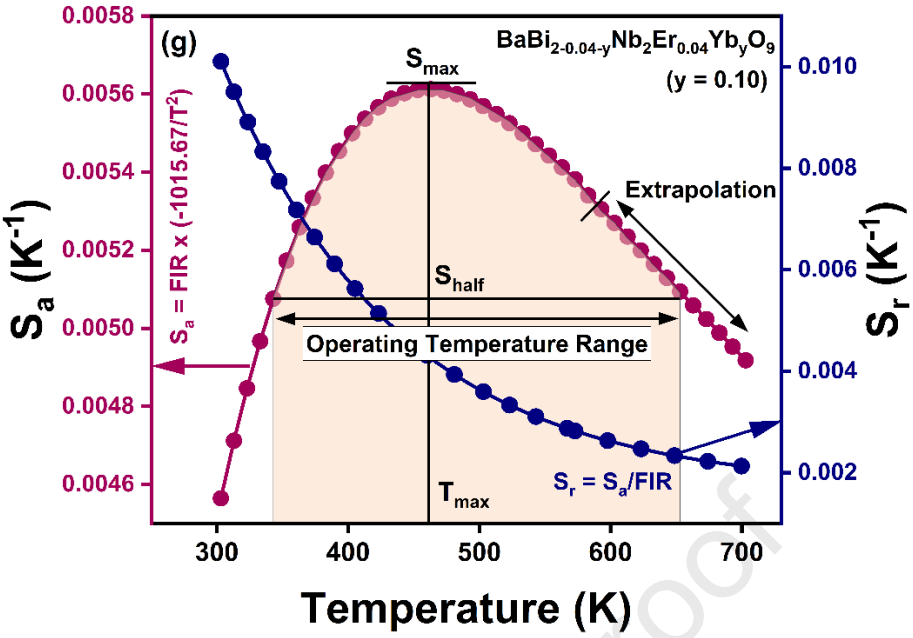

Fig. 7 (a, b) Time-dependent UC emission pattern of $BaBi_{2-0.04-y}Nb_2Er_{0.04}Yb_yO_9$ at y = 0.06 and 0.10 in the temperature range 303-573 K, respectively. (c) Evaluation of FIR vs. Temperature at two Yb^{3+} concentrations (y = 0.06 and 0.10). (d) The plot of Ln(FIR) with negative temperature for slope and intercept evaluations. (e) PRA values of thermally coupled levels ($^2H_{11/2}$ and $^4S_{3/2}$) at y = 0.06 and 0.10. (f) Absolute (S_a) and relative (S_r) sensitivity as a function of temperature for $BaBi_{2-0.04-y}Nb_2Er_{0.04}Yb_yO_9$ ceramic at y = 0.06. (g) 0.10 with operating temperature range (shaded region).

Table 2: Temperature sensing parameters of various Er^{3+}/Yb^{3+} co-doped host materials in the different temperature ranges.

Host material	ΔE (cm^{-1})	Temperature Range (K)	T_a (K)	S_a (K^{-1})	S_r (K^{-1})	T_r (K)	Published year	References
$CaBi_2Ta_2O_9$:Er/Yb	1181	153-603	590	0.39%	-	-	2014	[3]
$Na_{0.5}Er_{0.5}Bi_4Ti_4O_{15}$	500.1	175-500	380	0.17%	-	-	2014	[11]
La_2O_3:Er/Yb	566	303-600	303	0.91%	-	-	2014	[27]
$BaTiO_3$:Er/Yb	600	125-430	410	0.19%	-	-	2015	[2]
$Na_{0.5}Bi_{0.5}TiO_3$:Er/Yb	706.68	173-553	493	0.35%	-	-	2015	[26]
$La_2Ti_2O_7$:Er/Yb	683	93-773	493	0.29%	0.41 %	300	2023	[17]
BNT-SBT:Er/Yb	-	303-573	363	0.49%	-	-	2022	[18]
$La_2Ti_2O_7$:Er/Yb	760	333-553	525	0.57%	0.63%	333	2020	[32]
$Na_{0.5}Bi_{2.5}Ta_2O_9$: Er/Yb	-	153-483	483	0.78%	5.99%	153	2023	[31]
$Sr_{0.75}Ba_{0.25}Nb_2O_6$: Er/Yb	-	310-470	410	0.54%	0.85%	310	2023	[37]
$(Bi_{0.5}Er_{0.1}Yb_{0.4})Ta_7O_{19}$	660.65	303-693	475	0.162%	1.04%	303	2021	[38]
$BaGd_2O_4$:Er/Yb	873.94	298-573	573	0.42%	-	-	2023	[32]
$Ba_2NaNb_5O_{15}$:Er/Yb	735.5	298-573	373	0.68%	0.90%	298	2022	[15]
$BaBi_{2-0.04-y}Nb_2Er_{0.04}Yb_yO_9$ (y=0.06)	705	303-573	523	0.69%	1.10%	303	-	**This work**
$BaBi_{2-0.04-y}Nb_2Er_{0.04}Yb_yO_9$ (y=0.10)	645	303-573	463	0.58%	1.01%	303	-	**This work**

Journal Pre-proof

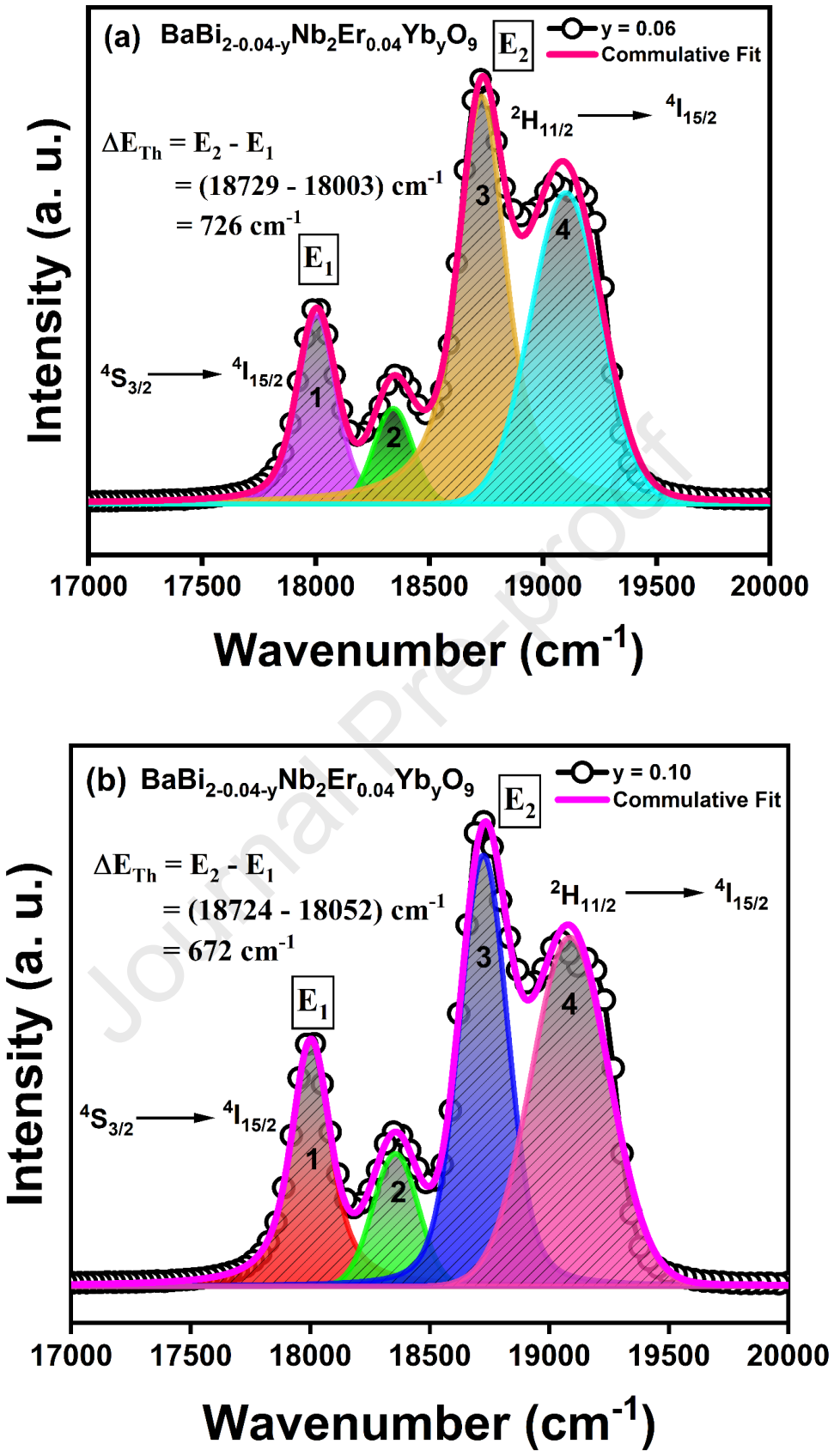

Fig. 8 (a, b) Deconvolution of time-dependent UC spectra by Voigt fit for $BaBi_{2-0.04-y}Nb_2Er_{0.04}Yb_yO_9$ at y = 0.06 and 0.10.

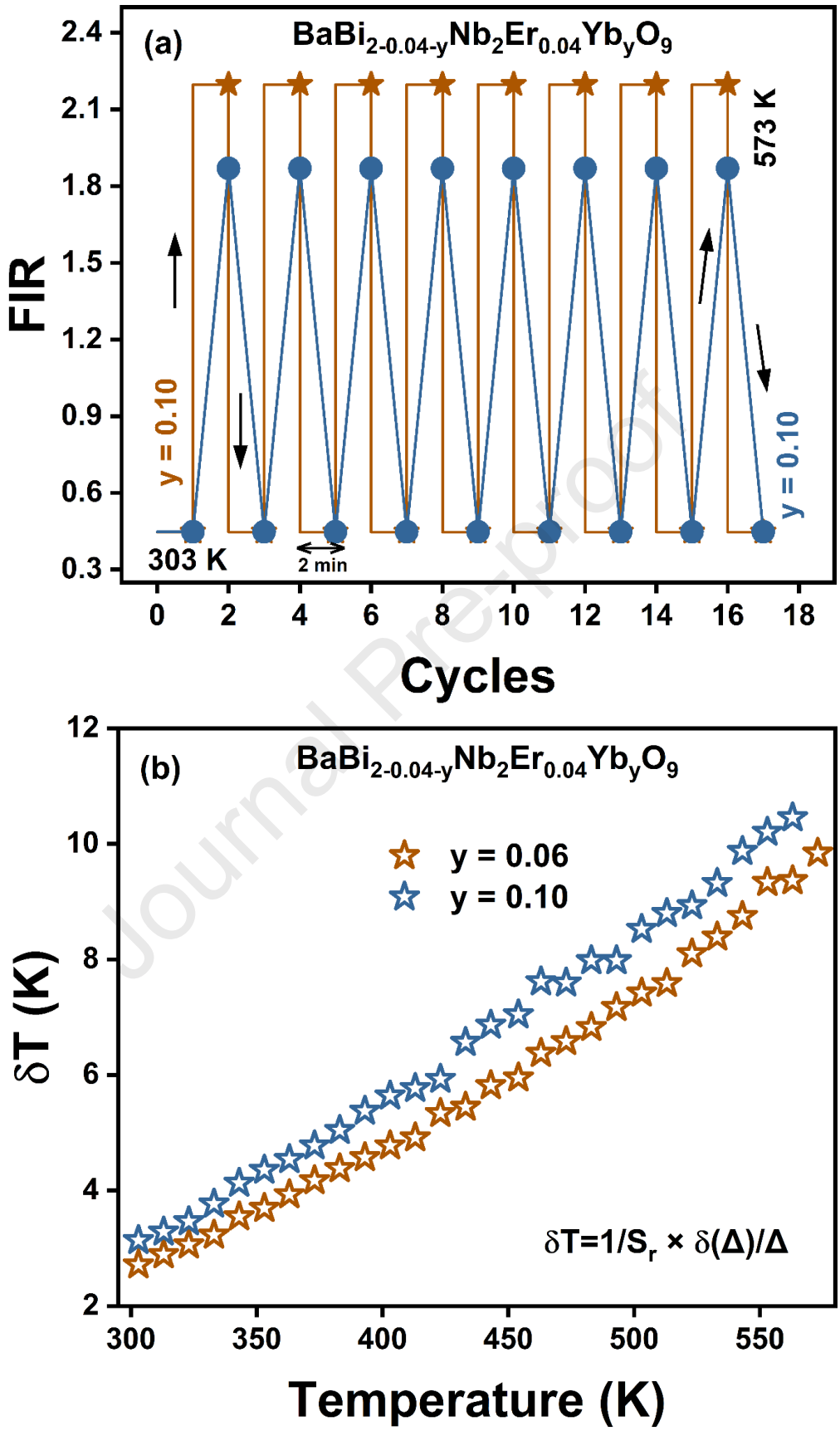

Fig. 9 (a) Reliablity test of $BaBi_{2-0.04-y}Nb_2Er_{0.04}Yb_yO_9$ ceramic in the temperature range (303-573 K) with a stabilization period of 2 minutes. (b) Resolution of temperature between 303 K to 573 K.

4. Conclusion

The co-doped Er^{3+}/Yb^{3+} ferroelectric ceramic $BaBi_{2-0.04-y}Nb_2Er_{0.04}Yb_yO_9$ (y = 0.00, 0.02, 0.04, 0.06, 0.08, 0.10, and 0.12) is produced by the solid-state reaction technique at 1050 °C have been studied for upconversion luminescence and temperature sensing applications. The XRD investigation confirmed the ceramic's orthorhombic geometry. The microstructure seen by SEM resembles plate-like formations and comprises non-uniform grains with irregular orientation. An increase in grain size with Yb^{3+} content up to y = 0.10 was found to promote upconversion luminescence. Two bright green bands at 535 and 557 nm and a detectable red spectrum nearby 672 nm were observed in upconversion luminescence (UCL) spectra, corresponding to an excitation wavelength of 980 nm. The effective energy transfer process from Yb^{3+} to Er^{3+} ions is supported by decay time measurements, which increases with increasing Er^{3+}/Yb^{3+} content because of the non-radiative transition at higher doping concentration. The pump power dependence upon the UC luminescence intensity for an optimum Yb^{3+} content y =0.10 reveals that green and red UC emissions involve two photons. Er^{3+}/Yb^{3+} co-doped $BaBi_{2-0.04-y}Nb_2Er_{0.04}Yb_yO_9$ ceramic system with y = 0.06 and 0.10 exhibit a maximum absolute sensitivity (S_a) of 0.69% K^{-1} and 0.58% K^{-1} at T_a = 523 K and 463 K, respectively, and maximum relative sensitivity (S_r) of 1.10% and 1.01% at T_r = 303 K, suggesting a viable contactless temperature sensor with tunable sensitivity.

Acknowledgment

The authors would like to thank the Department of Applied Physics at Delhi Technological University for making all of the necessary resources and facilities available to carry out this study. One of the authors, AB, is thankful to CSIR-HRDG ref no. Jan-Feb/06/21(i)EU-V for providing financial support.

References

[1] Z. Tianmin, Z. Yanqiu, W. Zhongli, and C. Baojiu, "Concentration effect and temperature quenching of upconversion luminescence in $BaGd_2ZnO_5:Er^{3+}/Yb^{3+}$ phosphor," *J. Rare Earth.*, vol. 33, no. 7, pp. 686, 2015, doi: 10.1016/S1002-0721(14)60471-3.

[2] M. K. Mahata, T. Koppe, T. Mondal, C. B. Sewitz, K. Kumar, V. K. Rai, H. Hofsass, and U. Vetter, "Incorporation of Zn^{2+} ions into $BaTiO_3:Er^{3+}/Yb^{3+}$ nanophosphor: an effective way to enhance upconversion, defect luminescence, and temperature sensing," *Phys. Chem. Chem. Phys.*, vol. 17, pp. 20741-20753, 2015, doi: 10.1039/c5cp01874a.

[3] Q. Cao, D. Peng, H. Zou, J. Li, X. Wang, and X. Yao, "Up-conversion luminescence of Er^{3+} and Yb^{3+} co-doped $CaBi_2Ta_2O_9$ multifunctional ferroelectrics," *J. Adv. Dielectr.*, vol. 4, no. 03, pp. 1450018, 2014, doi: 10.1142/s2010135x14500180.

[4] V. Lojpur, G. Nikoli, and M. D. Dramianin, "Luminescence thermometry below room temperature via up-conversion emission of $Y_2O_3:Yb^{3+}$, Er^{3+} nanophosphors," *J. Appl. Phys.*, vol. 115, pp. 203106, 2014, doi: 10.1063/1.4880158.

[5] R. Bokolia, O.P. Thakur, V. K. Rai, S. K. Sharma, and K. Sreenivas, "Electrical properties and light up conversion effects in $Bi_{3.79}Er_{0.03}Yb_{0.18}Ti_{3x}W_xO_{12}$ ferroelectric ceramic," *Ceram. Int.*, vol. 42, pp. 5718–5730, 2016, doi: 10.1016/j.ceramint.2015.12.103.

[6] R. D. Shannon, "Revised effective ionic radii and systematic studies of interatomic distances in halides and chalcogenides," *J. Acta Cryst.*, A32, pp. 751–767, 2016, doi: 10.1107/S0567739476001551.

[7] C. Kornphom, K. Saenkam, and T. Bongkarn, "Enhanced energy storage properties of BNT–ST-AN relaxor ferroelectric ceramics fabrication by the solid-state combustion technique," *Phys. Status Solidi A*, 2200240, 2022, doi: 10.1002/pssa.202200240.

[8] M. X. Façanha, J. P. C. do Nascimento, M. A. S. Silva, M. C. C. Filho, A. N. L Marques, A. G. Pinheiro, and A. S. B. Sombra, "Up-conversion emission of Er^{3+}/Yb^{3+} co-doped $BaBi_2Nb_2O_9$ (BBN) phosphors," *J. Lumin.*, vol. 183, pp. 102-107, 2017, doi: 10.1016/j.jlumin.2016.08.011.

[9] T. Wei, C. Z. Zhao, Q. J. Zhou, Z. P. Li, Y. Q. Wang, and L. S. Zhang, "Bright green upconversion emission and enhanced ferroelectric polarization in $Sr_{1-1.5x}Er_xBi_2Nb_2O_9$," *Opt. Mater.*, vol. 36, no. 7 pp. 1209-1212, 2014, doi: 10.1016/j.optmat.2014.03.001.

[10] Z. Yao, R. Chu, Z. Xu, J. Hao, W. Li, and G. Li, "Processing and enhanced electrical properties of $Sr_{1-x}(K_{0.5}Bi_{0.5})_xBi_2Nb_2O_9$

lead-free piezoelectric ceramics," *Ceram. Int.*, vol. 42, no. 9, pp. 10619-10623, 2016, doi: 10.1016/j.ceramint.2016.03.156.

[11] X. Hui, D. Peng, H. Zou, J. Li, Q. Cao, Y. Li, X. Wang, and X. Yao, "A new multifunctional Aurivillius oxide $Na_{0.5}Er_{0.5}Bi_4Ti_4O_{15}$: Up-conversion luminescent, dielectric, and piezoelectric properties," *Ceram. Int.*, vol. 40, part 4A, pp. 12477-12483, 2014, doi: 10.1016/j.ceramint.2014.04.102.

[12] A. Banwal, and R. Bokolia, "Phase evolution and microstructure of $BaBi_2Nb_2O_9$ ferroelectric ceramics," *Mater. Today Proc.*, vol. 46, part 20, pp. 10121-10124, 2021, doi: 10.1016/j.matpr.2020.09.380.

[13] Z. Chen, L. Sheng, X. Li, P. Zheng, W. Bai, L. Li, F. Wen, W. Wu, L. Zheng, and J. Cui, "Enhanced piezoelectric properties and electrical resistivity in W/Cr co-doped $CaBi_2Nb_2O_9$ high-temperature piezoelectric ceramics," *Ceram. Int.*, vol. 45, no. 05, pp. 6004-6011, 2019, doi: 10.1016/j.ceramint.2018.11.252.

[14] A. Banwal and R. Bokolia, "Effect of Er^{3+} ion doping on structural, ferroelectric and up/down conversion luminescence in $BaBi_2Nb_2O_9$ ceramic," *Mater. Today Proc.*, pp. 3–6, 2021, doi: 10.1016/j.matpr.2021.05.545.

[15] F. Luo, J. Xing, Y. Qin, Y. Zhong, F. Shang, and G. Chen, "Up-conversion luminescence, temperature sensitive and energy storage performance of lead-free transparent Yb^{3+}/Er^{3+} co-doped $Ba_2NaNb_5O_{15}$ glass-ceramics," *J. Alloy. Compd.*, vol. 910, pp. 164859, 2022, doi: 10.1016/j.jallcom.2022.164859.

[16] A. Pandey, S. Som, V. Kumar, V. Kumar, K. Kumar, V. K. Rai, and H.C. Swart, "Enhanced upconversion and temperature sensing study of Er^{3+}–Yb^{3+} co-doped tungsten–tellurite glass," *Sens. and Act. B: Chem.*, vol. 202, pp. 1305-1312, 2014, doi: 10.1016/j.snb.2014.06.074.

[17] R. Swami, A. Shandilya, A.K. Shukla, P. S. Kumar, and K. Sreenivas, "Luminescence intensity ratio based wide range contactless temperature sensing properties of Er3+/Yb3+ ions co-doped La2Ti2O7 ceramics," *J. Alloy. Compd.*, vol. 948, pp. 169610, 2023, doi: 10.1016/j.jallcom.2023.169610.

[18] P. Wang, X. Wang, G. Li, Y. Li, X. Yao, and Z. Pan, "Energy density capability and upconversion luminescence in Er^{3+}/Yb^{3+}-codoping BNT-based ferroelectric thin films," *Ceram. Int.*, vol. 48(19), pp. 28606-28613, 2022, doi: 10.1016/j.ceramint.2022.06.174.

[19] X. Liu, G. Hu, H. Wu, S. Shi, H. Wang, J. Xu, L. Yang, and W. Qiu, "Transmittance, Photoluminescence and Electrical Properties in Er-Doped $0.98K_{0.5}Na_{0.5}NbO_3$-$0.02Sr(Yb_{0.5}Ta_{0.5})O_3$ Ferroelectric Ceramics," *J. of Elec. Mat.*, vol. 51, pp. 3476–3484, 2022, doi: 10.1007/s11664-022-09626-3.

[20] A. Banwal, and R. Bokolia, "Enhanced upconversion luminescence and optical temperature sensing performance in Er^{3+} doped $BaBi_2Nb_2O_9$ ferroelectric ceramic," *Ceram. Int.*, vol. 48, no. 2, pp. 2230-2240, 2022, doi: 10.1016/j.ceramint.2021.09.314.

[21] R. Bokolia, O. P. Thakur, V. K. Rai, S. K. Sharma, and K. Sreenivas, "Dielectric, ferroelectric and photoluminescence properties of Er^{3+} doped $Bi_4Ti_3O_{12}$ ferroelectric ceramics," *Ceram. Int.*, vol. 41, no. 4, pp. 6055-6066, 2015, doi: 10.1016/j.ceramint.2015.01.062.

[22] L. Mukhopadhyay, V. K. Rai, R. Bokolia, and K. Sreenivas, "980 nm excited $Er^{3+}/Yb^{3+}/Li^{+}/Ba^{2+}$: $NaZnPO_4$ upconverting phosphors in optical thermometry" *J. Lumin.*, vol. 187, pp. 368–377, 2017, doi: 10.1016/j.jlumin.2017.03.035.

[23] A. Banwal, and R. Bokolia, "Thermometric sensing performance in Erbium modified $SrBi_{2-x}Nb_2Er_xO_9$ ferroelectric ceramic for optoelectronic devices," *Ceram. Int.*, vol. 48 part 23A, pp. 34405-34414, 2022, doi: 10.1016/j.ceramint.2022.08.019.

[24] F. Wang, Y. Han, C. S. Lim, Y. Lu, J. Wang, J. Xu, H. Chen, C. Zhang, M. Hong, and X. Liu, "Simultaneous phase and size control of upconversion nanocrystals through lanthanide doping," *Nature.*, vol. 463, pp. 1061-1065, 2010, doi: 10.1038/nature08777.

[25] P. Du, L. Luo, W. Li, and Q. Yue, "Upconversion emission in Er-doped and Er/Yb-codoped ferroelectric $Na_{0.5}Bi_{0.5}TiO_3$ and its temperature sensing application," *J. Appl. Phys.*, vol. 116, pp. 014102, 2014, doi: 10.1063/1.4886575.

[26] P. Du and J. S. Yun, "Effect of molybdenum on upconversion emission and temperature sensing properties in $Na_{0.5}Bi_{0.5}TiO_3$: Er/Yb ceramics," *Ceram. Int.*, vol. 41, pp. 6710–6714, 2015, doi: 10.1016/j.ceramint.2015.01.113.

[27] R. Dey and V. K. Rai, "Yb^{3+} sensitized Er^{3+} doped La_2O_3 phosphor in temperature sensors and display devices," *J Dalton Trans.*, vol. 43, pp. 111, 2014, doi: 10.1039/c3dt51773j.

[28] P. Du, L. Luo, and W. Li, "Upconversion emission in Er-doped and Er/Yb-codoped ferroelectric $Na_{0.5}Bi_{0.5}TiO_3$ and its temperature sensing application," *J. Appl. Phys.*, vol. 116, pp. 014102, 2014, doi: 10.1063/1.4886575.

[29] J. Shi, J. Suna, B. Fanga, Q. Dua, S. Zhanga, and J. Ding, "Photoluminescence performance of Er/Yb co-doped NBT ceramics prepared via hydrothermal method," *J. of Phys and. Chems.*, vol. 121, pp. 228-235, 2018, doi: 10.1016/j.jpcs.2018.05.031.

[30] R. Bokolia, M. Mondal, V. K. Rai, and K. Sreenivas, "Enhanced infrared-to-visible up-conversion emission and temperature sensitivity in (Er^{3+}, Yb^{3+}, and W^{6+}) tri-doped $Bi_4Ti_3O_{12}$ ferroelectric oxide," *J. Appl. Phys.*, vol. 121, no. 8, 2017, doi: 10.1063/1.4977006.

[31] P. Li, Z. Zhang, Z. Xu, H. Sun, Q. Zhang, and X. Hao, "Photomodulated cryogenic temperature sensing through a photochromic reaction in $Na_{0.5}Bi_{2.5}Ta_2O_9$: Er/Yb multicolour upconversion," *Opt Express.*, vol. 31(5), pp. 7047–7059, 2023, doi:

Journal Pre-proof

10.1364/OE.469538.

[32] Y. Liu, G. Bai, E. Pan, Y. Hua, L. Chen, and S. Xu, "Upconversion fluorescence property of Er^{3+}/Yb^{3+} co-doped lanthanum titanate microcrystals for optical thermometry," *J. of Alloys. and Compd.*, vol. 822, pp. 153449, 2014, doi: 10.1016/j.jallcom.2019.153449.

[33] Z. Guan, X. Li, R. Shen, Z. Tian, H. Yu, Y. Cao, Y. Wang, J. Zhang, S. Xu, and B. Chen, "Intense red up-conversion luminescence and temperature sensing property of Yb^{3+}/Er^{3+} co-doped $BaGd_2O_4$ phosphors," *Spectrochim. Acta A Mol. Biomol. Spectrosc.*, vol. 284, pp. 121805, 2023, doi: 10.1016/j.saa.2022.121805

[34] P. Du, L. Luo, W. Li, and Q. Yue, "Upconversion emission in Er-doped and Er/Yb-codoped ferroelectric $Na_{0.5}Bi_{0.5}TiO_3$ and its temperature sensing application," *J. of Appl. Phys.*, vol. 116, pp. 014102, 2014, doi: 10.1063/1.4886575.

[35] J. Xing, F. Shang, and G. Chen, "Upconversion luminescence of Yb^{3+}/Er^{3+} co-doped $NaSrPO_4$ glass ceramic for optical thermometry," *Ceram. Int.*, vol. 147, pp. 8330-8337, 2021, doi: 10.1016/j.ceramint.2020.11.195.

[36] M. D. Dramićanin, "Trends in luminescence thermometry," *J. Appl. Phys.*, vol. 128, pp. 040902, 2020, doi: 10.1063/5.0014825.

[37] J. Song, F. Luo, and G. Chen, "A new photoelectric niobate glass ceramic material: Up-conversion optical thermometry and dielectric energy storage," *Ceram. Int.*, 2023, doi: 10.1016/j.ceramint.2023.05.281.

[38] H. Cui, Y. Cao, Y. Zhang, L. Cao, S. Ran, X. Wang, D. Wu, X. Li, X. Zhang, and Baojiu Chen, "Extremely intense green up-conversion luminescent and ultra-high temperature sensitivity in Er^{3+}/Yb^{3+} co-doped $BiTa_7O_{19}$ phosphors," *J. Lumin.*, vol. 241, pp. 118484, 2022, doi: 10.1016/j.jlumin.2021.118484.

Journal Pre-proof

Journal Pre-proof

Dr. Renuka Bokolia
Department of Applied Physics
Delhi Technological University, Delhi – 110042, India

Mobile No. +919582610592
Email: renukabokolia@dtu.ac.in

To **19-06-2023**
The Editor
Journal of Luminescence

Dear Sir,

Sub: Revised manuscript submission to the journal "Journal of Luminescence"

We would like to submit our research paper for your kind consideration in the esteemed journal "**Journal of Luminescence**"

Title **Efficient tunable temperature sensitivity in thermally coupled levels of Er^{3+}/Yb^{3+} co-doped $BaBi_2Nb_2O_9$ ferroelectric ceramic**

Authors: First Author Ankita Banwal
Corresponding author Renuka Bokolia

First author's email: ankita.banwal25@gmail.com

Corresponding author's email: renukabokolia@dtu.ac.in

The authors further declare that:

i. The article is original and has been written by the stated author, who is ALL aware of its content and approves its submission.
ii. The article has not been published previously, and it is not under consideration for publication elsewhere.
iii. No conflict of interest exists.
iv. If the article is accepted, it will not be published elsewhere in the same form in any language without the written consent of the publisher.

Thanking You
Yours Sincerely

Dr. Renuka Bokolia

Journal Pre-proof

Journal Pre-proof

Declaration of interests

☒ The authors declare that they have no known competing financial interests or personal relationships that could have appeared to influence the work reported in this paper.

☐The authors declare the following financial interests/personal relationships which may be considered as potential competing interests:

Journal Pre-proof

Journal Pre-proof

Highlights:

- Contactless temperature sensitivity of Er/ Yb co-doped $BaBi_{2-0.04-y}Nb_2Er_{0.04}Yb_yO_9$ ceramic has been reported for the first time.
- The thermometric performance is observed in a wide temperature range (303K-573K).
- Efficient tunable sensitivity is achieved with varying Yb^{3+} concentration (S_a = 0.0069K^{-1} and 0.0058 K^{-1}).
- The energy transfer efficiency from Yb^{3+} to Er^{3+} ions increases by 32%, supported by time resolved measurements.

Journal Pre-proof

Journal Pre-proof

Author Statement

We the undersigned declare that this manuscript is original, has not been published before and is not currently being considered for publication elsewhere. We confirm that the manuscript has been read and approved by all named authors and that there are no other persons who satisfied the criteria for authorship but are not listed. We further confirm that the order of authors listed in the manuscript has been approved by all of us.

We understand that the Corresponding Author is the sole contact for the Editorial process. He/she is responsible for communicating with the other authors about progress, submissions of revisions and final approval of proofs.

Signed by all authors as follows:

Ankita Banwal

Dr. Renuka Bokolia

Journal Pre-proof

Journal Pre-proof

Declaration of interests

☒ The authors declare that they have no known competing financial interests or personal relationships that could have appeared to influence the work reported in this paper.

☐The authors declare the following financial interests/personal relationships which may be considered as potential competing interests:

Journal Pre-proof

2023 4th International Conference for Emerging Technology (INCET)
Belgaum, India. May 26-28, 2023

Electrical and Electronic Architecture of an ROV

1st Sriram Chava
dept. of Electrical Engineering
Delhi Technological University
New Delhi, India
sriramchava_2k19ee248@dtu.ac.in

2nd Saurav Ranjan
dept. of Electrical Engineering
Delhi Technological University
New Delhi, India
sauravranjan_2k19ee226@dtu.ac.in

3rd Shivang Dudani
dept. of Electrical Engineering
Delhi Technological University
New Delhi, India
shivangdudani_2k19ee236@dtu.ac.in

4th Dr Prakash Chittora
dept. of Electrical Engineering
Delhi Technological University
New Delhi, India
prakashchittora@dtu.ac.in

2023 4th International Conference for Emerging Technology (INCET) | 979-8-3503-3575-0/23/$31.00 ©2023 IEEE | DOI: 10.1109/INCET57972.2023.10170661

***Abstract*—A remotely operated underwater vehicle (ROV) is an unmanned vehicle which is controlled from an onshore operator for offshore tasks. ROV finds its use in many underwater applications where direct human interference is not possible. The remote control of an ROV is achieved using a tethered cable for power transmission and communication. In this research work focus has mainly been laid on the vehicle's embedded and electronic composition. The vehicle operates on a 48V power supply and communicates with the onshore system using the RS485 communication protocol.**

***Index Terms*—ROV, Power Distribution, Communication System**

I. Introduction

ROV is classified as an unmanned submersible vehicle that is tethered to the surface by a cable; it has multiple camera's, lights, and thrusters which provide three dimensional maneuverability, depth sensors, and wide array of manipulative and acoustic devices, as well as special instrumentation to perform a variety of work tasks [1]. An ROV is completely operated by a human operator. The human operator is on shore and can control the ROV using a controller additionally a camera feed is also received onshore from the vehicle so that the operator can control the vehicle and its actuators. ROVs have risen in popularity over the years as ROVs can access areas which are dangerous or impractical for a human to access, These vehicles are also low cost and modular. Mini ROV's have a higher freedom for movement and are very economical [2].

ROVs are disadvantageous in situations where freedom of movement is required. The tether for power and communication (Umbilical cord) restricts the vehicle's movement and provides limited movement. The disadvantages also include the fact that the human control is reduced, making visual surveys and analysis more difficult [3]. The first development of an ROV still remains unknown. The PUV (Programmable Underwater Vehicle) was developed by Luppis-Whitehead Automobile, Austria in 1864. It was a torpedo and it made notable contributions towards underwater robotics [4]. The first tethered ROV was developed by Dimitri Rebikoff in 1954 [5]. The United States Navy advanced the technology and developed underwater robots to recover weaponary lost during sea tests. US Navy CURV (Cable Controlled Underwater Recovery Vehicle) recovered an atomic bomb from Palomares Spain in 1966, ROVs also rescued the pilots of a sunken submersible from Ireland in 1973 [5].

Since their development the demand for ROVs has significantly risen. With the advent of new technologies applications of ROVs have diversified. One such appplication is that of pisciculture. An automated IOT based system for fish farming was developed which reduces the human interference. This system was placed in the center of a submersible ROV to explore underwater environments for real-time monitoring of aquatic flora and fauna [6]. This can maximize fish breeding and make the entire process of fish farming economical. Transmission networks are essential for a power transmission network, Hence it is necessary to continuously monitor these transmission lines to detect and repair different faults.

ROVs were implemented for this purpose. The operator can view the transmission lines remotely through a video stream from the ROV. Fault detection systems were also implemented to detect a fault and geo tag the point of failure [7]. This reduces human effort and also makes the fault ddetection systems more rigorous. The demand for oil and gas have risen significantly. Hence it becomes important to detect corrosion/mechanical failures in production, storage and manufacturing facilities. A range of vehicles can be implemented depending on the terrain. ROVs were implemented to monitor, detect and map failures in case of underwater oil and gas facilities [8]. An ROV is usually operated at minimum pitch and roll angles. However tasks can appear which require inspection in a range of angles. An ROV was implemented for ship hull inspection to detect mechanical failures. The ROV has both thrusters and wheels and can be maneuvered in a range of orientations [9]. Underwater mining is another application where ROVs can be utilised. European mine reserves at a depth of 500-1000m are valued at €100 billion [10]. Due to physical and environmental constraints these resources were unreachable. VAMOS (Viable alternative

Authorized licensed use limited to: DELHI TECHNICAL UNIV. Downloaded on July 20,2023 at 11:22:14 UTC from IEEE Xplore. Restrictions apply.

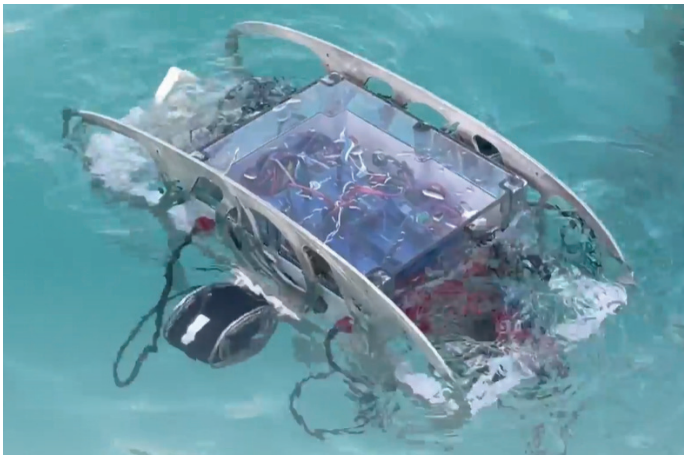

Fig. 1. Prototype ROV

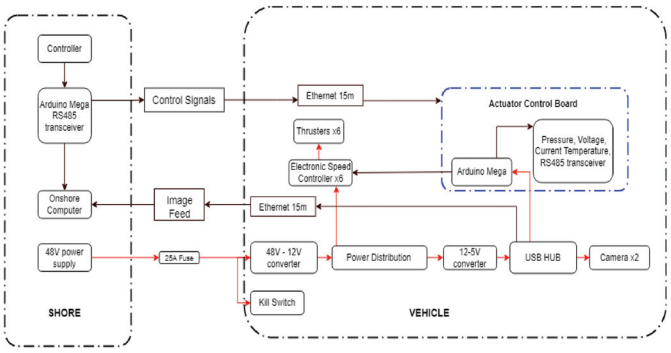

Fig. 2. Electrical and electronic architecture of the ROV

mining operating system) mining solution designed a variety of automated mining and environmental monitoring systems and was field tested successfully [10]. A hybrid ROV/AUV system was developed to support these automated mining systems. The hybrid ROV/AUV was also tested in VAMOS field trials in Lee Moor, United Kingdom [11].

Economical and modular ROVs continue to rise in demand due to their requirements in applications involving underwater inspection and exploration. In this research work we will present the electrical and electronic architecture of an ROV. This will make our vehicle capable of vision, control, manipulation and control. The electronic stack of our vehicle is compact, simple and economical. Further the use of electronic boards makes our vehicle modular and easy to assemble and disassemble. The main aim of this research work is to develop electronic architecture of an ROV which can serve a variety of applications ranging from a personal hobby robot to underwater inspection and exploration.

II. Conceptual Design

This section details the electronic design and architecture of the ROV. The ROV is powered by an onshore 48V power supply which is stepped down to 12V inside the vehicle. The vehicle is equipped with a camera for vision and has connections for 6 thruster's. An inertial measurement unit and a depth sensor are also present which help in pitch, roll and depth stabilisation. The onshore and on-vehicle micro controller communicate with each other using the RS485 protocol over an Ethernet cable. PCB's for power distribution and control were developed to make the system compact, modular and reduce the wiring in the electronic Assembly of the vehicle. The vehicle is controlled using a video game controller and the operator can utilise the camera feed for better control over the vehicle. Figure's 2 and 3 give a pictorial representation of the same. Pin outs for actuators and motors have also been provided on the control PCB for controlling different manipulators. In further sections the power, control and communication subsystem's will be covered in detail.

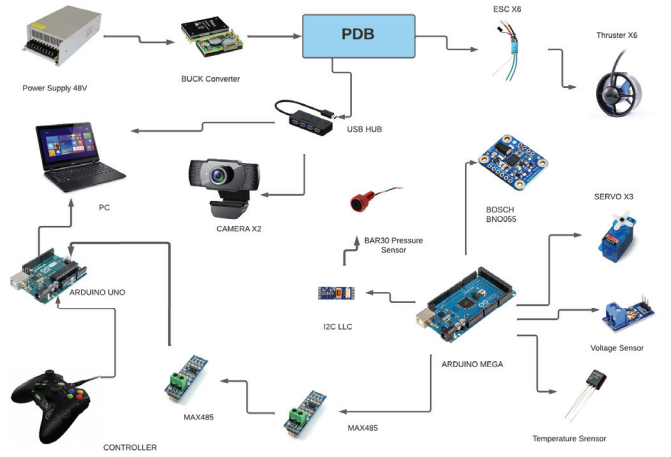

Fig. 3. Conceptual design of the ROV

III. Power Distribution Subsystem

The power subsystem consists of an onshore power supply and two buck converters on board the vehicle. A custom PCB was designed for effective power distribution to the control subsystem, actuators and sensors. The first on board buck converter is a quarter brick converter and it drops down the input 48V to 12V. A quarter brick converter was chosen for this purpose because of its compact size and high current output (75A). The power distribution board (PDB) was designed to make the system more modular and reduce the wiring within the system, this makes it easy to connect and disconnect the system and eliminates the chances of the system suffering a short circuit. The trace widths on the PDB were chosen after considering maximum input current with an additional 10 percent tolerance for all the components and an IPC 2221 PCB standard was also referred [12]. An additional buck converter drops the 12V on the PDB to 5V for the micro controller, camera and all the sensors. The power from the PDB is distributed to the control PCB, electronic speed controllers for the thruster's, camera, and to other actuators for the manipulator. Table 1 represents the current consumption of major components of the ROV.

Authorized licensed use limited to: DELHI TECHNICAL UNIV. Downloaded on July 20,2023 at 11:22:14 UTC from IEEE Xplore. Restrictions apply.

TABLE I
OPERATIONAL VOLTAGES AND CURRENTS OF MAJOR COMPONENTS IN THE ROV

S.No.	Components	Current rating	Voltage rating	Units
1	Thruster	6 A	12 V	6
2	Arduino	0.6 A	5 V	1
3	Pressure Sensor	1.25 mA	5 V	1
4	IMU	12 mA	5 V	1
5	Camera	0.5 A	5 V	2
6	Servo motor	1 A	12 V	2
7	RS485 module	0.5 mA	5 V	1

$$I_{Tot} = \Sigma(I_{Drawn} * N) \tag{1}$$

(6 x 6) + 0.6 + 0.00125 + 0.012 + (0.5 x 2) + (1 x 2) + 0.0005 = 39.6137A

Equation 1 represents the total current (I_{Tot}) drawn by the vehicle when all the components in the vehicle are assumed to be operational at the same time. N represents the number of installed units of each component on the vehicle and I_{Drawn} represents the current drawn by each component, the same can also be found in Table 1.

$$P_{Tot} = \Sigma(V_{Load} * I_{Drawn} * N) \tag{2}$$

72 x 6 + 3 + 0.00625 + 0.06 + 5 + 24 + 0.0025 = 464.06875W

Equation 2 represents the total power consumed by the vehicle when all the components in the vehicle are assumed to be operational at the same time. N represents the number of installed units of each component on the vehicle. V_{Load} represents the operational voltages of each component and I_{Drawn} represents the current drawn by each component. P_{Tot} is the total power consumed by the vehicle when all components are assumed to be operational at the same time and at maximum output. Figure 4 and 5 show the PCB and 3D schematic of the power distribution board.

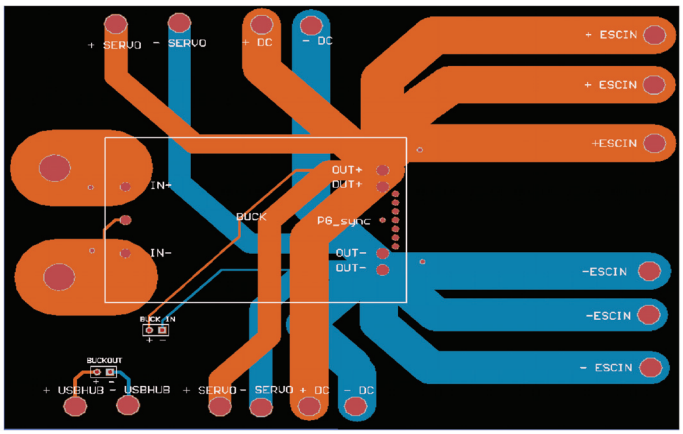

Fig. 4. Power distribution board PCB schematic

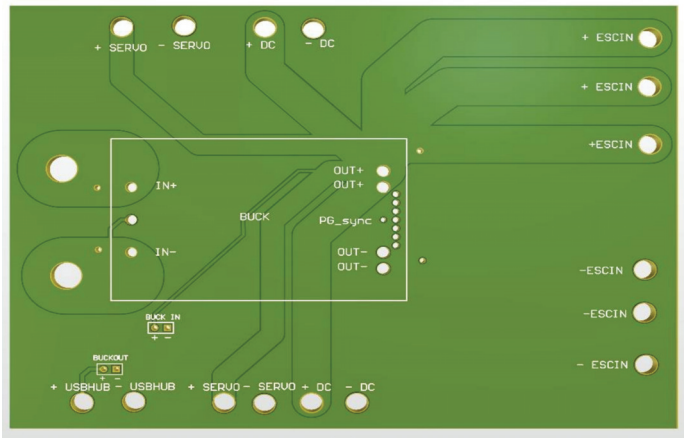

Fig. 5. Power Distribution Board 3D layout

IV. CONTROL SUBSYSTEM

The control subsystem of our vehicle consists of a micro controller, communication module, sensors and actuator connections. ATmega 2560 was utilised as the on board micro processor. ATmega 2560 has a high processing power to support communication and control of our vehicle additionally it also has multiple analog, digital, PWM and communication pins.

ATmega328P was utilised as the onshore microprocessor. A PCB was custom designed which acts as a shield for the for the onboard micro controller and is an interface between all the sensors, communication modules and the main micro controller. One of the challenges we encountered during the prototyping phase was wire management, with an increase in the number of components wire management had become extremely difficult. This arrangement reduces wiring and makes the system very modular. Voltage and current sensors can also be mounted on this PCB which find their use in the debugging phase in order to test a component's functionality.

The pressure sensor finds its use in depth stabilisation and can measure up to 300m depth with a resolution of 2mm. This sensor communicates over the I2C protocol and also includes a temperature sensor which can measure temperature with an accuracy of 1^oC. The inertial measurement unit (IMU) is a 9 axis absolute orientation sensor and communicates over the I2C protocol. The IMU finds its use in pitch and roll stabilisation.

The MAX 485 chip on this PCB acts as a receiver and is responsible for receiving the incoming signal. This signal is then decomposed by the onboard micro controller and signals are accordingly sent to all the peripheral components. The receiver and the sender chips are connected to each other through an Ethernet cable. UART communication pins on the micro controller are utilised for enabling communication between the two micro controllers. Figure 6 shows the 3D layout of the control board along with all the pin outs and connections to the peripheral components. RS485 provides effective communication over a very long range (1200 m) and

Authorized licensed use limited to: DELHI TECHNICAL UNIV. Downloaded on July 20,2023 at 11:22:14 UTC from IEEE Xplore. Restrictions apply.

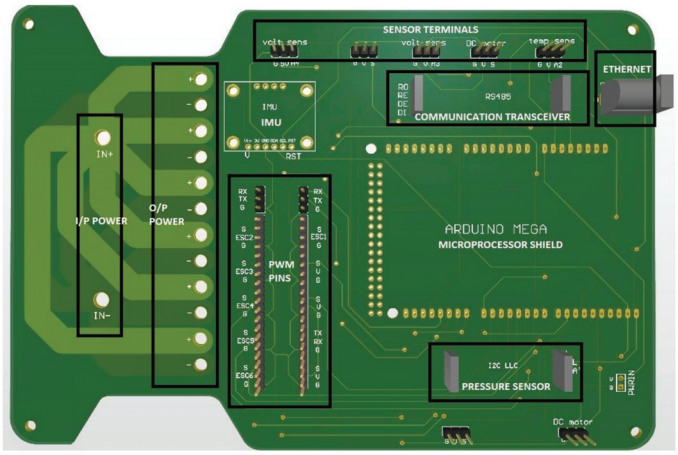

Fig. 6. Control board 3D layout

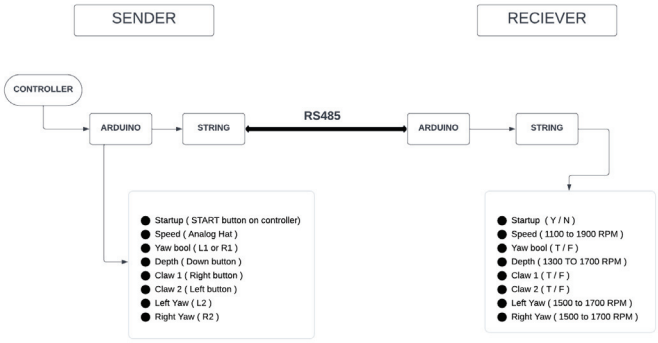

Fig. 7. Communication within the ROV

is easy to setup with the onboard micro controller.

Input power to this PCB comes from the power distribution board (PDB) and all the trace widths for the PCBs have been chosen according to the IPC 2221 norms with an additional 10% tolerance at maximum current consumption. The PCB traces have been extensively tested by running various tests on the sensors, the transceiver and the actuators. The input power at 12V is split into multiple branches to power all the 6 electronic speed controllers aboard the control PCB. This 12V is dropped down to 5V to power the micro controller, communication module, sensors and actuators for the manipulator.

V. Communication System

The communication subsystem of the vehicle covers the inter and intra communication techniques used.

Within the vehicle sensors like the pressure sensor and the inertial measurement unit communicate with the on board micro controller over the I2C (Inter Integrated Circuit) communication protocol. I2C is a bidirectional two-wire synchronous serial bus and requires only two wires to transmit information between devices connected to the bus. This communication protocol can support up to 128 slave devices to interact with a single master device. Each slave device is uniquely identified by the master by addressing each device. I2C was utilised for sensor communication as it is suitable at short range and a single micro controller master can communicate with multiple slave (sensor) devices at once [13]. I2C is also easy to set up as it only requires two wires to communicate. I2C communication protocol is only for devices within close proximity and has a range of up to 10m only.

The communication between the shore and the vehicle happens using RS485 protocol. Figure 7 shows the flow of data from the sender micro controller to the receiver micro controller. RS-485 is a duplex type of data transmission system based on the UART communication protocol. in which many devices on the same bus can send data in both directions. RS-485 is most often used as half-duplex with only a single data transmission line. The intended recipient will listen for its address and then that device will assert control and respond back. This communication protocol can support reliable communication up to 1200m [14]. RS485 was found to be superior over other communication protocols mainly due to effective and low noise data transfer at long ranges. Two RS485 transceivers are utilized for effective communication between the shore and the vehicle. The RS485 transceiver on the vehicle is responsible for receiving messages from the source and relaying it to the onboard microprocessor. The microprocessor then decomposes the incoming data and then accordingly controls different actuators to perform the desired action. The camera feed onboard the vehicle is transmitted to the shore via an Ethernet cable. The sender micro controller is mapped to a game controller and a stream of bits is continuously communicated from the sender to the receiver micro controller, onboard the vehicle. This stream of bits conveys information about the desired yaw, pitch, surge and depth speeds, further it also has information about the state of the vehicle and the manipulator claw motors (Y or N indicating whether the claw is closed or open respectively).

This stream is received by the onboard micro controller and is segmented accordingly into speeds for various thruster's and servo motors. This speed is sent to each actuator and also displayed to the operator at the shore, on the serial monitor. With the serial monitor data and the camera feed an operator can effectively control the ROV.

VI. Conclusion

In this research work an economical and modular electronic stack of an ROV was developed and tested. Different sections of the electronic stack like power distribution, control and communication systems were discussed. Printed circuit boards were also designed to reduce wiring and make the entire system more compact. The power distribution system is responsible for distributing power to all systems aboard the ROV. The control system integrates all the sensor's with the micro controller and is responsible for mapping the ROV's movement with the controller. Communication system discusses the inter and intra vehicle communication. The applications of this ROV can range from being a hobby robot to underwater exploration

Authorized licensed use limited to: DELHI TECHNICAL UNIV. Downloaded on July 20,2023 at 11:22:14 UTC from IEEE Xplore. Restrictions apply.

and inspection tasks. Further modifications will be required to make the vehicle more capable at industrial tasks. The electronic architecture of the ROV was extensively tested as shown in figure 8.

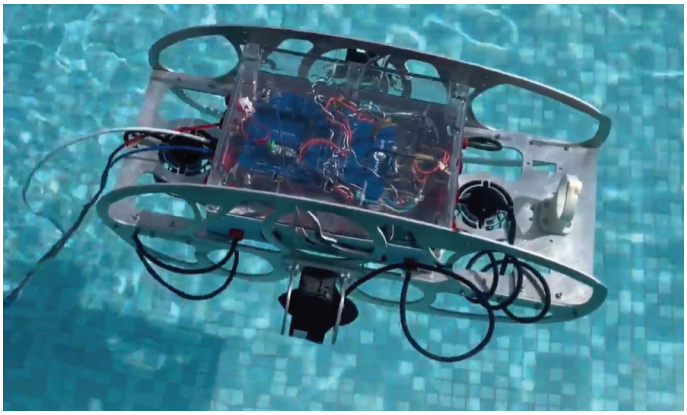

Fig. 8. Prototype ROV during maneuvering testing

REFERENCES

[1] F. A. Azis, M. S. M. Aras, M. Z. A. Rashid, M. N. Othman, and S. S. Abdullah, “Problem identification for underwater remotely operated vehicle (ROV): A case study,” 2012 Procedia Eng., vol. 41, pp. 554–560.

[2] S. Rubin, ”Mini-ROVs, going where no ROV has gone before,” 2013 OCEANS - San Diego, San Diego, CA, USA, 2013, pp. 1-4, doi: 10.23919/OCEANS.2013.6741385.

[3] S. S. Jarrett and W. Dave,T. Tom, “Deep-Sea ROV Cable,” in Proceedings of the 56th International Wire & Cable Symposium, 2007, pp. 401–408.

[4] Y. M. Ahmed, O. Yaakob, and B. K. Sun, “Design of a new low cost ROV vehicle,” J. Teknol., vol. 69, no. 7, 2014.

[5] Remotely Operated Vehicle Committee of the Marine Technology Society, ”History of the ROV Committee”, Marine Technology Society http://www.rov.org/history.cfm (Accessed March 2, 2023).

[6] M. H. Rohit, S. Barua, I. Akter, S. M. M. Karim, S. Akter and M. M. Lutfe Elahi, ”IOT Based Submersible ROV for Pisciculture,” 2019 28th IEEE International Conference on Robot and Human Interactive Communication (RO-MAN), New Delhi, India, 2019, pp. 1-6, doi: 10.1109/RO-MAN46459.2019.8956441.

[7] P. S. Ranaweera, D. C. Alahakoon, K. S. S. Prabhashwara and A. M. G. V. I. Lakmal, ”Autonomous Transmission Line Inspection and Fault Detection System,” 2018 Moratuwa Engineering Research Conference (MERCon), Moratuwa, Sri Lanka, 2018, pp. 402-407, doi: 10.1109/MERCon.2018.8421900.

[8] L. Yu et al., ”Inspection Robots in Oil and Gas Industry: a Review of Current Solutions and Future Trends,” 2019 25th International Conference on Automation and Computing (ICAC), Lancaster, UK, 2019, pp. 1-6, doi: 10.23919/IConAC.2019.8895089

[9] E. Gavrilina, V. Veltishev and A. Kropotov, ”Attitude Control System of a Highly Maneuverable Hybrid ROV for Ship-Hull Inspection,” OCEANS 2021: San Diego – Porto, San Diego, CA, USA, 2021, pp. 1-6, doi: 10.23919/OCEANS44145.2021.9705753.

[10] BMT Group Limited, ”¡Viable and Alternative Mine Operating System!”, European Commission CORDIS, https://cordis.europa.eu/project/id/642477 (Accessed March 3, 2023)

[11] A. Martins, J. Almeida, C. Almeida, B. Matias, S. Kapusniak and E. Silva, ”EVA a Hybrid ROV/AUV for Underwater Mining Operations Support,” 2018 OCEANS - MTS/IEEE Kobe Techno-Oceans (OTO), Kobe, Japan, 2018, pp. 1-7, doi: 10.1109/OCEANSKOBE.2018.8558880.

[12] ”IPC 2221A : Generic standard on printed board design”, IPC.org, https://www.ipc.org/TOC/IPC-2221A.pdf (accessed Dec. 4, 2022)

[13] Jonathan Valdez, Jared Becker,”Understanding the I2C bus”, Texas Instruments, shorturl.at/coPR2 (Accessed Nov 10, 2022)

[14] Thomas Kugelstadt, ”The RS-485 Design Guide”, Texas Instruments, shorturl.at/etES1 (Accessed Nov 7, 2022)

Authorized licensed use limited to: DELHI TECHNICAL UNIV. Downloaded on July 20,2023 at 11:22:14 UTC from IEEE Xplore. Restrictions apply.

Enhancing Accuracy in Handwritten Text Recognition with Convolutional Recurrent Neural Network and Data Augmentation Techniques

Shivanshu Minz*, Ritika Kanojia*, Tushar Yadav* and N.Jayanthi†
*Department of Electronics and Communication Engineering
Delhi Technological University, Delhi, 110042
Email:{minz.shivanshu, ritika29.edu, tusharyadavji15}@gmail.com
†Department of Electronics and Communication Engineering
Delhi Technological University, Delhi, 110042
Email: njayanthi@dce.ac.in

2023 Third International Conference on Secure Cyber Computing and Communication (ICSCCC) | 979-8-3503-0071-0/23/$31.00 ©2023 IEEE | DOI: 10.1109/ICSCCC58608.2023.10176601

***Abstract*—Handwriting recognition is a challenging research area in pattern recognition and image processing that has various applications, such as reading assistance for the blind and digitizing handwritten documents. This study proposes using a convolutional recurrent neural network (CRNN) architecture for handwritten text recognition without the need for segmentation, allowing for the image to be processed in one step. To improve the quality of results and the model, the study employs the CTC decoder to handle the unpredictability that arises when processing multiple alphabets and diverse handwriting. Data augmentation techniques are also utilized to increase the efficiency and accuracy of the model. The study provides detailed information on how to overcome these challenges and improve the accuracy of the proposed model.**

***Index Terms*—Handwritten text recognition, Convolutional Neural Network, Recurrent Neural Network, Data augmentation, CTC decoder**

I. Introduction

The capability of a machine to realize handwriting or analyze handwritten data from many sources such as documents, photos, touch elements, etc. and reading handwritten values is crucial to the cognitive process due to the large storage of facts available.

Morphing handwritten characters into formats that computers can understand is the aim of handwriting recognition techniques. Handwriting recognition software can deduce what is written in handwritten documents, allowing scholars to unearth valuable information hidden on old pages and manuscripts that are difficult to read with the human eye. Hand-written authentication systems are crucial for every organization, aside from past discoveries. Systematic uses of automatic note-taking include: To assist patients, employees, and pharmacists, recognition of scribbled health documents is needed. All of these channels demand large datasets, therefore systems for automatic recognition with higher detection capacity, fast processing, and accurate results. Furthermore, excellent identification precision is needed while designing recognition frameworks. Studies have suggested a multitude of options utilizing systems with manually coded features, neural nets, and other techniques to address these issues with computerized letter algorithms for handwriting and deep learning methods, etc.

In recent times, scholars have observed the usefulness of deep learning techniques, including Convolutional Neural Networks (CNNs) and Recurrent Neural Networks (RNNs). [1]. Without any human input, CNN can simply identify the distinctive elements of images. CNN is the (MLP) framework in its expanded form. The CNN framework's operation resembles the way the human brain processes information. People can help to identify stuff with their unaided eyes by viewing thousands of images of physical things. CNN consistently observes and distinguishes objects in the same way. The primary advantage of using CNN is that it makes use of the original sample's spatial information and is insensitive to thread alterations like scale adjustments, language, etc. Similarly, RNN is also utilised for handwriting recognition, allowing for either a superior or identical method. Given that RNN and CNN might complement each other's shortcomings, a hybrid involving both C-RNN was introduced to make the process more efficient. In this study, the use of the suggested machine-learning model in conjunction with the CTC approach and data augmentation is discussed to increase its overall accuracy [2].

A. Literature Review

The process of conversion of handwritten text into codes that are easy to understand on a computer or any device is known as offline handwritten text recognition. Some of the approaches to recognizing text involve lexically segmenting the sentences or paragraphs first to recognize them.

Segmenting sentences into words and then words into characters are required to recognize the whole sentences or even whole paragraphs as discussed in most related works. This implies that the model can recognize only a single character or a word at a time. Hence in this project, we implemented a model that focuses on recognition at the line level which makes the model independent of the segmentation technique.

Authorized licensed use limited to: DELHI TECHNICAL UNIV. Downloaded on July 20,2023 at 11:12:15 UTC from IEEE Xplore. Restrictions apply.

We've used deep learning techniques to tackle the problem of the robustness of human handwriting and also to deal with its variations.

Optical Character Recognition(OCR) [3] is another widely used technique that is used to convert printed or handwritten text into machine-encoded text [4]. The recognition of handwritten text is commonly divided into two types of techniques, which are analytic and holistic. Analytic techniques involve breaking down the text into individual components to recognize each character, while holistic techniques recognize the text as a whole.

A different approach, Hidden Markov Model (HMM) was discussed in [5] by Yusoff, Mohamed and Bakar. . It involves a probabilistic model which contains different sets of variables such as observational, hidden, or transitional in a matrix. This technique is considered superior as no segmentation was required and recognition was carried out by considering the content of the words for the determination of the next word in a sentence. One of the drawbacks of this technique is that it is still dependent on heavy feature extraction and poses a problem where the handwriting is cursive or the length of the characters is different from each other. In that case, language-specific knowledge is important to train the model. Hence, HMM is not dynamic to change according to such variations in handwriting.

Automatic feature extraction methodologies in deep learning such as CNN and RNN have been used in recent years in the computer vision domain. This has already caught the eyes of researchers who have previously attempted to use deep learning techniques in OCR. Recognition of handwritten text solutions is categorized into offline and online techniques. Online is when we deal with two-dimensional characters with the help of a digital device like a stylus while offline involves the processing of the whole image in which text is handwritten manually like pen on paper.

Since the convolutional neural network (CNN) only accepts inputs of fixed size as well as provide output for the same, fixed size, this causes a disadvantage in cases where different language with different character length are involved.

Wang et al. [6] tried to get rid of this issue by following the conventional flow which involves segmentation and individual recognition of each character. Pre-processing techniques such as Nonmaximald suppression as well as beam search were also used.

Another approach involves recognition as a classification problem which is a very inefficient as well as time-consuming technique for processing characters from different languages.

Another technique involving the use of feature extraction is recurrent neural networks (RNNs). Due to benign popularity in tasks such as NLP and speech recognition, RNN is also widely used for handwritten text recognition. One of the drawbacks of using RNN is that it is not able to process long sequences or datasets involving long-term dependencies.

Hochreiter and Schmidhuber introduced a solution to overcome the limitations of RNN by presenting Long Short Term Memory (LSTM) as a novel approach [7]. LSTM can be visualized as a three-block structure in increasing complexity order which is used to provide memory functionality to the RNN technique to handle long sequences or long-term dependencies. Problems such as vanishing gradients are also dealt with in the introduction of LSTM.

Handwritten text recognition using recurrent neural networks (RNN) has witnessed recent advancements with the introduction of various memory block variations like Multi-dimensional Long term Short Memory (MDLSTM). [7].

The introduction of offline handwritten text recognition which is globally trained and takes input in the form of raw pixel data without any need for linguistic preprocessing was done by Graves et al. Since this method was independent of characteristics of alphabets in language, it can be used for the recognition of various languages. This approach led the way to carry out less segmentation to recognize individual characters first and adopt approaches with which full text can be recognized at once.

Newer methods of handwritten Text Recognition use a combination of techniques such as Convolutional Recurrent Neural Networks(CRNN) to achieve better results [8] .

The architecture of the Convolutional Recurrent Neural Network begins with a conventional convolutional layer obtained from the CNN which has a two-dimensional layout [8]. The subsequent steps include batch normalization, activation through Exponential Linear Units (ELU), max pooling, and dropout, where the dropout rate is set to approximately 50 percent.Three layers are used which are stacked upon each other with their respective activations in a sequential manner. Permute and reshape layers follow convolutional layers as they are essential for CRNN implementation because of the difference in feature vectors in CNN and RNN. 3D layouts are used for convolutional layers feature vectors while 2D layouts are used for recurrent neural networks.

II. Motivation

Despite the advancement in recognition of handwritten words, the glory of the varied nature of one's writing remains a challenge. The IAM dataset, which is widely used for training models, only contains images of handwriting with wide linewidth, limiting the proficiency of models to that type of image. However, real-life handwriting images may have narrow linewidth, random noise, blurriness, and random stretching, making the current dataset less flexible and practical. Therefore, there is a need to find a way to introduce more variety into the dataset to enhance the performance of the models in recognizing words of various types. The proposed method of making the dataset more flexible and diverse could address the limitations of the current dataset and enhance the practicality of the recognition of handwritten words. This could significantly enhance the accuracy and efficiency of the models used for recognizing handwritten words.

III. Proposed Methodology

We approached the problem of offline handwritten text recognition using CRNN [7] in the following way in our

Authorized licensed use limited to: DELHI TECHNICAL UNIV. Downloaded on July 20,2023 at 11:12:15 UTC from IEEE Xplore. Restrictions apply.

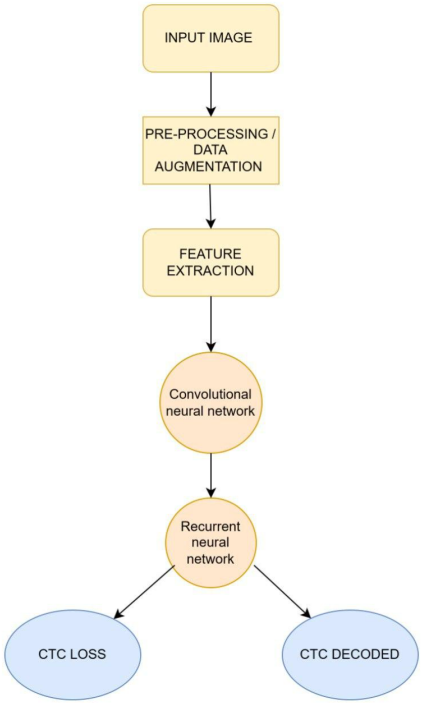

Fig. 1. Proposed Methodlogy Flowchart

paper. For extracting important features from the handwriting recognition dataset, convolutional neural is used first. Before this preprocessing of images takes place as well as date augmentation is carried out for increasing the variation in data in the dataset used. The result then gets passed on to the BLSTM layer to eradicate sequence dependency using time sequence operations. This results in 100 timestamps and 80 characters as output or 100x80, before getting passed on to CNN Fully connected layer of size 512x100. Possible outcomes or results are then observed with the help of labelling through the CTC algorithm.

A. Convolutional Neural Network

This passage provides an overview of the Convolutional Neural Network (CNN) architecture. The CNN design is based on layers, which serve as the basic building blocks, each with a specific task. These layers perform various operations, such as convolution, pooling, complete connection, ReLu, and softmax function. Normalization and dropout functions are also carried out through the layers. The number of layers in the architecture depends on the model function and utilization. In this particular model, there are [9]:

- 3 pooling layers
- 3 fully connected layers
- 5 convolutional layers

along with one layer for the softmax function. The passage provides a brief description of all the layers involved in the CNN architecture.

1) Convolutional Layer: Convolutional neural networks involve the convolution of feature vectors, for which one of the most important layers, i.e. convolutional layers are involved. These layers include structures for efficient implementation of feature convolution and are known as feature maps. These feature maps are formed in the form of a rectangle and involve other units known as neurons which share weights if they belong to the same feature maps and are known as convolutional kernels. These kernels are initialized similarly to random decimal arrays and during training, they can learn reasonable weights. One of the major advantages of these convolutional kernels is that they reduce the connections between layers of the network, hence keeping the whole model architecture less complex. Convolution is carried out by convolutional kernels convolving with upper neurons at a specific stride while the bias is kept adding and giving output simultaneously. The following figure explains the process of carrying out convolution having 0 bias.

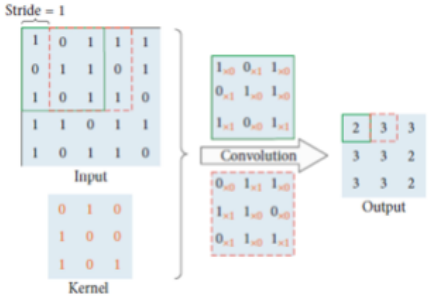

Fig. 2. Working of Convolutional Layer

2) The Pooling Layer: One of the layers that set convolutional neural layers different from other architectures is the inclusion of a pooling layer. The result of output neurons includes some of the information about the neurons at the input; hence, some of this information can be redundant, resulting in increased calculations and increased complexity. A pooling layer is used to carry out pooling operations for concluding convolution results. Another added advantage of pooling layers is that it helps reduce the input array's spatial size, retaining useful information while also preventing overfitting to some extent. Pooling included types such as max pooling and mean pooling. A modified version of pooling is max pooling and works better than mean pooling while working for CNN]. [10]

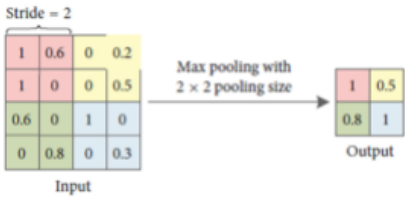

Fig. 3. Max Pooling Layer

3) Full Connection Layer: After the convolution operation, the full connection layer is utilized for logical inference, working similarly to a neural network. It mainly serves to convert the last convolutional layer's output, which is a 3-

Authorized licensed use limited to: DELHI TECHNICAL UNIV. Downloaded on July 20,2023 at 11:12:15 UTC from IEEE Xplore. Restrictions apply.

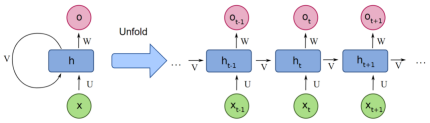

Fig. 4. Structure of Recurrent Neural Network

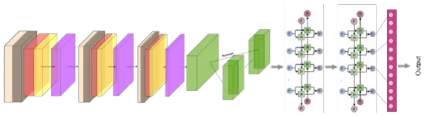

Fig. 5. Structure of Convolutional Recurrent Neural Network or CRNN

dimensional feature vector matrix, into a 1-dimensional output using convolution. The dimension of the kernel used depends on the input dimension in the full connection layer. As a result, the output of the convolutional layer is transformed into integers. The number of convolutional kernels, denoted by k, corresponds to the number of neurons in the first layer of the full connection layer.

4) Softmax Function: To transform numerical values into probabilities, neural networks use activation functions. A popular example of such a function is softmax, which outputs a vector representing the likelihood of each possible outcome. This vector is used to classify the input data. The sum of the probabilities for all possible outcomes in the vector is equal to one, which ensures that the probabilities are normalized.

B. Recurrent Neural Network

The recurrent neural network [11] is used for operating on sequential data in deep learning. This approach came forward before the emergence of CNN and contains the addition of feed-forward network architecture as the prime feature. One of the drawbacks of the RNN is its inability to generalize sequences having varying lengths.

In this network architecture same weights are used belonging to each element present in the given series which helps in reducing the number of parameters eventually adopting a generalized approach for working with handwritten text recognition as the type of alphabet of the language as well as length used will be of no matter at all while training the model. RNN as discussed earlier belongs to a feed-forward network working similarly to a human brain when it comes to using sequential data for training models and also helps in predicting or anticipating data.

C. Convolutional Recurrent Neural Network

The CRNN, which stands for Convolutional Recurrent Neural Network, combines two of the most well-known neural networks, the CNN and the RNN. The proposed CRNN architecture begins with a standard 2D CNN, followed by a sequence of Batch Normalization, Max-pooling, ELU activation layers and dropout with a 50% dropout rate. The architecture includes three convolution layers with their corresponding activations arranged in sequence. However, since the feature vector shape varies from CNN to RNN, a reshape and permute layer is added after the CNN layers to bridge this difference [8].

The feature vectors used in Recurrent Neural Networks are in two dimensions, whereas those in Convolutional Layers are in three dimensions. As CNN is followed by RNN, the conversion of the feature vector from three dimensions to two dimensions is accomplished by using reshape layers. In addition, permute layers and reshape layers are used to change the direction of the axes of the feature vectors.

The proposed model utilizes a pair of bidirectional GRU (Gated Recurrent Unit) layers, with each layer containing a variable number of GRU cells denoted as 'n'. The value of 'n' is dependent on the number of classes used for classification in a related network. It is advisable to steer clear of unidirectional RNN layers, as bidirectional GRU layers are capable of handling future timestamps and their respective representations [8]. The output from the bidirectional layers is ultimately inputted to time-distributed dense layers, followed by a Fully Connected Layer.

D. Connectionist Temporal Classification

Recognizing characters in handwritten text line images is a tough job because of the differences in writing styles. To tackle this issue, CNN models use a loss function called Connectionist Temporal Classification (CTC). CTC is beneficial because it can work with input sequences of varying lengths and does not require any alignment between input and output sequences. This makes it well-suited for recognizing words or sentences with varying lengths, which is frequently encountered in real-world scenarios.

To address the difficulty and time consumption in obtaining labeled data for training, CTC loss function offers a solution where a special "blank" label can be utilized to represent any character in the alphabet. The blank label can be inserted between any two characters or at the beginning or end of the sequence, allowing for variable-length outputs. This reduces the need for extensive labeling of the training data and allows for more efficient use of available labeled data.

The CTC loss function is defined as follows:

Let X be the input image sequence and Y be the corresponding output character sequence. Let B be the blank label. Then the CTC loss is given by:

$$L_{CTC}(X) = -\log \sum_{y \in B^{|Y|}} P(Y|X, y) \tag{1}$$

where $P(Y|X, y)$ is the probability of the output sequence Y given the input sequence X and label sequence y. The summation is over all possible label sequences of length —Y— that include blank labels.

During training, the CNN model is optimized to minimize the CTC loss function, which improves the model's ability to recognize variable-length handwritten text.

The simplest and quickest decoding algorithm in CTC is called Best Path decoding. This method selects the highest probability path as the output sequence. However, Beam

Authorized licensed use limited to: DELHI TECHNICAL UNIV. Downloaded on July 20,2023 at 11:12:15 UTC from IEEE Xplore. Restrictions apply.

Search decoding is a more sophisticated approach that examines multiple high-probability paths and attempts to locate the optimal sequence. However, it is more computationally expensive than Best Path decoding. to counter the inaccuracy issues associated with Best Path decoding, Data Augmentation is applied which is explained further in the next section.

IV. Results and Experiments

A. Dataset and Data Augmentation

To assess the efficiency of our proposed CNN-based approach for recognizing handwritten text, we performed experiments on the IAM dataset, a commonly used benchmark dataset in the field of handwriting recognition. The IAM dataset contains approximately 10,000 text lines written by 657 writers, with a total of 115,320 words that are both labeled and isolated. These text lines are collected from diverse sources like letters, newspaper articles, and stories, which cover an extensive range of content topics and writing styles. The dataset also comprises metadata like line IDs, writer IDs, and transcriptions of each word.

TABLE I
Summary of IAM Dataset

Set Name	*Number of Sentences*	*Number of Writers*
Train Set	6162	284
Validation-1	901	45
Validation-2	939	44
Test	1860	129
Total	9862	502

However, the dataset has some limitations that affect its representativeness for real-world applications. Firstly, the images only contain writings with thick line widths, while real-world handwritten texts can have various line widths and styles. Secondly, the images are pre-segmented and aligned, which may not reflect the actual variability of handwriting styles in unconstrained settings. Lastly, the dataset has a limited size and diversity, which may not be sufficient to train models that can generalize well to other domains. To address these challenges, we employed several data augmentation techniques, which we describe in detail in this section.

We found that applying four different techniques of data augmentations was sufficient for improving the recognition performance of our convolutional neural network (CNN) model. These techniques included varying the line thickness of the handwritten text (along with ref to image examples), adding random noise to the image, applying a blur filter to the image, and randomly stretching the image. Fig. 6 showcase the employed techniques at work. These data augmentation techniques helped to create a more diverse and representative dataset, which improved the robustness and accuracy of the CNN model in recognizing handwritten words with different styles and variations.

B. Results

The CNN model was trained using the IAM dataset for 15 epochs with a batch size of 1268. During training, the model

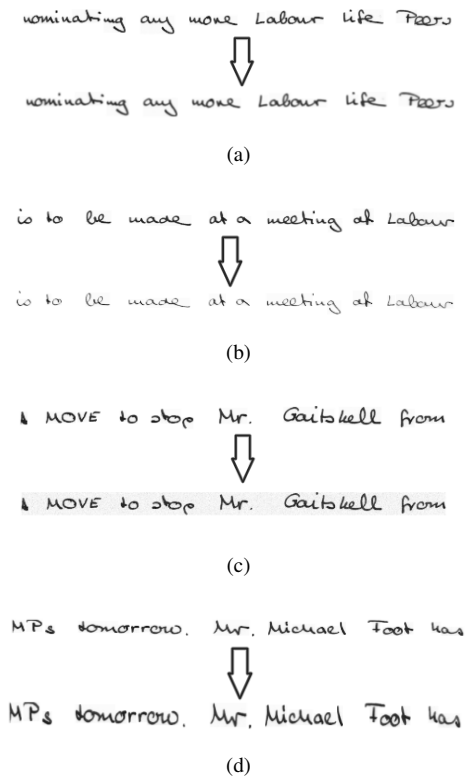

(a) (b) (c) (d)

Fig. 6. Various Data Augementaion Techniques. (a): Blur, (b): Reduced Line Thickness, (c): Random Noise, (d): Random Stretch

was set to save if the character error rate improved and stop if no improvement was observed for 5 epochs. The trained model achieved an accuracy of 0.97 on the validation set. Fig 7 demonstrate the progression through each epoch.

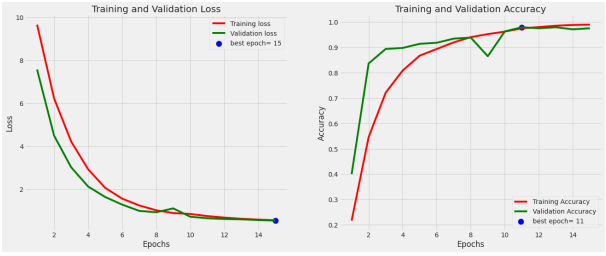

Fig. 7. Training and Validation data loss and accuracy per epoch

Recall is the measure of the ratio of the positives that are truly out of all positive samples which are actually indeed positive, while precision is the measure of the ratio of positives that were true out of all positive samples that were predicted. The F1 score refers to the mean calculated in a harmonical way using the values of precision and recall.

$$F_1 = 2 \cdot \frac{\text{precision} \cdot \text{recall}}{\text{precision} + \text{recall}} \tag{2}$$

In the context of the CNN model parameters, the recall, precision, and F1 score provide insight into the model's ability to correctly classify handwritten text. The high values achieved

Authorized licensed use limited to: DELHI TECHNICAL UNIV. Downloaded on July 20,2023 at 11:12:15 UTC from IEEE Xplore. Restrictions apply.

in this study (Table II) demonstrate the effectiveness of the proposed CNN model for handwritten text recognition.

TABLE II
PERFORMANCE METRICS OF THE MODEL

Metrics	*Values*
Accuracy	0.97
Precision	1
Recall	1
F1 Score	1

The effectiveness of the proposed method can be demonstrated through various examples presented in the figure 8. Each example includes an input image of handwritten text and the corresponding recognized text. In comparison to other

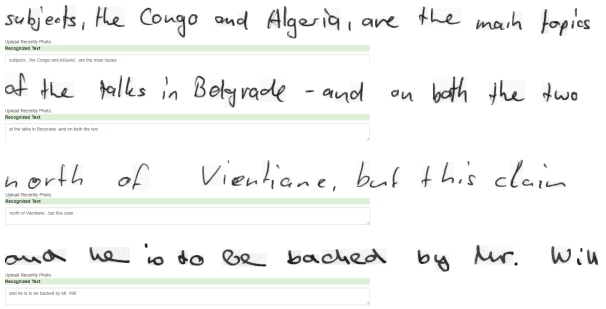

Fig. 8. Predicted texts on some example images from IAM dataset

studies, our proposed method achieved a high recognition rate of 97% on the largest dataset. This is an improvement in comparison to the work done by Marti and Bunke, which used HMM and Statistical Language Model for handwritten sentence recognition. Similarly, Dimla and Smith utilized CNN and beam search CTC decoding.In our study, we employed Best Path CTC decoding, which is faster but can be less accurate. However, we addressed this issue by integrating different data augmentation methods, leading to a high level of accuracy. Our proposed approach is compared to other studies on the biggest dataset, demonstrating its effectiveness as shown in Table III. Furthermore, we present examples of the recognition results of our system in Fig 8, which illustrates the input image and the recognized text.

TABLE III
COMPARISON WITH PREVIOUS WORKS

	Method Used	***Mean accuracy***
Bunke and Martin [12]	HMM and statistical language model	60.05%
Dimla and Smith [4]	CNN with Word Beam CTC decoder	93,31%
Implemented Method	**CNN with Best Path CTC decoder**	**97%**

V. CONCLUSION AND FURTHER IMPROVEMENT

The task of recognizing handwritten text was accomplished with an accuracy of more than 95% using the proposed CNN model with CTC decoder. To enable faster recognition, Best Path decoding was employed despite being more susceptible to inaccuracies. Nevertheless, data augmentation techniques such as blur filter, random noise, random stretch, and line thickness were integrated into the model to mitigate this issue. The batch size of 10 was determined based on the GPU memory limit of the computer system, and the training process was halted after 15 epochs as no further improvement was noted.

In order to further improve the performance of the proposed system for handwritten text recognition, there are several areas that could be explored. Firstly, better image preprocessing techniques could be applied to handle real-time images more accurately. For instance, edge detection and image binarization techniques could be applied to improve image quality, and hence recognition accuracy. Additionally, line segmentation could be added to the proposed system, to enable processing of whole paragraphs for handwritten text recognition. This could be achieved using existing line segmentation techniques, such as the Longest Path Algorithm or Vertical Projection. Finally, different CTC decoders, such as the Beam Search decoder or the Connectionist Decoding Time Warping (CDTW) decoder, could be experimented with to see which results in the highest recognition accuracies. By exploring these areas, the proposed system could potentially achieve even higher accuracies for handwritten text recognition.

REFERENCES

[1] A. J. Simon Fong, Nilanjan Dey, "Ict analysis and applications: Proceedings of ict4sd 2019," *Springer Science and Business Media LLC*, 2022.

[2] A. Khanna, D. Gupta, Z. Pólkowski, S. Bhattacharyya, and O. Castillo, "Ict analysis and applications: Proceedings of ict4sd 2019," *Springer Science and Business Media LLC*, 2022.

[3] H. Mule, N. Kadam, and D. Naik, "Handwritten text recognition from an image with android application," in *2022 IEEE Fourth International Conference on Advances in Electronics, Computers and Communications (ICAECC)*, 2022, pp. 1–5.

[4] H.-P. Tran, A. Smith, and E. Dimla, "Offline handwritten text recognition using convolutional recurrent neural network," in *2019 International Conference on Advanced Computing and Applications (ACOMP)*, 2019, pp. 51–56.

[5] I. M. M. I. Mohd Yusoff and M. R. A. Bakar, "Hidden markov models: An insigh," *Proceedings of the 6th International Conference on Information Technology and Multimedia*, pp. 259–264, 2014.

[6] T. Wang, D. J. Wu, A. Coates, and A. Y. Ng, "End-to-end text recognition with convolutional neural networks," in *Proceedings of the 21st International Conference on Pattern Recognition (ICPR2012)*, 2012, pp. 3304–3308.

[7] S. Hochreiter and J. Schmidhuber, "Long short-term memory," *Neural computation*, vol. 9, pp. 1735–80, 12 1997.

[8] H. Natarajan, D. Jos, O. Mahadik, and Y. Shahare, "Chapter 44 career advisor using ai," *Springer Science and Business Media LLC*, 2023.

[9] T. Gueye, Y. Wang, M. Rehma, R. T. Mushtaq, and A. Hassan, "Machine learning for control systems security of industrial robots: a post-covid-19 overview," *Research Square Platform LLC*, pp. 1–6, 2022.

[10] J. Zhang, Y. Ling, X. Fu, X. Yang, G. Xiong, and R. Zhang, "Model of the intrusion detection system based on the integration of spatial-temporal features," *Comput. Secur.*, vol. 89, 2020.

[11] Y. Zhou and X. Jiao, "Intelligent analysis system for signal processing tasks based on lstm recurrent neural network algorithm," *Neural Computing and Applications*, vol. 34, pp. 1–13, 08 2022.

[12] U.-V. Marti and H. Bunke, "The iam-database: An english sentence database for offline handwriting recognition," *International Journal on Document Analysis and Recognition*, vol. 5, pp. 39–46, 11 2002.

Authorized licensed use limited to: DELHI TECHNICAL UNIV. Downloaded on July 20,2023 at 11:12:15 UTC from IEEE Xplore. Restrictions apply.

ResearchGate

See discussions, stats, and author profiles for this publication at: https://www.researchgate.net/publication/371856149

EXPLORING THE DYNAMICS OF HEUTAGOGY IN STEM EDUCATION AND ITS POTENTIAL FOR ENHANCING LEARNING

Conference Paper · June 2023

CITATIONS
0

READS
20

5 authors, including:

Vaibhav Verma
Regional Institute of Education (NCERT), Ajmer
18 PUBLICATIONS **7** CITATIONS
SEE PROFILE

Charmy Panchal
Indian Institute of Teacher Education, Gandhinagar, Gujarat
5 PUBLICATIONS **1** CITATION
SEE PROFILE

Jijo Varghese
Regional Institute of Education Ajmer (NCERT)
16 PUBLICATIONS **6** CITATIONS
SEE PROFILE

Ranjan Kumar Singh
Central University of Bihar
7 PUBLICATIONS **33** CITATIONS
SEE PROFILE

Some of the authors of this publication are also working on these related projects:

A Comparative Study of Gurukul and Contemporary Education Systems View project

INDIAN HIGHER EDUCATION IN A GLOBAL SOCIETY View project

All content following this page was uploaded by Vaibhav Verma on 26 June 2023.

The user has requested enhancement of the downloaded file.

Research Article

EXPLORING THE DYNAMICS OF HEUTAGOGY IN STEM EDUCATION AND ITS POTENTIAL FOR ENHANCING LEARNING

Author 1: Mr. Vaibhav Verma, Post Graduate Scholar, Master of Education (M.Ed.), Department of Education, Regional Institute of Education (NCERT), Ajmer, Rajasthan, India – 305004. Email: vaibhav.rie@gmail.com

Author 2: Miss Charmy Panchal, Assistant Professor, Center of Education, Indian Institute of Teacher Education, Gandhinagar, Gujarat, India.

Author 3: Dr. Jijo Varghese, Assistant Professor, Department of Education, Regional Institute of Education (NCERT), Ajmer, Rajasthan, India – 305004.

Author 4: Mr. Ranjan Kumar Singh, Assistant Professor, Department of Education, Regional Institute of Education (NCERT), Ajmer, Rajasthan, India – 305004.

Author 5: Er. Rishabh Verma, Graduate Engineer, Alumni Department of Electronics and Communication, Delhi Technological University, New Delhi, India.

Author Note

Vaibhav Verma ORCID ID: 0000-0003-0024-1237

The authors declared no potential conflicts of interest concerning this article's research, authorship, and publication.

Correspondence concerning this article should be addressed to Vaibhav Verma, Post Graduate Scholar, Master of Education (M.Ed.), Department of Education, Regional Institute of Education (NCERT), Ajmer, Rajasthan, India - 305004. Phone: 8851556175. Email: vaibhav.rie@gmail.com

View publication stats

Abstract

The field of education is always developing to meet the ever-changing needs of students. The present study provides an overall understanding of Heutagogy, a learner-centered approach by encompassing its concept, principles, benefits & challenges and its potential to enhance learning in STEM education. It also reviews studies of the implementation of Heutagogy in various educational contexts and discusses the current status and integration of heutagogy in STEM education. The paper further presents a conceptualization of Heutagogy and a Reflective-Connective-Generative Model (RCG) as a tripolar conceptual framework for its implementation. The paper highlights the potential of Heutagogy to enhance learning outcomes in STEM education and identifies areas for future research. The research contributes to the ongoing discourse on innovative pedagogical approaches in STEM education and provides insights for educators and policymakers to design effective learning environments that foster self-determined learning.

Keywords: *Heutagogy, STEM education, Self-determined learning, Lifelong-learning,*

FACE RESTORATION VIA GENERATIVE ADVERSARIAL NETWORKS

Sonu Kumar
Dept. of Information Technology
Delhi Technological University
Delhi,India
sonuuno17@gmail.com

Soham Bhardwaj
Dept. of Information Technology
Delhi Technological University
Delhi,India
sohambhardwaj17@gmail.com,

Dinesh Kumar Vishwakarma
Dept. of Information Technology
Delhi Technological University
Delhi,India
dinesh@dtu.ac.in

2023 Third International Conference on Secure Cyber Computing and Communication (ICSCCC) | 979-8-3503-0071-0/23/$31.00 ©2023 IEEE | DOI: 10.1109/ICSCCC58608.2023.10176746

***Abstract*— The objective of face restoration or de-occlusion is to eliminate occluded regions in facial images that are caused by objects or disguises. This study proposes an innovative approach to address the challenge of facial image de-occlusion. Specifically, the proposed method employs a Deep Convolutional Generative Adversarial Network (DCGAN) to restore blocked regions of facial images, resulting in enhanced visual clarity and completeness. We utilize GANs which are trained on both occlusion-free and occluded images, enabling the restoration of corrupted facial regions. Furthermore, we achieve effective model training through mixed precision training. Our method shows promising results on testing images, successfully restoring facial images with up to 50% blocked regions.**

Keywords*— *Face de-occlusion, Generative Adversarial Network, Deep Convolutional Neural Network.

I. INTRODUCTION

As a result of the progress in the domain of computer vision, occluded face restoration has turned into a hot direction of computer vision. In the field of security, individuals engaged in illegal activities often conceal their faces. So people pay more and more attention to occluded face restoration. The combination of Convolution Neural Networks and Generative Adversarial Networks has demonstrated significant potential in the field of face restoration. Recent deep learning-based face recognition methods have surpassed or matched human performance. However, these algorithms are typically trained on image datasets consisting of occlusion-free facial images. Consequently, their ability to recognize distorted images, caused by occlusion or disguises, such as masks, sunglasses, scarves, objects, or hands, may be limited.

"Facial inpainting" is an intuitive approach to address this problem, involving the recovery of obscured areas of input images (also known as face completion).

Two types of face inpainting techniques are currently employed. The first group considers input images taken in restricted conditions (e.g., from a front view, with specific types of occlusion). Recursive PCA was used in [1] to rebuild eye regions covered by glasses or sunglasses, while Markov random field were used in [2] to ensure the local spatial continuity in the support for generated mistakes. However, the drawback of such techniques is that they require image samples of the intended painting subject in their training data, which may not always be feasible in real-world applications.

The second category of face inpainting techniques focuses on handling unconstrained input images. It was suggested to inpaint occluded or corrupted images using an already trained GAN in [3]. However, these techniques rely on pre-determined positions and sizes of the occluded regions, which may not be applicable in realistic scenarios (unless manual segmentation of occluded regions is performed). A generator based on embedding and a discriminator with a multi-model architecture were proposed in [4].

In this study, we address the problem of face restoration for images of unconstrained faces with occlusions. A black square is used as an occlusion instead of the actual occlusion (such as sunglasses) in order to effectively restore the large area of randomly occluded face images. We present an algorithm for face image restoration that takes an occluded face image and produces a de-occluded face image, wherein the blocked region is restored

II. PROPOSED METHOD

A. GANs History

This paper utilizes a GAN model as its basis, and thus it is essential to understand the fundamentals of GANs to fully comprehend the proposed approach. The original concept of GAN was presented in [5], and it comprises two key components; the generator & the discriminator.

$$\min \boldsymbol{G} \ \max \boldsymbol{D} \ V(D,G) = E_{x\sim P_{data}(x)} \log D_{\theta_d}(x) + E_{z\sim P_z(z)} \log\left(1 - D_{\theta_d}\left(G_{\theta_g}(z)\right)\right) \quad (1)$$

Here $\boldsymbol{G}$ refers to Generator (generate fake images i.e., generative model) $\boldsymbol{D}$ refers to Discriminator (Discriminate between original and fake image work as Binary classification model) refers to discriminator.

$P_{data}(x)$: Real data distribution

$P_z(z)$: Input data distribution

$G_{\theta_g}(z)$: Generated Distribution

θ_d and θ_g are respectively discriminator and generator parameters.

This equation represents the loss function of a GAN model, which is a deep learning framework for generating synthetic data that resembles real data.

Authorized licensed use limited to: DELHI TECHNICAL UNIV. Downloaded on July 20,2023 at 11:10:23 UTC from IEEE Xplore. Restrictions apply.

The equation consists of two main parts :

1. Discriminator loss term: the first term in the equation represents the expected value of the logarithm of the discriminator's probability output D(x) given real data samples x. The discriminator aims to maximize this term, so it learns to assign high probabilities to real samples.

2. Generator loss term: the second part of the above equation represents the expected value of the logarithm of the discriminator's probability output for the generated fake sample G(z). The objective of the generator is to minimize this term, which enables it to acquire the ability to generate samples which possess a significantly high likelihood of being identified as authentic by the discriminator.

The overall objective of the GAN is to find the optimal parameters for both the generator G and the discriminator D that minimize the generator loss while maximizing the discriminator loss.

B. Proposed Face De-Occlusion GAN

Our study involves the development of Deep Convolutional Generative Adversarial Network models for two distinct sets of images, each with varying image sizes of 64x64 and 128x128 pixels. The occluded face images are fed into the generator of our Generative Adversarial Network for restoration, while the discriminator is simultaneously prepared and trained against the generator. Both models are trained in a zero-sum manner, where each model competes with the other to establish its dominance. Specifically, the generator component strives to produce increasingly realistic images to deceive the discriminator, while the discriminator component aims to identify between the real and fake images produced by the generator model. Upon successful convergence of the algorithm, we obtained a trained generator model capable of producing high-quality, occlusion-free images when presented with occluded images as input.

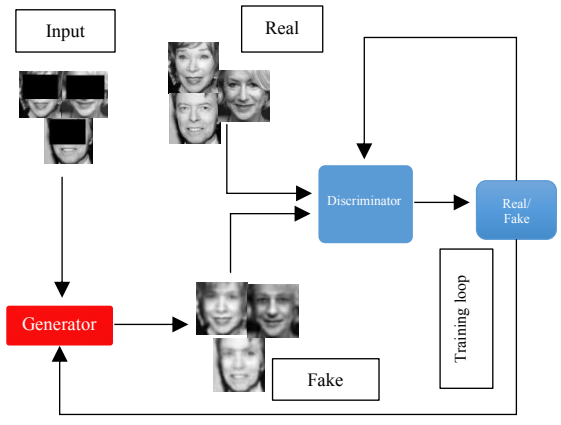

Fig. 1. Flowchart of Proposed GAN framework

Algorithm: Face restoration via Face De-Occlusion GAN

Input:
Set of face images with occlusion Z
Set of face images without occlusion X

Output: Set of restored face images Y

Notation :
$G \Longrightarrow$ Generator model
$D \Longrightarrow$ Discriminator model
$N \Longrightarrow$ Number of Epochs
$d_in \Longrightarrow$ Discriminator input
$d_out \Longrightarrow$ Discriminator output

Algorithm :
Initialize generator model G and discriminator model D

# Train the GAN model in a zero-sum manner to minimize
# the min-max loss function
for $i = 0$ *to* N **do**

Batch of face images with occlusion z from Z

Batch of face images without occlusion x from X

$y \longleftarrow$ Generate fake images for z by using G

If $i\%2 = 0$ **then**
$d_in = y$
$d_out = 0$

Else if $i\%2 != 0$ **then**
$d_in = x$
$d_out = 1$
End if

Discriminator loss for face images with or
without occlusion
Compute $logD_{\theta_d}(d_in)$

Update Discriminator weights
$W_d \longleftarrow$ Back-propagate gradients

Generator loss for generated face images
Compute $\log\left(1 - D_{\theta_d}(y)\right)$

Update Generator weights based on output y
and decision of discriminator for y
$W_g \longleftarrow$ Back-propagate gradients

End for

C. Mixed precision training

Mixed precision training is a technique that can significantly improve the speed of model training by using a combination of single precision (float32) and half-precision (float16) data

Authorized licensed use limited to: DELHI TECHNICAL UNIV. Downloaded on July 20,2023 at 11:10:23 UTC from IEEE Xplore. Restrictions apply.

types. However, to leverage this approach, access to a GPU with a compute compatibility score of 7.0 or higher is required. By utilizing mixed precision training, our model performs computations using half-precision and stores the final results in single precision. This technique is particularly effective as half-precision data types require fewer bits to store a number, which results in faster computational tasks and can lead to significant speed improvements of up to three times compared to single precision alone.

III. Experimental Results

A. Dataset

To train our Generative Adversarial Network (GAN), we utilized a subset of the CelebA dataset, consisting of 5000 face images. To create the input images for training, we overlaid a black mask on top of the original images, resulting in a set of 4471 pairs of face images with occlusion and their corresponding unobstructed counterparts. Similar kind of images have been used in [6]. We used 3000 pairs for training purpose, while the remaining pairs were reserved for validation and testing.

B. Implementation

Our work involves training two Generative Adversarial Networks (GANs) with different input and output image sizes. For each GAN model, we constructed two convolutional neural networks to facilitate the training. We have defined the building blocks of our model as follows:

Combo layer consists of a convolution layer, then batch normalization and an activation function; Reverse Combo layer is made up of a convolution transpose layer, then batch normalization & an activation function.

The generator model made of a sequence of combo layers. Each combo layer contains a convolution layer that convolve over the normalized data, followed by batch normalization to normalize it back and an activation function. To process 64x64 size face images, we employed three combo layers with dropout layer and two reverse combo layers. For 128x128 size face images, we used four combo layers with dropout layers and three reverse combo layers.

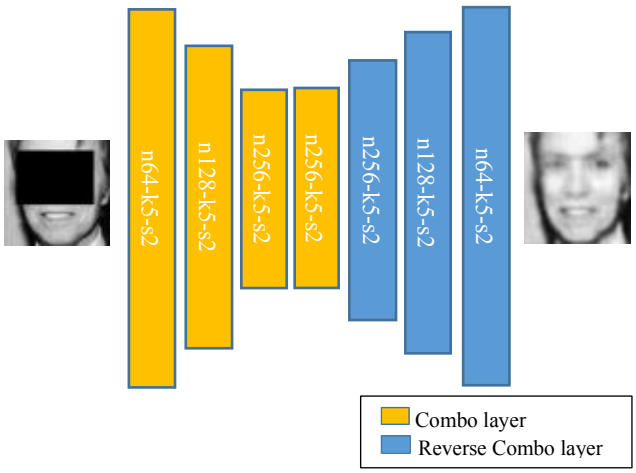

Fig. 2. Block diagram of Generator

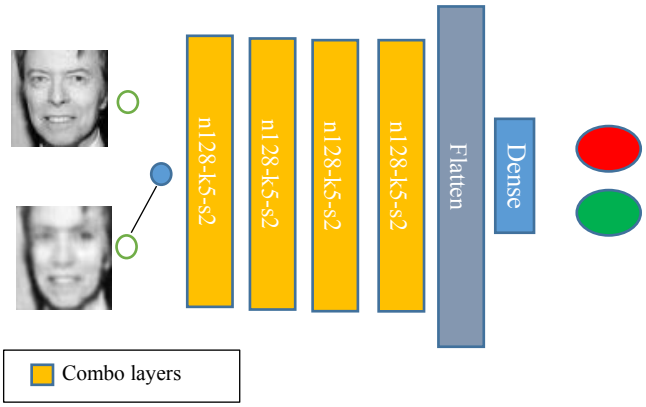

Fig. 3. block diagram of Discriminator

For the discriminator model, we utilized four combo layers combined with a dropout layer, which allowed for the differentiation between real and fake face images of sizes 64x64 and 128x128. To adding non-linearity, we have used Leaky-ReLU as our Activation function.

C. Qualitative Evaluation

To evaluate the performance of face restoration, we have chosen to evaluate its performance on images of faces that have been occluded by black masks. These occluded images and their corresponding original, unobstructed faces are used as test inputs. While our approach gives us promising restoration results, but it still has some drawbacks. We can see the input image that has occlusion has a face captured at a certain angle not a front view with some facial expression (upward eyebrows) which is covered by occlusion. We can say our model has certain limitations with pose variation.

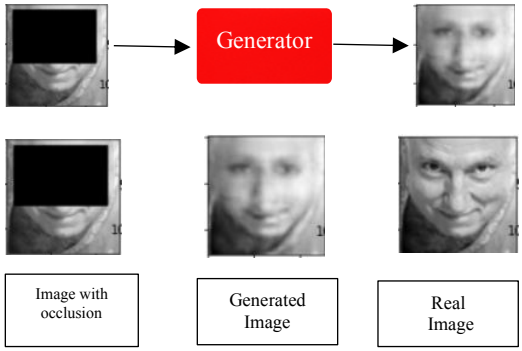

Fig.4. Image Generated by Generator

In Fig. , We can see that Generator starts converging around 100 epochs for performing face restoration via GAN and in Fig. 6. Images Generated by 100 epochs of generator model training for 64x64 image size the images generated by generator model after 100 epochs of training for 64x64 image size shows after 100 epochs of training generator gives us good results. It signifies the average rate of convergence of our proposed technique for the restoration of damaged regions within images. Additionally, the discriminator model's output value hovers around 0.5, indicating that the generated images are becoming increasingly realistic and more similar to the original images. Consequently, the discriminator becomes

Authorized licensed use limited to: DELHI TECHNICAL UNIV. Downloaded on July 20,2023 at 11:10:23 UTC from IEEE Xplore. Restrictions apply.

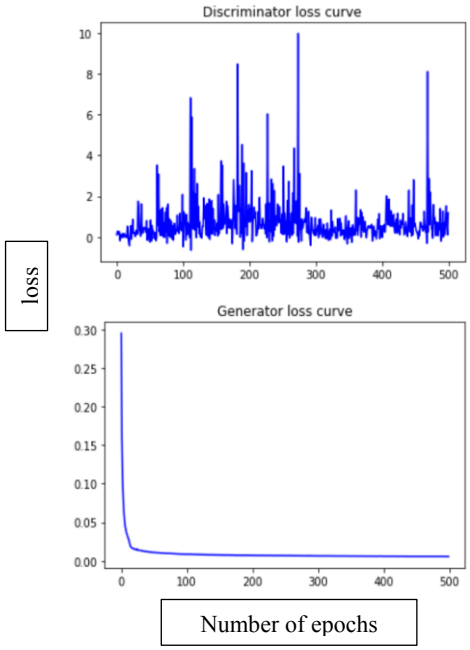

Fig. 5. 500 epochs of model training for 64x64 image size

less certain in differentiating between the generated and actual images. This outcome suggests that the generator dominates over the discriminator after some epochs of training, leading to the development of a generator that can produce highly realistic images.

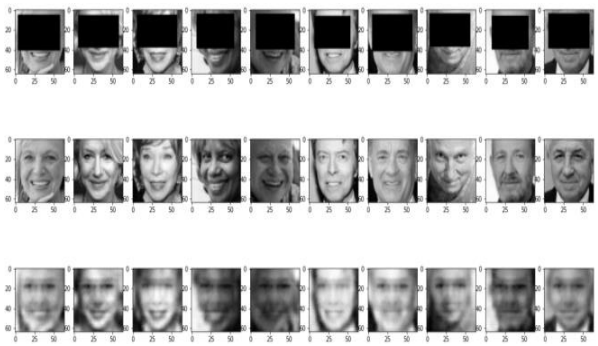

Fig. 6. Images Generated by 100 epochs of generator model training for 64x64 image size

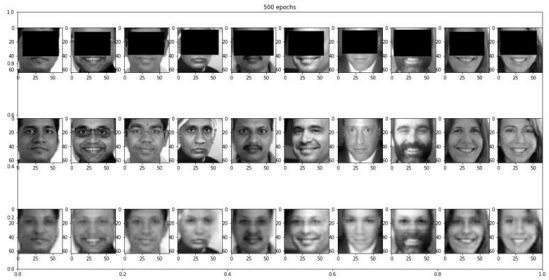

Fig. 7. Image generated by Generator after 500 epochs of training for 64x64 images size

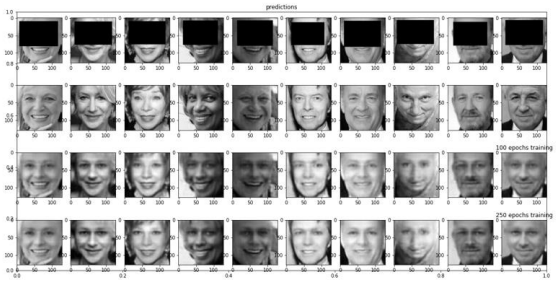

Fig. 8. Image generated by Generator after 100 and 250 epochs of training for 128x128 image size

D. Quantitative Evaluation

original images by generator so to measure performance of our generative model using a traditional approach of predictive model is not a good idea to evaluate our GAN model. It is proposed in [7] as a method for evaluation of the performance of GANs for image generation, they used the “Fréchet Inception Distance" (FID). In the field of deep learning, it is a commonly employed metric for evaluating the similarity between two probability samples. It is calculated by comparing the activations of a pre-trained neural network on real and de-occluded images. A lower FID score is indicative of a higher degree of resemblance between the generated images and the real ones, whereas a higher score implies the opposite. FID is considered to be a more robust and accurate evaluation metric compared to other methods, as it takes into account both the quality and diversity of the generated images. So, we also use this approach to evaluate our GAN model:

Fréchet Inception Distance = 85 %

The FID for our generator model is 82~87 %. It varies in this range for different sets of images.

Table I. Effect of mixed precision for training for 64x64 image size

Number of epochs	With Batching (in min)	With batch and mixed precision (in min)
5 epochs	6	2
500 epochs	210	75

As we used mixed precision training to train our model from Table I. Effect of mixed precision for training for 64x64 image size, we can see how fast our model trains without affecting the performance of our model.

IV. Conclusion

Through this paper, a face restoration algorithm is implemented to address the issue of restoring the corrupted regions of face images . The algorithm can recognize the occluded area in the face, and then repair the facial structure by leveraging both global features of the entire face as well as local characteristics of the non-occluded area. Experimental evaluation of the algorithm on relevant datasets demonstrates significant improvements in restoration

Authorized licensed use limited to: DELHI TECHNICAL UNIV. Downloaded on July 20,2023 at 11:10:23 UTC from IEEE Xplore. Restrictions apply.

accuracy for facial images with occlusion areas of up to 50%. The Generative Adversarial Network (GAN) models implemented with mixed precision training to reduce training time and encourage experimentation. Finally, Generator models (one for 64x64 image size and another for 128x28 image size) are created with a decent FID score.

V. Future Work

The proposed approach could be improved to handle occlusion in different facial poses. The current implementation demonstrates limitations with pose variations, indicating the potential for further development in this area. This can be done by using more diverse dataset with multi-angled facial images. Additionally, exploring the use of different types of occlusions beyond black masks could provide valuable insights into the algorithm's generalizability. Another potential direction for future work could be to evaluate the algorithm's performance on larger-scale datasets and conduct a comparative analysis with the existing state-of-the-art methods.

References

[1] Jeong-Seon Park, You Hwa Oh, Sang Chul Ahn, and Seong-Whan Lee, "Glasses removal from facial image using recursive error compensation," IEEE Trans Pattern Anal Mach Intell, vol. 27, no. 5, pp. 805–811, May 2005, doi: 10.1109/TPAMI.2005.103.

[2] Zihan Zhou, A. Wagner, H. Mobahi, J. Wright, and Yi Ma, "Face recognition with contiguous occlusion using markov random fields," in 2009 IEEE 12th International Conference on Computer Vision, IEEE, Sep. 2009, pp. 1050–1057. doi: 10.1109/ICCV.2009.5459383.

[3] R. Y. Yeh, C. Chen, T. Lim, M. Hasegawa-Johnson, and M. N. Do, "Semantic image inpainting with perceptual and contextual losses," 2016.

[4] X. Zhang et al., "DE-GAN: Domain Embedded GAN for High Quality Face Image Inpainting," Pattern Recognit, vol. 124, p. 108415, Apr. 2022, doi: 10.1016/j.patcog.2021.108415.

[5] I. J. Goodfellow et al., "Generative Adversarial Networks," Jun. 2014.

[6] Z. Li, H. Zhu, L. Cao, L. Jiao, Y. Zhong, and A. Ma, "Face Inpainting via Nested Generative Adversarial Networks," IEEE Access, vol. 7, pp. 155462–155471, 2019, doi: 10.1109/ACCESS.2019.2949614.

[7] M. Heusel, H. Ramsauer, T. Unterthiner, B. Nessler, and S. Hochreiter, "GANs Trained by a Two Time-Scale Update Rule Converge to a Local Nash Equilibrium," Jun. 2017.

Authorized licensed use limited to: DELHI TECHNICAL UNIV. Downloaded on July 20,2023 at 11:10:23 UTC from IEEE Xplore. Restrictions apply.

Journal of Public Health
https://doi.org/10.1007/s10389-023-01981-7

ORIGINAL ARTICLE

Financial burden of injury care in India: evidence from a nationally representative sample survey

Mehak Nanda[1] · **Rajesh Sharma**[2]

Received: 30 January 2023 / Accepted: 7 June 2023
© The Author(s), under exclusive licence to Springer-Verlag GmbH Germany, part of Springer Nature 2023

Abstract

Objective Injuries are a global public health concern, claiming a life every six seconds worldwide. Amidst the rising burden of injuries, this study comprehensively examines the out-of-pocket health expenditure (OOPE) and associated financial burden across seven categories of injuries in India.

Data and methodology This study used data from the latest nationally representative health survey, conducted by the National Sample Survey Organization (2017–18). Descriptive statistics and multivariable logistic regression were employed.

Results We found that 49.3% of injury-affected households experienced catastrophic health expenditure, with 17.8% of households falling into poverty, and 52.1% of households using distressed sources due to OOPE for hospitalization. Injuries such as intentional self-harm, burns or corrosions, and accidental injuries, road traffic accidents and falls imposed a colossal financial burden on households. The average loss of household income due to any injury was INR 3911.5 (USD 57.3). The brunt of OOPE was substantially higher when care was sought from private hospitals rather than public hospitals. Households residing in rural areas, belonging to lower economic quintiles, primarily earning from casual and other work, utilizing private health facilities, and lacking insurance coverage were more likely to experience higher financial burden when seeking care for injuries.

Conclusion High financial burden of injuries calls for policy measures such as increasing government health expenditure, strengthening public healthcare facilities, increasing health insurance enrolment, and prioritizing prevention strategies and safety interventions.

Keywords Out-of-pocket expenditure · Injuries · Distressed financing · Impoverishment · Catastrophic health expenditure

Introduction

Injuries are a major cause of death and disability, accounting for 8% of deaths and 10% of disability-adjusted life years worldwide (World Health Organization (WHO) 2019a). Globally, more than five million people die each year due to injuries, which is 1.7 times the number of fatalities from HIV/AIDS, tuberculosis, and malaria combined (WHO 2014). Nearly 90% of injury-related deaths occur in low and middle-income countries (WHO 2021). In 2016, India accounted for 36.6% of global suicide deaths among females and 24.3% of global suicide deaths among males (Dandona et al. 2018). Worldwide, India ranked first among 199 countries in terms of road accident mortality in 2018, accounting for nearly 11% of global accident-related deaths (Government of India (GOI) 2019a). Notably, India witnessed 54.9% increase in deaths due to unintentional injuries and 25.8% increase in suicide deaths from 1999 to 2019 (National Crime Records Bureau (NCRB) 2020). The economic consequences of any injury are dire, resulting in hefty medical and non-medical expenses, as well as productivity losses (WHO 2014). A recent study estimated that total medical costs due to road traffic accidents in India was USD 0.82–1.92 billion in 2019 (Kumaresh et al. 2021). Furthermore, India has one of the lowest public health expenditures (1.15% of gross domestic product) (National Health Policy 2017), as well as one of

✉ Rajesh Sharma
rajesh.sharma@nitkkr.ac.in

[1] University School of Management and Entrepreneurship, Delhi Technological University, New Delhi, India

[2] Humanities and Social Sciences, National Institute of Technology, Kurukshetra, Haryana, India

Published online: 14 July 2023

the highest out-of-pocket health expenditures (OOPE) (58.7% of total health expenditure) worldwide (National Health Systems Resource Centre 2019). Heavy reliance on OOPE exposes households to financial catastrophe, falling into or intensification of poverty, depletion of household assets, or even worse, treatment abstinence. In India, abysmally low health insurance coverage (GOI 2019b) coupled with a dominant fee-for-service private health sector forces households to rely on OOPE. Medical payments are a major cause of poverty in India, pushing nearly 32–39 million individuals below the poverty line every year (Bonu et al. 2007; Garg and Karan 2009; Van Doorslaer et al. 2006).

Estimating the cost and economic burden of injuries has been recognized as one of the priority areas to address the global burden of injuries (Chandran et al. 2010). However, limited literature is available on the financial burden associated with seeking care for injuries in India. Previous studies have only estimated the OOPE burden for specific injuries such as accidental injury, road traffic accidents, and falls (Goli et al. 2018; Pradhan et al. 2017; Ram and Thakur 2022), or drowning (Yadav et al. 2022), or were restricted to particular geographic areas (Kumar et al. 2012; Prinja et al. 2016, 2019). One study estimated the financial burden for all injuries combined and was based on an older dataset (Tripathy et al. 2018). Another study was limited to estimating only catastrophic health expenditure (CHE) due to injury care in India (Yadav et al. 2021). Moreover, to the best of our knowledge, no study in the Indian context has estimated CHE using the household's capacity-to-pay approach (Xu et al. 2003) for all categories of injuries.

Against this background, we provide a holistic examination of the financial burden due to hospitalization for seven categories of injuries, disaggregated by the type of healthcare facility, either public or private. Specifically, our study was guided by the following objectives. First, we estimated OOPE and determined the share of various components, such as medicines, doctors' fees, transportation costs, etc., in the total health expenditure. Second, we estimated the financial burden of OOPE using a battery of metrics, including incidence of incurring CHE, percentage of households falling into poverty due to OOPE, and incidence of using distressed financing. Third, we assessed the loss of household income resulting from hospitalization due to injuries. Last, we explored the factors associated with experiencing CHE, impoverishment, and distressed financing due to OOPE for injury care in India. Amidst the increasing burden of injuries in India, analyzing the financial impact of seeking care for these injuries using nationally representative estimates of healthcare costs could aid in the development of financial risk protection strategies for Indian households.

Data and methodology

Overview of data source

This study used data from the latest nationally representative health survey, entitled 'Household Social Consumption: Health,' conducted by the National Sample Survey Organization (NSSO). The survey was conducted between July 2017 and June 2018 and covered 555,115 individuals from 113,823 households across the country. It employed a stratified, multi-stage sampling design, with census villages in rural areas and urban blocks in urban areas as the first stage units, and households as the second stage units. The survey collected detailed information regarding diseases and injuries, utilization of healthcare facilities, healthcare expenditure, and demographic and socio-economic characteristics of households and their members.

Outcome variables

Out-of-pocket health expenditure (OOPE)

The NSSO survey collected information on expenses incurred for hospitalization during the past 365 days. The total expenditure was recorded under three subheads: 1) medical expenditure such as doctors' fees, expenses for medicines, bed, and diagnostic tests, other medical expenses, package component[1], 2) non-medical expenditure such as registration fees, food, lodging charges, etc., and 3) transportation expenditure. To estimate the OOPE, we deducted any reimbursements received from the total expenditure.

Catastrophic health expenditure (CHE)

The literature recommends two alternative methods to estimate CHE. Under the first method, health payments are defined as catastrophic if they exceed a

[1] Package component includes expenses for various items used in surgical or non-surgical treatment, such as operation theatre (OT) charges, OT consumables, bed charges, costs of medicines, and doctors' fees. However, it does not cover expenses associated with physiotherapy, additional diagnostic tests, blood, oxygen, personal medical appliances, attendant charges, etc. The package component is commonly provided by private hospitals (NSSO 2018).

certain fraction of the household's income or consumption expenditure (Berki 1986). However, this method does not account for the CHE of poorer households as the poor spend less on health due to their lower paying ability. Therefore, we used the capacity-to-pay approach, which defines health payments as catastrophic if they exceed 40% of the household's capacity to pay (Xu et al. 2003):

$$CHE_i = \begin{cases} 1, if \ \frac{OOPE_i}{CE_i - SE_i} > 0.4 \\ 0, if \ \frac{OOPE_i}{CE_i - SE_i} \leq 0.4 \end{cases}$$

In the above equation, $OOPE_i$ denotes the out-of-pocket health expenditure of i^{th} household, CE_i represents the consumption expenditure of i^{th} household, and SE_i is the subsistence expenditure of i^{th} household.

The subsistence expenditure is calculated using either food expenditure or the official poverty line (Mohanty and Kastor 2017). However, since the NSSO survey does not collect information on individual expenditure items, such as food and non-food items, the food expenditure was unavailable. Therefore, we used the inflation-adjusted, official poverty line issued by the Tendulkar Committee[2] (Planning Commission 2014) as a proxy for subsistence expenditure (Bonu et al. 2009; Mohanty and Kastor 2017). The poverty line was multiplied by the household size to determine a household's subsistence expenditure, which was then subtracted from household consumption expenditure to estimate a household's capacity to pay (Bonu et al. 2009; Engelgau et al. 2012).

The proportion of households experiencing CHE was estimated using the following formula:

$$Incidence\ of\ CHE = \frac{1}{N}\sum_{i=1}^{N} CHE_i$$

where N is the total number of households.

Poverty headcount ratio

The poverty headcount ratio estimates the proportion of households dragged below the poverty line due to OOPE (Yadav et al. 2022) and is calculated as follows:

$$Poverty\ headcount_i = \begin{cases} 1, & if\ CE_i \geq PL\ and\ \left(CE_i - OOPE_i\right) < PL \\ 0, & otherwise \end{cases}$$

In the above equation, $OOPE_i$ denotes the out-of-pocket health expenditure of i^{th} household and CE_i represents the consumption expenditure of i^{th} household. PL is the inflation-adjusted, official poverty line as defined by the Tendulkar Committee (Planning Commission 2014).

$$Poverty\ headcount\ ratio = \frac{1}{N}\sum_{i=1}^{N} poverty\ headcount_i$$

where N is the total number of households.

Incidence of using distressed sources to finance OOPE

We categorized a household as using distressed sources if it relied on borrowing, sale of physical assets, use of contributions from friends or relatives, or other sources to finance OOPE (Sangar et al. 2020).

The proportion of households employing various sources of finance to cope with OOPE was calculated as follows:

$$I = \frac{1}{N}\sum_{i=1}^{N} k_i$$

In the above equation, I is the incidence of employing a particular source of finance, and k is the number of households employing a particular source of finance.

The NSSO survey recorded sources of finance as major and second major sources, since households may have used more than one source to finance hospitalization-related OOPE. In this study, we combined both the first and second major sources of finance (Sangar et al. 2020). Hence, the cumulative incidence of all sources of finance may exceed 100% in some cases.

Statistical analysis

Descriptive statistics and multivariable logistic regression were employed in the study.

Multivariable logistic regression was used to gauge the factors associated with experiencing CHE, impoverishment, and distressed financing due to OOPE for injury care:

$$logit\left(\pi_i\right) = \beta_0 + \beta_1 X_1 + \beta_2 X_2 + \cdots + \beta_n X_n$$

In the above equation, π_i is the probability of occurrence of binary outcome variable, i.e. incurring CHE, impoverishment, and distressed financing for the i^{th} household. $X_1 \ldots X_n$ represent variables, namely economic quintiles, social group, household's principal source of income, religion, age, sex,

[2] In 2005, the Planning Commission constituted an expert group under the chairmanship of Professor Suresh D. Tendulkar (henceforth, Tendulkar Committee) to review the methodology for estimating poverty in India. The poverty line suggested by the Tendulkar Committee has been used by the government to publish official poverty estimates in India (Ministry of Rural Development 2020).

Table 1 OOPE and associated financial burden, and loss of household income due to various injuries

Injury	OOPE (INR)	Incidence of CHE (%)	Poverty headcount ratio (%)	Incidence of distressed financing (%)	Loss of household income (INR)
Accidental injury, road traffic accidents, and falls	29,966.5 [28,567.0–31,366.1]	49.7 [48.5–50.9]	18.1 [17.2–19.0]	52.5 [51.3–53.8]	4,101.1 [3,845.0–4,357.3]
Accidental drowning and submersion	24,823.9 [16,262.3–33,385.4]	41.6 [34.0–49.2]	8.5 [4.2–12.9]	52.4 [44.7–60.2]	3,592.1 [2,737.9–4,446.3]
Burns and corrosions	28,298.5 [21,141.0–35,455.9]	56.7 [49.4–64.1]	26.7 [20.1–33.2]	53.2 [45.8–60.6]	2,916.1 [2,356.5–3,475.8]
Poisoning	12,230.6 [8,362.7–16,098.4]	36.1 [28.4–43.9]	9.2 [4.6–13.9]	34.8 [27.1–42.5]	1,750.4 [1,369.9–2,130.9]
Intentional self-harm	35,028.9 [15,690.4–54,367.5]	65.9 [49.3–82.4]	33.7 [17.2–50.2]	67.7 [51.1–84.3]	2,777.4 [1,506.3–4,048.5]
Assault	16,585.9 [7,346.5–25,825.2]	43.7 [29.3–58.1]	15.9 [5.3–26.5]	50.1 [35.6–64.6]	3,102.2 [1,473.7–4,730.8]
Contact with venomous/harmful animals or plants	9,946.6 [5,218.0–14,675.2]	44.7 [36.4–53.0]	10.3 [5.2–15.3]	51.3 [43.0–59.7]	1,542.8 [1,147.0–1,938.6]
All injuries	28,754.5 [27,461.0–30,048.1]	49.3 [48.1–50.4]	17.8 [16.9–18.7]	52.1 [50.9–53.2]	3,911.5 [3,680.6–4,142.5]

OOPE, Out-of-pocket health expenditure; *CHE*, Catastrophic health expenditure

[ ] 95% confidence interval

educational status of household head, place of residence, health insurance status, and type of healthcare facility.

Results

Out-of-pocket health expenditure (OOPE) and share of various components

Table 1 shows the average OOPE of households by injury type. Intentional self-harm caused the highest OOPE (INR 35,028.9)[3], followed by accidental injuries, road traffic accidents, and falls (INR 29,966.5), and burns and corrosions (INR 28,298.5). The average hospitalization-related OOPE was fivefold higher when care was sought from private health facilities (INR 41,503.9) compared to public health facilities (INR 7,873.4). This trend was similar across almost all types of injuries (Table 2). The primary reasons for choosing private, rather than public health facilities were non-availability of doctors or unsatisfactory quality of public health facilities, preference for a trusted doctor/hospital, long waiting time at public health facilities, and required services not available (Fig. 1).

The cost of various components in total health expenditure varied considerably by the type of healthcare facility, although medicines constituted the largest share in the case of both public (30.0%) and private health facilities (23.5%) (Fig. 2). Notably, the relative burden of other non-medical expenses and transportation expenditure was higher in public health facilities (29.4% and 16.9%, respectively) compared with private health facilities (7.2% and 3.9%, respectively). In the case of private health facilities, doctors' fees (20.0%) and package component (15.5%) were the leading contributors to total health expenditure after medicines. A similar pattern was observed across most injuries.

Financial burden

Out of all households which sought hospitalization for any injury, 49.3% of households incurred CHE (Table 1). Households where a member inflicted intentional self-harm reported the highest CHE (65.9%), followed by households where a member suffered burns and corrosions (56.7%), and accidental injury, road traffic accidents, and falls (49.7%). The incidence of CHE was 1.5 times higher when care was sought from private health facilities (57.0%) than public health facilities (36.3%) (Table 2).

Table 1 shows that 17.8% of all injury-affected households which sought hospitalization were pushed below the poverty line due to OOPE. The percentage of households falling below the poverty line due to hospitalization-related OOPE was the highest for intentional self-harm (33.7%), burns and corrosions (26.7%), and accidental

[3] USD 1= INR 68.3 using average 2018 exchange rate.

Table 2 OOPE and associated financial burden by type of healthcare facility

Injury	Public health facilities				Private health facilities			
	OOPE (INR)	Incidence of CHE (%)	Poverty headcount ratio (%)	Incidence of distressed financing (%)	OOPE (INR)	Incidence of CHE (%)	Poverty headcount ratio (%)	Incidence of distressed financing (%)
Accidental injury, road traffic accidents, and falls	8,267.8 [7,625.5–8,910.2]	36.0 [34.1–37.8]	6.1 [5.2–7.0]	38.8 [37.0–40.7]	41,945.3 [39,776.1–44,114.4]	57.0 [55.4–58.6]	24.7 [23.3–26.1]	60.0 [58.4–61.6]
Accidental drowning and submersion	5,825.4 [3,686.3–7,964.6]	45.5 [32.1–59.0]	3.6 [0.9–6.4]	40.4 [27.2–53.7]	34,899.0 [21,931.9–47,866.0]	40.8 [31.2–50.3]	10.8 [4.8–16.9]	58.4 [48.8–68.0]
Burns and corrosions	6,897.0 [5,068.8–8,725.3]	43.6 [33.7–53.4]	5.5 [1.0–10.0]	47.8 [37.9–57.7]	38,359.5 [25,741.0–50,978.0]	64.1 [52.7–75.4]	40.3 [28.6–51.9]	54.4 [42.6–66.1]
Poisoning	4,483.4 [3,259.5–5,707.3]	27.6 [18.3–36.9]	6.4 [1.3–11.5]	30.2 [20.7–39.8]	33,023.0 [22,816.7–43,229.3]	58.1 [44.9–71.3]	16.9 [6.8–26.9]	45.9 [32.6–59.3]
Intentional self-harm	26,855.8 [4,659.6–49,051.9]	57.5 [35.1–79.9]	23.2 [4.0–42.3]	58.5 [35.5–81.5]	48,303.9 [6,594.5–90,013.4]	81.7 [67.3–96.1]	51.0 [27.9–74.2]	84.4 [69.9–98.7]
Assault	4,342.1 [2,957.3–5,727.0]	34.7 [16.6–52.8]	18.5 [3.7–33.2]	42.3 [23.6–61.1]	50,233.3 [24,664.7–75,801.9]	59.7 [34.7–84.8]	11.2 [0.7–21.9]	63.7 [39.1–88.3]
Contact with venomous/harmful animals or plants	4,102.3 [3,031.2–5,173.4]	39.7 [30.4–49.1]	5.2 [1.0–9.5]	43.2 [33.7–52.6]	29,312.3 [9,716.1–48,908.5]	61.0 [43.1–78.9]	27.0 [10.7–43.2]	78.3 [63.2–93.4]
All injuries	7,873.4 [7,295.6–8,451.2]	36.3 [34.6–38.0]	6.3 [5.5–7.2]	39.1 [37.4–40.8]	41,503.9 [39,441.1–43,566.7]	57.0 [55.4–58.5]	24.8 [23.4–26.1]	59.9 [58.4–61.4]

OOPE, Out-of-pocket health expenditure; *CHE*, Catastrophic health expenditure

[ ] 95% confidence interval

injuries, road traffic accidents, and falls (18.1%), whereas accidental drowning and submersion resulted in the lowest poverty headcount ratio (8.5%). The impoverishment impact was conspicuously higher among households which sought care in private health facilities compared to those treated in public health facilities (24.8% versus 6.3%). This trend was similar across most injuries (Table 2).

Furthermore, 52.1% of all injury-affected households relied on distressed sources to cope with the hospitalization-related cost of injuries (Table 1). Notably, more than 50% of households resorted to distressed financing for all injury categories, except poisoning. Borrowing (33.8%) and contributions from friends or relatives (15.6%) were the most common sources of distressed financing, whereas sale of physical assets (0.7%) was the least preferred coping mechanism (Fig. 3). The incidence of distressed financing was higher for households in which any member was treated in private health facilities (59.9%) compared to public health facilities (39.1%) (Table 2).

Loss of household income

In addition to the financial burden of OOPE, households also face indirect costs such as loss of earnings due to the inability of the patient or the caregiver to work. Table 1 shows that the average loss of household income due to hospitalization for any injury was INR 3,911.5, varying from INR 1,542.8 in case of contact with venomous or harmful animals or plants to INR 4,101.1 in case of accidental injury, road traffic accidents, and falls. Accidental drowning and submersion (INR 3,592.1), assault (INR 3,102.2), and burns and corrosions (INR 2,916.1) also inflicted losses in the household income.

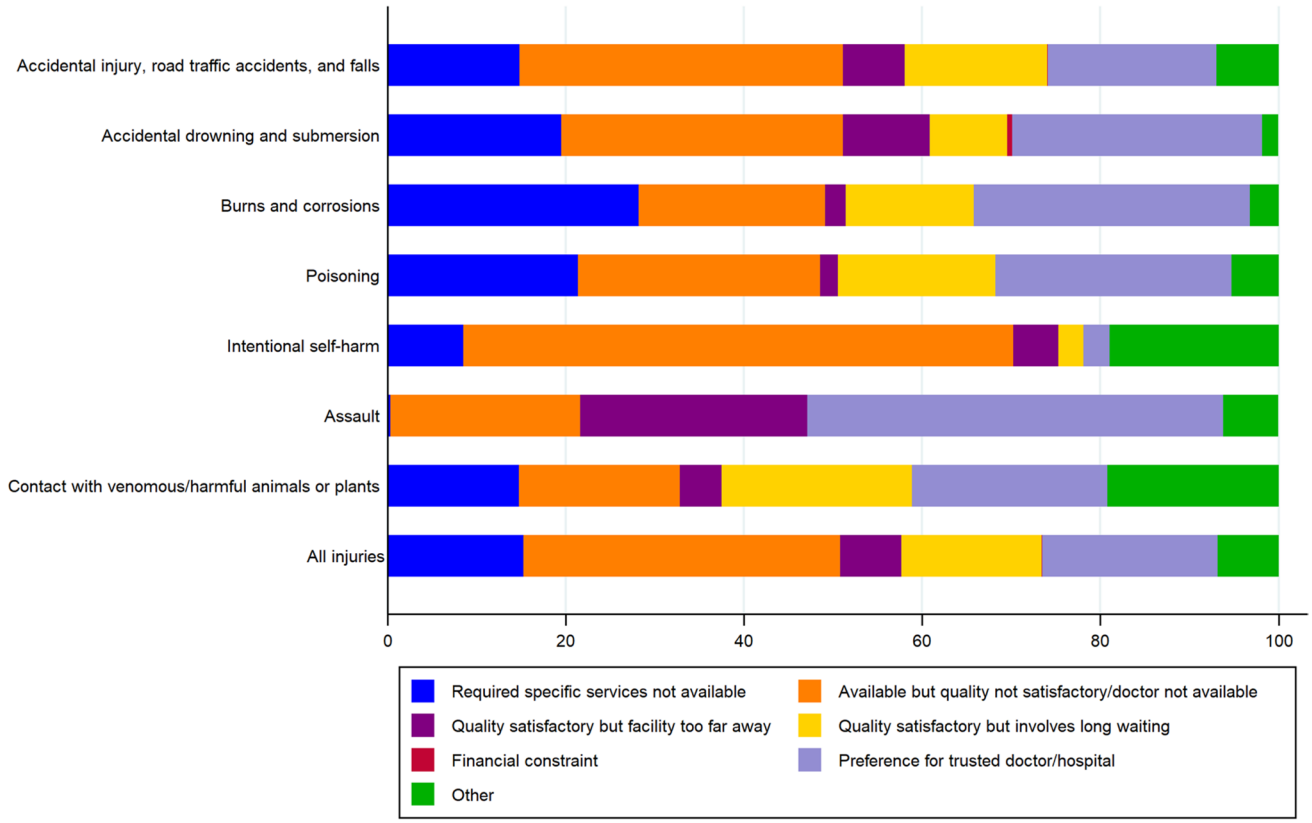

Fig. 1 Reasons for not choosing public healthcare facilities

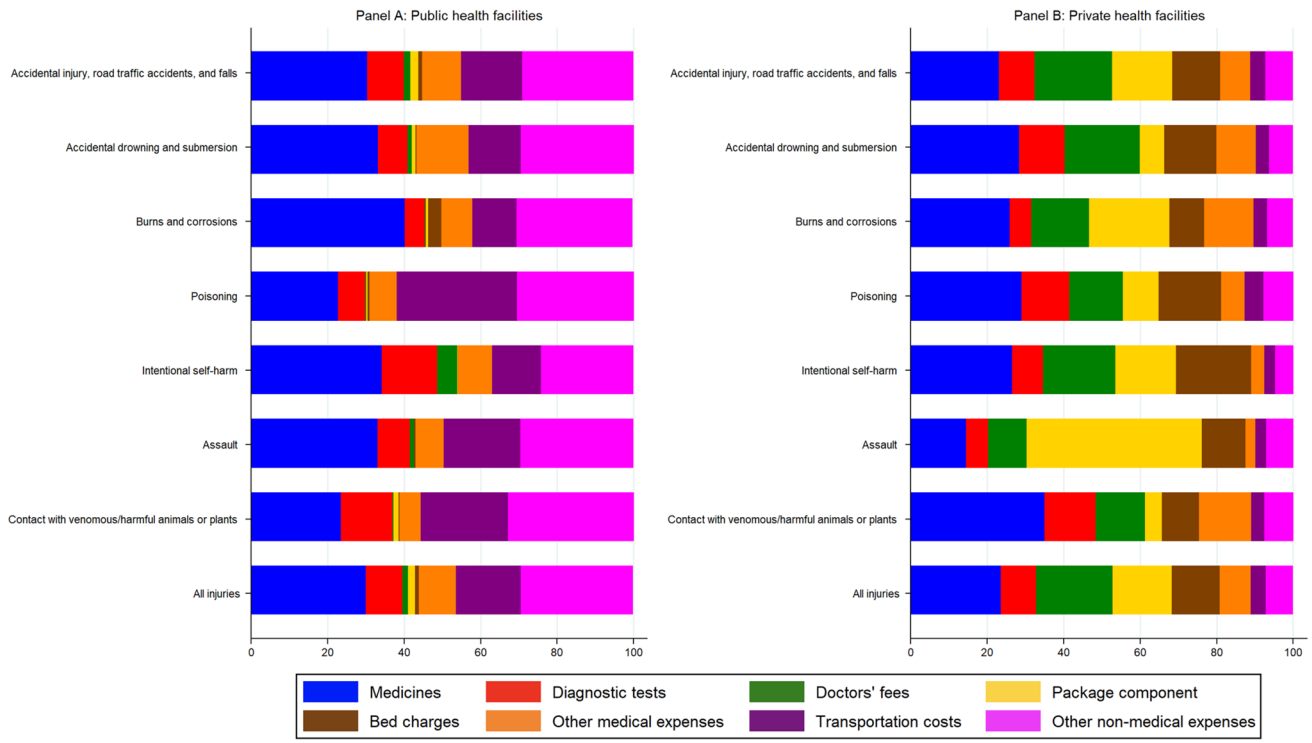

Fig. 2 Share of various components in total health expenditure by type of healthcare facility

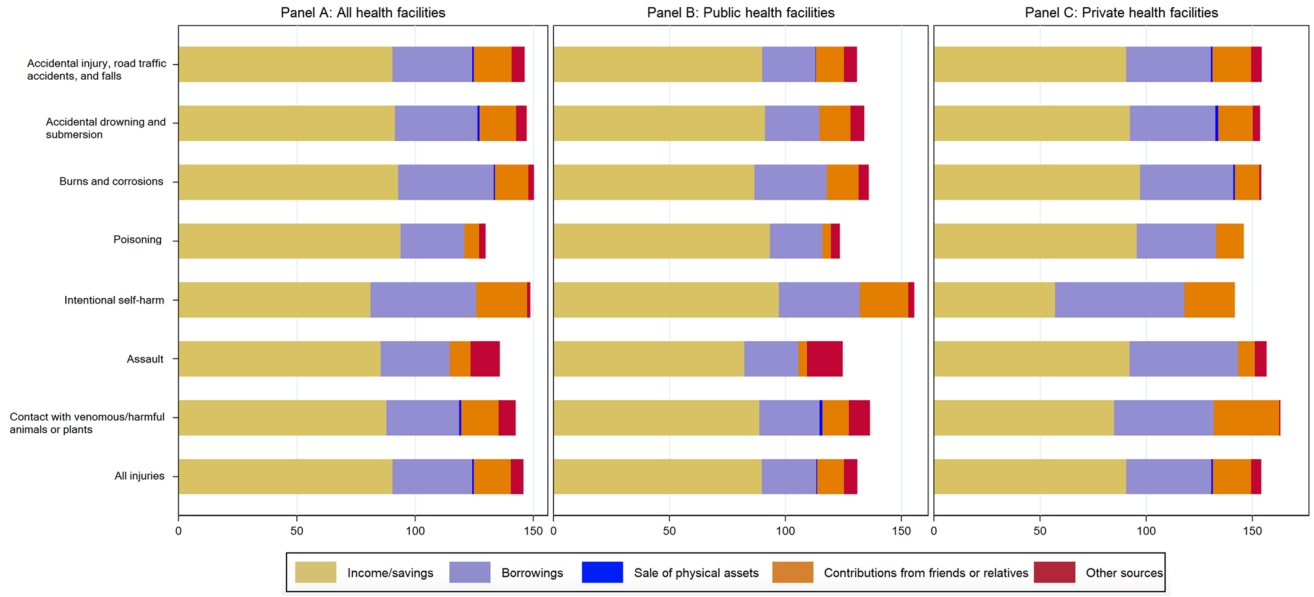

Fig. 3 Share of various sources of finance used as coping strategies

Multivariable logistic regression

Table 3 shows the results of multivariable logistic regression to reveal the impact of various factors on the likelihood of incurring CHE due to any injury. Urban households were statistically significantly less likely to experience CHE (odds ratio (OR): 0.11 [0.09–0.13]; $p < 0.05$) compared to their rural counterparts. The odds of experiencing CHE declined with each gradient of economic quintile ($p < 0.05$). Insurance coverage statistically significantly decreased the odds of incurring CHE (OR: 0.74 [0.64–0.86]; $p < 0.05$). Conversely, households whose principal source of earnings was from other sources reported higher odds of incurring CHE (OR: 1.89 [1.41–2.54]; $p < 0.05$) than those earning from self-employment. Utilization of private healthcare facilities increased the likelihood of experiencing CHE (OR: 8.69 [7.47–10.10]; $p < 0.05$).

The pattern of likelihood of falling below the poverty line and using distressed financing due to any injury was similar to experiencing CHE (Table 3). Households residing in urban areas, belonging to the wealthiest economic quintile, and headed by member with higher educational status were statistically significantly less likely to experience impoverishment and use distressed coping sources ($p < 0.05$). The odds of falling below the poverty line were statistically significantly lower for insured households (OR: 0.83 [0.69–0.99]; $p < 0.05$) compared to uninsured households. Conversely, households utilizing private health facilities and primarily earning from casual and other work were more likely to fall into poverty and employ distressed sources ($p < 0.05$). The odds of relying on distressed financing were also higher among the scheduled tribes, scheduled castes, and other backward classes ($p < 0.05$).

Discussion

This study provides holistic assessment of the financial burden due to injury care in India. We found that 49.3% of injury-affected households experienced CHE, 17.8% fell into poverty, and 52.1% used distressed sources due to OOPE for hospitalization. Injuries such as intentional self-harm, burns and corrosions, and accidental injury, road traffic accidents, and falls imposed a colossal financial burden on Indian households. Moreover, the brunt of OOPE was substantially higher when care was sought from private health facilities rather than public ones. Medicines were the key drivers of total health expenditure, irrespective of the type of healthcare facility, followed by doctors' fees in private facilities, and non-medical expenses in public facilities. Households residing in rural areas, belonging to lower economic quintiles, primarily earning from casual and other work, utilizing private health facilities, and lacking insurance coverage were more likely to experience higher financial burden when seeking care for injuries.

Notably, India reported the highest suicide rate (16.5 per 100,000) in the WHO South-East Asian region in 2016, which was even higher than the global average (10.5 per 100,000) (WHO 2019b). In agreement with a previous study (Yadav et al. 2021), we found that households in which a member inflicted intentional self-harm reported the highest OOPE (INR 35,028.9) and financial burden. This may

Table 3 Results of multivariable logistic regression

Variables	Odds ratio Catastrophic health expenditure	Odds ratio Impoverishment	Odds ratio Distressed financing
Place of residence			
Rural area ®			
Urban area	0.11* [0.09–0.13]	0.44* [0.37–0.52]	0.74* [0.66–0.82]
Economic quintile			
Quintile 1 ®			
Quintile 2	0.09* [0.07–0.12]	2.94* [2.32–3.72]	0.95 [0.81–1.12]
Quintile 3	0.023* [0.017–0.030]	2.32* [1.83–2.95]	1.05 [0.89–1.24]
Quintile 4	0.009* [0.006–0.012]	1.06 [0.82–1.36]	0.96 [0.81–1.13]
Quintile 5	0.004* [0.003–0.005]	0.45* [0.34–0.59]	0.79* [0.67–0.93]
Major source of household income			
Self-employment ®			
Regular wage or salary	1.06 [0.89–1.26]	0.94 [0.77–1.16]	1.10 [0.96–1.26]
Casual labour	1.05 [0.89–1.24]	1.25* [1.06–1.48]	1.49* [1.30–1.70]
Other	1.89* [1.41–2.54]	1.61* [1.19–2.19]	1.52* [1.22–1.90]
Social group			
Other ®			
Other Backward Classes	1.03 [0.88–1.20]	0.98 [0.83–1.16]	1.37* [1.21–1.54]
Scheduled Castes	0.89 [0.73–1.08]	0.94 [0.75–1.17]	1.42* [1.21–1.66]
Scheduled Tribes	0.98 [0.76–1.26]	0.57* [0.41–0.80]	1.40* [1.15–1.71]
Religion			
Hinduism ®			
Islam	0.81* [0.66–0.98]	0.88 [0.70–1.10]	1.03 [0.88–1.20]
Other	0.85 [0.68–1.07]	1.12 [0.85–1.49]	1.19 [0.99–1.43]
Educational level of household head			
Not literate/literate without schooling ®			
Up to primary	0.76* [0.63–0.91]	0.86 [0.70–1.05]	0.80* [0.69–0.92]
Up to secondary	0.84 [0.71–1.00]	0.88 [0.73–1.07]	0.79* [0.69–0.90]
Up to higher secondary	0.69* [0.54–0.89]	0.58* [0.43–0.78]	0.67* [0.55–0.81]
Graduation and above	0.80 [0.61–1.04]	0.64* [0.47–0.87]	0.50* [0.40–0.61]
Age of household head			
Less than 60 years ®			
60 years and above	1.20* [1.01–1.42]	1.20* [1.00–1.44]	0.86* [0.76–0.98]
Sex of household head			
Male ®			

Table 3 (continued)

Variables	Odds ratio Catastrophic health expenditure	Odds ratio Impoverishment	Odds ratio Distressed financing
Female	1.03 [0.82–1.29]	1.10 [0.86–1.40]	0.93 [0.78–1.11]
Insurance coverage			
No ®			
Yes	0.74* [0.64–0.86]	0.83* [0.69–0.99]	0.93 [0.82–1.04]
Healthcare facility			
Public ®			
Private	8.69* [7.47–10.10]	5.96* [4.99–7.11]	2.53* [2.28–2.81]

® Reference category; *$p < 0.05$; [ ] 95% confidence interval.

be due to the exclusion of any act of self-harm or suicide attempts from most health insurance plans (HDFC 2022; Sarkhel 2021). A study in South India reported that the median medical cost of hospitalization due to intentional self-harm was INR 13,690, and that deliberate self-harm with pesticide consumption increased the cost of treatment by 67% compared to non-pesticide poisoning (Barnabas et al. 2021). Hanging and consuming poison are common ways of committing suicide in India (NCRB 2020). While the former is difficult to control, the latter is amenable to legislation that regulates the sale or ban of highly hazardous pesticides (Lee et al. 2021; Menon et al. 2022). For instance, Sri Lanka and Bangladesh witnessed a significant decline in both overall and pesticide suicide rates after the ban of the most highly hazardous pesticides, without any apparent effect on agricultural output (Chowdhury et al. 2018; Knipe et al. 2017). Moreover, even though suicide was the leading cause of death in Indians aged 15–39 years in 2016 (Dandona et al. 2018), one study found that 86.4% of surveyed college students in India were unaware of any suicide support options (Cherian et al. 2022). The absence of a national suicide prevention strategy, inappropriate media reporting, such as potentially harmful reporting of practices and minimal educational and preventive information, and inadequate multisectoral engagement were reported to be major impediments to effective suicide prevention in India (Menon et al. 2021; Vijayakumar et al. 2022). In response, the Government of India recently launched the National Suicide Prevention Strategy on November 21, 2022, with the aim of reducing suicide mortality in the country by 10% by 2030 (GOI 2022). A scaffolding approach is helpful to reduce suicide rates, since interventions provided at the right time, and of the right intensity and duration, can help navigate situations in which an individual might be susceptible to and at risk of suicide (Vijayakumar et al. 2022).

Similar to previous studies (Nguyen et al. 2017), we observed that burns and corrosions imposed a copious financial burden on households and that they were the second leading cause of CHE, impoverishment, and distressed financing. Burn patients often require specialized treatment in a burn centre, surgery and wound care, and long periods of hospitalization and rehabilitation, leading to high treatment costs (Yu et al. 2020). In India, nearly seven million individuals sustain burn injuries each year, of which more than 0.7 million require hospitalization (National Health Portal 2016). However, studies have recognised inadequate infrastructure and human resource as big constraints for burn care in India (Jagnoor et al. 2018a, 2018b; National Academy of Burns 2016). Appallingly, only 15.9% of the Indian population resides within two hours of a burn centre with both an intensive care unit and a skin bank (Ranganathan et al. 2020). One study highlighted the lack of communication between healthcare professionals and burn survivors, limited rehabilitation services, transportation difficulties to healthcare facilities, and high cost of burn care as the key challenges to burn care and recovery in India (Jagnoor et al. 2018a).

In tandem with previous studies (Goli et al. 2018; Pradhan et al. 2017; Ram and Thakur 2022), we found that accidental injury, road traffic accidents, and falls imposed a severe financial burden, with CHE incidence of 49.7%, poverty headcount ratio of 18.1%, and distressed financing in case of 52.5% of households. India witnessed a 58.7% increase in mortality due to road injuries between 1990 and 2017 (Dandona et al. 2020). Importantly, road accidents mostly impact the economically-active younger age groups, with road injuries reported as the leading cause of mortality in males aged 15 to 39 years, and the second leading cause of death for both sexes combined in this age group in 2017 in India (Dandona et al. 2020). Consequently, road traffic accidents have far-reaching economic implications, such as costs of treatment, indirect expenses, and productivity losses (GOI 2019a). Goli et al. (2018) found that the share of OOPE in total healthcare expenditure was the highest for

accidents and injuries, and even greater than that of cancer, cardiovascular conditions, or any other causes of hospitalization. Other studies conducted in South Asian countries such as Pakistan (Razzak et al. 2011) and Vietnam (Nguyen et al. 2013) reported OOPE in the range of USD 300–400 for road traffic injuries, highlighting the grave economic consequences of accident care. In India, the enforcement of various national road safety legislations are lagging. For instance, the WHO rated enforcement of speed and seat-belt laws in India at three on a scale of 0 to 10, with 10 representing 'highly effective', and drunk-driving and motorcycle helmet laws were rated at four (WHO 2018). Another study found that enhanced enforcement of traffic regulations is the most cost-effective intervention, with an average cost of USD 64 per disability adjusted life year in lower and middle-income countries (Bishai and Hyder 2006). Therefore, amidst the rising burden of road traffic accidents and their concomitant financial impact, India must prioritize traffic law enforcement, improve road and vehicle designs, and enhance post-crash care (Dandona et al. 2020). The central government recently planned to introduce a scheme for cashless treatment of road accident victims during the 'golden hour', the period of up to an hour following an injury, when the chances of preventing death through prompt treatment are the highest (GOI 2019a).

We also noticed households with socio-economic lackings, such as households belonging to lower economic quintiles, residing in rural areas, primarily earning from casual and other work, and headed by members who were not literate, were exposed to greater financial risk due to injury care. As per WHO (2014), the poor and vulnerable have to deal with the double whammy of being at an increased risk of injuries plus the associated financial burden. We also found that health insurance statistically significantly decreased the odds of incurring CHE and falling below the poverty line. However, health insurance enrolment is abysmally low in India, with a mere 14% of rural and 19% of urban populations enrolled under health insurance schemes in 2018 (GOI 2019b). Inadequate awareness regarding various facets of health insurance, such as eligibility criteria, where and how to enrol, details about empanelled hospitals, and how to avail oneself of benefits, result in less than the desired coverage and benefits (Devadasan et al. 2013; Hooda 2020; Prinja et al. 2017; Thakur 2016). Moreover, social health insurance schemes only cover formal sector employees, and government-sponsored health insurance schemes (GSHIs), including the recently launched Pradhan Mantri Jan Arogya Yojana, cover only the poor and vulnerable population, leaving a significant portion of the Indian population with the choice to either enrol under private health insurance with the associated ability-to-pay premium constraints, or to remain uninsured (NITI Aayog 2021). As a result, a sizeable proportion of Indians remain uncovered, despite having the ability to pay nominal premiums (NITI Aayog 2021). Additionally, the GSHIs lag behind in covering the targeted poor and vulnerable families in India (Hooda 2020). Therefore, it is imperative to raise awareness and uptake of health insurance, and increase the affordability of health insurance products, especially for the 'missing-middle' population.

Our study highlights the important role of public hospitals in providing injury care, since the financial burden was invariably lower among households that sought care from public health facilities than private facilities across all injuries. However, deficiencies in the public health system, such as inadequate infrastructure, unavailable services, perceived low quality of care, and long waiting times, unfortunately forces people to use private facilities, exposing them to financial hardship. According to a recent report published by NITI Aayog[4] (2021), the capacity and quality of healthcare services in India's public health sector is restrained due to low government health spending, necessitating the need for higher public health expenditure and strengthening the public health system to safeguard against the burgeoning OOPE. Further, previous studies have reported numerous cases of overcharging, unnecessary tests and treatments, and malpractices in the private health sector, owing to inadequate monitoring by the government (Dehury et al. 2019; Phadke 2016; Times of India 2016). In addition, a well-established system of paying commissions to doctors when they refer patients for diagnostic testing is in place in the private sector (Baru et al. 2010). Selvaraj et al (2022) suggests that improved regulation is a key driver of decreasing costs and improving quality of care.

We found that medicines constituted the highest proportion of health expenditure due to injury care in India. The low availability of free or subsidized essential drugs in public healthcare facilities impels individuals to either purchase them from open markets, resulting in higher OOPE, or forgo treatment (Maiti et al. 2015). Several lessons can be learned from successful procurement models in states such as Tamil Nadu, Rajasthan and Delhi, which are able to provide free and readily available medicines in public healthcare facilities (Selvaraj et al. 2022). To curtail expenditure on drugs, the government of India has launched the Pradhan Mantri Bhartiya Janaushadhi Pariyojana scheme (2008) to ensure access to quality generic medicines at affordable prices (GOI 2008). However, the dominance of private healthcare providers who mostly prescribe branded medicines, necessitates the need for timely revision of the National List of Essential

[4] The National Institution for Transforming India (NITI Aayog) was established on 1 January 2015, as the premier policy think tank of the Government of India, providing directional and policy inputs (Press Information Bureau 2015).

Medicines along with appropriate price controls for branded drugs (Hooda 2017). Moreover, non-medical costs (29.4%) and transportation expenses (16.9%) often get overlooked, but were the leading contributors to total health expenditure when hospitalization was sought from public health facilities. India's rural healthcare system is marred by a shortage of public healthcare facilities, such as a 35% shortfall in community health centres (CHCs), and a dearth of workforce, particularly specialists. At the CHCs, for instance, there is an 80% shortage of specialists (GOI 2021). This forces individuals in rural areas to travel long distances to access treatment, resulting in two negative consequences, namely the enormous costs of travelling and lodging, and secondly, the loss of earnings due to travel. Moreover, previous studies have reported the unavailability of diagnostic tests and insufficient health infrastructure as the main reasons for medical travel (Arul and Babu 2017). This highlights the importance of a resilient healthcare system to expedite treatment, improve health outcomes, and facilitate a concomitant decline in OOPE.

Conclusion

This study highlights the onerous financial burden of OOPE experienced by Indian households suffering from any injury. Concerted efforts, such as increasing government health expenditure, ensuring quality provisioning of public healthcare facilities, and improving regulatory implementation for private healthcare providers, are imperative to alleviate financial hardships. There is an urgent need to ensure the availability and affordability of essential medicines and curtail non-medical costs while accessing public health facilities. Moreover, dismally low health insurance enrolment warrants policy measures to increase awareness and uptake of health insurance in India. Lastly, for long-term sustainability, policymakers must prioritize prevention strategies and safety interventions to reduce the burden of injuries and associated economic brunt. Correct helmet use and wearing seat belts, for example, can lead to a 42% reduction in the risk of fatal injuries and a 45–50% reduction in the risk of death among drivers and front seat occupants, respectively (WHO 2022). Moreover, several lessons can be learned from the successful multisectoral efforts of the Tamil Nadu state government in reducing road traffic mortalities by 54% from 2016 to 2020. Measures included the collection of robust accident data, identification and elimination of the most crash-prone hotspots, prompt provision of emergency and medical care, road safety awareness programs, and stringent enforcement of traffic regulations (Government of Tamil Nadu 2020; Worldbank Blogs 2018).

Authors' contributions All authors contributed to the conception and design of the study. MN conducted the data analysis and wrote the initial draft of the manuscript. RS reviewed the manuscript and supervised the work. All authors contributed to the study and approved the submitted version.

Funding This study received no specific grant from any funding agency in public, commercial, or not-for-profit sectors.

Data availability This study used data from the 75th round of the National Sample Survey on Health. Data are available in the public domain https://www.mospi.gov.in/

Declarations

Ethics approval and consent to participate This study was conducted using data available in the public domain and did not include any human participants or animals. Therefore, no ethical approval was required.

Consent to publish Not applicable

Conflict of interest The authors declare no competing interests.

References

Arul U, Babu S (2017) Domestic medical tourism in rural India: sociological perspective. J Res Dev (Srinagar) 5(4):51–54

Barnabas R, Yadav B, Jayakaran J et al (2021) Direct costs of health care among patients with deliberate self-harm: a pilot study from a tertiary care hospital in South India. Tablet 34:31–38. https://doi.org/10.5005/jp-journals-10071-24239

Baru R, Acharya A, Acharya S, Kumar AS, Nagaraj K (2010) Inequities in access to health services in India: caste, class and region. Econ Political Weekly 45(38):49–58

Berki SE (1986) A look at catastrophic medical expenses and the poor. Health Affairs 5(4):138–145. https://doi.org/10.1377/hlthaff.5.4.138

Bishai DM, Hyder AA (2006) Modeling the cost effectiveness of injury interventions in lower and middle income countries: opportunities and challenges. Cost Effect Resource Alloc 4:1–11. https://doi.org/10.1186/1478-7547-4-2

Bonu S, Bhushan I, Peters D (2007) Incidence, intensity, and correlates of catastrophic out-of-pocket health payments in India. Asian Development Bank. https://www.adb.org/sites/default/files/publication/28364/wp102.pdf

Bonu S, Bhushan I, Rani M, Anderson I (2009) Incidence and correlates of 'catastrophic' maternal health care expenditure in India. Health Policy Plann 24(6):445–456. https://doi.org/10.1093/heapol/czp032

Chandran A, Hyder AA, Peek-Asa C (2010) The global burden of unintentional injuries and an agenda for progress. Epidemiol Rev 32(1):110–120. https://doi.org/10.1093/epirev/mxq009

Cherian AV, Menon V, Rathinam B et al (2022) Awareness and preferences about suicide crisis support service options among college students in India: a cross sectional study. Asian J Psychiat 74:103172. https://doi.org/10.1016/j.ajp.2022.103172

Chowdhury FR, Dewan G, Verma VR et al (2018) Bans of WHO class I pesticides in Bangladesh—suicide prevention without hampering agricultural output. Int J Epidemiol 47(1):175–184. https://doi.org/10.1093/ije/dyx157

Dandona R, Kumar GA, Dhaliwal RS et al (2018) Gender differentials and state variations in suicide deaths in India: the Global Burden

of Disease Study 1990–2016. Lancet Public Health 3(10):e478–e489. https://doi.org/10.1016/S2468-2667(18)30138-5
Dandona R, Kumar GA, Gururaj G et al (2020) Mortality due to road injuries in the states of India: the Global Burden of Disease Study 1990–2017. Lancet Public Health 5(2):e86–e98. https://doi.org/10.1016/S2468-2667(19)30246-4
Dehury RK, Samal J, Coutinho S, Dehury P (2019) How does the largely unregulated private health sector impact the Indian mass? J Health Manag 21(3):383–393. https://doi.org/10.1177/0972063419868561
Devadasan N, Seshadri T, Trivedi M, Criel B (2013) Promoting universal financial protection: evidence from the Rashtriya Swasthya Bima Yojana (RSBY) in Gujarat, India. Health Res Policy Syst 11(1):1–8. https://doi.org/10.1186/1478-4505-11-29
Engelgau MM, Karan A, Mahal A (2012) The economic impact of non-communicablediseases on households in India. Glob Health 8(1):1–10. https://doi.org/10.1186/1744-8603-8-9
Garg CC, Karan AK (2009) Reducing out-of-pocket expenditures to reduce poverty: a disaggregated analysis at rural-urban and state level in India. Health Policy Plann 24(2):116–128. https://doi.org/10.1093/heapol/czn046
Goli S, Siddiqui MZ, Gouda J (2018) Road Traffic Accidents and Injuries in India. Econ Politic Weekly 53(14):52–60
Government of India (GOI) (2008) Pradhan Mantri Bhartiya Janaushadhi Pariyojana. http://janaushadhi.gov.in/pmjy.aspx. Accessed 12 Jan 2023
Government of India (GOI) (2019a) Road Accidents in India 2019. https://morth.nic.in/sites/default/files/RA_Uploading.pdf. Accessed 27 Nov 2022
Government of India (GOI) (2019b) Key indicators of social consumption in India: Health. https://www.mospi.gov.in/sites/default/files/publication_reports/KI_Health_75th_Final.pdf. Accessed 21 Nov 2022
Government of India (GOI) (2021) Rural Health Statistics 2020-2021. https://main.mohfw.gov.in/sites/default/files/rhs20-21_1.pdf. Accessed 5 Jan 2023
Government of India (GOI) (2022) National Suicide Prevention Strategy. https://www.mhinnovation.net/sites/default/files/downloads/resource/National%20Suicide%20Prevention%20Strategy.pdf. Accessed 12 Jan 2023
Government of Tamil Nadu (2020) Road Accident Analysis in Tamil Nadu. https://tnsta.gov.in/pdf/analysis_december2020.pdf. Accessed 13 Jan 2023
HDFC (2022) 4 Common Health Insurance Exclusions. https://www.hdfcergo.com/blogs/health-insurance/4-common-health-insurance-exclusions. Accessed 5 Jan 2023
Hooda SK (2017) Health payments and household well-being: How effective are health policy interventions? Econ Politic Weekly 52(16):54–65
Hooda SK (2020) Penetration and coverage of government-funded health insurance schemes in India. Clin Epidemiol Global Health 8(4):1017–1033. https://doi.org/10.1016/j.cegh.2020.03.014
Jagnoor J, Bekker S, Chamania S et al (2018a) Identifying priority policy issues and health system research questions associated with recovery outcomes for burns survivors in India: a qualitative inquiry. BMJ open 8(3):e020045. https://doi.org/10.1136/bmjopen-2017-020045
Jagnoor J, Lukaszyk C, Christou A et al (2018b) Where to from here? A quality improvement project investigating burns treatment and rehabilitation practices in India. BMC Res Notes 11(1):1–6. https://doi.org/10.1186/s13104-018-3314-9
Knipe DW, Gunnell D, Eddleston M (2017) Preventing deaths from pesticide self-poisoning—learning from Sri Lanka's success. Lancet Global Health 5(7):e651–e652. https://doi.org/10.1016/S2214-109X(17)30208-5
Kumar GA, Dilip TR, Dandona L, Dandona R (2012) Burden of out-of-pocket expenditure for road traffic injuries in urban India. BMC Health Serv Res 12(1):1–10. https://doi.org/10.1186/1472-6963-12-285
Kumaresh G, Saldanha F, Lich T, Moennich J (2021) Estimation of socio-economic loss due to road traffic accidents in India. SAE Int J Adv Curr Pract Mobil 4:774–784. https://doi.org/10.4271/2021-26-0012
Lee YY, Chisholm D, Eddleston M et al (2021) The cost-effectiveness of banning highly hazardous pesticides to prevent suicides due to pesticide self-ingestion across 14 countries: an economic modelling study. Lancet Global Health 9(3):e291–e300. https://doi.org/10.1016/S2214-109X(20)30493-9
Maiti R, Bhatia V, Padhy BM, Hota D (2015) Essential medicines: an Indian perspective. Indian J Commun Med 40(4):223. https://doi.org/10.4103/0970-0218.164382
Menon V, Mani AM, Kurian N et al (2021) Newspaper reporting of suicide news in a high suicide burden state in India: Is it compliant with international reporting guidelines? Asian J Psychiat 60:102647. https://doi.org/10.1016/j.ajp.2021.102647
Menon V, Cherian AV, Vijayakumar L (2022) Rising incidence and changing demographics of suicide in India: time to recalibrate prevention policies. Asian J Psychiatry 69:102983. https://doi.org/10.1016/j.ajp.2021.102983
Ministry of Rural Development (2020) Poverty measurement in India: a status update. https://rural.nic.in/sites/default/files/WorkingPaper_Poverty_DoRD_Sept_2020.pdf. Accessed 1 May 2023
Mohanty SK, Kastor A (2017) Out-of-pocket expenditure and catastrophic health spending on maternal care in public and private health centres in India: a comparative study of pre and post national health mission period. Health Econ Rev 7:1–15. https://doi.org/10.1186/s13561-017-0167-1
National Academy of Burns (2016) Burn Units and Burn Care providers in India. http://www.thenabi.org/bcp.php. Accessed 10 Jan 2023
National Crime Records Bureau (NCBR) (2020) Accidental Deaths & Suicides in India 2020. https://ncrb.gov.in/sites/default/files/ADSI_2020_FULL_REPORT.pdf. Accessed 18 Nov 2022
National Health Policy (2017). https://www.nhp.gov.in/nhpfiles/national_health_policy_2017.pdf. Accessed 19 Nov 2022
National Health Portal (2016) Burns. https://www.nhp.gov.in/disease/skin/burns. Accessed 10 Jan 2023
National Health Systems Resource Centre (2019) National Health Accounts Estimates for India (2016-17). https://nhsrcindia.org/sites/default/files/2021-06/FINAL%20National%20Health%20Accounts%202016-17%20Nov%202019-for%20Web%20%281%29.pdf. Accessed 19 Nov 2022
Nguyen H, Ivers R, Jan S, Martiniuk A, Pham C (2013) Catastrophic household costs due to injury in Vietnam. Injury 44(5):684–690. https://doi.org/10.1016/j.injury.2012.05.006
Nguyen H, Ivers R, Jan S, Pham C (2017) Analysis of out-of-pocket costs associated with hospitalised injuries in Vietnam. BMJ Glob Health 2(1):e000082. https://doi.org/10.1136/bmjgh-2016-000082
Niti Aayog (2021) Health Insurance for India's Missing Middle. https://www.niti.gov.in/sites/default/files/2021-10/HealthInsurance-forIndiasMissingMiddle_28-10-2021.pdf. Accessed 5 Jan 2023
NSSO (2018) India: Household Social Consumption: Health, NSS 75th Round Schedule-25.0: July 2017-June 2018. http://microdata.gov.in/nada43/index.php/catalog/152. Accessed 27 Nov 2022
Phadke A (2016) Regulation of doctors and private hospitals in India. Econ Political Wkly 51(6):46–55
Planning Commission (2014) Report of the expert group to review the methodology for measurement of poverty. https://forms.iimk.ac.in/libportal/reports/232858161-Planning-Commission-report-on-poverty-estimates.pdf. Accessed 1 Nov 2022

Pradhan J, Dwivedi R, Pati S, Rout SK (2017) Does spending matters? Re-looking into various covariates associated with out of pocket expenditure (OOPE) and catastrophic spending on accidental injury from NSSO 71st round data. Health Econ Rev 7(1):1–16. https://doi.org/10.1186/s13561-017-0177-z

Press Information Bureau (2015) NITI Aayog: Objectives and Composition. https://pib.gov.in/newsite/PrintRelease.aspx?relid=114273 Accessed: May 2, 2023

Prinja S, Jagnoor J, Chauhan AS et al (2016) Economic burden of hospitalization due to injuries in North India: a cohort study. Int J Environ Res Public Health 13(7):673. https://doi.org/10.3390/ijerph13070673

Prinja S, Chauhan AS, Karan A, Kaur G, Kumar R (2017) Impact of publicly financed health insurance schemes on healthcare utilization and financial risk protection in India: a systematic review. PloS one 12(2):e0170996. https://doi.org/10.1371/journal.pone.0170996

Prinja S, Jagnoor J, Sharma D et al (2019) Out-of-pocket expenditure and catastrophic health expenditure for hospitalization due to injuries in public sector hospitals in North India. PloS one 14(11):e0224721. https://doi.org/10.1371/journal.pone.0224721

Ram B, Thakur R (2022) Measuring the burden of accidental injuries in India: a cross-sectional analysis of the National Sample Survey (2017–18). Human Social Sci Commun 9(1):1–18. https://doi.org/10.1057/s41599-022-01369-0

Ranganathan K, Mouch CA, Chung M et al (2020) Geospatial mapping as a guide for resource allocation among burn centers in India. J Burn Care Res 41(4):853–858. https://doi.org/10.1093/jbcr/irz210

Razzak JA, Bhatti JA, Ali M, Khan UR, Jooma R (2011) Average out-of-pocket healthcare and work-loss costs of traffic injuries in Karachi, Pakistan. Int J Injury Control Safety Prom 18(3):199–204. https://doi.org/10.1080/17457300.2011.551942

Sangar S, Dutt V, Thakur R (2020) Coping with out-of-pocket health expenditure in India: evidence from NSS 71st round. Glob Social Welfare 7:275–284. https://doi.org/10.1007/s40609-019-00141-8

Sarkhel S (2021) Mental health insurance and attempted suicide: Need for a reappraisal. Ind J Psychiat 63(6):624–625. https://doi.org/10.4103/indianjpsychiatry.indianjpsychiatry_902_21

Selvaraj S, Karan KA, Srivastava S, Bhan N, Mukhopadhyay I (2022) India: health system review. World Health Organization, Regional Office for South-East Asia, New Delhi. https://apps.who.int/iris/handle/10665/352685

Thakur H (2016) Study of awareness, enrollment, and utilization of Rashtriya Swasthya Bima Yojana (national health insurance scheme) in Maharashtra, India. Front Public Health 3:282. https://doi.org/10.3389/fpubh.2015.00282

Times of India (2016) Greed and the rise of medical malpractice in India. https://timesofindia.indiatimes.com/blogs/the-irreverent-lawyer/greed-and-the-rise-of-medical-malpractice-in-india/. Accessed 15 Jan 2023

Tripathy JP, Jagnoor J, Prasad BM, Ivers R (2018) Cost of injury care in India: cross-sectional analysis of National Sample Survey 2014. Injury Prev 24(2):116–122. https://doi.org/10.1136/injuryprev-2017-042318

Van Doorslaer E, O'Donnell O, Rannan-Eliya RP et al (2006) Effect of payments for health care on poverty estimates in 11 countries in Asia: an analysis of household survey data. Lancet 368(9544):1357–1364. https://doi.org/10.1016/S0140-6736(06)69560-3

Vijayakumar L, Chandra PS, Kumar MS et al (2022) The national suicide prevention strategy in India: context and considerations for urgent action. Lancet Psychiat 9(2):160–168. https://doi.org/10.1016/S2215-0366(21)00152-8

World Health Organization (WHO) (2014) Injuries and Violence. The facts. https://apps.who.int/iris/bitstream/handle/10665/149798/9789241508018_eng.pdf?sequence=1&isAllowed=y Accessed: November 25, 2022

World Health Organization (WHO) (2018) Global status report on road safety 2018. https://www.who.int/publications/i/item/9789241565684. Accessed 10 Dec 2022

World Health Organization (WHO) (2019a) Global Health Estimates: Life expectancy and leading causes of death and disability. https://www.who.int/data/gho/data/themes/mortality-and-global-health-estimates Accessed: November 25, 2022

World Health Organization (WHO) (2019b) Suicide in the world: Global Health Estimates. https://apps.who.int/iris/bitstream/handle/10665/326948/WHO-MSD-MER-19.3-eng.pdf

World Health Organization (WHO) (2021) Injuries and violence. https://www.who.int/news-room/fact-sheets/detail/injuries-and-violence Accessed: November 25, 2022

World Health Organization (WHO) (2022) Road traffic injuries. https://www.who.int/news-room/fact-sheets/detail/road-traffic-injuries#:~:text=Road%20traffic%20injuries%20are%20the,pedestrians%2C%20cyclists%2C%20and%20motorcyclists. Accessed 18 Jan 2023

Worldbank Blogs (2018) Road safety: How a state in India is leading the way to lower road crash deaths. https://blogs.worldbank.org/endpovertyinsouthasia/road-safety-how-state-india-leading-way-lower-road-crash-deaths. Accessed 20 Jan 2023

Xu K, Evans DB, Kawabata K et al (2003) Household catastrophic health expenditure: a multicountry analysis. Lancet 362(9378):111–117. https://doi.org/10.1016/S0140-6736(03)13861-5

Yadav J, Menon G, Agarwal A, John D (2021) Burden of injuries and its associated hospitalization expenditure in India. Int J Injury Control Safety Prom 28(2):153–161. https://doi.org/10.1080/17457300.2021.1879163

Yadav J, John D, Menon GR et al (2022) Nonfatal drowning-related hospitalizations and associated healthcare expenditure in India: an analysis of nationally representative survey data. J Safety Res 82:283–292. https://doi.org/10.1016/j.jsr.2022.06.003

Yu TC, Zhang X, Smiell J et al (2020) Healthcare resource utilization, treatment patterns, and cost of care among patients with thermal burns and inpatient autografting in two large privately insured populations in the United States. Burns 46(4):825–835. https://doi.org/10.1016/j.burns.2019.10.019

Publisher's note Springer Nature remains neutral with regard to jurisdictional claims in published maps and institutional affiliations.

Springer Nature or its licensor (e.g. a society or other partner) holds exclusive rights to this article under a publishing agreement with the author(s) or other rightsholder(s); author self-archiving of the accepted manuscript version of this article is solely governed by the terms of such publishing agreement and applicable law.

2023 2nd International Conference on Vision Towards Emerging Trends in Communication and Networking Technologies (ViTECoN) | 979-8-3503-4798-2/23/$31.00 ©2023 IEEE | DOI: 10.1109/ViTECON58111.2023.10157581

Fingerprint and GSM based Security System for Banks

Dikshant Pabri
Department of Electrical Engineering
Delhi Technological University, Delhi, India
Delhi, India
dikshantpabri@gmail.com

Saurabh Mishra
Department of Electrical Engineering
Delhi Technological University, Delhi, India
Delhi, India
saurabhmishra@dtu.ac.in

Komal Meena
Department of Electrical Engineering
Delhi Technological University, Delhi, India
Delhi, India
komalmeena_2k19ee136@dtu.ac.in

Duli Chand Meena
Department of Electrical Engineering
Delhi Technological University, Delhi, India
Delhi, India
dcmeena@dce.ac.in

Gaurav Chhoker
Department of Electrical Engineering
Delhi Technological University, Delhi, India
Delhi, India
gauravchhoker_2k19ee101@dtu.ac.in

***Abstract*—Security has evolved into an issue that is now of the utmost importance for financial institutions. It is no longer adequate to safeguard critical information and assets by using standard passwords and PINs. Authentication based on biometric characteristics is widely regarded as one of the most trustworthy security solutions that can be used in circumstances like these. In this article, we suggest a security system that utilises fingerprint technology in conjunction with GSM technology. An Arduino microcontroller, a SIM900A GSM module, and a fingerprint sensor are the three components that make up this system, which gives financial organisations an increased degree of protection. The system is meant to use a fingerprint to identify the authorised person and to send an alarm message to both the authorised person and the management of the bank in the event that an unauthorised person accesses the system.**

Keyword— GSM, Fingerprint Sensor, Security, Arduino

I. INTRODUCTION

The usage of electronic devices for conducting financial transactions has significantly increased as a direct result of the progress that has been made in technology. One of the most important industries that has profited significantly from these technology improvements is the financial services industry. Yet, as a result of a surge in the usage of electronic devices for the processing of financial transactions, the problem of security has emerged as one of the most important concerns for financial institutions [1]. It is no longer adequate to safeguard critical information and assets by using standard passwords and PINs. Authentication based on biometric characteristics is widely regarded as one of the most trustworthy security solutions that can be used in circumstances like these [2].

The technique of validating a person's identification by employing the specific biological traits that are unique to that individual is referred to as biometric authentication. Recognition of a person's fingerprints, voice, face, or iris, as well as facial mapping and voice mapping, are all examples of biometric authentication technologies. Because of the distinctive qualities it has and the simplicity with which it may be implemented, fingerprint recognition is often regarded as one of the most trustworthy forms of biometric verification [3-5].

In this paper, we present a security system that utilises fingerprint technology in conjunction with GSM technology. An Arduino microcontroller, a SIM900A GSM module, and a fingerprint sensor are the three components that make up this system, which gives financial organisations an increased degree of protection. In the event that an unauthorised individual gains access to the bank's facilities, the system will use the authorised person's fingerprint to verify their identity before notifying the authorised person as well as the bank's management.

The process of identifying a person by analysing his or her unique fingerprint patterns is referred to as fingerprint recognition [6]. This process may be used to verify the identity of an individual. The legal system, the financial business, and the security

979-8-3503-4798-2/23/$31.00 ©2023 IEEE

Authorized licensed use limited to: DELHI TECHNICAL UNIV. Downloaded on July 03,2023 at 04:41:42 UTC from IEEE Xplore. Restrictions apply.

industry are examples of some of the many industries that make extensive use of fingerprint recognition technology. A technique to biometric identification known as fingerprint recognition is one that requires the use of a fingerprint sensor in order to obtain the one-of-a-kind fingerprint patterns of a person. This biometric identification method is known as fingerprint recognition [7,8].

GSM technology is a kind of communication technology that is quite widespread and permits for wireless connection between devices even across long distances [9]. This connection may occur even when there is a considerable deal of physical space between the devices. The GSM standard is widely implemented across a wide range of communication technologies, including but not limited to mobile phones. The SIM900A GSM module is a GSM module that is used widely and that is capable of giving applications of many different types with wireless communication capabilities. It does this by using a cellular system that is known as the global system for mobile communications (GSM) [10].

The Arduino platform is a well-known open-source microcontroller that may be used in a wide range of settings due to its adaptability. Arduino is a platform that enables the building of electrical devices, including sensors and actuators, that may be used in a variety of applications. Arduino is often used for a wide number of applications, including building security systems, home automation systems, and many other similar applications.

II. LITERATURE REVIEW

In recent years, fingerprint and GSM-based security systems have garnered substantial interest owing to the potential of these technologies to improve the safety of a variety of establishments, including financial institutions. The combination of GSM technology with fingerprint identification gives a solution that is both dependable and resilient for the problem of access control and detection of intrusion. The variety, low cost, and simplicity of use of systems that are based on Arduino have contributed to their meteoric rise in popularity. The research articles released after 2015 that investigate fingerprint and GSM-based security systems for banks utilising Arduino are the primary subject of this review of the relevant literature.

Akhtar and Vashist [1] suggested a biometric-based ATM security system that is controlled by an Arduino microcontroller. The method improves the safety of monetary transactions conducted at ATMs by combining the capabilities of fingerprint identification with GSM technology. The authors proved that the suggested system is successful in preventing unauthorised access and giving real-time warnings in the event of a breach in security.

Sharma and Kaur [2] developed a fingerprint-based bank locker system that makes use of GSM technology to enhance the safety of financial institutions. The authors showed the effectiveness and dependability of the suggested method by using a system that was based on Arduino. The method provides safe access to bank lockers and notifies appropriate individuals in the event that unwanted access attempts are made.

An Internet of Things (IoT)-based secure ATM banking system was developed by Abbas and Elasha [3]. This system makes use of fingerprint authentication and one-time password (OTP) verification that is communicated over GSM technology. The implementation of the system, which demonstrated the potential of biometric and GSM-based technologies to enhance ATM security, was carried out using the Arduino platform.

Kumar and Kaur [4] showed a biometric ATM system that was built using Arduino and included a high level of security. The use of fingerprint identification in conjunction with GSM technology allows for the provision of safe access to automated teller machines as well as the provision of real-time alerts in the event of unlawful access. The authors proved that the suggested approach is successful in increasing the level of safety associated with transactions conducted at ATMs.

Fingerprint recognition and GSM technology were used in the creation of a smart door lock system that was designed by Al-Khaldi and Al-Shaikhi [5]. The system, which was tested in a banking environment and showed promising results, was built using an Arduino platform, and it was designed to provide safe access management as well as real-time warnings in the event of a breach of security.

In conclusion, the research that was conducted after 2015 has shown that fingerprint and GSM-based security systems that use Arduino have the potential to significantly improve the safety of banking institutions.

Authorized licensed use limited to: DELHI TECHNICAL UNIV. Downloaded on July 03,2023 at 04:41:42 UTC from IEEE Xplore. Restrictions apply.

III. IMPLEMENTATION

Fingerprint and GSM technologies would be used as the foundation for the proposed security system. An Arduino microcontroller, a SIM900A GSM module, and a fingerprint sensor are the three components that make up this system, which gives financial organisations an increased degree of protection. In the event that an unauthorised individual gains access to the bank's facilities, the system will use the authorised person's fingerprint to verify their identity before notifying the authorised person as well as the bank's management.

The fig. 1 shows the block diagram of the implementation.

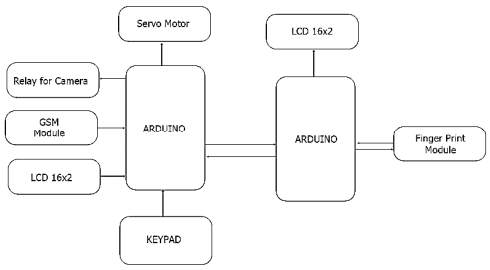

Fig. 1 Block Diagram

The following elements make up the various parts of the system:

Fingerprint sensor: The fingerprint sensor is what is utilised to collect the authorised person's unique fingerprint patterns in order to verify their identity.

Arduino is used throughout the system as the primary control unit for Arduino. Control of the fingerprint sensor as well as the GSM module is handled by Arduino.

If a person has long nails, it may make it more difficult to obtain clear and complete fingerprints because the nails can interfere with the contact between the fingertip and the surface of the scanning device. This can result in smudged or incomplete prints, which can make it more difficult to match against existing records in a database.

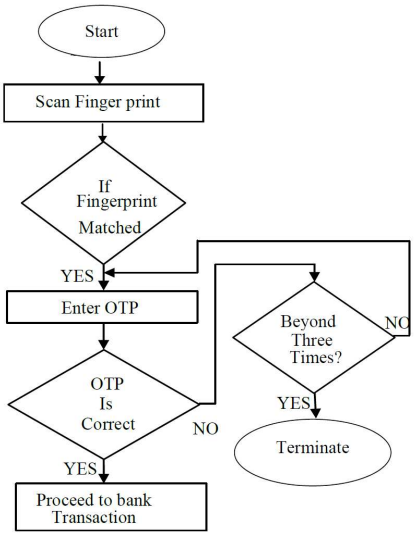

Fig. 2 Flowchart

SIM900A GSM module: In the event of unlawful access, the SIM900A GSM module is used to transmit alarm messages to the authorised individual as well as the management of the bank.

The following is how the system operates:

The finger of the authorised individual is placed on the fingerprint sensor.

The fingerprint sensor is able to record the individual's distinct print patterns in order to verify their identity.

Surveillance camera:

Video surveillance is an essential component of today's advanced security systems. It allows for round-the-clock monitoring and documenting of all events that take place inside a given area, in addition to serving as a deterrent. These systems are able to successfully increase security and promote safety by making use of cutting-edge technology and positioning cameras in key critical locations. When an individual's fingerprints have been validated, the addition of camera and relay technology to the current fingerprint and GSM-based security system offers an additional layer of protection via the capture of photographs of the persons in question. The successful recognition of a user's fingerprint activates a relay, which in turn causes the camera to take a picture of the person using the device. A relay is an electromagnetic switch.

The fingerprint patterns that were acquired by the Arduino are compared to the fingerprint patterns that were previously saved for the authorised individual.

Authorized licensed use limited to: DELHI TECHNICAL UNIV. Downloaded on July 03,2023 at 04:41:42 UTC from IEEE Xplore. Restrictions apply.

IV. RESULTS

Arduino, a fingerprint sensor, SIM900 for transmitting one-time passwords (OTPs), and a keypad to input OTPs were used in the successful design and implementation of a prototype of a fingerprint and GSM-based security system for banks. The prototype also included a servo motor for opening gates. The following is what the research found: Fig. 3 shows the OTP received.

The user's fingerprint was successfully used for identification and verification by the fingerprint sensor that was built into the system. The sensor has a high level of precision, as well as low levels of both false acceptance rates (FAR) and false rejection rates (FRR). This provided an extra degree of protection by ensuring that only authorised personnel were able to access the bank's protected sections.

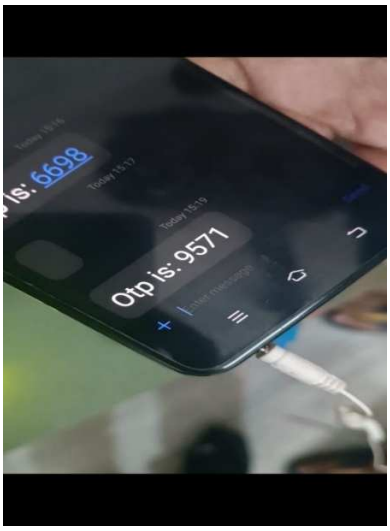

Fig. 3 OTP received screen

Upon the successful completion of fingerprint authentication, the SIM900 module was able to send one-time passwords (OTPs) to the approved users' registered mobile phone numbers. The process of generating OTPs was quick and dependable, which made it possible for users to get their OTPs in a very short amount of time. This enhancement included an extra authentication element, which resulted in the security system being improved even more (2FA).

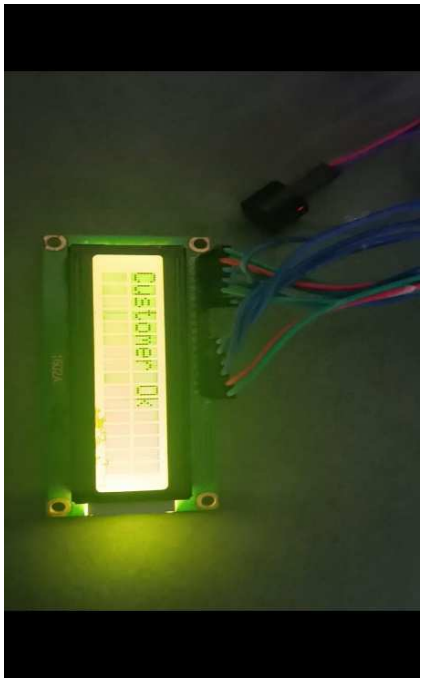

Fig. 4. Customer ID Screen

A user-friendly interface was given by the keypad for authorised users to input their own OTPs that they had received. The system performed a thorough check on the OTPs that were submitted, and it would only provide access if the appropriate OTP was provided. This additional step in the verification process offered an additional degree of protection to the system, assuring that even if an attacker managed to make a copy of a fingerprint, they would still be unable to access the system without the right OTP.

Fig. 5 Access Granted Screen

Authorized licensed use limited to: DELHI TECHNICAL UNIV. Downloaded on July 03,2023 at 04:41:42 UTC from IEEE Xplore. Restrictions apply.

When the one-time password had been checked and found to be correct, the servo motor that controlled the security gate was activated. The motor functioned faultlessly and dependably, allowing for the regulation of entry to the protected location. The servo motor was integrated with the other components of the security system to guarantee smooth functioning and to boost the bank's overall level of protection. Fig. 5 shows the access granted stage.

The results of the prototype demonstrated that the fingerprint and GSM-based security system for banks using Arduino, a fingerprint sensor, SIM900, a keypad, and a servo motor was effective in providing a secure and reliable access control solution. This was demonstrated by the fact that the system used all of these components. Several levels of protection were added to the bank's sensitive regions thanks to the combination of fingerprint authentication, OTP generation, and verification using GSM technology. This kept the bank's secure areas safe and preserved their integrity. To further improve the system's resilience and dependability, potential future study may investigate the possibility of including additional security features and technologies. Fig. 6 shows the project prototype

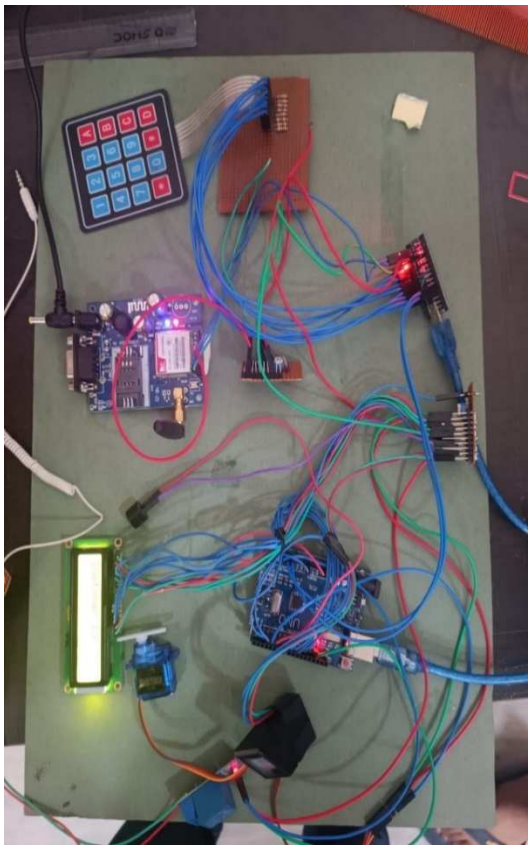

Fig. 6 Project Prototype

V. CONCLUSION

The prototype of the fingerprint and GSM-based security system for banks, which uses Arduino, a fingerprint sensor, SIM900 for sending one-time passwords (OTPs), a keypad to enter OTPs, and a servo motor to open gates, has demonstrated its effectiveness in providing a robust and reliable access control solution. The successful integration of multiple security measures, such as fingerprint authentication, OTP generation via GSM technology, and a user-friendly keypad interface for OTP verification, has significantly enhanced the overall security of the bank's secure areas. These measures include fingerprint authentication, OTP generation via GSM technology, and OTP verification.

By using this system, financial institutions are able to enjoy the benefits of many levels of protection, which helps to guarantee that only authorised personnel are able to access critical regions. The fingerprint sensor provides a means of identification that is based on biometrics, while the GSM module guarantees that one-time passwords (OTPs) are supplied in a secure manner to mobile numbers that have been registered. The one-time password (OTP) verification via a keypad provides an additional layer of security, which further restricts access to unapproved users and parties.

REFERENCES

[1] Akhtar, S., & Vashist, A. (2016). Biometric based ATM security system using Arduino. International Journal of Advanced Research in Computer and Communication Engineering, 5(6), 301-303.

[2] Sharma, N., & Kaur, P. (2017). Fingerprint-based bank locker system using GSM technology. International Journal of Advanced Research in Computer Science, 8(5), 29-31.

[3] Abbas, J., & Elasha, F. (2019). IoT-based secure ATM banking system using biometric and OTP authentication. International Journal of Computer Networks and Communications Security, 7(6), 100-107.

[4] Kumar, P., & Kaur, H. (2017). Design and implementation of highly secure biometric ATM system using Arduino. International Journal of Advanced Research in Computer Science and Software Engineering, 7(5), 292-296.

[5] Al-Khaldi, A. M., & Al-Shaikhi, A. A. (2020). Design and implementation of a smart door lock system based on fingerprint recognition and GSM technology. International Journal of Electrical and Computer Engineering, 10(1), 100-108.

[6] Bajaj, S., & Arora, S. (2018). Design and Implementation of GSM Based Bank Locker Security System using RFID and Fingerprint. International Journal of Engineering and Management Research (IJEMR), 8(2), 11-14.

Authorized licensed use limited to: DELHI TECHNICAL UNIV. Downloaded on July 03,2023 at 04:41:42 UTC from IEEE Xplore. Restrictions apply.

[7] Daniel, O., & Oyebode, A. (2017). Development of a microcontroller-based security system with GSM and smart card technology. International Journal of Scientific & Engineering Research, 8(4), 282-292.
[8] Kaur, J., & Kaur, M. (2016). Design of bank locker security system based on fingerprint sensor using GSM technology. International Journal of Engineering Research and Applications, 6(5), 45-49.
[9] Singh, P., & Shukla, A. K. (2019). Design and Implementation of a Biometric-Based Bank Locker Security System Using GSM Module. International Journal of Scientific Research in Computer Science, Engineering and Information Technology, 5(2), 305-309.
[10] Ullah, I., & Khan, S. A. (2017). Arduino based biometric locker security system using GSM module. In 2017 International Conference on Innovations in Electrical Engineering and Computational Technologies (ICIEECT) (pp. 1-6). IEEE.
[11] Faris, A. F., Al-Khafajiy, M., & Radi, N. (2020). Design of a smart security system based on IoT and GSM technologies. International Journal of Electrical and Computer Engineering (IJECE), 10(3), 2916-2923.
[12] Gupta, P., & Sharma, A. (2020). Fingerprint and OTP based dual security system using Arduino for bank lockers. International Journal of Innovative Technology and Exploring Engineering (IJITEE), 9(4), 1881-1884.
[13] Nabil, M., & Rizk, M. (2020). Arduino-based biometric access control system using GSM technology. International Journal of Computer Science and Network Security (IJCSNS), 20(5), 47-56.
[14] Singh, P., & Shukla, A. K. (2019). Design and Implementation of a Biometric-Based Bank Locker Security System Using GSM Module. International Journal of Scientific Research in Computer Science, Engineering and Information Technology, 5(2), 305-309.
[15] Ullah, S., & Suleman, I. (2020). Development of GSM and biometric-based bank security system. In Proceedings of the 2020 2nd International Conference on Computing, Mathematics and Engineering Technologies (iCoMET) (pp. 1-5). IEEE.

Authorized licensed use limited to: DELHI TECHNICAL UNIV. Downloaded on July 03,2023 at 04:41:42 UTC from IEEE Xplore. Restrictions apply.

Hand Gesture Based Sign Language Recognition Using Deep Learning

Roli Kushwaha
Department of Electronics & Communication Engineering
Delhi Technological University
Delhi, India
rolikushwaha_2k20phdec506@dtu.ac.in

Gurjit Kaur
Department of Electronics & Communication Engineering
Delhi Technological University
Delhi, India
gurjitkaur@dtu.ac.in

Manjeet Kumar
Department of Electronics & Communication Engineering
Delhi Technological University
Delhi, India
manjeetchhillar@dtu.ac.in

2023 Third International Conference on Secure Cyber Computing and Communication (ICSCCC) | 979-8-3503-0071-0/23/$31.00 ©2023 IEEE | DOI: 10.1109/ICSCCC58608.2023.10176912

***Abstract*— Sign Language Recognition (SLR) serves a very important role in creating a bridge between deaf/mute community and conventional society. SLR uses facial, head, arm, and hand motions to communicate linguistic information. Since mostly used body parts for communication are hands, therefore this paper is based on hand gesture sign language recognition system. The proposed method performs very well not only in detecting hand landmarks but also tracking of hand gesture continuously by using Google's MediaPipe. AlexNet classifier is used for classification of different gestures of Indian Sign Language (ISL) and also, comparison of the proposed method is done with some other existing SLR models. The dataset is a self-generated dataset which contains 15 classes for words and captured by stable webcam. This proposed method presents a system with recognition accuracy of 98.9% and its effectiveness is increased by translating the hand gesture recognition into readable text.**

Keywords*— *Sign Language Recognition, Indian Sign Language, Convolution Neural Network, MediaPipe.

I. INTRODUCTION

The World Health Organization has predicted that by 2050, there will be a considerable number of people, around 2.5 billion, who will suffer from hearing loss to some extent, with at least 700 million requiring hearing rehabilitation [1]. This is a significant public health issue that needs to be addressed. Hearing loss can greatly affect one's quality of life, resulting in social isolation, depression, and cognitive decline. It can also lead to economic losses due to reduced productivity and increased healthcare costs.

To address this issue, there is a need for improved access to hearing rehabilitation services, including Sign Language Recognition (SLR) technology. It can help people with hearing loss communicate with those who can hear, allowing for more effective communication and improved quality of life. Unfortunately, not everyone is familiar with sign language, which severely hinders communication. There are over 151 established sign languages [2], each with their own unique grammar rules and hand gestures that can differ not only between countries but also within regions. Sign language primarily relies on varying hand movements that differ in their shape, orientation, and location of articulation [3]. An efficient SLR system would not only benefit society but also helps in improvising the studies related to human machine tasks, such as gesture and pattern recognition. Unlike action recognition, surrounding objects shouldn't affect SLR's ability to recognize the gesture being signed. Gesture recognition system should be unaffected by the background, the signer's attire, or the color of their skin [4].

Therefore, it is essential to make sure that the processing of image/video to identify correct and discriminating features should be done effectively. Although SLR research has increased significantly in recent years [4], [5][6] creating an automated SLR system is still an open research challenge.

Both static and dynamic movements are used in sign language. The primary definition of a static gesture is the fingerspelling of a certain alphabetic or numerical symbol using a set finger configuration and fixed hand position [5]. In contrast, dynamic gestures could be single words or sentences [7]. Both contact-based systems and contactless-based systems are used by sign language recognition systems. In contact-based systems, the location of the skeleton joints in a series of postures or bodily motions serves as a signal to represent the gesture data, which is then recorded [3][8]. Whereas, Contactless approaches require the capturing of gestures through still/video camera. Flexibility, user friendly approach and more natural way of communication are various advantages of contactless approach over contact-based systems that can be uncomfortable and include risk of physical contact with sensors.

Deep learning techniques are currently advancing, and this has led to promising results in a variety of vision-based disciplines, including object detection, image categorization, and action recognition [9], [10].

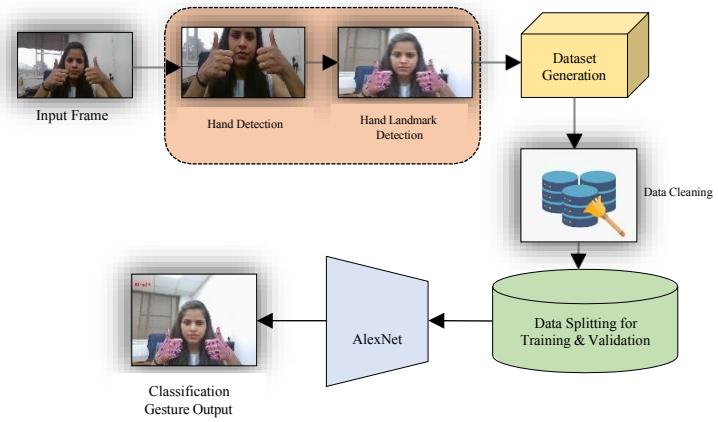

Fig. 1: Proposed Sign Language Recognition Architecture

The sign language used by the dumb and deaf communities in India is known as Indian Sign Language (ISL). The proposed approach seeks to identify words of ISL and translate them into text. The ISL recognition system uses self-created dataset from a stable web camera with an image size of 227×227. Hand and hand landmark detections are done by Mediapipe which is a comprehensive set of machine learning models that are capable of accurately detecting and

Authorized licensed use limited to: DELHI TECHNICAL UNIV. Downloaded on July 20,2023 at 11:05:43 UTC from IEEE Xplore. Restrictions apply.

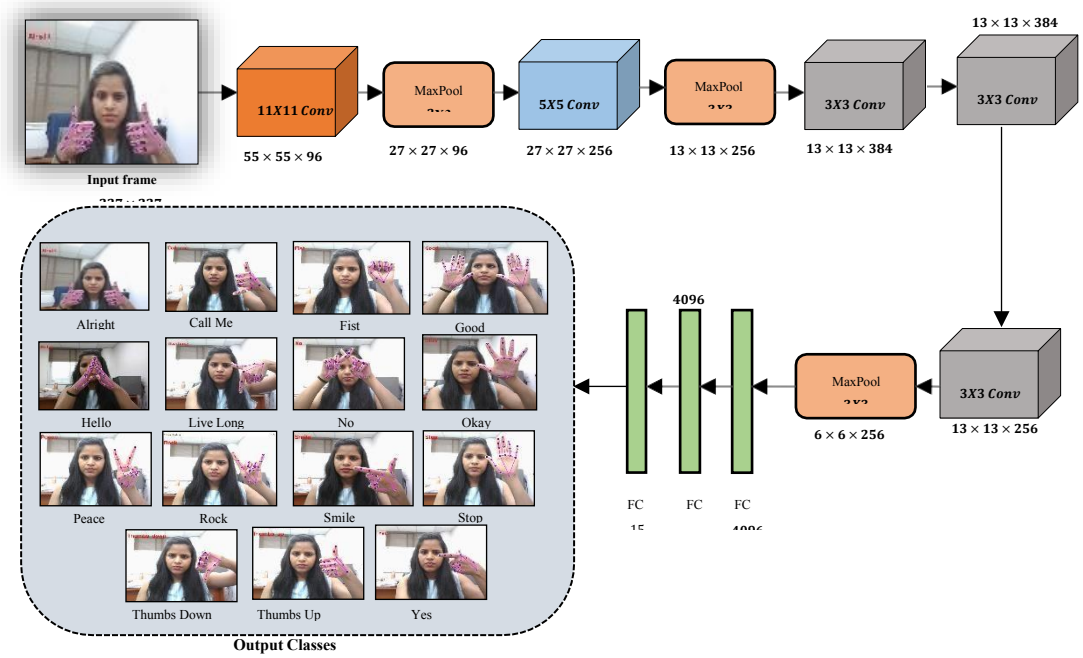

Fig. 2: The process flow for classification stage including deep feature extraction using AlexNet classifier.

tracking various parts of the human body. These modelshave been trained on large and diverse datasets from Google and can detect and track key points on different parts of the body as nodes and edges, with the nodes representing three-dimensional coordinate points that have been normalized. Fig. 1 illustrates the fundamental block diagram representation of the proposed methodology. The block diagram of the proposed methodology consists of data acquisition, pre-processing which includes hand detection and hand landmark detection, dataset generation, AlexNet classifier for classification [11] at the output stage.

The organization of the paper is: The related studies are briefly examined in Section II, the proposed work is discussed in Section III, the dataset generation is discussed in Section IV, results and discussion are discussed in Section V, Section VI concludes the proposed work with future scope.

II. Related Works

Understanding sign language is a challenging task because it varies from region to region. Various researches have been done in different languages but ISL recognition still needs to be improvise. This section briefly explained some latest research on gesture-based sign language recognition system.

In [12] authors explained sign language recognition during continuous movements of hands using Video Transformer Network and Long Short-Term Memory (LSTM) and recognition of Chinese sign language was done. Recent research [13] based on sentence recognition was done which used arm bands with inertial sensors for collection of electromyogram signals. The main limitation of contact-based approach is health hazardous and uncomfortable. In [14] human machine interaction for surgical robot was done by using LSTM and 3D user's fingers. It used Chinese language for recognition of ten gestures. The limitation of this research was that it only detects user's finger but it should combine multiple parameters like hand position and signer's body. In [15] , the proposed technique generates the predicted labels as both text and speech outputs after recognizing ISL alphabets and numbers in real time scenario. The main limitation of this study is usage of single-handed gestures whereas in real time gestures can be done by both hands. In [16] Bengali sign language (BSL) alphabets recognition introduced which also used three single handed gestures datasets with an accuracy of 94%, 99.06% and 99.06% respectively.

From the literature, it is evident that there is a significant research gap in the area of recognizing Indian Sign Language (ISL) words using hand gestures, thereby aiming to address the aforementioned research gap and improve the accuracy of recognition for ISL words.

III. Proposed Methodology

First step is to generate dataset as there is no publicly available datasets for words. Signs are captured from webcam and dataset was generated. The commonly used words in which only one hand represents a particular word are 'okay', 'yes' 'peace', 'thumbs up', 'call me', 'stop', 'live long', 'fist', 'smile', 'thumbs down', 'rock', and words which uses both hands are 'alright', 'hello', 'good', 'no'. After capturing 2536 images by stable camera, they are converted into frames. The dataset images are divided into 75% for training and 25% for testing.

Second step is to pass video frames to MediaPipe framework. Google's MediaPipe Hands [11] is a solution for accurate hand and finger tracking. It uses machine learning (ML) to deduce 21 3D hand landmarks from a single frame as shown in Fig. 3. Various existing state-of-the-art approaches [17][18]rely on desktop environments for inference whereas the proposed approach achieves real-time performance even on a mobile phone and scales to multiple hands. It consists of two model for extracting hand and its landmarks. First model is palm detection model which recognizes hand region from video frame. After that

Authorized licensed use limited to: DELHI TECHNICAL UNIV. Downloaded on July 20,2023 at 11:05:43 UTC from IEEE Xplore. Restrictions apply.

cropped hand region is sent to hand landmarks detection model which is used for recognizing position of landmarks.

For training the proposed model AlexNet Convolution Neural Network (CNN) model is used as shown in Fig. 2. The CNN model is the combination of convolution layer and pooling layer. The convolution layer extracts information from the hand landmarks obtained from MediaPipe hand landmarks detection model. Convolution layer is followed by pooling layer which down samples the feature map extracted from the convolution layer. This feature map contains the exact position the feature. The final pooling layer is then compressed out and transformed into 1D array. Final output is predicted by feeding one dimensional array obtained at pooling layer to the fully connected layer (FC). The proposed method used AlexNet classifier in which RGB images are used and it has 8 layers

with learnable parameters. Five convolution layers with a combination of max-pooling layers followed by three fully connected layers in which last fully connected layer is modified to recognize 15 classes. 'Relu' activation function used in all layers, two dropout layers and 'Softmax' activation function is used in output layer. Recognition of 15 classes is obtained with accuracy of 98.9% and translation of hand gesture recognition into readable text is also performed at the output stage.

IV. Dataset

The proposed methodology used self-generated dataset of 15 classes by capturing 2536 frames. Different classes of dataset are shown in Fig. 4. The size of the captured images is 227×227.

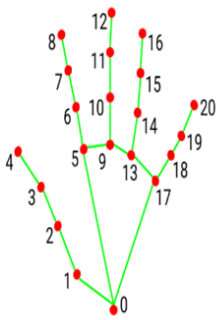

0. WRIST	11. MIDDLE_FINGER_PIP
1. THUMB_CMC	12.MIDDLE_FINGER_DIP
2. THUMB_MCP	13. MIDDLE_FINGER_TIP
3. THUMB_IP	14. RING_FINGER_MCP
4. THUMB_TIP	15. RING_FINGER_PIP
5. INDEX_FINGER_MCP	16. RING_FINGER_DIP
6. INDEX_FINGER_PIP	17. RING_FINGER_TIP
7. INDEX_FINGER_DIP	18. PINKY_MCP
8. INDEX_FINGER_TIP	19. PINKY_PIP
9. MIDDLE_FINGER_MCP	20. PINKY_DIP
10. MIDDLE FINGER MCP	21. PINKY TIP

Fig. 3. MediaPipe hand landmarks [11].

V. Results and Discussions

The proposed method's performance evaluation involves splitting the dataset into eight equal blocks and the 8-fold cross-validation technique is then applied. In each iteration of the process, the model is trained on 7 of these blocks and tested on the remaining block. This is done repeatedly for all 8 blocks, ensuring that each block serves as a test set once. After each iteration, the performance metrics of the model are recorded and averaged over the 8 folds to obtain an estimate of its performance on new, previously unseen data. For evaluation of the proposed model, the evaluation parameters are accuracy, precision, recall and F1 score.

Fig. 4. Different classes of self created dataset : (a) call me (b) thumbs up (c) thumbs up (d) peace (e) stop (f) rock (g) okay (h) fist (i) smile (j) alright (k) yes (l) no (m) live long (n) good (o) hello

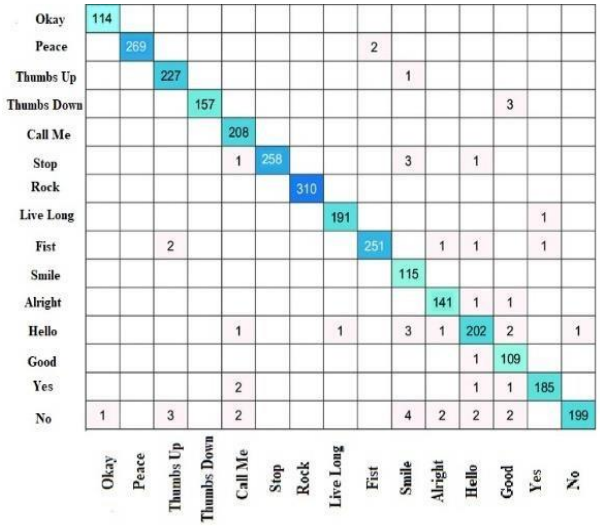

Fig. 5. Confusion matrix of proposed recognition system.

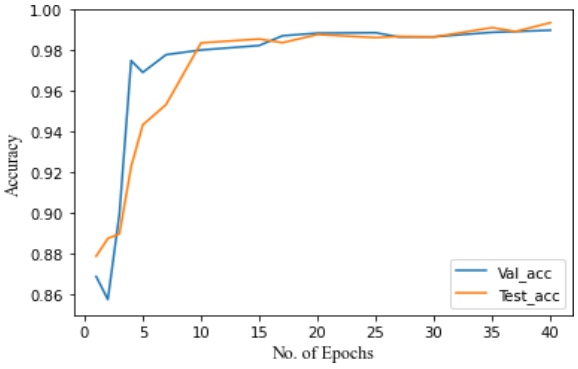

Fig. 6. Recognition accuracy curve for the proposed method (Val_acc: Validation accuracy and Test_acc: Test accuracy)

Authorized licensed use limited to: DELHI TECHNICAL UNIV. Downloaded on July 20,2023 at 11:05:43 UTC from IEEE Xplore. Restrictions apply.

Also, the comparison of the proposed model with the other state-of-the-art is shown in Table I and evaluation parameters of the proposed method is shown in Table II. It is evident from Table I that, when the proposed method is compared with [4][5][19]the proposed method provides 98.9% accuracy with the use of MediaPipe technique and AlexNet classifier. It has attained the accuracy of 98.9% and confusion matrix is shown in Fig. 5. The corresponding recognition accuracy curve and loss curve are shown in Fig 6 and Fig. 7 respectively.

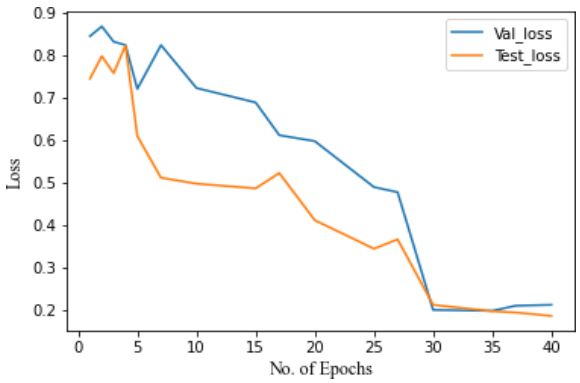

Fig. 7. Recogntion Loss curve for the proposed method (Val_loss: Validation loss and Test_loss: Test loss)

TABLE I. COMPARISON WITH SOME EXISTING METHODS.

Ref	***Dataset***	***Technique & Classifier***	***Accuracy***
[4]	American Sign Language dataset (ASL)	Microsoft Kinect sensor	91%
[5]	Self-generated dataset of 5 words using EMG	EMG and SVM	90%
[16]	BdSL Alphabet	Concatenate segmentation and BenSignNet CNN	94.0%
[13]	Chinese Sign Language (CSL) dataset	sEMG and CNN	94.2%
Proposed Model	Self-generated dataset of words	MediaPipe and AlexNet classifier	98.9 %

TABLE II. EVALUATION PARAMETERS FOR THE PROPOSEDMODEL.

Ref	***Accuracy***	***Precision***	***Recall***	***F1-score***
Proposed Model	98.9%	99.33%	99.07%	99.16%

VI. CONCLUSION

The proposed method recognizes 15 gestures which are then converted into readable texts. These gestures represent the words of ISL which are generally used in daily life. For detecting hand landmarks, Google's MediaPipe is used which is very effective in low illumination and complex background condition. With combination of AlexNet classifier which is used for recognition purpose, results in accuracy of 98.9%. As no standard dataset of words is publicly available, so dataset used in this method is a self-generated dataset of 15 words. The limitation of this method is that it is used for only 15 classes of words. Therefore, increasing the scope of future research with a greater number of classes. The dataset can also be extended with universally accepted words in ISL.

REFERENCES

[1] "Deafness and hearing loss." https://www.who.int/news-room/fact-sheets/detail/deafness-and-hearing-loss (accessed Feb. 21, 2023).

[2] "Eberhard, D. M., Simons, G. F., &Fennig, C. D. (2020.). Ethnologue Languages of the World (23rd ed.). SIL International. - References - Scientific Research Publishing." https://scirp.org/reference/referencespapers.aspx?referenceid=3057024 (accessed Feb. 27, 2023).

[3] U. Côté-Allard *et al.*, "Deep Learning for Electromyographic Hand Gesture Signal Classification Using Transfer Learning.," *IEEE Trans Neural Syst Rehabil Eng*, vol. 27, no. 4, pp. 760–771, Jan. 2019, doi: 10.1109/TNSRE.2019.2896269.

[4] H. V. Verma, E. Aggarwal, and S. Chandra, "Gesture recognition using kinect for sign language translation," *2013 IEEE Second International Conference on Image Information Processing (ICIIP-2013)*, pp. 96–100, 2013, doi: 10.1109/ICIIP.2013.6707563.

[5] B. Divya, J. Delpha, and S. Badrinath, "Public speaking words (Indian sign language) recognition using EMG," *2017 International Conference On Smart Technologies For Smart Nation (SmartTechCon)*, pp. 798–800, May 2017, doi: 10.1109/SMARTTECHCON.2017.8358482.

[6] M. Al-Hammadi, G. Muhammad, W. Abdul, M. Alsulaiman, M. A. Bencherif, and M. A. Mekhtiche, "Hand Gesture Recognition for Sign Language Using 3DCNN," *IEEE Access*, vol. 8, pp. 79491–79509, 2020, doi: 10.1109/ACCESS.2020.2990434.

[7] X. Zhang, X. Chen, Y. Li, V. Lantz, K. Wang, and J. Yang, "A framework for hand gesture recognition based on accelerometer and EMG sensors," *IEEE Transactions on Systems, Man, and Cybernetics Part A:Systems and Humans*, vol. 41, no. 6, pp. 1064–1076, Nov. 2011, doi: 10.1109/TSMCA.2011.2116004.

[8] N. Sarhan and S. Frintrop, "Transfer Learning for Videos: From Action Recognition to Sign Language Recognition," *Proceedings - International Conference on Image Processing, ICIP*, vol. 2020-October, pp. 1811–1815, Oct. 2020, doi: 10.1109/ICIP40778.2020.9191289.

[9] M. Shamim Hossain, M. Al-Hammadi, and G. Muhammad, "Automatic Fruit Classification Using Deep Learning for Industrial Applications," *IEEE Trans Industr Inform*, vol. 15, no. 2, pp. 1027–1034, Feb. 2019, doi: 10.1109/TII.2018.2875149.

[10] H. Altaheri *et al.*, "Deep learning techniques for classification of electroencephalogram (EEG) motor imagery (MI) signals: a review," *Neural Comput Appl*, 2021, doi: 10.1007/S00521-021-06352-5.

[11] "Hands mediapipe." https://google.github.io/mediapipe/solutions/hands

[12] W. Qin, X. Mei, Y. Chen, Q. Zhang, Y. Yao, and S. Hu, "Sign Language Recognition and Translation Method based on VTN," *2021 International Conference on Digital Society and Intelligent Systems, DSInS 2021*, pp. 111–115, 2021, doi: 10.1109/DSINS54396.2021.9670588.

[13] Z. Wang *et al.*, "Hear Sign Language: A Real-Time End-to-End Sign Language Recognition System," *IEEE Trans Mob Comput*, vol. 21, no. 07, pp. 2398–2410, Jul. 2022, doi: 10.1109/TMC.2020.3038303.

[14] W. Qi, S. E. Ovur, Z. Li, A. Marzullo, and R. Song, "Multi-Sensor Guided Hand Gesture Recognition for a Teleoperated Robot Using a Recurrent Neural Network," *IEEE Robot Autom Lett*, vol. 6, no. 3, pp. 6039–6045, Jul. 2021, doi: 10.1109/LRA.2021.3089999.

[15] S. Katoch, V. Singh, and U. S. Tiwary, "Indian Sign Language recognition system using SURF with SVM and CNN," *Array*, vol. 14, Jul. 2022, doi: 10.1016/J.ARRAY.2022.100141.

[16] A. S. M. Miah, J. Shin, M. A. M. Hasan, and M. A. Rahim, "BenSignNet: Bengali Sign Language Alphabet Recognition

Authorized licensed use limited to: DELHI TECHNICAL UNIV. Downloaded on July 20,2023 at 11:05:43 UTC from IEEE Xplore. Restrictions apply.

Using Concatenated Segmentation and Convolutional Neural Network," *Applied Sciences 2022, Vol. 12, Page 3933*, vol. 12, no. 8, p. 3933, Apr. 2022, doi: 10.3390/APP12083933.

[17] D. Li, X. Yu, C. Xu, L. Petersson, and H. Li, "Transferring Cross-Domain Knowledge for Video Sign Language Recognition," *Proceedings of the IEEE Computer Society Conference on Computer Vision and Pattern Recognition*, pp. 6204–6213, 2020, doi: 10.1109/CVPR42600.2020.00624.

[18] L. Pigou, A. van den Oord, S. Dieleman, M. van Herreweghe, and J. Dambre, "Beyond Temporal Pooling: Recurrence and Temporal Convolutions for Gesture Recognition in Video," *Int J Comput Vis*, vol. 126, no. 2–4, pp. 430–439, Apr. 2018, doi: 10.1007/S11263-016-0957-7.

[19] S. Adhikary, A. K. Talukdar, and K. Kumar Sarma, "A Vision-based System for Recognition of Words used in Indian Sign Language Using MediaPipe," *Proceedings of the IEEE International Conference Image Information Processing*, vol. 2021-November, pp. 390–394, 2021, doi: 10.1109/ICIIP53038.2021.9702551.

Authorized licensed use limited to: DELHI TECHNICAL UNIV. Downloaded on July 20,2023 at 11:05:43 UTC from IEEE Xplore. Restrictions apply.

2023 4th International Conference for Emerging Technology (INCET)
Belgaum, India. May 26-28, 2023

Heart Disease Prediction Using a Soft Voting Ensemble of Gradient Boosting Models, RandomForest, and Gaussian Naive Bayes

Kaustav Sen
Department of Information Technology
Delhi Technological University
Delhi, India
kaustavsen11@gmail.com

Bindu Verma
Department of Information Technology
Delhi Technological University
Delhi, India
binduverma@dtu.ac.in

2023 4th International Conference for Emerging Technology (INCET) | 979-8-3503-3575-0/23/$31.00 ©2023 IEEE | DOI: 10.1109/INCET57972.2023.10170399

***Abstract*—Heart disease is associated with a high mortality rate because it affects a significant number of people around the world. There is a pressing need for improved diagnostic methods that are both effective and accurate. Techniques from the field of machine learning have been put to extensive use on tabular data from the healthcare sector, where they have proven to be effective in prediction and analysis. To address the issue of the traditional machine learning model's low accuracy, precision, and recall value, we propose a soft voting meta classifier composed of Catboost, Light-Gradient Boosting Machine, Gaussian Naive Bayes , Random Forest, and XGBoost. The proposed soft voting ensemble outperformed the other models used in this experiment, which was conducted on a fused UCI heart disease and Statlog dataset. The proposed soft voting ensemble model achieved 91.85% accuracy and a 0.9344 Area Under The Curve Score.**

***Index Terms*—Heart Disease, Soft Voting Ensemble, Medical Analysis, Artificial Intelligence, Machine Learning**

I. Introduction

Heart disease is a group of illnesses that impact heart function; it is a subset of cardiovascular diseases (CVD). According to WHO, CVD deaths accounted for 32% of all deaths in 2019, with 17.9 million deaths [1]. CVD-related disorders are responsible for 38% of the 17 million premature deaths worldwide (aged 70 and lesser) in 2019 [1].The frequency of heart disease has continuously climbed, from 271 million cases in 1990 to 523 million in 2019 [2]. Heart disease is expected to increase due to population expansion and ageing since the number of older adults is expected to double in many parts of the world [2]. Hazardous lifestyle choices, such as drug or alcohol misuse, high cholesterol levels, obesity, increased triglyceride levels, hypertension, and other health problems, enhance an individual's heart disease [3]. It is critical to create heart disease prediction methods that can help medical practitioners to diagnose the disease. Patients use of smart bands and other forms of intelligent health wearable connected to the Internet of Things (IoT) has become an integral part of modern medical care [4], [5]. Researchers and medical professionals all over the world have used artificial intelligence and machine learning to increase the accuracy of predicting heart disease [6]–[8]. Deep learning and machine learning are commonly employed to detect health-related concerns [9]. Deep learning models have been created using medical data using pictures such as x-rays, chest scans [10]. Various machine learning models, such as CatBoost (CB), Decision Tree, Logistic Regression, Random Forest (RF) , XGBoost (XGB) , Light Gradient Boosting Machine (LGBM), Gaussian Nave Bayes classifier (GNB) and others, can be trained to diagnose, classify, or forecast heart diseases.

The paper proposed a voting ensemble that uses soft voting, and the five algorithms used are selected due to their performance as individual models in predicting heart disease. Gaussian Naive Bayes, XGBoost, Catboost, LGBM and Random forests are used to create the proposed model. An AUC of 0.9351 is found for the proposed soft voting ensemble model, and its accuracy is 0.9185. A combined Heart Dataset set consisting of the UCI (University of California Irvine) Heart disease dataset and the UCI Statlog dataset is used to conduct the experiment. The reason for developing a soft voting ensemble rather than individual models is that individual modes have higher False Negative and False Positive values. When predicting heart disease, a lower false negative value is preferred. Our proposed model minimized the false negative values compared to conventional machine learning models.

The paper is organized this way: Literature work is discussed in Section II. Section III describes the dataset description, pre-processing, the model proposed and other models in brief. In Section IV the detailed result analysis of the proposed soft voting ensemble. Finally, in section V the conclusion of the work is done.

II. Related Works

Heart disease prediction has received much attention, with many studies focusing on the UCI Cleveland dataset. On the combined UCI heart disease dataset, the UCI Irvine Statlog dataset, and other heart-related datasets like the Framingham heart study dataset, many researchers have studied the results of standard machine learning classifiers and ensemble techniques. In the work of Gárate-Escamila et al. [11], principal

Authorized licensed use limited to: DELHI TECHNICAL UNIV. Downloaded on July 20,2023 at 11:23:14 UTC from IEEE Xplore. Restrictions apply.

component analysis and Chi-Squared is used and experiments are conducted on Cleveland and Hungarian dataset from the UCI heart disease datasets. Compared to the results of ML models on raw datasets, using chi-square for feature selection and PCA to form new features significantly improves performance. Vivekanandan et al. [12] used a modified differential evolution algorithm with feature selection using combined model of fuzzy AHP and a neural network to predict heart disease. In their approach, Differential Evolution required a smaller number of generations. Ramalingam et al. [13] report in their paper that Random forest, ensemble-based techniques, and SVM performed well when used on the heart disease dataset.

On the Statlog heart disease dataset, Raza [14] discovered that a majority voting ensemble model consisting of logistic regression, nave Bayes, and multi-layer perceptron achieved 88% accuracy, f1 score of 0.87, and MCC of 0.77. Kim et al. [15] compared three oversampling techniques for the imbalanced dataset. Compared to Adasyn and the Borderline SMOTE oversampling technique, they found SMOTE to be the most promising. Ishaq et al. [16] used 299 samples from the UCI heart failure clinical records dataset. With an extra tree classifier model, they achieved 92.62% accuracy and 0.93 F1-score using random forest ranking for feature selection and SMOTE for oversampling. Kavitha et al. [17] used the UCI Cleveland dataset to create a combination model of random forest and decision tree with an accuracy of 88%. DBSCAN was used by Fitriyani et al. [18] to eliminate outliers in a heart disease prediction model. They used the SMOTE-ENN oversampling technique and XGBoost to balance the data to predict heart disease. The Statlog dataset had a 95.90% accuracy rate, while the UCI Cleveland dataset had a 98.40% accuracy rate. Wang et al. [19] developed a stacking-based model that achieved 95.43% accuracy and 95.84% recall and 94.44% specificity for coronary heart disease detection. Using data from a hospital in Beijing, China, Chang et al. [20] created a hybrid XGBSVM model to predict cardiovascular disease in hypertensive patients. While other machine learning models struggled on their dataset, XGBSVM performed admirably.

III. Methodology

The flowchart of the proposed soft voting ensemble model is shown in Figure 1. First, we convert the categorical features into numerical features using Label encoding. We split the heart dataset into the ratio of $80:20$ for training and testing data, respectively. We use a standard scalar to normalise the data for the models which are sensitive to scale of input features, and hyper-parameter tuning to improve the individual performance of all the models. The five best-performing models are used to create a soft voting ensemble for our work.

A. Dataset Description

UCI's heart disease dataset and Statlog dataset were used for this research, and the features employed here were derived from both of those sources. The number of samples from each of the datasets that are used is Cleveland (303), Hungarian (294), Switzerland (123), Long Beach, VA (200), and Statlog (Heart) Data Set (270). Out of which 272 are duplicated rows, therefore the total number of samples is 918. There are 11 features and one binary output variable named "heart disease". A detailed description of the features is shown in Table I. The datatype of the features is shown in Table II. The output variable has 508 samples with heart disease and 410 samples that do not have heart disease.

TABLE I
FEATURE DESCRIPTION TABLE

ID	Feature	Feature Description
1	Age	Age in years
2	Sex	Sex(Male:0 or female:1)
3	ChestPainType	Four Types of Chest Pain(TA:typical angina,ATA:atypical aninga,NAP:non-angina,ASY:asymptomatic)
4	RestingBP	Resting Blood pressure value(Unit mm hg)
5	Cholesterol	Serum Cholesterol concentration(Unit mm/dl)
6	FastingBS	Fasting Blood Sugar(1:blood sugar 120mg/dL,0:other)
7	RestingECG	Resting electrocardiogram (Normal: Normal, ST: having ST-T wave abnormalities(T wave inversions or ST elevation or depression of 0.05 mV), LVH: showing probable or definite left ventricular hypertrophy by Estes' criteria)
8	MaxHR	Maximum heart rate achieved(Values between 60 and 202)
9	ExcerciseAngina	Exercise-Induced Angina Presence:(1:Yes,0:No)
10	Oldpeak	St depression induced by exercise relative to rest
11	ST_Slope	The slope of the peak exercise ST segment(up, flat, down)

TABLE II
FEATURE TYPE

Feature Type	Feature Names
Categorical	Sex, ChestPainType, RestingECG, ExerciseAngina, ST_Slope
Numerical	Age, RestingBP, Cholesterol, FastingBS, MaxHR

B. Pre-processing

Data pre-processing is required before feeding data to the model to transform data into a valuable and efficient format. The dataset contained five categorical features, with the remaining features being numerical. Label Encoding is used to convert the absolute value of those features into a numerical data. The numerical data is scaled to a standard range for logistic regression and Support Vector Machine (SVM) . In Figure 2 shows the heat map of features and the binary output.

C. Methods

In this section we have discussed different machine learning methods that are used in the proposed work.

1) XGBoost: It is another ensemble machine learning algorithm that uses decision trees as weak learners based on a gradient boosting framework. It performs very well on structured data. The decision trees used by XGboost are called CART (Classification and Regression Trees). The leaf nodes

Authorized licensed use limited to: DELHI TECHNICAL UNIV. Downloaded on July 20,2023 at 11:23:14 UTC from IEEE Xplore. Restrictions apply.

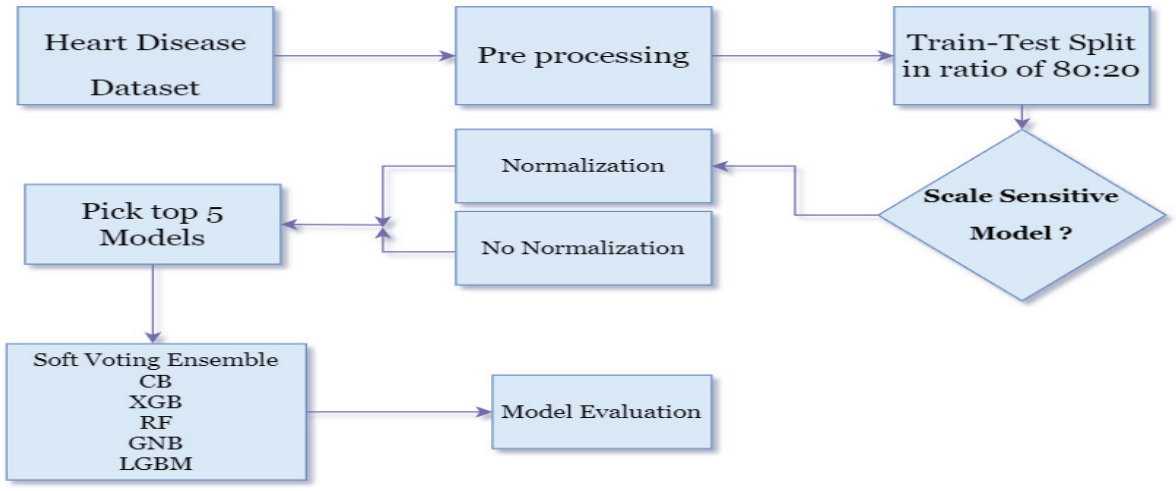

Fig. 1. Flowchart of Proposed soft voting ensemble

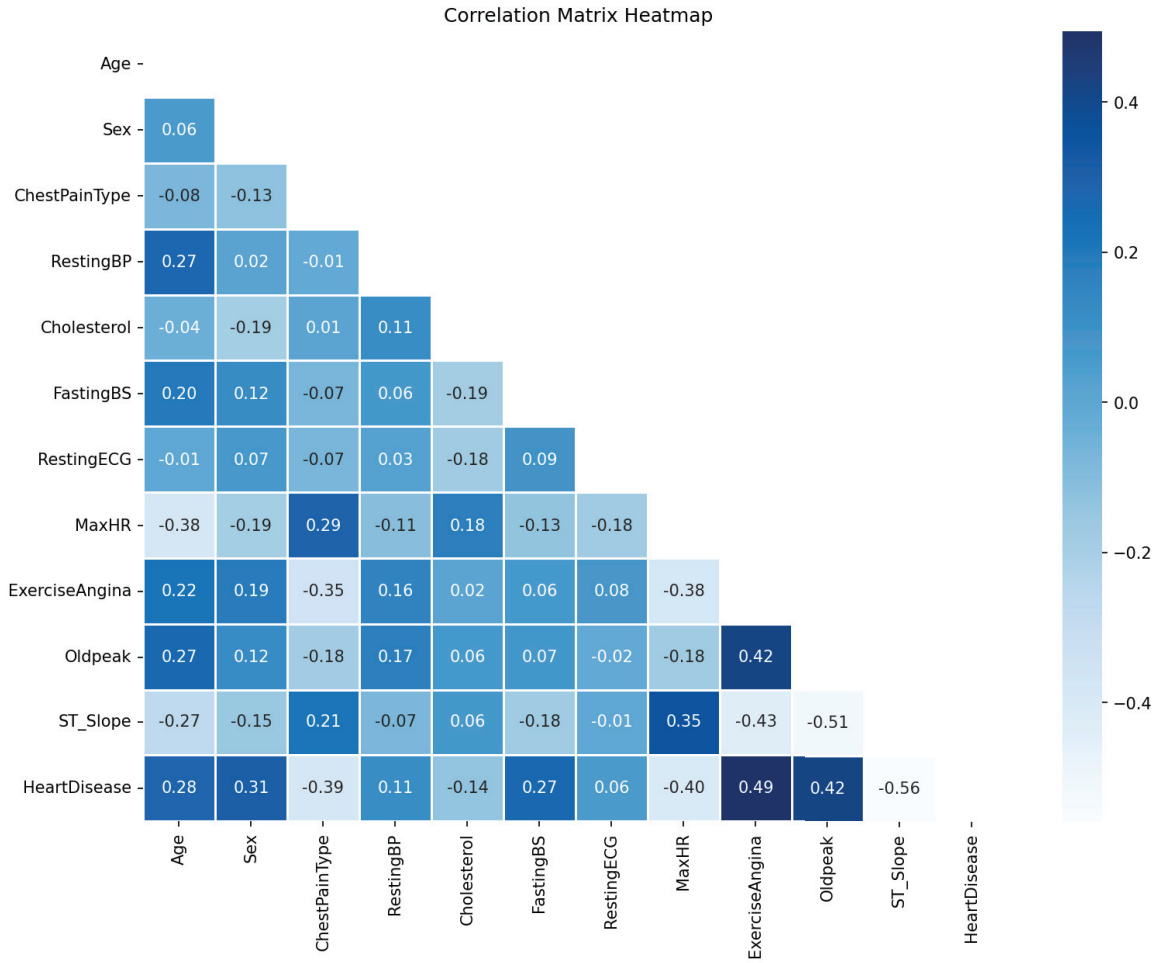

Fig. 2. Heatmap of the Features

Authorized licensed use limited to: DELHI TECHNICAL UNIV. Downloaded on July 20,2023 at 11:23:14 UTC from IEEE Xplore. Restrictions apply.

contain real-value scores of each instances belong to a class label. When the tree reaches its max depth, decisions are made by converting this score into categories using the threshold. The general formula of XGboost can be formed as :

$$\widehat{y}_i = \sum_{t=1}^{T} g_t\left(x_i\right), g_t \in G \tag{1}$$

Where T is the number of Trees, g is the functional space of G, G is the set of possible CARTS.

2) Random Forest: A random forest consists of many decision trees. The decision trees uses a subset of the original dataset as data with data replacement. After training the individual decision trees, a random forest picks the class that gets the maximum prediction vote from each tree. It helps random forests to overcome the problem of over-fitting. It uses the bagging concept of ensemble learning, which combines many weak classifiers to provide a solution. Mathematically it can be expressed as [6]: For a given Data $A = \{a_1, a_2, a_3, \ldots . a_n\}$with responses $O = \{a_1, a_2, a_3, \ldots . a_n\}$ the bagging is repeated from $b = 1\,to\,B$. By averaging the predictions $\sum_{b=1}^{B} fb\left(a^{'}\right)$ for every individual trees on $a^{'}$ the unseen samples $a^{'}$ is made :

$$K = \frac{1}{B}\sum_{b=1}^{B} fb\left(a^{'}\right) \tag{2}$$

3) Light Gradient Boosting Machine: It is a fast open-source gradient boosting derived framework. It's tree grows vertically compared to other algorithms whose level of use grows horizontally. Generally, it is used for larger datasets. LGBM removes instances with low gradients and keeps instances with more significant gradients. This technique is called Gradient-Based One-Side Sampling (GOSS), and it also has Exclusive Feature Bundling (EFB), which reduces the number of features while maintaining good accuracy. Given the Supervised training set $D = \{(x_i, y_i)\}_{i=1}^{m}$. LGBM attempts to find estimates $g\left(a\right)$ to a specific function $g^{*}\left(a\right)$ that restricts the normal estimation of a given loss function $F\left(c, g\left(a\right)\right)$ as shown in [21]:

$$g = argmin_g Q_{c,\mathbb{D}} F\left(c, g\left(a\right)\right) \tag{3}$$

4) Gaussian Naive Bayes: Gaussian Naive Bayes is a probabilistic machine learning classification approach that is based on the Bayes theorem and assumes that the features in the dataset are conditionally independent given the class label. Gaussian Naive Bayes is a continuous data model that models the likelihood of features given a class label using a Gaussian (normal) distribution. Despite its simplicity and strict independence assumptions, the method frequently performs unexpectedly well in practise, offering good classification accuracy and scalability. One disadvantage is its sensitivity to irrelevant traits, which might have a negative impact on its performance. Gaussian Naive Bayes is represented mathematically as follows:

$$P(z|x_1, x_2, ..., x_n) = \frac{P(z)\prod_{i=1}^{n} P(x_i|z)}{P(x_1, x_2, ..., x_n)} \tag{4}$$

where $P(z)$ is the prior probability of class z, $P(x_i|z)$ is the likelihood of feature x_i given class z (modeled using Gaussian distribution), and $P(x_1, x_2, ..., x_n)$ is the evidence.

5) Catboost: It is one of the algorithms based on gradient decision trees. There is no need to pre-process the categorical features as it automatically handles them. It does permutation-based boosting compared to the classic boosting algorithm. Gradient boosting is often overfitted on small datasets. Catboost is used to solve the overfitting problem on small datasets. Its general equation can be formed as [22]:

$$G_p\left(x\right) = G\left(p-1\right)\left(x\right) + \gamma_p K_p\left(x\right) \tag{5}$$

$$\gamma_p = argmin \sum_{c=1}^{c} Y\left(b_c, G\left(p-1\right)\left(x_c\right) + \gamma_p K_p\left(a_c\right)\right) \tag{6}$$

$G_p\left(x\right)$ is the final result, Y is the loss function, and $K_p\left(x\right)$ is the pseudo-residuals where p is the number of iterations,and γ_p is the multiplier in Equation 5 and 6.

6) Proposed Soft Voting Ensemble: A voting ensemble employs two voting methods: majority voting and soft voting. Majority voting establishes the final classification using the mode of all base classifier predictions. Soft voting computes the average of the predicted probabilities for class labels from all individual models in the ensemble. It then assigns the final class label based on the highest average probability. Our proposed soft voting ensemble is a meta-model composed of Catboost, LGBM, XGBoost, Random Forest, and Multilayer Perceptron models. We used equal weights for each classifier because all of the classifiers used in the soft voting ensemble have similar performances.Lets denote the probabilities predicted by each model as $P_{1,0}, P_{1,1}, P_{2,0}, P_{2,1}....P_{n,0}, P_{n,1}$.For binary classification, the probability for each class label (0 or 1) is computed by each model. The soft voting ensemble will compute the average of these probabilities and choose the class label with the highest average probability. Let $P_{i,0}$and $P_{i,1}$ epresent the predicted probabilities of class 0 and class 1, respectively, for the i-th model. The soft voting ensemble probabilities for each class can be calculated as:

$$P_{ensemble,0} = \frac{1}{n}\sum_{i=1}^{n} P_{i,0}, \tag{7}$$

$$P_{ensemble,1} = \frac{1}{n}\sum_{i=1}^{n} P_{i,1}, \tag{8}$$

After calculating the ensemble probabilities, the class label with the highest ensemble probability is chosen as the final prediction:

$$\hat{y}_{ensemble} = \begin{cases} 0 & \text{if } P_{ensemble,0} > P_{ensemble,1} \\ 1 & \text{if } P_{ensemble,1} \geq P_{ensemble,0} \end{cases} \tag{9}$$

IV. Results

For creating our proposed soft voting ensemble out of all the models, we picked the top-performing models: Catboost, GNB, LGBM, Random Forest, and XGboost. Hyperparameter

Authorized licensed use limited to: DELHI TECHNICAL UNIV. Downloaded on July 20,2023 at 11:23:14 UTC from IEEE Xplore. Restrictions apply.

TABLE III
COMPARATIVE ANALYSIS OF PROPOSED WORK WITH THE LITERATURE

Algorithm Used	**Accuracy(%)**	**F1-Score(%)**	**Precision(%)**	**Recall(%)**	**AUC**
Decision Tree	80.98	78.63	90.20	84.02	0.8677
Logistic Regression	86.41	85.32	91.18	88.15	0.8951
Support Vector Machine	86.41	85.32	91.18	88.15	0.8883
Gaussian Naïve Bayes	88.04	89.22	89.22	89.22	0.9241
Catboost	90.22	91.18	91.18	91.18	0.9313
LGBM	88.59	87.85	92.16	89.95	0.9264
Random Forest	88.59	88.57	91.18	89.86	0.9293
XGboost	90.22	90.38	92.16	91.26	0.9339
Soft Voting Ensemble (CB,XGB,RF, GNB,LGBM)	**91.85**	**91.43**	**94.12**	**92.75**	**0.9344**

TABLE IV
CONFUSION MATRICES OF ALL THE MODELS

Catboost		Decision Tree		SVM	
TP	FN	TP	FN	TP	FN
93	9	92	10	93	9
FP	TN	FP	TN	FP	TN
9	73	25	57	16	66
XGBoost		**RF**		**GNB**	
TP	FN	TP	FN	TP	FN
94	8	93	9	91	11
FP	TN	FP	TN	FP	TN
10	72	12	70	11	71
LR		**LGBM**		**Proposed Model**	
TP	FN	TP	FN	TP	FN
93	9	94	8	96	6
FP	TN	FP	TN	FP	TN
16	66	13	69	9	73

tuning was done for all of these models for was done using GridSearchCV technique from scikit-learn. Our proposed model achieved 91.85% accuracy, 92.75% f1-score, 91.43% precision, 94.12% recall, and the AUC score was 0.9344 In terms of accuracy, the ensemble model, with a score of 0.9185, outperforms the best individual classifier, XGBClassifier (0.9022), as well as other models. The detailed results of all the models are shown in Table III. Table IV show confusion matrix of all the models, and Fig 3 shows the receiver operating characteristics curve of all the models.

The ensemble model demonstrates superior performance across various metrics compared to individual classifiers and other models. With a precision of 0.9143, it effectively identifies true positive cases and reduces false positives. Its recall of 0.9412 indicates a higher effectiveness in detecting positive cases, minimizing false negatives. The ensemble model achieves the highest F1-score of 0.9275, reflecting a balanced performance between precision and recall, ensuring neither overly conservative nor aggressive predictions. Finally, its AUC of 0.9344, slightly higher than the best individual classifier, XGBClassifier (0.9339), highlights its enhanced discrimination ability, making it more effective in distinguishing between positive and negative instances.

The proposed ensemble had the lowest false positives and false negatives values compared to the other models used in the experiment, as shown in Table IV.The results discussion presented here highlights the key performance metrics of the ensemble model in comparison to the individual classifiers and other models. It emphasizes the improvements achieved by the ensemble model in accuracy, precision, recall, F1-score, and AUC. These performance enhancements can be attributed to the soft voting mechanism, which combines the complementary strengths of the individual classifiers, ultimately leading to a more accurate and reliable prediction of heart disease.

V. CONCLUSION

In conclusion, our soft voting ensemble model, which combines gradient-based boosting models (LightGBM, CatBoost, and XGBoost), Random Forest, and Gaussian Naive Bayes, has demonstrated superior performance in predicting heart disease. The improved metrics, including area under the curve (AUC), F1-score, and others, indicate the potential of this ensemble approach for more accurate and reliable disease prediction. The strength of our ensemble model lies in its ability to leverage the unique capabilities of each individual model. Gradient-based boosting models, such as LightGBM, CatBoost, and XGBoost, are well-suited to handling large datasets and can effectively model complex relationships in the data. Random Forest provides a robust approach, reducing overfitting by averaging multiple decision trees. Lastly, Gaus-

Authorized licensed use limited to: DELHI TECHNICAL UNIV. Downloaded on July 20,2023 at 11:23:14 UTC from IEEE Xplore. Restrictions apply.

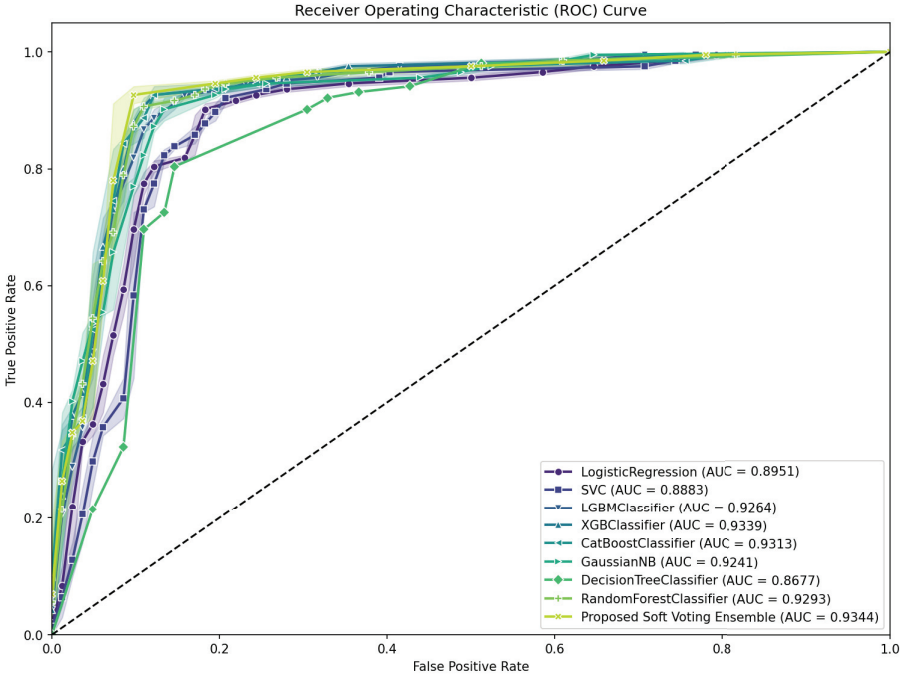

Fig. 3. Receiver operating characteristic curve of Proposed model and Other models

sian Naive Bayes offers a simple yet effective probabilistic approach, complementing the other methods in the ensemble. The soft voting technique employed in our model contributes to its success by combining the probability estimates from each individual model. This approach allows the ensemble to capture a more nuanced representation of the underlying data, resulting in improved performance over any single model.

For future research, several areas of exploration could further enhance the model's performance and utility:

- Feature engineering: Investigating additional features and feature transformations may lead to improved predictive power. Domain-specific knowledge could be leveraged to create new, meaningful features or to identify potential interactions among existing ones.
- Model diversity: Incorporating additional models, such as deep tabular learning techniques like TabNet, TabPfn, and others, could further improve the ensemble's performance. By adding models with different strengths and weaknesses, the ensemble may become more robust and less susceptible to the limitations of any single model.
- Real-world validation: Finally, validating the model using real-world data from various sources, such as electronic health records or biobanks, will be crucial for assessing its generalizability and applicability in clinical settings.

By exploring these avenues, our soft voting ensemble model could be further refined and expanded, potentially offering an even more powerful and practical tool for predicting heart disease .

REFERENCES

[1] "Cardiovascular diseases." [Online]. Available: https://www.who.int/health-topics/cardiovascular-diseases

[2] "Cardiovascular Disease Burden, Deaths Are Rising Around the World - American College of Cardiology." https://www.acc.org/about-acc/press-releases/2020/12/09/18/30/cvd-burden-and-deaths-rising-around-the-world (accessed Jun. 11, 2022).

[3] "Heart disease - Symptoms and causes - Mayo Clinic." [Online]. Available: https://www.mayoclinic.org/diseases-conditions/heart-disease/symptoms-causes/syc-20353118

[4] M. A. Khan and F. Algarni, "A Healthcare Monitoring System for the Diagnosis of Heart Disease in the IoMT Cloud Environment Using MSSO-ANFIS," IEEE Access, vol. 8, pp. 122259–122269, 2020, doi: 10.1109/ACCESS.2020.3006424.

[5] Y.-L. Zheng et al., "Unobtrusive Sensing and Wearable Devices for Health Informatics," IEEE Transactions on Biomedical Engineering, vol. 61, no. 5, pp. 1538–1554, Jun. 2014, doi: 10.1109/TBME.2014.2309951.

[6] S. Mohan, C. Thirumalai, and G. Srivastava, "Effective Heart Disease Prediction Using Hybrid Machine Learning Techniques," IEEE Access, vol. 7, pp. 81542–81554, 2019, doi: 10.1109/ACCESS.2019.2923707.

[7] P. Ghosh et al., "Efficient Prediction of Cardiovascular Disease Using Machine Learning Algorithms With Relief and LASSO Feature Selection Techniques," IEEE Access, vol. 9, pp. 19304–19326, 2021, doi: 10.1109/ACCESS.2021.3053759.

[8] A. Gani, A. v Gribok, S. Rajaraman, W. K. Ward, and J. Reifman, "Predicting Subcutaneous Glucose Concentration in Humans: Data-Driven Glucose Modeling," IEEE Transactions on Biomedical Engineering, vol. 56, no. 2, pp. 246–254, Jun. 2009, doi: 10.1109/TBME.2008.2005937.

[9] A. K. Sahoo, C. Pradhan, and H. Das, "Performance evaluation of different machine learning methods and deep-learning based convolutional neural network for health decision making," Studies in Computational Intelligence, vol. SCI 871, pp. 201–212, 2020, doi: 10.1007/978-3-030-33820-6_8/COVER/.

[10] Y. Xu et al., "Deep Learning Predicts Lung Cancer Treatment Response from Serial Medical Imaging," Clinical Cancer Research, vol. 25, no. 11, pp. 3266–3275, Jun. 2019, doi: 10.1158/1078-0432.CCR-18-2495.

[11] A. K. Gárate-Escamila, A. H. el Hassani, and E. Andrès, "Classification models for heart disease prediction using feature selection and PCA," Informatics in Medicine Unlocked, vol. 19, p. 100330, 2020.

Authorized licensed use limited to: DELHI TECHNICAL UNIV. Downloaded on July 20,2023 at 11:23:14 UTC from IEEE Xplore. Restrictions apply.

[12] T. Vivekanandan and N. C. S. N. Iyengar, "Optimal feature selection using a modified differential evolution algorithm and its effectiveness for prediction of heart disease," Comput Biol Med, vol. 90, pp. 125–136, 2017.
[13] V. v Ramalingam, A. Dandapath, and M. K. Raja, "Heart disease prediction using machine learning techniques: a survey," International Journal of Engineering & Technology, vol. 7, no. 2.8, pp. 684–687, 2018.
[14] K. Raza, "Improving the prediction accuracy of heart disease with ensemble learning and majority voting rule," in U-Healthcare Monitoring Systems, Elsevier, 2019, pp. 179–196.
[15] Y.-T. Kim, D.-K. Kim, H. Kim, and D.-J. Kim, "A comparison of oversampling methods for constructing a prognostic model in the patient with heart failure," in 2020 International Conference on Information and Communication Technology Convergence (ICTC), 2020, pp. 379–383.
[16] A. Ishaq et al., "Improving the prediction of heart failure patients' survival using SMOTE and effective data mining techniques," IEEE access, vol. 9, pp. 39707–39716, 2021.
[17] M. Kavitha, G. Gnaneswar, R. Dinesh, Y. R. Sai, and R. S. Suraj, "Heart disease prediction using hybrid machine learning model," in 2021 6th International Conference on Inventive Computation Technologies (ICICT), 2021, pp. 1329–1333.
[18] N. L. Fitriyani, M. Syafrudin, G. Alfian, and J. Rhee, "HDPM: An Effective Heart Disease Prediction Model for a Clinical Decision Support System," IEEE Access, vol. 8, pp. 133034–133050, 2020, doi: 10.1109/ACCESS.2020.3010511.
[19] J. Wang et al., "A Stacking-Based Model for Non-Invasive Detection of Coronary Heart Disease," IEEE Access, vol. 8, pp. 37124–37133, 2020, doi: 10.1109/ACCESS.2020.2975377.
[20] W. Chang, Y. Liu, X. Wu, Y. Xiao, S. Zhou, and W. Cao, "A New Hybrid XGBSVM Model: Application for Hypertensive Heart Disease," IEEE Access, vol. 7, pp. 175248–175258, 2019, doi: 10.1109/ACCESS.2019.2957367.
[21] X. Sun, M. Liu, and Z. Sima, "A novel cryptocurrency price trend forecasting model based on LightGBM," Finance Research Letters, vol. 32, p. 101084, Jan. 2020, doi: 10.1016/j.frl.2018.12.032.
[22] L. Prokhorenkova, G. Gusev, A. Vorobev, A. V. Dorogush, and A. Gulin, "CatBoost: unbiased boosting with categorical features," Advances in Neural Information Processing Systems, vol. 2018-December, pp. 6638–6648, Jun. 2017, doi: 10.48550/arxiv.1706.09516.

Authorized licensed use limited to: DELHI TECHNICAL UNIV. Downloaded on July 20,2023 at 11:23:14 UTC from IEEE Xplore. Restrictions apply.

2023 4th International Conference for Emerging Technology (INCET)
Belgaum, India. May 26-28, 2023

High Frequency DC-DC Isolated Converter with Rectification and Synchronous Rectification

Awanish Akash
Department of Electrical Engineering
Delhi Technological University,
Delhi, India
akashawanish29@gmail.com

Mini Sreejeth
Department of Electrical Engineering
Delhi Technological University,
Delhi, India
minisreejeth@dce.ac.in

2023 4th International Conference for Emerging Technology (INCET) | 979-8-3503-3575-0/23/$31.00 ©2023 IEEE | DOI: 10.1109/INCET57972.2023.10170293

***Abstract*—The use of Electric Vehicles (EVs) is increasing day by day and therefore chargers for electric vehicles play a vital role in the evolution of the industry. DC-DC converter is an important part of EV chargers. This paper presents the PSFB (phase-shifted full bridge) dc-dc converter with diode rectification and synchronous rectification. To obtain higher levels of efficiency, PSFB with synchronous rectification is preferred. The converter supports zero voltage switching (ZVS) which aids the converter to work at high frequencies along with advantages like less EMI (Electromagnetic Interference), less stress, lower switching losses, and better efficiency. The PSFB converter with the input DC voltage at 380 V under the zero voltage conditions for both the cases Rectification and Synchronous Rectification at different loads have been studied. A shift in the pulse between Diagonal switches has been maintained which helps in attaining the purpose of the proposed converter. The topology utilizes the resonance between the leakage inductor of high-frequency transformer and parasitic capacitances of full bridge MOSFETS for achieving ZVS. In the case of synchronous rectification, a lesser number of switches has been implemented which helps in having better efficiency than that conventional PSFB. These converters are preferred in medium and high-power applications. The system is designed for 1.1 kW, and the analysis is carried out using MATLAB/Simulink software.**

Keywords - dc-dc converter, isolated transformer, switching frequency, synchronous rectification, ZVS

I. INTRODUCTION

The use of Electric Vehicles (EVs) is increasing day by day and therefore chargers for electric vehicles play a vital role in the evolution of the industry. Technology and propulsion methods are undergoing a significant transformation in the car sector. More than ever, automakers and suppliers are prioritizing electrified powertrains above combustion engines for eco-friendly development. The transportation sector contributes to around 29% of greenhouse gas emissions in US, government, and industry are working together to develop EV infrastructure so that consumption of fossil fuels can be limited significantly,[2]. To build a sufficient DC fast-charging infrastructure, the government and private enterprises are investing millions of dollars. The absence of charging infrastructure is one of the major deterrents keeping consumers from purchasing EVs. As of now, reports from [3] the purchase of EVs has increased by over 43% in the year 2020 compared to the year 2019. With the increase in the trend of EVs, it is forecasted that the selling of EVs will increase in the upcoming years.

The EVs chargers play a vital role in the evolution of the industry. DC-DC converters are the basic unit of these chargers and there are different topologies available for battery charging applications. A DC-DC converter steps up or step down the voltage level depending on different applications. A typical electric vehicle (EV) powertrain is composed of several power electronics converter subsystems. Depending upon safe charging, DC-DC converter topologies are isolated and non-isolated dc-dc converters. When it comes to isolated topology then full-bridge configuration is most frequently implemented as it is suitable for high power transmission due to its characteristic feature of ZVS and switches working at high frequency. A high-frequency transformer is often used in isolated dc-dc converters. The use of high-frequency transformers makes the isolated converter different from the non-isolated converter which adds benefits to the isolated topology. Due to their compact size, high-frequency transformers can ignore undesirable characteristics including inductance leakage and eddy current losses [4]. To avoid bulky components. Since transformers need an AC supply, an inverter is required to convert dc into ac which is facilitated by the proposed full-bridge dc-dc converter.

Switching losses, poor efficiency, and voltage spikes are caused by oscillations at conventional FB-type converters between the parasitic capacitors of the power components and the leakage inductance of the transformer. To achieve Smooth Switching, the phase-shift control approach is used. A synchronous rectification at the secondary side enhances the efficiency further for the PSFB converter. The two MOSFET switches make the circuit more complex to control in the case of synchronous rectification [5],[6]. PSFB converter consists of three stages of power flow. The first stage is input dc then the second stage is dc to ac which is fed to the high-frequency transformer and later the third stage is ac to output dc which is fed to the load. For medium and high-power applications, PSFB converters are one of the most used dc/dc converters. Due to the soft switching capability of the major active switches, PWM control with a constant frequency, wide range, reduced current stress on the devices, and low electromagnetic interference, PSFB has come up for EV chargers. The phase shift between the diagonal switches affects the PSFB's output power. When the phase shift is zero, the duty cycle is 1, which causes the converter to operate in hard-switched mode. When

Authorized licensed use limited to: DELHI TECHNICAL UNIV. Downloaded on July 20,2023 at 11:25:35 UTC from IEEE Xplore. Restrictions apply.

the phase-shift angle is equal to 180 degrees, there is no power transmission and the duty cycle is zero. Soft switching is the alternative to hard switching.

If the current or voltage is zero during the transient in the MOSFET switch, the soft switching is visible. Zero current switching (ZCS) and zero voltage switching are two soft switching techniques (ZVS) [7],[8]. Here in the paper, Z VS has been implemented resulting in minimum switching losses. Electric vehicle loads ranging from 600 W to 3.3 kW can be handled by PSFB with ZVS architecture [9].

Section II describes the circuit configuration. Sections III and IV cover the design specifications, detailed analysis, and results. The study is validated using MATLAB/SIMULINK for a 1.1 kW system.

II. PHASE-SHIFT FULL-BRIDGE DC/DC CONVERTER

The phase-shifted PWM complete bridge converter is a two-stage device. To enable ZVS transition and make sure that the primary winding is shorted or connected to the input, the control signal to switches S3 and S4 is phase-shifted with regard to the gating signal to switches S1 and S2. It has also to be ensured that at no point in time, dc supply is shorted. The diode on the secondary side aids in rectification. Both center-tapped and full-bridge rectifiers, which use diodes, can be used for rectification. Synchronous rectification is a technique for rectification, in which MOSFETs are employed in place of diodes. By reducing the drain to source resistance while the MOSFET is ON, the voltage drop across the device can be reduced. Therefore, synchronous rectification may be more effective at some current levels. However, there are now two additional gate drive circuits and the control is more intricate. For simple control, full-wave diode rectification is utilized.

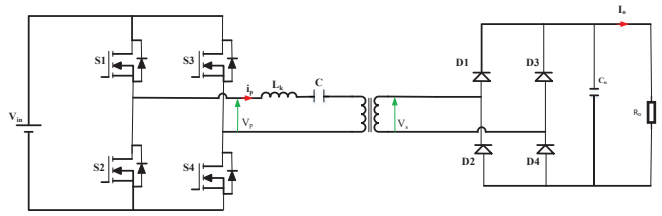

Fig. 1. Phase Shifted Full Bridge converter

Figure 1 depicts the structure of the ZVS phase-shift full bridge PWM converter, which differs from ordinary full bridge converters by having four switching elements and switching control signals.

PSFB with Synchronous Rectification

Here, the secondary side diodes have been replaced with Mosfet switches. The optimum value of R_{dson} for Mosfet will help in minimizing the switching losses. The two Mosfets are controlled by a pulse generator and help in completing the path for circuit operation at the secondary side.

Fig. 2 shows PSFB with Synchronous Rectification where two MOSFET and two inductors are present at the secondary side. The controlling of the switch at the Secondary side plays a key role.

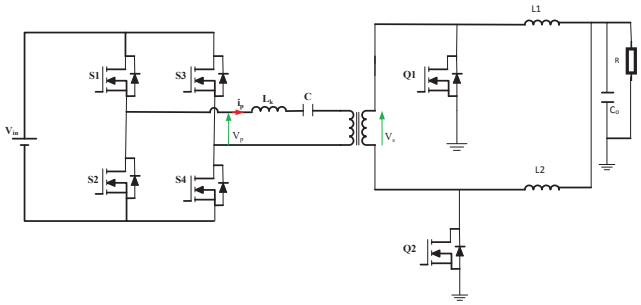

Fig. 2. PSFB with Synchronous Rectification

III. DESIGN AND ANALYSIS

A. Analysis of ZVS

By utilizing the energy stored in the transformer's leakage inductance to discharge the switches' output capacitance before turning them on, the Zero Voltage Turn ON is made possible. The energy stored in the leaking inductance must be greater than the energy stored in the output capacitances in order to accomplish ZVS.

$$E = \frac{1}{2} L_{lk} I^2 > \frac{4}{3} C_{MOS} V_{in}^{\ 2} + \frac{1}{2} C_{tr} V_{in}^{\ 2} \qquad (1)$$

where, C_{MOS} is the output capacitance of the switch

C_{tr} is the transformer winding capacitance

Consequently, in order to attain the ZVS, two key requirements must be fulfilled. Energy in the inductor must be enough to charge and discharge the capacitor. [9]Second, the transient should over before the switch gets ON.

For simplification the above equation can be written as:

$$\frac{1}{2} L_{lk} I^2 > \frac{1}{2} C_{eq} V_{in}^{\ 2} \qquad (2)$$

where C_{eq} is the equivalent capacitance

I is the primary current

On solving further input primary current can be written as:

$$I = \sqrt{\frac{C_{eq} * V_{in}^{\ 2}}{L_{lk}}} \qquad (3)$$

B. DESIGN SPECIFICATIONS

TABLE I. LISTS THE SPECIFICATIONS FOR A PSFB CONVERTER

Parameters	Units	Value
Input voltage	V	380
Output voltage	V	72
Switching frequency	kHz	200
Output current ripple	%	20
Output voltage ripple	%	40
Power Rating	kW	1.1

Choosing the duty ratio as *50%* and using the above design specifications, turns ratio N is calculated as:

Authorized licensed use limited to: DELHI TECHNICAL UNIV. Downloaded on July 20,2023 at 11:25:35 UTC from IEEE Xplore. Restrictions apply.

$$N = \frac{(V_{in} - 2V_{rdson})D}{V_o + V_d} \quad (4)$$

In equation (4) above V_{rdson} is a voltage drop over the MOSFET and V_d is a voltage drop across the rectifier diode. Since the output inductor ripple current is limited to 20%, so ΔIL can be calculated as:

$$\Delta I_L = \frac{P_{out}}{V_s} * 0.2 \quad (5)$$

The magnetizing inductance of the primary transformer is calculated as:

$$L_{mag} = \frac{V_{in}(1-D).N}{\Delta I_L.P_{out}.0.5} \quad (6)$$

The output filter inductor is given by:

$$L = \frac{V * D}{I * f} \quad (7)$$

The output filter capacitor is given by:

$$C_{out} = \frac{I_{ripple} * D}{V_{ripple} * f_s} \quad (8)$$

IV. Simulation Results

The results for the PSFB DC-DC Converter have been obtained at a switching frequency of 200 kHz with input Voltage 380 V, Output Voltage 72 V, and later the results have been obtained for PSFB with synchronous rectification.

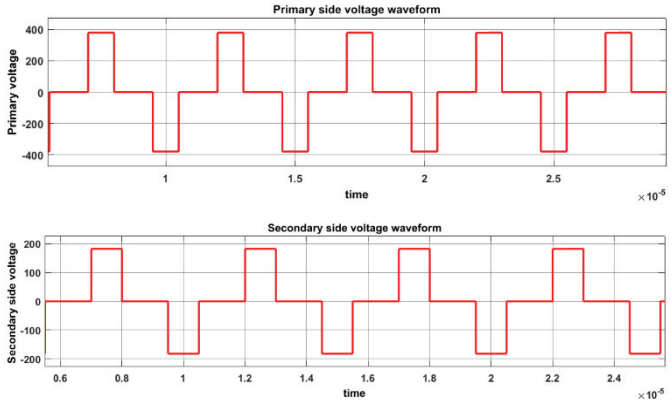

Fig. 3. Primary and secondary side voltage waveform

In Figure 3, the primary and secondary side voltage waveform has been shown. At the gate of the MOSFET, a pulse generator has been applied. With the help of a pulse generator square-shaped pulse of frequency, 200 kHz has been given to all four switches. A shift in the pulse between Diagonal switches has been maintained. With S_1, and S_4 ON the transformer is energized from the DC source and similar happens when S_4 and S_3 are ON, hence resulting in a Quasi square wave. The phase shift is given such that at any point in time two switches are operational. When S_1 and S_3 are ON for a short duration then, the primary of the transformer shows zero voltage across it which can be observed in the figure 3.

The phase shift between diagonal switches that is the starting time of conduction for diagonal switches varies by short duration. Thereby, the DC input to the transformer's primary winding varies accordingly.

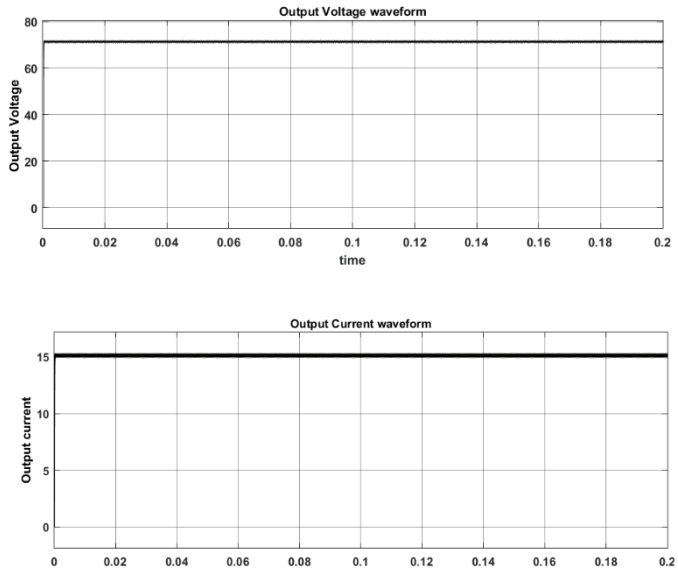

Fig. 4. Output Voltage and current waveform

In Figure 4, the output voltage and current waveform have been shown. The output of the transformer's secondary is fed to the full bridge rectifier which helps in attaining DC values. These DC quantities are passed through an LC filter at the output which improves the quality of the DC quantities and also gives gain for the circuit. Hence, on the output side, we are able to achieve the given specification values which fulfill the sole purpose of the given DC-DC converter. The output voltage achieved is 72 V and the output is 15 A.

In Figure 5, pulse generator waveforms have been shown. It can be observed from the figure that a pulse of constant amplitude, has been fed to the Gate of the MOSFET which controls the switch. A phase shift can also be observed between the diagonal switches that are S_1 - S_4, and S_3 - S_2. S_1 and S_4 conduct at a time than S_3 and S_2 conduct at a time. For a short duration, there is a common point of contact for S_1 and S_3 resulting in almost no voltage across the Transformer and the same happens for switches S_2 and S_4 also.

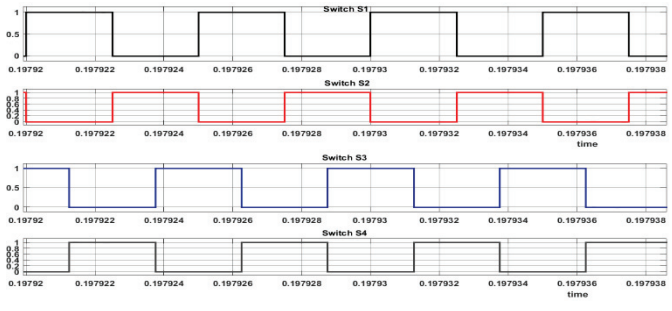

Fig. 5. Switching pulse waveforms

Authorized licensed use limited to: DELHI TECHNICAL UNIV. Downloaded on July 20,2023 at 11:25:35 UTC from IEEE Xplore. Restrictions apply.

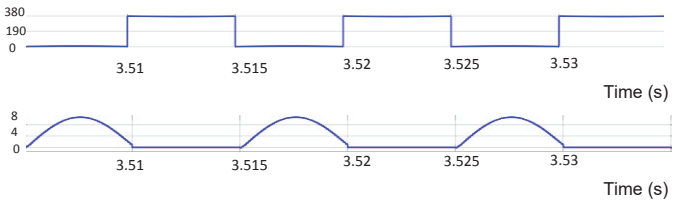

Fig. 6. ZVS across Switch S1

In Fig. 6, Zero Voltage Switching has been shown across Switch S_1. It can be observed that voltage across the switch is zero that is the inductive energy of the leakage inductor that has discharged the snubber capacitance of the switch then the switch starts conducting hence resulting in zero switching loss. It can also be observed across the other three switches also. The leakage inductor is a key element that controls the ZVS transitions.

TABLE II. LISTS THE EFFICIENCY FOR DIFFERENT VALUES OF LOAD CURRENT FOR DIODE RECTIFICATION

Load (%)	Efficiency (%)
Full load	92
80	90
50	87
30	80.56

A. PFSB with Synchronous Rectification:

Here, on the secondary side, two MOSFET switches have been used for the purpose of Rectification and two inductors have been connected at the load side for the splitting of the current into two parts. The control of the two MOSFETs at secondary is complex but it is efficient for the system. Fig. 7 shows the Primary and Secondary Voltage waveform across the transformer's primary winding.

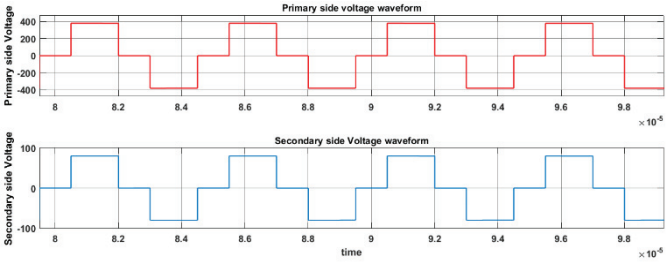

Fig. 7. Primary and Secondary voltage waveform across the transformer

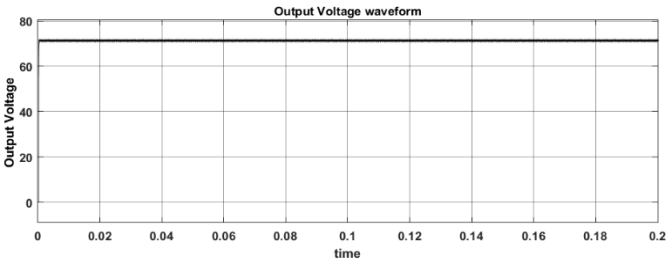

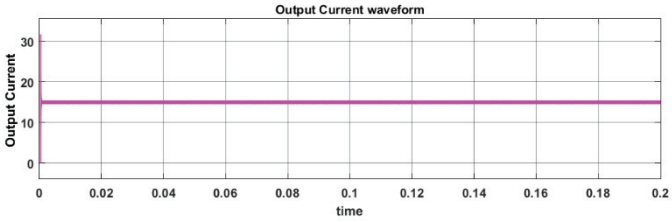

Fig. 8. Output Voltage and Current waveform at the Load side

Fig. 8 depicts the Output voltage and output current waveform at the Load side operated for Synchronous Rectification. The secondary side is connected to the Synchronous rectifiers thereby reducing switching power loss and improving heat dissipation. At a different value of load conditions, the magnitude of voltage and current will be different.

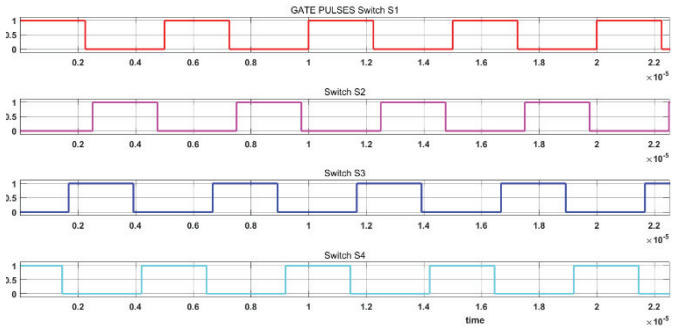

Fig. 9. Switching pulse waveforms applied to switches *S1*, *S2, S3, S4*

In Figure 9 Switching pulse fed to switches at the primary side is depicted. The phase shift has been maintained across Diagonal switches.

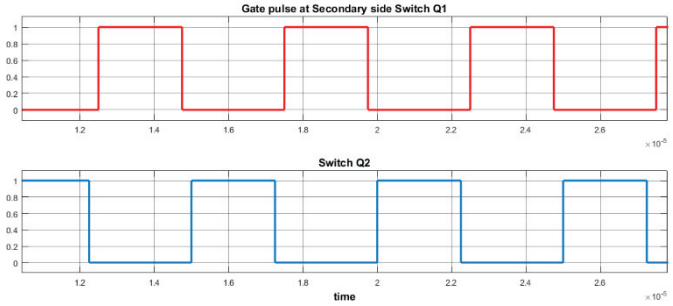

Fig. 10. Switching Pulse at Q1 and Q2

In Fig. 10. The switching pulse at Q_1 is the same that as fed to S_2 and the switching pulse at $Q2$ is the same as that fed to S_1. Switches Q_1, and Q_2 are at the secondary side thereby helping in completing the path at the load side.

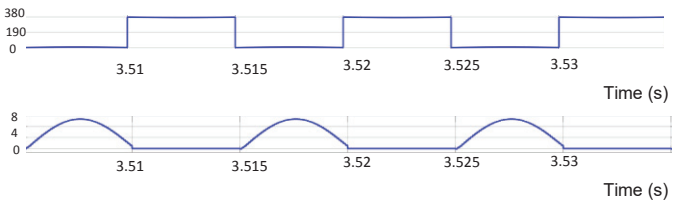

Fig. 11. ZVS across switch S_1

Authorized licensed use limited to: DELHI TECHNICAL UNIV. Downloaded on July 20,2023 at 11:25:35 UTC from IEEE Xplore. Restrictions apply.

In Figure 11, it shows the switches attaining ZVS as it can be observed that at zero voltage across Switches, the turn-on process occurs. At the secondary side current splits into two different paths and hence, conductivity losses reduce. If the drain-to-source resistance is reduced then the Voltage drop across the switch is low.

TABLE III. LISTS THE EFFICIENCY FOR DIFFERENT VALUES OF LOAD CURRENT FOR SYNCHRONOUS RECTIFICATION

Load	**Efficiency (%)**
Full load	95
80 % of the full load	93.20
50 % of the full load	90
30% of the full load	86

At a different load value, the converter has been analyzed thereby, efficiency has been calculated for different values of load current.

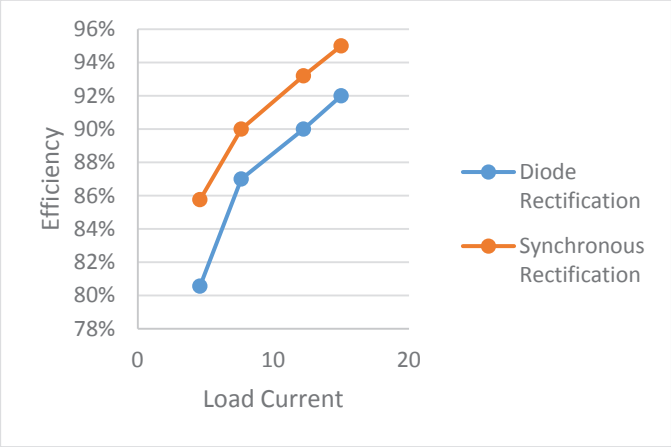

Fig. 12. Load Current vs Efficiency for PSFB

Fig 12 shows the variation of Efficiency as the load current is varied. The load current has been calculated at different values of R-load.

TABLE IV. LISTS THE COMPARISON FOR DIODE RECTIFICATION AND SYNCHRONOUS RECTIFICATION

PSFB with diode rectification	**PSFB with synchronous rectification**
Diode's forward voltage drop is more	MOSFETS R_{ds} (resistance across drain to source) ON will be less.
The switching speed is normal	Better switching speed
Conduction losses is more.	MOSFETS can be paralleled to have fewer conduction losses

V. CONCLUSION

A 200 kHz switching frequency ZVS PSFB dc-dc converter and PSFB with Synchronous Rectifier have been Modeled in the Simulink environment. PSFB is preferred in EV battery charging applications and it supports ZVS over a wide load range. It is more efficient to run PSFB with Synchronous Rectification for higher efficiency. PSFB with synchronous rectification is preferred over conventional PSFB. It is to be noted that MOSFET output capacitance should be kept low in order to extend the ZVS range. The model was analyzed under various loading conditions. Synchronous Rectification was able to deliver 95% efficiency at full load which was found to be better than conventional PSFB.

REFERENCES

[1] B. Maclnnis and J. A. Krosnick. (Oct. 2020). Climate insights 2020: Electric vehicles. Resources for the Future (RFF). [Online]. Available: https://www.rff.org/publications/reports/climateinsights2020- electric-vehicles.

[2] United States Environmental Protection Agency. (Apr. 2021). Inventory of U.S. Greenhouse Gas Emissions and Sinks. [Online]. Available: https://www.epa.gov/ghgemissions/inventory-us-greenhouse-gasemissions-and-sinks.

[3] International Energy Agency. (Apr. 2021). Global EV Outlook. [Online]. Available: https://iea.blob.core.windows.net/assets/ed5f4484-f556-4110- 8c5c-4ede8bcba637/GlobalEVOutlook2021.pdf

[4] S. Shankar, S. Lekshmi and M. R. Anaghakrishnan, "A novel AC-AC converter using bridgeless flyback rectifier and flyback CCM inverter", In *2016 Biennial International Conference on Power and Energy Systems: Towards Sustainable Energy,* pp. 1-6, 2016.

[5] S. Chothe, R. T. Ugale and A. Gambhir, "Design and modeling of Phase Shifted Full Bridge DC-DC Converter with ZVS," 2021 *National Power Electronics Conference (NPEC),* Bhubaneswar, India, 2021, pp. 01-06, doi: 10.1109/NPEC52100.2021.9672529.

[6] Texas Instruments, Phase-Shifted Full-Bridge, Zero-Voltage Transition Design Considerations - *Application report*", 2019.

[7] J. K. Sahoo and A. T. Mathew, "Design of a ZCS full — Bridge DC — DC converter for PV based electric vehicle fast charging station," *2017 IEEE Region 10 Symposium (TENSYMP),* 2017, pp. 1-5, doi: 10.1109/TENCONSpring.2017.8070079.

[8] E. Pool-Mazun, J. J. Sandoval, P. Enjeti and I. J. Pitel, "A Direct SwitchMode Three-Phase AC to DC Rectifier with High-Frequency Isolation for Fast EV Battery Chargers," 2019 *IEEE Applied Power Electronics Conference and Exposition (APEC)*, 2019, pp. 573-580, doi: 10.1109/APEC.2019.8722237.

[9] Chakraborty, Sajib et al. "DC-DC Converter Topologies for Electric Vehicles, Plug-in Hybrid Electric Vehicles and Fast Charging Stations: State of the Art and Future [1]Trends." *Energies* (2019).

Authorized licensed use limited to: DELHI TECHNICAL UNIV. Downloaded on July 20,2023 at 11:25:35 UTC from IEEE Xplore. Restrictions apply.

2023 4th International Conference for Emerging Technology (INCET)
Belgaum, India. May 26-28, 2023

Implementation of PSO based Controllers for Speed Control of BLDC Motor

Yashi Rani
Department of Electrical Engineering
Delhi Technological University
Delhi
yashirani_2k21psy06@dtu.ac.in

Dr. Uma Nangia
Department of Electrical Engineering
Delhi Technological University
Delhi
umanangia@dce.ac.in

Dr. Narender Kumar Jain
Department of Electrical Engineering
Delhi Technological University
Delhi
vnarender84@yahoo.com

2023 4th International Conference for Emerging Technology (INCET) | 979-8-3503-3575-0/23/$31.00 ©2023 IEEE | DOI: 10.1109/INCET57972.2023.10170535

***Abstract*— BLDC motor is a DC motor with concept of electronic commutation to provide better control over the speed characteristics of the motor compared to a mechanically commutated permanent magnet DC motor. This advantage comes at a cost of pulsating torque output from the motor, which makes the control strategy with speed reference more difficult as power will be pulsating if a constant voltage is set and under load there will be ripples in the actual motor speed.The control mechanism which uses feedback of the controlled parameter to calculate the error to a reference parameter and produces a control signal to minimize this error based on proportional and integral terms of the error signal by using any digital controller. Here we investigate a PID based control strategy v/s a PI control strategy using manual setting, auto-tuned and PSO algorithm. Application point of view we can use it in fully automatic machine, the behaviour of motor in that machines is continuously pulsating so the control factor comes into the role and we need the driver for it, the controlling part study with optimization that how truly we can enhance the result with our motor output. We do the study by simulating the BLDC motor on an industry standard software MATLAB Simulink.**

Keywords*— *BLDC motor control, Proportional and Integral controller, PI controller, Proportional, Integral and Derivative Controller (PIDC), PID controller, Brushless Direct Current motor, PSO algorithm, Speed control, DC motor, Back EMF (BEMF).

I. INTRODUCTION

With the recent emergence of interest in HVDC power, movement towards DC motors has started to become a viable and prospective thing for organizations to achieve. During the rotation of the machine, the impact of the BEMF can be seen while the motor is rotating. The frequency and of back emf are both proportional to the rotor speed for this type of motor. High torque output and self-starting characteristics of a typical DC motor help in shifting the tide even further. With such requirements BLDC motor shows a way for industry to opt for. BLDC motor by using specialized electronic circuitry also known as ESC (Electronic Speed Controller). The working principle of ESC is based on using solid state switching and position feedback from the BLDC motor to power the phases of a BLDC motor in a very specific manner. This electronic switching comes at a big cost of complicated speed control of the motor due to pulsating power output, in high load scenarios this can make the task of maintaining a steady reference speed at output a complicated task as normal PI/PID controller (With Saturation) become complicated to tune due to sudden spikes in the output speed due to dynamics from the varying load. In this paper we will take a deep dive into the responses and characteristics produced by both controllers, their shortcomings, and advantages in respective implementations. The paper is split into 4 Sections. In Section 1 we discuss prior work in this field from other authors. In Section 2 and 3 we will investigate the mathematical and modelling design used for the simulations. Section 4 will discuss our findings in the area, and we finally end the paper with Conclusions and possible future works.

For the purpose of comprehending and assessing the transient behaviour of BLDC motor, the dynamic equivalent circuit is used [1]. BLDC motor is more efficient in nature for electric vehicle and its efficiency is relatively higher than the other asynchronous motor, controlling capability is nice and precise [2]. The motor is continuously rotated by this electronic controller by turning a transistor on or other solid-state switches. The BLDC motor can be used both three phases plus a single phase [3]. Hysteresis current controller measures the error and gives result and controlling based upon that and hall effect sensors use current signal generated by the magnetic field [4].

PI controller uses the reference speed and actual measured speed for the controlling purpose [5]. The three components of a PID controller function as follows: the proportional part can lower the system's error response to disturbances; the integral part can eliminate steady-state error; and the dynamic response with system stability can be improved by the integral part [6]. Settling time and large overshoot can be reduced by using the windup PI control and hysteresis current controller [7]. The purpose of using hysteresis current controller and hall effect sensor is to take the position or displacement feedback for controlling speed of the motor. When there is less overshoot then the motor will produce less noise [9].By obtaining input data on the rotor position discovered by detecting the hall effect, a controller can control an electronic switch [10]. The proposed single Hall approach is used to compare various tactics, and it demonstrates the constancy of the speed-position estimator algorithm under a range of speeds and loads. Additionally, compared to the 120° and 150° techniques, the 160° strategy delivers higher RMS phase voltage, lower ripple for the produced torque and DC-link current, and overall superior BLDC motor performance [11].

The BEMF constant is made to be modest in order to minimise the voltage drop caused by BEMF when operating a BLDC motor at a high speed. However, due to the fact that the BEMF constant is the same as the torque constant, it produces a tiny initial torque and, as a result, has a long transient duration. One of a BLDC motor's shortcomings in high-speed applications [12]. In terms of cost and production efficiency, ferrite permanent magnets were discovered to be a solid alternative to magnetic rare-earth elements. The ferrite permanent magnet's residual magnetic flux density,

Authorized licensed use limited to: DELHI TECHNICAL UNIV. Downloaded on July 20,2023 at 11:21:47 UTC from IEEE Xplore. Restrictions apply.

however, is smaller than that of the neodymium permanent magnet. As a result, the ferrite permanent magnet is incapable of generating a large amount of torque. A ferrite permanent magnet motor has been created to address this issue; its torque is comparable to that of a neodymium permanent magnet motor, so neodymium permanent magnet stacking is used in BLDC motors [13]. Brush-less DC motor are efficient because of negligence of brush drop, they are suitable in terms of weight and efficiency. They can provide regenerative braking also [14].

II. Dynamic Modelling Of BLDC Motor And Its Controlling

BLDC motors are made up of a rotor/shaft assembly that is typically maintained in place by bearings installed at either end of the stator and a three-phase coil coiled on a cylindrically magnetic core (the stator). The stator and rotor are connected by a shaft that is fastened to the rotor, which is a smaller cylinder with numerous permanent magnets installed around it. For controlling of the motor we can use closed loop with a controller in series with the output of the motor and improve it using the PID controller [4]. A PI controller or proportional-integral controller is a control mechanism that bases its control signal to reduce this error on the proportional and integral terms of the error signal and uses feedback from the controlled parameter to determine the error relative to a reference parameter. Addition of derivative term to a PI controller makes the control be transformed to a three-term controller more commonly known as PID controller or proportional, integral, and derivative controller. It is expected that a PID controller would perform better for control application by minimizing the oscillations created by the integral portion of the controller. These controllers have been widely used in multiple real-world scenarios and simulated computer analysis.

BLDC motors are a relatively new application of such controllers. The brush less DC motor is likely the traditional DC motor with the point of view of working principle, but it is distinguished from designing purpose like in construction. The rotor of BLDC motor incorporates a permanent magnet and instead of brushes it uses an electronic controller for commutation purpose and its stator is identical to that of an induction machine, so it is regarded as a self-rotating synchronous motor.

$$\begin{bmatrix} v_{as} \\ v_{bs} \\ v_{cs} \end{bmatrix} = \begin{bmatrix} R_s & 0 & 0 \\ 0 & R_s & 0 \\ 0 & 0 & R_s \end{bmatrix} \begin{bmatrix} i_a \\ i_b \\ i_c \end{bmatrix} + \frac{d\begin{bmatrix} L_{aa} & L_{ab} & L_{ac} \\ L_{ba} & L_{bb} & L_{bc} \\ L_{ca} & L_{cb} & L_{cc} \end{bmatrix}}{dt} \begin{bmatrix} i_a \\ i_b \\ i_c \end{bmatrix} + \begin{bmatrix} e_a \\ e_b \\ e_c \end{bmatrix} (1)$$

Where, v_{as}, v_{bs}, and v_{cs} : The phase voltages of the stator

R_s : Resistance per phase of the stator

i_a, i_b and i_c : The phase currents of phase a, b, c

L_{aa}, L_{bb} and L_{cc} : The stated self-inductance of phases a, b, and c

L_{ab}, L_{bc} and L_{ca} : The stated mutual-inductances between phases a, b, and c

e_a, e_b and e_c : Phase back EMFs

It has been assumed that resistance of all the winding is same and equal.

In state space form,

$$\begin{bmatrix} v_{as} \\ v_{bs} \\ v_{cs} \end{bmatrix} = \begin{bmatrix} R_s & 0 & 0 \\ 0 & R_s & 0 \\ 0 & 0 & R_s \end{bmatrix} \begin{bmatrix} i_a \\ i_b \\ i_c \end{bmatrix} + \frac{d\begin{bmatrix} L-M & 0 & 0 \\ 0 & L-M & 0 \\ 0 & 0 & L-M \end{bmatrix}}{dt} \begin{bmatrix} i_a \\ i_b \\ i_c \end{bmatrix} + \begin{bmatrix} e_a \\ e_b \\ e_c \end{bmatrix} (2)$$

Where L shows the self-inductance and M represents the mutual inductance.

The basic motion system defined the governing equation with load inertia J, friction coefficient B, and load torque T_l is

$$J\,(d\omega_m)/dt + B\omega_m = T_e - T_l \quad (3)$$

The electrical rotor speed and position are related by

$$(d\theta_r)/dt = p/2\ \omega_m \quad (4)$$

Where, p: poles on the motor

ω_m : angular rotor speed in rad/sec

III. Design

For the objective of regulating the speed of brushless DC motors, there are two control loops. While the other loop is used to adjust the direct current bus voltage to control speed, inner loop is used to synchronize the gate pulse of the inverter with the EMF [2]. When a device is turned off during the reset phase, a significant event takes place when the motor winding current switches direction. In this instance, the current circulates through the free-wheeling diodes while continuing to flow in the same direction. We further try to use the property of BLDC motor having a specific KV rating per motor by having a proportional component of the reference speed being directly fed into the Voltage controlled voltage source, this allows the system to be inherently try to achieve the reference speed. We use the feedback loop with the PID controller in an additive parallel configuration only trying to minimize the difference created in the startup and loading/unloading conditions.

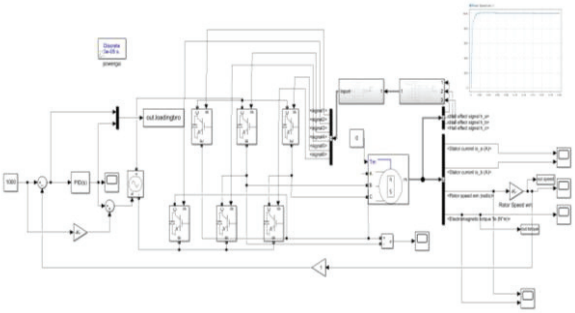

Fig. 1. Complete Model SET-UP

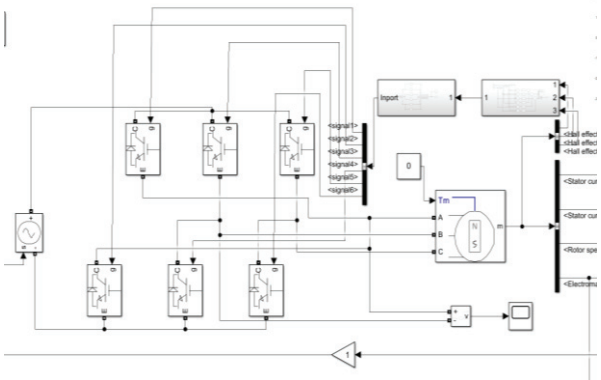

Fig. 2. BLDC Motor model with its Control Loops

Authorized licensed use limited to: DELHI TECHNICAL UNIV. Downloaded on July 20,2023 at 11:21:47 UTC from IEEE Xplore. Restrictions apply.

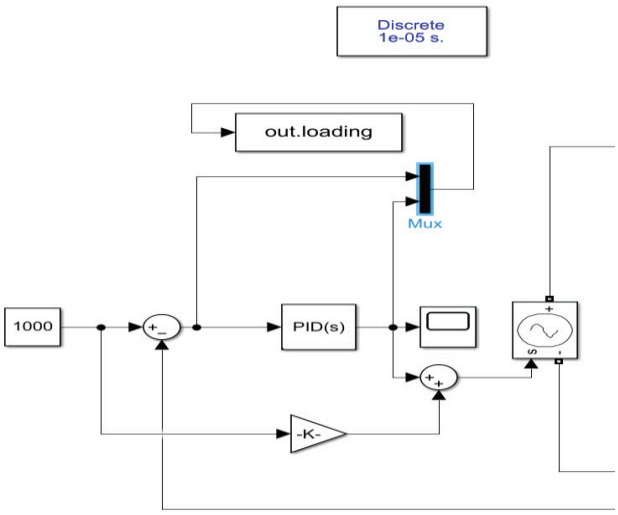

Fig. 3. PID controller with Control closed Loop with Reference speed

A. *PI and PID CONTROLLER:*

In this study the block named as PID controller from MATLAB Simulink is implemented as a digitally electronic PID controller. By simply varying parameters of PID. PI, PID is changed over to proportional integral and proportional integral derivative controller. Proportional integral and proportional integral derivative controller are then concurrently put in forward way of brush less DC model and the vast range of speed response signals are then assessed [1].

The Laplace transfer function equation for propotional integral derivative controller is given below,

$$G(s)=K_p + K_i/s + K_d*s \quad (5)$$

We limit the values of Kp,Ki and Kd parameters and filter coefficient (N) used in the PID controller to not have precision of more than 4 digits after decimal to estimate real world models.

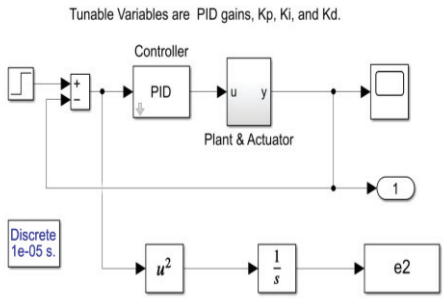

Fig. 4. Fig. 3.4. Model set-up for PSO optimization

The controllers were tuned using hit-and-trial method, MATLAB provided PID tuner and using PSO as described in [3] to find out the efficient parameters for both PI and PID controller. The PSO algorithm was modified to work using MSE (Mean Squared Error) and optimization for all three parameters Kp, Ki and Kd for the controller. A total of 1000 runs were performed of the PSO algorithm with different learning rates (C_1 and C_2) and the best performing parameters were chosen for the final results.

IV. RESULTS

The behaviour of the BLDC motor has been assessed at a variety of proportional, derivative, and integral coefficient values using manual, auto-tunned, and PSO algorithm. The results and graphs below highlight the most appropriate values. PID values are related to one another in several distinct ways.

The behaviour of BLDC motor with respect to speed is depicted in the accompanying figures, along with information about how it reaches steady state and with the help of controller the speed is compared with the reference speed with the assistance of a controller, which calculates the error from the reference speed using feedback from the controlled parameter and generates a control signal to reduce this error based on proportional and integral terms of the error signal.

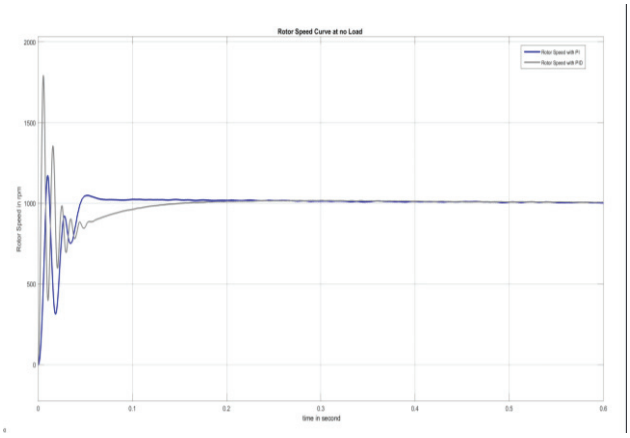

Fig. 5. Rotor Speed Control at No Load

Figure 5 shows the behaviour of motor using PI and PID controller at no load and it shows the different settling time and oscillations for both speed curves.

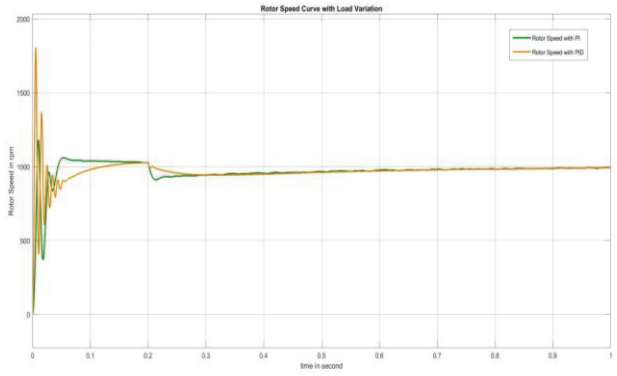

Fig. 6. Rotor Speed Control curve when load is provided on 0.2 second

Figure 6 shows the nature of PI and PID controller speed curve with settling time 0.05 seconds for PI controller and then giving load at 0.2 seconds and the behaviour of both controller is almost same but PI controller shows the decrement in speed. And then settles rapidly rather than slowly settling to the speed.

Authorized licensed use limited to: DELHI TECHNICAL UNIV. Downloaded on July 20,2023 at 11:21:47 UTC from IEEE Xplore. Restrictions apply.

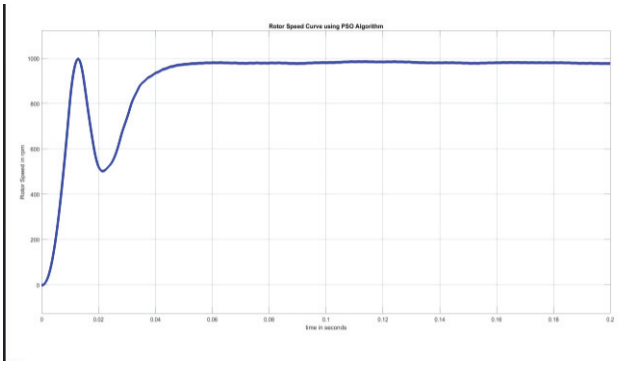

Fig. 7. Optimized PI controller result using PSO Algorithm at no load

Figure 7 shows the graph of Speed Curve which is settled in 0.05 seconds with less transients.

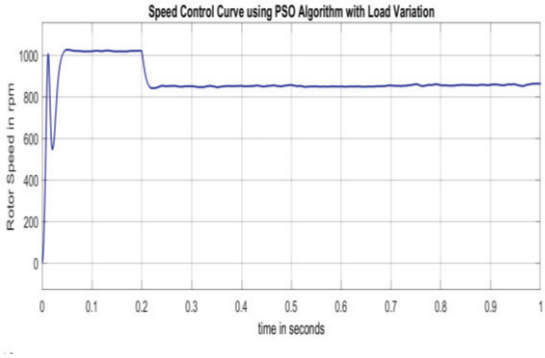

Fig. 8. Optimized PI controller result when load is provided at 0.2 seconds

Figure 8 shows the result of Load Variation at the 0.2 second in the duration of 1 second, using PSO Algorithm. The nature of Speed is shown when load is applied.

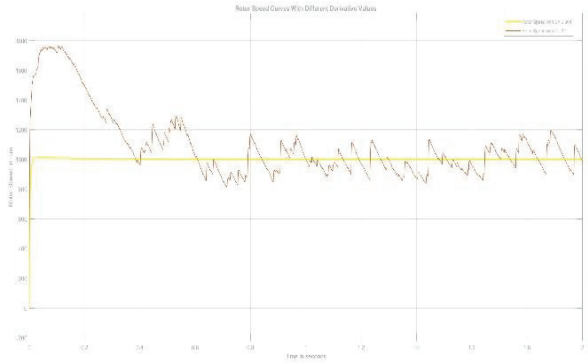

Fig. 9. Motor speed curve using auto-tunned PID Controller with Filter constant and without Filter Constant

Fig. 9 shows that the smooth nature of the speed curve when we use the Filter Constant with PID controller.

Figure 10 shows the speed curve of BLDC motor using PSO algorithm, the settling time for this curve is less than 0.02 seconds.

These results shows that the speed controlling settle time is less when we optimised the PID controller and PI controller with PSO algorithm and the first overshoot does not exceed the limited value.

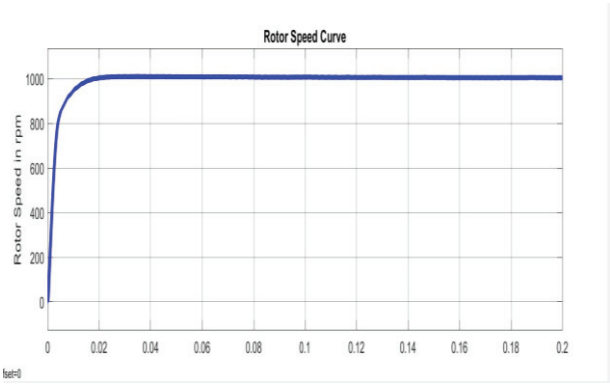

Fig. 10. Smooth controlling of BLDC motor using PSO Algorithm

Results are displayed in a table, based on parameters setting method, with the corresponding settling times and peak values summarized for PI and PID controller.

TABLE I. FOR PI CONTROLLER:

Parameters Setting Method	Settling Time (seconds)	Maximum Peak Value (rpm)
Manual Setting	0.055	1172
Auto Tuned	0.05	1060
PSO Algorithm	0.045	1057

TABLE II. FOR PID CONTROLLER:

Parameters Setting Method	Settling Time (seconds)	Maximum Peak Value (rpm)
Manual Setting	0.14	1793
Auto Tuned	0.06	985
PSO Algorithm	0.06	1007

V. CONCLUSION AND FUTURE WORK

It was found that the PI controller performed better in the case of startup characteristics of the motor whereas on loading and unloading the motor PID controller handled the event more gracefully by showing a gradual change in the speed rather than sudden change in the speed. The motor shows more oscillation s when derivative component is added to the motor. This behavior can be clarified by the fact that BLDC motor does not produce continuous time torque but rather has pulsations in the torque to the electronic commutation occurring from the IGBT. This pulsating effect is magnified by the derivative component as it produces significant output based on the high frequency micro-oscillations happening in the motor speed. Whereas a PI controller performs way better by just avoiding a component associated with the rate of change of motor speed.

We have done several assumptions in this simulation mainly in terms of the voltage controller being able to generate any voltage required from it, near instantaneous response of the inner loop feedback controller and outer loop PID controller, along with noiseless torque conditions. Although with PID controller the first swing (oscillation) magnitude reduced but settling time is more than PI controller. A practical in-depth analysis can provide us with much more insights in this area and possibly provide us more details with the practical constraints of the entire system being taken into consideration.

Authorized licensed use limited to: DELHI TECHNICAL UNIV. Downloaded on July 20,2023 at 11:21:47 UTC from IEEE Xplore. Restrictions apply.

REFERENCES

[1] H. Vítor, J. A. Pinto, and P. Gonçalves, "Introduction to DC Motors for Engineering Students based on Laboratory Experiments," in 6th International Conference on Control, Decision and Information Technologies (CoDIT), 2019, pp. 1522–1527.

[2] M. F. Bhuiyan, N. Sakib, M. R. Uddin, and K. M. Salim, "Experimental Results of a locally developed BLDC Motor Controller for electric tricycle," in 2019 1st International Conference on Advances in Science, Engineering and Robotics Technology (ICASERT), 2019.

[3] P. Suganthi, S. Nagapavithra, and S. Umamaheswari, "Modeling and simulation of closed loop speed control for BLDC motor," in 2017 Conference on Emerging Devices and Smart Systems (ICEDSS), 2017.

[4] D. Kumar, R. A. Gupta, and N. Gupta, "Modeling and simulation of four switch three-phase BLDC motor using anti-windup PI controller," in 2017 Innovations in Power and Advanced Computing Technologies (i-PACT), 2017.

[5] M. R. Haque and S. Khan, "The modified proportional integral controller for the BLDC motor and electric vehicle," in 2021 IEEE International IOT, Electronics and Mechatronics Conference (IEMTRONICS), 2021.

[6] H. S. Hameed, "Brushless DC motor controller design using MATLAB applications," in 2018 1st International Scientific Conference of Engineering Sciences - 3rd Scientific Conference of Engineering Science (ISCES), 2018.

[7] A. Shyam and Febin Daya J L, "A comparative study on the speed response of BLDC motor using conventional PI controller, anti-windup PI controller and fuzzy controller," in 2013 International Conference on Control Communication and Computing (ICCC), 2013.

[8] P. H. Krishnan and M. Arjun, "Control of BLDC motor based on adaptive fuzzy logic PID controller," in 2014 International Conference on Green Computing Communication and Electrical Engineering (ICGCCEE), 2014.

[9] M. Mahmud, S. M. A. Motakabber, A. H. M. Z. Alam, and A. N. Nordin, "Utilizing of flower pollination algorithm for brushless DC motor speed controller," in 2020 Emerging Technology in Computing, Communication and Electronics (ETCCE), 2020.

[10] S. Wongkhead, "State space model for speed control BLDC motor tuning by combination of PI - artificial neural network controller," in 2021 18th International Conference on Electrical Engineering/Electronics, Computer, Telecommunications and Information Technology (ECTI-CON), 2021.

[11] A. S. Al-Adsani, M. E. AlSharidah, and O. Beik, "BLDC motor drives: A single hall sensor method and a 160° commutation strategy," IEEE Trans. Energy Convers., vol. 36, no. 3, pp. 2025–2035, 2021.

[12] G. H. Jang and C. I. Lee, "Dual winding method of a BLDC motor for large starting torque and high speed," IEEE Trans. Magn., vol. 41, no. 10, pp. 3922–3924, 2005.

[13] H.-W. Kim, K.-T. Kim, Y.-S. Jo, and J. Hur, "Optimization methods of torque density for developing the neodymium free SPOKE-type BLDC motor," IEEE Trans. Magn., vol. 49, no. 5, pp. 2173–2176, 2013.

[14] P. Mishra, A. Banerjee, and M. Ghosh, "FPGA-based real-time implementation of quadral-duty digital-PWM-controlled permanent magnet BLDC drive," IEEE ASME Trans. Mechatron., vol. 25, no. 3, pp. 1456–1467, 2020.

Authorized licensed use limited to: DELHI TECHNICAL UNIV. Downloaded on July 20,2023 at 11:21:47 UTC from IEEE Xplore. Restrictions apply.

JMEPEG
https://doi.org/10.1007/s11665-023-08448-6

©ASM International
1059-9495/$19.00

ORIGINAL RESEARCH ARTICLE

Integration of Nanodiamonds and Graphene in Plasma-Sprayed Al_2O_3 Matrix for Enhancing the Tribological Properties

Shubhangi Chourasia, Qasim Murtaza, and Saurabh Agrawal

Submitted: 25 October 2022 / Revised: 23 May 2023 / Accepted: 11 June 2023

Graphene and nanodiamond are marvelous materials for wear-resisting coating, whose enhanced tribological properties are essential for its industrial development. Using a plasma spray process, we developed a method to fabricate graphene, nanodiamonds composite coating using the thermal spray coating technique. Nanodiamonds (0.1 wt.%) and Graphene nanoplatelets (GNP:1 wt.%) reinforced in Al_2O_3 hybrid carbon coating were deposited onto the (AISI 1020) steel substrate. Addition of 0.1 wt.% of ND and 0.1 wt.% of ND + 1 wt.% of GNP in alumina matrix has significantly enhanced relative density up to 97.25%, and improved wear resistance and wear rate at higher load are obtained. However, COF decreases with increasing loads. The maximum decrement in COF has been observed in 0.1 wt.% of ND + 1 wt.% of GNP in all the cases with decreasing drifts due to the self-lubricating properties of reinforced graphene nanoparticles and graphitization effect on the worn wear track during wear.

Keywords Al_2O_3, graphene (GNP), nano diamonds (NDs), plasma spray, wear

1. Introduction

Nowadays, industries and engineering services are working on various surfaces improving innovative and emerging technologies because of the fast degradation of parts during the operating time in harsh environments, which badly affects the industrial economy. It has been seen that industrial components and materials are speeded to failure due to the hostile, high-temperature environment, relative motion among the components, cyclic loading, and corrosive atmosphere. Industries are continuously working to attain higher efficiency and maximum productivity across the complete system to save the components from failures in the punitive environment during the daily processes. In this sense, plasma-sprayed Al_2O_3 coatings are the most promising due to their remarkable mechanical and electrical properties. It has been observed from previous studies that Al_2O_3 coatings possess excellent wear resistance properties with a significant elastic modulus value as well as anti-oxidant (Ref 1-6), thermal (Ref 7), friction (Ref 8-10), and erosion-resisting properties (Ref 11, 12) which make it more impeccable to protect the surfaces. However, Al_2O_3-based coatings are widely used in several areas such as aviation, automobiles, medical, and manufacturing due to their remarkable capability (mechanical and electrical properties) of safeguarding the surface of shafts, bio-implants, bearings, and running parts which are uninterruptedly open to high temperature (i.e., greater than 773 K) and facing a maximum degree of hotness and sliding motion (Ref 10). However, the major weakness of plasma-sprayed Al_2O_3 coatings is: the low value of fracture toughness (1.4 MPa $m^{1/2}$) and low value of hardness (8.5 GPa) when compared to bulk (Ref 13). It also produces several hindrances during its usage, where parts come in contact with each other and produce wear and friction (Ref 14). This shortcoming bounds alumina usage in wear and friction applications. The wear-resisting property of brittle material is connected to its fracture toughness and hardness (Ref 15). To improve the wear-resisting properties of alumina coatings, the above-discussed drawbacks must be mended. Thus, second-phase carbonaceous materials, such as GNP, NDs, YSZ, and cerium oxide, are added as reinforcement into the alumina matrix to reduce the drawbacks found by researchers. Among all the above-mentioned carbonaceous materials, GNP possesses the higher value of thermal conductivity:3000-5000 W/mk, low density:1.8-2.1 g/cc, tensile strength:11-63 GPa, modulus of elasticity:0.5-1TPa and electrical conductivity:$\sim 10^6$-10^8 S/cm (Ref 16, 17). In several prior research, the GNP graphitization effect has been studied at high temperatures, which shows promising results during the reinforcement of GNPs at high-temperature operating coatings (Ref 18). Therefore, adding these conductive materials in the alumina matrix as a reinforced material can uniformly distribute thermal energy in the alumina matrix; as a result, the alumina matrix's core and surface attain a high melting point and tend to higher densification. Due to high densification, it lowers the porosity matrix (Ref 19) and leads to an enhancement in tribological and mechanical properties. The state art of the present work is the combination of two second-phase materials with alumina. The developed coatings of considered material will improve the wear protection of industrial components and could promote wear resistance. The combination of ND and GNP in the coating enhances the wear resistance of the coating, making it

Shubhangi Chourasia, Qasim Murtaza, and **Saurabh Agrawal**, Delhi Technological University, Delhi, India. Contact e-mail: shubhangichourasia7@gmail.com.

Published online: 28 June 2023

suitable for use in harsh environments. This could result in increased durability of industrial components and reduced maintenance costs. The study of the properties and behavior of ND and GNP plasma-sprayed ceramic coatings will contribute to understanding how materials show wear-resisting properties under varying load conditions. This knowledge could be applied to other fields, leading to further advancements in materials science. As a result, the current work aims to develop a self-lubricating dense hybrid alumina coating reinforced by NDs and GNPs and examine their tribological behavior. In our research, the hybrid ceramic coating is developed using the plasma spray technique to save the components from friction and wear.

According to Gutierrez et al. Ref 20 investigation, the spark plasma-sintered reinforced GNP (0.22 wt.%) in Al_2O_3 matrix showed improved densification ($>$ 99 to 6.0%) and hardness and fracture toughness, i.e., about $\sim$ 6 to $\sim$ 50% correspondingly on mere addition of 0.22 wt.% of GNP in Al_2O_3 matrix, result received due to toughening brought by graphene because of its excellent connection with alumina and self-lubricating property (Ref 20). The tribological nature of 0-5 vol.% added GNPs in alumina using spark plasma sintered is also detected by Zhang et al. According to his team's research work, it has been observed that wear resistance improved up to 65% when 0.5 vol.% of GNP was reinforced to alumina (Al_2O_3). But in previously conducted research, the wear resistance was improved by only 53% when 5 vol.% GNP was added (Ref 21). From this study, it has been found that as the percentage of GNPs increases in composite, wear resistance tends to reduce as compared to the addition of a low percentage of GNPs. It occurred due to poor spreading and accumulation of GNPs with the formation of fractured Al_2O_3 grains at the time of wear.

The above literature also proves that the reduced percentage of carbonaceous material (GNPs) shows a significant improvement but sometimes converse also works. Many researchers also found that when CNTs or GNPs (Graphene Nanoparticles) or both are combined and reinforced into Al_2O_3 composite matrix, the mechanical, tribological, and electrical properties of plasma-sprayed coatings have shown significant improvement (Ref 3, 18-20, 22). This improvement is obtained by enriched dispersion of carbon nanotubes in Al_2O_3, strengthening the toughness process of coatings by connecting CNTs with the base matrix, crack deflection, and soaking CNTs in the Al_2O_3 matrix. And the same results were also observed in GNPs reinforcement in the Al_2O_3 (Ref 21-23) due to enhanced joint bonding among GNPs and base matrix, crack joining, and pulling out the concept of GNPs. As per the study performed by Evan and Marshall, the wear resistance of brittle material is straight reliant on the material mechanical properties like: fracture and hardness (Ref 24). As per the author's understanding, the reinforcement of GNPs in alumina has been found in studies, but the reinforcement of NDs and GNPs in alumina is not found in the literature. The novelty of the present research work is material combination, plasma spray technology, improved tribological properties, enhanced density, and wear resistance properties. The novelty of outlined work is as follows:

1. *Material Combination* Combining materials such as GNPs and NDs in alumina for developing the coatings will provide improved density, tribological properties and enhance the overall performance of the coating for wear protection in wear resistance applications.
2. *Plasma Spray Technology* The employability of the plasma spray technique in developing ceramic coatings is novel. The plasma spray technique is very effective for the uniform dispersion of NDs and GNPs during the reinforcement of Al_2O_3. Plasma spray technology permits precise control of the coating properties, developing a significant coating for wear-resistance applications.
3. *Improved Wear Resistance* The high self-lubricating properties of second-phase carbonaceous materials GNPs and NDs are attractive for wear-resisting applications. It shows a significant hike in density and tribological properties, offering improved performance compared to other coatings and making it suitable for wear-resistance applications. It can be predicted that uniform dispersion and high densification of coating could bring excellent interfacial bonding among the particles and provide outstanding wear resistance to the Al_2O_3 matrix. Therefore, an effort has been made to study the tribological performance of plasma-sprayed hybrid carbon ND and GNP-reinforced alumina coatings. Three different coatings will be developed, such as Al_2O_3 and Al_2O_3-0.1 wt.% ND and Al_2O_3-0.1 wt.% ND + 1 wt.% GNP using a plasma spray process. Dispersion effects on the densification of fabricated coatings and tribological properties will be investigated.

2. Experimental Setup

2.1 Groundwork of Powders

The cost-effective Al_2O_3 powder was acquired from Oerlikon Metco with a grain size of 15–45 micron meters, length of 2–5 micron meters, and 99.5% pure. The NDs with particle size 4–6 nm, the agglomerate size 200 nm, Graphene Nanoplatelets with a purity of 99.9%, flake size:5–10 micro-meter, 20–30 sheets of GNPS, the average surface area of 120–150 m^2g^{-1} were purchased from Plasma Chem GmbH and used as starting powders.

Due to high surface area of graphene and high antiparticle friction, the non-uniform flow could be lead in the plasma spray gun, and these nanoparticles could not be used directly in the plasma spray process. That's why the ultra sonicator and ball milling process were used to enhance the followability of considered powder and for a proper spray of nanoparticles through a plasma plume. The-received powders were ultrasonicated in a bath (ethanol as a medium) ultrasonicator for 30 min to mitigate agglomerations. This process helps produce spherical powders and homogenous distribution of nanodiamond and graphene in Al_2O_3 matrix. Different proportions of NDs and GNPs were mixed in a planetary ball mill (PM-100, Retsch Germany) with the Al_2O_3 powder for 150 minutes at 300 rpm by using 10 mm of tungsten carbide (WC) balls with the ball-to-powder ratio of 2:3 (in grams) for attaining the uniform dispersal of nanodiamonds and GNPs in the alumina matrix. Ball milling is used to grind the nanotubes/nano-synthesis/optimization of phase composite materials into very fine powders (Ref 25, 26). The ball milling process enhanced the material reactivity and uniformly distributed elements (Ref 27). In the ball milling process, the distinguished ratio of powers is ball milled using 10 mm of WC (Tungsten Carbide)

ball through a milling speed of 300 rpm for 150 min. The ball-to-powder ratio was 2:3 (in grams) for attaining the uniform dispersal of nanodiamonds and GNPs in the alumina matrix. During milling, the temperature rises due to the uninterruptedly running of the ball mill. To save the apparatus from damage due to high temperature during the milling process, after every twenty minutes, 5-min pause is provided to the ball milling cycle to acquire an adequate milling time and proper safety. Afterward, the ball-milled composite powder was collected and sent to the plasma powder feed system.

2.2 Fabrication of Composite Coatings by Plasma Spray

The three different powders, Al_2O_3 (named A-SD) and Al_2O_3-0.1 wt.% ND (named AND-SD), Al_2O_3-0.1 wt.% ND + 1 wt.% GNP (named ANDG-SD) was sprayed onto the steel substrate (AISI 1020) having a dimension of (100 × 20 × 3 mm) by using a plasma 9 MB spray gun made in Oerlikon Metco, USA, in the presence of plasma gases (Ar-H_2). Plasma spray is the process where mixed powders are fed into the powder feeder and exposed at a high temperature, i.e., 3000 °C in the presence of accelerated particles of primary gas. Before the coating deposition, the steel substrates (AISI 1020) were properly sanitary ultrasonically into the mixture of acetone. They passed to a grit blaster (MECPL, equipment India-based cabinet sort of grit blasting machine) using Al_2O_3 grit of 20 grit size to increase steel substrate surface roughness. The $\sim$ 2 μm of surface roughness on the steel substrate surface is obtained after grit blasting. Afterward, the melted powders are deposited onto the steel substrate and flattened continuously, followed by rapid solidification. Detailed information for synthesizing the A-SD, AND-SD, and ANDG-SD parameters is illustrated in Table 1.

2.3 Density Calculation for Fabricated Coatings

The HGP (helium gas pycnometer) Ultrapyc, Model 1200e, and Quanta chrome instrument made by the USA were used to calculate the true density of coatings. The helium gas pycnometer was operated at an exit gas pressure value of 0.34 bar in 0.25 cm^{-3} of the sample cell. The true density of the delaminated coating from the substrate sample is calculated. Theoretical density of Al_2O_3, NDs, and GNPs is considered 3.95 g/cm^{-3}, 3.52 g/cm^{-3}, and 1.8 g/cm^{-3} correspondingly (Ref 16, 17). The theoretical density was calculated for A-SD, AND-SD, and ANDG-SD with the rule of mixtures, and the value of RD (relative density) was calculated by dividing factual density by the theoretical density.

Table 1 Plasma-sprayed coating deposition factors

S.No	Parameters used	Standards
1	Powder feed rate	13 g/min
2	Used primary gas	Argon (SCFH):90
3	Power	22 KW
4	Stand-off distance (SOD)	100 mm
5	Surface pre-treatment	200 °C
6	Current	383 Ampere
7	Voltage	58 Volt
8	Secondary gas flow	Hydrogen (SCFH):10

2.4 Microstructural and Phase Characterization

The (FE-SEM, Zeiss, Sigma HD, UK) Field Emission Scanning Electron Microscope armed with EDS (Oxford-max made by the UK) was used for analyzing the morphology of ball-milled powder, interfacial bonding of coated samples, fracture surface, microstructure, thickness, elemental composition, elemental mapping of powders and developed coating from plasma sprayed at an operational voltage of 5KV.

Further, the XRD (x-ray diffraction) made in TRAX III, Rigaku, Japan method was used to analyze the phase changes using Cu Kα radiations with a wavelength of λ = 1.54 at 5 kW power scanning rate of 20°/min. Raman spectroscopy (Renishaw-based model 3900S made in the UK) enabled through an excitation laser (514 nm of wavelength) has been used to validate and measure the microstructural changes and retention in plasma-sprayed Al_2O_3-0.1 wt.% ND (named AND-SD), Al_2O_3-0.1 wt.% ND + 1 wt.% GNP (named ANDG-SD) in reinforced Al_2O_3 composite coating formerly and after wear test.

2.5 Tribo Test for Fabricated Coatings

The tribological wear tests were conducted on the fabricated hybrid coatings by using a ball on a disk tribometer (Ducom, Model: TR-20LE-CHM800, India) with the stationary pinball on the rotating samples to measure the wear weight loss, wear volume loss, wear rate, and COF of advanced coatings. Internal digital mettle analytical balance mettle Me204 was used to calculate weight loss. The apparatus has a maximum capacity to measure weight, up to 220 grams, with a minimum readability of 0.1 grams. For conducting the wear test, the dry room temperature was considered (298 K) to perform the test. All the tribological wear tests were performed under varying normal loads of 10 N, 15 N, and 20 N with constant sliding velocity (0.156 m/s) and constant speed of 250 rpm using a WC (tungsten carbide ball) having a diameter of 6 millimeters. For every wear test, 60 min was the total taken time where the ball on the disk took 15000 revolutions onto the coated samples covering a linear travel distance of 565 m. Throughout the tribo test, the COF of all the fabricated coatings is noted down rigorously. Before conducting and after the tribo test, the coated substrate weight was taken to calculate the wear weight loss. After wear weight loss, wear volume loss is calculated through the ratio of wear weight loss and density of the coating for further calculating wear rate.

For obtaining consistency in the value of the COF and volume loss, a wear test was performed at least 3 times. The wear rate was determined by using Eq 1 (Ref 1):

$$\text{Wear Rate} = \frac{\Delta V}{P \times L} \quad \text{(Eq 1)}$$

where ΔV depicts the (WVL) wear volume loss and (SL) sliding distance, (P) shows the load.

3. Results and Discussion

3.1 Microstructural Characterization

In the present study, Fig. 1 shows powder SEM images. The low-magnified images of FESEM for all the developed powders, such as A-SD, AND-SD, ANDG-SD, can be seen

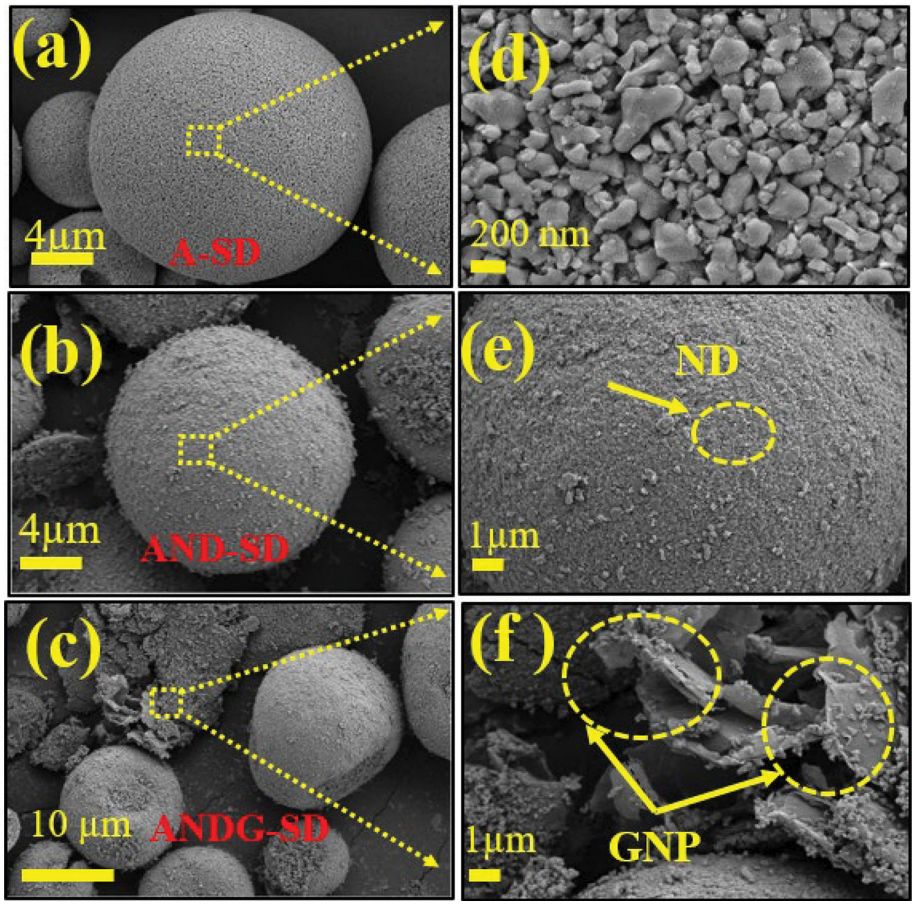

Fig. 1 (a-c) FESEM images (low magnification) of A-SD, AND-SD, and ANDG-SD powders, correspondingly, and (d-f) similar images display the FESEM (high magnification) images, whereas the arrow indicates the GNPs and NDs particles over the Al2O3 matrix.

in Fig. 1(a), (b), and (c). At the same time, high-magnified images of developed powders can be seen in corresponding Fig. 1(d), (e), and (f). Figure 1(a) shows the agglomerate Al_2O_3 powder range was 26.59 ± 14 μm on average. The spherical shape of agglomerates powder reduced inter-particle friction among the particles. The clogging of powders has reduced at the nozzle side, which played an incredible role in achieving uniformed and high-density coatings onto the substrate (Ref 28). While in Fig. 1(e) depicts the NDs particles having a particle size of 4-5 nm, which are reinforced into Al_2O_3. The NDs were balls milled with Al_2O_3 and 0.1 wt.% of ND, shown in Fig. 1(e), whereas 0.1 wt.% of ND and 1 wt.% of GNPs are shown in Fig. 1(f). NDs are unvaryingly distributed onto the Al_2O_3 matrix powders, as depicted in Fig. 2(e), and (f). GNPs have uniformly distributed into the alumina (Al_2O_3) powders. Figure 1(f) shows high-magnified images of 1 wt.% GNPs. All these powders show the spherical powder morphology that is uniformly distributed NDs and GNPs particles over the Al_2O_3 matrix. The ball milling operations and ultra-sonication of tailor-made powder are responsible for de-agglomeration and uniform dispersion of NDs and GNPs particles over the Al_2O_3 matrix. The uniform distribution of carbonaceous particles, i.e., NDs and GNPs, is achieved due to the proper interaction of NDs and GNPs with Al_2O_3 and the linking of GNPs with NDs (Ref 11).

3.2 Plasma-Sprayed Composite Coatings (A-SD, AND-SD, and ANDG-SD)

The cross-sectional sight of A-SD, AND-SD, and ANDG-SD coatings is shown in Fig. 2(a), (b), and (c). The developed coatings have no cracks and are properly adhesive to substrate materials. The thickness of coatings is approximately 100 micro mm observed. The cross-sectional FESEM images of developed coatings showed the uniform microstructure of coatings all over the length of the substrate. The coating nicely adheres to the surface of the substrate, and no boundaries and gaps are much visible at the border of the substrate material. The coating side shows the thickness of plasma-sprayed coatings onto the steel substrate. The same thickness, i.e., ∼ 253.25 μm, was received almost every time during the plasma spray process with spraying the same parameters.

The fracture surface of coatings was examined via field emission scanning electron microscope (FE-SEM) (Zeiss, EVO 18, UK) at a working voltage of 10-15 kV. Figure 3(a), (b), and (c) shows the FESEM images of the fractured surface of (a) A-SD, (b) AND-SD (c) ANDG-SD. This figure shows a completely melted coating region, re-solidified and partially melted, re-solidified coating regions, indicating the retention and stable dispersion of NDs and GNPs. Figure 3(a) depicts an incomplete and re-solidified arrangement with fully melted and re-solidified areas. The completely melted (fully melted) and incompletely melted (partially melted) regions are obtained by melting dried powders. The main powders agglomerate and

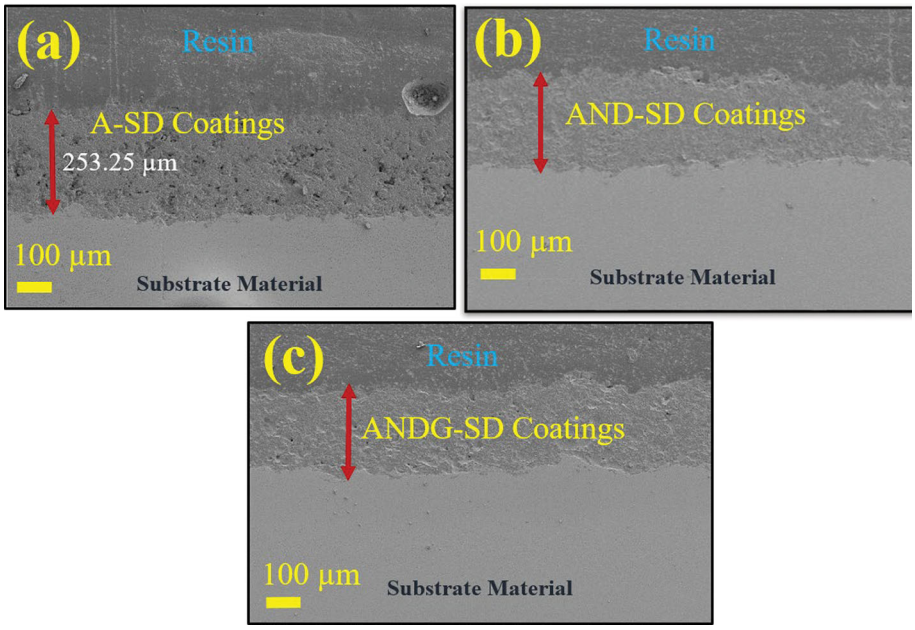

Fig. 2 FESEM images (cross-sectional surfaces) of (a) A-SD (b) AND-SD (c) ANDG-SD coatings.

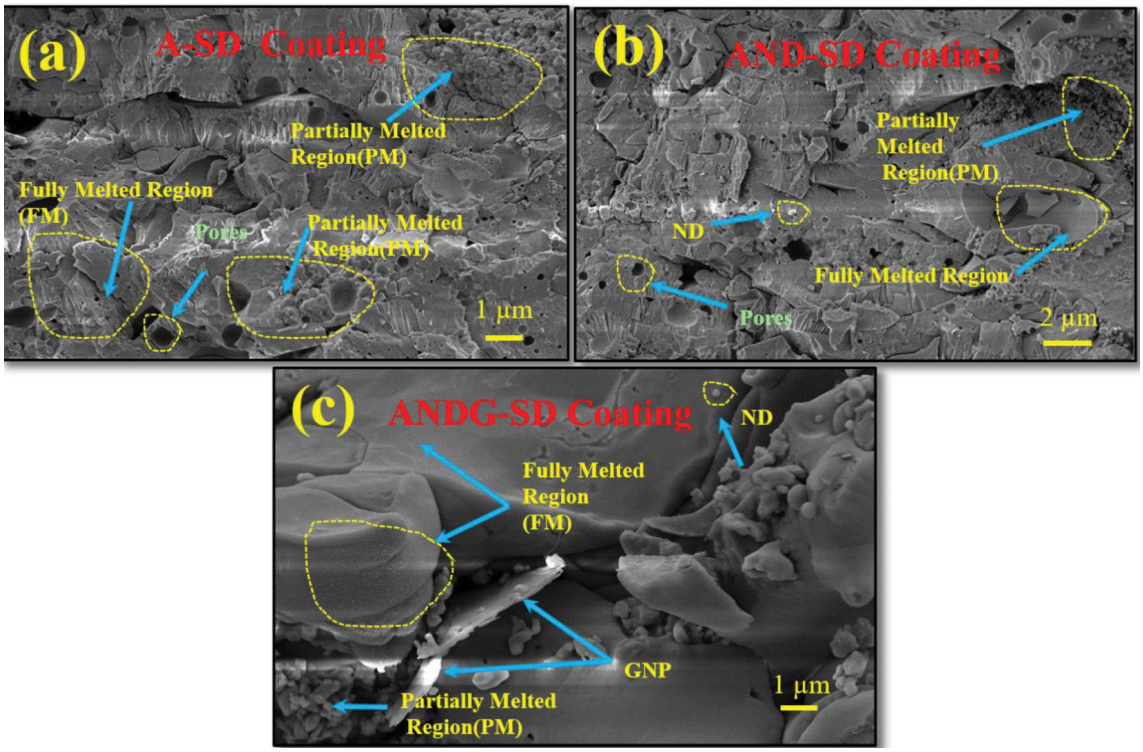

Fig. 3 Fractured surface FESEM images of (a-c) of a completely melted region and a half-melted region, and (b) AND-SD shows the constant dispersion and retention of NDs and GNPs

turn into solid-state form, responsible for forming the partially-melted and re-solidified regions. The partially-melted and re-solidified regions assist in the circulation of shock energy developed during the impact and create resistance to the transmission of cracks. At the same time, the completely melted region again solidifies and provides strength and uprightness to composite coatings. Figure 3(b) represents the dispersion of NDs in the A-SD coating. Figure 3(c) indicates the uniform dispersion of GNPs and NDs. In another part of FESEM images, fewer pores are visible in AND-SD and ANDG-SD coatings paralleled to A-SD coating. It occurred because of enhancement in the coating densification after reinforcement of the second phase of NDs and GNPs in the Al_2O_3 matrix.

The relative densities of developed coatings were calculated using (Mixture rule). The relative density measured is 94.45 ± 1.9, 95.45 ± 0.9, and 97.25 ± 1.9% for A-SD, AND-SD, and ANDG-SD correspondingly. The obtained result shows that the density improves after adding GNPs in the NDs in the Al_2O_3 matrix. The improved densification has been achieved due to a greater surface area versus volume ratio and high thermal conductivity of NDs (∼ 1000-W/m-k)(Ref 11, 15, 29-33) and GNP (∼ 5000 W/m) (Ref 34). Because of this property, NDs and GNPs can spread over a large surface area and uniformly dispersed all over the matrix (Ref 35, 36) and are responsible for the high melting of powders during plasma spray. Due to these results, dense coatings are obtained (Ref 37). The XRD pictures of plasma-sprayed coatings and powders are present in Fig. 4. The XRD results show similar powder and coatings peaks. In various peaks of Al_2O_3, the α-Al_2O_3 characteristics phase peak is visible in all the mixed powders phase, not in other phases, i.e., γ-Al_2O_3. But in plasma-sprayed coatings, γ-Al_2O_3 is present in some amount, i.e., approximately 15%. This phase (γ-Al_2O_3) is generally formed because of the fast solidification of splats in the plasma-sprayed coatings when lamellae are produced from melted α-Al_2O_3. Several researchers have also reported the occurrence of γ-Al_2O_3 (Ref 38-40). It has been found that 51% of γ-Al_2O_3 phase is formed in Al_2O_3 wt.% of ND after the execution of plasma spray (Ref 38). It has been also observed that the peaks are moving toward the right side concerning powders with higher intensities. This may occurred due to the plasma spraying process where particles are experienced compressive stress. Due to the contraction of lattice in crystals, the peak is started to shift in all developed coatings as strain is reproduced (Ref 39).

For investigating the retention of NDs and GNPs in the Al_2O_3 matrix, Raman spectroscopy was accomplished. Raman spectroscopy (Renishaw-based model 3900S made in the UK) enabled with an excitation laser (514 nm of wavelength) was used to validate and measure the microstructural changes and retention in plasma-sprayed A-SD, AND-SD, and ANDG-SD reinforced Al_2O_3 composite coating. Figure 5 shows the Raman spectra of powders and developed coatings of A-SD, AND-SD, and ANDG-SD. Powders and developed coatings exhibit the D and G bands at 1348 and 1583 cm^{-1}, correspondingly.

The "G" and "D" bands endorse the existence of NDs and GNPs in the Al_2O_3 matrix during the plasma spraying at high temperatures. No shifting has been seen in the D and G peaks in any direction; this validates that during the plasma spray process, the NDs and GNPs are not gone through any compressive or tensile stress, maybe because of their high value of elastic modulus (Ref 40). The EDS-based pictures of A-SD, AND-SD, and ANDG-SD developed coating can be seen in Fig. 6(a), (b), and (c). The EDS was employed to examine the elemental composition of the coatings to validate the presence of foreign particles in the Al_2O_3 matrix. The introduced table in Fig. 6(a), (b), and (c) shows the elemental compositions of developed coatings. EDS is proof of the occurrence of Al, O, and C in the developed coatings. In the EDS images, it can be seen that the intensity of carbon inclines to increase with the addition of 0.1 wt.% nanodiamonds (5.32 weight%) and 0.1 wt.% ND and 1 wt.% GNP (6.23 weight%) in the Al_2O_3 matrix.

Additionally, there is an increase in the peak of oxygen when NDs have added alone in the Al_2O_3 matrix. It shows the chance of oxidation when only NDs are added but tend to descend as NDs and GNPs are added together. This shows that as the GNPs are added to NDs, it reduces the formation of oxides in alumina during the high-temperature plasma spray. We can see that no foreign elements are present in the coatings through EDS.

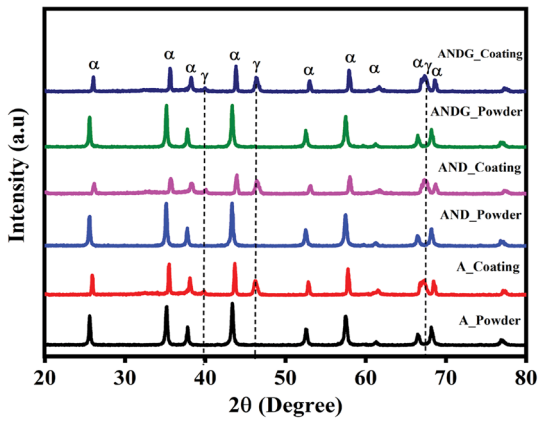

Fig. 4 Plasma-Sprayed Powders and Coatings XRD spectra of (a) A-SD (b) AND-SD (c) ANDG-SD

3.3 Tribological Behavior of Fabricated Coatings by Plasma Spray

To study the tribological behavior of fabricated samples, a tribometer, i.e., (pin on disk) was used for performing the wear test on different loads such as 10, 15 and 20 N at constant sliding velocity (0.156 m/s) and constant speed of 250 rpm by using a WC (tungsten carbide ball).

Figure 7(a), (b), and (c) shows the wear weight loss of the A-SD, AND-SD, and ANDG-SD coatings. The addition of nanodiamonds and graphene in the alumina shows a tremendous decrement in weight loss in all the composite coatings. Figure 7(a) spectacles the weight loss of bare Al_2O_3. The weight loss of Al_2O_3 was calculated at 98%, but adding 0.1 wt.% of ND in Al_2O_3 shows a 46% weight loss decrease compared to bare Al_2O_3 coatings. Figure 7(b) shows the weight loss at an applied load of 15 N, where adding 0.1 wt.% of ND in Al_2O_3 shows a 27.17% weight loss decrease compared to bare Al_2O_3 coatings.

Further, it tends to decrease when NDs and GNPs are reinforced into the Al_2O_3 matrix, i.e., a 53.03% decrease in wear weight loss has been observed. Figure 7(c) shows the weight loss at 20 N load. The weight loss by adding 0.1 wt.% of ND in Al_2O_3 shows a decrease of 33.67% in weight loss compared to bare Al_2O_3 coatings. Further, it tends to decline more when NDs and GNPs are reinforced into the Al_2O_3 matrix. At this time, a 44.70% decrement in wear weight loss has been observed. Through the wear test, it has to be concluded that wear weight loss is higher in ANDG-SD than in the AND-SD. The same result was observed in Sony et al. work (Ref 41).

It was observed from the obtained results that adding 0.1 wt.% ND in Al_2O_3, a 46.05% improvement in wear resistance, and wear rate tend to increase by 73.46% on adding NDs and GNPs to Al_2O_3 matrix. And at the applied load of 15 N, 27.17% improvement in wear resistance and 53.30% improvement in wear rate is seen, while at 20 N load, 33.67% improvement in wear resistance and 44.70% improvement in

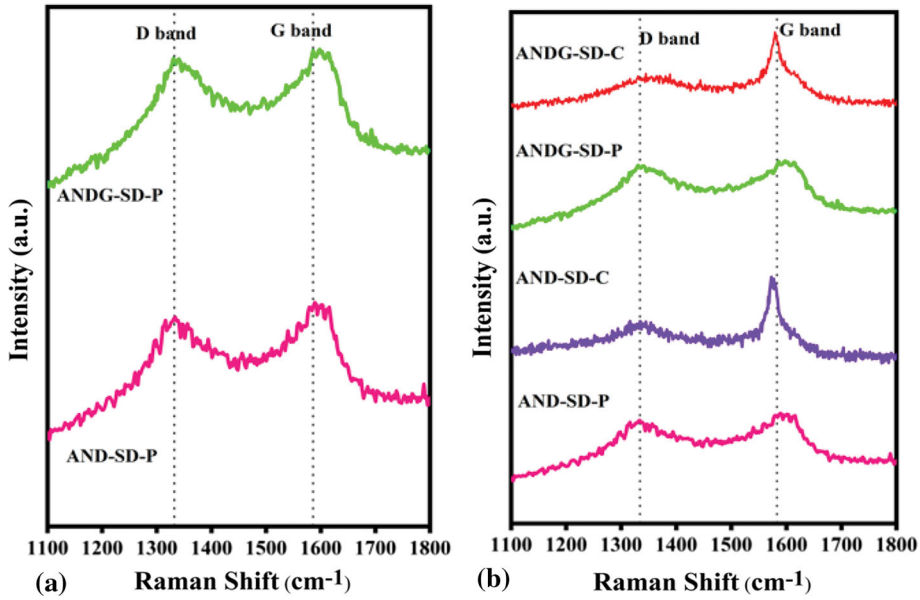

Fig. 5 Raman spectra (a) AND-SD and ANDG-SD plasma-sprayed powders (b) AND-SD and ANDG-SD powders and plasma-sprayed coatings.

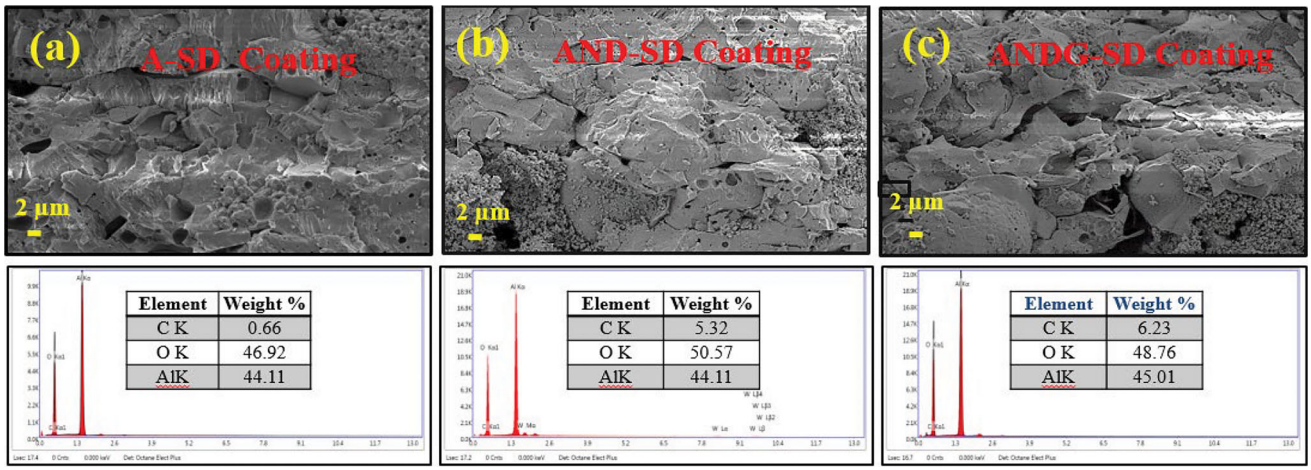

Fig. 6 EDS and elemental mapping of developed coatings (a) A-SD coating, (b)AND-SD coating and (c)ANDG-SD coating

wear rate are obtained, respectively. Figure 8(a), (b), and (c) shows the wear rate variations of A-SD, AND-SD, and ANDG-SD.

From the above results, the wear weight loss and wear rate among all fabricated coatings, A-SD, has the highest value. The lowest value is obtained from ANDG-SD coating when all coatings are passed through the WC counter body during the wear test. These results are obtained due to the formation of serval film from the counterparts, improved densification, and the resilient boundary between A-SD, AND-SD, and ANDG-SD.

Figure 9(a), (b), (c), and (d) shows the variations in COF by varying normal loads for A-SD, AND-SD, and ANDG-SD at sliding velocity (0.156 m/s) and constant speed of 250 rpm by using a WC (tungsten carbide ball) at room temperature in dry sliding condition. The obtained results show a decrease in the value of COF with elevating loads in all the cases with decreasing drifts. The low-value COF is found at higher loads as compared to other loads.

This result shows that the value of COF does not show the momentous change by adding 0.1wt %ND in the Al2O3 matrix due to the inadequate formation of solid lubricant at the interaction surface. Though,1 wt.% GNP in Al2O3 has shown a significant decrease in COF compared to other samples because of its self-lubricating properties. The same results are also seen in the research by Meysam et al. The average COF, the wear depth, wear track width, and lessening in wear depth of A-SD, AND-SD, and ANDG-SD plasma-sprayed coatings at varying loads (10, 15, and 20 N) for developed coatings are represented in Table 2.

The 3D optical microscope in Olympus, Japan, measured the wear depth on the formed track. During the study, wear volume loss is generalized by multiplying the area considered during the wear test and the depth of the wear track.

The FE-SEM pictures of the damaged surface of developed coatings A-SD, AND-SD, ANDG-SD at varying loads can be seen in Fig. 10(a), (b), (c), (d), (e), (f), (g), (h) and (i).

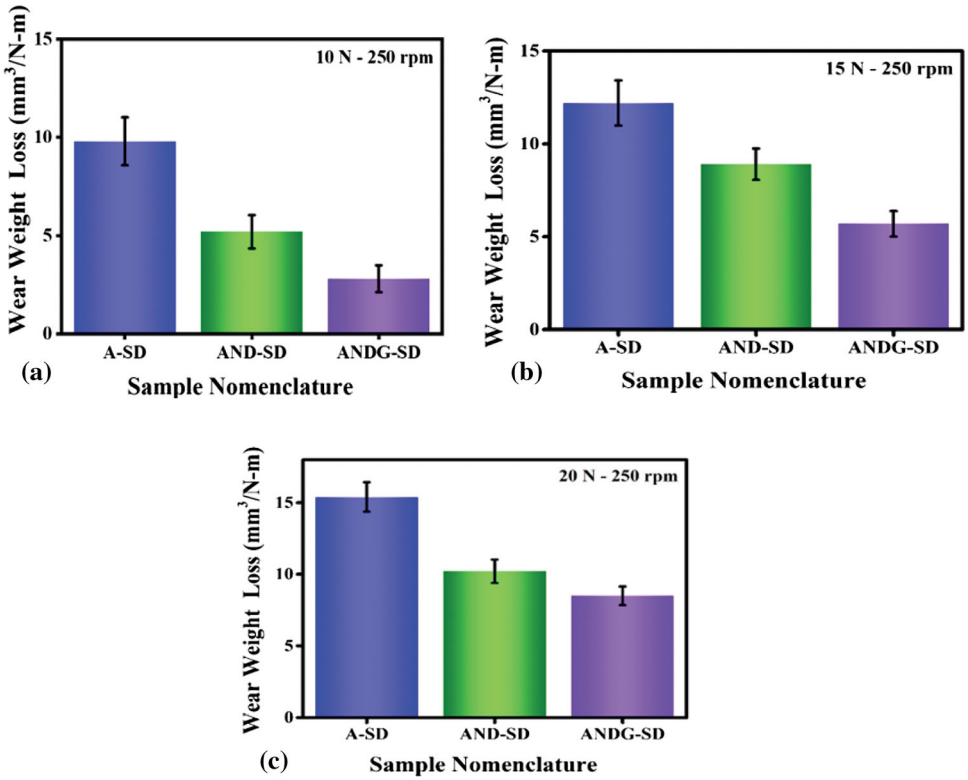

Fig. 7 (a-c) Wear weight loss A-SD, AND-SD, and ANDG-SD against the WC ball at normal load 10, 15, and 20 N.

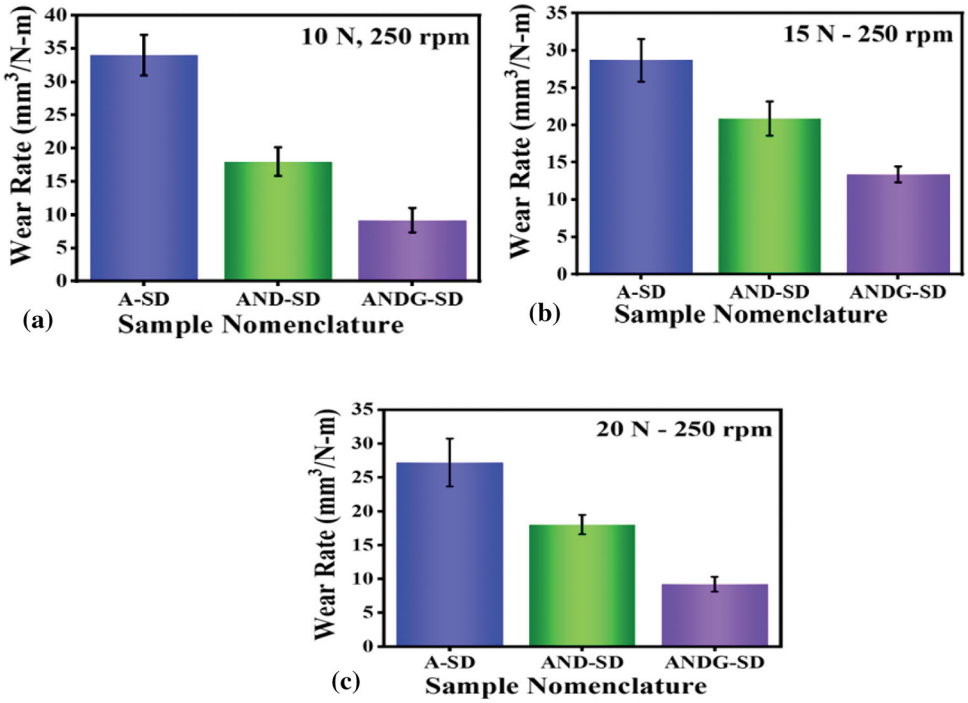

Fig. 8 (a-c) Wear rate variations in A-SD, AND-SD, and ANDG-SD at an applied load of 10, 15 and 20 N at 250 rpm.

Figure 10(a), (b), (c), (d), (e), (f), (g), (h) and (i) depicts the circular wear scratch developed at the time of the wear test by using a WC ball. From the obtained FESEM images, it can be perceived that the circular wear scratch of A-SD is much broader than the AND-SD, and the depth of AND-SD is more than the ANDG-SD**.** It is also observed by the researcher from obtained FESEM images that if carbonaceous materials like GNPs and NDs are added to the Al_2O_3 matrix, they tend to shrink the width and depth of the wear track.

The wear depth obtained from AND-SD at a 10 N load is $\sim$ 1.96 times, a 15 N load is $\sim$ 2.01 times, and a load of 20 N is $\sim$ 2.23, which is greater than the depth of the ANDG-SD.

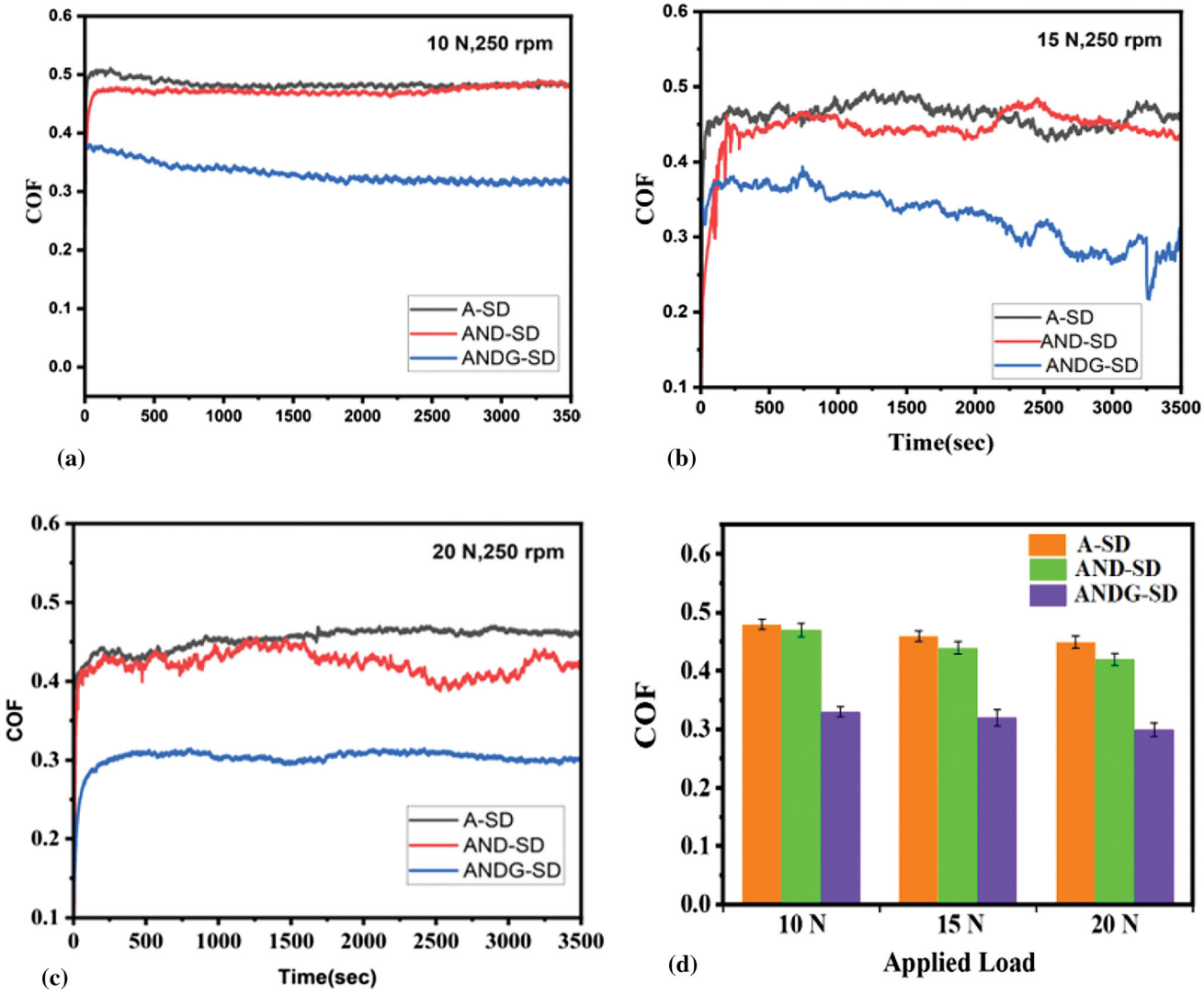

Fig. 9 (a-d) Variations in COF at varying normal loads for A-SD, AND-SD, and ANDG-SD at sliding velocity (0.156 m/s) and fixed speed of 250 rpm by using a WC (tungsten carbide ball).

Table 2 COF values, the wear depth, wear track width, and reduction in wear depth of A-SD, AND-SD & ANDG-SD for plasma-sprayed coatings.

S.No	Nomenclature used	Applied load	Value of COF	Reduction % as compared to A-SD coatings	Wear Depth, μm	Width of wear track, mm	Reduction in wear depth, mm
1	A-SD	10 N	0.48	…	573	2.25	…
2	AND-SD		0.47	0.28	292	1.76	~ 1.96 times
3	ANDG-SD		0.33	31.25	172	1.65	~ 3.33 times
4	A-SD	15 N	0.46	…	584	2.35	…
5	AND-SD		0.44	0.32	295	1.99	~ 1.97 times
6	ANDG-SD		0.32	30.43	165	1.72	~ 3.53 times
7	A-SD	20 N	0.45	…	591	2.88	…
8	AND-SD		0.42	0.30	313	1.82	~ 1.88 times
9	ANDG-SD		0.30	33.33	190	1.54	~ 3.10 times

GNPs can enhance wear resistance when reinforced with an Al_2O_3 matrix. The variations in values for all three coatings at various loads are shown in Table 2, which illustrates the width of the wear depth, wear track, and reduction in wear depth of A-SD, AND-SD, and ANDG-SD plasma-sprayed coatings in detail, respectively. In the next section in Fig. 11, the high-magnification FESEM images of the worn track are considered to understand the wear mechanism properly.

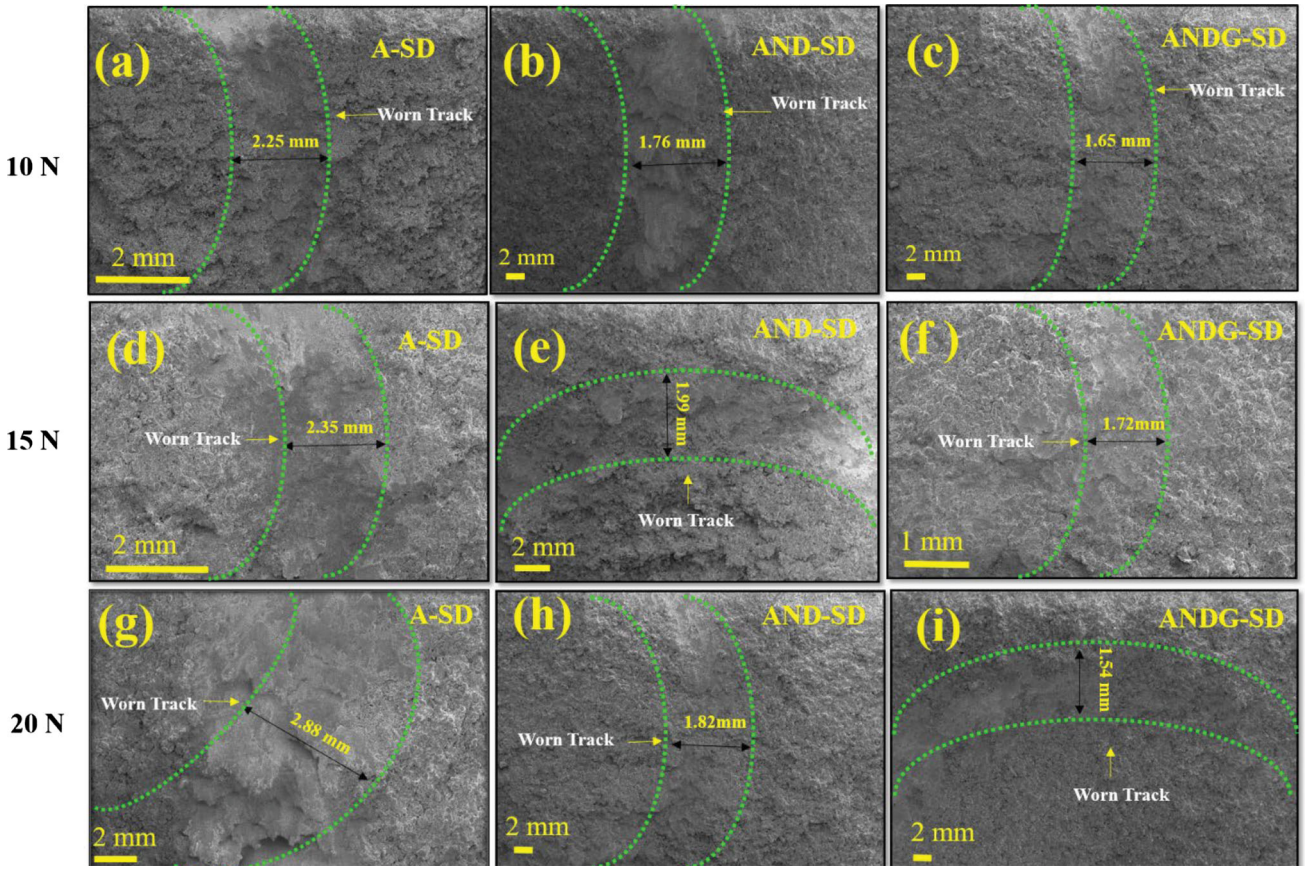

Fig. 10 FE-SEM images (a) A-SD (b) AND-SD (c) ANDG-SD coatings at an applied load of 10, 15, and 20 N, of worn surfaces, respectively. The 6 mm wide wear scar is left via a tungsten carbide ball.

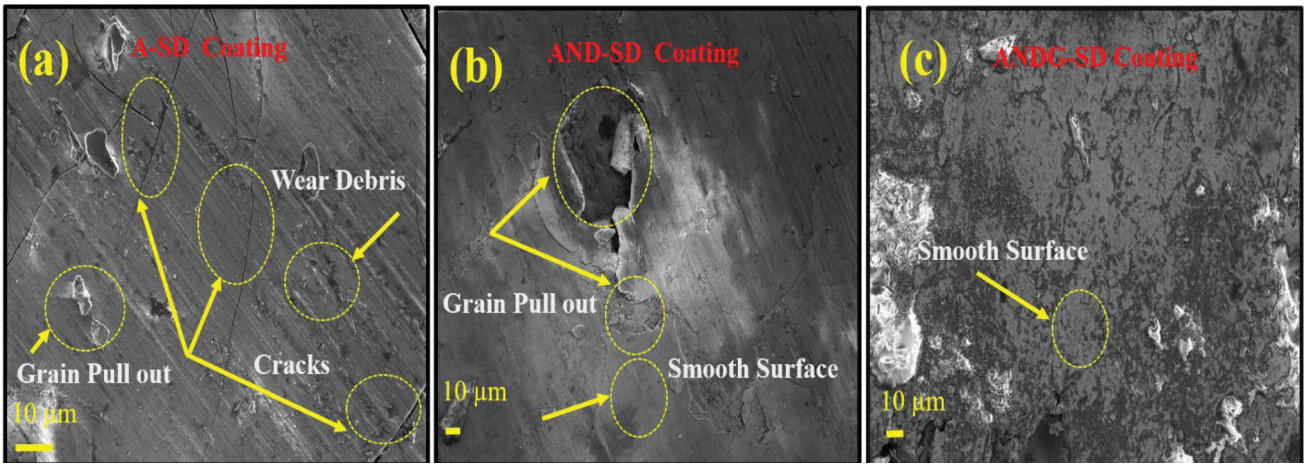

Fig. 11 High magnification FE-SEM images (a) A-SD, (b) AND-SD, and (c) ANDG-SD coatings of worn surfaces.

4. Wear Mechanism

Figure 11(a) shows the FESEM images of the Al_2O_3 worn surface of developed coatings. The wear debris, grain pulls out, and thin cracks can be observed in FESEM images. These occurred due to poor mechanical properties of Al_2O_3, which results in truncated densification of developed composite coatings. Figure 11(b) shows less severity in worn surfaces in AND-SD due to ND's high lubricating properties and density than Al_2O_3. As per the literature, the addition of NDs provides significant improvement in sliding resistance properties. It happens due to the lubricative nature and rolling effect of NDs that developed due to their spherical shape (Ref 42). The addition of ND in the nanocomposite powder encourages the up-surging of hardness and results of this hardness increase in the fabricated coatings. NDs are also able to deliver significant resistance to the insertion of abrasive particles and decrease the MRR (Material Removal Rate) (Ref 29).

This study also observed that the coating microstructure shows partially and fully melted zones, consisting of incompletely melted and re-solidified areas (Ref 3, 4). The same results were also found in the present study, where the incomplete melting of particles is the reason for poor cohesion forces among the splat of Al_2O_3 particles when the coating is performed by plasma spray. Al_2O_3 particles break and get stuck in wear debris into the counterpart in an incomplete melted region. Due to the incomplete melting of Al_2O_3 splat, they develop wear debris amid the coating and tungsten carbide ball (acts as a counterpart) and start acting as a third party, producing abrasion in the new coating surface. Henceforth, the coating surface suffers from a higher value of wear debris during wear. When the fully melted area of the developed coating comes across to the counterpart, it delivers the confrontation to fight against abrasion (Ref 4).

The low densification of the Al_2O_3 matrix might be the cause of wear. The slight wear, fewer micro-crack defects, formation of low wear debris, and grain pull-outs can be seen in AND-SD and ANDG-SD due to little increase in densification, rolling effect, and lubricating properties than A-SD coatings. To examine more about the layer transferred, EDS has been performed for worn surfaces. Figure 12(a), (b), and (c) shows the EDS of SEM images (A-SD, AND-SD ANDG-SD) of the worn-wear track. In EDS, elements such as aluminum, carbon, oxygen, and tungsten carbide are seen in the elemental distribution. The peaks of Carbon, Oxygen, Al, and WC of the worn surface are seen in the EDS image with an elemental percentage study of the worn surface. In the interest of brevity, the result of ANDG-SD has been explained here. The value received from elemental analysis of Carbon, Oxygen, Al, and WC of worn surface (ANDG-SD) is 3.94, 46.97, 47.41 and 1.68, respectively. As obtained images from EDS, it has been noticed that tungsten carbide and carbon were present on the shabby surface (worn) of ANDG-SD. This image information has confirmed that tungsten carbide is present in the transfer layer, causing wear between the developed coating and the tungsten carbide ball that worked as a counterpart. The carbon film layer is developed onto the surface of the worn surface due to NDs and GNPs reinforcement. The transfer of the WC layer onto the Al_2O_3 has added a smooth surface over the worn part surfaces, which behave like a shielding film to wear.

Higher densification and wear-resisting behavior can be seen in the developed coatings of ANDG-SD because of the solid interfacial connection among the NDs, GNPs, and Al_2O_3. Hereafter, the material taken off from ANDG-SD coating is less at the worn tie, improving the wear resistance property of developed coatings.

5. Conclusion

The current study studied the tribological nature of nanodiamonds and graphene nanoplatelet-reinforced plasma-sprayed alumina matrix. The tribological behavior of fabricated coatings is measured by the ball on a disk tribometer at room temperature. The two different compositions were prepared, such as 0.1 wt.% ND and 0.1 wt.%ND + 1 wt.%GNP reinforced in alumina, for studying the nature of distinguish reinforcement. The improved dense coating was obtained after adding NDs and GNPs in Al_2O_3. An excellent improvement in wear weight loss and wear rate is achieved with the addition of ND and GNP both in the alumina matrix. The wear weight loss and wear rate of pure Al_2O_3 and alumina matrix nanocomposites reinforced by NDs and GNPs tend to reduce with increasing normal loads. With an increasing load, the alumina matrix coefficient of friction decreases by adding 0.1 wt.%ND, 0.1 wt.%ND + 1 wt.%GNP with increasing loads. Adding 0.1 wt.%ND to the alumina matrix did not significantly change COF, but as the 1 wt.%GNP is added in alumina with 0.1 wt.%ND, the improved value of COF of alumina is achieved. The coefficient of friction reduces with increasing

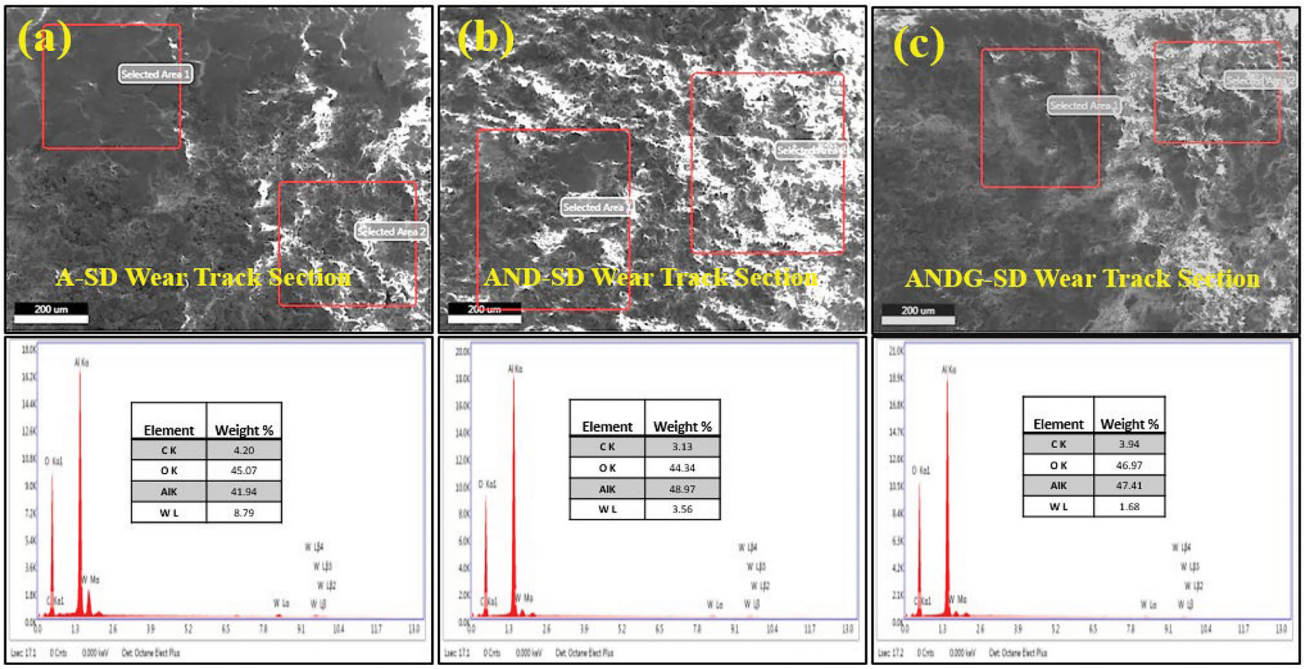

Fig. 12 EDS and elemental mapping of the worn wear track.

loads, in all the cases with decreasing drifts, and low-value COF is found at a higher load than other loads. Therefore, 1 wt.% GNP in Al_2O_3 has shown a significant decrease in COF compared to other samples due to its self-lubricating properties. This significant improvement is observed because of the following reasons (a) due to the formation of serval film from the counterparts, (b) improved densification, and (c) resilient boundary between A-SD, AND-SD, and ANDG-SD.

Acknowledgment

The authors of the present paper gratefully acknowledge the Thermal Plasma spray lab, Department of Metallurgical and Materials Engineering, IIT, Patna Bihta, for research facilities and guidance for effectively finishing the current research work.

References

1. M.M.J. Treacy, T.W. Ebbesen, and J.M. Gibson, Exceptionally High Young's Modulus Observed for Individual Carbon Nanotubes, *Nature*, 1996, **381**(June), p 678–680.
2. A.K. Keshri and A. Agarwal, Wear Behavior of Plasma-Sprayed Carbon Nanotube-Reinforced Aluminum Oxide Coating in Marine and High-Temperature Environments, *J. Therm. Spray Technol.*, 2011, **20**(6), p 1217–1230. https://doi.org/10.1007/s11666-011-9669-2
3. K. Balani and A. Agarwal, Process Map for Plasma Sprayed Aluminum Oxide–Carbon Nanotube Nanocomposite Coatings, *Surf. Coat. Technol.*, 2008, **202**(17), p 4270–4277. https://doi.org/10.1016/J.SURFCOAT.2008.03.024
4. E. H. Jordan and M. Gell, Nano Crystalline Ceramic and Ceramic Coatings Made by Conventional and Solution Plasma Spray Nano Crystalline Ceramic and Ceramic Coatings Made by Conventional and Solution Plasma Spray, *Meet. Proc. RTO-MP-AVT-122*, no. July 2015 (2006)
5. G.R. Karagedov and N.Z. Lyakhov, Preparation and Sintering of Nanosized α-Al_2O_3 Powder, *Nanostruct. Mater.*, 1999, **11**(5), p 559–572. https://doi.org/10.1016/S0965-9773(99)00331-1
6. H. Lou, D. Goberman, L. Shaw, and M. Gell, Identation Fracture Behavior of Plasma-Sprayed Nanostructured $A1_2O_3$-13 wt.%TiO_2 Coatings, *Mater. Sci. Eng. A*, 2003, **346**(1–2), p 237–245. https://doi.org/10.1016/S0921-5093(02)00523-3
7. L.L. Shaw et al., The Dependency of Microstructure and Properties of Nanostructured Coatings on Plasma Spray Conditions, *Surf. Coat. Technol.*, 2000, **130**(1), p 1–8. https://doi.org/10.1016/S0257-8972(00)00673-3
8. Y. Wang, S. Jiang, M. Wang, S. Wang, T.D. Xiao and P.R. Strutt, Abrasive Wear Characteristics of Plasma Sprayed Nanostructured Alumina/Titania Coatings, *Wear*, 2000, **237**(2), p 176–185. https://doi.org/10.1016/S0043-1648(99)00323-3
9. S.J. Bull, Comparison of the Erosive Wear Behavior of Vacuum Plasma Sprayed and Bulk Alumina, no. January 1991 (2014)
10. D.I. Pantelis, P. Psyllaki, and N. Alexopoulos, Tribological Behaviour of Plasma-Sprayed Al_2O_3 coatings under Severe Wear Conditions, *Wear*, 2000, **237**(2), p 197–204. https://doi.org/10.1016/S0043-1648(99)00324-5
11. Y. Naerheim, C. Coddet, and P. Droit, Effect of Thermal Spray Process Selection on Tribological Performance of Wc-Co and Al_2O_3-TiO_2 Coatings, *Surf. Eng.*, 1995, **11**(1), p 66–70. https://doi.org/10.1179/sur.1995.11.1.66
12. D.A.J. Ramm, T.W. Clyne, A.J. Sturgeon, and S. Dunkerton, Correlations Between Spraying Conditions and Microstructure for Alumina Coatings Produced By Hvof and Vps, *1994 Therm. Spray Ind. Appl.*, no. June, (1994), pp. 239–244
13. C. Muratore, J.J. Hu, and A.A. Voevodin, Adaptive Nanocomposite Coatings with a Titanium Nitride Diffusion Barrier Mask for High-Temperature Tribological Applications, *Thin Solid Films*, 2007, **515**(7–8), p 3638–3643. https://doi.org/10.1016/j.tsf.2006.09.051
14. S.C. Jambagi, S. Kar, P. Brodard, and P.P. Bandyopadhyay, Characteristics of Plasma Sprayed Coatings Produced from Carbon Nanotube Doped Ceramic Powder Feedstock, *Mater. Des.*, 2016, **112**, p 392–401. https://doi.org/10.1016/j.matdes.2016.09.095
15. T. Hansson, R. Warren, and J. Wasén, Fracture Toughness Anisotropy and Toughening Mechanisms of a Hot-Pressed Alumina Reinforced with Silicon Carbide Whiskers, *J. Am. Ceram. Soc.*, 1993, **76**(4), p 841–848. https://doi.org/10.1111/j.1151-2916.1993.tb05304.x
16. A. Nieto, J. Kim, O.V. Penkov, D.E. Kim, and J.M. Schoenung, Elevated Temperature Wear Behavior of Thermally Sprayed WC-Co/Nanodiamond Composite Coatings, *Surf. Coat. Technol.*, 2017, **315**, p 283–293. https://doi.org/10.1016/j.surfcoat.2017.02.048
17. H. Tang et al., Revealing the Formation Mechanism of Ultrahard Nanotwinned Diamond From Onion Carbon, *Carbon N. Y.*, 2018, **129**, p 159–167. https://doi.org/10.1016/j.carbon.2017.12.027
18. P. Singh, A. Islam, N. Pandit, S. Indupuri, and O.S.A. Rahman, Plasma Sprayed Graphene/Carbon Nanotube Reinforced Lanthanum Cerate Hybrid Composite Coating. Elesevier Ltd and Techna Grroup S.r.L. https://doi.org/10.1016/j.ceramint.2022.11.313
19. K.K. Mirche, K.K. Pandey, and S.M. Pandey, Microstructure and Corrosion Behavior of Plasma Sprayed Nanodiamond Reinforced NiAl Nanocomposite Coating, *J. Therm. Spary Technol.*, 2023 https://doi.org/10.1007/s11666-023-01558-6
20. B. Mukherjee, O.S. Asiq Rahman, A. Islam, M. Sribalaji, and A.K. Keshri, Plasma Sprayed Carbon Nanotube and Graphene Nanoplatelets Reinforced Alumina Hybrid Composite Coating with Outstanding Toughness, *J. Alloys Compd.*, 2017, **727**, p 658–670. https://doi.org/10.1016/j.jallcom.2017.08.160
21. C.F. Gutierrez-Gonzalez et al., Wear Behavior of Graphene/Alumina Composite, *Ceram. Int.*, 2015, **41**(6), p 7434–7438. https://doi.org/10.1016/j.ceramint.2015.02.061
22. J. Bai, X. Yang, S. Xu, Y. Shi, and J. Yang, Fabrication of Highly Dense Al_2O_3 Ceramics, *Scr. Mater.*, 2013, **68**(6), p 393–395. https://doi.org/10.1016/j.scriptamat.2012.10.054
23. C. Zhang, A. Nieto, and A. Agarwal, Ultrathin Graphene Tribofilm Formation during Wear of Al_2O_3-Graphene Nanoplatelet Composites, *Nanomater. Energy*, 2016, **5**(1), p 1–9. https://doi.org/10.1680/jnaen.15.00027
24. S.C. Jambagi and P.P. Bandyopadhyay, Plasma sprayed carbon nanotube reinforced splats and coatings, *J. Eur. Ceram. Soc.*, 2017, **37**(5), p 2235–2244. https://doi.org/10.1016/j.jeurceramsoc.2017.01.028
25. D.J. Woo et al., Synthesis of Nanodiamond-Reinforced Aluminum Metal Composite Powders and Coatings Using High-Energy Ball Milling and Cold Spray, *Carbon N. Y.*, 2013, **63**(1), p 404–415. https://doi.org/10.1016/j.carbon.2013.07.001
26. A. Katzensteiner, J.M. Rosalie, R. Pippan, and A. Bachmaier, Synthesis of Nanodiamond Reinforced Silver Matrix Nanocomposites: Microstructure and Mechanical Properties, *Mater. Sci. Eng. A*, 2020, **782**(December 2019), p 139254. https://doi.org/10.1016/j.msea.2020.139254
27. A.A. Kolchugin et al., Structural, Electrical and Electrochemical Properties of Calcium-Doped Lanthanum Nickelate, *Solid State Ion.*, 2016, **288**, p 48–53. https://doi.org/10.1016/j.ssi.2016.01.035
28. A. Nieto, D. Lahiri, and A. Agarwal, Synthesis and Properties of Bulk Graphene Nanoplatelets Consolidated by Spark Plasma Sintering, *Carbon N. Y.*, 2012, **50**(11), p 4068–4077. https://doi.org/10.1016/j.carbon.2012.04.054
29. M. Bao, C. Zhang, D. Lahiri, and A. Agarwal, The Tribological Behavior of Plasma-Sprayed Al-Si Composite Coatings Reinforced With Nanodiamond, *Jom*, 2012, **64**(6), p 702–708. https://doi.org/10.1007/s11837-012-0339-8
30. V.A. Sadykov et al., Cathodic Materials for Intermediate-Temperature Solid Oxide Fuel Cells Based on Praseodymium Nickelates-Cobaltites, *Russ. J. Electrochem.*, 2014, **50**(7), p 669–679. https://doi.org/10.1134/S1023193514070131
31. S. Simpson, A. Schelfhout, C. Golden, and S. Vafaei, Nanofluid Thermal Conductivity and Effective Parameters, *Appl. Sci.*, 2018 https://doi.org/10.3390/app9010087
32. V.N. Mochalin and Y. Gogotsi, Nanodiamond-polymer composites, *Diam. Relat. Mater.*, 2015, **58**, p 161–171. https://doi.org/10.1016/j.diamond.2015.07.003
33. V.I. Korepanov et al., Carbon Structure in Nanodiamonds Elucidated from Raman Spectroscopy, *Carbon N. Y.*, 2017, **121**, p 322–329. https://doi.org/10.1016/j.carbon.2017.06.012

34. L. Liu et al., Recent Advances in Friction and Lubrication of Graphene and Other 2D Materials: Mechanisms and Applications, *Friction*, 2019, **7**(3), p 199–216. https://doi.org/10.1007/s40544-019-0268-4
35. C. Li and A. Ohmori, Relationships Between the Microstructure, **11**(September), 365–374 (2002)
36. L. Zhao, K. Seemann, A. Fischer, and E. Lugscheider, Study on Atmospheric Plasma Spraying of Al_2O_3 Using On-line Particle Monitoring, *Surf. Coat. Technol.*, 2003, **168**(2–3), p 186–190. https://doi.org/10.1016/S0257-8972(03)00201-9
37. Y.J. Huang et al., Mechanical Properties and Tribological Behavior of Fe/Nano-Diamond Composite Prepared by Hot-Press Sintering, *Int. J. Refract. Met. Hard Mater.*, 2021, **95**(October 2020), p 105412. https://doi.org/10.1016/j.ijrmhm.2020.105412
38. S. Alleg, M. Ibrir, N.E. Fenineche, R. Bensalem, and J.J. Suñol, Microstructure and Magnetic Properties of HVOF Thermally Sprayed $Fe_{75}Si_{15}B_{10}$ Coatings, *Surf. Coat. Technol.*, 2010, **205**(2), p 281–286. https://doi.org/10.1016/j.surfcoat.2010.06.042
39. K.K. Pandey, R.K. Singh, O.A. Rahman, S. Choudhary, R. Verma, and A.K. Keshri, Insulator-Conductor Transition in Carbon Nanotube and Graphene Nanoplatelates Reinforced Plasma Sprayed Alumina Single Splat: Experimental Evidence by Conductive Atomic Force Microscopy, *Ceram. Int.*, 2020, **46**(15), p 24557–24563. https://doi.org/10.1016/j.ceramint.2020.06.243
40. S. Ranjan, B. Mukherjee, A. Islam, K.K. Pandey, R. Gupta, and A.K. Keshri, Microstructure, Mechanical and High Temperature Tribological Behaviour of Graphene Nanoplatelets Reinforced Plasma Sprayed Titanium Nitride Coating, *J. Eur. Ceram. Soc.*, 2020, **40**(3), p 660–671. https://doi.org/10.1016/j.jeurceramsoc.2019.10.043
41. S. Priyadershini, O.S.A. Rahman, K.K. Pandey, and A.K. Keshri, Remarkable Improvement in Tribological Behavior of Plasma Sprayed Carbon Nanotube and Graphene Nanoplatelates Hybrid Reinforced Alumina Nanocomposite Coating, *Ceram. Int.*, 2019, **45**(5), p 5768–5778. https://doi.org/10.1016/j.ceramint.2018.12.043
42. S. Singh, S. Sharma, and A.K. Keshri, Tribological Behaviour of Plasma-Sprayed Graphene Nanoplatelets Reinforced Hydroxyapatite Nanocomposite Coating, *Trans. Indian Inst. Met.*, 2021, **74**(11), p 2901–2907. https://doi.org/10.1007/s12666-021-02367-7

Publisher's Note Springer Nature remains neutral with regard to jurisdictional claims in published maps and institutional affiliations.

Springer Nature or its licensor (e.g. a society or other partner) holds exclusive rights to this article under a publishing agreement with the author(s) or other rightsholder(s); author self-archiving of the accepted manuscript version of this article is solely governed by the terms of such publishing agreement and applicable law.

2023 4th International Conference for Emerging Technology (INCET)
Belgaum, India. May 26-28, 2023

Investigations on Different Global Peak Tracking Algorithms for Extracting Maximum Power from Photovoltaic Systems

Mayank Ojha
Delhi Technological University
Department of Electrical Engineering
Delhi, India
mayankojha01@gmail.com

Vanjari Venkata Ramana
Delhi Technological University
Department of Electrical Engineering
Delhi, India
venkat.vr90@gmail.com

2023 4th International Conference for Emerging Technology (INCET) | 979-8-3503-3575-0/23/$31.00 ©2023 IEEE | DOI: 10.1109/INCET57972.2023.10170659

***Abstract*—In photovoltaic (PV) systems, various MPPT methods have certain merits and demerits. This paper focuses on different global peak tracking (GPT) algorithms for tracking peak power of PV array along with their comparison. Under non-uniform shading conditions, which involves change in environmental conditions like irradiance, many tracking techniques abort to track the global peak power (GPP) under partial shading conditions (PSC). This paper discusses investigations done under nonuniform shading conditions considering normal MPPT techniques compared with the modified MPPT algorithms to highlight the performance of different techniques. Simulation results comparing the effectiveness of the conventional Particle Swarm Optimization (PSO), Adaptive PSO and Hybrid PO-PSO have been done and it indicates that algorithms discussed here achieve global peak. A simulation model for 250W maximum power with a practical boost converter along with MPPT controller is used for investigation using MATLAB Simulink.**

Keyword Terms—global peak, maximum power point, power converter, partial swarm optimization, partial shading.

I. INTRODUCTION

Solar photovoltaic (PV) systems have emerged as a promising renewable energy source in recent years, and their use is rapidly expanding globally. However, the performance of these systems can be significantly affected by partial shading conditions, which can result in decreased energy yield and efficiency. This is mainly due to the mismatch between the maximum power point and the operating point which varies with shading conditions. The PV system characteristics are greatly dependent on the environmental conditions. The PV arrays are exposed to shaded conditions due to the surroundings such as buildings, tree shade etc. Under such circumstances, the *P-V* characteristics manifest multiple powers [1].

To solve the issue of partial shading, several maximum power point tracking (MPPT) techniques were proposed to optimize the energy yield of the system [1]-[8]. Among these techniques, global maximum power point tracking (GMPPT) is a promising approach that can identify the global MPP of the entire PV system, even in the presence of partial shading [7].

In this paper, a comparative analysis of different GMPPT techniques for partial shading conditions is presented. The performance of the different techniques is evaluated under different shading scenarios. The comparison is made among the particle swarm optimization (PSO) techniques with the conventional PSO [11], modified versions of PSO like hybrid PO-PSO [13] and adaptive PSO [8]. The simulation results show that the GMPPT techniques outperform the conventional MPPT techniques in terms of energy harvest. Specifically, the PSO based GMPPT techniques improve the energy harvest of the PV system as compared to conventional MPPT techniques. Therefore, the proposed study suggests that GMPPT techniques, particularly the non-linear optimization-based algorithm, are promising for designing efficient and cost-effective PV systems.

II. SYSTEM CONFIGURATION

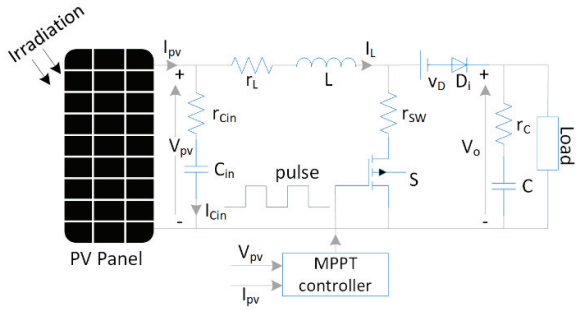

Fig. 1. Block diagram of Photovoltaic module comprising of DC-DC converter with a MPPT controller [10]

A PV array with boost converter along with MPPT controller is shown in Fig.1[10]. In PV applications, the modules are susceptible to partial shading that results in an uneven solar irradiance on different PV modules thus creating more peaks or MPPs. The local peaks are also referred as local MPPs, with one of them is the global maximum power point (GMPP)[7] . The global MPPs position correspondingly changes with respect to local MPPs on the *P-V* curve under partial shading conditions. To address this issue, the PV system employs a controller block i.e. MPPT controller that performs tracking to find the global peak point among the multiple local peaks which are effective under uniform insolation conditions and partial shading conditions[7]. However, the conventioanl methods may not be capable of tracking the GMPP under mismatched conditions, resulting in under-utilization of the PV system. To overcome this limitation, global peak tracking (GPT) techniques have been developed, which operate on a non-local search algorithm and can identify the global maxima even under non-uniform conditions. GPT techniques are

Authorized licensed use limited to: DELHI TECHNICAL UNIV. Downloaded on July 20,2023 at 11:23:44 UTC from IEEE Xplore. Restrictions apply.

considered more effective than conventional MPPT techniques, as they can optimize the energy yield of the PV system and minimize energy losses[3]. The changes in environment factors can alter the power charcteristics. These factors can be as follows:

A. Effect of Solar Irradiation:

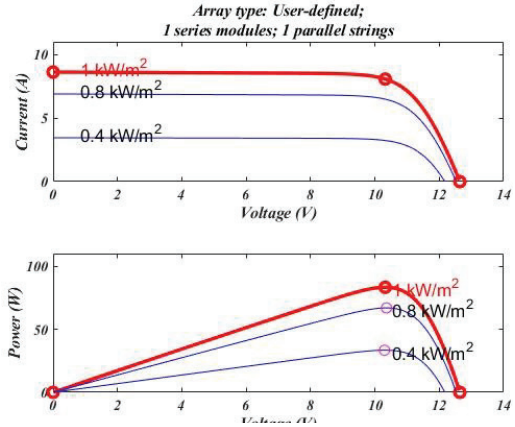

Fig. 2. *I- V* and *P- V* Characteristics for varying irradiance

The PV panel characteritics depends on solar irradiation as shown in Fig.2. A small change in irradiation pattern can bring around 2-5V difference in voltage and consequently current changes. As displayed in Fig. 3, for a definite amount of solar irradiation, when the temperature rises, subsequently V_{OC} decreases and I_{SC} escalates by small value[2].

B. Effect of Temperature variation :

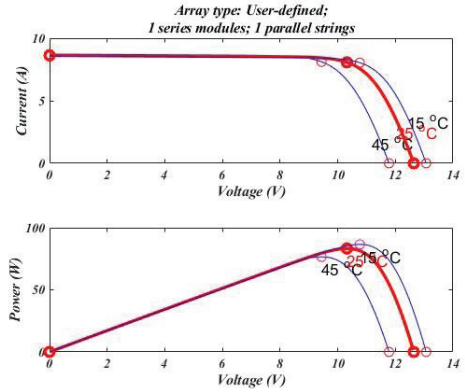

Fig. 3. *I- V* and *P- V* Characteristics for varying temperature

C. Effect of Partial Shading :

Partial shading has a considerable role in determining the output power. When irradiation received on a PV panel i.e. shaded cells is different to irradiation received on the unshaded cells, then $I_{unshaded} > I_{shaded}$. Then, this mismatch turns shaded cells to act as a sink. This power loss in the shaded cells leads to hot spot effect [6]. In order to bridle the issue, bypass diodes is connected in anti-parallel with PV sub-module. The string having four modules in series along with bypass diode in anti-parallel is considered in this work. The bypass diodes do not operate in reverse biased under uniform irradiance conditions. Bypass diode gets forward biased under partial shading conditions and irradiated cells will engage in generating power[2].

III. SOLAR PV SYSTEM CONFIGURATION

A. Boost converter parameter calculation

The boost converter [3] requires four components for its operation: inductor, MOSFET, diode, output capacitor, and an input capacitor. In general, the converter can be employed in the two modes: Discontinuous and Continuous (DCM and CCM). DCM is responsible for low power operation and other CCM is responsible for converting power efficiently. These modes depend on its switching period and energy storing capacity. However, for safe operation, it is generally recommended to operate boost converter in CCM mode only.

1) Selection of Inductor value

The large value of inductance increases the time constant while with the small value of inductance the converter goes into DCM. The boost inductor value is optimized to operate converter in the required range where we arrive at the concept of critical inductance [9].

$$L_{min} \geq \frac{R*(1-D)^2*D}{2*f_s} \quad (1)$$

From (1), L_{min} is defined as the minimum amount of inductance required to keep a continuous current. It plays a vital role in determining the performance of a converter. If $L>L_{min}$, then the converter operates in CCM, else it operates in DCM. f_s is the converter switching frequency. The value of the inductor computed is 3mH and its ESR is considered as 0.143 ohms.

2) Selection of Input Capacitor

To minimize the ripple in PV voltage, an input capacitor [6] is used to deliver current to the inductor with reduced ripple. The input current to capacitor is greater than zero, so the blue area in Fig. 4 is used to calculate the input capacitor value.

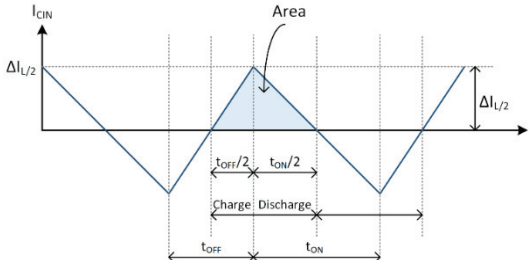

Fig. 4 Ripple Current waveform of Inductor at threshold in CCM mode[2].

The PV voltage is given by (2).

$$I_{Cin} = C_{in} \frac{\Delta V}{\Delta t} \quad (2)$$

From (2), (3) is obtained.

$$\Delta V = I_{in} \frac{\Delta t}{C_{in}} \quad (3)$$

From Fig.4. ΔV is calculated using (4).

$$\Delta V = \frac{\Delta I_L}{8*f_s*C_{in}} \quad (4)$$

Authorized licensed use limited to: DELHI TECHNICAL UNIV. Downloaded on July 20,2023 at 11:23:44 UTC from IEEE Xplore. Restrictions apply.

$$C_{in} = \frac{\Delta I_L}{8 * f_s * \Delta V} \quad (5)$$

The current in the ripple inductor is defined as [9]:

$$\Delta I_L = \frac{V * D}{f_s * L} \quad (6)$$

Substituting (6) in (5), (7) is obtained.

$$C_{in} = \frac{V * D}{8 * {f_s}^2 * L * \Delta V} \quad (7)$$

where, C_{in} is input capacitance, V is PV voltage, f_s is the switching frequency of the converter, D is the duty ratio and L is the inductance. The value of C_{in} is calculated by (7), where ΔV is considered as 1% of input voltage. Hence, (7) can be written as in (8).

$$C_{in} \geq \frac{D}{8 * {f_s}^2 * L * 0.01} \quad (8)$$

3) Calculation of Output Capacitance

The value is chosen from ripples present in output voltage [9]. During the turn-on time, the output current can be written as is given by (9).

$$I_o = C_o \frac{\Delta V}{T_{ON}} \quad (9)$$

In (9), T_{ON} is substituted as $D * f_s$, Therefore,

$$C_O = \frac{D * I_o}{\Delta V_o * f_s} \quad (10)$$

For desired voltage ripple (say 1%), output capacitor can be written as:

$$C_O \geq \frac{D}{0.01 * f_s * R} \quad (11)$$

Where R is the resistance or load connected at the output side and it is calculated from the values of output voltage and output curent. The capacitance value obtained using (11) is 100μF and ESR (r_c) of 0.3 ohms is considered.

B. PV array framework Characteristics

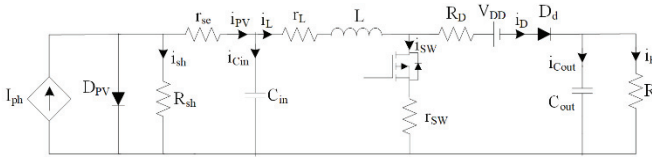

Fig. 5. Electrical Equivalent of Solar PV model [5]

This work utilized the equivalent circuit presented in [5] that is depicted in Fig. 5. A model of PV array consisting a dependent current source I_{ph} which depends on irradiance, anti-parallel diode, MOSEFT switch with a body diode, input and output capacitor, inductor and resistor load as shown in figure 5. The equation for the PV current can be represented as,

$$I = I_{ph} - I_s \left(\exp \frac{q(V + R_s I)}{aKTN_s} - 1\right) - \frac{(V + IR_s)}{R_s} \quad (12)$$

Where I_{ph} (13) is defined as[2],

$$I_{ph} = (I_{sc} + K_i(T - 298.5)) \frac{G}{1000} \quad (13)$$

And, I_s (14) is written as[2],

$$I_s = \frac{I_{sc} + K_i(T - 298.15)}{exp(q((V_{oc} + K_v(T - 298.15))/aKTN_s)) - 1} \quad (14)$$

The strings are integrated in a 1×3 matrix to obtain a maximum power approximately up to 250W under no partial shading condition at STC (usually T= 25°C and G=1000 W/m^2). Solar panels used are user defined as presented in Table I.

TABLE I. PV CHARACTERISTICS AT STC.

Parameters	Variable	Value
Maximum power	P_{max}	83.2824 W
V/T. coefficient	V_{coeff}	-0.339% /° C
A/T. coefficient	I_{coeff}	0.063%/° C
Voltage at Max. power	V_{mp}	10.32 V
Current at Max. power	I_{mp}	8.07 A
Short Circuit Current	I_{sc}	8.62 A
Open Circuit Voltage	V_{oc}	12.304 V
Number of Cells in Series	N_s	20

C. Steady State modeling of Boost converter

The small signal analysis is preferred for deriving the transfer function of any converter. The following assumptions are considered for practical boost converter for Small Signal Modelling [12]:

- L is large enough for current to remain constant.
- The MOSFET internal resistance (r_{sw}) and diode voltage drop (V_{DD}) are involved in the calculation.
- The switching duration is T, T_{on}= DT and T_{off} =(1-D) T
- The output voltage is kept constant by keeping large value of capacitor.

From state space representation, the ON and OFF state dynamic equations are derived. The closed loop transfer function (G_v) is calculated in equation (15) [1].

$$G_v = \frac{\widehat{V_{pv}}}{\widehat{V_{ref}}} = \frac{(K_p + K_i/S)|G_d|}{1 + (K_p + K_i/S)|G_d|H} \quad (15)$$

$\widehat{V_{pv}}$ *and* $\widehat{V_{ref}}$ are the perturbations in PV input voltage and reference voltage, G_d is forward path gain, H is feedback path gain.

D. MPPT Controller

The variation in irradiation and temperature are studied in Section I. The conventional methods like P and O and INC cannot achieve global peak in all the cases. Therefore, we need a more refined controller to track GMPPT to maximize power generated in any non-uniform conditions. An MPPT with PI controller block diagram is shown in Fig. 6.

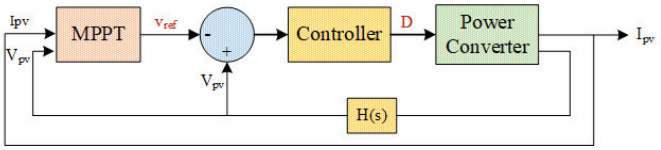

Fig. 6 MPPT controller with Boost converter and Feedback gain feedback loop[14]

Authorized licensed use limited to: DELHI TECHNICAL UNIV. Downloaded on July 20,2023 at 11:23:44 UTC from IEEE Xplore. Restrictions apply.

Vref is compared with the feedback block to obtain a correction factor required to optimize according to required profile[14]. PI tuning helps in reducing steady state error and gives a smooth output. Numerous MPPT techniques can be asserted a matter of study which are explained in Later stages.

IV. MPPT ALGORITHMS

A. Hybrid PO-PSO technique

The flowchart of Hybrid PO-PSO is presented in Fig. 7 [13] Firstly, perturb and observe algorithm is initiated to locate the nearest local maxima. Further, the PSO method is employed to locate the global maxima. The time required for convergence is reduced by limiting the search space. However, this technique cannot be used in the case of direct control of the converter duty cycle, as it uses the voltage of the photovoltaic system as a reference parameter, thus requiring a controller. Firstly, the complete search space is explored, and search is carried out in a reduced space until convergence. After a few calculation steps, it is possible to determine which particle is closest to the global maximum, then switches to the conventional P and O algorithm [1]. Starting from the best particle, will perform an adjustment to find the GMPP. Every particle has a velocity and position in space. The particle positions are defined as the duty ratio of converter. The starting positions of the particles can be defined or assigned randomly in the search space. The particles that were initialized at equidistant positions in the interval [d_{min}, d_{max}], where d_{min} and d_{max} highlight the minimum and maximum duty ratio, respectively, of the energy converter. As for initial velocities of the particles, they are randomly assigned.

Next, the best individual and data related to global peak are updated. The power obtained is compared with the value of the vector $P_m(i)$ as indicated in Fig.7. This vector is initially zero and is used to store the best result for each particle. If current power is greater, $P_m(i)$ is updated and the duty cycle value is saved in the d_p vector. In continuation, the current power is compared with the best global power value (G_m). If the current power value exceeds the G_m, the G_m vector is updated and the duty cycle value is stored in the d_g variable. This process repeats until all particles have been evaluated. The next step, velocity and position of every particle in the swarm gets reconditioned. In conventional PSO algorithm, this update was given by previous step in which the inertial weight and the cognitive and social coefficients are constant. Whereas to accelerate convergence the velocity update is given by [13].

$$v_i^{(k+1)} = w^k v_i^{(k+1)} + \emptyset_1^k a_1 (P_m - x_i^k) + \emptyset_2^k a_2 \, (G_m - x_i^k \,) \quad (16)$$

The term $w^k v_i^{(k+1)}$ determine the convergence behavior of the PSO. Initially, it is a common practice to set the foremost weight w^k, is kept at high quantity for more convergence, moderately reduce it to obtain inertial weight,

$$w^k = w_{max} - \frac{k}{k_{max}} (\emptyset_{1,max} - \emptyset_{1,min}) \quad (17)$$

Where, w_{max} and w_{min} are the upper and lower threshold of weights respectively; k represents current iteration; k_{max} corresponds to the max allowable iterations; $\emptyset_1^k$ and $\emptyset_2^k$ that represent the cognitive and social actions are defined in (18) and (19), in that order.

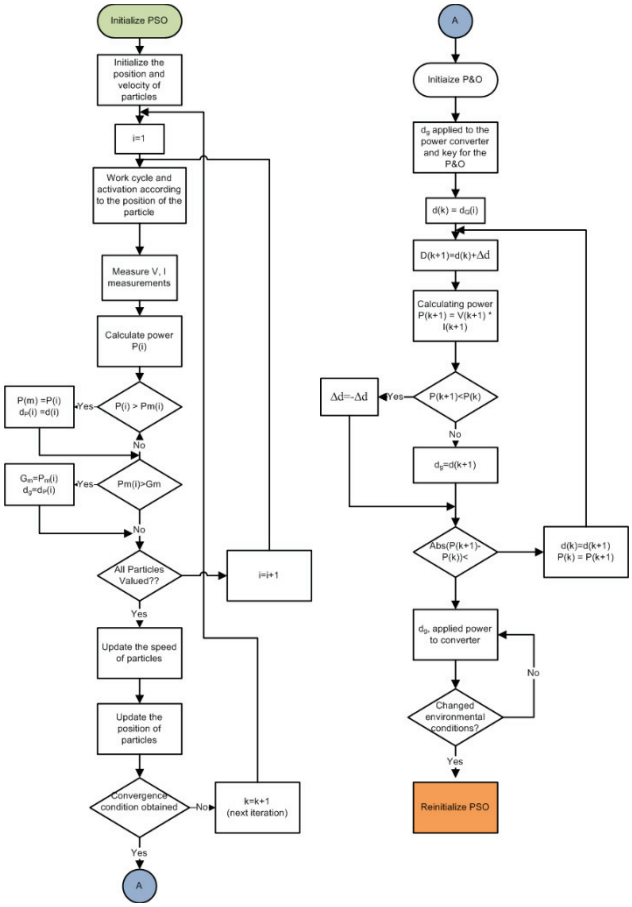

Fig. 7. Hybrid PO -PSO Algorithm flowchart

$$\emptyset_1^k = \emptyset_{1,max} - \frac{k}{k_{max}} (\emptyset_{1,max} - \emptyset_{1,min}) \quad (18)$$

$$\emptyset_2^k = \emptyset_{2,min} + \frac{k}{k_{max}} (\emptyset_{2,max} - \emptyset_{2,min}) \quad (19)$$

Where, $\emptyset_{1,max}$, $\emptyset_{1,min}$ and $\emptyset_{2,max}$, $\emptyset_{2,min}$ are upper and lower thresholds of $\emptyset_1$ and $\emptyset_2$. Completion of first part of algorithm, two convergence criteria are determined. Firstly, the difference in positions of the particles is less than a limit, and second, if the maximum number of iterations are reached. So, convergence limit must be chosen carefully, or the algorithm may go into later stage before reaching the global peak. Thus, in this research, the power limit was set to 10%, which is sufficient for the first stage to identify the proximities of the GMPP. As per empirical analysis, a limit of ten iterations are set to the first part of the algorithm. When one of the PSO convergence criteria is satisfied, the position of the particle that presents the highest power extracted from the system is stored in the d_g variable and transferred to the part of the hybrid algorithm that will perform a more refined adjustment. The second phase of the hybrid MPPT algorithm starts by applying the d_g work cycle in the converter. The value of power extracted from the photovoltaic system is tracked [13].

Authorized licensed use limited to: DELHI TECHNICAL UNIV. Downloaded on July 20,2023 at 11:23:44 UTC from IEEE Xplore. Restrictions apply.

After applying a disturbance (Δd) to the duty ratio of the power converter, the new power is extracted from the PV system. Then, the fine adjustment is effectively carried out, in which the current power is more than the power obtained before to keep the disturbance same. Above steps are repeated until the GMPP is tracked, or until the P and O convergence criteria is satisfied. The convergence criterion ithe difference of current power and the previous one should be less than predefined limit (1%) using the relation mentioned in [13]. The GMPP value changes with environmental conditions and load conditions. Therefore, in order to enable the use of this PSO and P and O hybrid MPPT technique in dynamic situations, a power variation should be less than 10% or algorithm will reset the particle position and process repeats.

B. *Adaptive PSO technique*

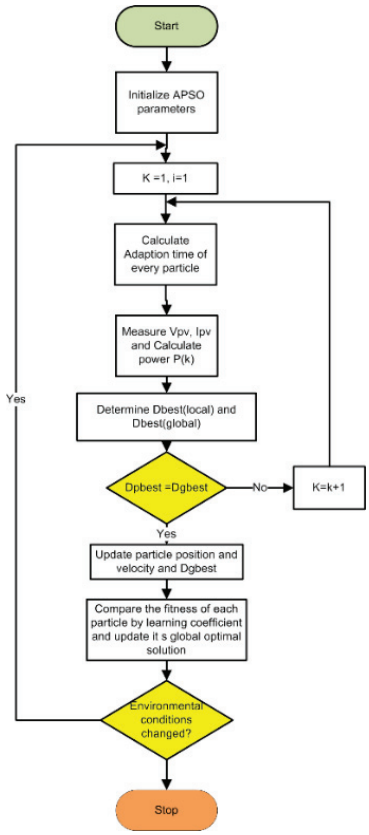

Fig. 8. Adaptive PSO Algorithm flowchart

The flowchart for adaptive PSO [8] is shown in Fig. 8. When the PSO convergence criteria is satisfied, the position of the particle represents maximum power taken from the system is stored as d_g. Next, a disturbance (Δd) is applied to duty cycle of the converter, and a new power is extracted from the PV system. Then, the fine adjustment is effectively carried out, in which the current power is more than the previous, the disturbance is kept in the similar direction. Above steps are repeated until the GMPP is tracked, or until the P and O convergence criteria is satisfied. The convergence criterion of is that the difference between the current and the previous power is less than the predefined limit as 1% using the relation mentioned in (20). In this application, the GMPP value generally changes with the environmental conditions.

$$\Delta P = \frac{Pm - P(m-1)}{Pm} < 1\% \tag{20}$$

The velocity of the algorithm is given by (21).

$$\omega = \left\{\frac{\omega min - (\omega max - \omega min)(f - fmin)}{favg - fmin}\right\}, f \le favg \tag{21}$$

$$\omega = \{\omega_{max}\},\ f \ge f_{avg} \tag{22}$$

In (21), the values of ω_{min} and ω_{max} are set as 0.5 and 0.9 respectively. The learning factor is introduced in the algorithm because each particle is different and changes dynamically according to its own fitness. As for the particle, the learning coefficient is given by (23) and (24).

$$c1(k) = c1(a1) + c1(b1)cos\frac{\pi k}{N_{max}} \tag{23}$$

$$c2(k) = c2(a2) - c2(b2)cos\frac{\pi k}{N_{max}} \tag{24}$$

The social cognitive coefficient is given by *c2*. *k* is iteration number; N_{max} is max iteration number. *c1* is individual cognitive coefficient of the particle learning from its maximum state. *c1* and *c2* in this paper are taken as *c1(b1)= c2(b2)* =1.2, *c1(a1)*= 1.8, *c2(a2)* =2. where *a1, a2*, *b1* and *b2* are the value of coefficients assigned to c1 and c2 taken from [8]. The conditions stated in (23) and (24) are used to identify reinitialization the APSO algorithm.

V. TESTBENCH CONFIGURARTION AND ANALYSIS

Three PV Modules which are defined in Table I is considered for evaluation in this work. All three module with uniform irradiance at STC condition can generate the maximum power of 250 W. The parameters of DC-DC Converter are calculated as per section II and values are presented in Table II.

TABLE II. POWER CONVERTER PARAMETERS

Parameter	Variable	Value
Inductance	*L*	3.3 mH
Inductor ESR	r_L	3 mΩ
Input Capacitor	*Cin*	100 µF
Cin, Cout ESR	r_c	0.03 Ω
Output Capacitor	*Cout*	100 µF
Load	*R*	30 Ω
MOSFET	*Vth*	5.7 mH
Internal Resistance	*Ron*	1 mΩ
Diode Knee voltage	*Vn*	0.7 V
Switching Frequency	*fs*	20kHZ

The effectiveness of all the algorithms are evaluated in terms of accuracy as per (25) [8].

$$Accuracy = \frac{P_{GMPP}}{P_{Steady\ state}} X100 \tag{25}$$

The simulation results are given in the Fig. 10 (a), (b), (c), (d).

The model is run for the simulation time of 2 sec. From the analysis, it depicts that at steady state, the expected maximum power comes out to be 249.93W, Conventional PSO has an accuracy of 99.29 %, Adaptive PSO has accuracy of 99.03%, and Hybrid PO-PSO has an accuracy of about 99.70. In second case dataset is taken as [1000 800 600] is shown in Fig.10(b). The expected maximum power is 166.49 W, whereas from the

Authorized licensed use limited to: DELHI TECHNICAL UNIV. Downloaded on July 20,2023 at 11:23:44 UTC from IEEE Xplore. Restrictions apply.

TABLE III. COMPARATIVE ANALYSIS FOR DIFFERENT TRACKING ALGORITHMS USED IN SIMULATION

Algorithm	*Irradiation Set*	*Duty ratio*	$P_{steady\ state}$ *(W)*	P_{GMPP}*(W)*	*Accuracy(%)*	*Transient Time(T_s)*
Conventional. PSO	[1000 1000 1000]	0.6273	249.93	248.18	99.29%	0.83s
	[1000 800 600]	0.530	166.49	164.423	98.75%	0.67s
	[800 600 400]	0.415	110.01	108.28	98.84%	0.77s
	[600 400 200]	0.525	69.70	67.61	97.00%	0.65s
Adaptive PSO	[1000 1000 1000]	0.641	249.93	247.65	99.03%	0.57s
	[1000 800 600]	0.542	166.49	165.29	99.27%	0.63s
	[800 600 400]	0.625	110.01	107.22	97.74%	0.55s
	[600 400 200]	0.550	69.70	68.75	98.63%	0.67s
Hybrid PO-PSO	[1000 1000 1000]	0.652	249.93	249.20	99.70%	0.95s
	[1000 800 600]	0.549	166.49	166.20	99.82%	0.84s
	[800 600 400]	0.441	110.01	109.85	99.85%	0.43s
	[600 400 200]	0.587	69.70	69.34	99.48%	0.73s

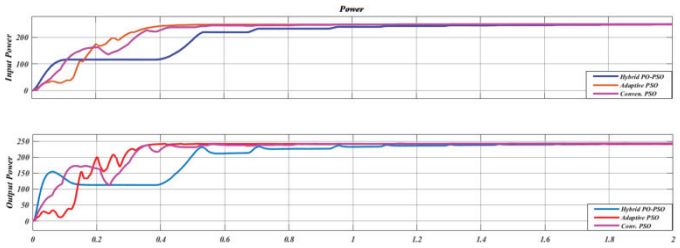

a) Power plots for irradiance [1000 1000 1000]

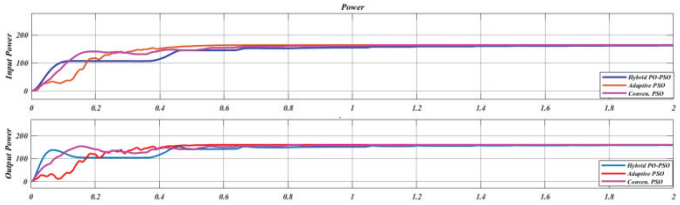

b) Power plots for irradiance [1000 800 600]

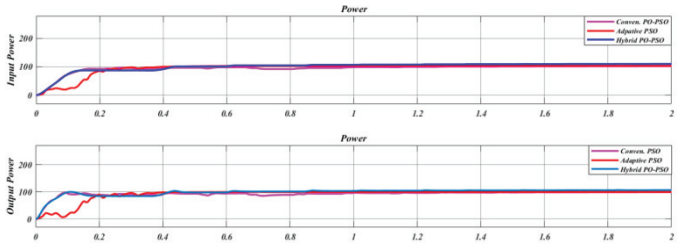

c) Power plots for irradiance [800 600 400]

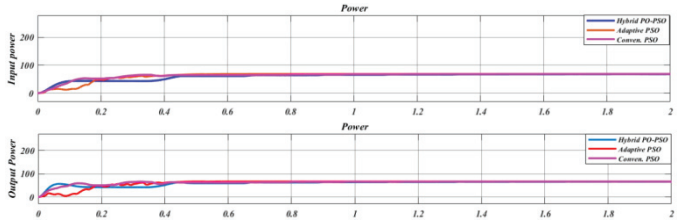

d) Power Plots for irrdiance [600 400 200]

Fig. 9.

simulation results, the conventional PSO has an accuracy of 98.75 %, adaptive PSO has accuracy of 99.27%, and hybrid PO-PSO has an accuracy of about 99.82%. From third case, the irradiance dataset taken is [800 600 400] as shown in Fig. 10(c).

The expected maximum power comes out to be 110.01W, whereas from our simulation results, we obtain that the conventional PSO has an accuracy of 98.84 %, adaptive PSO has accuracy of 97.74%, and hybrid PO-PSO has an accuracy of about 99.85%. The irradiance dataset in final stage taken is [600 400 200] as shown in Fig. 10(d). The expected maximum power comes out to be 69.70W, we obtain that the Conventional PSO has an accuracy of 97.00%, adaptive PSO has accuracy of 98.63%, and Hybrid PO-PSO has an accuracy of about 99.48%. Thus, Hybrid techniques bags the credit for average maximum accuracy among all three. However, if we observe the tracking time of simuation results of all algorithms, then Hybrid PO-PSO is slower in some cases than adaptive PSO. In a conclusion a tradeoff can be made between peak tracking time and performance accuracy for selecting a desired algorithm.

VI. CONCLUSION

In conclusion, our study contributes to the understanding of GMPPT techniques and provides valuable insights into the optimization of solar PV systems under partial shading conditions. Comparing the algorithms, the disadvantage of the Hybrid PO-PSO is it has longer tracked time but gives us a greater accuracy as compared to other two with least error margin. However, the other two algorithms have less tracking time but with smaller accuracy as compared to Hybrid PO-PSO. For higher accuracy, we prefer Hybrid PO-PSO for maximum extracted PV power. For least tracking time, it depends solely on a user needs and design. Thus, this study concludes under non -uniform partial shading conditions whose analysis can further studied by done by taking different shading patterns for different modules.

REFERENCES

[1] J M. A. Elgendy, B. Zahawi, and D. J. Atkinson, "Assessment of Perturb and Observe MPPT Algorithm Implementation Techniques for PV Pumping Applications," *IEEE Transactions on Sustainable Energy*, vol. 3, no. 1, pp. 21–33, 2011.

[2] S. Motahhir, A. El Ghzizal, S. Sebti, and A. Derouich, "Modeling of photovoltaic system with modified incremental conductance algorithm for fast changes of irradiance," *International Journal of Photoenergy*, vol. 2018, 2018.

[3] S. M. Adam, H. Wen, J. Ma, K. Wang, and K. L. Man, "An Improved P&O MPPT Method Using Boost Converter for Photovoltaic applications," in *International Conference on Recent Advancements in*

Authorized licensed use limited to: DELHI TECHNICAL UNIV. Downloaded on July 20,2023 at 11:23:44 UTC from IEEE Xplore. Restrictions apply.

Computing in AI, Internet of Things (IoT) and Computer Engineering Technology (CICET), 2020, pp. 26–28.

[4] A. Mohapatra, B. Nayak, and K. Mohanty, "Current Based Novel Adaptive P&O MPPT Algorithm for Photovoltaic System Considering Sudden Change in The Irradiance," in *2014 IEEE International Conference on Power Electronics, Drives and Energy Systems (PEDES)*. IEEE, 2014, pp. 1–4.

[5] M. Nasiri, S. Chandra, M. Taherkhani, and S. J. McCormack, "Impact of Input Capacitors in Boost Converters on Stability and Maximum Power Point Tracking in PV Systems," in *2021 IEEE 48th Photovoltaic Specialists Conference (PVSC)*. IEEE, 2021, pp. 1004–1008.

[6] S. Silvestre, A. Boronat, and A. Chouder, "Study of Bypass Diodes Configuration on PV Modules," *Applied Energy*, vol. 86, no. 9, pp. 1632– 1640, 2009.

[7] W. Hayder, E. Ogliari, A. Dolara, A. Abid, M. Ben Hamed, and L. Sbita, "Improved PSO: A Comparative Study in MPPT Algorithm for PV System Control Under Partial Shading Conditions," *Energies*, vol. 13, no. 8, p.2035, 2020.

[8] X. Chen, Y. Chai, and Y. Wang, "Application Of Adaptive Particle Swarm Optimization in Multi-Peak MPPT of Photovoltaic Array," in *2020 IEEE 4th Information Technology, Networking, Electronic and Automation Control Conference (ITNEC)*, vol. 1. IEEE, 2020, pp. 165–169.

[9] D. W. Hart, Power Electronics, McGraw-Hill New York, 2011.

[10] M. Arjun, V. V. Ramana, R. Viswadev, and B. Venkatesaperumal, "Small Signal Model for PV Fed Boost Converter in Continuous and Discontinuous Conduction Modes," *IEEE Transactions on Circuits and Systems II: Express Briefs*, vol. 66, no. 7, pp. 1192–1196, 2019.

[11] K. Ishaque, Z. Salam, M. Amjad, and S. Mekhilef, "An Improved Particle Swarm Optimization (PSO)–Based MPPT for PV with Reduced Steady-State Oscillation," *IEEE Transactions on Power Electronics*, vol. 27, no. 8,pp.3627–3638, 2012.

[12] R. W. Erickson and D. Maksimovic, Fundamentals of Power Electronics. Springer Science & Business Media, 2007.

[13] S. Figueiredo and R. Nayana Alencar Leão e Silva Aquino, "Hybrid MPPT Technique PSO-P&O Applied to Photovoltaic Systems Under Uniform and Partial Shading Conditions," *IEEE Latin America Transactions*, vol. 19, no. 10, pp. 1610-1617, Oct. 2021, doi: 10.1109/TLA.2021.9477222.

[14] E. I. Batzelis, G. Anagnostou and B. C. Pal, "A State-Space Representation of Irradiance-Driven Dynamics in Two-Stage Photovoltaic Systems," *IEEE Journal of Photovoltaics*, vol. 8, no. 4, pp. 1119-1124, July 2018, doi: 10.1109/JPHOTOV.2018.2839261.

Authorized licensed use limited to: DELHI TECHNICAL UNIV. Downloaded on July 20,2023 at 11:23:44 UTC from IEEE Xplore. Restrictions apply.

AIP Conference Proceedings

RESEARCH ARTICLE | JULY 14 2023

JTAG to AHB bridge FREE

Malti Bansal ✉; Harsh

Check for updates

AIP Conference Proceedings 2796, 150004 (2023)
https://doi.org/10.1063/5.0149168

View Online Export Citation CrossMark

20 July 2023 11:14:01

AIP Publishing

JTAG to AHB Bridge

Malti Bansal [a)], Harsh

Department of Electronics and Communication Engineering, Delhi Technological University (DTU), Delhi -110042, India

[a)]Corresponding author : maltibansal@gmail.com

Abstract: Design complexity of a chip is increasing day by day and because of which cost of testing is also increasing exponentially in terms of time and money and the remedy of this problem is DFT – Designfor testability which plays an importantpart in the ASIC design flow by reducing testing time and providing high fault coverage. Testing can be of two type Intest and Extest. In order to perform extest, we have to perform the boundary scan and for that we have an IEEE standard in DFT known asJTAG – Joint Test Action Group. JTAG is basically a design which we add as an additional circuitry to the system which makes input as controllable and output as observable. In DFT, we commonly use internal scan for testing but in some cases such as board-level test and diagnosis, test on-board interconnect among chips and test on-chip system logic makes boundary scan important which leads to JTAG as important part of DFT. This paper is primarily focused on the study of the logical functionalityof JTAG. We are going to do this by including JTAG into a design structure. The structure includes a master and a slave. Master have the JTAG for interface similarly slave have AHB for interface. Now, for communication we need a common bridge in- between. The data flow through the JTAG in order to perform are the sole purpose of this paper. We are going to design this structure in AMD Xilinx VIVADO 2019.2 and for the analysis and understanding purpose of the design, we will also perform theRTL analysis, Synthesis analysis which will create the netlist and at last we will use the netlist to generate the power report also.

20 July 2023 11:14:01

INTRODUCTION

The transfer of data from JTAG to AHB cannot be sent directly, this can be done using a Bridge. This bridge acts as a master to the JTAG and transfers data using AHB interface to the respective slave. The data initiated from JTAG tothe bridge is transferred through the AHB bus and is read back into the JTAG through the same bridge. This bridge works based on the TAP controller. Mainly two operations are performed by the bridge, it transfers data from JTAG to AHB for write operations and AHB to JTAG for read operations. TDI pin receives data for write operation and TDO pin receives data for read . Both the address and the data are present in this serial data frame. Using the control inputs, it is decided whether the data is to be written or read from the particular address. The configuration data is stored in the instruction register address that works based on the TAP controller state machine [1]. During write the data and address fields are set in the AHB interface with the control inputs, the communication happens between the AHB Master and AHB slave, if the AHB slave is ready to receive the data. During read, only the address is sent to the AHB interface with the control inputs this parallel data is received from the AHB slave and is sent as serial data through the TDO pin.

FEATURE LIST:

- Supports single transfer and four burst
- Status register to identify the status of the data transfer
- TAP Controller to control the data transfer

JTAG TO AHB BRIDGE ARCHITECTURE

This JTAG to AHB Bridge consist of different ports which controls and transacts data through the bridge. The data frame size is of 162 bit and is configured through the TDI pin based on the instruction register address.

Research Advancements and Innovations in Computing, Communications and Information Technologies
AIP Conf. Proc. 2796, 150004-1–150004-11; https://doi.org/10.1063/5.0149168
Published by AIP Publishing. 978-0-7354-4584-0/$30.00

ADDRESS[0:31]	READ/WRITE[32]	BURST SIZE[33]	DATA FRAME[34:161]

LSB → MSB

Signal Names	Description
Address	The 32-bit system address bus.
Write/Read	This bit represents the write or read function, High represents write function and low defines read operation
Burst/Single	This bit denotes that it processes a single or four bursts, low denotes a single transfer and high is for burst
Data Frame	Data is of 128 bits; we receive this data from JTAG only for write and not for read

TABLE 1: Data frame description

I/O DEFINATION

This JTAG to AHB Bridge consist of different ports which controls and transacts data through the bridge. The I/O pindiagram for the bridge is shown below.

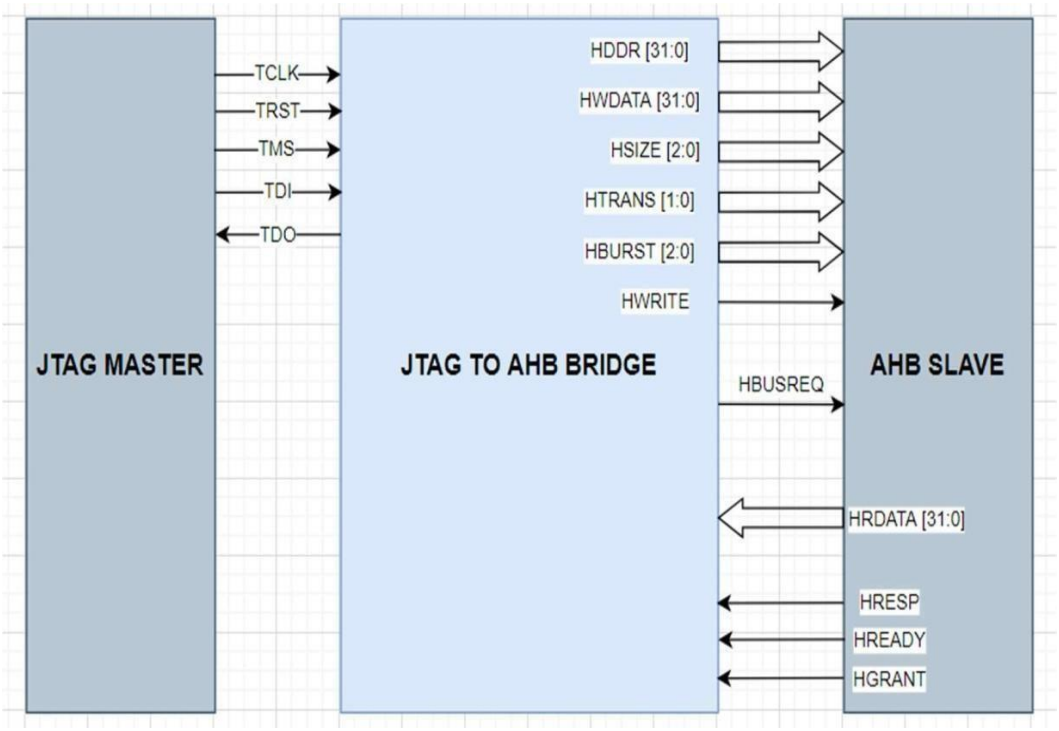

Figure 1: IO diagram

20 July 2023 11:14:01

JTAG SIGNALS

Signal name	I/O	Description
tck	Input	This port is the JTAG Test Clock.
tms	Input	This port is for mode selection and it is an input signal for the TAP controller. It is defined as TESTMODESELECT (TMS)
tdi	Input	This port is serial data input to all JTAG data registers and instruction registers.
trst	Input	This port is the JTAG Test reset. The JTAG reset canalso bedone by driving TMS high for five clock cycle
do	Output	This port is serial data output to all JTAG dataregisters andinstruction registers.

TABLE 2: JTAG signals description

AHB SIGNALS

hclk	Input	This port is the clock for the AHB signals
hrst	Input	This port act as a reset pin
haddr	Output	Indicates the AHB address bus. It is a 32-bit address
hwdata	Output	The write data bus is used to transfer data from the master to the bus slaves during write operations. A minimum data bus width of 32 bits is recommended.
hwrite	Output	When HIGH this signal indicates a write transfer and when LOW a read transfer.
hsize	Output	This size indicates the size of a transfer (Byte, Half word & Word)
htrans	Output	This port selects the signals as sequential, non-sequential, Idle or Busy
hburst	Output	This port indicates the size of the burst to be transferred (Single or Four burst)
hbusreq	Output	This Indicates the request from the corresponding Master to get the grant
hrdata	Input	This port gives parallel data as input from the AHB slave. And it is of 32 bits.
hready	Input	This ready signal indicates that the data is valid
hresp	Input	This gives the response for Ok or error
hgrant	Input	This is a grant signal, which enables the Master to process the transfer

20 July 2023 11:14:01

INTERNAL ARCHITECUTURE

This describes the whole top and internal architecture from JTAG to AHB. Below are the different blockswhich controls the data transfer from one end to other.

- Tap controller
- Instruction Register
- Configuration Register AHB Signal Generator
- Read Transfrer

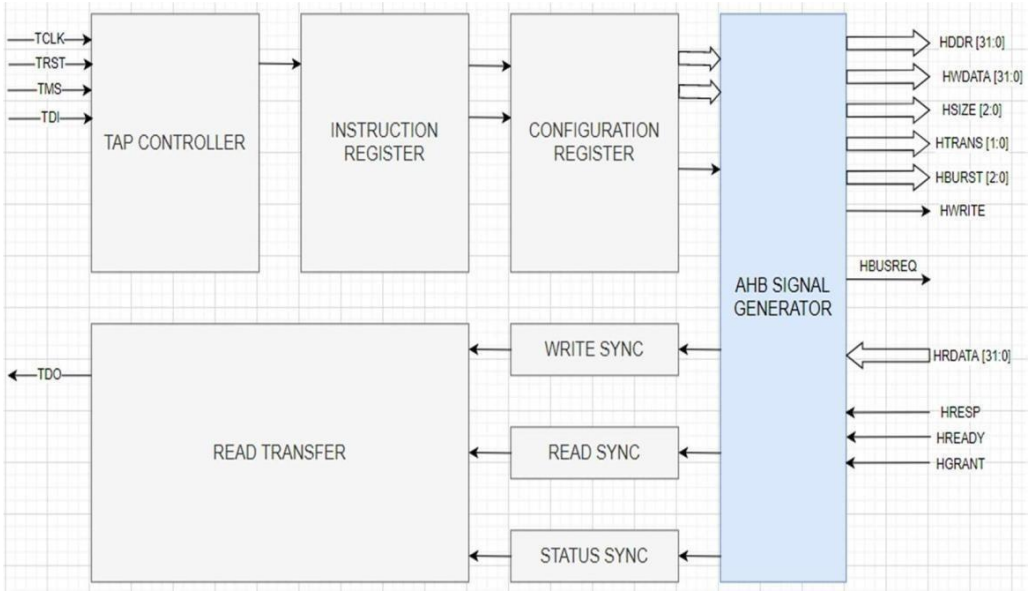

FIGURE 2: JTAG to AHB bridge architecture overview

TAP CONTROLLER

A TAP controller is a 16-state machine, programmed by the Test Mode Select (TMS) and Test Clock (TCK) inputs, which controls the flow of data bits to the Instruction Register (IR) and the Data Registers (DR). IR is the InstructionRegister column. Data instructions passed through this column affect the operation and contents of the Instruction Register, which is a mandatory component of every specified register. DR is the Data Registers column. Data instructions passed through this column affect the operation and contents of the data registers. The data registers can be the Boundary Register or Bypass Register, which all boundary-scan devices must contain, or they can be the optional IDCODE or USERCODE Registers, or even a designer-specified register (also known as Configuration Register) [2].

INSTRUCTION REGISTER

Instruction register basically works on the signals received from the TAP controller based on tck. The inputs and outputs given to the instruction register includes clock, TDI, shift enable, update enable and reset as inputs and data, valid, status as outputs [3]. The serial data tdi is converted into 3-bit parallel data which is given as an address to various data registers present. In the case of JTAG to AHB Bridge it is given to the configuration register, in order toconfigure the data register to be used. This Instruction register captures an address bit of 3 which is “100” and is sentas an address to the configuration module[4].

20 July 2023 11:14:01

CONFIGURATION REGSITER

This block is used to transfer a set of input signal to AHB signal generator which is in the form of frame structure. Once the data frame is received through the tdi pin, it stores the data in a buffer which consist of 162 bits, which has a Address bits, data bits, and control information. The Configuration register is split into 34 bits of Address_out, andremaining bits for data_out and it generates a valid signal along with it to identify the valid data available in the transmission path.

AHB SIGNAL GENERATOR

The AHB signals Generator is basic building block for generating AHB signals. It generates AHB signals based on the signals received from the AHB slave and the AHB input data. The inputs and outputs signals given to the AHB signalGenerator are shown in figure8. The AHB Signals generator receive the data frame which includes the data, address and control signals which are required for AHB slave. It will generate all the AHB signals like haddr, hwrite, hwdata, htrans, hburst, hsize and hbusreq based on AHB slave signals hck, hrst, hready, hresp, hgrant and hrdata. TheAHB Signals generator also generate internal signals like, ahb_valid and ahb_data which are required for read transferof JTAG based on hready, hrespand hrdata
[5].

- **AHB READ Transfer:**

When read transfer is initiated AHB_MASTER will send valid information with a specified address totheAHB_SLAVE interface and receives 32-bit data from AHB_SLAVE.

Single & Burst Read Transfer:

When the control information of the Bus pins are loaded the AHB_MASTER starts its transfer and based on the provided information its sends a data of 32bit to the Master interface. For read transfer also the same set of flow is followed. Once the AHB_MASTER is ready to receive a data from AHB_SLAVE, it starts with sending a hbusreq. Based on the request this master get a grant via hgrant signal. Once the grant goes high, master got the access and it will be ready to transfer the information to get the data from slave. It sends the address with a mentioned hburst and default hsize of 32 bit and htrans will start with non-Sequential and once the information is received by the slave, based on the control information it sends the data as a single or a burst. If this is for a single read, after each address istransferred for that corresponding address it gives or sends the valid data, its nearly same for the burst based on the Address it gives a valid data four time because it's of a burst and the address incrementing will be carried out inside a AHB_SLAVE interface and AHB_MASTER receive a 32 bit of data four times and its stored in a AHB interface[6].

- **AHB Write Transfer**:

The write data is received from the inputs as ahb_sync_data, ahb_sync_addr and when ahb_sync_valid is HIGH. ahb_sync_valid is HIGH for only one ahb_hclk clock cycle. Once the data and address are receivedit initially check forthe data is of WRITE or a READ, once it is defined it checks for it's a burst transferor a single transfer.

- **Single Write Transfer:**

Header is loaded with the sync_addr [31:0] and hsize is fixed to 32 bits (Word). hlock is not required in this transfer type, so it is set as LOW. htrans starts with non-Sequential and for each transfer it is set as Sequential. If it is of single transfer, hburst will be of "000" which denotes it's a single transfer. This will be taken from the sync_addr bitof [33] and hwrite will be set high for write transfer and this will be mentioned in the sync_addr bit of [32]. hprot will be assigned as "000" by default and hwdata consist of a 32-bit data which comes from the sync_data. In the depth of four, the first 32bit data from LSB is sent. When the hready and hresp is set high it denotes that the slave is ready to receive the transfer, then the transmission happens on the specified bus. Once the transfer is done the hready and hresp will be made LOW. Then the AHB Bus again request for a bus. Once the grant is set, it starts sending the next data frame to the AHB_Slave [7].

20 July 2023 11:14:01

- **Burst Write Transfer:**

This burst transfer start with the same set of process, it receives the address frame and data frame and based on the configuration defined it splits the frame to the corresponding AHB pins and initiate a transfer. In burst operation hburstis set as “010”and it defines a four burst. This will be taken from the sync_addr [33] and hwrite is set as low [8]. Once the hbusreq is initiated and when the hgrant is received, it starts the transfer. It sends the Address and control signals in the first clock cycle followed by data in the next clock cycle. This will be carried out for four clock cycles and once the transfer completes, the hready and hresp will be made LOW. [34]

STATUS REGISTER

This status register tells the status of the write, read, error and transfer complete. It is of 4 bits and each bit denotes thefunction or status of the operation which is carried out. The frame format defines with address bit of “010” and the frame structure defines the transfer completed for read and write operation and it gives the error in transfer. Till the new set of transfer starts, the data in the frame will remain the same. If other than the given pattern is sent just ignorethe data received and redo the same process to get the updated status.

- **ERROR TRANSFER STATUS:** If the status register is set as “1000” this denotes that there issome error inthe data transmission, the MSB bit of the status register will be set to HIGH.
- **OKAY TRANSFER STATUS:** This OKAY indicates that the transfer is done for Write or read, the statusregister is set as “0101” for Write transfer is done, if it for read it is setas “0110”.
- **INCOMPLETE TRANSFER**: If the status register is set as “0001” indicates that the write datais in progress,if it is of “0000” indicates that the read data is in progress.
- **READ DATA STATUS:** If the status register is set as “0010” it denotes that the read data isavailable in thebridge, and the JTAG can read the data from the bridge.

SIMULATIONS

The timing diagrams of all type of operations including read and write transfer in single andburst mode are shownbelow. The design is implemented in VIVADO 2019.2

Header is loaded with the sync_addr [31:0] and hsize is fixed to 32 bits (Word). hlock is not required in this transfer type, so it is set as LOW. htrans starts with non-Sequential and for each transfer it is set as Sequential. If it is of single transfer, hburst will be of “000” which denotes it’s a single transfer. This will be taken from the sync_addr bitof [33] and hwrite will be set high for write transfer and this will be mentioned in the sync_addr bit of [32]. hprot will be assigned as “000” by default and hwdata consist of a 32-bit data which comes from the sync_data. In the depth of four, the first 32bit data from LSB is sent. When the hready and hresp is set high it denotes that the slave is ready to receive the transfer, then the transmission happens on the specified bus. Once the transfer is done the hready and hresp will be made LOW. Then the AHB Bus again request for a bus. Once the grant is set, it starts sending the next data frame to the AHB_Slave [7].

When the control information of the Bus pins are loaded the AHB_MASTER starts its transfer and based on the provided information its sends a data of 32bit to the Master interface. For read transfer also the same set of flow is followed. Once the AHB_MASTER is ready to receive a data from AHB_SLAVE, it starts with sending a hbusreq. Based on the request this master get a grant via hgrant signal. Once the grant goes high, master got the access and it will be ready to transfer the information to get the data from slave. It sends the address with a mentioned hburst and default hsize of 32 bit and htrans will start with non-Sequential and once the information is received by the slave, based on the control information it sends the data as a single or a burst. If this is for a single read, after each address istransferred for that corresponding address it gives or sends the valid data, its nearly same for the burst.

20 July 2023 11:14:01

READ TRANSFER

- **SINGLE TRANSFER MODE**

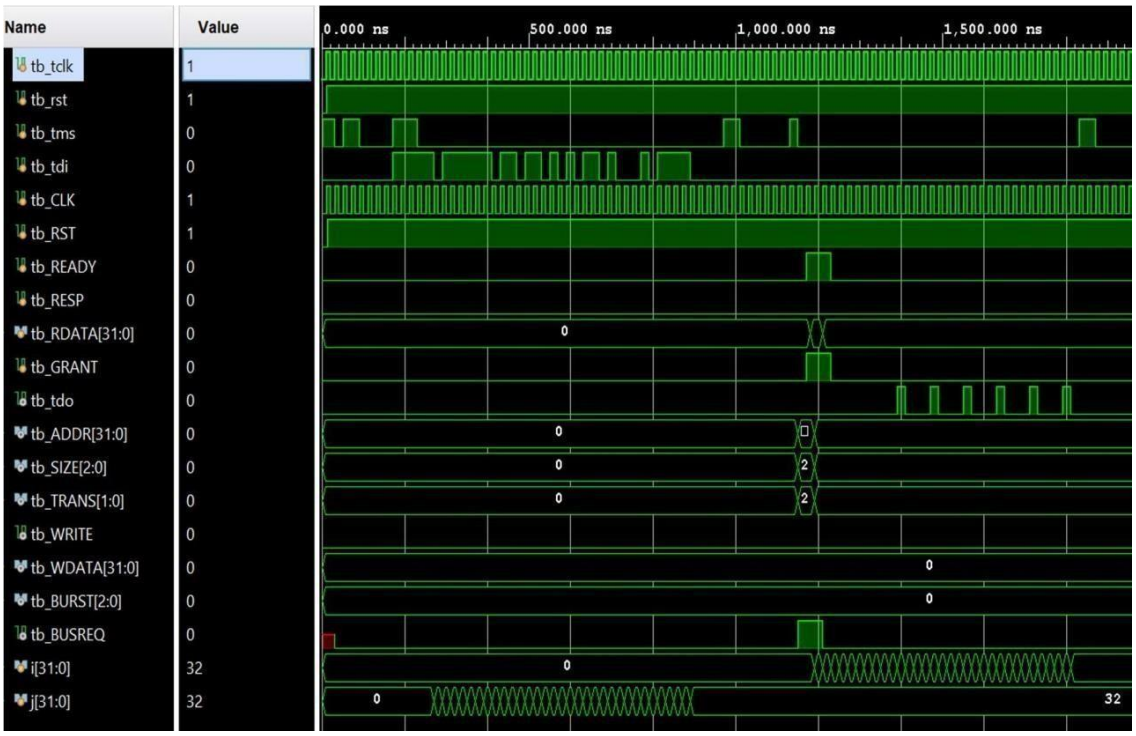

FIGURE 3: Waveform of read operation in single transfer mode

- **BURST TRANSFER MODE**

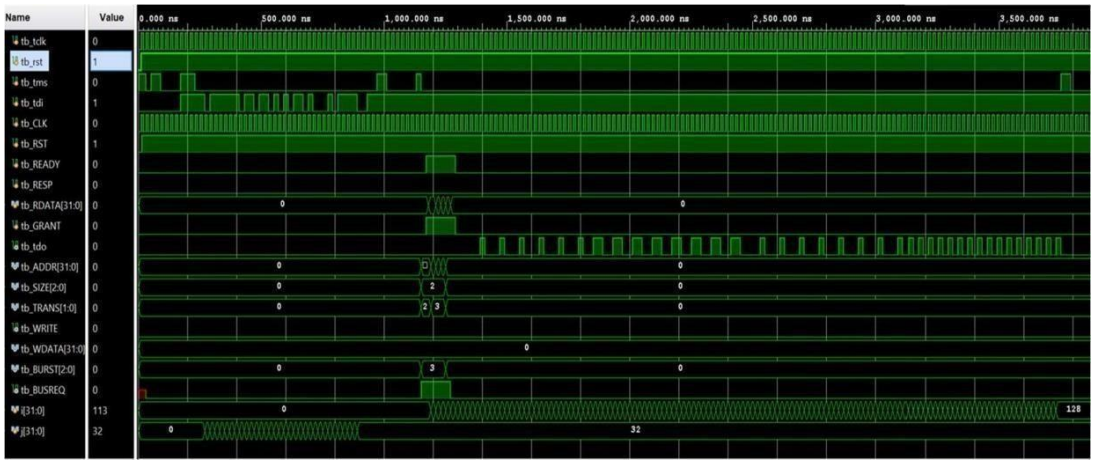

FIGURE 4: Waveform of read operation in burst transfer mode

20 July 2023 11:14:01

WRITE TRANSFER

- **SINGLE TRANSFER MODE**

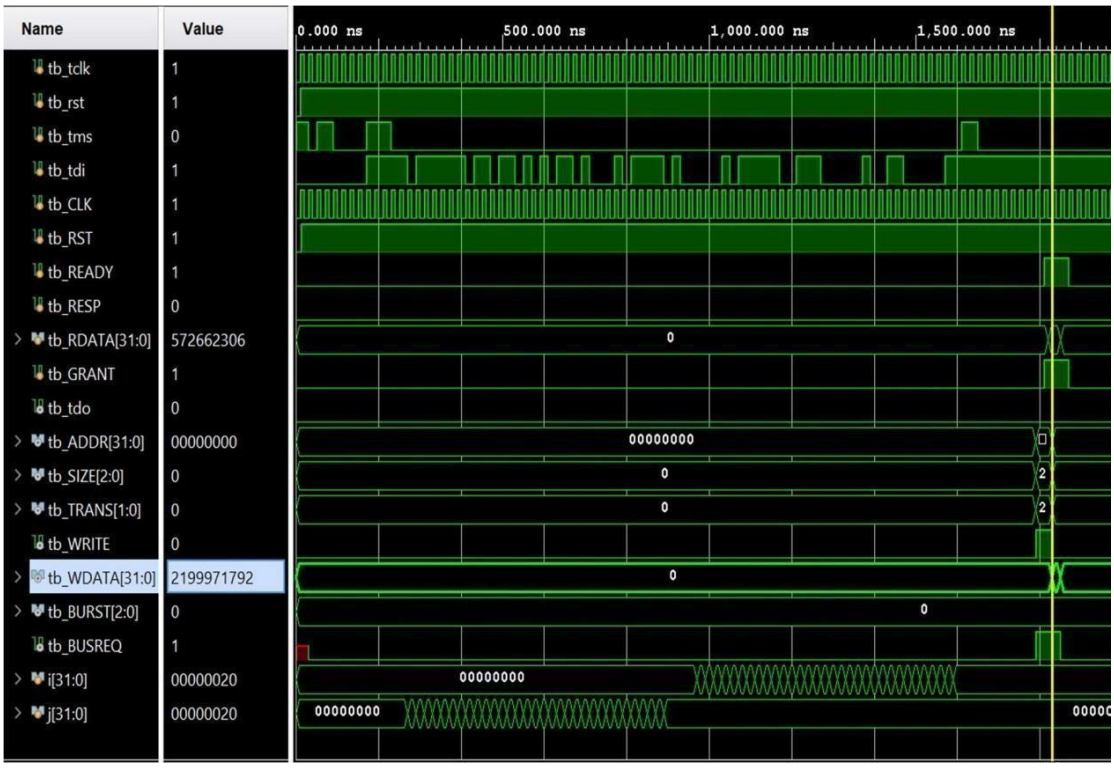

FIGURE 5: Waveform of write operation in single transfer mode

- **BURST TRANSFER MODE**

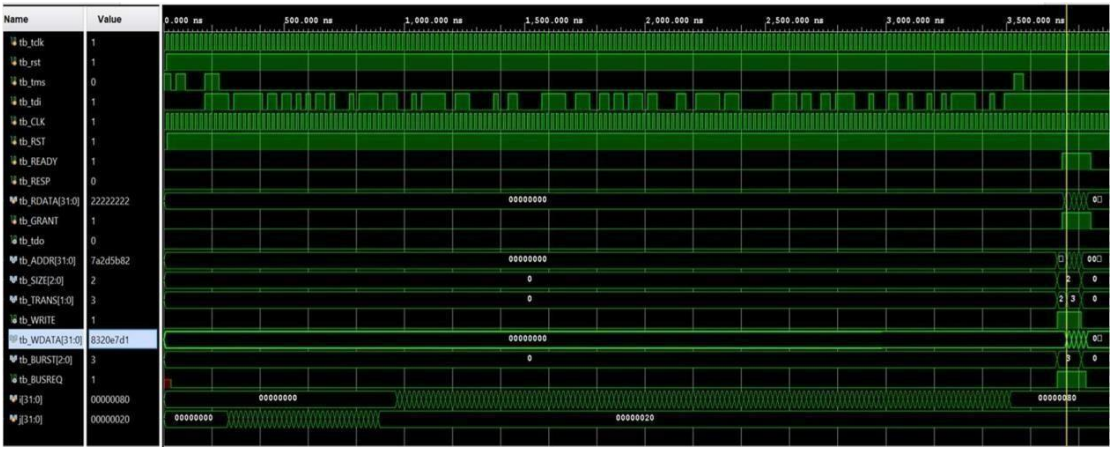

FIGURE 6: Waveform of write operation in burst transfer mode

DESIGN IMPLEMENTATION

The design is implemented using VIVADO 2019.2. The implementation analysis includes RTL schematicgeneration,synthesis analysis which generates netlist and at last power report.

20 July 2023 11:14:01

- **RTL ANALYSIS**

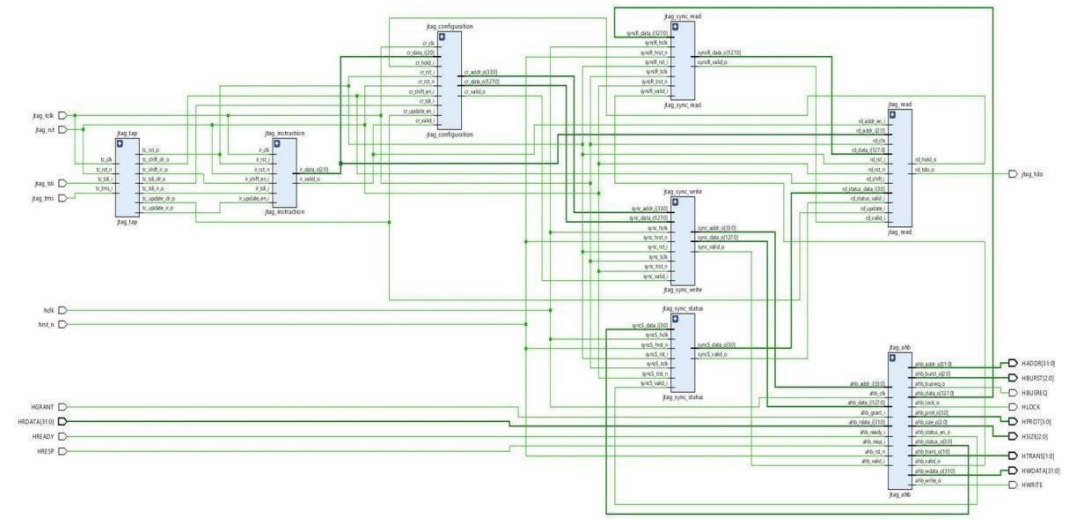

FIGURE 7: RTL schematic of the Design

- **SYNTHESIS ANALYSIS**

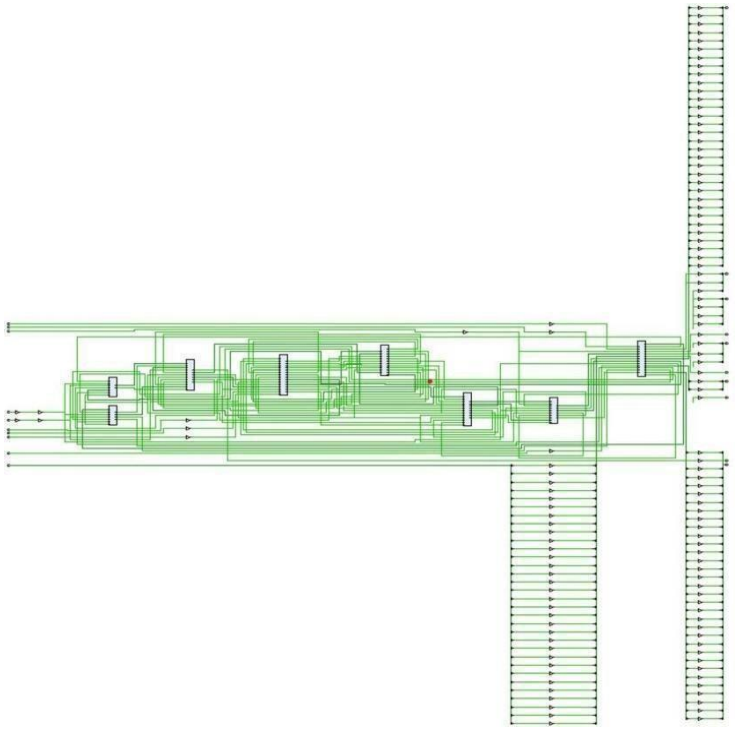

FIGURE 8: Netlist of the design

20 July 2023 11:14:01

- **POWER REPORT**

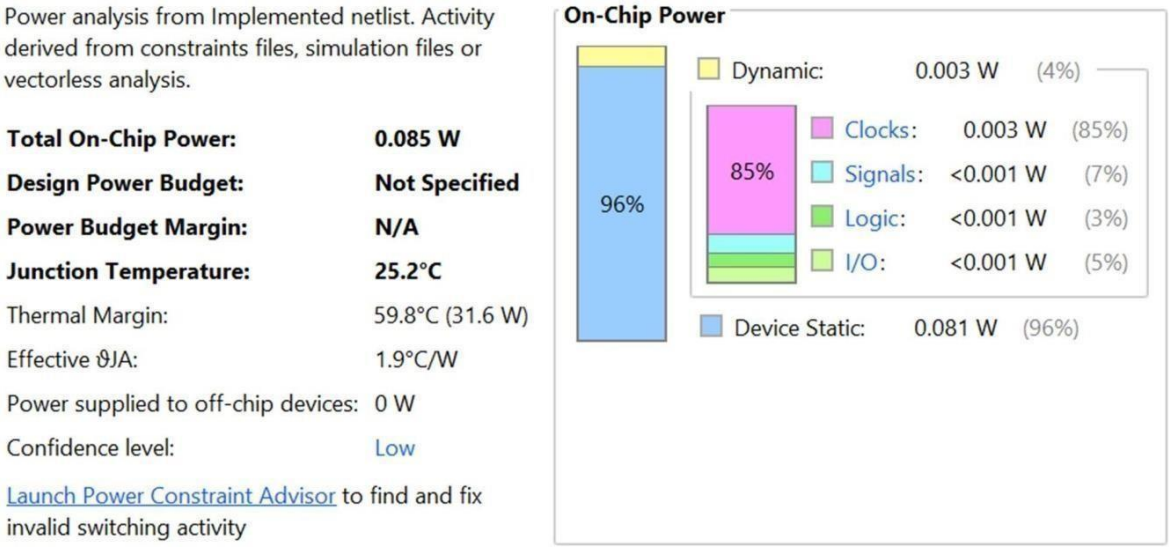

FIGURE 9: Power Report

CONCLUSION AND FUTURE SCOPE

The design is successfully coded using Verilog hardware description language in AMD Xilinx VIVADO 2019.2. In the results, waveform simulation of read and write operation in both single and burst mode is generated. Also, for the design implementation, RTL analysis and Synthesis analysis is done and as a result netlist and report power is generated. As per the power report, total 0.085 W on-chip power is consumed in which 96% is static power and 4% is dynamic power. For the future scope, we can use this design in design for testability (DFT) operations which includes scan boundary tests [9-13]. The scan boundary test basically includes the testing of I/O pins of the chip or module. For that we can use data registers of JTAG as boundary cells and the data we get for the data registers can be send to the processor through the JTAG to AHB bridge [14-19]. Also, for the improvement perspective, we can modify this design or add some low power circuitry in order to decrease the power consumption of the design [20- 22].

REFERENCES

1. Be Van Ngo, Peter Law, “Use of JTAG Boundary-Scan for Testing Electronic Circuit Boards andSystems”.
2. Shashidhara HB, Vasant Goudanavar, Dr. Siva yellampalii, “Board Level JTAG/Boundary Scan Test Solution”.
3. Huiguo Zhang, Yulan Tang, Zongguang Yu, “An FPGA Configuration Circuit Based on JTAG”.
4. Yassine Fkih, Pascal Vivet, “A JTAG based 3D DfT architecture using automatic die detection”.
5. Perumalla Giridhar, Dr Priyanka Choudhury, “Design and Verification of AMBA AHB”.
6. Poorani.P, Ms. Vijayashree.B M.E, “Implementation Of AHB Bus Protocol for System On ChipSecurity”.
7. Ashutosh Kumar Singh, Anurag Shrivastava, G.S. Tomar, “Design and Implementation of High Performance AHB Reconfigurable Arbiter for Onchip Bus Architecture”.
8. WANG Zhonghai, YE Yizheng, WANG Jinxiang, W Mingyan, “Designing AHB/PCI bridge”.
9. M. Bansal, R. Ranjan, “CMOS Instrumentation Amplifier Design”, International Journal of Electronics, Electrical and Computational System (IJEECS), 2017, Vol. 6, Issue 11, pp. 86-91.
10. M. Bansal and Priya, "Application Layer Protocols for Internet of Healthcare Things (IoHT)," 2020 Fourth International Conference on Inventive Systems and Control (ICISC), 2020, pp. 369-376, doi: 10.1109/ICISC47916.2020.9171092.
11. M. Bansal, Priya (2021) Performance Comparison of MQTT and CoAP Protocols in Different Simulation Environments. In: Ranganathan G., Chen J., Rocha Á. (eds) Inventive Communication and Computational

20 July 2023 11:14:01

Technologies. Lecture Notes in Networks and Systems, vol 145, pp. 549-560. Springer, Singapore. https://doi.org/10.1007/978-981-15-7345-3_47
12. M. Bansal, M. Nanda and M. N. Husain, "Security and Privacy Aspects for Internet of Things (IoT)," 2021 6th International Conference on Inventive Computation Technologies (ICICT), 2021, pp. 199-204, doi: 10.1109/ICICT50816.2021.9358665.
13. M. Bansal, P. "Machine Learning Perspective in VLSI Computer Aided Design at Different Abstraction Levels", S. Shakya et al. (eds.), Mobile Computing and Sustainable Informatics, Lecture Notes on Data Engineering and Communications Technologies vol. 68, pp. 95-112, Springer, Singapore 2021. https://doi.org/10.1007/978-981-16-1866-6_6
14. M. Bansal, S. Gupta and S. Mathur, "Comparison of ECC and RSA Algorithm with DNA Encoding for IoT Security," 2021 6th International Conference on Inventive Computation Technologies (ICICT), 2021, pp. 1340-1343, doi:10.1109/ICICT50816.2021.9358591.
15. M. Bansal, T. Chopra and S. Biswas, "Organ Simulation and Healthcare Services: An Application of IoT," 2021 6th International Conference on Inventive Computation Technologies (ICICT), 2021, pp. 205-208, doi: 10.1109/ICICT50816.2021.9358677.
16. M. Bansal and S. Garg, "Internet of Things (IoT) based Assistive Devices," 2021 6th International Conference on Inventive Computation Technologies (ICICT), 2021, pp. 1006-1009, doi: 10.1109/ICICT50816.2021.9358662.
17. M. Bansal, N. Adarsh, N. Kumar and M. Meena, "24×7 Smart IoT based Integrated Home Security System," 2020 Fourth International Conference on Inventive Systems and Control (ICISC), 2020, pp. 477-481, doi: 10.1109/ICISC47916.2020.9171051.
18. M. Bansal, G. Srivastava. (2020) Design and Implementation of LNA for Biomedical Applications. In: Pandian A., Ntalianis K., Palanisamy R. (eds) Intelligent Computing, Information and Control Systems. ICICCS 2019. Advances in Intelligent Systems and Computing, vol 1039, pp. 154-167, Springer, Cham. https://doi.org/10.1007/978-3-030-30465-2_18
19. M. Bansal and J. Singh, "Comparative Analysis of 4-bit CMOS Vedic Multiplier and GDI Vedic Multiplier using 18nm FinFET Technology," 2020 International Conference on Smart Electronics and Communication (ICOSEC), Trichy, India, 2020, pp. 1328- 1332, doi: 10.1109/ICOSEC49089.2020.9215317.
20. M. Bansal and J. Singh, "Qualitative Analysis of 2-bit CMOS Magnitude Comparator and GDI Magnitude Comparator using FinFET Technology (18nm)," 2020 International Conference on Smart Electronics and Communication (ICOSEC), Trichy, India, 2020, pp. 1323- 1327, doi: 10.1109/ICOSEC49089.2020.9215251.
21. M. Bansal, V. Sirpal, M. K. Choudhary, "Advancing e-Government using Internet of Things", S. Shakya et al. (eds.), Mobile Computing and Sustainable Informatics, Lecture Notes on Data Engineering and Communications Technologies vol. 68, pp. 123-137, Springer, Singapore 2021. https://doi.org/10.1007/978-981-16-1866-6_8
22. M. Bansal, V. Bharti, V. Chander, "Comparison between Conventional Fast Multipliers and Improved Fast Multipliers using PTL Logic", IOP Conf. Ser.: Mater. Sci. Eng., Vol. 1126, Issue 012041, pp. 1-12, 2021. doi:10.1088/1757-899X/1126/1/012041

20 July 2023 11:14:01

2023 2nd International Conference on Vision Towards Emerging Trends in Communication and Networking Technologies (ViTECoN) | 979-8-3503-4798-2/23/$31.00 ©2023 IEEE | DOI: 10.1109/ViTECON58111.2023.10157772

Lane-Line Segmentation Using YOLOv7

Dhruv Sharma
Department of Electronics and Communication
Delhi Technological University
New Delhi, India
dhrv99@gmail.com

S. Indu
Department of Electronics and Communication
Delhi Technological University
New Delhi, India
s.indu@dce.ac.in

N. Jayanthi
Department of Electronics and Communication
Delhi Technological University
New Delhi, India
njayanthi@dce.ac.in

***Abstract*—Lane-line segmentation has become increasingly significant in the contemporary times due to its compelling real-life applications in the diverse industries. The purpose of lane detection algorithms is to meticulously recognize the boundaries of the drivable-regions and carry out the localization. They form an enormously essential component of the Advanced Driver Assistance Systems (ADAS). Such systems would also help in significantly bringing down the accidents caused due to error by the human. In order to make such systems feasible, it's important to ensure they are reliable both in terms of inference speed and accuracy. Hence, this work proposes to use YOLOv7 model for the effective and efficient segmentation of the lane-lines from road-scene images. It follows the concept of trainable bag of freebies that allows the model to have both its performance as well as speed increase without negatively impacting each other. The Extended Efficient Layer Aggregation Network in its backbone network helps in improving the operation range while learning features. The performance of the model was compared to its predecessor YOLOv5. Results show that YOLOv7 outperforms with its optimal mean average precision of 92.4 for segmentation.**

Keywords—Lane-lines, Segmentation, You only look once.

I. INTRODUCTION

Lane-line segmentation is a crucial facet of computer vision that has become incrementally conspicuous in the contemporary times due to its compelling real-life applications in diverse industries. The essential purpose of lane detection algorithms is to meticulously recognize the boundaries of the drivable-regions and precisely locate the position of vehicles and localize while traversing them, thereby justifying their need in the Advanced Driver Assistance Systems (ADAS) and driverless-vehicles [1]. This can equip the drivers with significant information about their location and promptly alert them by accurately detecting lane lines in the real-time in case if they veer out of their designated lane, henceforth, minimizing the likelihood of accidents resulting from the human error. Over the past decade, an ever-growing human and industrial interest in the domain of lane-line segmentation has drawn upon keen interest amongst the researchers, leading to significant research in this field, leading to the development of several algorithms and techniques including the Hough transforms [2] and edge detection [3] to segment the lane- lines from road scenarios effectively and efficiently.

To minimize the hardware, deep learning mechanisms were introduced in this domain. Although such algorithms might be efficient at segmenting the lane-lines in terms of performance metrics and henceforth effectively locate them on roads, they aren't as capable in real-time scenarios where inference speed is the primary requirement. If separate algorithms are used for detecting each object on the road, the detection speed of the system will go down further. Hence, it is proposed to use the advance You Only Look Once (YOLO) [4] based encoder- decoder architectures that are capable of finding a trade-off between speed and metrics with the aid of trainable Bag of Freebies (BoF). In this work, YOLOv5 [5] and YOLOv7 models have been used to segment the lane-lines on drivable- region. These methods not only provide good inference speed but also show improved performance metrics and accuracy. However, as YOLOv7 utilizes Extended Efficient Layer Aggregation Network (E-ELAN) module, which employs the "Expand, Shuffle and Merge" cardinalities along with the group convolutional techniques to enhance the ability of the feature extraction network to learn important features, thereby increasing learning range manifolds, this would provide aid in segmenting and detecting thin lines on roads. The method also utilizes a dynamic label assignment process to acquire residual information, helpful in improving lane-line boundary segmentation. The main objectives achieved in this work are:

- YOLOv7 oriented encoder-decoder architecture has been proposed for segmentation of the lane-lines on roads effectively.
- To ensure complementary improvement in both performance metrics and speed, without any of them declining due to improvement in the other.
- Evaluation of the proposed method with YOLOv5 model to analyze the better performing method.

The rest of the paper is structured as follows. Literature Review is covered in Section II. This is followed by the Methodology in Section III, Results in Section IV that covers the results and comparative analysis. Section V is the concluding section that also covers and future scope.

II. LITERATURE REVIEW

Various deep learning algorithms have been employed in the past couple of years to implement lane-line detection systems. Convolutional Neural Networks (CNNs), a type of deep learning algorithm, have demonstrated impressive accuracy in object recognition and has been used for the detection of the lane-lines [6]. However, this accuracy often comes at the cost of longer inference times. LaneNet [7] was introduced specifically keeping this application in mind. It is a two-stage predictor meant for lane-line detection. The segmentation branch of the model was trained in order to produce binary masks for lane-lines. In [8], improved ripple-Generative Adversarial Networks (GAN) were used for lane-line detection. For effective learning of features they utilized quick connections and the gradient maps together. Methods including faster Region-based CNN (RCNN) [9] and mask RCNN [10] have also been used in detecting lane-lines and have yielded better results than CNN.

In [11], CNN in conjunction with Long Short Term Memory (LSTM) was used to construct an encoder-decoder

979-8-3503-4798-2/23/$31.00 ©2023 IEEE

Authorized licensed use limited to: DELHI TECHNICAL UNIV. Downloaded on July 03,2023 at 04:48:54 UTC from IEEE Xplore. Restrictions apply.

architecture. It helped in improving the speed as opposed to a conventional CNN. Detection rate was also improved. In Cross Layer Refinement Network (CLRNet) was based on extracting more of lane-line oriented information. This was achieved with the aid of low- and high-level aspect extraction [12]. Such methods were defined specifically to detect lane-lines. There were also techniques such as DLT-Net [13], YOLOP [14] and HybridNets [15] that would cover multiple elements on the roads that are required to be detected in order to ensure the drivable area is safe.

You Only Look Once (YOLO) is a swift object detector that uses single-detection architecture [4]. Utilizing the grid division technique, YOLO reduces the number of steps needed for object detection, leading to a faster inference speed that is ideal for real-time applications requiring quick detection. Nevertheless, there is typically a trade-off between speed and performance metrics, and as a result, YOLO experiences a decline in performance metrics. YOLOv2 [16] and YOLOv3 [17] object detectors were eventually developed. They are the improved versions of the original version. In [18], YOLOv3 Spatial Pyramidal Pooling (SPP) was utilized in detecting the lane-lines present in the road-scenes. In [19], YOLOv4 was used as the model to detect the lane-lines. The YOLOv4 approach surpasses YOLOv3 in both speed and metrics, thanks to its reliance on a trainable BoF that boosts its speed without compromising its metric performance.

III. Methodology

Methodologies that utilize encoder-decoder-oriented architectures have been employed in order to detect the lane-lines on the road. This involves segmentation method based on YOLOv7. [20] Both of these approaches involve annotating the lane-line-road images in txt format, where each value is normalized to a scale between 0 and 1 with respect to the image coordinates of the lane-line segmentation point. Subsequently, the annotated images are employed as inputs to train an encoder-decoder architecture-oriented segmentation model, which is a single-stage segmentation model operating at a rapid speed. This model utilizes the lane-line segmentation label to segment the lane-lines. After the model is trained, it is subjected to testing using new data to achieve the desired segmentation outcomes. The general process of segmentation of lane-lines is summarized in the proposed block diagram in Figure 1. Following architectures have been used to segment the lane-lines.

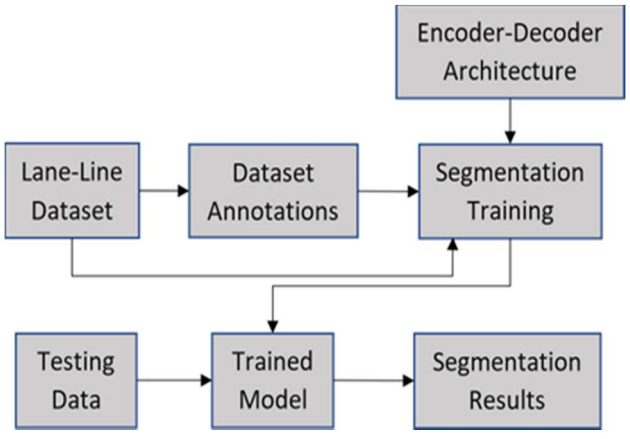

Fig. 1. Proposed Block Diagram for Lane-Line Segmentation

YOLOv7 segmentation utilizes an anchor-less approach. It consists of a backbone, that establishes the extraction of features of the road-scene images via feature maps of varying sizes *P1 = P/2, P2 = P/4, ... P5 = P/32*. Overall, these are covered over 50 layers of the backbone network. The backbone constitutes of E-ELAN module, which employs the ”Expand, Shuffle and Merge” cardinalities and group convolutional techniques to enhance upon the ability of the feature extraction network to learn important aspects. This method notably increases the range of features learned, while simultaneously preserving the gradient path without any adverse impact. The backbone further uses the Maxpool (MP) Layers with varying kernels with respect to sizes, with no compromise on input resolution. It also uses convolutional batch normalization to reduce to ameliorate the efficiency further by fusing into single convolutional layer.

The model adjusts scale factors such as depth, width, and resolution through a compound scaling approach in order to form models of varying sizes and speeds which helps it in achieving optimal throughput without altering the original architecture. It also combines Spatial Pyramidal Pooling and Cross-Stage Partial Network (SPPCSPNet) in the neck network, conventionally meant for detection and segmentation. SPP generates multi-scale region aspects. CSPNet, on the other hand, helps in mitigating any redundant gradient information. Additionally, the model employs a trainable Bag of Freebies (BoF) using a re-parameterized convolution technique and a module-level ensemble which utilizes the RepConvN method to preserve residuals and concatenation by skipping the identity connection. For the loss function, various losses including segmentation loss, bounding box loss, detection loss and classification loss have been considered.

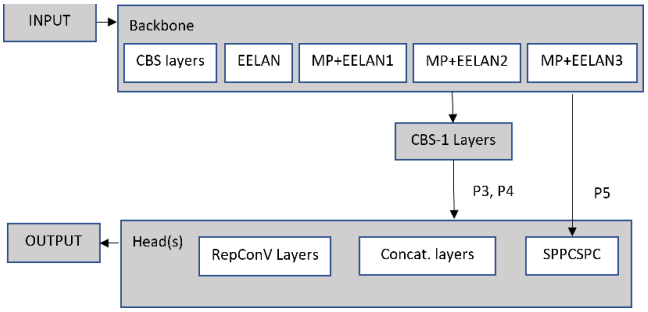

Fig. 2. YOLOv7 Segmentation Architecture

IV. Experimental Results

A. Dataset Acquisition

KITTI dataset [21], comprising of 15k images, was used to collect the training, testing and validation road-scene image data. The dataset has been designed to cover a wide range of applications, including detection, segmentation, and depth recovery, by incorporating eight distinct classes. We specifically chose according to the application requirement, i.e., lane-line segmentation. The images were annotated into txt format using manual annotators. Each annotation was brought down on a scale of 0 to 1. These images were then divided into training, testing and validation data.

B. Results and Discussion

In order to execute the proposed work, Linux Ubuntu (v22.04.01) was utilized. The training, testing and validation of the model utilized the Pytorch 1.10 library. Training was

Authorized licensed use limited to: DELHI TECHNICAL UNIV. Downloaded on July 03,2023 at 04:48:54 UTC from IEEE Xplore. Restrictions apply.

done on NVIDIA RTX A5000 GPU. The dataset was divided into training, testing and validation images. Both the models, YOLO- and YOLOv7 were then trained using the annotated training images with varying epochs and batch sizes, and then validated against the validation images. The Stochastic Gradient Descent (SGD) optimizer was used in training. The models were trained on different batch sizes and epochs till the optimal results were achieved. To evaluate the proposed model's effectiveness, it underwent a series of tests that involved randomly choosing lane-line images. Figure 3. shows the PR segmentation-curve for YOLOv7. The results of these tests, including both the ground truth and the output of the lane-line segmentation generated by the proposed method, are illustrated in Figure 4.

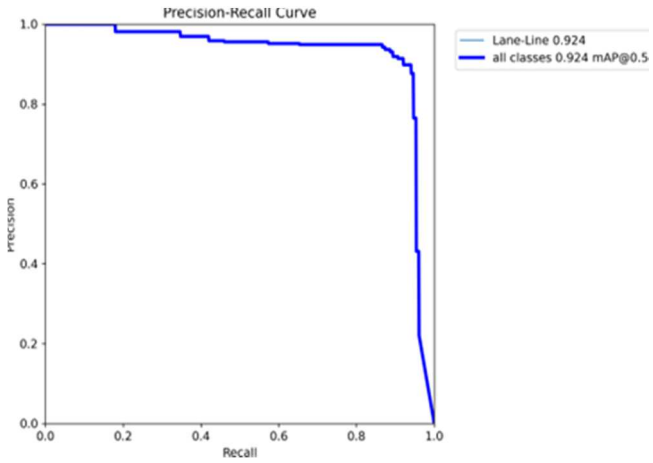

Fig. 3. Precision-Recall Curve (YOLOv7-seg)

The results of the two methods have been summarized in Table I, II and III. Table I shows the inference speeds of the two trained models. From Table I it may be concluded that YOLOv7 is the swifter architecture of the two proposed methods for segmenting the lane-lines, hence making it more feasible in the real-time applications.

TABLE I. COMPARISON OF SPEEDS

Method	Speed
YOLOv5	95 FPS
Proposed Method	123 FPS

These models were compared on different performance metrics including Recall, Precision, F1-score and mean Average Precision (mAP) as shown in table II and III. Not only in terms of inference speed, but YOLOv7 also outperforms YOLOv5 in the performance metrics, having a higher segmentation mAP of 92.4 and detection mAP of 95.7 as opposed to YOLOv5 which has an segmentation mAP of 86.7 and detection mAP of 86.7. This is owing to the fact that YOLOv7 has uses an improved trainable BoF, which helps in improving both accuracy as well as the speed together and find a perfect trade instead of downgrading the other despite conventionally the inverse relationship between the two for most of the other state-of- the-art deep learning models.

TABLE II. COMPARISON OF MEAN ACCURACY PRECISION

Method	Detection	Segmentation
YOLOv5	94.4	86.7
Proposed Method	95.7	92.4

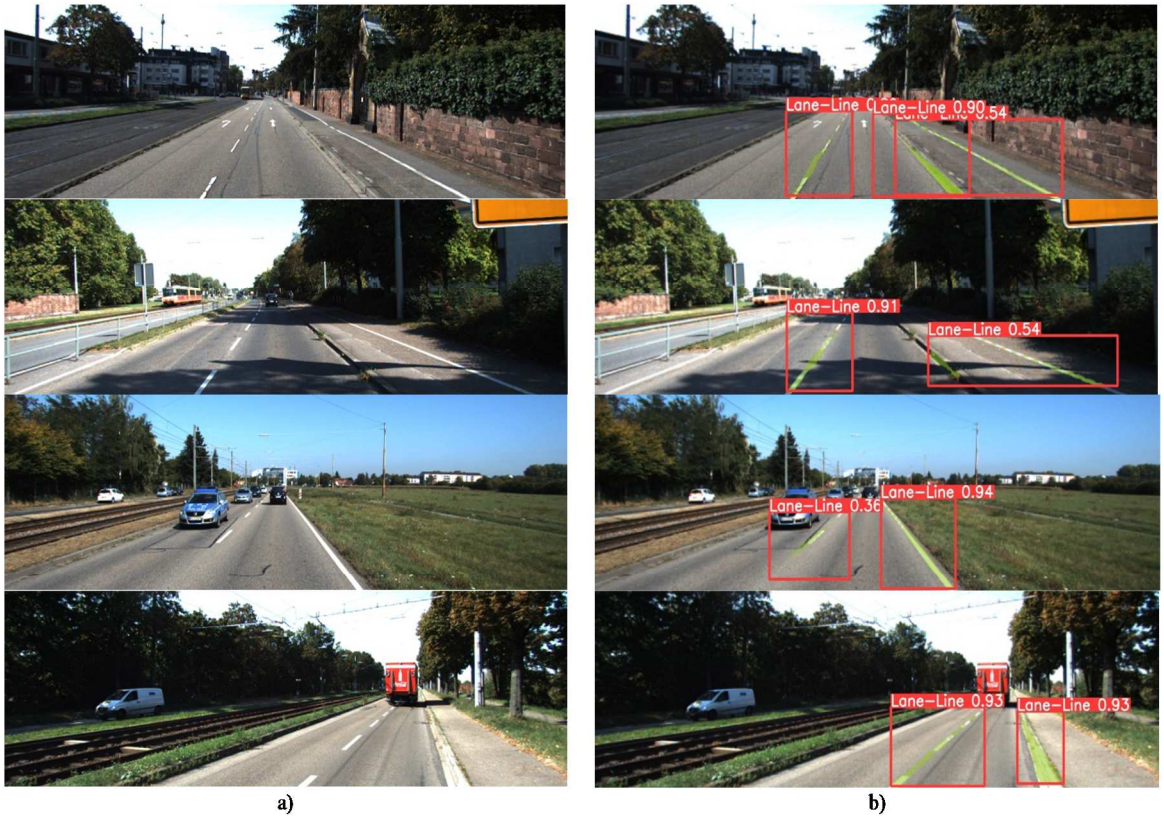

Fig. 4. Testing results a) Ground Truth b) Combined Segmentation and Detection Results for YOLOv7

Authorized licensed use limited to: DELHI TECHNICAL UNIV. Downloaded on July 03,2023 at 04:48:54 UTC from IEEE Xplore. Restrictions apply.

TABLE III. COMPARISON OF PERFORMANCE METRICS

Method	Precision	Recall	F1-Score
YOLOv5	89.1	85.2	87.15
Proposed Method-	94.4	90.5	92

V. CONCLUSION

Lane-line segmentation has become increasingly important in various industries due to its practical applications in computer vision. Lane detection algorithms are critical components of Advanced Driver Assistance Systems (ADAS), which require both reliable inference speed and accuracy. This work proposes using the YOLOv7 model for efficient and effective lane-line segmentation in road-scene images. YOLOv7 uses a trainable bag of freebies concept to improve both speed and performance without negatively impacting each other. The E-ELAN backbone network employs expand, shuffle, and merge cardinalities, along with group convolutional techniques to enhance feature extraction network capabilities for learning important features and detecting thin lines on roads. The method also uses a dynamic label assignment process to obtain residual information to improve lane-line boundary segmentation. YOLOv7 outperforms its predecessor, YOLOv5, with an optimal mean average precision of 92.4 for segmentation. For future scope, this method can be expanded to the other sub-systems of the ADAS as well.

REFERENCES

[1] A. Moujahid, M. E. Tantaoui, M. D. Hina, A. Soukane, A. Ortalda, A. ElKhadimi, and A. Ramdane-Cherif, "Machine learning techniques in ADAS: A review," in 2018 International Conference on Advances in Computing and Communication Engineering (ICACCE), pp. 235–242, IEEE, 2018.

[2] F. Zheng, S. Luo, K. Song, C.-W. Yan, and M.-C. Wang, "Improved lane line detection algorithm based on hough transform," Pattern Recognition and Image Analysis, vol. 28, pp. 254–260, 2018.

[3] W. Phueakjeen, N. Jindapetch, L. Kuburat, and N. Suvanvorn, "A study of the edge detection for road lane," in The 8th Electrical Engineering/Electronics, Computer, Telecommunications and Information Technology (ECTI) Association of Thailand-Conference 2011, pp. 995– 998, IEEE, 2011.

[4] J. Redmon, S. Divvala, R. Girshick, and A. Farhadi, "You only look once: Unified, real-time object detection," in Proceedings of the IEEE conference on computer vision and pattern recognition, pp. 779–788, 2016.

[5] G. Jocher, A. Chaurasia, A. Stoken, J. Borovec, Y. Kwon, K. Michael, J. Fang, Z. Yifu, C. Wong, D. Montes, et al., "ultralytics/yolov5: v7. 0-yolov5 sota realtime instance segmentation," Zenodo, 2022.

[6] J. Kim and M. Lee, "Robust lane detection based on convolutional neural network and random sample consensus," in Neural Information Processing: 21st International Conference, ICONIP 2014, Kuching, Malaysia, November 3-6, 2014. Proceedings, Part I 21, pp. 454–461, Springer, 2014.

[7] Z. Wang, W. Ren, and Q. Qiu, "LaneNet: Real-time lane detection networks for autonomous driving," arXiv preprint arXiv:1807.01726, 2018.

[8] Y. Zhang, Z. Lu, D. Ma, J.-H. Xue, and Q. Liao, "Ripple-GAN: Lane line detection with ripple lane line detection network and wasserstein gan," IEEE Transactions on Intelligent Transportation Systems, vol. 22, no. 3, pp. 1532–1542, 2020.

[9] M. Manana, C. Tu, and P. A. Owolawi, "Preprocessed faster RCNN for vehicle detection," in 2018 International Conference on Intelligent and Innovative Computing Applications (ICONIC), pp. 1–4, IEEE, 2018.

[10] B. Liu, H. Liu, and J. Yuan, "Lane line detection based on mask R-CNN," in 3rd International Conference on Mechatronics Engineering and Information Technology 2019, pp. 696–699, Atlantis Press, 2019.

[11] Y. Kortli, S. Gabsi, L. F. L. Y. Voon, M. Jridi, M. Merzougui, and M. Atri, "Deep embedded hybrid CNN–LSTM network for lane detection on NVIDIA Jetson Xavier NX," Knowledge-based systems, vol. 240, p. 107941, 2022.

[12] T. Zheng, Y. Huang, Y. Liu, W. Tang, Z. Yang, D. Cai, and X. He, "CLR-Net: Cross layer refinement network for lane detection," in Proceedings of the IEEE/CVF conference on computer vision and pattern recognition, pp. 898–907, 2022.

[13] Y. Qian, J. M. Dolan, and M. Yang, "DLT-Net: Joint detection of drivable areas, lane lines, and traffic objects," IEEE Transactions on Intelligent Transportation Systems, vol. 21, no. 11, pp. 4670–4679, 2019.

[14] D. Wu, M.-W. Liao, W.-T. Zhang, X.-G. Wang, X. Bai, W.-Q. Cheng, and W.-Y. Liu, "YOLOP: You only look once for panoptic driving perception," Machine Intelligence Research, pp. 1–13, 2022.

[15] D. Vu, B. Ngo, and H. Phan, "Hybridnets: End-to-end perception network," arXiv preprint arXiv:2203.09035, 2022.

[16] J. Redmon and A. Farhadi, "YOLO9000: Better, faster, stronger," in Proceedings of the IEEE conference on computer vision and pattern recognition, pp. 7263–7271, 2017.

[17] J. Redmon and A. Farhadi, "YOLOv3: An incremental improvement," arXiv preprint arXiv:1804.02767, 2018.

[18] Z. Fang, D. Yin, J. Xiao, and R. Guo, "Special lane detection based on YOLOv3-SPP," in CAIBDA 2022; 2nd International Conference on Artificial Intelligence, Big Data and Algorithms, pp. 1–4, VDE, 2022.

[19] Y. Ding, W. Li, and Y. Zhu, "Lane line detection based on YOLOv4," in 2021 IEEE International Conference on Signal Processing, Communi- cations and Computing (ICSPCC), pp. 1–5, IEEE, 2021.

[20] C.-Y. Wang, A. Bochkovskiy, and H.-Y. M. Liao, "YOLOv7: Trainable bag-of-freebies sets new state-of-the-art for real-time object detectors," arXiv preprint arXiv:2207.02696, 2022.

[21] A. Geiger, P. Lenz, and R. Urtasun, "Are we ready for autonomous driving? The KITTI vision benchmark suite," in 2012 IEEE conference on computer vision and pattern recognition, pp. 3354–3361, IEEE, 2012.

Authorized licensed use limited to: DELHI TECHNICAL UNIV. Downloaded on July 03,2023 at 04:48:54 UTC from IEEE Xplore. Restrictions apply.

Natl. Acad. Sci. Lett.
https://doi.org/10.1007/s40009-023-01310-2

NEWS/VIEWS AND COMMENTS

Lexical Semantics Identification Using Fuzzy Centrality Measures and BERT Embedding

Minni Jain[1] · Rajni Jindal[1] · Amita Jain[2]

© The Author(s), under exclusive licence to The National Academy of Sciences, India 2023

Abstract Lexical semantics identification is finding the correct meaning of an ambiguous word in the text. In the literature, WordNet, as a graph, has been widely used for lexical semantic identification, where words are represented by nodes and relations between words are represented by edges connecting the nodes. Researchers have considered all the relations between the words present in WordNet equally important. In actual, all relations do not have equal importance in identifying the appropriate meaning of the words in the sentence. To provide the required importance to the relations for the first time, fuzzy graphs with BERT embedding are used for Lexical semantic identification. The intended sense of the word is identified using various fuzzy graph centrality measures. BERT embeddings and cosine similarity are used to provide the fuzzy weight to the edges. The proposed method outperforms existing state-of-the-art methods on standard datasets.

Keywords Word embeddings · Fuzzy graphs · WordNet · Lexical semantic identification · Fuzzy graph connectivity measures

✉ Amita Jain
amitajain@aiactr.ac.in

Minni Jain
minnijain@dtu.ac.in

Rajni Jindal
rajnijindal@dce.ac.in

[1] Department of Computer Science and Engineering, Delhi Technological University, New Delhi, Delhi, India

[2] Department of Computer Science and Engineering, Netaji Subhas University of Technology, East Delhi Campus, New Delhi, Delhi, India

Introduction

The term ‘apple’ means the fruit or the company depending upon the context of the sentence in which it is used. Resolving the problem of semantic ambiguity in the words of a given sentence is known as lexical semantic identification or word sense disambiguation (WSD) [1]. This problem is crucial because it is often one of the intermediate steps in information retrieval, question answering, machine translation and many other natural language processing applications. The manual process of sense tagging is a tedious task; therefore, there is a need to automate this process. In this work, the terms WSD and LSI are used interchangeably.

In the literature, LSI has been performed in three ways that are knowledge based, supervised and unsupervised [1]. Although knowledge-based and supervised techniques have performed better than unsupervised techniques, their need for a large amount of sense-tagged corpora makes them less desirable. Creation of these data is a labor-intensive and challenging task which is not required in unsupervised methods [2]. A popular unsupervised method is graph-based approaches, which use an existing knowledge base for disambiguation and do not require any labeled data. In past research work, authors applied centrality measures on a graph to extract the correct sense of ambiguous words and provided better accuracy than supervised techniques [3]. Although the existing graph-based solutions eliminate the need for a labeled dataset, they do not consider the fuzziness or degree of connectedness between the words in the graph.

To overcome the mentioned problems, we propose a fuzzy graph-based approach. The core idea behind the proposed method is to use a fuzzy membership function to provide weight to the edges of the graph. In natural language, there is a degree to which the words are related to each other [4]. It is, therefore, possible to find the degree of association between

Published online: 29 June 2023

the words. The higher the degree, the more related the words are to each other. This degree can be a mapping $W \times W \rightarrow [0,1]$, that is, by a fuzzy membership function (μ).

The novelty of the proposed work can be mentioned as this is the first work that exploits the idea of assigning weights to the edges of the fuzzy wordnet graph for lexical semantic identification (LSI) using deep learning. The proposed work used deep learning-based word embedding, i.e., Bidirectional Encoder Representations from Transformers (BERT) for LSI task for the first time. The correct sense is further identified using fuzzy measures of centrality.

In recent years, WSD has garnered a lot of interest from researchers. Supervised, semi-supervised as well as unsupervised methods have been explored in the past [5]. Supervised machine learning techniques, along with topic modeling, have been used for disambiguation [6]. One of the semi-supervised methods used label propagation, that is, it provides labels to the unlabeled sentences with the help of the similarity between them and the labeled sentences [7]. Certain unsupervised techniques use knowledge bases and are hence called knowledge-based methods [3, 8, 9].

Graph-based methods have recently gained a lot of popularity. They have been able to provide superior results without using any training data. An extension is the usage of fuzzy graphs [10, 11, 22]. It has been observed that they provide better results than traditional supervised WSD systems. In a work, experts have been asked to provide the membership value between two nodes [4].

Word embeddings have also been used along with supervised methods [12]. In our proposed method, we use BERT embeddings for allocating fuzzy weight. BERT [13] are contextual embeddings. It gives a unique embedding for each sense of a word and is therefore used to provide the weight using cosine similarity [14] between the embeddings.

Fuzzy centrality measures [11, 14] (fuzzy degree, fuzzy betweenness and fuzzy PageRank) have been used in this work.

Fuzzy Degree

Degree centrality in an undirected graph is the number of edges connected to a given node. In a fuzzy graph, it is described as follows [15]

$$\deg_f(i) = \sum_{u:(u,i)\in E} \mu_{ui} \tag{1}$$

In Eq. 1, μ_{ui} refers to the fuzzy weight of the edge between node u and node i.

Fuzzy Betweenness

Betweenness centrality refers to the fraction of the number of shortest paths that pass through a given node. Higher the betweenness, the more important that node is. In a fuzzy graph, it is given by [16]

$$\text{between}(i) = \frac{\rho_i(s,t)}{\rho(s,t)} \tag{2}$$

In Eq. 2, $\rho_i(s,t)$ depicts the number of shortest paths between nodes s and t that pass through the node i.

Fuzzy PageRank

Fuzzy PageRank takes into account the fact that not all links are equal. The number and quality of the links are used to find the relevance of a node [17]. In a fuzzy graph, it is given a

$$\text{PR}_f(i) = \frac{(1-d)}{|V|} + d \times \sum_{j:(j,i)\in E} \frac{\mu_{ji}}{\sum\limits_{k:(j,k)\in E} \mu_{jk}} \times \text{PR}_f(j) \tag{3}$$

In Eq. 3, d refers to the damping factor [18] whose value is taken as 0.85 and μ_{ji} is the fuzzy weight assigned to the edge between nodes j and i.

The following are the steps of the proposed algorithm:

1. Initially, sentence S is the input sentence. Next pre-processing is performed that includes stop words removal using NLTK, the rest of the words are POS-tagged, and only nouns and verbs are considered. These words are known as content words.
2. A fuzzy graph is then created using WordNet, which can be perceived as a graph. The *synsets* are the nodes, and the relations (e.g. *hyponym, holonym*) between them are the edges. All the senses of the content words are taken as the initial set of vertices. DFS (Depth First Search) is then performed on WordNet (all relations are considered) starting from one of these initial vertices till another sense of this same set is reached. Intermediate vertices and edges of this path are then added to the set of vertices and edges of the graph.
3. Fuzzy weight is then provided to the edges using pre-trained BERT embeddings. BERT provides different embedding for each sense of a word. WordNet provides an example sentence for each sense which is used to calculate the embedding. Cosine similarity between embeddings of the two nodes making up an edge is calculated and used as the fuzzy edge weight.

4. Fuzzy centrality measures are then used to calculate the correct senses (please refer algorithm 1).

For the illustration of the proposed method, the sentence "*She is drinking milk*" is taken, and after pre-processing, we have left with "*drink*" and "*milk*" as the content words. The term "drink" has a total of eleven senses in WordNet, while "milk" has seven senses. These act as the initial vertices. DFS is then performed on the WordNet graph, and the fuzzy weight for each edge is calculated using pre-trained BERT embeddings. Figure 1 shows the formed graph for the example sentence.

Fuzzy measures of centrality are then used to obtain the correct senses. It can be seen from calculation that fuzzy degree and fuzzy PageRank have the highest value for "*drink.v.1*" and "*milk.n.1*." The values of fuzzy betweenness came out to be 0.0 for all the senses of "*milk*" and "*drink*." Highest fuzzy degree for *drink.v.1* is 1.420 and for *milk.n.1* is 0.374. Fuzzy PageRank for *drink.v.1* is 0.1 and for *milk.n.1* is 0.041.

According to WordNet, the definition of "*milk.n.1*" is "*a white nutritious liquid secreted by mammals and used as food by human beings*." Similarly, the definition of "*drink.v.1*" is "*take in liquids*." Both these definitions align with the intended meaning of the sentence.

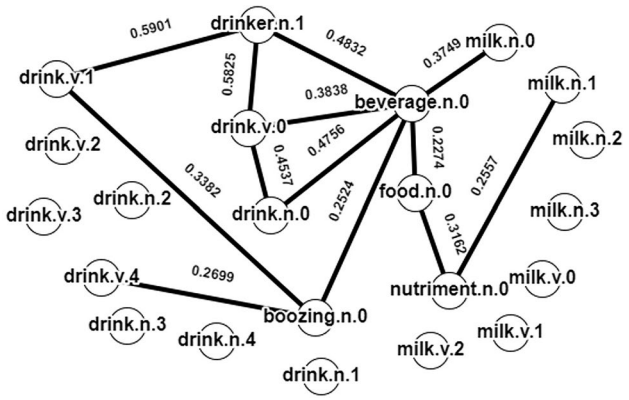

Fig. 1 Fuzzy graph of example sentence

SemCor and Senseval-3 are the two datasets that are used for evaluation [3, 4]. SemCor has been derived from the Brown corpus. It contains more than 2,00,000 content words which have been manually sensed tagged using WordNet sense. Senseval-3 [19] has been derived from the Penn Treebank corpus and consists of 2,018 content words annotated using WordNet senses. We compare our work with baseline models. The first baseline method, for each ambiguous content word, picks a sense randomly. Lesk's WSD model is another baseline method [8]. The next baseline method uses unweighted graphs and measures of centrality for disambiguating words [10]. Next is the comparison with the work, which is WSD using fuzzy semantic relations [10]. The proposed work also compared with the latest methods CEA [20] and SCSMM [21]. Both these approaches used crisp relations graph-based methods, whereas the proposed method fuzzified the network for more close analysis of the real world. The key player is measure of centrality for this method as it gave the best results. It has been observed that the first sense heuristic, that is, the sense for an ambiguous word with the highest frequency in SemCor, acts as an upper bound and unsupervised, as well as most supervised methods, as unable to outperform it [16].

Only words with more than one sense in WordNet are considered for disambiguation, that is, only polysemous words are considered. Table 1 depicts the precision (P), recall (R) and F-measure (F) values of the baseline models and the proposed method on the SemCor dataset. Table 1 depicts the results for Sensevel-3. Our method's performance is compared with the best semi-supervised and unsupervised systems for the same. Our method performs better than the best-unsupervised system (Sussex) and gives comparable results to the best semi-supervised method (IRST-DDD), which runs on an algorithm related to similarity. The fuzzy

Table 1 Results on datasets

SemCor dataset				Senseval-3 dataset			
Method	P	R	F	Method	P	R	F
Random	23.51	23.51	24.0	Lesk WSD [9]	44.05	32.91	37.67
Lesk WSD [9]	46.72	37.11	41.36	Unsupervised (Sussex)	47.80	41.26	44.28
Unweighted graph-based WSD (KPP) [12]	51.01	38.26	43.7	Semi-supervised (IRST-DDD)	55.36	42.95	43.11
WSD fuzzy semantic relations [10]	51.08	40.24	45.01	WSD Fuzzy semantic relations [10]	53.18	38.02	44.33
Proposed fuzzy degree	52.94	41.26	46.37	SCSMM [21]	56.2	41.4	47.7
Proposed fuzzy betweenness	52.63	37.32	43.64	CEA [20]	54.3	37.3	44.2
Proposed fuzzy PageRank	54.88	42.54	47.92	Proposed fuzzy degree	54.82	40.47	46.56
Proposed first sense	**72.45**	**69.37**	**70.87**	Proposed fuzzy betweenness	52.73	39.68	45.28
				Proposed fuzzy PageRank	**56.94**	**41.39**	**47.93**

Bold values signify the best results while comparing to other methods

PageRank measure of centrality gives the best results as it takes into account this fuzzy weight.

Fuzzy graphs consider membership functions to provide weight to the edges. In the proposed method, we consider cosine similarity between vectors provided by BERT embeddings.

It is found that the proposed fuzzy graph-based method, where the fuzzy weight is provided using BERT embeddings, incorporates the context of the word. Fuzzy centrality measures are further utilized for disambiguating the content word. The proposed work has been evaluated using SemCor and Senseval-3 datasets. It provides superior results than all the baseline models using SemCor dataset and the best-unsupervised system for Senseval-3. The proposed work shows that fuzzy PagerRank outperforms the other fuzzy measures of centrality. One limitation of the proposed method is the dependency on the WordNet for graph generation. Although with the help of WordNet, we are able to incorporate semantics in network, but still limited word sets and the absence of multi-words such as collocations, verbal phrases, idioms, etc. are its major constraints. In future work, this limitation may be mitigated by incorporating other knowledge bases for instance conceptNet. In the future, various other fuzzy measures of centralities can be tested for disambiguation. Also, other algorithms for generating embeddings can be used. Other applications, such as graph-based keyword extraction, text summarization etc., can also be explored using the proposed algorithm.

Algorithm 1: Lexical Semantic Identification using *BERT embeddings*

Input: Sentence $S = (s_1, s_2, s_3 \ldots\ldots s_n)$ where s_i are words in the sentence, $1 \leq i \leq n$

Step 1: Pre-process the sentence using the following steps

i. Remove stop words from S

ii. Remove words with pos tag other than *noun* and *verb*

$$S = (s_1, s_2, s_3 \ldots\ldots s_m)$$

where s_i is the content word left after pre-processing

Step 2: Create fuzzy graph $F = (V,E)$ where the set of vertices is represented by V the set of edges by E.

i. Initialise V by adding all the senses of the content words from WordNet

$$V = \bigcup_{i=1}^{m} (senses)$$

$$E = \phi$$

ii. For each node v in V perform the following steps

i. Take v as the starting node and perform DFS till level l (l is the limiting value and is usually between 5 and 8) or till a vertex $v`$ is reached where $v` \subset V$

ii. Add all the vertices in the formed path to V and edges between those to E

$$V = V \cup (v, v_1, v_2, \ldots\ldots v`)$$

$$E = E \cup ((v, v_1), (v_1, v_2) \ldots\ldots (v_i, v`))$$

iii. Provide each edge in E with a fuzzy weight using pre-trained BERT embeddings and examples of the two nodes from WordNet. Let M_i and M_j be the word embeddings for node i and node j of the graph

$$w_{ij} = cosine_similarity(M_i, M_j)$$

Step 3: Calculate the fuzzy measures of centrality using the equations 1 – 3

Step 4: For each content word the sense with the maximal value of a particular measure of centrality is taken as the correct sense

Acknowledgements The authors would like to thank Delhi Technological University, Delhi, for providing support and encouragement to proceed with the research.

Declarations

Conflict of interest The authors declare that they have no conflict of interest.

References

1. Pal AR, Saha D (2015) Word sense disambiguation: a survey. Int J Control Theory Comput Model (IJCTCM) 5(3):2
2. Yarowsky D (1995) Unsupervised word sense disambiguation rivaling supervised methods. In: 33rd annual meeting of the association for computational linguistics
3. Navigli R, Lapata M (2010) An Experimental study of graph connectivity for unsupervised word sense disambiguation. IEEE Trans Pattern Anal Mach Intell 3:678–692
4. Jain A, Lobiyal DK (2015) Fuzzy Hindi WordNet and word sense disambiguation using fuzzy graph connectivity measures. ACM Trans Asian Low-Resour Lang Inf Process 15:2
5. Miller G, Leacock C, Randee T, Bunker R (1993) A semantic concordance. In: Proceedings of third DARPA workshop human language technology, pp 303–308
6. Izquierdo R, Postma M, Vossen P (2015) Topic modeling and word sense disambiguation on the Ancora corpus. Proces Leng Nat 55:15–22
7. Yuan D, Richardson J, Doherty R, Evans C, Altendorf E (2016) Semi-supervised word sense disambiguation with neural models
8. Lesk M (1986) Automatic sense disambiguation using machine readable dictionaries: how to tell a pine cone from an ice cream cone. In: Proceedings of Fifth ACM SIGDOC, pp 24–26
9. Proceedings of COLING 2016, the 26th international conference on computational linguistics: technical papers, pp 1374–1385
10. Vij S, Jain A, Tayal DK, Castillo O (2018) Fuzzy logic for inculcating significance of semantic relations in word sense disambiguation using a WordNet graph. Int J Fuzzy Syst 20(2):444–459
11. Jain M, Bhalla G, Jain A, Sharma S (2022) Automatic keyword extraction for localized tweets using fuzzy graph connectivity measures. Multim Tools Appl 81:1–26
12. Abdalgader K, Al Shibli A (2021) Context expansion approach for graph-based word sense disambiguation. Expert Syst Appl 168:114313
13. Raganato A, Camacho-Collados J, Navigli R (2017) Word sense disambiguation: a unified evaluation framework and empirical comparison. In: Proceedings of the 15th conference of the European chapter of the association for computational linguistics, vol 1, Valencia, Spain, April 2017. Association for Computational Linguistic, Vancouver, pp 99–110
14. Devlin J, Chang MW, Lee K, Toutanova K (2019) BERT: pre-training of deep bidirectional transformers for language understanding. arXiv:1810.04805
15. Zedeh LA, Fu KS, Shimura M (1975) Fuzzy relations, fuzzy graphs, and their applications to clustering analysis. In: Fuzzy sets and their application to cognitive and decision processes. Academic Press, New York, p 125
16. McCarthy D, Koeling R, Weeds J, Carroll J (2004) Finding predominant senses in untagged text. In: Proceedings of 42nd annual meeting association for computational linguistics, pp 280–287
17. Freeman LC, Boragatti SP, White DR (1991) Centrality in valued graph: A measure of betweenness based on network flow. Soc Netw 13:141–154
18. Becchetti L, Carlos C (2006) The distribution of PageRank follows a power-law only for particular values of the damping factor. In: Proceedings of the 15th international conference on World Wide Web, pp 941–942
19. Snyder B, Palmer M (2004) The English all-words task. In: Proceedings of Senseval-3 Workshop, pp 41–43
20. Tsatsaronis G, Vazirgiannis M, Androutsopoulos I (2007) Word sense disambigu-ation with spreading activation networks generated from thesauri. IJCAI Int Jt Conf Artif Intell 41(2):1725–1730
21. Badaoui FE, Boulmakoul A, Lbath A, Thami ROH, Cherradi G, Karim L, Bouziri AE (2022) Fuzzy centrality measures: a survey. In: International conference on intelligent and fuzzy systems. Springer, pp 646–654
22. AlMousa M, Benlamri R, Khoury R (2022) A novel word sense disambiguation approach using WordNet knowledge graph. Comput Speech Lang 74:101337

Publisher's Note Springer Nature remains neutral with regard to jurisdictional claims in published maps and institutional affiliations.

Lightweight and Reliable Deep Learning Model for Plant Disease Detection

Shailender Kumar
Dept. of Computer Science & Engg.
Delhi Technological University Delhi, India
shailenderkumar@dce.ac.in

Garvit Kansal
Dept. of Computer Science & Engg.
Delhi Technological University Delhi, India
helewrer3@gmail.com

Jatin Pandey
Dept. of Computer Science & Engg.
Delhi Technological University Delhi, India
jatinpandey02@gmail.com

Harmeet Singh
Dept. of Computer Science & Engg.
Delhi Technological University Delhi, India
harmeetsingh_2k19co146@dtu.ac.in

2023 Third International Conference on Secure Cyber Computing and Communication (ICSCCC) | 979-8-3503-0071-0/23/$31.00 ©2023 IEEE | DOI: 10.1109/ICSCCC58608.2023.10176369

***Abstract*—With the continued penetration of smartphones among the current populace, tasks that were previously assigned to humans can now be done by our mobile devices with better efficiency. One such use case is found in the field of agriculture, from simple tasks like transferring farming news to meticulous ones like reading soil moisture, smartphones are on a clear path to becoming indispensable companions to our farmers. Contributing to nearly 20% of India's GDP (as of 2021), agriculture and its allied activities remain a relevant and powerful area of research, one such research is on the application of smartphones in the detection of crop plant diseases. One of the largest challenges faced by the agricultural industry is that of the onslaught ofplant diseases and pests, It has been estimated that around 30- 40% of global crop production is lost due to disease and pest attacks, so, rapid identification of crop diseases still remains a prevalent task in many parts of the world.**

With the advent of better and more efficient machine learning architectures, we are now ever so closer to the future of mobile crop disease diagnosis. Although, due to the limited processing powers of smartphones, especially in the budget category, image classification via more demanding, yet accurate deep learning models still seems to be impractical. In this paper, we research and propose the use of the EfficientNet family of deep learning models for the task of detecting crop plant diseases in a mobile setting, receiving an all-time high accuracy of 98.64% with significantly fewer model parameters than the other currently available deep learning models, we believe we are on a clearpath towards a more practical mobile crop disease diagnosis.

***Index Terms*—EfficientNet, smartphone, agriculture, disease, classification, deep-learning**

I. Introduction

The modern agriculture industry is plagued by several challenges more so than ever now. A. Sridhar, A. Balakrishnan, M. M. Jacob, M. Sillanpää, and N. Dayanandan [1] mentions that post covid, not only did the overall agricultural production in south-east Asia decrease by 3.11% (around 17 million in tons) but the demand for staple food crops saw an increase of over 150%. T. N. Liliane and M. S. Charles [2] mark factors such as climate change, natural resources depletion, pests, etc to be acting as barriers to global crop production. Suffice it to say a more efficient crop production procedure is a powerful and popular area of research.

Crop disease and pest attacks, however, continue to be the major roadblock faced by our farmers to this day, making a large hindrance to the constantly increased demand for agricultural produce. Traditionally, farmers especially those in India have been using the simple method of visual examination based on their past experience to search for the signs of any plant pathogens, this, however, is only possible after substantial damage has been done to the crop and moreoverthe result of such examination is dependent on a lot of factors both internal and external, like - stress, experience, health,age, etc., thus, these rudimentary perceptual measures have varying accuracy and might lead to wrong or undesirable results in certain situations. Ur Rehman, Fazal & Naz, Nageen& Kalsoom, Maria [3] records that plant diseases and pests account for about 20 to 40 percent of losses to global food production every year. Thus, one can see both the need andthe benefit of having a more objective, efficient system of crop disease diagnosis without all the factors and problems that are brought in by bringing a human touch.

There are several ways to the prediction of diseases in plants. A.-K. Mahlein [4] mentions how optical techniques, such as RGB imaging, thermography, 3D scanning, hyperspectral sensors, etc can be used for detecting diseases in plants. Y. Fang and R. Ramasamy [5] provides an analysis of the more laboratory-oriented techniques such as enzyme-linked immunosorbent assay, gas chromatography-mass spectrometry, fluorescence in-situ hybridization, etc among other such direct disease detection approaches. Despite their accuracyand validity, these methods are not feasible or practical for your common farmer due to the requirement of very specific hardware and environment. In situations like these, a more readily available, cost-effective, portable, and easy-to-use plant disease-detecting apparatus is the ideal choice. Liu and X. Wang [6] provides a review of the practical challenges faced by applying the current research on deep learning for detecting

Authorized licensed use limited to: DELHI TECHNICAL UNIV. Downloaded on July 20,2023 at 11:07:54 UTC from IEEE Xplore. Restrictions apply.

plant diseases and pests.

M. Halpern, Y. Zhu, and V. J. Reddi [7] documents the journey of mobile processors and how our smartphones have been seeing improvement in their processing power year after year. This, along with the continual spread of smartphones into even the remotest of lands thanks to the drop in prices makes them a very practical and ideal apparatus for detecting plant disease.

As for the technique, we propose to use deep learning to create a model that detects the disease a crop plant might be suffering from by looking at its leaf image. The last decade has seen a revolution in deep learning with massive improvements in performance and utilities. C. A. Dhawale, K. Dhawale, and R. Dubey [8] reviews how deep learning models are being used in linguistic models, audio infrastructures, and several more. The ability to have several thousand (maybe millions) of nodes all interconnected with each other, allow deep learning models today to do tasks previously thought only possible by the human brain. Deep learning models contain several nodes in several layers. The input layer takes the necessary inputs and then passes them through several layers of processing, each layer allowing it to extract information that helps in the task of that particular model be it regression or classification.

For training our models, we have made use of the excellent PlantVillage dataset from Project PlantVillage (our ”Previous Work” section goes into more detail about this dataset).

Detecting a result from images of crop plants or rather from any image in general calls for the task of image classification. For this task, we have decided to make use of convolutional neural networks. CNNs or Convolutional Neural Networks use a combination of convolutional layers along with several other techniques such as max pooling, etc, to work on image data providing much better results than a conventional deep learning model using way less number of computational nodes. A. Khan, A. Sohail, U. Zahoora, and A. S. Qureshi [9] provides a review of the path of evolution CNN has gone through in the last decade thanks to architectural innovations achieved by multi-path information processing, exploitation of spatial and channel information, etc resulting in the introduction of a number of family of models such as YOLO, Resnet, Alexnet to name a few. Similarly, one such family of models was introduced in 2019 by the name of EfficientNet.

EfficientNet (described in more detail later on) has the big advantage of using comparatively less amount of model parameters from its more contemporary deep learning models such as ResNet, VGC, etc. Making it ideal to be used in a mobile environment where the lack of processing power becomes quite apparent.

Being a relatively new model, EfficientNet has yet to have holistic research done on it for the prospects of crop plant disease detection.

For the methodology of our research, we ran the sub-variants of the EfficientNet model, b0-b6, across both the colored and leaf-segmented variants of the PlantVillage dataset for 20 epochs each. Totaling 14 experiments across 7 deep learning models. In the end, the measurement of performance for each experiment was marked and tabulated.

As a proof of concept, we have also developed an android app, Agro App, that, among other operations, provides a crop disease detection tool using the EfficientNet-b0 model. More about this application, its salient features, and differences from similar existing apps have been explained, in greater detail later on.

II. Previous Works

Over the past few years, research on the usage of machine learning and artificial intelligence in the field of agriculture has been on the rise, much effort has been done to attempt to bring about a positive change in quality and quantity in the end product of the traditional agricultural process by augmenting it with the cutting edge in technology. N. Yadav, S. M. Alfayeed, and A. Wadhawan [10] mentions amongst other things, the possible applications of machine learning in the field of agriculture and divides it neatly into 4 managerial roles - species management, field conditions management,crop management, and livestock management.

J. Dean, D. Patterson, and C. Young [11] records that the rate of publishing of machine learning papers has been doubling every two years to the point that more than 50 papers related to machine learning appear on arXiv alone every day.

L. Benos, A. C. Tagarakis, G. Dolias, R. Berruto, D. Kateris, and D. Bochtis [12] observes that the number of publications focusing on machine learning in the field of research papers in 2020 has increased by around 164% since 2018 i.e. 180 papers in 2020 to some 69 in 2018, 19% of these 180 papers were in the line of crop disease prediction.

With the gaining experience in image classification techniques over the years, the usage of machine learning to accurately predict the disease a particular crop is suffering from has been gaining momentum, in this regard several machine learning models and even more importantly, datasets have come up recently. Machine learning is governed by the process of induction wherein formal rules are made out of a series of observations, the rules formed out of these observations are then tested for their accuracy and subsequent validity. To facilitate such observations a quality training dataset is needed, several factors go into determining the quality and validity of a dataset, two key factors being - the high number of samples within the dataset, and the technical validity of the labels associated with these samples done with the process of peer-reviewing. The model trained on this dataset is then tested by passing it through a subset of data that it hasn’t been trained on, called the test dataset and is usually a certain percentageof the training dataset set aside for the process of testing.

Correlating to this, D. P. Hughes and M. Salathe [13] proposes PlantVillage, a crowdsourced, pathologically verified image dataset of leaves of infectious crop plants in an attemptto enable mobile disease diagnosis of the possible infected plants allowing crop growers to increase their agriculturalproduce. The dataset contains over 54,000 images spanning 26diseases across 14 crop species as of April 2016. Since 2019, over 45 open-access research papers have been published directly mentioning this dataset for image-based plant disease

Authorized licensed use limited to: DELHI TECHNICAL UNIV. Downloaded on July 20,2023 at 11:07:54 UTC from IEEE Xplore. Restrictions apply.

prediction.

Over the past few years, many deep learning publications have come up making use of PlantVillage for the classification of plant diseases.

J. P. Schwarz Schuler, S. Romani, M. Abdel-Nasser, H. Rashwan, and D. Puig [14] makes use of a modified Inception V3 architecture by infusing one branch for the L channel and the other for the AB channel, resulting in an accuracy of 99.48% on the PlantVillage dataset, this was done by feeding the 2-branch DCNN with CIE Lab color coordinates instead of RGB coordinates.

S. Ahmed, Md. B. Hasan, T. Ahmed, Md. R. K. Sony, and Md. H. Kabir [15] proposes a pre-trained lightweight MobileNet V2 architecture based on the transfer learning approach to detect diseases from tomato leaves. Utilizing an effective pre-processing method for enhancing leaf images with illumination correction they were able to achieve an accuracy of around 99.30% accuracy.

S. Osouli, B. B. Haghighi, and E. Sadrossadat [16] makes use of a combination of pre-trained MobileNet V2 and Inception architecture to detect disease specifically for the Maize plant with the help of the transfer learning approach and achieves an accuracy of 97% for its endeavors.

J. G. M. Esgario, R. A. Krohling, and J. A. Ventura [17] utilizes Resnet50 architecture in order to classify and estimate the stress caused due to the usage of biotic agents on coffee leaves, based on CNN, its proposed multi-task system results in an accuracy of 95.24% for classification and 86.51% for estimation of severity.

S. P. Mohanty, D. P. Hughes, and M. Salathe [18] provides a holistic view of the usage of various deep learning architectures for the purposes of image-based plant disease detection. It primarily compares two of the most popular deep learning architecture of the time, AlexNet and GoogleNet under various circumstances. It measures and compares the accuracy achieved by the aforementioned deep learning architectures by changing variables such as training mechanisms, type of dataset samples, and training-test set distribution. Overall, 60 experiments were run across both architectures for 30 epochs each (an epoch referring to a single pass-through of the neural network across the training dataset), achieving a top accuracy of 99.35% among all the experiments. Another point of interest was raised, although the training of the model takes multiple hours, the classification was in itself just a matter of a few seconds. Resulting in the possibility of a mobile crop disease diagnosis at a global scale.

Although feasible, multiple improvements can still be brought before we start utilizing deep learning models on a massive global scale. Chief among these being the computational requirements of the deep learning model itself. Traditional deep learning models make use of a large number of model parameters to facilitate image classification, for example, ResNeXt-101 has over 80 million trainable parameters, leading to high CPU cost during image classification making them unfit for a smartphone-assisted environment.

To combat this, we propose the use of EfficientNet architecture. M. Tan and Q. V. Le [19] introduce a new state-of-the- art CNN architecture that scales the dimensions of height, width, and resolution uniformly using a fixed set of scaling coefficients. The architecture has been recorded to achieve top-1 accuracy on ImageNet while still being over 8 times smaller than GPipe. Overall, EfficientNet has been shown to significantly outperform other CNNs while utilizing less number of model parameters by a wide margin.

Being a new deep learning architecture, research on Efficient-Net has been quite lacking when compared to more established models like ResNet, etc. As such only a handful have been used in the prospect of crop plant disease prediction. A. Bruno et al. [20] provides a cursory glance at the usage of EfficientNet architecture for crop disease prediction, however, it mainly focuses on the EfficientNet-b0 model variant of the architecture. Certainly, more holistic research is required for understanding the full potential of this architecture.

III. Agro App

To test out our research and check the feasibility of using EfficientNet for mobile crop plant disease detection, we created an android application made within the Flutter framework, named ”Agro App”, this app was created as a one-stop companion for the farmers of our country with variegated functionalities to help them become a more efficient version of themselves. Some of the salient features of this app are - crop disease prediction, providing a buyer and seller’s marketplace, showing live and forecasted weather, and providing the latest in farming-related news. More of these will be explained later in this section.

Over the past few years, Android has come to dominate the global smartphone market share, especially in the budget segment. F. Laricchia [21] calculates that globally, Android has a total market cap of over 71% in the smartphone operating system industry. Making this the ideal operating system of choice to build our application on, allowing us to test it on a wider variety of hardware specifications.

Despite this, as an attempt to future-proof our application, we have developed it using the Flutter framework. S. A. Bhagat [22] provides a review of the benefits of developing apps using Flutter, among other reasons, Flutter allows for the production of cross-platform code, i.e. using the same codebase, the product can be easily ported over to different hardware and systems. Currently, Flutter supports both the iOS and Android operating systems, with active development on support for web and desktop platforms as well. This allows us to write an iOS application in the possible future with relative ease.

A. Google Login and Signup

For authentication and authorization, we use the Auth0 API. It provides us with a callback-login method i.e. whenever the login request is received from our app, it opens up a login portal with the issued URI in our account. Once logged in,it sends us a callback response with the required data of the user (name, avatar, etc.) bundled into a JSON file.

Authorized licensed use limited to: DELHI TECHNICAL UNIV. Downloaded on July 20,2023 at 11:07:54 UTC from IEEE Xplore. Restrictions apply.

B. Aggregating Farming-related News

For obtaining news, we make use of the NewsCatcher API, which sources over 60,000 new sources covering various languages, regions, etc. To filter news of a particular topic/term, it uses NLP to process the text inside the news articles and index them based on the keywords which are then used as a search query by the end user ("agriculture" in our case). These News articles are presented in their clickable news-boxes, upon which the user is taken to the actual source of the news.

C. Live Weather Forecast

For obtaining weather details, we use OpenWeather API, to whose request we feed in the user's current latitudinal and longitudinal values, and in return, it provides us with the weather details of the location about the coordinates sent.

D. Marketplace

Allowing users to sell and buy products on a marketplace provided within the application. Sellers will be able to upload descriptions and prices of their products on the marketplace. Buyers, if interested, can contact the seller through the marketplace by accessing their mobile numbers. This was done as an attempt to provide total control and freedom over the 2 parties if they wished to continue the transaction.

E. Plant Disease Detection

The user has the option to either click from the camera or upload from the gallery, a leaf photo of the infected plant they want to check. Due to the small size of the Efficient-b0 model (at most 5MB) and low CPU usage during image classification, it allows us to bundle it with the app and just run it locally on the smartphone. This allows the user to run their app and detect plant diseases without the need for the internet and hence make it viable in even the remotest of places.

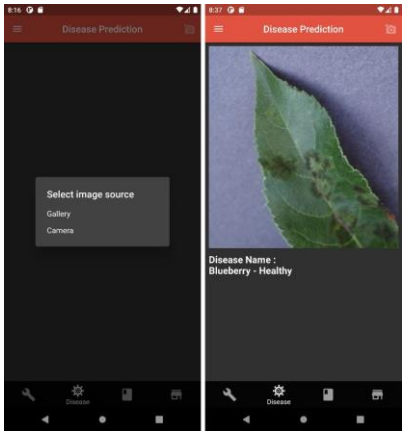

Fig. 1. App showcasing the detected disease of the leaf image provided by the user.

IV. Methodology of Research

A. Dataset

We used the publicly available plant disease dataset provided by Project PlantVillage. It has 54,306 images. These images are of 14 different crops which then contain 26 diseases. In total for all plant diseases and healthy plant classes, we have a total of 38 classes. As for the resolutionof the images, for different models of the EfficientNet family, different resolutions are recommended and are hence different for training each model. We use two different versions ofthe dataset for training on all the EfficientNet models thatare as it is and segmented. In the segmented dataset, onlythe leaf is kept in focus while the rest of the background is removed. This also gives us better confidence in our results across the board that our models have understood the problem of identifying plant diseases at least to a broader extent and not just performing on inherent biases.

TABLE I
Image resolution used by various models Efficient family of models

EfficientNet Model	Image Resolution
Efficient-b0	224
Efficient-b1	240
Efficient-b2	260
Efficient-b3	300
Efficient-b4	380
Efficient-b5	456
Efficient-b6	528

B. Training

For the training and validation of the models, all datasets are split in the ratio of 80%-20%(80% for training and 20% for validation). This split gives all models a balanced split to sufficiently train and understand the problem at hand and also leaves enough data points to check the performance of these models on the unseen dataset. All models are then trained on the training dataset for 20 epochs. 20 epochs give us information about training accuracy and loss and validation accuracy and loss so that we can come to firm conclusions about the models' performance. We consider the accuracy of the models to compare the performance of these models.

V. EfficientNet

While considering which model architectures to choose for our paper, we had several considerations to take. Herethe problem was not to simply take the best and maybe the largest model architecture to train upon and hope for the best results. While having almost perfect accuracy is a goal forus we also need to consider that this model will hopefullybe then implemented in mobile applications to be used by actual farmers. With the understanding that most farmers do not carry with them the most computationally powerful mobiles of the time, we need to make sure that the modelwe choose is able to deliver the best performance whilst also being lightweight and computationally less expensive.

Authorized licensed use limited to: DELHI TECHNICAL UNIV. Downloaded on July 20,2023 at 11:07:54 UTC from IEEE Xplore. Restrictions apply.

For this, we make use of the EfficientNet family of models. Introduced in 2019, Efficientnet Models were developed as a result of improving the performance of models but without necessarily increasing the size of these models. M. Tan and Q. V. Le [19] showed scaling techniques that were able to achieve significantly better results than a lot of conventional CNN models like ResNet-50, and Inception-v3 whilst using several times less amount of parameters in the models.
This makes EfficientNet a very viable choice for our research as it shows promising results whilst using very few resources on the system being used. This is ideal for our research as we wish to make models which can then be used on computationally less powerful handheld devices.

VI. Results

Throughout all the experimental configurations, for both the segmented and color versions of the PlantVillage dataset, the overall accuracy range varied from 97.33% (EfficientNet-b4, Segmented) to 98.64% (EfficientNet-b5, Color), showing strong potential for using EfficientNet family of deep learning models for use in mobile plant disease diagnosis. All the experiments were run for 20 epochs each, and the average of validation accuracy in the last 3 epochs for each experiment was considered as the resultant accuracy.

In the Segmented dataset, it was seen that EfficientNet-b4 performed the worst with an accuracy of 97.33% and EfficientNet-b5 performed the best with an accuracy of 98.05%. For the color version, EfficientNet-b1 (accuracy 98.16%) and EfficientNet-b5 (accuracy 98.64%) performed the worst and best respectively.

It can be seen that out of the two versions of the dataset, a noticeable difference in accuracy is present when all other experimentation variables are kept constant. The segmented version of the dataset was chosen to investigate the variance in accuracy caused by the presence of a background in the image. We had thought that the absence of background would lead to better accuracy, however, unexpectedly the color version of the dataset outperformed in every single experiment. In both cases, EfficientNet-b5 was recorded to have the best accuracy among all the other models in the respective dataset version.

TABLE II
Accuracy and loss across the experiments conducted on the color version of dataset

EfficientNet Model	Color Accuracy	Color Loss
Efficient-b0	0.9829	0.0485
Efficient-b1	0.9816	0.0552
Efficient-b2	0.9818	0.0534
Efficient-b3	0.9835	0.0503
Efficient-b4	0.9831	0.0558
Efficient-b5	0.9864	0.0443
Efficient-b6	0.9863	0.0447

TABLE III
Accuracy and loss across the experiments conducted on the segmented version of dataset

EfficientNet Model	Segmented Accuracy	Segmented Loss
Efficient-b0	0.9767	0.0767
Efficient-b1	0.9772	0.0750
Efficient-b2	0.9756	0.0756
Efficient-b3	0.9755	0.0775
Efficient-b4	0.9733	0.0819
Efficient-b5	0.9805	0.0675
Efficient-b6	0.9752	0.0775

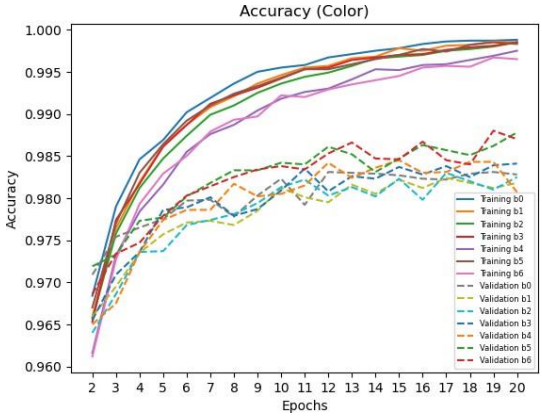

Fig. 2. Training and validation accuracy of the models as per the color version of the dataset.

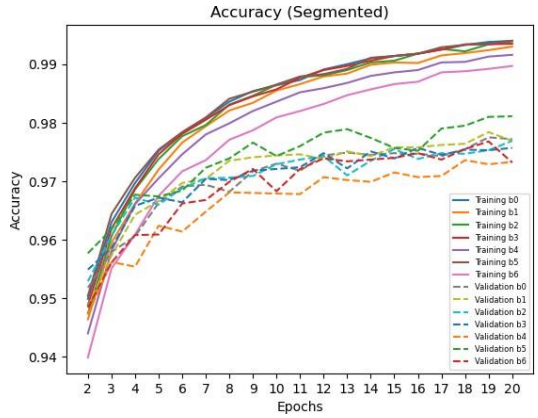

Fig. 3. Training and validation accuracy of the models as per the segmented version of the dataset.

VII. Conclusion

With the impressive progress of deep learning techniques in the last two decades, it was natural that it was also used to improve the efficiency and output of agriculture. With models being introduced larger and more complex with the ability to understand more difficult problems we wanted a model which while solving our problem of automating disease detection in crops, we also wanted it to be able to do so with the minimal resources required.

Even though the access to smartphones only increases day by day reaching more people, and hence farmers. There is still the

Authorized licensed use limited to: DELHI TECHNICAL UNIV. Downloaded on July 20,2023 at 11:07:54 UTC from IEEE Xplore. Restrictions apply.

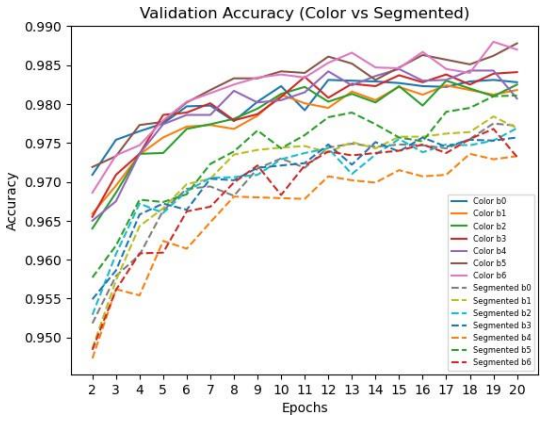

Fig. 4. Validation accuracy of the models across both the versions of the dataset

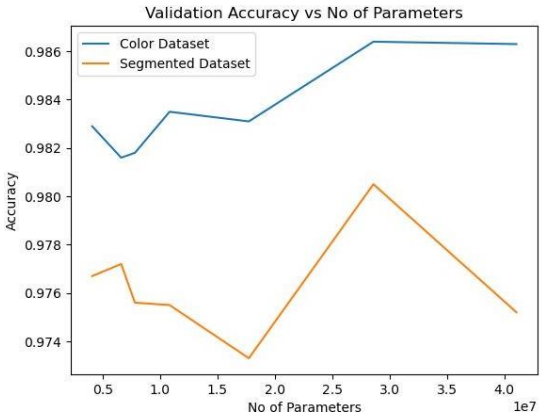

Fig. 5. Color validation accuracy in comparison with the number of trainable model parameters

constraint that not all these farmers are going to have access to top-end computationally powerful mobile phones. Therefore in our approach to this problem, we wanted our models to give the most accurate results but also make sure that they were minimal on resource demands. Naturally, this is a balancing act where we need to consider a lot of factors and test out several different models to first obtain the performance vs resource factor of all these models, and then make the decisionon which model to use in whatever particular environmentit is needed. Keeping this in mind we tested the models ofthe EfficientNet family (EfficientNetB0, EfficientNetB1,. ,
EfficientNetb6). These models introduced in 2019 had previously shown promising performance in comparison to other famous models whilst using significantly fewer resources. We saw EfficientNetB5 give the most accurate results but the rest of the models also performed very closely.

This problem can be further expanded upon by using different sets of models and using more robust datasets. Right now these models are only based on the 38 classes provided by the dataset. Another factor is that most of these images are taken under almost perfect conditions which is not the case during their actual use. This is expected to significantly hamper the accuracy of these models. With the availability of better data with more crops and more realistic image samples, further work can be done to make even more robust models. But still the results of our research point to the fact that deep learning can be used to assist farmers in disease detection while makingthe process less computationally expensive.

ACKNOWLEDGMENT

Firstly, we would like to thank Dr. Vinod Kumar (HOD, Dept. of Computer Science & Engg., DTU) and all the other staff members, and faculty of the department for their guidance and constant motivation and support for this work. Above all, we owe much of our gratitude to our supervisor and mentor, Prof. Shailender Kumar (Prof., Dept. of Computer Science & Engg., DTU) for constantly providing us with the motivation and zeal to tackle our project while simultaneously guiding us for the same whenever we needed it, without him we would not have been able to take on this endeavor.

REFERENCES

[1] A. Sridhar, A. Balakrishnan, M. M. Jacob, M. Sillanpää, and N. Dayanandan, “Global impact of COVID-19 on agriculture: role of sustainable agriculture and digital farming,” Environmental Science and Pollution Research, Mar. 2022, doi: 10.1007/s11356-022-19358-w.

[2] T. N. Liliane and M. S. Charles, “Factors Affecting Yield of Crops,” Agronomy - Climate Change & Food Security, Jul. 2020, doi: 10.5772/intechopen.90672.

[3] Ur Rehman, Fazal & Naz, Nageen & Kalsoom, Maria, “Plant Diseases and Food Security: An Overview,” Agrospheres: e-Newsletter, Jan. 2021, doi: 10.13140/RG.2.2.35480.52487.

[4] A.-K. Mahlein, “Plant Disease Detection by Imaging Sensors – Parallels and Specific Demands for Precision Agriculture and Plant Phenotyping,” Plant Disease, vol. 100, no. 2, pp. 241–251, Feb. 2016, doi: 10.1094/pdis-03-15-0340-fe.

[5] Y. Fang and R. Ramasamy, “Current and Prospective Methods for Plant Disease Detection,” Biosensors, vol. 5, no. 3, pp. 537–561, Aug. 2015, doi: 10.3390/bios5030537.

[6] J. Liu and X. Wang, “Plant diseases and pests detection based on deep learning: a review,” Plant Methods, vol. 17, no. 1, Feb. 2021, doi: 10.1186/s13007-021-00722-9.

[7] M. Halpern, Y. Zhu, and V. J. Reddi, “Mobile CPU’s rise to power: Quantifying the impact of generational mobile CPU design trends on performance, energy, and user satisfaction,” IEEE Xplore, Mar. 01, 2016. https://ieeexplore.ieee.org/document/7446054 (accessed Mar. 28, 2021).

[8] C. A. Dhawale, K. Dhawale, and R. Dubey, “A Review on Deep Learning Applications,” Advances in Systems Analysis, Software Engineering, and High Performance Computing, pp. 21–31, 2020, doi: 10.4018/978- 1-7998-1192-3.ch002.

[9] A. Khan, A. Sohail, U. Zahoora, and A. S. Qureshi, “A survey of the recent architectures of deep convolutional neural networks,” Artificial Intelligence Review, Apr. 2020, doi: 10.1007/s10462-020-09825-6.

[10] N. Yadav, S. M. Alfayeed, and A. Wadhawan, “MACHINE LEARNING IN AGRICULTURE: TECHNIQUES AND APPLICATIONS,” International Journal of Engineering Applied Sciences and Technology, vol. 5, no. 7, pp. 118–122, Nov. 2020, doi: 10.33564/ijeast.2020.v05i07.018.

[11] J. Dean, D. Patterson, and C. Young, “A New Golden Age in Computer Architecture: Empowering the Machine-Learning Revolu- tion,” IEEE Micro, vol. 38, no. 2, pp. 21–29, Mar. 2018, doi: 10.1109/mm.2018.112130030.

[12] L. Benos, A. C. Tagarakis, G. Dolias, R. Berruto, D. Kateris, and D. Bochtis, “Machine Learning in Agriculture: A Comprehensive Updated Review,” Sensors, vol. 21, no. 11, p. 3758, Jan. 2021, doi: 10.3390/s21113758.

Authorized licensed use limited to: DELHI TECHNICAL UNIV. Downloaded on July 20,2023 at 11:07:54 UTC from IEEE Xplore. Restrictions apply.

[13] D. P. Hughes and M. Salathe, “An open access repository of im- ages on plant health to enable the development of mobile disease diagnostics,” arXiv:1511.08060 [cs], Apr. 2016, [Online]. Available: https://arxiv.org/abs/1511.08060
[14] J. P. Schwarz Schuler, S. Romani, M. Abdel-Nasser, H. Rashwan, and D. Puig, “Color-Aware Two-Branch DCNN for Efficient Plant Disease Classification,” MENDEL, vol. 28, no. 1, pp. 55–62, Jun. 2022, doi: 10.13164/mendel.2022.1.055.
[15] S. Ahmed, Md. B. Hasan, T. Ahmed, Md. R. K. Sony, and Md. H. Kabir, “Less is More: Lighter and Faster Deep Neural Architecture for Tomato Leaf Disease Classification,” IEEE Access, pp. 1–1, 2022, doi: 10.1109/access.2022.3187203.
[16] S. Osouli, B. B. Haghighi, and E. Sadrossadat, “An EffectiveScheme for Maize Disease Recognition based on Deep Networks,” arXiv:2205.04234 [cs], May 2022, Accessed: Jan. 31, 2023. [Online]. Available: https://arxiv.org/abs/2205.04234v1
[17] J. G. M. Esgario, R. A. Krohling, and J. A. Ventura, “Deep learning for classification and severity estimation of coffee leaf biotic stress,” Computers and Electronics in Agriculture, vol. 169, p. 105162, Feb. 2020, doi: 10.1016/j.compag.2019.105162.
[18] S. P. Mohanty, D. P. Hughes, and M. Salathé, “Using Deep Learning for Image-Based Plant Disease Detection,” Frontiers in Plant Science, vol. 7, Sep. 2016, doi: 10.3389/fpls.2016.01419.
[19] M. Tan and Q. Le, ‘Efficientnet: Rethinking model scaling for convolutional neural networks’, in International conference on machine learning, 2019, pp. 6105–6114.
[20] A. Bruno et al., “Improving plant disease classification by adaptive minimal ensembling,” Frontiers in Artificial Intelligence, vol. 5, Sep. 2022, doi: 10.3389/frai.2022.868926.
[21] F. Laricchia, “Mobile OS market share 2019 — Statista,” Statista, Jun. 29, 2019. https://www.statista.com/statistics/272698/global-market-share-held-by-mobile-operating-systems-since-2009/
[22] N. Ahmad and S. Singh, "Comparative Study of Disease Detection in Plants using Machine Learning and Deep Learning," in 2021 2nd International Conference on Secure Cyber Computing and Communications (ICSCCC), pp. 54-59, 2021.
[23] S. A. Bhagat, “Review on Mobile Application Development Based on Flutter Platform,” International Journal for Research in Applied Science and Engineering Technology, vol. 10, no. 1, pp. 803–809, Jan. 2022, doi: 10.22214/ijraset.2022.39920.

Authorized licensed use limited to: DELHI TECHNICAL UNIV. Downloaded on July 20,2023 at 11:07:54 UTC from IEEE Xplore. Restrictions apply.

2023 3rd International Conference on Advance Computing and Innovative Technologies in Engineering (ICACITE) | 979-8-3503-9926-4/23/$31.00 ©2023 IEEE | DOI: 10.1109/ICACITE57410.2023.10183190

Linarin as an Anti-Cancer Therapeutic: In-Silico and Machine Learning Approach for HPV

Rati Bhardwaj
Department of Biotechnology
Delhi Technological University
New Delhi, India
bhardwajrati9412@gmail.com

Ananya
Department of Biotechnology
Delhi Technological University
New Delhi, India
ananya.pal1000@gmail.com

Dr. Asmita Das
Department of Biotechnology
Delhi Technological University
New Delhi, India
asmitadas1710@dce.ac.in

Abstract - Human Papillomavirus (HPV) is one of the principal causes of death among females in emerging nations. It is a sexually transmitted virus that shatters the cell cycle by two of its oncoproteins i.e., E6 and E7. HPV E7 oncoprotein binds to the pRb (Retinoblastoma tumor suppressor gene). This binding hinders the association of pRb with E2F causing the release of transcription factor E2F, vital for the cell cycle to proceed for the S phase thus causing abnormal unregulated cell division and growth. Precautionary HPV Vaccines are available, however infected populations are deprived of therapeutic treatments based on drugs. To rectify this issue, we try to recognize bioactive molecule inhibitors of the HPV E7 oncoprotein using bioinformatics softwares and in-silico molecular docking. In this in-silico study, flavonoid compounds were virtually screened and observed for their ability to inhibit E7 oncoprotein. The virtual screening was conducted in several steps starting with molecular docking to find their potential binding energy with the target followed by validating results with machine learning using Python. According to the literature review Baicalein is considered as a most potent inhibitor of E7 (taken as control). In this study, we worked on approximately 50 flavonoids out of which 15 have shown significant binding energies. Usually, the bioactive compounds present in flavonoids will not significantly cause a side effect. Linarin has shown maximum binding energy of ΔG -10.6 kcal/mol comparable to that of the standard inhibitor Baicalein with ΔG -7.36 kcal/mol. Docking results were further validated by machine learning. Linarin can be easily extracted from the Angiosperms and used as an herbal product to inhibit HPV E7 oncoprotein. The compounds identified here contribute to fascinating beginnings for further medical research and the development of therapeutic treatment.

Keywords: Human Papilloma Virus (HPV), HPV E7 oncoprotein, cervical cancer, Linarin, Flavonoids, In-silico molecular docking.

I. INTRODUCTION

The two major types of HPVs i.e mucosal and cutaneous consist of nearly 130 different varieties. HPV 6 & 11 are the low-risk variants that can cause benign cellular proliferation [1] while HPV16 & 18 are the high-risk ones and the possible causative for cervical cancer [2]. Moreover, HPV infection has been linked to around 35% of penile cancers, anal and vaginal cancers, as well as approximately 20% of head and neck cancer [3]. The high-risk strains of HPV produce oncoproteins E6 and E7 that interfere with the normal functioning of the p53 and Retinoblastoma (pRB) tumor suppressor proteins, resulting in dysregulation of the cell cycle and contributing to the virus's oncogenic properties.

It has also been proposed that pRb degradation is mediated by HPV E7 [4]. Although the HPV E7 oncoprotein interacts with pRb to disrupt the regulation of genes involved in the Synthesis phase of the cell cycle, in healthy uninfected cells, pRb cooperates with E2F/DP transcription factors to control the progression of the cell cycle into the Synthesis and Mitotic phases. P53 is often post-translationally altered and stabilized once the deregulated entry into the S phase is made, making cells to enter cell apoptotic pathway [5] However, HPV E6 picks out p53 and binds to it for deterioration through the ubiquitin-proteasomal pathway [6]. The E7 oncoprotein pathway will receive the majority of attention in our paper.

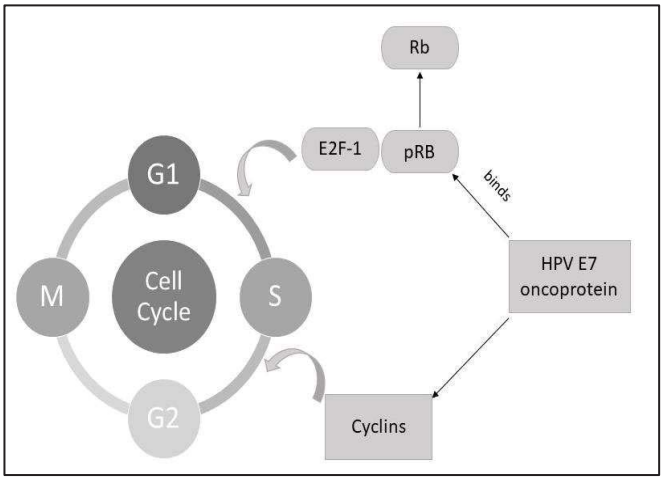

FIG. 1. Pathogenesis of HPV. The multifunctional proteins that are encoded by HPV E7 oncogenes bind predominantly to cellular pRB proteins, interfere with their regulatory cell cycle functions. pRB is tumor suppressor gene which when get activated leads to the apoptosis.

About 100 amino acids make up the small, acidic polypeptides known as E7 proteins. There may be an area of sequence similarity between the E7's amino acid terminus

Authorized licensed use limited to: DELHI TECHNICAL UNIV. Downloaded on August 08,2023 at 09:05:17 UTC from IEEE Xplore. Restrictions apply.

and the entirety of CR2 of Adenovirus (Ad) E1A. The preserved Leu-X-Cys-X-Glu (LXCXE) motif within the CR2 domain is crucial for the interaction between the E7 oncoprotein and pRb, the Retinoblastoma tumor suppressor gene. This interaction requires this specific motif and is found to be abundant [7].

After pharmacokinetics and pharmacodynamics research and limited in-silico docking analysis, the only molecule that was proven to be effective in cells blocking E7 oncoprotein at concentrations of higher micro-molarity was found to be Baicalein (Control) with a binding energy of ΔG= -7.36 [8]. We conducted an in-silico docking analysis to find inhibitors of the E7 oncoprotein interaction with pRb in order to find more novel and potent small molecule inhibitors because the pharmacophore-based in-silico screening campaign produced E7 inhibitors with favourable properties, despite their low potency [9]. In order to find small chemical E7 inhibitors, we devised a high throughput docking analysis method. Two inhibitors were identified in low-micromolar to a mid-nanomolar range of IC50 values that may precisely block pRb degradation in HPV-affected cells through the screening of about 50 different flavonoid compounds. These HPV E7 inhibitors offer a foundation for the development of potential therapeutic HPV inhibitors. After docking we performed Machine Learning to verify and validate the docking results.[10]Plant polyphenols provide a variety of biochemical and pharmaceutical benefits, including pro- and anti-oxidant potentials that are related to their structure-activity relationships. In the research and development of therapies for diseases like Parkinson's disease, cancer, Alzheimer's disease, Crohn's disease and cardiovascular diseases, flavonoids, in particular, have received considerable interest.

II. Methods and Methodology

A. *Pharmacological Properties:*

The study of compound, its composition and its effects on body constitute pharmacological properties. SMILES, Molecular Formula, Molecular Weight, Number of Hydrogen Acceptors and Donors are among the Pharmacological and Physicochemical properties prediction of a potent flavonoid compound. Studying secondary qualities included Leadlikeness, solubility, Lipinski, lipophilicity, and Bioavailability score.

B. *Ligand Receptor Preparation:*

The in-silico ligand structure data was obtained from Pubchem (https://pubchem.ncbi.nlm.nih.gov/) and the receptor studies were obtained from Protein Data Bank (PDB) https://www.rcsb.org/. The 3-D structure of target oncogene E7 i.e., 6E1I (PDB DOI: 10.2210/pdb6E1I/pdb) and 15 ligand that are flavonoids Linarin, Epigallocatechin, Flavopiridol, Quercetin, Acacetin, Fisetin, Naringenin, Genistein, Afzelin, Apigenin, Catechin, Kaempferol, Chrysin, Wogonin and Daidzein were prepared for docking using Biovia Discovery Studio Visualizer (https://discover.3ds.com/discovery-studio-visualizer-download). Preparing the ligand and receptor requires removing hetero atoms from substances like water, non-amino acid groups, and other ligand compound.

C. *Molecular Docking:*

In-silico Molecular Docking is usually started with the designing of ligands and receptors. Selected flavonoids were docked against the target protein using SWISSDOCK online server (http://www.swissdock.ch/docking#). The control inhibitor i.e., Baicalein was also docked against the target protein.

D. *Docking Interaction Analysis*

Affinity binding values (△G) were saved and analysed. Flavonoid compounds and the selected target (E7 oncoprotein) interactions were analyzed by UCSF Chimera. (https://www.cgl.ucsf.edu/chimera/). UCSF Chimera offers interactive molecular structure visualisation and analysis through the study of amino acids and associated information such as density maps and sequence alignments. The binding energies of ligands and control were compared and flavonoids with high binding energies were selected.

E. *Validating the Docking Results using Machine Learning*

A model for machine learning the Random Forest classifier was developed using 750 E7 oncoprotein inhibitors. This data was collected from the ChEMBL [11] data base by training the model with 307 molecular discriptors of above mention 750 inhibitory compounds using the python module Chembl_webresource_client (https://pypi.org/project/chembl-webresource-client/). The physical and chemical characteristics of a chemical substance are expressed as numerical numbers by molecular descriptors. Using the Python library Padelpy, the compound's molecular descriptors were produced. The model's training set consisted of these 307 molecular descriptors. 20:80 was used to divide the data into training and testing sets. Then, in order to identify the potential E7 oncoprotein inhibitor, the data was loaded into the machine learning RandomForestClassifier of the Python module scikit-learn. The model's cross-validation score ended out to be 85.6. The Python library Padelpy produced the molecular descriptors for the flavanoids. After that, the inhibitory phytochemicals were found using the trained machine learning model.

F. *Machine Learning Analysis*

The ChEMBL database was used to estimate the inhibitory potential of Linarin, a flavanoid compound and we chose the RF technique to train the target's structural interaction fingerprints. With the purpose of creating 307 dimensional features for 730 natural substances, latent knowledge, molecular interactions, and chemical property aspects were combined. The machine learning model was trained using the created characteristics and verified data on pharmaceutical indications[12]. When the properties of natural compounds were utilised as input, the trained model effectively predicted prospective efficacies with high accuracy, sensitivity, and specificity. The RF models prioritised phytochemicals with E7 binding potential: Linarin.

III. Results and Discussions

The study evaluated the potential of flavonoids as inhibitors of the HPV E7 oncoprotein by predicting the Gibbs free energy using Docking Score predicted values. The results suggest that flavonoids are likely to interact significantly with the E7 oncoprotein, with two natural inhibitors, Linarin and Afzelin, showing significant binding affinity.

Authorized licensed use limited to: DELHI TECHNICAL UNIV. Downloaded on August 08,2023 at 09:05:17 UTC from IEEE Xplore. Restrictions apply.

Table 1. In-silico docking results of ligands that are flavonoid compounds against the HPV E7 oncoprotein target.

S.No.	Ligands	ΔG	Amino acids
1.	Linarin	-10.6	Phe 80, Lys 82, Phe151, Ser 81, Ala 354, Thr 376, Tyr 50, Pro 378, Leu 89, Phe 384, Ser 79, Asp 173, Asp 172, Tyr 87, Thr 174, Gly 382, Gln 175, Tyr 170, Tyr 352, Ser 76
2.	Afzelin	-9.05	Asp 122, Pro 38, Thr 333, Hsd 331, Pro 39, Arg 21, Asp 120, Trp 119, Ser 35, Trp 347, Leu 349, Hsd 37, Tyr 34, Arg 377, Gln 385
3.	Hesperetin	-7.81	Gln 175, Tyr 170, Pro 378, Phe 384, Tyr 87, Ala 354, Thr 376, Glu 375, Thr 174, Asp 173, Leu 89, Tyr 50, Ser 81, Thr 52
4.	Epigallactechin	-7.77	Glu 375, Gln 53, Thr 52, Ser 81, Tyr 50, Pro 378, Tyr 170, Asp 173, Asp 172, Tyr 87, Phe 284, Ala 354, Thr 376
5.	Flavopiridol	-7.77	Pro 193, Ala 192, Arg 191, Gln 175, Asp 173, Tyr 352, Phe 384, Thr 383, Pro 378, Gly 382, Gly 380, Thr 174, Asp 381, Ala 379, Leu 89, Thr 321, Arg 324
6.	Acacetin	-7.70	Gln 175, Pro 378, Tyr 170, Phe 384, Asp 173, Ala 354, Thr 376, Tyr 87, Tyr 50, Ser 81, Thr 52, Glu 375, Gln 53
7.	Fisetin	-7.63	Gln175, Thr 174, Tyr 87, Phe 151, Asp 173, Tyr 170, Asp 172, Arg 149, Lys 82, Phe 384, Tyr 50, Pro 378, Leu 89
8.	Naringenin	-7.62	Gln 175, Thr 174, Thr 52, Pro 378, Ser 81, Phe 384, Tyr 87, Tyr 170, Asp 173, Glu 375, Gln 53, Tyr 50, Ala 354, Thr 376
9.	Genistein	-7.52	Asp 173, Pro 378, Ala 354, Tyr 50, Thr 376, Glu 375, Gln 53, Thr 52, Ser 81, Tyr 87, Phe 384, Tyr 170, Thr 174, Gln 175
10	Apigenin	-7.51	Ala 354, Thr 376, Tyr 170, Pro 378, Phe 384, Tyr 87, Asp 173, Tyr 50, Ser 81, Thr 52, Glu 375, Gln 53
11	Catechin	-7.49	Phe 384, Tyr 170, Thr 174, Gln 175, Ser 76, Arg 178, Asp 77, Arg 191, Met 75, Glu 74, HSe 91, Leu 89, Gly 380, Tyr 87, Pro 378, Asp 173
12	Kaempferol	-7.48	Gly 380, Leu 89, Pro 378, Ser 76, Tyr 50, Phe 384, Ser 81, Lys 82, Phe 151, Arg 149, Asp 172, Tyr 170, Asp 173, Tyr 87, Gln 175
13	Chrysin	-7.45	Tyr 170, Phe 384, Asp 173, Tyr 87, Tyr 50, Ser 81, Thr 52, Glu 375, Gln 53, Thr 376, Ala 354, Pro 378
14	Wogonnin	-7.27	Thr 376, Tyr 50, Leu 89, Pro 378, Phe 384, Gln, Thr 174, Tyr 87, Tyr 170, Asp 172, Asp 173, Phe 151, Lys 82, Ser 81
15	Daidzein	-7.23	Glu 375, Lys 82, Ser 81, Asp 173, Tyr 170, Ala 354, Phe 384, Thr 376, Tyr 87, Tr 50, Phe 86, Thr 52, Ser 85, Gln 53

Linarin demonstrated the highest binding affinity among all 15 ligands tested, with a ΔG value of -10.6 kcal/mol. This indicates that Linarin has a strong binding affinity with the E7 oncoprotein and is a promising inhibitor of the target. The ligand-target complex involved several important amino acids, including Phe384, Ala354, Ser81, Thr174, Leu89, and Asp.

To assess the pharmacokinetic properties of Linarin, ADME analysis was performed, which showed favorable results. The drug demonstrated good skin permeability with a logKp value of -9.56 cm/s and had good lipophilicity values with a Log Po/w (XLOGP3) of 0.50. Additionally, Linarin exhibited significant solubility in biofluids.

Overall, the study suggests that Linarin and Afzelin have the potential to be effective inhibitors of the HPV E7 oncoprotein, with Linarin showing the highest binding affinity. The favorable pharmacokinetic properties of Linarin further support its potential as a therapeutic drug candidate for the treatment of HPV-related cancers.

IV. Conclusion

Recent studies have revealed that synthetic medications used to treat cancer frequently have side effects and toxicity, which has caused the attention to shift towards non-toxic and widely accessible natural compounds that can be employed as anti-cancer agents, such as flavonoids. Linarin is a flavonoid compound found abundantly in angiosperms and is known for its numerous health benefits.

Authorized licensed use limited to: DELHI TECHNICAL UNIV. Downloaded on August 08,2023 at 09:05:17 UTC from IEEE Xplore. Restrictions apply.

In particular, Linarin is found in the roots of Valeriana Jatamnsi, a rhizome herb that is readily available in the market. This in-silico study aimed to explore the potential of Linarin as an inhibitor of the activity of the HPV E7 oncoprotein, a protein involved in HPV pathogenesis. The study utilized bioactive compounds derived from Linarin and found that Linarin exhibited a maximum binding affinity with a ΔG of -10.6, which was higher than the standard Baicalein with a ΔG of -7.36.

The study also considered additional parameters such as minimal cytotoxicity, maximum bioavailability, and bioactivity to evaluate Linarin as a potential therapeutic drug. Based on these parameters, Linarin was found to be a promising therapeutic drug candidate for inhibiting not only HPV E7 oncoprotein but also other proteins involved in HPV pathogenesis such as HPV E6 oncoprotein.

In summary, this study highlights the potential of natural compounds such as Linarin as effective and non-toxic alternatives to synthetic drugs for the treatment of cancer. The use of in-silico approaches to identify potential drug candidates can significantly reduce the time and cost required for drug development.

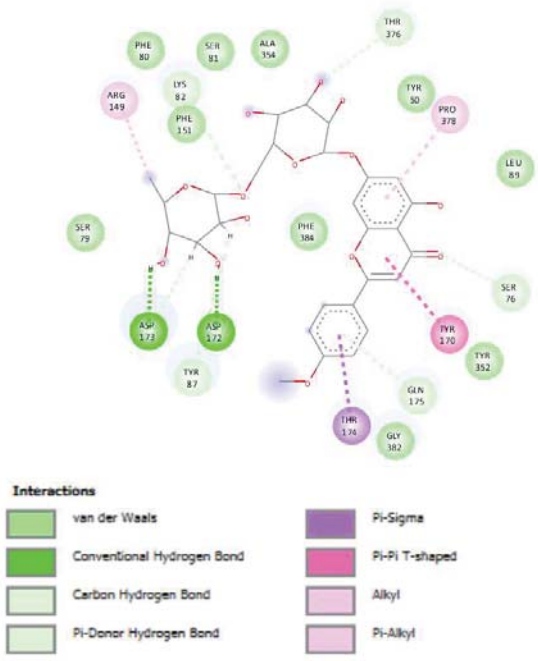

Figure 2. Molecular Interaction of ligand i.e. Linarin and target protein i.e. HPV E7 oncoprotein. https://discover.3ds.com/discovery-studio-visualizer-download

V. Acknowledgement

I am deeply thankful to Delhi Technological University for their generous financial assistance and granting me access to their research facilities and resources. I would like to acknowledge the invaluable guidance and support of my advisor, Dr. Asmita Das and colleagues who have contributed significantly to the success of this project. Thank You for their invaluable contributions. In this paper both the authors have contributed equally.

VI. References

[1] Zur Hausen, "Papillomaviruses and cancer: From basic studies to clinical application," Nature Reviews Cancer, vol. 2, no. 5. European Association for Cardio-Thoracic Surgery, pp. 342–350, 2002. doi: 10.1038/nrc798.

[2] A. R. Kreimer et al., "HPV16 semiquantitative viral load and serologic biomarkers in oral and oropharyngeal squamous cell carcinomas," Int J Cancer, vol. 115, no. 2, pp. 329–332, Jun. 2005, doi: 10.1002/ijc.20872.

[3] H. De Vuyst, G. M. Clifford, M. C. Nascimento, M. M. Madeleine, and S. Franceschi, "Prevalence and type distribution of human papillomavirus in carcinoma and intraepithelial neoplasia of the vulva, vagina and anus: A meta-analysis," Int J Cancer, vol. 124, no. 7, pp. 1626–1636, Apr. 2009, doi: 10.1002/ijc.24116.

[4] S. N. Boyer, D. E. Wazer, and V. Band, "E7 protein of human papilloma virus-16 induces degradation of retinoblastoma protein through the ubiquitin-proteasome pathway.," Cancer Res, vol. 56, no. 20, pp. 4620–4, Oct. 1996.

[5] M. Thomas, D. Pim, and L. Banks, "The role of the E6-p53 interaction in the molecular pathogenesis of HPV." [Online]. Available: http://www.stockton-press.co.uk/onc

[6] H. Zur Hausen, "Papillomaviruses and cancer: From basic studies to clinical application," Nature Reviews Cancer, vol. 2, no. 5. European Association for Cardio-Thoracic Surgery, pp. 342–350, 2002. doi: 10.1038/nrc798.

[7] K. Munger,', C. L. Yee, W. C. Phelps, J. A. Pietenpol, H. L. Moses, and P. M. Howley', "Biochemical and Biological Differences between E7 Oncoproteins of the High-and Low-Risk Human Papillomavirus Types Are Determined by Amino-Terminal Sequences," 1991. [Online]. Available: https://journals.asm.org/journal/jvi

[8] Q. Wang, H. Xu, and X. Zhao, "Baicalin inhibits human cervical cancer cells by suppressing protein kinase c/signal transducer and activator of transcription (PKC/STAT3) signaling pathway," Medical Science Monitor, vol. 24, pp. 1955–1961, Apr. 2018, doi: 10.12659/MSM.909640.

[9] J. J. Cherry et al., "Structure based identification and characterization of flavonoids that disrupt human papillomavirus-16 E6 function," PLoS One, vol. 8, no. 12, Dec. 2013, doi: 10.1371/journal.pone.0084506.

[10] R. Zhang, X. Li, X. Zhang, H. Qin, and W. Xiao, "Machine learning approaches for elucidating the biological effects of natural products," Natural Product Reports, vol. 38, no. 2. Royal Society of Chemistry, pp. 346–361, Feb. 01, 2021. doi: 10.1039/d0np00043d.

[11] A. Gaulton et al., "ChEMBL: A large-scale bioactivity database for drug discovery," Nucleic Acids Res, vol. 40, no. D1, Jan. 2012, doi: 10.1093/nar/gkr777.

[12] S. Krishna, S. Kumar, D. K. Singh, A. D. Lakra, D. Banerjee, and M. I. Siddiqi, "Multiple Machine Learning Based-Chemoinformatics Models for Identification of Histone Acetyl Transferase Inhibitors," Mol Inform, vol. 37, no. 8, Aug. 2018, doi: 10.1002/minf.201700150.

Authorized licensed use limited to: DELHI TECHNICAL UNIV. Downloaded on August 08,2023 at 09:05:17 UTC from IEEE Xplore. Restrictions apply.

Authorized licensed use limited to: DELHI TECHNICAL UNIV. Downloaded on August 08,2023 at 09:05:17 UTC from IEEE Xplore. Restrictions apply.

This article has been accepted for publication in IEEE Journal of Quantum Electronics. This is the author's version which has not been fully edited and content may change prior to final publication. Citation information: DOI 10.1109/JQE.2023.3292060

Link Optimisation of a Microwave Photonic Phase Shifter using Brillouin-Induced Low Biasing

Reena Parihar, Rajveer Dhawan, and Amol Choudhary, *Senior Member, IEEE, OSA*

***Abstract*— In this paper, we demonstrate a microwave photonic phase shifter using stimulated Brillouin scattering with Brillouin-induced low biasing of the carrier to improve the dynamic range of operation and the noise performance. Mathematical expressions for the analog photonic link's performance metrics are derived and experimentally optimized for the first time for a Brillouin-based microwave photonic phase shifter. Gain and loss responses are imparted on the carrier to induce a phase shift, and low-biasing of the carrier is achieved by using unbalanced loss and gain pumps, which results in a stronger Brillouin loss response compared to the gain response being imparted on the carrier, thereby improving the performance. The results indicate a 3 dB increase in link gain, a >2 dB improvement in noise figure, and >2 dB and >4 dB enhancements in compression dynamic range (CDR) and spurious free dynamic range (SFDR), respectively, when compared to the without low biasing while maintaining the same photocurrent. We also demonstrate the real-life application of the Brillouin RF phase shifter by transmitting 16- and 64-QAM signals using different Brillouin pump powers and have analysed its effect on the error vector magnitude, with minimal distortions being observed in the performance. Furthermore, a phase shift operation is performed on a linear frequency-modulated signal to demonstrate a potential application in RADAR systems.**

I. INTRODUCTION

MICROWAVE phase shifters are basic building blocks for realizing various sub-systems for various applications, including beam-steering, phased array antennae, communication systems, and frequency translators [1-3]. Microwave photonic (MWP) phase shifters are gaining popularity because of their numerous advantages over traditional RF phase shifters, including wide bandwidth tunability, significant phase tuning range, reliability, power efficiency, and immunity to electromagnetic interference [4-8]. There are several approaches to realize the microwave photonic phase shifters, including semiconductor optical amplifier (SOA) [10], micro-ring resonator (MRR) [11-15], fiber Bragg grating (FBG) [16], electro-optic modulator [17-20] and stimulated Brillouin scattering (SBS) [21]. Phase shifters based on these technologies require external control techniques such as thermal, electrical biasing, thermo-optic effect, or optical pumping to achieve the desired phase shift. The main requirement of a phase shifter is to provide a tunable phase shift while maintaining a flat amplitude response over a wide range of RF frequencies. Most of the above reports use optical carrier processing, where the phase is imparted onto the optical carrier modulated with an RF signal, which gets transferred to the RF domain through photodetection.

SBS [22-23] is an inelastic nonlinear three-wave interaction between a pump, a probe (Stokes), and an acoustic wave, which can be used for developing MWP phase shifters. SBS is gaining popularity since it enables rapid tuning and doesn't limit the lower frequency range due to its narrow bandwidth compared to ring resonators, for example. The SBS phase shifter technique relies on counter-propagating the single sideband (SSB)-modulated carrier with two pumps in a single-mode fiber using a gain response with a loss response [21] or two gain responses [24], which allows flat-amplitude phase shifters. In [24], for an emulated low-biasing configuration to improve linearity, an optical bandstop filter was used to suppress a sideband and to attenuate the carrier power making the system complex. SBS-based MWP phase shifters have also been demonstrated using chalcogenide chips [25, 26] and silicon chips [27]. While Brillouin-based approaches present an attractive way of implementing phase shifters, no efforts have been made to optimise the analog photonic link (APL) performance metrics [28-30], such as noise figure, link gain, spurious-free dynamic range, and compression dynamic range.

In the field of microwave photonics, there is a critical requirement to optimise the link performance parameters with advanced functionalities to enable the replacement of conventional RF devices. SBS-based phase shifters suffer from high noise figure dominated by spontaneous emission noise induced by Brillouin scattering [32]. Other factors contributing to noise delivered to the radio frequency signals are relative intensity noise (RIN), shot noise, thermal noise, and amplified spontaneous emission (ASE) noise. This leads to a high noise figure (NF) and results in degradation of the link performance. The modulator is typically operated at a low bias to improve APL noise performance, however, this causes even-order distortion, severely limiting the second-order spurious-free dynamic range ($SFDR_2$) [34].

Similarly, the linearity of the phase shifter plays an essential role in improving the dynamic range over which the microwave photonic phase shifter operates. This implies that a constant phase shift is applied for different RF powers when the phase shifter operates as a linear processor. Conversely, a nonlinear signal processor may display a specific frequency response while the input RF signal's power is weak, but the response of the nonlinear signal processor may change when the input RF signal power grows. In the linear regime, for a Brillouin phase shifter, the phase shift observed by the RF signal is directly proportional

The Manuscript was submitted on 15 March 2023.
This work is supported by the I-Hub Foundation for Cobotics.
R. Parihar, R. Dhawan, and A. Choudhary are with the UltraFast Optical Communications and High performance Integrated Photonics (UFO-CHIP) group, Department of Electrical Engineering, Indian Institute of Technology (IIT) Delhi, New Delhi 110016, India (e-mail: eez198567@ee.iitd.ac.in, eez188570@ee.iitd.ac.in, amol.choudhary@ee.iitd.ac.in.
(*Corresponding author: Reena Parihar*)

Authorized licensed use limited to: DELHI TECHNICAL UNIV. Downloaded on July 22,2023 at 05:16:02 UTC from IEEE Xplore. Restrictions apply.
© 2023 IEEE. Personal use is permitted, but republication/redistribution requires IEEE permission. See https://www.ieee.org/publications/rights/index.html for more information.

This article has been accepted for publication in IEEE Journal of Quantum Electronics. This is the author's version which has not been fully edited and content may change prior to final publication. Citation information: DOI 10.1109/JQE.2023.3292060

to the SBS pump power (or frequency detuning). However, in the pump-depletion (saturation) regime of SBS, which occurs for strong signals, the phase shift depends on the magnitude of gain and loss seen by the optical carrier [36].

In this work, we present the first demonstration of optimisation of the link performance metrics of a Brillouin-based phase shifter, which were not previously addressed. This is achieved by improving the linearity, noise figure and dynamic range of operation in terms of CDR and SFDR of the phase shifter using Brillouin-induced low biasing. To suppress the SBS pump-depletion issues, we low bias the carrier by imparting more SBS loss than gain on the carrier, which results in the improvement in the noise figure as well as in the dynamic range of operation. Imbalanced pumps are used that offer a significant loss response relative to the gain response on the carrier. In addition to reducing the amplitude of the carrier to emulate low biasing, which minimises the link noise, the stronger SBS loss response helps with further improvement of the noise figure and linear operation of the phase shifter since the anti-Stokes response depletes slower and does not lead to amplification of the spontaneous noise [35]. The operating point of the modulator can be directly controlled by the configurable SBS pump rather than by electronically controlling the modulator. Furthermore, in this approach, the low-biasing of the carrier using SBS prevents the generation of even-order nonlinear components as opposed to voltage-based low-biasing of modulators. This work is further extended to demonstrate an application in communication systems by transmitting 16 QAM/64 QAM signals through the phase shifter. We also demonstrate its potential for application in RADAR systems by transmitting a linear-frequency-modulated signal through the phase shifter. We present the principle of operation, theoretical background, and mathematical analysis in section II. Results and applications of the SBS phase shifter are discussed in sections III and IV, respectively, section V presents the discussion section. Also, conclusions and future work are outlined in section VI.

II. Principle of Operation

The proposed MWP phase shifter is realized by generating a single sideband (SSB) modulated signal, which forms the analog photonic link (APL) and imparting the anti-Stokes (loss) and Stokes (gain) resonance on the carrier. The optical carrier has a frequency ω_c and is modulated with an RF frequency (which requires the desired phase shift) at ω_{RF} to generate the single sideband. Photodetection of this signal results in an RF signal at a frequency of ω_{RF}. Additionally, any offset in the phase and amplitude of the optical carrier will be translated to the output RF signal upon photodetection. Based on this, the SBS gain and loss pump and associated phase are applied on the carrier to achieve the desired phase shift with a minimum variation of the magnitude response [24].

Since the SBS gain pump is depleted at high signal powers [33–35], leading to gain saturation, a new strategy is presented to address this, as shown in Fig.1. A laser at a frequency ω_c (① in Fig.1) is modulated with an RF frequency of ω_{RF} (② in Fig.1) to generate the upper sideband at $\omega_c + \omega_{RF}$. A laser at a frequency ω_c (③ in Fig.1) is intensity-modulated with an RF frequency (Ω_B), i.e. Brillouin shifts from the carrier frequency that generates the gain pump (pump 2) and the loss pump (pump 1) at a frequency of $\omega_c + \Omega_B$ and $\omega_c - \Omega_B$, respectively (④ in Fig.1). With the help of a programmable optical filter, the amplitude of the gain pump is attenuated by a factor of ΔP (with respect to the loss pump) to impart more Brillouin loss than the gain (⑤ in Fig.1), which effectively low biases [29] the carrier (⑥ in Fig.1). This can help to prevent the SBS gain pump depletion at high signal powers since this will not saturate the gain pump; therefore it will operate in the linear region. Furthermore, the noise added by the anti-Stokes (loss) response is lower than that added by the Stoke (gain) response [35] since the anti-Stokes response does not lead to amplification of the spontaneous noise, which improves the noise figure. Finally, reducing the carrier also improves the noise figure as it emulates the low-biasing technique of microwave photonics, where the modulator is operated close to the null point [34]. The phase shift imparted on the optical carrier is projected onto the output RF signal due to photodetection (⑦ in Fig.1). Phase shifting can be accomplished by adjusting the SBS pump frequency or the pump power. SBS has a narrowband phase response, which provides a phase shift over the RF range without affecting the optical sideband [31].

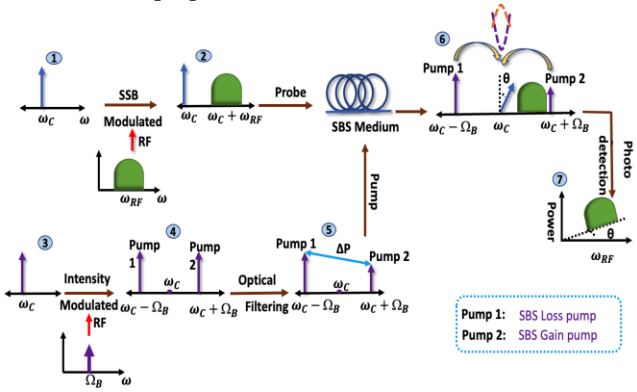

Fig. 1. Principle of operation of the SBS-based MWP phase shifter with Brillouin-induced low-biasing.

In this paper, we fixed the SBS pump frequency to $\pm\Gamma_B/2$ (where, Γ_B is the Brillouin linewidth) to achieve the maximum possible phase shift [24] and investigate the phase shift for various pump powers. In the next sub-section, we present the theoretical analysis of the linearity of an SBS-based MWP phase shifter.

A. *Theoretical Analysis of SBS Linearity*

In this section, the performance of the APL with the SBS-based phase shifter is described in detail. The metrics include various figures of merit (FOM) for quantifying the link performance, such as link gain (G), Noise figure (NF), compression dynamic range (CDR), and spurious-free dynamic range (SFDR) [37]. Before analysis of these parameters, the current at the output of the photodetector is derived for the APL, and all the parameters are explained.

Authorized licensed use limited to: DELHI TECHNICAL UNIV. Downloaded on July 22,2023 at 05:16:02 UTC from IEEE Xplore. Restrictions apply.
© 2023 IEEE. Personal use is permitted, but republication/redistribution requires IEEE permission. See https://www.ieee.org/publications/rights/index.html for more information.

This article has been accepted for publication in IEEE Journal of Quantum Electronics. This is the author's version which has not been fully edited and content may change prior to final publication. Citation information: DOI 10.1109/JQE.2023.3292060

The concept figure in Fig. 1 shows the APL, which consists of an electro-optic modulator used to generate the optical single sideband (SSB) and a single-mode fiber as the SBS medium. At the output of the modulator, the generalized equation for the electric field is given by [39]:

$$E_{mod} = \frac{1}{\sqrt{2}} E_o \sqrt{\alpha_{mod}} e^{i\omega_c t}\left[A_c e^{i\phi_c} + A_l e^{i(-\omega_{RF}t+\phi_l)} + A_u e^{i(\omega_{RF}t+\phi_u)}\right] \quad (1)$$

where, E_o is the magnitude of the optical carrier electric field, A_c, A_l and A_u are the optical carrier's, lower sideband's, and upper sideband's amplitudes, respectively. The associated phases are ϕ_c, ϕ_l and ϕ_u. Also, α_{mod} is the insertion loss of the modulator. When the modulator is biased to operate in the SSB modulation format and by taking the first-order sideband only, and considering the initial phases ϕ_c, ϕ_l and ϕ_u equal to zero, the expression for the single sideband can be simplified as:

$$E_{ossb} = \frac{1}{\sqrt{2}} \sqrt{\alpha_{mod}} E_o \left[J_o(m) e^{i\omega_c t} + J_1(m) e^{i(\omega_c+\omega_{RF})t}\right] \quad (2)$$

where m is the modulation index, ω_{RF} is the RF signal angular frequency, and $J_n(.)$ is the Bessel coefficient of the n[th]-order.

To induce the SBS effect on the optical carrier, the pump is generated by employing an intensity modulator (IM) at the minimum transmission point and a laser at the frequency ω_c is modulated with an RF signal at a frequency of Ω_B. Therefore, the two pumps can be represented as:

$$E_{pump} \propto E_{po}\left[J_1(m_p) e^{i(\omega_c+\omega_p)t} + J_1(m_p) e^{i(\omega_c-\omega_p)t}\right] \quad (3)$$

where, $\omega_p = \Omega_B \pm \Gamma_B/2$, and m_p is the modulation index of the intensity modulator represented as $m_p = \frac{\pi V_p}{V_{\pi,p}}$ and E_{po} is the magnitude of the electric field of the pump, V_p is the RF signal voltage and $V_{\pi,p}$ is the voltage required to produce relative π radian phase shift in the intensity modulator. A programmable optical filter (POF) creates a power difference of ΔP dB between the gain and loss pumps to low bias the carrier to avoid pump depletion of the SBS gain pump. Note that the combination of the IM and POF can be replaced by an IQ modulator where the relative amplitudes of the sidebands can be controlled via DC biasing to reduce the complexity of the system. The theoretical analysis of SBS linearity is presented in [36], where the evolution of the pump power and Stokes power along the SBS medium is evaluated by solving the coupled-mode differential equations.

For the linear regime, the power evolution of the carrier signal along the medium at a distance z can be defined as [36]:

$$P_c(z,\omega) = P_c(L,\omega) e^{-\alpha(L-z)} \exp\left[\frac{g_0(\omega) P_p(0)}{A_{eff}\alpha}\left(e^{-\alpha z} - e^{-\alpha L}\right)\right] \quad (4)$$

where $g_0(\omega)$ is Brillouin gain coefficient, $P_p(0)$ is total input pump power, A_{eff} and α are the effective mode area and fiber loss coefficient of the SBS media, respectively, $P_c(L)$ is the input carrier power at z = L, and L is the length of the SBS medium. However, the evolution of the carrier wave power under the un-depleted approximation can be numerically computed under the conditions:

$$\frac{g_0(\omega)}{A_{eff}} \int_0^L P_c(\xi,\omega).\, d\xi \ll 1 \quad (5)$$

Here, $\frac{g_0(\omega)}{A_{eff}} \int_0^L P_c(\xi,\omega).\, d\xi$ is an integrating factor governed by coupled equation and ξ is the length variable. The general solution is given by:

$$P_p(z) = P_p(0) e^{-\int_0^z [\frac{g_0(\omega)}{A_{eff}} P_c(\xi,\omega) + \alpha].d\xi} \quad (6)$$

The total pump power P_p is the sum of the anti-Stokes and Stokes pump powers, which is denoted as P_{pa} and P_{ps} respectively. For the depleted regime, the above condition is not satisfied, and the approximation does not hold, which gives:

$$\frac{g_0(\omega)}{A_{eff}} \int_0^L P_c(\xi,\omega).\, d\xi = \frac{P_c(L,\omega)}{P_p(0)} \frac{K}{\alpha} e^{-\alpha L} exp\left(\frac{K}{\alpha} e^{-\alpha L}\right).\left[\frac{K}{\alpha}\left(Ei\left(\frac{K}{\alpha}\right) - Ei\left(\frac{K}{\alpha} e^{-\alpha L}\right)\right) - e^{\frac{K}{\alpha}}\right] \quad (7)$$

Where $K = \frac{g_0(\omega)}{A_{eff}} P_p(0)$, and $Ei(x) = \int_{-\infty}^{x} \frac{e^{-\xi}}{\xi} d\xi$ is a function termed as the exponential integral.

In this work, a phase shifter is implemented such that the effect of the anti-Stokes response is considered stronger than the Stokes pump to low-bias the carrier. High signal powers cause the SBS gain to saturate, which reduces the dynamic range of an RF system. On the other hand, since the anti-Stokes response does not deplete as fast as the gain response, the anti-Stokes interaction can provide a way to ameliorate these problems [30, 35]. This helps to reduce the challenge of reduced SBS linearity brought on by pump depletion.

The SBS Stokes and Anti-Stokes pump can be represented as $M_s e^{i\phi_s}$ and $M_a e^{i\phi_a}$, respectively, where M_s, M_a and ϕ_s, ϕ_a are the magnitude and phase of the individual pump. However, The SBS-induced gain $G_{SBS}(\omega)$ and phase $\phi(\omega)$ response can be given as [31]:

$$G_{SBS}(\omega) = exp\left[\frac{g_0(\omega)}{1 + 4\left(\Delta\omega/\Gamma_B\right)^2}\right] \quad (8)$$

And,

$$\phi(\omega) = \frac{g_0(\omega).\left(\Delta\omega/\Gamma_B\right)}{1 + 4\left(\Delta\omega/\Gamma_B\right)^2} \quad (9)$$

where $\Delta\omega$ is frequency detuning in rad/sec and Γ_B is Brillouin linewidth. The electrical field at the output of the SBS medium after the interaction of the SBS gain and loss pumps with the optical signal is given by

$$E_{out} \propto \sqrt{\alpha_{mod}\alpha_o\alpha\, G_{probe}}\, E_o\left[M_s M_a J_0(m).\, e^{i(\omega_c t+\phi_s+\phi_a)} + J_1(m) e^{i(\omega_c+\omega_{RF})t}\right] \quad (10)$$

where α_o is the optical component loss in the setup, G_{probe} is the gain due to EDFA present in the link. Through square law photodetection, the electrical signal can be given as

$$I_{PD} \propto R_{pd} E_{out}.\, E_{out}^* \quad (11)$$

$$I_{PD} = I_{dc}[J_0^2(m) M_{sbs}^2 + 2J_1^2(m)] + 2\sqrt{2} I_{dc} J_0(m) J_1(m) M_{sbs} .\, cos(\omega_{RF} t - \phi_s - \phi_a) \quad (12)$$

Where, $I_{dc} = \frac{1}{2} R_{pd} \alpha_{mod} \alpha\, \alpha_o G_{probe} P_o$, $M_{sbs} = (M_s.M_a)$, R_{pd} is the responsivity of the photodiode. By considering small

Authorized licensed use limited to: DELHI TECHNICAL UNIV. Downloaded on July 22,2023 at 05:16:02 UTC from IEEE Xplore. Restrictions apply.
© 2023 IEEE. Personal use is permitted, but republication/redistribution requires IEEE permission. See https://www.ieee.org/publications/rights/index.html for more information.

This article has been accepted for publication in IEEE Journal of Quantum Electronics. This is the author's version which has not been fully edited and content may change prior to final publication. Citation information: DOI 10.1109/JQE.2023.3292060

signal approximation, the photodetector current can be represented as:

$$I_{PDss} = I_{dc}\left[M_{sbs}^2 + \frac{m^2}{2}\right] + \sqrt{2}\, I_{dc} m M_{sbs}\, cos(\omega_{RF} t - \phi_s - \phi_a) \quad (13)$$

This represents the photodetector current with the individual SBS response caused due to the Stokes and the anti-Stokes pump.

B. Link Gain

The ratio of the power of the RF signal delivered to the load to the power of the RF signal input at the source is known as the link gain (G). The frequency response of the electrical and optical components that are used to design the microwave photonic link determines the link gain, which is frequency dependent. In real-world scenarios, one wants to maximize link gain and prevent RF signal power loss. There is a significant impact on link gain due to power launched into the optical modulator and losses present in the MWP. The link gain can be derived as:

$$G = \frac{P_{PDss}}{P_{rf}} = G_{APL} * G_{RFamp} = \frac{2M_s^2 M_a^2 \pi^2 {I_{dc}}^2 R_{in} R_o G_{RFamp}}{{V_{\pi,rf}}^2} |H_{PD}|^2 \quad (14)$$

where R_{in} and R_o are input and load resistance, respectively, $|H_{PD}|$ is a photodiode circuit filter function, G_{APL} is the analog photonic link gain without RF amplifier and G_{RFamp} is the RF amplifier gain factor used in the APL.

C. Noise Figure

The noise factor is a common metric for describing an RF component or system's noise performance. The noise factor is defined as the ratio of the signal-to-noise (SNR) of an input RF signal to the SNR of the output RF signal of the link obtained at thermal noise-limited input. An alternative definition of the noise factor at a given input frequency is the ratio of the total noise power per unit bandwidth at a corresponding output frequency that is available at the output port when the input termination's noise temperature is standard (290K) to that portion of noise that is generated at the input frequency by the input termination [34]. Typically, the noise factor is represented in decibels known as Noise figure. Usually, the primary sources of noise to the signal along the MWP link are thermal, shot, RIN, and SBS-induced noise [30] and, EDFA ASE noise amplified by the SBS process, as shown in (15).

$$N_{total} = N_{thermal} + N_{shot} + N_{RIN,probe} + N_{SBS} + N_{ASE,EDFA+SBS} \quad (15)$$

where

$$N_{thermal} = (G+1)kTB$$
$$N_{shot} = 2qI_{PDDC}R_oB|H_{PD}|^2$$
$$N_{RIN,probe} = RIN_{probe}.{I_{Probe}}^2 R_oB|H_{PD}|^2$$
$$N_{SBS} = 2R_{PD}I_{Probe}P_{nsbs}R_oB_1|H_{PD}|^2$$
$$N_{ASE,EDFA+SBS} = 2R_{PD}I_{PDDC}\{G_{SBS}\alpha_l.2h\upsilon n_{sp}(G_{probe}-1)\}R_oB|H_{PD}|^2$$

where, k is the Boltzmann's constant, T is temperature, and B is the bandwidth over which noise is being measured. RIN is the relative intensity noise of the laser, q is the elementary charge constant, υ is the light signal frequency, h is the Planck's constant, n_{sp} is the spontaneous emission factor, I_{PDDC} is the photocurrent includes the reflected pump, I_{Pump} and the probe current, I_{Probe}. The ASE noise contribution due to the EDFA is represented by $N_{ASE,EDFA+SBS}$, which is enhanced by the SBS gain mechanism. However, ASE noise will experience optical loss α_l due to the SBS medium at the same time. The photocurrent is made up of numerous beat signals that occur between the optical noise and signal fields. N_{SBS} is the representation of the signal and spontaneous beat noises mixing product. One can roughly predict the evolution of SBS-induced thermal noise's optical power in the fiber as [40]:

$$P_{nsbs}(\Delta\omega, z) = \left(\frac{1}{A_{eff}}\right) h\nu g_0(\Delta\omega)(N+1)G_{SBS}(z) . \int_z^L P_p(z')G_{SBS}(z')^{-1}.dz'(W/Hz) \quad (16)$$

where N is the number of acoustic phonons at the thermal equilibrium. Therefore, one can write the noise figure as:

$$NF = \frac{N_{total}}{GkTB} \quad (17)$$

Biasing the modulator at low DC biases while maintaining the same current at the detector is a technique known as low-biasing and is commonly employed to reduce the noise figure [34]. A major contribution of this work is that we have used the Brillouin effect to induce low-biasing, where a stronger loss response effectively attenuates the carrier thereby reducing the noise faster than the reduction of the link gain.

D. Compression dynamic range (CDR)

It is the input power range at which the output signal is above the noise floor and output power is reduced by 1 dB compared to the linear response at the output [34]. The expression for the output power at 1-dB compression can be calculated by the fundamental component of current present at the output of the photodetector represented as P_{PDfun}

$$P_{PDfun,1dB} = P_{PDfun}\big|_{m=m_{1dB}} \quad (18)$$

Here, m= m_{1dB} stands for the value of m at which a 1-dB decrease in output RF power is noticed, also P_{PDfun} is given as

$$P_{PDfun} = \langle {I_{PDfun}}^2 \rangle R_o |H_{PD}|^2 \quad (19)$$

Therefore,

$$P_{PDfun,1dB} = 4{I_{dc}}^2 M_s^2 M_a^2 {J_0}^2(m){J_1}^2(m)R_o|H_{PD}|^2\Big|_{m=m_{1dB}} \quad (20)$$

The m_{1dB} quantity can be determined by setting the ratio of the linearized response, P_{PDss} to the actual response, P_{PDfun} at 1 dB compression, as shown in (21).

$$\frac{m_{1dB}}{J_0(m_{1dB})J_1(m_{1dB})} = 2 \times 10^{0.05} \quad (21)$$

Numerically, one can use the above expression to calculate m_{1dB} and compute output power at 1-dB compression. CDR_{1dB} can be written as [34]

$$CDR_{1dB} = \frac{P_{1dB}10^{0.1}}{N_{total}B} \quad (22)$$

E. Spurious free dynamic range (SFDR)

Due to the RF nonlinearities in the system, unwanted frequency components can be generated. SFDR is a metric that quantifies the nonlinearity of the system and is based on a two-tone

Authorized licensed use limited to: DELHI TECHNICAL UNIV. Downloaded on July 22,2023 at 05:16:02 UTC from IEEE Xplore. Restrictions apply.
© 2023 IEEE. Personal use is permitted, but republication/redistribution requires IEEE permission. See https://www.ieee.org/publications/rights/index.html for more information.

This article has been accepted for publication in IEEE Journal of Quantum Electronics. This is the author's version which has not been fully edited and content may change prior to final publication. Citation information: DOI 10.1109/JQE.2023.3292060

analysis. The primary spurs are the second-order harmonic distortion (HD2) at the frequency $2f_{RF1}$ and $2f_{RF2}$, the 2nd-order intermodulation distortions (IMD2) at $f_{RF1} - f_{RF2}$ and $f_{RF1} + f_{RF2}$ frequencies, the 3rd order intermodulation distortions (IMD3) at $2f_{RF1} - f_{RF2}$ and $2f_{RF2} - f_{RF1}$. SFDR can be defined as a range of input RF power over which the output RF power is above the output noise floor, and the undesired frequency component is either equal to or below the output noise floor. The average power of the fundamental component of photocurrent under small signal approximation is given by:

$$P_{PDss} \approx {I_{dc}}^2 m^2 M_{sbs}^2 R_o \, |H_{PD}|^2 \quad (23)$$

Higher-order intermodulation and harmonic distortions are frequently negligible and located distant from the signal of interest. Due to their proximity to the signal of interest and difficulty in being filtered away, IMD_3 distortions can be problematic. Hence, this paper focuses on calculating the spur present in the link due to the IMD_3 components. The average power of the IMD_3 component of photocurrent under small signal approximation can be derived as

$$P_{PDIMD3ss} = 2{I_{dc}}^2 \frac{m^6}{16} R_o \, |H_{PD}|^2 \langle [cos(2\omega_{RF1}t - \omega_{RF2}t)]^2 \rangle \quad (24)$$

$$P_{PDIMD3ss} = {I_{dc}}^2 \frac{m^6}{16} R_o \, |H_{PD}|^2 \quad (25)$$

The practical method for defining the nth-order SFDR is to locate the n[th]-order output intercept point (OIP_n). In most MWP links, the SFDR is third-order limited [37], necessitating the use of OIP_3. Since OIP_3 can be represented as [37]:

$$OIP_3 = \left(\frac{P_{PDss}^3}{P_{PDIMD3ss}} \right)^{\frac{1}{2}} \quad (26)$$

Therefore, inserting (23) and (25) in (26) results in

$$OIP_3 = \left(16 {I_{dc}}^4 M_{sbs}^6 \, {R_o}^2 \, |H_{PD}|^4\right)^{\frac{1}{2}} = 4{I_{dc}}^2 M_{sbs}^3 \, R_o \, |H_{PD}|^2 \quad (27)$$

So, $SFDR_3$ can be written as

$$SFDR_3 \, [\text{dB.Hz}^{2/3}] = \frac{2}{3}\{OIP_3[dBm] - N_{total}[\frac{dBm}{Hz}]\} \quad (28)$$

To measure the $SFDR_3$, the fundamental signal output powers (dB) and IMD3 are measured as a function of input RF powers (dB) and the intercept point of their extrapolated lines of fundamental signal, and IMD3 will give OIP_3. The IMD3 exhibits a slope of three with respect to the input power, whereas the output power of the fundamental signal has a slope of one.

III. Experimental Results and Discussion

A schematic diagram of the experimental setup of the optimised SBS-based phase shifter design is shown in Fig. 2. A laser is split into two equal parts using a 50:50 coupler. In the upper branch, a dual parallel Mach-Zehnder modulator (DPMZM) is employed for a single-sideband generation. The experimental configuration employed an RF amplifier with a gain of 26 dB preceding the 90° hybrid coupler. In the lower branch, an intensity (IM) is used for SBS pump generation. A 5-dB difference is produced between the anti-Stokes component (pump 1) and the Stokes component (pump 2) with a programmable optical filter (POF). Due to a significant SBS loss resonance compared to the gain pump, the interaction between the SBS pump and the carrier in the SBS medium results in attenuation of the optical carrier. In principle, the same configuration can be achieved by using a dual parallel Mach Zehnder Modulator (DPMZM) as a pump and controlling the amplitude of each pump via DC biases, thus reducing the complexity of the system. However, to demonstrate a proof-of-concept, we have utilised the combination of IM with POF.

Additionally, the decline in the link gain can be compensated by employing an Erbium-Doped Fiber Amplifier (EDFA) in the APL. Upon photodetection, the optical carrier's phase shift brought on by the interaction with the pump will be converted to an RF signal. The photodetector of responsivity 0.85 A/W has been used. This method improves the noise figure without DC biasing but through Brillouin-induced low-biasing and improves the linearity. In this analysis, the generation of even-order harmonics is neglected since these are significantly lower than the odd-order sideband. Placing the programmable filter on the pump side creates a strong anti-Stokes response since the anti-Stokes response saturates slower than the Stokes response. This effect cannot be achieved by placing a filter in the APL link after the SBS interaction or after the modulator.

A. *Phase shifter response*

This section illustrates the phase shifter response for various

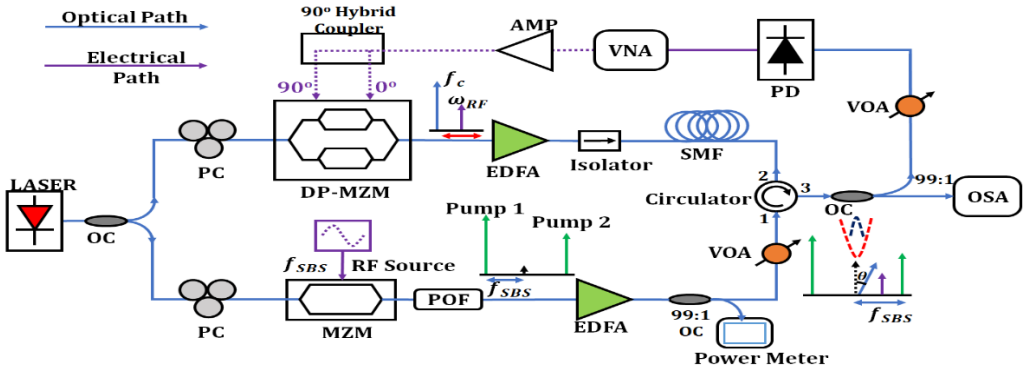

Fig. 2. Experimental setup of the microwave photonic phase shifter with Brillouin-induced low biasing. DPMZM: dual parallel Mach Zehnder Modulator (MZM), SG: signal generator, VNA: vector network analyser, VOA: variable optical attenuator, EDFA: Erbium-doped fiber amplifier, PD: photodetector, AMP: amplifier, PC: polarisation controller, SMF:, OSA: optical spectrum analyzer, OC: optical coupler POF: programmable optical filter.

Authorized licensed use limited to: DELHI TECHNICAL UNIV. Downloaded on July 22,2023 at 05:16:02 UTC from IEEE Xplore. Restrictions apply.
© 2023 IEEE. Personal use is permitted, but republication/redistribution requires IEEE permission. See https://www.ieee.org/publications/rights/index.html for more information.

This article has been accepted for publication in IEEE Journal of Quantum Electronics. This is the author's version which has not been fully edited and content may change prior to final publication. Citation information: DOI 10.1109/JQE.2023.3292060

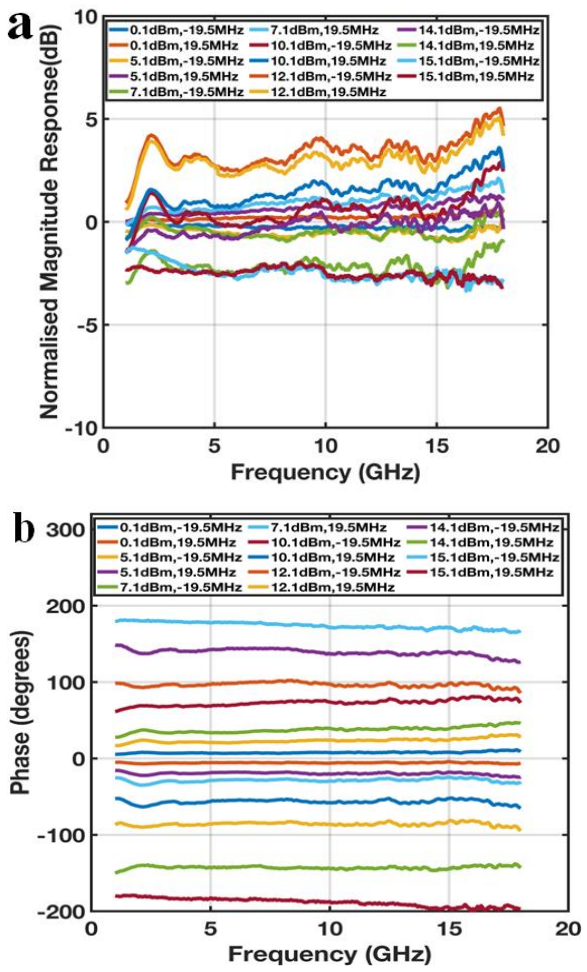

Fig. 3. Experimental SBS phase shifter response without low biasing of the carrier. (a) The magnitude response, and (b) the phase response. Here, the positive and negative phase shift was obtained by detuning pump frequency by -19.5 MHz and +19.5 MHz, respectively, at a photodetector current of 0.85 mA.

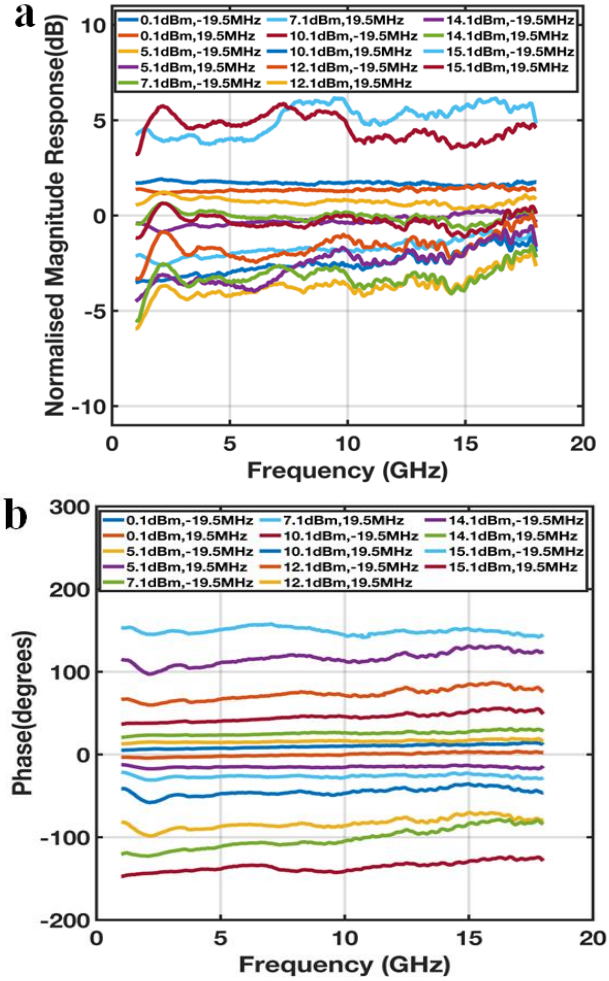

Fig. 4. Experimental SBS phase shifter response with low biasing of the carrier. (a) The magnitude response, and (b) the phase response at a photodetector current of 0.85 mA.

SBS pump powers. For the same MWP link depicted in Fig. 2, the normalised magnitude and the phase response in the case of without low biasing of the optical carrier are illustrated in Fig.3 at 0.85 mA of photodetector current. To measure the phase shift in the case of low biasing of the carrier, we set the experiment such that the photodetector receives the same optical power as in the case without low biasing. When the total pump power is tuned from 0.1 dBm to 15.1 dBm, it shows an equivalent deviation in the phase shift from ±5° to ±180°. As can be seen from Fig. 3, ±180° is obtained in case of without low bias at 15.1 dBm of total pump power. However, as shown in Fig. 4, in the case of low-biasing of the carrier, ±150 deg is recorded because the anti-Stokes response is much stronger than the Stokes response. Due to the frequency limitations of the hybrid coupler, the phase shift is measured for an RF sweep from 1-18 GHz. In Fig 3(a) and 4(a), the fluctuations in the gain response are within ± 5 dB due to slight variations in the relative powers of the two pumps. However, these fluctuations can be optimised by precisely controlling the pump power from the programmable optical filter.

B. Optimization of the APL Performance metrics

A phase shifter was implemented using the experimental setup described in Fig. 2, and related simulations were run to verify the experimental findings. To simulate the link gain and noise figure in MATLAB, a total pump power of 10 and 12 dBm has been used with a 5 dB difference in the SBS anti-Stokes and Stokes pump magnitude, respectively. The simulation also encompasses the depletion which happened at high carrier power as shown in equation (7). Additionally, an SSB modulator with an insertion loss of 5 dB, $V_{\pi,rf}$ value of 3.8 volts, a single mode fiber with a length of 3.2 km having an attenuation of 0.2 dB/km, a Brillouin shift of 10.86 GHz, a Brillouin linewidth of 39 MHz and an EDFA of 20 dB gain has been considered. For modelling the link gain in MATLAB, equation (14) along with equation (4) or (7) has been used depending on undepleted and depleted regime of operation, as shown in Fig. 5. Similarly, equations (15-17) have been used for the noise figure modelling with a laser RIN of -160.5 dBc/Hz and nsp of the EDFA of 2.75.

1) Link gain

Based on the experiment, the SBS phase shifter's link gain is measured at various pump power and photodetector current. The photocurrent is varied by tuning the VOA in the link to test

Authorized licensed use limited to: DELHI TECHNICAL UNIV. Downloaded on July 22,2023 at 05:16:02 UTC from IEEE Xplore. Restrictions apply.
© 2023 IEEE. Personal use is permitted, but republication/redistribution requires IEEE permission. See https://www.ieee.org/publications/rights/index.html for more information.

This article has been accepted for publication in IEEE Journal of Quantum Electronics. This is the author's version which has not been fully edited and content may change prior to final publication. Citation information: DOI 10.1109/JQE.2023.3292060

the insertion loss of the link on the VNA at a specific pump power from 1 GHz to 18 GHz. As illustrated in Fig. 5, the link gain has been compared for both scenarios with and without low-biasing of the carrier at a signal frequency of 5 GHz. Here, the photodetector current varies from 0.17 mA to 2.7 mA, and the link gain is measured for various pump powers. As shown in Fig. 5 (a), at 10 dBm of pump power and a photodetector current of 2.7 mA, the link gain observed is 6 dB and 9 dB, without and with low-biasing, respectively. Also, for the same photodetector current at an SBS pump power of 12 dBm, the link gain is almost the same without low biasing: 6 dB, whereas in the case with low-biasing, the achieved link gain is reduced to 7.9 dB. By doing low bias of the carrier, we are reducing the optical carrier power but increasing the contribution of the RF signal at photodetection (carried by the optical sidebands), so the overall link gain increases.

Similarly, at a signal frequency of 3 GHz, for a pump power of 10 dBm, and at a photodetector current of 2.7 mA, the achievable link gain is 7.6 dB and 10.9 dB, without and with low biasing, respectively. At a pump power of 12 dBm, for the same photodetector current, 8 dB of link gain is measured for without low-biasing and 9.86 dB for low-biasing.

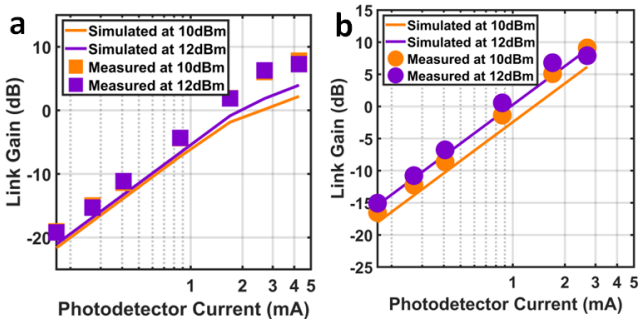

Fig. 5. Measured and simulated link gain vs. photodetector current at 10 dBm and 12 dBm of pump power for (a) without low biasing at 5 GHz RF signal, (b) with low biasing at 5 GHz RF signal.

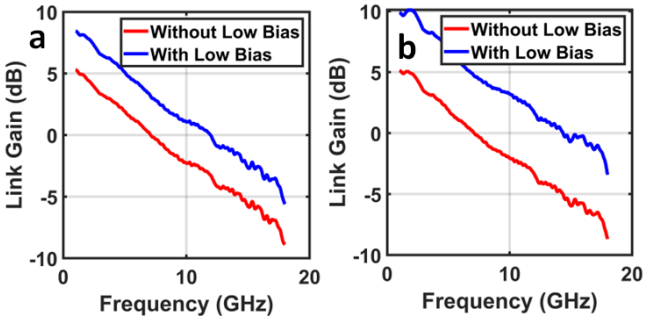

Fig. 6. Observed SBS phase shifter link gain vs. frequency for with and without low biasing of the carrier, at photodetector current of 1.7 mA for (a) 10 dBm of pump power, (b)12 dBm of pump power.

Fig. 6 presents a comparison between the link gain that has been observed with and without the low-biasing of the carrier. The measurements were taken at 10 and 12 dBm of pump power, with a photodetector current of 1.7 mA, and for an RF sweep ranging from 1 to 18 GHz. The data indicate that in both instances, there is a reduction in link gain as frequency increases. This is primarily due to the frequency response of the modulator and photodetector used in the link and also due to the frequency-dependent increase in the value of $V_{\pi,rf}$.

2) Noise Figure

The average optical power at the detector directly contributes to the noise power in the APL. Therefore, low-biasing of the carrier is beneficial to reduce the noise-inducing optical carrier to enhance the link noise performance. An electrical spectrum analyser measures the overall noise contribution in the SBS phase shifter link. Noise power is measured at individual frequencies (3,5,7,9,10.8,13,15, and 17 GHz). Fig. 7(a-b) shows the noise figure (NF) measurement at different pump power for both cases. Again, the photodetector current varies from 0.17 mA to 2.7 mA, and the corresponding NFs are observed. The noise is experimentally measured, and the calculation of the NF includes the noise sources described in section II and is used for simulating the NF. It is observed from fig. 7 (a-b) that when the SBS pump power is 10 dBm and the photodetector current is 2.7 mA, the measured NF is 27.3 dB and 24.7 dB, without and with low-biasing, respectively. We observe that in the case of low biasing of the carrier, the noise figure improves by >2 dB at a pump power of 10 dBm. Similarly, at a signal frequency of 3 GHz and photodetector current of 2.7 mA, at 10 dBm of the pump power, the measured NF is 29.9 dB and 26.8 dB without and with low-biasing of the carrier, respectively. It is observed that, when the SBS pump power is 12 dBm and photodetector current is 1.7mA, the measured NF is 27.4 dB and 24.4 dB, without and with low-biasing, respectively.

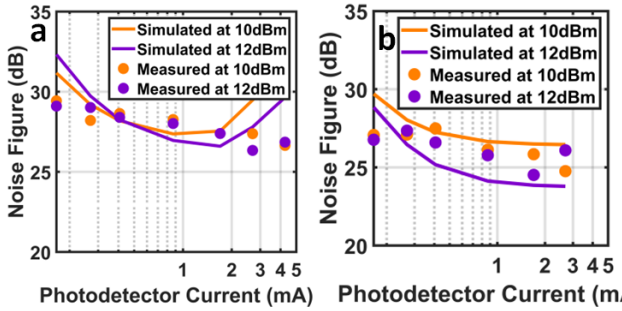

Fig. 7. Observed noise figure contributions as a function of photodetector current for an SBS phase shifter at different pump powers for (a)without low biasing at 5 GHz, and (b) with low biasing of the optical carrier at 5 GHz.

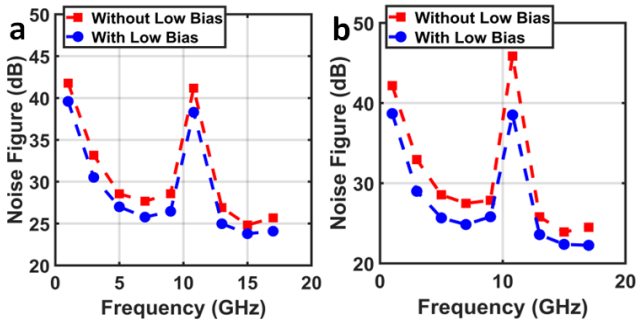

Fig. 8. Measured noise figure vs. frequency for the SBS phase shifter, at photocurrent of 1.7 mA for (a) with and without low biasing of the carrier at 10 dBm SBS pump power, and (b) with and without low biasing of the carrier at 12 dBm of pump power.

Authorized licensed use limited to: DELHI TECHNICAL UNIV. Downloaded on July 22,2023 at 05:16:02 UTC from IEEE Xplore. Restrictions apply.
© 2023 IEEE. Personal use is permitted, but republication/redistribution requires IEEE permission. See https://www.ieee.org/publications/rights/index.html for more information.

This article has been accepted for publication in IEEE Journal of Quantum Electronics. This is the author's version which has not been fully edited and content may change prior to final publication. Citation information: DOI 10.1109/JQE.2023.3292060

A plot of the noise figure vs. frequency is shown in Fig. 8. The comparative plot Fig 8. (a-b) shows improvement of the noise figure for low biasing at all frequencies compared to without low biasing. It has been observed that at 10.8 GHz we have a strong noise contribution due to SBS spontaneous response, which is improved significantly in the case of SBS-induced low biasing. Thus, the noise figure is improved using a strong SBS loss response compared to SBS gain response. This improvement is caused by a slower anti-Stokes wave build-up than the Stokes component, which reduces the noise-inducing effect of spontaneously created photons [35]. It is worth noting that link gain is independent of noise contribution due to SBS spontaneous noise.

3) CDR

As discussed in section II, for calculating the CDR, single-tone analysis is done to obtain $P_{1dB,}$ and for SFDR calculations, a two-tone test is carried out [34] to measure the OIP_3 value. As seen in Fig. 9 the input signal power ranges from -41 dBm to -19 dBm. At a signal frequency of 5 GHz, for 10 dBm of the pump power, at a photodetector current of 0.42 mA, the measured CDR_{1dB} is 124.6 dB.Hz and 126.2 dB.Hz in the case of without and with low-biasing, respectively. At the same signal frequency of 5 GHz and photodetector current for the pump power of 5 dBm (and 12 dBm), the observed CDR_{1dB} in the case of without low bias and with low biasing are 132 dB.Hz (and 127.9 dB.Hz), and 132.8 dB.Hz (and 131.7 dB.Hz), respectively. Clearly, at a signal frequency of 5 GHz, an improvement of roughly 1-4 dB is achieved.

Similarly, at a signal frequency of 3 GHz for a photodetector current of 0.42 mA, and pump power of 5 dBm, the measured CDR_{1dB} is 125.3 dB.Hz and 128.2 dB.Hz without and with low-biasing, respectively. At the same signal frequency of 3 GHz and photodetector current of 0.42 mA, for the pump power of 10 dBm (and 12 dBm), the observed CDR_{1dB} in the case of without and with low-biasing are 116.19 dB.Hz (and 116.97 dB.Hz), and 118.37 dB.Hz (and 119.8 dB.Hz), respectively. So, there is an improvement of >2 dB at the signal frequency of 3 GHz, as illustrated in Fig. 10.

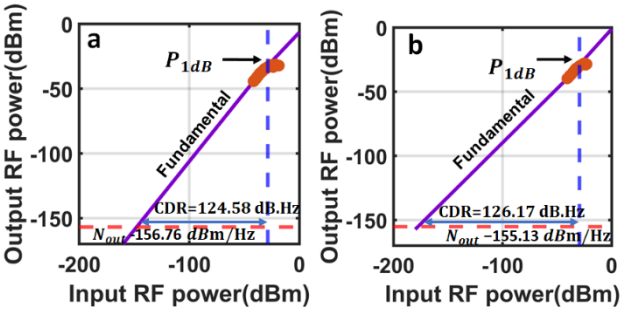

Fig. 9. Measurement of CDR of the phase shifter at a signal frequency of 5 GHz and photodetector current of 0.42 mA for (a) without low biasing at a pump power of 10 dBm, (b) with low biasing at a pump power 10 dBm.

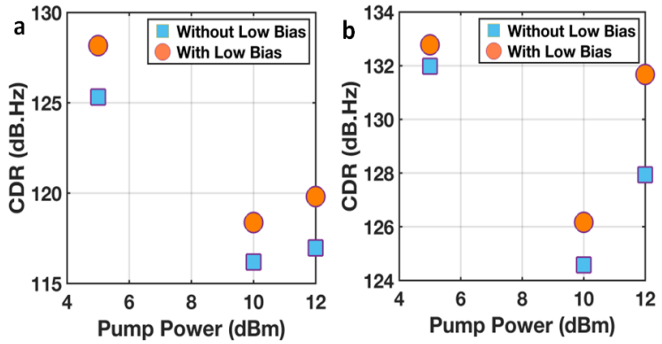

Fig. 10. Measurement of CDR vs pump power at signal frequencies of (a) 3 GHz, (b) 5 GHz, and photodetector current of 0.42 mA.

4) SFDR

Fig. 11 illustrates the measured $SFDR_3$ at a signal frequency of 5 GHz at a photodetector current of 0.42 mA. At a pump power of 10 dBm, the measured $SFDR_3$ is 91.1 $dB.Hz^{2/3}$ and 93.8 $dB.Hz^{2/3}$, without and with low biasing, respectively. At the same signal frequency of 5 GHz, for the pump power of 5 and 12 dBm, the observed $SFDR_3$ without low biasing (and with low biasing) are 91.2 $dB.Hz^{2/3}$ (and 91.6 $dB.Hz^{2/3}$) and 88.3 $dB.Hz^{2/3}$ (and 91 $dB.Hz^{2/3}$), respectively. As seen in Fig. 12, there is an improvement of >2-3 dB at a signal frequency of 5 GHz.

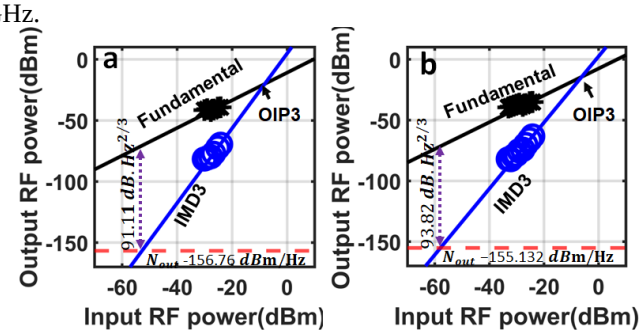

Fig. 11. Measurement of the SFDR of the phase shifter at a signal frequency of 5 GHz and photodetector current of 0.42 mA for (a) without low biasing at pump power 10 dBm, (b) with low biasing at pump power 10 dBm.

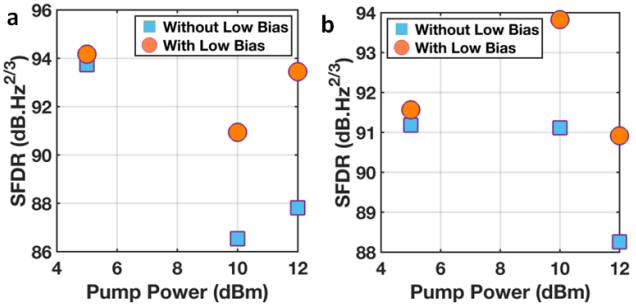

Fig. 12. Measurement of SFDR vs pump power at signal frequencies of (a) 3 GHz, (b) 5 GHz, and photodetector current of 0.42 mA.

Similarly, it is noted that at a signal frequency of 3 GHz, at the pump power of 5 dBm, the measured $SFDR_3$ without and with low biasing is 93.7 $dB.Hz^{2/3}$ and 94.2 $dB.Hz^{2/3}$,

Authorized licensed use limited to: DELHI TECHNICAL UNIV. Downloaded on July 22,2023 at 05:16:02 UTC from IEEE Xplore. Restrictions apply.
© 2023 IEEE. Personal use is permitted, but republication/redistribution requires IEEE permission. See https://www.ieee.org/publications/rights/index.html for more information.

This article has been accepted for publication in IEEE Journal of Quantum Electronics. This is the author's version which has not been fully edited and content may change prior to final publication. Citation information: DOI 10.1109/JQE.2023.3292060

respectively. Also, for the pump power of 10 and 12 dBm, the observed $SFDR_3$ without (and with low-biasing) are 86.5 dB.Hz$^{2/3}$ (and 90.9 dB.Hz$^{2/3}$) and 87.8 dB.Hz$^{2/3}$ (and 93.4 dB.Hz$^{2/3}$), respectively. Therefore, there has been an improvement of 1-5 dB at the signal frequency of 3 GHz. It is noted that at both frequencies, compared to those without low biasing, the SBS-induced low biasing shows better performance, as shown in Fig. 12.

Upon comparison of Fig. 9 and Fig. 11, it is observed that there exists a deviation in the link gain of the fundamental component due to the RF powers available for the experiments being different (more for CDR and lower for SFDR due to the need for power combiners and additional components). However, the link gain is within ±2 dB between both measurements. It can be noticed that we carried out the experiment to provide the proof-of-concept for a fixed 5 dB difference between the loss and gain pumps. The performance metrics could significantly improve with a different value for the power difference between the unbalanced pumps.

IV. APPLICATIONS

This section presents the application of our optimised microwave photonic phase shifter design. We discuss the results of transmitting a 16/64 QAM (quadrature amplitude modulation) signal through the APL in section IV(A), followed by transmitting linear frequency-modulated waveforms (LFM) in section IV(B). The demonstration is done for the without low bias case.

A. QAM Signals

We demonstrated an application of the SBS phase shifter by transmitting a 16-QAM and then a 64-QAM signal with a central frequency of 1 GHz at different SBS pump powers through the microwave photonic link and analysed its effect on the error vector magnitude (EVM). The present configuration employs a 16/64 QAM modulation scheme with a bandwidth of 150 kHz, as constrained by the instantaneous bandwidth of the signal generator. The primary purpose of demonstrating this application is to show that the SBS phase shifter did not affect the digital modulation scheme.

1) The phase shifter did not significantly affect the transmitted signal when a 16 QAM signal was sent through the APL. As illustrated in Fig. 13(a, b), the error vector magnitude (EVM) in this instance with a fixed carrier power of 5 dBm was calculated to be 4.5% (without SBS) and 5.8 % (with SBS at 10 dBm of pump power). When the pump power is increased further from 10 dBm to 12 dBm for the same optical carrier power, the reported EVM is 6.1%. Additionally, the EVM improves from 5.8 % to 5.2 % when the carrier power is increased from 5 dBm to 10 dBm at a fixed pump power of 10 dBm.

2) On transmitting a 64 QAM signal for fixed carrier power of 5 dBm, the EVM was measured to be 4.7% (without SBS) and 4.9% (with SBS at 10 dBm of pump power), as shown in Fig. 13 (c, d).

Fig. 13 illustrates that the Kerr effect has the potential to induce phase rotation of symbols [23], resulting in distortion of constellations, even in the absence of the SBS pump. Also, it has been observed that a slight degradation in EVM value has been observed in the case of using SBS due to the induced SBS noise.

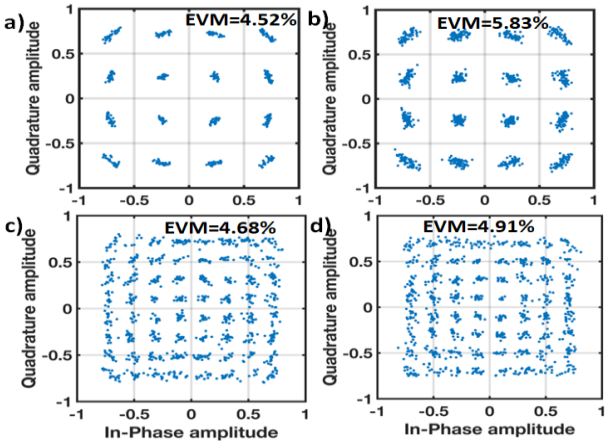

Fig. 13. Experimentally obtained constellation diagrams at 5 dBm of optical carrier power for (a) without SBS for 16 QAM, (b) with SBS for 16 QAM at 10 dBm of pump power, (c) without SBS for 64 QAM, and (d) with SBS for 64 QAM at 10 dBm of pump power.

B. LFM Signals

In the second application in the context of RADAR systems, we transmitted linear frequency modulated (LFM) waveforms through the APL, as LFM signals have better range resolution because of their excellent pulse compression property [37]. As shown in Fig. 14(a), an LFM signal of 10 μsec duration with a 900 MHz carrier is generated using an arbitrary waveform generator (AWG) with a chirp bandwidth of 100 MHz. It presents a comparison between two LFM waveforms, one before transmission through a link (blue) and the other after transmission through a link (orange). The objective was to demonstrate the latency associated with a fiber optic cable spanning a distance of 3.2 kilometres. The second part, denoted as b), involves comparing the signals after they have traversed the link (essentially a zoomed-in version of Fig. 14 (a)) to demonstrate the impact of the SBS phase shifter. Two LFM waveforms were compared, one with stimulated Brillouin scattering (SBS) enabled and the other with SBS disabled.

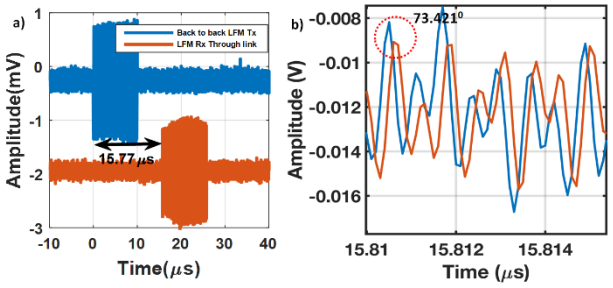

Fig. 14. a) Transmitted LFM waveforms monitored on an oscilloscope without sending it through the APL (blue), and the received LFM waveform sent through the APL (orange), (b) zoomed-in time trace of the received LFM without SBS (blue) and with SBS (orange) sent through the APL.

Authorized licensed use limited to: DELHI TECHNICAL UNIV. Downloaded on July 22,2023 at 05:16:02 UTC from IEEE Xplore. Restrictions apply.
© 2023 IEEE. Personal use is permitted, but republication/redistribution requires IEEE permission. See https://www.ieee.org/publications/rights/index.html for more information.

This article has been accepted for publication in IEEE Journal of Quantum Electronics. This is the author's version which has not been fully edited and content may change prior to final publication. Citation information: DOI 10.1109/JQE.2023.3292060

When a signal is sent across the link and then received back-to-back, a delay of 15.77 μsec is measured. This is consistent with the theoretically predicted delay of 3.2 km of Single-mode fiber. After passing the signal through the APL, we measured the phase change of 73.4 degrees at 10.1 dBm of pump power over a 10 μsec duration, which is within ±3° of the result shown in Fig. 3(b).

V. Discussions

The novel SBS-phase shifter system used in this work enables the independent link optimisation procedure without compromising the phase shifter features. The scheme applies SBS-induced low biasing to improve the linearity, dynamic range in terms of CDR and SFDR, and the noise figure. In section III, various performance metrics for phase shifter links are experimentally optimised, and a wide frequency range from 1 GHz to 18 GHz was used to characterise the link performance. The proposed phase shifter in terms of APL metrics (G, NF, CDR, and SFDR) performed better in the case of SBS-induced low-biasing compared to without low biasing of the carrier, even at a higher photodetector current. It has been observed that the phase shifter designed using SBS-induced low biasing performed optimally at a signal frequency of 5 GHz at a pump power of 10 dBm with positive link gain of 9 dB and NF of 24.7 dB, CDR_{1dB} and $SFDR_3$ of 132.8 dB.Hz and 93.8 $dB.Hz^{2/3}$ respectively.

The ASE noise from EDFA amplified by SBS gain process and the spontaneously generated photons from SBS are two of the key causes of performance degradation. By adopting low-noise EDFA in the MWP link, noise power caused by ASE can be reduced. As mentioned in section III, utilising a strong SBS loss response compared to the SBS gain response improves the noise figure. As was covered in section II, NF can be enhanced by improving the link gain. The link gain of the APL can be increased by feeding a strong laser signal into the modulator [41]. Since noise levels rise as laser power increases, the tradeoff can be mitigated by using a laser with a better RIN.

VI. Conclusion and Future Work

To the best of our knowledge, this paper is the first to model the Brillouin-based microwave photonic phase shifter's performance metrics and to demonstrate the technique for improving the analog performance metrics, including the linearity and noise performance of the phase shifter. We optimised the link parameters of the phase shifter through the SBS-induced low-biasing of the carrier. Additionally, this technique does not produce even-order harmonics since the carrier is low-biased due to Brillouin effects rather than voltage-based low-biasing, which generally produces even-order nonlinear components. The low biasing of the carrier is achieved by using unbalanced Stokes and anti-Stokes SBS components. The noise performance is also improved due to the use of dominant Anti-Stokes interactions compared to the Stokes interaction. The mathematical expressions for the analog photonic link performance metrics are derived, optimised, and the theoretical results are experimentally verified in terms of link gain, noise figure, spurious free dynamic range, and compression dynamic range.

In the SBS-induced low biasing regime, we observed enhancement in the performance in terms of linearity and noise figure by ~3 dB compared to without low biasing. Additionally, SBS-induced low-biasing of the carrier results in $SFDR_3$ improvement of 4 dB and CDR improvement of >2 dB. To demonstrate compatibility with real-life applications, 16-QAM and 64-QAM signals are passed through the designed phase shifter, which shows minimal degradation and is promising for digital communications applications. Additionally, linear frequency-modulated signals are sent through the phase shifter, which can have potential applications in RADAR systems, particularly in steerable communication links and radar pulse generation. The combination of a phase shifter and a linear frequency modulation (LFM) waveform exhibits potential for utilisation in low probability of intercept (LPI) radar and synthetic aperture radar (SAR) applications. This work can be further extended on an integrated platform for wireless applications. The incorporation of this phase shifter would enable its use in practical systems, increase robustness, the dynamic range of operation, and better noise performance, and decrease the size, cost, and power consumption.

References

[1] R. J. Mailloux, "Phased Array Antenna Handbook," Artech House, 2005.

[2] C. W. Yuan et al., "Designs and experiments of a novel radial line slot antenna for high-power microwave application," IEEE Trans. Antennas Propag. vol. 61 no. 10 pp. 4940-4946 Oct. 2013.

[3] Y. M. Yang et al., "A novel phase shifter for Ku-band high-power microwave applications" IEEE Trans. Plasma Sci. vol. 42 no. 1 pp. 51-54 Jan. 2014.

[4] L. McKay et al., "Broadband Brillouin phase shifter utilizing RF interference: Experimental demonstration and theoretical analysis," Journal of Lightwave Technology, 38, 3624-3636, 2020.

[5] W. Li et al., "A wideband 360° photonic-assisted microwave phase shifter using a polarization modulator and a polarization-maintaining fiber bragg grating," Opt. Express 20, 29838-29843 (2012).

[6] L. Bui, "Wideband RF photonic second order vector sum phase-shifter," IEEE Microw. Compon. Lett 15, 309-311, (2005).

[7] J. Capmany and D. Novak, "Microwave photonics combine two worlds," Nat. photonic, 1, pp. 319-330, 2007.

[8] J. Yao, "Microwave Photonics," J. of Lightwave Technol, vol. 27, no. 3, 314-335 (2009).

[9] R. Minasian, "Photonic signal processing of microwave signal," IEEE Trans. Microw. Theory Tech., vol. 54, no. 2, pp. 832-846, 2006.

[10] W. Xue et al., "Wideband 360° microwave photonic phase shifter based on slow light in semiconductor optical amplifiers," Opt. Express 18, 6156-6163 (2010).

[11] J. Sancho et al., "Fully tunable 360° microwave photonic phase shifter based on a single semiconductor optical amplifier," Opt. Express 19, pp.17421-17426 (2011).

[12] M. Pu et al., "Tunable Microwave Phase Shifter Based on Silicon-on-Insulator Microring Resonator," in IEEE Photonics Technology Letters, vol. 22, no. 12, pp. 869-871, 2010.

[13] M. Pu et al., "Widely tunable microwave phase shifter based on silicon-on-insulator dual-microring resonator," Opt. Express 18, 6172-6182 (2010).

[14] N. Ehteshami et al., "Optically tunable full 360° microwave photonic phase shifter using three cascaded silicon-on-insulator microring resonators," Opt. Comm., vol. 373, pp. 53-58, 2016.

[15] S. X. Chew et al., "Integrated microwave photonic phase shifter with full tunable phase shifting range (> 360°) and RF power equalization," Opt. Express 27, 14798-14808 (2019).

[16] W. Liu, W. Li and J. Yao, "An Ultra-Wideband Microwave Photonic Phase Shifter With a Full 360 degree Phase Tunable Range," in IEEE Photonics Technology Letters, vol. 25, no. 12, pp. 1107-1110, 2013.

[17] Y. Yin et al., "Frequency-Dependent and Full Range Tunable Phase Shifter" World Academy of Science, Engineering and Technology,

Authorized licensed use limited to: DELHI TECHNICAL UNIV. Downloaded on July 22,2023 at 05:16:02 UTC from IEEE Xplore. Restrictions apply.
© 2023 IEEE. Personal use is permitted, but republication/redistribution requires IEEE permission. See https://www.ieee.org/publications/rights/index.html for more information.

This article has been accepted for publication in IEEE Journal of Quantum Electronics. This is the author's version which has not been fully edited and content may change prior to final publication. Citation information: DOI 10.1109/JQE.2023.3292060

International Journal of Physical and Mathematical Sciences vol.12, no.10, 2018.

[18] E. H. W. Chan et al., "Photonic RF Phase Shifter Based on Optical Carrier and RF Modulation Sidebands Amplitude and Phase Control," in Journal of Lightwave Technology, vol. 30, no. 23, pp. 3672-3678, 2012.

[19] J.Shen et al., "A Photonic RF Phase Shifter Based on a Dual-Parallel Mach-Zehnder Modulator and an Optical Filter," Applied Physics Express, vol.5, no.7 , (2012).

[20] S. Pan and Y. Zhang, "Tunable and wideband microwave photonic phase shifter based on a single-sideband polarization modulator and a polarizer," Opt. Lett. 37, 4483-4485 (2019).

[21] A. Loayssa and F. J. Lahoz, "Broad-band RF photonic phase shifter based on SBS," Photon. Technol Lett 18, 208-210 (2006).

[22] D. Marpaung et al., "On-chip stimulated Brillouin scattering for microwave photonic signal processing," in Optical Fiber Communication Conference, OSA Technical Digest (online) (Optica Publishing Group, 2016), paper W1G.1.

[23] G. Agrawal, "Nonlinear Fiber Optics", Elsevier, 2012.

[24] M. Pagani, D. Marpaung, and B. J. Eggleton, "Ultra-wideband microwave photonic phase shifter with configurable amplitude response," Opt. Lett. 39, 5854-5857 (2014).

[25] M. Pagani et al., "Tunable wideband microwave photonic phase shifter using on-chip stimulated Brillouin scattering," Opt. Express 22, 28810-28818 (2014)

[26] I. Aryanfar et al., "Chip-based Brillouin radio frequency photonic phase shifter and wideband time delay," Opt. Lett. 42, 1313-1316 (2017).

[27] L. McKay et al., "Brillouin-based phase shifter in a silicon waveguide," Optica 6, 907-913 (2019).

[28] Y. Liu et al., "All-optimized integrated RF photonic notch filter," Opt. Lett. 42, 4631-4634 (2017).

[29] Y. Liu et al., "High-Performance Chip-Assisted Microwave Photonic Functionalities," in IEEE Photonics Technology Letters, vol. 30, no. 21, pp. 1822-1825, 1 2018.

[30] Y. Xie *et al*., "System-Level Performance of Chip-Based Brillouin Microwave Photonic Bandpass Filters," in Journal of Lightwave Technology, vol. 37, no. 20, pp. 5246-5258, 2019.

[31] R. Parihar, et al., "Design of Microwave Photonic Sub-system using stimulated Brillouin scattering," J. of Lightwave Technol, 39, 977-991 (2021).

[32] M. F. Ferreira, J. F. Rocha, J. L. Pinto, "Analysis of the gain and noise characteristics of fibre Brillouin amplifiers," Optical & Quantum Electronics, vol. 26, no. 1, pp. 35-44, 1994.

[33] A. Choudhary, et al., "Linearity and resolution of on-chip Brillouin filters for RF and optical communications," CLEO Pacific Rim, Singapore (2017).

[34] V. J. Urick, J. McKinney, K. J. Williams, "Fundamentals of microwave photonics", Wiley, 2015.

[35] A. Choudhary, et al., "Brillouin Filtering with Enhanced Noise Performance and Linearity using anti-Stokes Interactions," CLEO, San Jose, USA (2018).

[36] M. Pagani, et at., "A study of linearity performance of Stimulated Brillouin Scattering based microwave photonic bandpass filter," J. Lightwave Technol. 32, 999-1005 (2014).

[37] P. Zhou *et al.*, "Generation of LFM Waveforms by a Frequency-Sweeping Optoelectronic Oscillator," J. of Lightwave Technol. 36, 3927-3934 (2018).

[38] C.L. Tang, "Saturation and spectral characteristics of the Stokes emission in the Stimulated Brillouin process," J. Appl. Phys., vol. 37, no. 8, pp. 2945-2955, 1966.

[39] Y. Liu et al., "Integrated Microwave Photonic Filters", Advances in Optics and Photonics, 12, 485-555, 2020.

[40] Ferreira, M.F., Rocha, J.F. & Pinto, J.L. Analysis of the gain and noise characteristics of fibre Brillouin amplifiers. Opt Quant Electron 26, 35–44 (1994).

[41] Y. Liu, et al.,, "Link Performance Optimization of Chip-based Si3N4 Microwave Photonic Filters," J. of Lightwave Technol, vol. 36, pp. 4361-4370, 2018

Reena Parihar is a PhD student in the Department of Electrical Engineering at IIT Delhi. She joined the group in January 2020, and her research area is Microwave photonics and nonlinear optics. She is a recipient of the PMRF fellowship. She is also an active member of IEEE, Optica, and SPIE.

Rajveer is a research scholar in the Department of Electrical Engineering at IIT Delhi, India. He has a master's in engineering in wireless communication. He is involved in research on microwave photonics, which uses photonics to generate and process signals for various applications.

Amol is an Assistant Professor at the Department of Electrical Engineering at the Indian Institute of Technology (IIT), Delhi where he leads the UltraFast Optical Communications and High-performance Integrated Photonics (UFO-CHIP) group. He received his PhD from the Optoelectronics Research Center at the University of Southampton, MSc in Photonics from the University of St Andrews, Gent University, VUB Brussels and BEng from the Delhi College of Engineering. Before joining IIT Delhi, he was a DECRA fellow at the University of Sydney and an EPSRC Doctoral Prize fellow at the University of Southampton. His research areas are laser physics, nonlinear optics, microwave photonics, and optical communications. He received the 2020 Institute of Engineers India (IEI) Young Engineer Award and the 2018 Optica Ivan P Kaminow Outstanding Early Career Professional Prize.

Authorized licensed use limited to: DELHI TECHNICAL UNIV. Downloaded on July 22,2023 at 05:16:02 UTC from IEEE Xplore. Restrictions apply.
© 2023 IEEE. Personal use is permitted, but republication/redistribution requires IEEE permission. See https://www.ieee.org/publications/rights/index.html for more information.

ResearchGate

See discussions, stats, and author profiles for this publication at: https://www.researchgate.net/publication/371685423

Machine Learning & Artificial Intelligence in Production Planning and Control

Conference Paper · November 2022

DOI: 10.35629/5252-041111201126

CITATIONS
0

READS
8

5 authors, including:

Chitrasen Maitry
Delhi Technological University
2 PUBLICATIONS **0** CITATIONS
SEE PROFILE

Ashok Kumar Madan
Delhi Technological University
33 PUBLICATIONS **89** CITATIONS
SEE PROFILE

Aakarsh Dwivedi
Delhi Technological University
2 PUBLICATIONS **0** CITATIONS
SEE PROFILE

All content following this page was uploaded by Chitrasen Maitry on 19 June 2023.

The user has requested enhancement of the downloaded file.

International Journal of Advances in Engineering and Management (IJAEM)
Volume 4, Issue 11 Nov. 2022, pp: 1120-1126 www.ijaem.net ISSN: 2395-5252

Machine Learning & Artificial Intelligence in Production Planning and Control

Aakarsh Dwivedi[1], Chitrasen Maitry[2], Hrishikesh Raj[3], AshishGupta[4], Ashok Kumar Madan[5]

[1]*Student, Dept. of Production Engineering, Delhi Technological University, New Delhi, India*
[2]*Student, Dept. of Productionl Engineering, Delhi Technological University, New Delhi, India*
[3]*Student, Dept. of Production Engineering, Delhi Technological University, New Delhi, India*
[4]*Student, Dept. of Production Engineering, Delhi Technological University, New Delhi, India*
[5]*Associate Professor, Dept. of Mechanical Engineering, Delhi Technological University, New Delhi, India*

Date of Submission: 25-11-2022 Date of Acceptance: 06-12-2022

I. INTRODUCTION:

A new era of enhanced digitalization and connectivity is being ushered in by recent technical advancements in the industrial sector. The Fourth Industrial Revolution (i.e., Industry 4.0) and smart factory concepts have recently conceptualized a technology-oriented manufacturing paradigm that can accomplish flexibility, agility, personalization, and decentralization of the production processes. Industry 4.0 also denotes a paradigm change away from the conventional lean thinking philosophy, which is characterized by little adaptability, and toward the production management method. Currently, production procedures are dynamically changed to actively satisfy consumer wants and create a wide range of low-cost products. To this purpose, a reduced product life cycle, a high level of product variability, and an escalating level of international competition distinguish the manufacturing ecosystem of today.

Rüßmann et al. have recognised nine technologies as being essential industry 4.0 enablers (14.0). Big Data Analytics (BDA) is one of these technologies that is essential for utilizing the wealth of data coming from smart factories. BDA specifically uses machine learning (ML) techniques to enable computers to learn from the past and improve performance metrics at a particular activity. According to Cadavid et al., the recent development of powerful computing capabilities and an increase in storage capacity have made ML approaches an alluring approach to solving manufacturing-related problems.

Any manufacturing system must perform the essential task of production planning and control (PPC). Large-scale decision-making procedures about the production plans, delivery plans, productivity, and profitability are implied by this functionality. However, using machine learning (ML) techniques, the information gathered during the course of production could be useful in lowering costs while enhancing efficiency, quality, and sustainability. According to Cadavid et al., over 75% of the potential uses for ML in PPC are either not considered at all or minimally researched. This claim is supported by the rising body of conceptual research that suggests fresh methods for applying ML/AI in PPC. Nevertheless, the lack of expertise with the numerous application domains and their individual scopes is a significant barrier to the adoption of ML/AI in PPC. Because of this, the goal of this research is to outline the numerous PPC ML/AI application domains.

In order to comprehend the present state-of-the-art of ML/AI in manufacturing and supply chain systems, some recent studies have examined the literature. In order to describe the various approaches utilized in ML-aided PPC, Cadavid et al. reviewed 93 research application publications. They then presented a mapping to understand further research viewpoints. For ML in industrial applications since the year 2000, Bertolini et al. offered a thorough literature study, taking into account the application of ML algorithms in operations management.

This study is an expansion of the work done by, intending to further focus the analysis's focus on how current technical breakthroughs are being used to improve decision-intensive activities in PPC.

In essence, this literature review has two goals: first, it will conduct a general statistical analysis of contemporary manufacturing systems publications. After the recent rise of the idea of

International Journal of Advances in Engineering and Management (IJAEM)
Volume 4, Issue 11 Nov. 2022, pp: 1120-1126 www.ijaem.net ISSN: 2395-5252

Industry 4.0, this analysis tries to understand the main research trends and the most popular keywords for AI and ML in the manufacturing industry.

It also provides a mapping to identify the decision-intensive application domains for ML/AI in PPC.

The rest of this essay is structured as follows. First, Section 2 describes the methods used. A preliminary study of the prevalent trends in the literature on AI/ML enabled manufacturing systems is presented in Section 3. The recommended mapping for the use of AI/ML PPC-intensive tasks is discussed in Section 4. Finally, Section 5 offers some conclusions.

II. METHODOLOGY:

Forexamining, the scientific contributions found in the literature, this survey uses a methodical methodology. The three-step process depicted in Figure 1 provides a systematic framework for analysing the most recent papers in the field of AI & ML in industrial systems. The papers that will be examined for the analysis must first be gathered and chosen. The next step is to conduct a preliminary analysis with the goal of identifying the key research trends about AI/ML in manufacturing systems. Finally, the focus of this work is on ML/AI-based PPC decision assistance tools.

The scientific database Scopus was used to complete the first phase. The search was made to find research related to manufacturing and industry that contain the terms artificial intelligence or machine learning in their title, abstract, or keywords.

In order to accomplish this, the search string utilised was ((machine AND learning) OR (artificial AND intelligence)) AND TITLE-ABS-KEY .The following inclusion criteria were used to compile 1094 publications in order to more precisely tailor the analysis's scope:

Year of Publications: Since 2011 was the year that I4.0 was introduced, we restricted our search to papers from that year. The analysis did not include the Year 2021 because it had not been finalised at the time this report was produced.

Documents type: For this analysis, only journal publications were taken into account.

Final publication stage: This criterion's goal is to keep you away from documents that aren't ready for publication. As a result, the included documents are comprehensive, approved, and published in reputable scientific journals.

Language:English.

Source type: journals.

Subject area: “Computer Science” and “Engineering”.

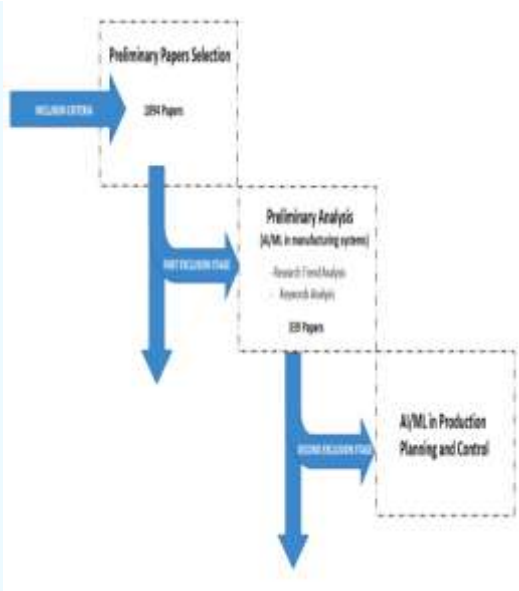

PRELIMINARY ANALYSIS:

We had to use a manual selection procedure to narrow the scope of the selected publications in order to conduct a preliminary study (i.e., first exclusion stage process). As a result, 339 papers were selected from the previously mentioned 1094 papers using the following criteria:

1. All studies that were reviews or surveys were not included in the study.
2. Due to several documents being outside the purview of the field of industry and manufacturing research, all out-of-scope papers were disregarded.
3. The exclusion of conceptual works. These publications offer a mathematical argument for an ML idea rather than any application or implementation.

Research Trend Analysis:

Industry 4.0 research has generally had a fairly positive trend in recent years. In the context of the Fourth Industrial Revolution, the concepts of machine learning and artificial intelligence are crucial. The number of publications on AI/ML in industrial systems increased modestly over the first five years after the advent of Industry 4.0, rising from six in 2011 to 19 in 2015. The quantity of journal papers on ML/AI in industrial systems, however, has increased dramatically in the years since, nearly doubling in 2016. The number of publications increased steadily over the ensuing years, reaching 95 in 2020. A graphic illustration of the research trend from 2011 to 2020 is shown in Figure.

International Journal of Advances in Engineering and Management (IJAEM)
Volume 4, Issue 11 Nov. 2022, pp: 1120-1126 www.ijaem.net ISSN: 2395-5252

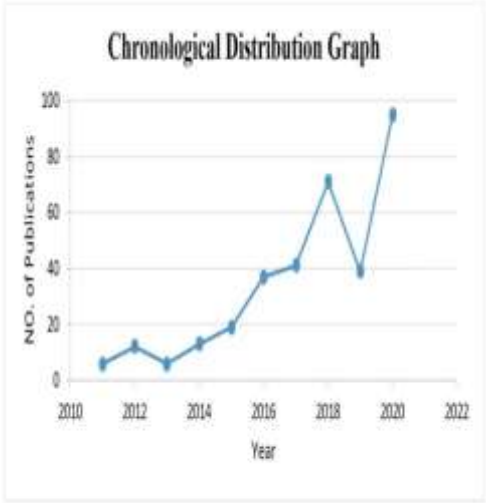

Fig. 2. Chronological distribution curve

We choose to take the minimum number of occurrences per keyword to be 10 in order to analyse the most popular keywords in the literature on machine learning and AI in industrial systems. However, we divided the keywords into four main groups based on their nature and scope: ML/AI methodology, industry applications, research disciplines, and research objectives.

1. **Research fields:** Broadly semantic keywords fall within this group. As a result, they speak about a general field of study, such as Industry 4.0, artificial intelligence, and machine learning. The variety of terms in this category suggests that machine learning and AI have been used in the industrial sector as part of a larger research framework. As seen in Figure 3, the terms "artificial intelligence" and "machine learning" are used the most. This is to be expected because these terms form the cornerstones of the literature study.

Similarly, industry 4.0 has 23 terms that are frequently repeated. Interesting terms that indicate their favourable link to the applications of ML/AI in the industrial systems research body include the internet of things, computer vision, information management, and intelligent systems.

2. **Research Objectives:** Keywords of this category provide a good insight into the major aims and research objectives of AI/ ML in the manufacturing industry. We utilized the Vosviewer software [10] to show patterns and relationships between the keywords representing these different research objectives.

Generally, Forecasting and Decision-making are the most common keywords in this category. Based on Figure 4, it is evident they are centred around various keywords shaping a green and red cluster, respectively. However, most of the other identified research objectives (i.e., Optimization, Prediction, Classification, and Scheduling) are orbiting on Forecasting and decision- making. This indicates an intertwined research body where research objectives have a broad and highly interrelated spectrum. On the other hand, the blue cluster is more difficult to define in terms of a particular research goal, but image recognition is still a key component of this cluster. Notably, the high frequency of process and quality control keywords stands out in the blue cluster, demonstrating a strong connection between image recognition as an imaging research goal and quality and process control.

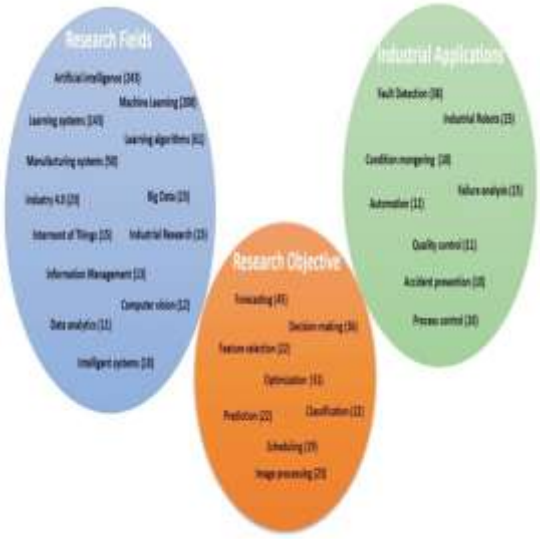

Fig. 3. Research Fields, Research objectives, and industrial Applications keywords with number of occurrences

3. **Industrial applications:** The most prevalent uses of AI/ML in manufacturing systems are denoted by keywords from this class. With 38 occurrences, fault detection is the keyword that appears the most frequently in this category. However, it is clear from Figure 4's term cloud that fault detection is closely related to other words in this category (e.g., failure analysis and condition monitoring). These terms are primarily associated with the maintenance industry, supporting the claim made in [9] that factory maintenance is a growing area of research. With 37 instances, the term "industrial robots" is also becoming increasingly popular, highlighting the recent trend of study in this

International Journal of Advances in Engineering and Management (IJAEM)
Volume 4, Issue 11 Nov. 2022, pp: 1120-1126 www.ijaem.net ISSN: 2395-5252

field. Evidently, the ten accidents prevention situations lay at the heart of an intriguing focus on the use of AI/ML in industrial safety. However, PPC-related tasks include those related to automation, quality control, and process control. As a result, the constant use of these keywords points to a growing yet extensive literature of AI/ML enabled PPC applications.

4. **Machine learning & AI methodologies:** This category comprises terms pertaining to applying an AI strategy or a particular ML method. The classification can be useful because it offers a useful perspective on the most popular AI/ML methodologies. The most often used keywords in the literature corpus are Support Vector Machines (SVM) and Neural Networks (NN) in this context. A significant adoption of artificial neural networks (ANN) in general is also indicated by the persistence of deep learning and deep neural networks. Notably, fuzzy logic and decision trees are also frequently used terms, indicating a rise in research on expert systems and black-box machine learning techniques. The relative frequency distributions for the most popular ML/AI methodology in this study field are shown in Figure below.

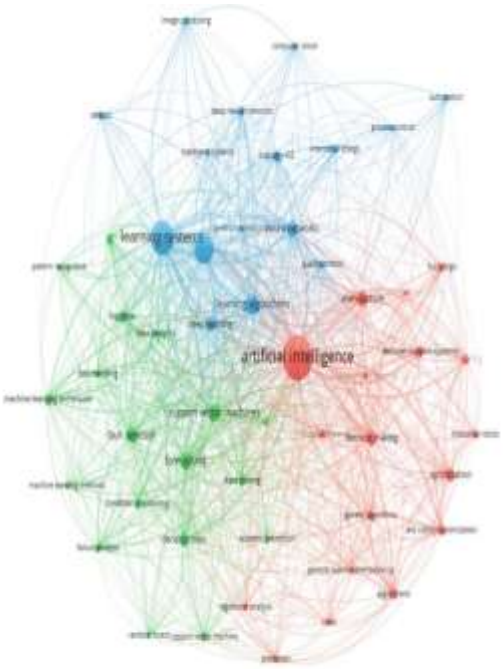

Fig. 4. Keywords cloud by VOSviewer [10]

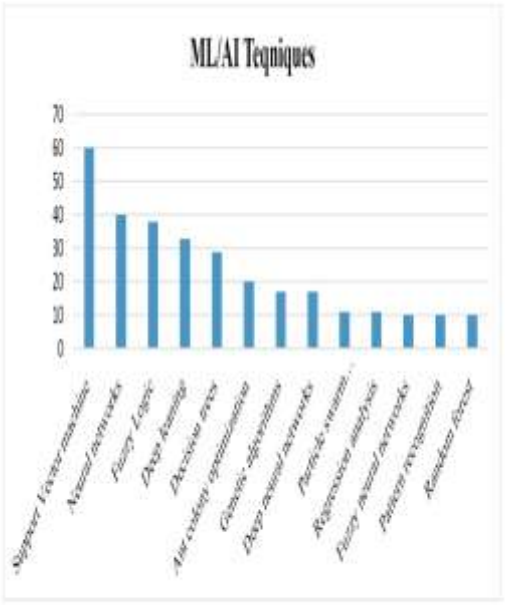

Fig. 5. Keywords occurrences of ML/AI methodologies

ML/AI FOR DECISION INTENSIVE TASKS IN PRODUCTION PLANNING AND CONTROL

In this section, we discuss the application areas of ML/AI in decision-intensive tasks within the function of PPC. With the aim to filter the relevant papers, some additional exclusion criteria were applied.

- We just looked at application materials. This criterion is meant to look into potential uses in production planning and control.
- We only included apps that entail making decisions on the shop floor.
- Papers that only deal with optimization and decision-making problems heuristically. But heuristic optimization techniques are taken into consideration when used in conjunction with ML/AI method.

We were able to locate some relevant publications that concentrate on decision-related activities in production planning and control using these criteria. These papers were grouped around the three main pillars that make up the most recent uses of AI/ML in PPC in the corpus of literature. As each category includes at least one study and suggests a potential use of AI/ML in PPC, each pillar was further divided into sub-categories.

International Journal of Advances in Engineering and Management (IJAEM)
Volume 4, Issue 11 Nov. 2022, pp: 1120-1126 www.ijaem.net ISSN: 2395-5252

One of the most notable examples of the use of AI/ML in production planning and management is considered to be smart scheduling. Due to the rise of industry 4.0, manufacturing systems are heading toward the seamless mass customisation of both products and production processes. Because the allotted apparitions can be rapidly redirected to other machines, the dynamic nature of industrial systems necessitates the adoption of a dynamic scheduling paradigm to deal with unforeseen events that interfere with the execution of a schedule. In the AI/ML-PPC literature, dynamic scheduling has three main forms. In terms of dynamic scheduling, it is either task-, resource-, or line-oriented:
Dynamic Scheduling

Tasks' Re-scheduling: It considers the rescheduling of a particular task as a response to a disruption in the original work plan inside the production process. The method suggested for ANN-enhanced evolutionary algorithm, which attempts to address the issue of simultaneous task processing on a particular computer, is an illustration of this application.

Resource Allocation: This category focuses on the use of dynamic scheduling on flexible shop floors with a resource-focused approach. The application of ML/AI should improve the capacity to allocate resources to deal with interruptions to plans in a dynamic production environment. For instance, suggests a resource allocation decision support system based on the (ANN) and fuzzy analytic network technique (FANP). In a flexible manufacturing environment, this application seeks to improve the machine selection process.

Line Balancing: This category of applications deals with rebalancing the manufacturing line following potential interruptions. In order to detect process anomalies and undertake dynamic reconfigurations for production line parameters, suggested an approach based on support vector machines (SVM).

Performance evaluation and monitoring

Monitoring and assessing the production metrics is a crucial role in production planning and control of industrial systems. The identification of bottlenecks is made possible by PPC's monitoring and evaluation of the various manufacturing performance parameters, which facilitates decision-making throughout production processes. The substantial body of research in this field is the result of the extensive use of industrial data that was produced by IoT, smart sensors, and cloud manufacturing technologies. In the context of production planning and control, we were able to identify two key study areas for performance evaluation and monitoring:

A) Performance Prediction & Optimization: Enhancing production metrics using past production instances and industrial data is the focus of this research topic. Analysing real-time data from machines and processes enables the identification of manufacturing bottlenecks and limits while taking the entire industrial environment into account. Additionally, by utilising AI/ML skills, it is possible to attain high performance with more adaptability.
AI/ML applications for performance prediction are significant in the context of production planning and control. To estimate the success of a deep drilling process under various cutting and cooling circumstances, Bustillo et al. used a hybrid approach combining conditional inference trees with dimensionality reduction using regression trees and Principal Component Analysis (PCA).

B) Process Fault Detection: The prevention of errors and preservation of the processes' overall quality are basic components of performance evaluation and monitoring, which is a crucial component of production planning and control in general. Here, we primarily concentrate on the ML/AI-based methodology, which attempts to improve the overall performance of manufacturing systems through the prediction and avoidance of production anomalies and failures.
In order to create an early warning system that can identify possible issues with egg production, Morales et al. suggested using a Support Vector Machine (SVM) technique.

International Journal of Advances in Engineering and Management (IJAEM)
Volume 4, Issue 11 Nov. 2022, pp: 1120-1126 www.ijaem.net ISSN: 2395-5252

Process Automation

The potential of AI/ML to automate various jobs and processes within the manufacturing industry is one of the important benefits of this technology as a key pillar of the fourth industrial revolution. Automating production strategies to achieve production goals would seem to be the main focus of automation in production planning. Automated control, the second process automation function, focuses on automating the manufacturing process to increase its overall adaptability and flexibility:

D) Automated planning: In the context of industry 4.0, the automation of industrial processes is met with a scaled requirement for assuring the adaptability of production facilities. An important factor in exploiting cutting-edge computation techniques and connectivity, which increases production flexibility and customization, is the modern application of information and communication technologies

But a crucial aspect of the industry 4.0 automation paradigm is automated planning. Automated planning, which has its roots in AI research, tackles the need for adequate strategies to automatically accomplish a particular goal. Due to its history, automated planning, commonly referred to as AI planning, provides the opportunity to greatly increase production autonomy, one of the key Industry 4.0 goals.

E) Automated control: The attainment of mass-customization of the processes and products within the industry 4.0 framework is compromised by process control's normal lack of flexibility and responsiveness to a significant degree. Higher flexibility can be achieved by automated control of the numerous process parameters inside the manufacturing system by utilising AI/ML that continuously leverages industrial data.

III. CONCLUSION

Due to the recent uptake of the idea of industry 4.0, trending applications of AI/ML in production and research necessitate a thorough examination of the state-of-the-art. The purpose of this article was to analyse the scholarly literature on the use of AI and ML in industrial systems. We therefore did a literature review to address the body of knowledge on AI/ML in manufacturing systems in order to identify the most frequently used terms and methods. However, in order to comprehend the Applications of ML/AI in decision-intensive activities of production planning and control, we reduced the field of analysis by a two-stage manual cross-check to the literature. The decision to manually choose the paper was made in order to include the papers that were the most pertinent to the focus of our analysis, particularly application articles that use ML/AI techniques to address an issue with production floor decision-making. In order to do this, the applications of AI/ML in PPC-intensive decision-making tasks can be categorised into three primary pillars: dynamic scheduling, performance evaluation and monitoring, and automated process control.

These three types of applications are a key development made possible by industry 4.0 to improve the automation of human-dependent operations that frequently require complex decision-making on the part of production workers or process supervisors. In order to overcome interruptions in the initial production plans, process rescheduling, for example, suggests dynamic assignments for resources, tasks, and production plans in real-time. Real-time analytics on the performance of the production are made possible by performance evaluation and monitoring, and this indicates potential operational changes to increase overall production efficiency. Process automation offers automated production planning and control, which also permits significant improvements for jobs requiring significant decision-making during production planning.

We were unable to go into further detail about the research methodology and the many papers we took into consideration for this study due to space restrictions associated with this conference paper. However, a further research project will identify and map the ML/AI approaches by application field in order to look into the popular methodologies and the factors that led to their popularity, among other things.

REFERENCES

[1]. Diaz-Rozo, J., Bielza, C. and Larrañaga, P. (2017). Machine Learning-based CPS for Clustering High throughput Machining Cycle Conditions.

[2]. Gyulai, D. et al. (2018). Lead time prediction in a flow-shop environment with analytical and machine learning approaches.

[3]. Lubosch, M., Kunath, M. and Winkler, H. (2018). Industrial scheduling with Monte Carlo tree search and machine learning.

[4]. Sharp, M., Ak, R. and Hedberg, T. (2018). A survey of the advancing use and development of machine learning in smart manufacturing. Journal of Manufacturing

Systems. The Society of Manufacturing Engineers.

[5]. Schuh, G. et al. (2017). Knowledge Discovery Approach for Automated Process Planning. Procedia CIRP. Rostami, H., Blue, J. and Yugma, C. (2018). Automatic equipment fault fingerprint extraction for the fault diagnostic on the batch process data.

[6]. Wodecki, A., Wodecki, & Harrison. (2019). Artificial Intelligence in Value Creation. Springer International Publishing.

[7]. Cadavid, J. P. U., Lamouri, S., Grabot, B., Pellerin, R., & Fortin, A. (2020). Machine learning applied in production planning and control: a state-of-the-art in the era of industry 4.0. Journal of Intelligent Manufacturing, 1-28.

[8]. Cheng, Y., Chen, K., Sun, H., Zhang, Y., & Tao, F. (2018). Data and knowledge mining with big data towards smart production. Journal of Industrial Information Integration.

View publication stats

Mathematical modeling and performance analysis of a solar assisted vapour absorption refrigeration system

Sanchita Singh[1*], *and Pushpendra* Singh[2]

[1]Dept. of Mechanical and Automation Engineering, Indira Gandhi Delhi Technical University for Women, Delhi, India
[2]Dept. of Mechanical Engineering, Delhi Technological University, Delhi, India

Abstract. Climate change is the hottest topic today on earth. Traditional HVAC's harm the environment and stand out to be a major contributor to global warming. One of the many techniques to mitigate the current climate crisis is by utilizing the abundantly available solar radiation. Solar evacuated tube collectors are used to absorb solar radiation. This solar power is used to provide solar cooling technologies. Unlike the conventional HVAC's thermally driven absorption cooling is a boon in today's era. In the following research work, the study aims to provide numerical modeling of a solar assisted air-conditioning unit through the first law of thermodynamics using mass balancing equations for the province of Delhi in July. This research work's aim is to build and evaluate a Li-Br absorption cooler with a capacity of 1 KW. This paper aims to provide characteristic design features of components and measures the efficiency of the system at operating conditions. PCM based thermal energy storage tank is adopted which helps to supply cold air even at no sunlight hours. As a result of this research study, such solar assisted air conditioners turn out to be a chosen solution for sustainability.

1 Introduction

Greenhouse gas emissions are directly responsible for the rising temperatures worldwide. Heating, ventilation air conditioners have large energy acquisition and pose a negative impact on the local environment. They have raised tremendous concerns about the current climate threat as they are responsible for ozone depletion and global warming. Many organizations are searching for ways to fight climate change and resorting to sustainable alternatives. Reciprocating sorption chillers can be one method of limiting the usage of conventional systems and hence reducing reliance on fossil fuels. In the 1950s, numerous nations developed tiny sun absorption refrigeration systems. In the area of solar refrigeration employing solar collectors (flat plate), American Professor G.O.G.L. is well known for his contribution [1]. Sorption cooling includes both absorption and adsorption. Absorption machines do not require much of input power (shaft power) as they are

* Sanchita Singh: sanchitaig20@gmail.com

© The Authors, published by EDP Sciences. This is an open access article distributed under the terms of the Creative Commons Attribution License 4.0 (https://creativecommons.org/licenses/by/4.0/).

thermally driven. In this way, absorption machines offer dependable and efficient cooling in areas with expensive or unreliable power sources, or in areas with access to waste, gas, geothermal, or solar heat. [2]. Traditional systems incorporate mechanical compression machines using electrical energy consumption whereas in absorption cooling thermal compression of refrigerant is employed. This area of research focuses discussion on an absorption system, which uses a refrigerant - absorbent pair that work together. The most commonly chosen working pairs are (1) lithium bromide – water, where the former is the absorbent and the latter is the refrigerant. It is one of the widely used pairs for space air-conditioning applications, (2) ammonia - water, where the refrigerant is ammonia & absorbent being water, but the lower efficiency of NH_3-H_2O compared with LiBr-H_2O restricts their use. NH_3 is poisonous and is not fit for residential applications.

[3] performed a life cycle analysis to examine the viability of the proposed design. COP achieved is bit lower but the system is economically friendly as compared to conventional HVAC's. [4] examined the system through a computational simulation using MATLAB. It incorporates analysis through 1st and 2nd law of thermodynamics. Various trends between the COP & temperatures of generator, absorber, and condenser are presented. [5] studies an ammonia - water absorption system for analysis. C-program is developed to find the thermodynamic properties of each component. Effect of various key parameters (eg. concentration effect, change in pressure) on performance of the structure is examined with graphs. [6] study the integration of PCM's with HVAC's to reduce energy consumption leading to maximization of the system's performance. The study also involves the making of 2 different systems and their efficiency is investigated. [7] includes construction and parameter analysis for each component of solar air conditioner. COP is calculated for two different working temperatures of the generator. A small thermal storage tank is also incorporated.

The study's goal is to analyse a LiBr-H_2O thermally driven absorption cooler which absorbs solar thermal energy using evacuated tube collectors. Practical problems that are faced by such an arrangement include crystallization, pressure drops & air leakage. To prevent crystallization to occur, the pressure of the condenser needs to be maintained at a particular value, irrespective of the temperature of the cooling water. This is achieved by monitoring the cooling water flow rate moving towards the condenser. Sometimes, addition of additives takes place to inhibit crystallization [1].

This paper reports design characteristics of different components of the system and presents a thermodynamic energy analysis of the vapour absorption refrigeration system under varied working conditions.

2 Geography description

The thermally powered solar absorption air-conditioning unit is planned and implemented for the province of Delhi, India. The site is located at 28.6° north latitude and 77.2° east longitude. In this area the average incident solar radiation is approximately 0.5 KWh/m2/day. In Delhi, for the month of July average ambient air temperature is 35℃ and humidity is 50% for the same. Under the current climatic conditions space air conditioning is required for human comfort.

3 System layout

The solar air conditioning system mainly comprises of evacuated tube solar collectors, a PCM thermal-storage unit & a vapor-absorption machine. The system's design and layout is depicted in Fig. 1.

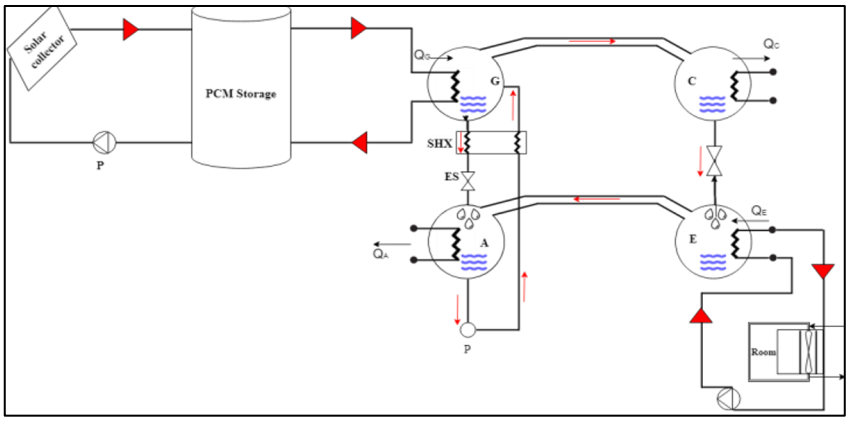

Fig. 1. Design layout for solar assisted water - libr absorption cooling system

4 Solar cycle system design

4.1 Solar collector

One of the crucial elements of a solar assisted air conditioning system, the solar collector, transforms the solar energy into thermal energy which further helps to drive the absorption chiller [8]. Evacuated tube collectors are used to absorb heat from sun's radiation. The heat transfer fluid incorporated for the solar system array is water because of a large value of thermal conductivity and heat capacity. Solar thermal energy then converts into heat output by the ETC collectors, which then uses that heat to warm water passing through them. In order to lessen losses from convection and re-radiation, the ETC collector is vacuumed [9]. The ETC collectors are placed under the sunlight to reach a temperature of 100℃. Once the given temperature is reached, the cycle starts. The amount of heat absorbed does not equal the actual heat that is transmitted to the heat transfer liquid because of the energy losses associated with the heat-transfer from the absorbent to the tubes.

Heat acquired by the solar collector is the useful heat required as an input to the generator in the absorption cycle. The following assumptions are adopted for the solar cycle system:

- Ambient temperature of the environment is 35℃ and the pressure is 1 atm.
- A temperature difference of about 20℃ is considered between the collector and the generator because of the losses that will take place.
- Area of each evacuated tube is 0.03 m^2.
- Efficiency of ETC is 0.70.
- Inlet heating water temperature to the generator is 92℃.
- Outlet temperature of water from generator is 88℃.

To find dimensions of the solar collector the following approach is used. The required area for the solar collector per cooling capacity is given as [10]:

1) Incident solar radiation for Delhi (G) = 0.5 KWh/m^2/day
2) Efficiency of solar collector (η) = 0.7 or 70%
3) Chiller COP = 0.76 or 76%

$$A = \frac{1}{G \cdot \eta \cdot COP} \frac{(m^2)}{(KW)}$$

$$= \frac{1}{0.5 * 0.7 * 0.76} \frac{(m^2)}{(KW)}$$

= 3.75 m^2 per KW

For 1KW absorption chiller, 3.75 m^2 coverage of area of the evacuated tubes is required. Area of each evacuated tube is 0.03 m^2 .

∴ 3.75 ÷ 0.03

= 125 evacuated tubes are required.

4.2 PCM storage

PCMs are materials that are ideal for energy transfer and conservation purposes as they are able to absorb, store, and emit a significant quantity of heat energy at fairly consistent temperatures [11], [12]. These are integrated to enhance the operational efficiency of solar assisted air conditioners. A thermal energy storage system is installed between ETC and the vapour absorption system to stock the thermal energy with the aid of PCMs. The primary elements of this unit are a solar collector & a storage tank. A cylindrical vessel which is filled with a dense bed of PCM spheres, serves as the storage unit [13]. Heat transfer during charging & discharging process takes place b/w the PCM and the heat-transfer fluid. Direct cooling occurs in the morning and early afternoon. The excess energy is utilized to create and stock up cooling energy in PCM once the specified temperature is reached and there is enough radiation of sun. The PCM storage is discharged in the night [14].

5 Thermally driven vapour absorption cooling system

5.1 Working principle of the cycle

The main components in the design of a vapour-absorption cycle include ‘generator’, ‘condenser’, ‘refrigerant expansion valve’, ‘evaporator’, ‘absorber’, ‘solution pump’, ‘solution expansion valve’ and ‘solution heat exchanger’.

The heat gained by the heat-transfer fluid in the solar cycle is further utilized by the system’s absorption unit for the purpose of cooling. In the generator, high temperature heat transfer fluid transfers its heat to the working pair, LiBr-H_2O solution which is pumped from the absorber. Hence, heat gain takes place in the generator. Water (refrigerant) evaporates from solution and this high pressure super-heated steam moves further to the condenser whereas the remaining strong solution with high percentage of Li-Br moves towards the absorber with the help of a solution heat exchanger. Inside the condenser, heat rejection takes place and the refrigerant changes to a high pressure saturated liquid. Pressure decreases as the saturated liquid moves through the expansion valve. Then it further enters the evaporator, where evaporation occurs and cooling takes place. Low pressure saturated-vapour exits through the evaporator, moves and enters the absorber where the solution present absorbs it. The heat gathered in the evaporator is released when the refrigerant vapour gets absorbed and is condensed from vapour to a liquid state. The heat generated by the condensation of vapour of the refrigerant, caused due to the absorption in mixture, is carried away through the cooling water as it moves along the bundle of absorber tubes. The weak absorbent mixture is then pushed towards the generator to drive off the refrigerant by heating it up [15].

6 Numerical modelling of the absorption system

6.1 Assumptions for thermodynamic analysis

- Steady-flow & steady-state analysis.
- Negligible changes in kinetic & potential energy are considered across each component.
- Pure refrigerant i.e. water, only boils in the generator.
- Cooling in room is provided at a temperature of 21℃, which lies in the temperature range for thermal comfort (20℃ - 25℃).
- There are two working pressures involved ($P_{evaporator}$ and $P_{condenser}$). Expansion valve reduces the working pressure of fluid from $P_{condenser}$ to $P_{evaporator.}$
- No temperature loss occurs between the expansion valve and the evaporator.
- Temperature of cooling coil of the evaporator is 15℃. Since losses are involved the working fluid has a temperature of 18℃. After leaving the cooling coil the working fluid gains about 3-4℃.

6.2 Design parameters for the absorption cycle

Fig. 2 represents a schematic diagram of the absorption cycle.

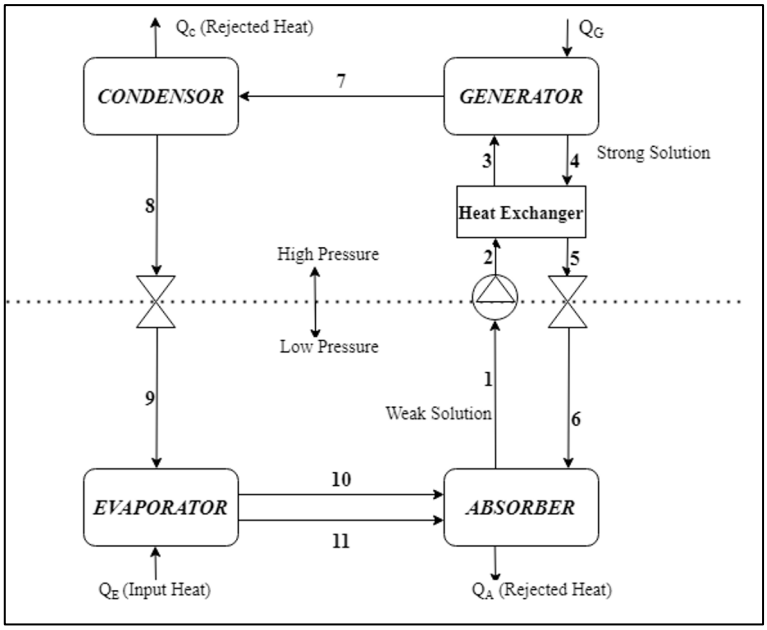

Fig. 2. Schematic diagram for absorption cooling system

Table 1 describes the operating conditions and temperatures of components that are adopted for carrying out the thermodynamic analysis.

Table 1. Design parameters

Parameters	***Symbol***	***Value***
Evaporator temperature	T_{10}	15℃
Generator solution exit temperature	T_4	75℃
Weak solution mass fraction	x_1	55% LiBr
Strong solution mass fraction	x_4	60% LiBr
Solution HX exit temperature	T_3	55℃
Generator (desorber) exit temperature	T_7	70℃

6.3 Thermodynamic model

Governing equations of mass balancing for a steady state & a steady flow model:

$$\sum \dot{m}_i - \sum \dot{m}_o = 0$$

Through the 1st law of thermodynamics and using mass balancing equations for every part :

$$\sum (\dot{m}h)_i - \sum (\dot{m}h)_o + \sum Q_i - \sum Q_o + W = 0$$

$$Also,\ Q_C + Q_A - Q_G - Q_E = 0$$

System calculations are performed at each point in Fig. 2 to specify values of P, T and h.

- Point 10:
  In the evaporator, the refrigerant is saturated water vapour.
  Temperature = T_{10} = 15℃ and saturation pressure = 1.7051 KPa
  Enthalpy = h_{10} = 2528.9 KJ/Kg {from steam table}
- Point 11:
  Refrigerant is a saturated liquid.
  h_{11} = 62.98 KJ/Kg
- Point 9:
  T_9 = 15℃ and P_9 = 1.7051 KPa
  $h_9 = h_8$ {since there is no loss in the expansion valve}
  h_9 = 131 KJ/Kg
- Point 8:
  At point 4, solution mass fraction = 60% Li-Br (strong solution) and temperature at the saturated state = 75℃
  → Saturation pressure = 4.82 KPa {LiBr-water chart}
  h_4 = 183.2 KJ/Kg
  At point 8, saturated liquid from condenser comes out. Temperature of condenser = 31.5℃
  Pressure at point 8 = pressure at point 4
  ∴ h_8 = 131 KJ/Kg {from steam table}
- Point 7:
  Exit temperature of superheated steam from the generator = 70℃

Pressure = 4.82 KPa
h_7 = 2612.2 KJ/Kg {from steam table}

- Point 6:
  Strong solution is obtained through the expansion valve and involves no losses.
  T_6 = 44.5℃
  P = 1.7051 KPa
  ∴ $h_6 = h_5$
  h_6 = 115.235818 KJ/Kg
- Point 1:
  Input mass fraction of saturated liquid = 55% {weak solution}
  Exit temperature of liquid = Temperature of Absorber = 34.9℃
  P = 1.7051 KPa
  h_1 = 62.3995 KJ/Kg {from steam table}
- Point 2:
  Pump work = $\dot{m}_2 h_2 - \dot{m}_1 h_1$
  $\dot{m}_2 = \dot{m}_1, x_2 = x_1$
  P = 4.82 KPa
  Since the work done by the pump is neglected.
  ∴ $h_2 = h_1$ = 62.3995 KJ/Kg
- Point 3:
  Exit temperature from solution heat exchanger = 55℃
  P = 4.82 KPa
  h_3 = 124.7 KJ/Kg {state: may be a sub-cooled liquid}
- Point 4:
  Generator solution exit temperature : T_4 = 75℃
  P = 4.82 KPa
  h_4 = 183.2 KJ/Kg {LiBr chart}
- Point 5:
  Exit Temperature of strong solution: T_5 = 51.5℃, P = 4.82 KPa
  Applying energy balance equation across solution heat exchanger:
  $\dot{m}_2 h_2 + \dot{m}_4 h_4 = \dot{m}_3 h_3 + \dot{m}_5 h_5$
  h_5 = 115.235818 KJ/Kg

Now,
Performing calculations across each component of the absorption cooler:
Capacity of single-effect water Li-Br absorption cooler = $\dot{Q}_E$ = 1KW {assumed}
Let, $\dot{m}$ = mass flow rate of the refrigerant (Kg/sec)
$\dot{m}_{ss}$= mass flow rate of the strong solution
Circulation ratio= $\lambda = \frac{\dot{m}_{ss}}{\dot{m}}$

1) Evaporator
   $\dot{Q}_E = \dot{m}_{10} h_{10} + \dot{m}_{11} h_{11} - \dot{m}_9 h_9$
   $\dot{m} = \dot{m}_{10} = 0.000417\ Kg/sec$
   $\lambda = \frac{\dot{m}_{ss}}{\dot{m}} = \frac{x_{ws}}{x_{ss} - x_{ws}} = \frac{55}{60-55} = 11$
   $\therefore Strong\ solution: \dot{m}_{ss} = \lambda \dot{m} = 0.004587\ Kg/sec$
   $Weak\ solution = \dot{m}_{ws} = (\lambda + 1)\dot{m} = 0.005004\ Kg/sec$
2) Absorber
   $Q_A = \dot{m}_6 h_6 + \dot{m}_{10} h_{10} + \dot{m}_{11} h_{11} - \dot{m}_1 h_1$
   $\therefore Q_A = 1.271546\ KW$ {heat rejected}
3) Pump work is neglected

4) Solution expansion valve
   There is no loss. → $\dot{m}_5 = \dot{m}_6, x_5 = x_6$
   $\therefore h_5 = h_6$
5) Solution heat exchanger
   $\dot{m}_2 h_2 + \dot{m}_4 h_4 = \dot{m}_3 h_3 + \dot{m}_5 h_5$
   $\therefore h_5 = 115.2358\ KJ/Kg$
6) Generator
   $Q_G = \dot{m}_4 h_4 + \dot{m}_7 h_7 - \dot{m}_3 h_3$
   $\therefore Q_G = 1.305\ KW$ {heat input to the generator}
7) Condenser
   $Q_C = \dot{m}_7 h_7 - \dot{m}_8 h_8$
   $\therefore Q_C = 1.034\ KW$ {heat rejected}
8) Refrigerant Expansion Valve
   Since there is no loss.
   $\dot{m}_8 = \dot{m}_9$ and $x_8 = x_9$
   $\therefore h_8 = h_9$

The COP for the absorption system is described through the following relation:

$$COP = \frac{Q_E\,(\text{evaporator heat load})}{Q_G(generator\ heat\ load)}$$

$$\therefore \boldsymbol{COP = 0.76}$$

6.4 Design of the generator heat-exchanger

Latent-heat of vaporization and sensible heat is obtained as an output when heat is fed into the generator. Experiments reveal that for such systems, the value obtained for heat-transfer coefficient, U ranges between 1600 -7500 W/m^2-℃. To evaluate the efficiency of a HX, the value of $(U.A)$ is used to represent the best heat transfer rate.

Employing single pass heat exchanger, the temperature b/w hot & cold fluid doesn't remain constant and varies with the distance along the heat-exchanger. For a HX that has two ends at which hot and cold streams enter or exit on either side, the logarithmic mean temperature difference is:

$$LMTD = \frac{\Delta T_O - \Delta T_I}{\ln(\frac{\Delta T_O}{\Delta T_I})}$$

Heat transfer is given by: $Q = U.A.LMTD$

$\Delta T_O = T_{12} - T_{13} = 92 - 55 = 37$℃
$\Delta T_I = T_7 - T_4 = 5$℃
$\therefore LMTD = 15.98$℃

Area of each evacuated tube is 0.03 m^2

$$U = \frac{Q_G}{A.LMTD}$$

∴ Heat transfer coefficient = 2711.72 W/m^2-℃, which lies between the said values.

7 Results

Results for the above research are tabulated in Table 2 for thermally driven water - libr absorption cooling system. Results for the above research are tabulated in Table 2 for thermally driven water - libr absorption cooling system. At each point h, P and T are specified along with the description of each part present in the absorption system. The COP evaluates the air-conditioner capacity. COP based on generator temperature = 75℃ is calculated to be equal to 0.76.

Table 2. Water-LiBr absorption cooling system calculations

Point	***h (KJ/Kg)***	***$\dot{m}$ (Kg/sec)***	***P (KPa)***	***T (℃)***	***%LiBr (x)***	***Remarks***
1	62.3995	0.005004	1.7051	34.9	55	
2	62.3995	0.005004	4.82	34.9	55	
3	124.7	0.005004	4.82	55	55	**'sub cooled liquid'**
4	183.2	0.004587	4.82	75	60	
5	115.235	0.004587	4.82	51.5	60	
6	115.235	0.004587	1.7051	44.5	60	
7	2612.2	0.000417	4.82	70	0	**'superheated steam'**
8	131	0.000417	4.82	31.5	0	**'saturated liquid'**
9	131	0.000417	1.7051	15	0	
10	2528.9	0.000417	1.7051	15	0	**'saturated vapour'**
11	62.98	0.000010	1.7051	15	0	**'saturated liquid'**

Description	***Working Temperature***	***KW***
Evaporator (Capacity)	T_{10} = 15℃	$Q_E = 1$
Absorber	T_1 = 34.9℃	$Q_A = 1.27$
Generator	T_4 = 75℃	$Q_G = 1.30$
Condenser	T_8 = 31.5℃	$Q_C = 1.03$
Coefficient of performance	COP	0.76

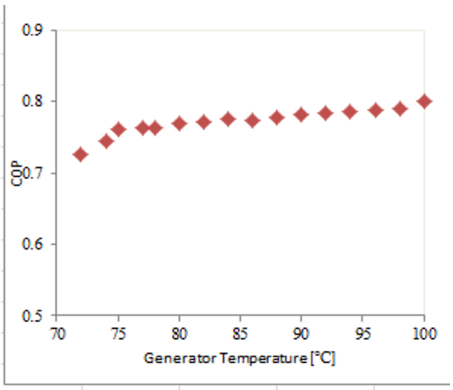

Fig. 3. Relation between COP and the generator temperature

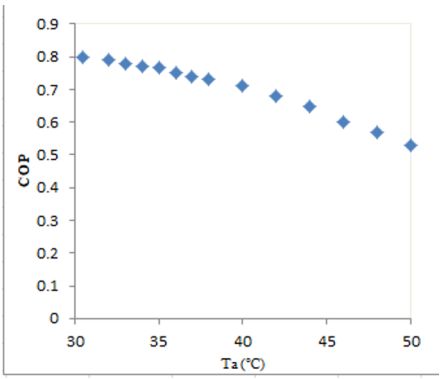

Fig. 4. Relation between COP and the absorber temperature

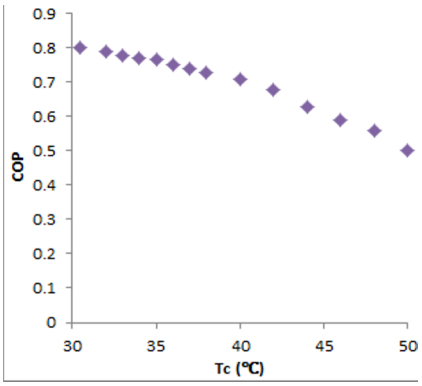

Fig. 5. Relation between COP and condenser temperature

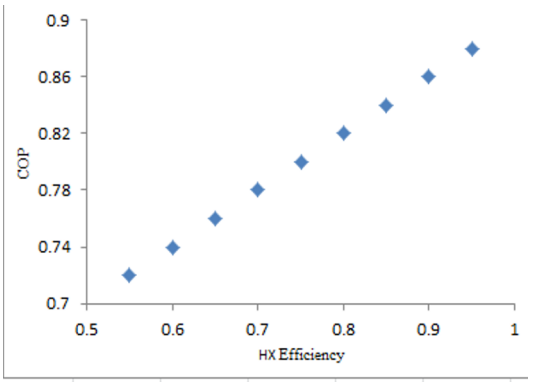

Fig. 6. Relation between COP of system and efficiency of HX

8 Discussions

Fig. 3 depicts the correlation between COP and different values of temperature of generator. It is noticed clearly that, as a rise occurs in the generator temperature, the value of coefficient of performance (COP) also increases. This implies that the system's performance is enhanced as the temperature of the generator rises. With Li-Br, the maximum attainable temperature is 100℃ as above that crystallization may take place.

Fig. 4 and fig. 5 shows that the system's COP decreases with a rise in the temperature of the absorber and condenser respectively. So, the system performance & the absorption reaction is improved by reducing the absorber temperature, this statement is explained through the fact that since water absorption by Li-Br is a chemical reaction therefore it requires to be cooled down for achieving an improved performance. To achieve a better condensation rate in the condenser, the water vapour ought to be cooled down which is done using cooling towers or through the phenomena of natural air cooling. Since, water -

libr pair is considered for analysis hence, for cooling purposes water will be a better choice than the other because of the problem of crystallization that may occur [16].

Fig. 6, tells that the COP is increased as heat-exchanger effectiveness increases. The amount of energy required for the overall process is reduced before moving into the generator as the HX aids in increasing the strong solution temperature. An improvement in the COP is noticed, with the increase in the heat-exchanger effectiveness and a reduction in the energy requirement of the generator [16].

9 Conclusions

In this analysis, a mathematical model is articulated by applying the 1st law of thermodynamics to a vapour absorption refrigeration system. This thermally driven solar absorption air conditioning unit is planned and implemented for the province of Delhi, India. The system is integrated with evacuated tube collectors which absorbs sun's radiation and then transforms it into heat output, which warms the water that is passing through the collectors. A well-defined approach is used to find the dimensions of the collector. Area for each of the collector is calculated to be 3.75 m^2. A thermal energy storage unit is incorporated to increase the system's operational efficiency. Numerical modeling of the absorption unit is accomplished with the help of energy calculations for each component of the system, at each of the points from thermodynamic characteristics of the working fluid at the given working parameters. The COP evaluates the capacity of the air conditioner and is calculated to be 0.76. Design for the generator heat exchanger is proposed. The value obtained for the coefficient of heat-transfer for heat exchanger is calculated through the LMTD method and the obtained value lies between the mentioned range.

From the results and discussion using appropriate graphical methods it is discovered that the cycle's COP increases as the generator's working temperature rises, indicating an improvement in efficiency and performance. While the COP value is decreased with a rise in temperatures of absorber and condenser. From the graph, it is observed that an increase in the heat exchanger effectiveness occurs with a decrease in the energy needed in the generator which further leads to an improvement in the performance of the system. Additionally, it has been found that raising the generator temperature improves the vapour absorption cycle's COP but, this increase in temperature negatively impacts the system's efficiency and performance. Thus, a special attention must be given to this dominant reverse effect. Finally, this research leads the way to an improved thermal system. Hence, this methodology can be used and applied to a similar suitable system which will be economical and sustainable.

References

1. W. Min'an, Refrigerator, Domest. Spaces Post-Mao China, 13–24, (2018), doi: 10.4324/9781315228372-2
2. American Society of Heating Refrigerating and Air-Conditioning Engineers, ASHRAE Handbook & Product Directory, 1977 fundamentals (1977)
3. S. Rahman, Z. Said, S. Issa, Energy Reports, **6**, 673–679, (2020), doi: 10.1016/j.egyr.2019.11.136
4. J. Abdulateef, S.D. Ali, M.S. Mahdi, J. Adv. Res. Fluid Mech. Therm. Sci., **60**, 233–246, (2019)
5. B.R. Narender, Int. J. Latest Trends Eng. Technol., **7**, 17–26, (2016), doi: 10.21172/1.74.003
6. Z. Ma, H. Ren, W. Lin, S. Wang, InTech, (2018) doi: 10.5772/intechopen.72187

7. A.K. Jairath, S. Kumar, G. Yadav, in International Conference on Advanced Computing and Communication Technologies, ACCT, 183–188, Feb (2015), doi: 10.1109/ACCT.2015.17
8. H.M. Henning, Appl. Therm. Eng., **27**, 1734–1749, Jul. (2007), doi: 10.1016/j.applthermaleng.2006.07.021.
9. D.K. Mohanty A. Padhiary, Sci. Technol. Eng., **4**, 45–54, June (2015)
10. L.C. Haw, K. Sopian, Y. Sulaiman, in Int. Conf. ENERGY Environ., 244–251, (2008)
11. Z. Ma, W. Lin, M.I. Sohel, Renewable and Sustainable Energy Reviews, **58**, 1256–1268, May (2016), doi: 10.1016/j.rser.2015.12.234
12. P.B. Salunkhe P.S. Shembekar, Renewable and Sustainable Energy Reviews, **16**, 5603–5616, Oct. (2012), doi: 10.1016/j.rser.2012.05.037
13. O.P. Ram, K.R. Subhramanyam, N. Jnana, S. Vamsidhar, N.S. Teja, Int. J. Mech. Eng. Technol., **10**, 149–159, (2019)
14. P. Byrne, Evergreen, **6**, 143–148, (2019), doi: 10.5109/2321009.
15. S. Kaushik S. Singh, Int. J. Res. Appl. Sci. Eng. Technol., **2**, 73–80, (2014)
16. O. Ketfi, M. Merzouk, N.K. Merzouk, S. Metenani, in Energy Procedia, **74**, 130–138, (2015), doi: 10.1016/j.egypro.2015.07.534.

The Open Chemical Engineering Journal

Content list available at: https://openchemicalengineeringjournal.com

RESEARCH ARTICLE

Mechanical and Structural Properties of Epoxy Resin-Allyl Guar Gum Composites

Gopal Arora[1,*] and A.P Gupta[2]

[1]*Department of Chemistry, SBAS Sanskriti University, Mathura 281401, India*
[2]*Department of Applied Chemistry, Delhi Technological University, Delhi 110042, India*

Abstract:

Introduction:

Guar gum is a non-ionic polysaccharide extracted from the endosperm of *Cyamopsistetragonalobus*. Guar gum and its derivatives are water-soluble hydrophilic polysaccharides, and hydrophobic modification is required to increase its compatibility in a polymer matrix.

Objectives:

The present study investigates the synthesis of allyl-modified guar gum (AGG) and epoxy resin composites. The mechanical properties of the prepared composites with varying concentrations of filler (allyl guar gum) in the range of 0.5-4.5 wt% have been evaluated. The mechanical and structural properties of the prepared composites have been investigated using Universal Testing Machine (UTM) and Scanning Electron Microscope (SEM), respectively.

Methods:

The epoxy composites were prepared by casting technique using allyl guar gum as the filler. The polymer-filler interactions varied with the contents of the filler.

Results:

The tensile strength was found to be enhanced up to 13% at 0.5% concentration of AGG. The % elongation at break values followed an opposite trend as compared to the tensile strength data of the composites. The observed mechanical properties have been correlated with the fracture morphology of the composites.

Conclusion:

A better dispersion, that is, polymer-filler interactions, improved the tensile strength of composites, while poor interactions declined the tensile strength. It is reported that max tensile strength can be obtained at 0.5% concentration of allyl guar gum (AGG1). The maximum increase in % elongation at break was 25% for AGG2-based epoxy composite at 3% of filler concentration.

Keywords: Allyl guar gum, Epoxy resin, Composites, Tensile strength, Impact strength, Scanning electron microscope.

Article History	Received: November 24, 2022	Revised: March 14, 2023	Accepted: March 29, 2023

1. INTRODUCTION

Plastics made from petroleum are widely used throughout the world for numerous applications. On the other hand, the disposal of waste plastic has become a serious environmental threat. Therefore, the development of novel plastic that could be degraded by indigenous microorganisms present in soil and water systems has recently attracted much attention. In this regard, biodegradable materials have been paid attention to as an alternative to petroleum-derived plastics [1]. A variety of natural biopolymers, including starch, cellulose, and chitosan, have been tested alone or combined with synthetic polymers for the possibility to develop fully or partially biodegradable films. Guar gum is the endosperm polysaccharide of the seed of *Cyamopsis tetragonolobus* [2]. It is a galactomannan consisting of backbones of α-1,4 D mannopyranosyl with every second unit bearing a β 1,6D–galactopyranosyl unit [3]. It is easily available and cheap in many parts of the world. India is

* Address correspondence to this author at the Department of Chemistry, SBAS Sanskriti University, Mathura – 281401;
E-mail:drgopalarora.chem@sanskriti.edu.in

the largest exporter of guar gum. Guar gum is extremely hydrophilic and water-soluble. The hydrophilic nature of guar gum hampers its interactions with the hydrophobic polymer matrix [4, 5]. Hydrophobic modification of guar gum is required to increase its compatibility with polymers. This integration has allowed these polymers and their derivatives to be commercialized in diverse fields, such as textiles, foods, cosmetics, pharmaceuticals, binders for electrodes and separators, and corrosion inhibition of iron-gall ink in paper works [6 - 10].

Epoxy resins are important thermosetting polymers and have a good combination of important properties, like excellent insulation, volatile less-flexible curing systems, and moisture resistance; epoxy resins are widely used as matrix resin in composites and as structural adhesives due to their remarkable bonding ability to various materials, including metals, ceramics, wood, and plastics [11].

The guar gum has been modified to prepare acryloyl, acetylated, and methacryloyl derivates of guar gum [12 - 14]. However, limited studies are available on the allyl etherification of guar gum. In a previous study [4], allyl guar gum was prepared by reaction of guar gum with allylchloride to effect etherification and it was characterized by FTIR, TGA, and SEM analyses. The different degree of substitution of AGG was realized by varying the concentration of sodium hydroxide and allyl chloride to guar gum (Table **1**). The free hydroxyl groups along the polysaccharide backbone of guar gum were substituted by allyl groups to improve the hydrophobicity and inhibit aggregation in an aqueous environment. In this study, the composites of epoxy resin with different % of allyl-modified guar gum as fillers have been prepared. The mechanical properties of these composites have been investigated. The fracture morphology of these composites has been recorded to decipher the observed mechanical properties.

Table 1. Properties of allylated guar gum.

Sample name	Volume of NaOH	Wt of allyl chloride	Temperature (^{o}C)	Time (hrs)	DS
AGG1	7	6.84	50	4	0.0389
AGG2	7	6.84	50	8	0.0625

2. MATERIALS AND METHODS

The epoxy composites were prepared by casting technique using allyl guar gum as the fillers. Epoxy resin (DGEBA) was purchased from Dow Chemicals. The allyl-modified guar gum was prepared as reported previously [15]. The degree of substitution of allyl guar gum was calculated by titration method [16]. A typical chemical structure of allyl guar gum (AGG) is shown in Fig. (**1**). The fillers were dispersed in the epoxy resin in different wt% of 0.5 to 4.5. Polyetheramine D230 was added as a curing agent and the composite was mixed thoroughly. The formulation was then de-aerated and poured into a preheated metal mold at 60 °C. The cure cycle adopted for the preparation of the epoxy composites was 60 °C for 4 h. The thickness of the prepared composites was found to be 3 mm. The composites were cut into the respective shapes for testing and the edges were uniformly ground to remove imperfections.

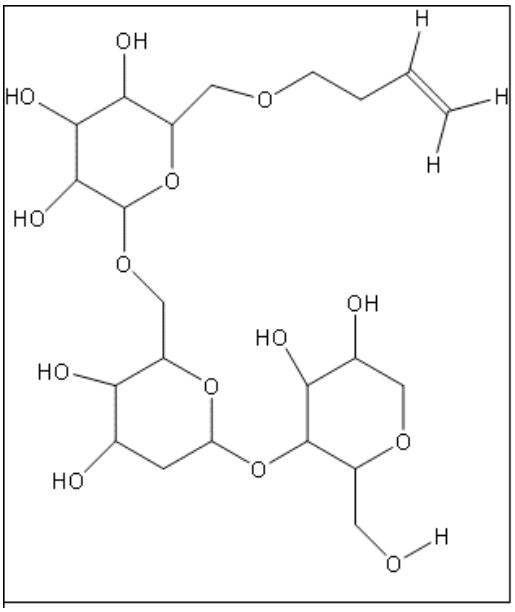

Fig. (1). Chemical structure of allyl guar gum (AGG); adapted from [4].

2.1. Characterization of the Prepared Composites

The morphology of the composite samples was investigated using scanning electron microscope (HITACHI S 3700N) at a voltage of 15KV. The samples were coated with gold for this analysis [17]. The mechanical properties (tensile strength, % elongation at break) of the prepared composites were analyzed using the universal testing machine (Instron 3369) with a crosshead speed of 5 mm/min. The dimensions of the specimen were 10 cm × 1 cm with a gauge length of 3.0 cm. The tensile strength was evaluated as per ASTM D638. The impact strength of the composites was measured using the Izod impact strength according to ASTM D790 at a crosshead speed of 2 mm/min.

3. RESULTS AND DISCUSSION

3.1. Mechanical Properties of the Synthesized Epoxy Allyl Guar Gum Composites

The tensile strength, elongation at break (%), and impact strength of the prepared epoxy composites with varying contents of two allyl guar gums (AGG1 and AGG2) are shown in Fig. (**2**). The tensile strength of the epoxy composites was found to increase at 0.5% concentrations of AGG1 and AGG2, and further addition resulted in a declining trend (Fig. **2A**). The tensile strength was enhanced by 13 and 8% in the case of AGG1 and AGG2-based composites, respectively. This decrease at higher filler concentration could be due to the presence of double bonds. The increase in tensile strength at lower concentration may be due to the reinforcing action of the fillers. Better filler-polymer interactions improved the tensile strength and decreased elongation at break values [18]. A lower value of tensile strength of the AGG2 epoxy composites at the same concentration of filler as compared to AGG1-based composites indicated that the higher degree of substitution hindered the filler-polymer interactions. The decrease in the

tensile strength was observed at filler concentrations above 0.5% due to poor interactions and phase separation. The impact properties of composites also followed a similar trend as tensile strength, as shown in Fig. (**2**). The impact strengths on the addition of AGG1 were greater than that of AGG2 concentration on the basis of increased interactions of epoxy resin. The maximum value of impact strength was observed at 1.5% of filler concentrations, which may be due to greater interaction resulting in composites with greater impact strength.

The % elongation at break of the composites displayed an initial decrease corresponding to the maximum value of tensile strength, as shown in Fig. (**2b**). There was a gradual increase in elongation at break values as the concentration of filler increased. The maximum elongation was observed at 3% of filler concentrations (Fig. **2b**). The % elongation at break values followed the reverse trend as compared to tensile and impact strength data, that is, better elongation was observed in AGG2 composites than in AGG1 at the same filler concentrations. The maximum increase in % elongation at break was 25% for AGG2-based epoxy composite at 3% of filler concentration. A further increase in filler concentrations above 3% resulted in a decrease of % elongation at break. However, % elongation at break was still greater than that of neat epoxy resin.

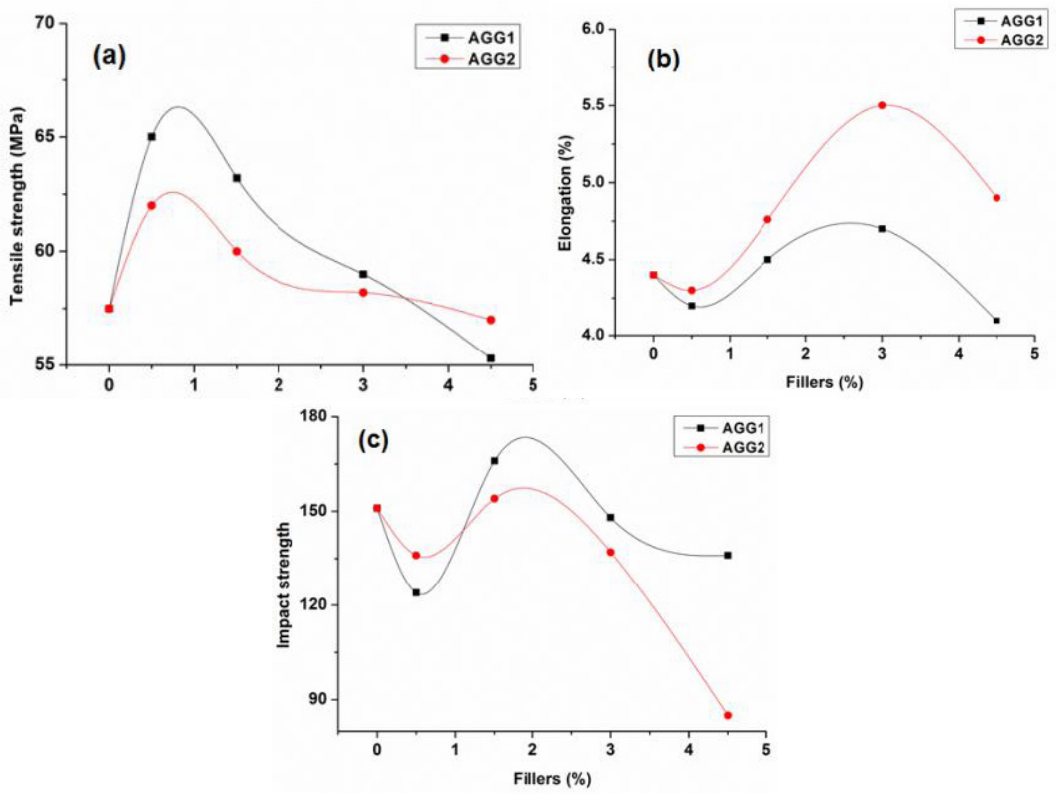

Fig. (2). Mechanical properties: (**a**) tensile strength; (**b**) % elongation, and (**c**) impact strength of epoxy allyl guar gum composites.

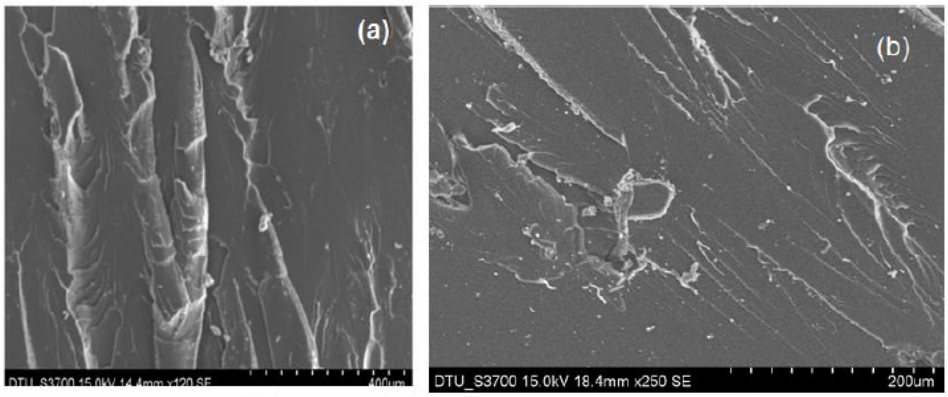

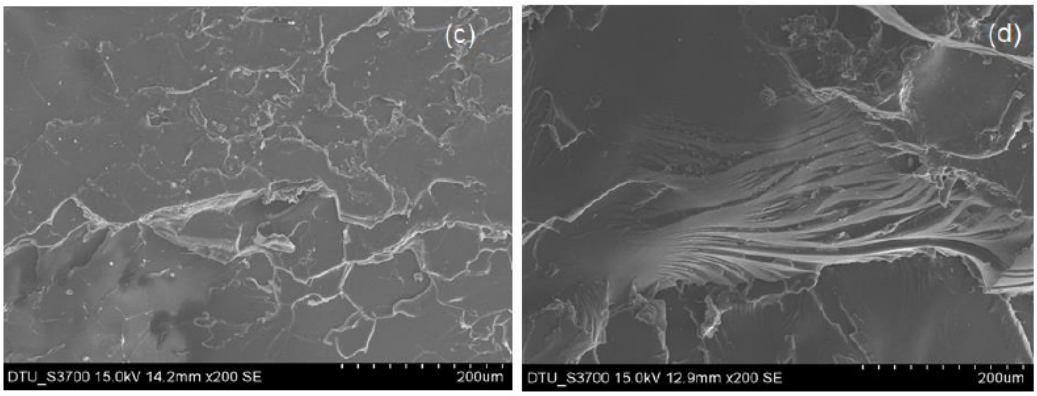

Fig. (3). SEM images of fractured surfaces of (**a**) neat epoxy resin; (**b**) epoxy allyl guar gum composite with 1.5% AGG1; (**c**) epoxy allyl guar gum composite with 1.5% AGG2; and (**d**) epoxy allyl guar gum composite with 4.5% AGG1.

3.2. Fracture Morphology of the Prepared Composites

The fracture morphology of neat epoxy resin and composites is shown in Fig. (**3**). The composites filled with low allyl guar gum showed an increase in matrix region as compared to composites with higher contents of allyl guar gum. The micrograph observed for the unmodified formulation was characteristic of a brittle system having a smooth glassy fractured surface with cracks in different planes, while rough fracture surfaces were observed for the composites. A similar morphology of neat epoxy resin was reported [9]. The composites containing 1.5% of AGG1 and AGG2 exhibited good dispersion of both phases and a lower extent of unreacted polymer (Fig. **3b - d**). This resulted in improved tensile strength and impact strength [11]. The fracture path of AGG1 showed a large breadth and parallel fibril structure, which indicated the stretching prior to fracture (Fig. **3b**). The formation of agglomerates was seen in the case of AGG2 due to reduced filler-polymer interaction [19 - 22] (Fig. **3c**). Therefore, composites with 0.5% of AGG1 resulted in higher tensile strength than the same contents of AGG2. A further increase in the content of modified guar gum resulted in poor dispersion of two phases. The extent of unreacted DGEBA and modified guar gum is shown by major black and white spots in the micrograph (Fig. **3d**), respectively. However, the fracture path of AGG2 was very narrow, and continuous rapid propagation along the axis of crack growth was observed (Fig. **3d**).

CONCLUSION

In the present study, allyl-modified guar gums (AGGs) were composited with epoxy resin. The AGG with two different degrees of substitutions was used. The polymer-filler interactions varied with the contents of filler (AGG) and degree of allyl substitutions, which in turn affected the mechanical properties of the composites. The mechanical properties of the composites showed a dual behavior depending on the contents of the filler. The tensile strength of the composites was found to be enhanced by 13% at a 0.5% concentration of AGG1 as compared to neat epoxy resin. The % elongation data exhibited an opposite trend as compared to the tensile strength of the composites. The maximum increase in % elongation at break was 25% for AGG2-based epoxy composite at 3% of filler concentration. The altered mechanical properties of the composites correlated with the dispersion of filler in the polymer matrix and phase separation.

LIST OF ABBREVIATIONS

AGG	=	Allyl Guar Gum
UTM	=	Universal Testing Machine
SEM	=	Scanning Electron Microscope

AUTHOR'S CONTRIBUTIONS

Dr. Gopal Arora is thankful to Chancellor, Dr. Sachin Gupta, Sanskriti University, Mathura, Dr. D S Tomar (Dean & HOD), and Sh Pooran Singh (Registrar), for help and support. Dr. Gopal Arora also thanks Mr. G.G. Kuswaha, Dr. Devender Kr Verma, Mr. B.K. Sharma, and Jeevan Ram for their valuable help during the work.

CONSENT FOR PUBLICATION

Not applicable.

AVAILABILITY OF DATA AND MATERIALS

The data supporting the findings of the article is available in the reference number [13].

FUNDING

None.

CONFLICT OF INTEREST

The authors declare no conflict of interest, financial or otherwise.

ACKNOWLEDGEMENTS

Declared none.

REFERENCES

[1] R.H.W. Wientjes, M.H.G. Duits, R.J.J. Jongschaap, and J. Mellema, "Linear rheology of guar gum solutions", *Macromolecules,* vol. 33, no. 26, pp. 9594-9605, 2000. [http://dx.doi.org/10.1021/ma001065p]

[2] A.P. Gupta, and A. Gopal, "Preperation and characterization of cross-linked guar-gum poly (vinylalcohol) green films", *Der Chimica Sinica,* vol. 3, no. 5, pp. 1191-1197, 2012.

[3] A.P. Gupta, and G. Arora, "Preparation and characterization of guar-gum/polyvinylalcohol blend films", *B is J. mater. sci. eng., B.,* vol. 1, no. 1B, p. 28, 2011.

[4] "Preparation and characterization of all modified guar gum",

[5] A. Tiwari, "Polysaccharide Development", In: *Properties and applications,* Nova Science Publiser, Inc, 2009.

[6] S. Sharma, P. Tiwari, and L. Pandey, *Identification of Various Metabolites like Gases, Biopolymers and Biosurfactants, Microbial Enhanced Oil Recovery.,* Springer, 2022, pp. 197-220.

[7] A. Katoch, and A. Roy Choudhury, "Understanding the rheology of novel guar-gellan gum composite hydrogels", *Mater. Lett.,* vol. 263, p. 127234, 2020.
[http://dx.doi.org/10.1016/j.matlet.2019.127234]

[8] M. Afsharpour, and S. Gilani, "Guar gum nanocomposites: Green corrosion inhibitors of iron-gall ink on paper artworks", *Stärke,* vol. 74, no. 1-2, p. 2100174, 2022.
[http://dx.doi.org/10.1002/star.202100174]

[9] M.A. Shenoy, and D.J. D'Melo, "Evaluation of mechanical properties of unsaturated polyester-guar gum/hydroxypropyl guar gum composites", *Express Polym. Lett.,* vol. 1, no. 9, pp. 622-628, 2007.
[http://dx.doi.org/10.3144/expresspolymlett.2007.85]

[10] D. Ray, A.K. Rana, N.R. Bose, and S.P. Sengupta, "Effect of guar-gum treatment on mechanical properties of vinylester resin matrix composites reinforced with jute yarns", *J. Appl. Polym. Sci.,* vol. 98, no. 2, pp. 557-563, 2005.
[http://dx.doi.org/10.1002/app.21995]

[11] R.Y. Ting, and A. Inc, *Epoxy resins Chemistry and Technology,* 2nd ed Marcel Dekker, Inc: New York, 1988, pp. 551-601.

[12] D.J. D'Melo, and M.A. Shenoy, "Evaluation of mechanical properties of acrylated guar gum – unsaturated polyester composites", *Polym. Bull.,* vol. 61, no. 2, pp. 235-246, 2008.
[http://dx.doi.org/10.1007/s00289-008-0941-7]

[13] M.A. Shenoy, and D.J. D'Melo, "Evaluation of mechanical properties of epoxy–guar gum composites", *Polym. Eng. Sci.,* vol. 48, no. 1, pp. 124-132, 2008.
[http://dx.doi.org/10.1002/pen.20925]

[14] W.F. Xiao, and L.T. Dong, "Studies on methacryloyl guar gum: Surface morphology, crystallinity, biodegradability and viscosity behavior of semi-dilute solutions", *Adv. Mat. Res.,* vol. 279, pp. 327-332, 2011.
[http://dx.doi.org/10.4028/www.scientific.net/AMR.279.327]

[15] M.B. Hoque, M.A. Hannan, M.Z.I. Mollah, M.R.I. Faruque, and R.A. Khan, "Physico-mechanical properties enhancement of pineapple leaf fiber (PALF) reinforced epoxy resin-based composites using guar gum (polysaccharide) filler: effects of gamma radiation", *Radiat. Eff. Defects Solids,* vol. 177, no. 3-4, pp. 401-416, 401-416, 2022.
[http://dx.doi.org/10.1080/10420150.2022.2043317]

[16] M. Li, Z. Zhu, and E. Jin, "Graft copolymerization of granular allyl starch with carboxyl-containing vinyl monomers for enhancing grafting efficiency", *Fibers Polym.,* vol. 11, no. 5, pp. 683-688, 2010.
[http://dx.doi.org/10.1007/s12221-010-0683-7]

[17] L.E. Nielson, *Mechanical properties of polymers and composites.,* Marcel Dekker: New York, 1974.

[18] J. Jain, and S. Sinha, "Pineapple leaf fiber polymer composites as a promising tool for sustainable, eco-friendly composite material", *J. Nat. Fibers,* 2021.
[http://dx.doi.org/10.1080/15440478.2021.1993478]

[19] S. Kaur, and S. Santra, "Application of guar gum and its derivatives as green binder/separator for advanced lithium-ion batteries", *ChemistryOpen,* vol. 11, no. 2, p. e202100209, 2022.
[http://dx.doi.org/10.1002/open.202100209] [PMID: 35103411]

[20] D. Mudgil, S. Barak, and B.S. Khatkar, "Guar gum: Processing, properties and food applications-A review", *J. Food Sci. Technol.,* vol. 51, no. 3, pp. 409-418, 2014.
[http://dx.doi.org/10.1007/s13197-011-0522-x] [PMID: 24587515]

[21] J. Aman, N.C. Shahi, U.C. Lohani, D. Balodhi, R. Singh, N. Kumar, M.I. Bhat, and A.P. Kumar, "Process optimization for development of guar gum-based biodegradable hydrogel film using response surface methodology", *Bioinorg Chem Appl.,* vol. 2022, p. 13, 2022.
[http://dx.doi.org/10.1155/2022/9180000]

[22] L. Qiu, Y. Shen, C. Wang, and X. Yang, "Scanning electron microscopy analysis of guar gum in the dissolution, gelation and gel-breaking process", *Polym. Test.,* vol. 68, pp. 95-99, 2018.
[http://dx.doi.org/10.1016/j.polymertesting.2018.04.001]

© 2023 Arora and Gupta

This is an open access article distributed under the terms of the Creative Commons Attribution 4.0 International Public License (CC-BY 4.0), a copy of which is available at: https://creativecommons.org/licenses/by/4.0/legalcode. This license permits unrestricted use, distribution, and reproduction in any medium, provided the original author and source are credited.

Arabian Journal for Science and Engineering
https://doi.org/10.1007/s13369-023-08115-x

RESEARCH ARTICLE-MECHANICAL ENGINEERING

Mechanical and Surface Wettability Analysis of Rare Earth Modified Composite Coating Developed Using Metal Spraying

Mohit Vishnoi[1,2] · **Qasim Murtaza**[1] · **Paras Kumar**[1]

Received: 6 August 2022 / Accepted: 13 July 2023
© King Fahd University of Petroleum & Minerals 2023

Abstract
The high pressure—high velocity oxy fuel (HP-HVOF) process is a thermal spraying process (TSP) for developing the high melting point powder ceramic coating over the surface. The mixture of used rare earth, the erbium oxide is an untouched rare earth oxide in the field of metal spraying and the likes of metal spraying such as the HP-HVOF process is a recently industrial opted process; which is the modified form of the HVOF process. This paper articulates the effects of rare earth ($La_2O_3/CeO_2/Er_2O_3$ −0.4 wt% each) addition on tungsten carbide coatings developed using high pressure-high velocity oxy fuel process on Martensitic steel having grade SS410. These effects have been analyzed using surface (like scanning electron microscope (SEM), porosity, surface roughness, wettability, and energy dispersive spectroscopy (EDS) test) and mechanical (such as tensile, flexural, and hardness test) characterization has been carried out on coated and uncoated samples. The porosity level of the coating was less than one percent, and the static water contact angle for coated sample (≈130º) was higher than the substrate (≈63º). This shows that fabricated coating is hydrophobic in nature. Moreover; the identification of doped elements has been done using EDS. The comparisons between the substrate and the coated samples have been done and the result shows that the coated sample possess enhanced surface and mechanical properties.

Keywords HP-HVOF · Wettability · Surface roughness · Porosity · Rare earth

1 Introduction

The elements (in limited quantities) which extraordinarily enhance the physical and chemical properties of metals by getting combined with them are called rare earth elements. Due to the high melting point, they are physically soft to the touch, appear silver in color, and get tarnished quickly in the air [1]. There is a total of seventeen elements that come under the group of rare earth elements (REEs) namely; lanthanum (La), cerium (Ce), praseodymium (Pr), neodymium (Nd), promethium (Pm), samarium (Sm), europium (Eu), gadolinium (Gd), terbium (Tb), dysprosium (Dy), holmium (Ho), erbium (Er), thulium (Tm), ytterbium (Yb), lutetium (Lu), which are fifteen lanthanides along with scandium (Sc) and yttrium (Y) [2]. Based on various physical and chemical properties, REEs are further classified into two sub-groups namely heavy rare earth elements (HREEs) which include Y, Tb, Dy, Ho, Er, Tm, Yb, and Lu, and light rare earth elements (LREEs) which include Sc, La, Ce, Pr, Nd, Pm, Sm, Eu, and Gd. The HREEs and LREEs are also known as the yttrium group and cerium group respectively [3]. Various elements such as hydrogen, oxygen, nitrogen, sulfur, and silicon interact with rare earth because of the large atomic radius and effective chemical activities and this plays a beneficial role in steel and its manufacturing [4]. REEs are useful in many surface engineering applications like surface modifications, surface chemical heat treatment, and electroplating [5]. Oxides of REEs find their application in diverse fields like chemical, metallurgy, and electronics engineering [6]. Clean and green energy comprises of wind turbines, Electric Vehicles, solar cells, etc. Terbium, dysprosium, neodymium, and yttrium are some of the rare elements which are advantageous for green energy science [7].

For industrial applications, the surface property of a material defines its performance. The surface alteration techniques

✉ Mohit Vishnoi
vishnoi.mohit06@gmail.com

Qasim Murtaza
qasimmurtaza@dce.ac.in

Paras Kumar
paraskumar@dtu.ac.in

[1] Department of Mechanical Engineering, Delhi Technological University, Delhi 110042, India

[2] Department of Mechanical Engineering, JSS Academy of Technical Education, Noida 201301, India

Published online: 25 July 2023

benefits as an economic substitute of the poor substrate with plated/coated substrate material producing desirable surface traits and performance. Surface tempering is very worthy in conditions where the material has to be protected from corrosion, wear, high temperature, and excessive stress.

In the latest studies, REEs have been used to achieve the desired surface properties of metals by applying a thin coating on metal surfaces using various thermal spray processes (TSP) and laser coating processes. Moreover, the effect of REE coating has been analyzed based on the corrosion resistance, wear, and microstructure of modified surfaces [8]. One of the techniques used for the deposition of REEs on base metal is the thermal spraying process. The thermal spraying technique is a straight shot process in which the feedstock material (powder, wire, rod, suspension) is placed in a spray torch, liquefied (fluid or semi-fluid state), and flanged onto a base material. The feedstock material (fluid or semi-fluid state) with very high velocity sticks to the substrate material [9, 10]. Due to high velocity, the impacting particle attains high kinetic energy which bridles surface tension energy, distorts the shape of the particles, and/or gets transmuted to heat because of viscous dissipation or reversible (adiabatic) shear instabilities while flattening for the construction of the splat [11–13].

The coating layer is in the form of a lamellar arrangement of splats due to TSP deposition manifests different physical characteristics from those of the coating bulk material. Phase change in the course of the build-up process, residual stresses in the stiffened splats, and the existence of porosities. Moreover, micro-structural faults could be the reason for these dissimilarities [14]. Even though there are various other surface deposition techniques available, for example, physical vapor deposition, chemical vapor deposition, and plasma-intensified chemical vapor deposition, these processes are comparatively expensive and are also not fit for the fabrication of coatings exceeding 100 μm thicknesses at a high rate of deposition [15–20]. On the contrary, the flexibility provided by the TSP is such that it can be engineered to bestow friction co-efficient adaptation, control, and restoration over dimensions, and strengthen thermal and electromagnetic properties of base materials already in service. The capabilities are for deposition of a coating on a complex-shaped substrate and to recoat defaced coatings, which proved to be beneficial [21, 22]. However, the base material may get damaged due to the occurrence of thermal degradation or char formation, which again is contingent on feedstock material temperature and the high temperature of gases during TSP deposition [23].

The efficiency of TSP deposition is defined as the quantitative relation between the deposited material weight and feedstock particles spattered within a given amount of time [24].

From the TSP emerge multiple other techniques which are classified based on heat source: (1) combustion heat source, for example, HVOF or HP-HVOF (high-velocity oxygen fuel/high-pressure high-velocity oxygen fuel), and detonation gun; (2) electrical energy as the heat source in the form of plasma, for example, atmospheric plasma spray (APS), and wire-arc spraying; and (3) energy from gas expansion as a heat source, for example, Cold Spray (CS) [25]. APS is one of the most flexible thermal spray techniques and it also has very few limitations regarding the feedstock materials that can be used. In APS, raw material is put into the plasma stream where melting of feedstock in partially or completely occurs which in the end gets deposited in a lamellar pattern on the base metal. APS is also cheaper as it is performed in the ambient environment. In-flight oxidation of feed material, it is the only major drawback of this technique and it is best fitted for less porous coating deposition [26]. Another TSP that makes use of electrical energy and is again cheaper, easy to use, and has a high rate of deposition is wire-arc spraying. In Wire-arc spraying, two wires which are made up of the same material that has to be coated on the substrate are fed continuously to the system. A strong arc is produced with the help of electrical energy between the two wires which leads to the immediate melting of the wires. High pressurized gas is further used which accelerates the molten droplets in the direction of the base material. The stockpile and solidification of molten droplets on the base material lead to the formation of coating in a layer-by-layer manner [27]. Metals that have a good aversion to corrosion, for example, zinc and aluminum, are well suited for the wire-arc spraying deposition technique for improving the anti-corrosion properties of base materials [28]. In-flight oxidation of feedstock can be avoided in cold spray (CS) technique. The CS, sometimes CS is also called 'kinetic spray', acceleration of feed material takes place by advancing a high-pressure gas past a de Laval nozzle [29, 30]. High velocity oxygen/air fuel (HVOF/HVAF) comes under the category of combustion spray technique. An oxidizing agent (oxygen/air) is used to set off a hydrocarbon fuel, usually kerosene, methane, propane, propylene, acetylene, or natural gas, into flames. The high pressure and high temperature required for melting and accelerating feedstock particles towards the base material comes from this ignition of hydrocarbon. For further speeding up the feedstock particle speed, de Laval nozzles are used. In HVOF, the gas mixture consists of a hydrocarbon fuel, nitrogen, and oxygen as an oxidizing agent whereas in HVAF oxygen is replaced by dry air. The flame temperature while spraying gets affected due to this change of oxidizing agent. HVOF exhibits a higher temperature range (2700–3100 °C) whereas HVAF exhibits a lower temperature range (1900–2000 °C). The pressure and particle velocity also differ in the case of HVOF and HVAF. HVOF handles the pressure of 1 MPa and particle velocity of 600–750 m/s whereas HVAF generates pressure up to 2 MPa which results to a velocity of 600–840 m/s to feedstock particles. As compared with plasma spray

techniques, HVOF/HVAF has low particle temperature but high velocity leads to a reduction of in-flight oxidation. Also, coating density is improved with very less porosity [31]. A detonation gun is another TSP that uses combustion as a heat source. Improved adhesion of coating material to a substrate, and low porosity coatings are some of the major advantages of this technique. A tube-shaped barrel closed at one end is used in which a combustion mixture containing oxygen and acetylene is fed through inlets. Nitrogen covering is used as a shield to prevent back-firing from gas inlets. A measured quantity of feedstock powder is put into the combustion chamber and spark plugs are used to burn up the gas mixture. High-pressure shock waves generated inside the combustion chamber move through the barrel and simultaneously melt the feedstock material and provide a very high velocity to it. The melted powder impacts the base material and the high kinetic energy of the particles leads to the development of a strong and dense layer on the base material [32].

In TSP, there are several process parameters but the decisive ones which determine the density, quality, and uniformity of coating on substrate material are gas flow rate, power input, carrier gas flow rate, stand-off distance, and power feed rate. The choice of a particular thermal spray technique to apply coating on base material should be based on feedstock material property and the desired coating microstructure [33–35].

There are some practical industrial applications such as metal structure in bridges and turbine blades (due to its good corrosion, erosion, and wear resistance); moreover in automotive such as shafts sleeves (due to their high hardness, and almost no pores after fusing) [36–38].

There are various thermal spraying processes listed as follows:

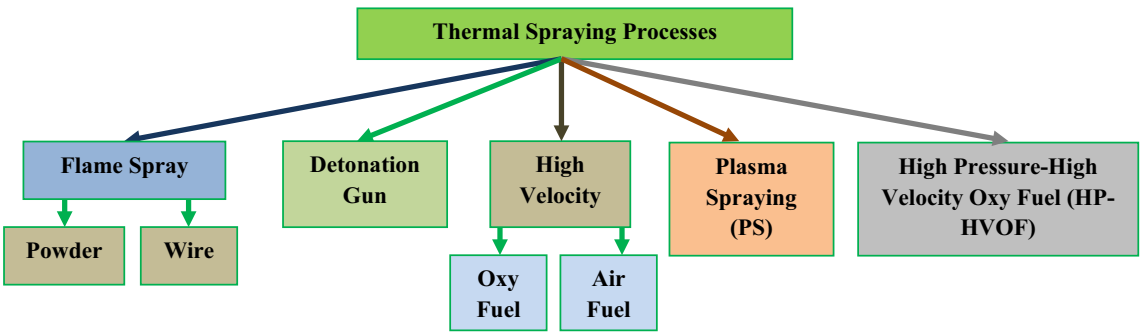

There are many available processes considered by different researchers in their experimentations. Though, there were very few works done on the (high pressure—high velocity oxy fuel) HP-HVOF process. This paper has considered the HP-HVOF as a thermal spraying process for the deposition of coating and substrate material as Martensitic steel having grade SS410. The coating powder is a mixture of various rare earths in their optimum quantity. Erbium oxide being heavy rare earth oxides has rarely (untouched) been used in the thermal spraying field. The developed coat has been characterized and obtained results have been discussed.

2 Experimental

2.1 Materials

The stainless steel having grade SS410, also known as Martensitic steel was used as a substrate material. The received substrate was in the form of a plate, having dimensions (12 inches *10 inches) with 0.2-inch thickness. The weight percentage of elements present is shown in Table 1.

The agglomerated sintered spheroidal shape carbide (WC-10Co-4Cr) powder with size (45/15) microns as shown in Table 2 was utilized for coating in which the doping of different rare earth elements was incurred in optimum quantity. The rare earth oxides such as lanthanum oxides (La_2O_3), cerium oxides (CeO_2), and erbium oxides (Er_2O_3) were used as the doping elements in carbide coating with equal (0.4% each) weight percentages. The morphology of carbide powder using scanning electron micrograph (SEM) has been shown in Fig. 1 at (1000X) magnifications. The spherical shape rare earth powder with 99% purity having a particle size in the range of 5–10 μm was used as doping element. The above quantity of rare earth oxides with micro-powders has been added and properly mixed with WC-Co-Cr.

The addition of RE; lanthanum oxides (La_2O_3—0.4 wt%), cerium oxides (CeO_2—0.4wt%), and erbium oxides (Er_2O_3—0.4 wt%) as shown in Table 2 were used as a doping element in carbide coating. The addition of optimum values (1.2 wt%) of RE was decided after reviewing previous literature. Various researchers have claimed that there are enhancements in coating properties with the addition of rare earth elements up to 1.2 wt% and beyond that is deterioration in the various coating properties [39–43].

Table 1 Weight percentage of elements present in SS410

Element	C	Si	Mn	P	S	Cr	Ni
Wt.%	0.14	0.54	0.64	0.04	0.005	12.44	0.17

Table 2 Chemical composition of rare earth (RE) doped coating powder

Powder	Chemical composition (wt.%)					Rare earth element (wt.%)		
	WC	Co	Cr	Fe	C	La_2O_3	CeO_2	Er_2O_3
WC-Co-Cr (86/10/4)	balance	9–11.5	3–5.5	0.03(max)	5–6.5	0.4	0.4	0.4

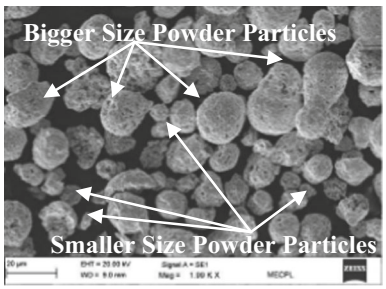

Fig. 1 SEM micrograph of carbides (WC-10Co-4Cr) powder

2.2 Method of Coating Deposition

The high pressure-high velocity oxy fuel (HP-HVOF) method has been opted for depositing of coating on Martensitic stainless steel as shown in Fig. 2a and the instrument used has been shown in Fig. 2b. The HP-HVOF is the modification of the HVOF process by incorporating the coating properties enhancing parameters. There were important steps involved in the thermal spraying process as shown in Fig. 3.

The coating on SS410 was developed at Metallizing Equipment Company (MEC) Pvt. Ltd. Jodhpur using HP-HVOF commercial high pressure—high-velocity oxy fuel (HVOF) thermal spraying system (model XPOJET-5000).

The following process parameters of the HP-HVOF system are considered in coating deposition as shown in Table 3.

The mechanism of formation of rare earth doped carbide coating on stainless steel has been shown in Fig. 4. The coating thickness is mainly depending upon the number of passes. The high temperature molten powder droplets have been accelerated using the nozzle and impact of molten powder on substrate SS410. Moreover, solidification of the molten droplets performed on the substrate turns the formation of a composite coating. Due to high velocity and temperature the deposited coating has shown high density and results in a reduction in porosity.

2.3 Characterization of Coating

The scanning electron microscope (JSM-6010 LA) (W-SEM) was used to know the morphology of coated and uncoated surfaces; which were represented as micrographs of the considered surface. The morphology of the used carbide powder was also done using SEM. To know the elemental identification on the coated surface, it was done using energy dispersive spectroscopy (EDS), which was attached to the scanning electron microscope. Further, the surface roughness

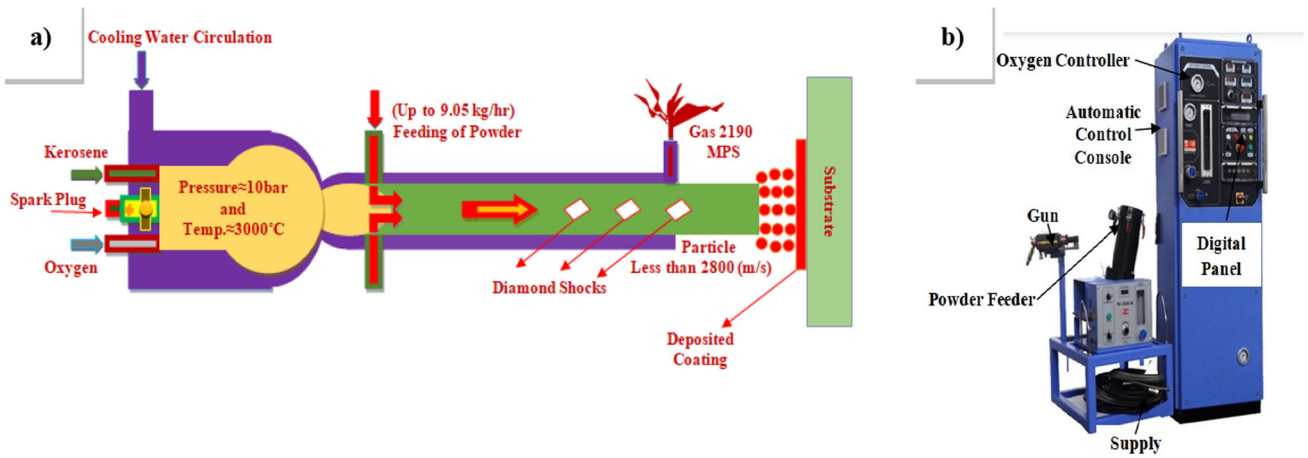

Fig. 2 **a** HP-HVOF as a method of coating deposition; and **b** Instrument of HP-HVOLF System

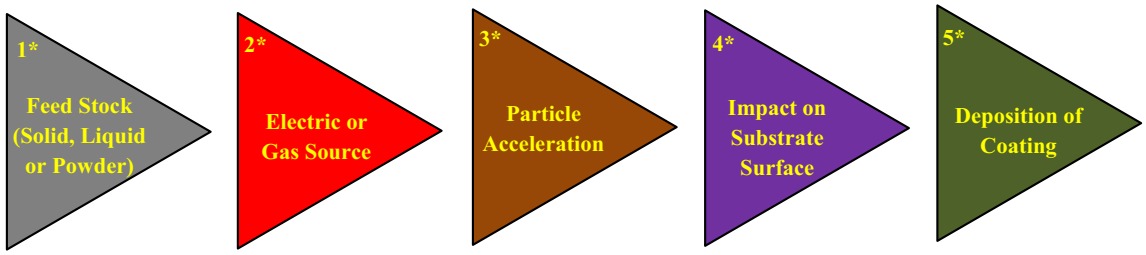

Fig. 3 Steps involved in coating

Table 3 Process parameters of HP-HVOLF coating

Gun	MJP-5000
Oxygen flow (SLPM)	850
Fuel flow (ml/min)	380
Chamber pressure (bar)	6.9
Powder feed rate (gm/min)	75
Spray distance (mm)	330
Particle velocity (m/sec)	785
Flame temperature (°C)	2630

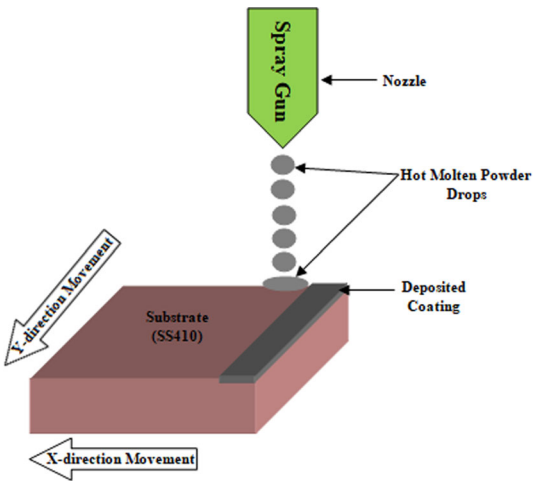

Fig. 4 Mechanism of coating formation on stainless steel

of the coated and uncoated substrate was carried out using a surface roughness tester (Model: Mitutoyo Surtest SJ301).

The porosity test was carried out on coated substrate using a metallurgical microscope (Axiovert A1, Make—Carl Zeiss, Magnification range: 100X to 1000X). The measurement of static water contact angle was carried out using a sessile droplet test. The contact angle meter having model (DMe-211 plus) was used.

The tensile test and three-point bend test (flexural test) were carried out to know the various mechanical properties of samples before and after coating. The Instron-1195; Universal Testing Machine (maximum capacity: 100kN, crosshead speed: 0.005–40 mm/min, and maximum crosshead displacement: 700 mm) was used to conduct the test at IIT Kanpur.

Table 4 Process parameters of EDS

Acquisition condition of EDS	
Volt	20.00 kV
Live time	196.60 s
Real time	203.04 s
Dead time	3.00%
Count rate	1849.00 CPS

The hardness test on the substrate and coated samples were carried out using Vicker's micro hardness tester (Model: Matrix DVS 1AT8, Maximum hardness: 1600HV and Maximum load: 1 kg).

3 Results and Discussion

3.1 Energy Dispersive x-ray (EDX) Analysis of Deposited Coating

The present elemental identification was done using energy dispersive x-ray analysis (EDS) as shown in Fig. 5h and individual element identification (such as C, Cr, Co, La, Ce, Er, and W) as shown in Fig. 5a–g with their different colors. The different process parameters of EDS have shown in Table 4. The measurement was carried out for approximately 203.04 s. The actual time (approximately 196.60 s) till the detector was active. The EDS spectrum of coating is shown in Fig. 5h; the peaks are x-ray given off as electron return to the K electron shell (C, Cr, and Co), to the L electron shell for rare earth elements, and only tungsten form M electron shell. The peak position identification has been done using Moseley's law.

3.2 Scanning Electron Microscope (SEM) Micrographs of the Substrate and Deposited Coating

The micrographs were taken using a scanning electron microscope (SEM) at 1000X magnification. The black spots on the substrate indicate the presence of a carbon-rich atmosphere

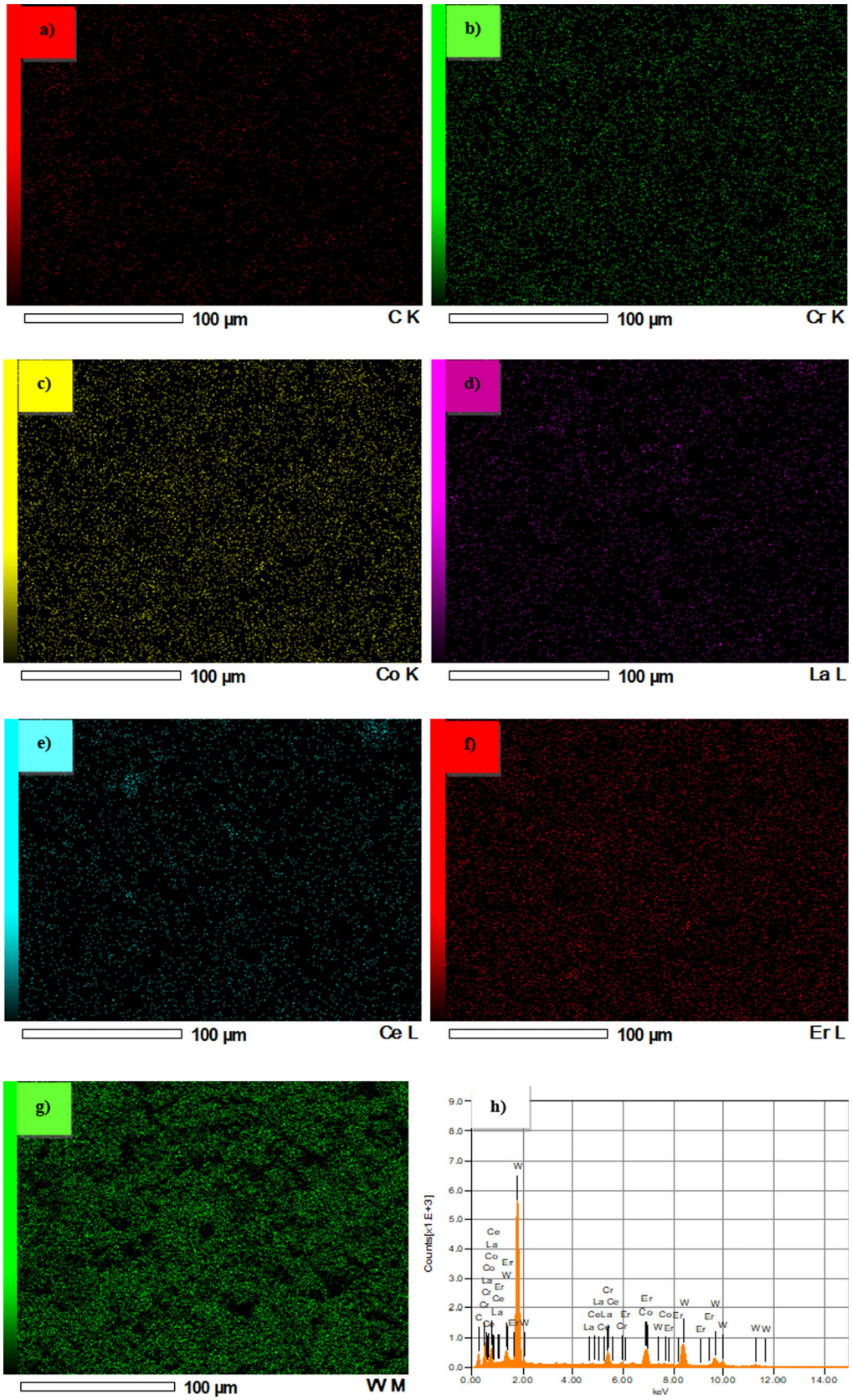

Fig. 5 The elements identification using EDX; **a** Carbon (C), **b** Chromium (Cr), **c** Cobalt (Co), **d** Lanthanum (La), **e** Cerium (Ce), **f** Erbium (Er), **g** Tungsten (W) and **h** Peaks of all identified elements

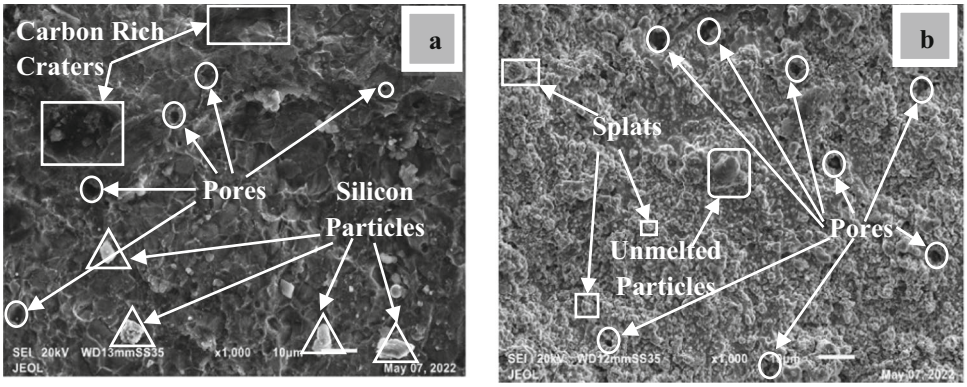

Fig. 6 Micrographs of **a** Uncoated; **b** Coated samples using SEM at 1000X

at many places on the surface of the samples. The numbers of pores on the surface of coated samples are more as compared to the substrate. This could be visualized in Fig. 6a and b. There are lots of splats as well as unbelted particles on the surface of coated sample.

3.3 Roughness Test

The surface roughness test was carried out using a roughness tester. The average values of all the experiments were considered as shown in Fig. 7 with deviations (approximately ± 5%). The average value of roughness is more for coated surfaces as compared to the substrate. The roughness of the coated surface is more due to the presence of several pores as compared to the substrate as shown in Fig. 6a and b.

3.4 Porosity Test of Coated Sample

The porosity test has been carried out on the rare earth doped thermal sprayed coatings using ASTM E standard 2L09-01 (reapproved 2007), Method A [44]. The porosity level was measured as < 1% in the 24 mm polished area. Figure 8 shows the microscopic image of the coated sample at 200X magnification. The roughness and porosity level test has been done for a better explanation of surface morphology.

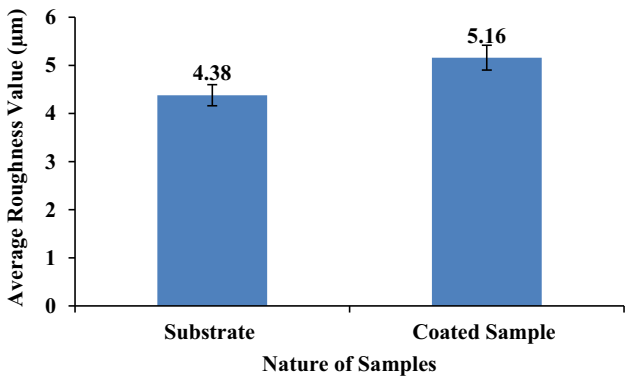

Fig. 7 Average surface roughness value for samples

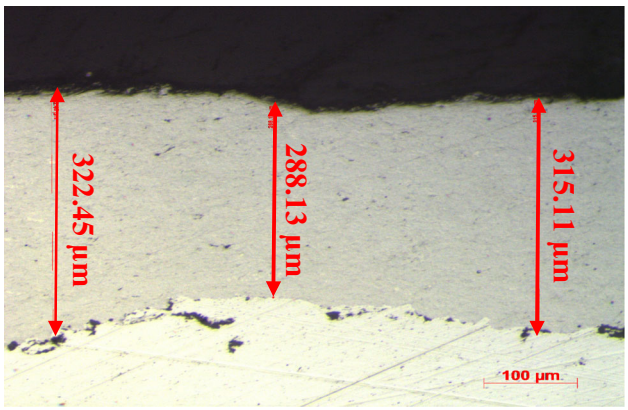

Fig. 8 Porosity test and thickness of coating

The different experiments on rare earth doped coating are conducted by various researchers and have suggested the outcome of each experiment. A comparison of porosity levels obtained from the current experiment and the other existing previous work is made in Table 5. The porosity level of current experimental work is very less as compared to existing experimentations. The rare earth doped coating obtained using HP-HVOF shows a better result as compared to others.

3.5 Wettability Analysis of Samples

The sessile droplet method was used to analyze the wettability behavior of substrate and coated surfaces. It is familiar that surface roughness is the prime parameter to decide the wetting behavior of the surface. The effect of roughness on wettability was discussed by Wenzel and Cassie Baxter's state model [45, 46]. There are two possibilities when a liquid droplet is placed on a solid surface, either it could spread or preserve over a finite area. It depends on the interactions between the liquid droplet and the solid surface.

Few researchers claims the demark line to categorize the surface, based on the static contact angle measurement the researchers generally recommended that the contact angle of any surface is in the range of acute angle (<90°), the surface is

Table 5 Comparison of porosity level of current work with other existing previous work

Coating powder	Rare earth (wt%)	Method	Porosity level	References
WC-10Co-4Cr	(La_2O_3 + CeO_2 + Er_2O_3-1.2%)	High pressure-high velocity oxy fuel	**< 1%**	Current experimentation
WC-12Co	(Cerium oxide-1%)	High velocity oxy fuel	**1.6%**	[39]
Nano (WC-12Co)	NA		**2.1%**	
NiCrBSi	(Cerium oxide)- 0%, 0.4%, 0.8%, 1.2%, 1.6% and 2%	Flame sprayed	6.2, 6.5, **5.2**, 6.8, 7.9 and 7.3	[42]
	(Lanthanum oxide)- 0%, 0.4%, 0.8%, 1.2%, 1.6% and 2%		6.2, 7.1, 6.2, **5.8**, 6.7 and 7.2	[43]

Bold values are the maximum values, which have been obtained in the respective literature

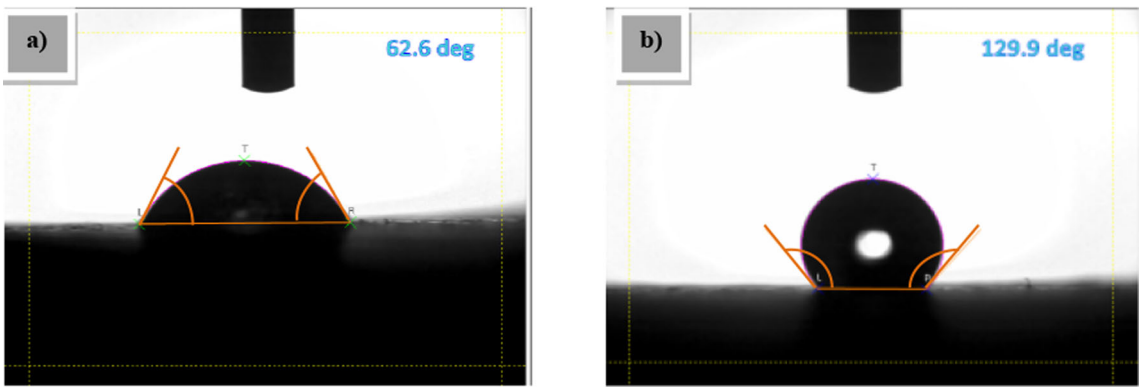

Fig. 9 Wettability behavior using contact angle measurement of **a** Substrate; **b** Coated samples

hydrophilic in nature otherwise it is described as hydrophobic (> 90°) surface [47–49].

Moreover, if the static water contact angle is greater than 150° then the surface shows super-hydrophobic behavior (in many plants leaves like the lotus and colrabi) [50, 51]. By increase in surface roughness, the nature of the surface leads towards hydrophobicity due to the trapping of air in the rough area [52, 53].

As shown in Fig. 9a and b, the coated sample shows a considerably larger static water contact angle (WCA) than the substrate.

The value of contact angle (CA) for uncoated surfaces was in the range of 60.7–62.6 degrees, which described the surface to be hydrophilic but the CA for the coated sample was 127.9–129.9 degrees, which characterized the surface as hydrophobic (very close to super-hydrophobicity).

3.6 Tensile Test Results

The Specimens were prepared using the ASTM- E8 standard. The average values of three experiments were considered with a deviation (approximately ± 5%).

The stress–strain diagram (as shown in Fig. 10a and b) for the substrate and the coated specimen was obtained from a tensile test using the universal testing machine.

The values of different mechanical properties were calculated from stress–strain as shown in Table 6. The percentage elongation indicates that the nature of the material, the value of percentage elongation is less in the case of coated sample. This means the coated sample is more brittle in nature. The strength of coated sample is more than the substrate due to its peak stress. The offset yield point at 0.02 and 0.2 is more for coated samples than the substrate. The modulus value for the coated sample is far greater than the substrate.

3.7 Three Point Test

The three experiments have been conducted and the average values of all the properties with a deviation (approximate ± 5%) were considered as shown in Table 7. The standard (ASTM-D790) has been used to make the specimens.

The stress–strain curve has been shown in Fig. 11a and b; for substrate and coated samples respectively. The curve has been obtained from the flexural (3-point bend) test and the different property values have been calculated using stress–strain curves.

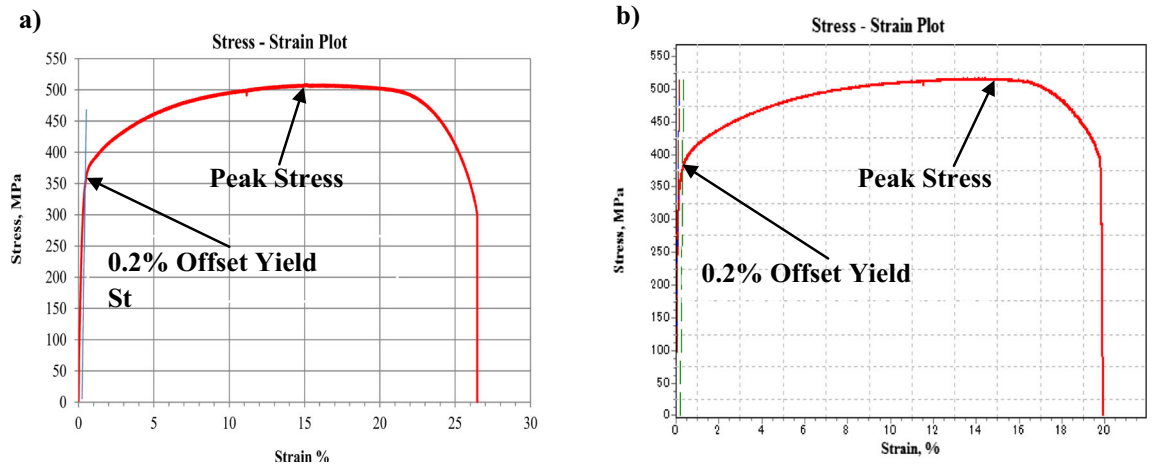

Fig. 10 Stress–strain curve obtained from tension test, **a** Substrate and; **b** Coated sample

Table 6 Different results obtained from the universal tensile machine (UTM)

Properties	Substrate	Coated sample	Change (%)
Peak stress (MPa)	508.7	516.27	1.49
Peak load (kN)	12.8	13.94	8.91
0.2% offset yield stress (MPa)	355	374.95	5.62
Yield strain (%)	0.47	0.31	34.041
Yield load (kN)	8.94	10.13	13.31
0.02% offset yield stress (MPa)	251	275.76	9.87
Modulus (GPa)	117	329.09	181.27
Elongation at break (using strain) (%)	26.48	19.93	24.74

The flexural peak stress value for the coated sample is considerably larger than the substrate, which indicates that the coated sample has a high capability to resist bending before yield. As shown in Table 7, the percentage change in the values of different properties is considerable, which could not be neglected.

3.8 Hardness Test

The Vickers hardness test (HV0.3) under a load of 300 g with 10 s dwell time has been conducted as per ASTM- A270 standard on uncoated and coated specimens. The average values of three readings were taken with a deviation (approximately ± 5%) as shown in Fig. 12.

The hardness value of substrate (≈HV194) was found to be lesser as compared to coated samples (≈HV932). This show after the deposition of the coating on SS410, the

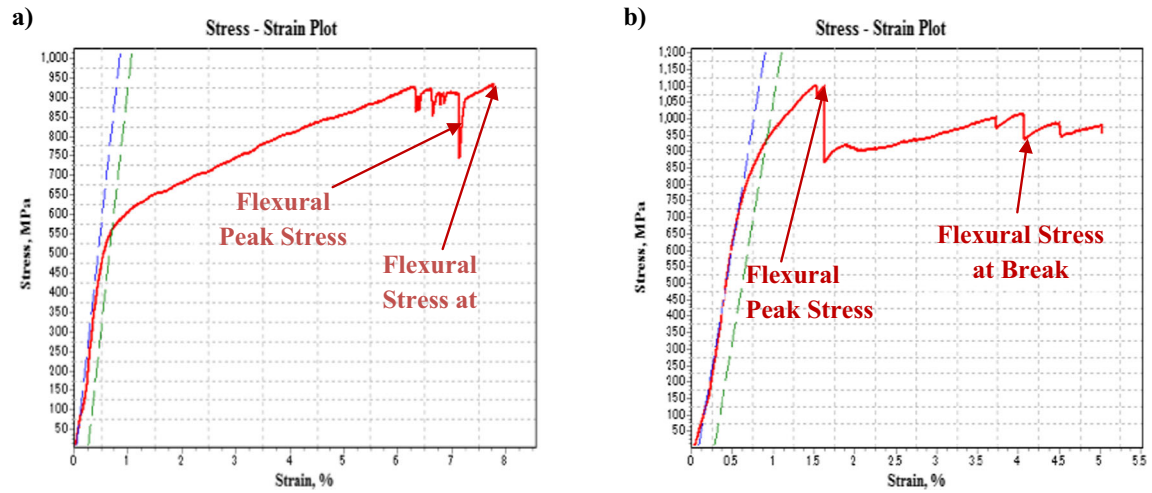

Fig. 11 Stress–Strain curve obtained from the flexural test (3-point bend test), **a** Substrate, and; **b** Coated sample

Table 7 Flexural (3-point bend) test results

Properties	Base Metal	Coated Sample	% change
Flexural peak stress (Mpa)	781.82	1101.17	40.85
Peak load (kN)	1.78	2.87	60.24
Offset flexural yield stress (Mpa)	0.72	1.16	61.11
Offset flexural yield load (kN)	0.72	1.16	61.11
Flexural stress at break (Mpa)	921.67	958.78	4.03

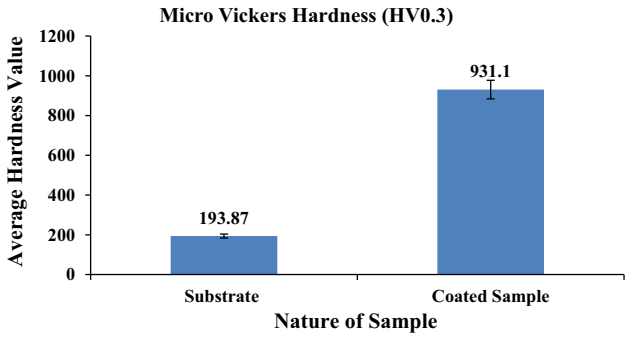

Fig. 12 Micro Hardness test on the substrate and coated sample

obtained coated samples shows better results than the substrate. The incorporation of rare earth in tungsten carbide powder enhanced the hardness of the coated sample. The reason for the increase in hardness of the coating was due to the presence of hard tungsten carbide particles and the addition of rare earth decreases the porosity level, this indicates the densification of the coating. The temperature of the heated powder was above the melting point of the material, which led to the formation of respective oxides in the coating. The nature of coating is ceramic due to the formation of oxides.

The various researchers have conducted their experiments and obtained different values of Vickers hardness as shown in Table 8. From Table 8, concludes that obtained hardness values form the current experimented work has a high hardness value among other existing work.

4 Conclusions

In this study, the contribution of optimum value of rare earth to WC-based coatings can be concluded as follows:

- The RE doped WC-10Co-4Cr coating has been successfully deposited on Martensitic steel using HP-HVOF process.

Table 8 Comparison of current work hardness value with other existing work

Powder used	Rare earth oxides	Vickers hardness	References
WC-10Co-4Cr	(La_2O_3 + CeO_2 + Er_2O_3) − 0.4 wt%. each	**931.1**	Current Work
NiCrBSi	(CeO_2) − 0, 0.4, 0.8, 1.2, 1.6 and 2 wt%	210, 215, **250**, 238, 221 and 226 respectively	[42]
NiCrBSi	(La_2O_3) − 0, 0.4, 0.8, 1.2, 1.6 and 2 wt%	≈210, 220, 230, **256**, 226 and 222 respectively	[43]

Bold values are the maximum values, which have been obtained in the respective literature

- The addition of rare earth makes the distribution of element uniform and inculcates a refined microstructure.
- There are various elements, identified in the coating such as Tungsten (W), Cobalt (Co), Chromium (Cr), Erbium (Er), etc. using energy dispersive x-ray analysis.
- The observed porosity level on surface of RE doped carbide coating was less than one percent.
- The average surface roughness value of the coated sample is about 5.16 μm, which is higher than compared to the uncoated sample (4.38 μm).
- The RE doped carbide coating showed the contact angle (of 129.9º), which turns out to be a hydrophobic surface than the substrate (62.6º) as hydrophilic.
- There was an enhancement of flexural strength of the RE doped carbide coating than the substrate.
- There was an increase in the hardness value (HV931.1) of the RE doped coated sample as compared to the uncoated sample (HV193.87).

5 Future scope

The tribological characterization can also be explored for the same composition. Apart from this composition, many other possible compositions can consider and optimize with various available optimization tools.

Acknowledgements The author wants to thank the JSS Academy of Technical Education, Noida, India for allowing me to pursue Ph.D. from the Department of Mechanical Engineering, Delhi Technological University, Delhi 110042, India. The author would like to thank Precision Manufacturing Lab at Delhi Technological University, Delhi, Metallizing Equipment Company Pvt. Ltd. Jodhpur for the fabrication of the

coating, and the Indian Institute of Technology, Kanpur for helping us in the Characterization (Mechanical and Surface) of the coating.

Author Contribution MV: conceptualization, investigation, data curation, writing—original draft. PK: review and editing, supervision. QM: review and editing, supervision.

Funding No funding has been involved in this work.

Declarations

Conflict of Interest The authors declare that they have no known competing financial interests or personal relationships that could have appeared to influence the work reported in this paper.

References

1. Wall, F.: Rare earth elements. Critical Metals Handbook. 312–339 (2013)
2. Li, H.; Wang, P.; Lin, G.; Huang, J.: The role of rare earth elements in biodegradable metals: a review. Acta Biomater. **129**, 33–42 (2021)
3. Rasoulnia, P.; Barthen, R.; Lakaniemi, A.-M.: A critical review of bioleaching of rare earth elements: the mechanisms and effect of process parameters. Crit. Rev. Environ. Sci. Technol. **51**, 378–427 (2020)
4. Wang, K.L.; Zhu, Y.M.; Zhang, Q.B.; Sun, M.L.: Effect of rare earth cerium on the microstructure and corrosion resistance of laser cladded nickel-base alloy coatings. J. Mater. Process. Technol. **63**, 563–567 (1997)
5. Yi, W., et al.: Effect of rare earth on oxidation resistance of iron base fluxing alloy spray-welding coating. J. Alloy. Compd. **311**, 65–68 (2000)
6. Wang, K.L.; Zhang, Q.B.; Sun, M.L.; Wei, X.G.; Zhu, Y.M.: Rare earth elements modification of laser-clad nickel-based alloy coatings. Appl. Surf. Sci. **174**, 191–200 (2001)
7. Jyothi, R.K., et al.: Review of rare earth elements recovery from secondary resources for clean energy technologies: grand opportunities to create wealth from waste. J. Clean. Prod. **267**, 122048 (2020)
8. Vishnoi, M.; Murtaza, Q.; Kumar, P.: Effect of rare earth elements on coatings developed by thermal spraying processes (TSP)—a brief review. In: Materials Today: Proceedings vol. 44, Elsevier Ltd, pp. 4053–4058 (2020)
9. Davis, J.R.: Handbook of Thermal Spray Technology. ASM International, Materials Park (2005)
10. Fauchais, P.L.; Heberlein, J.V., Boulos, M.I.: Overview of thermal spray. Thermal Spray Fundamentals. 17–72 (2013)
11. McDonald, A.; Lamontagne, M.; Moreau, C.; Chandra, S.: Impact of plasma-sprayed metal particles on hot and cold glass surfaces. Thin Solid Films **514**, 212–222 (2006)
12. Dewar, M.P.; McDonald, A.G.; Gerlich, A.P.: Interfacial heating during low-pressure cold-gas dynamic spraying of aluminum coatings. J. Mater. Sci. **47**, 184–198 (2012)
13. Schmidt, T.; Gärtner, F.; Assadi, H.; Kreye, H.: Development of a generalized parameter window for cold spray deposition. Acta Mater. **54**, 729–742 (2006)
14. Fauchais, P.; Fukumoto, M.; Vardelle, A.; Vardelle, M.: Knowledge concerning splat formation: an invited review. J. Therm. Spray Technol. **13**, 337–360 (2004)
15. McNaughton, T.G.; Horch, K.W.: Metallized polymer fibers as leadwires and intrafascicular microelectrodes. J. Neurosci. Methods **70**, 103–107 (1996)
16. Siegel, J.; Kotál, V.: Preparation of thin metal layers on polymers. Acta Polytechnica (2007). https://doi.org/10.14311/904
17. Duguet, T.; Senocq, F.; Laffont, L.; Vahlas, C.: Metallization of polymer composites by metalorganic chemical vapor deposition of Cu: Surface functionalization driven films characteristics. Surf. Coat. Technol. **230**, 254–259 (2013)
18. Gritsenko, K.P.: Metal-polymer optical storage media produced by PECVD. Thin Solid Films **227**, 1–2 (1993)
19. Voyer, J.; Schulz, P.; Schreiber, M.: Electrically conductive flame sprayed aluminum coatings on textile substrates. J. Therm. Spray Technol. **17**, 818–823 (2008)
20. Pawłowski, L.: The Science and Engineering of thermal spray coatings. Wiley, Chichester (2008)
21. Therrien, D.S.: Heat transfer analysis of flame-sprayed metal-polymer composite structures. Library and Archives Canada = Bibliothèque et Archives Canada, Ottawa (2013)
22. Fauchais, P.; Montavon, G.: Thermal and cold spray: recent developments. Key Eng. Mater. **384**, 1–59 (2008)
23. Katsoulis, C.; Kandola, B.K.; Myler, P.; Kandare, E.: Post-fire flexural performance of epoxy-nanocomposite matrix glass fibre composites containing conventional flame retardants. Compos. A Appl. Sci. Manuf. **43**, 1389–1399 (2012)
24. Vijay, M.; Selvarajan, V.; Yugeswaran, S.; Ananthapadmanabhan, P.V.; Sreekumar, K.P.: Effect of spraying parameters on deposition efficiency and wear behavior of plasma sprayed alumina-titania composite coatings. Plasma Sci. Technol **11**, 666–673 (2009)
25. Meghwal, A., et al.: Thermal Spray High-Entropy Alloy Coatings: A Review. J. Therm. Spray Technol. **29**, 857–893 (2020)
26. Alkhimov, A. P., Papyrin, A. N., Kosarev, V. F., Nesterovich, N. I., & Shushpanov, M. M.: U.S. Patent No. 5,302,414 (1994)
27. Darabi, A.; Azarmi, F.: Investigation on relationship between microstructural characteristics and mechanical properties of wire-arc-sprayed Zn-Al coating. J. Therm. Spray Technol. **29**, 297–307 (2020)
28. Gusev, V.M.; Nesterenko, N.S.; Il'ichev, M.V.; Konovalov, P.A.; Tyuftyaev, A.S.: Study of coating corrosion resistance for shelf structural objects and oil industry equipment. Chem. Petrol. Eng. **53**, 745–749 (2018)
29. Papyrin, A.; Fomin, V.M.; Alkhimov, A.; Klinkov, S.; Kosarev, V.: Cold Spray Technology. Elsevier, Oxford (2007)
30. Bulnes, A.G.; Fuentes, V.A.; Cano, I.G.; Dosta, S.: Understanding the influence of high velocity thermal spray techniques on the properties of different anti-wear wc-based coatings. Coatings **10**, 1–17 (2020)
31. Ang, A.S.M.; Berndt, C.C.: A review of testing methods for thermal spray coatings. Int. Mater. Rev. **59**, 179–223 (2014)
32. Singh, L.; Chawla, V.; Grewal, J.S.: A review on detonation gun sprayed coatings. J. Min. Mater. Characteriz. Eng. **11**, 243–265 (2012)
33. SudharshanPhani, P.; Srinivasa Rao, D.; Joshi, S.V.; Sundararajan, G.: Effect of process parameters and heat treatments on properties of cold sprayed copper coatings. J. Therm. Spray Technol. **16**, 425–434 (2007)
34. Szala, M.; Łatka, L.; Awtoniuk, M.; Winnicki, M.; Michalak, M.: Neural modelling of aps thermal spray process parameters for optimizing the hardness, porosity and cavitation erosion resistance of Al_2O_3–13 wt% TiO_2 coatings. Processes **8**, 1–15 (2020)
35. Kumar, S.; Handa, A.; Chawla, V.; Grover, N.K.; Kumar, R.: Performance of thermal-sprayed coatings to combat hot corrosion of coal-fired boiler tube and effect of process parameters and post-coating heat treatment on coating performance: a review. Surf. Eng. **37**, 833–860 (2021)

36. Vishnoi, M.; Kumar, P.; Murtaza, Q.: A review on coating for hydroturbine application by HVOF process. Adv. Mater. Eng. Manuf. Process. (2020). https://doi.org/10.1007/978-981-15-4331-9_8
37. Bhati, P.; Shrama, V.; Jha, R.; Gupta, S.; Vishnoi, M.; Mamatha, T.G.: The coatings developed by thermal spraying technique for hydroturbine applications—a brief review. Lecture Notes Mech. Eng. (2021). https://doi.org/10.1007/978-981-16-0159-0_50
38. Tripathi, A.; Pandey, A.; Rathore, A.; Singh, A.; Vishnoi, M.: Study on tribological behavior of HVOF developed coatings especially for Hydroturbine Runner application—a concise review. Lecture Notes Mech. Eng. (2021). https://doi.org/10.1007/978-981-16-0159-0_51
39. Hang, Z.Q.; Xi, N.Y.; Liu, Y.; Liu, Y.; Chen, H.: High-temperature oxidation behavior of HVOF-sprayed rare earth-modified WC–12Co coating. Rare Met. (2018). https://doi.org/10.1007/s12598-018-1075-1
40. Liu, Y., et al.: Effects of rare earth elements on the microstructure and mechanical properties of HVOF-sprayed WC-Co coatings. J. Therm. Spray Technol. **23**, 1225–1231 (2014)
41. Liu, Y., et al.: Erosion-corrosion property of CeO_2-modified HVOF WC-Co coating. J. Therm. Spray Technol. **25**, 815–822 (2016)
42. Sharma, S.P.; Dwivedi, D.K.; Jain, P.K.: Effect of CeO_2 addition on the microstructure, hardness, and abrasive wear behaviour of flame-sprayed Ni-based coatings. Proc. Inst. Mech. Eng. Part J **222**, 925–933 (2008)
43. Sharma, S.P.; Dwivedi, D.K.; Jain, P.K.: Effect of La_2O_3 addition on the microstructure, hardness and abrasive wear behavior of flame sprayed Ni based coatings. Wear **267**, 853–859 (2009)
44. American Society for Testing and Materials (ASTM).: Standard test methods for determining area percentage porosity in thermal sprayed coatings, ASTM E2109–01 (2014)
45. Wenzel, R.N.: Resistance of solid surfaces to wetting by water. Ind. Eng. Chem. **28**, 988–994 (1936)
46. Cassie, A.B.; Baxter, S.: Wettability of porous surfaces. Trans. Faraday Soc. **40**, 546 (1944)
47. Liu, W., et al.: Fabrication of the superhydrophobic surface on aluminum alloy by anodizing and polymeric coating. Appl. Surf. Sci. **264**, 872–878 (2013)
48. Vishnoi, M.; Muthupandi, V.; Murugan, S.S.: Characterization of hydrophobic coating developed by micro arc oxidation on AA2014 alloy. Indian J. Eng. Mater. Sci. **24**, 325–330 (2017)
49. Vishnoi, M.; Kumar, P.; Murtaza, Q.: Surface texturing techniques to enhance tribological performance: a review. Surf. Interfaces. **27**, 101463 (2021)
50. Barthlott, W.; Neinhuis, C.: Purity of the sacred lotus, or escape from contamination in biological surfaces. Planta **202**, 1–8 (2017)
51. Zhang, Y.: The effect of surface roughness parameters on contact and wettability of solid surfaces. (2007)
52. de Foggi, C.C.; Machado, A.L.; Zamperini, C.A.; Fernandes, D.; Wady, A.F.; Vergani, C.E.: Effect of surface roughness on the hydrophobicity of a denture-base acrylic resin and candida albicans colonization. J. Investig. Clin. Dent. **7**, 141–148 (2014)
53. Kittu, A. T.; Bulut, R.; Puckette, J.: Effects of Surface Roughness on Contact Angle Measurements on a Limestone Aggregate. in 1–8 (American Society of Civil Engineers (ASCE), (2014). https://doi.org/10.1061/9780784478493.001

Springer Nature or its licensor (e.g. a society or other partner) holds exclusive rights to this article under a publishing agreement with the author(s) or other rightsholder(s); author self-archiving of the accepted manuscript version of this article is solely governed by the terms of such publishing agreement and applicable law.

Indian Journal of Engineering & Materials Sciences
Vol. 30, April 2023, pp. 249-255
DOI: 10.56042/ijems.v30i2.1361

Microwave-based Transesterification of Waste Cooking Oil using Waste Aluminium Foil ($NaOH/\gamma\text{-}Al_2O_3$) as Catalyst

Naveen Kumar Garg*, & Amit Pal

Mechanical Engineering Department, Delhi Technological University, Delhi 110 042, India

Received: 30 December 2021; & Accepted 29 November 2022

In present study, the waste aluminium foil a menace to the environment and human health has been converted into catalyst. The prepared catalyst $NaOH/\gamma\text{-}Al_2O_3$ (3% by wt. of oil) has been used to transesterify waste cooking oil (WCO) in combination to methyl alcohol (CH_3OH) having a methyl alcohol to oil molar ratio of 15:1 for a reaction time of 1 hour in microwave based processor. The effect of different process affecting constraints such as catalyst amount, reaction temperature/time, the molar ratio of methyl alcohol to oil are also studied. The bio-diesel yield has been recorded as 98% and the physicochemical properties of bio-diesel found in reasonable agreement with ASTM bio-diesel standards.

Keywords: Biodiesel, Waste aluminium foil, Microwave, Transesterification

1 Introduction

The economic growth of the world is being severely hurt as fuel prices are rising high due to the high rate of fuel consumption and depletion of fossil fuel reserves with time. The uncertainty in the availability of fossil fuel is another concern which initiated the efforts for a search of alternative fuel. Rudolf Diesel, the father of the diesel engine, was first to use the engine to run on groundnut (peanut) oil in the year 1893 for farmers having a source of vegetable oil readily available. The high viscosity of the vegetable oil makes it not suitable to use directly in the internal combustion engine. There are various methods to reduce the viscosity of oil like mixing vegetable oil with diesel, thermal cracking, micro-emulsions and transesterification. Transesterification method is the best method to lower the oil viscosity and producing bio-diesel[1]. Therefore, an alternative fuel like bio-diesel becomes a necessity of the time for the energy security necessary for the economic development of a nation[2].Bio-diesel is biodegradable, sustainable and discharges fewer amounts of greenhouse gases. In Figure 1, unlike the petro-diesel, the oxygen content in the molecular structure of bio-diesel is 10-15%[3] which fastens the combustion process in compression ignition engines with less or nil emission of pollutants like oxides of Sulphur, oxides of Carbon and particulates[4-6]. The cetane value of bio-diesel is higher than diesel due to which ignition delay is smaller. The higher lubrication properties of bio-diesel reduce wear of the fuel injection pump and injectors resulting in an increased life[7]. The flashpoint of bio-diesel (100-170°C) is higher than petro-diesel oil (60-80°C) making it safe in storage, transportation and handling[8]. Thus, bio-diesel seems to be a better alternative substitute to petro-diesel fuel.

Bio-diesel has been vegetable oil/animal fat-based fuel composed of a long chain of fatty acid alkyl esters. Bio-diesel has many remarkable and favourable advantages over the other internal combustion engine fuel alternatives due to its physical characteristics very close to those of petro-diesel fuel and the production process is relatively easy and simple[9]. In addition to this bio-diesel can be ignited directly in conventional unmodified compressed ignition engines, with least deposition[10]. The viscosity of vegetable oil has been high enough to make it not

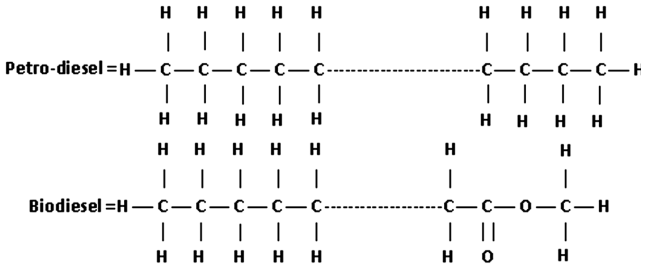

Fig. 1 — Dissimilarity in molecular structure of bio-diesel and petro-diesel.

*Corresponding author (E-mail: naveengarg452@gmail.com)

suitable to use in CI engines. Therefore, the viscosity of the oil is reduced by the transesterification reaction using methyl alcohol[11]. In addition to that, the properties of bio-diesel nearly similar to diesel fuels. According to ISO norms, bio-diesel is characterized by its properties like specific density, viscosity, cetane number, pour / cloud points, ignition points and high heating value (HHV) etc.

In the transesterification process, triglyceride in vegetable oil reacts with ethanol/methanol in the presence of alkaline catalysts as shown in Fig. 2. The use of a different type of catalyst in the transesterification reaction is a deciding factor in the conversion of triglycerides into bio-diesel. So the different types of catalysts are experimented to convert triglycerides into bio-diesel fuel. In general, there are two types of catalysts used to catalyze transesterification reaction i.e. homogeneous and heterogeneous catalysts. KOH and NaOH are popular base homogeneous catalysts soluble in methanol that give a higher yield of bio-diesel in transesterification reaction. But it generates a huge quantity of wastewater required for water-washing to neutralize and separate the catalyst from the methyl esters (bio-diesel). The byproduct of reaction i.e. glycerol is also obtained of poor quality due to the presence of water. These problems are easily rectified with the use of heterogeneous catalysts in the reaction due to its insolubility in methanol. The heterogeneous catalysts can be separated from the product of the reaction very economically. The recycling and reusability of the heterogeneous catalysts further make it more suitable than homogeneous catalysts leading to lower cost of production.

2 Materials and Methods

The vegetable oil after repeated frying becomes nonedible, is referred to here as waste cooking oil (WCO). On repeated frying of oil, total polar compounds (TPC) is formed in oil and the toxicity of TPC leads to diseases like hypertension, Alzheimer's diseases[12] and liver disease. A huge quantity of WCO is produced by caterers all over the world. Therefore it is essential to check the quality of vegetable oil during repeated frying[13]. As per the Food Safety and Standards Authority of India (FSSAI), the Total Polar Compounds (TPC) in vegetable oil should not be more than 25%. From 1st Jul 2018, all Food Business Operators (FBO) are required to monitor the quality of vegetable oil and comply with the regulations. In this work, WCO was collected from reputed caterers in kamla nagar, Delhi. WCO contains moisture and food particles. Food particles were removed by filtering through sieves and moisture was removed by heating the oil to 120°C. The WCO was then cooled and kept in an airtight glass container after filtration. FFA, iodine value, saponification, value, etc. of WCO were determined and recorded in table 1 by using standard methods. The Aluminium food wrap foil discarded from the lunch box was collected from local offices and educational institute, DTU in Delhi. The foil was used to convert into the catalyst required for the transesterification of WCO.

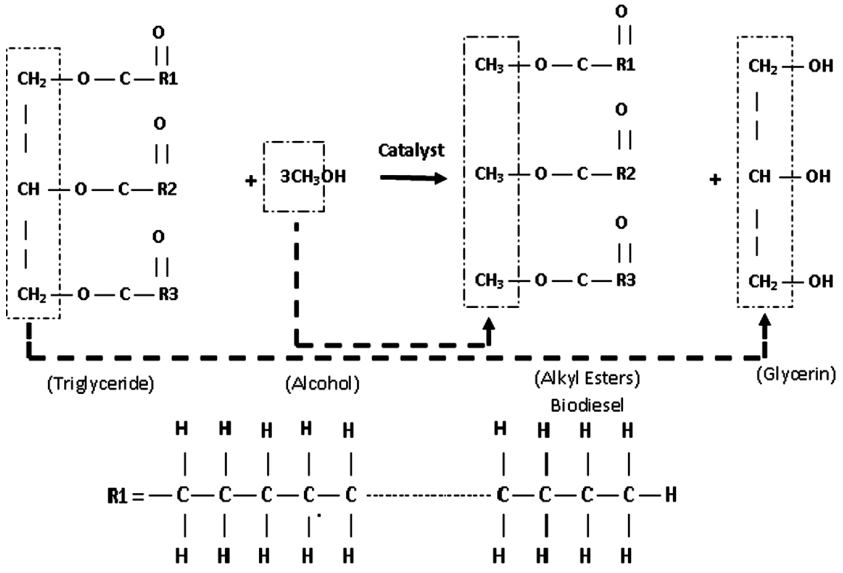

Fig. 2 — Transesterification reaction using alcohol and catalyst.

Table1 — Properties of WCO

Properties	Measured Value
Kinematic viscosity @ 40°C	51.5 mm^2/s
Acid Value	5.4 mg KOH/g
Iodine number	58.7 g I_2/100g
Saponification Value	203.7 mg KOH/g
FFA	1.04%

2.1 Catalyst from waste aluminium foil

Aluminium foil is emerging out as one of the most consumed aluminium products across the world due to its versatility and multiple uses. The demand of Aluminium foil may rise to 6.4 MMT by 2020. As per Aluminium Foils Market intelligence, aluminium foil is also used in the packaging of beverages and other liquids whose demand is also expected to grow at 4-5 percent by 2022. Growth in the consumption of aluminium foil is increasing due to the change in lifestyle and food habits. The high demand for ready to eat confectionaries and pharmaceutical products is also a reason for the growth of the aluminium foils industry. As per aluminium association, out of total aluminium foil produced in the world, more than 75% is used for food packaging which ends up in the local landfills Fig. 3.

The aluminium producing industries are optimistic to recover and recycle aluminium from the used foil. They want to get back all of the used metal at the expense of less energy than that is required to produce the pure metal. Industries are making significant efforts and investment to explore the different ways to recycle the aluminium from foil over several years. There are many companies in the world supplying the thin foils, used as laminates in drinks cartons. They have carried a feasibility study that shows the possibility to remove the aluminium from laminating material and return the used aluminium to produce more foil.

Aluminium oxide (Al_2O_3) known as alumina, is a compound of aluminium and oxygen. The oxides of aluminium are good in hardness, chemical inertness, high melting point, resistance to oxidation and corrosion, so broadly used in making ceramic refractory and abrasives[14]. The alumina as a catalyst is used in many chemical reactions. Aluminium oxide because of its properties like high dielectric constant, favourable thermal conductivity, excellent stability, low refractive index, and high hardness is used in electric batteries, thermal machinery, optics, and microelectronics. There are seven phases of polymorphs of transition alumina identified till now. These are named as phase γ (gamma), η (eta), δ (delta), θ (theta), χ (chi), κ (kappa), and ρ (rho). The phase-γ of transition alumina has a larger surface area in comparison to other phases and also has better structural stability. So it is widely used in industries for catalysis processes. The phase γ-alumina is formed conventionally by thermal dehydration of aluminium oxy-hydroxide above 450°C temperature. The γ-phase is a metastable phase which upon heating will form α-phase. The phase-γ of alumina is used as a catalyst in various processes due to its high surface area and mesoporous properties. Phase γ-alumina is usually used as a catalyst in various chemical processes such as ammonia synthesis, production of hydrogen gas, hydrogenation of oils, refining of petroleum, emissions control of automotive, etc.

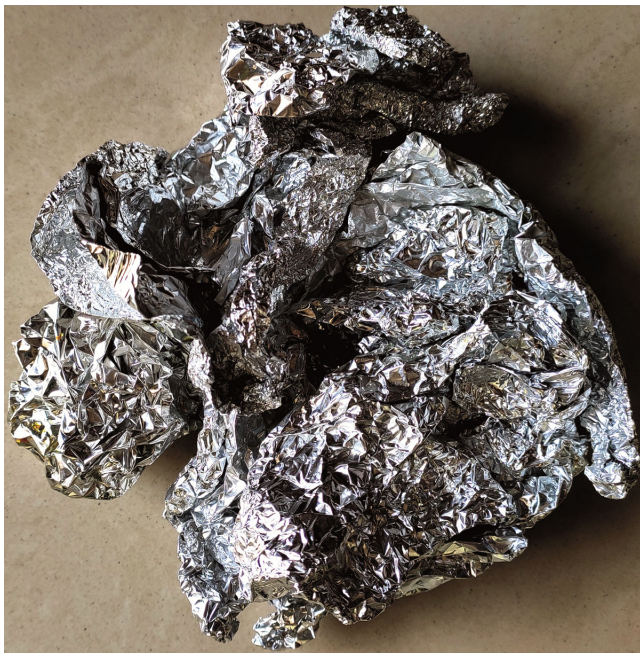

Fig. 3 — Waste Aluminium Foil.

2.2 Preparation of $AlCl_3.6H_2O$ from waste aluminium foil

Waste aluminium foil was cleaned using water and detergent to remove any dirt or oil. Dried foil was dissolved in a hydrochloric acid (HCl) solution containing 6 moles of hydrochloric acid. As aluminium being amphoteric, so can react with acid as well as with base. While reacting with acids, aluminium dissolves in hydrochloric acid to form solution of aluminium chloride and colourless gas hydrogen.

$$2Al + 6HCl = 2AlCl_3 + 3H_2$$

Aluminium chloride solution is kept for drying under desiccators to form crystalline aluminium

chloride hexahydrate ($AlCl_3.6H_2O$). These crystals were dissolved in distilled water and the solution is filtered to remove any soluble chloride. The solution is again dried to re-crystallize. The process of purifying the crystal is done 2-3 times. The complete removal of chloride was verified by adding a drop of silver nitrate ($AgNO_3$) in the sample of the solution. The presence of any chloride content will be indicated by a turbid solution. Finally, pure $AlCl_3.6H_2O$ is obtained.

2.3 Preparation of catalyst γ-Al_2O_3 from $AlCl_3.6H_2O$

The obtained precipitate of aluminium chloride hexahydrate was dispersed in distilled water. The pH value of the solution was regulated with ammonia solution NH_4OH drop by drop. The solution was stirred continuously at a speed of 200 rpm with a magnetic stirrer.

$AlCl_3(aq) + 3\ NH_4OH(aq) \rightarrow Al(OH)_3(s) + 3NH_4Cl\ (aq)$

The pale off-white precipitate of $Al(OH)_3$ was filtered, washed, and dried at 120°C. The substance was further calcined at 500°C and 600°C for a period of 2 hours in a muffle furnace to obtain γ-Al_2O_3.

2.4 X-Ray diffraction analysis

The crystalline phase was verified using X-ray diffraction (XRD) patterns, obtained with CuK radiation of λ = 1.54 A° in 2θ range varying from 20° to 80° at room temperature as shown in Fig. 4 and Fig. 5. The diffractograms for the samples at a calcination temperature of 500°C and 600°C have shown three distinctive reflections of 311, 400 and 440 at angle 2θs of 37.2°, 45.6°, and 66.8° respectively. These reflections are found in line with the gamma Al_2O_3 standards. The further increase in the calcination temperature did not have any effect in the position of peaks, therefore indicating no further change in the structure of γ-Al_2O_3.

2.5 Preparation of catalyst γ-Al_2O_3/NaOH/Na

The catalyst was prepared by employing the impregnation method using phase γ-Al_2O_3 and a solution of sodium hydroxide. The phase γ-Al_2O_3 was impregnated with 15 ml of sodium hydroxide solutions (50 wt.%). This impregnated γ-Al_2O_3 was then dried at a temperature of 120°C. The catalyst was then calcined at 650°C for 2 hours.

2.5.1 Transesterification of waste cooking oil (WCO)

a) A WCO sample was collected in a glass beaker. To eliminate any solid contaminants, it was filtered with a clean cloth. To eliminate any moisture existing in the oil, the oil was heated to 105°C. The oil was then allowed to cool to 60°C before being treated further.

b) The catalyst (γ-Al2O3 / NaOH) powder (3 % by weight of oil) was stirred in a molar ratio of 15:1 with heated methyl alcohol (CH_3OH) and poured into the glass beaker carrying oil.

c) 100 gm WCO sample was transferred to a round bottom flask. It has been treated with a CH_3OH solution and the prepared catalyst. The reactant mixture in the flask was treated in a microwave reactor[15]. The reaction temperature was recorded at 60°C. Throughout the reaction, the solution was constantly agitated. The speed of the turntable stirring was kept constant at 5 rpm throughout the process.

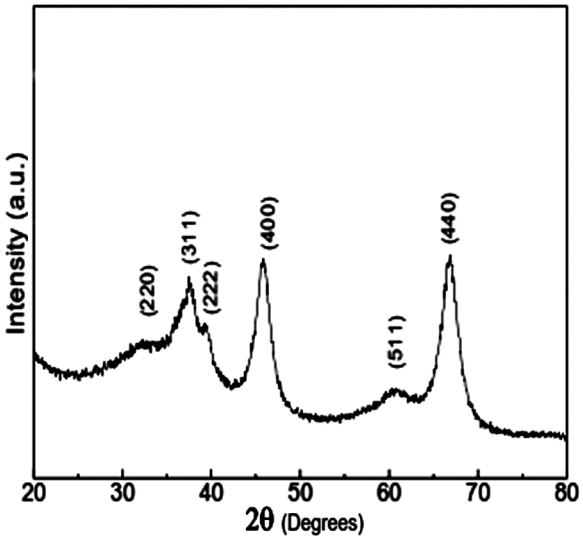

Fig. 4 — XRD pattern of γ-Al_2O_3 calcined at 500°C.

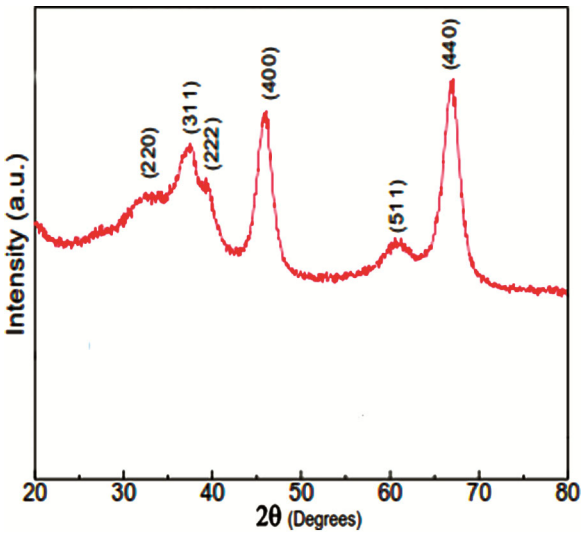

Fig. 5 — XRD pattern of γ-Al_2O_3 calcined at 600°C.

d) To avoid alcohol boiling, the reaction temperature of the solution was not allowed to increase over 60°C. The procedure was repeated for 60 minutes.
e) The reaction catalyst was removed from the reaction product. The remaining solution was allowed to settle in a separate funnel. The reaction products, bio-diesel, methyl alcohol, and glycerin, were separated based on their specific weight.
f) Because bio-diesel and methyl alcohol are lighter in weight, they settled on top of the solution, leaving glycerin at the bottom. The distillation procedure was used to extract the methanol from the bio-diesel.
g) Bio-diesel's physicochemical qualities were investigated. The bio-diesel's specific gravity (0.8849) and density (0.884 gm/cm^3) were determined using the DMA 4500 (Anton Paar) instrument, which was found to be in fair compliance with ASTM bio-diesel specifications. The product's kinematic viscosity was also determined to be 5.694 centistokes using a Stabinger Viscometer.

3 Results and Discussion

3.1 The Effect of Methanol/oil Molar Ratio

The molar ratio has been the most important element in the transesterification reaction, influencing both the bio-diesel output and the production cost. Three moles of methanol react stoichiometrically with one mole of triglyceride to form three moles of fatty acid methyl ester and one mole of glycerin. Because the reaction is seen as being reversible in nature, an excessive amount of methanol was required to drive the reaction towards the product side. The use of an excessive quantity of methanol in the process may increase the cost of bio-diesel, therefore it became critical to determine the ideal molar ratio to limit production costs. The addition of the methanol-oil molar ratio increased the bio-diesel output, as seen in the Fig. 6. A molar ratio of 15:1 produced the highest output. When the molar ratio exceeded 15, the yield % declined. This might be owing to an incomplete reaction and residual glycerol in the bio-diesel form.

3.2 The Effect of Catalyst Amount

The impact of catalyst loading on the reaction has been investigated. The method was evaluated by adjusting the amount of catalyst from 1 to 5 (wt%) of oil weight, and the effect on bio-diesel yield is shown in Fig. 7.

The yield increased when the catalyst was increased from 1 to 3 (wt %). A further increase in the amount of catalyst has lowered the yield. The addition of catalyst apparently made the liquid viscous enough to minimise the likelihood of reactants coming together for the reaction.

3.3 Reaction Time's Effect

For different samples, the reaction time ranged from 5 to 90 minutes. It was discovered that with a reaction period of 60 minutes, a maximum yield of 98 % was achieved. There was no apparent increase in yield afterwards.

3.4 The influence of Reaction Temperature

The transesterification reaction gets influenced by the reaction temperatures. The temperature of the reaction may vary depending on the type of alcohol and catalyst used. Figure 8 illustrates an example of the mixture prepared at five different temperatures. It can be noticed that the yield was decreased at a lower

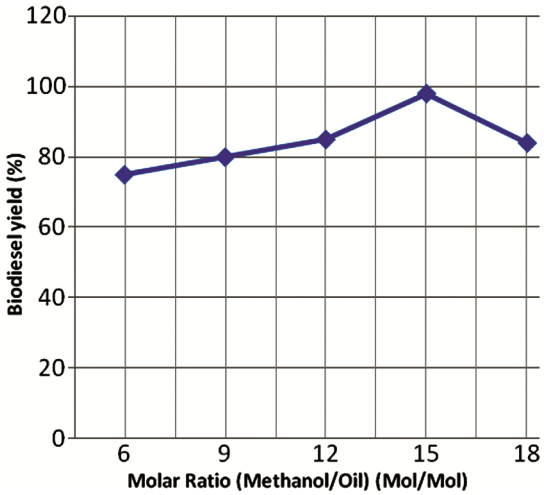

Fig. 6 — Impact of the molar ratio on yield.

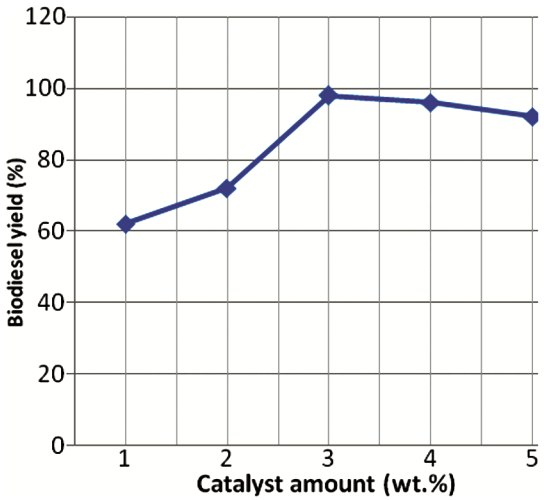

Fig. 7 — Impact of the catalyst on yield.

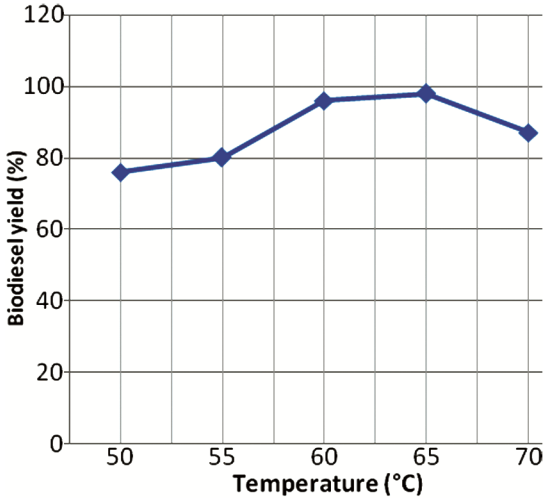

Fig. 8 — Impact of reaction temperature on bio-diesel yield.

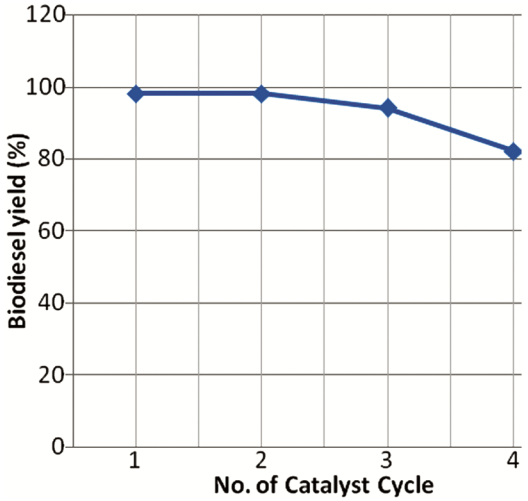

Fig. 9 — Reusability of catalyst.

temperature range of 50-55°C due to mass transfer and solubility issues.

The viscosity of the mixture was found to be reduced at higher temperatures, which is sufficient to increase the kinetic energy of the reactant and provide good mass transfer between oil and methanol to improve yield. The highest yield was found at reaction temperatures ranging from 60 to 65°C. Methanol began to boil at around 65°C, and methanol evaporate from the mixture, lowering the molar ratio and resulting in a reduced bio-diesel yield.

3.5 Reusability of catalyst

The cost of producing bio-diesel has been a determining element in bio-diesel manufacturing technologies. The cost of production can be lowered to some extent by reusing the same catalyst. The recovered catalyst γ-Al2O3 / NaOH has been washed with n-hexane and calcined again at 650°C temperature.

In the same experiment, the utilised and rejuvenated catalyst was employed in four successive transesterification reactions with similar regeneration strategies. No substantial loss of catalytic activity was seen in the first three consecutive uses of the catalyst, while catalytic activity was observed to be lowered in the fourth run of the experiment, as shown in Figure 9. This reduction of catalytic activity could be owing to the absorbed organic molecule blocking active sites on the catalyst surface, resulting in less surface area accessible for the reaction site.

3.6 Bio-diesel Properties and Their Significance

The characteristics of bio-diesel are mostly determined by the quality of the feedstock and the amount of free fatty acid present in it. In the laboratory of Delhi Technological University, the bio-diesel made from WCO has been tested for its chemical and physical attributes. As demonstrated in Table 2, the sample satisfies the ASTM D6751 standards.

Table 2 — Properties of bio-diesel produced

Parameter	Measured Value
Calorific Value	39MJ/kg
Flash point	146°C
Pour point	6°C
Kinematic viscosity @ 40°C	4.5 mm^2/s
Density at 30°C	0.884 g/cm^3
Specific gravity	0.8849
Acid value	0.77 mg KOH/g
Iodine number	86.4 g I_2/100g

The flash point would be a critical factor in the safe storage and handling of bio-diesel for fire safety. The minimal temperature at which the vapour of a liquid fuel forms an ignitable composition when mixed with air and produces a short flash in the presence of a small flame has been defined as the flash point. The flashpoint of bio-diesel produced in this study was determined to be 146°C, which is greater than the flashpoint of petro-diesel fuel (52 to 96°C)[16]. The pour point of fuel determines its ability to flow in the engine at lower temperatures. Fuels with a high pour point should not be used in engines at low temperatures[17]. When subjected to external forces, a fluid's resistance to flow is caused by internal friction. The viscosity of the fuel influences its atomization (spray properties and droplet volume). For the fuel injection system to function properly, the kinematic viscosity of the fuel should be close to that of petro-diesel[18]. At 40°C, the kinematic viscosity of the bio-diesel produced in this investigation was determined

to be 4.5mm^2/s. Bio-diesel with a higher density consumes more fuel, resulting in higher nitrogen oxide emissions. The higher the acid value of the fuel, the more likely it is to induce corrosion in the engine's fuel supply system. The acid value in this investigation was 0.77 mg KOH/g, which was close to the ASTM D-6751 norm of 0.8 mg KOH/g. The iodine number represents the occurrence of double bonds in bio-diesel, indicating the extent of unsaturation[19]. The iodine number has an effect on the oxidation stability of bio-diesel.

4 Conclusions

- Waste aluminium foil has been effectively employed to create a heterogeneous catalyst γ-Al_2O_3.
- The catalyst has been utilised to convert WCO into methyl ester, and a maximum yield of 98% is reached utilising a catalyst amount of 3 wt. %, a molar ratio of 15:1, and a reaction temperature of 60°C for 60 minutes.
- The catalyst has been optimally reutilized multiple (four) times in the bio-diesel conversion process.
- The microwave centred transesterification along with waste aluminium foil based catalyst has been effectively used to synthesize bio-diesel from WCO.
- The cost of bio-diesel production can be reduced to great extent by combination of microwave centred transesterification along with waste aluminium foil based catalyst and WCO.

References

1 Mythili R & Venkatachalam P & Subramanian P & Uma D, *Int J Energy Res,* 38 (2014) 1233
2 Alajmi FSMDA & Hairuddin AA & Adam NM & Abdullah LC, *Int J En Res*, 42 (2018) 885
3 Hwang J & Bae C & Gupta T, *Fuel* 176 (2016) 20
4 Anand K & Sharma RP &, Mehta PS, *Biomass Bioenergy,* 35 (2011) 533
5 Balat M & Balat H, *Applied Energy* 87 (2010) 1815
6 Kafuku G & Mbarawa M, *Applied Energy,* 87 (2010) 2561
7 Mofijur M &, Masjuki H, *Ren Sus Energy Rev,* 46 (2015) 51
8 Alagumalai A & Subramaniam D & Murugesan A (2014) *Ren Sus Energy Rev,* 29 (2014) 517
9 Kataria J & Mohapatra SK & Kundu K, *J Energy Inst,* 92 (2018) 1
10 Kumar R, & Dixit A, *J Ren Energy*, (2014) 1
11 Balasubramanian, D & Lalvani J & Murugesan P & Annamalai K *Energy Conv Mgmt,* 117 (2016) 466
12 Tetsumori Y, *J Alzheimers Dis Parkinsonism,* 7 (2017) 410
13 Farooq M & Ramli A & Naeem A & Perveen F, *Int J Energy Res,* 43 (2019)1
14 Itoh T & Uchida T, *Ceramics Int,* 41 (2015) 3631
15 Garg N & Pal A, *Proc Inst Mech Engr, Part E: J Pro Mech Engg,* 234 (2020) 394
16 Ismail S & Sinin H, *J Sci Tech Dev,* 31 (2014) 91
17 Lalvani J & Parthasarathy M, Ecotoxicol Environ Saf, 134 (2016) 336
18 Cataluna R & Silva R, *J Combustion,* (2012) 1
19 Verma P & Sharma & Dwivedi G, *Energy Rep*, 2 (2016) 8

Modeling and Analysis of Finger Splint for Mild to High-Grade Mallet Finger Fracture

Sahil Bansal[1], Aranyak Tripathi[1], Nikhil Kumar[1], Taruna Singh[2], Ranganath M.S[2,*]

[1]Department of Mechanical Engineering, Delhi Technological University, Delhi-110042

[2]Department of Design, Delhi Technological University, Delhi-110042

*Author to whom correspondence should be addressed:
E-mail: ranganath@dce.ac.in

(Received February 1, 2022; Revised May 14, 2023; accepted May 14, 2023).

Abstract: Fingers tend to be most prone to injuries in falls, accidents, and burns, and de-spite this, the treatment options tend to be highly limited, costly, deprived of ergonomics conforming to the patient requirements. CAD modeling offers a considerable solution for providing a product design for patient-specific splint for musculoskeletal while three dimensional model simulations provides a way to build comfortable splints with the least material use and most efficient mechanical and thermal capabilities. This hence benefits us in reducing material wastage and reducing cost. Reduction in material results in efficient heat dissipation which in-creases the breathability of the patient's finger inside the splint and makes the splint sweat efficient and hence conforming to the patient requirements with in-creased ergonomics and maintaining hygiene

Keywords: Product Design, Splint, CAD, Simulation, PLA

1. Introduction

Injuries occurring in the upper section of Mallet Finger happens to be the most generally occurring limb athletic injury[1)] and is also common among various age groups. Phalangeal fractures are commonly found in 9-12 aged children and metacarpal fractures are more common to older adolescents[2)]. This injury tends to affect the lifestyle of the patient by disrupting him/her from their daily activities involving both domestic and professional work-related life[3)].

Current treatment measures involve both surgical and non-surgical treatments de-pending on the extent of the fracture[4)]. Studies show that at least 70%–80% of fractures in hand can successfully be treated without surgery[5)]. Non- Surgical treatment on phalangeal fracture involves treatment is closed reduction and splinting[6)]. Splints made of thermoplastics are applied to the affected joint of the patient to immobilize it. Splints can be pre-fabricated, but widely splint is cast on the patient's finger. It can be seen that the effect of splinting is dependent on the skills and experience of the trained professional. And in many cases with trained professionals, the outcomes have been not satisfying due to non-adherence correlating to decreased outcomes[7)]. In addition to being a labor-intensive task, it also creates a lot of waste, and material consumption is fairly high. Advantages of 3D-manufacturing orthosis include cost reduction, easier modification concerning patients' parameters, and faster fabrication[8)].

Judicious and Efficient use of additive manufacturing process (3D printing) can offer a reduction of weight hence increasing breathability, improvement in heat dissipation, and making comfortable splints for the patient[9)].Furthermore, FEA can be used as an accurate method for computational analysis[10)] also helping in saving time and cost[11)]. This paper brings a study and investigation on the use of 3-D modeled patient-specific splint in reducing material wastage and cost, making the use of previous investigations done on mallet finger injuries.

1.1 Injury on the Mallet Finger

This happens to be the most commonly occurring limb injury on the finger, in this kind of injury the ability of extensor of the finger is disrupted, causing inaction to extend at distal interphalangeal joint[12)].

This is caused due to either the rupture of the extensor tendon or avulsion fracture[13)] of distal phalange. With the inability to extend to the distal phalanx, swelling and tenderness can also occur and an extension lag ranging from a couple of degrees to a couple of dozens can also occur.

The injury can be caused by either a distal phalanx facing a direct blow or else due to blunt injury caused on the distal interphalangeal joint[15)]. This injury is seen common in teens and children and athletes.

This injury can derive economic disruptions involving both direct, indirect, and many other intangible costs

which can differ with the severity of the injury. If left untreated, there can be functional shortfalls, impeding the whole hand in everyday motor tasks.

The treatment of the fracture can be done using two ways depending on the severity and type of fracture firstly surgically and secondly non-surgically, in most of the cases treatment using non-surgical are generally preferred over the surgical methods[16]. For Non-surgical treatment use of an immobilization device named Splint is made commonly. The splint is designed such that it immobilizes the affected region offering a limited flexion in some cases, while the avulsion fracture or tendon heals.

Currently used splints made of thermoplastics require the assistance of experts and in many cases with trained professionals also the results were not as desired. With material consumption being high and user comfort being disrupted, CAD modeling and simulation analysis can provide a way to eliminate the aforementioned issues.

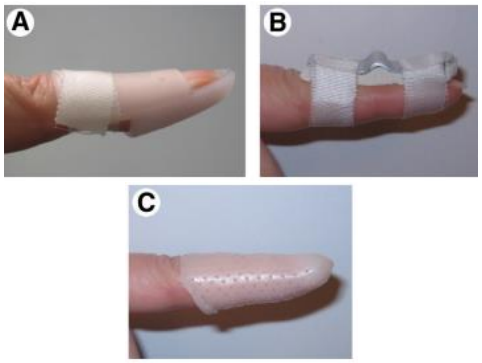

Fig. 2: Current treatments (A) an example of Stack split; B)making use of Dorsal aluminum; (C) by the means of Custom thermoplastic[17]

2. Design and Methods

2.1 Splint Material Selection

Multiple considerations for the materials for splints were made, in accordance that they can prove better than the thermoplastic splints applied previously, The materials include PLA (i.e., Poly-lactic-acid), ABS (i.e., acrylonitrile-butadiene-styrene), Polyurethane and polycarbonate, etc. As splint can't be passed on from patient to patient, wastage generation and composting ability were considered to be key criteria in material selection. According to a medical survey done by the N.A.M.C.S in collaboration with A.A.O, on an average 670,000 kg of waste occurring due to fractures, is produced per year[18]. PLA on the other hand is biodegradable, as it is derived from natural sources, and hence can be composted after its use**,** and has several uses in medical and packaging industries.[19]

Other Advantages of PLA**:**

1. Eco-Friendly
2. Bio-compatibility
3. Energy Saving
4. Processability

PLA is made using renewable sources which include corn, wheat, Rice hence is biodegradable, And compostable. Along with this during its Production it consumes CO2

Lactic acid is the main PLA Degradation Product which non-toxic organism itself

About 25–55% reduction in energy consumption takes in PLA against those of petroleum-based polymers.

It has an efficient thermal processing ability due to which it can be processed via multiple techniques.

Hence PLA is used for investigation in this study as it is suitable for the manufacturing of temporary fixtures for biomedical applications[21]

2.2 Modeling of Splint

The Personalized splint measurements were taken using the parameters derived from the index finger[3] of the user given in Figure 3.

Using Solidworks (2017) CAD modeling platform and the measurements of parameters taken from the patient's index finger, the splint has been constructed. The user can clinch his fist during some operation with the material not removed which can result in pushing of the skin of the region of mid-phalanx inside the splint to prevent this and provide some space is added to the design present on the back of splint. The front is provided with an open section for ventilation to occur so that air can pass and help in reducing sweat and will also provide opening to ensure washing. The upper face reaches to the proximal interphalangeal joint which will allow the patient to ensure flexion on the joint of the finger preventing any problems in the recovery. Finger regions have been kept exposed to the environment so that they can function during the recovery stage which could have not if thermoplastic settling was done. Slots and holes are provided in the splint so for the reasons of increasing breathability, reducing the weight, increasing limited flexibility, increasing heat dissipation and airflow which hence reduces sweat collection[22]

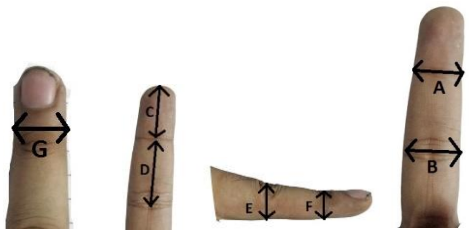

Fig. 3: (A) 7 parameters that were measured to create the CAD model of the splint

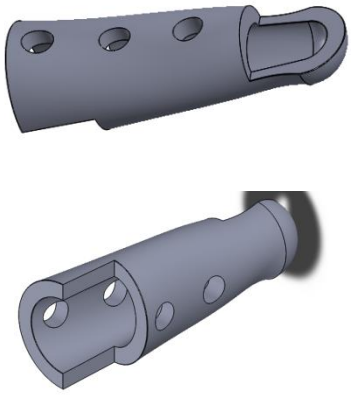

Fig. 3: (B) CAD model of the splint

The benefit of using Computer-Aided Modeling was that user's finger was not exposed to heating environments where thermoplastics are straightly set on their fingers. Splint's optimum thickness was taken 3.2mm providing a volume reduction of 35% against commercially available splints[23].

2.3 Analysis and Simulation of Splint

Finite element analysis has been conducted using ANSYS as it been used previously[24], to get desirable results.

Static Analysis. Static Structural Analysis on the splint was done using ANSYS 2016, Material taken was as mentioned PLA, with Young's Modulus 2850 MPa, Yield Strength 26.05 MPa Poisson's ratio 0.3 were defined as the mechanical properties during the testing of the splint. The maximum pressure applied on the splint was taken to be 0.66MPa[25].

The splint's rear face was taken as the fixed geometry shown in Figure 4 (A) and the tip of the splint was tested with the value of pressure applied taken 0.66MPa as shown in the Figure 4 (B). The impact of holes on the splint's strength was also investigated.

Thermal Analysis. Given splint was investigated for temperature distribution and total heat flux distribution was calculated. Using ANSYS 2016 Thermal analysis (steady state) was performed on the splint. Splint's interior was taken to be at 34 ° Celsius[26]. The ambient air temperature was taken to be 22° C, convection coefficient 10 Watt/meter^{2}K. and total thermal heat generated by the body of the user was taken as 110W with a surface area of 2m^2 [27-28].

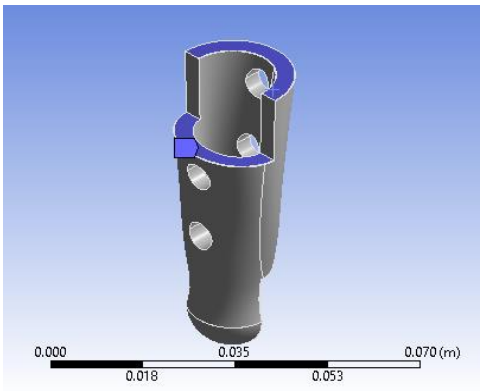

(A)

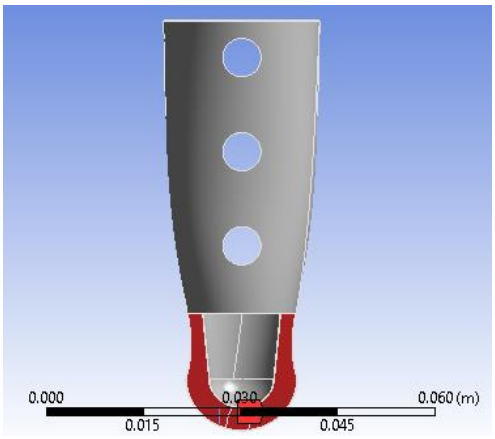

(B)

Fig. 4: (A) Fixed Geometry (B) Application of pressure

3 Result

The modeling of the splint was done is Solidworks 2017 using the parameters given in section 2.2. In the simulation of the splint, the fixture was taken as the rear part of the splint and was consistent during both thermal and static analysis. To implement the mesh convergence study in the simulation, the pressure value was applied at the tip of the splint (or front) as shown in Figure 4

In static analysis results of Von Mises deformation and Von Mises equivalent stress-plots were calculated after continuously refining the mesh. Stress and Deflection value was calculated using ANSYS 2016 to embed the best mechanical properties to the printed splint. Obtained Stress and deflection plot can be seen in the Figure 5A, B & C. Stress concentration was observed in the corner between the rim of the upper part of the splint and the rim containing the tip as can be seen in the Figure 5B. Above region was also the region where maximum stress was measured. The highest value of the deflection was derived at the pads rim.

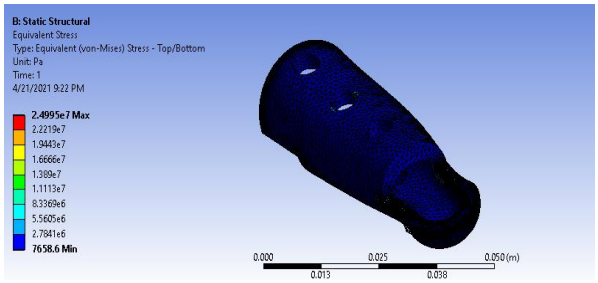

(A)

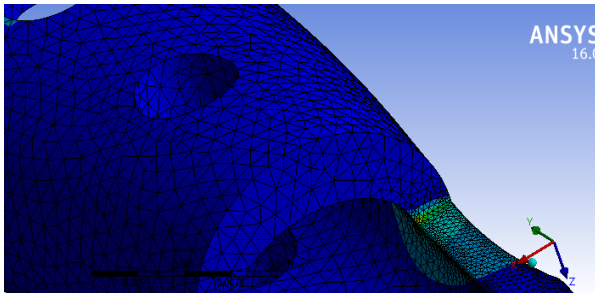

(B)

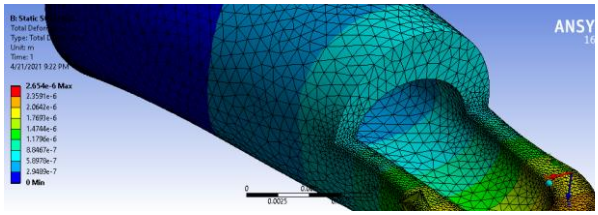

(C)

Fig. 5: (Up to bottom) (A) Equivalent Von-Mises stress distribution (B) Maximum Stress Region (C) Total Deformation distribution

For product designing of the splint, the thickness was taken to be 3.2mm which pro-vided reduction of material and hence increased breathability.

It can be seen in the static structural simulation that maximum stress (Equivalent Von mises stress) occurred in corners of the front rim touching the upper body rim with a magnitude 24.9 MPa which tends to be under the yield strength (26MPa) and hence showing that under the given thickness the material can perform well in distributing the load and withstanding real patient conditions. The maximum deflection (von mises) can be seen on the tip of splint which is 2.64e-06m (0.00264 mm) again showing that under the given thickness the splint performed better than the previous studies.

The results of total heat flux and temperature distribution across the splint and temperature distribution of the splints were analyzed and simulated whose results have been provided in Figures 6 A & B, in can be seen that the splint perform efficiently in heat dissipation and distributing the temperature.

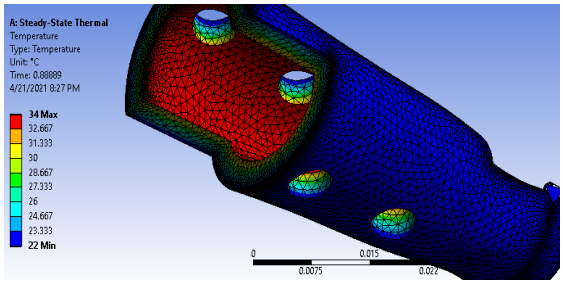

(A)

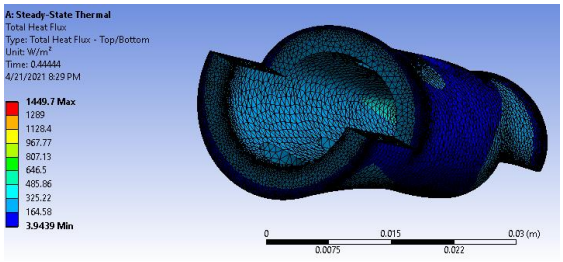

(B)

Fig. 6: (Up to bottom) (A) Temperature Distribution (B) Total Heat flux

The design was implemented with placement of holes and it can be seen that it not only reduced weight and increased breathability but also helped in improvement of heat dissipation and hasn't cost us reduction in mechanical parameters of the splint, hence proving to be a good trade in the splint

4 Conclusion

Applying the principles of Product Design, an efficient splint design was modeled on CAD modeling software (solidworks), it was investigated and verified that under the given material and parameters, the splint worked well in Static Structural analysis and Steady-State thermal analysis, the placement of holes helped in increasing breathability and didn't affect the mechanical parameters of the splint hence it can be used to increase the efficiency of a splint. The Material PLA not only will help in contributing its worth to the environment but also proved efficiently under simulations and was verified to be used as a material for the development of splints instead of the previously used thermoplastics. The results of this study will give the path to the interdisciplinary study between the medical and engineering industry to utilize advanced modeling and manufacturing methods for the development of sustainable splints and other related products.

Acknowledgements

The authors are grateful to Department of Design of Delhi Technological University for providing valuable technical support for conducting this Research Project.

Nomenclature

CAD:	Computer Aided Design
PLA:	Poly-lactic-acid
ABS:	acrylonitrile-butadiene-styrene
MPa:	Mega-Pascal
NAMCS:	National Ambulatory Medical Care Survey
AAO:	American Academy of Orthopedics

References

1) Pegoli L., and Pivato G. "Mallet Finger Injuries", Hayton M., Ng C., Funk L., Watts A., Walton M. (eds) *Sports Injuries of the Hand and Wrist,* 1-13(2019).doi:https://doi.org/10.1007/978-3-030-02134-4_1 .
2) Oetgen, Matthew E, and Seth D Dodds, Non-operative treatment of common finger injuries." *Current reviews in musculoskeletal medicine* **1**(2) 97-102 (2008) doi:10.1007/s12178-007-9014-z.
3) Zolfagharian, A., Gregory, T. M., Bodaghi, M., Gharaie, S., & Fay, P.,"Patient-specific 3D-printed Splint for Mallet Finger Injury." *International journal of bioprinting*, **6**(2), 259 (2020). https://doi.org/10.18063/ijb.v6i2.259
4) Tang, J. B., Blazar, P. E., Giddins, G., Lalonde, D., Martínez, C., & Solomons, M.,"Overview of indications, preferred methods and technical tips for hand fractures from around the world", *The Journal of hand surgery, European volume,* **40**(1), 88–97(2015),https://doi.org/10.1177/1753193414561942
5) MEH Boeckstyns," Current methods, outcomes and challenges for the treatment of hand fractures" *Journal of Hand Surgery (European Volume)*, **45**(6) 547–559(2020),doi.org/10.1177/1753193420928820
6) Caggiano, N. M., Harper, C. M., & Rozental, T. D. (2018),"Management of Proximal Interphalangeal Joint Fracture Dislocations" *Hand clinics*, **34**(2), 149–165(2018),https://doi.org/10.1016/j.hcl.2017.12.005
7) O'Brien, Lisa,"Adherence to Therapeutic Splint Wear in Adults With Acute Upper Limb Injuries: A Systematic Review." *Hand Therapy.* **15**(1). 3-12(2010), doi: 10.1258/ht.2009.009025
8) Nam, H. S., Seo, C. H., Joo, S. Y., Kim, D. H., & Park, D. S. ,"The Application of Three-Dimensional Printed Finger Splints for Post Hand Burn Patients: A Case Series Investigation."*Annals of rehabilitation medicine*,**42**(4),634–638.(2018), https://doi.org/10.5 5 35/arm.2018.42.4.634
9) Choi, H., Seo, A., & Lee, J. ," Mallet Finger Lattice Casts Using 3D Printing" *Journal of healthcare engineering,* (2019),. https://doi.org/10.1155/2019/4765043
10) Ismaiel, A. M. M., Metwalli, S. M., Elhadidi, B. M. N., & Yoshida, S."Fatigue analysis of an optimized HAWT composite blade" *Evergreen*, **4**(2-3), 1-6 (2017). https://doi.org/10.5109/1929656
11) Chauhan, Shailendra & Bhaduri, S." Structural analysis of a Four-bar linkage mechanism of Prosthetic knee joint using Finite Element Method" *Evergreen,* **7**(2), 209-215 (2020). https://doi.org/10.5109/4055220
12) A Zyluk and P. Bernard "Treatment of Mallet Finger", *polish journal of surgery,* **82**(4), 243-250(2010) DOI 10.2478/v10035-010-0034-9.
13) Bazavar M, Rouhani A, Tabrizi A.,"Simultaneous Dorsal Base Fracture and FDP Avulsion of Distal Phalanx of the Little Finger.", *Arch Bone Jt Surg,* **2**(1) 63-5.(2014).
14) Lamaris GA, Matthew MK.," The Diagnosis and Management of Mallet Finger Injuries." *Hand (N Y)*. **12**(3),223-228(2017). doi:10.1177/1558944716642763
15) Tuttle, H. G., Olvey, S. P., & Stern, P. J. "Tendon avulsion injuries of the distal phal-anx." *Clinical orthopaedics and related research,* **445**, 157–168.(2006) https://doi.org/10.1097/01.blo.0000205903.51727.62.
16) R. Glenn Gaston, MD Christopher Chadder-don, MD,"PhalangealFractures Displaced/Nondisplaced" *hand clinics,* **28**(3),395-401(2012) DOI:https://doi.org/ 10.1016/j.hcl.2012.05.032
17) O'Brien, Lisa J, and Michael J Bailey, " Single blind, prospective, randomized controlled trial comparing dorsal aluminum and custom thermoplastic splints to stack splint for acute mallet finger" *Archives of physical medicine and rehabil-itation* **92**(2) 191-8(2011). doi:10.1016/j.apmr.2010.10.035
18) Blaya, F., Pedro, P. S., Silva, J. L., D'Amato, R., Heras, E. S., & Juanes, J. A. " Design of an Orthopedic Product by Using Additive Manufacturing Technology: The Arm Splint" *Journal of medical systems,* **42**(3), 54(2018). https://doi.org/10.1007/s10916-018-0909-6
19) Maurya, Nagendra & Vikas, Rastogi & Singh, Pushpendra "Experimental and Computational Investigation on Mechanical Properties of Reinforced Additive Manufactured Component". *Evergreen,* **6**(3). 207-214 (2019). https://doi.org/10.5109/2349296
20) Farah, S., Anderson, D. G., & Langer, R. "Physical and mechanical properties of PLA, and their functions in widespread applications - A comprehensive review". *Advanced drug delivery reviews,* **107,** 367–392(2016). https://doi.org/10.1016 /j.addr.2016.06.012
21) Adrian J.T. Teo, Abhinay Mishra, Inkyu Park, Young-Jin Kim, Woo-Tae Park, and Yong-Jin Yoon ," Polymeric Biomaterials for Medical Implants and Devices"*ACS Biomaterials Science & Engineering* 2016 **2** (4), 454-472(2016) DOI:

10.1021/acsbiomaterials.5b00429
22) Lin, H., Shi, L. & Wang, D. "A rapid and intelligent designing technique for patient-specific and 3D-printed orthopedic cast." *3D Print in Medicine* **2(**4) (2016). https://doi.org/10.1186/s41205-016- 0007-7
23) Huang, T. H., Feng, C. K., Gung, Y. W., Tsai, M. W., Chen, C. S., & Liu, C. L. (2006). "Optimization design of thumbspica splint using finite element method". *Medical & biological engineering & computing*, **44**(12), 1105–1111(2006). https://doi.org/10.1007/s11517-006-0131-4
24) Sharma, Mehak & Soni, Manoj, "A musculoskeletal Finite Element Study of a Unique and Customised Jaw Joint Prosthesis for the Asian Populace". *Evergreen*, **7**(3), 351-358 (2020). https://doi.org/10.5109/4068615
25) Silva da SNP, Mattar Jr. R, Bolliger Neto R, Pereira CAM.,"Measurement of the flexing force of the fingers by a dynamic splint with a dynamometer." *Clinics*.**60**(5):381-8(2005). doi: 10.1590/s1807-5932 2005000500006
26) Price, Mike J, and Michelle Trbovich. "Thermoregulation following spinal cord injury." *Handbook of clinical neurology,* **157** 799-820(2018) doi:10.1016/B978-0-444-64074-1.00 050-1
27) Mathew Stevens," Human Body Heat as a Source for Thermoelectric Energy Generation", PH240,Stanford University, Fall (2016) htt p://large.stanford.edu/courses/2016/ph240/stevens1/.
28) Jain, Ankit, Cheruku Sandesh Kumar, and Yogesh Shrivastava. "Fabrication and Machining of Metal Matrix Composite Using Electric Discharge Machining: A Short Review." *Evergreen,* **8**(4),740-749 (2021). https://doi.org/10.5109/4742117

ResearchGate

See discussions, stats, and author profiles for this publication at: https://www.researchgate.net/publication/364336935

Monitoring Pressure in Controlled Ventilator System under Different Lung Settings

Preprint · March 2022

CITATIONS
0

READS
8

3 authors, including:

Palak Meena
Delhi College of Engineering
2 PUBLICATIONS **1** CITATION
SEE PROFILE

Palak Sharma
Delhi Technological University
5 PUBLICATIONS **1** CITATION
SEE PROFILE

Some of the authors of this publication are also working on these related projects:

Fetus heath risk predictor View project

Short Literature Review View project

All content following this page was uploaded by Palak Sharma on 12 July 2023.

The user has requested enhancement of the downloaded file.

International Journal of Scientific Research in Science, Engineering and Technology

Print ISSN - 2395-1990
Online ISSN : 2394-4099

Available Online at : www.ijsrset.com
doi : https://doi.org/10.32628/IJSRSET

Monitoring Pressure in Controlled Ventilator System under Different Lung Settings

Palak Meena, Palak Sharma, Kapil Sharma

Department of Information Technology Delhi Technological University, New Delhi, India

ARTICLEINFO

Article History :

Accepted: 01 July 2023
Published: 10 July 2023

Publication Issue :
Volume 10, Issue 4
July-August-2023

Page Number :
98-108

ABSTRACT

To support the weak human lungs with supply of continuous airway pressure in respiratory system throughout the time when patient is on life-support is quite a daunting and people-driven job. To reduce the stress on few doctors and nurses of saving innumerable lives in the time when the world is grappling with Covid-19 and its new deadly variants after every six months. In order to save patients life developing automated ventilation system is the need of the hour. We collected data from several simulations of test lung under different conditions. After preprocessing this dataset using NLP, cross-validation of train and test set. A range of different Machine Learning and Deep Neural Network Models are tried as they can better generalize across lungs with varying characteristics, we scored these models against several evaluation metrics such as MAE, MSE, RMSE. Lastly, we selected best model to predict the target pressure in the respiratory circuit. Through exhaustive clinical tests and accurate medical advice, it is practically possible to bring these results into practical application in future.

Keywords : Mechanical Ventilator System, Sedated Artificial Lung, Time-Series Prediction, Machine Learning, Deep Learning, Air Pressure, Covid-19 Variants.

I. INTRODUCTION

A patient enters a hospital who has trouble in breathing - a patient of COVID 19. The world saw a substantial increase in Covid-19 cases which in turn calls attention to quickly- deployable and cost-effective breathing machines to treat such respiratory ailments. Consequently, it caused a sudden rise of terminally ill patients, who require ventilation support. As mechanical ventilation is a clinically intensive process, one of the constraints that was faced during the early stage of COVID 19. Advancing any new methods for the control of mechanical ventilators is exorbitantly costly. Top notch simulators could diminish this obstruction. Each model of the current simulators simulates a sole lung setting. Simulators being used are prepared like an ensemble. For understanding the differences present in patients'

Copyright: © the author(s), publisher and licensee Technoscience Academy. This is an open-access article distributed under the terms of the Creative Commons Attribution Non-Commercial License, which permits unrestricted non-commercial use, distribution, and reproduction in any medium, provided the original work is properly cited

lungs, an approach with suitable parameters should be explored, as the lungs and their characteristics model a steady form. Different settings of mechanical ventilator are chosen relying upon the patient's lung state, and the determination of those boundaries relies upon the noticed patient's reaction and knowledge of the clinicians that are in question.

Essentially, this is not a usual time-series problem. Here we use values of different collections to predict the values of other series.

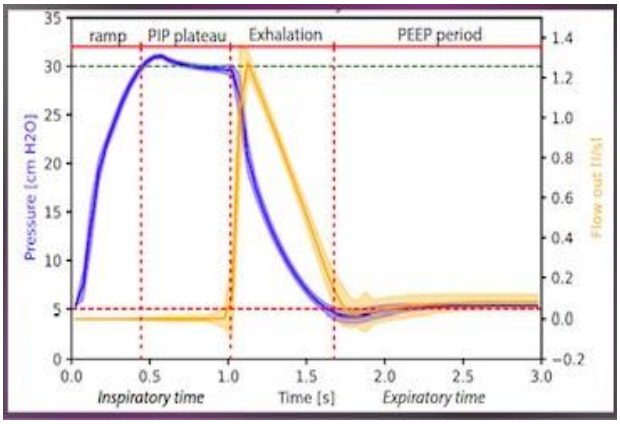

Fig. 1. A typical breath cycle

Great prediction models are constantly beneficial in additional developing setting exactness, decreasing treatment blunders, and fast weaning patients off of the ventilator support to help physicians with this dynamic interaction. It is important to note that positive mechanical breathing gives patients outside assistance till their health improves and they can reconcile with their devices. Volume and pressure control are the most frequent methods of mechanical ventilation. This is not the case with isometric tidal volume. Because of reduced compliance and aggressive exhalation in volume- controlled ventilation, the system may amplify the risk related to lung injury by adjusting pressure of the inspiratory flow and waveform features. Current mechanical ventilators enable doctors to modify a broad variety of parameters, including the mode and intensity of activity, to fit the patient's needs. It is important to know how many obligatory breaths a patient must take and how many extra breaths he or she may take if he or she chooses to do so. The amount of oxygen that is delivered into the body may be regulated from room air (21 percent oxygen) to 100%. To set the PCV air pressure that will be given to the patient, the SetP parameter may be utilized. All airway pressures, namely PEEP and SetP, are added together to calculate the peak inspiratory pressure (PIP). To avoid alveolar collapse between breaths, the ventilator may supply a continuous positive end-expiratory pressure (PEEP). It'll assist with conquering the expense barrier and growing new techniques for controlling mechanical ventilators.

Objective

The aim of this paper is to forecast the pressure within a mechanical lung at any given time step based on how much the inspiratory solenoid valve (u in; a number between 0 and 100) is opened. The purpose is to imitate a ventilator which is connected to a sedated patient's lung while accounting for lung properties such as compliance and resistance.

II. RELATED WORK

Over the past few years many traditional mechanical venti- lators prediction systems were introduced but they missed out on the expensive new developed methods and correct pressure as they were manually adjusted by a clinician. Previously a machine learning model based on ANN and optimization was trained with input/output data; it was used to predict mechanical ventilation parameters using the inverse mapping approach. [2] The unique GPSO approach was employed as an optimizer in inverse mapping computations. Extensive simulations were done to evaluate the GPSO's behavior in the feedback loop and to enhance the model's performance [3].

Mechanical ventilator settings were estimated using a ma- chine learning model based on ANN and optimization. After the ANN was trained with

input/output data, it was used to predict mechanical ventilation parameters using the inverse mapping approach. [2] The unique GPSO approach was employed as an optimizer in inverse mapping computations. Extensive simulations were done to evaluate the GPSO's behaviour in the feedback loop and to enhance the model's performance [4].

An AI model dependent on ANN and advancement was worked to assess mechanical ventilator boundaries. The pre- pared organizations were used to appraise mechanical ventila- tion boundaries utilizing the backwards planning procedure after the ANN was prepared with input/yield information.

[2] In reverse planning calculations, a one of a kind GPSO technique was utilized as an enhancer. To survey the conduct of the GPSO utilized in the input circle and to work on the model's exhibition, broad recreations were run [4]. Prediction for mechanical ventilation (MV) in hospitalised patients, including those with COVID-19, was done using generally accessible data from electronic health records, including the VentNet algorithm versus ROX and a logistic regression model that incorporated clinical factors. The algorithm's performance was evaluated based on its AUC, sensitivity, specificity, and positive predictive value (PPV).

Utilizing regularly accessible information from electronic wellbeing records, a straightforward DL calculation was utilized to anticipate the future requirement for MV in hospital- ized patients, incorporating those with COVID-19, utilizing the VentNet calculation against the ROX and a strategic relapse model dependent on generally utilized clinical factors. The region under the beneficiary working trademark bend (AUC), affectability, particularity, and positive prescient worth were utilized to survey the calculation's exhibition [3].

Kilkarni et al [5] By employing a well-known DenseNet121 deep learning architecture, an advanced model was constructed to predict the requirement for breathing using X-ray images three days in advance of the actual intubation incidence.

Ming-YenLin et al.[10] used three Machine Learning mod- els XGBoost, logistic regression(LR), and random forest (RF) to create an explainable weaning prediction model for patients requiring prolonged mechanical ventilation (PMV). The study established that the accuracy of the XGBoost and RF in prediction of successful weaning was high.

Researchers such as Yan Jia et al.[11] introduced Convolu- tion Neural Networks (CNN) for the prediction model in the coming hour for a given patient condition by using historical data from ICU which is extracted from MIMIC-III. The accuracy achieved was 86% by performing feature importance analysis for the CNN and interpreted the features by using the DeepLIFT method. Researchers like Schalekamp et al.[20] used multivariable logistic regression to build a risk model that took into account clinical, computed tomography (CT) scan, and laboratory data to predict severe illness (including invasive ventilation).

DBNet[21], a unique deep learning system that employs a relational database as input with multiple tables. There is no information loss or transformation due to the model's use of many tables from an EHR database. One layer of information that combines cross-sectional and longitudinal data utilising an integrated CNN-RNN encoder-decoder architecture that can handle varying durations of observations and several data modalities at the same time.

III. PROPOSED METHODOLOGY

Working to solve time-series forecasting problem by applying common machine learning methods and deep learning algorithms is not uncommon. As can be seen from the experimental results, generally deep learning approaches work better than traditional machine learning methods. Our project methodology revolves around some competent forecasting approaches such as LSTM and Bi-LSTM. All these sequential deep learning

models are nothing but subtypes of Recurrent Neural Networks (RNN). In case of sequential data like time-series data used here, data at time (t) depends on data at time (t-1). RNN being a feed forward neural network can easily remember what happened previously in sequential data which helps them in deriving correlations and patterns in the domain of predictive analytics.

4.1 Machine Learning

Linear Regression (LR): It is a renown supervised learning algorithm to perform regression tasks. It can also be defined as a statistical model which shows the relationship between two variables and forecasting with the linear equation.

Random Forest (RF): It is a versatile algorithm as it can perform regression and classification tasks both. It is an ensemble of decision trees on varying samples. It has an important feature of handling continuous dataset variables in case of regression.

K-Nearest Neighbour (kNN): It can also perform regression and classification tasks both. It calculates distance between two points in the dataset using similarity between attributes.

Light Gradient Boosting Machine (LGBM): It is a variant of the gradient boosting frameworks. It is supposed to be distributed, fast and also high-performance. It is based on the decision tree algorithm.

4.2 Deep Neural Networks

Multi-Layer Perceptron (MLP): This is a completely connected, feed forward neural network. This is a perceptron that attaches itself with several layers of additional perceptrons to solve numerous complex problems including time series data forecasting, recognition of gestures and prediction.

LSTM: For a variety of learning issues involving sequential input, recurrent neural networks (RNN) with long short-term memory (LSTM) have emerged as an efficient and robust technique. Because they are broad and effective, they are excellent for capturing long-term temporal dependencies.

Bi-directional LSTM: Bi-LSTM is known to train a network using both past and future data sequences as inputs. Two linked layers are used to process the input data. Bi-LSTM uses a finite sequence to forecast or tag the sequence of each element depending on the context of components in the past and future.

4.3 Optimization of hyperparameter

Adam Optimizer, a highly effective optimization algorithm, employed as an alternative to traditional gradient descent procedures for updation of weights in a neural network on the basis of training data. Parameters such as learning rate controls shifting of the rate of decays.

IV. EXPERIMENTAL SETUP

5.1 System Overview

To obtain medical data and test experiments a IOT-enabled system is developed by researchers and tech-professionals in the laboratory conditions. A lot of data was generated from a modified open-source mechanical ventilator (PVP-The People's Ventilator Project) [1] connected to an artificial test lung (Quick Test Lung) in a respiratory circuit. Artificial test lungs are more effective than the bladder-style test lung as they provide linear and predictable respiratory simulation. Pressure sensor records the amount of air absorbed and released by the test lung. This model helps in generation of dataset. A portion of this generated data for the use of medical and patient's treatment, including mechanical breathing.

The System software for the project is written in high-level Python (3.7) and even the hardware components are not medical-related devices but readily available components for instance specialized respiratory circuits and HEPA filters. In a real experimental set-up, an artificial bellow-style Lung along with a pressure analyzer is used for accurately testing the performance of mechanical ventilation in the presence of an open-

source, low-cost pressure control ventilation system developed in Princeton Lab intended for research purpose only in response to shortage of trained-professionals during Covid- 19 pandemic, to provide ventilation to patients mechanically who face trouble in regular breathing. In order to automate the ventilator, a control has been applied on air pressure in the ventilator in the Fig.2 mechanically so that it can respond accurately in different lung settings during the inspiratory phase in the human respiration.

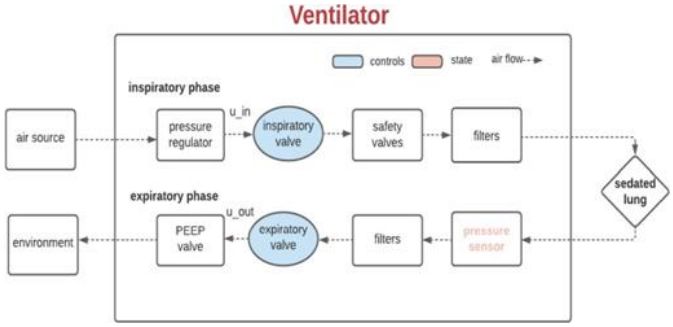

Fig. 2. Block Diagram of Mechanical Ventilator performing Simulation

5.2 Dataset

We performed our analysis on the research dataset launched by Google Brain in September 2021 on the kaggle platform. Ventilator Prediction dataset provides numerous time series of breaths and time series of control inputs of the mechanical ventilator data for training our time series models. It is a large- scale dataset with ventilator characteristics of multiple training samples where each sample is a time step in breath, giving two control signals, lung attributes and target airway pressure. Specifically, it is a time series data collected over a period as pressure data. Each time series represents approximately three seconds of a breath. The training set consists of 8 attributes of Ventilator, shown in the table I. In this ventilator-lung system, lung attributes are R and C and two control inputs each during inspiratory and expiratory phase in the given respiratory circuit. Here, our 'Target' is the dependent variable, which is nothing but a continuous variable, airway 'Pressure' during the inspiratory phase of the respiratory circuit. We are provided with csv file consisting of 7 attributes (except the 'Target') as a test data.

5.3 Exploratory Data Analysis

This step helped us to derive extra meaningful information from this huge ventilator dataset for our analysis besides what is already given. A set of python libraries is utilized to interpret the dataset in a better manner using statistical, graphics and other data visualization methods. Fig. 3 shows the visualization of a sample breath for a particular breath id (Breath id: 1, R: 20, C:50) we can observe that first the target pressure is uprising and then, after it when the u out becomes equal to 1, pressure drops abruptly.

A fairly balanced distribution of combinations of R and C data points is helpful in predicting each example in unknown

TABLE I. DESCRIPTION OF THE DATASET

Attributes	Accepted Value	Nature of Variable	Description
id	1 onwards	Continuous	Globally-unique time step identifier across an entire file
breath id	0 to 2245	Continuous	Globally-unique time step for breaths
R	[5,20,50]	Categorical	Represents the percentage of inspiratory solenoid valve open to let air into the lung(i.e., 0 is completely closed and no air is let in and 100 is completely open).
C	[10,20,50]	Categorical	Represents when the exploratory valve is open(1) or closed(0) to let the air out of the respiratory circuit.
time step	Actual time stamps	Continuous	It represents amount of time the breath took.
u in	0 to 100	Continuous	The control input for the inspiratory solenoid valve.
u out	0 or 1	Categorical	The control input for the exploratory solenoid valve.
pressure	measured in cmH20	Continuous	The airway pressure measured in the respiratory circuit.

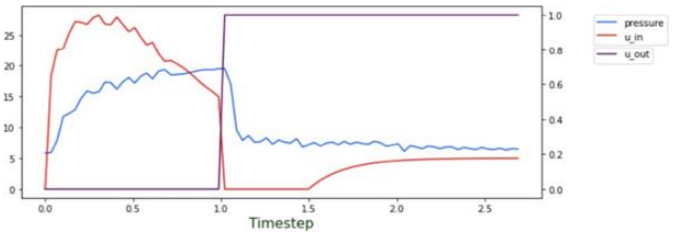

Fig. 3. Sample breath for a particular breath id in the train set

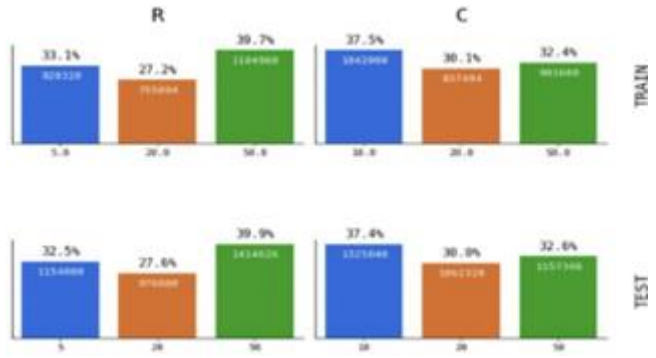

Fig. 4. Distribution of R and C values in the train and test set

Test data with equal probability. Fig. 4 shown above represents categorical variables such as R and C have identical distribution in train and test set. From the correlation matrix of features in Fig. 5, it is quite evident that, a moderately negative correlation exists between the target class 'pressure' and control input of exploratory solenoid valve 'u_out', also 'u out shows high positive correlation with time. Comparatively, 'u in' has a good positive correlation with 'pressure' than with other attributes.

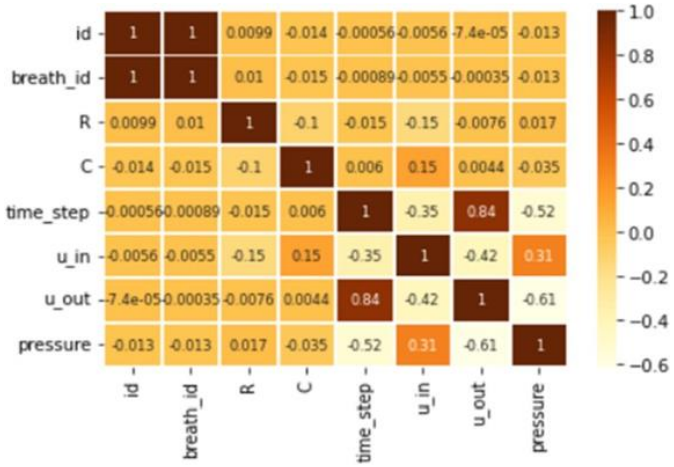

Fig. 5. Pearson correlation of Features for the ventilator dataset

5.4 Preprocessing and Feature Engineering

We checked for any null or duplicate values in both test and train set and removed these examples when found. Before feeding this complex real-time data to the neural network, it is important to remove certain unexpected observations by normalization on rare instances of both test and train set using the transform method of robust scaler class in scikit-learn library. Compared to other normalizers, it removes median and scales of data using the range between quantiles.

This was followed by feature engineering in which we selected few important features and and transformed them to generate additional attributes which could help in training the model. Here, for instance by grouping u in of a particular breath id. In that particular breath we can find the maximum amount of air inhaled ('breath id u in max'), mean amount of air inhaled for a breath ('breath id u in mean') and also find out how much u in in each sample for a particular breath deviate from max u in value ('breath id u in diffmax') and from mean u in value ('breath id u in diffmean').

5.5 Experimental Configuration of ML Models

After feature engineering, we split the training and test set in the 7:3 ratio. We scaled the dataset by performing 5-fold cross- validation on this train set and test set. We used a collection of machine learning regressors here, such as Linear Regression, kNN, XGBoost, Light Gradient Boosted Machine and Random Forest.

TABLE II. SCORING SUPERVISED MACHINE LEARNING MODELS

Supervised ML Algorithms	R-squared	MAPE
Linear Regression	0.380519	37.565245
LightGBM Regression	0.443025	34.115820
K-Nearest Neighbors	0.702278	22.119794
XGBoost	0.434124	34.245190
Random Forest	0.295020	36.808463

5.6 Experimental Configuration of Neural Networks

We constructed a bunch of DNN models based on MLP, LSTM with two hidden layers and Bi-LSTM with eight hidden layers. After this, these neural network models were trained for updation of weights to learn

the behavior of data, here, we tried to minimize the time taken to perform update using adam optimization algorithm where the parametric value for the learning rate equals to (1 x 10–3 for Bidirectional LSTM) and (0.5 x 10–3 for LSTM) models.

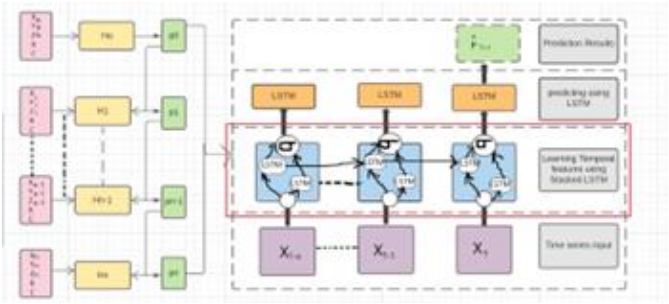

Fig. 6. Network Architecture for our implemented Bi-LSTM Model. For the architecture of our implemented LSTM Model just remove the Stacked LSTM layer.

V. Evaluation and Comparison of Results

During the evaluation, we calculated training error loss to compare performance of the models based on different algorithms. Score of mean absolute error i.e MAE, (also called as L1 loss) , mean square error (MSE) and root mean square error (RMSE) between the predicted and actual pressures during the inspiratory phase of each breath was recorded for each trained model. We can clearly see the expiratory phase is not scored here. Probably, the scores are only calculated during the inspiratory phase because u in profiles in the expiratory phase didn't change much across different simulations and would not be much valuable to study. Score of evaluation metrics used are given by:

$$MAE(X, Y) = |X - Y| \quad (1)$$

$$MSE(X, Y) = (X - Y)^2 \quad (2)$$

$$RMSE(X, Y) = \overline{(X - Y)^2} \quad (3)$$

where X is the vector of predicted pressure and Y is the vector of actual pressures across all breaths in the test set. At the end of each iteration, loss is recorded while training our models with training set. Similarly, loss for the validation set is calculated after recording the error after each epoch. We observed that loss during each epoch dropped, this decreasing loss with respect to epochs is the learning curve for LSTM (as shown in Fig. 7) and Bi-LSTM (as shown in Fig. 8) models implemented here.

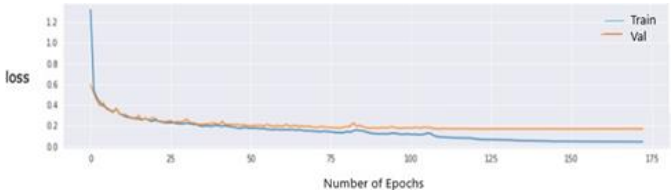

Fig. 7. Variation of the training loss and validation loss over time for LSTM Model

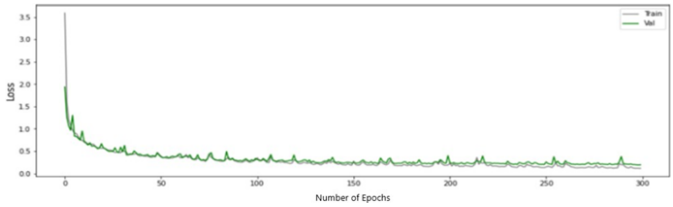

Fig. 8. Variation of the training loss and validation loss over time for Bi-LSTM Model

We have mentioned Overall L1 Loss,MSE and RMSE of all the algorithms we used in the Table III. From the column of mean absolute error loss (0.161112) in Table III, we can observe that Bi-LTSM model gives minimum loss (4.029514) among all, whereas the performance of supervised machine learning algorithm i.e. Linear Regression is worst among them all. From the mean square error loss in Table III, we can observe that Bi-LTSM model gives minimum loss (1.05818) among all, whereas the Linear Regression Model gives maximum mean square error (20.26328) in the computation of predictions. Based on the results, root mean square error for Linear Regression is 4.50148 whereas LSTM model with 1.65735 and Bi-LSTM model with 1.02868 loss impressively, outperforms rest of the techniques used.

TABLE III. COMPARISON OF RESULTS

Algorithm Used	Overall L1 Loss	MSE	RMSE
Linear Regression	4.029514	20.26328	4.50148
K-Nearest	2.211979	19.576831	4.42457
Neighbors	2.557977	12.86334	3.58655
Multi-Layer	2.125771	10.68989	3.26954
Perceptron	1.308497	6.58006	2.56516
LightGBM	0.418213	2.74681	1.65735
Random Forest	0.161112	1.05818	1.02868
LSTM			
Bi-LSTM			

VI. LIMITATIONS OF THIS WORK

On the basis of our results of our proposed work, post the training and evaluation of our models on the dataset. We can draw some observations on the possible drawbacks of our study, a few of which are listed below:

1) Given the dataset we have, the solution might not be able to generalize to real word scenarios.

2) Simulated data is not considered real environment data even though the neural network model was learning the pattern existed in data. But since it was driven by a PID Controller we ended up learning the behavior of PID Controller while training our model.

3) Though we could fit in the data, but the way data was generated could have improved a bit.

4) Values of pulmonary parameters such as R and C, didn't have any considerable effect on our results. From the experimental observations we observed that even after changing R and C values and training the model deep enough didn't have much impact. We assume this could be because the pressure is only dependent on immediate previous u in values.

VII. CONCLUSION

In this paper we have used ventilator pressure prediction dataset published by Google Brain on the Kaggle platform using the data generated by the open-source ventilation system developed by Princeton Lab researchers for our analysis. We performed exploratory data analysis on the large dataset followed by data pre-processing. We considered this as a regression problem and split the dataset into train and test data. After this various machine learning algorithms and a bunch of deep learning algorithms were used for training our model separately. Out of which the deep learning approaches such as LSTM and Bi-LSTM outperformed outperformed the machine learning-based and other deep learning-based regression models in terms of prediction. Further, the results revealed that BiLSTM-based modelling, which incorporates additional data training, provides better forecasts than normal LSTM-based models. Thus, providing the model with additional training data can be useful for future predictions.The proposed study utilizes data analysis, deep learning architectures and machine algorithms to optimize the control of ventilator, showed what can be accomplished by learning the whole pressure-control system from the ground up. Practically, in the wake of the unforeseen outbreak of Covid- 19 pandemic, the deep neural network models developed in this work may be useful in forecasting mechanical ventilation settings for the survival of patients inflicted with respiratory diseases. Using a neural network, it is possible to replicate the lung-ventilator system's nonlinear dynamical system more precisely than with earlier physics-based models. But as the dataset was taken from a simulator-based lung setting which is not clinically validated results in uncertainty for the real-world scenarios, to test its efficacy on living organisms correct medical recommendations are required. To initiate its regular operation few changes in design of the device are essential to make it portable and convenient for everyday use in homes and hospitals by any individual.

VIII. FUTURE SCOPE

In our future work, we would like to use a transformer-based framework for multivariate time series analysis. Instead of using mean as done in our technique, in future, median can be used as a statistical measure to

ensemble fold predictions of the model in consideration. To increase the accuracy of predictions, rounding of the actual pressure in the training data can also be done to closely match with the discrete target predictions. To reduce training error in future notebooks, we have to avoid over-fitting the training set with several features. We can fix this by adding regularization and also through early stopping to avoid overt-raining neural networks. Since, we also have multiple attributes in the dataset some of which have categorical values too, we can consider this problem as a classification problem instead of regression as done here to predict the pressure for each training example. Further, we could also try experimenting with other neural networks like multilayer perceptrons, convolution neural network ensemble of LSTM or BILSTM-CNN. Additionally, we can aim to use a powerful GPU to speed up the training process.

IX. REFERENCES

[1]. PVP1–The People's Ventilator Project: A fully open, low-cost, pressure-controlled ventilator. Julienne LaChance, Tom J. Zajdel, Manuel Schottdorf, Jonny L. Saunders, Sophie Dvali, Chase Marshall, Lorenzo Seirup, Daniel A. Notterman, Daniel J. Cohen medRxiv 2020.10.02.20206037; DOI: https://doi.org/10.1101/2020.10.02.20206037.

[2]. Oruganti Venkata SS, Koenig A, Pidaparti RM. Me- chanical Ventilator Parameter Estimation for Lung Health through Machine Learning. Bioengineering (Basel, Switzerland). 2021 May;8(5). DOI: 10.3390/bioengineer-ing8050060. PMID: 34067153; PMCID: PMC8150272.

[3]. Supreeth P. Shashikumar, Gabriel Wardi, Paulina Paul, Morgan Carlile, Laura N. Brenner, Kathryn A. Hib- bert, Crystal M. North, Shibani S. Mukerji, Gregory K. Robbins, Yu-Ping Shao, M. Brandon Westover, Shamim Nemati, Atul Malhotra, Development and Prospective Validation of a Deep Learning Algorithm for Predicting Need for Mechanical Ventilation,Chest,Volume 159, Issue 6,2021

[4]. Sanjay S.O., Pidaparti R.M. Graded Particle Swarm Op- timization (GPSO); Proceedings of the 2016 Interna- tional Conference on Robotics: Current Trends and Future Challenges (RCTFC); Thanjavur, India. 19–20 December 2016;

[5]. Kulkarni AR, Athavale AM, Sahni A, et alDeep learning model to predict the need for mechanical ventilation using chest X-ray images in hospitalised patients with Covid- 19BMJ Innovations 2021;7:261-270.

[6]. Chen T, Guestrin C. XGBoost. Proceedings of the 22nd ACM SIGKDD International Conference on Knowledge Discovery and Data Mining; San Francisco, California, USA: Association for Computing Machinery; 2016.

[7]. Arvind V, Kim JS, Cho BH, Geng E, Cho SK. De-velopment of a machine learning algorithm to predict intubation among hospitalized patients with COVID-19. Journal of Critical Care. 2021; 62:25–30. https:// doi.org/10.1016/j.jcrc.2020.10.033 PMID: 33238219

[8]. Siami-Namini, Sima et al. "The Performance of LSTM and BiLSTM in the Forecasting Time Series." 2019 IEEE International Conference on Big Data (Big Data) (2019): 3285-3292.

[9]. Rehm GB, Kuhn BT, Nguyen J, Anderson NR, Chuah CN, Adams JY. Improving Mechanical Ventilator Clin- ical Decision Support Systems with a Machine Learn- ing Classifier for Determining Ventilator Mode. Stud Health Technol Inform. 2019 Aug 21;264:318-322. doi: 10.3233/SHTI190235. PMID: 31437937

[10]. Yu L, Halalau A, Dalal B, Abbas AE, Ivascu F, Amin M, et al. (2021) Machine learning methods to predict mechanical ventilation and mortality in pa- tients with COVID-19. PLoS ONE 16(4):

e0249285.
https://doi.org/10.1371/journal.pone.0249285

[11]. Lin M-Y, Li C-C, Lin P-H, Wang J-L, Chan M-C, Wu C- L and Chao W-C (2021) Explainable Machine Learning to Predict Successful Weaning Among Patients Requiring Prolonged Mechanical Ventilation: A Retrospective Co-hort Study in Central Taiwan. Front. Med. 8:663739. doi: 10.3389/fmed.2021.663739

[12]. Jia Y, Kaul C, Lawton T, Murray-Smith R, Habli I. Prediction of weaning from mechanical ventilation us- ing Convolutional Neural Networks. Artif Intell Med. 2021 Jul;117:102087. doi: 10.1016/j.artmed.2021.102087. Epub 2021 May 5. PMID: 34127233.

[13]. Chang, W.; Ji, X.; Wang, L.; Liu, H.; Zhang, Y.; Chen, B.; Zhou, S. A Machine-Learning Method of Predicting Vital Capacity Plateau Value for Ventilatory Pump Fail- ure Based on Data Mining. Healthcare 2021, 9, 1306. https://doi.org/10.3390/healthcare9101306

[14]. Rehm GB, Kuhn BT, Nguyen J, Anderson NR, Chuah CN, Adams JY. Improving Mechanical Ventilator Clin- ical Decision Support Systems with a Machine Learn- ing Classifier for Determining Ventilator Mode. Stud Health Technol Inform. 2019 Aug 21;264:318-322. doi: 10.3233/SHTI190235. PMID: 31437937.

[15]. Strodthoff, Claas Frerichs, Ine´z Weiler, Nor-bert Bergh, Bjo¨rn. (2021). Predicting and simulating effects of PEEP changes with machine learning. 10.1101/2021.01.28.21250212.

[16]. Zhang L, Mao K, Duan K, Fang S, Lu Y, Gong Q, Lu F, Jiang Y, Jiang L, Fang W, Zhou X, Wang J, Fang L, Ge H, Pan Q. Detection of patient-ventilator asynchrony from mechanical ventilation waveforms us- ing a two-layer long short-term memory neural net- work. Comput Biol Med. 2020 May; 120:103721. doi: 10.1016/j.compbiomed.2020.103721. Epub 2020 Mar 26. PMID: 32250853

[17]. Zhang, K., Karanth, S., Patel, B., Murphy, R., Jiang, X. (2021). Real-time Prediction for Mechanical Ventilation in COVID-19 Patients using A Multi-task Gaussian Process Multi-objective Self-attention Network. arXiv preprint arXiv:2102.01147.

[18]. Oruganti Venkata SS, Koenig A, Pidaparti RM. Me- chanical Ventilator Parameter Estimation for Lung Health through Machine Learning. Bioengineering (Basel). 2021 May 7;8(5):60. doi: 10.3390/bioengineering8050060. PMID: 34067153; PMCID: PMC8150272.

[19]. Machine Learning for Mechanical Ventilation Control Daniel Suo, Cyril Zhang, Paula Gradu, Udaya Ghai, Xinyi Chen, Edgar Minasyan, Naman Agarwal, Karan Singh, Julienne LaChance, Tom Zajdel, Manuel Schottdorf, Daniel Cohen, Elad Hazan medRxiv 2021.02.26.21252524; doi: https://doi.org/10.1101/2021.02.26.21252524

[20]. Schalekamp, Steven Huisman, Merel Dijk, Rogier Boomsma, Martijn Jorge, Pedro Boer, Wytze Herder, Gerada Bonarius, Marja Groot, Oscar Jong, Eefje Schreuder, Anton Schaefer-Prokop, Cornelia. (2020). Model-based Prediction of Critical Illness in Hospital- ized Patients with COVID-19. Radiology. 298. 202723. 10.1148/radiol.2020202723.

[21]. Cvitkovic, Milan. “Supervised Learning on Rela-tional Databases with Graph Neural Networks.” ArXiv abs/2002.02046 (2020): n. pag.

[22]. Sathesh, A. ”Computer Vision on IOT Based Patient Preference Management System.” Journal of Trends in Computer Science and Smart Technology 2, no. 2 (2020): 68-77.

[23]. Murthy, Shrujana, and C. R. Kavitha. ”A Smart and Secure Framework for IoT Device Based Multimedia Medical Data.” In International Conference On Computa- tional Vision and Bio

Inspired Computing, pp. 583-588. Springer, Cham, 2019.

[24]. P. Meena, P. Sharma and K. Sharma, ”Optimizing Control of IOT Device using Traditional Machine Learning Mod- els and Deep Neural Networks,” 2022 6th International Conference on Computing Methodologies and Commu- nication (ICCMC), 2022, pp. 445-451, doi: 10.1109/IC- CMC53470.2022.9753943.

Cite this article as :

Palak Meena, Palak Sharma, Kapil Sharma, "Monitoring Pressure in Controlled Ventilator System under Different Lung Settings", International Journal of Scientific Research in Science, Engineering and Technology (IJSRSET), Online ISSN : 2394-4099, Print ISSN : 2395-1990, Volume 10 Issue 4, pp. 98-108, July-August 2023.
Journal URL : https://ijsrset.com/IJSRSET23103190

View publication stats

Multi-factor Assymetric Key Encryption (MAKE) for Mutual Authentication in IoMT

Sristi Mitra
Department of Computer Engineering, Delhi Technological University
Bawana Road, Rohini - 110042, Delhi, India
ratrimitra16@gmail.com,

Zishnendu Sarker
Department of Computer Engineering, Delhi Technological University
Bawana Road, Rohini - 110042, Delhi, India
zzishnusarker@gmail.com,

Priyanka Patel
Department of Computer Engineering, Delhi Technological University
Bawana Road, Rohini - 110042, Delhi, India
piyapatel2057@gmail.com

Pawan Singh Mehra
Department of Computer Engineering, Delhi Technological University
Bawana Road, Rohini - 110042, Delhi, India
pawansinghmehra@gmail.com

2023 Third International Conference on Secure Cyber Computing and Communication (ICSCCC) | 979-8-3503-0071-0/23/$31.00 ©2023 IEEE | DOI: 10.1109/ICSCCC58608.2023.10176485

***Abstract*—Digital health, smart hospitals, and other uses of the Internet of Things (IoT) generate enormous amounts of heterogeneous data. Sensor nodes of IOT are incorporated with medical apparatus so that medical staff may continuously check patients' health and appliances. However, due to security flaws, an unauthorized person might access patient health data or manage the IoT nodes linked to their bodies, leading to results that were previously unheard of. Because wireless channels are used as a communication medium, IoT presents a number of risks to the security and privacy of IoT networks. We proposed a multifactor-oriented protocol which provides mutual authentication for transmission of data between patient and doctor by maintaining secrecy among smart card, sensor node, server, gateway and IoMT devices. We use the concept of assymetric key, XOR operation and the fuzzy extractor for better and more secure encryption. We proved the protocol formally by BAN logic and informally and then finally calculated the computational cost.**

Keywords—mutual authentication, IoMT, WBAN, BAN logic, session key agreement.

I. Introduction

The Internet of Things (IoT) has developed into a crucial component in order to meet the connection requirements of modern smart healthcare systems. IoT is sometimes referred to as the Internet of Medical Things in the healthcare sector. The Internet of Medical Things (IoMT) is an interconnected network of medical devices that track patients' vital signs and send that information to healthcare professionals so they may administer remote medical care. [2] To prevent the abuse of the patient's sensitive information, IoMT security is a crucial prerequisite that calls for more study [19]. IoMT apps must follow stringent authentication procedures to prevent unauthorised access to patient data and IoMT resources as well as to safeguard the overall system from any threats. One of the WBAN (Wireless Body Area Network) technologies is the Telecare Medical Information System (TMIS), which may deliver a range of healthcare services to far-flung patients via telecare servers. Using the telecare server or an online database, the patient, doctors, and hospital will mutually authenticate one another in this situation. [6]

A. Research Motivation

- Smart pharmaceuticals, onsite and remote monitoring of medical resources, patient treatment compliance, and behavioural modification are just a few of the applications that the IoMT has made possible, considerably advancing smart healthcare. The authentication of IoMT users and devices serves as the first barrier to access into systems using this technology.
- In light of the most recent COVID-19 problem, people are getting increasingly interested in distant services to minimise social connection. In addition, some people could find it challenging to go to the hospital because of their health or other circumstances.

TABLE I ABBREVIATION TABLE

Abbreviation		Full Form
IoT	-	Internet of Things
IoMT	-	Internet of Medical Things
MA	-	Mutual Authentication
PP	-	Privacy Prevention / Protection
SN	-	Sensor Node
SC	-	Smart Card
SK	-	Session Key
WBAN	-	Wireless Body Area Network

B. Our Contribution

- Firstly, we have reviewed 4 recent papers on this topic consisting of different protocols and mentioned the achieved factors and the limitations of the protocol to understand the work done and the lacking on this respective topic in Section II
- Section IV depicts as we proposed a mutual authentication model to ensure secure communication between patients and doctors/smart healthcare centers using a trusted telecare server and database on the Internet.
- We performed theoretical formal and informal analysis on our model which led to a better understanding of the pre-existing models used in recent times in Section V.

C. Paper Organization

The paper has been arranged as follows: i) Section II mentions the overview of the previous work done; their achieved factors and the limitations of the protocols. ii) Section III will describe the preliminaries of our model and the basic concept of understanding the model better. iii) Section IV will unfold our model of mutual authentication. iv) Section V will depict the authentication analysis where we will show the security analysis and comparison analysis and v) Concluding with the future work and further scope of this field of authentication.

Authorized licensed use limited to: DELHI TECHNICAL UNIV. Downloaded on July 20,2023 at 11:09:19 UTC from IEEE Xplore. Restrictions apply.

II. Related Work

Almulhim et al. [8] put forth an elliptic curve cryptography-based protocol that authenticates and establishes secure channels between sensor nodes and base stations, allowing sensors to save energy, increase the network's longevity, and be resistant to a variety of attacks. The suggested system will use less energy and use less energy because of its group-based node functionality.

Binu et al. [9] discussed the authentication process for mutual user and medical server authentication while presenting a sign-based approach for remote health assessment. They have used the Scyther tool to do both quick and in-depth security evaluations. The findings demonstrate that the protocol is robust to a number of prevalent and automated attacks.

Sharma et al. [10] put up a framework for application layer security, to fend off any assaults from public access networks.The protocol prevents several attacks that could aim to compromise availability, confidentiality, or integrity.

Radhakrishnan et al. [11] proposed a system that utilised the well-known random Oracle model to demonstrate the security of the recommended systems by offering an improved trade-off between security and efficiency as compared to other pertinent contemporary methodologies.

In the next section, we will describe the IoMT context and architecture, mutual authentication, and fuzzy extractor as preliminaries of our study. In the later part of the section, system model and the adversary model is also shown.

TABLE II
NOTATION TABLE

Abbreviation		Full Form
P_i	-	Patient
IP_i	-	Patient Identity
R_{GW}	-	Gateway
D_i	-	Doctor
DW_i	-	Doctor's Password
P_{TID}	-	Patient temporary ID
D_{TID}	-	Doctor temporary ID
SCI_i	-	Imprints of smart card
h	-	Hash function
PW_i	-	Patient Password
SN	-	Sensor Node
SC	-	Smart Card
RC	-	Registration Center
RS	-	Random Secret Number generated by R_{GW}
Db_i	-	Database
K	-	Key generated by smart card
K_{USG}	-	Session key for communication between Doctor and Patient
K_{SG}	-	Session key for communication between Telecare Server and Gateway
K_{GS}	-	Session key for communication between Gateway and Telecare Server
K_{SS}	-	Session key for communication between Telecare Server and Patient
K_{DP}	-	Session key for communication between Doctor and Patient
K_{SN}	-	Session key for communication between Gateway and Patient
x y	-	Private keys of Registration Center
TS_i	-	Telecare Server
N_P	-	Nonce of Patient
N_D	-	Nonce of Doctor
N_S	-	Nonce of Telecare Server
IR_{GW}	-	Identity of Gateway
N_G	-	Nonce of Gateway

III. Preliminaries

A. Mutual Authentication:

The first stage in establishing formal and secure data transmission or communication between various IOT devices is mutual authentication. The doctor and the patient must increase the security for sending or receiving information since the patient and the healthcare provider are mutua1lly authenticated. MA is accomplished through a strong password authentication system that enables both the server and the user to independently verify the other party's validity. [1] Furthermore, neither illegal users nor servers are permitted to assume the identity of authorized users or servers.

B. Fuzzy extractor:

The fuzzy extractor functions as a biometric tool, and users' biometric templates created from their biometric data serve as secret keys. We briefly define the terms reproduce function Rep and generate function, Gen.

- The fuzzy extractor creates helper data (public information) and a consistent secret key from an input (such as a biometric reading). Although the assistance data doesn't reveal anything about the input, it is used to subsequently retrieve the secret key. [15]
- The fuzzy extractor can recreate the same secret key created during the enrollment step given the same input (for instance, another biometric reading from the same person) and the auxiliary data, notwithstanding the tiny variations between the two inputs.

C. System Model:

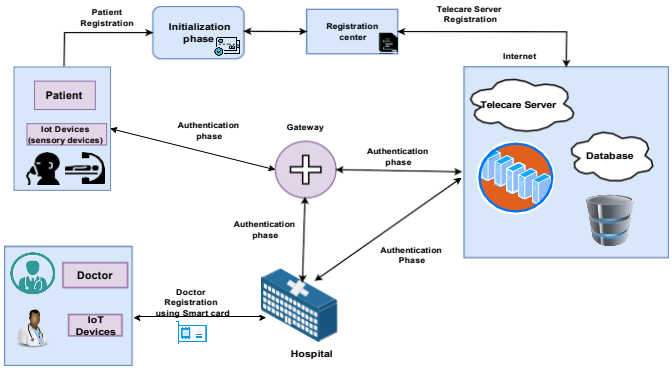

Fig. 1. Systematic Model View

- Patient: The patient must register using a mobile device at the registration centre before obtaining the medical services offered by the telecare server. After registering, the patient can use a mobile device to send the data they've acquired to the telecare servers.
- Registration Center: The registration centre is a reputable authority that creates system parameters and distributes open data. The registration centre manages the telecare servers and patient registration.
- Gateway: Between the physician and the patient sensor node, the gateway serves as a hub. It is important to remember that the gateway does not lack resources.
- Telecare Server: To be a valid organization, the telecare server has to register with the registration center. The telecare server gets the patient's medical information after registration from their mobile devices.

D. Adversory Model:

The proposed model considers WBAN and Dolev-Yao network model which consists of a patient, sensory nodes, a registration center, a server in the cloud, a gateway, a doctor,

Authorized licensed use limited to: DELHI TECHNICAL UNIV. Downloaded on July 20,2023 at 11:09:19 UTC from IEEE Xplore. Restrictions apply.

and IoT devices. [4] Using power analysis assaults, an attacker can seize a valid patient's mobile device and retrieve all the information that is stored on it. A rival may be a trusted insider at the registration center or a real patient. Users using WBAN may be at risk. Users who have been compromised are able to work together with any adversary or cloud server to get other users' private information or assist the adversary with bypassing authentication. However, we do not believe that compromised consumers provide the adversary access to all of their private information for the impersonation assault. [6]

The next section will unfold our proposed model, the aim of the model and the architecture of the model.

IV. Proposed Model

The proposed model mainly consists of three phases: i) the Initialization phase; ii) the Login and Registration phase; iii) the Authentication phase. We have used the Hash function, OR, and XOR operation for a lightweight and mutually authenticated model.

A. Architecture

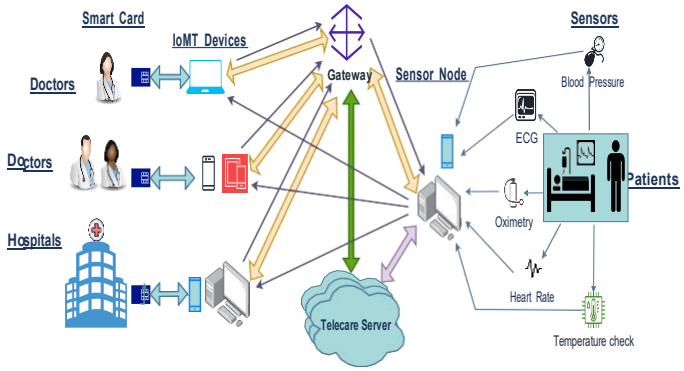

Fig. 2. Basic architecture of our model

B. Aim of Model

We are aiming for a protocol that has

- Device authentication: Before a device is permitted to connect with the network, it must first be given a unique identification and authenticated.
- Secure Communication: The protocol must make sure that data exchanges between devices and the network are secure. Authentication and encryption techniques can be used to accomplish this.
- Access Control: To prevent unauthorized access to the network and devices, the protocol should incorporate access control methods.
- Data Privacy: By using access restriction, anonymization, and encryption techniques, the protocol should guarantee the confidentiality of patient data.
- Threat Detection and Response: Real-time detection and reaction to security risks or assaults should be possible using the protocol. Implementing intrusion detection and prevention techniques can help with this.

C. Model Phase

1) Initialization Phase: Since WBAN is being used, the nodes are fixed on the human body for the collection of data which are wearable, portable, and very light. Again as we are using WBAN in Dolev-Yao model, we are initiating a Registration Center (RC) where both the patient and the teleserver will register and store the necessary values which can be used in the later authentication process. The parameters of the WBAN are generated in this phase. A number of assumptions are also done like [17];

- The medical device and the IoT sensor node are resource-constrained in comparison to the gateway, which is connected to the main power supply and has no computational or storage restrictions.
- The gateway and the registration center is always a trusted entity and cannot be tampered.
- Upto the registration phase, a secured channel is used, and after that public channels can be used as well.

In this phase, the RC decides on a two-way factor authentication system where the private key also gets decided. Therefore, RC publishes the system parameters also which is shown later in the paper.

2) Registration Phase: The registration phase can mainly be divided into two parts; i) User registration and ii) Teleserver registration. The initialization and registration information is stored in the Registration Center for further use. This registration is done through the gateway where mutual authentication can also be seen.

- **User Registration phase:**
  - **Step 01:** The Gateway, R_{GW} generates a Random Secret which is denoted by RS. Patients and doctors will register themselves from their side in which case of the patient; $a_i = (IP_i \oplus RS) \oplus PWi$ and with this calculation, R_{GW} will generate a temporary ID for the patient. The calculated value of a_i is sent to the patient within a secure communication channel and the patient will derive the temporary ID, P_{TID}, and store it. Finally, it computes $b = (PW_i || RS) \oplus P_{T\,ID}$. Now, from the doctor's side, the gateway will generate $p = (D_i\ RS) \oplus DW_i$, and here the temporary ID for the doctor is generated, D_{TID}. The value of p is sent to the doctor and the doctor will derive the temporary ID and calculate $q = (DW_i || RS) \oplus D_{TID}$. [17]
  - **Step 02:** During the registration phase, the value of b and q is verified whether the registration will go on or not.
- **Teleserver registration phase:**
  - **Step 01:** The Registration Center will provide the private keys x and y to the teleserver and a random number R is generated.
  - **Step 02:** Calculating the $R = h(R || h(x||y))$. The Registration center will the pseudo-identity of the teleserver; makes it public and sends it to the teleserver. [18]

Authorized licensed use limited to: DELHI TECHNICAL UNIV. Downloaded on July 20,2023 at 11:09:19 UTC from IEEE Xplore. Restrictions apply.

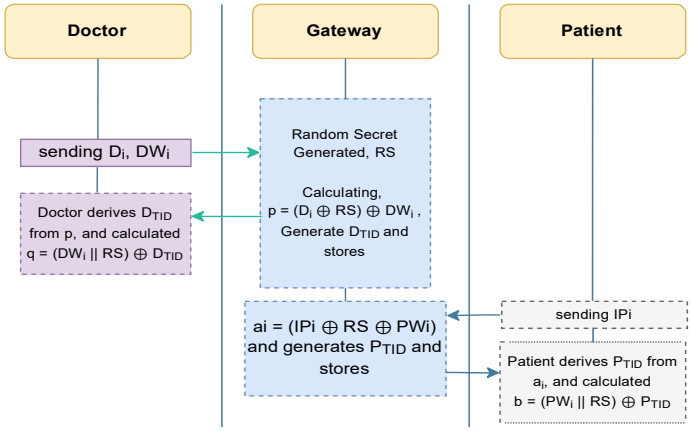

Fig. 3. Registration Phase

3) Login Phase: The login phase will be done through a biometric smart card or through the same credentials on your smartphone which has an unique imprint which we denoted by SCI_i.

- **Step 01:** The Registration center will have to calculate the Hash of patient identity, patient's password and the imprint of the smart card denoted as,
  $SC_i = h(IP_i||PW_i||SCI_i)$
- **Step 02:** By using the fuzzy extractor, $Gen(SC_i) = (\sigma i, \vartheta i)$; here the parameter ϑ_i is considered as the reproduction parameter where it has been derived from a physical channel and it is not found publicly and the parameter σ_i is always kept secured as secret.
  $\sigma_i^* = Rep(SC_i, \vartheta_i)$
  $PW_i^* = h(PW_i||\sigma_i^*)$
  $SC_i^* = h(IP_i||PW_i^*||SCI_i)$
- **Step 03:** Now, we have to match $SC_i^* = SC_i$; if it matches the login process will continue otherwise the login phase will be terminated. [15]

4) Authentication phase:: As we are giving a theoretical model for the authentication protocol, we can unfold the layers of mutual authentication as;

- **Step 01**: We have to mutually authenticate between Doctor and Patient where we have to use Key of the smart card and keys generated between the doctor and patient communication.
  - Step 01: Then authenticating patient and the telecare server with the help of session key, K_{SS}.
  - Step 02: The telecare server reconstructs K using SC_i^* using fuzzy extractor.
  - Step 03: Now, telecare server and the patient is authenticating with the help of K_{DP}.
  - Step 04: Finally mutual authentication of patient and doctor takes place.
- **Step 02**: It is to mutually authenticate between patient and gateway where we use session keys like K_{SG} and K_{SN}.
  - Step 01: Authentication between patient and gateway are taking place in this step firstly using K_{DP}.
  - Step 02: We authenticate gateway and telecare server in this case with the help of K_{SG}
  - Step 03: Then, authenticating server and gateway with help of session key, K_{GS}.
  - Step 04: Lastly we authenticate gateway and patient communication with session key K_{SN}.
- **Step 03**: In this step we authenticate Gateway to the Telecare Server funding on the authentication of patient and doctor as it consists only two steps.
  - Step 01: Authentication between gateway and telecare server with the help of K_{SG}
  - Step 02: We authenticate gateway and telecare server and gateway in this case with the help of K_{GS}
- **Step 04**: Finally, it is to authenticate Doctor, Patient and the gateway altogether so that the data transmission is via a secured channel in real time where using XOR propertice with key K_{USG} for secrecy.

In the next section, the security analysis is depicted according to the factors we aimed to use in our protocol.

V. Security Analysis

A. Formal Security Analysis with BAN logic

Idealized messages:

- M1: $D_i \Rightarrow SC : D_i, SCI_i$
- M2: $SC \Rightarrow D_i : D_i \oplus K, R$
- M3: $D_i \Rightarrow IP_i : D_i \oplus K, R, N_D$
- M4: $IP_i \Rightarrow TS_i : D_i \oplus K, R, N_D, IP_i, N_p$
- M5: $TS_i \Rightarrow IP_i : D_i \oplus K, N_D, IP_i, N_p, K_{USG}$
- M6: $IP_i \Rightarrow D_i : IP_i \oplus K_{USG}, N_P, N_D$

Assumptions:

- D_i believes SC controls K
- SC believes D_i controls SCI_i
- IP_i believes TS_i controls K_{DP}
- R_{GW} believes TS_i controls K_{USG}
- TS_i believes R_{GW} controls K_{GS}

Step 1: Doctor $\Leftarrow\Rightarrow$ Smartcard Authentication

- D_i sees D_i, SCI_i
- D_i believes SC said D_i, SCI_i
- D_i believes fresh SCI_i
- D_i believes SC said $D_i \oplus K, R$

Step 2: Doctor $\Leftarrow\Rightarrow$ Patient Mutual Authentication

- D_i sees D_i, K, R, N_D
- D_i believes fresh N_D
- D_i believes IP_i said $D_i \oplus K, R, N_D$
- IP_i sees $D_i \oplus K, R, N_D$
- IP_i believes fresh N_D
- IP_i believes IP_i said $D_i \oplus K, R, N_D$

Step 3: Patient $\Leftarrow\Rightarrow$ Gateway Mutual Authentication

- IP_i sees IP_i, N_P
- IP_i believes fresh N_P
- D_i believes R_{GW} said IP_i, N_P
- R_{GW} sees IP_i, N_P

Authorized licensed use limited to: DELHI TECHNICAL UNIV. Downloaded on July 20,2023 at 11:09:19 UTC from IEEE Xplore. Restrictions apply.

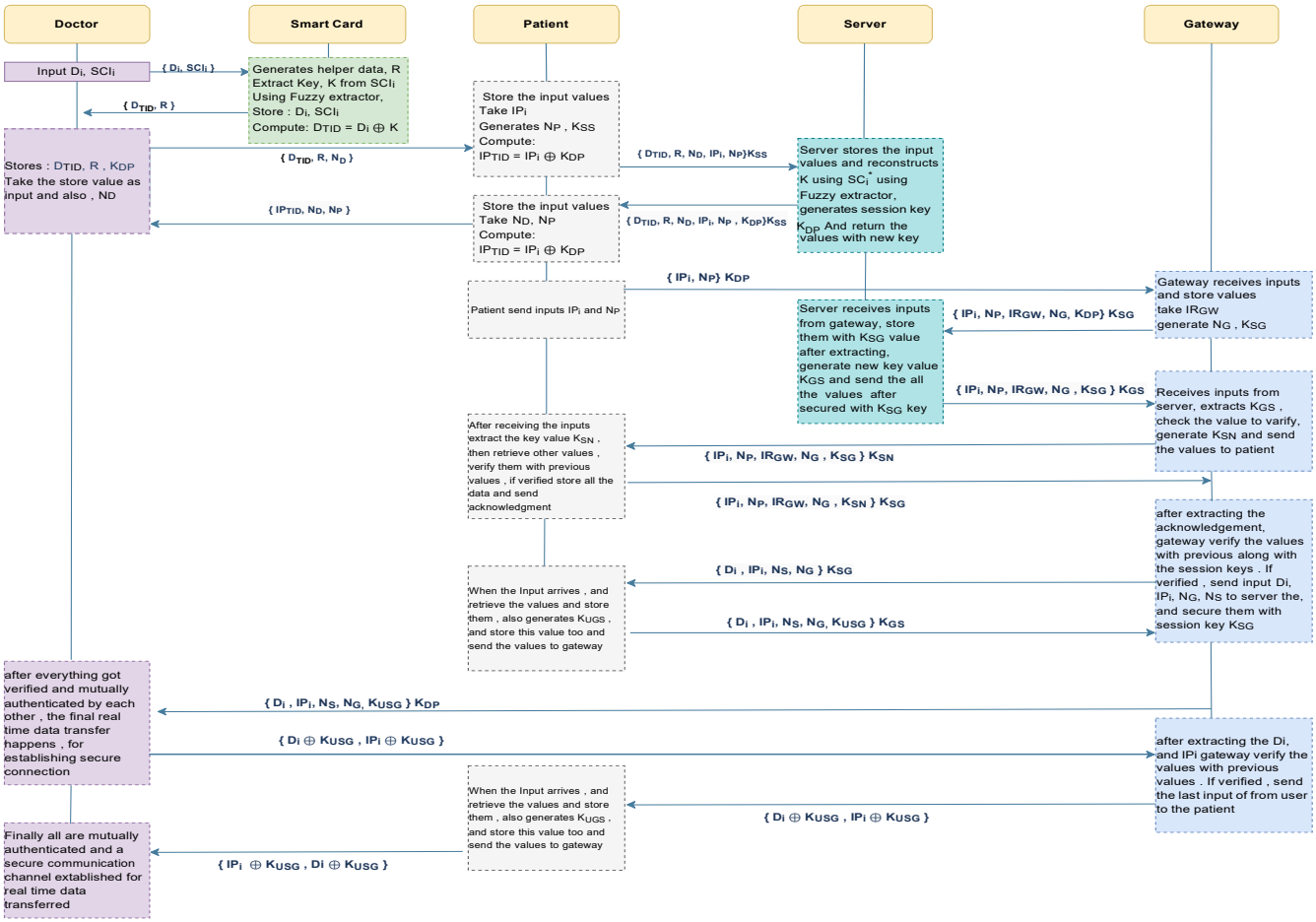

Fig. 4. Authentication Phase

- R_{GW} believes fresh N_P
- R_{GW} believes IP_i said D_i, N_P

Step 4: Gateway $\Longleftrightarrow$ Server Authentication of User and Sensor Node

- R_{GW} sees D_i, IP_i, N_G, N_S
- R_{GW} believes fresh N_P, N_S
- R_{GW} believes TS_i said D_i, IP_i, N_G, N_S
- TS_i sees D_i, IP_i, N_G, N_S
- TS_ibelieves fresh N_G, N_S
- TS_i believes D_i, IP_i, N_G, N_S

Step 5: User, Sensor Node, and Gateway Establish Secure Communication

- D_i sees $IP_i \oplus K_{USG}$, N_P, N_D
- D_i believes fresh K_{USG}
- D_i believes IP_i said $IP_i \oplus K_{USG}$, N_P, N_D
- IP_i sees $IP_i \oplus K_{USG}$, N_P, N_D
- IP_i believes fresh K_{USG}
- IP_i believes D_i said $IP_i \oplus K_{USG}$, N_P, N_D

By employing the session keys K_{USG} andK_{DP} , we can now say that all involved parties - User, Smart card, Sensor Node, Gateway, and Server - have mutually authenticated one another and created secure communication channels.

B. Informal Security Analysis

- Step 01: Without precise knowledge of the smart card imprint SCI_i, an attacker cannot get K. K's key is therefore kept safe.
- Step 02: Only the intended recipients will be able to accurately retrieve the original messages because of encrypted messages using XOR operations in this stage. Without the key K, an attacker cannot recover the original message. Consequently, the patient and the doctor may verify one another.
- Step 03: Using shared keys that are protected against DY attack, all messages are encrypted. Because they cannot decrypt the communications, the attacker is unable to change or insert false messages. Patient and gateway can therefore verify one other's identities.
- Step 04: The messages exchanged in this step are encrypted using XOR operations with K_{UGS} or K_{USN}. The attacker cannot retrieve the original message without knowing the keys K_{UGS}or K_{USN} , ensuring secure communication among doctor, patient, and gateway.

Authorized licensed use limited to: DELHI TECHNICAL UNIV. Downloaded on July 20,2023 at 11:09:19 UTC from IEEE Xplore. Restrictions apply.

C. Computational Cost

There are two fuzzy extractor processes (one for creating R and K and the other for reconstructing K). 10 sessions for encryption and decryption (four encryption and four decryption operations) along with in smartcard and server 2 fuzzy extractor used for key extraction and total 8 Xor function used for secrery maintaining.

Total computational cost: 2 (fuzzy extractor) + 10 (encryption/decryption) + 8 (XOR operation) = 20 operations

This is only the theoretical aspect of calculating computational value and does not consider the actual computational time for each operation, which can vary based on the specific algorithms and hardware used.

TABLE III
A COMPARISON ON COMPUTATIONAL COST

Ref.	Framework/scheme	User / SC	Sensor / Server	Gateway / RC	Total
[1] / 2022	Mutually authenticated cryptograpic protoco	6 T_h	5 T_h	3 T_h	14 T_h
[2] / 2021	ECC-Based Three-Factor Multiserver Authentication Scheme	3 T_{cpm} + 1T_s	2 T_{cpm} + 1T_s	2 T_{cpm} + 2T_s	7 T_{cpm} + 4T_s
[3] / 2016	Decentralized Car-sharing System Using Blockchain	3 T_{cpm} + 13T_h	7 T_{cpm} + T_p + 9T_h	7 T_{cpm} + T_p + 9T_h	17 T_{cpm} +2T_p +31T_h
[4] / 2021	Anonymous Device to Device Access Control based on Secure Certificate	-	-	-	14 T_{cpm} +6T_p +10T_h
[9] / 2020	Signature-Based Mutual Authentication Protocol	-	-	-	59 T_h + 15T_{xor}
[11] / 2018	mutual authentication scheme using smart cards	8 T_h	7 T_h + T_{ex}	-	15 T_h + 1T_{ex}
[12] / 2023	Dynamic Anonymous Authentication Protocol	6 T_h + 2T_s + 2T_{cpm}	4 T_h + 6T_s	2 T_h + 2T_s + 2T_{cpm}	12 T_h +10T_s +4T_{cpm}
[14] / 2022	Signature-Based Authenticated Key Establishment Scheme	5 T_{cpm} + 5T_h	4 T_{cepm} + 3T_h	5 T_{cpm} + 4T_h	14 T_{cpm} + 12T_h
Ours / 2023	Multi-factor Assymetric Key Encryption(MAKE) for Mutual Authentication	1 F_e + 3T_{xor}	6 T_s + 1F_e + 3T_{xor}	4 T_s + 2T_{xor}	10 T_s + 2F_e + 8T_{xor}

T_h = The execution time of a hash function is almost equal to that of symmetric encryption or decryption , T_{cpm} = time for executing elliptic curve scalar point multiplication. T_p = time for performing elliptic curve point addition operation. T_s = time for executing symmetric encryption/decryption operation. T_{ex} = the computational cost of a modular exponent operation, T_{xor} = the computational cost of a XOR operation, T_{pm} = the time for executing a point multiplication operation.

VI. Conclusion and Future Work

An innovative and portable mutual multi-factor authentication technique for Internet of Things applications is put forth in this work. In this study, a theoretical model of a resource-constrained IoT-based digital health networks' lightweight user authentication mechanism is presented. The suggested paradigm is theoretically supported by BAN logic and effective cryptographic primitives for user authentication, such as the one-way hash function, bit-wise XOR, and the nonce. We'll be using AVISPA to implement our model in further work. Up to this point, we have conducted formal and informal analyses as well as comparative security analyses, which show how the suggested protocol is efficient and resilient, making it appropriate for a range of WBAN applications.

References

[1] El-Meniawy, N., Rizk, M. R. M., Ahmed, M. A., Saleh, M., "An Authentication Protocol for the Medical Internet of Things," Symmetry, 14(7), 2022. https://doi.org/10.3390/sym14071483

[2] JWu, T. Y., Yang, L., Lee, Z., Chen, C. M., Pan, J. S., Islam, S. K. H., "Improved ECC-Based Three-Factor Multiserver Authentication Scheme. Security and Communication Networks," 2021. https://doi.org/10.1155/2021/6627956

[3] Kim, M., Lee, J., Park, K., Park, Y., Park, K. H., Park, Y., Design of Secure Decentralized Car-Sharing System Using Blockchain. IEEE Access, 9, pp. 54796–54810, 2021. https://doi.org/10.1109/ACCESS.2021.3071499

[4] Ashraf Chaudhry, S., Irshad, A., Nebhen, J., Kashif Bashir, A., Moustafa, N., Al-Otaibi, Y. D., bin Zikria, Y. (n.d.), "An Anonymous Device to Device Access Control based on Secure Certificate for Internet of Medical Things Systems."

[5] Vaiyapuri, T., Binbusayyis, A., Varadarajan, V. (n.d.). "Related papers Security, Privacy and Trust in IoMT Enabled Smart Healthcare System: A Systematic Review of Current and Future Trends," In IJACSA) International Journal of Advanced Computer Science and Applications, Vol. 12, Issue 2. www.ijacsa.thesai.org

[6] Rahman, M. A., Shamim Hossain, M., Islam, M. S., Alrajeh, N. A., Muhammad, G., "Secure and provenance enhanced internet of health things framework: A blockchain managed federated learning approach," IEEE Access, 8, pp. 205071–205087, 2020. https://doi.org/10.1109/ACCESS.2020.3037474

[7] Pathinarupothi, R. K., Durga, P., Rangan, E. S., "IoT-based smart edge for global health: Remote monitoring with severity detection and alerts transmission," IEEE Internet of Things Journal, 6(2), pp. 2449–2462, 2019. https://doi.org/10.1109/JIOT.2018.2870068

[8] Almulhim, M., Islam, N., Zaman, N., "A Lightweight and Secure Authentication Scheme for IoT Based E-Health Applications," In IJCSNS International Journal of Computer Science and Network Security Vol. 19, Issue 1, 2019.

[9] Binu, S., Misbahuddin, M., Paulose, J., "A Signature-Based Mutual Authentication Protocol for Remote Health Monitoring," SN Computer Science, 1(1), 2020. https://doi.org/10.1007/s42979-019-0010-3

[10] Chanana, R., Singh, A. K., Killa, R., Agarwal, S., Mehra, P. S., "Blockchain Based Secure Model for Sensor Data in Wireless Sensor Network," In 2020 6th International Conference on Signal Processing and Communication (ICSC), pp. 288-293, March-2020, IEEE.

[11] Radhakrishnan, N., Karuppiah, M., "An efficient and secure remote user mutual authentication scheme using smart cards for Telecare medical information systems," Informatics in Medicine Unlocked, 16, 2019. https://doi.org/10.1016/j.imu.2018.02.003

[12] Ding, Z., Xie, Q., "Provably Secure Dynamic Anonymous Authentication Protocol for Wireless Sensor Networks in Internet of Things," Sustainability, 15(7), 5734, 2023. https://doi.org/10.3390/su15075734

[13] Hossain, M. S., "Cloud-supported cyber-physical localization framework for patients monitoring," IEEE Systems Journal, 11(1), pp. 118–127, 2017. https://doi.org/10.1109/JSYST.2015.2470644

[14] Challa, S., Wazid, M., Das, A. K., Kumar, N., Goutham Reddy, A., Yoon, E. J., Yoo, K. Y., "Secure Signature-Based Authenticated Key Establishment Scheme for Future IoT Applications," IEEE Access, 5, pp. 3028–3043, 2017. https://doi.org/10.1109/ACCESS.2017.2676119

[15] S. S. Sahoo, S. Mohanty, and B. Majhi, "A secure three factor based authentication scheme for health care systems using IoT enabled devices," J. Ambient Intell. Humanized Comput., vol. 12, no. 1, pp. 1419–1434, Jan. 2021.

[16] Zhang, L., Zhu, S., "Robust ECC-based Authenticated Key Agreement Scheme with Privacy Protection for Telecare Medicine Information Systems," Journal of Medical Systems, 39(5), pp. 1–11, 2015. https://doi.org/10.1007/s10916-015-0233-3

[17] Masud, M., Gaba, G. S., Choudhary, K., Hossain, M. S., Alhamid, M. F., Muhammad, G., "Lightweight and Anonymity-Preserving User Authentication Scheme for IoT-Based Healthcare," pp. 2649–2656, 2022. https://doi.org/10.1109/JIOT.2021.3080461

[18] Ryu, J., Oh, J., Kwon, D., Son, S., Lee, J., Park, Y., Park, Y., "Secure ECC-Based Three-Factor Mutual Authentication Protocol for Telecare Medical Information System," IEEE Access, pp. 11511–11526, 2022. https://doi.org/10.1109/ACCESS.2022.3145959

[19] Dwivedi, A. K., Mehra, P. S., Pal, O., Doja, M. N., Alam, B., "EETSP: Energy-efficient two-stage routing protocol for wireless sensor network-assisted Internet of Things," International Journal of Communication Systems, 34(17), e4965, 2021.

Authorized licensed use limited to: DELHI TECHNICAL UNIV. Downloaded on July 20,2023 at 11:09:19 UTC from IEEE Xplore. Restrictions apply.

Ageing Research Reviews 90 (2023) 102013

Contents lists available at ScienceDirect

Ageing Research Reviews

journal homepage: www.elsevier.com/locate/arr

Review

New era of artificial intelligence and machine learning-based detection, diagnosis, and therapeutics in Parkinson's disease

Rohan Gupta [a,*], Smita Kumari [a], Anusha Senapati [b], Rashmi K. Ambasta [a], Pravir Kumar [a,**,1,2]

[a] Molecular Neuroscience and Functional Genomics Laboratory, Department of Biotechnology, Delhi Technological, University, USA
[b] Acton Boxborough Regional High School, MA, USA

ARTICLE INFO

Keywords:
Parkinson's disease
Artificial intelligence
Internet of things
Gait abnormalities
Telemedicine systems
Machine learning

ABSTRACT

Parkinson's disease (PD) is characterized by the loss of neuronal cells, which leads to synaptic dysfunction and cognitive defects. Despite the advancements in treatment strategies, the management of PD is still a challenging event. Early prediction and diagnosis of PD are of utmost importance for effective management of PD. In addition, the classification of patients with PD as compared to normal healthy individuals also imposes drawbacks in the early diagnosis of PD. To address these challenges, artificial intelligence (AI) and machine learning (ML) models have been implicated in the diagnosis, prediction, and treatment of PD. Recent times have also demonstrated the implication of AI and ML models in the classification of PD based on neuroimaging methods, speech recording, gait abnormalities, and others. Herein, we have briefly discussed the role of AI and ML in the diagnosis, treatment, and identification of novel biomarkers in the progression of PD. We have also highlighted the role of AI and ML in PD management through altered lipidomics and gut-brain axis. We briefly explain the role of early PD detection through AI and ML algorithms based on speech recordings, handwriting patterns, gait abnormalities, and neuroimaging techniques. Further, the review discuss the potential role of the metaverse, the Internet of Things, and electronic health records in the effective management of PD to improve the quality of life. Lastly, we also focused on the implementation of AI and ML-algorithms in neurosurgical process and drug discovery.

1. Introduction: emergence of AI and ML

The term artificial intelligence (AI) was first introduced by John McCarthy in 1956 to describe machines that can perform cognitive functions, such as learning and problem solving, resembling the human mind. The foundation of AI lies in machine learning (ML), which is a compilation of complex algorithms to perform functions, namely decision-making, speech recognition, and visual perception. With the advent of technology, the implementation of AI in the healthcare industry for disease diagnosis, disease prediction, patient monitoring, and surgery strategies has increased. Further, in today's scenario, the volume of healthcare data is rising exponentially, which can be analyzed with the help of AI. AI enables clinicians and physicians to analyze only clinically relevant information and remove the non-significant information (Fig. 1**a**).

ML algorithms are classified into supervised and unsupervised algorithms. Linear regression, decision tress (DT), random forest (RF), K-nearest neighbor (KNN), support vector machine (SVM), logistic

List of abbreviations: AI, Artificial Intelligence; ML, Machine Learning; AD, Alzheimer's disease; PD, Parkinson's disease; SVM, Support Vector Machine; KNN, K-nearest neighbour; Rf, Random Forests; DT, Decision Tree; MLP, Multiplayer Perceptron; SC, Stacking Classifier; LR, logistic regression; ANN, Artificial Neural Network; DNN, Deep Neural Networks; CNN, Convolutional Neural Networks; ALFF, Amplitude of Low-Frequency Fluctuation; α-Syn, alpha-synuclein; NDDs, Neurodegenerative Disorders; SCFAs, Short-Chain Fatty Acids; EEG, Electroencephalogram; DBS, Deep Brain Stimulations; DL, Deep Learning; SGD, Stochastic Gradient Descent; SG, Smart Gait; IoT, Internet of Things; PTSD, Post-Traumatic Stress Disorder; EHRs, Electric Health Records.

* Correspondence to: Molecular Neuroscience and Functional Genomics Laboratory, Delhi Technological University (Formerly Delhi College of Engineering), Shahbad Daulatpur, Bawana Road, Delhi 110042.

** Correspondence to: Department of Biotechnology, Dean (International Affairs), Molecular Neuroscience and Functional Genomics Laboratory, Delhi Technological University (Formerly Delhi College of Engineering), Shahbad Daulatpur, Bawana Road, Delhi 110042.

E-mail addresses: rohangupta1394@gmail.com (R. Gupta), kpravir@gmail.com, pravirkumar@dtu.ac.in (P. Kumar).

[1] ORCID ID: 0000-0001-7444-2344

[2] Scopus ID: 14831447800

https://doi.org/10.1016/j.arr.2023.102013
Received 29 May 2023; Received in revised form 26 June 2023; Accepted 6 July 2023
Available online 8 July 2023
1568-1637/© 2023 Elsevier B.V. All rights reserved.

regression (LR), neural networks, and Naïve-Bayes are grouped into supervised ML algorithms, whereas, clustering and hidden Markov models are categorized as unsupervised ML algorithms (Sarker, 2021). DT is a predictive modelling method that are built using an algorithmic method that finds ways divide a data set depending on several criteria. A non-parametric supervised learning technique called DT s is utilized for both classification and regression applications. The objective is to learn straightforward decision rules derived from the data characteristics in order to build a model that predicts the value of a target variable (Song, Lu, 2015). KNN depends on computing distances, it is quite sensitive to the quantity of training data. This method does not retrieve results based on presumptions regarding the training set of data (Narayan and Daniel, 2022). In SVM technique the data is classified by plotting the raw data as dots into an n-dimensional (where n represent number of features). Now the data can be easily classified as each feature's value is connected to a specific coordinate. The data may be grouped and displayed on a graph using classifiers (Almansour et al., 2019; Okwuashi and Ndehedehe, 2020). Further, RF due to its great flexibility and simplicity of use, it is one of the most preferred ML algorithms. Compared to the majority of non-linear classifiers, the RF approach is substantially more accurate. Because it generates its output using many decision trees, this method is also quite reliable. Because the RF classifier averages all predictions, eliminating out biases and resolving the overfitting issue, it does not experience the overfitting problem (Bi et al., 2020; Jackins et al., 2021).

Artificial neural networks (ANN) are used in the machine learning subfield known as deep learning (DL). Deep neural networks deep belief networks, recurrent neural networks, and convolutional neural networks are examples of deep learning architectures (Sivaranjini and

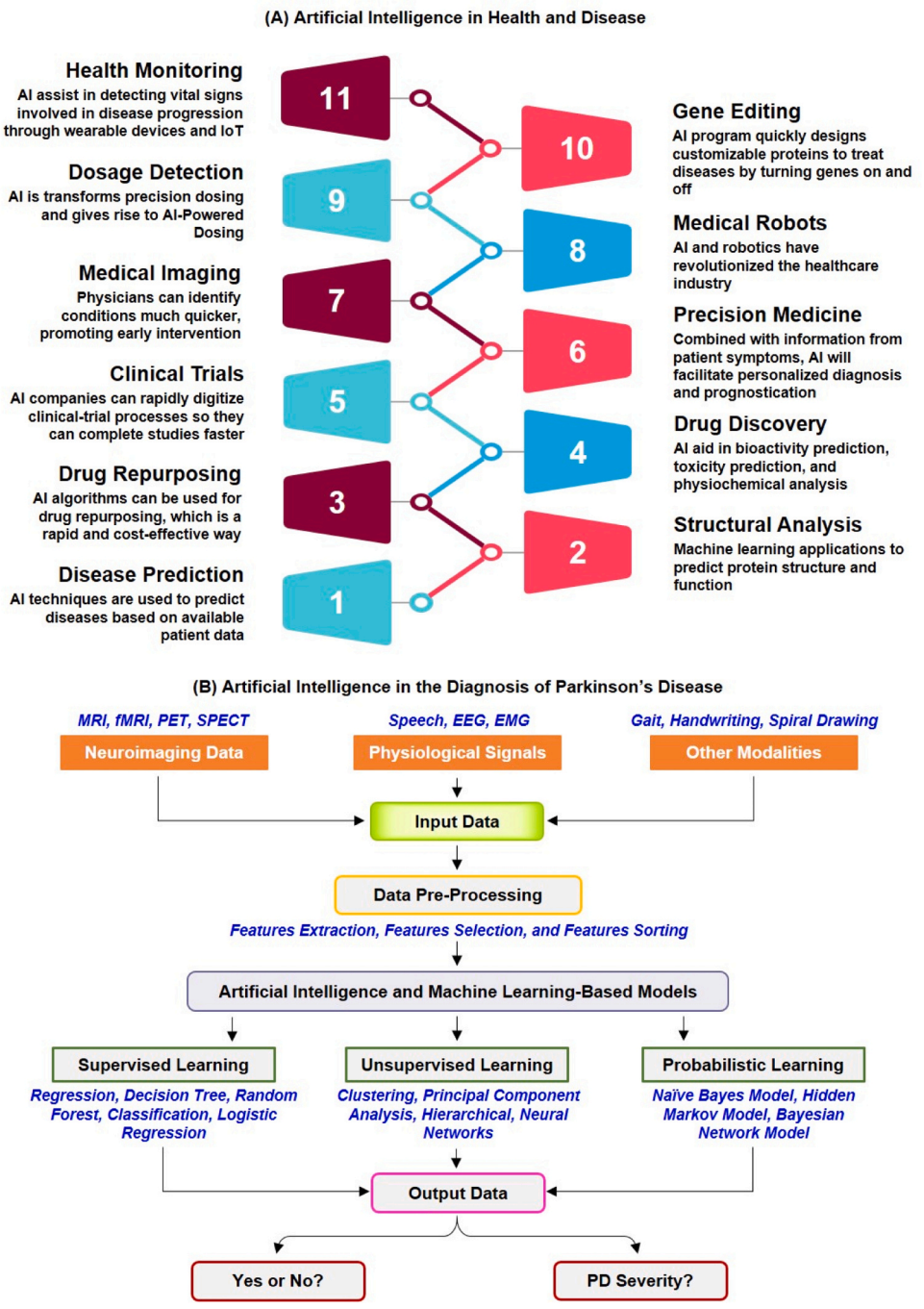

Fig. 1. (A) Artificial intelligence has revolutionized the healthcare sector and shifted towards digital healthcare through health monitoring, dosage detection, medical imaging, clinical trials, drug repositioning, disease prediction, gene editing techniques, medical robots, precision medicine, drug discovery and development, and structural analysis. (B) Neuroimaging data, physiological signal data, gait parameters, handwriting patterns, and spiral drawing parameters are commonly used as input data, which should be pre-processed. Machine learning models, namely supervised learning, unsupervised learning, and probabilistic learning were made using the above-mentioned features that can be used for early diagnosis of Parkinson's disease severity.

Sujatha, 2020). These have found extensive use in a variety of research fields, including speech recognition, natural language processing, audio recognition, computer vision, gaming, and many more. An input layer, a number of hidden layers, and an output layer make up a DNN (Jain et al., 2019). Additionally, the much more complicated design of ANN is defined by the multi-layer perceptron (MLP). It is largely constructed from several perceptron layers. A directed graph connecting the input and output layers of an MLP is made up of many layers of input nodes. Back propagation is used by MLP to train the network (Juanjuan et al., 2020; Martinez-Eguiluz et al., 2023). Further, the Bayesian theorem is the foundation of the probabilistic classifier Naive Bayes. Because the classifier operates under the strong features independence assumption, it is termed naïve (Mostafa et al., 2019; Nancy Noella and Priyadarshini, 2022). Boosting is a class of machine learning techniques that turns weak learners into superior and is a machine learning ensemble meta-algorithm for decreasing bias and variation in reinforcement methods (Nishat et al., 2021). The Boosting technique known as AdaBoost algorithm, sometimes known as Adaptive Boosting, is used as an Ensemble Method in machine learning. The weights are redistributed to each instance, with higher weights being given to instances that were mistakenly categorized, hence the name "adaptive boosting" (Soumaya et al., 2022).

Neurological disorders are complex brain diseases that result in cognitive decline and ultimately lead to death. With the growing population size, the burden of chronic brain diseases has been rising rapidly, impacting the global economy. Further, the diagnosis and management of neurological disease come up with multifaced challenges. However, the involvement of AI in neurological disease diagnosis, treatment, and management has gained a lot of attention in recent years because of its positive outcomes. Currently, neuroscientists and neurologists in collaboration with computer science engineers develop novel tools and algorithms to unravel the complex organization of the brain and the mechanism of neurological diseases, namely Alzheimer's disease (AD), Parkinson's disease (PD), traumatic brain injury, and others. For instance, Sudar et al., 2022 analyzed AD using explainable AI (XAI) using algorithms, such as layer-wise relevance propagation algorithm and convolutional neural network (Sudar et al., 2022). Likewise, Wu et al., 2023 employed XGBoost and SVM mortality prediction in severe traumatic brain injury (Wu et al., 2023).

Moreover, PD is one of the major life-threatening complex diseases of the brain, which is characterized by neuronal cell death. The diagnosis of PD is based on motor symptoms, whereas, non-motor symptoms, such as sleep disorders, attention problems, olfactory dysfunction, and others failed to diagnose PD independently (Mei et al., 2021). Recent years have seen the development and establishment of various tools and algorithms that have been used for the diagnosis of PD, including both motor symptoms and non-motor symptoms (Govindu and Palwe, 2023; Kurbatskaya et al., 2023; Martinez-Eguiluz et al., 2023; Nancy Noella and Priyadarshini, 2022). For example, Mall et al., 2022 predicted early warning signs of PD using web-based ML framework, such as SVM, KNN, RF, DT, MLP, stacking classifier (SC), and LR, which enables patients with PD to easy management of disease with the increase in age (Kumar Mall et al., 2022). Similarly, Rahman et al., 2023 employed python-based ML algorithms, namely DT, XGBoost, SVM, Naïve Bayes, deep neural networks (DNN), and others with an accuracy of over 95% for the classification of PD using speech signals (Rahman et al., 2023). Additionally, Valla et al., 2022 introduced a database, namely DraWritePD for tremor-related differential and angular features-based PD diagnostics (Valla et al., 2022). Alexander et al., 2023 predicted quality of life changes in patients with PD through ANN as web-based application. The authors concluded that the learning model has the potential to rule in patients who may exhibit clinically significant worsening in QoL at 12 months (Alexander et al., 2023).

2. AI and ML framework: a story for diagnosis and treatment of Parkinson's disease

With the increase in healthcare data, the implementation of ML and AI algorithms in healthcare is increasing exponentially. AI and ML algorithms can be used for disease diagnosis, prediction, and treatment (Kohli and Arora, 2018) **(**Fig. 1**b)**. However, it is of utmost importance to design a framework of AI and ML algorithms for effective disease prediction and treatment (S. S. Uddin et al., 2019; M. Uddin et al., 2019). A fundamental framework consists of six steps, namely data acquisition, data visualization, data preprocessing, ML classification algorithms, model tuning, and model evaluation (McArthur et al., 2018). Data acquisition is the most vital step in designing the ML framework for disease prediction, which hampers the model performance (Mishra and Mohapatro, 2019). However, the acquisition of high-quality data for model training remains a huge challenge for AI and ML projects. Liu et al., 2021 constructed a novel system, automatic data acquisition (AutoData) that searches training data automatically within the heterogenous data repository, and ultimately increases the accuracy of the prediction model (Liu et al., 2021). Similarly, Li et al., 2021 proposed two novel strategies for data acquisition, namely estimation and sequential predicate selection to improve the accuracy of AI and ML models (Li et al., 2021). Data visualization helps to understand the data by demonstrating the data in a bar format. It can help in identifying the hidden information in big healthcare data (Kunjir et al., 2017; Olshannikova et al., 2015). However, due to the high demand for data processing, there is a growing need for database experts to improve data visualization methods. The data visualization pipeline includes data import, data preparation, data manipulation, mapping, and rendering (Qin et al., 2020; Zudilova-Seinstra et al., 2008). To date, various data visualization tools have been developed for the diagnosis and treatment of PD. For example, Pun et al., 2016 developed a data mining method for a statistical diagnostic test based on the regression model, which classifies and visualizes the PD through gait data (Pun et al., 2016). Likewise, Oliveira et al., 2018 classified individuals with PD through t-distributed stochastic neighbor embedding for data visualization. The authors implemented the scatter plots from the t-SNE algorithm for patients with normal and abnormal motor behaviors that could be involved in the treatment management (Oliveira et al., 2018). Data preprocessing is considered a crucial step in establishing a pipeline for disease diagnosis and prediction, which ensures effectiveness and transparency in the ML protocol (Gonzalez Zelaya, 2019). Data preprocessing aims to transform the raw data into a prescribed format that can be used for further steps or building an ML framework (Ahmad and Aziz, 2019; Kazmaier and van Vuuren, 2020). Data normalization improves the training time, whereas, data discretization converts the value of the continuous data attributes into a series to prevent the loss of information (Borkin et al., 2019). Further, the development of the ML classification model is the most crucial step in the pipeline, which helps clinicians and physicians to detect the disease at early stages and improves the treatment. Several ML classification models have been employed previously to detect PD, namely SVM, KNN, artificial neural networks (ANN), MLP, and others (Pahuja and Nagabhushan, 2018; Salari et al., 2022). For example, Shi et al., 2022 proposed an SVM-based model that can classify patients with PD and healthy controls through the amplitude of the low-frequency fluctuation (ALFF)-based radiomics method. In the study, the authors selected brain region ROIs and extracted radiomics features based on Brainnetome 246 atlas, including intensity histogram-, texture-, and wavelet transformation-based features (Shi et al., 2022). Pantaleo et al., 2022 developed an ML algorithm-based on RF and XGBoost to classify PD patients and healthy controls (Pantaleo et al., 2022).

Salari et al., 2022 performed a comparative analysis of different ML algorithms among 82 studies for early prediction of PD, where the authors concluded that RF, SVM, and LR have performed best among the other algorithms with an accuracy of approximately 98% (Salari et al.,

2022). Similarly, Yadav and Jain, 2022 performed the comparative analysis of six ML algorithms, such as KNN, LR, SVM, RF, and DT for early prediction of PD. The authors concluded that among the six ML algorithms, KNN performed best with an accuracy of 92.058 and an F-1 score of 94.482 (Yadav and Jain, 2022). Moreover, Valla et al., 2022 proposed a novel ML framework for PD diagnostics, where the authors employed micro-changes in handwriting patterns. In the study, six ML classifiers were used on two datasets, and concluded that a nested wrapper-type feature selection method combined with the ensemble classifiers predicted a disease with an accuracy of 84.33% and 73.71% for DraWritePD and PaHaW, respectively (Valla et al., 2022). Despite having the advantages of ML framework in the classification and treatment of PD, still there is growing need to enhance accuracy of the classifiers, which improves the treatment and diagnostic efficiency.

3. Targeting Parkinson's disease: applications of AI and ML in altered brain homeostasis

3.1. Altered brain lipidomics

Lipids are "bioactive lipids" because they are essential signaling regulators besides being components of cellular membranes. Bioactive lipids serve a significant role in immunological control, inflammation, and homeostasis maintenance (Shimizu, 2009). Due to the BBB's unique regulation of lipid flux, the brain, a lipid-rich organ, has high concentrations of glycerophospholipids, sphingolipids, and cholesterol. Consequently, its dysregulation can result in neurodegenerative disorders (NDDs) like PD (Pifferi et al., 2021). The lipid profile change in alpha-synuclein (α-Syn) mutant models in humans and cells (Avisar et al., 2022). Lipid dysregulation triggers many a-Syn multimerization pathways that result in the generation of Lewis Bodies. Dopaminergic neurons are diminished and cellular death is triggered by Lewis's body development and neuroinflammation. Additionally, neuroinflammation is brought on by elevated levels of oxidative stress as well as higher amounts of ceramides and gangliosides (Castellanos et al., 2021). Lipids play an essential part in oxidative stress, which is a hallmark of many neurodegenerative diseases, through lipid peroxidation (Stern et al., 2016). It might cause acrolein to develop and react with DNA bases. Interesting research has linked neurodegeneration with increased acrolein concentrations (Shamim et al., 2018). Accumulated evidence indicates that immune and nervous systems are thought to interact in a bidirectional manner, and lipids can especially affect the aggregation and spread of numerous pathogenic proteins, which are well-known characteristics of various NDDs, including AD and PD (Chiurchiù et al., 2022). Brain lipidomics has been actively researched in pursuit of possible biomarkers for the development of therapeutic and diagnostic techniques (Czubowicz et al., 2019). Currently, liquid chromatography, gas chromatography-mass spectrometry (GC-MS), or mass spectrometry imaging (MS) are used for measuring several superfamilies of bioactive lipids in the tissues and bodily fluids of patients (Zardini Buzatto et al., 2021). However, in light of the molecular and clinical heterogeneities in neurological conditions, integrated omics, MS, including lipidomics, acts as an essential technique to find reliable biomarkers by examining the interactions between many biological systems (Garcia-Segura et al., 2023; Guan, 2009). Hence, considering lipidomic indicates changes in the genome, transcriptome, and proteome, it is crucial in brain research for bridging the gap between the phenotype and genotype related to the disorder (Yoon et al., 2022). In addition, changes in lipid homeostasis or α-syn formation and aggregation are caused by changes in membrane lipid composition. (Sarchione et al., 2021). Additionally, several recognized PD-risk genes, including parkin (PARK2), leucine-rich repeat kinase 2 (LRRK2), and glucocerebrosidase (GBA), exhibit a pronounced connection with lipid metabolism, notably accumulation of lipids. (Fais et al., 2021). Further, an innovative machine-learning approach is being developed to correlate the lipidome data of PD patients. The broad types of ML techniques are supervised learning, semi-supervised learning, and unsupervised learning. For instance, Lotsch et al.'s 2018 work implemented unsupervised ML (emergent self-organizing feature maps, ESOM/U-matrix approach) on 200 blood plasma samples to find physiologically plausible patterns in high-dimensional biomedical data of both PD or healthy controls (Lötsch et al., 2018). Furthermore, Hila et al., 2021 discovered lipid markers (dihydrosphingomyelin (dhSM), GlcCer, dihydro globotriaosylceramide (dhGB3), and dihydro GM3 ganglioside (dhGM3)) that allow forecasting motor severity in PD employing RF-ML algorithm assisted by traditional statistical approaches (Avisar et al., 2021). However, α-Syn affects the modulation of mitochondrial-associated endoplasmic reticulum membrane activities, which helps to regulate lipid homeostasis in a patient's serum (Guardia-Laguarta et al., 2015). For instance, using an RF algorithm, Avisar et al., 2022 measured 530 lipids in the serum of 22 PD patients bearing the α-Syn mutation (A53T) and 30 healthy controls (Avisar et al., 2022). As discussed above, using ML algorithms to assess lipidomics and metabolomics data in neurodegeneration (as in other domains) is a potential strategy for improving comprehension of these diseases and supporting the development of innovative drugs and therapies **(**Table 1**)** **(**Fig. 2**a)**.

3.2. Dysregulated gut microbiome status

The gut microbiota profoundly influences the brain-gut axis via immunological, neuroendocrine, and direct neuronal pathways (Mulak and Bonaz, 2015). The gut appears to be crucial to the pathophysiology of PD, acting as an entrance point for a potential environmental trigger that could start the pathological process. The etiology of PD may be greatly influenced by the disruption of the brain-gut-microbiota axis (Vascellari et al., 2020). The ability of gut bacteria to produce metabolites such as short-chain fatty acids (SCFAs), that exhibit neuroactive properties, in addition to their capacity to synthesize neurotransmitters such as -amino butyric acid, noradrenaline, and dopamine, influences central processes. (Sherwin et al., 2018). For instance, a study conducted by Aho et al., in 2021 revealed a sex-dependent rise in calprotectin (neutrophil-associated protein) and a decrease in fecal SCFAs in 55 PD patients (Aho et al., 2021). Additionally, the vagus system and the modulation of important dietary amino acids, such as tryptophan, are two avenues via which the gut bacteria and the brain are connected (Sherwin et al., 2018). Numerous research has examined the metabolomics characteristics of PD patients in various biological samples, including cerebrospinal fluid, blood, urine, and feces, and they reveal that altered metabolic rates in PDs are correlated with gut bacteria (Aho et al., 2021; Vascellari et al., 2020). Given their enormous potential as treatments for or preventative measures against neurodegeneration, the use of probiotics, prebiotics, synbiotics, and TLRs modulators seems to be a promising approach (Caputi and Giron, 2018; Lorente-picón and Laguna, 2021). In addition, the science of ML presents the field of PD with previously unheard-of prospects. ML entails the creation and use of computer algorithms that get stronger with utilization, making them suitable building blocks for the categorization of biological data and the identification of biomarkers through a process of training (Pasolli et al., 2016). In a recent study, Pietrucci et al., 2020 processed 846 16 S rRNA gene sequencing microbiota published data sets from six different studies (472 from PD patients and 374 from healthy controls) and used ML algorithms (RF, neural networks, and SVM) in Python 3.6.7 language, using the sci-kit learn package to develop a classifier that could recognize the pathological state of PD patients compared to healthy control (Pietrucci et al., 2020). Besides that, they have found a selected group of 22 bacterial families that were discriminative for the forecasting, and interestingly, not all the families obtained by the algorithm have been reported in the literature **(**Table 1**)**.

The discovery of novel bacterial families that may be crucial in PD status prediction demonstrates the potency of a prediction analysis utilizing ML algorithms (Pietrucci et al., 2020). Further, the researchers who are motivated to undertake predictive research on microbiome data

Table 1
Machine learning-based tools and databases for altered brain lipidomics and gut-microbiome axis.

Name	Utility	Model	Accuracy	Description	Link	References
MetAML	Web-based tool	SVM, RF, Lasso, and ENet	0.963	Assess approaches to metagenomics-based prediction tasks and for quantitative assessment of microbiome-phenotype associations	http://segatalab.cibio.unitn.it/tools/metaml	(Pasolli et al., 2016)
DeepMicro	Python-based application	Deep representation learning	0.803	DeepMicro accelerates the model training and hyperparameter optimization procedure with 8X–30X speedup over the basic approach	https://github.com/minoh0201/DeepMicro	(Oh and Zhang, 2020)
GutBug	Web-based tool	Machine learning, neural networks and chemoinformatic methods	0.97	Tool for prediction of human gut bacteria mediated biotransformation of biotic and xenobiotic molecules using machine learning	https://metabiosys.iiserb.ac.in/gutbug	(Malwe et al., 2023)
Seeker	Web-based tool	LSTM and RNN	0.90	Alignment-free identification of bacteriophage genomes by DL	https://seeker.pythonanywhere.com/	(Auslander et al., 2020)
CHEER	Web-based application	CNN	_	Hierarchical taxonomic classification for viral metagenomic data via DL	https://github.com/KennthShang/CHEER	(Shang and Sun, 2021)
iProbiotics	Web-based tool	SVM	0.98	A machine learning platform for rapid identification of probiotic properties from whole-genome primary sequences	http://bioinfor.imu.edu.cn/iprobiotics/public/	(Sun et al., 2022)
NEURO-LEARN	Web-based tool	SVM, RF, LDA, LR, and KNN	0.917	Integrated framework of machine learning and used the combination of multi-biological data to discriminate patients with SZ from healthy controls	https://github.com/Raniac/NEURO-LEARN	(Ke et al., 2021)
SIAMCAT	R-based app	LASSO	0.96	SIAMCAT (Statistical Inference of Associations between Microbial Composition And host phenoTypes), a comprehensive toolbox for comparative metagenome analysis using ML, statistical modeling, and advanced visualization approaches	https://github.com/zellerlab/siamcat_paper	(Wirbel et al., 2020)
Cronos	R-based app	Clustering	_	A machine learning pipeline for description and predictive modeling of microbial communities over time	https://github.com/Lagkouvardos/Cronos	(Litos et al., 2022)
iPHoP	Web-based tool	RF	0.90	An integrated machine learning framework to maximize host prediction for metagenome-derived viruses of archaea and bacteria	https://bitbucket.org/srouxjgi/iphop	(Roux et al., 2023)
QSRR Automator	————	SVM, MLR, RF, and RBF	0.9942	A tool for automating retention time prediction in lipidomics and metabolomics	https://github.com/UofUMetabolomicsCore/QSSR_Automator	(Naylor et al., 2020)
LipidSig	Web-based tool	Machine learning	_	A web-based tool for lipidomic data analysis	http://chenglab.cmu.edu.tw/lipidsig	(Lin et al., 2021)
ADViSELipidomics	R-based Shiny app	PCA and PLS	_	A workflow for analyzing lipidomics data	https://github.com/ShinyFabio/ADViSELipidomics	(Del Prete et al., 2022)
LipidCCS	Web-based tool	SVR	0.99	Prediction of collision cross-section values for lipids with high precision to support ion mobility–mass spectrometry-based lipidomics	http://www.metabolomics-shanghai.org/LipidCCS/	(Zhou et al., 2017)

use statistical ML techniques such as the LASSO multinomial LR model to forecast phenotypes based on microbial composition (Dong et al., 2020). Furthermore, Y.W. Wang et al. (2020); L. Wang et al. (2020) conducted a comparison of 29 human microbiome data using an elastic net, SVM, RF, and extreme gradient boosting DT (XGBoost). Meanwhile, XGBoost performs better than RF, ENET, and SVM (Wang and Liu, 2020). According to a recent study by Boodaghidizaji et al., in 2023, ML algorithms were used to accurately distinguish between subjects with PD, Crohn's disease, ulcerative colitis, human immunodeficiency virus, and healthy control subjects in the presence and absence of dietary fiber treatments (Boodaghidizaji et al., 2023). However, the association between gut microbes and drug response was also shown. To forecast drug-microbiome interactions in patients, they used ML (McCoubrey et al., 2022). In accordance with mentioned studies, if it is successfully exploited ML might influence the way the pharmaceutical industry and medical professionals perceive the drug-microbiome axis in patient care.

4. AI and ML aid in the identification of novel potential biomarkers in Parkinson's disease

Evidently, there is no set methodology for making the diagnosis of PD, which makes it a challenging and time-consuming task. Finding efficient PD biomarkers has been the subject of numerous investigations (Barcelon et al., 2019). The use of biomarkers that precisely indicate the beginning and course of the pathology may have an enormous effect on the disease's recognition and diagnosis. Therefore, finding clinically relevant biomarkers for the initial clinical phases of PD will not only aid in making clinical diagnoses but also assist in tracking the progression of the disease, allow for personalized therapeutics, and provide an avenue for disease-modifying drugs (Li and Le, 2020). Although biomarkers for the diagnosis of PD have been thoroughly studied, their clinical usefulness currently requires more investigation (Miller and O'Callaghan, 2015). Multiple imaging techniques have been established to provide comprehensive details on the anatomy and functioning of the brain (Algarni and Stoessl, 2016). However, due to the significant expenses and demands on infrastructure, these approaches are difficult to deploy in the clinical setting and have little utility when it comes to routine use for early detection. The best method for facilitating clinical diagnosis has been proposed to be the incorporation of molecular biomarkers that can be identified in the body's fluids. Due to its purported surrogacy to the brain, past research has shown that cerebrospinal fluid is the preferable biofluid for biomarker examinations (Olsson et al., 2016). In a study by Cristina et al., 2018, a panel of markers, including α-syn, S100, and UCHL1, were identified that could help with clinical diagnosis. Aβ42 was shown to be the sole reproducible prospective biomarker while the suggested potential biomarkers lacked robustness and

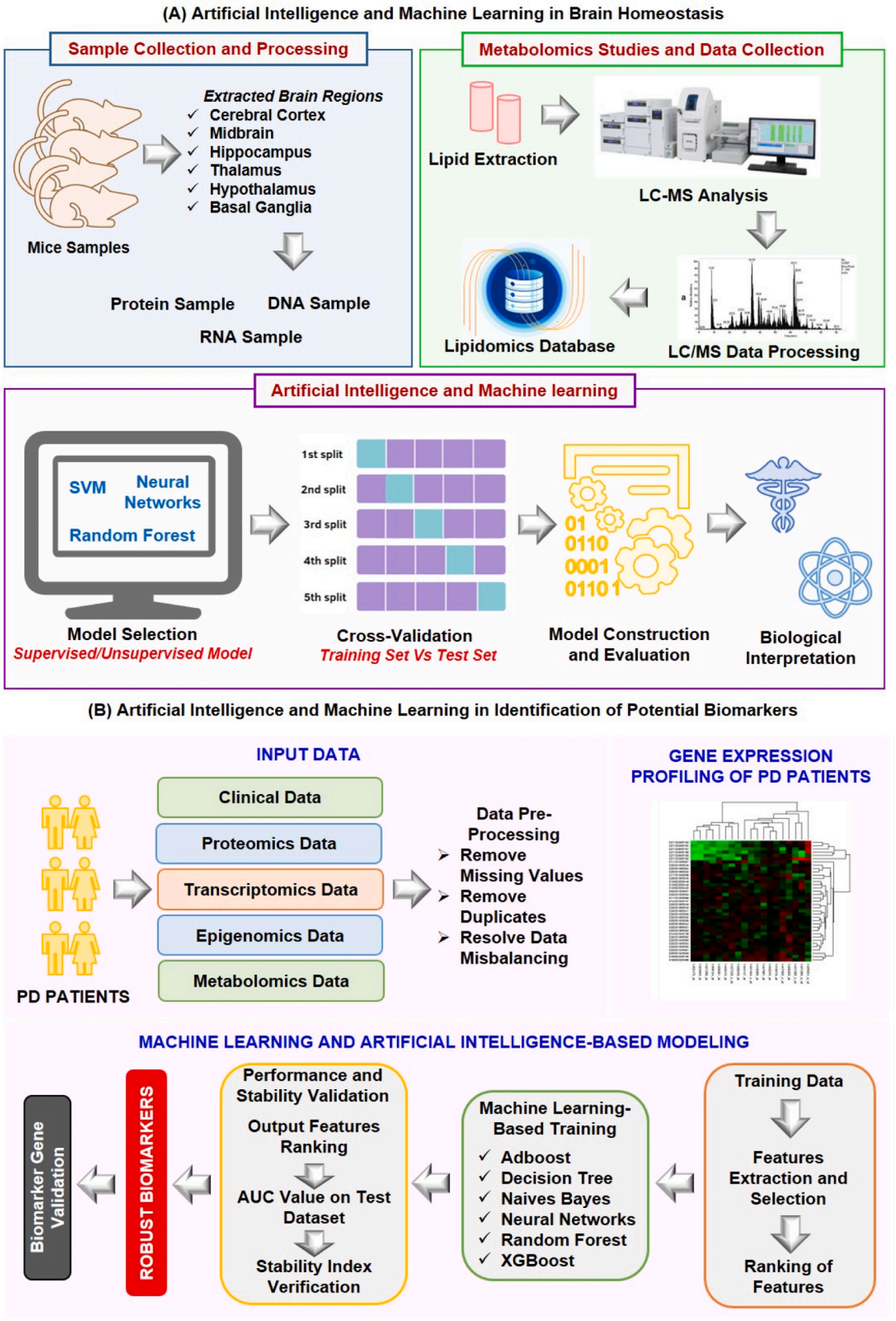

Fig. 2. (A) Altered brain homeostasis is the characteristic feature of Parkinson's disease, which leads to neuronal cell death. Currently, artificial intelligence and machine learning are involved in the progression of Parkinson's disease, which improves motor and non-motor functions through the regulation of brain homeostasis. DNA, RNA, and protein samples were extracted from the mice samples followed by LC-MS analysis. Lipid databases were constructed and machine learning models were constructed followed by cross-validation for biological interpretation. (B) Clinical data, proteomic data, transcriptomics data, epigenomics data, and metabolomics data were pre-processed for gene expression profiling, which should be trained for identifying potential biomarkers involved in the progression of Parkinson's disease.

reproducibility (Dos Santos et al., 2018). Another research team has shown how iMotor, an AI-powered (Neural Network Construction, NNC technique), cloud-based digital platform, can distinguish patients with PD and healthy volunteers by using an array of upper limb functional tests. It can also identify different disease features within a cohort consisting of individuals with PD. The accuracy of the NNC algorithm's discrimination between individual PD patients and healthy volunteers was 93.11%, and its ability to differentiate between ON and OFF states was 76.5% (Tsoulos et al., 2019). In addition, ML algorithms may extract common patterns from large amounts of data in order to assist clinicians in simultaneously identifying patients based on several factors (Landolfi et al., 2021). One strategy employed in the quest for biomarkers is the examination of electroencephalogram (EEG) output characteristics (Coelho et al., 2023). A different team has used ML techniques to investigate the most significant EEG information characteristics that enable patients and controls to be distinguished during visual stimulation. These techniques include LR, DT, SVMs, and extra trees (Vanegas et al., 2019). However, Geraedts et al., 2021 employed an entirely automated EEG-based ML workflow to accurately identify (0.65) deep brain stimulation (DBS) candidates with PD (Geraedts et al., 2021). Additionally, Costantini and colleagues in 2023, examined and distinguished HVs, early, full-blown PD, and L-Dopa treated patients based on the examination of their speech features by utilizing feature-based ML and deep learning (DL) techniques such as KNN, SVM, and naive Bayes classifiers (Costantini et al., 2023). In contrast to previously mentioned studies which uses single regions of interest (ROIs), Peng et al. (2017) have proposed a multilevel-ROIs-features-based ML technique for the identification of morphometric biomarkers of PD with a precision of 85.78%, a specificity of 87.79%, and a sensitivity of 87.64% on brain structure-based MRI images. Further, one of the most common non-motor symptoms of PD is sleep disorders, which have a significant negative impact on quality of life. According to Baumgartner et al., in 2021 DBS in PD demonstrated Basal Ganglia local field potentials as potential biomarkers for sleep disturbance as well as a great signal for an adaptive DBS system that seeks sleep disturbance by ranging activation according to alterations in the sleep-wake state during the night (Baumgartner et al., 2021). In a recent PD Digital Biomarker (PDDB) Challenge, the Dialog for Reverse Engineering Assessments and Methods (DREAM) asked for approaches to precisely diagnose PD in people of all ages using smartphone accelerometers and gyroscope records. For chronic, neurodegenerative diseases like PD, which may be tracked by wearable technology from its motor-related symptoms, in-home digital surveillance is being suggested as a potential solution (Zhang et al., 2020). These techniques offer a very reliable and accurate approach that may support medical examinations and the diagnosis of PD **(**Fig. 2**b)**.

5. AI and ML techniques promote the early detection of Parkinson's disease

Recently, AI has taken over the healthcare industry, especially in medical imaging (Saba et al., 2019; Tandel et al., 2019). The capacity to diagnose a variety of illnesses quickly and reliably has been greatly improved through ML. In recent times, there have been emerged attempts to use AI, particularly ML and DL algorithms, to identify PD early (Alzubaidi et al., 2021). The ML and DL algorithms are susceptible to the sample size when creating training models, and they are further biased by a lack of clinical testing, scientific validation, and big data setup (Jo et al., 2019). Therefore, it is important to ensure that the AI system is trustworthy, accurate, and has less AI bias when PD symptoms are considered as input to the AI model. The possibility of employing ML methods like DT, SVM, LR, ANN, CART, KNN, naive Bayes, etc. to accurately assess the severity of PD, as indicated by clinical measures (Rana et al., 2018). In problems with regression and classification, where existing adjacent characteristics are thought to be related, ANN is most frequently utilized. The ML algorithm uses test data and training datasets. The term "ML" refers to a method that learns from its prior data and advances as a result (Rana et al., 2022). In essence, it is a study of algorithms that produce data automatically. There are two types of ML classifiers: supervised and unsupervised. Labeled data comes within the category of supervised learning, where several techniques are employed to train the model (Rana et al., 2018). With the advancement in technology, multiple criteria have been discussed below that have been set to detect PD **(**Fig. 3**) (**Table 2**).**

5.1. Speech recording to detect Parkinson's disease

Since 90% of people with Parkinson's have speech as well as voice acoustic issues, such as dysphonia dysarthria, and monotone, the first symptom seen in patients with this illness is voice loss, according to several studies done by researchers (Perez et al., 1996; Upadhya and Cheeran, 2018). There is now no known cure for the illness, however, there is some pharmaceutical therapy that can dramatically lessen symptoms, especially in the initial phases. The examination of voice frequency is quick and painless (Bugalho and Viana-Baptista, 2013). Therefore, it is possible to monitor the development of this subjective sickness using voice frequency (Rahn et al., 2007). Many speech trials are being carried out to monitor the disease's course. We may use ML algorithms to identify the pertinent characteristics that aren't often used in the clinical evaluation of PD and rely on these alternative indications to identify the disease in its preclinical stages (Ahlrichs and Lawo, 2013). The identification of this condition typically involves three steps: pre-processing information, retrieving the features, and employing classification techniques. Speech signals are initially classified using time frames in the first phase. Any possible noise is eliminated using the filter approach (Mei et al., 2021). In the following stage, each segment's commonly utilized characteristics are extracted. The classification approaches are used in the final stage. The effectiveness of the classification technique has a big impact on the feature extraction strategy. Hence choosing accurate classification requires special consideration for the detection of this disease (Rana et al., 2022)**.** The authors of a research paper suggested a technique for diagnosing PD utilizing stochastic gradient descent (SGD), RF, LR, DT-ML classifier, Extreme Gradient Boosting (XGB), and KNN (Alzubaidi et al., 2021). To categorize specific features in their study for better comprehension, the authors first extracted them. Feature extraction increases the precision of trained models by extracting characteristics from the input data. This stage reduces the data's dimensionality by eliminating the superfluous records. Naturally, classification is accelerated (Maitín et al., 2020). Selecting and combining variables into features enables the acquisition of the best feature from such big data sets while also drastically lowering the amount of data. These features properly and distinctively describe the actual data set while being straightforward to utilize. To forecast the accuracy rate, they also used certain data mining techniques to categorize the afflicted patients and healthy controls based on different acoustic voice parameters. The health state of PD patients was the goal variable that the authors originally established for this purpose (Ahmed et al., 2021). They updated the data collection column that was utilized as the input after being pulled from the dataset once the target attribute had been defined. The best accuracy result was attained using an RF classifier with a classification accuracy of 97.10%, alongside the least reliability was acquired through SGD as well as LR, with a certainty rate of 91.66% for both classifiers, in the authors' final comparison of all the ML algorithms (Ahmed et al., 2021). In the similar manner, various other studies have been conducted and various datasets are been used to study the detection of PD.

5.2. Techniques based on handwriting pattern

Handwriting requires precise and intricate manual skills as well as a sophisticated blend of cognitive, sensory, and motor abilities. It is an activity that is made up of consecutive actions. This explains how PD sufferers' handwriting displays aberrant characteristics (Seo, 2018). The

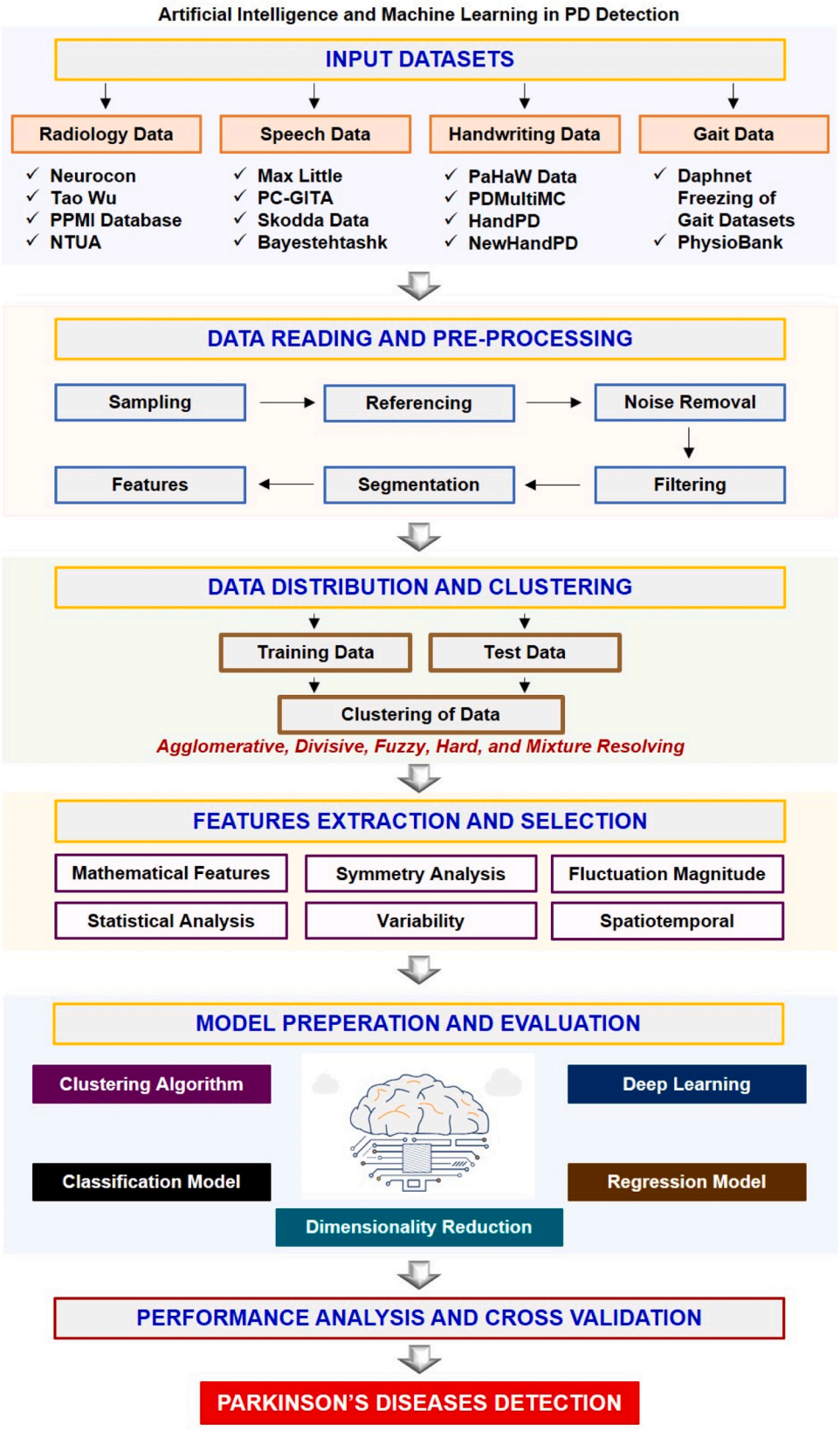

Fig. 3. Machine learning and artificial intelligence-based algorithms have been involved in the detection of Parkinson's disease. Input datasets, namely radiology data, speech data, handwriting data, and gait data were extracted from various databases that were undergone through pre-processing methods, namely sampling, noise removal, segmentation, and features. The processed data were distributed and clustered into training and test data followed by features selection, such as variability, symmetry analysis, and others. Supervised and unsupervised algorithms were applied to construct a model. Once the model is prepared performance evaluations were done to identify the accuracy and precision of the constructed model.

obstacles in the handwriting procedure that PD patients experience are primarily two: bradykinetic movements that are not regular, resulting in longer movement durations, slower speeds and accelerations, and uncertain velocity and acceleration; and challenges associated with the control they have over the movement amplitude, such as failing to maintain the stroke width of the letters constant as the writing advances (Drotár et al., 2013). This is also termed micrographia (McLennan et al., 1972; Teulings et al., 2002). Several research teams have looked at how

Table 2
Artificial intelligence and machine learning-based tools and databases for early detection of Parkinson's disease.

Algorithm	Tool or Software	Data Source	Accuracy	Results	References
Speech Recordings					
Artificial Bee Colony Algorithm	Python-based tool	Mobile device voice recordings at King's College London (MDVR-CKL) dataset	0.96	The proposed auxiliary diagnosis system shows better classification performance on the dataset within limited time and resources	(Wang et al., 2023)
KNN and SVM	Python-based tool	Mobile device voice recordings at King's College London (MDVR-CKL) dataset	0.997	New technique in extracting the features from the voice dataset based on the segmentation of variable speech-signal-segment-durations, i.e., the use of different durations in the segmentation phase	(Yousif et al., 2022)
Gradient Boosting with LASSO and ElasticNet	PD Predict (Web-based Application)	Participants who were 40 years of age and older	0.65 and 0.75	PD Predict is a two-component system: a desktop application that records audio recordings, extracts audio features, and makes predictions; and a server-side web application that implements the machine learning pipelines and processes incoming requests with the extracted audio features to make predictions	(Tougui et al., 2022)
1D and 2D Convolutional neural network	___	German corpus Saarbruecken Voice Database (SVD)	0.93 and 0.84	Implying that a model trained on handcrafted features is better for speech processing than a model that extracts features directly	(Alghamdi et al., 2022)
SVM, KNN, and DT	Python and MATLAB-based framework	756 samples containing 564 PD classes and 192 Healthy classes	0.954	The proposed approach was evaluated using a 10-fold cross-validation technique on a dataset containing PD and normal classes, and a classification accuracy of 95.4% was achieved	(Demir et al., 2022)
Six different machine learning classifiers	Android app	UEX database and mPower-based database	0.92 and 0.71	The results clearly show the potential of the proposed system as an aid for general practitioners to conduct triage or an additional tool for neurologists to perform diagnosis	(Carrón et al., 2021)
XGBoost-a gradient-boosted DT model	Web-based framework	726 unique participants (262 PD and 464 healthy)	0.753	The model performed equally well on data collected in a controlled laboratory environment and in the wild across different gender and age groups	(Rahman et al., 2021)
Light Gradient Boosting	Web-based framework	80 subjects (40 PD and 40 healthy)	0.946–0.955	Machine learning can accurately detect Parkinson's disease using an inexpensive and non-invasive voice recording	(Karabayir et al., 2020)
Convolutional neural network	Web-based framework		0.90	DeepVoice could successfully achieve PD identification with an accuracy of 90.45 ± 1.71% with only a 10-second long audio segment.	(Zhang et al., 2018)
Handwritten Patterns					
Deep neural network	___	Multiple PD handwriting datasets	0.99	The proposed approach achieved excellent PD identification performance with 99.22% accuracy on the illuminated task of combined HandPD, NewHandPD, and Parkinson's Drawing datasets, demonstrating the superiority of our approach over current state-of-the-art methods	(Kamran et al., 2021)
Convolutional neural networks	___	HandPD Dataset	0.98	CNNs can learn relevant information, thus outperforming results obtained from raw data	(Pereira et al., 2017)
Convolutional neural networks	___	204 (102 negatives and 102 positives)	0.87	The model achieved an accuracy of 87% and an F1 score of 83.21%, which outperforms state-of-the-art clinical diagnosis techniques	(Aghzal and Mourhir, 2020)
Optimum-Path Forest, SVM remove, and Naive Bayes	___	76 data for the cube pattern, 80 for the spiral Archimedean pattern, and 85 for the triangle pattern	0.83, 0.96, and 0.85	Machine learning techniques such as Optimum-Path Forest, SVM remove, and Naive Bayes use the dataset to search and learn of the characteristics for the process of classifying individuals distributed into two classes: sick and healthy	(Bernardo et al., 2019)
Gait Parameters					
Machine learning algorithms	___	63 people with PD and 63 matched-control group individuals	0.84	The results showed that the studied ML algorithms have the potential both for PD diagnosis and stage identification by analyzing gait parameters.	(Ferreira et al., 2022)
SVM	___	15 PD patients	0.83	These feature vectors are then individually analyzed to extract the best 7 feature vectors which are then classified using a Gaussian radial basis function kernel-based SVM classifier. Results show that the 7 features selected for SVM achieve good overall accuracy of 83.33%, a good detection rate for PD is 75%, and low false positive results of 16.67%	(Shetty and Rao, 2016)
SVM	Portable device	18 normal subjects and 29 PD subjects.	0.95	A 95% overall classification accuracy has been achieved using a linear decision boundary	(Alkhatib et al., 2020)
SVM, artificial neural network, DT, RF, and KNN	Python and MATLAB-based framework	PD (25 females and 56 males, aged 72.1 ± 6.7 years)	0.87, 0.82, 0.82, 0.81, 0.77	The proposed model could reduce the risk of overrepresenting multicollinear gait features in the model, reducing the risk of overfitting in the test performances while fostering the explainability of the results	(Trabassi et al., 2022)
ANN	Tracking system	76 PD patients	0.82–0.98	The ANN approach enabled automated diagnosis of gait deficits in several symptomatic stages of PD	(Varrecchia et al., 2021)
Neuroimaging Data					

(*continued on next page*)

Table 2 (*continued*)

Algorithm	Tool or Software	Data Source	Accuracy	Results	References
SVM	Matlab and R-based application	FDOPA PET in 44 patients and 14 controls and FDG PET in 51 patients and 16 controls	0.98	Integrating blood metabolomics data combined with PET data considerably enhances the diagnostic discrimination power. Metabolomic signatures also indicate interesting disease-inherent changes in cellular processes, including oxidative stress response and inflammation.	(Glaab et al., 2019)
Linear discriminant analysis	Art toolbox-based framework	67 PD patients	0.88	The model predicts optimal stimulation settings in unseen datasets: a priori clinically optimized and stimulation-naïve PD patients.	(Boutet et al., 2021)
Global graph theoretical metrics	___	18 healthy controls and 19 patients	0.95	Classifier was able to achieve a diagnosis accuracy of ~95% when subjected to a leave-one-out cross-validation test. These features belonged to cuneus (right hemisphere), precuneus (left), superior (right), and middle (both) frontal gyri which were all previously reported to undergo alterations in PD	(Kazeminejad et al., 2018)
Regression	___	238 subjects from the PPMI dataset	0.75–0.80	The results demonstrate that our proposed method is more efficient and achieves promising performance on both longitudinal early diagnosis and clinical scores prediction compared to state-of-the-art methods	(Lei et al., 2023)
SVM	___	400 PD patients and 200 health controls	0.75–0.83	It is anticipated that machine-learning techniques will further help improve the differential diagnosis of parkinsonism and early detection of PD, which may reduce the error rate of PD diagnosis and help detect PD at a pre-motor stage to make it possible for early treatments (e.g., neuroprotective treatment) to slow down PD progression, prevent severe motor symptoms from emerging, and relieve patients from suffering	(Zhang, 2022)

to categorize PD individuals as well as healthy people using handwriting characteristics. In a study paper, a structural Co-occurrence Matrix (SCM)-based method to identify PD was developed. The characteristics used in their study were taken from the Hand PD databases' spiral as well as meander handwriting assessments (Souza et al., 2018). Initially, the examination segmentation is carried out, producing two new images: a handwritten trace and an exam template. These pictures are created by applying digital image processing methods to a handwritten trace. Second, the exam's segmentation is changed to grayscale for the following level. The third step is the extraction of features from the segmented and converted grayscale pictures (Pereira et al., 2016). Integrating the handwritten trace along with the handwriting in spiral style and applying SVM yielded the maximum accuracy (85.54%).

5.3. A model incorporating gait-based datasets

The healthy controls and PD patients of identical age can be classified in a binary manner for the PD identification task. In earlier studies, the efficiency and precision of several gait analysis methods along with algorithms for classification in gait-based detection of PD were examined (L. L. Wang et al., 2020; Y.W. Wang et al., 2020; A. H. Zhao et al., 2022; A. Zhao et al., 2022). The capacity to categorize various neurodegenerative disorders was also investigated by Wang et al. and H. Zhao et al., 2022; A. Zhao et al., 2022 besides this binary detection task. Recently, Guayacán and Martnez, 2021 suggested a 3D CNN model for vision-based systems that used the spatiotemporal saliency maps of RGB pictures as input, and it was successful in achieving 94.1% correctness with 11 PD and 11 healthy controls in the context of LOSO validation (Guayacán and Martínez, 2021). Leveraging the highly precise spatiotemporal as well as kinematic gait metrics acquired by the Mocap system, Park et al., 2021 reported a detection rate of 98.1% (77 PD and 34 healthy controls). As it can be observed, marker-based systems can perform better at PD detection since they can capture human skeletons with high accuracy, but markerless methods may be used in situations with free-living organisms (Park et al., 2021). Further, for PD detection, inertial sensors were additionally thoroughly investigated. Zhang et al. (2020))used a smartphone's 3-axis accelerometer to capture gait data to create a sizable dataset consisting of 656 PD and 2148 healthy controls. Eight IMUs were used by Caramia et al., 2018 to collect spatiotemporal and kinematic gait data, which were then combined with six ML classifiers to achieve an accuracy rate for classification of 96.0% (Caramia et al., 2018). Additionally, vertical GRF data gathered by force sensors may effectively identify the PD gait. But it would be inappropriate to analyze the detection efficacy of various works directly because the algorithms were created using various datasets, individuals, data modalities, and assessment techniques. The short dataset sizes that are typically associated with PD detection present intrinsic difficulties that may make it difficult to create data-driven deep models. It may be simple to gather information from volunteers who are healthy but challenging to gather PD gait data, which may result in an unbalanced distribution of data. Future research should address these issues to develop accurate as well as generalized detection models (Guo et al., 2022).

5.4. Neuroimaging techniques as input data to detect Parkinson's disease

The influence on common structural imaging results is modest until approximately half of the nigral dopamine neurons have been destroyed before the symptoms of PD start to manifest (Braak et al., 2003). As a result, structural imaging has generally proven unsuccessful, while certain more recent MRI methods, such as diffuse tensor imaging as well as shape analysis, show some signs of promise (Stoessl, 2011). The cortical-striatal-pallidal-thalamic-cortical circuitry is significantly functionally impacted by the estimated 80% reduction in striatal DA that occurs before the onset of typical motor symptoms, despite the anatomical alterations being relatively minimal. Therefore, PD is the perfect situation for the use of functional imaging methods (Yoshikawa et al., 2004). Given that a diagnostic imaging test has thus far been unable to replace a clinical diagnosis in cases of established Parkinson's, creating one for pre-clinical or prodromal Parkinson's disorder is a big problem (Barber et al., 2017)v. However, this is a fast-developing subject with enormous near-term promise due to the recent increase in the total amount of prodromal cohorts undergoing examination and the introduction of innovative imaging tools. The numerous imaging techniques that have been researched may be roughly categorized into three methods: the ones which aim for dopaminergic activity in the area of the basal ganglia, those that explicitly scan the substantia nigra, as well as those that evaluate changes in disease-related brain networks (Saeed et al., 2020). Although there is a general association between the

severity of the disease and the intensity of imaging abnormalities, investigations have often been unable to detect a meaningful correlation between the development of motor dysfunction and the development of image markers (Schapira and Olanow, 2004). There is a lot of interest in imaging's potential use as a biomarker to evaluate the impact of possible disease-modifying medications as a result of its potential value in quantitatively assessing the course of dopaminergic dysfunction. There are several neuroimaging biomarkers for PD (Zeighami et al., 2015). However, some biomarkers could be more appropriate for evaluating the neurodegeneration procedure at various PD development stages. About 50% of individuals experiencing idiopathic rapid eye movement sleep behavior disorder (iRBD) have a dopaminergic deficiency, according to PET/SPECT imaging of striatal membrane dopamine transporters (Pont-Sunyer et al., 2017). Although neuroimaging has not provided prominent results in wider scenarios for the detection of PD, with the advents of innovations in science these limitations will diminish and a highly advanced level of data would be present.

6. AI and ML accelerate Parkinson's disease therapeutics

The implication of technological devices in neuroscientific research has been demonstrated by the development of brain augmentation devices, such as nanorobots, which enhance the cognitive abilities of the brain (Saniotis et al., 2018). Nanorobots are AI and ML-based devices that are small in size and would require huge numbers to perform microscopic as well as macroscopic tasks, especially in the medical field (Verma and Chauhan, 2014). For instance, Martins et al., 2012 demonstrated the potential of nanorobotic devices to achieve comprehensive non-destructive real-time in vivo monitoring of the brain (Martins et al., 2012). One of the major applications of nanorobots in the treatment of PD is targeting neural regeneration in dopamine-releasing cells. **(**Fig. 4**a)**.

Moreover, the assessment of gait is one of the most challenging and fruitful parts of the neurological assessment because gait problems are widespread, considerably increase morbidity from falls, and may provide information about illnesses affecting various parts of the nervous system (Society et al., 2001). About 1 in 3 people who live in the community over the age of 60 have an abnormal gait, making it especially common among the elderly. In this demographic, gait problems are linked to lower life satisfaction and nursing home placement, and they may be a sign that dementia is developing in people with moderate cognitive impairment (Mahlknecht et al., 2013). An underlying gait issue may be suggested by a past that includes leg weakness, instability, unsteadiness on one's feet, or numerous falls. Any comprehensive human gait data analysis system that makes use of AI is referred to as "Smart Gait" (SG). It is a developing area of study that benefits from developments in cloud computing, parallel processing, data analytics, current sensing technologies, and the Internet of Things (IoT) (Fang et al., 2019). Further, Gait phase detection, human activity recognition, gait event prediction, fall detection, age recognition, gender recognition, recognition of the walking person's intent and trajectory prediction, estimation of joint angles and moments, authentic person identification, human pose estimation, re-identification, localization, and mapping are some of the most prominent tasks that SG performs (Harris et al., 2022) **(**Fig. 4**b)**. SG is frequently a component of a sophisticated IoT system that includes linked, always-on actuators, monitoring equipment, and AI-enabled sensors. Smart gadgets, smart homes, smart schools, smart automobiles, smart retail, smart cities, and smart energy grids all use SG. Future developments in other technologies including 5 G, sensors, cloud computing, blockchain, and big data, will help the fast-growing field of smart gait study (Sedighi Maman et al., 2020). For research on smart gait, these emerging innovations will also provide new needs and possibilities. The continued focus of SG research will be on user privacy concerns, health data security, patient comfort, workplace worker safety, improved user experience, tiredness monitoring, as well as preventing injuries in sports.

Additionally, Disruption of day-to-day tasks often leads to the difficulties in accessibility of quality healthcare services in remote areas. Further, the unavailability of highly qualified professional healthcare providers also imposes challenges in treating PD. However, the recent COVID pandemic has highlighted the potential of home-based telemedicine in the treatment NDDs, such as AD and PD (Angelopoulou et al., 2023) **(**Fig. 4**c)**. AI and ML-based e-health interventions, such as telecommunications in the diagnosis, monitoring, and treatment of PD prove to be a beneficial strategy that reduces the cost of in-patient visits. Thus, several applications and algorithms have been developed to ease the accessibility of telemedicine in remote areas. For instance, Ahmed and Sankar, 2019 developed an optimized real-time signal re-generator and validator algorithm based on neural networks for biomedical signal transmission and regeneration in a telemedicine environment. The study concluded that the proposed method provides a performance of 1.16 over 767 EEG samples with 0.65 s as an average processing time for the regeneration of signals (Ahmed et al., 2019). Likewise, Ramkumar et al., 2018 provided a motion-based ML software development kit that will likely eliminate the incorporation of the goniometer. The results highlighted that the proposed kit can substitute for a shoulder range of motion examination within 5 degrees of goniometer measurements (Ramkumar et al., 2018). Ahmed and Sandhya, 2018 developed a technique for biomedical recursive image detection, which is based on pixel value density matching with edge extraction (Thouheed Ahmed and Sandhya, 2019). Recently, Kadum et al., 2023 proposed an ML-based telemedicine framework to prioritize remote patients with multi-chronic diseases for emergency healthcare services. The study highlighted that the DT algorithm has the most accurate results as compared to the other relevant algorithms, such as neural networks, SVM, and RF (Kadum et al., 2023) **(**Table 3**)**.

7. Emerging AI and ML-based technologies assisting in the effective management of Parkinson's disease

A longer life expectancy and better therapeutic care have directly contributed to an increase in the number of people with late stages of PD. Although PD pharmaceutical therapy has made significant strides in the past ten years, particularly in the later stages, with time the treatment diminishes its effectiveness, thereby shortening the patient's quality of life and lifetime (Pedersen et al., 2017). A multidisciplinary team is focused on pharmacological therapy for the advanced stages of PD, which is completely different from treatment for the earlier stages and aims to treat critical non-motor symptoms. Even though the current therapeutic recommendations are thorough and accurate, individualized therapy is still advised for each patient (Amjad et al., 2019). This strategy calls for a thorough evaluation of a wide range of resources, including specialist employees, multidisciplinary teams, professional healthcare systems, and coordinated medical treatments. Unluckily, the globe is always experiencing a severe lack of healthcare professionals, and AI-based healthcare innovations have appeared as one of the most potential answers to this issue (Perju-Dumbrava et al., 2022). Currently, a limited but precise range of AI-based applications is present in the industry which is highly beneficial for the diagnosis and treatment of the disease **(**Fig. 5**a)**.

7.1. Decoding metaverse for the intervention of cognitive decline in Parkinson's disease

The implementation of telehealth care in the therapy and study of intellectual developmental problems serves as a paradigm for the application of metaverse technology to intervene in cognitive decline (M. M. Uddin et al., 2019; S. Uddin et al., 2019). "Metaverse" is a cutting-edge, 3D (three-dimensional) internet application and social media platform that has all the characteristics of a manufactured virtual environment. It is anticipated that the service models for the elderly will be rebuilt by including the metaverse's framework in the intervention

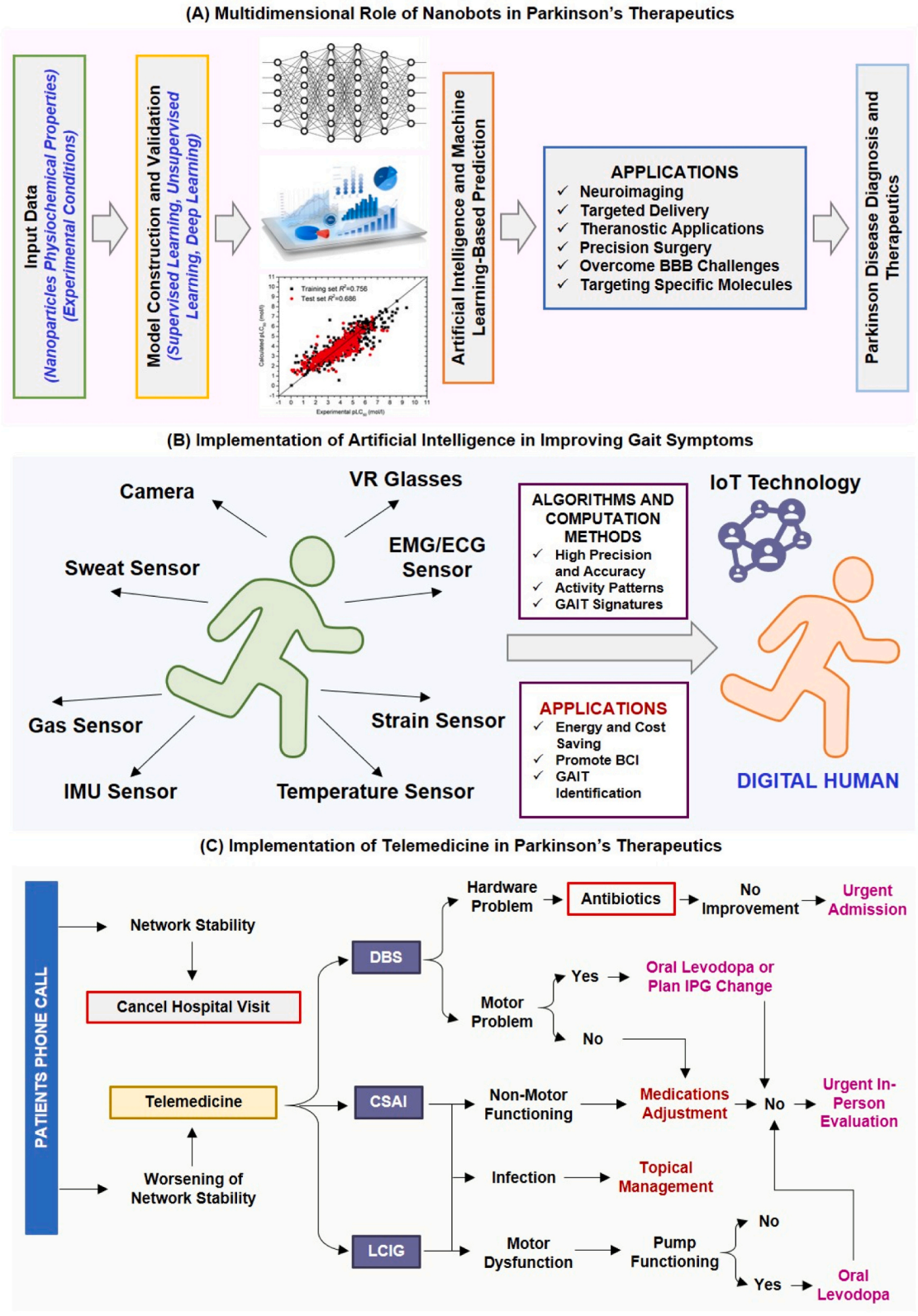

Fig. 4. (A) Discuss the involvement of nanobots in Parkinson's therapeutics. (B) Explain the applicability of artificial intelligence and the Internet of Things in improving GAIT abnormalities through the implementation of sensors and cameras. (C) Recently, telemedicine has emerged as a potential strategy in Parkinson's disease treatment that reduces hospital visits and financial burdens. Telemedicine depends on the network stability of the patient. If the network is stable then cancel the hospital visit otherwise, the patient has gone through the telemedicine procedure.

Table 3
Artificial intelligence and machine learning-based technologies, namely metaverse, Internet of Things, telemedicine, wearable devices, augmented reality, and virtual reality in the management of Parkinson's disease.

Technology	Artificial Intelligence or Machine Learning Model	Outcome Measures	Participants and Duration	Outcomes	References
Telemedicine	AI-based chatbot app; ASR and NLP	Facial expression and voice data	20 PD patients for 5 months	Daily chatbot conversations enhanced smile and speech features in Parkinson's disease	(Ogawa et al., 2022a)
Telemedicine	Automated telephone call service	Answer questions simply by pressing the numbers #1, #2 or #3	104 NDD patients and caregivers, including 27 PD patients and caregivers for 3 months	Suggests that there is a positive effect of using an automated telephone call service for anxiety in neurological disease patients and caregivers	(Ohta et al., 2018)
Telemedicine	Regular visits every two months with intermediate video calls via an iPad mini	Visual analog	10 PD patients for 6 months	Telemedicine was comparable to those of regular, face-to-face visits and suggest that a tablet device, such as an iPad, is a feasible method to administer telemedicine in real-time situations	(Sekimoto et al., 2019)
Telemedicine	Questionnaire	Response to questionnaire	52 PD patients	In a specific cohort in Japan, patients with PD and their caregivers were mostly satisfied with the telemedicine service	(Ogawa et al., 2022b)
Virtual reality	Nintendo Wii Fit	Cognitive skills	16 PD patients for 60 days	The ability of patients with PD to learn, retain and transfer performance improvements after training on the Nintendo Wii Fit depends largely on the demands, particularly cognitive demands, of the games involved	(Mendes et al., 2012)
Virtual reality	VR rehabilitation program	Balance berg scale and dynamic gait index	51 PD patients for 6 consecutive weeks	VR rehabilitation program was more effective in determining overall improvement than the conventional rehabilitation program	(Pazzaglia et al., 2020)
Virtual reality	Home-based virtual reality balance training	Balance berg scale, dynamic gait index, timed Up-and-Go test, and PD questionnaire	23 PD patients for 8 weeks	The training option was effective in improving balance, walking, and quality of life among community-dwelling patients with PD	(Yang et al., 2016)
Virtual reality	Immersive 3D virtual reality-based physiotherapy	Box and block tests shortened unified PD rating scale	20 PD patients	The outcomes of the study demonstrated that the immersive 3D technology may bring increased interest/enjoyment scores resulting in faster and more efficient functional performance (NCT03515746)	(Cikajlo and Peterlin Potisk, 2019)
Virtual reality	VR-based visual perturbation standing balance task	Visual sensory inputs during balance tasks	40 PD patients	The VR-based balance assessment protocol is safe and feasible for use in PD and provides a portable objective measure of balance performance with visual perturbation	(Hawkins et al., 2021)
Virtual reality	VR-graded exercise-based intervention	Trunk and postural control	11 PD patients	The results provide early safety, usability, and feasibility outcomes for VR interventions that require specific trunk excursions	(Stamenkovic et al., 2023)
Augmented reality	AR systems with contactless tracking of the hand and upper body using an AIRO II head-mounted display	Speed and goal-directedness of movements, an adaptation of hand opening to objects	10 PD patients	Implemented three AR games using an optical see-through HMD and contactless hand and body tracking to evaluate key aspects of motor function	(Bank et al., 2018)
Augmented reality	AR visual cues	Improvement in freezing of gait	16 PD patients	The AR visual cues in this study did not reduce FOG, and worsen some measures of axial kinematics, and turn scaling and timing (NTR6409)	(Janssen et al., 2020)
Augmented reality	Mobile dance intervention	Changes in motor functions (balance, mobility) and non-motor functions (mood, quality of life) were evaluated	7 PD patients for 3 weeks	The outcomes of this pilot study suggest that Moving Through Glass, as a mobile dance intervention, may be a safe way to increase physical activity through dance in individuals with PD	(Tunur et al., 2020)
Augmented reality	AR-based game	Improvements in gait and a sense of balance	5 PD patients for 3 weeks	The game was designed to allow patients with PD to ambulate while following virtual visual cues in a real environment as well as incorporated levels with increasing difficulty	(Y. W.L. Wang et al., 2020; Y.W. Wang et al., 2020)
Augmented reality	AR-based dual-task training platform	Feasibility and usability	48 PD patients	Individuals with PD were able to effectively and safely use a head-mounted AR device that provoked dual-task declines. The DART platform provides objective and quantitative outcomes related to gait across a continuum of task difficulty, from simple continuous walking to conditions in which participants are avoiding digital obstacles (NCT04634331)	(Alberts et al., 2022)
Augmented reality	AR-based game	Free hand and body tracking	20 PD patients	Improves the motor dysfunction	(Cidota et al., 2017)

(*continued on next page*)

Table 3 (*continued*)

Technology	Artificial Intelligence or Machine Learning Model	Outcome Measures	Participants and Duration	Outcomes	References
Internet of Things	EMPARK	Medication compliance, sleep and motor function	—	The EMPARK system is a novel home monitoring system for providing patients with PD and the care team with feedback on longitudinal disease activities	(Karni et al., 2022)
Internet of Things	Smart FOG	Pathological speech data	—	The proposed architecture is promising for low-resource machine learning. It could be useful for other applications within wearable IoT for smart telehealth scenarios by translating machine learning approaches from the cloud backend to edge computing devices such as Fog	(Borthakur et al., 2018)
Internet of Things	Fast healthcare interoperability resources platform	Foot pressure data	—	The platform can be used to collect the foot pressure of a large number of Parkinson's patients. Based on the accumulated data, it is possible to identify abnormal behaviors such as walking pattern, tilt, and instability of stride length in patients with PD	(Kim et al., 2017)
Internet of Things	Wearable devices	EEG data	—	This is required for those people who are suffering from this disease and could not able to communicate with another people just because they cannot able to send their signals properly to the brain because they do not get the signals on time because of dead neurons	(Pathak et al., 2020)
Internet of Things	PD remote monitoring architecture	Recording data of edge/fog system	—	An IoT Architecture for CLTM, adaptable in terms of monitoring time and edge configuration. A multi-parameter App for the continuous monitoring of Parkinson's disease patients.	(d'Angelis et al., 2022)
Wearable devices	PDMeter	Assessment of the PD rigidity	7 PD patients	The device allowed to discriminate of both Healthy subjects from PD subjects and PD subjects in OFF condition from PD subjects in ON condition.	(Raiano et al., 2020)
Wearable devices	Wrist-watch-type wearable device	Classification of tremor severity	85 PD patients	It provides a predicted UPDRS with a high accuracy using a wearable device, which is most similar to neurologist-evaluated tremor scores in routine clinical practice using classical rating methods and can effectively be used in a home environment	(Jeon et al., 2017)
Wearable devices	PDMonitor	Evaluation of the PD motor symptom	22 patients and 29 sessions in the pilot study	The studies confirmed the effectiveness of the system as a continuous telemonitoring solution, easy to be used to facilitate decision-making for the treatment of patients with PD	(Antonini et al., 2023)
Wearable devices	Wrist watch-based device	Timed Up and Go test	96 PD patients	In contrast to older adults without PD, most patients with PD utilize the overlapping strategy. Poorer postural and gait control are associated with the strategy choice and with the duration of concurrent performance of turning and sitting	(Weiss et al., 2019)

for cognitive decline (Caldwell et al., 2022). The need for non-face-to-face healthcare developed, and the metaverse's application field expanded, particularly during the worldwide COVID-19 epidemic. The metaverse in education employs metaverse technology in the teaching and learning sectors, while the metaverse in healthcare along with the Metaverse in Medication applies it in the healthcare and medical sectors (Zhou et al., 2022). The medical IoT executed through augmented reality technology via augmented reality glasses or virtual reality glasses is referred to as the "Metaverse in Medicine," according to an Expert Consensus published by the International Association and Alliance of Metaverse in Medicine (IAMM), which identifies 2022 as the first year of the field (Cho et al., 2023). The four categories of the metaverse in medicines that Kye et al., 2021 identified are mirror worlds, augmented reality, virtual reality, and lifelogging (Kye et al., 2021). The bottleneck of early prediction and PD intervention can be overcome thanks to AI technology's trustworthy outcomes in genetic diagnosis along with neuropsychological diagnoses of neurological diseases based on brain development like intellectual disability, depression, and autism (Shivkumar et al., 2021). The metaverse, as well as an algorithm-based platform created for the prevention of cognitive decline, may intervene at an early stage by training the brain, promoting neural function, healing memory loss, and delaying degradation to provide personalized cognitive decline prevention (Shu and Woo, 2023). The better the reasoning, which ensures the capacity for quicker reaction and processing, intending to reestablish fluid intelligence and cognition, the more communication there is among certain brain areas. The game-based platform has been employed in the management of neuropsychological disorders, including PD, post-traumatic stress disorder (PTSD), depression, pain relief, amblyopia improvement, and postponing cognitive deterioration (Riva et al., 2023). In 2015, consultation and therapy for mental diseases through man-machine dialogue were made possible. Virtual reality is a useful rehabilitation technique for neurological conditions including Parkinson's, stroke, and other neuropathic conditions (M. M. Uddin et al., 2019; S. Uddin et al., 2019). The virtual reality platform's sports components are advantageous for enhancing senior people's cognitive capacity. It has been

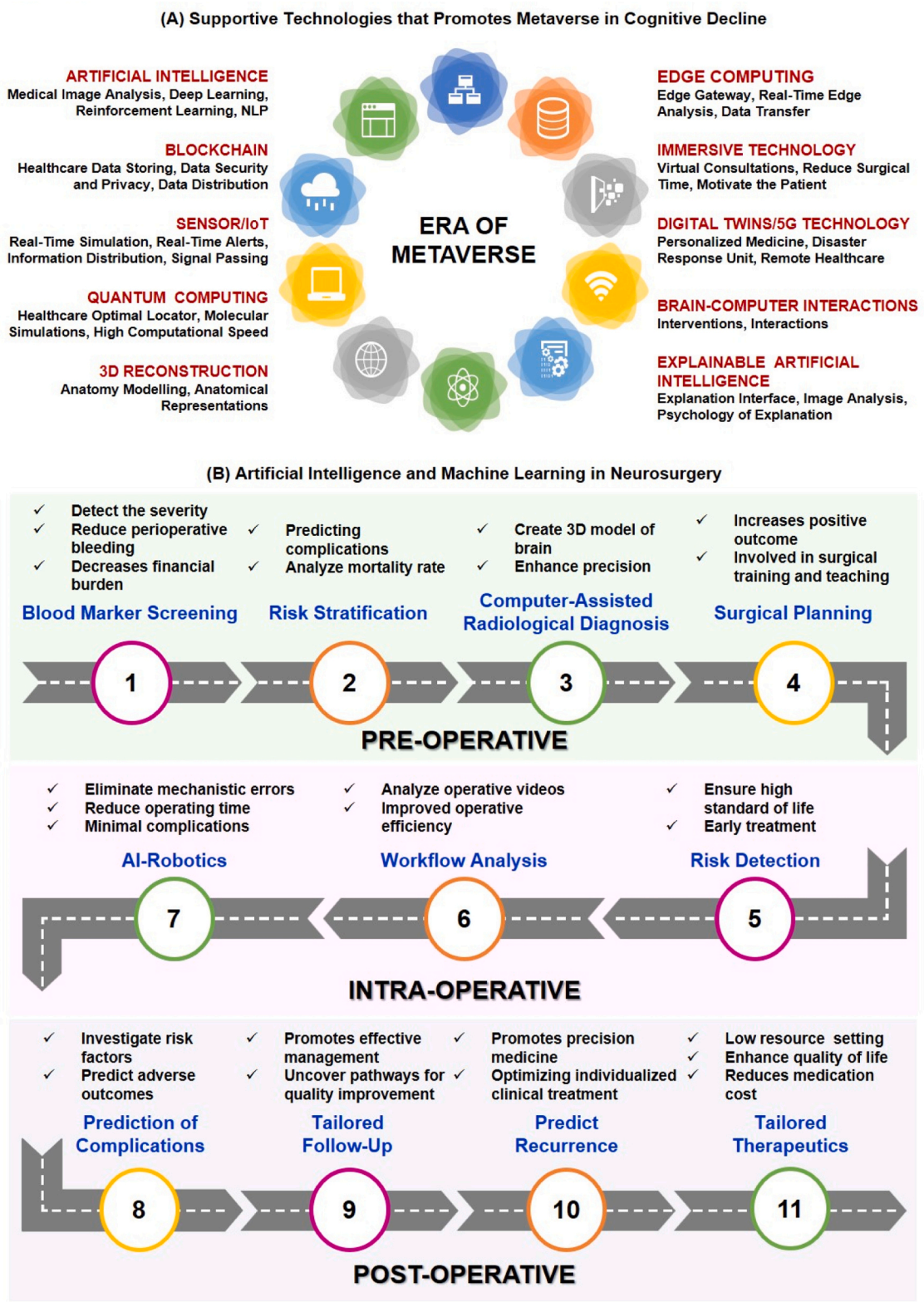

Fig. 5. (A) Metaverse, an emerging Internet of Things has revolutionized the paradigm of Parkinson's therapeutics through improving cognitive functions. (B) Flowchart discusses the involvement of artificial intelligence and machine learning algorithms in different phases of neurosurgery, namely pre-operative, intra-operative, and post-operative.

shown to be an effective strategy. The application of virtual reality in the intervention of cognitive as well as motor functioning in older people with mild cognitive impairment was thoroughly examined by Zhu et al., 2021 The general level of executive function, mental abilities, and focus, have all improved (Zhu et al., 2021) **(**Table 3**).**

7.2. Internet of things: applications of smart assisted devices based on artificial intelligence

AI and IoT or Internet technologies can support equally the phase identification of PD and the monitoring of PD patients. These

technologies aim to develop individualized therapies and evaluate the ones that have been presented, supplementing the well-established conventional approaches (Espay et al., 2016). Additionally, the evaluation of the efficacy of currently prescribed medications, along with the enhancement of surgical treatments, predictability of the course of the disease, and the prevention of negative consequences even in real-time, can be facilitated by preparing ML algorithms based on sensory information obtained from PD patients (Giannakopoulou et al., 2022). These treatments facilitate the shift from clinic-centric to patient-focused medical practices and pave the way for precision therapy in PD and other chronic illnesses (Miele et al., 2020). Lastly, in the COVID-19 pandemic era, the possibilities that come from remote monitoring with the aid of wireless sensors, other wearables, and telemedicine applications may cover the corresponding urgent need and assist PD patients in continuing their medical treatment and care without laying themselves at risk, while simultaneously overcoming the existing spatial and temporal constraints. Inertial sensors and inertial measurement units or IMUs, which include accelerometers, magnetometers, and gyroscopes, in addition to pressure sensors alongside ground reaction force (GRF) plates monitoring features related to PD motor symptoms, make up the great bulk of the deployed sensors (Giannakopoulou et al., 2022; Suzuki et al., 2017). In addition, several additional technologies have been implemented at varying stages of technological maturity, as stated by Monje et al., 2019 For instance, picture, depth, sound, and audio sensors have all been utilized to record both motors as well as non-motor PD signs (Monje et al., 2019). electroencephalography (EEG), electrocardiography (ECG), electromyography (EMG), pain measurement devices, portable sleep measurement devices, temperature sensors, polysomnography (PSG) sensors, heart rate, eye tracking systems, among others, are other deployed sensors that capture various bio-signals (Abou et al., 2021). Finally, to enhance the patient's quality of life, these data sources and the corresponding ML and DL models learned are sometimes incorporated into smartphone applications, conversational agents or chatbots, and serious games, and can be paired with controllers (Little, 2021). Further, due to a lack of resources or the patient's disability, patients also have restricted access to occupational therapists and specialized nurses. It is now possible to continuously monitor PD symptoms at home using new technologies, such as the IoT, in the form of wearable sensors that can record changing disease actions, possibly fatal incidents like falls or gait freezing, or support for the medication strategy (Pasluosta et al., 2015). There is also a possibility that technology-based objective assessments could eventually replace or modify the way illness severity is now assessed and tracked, which mostly relies on patient feedback and clinical scales (Marxreiter et al., 2018) (Table 3).

7.3. Electronic health records and mobile health technologies: shifting the paradigm in Parkinson's care

With an emphasis on PD management, the viewpoint attempts to describe the existing status and probable future development of electronic health records (EHRs) and technical equipment. An interactive and adaptable health data collecting system, like an EHR, is especially helpful for them since the condition necessitates extensive interaction from both patients as well as medical practitioners (Van Uem et al., 2016). The illness also involves a variety of motor symptoms, and since mobile healthcare technology has made significant strides in evaluating movement and mobility, it will eventually be feasible to use applications and devices to evaluate non-motor symptoms as well. All these advancements guarantee an ongoing, pertinent examination of a wide range of PD symptoms without becoming overly taxing (Sánchez-Ferro et al., 2016). Moreover, many health records are now kept on paper and are controlled by medical institutions, many of which have poor communication capabilities. Some medical records have already transitioned from paper charts to EHR, but these EHRs are primarily digital copies of their paper-based forebears and do not include all the technological alternatives that are presently available to help clinical decision-making (Choi et al., 2018). EHRs will be able to interface via clinical data centers that combine data from hospitals and practices, population-based health analytics databases that offer details on disease risk as well as prevention, and digital devices used by the patient who owns the EHR (Althoff et al., 2017). The ability to continuously evaluate illness symptoms and resource usage in the user's everyday surroundings is becoming more and more possible thanks to digital technology, which includes accelerometers, barometers, gyroscopes, galvanic skin resistors, magnetometers, and heart rate monitors. Some of these gadgets, mostly mobile ones, are currently on the market and well-liked, especially when they are created as stylish accessories like watches, flexible forms worn on the arms as well as feet, or components of footwear (Bernhard et al., 2018). The likelihood that individuals will be empowered to input information directly into their personal EHR from various sources is increasing. These sources can include the medical digital systems mentioned above as well as patient-owned "satellite" (mobile) technologies from the fitness and health sector. There will likely be a market for algorithm and app developers where they may contend against third-party applications along with sensor systems on factors like quality, price, value, and user experience (Mandl and Kohane, 2016). It is expected that individuals will soon be able to add or delete information from the EHR just like they can on a smartphone. Regulation of APIs, or application programming interfaces, is required in light of this situation. Two distinct digital systems can communicate with each other through an API, and standardization makes this possible in predictable ways. Such a consistent API is already necessary for US-made EHRs (Maetzler et al., 2016). All things considered, it is predicted that after a few years, most PD patients would utilize a personal EHR together with interchangeable and interoperable technologies that can communicate with this EHR. To improve information about individual illness courses and treatment responses, this combination will enable the incorporation of daily-relevant information by algorithms that remain in development but guarantee the valid evaluation of typical performance (Mandl and Kohane, 2017).

8. Rise of AI and ML-based technologies in neurosurgical care

Over the three decades, the implementation of AI and ML algorithms has been increasing at a rapid pace. Additionally, the digitalization of healthcare and the emergence of big data analytics have provided an enormous amount of both structured and unstructured neuroimaging data, which helps surgeons and clinicians in brain tumor diagnosis and other neurological diseases, especially PD (Schilling et al., 2022). For instance, Hosny et al., 2022 developed a novel DL algorithm for subthalamic nucleus localization from local field potentials in PD patients. The authors employed CNN and KNN classifiers to predict the leave-one patient-out strategy. The results demonstrated that CNN-GA-KNN has tremendous potential to divulge informative features concerning STN taking advantage of a robust feature extraction strategy that combines the repeatability and learnability of GA and KNN (Hosny et al., 2022). Likewise, a study in 2022 processed intraoperative recordings during neurosurgery in patients with PD, where the authors incorporated an ML classifier, namely DT on 36 PD patients that acquired an accuracy of 92.1% (Figliolo Cajal, 2022). Additionally, a systematic review published in 2018 highlighted the importance of ML in neurosurgery to improve decision-making in patient care (Senders et al., 2018). Tonutti et al., 2017 demonstrated the involvement of AI and ML models in real-time modeling of tissue deformation during image-guided neurosurgery, which leads to a low rate of errors and promotes high-patient specificity (Tonutti et al., 2017). Further, AI and ML help in various other tasks, namely tumor segmentation and tumor resection during surgery, which help clinicians and neurosurgeons to carry out successful neurosurgery. For example, Cardone et al., 2023 demonstrated that thermal infrared imaging might be a promising approach for neurosurgeons that leads to the segmentation of tumors, whereas, Siyar et al.,

2020 developed a virtual reality-based tool to design an apprenticeship program to improve performance (Cardone et al., 2023; Siyar et al., 2020). Further, surgical phase recognition is an emerging technology that uses the data from the operative video to train AI and ML models for the identification of different surgical phases (Jumah et al., 2022). Despite the enormous advancements in technology and healthcare, the incorporation of AI and ML algorithms and models, such as surgical robots are still ineffective due to the ethical issues concerned with it and the low success rate. Thus, more research should be done to harness the potential AI and ML algorithms in neurosurgery to improve outcomes and patient response (Fig. 5**b**).

9. Artificial intelligence and machine learning-based drug discovery in Parkinson's disease therapeutics

Currently, the application of AI and ML accelerates the process of drug discovery and development as compared to traditional methods. Further, AI and ML promote the reduction in time and cost of the

Table 4
List of drugs identified against Parkinson's disease through the implication of artificial intelligence and machine learning algorithms.

Name of the drug	Target	Signaling pathway	Input datasets	Artificial intelligence and machine learning model	Outcomes	References
Compound 1, Compound 2, Compound 3, Compound 4, Compound 5	MAO-A and MAO-B	__	Piperine and 57423 compounds were used for the training and testing of the dataset	Deep learning	Integrated MD simulations and free energy calculations revealed that the predicted compounds possessed stronger inhibitory potential than those of the already FDA-approved compounds	(Khan et al., 2019)
Tetrahydrocannabinol (THC)	Dopamine receptors	Dopamine signaling event	Tox21 datasets	Support vector machine	THC may affect dopamine receptors directly and could be useful for Parkinson's disease	(Yucel et al., 2023)
Indolyl-piperazinyl-pyrimidines derivatives	Adenosine A2A and dopamine D2 receptors	Dopamine signaling event	PubChem & MDDR Databases	Support vector machine	Moreover, compound 5 showed improvement in movement and mitigation of the loss of dopaminergic neurons in Drosophila models of PD	
Sulfonamide diuretics (ATC-C03CA)	β2-adrenergic	__	French national health data system and SNDS data	lasso logistic regression	identified several signals that deserve to be confirmed in large studies with appropriate consideration of the potential for reverse causation. The results illustrate the value of ML-based signal detection algorithms for identifying drugs inversely associated with PD risk in health-care databases	(Courtois et al., 2022)
36 repurposed drugs	M1-M5 receptors	__	ChEMBL 30 Database	Dual Structural Activity Landscape Index (D-SALI)	Cheminformatics methods identified 36 polypharmacological chemical scaffolds related to Parkinson's disease	(Michelet et al., 2022)
2007_22057, 2007_22325, 2007_15317	NLRP3	Inflammatory response	TCM Database	3D-QSAR and AI model	The results showed that 2007_22057 (an indole derivative), 2007_22325 (a valine anhydride) and 2007_15317 (an indole derivative) might be a potential medicine formula for the treatment of PD	(Chen et al., 2020)
Dabrafenib	ERK	Apoptosis pathway	GWAS data and 57 FDA-approved drug families	Network biology	suggest that this in silico drug screening system is useful in not only neurodegenerative diseases but also other common diseases such as diabetes mellitus and hypertension	(Uenaka et al., 2018)
5 chemical inhibitors	MAO-B	Apoptosis pathway	ChEMBL database	LR	Five molecules showed a high binding affinity; they are − 10.917, − 10.154, − 10.223, − 10.858, and − 9.629 Kcal/mol, respectively. Additionally, the selected inhibitors were further examined by in vitro activity, and their binding affinity was confirmed using an enzyme-based assay	(Siddiqui et al., 2023)
Amantadine and clonidine	_	_	MEDLINE, PubMed, and PubMed Central (PMC) database	LR, RF, DT, and Naïve Bayes	The proposed strategy was used to mine information pertaining to the mechanisms of disease treatment from known treatment relationships and predict drugs for repurposing against Parkinson's disease. The F1 score of the best-performing method was 0.97, indicating the effectiveness of the proposed approach	(Zhu et al., 2020)
Ponatinib analogs	hERG	hERG channel	In-house datasets	Naïve Bayes	The best compound exhibited a hERG IC50 of 12.1 μM (compared to nilotinib with an IC50 of 0.45 μM and ponatinib with an IC50 of 0.767 μM)	(Kaiser et al., 2020)
DHP-CCB blockers	_	aSyn oligomerization	IBM MarketScanâ Research Databases	IBM Watson for Drug Discoveryâ (WDD)	Computational approach can efficiently identify leads for disease-modifying drugs. Identified the combination of ARBs and DHP-CCBs as of particular interest in PD	(Visanji et al., 2021)

traditional drug discovery and development process (Vamathevan et al., 2019). ML and AI approaches provide a set of tools and algorithms that enable improved decision-making processes and minimize the reduction in data errors. Additionally, AI and ML-based procedures increase the speed of the process and minimize the failure rates (Dara et al., 2021). In neurological diseases, such as AD, PD, and others, drug discovery is considered as a major challenging event to inhibit the formation of misfolded protein aggregates. However, mounting evidence has highlighted the crucial involvement of AI and ML-based models to accelerate drug development. For instance, Kulkarni et al., identified alkaloid inhibitors of PD-associated proteins through computer-aided methods. The authors found out that metergoline, pipercallosine, hookerianamide J, and lobeline as effective POP inhibitors against PD through molecular docking and molecular dynamic simulation studies (Kulkarni et al., 2021). Likewise, Visanji et al., 2020 incorporated an AI model to identify putative anti-hypertensives as possible disease-modifying agents. The authors demonstrated that the combination of angiotensin receptor II blockers (ARBs) and dihydropyridine calcium channel blockers and angiotensin converting enzyme inhibitors might recue neuronal loss in PD (Visanji et al., 2021). Table 4 discuss the potential PD modifying drug candidates that are identified through AI and ML algorithms and tools.

10. Discussion: current limitations, challenges, and future perspectives

PD is one of the deadliest diseases of the brain, which is characterized by the loss of neuronal cells leading to memory impairment and synaptic dysfunction (Azam et al., 2021). PD is also recognized by tremors that are associated with the symptoms, such as movement problems, speaking and writing pattern changes, and walking disabilities (Greenland and Barker, 2018). The diagnosis of PD is based on either motor symptoms or non-motor symptoms. Motor system disorder consists of bradykinesia, rigidity, postural instability, and tremor, whereas, non-motor system dysfunctions include urinary dysfunction, depression, psychosis, apathy, and sleep disorders (Cahill and Huang, 2021). To date, the first line of defense against PD is dopamine replacement through oral administration of levodopa or carbidopa. Additionally, alternative treatment regimens have been also proposed, such as complementary and alternative medicine and integrative medicine strategies to improve brain conditions (Ahlskog, 2011; Hall and Church, 2020; Manyam, 2007). Apart from the pharmacological interventions, moderation in lifestyle also improve cognitive function that might prevent the occurrence of PD or improve the quality of life (Ellis and Rochester, 2018; Paillard et al., 2015). Other treatment options that might be beneficial in the treatment of patients with PD are rehabilitation, surgery, maintenance, and restorative therapy. However, despite the advancements in therapeutic approaches, the overall rescue rate of PD is still low due to early diagnosis and detection. Further, the availability of novel biomarkers in patients with PD possess a hindrance to the treatment strategy. Further, managing PD in day-to-day life also imposes issues, which are very difficult for an individual to manage. Thus, to overcome the challenges faced by clinicians and physicians in the treatment of patients with PD, researchers or clinicians across the globe have shifted towards the implementation of AI and ML-based tools, algorithms, and devices to support patients with PD that might improve the quality of life. AI and ML algorithms have been involved in a screening procedure, especially, where there is no need for physical evaluation. For example, Makarious et al., 2022 developed a novel tool, namely GenoML to improve the prediction of PD based on multi-model data. The authors concluded that the proposed model is best for identifying a large group of individuals to monitor (Makarious et al., 2022). Likewise, Dadu et al., 2022 incorporated supervised and unsupervised ML algorithms on clinical data to identify patient subtypes and disease progression (Dadu et al., 2022). Further, AI and ML methods can be applied to additional features of PD, namely speech recordings and neuroimaging pictures to predict PD progression and diagnosis. For instance, Zhao et al., acquired diffusion-weighted images were acquired from a 3 T scanner to build a DL-based model with an accuracy of 94.1% to distinguish PD patients and healthy controls (H. A. Zhao et al., 2022; H. Zhao et al., 2022). Similarly, Hires et al., 2022 applied CNN on 50 healthy people and 50 people with PD obtained from PC-GITA to detect PD from voice recordings (Hireš et al., 2022). Moreover, recent years have witnessed the implication of AI-based machines, such as nanobots, virtual reality and augmented reality-based appliances, telemedicine, and others that are involved in the diagnosis, detection, and treatment of PD patients to enhance the quality of life (Cubo and Delgado-López, 2022). A recent survey has highlighted that using the telemedicine system enhances satisfaction among patients with PD (Ogawa et al., 2022b). A systematic review and meta-analysis studies have confirmed the positive results of virtual reality-based balance training in patients with PD (Wu et al., 2022). The advent of AI and ML has beneficial effects on the treatment and management of PD. However, every technology comes with several limitations and challenges, yet the involvement of AI and ML is no apart from it, and issues such as accuracy, precision, and dependency still need to be resolved. This review highlighted the different aspects of AI and ML in the management of PD that provide valuable insights and guidelines for future progress.

CRediT authorship contribution statement

Conceived and designed by P.K. and R.G. Materials collected and artwork done by R.G., S.K., and A.S. Critical evaluation and analysis of data done by R.K.A., R.G., and PK. Manuscript written by R.G., S.K., A.S., R.K.A., and P.K. All authors read the manuscript and agreed to submit.

Declaration of Competing Interest

The authors declare that there is no conflict of interest.

Data Availability

No data was used for the research described in the article.

Acknowledgment

We would like to thank the senior management of Delhi Technological University for their constant support and guidance.

References

Abou, L., Peters, J., Wong, E., Akers, R., Dossou, M.S., Sosnoff, J.J., Rice, L.A., 2021. Gait and balance assessments using smartphone applications in parkinson's disease: a systematic. Rev. J. Med. Syst. 45. https://doi.org/10.1007/S10916-021-01760-5.

Aghzal, M., Mourhir, A., 2020. Early diagnosis of Parkinson's disease based on handwritten patterns using deep learning. 4th Int. Conf. Intell. Comput. Data Sci. ICDS 2020. https://doi.org/10.1109/ICDS50568.2020.9268738.

Ahlrichs, C., Lawo, M., 2013. Parkinson's disease motor symptoms in machine learning: a review. Heal. Inform. - Int. J. 2. https://doi.org/10.5121/hiij.2013.2401.

Ahlskog, J.E., 2011. Cheaper, simpler, and better: tips for treating seniors with Parkinson disease. Mayo Clin. Proc. 86, 1211–1216. https://doi.org/10.4065/MCP.2011.0443.

Ahmad, T., Aziz, M.N., 2019. Data preprocessing and feature selection for machine learning intrusion detection systems. ICIC Express Lett. 13, 93–101. https://doi.org/10.24507/ICICEL.13.02.93.

Ahmed, I., Aljahdali, S., Khan, M.S., Kaddoura, S., 2021. Classification of Parkinson disease based on patient's voice signal using machine learning. Intell. Autom. Soft Comput. 32, 705–722. https://doi.org/10.32604/IASC.2022.022037.

Ahmed, S.T., Sandhya, M., Sankar, S., 2019. An optimized RTSRV machine learning algorithm for biomedical signal transmission and regeneration for telemedicine environment. Procedia Comput. Sci. 152, 140–149. https://doi.org/10.1016/J.PROCS.2019.05.036.

Aho, V.T.E., Houser, M.C., Pereira, P.A.B., Chang, J., Rudi, K., Paulin, L., Hertzberg, V., Auvinen, P., Tansey, M.G., Scheperjans, F., 2021. Relationships of gut microbiota, short-chain fatty acids, inflammation, and the gut barrier in Parkinson's disease. Mol. Neurodegener. 16, 1–14. https://doi.org/10.1186/s13024-021-00427-6.

Alberts, J.L., Kaya, R.D., Scelina, K., Scelina, L., Zimmerman, E.M., Walter, B.L., Rosenfeldt, A.B., Alberts, J.L., Kaya, R.D., Scelina, Kathryn, Scelina, Logan, Zimmerman, E.M., Walter, B.L., Rosenfeldt, Anson B., 2022. Digitizing a therapeutic: development of an augmented reality dual-task training platform for Parkinsons

disease, 8756 Sensors 2022 Vol. 22 (22), 8756. https://doi.org/10.3390/S22228756.
Alexander, T.D., Nataraj, C., Wu, C., 2023. A machine learning approach to predict quality of life changes in patients with Parkinson's Disease. Ann. Clin. Transl. Neurol. 10, 312–320. https://doi.org/10.1002/ACN3.51577.
Algarni, M.A., Stoessl, A.J., 2016. The role of biomarkers and imaging in Parkinson's disease. Expert Rev. Neurother. 16, 187–203. https://doi.org/10.1586/14737175.2016.1135056.
Alghamdi, N.S., Zakariah, M., Hoang, V.T., Elahi, M.M., 2022. Neurogenerative disease diagnosis in cepstral domain using MFCC with deep learning. Comput. Math. Methods Med 2022. https://doi.org/10.1155/2022/4364186.
Alkhatib, R., DIab, M.O., Corbier, C., Badaoui, M.El, 2020. Machine learning algorithm for gait analysis and classification on early detection of parkinson. IEEE Sens. Lett. 4 https://doi.org/10.1109/LSENS.2020.2994938.
Almansour, N.A., Syed, H.F., Khayat, N.R., Altheeb, R.K., Juri, R.E., Alhiyafi, J., Alrashed, S., Olatunji, S.O., 2019. Neural network and support vector machine for the prediction of chronic kidney disease: a comparative study. Comput. Biol. Med. 109, 101–111. https://doi.org/10.1016/J.COMPBIOMED.2019.04.017.
Althoff, T., Sosič, R., Hicks, J.L., King, A.C., Delp, S.L., Leskovec, J., 2017. Large-scale physical activity data reveal worldwide activity inequality, 547 Nat 2017 (5477663), 336–339. https://doi.org/10.1038/nature23018.
Alzubaidi, M.S., Shah, U., Dhia Zubaydi, H., Dolaat, K., Abd-Alrazaq, A.A., Ahmed, A., Househ, M., 2021. The role of neural network for the detection of Parkinson's disease: a scoping review. Healthc. (Basel, Switz.) 9. https://doi.org/10.3390/HEALTHCARE9060740.
Amjad, F., Bhatti, D., Davis, T.L., Oguh, O., Pahwa, R., Kukreja, P., Zamudio, J., Metman, L.V., 2019. Current practices for outpatient initiation of levodopa-carbidopa intestinal gel for management of advanced parkinson's disease in the United States. Adv. Ther. 36, 2233–2246. https://doi.org/10.1007/S12325-019-01014-4/TABLES/2.
Angelopoulou, E., Stanitsa, E., Fragkiadaki, S., Kontaxopoulou, D., Pavlou, D., Papatriantafyllou, I., Papageorgiou, S.G., 2023. Telemedicine in neurodegenerative diseases: opportunities and challenges. Arch. Hell. Med. 92–101.
Antonini, A., Reichmann, H., Gentile, G., Garon, M., Tedesco, C., Frank, A., Falkenburger, B., Konitsiotis, S., Tsamis, K., Rigas, G., Kostikis, N., Ntanis, A., Pattichis, C., 2023. Toward objective monitoring of Parkinson's disease motor symptoms using a wearable device: wearability and performance evaluation of PDMonitor®. Front. Neurol. 14, 721. https://doi.org/10.3389/FNEUR.2023.1080752.
Auslander, N., Gussow, A.B., Benler, S., Wolf, Y.I., Koonin, E.V., 2020. Seeker: alignment-free identification of bacteriophage genomes by deep learning. e121–e121 Nucleic Acids Res 48. https://doi.org/10.1093/NAR/GKAA856.
Avisar, H., Guardia-Laguarta, C., Area-Gomez, E., Surface, M., Chan, A.K., Alcalay, R.N., Lerner, B., 2021. Lipidomics prediction of Parkinson's disease severity: a machine-learning analysis. J. Park. Dis. 11, 1141. https://doi.org/10.3233/JPD-202476.
Avisar, H., Guardia-Laguarta, C., Surface, M., Papagiannakis, N., Maniati, M., Antonellou, R., Papadimitriou, D., Koros, C., Athanassiadou, A., Przedborski, S., Lerner, B., Stefanis, L., Area-Gomez, E., Alcalay, R.N., 2022. Lipid level alteration in human and cellular models of alpha synuclein mutations. npj Park. Dis. 8. https://doi.org/10.1038/s41531-022-00313-y.
Azam, S., Haque, M.E., Balakrishnan, R., Kim, I.S., Choi, D.K., 2021. The ageing brain: molecular and cellular basis of neurodegeneration. Front. Cell Dev. Biol. 9, 2120. https://doi.org/10.3389/FCELL.2021.683459/BIBTEX.
Bank, P.J.M., Cidota, M.A., Ouwehand, P., (Elma), W., Lukosch, S.G., 2018. Patient-tailored augmented reality games for assessing upper extremity motor impairments in Parkinson's disease and stroke. J. Med. Syst. 42, 1–11. https://doi.org/10.1007/S10916-018-1100-9/FIGURES/5.
Barber, T.R., Klein, J.C., Mackay, C.E., Hu, M.T.M., 2017. Neuroimaging in pre-motor Parkinson's disease. NeuroImage. Clin. 15, 215–227. https://doi.org/10.1016/J.NICL.2017.04.011.
Barcelon, E.A., Mukaino, T., Yokoyama, J., Uehara, T., Ogata, K., Kira, J. ichi, Tobimatsu, S., 2019. Grand total EEG Score Can Differentiate Parkinson's disease from parkinson-related disorders. Front. Neurol. 10. https://doi.org/10.3389/FNEUR.2019.00398.
Baumgartner, A.J., Kushida, C.A., Summers, M.O., Kern, D.S., Abosch, A., Thompson, J. A., 2021. Basal ganglia local field potentials as a potential biomarker for sleep disturbance in Parkinson's disease. Front. Neurol. 12, 1–13. https://doi.org/10.3389/fneur.2021.765203.
Bernardo, L.S., Quezada, A., Munoz, R., Maia, F.M., Pereira, C.R., Wu, W., de Albuquerque, V.H.C., 2019. Handwritten pattern recognition for early Parkinson's disease diagnosis. Pattern Recognit. Lett. 125, 78–84. https://doi.org/10.1016/J.PATREC.2019.04.003.
Bernhard, F.P., Sartor, J., Bettecken, K., Hobert, M.A., Arnold, C., Weber, Y.G., Poli, S., Margraf, N.G., Schlenstedt, C., Hansen, C., Maetzler, W., 2018. Wearables for gait and balance assessment in the neurological ward - study design and first results of a prospective cross-sectional feasibility study with 384 inpatients. BMC Neurol. 18, 1–8. https://doi.org/10.1186/S12883-018-1111-7/TABLES/1.
Bi, X.A., Hu, X., Wu, H., Wang, Y., 2020. Multimodal data analysis of Alzheimer's Disease based on clustering evolutionary random forest. IEEE J. Biomed. Heal. Inform. 24, 2973–2983. https://doi.org/10.1109/JBHI.2020.2973324.
Boodaghidizaji, M., Jungles, T., Chen, T., Zhang, B., Landay, A., 2023. Machine learning based gut microbiota pattern and response to fiber as a diagnostic tool for chronic inflammatory diseases 1–15.
Borkin, D., Némethová, A., Michaľconok, G., Maiorov, K., 2019. Impact of data normalization on classification model accuracy. Res. Pap. Fac. Mater. Sci. Technol. Slovak Univ. Technol. 27, 79–84. https://doi.org/10.2478/RPUT-2019-0029.
Borthakur, D., Dubey, H., Constant, N., Mahler, L., Mankodiya, K., 2018. Smart fog: fog computing framework for unsupervised clustering analytics in wearable Internet of Things. 2017 IEEE Glob. Conf. Signal Inf. Process. Glob. 2017 - Proc. 2018 (January), 472–479. https://doi.org/10.1109/GLOBALSIP.2017.8308687.
Boutet, A., Madhavan, R., Elias, G.J.B., Joel, S.E., Gramer, R., Ranjan, M., Paramanandam, V., Xu, D., Germann, J., Loh, A., Kalia, S.K., Hodaie, M., Li, B., Prasad, S., Coblentz, A., Munhoz, R.P., Ashe, J., Kucharczyk, W., Fasano, A., Lozano, A.M., 2021. Predicting optimal deep brain stimulation parameters for Parkinson's disease using functional MRI and machine learning, 12 Nat. Commun. 2021 (121), 1–13. https://doi.org/10.1038/s41467-021-23311-9.
Braak, H., Del Tredici, K., Rüb, U., De Vos, R.A.I., Jansen Steur, E.N.H., Braak, E., 2003. Staging of brain pathology related to sporadic Parkinson's disease. Neurobiol. Aging 24, 197–211. https://doi.org/10.1016/S0197-4580(02)00065-9.
Bugalho, P., Viana-Baptista, M., 2013. REM sleep behavior disorder and motor dysfunction in Parkinson's disease–a longitudinal study. Park. Relat. Disord. 19, 1084–1087. https://doi.org/10.1016/J.PARKRELDIS.2013.07.017.
Cahill, C., Huang, X., 2021. Treatment options for motor and non-motor symptoms of Parkinson's disease, 11 Biomol 2021 Vol. 11 (612), 612. https://doi.org/10.3390/BIOM11040612.
Caldwell, A.B., Liu, Q., Zhang, C., Schroth, G.P., Galasko, D.R., Rynearson, K.D., Tanzi, R. E., Yuan, S.H., Wagner, S.L., Subramaniam, S., 2022. Endotype reversal as a novel strategy for screening drugs targeting familial Alzheimer's disease. Alzheimers Dement. 18, 2117–2130. https://doi.org/10.1002/ALZ.12553.
Caputi, V., Giron, M.C., 2018. Microbiome-gut-brain axis and toll-like receptors in parkinson's disease. Int. J. Mol. Sci. 19. https://doi.org/10.3390/ijms19061689.
Caramia, C., Torricelli, D., Schmid, M., Munoz-Gonzalez, A., Gonzalez-Vargas, J., Grandas, F., Pons, J.L., 2018. IMU-based classification of Parkinson's disease from gait: a sensitivity analysis on sensor location and feature selection. IEEE J. Biomed. Heal. Inform. 22, 1765–1774. https://doi.org/10.1109/JBHI.2018.2865218.
Cardone, D., Trevisi, G., Perpetuini, D., Filippini, C., Merla, A., Mangiola, A., 2023. Intraoperative thermal infrared imaging in neurosurgery: machine learning approaches for advanced segmentation of tumors. Phys. Eng. Sci. Med 46, 325–337. https://doi.org/10.1007/S13246-023-01222-X/TABLES/3.
Carrón, J., Campos-Roca, Y., Madruga, M., Pérez, C.J., 2021. A mobile-assisted voice condition analysis system for Parkinson's disease: assessment of usability conditions. Biomed. Eng. Online 20. https://doi.org/10.1186/S12938-021-00951-Y.
Castellanos, D.B., Martín-Jiménez, C.A., Rojas-Rodríguez, F., Barreto, G.E., González, J., 2021. Brain lipidomics as a rising field in neurodegenerative contexts: Perspectives with Machine Learning approaches. Front. Neuroendocr. 61. https://doi.org/10.1016/j.yfrne.2021.100899.
Chen, Z.D., Zhao, L., Chen, H.Y., Gong, J.N., Chen, X., Chen, C.Y.C., 2020. A novel artificial intelligence protocol to investigate potential leads for Parkinson's disease. RSC Adv. 10, 22939–22958. https://doi.org/10.1039/D0RA04028B.
Chiurchiù, V., Tiberi, M., Matteocci, A., Fazio, F., Siffeti, H., Saracini, S., Mercuri, N.B., Sancesario, G., 2022. Lipidomics of bioactive lipids in Alzheimer's and Parkinson's diseases: where are we? Int. J. Mol. Sci. 23. https://doi.org/10.3390/IJMS23116235.
Cho, K.H., Park, J.B., Kang, A., 2023. Metaverse for exercise rehabilitation: possibilities and limitations. Int. J. Environ. Res. Public Health 20. https://doi.org/10.3390/IJERPH20085483.
Choi, K., Gitelman, Y., Asch, D.A., 2018. Subscribing to your patients — reimagining the future of electronic health records. N. Engl. J. Med 378, 1960–1962. https://doi.org/10.1056/NEJMP1800874/SUPPL_FILE/NEJMP1800874_DISCLOSURES.PDF.
Cidota, M.A., Lukosch, S.G., Bank, P.J.M., Ouwehand, P.W., 2017. Towards engaging upper extremity motor dysfunction assessment using augmented reality games. Adjun. Proc. 2017 IEEE Int. Symp. Mix. Augment. Real., ISMAR-Adjun. 2017, 275–278. https://doi.org/10.1109/ISMAR-ADJUNCT.2017.88.
Cikajlo, I., Peterlin Potisk, K., 2019. Advantages of using 3D virtual reality based training in persons with Parkinson's disease: a parallel study. J. Neuroeng. Rehabil. 16, 1–14. https://doi.org/10.1186/S12984-019-0601-1/FIGURES/7.
Coelho, B.F.O., Massaranduba, A.B.R., Souza, C.A., dos, S., Viana, G.G., Brys, I., Ramos, R.P., 2023. Parkinson's disease effective biomarkers based on Hjorth features improved by machine learning. Expert Syst. Appl. 212, 118772 https://doi.org/10.1016/J.ESWA.2022.118772.
Costantini, G., Cesarini, V., Leo, P. Di, Amato, F., Suppa, A., Asci, F., Pisani, A., Calculli, A., Saggio, G., 2023. Deep-Learning Comparison.
Courtois, É., Nguyen, T.T.H., Fournier, A., Carcaillon-Bentata, L., Moutengou, É., Escolano, S., Tubert-Bitter, P., Elbaz, A., Thiébaut, A.C.M., Ahmed, I., 2022. Identifying protective drugs for Parkinson's disease in health-care databases using machine learning. Mov. Disord. 37, 2376–2385. https://doi.org/10.1002/MDS.29205.
Cubo, E., Delgado-López, P.D., 2022. Telemedicine in the management of parkinson's disease: achievements, challenges, and future perspectives, 1735 Brain Sci. 2022 Vol. 12 (12), 1735. https://doi.org/10.3390/BRAINSCI12121735.
Czubowicz, K., Jęśko, H., Wencel, P., Lukiw, W.J., Strosznajder, R.P., 2019. The role of ceramide and sphingosine-1-phosphate in Alzheimer's disease and other neurodegenerative disorders. Mol. Neurobiol. 56, 5436–5455. https://doi.org/10.1007/s12035-018-1448-3.
d'Angelis, O., Di Biase, L., Vollero, L., Merone, M., 2022. IoT architecture for continuous long term monitoring: Parkinson's Disease case study. Internet Things 20, 100614. https://doi.org/10.1016/J.IOT.2022.100614.
Dadu, A., Satone, V., Kaur, R., Hashemi, S.H., Leonard, H., Iwaki, H., Makarious, M.B., Billingsley, K.J., Bandres-Ciga, S., Sargent, L.J., Noyce, A.J., Daneshmand, A., Blauwendraat, C., Marek, K., Scholz, S.W., Singleton, A.B., Nalls, M.A., Campbell, R. H., Faghri, F., 2022. Identification and prediction of Parkinson's disease subtypes

and progression using machine learning in two cohorts. npj Park. Dis. https://doi.org/10.1038/s41531-022-00439-z.
Dara, S., Dhamercherla, S., Jadav, S.S., Babu, C.M., Ahsan, M.J., 2021. Machine learning in drug discovery: a review. Artif. Intell. Rev. 1947–1999. https://doi.org/10.1007/S10462-021-10058-4.
Del Prete, E., Campos, A.M., Della Rocca, F., Gallo, C., Fontana, A., Nuzzo, G., Angelini, C., 2022. ADViSELipidomics: a workflow for analyzing lipidomics data. Bioinformatics 38, 5460–5462. https://doi.org/10.1093/BIOINFORMATICS/BTAC706.
Demir, F., Siddique, K., Alswaitti, M., Demir, K., Sengur, A., 2022. A simple and effective approach based on a multi-level feature selection for automated Parkinson's disease detection. J. Pers. Med 12, 55. https://doi.org/10.3390/JPM12010055.
Dong, M., Li, L., Chen, M., Kusalik, A., Xu, W., 2020. Predictive analysis methods for human microbiome data with application to Parkinson's disease. PLoS One 15, 1–18. https://doi.org/10.1371/journal.pone.0237779.
Dos Santos, M.C.T., Scheller, D., Schulte, C., Mesa, I.R., Colman, P., Bujac, S.R., Bell, R., Berteau, C., Perez, L.T., Lachmann, I., Berg, D., Maetzler, W., Da Costa, A.N., 2018. Evaluation of cerebrospinal fluid proteins as potential biomarkers for early stage Parkinson's disease diagnosis. PLoS One 13, 1–17. https://doi.org/10.1371/journal.pone.0206536.
Drotár, P., Mekyska, J., Smékal, Z., Rektorová, I., Masarová, L., Faundez-Zanuy, M., 2013. Prediction potential of different handwriting tasks for diagnosis of Parkinson's. 2013 E-Health Bioeng. Conf. EHB 2013. https://doi.org/10.1109/EHB.2013.6707378.
Ellis, T., Rochester, L., 2018. Mobilizing Parkinson's disease: the future of exercise. J. Park. Dis. 8, S95–S100. https://doi.org/10.3233/JPD-181489.
Espay, A.J., Bonato, P., Nahab, F.B., Maetzler, W., Dean, J.M., Klucken, J., Eskofier, B.M., Merola, A., Horak, F., Lang, A.E., Reilmann, R., Giuffrida, J., Nieuwboer, A., Horne, M., Little, M.A., Litvan, I., Simuni, T., Dorsey, E.R., Burack, M.A., Kubota, K., Kamondi, A., Godinho, C., Daneault, J.F., Mitsi, G., Krinke, L., Hausdorff, J.M., Bloem, B.R., Papapetropoulos, S., 2016. Technology in Parkinson's disease: challenges and opportunities. Mov. Disord. 31, 1272–1282. https://doi.org/10.1002/MDS.26642.
Fais, M., Dore, A., Galioto, M., Galleri, G., Crosio, C., Iaccarino, C., 2021. Parkinson's disease-related genes and lipid alteration. Int. J. Mol. Sci. 22. https://doi.org/10.3390/IJMS22147630.
Fang, J., Wang, T., Li, C., Hu, X., Ngai, E., Seet, B.C., Cheng, J., Guo, Y., Jiang, X., 2019. Depression prevalence in postgraduate students and its association with gait abnormality. IEEE Access 7, 174425–174437. https://doi.org/10.1109/ACCESS.2019.2957179.
Ferreira, M.I.A.S.N., Barbieri, F.A., Moreno, V.C., Penedo, T., Tavares, J.M.R.S., 2022. Machine learning models for Parkinson's disease detection and stage classification based on spatial-temporal gait parameters. Gait Posture 98, 49–55. https://doi.org/10.1016/j.gaitpost.2022.08.014. ISSN 0966-6362.
Figliolo Cajal, C., 2022. Processing of intraoperative recordings during Subthalamic Nucleus Deep Brain Stimulation Neurosurgery in patients with Parkinson Disease.
Garcia-Segura, M.E., Durainayagam, B.R., Liggi, S., Graça, G., Jimenez, B., Dehghan, A., Tzoulaki, I., Karaman, I., Elliott, P., Griffin, J.L., 2023. Pathway-based integration of multi-omics data reveals lipidomics alterations validated in an Alzheimer's disease mouse model and risk loci carriers. J. Neurochem. 164, 57–76. https://doi.org/10.1111/jnc.15719.
Geraedts, V.J., Koch, M., Contarino, M.F., Middelkoop, H.A.M., Wang, H., van Hilten, J. J., Bäck, T.H.W., Tannemaat, M.R., 2021. Machine learning for automated EEG-based biomarkers of cognitive impairment during Deep Brain Stimulation screening in patients with Parkinson's Disease. Clin. Neurophysiol. 132, 1041–1048. https://doi.org/10.1016/J.CLINPH.2021.01.021.
Giannakopoulou, K.M., Roussaki, I., Demestichas, K., 2022. Internet of things technologies and machine learning methods for Parkinson's disease diagnosis, monitoring and management: a systematic review. Sens. (Basel) 22. https://doi.org/10.3390/S22051799.
Glaab, E., Trezzi, J.P., Greuel, A., Jäger, C., Hodak, Z., Drzezga, A., Timmermann, L., Tittgemeyer, M., Diederich, N.J., Eggers, C., 2019. Integrative analysis of blood metabolomics and PET brain neuroimaging data for Parkinson's disease. Neurobiol. Dis. 124, 555–562. https://doi.org/10.1016/J.NBD.2019.01.003.
Gonzalez Zelaya, C.V., 2019. Towards explaining the effects of data preprocessing on machine learning. Proc. - Int. Conf. Data Eng. 2019-April 2086–2090. https://doi.org/10.1109/ICDE.2019.00245.
Govindu, A., Palwe, S., 2023. Early detection of Parkinson's disease using machine learning. Procedia Comput. Sci. 218, 249–261. https://doi.org/10.1016/J.PROCS.2023.01.007.
Greenland, J.C., Barker, R.A., 2018. The differential diagnosis of Parkinson's disease. Neurology 43, S1–S11. https://doi.org/10.15586/CODONPUBLICATIONS.PARKINSONSDISEASE.2018.CH6.
Guan, Z., 2009. Discovering novel brain lipids by liquid chromatography/tandem mass spectrometry. J. Chromatogr. B. Anal. Technol. Biomed. Life Sci. 877, 2814–2821. https://doi.org/10.1016/J.JCHROMB.2009.03.002.
Guardia-Laguarta, C., Area-Gomez, E., Schon, E.A., Przedborski, S., 2015. A new role for α-synuclein in Parkinson's disease: Alteration of ER-mitochondrial communication. Mov. Disord. 30, 1026–1033. https://doi.org/10.1002/MDS.26239.
Guayacán, L.C., Martínez, F., 2021. Visualising and quantifying relevant parkinsonian gait patterns using 3D convolutional network. J. Biomed. Inf. 123, 103935 https://doi.org/10.1016/J.JBI.2021.103935.
Guo, Y., Yang, J., Liu, Y., Chen, X., Yang, G.Z., 2022. Detection and assessment of Parkinson's disease based on gait analysis: a survey. Front. Aging Neurosci. 14, 837. https://doi.org/10.3389/FNAGI.2022.916971/BIBTEX.
Hall, M.F.E., Church, F.C., 2020. Integrative medicine and health therapy for Parkinson disease. Top. Geriatr. Rehabil. 36, 176–186. https://doi.org/10.1097/TGR.0000000000000278.
Harris, E.J., Khoo, I.H., Demircan, E., 2022. A survey of human gait-based artificial intelligence applications. Front. Robot. AI 8, 370. https://doi.org/10.3389/FROBT.2021.749274/BIBTEX.
Hawkins, K.E., Paul, S.S., Chiarovano, E., Curthoys, I.S., 2021. Using virtual reality to assess vestibulo-visual interaction in people with Parkinson's disease compared to healthy controls. Exp. Brain Res. 239, 3553–3564. https://doi.org/10.1007/S00221-021-06219-0/TABLES/3.
Hireš, M., Gazda, M., Drotár, P., Pah, N.D., Motin, M.A., Kumar, D.K., 2022. Convolutional neural network ensemble for Parkinson's disease detection from voice recordings. Comput. Biol. Med. 141, 105021 https://doi.org/10.1016/J.COMPBIOMED.2021.105021.
Hosny, M., Zhu, M., Gao, W., Fu, Y., 2022. A novel deep learning model for STN localization from LFPs in Parkinson's disease. Biomed. Signal Process. Control 77, 103830. https://doi.org/10.1016/J.BSPC.2022.103830.
Jackins, V., Vimal, S., Kaliappan, M., Lee, M.Y., 2021. AI-based smart prediction of clinical disease using random forest classifier and Naive Bayes. J. Supercomput. 77, 5198–5219. https://doi.org/10.1007/S11227-020-03481-X/FIGURES/10.
Jain, R., Jain, N., Aggarwal, A., Hemanth, D.J., 2019. Convolutional neural network based Alzheimer's disease classification from magnetic resonance brain images. Cogn. Syst. Res. 57, 147–159. https://doi.org/10.1016/J.COGSYS.2018.12.015.
Janssen, S., de Ruyter van Steveninck, J., Salim, H.S., Cockx, H.M., Bloem, B.R., Heida, T., van Wezel, R.J.A., 2020. The effects of augmented reality visual cues on turning in place in parkinson's disease patients with freezing of gait. Front. Neurol. 11, 185. https://doi.org/10.3389/FNEUR.2020.00185/BIBTEX.
Jeon, H., Lee, W., Park, H., Lee, H.J., Kim, S.K., Kim, H.B., Jeon, B., Park, K.S., 2017. Automatic classification of tremor severity in Parkinson's disease using a wearable device, 2067 Sensors 2017 Vol. 17 (17), 2067. https://doi.org/10.3390/S17092067.
Jo, T., Nho, K., Saykin, A.J., 2019. Deep learning in Alzheimer's disease: diagnostic classification and prognostic prediction using neuroimaging data. Front. Aging Neurosci. 11, 220. https://doi.org/10.3389/FNAGI.2019.00220/BIBTEX.
Juanjuan, H., Zhiming, Y., Jianguo, W., Bochen, L., Xianjun, Y., 2020. An automatic detection method for bradykinesia in Parkinson's disease based on inertial sensor. 2020 IEEE 3rd Int. Conf. Electron. Technol. ICET 2020, 166–169. https://doi.org/10.1109/ICET49382.2020.9119604.
Jumah, F., Raju, B., Nagaraj, A., Shinde, R., Lescott, C., Sun, H., Gupta, G., Nanda, A., 2022. Uncharted waters of machine and deep learning for surgical phase recognition in neurosurgery. World Neurosurg. 160, 4–12. https://doi.org/10.1016/J.WNEU.2022.01.020.
Kadum, S.Y., Salman, O.H., Taha, Z.K., Said, A.B., Ali, M.A.M., Qassim, Q.S., Aal-Nouman, M.I., Mohammed, D.Y., Al baker, B.M., Abdalkareem, Z.A., 2023. Machine learning-based telemedicine framework to prioritize remote patients with multi-chronic diseases for emergency healthcare services. Netw. Model. Anal. Heal. Inform. Bioinforma. 12, 1–12. https://doi.org/10.1007/S13721-022-00407-W/TABLES/5.
Kaiser, T.M., Dentmon, Z.W., Dalloul, C.E., Sharma, S.K., Liotta, D.C., 2020. Accelerated discovery of novel ponatinib analogs with improved properties for the treatment of Parkinson's disease. ACS Med. Chem. Lett. 11, 491–496. https://doi.org/10.1021/ACSMEDCHEMLETT.9B00612/ASSET/IMAGES/LARGE/ML9B00612_0004.JPEG.
Kamran, I., Naz, S., Razzak, I., Imran, M., 2021. Handwriting dynamics assessment using deep neural network for early identification of Parkinson's disease. Futur. Gener. Comput. Syst. 117, 234–244. https://doi.org/10.1016/J.FUTURE.2020.11.020.
Karabayir, I., Goldman, S.M., Pappu, S., Akbilgic, O., 2020. Gradient boosting for Parkinson's disease diagnosis from voice recordings. BMC Med. Inform. Decis. Mak. 20. https://doi.org/10.1186/S12911-020-01250-7.
Karni, L., Jusufi, I., Nyholm, D., Klein, G.O., Memedi, M., 2022. Toward improved treatment and empowerment of individuals with Parkinson disease: design and evaluation of an internet of things system. JMIR Form. Res 2022 6 (6), e31485 https//formative.jmir.org/2022/6/e31485 6, e31485. https://doi.org/10.2196/31485.
Kazeminejad, A., Golbabaei, S., Soltanian-Zadeh, H., 2018. Graph theoretical metrics and machine learning for diagnosis of Parkinson's disease using rs-fMRI. 19th CSI Int. Symp. Artif. Intell. Signal Process. AISP 2017 2018-Jan. 134–139. https://doi.org/10.1109/AISP.2017.8324124.
Kazmaier, J., van Vuuren, J.H., 2020. A generic framework for sentiment analysis: leveraging opinion-bearing data to inform decision making. Decis. Support Syst. 135, 113304 https://doi.org/10.1016/J.DSS.2020.113304.
Ke, P. fei, Xiong, D. sheng, Li, J. hui, Pan, Z. lin, Zhou, J., Li, S. jia, Song, J., Chen, X. yi, Li, G. xiang, Chen, J., Li, X. bo, Ning, Y. ping, Wu, F. chun, Wu, K., 2021. An integrated machine learning framework for a discriminative analysis of schizophrenia using multi-biological data. Sci. Rep. 2021 111 (11), 1–11. https://doi.org/10.1038/s41598-021-94007-9.
Khan, A., Chandra Kaushik, A., Ali, S.S., Ahmad, N., Wei, D.Q., 2019. Deep-learning-based target screening and similarity search for the predicted inhibitors of the pathways in Parkinson's disease. RSC Adv. 9, 10326–10339. https://doi.org/10.1039/C9RA01007F.
Kim, D.Y., Hwang, S.H., Kim, M.G., Song, J.H., Lee, S.W., Kim, I.K., 2017. Development of parkinson patient generated data collection platform using FHIR and IoT devices. Stud. Health Technol. Inf. 245, 141–145. https://doi.org/10.3233/978-1-61499-830-3-141.
Kohli, P.S., Arora, S., 2018. Application of machine learning in disease prediction. 2018 4th Int. Conf. Comput. Commun. Autom. ICCCA 2018. https://doi.org/10.1109/CCAA.2018.8777449.

Kulkarni, A.M., Rampogu, S., Lee, K.W., 2021. Computer-aided drug discovery identifies alkaloid inhibitors of Parkinson's disease associated protein, Prolyl Oligopeptidase. Evidence-based Complement. Altern. Med 2021. https://doi.org/10.1155/2021/6687572.

Kumar Mall, P., Kumar Yadav, R., Rai, A.K., Narayan, V., Srivastava, S., 2022. Early warning signs of Parkinson's disease prediction using. Mach. Learn. Tech. J. Pharm. Negat. Results 13, 4784–4792. https://doi.org/10.47750/PNR.2022.13.S10.579.

Kunjir, A., Sawant, H., Shaikh, N.F., 2017. Data mining and visualization for prediction of multiple diseases in healthcare. Proc. 2017 Int. Conf. Big Data Anal. Comput. Intell. ICBDACI 2017, 329–334. https://doi.org/10.1109/ICBDACI.2017.8070858.

Kurbatskaya, A., Jaramillo-Jimenez, A., Ochoa-Gomez, J.F., Brønnick, K., Fernandez-Quilez, A., 2023. Machine Learning-Based Detection of Parkinson's Disease From Resting-State EEG: A Multi-Center Study.

Kye, B., Han, N., Kim, E., Park, Y., Jo, S., 2021. Educational applications of metaverse: possibilities and limitations. J. Educ. Eval. Health Prof. 18. https://doi.org/10.3352/JEEHP.2021.18.32.

Landolfi, A., Ricciardi, C., Donisi, L., Cesarelli, G., Troisi, J., Vitale, C., Barone, P., Amboni, M., 2021. Machine learning approaches in Parkinson's disease. Curr. Med. Chem. 28, 6548–6568. https://doi.org/10.2174/0929867328999210111211420.

Lei, H., Lei, Yukang, Chen, Z., Li, S., Huang, Z., Zhou, F., Tan, E.-L., Xiao, X., Lei, Yi, Hu, H., Huang, Y., Liu, C.-H., Lei, B., 2023. Early diagnosis and clinical score prediction of Parkinson's disease based on longitudinal neuroimaging data. Neural Comput. Appl. 2023, 1–27. https://doi.org/10.1007/S00521-023-08508-X.

Li, T., Le, W., 2020. Biomarkers for Parkinson's disease: how good are they? Neurosci. Bull. 36, 183. https://doi.org/10.1007/S12264-019-00433-1.

Li, Y., Yu, X., Koudas, N., 2021. Data acquisition for improving machine learning models. Proc. VLDB Endow. 14, 1832–1844. https://doi.org/10.14778/3467861.3467872.

Lin, W.J., Shen, P.C., Liu, H.C., Cho, Y.C., Hsu, M.K., Lin, I.C., Chen, F.H., Yang, J.C., Ma, W.L., Cheng, W.C., 2021. LipidSig: a web-based tool for lipidomic data analysis. Nucleic Acids Res 49, W336–W345. https://doi.org/10.1093/NAR/GKAB419.

Litos, A., Intze, E., Pavlidis, P., Lagkouvardos, I., 2022. Cronos: a machine learning pipeline for description and predictive modeling of microbial communities over time. Front. Bioinforma. 2, 77. https://doi.org/10.3389/FBINF.2022.866902.

Little, M.A., 2021. Smartphones for remote symptom monitoring of Parkinson's disease. J. Park. Dis. 11, S49–S53. https://doi.org/10.3233/JPD-202453.

Liu, J., Zhu, F., Chai, C., Luo, Y., Tang, N., 2021. Automatic data acquisition for deep learning. Proc. VLDB Endow. 14, 2739–2742. https://doi.org/10.14778/3476311.3476333.

Lorente-picón, M., Laguna, A., 2021. New avenues for parkinson's disease therapeutics: disease-modifying strategies based on the gut microbiota. Biomolecules 11, 1–39. https://doi.org/10.3390/biom11030433.

Lötsch, J., Lerch, F., Djaldetti, R., Tegder, I., Ultsch, A., 2018. Identification of disease-distinct complex biomarker patterns by means of unsupervised machine-learning using an interactive R toolbox (Umatrix). Big Data Anal. 3, 1–17. https://doi.org/10.1186/s41044-018-0032-1.

Maetzler, W., Klucken, J., Horne, M., 2016. A clinical view on the development of technology-based tools in managing Parkinson's disease. Mov. Disord. 31, 1263–1271. https://doi.org/10.1002/MDS.26673.

Mahlknecht, P., Kiechl, S., Bloem, B.R., Willeit, J., Scherfler, C., Gasperi, A., Rungger, G., Poewe, W., Seppi, K., 2013. Prevalence and burden of gait disorders in elderly men and women aged 60–97 years: a population-based study. PLoS One 8, e69627. https://doi.org/10.1371/JOURNAL.PONE.0069627.

Maitín, A.M., García-Tejedor, A.J., Muñoz, J.P.R., 2020. Machine learning approaches for detecting Parkinson's disease from EEG analysis: a systematic review, 8662 Appl. Sci. Vol. 10 (10), 8662. https://doi.org/10.3390/APP10238662.

Makarious, M.B., Leonard, H.L., Vitale, D., Iwaki, H., Sargent, L., Dadu, A., Violich, I., Hutchins, E., Saffo, D., Bandres-Ciga, S., Kim, J.J., Song, Y., Maleknia, M., Bookman, M., Nojopranoto, W., Campbell, R.H., Hashemi, S.H., Botia, J.A., Carter, J. F., Craig, D.W., Van Keuren-Jensen, K., Morris, H.R., Hardy, J.A., Blauwendraat, C., Singleton, A.B., Faghri, F., Nalls, M.A., 2022. Multi-modality machine learning predicting Parkinson's disease. npj Park. Dis. 2022 81 (8), 1–13. https://doi.org/10.1038/s41531-022-00288-w.

Malwe, A.S., Srivastava, G.N., Sharma, V.K., 2023. GutBug: a tool for prediction of human gut bacteria mediated biotransformation of biotic and xenobiotic molecules using machine learning. J. Mol. Biol., 168056 https://doi.org/10.1016/J.JMB.2023.168056.

Mandl, K.D., Kohane, I.S., 2016. Time for a patient-driven health information economy? N. Engl. J. Med 374, 205–208. https://doi.org/10.1056/NEJMP1512142.

Mandl, K.D., Kohane, I.S., 2017. A 21st-century health IT system - creating a real-world information economy. N. Engl. J. Med. 376, 1905–1907. https://doi.org/10.1056/NEJMP1700235.

Manyam, B.V., 2007. An Alternative Medicine Treatment for Parkinson's Disease: Results of a Multicenter Clinical Trial. https://home.liebertpub.com/acm 1, 249–255. https://doi.org/10.1089/ACM.1995.1.249.

Martinez-Eguiluz, M., Arbelaitz, O., Gurrutxaga, I., Muguerza, J., Perona, I., Murueta-Goyena, A., Acera, M., Del Pino, R., Tijero, B., Gomez-Esteban, J.C., Gabilondo, I., 2023. Diagnostic classification of Parkinson's disease based on non-motor manifestations and machine learning strategies. Neural Comput. Appl. 35, 5603–5617. https://doi.org/10.1007/S00521-022-07256-8/TABLES/5.

Martins, N.R.B., Erlhagen, W., Freitas, R.A., 2012. NON-DESTRUCTIVE WHOLE-BRAIN MONITORING USING NANOROBOTS: NEURAL ELECTRICAL DATA RATE REQUIREMENTS. https://doi.org/10.1142/S1793843012400069 4, 109–140. https://doi.org/10.1142/S1793843012400069.

Marxreiter, F., Gaßner, H., Borozdina, O., Barth, J., Kohl, Z., Schlachetzki, J.C.M., Thun-Hohenstein, C., Volc, D., Eskofier, B.M., Winkler, J., Klucken, J., 2018. Sensor-based gait analysis of individualized improvement during apomorphine titration in Parkinson's disease. J. Neurol. 265, 2656–2665. https://doi.org/10.1007/S00415-018-9012-7/FIGURES/4.

McArthur, J.J., Shahbazi, N., Fok, R., Raghubar, C., Bortoluzzi, B., An, A., 2018. Machine learning and BIM visualization for maintenance issue classification and enhanced data collection. Adv. Eng. Inform. 38, 101–112. https://doi.org/10.1016/J.AEI.2018.06.007.

McCoubrey, L.E., Gaisford, S., Mine Orlu, A.W.B., 2022. Predicting drug-microbiome interactions with machine learning. Biotechnol. Adv. 54, 107797 https://doi.org/10.1016/J.BIOTECHADV.2021.107797.

McLennan, J.E., Nakano, K., Tyler, H.R., Schwab, R.S., 1972. Micrographia in Parkinson's disease. J. Neurol. Sci. 15, 141–152. https://doi.org/10.1016/0022-510X(72)90002-0.

Mei, J., Desrosiers, C., Frasnelli, J., 2021. Machine learning for the diagnosis of Parkinson's disease: a review of literature. Front. Aging Neurosci. 13, 184. https://doi.org/10.3389/FNAGI.2021.633752/BIBTEX.

Mendes, F.A., dos, S., Pompeu, J.E., Lobo, A.M., da Silva, K.G., Oliveira, T., de, P., Zomignani, A.P., Piemonte, M.E.P., 2012. Motor learning, retention and transfer after virtual-reality-based training in Parkinson's disease – effect of motor and cognitive demands of games: a longitudinal, controlled clinical study. Physiotherapy 98, 217–223. https://doi.org/10.1016/J.PHYSIO.2012.06.001.

Michelet, E., Romero, G.-, López-López, E., Soriano-Correa, C., Medina-Franco, J.L., Barrientos-Salcedo, C., Rastelli, G., 2022. Polypharmacological drug design opportunities against Parkinson's disease. F1000Research 2022 111176 (11), 1176. https://doi.org/10.12688/f1000research.124160.1.

Miele, G., Straccia, G., Moccia, M., Leocani, L., Tedeschi, G., Bonavita, S., Lavorgna, L., 2020. Telemedicine in Parkinson's Disease: How to Ensure Patient Needs and Continuity of Care at the Time of COVID-19 Pandemic. Telemed. J. E. Health 26, 1533–1536. https://doi.org/10.1089/TMJ.2020.0184.

Miller, D.B., O'Callaghan, J.P., 2015. Biomarkers of Parkinson's disease: present and future. Metabolism 64 S40–S46. https://doi.org/10.1016/J.METABOL.2014.10.030.

Mishra, A., Mohapatro, M., 2019. An IoT framework for Bio-medical sensor data acquisition and machine learning for early detection Wireless Sensor Networks (WSN Technology) View project Machine Learning View project. Artic. Int. J. Adv. Technol. Eng. Explor. https://doi.org/10.19101/IJATEE.2019.650027.

Monje, M.H.G., Foffani, G., Obeso, J., Sánchez-Ferro, A., 2019. New sensor and wearable technologies to aid in the diagnosis and treatment monitoring of Parkinson's disease. Annu. Rev. Biomed. Eng. 21, 111–143. https://doi.org/10.1146/ANNUREV-BIOENG-062117-121036.

Mostafa, S.A., Mustapha, A., Mohammed, M.A., Hamed, R.I., Arunkumar, N., Abd Ghani, M.K., Jaber, M.M., Khaleefah, S.H., 2019. Examining multiple feature evaluation and classification methods for improving the diagnosis of Parkinson's disease. Cogn. Syst. Res. 54, 90–99. https://doi.org/10.1016/J.COGSYS.2018.12.004.

Mulak, A., Bonaz, B., 2015. Brain-gut-microbiota axis in Parkinson's disease. World J. Gastroenterol. 21, 10609. https://doi.org/10.3748/WJG.V21.I37.10609.

Nancy Noella, R.S., Priyadarshini, J., 2022. https://doi.org/10.1080/03091902.2022.2097326 Mach. Learn. Algorithms Diagn. Alzheimer Park. Dis. 47, 35–43. https://doi.org/10.1080/03091902.2022.2097326.

Narayan, V., Daniel, A.K., 2022. CHHP: coverage optimization and hole healing protocol using sleep and wake-up concept for wireless sensor network. Int. J. Syst. Assur. Eng. Manag 13, 546–556. https://doi.org/10.1007/S13198-021-01538-5.

Naylor, B.C., Leon Catrow, J., Alan Maschek, J., Cox, J.E., 2020. QSRR automator: a tool for automating retention time prediction in lipidomics and metabolomics. Metab 2020 Vol. 10 (10), 237, 237. https://doi.org/10.3390/METABO10060237.

Nishat, M.M., Hasan, T., Nasrullah, S.M., Faisal, F., Asif, M.A.A.R., Hoque, M.A., 2021. Detection of Parkinson's Disease by Employing Boosting Algorithms. 2021 Jt. 10th Int. Conf. Informatics, Electron. Vision, ICIEV 2021 2021 5th Int. Conf. Imaging, Vis. Pattern Recognition, icIVPR 2021. https://doi.org/10.1109/ICIEVICIVPR52578.2021.9564108.

Ogawa, M., Oyama, G., Morito, K., Kobayashi, M., Yamada, Y., Shinkawa, K., Kamo, H., Hatano, T., Hattori, N., 2022a. Can AI make people happy? The effect of AI-based chatbot on smile and speech in Parkinson's disease. Park. Relat. Disord. 99, 43–46. https://doi.org/10.1016/J.PARKRELDIS.2022.04.018.

Ogawa, M., Oyama, G., Sekimoto, S., Hatano, T., Hattori, N., 2022b. Current status of telemedicine for Parkinson's disease in japan: a single-center cross-sectional questionnaire survey. J. Mov. Disord. 15, 58. https://doi.org/10.14802/JMD.21096.

Oh, M., Zhang, L., 2020. DeepMicro: deep representation learning for disease prediction based on microbiome data. Sci. Rep. 2020 101 (10), 1–9. https://doi.org/10.1038/s41598-020-63159-5.

Ohta, Y., Yamashita, T., Hishikawa, N., Sato, K., Hatanaka, N., Takemoto, M., Doutare, S., Abe, K., 2018. Affective improvement of neurological disease patients and caregivers using an automated telephone call service. J. Clin. Neurosci. 56, 74–78. https://doi.org/10.1016/J.JOCN.2018.07.006.

Okwuashi, O., Ndehedehe, C.E., 2020. Deep support vector machine for hyperspectral image classification. Pattern Recognit. 103, 107298 https://doi.org/10.1016/J.PATCOG.2020.107298.

Oliveira, F.H.M., MacHado, A.R.P., Andrade, A.O., 2018. On the use of t -distributed stochastic neighbor embedding for data visualization and classification of individuals with Parkinson's disease. Comput. Math. Methods Med 2018. https://doi.org/10.1155/2018/8019232.

Olshannikova, E., Ometov, A., Koucheryavy, Y., Olsson, T., 2015. Visualizing Big Data with augmented and virtual reality: challenges and research agenda. J. Big Data 2, 1–27. https://doi.org/10.1186/S40537-015-0031-2/FIGURES/14.

Olsson, B., Lautner, R., Andreasson, U., Öhrfelt, A., Portelius, E., Bjerke, M., Hölttä, M., Rosén, C., Olsson, C., Strobel, G., Wu, E., Dakin, K., Petzold, M., Blennow, K., Zetterberg, H., 2016. CSF and blood biomarkers for the diagnosis of Alzheimer's

disease: a systematic review and meta-analysis. Lancet Neurol. 15, 673–684. https://doi.org/10.1016/S1474-4422(16)00070-3.
Pahuja, G., Nagabhushan, T.N., 2018. A Comparative Study of Existing Machine Learning Approaches for Parkinson's Disease Detection. https://doi.org/10.1080/03772063.2018.1531730 67, 4–14. https://doi.org/10.1080/03772063.2018.1531730.
Paillard, T., Rolland, Y., Barreto, P., de, S., 2015. Protective effects of physical exercise in Alzheimer's disease and Parkinson's disease: a narrative review. J. Clin. Neurol. 11, 212–219. https://doi.org/10.3988/JCN.2015.11.3.212.
Pantaleo, E., Monaco, A., Amoroso, N., Lombardi, A., Bellantuono, L., Urso, D., Giudice, C., Lo, Picardi, E., Tafuri, B., Nigro, S., Pesole, G., Tangaro, S., Logroscino, G., Bellotti, R., 2022. A machine learning approach to parkinson's disease blood transcriptomics, 727 Genes 2022 Vol. 13 (13), 727. https://doi.org/10.3390/GENES13050727.
Park, H., Shin, S., Youm, C., Cheon, S.M., Lee, M., Noh, B., 2021. Classification of Parkinson's disease with freezing of gait based on 360° turning analysis using 36 kinematic features. J. Neuroeng. Rehabil. 18, 1–18. https://doi.org/10.1186/S12984-021-00975-4/FIGURES/7.
Pasluosta, C.F., Gassner, H., Winkler, J., Klucken, J., Eskofier, B.M., 2015. An emerging era in the management of Parkinson's disease: wearable technologies and the internet of things. IEEE J. Biomed. Heal. Inform. 19, 1873–1881. https://doi.org/10.1109/JBHI.2015.2461555.
Pasolli, E., Truong, D.T., Malik, F., Waldron, L., Segata, N., 2016. Machine learning meta-analysis of large metagenomic datasets: tools and biological insights. PLOS Comput. Biol. 12, e1004977 https://doi.org/10.1371/JOURNAL.PCBI.1004977.
Pathak, V., Singh, K., Aziz, A., Dhoot, A., 2020. Efficient and compressive iot based health care system for Parkinson's disease patient. Procedia Comput. Sci. 167, 1046–1055. https://doi.org/10.1016/J.PROCS.2020.03.441.
Pazzaglia, C., Imbimbo, I., Tranchita, E., Minganti, C., Ricciardi, D., Lo Monaco, R., Parisi, A., Padua, L., 2020. Comparison of virtual reality rehabilitation and conventional rehabilitation in Parkinson's disease: a randomised controlled trial. Physiotherapy 106, 36–42. https://doi.org/10.1016/J.PHYSIO.2019.12.007.
Pedersen, S.W., Suedmeyer, M., Liu, L.W.C., Domagk, D., Forbes, A., Bergmann, L., Onuk, K., Yegin, A., van Laar, T., 2017. The role and structure of the multidisciplinary team in the management of advanced Parkinson's disease with a focus on the use of levodopa–carbidopa intestinal gel. J. Multidiscip. Health 10, 13–27 https://doi.org/10.2147/JMDH.S111369.
Peng, B., Wang, S., Zhou, Z., Liu, Y., Tong, B., Zhang, T., Dai, Y., 2017. A multilevel-ROI-features-based machine learning method for detection of morphometric biomarkers in Parkinson's disease. Neurosci. Lett. 651, 88–94. https://doi.org/10.1016/j.neulet.2017.04.034.
Pereira, C.R., Pereira, D.R., Silva, F.A., Masieiro, J.P., Weber, S.A.T., Hook, C., Papa, J.P., 2016. A new computer vision-based approach to aid the diagnosis of Parkinson's disease. Comput. Methods Prog. Biomed. 136, 79–88. https://doi.org/10.1016/J.CMPB.2016.08.005.
Pereira, C.R., Weber, S.A.T., Hook, C., Rosa, G.H., Papa, J.P., 2017. Deep learning-aided Parkinson's disease diagnosis from handwritten dynamics. Proc. - 2016 29th SIBGRAPI Conf. Graph. Patterns Images, SIBGRAPI 2016, 340–346. https://doi.org/10.1109/SIBGRAPI.2016.054.
Perez, K.S., Ramig, L.O., Smith, M.E., Dromey, C., 1996. The Parkinson larynx: tremor and videostroboscopic findings. J. Voice 10, 354–361. https://doi.org/10.1016/S0892-1997(96)80027-0.
Perju-Dumbrava, L., Barsan, M., Leucuta, D.C., Popa, L.C., Pop, C., Tohanean, N., Popa, S.L., 2022. Artificial intelligence applications and robotic systems in Parkinson's disease (Review). Exp. Ther. Med. 23, 1–11. https://doi.org/10.3892/ETM.2021.11076.
Pietrucci, D., Teofani, A., Unida, V., Cerroni, R., Biocca, S., Stefani, A., Desideri, A., 2020. Can gut microbiota be a good predictor for Parkinson's disease? A machine learning approach. Brain Sci. 10. https://doi.org/10.3390/brainsci10040242.
Pifferi, F., Laurent, B., Plourde, M., 2021. Lipid transport and metabolism at the blood-brain interface: implications in health and disease. Front. Physiol. 12. https://doi.org/10.3389/fphys.2021.645646.
Pont-Sunyer, C., Tolosa, E., Caspell-Garcia, C., Coffey, C., Alcalay, R.N., Chan, P., Duda, J.E., Facheris, M., Fernández-Santiago, R., Marek, K., Lomeña, F., Marras, C., Mondragon, E., Saunders-Pullman, R., Waro, B., 2017. The prodromal phase of leucine-rich repeat kinase 2–associated Parkinson disease: clinical and imaging Studies. Mov. Disord. 32, 726–738. https://doi.org/10.1002/MDS.26964.
Pun, U.K., Gu, H., Dong, Z., Artan, N.S., 2016. Classification and visualization tool for gait analysis of Parkinson's disease. Annu. Int. Conf. IEEE Eng. Med. Biol. Soc. IEEE Eng. Med. Biol. Soc. Annu. Int. Conf. 2016, 2407–2410. https://doi.org/10.1109/EMBC.2016.7591215.
Qin, X., Luo, Y., Tang, N., Li, G., 2020. Making data visualization more efficient and effective: a survey. VLDB J. 29, 93–117. https://doi.org/10.1007/S00778-019-00588-3/TABLES/7.
Rahman, S., Hasan, M., Sarkar, A.K., Khan, F., 2023. Classification of Parkinson's disease using speech signal with machine learning and deep learning approaches. Eur. J. Electr. Eng. Comput. Sci. 7, 20–27. https://doi.org/10.24018/EJECE.2023.7.2.488.
Rahman, W., Lee, S., Islam, M.S., Antony, V.N., Ratnu, H., Ali, M.R., Mamun, A., Al, Wagner, E., Jensen-Roberts, S., Waddell, E., Myers, T., Pawlik, M., Soto, J., Coffey, M., Sarkar, A., Schneider, R., Tarolli, C., Lizarraga, K., Adams, J., Little, M.A., Dorsey, E.R., Hoque, E., 2021. Detecting Parkinson disease using a web-based speech task: observational study. J. Med. Internet Res 23. https://doi.org/10.2196/26305.
Rahn, D.A., Chou, M., Jiang, J.J., Zhang, Y., 2007. Phonatory impairment in Parkinson's disease: evidence from nonlinear dynamic analysis and perturbation analysis. J. Voice 21, 64–71. https://doi.org/10.1016/J.JVOICE.2005.08.011.
Raiano, L., Di Pino, G., Di Biase, L., Tombini, M., Tagliamonte, N.L., Formica, D., 2020. PDMeter: a wrist wearable device for an at-home assessment of the Parkinson's disease rigidity. IEEE Trans. Neural Syst. Rehabil. Eng. 28, 1325–1333. https://doi.org/10.1109/TNSRE.2020.2987020.
Ramkumar, P.N., Haeberle, H.S., Navarro, S.M., Sultan, A.A., Mont, M.A., Ricchetti, E.T., Schickendantz, M.S., Iannotti, J.P., 2018. Mobile technology and telemedicine for shoulder range of motion: validation of a motion-based machine-learning software development kit. J. Shoulder Elb. Surg. 27, 1198–1204. https://doi.org/10.1016/J.JSE.2018.01.013.
Rana, A., Rawat, A.S., Bijalwan, A., Bahuguna, H., 2018. Application of multi layer (perceptron) artificial neural network in the diagnosis system: a systematic review. Proc. 2018 3rd IEEE Int. Conf. Res. Intell. Comput. Eng. RICE 2018. https://doi.org/10.1109/RICE.2018.8509069.
Rana, A., Dumka, A., Singh, R., Panda, M.K., Priyadarshi, N., Twala, B., 2022. Imperative role of machine learning algorithm for detection of Parkinson's disease: review, challenges and recommendations. Diagnostics 12. https://doi.org/10.3390/DIAGNOSTICS12082003.
Riva, G., Wiederhold, B.K., Mantovani, F., 2023. Searching for the metaverse: neuroscience of physical and digital communities. Cyber Behav. Soc. Netw. https://doi.org/10.1089/CYBER.2023.0040.
Roux, S., Camargo, A.P., Coutinho, F.H., Dabdoub, S.M., Dutilh, B.E., Nayfach, S., Tritt, A., 2023. iPHoP: an integrated machine learning framework to maximize host prediction for metagenome-derived viruses of archaea and bacteria. PLOS Biol. 21, e3002083 https://doi.org/10.1371/JOURNAL.PBIO.3002083.
Saba, L., Biswas, M., Kuppili, V., Cuadrado Godia, E., Suri, H.S., Edla, D.R., Omerzu, T., Laird, J.R., Khanna, N.N., Mavrogeni, S., Protogerou, A., Sfikakis, P.P., Viswanathan, V., Kitas, G.D., Nicolaides, A., Gupta, A., Suri, J.S., 2019. The present and future of deep learning in radiology. Eur. J. Radio. 114, 14–24. https://doi.org/10.1016/J.EJRAD.2019.02.038.
Saeed, U., Lang, A.E., Masellis, M., 2020. Neuroimaging advances in Parkinson's disease and atypical parkinsonian syndromes. Front. Neurol. 11, 1189. https://doi.org/10.3389/FNEUR.2020.572976/BIBTEX.
Salari, N., Kazeminia, M., Sagha, H., Daneshkhah, A., Ahmadi, A., Mohammadi, M., 2022. The performance of various machine learning methods for Parkinson's disease recognition: a systematic review. Curr. Psychol. 1, 1–24. https://doi.org/10.1007/S12144-022-02949-8/TABLES/2.
Sánchez-Ferro, Á., Elshehabi, M., Godinho, C., Salkovic, D., Hobert, M.A., Domingos, J., van Uem, J.M.T., Ferreira, J.J., Maetzler, W., 2016. New methods for the assessment of Parkinson's disease (2005 to 2015): a systematic review. Mov. Disord. 31, 1283–1292. https://doi.org/10.1002/MDS.26723.
Saniotis, A., Henneberg, M., Sawalma, A.R., 2018. Integration of nanobots into neural circuits as a future therapy for treating neurodegenerative disorders. Front. Neurosci. 12, 153. https://doi.org/10.3389/FNINS.2018.00153/BIBTEX.
Sarchione, A., Marchand, A., Taymans, J.M., Chartier-Harlin, M.C., 2021. Alpha-synuclein and lipids: the elephant in the room? Cells 10. https://doi.org/10.3390/CELLS10092452.
Sarker, I.H., 2021. Machine learning: algorithms, real-world applications and research directions. SN Comput. Sci. 2, 1–21. https://doi.org/10.1007/S42979-021-00592-X/FIGURES/11.
Schapira, A.H.V., Olanow, C.W., 2004. Neuroprotection in Parkinson disease: mysteries, myths, and misconceptions. JAMA 291, 358–364. https://doi.org/10.1001/JAMA.291.3.358.
Schilling, A.T., Shah, P.P., Feghali, J., Jimenez, A.E., Azad, T.D., 2022. A brief history of machine learning in neurosurgery. Acta Neurochir. Suppl. 134, 245–250. https://doi.org/10.1007/978-3-030-85292-4_27/COVER.
Sedighi Maman, Z., Chen, Y.J., Baghdadi, A., Lombardo, S., Cavuoto, L.A., Megahed, F. M., 2020. A data analytic framework for physical fatigue management using wearable sensors. Expert Syst. Appl. 155, 113405 https://doi.org/10.1016/J.ESWA.2020.113405.
Sekimoto, S., Oyama, G., Hatano, T., Sasaki, F., Nakamura, R., Jo, T., Shimo, Y., Hattori, N., 2019. A randomized crossover pilot study of telemedicine delivered via iPads in Parkinson's disease. Park. Dis. 2019. https://doi.org/10.1155/2019/9403295.
Senders, J.T., Staples, P.C., Karhade, A.V., Zaki, M.M., Gormley, W.B., Broekman, M.L.D., Smith, T.R., Arnaout, O., 2018. Machine learning and neurosurgical outcome prediction: a systematic review. World Neurosurg. 109 (476–486), e1 https://doi.org/10.1016/J.WNEU.2017.09.149.
Seo, S.-M., 2018. The effect of fine motor skills on handwriting legibility in preschool agechildren. J. Phys. Ther. Sci. 30, 324. https://doi.org/10.1589/JPTS.30.324.
Shamim, A., Mahmood, T., Ahsan, F., Kumar, A., Bagga, P., 2018. Lipids: an insight into the neurodegenerative disorders. Clin. Nutr. Exp. 20, 1–19. https://doi.org/10.1016/J.YCLNEX.2018.05.001.
Shang, J., Sun, Y., 2021. CHEER: HierarCHical taxonomic classification for viral mEtagEnomic data via deep leaRning. Methods 189, 95–103. https://doi.org/10.1016/J.YMETH.2020.05.018.
Sherwin, E., Dinan, T.G., Cryan, J.F., 2018. Recent developments in understanding the role of the gut microbiota in brain health and disease. Ann. N. Y. Acad. Sci. 1420, 5–25. https://doi.org/10.1111/nyas.13416.
Shetty, S., Rao, Y.S., 2016. SVM based machine learning approach to identify Parkinson's disease using gait analysis. Proc. Int. Conf. Inven. Comput. Technol. ICICT 2016, 2. https://doi.org/10.1109/INVENTIVE.2016.7824836.
Shi, D., Zhang, H., Wang, G., Wang, S., Yao, X., Li, Y., Guo, Q., Zheng, S., Ren, K., 2022. Machine learning for detecting Parkinson's disease by resting-state functional magnetic resonance imaging: a multicenter radiomics analysis. Front. Aging Neurosci. 14, 82. https://doi.org/10.3389/FNAGI.2022.806828/BIBTEX.

Shimizu, T., 2009. Lipid mediators in health and disease: enzymes and receptors as therapeutic targets for the regulation of immunity and inflammation. Annu. Rev. Pharmacol. Toxicol. 49, 123–150. https://doi.org/10.1146/ANNUREV.PHARMTOX.011008.145616.

Shivkumar, V., Subramanian, T., Agarwal, P., Mari, Z., Mestre, T.A., 2021. Uptake of telehealth in Parkinson's disease clinical care and research during the COVID-19 pandemic. Park. Relat. Disord. 86, 97. https://doi.org/10.1016/J.PARKRELDIS.2021.03.032.

Shu, S., Woo, B.K.P., 2023. Pioneering the metaverse: the role of the metaverse in an aging population. JMIR Aging 6, e40582. https://doi.org/10.2196/40582.

Siddiqui, A.J., Jahan, S., Siddiqui, M.A., Khan, A., Alshahrani, M.M., Badraoui, R., Adnan, M., 2023. Targeting monoamine oxidase b for the treatment of Alzheimer's and Parkinson's diseases using novel inhibitors identified using an integrated approach of machine learning and computer-aided drug design. Mathematics 11, 1464. https://doi.org/10.3390/MATH11061464/S1.

Sivaranjini, S., Sujatha, C.M., 2020. Deep learning based diagnosis of Parkinson's disease using convolutional neural network. Multimed. Tools Appl. 79, 15467–15479. https://doi.org/10.1007/S11042-019-7469-8/TABLES/3.

Siyar, S., Azarnoush, H., Rashidi, S., Winkler-Schwartz, A., Bissonnette, V., Ponnudurai, N., Del Maestro, R.F., 2020. Machine learning distinguishes neurosurgical skill levels in a virtual reality tumor resection task. Med. Biol. Eng. Comput. 58, 1357–1367. https://doi.org/10.1007/S11517-020-02155-3/TABLES/6.

Society, A.G., Society, G., Of, A.A., Prevention, O.S.P.O.F., 2001. Guideline for the prevention of falls in older persons. J. Am. Geriatr. Soc. 49, 664–672. https://doi.org/10.1046/J.1532-5415.2001.49115.X.

Song, Y.-Y., Lu, Y., 2015. Decision tree methods: applications for classification and prediction. Psychiatry 27, 130–135. https://doi.org/10.11919/j.issn.1002-0829.215044.

Soumaya, Z., Benayad, N., Taoufiq, B.D., Abdelkrim, A., 2022. Predicting Parkinson's disease based on transformed speech signal by DWT with two methods for features selection: GA-AdaBoost and BPSO. Proc. - 2022 7th Int. Conf. Math. Comput. Sci. Ind. MCSI 2022, 121–130. https://doi.org/10.1109/MCSI55933.2022.00026.

Souza, J.W.M.D., Alves, S.S.A., Rebouças, E.D.S., Almeida, J.S., Rebouças Filho, P.P., 2018. A new approach to diagnose parkinson's disease using a structural cooccurrence matrix for a similarity analysis. Comput. Intell. Neurosci. 2018. https://doi.org/10.1155/2018/7613282.

Stamenkovic, A., Underation, M., Cloud, L.J., Pidcoe, P.E., Baron, M.S., Hand, R., France, C.R., van der Veen, S.M., Thomas, J.S., 2023. Assessing perceptions to a virtual reality intervention to improve trunk control in Parkinson's disease: a preliminary study. Virtual Real. 27, 465–479. https://doi.org/10.1007/S10055-022-00657-Z/TABLES/2.

Stern, J.H., Rutkowski, J.M., Scherer, P.E., 2016. Adiponectin, leptin, and fatty acids in the maintenance of metabolic homeostasis through adipose tissue crosstalk. Cell Metab. 23, 770–784. https://doi.org/10.1016/J.CMET.2016.04.011.

Stoessl, A.J., 2011. Neuroimaging in Parkinson's disease. Neurotherapeutics 8, 72–81. https://doi.org/10.1007/S13311-010-0007-Z/FIGURES/6.

Sudar, K.M., Nagaraj, P., Nithisaa, S., Aishwarya, R., Aakash, M., Lakshmi, S.I., 2022. Alzheimer's disease analysis using explainable artificial intelligence (XAI). Int. Conf. Sustain. Comput. Data Commun. Syst. ICSCDS 2022 - Proc. 419–423. https://doi.org/10.1109/ICSCDS53736.2022.9760858.

Sun, Y., Li, H., Zheng, L., Li, J., Hong, Y., Liang, P., Kwok, L.Y., Zuo, Y., Zhang, W., Zhang, H., 2022. iProbiotics: a machine learning platform for rapid identification of probiotic properties from whole-genome primary sequences. Brief. Bioinf. 23. https://doi.org/10.1093/BIB/BBAB477.

Suzuki, M., Mitoma, H., Yoneyama, M., 2017. Quantitative analysis of motor status in Parkinson's disease using wearable devices: from methodological considerations to problems in clinical applications. Park. Dis. 2017. https://doi.org/10.1155/2017/6139716.

Tandel, G.S., Biswas, M., Kakde, O.G., Tiwari, A., Suri, H.S., Turk, M., Laird, J.R., Asare, C.K., Ankrah, A.A., Khanna, N.N., Madhusudhan, B.K., Saba, L., Suri, J.S., 2019. A review on a deep learning perspective in brain cancer classification, 111 Cancers 2019 Vol. 11 (11), 111. https://doi.org/10.3390/CANCERS11010111.

Teulings, H.L., Contreras-Vidal, J.L., Stelmach, G.E., Adler, C.H., 2002. Adaptation of handwriting size under distorted visual feedback in patients with Parkinson's disease and elderly and young controls. J. Neurol. Neurosurg. Psychiatry 72, 315–324. https://doi.org/10.1136/JNNP.72.3.315.

Thouheed Ahmed, S., Sandhya, M., 2019. Real-time biomedical recursive images detection algorithm for indian telemedicine environment. Adv. Intell. Syst. Comput. 768, 723–731. https://doi.org/10.1007/978-981-13-0617-4_68/COVER.

Tonutti, M., Gras, G., Yang, G.Z., 2017. A machine learning approach for real-time modelling of tissue deformation in image-guided neurosurgery. Artif. Intell. Med. 80, 39–47. https://doi.org/10.1016/J.ARTMED.2017.07.004.

Tougui, I., Jilbab, A., El Mhamdi, J., 2022. Machine learning smart system for parkinson disease classification using the voice as a biomarker. Healthc. Inform. Res. 28, 210. https://doi.org/10.4258/HIR.2022.28.3.210.

Trabassi, D., Serrao, M., Varrecchia, T., Ranavolo, A., Coppola, G., De Icco, R., Tassorelli, C., Castiglia, S.F., 2022. Machine learning approach to support the detection of Parkinson's disease in IMU-based gait analysis. Sensors 22, 3700. https://doi.org/10.3390/S22103700/S1.

Tsoulos, I.G., Mitsi, G., Stavrakoudis, A., Papapetropoulos, S., 2019. Application of machine learning in a parkinson's disease digital biomarker dataset using Neural Network Construction (NNC) methodology discriminates patient motor status. Front. ICT 6, 1–7. https://doi.org/10.3389/fict.2019.00010.

Tunur, T., DeBlois, A., Yates-Horton, E., Rickford, K., Columna, L.A., 2020. Augmented reality-based dance intervention for individuals with Parkinson's disease: A pilot study. Disabil. Health J. 13, 100848 https://doi.org/10.1016/J.DHJO.2019.100848.

Uddin, M., Wang, Y., Woodbury-Smith, M., 2019. Artificial intelligence for precision medicine in neurodevelopmental disorders. npj Digit. Med. 2019 21 (2), 1–10. https://doi.org/10.1038/s41746-019-0191-0.

Uddin, S., Khan, A., Hossain, M.E., Moni, M.A., 2019. Comparing different supervised machine learning algorithms for disease prediction. BMC Med. Inform. Decis. Mak. 19, 1–16. https://doi.org/10.1186/S12911-019-1004-8/FIGURES/12.

Uenaka, T., Satake, W., Cha, P.-C., Hayakawa, H., Baba, K., Jiang, S., Kobayashi, K., Kanagawa, M., Okada, Y., Mochizuki, H., Toda, T., 2018. In silico drug screening by using genome-wide association study data repurposed dabrafenib, an anti-melanoma drug, for Parkinson's disease. Hum. Mol. Genet 27, 3974–3985. https://doi.org/10.1093/hmg/ddy279.

Upadhya, S.S., Cheeran, A.N., 2018. Discriminating Parkinson and healthy people using phonation and cepstral features of speech. Procedia Comput. Sci. 143, 197–202. https://doi.org/10.1016/J.PROCS.2018.10.376.

Valla, E., Nõmm, S., Medijainen, K., Taba, P., Toomela, A., 2022. Tremor-related feature engineering for machine learning based Parkinson's disease diagnostics. Biomed. Signal Process. Control 75, 103551. https://doi.org/10.1016/J.BSPC.2022.103551.

Vamathevan, J., Clark, D., Czodrowski, P., Dunham, I., Ferran, E., Lee, G., Li, B., Madabhushi, A., Shah, P., Spitzer, M., Zhao, S., 2019. Applications of machine learning in drug discovery and development. Nat. Rev. Drug Discov. 2019 186 (18), 463–477. https://doi.org/10.1038/s41573-019-0024-5.

Van Uem, J.M.T., Isaacs, T., Lewin, A., Bresolin, E., Salkovic, D., Espay, A.J., Matthews, H., Maetzler, W., 2016. A viewpoint on wearable technology-enabled measurement of wellbeing and health-related quality of life in Parkinson's disease. J. Park. Dis. 6, 279–287. https://doi.org/10.3233/JPD-150740.

Vanegas, M.I., Ghilardi, M.F., Kelly, S.P., Blangero, A., 2019. Machine learning for EEG-based biomarkers in Parkinson's disease. Proc. - 2018 IEEE Int. Conf. Bioinforma. Biomed. BIBM 2018, 2661–2665. https://doi.org/10.1109/BIBM.2018.8621498.

Varrecchia, T., Castiglia, S.F., Ranavolo, A., Conte, C., Tatarelli, A., Coppola, G., Di Lorenzo, C., Draicchio, F., Pierelli, F., Serrao, M., 2021. An artificial neural network approach to detect presence and severity of Parkinson's disease via gait parameters. PLoS One 16, e0244396. https://doi.org/10.1371/JOURNAL.PONE.0244396.

Vascellari, S., Palmas, V., Melis, Marta, Pisanu, S., Cusano, R., Uva, P., Perra, D., Madau, V., Sarchioto, M., Oppo, V., Simola, N., Morelli, M., Santoru, M.L., Atzori, L., Melis, Maurizio, Cossu, G., Manzin, A., 2020. Gut microbiota and metabolome alterations associated with Parkinson's disease. mSystems 5.

Verma, S.K., Chauhan, R., 2014. Nanorobotics in dentistry – a review. Indian J. Dent. 5, 62–70. https://doi.org/10.1016/J.IJD.2012.12.010.

Visanji, N.P., Madan, P., Lacoste, A.M.B., Buleje, I., Han, Y., Spangler, S., Kalia, L.V., Hensley Alford, S., Marras, C., 2021. Using artificial intelligence to identify anti-hypertensives as possible disease modifying agents in Parkinson's disease. Pharmacoepidemiol. Drug Saf. 30, 201–209. https://doi.org/10.1002/PDS.5176.

Wang, L., Sun, Y., Li, Q., Liu, T., Yi, J., 2020. Two shank-mounted IMUs-Based gait analysis and classification for neurological disease patients. IEEE Robot. Autom. Lett. 5, 1970–1976. https://doi.org/10.1109/LRA.2020.2970656.

Wang, X., Li, S., Pun, C.M., Guo, Y., Xu, F., Gao, H., Lu, H., 2023. A Parkinsons Auxiliary diagnosis algorithm based on a hyperparameter optimization method of deep learning. IEEE/ACM Trans. Comput. Biol. Bioinforma. https://doi.org/10.1109/TCBB.2023.3246961.

Wang, X.W., Liu, Y.Y., 2020. Comparative study of classifiers for human microbiome data. Med. Micro 4, 100013. https://doi.org/10.1016/j.medmic.2020.100013.

Wang, Y.W., Chen, C.H., Lin, Y.C., 2020. Balance rehabilitation system for Parkinson's disease patients based on augmented reality. 2nd IEEE Eurasia Conf. IOT, Commun. Eng. 2020, ECICE 2020, 191–194. https://doi.org/10.1109/ECICE50847.2020.9302018.

Weiss, A., Herman, T., Mirelman, A., Shiratzky, S.S., Giladi, N., Barnes, L.L., Bennett, D. A., Buchman, A.S., Hausdorff, J.M., 2019. The transition between turning and sitting in patients with Parkinson's disease: a wearable device detects an unexpected sequence of events. Gait Posture 67, 224–229. https://doi.org/10.1016/J.GAITPOST.2018.10.018.

Wirbel, J., Zych, K., Essex, M., Karcher, N., Kartal, E., Salazar, G., Bork, P., Sunagawa, S., Zeller, G., 2020. SIAMCAT: user-friendly and versatile machine learning workflows for statistically rigorous microbiome analyses. bioRxiv 2020.02.06.931808. https://doi.org/10.1101/2020.02.06.931808.

Wu, J., Zhang, H., Chen, Z., Fu, R., Yang, H., Zeng, H., Ren, Z., 2022. Benefits of virtual reality balance training for patients With Parkinson disease: systematic review, meta-analysis, and meta-regression of a randomized controlled trial. JMIR Serious Games 2022;10(1)e30882 https//Games. jmir. Org. /2022/1/e30882 10, e30882. https://doi.org/10.2196/30882.

Wu, X., Sun, Y., Xu, X., Steyerberg, E., Retel Helmrich, I.R.A., Lecky, F., Guo, J., Li, X., Feng, J., Mao, Q., Xie, G., Maas, A., Gao, G., Jiang, J., 2023. Mortality Prediction in Severe Traumatic Brain Injury Using Traditional and Machine Learning Algorithms. ⟨https://home.liebertpub.com/neu⟩. https://doi.org/10.1089/NEU.2022.0221.

Yadav, D., Jain, I., 2022. Comparative analysis of machine learning algorithms for Parkinson's disease prediction. Proc. - 2022 6th Int. Conf. Intell. Comput. Control Syst. ICICCS 2022, 1334–1339. https://doi.org/10.1109/ICICCS53718.2022.9788354.

Yang, W.C., Wang, H.K., Wu, R.M., Lo, C.S., Lin, K.H., 2016. Home-based virtual reality balance training and conventional balance training in Parkinson's disease: a randomized controlled trial. J. Formos. Med. Assoc. 115, 734–743. https://doi.org/10.1016/J.JFMA.2015.07.012.

Yoon, J.H., Seo, Y., Jo, Y.S., Lee, S., Cho, E., Cazenave-Gassiot, A., Shin, Y.S., Moon, M. H., An, H.J., Wenk, M.R., Suh, P.G., 2022. Brain lipidomics: from functional landscape to clinical significance. Sci. Adv. 8, 1–15. https://doi.org/10.1126/sciadv.adc9317.

Yoshikawa, K., Nakata, Y., Yamada, K., Nakagawa, M., 2004. Early pathological changes in the parkinsonian brain demonstrated by diffusion tensor MRI. J. Neurol. Neurosurg. Psychiatry 75, 481–484. https://doi.org/10.1136/JNNP.2003.021873.
Yousif, N.R., Balaha, H.M., Haikal, A.Y., El-Gendy, E.M., 2022. A generic optimization and learning framework for Parkinson disease via speech and handwritten records. J. Ambient Intell. Humaniz. Comput. 1, 1. https://doi.org/10.1007/S12652-022-04342-6.
Yucel, M.A., Ozcelik, I., Algul, O., 2023. Machine learning study: from the toxicity studies to tetrahydrocannabinol effects on Parkinson's disease. Future Med. Chem. 15, 365–377. https://doi.org/10.4155/FMC-2022-0181.
Zardini Buzatto, A., Tatlay, J., Bajwa, B., Mung, D., Camicioli, R., Dixon, R.A., Li, L., 2021. Comprehensive serum lipidomics for detecting incipient dementia in Parkinson's disease. J. Proteome Res. 20, 4053–4067. https://doi.org/10.1021/ACS.JPROTEOME.1C00374.
Zeighami, Y., Ulla, M., Iturria-Medina, Y., Dadar, M., Zhang, Y., Larcher, K.M.H., Fonov, V., Evans, A.C., Collins, D.L., Dagher, A., 2015. Network structure of brain atrophy in de novo parkinson's disease. Elife 4. https://doi.org/10.7554/ELIFE.08440.
Zhang, H., Wang, A., Li, D., Xu, W., 2018. DeepVoice: a voiceprint-based mobile health framework for Parkinson's disease identification. 2018 IEEE EMBS Int. Conf. Biomed. Heal. Inform., BHI 2018 2018-Jan. 214–217. https://doi.org/10.1109/BHI.2018.8333407.
Zhang, H., Deng, K., Li, H., Albin, R.L., Guan, Y., 2020. Deep learning identifies digital biomarkers for self-reported Parkinson's disease. Patterns 1, 100042. https://doi.org/10.1016/j.patter.2020.100042.
Zhang, J., 2022. Mining imaging and clinical data with machine learning approaches for the diagnosis and early detection of Parkinson's disease. npj Park. Dis. 2022 81 (8), 1–15. https://doi.org/10.1038/s41531-021-00266-8.
Zhao, A., Li, J., Dong, J., Qi, L., Zhang, Q., Li, N., Wang, X., Zhou, H., 2022. Multimodal gait recognition for neurodegenerative diseases. IEEE Trans. Cyber 52, 9439–9453. https://doi.org/10.1109/TCYB.2021.3056104.
Zhao, H., Tsai, C.C., Zhou, M., Liu, Y., Chen, Y.L., Huang, F., Lin, Y.C., Wang, J.J., 2022. Deep learning based diagnosis of Parkinson's Disease using diffusion magnetic resonance imaging. Brain Imaging Behav. 16, 1749–1760. https://doi.org/10.1007/S11682-022-00631-Y/TABLES/2.
Zhou, H., Gao, J.Y., Chen, Y., 2022. The paradigm and future value of the metaverse for the intervention of cognitive decline. Front. Public Heal 10. https://doi.org/10.3389/FPUBH.2022.1016680.
Zhou, Z., Tu, J., Xiong, X., Shen, X., Zhu, Z.J., 2017. LipidCCS: prediction of collision cross-section values for lipids with high precision to support ion mobility-mass spectrometry-based lipidomics. Anal. Chem. 89, 9559–9566. https://doi.org/10.1021/ACS.ANALCHEM.7B02625/SUPPL_FILE/AC7B02625_SI_002.ZIP.
Zhu, S., Sui, Y., Shen, Y., Zhu, Y., Ali, N., Guo, C., Wang, T., 2021. Effects of virtual reality intervention on cognition and motor function in older adults with mild cognitive impairment or dementia: a systematic review and meta-analysis. Front. Aging Neurosci. 13. https://doi.org/10.3389/FNAGI.2021.586999.
Zhu, Y., Jung, W., Wang, F., Che, C., 2020. Drug repurposing against Parkinson's disease by text mining the scientific literature. Libr. Hi Tech. 38, 741–750. https://doi.org/10.1108/LHT-08-2019-0170/FULL/PDF.
Zudilova-Seinstra, E., Yang, N., Axner, L., Wibisono, A., Vasunin, D., 2008. Service-oriented visualization applied to medical data analysis. Serv. Oriented Comput. Appl. 2, 187–201. https://doi.org/10.1007/S11761-008-0031-6/METRICS.

Dr. Rohan Gupta finished his Ph.D. from Department of Biotechnology, Delhi Technological University under the supervision of Prof. Pravir Kumar. His area of research is "Acetylation Mechanism and HDAC enzymes in neurodegenerative disease". His current research interests are neuroinformatics, in-silico biology, medical bioinformatics, drug discovery and development, computational biology, and machine learning.

Smita Kumari is pursuing her PhD from Department of Biotechnology, Delhi Technological University under the supervision of Prof. Pravir Kumar. H Her academic training, research experience, teaching assistance, and scientific training experience have provided me with excellent background on multiple disciplines, such as computational biology, biomedical informatics, drug designing, drug discovery, proteomic studies, genetics, and molecular biology.

Anusha Senapati is a project trainee under Prof. Pravir Kumar and student of Acton Boxborough Regional High School, MA, USA.

Dr. Rashmi K Ambasta has finished her Master's degree from the Department of Zoology, Banaras Hindu University. She has qualified national level exam for CSIR-JRF, ICMR-JRF, and ASRB-LS. She has joined J W Goethe University for her PhD in Frankfurt Germany. She has finished her PhD in 2004 and joined Boston, MA, USA for her two Postdoctoral training sponsored by NIH. She joined the faculty position at VIT, Vellore, India as an Assistant Professor and was promoted to Associate Professor. She was awarded with DST-Young Scientist Award under fast-track scheme, CSIR scientific pool officer at Delhi Technological University.

Prof. Pravir Kumar is working as a Professor and Head of the Department in the Department of Biotechnology and Dean of International Affairs at Delhi Technological University, New Delhi, India.

2023 4th International Conference for Emerging Technology (INCET)
Belgaum, India. May 26-28, 2023

Performance Analysis of DC Motor using GWO and FPA

Abhigyan Adarsh
Dept. of Electrical Engineering
Delhi Technological University
Delhi, India
abhigyanadarsh_2k19ee005@dtu.ac.in

Amal Chawla
Dept. of Electrical Engineering
Delhi Technological University
Delhi, India
amalchawla_2k19ee032@dtu.ac.in

Anirudh Singh
Dept. of Electrical Engineering
Delhi Technological University
Delhi, India
anirudhsingh_2k19ee042@dtu.ac.in

Bharat Bhushan
Dept of Electrical Engineering
Delhi Technological University
Delhi, India
bharat@dce.ac.in

2023 4th International Conference for Emerging Technology (INCET) | 979-8-3503-3575-0/23/$31.00 ©2023 IEEE | DOI: 10.1109/INCET57972.2023.10170189

***Abstract*—This paper aims at comparing various PID tuning methodologies. An armature-controlled DC motor has been modeled in Simulink using its actual parameters for the study. The metaheuristic approaches i.e., Flower Pollination Algorithm and Grey Wolf Optimization have been coded on MATLAB and the tuned parameters have been imported on Simulink to check their response. These algorithms work on ITAE as their objective function. Finally, the results of the controllers are analyzed and distinguished by values of Rise Time (Tr), Peak Overshoot (Mp), and Peak Time (Tp).**

***Index Terms*—DC Motor, SIMULINK, PID, GWO, FPA, ITAE, Objective function.**

I. Introduction

Engineers rely on motion-control devices to improve efficiency and production rates on automated factory floors, or at least maintain them. One of the earliest devices designed to transform electrical power into mechanical power was the DC motor. Due to their high levels of dependability, versatility, and affordability[1], DC motors are frequently used when speed of motor and position control are essential in industrial settings, robot manipulators, and appliances.

Motor control applications frequently use PID controllers because of their straightforward topologies and easily understandable control algorithms. Proportional-integral-derivative (PID) control offers a simple and incredibly useful solution to many concerns in the real world due to its three-term structure. Both transient and steady-state behaviors may be governed by all this. As a result, PID controllers are frequently used in traditional speed control loops[2]. The drawbacks of conventional PID controllers include unwanted overshoot, slow response, sensitivity to controller gains, and rapid changes in load torque[3]. The varied behavior of the system parameters under operating environment and the noise that is present in the circuit are the two main issues with motor control[4]. As a result, it is difficult to use standard techniques for motor control of sophisticated, nonlinear, and time-varying systems. To achieve an ideal state under field conditions, tuning the PID controller's parameters is therefore obviously necessary[5].

The metaheuristic algorithms [6] like Flower Pollination Algorithm and Grey Wolf Optimization use ITAE as an objective function for optimization. This objective function is minimized using a global minimization approach. These algorithms are inspired by nature and approach optimization of PID irrespective of plant model, thus providing robust results.

This paper is organized into seven segments: Section II goes on to discuss the mathematical model; Section III aims to discuss the metaheuristic approach to PID tuning and objective functions; Section IV explores Grey Wolf Optimization; Section V explains the Flower Pollination Algorithm; Section VI mentions simulation results and discussions; Section VII analyses conclusions; and Section VIII concludes. These sections are followed by an acknowledgment and a list of references.

II. Mathematical Model

The voltage applied to the motor can be changed while the field remains constant in separately excited DC Motors.

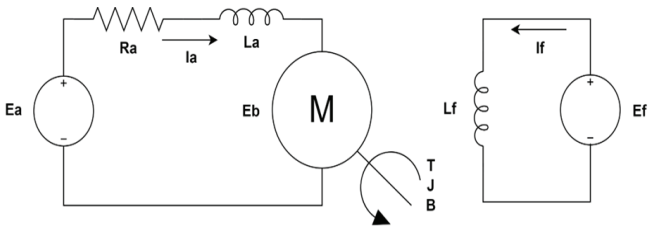

Fig. 1. Equivalent Circuit of Armature Controlled DC Motor.

TABLE I
Equivalent circuit parameters and values

Parameter	Nomenclature	Values
Moment of Inertia	J	$0.093Kg-m^2$
Friction Coefficient	B	$0.007N-ms$
Back Emf Constant	K_b	$0.6V/rad-s^-1$
Torque Constant	K_T	$0.7273Nm/A$
Armature Resistance	R_a	0.6
Armature Inductance	L_a	$0.006H$

Authorized licensed use limited to: DELHI TECHNICAL UNIV. Downloaded on July 20,2023 at 11:18:33 UTC from IEEE Xplore. Restrictions apply.

The mathematical equations of the Armature Controlled DC Motor are as follows:

$$\Phi \propto i_f$$

$$\Phi = K_f i_f \tag{1}$$

Where,

$$T \propto \Phi i_a$$

$$T = K_a \Phi i_a = K_a K_f \Phi i_a$$

$$T = K_T i_a \tag{2}$$

$$E_b \propto \Phi \omega$$

$$E_b = K_b \omega \tag{3}$$

Applying KVL,

$$V = i_a R_a + L_a \frac{di_a}{dt} + E_b \tag{4}$$

And,

$$T = J\frac{d^2\theta}{dt^2} + B\frac{d\theta}{dt} \tag{5}$$

Load Torque,

$$T = J\frac{d^2\theta}{dt^2} + B\frac{d\theta}{dt} + T_L \tag{6}$$

By Laplace Transform,

$$V(s) = i_a(s)(R_a + sL_a) + E_b$$

$$V(s) - E_b(s) = i_a(s)(R_a + sL_a)$$

$$E_b(s) = K_b s\theta(s)$$

$$T(s) = Ki_a(s)$$

$$T(s) = \theta(s)(Js^2 + sB)$$

$$T(s) = \omega(s)(Js + B)$$

$$T(s) = K_T i_a I(s)$$

$$T(s) = \frac{\omega(s)}{V(s)} = \frac{K_T}{(R_a + sLa)(Js + B) + K_b K_T} \tag{7}$$

The transfer function of the DC Motor obtained after putting Equivalent circuit Parameters defined in Table I is as follows:

$$T(s) = \frac{1}{0.0007671s^2 + 0.076785s + 0.60654} \tag{8}$$

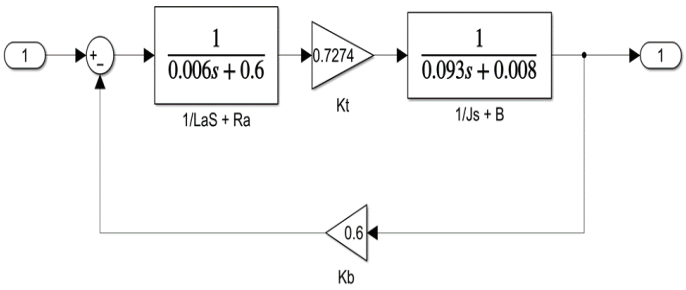

Fig. 2. Block Diagram of DC Motor designed in SIMULINK

Figure 2, depicts the block diagram modeled in SIMULINK using Equation (7).

III. Metaheuristic approach of PID Tuning and Objective Functions

A. Metaheuristic approach of PID Tuning

Process control makes considerable use of metaheuristic algorithms [7] because of their quick response times, high optimization capabilities, and simple architectural design. Metaheuristic algorithms are more effective at resolving higher-dimensional optimization issues than conventional optimization techniques. They are easily adaptable to modern classical controller design approaches due to their durability. Metaheuristic algorithms can be used as a fundamental method for creating a uniform and enhanced set of resilient operational models that require structured controllers, regardless of the order in which the models are developed.

B. Objective Functions

The real-valued function whose value is to be either minimized or maximized over the range of feasible solutions is characterized as the objective function[8] in a mathematical optimization problem. In this case, our optimization goal function would be the Integral Time Absolute Error (ITAE)[9]: ITAE =$\int_0^\tau t|e(t)|$

IV. Grey Wolf Optimization (GWO)

A. Implementation

The grey wolf, which hunts massive prey in gangs and thrives on individual wolf coordination, inspired this algorithm. This behavior is notable for two reasons:

1) Social hierarchy
2) Hunting mechanism.

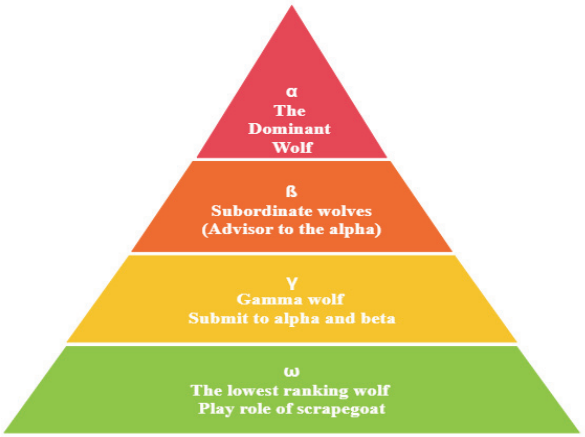

Fig. 3. Grey Wolf Algorithm dominance hierarchies

The grey wolf has a sophisticated social structure due to its gregarious nature. The phrase ”dominance hierarchies” refers to the hierarchical order depicted in Fig 3, in which wolves are ranked according to their authority and strength[10]. As a result, alphas, betas, deltas, and omegas exist.

1) At the top of the pack’s hierarchy are the alpha male and female. Each member of the pack has been assigned a rank. The wolf’s hierarchical order is about more than

Authorized licensed use limited to: DELHI TECHNICAL UNIV. Downloaded on July 20,2023 at 11:18:33 UTC from IEEE Xplore. Restrictions apply.

just dominance and aggression; it also assists vulnerable members of the pack who are unable to hunt for themselves.

2) The beta wolf comes next, who supports the alpha wolf's decisions and helps to preserve pack discipline.
3) The delta wolf is inferior to the beta wolf. They are frequently powerful, but lack the necessary leadership qualities and self-confidence to take on leadership responsibilities.
4) Eventually, the omega wolf wields little power, and other wolves will quickly chase him. Omega wolf is also in charge of monitoring the younger wolves.

At each level, we will use the previously described methods to indicate the three best solutions by alpha, beta, and delta, as well as alternative options by omega. This essentially means that the optimization process is guided by the flow of the three best solutions. In addition, the prey will be the best optimization solution[11].
Most of the logic follows the equations:

$$\overrightarrow{D} =\mid \overrightarrow{C}.\overrightarrow{X_p}(t) - \overrightarrow{X}(t) \mid \tag{9}$$

$$\overrightarrow{X}(t+1) =\mid \overrightarrow{X_p}(t) - \overrightarrow{A}.\overrightarrow{D} \mid \tag{10}$$

where t indicates the latest iteration, A and C are regression coefficients, Xp is the vector of the prey's movement, and X is the vector of the wolf's position. Cartesian coordinates A and B seem to be similar.

$$\overrightarrow{A} = 2\overrightarrow{a}.\overrightarrow{r_1} - \overrightarrow{a} \tag{11}$$

$$\overrightarrow{C} = 2\overrightarrow{r_2} \tag{12}$$

where a's components decline linearly from 2 to 0 over iterations and r1, r2 are random vectors with values ranging from [0, 1] computed for each wolf at each iteration[12]. Vector A governs the trade-off between exploration and exploitation, whereas vector C always includes some unpredictability. This is crucial because our agents can become stranded in local optima, which most metaheuristics can avoid. Because we don't know the true position of the optimal solution, Xp is determined by the three best answers.

B. PID Tuning using GWO

The tuning parameters of our PID controller, namely Kp, Ki, and Kd, will be modified by assessing the fitness of our DC motor system's objective function, namely ITAE (Integral Time Absolute Error). These parameters are then fed into our DC motor model's PID controller. Figure 5 shows a block schematic for a PID-fed DC motor with parameters optimised using the GWO Algorithm.

The Grey Wolf Optimisation algorithm will be applied as defined in the flowchart shown in Fig 6 with the initialisation parameters being[13]:

1) Number of iterations.
2) Size of the population (search area).
3) Number of variables (Kp, Ki, Kd).

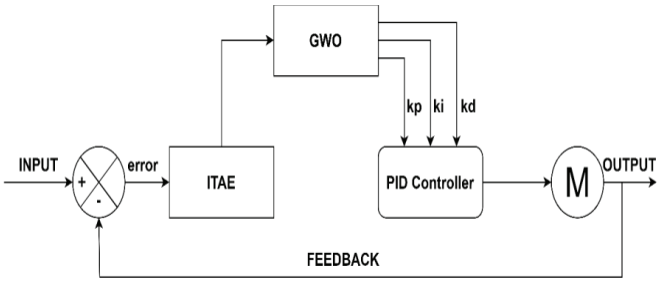

Fig. 4. DC motor drive speed with PID tuning in closed loop control

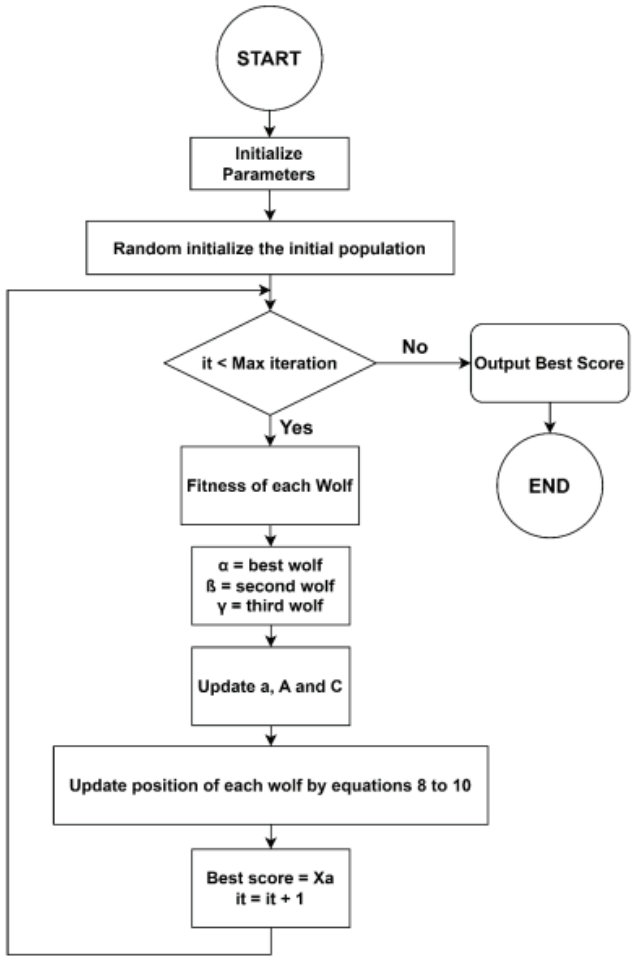

Fig. 5. Flowchart of Grey Wolf Optimization Algorithm

V. Flower Pollination Algorithm(FPA)

A. Algorithm

Pollen transmission is often a component of flower pollination[14], and it frequently involves pollinators which contain animals such as birds, and bugs, among others. In real world, a highly specialised flower-pollinator partnership has co-evolved as a result of specific blooms and insects. For optimal pollination, some blooms, for example, can only draw and depend on a certain species of insect. Pollinators, also referred to as pollen vectors, appear in great diversity. At least

Authorized licensed use limited to: DELHI TECHNICAL UNIV. Downloaded on July 20,2023 at 11:18:33 UTC from IEEE Xplore. Restrictions apply.

200,000 different pollinators, including birds and insects[15], are thought to exist. A notable example of a pollinator is the honeybee, which has the capacity to achieve what is known as blossom constancy. In terms of behavior, these pollinators frequently visit only a few flower types while avoiding others. Floral constancy may have evolutionary benefits since it will improve the transmission of pollen to related or identical plants, maximizing the continuation of a particular genus of flowers. Such floral stability can be beneficial. Figure 6 shows a block schematic for a PID-fed DC motor with parameters optimised using the Flower Pollination Algorithm[16,17].

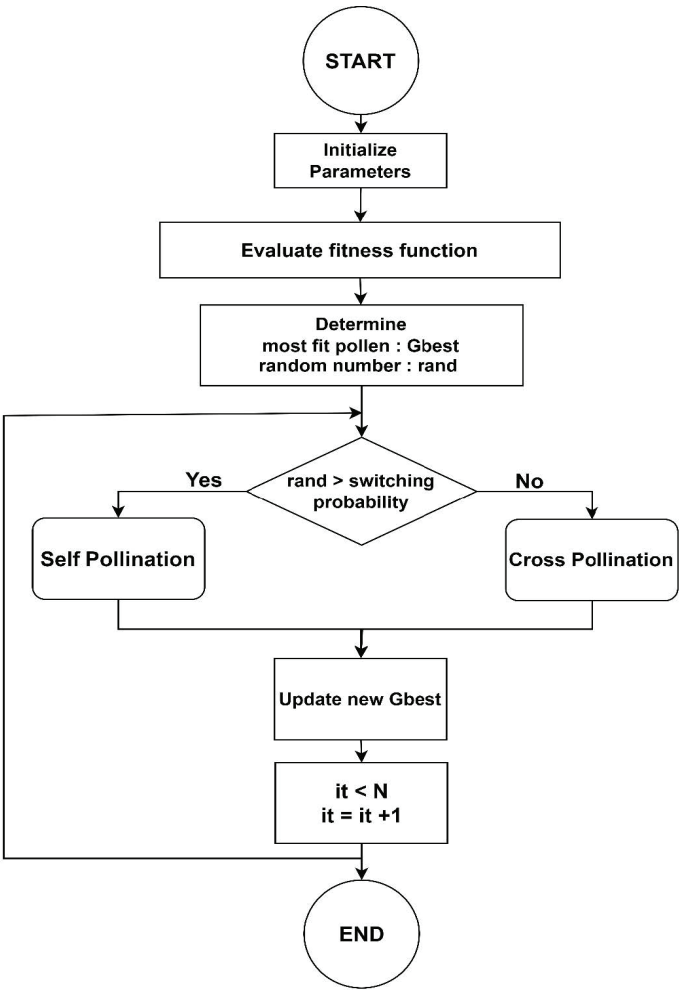

Fig. 6. Flowchart of Flower Pollination Optimization Algorithm

B. PID Tuning using FPA

The values of the controller parameters for our analysis of the performance of DC motors[18] can be obtained by applying the flower pollination algorithm with K_p, K_i, K_d.

The following four guidelines are employed for simplicity[19]:

1) Lévy flights are followed by pollen-carrying pollinators, and biotic and cross-pollination are considered to be global pollination processes. (Rule 1).
2) Local pollination techniques include self-pollination and abiotic pollination. (Rule 2).

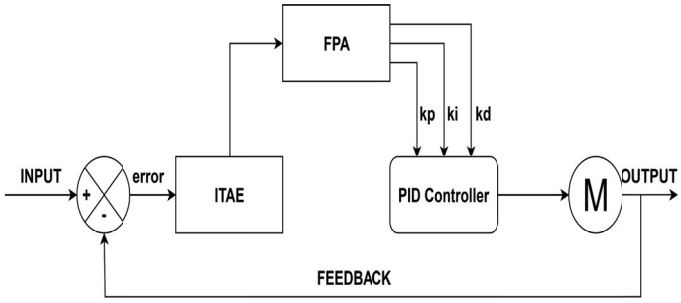

Fig. 7. DC motor drive speed with PID tuning using FPA in closed loop control

3) Pollinators like insects can develop flower constancy, which is compared to a reproduction likelihood proportionate to the similarity of the two flowers involved. (Rule 3).
4) Switch likelihood p[0,1] that is somewhat biased in favor of local pollination can be used to influence how local and global pollination interacts or switch. (Rule 4).

VI. Simulation Results and Discussion

1. Convergence of Objective Function

Figure 8 and Figure 9 demonstrates how objective function ITAE is converging for Grey Wolf Optimization and Flower Pollination ALgorithm run in MATLAB to obtain parameter for PID Controller.

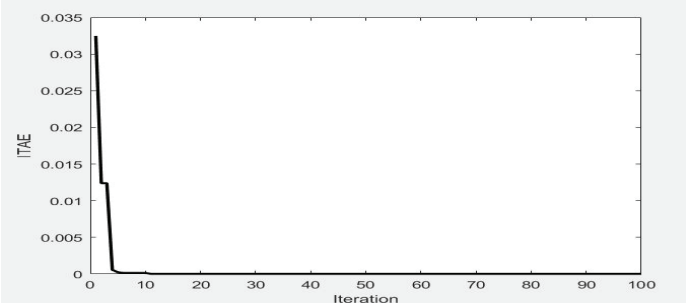

Fig. 8. Convergence of Objective Function for GWO

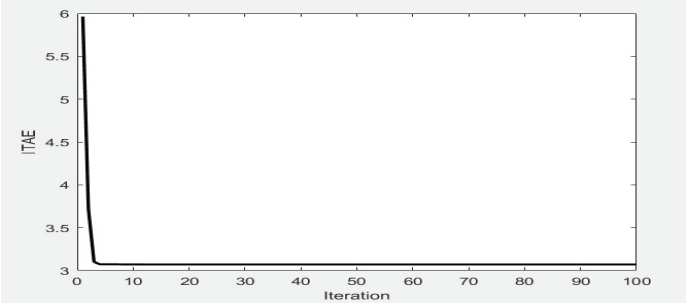

Fig. 9. Convergence of Objective Function for FPA

2. Comparative Analysis of GWO and FPA

Figure 10 shows Combined Response of GWO and Flower Pollination Algorithm with respect to Step Input. Flower pollination can provide better results in every aspect as compared

Authorized licensed use limited to: DELHI TECHNICAL UNIV. Downloaded on July 20,2023 at 11:18:33 UTC from IEEE Xplore. Restrictions apply.

to Grey Wolf optimisation. FPA tuning provide us with less overshoot and the system is becoming stable faster. Table II

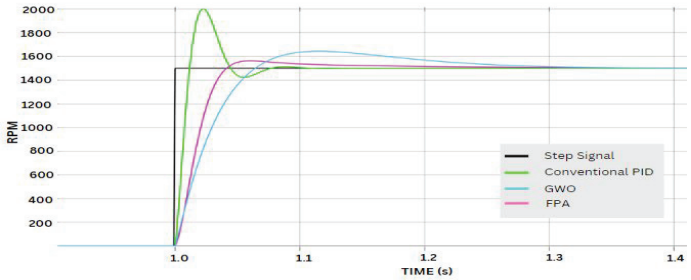

Fig. 10. Comparative Analysis of all the Tuning Methodologies

shows the results obtained by different Algorithms for various Parameters involving Peak Overshoot(M_p), Peak Time(T_p) and Rise Time(T_r).

TABLE II
SYSTEM CHARACTERISTICS FOR TUNED PARAMETERS OF FPA AND GWO

Tuning Algorithm	Tr(ms)	Mp(%)	Tp(ms)
Conventional PID Tuning	10	33.4	22
Grey Wolf Optimisation	49	9.6	115
Flower Pollination	14	2.7	27

VII. CONCLUSION

Using MATLAB/Simulink, a DC motor is simulated and its speed is controlled. We have employed metaheuristic methods of optimization: Grey Wolf Optimisation, and Flower Pollination Algorithm. The nature-inspired metaheuristic approaches for tuning PID provide robust results and are irrespective of the plant model. The use of the objective function for optimization in these techniques provides better stability with changes. Thus, we have a minimum rise time for a plant model. Considering the individual algorithms we see faster settling in FPA, along with better rise time and also lesser overshoot. Hence, Flower pollination with cross-pollination and self-pollination provides a better methodology for tuning compared to conventional techniques, while metaheuristic approach is superior in general.

ACKNOWLEDGMENT

We would like to convey our sincere gratitude to Professor Bharat Bhushan of the Electrical Engineering Department, Delhi Technological University for providing us with the chance to conduct this research and for his helpful advice. His enthusiasm, vision, sincerity, and drive have greatly motivated us. It was a great honor and joy to be able to work and study under his leadership. We are immensely grateful for everything he has given us. He has always been an inspiration to me. We also like to express our gratitude to all of the teaching and support personnel at Delhi Technological University's Electrical Engineering Department for their direct and/or indirect contributions to the project.

REFERENCES

[1] T. Thu Lynn and E. Eaint, "Position Control of DC Servo Drive by Fuzzy Logic Controller in Flat-Bed Screen Printing Machine", ASRJETS-Journal, vol. 26, no. 1, pp. 8–19, Oct. 2016.
[2] A. Kiam Heong, G. Chong, and L. Yun, "PID control system analysis, design, and technology," IEEE Transactions on Control Systems Technology, vol. 13, pp. 559-576, 2005.
[3] R. Kandiban and R. Arulmozhiyal, "Speed Control of BLDC Motor Using Adaptive Fuzzy PID Controller," Procedia Engineering, vol. 38, pp. 306-313, 2012/01/01 2012
[4] M. Kushwah and A. Patra, "Tuning PID controller for speed control of dc motor using soft computing techniques-a review," Advance in Electronic and Electric Engineering, vol. 4, pp. 141-148, 2014.
[5] W. Gubara, M. Elnaim, and S. F. Babiker, "Comparative study on the speed of DC motor using PID and FLC," in 2016 Conference of Basic Sciences and Engineering Studies (SGCAC), 2016, pp. 24-29.
[6] George Ellis, Chapter 6 - Four Types of Controllers, Editor(s): George Ellis, Control System Design Guide (Fourth Edition), Butterworth-Heinemann, 2012, Pages 97-119, ISBN 9780123859204.
[7] Joseph, Stephen Dada, Emmanuel Abidemi, Afeez Oyewola, David Mohammed, Ban. (2022). Metaheuristic Algorithms for PID Controller Parameters Tuning: Review, Approaches and Open Problems. Heliyon.
[8] Stephen Bassi Joseph, Emmanuel Gbenga Dada, Afeez Abidemi, David Opeoluwa Oyewola, Ban Mohammed Khammas. Metaheuristic algorithms for PID controller parameters tuning: review, approaches and open problems.
[9] Abushawish, Eng. Abdallah Hamadeh, Mohammed Nassif, Ali. (2020). PID Controller Gains Tuning Using Metaheuristic Optimization Methods: A survey. International Journal of Computers.
[10] Mirjalili, Seyedali Mirjalili, Seyed Lewis, Andrew. (2014). Grey Wolf Optimizer. Advances in Engineering Software.
[11] Wang, JS., Li, SX. An Improved Grey Wolf Optimizer Based on Differential Evolution and Elimination Mechanism. Sci Rep 9, 7181 (2019).
[12] Aala Kalananda, V.K.R., Komanapalli, V.L.N. A competitive learning-based Grey wolf Optimizer for engineering problems and its application to multi-layer perceptron training. Multimed Tools Appl (2023).
[13] Almufti, S.M., Ahmad, H.B., Marqas, R.B. Asaad, R.R. (2021). Grey wolf optimizer: Overview,modifications and applications. International Research Journal of Science, Technology, Education, and Management, 1(1), 44-56.
[14] Xin-She Yang, Yu-Xin Zhao, Chapter 3 - Firefly algorithm and flower pollination algorithm, Editor(s): Xin-She Yang, Nature-Inspired Computation and Swarm Intelligence, Academic Press,2020,Pages 35-48.
[15] Yang, XS. (2012). Flower Pollination Algorithm for Global Optimization. In: Durand-Lose, J., Jonoska, N. (eds) Unconventional Computation and Natural Computation. UCNC 2012. Lecture Notes in Computer Science, vol 7445. Springer, Berlin, Heidelberg.
[16] S. Lalljith, I. Fleming, U. Pillay, K. Naicker, Z. J. Naidoo and A. K. Saha, "Applications of Flower Pollination Algorithm in Electrical Power Systems: A Review," in IEEE Access, vol. 10, pp. 8924-8947, 2022.
[17] Weijia Cui, Yuzhu He, "Biological Flower Pollination Algorithm with Orthogonal Learning Strategy and Catfish Effect Mechanism for Global Optimization Problems", Mathematical Problems in Engineering, vol. 2018, Article ID 6906295, 16 pages, 2018.
[18] C. Thammarat, A. Nawikavatan and D. Puangdownreong, "Application of Flower Pollination Algorithm to PID Controller Design for Three-Tank Liquid-Level Control System," Proceedings of the 9th International Conference on Sciences, Technology and Innovation for Sustainable Well-Being (STIWB), pp.42-46, 2017.
[19] Mohamed, R., Saber, S., Askar, S. S., Abouhawwash, M. (2021). Modified Flower Pollination Algorithm for Global Optimization. Mathematics, 9(14), 1661.

Authorized licensed use limited to: DELHI TECHNICAL UNIV. Downloaded on July 20,2023 at 11:18:33 UTC from IEEE Xplore. Restrictions apply.

Computers and Electrical Engineering 110 (2023) 108849

Contents lists available at ScienceDirect

Computers and Electrical Engineering

journal homepage: www.elsevier.com/locate/compeleceng

Performance evaluation and optimization of albedo and tilt angle for solar photovoltaic system☆

Neelam Baghel [a], K. Manjunath [a], Anil Kumar [a,b,*]

[a] Department of Mechanical Engineering, Delhi Technological University, Delhi 110042, India
[b] Centre for Energy and Environment, Delhi Technological University, Delhi 110042, India

ARTICLE INFO

This paper is for CAEE special section VSI-hres. Reviews processed and recommended for publication to the Editor-in-Chief by Guest Editor Dr R. K. Saket.

Keywords:
Photovoltaic
Economic
Specific energy production
Carbon emissions
RSM

ABSTRACT

This research focuses on the UN sustainable development goal (SDG)7 i.e., affordable and clean energy. As per goal 7, renewable energy sources are the cleanest sources and will help to reach net zero emissions. Performance of solar photovoltaic (PV) systems is analysed using PVsyst and Response Surface Methodology (RSM) for composite climatic conditions. Two critical parameters i.e., tilt angle and albedo are investigated. Specific production increases as albedo and tilt angle increase. Optimum tilt angle is 25° at 0.54 albedo with a maximum specific production of 1643.3 $kWh/kW_p/year$. Payback period is 5.8 years, the return of investment (ROI) is at 469.2% and the levelized cost of energy (LCOE) is 2.298 ₹/kWh. During its lifetime, the system reduces 3470.5 tCO_2 carbon emission compared to the conventional plant. Therefore, installing such a system will dramatically reduce CO_2 emissions, encourage environmental sustainability and enhance the number of claimed carbon credits.

1. Introduction

Energy is considered a significant factor for economic growth, communal expansion and human welfare. As their exploration, conventional energy has continued as the primary energy source. With the rising tendency of industrialization, the world energy requirement is also growing faster. To cope with the increasing requirement, most developing countries are switching to non-conventional energy resources from conventional ones. The most significant predicament for a sustainable future is the everyday increase in requirements for electrical energy, power pricing, and CO_2 emissions. Electricity consumption in industrialized and developing countries is increasing at 1% and 5% per year, respectively [1]. Nowadays, 80% of power is generated by the combustion of traditional resources such as coal, oil, and gas, increasing the cost of electricity and destroying our environment [2]. A high carbon dioxide concentration causes global warming. By the end of this century, the global temperature is projected to rise by 3°C–6°C. Solar photovoltaics is an excellent solution to the above problems.

Sharma et al. analysed a solar PV system based on different load scenarios in a building to acquire maximum power, performance ratio, efficiency, and more specific production and enhanced system efficiency. The system is tested for one laboratory load with a fixed tilt and variable azimuth angles, and it is found that when the system has zero azimuth angle, the specific production is maximum with 1.7% increase in efficiency [3]. Asgharzadeh et al. analyzed the effect of module height, tilt angle and albedo on the energy yield and bifacial gain of solar PV arrays. It is found that with a ground albedo of 21%, the energy production of the center module in a large

☆ This paper was recommended for publication by Associate Editor Dr R. K. Saket.

* Corresponding author at: Department of Mechanical Engineering, Delhi Technological University, Delhi 110042, India.
E-mail address: anilkumar76@dtu.ac.in (A. Kumar).

https://doi.org/10.1016/j.compeleceng.2023.108849
Received 16 April 2023; Received in revised form 25 June 2023; Accepted 27 June 2023
Available online 5 July 2023
0045-7906/© 2023 Elsevier Ltd. All rights reserved.

Nomenclature

A_m	module area
C_t	temperature coefficient
DiffHor	horizontal diffuse irradiation
E_{DC}	energy produced through PV system
E_{AC}	energy fed to the utility grid
$E_{DC,m}$	monthly DC energy output
E_{Array}	effective energy at the output of the array
E_Grid	energy injected into the grid
$E_{DC,d}$	generated DC energy per day
$E_{DC,d}$	rated value of PV power plant
G_i	global solar irradiance
GlobHor	global horizontal irradiation
GlobInc	global incident in coll. plane
GlobEff	effective global, corr. for IAM and shadings
N	no. of observations
P	regression coefficient number
R	coefficient of determinations
R_{adj}	coefficient of adjusted determinations
SS_T	sum of squares
SS_E	sum of residuals
T_Amb	ambient temperature
T_r	time intermission of recording
T_{rp}	duration of reporting
T_m	module temperature
T_{STC}	ambient temperature
Y	response
y_i and $\widehat{y}$	observations and fitted values
Y_a	array yield
Y_f	final yield
$Y_{a,m}$	monthly mean value of array yield
Y_r	reference yield

Greek Symbols

β_0	constant coefficient
β_i	linear coefficient
β_{ii}	quadratic coefficient
β_{ij}	interaction coefficient
η_{degr}	degradation efficiency
η_{temp}	temperature efficiency
η_{soil}	soiling efficiency
η_{inv}	inverter efficiency
η_{sys}	system efficiency
η_{PV}	PV module efficiency

Abbreviation

ANOVA	Analysis of variance
AC	Alternating current
CRF	Capital recovery factor
COE	Cost of energy
DC	Direct current
₹	Indian National Rupees
LCOE	Levelized cost of energy
LCE	Life cycle emissions
LCC	Life cycle cost
NPC	Net present cost
PR	Performance ratio
PV	Photovoltaics
RSM	Response surface methodology

ROI	Return of investment
SDG	Sustainable development goals
UN	United Nations

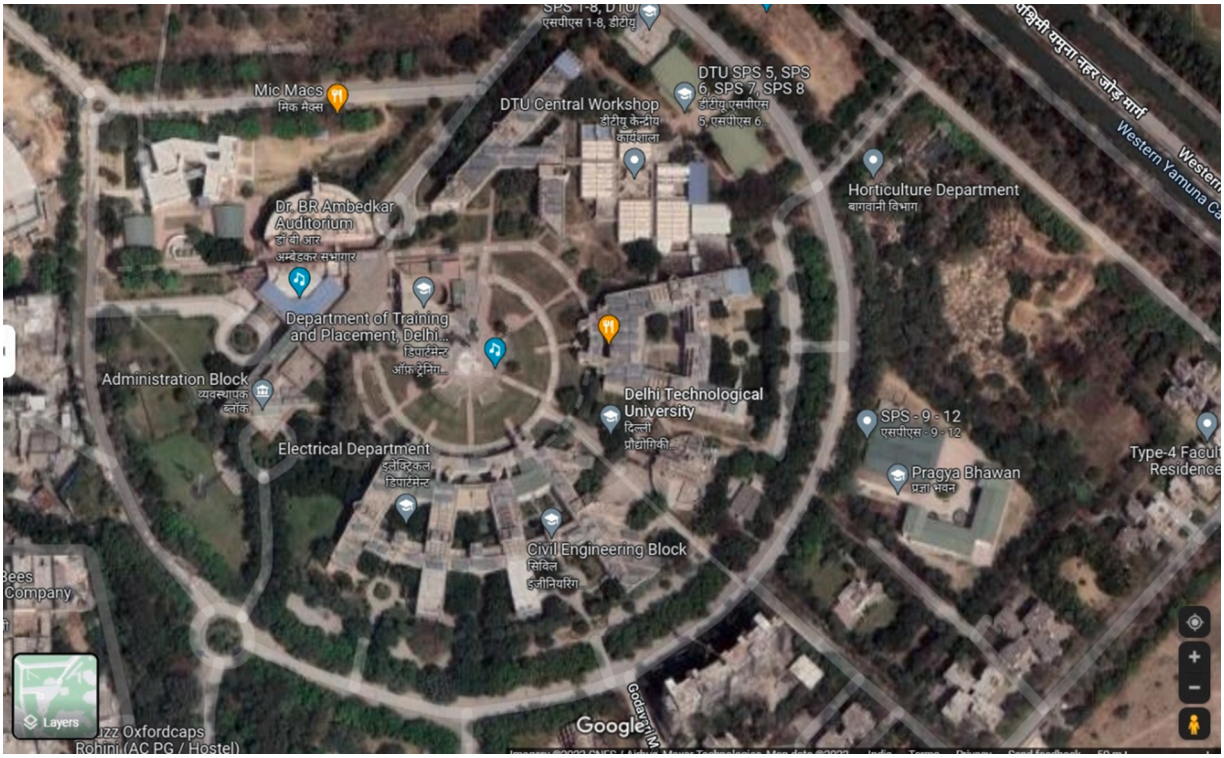

Fig. 1. Location of the site.

array can drop by up to 7% (compared to a single module system) [4]. Yakubu et al. determined that factors such as albedo tilt angle and module height above ground should be tuned to enhance the energy generation from bifacial PV modules. It is concluded that there is around 3.7 to 4.3% increase in annual energy yield in bifacial modules compared to mono-facial modules at different climatic conditions [5]. Asgharzadeh et al. discovered that modules installed at the greatest possible albedo with a sufficient height had higher productivity [6]. Nussbaumer et al. investigated solar PV array energy yield production using miniature test rig assembly. Variations (1 for single-day and short-term observations) vary from 2% to 6.5% depending on the tilt angle. A mean standard deviation of $< 1\%$ was attained for the specified long-term measurement period [7]. Ghenai et al. analysed the effect of tilt angle, height and albedo on the performance of bifacial solar PV systems using RSM. The findings demonstrated a linear relationship between bifacial PV energy yield and albedo [8]. Stein et al. observed that bifacial PV modules system produce more energy than identical modules with the same orientation [9]. Turjman et al. suggested a system that has a life cycle savings of 788 $/year, a payback period of 10.9 years, and NPV and International Rate of Return (IRR) is around 11k $ and 10%, respectively and it provides a sustainable environment, free from CO_2 emissions [10]. Jang et al. used three test beds to experiment with a bifacial PV module and a bifacial PV system, changing the size of the reflecting material, vertical installation, location of the modules for temperature mismatch, and PM concentration. The bifacial gain rose 4% in clear sky circumstances when the PM10 concentration changed by 100 g/m^3. When the PM 10 concentration changed in cloudy circumstances by 100 g/m^3, the bifacial gain fell by 0.9% [11]. Sreenath et al. determined that installing a bifacial solar PV module with a high albedo factor on the ground surface is appropriate for maximizing energy output. The minimal albedo factor of 0.15 is estimated to provide 164.5 MWh of energy annually. An albedo factor of 0.85 at its highest is predicted to produce 175.8 MWh annually [12]. Sanchez et al. used existing algorithms to investigate the influence of clearance height, albedo, tilt, and azimuth angle on bifacial PV energy calculation [13]. Many researchers used RSM for optimizing operating and design parameters. Varun et al. used PVsyst to examine the performance of bifacial modules in vertical and latitude mounting and determined that a latitude-tilted bifacial panel produced 1000 kW_p more than a vertically oriented N-S panel [14]. Osmani et al. investigated the impact of solar PV tilt angle variation on the PV network's cost-effectiveness. Results suggested that for Tripoli, Belfort, and Tantan, respectively, the levelized cost of energy is reduced by 4.32, 3.73, and 4.35%, and generated power is raised by 49.67, 50.36, and 26.83%, while the power cost is dropped by 4.43, 4.48, and 4.47% [15]. Kamalapur et al. assessed the features of rural electrification in India and the feasibility of solar PV home systems [16]. Adaramola et al. investigated that the level of solar radiation on earth strongly influences the economic

Table 1
Specifications of solar module [19].

S.No.	Parameters (All data refers to STC)	Data
1.	Peak Power (0–4.99W_p) P_{max} (W_p)	315
2.	Maximum Voltage V_{mpp} (V)	38.33
3.	Maximum Current I_{mpp} (A)	8.22
4.	Open Circuit Voltage V_{oc} (V)	46.04
5.	Short Circuit Current I_{sc} (A)	8.85
6.	Module Efficiency (%)	16.23
7.	Length × Width × Height	1956 mm × 992 mm × 40 mm
8.	Weight	27 kg
9.	Junction Box	IP67, 3 bypass diodes
10.	Cells	72 polycrystalline solar cells, 3 bus bars
11.	Cell Encapsulant	EVA (Ethylene Vinyl Acetate)
12.	Back Sheet	Composite film
13.	Frame	Anodized aluminium frame with twin wall profile
14.	Mechanical Load Test	5400 Pa
15.	Maximum Series Fuse Rating	15 A

feasibility of the system. This energy system generates 331,536 kWh of electricity annually, 40.4% of electricity coming from solar PV. The levelized cost of energy was determined to be $0.103/kWh based on the assumptions utilized. Integrating solar PV with grid technology is anticipated to lower carbon dioxide and other pollution emissions linked to energy generated by conventional power plants [17]. Sandwell et al. presented a model that can assess the levelized cost and life-cycle emissions intensity of various established and developing PV technologies for rural electrification. It can also reduce greenhouse gas emissions as compared to the conventional mode of electricity generation [18].

Various studies on the solar PV system's performance, techno-economic, environmental and optimization have been analyzed. The literature reveals that no detailed performance analysis of solar PV system i.e., economic, environmental and optimization using RSM has been carried out based on meteorological data for composite climatic conditions. Meanwhile, the influence of two major process parameters, tilt angle and albedo on the performance of the solar PV system is explored in this current research. The specific production of solar PV system will increase with the increase in tilt angle and albedo according to the latitude of the location. Also, it was observed that the installation of such a system will significantly lower CO_2 emissions, promote environmental sustainability, and increase the amount of claimed carbon credits. The findings presented in this study will help investors and regulators discover location-based technologies that will provide the best return on investment for large-scale projects in the home and industrial sectors.

This paper is organized as follows: In Section 2 simulation modelling and optimization of the system are discussed. Section 3 presents a detailed discussion of the results. Section 4 draws out some conclusions and benefits of the system.

2. Methodology

2.1. Simulation modelling of a solar photovoltaic system

PVsyst 7.2.11 is a complete software package to design and simulate a solar PV system. It is also a straightforward and user-friendly simulation tool with few known parameters. It provides a detailed solution of grid-connected, pumping, standalone, and DC grid PV systems about the sizing, no. of inverters, no of PV array, and detailed analysis of solar PV systems. Delhi Technological University, Delhi-India (77.23° E and 28.65° N), is considered as a site (Fig. 1) for analysis and simulation using PVsyst and system is designed for 108 kW_p load. Input data are required for the design simulation in PVsyst. After substituting the value of the longitude and latitude of the above-selected site, solar irradiance is calculated. Fundamentally, designing the solar PV system depends on the availability of solar irradiance. Performance analysis of grid-connected plants has been done at various tilt angle orientations of solar panels. Two cases have been considered for the analysis and simulation. Solar PV panels are mounted at an inclination of 20° tilt angle for the yearly irradiation yield value for the 108 kW_p unit. An identical solar PV system has been analysed at an inclination of 28° to check the existing plant performance according to the existing plant latitude. RPI-M50A inverter and Eldora 300P as a PV array is chosen to meet the 108 kW_p. The detailed specifications of the solar module are given in Table 1.

Following design parameters of the solar photovoltaic system are considered in simulation and modelling:

i **Azimuth Angle**: Azimuth angle is required to define the trend of the sunshine. If the solar panels are in the northern hemisphere and face south, the value is zero. The "Azimuth angle" is the angle created by the sun's rays and true south. A positive azimuth angle indicates an east-south orientation, whereas a negative azimuth angle indicates a west-south orientation.
ii **PV Array specifications:** To design the unit of 108 kW_p for Delhi Technological University, Delhi. Solar PV panels of "Vikram Solar" manufacture model no. Eldora 300P, rated peak power of 300 W each, polycrystalline solar PV modules are considered [19].
iii **Inverter specification**: To design the unit of 108 kW_p for Delhi Technological University, Delhi. Delta Inverter capacity of 50 kW_p each with model number RPI-M50A by Delta Power Solutions is considered [20].

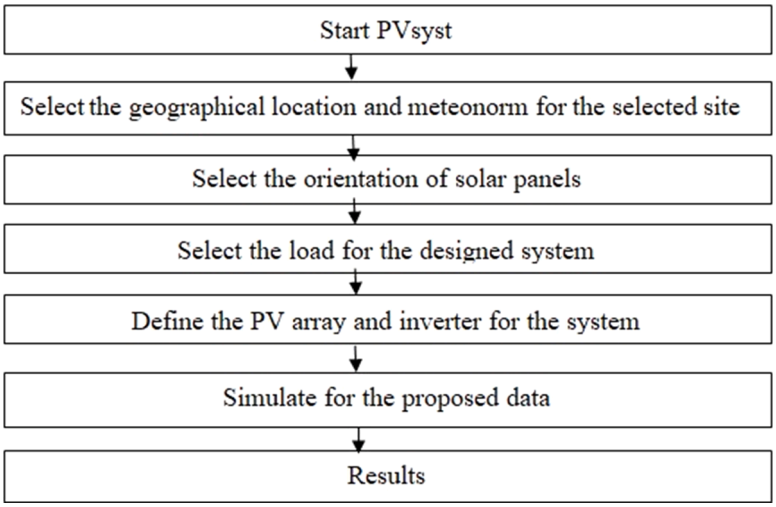

Fig. 2. Flowchart of simulation in PVsyst.

iv **Solar irradiance:** The average sun irradiation at 28.650° N and 77.230° E is around 5.477 kWh/m^2/day, which is an adequate number for producing electrical energy. Solar irradiance is the amount of solar energy received per unit area. This irradiance has the maximum value in the summer and the lowest value in the winter and it is measured in W/m^2.

The steps followed for the simulation in PVsyst are shown in Fig. 2.
Performance analysis parameters for evaluating grid-connected solar PV systems are discussed as follows:

Energy fed to the utility grid (E_{AC}): The entire day evaluation of AC energy generation is evaluated by Eq. (1)[21]:

$$E_{AC,d} = \sum_{t=1}^{t=T_{rp}} V_{AC} \times I_{AC} \times T_r \tag{1}$$

AC output generated in a month is presented by Eq. (2) [21]as:

$$E_{AC,m} = \sum_{d=1}^{N} E_{AC,d} \tag{2}$$

Energy produced through PV system (E_{DC}): The complete monitored everyday DC power is given by Eq. (3)[21]:

$$E_{DC,d} = \sum_{t=1}^{t=T_{rp}} V_{DC} \times I_{DC} \times T_r \tag{3}$$

The monthly generated DC energy is given by Eq. (4)[21]:

$$E_{DC,m} = \sum_{d=1}^{N} E_{DC,d} \tag{4}$$

where, N denotes the number of working days of a plant in a month, subscript m indicates monthly value and subscript d indicates daily value.

Final yield (Y_f): The ratio of final produced power to rated PV power specified by the manufacturer under standard temperature conditions. It denotes the amount of time the PV system requires to create the concluding output concerning its nominal power capability. Eqs. (5) and (6) give the daily (Y_f,d) and monthly (Y_f,m) average final yields as [22]:

$$Y_{f,d} = \frac{E_{AC,d}}{P_{PV,rated}} \tag{5}$$

$$Y_{a,m} = \left(\frac{1}{N}\right) \times \sum_{d=1}^{N} \mathrm{Y_{a,d}} \tag{6}$$

Array yield (Y_a): The array yield is calculated by taking the ratio of generated DC energy to the rated value of the PV power plant system. The daily array yield ($Y_{a,d}$) is presented by Eq. (7) [22]:

$$Y_{a,d} = \frac{E_{DC,d}}{P_{PV,rated}} \tag{7}$$

The monthly mean value of array yield ($Y_{a,m}$) is presented by Eq. (8):

$$Y_{a,m} = \left(\frac{1}{N}\right) \times \sum_{d=1}^{N} \mathrm{Y_{a,d}} \tag{8}$$

Array yield denotes the time the PV system acquires to operate at nominal power generation in the unit of h/day.

Reference yield (Y_r): The total in-plane solar insolation ratio to reference irradiance under standard temperature conditions of 1 kW/m^2. It is represented by Eq. (9) as:

$$Y_{r,d} = T_r \times \frac{\sum_{day} G_i}{G_{STC}} \tag{9}$$

Furthermore, the corrected reference yield is evaluated by taking into account the module's modification impact and the ambient temperature, as shown in Eq. (10):

$$\mathrm{Y_{cr}} = \mathrm{Y_r}\ [1 - \mathrm{C_t}(\mathrm{T_m} - \mathrm{T_{STC}})] \tag{10}$$

PV module efficiency (η_{PV}): The efficiency of a PV module reveals how much energy the module generates compared to the available radiation. Eq. (11) expresses it as follows:

$$\eta_{\mathrm{PV}} = \left[\frac{\mathrm{P_{DC}}}{\mathrm{G_i} \times \mathrm{A_m}}\right] \times\ 100\% \tag{11}$$

The monthly module efficiency is given by Eq. (12) as follows:

$$\eta_{\mathrm{PV,m}} = \left[\frac{\mathrm{E_{DC,m}}}{\mathrm{G_i} \times \mathrm{A_m}}\right] \times\ 100\% \tag{12}$$

Inverter efficiency (η_{inv}): The inverter efficiency is estimated by dividing the inverter's generated AC power by the PV array system's generated DC power. When calculating inverter efficiency, it is considered that system efficiency and module efficiency are the greatest since it is the conversion efficiency of DC to AC power. Eq. (13) gives the instantaneous inverter efficiency as follows:

$$\eta_{\mathrm{inv}} = \left[\frac{\mathrm{P_{AC}}}{\mathrm{P_{DC}}}\right] \times\ 100\% \tag{13}$$

The inverter efficiency may also be estimated using Eq. (14) with monthly values of DC energy generated ($E_{DC,m}$) and AC energy generated ($E_{AC,m}$).

$$\eta_{\mathrm{inv,m}} = \left[\frac{\mathrm{E_{AC,m}}}{\mathrm{E_{DC,m}}}\right] \times\ 100\% \tag{14}$$

System efficiency (η_{sys}): The photovoltaic system efficiency is characterized by the product of PV module efficiency (η_{PV}) and inverter efficiency (η_{inv}), as shown in Eq. (15):

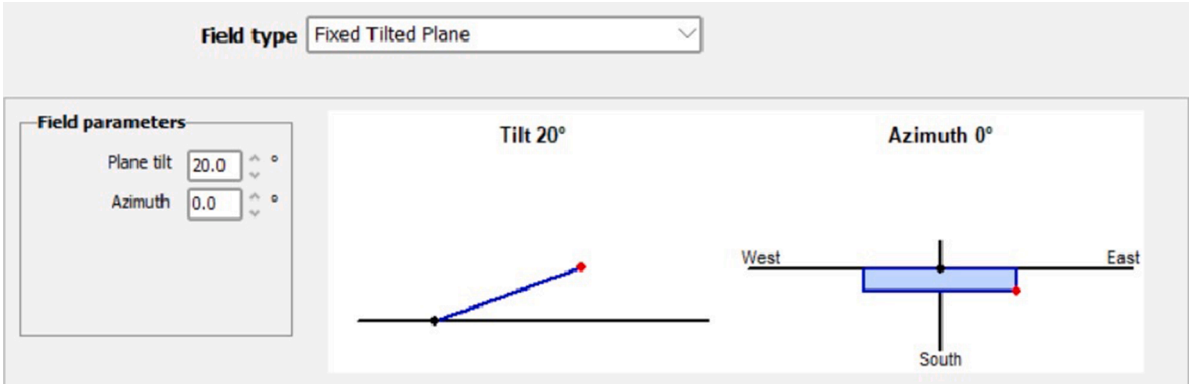

Fig. 3. Orientation of PV system at 20° tilt angle.

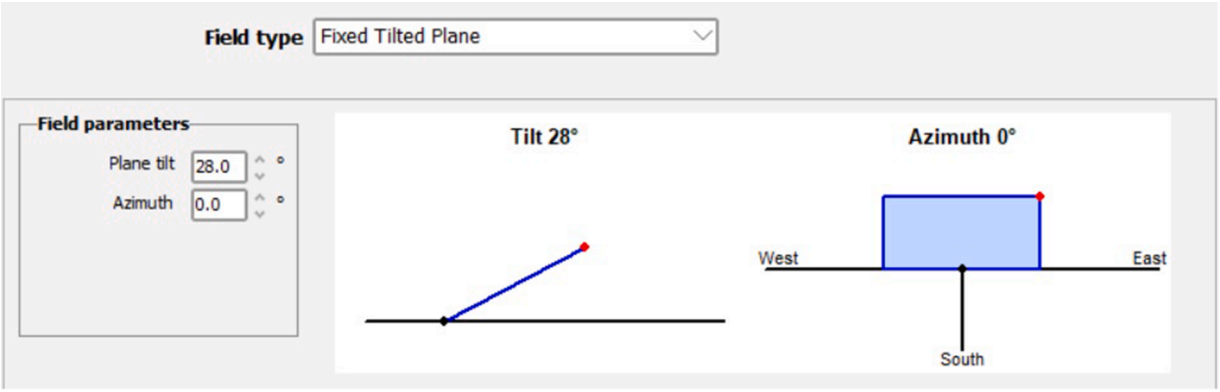

Fig. 4. Orientation of PV system at 28° tilt angle.

$$\eta_{sys} = \eta_{PV} \times \eta_{inv} \tag{15}$$

Capacity factor (CF): It is the ratio of real yearly energy production to the quantity of energy that can be produced by the rated capacity of the PV system for 24 h per day during one year, as stated by Eq. (17) as:

$$CF = \frac{Y_{f,annual}}{24 \times 365} = \frac{E_{AC,annual}}{P_{PV,rated} \times 8760} \tag{16}$$

$$CF = \frac{\frac{h}{day} \text{of the peak sun}}{24 \text{ hours/day}} \tag{17}$$

The CF fluctuates in a similar ratio as the ultimate yield. It is a means of displaying the energy carried by an electrical power distribution system. If the system delivered full-rated power constantly, the CF would be 1.

Performance ratio (PR): It is defined as the ratio of the final yield (Y_f) to the array yield (Y_a), as stated in Eq. (18)[23]:

$$PR = Y_f / Y_a \tag{18}$$

As demonstrated in Eq. (19), it may alternatively be characterized as a function of degradation efficiency (η_{degr}), soiling efficiency (η_{soil}), temperature efficiency (η_{temp}), and inverter efficiency (η_{inv}):

$$PR = \eta_{degr} \times \eta_{temp} \times \eta_{soil} \times \eta_{inv} \tag{19}$$

This ratio depicts the real proximity to the ideal efficiency and the influence of photovoltaic system losses. Optimizing system orientation with variation in the tilt angle of PV panels is studied. The panels are facing true south tilted with angles of 20and 28°. The comparative analysis is done based on different tilt angle positions of PV panels to maximize the module's output. Figs. 3 and 4 indicate the PV system's orientation at 20° and 28° tilt angles for the 108 kW_p systems. A Grid-Connected system with different tilt angles has been chosen for the simulation. According to the site specification and solar irradiation, two tilt angles 20° and 28° and azimuth angle 0° are considered for the analysis.

2.1.2. Case: I and II – 108 kW_p system at an inclination of 20° and 28°

Figs. 3 and 4.

2.2. Optimization using RSM

Response surface methodology (RSM) is a compilation of arithmetical and statistical methodologies. RSM's capacity to establish a model between the response and input variables using analysis of variance (ANOVA) is one of its beneficial qualities. The polynomial regression model is used, and it is written in Eq. (20) [8]:

$$y = \beta_0 + \sum_{i=1}^{n} \beta_i \chi_i + \sum_{i=1}^{n} \beta_{ii} \chi_i^2 + \sum_{i=1}^{n-1} \sum_{j-i+1}^{n} \beta_{ij} \chi_i \chi_j \tag{20}$$

The adjusted multiple determination coefficient tests the precision of the regression model (R^2_{adj}) and the coefficient of multiple determinations (R^2_{adj}) is calculated by the following expressions Eq. (21):

$$R^2_{adj} = 1 - \left(1 - R^2\right) \frac{n-1}{n-P} \tag{21}$$

where, y is the response; β_0, β_i, β_{ii}, and β_{ij} are the constant, linear, quadratic, and interaction coefficients, respectively; n designates the number of the factors $(x)_i$. P is the regression coefficient number. The coefficient of determination is determined by using Eq. (22).

$$R^2 = 1 - \frac{SS_E}{SS_T} \tag{22}$$

where, SS_T and SS_E are the sum of the squares and the sum of the residuals

$$SS_T = \sum_{i=1}^{n} y_i^2 - \frac{\sum_{i=1}^{n} y_i^2}{n} \tag{23}$$

$$SS_E = \sum_{i=1}^{n} \left(y_i - \hat{y}\right)^2 \tag{24}$$

where, y_i and $\hat{y}$ are the observations and fitted values, and N designates the number of observations. The impacts of two predominantly major installation parameters on a solar PV system's performance have been determined. As input variables, tilt angles 20° and 28° and albedo of 0.2 and 0.8 are examined.

2.3. Economic analysis

Economic variables should be considered to assess the advantages of investing in PV power systems. The feasibility of the PV system investment may be guaranteed by appropriate economic analysis, which includes life cycle cost (LCC), cost of energy (COE), and payback period.

2.3.1. Net present cost

Net Present Cost (NPC) is the difference between total paid expenses and total received income during the project's life. Capital expenses, replacement costs, maintenance and operations costs, fuel costs, and grid electric purchase prices are all possible. The cash might come from selling the energy to the grid and salvage value. Eq. (25) defined the NPC as follows:

$$\mathrm{NPC} = \frac{C_{total}}{\mathrm{CRF}\left(i, T_p\right)} \tag{25}$$

2.3.2. Payback period

Payback period is the amount of time it takes for a project to recoup its original investment through income. The payback method's core concept is to assess the likelihood of investment. It is defined by Eq. (26) [24].

$$\text{Payback period} = \frac{\text{Initial Investment}}{\text{Annual Savings}} \tag{26}$$

Table 2
PVsyst simulation results at different tilt angles.

Power (kWh)	108 kW_p	
Tilt Angle	20° (Simulated)	28° (Simulated)
Produced Energy	172.4 MWh/year	174.3 MWh/year
Performance Ratio	80.77%	80.92 %
Specific Production	1600 kWh/kW_p/year	1618 kWh/kW_p/year

Table 3
Balance sheet simulation result in PVsyst at 28° tilt angle.

	GlobHr kWh/m^2	DiffHor kWh/m^2	T_Amb °C	GlobInc kWh/m^2	GlobEff kWh/m^2	EArray MWh	E_Grid MWh	PR Ratio
January	106.2	45.0	13.08	147.1	140.0	13.91	13.67	0.863
February	126.2	46.9	17.36	162.7	154.7	14.95	14.68	0.838
March	174.6	63.9	23.65	201.5	191.0	17.88	17.55	0.809
April	198.4	76.5	29.58	204.9	194.1	17.62	17.27	0.782
May	203.4	98.5	33.40	192.7	181.8	16.38	16.07	0.774
June	182.7	104.9	33.11	167.6	157.8	14.41	14.15	0.784
July	154.5	100.1	31.48	142.8	134.1	12.43	12.21	0.794
August	153.9	93.0	30.53	150.6	141.9	13.16	12.93	0.797
September	148.4	75.0	29.09	159.2	150.4	13.90	13.65	0.796
October	147.0	67.6	26.31	177.2	168.4	15.68	15.39	0.807
November	111.2	52.7	19.88	148.2	140.8	13.56	13.34	0.836
December	101.6	44.1	14.72	144.7	137.8	13.58	13.34	0.856
Year	**1808.1**	**868.3**	**25.22**	**1999.1**	**1892.8**	**177.46**	**174.26**	**0.809**

2.3.3. Levelized cost of electricity

Levelized cost of electricity (LCOE) of a solar PV system is the total cost of installation and operation in terms of the present currency per kilowatt-hour. It is expressed by Eq. (27) [24].

$$\mathrm{LCOE} = \frac{\text{Total life cycle cost (in Rs.)}}{\text{Total lifetime energy production (in kWh)}} \tag{27}$$

2.3.4. Annualized capital cost (C_a)

It is determined by adding the capital recovery factor (CRF), which depends on the actual discount rate, i and the payment period (in years), n, to the total cost of all components, Ci. It is represented by Eq. (29).

$$\mathrm{CRF} = \frac{i(1+i)^n}{(1+i)^n - 1} \tag{28}$$

$$C_a = C_i * \mathrm{CRF} \tag{29}$$

2.4. Environmental analysis

The power grid provides the electrical energy utilized in government facilities and academic campuses. Conventional, nuclear, hydroelectric, and renewable energy sources power the grid. As a result, a significant quantity of CO_2 is emitted during the creation of this power. Grid electricity would be replaced with solar PV-based electricity. The emissions reductions from not utilizing grid electricity are evaluated using emission factors from the Central Electricity Authority of India (CEA 2019). Grid power is being replaced with solar PV-based electricity, the reductions in CO_2 emissions and not utilizing grid electricity are evaluated using emission factors given by the Central Electricity Authority of India (CEA 2019). CO_2 emission factor is given by Eq. (30)[24].

$$CO_2\mathrm{emissionfactor} = 0.9247 t CO_2/\mathrm{MWh} \tag{30}$$

3. Results and discussion

3.1. Performance analysis

The performance analysis of the solar PV system depends upon factors like longitude, latitude conditions and climatic conditions like wind speed, temperature and sun-oriented irradiance. Analysis is performed for the specified location by evaluating these factors. Simulation results at different tilt angles are given in Table 2.

Table 3 represents the values of global horizontal radiation, diffuse radiations, ambient temperature, and global incident coll.

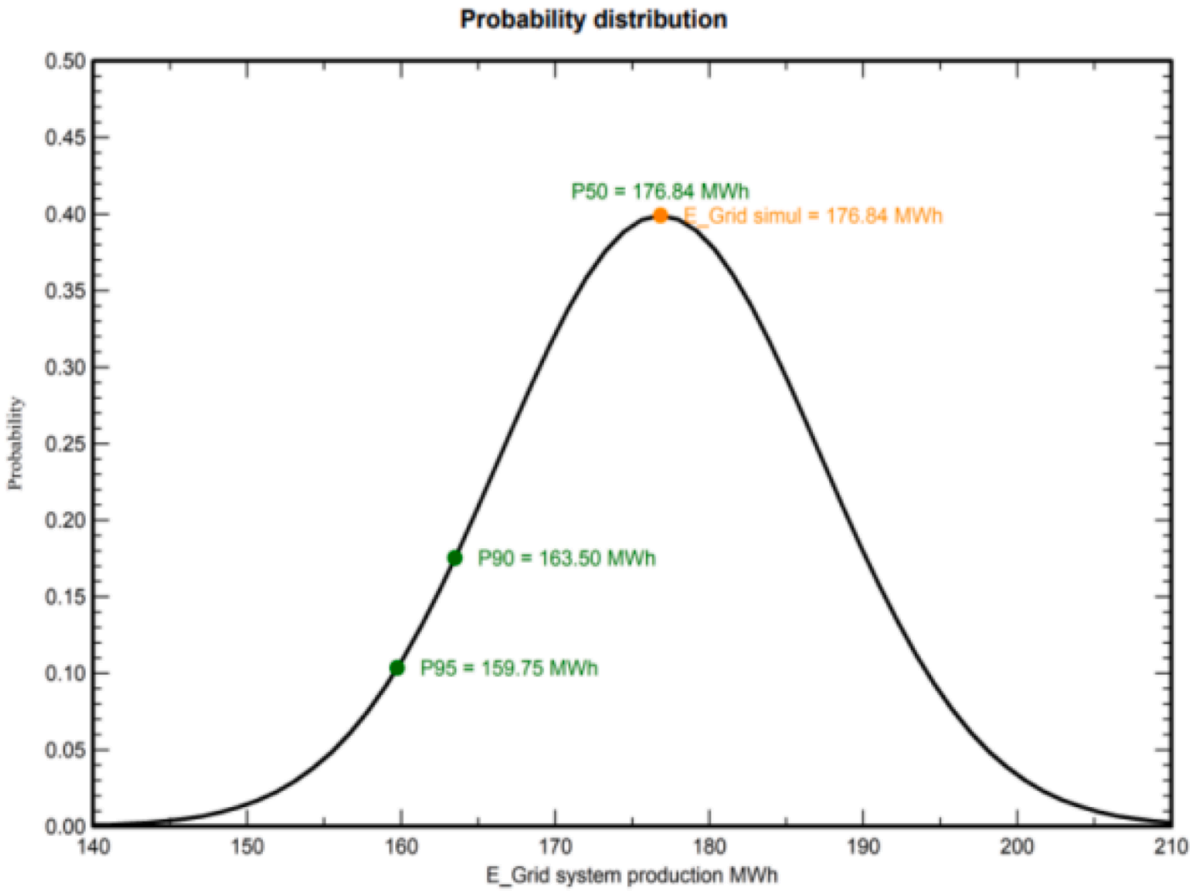

Fig. 5. Probability distribution of the system.

Table 4
Input variable and output response for the simulation.

Type	Description	Unit	Levels	
			Minimum	Maximum
Input Variable	Tilt Angle	Degree	20°	28°
	Albedo	–	0.2	0.8
Output Response	Specific Production	kWh/kW$_p$/year	1600	1670

plane, effective global correlations for IAM shadings, effective energy at the array output, energy injected into the grid and performance ratio at the tilt angle of 28°. Yearly total incident global horizontal radiation (GlobHor) of 1808.1 kWh/m^2 is fed into the system, and the result increases to 1999.1 kWh/m^2 after adding a particular inclination to the global horizontal radiation (GlobInc). The performance ratio (PR) determines a PV facility's efficiency. It is the ratio of the system's energy production to the radiation incident in the specified region.

P50-P90 evaluation is a probabilistic approach for the interpretation of the simulation results, as a Gaussian probability distribution during the entire project life. The probability distribution at P50, P90 and P95, i.e., 176.84 MWh, 163.50 MWh and 159.75 MWh, respectively, for the existing system is shown in Fig. 5.

The albedo varies from zero (blackbody - a surface that absorbed all incident radiation) to one (the surface that reflects all the incident radiation). The bifacial solar panels are intended to be installed on the building's roof. If the roof surface is black or grey, the albedo will be close to 10% (gravel, tar, or bitumen). In addition, if the roof surface is painted white or heat-reflecting paint (cool roof-high albedo and high solar reflectance index SRI), the visible solar reflectance spectrum albedo value may exceed 90%. The solar cell does not react to extended wavelengths (>900 nm). The use of cool roof technology boosts the effectiveness of bifacial solar PV systems (white paint with a high solar reflectance index).

This high albedo level is achievable with cool roof technology (white roof paint) and a clean roof surface (no dust collection on the roof surface). Minimum and maximum tilt angle level is taken from 20° to 28° and albedo from 0.2 to 0.8 as shown in Table 4. Various

Table 5
Specific production of solar photovoltaic system at different tilt angles and albedo.

Run	Tilt Angle (° C)	Albedo	Specific energy production (kWh/kW$_p$/year)
1.	20	0.8	1628
2.	20	0.5	1618
3.	24	0.5	1636
4.	20	0.2	1600
5.	24	0.5	1636
6.	28	0.8	1670
7.	28	0.2	1618
8.	28	0.8	1670
9.	20	0.8	1628
10.	20	0.2	1600
11.	20	0.2	1600
12.	28	0.8	1670
13.	20	0.2	1600
14.	24	0.8	1651
15.	28	0.8	1670
16.	20	0.2	1600
17.	28	0.8	1670
18.	28	0.2	1600
19.	24	0.5	1636
20.	28	0.2	1628
21.	24	0.5	1636
22.	28	0.5	1648
23.	28	0.2	1618
24.	24	0.5	1636
25.	28	0.2	1618
26.	24	0.5	1636
27.	20	0.8	1628
28.	24	0.5	1636
29.	20	0.8	1628

Table 6
ANOVA for specific production of solar PV system.

Source	Sum of squares	Df	Mean Square	F-value	P-value	
Model	14,537.19	5	2907.44	162.29	<0.0001	**Significant**
A-Tilt angle	4465.78	1	4465.78	249.27	<0.0001	
B-Albedo	8084.04	1	8084.04	451.23	<0.0001	
AB	772.98	1	772.98	43.15	<0.0001	
A^2	17.05	1	17.05	0.9516	0.3395	
B^2	59.06	1	59.06	3.30	0.0825	
Residual	412.05	23	17.92			
Lack of fit	0.8538	2	0.4269	0.0218	0.9785	**Not significant**
Pure error	411.20	21	19.58			
Cor Total	14,949.24	28				

combinations of tilt angle and albedo have been run to find out the optimum value of specific energy production as per the minimum and maximum levels of tilt angle and albedo (Table 5).

The analysis of variance (ANOVA) is used to describe the significance and fitness of the coupled RSM model using mathematical results given by PVsyst. Table 6 displays the ANOVA findings and linear variable (Albedo, tilt Angle). In the event of the RSM model's yearly specific production by the solar PV system, coefficient determination (R^2) and adjusted coefficient determination (Adj R^2) are established as 0.9989 and 0.9983, respectively. The (F-test) value of 1652.49 is obtained, indicating the importance of the proposed model. As a result, a regression model is designed to characterize the correlation between the parameters and the yearly specific production of the solar PV system. This indicates that the RSM's fitness has been estimated, the model's accuracy is adequate, and it provides a decent match. Eq. (31) gives the second-order equation in coded terms (+1 for the high level of input factors and 1 for the low level of input factors) developed to forecast the yearly specific production by the solar PV module. Eq. (3) calculates specific production.

$$\text{Specific Production} = 1470.20 + 8.89A - 7.81B + 5.33AB - 0.164\ A^2 - 52.41B^2 \tag{31}$$

3.2. Effect of albedo on specific production

The effectiveness of a PV array is also dependent on various factors like climatic conditions, the height of the structure etc. The ability of a surface to reflect solar radiation is referred to as albedo. The primary source of rear irradiance is reflected radiation from the

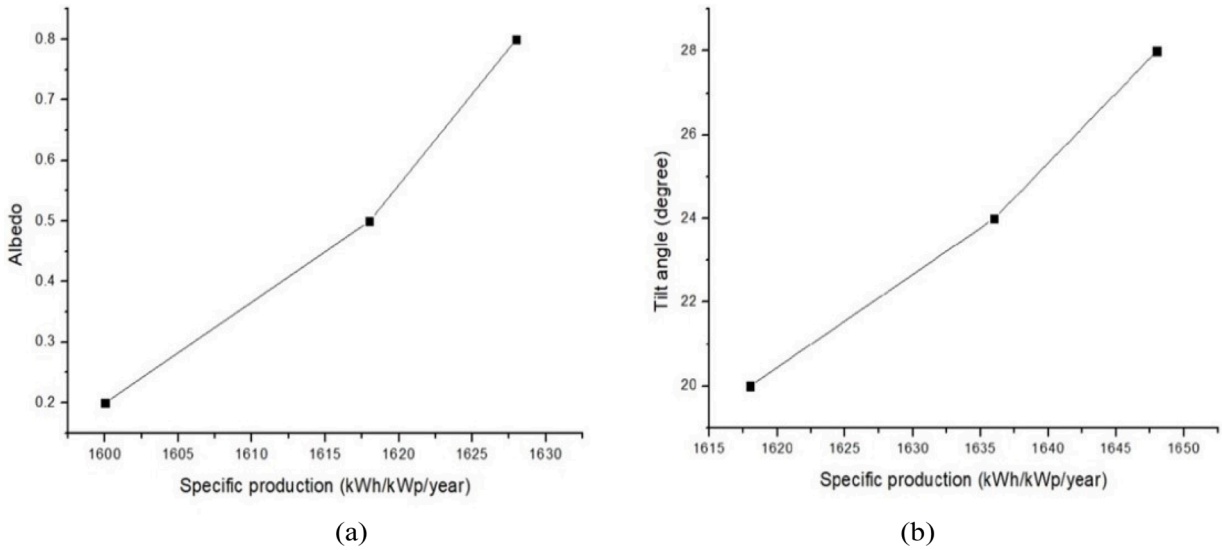

Fig. 6. Specific production of energy (a) effect of albedo (b) effect of tilt angle.

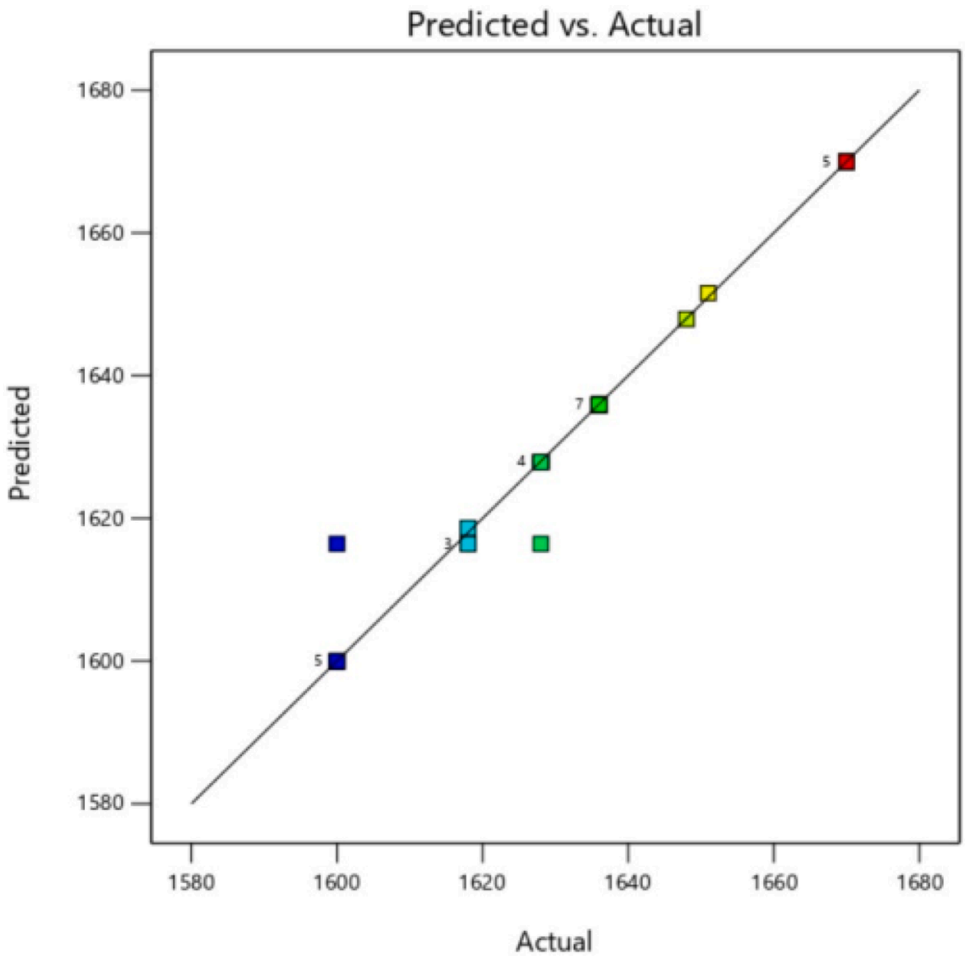

Fig. 7. Predicted vs. actual specific production.

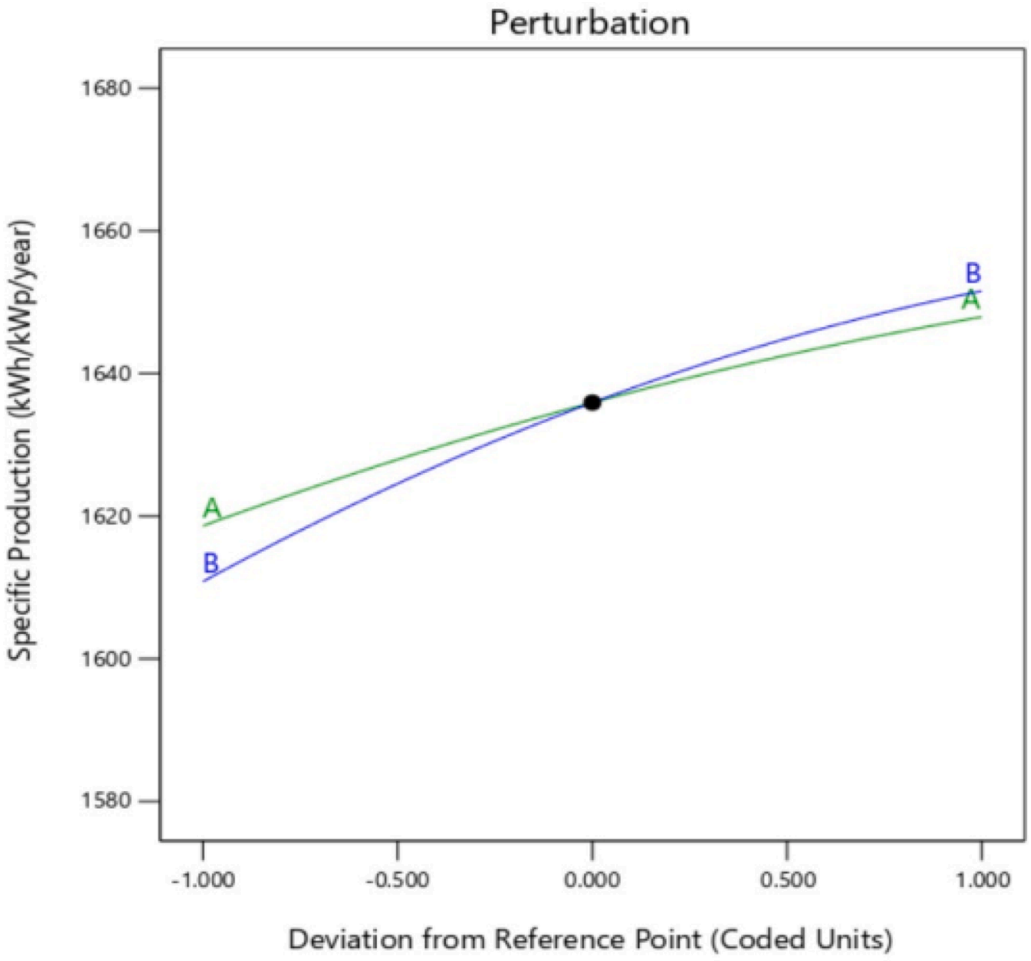

Fig. 8. Perturbation plot of specific production.

ground, increasing albedo, and specific production is also increasing (Fig. 6(a)).

3.3. *Effect of tilt angle on specific production*

The tilt angle determines the solar irradiance received by the plane of the PV array. As a result, it directly influences the PV system's performance. The angle of inclination has been examined and determined by the geographical characteristics of the area. Specific production increases yearly with increasing tilt angle, reaching a peak at 28° (Fig. 6(b)). As a result, 28° may be the best tilt angle for solar PV under the considered geographical location. The optimal tilt angle for solar PV depends on other characteristics, such as albedo. Hence, investigating these component's interplay is essential to identify optimum circumstances. The comparison of specific energy production by the solar PV module generated by the PVsyst (actual) and the predicted assessments using the polynomial regression model stated in Eq. (31) (Fig. 7), verifies the adjacency of predicted data and actual data.

Expected values of the solar PV annual energy output are close to and well-matched to the actual simulation values. The R^2 indicates how effectively a linear regression model fits a data set. As a result, $R^2 = 1$ means that the predictor variable can describe the responder variable without a mistake. The R^2 and adjusted R^2 values for yearly specific energy production are 0.9724 and 0.9664, respectively. As a result, the produced response surface model is credible, and the suggested correlation in Eq. (31) is valid and correct for the yearly specific energy production by solar PV using two input parameters. The effects of tilt angle and albedo on specific energy production are presented in perturbation plots as shown in Fig. 8. It can be noted that the albedo and tilt angle is the most important parameter for specific energy production.

The slope of curvature indicates that the intention of the reaction is sensitive to the specified factor. It is worth noting that the albedo is the main critical parameter for specific energy production. Increasing the tilt angle and albedo increases the yearly specific energy production. However, the effect of both parameters is analyzed on specific energy production. 3D-response surface graph that depicts the interface impact of tilt angle and albedo (Fig. 9). Fig. 10 depicts the contours plot of specific albedo and tilt angle. The specific energy production of PV is most significant with a tilt angle of 28° and an albedo of 0.8. Specific energy production is low at 20°

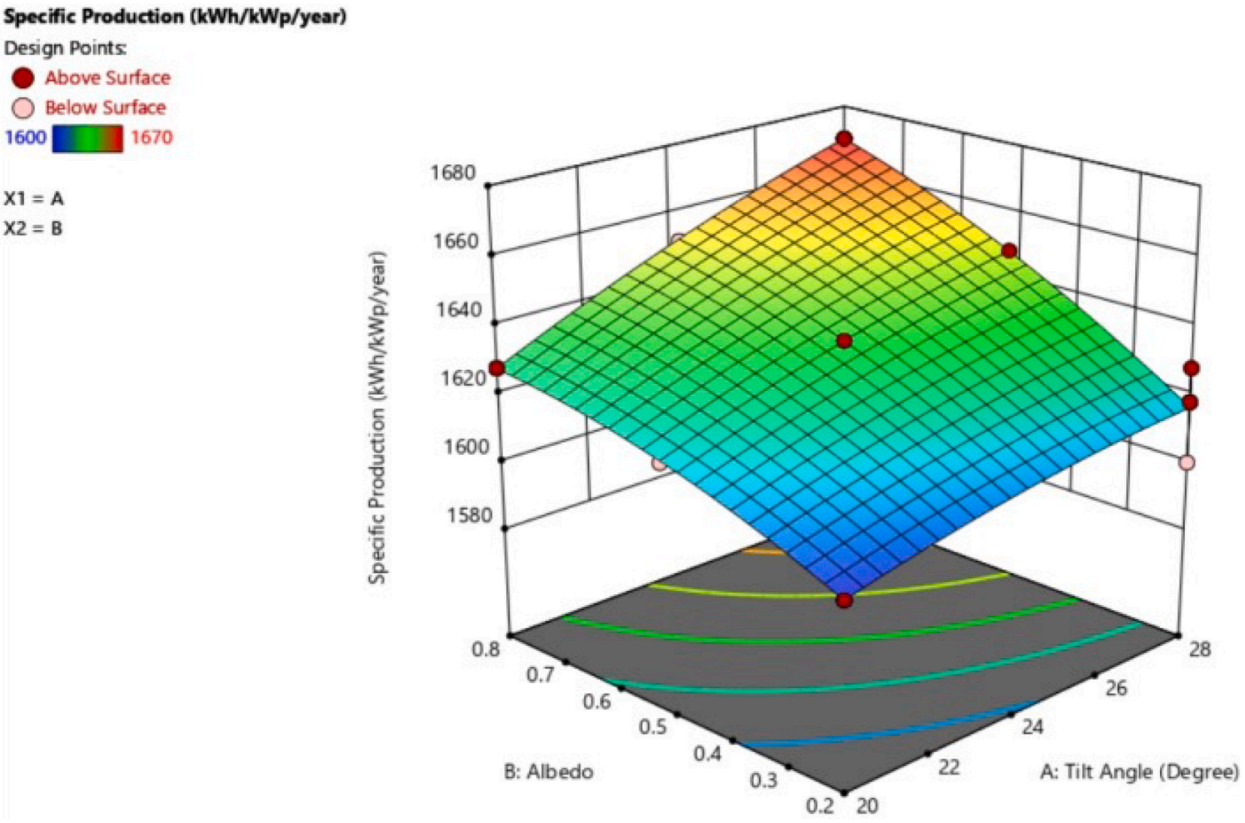

Fig. 9. 3D Surface plots of specific production vs. albedo and tilt angle.

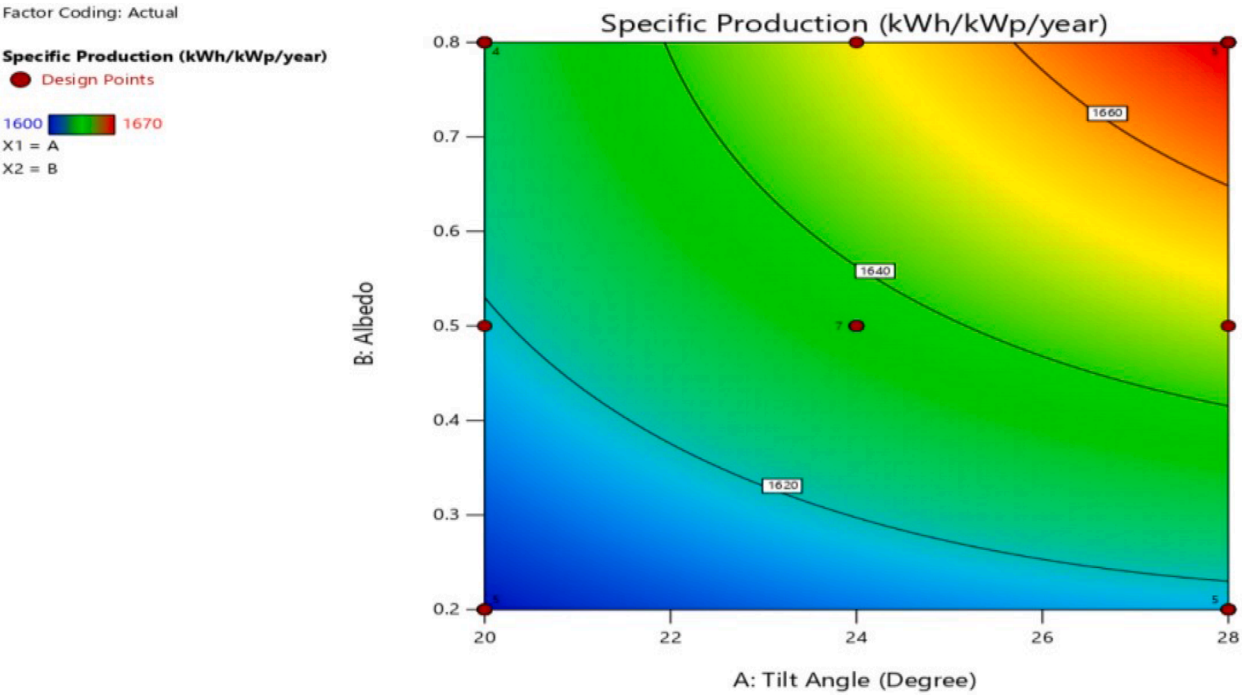

Fig. 10. Contour plots of specific albedo and tilt angle.

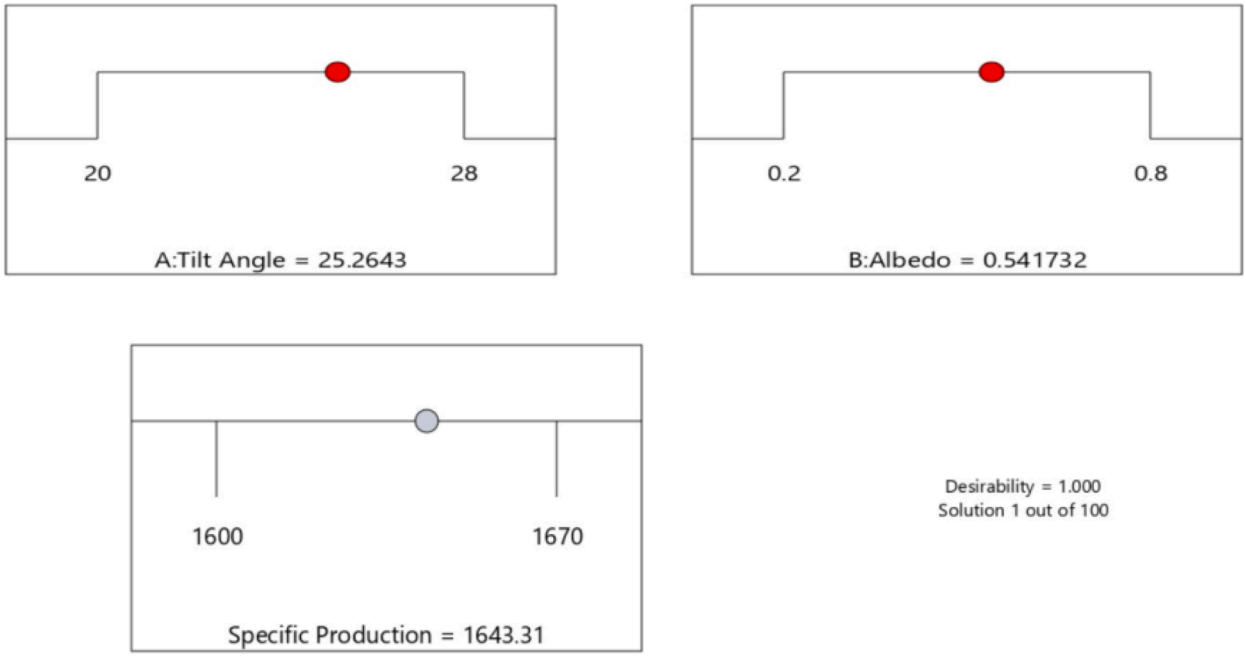

Fig. 11. Optimum conditions of tilt angle, albedo for maximum specific energy production.

Table 7
Financial summary of the system for project lifetime (25 years).

S.No.	Cost component	Details
1.	Total installation cost	₹ 5,138,721.00
2.	Operating cost (including inflation 2% per year)	69,012.48 ₹/year
3.	Produced energy	177 MWh/year
4.	Cost of produced energy	2.298 ₹/kWh
5.	Feed-in tariff	7.75 ₹/kWh
6.	Payback period	5.8 years
7.	Net present value	₹ 24,109,600.38
8.	Return on investment (ROI)	469.2%

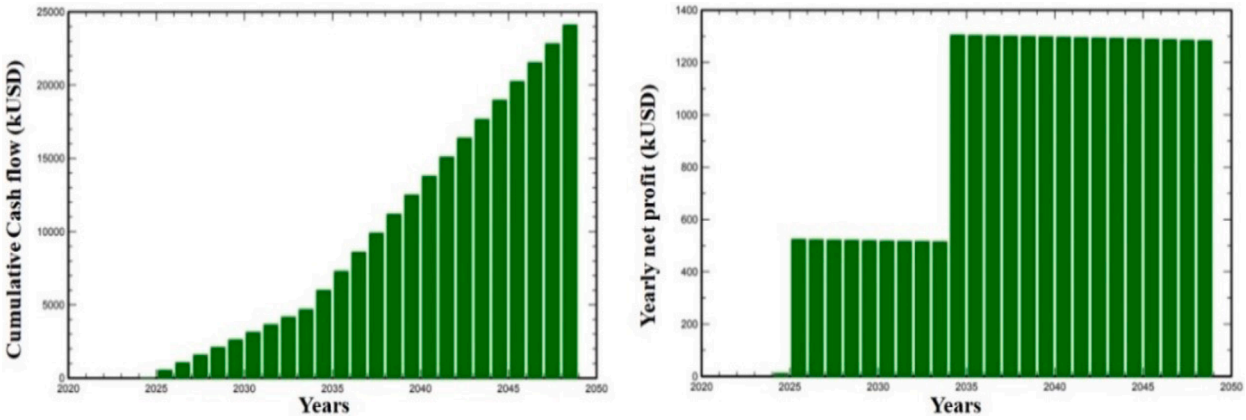

Fig. 12. (a) Cumulative cash flow of the system (b) Yearly net profit for the system.

tilt angle and 0.2 albedo. In comparison, the specific energy production is increased by 1.85% with increased tilt angle from 20° to 28° and 1.75% increases with albedo increase from 0.2 to 0.8 using PVsyst. Optimum results are found at a tilt angle of 25°, albedo 0.54, with specific production of 1643.3 kWh/kW$_p$/year for the solar PV system (Fig. 11).

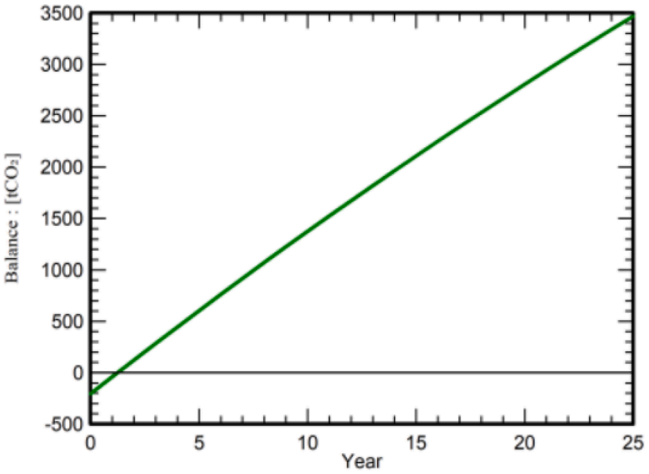

Fig. 13. Saved CO_2 emission vs. time.

Table 8
Details of system emission balance.

Total	3470.5 tCO_2
Generated Emissions	
Total	207.10 tCO_2
Replaced Emissions	
Total	4138.1 tCO_2
System production	176.84 MWh/yr
Grid Life cycle emissions	936 gCO_2/kWh
Lifetime	25 years
Annual degradation	1.0 %

Table 9
Life cycle emission details of the system.

S. No.	Item	LCE	Quantity	Subtotal ($kgCO_2$)
1.	Modules	1713 $kgCO_2/kW_p$	108 kW_p	184,511
2.	Supports	6.24 $kgCO_2$/kg	3420 kg	21,351
3.	Inverters	619 $kgCO_2$/units	2.00 units	1237

3.4. Economic and environment analysis

Table 7 elaborates the financial summary of the system for a project lifetime of 25 years including various cost like total installation cost, operating cost, produced energy, levelized cost of energy and feed-in-tariff. The total net present value of the system is ₹ 24,109,600.38 with a payback period of 5.8 years and 469.2% of return on investment. Cumulative cash flow is calculated by adding the present value of cash flows to the previous year's cash flow balance. As seen in Fig. 12(a) cumulative cash flow is increasing with every ongoing year. The yearly net profit of the system is increasing constantly up to the year 2034 and then it grows rapidly to the maximum during the remaining years of project life as shown in Fig. 12(b).

Total installation cost is ₹ 5,138,721 and the operating cost is 69,012.48 ₹/year, including 2% inflation annually. The system produces 177 MWh energy per year with a payback period of 5.8 years. Fig. 13 shows the emission details of the system for 25 years. Table 8 shows that a significant reduction in carbon emissions leads to a green and clean environment with annual degradation of 1%. Table 9 indicates the life cycle emission details of major components like modules, supports and inverters of the system. The maximum emission is generated by the PV modules as compared with the inverter and other components of the system.

4. Conclusion

Techno-economic and environmental viability of Solar PV system is evaluated based on two significant components, i.e. albedo and tilt angle for the specific energy production under composite climatic conditions. PVsyst is used to analyze the solar PV system's specific energy production, and RSM is used to optimize the results to get maximum output. The following concluding remarks are

drawn based on the analysis:

- Tilt angle and albedo show a linear relationship with the specific energy production.
- Specific production is 1600, 1618 and 1628 kWh/kW_p/year at albedo 0.2, 0.5 and 0.8. It indicates that specific production increases with the increase in albedo.
- Specific production is 1618, 1636 and 1648 kWh/kW_p/year at tilt angles 20°, 24° and 28°. It increases with the increase in tilt angle.
- Using RSM, the optimum condition for the maximum specific production, i.e., 1643.3 kWh/kW_p/year, is found at the tilt angle of 25°, albedo 0.54 for the solar PV system.
- The system's payback period is 5.8 years, ROI is 469.2% and LCOE is 2.298 ₹/kWh.
- During the operational years (25 years), the solar PV system will reduce 3470.5 tCO_2 carbon emission compared to the conventional plant.

The current study would benefit the allocation of solar PV power plants in various climatic conditions. According to the latitude of the site, the specific output of the solar PV system will rise as the tilt angle and albedo increase. Also, noted that installing such a system would greatly reduce CO_2 emissions, advance environmental sustainability, and raise the number of claimed carbon credits. These findings will help in the selection of solar photovoltaic technologies suitable for different climate locations and provide important insights to policymakers and the public on the effectiveness and viability of installing grid-connected PV systems on building roofs.

Declaration of Competing Interest

The authors declare that they have no known competing financial interests or personal relationships that could have appeared to influence the work reported in this paper.

Data availability

Data will be made available on request.

Acknowledgment

The first author would like to thank Delhi Technological University, Delhi (India), for awarding the fellowship for pursuing the Ph. D. in the Mechanical Engineering Department and gratefully acknowledge centre for Energy and Environment, DTU-Delhi for supporting the present work.

References

[1] Stambouli AB, Koinuma H. A primary study on a long-term vision and strategy for the realisation and the development of the Sahara Solar Breeder project in Algeria. Renew Sustain Energy Rev 2012;16(1):591–8. https://doi.org/10.1016/j.rser.2011.08.025.
[2] Sohail M, Afrouzi HN, Ahmed J, Mehranzamir K, Tabassum M, Mobin Siddique MB. A comprehensive scientometric analysis on hybrid renewable energy systems in developing regions of the world. Results Eng 2022;16:100481. https://doi.org/10.1016/j.rineng.2022.100481.
[3] Sharma S, Kurian CP, Paragond LS. Solar PV system design using PVsyst: a case study of an academic institute. In: Proceedings of the 2018 international conference on control, power, communication and computing technologies, ICCPCCT 2018; 2018. p. 123–8. https://doi.org/10.1109/ICCPCCT.2018.8574334.
[4] Asgharzadeh A, Marion B, Deline C, Hansen C, Stein JS, Toor F. A sensitivity study of the impact of installation parameters and system configuration on the performance of bifacial PV arrays. IEEE J Photovoltaics 2018;8(3):798–805. https://doi.org/10.1109/JPHOTOV.2018.2819676.
[5] Yakubu RO, Mensah LD, Quansah DA, Adaramola MS, Hammed Y. Performance evaluation of bifacial solar PV modules under different climatic regions in Nigeria. E3S Web Conf. 2022;354:02006. https://doi.org/10.1051/e3sconf/202235402006.
[6] Asgharzadeh A, et al. Analysis of the impact of installation parameters and system size on bifacial gain and energy yield of PV systems. In: Proceedings of the IEEE 44th photovoltaic specialist conference; 2017. p. 3333–8. https://doi.org/10.1109/pvsc.2017.8366690.
[7] Jouttijärvi S, Lobaccaro G, Kamppinen A, Miettunen K. Benefits of bifacial solar cells combined with low voltage power grids at high latitudes. Renew Sustain Energy Rev 2021;161:2022. https://doi.org/10.1016/j.rser.2022.112354. April.
[8] Ghenai C, Ahmad FF, Rejeb O, Hamid AK. Sensitivity analysis of design parameters and power gain correlations of bi-facial solar PV system using response surface methodology. Sol Energy 2021;223(April):44–53. https://doi.org/10.1016/j.solener.2021.05.024.
[9] Stein JS, Riley D, Lave M, Hansen C, Deline C, Toor F. Outdoor field performance from bifacial photovoltaic modules and systems. In: Proceedings of the 2017 IEEE 44th photovoltaic specialist conference (PVSC); 2018. p. 3184–9. https://doi.org/10.1109/pvsc.2017.8366042.
[10] Al-Turjman F, Qadir Z, Abujubbeh M, Batunlu C. Feasibility analysis of solar photovoltaic-wind hybrid energy system for household applications. Comput Electr Eng 2020;86. https://doi.org/10.1016/j.compeleceng.2020.106743.
[11] Jang J, Lee K. Practical performance analysis of a bifacial PV module and system. Energies 2020;13(17):4389. https://doi.org/10.3390/en13174389.
[12] Sreenath S, Sudhakar K, Yusop AF. Performance assessment of conceptual bifacial solar PV system in varying albedo conditions. IOP Conf Ser Mater Sci Eng 2021;1078(1):012033. https://doi.org/10.1088/1757-899x/1078/1/012033.
[13] Sánchez A, Zhang Q, Martín M, Vega P. Towards a new renewable power system using energy storage: an economic and social analysis. Energy Convers Manag 2022;252. https://doi.org/10.1016/j.enconman.2021.115056.
[14] Manikandan S, Varun M, Manikandan S. Performance Evaluation of Bifacial and Monofacial modules in vertical and latitude mounting at South India using PVsyst. IOP Conf Ser Mater Sci Eng 2020;912(4). https://doi.org/10.1088/1757-899X/912/4/042066.
[15] Osmani K, Ramadan M, Lemenand T, Castanier B, Haddad A. Optimization of PV array tilt angle for minimum levelized cost of energy. Comput Electr Eng 2021;96:107474. https://doi.org/10.1016/j.compeleceng.2021.107474.
[16] Kamalapur GD, Udaykumar RY. Rural electrification in India and feasibility of Photovoltaic Solar Home Systems. Int J Electr Power Energy Syst 2011;33(3):594–9. https://doi.org/10.1016/j.ijepes.2010.12.014.

[17] Adaramola MS. Viability of grid-connected solar PV energy system in Jos, Nigeria. Int J Electr Power Energy Syst 2014;61:64–9. https://doi.org/10.1016/j.ijepes.2014.03.015.
[18] Sandwell P, et al. Off-grid solar photovoltaic systems for rural electrification and emissions mitigation in India. Sol Energy Mater Sol Cells 2016;156:147–56. https://doi.org/10.1016/j.solmat.2016.04.030.
[19] "Eldora solar 300P" https://www.vikramsolar.com/wp-content/uploads/2016/03/ELDORA-neo-72-Series_printable.pdf (Access on 10-04-2023).
[20] "DELTA RPI-M50A." https://www.filatech.in/datasheet/50KW-RPI-M50A_Data_Sheet_V8-17-Commercial-Series.pdf (Access on 10-04-2023).
[21] Singh S, Alharthi M, Anand A, Shukla A, Sharma A, Panchal H. Performance evaluation and financial viability analysis of grid associated 10 MWP solar photovoltaic power plant at UP India. Sci Rep 2022;12(1):1–18. https://doi.org/10.1038/s41598-022-26817-4.
[22] Ibrik IH. Techno-economic assessment of on-grid solar PV system in Palestine. Cogent Eng 2020;7(1). https://doi.org/10.1080/23311916.2020.1727131.
[23] Sharma GS, et al. Performance evaluation of a MW-size grid-connected solar photovoltaic plant considering the impact of tilt angle. Sustainability 2022;14(3):1–28. https://doi.org/10.3390/su14031444.
[24] Saxena AK, Saxena S, Sudhakar K. Energy, economic and environmental performance assessment of a grid-tied rooftop system in different cities of India based on 3E analysis. Clean Energy 2021;5(2):288–301. https://doi.org/10.1093/ce/zkab008.

Neelam Baghel is currently working as a full-time research scholar at Delhi Technological University, Delhi (India). She has completed his B.E. from Madhav Institute of Technology and Science, Gwalior and M.Tech. from Delhi Technological University, Delhi. His area of interest is solar photovoltaics and hybrid renewable energy systems.

Manjunath K. completed his Ph.D. at Indian Institute of Technology, Delhi. He currently holds the position of Assistant Professor in Department of Mechanical Engineering Delhi Technological University, Delhi (India). His areas of expertise are thermal engineering and renewable energy technologies.

Anil Kumar received his Ph.D. in Solar Energy from IIT Delhi in 2007. He was Post-Doctoral Researcher at Energy Technology Research Center, Prince of Songkla University, Thailand. Currently working as Associate Professor, Department of Mechanical Engineering with additional charge of Coordinator, centre for Energy and Environment, Delhi Technological University, Delhi (India). His area of expertise is renewable energy technology.

Environmental Science and Pollution Research
https://doi.org/10.1007/s11356-023-28857-3

REVIEW ARTICLE

Perspective: The unexplored dimensions behind the foam formation in River Yamuna, India

Garima Sejwal[1] · **Santosh Kumar Singh**[2]

Received: 1 March 2023 / Accepted: 14 July 2023
© The Author(s), under exclusive licence to Springer-Verlag GmbH Germany, part of Springer Nature 2023

Abstract

For nearly two years, a persistent foam cover has been observed during the post-monsoon season in the Yamuna River beneath the barrage near Okhla in Delhi, India. This affair has been a matter of public concern now, after the gigantic appearance of foam in November 2021, as the visibility of foam has awakened people's environmental 'conscience' over the 'concealed' chemical pollution. The mechanisms of agents responsible for foaming in rivers, particularly surfactants and phosphates, have received wide attention in the dynamic community of river pollution. Many studies in the past, around the globe, have evidently provided different rationales behind the dense foam formation in rivers, yet the Concerned Govt. Authorities have highlighted the cause of foam formation in the river Yamuna is associated with the presence of detergents and phosphates as foaming agents. Despite this, an aperture with copious unaccounted factors or underlying agents still exists to rationalize the foam formation and persistence. In this article, we outline these unaccounted factors which might be responsible for the foam formation and stabilization and give indications for future research directives towards the emergence of studies regarding the dense foam formation in river Yamuna.

Keywords Foam formation · Freshwater pollution · Ostwald ripening · Policy implementation · Yamuna

Introduction

River Yamuna is the longest tributary of India and the largest tributary of river Ganga originating from Saptarishi Kund, Yamunotri glacier at a height of 20,955 ft. on the south-western slopes of Lower Himalaya in Uttarakhand, travelling 1,376 kms, having a drainage system of 366,223 square kilometres, and finally merging with river Ganga at Prayagraj. The National Capital Region (NCR) of Delhi relies on the river Yamuna for its water requirements including irrigation, fishing, hydropower generation, livestock husbandry, bathing and washing activities (Christopher et al. 2012; Sehgal et al. 2011; Upadhyay et al. 2011).

In Hinduism, the river Yamuna is considered a sacred river and is worshipped as a Hindu goddess. In early texts, Yamuna is referred to as Yami and in later literature, as Kalindi. According to the Hindu scriptures, she is the daughter of Surya (the Sun god) and Sanjna (cloud goddess) and the twin sister of Yama, the god of death. People in India's northern region believe bathing in or drinking Yamuna's waters removes sin. However, in 2019 during the Chhath Puja Hindu religious festival, thousands of devotees dressed in traditional clothes took a dip in water and worshipped the rising sun, with knee-dip in the froth layer formed in the polluted river (Zargar 2019). The same has now been observed in consecutive years (ANI 2020; India News 2021; Zargar 2019).

People alive today are witnessing the consequences of unplanned biological and chemical experiments resulting from the anthropogenic activities of the growing human population. Since the Age of Enlightenment, there have been enormous scientific changes, particularly in the discovery of chemicals. Some chemicals introduced are first considered a boon but later turned out to be a curse, as in the case of plastics and chlorofluorocarbons (CFCs). These discoveries, however, have led to the rise of contaminants

Responsible Editor: Christian Gagnon

✉ Garima Sejwal
garima_2k22phden01@dtu.ac.in; ggarima641@gmail.com

Santosh Kumar Singh
sksinghdce@gmail.com

[1] Department of Environmental Engineering, Delhi Technological University, Delhi 110042, India

[2] Rajasthan Technical University, Rajasthan 324010, India

Published online: 21 July 2023

and pollutants, which changes the composition of the biota of the Earth.

River Yamuna is one example where rapid urbanization has taken a toll on it. Despite being a significant ecological habitat for sustaining various life forms, the river has been facing an increase in pollution load significantly.

The river Yamuna enters Delhi at 1.5 km upstream of Palla and leaves at Okhla in the south, having a stretch of 22 km. The Delhi stretch is less than 2% of the river's total length; however, it is responsible for 79% of the entire pollution load in the river (CPCB 2006; B. Kumar et al. 2018). During the last few decades, river Yamuna has been considered the most polluted river in India and has been fighting for its survival, mainly due to the anthropogenic pressures deteriorating the water quality by the vast amounts of industrial, agricultural, and domestic wastewater discharge (Misra and Misra 2010; Sharma et al. 2015) (approx. 3296 MLD) (CPCB 2004; Gautam et al. 2017; Paliwal et al. 2007; Upadhyay et al. 2011), or treated waste from urban local bodies (ULB) discharging directly into the river. Delhi has the highest number of working Sewage Treatment Plants (STP) in India with the highest sewage treatment capacity (Mutiyar et al. 2018); despite this, partially treated and untreated sewage directly flows into the river due to the non-operationality of STPs, the reasons being power failures, mechanical problems or maintenance issues (Babu and Seth 2007; CPCB 2006). In Delhi, water quality monitoring of water bodies is being carried out by Central Pollution Control Board (CPCB) and Delhi Pollution Control Committee (DPCC) (Fig. 1(b)) every month (CPCB 2004, 2006).

The nationwide lockdown enforced in India from 25 March 2020 due to Covid-19 enlightened a ray of hope. Studies (CPCB 2020; Lokhandwala and Gautam 2020; Mallik et al. 2022; Patel et al. 2020; Singh and Mishra 2021; Somani et al. 2020) across India have demonstrated the improvement in the water quality of river Yamuna by comparing the water quality in pre-lockdown and post-lockdown phases. The lockdown restrictions were lifted from 1 June 2020, while the lockdown was further extended until 30 June 2020 for the containment zones. The "Unlock 1.0" started on 8 June 2020, as the services were resumed. Looking at the improved air and water quality in India, it was presumed that the foam episode would not resurface. However, in November 2020, the foam appeared again (Fig. 2).

Despite several attempts and legal frameworks like banning non-degradable detergents for washing activities (Express News Service 2021), upgradation and installment of Sewage Treatment Plants (STP) and maintenance of Common Effluent Treatment Plants (CETP) (Singh 2020), every year in Delhi during the winter season, the prominent headline "Toxic Foam Formation in River Yamuna" is a recurring phenomenon in the news now.

Foam formation in River Yamuna, the scenario

Rivers receive and carry wastewater from municipal and industrial areas and runoff from agricultural areas, roadways, and streets, which are responsible for introducing pollutants into the river. Environmental concerns regarding the deteriorating surface water quality due to eutrophication, heavy metals (Bhardwaj et al. 2017), antibiotics (Lamba et al. 2018), and pharmaceutically active compounds (Mutiyar et al. 2018) are usually accentuated (Ouyang et al. 2006). However, comparatively, foam formation on surface water is at present overlooked. Although there have been some studies regarding foam formation in the marine environment (Bärlocher et al. 1988; Bätje and Michaelis 1986; Craig et al. 1989; Eberlein et al. 1985; Myres 1939) and wastewater treatment plants (Defrain and schulze-Rettmer 1989; Dillner Westlund et al. 1998; Hladikova et al. 2002; Lánský et al. 2005; Schilling and Zessner 2011; Torregrossa et al. 2005), literature concerning the rivers is rare.

A considerable amount of early literature has identified the sources of foam formation in freshwater systems across the globe (Fisenko 2004; Madrange et al. 1993; Ruzicka et al. 2009; Wegner and Hamburger 2002). Foam production is associated with multiple factors from different industrial sources, such as cosmetic and detergent (Buzzacchi et al. 2006; Regismond et al. 1998; Zhang et al. 2003), food (Dale et al. 1999; Piazza et al. 2008; Vanrell et al. 2007), paper (Craig et al. 1990; Ettema et al. 1989), tannery (Ruzicka et al. 2009), cement (Pedersen et al. 2007), and fire-fighting (Figueredo and Sabadini 2003; Tafreshi and Marzo 1999) industries. However, some studies suggest detergents as the main driver of foam formation in rivers across the globe (Gagnon 1983; Hand et al. 1990; Kikuchi et al. 1986; Kumar et al. 2021; McAvoy et al. 1993; Waters and Garrigan 1983).

Nowadays, the issues concerning the deteriorating water quality of rivers have been of great concern not only for scientists but for policymakers and the public too. The foams are usually associated with detergents or pollution (Schilling and Zessner 2011), and such is now the case with the river Yamuna.

The presence and persistence of a stable foam on the river Yamuna beneath the barrage at Okhla in Delhi, India has been a recurring phenomenon in winter ever since its appearance in 2019 (Zargar 2019). Accumulation of massive lumps of froth is observed at the outlet of the barrages. The foam usually covers up to half of the river's surface and gradually disappears several kilometres downstream. This phenomenon has now been highlighted as the foam's visibility has awakened the environmental 'conscience' of people over the 'concealed' chemical pollution. From

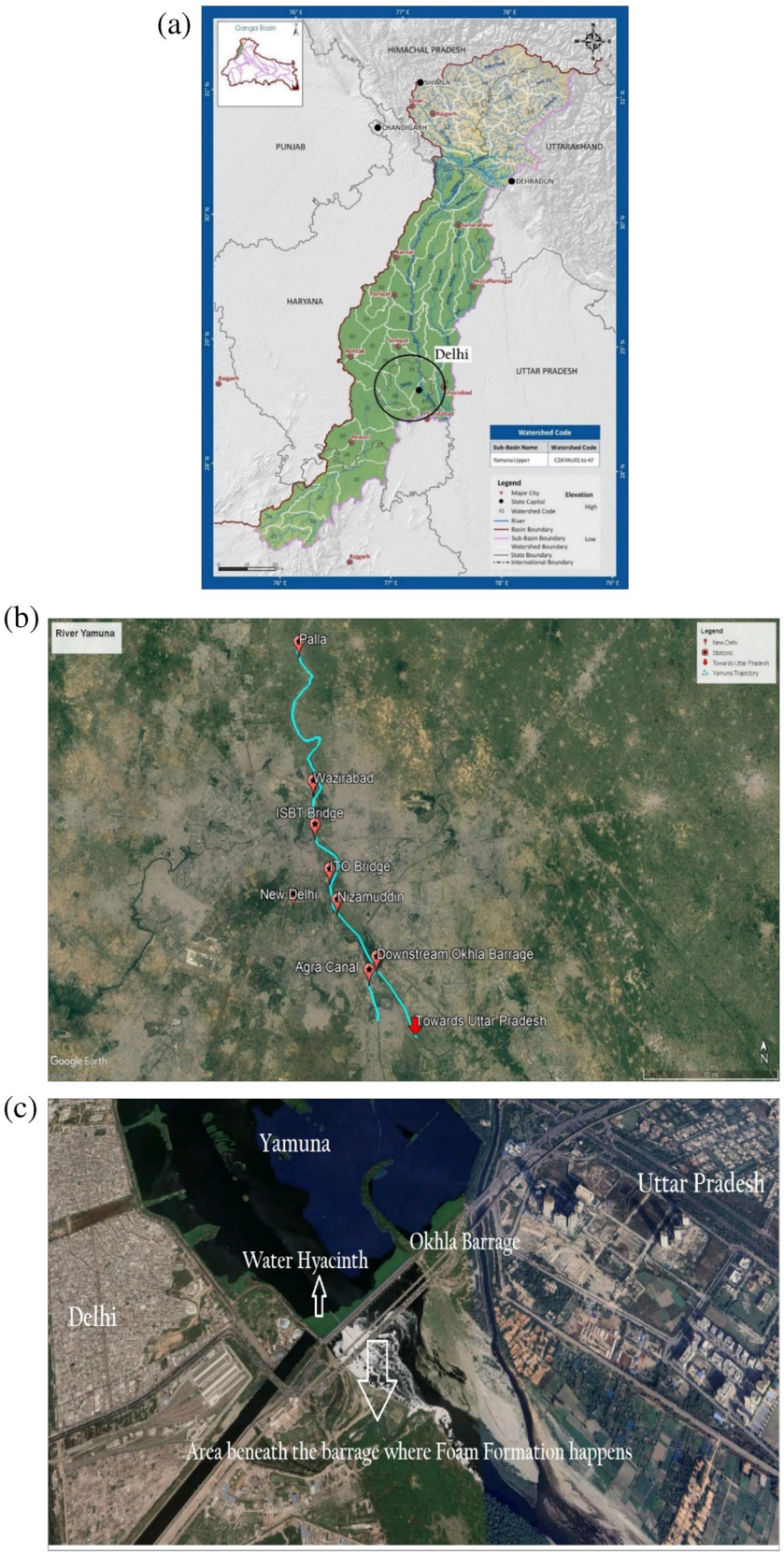

Fig. 1 Zeroing in on a specific study site: Okhla Barrage. (**a**) Yamuna Upper Sub-Basin (Source: WRIS); (**b**) Sampling locations of River Yamuna by DPCC. The base image is provided by ESRI and projection and river highlights are done using ArcGIS; (**c**) Location of Okhla Barrage. The base image is provided by Google maps

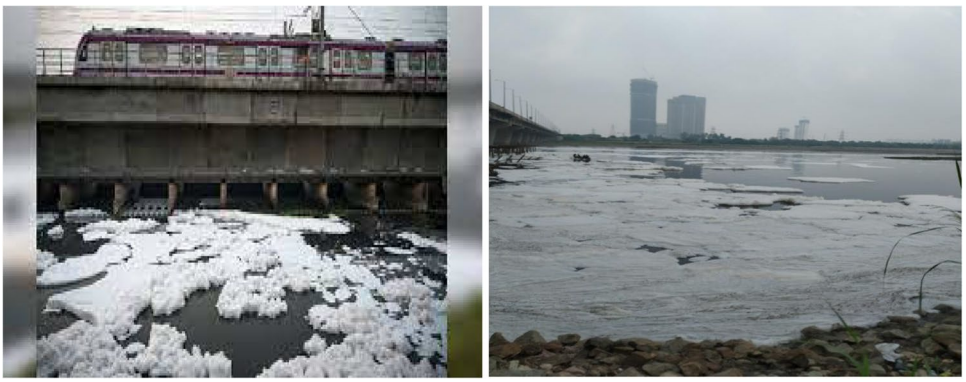

Fig. 2 Foam patches in River Yamuna

Table 1 Concentrations of Detergents, Phosphate and Ammoniacal Nitrogen at Palla and Okhla

Sl. No	Sampling Locations	Sampling Date	Detergent (mg/L)	Phosphate (mg/L)	Ammoniacal Nitrogen (mg/L)
1	Palla	09.11.2021	BDL	0.2	4
2	Okhla	08.11.2021	1.8	1.05	15.8
		11.11.2021	2	0.66	13.3

BDL = below detection limit;

Source: CPCB (Central Pollution Control Board (CPCB) 2021b)

2019 onwards, the concerned authorities have been looking for the possible reasoning behind this phenomenon.

In 2021, Central Pollution Control Board (CPCB) monitored different locations of river Yamuna, and the concentrations of detergents and phosphate were reported (Central Pollution Control Board (CPCB) 2021a) (Table 1).

However, Delhi Pollution Control Committee (DPCC) reported the concentrations of surfactants and phosphate at Okhla on 08.11.2021 to be 2.77 mg/L and 62.42 mg/L, respectively.

According to CPCB and DPCC, the reason behind the foam formation is the high concentration of detergents and laundry chemicals, which contains phosphate (sodium tri-poly-phosphate) being released from industrial and household activities (Central Pollution Control Board (CPCB) 2021a).

This rationale can, however, be ruled out by monitoring the possible sources rather than the analytical experimentation of water and foam samples for phosphates and surfactants, as the fundamental potential sources have largely been neglected.

Probing the other potential dimensions in foam formation

Fostering the scientific culture of looking into the existing literature is the sine qua non of exploring the 'hidden' potential sources of an existing problem.

In 1976, a hypothesis was postulated between the aquatic plant *Ranunculus fluitans* Lamk. and the occurrence of the foam in the river Rhine, but it was disregarded as it was not supported by experimental data (Wegner et al. 2000; Wegner and Hamburger 2002). After numerous reporting on the occurrence of foam, a study by C. Wegner and M. Hamburger was carried out backed up by experimental findings of two classes of tensioactive metabolites occurring in the aquatic plant *Ranunculus fluitans* Lamk. (Ranunculaceae) in river water and foam samples. It was then proven that saponin concentration paralleled foam occurrence and with the amounts of detached *Ranunculus fluitans* biomass accumulated at the dam above the Rhine Falls and not with the synthetic detergents (Wegner and Hamburger 2002).

This study might provide an auxiliary factor by linking the widespread notorious invasive species *Eichhornia crassipes*, commonly known as water hyacinth, with the foam formation in river Yamuna.

Since the Age of Exploration, numerous biotic exchanges have directly impacted the evolutionary processes. The resultant trajectories of drastic alteration in the biotic community composition by 'introducing' species in different geographical realms are becoming clear with the increasing research.

Vast land and waterscapes, in certain regions, have been entirely dominated by invasive species, such as water hyacinths in many tropical lakes and rivers (Mooney and Cleland 2001). In backwater areas of river Yamuna at Okhla barrage, water hyacinth has profoundly exploded (Mehra et al. 2000) – the so-called lag effect (Mooney and Cleland 2001), which may be due to the normal increase in size and distribution of population. Invasive species have been tested to be phytochemically unique in their

new habitats (Cappuccino and Arnason 2006; Peter et al. 2021). Contrastingly, they are more likely to have potent secondary compounds in their introduced regions over their native region (Macel et al. 2014).

With these insights, we hypothesize that the water hyacinth present in the backwaters of river Yamuna (Fig. 1(c)) might play a crucial role as a biogenic origin of this foam phenomenon. Considering the wide proportion of phytochemicals (Harun et al. 2021) and high biomass, water hyacinths might be releasing an exceptional amount of phosphates (Masifwa et al. 2004), saponins (Ben Bakrim et al. 2022), lipids, proteins, and carbohydrates into the waterways, since natural foams are usually linked with these factors (Bätje and Michaelis 1986; Eberlein et al. 1985; Napolitano and Richmond 1995; Pojasek and Zajicek 1978; Schilling and Zessner 2011; Seuront et al. 2006; Wegner and Hamburger 2002). These compounds have a surface-active character causing a reduction of surface tension and creating favourable conditions for foaming (Ruzicka et al. 2009; Schilling and Zessner 2011).

Moreover, due to excess nutrients flowing into the river, eutrophication has been reported as a problem in the river. Eutrophication can favour the formation of plankton blooms resulting in the formation of biogenic surface-active compounds. These surface-active compounds could also help in foam formation.

The secondary condition for foam formation is the injection of gas bubbles (Heard et al. 2008) at a higher rate (Napolitano and Cicerone 1999) into the water by the mechanical impact (Poremba et al. 1991) caused by the barrage (Craig et al. 1989; Ettema et al. 1989; Fisenko 2004) at Okhla (Central Pollution Control Board (CPCB) 2021a). Hence, these surface-active agents get agitated by the turbulence caused after the release of water from the barrage or reservoir at a particular height, forming the dense foam layer on the river bed.

However, this hypothesis is yet to be verified by the experimental data after the continuous monitoring of these foaming agents in the water and foam samples, which can henceforth provide a clearer picture of the foaming phenomenon (Fig. 3).

Foam persistence

The foam destabilisation is due to the three known mechanisms: drainage, coalescence, and coarsening (Fameau and Salonen 2014). The stabilization of foam could also be achieved by the presence of high diversity and large biomass of filamentous bacteria like *Microthrix parvicella* and nocardioform actinomycetes (Blackall et al. 1991; Blackall and Marshall 1989; Heard et al. 2008; Lemmer et al. 2005). With insufficient hydrophobic cells, the unstable foam will be generated (Petrovski et al. 2011).

Foams are thermodynamically unstable due to their high interfacial energy and disappear with time (Fameau and Salonen 2014), yet the foam layer persists on the river Yamuna for months.

Foam stability to water drainage

The characteristic time for foam drainage in the regimes could be expressed as:

$$t_{DR} \approx H_F\, \mu/K_m\, \rho g\, {R_B}^2\, {\Phi_L}^m \quad m = 1 \text{ or } {}^1/_2 \qquad (1)$$

H_F is foam height, μ is viscosity, if $m = 1$, $K_m \equiv K_1 \approx 6 \times 10^{-3}$ for immobile interfaces, if $m = ½$, $K_m \equiv K_2 \approx 2 \times 10^{-3}$ for mobile interfaces, ρ is the mass density of the

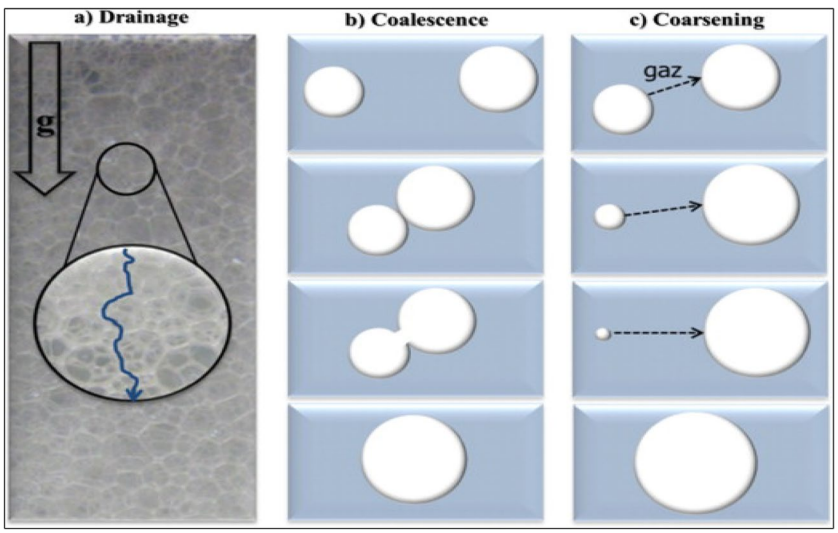

Fig. 3 Foam stability to drainage, coarsening and coalescence (Figure reproduced from Fameau and Salonen (2014) Effect of particles and aggregated structures on the foam stability and aging, Comptes Rendus Physique,15, 748–760, 10.1016/j.crhy.2014.09.009)

continuous phase, g is gravity acceleration, R_B is bubble size and $\phi_L = (1\text{-}\phi)$ is liquid volume fraction.

Sewage and other sources like algae and bacteria are associated with the introduction of long-chain fatty acids into the river system (Jiménez Martínez et al. 2019). These long-chain fatty acids (C14 – C16) act as cosurfactants by increasing the surface viscoelasticity as they create condensed mixed adsorption layers with the surfactants, thus decelerating the foam drainage (Mitrinova et al. 2018).

Drainage can be decelerated by creating yield stress via confining particles or oil drops in the Plateau channels. According to Lesov et al. (Lesov et al. 2014, 2017), when the fluid yield stress, τ_{Y0}, exceeds a critical value, the liquid drainage would stop, implying:

$$\tau_{Y0} > \tau_D \approx 2\ \rho g\ R_{32} \tag{2}$$

τ_D is the stress to be overcome by the yield stress fluid and R_{32} is the volume-surface radius (also called 'Sauter mean radius').

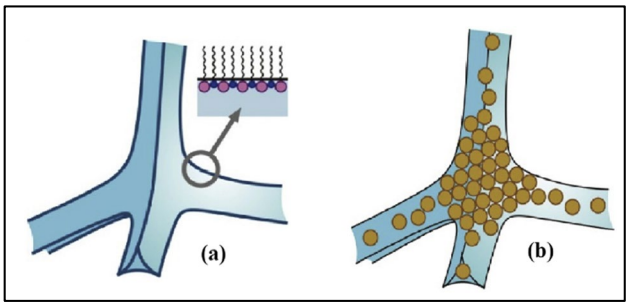

Fig. 4 Slowing of foam drainage: (**a**) formation of viscoelastic surface layer on the bubbles' surfaces; (**b**) trapping of oil drops in the Plateau channels. (Figure reproduced from Denkov et al. (2020). Physicochemical control of foam properties. Curr. Opin. Colloid Interface Sci. 50, 101,376, 10.1016/j.cocis.2020.08.001)

Therefore, the oil discharged from different sources into the river Yamuna can also act as a stabilizing agent, as it can be densely packed and jammed in the Plateau channels, increasing the viscosity, and slowing the channel shrinking and the foam film thinning (Fig. 4).

Foam stability to coarsening

Princen and Mason (Princen and Mason 1965) proposed the following expression for the flux of gas molecules across the foam film separating two neighbouring bubbles:

$$J_{ij} = \frac{dnij}{dt} \approx \frac{Aij\ HD}{kBT}\left(\frac{\sigma i}{Ri} - \frac{\sigma j}{Rj}\right)/\left(h + 2D/K_{al}\right) \tag{3}$$

J_{ij} is gas flux across the foam film separating two bubbles (i and j) in the foam per unit time, Aij is the area of the foam film, H is the gas solubility and D is gas diffusion coefficient in the continuous medium, kBT is the thermal energy, $\sigma i,j$ and Ri,j are surface tensions and radii of the contacting bubbles, h is the thickness of the foam film and K_{al} is the gas permeability of the surfactant adsorption layer.

Several studies have proposed slowing Ostwald ripening in foams based on this concept. One such approach is by the use of a poorly soluble gas such as N_2 (Fameau and Salonen 2014; Weaire and Pageron 2006). Since the transfer of the more soluble gas will be faster, the smaller and larger bubbles will have different gas compositions, leading to differences in osmotic pressures and thereby balancing the Laplace pressure (Webster and Cates 2001), and thus, decelerating Ostwald ripening. Therefore, the foam stability is higher in the presence of N_2 gas (Fig. 5).

Considering the river Yamuna dynamics, the dissolved oxygen concentration at Okhla barrage throughout the year has been reported as nil (approx.) by DPCC (Delhi Pollution Control Committee n.d.), defining the system

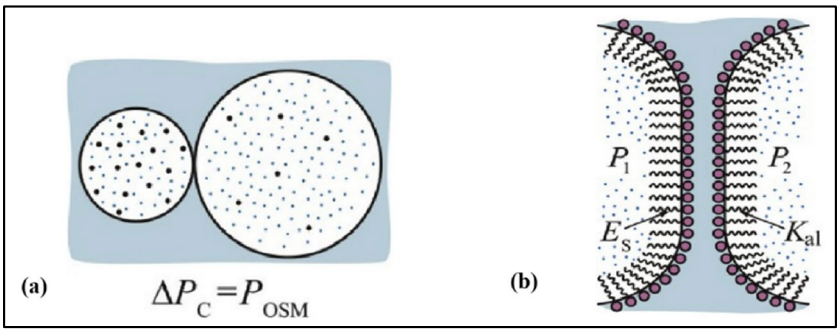

Fig. 5 Slowing down Ostwald ripening: (**a**) use of gas mixture in foaming with a gas of low solubility in water, the osmotic pressure formed between the expanding and shrinking bubbles will oppose the difference in their capillary pressure; (**b**) formation of highly viscoelastic layers, reducing the gas permeability across the foam film. (Figure reproduced from Denkov et al. (2020). Physicochemical control of foam properties. Curr. Opin. Colloid Interface Sci. 50, 101,376, 10.1016/j.cocis.2020.08.001)

at Okhla as an oxygen-deficient zone (ODZ). In ODZ, denitrification and anammox prevail over other processes leading to the formation of gaseous dinitrogen (and N_2O in the former case) by consuming the dissolved inorganic nitrogen (Voss et al. 2013). Moreover, with no available oxygen, denitrifying bacteria use the oxygen present in the nitrate to oxidize the carbon, forming N_2 gas from nitrates, which then bubbles up out of the waterways (Pajares and Ramos 2019). Parween et al. (Parween et al. 2017) have documented the significant levels of nitrates and total phosphate in River Yamuna.

The N_2 gas, hence, might be cumulatively responsible for the foam stabilization and its persistence over the river bed. The high amount of dinitrogen might also be associated with the exploding population of water hyacinth at the barrage as this species proliferates in areas rich with nutrients like nitrogen (Gichuki et al. 2012; Harun et al. 2021; Wilson et al. 2005; Zarkami et al. 2021).

There have been cases where a high concentration of ammoniacal nitrogen has been reported. CPCB has received enormous complaints regarding the high rise in ammoniacal nitrogen in the river Yamuna during the time of foam occurrence (Central Pollution Control Board (CPCB) 2021a, 2021b). Furthermore, every year public notices have been issued by the Delhi Jal Board (DJB) informing the availability of water supply at low pressure, due to the high ammonia level in River Yamuna, affecting the water production at Chandrawal, Wazirabad and Okhla Water Treatment Plants (Express News Service 2022; The Times of India 2021). After monitoring, CPCB reported the concentrations of Amm. Nitrogen to be high (Table 1), approx. 15 times higher than the limit of Amm. Nitrogen treatment (1 ppm) by Water Treatment Plants (WTP) designed in Delhi and 28 times higher than the prescribed limit of ammonia in drinking water (0.5 ppm) as per BIS standards (IS 10500:2012).

Not constraining ourselves only to dinitrogen behind the foam stability, it has been reported that ammonium ions (He et al. 2017) and fatty acids (Atrafi and Pawlik 2017) also increase the foam formation and stability. Also, NH^{4+} ions can form ammonium soaps with long-chain fatty acids (Pest Management Regulatory Agency 2017) which act as surface–active materials augmenting the foam formation and stability.

Furthermore, the formation of highly viscoelastic layers on the bubble surface by the addition of some constituents can also reduce Ostwald ripening in foams. The effect of surface elasticity can be described by the classical prediction given by Gibbs (Gibbs 1993):

$$\frac{\partial \Delta p}{\partial R} = 2(2\mathrm{E} - \sigma)/\mathrm{R}^2 \tag{4}$$

where Δp is the pressure drop, R is the radius of the bubble, E is the dilational elastic surface modulus and σ is the surface tension. When $\frac{E}{\sigma} \geq ½$, the bubble evolution is stopped, which is known as the Gibbs criterion. However, in the presence of gravity or fast adsorption, the coarsening is predicted by a modified Gibbs criterion, given by Salonen et al. (Salonen et al. 2016):

$$\frac{E}{\sigma} \geq \mathrm{k_{ads}}\left(1 + (2\mathrm{R}^2/3\mathrm{l_{cap}}^2\right) \tag{5}$$

and, $\mathrm{l_{cap}} = \sqrt{\sigma/(\rho g)}$ where, $\mathrm{k_{ads}} = ½$ when no adsorption takes place and $\mathrm{k_{ads}} = 1$ for fast adsorption, and where the capillary length, $\mathrm{l_{cap}} \rightarrow \infty$ in the zero gravity limit.

The triterpenoid saponins (from water hyacinth) can significantly increase surface elasticity, even at meagre rates of surface deformation, by forming the viscoelastic adsorption layers. The saponin molecules are larger, and their desorption from bubble surfaces is reduced by strong intermolecular attraction inside the adsorbent layer (Pagureva et al. 2016; Tcholakova et al. 2017). The H-bond formation between the head groups of the adsorbate surfactant molecules induces short-range attraction, increasing the rigidity and elasticity of the surfactant adsorbent layer (Stubenrauch et al. 2017). Also, the rigid hydrophobic framework of the saponin molecules and the strong dipole–dipole interactions block the adsorbent layer, enhance molecular packing, reduce molecular desorption and thus, maintain the high surface elasticity (Tcholakova et al. 2017; Tsibranska et al. 2019). Hence, the amalgamation of all these effects suppresses the gas permeability across the film (Ostwald ripening) by larger orders of magnitude.

Foam stability to coalescence

The modification of foam films can control thin film drainage and provide stability against coalescence. Particles present in river Yamuna can combine with surfactants to improve foam stability by armouring the bubble surfaces ensuring capillary stabilization (Denkov et al. 2020) of the bubbles.

Sodium dodecyl sulfate (SDS) is widely used in domestic (household detergents), industrial and research applications (Arslan et al. 2018). Due to improper or partial treatment and/or non-functionality of STPs and CETPs, these anionic detergents are directly discharged into the river Yamuna, which can form surfactant crystals due to the precipitation of SDS in the presence of divalent Mg^{2+} counter ions. Binks and Shi (Binks and Shi 2020) in their study have observed the relationship between these surfactant crystals and foam stability. Unstable foams were obtained at low crystal adsorption, whereas long-term stability was observed in foams with closely packed surfactant crystals adsorption.

Surfactant crystal partitioning between the bulk solution and bubble surfaces can, therefore, suppress coalescence and coarsening.

Proteins, likely, also have been cited to be a very good foaming agent as well as foam stabilizing agent (Shen et al. 2022; Zayas 1997), hence, foaming is a problem due to protein-bearing waste (Borja 2011). Proteins and protein-derived substances are active ingredients in hair conditioners (D'Souza and Rathi 2015), which find their way into the wastewater. Therefore, the protein sources in the wastewater effluent could be the undigested influent proteins or soluble microbial products (SMPs) eg. tryptophan-like material, which are products of microbial metabolism in the activated sludge secondary treatment process (Westgate 2009). Proteins decrease interfacial tension and increase the viscosity and elastic properties of the liquid phase to promote foam formation and stabilization by adsorbing at the interface and forming stabilizing film (Zayas 1997) (Fig. 6).

Outlook, attention points

Ever since the introduction of synthetic detergents on a large scale after the Second World War, foam elimination has been a worldwide concern (Anonymous 1964). However, some studies have shown that foam formation can be associated with remediation processes for removing pollutants from the wastewater; on that account, the 'problem' of foam formation in river Yamuna can be transmogrified into a 'temporary solution' for pollutant removal.

Fisenko (Fisenko 2004) has documented that nature "uses" the "foam fractionation and floatation technique" as a process of self-purification, as substances like petroleum compounds, synthetic pesticides, herbicides and surfactants are accumulated in the surface microlayer (SML) (Eisenreich et al. 1978; Johnson et al. 1989; Napolitano and Richmond 1995; Parker and Barsom 1970; Pojasek and Zajicek 1978) by adsorbing onto bubbles as they rise through the water column (Harden and Williams 1989).

Eisenreich et al. (Eisenreich et al. 1978), Szekielda et al. (Szekielda et al. 1972), Elzerman (Elzerman 1949), and Johnson et al. (Johnson et al. 1989) have highlighted the enrichment of metals in Lake Mendota, Delaware Bay, Lake Michigan and Niagara Falls respectively. Moreover, Eisenreich et al. (Eisenreich et al. 1978) also reported high concentrations of pesticides like dieldrin and DDT-group in the foam of Lake Mendota compared to the underlying water.

Similarly, an experimental setup can be formulated to study the enrichment of metals in the dense foam generated on the river bed of Yamuna. which can provide some useful insights concerning the toxicity of foam.

Furthermore, since vast and extensive literature exists regarding the analysis of spatiotemporal variability of heavy metals contamination in the river Yamuna (Bhardwaj et al. 2017; Parween et al. 2021; Singh et al. 2020; Singh Sankhla et al. 2022; Yadav and Khandegar 2019), we hypothesize that heavy metals might also be present in the foam, contributing to its toxicity. However, this foam can serve as a 'temporary solution' for removing the heavy metals and other accumulated contaminants which might have escaped from wastewater treatment plants (WWTP). The foam formed on river Yamuna is so thick that it can be collected via loose net sheets (from the surface) or bamboo sheets (Express Web Desk 2021) and transferred into a giant electric mixer where biodegradable anti-foaming agent or defoamers can be added to the system to eliminate the foam. The wastewater generated can be cycled back to the WWTPs for the treatment and removal of significant contaminants (like heavy metals and surfactants) extracted from the foam. The excessive amount of surfactants extracted can then be removed by treating with chemical, physical, biological or acoustic methods (or maybe a hybrid of two or more methods) (Badmus et al. 2021). This model might serve as a prelude to the upcoming foam episode. We would, however, like to highlight that this model is only a temporary solution.

Conclusion

The occurrence of foam in River Yamuna has taken nationwide attention, yet no such study has been conducted to substantiate the phenomenon. Although surfactants (primarily

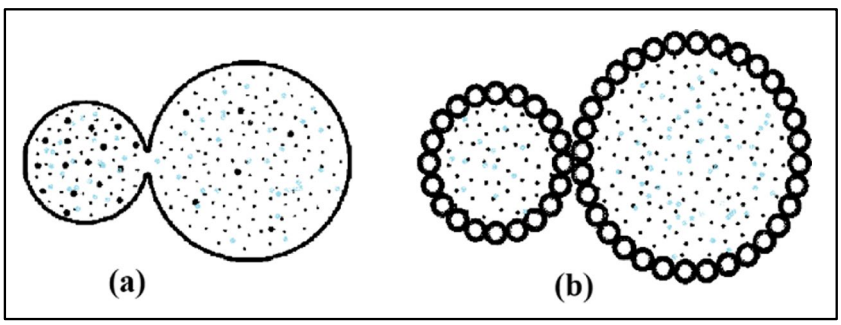

Fig. 6 (**a**) Coalescence of bubbles in the absence of particles; (**b**) adsorption of solid particles on the bubble surface which produces structured stable foams

detergents) and phosphates are defined to be causative, in this *article*, we have highlighted the other potential factors that might be playing a pivotal role in this foam-river dynamics, considering that foam formation is a sum effect of all the surface-active agents and a mixture of various components present in water.

The common solution involves the sprinkling of water (Lemmer et al. 2005) and the application of anti-foaming agents (Hwang and Tanaka 1998; Ruzicka et al. 2009), but the latter cannot be applied when considering the river dynamics. Such measures are only temporary and do not eliminate the reasons. Therefore, the identification, source and elimination of active agents, with the legal aspects and public concern have now been a new challenge, which requires a fast and effective solution.

In order to frame and implement cost-effective measures, studies are required to develop a model to quantify the impact of the foam-causing agents in the river basin as the potential sources listed in this *article* are maybe interacting synergistically.

Through this *article*, we have provided a series of attention points and recommendations for futuristic research avenues in the foam–river system.

Author contributions Garima Sejwal: conceptualization, data analysis, literature survey, and first draft of the manuscript.

Santosh Kumar Singh: conceptualization, data analysis, and critical review of the draft.

Funding Not applicable.

Data Availability All the data used in the present study is freely available in the public domain and citations have been provided in the manuscript, however, we will provide data to all the interested scientists.

Declarations

Competing interests The authors declare that they have no known competing financial interests or personal relationships that could have appeared to influence the work reported in this paper.

References

ANI (2020) Delhi's air pollution remains in "poor" category, toxic foam floats on Yamuna river. The New Indian Express. https://www.newindianexpress.com/cities/delhi/2020/nov/04/delhis-air-pollution-remains-in-poor-category-toxic-foam-floats-on-yamuna-river-2219244.html

Anonymous (1964) Eliminating Detergent Foam. Nature 203(4945):587–588. https://doi.org/10.1038/203587b0

Arslan A, Topkaya E, Bingöl D, Veli S (2018) Removal of anionic surfactant sodium dodecyl sulfate from aqueous solutions by O3/UV/H2O2 advanced oxidation process: Process optimization with response surface methodology approach. Sustain Environ Res 28(2):65–71. https://doi.org/10.1016/J.SERJ.2017.11.002

Atrafi A, Pawlik M (2017) Foamability of fatty acid solutions and surfactant transfer between foam and solution phases. Miner Eng 100:99–108. https://doi.org/10.1016/j.mineng.2016.10.012

Babu SVS, Seth BL (2007) Sewage Canal: How to Clean the Sewage Canal: How to Clean the Yamuna Yamuna. https://www.indiawaterportal.org/sites/default/files/iwp2/Sewage_Canal___How_to_Clean_the_Yamuna_CSE_Presentation_2007.pdf

Badmus SO, Amusa HK, Oyehan TA, Saleh TA (2021) Environmental risks and toxicity of surfactants: overview of analysis, assessment, and remediation techniques. Environ Sci Pollut Re 28. https://doi.org/10.1007/s11356-021-16483-w/Published

Bärlocher F, Gordon J, Ireland RJ (1988) Organic composition of seafoam and its digestion by Corophium volutator (Pallas). J Exp Mar Biol Ecol 115(2):179–186. https://doi.org/10.1016/0022-0981(88)90102-5

Bätje M, Michaelis H (1986) Phaeocystis pouchetii blooms in the East Frisian coastal waters (German Bight, North Sea). Mar Biol 93(1):21–27. https://doi.org/10.1007/BF00428651

Ben Bakrim W, Ezzariai A, Karouach F, Sobeh M, Kibret M, Hafidi M, Kouisni L, Yasri A (2022) Eichhornia crassipes (Mart.) Solms: A Comprehensive Review of Its Chemical Composition, Traditional Use, and Value-Added Products. Front Pharmacol 13. https://doi.org/10.3389/FPHAR.2022.842511/

Bhardwaj R, Gupta A, Garg JK (2017) Evaluation of heavy metal contamination using environmetrics and indexing approach for River Yamuna, Delhi stretch, India. Water Sci 31(1):52–66. https://doi.org/10.1016/j.wsj.2017.02.002

Binks BP, Shi H (2020) Aqueous Foams in the Presence of Surfactant Crystals. Langmuir 36(4):991–1002. https://doi.org/10.1021/ACS.LANGMUIR.9B03862/SUPPL_FILE/LA9B03862_SI_001.PDF

Blackall LL, Marshall KC (1989) The mechanism of stabilization of actinomycete foams and the prevention of foaming under laboratory conditions. J Ind Microbiol 4(3):181–187. https://doi.org/10.1007/BF01574075

Blackall LL, Harbers AE, Hayward AC, Greenfield PF (1991) Activated sludge foams: Effects of environmental variables on organism growth and foam formation. Environ Technol 12(3):241–248. https://doi.org/10.1080/09593339109385001

Borja R (2011) Biogas Production. Comprehensive Biotechnology, Second Edition, 2:785–798.https://doi.org/10.1016/B978-0-08-088504-9.00126-4

Buzzacchi M, Schmiedel P, Von Rybinski W (2006) Dynamic surface tension of surfactant systems and its relation to foam formation and liquid film drainage on solid surfaces. Colloids Surf, A 273(1–3):47–54. https://doi.org/10.1016/J.COLSURFA.2005.06.074

Cappuccino N, Arnason JT (2006) Novel chemistry of invasive exotic plants. Biol Let 2(2):189–193. https://doi.org/10.1098/rsbl.2005.0433

Central Pollution Control Board (CPCB) (2021a) Directions under section 18 (1) (b) Of the water (Prevention and control of pollution) Act, 1974 In the matter of control of pollution in River Yamuna. www.cpcb.nic.in

Central Pollution Control Board (CPCB) (2021b) Study Group Report on Increase of Pollution in River Yamuna. https://cpcb.nic.in/yamuna-monitoring-committee/

Christopher D, Kaur S, Singh R (2012) Water quality status of River Yamuna in Delhi with reference to presence of heavy metals: a review. International Journal of Pharma Medicine and Biological Sciences 1(2):266–271. http://www.ijpmbs.com/uploadfile/2015/0412/20150412030949497.pdf

CPCB (2004) Annual Report, 2004–2005. http://www.cpcbenvis.nic.in/annual_report/AnnualReport_9_annualreport2004-2005.pdf

CPCB (2006) Water quality status of Yamuna River (1999 – 2005). http://www.cpcb.nic.in

CPCB CPCB (2020) Assessment of Impact of Lockdown on Water Quality of Major Rivers . Monitoring of Indian National Aquatic Resources Series (MINARS) , 38. https://cpcb.nic.in/upload/Assessment-of-Impact-Lockdown-WQ-MajorRivers.pdf

Craig D, Ireland RJ, Bärlocher F (1989) Seasonal variation in the organic composition of seafoam. J Exp Mar Biol Ecol 130(1):71–80. https://doi.org/10.1016/0022-0981(89)90019-1

Craig GR, Orr PL, Robertson JL, Vrooman WM (1990) Toxicity and bioaccumulation AOX and EOX. Pulp and Paper Canada 91:39–45. https://www.researchgate.net/publication/279958618_Toxicity_and_bioaccumulation_of_AOX_and_EOX

D'Souza P, Rathi SK (2015) Shampoo and Conditioners: What a Dermatologist Should Know? Indian J Dermatol 60(3):248. https://doi.org/10.4103/0019-5154.156355

Dale C, West C, Eade J, Rito-Palomares M, Lyddiatt A (1999) Studies on the physical and compositional changes in collapsing beer foam. Chem Eng J 72(1):83–89. https://doi.org/10.1016/S1385-8947(98)00141-7

Defrain M, Schulze-Rettmer R (1989) Schaumentwicklung in biologisch gereinigtem Abwasser und im Gewässer. I: Voruntersuchungen zur Schaumentstehung auf Abwässern. Vom Wasser 73:251–257

Delhi Pollution Control Committee (n.d.) Monthly Analysis Report of River Yamuna. Retrieved August 26, 2022, from https://www.dpcc.delhigovt.nic.in/home/monthly_analysis_report#gsc.tab=0

Denkov N, Tcholakova S, Politova-Brinkova N (2020) Physicochemical control of foam properties. Curr Opin Colloid & Interface Sci 50:101376. https://doi.org/10.1016/J.COCIS.2020.08.001

Dillner Westlund Å, Hagland E, Rothman M (1998) Foaming in anaerobic digesters caused by Microthrix parvicella. Water Sci Technol 37(4–5):51–55. https://doi.org/10.1016/S0273-1223(98)00083-3

Eberlein K, Leal MT, Hammer KD, Hickel W (1985) Dissolved organic substances during a Phaeocystis pouchetii bloom in the German Bight (North Sea). Mar Biol 89(3):311–316. https://doi.org/10.1007/BF00393665

Eisenreich SJ, Elzerman AW, Armstrong DE (1978) Enrichment of Micronutrients, Heavy Metals, and Chlorinated Hydrocarbons in Wind-Generated Lake Foam. Environ Sci Technol 12(4):413–417. https://doi.org/10.1021/ES60140A015/ASSET/ES60140A015.FP.PNG_V03

Elzerman AW (1976) Surface microlayer-microcontaminant interactions in freshwater lakes. PhD Thesis. Madison, Wis. : University of Wisconsin ©1976

Ettema R, Johnson JK, Schaefer JA (1989) Foam-initiated ice covers on small rivers and streams: An observation. Cold Reg Sci Technol 16(1):95–99. https://doi.org/10.1016/0165-232X(89)90011-6

Express News Service (2021) Delhi bans soaps, detergents not conforming to latest BIS standards to curb pollution in Yamuna. The Indian Express. https://indianexpress.com/article/cities/delhi/delhi-bans-soaps-detergents-yamuna-pollution-7359122/

Express News Service (2022) High ammonia levels in Yamuna briefly hit water supply to parts of Delhi | Cities News,The Indian Express. The Indian Express. https://indianexpress.com/article/cities/delhi/high-ammonia-level-yamuna-delhi-water-supply-7871182/

Express Web Desk (2021) How Delhi govt is controlling toxic froth over Yamuna for Chhath. The Indian Express. https://indianexpress.com/article/cities/delhi/delhi-govt-clear-off-toxic-froth-yamuna-chhath-7616204/

Fameau AL, Salonen A (2014) Effect of particles and aggregated structures on the foam stability and aging. In Comptes Rendus Physique, vol 15. Elsevier Masson SAS, Issues 8–9, pp. 748–760. https://doi.org/10.1016/j.crhy.2014.09.009

Figueredo RCR, Sabadini E (2003) Firefighting foam stability: the effect of the drag reducer poly(ethylene) oxide. Colloids Surf, A 215(1–3):77–86. https://doi.org/10.1016/S0927-7757(02)00425-9

Fisenko AI (2004) A new long-term on site clean-up approach applied to non-point sources of pollution. Water Air Soil Pollut 156(1–4):1–27. https://doi.org/10.1023/B:WATE.0000036822.97934.7B

Gagnon MJ (1983) Monitoring anionic surfactants at a sea outfall, Halifax Harbour, Canada. Water Res 17(11):1653–1659. https://doi.org/10.1016/0043-1354(83)90025-8

Gautam RK, Islamuddin, More N, Verma S, Pandey S, Mumtaz N, Kumar R, Md. Usama (2017) Sewage Generation and Treatment Status for the City of Delhi, its Past, Present and Future Scenario- A Statistical Analysis. International Journal for Research in Applied Science & Engineering Technology (IJRASET). https://www.researchgate.net/publication/335228238_Sewage_Generation_and_Treatment_Status_for_the_City_of_Delhi_its_Past_Present_and_Future_Scenario-_A_Statistical_Analysis

Gibbs JW (1993) A method of geometrical representation of the thermodynamic properties of substances by means of surfaces. The Scientific Papers of J. Willard Gibbs (Oxbow Press, Woodridge). https://www3.nd.edu/~powers/ame.20231/gibbs1873b.pdf

Gichuki J, Omondi R, Boera P, Okorut T, Matano AS, Jembe T, Ofulla A (2012) Water hyacinth eichhornia crassipes (Mart.) solms-laubach dynamics and succession in the nyanza gulf of Lake Victoria (East Africa): Implications for water quality and biodiversity conservation. Sci World J 2012. https://doi.org/10.1100/2012/106429

Hand VC, Rapaport RA, Pittinger CA (1990) First validation of a model for the adsorption of linear alkylbenzenesulfonate (LAS) to sediment and comparison to chronic effects data. Chemosphere 21(6):741–750. https://doi.org/10.1016/0045-6535(90)90261-Q

Harden SL, Williams DF (1989) Stable carbon isotopic evidence for sources of particulate organic carbon found in sea foam. Estuaries 12(1):49–56. https://doi.org/10.2307/1351450

Harun I, Pushiri H, Amirul-Aiman AJ, Zulkeflee Z (2021) Invasive water hyacinth: Ecology, impacts and prospects for the rural economy. In Plants vol 10, Issue 8. MDPI AG. https://doi.org/10.3390/plants10081613

He Q, Li L, Zhao X, Qu L, Wu D, Peng X (2017) Investigation of foaming causes in three mesophilic food waste digesters: Reactor performance and microbial analysis. Sci Rep 7(1). https://doi.org/10.1038/s41598-017-14258-3

Heard J, Harvey E, Johnson BB, Wells JD, Angove MJ (2008) The effect of filamentous bacteria on foam production and stability. Colloids Surf, B 63(1):21–26. https://doi.org/10.1016/J.COLSURFB.2007.10.011

Hladikova K, Ruzickova I, Klucova P, Wanner J (2002) An investigation into studying of the activated sludge foaming potential by using physicochemical parameters. Water Sci Technol 46(1–2):525–528. https://doi.org/10.2166/WST.2002.0529

Hwang Y, Tanaka T (1998) Control of Microthrix parvicella foaming in activated sludge. Water Res 32(5):1678–1686. https://doi.org/10.1016/S0043-1354(97)00380-1

India News (2021) Toxic foam floats on Yamuna as Delhi gasps to breathe clean air. Hindustan Times. https://www.hindustantimes.com/india-news/toxic-foam-floats-on-yamuna-as-delhi-gasps-to-breathe-clean-air-101636266906932.html

Jiménez Martínez AE, Schleder A, Sanez J, Bahniuk A, Froehner S (2019) Use of fatty acids as tracer of organic matter input associated with level of land urbanization. Environ Sci Pollut Res 26(31):31685–31698. https://doi.org/10.1007/S11356-019-06257-W

Johnson BD, Zhou X, Parrish CC, Wangersky PJ, Kerman BR (1989) Fractionation of Particulate Matter, the Trace Metals Cu, Cd, and Zn, and Lipids in Foam and Water Below Niagara Falls. J Great Lakes Res 15(2):189–196. https://doi.org/10.1016/S0380-1330(89)71474-X

Kikuchi M, Tokai A, Yoshida T (1986) Determination of trace levels of linear alkylbenzenesulfonates in the marine environment by high-performance liquid chromatography. Water Res 20(5):643–650. https://doi.org/10.1016/0043-1354(86)90029-1

Kumar B, Singh UK, Ojha SN (2018) Evaluation of geochemical data of Yamuna River using WQI and multivariate statistical analyses: a case study. Int J River Basin Manag 17(2):143–155. https://doi.org/10.1080/15715124.2018.1437743

Kumar V, Sahu P, Singh PK, Shukla NK, Mishra DP, Markandeya, Kumar V, Sahu P, Singh PK, Shukla NK, Mishra DP, Markandeya (2021) Evaluation and Quantification of Anionic Surfactant in the Gomti River at Lucknow City, India. Promising Techniques for Wastewater Treatment and Water Quality Assessment.https://doi.org/10.5772/INTECHOPEN.93517

Lamba M, Sreekrishnan TR, Ahammad SZ (2018) Sewage mediated transfer of antibiotic resistance to River Yamuna in Delhi, India. J Environ Chem Eng December, 0–1. https://doi.org/10.1016/j.jece.2017.12.041

Lánský M, Ružičková I, Benáková A, Wanner J (2005) Effect of coagulant dosing on physicochemical and microbiological characteristics of activated sludge and foam formation. Acta Hydrochim Hydrobiol 33(3):266–269. https://doi.org/10.1002/AHEH.200400569

Lemmer H, Lind G, Müller E, Schade M (2005) Non-famous Scum Bacteria: Biological Characterization and Troubleshooting. Acta Hydrochim Hydrobiol 33(3):197–202. https://doi.org/10.1002/AHEH.200400567

Lesov I, Tcholakova S, Denkov N (2014) Factors controlling the formation and stability of foams used as precursors of porous materials. J Colloid Interface Sci 426:9–21. https://doi.org/10.1016/J.JCIS.2014.03.067

Lesov I, Tcholakova S, Kovadjieva M, Saison T, Lamblet M, Denkov N (2017) Role of Pickering stabilization and bulk gelation for the preparation and properties of solid silica foams. J Colloid Interface Sci 504:48–57. https://doi.org/10.1016/J.JCIS.2017.05.036

Lokhandwala S, Gautam P (2020) Indirect impact of COVID-19 on environment: A brief study in Indian context. Environ Res 188:109807. https://doi.org/10.1016/J.ENVRES.2020.109807

Macel M, de Vos RCH, Jansen JJ, van der Putten WH, van Dam NM (2014) Novel chemistry of invasive plants: Exotic species have more unique metabolomic profiles than native congeners. Ecol Evol 4(13):2777–2786. https://doi.org/10.1002/ece3.1132

Madrange L, Chaboury P, Ferrandon O, Mazet M, Rodeaud J (1993) Study of the formation and stability of chemical foam on the Vienne river between Limogesançi Confolens. Revue Des Sciences De L'eau / J Water Sci 6(3):315–335. https://doi.org/10.7202/705178AR

Mallik A, Chakraborty P, Bhushan S, Nayak BB (2022) Impact of COVID-19 lockdown on aquatic environment and fishing community: Boon or bane? Mar Policy 141:105088. https://doi.org/10.1016/J.MARPOL.2022.105088

Masifwa WF, Okello W, Ochieng H, Ganda E (2004) Phosphorus release from decomposing water hyacinth and effects of decomposition on water quality. Uganda Journal of Agricultural Sciences 9(1):389–395. https://www.ajol.info/index.php/ujas/article/view/134975/124479

McAvoy DC, Eckhoff WS, Rapaport RA (1993) Fate of linear alkylbenzene sulfonate in the environment. Environ Toxicol Chem 12(6):977–987. https://doi.org/10.1002/ETC.5620120604

Mehra A, Farago ME, Banerjee DK (2000) A Study of Eichhornia crassipes Growing in the Overbank and Floodplain Soils of the River Yamuna in Delhi, India. Environ Monit Assess 60(1):25–45. https://doi.org/10.1023/A:1006181516828

Misra AK, Misra AK (2010) A River about to Die: Yamuna. J Water Resour Prot 2(5):489–500. https://doi.org/10.4236/JWARP.2010.25056

Mitrinova Z, Tcholakova S, Denkov N (2018) Control of surfactant solution rheology using medium-chain cosurfactants. Colloids Surf, A 537:173–184. https://doi.org/10.1016/J.COLSURFA.2017.10.018

Mooney HA, Cleland EE (2001) The evolutionary impact of invasive species. Proc Natl Acad Sci USA 98(10):5446–5451. https://doi.org/10.1073/PNAS.091093398

Mutiyar PK, Gupta SK, Mittal AK (2018) Fate of pharmaceutical active compounds (PhACs) from River Yamuna, India: An ecotoxicological risk assessment approach. Ecotoxicol Environ Saf 150(December 2017):297–304. https://doi.org/10.1016/j.ecoenv.2017.12.041

Myres JL (1939) Foam on the dead sea-and off the meander river. Nature 143:564. https://www.nature.com/articles/143564a0.pdf

Napolitano GE, Cicerone DS (1999) Lipids in Water-Surface Microlayers and Foams. Environ Sci 235–262. https://doi.org/10.1007/978-1-4612-0547-0_11

Napolitano GE, Richmond JE (1995) Enrichment of biogenic lipids, hydrocarbons and PCBs in stream-surface foams. Environ Toxicol Chem 14(2):197–201. https://doi.org/10.1002/ETC.5620140203

Ouyang Y, Nkedi-Kizza P, Wu QT, Shinde D, Huang CH (2006) Assessment of seasonal variations in surface water quality. Water Res 40(20):3800–3810. https://doi.org/10.1016/J.WATRES.2006.08.030

Pagureva N, Tcholakova S, Golemanov K, Denkov N, Pelan E, Stoyanov SD (2016) Surface properties of adsorption layers formed from triterpenoid and steroid saponins. Colloids Surf, A 491:18–28. https://doi.org/10.1016/J.COLSURFA.2015.12.001

Pajares S, Ramos R (2019) Processes and Microorganisms Involved in the Marine Nitrogen Cycle: Knowledge and Gaps. In Frontiers in Marine Science vol 6. Front Media S.A. https://doi.org/10.3389/fmars.2019.00739

Paliwal R, Sharma P, Kansal A (2007) Water quality modelling of the river Yamuna (India) using QUAL2E-UNCAS. J Environ Manag 83(2):131–144. https://doi.org/10.1016/J.JENVMAN.2006.02.003

Parker B, Barsom G (1970) Biological and Chemical Significance of Surface Microlayers in Aquatic Ecosystems. Bioscience 20(2):87–93. https://doi.org/10.2307/1294827

Parween M, Ramanathan A, Raju NJ (2017) Waste water management and water quality of river Yamuna in the megacity of Delhi. Int J Environ Sci Technol 14(10):2109–2124. https://doi.org/10.1007/S13762-017-1280-8

Parween M, Ramanathan AL, Raju NJ (2021) Assessment of toxicity and potential health risk from persistent pesticides and heavy metals along the Delhi stretch of river Yamuna. Environ Res 202:111780. https://doi.org/10.1016/J.ENVRES.2021.111780

Patel PP, Mondal S, Ghosh KG (2020) Some respite for India's dirtiest river? Examining the Yamuna's water quality at Delhi during the COVID-19 lockdown period. Sci Total Environ 744:140851. https://doi.org/10.1016/J.SCITOTENV.2020.140851

Pedersen KH, Andersen SI, Jensen AD, Dam-Johansen K (2007) Replacement of the foam index test with surface tension measurements. Cem Concr Res 37(6):996–1004. https://doi.org/10.1016/J.CEMCONRES.2007.02.007

Pest Management Regulatory Agency HC (2017) Ammonium salt of fatty acid 36. https://www.canada.ca/content/dam/hc-sc/migration/hc-sc/cps-spc/alt_formats/pdf/pubs/pest/_decisions/rd2017-09/RD2017-09-eng.pdf

Peter A, Žlabur JŠ, Šurić J, Voća S, Purgar DD, Pezo L, Voća N (2021) Invasive plant species biomass—evaluation of functional value. Molecules 26(13). https://doi.org/10.3390/molecules26133814

Petrovski S, Dyson ZA, Quill ES, McIlroy SJ, Tillett D, Seviour RJ (2011) An examination of the mechanisms for stable foam formation in activated sludge systems. Water Res 45(5):2146–2154. https://doi.org/10.1016/J.WATRES.2010.12.026

Piazza L, Gigli J, Bulbarello A (2008) Interfacial rheology study of espresso coffee foam structure and properties. J Food Eng 84(3):420–429. https://doi.org/10.1016/J.JFOODENG.2007.06.001

Pojasek RB, Zajicek OT (1978) Surface microlayers and foams—source and metal transport in aquatic systems. Water Res 12(1):7–10. https://doi.org/10.1016/0043-1354(78)90188-4

Poremba K, Gunkel W, Lang S, Wagner F (1991) Toxicity testing of synthetic and biogenic surfactants on marine microorganisms. Environ Toxicol Water Qual 6(2):157–163. https://doi.org/10.1002/TOX.2530060205

Princen HM, Mason SG (1965) The permeability of soap films to gases. J Colloid Sci 20(4):353–375. https://doi.org/10.1016/0095-8522(65)90082-6

Regismond STA, Winnik FM, Goddard ED (1998) Stabilization of aqueous foams by polymer/surfactant systems: effect of surfactant chain length. Colloids Surf, A 141(2):165–171. https://doi.org/10.1016/S0927-7757(98)00336-7

Ruzicka K, Gabriel O, Bletterie U, Winkler S, Zessner M (2009) Cause and effect relationship between foam formation and treated wastewater effluents in a transboundary river. Phys Chem Earth 34(8–9):565–573. https://doi.org/10.1016/j.pce.2009.01.002

Salonen A, Gay C, Maestro A, Drenckhan W, Rio E (2016) Arresting bubble coarsening: A two-bubble experiment to investigate grain growth in the presence of surface elasticity. EPL 116(4). https://doi.org/10.1209/0295-5075/116/46005

Schilling K, Zessner M (2011) Foam in the aquatic environment. In Water Research vol 45, Issue 15. Elsevier Ltd., pp. 4355–4366 https://doi.org/10.1016/j.watres.2011.06.004

Sehgal M, Garg A, Suresh R, Dagar P (2011) Heavy metal contamination in the Delhi segment of Yamuna basin. Environ Monit Assess 184(2):1181–1196. https://doi.org/10.1007/S10661-011-2031-9

Seuront L, Vincent D, Mitchell JG (2006) Biologically induced modification of seawater viscosity in the Eastern English Channel during a Phaeocystis globosa spring bloom. J Mar Syst 61(3–4):118–133. https://doi.org/10.1016/J.JMARSYS.2005.04.010

Sharma D, Kansal A, Pelletier G (2015) Water quality modeling for urban reach of Yamuna river, India (1999–2009), using QUAL2Kw. Appl Water Sci 7(3):1535–1559. https://doi.org/10.1007/S13201-015-0311-1

Shen Y, Hong S, Li Y (2022) Pea protein composition, functionality, modification, and food applications: A review. Adv Food Nutr Res 101:71–127. https://doi.org/10.1016/BS.AFNR.2022.02.002

Singh V, Mishra V (2021) Environmental impacts of coronavirus disease 2019 (COVID-19). Bioresour Technol Rep 15:100744. https://doi.org/10.1016/J.BITEB.2021.100744

Singh P, Purakayastha TJ, Mitra S, Bhowmik A, Tsang DCW (2020) River water irrigation with heavy metal load influences soil biological activities and risk factors. J Environ Manag 270:110517. https://doi.org/10.1016/J.JENVMAN.2020.110517

Singh Sankhla M, Kumar R, Prasad L (2022) Impact of Variation in Climatic Changes in Concentration of Lead & Nickel in Yamuna River Water, Delhi, India. Mater Today: Proc. https://doi.org/10.1016/J.MATPR.2022.05.242

Singh DK (2020) Action plan for Prevention of Froth / Foam Formation in River Yamuna. Delhi Pollution Control Committee. https://www.dpcc.delhigovt.nic.in//uploads/pdf/ACTION-PLAN-RIVER-YAMUNA-PDF-6f6276ee9bbc75b46106fdc56d9d674d.PDF

Somani M, Srivastava AN, Gummadivalli SK, Sharma A (2020) Indirect implications of COVID-19 towards sustainable environment: An investigation in Indian context. Bioresour Technol Rep 11:100491. https://doi.org/10.1016/J.BITEB.2020.100491

Stubenrauch C, Hamann M, Preisig N, Chauhan V, Bordes R (2017) On how hydrogen bonds affect foam stability. Adv Coll Interface Sci 247:435–443. https://doi.org/10.1016/J.CIS.2017.02.002

Szekielda K-H, Kupferman SL, Klemas V, Polis DF (1972) Element enrichment in organic films and foam associated with aquatic frontal systems. J Geophys Res 77(27):5278–5282. https://doi.org/10.1029/JC077I027P05278

Tafreshi AM, Marzo MD (1999) Foams and gels as fire protection agents. Fire Saf J 33(4):295–305. https://doi.org/10.1016/S0379-7112(99)00031-4

Tcholakova S, Mustan F, Pagureva N, Golemanov K, Denkov ND, Pelan EG, Stoyanov SD (2017) Role of surface properties for the kinetics of bubble Ostwald ripening in saponin-stabilized foams. Colloids Surf, A 534:16–25. https://doi.org/10.1016/J.COLSURFA.2017.04.055

The Times of India (2021) High ammonia content in Yamuna, water supply to remain affected in parts of Delhi | Delhi News - Times of India. https://timesofindia.indiatimes.com/city/delhi/high-ammonia-content-in-yamuna-water-supply-to-remain-affected-in-parts-of-delhi/articleshow/80237802.cms

Torregrossa M, Viviani G, Vinci V (2005) Foaming estimation tests in activated sludge systems. Acta Hydrochim Hydrobiol 33(3):240–246. https://doi.org/10.1002/AHEH.200400578

Tsibranska S, Ivanova A, Tcholakova S, Denkov N (2019) Structure of Dense Adsorption Layers of Escin at the Air-Water Interface Studied by Molecular Dynamics Simulations. Langmuir 35(39):12876–12887. https://doi.org/10.1021/ACS.LANGMUIR.9B02260/SUPPL_FILE/LA9B02260_SI_001.PDF

Upadhyay R, Dasgupta N, Hasan A, Upadhyay SK (2011) Managing water quality of River Yamuna in NCR Delhi. Phys Chem Earth 36(9–11):372–378. https://doi.org/10.1016/j.pce.2010.03.018

Vanrell G, Canals R, Esteruelas M, Fort F, Canals JM, Zamora F (2007) Influence of the use of bentonite as a riddling agent on foam quality and protein fraction of sparkling wines (Cava). Food Chem 104(1):148–155. https://doi.org/10.1016/J.FOODCHEM.2006.11.014

Voss M, Bange HW, Dippner JW, Middelburg JJ, Montoya JP, Ward B (2013) The marine nitrogen cycle: Recent discoveries, uncertaintiesand the potential relevance of climate change. Philos Trans R Soc B: Biol Sci 368(1621). https://doi.org/10.1098/rstb.2013.0121

Waters J, Garrigan JT (1983) An improved microdesulphonation/gas liquid chromatography procedure for the determination of linear alkylbenzene sulphonates in U.K. rivers. Water Res 17(11):1549–1562. https://doi.org/10.1016/0043-1354(83)90011-8

Weaire D, Pageron V (2006) Frustrated froth: Evolution of foam inhibited by an insoluble gaseous component. Philos Mag Lett 62(6):417–421. https://doi.org/10.1080/09500839008215544

Webster AJ, Cates ME (2001) Osmotic Stabilization of Concentrated Emulsions and Foams. Langmuir 17(3):595–608. https://doi.org/10.1021/LA000699M

Wegner C, Hamburger M (2002) Occurrence of stable foam in the upper Rhine River caused by plant-derived surfactants. Environ Sci Technol 36(15):3250–3256. https://doi.org/10.1021/es025532p

Wegner C, Hamburger M, Kunert O, Haslinger E (2000) Tensioactive Compounds from the Aquatic Plant Ranunculus fluitans L (Ranunculaceae) | Request PDF. Helvetica Chimica Acta 83(7):1454–1464. https://doi.org/10.1002/1522-2675(20000705)83:7%3c1454::AID-HLCA1454%3e3.0.CO;2-7

Westgate PJ (2009) Characterization of Proteins in Effluents from Three Wastewater Treatment Plants that Discharge to the Connecticut River. Environ Water Resour Eng Masters Projects 42:1–56. https://doi.org/10.7275/9REW-AG73

Wilson JR, Holst N, Rees M (2005) Determinants and patterns of population growth in water hyacinth. Aquat Bot 81(1):51–67. https://doi.org/10.1016/J.AQUABOT.2004.11.002

Yadav A, Khandegar V (2019) Dataset on assessment of River Yamuna, Delhi, India using indexing approach. Data Brief 22:1–10. https://doi.org/10.1016/J.DIB.2018.11.130

Zargar AR (2019) Air pollution in India and Yamuna River toxic foam mar Hindu festival in India - CBS News. CBS News. https://www.cbsnews.com/news/yamuna-rivers-toxic-foam-and-delhi-air-pollution-greet-india-hindu-devotees-for-chhath-puja-festival/

Zarkami R, Esfandi J, Sadeghi R (2021) Modelling Occurrence of Invasive Water Hyacinth (Eichhornia crassipes) in Wetlands. Wetlands 41(1). https://doi.org/10.1007/S13157-021-01405-W

Zayas JF (1997) Foaming Properties of Proteins. Functionality of Proteins in Food 260–309. https://doi.org/10.1007/978-3-642-59116-7_6

Zhang H, Miller CA, Garrett PR, Raney KH (2003) Mechanism for defoaming by oils and calcium soap in aqueous systems. J Colloid Interface Sci 263(2):633–644. https://doi.org/10.1016/S0021-9797(03)00367-9

Publisher's note Springer Nature remains neutral with regard to jurisdictional claims in published maps and institutional affiliations.

Springer Nature or its licensor (e.g. a society or other partner) holds exclusive rights to this article under a publishing agreement with the author(s) or other rightsholder(s); author self-archiving of the accepted manuscript version of this article is solely governed by the terms of such publishing agreement and applicable law.

Proceedings of the International Conference on Sustainable Computing and Smart Systems (ICSCSS 2023)
IEEE Xplore Part Number: CFP23DJ3-ART; ISBN: 979-8-3503-3360-2

Plant Disease Detection using Deep Learning

Tejas Gupta
Dept of Computer Engineering
Delhi Technological University
New Delhi, India
tejasgupta.2003@gmail.com

Titunath
Dept of Computer Engineering
Delhi Technological University
New Delhi, India
titunathchauhan@gmail.com

Vibhor Jain
Dept of Computer Engineering
Delhi Technological University
New Delhi, India
290901vibsjain@gmail.com

2023 International Conference on Sustainable Computing and Smart Systems (ICSCSS) | 979-8-3503-3360-2/23/$31.00 ©2023 IEEE | DOI: 10.1109/ICSCSS57650.2023.10169268

***Abstract*—Plants play an essential role in the ecosystem of our planet, and their significance is immeasurable. Detection of plant disease at an early stage is very important. It aids in minimizing crop losses, which can have severe consequences on the livelihoods of farmers as well as global food security. By identifying plant diseases early, the spread of the disease can be stopped, reducing crop losses. Detecting plant diseases accurately enables farmers and researchers to select the most effective treatment or management strategy, saving time, money, and resources by preventing the unnecessary use of pesticides or other interventions that may not work. The potential use of Deep Learning techniques, particularly transfer learning, for the detection of plant diseases could provide valuable support to farmers who may not have the resources or expertise to hire specialized experts. We are proposing a technique to classify plant disease by images of the plants by using transfer learning models. The paradigm is to use numerous models which then will be used to put out a comparative analysis where we put out different results to assert the viability of using the defined methods in order to visually categorize the plant diseases.**

***Index Terms*—Transfer Learning, Deep Learning, AlexNet, Inception V3**

I. Introduction

With the help of modern technology, civilization can now generate sufficient bread to fill the planet's population. There are many factors that still are a threat to food security such as the dwindling number of pollinators, climate change, plant diseases, etc. Causing a threat to the world's food safety, plant infections could have catastrophic effects on midget farmers who are only dependent on robust harvests. Over 75% of irrigated food supply in the world is grown by midgets farmers, and almost 45% of the total produced because of infections are frequent. Additionally, most people (55%) who does not get food reside at homes with midget farmers, creating this population herd at risk of interruptions in the food brought on by pathogens. To avoid agricultural loss brought on by diseases, several initiatives have been established. In the previous decade, alternative procedures would increasingly use to augment traditional methods of applying pesticides widely by IPM (integrated pest management) techniques. Regardless of the strategy, Identifying the disease is the first thing in the queue of accurate disease identification. Historically, Leaves health centers or other institutions like irrigation groups have helped with infection detection. In more recent years, such drives have also benefited from internet resources for illness detection.

Fig. 1. Rot Plant Leaves (Plant Village)

In recent years, object identification and computer vision in general have made significant strides. ILSAVRC built on the ImageNet dataset and the PASCAL VOC Challenge have lately been utilized as a criterion for several perception-related issues, together with object classification. In 2013, a large, CNN classified photos in 1,000 different groups with a top-8 error of 15.3%. The error was lessened to 3.57% during the course of the next three years as a result of several deep convolutional neural network advancements. Despite the time-consuming nature of training massive neural networks, trained models are capable of classifying pictures. We need a sizable, validated dataset of pictures of infected and in good-shape plants in order to create trustworthy picture classification for leaf infection detection. Image sets like this weren't available, and tiny Image sets were not freely accessible, until quite recently. The Plant Village initiative has started collecting images and made around fifty thousand till now of pictures of both well and sick agricultural plants to solve this issue. Here, we report on a convolutional neural network-based analysis of 54,306 pictures to classify 26 illnesses across 14 crop species. By predicting the right crop-disease match out of 38 different classes, our models' performance is evaluated. The model that performs the best obtains a mean F1.

What is Transfer Learning? The practice of applying a model that has already been learned to address the latest difficulty is called transfer learning. Transfer Learning is especially well-liked in the domain of DL since neural networks could currently be taught with the help of little to no input. Since most real-world events don't require training complex models employing millions of labeled data points, this is very helpful in the field of data science. For instance, when training a categorizer to decide if the picture consists of food, one

Authorized licensed use limited to: DELHI TECHNICAL UNIV. Downloaded on July 22,2023 at 05:07:04 UTC from IEEE Xplore. Restrictions apply.

can work with the information we grasped to differentiate beverages. The skill of a machine learning model that has already been trained is applied to an unrelated but firmly related difficulty through this method. For instance, if we coached an uncomplicated classifier to identify if a photo has a carry bag, you might apply that information to judge other things, like shoes. With this technique, we essentially try to apply the knowledge we have learned to fresh contexts in order to better understand the ideas. Weights are immediately moved from a network that finished the brand-new "task B" to a network that was working on "task A. Transfer learning refers to the technique of using a pre-trained model to solve a new problem. It is presently particularly well-liked in deep learning because of its capacity to coach deep NN in the company of relatively minimal information. This could be incredibly helpful in data technology because the bulk of real-world scenarios frequently does not contain thousands of labeled points of data to coach complex prototypes. We'll look at the definition, approach, advantages, and suitable applications of transfer learning. We'll also go over a few transfer learning techniques and offer you access to some pre-trained model resources.

The essay is organized as follows: Section II presents the related work, while Section III details the proposed plant disease detection method. Section IV provides an overview of the dataset used in the study. The experimental results are presented in Section V.

II. Literature Review

Saradhambal et al. [1] used image classification to study plant disease. They collect an image set constituted of 75 samples of diverse plant leaves with the disease, including those with bacterial blight and other diseases, for their methodology. There were five groups altogether, including one for healthy, normal leaves, and four for illnesses. A lab color model conversion was done after a little amount of image preprocessing to reduce noise. To segment the image, they applied Otsu's method along with clustering.

Melike et al. [2] employed the CNN model for the classification of leaf illnesses, utilizing a dataset of 500 photos, which was split into 400 training images and 100 testing images. There were a total of five classification categories, one of which was for healthy individuals. The image size of 512*512 that was selected was an acceptable size. The CNN model used three R, G, and B channel matrices as input, and the LVQ neural network received the output (Learning Vector Quantization). On average, 88 percent accuracy was reached. Their proposed model only included illnesses related to tomatoes.

K.Elangovan et al. [3]use SVM for classification in their study "Plant Disease Classification Using Image Segmentation and SVM Techniques." As part of their strategy, the image was converted into a separate color space. Image preparation methods were used to remove noise after cropping, smooth the image, and convert it to a greyscale image. Additionally, segmentation was done, after which characteristics were extracted. They used characteristics like color, shape, and texture for categorization. By constructing an architecture with a sub-path dedicated to light and another sub-path dedicated to color channels, can classify the CIFAR-10 dataset more efficiently and accurately. Using input photos encoded in the CIE Lab color space, a CNN was trained to accomplish this. Only the first convolution layer for the L and AB channels is reserved for each sub-path in this study. Toda et al. [3] shown that DCNNs can learn the distinct colors and textures of plant leaf diseases in a manner similar to human-made classification. Yang employed decision trees and logistic regressions to identify hyperspectral images, and decision trees were found to be more precise. Artificial neural networks (ANNs) are mathematical models that imitate the biological neural networks in animal brains and are used for processing complex input data. Recently, a 13-layer convolutional neural network has been created for the purpose of classifying fruit images by learning high-level features through data augmentation techniques and stochastic gradient descent with momentum. In the final experiment, this network achieved a classification accuracy of 94.94%. Convolutional neural networks may also be used for the categorization of multi-temporal crops.

Simulated Annealing (SA), in addition to ELM, is a new way of categorizing the Jatropha Curcas Disease suggested by Saragih et al. [4]. This work makes use of the jatropha disease dataset for model testing, training, and SA weight output optimization. The SA will modify the ELM classifier's neuron's ideal weight. The model is further enhanced by recognizing the jatropha seed disease using the decision tree classifier. The development of a model that can make judgments based on specialized information is the aim of the decision tree classifier. The result of this approach has a far higher acceptable accuracy rate of 94.74% compared to pure ELM, which has an accuracy rate of 66.67%. A comparison of different ML models, including the(SVM), (KNN), RF, and Bayes method, is advised by Maniyath et al. [5]. For training and testing, the method takes advantage of the existing datasets of diseased leaves. Additionally, features such as hu moments, Haralick textures, and color histograms are extracted using the histogram of oriented gradients (HOG). Following that, the datasets of sick and healthy leaves are jointly coached using the aforementioned models. Random forests had the highest accuracy in the comparison, scoring 70.14%. Implementing the ELM model can enhance the model since it scales better with the number of characteristics than the random tree does.

III. PROPOSED WORK

To find the best transfer learning model for plant disease classification, two models were used InceptionV3 and AlexNet. Also, three different versions of images have been used - colored image, grey scaled, and segmented images. Images were segmented using the SRCNN model that return the high-resolution images and also give extra information on the background image.

Authorized licensed use limited to: DELHI TECHNICAL UNIV. Downloaded on July 22,2023 at 05:07:04 UTC from IEEE Xplore. Restrictions apply.

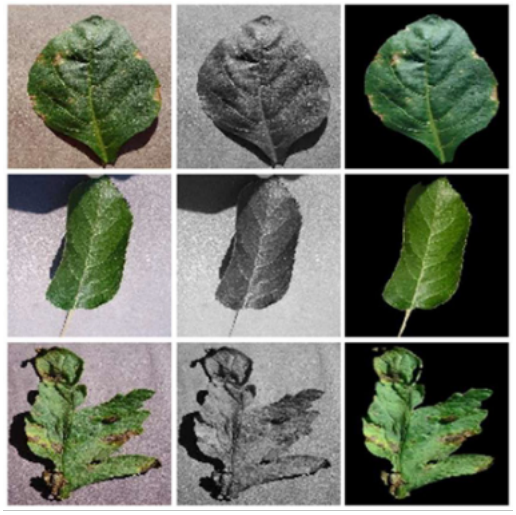

Fig. 2. Different type of image variations used to perform tests

A. InceptionV3

This model architecture has 22 layers. This model achieves high efficiency by reducing input image size and keeping important spatial information simultaneously. The first convolution layer of GoogleNet uses a filter size of 7*7. This layer reduces the image size and keeps spatial information of the images. At the second convolution layer size of the image is reduced by four and further by 8 before passing the input to the inception layer. Its architecture consists of nine inception modules. Two max-pooling layers are also present between the inception modules.

B. AlexNet

This model architecture has eight layers with learnable parameters. It uses relu-activation functions in each layer except the output layer. In this model, dropout layers are also used that prevents overfitting. Out of eight layers, five layers are used with the combination of max pooling layers and rest are the fully connected layers. In the output layer soft-max function is used as an activation function.

C. Image preprocessing

The collection contains various photos of arbitrary sizes and needs to be processed. Deep learning uses image preprocessing to improve model performance. Pictures are downsized to 128x128 before being used to train and test the model. After dividing each pixel's value by 255, augmentation is applied to the data. An additional 90 degrees of rotation, 0.1 degrees of breadth shift, 0.1 degrees of height shift, and 0.2 degrees of the shear range were added to the data. The 0.2 zoom range was chosen.

D. SRCNN

It is used for increasing the resolution of the images. This model consists of 3 parts - patch extraction and representation, non-linear mapping, and reconstruction. In this first images are converted into desired size by bicubic interpolation and then given input to SRCNN Network. Fig. 3 depicts the basic architecture of the SRCNN model.

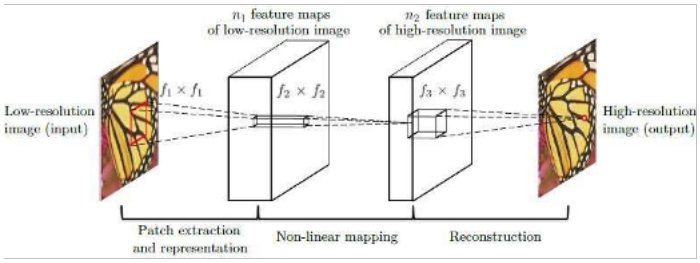

Fig. 3. SRCNN Model

Layer (type)	Output Shape	Param #
input_1 (InputLayer)	(None, 33, 33, 3)	0
conv2d_1 (Conv2D)	(None, 25, 25, 64)	15616
conv2d_2 (Conv2D)	(None, 25, 25, 32)	2080
conv2d_3 (Conv2D)	(None, 21, 21, 3)	2403

Total params: 20,099
Trainable params: 20,099
Non-trainable params: 0

Fig. 4. SRCNN Structure

IV. Dataset

The Plant Village dataset, which consists of 54,306 raw images distributed among 38 labels corresponding to pairs of crop-disease with accompanying images of plant leaves, is utilized. Figure 1 displays one example from each pair of crops and disease in the Plant Village dataset. In all approaches, the images were first resized to 128*128 pixels after which models were trained and tested. Fig. 5 shows the heat map of the disease and specie image set.

V. Results

A. Naive Approach

The first approach that was incorporated was the random guessing model which intakes the random modeling issues and was incorporated into the model and we obtained a result of 3.79% accuracy. However, when the information about the crop that the particular image belongs to was provided, the accuracy of the prediction increased to 49.23%.

B. Transfer Based

We perform all of our experiments across a wide range of train-test set splits to keep track of whether any of our techniques are over fitting.

We can notice that Inception_V3 has outperformed the majority of the results in the above specification. Hence we went deep into the technical details. Heatmap Fig. 6 shows

Authorized licensed use limited to: DELHI TECHNICAL UNIV. Downloaded on July 22,2023 at 05:07:04 UTC from IEEE Xplore. Restrictions apply.

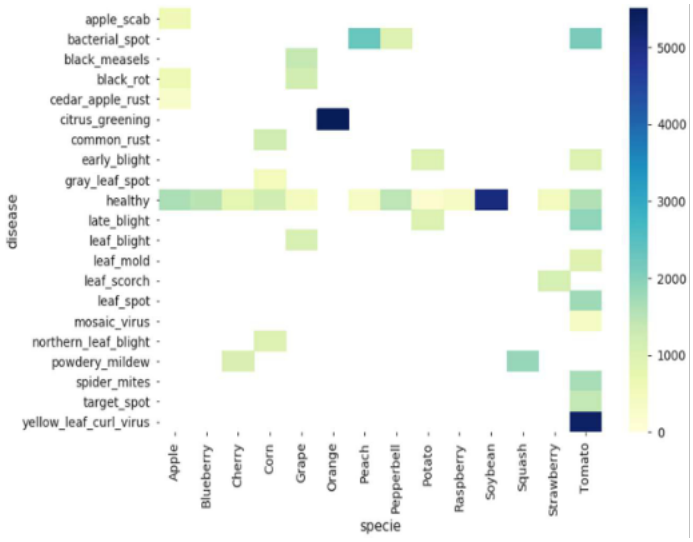

Fig. 5. Heat Map of the disease-specie image set in the Data

Model Type	Image Type	Data Split	Accuracy(in%)
GoogleNet/Inception	Color	70 – 30	99.57
		50 – 50	99.34
		30 – 70	99.32
	Grey scale	70 – 30	98.82
		50 – 50	92.74
		30 – 70	97.52
	Segmented	70 – 30	99.12
		50 – 50	96.85
		30 – 70	98.17
AlexNet	Color	70 – 30	99.17
		50 – 50	98.76
		30 – 70	97.11
	Grey Scale	70 – 30	97.15
		50 – 50	96.41
		30 – 70	96.52
	Segmented	70 – 30	98.91
		50 – 50	98.47
		30 - 70	97.24

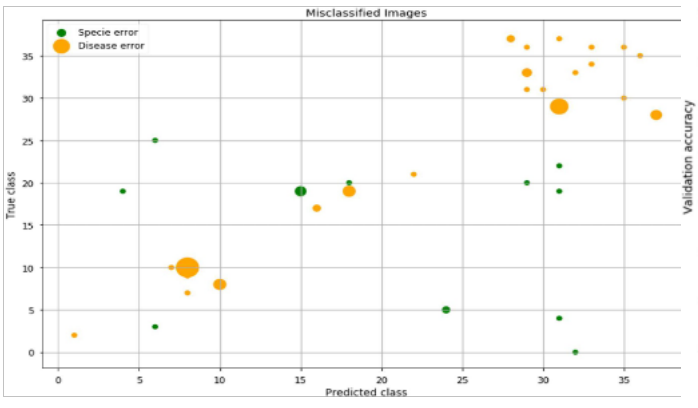

Fig. 6. Perception of errors in species vs disease

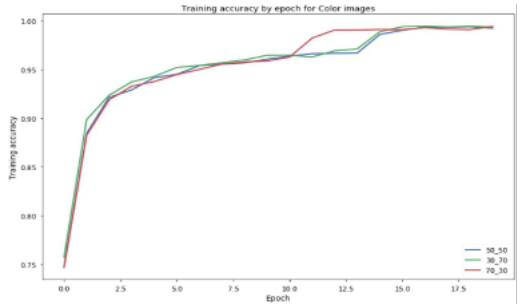

Fig. 7. Training Accuracy for the color images

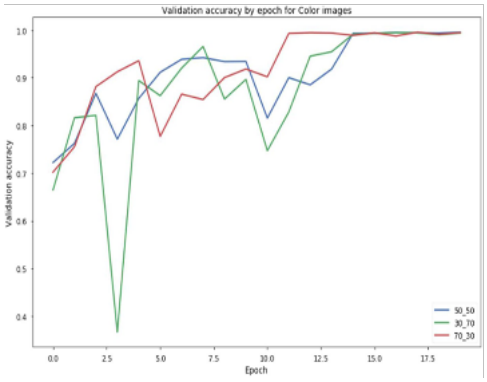

Fig. 8. Validation Accuracy for the color images

that major of the classification errors are within the specie errors and only a handful of cases have out to be on the model inconsistent with the suggested by novel considerations.

Fig. 7 and Fig. 9 are the depiction of Training accuracy and Validation accuracy of color images that were run on the three different splits of 30-70 (30% training and 70% validation), 50 – 50 (50 data for training and 50% data for validation), and 70-30 (70% training and 30% validation).

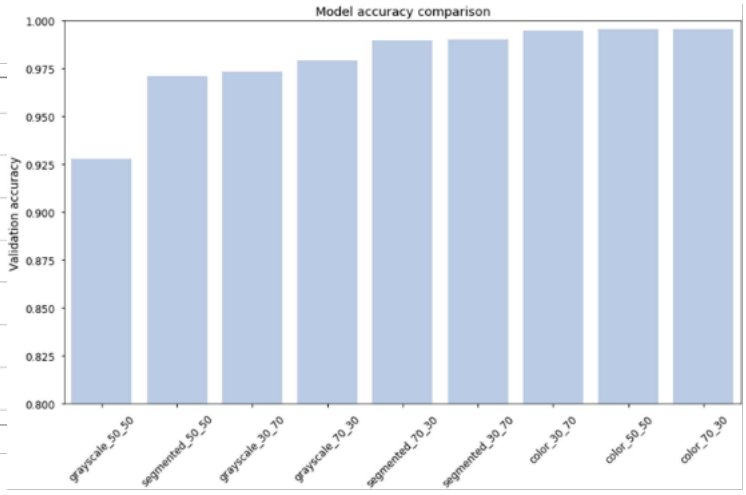

Fig. 9. Comparison of the various combinations in altogether

Authorized licensed use limited to: DELHI TECHNICAL UNIV. Downloaded on July 22,2023 at 05:07:04 UTC from IEEE Xplore. Restrictions apply.

VI. Conclusion

As plant diseases can impact our health and lifestyle, it is very important to classify plant diseases and provide medication for the same. By establishing the relationship between available data sets and various methodologies available for classifying plant disease this study established that by using a random guess model without providing species of the plant we achieved an accuracy of 3.79%, however by providing species name we achieved an accuracy of 49.23%. Further using Inception_V3 and Alexnet provided the highest accuracy of 99.57% for colored images. Even maximum accuracy is achieved in Alexnet when the dataset is split into 70%-30% for test-train simultaneously. Further research into plant disease classification should be done into the implementation of the above approach practically. While this study uses plant images for classifying disease, observational studies are required to gain more insights into different plants to identify whether the disease is common in all plants or some specific types of plants.

References

[1] Y Saradhambal.G, Dhivya.R, Latha.S, R.Rajesh, "Plant Disease Detection And Its Solution Using image Classification," International Journal of Pure and Applied Mathematics Volume 119 No. 14 2018, 879-884 ,ISSN: 1314-3395

[2] M. Sardogan, A. Tuncer and Y. Ozen, "Plant Leaf Disease Detection and Classification Based on CNN with LVQ Algorithm," 2018 3rd International Conference on Computer Science and Engineering (UBMK), Sarajevo, Bosnia and Herzegovina, 2018, pp. 382-385, doi: 10.1109/UBMK.2018.8566635.

[3] K. Elangovan,S. Nalini,"Plant Disease Classification Using Image Segmentation and SVM Techniques," International Journal of Computational Intelligence Research ISSN 0973-1873 Volume 13, Number 7 (2017), pp. 1821-1828

[4] Saragih, Triando Hamonangan Fajri, Diny Mahmudy, Wayan Abadi, Abdul Anggodo, Yusuf Priyo. (2018). Jatropha Curcas Disease Identification With Extreme Learning Machine. Indonesian Journal of Electrical Engineering and Computer Science. 12. 883. 10.11591/ijeecs.v12.i2.pp883-888.

[5] Ramesh Maniyath, Shima P V, Vinod M, Niveditha R, Pooja N, Prasad N, Shashank Ram, Hebbar. (2018). Plant Disease Detection Using Machine Learning. 41-45. 10.1109/ICDI3C.2018.00017.

[6] J. G. A. Barbedo, "Impact of dataset size and variety on the effectiveness of deep learning and transfer learning for plant disease classification," Comput. Electron. Agric., vol. 153, no. October, pp. 46–53, 2018.

[7] P. B. Padol and A. A. Yadav, "SVM classifier based grape [20] leaf disease detection," Conf. Adv. Signal Process. CASP 2016, pp. 175–179, 2016.

[8] K. P. Ferentinos, "Deep learning models for plant disease detection and diagnosis," Comput. Electron. Agric., vol. 145, no. February, pp. 311–318, 2018.

[9] M. J. Khan, H. S. Khan, A. Yousaf, K. Khurshid, and A. Abbas, "Modern Trends in Hyperspectral Image Analysis: A Review," IEEE Access, vol. 6, pp. 14118–14129, 2018.

[10] K. Elangovan , S. Nalini "Plant Disease Classification Using Image Segmentation and SVM Techniques" IJCIRV I

[11] H. Al-Hiary, S. Bani-Ahmad, M. Reyalat, M. Braik and Z. ALRahamneh, "Fast and Accurate Detection and Classification of Plant Diseases", International Journal of Computer Applications (0975 – 8887)Volume 17– No.1, March 2011

[12] Zulkifli Bin Husin, Abdul Hallis Bin Abdul Aziz, Ali Yeon Bin MdShakaffRohaniBinti S Mohamed Farook, "Feasibility Study on Plant Chili Disease Detection Using Image Processing Techniques", 2012 Third International Conference on Intelligent Systems Modelling and Simulation.

[13] RajneetKaur , Miss. ManjeetKaur"A Brief Review on Plant DiseaseDetection using in Image Processing"IJCSMC, Vol. 6, Issue. 2, February 2017

[14] Dr.K.Thangadurai, K.Padmavathi, "Computer Vision image Enhancement For Plant Leaves Disease Detection", 2014 World Congress on Computing and Communication Technologies.

[15] V Suresh , Mohana Krishnan , M Hemavarthini , K Jayanthan, D Gopinath, 2020, Plant Disease Detection using Image Processing, INTERNATIONAL JOURNAL OF ENGINEERING RESEARCH TECHNOLOGY (IJERT) Volume 09, Issue 03 (March 2020),

Authorized licensed use limited to: DELHI TECHNICAL UNIV. Downloaded on July 22,2023 at 05:07:04 UTC from IEEE Xplore. Restrictions apply.

2023 3rd International Conference on Advance Computing and Innovative Technologies in Engineering (ICACITE) | 979-8-3503-9926-4/23/$31.00 ©2023 IEEE | DOI: 10.1109/ICACITE57410.2023.10182822

PM2.5 Level Forecasting using Transformer-Based Model

Varang Rai
Department of Electronics and Communication Engineering
Delhi Technological University
New Delhi, India
varangrai@gmail.com

Sanidhya Kumar
Department of Electronics and Communication Engineering
Delhi Technological University
New Delhi, India
sanidhyakumar_2k19ec171@dtu.ac.in

Tamandeep Singh
Department of Electronics and Communication Engineering
Delhi Technological University
New Delhi, India
tamandeepsingh_2k19ec193@dtu.ac.in

Rajiv Kapoor
Department of Electronics and Communication Engineering
Delhi Technological University
New Delhi, India
rajivkapoor@dce.ac.in

Abstract— Air pollution is a significant public well-being concern in Indian cities, and forecasting PM 2.5 levels is important for effective air quality control. In this paper, we present a novel technique for PM2.5 level forecasting using transformer-based models, specifically the encoder part of the Transformer with modifications employed for the prediction of the concentration levels of PM2.5 particles using the previous years of data available to us. The proposed model makes use of historical PM 2.5 data to make predictions for multiple cities in India. Our experimental results indicate that the presented model surpasses previously used time series forecasting methods, achieving average error of 7.69% on the test set. Additionally, the given model can comprehend the complex temporal dependencies in the data and handle missing values effectively. These results demonstrate the potential of transformer-based models for PM2.5 level forecasting in Indian cities and have important implications for air quality management and public health policy.

Keywords—Transformers, LSTM, Bi-directional LSTM, RNN, CNN, PM2.5

I. INTRODUCTION

Deep learning is a field of machine learning that takes inspiration from the structure & function of the Human Brain, particularly from the neural networks that make up the brain. A neural network can learn the patterns and relationships directly from the raw data rather than relying on pre-defined features that may only capture some of the relevant details in the data. It has been successfully applied to different tasks like NLP (natural language processing), image recognition and speech recognition. It has also been used for prediction using time series data, which uses previous data to predict events in the future.

Time series forecasting is a common problem in many fields, including finance, economics, and meteorology. Accurate forecasts can be used to make informed decisions about the allocation of resources, the planning of future tasks, and the assessment of risk. Several approaches to time series forecasting exist, not limited to traditional statistical methods and ML algorithms. However, deep learning techniques have recently attained popularity due to their power to handle extensive and complex datasets and learn from long-term data dependencies.

There are several other types of neural networks which can be used for the purpose of time-series prediction, such as LSTM (long short-term memory) [1] & CNNs (convolutional neural networks) [2]. LSTM networks are notably well-suited for time series forecasting due to their power to recollect and learn from long-term dependencies in the data. Air pollution is a matter of great concern, especially in dense countries like India, the USA, China, UK. Average PM_2.5 level in the Capital of India, New Delhi, has been over 300 μg/m^3 whereas the acceptable level is 100 μg/m^3 [1]. PM_2.5 (Particulate Matter) is one of the pollutants of that affects our health, especially respiratory health. In this paper, we work on forecasting PM_2.5 levels

Transformers[2] are neural network architectures that succeeded precisely in machine translational, which is an NLP (natural language processing) task. The key idea behind transformers is self-attention, which allows the model to consider the relationships between all input tokens simultaneously rather than processing them in a predetermined order as in traditional sequential models like LSTMs (Long short-term memory cells) or RNNs (recurrent neural networks).

Transformers are particularly useful in natural language processing, where input sequences can be very long due to the complexity and structure of natural language. It has also been applied to other domains, such as time series forecasting. In time-series forecasting, the input to the Transformer can be a sequence of past weights of the time series, and the aim is to predict the forthcoming values of time-series data.

One way is to consider the time series as a sequence of tokens, with each token representing a single time point. The Transformer can then predict future time series values using the mechanism of self-attention to learn and understand intricate patterns in the time series data. This can be useful if the Transformer can learn more relevant and informative features than those that can be engineered manually.

Authorized licensed use limited to: DELHI TECHNICAL UNIV. Downloaded on August 08,2023 at 09:06:03 UTC from IEEE Xplore. Restrictions apply.

The major contributions of the paper are as follows:

1) We have gathered an hourly PM2.5 levels dataset for various Indian cities and designed a modified transformer-based model to perform prediction on this dataset. To our knowledge, this is the first such attempt at Indian Pollution levels.

2) Further we have compared the results of our models with various previously used models for time series forecasting. The proposed method enables faster training time, because of parallelism in transformer architecture, further transformer models can also take care of missing values in the dataset. Experimentations suggest that our model performs better as compared to previously used models, with MAPE as the testing metric.

II. Related Work

In [1], the authors proposed an LSTM deep learning model. They used hourly air quality data from India's CPCB (Central Pollution Control Board). The model was trained and tested on the 2018 to 2020 dataset, with a particular focus on the period of the COVID-19 lockdown in 2020. The study showed that the LSTM deep learning model could accurately predict air quality in Delhi, with an error of less than 5% for most pollutants. The authors also found the effect of COVID-19 lockdown significantly degraded air quality in Delhi, with a reduction in the levels of contaminants such as PM2.5 and NO2.

According to the study [2], a mixture of CNN and LSTM developed model was used to forecast the levels of PM2.5. To train and evaluate the model, a dataset of PM2.5 levels from Beijing, China is used. The model fully utilises its advantages, such as CNN's effectiveness in extracting characteristics relevant to the air quality & the LSTM's capacity to replicate the long ranged previous data which is used as an input. Four models were used - multivariate LSTM model, univariate LSTM model, univariate LSTM-CNN model, and multivariate LSTM-CNN model for predicting PM 2.5 concentrations levels. Further the implementation of all these models is evaluated utilising RMSE & MAE. Consequently, the Resulting from its low error and rapid training period, the suggested multivariate CNN-LSTM model outperformed all others. It fared better than a single CNN, a single LSTM, and a linear regression model, among other baseline models.

In [5], the authors proposed a combination of three different techniques for predicting AQI: the CEEMDAN [5] method, the ARMA [5] model, and the LSTM model. The authors test their method on AQI data from Beijing, China. The data from 2014 January to 2019 December are used as the training set. The test set includes data from January 2020 to December 2021 compared to several other methods for AQI prediction. The outcomes demonstrated that this model's MAPE, MAE, RMSE and MSE are the least. MAE increased by 22.5%, 53.4%, and 21.5% compared to the LSTM-CEEMDAN, GARCH-ARMA and LSTM models, MAPE increased by 21.4%, 55.3%, and 26.1%, MSE increased by 39.9%, 76.9%, and 28.5%, and RMSE increased by 22.5%, 52.0%, and 15.4%, respectively. They found that their method outperformed the other methods regarding prediction accuracy and stability.

In [6], the authors suggested a mixed model based on the Attention Gate Unit and Convolutional Neural Network for Air Quality Index Forecasting. They used PM2.5 data from the Beijing-Tianjin-Hebei region in China to train and evaluate their model. For validation of the proposed AGU-CNN model, the prediction results were compared with 9 other models using MSE, MAE and R2. The outcomes showed that the evaluation indexes of the AGU-CNN forecast model are more valuable than CNN-GRU, AGU, GRU, BD-LSTM, CNN-LSTM, LSTM, SVR, RFR and MLR models.

In addition to taking into account meteorological aspects, the research[7] recommended employing PSOGSA with the SVR algorithm based on GRNN, GCA and CEEMD for PM 2.5 forecasting. The efficiency of the suggested instance was tested using PM2.5 data from Harbin, Jinan and Chongqing in China from Dec 2013 to Aug 2015. When compared to the SVR-CEEMD-PSO, SVR-CEEMD-GSA, EEMD-SVR-PSOGSA, SVR-PSOGSA and SVR-CEEMD-GWO models based on MAE, RMSE, R, MAPE and I, findings of the proposed CEEMD-PSOGSA-SVR-GRNN for Chongqing exhibit the same instabilities as real PM 2.5 series. The other two cities, Harbina and Jinan, where the suggested model performed better, continued the trend.

Another model based on WT-LSTM-SAE (wavelet transform - stacked autoencoder - Long short-term memory) is suggested in [8] to forecast PM2.5. The information offered the foundation for online tracking and evaluation of China's air quality. Based on a variety of samples, WT separates PM 2.5 time series into different frequency components. As examples, six study locations in China were selected. LSTM-SAE is then used to predict the deconstructed elements [8]. The results show that for six different PM2.5 instances, SAE-forecasting LSTM outperforms other models (such as backpropagation), with the most effective models being 4 orders 5 layers, 5 orders 6 layers, 5 orders 7 layers, 3 orders 6 layers, 5 orders 7 layers, and 5 orders 6 layers.

The [9] study's goals are to devise and estimate the deployment of 4 unique Deep Neural Network topologies, as well as to look at how feature augmentation affects the ability to predict PM2.5 concentrations utilising five discrete wavelet levels (DWT). Four models—multi layer neural network, long short-term memory (LSTM), 1D convolutional neural network (1D-CNN) and an ensemble model consisting of 1D-CNN and LSTM are trained & experimented with using datasets collected from busy highways in Guildford, England. Through the use of statistical criteria, the precision of each model's predictions for the next 24 hour was quantitatively examined. The models were evaluated using MSE, MAE, NMSE, Pearson (r), and R2. The developments indicate that using wavelets enhances predicting outcomes. Wavelet transform is a helpful method to improve the implementation of DNN topologies, focusing on the mixture topology, which beats all other applied models in outcome predictions.

In [10], the authors proposed Transformer based Models for Time-Series Forecastings. They highlighted the limitations of traditional approaches such as ARIMA models and the use of conventional statistical methods for time series forecastings, like SVMs and LSTM networks. They tested the model using the available data of the stated-level and country level historical data from 2010 to 2018 from the CDC. When the outcomes were compared with the ARGONet ILI forecasting data, it was found that the Transformer-based model performed equally with ARGONet. Improvement in mean correlation was observed in the case of Transformer (0.931) compared to ARGONet (0.912). The mean RMSE

Authorized licensed use limited to: DELHI TECHNICAL UNIV. Downloaded on August 08,2023 at 09:06:03 UTC from IEEE Xplore. Restrictions apply.

value was slightly degraded for Transformer (0.593) compared to ARGONet (0.550).

III. Methodology

A. Description

The problem can be interpreted as a supervised learning problem with features & labels. From the PM2.5 levels time series, we take the previous N values as features and the subsequent M values as labels, where N is the history window size and M is the forecast window size. Here for our research work, we have taken N as 24 and M as 12.

For every point xi in time series data, the n points ranging from x_(i-n+1) to ⟦ x⟧ _i will be considered features, and the m points from x_(i+1),to x_(i+m) will be considered labels for those features. For the evaluation of the model, we will use Two common measures used to assess a model's accuracy are MSE and MAPE. To compare a model's forecasted values to the real values of the target variable, both metrics are employed. The average squared difference between the anticipated values and the real values is measured by MSE and the formula for it is given in equation 1 below:

$$MSE = \frac{1}{n}\sum(\hat{y} - y)^2 \qquad (1)$$

In the formulae above ŷ is the forecasted value, y is the ground truth value and n is the number of observations. Similar notation is followed throughout the paper.

The average absolute percentage difference between the expected and actual values is measured by the term MAPE. It is determined in accordance with equation 2:

$$MAPE = \frac{1}{n}\sum|\frac{\hat{y} - y}{y}| \qquad (2)$$

A model's performance can be assessed using MSE and MAPE, but there are some significant discrepancies between the two. MSE is sensitive to large errors since it calculates the average squared difference between the expected and true values. This can make MSE a wise decision when avoiding huge errors is more important. The average absolute percentage difference between the projected and actual values is measured by MAPE, so it is more robust to large errors. This can make MAPE a good choice when it is essential to understand the average magnitude of the error, regardless of whether it is positive or negative.

B. Dataset and Dataset windowing

The dataset we have taken from the official Indian Pollution board website[3] with PM_2.5 as the only feature in the dataset. It covers four years and has value for every hour, so the total data points will be 4×365×24. The data from 5 major cities were considered, New Delhi, Mumbai, Gurugram, Bengaluru, and Chennai. All this data has been put into matrix form where each row represents a city and has 4×365×24 entries representing time series value from 2016-2020. Every supervised model requires x values, which are features that will be fed into the model, and it will predict y values. We need (x,y) pairs to train our model on these values. This is a problem in which we have multiple input and output values, which is a classic NLP problem that also takes a vector of words and tries to predict the vector of words that can come after those words. We have implemented a similar approach to this. We have taken 24 previous data points as x values and 12 future data points as y values. We have taken a window of 36 data points (24,12) as (x,y), windows are formed with 1 step size.

To implement and retrieve this dataset from our available data matrix, which we mentioned, for every row, we used the sliding window algorithm, which has a window of 36 data points. This window is inserted in a new Dataframe. We shifted the window by one data point to the right and continued the process till the end of the row. This is done for all five rows.

C. Previous forecasting models experimented with.

Usually, time series forecasting problems involve recurrent deep learning models, which process on each step of the time series individually. There are various variants of recurrent models. The formulation of the models are given below.

1) RNN

In order to analyse sequential data, such as time series data or spoken language, recurrent neural networks (RNNs) were developed. The "neurons" that make up RNNs process the incoming data and send it via a network of linked layers. Typical architecture of a RNN is shows in figure 1.

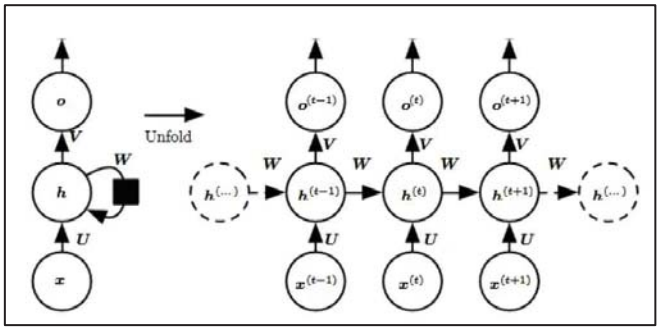

Fig. 1. Sequential units of RNN, unrolled across time.[12]

Equations of RNN forward pass are given in the equations below

$$a^{(t)} = h^{(t-1)}W + x^{(t)}U + b \qquad (3)$$

$$h^{(t)} = \tanh(a^{(t)}) \qquad (4)$$

$$o^{(t)} = h^{(t)}V + c \qquad (5)$$

$$y^{(t)} = softmax(o^{(t)}) \qquad (6)$$

RNNs have a "memory" that allows them to retain information from previous time steps. They are therefore suitable for jobs that require the consideration of contextual information, such as language translation or speech recognition. The outcome of the RNN is subjected to a nonlinear activating function at each timestep, enabling the RNN to simulate intricate interactions between the input and output data.

2) LSTM

RNNs have limitations, including vanishing gradients, exploding long sequences, etc. This problem is addressed by LSTM and designed in such a way as to do so. It has three gates: an input gate, forget gate (one of the most important ones) and an output gate. The architecture of an LSTM block is given in figure 2.

Authorized licensed use limited to: DELHI TECHNICAL UNIV. Downloaded on August 08,2023 at 09:06:03 UTC from IEEE Xplore. Restrictions apply.

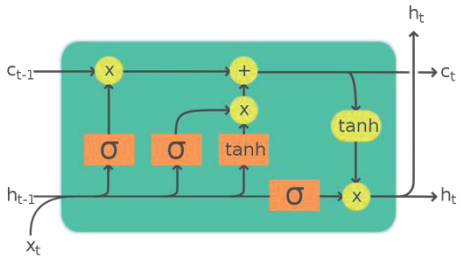

Fig. 2. Architecture of an LSTM unit.[13]

Equations are as follows:

$$f_t = \sigma\left(x_t \times W_f + h_{t-1} \times U_f + b_f\right) \quad (7)$$

$$i_t = \sigma(x_t \times W_i + h_{t-1} \times U_i + b_i) \quad (8)$$

$$o_t = \sigma(x_t \times W_o + h_{t-1} \times U_o + b_o) \quad (9)$$

$$\bar{c}_t = tanh(x_t \times W_c + h_{t-1} \times U_c + b_c) \quad (10)$$

$$c_t = f_t \cdot c_{t-1} + i_t \cdot \bar{c}_t \quad (11)$$

$$h_t = o_t \cdot \tanh(c_t) \quad (12)$$

The input gate determines what information from the input should be passed through to the cell state. It is given by equation 8. Whether to ignore the information obtained from the cell state is decided by the forget gate given by equation 7.

Further the output gate determines what cell state information obtained should be passed to the result. The cell state and hidden state are updated using equation 11, 12 respectively.

The equation W is a weight matrix, and × represents matrix multiplication between weights and input vector values. The sigmoid function squashes the values between 0 and 1.

3) Bidirectional LSTM

A bi-directional LSTMs (Bi-LSTM), is a special type of RNN capable of processing information not only in forward direction but also in reverse direction. Architecture is shows in figure 3. To obtain complex information in the input data, natural language processing (NLP) like translation of languages or modelling are frequently used. The goal of an LSTM is to identify long-term dependencies in sequential data by employing "memory cells" that can store information for extended periods of time. Similar to a standard LSTM is a Bi-LSTM. It nevertheless analyses the incoming data in both ways, enabling it to record contextual data from the present as well as the future. A Bi-LSTM is made up of two LSTM networks, one of which processes the input data forward and the other of which processes it backward. In Bi-LSTM architecture, the input data is processed in a bidirectional manner using a forward LSTM reading it from left-to-right and a backward LSTM reading it from right-to-left. The ultimate output is obtained by concatenating the results of the forward and backward LSTMs and passing them through a final layer. The accompanying figure provides a visual depiction of this process.

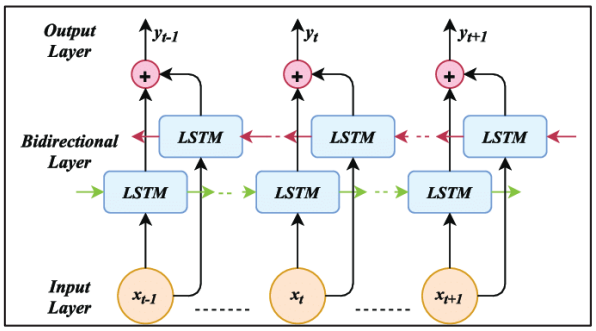

Fig. 3. Architecture of Bi directional LSTM. Green arrows indicate the information propagation in the forward direction, while the red arrow is in the backward.[14]

D. Transformer-Based Architecture

Transformers models have been growing tremendously in recent years after google research was first introduced in 2018. It gained much attraction due to its outstanding results compared to other available models in the research community. Transformers have broadly two components: Encoder and Decoder. The encoder consists of the positional encoding layer, multi-head attention and addition and normalization layers. The modified transformer architecture used in the study is shows in figure 4 and described in detail below.

1) Positional Encoding

The encoder is a component of the transformer architecture that processes the input data and encodes it into a compact and valuable representation. Firstly, positional embeddings is done on the input data. It is done to capture the position of time where this data point is noted so that we know which values occur at which point. It is essential to do so because it can be related to the actual scenario. Considering that pollution in Delhi is increasing yearly, we should know which values are from what time point, as 2016 might be much different than 2020.

2) Multi-head Attention

After the positional embeddings part, outputs are now input to eight self-attention blocks, which form one of the key components of this architecture, the multi-head attention mechanism. Multihead attention allows the model to look after the other areas of the input sequence by linearly projecting the input multiple times with different weights. Mathematically, the multihead attention mechanism can be represented as:

$$MultiHead(Q,K,V) = Concat(head_1,\ldots,head_h)W^O \quad (13)$$

Where Q, K and V are the query, key and value matrices respectively. The attention is computed by taking the dot product of the query with the key, then applying a scaling factor and passing the result through a softmax function. This process is repeated for h heads, where each head has its own set of weights. The output of each head is concatenated and passed through a linear projection, represented by W^O , to produce the final output.

In our application we have used 8 heads in the multi head attention. Recently, multihead attention has also been applied to time series forecasting tasks. In these scenarios, the input sequence is typically a sequence of past values of a time series,

Authorized licensed use limited to: DELHI TECHNICAL UNIV. Downloaded on August 08,2023 at 09:06:03 UTC from IEEE Xplore. Restrictions apply.

represented by X = {x_1,x_2,...,x_t}, and the goal is to make predictions for future values represented by Y = {y_1,y_2,...,y_t}. By using multihead attention, the model can attend to different parts of the input sequence, such as short-term and long-term dependencies, and make more accurate predictions.

The intuition behind self-attention is to focus on specific aspects of input sequences relevant to our case. After passing through the 8 self-attention modules it is send to an addition and normalization layer.

3) Addition and Normalization layer

The addition layer is used to combine the input of the attention mechanism with the outcome of the previous layer. Mathematically, we can represent the relation as y = x + Layer(x), where x is the input and Layer(x) is the output of the previous layer. The addition layer allows the model to learn residual functions, which can simplify the optimization process and stabilize the training process.

Normalization layers, such as Layer Normalization (LN) or Batch Normalization (BN), are used to normalize the inputs and outputs of the layers which ensures that the inputs to the next layer have zero mean and unit variance. This helps to emhance the stability and effect of the model. In the transformer architecture, both layers are used together to form the Add and Normalize (AddNorm) block.The output of this block then passes to a fully connected neural network layer, and then we again add and normalized to get the encoder input data. Finally, there is a straightforward feed network in the end which acts like the decoder to get the forecasted data.

4) Experimentation and Results

We began our experiments using previously used models for time series forecasting. We choose RNN, LSTM and bi-directional LSTM which are of increasing order of complexity to see how well they were able to model the complexity of the data. These serve as a baseline for analyzing the performance of our modified transformer model. We make use of Mean Squared Error (MSE) and Mean Absolute Percentage Error (MAPE) to quantify our effects. These are usually utilized metrics for regression problems. Final results of all models are given in table I.

In this section we first explain the transformations applied on the data and the preprocessing techniques. Then we demonstrate the results of the recurrent models experimented with. Finally, we conclude with the proposed transformer architecture used for forecasting.

We pre-processed our data before applying any model.

For every row in the data matrix, we had just described in the above paragraphs, x = np. diff(np.log(x)), then x = x.csum(). Where np is used for the NumPy library.

Here, pre-processing is an important step in the data analytics because it helps to make sure that the data is accurate & ready for experimentation.

Dataset has been has been split 60-20-20 ratio for training ,validation and test set respectively. We have trained the model on our data for 100 epochs.

Results from recurrent networks, LSTM and bi-directional LSTM: With a history size of 48-time steps, looking at the histogram, the MAPE and MSE are higher for all the above three models compared to transformers. First, we implemented the RNN algorithm to see how it works on this time series data and what we found is that it performs the worst among all the algorithms As MAPE came out to be 47%. We applied another algorithm with a better memory for past values to improve this. For this, we tried LSTM, which improved MAPE by 27.01%. To strengthen further, we went with bi-directional LSTM, which also improved to 13.4% but still isn't adequate, so now we thought of implementing something else. Then we got the idea of using Transformers.

Results from Transformers: Transformers produce the most satisfactory results: The MAPE we got is 7.69%, as evident from the training and validation loss graph vs epochs shows in figure 6. We tuned with various hyperparameters, including windows size and dimensionality of the transformer model, which is the dimension input to multi-head attention. Three window sizes were tried, using past 12, 24, and 48 hours data, and got a validation MAPE of 17.76, 7.54, and 7.6. Consequently, we use the past 24 hours' data to predict the future 12 hours. Further, upon changing the model dimensionality, it was observed that a small dimensionality of 128 gave the best results compared to 256 and 512. Sample forecasting results is shown in figure 5.

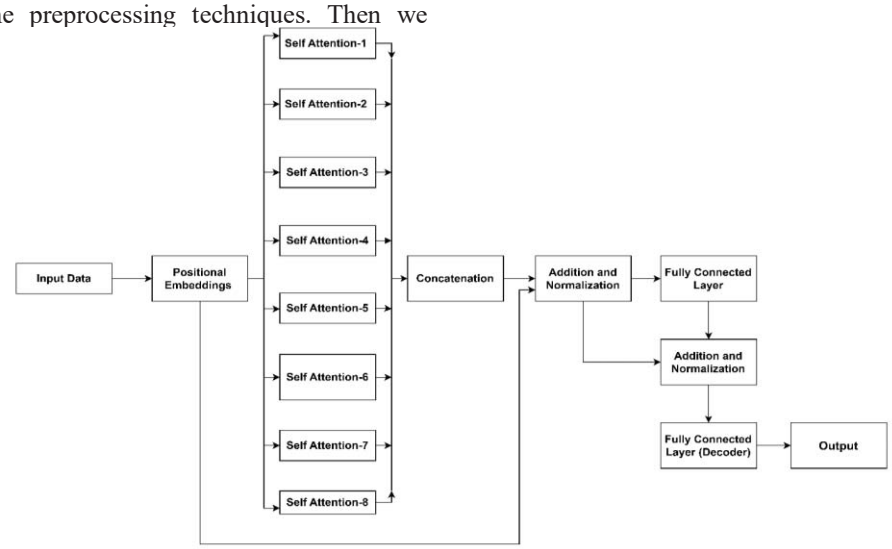

Fig. 4. Modified transformer architecture used in the study

Authorized licensed use limited to: DELHI TECHNICAL UNIV. Downloaded on August 08,2023 at 09:06:03 UTC from IEEE Xplore. Restrictions apply.

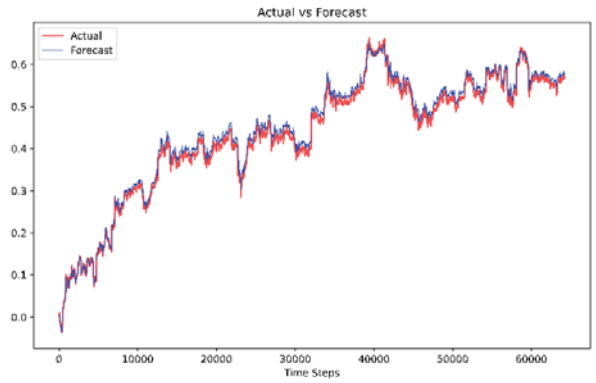

Fig. 5. Actual vs Forecasted values on validation and test dataset.

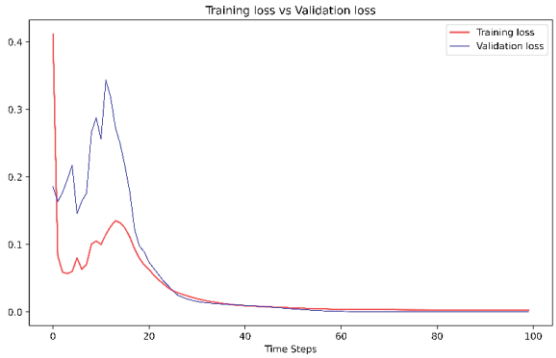

Fig. 6. Training and validation loss graph.

TABLE I. MEAN AVERAGE PERCENTAGE ERROR OF VARIOUS MODELS

Model	*MAPE score (%)*
RNN	47.01
LSTM	27.01
Bidirectional LSTM	13.4
Modified Transformers(Our Model)	7.69

IV. CONCLUSION AND FUTURE WORK

It can be concluded from above discussions that transformers provide promising results in time series forecasting tasks. We have also investigated previously used methods, and transformers have outperformed them in terms of performance. Further the proposed model can also be extended to other types of time series. The current applications of our work can be used to predict the pollution of cities hourly, which can be of utmost importance. Depending on the pollution prediction, people can go outside and plan their day accordingly. Future work can also include associating different cities together in a graphical representation and taking into account intercity pollution level. We can further enhance the model by introducing other parameters like average temperature, average pressure, wind speed, humidity etc. and other weather parameters [15] and see their dependance on pollution levels. Overall, weather conditions can have a significant impact on the pollution levels.

REFERENCES

[1] A. Tiwari, R. Gupta, and R. Chandra, "Delhi air quality prediction using LSTM deep learning models with a focus on COVID-19 lockdown," Feb. 2021, [Online]. Available: http://arxiv.org/abs/2102.10551

[2] T. Li, M. Hua, and X. Wu, "A Hybrid CNN-LSTM Model for Forecasting Particulate Matter (PM2.5)," IEEE Access, vol. 8, pp. 26933–26940, 2020, doi: 10.1109/ACCESS.2020.2971348.

[3] "Delhi Air Pollution Facts & Stats - Gifographic | Mocomi Kids." https://mocomi.com/delhi-air-pollution/ (accessed Dec. 30, 2022).

[4] A. Vaswani et al., "Attention Is All You Need."

[5] Y. Sun and J. Liu, "AQI Prediction Based on CEEMDAN-ARMA-LSTM," Sustainability (Switzerland), vol. 14, no. 19, Oct. 2022, doi: 10.3390/su141912182.

[6] J. Wang, L. Jin, X. Li, S. He, M. Huang, and H. Wang, "A Hybrid Air Quality Index Prediction Model Based on CNN and Attention Gate Unit," IEEE Access, vol. 10, pp. 113343–113354, Nov. 2022, doi: 10.1109/access.2022.3217242.

[7] S. Zhu et al., "PM2.5 forecasting using SVR with PSOGSA algorithm based on CEEMD, GRNN and GCA considering meteorological factors," Atmos Environ, vol. 183, pp. 20–32, Jun. 2018, doi: 10.1016/J.ATMOSENV.2018.04.004.

[8] W. Qiao, W. Tian, Y. Tian, Q. Yang, Y. Wang, and J. Zhang, "The Forecasting of PM2.5 Using a Hybrid Model Based on Wavelet Transform and an Improved Deep Learning Algorithm," IEEE Access, vol. 7, pp. 142814–142825, 2019, doi: 10.1109/ACCESS.2019.2944755.

[9] S. L. J. Galvão et al., "Particulate Matter Forecasting Using Different Deep Neural Network

[10] Topologies and Wavelets for Feature Augmentation," Atmosphere (Basel), vol. 13, no. 9, p. 1451, Sep. 2022, doi: 10.3390/atmos13091451.

[11] N. Wu, B. Green, X. Ben, and S. O'Banion, "Deep Transformer Models for Time Series Forecasting: The Influenza Prevalence Case," Jan. 2020, [Online]. Available: http://arxiv.org/abs/2001.08317

[12] "CPCB | Central Pollution Control Board." https://cpcb.nic.in/ (accessed Dec. 30, 2022).Machine Learning Approaches for Time Series." https://dida.do/blog/machine-learning-approaches-for-time-series (accessed Apr. 22, 2023).

[13] "Long short-term memory - Wikipedia." https://en.wikipedia.org/wiki/Long_short-term_memory (accessed Apr. 22, 2023).

[14] S. Cornegruta, R. Bakewell, S. Withey, and G. Montana, "Modelling Radiological Language with Bidirectional Long Short-Term Memory Networks," EMNLP 2016 - 7th International Workshop on Health Text Mining and Information Analysis, LOUHI 2016 - Proceedings of the Workshop, pp. 17–27, Sep. 2016, doi: 10.18653/v1/w16-6103.

[15] J. P. Buckley, J. M. Samet, and D. B. Richardson, "Does air pollution confound studies of temperature?," Epidemiology, vol. 25, no. 2, pp. 242–245, Mar. 2014, doi: 10.1097/EDE.0000000000000051.

Authorized licensed use limited to: DELHI TECHNICAL UNIV. Downloaded on August 08,2023 at 09:06:03 UTC from IEEE Xplore. Restrictions apply.

Prediction of Surface Roughness of Mild Steel finished with Viscoelastic Magnetic Abrasive Medium

Anushka Sharma[1], Himagra Chawla[2], Krovvidi Srinivas[3,*]

[1,2]Delhi Technological University, New Delhi 110042, India

[3]Faculty of Delhi Technological University, New Delhi 110042, India

*Author to whom correspondence should be addressed:

E-mail: srinivaskrovvidi@dtu.ac.in

(Received month date, year; Revised month date, year; accepted month date, year).

Abstract: In this investigation on Viscoelastic magnetic abrasive finishing process, a deep learning model is applied to predict the change in surface roughness. A dedicated experimental setup along with the abrasive media was prepared to carry out the finishing process. Experiments were performed on mild steel to inspect the effect of several parameters such as finishing time, magnetic flux density, abrasive mesh number, magnetic tool rotational speed, feed, ultrasonic amplitude on the surface roughness. The paper aims to provide a cost-effective as well as time-effective predictive method to depict the change in surface roughness.

Keywords: Viscoelastic magnetic abrasive finishing, Surface Roughness, Artificial neural network modeling

1. Introduction

Finishing, in a manufacturing process, is employed to add an appealing texture to the workpiece. It enables us to achieve the desired surface finish, geometric structure, and accuracy through various operations that come under its umbrella. It can be classified into conventional and non-conventional finishing processes. Non-conventional finishing processes provide a multitude of advantages over the traditional processes, including better tool life and higher precision. One of the favourable non-conventional finishing processes is Magnetic Field Assisted Finishing. It employs a magnetic field generated by a temporary or permanent magnet, which provides the necessary finishing force to abrasive particles causing them to press against the workpiece, thus generating abrasion. One of its major attractions include being able to finish both internal and external surfaces with high precision and minimum surface damage. It can be further classified into three sub-categories, namely magnetic abrasive finishing (MAF), magnetorheological finishing (MRF), and Viscoelastic magnetic abrasive finishing (VEMAF). The fundamental idea behind all of these processes is the use of abrasive media which have multiple random cutting edges and no definite orientation, which finishes the surface much more efficiently when compared with a cutting tool with definite edges. In our study, we have used Viscoelastic magnetic abrasive finishing wherein Viscoelastic material is added to prevent the abrasive particles from disintegrating due to the centrifugal force of the magnetic field.

1.1 Viscoelastic Magnetic Abrasive Finishing

Li et al.[1)] first presented the technology of VEMAF, which effectively integrated the advantages of solid magnetic abrasive and abrasive flow finishing providing a whole new effective method to solve surface finishing problems of complex surfaces. In this study, an experimental setup for Viscoelastic magnetic abrasive finishing (VEMAF) was established to record and analyze the effect of process parameters on the finishing characteristics of the workpiece, followed by the analysis of this process through an artificial neural network model. A new type of polishing tool was designed and manufactured along with the Viscoelastic magnetic abrasive. This abrasive mixture comprises polymer, gel, CIP, and SIC, which, under the influence of a magnetic field, forms a magnetic brush. The strength of the magnetic field controls the finishing pressure, which affects the finishing characteristics of the workpiece. It is possible to achieve a nano-level finish of the workpiece with hardly any surface damage through this process.

1.2 Artificial Neural Networks

Neural network, also referred to as Deep Learning, is an approach to Artificial Intelligence that is applied to almost all engineering applications. A neural network, a massively parallel distributed processing system, is a simplified model of our biological neuron system. Neural networks learn by training over the training data, and their accuracy is measured by testing them over the testing data

or validation data, with the use of various metrics and scores. They are particularly fundamental in explaining non-linear relationships between the process parameters. They enable obtaining complex connections between dependent and independent variables with the application of activation functions. Neural networks are encouraged because of their tolerance to high levels of noise and non-linearities in the datasets. The promptness and quickness of the operation of neural networks in terms of working and producing accurate results can be seen both in software and in real-time in hardware. This is one of the many reasons they're implemented and preferred over other conventional multiple regression models. Three key features define a neural network; topology, functionality, and learning. Topology refers to the quantity of nodes in each layer and the interconnection between these nodes. Functionality entails the transfer function and the cost function of network outputs. Learning refers to the way in which the network trains itself, which is determined by parameters such as the learning rate. A neural network has various types, but the most commonly used is the back-propagation network. Back-propagation works by feeding the input to the entire network (input layer, hidden layers and the output layer) and predicting an output. The error in the output is then computed and this error is back propagated upon which the network is fine-tuned to minimise this error in the next iteration. The number of iterations is defined by the parameter 'epochs,' and the aim of running multiple iterations is to ensure that after every iteration, the loss/error is decreasing, which proves the efficiency of the neural network.

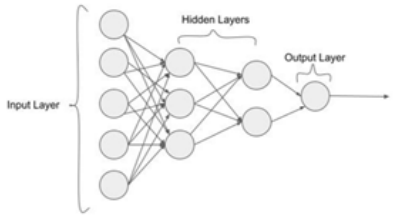

Fig. 1 General Artificial Neural Network Architecture

In recent times, the application of neural networks has been found in precision manufacturing, and it is being implemented to analyse various machining phenomena along with machining quality. Numerous researchers have utilized neural networks for the prediction of surface roughness parameters in other finishing processes. However, on the other hand, there is very little contribution of significance in the employment of neural network architectures in the modeling and simulation of the VEMAF process. The purpose of this research is to employ a neural network to analyse, and predict the surface roughness in a Viscoelastic magnetic abrasive finishing process. The impact of process parameters, namely finishing time, magnetic flux density, abrasive mesh number, magnetic tool rotational speed, feed and ultrasonic amplitude on the corresponding surface roughness has been analysed.

2. Related Work

After the invention of magnetic field assisted finishing process in early 20th century, many researchers have since developed various novel ideas to improve the key parameters, and many publications have been introduced in this field some of which are outlined below:

Earliest technique of Abrasive finishing in a Magnetic Field was outlined by Baron, Y.M[2]. Process principles and the influence of abrasive particle size on the surface finish was demonstrated by Shinmura et al.[3] on ceramic bars, using diamond-coated abrasive particles. Fox et al.[4] presented a technique and investigated experimentally the application of this technology. A pole rotating system for internal magnetic abrasive finishing, was proposed by Yamaguchi & Shinmura[5] which characterised in-process abrasive behaviour by the magnetic field, acting on the magnetic abrasive. Singh et al.[6] measured experimentally the forces acting on their workpiece. They also found out the percentage contribution, of various experimental operating factors, on the forces and change in surface roughness. Srinivas et al.[7] studied the effect of various process parameters in the viscoelastic magnetic abrasive finishing arrangement using Ansys Maxwell.Li et al.[8] established a mathematical model of interfacial debonding while using coupling agents and also determined the effect of these agents on change in surface roughness. Li et al.[9] developed a new d surfaces in face milling process, by means of a feed-forward back-propagation neural network model. Their work could help achieve the desired surface roughness profile geometry by appropriately determining the cutting conditions. Djavanroodi F.[11] examined the effectiveness of back-propagation neural network models for predicting the surface roughness variation in the MAF process. Numerous researchers have also utilized neural networks for the prediction of surface roughness parameters (Petri et al.[12], Singh et al.[13], however, no concrete employment of ANN has been seen in the VEMAF process. Therefore, in order to optimise VEMAF through a machine learning technique, in our study, we have employed an artificial neural network model to predict the change in surface roughness. magnetic finishing media for the magnetic abrasive finishing process on rotary surfaces. El-Sonbaty et al.[10] analysed and anticipated the connection between cutting conditions and comparing fractal boundaries of machine

3. Experimental Setup

The schematic diagram of the Viscoelastic magnetic abrasive finishing operation is illustrated in fig. 2. A CNC tapping and drilling machine was used for the experiment, consisting of a polishing tool, ultrasonic generator, Viscoelastic magnetic abrasive polishing medium, workpiece, and fixture, as shown in fig. 3.

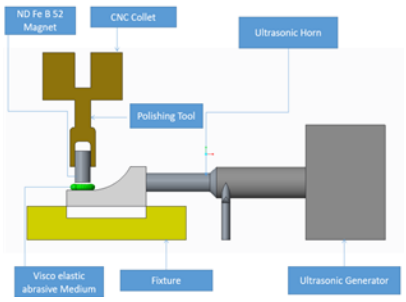

Fig. 2 Schematic Diagram of Setup

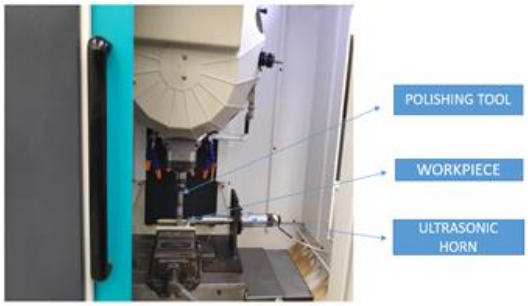

Fig. 3 CNC Machine Setup

The polishing tool is shown in fig. 4, it consists of a mild steel tool holder having a length of 95 cm and an outer diameter of 20 mm. The top of the tool holder holds the polishing tool to the spindle of the CNC machine. An N52 permanent magnet with a diameter of 20 mm and a height of 20 mm is used to generate magnetic field, which provides magnetic force. This force helps build a magnetic abrasive brush which generates abrasion pressure. The distribution of flux densities generated during finishing, for 3 different working gaps, through Ansys Maxwell Anosoft is as shown in fig. 5. The flux densities measured using Gauss Meter are shown in fig. 6. The readings are 3.11 T, 2.99 T, 2.8T, and 2.59 respectively. Ultrasonic generator used for the present research work produces fixed frequency ultrasonic waves of 25kHz and can produce ultrasonic waves ranging from 11µm to 99 µm as shown in fig. 7 . The viscoelastic abrasive was taken of 3 sizes, 400 microns, 600 microns and 800 microns. We could not take up bigger sizes because when experimented with abrasives of 1000 microns, scratches were observed. This could possibly be due to their deposit on the workpiece surface, which is not removable[14-17].

For the preparation of a flexible magnetic abrasive brush, a Viscoelastic medium was prepared. First, a polymer was prepared with silicon base oil mixed with boric acid with the further addition of lewis acid and NH_4CO_3. Separately hydrocarbon oil was mixed with aluminium stearate and heated to 100°C to produce a gel, and the mixing of polymer and gel at 50°C resulted in the preparation of the Viscoelastic medium. Mixing CIP and SiC with this medium resulted in the final Viscoelastic magnetic abrasive medium, as shown in fig 8. This medium helps reduce the segregation of the CIP and abrasive mixture in the absence of a magnetic field. Since we are using a permanent magnet in the current experiment, hence the particles will not have any tendency to get segregated. A viscosity test of the final medium was done and came out to be 954 mPa-S. It was also assumed that throughout the finishing operation there wasn't any appreciable change in the viscosity of the medium[18-22].

Nine different samples of mild steel have been used in the experiment and subjected to three cycles of operation to study the effect of process parameters on surface roughness. The pictorial view, same for each workpiece, is shown in fig. 9. For each experiment the workpiece was mounted on a vice which was bolted on the machine table. A closed-loop magnetic field was formed between the magnetic pole and the ferromagnetic workpiece. This led to the formation of a magnetic abrasive brush responsible for cutting action until the desired finish as shown in the fig. 10 was obtained[23-26].

Fig. 4 Polishing Tool

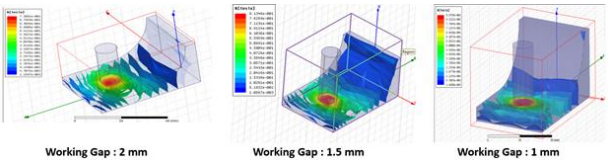

Fig. 5 Flux density simulation for different working gaps

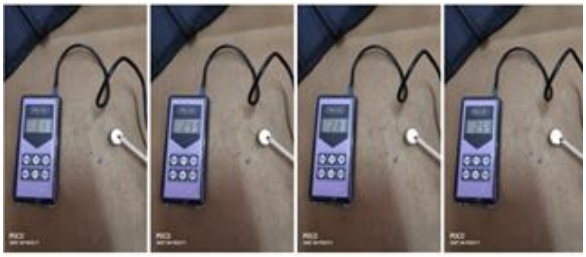

Fig. 6 Flux Density measurement

Fig. 7 Ultrasonic Generator (Fixed Frequency)

Fig. 8 Viscoelastic Abrasive Medium

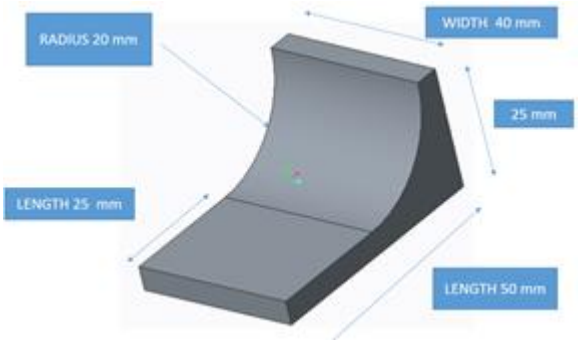

Fig. 9 Pictorial view of the workpiece

Fig. 10 Finished Specimen

4. Model development

4.1 Data Set

After completion of the experiment with several combinations of process parameters, i.e. finishing time, magnetic flux density, abrasive mesh number, magnetic tool rotational speed, feed and ultrasonic amplitude, the output in terms of surface roughness for each experiment was recorded. Instrument used for recording the surface roughness is known as TalySurf as shown in fig.11. The characteristics of change in surface roughness (ΔRa) were analyzed for 27 observations using neural network modeling. The input variables of the training dataset were standardised to ensure that all the variables were analysed over the same range of values. This was necessary because while an input variable like magnetic flux density has values less than one, another input variable, namely abrasive mesh number, has values in hundreds. Therefore, to prevent the higher values of one variable from influencing the model more strongly, than the one with much smaller values, standardisation was deemed necessary. The utility class used to perform this preprocessing of the dataset is StandardScaler. StandardScaler standardises all the values of all the variables in the range of -1 to 1. Therefore, every variable now impacts the output variable genuinely, and the model can now justly analyse the correlation of each input variable with the output variable. Once the training input variables have been standardised, utilising the same mean and standard deviation, the input variables of the testing dataset are also standardised. However, not all variables have been passed on as input variables to our neural network. Once we defined the correlation factor between various variables and the outfit, we found out that two variables out of the six were having very low correlation values and therefore were eliminated during the feature selection process. Therefore, our neural network was fed four input variables, namely magnetic flux density, abrasive mesh number, magnetic tool rotational speed, and feed, along with the output variable change in surface roughness[27-28].

Table 1. Input Variables

Variable	Values Taken
Magnetic Flux Density (Tesla)	0.7208, 0.8134, 0.8875
Abrasive Mesh Number	400, 600, 800
Magnetic Tool Rotational Speed (rpm)	480, 600, 720
Finishing Time (mins)	6, 9, 12
Feed (mm/min)	12, 18, 24
Ultrasonic Amplitude (μm)	15, 30, 45

Fig. 11 TalySurf Instrument

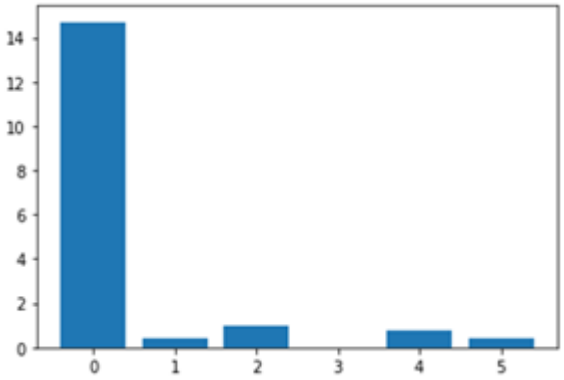

Fig. 12 Correlation Graph

4.2 Neural Network Architecture

The architecture of our model was determined through experimentation. The model consisted of 4 layers comprising the input layer, 2 hidden layers, and one output layer. Components of the model are as follows:

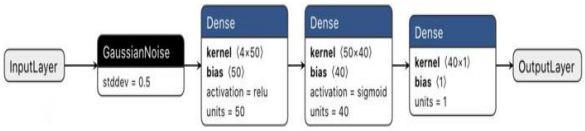

Fig. 13 Model Architecture

Table 2. Model Hyperparameters

Optimiser	Adam
Loss	Mean Squared Error
Metrics	Mean Squared Error
Batch Size	1
Epochs(Iterations)	100

Training a neural network on a small dataset can lead to overfitting which reduces the learning abilities of the network by manifolds. Adding noise to such a dataset regularises the data and helps in reducing overfitting. Gaussian noise, also known as white noise, has a mean of zero and standard deviation of one. Thus, to reduce overfitting and train the model well on our small dataset, we have introduced Gaussian noise in our input layer, by adding the Gaussian Noise layer.

5. Results and Discussion

A seven-fold cross-validation approach was used, which utilised the entire data set for model evaluation. The data set, of 27 data points, was split into seven mutually exclusive data sets. The neural network was trained with six of the seven datasets and tested on the test set, each of the seven times any six datasets were used for training while the remaining one was utilised for testing. Cross-validation is an evaluation technique primarily used for a small dataset. This is necessary for two reasons :

1. To avoid overfitting by preventing the model from learning a particular training data which it is trained upon. This results in overfitting and does not result in a successful model.

2. To enable the model to be able to predict unseen data with a low error, which can otherwise be an issue because if the model is training only on a particular part of the dataset then it is completely unaware of the rest of it, and since the dataset already is small, the training dataset is even smaller. Hence, the learning curve of the model can be quite small. Instead, through cross-validation, depending on the number of chosen folds, the model is trained on all different kinds of data points and tested on all the others, and therefore is fit enough to be able to deal with external data.

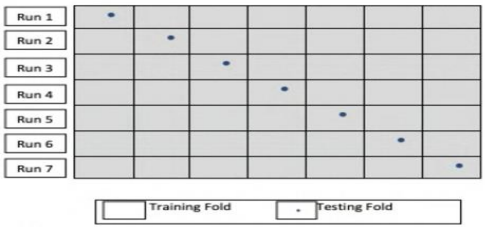

Fig. 14 Seven fold cross-validation

The result was evaluated through two metrics, namely the mean absolute error and the R^2 value (coefficient of determination).

Mean absolute error is the mean of the difference between the predicted values and the experimental values. It is calculated using the following equation :

$$MAE = \frac{\Sigma\,(y_{pred} - y_{exp})}{N}$$

In which y_{pred} and y_{exp} are predicted, and experimental values respectively, and N indicates the number of data points.

Coefficient of determination helps in determining the amount of variance of the dataset that the model is able to understand and learn. It is calculated through the following equation :

$$R^2 = 1 - \frac{\Sigma\,(y_{exp} - y_{pred})^2}{\Sigma\,(y_{exp} - y_{mean})^2}$$

Table 3. Result Metrics

Mean Absolute Error	0.032
R2	0.62

Modeling Results of the Neural Network for the testing data :

Table 4. Network Prediction on testing data

S.No.	MFD	AMN	MTRS	FEED	Experimental ΔRa	Predicted ΔRa
1	0.814	600	720	18	0.076	0.066
2	0.72	800	720	12	0.007	0.0025
3	0.72	400	480	24	0.008	0.0039
4	0.887	400	720	12	0.1077	0.1007
5	0.814	600	720	12	0.064	0.0632
6	0.814	400	600	18	0.104	0.1028
7	0.72	600	600	12	0.108	0.1063
8	0.887	800	600	12	0.142	0.141
9	0.887	800	600	24	0.18	0.148

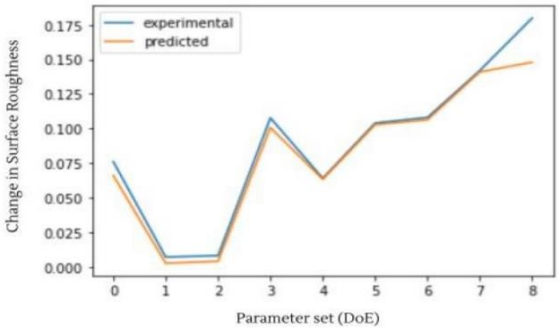

Fig. 15 Graphical Depiction of the experimental and predicted test dataset

6. Conclusion

As a consequence of the above-mentioned results, it seems suitable to conclude that :

1. The efficacy of this neural network model in predicting the change in surface roughness for Magnetic Abrasive Finishing has been affirmed.
2. A suitably trained network effectively blends optimal input conditions for Magnetic Abrasive Finishing.
3. Feature selection, in the case of datasets with large variances, is a key component of data preprocessing in order to effectively train a model.
4. Adding noise to a neural network model training on a small dataset can lead to regularization and help lessen overfitting.
5. Flux density varies depending upon the distance between the magnet and the area to be machined.
6. The base for flux density values has been set as 0.5 because upon lowering the flux density below this value, scratches were observed.
7. Maximum flux density has been adopted for Mild Steel because most of the machining zone came under the influence of maximum flux density.

References

1) Li, W. H., Yang, S. Q., Li, X. H., Zhai, H. F., & Shi, J. T. (2013). Mechanism research and experimental study of viscoelastic magnetic abrasive tools finishing. Journal of Chemical and Pharmaceutical Research, 5(9), 278-285. https://www.jocpr.com/articles/mechanism-research-and-experimental-study-of-viscoelastic-magnetic-abrasive-tools-finishing.pdf
2) Baron, Y.M., Technology of Abrasive Machining in a magnetic field, (in Russian), 1975, Masino strojenije, Leningrad
3) Shinmura, T., Takazawa, K., Hatano, E., Matsunaga, M., & Matsuo, T. (1990). Study on Magnetic Abrasive Finishing. CIRP Annals - Manufacturing Technology, 39(1), 325-328. 10.1016/S0007-8506(07)61064-6
4) Fox, M., Agrawal, K., Shinmura, T., & Komanduri, R. (1994). Magnetic Abrasive Finishing of Rollers. CIRP Annals - Manufacturing Technology, 43(1), 181-184. 10.1016/S0007-8506(07)62191-X
5) Yamaguchi, H., & Shinmura, T. (2000). Study of an internal magnetic abrasive finishing using a pole rotation system. Discussion of the characteristic abrasive behavior. Precision Engineering, 24(3), 237-244. 10.1016/S0141-6359(00)00037-4
6) Singh, D. K., Jain, V. K., & Raghuram, V. (2006). Experimental investigations into forces acting during a magnetic abrasive finishing process. The International Journal of Advanced Manufacturing Technology, 30(7), 652-662. https://link.springer.com/article/10.1007/s00170-005-0118-6
7) Srinivas K, Murtaza Q, Aggarwal AK (2019) Variation of flow parameters and magnetic flux in viscoelastic magnetic abrasive finishing process. 14:1940–1946. ISSN: 0973-4562
8) Li X, Li W, Yang S Effect of coupling agent on interfacial bonding properties of viscoelastic magnetic abrasive tools and finishing performance. ISSN: 1473-804, online 1473-8031. print https://doi.org/10.5013/ijssst.a.17.28.17
9) Li W, Li X, Yang S, Li W (2018) A newly developed media for magnetic abrasive finishing process: material removal behaviour and finishing performance. J Mater Process Tech 260:20–29
10) El-Sonbaty, I. A., & Selmy, A. I. (2008). Prediction of surface roughness profiles for milled surfaces using an artificial neural network and fractal geometry approach. Journal of Materials Processing Technology, 200(1-3), 271-278. 10.1016/j.jmatprotec.2007.09.006
11) Djavanroodi, F. (2013). Artificial Neural Network Modeling of Surface Roughness in Magnetic Abrasive Finishing Process. Research Journal of Applied Sciences, Engineering and Technology, 6(11), 1976-1983. 10.19026/rjaset.6.3812
12) Petri, K. L., Billo, R. E., & Bidanda, B. (1998). A neural network process model for abrasive flow machining operations. Journal of Manufacturing

Systems, 17(1), 52-64. https://doi.org/10.1016/S0278-6125(98)80009-5

13) Singh, R. K., Gangwar, S., Singh, D. K., & Pathak, V. K. (2019). A novel hybridization of artificial neural network and moth-flame optimization (ANN–MFO) for multiobjective optimization in magnetic abrasive finishing of aluminium 6060. Journal of the Brazilian Society of Mechanical Sciences and Engineering, 41(6), 1-19. 10.1007/s40430-019-1778-8
14) Manish Maurya, Nagendra Kumar Maurya, and Vivek Bajpai, "Effect of Sic Reinforced Particle Parameters in the Development of Aluminium Based Metal Matrix Composite", *EVERGREEN Joint Journal of Novel Carbon Resource Sciences & Green Asia Strategy,* **6**(3) 200-206 (2019). https://doi.org/10.5109/2349295
15) Shashi Prakash Dwivedi, Nagendra Kumar Maurya, and Manish Maurya, "Assessment of Hardness on Aa2014/Eggshell Composite Produced Via Electromagnetic Stir Casting Method", *Evergreen Joint Journal of Novel Carbon Resource Sciences & Green Asia Strategy,* **6**(4) 284-94 (2019). https://doi.org/10.5109/2547354
16) P Wahyu Raharjo, Rudy Soenoko, Anindito Purnowidodo, and Agus Choiron, "Characterization of Sodium Bicarbonate Treated Zalacca Fibers as Composite Reinforcements", *Evergreen,* **6**(1) 29-38 (2019). https://doi.org/10.5109/2321001
17) Endah R Dyartanti, I Nyoman Widiasa, Agus Purwanto, and Heru Susanto, "Nanocomposite Polymer Electrolytes in Pvdf/Zno Membranes Modified with Pvp for Lifepo_4 Batteries", *Evergreen,* **5**(2) 19-25 (2018). https://doi.org/10.5109/1936213
18) Hiroshi Naragino, Mohamed Egiza, Aki Tominaga, Koki Murasawa, Hidenobu Gonda, Masatoshi Sakurai, and Tsuyoshi Yoshitake, "Fabrication of Ultrananocrystalline Diamond/Nonhydrogenated Amorphous Carbon Composite Films for Hard Coating by Coaxial Arc Plasma Deposition", *EVERGREEN Joint Journal of Novel Carbon Resource Sciences & Green Asia Strategy,* **3**(1) 1-5 (2016). https://doi.org/10.5109/1657379
19) Mohamed Egiza, Hiroshi Naragino, Aki Tominaga, Kouki Murasawa, Hidenobu Gonda, Masatoshi Sakurai, and Tsuyoshi Yoshitake, "Si and Cr Doping Effects on Growth and Mechanical Properties of Ultrananocrystalline Diamond/Amor-Phous Carbon Composite Films Deposited on Cemented Carbide Substrates by Coaxial Arc Plasma Deposition", *Evergreen: joint journal of Novel Carbon Resource Sciences & Green Asia Strategy,* **3** (1) 32-36 (2016). https://doi.org/10.5109/1657738
20) Ashish Kumar Srivastava, Shashi Prakash Dwivedi, Nagendra Kumar Maurya, and Manish Maurya, "3d Visualization and Topographical Analysis in Turning of Hybrid Mmc by Cnc Lathe Sprint 16tc Made of Batliboi", *Evergreen,* **7**(2) 202- 208 (2020). https://doi.org/10.5109/4055217
21) Dharu Feby Smaradhana, Dody Ariawan, and Rafli Alnursyah, "A Progress on Nanocellulose as Binders for Loose Natural Fibres", *Evergreen,* **7**(3) 436- 443 (2020). https://doi.org/10.5109/4068624
22) Nagendra Kumar Maurya, Vikas Rastogi, and Pushpendra Singh, "Experimental and Computational Investigation on Mechanical Properties of Reinforced Additive Manufactured Component", *EVERGREEN Joint Journal of Novel Carbon Resource Sciences & Green Asia Strategy,* **6**(3) 207-214 (2019). https://doi.org/10.5109/2349296
25) Ang Li, Azhar Bin Ismail, Kyaw Thu, Muhammad Wakil Shahzad, Kim Choon Ng, and Bidyut Baran Saha, "Formulation of Water Equilibrium Uptakes on Silica Gel and Ferroaluminophosphate Zeolite for Adsorption Cooling and Desalination Applications", *Evergreen,* **1**(2) 37-45 (2014). https://doi.org/10.5109/1495162
26) Jabir Al Salami, Changhong Hu, and Kazuaki Hanada, 'A Study on Smoothed Particle Hydrodynamics for Liquid Metal Flow Simulation' *Evergreen,* 6(3) 190-199 (2019). https://doi.org/10.5109/2349294
27) Matheus Randy Prabowo, Almira Praza Rachmadian, Nur Fatiha Ghazalli, and Hendrik O Lintang, "Chemosensor of Gold (I) 4-(3, 5-Dimethoxybenzyl)-3, 5-Dimethyl Pyrazolate Complex for Quantification of Ethanol in Aqueous Solution", *Evergreen,* **7**(3) 404-408 (2020). https://doi.org/10.5109/4068620
28) Jain, Ankit, Cheruku Sandesh Kumar, and Yogesh Shrivastava. "Fabrication and Machining of Metal Matrix Composite Using Electric Discharge Machining: A Short Review." *Evergreen,* 8(4) 740-749 (2021). https://doi.org/10.5109/4742117

2023 4th International Conference for Emerging Technology (INCET)
Belgaum, India. May 26-28, 2023

Proof of Opinion (PoO): A New Consensus Algorithm for Decentralized Blockchain Networks

Rumit Garg
Delhi Technological University
New Delhi, India
rumit0406@gmail.com

Nandika Arora
Delhi Technological University
New Delhi, India
nandika2709@gmail.com

Shagun Uppal
Delhi Technological University
New Delhi, India
uppalshagun18@gmail.com

Dhirendra Kumar
Delhi Technological University
New Delhi, India
dhirendrakumar@dtu.ac.in

2023 4th International Conference for Emerging Technology (INCET) | 979-8-3503-3575-0/23/$31.00 ©2023 IEEE | DOI: 10.1109/INCET57972.2023.10170143

***Abstract*—This paper introduces the Proof of Opinion (PoO) consensus algorithm as an alternative to the traditional Proof of Work (PoW) and Proof of Stake (PoS) algorithms. PoO is designed to address the issues of energy efficiency, decentralization, privacy protection, scalability, and incentivization that are associated with PoW and PoS. PoO relies on the collective opinion of network nodes to reach consensus, which reduces the computational and energy requirements compared to PoW and PoS. PoO can be customized to provide a greater degree of privacy protection, such as by enabling private transactions and hiding transaction details from other nodes. PoO is designed to be more scalable than PoW and PoS, as it relies on the collective opinion of nodes, which reduces the computational requirements and enables greater scalability. PoO's reputation-based approach incentivizes nodes to act honestly and perform their duties diligently, which promotes network security, stability, and better consensus decision-making. Our simulation results show that PoO can achieve comparable performance to PoW and PoS while consuming significantly less energy. PoO also provides greater decentralization, privacy protection, and scalability compared to PoW and PoS.**

***Index Terms*—consensus algorithm, decentralization, opinion**

I. Introduction

Blockchain technology has gained immense popularity in recent years, particularly due to its association with cryptocurrencies such as Bitcoin. However, the potential applications of blockchain extend far beyond cryptocurrencies, with the technology being explored for use cases in a wide range of industries such as Healthcare, Supply Chain Management and Finance.

A blockchain is a distributed database which has a regularly increasing list of ordered data, known as blocks, that are connected using cryptography. Each and every block has transaction data, a timestamp, and a cryptographic hash of the block previous to it. A blockchain is a distributed, decentralized, and open digital ledger that is used to log transactions across many computers in a way that prevention of the record from being altered retrospectively without changing all succeeding blocks and getting network consent takes place [5].

The following are the four main concepts of blockchain:

Shared ledger: Shared ledger is a distributed and "append-only" system of records which is disseminated throughout a company network. The repetition of effort is lowered as transactions are recorded just once via a shared ledger [8].

Permissions: Permissions guarantee protection,verification and validation of the transactions. Given the flexibility to minimize network membership, enterprises can more easily adhere to the data protection laws [2].

Smart contracts: List of rules that regulate any transaction is known as a smart contract. A smart contract is kept on the blockchain system and executed automatically as part of a transaction [7].

Consensus: Through the consensus, all the parties consent to the network verified transaction. It ensures the engagement and inclusion of all the participants in decision making related to the blockchain system. The consensus algorithm establishes a threshold—the minimum number of members required to gain consensus or basically the agreement on the decisions of that blockchain system. Blockchains have a variety of consensus mechanisms, such as multisignature and proof of stake.

The most popular application of the blockchain technology is for keeping a decentralized and secured record of the transactions in cryptocurrency systems like 'Bitcoin' [4]. The innovative concept of the blockchain is that it instills confidence without requiring a reliable third party by guaranteeing the truthfulness and security of a data record.

Blockchain technology has a subtype known as the consortium blockchain. These networks consist of presently operating nodes and have access restrictions. As compared to public blockchain, this network has lesser or fewer nodes, but it is more scalable and secure. Also, it as a result provides reduced network load and greater security. But it has a few hazards despite having lower transparency than a public chain. In this

Authorized licensed use limited to: DELHI TECHNICAL UNIV. Downloaded on July 20,2023 at 11:26:02 UTC from IEEE Xplore. Restrictions apply.

type of network, fewer participants are well-known. In order to minimize latency and achieve excellent speed, a voting based approach is adopted. Any node may write a transaction, however addition of a new block cannot be done by a node itself. On the other hand, prior to a block addition to the network by another node, it must be confirmed first. More innovation and exposure are made feasible this way [3]. It is a semi-decentralized network in which membership is not awarded to a single or particular entity. Instead, a collection of people, or 'node' receives it. Network security is provided, that public chains do not offer. Also, consortium blockchain provides a high degree of control, fast processing and many more improvements that enhance its security and effectiveness.

Here are some characteristics of Consortium Blockchain due to which it is highly in demand:

Rules and Regulations- Regulations are much more essential to keep the consortium's creative juices flowing because it was specifically created for various enterprises and organizations. Nodes must abide by the network's regulations in this situation. By doing so, a team environment is created and efficiency is increased quickly.

Fast Pace Transaction- Blockchain consortiums have few users. Because of this, there is less competition for validation of transaction across nodes from various firms. Regulated user groups can potentially speed up the consensus-building process. All of these elements help make transactions happen more quickly.

Secrecy of Data - Data privacy is supported by fewer nodes in addition to a lighter load of network. Here, unlike private blockchains, only a select few people have access to the datasets. The safety and originality of the information in the blocks are exploited by this approach. The network's information cannot be changed without the approval of some nodes.

Change of Data- A data modification on a public blockchain is essentially impossible. The cause includes a huge number of users. While fewer users can easily update the data using the consensus rule in the consortium. Here, there are no monopolies on any judgment and every node has an equal voice.

No chances of 51% act- Attacks by 51% of users could be disastrous for the blockchain network. A private blockchain is especially vulnerable to this problem since many organizations' members can work together to veto or even do reverse transactions.The consortium is exempt from this problem, though, because specific nodes from numerous businesses properly authenticate each transaction. The difficulty of working with other businesses to commit fraud in the network accounts for 51% of the cause.

Zero chances of Criminal Act- Because most anonymous users are renowned for clogging up a network's procedures, the potential of illicit or unlawful activity is completely eliminated when a federated blockchain is connected with a small number of well-known individuals. This chain's familiarity with one another fosters a system of checks and balances that reduces the likelihood of illicit activities, making this platform a secure choice for businesses.

Scalability- Scalability problems with the consortium blockchain will only be mildly present. For confirmation, this chain does have controlled nodes. As a result, managing the network effectively by a few chosen nodes within a consortium is a smart feature that lowers the likelihood of network's slow output and delayed transactions. Federated provides a better user experience with a time-saving function as a permission blockchain.

Reduced Transaction Costs- Users can access this platform from consortium blockchain providers for cheap transactions. In contrast to a public blockchain, where increasing the number of users might increase transaction costs, in a federated network, transaction fees are fixed regardless of the user base. In fact, this network is much more affordable for businesses than conventional banking methods.

Some applications of the Consortium Blockchain are:

Finance and Banking - This sector deals with the issuing, trading, and KYC of assets. All the banks in a partnership put their data on datasets at one location. This distributed ledger will be available to assist banks whenever they need to confirm or access the information about the creditor.The consortium is the most advantageous choice for cross-sector deployment, according to a datolite research [1].

Logistics- In order to benefit businesses and customers, logistics is a sophisticated process that involves the management of goods from their point of origin to their final destination. By connecting all the actors in the supply chain to a single network, the consortium can simplify this procedure. It will assist in maintaining a clear record of logistics from the point of origin to the end of the shipping process [6].

Insurance and Health- If you choose health insurance, you can use it as reimbursement for any time spent in the hospital. Hospitals and insurance providers can work together to share funds and info through the consortium to quicken the process and save time [13].

In section II we talk about some existing consensus algorithms and their advantages and disadvantages. In section III we describe our proposed methodology and the advantages and disadvantages it has over the existing consensus algorithms. In section IV we run simulation and analysis over our proposed approach. In section V we provide the conclusion on our findings.

II. Background and Preliminaries

A. Consensus Algorithms

Consensus algorithms are a crucial component of blockchain technology, as they enable multiple parties in a distributed system to reach agreement on a shared state. In essence, consensus algorithms ensure that all nodes in a network have the same copy of the blockchain ledger, and that all transactions added to the blockchain are valid and consistent. There are several consensus algorithms that have been developed for blockchain, each with its own strengths and weaknesses. Some of the most commonly used consensus

Authorized licensed use limited to: DELHI TECHNICAL UNIV. Downloaded on July 20,2023 at 11:26:02 UTC from IEEE Xplore. Restrictions apply.

algorithms include Proof-of-Work (PoW) and Proof-of-Stake (PoS). While these algorithms differ in their approach to achieving consensus, they all share the goal of creating a decentralized, trustless network that can operate without the need for a central authority. As blockchain technology continues to evolve and become more widely adopted, consensus algorithms will play an increasingly important role in ensuring the integrity and security of distributed systems.

B. Proof of Work

Proof of Work (PoW) is a consensus algorithm used in blockchain networks to validate transactions and add new blocks to the chain. It requires a network of miners to compete to solve a complex mathematical puzzle, with the first one to solve it receiving the right to add a new block to the blockchain. This process of solving the puzzle is called mining [9]. The concept behind PoW is to make it computationally difficult to add new blocks to the blockchain, ensuring that the network remains secure from malicious attacks. The algorithm also ensures that new blocks are added at a consistent rate, maintaining the stability of the network. One of the primary benefits of PoW is its **security**. It is highly resistant to attacks, as a malicious user would need to control over 51% of the computing power on the network to launch a successful attack [9]. This makes it a reliable and secure algorithm for blockchain networks. However, PoW also has several drawbacks. The first and most significant of these is its **high energy consumption** [9]. Mining requires a significant amount of computational power, which requires a lot of energy, often from non-renewable sources. This leads to high operating costs for miners and has been criticized for its environmental impact. Another issue with PoW is its **scalability**. As the number of miners on the network grows, the difficulty of the mathematical puzzle increases, making it more challenging to solve. This, in turn, leads to longer block times, slowing down the network's transaction processing speed.

Finally, PoW also **suffers from centralization**. As the cost of mining increases, smaller miners may be forced out of the network, leaving only the most significant players to dominate the mining process. This creates a risk of centralization and can compromise the decentralization of the network.These challenges have led to the development of alternative consensus algorithms, such as Proof of Stake, which attempt to address these issues.

C. Proof of Stake

Proof of Stake (PoS) is a consensus mechanism used in blockchain networks to validate transactions and create new blocks. In PoS, validators are chosen to create new blocks based on the amount of cryptocurrency they hold and are willing to lock up as collateral. The more cryptocurrency a validator holds, the higher the chances they have of being chosen to validate the next block[10]. One of the major advantages of PoS is that it is **energy-efficient** compared to Proof of Work (PoW), which requires miners to solve complex mathematical problems to create new blocks. However, there are also some drawbacks to PoS, including:

Centralization : PoS can lead to centralization since validators with more cryptocurrency have a greater chance of being chosen to create new blocks. This means that those who already hold a significant amount of cryptocurrency will have a greater advantage over smaller holders, making it difficult for new entrants to join the network [12].

Sybil attacks : In PoS, an attacker can create multiple identities or nodes to gain control of the network. This is known as a Sybil attack and can be challenging to prevent since there is no way to identify whether a node is legitimate or not based on its computational power.

Nothing at stake problem : The nothing at stake problem occurs when validators have nothing to lose by participating in multiple blockchain forks. This can result in validators voting for multiple blocks, leading to a network split and double-spending attacks [9].

Long-range attacks : In PoS, attackers can carry out long-range attacks by acquiring a large amount of cryptocurrency that was held at an earlier time and using it to create a new blockchain branch [12]. This can be challenging to detect and prevent, and can lead to double-spending attacks.

In the context of consensus algorithms, both Proof of Work (POW) and Proof of Stake (POS) have been used extensively in blockchain networks. However, these algorithms have several limitations and drawbacks that can affect their scalability, security, and energy efficiency. In response, we have proposed an alternative consensus algorithm Proof of Opinion (POO) that aims to address these issues.

III. Proposed Methodology

The concept behind **Proof of Opinion** is simple: instead of relying on computational power or stake to validate transactions, it relies on the collective opinion of network nodes. In this consensus algorithm, nodes express their opinion about the validity of a transaction by casting a vote, and the transaction is validated if a sufficient number of nodes agree.

The proof of opinion algorithm can be customized to suit different use cases, such as privacy protection, scalability, or decentralized governance. It can be designed to be more energy-efficient and scalable than proof of work and proof of stake, while also being more decentralized and providing a greater degree of privacy for users. In PoO, nodes with higher reputation scores are given more weight in decision-making processes, such as leader selection. Reputation scores are calculated based on various factors, such as the number of successfully validated blocks, the number of times a node has participated in decision making, the opinion of the node held by the other nodes. The more a node contributes to the network, the higher their reputation score, and the more influence they have in decision-making processes.

$$Rep(i) = \frac{2}{1 + \exp^{-VT^{(1+B)}}} - 1 \tag{1}$$

Rep(i) = Reputation of the node i

Authorized licensed use limited to: DELHI TECHNICAL UNIV. Downloaded on July 20,2023 at 11:26:02 UTC from IEEE Xplore. Restrictions apply.

V = The number of times the node has cast a vote in the blockchain

T = The number of nodes in the blockchain which have given a positive rating to the node

B = blocks added by the node in the blockchain

The range of Rep(i) is [0, 1]. The reputation-based approach is designed to incentivize nodes to act honestly and perform their duties diligently. The more a node contributes to the network, the higher their reputation score, and the more rewards they can receive. This promotes network security, stability, and better consensus decision-making.

Here are some of the strengths and weaknesses of proof of opinion: Strengths:

Decentralization: Proof of opinion is designed to be more decentralized than many other consensus algorithms, as it does not rely on a small group of nodes or a large amount of computational power to validate transactions.

Energy-efficient: Proof of opinion is designed to be more energy-efficient than proof of work and proof of stake, as it does not require nodes to perform complex calculations or use large amounts of electricity to validate transactions.

Scalability: Proof of opinion is designed to be more scalable than proof of work and proof of stake, as it can support a larger number of transactions per second without requiring significant increases in computational power or network bandwidth.

Privacy: Proof of opinion can be designed to protect the privacy of users by allowing them to submit transactions anonymously and without revealing their identities.

Better network security: The reputation and opinion-based approach encourages nodes to act honestly and perform their duties diligently to earn and maintain their reputation scores. This incentivizes nodes to act in the best interest of the network, leading to better network security.

Promotes stability: By assigning leader selection based on reputation and opinion scores, the network can maintain a stable and consistent leadership, promoting more consistent network performance.

Better consensus : The use of reputation and opinion-based scores to influence decision-making can lead to more effective consensus decisions. Nodes with higher reputation scores are given more influence and decision-making power, which promotes more trustworthy decision-making.

More resistant to attacks: The use of reputation and opinion-based scores can make it more difficult for attackers to gain control of the network. Attacking nodes would need to accumulate reputation and opinion scores to have any chance of becoming leaders, which can be a time-consuming and difficult task. **Weaknesses** :

Lack of Security: Proof of opinion is a relatively new consensus algorithm and has not yet been extensively tested in real-world conditions. It may be vulnerable to attacks and exploits that have not yet been discovered.

Dependence on Human Judgment: Proof of opinion relies on human judgment to determine the validity of transactions. This introduces the risk of human error, bias, or manipulation.

Potential for Collusion: There is a risk that nodes may collude to manipulate the consensus process and validate invalid transactions. This risk is particularly high if a small group of nodes control a significant portion of the network.

Difficulty in measuring opinions: Measuring and quantifying opinions can be a difficult and subjective task. Different nodes may have different opinions on the same issue, and it may be challenging to reach a consensus on which opinions are more valid than others.

Centralization risk: The reputation and opinion-based approach can potentially lead to centralization of decision-making power in the hands of a few nodes with high reputation scores. This can lead to reduced decentralization and potentially harm network security.

Potential for manipulation: Reputation and opinion-based scores can be manipulated by nodes to influence decision-making in their favor. This can lead to a distorted network view and affect network performance.

Higher computational overhead: Calculating and managing reputation and opinion scores for each node can require additional computational resources and increase the complexity of the consensus algorithm.

A. Comparison with PoW and PoS

Proof of Opinion (PoO) consensus algorithm is designed as an alternative to Proof of Work (PoW) and Proof of Stake (PoS) consensus algorithms. PoO provides several advantages over these traditional algorithms, making it a better choice for blockchain networks in several ways:

Energy efficiency: PoW consensus algorithm requires nodes to perform complex calculations to validate transactions, which requires significant computational power and energy. This results in high electricity consumption and environmental concerns. PoS also has high energy consumption as nodes need to constantly validate transactions. PoO, on the other hand, relies on the collective opinion of network nodes, which is a more energy-efficient approach.

Decentralization: In PoW, a large portion of network power can be controlled by a few miners, which can lead to centralization of the network. In PoS, the concentration of power among nodes that hold a large stake in the network can also lead to centralization. In contrast, PoO ensures that all nodes have an equal say in the consensus process, which promotes greater decentralization.

Privacy protection: PoW and PoS do not provide any privacy protection to users. PoO can be customized to provide a greater degree of privacy protection, such as by enabling private transactions and hiding transaction details from other nodes.

Scalability: PoW and PoS can suffer from scalability issues due to the high computational and energy requirements. PoO is designed to be more scalable as it relies on the collective opinion of nodes, which reduces the computational requirements and enables greater scalability.

Incentivization: PoO's reputation-based approach incentivizes nodes to act honestly and perform their duties dili-

Authorized licensed use limited to: DELHI TECHNICAL UNIV. Downloaded on July 20,2023 at 11:26:02 UTC from IEEE Xplore. Restrictions apply.

gently. The more a node contributes to the network, the higher their reputation score, and the more rewards they can receive. This promotes network security, stability, and better consensus decision-making.

In summary, PoO is a better choice for blockchain networks compared to PoW and PoS as it is more energy-efficient, decentralized, provides greater privacy protection, is more scalable, and incentivizes nodes to contribute to the network's security and stability.

B. Leader selection algorithm

Calculate the reputation score for each node in the network based on their past behavior and performance.

Now we will calculate a leader score [13] for each node which would be the sum of its own reputation times the number of nodes from which it has received a positive rating and the sum of reputations of all the nodes which have given a positive rating to the node.

Suppose we have to select n leaders then we will take the n nodes with the best leader score.

$$Leader_Score(i) = TRep(i) + \sum_{j=1}^{T} Rep(j) \tag{2}$$

T = number of nodes which have given a positive rating to the node

C. Transaction Validity Algorithm

Have all the nodes participating the transaction express an opinion (boolean) about it.

The opinion score for each node will be calculated as product of its reputation and its opinion

Transaction score will be calculated by summing up all the individual opinion scores

A threshold value will be determined according to the use case. An example threshold value could be 0.3 times the number of nodes.

If the transactions score if greater than or equal to the threshold value the transaction will be taken as valid.

$$OS(i) = Rep(i)O(i) \tag{3}$$

$$TS = \sum_{i=1}^{n} OS(i) \tag{4}$$

Rep(i) = Reputation of the node i
O(i) = Opinion of the node i
n = number of nodes participating in the blockchain
OS(i) = Opinion score of the node i
TS = Transaction score of the transaction

IV. Simulation results and analysis

We wrote a python script which simulates the proposed Proof of Opinion (PoO) consensus algorithm and measures the time taken by the transaction to validate for different numbers of nodes (100, 500, 1000, 10000, 50000, 100000, 200000) and plots the results on a bar graph that shows the transaction time (in seconds) on the y-axis and the number of nodes on the x-axis.

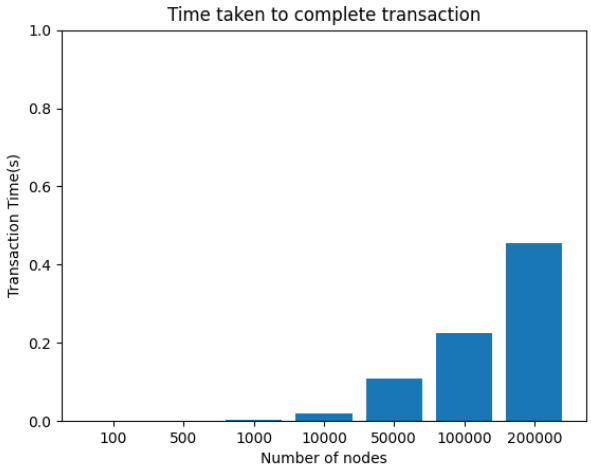

The simulation results show that as the number of nodes increases, the transaction time also increases. This is expected since the more nodes there are in the system, the more time it takes to reach consensus. Overall, the simulation results demonstrate the effectiveness of Proof of Opinion consensus algorithm in reaching consensus in a distributed system, while also highlighting the trade-off between the number of nodes and the time taken to validate transactions

V. Conclusion

Reputation-based proof of opinion is a promising approach to achieving consensus in blockchain networks. It has the potential to improve network security, promote stability, and lead to better consensus decisions. However, it also has some potential challenges, including difficulty in measuring opinions, centralization risk, potential for manipulation, and higher computational overhead. Future research can focus on developing strategies to mitigate these challenges and further explore the potential of reputation-based proof of opinion in achieving blockchain consensus.

References

[1] Nikita Rajeshkumar Bagrecha, Ishaq Mustafa Polishwala, Pragya Abhai Mehrotra, Rishabh Sharma, and B.S. Thakare. Decentralised blockchain technology: Application in banking sector. In 2020 International Conference for Emerging Technology (INCET)pages 1–5, 2020.

[2] Bharat Bhushan, Preeti Sinha, K. Martin Sagayam, and Andrew J. Untangling blockchain technology: A survey on state of the art, security threats, privacy services, applications and future research directions.Computers Electrical Engineering, 90:106897, 2021..

[3] Omar Dib, Kei-L eo Brousmiche, Antoine Durand, Eric Thea, and Elyes Ben Hamida.Consortium blockchains:Overview, applications and challenges.International Journal On Advances in Telecommunications, 2018.

[4] Enis Karaarslan and Enis Konacaklı.Data storage in the decentralized world: Blockchain and derivatives.In Who Runs the World: Data, pages 37–69. Istanbul University Press, dec 2020.

[5] Sunny Pahlajani, Avinash Kshirsagar, and Vinod Pachghare. Survey on private blockchain consensus algorithms. In 2019 1st International Conference on Innovations in Information and Communication Technology (ICIICT),pages 1–6, 2019.

[6] Arief Rijanto. Blockchain technology adoption in supply chain finance.Journal of Theoretical and Applied Electronic Commerce Research, 16(7):3078–3098, 2021.

Authorized licensed use limited to: DELHI TECHNICAL UNIV. Downloaded on July 20,2023 at 11:26:02 UTC from IEEE Xplore. Restrictions apply.

[7] Shuai Wang, Yong Yuan, Xiao Wang, Juanjuan Li, Rui Qin, and Fei-Yue Wang. An overview of smart contract: Architecture, applications, and future trends. In 2018 IEEE Intelligent Vehicles Symposium (IV), pages 108–113,2018.
[8] Dylan Yaga, Peter Mell, Nik Roby, and Karen Scarfone.Blockchain technology overview. Technical report, oct 2018.
[9] Nakamoto, S., Bitcoin, A. (2008). A peer-to-peer electronic cash system. Bitcoin.–URL: https://bitcoin. org/bitcoin. pdf,
[10] Kiayias, A., Russell, A., David, B., Oliynykov, R. (2017, July). Ouroboros: A provably secure proof-of-stake blockchain protocol. In Advances in Cryptology–CRYPTO 2017: 37th Annual International Cryptology Conference, Santa Barbara, CA, USA, August 20–24, 2017, Proceedings, Part I (pp. 357-388). Cham: Springer International Publishing.
[11] Alzaid, H., Alfaraj, M., Ries, S., Jøsang, A., Albabtain, M., Abuhaimed, A. (2013). Reputation-based trust systems for wireless sensor networks: A comprehensive review. In Trust Management VII: 7th IFIP WG 11.11 International Conference, IFIPTM 2013, Malaga, Spain, June 3-7, 2013. Proceedings 7 (pp. 66-82). Springer Berlin Heidelberg.
[12] Šimunić, S., Bernaca, D., Lenac, K. (2021). Verifiable computing applications in blockchain. IEEE Access, 9, 156729-156745.
[13] Li, D., Han, D., Zheng, Z., Weng, T. H., Li, H., Liu, H., ... Li, K. C. (2022). MOOCsChain: A blockchain-based secure storage and sharing scheme for MOOCs learning. Computer Standards Interfaces, 81, 103597.

Authorized licensed use limited to: DELHI TECHNICAL UNIV. Downloaded on July 20,2023 at 11:26:02 UTC from IEEE Xplore. Restrictions apply.

2023 2nd International Conference on Vision Towards Emerging Trends in Communication and Networking Technologies (ViTECoN) | 979-8-3503-4798-2/23/$31.00 ©2023 IEEE | DOI: 10.1109/VITECON58111.2023.10157250

Realization of DTMOS based 6T SRAM cells and their performance analysis at 32nm technology node

Divesh
Department of Electronics and Communication
Delhi Technological University,
New Delhi, India
diveshgopal44@gmail.com

Jatin
Department of Electronics and Communication
Delhi Technological University,
New Delhi, India
jatinbhola9599@gmail.com

Keshav
Department of Electronics and Communication
Delhi Technological University,
New Delhi, India
keshav312000@gmail.com

Neeta Pandey
Department of Electronics and Communication
Delhi Technological University,
New Delhi, India
n66pandey@rediffmail.com

***Abstract*— The SRAM cells are extensively used in on-chip cache memory in devices such as microprocessors, computers, games controller, and mobile phones etc. This paper examines the performance of six transistor SRAM cell with DTMOS as access/ pull-up/ pull-down transistors and in combination totaling to seven topologies. Copious simulations in LTspice environment have been performed to compute static and dynamic performance of all the seven topologies using 32 nm PTM model parameters. It is found that pull-up and pull-down based DTMOS structure gives best matrices for stability while access only DTMOS structure gives best delay performance.**

Keywords—SRAM cell, DTMOS, SNM, WTP, WTV, WVI, SVNM, SPNM, SINM, Power Delays

I. INTRODUCTION

Over the past five decades, the semiconductor industry has seen significant advancements in terms of scaling. The semiconductor industry has introduced new process technology generations every two to three years to meet the growing demands of customers for enhanced performance and functionality at reduced costs. SRAM has become a crucial component in System-on-chip (SoC) and has gained popularity quickly. Nowadays CMOS SRAM memory architecture confronts a number of difficulties, such as decreasing noise margins and rising unpredictability with scaling. Further, SRAM power consumption accounts for a sizable amount of the total chip energy usage. Therefore, SRAM module power consumption needs to be decreased. The speed and power consumption of SRAM are important issues that have prompted several designs aimed at reducing the power consumption during read/ write operations [1,2]. However, conventional SRAM structures have limitations on Static Noise Margin (SNM) and N-curve properties that affect the overall performance and power consumption of the circuit. These properties, therefore, need improvement in order to meet the demands of modern technology. One way to achieve this is through the use of Dynamic Threshold Metal Oxide Semiconductor (DTMOS) structures in SRAM design [3-7].

The DTMOS is used 6T SRAM cell in [3,5,6]. It is applied in only pull up transistors in [3] whereas all transistors use DTMOS in [5,6]. The SRAM cell presented in [4] uses two additional inverters and uses DTMOS in rest of the six transistors. Eight DTMOS SRAM cell [7] uses transmission gates as access transistors to improve access time.

It is clear that no comprehensive study has been carried out on DTMOS based 6T SRAM cell to evaluate performance when DTMOS is used as only access/ only pull-up/ only pull-down transistors and in combination.

II. BACKGORUND

In this Section, DTMOS and Conventional 6T SRAM cell are briefly described.

A. DTMOS

DTMOS stands for Dynamic Threshold Metal Oxide Semiconductor. Here substrate and gate terminals are connected together resulting in dynamic change in threshold voltages of PMOS and NMOS. This dynamic adjustment leads to lowering of threshold voltage and provides higher current at low supply voltages [3].

B. The 6T SRAM Cell

The 6T SRAM cell stores one-bit of information and made up of 6 transistors. It consists of two back-to-back connected CMOS inverters which forms a bi-stable circuit. The cell stores complementary values at internal nodes (Q and QB). The bitcell is connected to bit and word lines for reading and writing data by enabling access transistors. The 6T SRAM cell is a compact and efficient way for storing data.

C. Operation of 6T SRAM Cell

The bitlines (BL and BLB) are precharged to the supply voltage (VDD) to perform read operation. The wordline (WL) is also enabled. The bitline connected to the storage node storing '0' gets discharged through the access and pull-down transistors and inferred as read 0 operation. On the other hand, if no discharge of BL occur it is treated as read 1 operation [2].

Let's assume that the internal data storage nodes Q are at '0' for write operations. WL is enabled to enable write 1 operation, and write driver drives BL to 1 and BLB to 0. The write 1 operation of a cell is completed when the storage node Q is driven to 1 through the active PG. The write 0 procedure can be carried out similarly [2].

979-8-3503-4798-2/23/$31.00 ©2023 IEEE

Authorized licensed use limited to: DELHI TECHNICAL UNIV. Downloaded on July 03,2023 at 04:45:57 UTC from IEEE Xplore. Restrictions apply.

III. DTMOS BASED SRAM STRUCTURES

In this section, we delve into the intricacies of obtaining diverse structures of SRAM through utilization of DTMOS technology. Our objective is to compare and evaluate the various SRAM structures to determine which design surpasses conventional SRAM in various performance parameters. These structures were made by swapping out the access, pull-up, and pull-down transistors with DTMOS. By applying different combinations, seven structures were produced. The structure-1 of the 6T SRAM is obtained by connecting the gates of the M5 and M6 transistors to their respective bulk, as shown by the red dotted line in Fig. 1. It results in dynamically variation of the access transistor threshold voltage and thereby impacting the cells' performance.

Fig. 2. shows structure-2 of the 6T SRAM cell wherein the bulk of the pull-down transistors are connected to their respective gates. This connection results in the pull-down transistors threshold voltages are contingent on the charge stored at Q and QB.

The structure-3, as depicted in Fig.3, leverages the benefits of DTMOS technology specifically for the pull-up transistors. This configuration is same as [3]. This design results in the threshold values of the PMOS transistors being dictated by the charge stored at Q and QB.

The structure-4 as shown in Fig. 4, combines the best of both structures 1 and 2 by incorporating DTMOS technology for both pull-down and access transistors. So, the threshold values of the transistors are contingent on the input applied to the gate, leading to a synergistic improvement in performance.

The structure-5 depicted in Fig. 5, represents an optimized implementation of DTMOS technology, as it combines the best of both the first and third structures. By employing DTMOS technology for both access and the pull-up transistors, this configuration provides a superior performance compared to conventional SRAM architectures. The interplay between the input applied to the gate and the charge stored at Q and QB determines the threshold values of the transistors.

The structure-6 represents a significant advancement in the utilization of DTMOS technology for SRAM structures. This configuration employs DTMOS technology for both the pull-up and pull-down transistors, with the gates of M1, M2, M3, and M4 transistors connected to their respective bulks as shown in Fig. 6. The threshold values of the transistors in this design are dependent on the input applied to the gate, leading to improved stability and performance during read and write operations.

The final structure-7, as shown in Fig.7, incorporating DTMOS technology for all transistors in the 6-T bit cell [5,6]. The integration of DTMOS technology in such a comprehensive manner underscores its versatility and efficacy in enhancing SRAM structures.

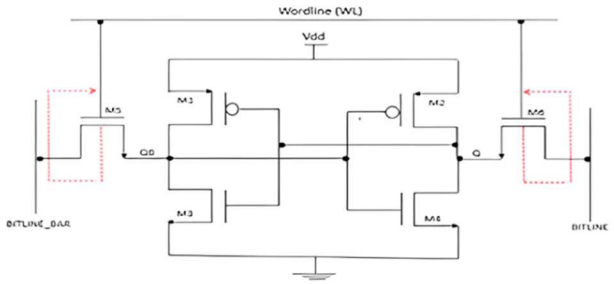

Fig. 1. Structures with DTMOS in Access transistors

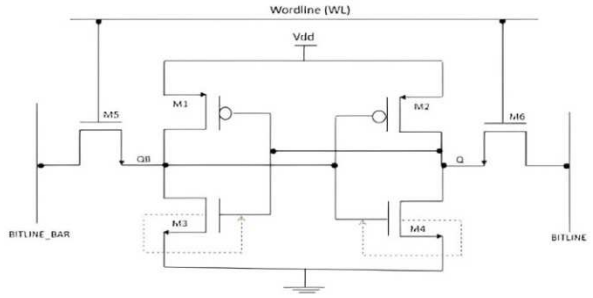

Fig. 2. Structures with DTMOS in PDN transistors

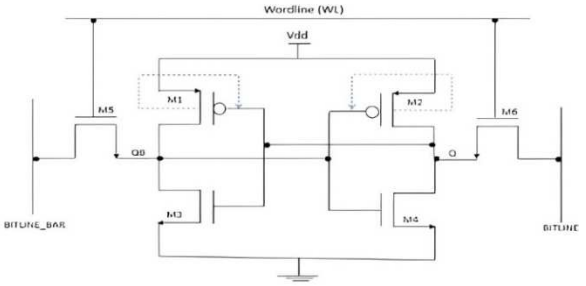

Fig. 3. Structures with DTMOS in PUP transistors

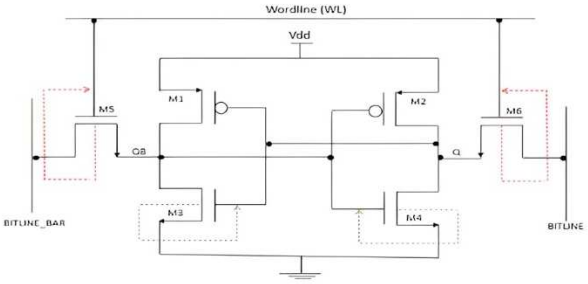

Fig. 4. Structures with DTMOS in Access and PDN transistors

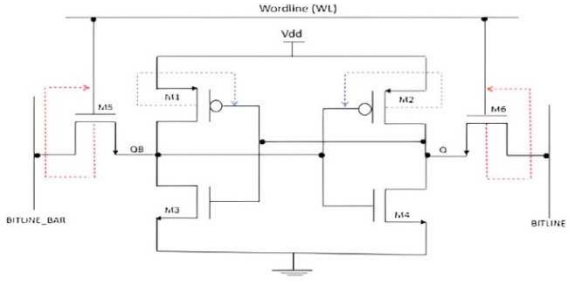

Authorized licensed use limited to: DELHI TECHNICAL UNIV. Downloaded on July 03,2023 at 04:45:57 UTC from IEEE Xplore. Restrictions apply.

Fig. 5. Structures with DTMOS in Access and PUP transistors

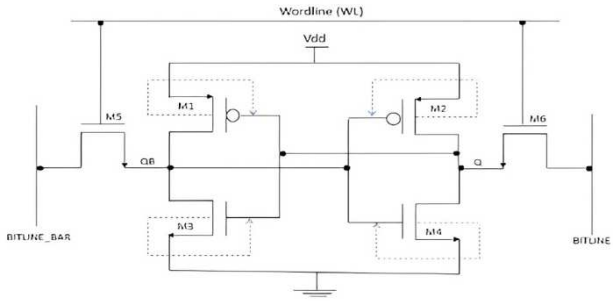

Fig. 6. Structures with DTMOS in PDN and PUP transistors

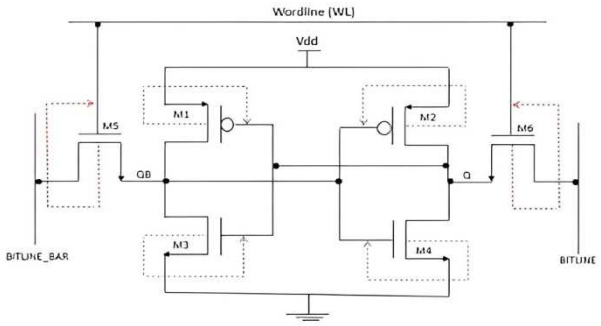

Fig. 7. Structures with DTMOS in Access, PDN and PUP transistors

IV. RESULTS AND DISCUSSION

All the structures are simulated using 32nm PTM model parameters in LTspice XVII environment at power supply of 400mV. The cell ratio (W/L ratio of the pull-down transistor to the access transistor) is β= 12/11=1.09 and pull up ratio (W/L ratio of pull-up transistor to the access transistor) is = 10/11= 0.91. The stability of both the conventional and alternative structures have been obtained using butterfly curves for comparison. In addition to the SNM, read-write latency, N-curve metrics (SPNM, WTP, SVNM, SINM, WTV, WTI), and power consumption while reading and writing all have been determined.

A. Static Noise Margin (SNM)

The Static Noise Margin (SNM) is a measure of the highest amount of DC noise voltage that an SRAM cell can withstand without affecting the stored bit. In Butterfly Curve, the SNM measure as the length of the side of the largest square that are inside within the lobes. The Butterfly Curve method is used to find the read, write and hold SNM of each structure and is abbreviated as RSNM, WSNM and HSNM respectively. The results of this analysis are depicted in fig. 8, fig. 9 and fig. 10 respectively, where the RSNM, WSNM and HSNM of Fig. 3 has been calculated and similarly we have obtained SNM's of different structure and presented in tabular form in Table 1.

This information provides valuable insight into the relative strengths and weaknesses of each structure, and allows us to make informed decisions about the optimal design for a given application. By utilizing the Butterfly Curve method, we can ensure the reliability and robustness of our SRAM structures in real-world operating conditions.

In the structure-1, the RSNM is 18.87mV, which is one-third of the conventional bitcell. This is likely due to the use of DTMOS in the access transistors. The access transistors' threshold voltage decreases during the read operation thus allowing for fluctuations with even lower voltage to pass, resulting in a lower static noise margin.

The RSNM of structures 2 and 3 is greater than that of the conventional SRAM, due to the use of positive feedback from the pull-up and pull-down transistors inverter respectively. These dynamically alter the inverter trip voltage in accordance with the state transition's direction, providing the cell with optimal inverter properties for reliable memory operation. The use of DTMOS in the circuit shifts the VTC curve of the inverter either towards the right or left side.

It's noted that the use of DTMOS in access transistors shifts the VTC curve of the inverter towards the right side, implying a higher switching threshold voltage. As a result, all the structures that have access transistors as DTMOS have a lower RSNM. However, the usage of DTMOS in place of

pull-up or pull-down transistors enhances RSNM of bitcell. As a consequence, structures 2, 3, and 6 (Fig. 2, 3 and 6) have a greater RSNM than other structures. The DTMOS in access transistors leads to speeding up of QB discharge, resulting in improvement of 23.51% in WSNM in comparison to conventional 6T SRAM cell.

Further, the use of DTMOS transistors instead of traditional pull-up or pull-down transistors results in a slight reduction in WSNM, as seen in structures 2 and 3 (Fig. 3 and 3). However, other structures such as 4, 5, and 7 (Fig. 4, 5 and 7) have even better WSNM than structures 2 and 3 due to the inclusion of DTMOS access transistors.

The WSNM of structure-1 is found to be comparable to that of structure-2 due to the absence of access transistors' involvement in shaping the voltage-transfer characteristics (VTC) curve of the inverter.

The use of DTMOS transistors in place of pull-up transistors causes the VTC curve of inverter-2 to shift towards the left, resulting in a lower HSNM. Conversely, the incorporation of DTMOS transistors in place of pull-down transistors shifts the VTC curve of the second inverter to the right, leading to a higher HSNM. This explains why structures 3 and 5 (Fig. 3 and 5) exhibit a greater HSNM than the other structures. By replacing the pull-up transistors with DTMOS transistors in structures 2 and 4 (Fig. 2 and 4), the HSNM is reduced. In the 7th structure, the (Fig. 7) VTC curve is balanced as DTMOS transistors are utilized in both pull-up and pull-down transistors. As a result, this structure has the same hold SNM as that of a standard bit cell.

We have meticulously calculated the SNMs of each structure but here we are displaying SNM of Structure 3 (Fig. 3) only as it's consistently outperforming the other structures in terms of SNM criteria. Using the similar method, we have obtained SNM of other 6 structures.

Authorized licensed use limited to: DELHI TECHNICAL UNIV. Downloaded on July 03,2023 at 04:45:57 UTC from IEEE Xplore. Restrictions apply.

TABLE I. SNM OF DIFERENT STRUCTURES

Structure	RSNM	WSNM	HSNM
Conventional SRAM	56.81mV	168.4mV	140mV
Structure-1	18.87mV	208mV	140mV
Structure-2	65.36mV	149mV	128.3mV
Structure-3	69.93mV	166mV	149.2mV
Structure-4	33.90mV	188mV	129mV
Structure-5	33.0mV	197.5mV	150mV
Structure-6	81.0mV	152.2mV	143mV
Structure-7	48.0mV	174mV	140mV

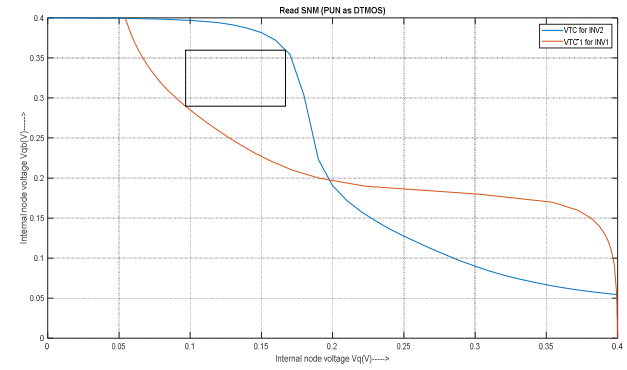

Fig. 8. Butterfly curve for RSNM (Structure-3)

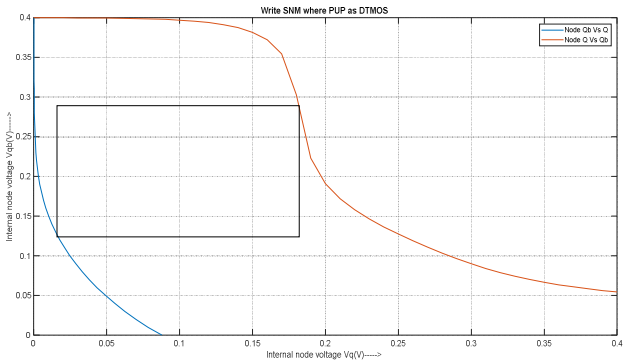

Fig. 9. Butterfly curve for WSNM (Structure-3)

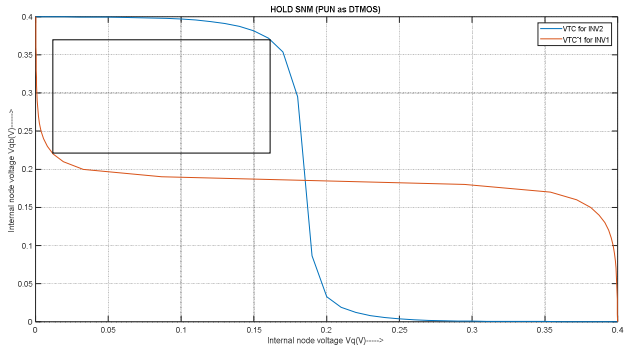

Fig. 10. Butterfly curve for HSNM (Structure-3)

B. Read-Write Delay/Latency

The read delay or read access time is the period of time between the assertion of WL and the occurrence of the 50-mV difference between BITLINE and BITLINE_BAR in the differential BL structure.

This voltage difference then be sensed by the sense amplifier. The read delay of Structure-1 (Fig. 1) in the 6T SRAM architecture has been found to be 0.325 ns, which represents a 57.68% improvement over that of a standard bit cell. The use of DTMOS transistors in place of access transistors in this structure has been found to provide high current drive and low threshold voltage, which enables faster access to the stored data. However, it should be noted that replacing pull-down transistors with DTMOS only results in a minimal improvement in read access time. Conversely, when DTMOS transistors are used in place of pull-up transistors, the access time or read delay of the circuit increases significantly. In particular, Structure-4 (Fig. 4) in our circuit has been found to take 62.63% less time than a standard bit cell to access the same data. Additionally, when other combinations of DTMOS transistors are used, the read delay or access time varies between 1.32-1.36 ns.

An SRAM bitcells write delay or write access time shows how quickly it completes the write operation.

When the WL is turned on, the write "1" delay is the amount of time it takes for an internal node to increase to 90% of the supply voltage. Similarly, during WL activation, the write "0" delay is defined as the time required by the storage node voltage reaching 10% of the supply voltage. The utilization of DTMOS transistors in place of access transistors in the 6T SRAM cell has minimal impact on the write delay of the circuit.

However, when DTMOS transistors are implemented in place of pull-down transistors, the write access time of the circuit increases. On the other hand, incorporating DTMOS transistors in place of pull-up transistors leads to a reduction in write access time. As a result, structures 3, 5, 6, and 7 (Fig. 3, 5, 6, and 7) in our circuit exhibit low write access time.

TABLE II. READ AND WRITE DELAY OF DIFERENT STRUCTURES

Structures	Read Delay (in ns)	Write Delay (in ns)
Conventional Bitcell	0.768	2.21
Structure-1	0.325	2.22
Structure-2	0.733	2.81
Structure-3	1.730	1.60
Structure-4	0.287	2.36
Structure-5	1.360	1.70
Structure-6	1.320	1.62
Structure-7	1.360	1.60

C. N-Curve Stability Metrics

The N-curves provide a comprehensive analysis of a 6T-SRAM conventional bitcell, including power and current metrics as well as Static Noise Margins (SNMs). Three places - A, B, and C, where these curves cross the voltage axis, are defined by the relative sizes of the transistors inside the cell.

Authorized licensed use limited to: DELHI TECHNICAL UNIV. Downloaded on July 03,2023 at 04:45:57 UTC from IEEE Xplore. Restrictions apply.

The locations A, B, and C, are evaluated by the Bit cell ratio, both the bit cell and pull up ratio and pull up ratio respectively.

To evaluate the stability of the cell during read operations, the Static Voltage Noise Margin (SVNM) and Static Current Noise Margin (SINM) are utilized. The SVNM and SINM are measured as the potential difference and the highest level of current between points B and A respectively. Similarly, for write operations, the Write Trip Voltage (WTV) and Write Trip Current (WTI) are calculated as the voltage difference between points C and B and the highest level of current between points C and B respectively. These metrics provide insight into the performance and stability of the cell during both read and write operations. The access transistor (M6) and the transistor M4 are in the velocity exhaustion and linear zones, respectively, at the beginning when the input voltage (Vin) and node Q are both at 0 volts. Therefore, M6's drain current is higher than M4's drain current. This drain current will be more in structure-1 (Fig. 1), as it's using DTMOS which has high current drive. Additionally, power stability can be evaluated by analysing the area under the N-Curves, where a larger Specific Power Noise Margin (SPNM) and smaller Write Trip Power (WTP) indicate improved power stability. Certain structures demonstrate enhancements in specific parameters.

TABLE III. N-CURVE PARAMETERS OF DIFERENT STRUCTURES

Structure	SPNM (µW)	WTP (µW)	SVNM (V)	SINM (µA)	WTV (V)	WTI (µA)
Conventional Bitcell	1.07	0.23	0.13	14.46	0.2115	1.82
Structure-1	0.29	0.04	0.17	81.23	0.12	0.57
Structure-2	1.77	0.30	0.13	25.46	0.29	2.64
Structure-3	1.52	0.55	0.14	16.63	0.20	4.21
Structure-4	0.88	0.15	0.12	16.22	0.19	1.34
Structure-5	0.65	0.16	0.12	10.54	0.173	1.71
Structure-6	1.53	0.80	0.12	19.61	0.215	5.71
Structure-7	0.67	0.28	0.11	12.38	0.184	2.69

D. Read and Write Power

The read power is equal to the product of the voltage of the Bitline bar (BL') and the current flowing through the M5 drain or the product of the voltage of the Bitline (BL) and the current flowing through the M6 drain. The write power is equal to the product of the voltage applied to the PMOS in a bit cell and the current flowing through VDD.

TABLE IV. READ AND WRITE POWER OF DIFERENT STRUCTURES

Structures	Read Power (µW)	Write Power (µW)
Conventional Bitcell	0.61	2.84
Structure-1	0.76	2.48
Structure-2	0.63	2.92
Structure-3	0.05	3.14
Structure-4	0.77	2.65
Structure-5	0.16	4.21
Structure-6	0.05	3.14
Structure-7	0.16	4.21

V. CONCLUSION

In this paper, use of DTMOS (Dynamic threshold metal-oxide-semiconductor) structures in conventional 6T SRAM cell has been examined. The simulation results demonstrate that the use of DTMOS transistors in SRAM cell structures can significantly improve the stability and performance of the cell, with improved read delay, minimal impact on write delay, and improved stability metrics such as SVNM, SINM, WTV, and WTI. Structure-7 is an optimal choice for high frequency operation alternatively, structure-6 can be used as it offers the highest read SNM and low power consumption. To prioritize read speed, structure-1 can be employed, although it may result in a trade-off with the read SNM of the circuit. For applications where power conservation is a primary concern, structure-3 is a suitable option. Ultimately, the appropriate structure should be selected based on the specific demands of the application. Overall, the use of DTMOS transistors in SRAM design has the potential to improve the performance and efficiency of SRAM-based devices.

REFERENCES

[1] J. Singh, S. P. Mohanty and D. K. Pradhan, Robust SRAM design and analysis, Springer, 2013.

[2] Pavlov and M. Sachdev, CMOS SRAM circuit design and parameteric test in nano-scaled technologies: Process-aware SRAM design and Test, Dordrecht: Springer Science + Business Media B.V, 2008.

[3] S. Sharan, A. Chandra, N. Goel and A. Kumar, "Comparison of 6T-SRAM cell designs using DTMOS and VTMOS for low power applications," *2016 IEEE 1st International Conference on Power Electronics, Intelligent Control and Energy Systems (ICPEICES)*, Delhi, India, 2016, pp. 1-5.

[4] S. Soleimani-Amiri, A. Afzali-Kusha and A. Sammak, "Design and analysis of a new sub-threshold DTMOS SRAM cell structure," *The 16th CSI International Symposium on Computer Architecture and Digital Systems (CADS 2012)*, Shiraz, Iran, 2012, pp. 50-53.

[5] S. Pal and A. Islam, "Device bias technique to improve design metrics of 6T SRAM cell for subthreshold operation," *2015 2nd International Conference on Signal Processing and Integrated Networks (SPIN)*, Noida, India, 2015, pp. 865-870.

[6] Chunn, A. Agrawal and A. Naugarhiya, "An 8T TG-DTMOS Based Subthreshold SRAM Cell with Improved Write Ability and Access Times," 2020 24th International Symposium on VLSI Design and Test (VDAT), Bhubaneswar, India, 2020, pp. 1-6.

[7] M. E. Hwang and K. Roy, "A 135mV 0.13µW process tolerant 6T subthreshold DTMOS SRAM in 90nm technology," *2008 IEEE Custom Integrated Circuits Conference*, San Jose, CA, USA, 2008, pp. 419-422.

Authorized licensed use limited to: DELHI TECHNICAL UNIV. Downloaded on July 03,2023 at 04:45:57 UTC from IEEE Xplore. Restrictions apply.

Reversible Data Hiding for Interpolated Images using CNN based Nearest Neighbour Interpolation

Praveen Kumar, Prateek Ravi, Rajeev Kumar
Department of Computer Engineering
Delhi Technological University
Delhi, India
p01maurya@gmail.com, prateek38gautam@gmail.com, rajeevkumar@dtu.ac.in

2023 Third International Conference on Secure Cyber Computing and Communication (ICSCCC) | 979-8-3503-0071-0/23/$31.00 ©2023 IEEE | DOI: 10.1109/ICSCCC58608.2023.10176624

***Abstract*—Interpolation based reversible data hiding (RDH) has gained plenty of research interest because to its ability to increase large amount of secret information in an image. However, one of the issues is that it involves approximating pixel values, which can result in a loss of image detail or in other words deteriorated image quality. To resolve this issue, this paper defines an innovative RDH method for interpolated images using convolution neural network based nearest neighbor interpolation (CNN-NNI). The CNN-NNI generates high-resolution image that closely matches the original image by processing through a series of convolutional layers. On the other hand, the strategy for embedding data involves using both interpolated pixels as well as reference pixels for data insertion in each block. Experimental findings indicate that the suggested approach beats recently developed and comparable techniques not only on final visual quality yet also at the maximum embedding ability i.e., higher than 1.75 bpp including an average PSNR value higher than 30 dB .**

***Index Terms*—Reversible Data Hiding, convolution neural network, CNN, RDH, Nearest neighbor, Interpolation**

I. Introduction

The secure exchange of confidential information is a crucial necessity for both individuals and organizations within society [**?**], [**?**]. The transmission of confidential data through public networks has demonstrated its vulnerability, making it imperative to adopt secure methods for sharing secret information. The conventional approach for safeguarding information is through cryptography [**?**], but it does have some limitations. While encrypted data provides protection, it can be noticeable during transmission, which may draw unwarranted attention to the confidential information. Data hiding is another technique that can be utilized to secure sensitive data [**?**], [**?**], [**?**]. Unlike cryptography, which shields the material of messages, data hiding safeguards the existence of sensitive data. However, using traditional techniques to embed confidential data within the cover signal often leads to irreversible distortion, rendering it unsuitable for certain fields [**?**]. Reversible data hiding (RDH), however, is one such way of data hiding, permitting concealment of data without sacrificing its quality or integrity [**?**], [**?**], [**?**] at the receiving end. RDH is helpful in many different areas, including diagnostic imaging, wherein medical images can be used to obfuscate data regarding patients without permanently changing the medical information. This lessens the risk of patient data being lost or misidentified [**?**]. RDH can also be used to embed digital watermarks or copyright information within multimedia content to safeguard against unlicensed use, distribution, or copying.

Due to its adaptability, RDH has attracted a lot of interest. As as result, many high-performance techniques such as lossless compression [**?**], [**?**], prediction-error expansion [**?**], [**?**], [**?**], histogram shifting [**?**], [**?**], [**?**], difference expansion [**?**], [**?**], [**?**], and interpolation [**?**], [**?**], [**?**], [**?**], [**?**], [**?**] based RDH techniques. However, most of the aforementioned techniques (except Interpolation based RDH) require a location map to prevent the overflow/underflow issue, which can lead to loss of data and degradation of visual quality. Interpolation solves this by embedding mainly in the interpolated pixels. Additionally, interpolation-based data hiding methods can provide higher embedding rates while maintaining good visual quality [**?**]. Interpolation techniques are usually utilized to transform a low visual quality image into a higher quality one that maintains resemblance to the original input image. For this, there have been introduced various interpolation techniques such as Nearest Neighbor interpolation (NNI) [**?**], Bilinear Interpolation (BI) [**?**], Cubic Interpolation (CI) [**?**] etc. These technique have also been additionally used in the course of inserting secret data, as embedding capacity grows with the increase in pixels available for implanting data.

The crucial inputs of this paper are as follows:

1. The CNN-NNI resolves issue that occurs through secondary embedding by achieving high-resolution image and a high data concealment ability.

2. The model is a nearest neighbour approach based on CNN to create an interpolated illustration. During data insertion process the interpolated illustration is partitioned into 3×3 blocks and 2 pixels are inserted in interpolated pixels using modulo and difference operation and 1 pixel into reference pixel through Prediction Error Expansion (PEE).

3. The model was able to achieve good watermarked image quality, higher BPP and an high average PSNR at the given embedding capability.

The remaining paper is structured as given. Section II explores the current relevant works in the domain of interpolation based RDH methods. Section III gives a glimpse of CNN-NNI method for Image Interpolation, data insertion, extraction and image recovery. Section IV highlights experimental findings along with a comparative assessment with recent methods. In Section V, paper is concluded.

Authorized licensed use limited to: DELHI TECHNICAL UNIV. Downloaded on July 20,2023 at 11:11:06 UTC from IEEE Xplore. Restrictions apply.

II. Related Work

In 2009, Jung et al. [**?**] discussed earliest image interpolation based RDH method. The method presents a fresh method of interpolation popularly known as Neighbor Mean Interpolation (NMI) which enlarges the original image using Eq. (1) to create an image that can be used as a cover for embedding data. Utilising median of laterally nearby pixel values, the NMI predicts the lateral pixels in 3×3 blocks. Similarly, the upright pixels are predicted using the median of the upright nearby pixels. The diagonal pixels are then assessed by taking the average of the other three pixels. Since, the volume of data that can be embedded was assessed from the difference of interpolated and a reference pixel, it was limited.

$$\begin{aligned} P(0,1) &= (P(0,0) + P(0,2))/2 \\ P(1,0) &= (P(0,0) + P(2,0))/2 \\ P(1,1) &= (P(0,0) + P(0,2) + P(2,0))/3. \end{aligned} \tag{1}$$

Liu et al. [**?**] extends the Jung's method [**?**] by integrating a better NMI algorithm and a random block partition method. This led to increased hiding capacity and improved standard of steganographic images. To further improve the performance, Lee et al. [**?**] discuss an Interpolation by neighboring pixels (INP) technique which increases the difference compared to the earlier method and also enhanced the quality of illustrations. Similarly, Chang et al. [**?**] utilized an enhanced neighbor mean interpolation (ENMI) method, which evaluates offset interpolated pixel value by using median of four closest reference pixels while calculation for horizontal and upright pixels remains the same as shown in Eq. (2).

$$\begin{aligned} P(0,1) &= (P(0,0) + P(0,2))/2 \\ P(1,0) &= (P(0,0) + P(2,0))/2 \\ P(1,1) &= (P(0,0) + P(0,2) + P(2,0) + P(2,2))/4. \end{aligned} \tag{2}$$

Malik et al. discuss modified neighbor mean interpolation (MNMI) technique based RDH method [**?**], [**?**] by assigning weights in proximity to the pixels, while also utilizing better accurate estimated values to find the dissimilarity between the embedded pixels. This method effectively preserve visual quality, but with low concealing capability. In 2021, Xiong et al. [**?**], [**?**] discussed an adaptive RDH methods for interpolated illustrations to achieve good PSNR, by optimally using all the available interpolation techniques. Mandal et al. [**?**] introduce a technique that utilized interpolation and difference expansion methods, resulting in a high embedding capability and Bpp. Another study by Mengting et al. [**?**] discuss a RDH method that employs an enhanced NMI for interpolation and divided the interpolated figure into coinciding 3×3 blocks for data embedding. They also employ a pixel pre-processing technique to alter each value of pixels to a proper span before inserting. Despite having high embedding capacity, this method results in low-quality images. To overcome the aforementioned issues, we propose a new convolution neural network based Nearest neighbour interpolation (CNN-NNI) which is to be discussed in brief in upcoming section.

III. The Proposed Method

The proposed method is split into several stages which include Image interpolation, data insertion, extraction, and image recovery discussed in subsequent sub-sections. The complete mechanism of the CNN-NNI is shown in Fig. 1.

A. Image interpolation

The proposed image interpolation technique is based on convolution neural network which requires training and testing. So for training and testing, we have created our own custom data-set that consists of 7900 images of 512×512 size, by scrapping through the internet. This data-set is divided in a 90:10 proportion amongst training and testing. In the image interpolation stage, the original image is first down-sampled and then nearest neighbor is applied creating the interpolated image. This interpolated image is passed through our CNN model as shown in Fig. 2 which enhances the inserted image and brings it as close as possible to the original image. In the CNN architecture, five layers of convolution + ReLU activation function have been used. ReLU is applied element-wise to outcome of each filter in the convolutional layer. In the proposed model, MSE is used as loss function and Adam optimizer is preferred due to its ability to adapt the learning rate for each parameter based on slope of the loss function in relation to that parameter, and provided with better interpolation performance. The details of hyper-parameters is provided in Table I. The complete step by step process of our image interpolation is given as follows: The CNN-NNI model is shown in Fig. 2.

Step 1: The original inserted image I with dimensions $w \times h$ is down sampled to generate an intermediate image I_m with half the size, by eliminating even rows and columns.

Step 2: The nearest neighbor algorithm is applied on intermediate image I_m as shown in Fig. 3, pixels in gray are reference pixels. Thus, the image is then up sampled to give an interpolated image (F) with dimensions $w \times h$. The basic idea behind nearest neighbor algorithm is to look at the closest pixel to the interpolated point, and assign that pixel value to the interpolated point.

Step 3: The image F is fed through the trained CNN-NNI in order to increase its resemblance with I.

TABLE I: Hyper parameters

Hyper parameters	
Batch size	16
Learning rate	0.0001
Optimizer	Adam
Loss	Mean Squared Error(MSE)
Metrics	PSNR
Layers of CNN	5
Kernel	3
Stride	1×1
Filter	32

B. Underflow / Overflow Conditions

It is possible that during embedding process some pixel values may surpass the acceptable range of values [0, 255],

Authorized licensed use limited to: DELHI TECHNICAL UNIV. Downloaded on July 20,2023 at 11:11:06 UTC from IEEE Xplore. Restrictions apply.

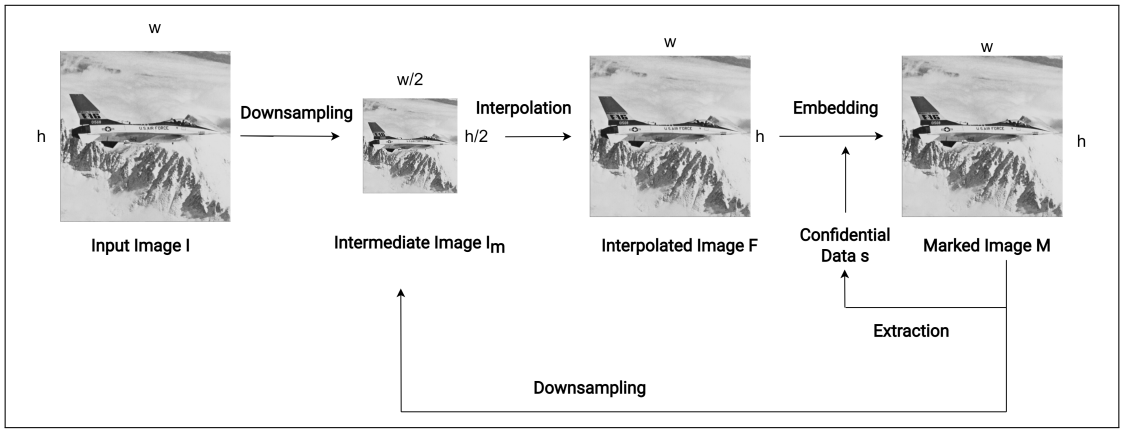

Fig. 1: Complete framework of the presented method

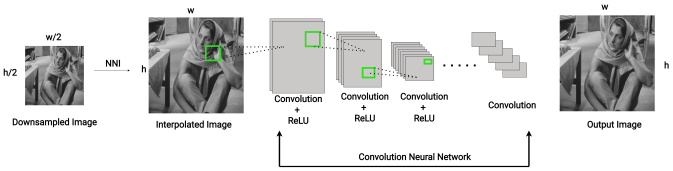

Fig. 2: The proposed CNN-NNI for image interpolation

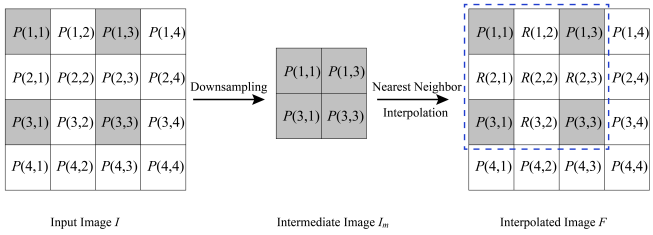

Fig. 3: Nearest Neighbor Interpolation

resulting in underflow/overflow. To address this, a pixel pre-processing method is used which adjusts the values of each boundary pixel, to ensure that they fall within the permissible interval before the embedding step. For this, first, the two secret data bits are converted into decimal that will be within the range [0,3]. Then the modulo and difference operation is applied to three interpolated pixels denoted as F_n, for embedding. Also a pixel pre-processing method is used to adjust the values of the pixels within the valid range before embedding data. The difference between interpolated pixels and modulo results falls in the range of [-3, 3] while interpolated pixels themselves are in range of [3, 252]. To resist any underflow or overflow, the pixels values in between [0, 2] and [253, 255] are pre-processed using following Eq. (3)

$$F_n = \begin{cases} 3, \text{ if } 0 \le F_n \le 2 \\ 252, \text{ if } 253 \le F_n \le 255 \end{cases}, n = 1, 2, 3 \quad (3)$$

During embedding top left reference pixel(P_1) of every block may be at most changed by '1'. so to avoid the probable underflow/overflow scenario, the boundary pixels are pre-processed using Eq. (4). Since we need their original value at the time of extraction and recovery, the changes are tracked using a location map (L) constructed using Eq. (5).

$$P_1 = \begin{cases} 1, \text{ if } P_1 = 0 \\ 254, \text{ if } P_1 = 255 \end{cases} \quad (4)$$

$$L = \begin{cases} 1, \text{ if } P_1 \in \{0, 255\} \\ 0, \text{ otherwise} \end{cases} \quad (5)$$

C. Data Embedding

The data insertion is done in two phases. In first phase, embedding is done in interpolated pixels using modulo and difference expansion and then in the reference pixels using PEE. However, prior to this, the interpolated illustration is split into 3×3 overlapping chunks for embedding. The complete step by step embedding process is defined as follows.

Step 1: Firstly, F is partitioned into overlapping/coinciding 3×3 blocks. In each block, there will be a reference pixel $P(x, y)$ with P_1 value, and three interpolated pixels $F(x, y+1)$, $F(x+1, y)$ and $F(x+1, y+1)$ with value F_1, F_2 and F_3.

Step 2: In each block of F, first modulo operation is applied to the three pre-processed interpolated pixels using Eq. (6):

$$B_n = F_n \ modK \quad n = 1, 2, 3 \quad (6)$$

Step 3: For each of the interpolated pixels, two-bits are taken out of confidential data and then changed to decimal number, S_n. Then the difference(D_n) of confidential data S_n and B_n is evaluated using Eq. (7):

$$D_n = S_n - B_n \quad n = 1, 2, 3 \quad (7)$$

Step 4: Evaluate marked pixel values using Eq. (8):

$$M_n = F_n + D_n \quad n = 1, 2, 3 \quad (8)$$

Step 5: Once each and every 3×3 blocks have been processed, M is derived. Then at most single bit of confidential data is inserted into P_1 of each 3×3 block using PEE. For each block, the pixel values $M(1, 2)$, $M(2, 1)$ and $M(2, 2)$,

Authorized licensed use limited to: DELHI TECHNICAL UNIV. Downloaded on July 20,2023 at 11:11:06 UTC from IEEE Xplore. Restrictions apply.

are denoted as M_1, M_2, M_3 respectively. Use M_1 and M_2 to predict P_1 and obtain the corresponding prediction value of P_1 using Eq. (9).

$$\begin{cases} a = \max(M_1, M_2) \\ b = \min(M_1, M_2) \end{cases}$$
$$P_1 = \begin{cases} a, \text{ if } P_1 \geq a \\ b-1, \text{ if } P_1 < b \end{cases} \quad (9)$$

Step 6: Evaluate the prediction error using Eq. (10):

$$p_e = P_1 - P_1 \quad (10)$$

Step 7: Evaluate the embedding and shifting rules using the error (p_e) and the confidential data s using Eq. (11):

$$p_e = \begin{cases} p_e + s, \text{ if } P_1 = a \\ p_e + 1, \text{ if } P_1 > a \\ p_e - s, \text{ if } P_1 = b-1 \\ p_e - 1, \text{ if } P_1 < b-1 \end{cases} \quad (11)$$

Step 8: Calculate the marked pixel value using the prediction error through Eq. (12):

$$P_1 = P_1 + p_e \quad (12)$$

Step 9: After using PEE for P_1 in every 3×3 blocks, lastly marked image M is produced.

D. Data Extraction And Image Recovery

The steps for extracting data and recovering illustration in its actual form are as follows:

Step 1: Divide M into coinciding 3×3 blocks, and evaluate a predicted value P_1 of marked pixel P_1 in each block using Eq. (9) of Step 5 of embedding.

Step 2: To evaluate p_e, subtract the predicted pixel value (obtained in step 1) from the actual marked pixel value. Then obtain the confidential data from M using Eq. (13):

$$s = \begin{cases} 0, \text{ if } p_e = 0 \\ 1, \text{ if } p_e \in \{-1, 1\} \end{cases} \quad (13)$$

Step 3: Retrieve p_e using the extracted secret data and the predicted value calculated in step 1 using Eq. (14):

$$p_e = \begin{cases} p_e - 1, \text{ if } P_1 > a \\ p_e + 1, \text{ if } P_1 < b-1 \\ p_e, \text{ if } P_1 \in \{a, b-1\} \end{cases} \quad (14)$$

Step 4: Retrieve the reference pixel value using the recovered prediction error and the actual marked pixel value using Eq. (15):

$$P_1 = P_1 + p_e \quad (15)$$

Step 5: Combine the reference pixel value with the L to obtain the final pixel value using Eq. (16). The L determines whether the pixel value should be 0 or 255.

$$P_1 = \begin{cases} 0, \text{ if } P_1 = 1 \text{ and } L = 1 \\ 255, \text{ if } P_1 = 254 \text{ and } L = 1 \end{cases} \quad (16)$$

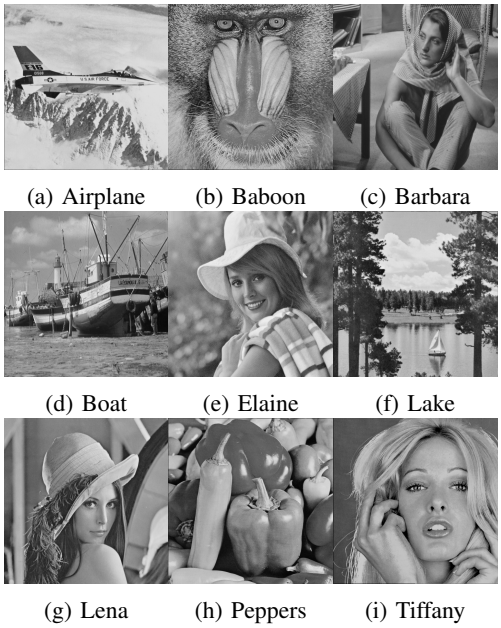

(a) Airplane (b) Baboon (c) Barbara

(d) Boat (e) Elaine (f) Lake

(g) Lena (h) Peppers (i) Tiffany

Fig. 4: Test Images

Step 6: Reiterate the same steps for every blocks to restore M and retrieve the embedded confidential data using the modulo operation as Eq. (17).

$$S_n = M_n \ mod K \quad n = 1, 2, 3 \quad (17)$$

Step 7: Transform the retrieved data into a two-bits format and affix with data obtained. Obtain the original image O by reducing the resolution of M.

IV. Experimental Results

To assess the suggested approach, few standard test images Airplane, Baboon, Barbara, Boat, Elaine, Lake, Lena, Peppers and Tiffany have been chosen as shown in Fig. 4 . To assess how well the method performs, two metrics are used: PSNR, and BPP. As per the provided results in Table II, the BPPs of CNN-NNI is 1.75 showcasing that it has a significant capability to incorporate a lot of information. Also the average PSNR between the watermarked and interpolated image are higher than 30 dB showing that given method has high visual quality as well.

TABLE II: Maximum BPP and corresponding PSNR

	BPP	**PSNR**
Airplane	1.7542	30.5227
Baboon	1.7553	28.7419
Barbara	1.7560	28.2776
Boat	1.7558	29.8350
Elaine	1.7587	33.8980
Lake	1.7550	30.3335
Lena	1.7574	31.2301
Peppers	1.7575	31.7128
Tiffany	1.7539	33.6983
Average	1.7559	30.9166

Authorized licensed use limited to: DELHI TECHNICAL UNIV. Downloaded on July 20,2023 at 11:11:06 UTC from IEEE Xplore. Restrictions apply.

A. COMPARISON WITH RECENTLY DEVELOPED RELATED METHODS

To assess the effectiveness of approach, a comparison with other recently reported methods that are similar in nature on standard test images is conducted. Table III shows comparison of PSNR amongst interpolated and marked images of standard test images on the CNN-NNI method and method given in [**?**]. Irrespective of the images, our method performs significantly superior in terms of PNSR.

TABLE III: PSNR comparison of the CNN-NNI with [**?**]

	[?]	**Proposed**
Airplane	23.88	30.5227
Boat	24.02	29.8350
Lena	25.26	31.2301
Peppers	24.98	31.7128
Tiffany	28.81	33.6983
Average	25.39	31.3997

Further, a comparison of interpolation techniques asuch as NMI [**?**], INP [**?**], ENMI [**?**], MNMI [**?**] and the proposed CNN-NNI is carried out as shown in Table IV. On comparing the PSNR between interpolated image and corresponding original inserted image, it is visible that the given method achieves greater average PSNR for the test images especially in comparison to other interpolation techniques.

TABLE IV: PSNR comparison of proposed CNN-NNI with alternative interpolation methods

Test Image	**NMI**	**INP**	**ENMI**	**MNMI**	**Proposed**
Airplane	28.93	28.04	30.12	29.98	30.66
Boat	29.22	28.30	30.53	30.39	29.80
Baboon	22.23	21.72	22.69	22.70	22.85
Peppers	30.07	28.98	31.70	31.60	32.48
Average	27.61	26.76	28.76	28.66	28.94

B. HISTOGRAM ANALYSIS

The typical technique of histogram analysis has been utilized to assess efficacy of the method in terms of robustness against malicious attacks. This evaluation requires a comparison of the histograms for both the interpolated and marked images to determine whether embedding of confidential information has made any vital change in the characteristics of images. For this the results are presented in Fig. 5. As evident from the aforementioned results, both the histograms are almost same with no noticeable change which in turn suggest that CNN-NNI method can withstand histogram interpretation.

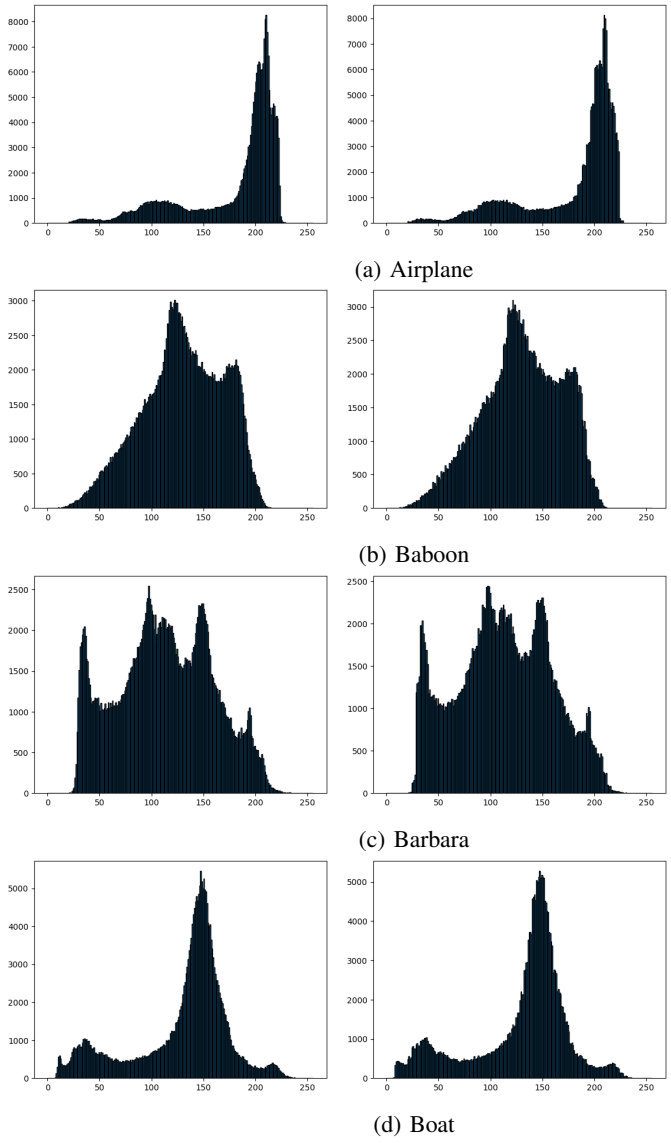

(a) Airplane

(b) Baboon

(c) Barbara

(d) Boat

Fig. 5: Histogram analysis of the CNN-NNI for interpolated images with respect to the watermarked images

V. CONCLUSION

In this paper, a interesting CNN-NMI based RDH method was introduced. Unlike most existing interpolation based RDH methods, the given method embeds two bits of confidential data in three interpolated pixels of each block using modulo and difference operation. Additionally, PEE embeds a maximum of single bit of confidential data in reference pixel of each block while addressing issue of severe image deformation. Also, the associated values of pixels have been processed beforehand prior to the data insertion process to avoid any potential underflow/overflow of marked values of pixels. Experimental findings demonstrates that presented CNN-NNI gives BPP of 1.75 and also it results in an improvement in the PSNR contrasted to recent comparable techniques. Furthermore, the method can withstand histogram analysis.

In future, proposed work can be tried and tested on other algorithms as well in order to test robustness of model and improve accuracy achieved in regenerating images. Also it is necessary to directly interpolate the input image, otherwise it can have the effect of increasing the size of interpolated image and can seriously impact the communication.

REFERENCES

[1] A. Fahim, A. Salem, F. A. Torkey, and M. Ramadan, "An efficient enhanced k-means clustering algorithm," *Journal of Zhejiang University-Science A*, vol. 7, pp. 1626–1633, 2006.

Authorized licensed use limited to: DELHI TECHNICAL UNIV. Downloaded on July 20,2023 at 11:11:06 UTC from IEEE Xplore. Restrictions apply.

[2] A. K. Jain and R. C. Dubes, *Algorithms for clustering data*. Prentice-Hall, Inc., 1988.
[3] S. Na, L. Xumin, and G. Yong, "Research on k-means clustering algorithm: An improved k-means clustering algorithm," in *2010 Third International Symposium on intelligent information technology and security informatics*. Ieee, 2010, pp. 63–67.
[4] W. H. Day and H. Edelsbrunner, "Efficient algorithms for agglomerative hierarchical clustering methods," *Journal of classification*, vol. 1, no. 1, pp. 7–24, 1984.
[5] J. Leskovec, A. Rajaraman, and J. D. Ullman, *Mining of massive data sets*. Cambridge university press, 2020.
[6] S. Guha, R. Rastogi, and K. Shim, "Cure: An efficient clustering algorithm for large databases," *ACM Sigmod record*, vol. 27, no. 2, pp. 73–84, 1998.
[7] A. S. Acharya, A. Prakash, P. Saxena, and A. Nigam, "Sampling: Why and how of it," *Indian Journal of Medical Specialties*, vol. 4, no. 2, pp. 330–333, 2013.
[8] I. Etikan and K. Bala, "Sampling and sampling methods," *Biometrics & Biostatistics International Journal*, vol. 5, no. 6, p. 00149, 2017.
[9] A. K. Jain and M. H. Law, "Data clustering: A user's dilemma," in *Pattern Recognition and Machine Intelligence: First International Conference, PReMI 2005, Kolkata, India, December 20-22, 2005. Proceedings 1*. Springer, 2005, pp. 1–10.
[10] A. Gionis, H. Mannila, and P. Tsaparas, "Clustering aggregation," *Acm transactions on knowledge discovery from data (tkdd)*, vol. 1, no. 1, pp. 1–30, 2007.
[11] C. J. Veenman, M. J. T. Reinders, and E. Backer, "A maximum variance cluster algorithm," *IEEE Transactions on pattern analysis and machine intelligence*, vol. 24, no. 9, pp. 1273–1280, 2002.
[12] Manoj, "Cluster," 2021. [Online]. Available: https://www.kaggle.com/datasets/sai1881/cluster
[13] D. Dua and C. Graff, "UCI machine learning repository," 2017. [Online]. Available: http://archive.ics.uci.edu/ml

Authorized licensed use limited to: DELHI TECHNICAL UNIV. Downloaded on July 20,2023 at 11:11:06 UTC from IEEE Xplore. Restrictions apply.

2023 4th International Conference for Emerging Technology (INCET)
Belgaum, India. May 26-28, 2023

SEMC-Net: A Shared-Encoder Multi-Class Learner

Rahul Jain
Dept. of Information Technology
Delhi Technological University
Delhi, India
rahuljain_2k19it103@dtu.ac.in

Satvik Dixit
Dept. of Information Technology
Delhi Technological University
Delhi, India
satvikdixit_2k19it116@dtu.ac.in

Vikas Kumar
Dept. of Information Technology
Delhi Technological University
Delhi, India
vikaskumar_2k19it143@dtu.ac.in

Bindu Verma
Dept. of Information Technology
Delhi Technological University
Delhi, India
binduverma@dtu.ac.in

2023 4th International Conference for Emerging Technology (INCET) | 979-8-3503-3575-0/23/$31.00 ©2023 IEEE | DOI: 10.1109/INCET57972.2023.10170284

Abstract— **Brain tumour segmentation is a crucial task in medical imaging that involves identifying and delineating the boundaries of tumour tissues in the brain from MRI scans. Accurate segmentation plays an indispensable role in the diagnosis, treatment planning, and monitoring of patients with brain tumours. This study presents a novel approach to address the class imbalance prevalent in brain tumour segmentation using a shared-encoder multi-class segmentation framework. The proposed method involves training a single encoder class learner and multiple decoder class learners, which are designed to learn feature representation of a certain class subset, in addition to a shared encoder between them that extracts common features across all classes. The outputs of the complement-class learners are combined and propagated to a meta-learner to obtain the final segmentation map. The authors evaluate their method on a publicly available brain tumour segmentation dataset (BraTS20) and assess performance against the 2D U-Net model trained on all classes using standard evaluation metrics for multi-class semantic segmentation. The IoU and DSC scores for the proposed architecture stands at 0.644 and 0.731, respectively, as compared to 0.604 and 0.690 obtained by the base models. Furthermore, our model exhibits significant performance boosts in individual classes, as evidenced by the DSC scores of 0.588, 0.734, and 0.684 for the necrotic tumour core, peritumoral edema, and the GD-enhancing tumour classes, respectively. In contrast, the 2D-Unet model yields DSC scores of 0.554, 0.699, and 0.641 for the same classes, respectively. The approach exhibits notable performance gains in segmenting the T1-Gd class, which not only poses a formidable challenge in terms of segmentation but also holds paramount clinical significance for radiation therapy.**

Keywords — segmentation, brain tumour, BraTS2020, class imbalance, shared encoder, class learner

I. INTRODUCTION

A brain tumour denotes an anomalous growth of cells in the cranial cavity or the central spinal canal. These tumours may assume a benign (non-cancerous) or malignant (cancerous) nature and can originate from diverse cell lineages within the brain, including the glial cells responsible for neuronal sustenance and the meningeal cells lining the brain and spinal cord [14].

A tumour that originates in the brain or spinal cord is referred to as a primary brain or spinal cord tumour. According to statistics from the American Society of Clinical Oncology (ASCO), in 2020 alone, 308,102 individuals were diagnosed with primary brain tumour worldwide.

Survival of individuals diagnosed with brain tumours is influenced by several factors, including age. Notably, the study highlights that advanced age is associated with a reduced probability of survival. For instance, the analysis reveals that individuals within the age bracket of 55-64 years have a one-year survival rate of 46.1%, whereas the survival rate drops to 29.3% for patients aged 65-74 years [3]. Achieving maximum resection of both the enhancing tumour (ET) and non-enhancing tumour (NET) sub-regions of a brain tumour is a viable strategy for improving the overall survival rate [1]. Therefore, it is crucial to determine the extent of the tumour in a non-invasive manner prior to any invasive procedures. As a result, it is important to perform imaging and precise identification of tumours using MRI technique before any medical procedures. Advancements in medical image segmentation have the potential to automate the task of detecting and outlining tumour growth, which can significantly reduce the time and cost associated with the process. This, in turn, can help prevent manual errors and minimize subjectivity, thereby improving both accuracy and reliability of the results.

A. Related Work

Persistent research efforts have been dedicated to exploring deep learning-based image segmentation techniques. However, accurate and automatic partitioning of tumour sub-regions from MRI scans is often hindered by the complexity arising from two major sources: First, the heterogeneity and infiltrative nature of gliomas, and second, the disproportionate prevalence of non-tumour pixels in comparison to tumour pixels in brain MR images, leading to a significant class imbalance. Convolutional neural networks (CNNs) have emerged as a groundbreaking tool in medical image analysis and have demonstrated quite impressive performance in semantic segmentation tasks. [22] Among these, the encoder-decoder architecture, such as the widely adopted U-Net model, has captured attention for its capacity to extract rich semantic features from medical images. Originally introduced by Ronneberger et al. [17], the U-Net model incorporates skip connections between decoder and encoder blocks to facilitate propogation of high level features. Since the original proposal of U-Net, numerous studies have been carried out in various fields using this architecture as a fundamental model, including Residual U-Net [10], which uses residual skip connections in each block

Authorized licensed use limited to: DELHI TECHNICAL UNIV. Downloaded on July 20,2023 at 11:19:31 UTC from IEEE Xplore. Restrictions apply.

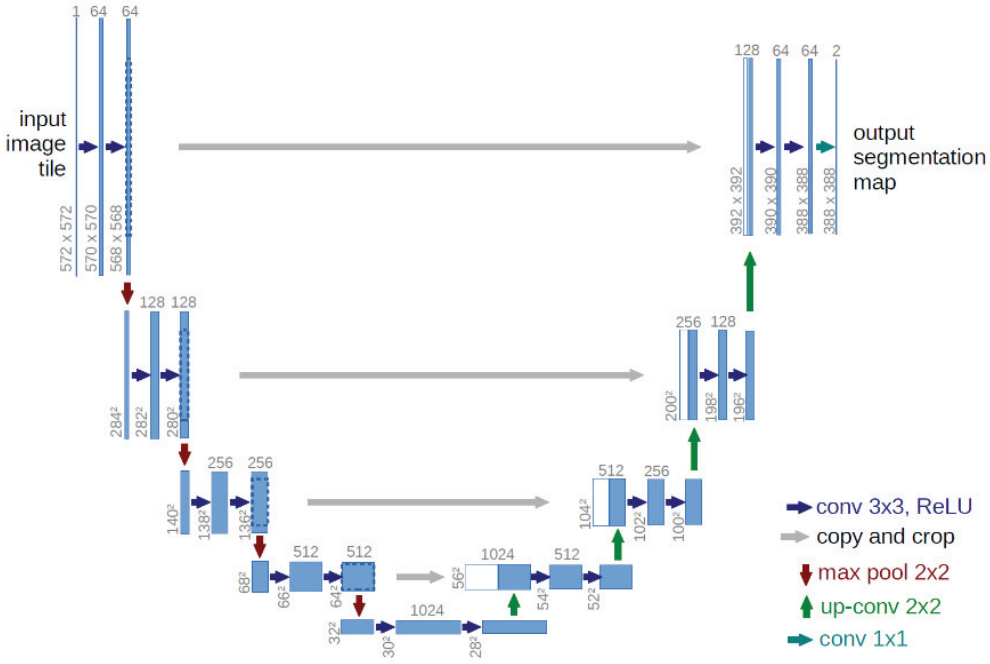

Fig. 1. The U-net architecture [17]

of the model architecture to alleviate the problem of vanishing gradients in very deep neural networks or the Dense U-net[8], which also aims to solve exploding gradients by building a U-net over a DenseNet backbone, essentially providing each layer in the model the outputs of each preceding layer.

U-net++ [23] utilizes a dense network of skip connections to establish an intermediate grid between the contracting and expansive paths, which aids the network in propagating greater semantic information between the two paths. This, in turn, enables the network to perform image segmentation tasks with enhanced accuracy. LadderNet [11], utilised the idea of concatenating multiple U-net layers and adding skip connections [9] between them for more efficient information flow across layers.

B. Our Contribution

The central contribution of this paper is to present a model that utilizes –

Class learners, where each learner is geared towards the accurate identification of a single label and multi-class learners, which better learn the relationships and associations between different classes. This methodology is useful when working with datasets that require focused analysis and precise categorization. By prioritizing a particular label, these learners have the potential to offer profound insights into the interrelationships among diverse classes within a given dataset.

The present study proposes a shared encoder architecture wherein the underlying encoder is trained on all classes to acquire a generalized understanding of the associations within the dataset, resulting in more efficient input embeddings. Specifically, our paper showcases how leveraging such an encoder, and subsequently passing these latent space features into both single and multi-class decoders, enhances the ability to precisely identify each class while simultaneously learning the inter-class correlations present. Our experimental results demonstrate the effectiveness of this technique in improving the accuracy and performance of the model on various tasks.

This study also investigates a compound loss function that incorporates both the categorical class entropy and dice loss, which are combined to obtain the final loss. The compound loss function is designed to effectively handle cases of class imbalance, which otherwise pose a significant challenge for deep learning models. Although dice loss has been shown to be effective in addressing skewed distributions, it suffers from the issue of unstable gradients. On the other hand, categorical cross entropy provides a more stable gradient change [15] . The findings suggest that the use of a hybrid loss function which incorporates both the dice loss and the cross-entropy, yields favourable results , outperforming other alternatives on evaluation metrics.

II. METHODOLOGY

A. Dataset Description

BraTS20 dataset [2, 18, 19, 20, 21, 23] was employed for training and testing the model. BraTS20 (Brain Tumour Segmentation) dataset is a benchmark dataset used for evaluating state-of-the-art algorithms present for brain tumour segmentation, classification, and survival prediction. The dataset comprises of clinically acquired multimodal magnetic resonance images (MRIs) of brain tumors, specifically referred to as glioblastomas (GBM, HGG) and low-grade gliomas (LGG).

The dataset consists of 369 pixelwise annotated 3D volumes of dimensions 240*240*155 described as namely native (T1), post-contrast T1-weighted (T1Gd), T2-weighted (T2), and T2 Fluid Attenuated Inversion Recovery (T2-FLAIR) volumes. These scans were obtained using distinct clinical protocols and 19 scanners from various institutions. The annotations were done manually by experienced neuroradiologists. All images were present in Nifty format. The annotations in the dataset comprise of the necrotic and non-enhancing tumor core (NCR/NET - label 1), the peritumoral edema (ED - label 2), and the GD-enhancing

Authorized licensed use limited to: DELHI TECHNICAL UNIV. Downloaded on July 20,2023 at 11:19:31 UTC from IEEE Xplore. Restrictions apply.

tumor (ET - label 4) .The dataset is particularly challenging due to the presence of heterogeneous tumours.

B. *Dataset Pre-processing*

In this study, we employed a dataset comprising 369 volumes of cerebral MRI scans, which were partitioned into training, validation, and testing, in a proportion of 6:2:2, respectively. To facilitate training procedure for our model, preprocessing steps were carried out, which involved the selection of the 100 slices and cropping a central portion with dimensions of 128x128. This measure was undertaken to mitigate the computational burden of processing the images, given that the full 240x240 size was deemed unnecessary, as it primarily consisted of vacuous space enveloping the MRI scan.

We stacked the T1-weighted with contrast enhancement (T1Gd), Fluid Attenuated Inversion Recovery (FLAIR) and T1-weighted (T2) scans on top of each other to create a 3-channel image, which was used as input to the model. This was motivated by the fact that these modalities provide complementary information about the brain tissues, which can be used to accurately segment the tumour region. However, the native T1 modality was excluded from the input channels, as it does not provide enough contrast between the tumour and surrounding brain tissues and T1Gd already has the highest spatial resolution in most cases. [12]

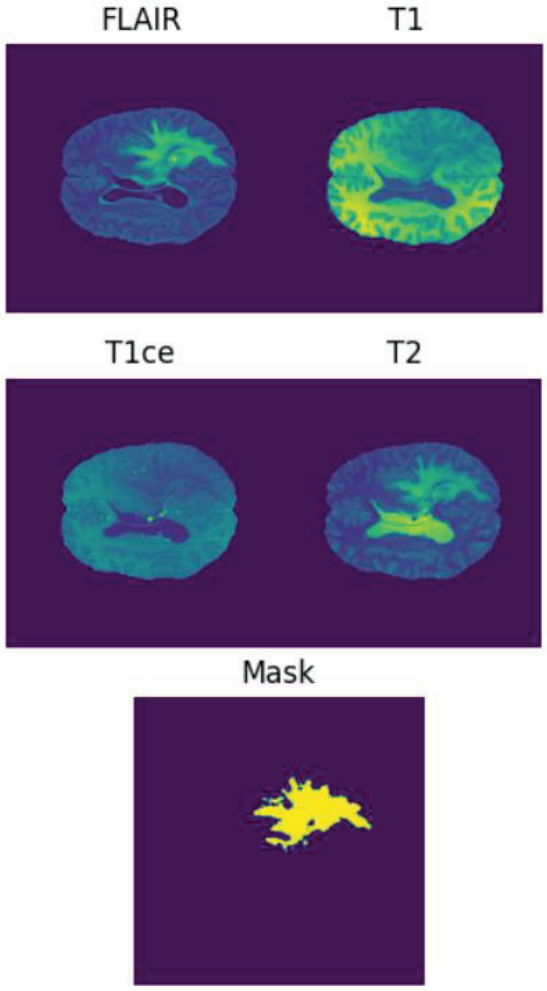

Fig. 2. Dataset Instance

Normalization of the data was done using the min-max scaling technique to ensure that all features contributed equally to the analysis and to prevent any bias towards a particular modality. To facilitate the one-hot encoding of the output mask, the numerical labels of the classes in the original dataset were modified. Specifically, the labels with a value of 4 were transformed to a value of 3 prior to the one-hot encoding procedure. This transformation enabled the encoding of the categorical labels as binary vectors with elements of 0 and 1, allowing for more efficient and flexible handling of the segmentation task.

Finally, we passed the pre-processed data into the model for training. Our results demonstrate the effectiveness of this approach in accurately segmenting brain tumours and hold promise for further developments in this field.

C. *Architecture*

This study proposes an extension to the U-net architecture [10] by introducing a hierarchical learning approach using a shared encoder and multiple specialized decoders, known as class learners. These learners are tailored to capture specific patterns between each class present in the segmentation voxels. Specifically, 7 class learners are trained on all possible combinations of the three tumour classes: (T1-Gd), (T2), and (FLAIR). The outputs of the individual class learners, along with the original image input, are subsequently passed to the meta learner, which comprises of a similar base U-net architecture as shown in Fig 1.

Encoder and Decoder Class Learners

A foundational U-net model trained on all three classes (T1-Gd, T2, FLAIR) was used as the representative encoded class learner. Training a model using all available labels enables it to acquire a more comprehensive understanding of the input space representations within the context space compared to other subset learners, acquiring a more robust feature embedding space. This encoding space facilitates the training of the decoders of the six additional class learners allowing for a more efficient and effective correlation learning for the inter-class characteristics in the input space.

Furthermore, the utilization of the shared encoder enabled the decoders to learn from a more diverse and salient feature latent space, as opposed to being restricted to the information available in specific encoders trained for separate class subsets. This also capitalizes on the powerful transfer learning capabilities of the shared weight architecture between models aiding in more high-level contextual information being transferred in skip connections [11], while also achieving significant computational gains as compared to training the class-specific encoder

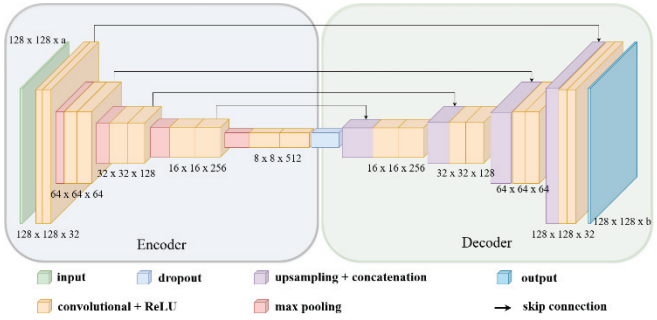

Fig. 3. Encoder and Decoder Block

Authorized licensed use limited to: DELHI TECHNICAL UNIV. Downloaded on July 20,2023 at 11:19:31 UTC from IEEE Xplore. Restrictions apply.

Meta Learner

The decoder-only class learners and the encoder class learner outputs were subsequently fed into the meta-learner.

The inputs were formed by selecting a pair of complement target learners in the set of all base learners, combining inputs of (T1-Gd) and (T2, FLAIR), (T2) and (T1-Gd, FLAIR), and (FLAIR) and (T1-Gd, T2) models, resulting in a uniform input voxel dimension of 128x128x16 for the stacked ensemble model.

To address the presence of non-tumour pixels in both the complement class learners, a pixel-wise minimum operation was carried out on the corresponding slice. This was done to minimize the influence of probabilities coming from the single-class learners. In addition, the input image of size 128x128x3 was concatenated to the input to add spatial learning capabilities for the meta-learner giving it a more comprehensive understanding of the input domain space.

Loss Function

Medical image segmentation poses a significant challenge in the form of class imbalance, which may adversely affect the efficacy of traditional loss functions like categorical cross-entropy [7, 13, 15]. Given the prevalent class disparity within the data distribution, it is evident that a compound loss function would prove more effective in achieving optimal segmentation outputs [4]. Thus, a combination of Multiclass Dice Loss [6, 7] as given in (2) and categorical cross entropy shown in (1) was used for training the weak learners (4) and an additional penalty factor of 2 was introduced on the Dice Loss to train the Meta Learner given in (5).

Let $y_{i,c}$ be the one-hot encoded vector of ground truth labels and $p_{i,c}$ be the predicted value matrix for each class, then the categorical cross entropy loss $\mathcal{L}_{CCE}$ is represented as:

$$\mathcal{L}_{CCE}(y,p) = -\frac{1}{N}\sum_{i=1}^{N}\sum_{c=1}^{C} y_{i,c}\cdot log\left(p_{i,c}\right) \quad (1)$$

Where indices c and i iterate over all classes and pixels, respectively. The Dice loss can be expressed as the complement of the Dice similarity coefficient (DSC), which quantifies the dissimilarity between two given sets of data and is widely used as an objective measure in various image segmentation tasks. Dice Loss ($\mathcal{L}_{DSC}$) is computed as:

$$DSC = \frac{2\cdot TP}{2\cdot TP + FP + FN} \quad (2)$$

$$\mathcal{L}_{DSC} = 1 - DSC \quad (3)$$

where the notations TP, FP and FN represent the True Positive, False Positive and False Negative per voxel classifications respectively.

$$\mathcal{L}_{Weak\ Learner} = \mathcal{L}_{CCE} + \mathcal{L}_{DSC} \quad (4)$$

$$\mathcal{L}_{Meta\ Learner} = \mathcal{L}_{CCE} + 2\cdot\mathcal{L}_{DSC} \quad (5)$$

Evaluation Metrics

To evaluate our model against the 2D U-net Model trained on all the 3 classes, we employed the commonly adopted evaluation criterion in semantic image segmentation, DSC as previously demonstrated in (2), as well as the Intersection over Union (IoU) metric (6). Additionally, we performed a comparative assessment of the DSC for each specific tumour class to see the impact of the shared latent space on the performance of individual class learners.

III. Results and Discussion

The proposed architecture was tested over the BraTS2020 dataset. The encoder was first trained for 50 epochs with Adam optimizer [5] and the hybrid loss function given in (4) suggested above. The starting learning rate was set at 0.001 and then further reduced when a plateau was reached over the validation loss with a patience of 2 epochs.

Subsequently, the training for each of the independent decoder class learners was also done for 50 epochs with the same learning rate reduction strategy as mentioned. In this part of the training process, the encoder weights were set to be untrainable. This reduced the computation cost for each class learner by reducing the number of trainable parameters from approximately 7.5 million to around 4 million.

Finally, the meta learner was trained on the original image and results from all the preceding learners for 15 epochs with the compound loss function given in (5).

The proposed model showed significant performance over the base 2D U-net model. The IoU and DSC scores for the proposed architecture stands at 0.644 and 0.731, respectively, as compared to 0.604 and 0.690 obtained by the base models. Furthermore, our model exhibits significant performance boosts in individual classes, as evidenced by the DSC scores of 0.588, 0.734, and 0.684 for the necrotic

$$IoU = \frac{TP}{TP + FP + FN} \quad (6)$$

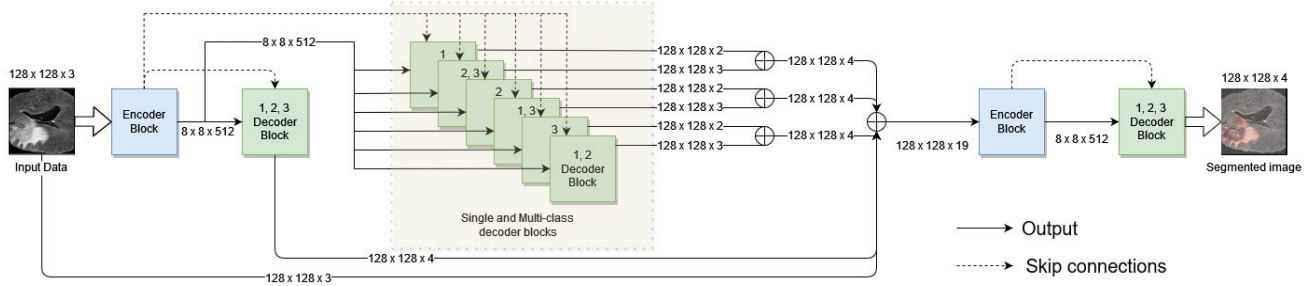

Fig. 4. Proposed Model Architecture

Authorized licensed use limited to: DELHI TECHNICAL UNIV. Downloaded on July 20,2023 at 11:19:31 UTC from IEEE Xplore. Restrictions apply.

tumour core, peritumoral edema, and the GD-enhancing tumour classes, respectively. In contrast, the 2D-Unet model yields DSC scores of 0.554, 0.699, and 0.641 for the same classes, respectively.

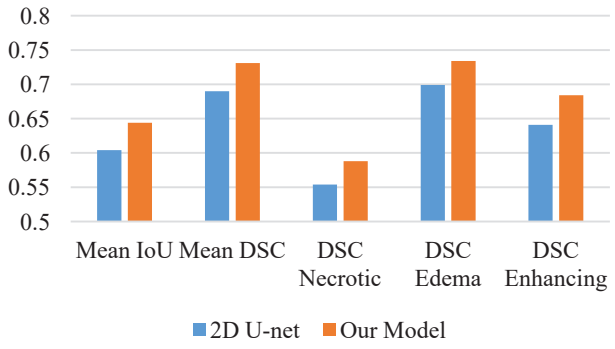

Fig. 5. Performance over BraTS2020 Dataset

Table I presents the comparison between independently trained class learners and decoders trained over a latent space representation of the complete data labels.

The shared encoder class learners consistently surpass the independent learners in IoU and Dice scores. This showcases how by employing a shared encoder approach, the skip connections to the decoders provided a more enriched high-level information from a robust feature latent space.

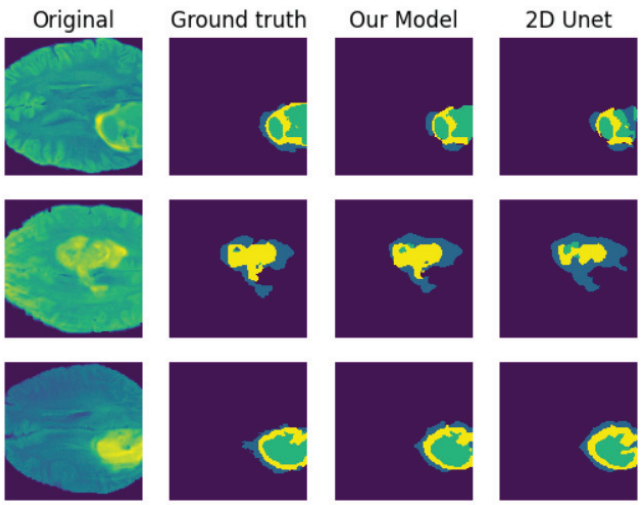

Fig. 6. Test Results on BraTS2020 Dataset

IV. Conclusion

This work aims to bring together class-based learning together with a shared encoder approach across the networks for better multi-class association learning to boost model performance across all the class labels.

The proposed framework of stacking a meta-learner on top of the base learners through the integration of outputs of complement classes and combining the input image for additional spatial learning outperforms the base U-Net Model across all evaluation metrics. Having a shared encoder approach as opposed to training class encoders from scratch also benefits from both computational and performance results with better representation learning through skip connections from a richer embedding space. This hierarchical learning approach beats the 2D U-Net Model achieving an IoU score of 0.644 and DSC of 0.731 compared to 0.604 and 0.690 on the metrics respectively.

TABLE I. Comparison of Independent and Shared Encoder Class Learners

Model	IoU	Dice	Necrotic	Edema	Enhancing
Independent Learner (Class-1)	0.693	0.746	0.529	-	-
Shared Encoder Leaner (Class-1)	**0.714**	**0.776**	**0.576**	-	-
Independent Learner (Class-2)	0.743	0.808	-	0.682	-
Shared Encoder Leaner (Class-2)	**0.761**	**0.831**	-	**0.697**	-
Independent Learner (Class-3)	0.739	0.796	-	-	0.625
Shared Encoder Leaner (Class-3)	**0.763**	**0.815**	**-**	**-**	**0.636**
Independent Learner (Class-1, 2)	0.521	0.713	0.486	0.439	-
Shared Encoder Leaner (Class-1, 2)	**0.653**	**0.774**	**0.575**	**0.699**	-
Independent Learner (Class-1, 3)	0.646	0.764	0.573	-	0.647
Shared Encoder Leaner (Class-1, 3)	0.643	**0.773**	**0.575**	-	**0.647**
Independent Learner (Class-2, 3)	0.637	0.777	-	0.632	0.625
Shared Encoder Leaner (Class-2, 3)	**0.679**	**0.827**	**-**	**0.698**	**0.656**

Authorized licensed use limited to: DELHI TECHNICAL UNIV. Downloaded on July 20,2023 at 11:19:31 UTC from IEEE Xplore. Restrictions apply.

V. Future Work

Deep learning has transformed computer vision, particularly in semantic segmentation tasks. Different approaches, like the U-Net [17], U-Net++ [24], and V-Net [6] excel at learning high-level features from raw input data and have achieved state-of-the-art performance across a range of image segmentation applications. The field of semantic segmentation is continually evolving intending to develop more accurate, efficient, and robust models for real-world applications.

In further research, we plan to extend the generalizability of our proposed methodology to diverse multi-class image segmentation datasets, beyond the domain of medical imaging. Additionally, we aim to investigate the integration of attention gates to skip connections [16] of the shared-encoder , to enhance the high-level semantic information from hidden feature representations, albeit at the expense of increased computational complexity.

The inclusion of a 3D Convolution in the model's architecture can confer considerable advantages as it would provide the model with a contextual understanding of the layers that constitute the volume, thereby augmenting the model's capacity to discern relevant contextual information. [24]

Further studies would try to improve the complexity of this approach to better scale for problem definitions with more labels by learning relevant class relations through only single-class learners.

References

[1] A. M. Molinaro et al., "Association of maximal extent of resection of contrast-enhanced and non–contrast-enhanced tumor with survival within molecular subgroups of patients with newly diagnosed glioblastoma," *JAMA Oncology*, vol. 6, no. 4, p. 495, 2020.

[2] B. H. Menze et al., "The Multimodal Brain Tumor Image Segmentation Benchmark (brats)," *IEEE Transactions on Medical Imaging*, vol. 34, no. 10, pp. 1993–2024, 2015.

[3] B. Yavuz, G. Kanyilmaz, and M. Aktan, "Factors affecting survival in glioblastoma patients below and above 65 years of age: A retrospective observational study: Semantic scholar," *Indian Journal of Cancer*, vol. 58, pp. 210-26, 2021

[4] C. Mathews and A. Mohamed, "Nested U-Net with enhanced attention gate and compound loss for semantic segmentation of brain tumor from multimodal MRI," *International Journal of Intelligent Engineering and Systems*, vol. 15, no. 4, 2022.

[5] D. P. Kingma and J. Ba, "Adam: A method for stochastic optimization," *arXiv.org*, 30-Jan-2017. [Online]. Available: https://arxiv.org/abs/1412.6980. [Accessed: 04-Apr-2023].

[6] F. Milletari, N. Navab, and S.-A. Ahmadi, "V-net: Fully convolutional neural networks for volumetric medical image segmentation," *arXiv.org*, 15-Jun-2016. [Online]. Available: https://arxiv.org/abs/1606.04797. [Accessed: 05-Apr-2023].

[7] F. Isensee, P. Kickingereder, W. Wick, M. Bendszus, and K. H. Maier-Hein, "Brain tumor segmentation and radiomics survival prediction: Contribution to the brats 2017 challenge," *arXiv.org*, 28-Feb-2018. [Online]. Available: https://arxiv.org/abs/1802.10508. [Accessed: 04-Apr-2023].

[8] G. Huang, Z. Liu, L. van der Maaten, and K. Q. Weinberger, "Densely connected Convolutional Networks," *arXiv.org*, 28-Jan-2018. [Online]. Available: https://arxiv.org/abs/1608.06993. [Accessed: 05-Apr-2023].

[9] H. Huang et al., "UNet 3+: A full-scale connected unet for medical image segmentation," *ICASSP 2020 - 2020 IEEE International Conference on Acoustics, Speech and Signal Processing (ICASSP)*, 2020.

[10] H. Zhao and N. Sun, "Improved U-net model for nerve segmentation," *Lecture Notes in Computer Science*, pp. 496–504, 2017.

[11] J. Zhuang, "LadderNet: Multi-path networks based on U-Net for Medical Image segmentation," *arXiv.org*, 28-Aug-2019. [Online]. Available: https://arxiv.org/abs/1810.07810. [Accessed: 05-Apr-2023].

[12] K. Usman and K. Rajpoot, "Brain tumor classification from multi-modality MRI using wavelets and machine learning," *Pattern Analysis and Applications*, vol. 20, no. 3, pp. 871–881, 2017.

[13] L. Sun, S. Zhang, H. Chen, and L. Luo, "Brain tumor segmentation and survival prediction using multimodal MRI scans with Deep Learning," *Frontiers in Neuroscience*, vol. 13, 2019.

[14] M. Adel Fahmideh and M. E. Scheurer, "Pediatric brain tumors: Descriptive epidemiology, risk factors, and future directions," *Cancer Epidemiology, Biomarkers & Prevention*, vol. 30, no. 5, pp. 813–821, 2021.

[15] M. Yeung, E. Sala, C.-B. Schönlieb, and L. Rundo, "Unified focal loss: Generalising dice and cross entropy-based losses to handle class imbalanced medical image segmentation," *arXiv.org*, 24-Nov-2021. [Online]. Available: https://arxiv.org/abs/2102.04525. [Accessed: 05-Apr-2023].

[16] O. Oktay et al., "Attention U-net: Learning where to look for the pancreas," *arXiv.org*, 20-May-2018. [Online]. Available: https://arxiv.org/abs/1804.03999. [Accessed: 05-Apr-2023].

[17] O. Ronneberger, P. Fischer, and T. Brox, "U-Net: Convolutional Networks for Biomedical Image Segmentation," *arXiv.org*, 18-May-2015. [Online]. Available: https://arxiv.org/abs/1505.04597. [Accessed: 04-Apr-2023].

[18] S. Bakas et al., "Advancing the cancer genome Atlas Glioma MRI collections with expert segmentation labels and Radiomic features," *Scientific data*, 05-Sep-2017. [Online]. Available: https://pubmed.ncbi.nlm.nih.gov/28872634/. [Accessed: 05-Apr-2023].

[19] S. Bakas et al., "Identifying the best machine learning algorithms for brain tumor segmentation, progression assessment, and overall survival prediction in the brats challenge," *arXiv.org*, 05-Nov-2018. [Online]. Available: https://arxiv.org/abs/1811.02629v1. [Accessed: 05-Apr-2023].

[20] S. Bakas et al., "Segmentation Labels and Radiomic Features for the Pre-operative Scans of the TCGA-GBM collection", *The Cancer Imaging Archive*, 2017. DOI: 10.7937/K9/TCIA.2017.KLXWJJ1Q

[21] S. Bakas et al., "Segmentation Labels and Radiomic Features for the Pre-operative Scans of the TCGA-LGG collection", *The Cancer Imaging Archive*, 2017. DOI: 10.7937/K9/TCIA.2017.GJQ7R0EF

[22] S. Pereira, A. Pinto, V. Alves, and C. A. Silva, "Brain tumor segmentation using convolutional neural networks in MRI images," *IEEE Transactions on Medical Imaging*, vol. 35, no. 5, pp. 1240–1251, 2016.

[23] Z. Zhou, M. M. Rahman Siddiquee, N. Tajbakhsh, and J. Liang, "UNet++: A nested U-Net Architecture for Medical Image segmentation," *Deep Learning in Medical Image Analysis and Multimodal Learning for Clinical Decision Support*, pp. 3–11, 2018.

[24] Ö. Çiçek, A. Abdulkadir, S. S. Lienkamp, T. Brox, and O. Ronneberger, "3D U-Net: Learning dense volumetric segmentation from sparse annotation," *Medical Image Computing and Computer-Assisted Intervention – MICCAI 2016*, pp. 424–432, 2016.

Authorized licensed use limited to: DELHI TECHNICAL UNIV. Downloaded on July 20,2023 at 11:19:31 UTC from IEEE Xplore. Restrictions apply.

Proceedings of the International Conference on Sustainable Computing and Smart Systems (ICSCSS 2023)
IEEE Xplore Part Number: CFP23DJ3-ART; ISBN: 979-8-3503-3360-2

Social Networks Analysis and Machine Learning: an Overview of Approaches and Applications

Ms. Sonia Choudhary
Information Technology
Delhi Technological University
New Delhi, India
er.soniyachoudhary@gmail.com

Prof. Kapil Sharma
Information Technology
Delhi Technological University
New Delhi, India
kapil@ieee.org

Dr. Monika Bajaj
Department of Computer Science
University Of Delhi
New Delhi, India
mbajaj@du.ac.in

2023 International Conference on Sustainable Computing and Smart Systems (ICSCSS) | 979-8-3503-3360-2/23/$31.00 ©2023 IEEE | DOI: 10.1109/ICSCSS57650.2023.10169353

Abstract— **A significant data mining challenge is social network analysis. To effectively retain the network topological structure and other attribute information, it is essential to encode network data into low-dimensional representations, or network embeddings, before doing social network analysis. Classification, link prediction, anomaly detection, and clustering are further applications made easier by network representation learning. Machine learning-based approaches have also gained a lot of attention in recent years. This study performs a thorough analysis of the recent literature on network representation learning by utilizing neural network models. A study of past research works in social network analysis reveals that most of them used methods based on matrices and graphs. The same methodology is used in several studies that concentrate on various facets of society. The antiquated techniques, which mostly rely on visual analysis, are suitable for usage with more controllable datasets. Although it is possible to automate the process of extracting the information while also reducing bias, one could argue that a study of social networks based on machine learning could perform better even now, in unpredictable circumstances. This is because the data extraction based on machine learning has delivered better results.**

Keywords—Social networking, Machine learning, Graph-Based Representation

I. INTRODUCTION

A social structure that consists of a selected group of players and their interactions is described as "Social Network". This theoretical framework helps to examine how people, groups, organizations, and even societies are interconnected. Researchers also looked at how these social formations affect other factors, how they alter the relative density of relationships, or how they alter through time (network dynamics). Identification among the most important, prestigious, and central actors; recognition of hubs and authority; and community discovery are a few of the common tasks in social network analysis. The method for obtaining knowledge via networks and, as a result, the issue resolution process of issue resolution both greatly benefit from these tasks. Social network research is becoming popular as a common method in various domains, from statistics to machine learning, due to the allure of such problems and the strong probability provided by this form of analysis[1]. The way that society as a whole uses computers to mine and analyze data is changing in a significant way. Machine-learning algorithms have been used to evaluate historical data over the last ten years, frequently showing trends and patterns that are simply too subtle even for humans to see. Examples include using credit card data mining to find fraudulent activity trends and using scientific data mining to find empirical laws. To enhance social interactions, researchers have recently started to apply these techniques to real-time data that records individual activities, talks, and movements. Changes to systems that carry out activities connected to artificial intelligence are referred to as machine learning. Support vector machines, fuzzy theories, neural networks, and evolutionary algorithms are a few examples of machine learning components. further information on machine learning. Researchers from various fields, including sociology, humanities, psychology, political science, information science, economics, medicine, management, and business, are drawn to social networks because of the vast amounts of hidden information variety of fields, including sociology, humanities, psychology, politics, information science, economy, medical, management, and business, are drawn to social networks because of the vast amounts of hidden information that are there. These researchers are looking for patterns of interest. While the majority of them concentrate on the formation and structure of networks, others focus on the dissemination of knowledge, similar to the spread of disease; still, others concentrate on the extraction of network information from diverse data sources, such as online and social communities, the web, communication networks, and blogs[2]. Some of them, such as security analysis, significance recognition, boundary analysis, performance analysis, and many more, concentrate on the many types of information that can be retrieved. The research that has already been done on the various topics is provided here. We also include a section with contributions by machine learning academics.

A. Problem Statement

- An uptick in utilization. Social anxiety, social anxiety disorder, sadness, and exposure to inappropriate content can all result from spending more time on social media.

- Addiction to social media exists. User aim to perform a task or play a game as skillfully as possible. Once the user achieves the goal,

Authorized licensed use limited to: DELHI TECHNICAL UNIV. Downloaded on July 22,2023 at 05:11:46 UTC from IEEE Xplore. Restrictions apply.

dopamine and other feel-good hormones are released from brain, making the user happy. Posting a photo to Instagram or Facebook uses the same method. The subconscious mind will start to perceive the notifications for likes and supportive remarks as rewards once they start to appear on the screen. However, there are also many mood-altering experiences on social media.

- The fear of being left out. FOMO has emerged as a prominent motif that frequently encourages frequent scanning of social media platforms. Your mental health may be impacted by the fear of missing out if you aren't online.

B. *Objectives*

- Social Network Analysis (SNA) can reveal the social influence that exist inside teams and pinpoint cultural difficulties.
- The study done for SNA is interested in people but the analysis itself is concerned with connectivity: how people work together.

II. Social Networks and Machine Learning

A. *Graphical Representation of Social Networks*

Graphs and matrices are used to represent networks. In the original depiction of social networks, persons are represented as points and lines that show their connections to one another. One of the most popular structural representations is this graph-based perspective using graph theory. The characteristics or type of the actor are specified using various colors, shades, symbols, and sizes. Dotted lines, bold lines, multiple lines, arrow-headed line segments indicating direction, etc. were used along with various colors to denote different types of relationships using ties. This clarifies the layered relationships between the actors. Figure 1 shows a graphic representation of the network's history.

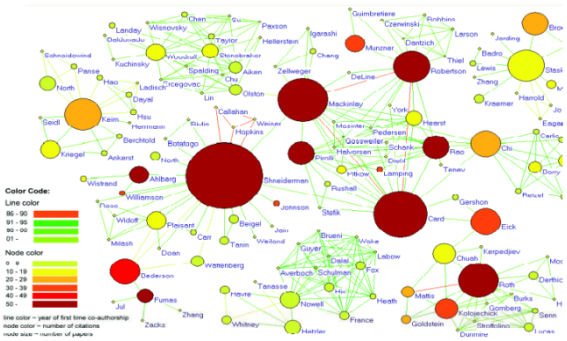

Fig.1. Graphical representation of Social Network

Researchers from a variety of fields, including sociology, the humanities, psychology, politics, information systems, economics, medicine, management, and business, are drawn to social networks because of the vast amounts of hidden information that are there. These researchers are looking for patterns of interest. Some of them concentrate on obtaining network information from diverse data sources, including online and social communities, the web, communication networks, and blogs. The majority of them concentrate on the structure and development of connections, while others focus just on the spread of information like the spread of disease. Several of them concentrate on various information types that can be collected, including security analysis, importance recognition, boundary analysis, performance analysis, and many more.

B. *Overview of Social Networks and Social Network Analysis*

The idea of social networks was created about a century ago. The theories which have emerged have focused on the complex relationships between the many parts of social systems. Consequently, relational theory must serve as the foundation of any analysis of social networks.

Terminologies

a) Networks are made up of nodes that are connected by a set of ties in a graph.
b) Networks are homogenous if they contain just one kind of node; otherwise, they are heterogeneous. Depending on the sort of relationship between the participants, a network could be simplex or multiplex.
c) If each actor selects a different actor, the group of actors is said to be reciprocal.
d) When an actor has just one connection to the ensemble, they are considered pendants.
e) Relational data refers to a network's collection of ties, while network size refers to the total number of actors in a network.
f) A network is referred to as a valued network if its connections are connected by a scale of magnitude or strength.

B. *Social Network Analysis*

Social network analysis is an interdisciplinary field that examines social structures, relationships, and interactions through the use of network theory and methods. This approach allows for the visualization and analysis of complex social systems, revealing patterns of connection, influence, and information flow that may be difficult to discern otherwise. This paper provides an overview of social network analysis, its history, and key concepts, as well as its applications in various fields including sociology, psychology, business, and public health.

One of the earliest and most influential works in social network analysis is the book "The Strength of Weak Ties" by Mark Granovetter (1973). Granovetter argues that weak ties, or the connections between people who are not closely related, are often more valuable than strong ties because they provide access to new information and resources. Another important concept in social network analysis is centrality, which refers to the extent to which an individual or node is connected to other nodes in a network. Freeman (1979) proposed several measures of centrality, including degree centrality, betweenness centrality, and eigenvector centrality, each of which captures different aspects of an individual's position in a network

Authorized licensed use limited to: DELHI TECHNICAL UNIV. Downloaded on July 22,2023 at 05:11:46 UTC from IEEE Xplore. Restrictions apply.

Social network analysis has been applied to a wide range of topics, including the spread of disease, the diffusion of innovation, and the formation of social movements. For example, Christakis and Fowler (2007) used social network analysis to study the spread of obesity in a large social network, demonstrating that the likelihood of obesity was influenced not only by an individual's behavior but also by the behavior of their friends, their friend's friends, and so on. Another example is the study by Gladwell (2000) on the power of social networks in the civil rights movement, showing how the strength of weak ties played a critical role in the success of the movement.
social network analysis provides a powerful framework for studying social structures and interactions, revealing patterns that might otherwise be difficult to detect. Its application in a wide range of fields demonstrates its versatility and potential for further research.

C.Machine Learning for Social Network Analytics

Over the past ten years, algorithms for machine learning have been employed to analyze historical data, frequently revealing patterns and trends that are just subtle even for people to notice[1]. Examples include utilizing scientific information mining to discover empirical laws and using credit card information mining to identify trends in fraudulent behavior. Researchers have lately begun to apply similar algorithms to real-time data which records individual activities, discussions, and movements to improve social interactions. Highlighting the visual clarity and algorithmic complexity of social networks. They used reduction techniques to demonstrate the type of information loss that occurs during extensive analysis. Similar Communities & associations have been grouped using clustering algorithms.[2] Listed causes for finding clusters. The foundation of member collaboration is membership in detected communities, which enables the deployment of group-focused services[2].[3] Demonstrated the value of the clustering coefficient. Fortunato (2010) suggested a dynamic synchronization-based approach for community detection. The term "Machine Social Network," which describes a social media network among active machines through the Internet, has recently attracted some investigation. According to research, MSN has some difficulties, including message communication delays and a distrustful device community[4].
Machine learning is the process of making adjustments to computer systems that carry out artificial intelligence-related tasks. Neural networks, fuzzy, and genetic algorithms are some of the elements of machine learning. Machine-learning algorithms have aided in the analysis of historical data, frequently finding patterns and trends minute for people to see. A couple of examples are mining scientific data to find empirical laws and mining credit card information to find patterns of activity that point to fraud. Recently, some study on "Machine Social Networks," or social networks among online active gadgets, has been initiated. The study discovered some MSN problems, including message communication delays and a lack of a trusted device community. To reduce the sparsity issue in recommender systems, an integrated recommendation method based on network science tools is used. Using information network concepts, they calculated the similarity network and used link prediction & diffusion methods to take into account user ratings and hidden connections. The tools required to examine such vast, complicated, and constantly changing social media information are made available to researchers through data mining techniques.

III. Approaches and Applications of Social Network Analysis

The last two decades have seen a rise in the importance of social network analysis (SNA), both as a research program and as a tool for network analysis applications in various contexts. SNA has created a new paradigm for research in the social and behavioral sciences that conceptually and methodologically focuses on the relational aspects of social phenomena and behavior patterns. It sets itself apart from conventional scientific methods that frequently analyze—at least methodologically—the various objects of the investigative process as independent from one another. SNA has proven to be an effective method for examining the interconnectivity of individual or group actors in social processes like communication channels or deliberative processes in practical applications of network analysis techniques and tools. Due to the practical utility of its relatively simple-to-understand mental concepts and techniques, SNA also has piqued the interest of practitioners, whether as sponsors or contractors for network studies or even as users of network analytical applications and tools.
Different participatory network mapping approaches have been successful in using social network analysis as an instrument for facilitating change. Here, participants and interviewees contribute network data by drawing a physical map of the network (either on paper or digitally) while the data is being collected. The Net-map toolbox is an illustration of a pen-and-paper network mapping method that also includes the gathering of some actor attributes (perceived influence as well as goals of actors). The ability to gather qualitative information and pose clarifying queries while network data is being gathered is one advantage of this strategy.

A. Machine Learning and Social Network Analysis Approaches and Applications

Different machine learning and social network analysis approaches and applications are discussed in Table 1.

Haque's machine learning-based multi-class sentiment assessment of Bengali comments on social media [7] conducted a side-by-side comparison of the suggested model and the reference models. Six machine learning models that used two different feature extraction techniques were recognized as baseline models. On a labeled dataset identifying 42036 Facebook comments, our suggested CLSTM architecture significantly outperforms SA with 85.8% accuracy & 0.86 F1 scores. To identify the true emotion of social media comments, a web application was created utilizing only the proposed model and the best base model[7]. Ma [8] In the experiment Modeling Major League Sports Athletes' Social Media Sites Using Machine-Learning Techniques cumulatively models a sports athlete's social media network. The following model displays the experiment's results: Images from the machine learning-

Authorized licensed use limited to: DELHI TECHNICAL UNIV. Downloaded on July 22,2023 at 05:11:46 UTC from IEEE Xplore. Restrictions apply.

optimized athletic social networks consist of 1,200 male athletes, 48%, and 1,000 female athletes, 40%. Before the

TABLE I. APPLICATIONS OF SNA AND MACHINE LEARNING

Author/ Year	Title	Method
Norz/2023 [5]	Using log data and social network analysis, an exploration route analysis was conducted to assess social presence in online learning.	carried out an exploratory route analysis to determine which metrics best reflect social presence.
Alzahrani/ 2022 [6]	Machine Learning Approaches for Developing Land Cover Mapping	proposed a method using a recent dataset of 9 different kinds of urban land cover. According to experimental findings, the suggested technique outperformed the RF classifier by only using 27% of the information.
Veeramakali/2022 [7]	Healthcare Data in Social Networks Can Be Kept Private Using Machine Learning	Based on reliable outcomes, machine learning approaches should be selected. To do this, one must apply each strategy to the outcomes.
Alshari/2022 [8]	Sentinel-2A Satellite Image Analysis Using Machine Learning Methods	Describe the fundamentals of supervised learning, its pros and disadvantages, and the experimental findings obtained with 12 classifiers.
MacDermott/2022 [9]	Using deep learning to detect social media 'trolls'	Discuss the findings of our study utilising deep learning algorithms to find damaging information and "trolls" on social media.

optimization, there were 22.58 percent fewer athletes overall and 23.07 percent fewer female athletes than there were male athletes (70.58% vs. 16.3%)[8]. From the facts above, it is clear that machine learning research on athletes' social networking within sports has a favorable impact on the growth of an athlete's social media network. Ahmed's scoping investigation of social media depression and anxiety detection using machine learning [9] Studies have used social media data from a variety of different platforms to develop forecasting analytics again for the diagnosis of anxiety or depression. These posts were published on numerous social media sites, such as Twitter, Facebook, Instagram, Reddit, Weibo, and others. provide the recognized machine learning models that are most prevalent. Prediction models that identify user language on social networks can be used to identify people with anxiety and depressive problems, which has the possibility of enhancing current screening methods. Such research could reveal information on the mental health of a general populace, particularly when access to healthcare providers may be hampered by lockdowns and temporary service closures like those seen at the height of the COVID-19 pandemic[9]. Hinduja[10] These are difficult to use in early detection but do offer an online detection for mental disorders. In this article, a general architecture for supporting active psychiatric monitoring is created with a focus on the Twitter platform. Comprehensive data cleaning & pre-processing of tweets is provided based on known trends to achieve precise sentiment analysis results. Machine learning techniques, particularly LSTM, are used for the early detection of social sensors that pose risks to overcome the limits of traditional classifiers. According to experimental findings, The suggested methodology performs better in terms of precise prediction than the present methods[10].[11] Drury evaluated a wide variety of studies that looked at particular crimes committed through social media sites, the utilization of social networks in crime, as well as the detection of such crimes. There is currently no review article available that examines the many types of crimes committed via social media, their commonalities, or how they might be recognized. It is possible to share procedures & data between domains by comparing crimes and the detection techniques used to catch them. This study will collect a list of crimes carried out using social media platforms to demonstrate how comparable they are. A list of publicly accessible datasets is also included in this study. Lastly, this poll makes recommendations for additional research in this area[11].

B. Deep Learning and (Sna) Social Network Analysis Approaches and Applications

Ties' strength

One of the first methods of SNA in the 20th century was measuring and analyzing the strength of links. Even in the twenty-first century, it is an interesting subfield of SNA. Information dispersal, churning prediction, involvement within the system, link forecasting, etc. are just a few of the SNA issues that have been addressed using strength-of-ties methodologies. By analyzing one or more indications of tie strength, predictors of connection strength are created, which are then used in this procedure (friends, family, coworkers, etc.). (such as the volume, intensity, regularity, length, or subject of a discourse).

Churn Prediction

Numerous published studies in the area of SNA that used the Strength-of-Ties approach tackled the issue of Churn Prediction. The authors essentially developed new metrics or used existing ones to measure the adhesive force binding links and connections in SN architectures (s). These metrics often consist of probability distributions that give values such as "xi: 0 xi 1," where "xi" denotes the degree of a particular link. To identify which (weak) links and relationships have a propensity to churn, a preset cutoff threshold (e.g., xi = 0.5) is employed. Any (strong) connections which would still need to be retained are then identified (like xi 0.5). This method of churn forecasting does not seem to be beneficial and accurate because weak relationships are relevant, influential, helpful, or favorable to the pairs of associated players as well as the SN structure.

Link Prediction

In SNA, Link Prediction (LP) is still an unresolved research issue. To forecast newer edges as likely links and relationships for merely a conceivable SN structure extension, LP investigates & analyses SN structures. Numerous strategies have been put forth over time to address

Authorized licensed use limited to: DELHI TECHNICAL UNIV. Downloaded on July 22,2023 at 05:11:46 UTC from IEEE Xplore. Restrictions apply.

this SNA issue. The most important developments in this area are highlighted in the overview that follows.

C. Literature Survey

Cuzzocrea 2020 et al. To further boost the potency of this strategy, the graph convolutional network model incorporates a teleport probability t from the page rank domain. When compared to previous techniques, the combination personalized propagation of neural predictions (CPPNP) method also achieves a remarkable level of prediction accuracy. According to evaluation results utilizing three well-known datasets, altering t improves CPPNP performance. This deep learning plus transfer learning combined approach offers strong support for predictions of social influence[12].

Arasu 2020 et al. To develop a social media strategy, this study evaluates social data analytics employing machine learning approaches using a Waikato Environment of Knowledge Analysis (WEKA). When compared to other relevant algorithms, WEKA performs better than the competition, notably in terms of metrics like precision, recall, or F-measure, demonstrating that it is more effective than alternative methods[13].

Ganguli 2020 et al. Online social network analysis encompasses a variety of techniques, such as spammer detection, user classification, link prediction, troll page sensing, friend referrals, community & cluster identification, trends, sentiment classification on political blogs, etc. This article reviews the most recent findings in machine learning-based depression diagnosis, false profile detection, personality trait identification, and social media network analysis-based depression identification. Additionally, it compares the various techniques[14].

Birjali 2017 et al. Place a person in a challenging situation and focus on the feelings that might give rise to suicidal thoughts. We specifically suggest a technique of creating a language related to suicide to overcome the paucity of terminological people could afford with suicide. Then, for a more in-depth examination, we suggest taking a look at Weka, a machine learning-based information mining program that may extract important information from the Twitter data Twitter4J has collected. A WordNet-based method is suggested to calculate sentiment classification for tweets within the training sample using tweeting inside the data set. Experiments show that our approach, which is based on algorithms for machine learning & semantic sentiment analysis, can extract predictions about suicidal thoughts using Twitter Data. This analysis also supports the performance's efficacy in terms of both precision and precision in classifying semantic sentiments that may indicate suicidal intent. The meeting program chairs will direct the peer review process[3].

Fersini 2017 et al. Examine the research on the classification of polarity in social networks using semi supervised, supervised, & supervised machine learning techniques. The most current advancements in the field are presented in detail, with a focus solely on the true nature of communications that are offered in a casual and networked context[15].

IV. Conclusion

Graph- or matrix-based approaches were used most frequently in early social network analysis studies. A similar approach is used by numerous other research that looks into a range of social issues. Smaller datasets can be used with these antiquated techniques, which primarily rely on visual judgment. Although, arguably, social network analysis that is based on machine learning algorithms can extract data while reducing bias and performing well for large amounts of data in even uncertain contexts, it is still possible to make the case that this method is superior to traditional methods.

Social network analysis and machine learning approaches have shown tremendous potential in various fields, including sociology, marketing, politics, and healthcare, to name a few. Through the integration of social network data with machine learning algorithms, researchers can gain deeper insights into complex social systems, discover patterns and trends, and predict outcomes

One significant benefit of social network analysis and machine learning is the ability to identify key influencers or individuals within a network who play a crucial role in the spread of information, behaviors, or opinions. This can have implications for targeted marketing, political campaigning, and public health interventions

However, there are also potential ethical concerns related to the use of social network analysis and machine learning. Privacy concerns, algorithmic bias, and the potential for unintended consequences are all important considerations that must be addressed as these methods become more prevalent.

Looking to the future, there is a growing need for multidisciplinary collaborations between social scientists, computer scientists, and domain experts to address the challenges and opportunities presented by social network analysis and machine learning. As technology continues to evolve and new data sources become available, there is no doubt that social network analysis and machine learning will play an increasingly important role in our understanding of complex social systems.

References

[1] X. Hong-Lin, Y. Han-Bing, G. Cui-Fang, and Z. Ping, “Social network analysis based on network motifs,” J. Appl. Math., vol. 2014, 2014, doi: 10.1155/2014/874708.

[2] H. J. Yin, H. Yu, Y. L. Zhao, Z. L. Zhu, and W. Zhang, “Analysis of the Dynamic Influence of Social Network Nodes,” Sci. Program., vol. 2017, 2017, doi: 10.1155/2017/5046905.

[3] M. Birjali, A. Beni-Hssane, and M. Erritali, “Machine Learning and Semantic Sentiment Analysis based Algorithms for Suicide Sentiment Prediction in Social Networks,” Procedia Comput. Sci., vol. 113, pp. 65–72, 2017, doi: 10.1016/j.procs.2017.08.290.

[4] J. Meghana, J. Hanumanthappa, and S. P. S. Prakash, “Performance comparison of machine learning algorithms for data aggregation in social internet of things,” Glob. Transitions Proc., vol. 2, no. 2, pp. 212–219, 2021, doi: 10.1016/j.gltp.2021.08.032.

Authorized licensed use limited to: DELHI TECHNICAL UNIV. Downloaded on July 22,2023 at 05:11:46 UTC from IEEE Xplore. Restrictions apply.

[5] A. Gupta and R. Katarya, "Social media based surveillance systems for healthcare using machine learning: A systematic review," J. Biomed. Inform., vol. 108, no. June, p. 103500, 2020, doi: 10.1016/j.jbi.2020.103500.

[6] R. Rothenberg and E. Costenbader, "Empiricism and theorizing in epidemiology and social network analysis," Interdiscip. Perspect. Infect. Dis., vol. 2011, 2011, doi: 10.1155/2011/157194.

[7] R. Haque, N. Islam, M. Tasneem, and A. K. Das, "Multi-class sentiment classification on Bengali social media comments using machine learning," Int. J. Cogn. Comput. Eng., vol. 4, no. December 2021, pp. 21–35, 2023, doi: 10.1016/j.ijcce.2023.01.001.

[8] Y. Ma, "Modeling Social Network of Professional Sports Athletes Based on Machine Learning Algorithms," Int. Trans. Electr. Energy Syst., vol. 2022, 2022, doi: 10.1155/2022/6283618.

[9] A. Ahmed et al., "Machine learning models to detect anxiety and depression through social media: A scoping review," Comput. Methods Programs Biomed. Updat., vol. 2, no. August, p. 100066, 2022, doi: 10.1016/j.cmpbup.2022.100066.

[10] S. Hinduja, M. Afrin, S. Mistry, and A. Krishna, "Machine learning-based proactive social-sensor service for mental health monitoring using twitter data," Int. J. Inf. Manag. Data Insights, vol. 2, no. 2, p. 100113, 2022, doi: 10.1016/j.jjimei.2022.100113.

[11] B. Drury, S. M. Drury, M. A. Rahman, and I. Ullah, "A social network of crime: A review of the use of social networks for crime and the detection of crime," Online Soc. Networks Media, vol. 30, no. May, p. 100211, 2022, doi: 10.1016/j.osnem.2022.100211.

[12] A. Cuzzocrea, C. K. Leung, D. Deng, J. J. Mai, F. Jiang, and E. Fadda, "A combined deep-learning and transfer-learning approach for supporting social influence prediction," Procedia Comput. Sci., vol. 177, no. 2018, pp. 170–177, 2020, doi: 10.1016/j.procs.2020.10.025.

[13] B. S. Arasu, B. J. B. Seelan, and N. Thamaraiselvan, "A machine learning-based approach to enhancing social media marketing," Comput. Electr. Eng., vol. 86, p. 106723, 2020, doi: 10.1016/j.compeleceng.2020.106723.

[14] R. Ganguli, A. Mehta, and S. Sen, "A Survey on Machine Learning Methodologies in Social Network Analysis," ICRITO 2020 - IEEE 8th Int. Conf. Reliab. Infocom Technol. Optim. (Trends Futur. Dir., pp. 484–489, 2020, doi: 10.1109/ICRITO48877.2020.9197984.

[15] E. Fersini, Sentiment Analysis in Social Networks: A Machine Learning Perspective. Elsevier Inc., 2017. doi: 10.1016/B978-0-12-804412-4.00006-1.

[16] L. M. Norz, V. Dornauer, W. O. Hackl, and E. Ammenwerth, "Measuring social presence in online-based learning: An exploratory path analysis using log data and social network analysis," Internet High. Educ., vol. 56, no. October 2022, p. 100894, 2023, doi: 10.1016/j.iheduc.2022.100894.

[17] A. Alzahrani and A. Kanan, "Machine Learning Approaches for Developing Land Cover Mapping," Appl. Bionics Biomech., vol. 2022, 2022, doi: 10.1155/2022/5190193.

[18] T. Veeramakali, A. Shobanadevi, N. R. Nayak, S. Kumar, S. Singhal, and M. Subramanian, "Preserving the Privacy of Healthcare Data over Social Networks Using Machine Learning," Comput. Intell. Neurosci., vol. 2022, no. June 2012, 2022, doi: 10.1155/2022/4690936.

[19] E. A. Alshari and B. W. Gawali, "Analysis of Machine Learning Techniques for Sentinel-2A Satellite Images," J. Electr. Comput. Eng., vol. 2022, 2022, doi: 10.1155/2022/9092299.

[20] Á. MacDermott, M. Motylinski, F. Iqbal, K. Stamp, M. Hussain, and A. Marrington, "Using deep learning to detect social media 'trolls,'" Forensic Sci. Int. Digit. Investig., vol. 43, p. 301446, 2022, doi: 10.1016/j.fsidi.2022.301446.

Authorized licensed use limited to: DELHI TECHNICAL UNIV. Downloaded on July 22,2023 at 05:11:46 UTC from IEEE Xplore. Restrictions apply.

Proceedings of the International Conference on Sustainable Computing and Smart Systems (ICSCSS 2023)
IEEE Xplore Part Number: CFP23DJ3-ART; ISBN: 979-8-3503-3360-2

2023 International Conference on Sustainable Computing and Smart Systems (ICSCSS) | 979-8-3503-3360-2/23/$31.00 ©2023 IEEE | DOI: 10.1109/ICSCSS57650.2023.10169690

Store and Restore Delay Reduction Techniques of Non-volatile SRAM cells

Damyanti Singh
Dept. of ECE
Delhi Technological University
Delhi, India-110042
damyanti_singh@rediffmail.com

Neeta Pandey
Dept. of ECE
Delhi Technological University
Delhi, India-110042
neetapandey@dce.ac.in

Kirti Gupta
Dept. of ECE
Bharati Vidyapeeth's College of Engineering
Delhi, India-110063
kirti.gupta@bharatividyapeeth.edu

***Abstract*—The incorporation of memristor with static random access memory (SRAM) cell, known as non-volatile SRAM (nvSRAM) cell, not only introduces non-volatile feature in it but also enhances stability and reduces power consumption. With the development in technology, this has become a mainstream development focus. During the analysis of nvSRAM cell, the store and restore delays become a major concern as the longer time duration leads to memory failure. Limited work is done to address this problem, which increases complexity during non-volatile operation. In this work, different techniques are introduced to reduce the store and restore delays. These delay reduction techniques deal with the control signals required to perform non-volatile operation. The maximum reduction of 19.41% is achieved in the store delay, while the restore delay is reduced by 21.74%. The SPICE simulations are carried out using 32nm PTM CMOS model at Vdd=1.0V.**

***Index Terms*—Memristor, non-volatile operation, non-volatile static random access memory (nvSRAM), store delay, restore delay**

I. Introduction

The continuous growth in semiconductor industry has increased the demand of portable devices like mobile phones, tablet computers, laptops and many more. This leads to increment in amount of data to be stored in memory system. Also, the device size is continuously shrinking due to the technology scaling. It causes increase in leakage during idle state and leads to increment in power consumption [1]–[3]. Further, there is a possibility of data loss due to leakage which may result in memory failure. One of the possible ways to reduce leakage is turning of the device during idle mode, however, this is not feasible due to volatile nature of SRAM cell. The researchers have provided the solution of this issue by adding non-volatile memory (NVM) device with SRAM cell and make it non-volatile in nature [4], [5].

With the advancement in technology, it become possible to fabricate NVM device on SRAM cell leading to development of non-volatile SRAM (nvSRAM) cell. Memristor (also known as RRAM) is considered as the best candidate among existing NVM devices due to its compatibility with CMOS technology [5]. The nvSRAM cell exhibits feature of regular SRAM cell as well as non-volatile functionality. This ensures that the real time data can be stored in advanced electronic devices [6]. The nvSRAM cells find their application in ATM, electronic equipment, printing devices, industrial products and many more [7], [8].

In the literature, there are several nvSRAM cells available that have their own merits and demerits [9]–[23]. The 6T2R nvSRAM cell was proposed to introduce non-volatile feature in conventional 6T SRAM cell [9]. However, the direct connection of memristor with the internal nodes cause leakage that affects the cell stability. To reduce leakage,7T2R [10], [11] and 8T2R [12] nvSRAM cells are introduced. In 7T2R [10] and 8T2R [12] nvSRAM cells switch transistor(s) is(are) used to control the memristor operation which helps in leakage reduction. The 7T2R nvSRAM cell [11] uses self-controllable voltage level (SVL) method to decrease leakage in the cell. Although, the leakage issue is resolved in these cells, the stability is of a bit concern. To overcome the stability concern, Avg.7T1R [13], MS 7T1R [14], 8T3R [15], RD 8T1M [16], [17], ST 12T1M [18] and ST 13T1M [19] nvSRAM cells are introduced. The nvSRAM cells [13]–[15] enhance cell stability by reducing the strength of pull-down path, while in RD 8T1M cell [16], [17], an isolated read port is used. In nvSRAM cells, the power consumption is also an important issue as the programming of memristor may increase power consumption of the cell. The 8T2R [12], Avg.7T1R [13], 8T1M [20] and TG 7T1R [21] nvSRAM cells propose different techniques to reduce the power consumption. Other than the leakage, stability and power consumption issues, the delay reduction is also an important concern that is not discussed in the aforementioned cells. The longer delays may lead to extended power on/off time and causes data loss at the time of sudden power failure. The 8T1R [22] and 8T2R [23] nvSRAM cells are introduced to fasten the store/restore operation, however, the method increases the complexity of the cell during non-volatile mode.

From the literature, it is observed that limited work is done to reduce store and restore delay. There is enough scope to work in this direction as it is an important parameter in nvSRAM cells. In this work, some schemes are introduced which help in the reduction of store and restore delay. Section II gives a description of different delay reduction techniques. These techniques are applicable to nvSRAM cells which use one transistor and one memristor (1T1M) configuration to conduct non-volatile operation. In section III, the delay reduction tech-

Authorized licensed use limited to: DELHI TECHNICAL UNIV. Downloaded on July 22,2023 at 05:12:26 UTC from IEEE Xplore. Restrictions apply.

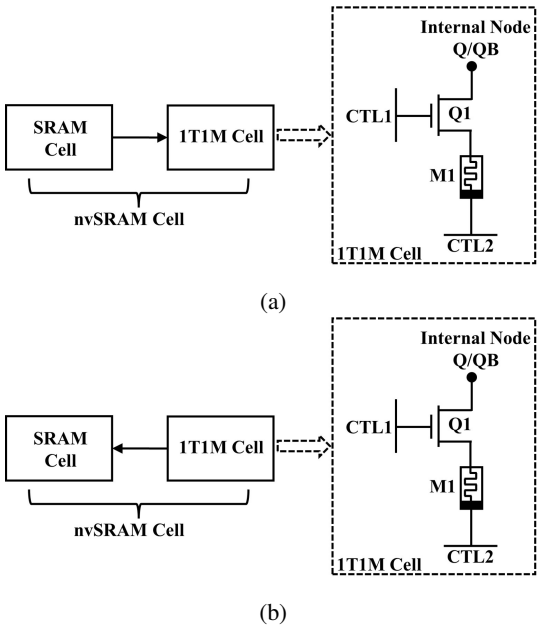

Fig. 1. Generic structure of nvSRAM cell with 1T1M configuration; flow of data during (a) store operation and (b) restore operation.

niques are applied on existing 8T1M nvSRAM cell [20]. The timing waveform during non-volatile operation, store/restore delay and power consumption are analyzed and discussed in this section. This study is carried out at Vdd=1.0V. The effect of voltage variation on the performance parameters is also discussed. The last section IV concludes the paper.

II. Proposed Store and Restore Delay Reduction Techniques

The generic structure of nvSRAM cell with 1T1M configuration is shown in Fig.1. The non-volatile operation consists of four modes: normal, store, power-down and restore. The status of control signals CTL1 and CTL2 during different operations are given in Table I. In normal mode, SRAM operations (write, read and hold) are carried out. During store operation, the data transfer takes place as depicted in Fig.1(a). The logic '1' at internal node develops a potential difference across memristor. This causes change in memristor state from high resistance state (HRS) to low resistance state (LRS). If logic '0' is stored at internal node, memristor remain in HRS state. The power supply is shut off after store operation. Memristor preserves its state even after the internal node loses its data. In restore mode, the power supply is turned on again to recover the data from memristor as shown in Fig.1(b). A significant current can flow through a memristor in its LRS state, charging the internal node to Vdd i.e., logic '1'. When the memristor is in the HRS state, a modest current flows, but it cannot charge the internal node up to Vdd, hence, remains at GND i.e., logic '0'. After recovery of data, memristor regains its initial state i.e., HRS state and SRAM mode is performed again.

TABLE I. Status of Control Signals During Different Operations

Operation	Control Signals	
	CTL1	*CTL2*
SRAM Mode	LOW	LOW
Store	HIGH	LOW
Power Down	LOW	LOW
Restore	HIGH	HIGH

In nvSRAM cells, the long store and restore time may lead to the loss of data at the time of sudden power failure. From the literature survey, it is observed that nvSRAM cells with 1T1M configuration avoid the complexity during non-volatile operation. This configuration also improves delay and power consumption of the nvSRAM cells during storage and recovery of the data. In the subsections below, the techniques to reduce the store and restore delays are introduced.

A. Negative CTL2 Technique

This technique is applicable for store delay reduction only. In this method, the signal CTL2 is pulled to a negative voltage instead of ground potential during store operation only, and it is shown in Fig.2(a). The negative voltage at CTL2 is achieved by coupling capacitance method suggested in [24], [25]. The increased potential difference across memristor results in large memristor current which causes faster change in memristor state from HRS to LRS or vice versa. Due to this, the store delay is reduced effectively. Although, the negative CTL2 technique fastens the store operation speed, its increases store energy consumption also.

B. Boosted CTL1 Technique

This technique is applicable for the reduction of both store and restore delays. The boosted control signal CTL1, shown in Fig.2(b), is achieved by charge pump circuit [26] or capacitive coupling method [27]. This increases the strength of pass transistor Q1 during store and restore operation. Due to this, the drain current of the transistor Q1 is increased which fastens both the transfer of data into memristor during store operation and recovery of data to the cell during restore operation. Hence, the store and restore delays are reduced. However, this is achieved at the cost of increased store and restore energy consumption.

C. Floating Vss Technique

This technique is significant for restore delay reduction only. In nvSRAM cell, Vss is the source potential of pull-down transistors which generally remain at ground (GND) potential. In this approach, the Vss is raised to few hundred mV instead of GND [28], as shown in Fig.2(c). This reduces the strength of pull-down path of the cell. When the data is restored at the internal nodes, the high potential of Vss makes it easy to recover the data. It results in fast restore operation and reduces the restore delay of the cell.

Authorized licensed use limited to: DELHI TECHNICAL UNIV. Downloaded on July 22,2023 at 05:12:26 UTC from IEEE Xplore. Restrictions apply.

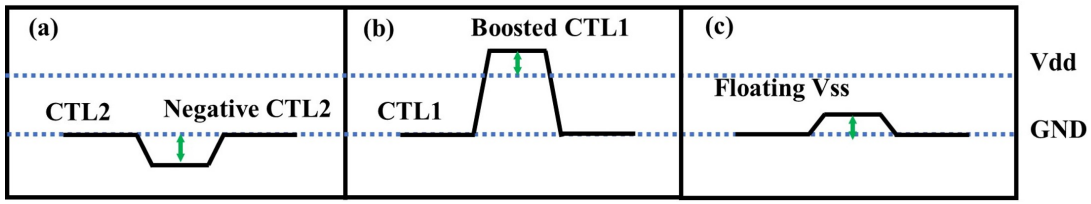

Fig. 2. Different techniques (a) negative CTL2, (b) boosted CTL1 and (c) floating Vss for store and restore delay reduction.

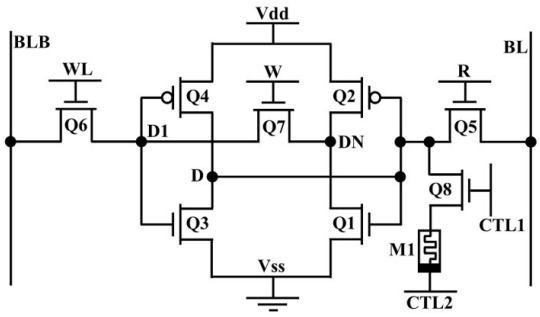

Fig. 3. Schematic of 8T1M nvSRAM cell [20].

III. Simulation and Discussion

The memristor model suggested in [29] is used for the analysis with the following parameter values: R_{ON}=100Ω, R_{OFF}=16KΩ, mobility $\mu v = 10^{-14} m^2 V^{-1} s^{-1}$ and thickness D=10nm. Figure 3 shows the schematic of existing 8T1M nvSRAM cell [20] and the aspect ratio of transistors is given in Table II. To study the effectiveness of the proposed techniques, Figure 4, 5, 6 and 7 show timing waveforms, delay and power consumption with different delay reduction techniques for store and restore operations of 8T1M nvSRAM cell [20]. For the sake of completeness, the voltage variation study on performance parameters like delay and power consumption is also carried out.

TABLE II. Aspect Ratio of Transistors used in 8T1M nvSRAM Cell [20]

Operation	Aspect Ratio (W/L)
Q1	211.2nm/32nm
Q2	128nm/32nm
Q3	166.4nm/32nm
Q4	64nm/32nm
Q5	64nm/32nm
Q6	83.2nm/32nm
Q7	256nm/32nm
Q8	64nm/32nm

A. Store Operation

The timing waveforms for variation in memristance and current flowing through memristor are depicted in Fig.4(a). The store delay is observed as 38.54ps at Vdd=1.0V. Figure 4(b) depicts the timing waveform for negative CTL2 technique. It is observed that a large current flows through memristor M1 when signal CTL2 is negative. It is due to the increased potential difference across memristor M1 and the store delay is reduced to 30.98ps. Figure 4(c) depicts timing waveform for boosted CTL1 technique. The boosted signal CTL1 increases the gate voltage of transistor Q1 and hence, the amount of drain current is also increased. The increased amount of current increases the speed of change in memristor state and hence, the store delay is reduced upto 34.52ps.

The impact of power supply scaling is also observed on store delay and power consumption of 8T1M nvSRAM cell [20] and the findings are summarized in Fig.5(a) and 5(b), respectively. Figure 5(a) shows the store delay of 8T1M nvSRAM cell [20] with different store delay reduction techniques. It is observed that with reduction of signal CTL2 to negative value, the store delay is reduced by 19.41%, while the reduction of 10.33% is observed in store delay by boosting the voltage level of signal CTL1 in comparison to normal store delay at Vdd=1.0V. This reduction in store delay is achieved at the cost of increased store power consumption which is shown in Fig.5(b). It is observed that the store power consumption is increased by 43.5% and 29.3% using negative CTL2 and boosted CTL1 techniques, respectively, in comparison to normal store power consumption at the same supply voltage. Also, Fig. 5 depicts the reduction in store delay and enhancement in store power consumption with an increase in supply voltage.

B. Restore Operation

The timing waveforms for data recovery at internal node Q and the current flowing through memristor are shown in Fig.6(a). The restore delay is observed as 24.56ps at Vdd=1.0V. The timing waveform for floating Vss technique are shown in Fig.6(b). This approach reduces the restore delay to 19.26ps. In floating Vss technique, the absence of pull-down path helps in data recovery. Figure 6(c) depicts the timing waveform for boosted CTL1 technique. This technique increases the amount of drain current due to the increased gate potential of transistor Q1 and reduces the restore delay upto 20.95ps.

The effect of power supply scaling on restore delay and power consumption of 8T1M nvSRAM cell [20] is also observed and the results are shown in Fig.7(a) and 7(b), respectively. Form Fig.7(a), it is observed that the restore delay is reduced by 21.74% and 14.54% due to floating Vss technique and boosted control signal CTL1 method, respectively, in comparison to normal restore delay at Vdd=1.0V. Figure 7(b)

Authorized licensed use limited to: DELHI TECHNICAL UNIV. Downloaded on July 22,2023 at 05:12:26 UTC from IEEE Xplore. Restrictions apply.

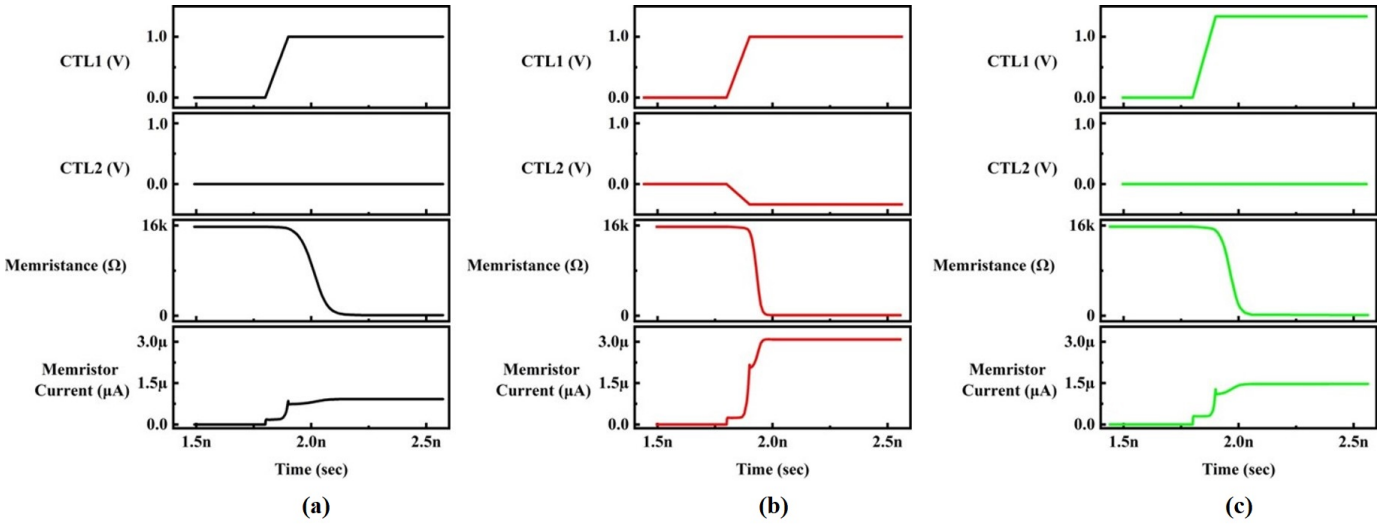

Fig. 4. Timing waveform for store operation using (a) normal values (b) negative CTL2 technique and (c) boosted CTL1 technique of 8T1M nvSRAM cell [20].

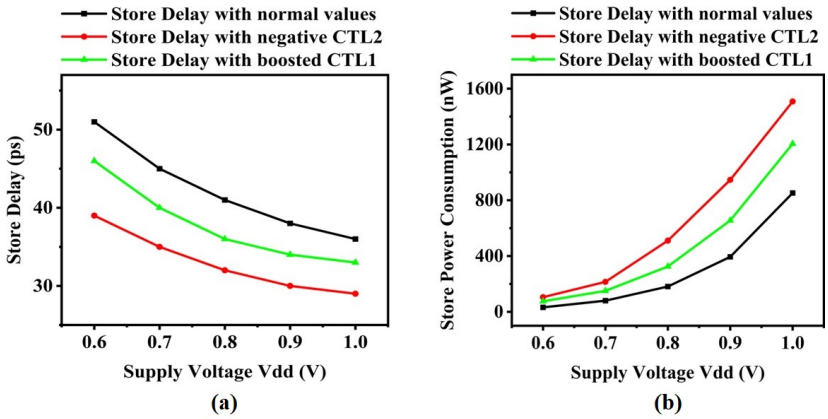

Fig. 5. (a) Store delay and (b) store power consumption of 8T1M nvSRAM cell [20].

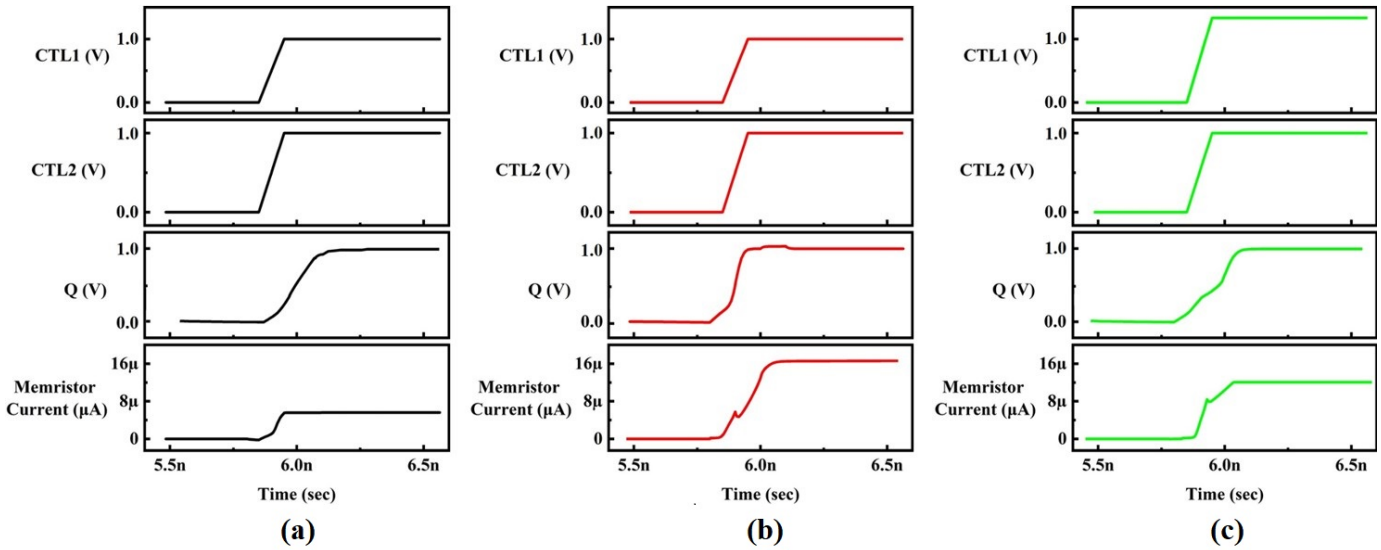

Fig. 6. Timing waveform for restore operation using (a) normal values (b) floating Vss technique and (c) boosted CTL1 technique of 8T1M nvSRAM cell [20].

Authorized licensed use limited to: DELHI TECHNICAL UNIV. Downloaded on July 22,2023 at 05:12:26 UTC from IEEE Xplore. Restrictions apply.

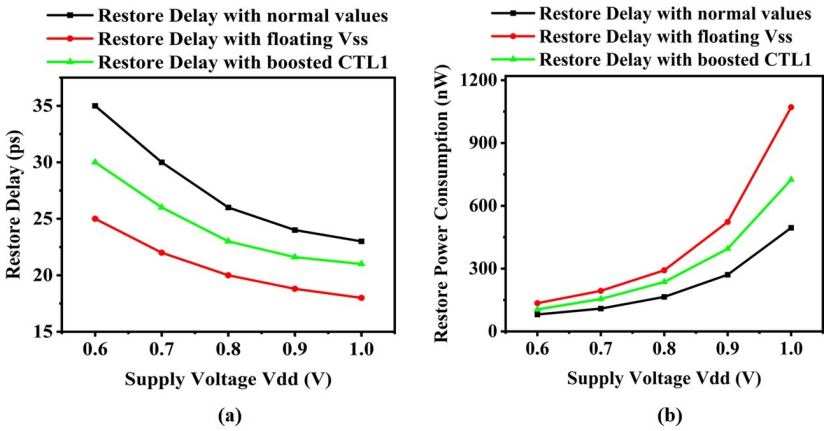

Fig. 7. (a) Restore delay and (b) restore power consumption of 8T1M nvSRAM cell [20].

shows the restore power consumption using different restore delay reduction techniques. Although the floating Vss method gives a maximum reduction in restore delay, it increases the restore power consumption by 53.8% at Vdd=1.0V. The boosted CTL1 method increases the restore power consumption by 31.7% at the same supply voltage. Further, Fig. 7 depicts the reduction in restore delay and enhancement in restore power consumption with an increase in supply voltage.

IV. Conclusion

The proposed work presents different techniques for the reduction of store and restore delay of nvSRAM cells. The negative CTL2 and boosted CTL1 techniques are introduced to reduce store delay. The floating Vss and boosted CTL1 techniques are introduced to reduce restore delay of the nvSRAM cell. Out of the discussed techniques, it is observed that the negative CTL2 technique gives a maximum reduction of 19.41% in store delay at Vdd=1.0V. The floating Vss technique shows the best performance in restore delay reduction and it is reduced by 21.74% at the same supply voltage. However, the reduction in store and restore delays is achieved at the cost of increased store/restore power consumption.

References

[1] Y. Nakagome, M. Horiguchi, T. Kawahara, and K. Itoh, "Review and future prospects of low-voltage RAM circuits," *IBM Journal of Research and Development*, vol. 47, no. 5-6, pp. 525–552, 2003.

[2] A. J. Bhavnagarwala, X. Tang, and J. D. Meindl, "The impact of intrinsic device fluctuations on CMOS SRAM cell stability," *IEEE Journal of Solid-State Circuits*, vol. 36, no. 4, pp. 658–665, 2001.

[3] S. Mukhopadhyay, H. Mahmoodi, and K. Roy, "Modeling of failure probability and statistical design of SRAM array for yield enhancement in nanoscaled CMOS," *IEEE Transactions on Computer-Aided Design of Integrated Circuits and Systems*, vol. 24, no. 12, pp. 1859–1879, 2005.

[4] G. W. Burr, B. N. Kurdi, J. C. Scott, C. H. Lam, K. Gopalakrishnan, and R. S. Shenoy, "Overview of candidate device technologies for storage-class memory," *IBM Journal of Research and Development*, vol. 52, no. 4-5, pp. 449–464, 2008.

[5] J. S. Meena, S. M. Sze, U. Chand, and T. Y. Tseng, "Overview of emerging nonvolatile memory technologies," *Nanoscale Research Letters*, vol. 9, no. 1, pp. 1–33, 2014.

[6] H. Bazzi, A. Harb, H. Aziza, M. Moreau, and A. Kassem, "RRAM-based non-volatile SRAM cell architectures for ultra-low-power applications," *Analog Integrated Circuits and Signal Processing*, vol. 106, no. 2, pp. 351–361, 2021. [Online]. Available: https://doi.org/10.1007/s10470-020-01587-z

[7] M. F. Chang, A. Lee, C. C. Kuo, S. S. Sheu, F. T. Chen, T. K. Ku, Y. P. Liu, H. Z. Yang, and P. C. Chen, "Challenges at circuit designs for resistive-type Nonvolatile memory and nonvolatile logics in mobile and cloud applications," in *Proceedings - 2014 IEEE 12th International Conference on Solid-State and Integrated Circuit Technology, ICSICT 2014*, 2014, pp. 5–8.

[8] W. H. Chen, W. S. Khwa, J. Y. Li, W. Y. Lin, H. T. Lin, Y. Liu, Y. Wang, H. Wu, H. Yang, and M. F. Chang, "Circuit design for beyond von Neumann applications using emerging memory: From nonvolatile logics to neuromorphic computing," in *Proceedings - International Symposium on Quality Electronic Design, ISQED*. IEEE, 2017, pp. 23–28.

[9] W. Wang, A. Gibby, Z. Wang, T. W. Chen, S. Fujita, P. Griffin, Y. Nishi, and S. Wong, "Nonvolatile SRAM cell," in *Technical Digest - International Electron Devices Meeting, IEDM*. IEEE, 2006, pp. 1–4.

[10] S. S. Sheu, C. C. Kuo, M. F. Chang, and et al., "A ReRAM integrated 7T2R non-volatile SRAM for normally-off computing application," in *Proceedings of the 2013 IEEE Asian Solid-State Circuits Conference, A-SSCC 2013*. IEEE, 2013, pp. 245–248.

[11] C. H. Kumar and B. Kariyappa, "Node voltage and KCL model-based low leakage volatile and non-volatile 7T SRAM cells," *IETE Journal of Research*, pp. 1–17, 2022.

[12] P.-F. Chiu, M.-F. Chang, C.-W. Wu, C.-H. Chuang, S.-S. Sheu, Y.-S. Chen, and M.-J. Tsai, "Low store energy, low VDDmin, 8T2R nonvolatile latch and SRAM with vertical-stacked resistive memory (memristor) devices for low power mobile applications," *IEEE Journal of Solid-State Circuits*, vol. 47, no. 6, pp. 1483–1496, 2012.

[13] C. Peng, S. Xiao, W. Lu, J. Zhang, X. Wu, J. Chen, and Z. Lin, "Average 7T1R Nonvolatile SRAM with R/W Margin Enhanced for Low-Power Application," *IEEE Transactions on Very Large Scale Integration (VLSI) Systems*, vol. 26, no. 3, pp. 584–588, 2018.

[14] Z. Lin, Y. Wang, C. Peng, X. Wu, X. Li, and J. Chen, "Multiple Sharing 7T1R Nonvolatile SRAM with an Improved Read/Write Margin and Reliable Restore Yield," *IEEE Transactions on Very Large Scale Integration (VLSI) Systems*, vol. 28, no. 3, pp. 607–619, 2020.

[15] U. M. Janniekode, R. P. Somineni, O. I. Khalaf, M. M. Itani, J. Chinna Babu, and G. M. Abdulsahib, "A Symmetric Novel 8T3R Non-Volatile SRAM Cell for Embedded Applications," *Symmetry*, vol. 14, no. 4, p. 768, apr 2022. [Online]. Available: https://www.mdpi.com/2073-8994/14/4/768

[16] D. Singh, K. Gupta, and N. Pandey, "A novel read decoupled 8T1M nvSRAM cell for near threshold operation," *Microelectronics Journal*, vol. 126, no. May, p. 105496, 2022. [Online]. Available: https://doi.org/10.1016/j.mejo.2022.105496

[17] D. Singh, N. Pandey, and K. Gupta, "A novel read decoupled 8T1M nvSRAM cell with improved read/write margin," *Analog Integrated*

Authorized licensed use limited to: DELHI TECHNICAL UNIV. Downloaded on July 22,2023 at 05:12:26 UTC from IEEE Xplore. Restrictions apply.

Circuits and Signal Processing, vol. 114, no. 1, pp. 89–101, 2023. [Online]. Available: https://doi.org/10.1007/s10470-022-02121-z

[18] D. Singh, N. Pandey, and K. Gupta, "Schmitt Trigger 12T1M Non-volatile SRAM cell with improved process variation tolerance," *AEU-International Journal of Electronics and Communications*, vol. 162, p. 154573, 2023.

[19] D. Singh, N. Pandey, and K. Gupta, "Process invariant Schmitt Trigger non-volatile 13T1M SRAM cell," *Microelectronics Journal*, vol. 135, no. January, p. 105773, 2023. [Online]. Available: https://doi.org/10.1016/j.mejo.2023.105773

[20] D. Singh, K. Gupta, and N. Pandey, "A Novel Low-Power Nonvolatile 8T1M SRAM Cell," *Arabian Journal for Science and Engineering*, vol. 47, no. 3, pp. 3163–3179, 2022. [Online]. Available: https://doi.org/10.1007/s13369-021-06035-2

[21] Y. Zhu, Y. Xia, S. Cheng, Y. Sun, and X. Wang, "A 7T1R Nonvolatile SRAM with High Stability, Low Delay and Low Power Consumption Embedded with Transmission Gates (TGs)," in *Proceedings of 2022 IEEE 16th International Conference on Solid-State and Integrated Circuit Technology, ICSICT 2022*. IEEE, 2022, pp. 1–3.

[22] A. M. Tosson, A. Neale, M. Anis, and L. Wei, "8T1R: A novel low-power high-speed RRAM-based Non-volatile SRAM Design," in *Proceedings of the ACM Great Lakes Symposium on VLSI, GLSVLSI*, 2016, pp. 239–244.

[23] J. Yin, W. Liao, Y. Zhang, J. Jiang, and C. Chen, "An 8kb RRAM-Based Nonvolatile SRAM with Pre-Decoding and Fast Storage/Restoration Time," *Applied Sciences*, vol. 13, no. 1, p. 531, 2023.

[24] M. Yabuuchi, K. Nii, Y. Tsukamoto, S. Ohbayashi, Y. Nakase, and H. Shinohara, "A 45nm 0.6V cross-point 8T SRAM with negative biased read/write assist," in *IEEE Symposium on VLSI Circuits, Digest of Technical Papers*. IEEE, 2009, pp. 158–159.

[25] H. Mizuno and T. Nagano, "Driving source-line cell architecture for sub-1-V high-speed low-power applications," *IEEE Journal of Solid-State Circuits*, vol. 31, no. 4, pp. 552–557, 1996.

[26] C. C. Wang, Y. H. Hsueh, T. W. Kuo, and R. Hu, "A boosted wordline voltage generator for low-voltage memories," in *Proceedings of the IEEE International Conference on Electronics, Circuits, and Systems*, vol. 2, 2003, pp. 806–809.

[27] M. Iijima, K. Seto, M. Numa, A. Tada, and T. Ipposhi, "Low power SRAM with boost driver generating pulsed word line voltage for sub-1V operation," *Journal of Computers*, vol. 3, no. 5, pp. 34–40, 2008.

[28] A. Bhavnagarwala, S. Kosonocky, Y. Chant, K. Stawiasz, U. Srinivasant, and M. Ziegler, "A Sub-600mV, Fluctuation tolerant 65nm CMOS SRAM Array with Dynamic Cell Biasing," in *2007 Symposium on VLSI Circuits Digest of Technical Papers*, 2007, pp. 78–79.

[29] D. Biolek, M. Di Ventra, and Y. V. Pershin, "Reliable SPICE simulations of memristors, memcapacitors and meminductors," *Radioengineering*, vol. 22, no. 4, pp. 945–968, 2013.

Authorized licensed use limited to: DELHI TECHNICAL UNIV. Downloaded on July 22,2023 at 05:12:26 UTC from IEEE Xplore. Restrictions apply.

arXiv:2307.00454v1 [cond-mat.mtrl-sci] 2 Jul 2023

Structural, vibrational and electronic properties of Nb substituted orthovanadates $LaV_{1-x}Nb_xO_4$

Ashok Kumar,[1,2] Anurag Sharma,[3] Madhav Sharma,[3] Vinod Singh,[1] Anita Dhaka,[4] and Rajendra S. Dhaka[3,*]

[1] *Department of Applied Physics, Delhi Technological University, Delhi-110042, India*
[2] *Department of Physics, Atma Ram Sanatan Dharma College, University of Delhi, New Delhi-110021, India*
[3] *Department of Physics, Indian Institute of Technology Delhi, Hauz Khas, New Delhi-110016, India*
[4] *Department of Physics, Hindu College, University of Delhi, New Delhi-110007, India*

(Dated: July 4, 2023)

We investigate the structural, vibrational, morphological, and electronic properties of Nb substituted orthovanadate $LaV_{1-x}Nb_xO_4$ samples prepared by the solid-state reaction method. The x-ray diffraction (XRD) analysis reveals the presence of three crystal structures [monoclinic monazite ($m-m$) type for the $x = 0$, two-phase equilibrium of monoclinic monazite ($m-m$) and tetragonal scheelite ($t-s$) type for the $0.2 \leq x \leq 0.8$, and monoclinic fergusonite ($m-f$) type for the $x = 1$ samples] with an increase in Nb^{5+} concentration. The Raman spectroscopy and x-ray photoelectron spectroscopy (XPS) were employed to study the vibrational and electronic properties of all the samples, respectively. In order to choose an excitation wavelength that does not cause undesirable fluorescence and has observable intensities of all the vibrational modes, the Raman spectra are collected using 532 nm, 633 nm, and 785 nm laser lines. With increasing the Nb^{5+} concentration, new Raman modes associated with Nb-bonds are clearly visible and the intensity of V-bonds assigned modes is decreasing. The XPS analysis shows the unchanged 3+ oxidation state of La ion where the intensity of the V $2p$ core-level decreases while the Nb $3d$ core-level increases with x. The equal spin-orbit energy splitting of the states is confirmed by the average energy difference (across La core-level spectra for all the samples) for state I as well as bonding and anti-bonding of state II. Interesting, the relative intensity of La $3d$ state I and state II show systematic change with Nb doping altering the metal ligand overlap. We discuss and provide insight into the evolution of the structural, morphological, and chemical features with Nb substitution in $LaV_{1-x}Nb_xO_4$ samples.

I. INTRODUCTION

In various polycrystalline oxides, rare earth orthovanadates (RVO_4; R-Rare earth elements) are interesting because of their potential applications in catalysis, polarizers, luminescent materials, and laser host materials [1–3]. Also, researchers have reported that complex oxide materials show interesting structural, magnetic and electronic properties [4–7], and may be utilized for various applications such solid oxide fuel cells and as an electrode material for Lithium-ion batteries due of their high specific capacity and cycle stability [8]. It is interesting to note that the lanthanum based orthovanadates $LaVO_4$ shows the structural trend in rare-earth family, it crystallizes in tetragonal–zircon ($t-z$) type polymorphs with space group $I4_1/amd$ and monoclinic–monazite ($m-m$) type polymorph with space group $P2_1/n$. However, it thermally stabilizes in $m-m$ type, whereas the $t-z$ structure remains in metastable state at room temperature, because of the largest ionic radius of La^{3+} in lanthanide series, it has a higher oxygen coordination number (9) in $m-m$ type structure as compared to 8 in $t-z$ type [9]. The zircon structure contains a pattern of VO_4 tetrahedra (having four identical V-O bonds) [10] and RO_8 dodecahedra (coordination no. 8), sharing their edges alternatively and linked together in chains along the $c-$axis. In the monazite structure, deformed VO_4 tetrahedra with four different V-O bonds [11] are connected to RO_9 polyhedra (coordination no. 9) and sharing their edges. The zircon type $LaVO_4$ sample is difficult to prepare at ambient conditions by conventional solid state reaction method but few reports say that it can be synthesized and stabilized by hydrothermal and precipitation methods [12–14].

The structural and electronic properties of lanthanum orthovanadate with pentavalent niobium substitution are vital to understand for their practical use. Though the parent compound $LaVO_4$ with substitution at the La site has been extensively explored [15, 16], there are very few studies to understand the effect of substitution at V site [17, 18]. As the niobium is located just below vanadium in the periodic table and has many advantages like Vanadium prices have recently risen to about 300% higher, niobium (Nb^{5+}) is biocompatible, isoelectronic to vanadium ion and has a larger ionic radius (0.48 Å) with four coordination numbers in comparison to vanadium ion (0.36 Å) [19]. The $LaNbO_4$ is a rare-earth niobate and shows a well-known temperature and composition/substitution-induced structural transformation. For example, the $LaNbO_4$ undergoes a thermally induced structural transition from monoclinic fergusonite ($m-f$) with space group I2/a to tetragonal scheelite ($t-s$) with space group $I4_1/a$) phase at ∼495°C [20]. Similarly, it undergoes structural transformation by substituting Nb^{5+} at V^{5+} site [21]. It has been reported that lanthanum niobate shows interesting properties and very useful for technological applications such as proton con-

* rsdhaka@physics.iitd.ac.in

ductivity [22, 23], good dielectric, high energy emission using X-ray excitation [24] and its potential for applications in a variety of fields, including sensors [25], contrast agents, waveguides, ferroelectrics [26], phosphors [27], laser crystals [28], luminophores, LEDs [29], etc.

In this paper, we study the structural, vibrational, morphological, and electronic properties of $LaV_{1-x}Nb_xO_4$ using various experimental tools like x-ray powder diffraction (XRD), scanning electron microscopy (SEM), high resolution transmission electron microscopy (HR-TEM), selected area electron diffraction (SAED), Raman spectroscopy, and x-ray photoelectron spectroscopy (XPS). We find the phase purity and structural transition by performing the Rietveld refinement of the measured XRD patterns at room temperature. The Raman spectra of $LaV_{1-x}Nb_xO_4$ samples are measured with different excitation wavelengths of 532 nm, 633 nm, and 785 nm, where we find significant intensity of all the Raman active modes as well as interesting changes with Nb substitution. The Raman spectra exhibit a pattern of maximum intensity peaks that is compatible with Badger's rule. The structural phase transition observed in the XRD analysis of $LaV_{1-x}Nb_xO_4$ is also supported by the intensity variation in the Raman mode observed in the samples with increasing Nb concentration. Through the SEM micrographs, we identify that the samples contain fine particles along with pores as well as changes in particle size and shape can be seen in the surface images of the samples. The core-level photoemission reveals the oxidation state and electronic structure of the constitute elements in these samples. The intensity of the core-level spectra of all the samples varied systematically with an increase in Nb^{5+} concentration, as shown by XPS analysis. The average energy difference (for the La core-level spectra of all the samples) for state I, state II bonding, and state II anti-bonding verified the equal spin-orbit energy splitting of the states. Moreover, we find a systematic change in the relative intensity of La $3d$ state I and state II with Nb doping, which suggest an altering in the metal ligand overlap.

II. EXPERIMENTAL

We use solid-state reaction method to prepare $LaV_{1-x}Nb_xO_4$ ($x = 0$ to 1) samples by mixing V_2O_5 (99.6%, Sigma), Nb_2O_5 (99.99%, Sigma), and La_2O_3 (99.99%, Sigma) as precursors in the stoichiometric proportions. The La_2O_3 was pre-dried for 6 hrs at 900°C to remove the moisture. After that the mixture was ground evenly for 8 hours, then heated for 17 hrs at 1000°C. The mixture was then reground and sintered at 1250°C for 13 hrs to improve the crystallinity of the samples. The phase purity and structural parameters of $LaV_{1-x}Nb_xO_4$ were determined using Panalytical XPert^3 powder x-ray diffractometer at room temperature using the Cu source of Kα radiation ($\lambda = 1.5406$ Å). We use the step size of 0.033° for each XRD scan taken in the 2θ range from 10° to 90°. The lattice parameters are extracted by the Rietveld refinement of XRD patterns using FullProf software, where linear interpolation is used to fit the background. We use Jeol JSM-7800F Prime field emission scanning electron microscope (FE-SEM) with LN_2 free SDD X-max 80 EDS detector in high vacuum mode to produce the scanning electron microscope (SEM) micrographs of the materials' surfaces. The analysis of particle size and change in morphology of $LaV_{1-x}Nb_xO_4$ was done using ImageJ software by analyzing SEM micrographs at the surface of the pellet samples. In order to execute FE-SEM, the non-conducting $LaV_{1-x}Nb_xO_4$ pellets were turned into conducting by coating the surface with a thin layer of Au using a sputter coater. We use the JEOL/JEM-F200 microscope, equipped with thermal electron field emission and OneView CMOS camera (4k × 4k pixels), to collect HR-TEM data by operating the system at an acceleration voltage of 200 keV.

The Raman spectra were recorded at room temperature with the Renishaw inVia confocal Raman microscope using 2400 lines/mm grating, 10X objective, and three different wavelengths; (i) 532 nm, gas laser with a power of 1 mW, (ii) 633 nm, where the semiconductor diode laser with a power of 1 mW, (iii) 785 nm semiconductor diode laser with a power of 0.1 mW. The samples can be identified by their particular Raman fingerprint, and their structural and chemical information can be discovered through the examination of several Raman active modes in $LaV_{1-x}Nb_xO_4$. The x-ray photo emission spectroscopy (XPS) measurements are done using AXIS Supra instrument (Kratos Analytical Ltd). The survey spectra and core level spectra (La $3d$, Nb $3d$, V $2p$, and O $1s$, for each sample), were recorded at room temperature using the monochromatic X-ray source: Al Kα-1486.6 eV(step size 1 eV for the survey and 0.1 eV for core level spectra), with a charge neutralizer, is used to offset the charging impact in these insulating materials. The pass energy of the analyzer was 160 eV and 20 eV for the survey and core-level spectra, respectively. For all the wide scans and core-level spectra, the C $1s$ peak is fitted to obtain the peak binding energy (BE) and the calibration for charge correction was done using the C $1s$ BE reference at 284.6 eV for each sample. We utilize the Igor Pro 9 software to analyze the observed Raman spectra and fitted the modes using the Lorentzian peak function as well as XPS spectra using the Voigt function.

III. RESULTS AND DISCUSSION

The Rietveld refined room-temperature x-ray diffraction (XRD) patterns of the polycrystalline $LaV_{1-x}Nb_xO_4$ ($x = 0$–1) samples are displayed in Fig. 1 and lattice parameters of the samples are summarised in Table I, where we can see that angle β is increasing in the $m-m$ type phase of $LaV_{1-x}Nb_xO_4$ samples with Nb^{5+} substitution due to higher ionic size of Nb^{5+} as compared to V^{5+}. The crystallization of $LaV_{1-x}Nb_xO_4$

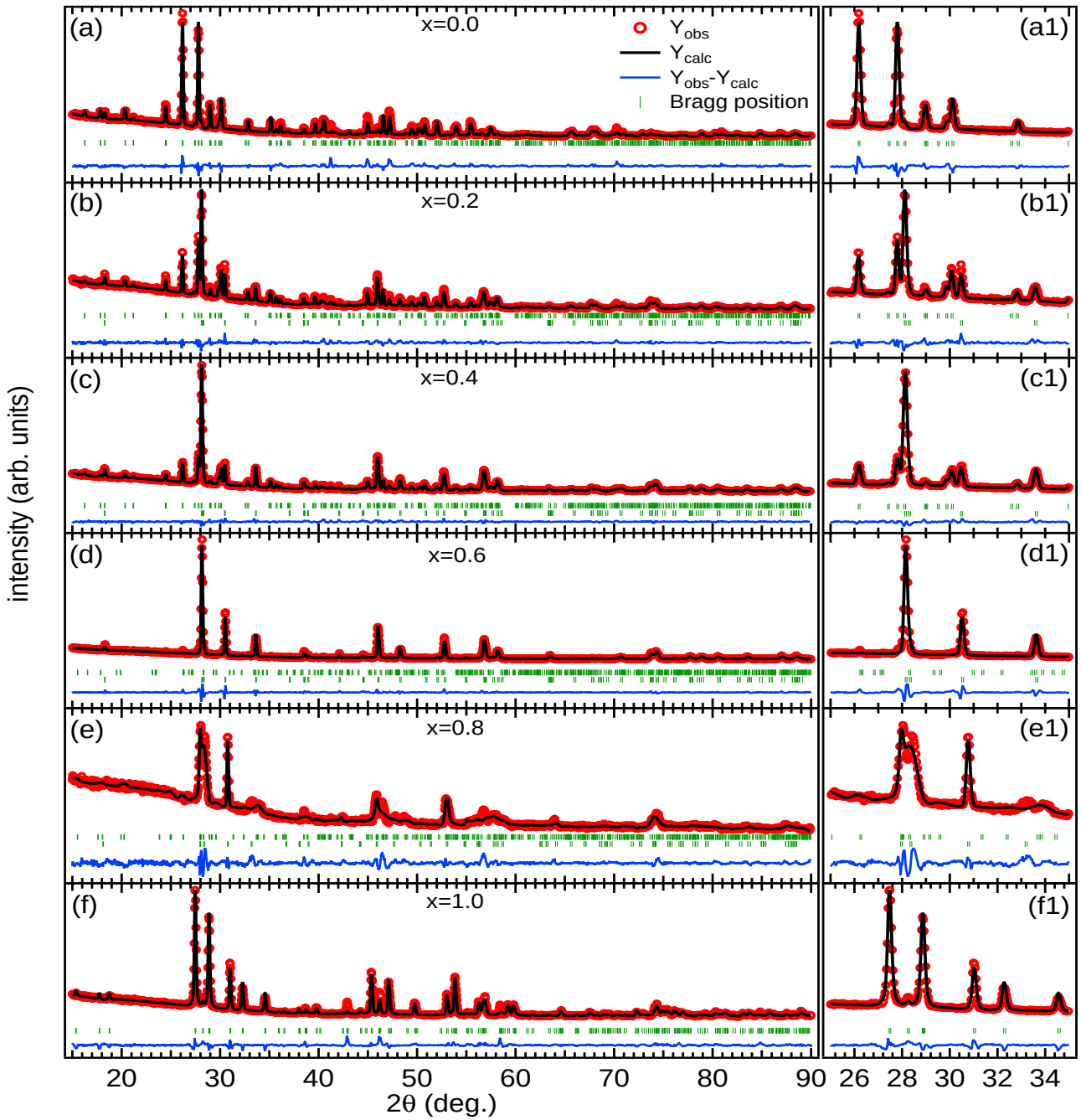

FIG. 1. (a–f) The Rietveld refined x-ray diffraction patterns of $LaV_{1-x}Nb_xO_4$ ($x = 0$–1) samples. The experimental, simulated, and difference between the experimental and simulated spectra are shown by open red circles, black solid lines, and blue solid lines, respectively. The Bragg positions corresponding to their respective space groups are shown by green vertical markers. In the side of each panel (a1–f1), we show partial amplification for clarity between $2\theta = 25$–35° for all the samples.

is clearly observed in three different phases depending on the substitution of Nb^{5+} at the site of V^{5+}, and also been reported by Aldred *et al.* in ref. [21]. We observe that the structure changes from $m - m$ to $m - f$ with increase in the Nb^{5+} concentration from 0 to 100%. For the $x = 0$ and 1, a pure monoclinic phase is obtained with no impurity peaks. In between $x = 0.2$ and 0.8, a monoclinic monazite ($m - m$) and a tetragonal scheelite ($t - s$) type phases coexist. Moreover, all the Bragg reflections of $LaVO_4$ and $LaNbO_4$ can easily be indexed to the $m - m$ and $m - f$ phases with the space group $P2_1/n$ and $I2/a$ for the $x = 0$ and 1 samples, respectively. We find that the contribution of space group $I4_1/a$ is increasing from the $x = 0.2$ to 0.8 samples (see Table I)

due to the increase of $t-s$ phase with the substitution of Nb^{5+} at the site of V^{5+} in $LaV_{1-x}Nb_xO_4$ samples. So, it can clearly be seen that the $LaV_{1-x}Nb_xO_4$ samples crystallize in monoclinic monazite $(m-m)$ type $(x = 0)$, coexistence of monoclinic monazite $(m-m)$ and tetragonal scheelite $(t-s)$ type $(0.2{\leq}x{\leq}0.8)$, and monoclinic fergusonite $(m-f)$ type $(x = 1)$ [21, 30].

Moreover, for the $x = 0$ sample, the $m-m$ type crystal structure shows high intensity diffraction peaks corresponding to (200) as well as (120) crystal planes at 26.17° and 27.78°, respectively. However, the $t-s$ type structure contains a peak corresponding to (112) plane at 28.08°, and the $m-f$ type structure shows high intensity peaks for the $(\bar{1}21)$ and (121) planes at 27.5^o and 28.9^o respectively. In the measured XRD pattern for the $x = 0.2$ to 0.8 samples, the diffraction peaks for the (200), (120) and (112) planes are present, which clearly indicate the co–existence of both the $m-m$ or $t-s$ type structures. The presence of (110) plane at 17.65° for the $x = 0.2$ and 0.4 samples is due to the dominance of $m-m$ type structure in the $LaV_{1-x}Nb_xO_4$. The (200) and (120) peaks are also present in these samples; however, their intensity decreasing with higher concentration of Nb substitution and become negligible for the $x \geq 0.6$ sample. As the Nb^{5+} concentration becomes more than V^{5+} concentration the $t-s$ type structure dominates, which results in the reduction/absence of diffraction peaks corresponding to (200) and (120) planes. The variation in peak intensity corresponding to (200) and (120) crystal planes and the presence of (112) plane indicate the co–existence of $t-s$ and $m-m$ type structures for the $x = 0.2$ to 0.8 samples. This also validates that the $m-m$ type structure ($P2_1/n$) is decreasing and $t-s$ type structure ($I4_1/a$) is increasing with increasing the Nb concentration, i.e., from the $x = 0.2$ to 0.8 samples. The determined % of phases by Rietveld refinement of XRD data is presented in Table I. For the $x = 1$ sample, the presence of $(\bar{1}21)$ and (121) peaks further confirms the $m-f$ type structure of $LaNbO_4$ and consistent with literature [31].

Note that pure $m-m$ and $m-f$ phases are observed for the $x = 0$ and 1 samples, respectively. However, for the $x = 0.2$–0.8 samples, both the monoclinic and scheelite-tetragonal phases coexist in a certain ratio. These results reveal that $LaV_{1-x}Nb_xO_4$ samples undergo three phase transformation; monoclinic monazite $(m-m)$ type (for the $x = 0$), two-phase equilibrium of monoclinic monazite $(m-m)$ and tetragonal scheelite $(t-s)$ type $(0.2{\leq}x{\leq}0.8)$, and monoclinic fergusonite $(m-f)$ type (for the $x = 1$) with increased substitution of Nb^{5+} at the V^{5+} site. It is quite interesting to note that small amount of Nb^{5+} substitution can transform $LaVO_4$ from $m-m$ phase to mix of $m-m$ and $t-s$ phases. It has also been observed that $LaNbO_4$ shows structural transition from monoclinic to a tetragonal phase at ∼495°C. This structural transformation is very important in governing the protonic conductivity of $LaNbO_4$ [32]. For some compositions of $LaV_{1-x}Nb_xO_4$, this transition temperature shifts near room temperature. The reported temperature-dependent XRD measurements also suggest that at $x = 0.75$ (25% substitution of V^{5+} at Nb^{+5} sites in $LaNbO_4$) [21], it possess a tetragonal structure at room temperature as its transition temperature is 250 K. The XRD pattern below 250 K shows some residual intensity (broadened lines) of tetragonal structures because of precursor effects. Similarly, we can see broad peaks in XRD patterns for the $x = 0.8$ sample due to the above mentioned effect [21]. As we increase the Nb concentration, we find some new peaks appearing in the $x = 0.2$ sample at 33.56^o, 52.68^o, 56.69^o, and 58.06^o. All these peaks are the symbols of t–s structure that belongs to (020), (116), (312), and (224) planes, respectively [33]. These peaks maintained up to the $x = 0.8$ sample, which confirms presence of some $t-s$ phase, and also indicate the substitution-induced phase transformation. This is an important finding that $LaNbO_4$ can possess a tetragonal structure at room temperature by just 20% replacement of Nb^{5+} sites by the V^{5+} sites. This result opens the possibility for a wide range of applications of $LaNbO_4$ at room temperature. All these patterns discussed above suggest that substitution of larger Nb^{5+} ($r = 0.48$ Å) ion for V^{5+} ($r = 0.36$ Å) affects the lattice constant of $LaV_{1-x}Nb_xO_4$ and confirms the transformation of 3 different phases with increasing concentrations of Nb^{5+}.

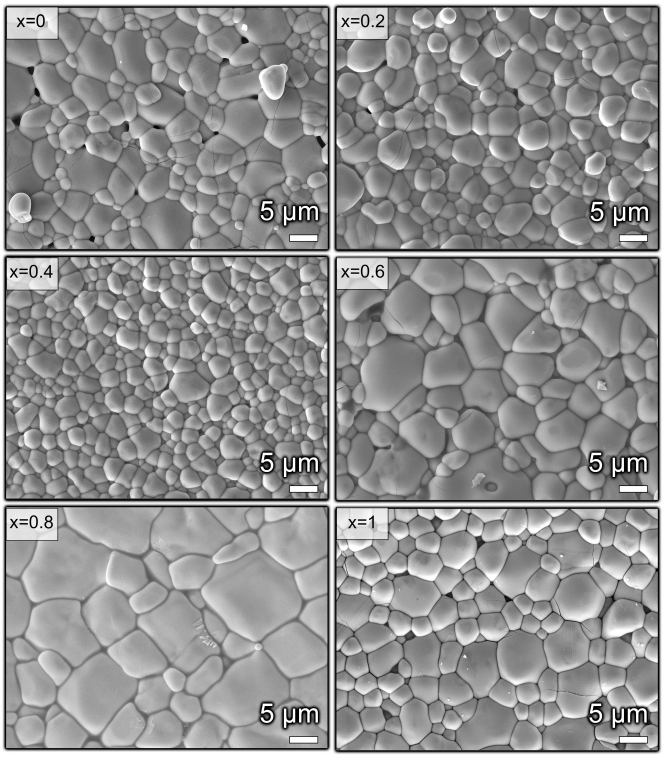

FIG. 2. The scanning electron microscope images of the $LaV_{1-x}Nb_xO_4$ ($x = 0$–1) samples.

The scanning electron microscope images of the $LaV_{1-x}Nb_xO_4$ for the $x = 0$–1 are shown in Fig. 2, which depict the closed packed surface morphology in all the

TABLE I. The Rietveld refinement parameters of polycrystalline $LaV_{1-x}Nb_xO_4$ (x = 0–1) samples with Nb substitution induced metastable tetragonal–scheelite phase for the $x = 0.2$ to 0.8 samples, determined using the FullProf software.

x	χ^2	Space Group	a (Å)	b (Å)	c (Å)	β(°)	Volume (Å^3)
0	1.09	$P2_1/n$	7.042(3)	7.276(4)	6.724(7)	104.88 (6)	333.033(5)
0.2	2.63	$P2_1/n$ - 84% $I4_1/a$ - 16%	7.046(1) 5.336(1)	7.278(2) 5.336(1)	6.733(3) 11.731(2)	104.91(1) 90	333.685(4) 334.042(4)
0.4	2.46	$P2_1/n$ - 78% $I4_1/a$ - 22%	7.043(0) 5.332(3)	7.276(3) 5.332(3)	6.732(4) 11.735(2)	104.91(2) 90	333.397(3) 333.509(6)
0.6	3.70	$P2_1/n$ - 45% $I4_1/a$ - 55%	6.818(9) 5.329(8)	7.596(5) 5.329(8)	8.030(0) 11.714(8)	105.21(7) 90	401.383(6) 332.787(0)
0.8	4.31	$P2_1/n$ - 4% $I4_1/a$ - 96%	6.878(5) 5.375(4)	7.459(4) 5.375(42)	7.679(8) 11.624(0)	105.61(1) 90	379.517(2) 335.869(7)
1	4.91	I2/a	5.558(5)	11.529(1)	5.201(8)	93.99(2)	332.546(3)

samples and some variation in the particle size is clearly visible. The pores are clearly visible from the top view of the surface. We can see that with the increase in Nb^{5+} concentration, the particle size slightly decreases from $x = 0$ to $x = 0.4$ sample, then increases and becomes maximum at $x = 0.8$ and again decreases for the $x = 1$ sample. An average particle size (D) of $LaV_{1-x}Nb_xO_4$ is 5.14 µm for the $x = 0$, 4.22 µm for the $x = 0.2$, 3.56 µm for the $x = 0.4$, 8.73 µm for the $x = 0.6$, 11.31 µm for the $x = 0.8$, and 5.70 µm for the $x = 1$ samples. It is found that the change in crystal surface morphology of $LaV_{1-x}Nb_xO_4$ samples with increasing Nb^{5+} concentration causes variation in the particle size and shape.

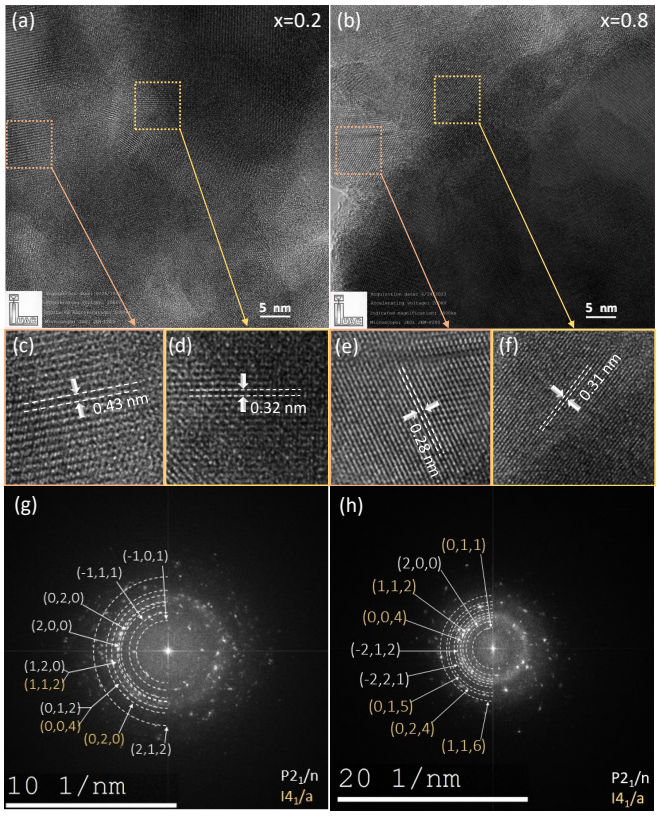

FIG. 3. The HR-TEM images of $LaV_{1-x}Nb_xO_4$ for the (a) $x = 0.2$ and (b) $x = 0.8$ samples. The magnified view of HR-TEM images in (c, d) for the $x = 0.2$ sample, and (e, f) for the $x = 0.8$ sample. (g, h) The SAED patterns for the $x = 0.2$ and 0.8 samples, respectively.

Further, in Figs. 3 (a, b) we display the HR-TEM images indicating distinct sets of planes with characteristic spacing for the $x = 0.2$ and 0.8 samples. The images in Figs. 3(c, d) and (e, f) for the samples $x = 0.2$ and $x = 0.8$, respectively, show these plane sets in magnified view. The spacing between the planes is determined using ImageJ software, and we find the $d-$spacings of 0.43 and 0.32 nm for the (-1,1,1) and (1,2,0) planes in the $P2_1/n$ phase for the $x = 0.2$ sample, and 0.28 and 0.31 nm for the (0,0,4) and (1,1,2) planes in the $I4_1/a$ phase for the $x = 0.8$ sample. However, these planes only correspond to the dominating phase of the mixed-phase samples. The selected area electron diffraction (SAED) patterns in Figs. 3(g, h) indicate the contributions from both the phases. The indexed (h, k, l) planes that relate to $P2_1/n$ are coloured in white and yellow colour is designated to the $I4_1/a$ space group, as marked in Figs. 3(g, h). We find that the analysis of HR-TEM and SAED results is consistent with the XRD refinement data for these samples, as presented in Figs. 1(b, e).

The Raman spectra of $LaV_{1-x}Nb_xO_4$ measured at three different excitation wavelengths, 532 nm, 633 nm, and 785 nm are presented in Fig. 4 for all the samples (x = 0–1). Three different excitation wavelengths are used to distinguish the fluorescence effect on the Raman signal and to avoid the background effects from the sample. We use Lorentzian line shape function to deconvolute and fit the observed individual Raman peaks, as marked in Table I. We find that all the specific Raman peak positions (Raman shift) are independent of excitation wavelength for a sample, which confirm their inherent characteristic of that particular sample, as shown in Fig. 4. The intensity of the modes may vary due to several reasons like the polarizability of the molecule, ex-

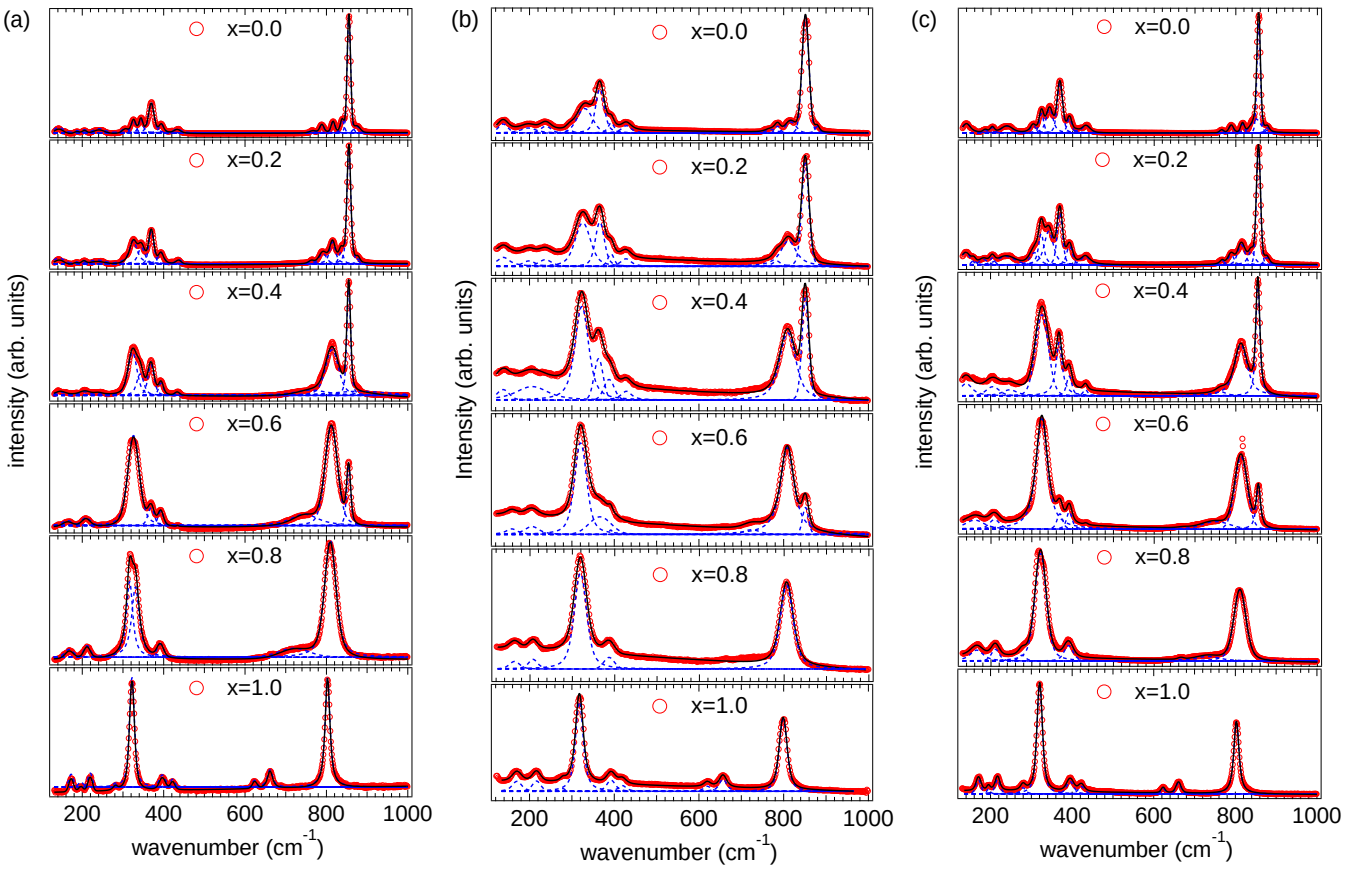

FIG. 4. The room temperature Raman spectra of $LaV_{1-x}Nb_xO_4$ ($x = 0$ to 1) samples using (a) 532 nm, (b) 633 nm, and (c) 785 nm excitation wavelengths. The dotted blue lines represent the Lorentzian line shape to deconvolute the individual modes.

citation wavelength of the laser source, and the concentration of the active group [34]. Though there are minor changes in the intensity variation of Raman modes measured with different excitation wavelengths, we can see that Raman active peaks are changing systematically for all the measured samples in Fig. 4.

In the measured spectra we see 20 peaks corresponding to $LaVO_4$ and 17 peaks for $LaNbO_4$. According to the Group theory calculations $LaVO_4$ contains 72 vibrational modes and out of them, 36 modes are Raman active modes ($18A_g + 18B_g$) [35–37] (here, A and B denote symmetric and antisymmetric vibrations about the principal axis of symmetry and subscripts g indicates that the vibrations are symmetric relative to a symmetry center, respectively). All the 20 Raman peaks for the $x = 0$ sample are represented from S_0 to S_{19}, as shown in the Table II. The theoretical approach predicted that the $8A_g$+$10B_g$ modes are for $m - f$ structure, and 13 Raman-active modes in $t - s$ structure (as observed in the $x = 0.6$ sample), which are summarized in Table II. The reason for the absence of some of the peaks could be due to the overlap of several A_g and B_g modes and their low Raman scattering cross-section. All the assignments related to each Raman peak in $LaV_{1-x}Nb_xO_4$ are summarised in Table III. We can see in Table II that the S_0 mode (127.24 cm^{-1}) is present only in $LaVO_4$ and $LaNbO_4$ samples and absent for rest of the intermediate samples. The reason for origin of S_0 mode is translational motion of La atoms in the monoclinic phase. All the concentrations from $x = 0.2$ to 0.8 in $LaV_{1-x}Nb_xO_4$ results in the formation of $t - s$ type structure or $m - m$ and $t - s$ in equilibrium type structure. So, the formation of mixed phase may result in the disappearance of S_0 mode. The S_{18} is the most intense mode for the $LaVO_4$ sample, which decreases with Nb substitution. Whereas, we find that the intensity of S_{16} mode increases with Nb substitution and the same becomes the most intense mode for the $LaNbO_4$ sample, as can be seen in Fig. 4(a). For the $x = 0.8$ sample, the S_{18} mode completely disappears, which indicates that crystal phase transformation from a mixed phase of $m - m$ and $t - s$ in equilibrium to turning into an approximately pure (96%) $t - s$ phase [38]. This behaviour of S_0, S_{16} and S_{18} corroborate with the structural phase transformation with Nb^{+5} substitution, as has been observed in XRD analysis. Furthermore, the presence of S_8, S_9, S_{10}, S_{13}, S_{14}, S_{15}, S_{17} and S_{18} modes in the $x = 0$ sample confirms the existence of VO_4^{3-} ions since none of these modes are visible in $LaNbO_4$ [39–42].

All the Raman peaks arise due to different vibrational modes, i.e., bonds between different constituent elements,

TABLE II. The experimentally observed frequencies ω_{obs} of the individual Raman modes in $LaV_{1-x}Nb_xO_4$ ($x = 0$–1) samples measured at room temperature.

x	0	0.2	0.4	0.6	0.8	1
Peak	ω_{obs}	ω_{obs}	ω_{obs}	ω_{obs}	ω_{obs}	ω_{obs}
S_0	$B_g(127.24)$					$B_g(121.86)$
S_1	$A_g(141.99)$	$A_g(140.66)$	$A_g(140.66)$	$A_g(140.66)$		
S_2	$B_g(154.05)$	$B_g(155.39)$	$B_g(152.71)$			
S_3	$A_g(187.44)$	$A_g(187.44)$	$A_g(186.11)$			
S_4	$B_g(206.07)$	$B_g(206.07)$	$B_g(206.079)$	$B_g(207.40)$	$B_g(211.39)$	$A_g(219.35)$
S_5	$A_g(235.26)$	$A_g(233.94)$	$A_g(233.94)$			
S_6	$A_g(245.84)$	$A_g(244.52)$	$A_g(244.52)$			
S_7	$B_g(305.11)$	$B_g(305.11)$				
S_8	$A_g(326.07)$	$A_g(326.07)$	$A_g(326.07)$	$A_g(324.76)$	$A_g(328.69)$	
S_9	$A_g(344.36)$	$A_g(344.36)$	$A_g(344.36)$			
S_{10}	$A_g(370.41)$	$A_g(370.41)$	$A_g(369.11)$	$A_g(369.11)$		
S_{11}	$B_g(393.78)$	$B_g(393.78)$	$B_g(391.19)$	$A_g(391.19)$	$A_g(388.60)$	$B_g(396.38)$
S_{12}	$A_g(420.96)$	$A_g(418.37)$	$A_g(418.37)$			
S_{13}	$B_g(436.44)$	$B_g(435.15)$	$B_g(433.86)$	$B_g(436.44)$		
S_{14}	$A_g(765.31)$	$A_g(765.31)$	$A_g(766.54)$	$A_g(766.54)$		
S_{15}	$B_g(788.68)$	$B_g(788.68)$	$B_g(788.68)$	$B_g(788.68)$		
S_{16}	$A_g(816.86)$	$A_g(815.63)$	$A_g(814.41)$	$A_g(811.96)$	$A_g(807.07)$	$A_g(803.39)$
S_{17}	$A_g(840.06)$	$A_g(840.06)$	$A_g(840.06)$	$A_g(840.06)$		
S_{18}	$B_g(855.88)$	$B_g(855.88)$	$B_g(854.67)$	$B_g(854.67)$		
S_{19}	$B_g(874.10)$	$B_g(874.10)$	$B_g(874.10)$			
S_{20}				$A_g(170.10)$	$A_g(168.76)$	$A_g(174.10)$
S_{21}						
S_{22}					$A_g(108.41)$	$A_g(105.72)$
S_{23}						$B_g(164.75)$
S_{24}						$B_g(198.09)$
S_{25}						$B_g(282.77)$
S_{26}					$B_g(316.91)$	$A_g(322.14)$
S_{27}						$A_g(331.30)$
S_{28}					$A_g(345.67)$	$B_g(343.06)$
S_{29}						$B_g(405.44)$
S_{30}						$A_g(422.25)$
S_{31}						$B_g(623.49)$
S_{32}						$A_g(648.58)$
S_{33}				$B_g(669.83)$	$B_g(661.08)$	$B_g(661.08)$

i.e., the La^{3+}, V^{5+}, Nb^{5+} and O^{2-}. The comparison of experimentally observed peak positions of distinct Raman modes, fitted using Lorentzian function, with the reported data [9, 35, 43–45], shows a high degree of similarity, as presented in Table II. In the $m - m$ structured $LaVO_4$ crystal, nine O^{2-} atoms are linked to La^{3+} whereas four O^{2-} atoms and V^{5+} are joined in a tetrahedral shape. There are four different O^{2-} locations and it is bound in a 3-coordinate geometry to two equivalent La^{3+} and one equivalent V^{5+} atoms at the first site. Also, it is bound to two comparable La^{3+} and one equivalent V^{5+} atoms in a deformed single-bond geometry in the second site. Three comparable La^{3+} and one equivalent V^{5+} atoms are linked to O^{2-} in a 3-coordinate geometry at the third O^{2-} site and it is bound in a deformed single-bond geometry to three equivalent La^{3+} and one equivalent V^{5+} atom in the fourth O^{2-} site [46]. In the $m - f$ structured $LaNbO_4$ crystal, the La^{3+} is joined to eight O^{2-} atoms in an 8-coordinate geometry and six O^{2-} atoms are bound to Nb^{5+} to create the deformed, edge-sharing NbO_6 tetrahedra. There are two different sites for O^{2-} and it is linked in a 4-coordinate geometry to two equivalent La^{3+} and two equivalent Nb^{5+} atoms at the first O^{2-} site. Also, it is bound in a 3-coordinate geometry to two equivalent La^{3+} and one Nb^{5+} atoms at the second O^{2-} site. In the analysis of vibrational modes, it has been assumed that the $LaNbO_4$ crystal is made up of La^{3+} cations and NbO_4^{3-} molecular anions [43, 46]. It is revealed experimentally that on the addition of Nb^{5+}, it replaces V^{5+} from its site and distorts $LaVO_4$'s unit cell [30]. The mode of vibrations for $LaVO_4$ is categorised as follows: (I) the zone of high wavenumber (765–874 cm^{-1}) resulting from O-V-O bond's stretching vibration (II) the intermediate (305–436 cm^{-1}) region resulting from O-V-O bond's bending vibration, and (III) the zone of low wavenumber (< 285 cm^{-1}) resulting from La atom's translation modes as the La atoms have high mass [9, 17], and the results are presented in Table III. Similarly, the vibrational modes of $LaNbO_4$ are also categorized as follows: (I) high wavenumber zone (623–803 cm^{-1}) for stretching modes of Nb-O bonds, (II) intermediate zone (322–422 cm^{-1}) for deformation/scissor

TABLE III. Summary of all the 34 Raman active modes and their assignments with the help of literature (cited in the last coloum of the table) for the $LaVO_4$ and $LaNbO_4$ samples.

	$LaVO_4$		$LaNbO_4$		
Peak	ω_{th}	Assignments	ω_{th}	Assignments	Refs.
S_0	$B_g(127)$	Translation mode of La atoms in monoclinic phase	$B_g(125.1)$	Coupled translation-rotational mode of La atoms in monoclinic phase and NbO_4^{3-} around an axis perpendicular to b-axis	[19, 43, 45]
S_1	$A_g(143)$	Translation mode of La–O bonds			[45, 47]
S_2	$B_g(158)$	Translation mode of La–O bonds			[47]
S_3	$A_g(188)$	Translation mode of La–O bonds			[45, 47]
S_4	$B_g(204)$	Translation mode of La–O bonds	$A_g(222.3)$	Translational mode of La–O bonds along b-axis	[43, 48]
S_5	$A_g(230)$	Translation mode of La–O bonds			[47]
S_6	$A_g(252)$	Translation mode of La–O bonds			[45, 47]
S_7	$B_g(316)$	Bending vibration of O–V–O bonds			[45, 49]
S_8	$A_g(336)$	Bending vibration of O–V–O bonds			[45, 49]
S_9	$A_g(355)$	Bending vibration of O–V–O bonds			[45, 49]
S_{10}	$A_g(380)$	Bending vibration of O–V–O bonds			[45, 49]
S_{11}	$B_g(389)$	Bending vibration of O–V–O bonds	$B_g(398.1)$	Triply degenerate deformation mode (Rocking mode of NbO_4^{3-})	[43, 45, 49]
S_{12}	$A_g(423)$	Bending vibration of O–V–O bonds			[45, 49]
S_{13}	$B_g(427)$	Bending vibration of O–V–O bonds			[45, 49]
S_{14}	$A_g(784)$	Stretching vibration of V–O bonds			[50]
S_{15}	$B_g(799)$	Stretching vibration of V–O bonds			[50]
S_{16}	$A_g(806)$	Stretching vibration of V–O bonds	$A_g(805.2)$	Non degenerate Stretching mode of Nb–O bonds	[43, 50–52]
S_{17}	$A_g(836)$	Stretching vibration of V–O bonds			[50]
S_{18}	$A_g(861)$	Non degenerate stretching mode of shortest V–O bonds			[45, 50]
S_{19}	$B_g(892)$	Stretching vibration of O–V–O bonds			[45, 51, 52]
S_{20}			$A_g(177.1)$	Translational mode along b axis	[43]
S_{21}			$B_g(114)$	Rotational mode of NbO_4^{3-} along an axis perpendicular to b-axis	[43]
S_{22}			$A_g(108.6)$	Rotational mode of NbO_4^{3-} along b-axis	[43, 48]
S_{23}			$B_g(170)$	Translational mode parallel to ac-plane	[43]
S_{24}			$B_g(200.2)$	Translational mode parallel to ac-plane	[43]
S_{25}			$B_g(284.9)$	Translational mode parallel to ac-plane	[43]
S_{26}			$A_g(321.7)$	Doubly degenerate scissors mode of NbO_4^{3-})	[43, 48]
S_{27}			$A_g(326.9)$	Doubly degenerate scissors mode of NbO_4^{3-})	[43, 48]
S_{28}			$B_g(344)$	Translational mode parallel to ac-plane	[43]
S_{29}			$B_g(404.9)$	Triply degenerate deformation mode (Rocking mode of NbO_4^{3-})	[43]
S_{30}			$A_g(425.8)$	Triply degenerate deformation mode (Twist mode of NbO_4^{3-})	[43]
S_{31}			$B_g(625.5)$	One of triply degenerate Stretching mode of Nb–O bonds	[43, 48, 51]
S_{32}			$A_g(649)$	One of triply degenerate Stretching mode of Nb–O bonds	[43, 48, 51]
S_{33}			$B_g(664.9)$	One of triply degenerate Stretching mode of Nb-O bonds	[43, 48, 51]

modes of NbO_4^{3-}, and (III) low wavenumber zone (121–282 cm^{-1}) for rotational modes of NbO_4^{3-} and translational lattice modes that include the relative translations of anions and cations [43].

The $LaNbO_4$ contains a total of three different modes; rotational modes of NbO_4^{3-}, vibrational modes of NbO_4^{3-} and translation modes of La–O and O–La–O bonds. The S_0, and S_{22} peaks are visible corresponding to the combined translation-rotational (B_g) and rotational mode (A_g), respectively, while the third rotational B_g mode (S_{21}) is absent in the observed experimental Raman spectra. The vibrational modes can be categorized into (I) doubly degenerated scissor modes, (II) triply degenerated deformation mode, which further splits into a pair of degenerated rocking mode and one twist mode, (III) stretching mode, a non-degenerate and a triply degenerated with increasing order of wave number [43]. The remaining modes are all translational modes. From the Table III, we can easily identify that $LaNbO_4$ Raman modes are matching well with the reported one. Two NbO_4^{3-}

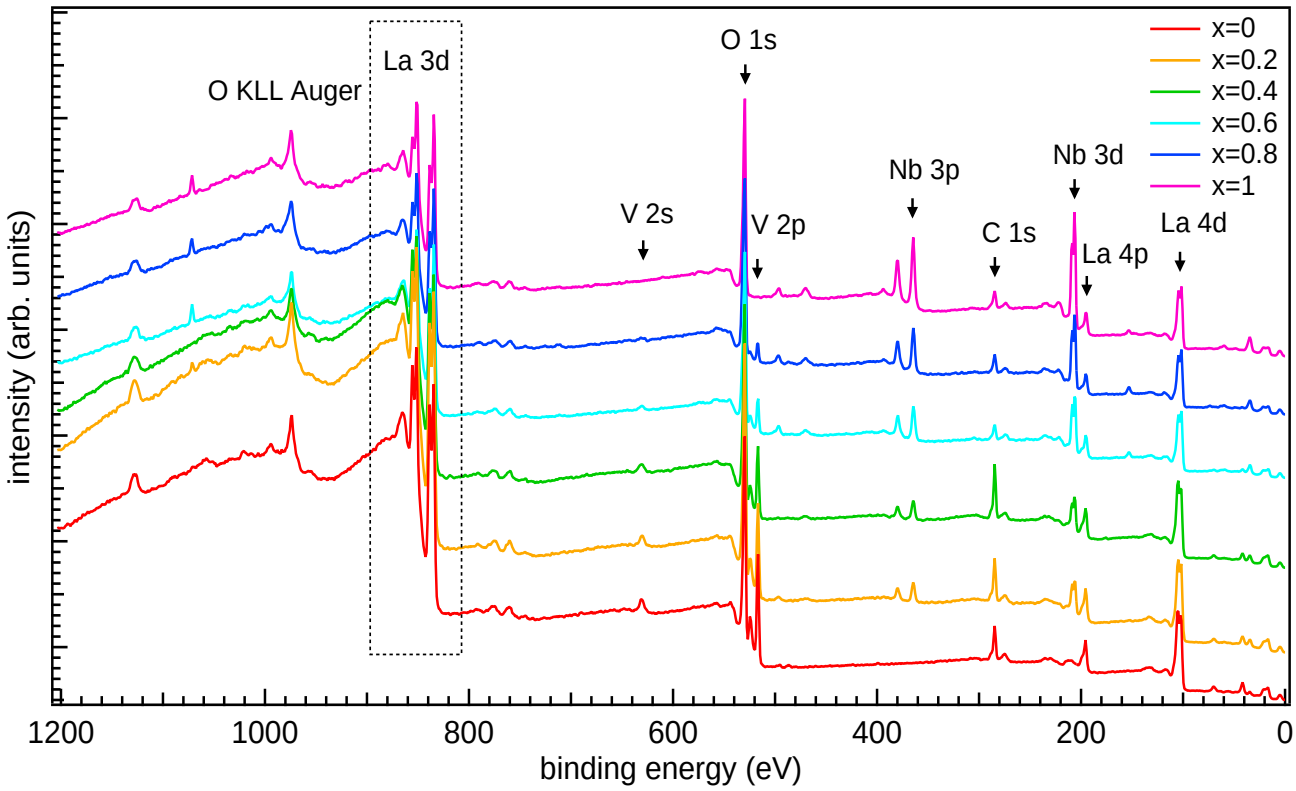

FIG. 5. The room temperature XPS survey spectra of $LaV_{1-x}Nb_xO_4$ ($x = 0$ to 1) samples.

scissor modes with almost degenerated wave numbers are projected to be seen in the A_g spectrum. Out of all, the most obvious choices are S_{26} and S_{27} because the remaining A_g band's wavenumbers are too low to allocate them. In the $LaNbO_4$, as already discussed, the deformation modes are believed to be divided into two almost degenerated rocking modes (S_{11} and S_{29}) with B_g symmetry and a twist mode (S_{30}) with A_g symmetry. These modes are also present in the region of intermediate wave numbers. The stretching modes are high energy vibrations and here they are recognised as S_{16}, S_{31}, S_{32} and S_{33} peaks. As the non-degenerate symmetric mode is expected to provide the strongest band, band S_{16} is allocated to it. The remaining S_{31}, S_{32}, and S_{33} peaks are assigned to other three degenerate stretching modes. The invariance of the S_4, S_{11} and S_{16} peak positions, all through, from the $x = 0$ to 1 samples indicates no effect on translational mode along the $b-$axis, the B_g frequency of VO_4^{3-} and NbO_4^{3-} for rocking and stretching modes. The S_8 peak disappears only in $LaNbO_4$ spectrum because of absence of O-V-O bending vibrations [17, 43]. Interestingly, the S_2, S_3, S_5, S_6, S_9, S_{12} and S_{19} peaks vanished just before Nb concentration exceeds V (at $x = 0.4$) and also S_1, S_{10}, S_{13}, S_{14}, S_{15}, S_{16}, S_{17} and S_{18} peaks vanished just after Nb concentration became more than V. It is quite possible that the low concentration of Nb in the sample results in the weakening and then disappearance of some of the spectral peaks. Due to the same reason some new peaks (S_{20} and S_{33}) appeared in $x = 0.6$–1 samples. Furthermore, the S_{20} peak arises due to translational mode along the $b-$axis, and S_{33} peak appeared due to one of three triply degenerate stretching modes of NbO_4^{3-} in the sample.

The most intense peak in $LaNbO_4$ (S_{16}) and $LaVO_4$ (S_{18}) at higher wavenumber is due to the stretching of Nb-O_t and V-O_t bonds, where O_t represents the oxygen atoms in the terminal position [53]. The terminal position of oxygen is that where it connects the LaO_8 dodecahedra and NbO_6 octahedra in case of $LaNbO_4$ and LaO_9 muffin [54] and VO_4 tetrahedra in case of $LaVO_4$ [53]. Since the VO_4 tetrahedra appears to be intrinsic in the peak broadening, it has been found that this broadening in the Raman peaks spreads along samples with intermediate Nb and V compositions. However, in certain samples, Nb^{5+} and V^{5+} cation-related variables may also play an important role in the increasing the broadening of the peak. The broad peaks are made up of multiple modes which are normally difficult to distinguish from one another [53]. The strongest peak of $LaVO_4$ (S_{18}) is in the high wavenumber region which lies approximatly 52.5 cm^{-1} on higher side of the spectrum with respect to the strongest peak of $LaNbO_4$ (S_{16}). This difference in wavenumber (Δ) is related to average bond length (d) of the atoms by $\Delta \propto 1/d^{3/2}$, as stated by the Badger

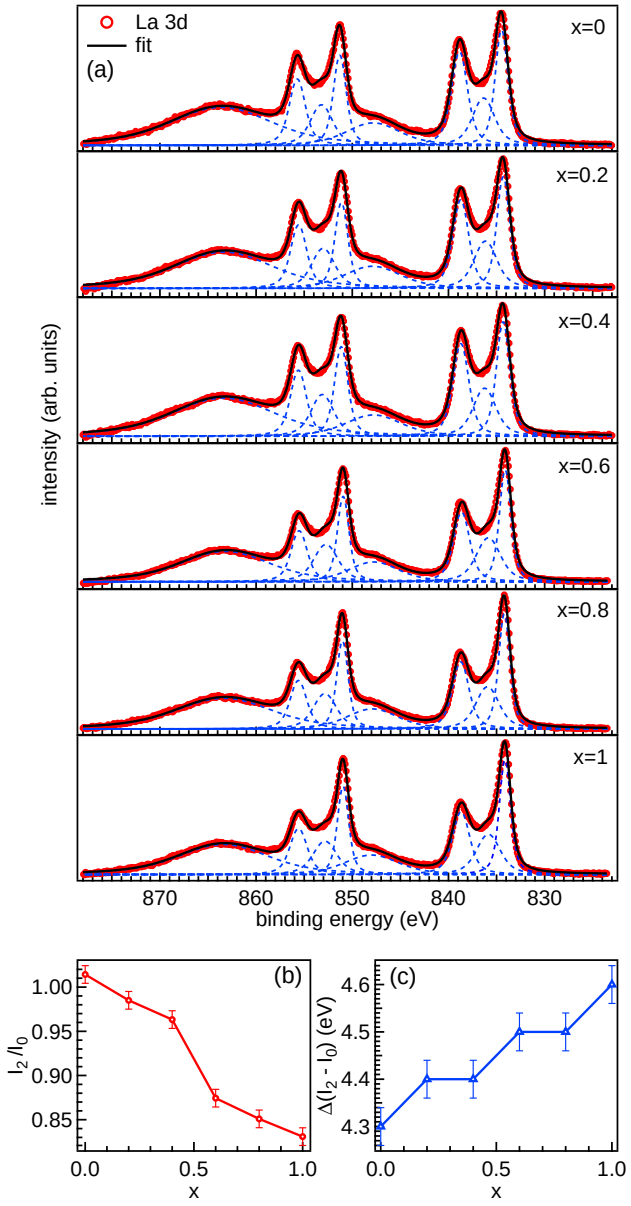

FIG. 6. (a) The La 3d core-level spectra of $LaV_{1-x}Nb_xO_4$, $x = 0$–1 samples. (b) The intensity ratio I_2/I_0, and (c) energy separation I_2 - I_0 as a function of doping level x. The fitted spin-orbit split components are also shown for each sample.

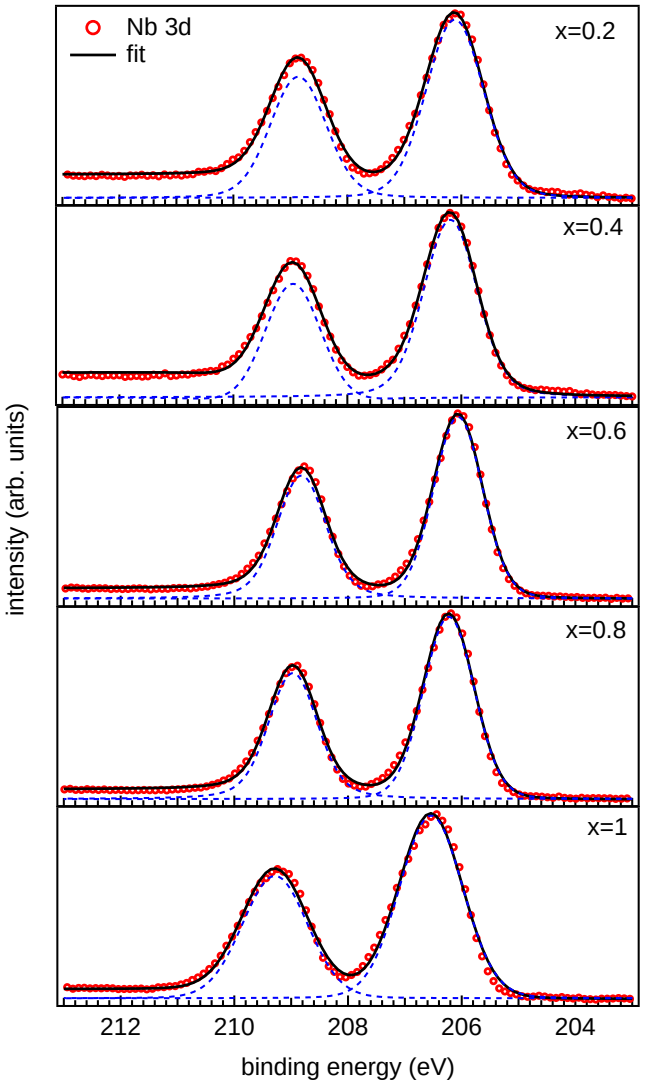

FIG. 7. Tha Nb 3d core level spectra of $LaV_{1-x}Nb_xO_4$, $x = 0$–1 samples. The fitted spin-orbit split components are also shown for each sample.

rule [55]. The bond lengths V–O_t in $LaVO_4$ and Nb–O_t in $LaNbO_4$ are ∼1.72 Å [9] and ∼1.90 Å [53], respectively. The changes observed in the Raman sepctra of the samples is quite consistent with the Badger's rule.

Finally we use x-ray photoemission spectroscopy (XPS) to investigate the electronic structure by measuring the survey scan and particular elemental core-level spectra of all the prepared samples. The identified peaks in the survey spectra according to their binding energies are labeled and are in agreement with reported values, as shown in Fig. 5. The characteristic La 3d peaks cluster (830–870 eV), 4d (4$d_{5/2}$ at 101 eV and 4$d_{3/2}$ at 104 eV), and 4p (centered around 195 eV) [56]. The presence of these peaks of La are clearly visible for every synthesised sample, and they are all remarkably comparable. A consistent rise in Nb 3d (discussed later) and Nb 3p (3$p_{3/2}$ at 364 eV and 3$p_{1/2}$ at 379 eV) is observed along with an increase in Nb doping and this feature of Nb is absent in the $x = 0$ sample [57]. For the V 2p (2$p_{3/2}$ at 517 eV and 2$p_{1/2}$ at 525 eV) and V 2s (630 eV) core-level peaks, the reverse behavior is anticipated and it is quite evident as clearly visible in Fig. 5 [58]. The Voigt function has been used to fit the core level spectra of the constituent elements. The fitted La 3d core-levels are shown in Fig. 6(a). The spin-orbit splitting peaks present in all the samples, have been de-convoluted at binding energies 834.3±0.2 eV, 836.0±0.3 eV, 838.7±0.1 eV, 847.9±0.1 eV, 851.1±0.2 eV, 853.0±0.3 eV, 855.6±0.1

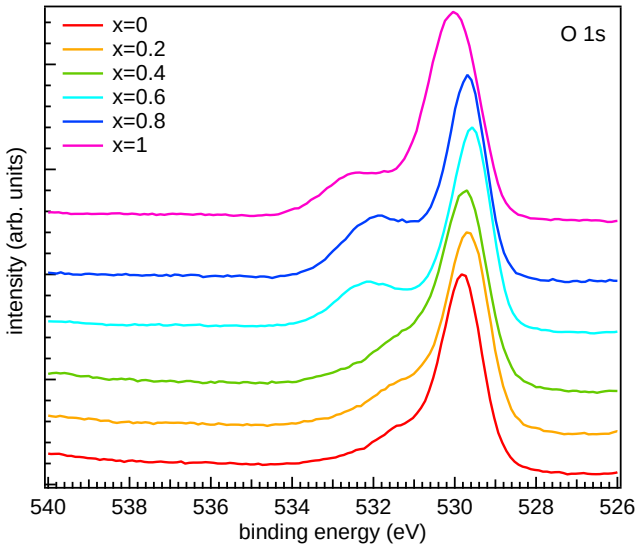

FIG. 8. Tha O 1*s* core level spectra of $LaV_{1-x}Nb_xO_4$, $x = 0$–1 samples. Each spectrum is shifted vertically for the clarity.

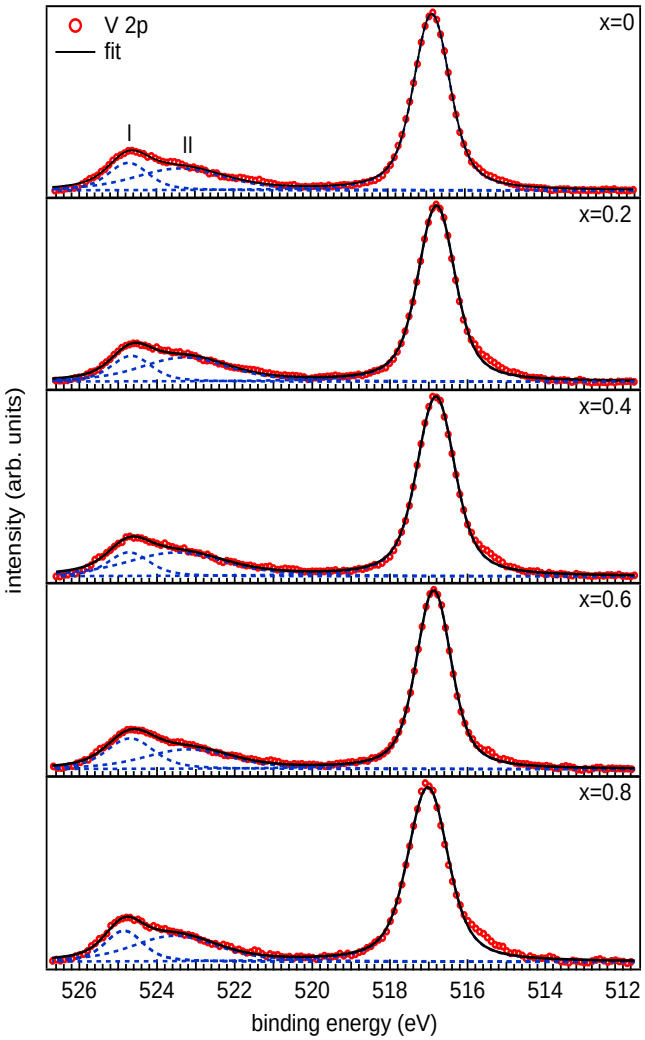

FIG. 9. Tha V 2*p* core level spectra of $LaV_{1-x}Nb_xO_4$, $x = 0$–1 samples. The fitted spin-orbit split components are also shown for each sample.

eV, and 863.4±0.2 eV (average B.E. of all the samples ± ΔB.E., calculated for the $x = 0$–1 samples). The broad diffusive satellite peaks at 847.7 eV and 863 eV in the locality of La 3*d* core-level are coming from plasmons. Because of the two final states I and II, and the subsequent spin-orbit splitting between each state, making the structure complex. The primary strong peaks ($3d_{5/2}$ at 834.3 eV and $3d_{3/2}$ at 851.1 eV, respectively) are associated with the final state I (La^{4+} $3d^94f^0$, L), which involves electron transfer to the continuum from the 3*d* core-level. The peaks at higher binding energies are features of final state II (La^{3+} $3d^94f^1$, L, -e) and this feature is experimentally unresolved which indicates multiplet structure, as has been suggested by Mullica *et al.* [56]. This corresponds to the electron transfer from ligand (L, O_{2p} in our case) valance band to the empty 4*f* orbitals of La [56, 59]. This multiplet structure of state II is composed of two bonding and anti-bonding states. The prominent signals at higher binding energies ($3d_{5/2}$ at 838.7 eV and $3d_{3/2}$ at 855.6 eV) are due to bonding of state II and the weak signals at lower binding energies ($3d_{5/2}$ at 836.0 eV and $3d_{3/2}$ at 853 eV) are because of anti-bonding. The average energy difference (over La core-level spectra of all the samples) between these three pairs of peaks is nearly the same (16.9 eV) for the state I, state II bonding, and state II anti-bonding, respectively. This verifies the unaltered spin-orbit energy splitting of the states of La on Nb substitution [60]. Interestingly, we find a significant and systematic change in the intensity variation of the peak at 838.7 eV (I_2) relative to the primary peak at 834.3 eV (I_0) with Nb doping. The metal-ligand orbital overlaps are reported to be accountable for such doping-induced intensity variations [61, 62] where strong ligands are found to populate the (La^{3+} $3d^94f^1$, L, -e) state, intensifying I_2 [63]. The intensity ratio I_2/I_0 is shown in Fig. 6(b), which shows a consistent decrease as a function of doping x. This signifies that with Nb substitution, the extent of overlapping between La(4f)-O(2p) orbitals decreases monotonically. This conclusion can also be drawn from the trend in the energy separation between I_2 and I_0 as a function of x, as shown in Fig. 6(c). However, the separation is minute in the subsequent samples, but for the $x = 0$ and $x = 1$ the energy difference (I_2 - I_0) is found to be of the order of 0.3 eV. The value of I_2 - I_0 was found to be varying for a variety of La-containing compounds majorly because of the crystal structure, like 3.8 eV for $La_{0.5}Sr_{0.5}Co_{1-x}Nb_xO_3$ and 5.3 eV $La_{1.85}Ba_{0.15}CuO_4$ [60, 62]. Notably, this energy separation could be related to the ease of electron transfer between the ligand and the more ionic state of La, therefore having an opposite trend with the tendency of ligand's overlapping with the La 4*f* orbitals [62].

The Nb 3d core level spectra are shown in Fig. 7 where the spin-orbit doublet of Nb 3d core levels are fitted with a single peak for each component and the calculated peak positions for the Nb-doped samples are found to be $3d_{5/2}$ at 206.2±0.2 eV and $3d_{3/2}$ at 209.0±0.2 eV [64, 65]. This confirms the presence of prevailed 5+ oxidation state of Nb atom [57] in all the samples. However, for the $x = 1$ sample the Nb $3d_{5/2}$ is at a higher binding energy as compared to the other Nb-containing samples, which could be due to the charging effects and the change in chemical environments. Therefore, Atuchin *et al.* characterized the Nb state by using energy difference Δ (Nb $3d_{5/2}$ – O 1s) instead of solely relying on Nb $3d_{5/2}$ binding energy position [66]. The evaluated Δ (Nb $3d_{5/2}$ – O 1s) values are found to be around 323.5 eV. The calculated energy difference with respect to O 1s is independent of the carbon correction. The obtained binding energy difference ≈323.5 eV is reported to be a fairly highest value for the 5+ oxidation state of Nb. We can also see that the error in the value of binding energy position Δ is only 0.1 eV in this case, while for the Nb $3d_{5/2}$, and O 1s, it is 0.3, and 0.2 eV, respectively. In Fig. 8 we can also see that the O 1s peak is shifting to higher binding energy for the $x = 1$ sample as compared to the $x = 0$. Similarly, for the Nb $3d_{5/2}$ core-level, it is shifting to higher binding energy. The Δ(Nb $3d_{5/2}$ - O 1s) value for the $x = 1$ sample is quite consistent for all the samples, which strongly supports the electronic characterization using energy difference with respect to O 1s instead of absolute peak positions.

In Fig. 9, we present the V 2p core level spectra for all the samples, which shows spin orbit components of $2p_{3/2}$, and $2p_{1/2}$ at 516.9 and 524.8 eV, respectively indicating V in 5+ state. Interestingly, an unusual broadening in the V $2p_{1/2}$ component is observed for all the samples, whereas no such additional component is evident in the V $2p_{3/2}$ peak at 516.9 eV. More importantly, the deconvolution of the V $2p_{1/2}$ component reveals that the FWHM of the higher energy feature (denoted by I) (1.2 eV) is nearly the same as that of $2p_{3/2}$ component (1.1 eV). In contrast, the lower energy feature (II) is significantly broader (2.8 eV). Moreover, the area ratio of the combined I and II with $2p_{3/2}$ is close to 1/2, which clearly indicates the intrinsic origin of these two features from the vanadium. In contrast to metallic V 2p core-level, the vanadium based compounds have often been reported to exhibit an anomalous V $2p_{1/2}$ width as a consequence of Coster-Kronig (C-K) transitions [68]. The C-K type transition is a class of Auger transition in which an electron from a higher sub-shell of the same shell fills the core hole [67]. In the present case, the filling of $2p_{1/2}$ core hole by an electron from $2p_{3/2}$ may give rise to the C-K transitions and that can result in an additional feature in the $2p_{1/2}$ component. Therefore, it is likely that the component I is attributed to the core-hole recombination with the screening electrons, analogous to the $2p_{3/2}$, whereas an additional L_2-L_3 (C-K) relaxation process gives rise to the feature II in $2p_{1/2}$ peak [69]. No significant change in these components has been observed with the Nb substitution, indicating the robust nature of the underlined system. Further, the approach of O 1s energy difference is also implemented in this case as for vanadium oxides, the energy difference Δ(V $2p_{3/2}$ - O 1s) is an advantageous reference [70]. The average Δ(V $2p_{3/2}$ - O 1s) magnitude is 12.8∓0.1 eV, which is in good agreement with the literature for V^{5+} oxidation state [71].

CONCLUSIONS

In conclusion, the solid state reaction method was used to prepare $LaV_{1-x}Nb_xO_4$ samples successfully with regular variable Nb^{5+} concentration. The XRD measurements established that the substitution of larger Nb^{5+} ion for V^{5+} affects the lattice constant of $LaV_{1-x}Nb_xO_4$ and goes through three different phase transformations [monoclinic monazite ($m - m$) type ($x = 0$), two-phase equilibrium of monoclinic monazite ($m - m$) and tetragonal scheelite ($t - s$) type ($0.2 \leq x \leq 0.8$) and monoclinic fergusonite ($m - f$) type ($x = 1$)]. The SEM micrographs helped in analyzing that the particle size and shape altered due to the change in crystal phases of these samples with increasing Nb^{5+} concentration. The analysis of HR-TEM and SAED data found to be consistent with the XRD refinement data. The Raman spectra of $LaV_{1-x}Nb_xO_4$ were studied using 532 nm, 633 nm, and 785 nm excitation wavelengths. All the Raman assignments were found to have well-ordered enhancement/diminution with the increase in Nb^{5+} doping. The variation in the intensity as well as appearance/disappearance of the Raman mode with Nb concentration are coinciding with the change in the structural phases, as observed in XRD analysis. This further confirms that the phase transformation in $LaV_{1-x}Nb_xO_4$ agrees with the maximum intensity peak patterns shown in the Raman spectra of these samples and are consistent with the Badger's rule. The XPS analysis reveal the changes in Nb 3d and V 2p core-level spectral intensities of the samples with the increase in Nb^{5+} concentration. The equal spin-orbit energy splitting of the states was confirmed by the average energy difference (over La core spectra of all samples) for state I, state II bonding, and state II anti-bonding and the observed changes in their relative intensities with Nb substitution are due to the metal ligand orbitals overlap. These findings provide valuable insights into the structural and electronic properties of $LaV_{1-x}Nb_xO_4$ samples and their potential use in different fields of practical applications.

ACKNOWLEDGMENT

AS and MS thank MHRD and CSIR, respectively for the fellowship. The authors acknowledge IIT Delhi's FIST (DST, Govt. of India) UFO scheme for providing the physics department with the Raman facility. We

thank the Physics Department at IIT Delhi for the XRD and the Central Research Facility (CRF) for the FESEM, EDX, and XPS. We also thank Ambuj Mishra for providing HR-TEM facility at IUAC, New Delhi. The preparation of the samples was done in a high-temperature furnace (from Nabertherm GmbH, Germany), funded by BRNS through the DAE Young Scientist Research Award (Project Sanction No. 34/20/12/2015/BRNS). RSD acknowledges SERB–DST for the financial support through a core research grant (project reference no. CRG/2020/003436).

[1] E. Varghese, S. Kumar, B. Pathak, and S. Sen, Temperature-induced crystallinity and vibrational properties in samarium orthovanadate, Phys. Rev. B 101 (2020) 174112.

[2] S. Huang, Z. Wang, Q. Zhu, X. Shi, X. Wang, X. Li, X. Sun, and J.-G. Li, A new protocol for templated synthesis of YVO_4:Ln luminescent crystallites (Ln=Eu, Dy, Sm), Journal of Alloys and Compounds 776 (2019) 773.

[3] T. Carbonati, C. Cionti, E. Cosaert, B. Nimmegeers, D. Meroni, and D. Poelman, NIR emitting $GdVO_4$:Nd nanoparticles for bioimaging: The role of the synthetic pathway, Journal of Alloys and Compounds 862 (2021) 158413.

[4] Ajay Kumar, A. Jain, S. M. Yusuf, and R. S. Dhaka, Observation of Anisotropic Thermal Expansion and the Jahn-Teller Effect in Double Perovskites $Sr_{2-x}La_xCoNbO_6$ Using Neutron Diffraction, J. Phys. Chem. Lett. 13 (2022) 3023.

[5] Ajay Kumar, R. Shukla, R. Kumar, R. J. Choudhary, S. N. Jha, and R. S. Dhaka, Probing the electronic and local structure of $Sr_{2-x}La_xCoNbO_6$ using near-edge and extended x-ray absorption fine structures, Phys. Rev. B 105 (2022) 245155.

[6] Ajay Kumar and R. S. Dhaka, Unraveling magnetic interactions and the spin state in insulating $Sr_{2-x}La_xCoNbO_6$, Phys. Rev. B 101 (2020) 094434.

[7] Ajay Kumar, B. Schwarz, H. Ehrenberg, and R. S. Dhaka, Evidence of discrete energy states and cluster-glass behavior in $Sr_{2-x}La_xCoNbO_6$, Phys. Rev. B 102 (2020) 184414.

[8] M. Yi, S.-K. Park, C.-Y. Seong, Y. Piao, and T. Yu, The general synthesis and characterization of rare earth orthovanadate nanocrystals and their electrochemical applications, Journal of Alloys and Compounds 693 (2017) 825.

[9] L. Sun, X. Zhao, Y. Li, P. Li, H. Sun, X. Cheng, and W. Fan, First-principles studies of electronic, optical, and vibrational properties of $LaVO_4$ polymorph, J. Appl. Phys. 108 (2010) 093519.

[10] B. C. Chakoumakos, M. M. Abraham, and L. A. Boatner, Crystal structure refinements of zircon-type MVO_4 (M = Sc, Y, Ce, Pr, Nd, Tb, Ho, Er, Tm, Yb, Lu), J. Solid State Chem. 109 (1994) 197.

[11] C. E. Rice and W. R. Robinson, Lanthanum Orthovanadate, Acta Crystallogr B Struct. Sci. 32 (1976) 2232.

[12] W. Fan, X. Song, Y. Bu, S. Sun, and X. Zhao, Selected-Control Hydrothermal Synthesis and Formation Mechanism of Monazite- and Zircon-Type LaVO4 Nanocrystals, J. Phys. Chem. B 110 (2006) 23247.

[13] C. K. Rastogi, S. K. Sharma, A. Patel, G. Parthasarathy, R. G. S. Pala, J. Kumar, and S. Sivakumar, Dopant Induced Stabilization of Metastable Zircon-Type Tetragonal $LaVO_4$, J. Phys. Chem. C 121 (2017) 16501.

[14] B. Xie, G. Lu, Y. Wang, Y. Guo, and Y. Guo, Selective synthesis of tetragonal $LaVO_4$ with different vanadium sources and its luminescence performance, Journal of Alloys and Compounds 544 (2012) 173.

[15] Suzuki, N., Noritake, T., and Hioki, T. Structural analysis and physical properties of $Sr_{2-x}La_xVO_{4-\delta}$. Journal of Alloys and Compounds 612 (2014) 114.

[16] Liu, H., Yuan, J., Jiang, Z., Shangguan, W., Einaga, H., and Teraoka, Y., Roles of Bi, M and VO_4 tetrahedron in photocatalytic properties of novel $Bi_{0.5}M_{0.5}VO_4$ (M=La, Eu, Sm and Y) solid solutions for overall water splitting. Journal of Solid State Chemistry 186 (2012) 70.

[17] Himanshu Dua, Rishabh Shukla, and R. S. Dhaka, Structural phase transition and its consequences for the optical behavior of $LaV_{1-x}Nb_xO_4$, Phys. Rev. B 103 (2021) 174107.

[18] S. Verma, B. N. Wani, and N. M. Gupta, Synthesis, characterisation, TPR/TPO and activity studies on $LaMn_xV_{1-x}O_{4-\delta}$–catalysts, Appl. Catal. A: Gen. 205 (2001) 295.

[19] D. Errandonea and F. J. Manjón, Pressure effects on the structural and electronic properties of ABX4 scintillating crystals, Progress in Materials Science 53 (2008) 711.

[20] H. Takei and S. Tsunekawa, Growth and properties of $LaNbO_4$ and $NdNbO_4$ single crystals, Journal of Crystal Growth 38 (1977) 55.

[21] A. T. Aldred, Unusual cell volume behavior in the $LaNb_{1-x}V_xO_4$ system, Materials Letters 1 (1983) 197.

[22] R. Haugsrud, and T. Norby, Proton conduction in rare-earth ortho-niobates and ortho-tantalates, Nature Mater. 5 (2006) 193.

[23] L. Hakimova, A. Kasyanova, A. Farlenkov, J. Lyagaeva, D. Medvedev, A. Demin, and P. Tsiakaras, Effect of Isovalent Substitution of La^{3+} in Ca-Doped $LaNbO_4$ on the Thermal and Electrical Properties, Ceramics International 45 (2019) 209.

[24] G. Blasse, and L. H. Brixner, Ultraviolet emission from ABO_4-type niobates, tantalates and tungstates, Chem. Phys. Lett. 173 (1990) 409.

[25] H. Liu, H. Yu, J. Wang, F. Xia, C. Wang, and J. Xiao, $LaNbO_4$ as an electrode material for mixed-potential CO gas sensors, Sensors and Actuators B: Chemical 352 (2022) 130981.

[26] D. Zhou, H.-H. Guo, M.-S. Fu, X.-G. Yao, H.-X. Lin, W.-F. Liu, L.-X. Pang, C. Singh, S. Trukhanov, A. Trukhanov, and I. M. Reaney, Anomalous dielectric behaviour during the monoclinic to tetragonal phase transition in $La(Nb_{0.9}V_{0.1})O_4$, Inorg. Chem. Front. 8 (2021) 156.

[27] J. Xue, Z. Yu, H. M. Noh, B. R. Lee, B. C. Choi, S. H. Park, J. H. Jeong, P. Du, and M. Song, Designing multi-mode optical thermometers via the thermochromic $LaNbO_4$:Bi^{3+}/Ln^{3+} (Ln = Eu, Tb, Dy, Sm) phosphors,

Chemical Engineering Journal 415 (2021) 128977.
[28] S. Ding, Q. Zhang, W. Liu, J. Luo, F. Peng, X. Wang, G. Sun, and D. Sun, Crystal growth and characterization of a mixed laser crystal: Nd-doped $Gd_{0.89}La_{0.1}NbO_4$, RSC Adv. 7 (2017) 35666.
[29] F. B. Xiong, F. X. Xu, H. F. Lin, Y. P. Wang, E. Ma, and W. Z. Zhu, Synthesis and luminescent properties of novel thermal-stable orangish-red-emitting $LnNbO_4$: Sm^{3+} (Ln=La, Y) phosphors, Appl. Phys. A 126 (2020) 908.
[30] P. Sun, P. Dai, J. Yang, C. Zhao, and X. Zhang, Enhanced upconversion luminescence induced by structural evolution of Lanthanum Niobate Phosphor, Ceramics International 41 (2015) 3009.
[31] S. Wachowski, A. Mielewczyk-Gryn, and M. Gazda, Effect of isovalent substitution on microstructure and phase transition of $LaNb_{1-x}M_xO_4$ (M=Sb, V or Ta; $x = 0.05$–0.3), J. Solid State Chem. 219 (2014) 201.
[32] M. Huse, A. W. B. Skilbred, M. Karlsson, S. G. Eriksson, T. Norby, R. Haugsrud, and C. S. Knee, Neutron Diffraction study of the monoclinic to tetragonal structural transition in $LaNbO_4$ and its relation to proton mobility, Journal of Solid State Chemistry 187 (2012) 27.
[33] W. I. F. David, The high-temperature paraelastic structure of $LaNbO_4$, Mater. Res. Bull. 18 (1983) 749.
[34] Rishabh Shukla, Clemens Ulrich, and R. S. Dhaka, Investigation of lattice dynamics, magnetism and electronic transport in β-$Na_{0.33}V_2O_5$, Phys. Rev. B 106 (2022) 125148.
[35] X. Cheng, D. Guo, S. Feng, K. Yang, Y. Wang, Y. Ren, and Y. Song, Structure and stability of monazite- and zircon-type $LaVO_4$ under hydrostatic pressure, Opt. Mater. 49 (2015) 32.
[36] C. C. Santos, E. N. Silva, A. P. Ayala, I. Guedes, P. S. Pizani, C.-K. Loong, and L. A. Boatner, Raman investigations of rare earth orthovanadates, J. Appl. Phys. 101 (2007) 053511.
[37] V. Panchal, S. López-Moreno, D. Santamaría-Pérez, D. Errandonea, F. J. Manjón, P. Rodríguez-Hernandez, A. Muñoz, S. N. Achary, and A. K. Tyagi, Zircon to monazite phase transition in $CeVO_4$: X-ray diffraction and Raman-scattering measurements, Phys. Rev. B 84 (2011) 024111.
[38] R. Okram, N. R. Singh, and Ak. M. Singh, Simple preparation of Eu^{3+}-Doped $LaVO_4$ by ethylene glycol route: A luminescence study, Micro Nano Lett. 6 (2011) 165.
[39] N. Clavier, R. Podor, N. Dacheux, Crystal chemistry of the monazite structure, J. Eur. Ceram. Soc. 31 (2011) 941.
[40] R.K. Selvan, A. Gedanken, P. Anilkumar, G. Manikandan, C. Karunakaran, Synthesis and characterization of rare earth orthovanadate (RVO_4; R = La, Ce, Nd, Sm, Eu and Gd) nanorods/Nanocrystals/Nanospindles by a facile sonochemical method and their catalytic properties, J. Cluster Sci. 20 (2009) 291.
[41] Z. Huang, S. Huang, G. Ou, and W. Pan, Synthesis, phase transformation and photoluminescence properties of Eu:$La_{1-x}Gd_xVO_4$ nanofibers by electrospinning method, Nanoscale 4 (2012) 5065.
[42] L. Wang, Q. Xu, L. Liu, Q. Song, H. Lv, G. Zhu, D. Zhang, Single-hole hollow tetragonal LaVO4:Eu^{3+} microspheres prepared by Ostwald ripening and their luminescence property, J. Lumin. 192 (2017) 1020.
[43] K. Ishii, N. Morita, H. Nakayama, S. Tsunekawa, and T. Fukuda, Raman Spectra of $LaNbO_4$ in the ferroelastic phase and the relaxation after the state shift, Phys. Stat. Sol. (a) 112 (1989) 207.
[44] C. J. Jia, L. D. Sun, Z. G. Yan, Y. C. Pang, S. Z. Lü, and C. H. Yan, Monazite and zircon type $LaVO_4$:Eu nanocrystals-synthesis, luminescent properties, and spectroscopic identification of the Eu^{3+} sites, Eur. J. Inorg. Chem. 18 (2010) 2626.
[45] D. Errandonea, J. Pellicer-Porres, D. Martínez-García, J. Ruiz-Fuertes, A. Friedrich, W. Morgenroth, C. Popescu, P. Rodríguez-Hernández, A. Muñoz, and M. Bettinelli, Phase stability of lanthanum orthovanadate at high-pressure, J. Phys. Chem. C 120 (2016) 13749.
[46] A. Jain, S. P. Ong, G. Hautier, W. Chen, W. D. Richards, S. Dacek, S. Cholia, D. Gunter, D. Skinner, G. Ceder, K. A. Persson, Commentary: the materials project: A materials genome approach to accelerating materials innovation, APL Materials 1 (2013) 011002.
[47] D. Errandonea and A. B. Garg, Recent progress on the characterization of the high-pressure behaviour of AVO_4 orthovanadates, Prog. Mater. Sci. 97 (2018) 123.
[48] J. Pellicer-Porres, A. B. Garg, D. Vázquez-Socorro, D. Martínez-García, C. Popescu, and D. Errandonea, Stability of the fergusonite phase in $GdNbO_4$ by high pressure XRD and Raman experiments, Journal of Solid State Chemistry 251 (2017) 14.
[49] G. Herzberg and G. Herzberg, Infrared and Raman spectra of polyatomic molecules, van Nostrand, New York, **22** 1987.
[50] M. Ishaque Khan, T. Hope, and S. Tabassum, Synthesis, reactivity, X-ray structure and thermal study of the mixed-metal oxide hydrate $[Mn(H_2O)_2V_2O_6]$, Solid State Sciences 1 (1999) 163.
[51] F. D. Hardcastle and I. E. Wachs, Determination of Vanadium-Oxygen bond distances and bond orders by Raman spectroscopy, J. Phys. Chem. 95 (1991) 5031.
[52] L. Liu, M. Knapp, H. Ehrenberg, L. Fang, H. Fan, L. A. Schmitt, H. Fuess, M. Hoelzel, H. Dammak, M. P. Thi, M. Hinterstein, Average vs. local structure and composition-property phase diagram of $K_{0.5}Na_{0.5}NbO_3$-$Bi_{0.5}Na_{0.5}TiO_3$ system, Journal of the European Ceramic Society 37 (2017) 1387.
[53] J. P. Peña, P. Bouvier, and O. Isnard, Structural properties and Raman spectra of Columbite-type $NiNb_{2-x}V_xO_6$ synthesized under high pressure, Journal of Solid State Chemistry 291 (2020) 121607.
[54] A. Ruiz-Martínez, D. Casanova, and S. Alvarez, Polyhedral structures with an odd number of vertices: Nine-coordinate metal compounds, Chem. Eur. J. 14 (2008) 1291.
[55] R. M. Badger, A relation between internuclear distances and bond force constants, The Journal of Chemical Physics 2 (1934) 128.
[56] D. F. Mullica, C. K. C. Lok, H. O. Perkins, and V. Young, X-ray photoelectron final-state screening in $La(OH)_3$: A multiplet structural analysis, Phys. Rev. B 31 (1985) 4039.
[57] P. Steiner and H. Höchst, X-ray excited photoelectron spectra of $LiNbO_3$: a quantitative analysis. Z Physik B 35 (1979) 51.
[58] A. Lebugle, U. Axelsson, R. Nyholm, and N. Mårtensson, Experimental L and M core level binding energies for the

metals ^{22}Ti to ^{30}Zn, Phys. Scr. 23 (1981) 825.

[59] R. Shukla, A. Jain, M. Miryala, M. Murakami, K. Ueno, S. M. Yusuf, and R. S. Dhaka, Spin dynamics and unconventional magnetism in insulating $La_{(1-2x)}Sr_{2x}Co_{(1-x)}Nb_xO_3$, J. Phys. Chem. C 123 (2019) 22457.

[60] Rishabh Shukla and R. S. Dhaka, Evolution of complex magnetic phases and metal-insulator transition through Nb substitution in $La_{0.5}Sr_{0.5}Co_{1-x}Nb_xO_3$, Phys. Rev. B 107 (2023) 165108.

[61] P. V. Kamath and D. D. Sarma, Charge Transfer Satellites in X-Ray Photoelectron Spectra of Lanthanum Compounds, Indian J. Chem. 23A (1984) 292.

[62] R. P. Vasquez, X-Ray Photoemission Measurements of $La_{1-x}Ca_xCoO_3$ (x = 0, 0.5), Phys. Rev. B 54 (1996) 14938.

[63] A. J. Signorelli and R. G. Hayes, X-Ray Photoelectron Spectroscopy of Various Core Levels of Lanthanide Ions: The Roles of Monopole Excitation and Electrostatic Coupling, Phys. Rev. B 8 (1973) 81.

[64] Rishabh Shukla and R. S. Dhaka, Anomalous magnetic and spin glass behavior in Nb-substituted $LaCo_{1-x}Nb_xO_3$, Phys. Rev. B 97 (2018) 024430.

[65] K. Isawa, R. Itti, J. Sugiyama, N. Koshizuka, and H. Yamauchi, Photoelectron spectroscopic study of Sr_xNbO_3, Phys. Rev. B 49 (1994) 3534.

[66] V. V. Atuchin, I. E. Kalabin, V. G. Kesler, and N. V. Pervukhina, Nb 3d and O 1s core levels and chemical bonding in niobates, Journal of Electron Spectroscopy and Related Phenomena 142 (2005) 129.

[67] E. Antonides, E. C. Janse, and G. A. Sawatzky, LMM Auger spectra of Cu, Zn, Ga, and Ge, II. Relationship with the L_{23} photoelectron spectra via the $L_2L_3M_{45}$ Coster-Kronig process, Phys. Rev. B 15 (1977) 4596.

[68] G. A. Sawatzky and D. Post, X-Ray photoelectron and Auger spectroscopy study of some vanadium oxides, Phys. Rev. B 20 (1979) 1546.

[69] M. Ohno, The effect of Coster–Kronig transition on the Auger-photoelectron coincidence spectroscopy spectra of early $3d-$transition metals, Journal of Electron Spectroscopy and Related Phenomena 136 (2004) 221.

[70] J. Mendialdua, R. Casanova, and Y. Barbaux, XPS studies of V_2O_5, V_6O_{13}, VO_2 and V_2O_3, Journal of Electron Spectroscopy and Related Phenomena 71 (1995) 249.

[71] G. Silversmit, D. Depla, H. Poelman, G. B. Marin, and R. De Gryse, Determination of the V 2p XPS binding energies for different Vanadium oxidation states (V^{5+} to V^{0+}), Journal of Electron Spectroscopy and Related Phenomena 135 (2004) 167.

2023 Third International Conference on Secure Cyber Computing and Communication (ICSCCC)

Study and Comparative Analysis of Data Hiding Methods for Animated GIFs

Pratham
Department of Computer Science & Engineering,
Delhi Technological University,
Delhi, India
prathams1310@gmail.com

Nikhil Kansal
Department of Computer Science & Engineering,
Delhi TechnologicalUniversity,
Delhi, India
nikhilkansal09@gmail.com

Nikhil Tawar
Department of Computer Science & Engineering,
Delhi Technological University,
Delhi, India
nikhil.ab24@gmail.com

Rajeev Kumar
Department of Computer Science & Engineering,
Delhi TechnologicalUniversity,
Delhi, India
rajeevkumar@dtu.ac.in

2023 Third International Conference on Secure Cyber Computing and Communication (ICSCCC) | 979-8-3503-0071-0/23/$31.00 ©2023 IEEE | DOI: 10.1109/ICSCCC58608.2023.10176440

***Abstract*—In this paper, we study and comparatively analyze the available data hiding methods for animated GIFs. Since there exist different data hiding techniques, and the choice of technique can greatly affect the security and robustness of the resulting stego-media. So, to provide guidance to the prospective researchers and users, an evaluation of several popular animated GIF based data hiding techniques which include LSB substitution, palette-based, frame-based, among others. Our experiments involve analyzing those data hiding techniques based on their imperceptibility, payload capacity, and resistance to common attacks such as visual inspection and statistical analysis. The findings suggest that while some techniques offer better payload capacity, others provide stronger security and resistance to detection. Finally, we conclude by summarizing the strengths and weaknesses of each technique and providing recommendations for their practical use in various data hiding applications.**

***Index Terms*— Data Hiding, Animated GIFs, LSB (Least Significant Bits), Palette-based Techniques, Frame-based, Robustness.**

I. INTRODUCTION

In today's rapidly evolving digital landscape, the amount of data being produced at an unprecedented rate in the quickly changing digital environment. Data security and integrity are now top priorities because they affect everything from private information to trade secrets. Protecting sensitive information has become increasingly difficult due to the sophistication of cyberthreats and the possibility of unauthorized access, detection, or modification. Techniques for data hiding provide a potent response to these security issues. Data hiding techniques offer a way to shield information from prying eyes and guarantee its confidentiality, integrity, and authenticity by hiding it within unnoticeable carriers.

Data hiding has been an active research topic in recent years, and many techniques like steganography, cryptography, watermarking, and various others have been proposed for hiding data in various types of images, such as JPEG, PNG and BMP. However, dynamic GIF images have not received much attention in data hiding research. Steganography refers to the practice of hiding secret information within innocuous cover media, such as images, videos, or audio files. The use of steganography has become increasingly important in the era of digital communication, where privacy and confidentiality are essential for various applications, such as military, law enforcement, intelligence, and personal communication.

In recent years, animated GIFs have emerged as apopular form of digital media that can be used as cover objects for data hiding. Animated GIFs are a type of image filethat contains multiple frames or images that are displayed in a sequence to create a moving picture, due to their ability to store multiple frames of images in a single file, making them an attractive option for embedding secret information.

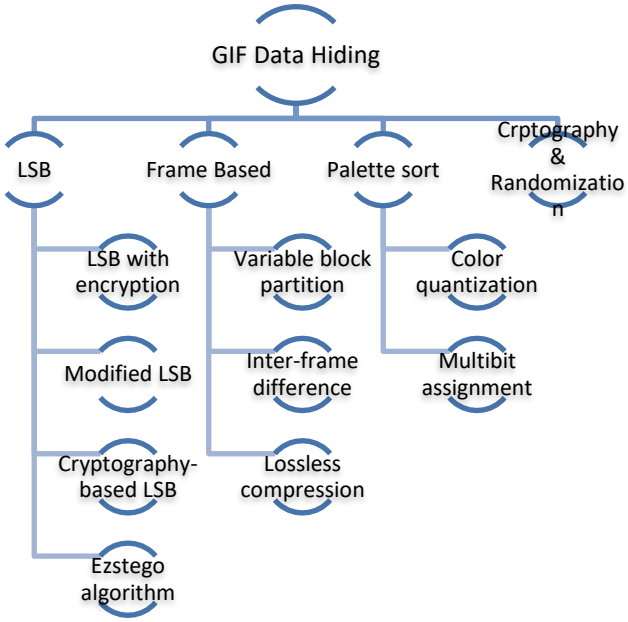

Fig. 1 GIF Data Hiding Techniques

979-8-3503-0071-0/23/$31.00 ©2023 IEEE

Authorized licensed use limited to: DELHI TECHNICAL UNIV. Downloaded on July 20,2023 at 11:16:05 UTC from IEEE Xplore. Restrictions apply.

They are widely used on the internet for various purposes, such as memes, advertisements, and instructional videos. However, the use of animated GIFs for data hiding poses several challenges, including limited payload capacity, low imperceptibility and susceptibility to detection by various attacks, such as visual inspection and statistical analysis.

To address these challenges, various techniques have been proposed to embed secret data into animated GIFs, including those based on LSB substitution, modified LSB, frame based, palette based as shown in Fig. 1 . The data hiding in GIF is divided into many categories where some of the important ones are LSB (Least Significant Bit) substitution, the technique which is used to embed a secret message or data inside the pixel values of GIF images. In this method, each pixel's least significant bit is modified to encrypt a part of the secret message, it is further divided in more different methodologies like LSB with AES encryption, Modified LSB and Cryptography based LSB. The other frame-based technique involves hiding messages in individual frames of a GIF animation. These techniques can increase the overall capacity of the message that can be hidden in the GIF and provide a higher level of security, this also includes some modified techniques Inter-frame differences, variable partition block and lossless compression. The other palette-based method for data hiding in GIF is a technique used to hide secret messages within the color palettes of a GIF image. This method relies on the fact that GIF images can have up to 256 colors in their palettes, this involves color quantization and multibit assignment or embedding methods. The voicing in GIF is a method to add sound bits to the GIF using data hiding method. The main goal of this research paper is to present a comparative analysis of various animated data hiding techniques in GIF. The choice of technique can greatly affect the security and robustness of the resulting stego-media. This paper presents a comparative analysis of these popular animated GIF data hiding techniques. Our objective is to evaluate and compare the strengths and weaknesses of each technique in terms of their imperceptibility, data-hiding capacity, and resistance to common attacks.

The rest of the paper is organized as follows. Section II provides a Literature Review. In section III, a comparative analysis based on the experimental results is provided. Section IV concludes the paper while discussing possible directions for future research.

II. LITERATURE REVIEW

The use of animated GIFs for data hiding has been an active research area in recent years. For this, various techniques have been proposed to embed secret information within animated GIFs while maintaining their visual quality and avoiding detection. Here, we review the various available data hiding works by highlighting their important points as follows:

Table I: LSB substitution-based Techniques

Year & References	Methodology	Results
1999 **[1]**	In this method, each secret message binary bits is embedded into every single pixel. The pixels for embedding are selected randomly with the help of pseudo random number generator (PRNG) and a secret key is seeded into it.	There is less distortion to the stego image. It is having a limitation of that message length in binary bits should be lesser than the number of pixels in the (GIF) image
2011 **[14]**	A frame-based technique on GIF images is suggested using a secret key and a modified least significant bit (LSB) approach. This method makes use of the GIF animation format's frame-by-frame structure to hide data in each frame.	Dividing the hidden data into smaller chunks (called frames) makes it harder for hackers to discover and extract the information. Secret Key shields the private information from tampering or unauthorised access. However, there is distortion in images and its application is also complex.
2015 **[8]**	It uses an LSB technique to conceal the secret message within the colours of every pixels within the frames of the GIF image. Each frame of the GIF image is processed to a 256 color (BMP) image and the color palette of these images is sorted, then each pixel is assigned a new index. The message is also encrypted using the LZW compression.	LZW, cryptography and GIF picture steganography work together to provide a high level of security. Unauthorised individuals can hardly ever access your data. Compression makes efficient use of storage space. However, there is some distortion in images and is complex to implement. Also, not compatible with every software.
2016 **[15]**	The upgraded EZstego allows for the arbitrary insertion of message fragments into the image. Each frame contains a random assortment of message fragments. Additionally, frames can be chosen at random to boost security. Before embedding, the message is encrypted with a secret key to make it safer.	The pixel values are rearranged randomly, making it far more difficult for an attacker to figure out the secret message. It is a straightforward method that is both extremely effective and computationally light. It has High Payload and Low distortion and is an improvement over the original EZstego.
2018 **[10]**	The proposed method involves dividing each frame of the GIF into blocks of pixels, and then embedding the message which is converted into bit stream, into these blocks using the LSB technique. The length of the message that can be	This method helps in optimizing the storage capacity of GIF images by using multiple frames for embedding data. This increases the overall efficiency of the technique. The use of LSB technique combined with variable message length ensures

Authorized licensed use limited to: DELHI TECHNICAL UNIV. Downloaded on July 20,2023 at 11:16:05 UTC from IEEE Xplore. Restrictions apply.

	embedded in each block varies based on the number of available LSBs in the pixel values. To improve efficiency, a variable message length technique is employed, which allows the message to be embedded in different blocks of pixels by dividing them into small segments.	a higher level of security and makes it harder for unauthorized parties to detect the embedded data. However, there is some degradation in image quality and its implementation is complex and is slower and requires higher hardware requirements.
2020 **[18]**	The LSB approach is the frequently used and industry standard method to do data hiding whereas, in spread spectrum, the energy signal is distributed along a communications line with a broader bandwidth using spread spectrum transmission, which uses pseudo-noise code, a separate waveform modulator from the data information.	Spread Spectrum method had a higher capacity for hiding a secret message than the LSB method, as it was able to embed a larger amount of data in the GIF images. Also, it is more secure than LSB.
2020 **[12]**	The authors propose a novel approach to embedding the chat message within a GIF image frames by using the LSB substitution method. The GIF frame is first converted into the BMP images, then chat message is first encrypted using AES encryption before being embedded within the image.	It can improve the security of online communication. This also works well with PNG image format. It maintains a high degree of image quality. To reduce the size of stego-image it uses lossless compression technique.

Table II: Frame-Based Techniques

Year & References	Methodology	Results
2013 **[13]**	In this method, we can insert secret data without drastically changing the overall appearance of image by altering the LSBs of the pixel values that vary between two frames. We choose the frames to be utilised for embedding at random and use a pseudorandom sequence to pinpoint the changed pixels' locations in order to make sure they are difficult to spot.	The steganography methodology proposed in this article performed well based on their capacity, distortion, and compatibility. The embedding and extraction procedures are quick and effective, which makes the method perfect for usage in real-time applications.
2021 **[3]**	A novel method for data hiding in animated GIF images using lossless compression technique RZL. In which a new frame is placed in between the two consecutive original frames with same indices of previous frame. Then the pre-processing of Gif and data hiding is done, by pre-processing all the transparent pixel of new frame is removed within the Gif by copying the same color of previous pixel. As adding new frames increases the size, reverse zero run length encoding compression technique is used to limit this file size expansion.	To ensure that the length of the animated Gif remains intact, complete quality preservation can be achieved by modifying the delay time of each frame. As the Gif can be restored perfectly, it means method is reversible. The method is scalable.
2021 **[11]**	The suggested method takes, resize, alter the colour, and filter the GIF image and its frame using a Gaussian filter, it embeds data in GIF files by applying variable partition block. Then the (GIF) frame is divided into variable blocks, then data bits were put in to those variable blocks. Variable-sized data will also be embedded in the blocks because the blocks themselves have variable sizes.	It offers the highest level of imperceptibility and produces good-quality stego-image. Having higher capacity of around 93 kilobytes of secret data. Choosing random partition block and random frames provides better security than other methods.

Table III: Palette-Sort Technique

Year & References	Methodology	Results
2005 **[2]**	To reduce the number of colors in the image, the color palette of GIF image is quantized. The only way to perform the quantization is to combine two similar color entries from the palette into one color. To represent the stego message, the positions is assigned using the binary values 0 and 1. A 256-color image format is frequently divided into 128 colours in this context.	The results show that this method has high hiding capacity and low distortion, making it a suitable method for practical applications. The method is also shown to be resistant to common attacks such as histogram equalisation and noise addition.
2012 **[17]**	For palette-based photos, this article suggests a high-capacity data concealing approach that doesn't significantly impair the image quality. By utilising Euclidean distance, this technique can help to hide a multiple-bit message within a pixel matrix unit. The stego-images produced with our method have a higher quality and can be implemented at a lower cost.	The palette-based images can be more effectively hidden thanks to the multibit embedding approach. Reduced Distortion because changes are made in the least important bits. Its implementation is simple. It is better than traditional methods. However, it is vulnerable to attack Because it does not use any encryption to secure data.

Authorized licensed use limited to: DELHI TECHNICAL UNIV. Downloaded on July 20,2023 at 11:16:05 UTC from IEEE Xplore. Restrictions apply.

2012 **[6]**	One secret message bit is embedded into each pixel using this technique in which message is first converted into a binary stream. The pixels for message embedding choose at random using PRNG method which is seeded with an input key. The palette is searched for the closest colours for each pixel at which one message bit is to be embedded. The index for the pixel is modified to point to the new colour once the colour has been found.	By improving the quality of stego-images, it becomes much more difficult for unauthorized parties to detect the hidden data in the image and Easy to implement. However, it has limited applications.
2016 **[4]**	The GIF images are divided into frames using this technique. After choosing a frame, the usable multibit assignment is produced using the threshold D and a input key, with some modifications based on the colour palette of the frame. Before embedding the message, the message can be encrypted using AES and the input key after the frame and pixel are chosen.	There is nearly no distortion in the stego image and stego image is in good quality. Here, the method is prone to attack as it fully depends on color of GIF image.
2020 **[7]**	A GIF image consists of a color palette and a series of frames that are displayed in a specific sequence, creating the illusion of animation. A small amount of colours are utilised to represent the image in the colour palette. The palette sort method for data hiding involves changing a GIF image's colour scheme to incorporate hidden data. The goal is to rearrange the colours in a manner that represents the secret data. It is possible to encrypt more information into the image by rearranging the colours in the palette.	This method ensures a higher level of security when compared to traditional techniques when experiments performed on 500 dynamic GIFs. This method also provides that there is no degradation in the image. Limited Storage capacity because palette sizes are frequently modest. Vulnerable to attacks because the method doesn't safeguard the data using encryption or compression. There are also Complexity and Performance issues.

Table IV: Miscellaneous Techniques

Year & References	Methodology	Results
2018 **[16]**	This article combines cutting-edge strategies like steganography, cryptography, and randomization to achieve a high level of security. It uses PCG (Permuted Congruential Generator) technique for random selection of frames and Viginere cypher to encrypt messages into Base64 Code.	This technology lowers the possibility of unauthorised access and information leakage. It provides Efficient Data Integration and also increases the range of Applications such as digital forensics, content protection, and internet data transmission. However, there is distortion in images and is very complex to implement and also requires appropriate tools for implementation.
2015 **[5]**	A novel and simple method for adding sounds to animated GIF. It is based on Fridrich's[1] data hiding technique, here, digital sound is divided into sub vectors, then sound bits are embedded in the pixels of the GIF frames. And the parity bits of the RGB colours of the frame pixels are used to extract the inserted data bits.	The GIF voicing application is not concerned with pirate attacks as it has no security issues. The proposed method can embed audio data with good quality while maintaining the visual quality. This method preserves compatibility and portability of the animated GIF with small amount of distortion.

III. Experimental Results and Their Analysis

As discussed in Table I, the LSB technique discussed by Fridrich [1] gives lesser distortion than other standard EZstego[21]techniques but it provides less security so the algorithm is not robust. The other technique, Frame based method provides better security by dividing the data into smaller chunks, which makes it harder for attacker to discover and extract the data from the GIF images but it having the distortion in image and also complex. The other technique of data hiding using LZW compression, cryptography and GIF image provides a high level of security but the distortion is available and also it is not compatible on every software. The other techniques use modified EZstego algorithm provides less distortion than other LSB techniques, which preservers the quality of GIF image and as pixels are modified and rearranged randomly which provides great robustness from attacking, also it provides high payload capacity. The other technique which uses LSB with encryption provides a high visual quality and uses lossless compression to maintain the size of GIF image but it is not compatible with other formats and many software. So, the best LSB technique among them is the modified EZstego algorithm [15] in terms of visual quality and simplicity and also the payload capacity.

Now, As discussed in Table II (Frame-based techniques), the Inter-frame pixel differences provide embedding and extraction procedures are quick and effective but by altering the LSBs of pixel values that vary between two frames will not able to provide high level or hiding capacity, and also some distortion is also visible. The other technique which uses RZL a lossless compression technique to hide data in frames of GIF image by putting a transparent frame between them, provides complete quality preservation by modifying the delay time of each frame, also it is reversible means the original image can be restored from the stego image. The other frame-based technique to embed data in GIF file by applying block partition achieves highest level of imperceptibility and produces a good-quality stego-image. Also, it gives higher

Authorized licensed use limited to: DELHI TECHNICAL UNIV. Downloaded on July 20,2023 at 11:16:05 UTC from IEEE Xplore. Restrictions apply.

capacity of around 93 kilobytes of secret data for images with dimensions 512 × 512, and provides better security than other methods as it chooses random partition block and frames respectively.

Now, as discussed in Table III, Palette sort technique using color quantization[2] in which it allocates a new color to a entry in the palette of images such that they become identical to its following color. Thus, this will increase the computational cost of the calculation. But it is better than standard method [1] and [21] as it has more PSNR (peak signal to noise ratio) and having high embedding capacity with low degradation. The other technique uses multibit embedding it gives high embedding capacity with low degradation. It also gives more PSNR value than [22]. However, it is not so much secure than them as not using any method to secure the message. The other technique to improve the stego image quality in which it removes the color entry from the palette to mark it as empty and new entry occupy that empty space which helps to reduce the RMS (root means square) error than other data hiding methods. It also increases the computational cost for calculation by removing the entry. The other technique uses multibit assignment method in which the visual quality of stego image depends on the threshold D, it gives better result with small value of threshold D. Also, this method can be detected by the statistical analysis which maybe attack by attackers. The other technique uses data hiding in dynamic images which uses palette sort algorithm which ensures high level of security as compare to the previous works and also the stego image has no such distortion. Now there are some more techniques shown in Table IV like data hiding using randomization and cryptography, which uses viginere cipher to encrypt and decrypt the data. Randomization gif frames provides high level of security, it provides good visual quality but have limited hiding capacity. The other technique of voicing in animated GIF uses embedding sound bits in GIF by using data hiding methods based on the technique used in [1] method. As we discussed above, we get four best techniques in terms of their hiding capacity, visual quality and security from attacks. These are chosen from our analysis from LSB, Frame based and palette sort method in which a method proposes by Munir a modified EZstego[15], A variable block partition method[11] Method to embedding in dynamic Gif images[7] respectively, and also a cryptography and steganography method which uses viginere cipher and randomization.

Now, we analyze the above best methods [15], [11], [7] and [16] in terms of their hiding capacity, Visual quality and robustness to attacks. In modified Ez-stego method the pixel values of GIF images are rearranged randomly making it far more difficult for an attacker to figure out the secret message means it provides robustness to attacks. Also, It is a simple method to implement which is both extremely effective and computationally light. It has High capacity and Low distortion and is an improvement over the original EZstego. In palette sort method to hide data in dynamic GIF images, this method ensures a higher level of security when compared to previous work when experiments performed on 500 dynamic GIF. Also, there is no degradation in the visual quality of the embedded animated GIF. But this method is vulnerable to attacks as does not provide any encryption to data. And also, it is complex for calculations. [11]In the block partition method It offers the highest level of imperceptibility and produces good-quality stego-image. Also having higher capacity of around 93 kilobytes of secret data. Choosing random partition block and random frames provides better security than other methods. In the cryptography & steganography method to encrypt and decrypt the data using vigenere cipher and embed it by using the randomization, in which Randomizing gif frames provides high level of security, it provides very good visual quality but have limited hiding capacity. By above analysis, we can conclude that the data embedding using variable partition block technique achieves no distortion in visual quality of the GIF image as compared to other techniques, the other techniques produce distortion in images as noise maybe increase after embedding and also this technique provide more security as compared to the other techniques. Additionally, it can also be said that though there exist various good reversible data hiding methods [23-29] for simple gray-scale images, but embedding in GIFs has not been explored much to achieve comparable performance.

IV. Conclusion

This paper presents a study on information-hiding techniques for the animated GIF images. First, a categorization of algorithms which include LSB substitution techniques, Frame-based technique, palette-based technique, and one that rely on randomization and cryptography, according to their embedding technique, is provided. It has been observed that the works in all aforementioned categories seem to address all three key features such as undetectability or security, visual quality and hiding capacity. However, after the comparative analysis, it is concluded that, the frame-based technique using the variable partition block method[11] usually have the superior performance performs than the other ones. These methods show no visible distortion in the GIF image's visual quality; whereas other categories of methods, produce some distortion in images after embedding. Additionally, it offers a good amount of storage capacity around 93 kilobytes of data in a GIF file. However, it has also been observed that each method has its own benefits and drawbacks. Therefore, it is unfair to label any method as the worst or the best of all. In the future works, the data hiding in animated GIFs can be extended to encryption domain so that the confidentiality of cover media can also be ensure while maintaining the security of the hidden data.

REFERENCES

[1] Fridrich, J.: A new steganographic method for palette-based images. In: PICS 1999: Proceedings of the Conference on Image Processing, Image Quality and Image Capture Systems (PICS-99), Savannah, Georgia, USA, April 25-28 1999. pp. 285– 289. IS&T - The Society for Imaging Science and Technology (1999)

[2] Wang, X., Yao, T., Li, C.T.: A palette-based image steganographic method using colour quantisation. In: IEEE International Conference on Image Processing 2005.

Authorized licensed use limited to: DELHI TECHNICAL UNIV. Downloaded on July 20,2023 at 11:16:05 UTC from IEEE Xplore. Restrictions apply.

vol. 2, pp. II–1090 (Sep 2005). https://doi.org/10.1109/ICIP.2005.1530249

[3] Wong, K., Nazeeb, M.N.M., Dugelay, JL. (2021). Complete Quality Preserving Data Hiding in Animated GIF with Reversibility and Scalable Capacity Functionalities. In: Zhao, X., Shi, YQ., Piva, A., Kim, H.J. (eds) Digital Forensics and Watermarking. IWDW 2020. Lecture Notes in Computer Science(), vol 12617. Springer, Cham. https://doi.org/10.1007/978-3-030-69449-4_10

[4] M. T. Juzar and R. Munir, "Message hiding in animated GIF using multibit assignment method," 2016 International Symposium on Electronics and Smart Devices (ISESD), Bandung, Indonesia, 2016, pp. 225-229, doi: https://doi.org/10.1109/ISESD.2016.7886723

[5] Sonia Djaziri-Larbi, Awatef Zaien, Sylvie Sevestre-Ghalila. Voicing of Animated GIF by Data Hiding A Technique to Add Sound to the GIF Format. Multimedia Tools and Applications, 2015, ⟨10.1007/s11042-015-2491-y⟩. ⟨hal-01371344⟩

[6] M.-Y. Wu, Y.-K. Ho, and J.-H. Lee, "A Method to Improve the Stego-Image Quality for Palette-Based Image Steganography," in 2012 International Symposium on Computer, Consumer and Control (IS3C), 2012, pp. 62-65.

[7] Lin, Jingzhi, Zhenxing Qian, Zichi Wang, Xinpeng Zhang and Guorui Feng. "A New Steganography Method for Dynamic GIF Images Based on Palette Sort." *Wirel. Commun. Mob. Comput.* 2020 (2020): 8812087:1-8812087:13.

[8] Saleh, Intisar Majeed. "EFFICIENT DATA HIDING SYSTEM USING LZW, CRYPTOGRAPHY AND GIF IMAGE." (2015). https://www.ijtra.com/view/efficient-data-hiding-system-using-lzw-cryptography-and-gif-image-steganography.pdf

[9] Fang Cao ,Yujie Fu, Heng Yao,Mian Zou , Jian Li and Chuan Qin :Separable Reversible Data Hiding in Encrypted VQ-Encoded Images. (2022) https://www.hindawi.com/journals/scn/2022/1227926/

[10] Kumar, D., & Kaur, M. (2018). Inter-Frame Steganography in GIF Images using LSB Technique and Variable Message Length. International Journal of Computer Applications, 180(35), 8-13.

[11] Alyahya, M. A. M., Ansari, A. S., & Mohammadi, M. S. (2021). An Animated GIF Steganography Using Variable Block Partition Scheme. International Journal of Emerging Trends in Technology in Computer Science, 10(2), 206-211

[12] Himanshu Pise , Vidhi Kala , Saurabh Somkuwar , Nidhi Dev, Prajwali Korde, 2020, Obscuration of Chat using Steganography and AES on GIF image format, International Journal Of Engineering Research & Technology (IJERT) Volume 09, Issue 04 (April 2020)

[13] S. Goyal and S. Singh. (2013). A Novel Steganography Technique for GIF Images Based on Inter-Frame Pixel Differences. International Journal of Computer Applications, Vol. 79, No. 14, pp. 13-18.

[14] R. Ali, M. Ikram, and H. U. Asghar. (2011). Frame Based Steganography on GIF Images Using Modified LSB Technique. International Journal of Computer Science Issues, Vol. 8, Issue 3, No. 2, pp. 311-316.

[15] R. Munir, "Application of the modified EZstego algorithm for hiding secret messages in the animated GIF images," 2016 2nd International Conference on Science in Information Technology (ICSITech), Balikpapan, Indonesia, 2016, pp. 58-62, doi: 10.1109/ICSITech.2016.7852608.

[16] Perumal, V. (2018). An Innovative Methodology of Steganography and Cryptography Elicited from Randomization and Base64 Code in GIF images. International Journal of Computer Applications, 179(27), 22-25

[17] Imaizumi, S., & Ozawa, K. (2012). Multibit Embedding Algorithm for Steganography of Palette-Based Images. IEEJ Transactions on Electrical and Electronic Engineering, 7(6), 636-643

[18] Andika Amirulhaqi, Tito Waluyo Purboyo and Ratna Astuti Nugrahaeni, 2020. A Comparison of Steganography in the GIF Image using LSB and Spread Spectrum Method. *Journal of Engineering and Applied Sciences, 15: 247-251.* https://dx.doi.org/10.36478/jeasci.2020.247.251

[19] Chen, C. H., & Hsieh, C. T. (2009). Color Image Protection with Palette Information Embedded into Its Grayscale Image. Journal of Electronic Imaging, 18(3), 033001.

[20] Al-Haj, A., & Al-Ma'adeed, S. (2016). A Block Based Adaptive Video Data Hiding Method Using Forbidden Zone Data Hiding. Journal of King Saud University-Computer and Information Sciences, 28(4), 419-430.

[21] Machado, R.: EZstego. <http://www.stego.com/> (1997)

[22] Tanaka, G., Suetake, N., Uchino, E.: A steganographic method realizing high capacity data embedding for palette-based images. In: Proc. of International Workshop on Smart Info-Media Systems in Asia, pp.92-95 (2009)

[23] Kumar, R.; Chand, S. A reversible high capacity data hiding scheme using pixel value adjusting feature. Multi. Tools Apps. 2016, 75, 241–259.

[24] Kumar, R.; Chand, S. A reversible data hiding scheme using pixel location. Int. Arab J. Info. Tech. 2018, 15, 763–768.

[25] Malik, A.; Singh, S.; Kumar, R. Recovery based high capacity reversible data hiding scheme using even-odd embedding. Multi. Tools Apps. 2018, 77, 15803–15827S.

[26] Kaur, G.; Singh, S.; Rani, R.; Kumar, R.; Malik, A. High-quality reversible data hiding scheme using sorting and enhanced pairwise PEE. IET Image Process. 2022, 16, 1096–1110.

[27] Kaur, G.; Singh, S.; Rani, R.; Kumar, R. A comprehensive study of reversible data hiding (RDH) schemes based on pixel value ordering (PVO). Arch. Comput. Methods Eng. 2021, 28, 3517–3568.

[28] Kumar, R.; Jung, K.H. Enhanced pairwise IPVO-based reversible data hiding scheme using rhombus context. Inf. Sci. 2020, 536, 101–119.

Authorized licensed use limited to: DELHI TECHNICAL UNIV. Downloaded on July 20,2023 at 11:16:05 UTC from IEEE Xplore. Restrictions apply.

九州大学学術情報リポジトリ
Kyushu University Institutional Repository

Synthesis of a Novel Raw Wool and Polyacrylamide-BasedHydrogel as a Colorimetric Sensor

SachinGupta
Department of Applied Chemistry, Delhi Technological University

Chauhan, Deepti
Department of Applied Chemistry, Delhi Technological University

Rana, Atul
Department of Applied Chemistry, Delhi Technological University

Singh, Drishti
Department of Applied Chemistry, Delhi Technological University

他

https://doi.org/10.5109/6793664

出版情報：Evergreen. 10 (2), pp.1068-1073, 2023-06. 九州大学グリーンテクノロジー研究教育センター
バージョン：
権利関係：

Synthesis of a Novel Raw Wool and Polyacrylamide-Based Hydrogel as a Colorimetric Sensor

SachinGupta[1], Deepti Chauhan[2], Atul Rana[3], Drishti Singh[4], Anil Kumar[5,*]
Sudhir G. Warkar[6,*]
Department of Applied Chemistry, Delhi Technological University, Bawana Road, New Delhi 110042, India

*Author to whom correspondence should be addressed:
*E-mail:anil_kumar@dce.ac.in

(Received February 1, 2022; Revised May 14, 2023; accepted May 14, 2023).

Abstract: We have developed a robust method for the detection of heavy metal ions zinc, cadmium, and mercury in water. In this study we have synthesized a hydrogel based on biopolymer that is raw wool obtained from eszvMarino sheep and used this hydrogel as heavy metal ion sensor in the water. We have incorporated meta- benziporphodimethene ligand in-situ in the hydrogel synthesis, which shows selectively color-changing characteristics when immersed in Zn2+, Cd2+ and Hg2+ metal ions aqueous solution. This hydrogel shows selective response towards Zn2+, Cd2+ and Hg2+ metal ions in a competitive environment. Meta-BPDM was responsible for the selectivity of hydrogel towards Zn2+, Cd2+ and Hg2+ metal ions in water. This selective sensing behavior of raw wool based hydrogel has given a novel existence to our study. The synthesized hydrogel was studied for sensing applications and characterized by using FTIR, TGA, and SEM techniques.

Keywords: Hydrogel, Colorimetric Sensor, Heavy Metal, meta-Benziporphodimethene.

1. Introduction

Environmental contamination by heavy metal ions is a real and growing problem that urgently needs to be monitored. Heavy metals have high atomic weights and densities initially known heavy metals are thallium, gallium, and hafnium. Heavy metals are essential nutrients in small amounts but are toxic in large quantities. They are non-biodegradable, toxic and are responsible for the contamination of the natural resources in the environment including water. Some of the heavy metals are hazardous even at trace levels such as Arsenic, Lead, Cadmium, Mercury, and Chromium. They are considered to be highly harmful and toxic to human health. This results to the requirement of efficient, easy and accurate techniques for the detection of heavy metal ions in water. Heavy metals are commonly released in wastewaters by various industries such as chemical manufacturing, mining, paint, coating, extractive metallurgy, and nuclear power plants. Polymers containing one or more electron donor atoms like O, N, P and S that can easily form coordinate bonds and chelation with metal are known as poly-chelatogens. Polymeric hydrogels having hydroxyl, amide, amine, ammonium, and carboxylic acid groups can bind with heavy metal ions and act as a good poly-chelatogens. Therefore, they can be used for water purification applications. Forinstance, Acrylamide and its N- substituted derivatives based polymeric hydrogels are widely used for the applications in various fields[1)]. Zinc is essential for human beings, animals, and plants but excess consumption can cause severe health effects. Heavy metals ions are bio accumulative, non-biodegradable, and emit toxic pollutants in the environment. Mercury and cadmium metal ions are becoming increasingly crucial for determination due their toxicity in the environment. Their contamination can lead to various health issues, like kidney toxicity, paralysis, physiological metabolic disorders, birth and genetic defects. Mercury inorganic salts can even be corrosive to our eyes and skin. It gets very easily absorbed by the body of human beings and its discharge occurs at a very slow rate[2, 3, 4)].

Cadmium is a soft and silvery white metal that is chemically similar to zinc and mercury due to filled d-orbital. They are spectroscopically silent metal ions hence their detection in water is difficult. Cadmium metal is widely used in batteries, pigments, corrosion resistant steel plating, plastics stabilizers and solar panels. It can cause acute and chronic disease. It can cause bone mineralization, fragile bones, kidney intoxication and damage our heart. Zinc has numerous applications in our industry such as in galvanization of iron, cathode in batteries, pharmaceuticals, pigments and as catalysts. Small amounts of zinc do not have considerable effects on human body but large quantities can cause damage to pancreas, and arteriosclerosis[5)].

A hydrogel firstly appeared in 1894, is a 3-Dimensional, cross-linked polymer solid prepared from physical and chemical crosslinking. These soft and wet materials can

be made into smart materials by chemical modifications[1]. These are the polymeric network formed by hydrophilic polymer chains. The hydrophilicity provides ease in the absorption of big quantities of water, which causes the gel to swell and maintain its 3-D structure[6]. Swelling behaviour depends on the pH, temperature and ionic strength of the solution. A hydrogel can even contain more than 90% water[1]. Hydrogel emit various properties like mechanical flexibility, opacity, porosity, etc.

Acrylamide is an organic compound, its chemical formula CH2=CHC (O) NH2. Acrylamide is an odourless white crystalline solid, soluble in water [7]. It is also soluble in various other organic solvents. Acrylamide is stable at room temperature. Under UV light or at its melting point, acrylamide can violently polymerize. Acrylamide monomers can easily copolymerize by free radical mechanism under mild conditions with various functional groups which are ionizable, reactive, thermosensitive etc.[8]. Wool is made from natural fibres; it is a fibrous covering from sheep. It is a protein fibre, primarily made of keratin-based proteins which contributes in its high elasticity. This fibre is the earliest known, can be spun and women by various methods into cloth. Production of wool has declined over the years, highly used in 1990, but now it is fairly stable[9]. Raw wool constitutes of some contaminants. These also depends on the breed, environment, nutrition etc. Some animals producing wool fibres are Merino, Angora, Cashmere, Mohair, Yak, Camel, etc. The quality of wool fibre is based on its breeding conditions, food, weather conditions and general care. Protein chains are contained within the twisted molecular chain. The protein chains are coiled in a helical shape like a spring. It is a stiff structure due to the presence of hydrogen and disulphide bonds. Each helix is coiled together for stiffening. The coil provides the wool with the desired flexibility and resilience[10]. The surface morphology is shown in Fig. 1.

Colorimetric sensors have gained wise popularity in recent years. Colorimetry is a scientific technique, sensors belonging to the optical sensors. This technique is used to determine the concentration of coloured compounds [11]. Sensors change colour when regulated by an external stimulus. This technique is the application of Beer-Lambert law, pronouncing that the concentration of a solute is proportional to the absorbance and the length of light path through the solution[12]. In comparison to fluorescent sensors, this offers some obvious advantages. Colorimetric sensors have low cost, high accessibility, ease of usage. These have gained popularity over the years due to sensitive and selective response towards various analytes. Numerous methods have been deployed to detect metal ions typically, the systems used to detect metal ions require high-efficiency liquid chromatography, atomic absorption spectrometry (AAS), ICP-MS, and fluorescent sensors have been used for the detection of metal ions. These are used because of their simplicity and ease in operation[6, 2] but there are many limitations have been faced while using these techniques. For instance, fluorescent probes are associated with background fluorescence and are relatively dispersed in the entire solution which affects the sensitivity for detection[1]. It is difficult to separate a fluorescent probe from a solution which limits its reuse, AAS and ICP-MS techniques are expensive and require highly trained personnel[3] Although, such methods can pose ultrasensitive analytic results. These require expensive types of equipment, complicated and time taking experiments.

To overcome this, we have devoted our effort towards obtaining elementary and inexpensive methods that allow us to visual detection of heavy metal ions in water. In this study, we have employed a new strategy for designing sensors for Zn2+, Cd2+ and Hg2+ metal ions in water. We have used acrylamide to improve extraction capacity and N, Ń- methylenebisacrylamide (MBA) was used as a cross-linker. We have obtained raw wool from Merino sheep. Heavy metals are harmful and toxic, so we have focused on a selective and sensitive method. Our method is easy to operate and helps in viable and simple visual detection.

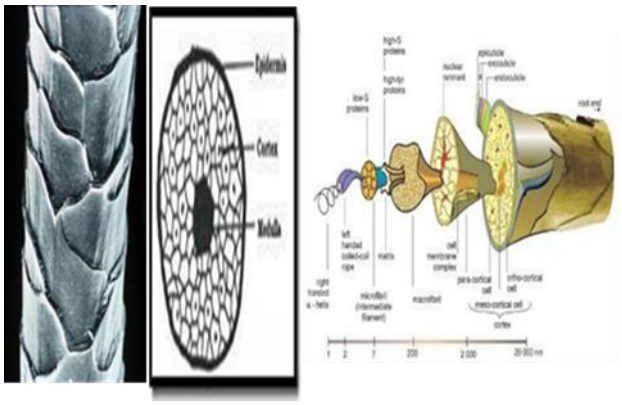

Fig.1: Microscopic appearance of wool [13-14].

2. Experimental Section

2.1 Chemical Used

Sodium hydroxide (NaOH), Hydrochloric acid (HCl), Acrylamide, Potassium persulfate (K2S2O8), Acetone and N, Ń-methylenebisacrylamide. They are obtained from SRL and used as supplied. Raw wool obtained from merino sheep. Meta-Benziporphodimethene was synthesized in lab according to our previous reports[15-20]. Deionized water was used for sample preparations.

2.1 Instrumentation

Magnetic Stirrer, pH meter, weighing balance, The Fourier-transform infrared spectrophotometer (NICOLET 380 FTIR), Thermogravimetric analysis (Perkin Elmer TGA 4000), Scanning electron microscopy (JEOLJSM-6610LV).

2.3Synthesis

Preparation of Wool solution: 0.625 molar solution of

NaOH was prepared and mixed with 1.5 gm. of raw wool using a magnetic stirrer under boiling temperature at 200 rpm. Cooled the solution for 30 min and maintained neutral pH using HCl. Added distilled water to increase solution volume to 100 ml.

Preparation of hydrogel: 1gm of Acrylamide was dissolved in 10 mL of distilled water and 5ml of fresh wool solution added into the acrylamide solution. Fresh meta-BPDM was dissolved in 2mL of acetone which was then added to the first solution. After 15 min 1gm of K2S2O8 initiator added gently and mixed for next 30 min and then added 0.03gm of MBA crosslinker and mixed it well for 40 min. Poured the reaction mixture into a test tube and kept at 75 ℃ for 1 h, 30 minutes underwater bath for the solidifying process. The obtained hydrogel was washed using deionized water to remove unreacted chemicals and cut into slices, dried at room temperature first and then in oven for overnight

3. Result and Discussion

3.1 Characterization

Thermo gravimetric Analysis (TGA): This is a technique by which thermal stability of a material is determined by monitoring the materials mass with the change in temperature. This can be done in different atmospheres like air, vacuum, inert gas, etc. This data is then represented on a graph with percentage of initial mass on Y-axis and time or temperature on X-axis. This plot is called the TGA curve. The TGA curve appears as steps with horizontal and curved points. It can be used to determine the composition of material, kinetics of reaction in fields of pharmaceuticals, food, polymer applications. Fig.2 shows TGA curves plotted with temperature against percentage weight loss in nitrogen environment. By using TGA curves we determined thermal stability of our polymeric materials and observed the weight change starting from 40 °C to 800 °C. Finally, the sample has been degraded and turned to ash. TGA for meta- BPDM raw wool polyacrylamide hydrogel shows that initial loss of weightof about 10% around 40 to 100 ℃ is due to loss of water in form of vapors and other components which are attached to sample surface physically. The second stage of weight loss at about 250 ℃shows the degradation of wool fiber, the amide group, breaking of hydrogen and sulfide bonds. The final decomposition was observed above 400 ℃ due to the degradation of polymeric backbone and the structure starts losing its strength. The TGA curve of metalated m-BPDM raw wool acrylamide hydrogel shows that slow loss in the weight starts from 100℃ and continues till 220℃ due to detachment of physically attached components and vaporization. The main stage of weight loss starting from 270℃ to around 320℃ and around 25-30% weight is lost, leaving ~60% of material. Degradation from 375℃to 430℃ is result of breaking of crosslinking. The decomposition of material starts above 500℃ due to degradation of organic backbone of hydrogel. The results obtained from thermo gravimetric analysis of wool shows that the initial weight loss between 50 to 100 ℃ is due to the vaporization of water and some components that are physically attached to the sample. The second stage of weight loss starts at about 270 ℃ due to degradation of the wool fiber, hydroxyl, and amide group's starts. Degradation from 350 to 400℃ was due to breaking of sulfide linkage, crosslinking. Final decomposition above 500 ℃ was due to organic backbone degradation of hydrogel,

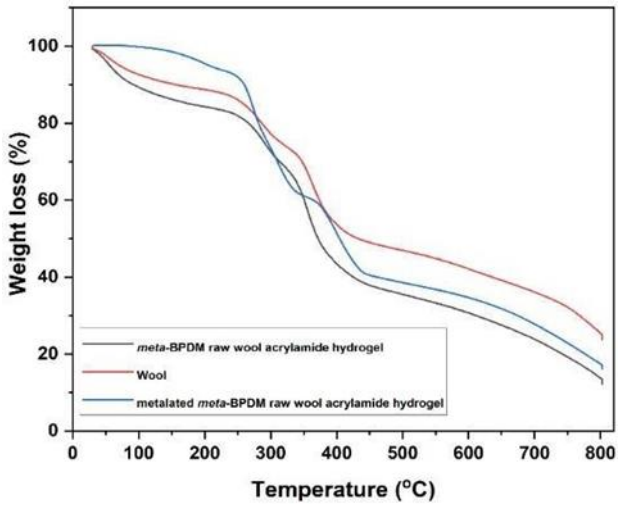

Scanning electron microscopy (SEM): This is used in studying the surface of material with the help of a focused electron beam. This high energy electron beam creates various signals on interaction with various atoms and helps in understanding surface topography and composition of material. Fig. 3. Showing surface morphology of raw wool- acrylamide hydrogel is rough, porous and uneven which is remains unaffected by embedded meta- BPDM However, metalation make the morphology more connected and compact due to complexation with metal ions.

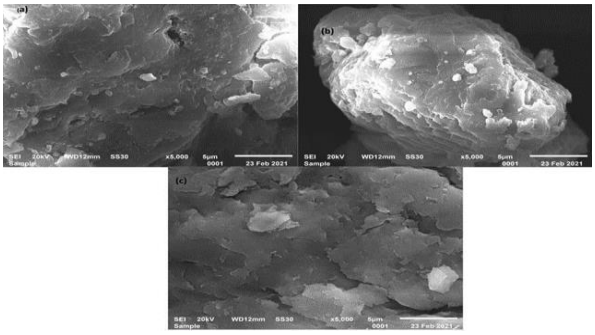

Fig.3: Showing surface morphology of (a) Raw wool-acryloamide hydrogel (b) meta-BPDM raw wool-acrylamide hydrogel and (c) metalated meta-BPDM raw wool-acryalamide hydrogel.

Fourier Transform Infrared spectroscopy (FTIR): FTIR spectra of metalated meta-BPDM raw wool

acrylamide hydrogel showing the broad peak around 3450cm-1 is characterization of OH stretch and the peak observed at 3300 cm-1 is due to presence of amide group i.e., CONH2. The sharp peak due to carbonyl group is observed at ~1690 cm-1 and in the fingerprint region the small peak at ~1450 cm-1 is due to OH bending. The C-H bending peak is observed at ~1380 cm-1. No peak is observed around 2000-2500 cm-1 indicates that no triple bonded C is present in the structure. In meta-BPDM raw wool acrylamide hydrogel FTIR spectra the broad peak at around 3430 cm-1 is the characteristic peak of hydroxyl group stretch. Peak adjacent to the OH is due to amide group which is observed with the help of peak around 3310 cm-1. The sharp and clear peak at 1690 cm- 1 shows the presence of C=O stretching. The dual peaks around 1400 cm-1 are again for hydroxyl group but this time for OH bend. Small peak around 1370 cm-1 is characterisation of vinylidene C-H bending. Another peak in the finger print region at ~1150 cm-1 could be for C-H bond. For raw wool acrylamide hydrogel, the peak observed at ~3400 cm-1 shows characteristics of stretching vibration of hydroxyl group (OH). The peak ~3300 cm-1 is related to the amide group (CONH2). The clear peak around 1700 cm-1 shows characteristics of the carbonyl group present in acrylamide, wool and hydrogel. The small peak at around 1400cm-1 shows characteristics of -OH bending.

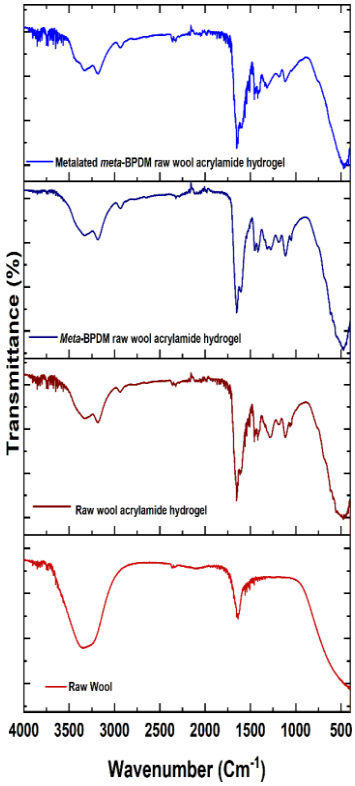

Fig.4: Showing FTIR spectra.

The disturbance peaks around ~1350 is due to Vinylidene C-H in- plane bending. Metalated meta-BPDM raw wool acrylamide hydrogel and meta-BPDM raw wool acrylamide hydrogel shows identical spectra with raw wool-acrylamide hydrogel. Which indicates that the insertion of this ligand does not affect the IR spectra of hydrogel. The ATR-FTIR spectrum of the wool fibre solution showing peaks between 3300 and 3500 cm-1 is due to the presence of an amide group O-H stretching. The peak observed at 3278cm-1 shows characterization of N-H group present in wool chemical structure as shown in Fig. 1. The clear peak at 1680 cm-1 shows the presence of carbonyl group (C=O) stretching in the structure[20-25].

Sensing Application of Synthesized Hydrogel: The sensing behavior of the synthesized polymeric hydrogel was performed in aqueous solutions of metal ions. It was found that the hydrogel changes its colour only with Zn2+, Cd2+ and Hg2+ in the presence of other alkali, alkaline metal ions aqueous solutions. The meta-BPDM organic ligand a red- coloured molecule is responsible for this selective nature. This was incorporated in situ in hydrogel synthesis. The hydrogel changes its colour upon metalation from red to dark blue. The binding constant of these metal ions with the meta-BPDM present in polymeric network is responsible for selectivity in sensing. The hydrogel was allowed to disperse in aqueous metal ion solution and observed the colour change in them with time at room temperature. The sensitivity of the polymeric hydrogel was found to be 1, 1.5, and 4 mg/L with Hg2+, Zn2+ and Cd2+ in 1.5 h, 2 h and 4 h respectively at 60 °C. Minimum time and high sensitivity were shown by mercury metal ions detection followed by zinc and cadmium respectively. This can be explained by the kind of interaction occurring between metal ions and meta-BPDM.[25-32].

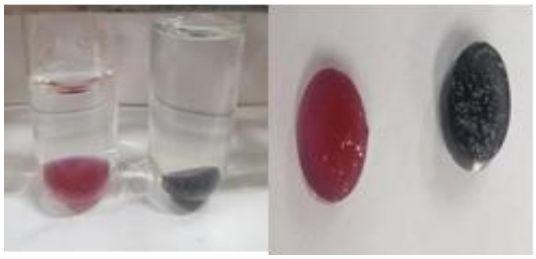

Fig.5: Showing color change property of hydrogel.

4. Conclusion

In a nutshell, a novel meta-benziporphodimethene incorporated raw wool- polyacrylamide based polymeric hydrogel was synthesized via free radical mechanism successfully using water as a solvent. Thermogravimetric analysis has shown that this hydrogel has adequate thermal stability and was potentially applied for the sensing of Zn2+, Cd2+ and Hg2+ in aqueous metal ion solution. This is the first report on raw wool-polyacrylamide based polymeric hydrogel used for sensing zinc, cadmium and mercury metal ions in water. The hydrogel changes its color from red to dark blue which is visually detected hence, showing easy to use. The

minimum detectable concentration of metal ions by the polymeric hydrogel was found to be 1, 1.5, and 4 ppm with Hg2+, Zn2+ and Cd2+ in 1.5 h, 2 h and 4 h respectively at 60 ℃. Further this application can be explored for real time sensing of these metal ions in industrial wastewater. Potential application of this hydrogel can be explored in heavy metal ions removal from the real wastewater. Removal of heavy metal ions from wastewater using this hydrogel is the current focus of our lab.

Acknowledgements

Authors thank to Delhi Technological University, New Delhi 110042 for providing lab facilities and CSIRO Science images for wool microscopic structure.

References

1) Atta, Ayman & Husein, Sadam & Elsaeed, Ashraf. (2012). Application of Anionic Acrylamide-Based Hydrogels in the Removal of Heavy Metals from Waste Water. Journal of Applied Polymer Science. 123. 10.1002/app.34798.
2) Hong M, Lu X, Chen Y, Xu D, (2016) A novel rhodamine-based colorimetric and fluorescent sensor for Hg2+ in water matrix and living cell, Sensors Actuators, B Chem. 232 28–36. https://doi.org/10.1016/j.snb.2016.03.125.
3) Kumar V. Vinod, Anthony S.P, (2014) Silver nanoparticles based selective colorimetric sensor for Cd 2+, Hg2+ and Pb2+ ions: Tuning sensitivity and selectivity using co-stabilizing agents, Sensors Actuators, B Chem. 191 31–36. https://doi.org/10.1016/j.snb.2013.09.089.
4) Lv J, Liu G, Fan C, Pu S, (2020) A highly sensitive fluorescent sensor for Cd2+ and Zn2+ based on diarylethene with a pyrene unit, Spectrochim. Acta - Part A Mol. Biomol. Spectrosc. 227 117581. https://doi.org/10.1016/j.saa.2019.117581.
5) M. Parmar, L.S. Thakur, Heavy metal Cu, Ni and Zn: toxicity, health hazards and their removal techniques by lowcost adsorbents: a short overview international journal of plant, Animal Environ. Sci. 3 (2013) 143–157.
6) L. Zhang, D. Peng, R.-P. Liang, J.-D. Qiu, Graphene-based optical nanosensors for detection of heavy metal ions, TrAC Trends in Analytical Chemistry. 102 (2018) 280-289.
7) Hydrogel Market Size, Share | Industry Analysis & Forecast, 2027; available via the Internet at: https://www.alliedmarketresearch.com/ hydrogel-market (accessed Aug. 10, 2020).
8) Y. Zhou, H. Zhao, Y. He, N. Ding, Q. Cao, Colorimetric detection of Cu2þ using 4-mercaptobenzoic acid modified silver nanoparticles, Colloids Surf. Physicochem. Eng. Asp. 391 (2011) 179–183.
9) D.W. Domaille, E.L. Que, C. Chang, Synthetic fluorescent sensors for studying the cell biology of metals, J. Nat. Chem. Biol. 4 (2008) 168– 175.
10) Kim, S.; Laschi, C.; Trimmer, B. Soft Robotics: A Bioinspired Evolution in Robotics. Trends Biotechnol. 2013, 31 (5), 287−294.
11) L. Zhang, B. Zhao, G. Xu, Y. Guan, Characterizing fluvial heavy metal pollutions under different rainfall conditions: Implication for aquatic environment protection, Science of The Total Environment. 635 (2018) 1495-1506.
12) Gul, J. Z.; Sajid, M.; Rehman, M. M.; Siddiqui, G. U.; Shah, I.; Kim,K. H.; Lee, J. W.; Choi, K. H. 3D Printing for Soft Robotics A Review. Sci. Technol. Adv. Mater. 2018, 19 (1), 243−262.
13) Textileapex homepage, https://textileapex.blogspot.com/2015/07/how- to-identify-wool-and-silk-fibre.html , last accessed 2021/03/10.
14) Sciencelearn-wool-fibre-structure-and-properties, https://cutt.ly/RzPmpJF, Last accessed 2021/03/10.
15) Deepti Chauhan, Anil Kumar & Sudhir Warkar (2020). Synthesis, Characterization and Metal Ions Sensing Applications of meta - Benziporphodimethene Embedded Polyacrylamide/ Carboxymethyl Guargum Polymeric Hydrogels in Water. Environmental Technology. 1-28. 10.1080/09593330.2020.1812730.
16) Nandiyanto, Asep & Oktiani, Rosi & Ragadhita, Risti. (2019). How to Read and Interpret FTIR Spectroscope of Organic Material. Indonesian Journal of Science and Technology. https://doi.org/10.1080/09593330.2021.1928294
17) Sharma R.K, Maurya A, Kumar A, et. al. meta-benziporphodimethenes: New Cell Imaging Porphyrin Analogue Molecules, ChemistrySelect. 2016;1: 3502–3509. https://doi.org/10.1002/slct.201600812.
18) Sharma R.K, Gajanan L.K, Kumar A, et. al. Synthesis, characterization and fluorescence turn-on behavior of new porphyrin analogue: meta - benziporphodimethenes, Spectrochim. Acta Part A Mol. Biomol. Spectrosc. 2016;169: - https://doi.org/10.1016/j.saa.2016.06.020. 20
19) Muhamad Allan Serunting, Okky Fajar Tri Maryana, Erga Syafitri, Solina Balqis- Green Synthesis Silver Nanoparticles (AgNPs) Using Lamtoro Pods Extract (Leucaena leucocephala) and Their Potential for Mercury Ion Detection- http://doi.org/10.5109/4372261
20) Md. Amirul Islam, Kyaw Thu, Bidyut Baran Saha Specific heat capacity of mesoporous silica gel for adsorption heat pump applications-2017;
21) Muhammad Hamid Mahmood , Muhammad Sultan , Takahiko Miyazaki- 2019, Study on Water-Vapor Adsorption onto Polymer and Carbon Based Adsorbents for Air-Conditioning Applications

22) Muñoz-García,Rubén O. et al.- Química Nova(2015) A novel Polyacrylamide-based hydrogel crossinked with cellulose acetate and prepared by precipitation polymerization-http://dx.doi.org/10.5935/0100-4042.20150119
23) Venkatadri Tekuri, Darshak R. Trivedi-2017, A new colorimetric chemosensors for Cu2+ and Cd2+ ions detection: Application in environmental water samples and analytical method validation- - https://doi.org/10.1016/j.aca.2017.03.035
24) Nergiz Cengiz-(2019) Fabrication of Multifunctional stimuli-responsive hydrogels susceptible to both ph and Metal cation for visual detection-- https://doi.org/10.1002/macp.201900212.
25) Mohamed Egiza, Hiroshi Naragino, Aki Tominaga, Kouki Murasawa, Hidenobu Gonda, Masatoshi Sakurai, and Tsuyoshi Yoshitake, "Si and Cr Doping Effects on Growth and Mechanical Properties of Ultrananocrystalline Diamond/Amor-Phous Carbon Composite Films Deposited on Cemented Carbide Substrates by Coaxial Arc Plasma Deposition", *Evergreen: joint journal of Novel Carbon Resource Sciences & Green Asia Strategy,* **3**(1), 32-36 (2016). https://doi.org/10.5109/1657738
26) Ashish Kumar Srivastava, Shashi Prakash Dwivedi, Nagendra Kumar Maurya, and Manish Maurya, "3d Visualization and Topographical Analysis in Turning of Hybrid Mmc by Cnc Lathe Sprint 16tc Made of Batliboi", *Evergreen,* **7**(2), 202-208 (2020). https://doi.org/10.5109/4055217
27) Dharu Feby Smaradhana, Dody Ariawan, and Rafli Alnursyah, "A Progress on Nanocellulose as Binders for Loose Natural Fibres", *Evergreen,* **7**(3), 436-443 (2020). https://doi.org/10.5109/4068624
28) Nagendra Kumar Maurya, Vikas Rastogi, and Pushpendra Singh, "Experimental and Computational Investigation on Mechanical Properties of Reinforced Additive Manufactured Component", *EVERGREEN Joint Journal of Novel Carbon Resource Sciences & Green Asia Strategy,* **6**(3), 207-214 (2019). https://doi.org/10.5109/2349296
29) Ang Li, Azhar Bin Ismail, Kyaw Thu, Muhammad Wakil Shahzad, Kim Choon Ng, and Bidyut Baran Saha, "Formulation of Water Equilibrium Uptakes on Silica Gel and Ferroaluminophosphate Zeolite for Adsorption Cooling and Desalination Applications", *Evergreen,* **1**(2), 37-45 (2014). https://doi.org/10.5109/1495162
30) Jabir Al Salami, Changhong Hu, and Kazuaki Hanada, 'A Study on Smoothed Particle Hydrodynamics for Liquid Metal Flow Simulation', *Evergreen,* **6**(3), 190-199 (2019). https://doi.org/10.5109/2349294
31) Matheus Randy Prabowo, Almira Praza Rachmadian, Nur Fatiha Ghazalli, and Hendrik O Lintang, "Chemosensor of Gold (I) 4-(3, 5-Dimethoxybenzyl)-3, 5-Dimethyl Pyrazolate Complex for Quantification of Ethanol in Aqueous Solution", *Evergreen,* **7**(3), 404-408 (2020). https://doi.org/10.5109/4068620
32) Jain, Ankit, Cheruku Sandesh Kumar, and Yogesh Shrivastava. "Fabrication and Machining of Metal Matrix Composite Using Electric Discharge Machining: A Short Review." *Evergreen,* **8**(4), 740-749 (2021). https://doi.org/10.5109/4742117.

Systematic Literature Review of Current Trends in Artificial Intelligence-Based Intrusion Detection Systems

Apoorva Aggarwal[1], Kushagra Keserwani[2], and Anamika Chauhan[3]

Department of Information Technolgy,Delhi Technological University, Delhi, India

E-mail address: apoorva27sep@gmail.com, kushagrakeserwani@gmail.com, anamika@dtu.ac.in

Abstract: An intrusion detection system (IDS) is a crucial part of network security, but historical models aren't always the best way to deal with today's problems. The problem occurs in the accuracy of detection, with high false alarm being raised, which the researchers have been working over for decades. Some of the solutions proposed include improving the methodologies for detection by using machine learning. Despite the significance of this subject, there aren't many thorough and systematic reviews regarding exploring and delving into its key mechanisms. As a result, the current paper presents a Systematic Literature Review (SLR) of the IDSs that have been put forth over the past few years, and they are categorized according to the kind of approach used. Then, utilising shared characteristics, extensive classifications of the IDS techniques (classical machine learning-based IDS, hybrid IDS, deep learning-based IDS, graph-based IDS, streaming data-based IDS, and cloud-based IDS) have been provided. The benefits and drawbacks of the chosen mechanisms are then discussed. The report also provides an outline of the current difficulties, unresolved problems and the directions for future trends.

Keywords: Cloud, Deep Learning, Ensemble, Graph, IDS, Intrusion Detection, Machine Learning, Real-Time

1. Introduction

In this modern world, keeping in touch with the ever-changing world is made possible using computer networks, where one of the key aspects of the networks is security. The easier it has come for people to share their knowledge across the globe, the more the threats surrounding it have also tremendously increased. This makes intrusion detection systems a critical component in network security because they monitor network traffic for any malicious activity in order to keep the network operating as intended. However, the different traditional intrusion detection models based on signature matching are not always the best at coping with the current network challenges. The problem occurs in the accuracy of detection, with high false alarms being raised, which the researchers have been working over for decades. One solution that has been suggested is to use machine learning to improve the ways that things can be found. Some researchers believe that artificial intelligence-based techniques can improve the system by distinguishing between normal and suspicious data and detecting previously unknown threats. Also, Intrusion Detection Systems (IDSs) that are based on such methodologies don't need to know a lot about the structure of the network. In this paper, the different (Intrusion detection system)IDS methodologies are proposed to improve performances keep focus on machine learning and hybrid techniques proposed over recent years and classify them based on the type of technique used. The paper also overviews the current challenges faced by the researchers in the field of intrusion detection. For this, papers were chosen and analyzed based on the techniques they used, to show how intrusion detection technologies are changing.

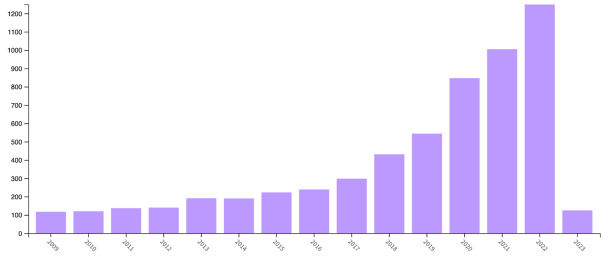

Figure 1. Number of articles on IDS in WoS Database

Figure 1. clearly shows that the number of published studies has increased significantly between 2000 and 2022 and it is one of the topic of interest of 2023. Hence, to explore this topic, this is a systematic literature review on the advancements made by the researchers in the field of intrusion detection. This systematic literature review is divided into number of sections for the ease of readers. The background of the IDS and this study is thoroughly discussed in Section 1. Section 2 describes about SLR the methodology that is incorporated to search, select and compare the papers. The various datasets that are used to test and train the ML based IDS are detailed in section 3. Section 4 presents a detailed discussion of each ML and AI technique used to detect malicious activity along with its advantages of it over existing solutions. Next in

section 5, discusses and compare in detail the various IDS methods proposed based on the techniques, their pros and cons (such as less accuracy, no protection against zero-day attacks, etc.), and what researchers have come up with over time to make the existing solutions better. The challenges that we found after reviewing the selected pacers are discussed in section 6. Finally conclusion of the work in given in section 7 followed by identifying the future scope in ML based IDS.

a. Background

A. Intrusion Detection Systems

"The term "intrusion" refers to attempts to compromise the confidentiality, integrity, or availability of a resource or to bypass the security mechanism of a computer or network system. An intrusion detection system (IDS) watches what happens in a computer system or network and looks for signs that someone is trying to get in. It can generate and report alarms to system operators when it detects intrusive or abnormal" [41]. The components of IDS can be defined based on their functions as shown in Figure 2.

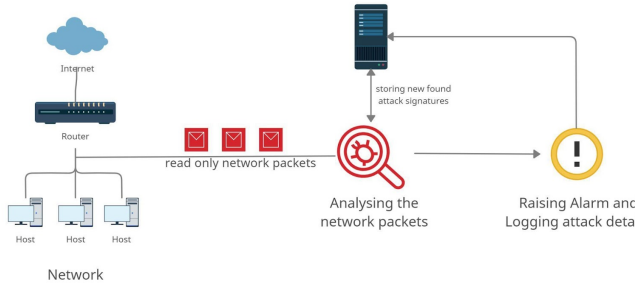

Figure 2. Components of an Intrusion Detection System

The components of IDS can be described as follows:
• monitoring network traffic
• gathering data from the flow of network traffic
• making sense traffic by analyzing patterns or characteristics of data
• storing the any new found attack signature in the database
• generating alerts if any signature matches.

i. B. Intrusion Detection Systems Classifications

1) Classification based on source of data

The data used to analyze the intrusion might come from a variety of sources. Hence, intrusion detection systems are classed into host-based and network-based IDS based on the information sources. [42] Host-based intrusion detection systems (HIDS) monitor a host's attributes and behaviors in order to detect possible attacks. A host-based intrusion detection system (IDS) monitors data such as network traffic statistics, system logs, and access controls and alteration. The network-based intrusion detection system (NIDS) on the other hand, examines network traffic to ensure that network devices are secure and assesses the protocols (network, application, transport, and so on) that have been utilized to detect suspicious activity.

2) Classification based on IDS methodologies

In order to identify malicious actions and invasive behavior in the system, the IDS can implement different methodologies, often categorized as: anomaly-based IDS and misuse-based IDS. [42] Detecting any potential attacks via signature-based or misuse-based detection is the act of correlating signatures with observed events in order to identify possible attacks. In the event that a match is found during the comparison process, the system will provide a notification. Because of this, IDSs that use signatures are very good at finding known attacks, but they aren't very good at finding new threats or new versions of known threats [42]. In order to identify abnormal occurrences, anomaly-based detection compares observed activity with criteria of what is deemed normal. An intrusion detection system that employs an anomaly-based detection method contains rules that describe the usual behavior of users, hosts, network connections, and applications.

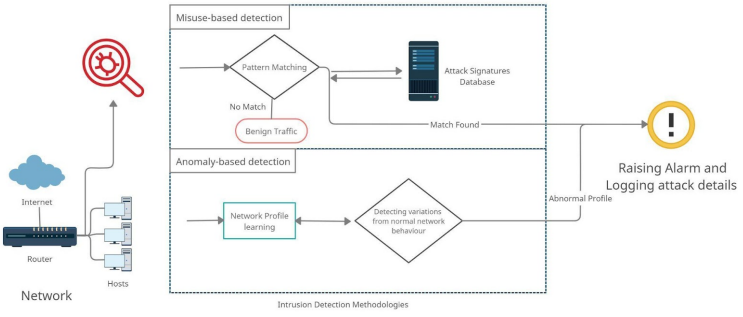

Figure 3. Misuse-based and Anomaly-based IDS

2. METHODOLOGY

A systematic literature review (SLR) is a thorough evaluation of all exploratory studies and papers on a certain topic.

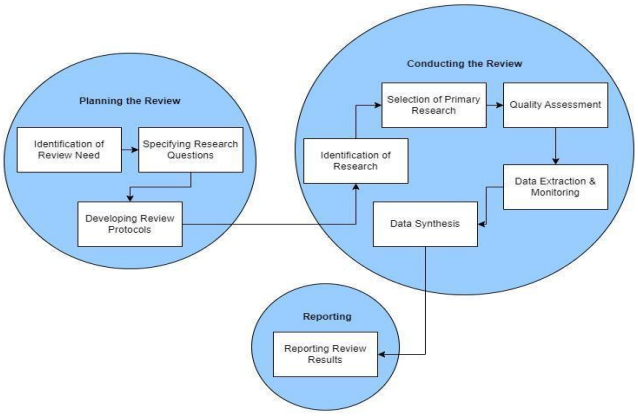

Figure 4. Research Methodology

a. Method

The planning, conducting, and reporting phases of the SLR are carried out using the methods illustrated in [20, 21]. The SLR presented methods in [22, 23] are also taken into account, and some of their techniques are applied in this paper. The necessary steps in the SLR are shown in Figure 2. The first point made is the requirement for a thorough analysis of the most recent developments in AI-based IDS. The shortcomings and advantages of the current approaches are also identified. The research questions are then specified in Table 1. The research methodology is then identified, along with the search terms and sources used. The next step is to identify relevant studies based on the research questions. The inclusion and exclusion criteria are also established in this step. The study analysis and evaluation results are presented after creating a quality evaluation questionnaire. Designing a data extraction process to combine the required data and provide answers to the research questions is the next step. Finally, a process for analysing data and reporting review findings is developed.

b. Research questions

TABLE I. RESEARCH QUESTIONS

RQ#	Research Questions	Motivation
1	Which AI Based algorithm/ method is used to implement IDS	To Identify what are recent trends in AI based technique used to detect intrusion in a system or network
2	Which datasets are trending nowadays to train/test/evaluate IDS.	To Identify the currently trending datasets used to train, test or evaluate IDS
3	What are the main merits and demerits of the proposed AI based IDS method	Identifying thepros and cons of using that AI based IDS method
4	Which algorithm/Method is better for implementing AI-based IDS	To know which AI based IDS algorithm has a good performance in terms of accuracy, implementation etc. and to show how accuracy improves from classical algorithms to novel technologies
5	What are the challenges and future scope of the ML approaches for implementing IDS.	To find out the existing research gap in ML based IDS which gives possibilities of improvisations in existing models to formulate better models

c. Search strategy and study selection

For each of the dubious terms, the synonyms and alternate spellings are provided, and they are then combined using Boolean OR and Boolean AND to create search strings. As a result, seven keywords have been chosen, including "artificial intelligence," "intrusion detection system," "machine learning," "deep learning," "graph-based," "real time," and "data streaming." The following search string was used for selection of main studies:

"(((((TS=(intrusion detection system AND (Machine Learning OR ML))) OR TS=((intrusion detection system AND (Deep Learning OR IoT))) OR TS=(intrusion detection system AND ((graph AND based) OR graph))) OR TS=(intrusion detection system AND ((cloud AND based) OR cloud))) OR TS=(intrusion detection system AND ((real AND time) OR (data streaming)))) OR TS=(intrusion detection system AND ensemble based))"

These search strings are given to the WoS/SSCI electronic database to get the latest articles. This database was selected because it is one of the largest repositories and covers a wide range of excellent publications on all academic fields.

Since the IoT was introduced in the late 1990s, the search is limited to years 2010 to as recently as 2022. The full-text of the pertinent papers is obtained after the candidate found papers have been identified. After going through the inclusion and exclusion criteria manually listed in Table 2, 21 papers are selected for further evaluation in the following phase.

TABLE II. INCLUSION EXCLUSION CRITERIA

Criteria	Rational
Inclusion 1: A study that have proposed a new AI based IDS	To examine current IDS trends using AI-ML.
Inclusion 2: The method or technique is clearly explained	To investigate the novel techniques employed in IDS
Inclusion 3: The IDS method proposed in the paper has been trained/tested using the datasets listed above	In order to learn more about the popular datasets
Exclusion 2: Review Studies	The review studies are disregarded because no novel concepts were presented in them.
Exclusion 3: Non English Papers	These papers are not included because they were not published in English.

d. Quality assessment criteria

The studies are weighed using the quality assessment. The questions for the quality assessment that are incorporated are shown in Table 3. The questions are ranked 1 (yes) and 0 (no). The review only includes the studies that received two yes votes. This process results in the selection of 21 studies, which are reviewed in Section 5 of this paper. This step is also depicted in Figure 3's stage 3 .

TABLE III. QUALITY ASSESSMENT QUESTIONS

Q#	Quality Question
Q1	Does the research paper evaluate or simulate the suggested method?
Q2	Does the chosen paper come from a legitimate publication?

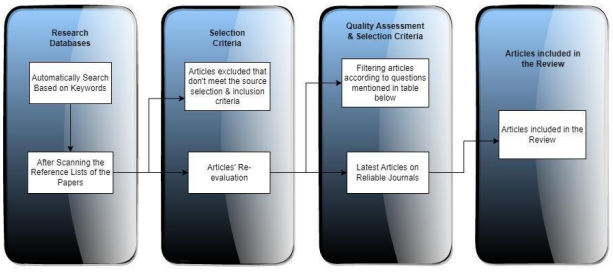

Figure 5. Selection Process of Articles

a. Results and discussion

The objective of the current review is to examine the chosen articles and determine the answers to the issues posed. The pros and cons of IDSs are then discussed, along with a categorization of different IDSs. The quantitative data, including indicators such as detection accuracy, f1 score, rate of false positives, consumption of resources, real-time, flexibility, reliability, and scalability, is evaluated and examined. Charts and tables like Tables 4, 6, have been used to present the results of this review and respond to the aforementioned research questions.

3. INTRUSION DETECTION DATASETS

Studies on improving the performance of intrusion detection systems is not a newly recognized proposition. Multiple researchers have been working on it however the proposed models need to be evaluated or if as in several more recent papers focusing on machine learning based IDS requires network traffic based data. This is where the intrusion detection datasets come into play, which usually tries to replicate a particular real world network scenario, which can be then used to either train or assess the effectiveness of the proposed models by the researchers.

In this section, some of the more popular IDS datasets over the years have been discussed and tabulated. For a dataset to be advantageous for a study there are a few parameters as the types of attacks present, the nature of network traffic, up-to-dateness with the current standards, the type of attributes defining a sample of the dataset, the number of samples present,etc. based on which a researcher can decide how to utilise the dataset to its best. For evaluating the intrusion detection model it is required that the data which is being used is to be labelled, hence in this section mentions those datasets having labels defining attack or neingn data. Table 4, overviews the more popular datasets in the field of intrusion detection.

TABLE IV. OVERVIEW OF POPULAR IDS DATASETS

Dataset	Release Year	No. of Features	Types of Attack in Dataset	Attack Sample Count	Total Samples (approx.)	Labelled
NSL-KDD [14]	1998	43	DoS, U2R, R2L, Probe	72k	150k	Yes
DAPRA [15]	1998	43	DoS, U2R, R2L, Probe	N/A	N/A	Yes
KDDCUP99 [16]	1998	43	DoS, U2R, R2L, Probe	3.9million	4.9million	Yes
ISCX 2012 [17]	2012	80	Brute Force SSH, Infiltra- tion, DoS, and DDoS	69k	2.4million	Yes
UNSW-NB15 [18]	2015	49	Fuzzers, Analysis, Back doors, DoS, Exploits, Generic, Reconnaissance, Shell Code, Worms	321k	2.5million	Yes
CICIDS17 [19]	2017	80	Brute Force, Heartbleed, DoS, Web Attack, Infiltra- tion, Botnet, PortScan and DDoS	472k	3.1million	Yes
CSECICIDS 2018 [19]	2018	80	Brute Force, Heartbleed, DoS, Web Attack, Infiltra- tion, Botnet, PortScan and DDoS	2.8million	16.2million	Yes
AWID2 [35]	2016	154	Impersonation, Injection, Normal, flooding	220K	2.3 million	Yes
BoT-IoT [36]	2019	47	DoS, DDoS, Information Theft	3.6 million	3.6 million	Yes
ToN-IoT [37]	2019	44	DDoS, DoS, password cracking attacks, reconnaissance or verification, MITM, ransomware, backdoors, and injection attacks	21.5 million	22.3 million	Yes
NF-ToN-IoT and NF-BoT-IoT [38]	2020	12	XSS, Benign, DDoS, DoS, password cracking attacks, MITM, ransomware, backdoors, Reconnaissance, theft and scanning attacks	1.6 million	1.9 million	Yes
Edge-IIoTset [39]	2022	61	DoS/DDoS attacks, informationInformation gathering, Man in the middle attacks, Injection attacks, and Malware attacks,	209K	1.9 million	Yes

4. AI TECHNIQUES USED TO IMPLEMENT INTRUSION DETECTION SYSTEM

b. Classical Machine Learning

Machine Learning is seen as a thriving research field that can tackle the issue of traditional IDS methods that require dedicated manual labour to maintain the signature record or identify the attack patterns. Machine learning can easily distinguish such patterns, which relates closely to how intrusion detection works. Hence, researchers came up with IDS methods that use machine learning models to improve the system's performance. This section explains machine learning techniques that have been suggested as alternatives to traditional IDS models and classifies them into groups based on their work & model used. The paper divided the machine learning models into the following categories:

ii. Classification

The classification-based approach builds a detection model by training it on the labels available in the training set, and it classifies a sample of data from the test set by using the classifications discovered during the training of the training set. The three main classification techniques found in IDS were tree-based, naive-bayes, and SVM-based models. Different classification techniques were used over NSL-KDD, UNSW-15, and CICIDS-17 in the studies under consideration [4,5,6], and their performance was evaluated based on accuracy and false alarm rate. Compared to other machine learning

techniques, the model training time is shorter, which gives it an advantage. However, these techniques cannot be used alone due to the recent rise in data complexity and the inefficiency of their output. Table 6 contains a summary of the studied works in classification-based IDS.

iii. Clustering

The network traffic datasets are often found to be unlabelled in nature, which raises the issue of usability with supervised machine learning techniques, to which clustering-based approach was proposed by the researchers in their studies. The process of grouping unlabeled network records according to similarity is known as clustering. Clustering-based machine learning methods enable us to work with unlabeled traffic data where clusters of similar records are created to determine if there is a possible intrusion in the network. These strategies' main objective is to combine data samples based on their homogeneity. K-means and hierarchical clustering were the main clustering techniques used in IDS, but in recent years, other techniques have become more popular. Most of the time, clustering-based models were used along with other models because single clustering methods were not good enough to use. This can be seen in the studies [7,8], where the accuracy got better as the number of clusters went up, but the false alarm rate went as high as 16. The studies in clustering-based IDS are tabulated in Table 6.

c. Hybrid

In recent years, studies based on machine learning-based IDS have seen a shift from using a single classifier to a combination of multiple methods, given that the networks as known now have been evolving quite rapidly. The attackers have been perfecting their strategies, which makes it much easier to fool an IDS based on simpler methods. Researchers there have made attempts to come up with and use hybrid techniques to get better results. To improve the attack detection and classification rates, to tackle the drawbacks of other proposed models, as in, there was a tradeoff between accuracy, false alarm rate, and model training time.

iv. Ensemble-Based

This type of approach helps in improving the accuracy, decrease the false alarm rate, and as the model will be using computationally less expensive machine learning models, hence faster training times. Ensemble-based IDS can be based on the different ensembling techniques available as bagging, boosting, stacking, and many other variants. In 2011 [6], C4.5 which is a variant of decision tree is boosted homogeneously, to improve the accuracy by 5.5% over its singular C4.5 model. Another instance of homogeneous ensemble was seen in [7], where Na¨ıve Bayes was ensembled over bagging, boosting and stacked over decision trees base classifier, where stacked model showed best results by improving accuracy and reducing false alarm rate to as much as 0.3%. Heterogeneous ensemble models were also seen to be applied in intrusion detection, as in [8], an ensemble of 7 different classifiers were made, where the best classifier was used to make the predictions. In [9], SVM was stacked with 3 different base classifiers, Random Forest, Logistic Regression, and k-NN, and evaluated on UNSW-15 and UGR-16 datasets, showing lowered false alarm rates. From the above studies, it can be seen that the ensemble-based intrusion detection methods were successful in reducing false alarm rate and improving overall accuracy.

v. Signature + Anomaly based

Some researchers have made use of machine learning to create a layered hierarchical detection system where either anomaly or misuse-based method is deployed followed by the misuse or anomaly-based or a combination to filter out the network data. Here the network traffic is analysed by first checking on a misuse-based detection model for any known attacks, where any known attacks are filtered out and the reduced network traffic is classified as normal and passed to the anomaly based model where it will be detected for any unknown attacks, or vice versa. This was also seen in studies where the anomaly based model checks first on the network traffic to reduce the data by eliminating the data classified as normal, since majorly in network traffic there is the normal data, this will reduce the load on next level of detection system where it will only have to consider a less data and hence a more accurate model can be deployed here. In [10], the proposed model uses Snort, to detect any known attacks. If any unknown attacks are missed, they are detected using clustering based methods. This approach was validated using DARPA 2000 and private banking dataset, where it achieved 98.7% and 99.9% accuracies and a 0.7% and 0.01% FAR, respectively. A similar approach was seen in [13],where a decision tree-based model was used for checking known attacks and association rule mining for anomaly detection. A different approach was seen in [11], [12], and [13], where the anomaly detection was done first to reduce the data and use a stronger algorithm for final detection. The results in all the studies were very excellent accuracy and much reduced false alarms.

d. Deep Learning

Modern attacks cannot be defended against with conventional methods. Advanced deep learning approaches have been developed for the automatic detection of intrusions and the detection of strange network behaviour.

Due to their capacity to spot previously unnoticed patterns in the raw data, deep learning techniques outperform machine learning-based ones when working with large datasets and solve all pattern recognition problems. It uses multiple layers of adjustments to find higher-level traits. To choose the optimal features for pattern recognition, it automatically uses numerous hidden layers. The foundation of deep learning models is the structure of a feed-forward neural network.

Over the past 20 years, many researchers have suggested using machine learning (ML) and deep learning (DL) to enhance intrusion detection (ID) systems. However, the earlier ML methods show subpar classification performance in an ID system with the largest false alarm rate (FAR) and low attack detection rate (DR). The research put the models into groups based on classification algorithms that pull out features that are spatial, temporal, or both.

vi. Spatial Features

It focuses mostly on the interactions between spatial objects' orientation, connection, and distance. The technique is based on studies in which a lightweight CNN-based IDS for Wi-Fi networks uses the EfficientNet-B0 architecture (convolutional neural networks classifiers to which data is fed) and a zigzag scan pattern created using the JPEG image compression method on the basis of feature importance. It is handled to convert the IDS data into a graphical numerical format that depicts the attribute value of each characteristic. The framework investigates feature selection using cross-validated random forest models. The best performance of 99.91% of F1 score is reached by utilising Feature Ranking and the EfficientNet classifier, successfully maintaining the false positive rate of roughly 0.11%.

Limitations: In IoT traffic communications, samples taken in close proximity are linked to each other. Another biggest problem with Via CNN is that it takes a long time to train the model, even though it works well at classifying tabular data sets using picture projection.

vii. Temporal Features

Temporal features (TFs), such as rhythmic traits or temporal transitions, reflect the relatively long-term dynamics of a music signal throughout time. An LSTM network allows you to input sequence data and produce predictions based on each of the different time steps in the sequence data.

A higher-quality ID system uses Spark MLlib (Stage-1 Anomaly detection using a number of reliable classification algorithms, such as LR and XGB), as as well as cutting-edge DL methods like LSTM-AE (Stage-2 Misuse detection), which combines shallow and deep networks to reduce their analytical costs and take advantage of their strengths (LSTM to find temporal features and an AE to find global features more quickly). When full feature datasets are used, the two steps of the ID framework are efficient in terms of the amount of work they require and give more accurate results with less FAR. It quickly and automatically figures out how to represent key features from a huge amount of unlabeled raw network traffic data in order to find and classify attacks that weren't expected. The proposed HIIDS, which is based on DL classification, improves ID accuracy and DR while making the system as easy to use as possible. It incorporates the advantages of both signature-based (SB) and anomaly-based (AB) techniques.

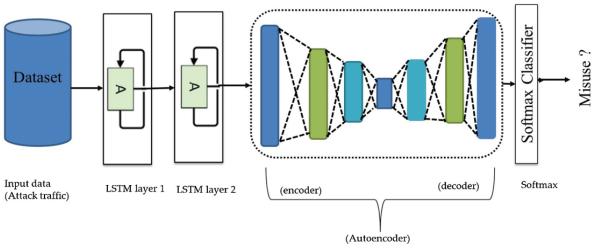

Figure 6. The micro-overview of LSTMAE [25]

The results show that when the HIIDS method is compared with other traditional ML methods, the HIIDS method is a good fit for finding harmful traffic. It was discovered through 10-fold cross-validation that it correctly identified network misuses in 97.52% of cases for the ISCX-UNB dataset, which is superior to other ID techniques.

Limitations: Since IoT traffic samples taken at close-together times are so similar, new IDS must take into account the time context.

viii. Spatial + Temporal Features

Semi-supervised methods, especially when only a small number of labelled examples are available, a given classifier is trained using annotated and unannotated samples. The focus is on the use of these methods in creating spatial-temporal models for data gathered over time and location. A semi-supervised deep learning model called SS-DeepID has been introduced to efficiently learn from both labelled and unlabeled IoT traffic logs. The model has a unique architecture that includes a DC-Conv, a multiscale residual temporal convolution block, and an attention module. Results from empirical analysis of two datasets have shown that the proposed method improves performance, intrusion detection efficiency and computational efficiency. However, the limitations of the method include its

efficiency with large amounts of IoT traffic data, lack of consideration for privacy protection, and uncertainty in data interpretation. Federated learning may be used in the future to address the privacy protection issue.

a. Graph-Based

Current ML-based NIDS's limited ability to defend against common adversarial attacks limits their applicability in real-world networks. These systems have a fundamental issue in that they treat and categorise flows differently. It is crucial to record significant structural flow patterns that represent various attack types, such as DDoS, port/network scans, and brute-force attacks, in order to have a successful ML-based NIDS.

According to Perich et al.[27], a graph representation accurately captures the characteristics of flows and their connections in the network. Then it introduces a novel GNN architecture explicitly created to learn from and generalise the prior graph-structured data. Tests of the proposed GNN model's accuracy using the CIC-IDS2017 dataset show that it is fully robust to detecting these attacks more accurately than other existing ML-based IDS. This is largely due to the proposed GNN model's capacity to learn the structural flow patterns that distinguish various attacks. These structural patterns give us more information about attacks because they usually don't change over time or between networks.

Most GNN models use the Message-Passing Neural Network (MPNN) [29] as their fundamental framework. MPNN operates on a graph in which each node is defined by an initial set of features that are used to encode its initial hidden state. After that, the MPNN moves on to the message-passing phase, which is iterated T times. Formally, the following operations (1) and (2) are applied in each message-passing step.

$$h_i^{(l+1)} = \sigma\left(b^l + \varphi\left(h_i^l, w^l, m^{l+1}\right)\right) \quad (1)$$

$$m_i^{l+1} = \varphi\left(X_{i,j}\right) \quad (2)$$

The ML-based NIDS that was suggested earlier looks at flow data records in isolation, without taking into account how they relate to each other or the traffic pattern as a whole. Therefore, using these techniques will not be able to detect more complex IoT network attacks like botnet attacks [30], distributed port scans [31], or DNS amplification attacks [32], which need a deeper comprehension of the network and traffic flow. When identifying distributed attacks in the IoT, researchers advise taking into account traffic patterns on a more global scale and, consequently, flow interrelationships. Lo et al.[28] suggest E-GraphSAGE, another GNN model that is meant to get around the problems that NIDSs have right now for IoT. The E-GraphSAGE makes it possible to collect information on flow-based features and topological patterns to understand how network flows are connected. E-GraphSAGE thus supports the edge classification procedure and, as a result, the detection of malicious network flows.

E-graph convolution layer is a graph convolution layer modification for graphs with multi-dimensional edge features that uses a message passing function to aggregate the edge features of all the node's neighbouring edges. A layer of e-graph convolution can be described as, for each node i: aggregating the neighbouring node features of node i, and transforming the aggregated form with a linear transform followed by a nonlinear function. As shown in Table 6, the E-GraphSAGE-based NIDS outperformed other algorithms in key classification metrics across four benchmark datasets.

b. Streaming Data

A real-time network IDS is required because the internet is getting faster and more complex thanks to technologies like 5G, and it must be able to process large amounts of network traffic data quickly in order to identify malicious traffic as early as possible. Such high-speed traffic data cannot be detected by a conventional intrusion detection system (IDS). Zhang et. al. [33] propose a distributed RF detection model built on Spark The CICIDS2017 intrusion dataset is used to simulate the complete system in a framework made up of Spark distributed cluster, logstash and kafka. Softflow distributes PCAP file from the dataset in order to simulate network data traffic. The distributed RF detection model is then included in a Spark cluster, where the data are sent for detection using logstash and kafka.

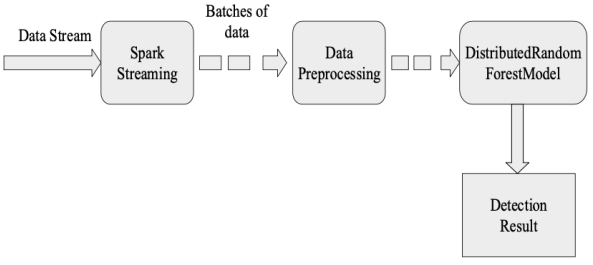

Figure 5. The real-time detection flow based on spark internal topology

Existing intrusion detection systems try to find odd events or edges in streams of dynamic graphs. However, this means that extra information about each entry can't be taken into account. This study by Bhatia et al.[34] suggests the MStream framework for streaming multi-aspect data anomaly identification, which may dynamically identify unexpected group abnormalities as they happen. The features of MStream include (a) its

ability to identify outliers in multi-aspect data, which includes both categorical and numerical attributes; (b) its online operation, which allows it to process each record in an equal amount of time and memory; and (c) its ability to identify correlations between various components of the data. The paper goes into further detail regarding the MStream approach as well as its modifications, the MStream-PCA, MStream-AE, and MStream-IB approaches, which incorporate feature correlation in an unsupervised manner. Principal component analysis is used by MStream-PCA, information bottlenecking is used by MStream-IB, and an autoencoder is used by MStream-AE to compress the original features before applying MStream in the compressed feature space. According to the experimental findings and comparisons presented in Table 6, the suggested MStream detection model can achieve real-time intrusion detection in a high-speed network environment and has a shorter detection time and higher accuracy.

c. G. Cloud-based solutions

The intrusion detection systems' limited data processing capacity limits the effectiveness and timeliness of the system's detection while also slowing down the pace of IDS development due to the constantly growing volume of network detection data. But this problem can be fixed by making intrusion detection systems work with powerful cloud computing. Mobile cloud computing (MCC) also enables smart mobile devices (SMDs) to access cloud resources, offload data from smartphones, and purchase computational services for application processing. You and Wang [40] conduct an empirical study on the design of a cloud-based network intrusion detection system using the 10% training datasets from KDDCup99. The results show that a cloud-based network IDS is capable of detecting four common types of attacks, including U2R, Probe, R2L and DoS, with detection rates all greater than 94%, the highest false alarm rate is 4.32%, and the fastest detection time is only 50 seconds. This proves the viability of the system detection. The architecture of the network intrusion detection system based on cloud computing that is discussed in this paper is shown in Figure 6.

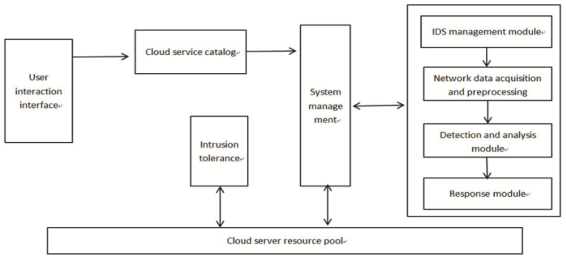

Figure 6. Model of network intrusion detection system based on cloud computing.

[1] 5. Comparison Analysis - A side-by-side comparison of the selected IDS techniques

TABLE V. Advantages And Disadvantages Of ML Based IDS

ML Based Method	Advantages	Disadvantages
Classical Machine Learning	- less information is required to solve the problem because the algorithm is given specific features by the user.	- the extensive training period is needed to process large dataset from the network's earlier data flow. - a low attack detection rate (DR) and the largest false alarm rate (FAR) in an ID system, respectively, show poor classification performance.
Hybrid	- eliminates the shortcomings of the two legacy IDSs - signature & anomaly-based - have better performance compared to single IDS - these record a greater detection rate with a lesser false alarm rate than a single algorithm.	- can't learn its environment and update itself without human input.
Deep Learning	- using big data, which has a unique learning mechanism, with little training time and high accuracy and detection rates. - it automatically pulls parts of the problem without needing a lot of information beforehand. - it reduces their analytical costs - it gives more accurate results with less FAR while making the system as easy to use as possible.	- To get the algorithm structure to its ideal state, too much data is required.
Graph - based	- takes a broad view of the network and traffic flow into account - Able to detect advanced IoT network attacks like distributed port scans, botnet attacks etc	- Extensive computation power - Require more memory to store and analyse the global view of network traffic
Streaming Data	detect malicious traffic as early as possible on high speed networks	- Sometimes results in lower accuracy
Cloud - based	- no need of high processing power and data storage - IDS as a SAAS on cloud platform	- Weak communication link between cloud IDS and Device - Prone to data leak

TABLE VI. Accuracy Analysis Of ML Based IDS

Ref.	Year	Dataset Used	Detection Technique Used	Results	
				Acc.	FAR
Classification-based ML					
[1]	2020	UNSW-NB15	Random Forest	85.10%	13.90%
[2]	2020	CICIDS-17	Naive Bayes	67.50%	7%
			Random Forest	96.50%	3.40%
[3]	2021	NSL-KDD	Decision Tree	93.70%	N/A
			Random Forest	92.10%	
			Logistic Regression	86.80%	
			Support Vector Machine	93.00%	
			Naive Bayes	92.20%	
			k-NN	86.70%	
Clustering-based ML					
[4]	2005	KDDCUP 99	k-means (k=4)	15.50%	0.20%
			k-means(k=15)	90%	16%
[5]	2016	DARPA	k-means	40.50%	N/A
			Hierarchical Clustering	85.60%	
Ensemble-based IDS					
[6]	2011	KDD-99	C4.5	83.30%	N/A
			Boosted C4.5	88.80%	
[7]	2014	KDD99	Naive Bayes	89.50%	10.60%
			Bagged -NB	89.50%	10.70%
			Boosted -NB	94.50%	5.30%
			Stacked-NB with DT-base	99.70%	0.25%
[8]	2018	NSL-KDD	Ensemble of 7 Classifiers (J48 + Meta-Pagging + RandomTree + REPTree + AdaBoostM1 + DecisionStump + NaîveBayes)	99.80%	0.25%
[9]	2020	UNSW-15	Stacked SVM with (RF+LR+KNN) base classifiers	94.00%	5.20%
		UGR 16		97.10%	1.00%
Hierarchical hybrid IDS					
[10]	2016	DARPA	Snort for known attack detection + Gaussian Mixture Model (GMM) clustering for anomaly detection	98.70%	0.73%
		Private		99.90%	0.01%
[11]	2016	NSL-KDD	SVM for anomaly detection + ANN for reducing false alarm rate	99.90%	0.20%
[12]	2018	ISCX 2012	k-means for reducing normal data + Random Forest	99.90%	0.05%
[13]	2019	NSL-KDD	Decision Tree for known attacks + Association Rule Mining to determine based on association rule over reduced normal data	99.70%	0.17%
Deep Learning					
[24]	2022	AWID2	CNN	99.89%	2.43%
[25]	2021	ISCX-2012	LSTM + Autoencoder	97%	1.20%
[26]	2021	CICIDS-17	DC-Conv	99.60%	
		CICIDS-18		99.69%	
Graph Based IDS					
				Weighted F1 Score	
[27]	2021	CICIDS-17	GNN - Global view of network traffic	0.99	
[28]	2022	BoT-IoT	E-GraphSAGE - a GNN model using edge classification	1	
		NF-BoT-IoT		0.81	
		ToN-IoT		0.87	
		NF-ToN-IoT		0.63	
Streaming Data / Real Time Data IDS					
				Acc	Running Time

Ref.	Year	Dataset Used	Detection Technique Used	Results	
				Acc.	FAR
[33]	2018	CICIDS-17	Distributed Random-Forest using Apache Spark	96%	0.04s
[34]	2020	KDD	M-Stream	96%	3.1s
		CICIDS 2018 Dos		94%	5.1s
		UNSW		90%	8.0s
		CICIDS 2018 DDoS		93%	27.7s
Cloud Based Data IDS					
				Acc, FAR	Running Time
[40]	2022	KDD	K-Means Clustering	96%, 4%	50s

[2] 6. Intrusion Detection Systems Challenges

Although machine learning techniques have made significant progress in the field of intrusion detection, the following problems still need to be solved.

• The most widely used datasets for IDS for many years included KDD99, NSL-KDD, a more recent CICIDS 17 was also seen in some studies. However, with the ever changing networks, and newer attack types, makes the models of proposed studies on any older dataset questionable. There is a need for datasets that are regularly updated.

• Decreased detection accuracy in real-world settings. Despite the fact that machine learning algorithms have a certain capacity to identify intrusions, they often do not perform well on data that is entirely novel to them. The majority of the available studies were carried out using labelled datasets as their starting point. As a result, when the dataset does not include all of the usual real-world examples, good performance in real-world situations is not guaranteed—even if the models achieve high accuracy on test sets, good performance in real-world situations is not guaranteed.

• Because detection outcomes are so important in most studies, sophisticated models and extensive data preparation procedures are frequently used, resulting in better performance but longer training and detection times, resulting in poor efficiency. But for intrusion detection systems (IDSs) to do the least amount of damage, attacks must be found in real time. Many researchers are working on different techniques to improve this situation, as it is also important to reduce the amount of resources used.

• When it comes to practical intrusion detection systems, interpretability is critical for detection because the intrusions detected must be analysed by a human. An intrusion detection model that makes analysis difficult to understand, particularly deep learning models, has low interpretability and makes no sense. On the other hand, every cyber security choice should be made with care, not based on a weak output that can't be traced back to its source.

[3] 7. Conclusion & Future Scope

This work has suggested a thorough, detailed, and consolidated review of IDSs in the context of IoT ecosystems. The various state-of-the-art IDS approaches were examined in light of the benefits of using machine learning for intrusion detection, and classification was carried out according to the kind of technology employed. The shortcomings of the conventional intrusion detection methods were examined and highlighted.

The identified papers are divided into six primary categories based on the readily available literature: classical machine learning-based IDS, hybrid IDS, deep learning-based IDS, graph-based IDS, streaming data-based IDS, and cloud-based IDS. Twenty more attack categories are taken into account, including DoS, U2R, R2L, Probe, Brute Force SSH, Brute Force, Infiltration, DDoS, Fuzzers, Analysis, Backdoors, Exploits, Generic, Reconnaissance, Shell Code, Worms, Heartbleed, Web Attack, Botnet, and Port Scan.

The benefits and drawbacks of many IDSs are discussed that includes comparing and contrasting the different approaches. Based on the strategy, dataset, and effectiveness of the claimed intrusion detection technology, many researchers' ideas for improving accuracy, false alarm rate, training duration, interpretability, and other aspects of intrusion detection were seen and listed. This is a description of the problems that exist in intrusion detection right now, which can be seen as the future potential of the field. IDS that are more effective and beneficial might be a major area of focus instead of complex black box systems. Using simulation software or test environments to evaluate a system helps make sure that it will work well when used in real networks.

KDDCup99 and NSL-KDD are two datasets that showed high usage in the papers that were analysed. Researchers have criticised these datasets despite their high observed popularity as they are outdated. As a solution to this problem, the literature review found that there are more and more databases that keep track of recent invasions. These consist of the datasets from CICIDS2017, UNSW-NB15, CSE-CIC-IDS2018, and Bot-IoT. The majority of the research still makes use of outdated datasets, which is an issue. Researchers in this area of intrusion detection systems (IDS) must be willing to use

the updated datasets if they want to make IDS that works well.

Future research should take CPU usage and detection time into account as performance measures. The detection period should be as short as feasible because intrusion should be detected immediately before any damage is done. Resource utilisation should be taken into account while developing intrusion detection systems.

This research is a good place to start when coming up with research problems for future researchers because it shows where there are gaps and where there are overlaps. Overall, the definitional questions' responses highlight the primary objective of intrusion detection, as well as its current issues, unresolved issues, and potential applications in the Internet of Things.

● REFERENCES

[4] Dutta, Vibekananda, Michał Choras´, Rafał Kozik, and Marek Pawlicki. ”Hybrid model for improving the classification effectiveness of network intrusion detection.” In Computational Intelligence in Security for Information Systems Conference, pp. 405-414. Springer, Cham, 2019.

[5] Ahmim, Ahmed, Mohamed Amine Ferrag, Leandros Maglaras, Makhlouf Derdour, and Helge Janicke. ”A detailed analysis of using supervised machine learning for intrusion detection.” In Strategic Innovative Marketing and Tourism, pp. 629-639. Springer, Cham, 2020.

[6] Thakkar, Ankit, and Ritika Lohiya. ”Attack classification using feature selection techniques: a comparative study.” Journal of Ambient Intelligence and Humanized Computing 12, no. 1 (2021): 1249-1266.

[7] Zhang,Yu-Fang,Zhong-YangXiong,andXiu-QiongWang.”Distribut ed intrusion detection based on clustering.” In 2005 International Conference on Machine Learning and Cybernetics, vol. 4, pp. 2379-2383. IEEE, 2005.

[8] [5] Alhaj TA, Siraj MM, Zainal A, Elshoush HT, Elhaj F (2016) Feature selection using information gain for improved structural-based alert correlation. PLoS ONE 11(11):e0166017

[9] Bahri, Emna, Nouria Harbi, and Hoa Nguyen Huu. ”Approach based ensemble methods for better and faster intrusion detection.” In Computational intelligence in security for information systems, pp. 17-24. Springer, Berlin, Heidelberg, 2011.

[10] Syarif, Iwan, Ed Zaluska, Adam Prugel-Bennett, and Gary Wills. ”Application of bagging, boosting and stacking to intrusion detection.” In International Workshop on Machine Learning and Data Mining in Pattern Recognition, pp. 593-602. Springer, Berlin, Heidelberg, 2012.

[11] Aljawarneh, Shadi, Monther Aldwairi, and Muneer Bani Yassein. ”Anomaly-based intrusion detection system through feature selection analysis and building hybrid efficient model.” Journal of Computational Science 25 (2018): 152-160.

[12] Rajagopal, Smitha, Poornima Panduranga Kundapur, and Katiganere Siddaramappa Hareesha. ”A stacking ensemble for network intrusion detection using heterogeneous datasets.” Security and Communication Networks 2020 (2020).

[13] O ¨ Cepheli, S. Bu ¨yu ¨kc orak, and G. Karabulut Kurt, “Hybrid Intrusion Detection System for DDoS Attacks,” J. Electr. Comput. Eng., vol. 2016, 2016, doi: 10.1155/2016/1075648.

[14] Hussain, Jamal, Samuel Lalmuanawma, and Lalrinfela Chhakchhuak. ”A two-stage hybrid classification technique for network intrusion detection system.” International Journal of Computational Intelligence Systems 9, no. 5 (2016): 863-875

[15] Soheily-Khah S, Marteau PF, Be´chet N (2018) Intrusion detection in network systems through hybrid supervised and unsupervised machine learning process: a case study on the ISCX dataset. In: 2018 1st international conference on data intelligence and security (ICDIS). IEEE, pp 219–226

[16] Adhanom and H. M. Melaku, “A hybrid behavioural-based cyber intrusion detection system,” Int. J. Commun. Networks Distrib. Syst., vol. 23, no. 4, pp. 473–498, 2019, doi: 10.1504/IJCNDS.2019.102986.

[17] Bourou, Stavroula, Andreas El Saer, Terpsichori-Helen Velivassaki, Artemis Voulkidis, and Theodore Zahariadis. ”A review of tabular data synthesis using gans on an ids dataset.” Information 12, no. 9 (2021): 375.

[18] Thomas, Ciza, Vishwas Sharma, and N. Balakrishnan. ”Usefulness of DARPA dataset for intrusion detection system evaluation.” In Data Mining, Intrusion Detection, Information Assurance, and Data Networks Security 2008, vol. 6973, pp. 164-171. SPIE, 2008.

[19] Kumar, Satish, and Sakshi Arora. ”A Statistical Analysis on KDD Cup’99 Dataset for the Network Intrusion Detection System.” In International conference on advanced communication and networking, pp. 131-157. Springer, Singapore, 2019.

[20] Shiravi, Ali, Hadi Shiravi, Mahbod Tavallaee, and Ali A. Ghorbani. ”Toward developing a systematic approach to generate benchmark datasets for intrusion detection.” computers security 31, no. 3 (2012): 357-374.

[21] Moustafa, Nour, and Jill Slay. ”UNSW-NB15: a comprehensive data set for network intrusion detection systems (UNSW-NB15 network data set).” In 2015 military communications and information systems conference (MilCIS), pp. 1-6. IEEE, 2015.

[22] Sharafaldin, Iman, Arash Habibi Lashkari, and Ali A. Ghorbani. ”To- ward generating a new intrusion detection dataset and intrusion traffic characterization.” ICISSp 1 (2018): 108-116.

[23] S. Keele, Guidelines for performing systematic literature reviews in software engineering, Technical report, Ver. 2.3 EBSE Technical Report. EBSE, 5, 2007.

[24] B.A. Milani, N.J. Navimipour, A systematic literature review of the data replication techniques in the cloud environments, Big Data Res. 10 (2017) 1–7.

[25] A.S. Milani, N.J. Navimipour, Load balancing mechanisms and techniques in the cloud environments: systematic literature review and future trends, J. Netw. Comput. Appl. 71 (2016) 86–98.

[26] A.A. Neghabi, N.J. Navimipour, M. Hosseinzadeh, A. Rezaee, Load balancing mechanisms in the software defined networks: a systematic and comprehensive review of the literature, IEEE Access 6 (2018) 14159–14178.

[27] M. Erza Aminanto, I. Rifqi Purbomukti, H. Chandra and K. Kim, "Two-dimensional projection-based wireless intrusion classification using lightweight efficientnet," Computers, Materials & Continua, vol. 72, no.3, pp. 5301–5314, 2022.

[28] M. Ashfaq Khan and Y. Kim, "Deep learning-based hybrid intelligent intrusion detection system," Computers, Materials & Continua, vol. 68, no.1, pp. 671–687, 2021.

[29] M. Abdel-Basset, H. Hawash, R. K. Chakrabortty and M. J. Ryan, "Semi-Supervised Spatiotemporal Deep Learning for Intrusions Detection in IoT Networks," in IEEE Internet of Things Journal, vol. 8, no. 15, pp. 12251-12265, 1 Aug.1, 2021, doi: 10.1109/JIOT.2021.3060878.

[30] David Pujol-Perich, Jose Suarez-Varela, Albert Cabellos-Aparicio, and Pere Barlet-Ros. 2022. Unveiling the potential of Graph Neural Networks for robust Intrusion Detection. SIGMETRICS Perform. Eval. Rev. 49, 4 (March 2022), 111–117. https://doi.org/10.1145/3543146.3543171

[31] Wai Weng Lo, Siamak Layeghy, Mohanad Sarhan, Marcus Gallagher, and Marius Portmann. 2022. E-GraphSAGE: A Graph Neural Network based Intrusion Detection System for IoT. In NOMS 2022-2022 IEEE/IFIP Network Operations and Management Symposium. IEEE Press, 1–9. https://doi.org/10.1109/NOMS54207.2022.9789878

[32] Justin Gilmer, Samuel S. Schoenholz, Patrick F. Riley, Oriol Vinyals, and George E. Dahl. 2017. Neural Mes- sage Passing for Quantum Chemistry. In Proceedings of the International Conference on Machine Learning (ICML), Vol. 70. 1263–1272.

[33] G. Vormayr, T. Zseby, and J. Fabini, “Botnet com- munication patterns,” IEEE Communications Surveys Tutorials, vol. 19, no. 4, pp. 2768–2796, 2017. DOI: 10.1109/COMST.2017.2749442.

[34] M. H. Bhuyan, D. K. Bhattacharyya, and J. K. Kalita, “Surveying port scans and their detection methodologies,” The Computer Journal, vol. 54, no. 10, pp. 1565– 1581, 2011.

[35] G. Kambourakis, T. Moschos, D. Geneiatakis, and S. Gritzalis, “Detecting dns amplification attacks,” in International workshop on critical information infrastructures security, Springer, 2007, pp. 185–196.

[36] H. Zhang, S. Dai, Y. Li and W. Zhang, "Real-time Distributed-Random-Forest-Based Network Intrusion Detection System Using Apache Spark," 2018 IEEE 37th International Performance Computing and Communications Conference (IPCCC), Orlando, FL, USA, 2018, pp. 1-7, doi: 10.1109/PCCC.2018.8711068.

[37] Siddharth Bhatia, Arjit Jain, Pan Li, Ritesh Kumar, and Bryan Hooi. 2021. MStream: Fast Anomaly Detection in Multi-Aspect Streams. In Proceedings of the Web Conference 2021 (WWW '21), April 19–23, 2021, Ljubljana, Slovenia. ACM, New York, NY, USA 12 Pages.

[38] Kolias, Costantinos & Kambourakis, Georgios. (2015). Aegean Wi-Fi Intrusion Dataset (AWID).

[39] N. Koroniotis, N. Moustafa, E. Sitnikova, and B. Turnbull, “Towards the development of realistic botnet dataset in the Internet of Things for network forensic an- alytics: Bot-IoT

dataset," Future Generation Computer Systems, 2019, ISSN: 0167739X. DOI: 10.1016/j.future. 2019.05.041. arXiv: 1811.00701.

[40] A. Alsaedi, N. Moustafa, A. M. Z. Tari, and A. Anwar, "TON IoT telemetry dataset: A new generation dataset of iot and iiot for data-driven intrusion detection systems," IEEE Access, vol. 8, pp. 165 130–165 150, 2020. DOI: 10.1109/ACCESS.2020.3022862.

[41] M. Sarhan, S. Layeghy, N. Moustafa, and M. Portmann, Netflow datasets for machine learning-based network intrusion detection systems, Nov. 2020. arXiv: 2011. 09144.

[42] Mohamed Amine Ferrag, Othmane Friha, Djallel Hamouda, Leandros Maglaras, Helge Janicke, January 17, 2022, "Edge-IIoTset: A New Comprehensive Realistic Cyber Security Dataset of IoT and IIoT Applications: Centralized and Federated Learning", IEEE Dataport, doi: https://dx.doi.org/10.21227/mbc1-1h68.

[43] L. You and Z. Wang, "A Cloud Based Network Intrusion Detection System", Tehnički vjesnik, vol.29, no. 3, pp. 987-992, 2022. [Online]. https://doi.org/10.17559/TV-20211130024245

[44] Yu,Zhenwei.,Tsai,JeffreyJP.IntrusionDetection:AMachineLearning Approach. Singapore: World Scientific Publishing Company, 2011.

[45] Ozkan-Okay,Merve,RefikSamet,O ¨merAslan,andDeeptiGupta."A Comprehensive Systematic Literature Review on Intrusion Detection Systems." IEEE Access (2021).

Author 1 Apoorva Aggarwal, final year undergraduate pursuing B. Tech. from Delhi Technological University under Department of Information Technology. She is an AI-ML enthusiast, and has experience working as a machine learning engineer. Her research interests include Network Security, IoT, Machine Learning, Natural Language Processing and Automatic Speech Recognition.

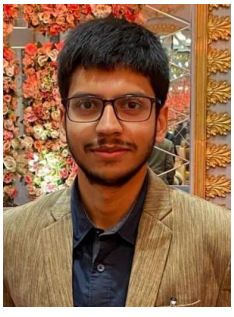

Author 2 Kushagra Keserwani, final year undergraduate pursuing B.Tech from Delhi Technological University under Department of Information Technology. He is a tech enthusiast, passionate about coding and has experience working as a backend developer. His research interests include Network Security, IoT, Machine Learning and Natural Language Processing.

Author 3 Anamika Chauhan, Member IEEE (M.Tech, B.Tech) has published more than ten international journal/conference papers/book chapters. Her research interests include computer networks , Internet of Things , Smart cities, Blockchain applications etc. She is the reviewer of several IEEE conferences. She is a member of many technical and professional societies. She possesses more than fifteen years of research and academic experience and presently, working as Assistant Professor in the department of IT at DTU, Delhi, India.

ResearchGate

See discussions, stats, and author profiles for this publication at: https://www.researchgate.net/publication/372486542

Tackling class imbalance in computer vision: a contemporary review

Article *in* Artificial Intelligence Review · July 2023

DOI: 10.1007/s10462-023-10557-6

CITATIONS
0

READS
128

2 authors:

Manisha Saini
Delhi Technological University
11 PUBLICATIONS **152** CITATIONS

SEE PROFILE

Seba Susan
Delhi Technological University
134 PUBLICATIONS **1,425** CITATIONS

SEE PROFILE

All content following this page was uploaded by Manisha Saini on 21 July 2023.

The user has requested enhancement of the downloaded file.

This article has been accepted for publication in a future issue of this journal, but has not been fully edited. Content may change prior to final publication. Citation information: DOI 10.1007/s10462-023-10557-6, Artificial Intelligence Review

Tackling class imbalance in computer vision: A contemporary review

Manisha Saini* and Seba Susan
Delhi Technological University, Delhi, India
*Email: manisha.saini44@gmail.com

Abstract

Class imbalance is a key issue affecting the performance of computer vision applications such as medical image analysis, objection detection and recognition, image segmentation, scene understanding, and many others. Class imbalance refers to the situation when the number of samples in the majority classes outnumber the minority class populations. The model might then get biased towards the majority classes while neglecting the minority classes, adversely affecting the classification performance. In this paper, an extensive literature survey has been conducted to discuss in depth about the class imbalance issues affecting various classification tasks in computer vision. The study analyzes the performance of several contemporary machine learning algorithms such as chi-square support vector machine and gradient boosted decision trees, and deep learning models such as deep pre-trained convolutional networks, generative adversarial networks and vision transformers, for effective learning from imbalanced computer vision datasets. Most of these models either perform data-level manipulation (data augmentation) or cost-sensitive learning (loss functions) or a combination of the two. This survey also includes a summary of novel deep learning frameworks customized to mitigate the effect of class imbalance. It has included recent advancement and new developments in this field such as Explainable AI. The scrutiny of various popular and benchmark imbalanced datasets in computer vision and performance evaluation metrics are also included as a part of this study. Along with that it has emphasized on the research gaps in contemporary literature which would contribute towards future artificial vision models that can learn effectively from imbalanced datasets.

Keywords: Class imbalance, Computer vision, Data-level manipulation, cost-sensitive learning, Deep learning

1. Introduction

Nowadays, due to a vivid increase in the visual data from multiple sources, there is an exponential rise in the cases of class imbalance occurring in real-world computer vision datasets. Class imbalance is the situation where the classes present in a dataset are unevenly distributed. This problem is highlighted when the sample distribution in one or more classes is more in comparison to other classes due to which priority during the learning process is given to the class which has more sample size distribution in comparison to others [1]. Generally, when one class is much more prevalent than the others, the algorithm will prioritize minimizing errors for the more prevalent class at the expense of the less prevalent classes. This can degrade the performance of the less prevalent classes which brings down the overall classification performance [2]. Even if a model exhibits high classification accuracy, there are higher chances of misleading results due to inaccurate predictions for the underrepresented classes. The topic has been

extensively researched in the data mining community [3], but not so satisfactorily in the computer vision field. The handling of class imbalance in image datasets remains one of the persistent challenges in the field of computer vision. It is crucial to address this issue to ensure fair and accurate classification performance in computer vision tasks.

In this section, the paper delves deeper into the issue of class imbalance, examining it from various perspectives. It begins with section 1.1 which sheds light on the generic problem of class imbalance that is prevalent in real-world applications. Next, section 1.2 explores the potential causes of class imbalance, aiming to understand the factors contributing to this issue. Moving on to section 1.3, the study takes a closer look at the specific challenges posed by class imbalance in both binary and multi-class datasets. In section 1.4, this study delves into a discussion of the traditional methods in data mining that have been employed to tackle this problem, and that can be easily adapted to the computer vision domain. In section 1.5, the focus is directed towards class imbalance in the domain of computer vision while section 1.6 gives an overview of some popular solutions for mitigating the class imbalance in computer vision. A summary of other surveys, contributions of the current survey, and the organization of the paper are outlined in sections 1.7, 1.8 and 1.9, respectively. By understanding these details, the reader can better appreciate the significance of addressing class imbalance to ensure fair and accurate performance in computer vision applications.

1.1 Some real-world instances of class imbalance

The class imbalance problem is prevalent in a variety of real-world applications including diagnostic procedures in the biomedical domain, credit card fraud detection, surveillance, biometric verification etc. In most cases, it is the minority class that is of more interest, hence a lot is at stake for finding effective solutions for learning from such a flawed dataset. Alam et al. have worked on credit card imbalanced datasets [150]. The major finding of their study is that the performance of over-sampling techniques like synthetic minority oversampling (SMOTE) [177] is better than under-sampling techniques applied at data level. According to the experimental results it was proved that the Gradient Boosted Decision Trees works well in comparison to other machine learning classifiers for imbalanced datasets. Yang et al. (2020) emphasized on feature engineering by selecting appropriate features which can overall improve the early prediction of ovarian cancer [153]. The experimental analysis proved that the decision tree in combination with SVM-SMOTE gives overall better performance in comparison to other traditional classifiers. The decision tree classifier has already proved to be a reliable machine learning strategy in various domains of data mining [154][155].

In the biomedical domain, class imbalance occurs when certain disease conditions are rare, as is the case with certain cancer subtypes, as compared to healthy individuals [4]. The model may not accurately identify individuals with the disease in this case, which can have serious consequences in healthcare settings. In case of credit card fraud detection, class imbalance occurs when fraudulent transactions are much less common than legitimate transactions [5]. A model which is trained on this kind of dataset may prioritize minimizing the errors for the majority class (transactions which are legitimate) at the expense of the minority class (transactions which are fraudulent), which ultimately leads to poor performance of the minority class.

Similarly, in surveillance and biometric applications, class imbalance can occur when certain events or individuals are much less common than others [6]. Class imbalance in computer vision may induce a rise in the numbers of false negatives and false positives degrading the system performance. For example, a surveillance system that is trained to detect criminal activity may perform poorly on the minority class

(activities which are suspected as criminal) because it has very few examples to learn from. This can lead to false negatives, where the system fails to detect criminal activity that is actually occurring. The foreground-background imbalance is a typical instance of class imbalance in video surveillance applications. An innovative approach to anomaly detection known as Attention-loss driven anomaly detection method is introduced in [7] to address the foreground-background imbalance by assigning distinct weights to the foreground and background in order to mitigate the foreground-background imbalance. Another popular classification task in video surveillance is the detection of small objects such as weapons and purses whose samples in the training set are in minority as compared to the background clutter; many objects in the background may resemble the small objects under consideration leading to a rise in the number of false positives. An improvised approach was proposed in [8] for detecting small objects using binary classifiers. The number of false positives were found to be significantly reduced by this approach. The initial stage involves selecting candidate regions from the input frame and gradually shifting towards applying a binarization technique based on a convolutional neural network classifier.

1.2 Factors contributing to class imbalance

The occurrence of imbalanced datasets in the real-world may be due to some common factors as illustrated below for the example of biomedical image datasets: (a) Improper manner of data collection that may occur due to lack of technology or due to the lack of proper equipment leading to improper data acquisition. This is generally observed in the biomedical domain where there are possibilities of equipment failure or lack of modern diagnostic procedures (b) A lot of manual effort is required for the collection of a labeled and annotated dataset which can also contribute towards class imbalance. The lack of availability of medical professionals/experts for huge data collection and annotation have rendered several biomedical datasets to have an imbalanced class distribution profile (c) Imbalance situation can also occur due to the actual lack of samples in different classes which are termed as minority classes. This may be observed for images of cancerous tissues that occur in a minority as compared to the healthy tissues (d) Class overlapping could be another reason where there might be more than two groups (such as various subtypes of cancers) and further noise caused due to class label and unclear separation of borders/boundaries between various classes can also cause significant impact on the model performance. The mistakenly defined wrong labels can also cause the increase in the imbalance scenario. In this type of situation there is a need to have clearly defined strategies for labeling the classes in an appropriate manner so that there is no overlapping of the class boundaries.

1.3 Binary versus multi-class imbalanced datasets

Imbalanced datasets found in literature are broadly categorized into two groups i.e. binary and multi-class. While a binary imbalanced dataset has two classes (one is majority and another one is minority), in the case of multi-class imbalanced dataset there are multiple classes (there could be multiple majority or minority classes). Different types of solutions are proposed in literature for binary and multi-class imbalanced datasets though the works on multi-class datasets are relatively rare to find. Fig. 1. shows instances of balanced and imbalanced class distributions of the samples of images in a biomedical dataset in the cases of both binary and multi-class scenarios. In comparison to the binary dataset, there are more difficulties and challenges involved in addressing the concerns related to multi-class imbalance problems. There is a possibility of occurrence of various combinations in multi-class imbalanced datasets which includes: (1) presence of more minority classes as compared to the majority classes in the dataset (2) occurrence of fewer minority classes and more majority classes. Moreover, in the case of the multi-class

imbalanced dataset, it is difficult to set a proper definition for deciding which are the majority or minority categories solely based upon the sample distribution in each class [9].

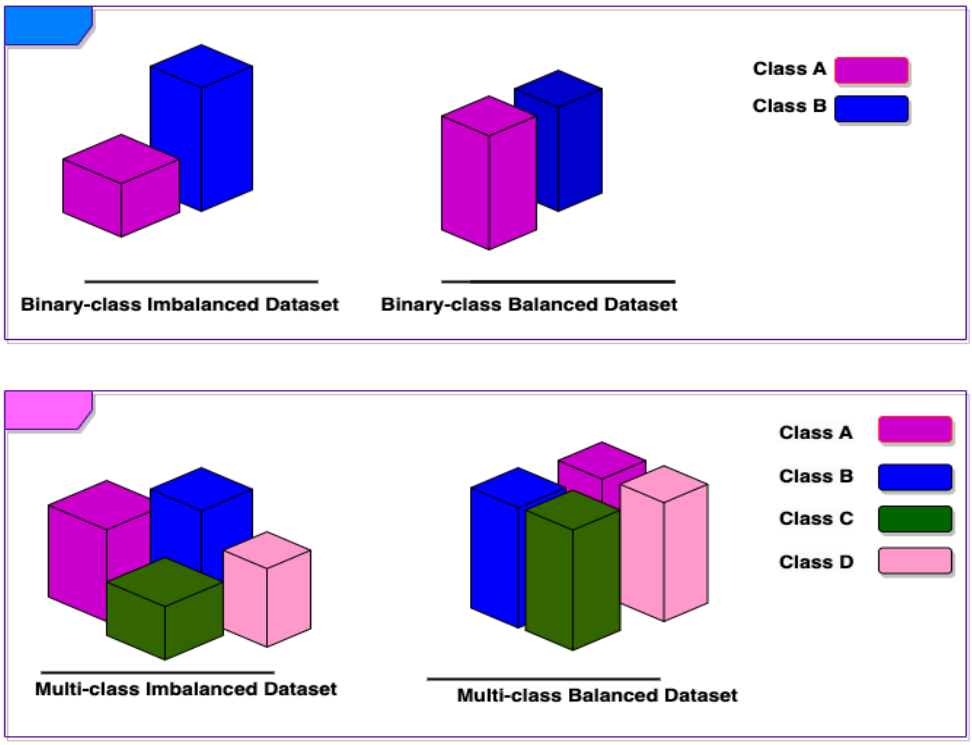

Fig. 1. Visual representation of imbalanced and balanced class distributions for binary- and multi-class datasets

Long-tailed class imbalance [67] is a problem in visual recognition tasks where the system is biased towards the dominant classes but performs adversely on the tail classes. Balanced group softmax (BAGS) is used in [68] to mitigate long-tailed class imbalance by ensuring that the training process for the head and tail classes are done in such a way that they are both trained equally well. They also emphasized that the reason for the down performance on long-tailed data is that the classifier becomes imbalanced in the presence of insufficient training on few-shot class. Fig. 2. illustrates a long-tailed data distribution showcasing the contrast between the dominant or majority classes and the tail classes which are the minority classes.

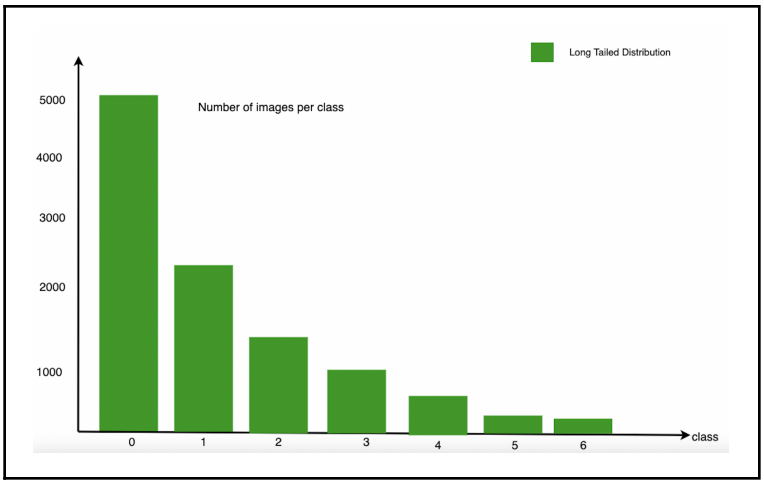

Fig. 2. Illustration of long-tailed data distribution in an imbalanced dataset.

1.4 An overview of traditional strategies used for imbalanced learning in data mining

To address class imbalance issues in data mining, various researchers have proposed solutions at data, algorithm and hybrid levels [10][11]. These are known as the traditional approaches and use machine learning for the classification. Data level approaches aim to balance the class distributions by resampling [3] which can be of three forms: (i) oversampling the under-represented minority class (ii) under sampling the over-represented majority class (iii) hybrid approaches involving both under sampling and oversampling procedures. Data-level manipulations help to create a balanced dataset having more or less equal samples in each class and helps to remove any kind of bias towards a particular class. Applying data level approaches on the training dataset can act as a regularization technique and reduces the chance of overfitting the model in case there is an increase in the number of samples (oversampling), however, decreasing the number of samples (under sampling) can lead to under-fitting issues [12]. Hybrid sampling techniques that involve sampling the majority class and oversampling the minority class have been found to yield improved performance [13]. Such data level manipulations can be termed as intelligent data pruning techniques [14] that retain only those samples that help in effective classification. Data pruning has thus two objectives (i) to maintain a balanced class distribution (ii) retain the 'significant' samples that maintain the diversity in the data.

Fig. 3 depicts a taxonomy of various popular approaches used at data, algorithm and hybrid levels for handling imbalanced datasets. As illustrated in Fig. 3, data augmentation using image transformations, synthetic image generation using generative adversarial networks (GAN) [179], SMOTE and its variants, and over- and under-sampling algorithms are popular data level approaches which are applied to balance the dataset for binary and multi-class imbalanced datasets. Algorithm level approach, on the other hand, aims to modify the learning algorithm such that it pays more attention towards the under-represented class. An example of algorithm approach is cost-sensitive learning that assigns a higher weight to the loss function emanating from the minority class and a lower weight to the loss function emanating from the majority class [15]. Design of optimal loss functions for mitigating class imbalance in computer vision is a significant research direction. Application of class weights is another algorithmic approach to address class imbalance in computer vision by assigning different weights to samples of majority and minority classes present during the training process to account for the disproportionate representation of the

classes. By adjusting the weights, the algorithm can give more importance to the minority class and help mitigate the effects of class imbalance. Hybrid methods mainly focus on merging the data level and algorithm level approaches to create effective combinations. There exist several hybrid approaches such as RUSBoost which is a hybrid of resampling and boosting [17]; more generically these are known as the ensemble approaches [18]. Ensemble classifiers, such as bagging and boosting classifiers, are created by combining the strong and weak classifiers together that makes way for efficient learning. A recent work by Chen et al. [19] introduces a novel combination called balance cascade that initially samples the imbalanced data using Up-Down sampling strategy that initially upsamples and then downsamples the minority class, and later on the balanced dataset is trained on a "growing" multi-channel cascade forest, hence the name balance cascade. The channels that do not give good performance are terminated.

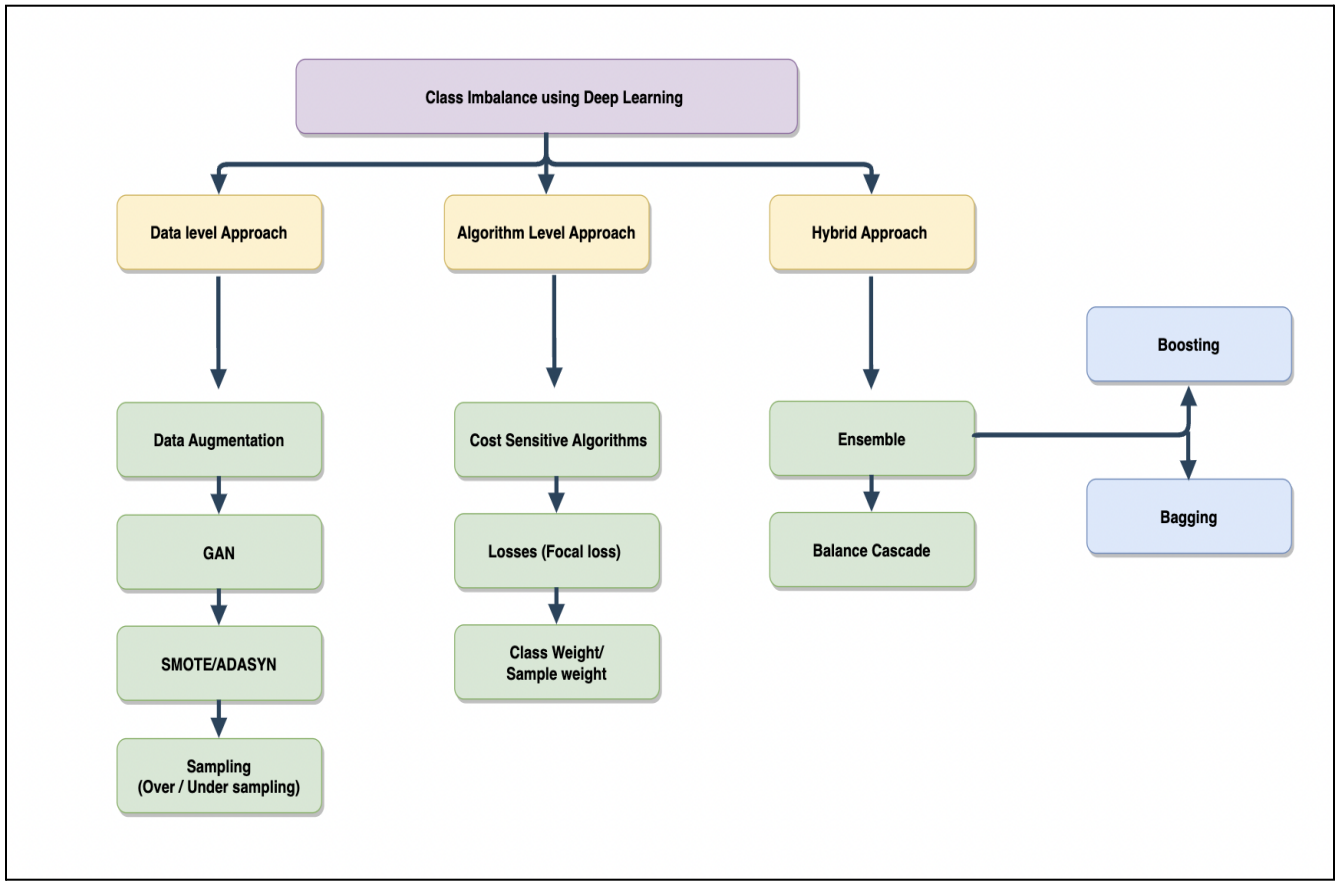

Fig. 3. Taxonomy of imbalanced learning solutions at the data, algorithm and hybrid levels

1.5 Class imbalance in computer vision-An overview of the problem

Object detection, localization, segmentation and classification are important tasks in the field of computer vision, and are used in a wide range of applications ranging from images and video analysis, robotics to autonomous vehicles etc. Class imbalance is a common problem in the computer vision domain, particularly in numerous tasks associated with classification, object detection, and semantic segmentation [20]. In image classification tasks, class imbalance can occur when some classes are much more in

number than others. There are various application domains in computer vision where imbalanced datasets are characteristically found [163]; some of these research areas are mentioned below for reference:
(1) *Biomedical domain*: Imbalanced datasets are common in the biomedical domain [116]. In the case of diagnostic systems for detecting rare diseases, the number of samples for the rare disease may be much smaller than the number of samples for more common disease types or the healthy samples. Examples in the biomedical domain are: a) ECG Heartbeat classification dataset: - This dataset contains ECG readings taken from individuals and is used to evaluate the performance of systems in detecting abnormalities in heart rhythms. b) Another example could be cancer detection from MRI/CT scan images - the cancerous samples being smaller in number in comparison to the non-cancerous samples.
(2) *Biometrics recognition:* Biometric domain consists of facial, fingerprints and iris patterns. Behavioral biometrics such as gait recognition is also well researched [174]. The class profile of biometric datasets is mostly imbalanced for most real-world datasets [148]. For example, in case of face recognition system, the number of samples for certain individuals may be much smaller in number in comparison to the other individuals present in the dataset.
(3) *Defect detection in industrial processes*: Another common imbalanced dataset is the one used for defect detection in fabrics or in surface inspection in industrial processes [105, 106]. Here, the number of image patches containing the defect are far less as compared to the defect-free image patches.
(4) *Pedestrian detection in traffic surveillance*: This is a commonly found imbalanced dataset useful in self-driving cars and video and traffic surveillance [115]. The dataset is imbalanced because the number of negative samples (non-pedestrian images) is much greater in number than positive samples (i.e. pedestrian images).
(5) *Object recognition*: Effective classification of the objects in a scene is tremendously affected by the distribution of object classes in the training set [175]. For example, in a dataset of objects, the class "object1" may have many more samples than the class "object2". This can lead to a model that performs well on the majority class (object1), but poorly on the minority class (object2).
(6) *Human activity recognition*: Likewise, in human activity datasets, the less frequent activities have fewer samples, resulting in an uneven class distribution [176]. Human activity recognition from videos is challenging when the intra-class variation is high and the inter-class variation is low. For instance, sports activities such as jumping, running and walking have overlapping contexts; this scenario is critically affected when a few of the classes are inadequately represented in the learning process.
(7) *Agriculture*: Some popular computer vision experiments related to agriculture are plant disease classification, weeds classification etc. [110][111]. The class imbalance issue is prevalent in this field due to the common occurrences of certain types of plant diseases as opposed to the rarely occurring ones.
(8) *Object detection and image segmentation*: Object detection and semantic segmentation tasks are also affected by class imbalance. For example, in a dataset of traffic scenes, the "pedestrian" class may be rarer than the "car class". This can lead to a model that has difficulty in detecting pedestrians, even if it performs well on other classes. In case of object detection, the main challenge involves identifying the location and class of numerous objects present in a given image; the problem is complicated when the size of the object is small. One major instance of class imbalance in computer vision is the smaller foreground (objects) area as compared to the larger (and cluttered) background area. As the object occupies a smaller portion of the image, there are multiple background pixels in comparison to the foreground pixels. This class imbalance can affect the performance of algorithms, particularly if the model is biased towards the background class. Fig. 4. depicts the object detection case where a class imbalance situation occurs in the

real-world example consisting of two categories: Minority (Foreground) and majority (Background). The number of background pixels were found to be significantly higher in this case.

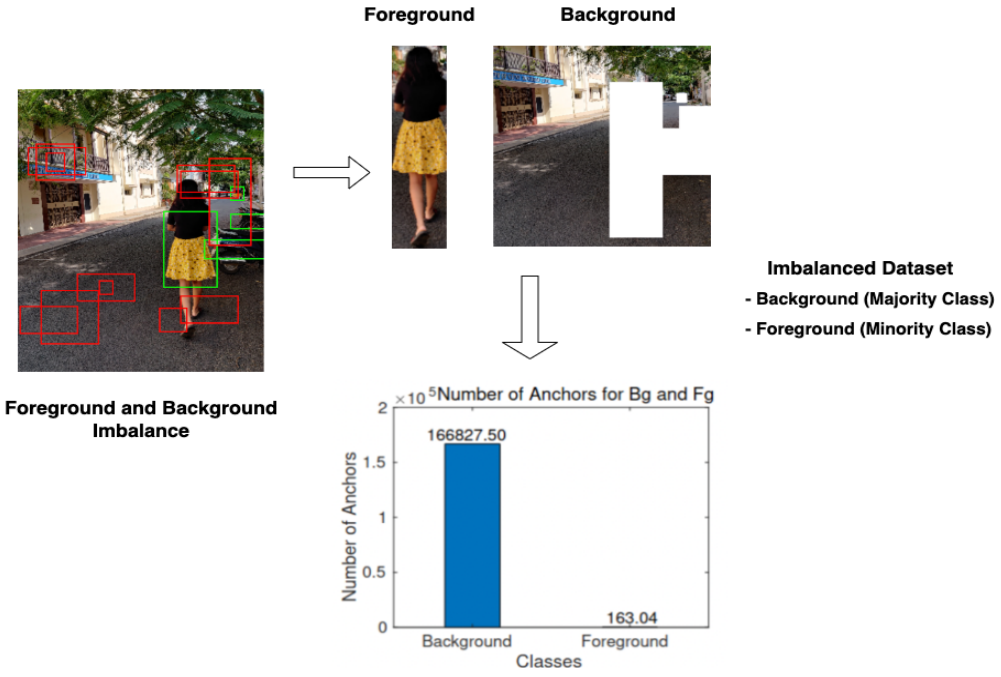

Fig. 4. Illustration of class imbalance in the form of smaller foreground area versus larger background area for the object detection task.

The object detection and segmentation tasks can be adversely affected by the class imbalance when particularly there are large numbers of classes having small number of instances. There could be multiple reasons for class imbalance, such as the relative rarity of certain objects in the dataset, or the difficulty of collecting and labeling data for certain classes. Object detection, localization, and classification can be together used to identify and classify objects in an image or video. For example, in the case of a self-driving car, object detection is used to identify the pedestrians, cars, and other objects in its environment, and then further use object classification to determine the type of each object. Discussion related to the impact of class imbalance on the perceptive capacity of self-driving cars is provided in [21] with a comprehensive overview of the application of deep learning techniques in the context of self-driving cars.

1.6 Class imbalance in computer vision- popular solutions adapted from data mining to computer vision

It is generally acknowledged that the traditional machine learning solutions discussed previously are applicable to the imbalanced image datasets available in computer vision and deep learning; however, there are rare works that embed class imbalance solutions into deep neural network architectures as per the survey in [22]. There are two popular and effective solutions adapted from data mining studies into computer vision – (i) cost-sensitive learning and (ii) data augmentation which is equivalent to oversampling of the minority class. Many researchers have tested and tried different combinations of loss

functions and data augmentation techniques for different computer vision tasks [142]. Data augmentation of the minority class is the most simple and well-tried remedy for mitigating class imbalance issues in deep learning [69]. The data is augmented synthetically through various image transformations such as scaling, rotation, flipping etc., and in some cases the Generative Adversarial Network (GAN) is used to generate the fake or synthetic images [78]. Fig. 5. illustrates data augmentation on image samples of the UC Merced Land Use Dataset. Simple image transformations such as rotation, scaling, horizontal flipping, vertical flipping, shearing, and zooming, are applied to create a whole set of synthetic images that look totally alike the natural images in the dataset.

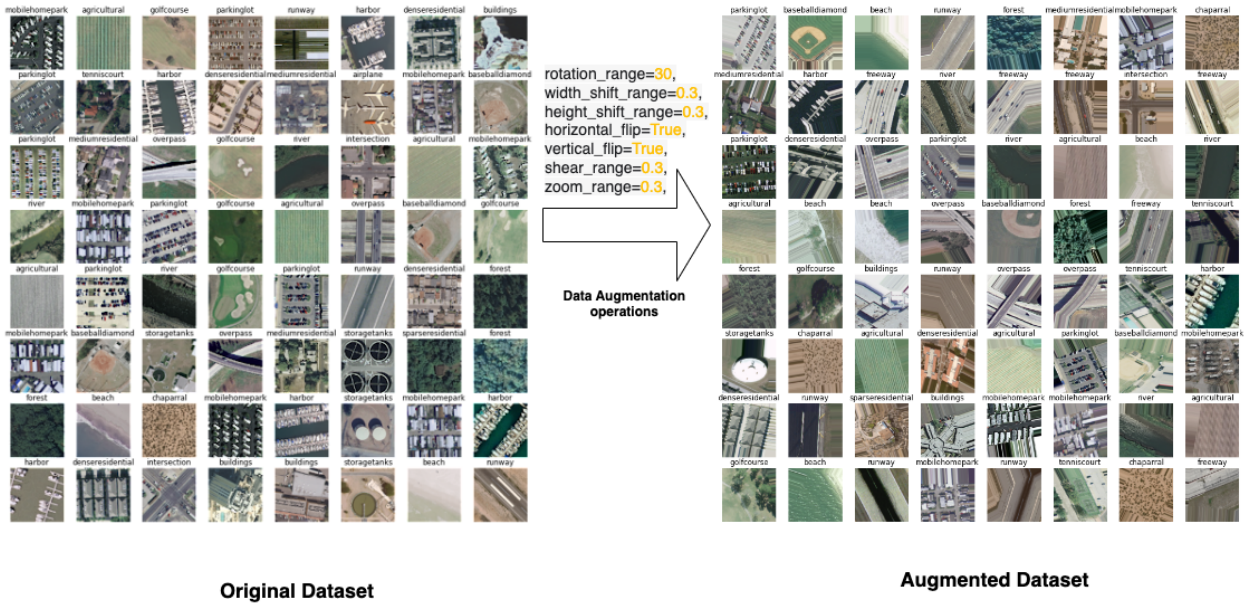

Fig. 5. Illustration of applying data augmentation on the image Samples of UC Merced Land Use Dataset

Most researchers have focused on simply comparing the performance of different pre-trained deep convolutional neural networks (CNNs) for learning from imbalanced datasets; data augmentation is applied in some cases to increase the samples in the minority class for improving the classification performance [23][24][86]. Saini and Susan [69] applied data augmentation only on the minority class of the BreakHis breast cancer dataset using image transformations such as shear, zoom, horizontal flip and resizing. From the experimental analysis, they found that data augmentation when applied only on minority classes proves to be effective for imbalanced datasets. A detailed discussion on different loss functions used in cost-sensitive learning to mitigate class imbalance is given in the later sections of this paper. The loss function which is also the fitness function of the neural network pertaining to the minority class is weighted by a higher value (w>1) as shown in (1).

$$Loss = Majority_{loss} + Minority_{loss} * w \quad (1)$$

Table 1 presents some updates on recent progress in imbalanced learning for vision-related classification tasks. The application, dataset and remedy for class imbalance is discussed.

Table 1. Some recently introduced computer vision applications involving imbalanced datasets

Author & year	Computer vision application	Imbalanced dataset	Solution proposed – Data augmentation vs Cost-sensitive learning
Sarafianos et al. (2018) [25]	Visual attribute classification challenges	The authors have used highly imbalanced datasets: (1) PETA (2) WIDER	- They have introduced a loss function that handles instance- and class-level class imbalance, and have achieved results using PETA and WIDER attribute datasets by using attention mechanisms. - The focal loss weighted-variant works better for handling imbalance and also focuses on hard examples.
Sambasivam et al. (2021) [26]	-Cassava leaf disease detection and classification	Authors have created their dataset which consists of fine-grained cassava leaf disease categories having 10,000 labeled images. (This dataset has high imbalance ratio)	- Class-weight, Synthetic Minority Oversampling Technique (SMOTE), focal loss techniques have helped to improve performance of the model to a great extent
Yeung et al. (2022) [27]	-Biomedical application	The authors have used five different types of publicly available imbalanced datasets: - (1) CVS-ClinicDB (2) Digital Retinal Images for Vessel Extraction (DRIVE) (3) Breast Ultrasound 2017 (BUS2017) (4) Brain Tumor Segmentation 2020 (BraTS20) (5) Kidney Tumor Segmentation 2019 (KiTS19)	- Proposed the unified focal loss for class imbalance scenario. -Evaluated performance on five different image segmentation datasets (3D binary as well as 3D multi-class), and found that their loss function works better in comparison to other state-of-the-art loss functions using DSC (Dice similarity cosine) and IoU (Intersection Over Union) scores.
Carranza-García et al. (2021) [28]	-Autonomous driving	Waymo Open Dataset	- Designed an ensemble model which combines numerous learning strategies, and addresses the class imbalance problem by using a reduced focal loss that can significantly improve the detection of tough objects in two-stage detectors.
Dong et al.	-shop domain	They have used popular large-scaled imbalanced datasets:	- Formulated the novel idea corresponding to the batch incremental hard sample mining of minority attribute classes, and developed the deep learning approach to reduce the impact of the

(2017) [29]	(Recognizing detailed facial or clothing attributes in images of people)	(1) CelebA facial attribute dataset (2) X-Domain clothing attribute dataset	majority class using class rectification loss (CRL).
Ngo and Yoon (2020) [30]	Facial expression recognition	AffectNet database	- Formulated a novel loss function named weighted-cluster loss.
Yang et al. (2022) [31]	Satellite remote sensing	Three remote sensing image datasets have been used: (1) DOTA-v1.5 (2) TGRS-HRRSD (3) RSOD	- They have proposed the variant of YOLO as RS-YOLOX, and along with it used Varifocal Loss function to balance the number of samples. (positive as well as negative). - They have also used Efficient Channel Attention (ECA) and Adaptively Spatial Feature Fusion (ASFF) to improvise the feature learning ability along with enhancing the power to improve the performance of the model in identifying even the smallest targets.
Alaba et al. (2022) [32]	Fish species recognition	SEAMAP 21 (Highly imbalanced reef fish dataset)	- Proposed a deep framework involving a MobileNetv3 deep neural network, and proposed the class-aware loss function which gives more weightage to the minority class (species having a smaller number of image samples) in comparison to the majority class.
Liu et al. (2017) [33]	Traffic surveillance systems/ Transport systems	MIO-TCD classification challenge dataset	- Proposed a deep learning based method consisting of two phases: (1) First phase: -Data augmentation at data level is applied along with balanced sampling. (2) Second phase: - Ensemble approach is designed using different convolutional neural network models having varied architectures.
Susan and Kaushik (2022) [34]	Face classification	Labeled Faces in the Wild (LFW)	-Authors have proposed localized metric learning for extremely large multi class imbalanced face databases. -Extracted Histogram of Gradient (HOG) features from images which are passed as input for metric learning.
Alam et al.	Biomedical-	MNIST: HAM10000 dataset	-RegNetY-320 deep learning model outperforms AlexNet, InceptionV3 deep learning models.

(2022) [35]	Skin lesion cancer detection		- RegNetY-320 is a variant of ResNet that uses the RegNet module which is based on the basic ResNet building block in order to tackle large-scale images.

Table 1 showcases a variety of computer vision applications ranging from biomedical or satellite image classification to plant disease and fish species recognition, to highlight the extent of the problem. One notable fact from Table 1 is the exploration of efficient loss functions for deep models which has surfaced to be the most effective deep learning solution to date for imbalanced learning followed by ensemble learning and application of SMOTE variants. The focal loss function appears to be a popular choice. Some new loss functions introduced over the last three years are observed to be the class-aware loss function and weighted cluster loss. Distance metric learning is observed to be another imbalance treatment strategy, though the works incorporating metric learning for vision datasets are relatively less.

1.7 Other surveys

It is vividly observed that the existing state-of-the-art survey papers mostly focused on narrowing down areas associated with imbalanced datasets or focusing particular on techniques/approaches/application/task in depth. But the overall perspective and a common solution related to the computer vision field while working with imbalanced datasets is missing which has motivated us to write this survey. Table 2 illustrates the in-depth study conducted related to the recently published existing state-of-the-art survey papers whwich illustrates how the proposed work is distinguished from the existing research works.

Table 2. Summary of related survey papers published recently in the field of computer vision

Reference	Imbalanced dataset	Machine Learning approaches	Deep Learning approaches	Data augmentation	GAN	Vision Transformer	Image classification	Segmentation	Object detection
[162]	✓	✗	✓	✗	✓	✓	✓	✓	✓
[164]	✓	✗	✓	✓	✓	✗	✓	✓	✓
[159]	✗	✗	✓	✗	✓	✓	✓	✓	✓
[161]	✗	✓	✓	✓	✓	✗	✓	✓	✗
[42]	✓	✓	✗	✗	✗	✗	✓	✗	✗
[22]	✓	✓	✓	✓	✗	✗	✓	✓	✓
[165]	✗	✗	✓	✓	✗	✓	✓	✓	✓
[166]	✓	✓	✓	✗	✗	✗	✓	✗	✓

This Survey	✓	✓	✓	✓	✓	✓	✓	✓	✓

As represented in Table 1, most of the surveys covered few aspects as observed from the number of ticks in each row. Sampath et al. had published a survey in the field of Generative adversarial networks (GAN) [162]. This included an elaborate discussion on the latest advancements associated with GAN and various GAN-based architectures in order to address the imbalance problems in image datasets. The survey was conducted in a very systematic way but the overall main focus was on how GAN can mitigate the effect of class imbalance. Xu et al. have done a comprehensive survey of the application of data augmentation techniques for deep learning in the computer vision domain [164]. However, the discussion related to challenges associated with class imbalance is lacking, and solutions to mitigate the effect of class imbalance is not emphasized upon in detail, as the main focus of the paper was on augmentation and how they could improve the performance, including the specific challenges which included domain shift and intensity transformations for occlusion. Most surveys found contained a few aspects which were not covered in other state-of-the-art surveys and also were specific to one application domain. Shamshad et al. conducted a survey related to transformers, which is recently trending in the computer vision domain, by focusing on medical imaging [159]. They surveyed the application of transformers in classification, detection, segmentation, reconstruction, synthesis, registration, clinical report generation, and various other tasks associated with medical images without putting separate emphasis on class imbalance scenarios and solutions for mitigating the class imbalance. Castiglioni et al. has also conducted a survey on the biomedical domain; they discussed the pros as well as cons along with the recommendations for selecting any machine learning or deep learning approaches on the medical imaging [161]. There are other surveys which have mostly focused on machine learning approaches to address the class imbalance problems. Kaur et al. had done an extensive survey of challenges and solutions associated with machine learning covering various applications such as marketing sector, information security, bioinformatic in text and image processing-based applications [42]. Johnson et al. conducted an extensive survey in an elaborative and structured way by including machine learning and deep learning approaches in computer vision which motivated us to conduct the survey on imbalanced datasets [22]. Few approaches such as generative models and vision transformers have not been detailed in the survey. Zaidi et al. had presented the survey on object detection and recent developments associated with object detectors based on deep learning and associated performance metrics [165]. This survey covers in depth about object detection, but not the approaches associated with class imbalances in object detection particularly. Chen et al. combined the discussion on ensemble learning and deep convolutional neural networks (CNNs) in order to tackle the class imbalanced problem more effectively [166]. Data augmentations, transformers and GAN are not part of the survey. The current research survey covers all the aspects as observed from Table 2, including imbalanced datasets, deep learning, machine learning, data augmentations, GAN, vision transformers, image classification, segmentation and object detection.

1.8 Chief contributions of this survey

Unlike the state-of-the-art survey, the analysis conducted in this study aims to include the numerous real world domain applications ranging from biomedical to satellite images and along with in depth description of various techniques which are proposed in recent times in the field of computer vision and

deep learning for imbalanced datasets. Instead of narrowing down on specific domains or techniques, it has included recognition, segmentation, classification and object detection applications by using data, algorithmic, and hybrid approaches to mitigate the effect of class imbalance problem. In this survey, a thorough review of the existing literature, which includes recent advancements, is included to offer a comprehensive understanding of this research field. The emphasis is upon the insight into the future trends associated with the class imbalance problem in the computer vision area. The time complexity involved in deep learning models is discussed in this survey. It has included recent advancement and new developments in this field such as Transformers, GAN and Explainable AI. Additionally, certain benchmark and popular imbalanced datasets are identified and illustrated along with an associated discussion of the characteristics of the datasets and attributes. The study also discusses the challenges and constraints faced when applying these methods to real-world scenarios, and provides insights into the potential impact and practical implications of the mentioned techniques. This survey highlights trends, challenges and future directions in the area of class imbalance in computer vision which will enable readers to stay updated with the latest research developments and challenges involved in this evolving and promising domain which might impact real-world applications. By addressing these aspects, the main aim was to provide a valuable resource for researchers, practitioners, in understanding and addressing class imbalance in computer vision tasks. An overview of the appropriate evaluation metrics used on popular benchmark imbalanced datasets is included in the study to promote unbiased and fair decisions or predictions in the classification experiment. This detailed analysis was missing in the previous state-of-the-art surveys.

An in-depth discussion is illustrated in this section related to the existing state-of-the-art research survey works, and the proposed survey work is differentiated and distinguished from the previous state-of-the-art works. The extensive searches were conducted using numerous combinations of keywords/ search strings, including ‘deep learning and class imbalance’, 'machine learning and class imbalance’, ‘GAN and class imbalance’ and ‘transformers and class imbalance’ in order to gather peer-reviewed research articles from various sources such as conference, journals, book chapters, and reports as inspired by previous works present in literature. This search spanned across prominent databases such as: IEEE, Scopus, ScienceDirect, SpringerLink, ACM Digital Library, and Web of Science from January 2005 to January 2023 (with a focus on the recent advancements in the last five years); this analysis was found approximately equivalent to 1000 plus relevant articles which were further filtered to extract relevant 180 articles emphasizing on the different application domains without any repetition. Fig. 6. (i) illustrates the pie-chart depicting the statistics of the papers mentioned in this survey, and Fig. 6 (ii) illustrates the pie chart of application-wise categories included in this survey. Further Fig. 7 presents a timeline of curated techniques developed for imbalanced image classification between 2005 and the present. As observed, the earlier works relied on sampling strategies based on SMOTE and its variants to balance the distribution, while after 2010, the attention shifted to cost-sensitive learning and testing and trying different loss functions for imbalanced learning. However, ever since deep learning resurged in 2012, there has been an increased interest in addressing class imbalance in deep learning, though deep learning specific solutions are more difficult to find.

However, there is a research gap in the literature work which motivated us to compile and do analysis of various deep learning-based approaches in computer vision domain for imbalanced datasets. There are limited studies associated with imbalanced datasets in computer vision domain using deep learning while considering the numerous applications in various domains. The combination of new advanced approaches such as GAN and vision have proved to contribute towards mitigating the impact of class imbalance. Also

the performance evaluation in several experiments is flawed since the models are judged on the basis of wrong evaluation metrics. Our survey aims to address all these issues, and identify generic solutions for mitigating the class imbalance, cutting across a broad spectrum of computer vision applications.

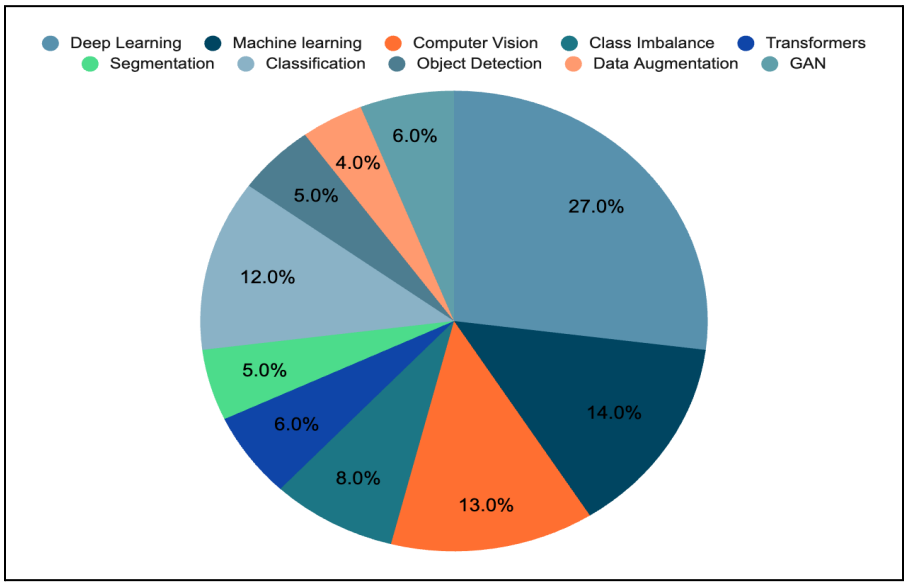

(a)

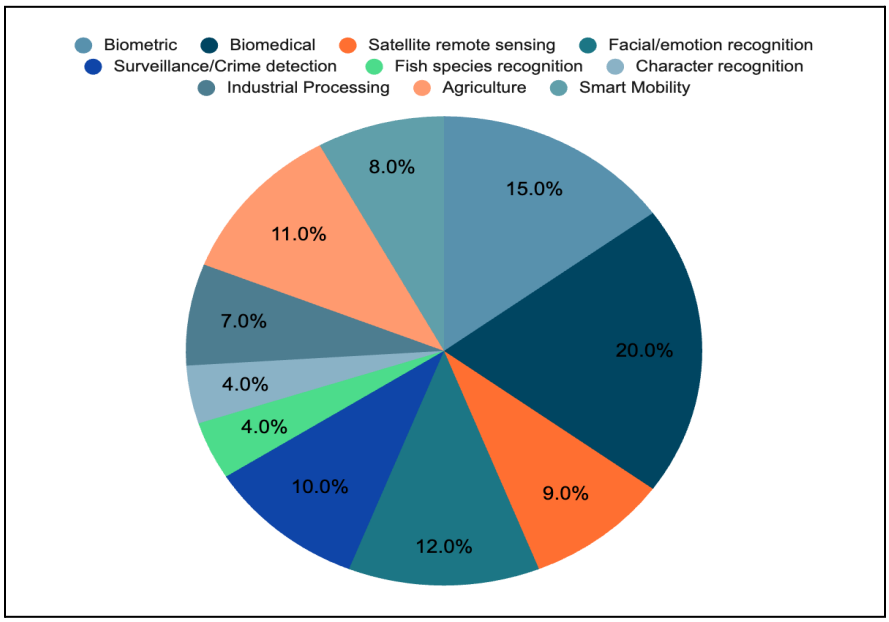

(b)

Fig. 6. (Top) The pie-charts depicting the statistics of the papers mentioned in this survey. (Bottom) Pie chart of application-wise categories included in this survey.

Fig. 7. Timeline of curated techniques popularly used for imbalanced image classification between 2005 and present.

The significant contributions of the paper are highlighted briefly: (1) The survey conducted in this paper provides a detailed analysis of various machine learning and deep learning methods for addressing class imbalance situations, along with a summarization of related works for binary and multi-class imbalanced datasets (2) Discussion related to the time complexity factor of AI models is elaborated. (3) Research challenges, insights and limitations are discussed in depth associated with learning from imbalanced datasets (4) Performance evaluation and details of some popular imbalanced datasets in computer vision are included (5) The scope of the paper is not restricted towards a discussion about imbalanced datasets, but to discuss in depth about the open challenges and application domains, and associated solutions in the computer vision domain, and provide future research insights and directions to address this challenging problem in a structured fashion.

1.9 Organization of the paper

The paper is organized as follows: in Section 2 the study includes a discussion on machine learning techniques adapted from the data mining field that have been applied successfully for handling class imbalance in computer vision. Further, Section 3 expands upon the current crop of deep learning techniques incorporating some mechanism for mitigating class imbalance. Deep learning techniques incorporating data augmentation and loss functions, which are two of the most popular remedies for class imbalance till date, are emphasized in a more curated and detailed way in Section 4. Further in Section 5, the emphasis is on popular imbalanced datasets and their performance evaluation metrics for numerous real-world challenging problems. The open research problems and future research directions are outlined in Section 6. The paper is concluded in Section 7.

2. Machine learning solutions for class imbalance in computer vision

Machine learning can be categorized as a subfield of Artificial Intelligence that aims to learn from data with the help of algorithms, and is able to execute tasks with human-like intelligence without being explicitly programmed [36][155][156]. In machine learning, tasks are subdivided into different modules. First features are extracted from the data, which comes under the category of feature engineering, then features extracted are passed to a machine learning classifier. Machine learning models do not require large computational resources such as cloud Graphical processing units (GPU), and the data can be easily processed, loaded and models can be easily trained using Central processing units (CPU). It can even work well with smaller datasets and the model is trained quickly also, and gives promising results. Machine learning can be classified into: (1) Supervised (2) Unsupervised (3) Reinforcement learning [37]. In supervised learning, there is labeled data, but in case of unsupervised learning the dataset is not labeled, while reinforcement learning is based upon maximizing rewards and minimizing punishments. The class imbalance issue affects supervised, unsupervised and reinforcement learning techniques all three alike; therefore, some type of mechanism needs to be incorporated to counter its effect.

There are efficient machine learning and pattern recognition approaches to tackle the class imbalance problem in literature. Data augmentation is one of the most widely used technique to increase the set of samples so as to enhance the diversity of samples to enhance the performance of the imbalanced dataset. The aim is to increase the sample set by synthesizing numerous samples from the minority class also so that ultimately the model performance is not biased towards the majority class. Various popular

data augmentation techniques available in literature are image transformations like Rotation, Scaling, and Translation, Flip, Hue, saturation and Random Erasing. The choice of application of data augmentation techniques can vary based upon the dataset and also on the characteristics of the classes present in the dataset. In order to find the right data augmentation techniques for a specific dataset, it is required to conduct multiple trials of combinations of image transformations. Even GAN and Synthetic Minority Over-sampling Technique (SMOTE) can be a form of data augmentation technique. SMOTE is also amongst the popular techniques, which generates the synthetic samples for the minority class by interpolating between feature vectors of neighboring samples. SMOTE can help to enhance the diversity of the samples by taking minority classes without focusing on the duplication of the existing samples. Another technique is ADASYN [178] which is an extension of SMOTE that introduces adaptivity to the synthetic sample generation process. In ADASYN, different weights are assigned to the minority class samples as it will generate more synthetic samples for the minority class samples that are harder to classify and focus on the more challenging regions of the feature space. Generative Adversarial Network (GAN) approach is often used nowadays in order to address class imbalance at the data level in computer vision tasks by generating the realistic fake samples. The quality of the generated samples plays a crucial role to ensure that images appear to be more realistic and better representative of the minority class.

Guillaume et al. (2017) had created an open course python toolbox in 2017 named imbalanced-learn API [38] which includes several machine learning algorithms to tackle class imbalance. They have made available tools for undersampling, oversampling, and combinations of both oversampling and undersampling, along with ensemble learning methods together in one toolbox. Data mining researchers seeking quick-fix problems to class imbalance often make use of imbalanced-learn. However, the application to computer vision datasets is not so easy due to the scalability of the data and the two-dimensional spatial layout of images that renders simple interpolation based resampling strategies ineffective in some cases. SMOTE and its variants like Borderline SMOTE and ADASYN have therefore been applied limitedly in computer vision for resampling of hyperspectral or satellite images [39] or biomedical images such as histopathological images or X-ray images [4] [40]. In such a scenario, many researchers confined their efforts to finding the optimal combination of image features and machine learning classifiers to mitigate the effect of class imbalance. A novel approach is introduced in [41] related to multi-class imbalanced datasets constructed from a dictionary of bag-of-visual-words using deep features extracted from the ResNet pre-trained neural network and applied to the non-linear Chi^2 SVM classifier for the multi-class classification task. They validated their approach on the Graz-02 and TF-Flowers datasets, and stated that the choice of ResNet deep features with Chi^2 SVM classifier is a perfect combination of features with classifiers for imbalanced datasets. Overall SVM is considered an effective classifier for imbalanced datasets; it is considered as the base classifier for ensemble learning of imbalanced data [42].

The cost-sensitive methods however, are amply used in computer vision since it does not involve data level manipulation. Cost-sensitive learning uses a cost matrix [16] and pays attention to the misclassification that involves cost. These algorithms aim to do adjustment of the misclassification costs or decision thresholds to account for the imbalanced class distribution. Several combinations of features and classifiers have been tested for cost-sensitive learning where the misclassification cost for the minority class is given more bias. Zhang et al.(2016) [43] tried cost-sensitive learning on the combination of wavelet entropy features with three different classifiers: - SVM, K-Nearest Neighbor (kNN) and decision trees, and found that kNN performed best. In contemporary times, cost-sensitive learning is integrated into deep networks, this study has included detailed discussion on this topic in subsequent

sections. It therefore concludes that the resampling strategies popular in data mining are not advisable in computer vision. In the absence of any class imbalance correction, SVM is found to be an effective machine learning classifier for learning directly from imbalanced datasets. However, cost-sensitive learning is an effective strategy for imbalanced learning that has been adapted successfully to deep learning models.

Focal Loss is introduced specifically to address class imbalance even when there is presence of a large number of easy examples (majority class) and a small number of difficult examples (minority class). There are two crucial parameters present in focal Loss, focusing parameter (gamma) and the balancing parameter (alpha). The focusing parameter (gamma) controls the degree of down weighting for well-classified examples and the balancing parameter adjusts the balance between the positive (minority) and negative (majority) class while training.

Hybrid approaches combine data level and algorithmic level approaches. Ensemble methods like bagging and boosting are helpful for dealing with class imbalance in computer vision tasks. These methods combine multiple models to improve performance and handle imbalanced classes effectively. Bagging involves training several classifiers independently on different subsets of the training data, where each classifier is trained on a random sample with replacement. This ensures that minority class samples are included in the subsets. By combining the predictions of all classifiers, bagging reduces variance and makes predictions more stable. It helps improve overall performance by giving minority class samples a chance to be included in training. Boosting, on the other hand, trains classifiers sequentially and focuses more on misclassified examples from previous models. It adapts by assigning higher weights to misclassified minority class samples. Boosting combines weak learners into a strong learner, performing well on imbalanced datasets. Boosting algorithms like AdaBoost, Gradient Boosting, or XGBoost can handle class imbalance by assigning higher weights to minority class samples during each iteration. The proficient method is devised that involves constructing weak and strong classifiers using different subsets of the imbalanced data, exemplifying the fusion of resampling techniques with the learning process helps to address the challenge associated with imbalanced data. However the impact of hybridization of data level manipulations and learning strategies has become trending research in current times.

3. Deep learning solutions for class imbalance in computer vision

The Deep Convolutional Neural Network, a term that came into use due to the many hidden layers in the neural network architecture, is widely used nowadays in numerous applications in various domains. The overall usage of deep learning has been tremendously increased in various applications ranging from computer vision, speech recognition, video processing, activity recognition and natural language processing. The hype of deep learning has been enhanced to a great extent nowadays due to the easy availability of computing power resources such as Graphic processing units (GPUs) as well as high usage of distributed and parallel systems which makes it easier to train huge datasets. To understand how class imbalance solutions may be incorporated into deep learning, it is necessary to start with the deep neural network architecture and the computation of feature maps, and then foray into the topic of transfer learning using pre-trained networks.

In this section, the paper delves further into the different approaches in deep learning aimed at addressing class imbalance in computer vision. Section 3.1 provides a comprehensive explanation of the process of training a deep neural network from scratch. Section 3.2 further explores the utilization of pre-trained

networks specifically tailored for tackling class imbalance in computer vision tasks. Section 3.3 discusses new developments in the field of computer vision such as vision transformers and explainable AI to address class imbalance in computer vision, and also offers promising avenues for improving the fairness, generalizability and interpretability of models in imbalanced settings. Lastly, section 3.4 provides a comprehensive analysis of these approaches from the perspective of time complexity and their practical utility. Considering the computational demands and real-world applicability, this section offers valuable insights into the feasibility and scalability of the discussed methods for handling class imbalance in computer vision tasks.

3.1 Training a deep neural network from scratch

Deep learning and machine learning differ in the complexity of the model, the feature extraction and learning process. In machine learning, features are extracted separately then the extracted features are passed to train the classifier model, thus there is separate feature engineering and classification step. However, in deep learning, feature extraction and classification are performed together in a single step as shown in Fig. 8.

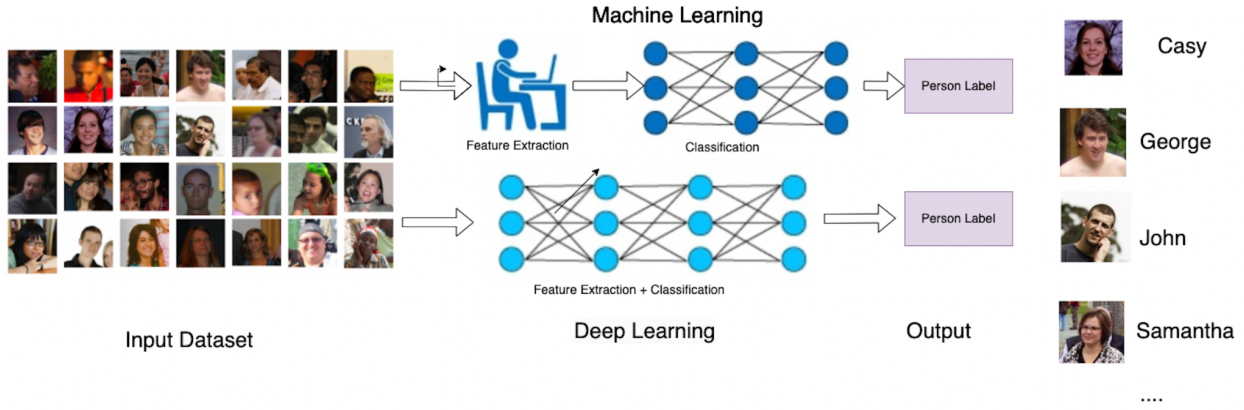

Fig. 8. Illustration of feature extraction and classification in machine learning and deep learning using a facial dataset as example

Deep learning therefore learns features directly from the data in an end-to-end fashion, and it scores over machine learning in terms of the high accuracies achieved for various computer vision tasks [44]. Also, deep neural network architectures are much more complex and have multiple hidden layers, with some of the latest deep models like DenseNet [45] having more than 100 layers. Srinivas et al. presented that VGG-16 gives better accuracy in comparison to Inception-v3, and ResNet50 pre-trained networks for classification of brain MRI images into benign and malignant tumor classes [151]. Fig. 9. illustrates the multiple layers generally found in deep learning models: convolution, pooling, fully-connected layers and the softmax or classification layer, is shown for an input satellite image along with the feature map representations extracted from intermediate layers.

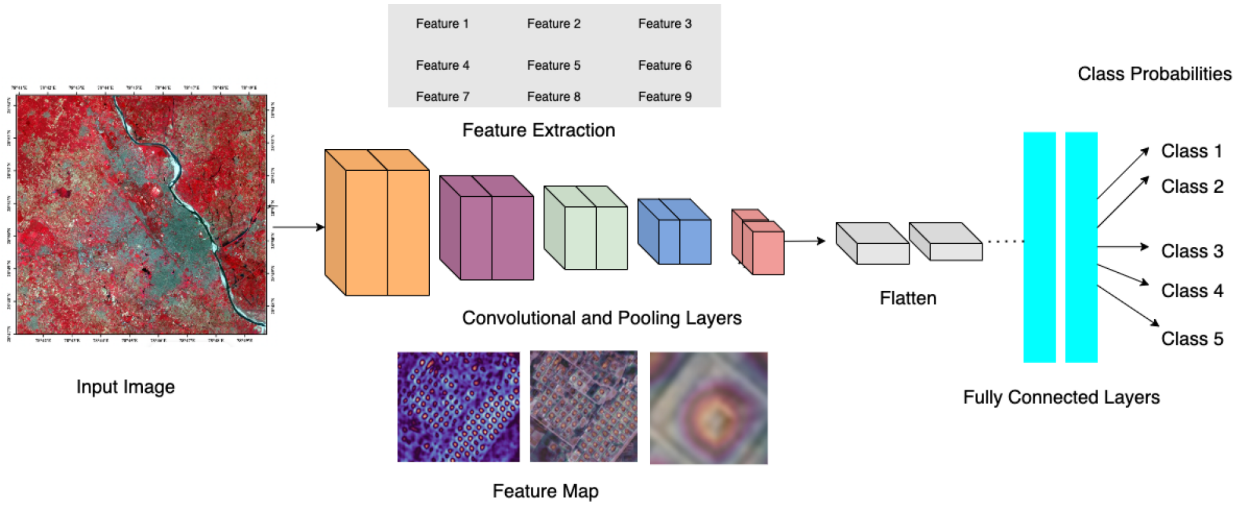

Fig. 9. Deep learning model comprising of multiple layers with satellite image as input

Each layer in a CNN typically consists of a set of filters, which are used to detect specific patterns or features in the input data. As the data passes through the layers of the network, the filters are applied to the data and the resulting feature maps are combined and processed by the next layer in the network as illustrated in Fig. 10. where visualization of features representations at five different layers of a deep learning model is shown for some sample images from the MNIST numeral recognition database. One of the key features of CNNs is their ability to learn hierarchical representations of the data, which allows them to automatically learn and extract useful features from the data without the need for manual feature engineering.

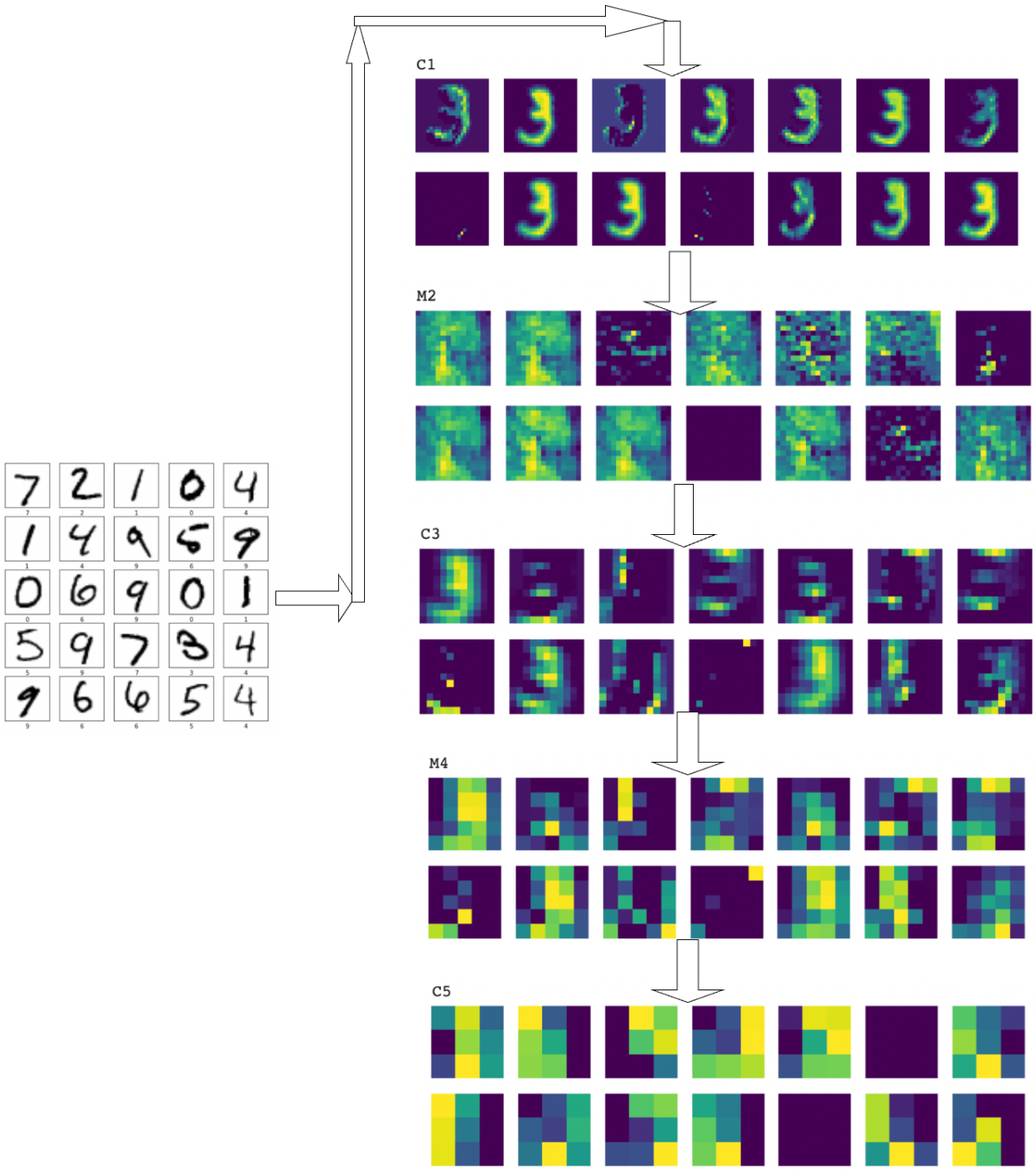

Fig. 10. Visualization of features maps computed for MNIST numeral images at subsequent layers of a five-layer deep learning model (C1: convolutional layer, M2: max-pooling, C3: convolutional layer, M4: max-pooling, C5: convolutional layer)

Deep CNNs have been widely used in a variety of applications, including image and video analysis, natural language processing, and speech recognition. Training a deep CNN from scratch is a computationally extensive process and requires adequate training using labeled samples for effective

performance. In this scenario, the presence of class imbalance in the image dataset deters the effective working of the classifier. Just as for machine learning, for Deep CNNs trained from scratch, the two most popular solutions for class imbalance in deep learning are (i) data augmentation where the samples are synthetically increased [137][138] and (ii) cost-sensitive learning wherein the loss function of the minority class is given a boost during the network optimization [95][139][143]. It is notable that Deep CNNs trained from scratch are not suitable for small datasets [140]; large pre-trained networks are advisable in this case, which is the topic of discussion in the next subsection.

3.2 Transfer learning using pre-trained networks

An alternative to the CNN networks which are trained from scratch are pre-trained networks which are already trained on a very large dataset and can be fine-tuned for a specific task using a smaller dataset [47]. Even with the huge availability of resources, the time taken to train deep neural networks from scratch is very high, and also large labeled datasets are required for effective learning. This led to the development of pre-trained models that have an advantage when dealing with smaller datasets, and in that case the time taken to train the network is significantly less since the learning process is bootstrapped for the smaller dataset using transfer learning [48]. Several researchers have proved that pre-trained networks with fine tuning outperforms deep CNNs trained from scratch [136].

Various examples of popular pre-trained networks in the computer vision domain: (1) VGG (Visual Geometry Group) [49]: VGG is a pre-trained convolutional neural network (CNN) that was developed by researchers at the University of oxford. It was trained on the ImageNet dataset and is commonly used as a starting point for image classification tasks. (4) ResNet (Residual Network) [50], is another popular pre-trained CNN that was developed by researchers at Microsoft. It is notable for its use of residual connections, which allows the network to learn more complex patterns and achieve better performance on tasks such as image classification. Besides this there are pre-trained networks that can be very useful in a variety of scenarios, such as when training data is limited or when a model needs to be quickly deployed for a new task. By starting with a pre-trained network, it is often possible to achieve good performance with relatively little additional training, and they can serve as strong baselines for comparison with other models. There are many different types of pre-trained networks available, and the most appropriate type will depend on the specific task and dataset. The popular pre-trained networks utilized for various vision-related tasks are discussed next.

(1) *Pre-trained networks for image classification*: These are pre-trained networks that have been trained on large datasets of images for the task of image classification. Examples include VGG [49], ResNet [50], Inception [51], DenseNet [45], MobileNet [52], Efficient Net [53], InceptionResNet [54] etc. The pre-trained networks that have been trained on a large dataset can then be fine-tuned or used as a starting point for training on a new task. Transfer learning can be useful when training data is limited or when it is desirable to leverage the knowledge learned on a related task. Even when there is a limited dataset, it is best to train using pre-trained networks since the training of the model would be better due to the presence of pre-trained weights that enforces the model to learn better from the smaller dataset and make accurate predictions. The development of deep learning architectures that support imbalanced datasets is upcoming research. One example is VGGIN-Net [24][86] that integrates the lower layers of VGG16 and Inception block in its architecture. The result is improved classification as compared to the baseline deep models.
(2) *Pre-trained networks for object detection*: These are various pre-trained networks that have been trained to detect and classify objects in images. They are typically based on CNNs and may also include

additional components such as region proposal networks (RPNs) and anchor boxes. Examples are Faster RCNN [55], RetinaNet [56], EfficientDet [57] etc. The extensive comparative analysis of pre-trained networks for diabetic retinopathy screening for object detection, segmentation and classification tasks is performed in [23], wherein all the three tasks can be converged into a single problem for an application. From the analysis they inferred that in the scenario of class imbalance, (1) EfficientDet-D0 and SSD (MobileNetV1) pre-trained models are most suited for performing object detection (2) PSPNet (with focal loss) works effectively for the segmentation task (3) DenseNet121 pre-trained model performs effective classification.

(3) *Pre-trained networks for* i*mage segmentation*: Similarly for image segmentation there are pre-trained networks available such as Deeplabv3 [58], PSPNet [59] etc. A few years ago, segmentation was considered an unsupervised image processing task achieved through clustering or region growing and merging techniques [132][133] . Present-day image segmentation, however, uses deep learning in the form of fully convolutional pixel-labeling networks, semantic (pixel-level) and instance-level (object-level) segmentation, recurrent neural networks and attention-based models, generative adversarial networks etc. [134]. The application of deep learning thus reduces segmentation to an end-to-end classification task; hence class imbalance affects the image segmentation task as well. There are very few works that deal with class imbalance in image segmentation. One of the rare works is that of Milletari et al. [135] who proposed a fully convolutional neural network called V-Net with an objective function based on the Dice coefficient. The new objective function was successful in mitigating the strong class imbalance between foreground versus background pixels in the 3D medical image segmentation task.

(4) *Generative models for data augmentation*: These are pre-trained networks that have been trained to generate new data that is similar to a given training dataset in various applications associated with computer vision [160]. Examples include GANs [60] and Variational Autoencoders (VAEs) [61]. GAN has proved to be one of the most effective techniques to synthetically increase the minority class samples at data level which overall helps to deal with cases of imbalance scenarios. Goodfellow et al. proposed that GAN has two components: generator (G) and discriminator (D) [60]. The generator module helps to generate the fake image samples and the role of the discriminator is to detect whether the fake images generated are actually fake images or real. In GAN, the generator G and discriminator D are continually competing with one another by following the min-max strategy algorithm as represented in the equation below.

$$min_G max_D V(D,G) = \mathrm{E}_{x\sim p_{data}(x)}[logD(x)] + E_{z\sim p_{z\,(z)}}[log(1 - D(G(z)))] \qquad (2)$$

Tanaka et al. had conducted an extensive survey on different GAN architectures; the authors proved that data augmentation by generating synthetic images using GAN is more effective than traditional approaches for imbalance treatment [73]. Some applications of GANs for imbalanced datasets are summarized in Table 3 in section 4. Fig. 11. depicts the Generative adversarial network having generator and discriminator components. The generator after adding noise will generate fake images, and further fake and real images are passed into the discriminator to distinguish between real and fake images.

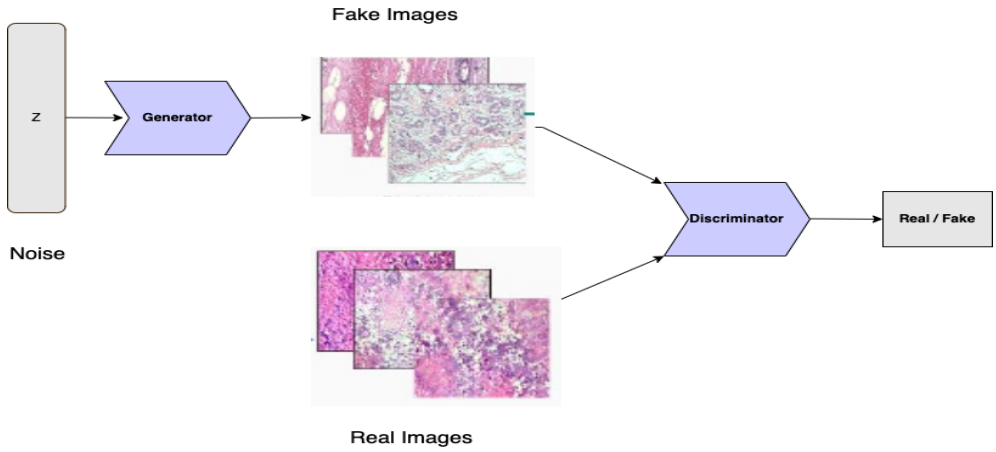

Fig. 11. Generative adversarial network having generator and discriminator components

In Table 3, a detailed discussion related to various popular state-of-the-art pre-trained networks and their key factors is presented.

Table 3. Discussion of state-of-the-art pre-trained networks and key factors

References	Pre-trained networks	Key factors
[49]	VGG	VGG architecture consists of stacking multiple convolutional layers with the filter size and pooling layers. VGG consists of approximately 138 million parameters which makes this network bulky.
[51]	Inception	The Inception network consists of an Inception module having filters of 1x1, 3x3, 5x5 convolutions followed by concatenation or pooling. This allows the model to capture features at multiple levels of abstraction and enables it to learn both local and global information.
[50]	ResNet	ResNet architecture is formulated with multiple residual networks having skip connections which helps the gradient to smoothly flow during backpropagation
[45]x	DenseNet	DenseNet architecture has dense blocks where each block contains multiple layers with the same number of feature maps. This dense block structure encourages the reusability of features and strengthens the feature propagation across layers. In DenseNet architecture the summation of output feature maps with the incoming feature maps is there, followed by concatenation.

[55]	Faster RCNN	Fast RCNN performs detection on multiple region proposals and it is based upon the Region Proposal Network (RPN). The RPN generates the region proposals which are potential bounding box locations and also the containing objects of interest.
[167]	YOLO	One of the most popular object detection algorithms is YOLO (You Only Look Once) having multiple variants. The latest variant is YOLO-NAS, YOLOv8. The various object detection algorithms use sliding windows or region proposal methods but the key factor which distinguishes them from others is that YOLO divides the input image into a various grid and finally predicts bounding boxes and class probabilities directly on the basis of the grid which makes YOLO significantly faster than many other object detection algorithms.
[168]	U-Net	The popular pre-trained network that is most widely used for segmentation is U-Net. The distinctive factor about U-Net is its U-shaped architecture consisting of encoder and a decoder. The U-Net consists of skip connections between the corresponding encoder and decoder layers. Overall, these connections help to preserve spatial information and also enable decoders to access lower-level features.
[169]	Swin Transformer	The Swin Transformer has an architecture that combines the goodness of vision transformers and convolutional neural networks (CNNs). The introduction of hierarchical structure and window-based self-attention mechanism makes efficient processing of images at different scales appropriate.

3.3 New developments –Transformers and Explainable AI

As an alternative to CNNs, Transformers [62] and Explainable AI (XAI) [63] have brought in a revolution in recent times. Transformers have been widely adapted for use in computer vision in applications such as object detection, classification, and image generation; they rely on self-attention modules instead of convolution layers [62][159]. The transformers in the computer vision domain can be categorized into Vision Transformer (ViT), 3D Transformer, Two-Stream Transformer, Detr/ Detection Transformer, etc. [64].

Transformers can be adapted to address class imbalance challenges by using an adaptive weight-based sampling strategy [141] that assigns more weights to the minority classes to provide higher probability of being sampled during training. The imbalanced learning strategies are merged into the pre-training stage itself. Another approach is to use a transformer-based model with a loss function that is

designed to address class imbalance such as focal loss which helps to focus on the hard examples/ samples [142]. Recent literature highlights various application domains where the transformers can be applied to alleviate the effect of imbalanced datasets. Bai et al. (2022) applied the Vision Transformer (ViT) on a small medical capsule endoscopy imbalanced dataset [65]. ViT uses self-attention which enables it to capture effectively long-range information. The authors emphasized upon three step pooling in order to reduce the spatial dimension by approximately three times. Kaselimi et al. (2022) had proposed the ForestViT and achieved superlative performance in comparison to other well-known state-of-the-art deep learning models for imbalanced datasets [66]. The superiority was more noticeable in case of the minority classes.

Moreover, there is a rising need of having explainable deep learning models instead of considering deep learning models as a black box. Considering the fact it works as a black box, it is difficult to understand how a model actually works between taking the input and finally making predictions, which makes it difficult to understand how the deep working model can help to tackle imbalance challenges [144]. Explainable AI models provide clear justification and explanation of decisions and how each and every component are connected together to create the impact. These models are created and designed in such a way that it can be transparent and interpretable so that being a user, someone can exactly understand how the model is making its decisions and can trust the outcomes of the model [145]. SHapley Additive exPlanations (SHAP) tools are now increasingly being used [173] to analyze the decisions of deep convolutional networks in order to assess the explainability and interpretability of the classification outcomes of imbalanced datasets.

3.4 Time Complexity of AI models

The time complexity of an algorithm is the amount of time and computational resources required to execute the algorithm [158]. The time complexity of AI (Artificial Intelligence) specifically DL (Deep Learning) models can vary significantly depending on numerous factors, including the architecture of the model, size of the input data, complexity of the task, and even it can be based on the hardware used for computation. Also while training a DL model, the training time complexity is influenced by the number of trainable parameters in the model and also by the size of the training dataset. It is observed that as the number of parameters increases then the time required for model optimization through techniques like backpropagation and gradient descent will also increase in parallel. Additionally, it is also dependent on the size of the training datasets i.e. if it involves larger datasets, it is generally observed that it requires more time for processing and iteration through the training steps. Time complexity is also calculated to observe the complexity associated with the AI/DL model.

The Inference time complexity refers to the time required to do predictions while using a trained AI/DL model with different test samples. The complexity is also again dependent on a few factors such as model architecture, input data size, and considering the computational requirements while performing underlying operations. The complex models involving more layers and complex operations involving convolutions generally have higher inference time complexity in comparison to less-complex models. For example, the basic Conv2D and Conv2DTranspose layers, if present in the architecture, have more parameters that need to be trained than a simple dense layer present in the architecture. The input data size also has an effect on the inference time, as larger inputs require more computations. Overall, the model architecture plays a crucial role in calculating the overall performances as well as inference time. However different AI/DL model architectures have different complexity involved in their architecture so have varying time complexities. Generally, CNNs architectures involved in the computer vision tasks, can

be computationally intensive due to presence of the multiple layers and convolutions in their architecture. Vision transformers have complex attention mechanisms present in their architecture that are also involved in their higher time complexity. The parameter which is generally ignored is the choice of hardware acceleration which has an impact on the overall time complexity involved associated with AI/DL models. The specialized hardware, such as GPUs (Graphics Processing Units) or TPUs (Tensor Processing Units). The model training and inference due can be accelerated to an extent based upon their parallel processing capabilities. By using hardware accelerators tailored for AI/DL workloads can help to overall reduce the overall time required for computations. In the case of GAN, while training a generator and discriminator, it takes much more training and pre-processing time than a very deep dense neural network; this will have an impact on the involved complexity. Also, it depends on the width (less layers but more filters in the layers) and depth (less filters in the layers but more layers) effects.

4. Extensive survey of contemporary literature on data augmentation and loss functions used in deep learning frameworks involving imbalanced datasets

This study has reviewed in depth various data augmentation procedures, loss functions and deep learning architectures that have been introduced over the past five years to tackle class imbalance. The majority of these works were published in the last two years. Table 4. presents a detailed analysis of various applications where data augmentation is used with deep learning models to mitigate the effect of class imbalance in various application domains considering different tasks of computer vision including classification, segmentation, object detection, recognition. Table 5 presents an exclusive study on data augmentation using GAN which is trending research on fake image generation and proves to increase the efficiency of the models to a great extent in numerous applications.

Table 4. A summary of data augmentation procedures used along with deep learning models to mitigate the effect of class imbalance (*from past five years data*)

References	Task	Imbalanced dataset	Data augmentation details	Contribution
[71]	Classification - Alzheimer's detection	Open Access Series of Imaging Studies (OASIS)	-Some data augmentation operations applied were Rotation, Cropping applied from right, bottom, left, corner, top, having parameters equivalent to (90˚,270˚, 180˚) set while cropping.	-Proposed transfer learning for Magnetic Resonance Imaging (MRI) and 3D MRI views of the brain along with image augmentation in order to avoid overfitting. -From the analysis it was found that the main view of the brain along with augmentation gave higher performance in comparison with the 3D view of the brain.
[72]	Character recognition	Dataset is taken from the digital	-Applied different image processing	-Have emphasized on the fact that robust data

		collection of Southeast Asian palm leaf manuscripts.	operations including noise, background, brightness adjustment and affine transformations. The Affine transformation operations include horizontal and vertical translations, rotations, zoom, or compositions of two or more transformations together.	augmentation operations can improve the overall performance of the CNN-based ancient Sundanese model.
[33]	Classification - traffic surveillance	MIO vision traffic camera dataset (MIO-TCD)	- Applied random rotations, cropping, flips and shifts. - For extremely imbalanced data an oversampling strategy with random shuffle is proposed.	-Proposed an ensemble deep learning model using different CNN architectures along with balanced sampling. -Adapted maximum majority voting for the classification of images.
[74]	Classification-Biomedical images	-Skin melanomas diagnosis -Histopathological images - Magnetic resonance imaging (MRI) scans analysis	-Applied classical image transformation operations ranging from zoom, rotate, crop, histogram-based methods and style transfer and generative adversarial networks. - Created a method of data augmentation using image style transfer	- Have compared different data augmentation operations for image classification. - They have proposed a method of data augmentation using image style transfer to generate new image samples of high-quality perceptual images which are further used to train the network in order to improve the training efficiency.
[75]	Segmentation	IPPN dataset	-Introduced a method of image augmentation for segmentation tasks which takes image mask pairs and transforms them to capture numerous scenes.	- They have compared the performance of their proposed augmentation with and without basic augmentation operations and found that there is relative increase in F1-score using the DeepLabV3 model in comparison to basic augmentations.
[76]	Object detection	Collected labeled dataset consisting of individual	Rotated crop images by 90˚, which augmented underrepresented cell	-Used Faster Region-based Convolutional Neural

		cells.	counts by roughly four times and removed crop images containing only RBCs.	Network (Faster R-CNN), for object detection

Table 5. A summary of GANs used for data augmentation in various computer vision applications (*from past five years data*)

References	**Task**	**Imbalanced dataset**	**GAN type**	**Details of data augmentation using GAN**
[77]	Defect spot welds detection	Industrial spot welding defects images dataset	Balancing GAN and gradient penalty (BAGAN-GP)	-Extensive experiments showed that the proposed approach can generate spot welds, defect images efficiently, and improve performance of the classification for industrial inspection with annotation-lack or class-imbalanced dataset. -This work provides a valuable reference for industry defect image analysis based on deep learning.
[78]	Breast Cancer classification	Breast cancer histopathology dataset (BREAKHIS)	Deep Convolutional Generative Adversarial network (DCGAN)	-DCGAN is used at the data level which is applied to the samples present at the minority class. - The balanced binary dataset after applying DCGAN is passed to the proposed modified VGG16 architecture.
[79]	Mammogram classification	Digital Database for Screening Mammography (DDSM)	Class conditional GAN with mask infilling (ciGAN)	- Proposed the novel approach ciGAN using multi scale generator architecture. - The proposed approach has a generator which uses a cascading refinement network to generate the multiple scale features.

[80]	X-ray image classification	Large-scale dataset X-ray images	Deep Convolutional GAN (DCGAN) and Cycle-GAN	-Have proposed the use of DCGAN to generate new image samples of the X-ray for the threat objects -Cycle-GAN has been adapted for the translation of camera images of threat objects into the X-ray images. -Then they have trained using various Region Based Convolutional Neural Network (R-CNN) models along with numerous augmentation approaches
[81]	Digit recognition	-MNIST -E-MNIST -SVHN -CIFAR-10	-Multiple Fake Class Generative Adversarial Networks (MFC-GAN)	-Have proposed novel GAN approach called MFC-GAN which uses multiple fake classes to make sure there occurs fine-grained generation and classification of minority class instances. -Performed augmentation using MFC-GAN; achieved superlative performance in comparison to other traditional augmentation or oversampling techniques.
[82]	Facial emotion Classification	-Facial Expression Recognition Database (FER 2013) - Static Facial Expressions in the Wild (SFEW) - Japanese Female Facial Expression (JAFFE)	-Cycle-consistent adversarial networks (CycleGAN) -GAN	-Performed augmentation using cycle-consistent adversarial networks (CycleGAN) along with CNN as the classifier with least-squared loss as adversarial loss to prevent the gradient vanishing issue.
[83]	Weather classification	-Multi-class Weather Image (MWI) -Multi-class weather dataset (MWD) -Self-made	-GAN -Deep Convolutional Adversarial networks (DCGANs)	- Proposed an ensemble approach (using KNN, SVM, RF and AdaBoost) incorporating advanced GANs, along with efficient data cleaning technique (Edited Nearest Neighbor

		laboratory dataset		(ENN) Rule) to remove outlier images generated using GANs, for dealing with the class imbalance scenario tested on various weather classification datasets.
[84]	Plant Disease classification	Prepared a small tomato plant disease image dataset generated in different circumstances of varying lightning, temperature, season, humidity and also different places using a camera.	-Introduced a U-net integrated in CycleGAN in order to improvise the perceptual quality of generated image samples.	- Generated synthetic fake samples at data level using the proposed GAN approach. -Improvised approach that can improve learning with respect to data sample distributions which helps to further reduce the partiality which is inculcated using class imbalance.
[85]	Medical image semantic segmentation	-LiTS-2017-liver lesion segmentation -MDA231, PhCHeLa-microscopic cell segmentation -BraTS-2017-brain tumor segmentation.	-Conditional Generative Adversarial Network -Recurrent conditional GAN.	-Have proposed conditional generative refinement network for biomedical image segmentation which consists of: (1) Generative network: - helps to segment pixels labels. (2) Discriminative network: - helps in classification of segmented output to real or fake category. (3) Refinement network: - which is further trained on prediction of false positive and negative masks which is predicted by the generator.

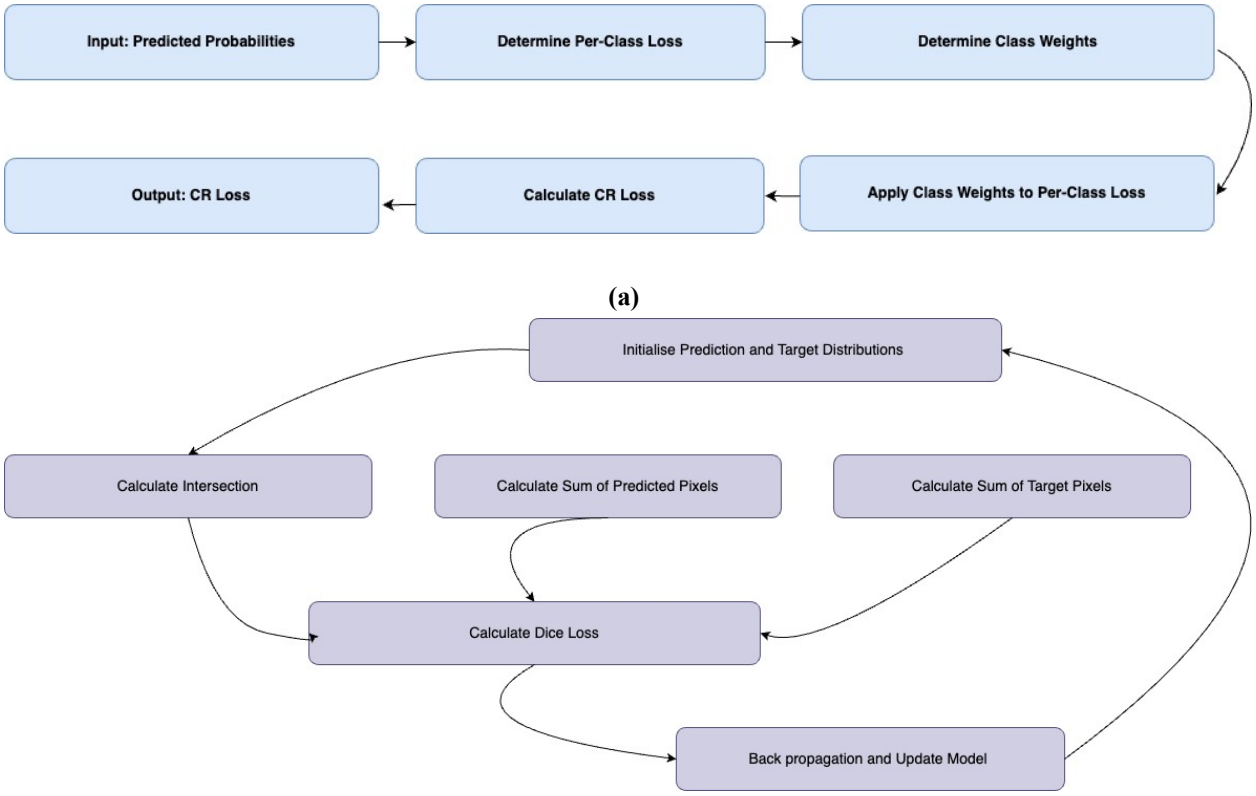

Fig. 12. (a) Class rectification loss (b) Dice Loss for imbalanced data learning.

Fig. 12 illustrates the computation and updation process of two popular loss functions used for imbalanced datasets. Fig. 12. (a) illustrates the Class Rectification Loss (CRL) based regularization approach for imbalanced data learning where the imbalanced dataset is provided in batches to the CNN along with the class rectification loss. In each batch of training, it is profiled to find the majority and minority classes, respectively. Fig. 12 (b) shows the Dice loss computation and updation in the learning process. Yeung et al. in a recent work had emphasized upon the usage of the correct focal loss function while training any deep learning model as it can have an impact on the overall performance and convergence of the model [70]. In Table 6, a discussion on different loss functions infused in the deep learning models for imbalanced datasets is present. A variety of loss functions are covered, including focal loss, dice loss, CRL etc. for a variety of computer vision tasks.

Table 6. A summary of loss functions used to mitigate the effect of class imbalance (*from past five years data*)

References	Task	Dataset	Loss	Analysis
[87]	Classification	Have constructed an imbalanced	Cross entropy (CCE) loss	Proposed cross entropy (CCE) loss for imbalanced

		dataset from popular balanced datasets -CIFAR -Fashion MNIST -Tiny ImageNet		classification which emphasizes upon suppressing the probabilities of incorrect classes to help the deep learning models to learn discriminative information.
[88]	Human attribute analysis	-Face attribute dataset-CelebA -pedestrian attribute dataset RAP	Dynamic Curriculum Learning (DCL)	-Proposed the approach named as Dynamic Curriculum Learning which incorporates the adjustment of the sampling strategy adaptively to generalize in a much better way.
[89]	Object detection	-BDD100K (highly imbalanced driving database)	weighted Cross Entropy Loss	Proposed the weighted variant of the original Cross Entropy loss named as weighted Cross Entropy Loss that assigns suitable weights to each object class present in the dataset.
[90]	Deep Regression Tracking	Five benchmark datasets including OTB-2013, OTB-2015, Temple-128, UAV-123 and VOT-2016	Shrinkage Loss	Shrinkage loss has been proposed by authors to balance the training data by penalizing the importance of easy training samples, and along with that applied residual connections in order to integrate the multiple convolutional layers as well as their output response maps to facilitate faster convergence of regression networks.
[91]	Lung nodule classification	LIDC/IDRI dataset	Focal loss	-Author uses a 15-layer 2D deep convolutional neural network named as LdcNet along with focal loss function to classify lung CT scans into nodule or non-nodule category.
[46]	Medical image segmentation	Multimodal brain tumor segmentation dataset (BraTS2018)	Focal Dice loss	Dice loss enables foreground-background separation under class imbalance, however, focal dice loss helps to reduce the contribution from easy examples during the

				learning process.
[92]	Imbalanced regression	-Imbalanced Human Mesh Recovery (IIHMR) -Age and Depth Estimation	Balanced Mean Square Error (MSE) loss	-Have proposed the Balanced MSE which was found effective for high-dimensional imbalanced regression.
[93]	Visual Classification	-CIFAR-10 -CIFAR-100 - Tiny ImageNet - iNaturalist 2018	Influence-Balanced Loss	-Proposed the Influence balanced Loss which is used for balancing in order to remove the significance of samples that cause an overfitted decision boundary.
[94]	Medical image segmentation	-Digital Retinal Images for Vessel Extraction (DRIVE) -CVC-ClinicDB -Brain Tumor Segmentation 2020 (BraTS20) -Breast ultrasound 2017 (BUS2017) -Kidney Tumor Segmentation 2019 (KiTS19)	Unified Focal loss	-Have proposed the Unified Focal loss for medical image segmentation in case of imbalanced datasets for 2D and 3D multi-class segmentation. Results show significant improvement in comparison to other loss functions in most of the cases.
[95]	Lung nodule classification	LIDC-IDRI dataset	Class-Weighted loss	-Proposed the loss function using class-weight concept that loss function associated with each class is weighted by the ratio of the total population to the class population.

Sivapuram et al. in 2023 [170] proposed a novel learning strategy called VISAL to address the challenges of class imbalance in classification tasks. The aim of VISAL is to improve the generalization of samples from the minority class by combining angular and Euclidean margins within the cross-entropy (CE) learning strategy. The researchers evaluate their approach on various imbalanced datasets, including CIFAR, COVIDx, IMDB reviews, and Tiny ImageNet. One of the key advantages of VISAL is its seamless integration into existing deep neural network (DNN) models. The idea of VISAL is incorporated into a well-designed CE loss function, making it easy to incorporate into different DNN frameworks. This flexibility enables it to effectively tackle class imbalance issues in high level vision applications, including image segmentation and object detection. A deep neural network named BiLSTM for imbalanced medical data of IoT systems was proposed in [171] by combining the decision tree model

with BiLSTM deep learning and by using data balancing strategy. In Table 7, a discussion related to various deep learning frameworks that are customized to mitigate the effect of class imbalance is presented. A scrutiny of this Table reveals some unique ideas in the form of iterative learning mechanisms, weighted ensemble formation, smart combination of classifiers, novel architecture etc., that were proposed as alternatives to the more popularly used data augmentation and cost-sensitive learning. Table 7 illustrates some of the latest research works including different variants of vision transformers, enhanced ensemble based deep learning approaches, and advanced deep learning architectures. These works pave the way for intelligent design of futuristic models that can be generalized to any type of imbalanced dataset and can achieve optimal performance in any field of computer vision.

Table 7. A summary of novel deep learning frameworks customized to mitigate the effect of class imbalance
(*From past five years data*)

Field of computer vision	**Classification task**	**Deep Learning framework**	**Reference**
Biomedical	Histopathological image classification	-Proposed a combination of different pre-trained networks using Coalition game theory, Choquet fuzzy integral, and Information theory. -The pre-trained networks used for the combination are: VGG16, VGG19, Inception V3, Xception and InceptionResnetV2 -The fuzzy ensemble considers subsets of classifiers and hence is effective for imbalanced classification	[96]
	Lung cancer detection from CT scan	-DFD-Net has been proposed for lung cancer detection from CT scan images. -A retraining strategy assures fine-tuning of only some layers of the network which ensures improved detection of the minority class.	[97]
	Heart disease detection	-Proposed a combination of GAN and LSTM, named as GAN-LSTM, for imbalanced data by synthetically generating fake samples for detection.	[98]
	Alzheimer's disease detection from Brain MRI images	-12-layer CNN architecture trained on the OASIS dataset -Data pre-processing steps: 1) Image resizing, and 2) Image denoising -The customized CNN outperformed pre-trained CNNs for the classification of the imbalanced data.	[99]
	Cervical cancer detection	-Proposed a Token-to-Token Vision Transformer (T2T-ViT) in combination with SMOTE-Tomek Links in order to balance the dataset along with the	[100]

		weights of the images and number of image samples.	
Surveillance for Crime detection	Weapon detection	-Have emphasized on the small regions of interest in the image using the YOLOV4 object detection model -YOLOV4 model is used along with Partial-ResNet with multi-scale fusion of fine semantic features of small objects, in order to gather more information about the minority class.	[101]
	Pose/ postures tracking	-Proposed Sensor-independent Parallel dEep ConvoluTional leaRning nEtwork (SPECTRE) deep learning network using convolutional networks in order to perform classification of various postures at workplace. -SPECTRE is able to extrapolate using explainable AI the patterns are significant for learning	[102]
	Human activity recognition	-Proposed an approach using LSTM infused with 1-D ConvNet, named as the joint diverse temporal learning framework -The joint learning of the two temporal models, using fuzzy temporal windows and multiple sensors, ensures improved classification of the minority classes.	[103]
	Event detection	-Proposed an enhanced ensemble based deep learning framework in which SVM classifiers are used as weak learners in order to eradicate the class imbalance issues. -Weight coefficients of the classifiers in the ensemble are adjusted according to classification performance.	[104]
Industrial Processing	Fabric defect detection	-Proposed a novel deep CNN named as Mobile-Unet for learning effectively from imbalanced defect/non-defect data. -Depth-wise separable convolution with a median frequency balancing loss function helps to mitigate the class imbalance	[105]
	Surface defect inspection	-Proposed a deep ensemble framework with dynamic fluctuation adaptation. -Weight adjustment is performed after every iteration so that the sub-models are fine-tuned on new data characteristics.	[106]

	E-commerce image classification	-Proposed approach related to deep learning and computer vision-based system for segregating, detecting and also removing the offensive and non-compliant images from e-commerce catalog. -They initially started with limited samples to fine-tune Resnet50 and Inception-V3 deep learning models, and then improved the training set iteratively; they have also used YOLOV3 and Faster R-CNN object detection model for creating the proposed system.	[107]
	Material identification	-Proposed a Vision Transformer (ViT) for classification as well as detection of construction materials. -It was observed that the model can be easily generalized to other imbalanced datasets.	[108]
Agriculture	Weeds classification	-Proposed a deep learning based approach for weed classification using a voting method by combining the multimodal Deep CNNs: VGG, NASNet, ResNet, MobileNet, and InceptionResNet together. -In this approach the score vector is adapted for the voting mechanism with priority weights determination in order to identify the better DNN models which have a greater contribution in scoring.	[109]
	Defect detection on tomatoes	-The ResNet50 model with fine tuning of all the layers of the model was found to be an effective solution for the imbalanced dataset which is biased towards the healthy class.	[110]
	Leaf disease identification	-Proposed a lightweight convolutional neural network RegNet for the small imbalanced apple leaf diseases dataset. -The results depict that RegNet using Adam optimizer having learning rate set to 0.0001 proves to be effective in comparison to other state-of-the-art deep learning including Vision Transformer.	[111]
	Classification of biotic stress in coffee plantation	-Proposed a multi-task system using convolutional neural networks which uses ResNet50 model along with data augmentation technique using leaf image for the identification of severity and	[112]

		classification of biotic stress for the coffee plantations. -All layers of ResNet50 were made trainable for effective separation of the imbalanced classes.	
Smart Mobility	Surveillance of urban road traffic	-Proposed a novel approach for surveillance and traffic monitoring for an aerial image imbalanced dataset by using YOLOv4 object detection models along with basic augmentation such as saturation, hue, flip, rotation, brightness, zoom, shearing, crop. -This proposed approach is able to effectively recognize the different traffic components from the aerial images from different angles and altitude.	[113]
	Vehicle detection/classification	-A deep learning architecture was proposed for surveillance images by combining bagging and convolutional neural networks together in a single framework.	[114]
	Pedestrian detection	-Proposed a hybrid patch-based deep learning approach using EfficientNet-B0 based classifier and a false positive reduction algorithm	[115]

5. An analysis of popular imbalanced datasets and performance evaluation metrics

Further into this section, Section 5.1 provides a comprehensive list of popular as well as benchmark datasets widely employed by researchers across diverse fields with inherent class imbalance. Lastly, section 5.2 is dedicated to discussing the evaluation metrics and their applicability in different scenarios. Overall, these three sections collectively contribute to an understanding of class imbalance challenges in different research areas, provide a list of popular and relevant datasets, and guide researchers in selecting appropriate evaluation metrics for effective assessment.

5.1 Popular imbalanced datasets in computer vision

In an imbalanced dataset, generally the minority classes are of great interest and which needs to be handled carefully especially in the biomedical sector where there is high risk of misdiagnosis. In this section, the study reviews several popularly used datasets in computer vision belonging to different application domains. These benchmark datasets can serve as starting points for evaluating the performance of algorithms and techniques in handling imbalanced data in computer vision tasks. The datasets in computer vision can be broadly categorized on the basis of their imbalance distribution and also on the basis of the size of the datasets into the following groups:

1. The dataset having an adequate number of samples present in each class. While training the model the probability associated with each class is equal.

2. Another category of datasets is the one having adequate number of samples; however, instances of some classes are rarer than that of other classes; such datasets are termed as uneven datasets.
3. Another type of dataset is the small size dataset having a smaller number of samples present; such datasets can have samples present in each class which could be equal or unequal.

It is very difficult for the model to learn from datasets belonging to categories 2 and 3. Uneven or inadequate class population arises due to the non-availability of samples in the acquisition stage since due to the privacy concerns or restrictions it becomes difficult to collect samples for every class or category. The most common reason for the occurrence of class imbalance could be possibly due to the existence of a smaller number of expert professionals for the acquisition of the appropriate and correct samples. Other reasons could be due to manual data collection for labeled dataset and deficiency of the sample's presence in particular classes. Both the factors such as class imbalance and size of dataset can have a tremendous impact on the overall performances of the CNNs which form the backbone of deep neural networks [146]. However, in machine learning, classifiers like XGBoost are known to perform well even in the presence of class imbalance [147].

Some popular imbalanced datasets in computer vision are listed below.

(1) CI-MNIST (Correlated and Imbalanced MNIST) dataset [117] consists of imbalanced handwritten digits; it is a variant of the MNIST dataset. MNIST dataset is a popular dataset used for image classification, which has 60,000 grayscale images of handwritten digits (0-9). The dataset is not inherently imbalanced; researchers often create imbalanced versions by artificially manipulating the distribution representation of samples present in classes.

(2) ISIC 2018 Melanoma Detection Challenge and Dataset [118] which has images of benign lesions much more in number in comparison to the malignant melanoma.

(3) Mammographic Masses (DDSM) consists of mammographic images where benign masses have a high number of samples in comparison to the malignant masses [119].

(4) PASCAL VOC [149] consists of annotated images for object detection, segmentation and classification tasks, where some classes are more common than others having more sample size due to the presence of more images.

(5) COVID-19 X-ray image classification [120] and COVID-19 lung CT image segmentation [121] are imbalanced datasets having more images present of COVID-19 abnormalities in comparison to normal images.

(6) CelebA is a celebrity image imbalanced dataset having few celebrity classes having a disproportionate number of samples in comparison to other majority classes [122]. RAP [123] is a highly imbalanced dataset used for pedestrian attribute recognition with an imbalance ratio of 1:1800.

(7) Popular Diabetic retinopathy imbalanced datasets are: Kaggle DRD Dataset [124], DDR Dataset [125] and Indian Diabetic Retinopathy image (IDRiD) Dataset [126].

(8) Intel and MobileODT- cervical cancer screening dataset [127] available at Kaggle is a smaller imbalanced dataset consisting of different images of women's cervix type present in images.

(9) BreakHis Histopathological dataset [128] and Breast-Histopathological-Images dataset [129] are two very popular breast cancer datasets having histopathological images of breast cancer images with the benign image samples being less in number in comparison to the malignant samples, but in case of Breast-Histopathological-Images dataset the class distribution is different as IDC -ve class is in majority in comparison to the IDC +ve classes.

3.1 Performance metrics for evaluating imbalanced datasets

There are standard performance evaluation metrics that are commonly used for imbalanced datasets in real-world challenging computer vision problems [130] [131]. Some of these performance evaluation metrics are discussed as follows: (1) Precision measures the proportion of true positive predictions made by the model to the total number of positive predictions made. (2) Recall measures the proportion of true positive predictions made by the model to the total number of actual positive samples in the dataset. (3) F1-score is the harmonic mean of precision and recall, and is one good metric to measure for imbalanced dataset. (4) Area under the precision-recall curve (AUPRC) metric measures the performance of the model over a range of different classification thresholds, and is a good metric to use when the positive class is rare. (5) Classification accuracy is the most commonly used performance evaluation metric for classification tasks. It is simply the percentage of test examples that are correctly classified by the model. Accuracy should not be the only evaluation measure while measuring the performance of an imbalanced dataset as it can lead to false predictions sometimes. (6) AUC-ROC: The AUC-ROC (area under the receiver operating characteristic curve) is a measure of the model's ability to distinguish between positive and negative examples. It is often used for binary classification tasks. (7) G-mean metric is the geometric mean of sensitivity (recall) and specificity, and is also a good metric to use when the classes are imbalanced and both false positives and false negatives are important to minimize. (8) Training time: The time required to train a model can be an important factor in certain situations, such as when working with large datasets or when model training needs to be completed within a certain time frame. (9) Inference time: The time required to make predictions with the model can also be an important factor, particularly for applications where real-time performance is required. It is equally important to note that no single metric can provide a complete picture of a model's performance, and it is often necessary to consider multiple metrics in order to get a comprehensive understanding of a model's strengths and weaknesses. (10) Matthew's Correlation Coefficient (MCC) is a statistical measure for binary classification which is used to balance the impact of false negative and false positive which will be useful in the applications involving errors with different costs. (11) Cohen's kappa coefficient is a statistical measure which is used to measure the level of agreement between two annotators. (12) Indexed Balanced accuracy (IBA) metric gives maximum weight to minority classes and also penalizes the classifiers which perform well on the majority class but not well on the minority class. (13) Intersection over Union (IoU) and Dice score are the performance evaluation metrics for segmentation and object detection. Intersection over Union (IoU) measures the overlap which occurs between the ground and predicted truth regions and is used as the ratio of the area of the intersection between the two regions to the area of their union. There are few variants of IOU which can be used such as frequency-weighted IoU, mean IoU and per-class IoU for an imbalanced dataset. The Dice Coefficient is twice into the Area of Overlap divided by the total number of pixels in both images. The variants of Dice score such as weighted Dice score and generalized Dice score can be used for imbalanced datasets. There are many different ways to compare the performance of deep learning models, and the most appropriate method will depend on the specific goals and requirements of the task at hand as illustrated in Table 8.

Table 8. Various performance metrics used for the evaluation of imbalanced datasets.

Evaluation Parameters	
Accuracy	$\frac{TP+TN}{TP+TN+FP+FN}$

Precision	$\frac{TP}{TP+TN}$
Recall	$\frac{TP}{TP+FN}$
F1-Score	$\frac{2*(Precision*Recall)}{(Precision+Recall)}$
Matthew's Correlation Coefficient (MCC)	$\frac{TP*TN-FP*FN}{\sqrt{(TP+FP)(TP+FN)\ (TN+FP)(TN+FN)}}$
Cohen Kappa	$\frac{p_0-p_c}{1-p_0}$
Geometric Mean	$TPrate = TP/(TP + FN)$ $TNrate = TN/(TN + FP)$ $Gmean = \sqrt{TPrate * TNrate}$
Index Balanced Accuracy (IBA)	$Dominance = (TPrate - TNrate)$ $IBA = (1 + Dominance) * Gmean^2$
Intersection over Union (IoU)	$\frac{Area\ of\ Intersection}{Area\ of\ Union}$
Dice Score	$\frac{2 * Area\ of\ Intersection}{Area\ of\ Union}$

4. Discussion and future insights of the trends associated with class imbalance problem

The study has been conducted in depth about various data augmentation procedures, loss functions and deep learning architectures widely used to tackle class imbalance in various computer applications. Different tasks of computer vision are covered in this study including classification, segmentation, object detection and recognition. Also, an exclusive study on data augmentation using GAN which is trending research on fake image generation is included; this technique was found to enhance the overall efficiency of the models to a great extent in various real-world applications. The various deep learning frameworks that are customized to mitigate the effect of class imbalance are presented including vision transformers and ensemble transformers that is trending research nowadays. A scrutiny of all the Tables presented reveals some unique ideas in forms of the use of iterative learning, weighted ensembles, appropriate loss functions and smart combination of classifiers and data augmentation, novel architectural layers etc. for mitigating the effect of class imbalance. This work paves the way for intelligent design of futuristic models that can be generalized on an imbalanced dataset in real world applications. The limitations, open issues, potential insights, future trends and directions that may shape the future of addressing class imbalance in the computer vision domain are further highlighted in this section.

4.1 More challenging application areas and customized solutions

As the computer vision models are increasingly being deployed in more real-world scenarios such as medical imaging and automated diagnostic procedures, autonomous driving and surveillance, multimodal biometric recognition and many more, where few classes may be rare (minority) in comparison to others or in other words there might be imbalanced class representation due to the performance of the

underrepresented classes is downgraded. Therefore, new application domains in computer vision need to be identified and customized imbalanced learning procedures need to be adopted to suit the classification task at hand.

4.2 Active learning with hyperparameter tuning for few-shot learning

Further, integration of active learning and automated selection of models with appropriate hyperparameters may also play a more significant role in addressing class imbalance when the class definition is ambiguous and the majority and minority samples overlap to a large extent. Even after selectively choosing the most informative samples for annotation, active learning can help to mitigate the impact of class imbalance by focusing on underrepresented or on more difficult instances/samples which can overall improve the performance of models while reducing the annotation efforts. This would help to address the cases of few-shot or zero-shot learning which deals with test samples having new class definitions; semi-supervised techniques are found to be more successful for this case than supervised learning [172].

4.3 Generalizability of transfer learning to unseen classes

Transfer learning and domain adaptation wherein pre-trained networks are fine-tuned on target domains still remain a crucial factor in handling the class imbalance situation. The transfer of knowledge should be such that the fine-tuned model is able to identify new unseen classes. In the new era, it is expected that there will be more design and development of new specialized advanced approaches/ packages or open-source frameworks to tackle class imbalance in computer vision; the overall goal will be to improve the performance of models and make it more generalized to work well on learning representations from the minority classes in real world applications.

4.4 Interpretability and explainability of learning frameworks

Modifying the existing learning algorithms to make it more explainable and interpretable is ongoing research. Explainable deep learning is still not fully achievable, and the problem is complicated in the background of class imbalance. As AI technologies become more pervasive, ethical considerations surrounding class imbalance in computer vision will gain significance. Bias and fairness concerns in algorithmic decision-making may drive the development of more comprehensive frameworks for addressing class imbalance to ensure equitable outcomes across various demographic groups/ applications.

4.5 Effect of adversarial learning on the minority classes

Adding adversarial samples (such as in GAN) can exacerbate the challenges of addressing class imbalance. Adversarial samples are deliberately crafted input patterns that can be created for any class, including both majority and minority classes [157]. However, the impact of adversarial samples can be particularly severe for minority classes in imbalanced datasets. When a computer vision model is trained on imbalanced data, it may already have difficulty learning representations for the minority classes due to the limited number of examples available. Adversarial samples can further exacerbate this problem by introducing additional sources of misclassification, making it even more challenging for the model to accurately classify instances from the minority classes. To tackle these vulnerabilities, researchers have been actively investigating adversarial samples and working on methods to mitigate their impact. Overall,

this integration will help in creation of more equitable and reliable computer vision models in the terms of class imbalance and adversarial samples.

4.6 Limitations of current research

The limitations of contemporary research on imbalanced learning are summarized below.

(i) Despite the advancements made in the field of machine learning and deep learning; the system is still data driven. Changing the dataset will bring in a lot of changes in the performance. Therefore, the current crop of balancing strategies do not have generalization ability.

(ii) Data augmentation may in some cases (minority samples are too few) lead to repetitive samples, which may in turn lead to overfitting of the model.

(iii) Designing loss functions for cost-sensitive learning is effective, however, they are usually customized for the task at hand and the imbalance ratio of the dataset.

(iv) There are relatively fewer works on extremely imbalanced datasets. The handful of samples in the minority class would bring down the system performance.

7. Conclusion

This survey includes a comprehensive analysis of machine learning and deep learning methods for addressing the challenges of class imbalance in computer vision, with an increased focus on deep learning solutions that form the state-of-the-art today. Class imbalance is prevalent in real-world image datasets such as biomedical datasets where the number of healthy or control samples heavily outnumber the diseased samples. Addressing the class imbalance issue is therefore a crucial step to improve the performance. There are very few surveys conducted in a structured manner related to data augmentation, loss functions and deep learning frameworks in the context of class imbalance.

From this study, the two most popular solutions for class imbalance in deep learning frameworks in numerous applications appear to be (i) pre-trained CNNs with data augmentation which is a form of data-level augmentation (ii) cost-sensitive learning for both CNNs trained from scratch and pre-trained CNNs which aims to improve the learning process without manipulating the input data. Fine-tuning with data augmentation is one of the best available solutions to prevent overfitting when the dataset is small in size. Most of the researchers have experimented on different combinations of loss functions and data augmentation. As per the findings, the choice of the loss function, system components, architectural blocks or layers, and applying various balancing strategies approaches at data level, plays a crucial role in how effectively the system is able to combat class imbalance. The study has also reviewed some deep neural network frameworks that have been designed keeping class imbalance in mind, though such works are rarer to find. The pre-trained network ResNet50 was found to mitigate class imbalance even in the absence of data augmentation or cost-sensitive learning as compared to all other pre-trained networks, emphasizing the role of residual connections for improving the classification of minority classes. The YOLO object detection models also were found helpful for imbalanced learning since these models identify the points of interest in an image. When integrated with data augmentation techniques, this method helps to mitigate class imbalance as proved by surveyed works.

This study would be useful for the creation of new deep learning frameworks that can learn effectively from imbalanced datasets, and also inspires development of hybrid machine learning and deep learning approaches involving manipulations at both data-level and algorithm-level. Overall these techniques can be used in various domains or applications eradicating the problems or challenges associated with the class imbalanced datasets. Also discussed the challenges and constraints faced when applying these methods to real-world scenarios. This survey highlights trends, challenges and future directions in the field of class imbalance in computer vision and deep learning which will enable readers to stay updated with the latest research developments and challenges involved in this evolving and promising domain which might impact real-world applications. The paper reviews a large variety of imbalanced datasets used in various applications of computer vision, and multiple complementary performance metrics such as F1-score, IBA, MCC and Geometric mean, which would help to identify the preferred deep/non-deep learning methodology for various computer vision applications having class imbalance situations. Lastly, research that evaluates the use of deep learning to address class imbalance in non-image data is limited which needs to be expanded upon in future works. The current study has limitations as it is focused in the computer vision domain. Future studies should integrate the interdisciplinary works of various domains linking computer vision with other fields of Artificial intelligence such as Internet of Things (IoT), Robotics, and Natural language processing (NLP), and also extend and streamline this study to explore further into specific classification tasks in the biomedical domain.

References

1. Fernández, Alberto, Salvador García, Mikel Galar, Ronaldo C. Prati, Bartosz Krawczyk, and Francisco Herrera. *Learning from imbalanced data sets*. Vol. 10. Cham: Springer, 2018.
2. Krawczyk, Bartosz. "Learning from imbalanced data: open challenges and future directions." *Progress in Artificial Intelligence* 5, no. 4 (2016): 221-232.
3. Susan, Seba, and Amitesh Kumar. "The balancing trick: Optimized sampling of imbalanced datasets—A brief survey of the recent State of the Art." *Engineering Reports* 3, no. 4 (2021): e12298.
4. Reza, Md Shamim, and Jinwen Ma. "Imbalanced histopathological breast cancer image classification with convolutional neural network." In *2018 14th IEEE International Conference on Signal Processing (ICSP)*, pp. 619-624. IEEE, 2018.
5. Kulatilleke, Gayan K. "Challenges and complexities in machine learning based credit card fraud detection." *arXiv preprint arXiv:2208.10943* (2022).
6. Bailey, Kyle O., James S. Okolica, and Gilbert L. Peterson. "User identification and authentication using multi-modal behavioral biometrics." *Computers & Security* 43 (2014): 77-89.
7. Zhou, Joey Tianyi, Le Zhang, Zhiwen Fang, Jiawei Du, Xi Peng, and Yang Xiao. "Attention-driven loss for anomaly detection in video surveillance." *IEEE transactions on circuits and systems for video technology* 30, no. 12 (2019): 4639-4647.
8. Pérez-Hernández, Francisco, Siham Tabik, Alberto Lamas, Roberto Olmos, Hamido Fujita, and Francisco Herrera. "Object detection binary classifiers methodology based on deep learning to identify small objects handled similarly: Application in video surveillance." *Knowledge-Based Systems* 194 (2020): 105590.
9. Tanha, Jafar, Yousef Abdi, Negin Samadi, Nazila Razzaghi, and Mohammad Asadpour. "Boosting methods for multi-class imbalanced data classification: an experimental review." *Journal of Big Data* 7, no. 1 (2020): 1-47.

10. Kotsiantis, Sotiris, Dimitris Kanellopoulos, and Panayiotis Pintelas. "Handling imbalanced datasets: A review." *GESTS international transactions on computer science and engineering* 30, no. 1 (2006): 25-36
11. Guo, Xinjian, Yilong Yin, Cailing Dong, Gongping Yang, and Guangtong Zhou. "On the class imbalance problem." In *2008 Fourth international conference on natural computation*, vol. 4, pp. 192-201. IEEE, 2008.
12. Barandela, Ricardo, Rosa M. Valdovinos, J. Salvador Sánchez, and Francesc J. Ferri. "The imbalanced training sample problem: Under or over sampling?." In *Structural, Syntactic, and Statistical Pattern Recognition: Joint IAPR International Workshops, SSPR 2004 and SPR 2004, Lisbon, Portugal, August 18-20, 2004. Proceedings*, pp. 806-814. Springer Berlin Heidelberg, 2004.
13. Susan, Seba, and Amitesh Kumar. "Hybrid of intelligent minority oversampling and PSO-based intelligent majority undersampling for learning from imbalanced datasets." In *Intelligent Systems Design and Applications: 18th International Conference on Intelligent Systems Design and Applications (ISDA 2018) held in Vellore, India, December 6-8, 2018, Volume 2*, pp. 760-769. Springer International Publishing, 2020.
14. Susan, Seba, and Amitesh Kumar. "SSOMaj-SMOTE-SSOMin: Three-step intelligent pruning of majority and minority samples for learning from imbalanced datasets." *Applied Soft Computing* 78 (2019): 141-149.
15. Sun, Yanmin, Mohamed S. Kamel, Andrew KC Wong, and Yang Wang. "Cost-sensitive boosting for classification of imbalanced data." *Pattern recognition* 40, no. 12 (2007): 3358-3378.
16. Zhou, Zhi‐Hua, and Xu‐Ying Liu. "On multi‐class cost‐sensitive learning." *Computational Intelligence* 26, no. 3 (2010): 232-257.
17. Seiffert, Chris, Taghi M. Khoshgoftaar, Jason Van Hulse, and Amri Napolitano. "RUSBoost: A hybrid approach to alleviating class imbalance." *IEEE Transactions on Systems, Man, and Cybernetics-Part A: Systems and Humans* 40, no. 1 (2009): 185-197.
18. Yijing, Li, Guo Haixiang, Liu Xiao, Li Yanan, and Li Jinling. "Adapted ensemble classification algorithm based on multiple classifier system and feature selection for classifying multi-class imbalanced data." *Knowledge-Based Systems* 94 (2016): 88-104.
19. Chen, Hao, Chaoshun Li, Wenxian Yang, Jie Liu, Xueli An, and Yujie Zhao. "Deep balanced cascade forest: An novel fault diagnosis method for data imbalance." *ISA transactions* 126 (2022): 428-439.
20. Rahman, M. Mostafizur, and Darryl N. Davis. "Addressing the class imbalance problem in medical datasets." *International Journal of Machine Learning and Computing* 3, no. 2 (2013): 224.
21. Gupta, Abhishek, Alagan Anpalagan, Ling Guan, and Ahmed Shaharyar Khwaja. "Deep learning for object detection and scene perception in self-driving cars: Survey, challenges, and open issues." *Array* 10 (2021): 100057.
22. Johnson, Justin M., and Taghi M. Khoshgoftaar. "Survey on deep learning with class imbalance." *Journal of Big Data* 6, no. 1 (2019): 1-54.
23. Saini, Manisha, and Seba Susan. "Diabetic retinopathy screening using deep learning for multi-class imbalanced datasets." *Computers in Biology and Medicine* 149 (2022): 105989.
24. Saini, Manisha, and Seba Susan. "Vggin-net: Deep transfer network for imbalanced breast cancer dataset." IEEE/ACM Transactions on Computational Biology and Bioinformatics (2022).
25. Sarafianos, Nikolaos, Xiang Xu, and Ioannis A. Kakadiaris. "Deep imbalanced attribute classification using visual attention aggregation." In Proceedings of the European Conference on Computer Vision (ECCV), pp. 680-697. 2018.
26. Sambasivam, G. A. O. G. D., and Geoffrey Duncan Opiyo. "A predictive machine learning application in agriculture: Cassava disease detection and classification with imbalanced dataset using convolutional neural networks." *Egyptian informatics journal* 22, no. 1 (2021): 27-34.
27. Yeung, Michael, Evis Sala, Carola-Bibiane Schönlieb, and Leonardo Rundo. "Unified focal loss: Generalising dice and cross entropy-based losses to handle class imbalanced medical image segmentation." *Computerized Medical Imaging and Graphics* 95 (2022): 102026

28. Carranza-García, Manuel, Pedro Lara-Benítez, Jorge García-Gutiérrez, and José C. Riquelme. "Enhancing object detection for autonomous driving by optimizing anchor generation and addressing class imbalance." *Neurocomputing* 449 (2021): 229-244.
29. Dong, Qi, Shaogang Gong, and Xiatian Zhu. "Class rectification hard mining for imbalanced deep learning." In Proceedings of the IEEE International Conference on Computer Vision, pp. 1851-1860. 2017
30. Ngo, Quan T., and Seokhoon Yoon. "Facial expression recognition based on weighted-cluster loss and deep transfer learning using a highly imbalanced dataset." *Sensors* 20, no. 9 (2020): 2639.
31. Yang, Lei, Guowu Yuan, Hao Zhou, Hongyu Liu, Jian Chen, and Hao Wu. "RS-YOLOX: A High-Precision Detector for Object Detection in Satellite Remote Sensing Images." Applied Sciences 12, no. 17 (2022): 8707
32. Alaba, Simegnew Yihunie, M. M. Nabi, Chiranjibi Shah, Jack Prior, Matthew D. Campbell, Farron Wallace, John E. Ball, and Robert Moorhead. "Class-Aware Fish Species Recognition Using Deep Learning for an Imbalanced Dataset." Sensors 22, no. 21 (2022): 8268
33. Liu, Wei, Miaohui Zhang, Zhiming Luo, and Yuanzheng Cai. "An ensemble deep learning method for vehicle type classification on visual traffic surveillance sensors." *IEEE Access* 5 (2017): 24417-24425.
34. Susan, Seba, and Ashu Kaushik. "Localized Metric Learning for Large Multi-class Extremely Imbalanced Face Database." In Database Systems for Advanced Applications. DASFAA 2022 International Workshops: BDMS, BDQM, GDMA, IWBT, MAQTDS, and PMBD, Virtual Event, April 11–14, 2022, Proceedings, pp. 64-78. Cham: Springer International Publishing, 2022.
35. Alam, Talha Mahboob, Kamran Shaukat, Waseem Ahmad Khan, Ibrahim A. Hameed, Latifah Abd Almuqren, Muhammad Ahsan Raza, Memoona Aslam, and Suhuai Luo. "An Efficient Deep Learning-Based Skin Cancer Classifier for an Imbalanced Dataset." Diagnostics 12, no. 9 (2022): 2115.
36. Mahesh, Batta. "Machine learning algorithms-a review." International Journal of Science and Research (IJSR).[Internet] 9 (2020): 381-386.
37. Carbonell, Jaime G., Ryszard S. Michalski, and Tom M. Mitchell. "An overview of machine learning." *Machine learning* (1983): 3-23.
38. Lemaître, Guillaume, Fernando Nogueira, and Christos K. Aridas. "Imbalanced-learn: A python toolbox to tackle the curse of imbalanced datasets in machine learning." The Journal of Machine Learning Research 18, no. 1 (2017): 559-563.
39. Feng, Wei, Wenjiang Huang, and Wenxing Bao. "Imbalanced hyperspectral image classification with an adaptive ensemble method based on SMOTE and rotation forest with differentiated sampling rates." *IEEE Geoscience and Remote Sensing Letters* 16, no. 12 (2019): 1879-1883.
40. Chamseddine, Ekram, Nesrine Mansouri, Makram Soui, and Mourad Abed. "Handling class imbalance in COVID-19 chest X-ray images classification: Using SMOTE and weighted loss." *Applied Soft Computing* 129 (2022): 109588.
41. Saini, Manisha, and Seba Susan. "Bag-of-Visual-Words codebook generation using deep features for effective classification of imbalanced multi-class image datasets." Multimedia Tools and Applications 80, no. 14 (2021): 20821-20847.
42. Kaur, Harsurinder, Husanbir Singh Pannu, and Avleen Kaur Malhi. "A systematic review on imbalanced data challenges in machine learning: Applications and solutions." *ACM Computing Surveys (CSUR)* 52, no. 4 (2019): 1-36.
43. Zhang, Yudong, Siyuan Lu, Xingxing Zhou, Ming Yang, Lenan Wu, Bin Liu, Preetha Phillips, and Shuihua Wang. "Comparison of machine learning methods for stationary wavelet entropy-based multiple sclerosis detection: decision tree, k-nearest neighbors, and support vector machine." *Simulation* 92, no. 9 (2016): 861-871.
44. LeCun, Yann, Yoshua Bengio, and Geoffrey Hinton. "Deep learning." *nature* 521, no. 7553 (2015): 436-444.
45. Huang, Gao, Zhuang Liu, Laurens Van Der Maaten, and Kilian Q. Weinberger. "Densely connected convolutional networks." In *Proceedings of the IEEE conference on computer vision and pattern recognition*, pp. 4700-4708. 2017.

46. Zhao, Rongjian, Buyue Qian, Xianli Zhang, Yang Li, Rong Wei, Yang Liu, and Yinggang Pan. "Rethinking dice loss for medical image segmentation." In *2020 IEEE International Conference on Data Mining (ICDM)*, pp. 851-860. IEEE, 2020.
47. Cetinic, Eva, Tomislav Lipic, and Sonja Grgic. "Fine-tuning convolutional neural networks for fine art classification." *Expert Systems with Applications* 114 (2018): 107-118.
48. Huang, Zhongling, Zongxu Pan, and Bin Lei. "Transfer learning with deep convolutional neural network for SAR target classification with limited labeled data." *Remote Sensing* 9, no. 9 (2017): 907.
49. Simonyan, Karen, and Andrew Zisserman. "Very deep convolutional networks for large-scale image recognition." *arXiv preprint arXiv:1409.1556* (2014).
50. He, Kaiming, Xiangyu Zhang, Shaoqing Ren, and Jian Sun. "Deep residual learning for image recognition." In *Proceedings of the IEEE conference on computer vision and pattern recognition*, pp. 770-778. 2016.
51. Szegedy, Christian, Vincent Vanhoucke, Sergey Ioffe, Jon Shlens, and Zbigniew Wojna. "Rethinking the inception architecture for computer vision." In *Proceedings of the IEEE conference on computer vision and pattern recognition*, pp. 2818-2826. 2016.
52. Sandler, Mark, Andrew Howard, Menglong Zhu, Andrey Zhmoginov, and Liang-Chieh Chen. "Mobilenetv2: Inverted residuals and linear bottlenecks." In *Proceedings of the IEEE conference on computer vision and pattern recognition*, pp. 4510-4520. 2018.
53. Tan, Mingxing, and Quoc Le. "Efficientnet: Rethinking model scaling for convolutional neural networks." In *International conference on machine learning*, pp. 6105-6114. PMLR, 2019.
54. Szegedy, Christian, Sergey Ioffe, Vincent Vanhoucke, and Alexander Alemi. "Inception-v4, inception-resnet and the impact of residual connections on learning." In *Proceedings of the AAAI conference on artificial intelligence*, vol. 31, no. 1. 2017
55. Ren, Shaoqing, Kaiming He, Ross Girshick, and Jian Sun. "Faster r-cnn: Towards real-time object detection with region proposal networks." *Advances in neural information processing systems* 28 (2015).
56. Lin, Tsung-Yi, Priya Goyal, Ross Girshick, Kaiming He, and Piotr Dollár. "*Focal loss for dense object detection*." In Proceedings of the IEEE international conference on computer vision, pp. 2980-2988. 2017.
57. Tan, Mingxing, Ruoming Pang, and Quoc V. Le. "Efficientdet: Scalable and efficient object detection." In *Proceedings of the IEEE/CVF conference on computer vision and pattern recognition*, pp. 10781-10790. 2020.
58. Chen, Liang-Chieh, George Papandreou, Florian Schroff, and Hartwig Adam. "Rethinking atrous convolution for semantic image segmentation." *arXiv preprint arXiv:1706.05587* (2017).
59. Zhao, Hengshuang, Jianping Shi, Xiaojuan Qi, Xiaogang Wang, and Jiaya Jia. "Pyramid scene parsing network." In *Proceedings of the IEEE conference on computer vision and pattern recognition*, pp. 2881-2890. 2017.
60. Goodfellow, Ian, Jean Pouget-Abadie, Mehdi Mirza, Bing Xu, David Warde-Farley, Sherjil Ozair, Aaron Courville, and Yoshua Bengio. "Generative adversarial networks." *Communications of the ACM* 63, no. 11 (2020): 139-144.
61. Doersch, Carl. "Tutorial on variational autoencoders." *arXiv preprint arXiv:1606.05908* (2016).
62. Khan, Salman, Muzammal Naseer, Munawar Hayat, Syed Waqas Zamir, Fahad Shahbaz Khan, and Mubarak Shah. "Transformers in vision: A survey." *ACM computing surveys (CSUR)* 54, no. 10s (2022): 1-41.
63. Xu, Feiyu, Hans Uszkoreit, Yangzhou Du, Wei Fan, Dongyan Zhao, and Jun Zhu. "Explainable AI: A brief survey on history, research areas, approaches and challenges." In *Natural Language Processing and Chinese Computing: 8th CCF International Conference, NLPCC 2019, Dunhuang, China, October 9–14, 2019, Proceedings, Part II 8*, pp. 563-574. Springer International Publishing, 2019.
64. Han, Kai, Yunhe Wang, Hanting Chen, Xinghao Chen, Jianyuan Guo, Zhenhua Liu, Yehui Tang et al. "A survey on vision transformer." *IEEE transactions on pattern analysis and machine intelligence* 45, no. 1 (2022): 87-110.
65. Bai, Long, Liangyu Wang, Tong Chen, Yuanhao Zhao, and Hongliang Ren. "Transformer-based disease identification for small-scale imbalanced capsule endoscopy dataset." Electronics 11, no. 17 (2022): 2747.

66. Kaselimi, Maria, Athanasios Voulodimos, Ioannis Daskalopoulos, Nikolaos Doulamis, and Anastasios Doulamis. "A vision transformer model for convolution-free multilabel classification of satellite imagery in deforestation monitoring." *IEEE Transactions on Neural Networks and* Learning Systems (2022).
67. Zhang, Yifan, Bingyi Kang, Bryan Hooi, Shuicheng Yan, and Jiashi Feng. "Deep long-tailed learning: A survey." *arXiv preprint arXiv:2110.04596* (2021).
68. Li, Yu, Tao Wang, Bingyi Kang, Sheng Tang, Chunfeng Wang, Jintao Li, and Jiashi Feng. "Overcoming classifier imbalance for long-tail object detection with balanced group softmax." In *Proceedings of the IEEE/CVF conference on computer vision and pattern recognition*, pp. 10991-11000. 2020.
69. Saini, Manisha, and Seba Susan. "Data augmentation of minority class with transfer learning for classification of imbalanced breast cancer dataset using inception-V3." In Pattern Recognition and Image Analysis: 9th Iberian Conference, IbPRIA 2019, Madrid, Spain, July 1–4, 2019, Proceedings, Part I 9, pp. 409-420. Springer International Publishing, 2019.
70. Yeung, Michael, Evis Sala, Carola-Bibiane Schönlieb, and Leonardo Rundo. "Unified focal loss: Generalising dice and cross entropy-based losses to handle class imbalanced medical image segmentation." Computerized Medical Imaging and Graphics 95 (2022): 102026.
71. Afzal, Sitara, Muazzam Maqsood, Faria Nazir, Umair Khan, Farhan Aadil, Khalid M. Awan, Irfan Mehmood, and Oh-Young Song. "A data augmentation-based framework to handle class imbalance problem for Alzheimer's stage detection." IEEE access 7 (2019): 115528-115539.
72. Hidayat, Alam Ahmad, Kartika Purwandari, Tjeng Wawan Cenggoro, and Bens Pardamean. "A convolutional neural network-based ancient sundanese character classifier with data augmentation." Procedia Computer Science 179 (2021): 195-201.
73. Tanaka, Fabio Henrique Kiyoiti dos Santos, and Claus Aranha. "Data augmentation using GANs." arXiv preprint arXiv:1904.09135 (2019).
74. Mikołajczyk, Agnieszka, and Michał Grochowski. "Data augmentation for improving deep learning in image classification problem." In 2018 international interdisciplinary PhD workshop (IIPhDW), pp. 117-122. IEEE, 2018
75. Nesteruk, Sergey, Dmitrii Shadrin, and Mariia Pukalchik. "Image augmentation for multitask few-shot learning: Agricultural domain use-case." arXiv preprint arXiv:2102.12295 (2021)
76. Hung, Jane, and Anne Carpenter. "Applying faster R-CNN for object detection on malaria images." In Proceedings of the IEEE conference on computer vision and pattern recognition workshops, pp. 56-61. 2017.
77. Dai, Wei, Dayong Li, Ding Tang, Huamiao Wang, and Yinghong Peng. "Deep learning approach for defective spot welds classification using small and class-imbalanced datasets." Neurocomputing 477 (2022): 46-60.
78. Saini, Manisha, and Seba Susan. "Deep transfer with minority data augmentation for imbalanced breast cancer dataset." Applied Soft Computing 97 (2020): 106759.
79. Wu, Eric, Kevin Wu, David Cox, and William Lotter. "Conditional infilling GANs for data augmentation in mammogram classification." In Image analysis for moving organ, breast, and thoracic images, pp. 98-106. Springer, Cham, 2018.
80. Dumagpi, Joanna Kazzandra, and Yong-Jin Jeong. "Evaluating gan-based image augmentation for threat detection in large-scale xray security images." Applied Sciences 11, no. 1 (2020): 36.
81. Ali-Gombe, Adamu, and Eyad Elyan. "MFC-GAN: Class-imbalanced dataset classification using multiple fake class generative adversarial network." Neurocomputing 361 (2019): 212-221.
82. Zhu, Xinyue, Yifan Liu, Jiahong Li, Tao Wan, and Zengchang Qin. "Emotion classification with data augmentation using generative adversarial networks." In Advances in Knowledge Discovery and Data Mining: 22nd Pacific-Asia Conference, PAKDD 2018, Melbourne, VIC, Australia, June 3-6, 2018, Proceedings, Part III 22, pp. 349-360. Springer International Publishing, 2018.
83. Huang, Yangru, Yi Jin, Yidong Li, and Zhiping Lin. "Towards imbalanced image classification: a generative adversarial network ensemble learning method." IEEE Access 8 (2020): 88399-88409.
84. Nazki, Haseeb, Jaehwan Lee, Sook Yoon, and Dong Sun Park. "Image-to-image translation with GAN for synthetic data augmentation in plant disease datasets." Smart Media Journal 8, no. 2 (2019): 46-57

85. Rezaei, Mina, Haojin Yang, and Christoph Meinel. "Conditional generative refinement adversarial networks for unbalanced medical image semantic segmentation." arXiv preprint arXiv:1810.03871 (2018).
86. Saini, Manisha, and Seba Susan. "Cervical Cancer Screening on Multi-class Imbalanced Cervigram Dataset using Transfer Learning." In *2022 15th International Congress on Image and Signal Processing, BioMedical Engineering and Informatics (CISP-BMEI)*, pp. 1-6. IEEE, 2022.
87. Kim, Yechan, Younkwan Lee, and Moongu Jeon. "Imbalanced image classification with complement cross entropy." Pattern Recognition Letters 151 (2021): 33-40.
88. Wang, Yiru, Weihao Gan, Jie Yang, Wei Wu, and Junjie Yan. "Dynamic curriculum learning for imbalanced data classification." In Proceedings of the IEEE/CVF international conference on computer vision, pp. 5017-5026. 2019.
89. Phan, Trong Huy, and Kazuma Yamamoto. "Resolving class imbalance in object detection with weighted cross entropy losses." arXiv preprint arXiv:2006.01413 (2020).
90. Lu, Xiankai, Chao Ma, Bingbing Ni, Xiaokang Yang, Ian Reid, and Ming-Hsuan Yang. "Deep regression tracking with shrinkage loss." In Proceedings of the European conference on computer vision (ECCV), pp. 353-369. 2018
91. Tran, Giang Son, Thi Phuong Nghiem, Van Thi Nguyen, Chi Mai Luong, and Jean-Christophe Burie. "Improving accuracy of lung nodule classification using deep learning with focal loss." Journal of healthcare engineering 2019 (2019).
92. Ren, Jiawei, Mingyuan Zhang, Cunjun Yu, and Ziwei Liu. "Balanced mse for imbalanced visual regression." In Proceedings of the IEEE/CVF Conference on Computer Vision and Pattern Recognition, pp. 7926-7935. 2022.
93. Park, Seulki, Jongin Lim, Younghan Jeon, and Jin Young Choi. "Influence-balanced loss for imbalanced visual classification." In Proceedings of the IEEE/CVF International Conference on Computer Vision, pp. 735-744. 2021.
94. Yeung, Michael, Evis Sala, Carola-Bibiane Schönlieb, and Leonardo Rundo. "Unified focal loss: Generalising dice and cross entropy-based losses to handle class imbalanced medical image segmentation." Computerized Medical Imaging and Graphics 95 (2022): 102026
95. Susan, Seba, Dhaarna Sethi, and Kriti Arora. "CW-CAE: pulmonary nodule detection from imbalanced dataset using class-weighted convolutional autoencoder." In *International Conference on Innovative Computing and Communications: Proceedings of ICICC 2020, Volume 2*, pp. 825-833. Springer Singapore, 2021.
96. Bhowal, Pratik, Subhankar Sen, Juan D. Velasquez, and Ram Sarkar. "Fuzzy ensemble of deep learning models using choquet fuzzy integral, coalition game and information theory for breast cancer histology classification." Expert Systems with Applications 190 (2022): 116167
97. Sori, Worku J., Jiang Feng, Arero W. Godana, Shaohui Liu, and Demissie J. Gelmecha. "DFD-Net: lung cancer detection from denoised CT scan image using deep learning." Frontiers of Computer Science 15 (2021): 1-13.
98. Rath, Adyasha, Debahuti Mishra, Ganapati Panda, and Suresh Chandra Satapathy. "Heart disease detection using deep learning methods from imbalanced ECG samples." Biomedical Signal Processing and Control 68 (2021): 102820.
99. Hussain, Emtiaz, Mahmudul Hasan, Syed Zafrul Hassan, Tanzina Hassan Azmi, Md Anisur Rahman, and Mohammad Zavid Parvez. "Deep learning based binary classification for alzheimer's disease detection using brain mri images." In 2020 15th IEEE Conference on Industrial Electronics and Applications (ICIEA), pp. 1115-1120. IEEE, 2020.
100. Zhao, Chen, Renjun Shuai, Li Ma, Wenjia Liu, and Menglin Wu. "Improving cervical cancer classification with imbalanced datasets combining taming transformers with T2T-ViT." Multimedia tools and applications 81, no. 17 (2022): 24265-24300.
101. Wang, Guanbo, Hongwei Ding, Mingliang Duan, Yuanyuan Pu, Zhijun Yang, and Haiyan Li. "Fighting against terrorism: A real-time CCTV autonomous weapons detection based on improved YOLO v4." *Digital Signal Processing* 132 (2022): 103790.

102. Ciccarelli, Marianna, Flavio Corradini, Michele Germani, Giacomo Menchi, Leonardo Mostarda, Alessandra Papetti, and Marco Piangerelli. "SPECTRE: a deep learning network for posture recognition in manufacturing." Journal of Intelligent Manufacturing (2022): 1-13
103. Hamad, Rebeen Ali, Longzhi Yang, Wai Lok Woo, and Bo Wei. "Joint learning of temporal models to handle imbalanced data for human activity recognition." Applied Sciences 10, no. 15 (2020): 5293.
104. Pouyanfar, Samira, and Shu-Ching Chen. "Automatic video event detection for imbalance data using enhanced ensemble deep learning." International Journal of Semantic Computing 11, no. 01 (2017): 85-109.
105. Jing, Junfeng, Zhen Wang, Matthias Rätsch, and Huanhuan Zhang. "Mobile-Unet: An efficient convolutional neural network for fabric defect detection." *Textile Research Journal* 92, no. 1-2 (2022): 30-42.
106. Liu, Yuekai, Hongli Gao, Liang Guo, Aoping Qin, Canyu Cai, and Zhichao You. "A data-flow oriented deep ensemble learning method for real-time surface defect inspection." *IEEE Transactions on Instrumentation and Measurement* 69, no. 7 (2019): 4681-4691.
107. Gandhi, Shreyansh, Samrat Kokkula, Abon Chaudhuri, Alessandro Magnani, Theban Stanley, Behzad Ahmadi, Venkatesh Kandaswamy, Omer Ovenc, and Shie Mannor. "Scalable detection of offensive and non-compliant content/logo in product images." In Proceedings of the IEEE/CVF Winter Conference on Applications of Computer Vision, pp. 2247-2256. 2020.
108. Soleymani, Maryam, Mahdi Bonyani, Hadi Mahami, and Farnad Nasirzadeh. "Construction material classification on imbalanced datasets using Vision Transformer (ViT) architecture." arXiv preprint arXiv:2108.09527 (2021).
109. Trong, Vo Hoang, Yu Gwang-hyun, Dang Thanh Vu, and Kim Jin-young. "Late fusion of multimodal deep neural networks for weeds classification." Computers and Electronics in Agriculture 175 (2020): 105506.
110. Da Costa, Arthur Z., Hugo EH Figueroa, and Juliana A. Fracarolli. "Computer vision based detection of external defects on tomatoes using deep learning." Biosystems Engineering 190 (2020): 131-144.
111. Li, Lili, Shujuan Zhang, and Bin Wang. "Apple leaf disease identification with a small and imbalanced dataset based on lightweight convolutional networks." Sensors 22, no. 1 (2022): 173.
112. Esgario, José GM, Renato A. Krohling, and José A. Ventura. "Deep learning for classification and severity estimation of coffee leaf biotic stress." Computers and Electronics in Agriculture 169 (2020): 105162.
113. Gupta, Himanshu, and Om Prakash Verma. "Monitoring and surveillance of urban road traffic using low altitude drone images: a deep learning approach." Multimedia Tools and Applications (2022): 1-21.
114. Kim, Pyong-Kun, and Kil-Taek Lim. "Vehicle type classification using bagging and convolutional neural network on multi view surveillance image." In Proceedings of the IEEE conference on computer vision and *pattern recognition workshops*, pp. 41-46. 2017.
115. Alia, Ahmed, Mohammed Maree, and Mohcine Chraibi. "A hybrid deep learning and visualization framework for pushing behavior detection in pedestrian dynamics." Sensors 22, no. 11 (2022): 4040.
116. Haixiang, Guo, Li Yijing, Jennifer Shang, Gu Mingyun, Huang Yuanyue, and Gong Bing. "Learning from class-imbalanced data: Review of methods and applications." Expert systems with applications 73 (2017): 220-239.
117. Reddy, Charan, Deepak Sharma, Soroush Mehri, Adriana Romero-Soriano, Samira Shabanian, and Sina Honari. "Benchmarking bias mitigation algorithms in representation learning through fairness metrics." In *Thirty-fifth Conference on Neural Information Processing Systems Datasets and Benchmarks Track (Round 1)*. 2021. url: https://paperswithcode.com/dataset/ci-mnist
118. Codella, Noel, Veronica Rotemberg, Philipp Tschandl, M. Emre Celebi, Stephen Dusza, David Gutman, Brian Helba et al. "Skin lesion analysis toward melanoma detection 2018: A challenge hosted by the international skin imaging collaboration (isic)." *arXiv preprint arXiv:1902.03368* (2019).
119. Heath, Michael, Kevin Bowyer, Daniel Kopans, Philip Kegelmeyer, Richard Moore, Kyong Chang, and S. Munishkumaran. "Current status of the digital database for screening mammography." *Digital Mammography: Nijmegen, 1998* (1998): 457-460.
120. Ortiz, Julian Albert Aviles. *COVID-19 X-ray Image Classification: A Transfer Learning Approach*. University of California, Los Angeles, 2021.

121. Saood, Adnan, and Iyad Hatem. "COVID-19 lung CT image segmentation using deep learning methods: U-Net versus SegNet." *BMC Medical Imaging* 21, no. 1 (2021): 1-10.
122. Liu, Ziwei, Ping Luo, Xiaogang Wang, and Xiaoou Tang. "Deep learning face attributes in the wild." In Proceedings of the IEEE international conference on computer vision, pp. 3730-3738. 2015.
123. Li, Dangwei, Zhang Zhang, Xiaotang Chen, Haibin Ling, and Kaiqi Huang. "A richly annotated dataset for pedestrian attribute recognition." *arXiv preprint arXiv:1603.07054* (2016).
124. Eyepacs and Kaggle. Diabetic retinopathy detection. 2015. url: https://www.kaggle.com/c/diabetic-retinopathy-detection/data
125. Shao, Shuai, Zeming Li, Tianyuan Zhang, Chao Peng, Gang Yu, Xiangyu Zhang, Jing Li, and Jian Sun. "Objects365: A large-scale, high-quality dataset for object detection." In *Proceedings of the IEEE/CVF international conference on computer vision*, pp. 8430-8439. 2019. url: https://github.com/nkicsl/DDR-dataset
126. Li, Tao, Yingqi Gao, Kai Wang, Song Guo, Hanruo Liu, and Hong Kang. "Diagnostic assessment of deep learning algorithms for diabetic retinopathy screening." *Information Sciences* 501 (2019): 511-522.
127. MobileODT, "Intel and mobileodt cervical can cer screening." [Online]. Available: https://www.kaggle.com/c/intel-mobileodt- cervical-cancer-screening/data
128. Databases–Laboratório Visão Robótica e Imagem, 2019, https://web.inf.ufpr.br/vri/databases/. (Accessed 28 November 2019).
129. Mooney, Paul. "Breast Histopathology Images. Kaggle." (2020). Accessed October 09, 2020. https://www.kaggle.com/datasets/paultimothymooney/breast-histopathology-images
130. Wardhani, Ni Wayan Surya, Masithoh Yessi Rochayani, Atiek Iriany, Agus Dwi Sulistyono, and Prayudi Lestantyo. "Cross-validation metrics for evaluating classification performance on imbalanced data." In 2019 International conference on computer, control, informatics and its applications (IC3INA), pp. 14-18. IEEE, 2019.
131. Japkowicz, Nathalie. "Assessment metrics for imbalanced learning." Imbalanced learning: Foundations, algorithms, and applications (2013): 187-206.
132. Zaitoun, Nida M., and Musbah J. Aqel. "Survey on image segmentation techniques." Procedia Computer Science 65 (2015): 797-806.
133. Susan, Seba, and Ankit Kumar. "Auto-segmentation using mean-shift and entropy analysis." In *2016 3rd international conference on computing for sustainable global development (INDIACom)*, pp. 292-296. IEEE, 2016.
134. Minaee, Shervin, Yuri Boykov, Fatih Porikli, Antonio Plaza, Nasser Kehtarnavaz, and Demetri Terzopoulos. "Image segmentation using deep learning: A survey." *IEEE transactions on pattern analysis and machine intelligence* 44, no. 7 (2021): 3523-3542.
135. Milletari, Fausto, Nassir Navab, and Seyed-Ahmad Ahmadi. "V-net: Fully convolutional neural networks for volumetric medical image segmentation." In *2016 fourth international conference on 3D vision (3DV)*, pp. 565-571. Ieee, 2016.
136. Tajbakhsh, Nima, Jae Y. Shin, Suryakanth R. Gurudu, R. Todd Hurst, Christopher B. Kendall, Michael B. Gotway, and Jianming Liang. "Convolutional neural networks for medical image analysis: Full training or fine tuning?." *IEEE transactions on medical imaging* 35, no. 5 (2016): 1299-1312.
137. Alghamdi, Hanan S., Ghada Amoudi, Salma Elhag, Kawther Saeedi, and Jomanah Nasser. "Deep learning approaches for detecting COVID-19 from chest X-ray images: A survey." *Ieee Access* 9 (2021): 20235-20254.
138. Mushtaq, Zohaib, Shun-Feng Su, and Quoc-Viet Tran. "Spectral images based environmental sound classification using CNN with meaningful data augmentation." *Applied Acoustics* 172 (2021): 107581.
139. Fuqua, Donovan, and Talayeh Razzaghi. "A cost-sensitive convolution neural network learning for control chart pattern recognition." *Expert Systems with Applications* 150 (2020): 113275.
140. Papathanasiou, Nikolaos D., Trifon Spyridonidis, and Dimitris J. Apostolopoulos. "Automatic characterization of myocardial perfusion imaging polar maps employing deep learning and data augmentation." *Hell J Nucl Med* 23 (2020): 125-132.

141. Hou, Rujie, Jinglong Chen, Yong Feng, Shen Liu, Shuilong He, and Zitong Zhou. "Contrastive-weighted self-supervised model for long-tailed data classification with vision transformer augmented." *Mechanical Systems and Signal Processing* 177 (2022): 109174.
142. Han, Sangwoo, Chan Lim, Bonggeon Cha, and Jongwuk Lee. "An empirical study for class imbalance in extreme multi-label text classification." In *2021 IEEE international conference on big data and smart computing (BigComp)*, pp. 338-341. IEEE, 2021.
143. Kuo, Weicheng, Christian Häne, Esther Yuh, Pratik Mukherjee, and Jitendra Malik. "Cost-sensitive active learning for intracranial hemorrhage detection." In *Medical Image Computing and Computer Assisted Intervention–MICCAI 2018: 21st International Conference, Granada, Spain, September 16-20, 2018, Proceedings, Part III 11*, pp. 715-723. Springer International Publishing, 2018.
144. Ghosh, Kushankur, Colin Bellinger, Roberto Corizzo, Paula Branco, Bartosz Krawczyk, and Nathalie Japkowicz. "The class imbalance problem in deep learning." *Machine Learning* (2022): 1-57.
145. Adadi, Amina, and Mohammed Berrada. "Explainable AI for healthcare: from black box to interpretable models." In *Embedded Systems and Artificial Intelligence: Proceedings of ESAI 2019, Fez, Morocco*, pp. 327-337. Springer Singapore, 2020.
146. Buda, Mateusz, Atsuto Maki, and Maciej A. Mazurowski. "A systematic study of the class imbalance problem in convolutional neural networks." *Neural networks* 106 (2018): 249-259.
147. Rácz, Anita, Dávid Bajusz, and Károly Héberger. "Effect of dataset size and train/test split ratios in QSAR/QSPR multiclass classification." *Molecules* 26, no. 4 (2021): 1111.
148. Akhtar, Zahid, Christian Micheloni, and Gian Luca Foresti. "Biometric liveness detection: Challenges and research opportunities." *IEEE Security & Privacy* 13, no. 5 (2015): 63-72.
149. Vicente, Sara, Joao Carreira, Lourdes Agapito, and Jorge Batista. "Reconstructing pascal voc." In *Proceedings of the IEEE conference on computer vision and pattern recognition*, pp. 41-48. 2014.
150. Alam, Talha Mahboob, Kamran Shaukat, Ibrahim A. Hameed, Suhuai Luo, Muhammad Umer Sarwar, Shakir Shabbir, Jiaming Li, and Matloob Khushi. "An investigation of credit card default prediction in the imbalanced datasets." IEEE Access 8 (2020): 201173-201198.
151. Srinivas, Chetana, Nandini Prasad KS, Mohammed Zakariah, Yousef Ajmi Alothaibi, Kamran Shaukat, B. Partibane, and Halifa Awal. "Deep transfer learning approaches in performance analysis of brain tumor classification using MRI images." Journal of Healthcare Engineering 2022 (2022).
152. Alam, Talha Mahboob, Kamran Shaukat, Haris Mahboob, Muhammad Umer Sarwar, Farhat Iqbal, Adeel Nasir, Ibrahim A. Hameed, and Suhuai Luo. "A machine learning approach for identification of malignant mesothelioma etiological factors in an imbalanced dataset." The Computer Journal 65, no. 7 (2022): 1740-1751.
153. Yang, Xiaoyan, Matloob Khushi, and Kamran Shaukat. "Biomarker CA125 feature engineering and class imbalance learning improves ovarian cancer prediction." In 2020 IEEE Asia-Pacific Conference on Computer Science and Data Engineering (CSDE), pp. 1-6. IEEE, 2020.
154. Shaukat, Kamran, Suhuai Luo, Nadir Abbas, Talha Mahboob Alam, Muhammad Ehtesham Tahir, and Ibrahim A. Hameed. "An analysis of blessed Friday sale at a retail store using classification models." In 2021 The 4th International Conference on Software Engineering and Information Management, pp. 193-198. 2021.
155. Shaukat, Kamran, Suhuai Luo, Vijay Varadharajan, Ibrahim A. Hameed, Shan Chen, Dongxi Liu, and Jiaming Li. "Performance comparison and current challenges of using machine learning techniques in cybersecurity." Energies 13, no. 10 (2020): 2509.
156. Shaukat, Kamran, Suhuai Luo, Vijay Varadharajan, Ibrahim A. Hameed, and Min Xu. "A survey on machine learning techniques for cyber security in the last decade." IEEE Access 8 (2020): 222310-222354.
157. Shaukat, Kamran, Suhuai Luo, and Vijay Varadharajan. "A novel deep learning-based approach for malware detection." Engineering Applications of Artificial Intelligence 122 (2023): 106030.
158. Shaukat, K., Luo, S., Chen, S. and Liu, D., 2020, October. Cyber threat detection using machine learning techniques: A performance evaluation perspective. In 2020 international conference on cyber warfare and security (ICCWS) (pp. 1-6). IEEE.

159. Shamshad, Fahad, Salman Khan, Syed Waqas Zamir, Muhammad Haris Khan, Munawar Hayat, Fahad Shahbaz Khan, and Huazhu Fu. "Transformers in medical imaging: A survey." Medical Image Analysis (2023): 102802
160. Iglesias, Guillermo, Edgar Talavera, and Alberto Díaz-Álvarez. "A survey on GANs for computer vision: Recent research, analysis and taxonomy." Computer Science Review 48 (2023): 100553.
161. Castiglioni, Isabella, Leonardo Rundo, Marina Codari, Giovanni Di Leo, Christian Salvatore, Matteo Interlenghi, Francesca Gallivanone, Andrea Cozzi, Natascha Claudia D'Amico, and Francesco Sardanelli. "AI applications to medical images: From machine learning to deep learning." *Physica Medica* 83 (2021): 9-24.
162. Sampath, Vignesh, Iñaki Maurtua, Juan Jose Aguilar Martin, and Aitor Gutierrez. "A survey on generative adversarial networks for imbalance problems in computer vision tasks." *Journal of big Data* 8 (2021): 1-59.
163. Krawczyk, Bartosz. "Learning from imbalanced data: open challenges and future directions." *Progress in Artificial Intelligence* 5, no. 4 (2016): 221-232.
164. Xu, Mingle, Sook Yoon, Alvaro Fuentes, and Dong Sun Park. "A comprehensive survey of image augmentation techniques for deep learning." *Pattern Recognition* (2023): 109347.
165. Zaidi, Syed Sahil Abbas, Mohammad Samar Ansari, Asra Aslam, Nadia Kanwal, Mamoona Asghar, and Brian Lee. "A survey of modern deep learning based object detection models." *Digital Signal Processing* (2022): 103514.
166. Chen, Zhi, Jiang Duan, Li Kang, and Guoping Qiu. "Class-imbalanced deep learning via a class-balanced ensemble." *IEEE transactions on neural networks and learning systems* 33, no. 10 (2021): 5626-5640.
167. Redmon, Joseph, Santosh Divvala, Ross Girshick, and Ali Farhadi. "You only look once: Unified, real-time object detection." In *Proceedings of the IEEE conference on computer vision and pattern recognition*, pp. 779-788. 2016.
168. Ronneberger, Olaf, Philipp Fischer, and Thomas Brox. "U-net: Convolutional networks for biomedical image segmentation." In *Medical Image Computing and Computer-Assisted Intervention–MICCAI 2015: 18th International Conference, Munich, Germany, October 5-9, 2015, Proceedings, Part III 18*, pp. 234-241. Springer International Publishing, 2015.
169. Liu, Ze, Yutong Lin, Yue Cao, Han Hu, Yixuan Wei, Zheng Zhang, Stephen Lin, and Baining Guo. "Swin transformer: Hierarchical vision transformer using shifted windows." In Proceedings of the IEEE/CVF international conference on computer vision, pp. 10012-10022. 2021.
170. Sivapuram, Arun Kumar, Vaishnavi Ravi, Gowtham Senthil, and Rama Krishna Gorthi. "Visal—A novel learning strategy to address class imbalance." Neural Networks (2023)
171. Woźniak, Marcin, Michał Wieczorek, and Jakub Siłka. "BiLSTM deep neural network model for imbalanced medical data of IoT systems." Future Generation Computer Systems 141 (2023): 489-499.
172. Xu, Bingrong, Zhigang Zeng, Cheng Lian, and Zhengming Ding. "Semi-supervised low-rank semantics grouping for zero-shot learning." *IEEE Transactions on Image Processing* 30 (2021): 2207-2219.
173. Anand, Atul, Tushar Kadian, Manu Kumar Shetty, and Anubha Gupta. "Explainable AI decision model for ECG data of cardiac disorders." *Biomedical Signal Processing and Control* 75 (2022): 103584.
174. Sundararajan, Kalaivani, and Damon L. Woodard. "Deep learning for biometrics: A survey." *ACM Computing Surveys (CSUR)* 51, no. 3 (2018): 1-34.
175. Zhang, Linbin, Caiguang Zhang, Sinong Quan, Huaxin Xiao, Gangyao Kuang, and Li Liu. "A class imbalance loss for imbalanced object recognition." *IEEE Journal of Selected Topics in Applied Earth Observations and Remote Sensing* 13 (2020): 2778-2792.
176. Sozykin, Konstantin, Stanislav Protasov, Adil Khan, Rasheed Hussain, and Jooyoung Lee. "Multi-label class-imbalanced action recognition in hockey videos via 3D convolutional neural networks." In *2018 19th IEEE/ACIS International Conference on Software Engineering, Artificial Intelligence, Networking and Parallel/Distributed Computing (SNPD)*, pp. 146-151. IEEE, 2018.
177. Chawla, Nitesh V., Kevin W. Bowyer, Lawrence O. Hall, and W. Philip Kegelmeyer. "SMOTE: synthetic minority over-sampling technique." *Journal of artificial intelligence research* 16 (2002): 321-357.

View publication stats

178. He, Haibo, Yang Bai, Edwardo A. Garcia, and Shutao Li. "ADASYN: Adaptive synthetic sampling approach for imbalanced learning." In *2008 IEEE international joint conference on neural networks (IEEE world congress on computational intelligence)*, pp. 1322-1328. IEEE, 2008.
179. Creswell, Antonia, Tom White, Vincent Dumoulin, Kai Arulkumaran, Biswa Sengupta, and Anil A. Bharath. "Generative adversarial networks: An overview." *IEEE signal processing magazine* 35, no. 1 (2018): 53-65.

Time Series Approach for Visual Servoing Using Transformers

Tushar Singh
Department of Electrical Engineering
Delhi Technological University
Delhi, India
tushar300101@gmail.com

Jayant Prakash
Department of Electrical Engineering
Delhi Technological University
Delhi, India
jayant21prakash@gmail.com

Tushar Bharti
Department of Electrical Engineering
Delhi Technological University
Delhi, India
tbharti2001@gmail.com

Dr. Anup Kumar Mandpura
Department of Electrical Engineering
Delhi Technological University
Delhi, India
kanup@dtu.ac.in

2023 12th Mediterranean Conference on Embedded Computing (MECO) | 979-8-3503-2291-0/23/$31.00 ©2023 IEEE | DOI: 10.1109/MECO58584.2023.10154996

***Abstract*—We introduce Visual servoing using a novel deep-learning time-series architecture to control an unmanned aerial vehicle (UAV) with a mounted camera to track a target consisting of a finite set of stationary points lying in a plane. Many visual servoing approaches use computer vision along with estimation algorithms, sensors, and actuators' feedback to solve tasks like, tracking, obstacle avoidance, and localization. Nowadays, deep neural networks are gaining popularity in such tasks owing to their accuracy, adaptability, and flexibility. We propose a solution that employs a time-series architecture to learn temporal data from sequential values to output the control cues to the flight controller. Because of its low computational expense, the solution is deployable on less powerful onboard computers present on the UAV, ensuring real-time tracking of the target. The solution is tested both in a simulation environment and in real life, outperforming the current state-of-the-art in terms of time efficiency and accuracy.**

Keywords— Visual Servoing, Deep Learning, Transformers, Image-Based Visual Servoing.

I. INTRODUCTION

Visual servoing is termed as a control for robotic maneuvers using optical data from the present sensors. It is aimed at a robot to travel in space from one point to another(specified/unspecified destination) by iteratively reducing the error in present and target positions. Visual servoing has numerous applications, including autonomous navigation and robotic surgery[1].

The problem of visual servoing can be approached mathematically in two conventional ways: Position-Based Visual Servoing (PBVS) and Image-Based Visual Servoing (IBVS). In PBVS, the error is defined in Euclidean space with an inertial frame of reference, resulting in simple control laws but with an error-prone Perspective-n-Point problem that requires filtering the results to achieve accuracy[2]. On the other hand, In IBVS, the error is defined in an image plane by extracting a set of visual features, designing the control around the image jacobian/Interaction matrix, and approximating its pseudo inverse.[3] However efficient, Both IBVS and PBVS are camera dependent and rely highly on the intrinsic parameters of a camera and strict calibration.

Our research suggests a new method of conducting visual servoing by viewing it as a problem of a time-varying neural network in a sequential manner. Similar to IBVS, we also define the error in the image plane by calculating the Image Jacobian and control using separate computer vision algorithms. We use a Deep neural network containing Long Short-Term Memory(LSTM) [8] layers and a Transformer [9], with a set of self-created (using a custom environment of Robotic Operating System(ROS)) time-series data to solve the perceived problem of visual servoing.

The paper is organized as follows: Section II provides an elaborate review of various deep learning methods that have been applied to approach the visual servoing problem. In Section III, the traditional IBVS algorithm is first discussed for dataset collection. Then, a new Deep learning architecture is introduced. The training setup and results for testing are presented in Section IV. Finally, the research is concluded, and future works are stated in Section V of the research paper, followed by future work in Section VI.

II. RELATED WORKS

The research in [4] utilized techniques that involve manually designing visual features to represent images and control laws that are determined through backpropagation of gradient descent on spatial information errors. This approach necessitates numerical or analytical estimation of the camera and interaction matrix. The algorithm was subsequently applied to a deep learning-based architecture and adapted for reinforcement learning-based methodology, which is commonly employed in deep reinforcement learning. The

979-8-3503-2291-0/23/$31.00 ©2023 IEEE

Authorized licensed use limited to: DELHI TECHNICAL UNIV. Downloaded on July 03,2023 at 04:47:38 UTC from IEEE Xplore. Restrictions apply.

results indicated that the model's learned parameters are context-specific and cannot be generalized to unknown environments or tasks.

In another research, FlowNet Convolutional Neural Networks were employed to carry out visual servoing[5]. The primary technique entails using pairs of images as inputs and their corresponding x-y flow fields as actual data to make predictions about optical flow. This information is then passed through multiple ConvNets and ReLu activations. It is essential to consider the practical implementation of the architecture, as it must be trained on various environments and camera settings[9].

In [12], EfficientNet Convolutional Neural Network(CNN) is employed to estimate the relative pose difference between the current images and the desired ones. Then a PBVS control strategy is used to reach the desired pose. The researchers also suggest an autonomous dataset collection methodology to train the neural network in various lighting environments and occlusions. The method is validated on a 6-degree-of-freedom (DOF) robot in simulation.

In the Proposed solution, the estimation of control cues depends upon the time-varying pixel error values, which can be inferred in any environment hence making the proposed solution independent of the visual environment. Furthermore, the architectures used in the above studies are computationally expensive. Hence, they cannot be deployed on a low-power onboard computer, leading to the requirement of on-ground processing, making it prone to communication delay and errors. The proposed solution is a lightweight architecture that can be easily deployed on such systems for faster and more accurate servoing.

III. METHODOLOGY

A. Image-Based Visual Servoing

Image-Based Visual servoing, Like other vision-based control methods, works on minimizing the error e(t), defined as

$$e(t) = s - s^* \tag{1}$$

Where the vector s represents the locations of a set of features in the image and s* represents the desired locations of these features in the image plane. The velocity controller is designed by differentiating the error term. The spatial velocity of the UAV/Camera is established as $V_c = (v_c, w_c)$, where v_c and w_c stand for instantaneous linear velocity and instantaneous angular velocity, respectively. For UAV being an underactuated system, only the linear velocities are calculated and controlled. The relationship is established as

$$de/dt = L_s v_c \tag{2}$$

Where $L_s \in R^{k*6}$ is the interaction matrix/feature jacobian matrix. To decrease the error term exponentially, we use the following control law.

$$v_c = -\lambda L_e^+ e \tag{3}$$

Where L_e^+ is the Moore-Penrose pseudoinverse of the L_e. Both of them are approximated, as they cannot be known certainly for a real visual servo system.

The feature points in the image plane with coordinates **x** = $(x, y)_{\text{in pixels}}$ are projected from a 3D point of view with respect to the camera frame with Coordinates **X** = (X, Y, Z). The relationship between **x** and **X** is established using the following equations

$$x = X/Z = (u - c_u)/f\alpha \tag{4}$$

$$y = Y/Z = (v - c_v)/f \tag{5}$$

Here, c_u, c_v, f, α is a set of the intrinsic camera parameters. c_u and c_v are principal coordinate points, f is the camera's focal length, and α is the pixel dimension ratio (usually equal to 1). These parameters were denied in the simulation environment in ROS for dataset collection and testing. Using the above relations, we calculated the interaction matrix to be.

$$Lx = \begin{bmatrix} -1/Z & 0 & x/Z & xy & -(1+x^2) & y \\ 0 & -1/Z & y/Z & 1+y^2 & -xy & -x \end{bmatrix}$$

where Z represents the depth of the point from the camera.

B. Dataset Collection

Sequential deep learning models require a voluminous dataset for training and inference of the model. Since there is no publicly available dataset for such an application of visual servoing, the data for the problem statement is collected manually by executing IBVS control in the custom-developed simulation environment on ROS and Gazebo 3D simulator[6],[7] by varying the location and velocity of the target(ArUCo marker), and the altitude of the UAV. The input vector includes the error component (e) in both the x and y dimensions of the image plane (ex, ey), as well as the altitude of the unmanned aerial vehicle. On the other hand, the output vector contains the control cues of the UAVs i.e. the desired velocity calculated using the IBVS control algorithm.

$$Input = [e_x, e_y, Alt]$$

$$Output = [Vel_x, Vel_y]$$

Authorized licensed use limited to: DELHI TECHNICAL UNIV. Downloaded on July 03,2023 at 04:47:38 UTC from IEEE Xplore. Restrictions apply.

C. *Transformers and time series prediction*

Transformers are widely used in Natural Language Processing. However, transformers have recently gained popularity as competition to RNNs and LSTMs in time series prediction/forecasting[11]. For multivariate time series predictions, the transformers use a multi-head self attention (MSA) technique, comparing each token and the input sequence with every other token to learn contextual information dynamically. Moreover, Transformers allow parallelism into the sequential time series problems that help in overcoming the vanishing gradient problem faced in RNNs.

D. *Proposed Architecture*

The proposed architecture is a single-phase regression architecture, where the main task of the model is to extract the temporal information from the sequential data given(error e(t)) as an input to the model and predict the control cues(UAV's velocity).

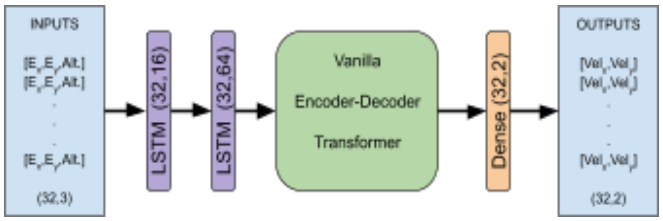

Fig 1.a: Proposed network architecture, where input is a vector containing pixel errors in the x and y direction along with altitude value. After recollecting all the shared information, the architecture outputs a final velocity vector a UAV should opt for target tracking.

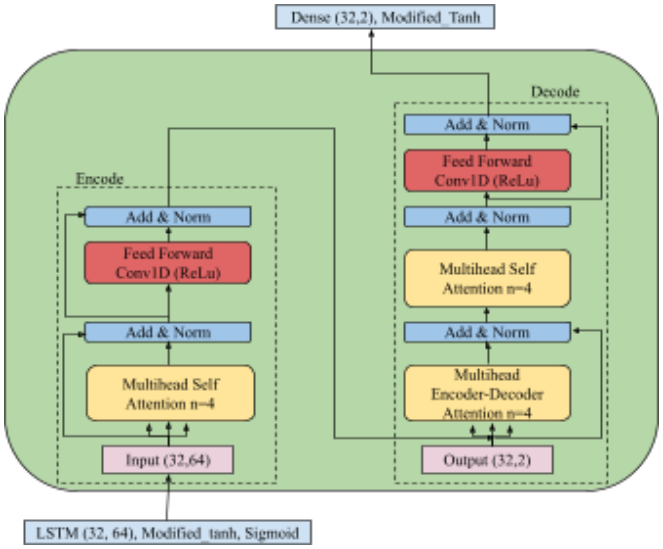

Fig 1.b. Proposed transformer model with multi-head attention encoder-decoder pair. It takes the input from the preceding LSTM layer in (32,64) format and encodes it with attention given to each variable. The decoder decodes the encoder output parallelly, comparing it with the actual velocity output of the size (32,2).

As displayed in Fig 1.a, the input layer feeds the error inputs and the altitude to the model in a stacked array in the shape of (32x3). Further, the consequent LSTM layers increase the dimensionality of the input to the values of 16 and 64 for preprocessing the input to understand the principal features from the input sequence. The output of the shape (32x64) is forwarded to an encoder-decoder transformer, as presented in Fig 2, for the time series prediction of the control cues. The transformer comprises an encoder-decoder pair with multi-head attention blocks. It splits the key(K), value(V), and query (Q) parameters into four ways that are passed independently through the separate head. The MSA mechanism allows the transformer to encode and decode multiple relations between each channel value robustly. The following relations explain the multi-head attention block vividly.

$$attention(Q,K,V) = softtmax(\frac{QK^T}{\sqrt{d}})V \quad (6)$$

$$MultiHead(H) = concat(head_1, head_2, \ldots\ldots head_h)W^0 \quad (7)$$

$$head_i = attention(HW_i^Q, HW_i^K, HW_i^V) \quad (8)$$

$$W_i^Q, W_i^K, W_i^V \in R^{\frac{d\times d}{h}}, W^0 \in R^{d\times d} \quad (9)$$

The feed-forward networks consist of the Conv1D layer with ReLu activation in both encoder and decoder containing the trainable weights, trained throughout the training. Finally, a dense layer outputs the (32,2) vector of predicted probable velocities. Alongside the decision-making, the Sigmoid activation function is used as recurrent activation for the input, forget, and output gates of the LSTM layers. Whereas a custom Modified_tanh function (explained in the next section) is used as the memory state activation function to counter the vanishing gradient problems in recurrent neural networks.

E. *Activation Function*

It is empirical that in a large neural network, back-propagation learning using asymmetric activation functions can yield faster convergence. Hence, the non-linearity is introduced in the proposed network architecture with a modified version of the hyperbole tangent activation function defined as

$$y = 10 \times ((e^{x/10} - e^{-x/10})/(e^{x/10} + e^{-x/10})) \quad (10)$$

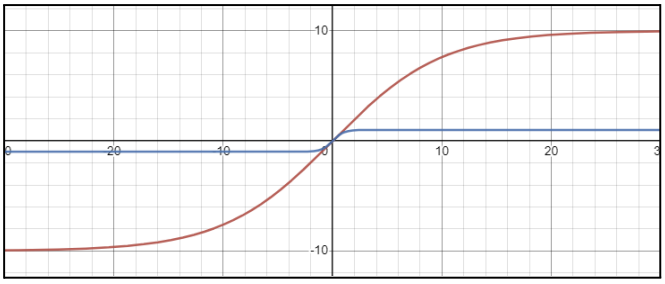

Fig 2: Activation function plots: "modified_tanh" (red), regular "tanh" (blue).

Authorized licensed use limited to: DELHI TECHNICAL UNIV. Downloaded on July 03,2023 at 04:47:38 UTC from IEEE Xplore. Restrictions apply.

The output values of the tanh activation function are in the range of [-1,1], which limits the capability of the UAV to attain higher velocities. Hence, to overcome this bottleneck, a novel modified tanh activation function, as explained in (10), is proposed that permits the output value to range between [-10,10], with a similar behavior as that of a regular tanh function as shown in Fig 2.

F. Loss Function

In order to illustrate the results of feature extraction in the form of error values and predict the velocities of the UAV, we trained the model using backpropagation of the sum of L1 and L2 regularisation losses, i.e., minimizing the sum of all absolute and squared differences between the true and predicted values. The Loss function is defined as

$$Loss = \sum_{i=0}^{n} \{|y_i - y'_i| + (y_i - y'_i)^2\} \quad (11)$$

Where y_i, and y'_i, are the ground truth and predicted values of UAVs velocity in X and Y directions and n is a batch's total number of outputs.

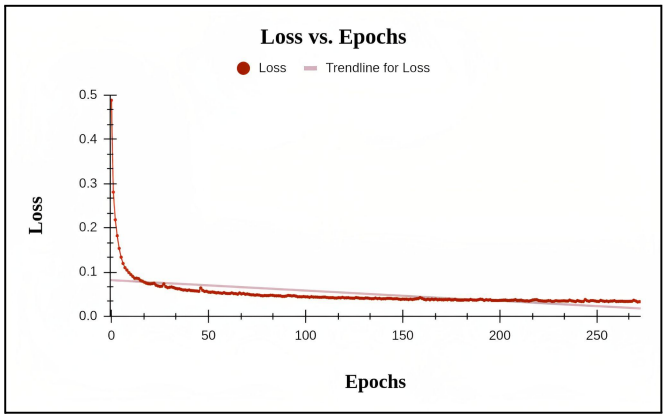

Fig 3: Loss curve of the model along the epochs.

The loss curve presented in fig 3 deals with the regression task of multiple probability distributions, as the predicted UAV maneuvers belong to many possible categories. The Modified_tanh is the sole activation function used in conjunction with the above mentioned loss function.

IV. EXPERIMENTAL RESULTS

A. Training Details

We used the tensorflow library to design, train, and implement the proposed architecture. We used the adaptive momentum optimizer to control the sparse gradients in noisy problems.[10] The model is trained, inferred, and validated on a self-collected dataset of variable altitude and dynamic target dataset. The model is trained for 150 epochs with a learning rate of 0.001 for the first 100 epochs and then on the scheduled learning rate. The input is selected to be a batch size of 32, i.e., errors in x and y, and UAVs altitude values in 32 consecutive frames are fed as the input to the network. The network is trained for variable altitudes and dynamic targets. The network is trained on a Quadro P5000 GPU. The entire network comprises approximately 13.2 million parameters that help accumulate the trainable features and predict the UAV's velocities.

Moreover, the Root Mean Square Error matrix is used to evaluate the quantitative results of the architecture to check for the similarity between the predicted velocity and the ground truth.

$$RMSE = \sqrt{1/n(\sum_{i=0}^{n} (y_i - y'_i)^2} \quad (12)$$

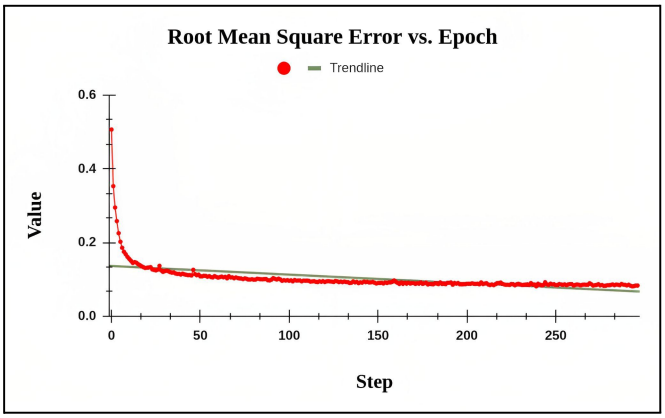

Fig 4: RMSE at each time-step of training

B. Ablation Study

The architecture learns the temporal data using the Transformer based encoding and decoding of a stack of consecutive 32 timestep error values to achieve desired results. To decide the length of the stacked values to be 32, experiments were performed for 8, 16, 32, and 64 stack values. For 8 and 16 stacked frames, temporal details were not sufficient to train the model. Whereas for 32 frames, maximum recognition accuracy was achieved. As for the case of 64 frames, we observed similar performance in terms of relative accuracy at the cost of handling larger stacks(Fig 4). Hence, the stack of 32 frames was chosen.

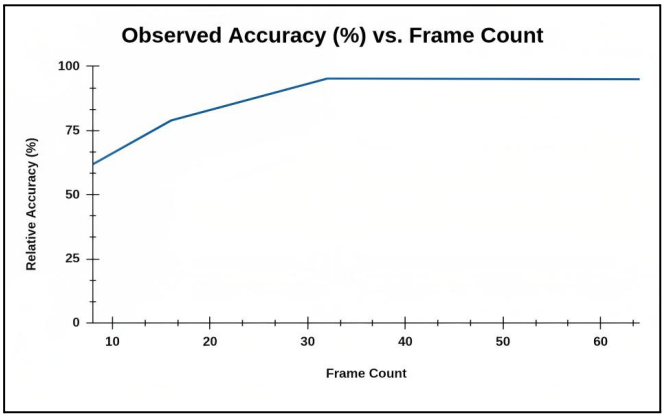

Fig 5: Effect of size of input on the performance of the proposed algorithm.

Authorized licensed use limited to: DELHI TECHNICAL UNIV. Downloaded on July 03,2023 at 04:47:38 UTC from IEEE Xplore. Restrictions apply.

C. *Real-Time Testing*

The algorithm is evaluated both in simulation as well as in the real world. The algorithm is tested in a custom environment on ROS. ROS is an open-source robotics middleware that has a collection of various software frameworks to simulate the hardware abstractions of a robot. For our simulation, we used Gazebo as the 3D simulator, Iris UAV with a gimbal-stabilized camera mounted under the UAV, and a ground vehicle with the ArUco marker on top as the target to be tracked. Figure 5 depicts the simulation environment.

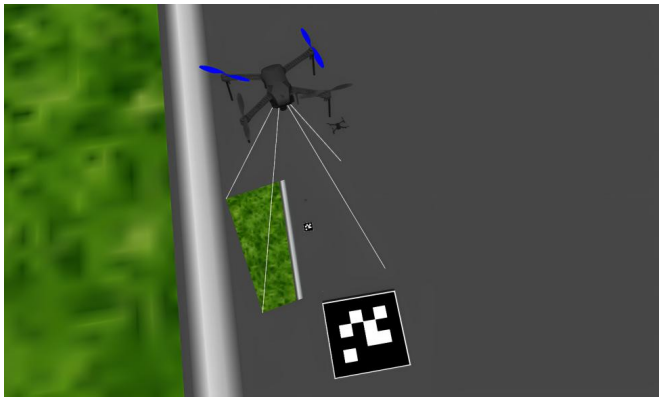

Fig 5: A camera mounted on an Iris Drone capturing a frame consisting of ArUco marker in the Gazebo simulation environment.

For the real-world testing, as displayed in Fig 6, we used a Tarot 650 UAV, a pixhawk cube flight controller, and jetson nano 2.0 as the onboard computer along with a git2p camera for detection and tracking stabilized using a Tarot TL3T05 gimbal.

The problem of visual servoing requires real-time velocity prediction and control. The algorithm has to be implemented on the onboard computer. Since the trained architecture uses 13.2 million parameters to predict the control cues of the UAV and the only available onboard computer at the time of research was Jetson Nano 2.0, We converted the trained tensorflow model to the TFlite version. The model is quantized, and its weights are pruned using the TFlite for the optimized deployment of the model on the aforementioned OBC.

Once the program is triggered, the frames captured by the camera are fed to the OBC to detect the AruCo marker. Upon detection, the resultant errors and the altitude of the UAV are fed to the deep learning model that predicts the velocity to control the UAV. These output velocities are then fed to the pixhawk flight controller as mavlink messages that in turn, controls the UAV's maneuver to track the ArUco target.

Fig 6: Real-life tracking of ArUco Marketushar300101@gmail.comr using Tarot-650 UAV.

V. CONCLUSION

The research presents visual servoing with a novel time series approach along with autonomous tracking on the present target. The proposed solution is a fusion of computer vision for object detection with a Transformer based deep-learning neural network. The suggested structure employs encrypted error data that is generated by measuring the distance between the center of the frame and the pixels of the desired AruCo marker to generate the control signals for the UAV. For training the time-series model, a custom dataset was generated using the ROS and Gazebo Simulator. Further, the algorithm was validated in both simulation and real-life using a self-built/assembled quadcopter. Once satisfactory results were obtained, we culminated the research with various applications of the solution in the fields of UAVs ranging from autonomous landing to kinetic strike.

VI. FUTURE WORK

For the future perspective of the research, we aim

- Using Self-Supervised transformers to learn and estimate the control cues of the UAv based on more variable features like the target's velocities.
- Extending the research for the control of fixed-wing UAVs by generating more data both in real-time and in simulations with different control laws.

VII. REFERENCES

[1] W. Fu, H. Hadj-Abdelkader and E. Colle, "Visual servoing based mobile robot navigation able to deal with complete target loss," 2013 18th International Conference on Methods & Models in Automation & Robotics (MMAR), 2013, pp. 502-507, doi: 10.1109/MMAR.2013.6669961.

Authorized licensed use limited to: DELHI TECHNICAL UNIV. Downloaded on July 03,2023 at 04:47:38 UTC from IEEE Xplore. Restrictions apply.

[2] Marinela G. Popova and Hugh H. Liu. "Position-Based Visual Servoing for Target Tracking by a Quadrotor UAV," AIAA 2016-2092. AIAA Guidance, Navigation, and Control Conference. January 2016.

[3] F. Chaumette and S. Hutchinson, "Visual servo control. I. Basic approach," in IEEE Robotics & Automation Magazine, vol. 13, no. 4, pp. 82-90, Dec. 2006, DOI: 10.1109/MRA.2006.250573.][F. Chaumette and S. Hutchinson, "Visual servo control. II. Advanced approach [Tutorial]," in IEEE Robotics & Automation Magazine, vol. 14, no. 1, pp. 109-118, March 2007, DOI: 10.1109/MRA.2007.339609.

[4] Q. Bateux, E. Marchand, J. Leitner, F. Chaumette and P. Corke, "Training Deep Neural Networks for Visual Servoing," 2018 IEEE International Conference on Robotics and Automation (ICRA), 2018, pp. 3307-3314, doi: 10.1109/ICRA.2018.8461068

[5] J. Long, E. Shelhamer, and T. Darrell, "Fully convolutional networks for semantic segmentation," 2015 IEEE Conference on Computer Vision and Pattern Recognition (CVPR), Boston, MA, USA, 2015, pp. 3431-3440, doi: 10.1109/CVPR.2015.7298965.

[6] Quigley, Morgan, et al. "ROS: an open-source Robot Operating System." ICRA Workshop on open-source software. Vol. 3. No. 3.2. 2009.

[7] N. Koenig and A. Howard, "Design and use paradigms for Gazebo, an open-source multi-robot simulator," 2004 IEEE/RSJ International Conference on Intelligent Robots and Systems (IROS) (IEEE Cat. No.04CH37566), 2004, pp. 2149-2154 vol.3, DOI: 10.1109/IROS.2004.1389727.

[8] Sepp Hochreiter, Jürgen Schmidhuber; Long Short-Term Memory. Neural Comput 1997; 9 (8): 1735–1780. doi: https://doi.org/10.1162/neco.1997.9.8.1735

[9] Vaswani, A., Shazeer, N., Parmar, N., Uszkoreit, J., Jones, L., Gomez, A. N., Kaiser, Ł., & Polosukhin, I. (2017). Attention is all you need. In Advances in Neural Information Processing Systems (pp. 5998-6008).

[10] Vempati, Anurag Sai & Choudhary, Vipul & Behera, Laxmidhar. (2014). Quadrotor: Design, Control and Vision Based Localization. IFAC Proceedings Volumes (IFAC-PapersOnline).3.1104-1110.10.3182/20140313-3-IN-3024.00229.

[11] Wen, Qingsong & Zhou, Tian & Zhang, Chaoli & Chen, Weiqi & Ma, Ziqing & Yan, Junchi & Sun, Liang. (2022). Transformers in Time Series: A Survey.

[12] FELTON, S., BRAULT, P., FROMONT, E., & MARCHAND, E., [2022], Visual Servoing in Autoencoder Latent Space [Also presented at ICRA'22, Philadelphia, June 2022], IEEE Robotics and Automation Letters, 7[2], 3234-3241

[13] Kingma, D.P., & Ba, J. (2014). Adam: A Method for Stochastic Optimization. CoRR, abs/1412.6980.

[14] Lim, Jae Hyun and J. C. Ye. "Geometric GAN." ArXiv abs/1705.02894 (2017): n. Pag.

[15] Bateux, Quentin et al. "Visual Servoing from Deep Neural Networks." ArXiv abs/1705.08940 (2017): n. pag.

Authorized licensed use limited to: DELHI TECHNICAL UNIV. Downloaded on July 03,2023 at 04:47:38 UTC from IEEE Xplore. Restrictions apply.

To Determine the Futures pricing of Metal Commodities using Deep Learning

Vrinda Aggarwal[1*], Arman Ranjan[1], Shivam Shaurya[1], S. K. Garg[1]
[1]Delhi Technological University, Delhi, India

*Author to whom correspondence should be addressed:
*Email: vrindaaggarwal67@gmail.com

(Received February 1, 2022; Revised May 14, 2023; accepted May 14, 2023).

Abstract. Manufacturing industries have been growing in terms of their market size and their revenue generated in the past decade. With rapidly evolving technologies, accurate forecasting and predictions act as a strong pillar in strategic planning. Predicting the prices of commodities helps in reducing the financial losses incurred while procurement of the inventory. In this paper, we used the deep learning methods to develop some models for predicting the prices. Deep learning is basically a part of the bigger sphere of machine learning and artificial intelligence. It is based on artificial neural networks with representation learning. The models based on deep learning are superior to any machine learning models in predicting the prices, hence our methodology consists of such techniques. This paper is a preliminary attempt to predict the future prices by using hybrid LSTM-Attention-CNN model with the help of the past 10 years data. The proposed model performed significantly better than traditional ARIMA model which has been a benchmark in time-series for a long time.

Keywords: Metal Commodities, Deep learning, CNN, LSTM, Attention, Time series models.

1. Introduction

Commodities are the common materials used in industries and businesses which can be traded for or exchanged with the materials of the same type. Trading of these commodities and establishing commodity exchanges are very important as they establish worldwide standard prices, and are essential for both producers and consumers[1)]. These commodities are traded through future contracts. A future contract is basically a contract between the two parties where an agreement of buying and selling a specific amount of any commodity is signed. This agreement is done at a predetermined price and at a specified date in the future. A commodity exchange is the legal body or an entity which is responsible for the rules and regulations for trade of commodities. It may also refer to an actual physical space where this trading takes place. The interested buyers use future contracts to fix prices of certain commodities, which reduces the risk of price hike. The commodity centric industries, manufacturers and service providers often participate actively in these exchanges and markets to reduce the risks of financial losses due to changing prices[2)]. The rise of the industrial economy has fuelled the rise of the commodities market over the last few decades[3)]. Many traders have switched to commodity markets in search of new trading options, as capital markets have become more available. The commodities market is notorious for its high uncertainty, which can influence a trader's trading strategy. The extreme volatility of the commodities market can be attributed to a number of reasons, including commodity supply and demand, currency fluctuations, geopolitical conditions, government policies, and economic development[4-5)].

Over the past years, the economies of the world have been evolving and the trade of basic commodities have seen a diminishing trend. Taking the developing nations into perspective, the primary commodities are an important export earning source and the fluctuations and movements in prices of these commodities affect their economic conditions[6)].

The pricing of metals in the markets directly affects the mineral industry and hence the forecasting of the metal markets have been receiving a lot of light in the past decade. The prediction of these markets starts with the analysis of past accumulated data which help in selecting an accurate machine learning model to perform accurate predictions[6)]. To forecast these prices, methods such as econometric, time series models, qualitative, have been used[7-8)].

Copper is one of the most important industrial commodities and has a strong impact on the global economy. It is a widely used alloy with strong resistance to corrosion and acts as a very strong conductor for heat and electricity. Hence being of extreme importance for the electrical power industry and manufactures of electronic

products. Given the industrial importance of this metal, its consumption and rising prices reflect upon a good economic health. India is currently ranked 30th in copper producers and given the industrialization the demand of this metal is growing per year. Gold has since long been present in our heritage as one of the most precious metals. And due to its limited supply and the inability to dilute it enables the retention of its value. Hence is very useful in hedging against inflation. India being the world's most ardent gold buyer, is also one of the world's most important Gold markets today. However, due to limited domestic gold supply, imports are the primary source of supply. Our gold market is mainly dominated by the gems and jewellery industry which contributes to 7% of our GDP. Silver is the most ideal metal for electrical applications, and its non toxic composition makes it useful in the medical and consumer product industry. India is one of the largest consumers of silver and hence our demand impacts the global markets. The industrial demand of silver is more than 50% of the worldwide demand. Solar energy is also a major consumer of silver as it is used in fabrication of photovoltaic cells.

In this research, we aim to forecast metal prices for the commodities using a hybrid LSTM - Attention - CNN model. The metals we are considering for our research are Gold, Copper, and Silver. The paper will begin with a Review of the past research, followed by the Research Methodology and Results[9].

2. Literature Review

Forecasting the future prices plays an important role in trading of goods and services in today's world. A challenging area in the field of prediction is selecting or designing the appropriate and accurate model for the prediction. Various methods were implemented in the past decade for accurate prediction of the price in the market of the specific commodity.

There is a considerable amount of literature on the prediction of prices using different models. The models are categorised into two main segments; (i) econometric models such as time series, regression analysis, ARIMA, GARCH, and SARIMA and (ii) computing techniques such as ANN, CNN, and LSTM driven models. Now, the models based on traditional econometrics pose a strong challenge as they fail to detect the hidden non linear patterns in the price series[10]. When compared to the models utilising soft computing techniques, they tend to perform better as they are more robust and have the ability to forecast the volatility[11].

Deep learning is a subset of machine learning and is widely applied in today's day and age. The effectiveness of deep learning and its models are so remarkable, that many organizations are pouring capital and resources into developing this architecture. In recent years, highly efficient deep learning based models are being used for predictive applications. The Long Short Term Memory (LSTM) based models have proven their high degree of accuracy and have been successfully applied for various price forecasting related objectives[12]. Recent studies have also indicated the better performance of the models based on machine learning and neural networks than stochastic methods in prediction of commodity prices[6) 13)].

For instance, a study based on Korean stock exchange through two models (autoregressive & deep learning) was performed and upon comparison of results, deep learning models outperformed the linear autoregressive models [14]. Artificial Neural Network based models were tested on the New York Stock exchange and its efficiency was compared with ARIMA linear model, it was found that the Convolutional neural network (CNN) was more accurate than the other neural networks used and the CNN networks were capable of capturing the changes in trends [15-16]. An experiment was conducted with LSTM prediction models, and these neural network based models were getting upwards of 55% accuracy while predicting the movement of a stock price[17]. Efficient models based on support vector machines and artificial neural networks were tested on the Istanbul Stock Exchange National 100 Index and the results showed the accuracy of the predictions to be in the range of 70% to 75%[18].

On the other hand, he stated that computational complexities and constant error flow through CECs have been some of the limitations of that model. In 2021, LSTM is in third place in the Large Text Compression Bench.[19-20]

Squared regression models usually impose an uncompromising requirement on the real-world data, whereas the time series and Econometric models depend on the trend and seasonality for forecasting with higher accuracy and prediction. The randomness exhibited by the time series models drastically decreases the accuracy of the existing models[21].

3. Approach

To have a high level of accuracy, we propose a hybrid LSTM (Long-and-Short-Term-Memory) - Attention - CNN (Convolutional Neural Network) model. This section talks about our approach towards building a forecasting model for metal commodities. In this study, we have used the LSTM (GRU) - attention-CNN model to forecast using 10 years data respectively for three metals Gold, Copper and Silver. The LSTM GRU model uses CNN to memorize short- and long-term patterns. Due to gradient vanishing and training instability, LSTM or GRU models cannot memorize very long-term independencies. LSTM along with the attention model is used to smoothen out the data[22]. In alignment, we identified the parts of the input sequence that are relevant to each word in the output, whereas in translation we used relevant information to select the appropriate output. Here after, we used CNN to compile all the layers and produce the desired forecasted output[23]. At last we have concluded our results by detecting the RMSE (Root mean squared error), RMAE(Root Mean Absolute Error) and MAPE (Mean

Absolute Percentage Error).[24-25)]

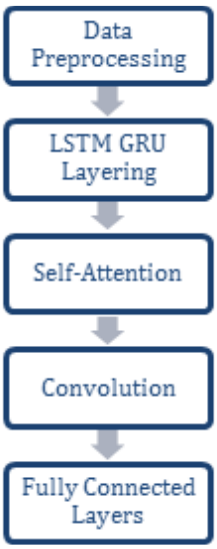

Fig. 1: Flowchart of model

3.1 Data Extraction

We have extracted the 10 years historical pricing data of three of the most commonly traded metals which are Gold, Silver and Copper from Yahoo Finance. All of these metals are widely used in industries as well as retained by individuals as a mode of investment[26)].

3.2 Data Preparation

During data extraction, to remove the null values we have used interpolation. As we were dealing with prices of the metal commodities which turns out to have somewhat of a polynomial growth, for this reason we have used polynomial interpolation in this study to fill in the missing values in the series. Polynomial interpolation uses the minimum polynomial that passes the resulting graph and predicts the values of the missing points from the same. The degree of the polynomial interpolation that we have considered here is quadratic.

3.3 Long Short-Term Memory (LSTM) - Gated recurrent units (GRU)

LSTM is a part of a family of Recurrent Neural Networks (RNNs). These layers have a special property of retaining the information extracted from the previous state. This fundamental property makes them particularly useful in time series analysis, as they can account for the historic trend in the time series.

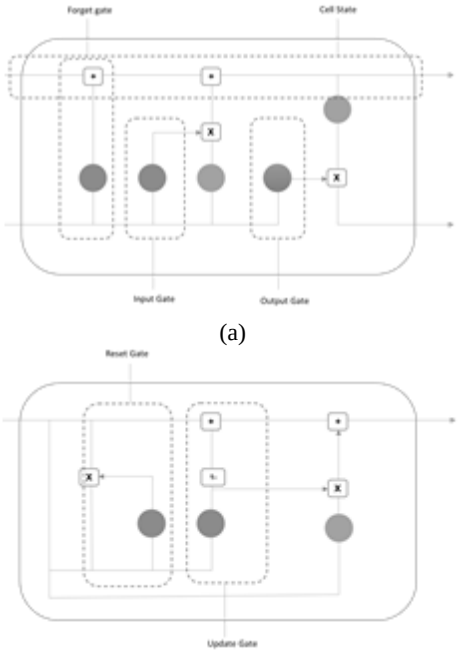

(a)

(b)

Fig. 2: Gate system of (a)LSTM and (b)GRU.

3.4 Attention Model

Attention models are relatively new in deep learning and are finding their extensive use in Natural Language Processing and Machine Translations. They can be used to assign different weights to different time-steps, and this determines how much weight-age should be given to each point to forecast the time-series[27-29)].

In this research, we have created three vectors namely, Query, Key and Value vector from the encoder's input vector. Using the dot product of the Query and Key vector we have calculated the score which helps us to determine how the focus on the different inputs needs to be distributed. Here after, for a stable gradient we divided the scores by 8 which is a default value for the same and the result has been passed to the softmax operation which normalizes the score i.e scores turn to be positive and add up to 1. We multiplied values of the vector by the normalized scores and added the weighted value error[30-33)].

To form the self-attention matrix, we packed the resulting vectors in the form of matrix and condensed them into a layer using the formula:

$$\text{Softmax}\ \left(\frac{QxK^T}{\sqrt{d_K}}\right) V = Z \qquad (1)$$

In the following model we have used 8 similar layers for the data prediction.

3.5 Convolutional Neural Network (CNN)

A typical CNN has a sequence of layers stacked together. Mainly, a convolutional layer, a ReLU Layer, a pooling layer and a fully connected layer. In the First layer, the convolutional procedure is followed wherein the exact

features are extracted. Then an activation function is used to give the final result. The pooling layer has the purpose of reducing the spatial size of the map of features and gives the most feasible learning results for the data that is provided as input. The output is then passed through the next layer where the entire process is repeated. This ensures that the most optimal solutions are received at every stage. Finally, the classification and regression are obtained through the fully connected layer.

Fig. 5: Structure of a typical Convolutional Neural Network

3.6 Error Measurement

To evaluate the performance of our model we use different error metrics namely, Root Mean Square Error, Root Mean Absolute Error and Mean Absolute Percentage Error.

Root Mean Square Error is calculated by the formula:

$$\text{RMSE} = \sqrt{\frac{\Sigma(Pi - Oi)2}{n}} \quad (2)$$

Root Mean Absolute Error is calculated by the formula:

$$\text{RMAE} = \sqrt{\frac{\Sigma_{i=0}^{n}(Pi - Oi)}{n}} \quad (3)$$

Root Mean Square Error is more sensitive to the outliners than RMAE hence mostly RMSE is used for the error prediction.

$$\text{MAPE} = \frac{1}{n}\Sigma_{t=1}^{n}\left|\frac{At - Ft}{At}\right| \quad (4)$$

4. Results & Discussions

A Keras environment was used to implement the model. We trained and tested our model on three different commodities, namely Gold, Copper and Silver. This was done to make sure that the model was generic in nature rather than being specific to a single commodity. Initial data pre-processing was done and the missing data points were calculated using spline interpolation. We then divided the data into training and testing sets and trained the model. Different window sizes were tried for the CNN and ultimately we worked with a window of size 7 as it was found to give the optimum look back window. Ultimately, the three error metrics namely Root Mean Square Error, Root Mean Absolute Error and Mean Absolute Percentage.

5. Conclusion and Future Scope of Work

Precious metal price forecasting can be a much significant and challenging task. Precious metals find their usage in industry and households and are an important financial holding all over the world.

This study proposed a new deep learning-based model featuring CNN, LSTM and Attention mechanism for price forecasting. This method is different from traditional statistical and data-based techniques and takes into account both the historical trend and the signal of the time series.

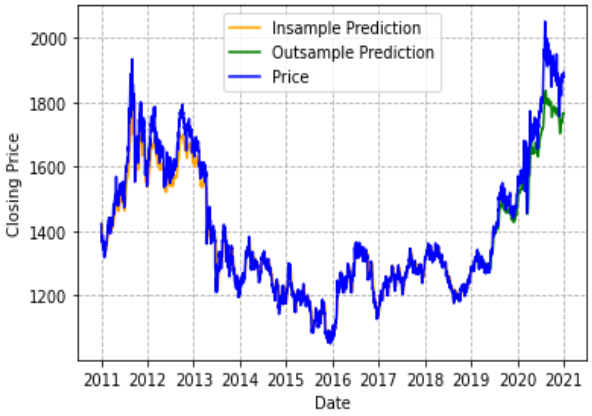

Fig. 3 (a)

Fig. 3 (b)

Fig. 3 (c)

Fig. 3: Predicted price vs Actual Price for (a) Gold, (b) Silver, (c) Copper

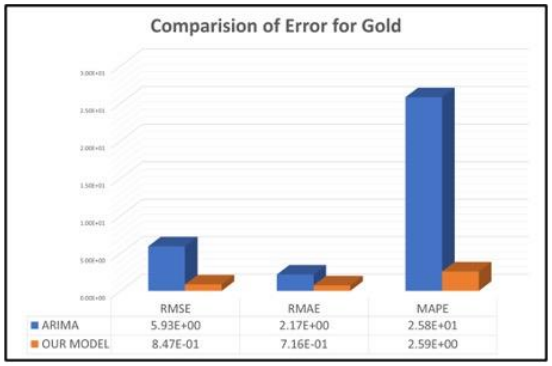

Fig. 4 (a)

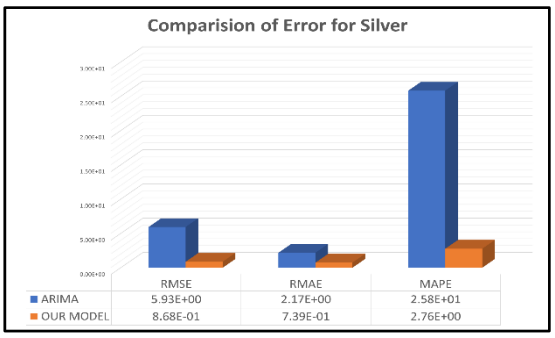

Fig. 4 (b)

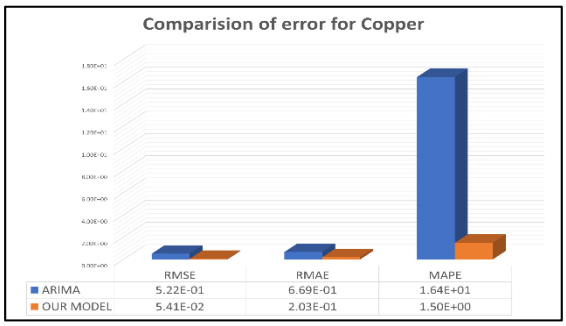

Fig. 4 (c)

Fig. 4: Comparison between the error of Arima model and proposed model prediction for (a) Gold, (b) Silver and (c) Copper.

In our empirical results we found out that the proposed model performed significantly better than traditional ARIMA model which has been a benchmark in time-series for a long time. This work may be further improved by accounting for the correlation between different commodities and using signal processing techniques like Fourier analysis.

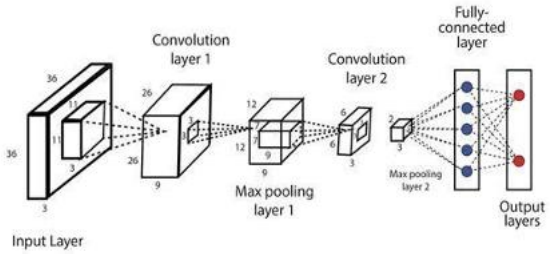

Fig. 5: Structure of a typical Convolutional Neural Network 3`21`21`

Acknowledgements

The authors are thankful to the Central Library, Delhi Technological University, New Delhi, India for providing them access to resources for conducting the research.

Nomenclature

CNN	Convolutional Neural Network
LSTM	Long-Short Term Memory
ARIMA	Auto-Regressive Integrated Moving Average
GARCH	Generalized Auto-Regressive Conditional Heteroskedasticity
ReLU	Rectified Linear Unit
GRU	Gated Recurrent Unit
RMSE	Root Mean Squared Error
RMAE	Root Mean Absolute Error
MAPE	Mean Absolute Percentage Error

References

1) Commodities: What Are They? (n.d.). https://www.thebalance.com/what-are-commodities-356089
2) Raikes, P., Jensen, M. F., & Ponte, S. (2000). Global commodity chain analysis and the French filière approach: Comparison and critique. Economy and Society, 29(3), 390–417. https://doi.org/10.1080/03085140050084589
3) Jones, S. (1986). Future demand for selected industrial commodities.
4) Cox, C. C., & Michael, D. C. (1986). The Market for Markets: Development of International Securities and Commodities Trading. Catholic University Law Review, 36.
5) Evans, G. (1990). Industrial Commodities. In ICCH Commodities Yearbook 1990 (pp. 143–176).

Palgrave Macmillan UK. https://doi.org/10.1007/978-1-349-11268-5_11

6) Tapia Cortez, C. A., Saydam, S., Coulton, J., & Sammut, C. (2018). Alternative techniques for forecasting mineral commodity prices. International Journal of Mining Science and Technology, 28(2), 309–322. https://doi.org/10.1016/j.ijmst.2017.09.001
7) Moroga, K. (n.d.). Effect of Investment Regulations and Subsidies on the Proliferation of Next Generation Vehicles in China. https://doi.org/10.5109/1500424
8) Sato, T. (n.d.). How is a Sustainable Society Established? : A Case Study of Cities in Japan and Germany How is a Sustainable Society Established? A Case Study of Cities in Japan and Germany. 2, 25–35. https://doi.org/10.5109/1800869
9) FAMA, E. F., & FRENCH, K. R. (1988). Business Cycles and the Behavior of Metals Prices. The Journal of Finance, 43(5), 1075–1093. https://doi.org/10.1111/j.1540-6261.1988.tb03957.x
10) Ciner, C. (2017). Predicting white metal prices by a commodity sensitive exchange rate. International Review of Financial Analysis, 52, 309–315. https://doi.org/10.1016/j.irfa.2017.04.002
11) Ding, S., & Zhang, Y. (2020). Cross market predictions for commodity prices. Economic Modelling, 91, 455–462. https://doi.org/10.1016/j.econmod.2020.06.019
12) Yu, L., Wang, S., & Lai, K. K. (2008). Forecasting crude oil price with an EMD-based neural network ensemble learning paradigm. Energy Economics, 30(5), 2623–2635. https://doi.org/10.1016/j.eneco.2008.05.003
13) Nelson, D. M. Q., Pereira, A. C. M., & De Oliveira, R. A. (2017). Stock market's price movement prediction with LSTM neural networks. Proceedings of the International Joint Conference on Neural Networks, 2017-May, 1419–1426. https://doi.org/10.1109/IJCNN.2017.7966019
14) Bakir, H., Chniti, G., & Zaher, H. (2018). E-Commerce price forecasting using LSTM neural networks. International Journal of Machine Learning and Computing, 8(2), 169–174. https://doi.org/10.18178/ijmlc.2018.8.2.682
15) Ryll, L., & Seidens, S. (2019). Evaluating the Performance of Machine Learning Algorithms in Financial Market Forecasting: A Comprehensive Survey. ArXiv. http://arxiv.org/abs/1906.07786
16) Anomaly Detection Using LSTM-Autoencoder to Predict Coal Pulverizer Condition on Coal-Fired Power Plant. EVERGREEN Joint Journal of Novel Carbon Resource Sciences & Green Asia Strategy, 8(1), 89–97 (2021). https://doi.org/10.5109/4372264
17) Hiransha, M., Gopalakrishnan, E. A., Menon, V. K., & Soman, K. P. (2018). NSE Stock Market Prediction Using Deep-Learning Models. Procedia Computer Science, 132, 1351–1362. https://doi.org/10.1016/j.procs.2018.05.050
18) Selvin, S., Vinayakumar, R., Gopalakrishnan, E. A., Menon, V. K., & Soman, K. P. (2017). Stock price prediction using LSTM, RNN and CNN-sliding window model. 2017 International Conference on Advances in Computing, Communications and Informatics, ICACCI 2017, 2017-January, 1643–1647. https://doi.org/10.1109/ICACCI.2017.8126078
19) Selvin, S., Vinayakumar, R., Gopalakrishnan, E. A., Menon, V. K., & Soman, K. P. (2017). Stock price prediction using LSTM, RNN and CNN-sliding window model. 2017 International Conference on Advances in Computing, Communications and Informatics, ICACCI 2017, 2017-January, 1643–1647. https://doi.org/10.1109/ICACCI.2017.8126078
20) Kara, Y., Acar Boyacioglu, M., & Baykan, Ö. K. (2011). Predicting direction of stock price index movement using artificial neural networks and support vector machines: The sample of the Istanbul Stock Exchange. Expert Systems with Applications, 38(5), 5311–5319. https://doi.org/10.1016/j.eswa.2010.10.027
21) Hochreiter, S., & Schmidhuber, J. (1997). Long Short-Term Memory. Neural Computation, 9(8), 1735–1780. https://doi.org/10.1162/neco.1997.9.8.1735
22) Do, Q. H., & Yen, T. T. H., "Predicting primary commodity prices in the international market: an application of group method of data handling neural network." (2019)
23) Dooley, G., & Lenihan, H. (2005). An assessment of time series methods in metal price forecasting. Resources Policy, 30(3), 208–217. https://doi.org/10.1016/j.resourpol.2005.08.007
24) Rafei, S., Esmaelian, M., & Botshekan, M. (2018). The Efficinecy and Predictability of Industrial Commodities using Fundamental and Technical Approaches. In Journal of Industrial Management Perspective (Vol. 7, Issue Issue 4, Winter 2018). دانشگاه شهید بهشتی. https://jimp.sbu.ac.ir/article_87188.html
25) Baldursson, F. M. (1999). Modelling the price of industrial commodities. Economic Modelling, 16(3), 331–353. https://doi.org/10.1016/S0264-9993(99)00003-6
26) Dharu Feby Smaradhana, Dody Ariawan, and Rafli Alnursyah, "A Progress on Nanocellulose as Binders for Loose Natural Fibres", Evergreen, 7(3), 436-443 (2020). https://doi.org/10.5109/4068624
27) Nagendra Kumar Maurya, Vikas Rastogi, and Pushpendra Singh, "Experimental and Computational Investigation on Mechanical Properties of Reinforced Additive Manufactured Component", EVERGREEN Joint Journal of Novel Carbon Resource Sciences & Green Asia Strategy, 6 (03), 207-214 (2019). https://doi.org/10.5109/2349296

28) Ang Li, Azhar Bin Ismail, Kyaw Thu, Muhammad Wakil Shahzad, Kim Choon Ng, and Bidyut Baran Saha, "Formulation of Water Equilibrium Uptakes on Silica Gel and Ferroaluminophosphate Zeolite for Adsorption Cooling and Desalination Applications", Evergreen, 1(2), 37-45 (2014). https://doi.org/10.5109/1495162
29) Jabir Al Salami, Changhong Hu, and Kazuaki Hanada, 'A Study on Smoothed Particle Hydrodynamics for Liquid Metal Flow Simulation', Evergreen, 6(3), 190-199 (2019). https://doi.org/10.5109/2349294
30) Matheus Randy Prabowo, Almira Praza Rachmadian, Nur Fatiha Ghazalli, and Hendrik O Lintang, "Chemosensor of Gold (I) 4-(3, 5-Dimethoxybenzyl)-3, 5-Dimethyl Pyrazolate Complex for Quantification of Ethanol in Aqueous Solution", Evergreen, 7(3), 404-408 (2020). https://doi.org/10.5109/4068620
31) Jain, Ankit, Cheruku Sandesh Kumar, and Yogesh Shrivastava. "Fabrication and Machining of Metal Matrix Composite Using Electric Discharge Machining: A Short Review." Evergreen, 8(4), 740-749 (2021). https://doi.org/10.5109/4742117
32) Mohamed Egiza, Hiroshi Naragino, Aki Tominaga, Kouki Murasawa, Hidenobu Gonda, Masatoshi Sakurai, and Tsuyoshi Yoshitake, "Si and Cr Doping Effects on Growth and Mechanical Properties of Ultrananocrystalline Diamond/Amor-Phous Carbon Composite Films Deposited on Cemented Carbide Substrates by Coaxial Arc Plasma Deposition", Evergreen: joint journal of Novel Carbon Resource Sciences & Green Asia Strategy, 3(1), 32-36 (2016). https://doi.org/10.5109/1657738.
33) Ashish Kumar Srivastava, Shashi Prakash Dwivedi, Nagendra Kumar Maurya, and Manish Maurya, "3d Visualization and Topographical Analysis in Turning of Hybrid Mmc by Cnc Lathe Sprint 16tc Made of Batliboi", *Evergreen*, 7(2), 202-208 (2020). https://doi.org/10.5109/4055217.

ResearchGate

See discussions, stats, and author profiles for this publication at: https://www.researchgate.net/publication/371963691

Total Quality Management in Higher Technical Education

Article *in* International Journal of Innovative Technology and Exploring Engineering · June 2023

DOI: 10.35940/ijitee.G9593.0612723

CITATIONS
0

READS
21

4 authors, including:

Anshuman Pandey
Delhi Technological University
2 PUBLICATIONS **0** CITATIONS
SEE PROFILE

Aryan Rana
Delhi Technological University
1 PUBLICATION **0** CITATIONS
SEE PROFILE

Some of the authors of this publication are also working on these related projects:

STRUCTURAL ANALYSIS OF DRILL BIT USING ANSYS View project

All content following this page was uploaded by Anshuman Pandey on 02 July 2023.

The user has requested enhancement of the downloaded file.

International Journal of Innovative Technology and Exploring Engineering (IJITEE)
ISSN: 2278-3075 (Online), Volume-12 Issue-7, June 2023

Total Quality Management in Higher Technical Education

RS Mishra, Anshuman Pandey, Aryan Rana, Aakash Mehta

Abstract: ***The paper determines the behavior of Indian Technical Educational through the Total quality management tools and techniques, in this we tend to find the research gaps by reviewing some already existing research papers, and giving the solution through the analytical process of data analysis, we will majorly focus on the higher educational institutions. we will review the methodology that is currently being used by universities and how can they come at par as compared to the foreign universities. The reviewed papers will be used to find the shortcomings of the research and will be taken into consideration of analyzing it. Then we will be doing the quantitative data analysis of some collected data from google form and internet sources regarding the six TQM factors that influence the enrolment and hence the quality of institutions and determining the hypothesis result, then we will discuss the results and shortcomings of the analysis and will bridge those shortcomings by providing various possible solutions in that regards. In the whole process we have used data gathering, analyzing it and hence giving the solution. We have basically used IBM SPSS AND AMOS software to construct TQM models and their covariance relations. Now the future aspect of this paper is confirmed that the same procedure can be adopted to any industry for analyzing the quality of that organization.***

Index Terms: ***Total Quality Management, Technical Institutions, AMOS & SPSS.***

I. INTRODUCTION

"Quality" is a relative word, a multifaceted concept that is contingent on the viewpoint of the consumer and the supplier. Usability (from a user-based perspective), requirement compliance (from a manufacturer-based perspective), gradation of penchant (from a value-based perspective), and gradation of perfection (from an excellence -based perspective) are all ways that quality may be communicated (transcendental approach). The level of the produced product's ability to confirm the design requirements is referred to as its conformance quality. [1-6]

Manuscript received on 11 May 2023 | Revised Manuscript received on 24 May 2023 | Manuscript Accepted on 15 June 2023 | Manuscript published on 30 June 2023.
*Correspondence Author(s)
Prof. RS Mishra, Department of Mechanical Engineering, Delhi Technological University, Delhi, India. E-mail rsmishra@dce.ac.in
Anshuman Pandey*, Department of Mechanical Engineering, Delhi Technological University, Delhi, India. E-mail anshumanp571@gmail.com, ORCID ID: 0009-0000-7977-4962
Aryan Rana, Department of Mechanical Engineering, Delhi Technological University, Delhi, India. E-mail aryanrana036@gmail.com
Aakash Mehta, Department of Mechanical Engineering, Delhi Technological University, Delhi, India. E-mail aakashmehta880@gmail.com

© The Authors. Published by Blue Eyes Intelligence Engineering and Sciences Publication (BEIESP). This is an open access article under the CC-BY-NC-ND license http://creativecommons.org/licenses/by-nc-nd/4.0/

A. Quality in terms of educational system

A good education is one which provides all students with assistance that they require to become economically productive, sustainable lives and contribute to peace and democratic societies and enhance individual well-being. Quality in education is one which can provide desired knowledge and understanding in respective field. Learning outcomes vary according to different objectives or goals which can be classified under TQM goals, but at the end basic education must include initial levels of literacy, basic science knowledge and life skills learning including all basic required trainings [7-9]. Moreover, other stake holders of education and teachers' quality should be improvised.

B. Education Scenerio in India

India is a place in the world which holds a good rank in world education industry. India is also a home for many foreign international students, with more than 260 million students,760 university and 35,537 colleges. India has biggest advanced educational systems. But there is still a scope of growth in and around by implementing new policies [10]. But projected is the good growth ahead coming in recent years and India will become the biggest industry in world by expanding its ties and network worldwide.[11]

C. Primary Education

Lower elementary (Class I–V) and Upper Primary (Middle School, Class VI–VIII) are the two divisions of elementary education in India. For children between the ages of 6 and 14, the Indian government places a strong focus on primary education (Class I–VIII), often known as elementary education. The elementary school visits vary between Indian states since education rules are determined by the governments [12]. In order to prevent children from working in hazardous settings, the Indian government has officially outlawed child employment. Due to social injustice and economic inequality, it is challenging to implement both the right to free education and the prohibition on child work. At the primary level, 80% of all certified schools are managed or sponsored by the government, making it the biggest sector.

II. SECONDARY EDUCATION

Secondary education covers children aged 14 to 18, a group comprises of millions of children. The last two years of secondary is often called Higher Secondary (HS), Senior Secondary.

The two of secondary education are each an important stage for which passing certificate is necessary, hence are affiliated by boards of education under education ministry, before one can pursue higher education, including college or professional courses. [13]

III. HIGHER TECHNICAL EDUCATION

From the early five-year plan, India's focus was to develop a pool of scientific and technologically inclined power. India's National Policy on Education (NPE) has a prove for an apex body for regulation and development of higher technical education, which came into being as the (AICTE) in 1987 through an act of the Indian parliament. At the central level, the Indian Institute of Technology, the Indian Institute of Space Science and Technology, the National Institute of technology and the IIIT are deemed of national importance. according to one study, 75% of technical graduates and more than 85% of general graduates lack the skills needed in India's most demanding and high-growth global industries such as Information Technology[14]. As the government has made so much efforts for the upliftment of the higher technical education. So, it is important to figure out if the goal which are set out by the GOI can be accomplished. The method of Total quality management can link the goal of TQM with the Critical success factor and based on hypothesis testing we can figure it out if the desired model can be used to figure out the actual implication based on data collected.

A. Need for the Research

Basically, our review work in the thesis shows that there are ample of researchers who have contributed in the field of higher education quality management and have done the qualitative analysis which uses country, ministry information. Thus, they lack the quantitative part of the study. We have collected data from different universities(technical) and have done the quantitative analysis on the same.

IV. METHODOLOGY

A. Conceptual Development and Research variables

The use of mediation analysis as a tool for determining the causal pathway(s) that connect an independent variable and a dependent variable via the use of an intermediary variable has become more common (s). yet, when the intermediate variables (mediators) are high-dimensional cross-functional and the result is a survival endpoint, there has been very little research done in this area. this work makes an effort to model [15,16]. a complicated structure of a TQM system and link the critical success factors with the performance of the system in order to provide credible evidence for the hypotheses of interest. this questionnaire has been developed for the purposes of research in order to carry out a survey and gather data for the goal of analyzing the impact of csf's on the performance of TQM using amos 22 software.

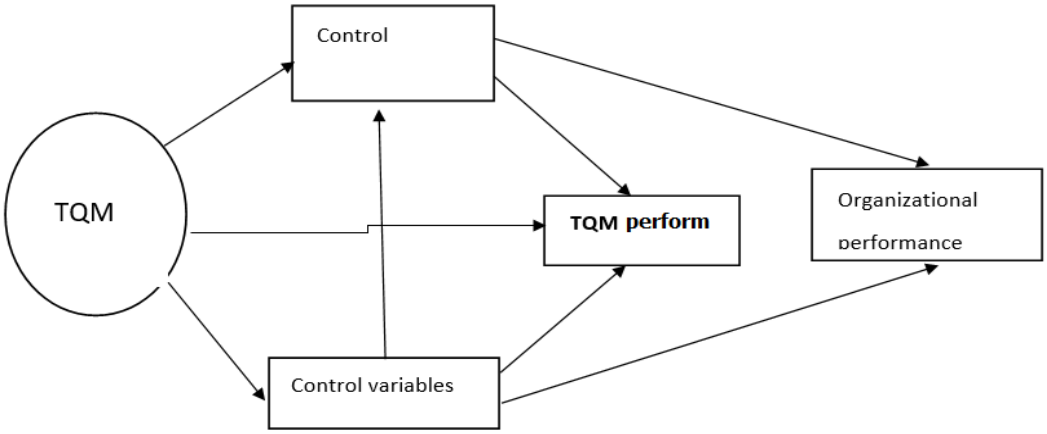

Fig. 1- The basic usage of structural equation modelling (SEM) in path analysis with mediation

The survey was given to two hundred and fifty students attending a variety of educational institutions in India. There was a total of 150 people who responded, and out of those 150 replies, 20 responses were eliminated because their answers were insufficient. Because of this, the total number of participants in the sample for this study is 130, and the percentage of response was 52%. Both the primary data (quantitative) and the secondary data (data obtained from already existing sources such as books, papers, websites, reports, and journals) were gathered. The primary data were obtained via the use of a targeted questionnaire consisting of structurally targeted questions. The secondary data was discovered to be a rapid, readily accessible, and low-cost method of gathering data that might be used to further characterize the issue. According to the findings of the examination of the reliability of the questionnaire in its whole, the Cronbach's value for the questionnaire as a whole is 0.891, which is very near to 0.9, indicating that the questionnaire has a high degree of reliability.

If the value is more than 0.8, then the reliability of the questionnaire is very excellent. If the value is between 0.8 and 0.9, then the reliability of the questionnaire is good. In general, people consider that the questionnaire's reliability must be better than 0.5 in order to be rational. At the same interval of time, the calculated Cronbach's magnitude of each and every influential component is more than the value 0.6, which indicates that the credibility and dependability of each and every influential factor is improving as well.

Published By:
Blue Eyes Intelligence Engineering
and Sciences Publication (BEIESP)
© Copyright: All rights reserved.

The purpose of this study is to establish connections between many distinct categories of data. Data on TQM performance at three engineering institutions in India, namely DTU, NSIT, and Jamia Millia Islamia, is collected via the use of questionnaires. Answers are provided in a five-point Likert scale. The data we collected on TQM drivers and enablers, which, after being combined, were referred to as important success factors. These criteria included the Quality of Education (QE), infrastructure, Students and faculties, and Placements [17]

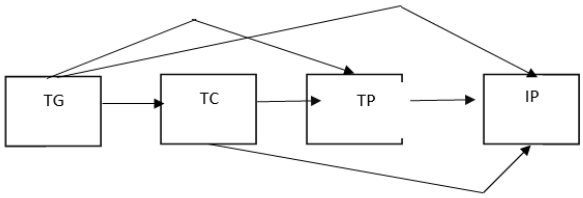

Fig. 2- Relations between TQM Goal (TG), TQM CSFs (TC), TQM Performance (TP) and Institutional Performance (OP).

These three assumptions—the relationship between TC-OP, TP-OP, and TC-TP confounding—essentially equivalent to controlling for the variables TQM Goal in Figure which corresponds with the variables that are found in the TC-OP, TP-OP, and TC-TP categories, respectively. In actual fact, it's possible that some of the variables will have an effect on all of the TG, TC, and TP, and the covariates themselves could have an effect on one another. There are no issues with any of this, and the covariate groups that are being studied do not need to be differentiated from one another. The fact that the variables that were included in the regression models described above were enough to adjust for TC-OP, TP-OP, and TC-TP confounding is very relevant [18]. For assessing high-dimensional mediation hypotheses, we use a process called Structural Equation Modelling (SEM) to evaluate the links between TQM Critical Success Factors and TQM Performance Variables. In order to complete this section of the task, the structural equation modelling (SEM) application known as Amos is used

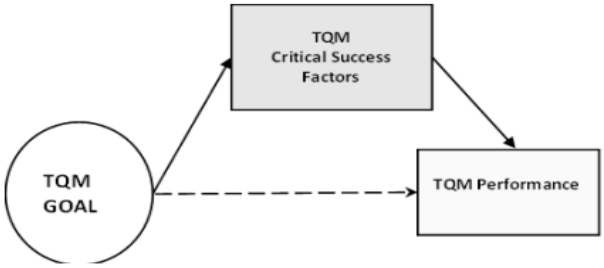

Fig. 3- proposed research model

As we know that the organizations have certain goal which they tend to accomplish. Our study aims at defining the CSF (critical success factor) in which we categorize the TQM drivers to main TQM factors (TQM enablers) this helps us to reduce the amount of data Using this method to recognize a domain has led to the development of many specific approaches; however, the majority of these approaches entail much more strict rules on data generation, variabilities, and observability of all relevant information than in typical cases. This is because SEM seeks to understand domains, not just the causal relationships between different variables. With sufficient sample sizes, structural equation modelling (SEM) has the potential to be one of these methodologies since it enables the modelling of behavioral complexity such as model loops, cross-lagged effects, autocorrelation structures, and so on [19]. The versatility of structural equation modelling (SEM) is one of its advantages. This flexibility makes it possible to examine intricate relationships, make use of many kinds of data (such as category, dimensional, censored, and count variables), and compare several alternative models. On the other hand, due to the characteristics of SEM, it is impossible to formulate broad standards about the needs for sample size (MacCallum et al. 1999). The success of any system, or more accurately, of any organization in relation to its goals, may be determined via performance assessment. Measurement of performance is a process-focused strategy that connects the performance of vital processes to strategic objectives by measuring and improving what is most important to a company. This is accomplished via the use of performance metrics. Establishing dimensions and keeping track of everything are the two most important aspects of measurement. According to Oakland (2003), in order to acquire accurate measurements of the efficacy of TQM, it is necessary to investigate all three aspects of TQM: the human, the technical, and the commercial aspects. Monitoring the effects of “Total Quality Management” (TQM) may be accomplished by analyzing many aspects of performance with the assistance of crucial success criteria, which are chosen on the basis of the TQM target [20-25]. “Total Quality Management” (TQM) is a dynamic system that may be tamed, as described by Pirsig (1991), and its dynamism is directed and controlled by its key success factors or critical success factors (CSFs), which are assigned as a combination of their drivers and enablers. The drivers and facilitators of “total quality management” differ from one organization to another depending on the aim that is being pursued. The drivers are the constructions that will define not only the performance level of TQM but also the performance level of the company. The empirical drivers, such as education and training, as well as the TQM drivers, were made possible by the enablers. Enablers are there to help ensure that the system's drivers continue to be dynamic so that continual development may take place. Since enablers are regarded to be variables, it is possible to preserve consistency even while using them.

The elements that were rigorously analyzed and shown to be responsible for the success of the system in question in terms of achieving the intended aim are considered crucial success factors of that system. After an explanation of how the research variables were operationalized and quantified, this part provides a short description of the sample and an overview of the survey process that was employed in this study. It was decided that the best way to gather data would be via a survey. Just one step of data collecting was carried out, and that was the questionnaire survey phase.

Published By:
Blue Eyes Intelligence Engineering
and Sciences Publication (BEIESP)
© Copyright: All rights reserved.

The study is carried out primarily at two engineering institutions: the Netaji Subhas Institute of Technology and the Delhi Technological University (Delhi Technological University). The final sample contained responses from these and other other institutions as well.

Table1: characteristics of the responding institutes

Institute name	Students participated
Delhi Technological University	152
Netaji Subhash Institute of Technology	60
Jamia millia islamia	25
Others (VIPS, DU colleges, VIT, etc)	13

V. RESULT AND DISCUSSION

Now Let Us Discuss The Model And Check The Reliability Of The Hence Got Model

1) **Reliability of the Model- Cronbach's Alpha Value**

Reliability Statistics

Cronbach's Alpha	N of Items
.896	22

- Basically, this provides the inter-consistency of the model so as to how the inter questionnaires are linked with each other.
- The Cronbach alpha value for our model came out to be 0.896 which is considered to be a very good result so our model is internet-reliable.
- For seeing the reliability of each TQM driver we have a table of (if item deleted) that was not up to the mark for that we deleted four drivers from the analysis these are-I5,O2,Q6,P4 and then the results were excellent.

Item-Total Statistics

	Scale Mean if Item Deleted	Scale Variance if Item Deleted	Corrected Item-Total Correlation	Squared Multiple Correlation	Cronbach's Alpha if Item Deleted
Q1	78.16	87.236	.625	.603	.888
Q2	78.03	88.782	.525	.545	.891
Q3	78.01	88.014	.554	.544	.890
Q4	77.94	87.620	.576	.739	.889
Q5	78.14	87.429	.581	.639	.889
I1	78.04	86.650	.558	.614	.890
I2	78.21	85.794	.612	.827	.888
I3	78.20	88.336	.524	.709	.891
I4	78.41	87.898	.542	.694	.890
I6	78.26	89.121	.524	.509	.891
I7	78.10	88.671	.515	.554	.891
S1	78.14	88.269	.416	.663	.894
S2	77.91	87.268	.497	.657	.892
S3	78.17	90.985	.315	.566	.896
O1	78.07	90.125	.459	.519	.892
O3	77.81	89.400	.436	.636	.893
O4	77.91	88.427	.530	.580	.891
O5	78.01	88.507	.550	.729	.890
O6	78.01	90.681	.377	.634	.894
P1	77.96	88.621	.475	.643	.892
P2	78.30	91.025	.406	.513	.894
P3	77.97	89.419	.467	.533	.892

Fig. 4-Scale & Correlated Table

A. Factor Analysis

For factor analysis we used spss dimension reduction techniques so that we can suggest if the csf are in a good place to show the reliability of the model/questionnaire results Process-

1. All the questions were taken and later the questions which failed the reliability were deleted.
2. Rotation type was chosen to be varimax.
3. Scale items were also chosen (original vs if deleted)

Retrieval Number: 100.1/ijitee.G95930612723
DOI: 10.35940/ijitee.G9593.0612723
Journal Website: www.ijitee.org

Published By:
Blue Eyes Intelligence Engineering and Sciences Publication (BEIESP)
© Copyright: All rights reserved.

Basically, this is the proportion of each variable's variance that can be explained by the factors (e.g., the underlying latent continua). It is also noted as h2 and can be defined as the sum of squared factor loadings for the variables.

- The communalities of each question were above 0.5 suggest that nothing is wrong in the communalities
- Before removing the unwanted questions according to the reliability factor, we had the result of worst but after removing the unwanted we got very good result as shown in table on the left-hand side.
- Now only this test cannot give the only result we want, for that one needs to check many more parameters. And for the adequacy of the model, we used KMO test.

B. Kmo And Bartlett's Test

- KMO's measure of the sampling adequacy is a test performed to assess the appropriateness of accepting factor analysis on the data set available. Additionally, Bartlett test of sphericity is applied to test the null hypothesis that the different variables in the population correlation matrix are not correlated.
- KMO AND BARTLETT TEST THRESHOLD VALUES - KMO value of over 0.5 and a visible significance level for the Bartlett test below the value of 0.05 suggests there is considerable correlation in the data.
- Now as far as our data is concerned, it consists of a large number of inputs and it gives us near accurate results.

The Kaiser-meyer-olkin measurement of the sampling adequacy = 0.752(well above the threshold) bartlett test of sphericity-approx. = 788.499, ∂f = 231.Based on correlations it is a very good score.

C. Scree Plot

A scree plot is a line plot that shows the eigenvalues of the factors or main components in an analysis. This kind of graphic is used in multivariate statistics. While doing an exploratory factor analysis or a principal component analysis, the scree plot may be used to ascertain the number of factors or principal components that should be maintained in the investigation.

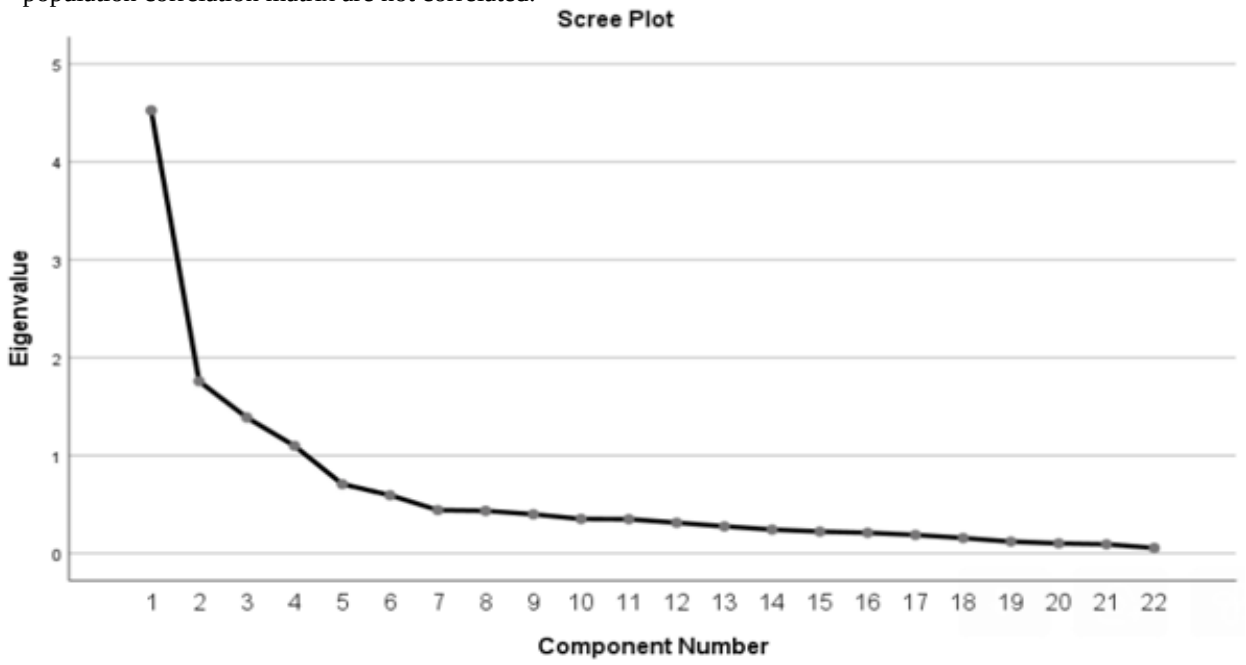

Fig. 5 Scree Plot

The following graph shows the relationship between the Eigenvalue and the number of components; in our example, there are 22 components in the questionnaire. A decent scree plot has a graph that has a downward slope and is formed like an elbow; this is one of its defining characteristics.

VI. ROTATED COMPONENT MATRIX

You will be able to determine what the components stand for with the help of the rotated component matrix. The first component has the highest degree of correlation, whereas the succeeding components have a lower degree. The major outcome of principal components analysis is the loadings, which are also frequently referred to as the loadings. It includes estimates of the correlations that exist between each of the variables and the components that have been calculated. We can see that all of the capabilities of TQM are connected with each other in this image, and this is done entirely by spss with no interference. This is the case in our particular scenario. This leads us to believe that if we rotate our system or collection of questions, they will remain tightly associated under one head, such as I with all I's alone, O with O's only, and not with any other variable.

Published By:
Blue Eyes Intelligence Engineering
and Sciences Publication (BEIESP)
© Copyright: All rights reserved.

Raw

	Component				
	1	2	3	4	5
I4	.692				
I2	.761				
I3	.600				
I1	.639				
I6	.384				
I7					
O6		.598			
O4		.586			
O5		.552			
O3		.597			
O1		.466			
Q4			.670		
Q5			.526		
Q1			.481		
Q3			.485		
Q2			.432		
S1				.841	
S2				.749	
S3				.665	
P3					.605
P1					.655
P2					.473

Fig. 6- Rotated component matrix

VII. CONFIRMATORY FACTOR ANALYSIS

Once one has a conceptual model which is a simple sketch on a paper with arrows pointing between the variables showing how influences predicts, one may proceed to the "testing". CFA is accomplished with SEM. Once you have the conceptual model, you can attain CFA with SEM. And now the person has to deal with the sort of SEM which is appropriate for testing. One further angle from which to examine this problem is to begin with the various modelling approaches. PLS modelling or covariance-based modelling are two options that are available to us. It goes without saying that we would not continue testing or creating models just because EFA indicates certain fundamental structures. Rather, your EFA should first be guided by a number of dogmatic or theoretical considerations. The meanings of the symbols in this graphic may be found in their respective definitions. The newly formed representations are the functions that give a generic method which expresses the relationships between the involved variables that are included inside the parenthesis and those that are located on the left-handed side of every node.

This is an early model that was fit using the rotated component matrix in the study; it was created using those data. But, at this point, we are interested in determining whether or not this model is appropriate when it is associated with the TQM enablers (five of them in our instance), i.e. As we are primarily interested in analyzing technical schools, the areas of focus will be on the Quality of Education, Infrastructure, Students and Faculty Information, Other General Aspects, and Placements.

Retrieval Number: 100.1/ijitee.G95930612723
DOI: 10.35940/ijitee.G9593.0612723
Journal Website: www.ijitee.org

Published By:
Blue Eyes Intelligence Engineering and Sciences Publication (BEIESP)
© Copyright: All rights reserved.

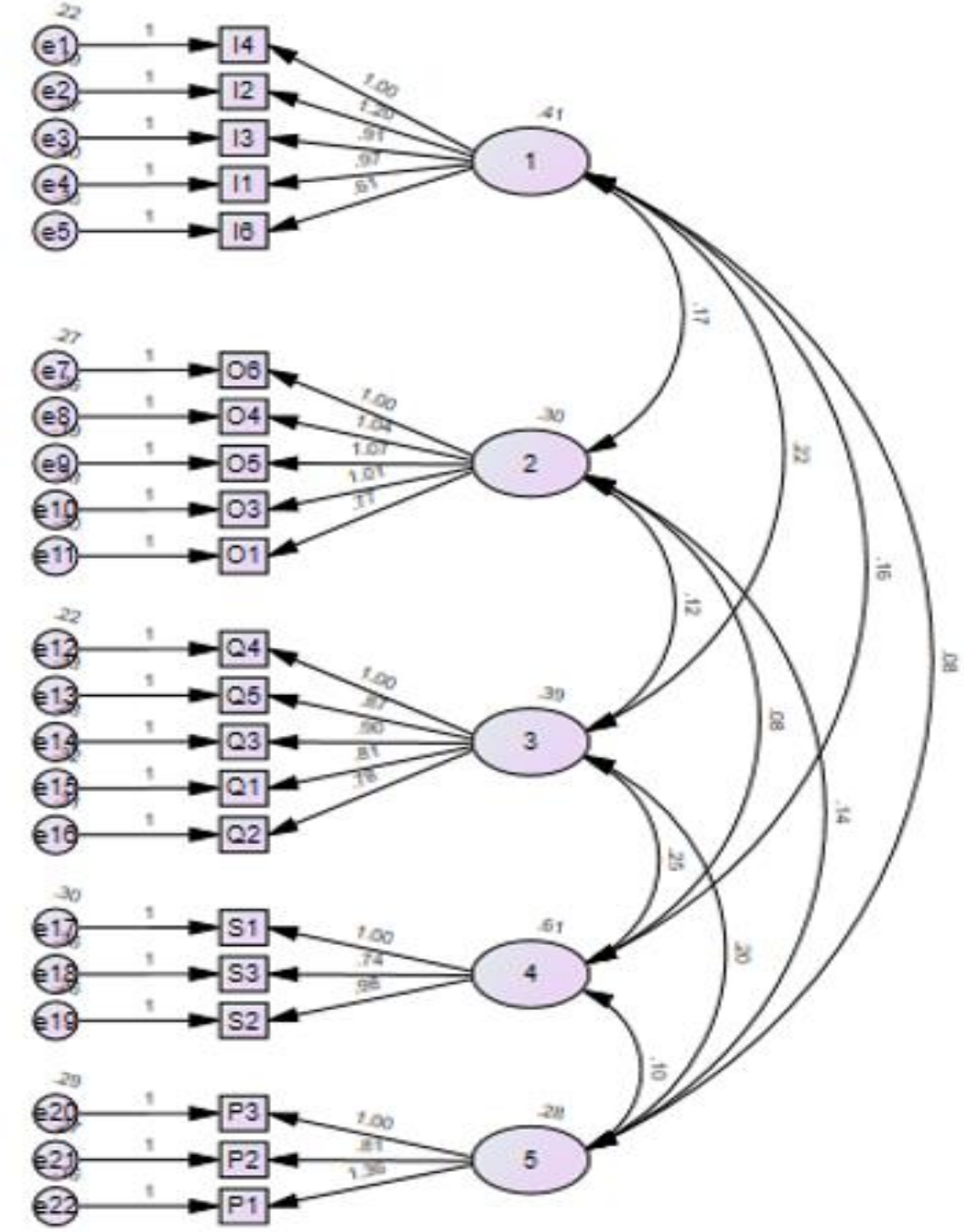

Fig. 7- Confirmatory Factor Analysis

This is an early model that was fit using the rotated component matrix in the study; it was created using those data. But, at this point, we are interested in determining whether or not this model is appropriate when it is associated with the TQM enablers (five of them in our instance), i.e. As we are primarily interested in analyzing technical schools, the areas of focus will be on the Quality of Education, Infrastructure, Students and Faculty Information, Other General Aspects, and Placements.

This model establishes a connection between the aforementioned fit model and the many TQMs that fall under the umbrella of the five TQM enablers. I, O, Q, S, and P (numeric) are the different drivers, and they are directly tied to their respective headings. The headings, in turn, are related to the overall performance of the institution or the primary TQM aim, which is related to the numerous TQM enablers head (i.e., I, O, Q, S, and P). TQM1, TQM2, TQM3, and so on. Since the majority of our data came from Delhi Technological University, we compared it to that of other reputable universities from around the world that are ranked similarly to our own institution.

Published By:
Blue Eyes Intelligence Engineering
and Sciences Publication (BEIESP)
© Copyright: All rights reserved.

The table that follows provides a comparison between DTU and other institutes from around the world in terms of teaching and research, which was identified as the most prevalent TQM DRIVER in our analysis. DTU received certain low scores and has a lot of room for improvement in both of these areas, but the university is making progress in both areas, according other requirements include making steady progress towards improvement and, in the not-too-distant future, competing on an equal footing with the nation's leading educational institutions.

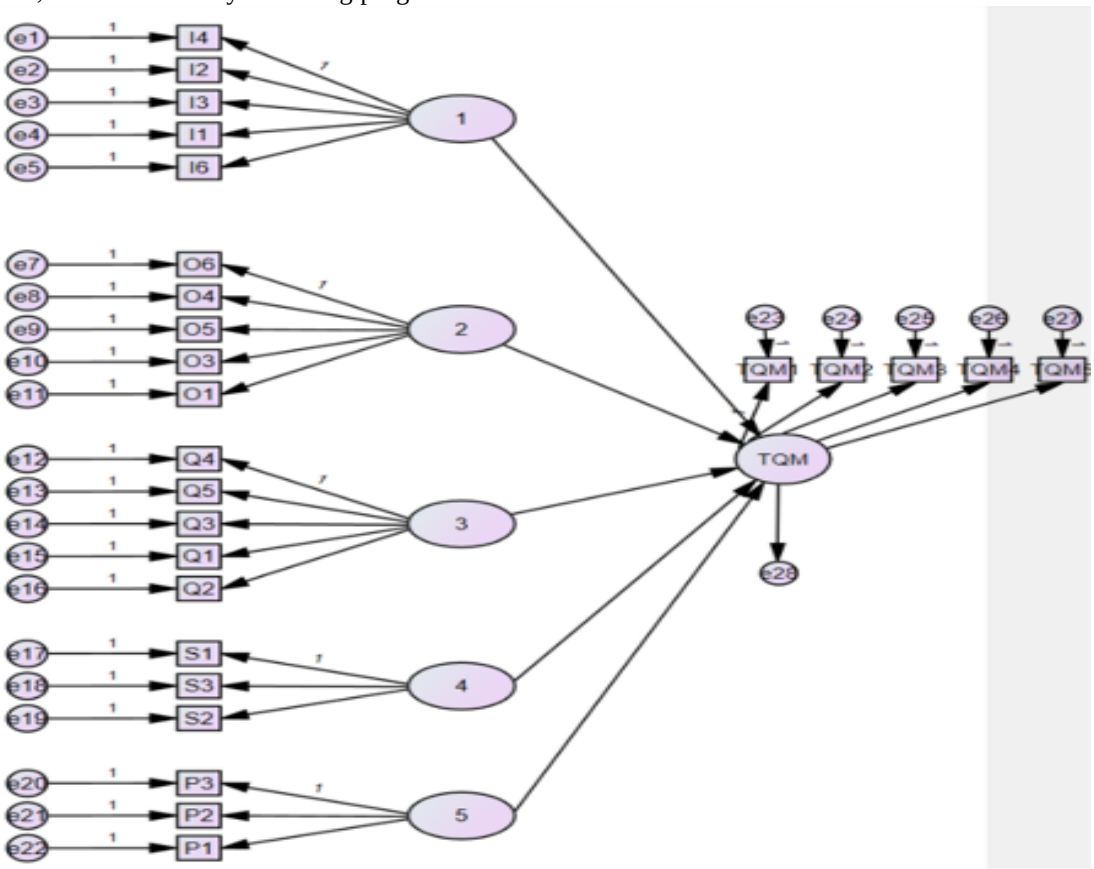

Fig. 8- linkage enablers vs. drivers

Now as we have explained the model and their linkage now it's the time when ve see if this model well fits the analysis or not. For model being fit it has to be passed through some cut-off criteria. Lets see that vs. our scores in front of it

Cutoff Criteria*

Measure	Terrible	Acceptable	Excellent
CMIN/DF	> 5	> 3	> 1
CFI	<0.90	<0.95	>0.95
SRMR	>0.10	>0.08	<0.08
RMSEA	>0.08	>0.06	<0.06
PClose	<0.01	<0.05	>0.05

Fig. 9- cutoff criteria for model fit

Measure	Estimate	Threshold	Interpretation
CMIN	229.138	--	--
DF	179.000	--	--
CMIN/DF	1.280	Between 1 and 3	Excellent
CFI	0.920	>0.95	Acceptable
SRMR	0.084	<0.08	Acceptable
RMSEA	0.064	<0.06	Acceptable
PClose	0.188	>0.05	Excellent

Congratulations, your model fit is excellent!

Fig. 10- our model fit or not

This we have found out that our hence produce model was fit and the factors were accordingly placed with the ratings received through questionires.

Table 2 – influence of inividual factor linkage

Estimate p value result	linkage
.662 *** Fail to reject	Infrastructure→ tqm1
.573 *** Fail to reject	Quality education→ tqm2
.509 *** Fail to reject	Student faculty info→ tqm3
.475 *** Fail to reject	Important aspects→tqm4
.438 *** Fail to reject	Placements→ tqm5

Retrieval Number: 100.1/ijitee.G95930612723
DOI: 10.35940/ijitee.G9593.0612723
Journal Website: www.ijitee.org

Published By:
Blue Eyes Intelligence Engineering and Sciences Publication (BEIESP)
© Copyright: All rights reserved.

Fig. 11, 12-Research score and teaching score with near ranked college

As we have collected data majorly from Delhi technological university we have compared the data with the world wide good universities which possess near ranking with our university.Above is the comparison between DTU and other worldwide institutes in terms of teaching & research which is the most prevalent TQM DRIVER in our analysis which got certain low scores and need to be improved but DTU is improving in terms of both as further analysis suggest that delhi technological university has approximately all the teaching staff who are well versed in their PHD and are well qualified in the respective fields also as far as research is concerned many programs are bring run in the university. further needs are to continuously work towards improving and make it stand head to head with top institutes in near future.

VIII. CONCLUSION

Our model of analysis passed all the testing's and can be used to examine the quality management of any institution or organization. Moreover, we found that these factors help understanding the real time demand of the students and attempts can be made to fulfill them. In our attempt to find out the success criteria we found that real-time data collection is very essential. The changes in economics, society, culture, and technology all contribute to the development of the knowledge society. If India were to become a superpower in the knowledge sector, this would allow for a significant acceleration of the current rate of economic development. In this respect, we have made an effort to examine by collecting data and analyzing it using the software IBM SPSS AND AMOS. As a result of these efforts, we discovered that statistical methods are effective for analyzing and forecasting the nature of the input provided by the general population. In our study, the primary emphasis was on establishing a connection between quality management and essential success criteria, and we also conducted an in-depth examination of the primary elements that, if addressed, may result in a significant improvement for the organization.

Published By:
Blue Eyes Intelligence Engineering and Sciences Publication (BEIESP)
© Copyright: All rights reserved.

The implementation of total quality management inside the company enables the company to realize greater levels of productivity and success by honing in on the most effective means of accomplishing their objectives. In order to conduct a successful study of the students' actions, we relied on reliability factors and model fit analysis. A conceptualized TQM model for achieving excellence in higher education institutes is suggested, and is dependent on the following characteristics, all of these lead to satisfied students.

DECLARATION

Funding/ Grants/ Financial Support	No, I did not receive it.
Conflicts of Interest/ Competing Interests	No conflicts of interest to the best of our knowledge.
Ethical Approval and Consent to Participate	No, the article does not require ethical approval and consent to participate with evidence.
Availability of Data and Material/ Data Access Statement	Not relevant.
Authors Contributions	All authors have equal participation in this article.

REFERENCES

1. Pravin kumar (2015) Industrial Engineering and Management, Delhi Technological University.
2. Bollen, K. A. (1989). Structural equations with latent variables. New York: Wiley. [CrossRef]
3. Bolwijn PT, Kumpe T. (1990). Manufacturing in the 1990s—productivity, flexibility, and innovation. Long Range Planning, 23(4), 44–57. [CrossRef]
4. Brotherton, B., & Shaw, J. (1996). Towards an identification and classification of critical success factors in UK hotels Plc. International Journal Hospitality Management, 15(2), 113-135. [CrossRef]
5. Claver, E., Tari, J.J. and Molina, J.F. (2003), "Critical factors and results of quality management: an empirical study", Total Quality Management and Business Excellence, Vol. 14 No. 1, pp. 91-118. [CrossRef]
6. Demirbag M, Tatoglu E, Tekinkus M, Zaim S. (2006). An analysis of the relationship between TQM implementation and organizational performance: Evidence from Turkish SMEs. Journal of Manufacturing Technology Management, 17(6), Pp. 829–847. [CrossRef]
7. https://economictimes.indiatimes.com/industry/services/education/budget-2023-education-gets-highest-ever-allocation-share-in-gdp-remains-stagnant-at-2-9/articleshow/97534802.cms. *Retrieved 5 March 2023.* {{cite web}}: Missing or empty |title= (help)
8. *"India Literacy Rate". UNICEF. Retrieved 10 October 2013.*
9. *Kumar, Vinay (31 March 2011). "Census 2011: population pegged at 1,210.2 million". The Hindu. Retrieved 9 April 2021.*
10. Jump up to:[a] [b] *"World Development Indicators: Participation in education". World Bank. Retrieved 21 August 2014.*
11. *"Education in India". World Bank. Retrieved 9 April 2021.*
12. Jump up to:[a] [b] [c] *"Educational Statistics At a Glance – Government of India" (PDF). education.gov.in. Retrieved 17 March 2021.*
13. *Kingdon, Geeta Gandhi (2 October 2020). "The Private Schooling Phenomenon in India: A Review". The Journal of Development Studies.* ***56*** *(10): 1795–1817. doi:10.1080/00220388.2020.1715943. ISSN 0022-0388. S2CID 158006322.* [CrossRef]
14. *Little, Angela W.; Lewin, Keith M. (11 July 2011). "The policies, politics and progress of access to basic education". Journal of Education Policy.* ***26*** *(4): 477–482. doi:10.1080/02680939.2011.555004. ISSN 0268-0939. S2CID 145170025.*^ NSO 2018, pp. 43. [CrossRef]
15. Dixon, J.R., Nanni, A.J., Vollmann, T.E. (1990). The new performance challenge: Measuring operations for world-class competition, Homewood, IL, Dow Jones-Irwin.
16. Kumar, V., Choisne, F., Grosbois, D. and Kumar, U. (2009) Impact of TQM on Company's Performance. International Journal of Quality & Reliability Management, 26, 23-37. https://doi.org/10.1108/02656710910924152. [CrossRef]
17. Venkatraman, S. (2007) A Framework for Implementing TQM in Higher Education Programs. Quality Assurance in Education, https://doi.org/10.1108/09684880710723052. [CrossRef]
18. TOTAL QUALITY MANAGEMENT IN HIGHER EDUCATION: A REVIEW Naveen Kumar Research Scholar Department of Commerce, M.D.U, Rohtak, Haryana, India
19. Barros, S., Sampaio, P., and Saraiva, P. (2014). The Relationship between Quality Approaches and their Impact on Portuguese Companies´ Quality Performance", International Conference on Industrial Engineering and Operations Management, Bali, Indonesia.
20. Kumar, s.(2009). Total Quality Management. New Delhi: University Science Press. [CrossRef]
21. R.S. Mishra, Rakesh Kumar, Effect of mediation using critical success factors in the TQM fororganizational performance evaluation, International journal of research in engineering and innovation (IJREI), vol 5, issue 6(2021), 387-396. https://doi.org/10.36037/IJREI.2021.5607
22. National Assessment and Accreditation Council (NAAC), 2004. Guidelines for Re- Accreditation, Bangalore: NAAC, Retrieved from: http://uphed.up.nic.in/sNAAC- N.pdf
23. Sangeeta, et al., 2004. Conceptualising total quality management in higher education. The TQM Magazine, 16(2): 145-159. [CrossRef]
24. Srivanci, M.B., 2004. Critical issues for TQM implementation in higher education. The TQM Magazine, 16(6): 382-386 [CrossRef]
25. Wing, C. (1998). Applying Total Quality Management to the Educational Process. Int. J. Engng Ed, 14(1),

AUTHORS PROFILE

Prof. RS Mishra is a senior professor and ex HOD in department of mechanical engineering, delhi technological university. He is a well qualified and versed in PHD degree. His area of interest includes majorly Thermal engineering and related areas such as heat transfer, Alternate Energy sources, RAC and quality management. He has guided many phd holders and mtech students to complete their degree. From 1997 till date he is giving his best to the university and under him the department is fulfilling all requirements of the authority.

Anshuman Pandey is a Btech undergraduate in department of mechanical engineering, Delhi Technological University. He was born on 10 december 2001 and his major contribution is in design engineering and Total Quality Management and data analysis. He works on several projects which deals with mechanical design and computer aided projects. He is also involved in futuristic work related to the enhancement of existing functions and the development of new features based on the requirements of design constraints. He will be working in power and design sector in near future

Aryan Rana is a B.tech undergraduate in department of mechanical engineering, Delhi Technological University. His major contribution is in design engineering and Total Quality Management and data analysis. He works on several projects which deals computer aided projects. He is also involved in futuristic work related to the enhancement of existing functions and the development of new features based on the requirements of analysis techniques. He will be working in consultant sector in near future

© Copyright: All rights reserved.

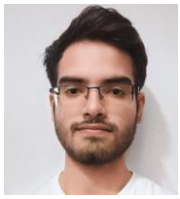

Aakash Mehta is a Btech undergraduate in department of mechanical engineering, Delhi Technological University. He was born on 8 march 2001 and his major contribution is in automobile and Total Quality Management. He works on several projects which deals with cam projects. He is also involved in futuristic work related to the enhancement of existing functions and the development of new features based on the requirements of design constraints. He will be working in automobile sector in near future.

Disclaimer/Publisher's Note: The statements, opinions and data contained in all publications are solely those of the individual author(s) and contributor(s) and not of the Blue Eyes Intelligence Engineering and Sciences Publication (BEIESP)/ journal and/or the editor(s). The Blue Eyes Intelligence Engineering and Sciences Publication (BEIESP) and/or the editor(s) disclaim responsibility for any injury to people or property resulting from any ideas, methods, instructions or products referred to in the content.

© Copyright: All rights reserved.

View publication stats

2023 4th International Conference for Emerging Technology (INCET)
Belgaum, India. May 26-28, 2023

UAV Swarm Navigation in GNSS Denied Region with Formation Control

Priyanshi Jain
Electronics and Communication Engineering, Delhi Technological Univeristy,
Delhi, India
priyanshijain1610@gmail.com

Rohaan Qureshi
Electronics and Communication Engineering, Delhi Technological Univeristy,
Delhi, India
qureshirohaan1@gmail.com

Raghava Nallanthighal
Electronics and Communication Engineering, Delhi Technological Univeristy,
Delhi, India
nsraghava@dtu.ac.in

2023 4th International Conference for Emerging Technology (INCET) | 979-8-3503-3575-0/23/$31.00 ©2023 IEEE | DOI: 10.1109/INCET57972.2023.10170669

***Abstract*—UAVs are becoming extremely essential these days for many applications such as HADR missions. During these missions, there can be a loss of GPS signal due to challenging environments and terrains, and this can hinder the missions so there is a need for a system that provides UAVs the capability to do these missions even in GPS-denied environments. In most of such missions, swarms of UAVs are working. Hence, the aim of this research paper is to propose a reliable GPS-denied navigation system for swarms. The major challenge with the swarm navigation is to achieve inter-UAV collision avoidance. So, this paper mainly focuses on prevention of inter UAV collision. Therefore, to accomplish this objective, the integration of estimations by Visual Odometry and UWB module is proposed in this paper.**

Keywords—GPS-Denied, Visual Odometry, UWB Module, Unmanned Aerial Vehicle, swarm, outdoor navigation

NOMENCLATURE

UAV	Unmanned Aerial Vehicle
GPS	Global positioning system
HADR	Humanitarian assistance and disaster relief
NED	North East Down
fps	Frames per second
UWB	Ultra-Wide Band
TDoA	Time Difference of Arrival
SWaP	Size, Weight and Power
ϕ	Roll angle about x axis
θ	Pitch angle about y axis
ψ	Yaw angle about z axis
d_{ij}	Desired distance between i^{th} and j^{th} UAV
d'_{ij}	Current distance between i^{th} and j^{th} UAV
dd_{ij}	Displacement vector of j^{th} UAV w.r.t i^{th} UAV
α_{ij}	Angle formed by vector dd_{ij} with d_{ij} and d'_{ij}
m	Mass of the UAV
g	Gravitational constant
H	Heading of the UAV
k	Proportional constant for Roll
k'	Proportional constant for Pitch

I. INTRODUCTION

In the modern world, unmanned aerial vehicles (UAVs) have become an essential gadget for a wide range of applications including military, civilian, and commercial applications. UAVs are being used in agriculture, remote sensing, long-range environment monitoring, coastal surveillance, search and rescue missions, and many more applications [1]. Humanitarian assistance and disaster relief (HADR) missions are critical operations that require fast and effective responses to save live and provide aid to affected populations. UAVs play an important role in HADR missions due to their ability to provide rapid situational awareness and support rescue operations in areas that are difficult to access. During these missions, UAVs can face a loss in GPS due to navigation in hilly terrain, the presence of jammers, low signal patches, faulty sensors, etc. This can lead to the failure of rescue missions.

GPS-denied swarms are becoming increasingly important in modern warfare and other applications where GPS navigation may not be reliable or available. These swarms are typically composed of multiple autonomous vehicles that work together to achieve a common goal, such as search and rescue missions or surveillance operations. However, navigating without GPS presents several challenges, including limited range, high power consumption, and the need for accurate and reliable sensors.

The development of GPS-denied swarm navigation systems has important implications for modern warfare and other domains, such as disaster response and environmental monitoring. By enabling swarms to navigate without relying on GPS, these systems can improve the resilience and effectiveness of autonomous vehicles in challenging environments. In this research paper, we present a GPS-denied swarm navigation system with formation control.

GPS can be lost during a mission due to many reasons, i.e., the presence of jammers, faulty sensors, hilly regions or low signal areas, etc. This can make the UAV abort the missions in the middle and sometimes it's a critical mission like human rescue in disaster areas. For these critical missions, it is very important for a UAV to be able to work in GPS-denied conditions. Many solutions have been proposed to tackle the issue but they mostly are focused on indoor navigation. A comparative study for indoor navigation techniques is done in [2]. In [3], GPS Denied navigation is done using AprilTags that are linked to coordinate 3D building information model. Occupancy grid mapping enhanced visual SLAM for real time locating applications is proposed in [4]. In [5], location has been done using optimized beacon placement.

Various studies have been done for outdoor navigation also. A highspeed laser scan matching algorithm is used for mapping by researchers in [6]. In [7], an error state Kalman Filter approach for GPS-INS integration is used for outdoor navigation. A fusion of wheel odometry, inertial

Authorized licensed use limited to: DELHI TECHNICAL UNIV. Downloaded on July 20,2023 at 11:20:47 UTC from IEEE Xplore. Restrictions apply.

measurement unit (IMU), and visual odometry is proposed in [8]. A micro-electro mechanical system (MEMS) sensors-based navigation technique is proposed in [9]. A long-range GOS denied aerial inertial navigation is proposed using LIDAR localisation technique in [10]. In [11], localisation is achieved by using optical flow sensors and ultrasound sensors. However, these solutions can be applied to a single UAV and if applied to multiple UAV, they may cause various problems.

From the above-mentioned research papers, it can be concluded that both indoor and outdoor GPS-denied navigation solutions have been well-developed but mostly for single UAV navigation, and not much research on outdoor GPS-denied swarm navigation. The aim of this paper is to provide a solution sensor fusion-based approach to outdoor GPS-denied swarm navigation using a monocular camera and UWB module.

In this paper, a co-operative localization algorithm is presented in reference to the above-mentioned problem. The algorithm is tested and validated in simulations. The hardware includes UWB module and monocular camera in addition to UAV basic hardware with the onboard computational board. A sensor fusion algorithm is proposed to fuse the estimations of visual odometry with the UWB module. The paper covers the relative localization strategy using both sensors separately which is followed by their fusion algorithm which will result in the improvement of both of their estimations separately along with formation control.

The remaining paper is structured as follows. Section II is devoted to the background study and testing of the relative localization algorithms using both sensors separately with their results. It also contains the problems which mandated the need for the fusion algorithm. Section III proposes the fusion algorithm and also explains how the fusion algorithm itself controls the formation. Section IV is contributed to the simulation and results followed by the conclusion and scope for future work in section V.

II. BACKGROUND

In this paper, we are using two reference frames: Inertial frame and Body frame. We are using the conventional NED frame as the inertial frame orientation. x axis represents positive towards north, y axis represents positive towards east and z axis represents downward positive i.e. , towards gravity, respectively.

The origin of inertial frame is taken as the takeoff point of the UAV. The body frame is the frame in the UAV initially is in.

The state of the UAV at any point is defined as:

$$[x \quad y \quad z \quad \phi \quad \theta \quad \psi]^T \tag{1}$$

where UAV position is represented by (x,y,z) w.r.t. the inertial frame and the attitude of UAV is represented by (ϕ, θ, ψ).

The body frame is converted to the NED frame using a rotation matrix [12].

$$R_M = \begin{bmatrix} C_\psi C_\theta & C_\psi S_\theta S_\phi - S_\psi C_\phi & C_\psi S_\theta C_\phi + S_\psi S_\phi \\ S_\psi C_\theta & S_\psi S_\theta S_\phi + C_\psi C_\phi & S_\psi S_\theta C_\phi - C_\psi S_\phi \\ -S_\theta & C_\theta S_\phi & C_\theta C_\phi \end{bmatrix} \tag{2}$$

where S_ψ is sin ψ and C_ψ is cos ψ, and so on.

In our system, we have maintained $\psi = 0$. That means that the UAV is always pointing towards north. So, the rotaion matrix get simplified into:

$$R_M = \begin{bmatrix} C_\theta & S_\theta S_\phi & S_\theta C_\phi \\ 0 & C_\phi & -S_\phi \\ -S_\theta & C_\theta S_\phi & C_\theta C_\phi \end{bmatrix} \tag{3}$$

The upward force caused by propulsion is the sole force acting on the UAV's frame (body frame), disregarding the drag caused by translational motion. F_B is hence the force at work in the bodily frame. To convert this force and the roll pitch angles to the inertial frame of reference [13], the following equation is used:

$$\begin{bmatrix} \ddot{x} \\ \ddot{y} \\ \ddot{z} \end{bmatrix} = \frac{1}{m}\left(\begin{bmatrix} 0 \\ 0 \\ mg \end{bmatrix} + R_M \begin{bmatrix} 0 \\ 0 \\ -F_B \end{bmatrix}\right) \tag{4}$$

The link between the roll angle, pitch angle, and thrust and the linear accelerations of the UAV in its inertial frame is found by rearranging the aforementioned equations.

$$\begin{bmatrix} \ddot{x} \\ \ddot{y} \\ \ddot{z} \end{bmatrix} = \frac{1}{m}\left(\begin{bmatrix} -F_B S_\theta C_\phi \\ F_B S_\phi \\ -F_B C_\theta C_\phi + mg \end{bmatrix}\right) \tag{5}$$

A. Visual Odometry

GNSS-Denied UAV Navigation using Monocular Camera is beautifully proposed in [13]. Our paper is extension to the research conducted in this paper. In Visual Odometry, two reference frames are defined: Inertial frame and the Body frame. The Inertial frame we are using is NED frame.

In Visual Odometry, we mount a monocular camera on a 3-axis gimbal which keep the camera facing downwards. The camera captures continuous images of ground at a specific frame rate. The motion of the UAV is calculated by detecting the distinct features between consecutive two image frames and the displacement vector is formed from one point to another point.

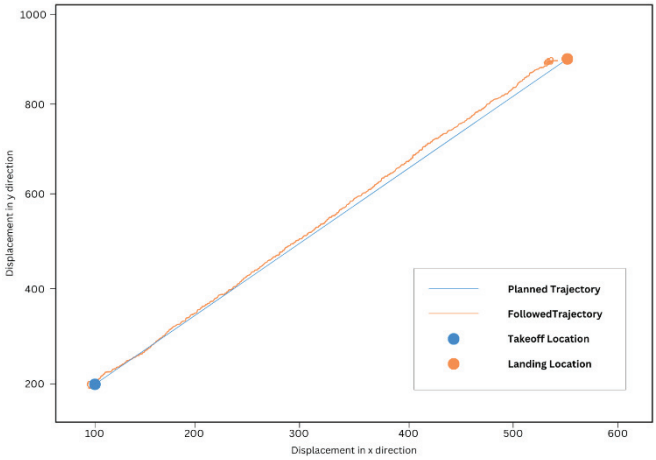

Fig. 1. Plot of planned trajectory and actual trajectory in outdoor flight of visual odometry

Authorized licensed use limited to: DELHI TECHNICAL UNIV. Downloaded on July 20,2023 at 11:20:47 UTC from IEEE Xplore. Restrictions apply.

The above graph shows that the UAV is following the trajectory perfectly well but with time an error is accumulated. This error is small but it will affect the system in the long run. So, there must be a system to remove this error or minimize this error.

B. UWB Module

In this paper, we are using Decawave DWM1001 UWB module. The module gives accuracy up to 5 cm. The localisation through UWB is based on TDoA measurements [14]. The module can be configured as anchor, active tag and passive tag. The anchor works as the satellite to the system and the tag works as a receiver. Their working is exactly like GPS module and satellite. They just create a fake GPS environment in a small area. The range of the module is 30 meters. The anchor was fixed in our laboratory and a UAV with a tag was tested for an indoor flight. The resulting UAV position is presented in the figure 3.

The position as shown in figure 5 is following the line but is giving a noisy error for which we are using low pass filter and a moving average filter [15].

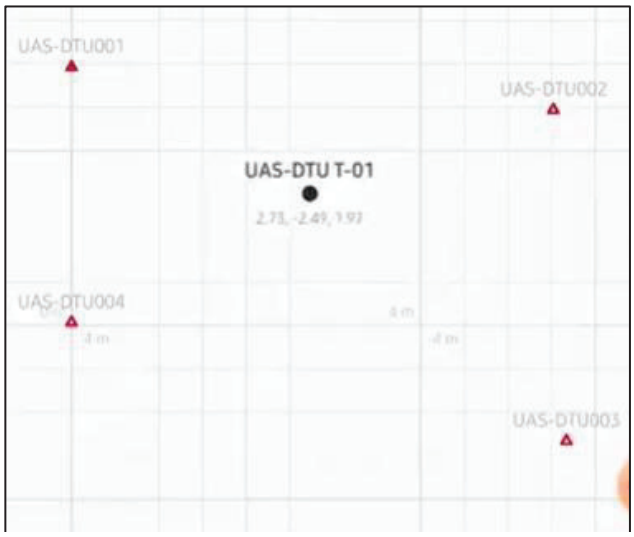

Fig. 2. UAV position given by UWB Module in indoor flight

Fig. 3. Indoor UAV flight

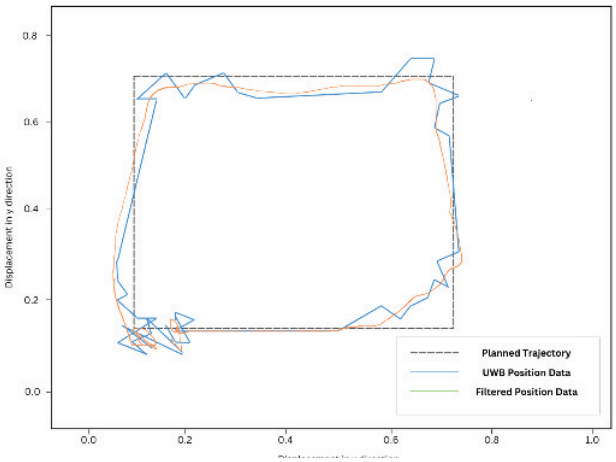

Fig. 4. Plot of UAV planned trajectory with UWB positioning data

The above graph shows that UWB modules give very accurate positioning information but their range is less.

III. PROPOSED SOLUTION

Given the issues with both of the above solutions, a fusion algorithm is designed to solve both issues using their advantageous characteristics. Visual odometry gives an accumulation of error over time while UWB gives the position in the correct range. Visual odometry is not dependent on any ground module and is not bound by range while UWB is dependent on other modules' positioning and has a limited range. The paper presents a model which gives a better positioning in a long run too, i.e., the paper aims to minimize the accumulation of errors in Visual odometry using UWB modules.

Consider a swarm of N UAVs moving towards a target in a stochastic region. The swarm faces a no GPS region during the journey. The aim of the swarm is to fly across the GPS-denied region without disturbing the formation and predicting its current location. Each UAV is communicating with each and every UAV in its range. Each UAV is installed with a monocular camera and UWB module. Let D and A are the distance matrix and angle matrix respectively where d_{ij} and a_{ij} are the distance between i^{th} and j^{th} UAV and the angle formed by the line passing through i^{th} and j^{th} UAV with the heading respectively.

$$D = \begin{bmatrix} d_{11} & \cdots & d_{1N} \\ \vdots & \ddots & \vdots \\ d_{N1} & \cdots & d_{NN} \end{bmatrix} \text{ and } A = \begin{bmatrix} a_{11} & \cdots & a_{1N} \\ \vdots & \ddots & \vdots \\ a_{N1} & \cdots & a_{NN} \end{bmatrix}$$

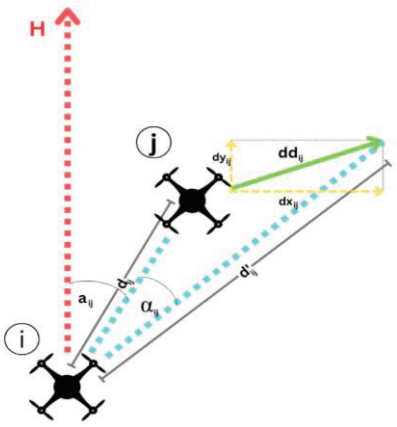

Fig. 5. Analysis of UAV's i and j

Authorized licensed use limited to: DELHI TECHNICAL UNIV. Downloaded on July 20,2023 at 11:20:47 UTC from IEEE Xplore. Restrictions apply.

The matrices A and D are updated in real-time during GPS region and fixed during the no GPS region. The system has to maintain this formation after the loss of GPS. After entering the no GPS region, the system starts computing vector dd, i.e., the relative change in position of i^{th} and j^{th} UAVs. In visual odometry, the error was reduced by generating roll or pitch in the direction opposite to the error. In this fusion algorithm, we are calculating the roll and pitch in a different manner using the relative distance from the UWB module.

Here, using basic trigonometry, we know

$$\alpha_{ij} = cos^{-1}\frac{d_{ij}^2+dd_{ij}^2-d'^2_{ij}}{2d_{ij}.dd_{ij}} \quad (6)$$

By observing the diagram, we can say,

$$(d'_{ij}\cos\alpha_{ij} - dy_{ij})^2 + (d'_{ij}\sin\alpha_{ij} - dx_{ij})^2 = d_{ij}^2 \quad (7)$$

$$dx_{ij}\sin\alpha_{ij} + dy_{ij}\cos\alpha_{ij} = \frac{d'^2_{ij}+dx_{ij}^2+dy_{ij}^2-d_{ij}^2}{2d'_{ij}} \quad (8)$$

$$\sin(\alpha_{ij}+\beta_{ij}) = \frac{d'^2_{ij}+dx_{ij}^2+dy_{ij}^2-d_{ij}^2}{2d'_{ij}.\sqrt{dx_{ij}^2+dy_{ij}^2}} \quad (9)$$

where $\tan\beta_{ij} = \frac{dy_{ij}}{dx_{ij}}$ or $\beta_{ij} = \tan^{-1}\frac{dy_{ij}}{dx_{ij}}$ (10)

and $dd_{ij} = \sqrt{dx_{ij}^2 + dy_{ij}^2}$

$$\sin(\alpha_{ij}+\beta_{ij}) = \frac{d'^2_{ij}+dd_{ij}^2-d_{ij}^2}{2d'_{ij}.dd_{ij}} \quad (11)$$

$$\alpha_{ij}+\beta_{ij} = \sin^{-1}\frac{d'^2_{ij}+dd_{ij}^2-d_{ij}^2}{2d'_{ij}.dd_{ij}} \quad (12)$$

Similarly,

$$|\beta_{ij}-\alpha_{ij}| = \cos^{-1}\frac{d'^2_{ij}+dd_{ij}^2-d_{ij}^2}{2d'_{ij}.dd_{ij}} \quad (13)$$

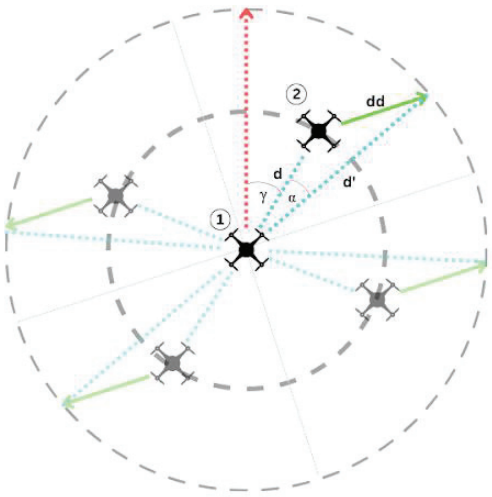

Fig. 6. Calculation of desired angle for roll and pitch

It is observed that with the given information, the relative positioning of UAV can be observed in four cases as shown in Figure (6). Where it is observed that cases (2), and (3) are separated from cases (1) and (4) by the direction of the vector dd with the heading. On an experimental and observational basis, it is observed that if u_1 and u_2 are the modified angles of their relative positions for both cases, then the corrective roll and pitch are calculated as follows:

$$u_{1_{ij}} = \beta_{ij} - \alpha_{ij} \text{ and } u_{2_{ij}} = \alpha_{ij} + \beta_{ij} \quad (14)$$

$$\varphi_j = k(d'_{ij}.\sin u_{ij} - d_{ij}.\sin a_{ij}) \quad (15)$$

$$\theta_i = k'\,(d'_{ij}\,.\cos u_{ij} - d.\cos a_{ij})\,, \quad (16)$$

$$\text{where } u = \min\left(\left|u_{1_{ij}}\right|, \left|u_{2_{ij}}\right|\right) \quad (17)$$

and k and k' are constants

As mentioned in previous section, the target of the paper is to find a solution better than previously done solutions and make it useful for a UAV swarm. Our solution is constantly correcting its position with the UWB data which is more accurate and does not provide an accumulation of errors over time. Hence, our algorithm minimizes the error and prevents inter-UAV collision. Moreover, the solution also maintains the formation with which the swarm entered the GPS denied region.

IV. RESULT

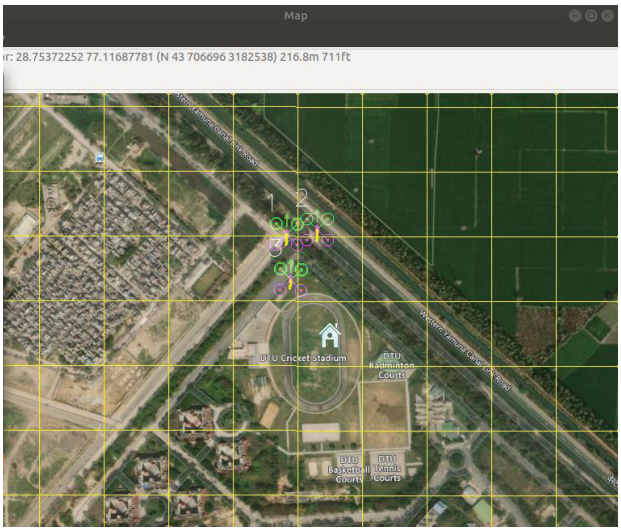

Fig. 7. Simulation of fusion algorithm in SITL

The simulations and testing of algorithm are done using a software called Ardupilot SITL as shown in Fig. 7. Result of testing of the algorithm in ideal case without introducing an error is shown in Fig. 8. The deflection in the midway is due to presence of a conditional statement in equation. (17). Fig. 9 shows the results of the testing of the algorithm by introducing small errors in the distance readings which were observed when the separate testing of UWB modules was being done. The solution shows decent results in this scenario too. The main concern in real world applications is avoiding an inter-UAV collision and this can be concluded that the UAVs are not colliding at any point of time and maintaining the same formation throughout the journey. So, this show that the algorithm is ready to be tested in a real

Authorized licensed use limited to: DELHI TECHNICAL UNIV. Downloaded on July 20,2023 at 11:20:47 UTC from IEEE Xplore. Restrictions apply.

environment. To increase the accuracy of the algorithm, the work is being extended to using Kalman filter which will be the extension of this work.

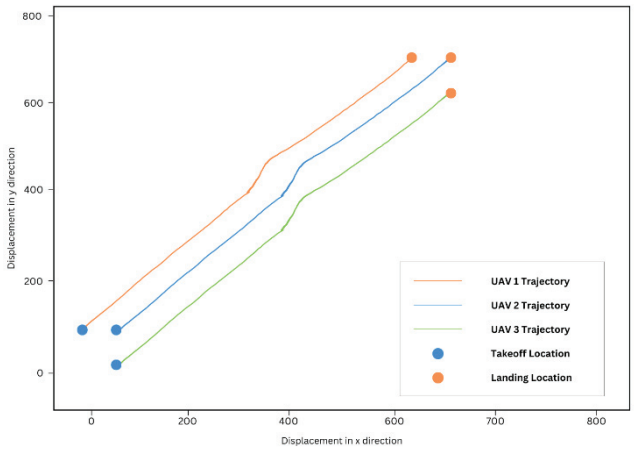

Fig. 8. Plot of trajectory followed by three UAVs and testing of algorithm without error

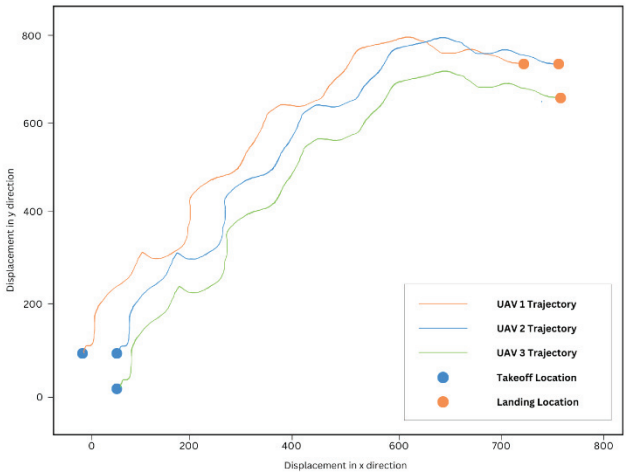

Fig. 9. Plot of trajectory followed by three UAVs and testing of algorithm with error

V. CONCLUSION

Through this paper, the problem of GPS-denied during outdoor navigation is addressed by a fusion algorithm for making a more reliable solution for outdoor navigation which can be applied to swarms. The hardware used in this process is low-cost and SWaP optimized that is making our solution more reliable. In future comings, we will be testing the algorithm in flights.

ACKNOWLEDGMENT

The authors would like to thank Delhi Technological University and team UAS-DTU Laboratory for allowing them to conduct the research. The authors duly acknowledge the help of the professors and the team members for the same

REFERENCES

[1] N. Muchiri, S. Kimathi, "A review of applications and potential Applications of UAV", 2016 Annual Conference on Sustainable Research and Innovation

[2] Balamurugan G, Valamathi J, VPS Naidu, "Survey on UAV Navigation in GPS Denied enviroment", International conference on Signal Procesing, Communication, Power and Embedded System (SCOPES)-2016

[3] Mohammad Nahangi, Adam Heins, Brenda McCabe, Angela Schellig, "Automated Localisation of UAVs in GPS-Denied Indoor Constrction Environemtn Using Fiducial Markers" 35th International Symposiuam on Automation and Robotics in Construction (ISARC 2018)

[4] Lichao Xu, Chen Feng, Vineet R. Kamat, Carol C. Menassa, "An occupancy grid mapping enhanced visual SLAM for eal-time locating applications in indoor gps- denied Environments"

[5] Alireza Famili, Angelos Stavrou, Haining Wang, Jun-Min (Jerry) Pack "iDROP: Robust Localisation for Navigation of Drones with Optimized Beacon Placement", Famili and Stavrou, et al.

[6] Abraham Bachrach Samuel Prentice, Ruijie He, Nicholas Roy, "Range – Robust autonomous navigation in GPS denied environments", journal of Field Robotics, Volume 28, Isue 5, p.644-666

[7] Markus Kleinert, Sebestian Schleith, "Inertail Aidede monocular SLAM for GPS denied navigation", 2010 IEEE International Conference on Multisensor Fusion and Integration for Intelligent Systems, University of Utah, Salt Lake City, UT, USA, Sept. 5-7, 2010

[8] Yaxuan Yan, Baohua Zhang, Jun Zhou, Yibo Zhang, Xiao'ang Liu, "Real Time localisation and Mapping Itilizing Multi-Sensor Fusion and Visual-IMU-Wheel odometry for Agriculatureal Robots in Unstrctured, Dynamic and GPS-Denied Greenhouse environments", Agronomy 2022, 12, 1740.

[9] Abdelrahman Ali, Naser El-Sheimy, "Low-Cost MEMS-Based Pedestrain navigation Technique for GPS-Denied Areas", Hindawi Publishing Corporation, Journal of Sensors, Volume 2013, Article ID 197090

[10] Garrett Hemann, Sanjiv Singh, and Michael Kaess, "Long range GPS Denied aerial inertial navigation with LIDAR localisation.", 2016 IEEE/RSJ International Conference on Integent Robots and Systems(IROS), Daejeon Convention Center, October 9-14, 2016, Daejeon, Korea

[11] Shang-En Tsai, Shih-Hsien Zhuang, "Optical flow sensor integrated navigation system for quadrotor in GPS-denied environment", 2016 International Conference on Robotics and Automation Engineering (ICRAE)

[12] K. Thu, and A. I. Gavrilova, "Designing and modeling of quadcopter control system using L1 adaptive control", 12th International Symposium Intelligent Systems INTELS'16, Oct. 2016

[13] Joyraj Bhowmick, Anurag Singh, Harshit Gupta, Raghava Nallanthighal, "A Novel Approach to Computationally Lighter GNSS-DEied UAV Navigation Using Monocular Camera", 2021 International Conference on Automation, Robotics and Applications

[14] Thein Minh Nguyen, Abdul Hanif Zaini, Kexin Guo and Lihua Xie, "An Ultra Wideband-based Multi-UAV Localisation System in GOS-Denied environments", IMAV2016-9

[15] Belyaev Alexander, Tutov Ivan, Butuzon Denis, "Analysis of noisy signal signal restoration quality with exponential moving avrage filter.", 2016 International Siberian Conference on Control and Communications (SIBCON).

Authorized licensed use limited to: DELHI TECHNICAL UNIV. Downloaded on July 20,2023 at 11:20:47 UTC from IEEE Xplore. Restrictions apply.

Uncovering Political Hate Speech During Indian Election Campaign: A New Low-Resource Dataset and Baselines

Farhan Ahmad Jafri[1], Mohammad Aman Siddiqui[1], Surendrabikram Thapa[2], Kritesh Rauniyar[3], Usman Naseem[4], Imran Razzak[5]

[1] Jamia Millia Islamia, India
[2] Department of Computer Science, Virginia Tech, USA
[3] Department of CSE, Delhi Technological University, India
[4] School of Computer Science, The University of Sydney, Australia
[5] School of Computer Science and Engineering, University of New South Wales, Australia

Abstract

The detection of hate speech in political discourse is a critical issue, and this becomes even more challenging in low-resource languages. To address this issue, we introduce a new dataset named IEHate, which contains 11,457 manually annotated Hindi tweets related to the Indian Assembly Election Campaign from November 1, 2021, to March 9, 2022. We performed a detailed analysis of the dataset, focusing on the prevalence of hate speech in political communication and the different forms of hateful language used. Additionally, we benchmark the dataset using a range of machine learning, deep learning, and transformer-based algorithms. Our experiments reveal that the performance of these models can be further improved, highlighting the need for more advanced techniques for hate speech detection in low-resource languages. In particular, the relatively higher score of human evaluation over algorithms emphasizes the importance of utilizing both human and automated approaches for effective hate speech moderation. Our IEHate dataset can serve as a valuable resource for researchers and practitioners working on developing and evaluating hate speech detection techniques in low-resource languages. Overall, our work underscores the importance of addressing the challenges of identifying and mitigating hate speech in political discourse, particularly in the context of low-resource languages. The dataset and resources for this work are made available at https://github.com/Farhan-jafri/Indian-Election.

Introduction

In today's world, social media has become increasingly popular for expressing opinions and engaging in online discussions. Social media has turned out to be a key influence in amplifying economic, political, and cultural disparities globally, thereby impacting politics in democratic as well as autocratic regimes (Zhuravskaya, Petrova, and Enikolopov 2020). Opinions on social media vary on a vast spectrum of emotions. During events such as elections, the users on the platforms tend to be more active by voicing support or criticism for the people and parties contesting in the election. The ease of access and vast reach of social media combined with some degree of anonymity options has facilitated a hostile and offensive environment on it (Beddiar, Jahan, and Oussalah 2021). During elections, supporters of respective parties tend to gain support on social platforms by criticizing their opposition through accusations, highlighting issues, and failures. Politics is impossible to separate from sensitive topics such as Religion, Sex, Race, Culture, etc.; hence political competition becomes a forefront for hateful content online. Hate speech encompasses various types of language, such as name-calling, defamation of political rivals, false accusations, targeted sarcasm, references to historical wrongdoings, and more. Minimizing hate speech is thus important because it harms individuals and groups, fosters division and prejudice, and erodes social cohesion (Parihar, Thapa, and Mishra 2021).

India is a country of 1.21 billion people (Chandramouli and General 2011). With such a vast population and enormous diversity, hate speech on online platforms is an inevitable issue that needs to be tackled. In the Indian General elections of 2009, social media was first used to engage voters politically. In the General Elections of 2014 and 2019, the strategic use of social media by the BJP prompted other political parties to adopt it as part of their political campaigns (Mir and Rao 2022). This fierce contest on social media among the parties led to accusations and defamation among political leaders and ordinary citizens. The subtle religious difference in India have been exploited in the past and have resulted in communal violence. In the digital age, the propagation of hateful religious views has also been accelerated by the circulation of fake news and hate speech on digital platforms, serving as propaganda to influence voters' decision-making (Parwez 2022).

According to the 2011 Census, there are 43.63 percent of Indians that speak Hindi as their mother tongue (Chandramouli and General 2011). Hindi is based on the Devanagari script, which comprises 47 characters with 33 consonants and 14 vowels (Templin 2013). With the vast usage of the Hindi language on social media, the usage of NLP techniques for a low-resource language like Hindi can aid to minimize the problem of Hate Speech. To create a bridge to combat hate speech

and invite more research in hate speech detection in the Hindi language, we have created "IEHate", a dataset of 11,457 Tweets collected during state assembly elections in the states of Goa, Uttarakhand, Uttar Pradesh, Punjab, and Manipur, all conducted in the year 2022. The tweets are manually annotated as "Hate" and "Non-Hate" by four annotators. Our contributions are as follows:

- We create and release a new low-resource dataset of 11,457 Hindi tweets labeled for the presence of hate speech during Indian assembly election campaign.
- Our experimental analysis shows that state-of-the-art transformer-based models are important and further research can be done in this direction.
- Our analysis shows that the algorithms showed lower performance compared to human evaluation for detecting instances of hate speech. These findings emphasize the need for developing more advanced and robust automated systems for hate speech detection during the Indian election campaign.

Related Works

Several studies have been conducted to detect hate speech on social media platforms. Vidgen and Yasseri (2020) annotated 109,488 tweets for the identification of Islamophobic hate speech, categorizing the annotation into none, weak, and strong. Similarly, Waseem and Hovy (2016) collected 16,914 tweets which had three labels as racist, sexiest, and none. They also showed the gender distribution for the detection of hate speech. Meanwhile, Vadesara and Tanna (2023) annotated 10,000 tweets for hate speech collected using keywords such as religion, sport, politics, and celebrity, categorizing them as hate or non-hate. Mulki et al. (2019) compiled 5,846 Arabic-language tweets about political events and categorized them as regular, abusive, or hateful. These studies demonstrate the widespread use of hate speech in relation to political issues across many languages and the importance of developing effective detection methods.

In addition to the above works, several studies have been conducted on hate speech detection in the Hindi and Hindi code-mixed languages. Bohra et al. (2018) developed a dataset of 4,575 Hindi-English code-mixed tweets manually annotated for hate speech and normal speech. Similarly, Kumar et al. (2018) proposed a multilingual dataset containing Hindi, English, and mixed tweets annotated for aggression. Similarly, Modha et al. (2020) curated the data from Twitter and Facebook where they extracted code-mixed Hindi language as well as English. The task was set for online aggression detection where they used 15,001 data samples to train the models. Sreelakshmi, Premjith, and Soman (2020) made use of three existing data sources to create a pool of 10,000 data samples with two classes (Hate and Non-hate). The performance of various models was compared using different word embeddings like word2vec, fastText, and doc2vec.

Despite these efforts for the detection of hate and aggression in Hindi and Hindi-English code-mixed data, there is a need for more research and data specifically focused on detecting hate speech in political discourse in the Hindi language. As political discourse is a crucial aspect of any democracy, the spread of hate speech in this domain can have serious consequences on society. Realizing this need, our dataset, IEHate can be used to train machine learning models for hate speech detection in political discourse. By developing such models, it will be possible to monitor and control the spread of hate speech in political discourse, thus promoting a healthier and more inclusive democracy.

Dataset

On March 10, 2022, the results of the state election in India were announced after the votes had been counted. To investigate the role of hate speech in political discourse leading up to the election, we collected tweets using the Twitter API between November 1, 2021, and March 9, 2022, which covered the period of the election campaign. We used Twitter API[1] to gather the tweets from this time period.

Data Collection

In order to find relevant tweets, we used various hashtags like #UttarPradeshElections2022, #GoaElections2022, #PunjabElections2022, #IndianElections2022, #StateElections2022, #AssemblyElections2022, #UttarakhandElections2022 and #ManipurElections2022.

We used tweets that predominantly had Hindi text. In order to filter the tweets for our dataset, we set criteria that included retaining tweets that contained a few non-Hindi words or phrases as long as the majority of the tweet was in Hindi. However, we eliminated tweets that were deemed non-informative, such as spam or advertisements, and those that used election-related hashtags only for spamming. Additionally, we excluded tweets that lacked clear context related to the assembly election and might be influenced by local contexts, as they could introduce ambiguity and hinder the accurate categorization of hate speech. After applying these criteria, we were left with 11,457 labeled tweets that were annotated for their text.

Annotation

The dataset was manually annotated by a team of four individuals with diverse educational backgrounds and experience in NLP and data collection. The annotators were from different regions in India and had different political and religious beliefs. Having such diverse backgrounds helps minimize bias, which is crucial in ensuring accurate labeling (Vargas et al. 2022).

The data was annotated into two binary classes, namely hate speech and no hate speech, to categorize

[1]https://developer.twitter.com/en/docs/twitter-api

the tweets. To accomplish this, annotators were provided with guidelines to assign labels to the tweets. In cases where the annotators were unsure about the label for a tweet, it was marked as 'Non-Informative' and eventually excluded from the dataset. The annotation guidelines are mentioned below.

Hate Speech: Hate speech during political events such as election campaigns often targets specific groups based on their political beliefs or affiliations and expresses hostility or aggression towards them. It can also include the use of satires to disseminate harmful messages that are intended to demean, degrade or dehumanize a particular political group or individual.

> ➢AAP की सोच पाकिस्तान जैसी. पंजाब के ख़िलाफ साज़िश रची गई. वोट से अपराधों का हिसाब करें
> Translation: *AAP's ideology is like that of Pakistan. A conspiracy has been hatched against Punjab. Criminals should be held accountable through votes.* ***(Hostile/ Demeaning)***
> ➢सुनने में आ रहा है की जिन आतंकियों को मृत्युदंड दिया गया है उनमे से एक आजमगढ़ का है और उसका बाप समाजवादी पार्टी में है। तो बात हुई ना सही की समाजवादी की लाल टोपी निर्दोष भारतीयों के रक्त से रंगा हुआ है।
> Translation: *It is being heard that one of the terrorists who has been given the death penalty is from Azamgarh and his father is associated with the Samajwadi Party. So it is correct to say that the red cap of Samajwadi Party is stained with blood of innocent Indians.* ***(Misinformation)***

No Hate Speech: The characteristics of non-hate speech were defined as part of the annotation guidelines for a study on hate speech during the Indian election campaign. These include constructive criticism of political figures, policies, or parties, factual and informative content, lack of hostility, and absence of misinformation or fake news. Non-hate speech during the Indian election campaign also does not target specific groups of people based on their political beliefs or affiliations. These guidelines were provided to annotators to help them identify and label tweets as non-hate speech.

> ➢काम करते तो जनता खुद मन से वोट देते । अभी जनता जागरूक हो गइ है ।
> Translation: *If you had done your work, people would have voted with their heart. People have become aware now.* ***(Constructive Criticism)***
> ➢कोविड से आपकी सुरक्षा के लिए मतदान केंद्रों पर होंगे कई इंतज़ाम। अब आप भी हो जाइये, मतदान के लिए तैयार।
> Translation: *Arrangements to prevent you from COVID has been done. Now, you should also be ready for voting.* ***(No Misinformation)***

Labeling tweets for hate speech can be challenging (Thapa et al. 2022). Thus, a multi-phase approach was taken to ensure high-quality annotations. First, a pilot annotation of 100 tweets was conducted with all four team members to confirm their understanding of the instructions. The instructions were revised based on the feedback received to address any confusion. In the second phase, all four annotators were tasked with labeling 250 tweets to assess the clarity of the revised instructions. Finally, a group discussion was conducted to resolve any conflicts in the annotations. This multi-phase approach ensures consistency and accuracy in the annotation process, even when the content of the tweet is challenging. The inter-annotator agreement score, Fleiss's Kappa (κ), was 0.49 and 0.72 for pilot and final annotations, respectively.

Dataset Statistics and Analysis

Our new dataset included 11,457 tweets, with 970 (8.46%) of them annotated as "Hate Speech" and 10,487 (91.53%) as "No Hate" (Table 1). Dataset statistics reflect a real-world scenario where most posts are neutral, and only a few contain hate speech.

Labels	Tweets	Avg. Char	Avg. words
Hate	970	158.37 (145.02)	27.39 (25.37)
Non-Hate	10487	150.06 (136.70)	24.51 (22.69)

Table 1: Dataset Statistics for "IEHate" dataset. The values in parentheses in average characters per tweet (Avg. Char) and average words per tweet (Avg. words) are calculated after preprocessing of text.

Exploratory Data Analysis

The top 5 words in our entire dataset, as well as the categories of hate speech and non-hate speech, are shown in Table 2. In addition to the matching TF-IDF score for words, translations or transliterations are provided. Words with high TF-IDF scores are deemed to be more significant to the document. The terms Election (चुनाव), vote (मतदान), and Congress (कांग्रेस) have a high significance in majority of the courses, according to Tables 2. The histogram for the total number of words across both classes is displayed in Figure 1. The average number of words and characters per tweet for each class are shown in Table 2 as well. A relatively higher number of words in "Hate Speech" tweets show that people frequently engaged in lengthy discussions about how the current political system is flawed in "Hate" tweets.

Experimental Results

We used various machine learning, deep learning, and state-of-the-art transformer-based methods to establish baselines. We further evaluated our test data using two human evaluators. They were made to label the tweets based on whether they contained hate or not. Instructions were provided to human evaluators. We employed

All Posts			No Hate Speech Posts			Hate Speech Posts		
Words	**Translation**	**TF-IDF**	**Words**	**Translation**	**TF-IDF**	**Words**	**Translation**	**TF-IDF**
चुनाव	Election	0.1327	चुनाव	Election	0.1389	नहीं	No	0.1290
कांग्रेस	Congress	0.0855	मतदान	Vote	0.0906	कांग्रेस	Congress	0.0959
मतदान	Vote	0.0843	कांग्रेस	Congress	0.0838	भाजपा	BJP	0.0869
गोवा	Goa	0.0757	विधानसभा	Assembly	0.0793	पंजाब	Punjab	0.0806
विधानसभा	Assembly	0.0741	गोवा	Goa	0.0782	सरकार	Government	0.0608

Table 2: Top-5 most frequent words in the overall dataset and also for each sub-classes viz. "Hate Speech" and "Non-Hate Speech" along with their TF-IDF values

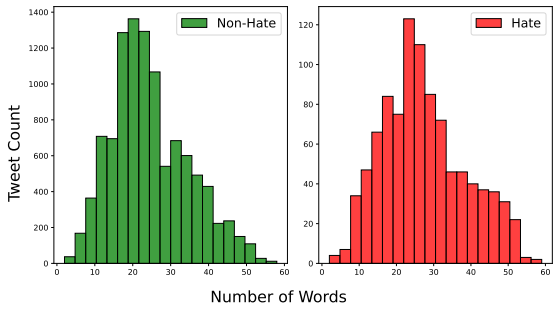

Figure 1: Histogram of the number of words used in Hate Speech and Non-Hate speech tweets

accuracy, macro-mean-squared-error (MMAE), and F1-score (macro) as evaluation measures to determine each baseline's results.

Machine Learning Algorithms: In traditional machine learning algorithms, we used Naive Bayes (Rish et al. 2001), Decision Tree (Rokach and Maimon 2005), Logistic Regression (Stoltzfus 2011), Support Vector Machine (SVM) (Cortes and Vapnik 1995) with TF-IDF vectorizer.

Deep Learning Algorithms: In deep learning algorithms, we used Long-Short-Term-Memory (LSTM) (Hochreiter and Schmidhuber 1997), Bidirectional-LSTM, Bi-LSTM + Convolutional Neural Networks (CNN). We employed TensorFlow Tokenizer embedding for word embeddings.

Transformer based algorithms: In transformer-based models, we have used XLM-RoBERTa-base (Barbieri, Anke, and Camacho-Collados 2022) trained on 198M multilingual tweets, BERT (HAM: Hindi-abusive-MuRIL) (Das, Banerjee, and Mukherjee 2022) trained on Devanagari Hindi and was finetuned on MuRIL model, BERT (HCMAM: Hindi-codemixed-abusive-MuRIL) (Das, Banerjee, and Mukherjee 2022) and RoBERTa (hate-roberta-hasoc-hindi) (Velankar et al. 2021) model fine-tuned on Hindi HASOC Hate Speech Dataset 2021. All models were imported from huggingface[2] library.

Results

Table 3 show the results for the classification of hate and non-hate speech. Among all the algorithms, the

[2]https://huggingface.co/

Models	**Acc↑**	**MMAE↓**	**F1-Score↑**
Naive Bayes	0.766	0.410	0.589
Decision Tree	0.849	0.438	0.568
Logistic Regression	0.820	0.410	0.604
SVM	0.916	0.303	0.533
LSTM (Upscaled)	0.892	0.350	0.639
Bi-LSTM	0.901	0.367	0.585
Bi-LSTM + CNN	0.873	0.391	0.616
XLM-Roberta	0.906	0.322	0.603
BERT (HAM)	0.913	0.272	0.706
BERT (HCMAM)	0.905	0.307	0.659
RoBERTa	**0.923**	**0.230**	**0.725**
Human Evaluator-A	0.959	0.126	0.847
Human Evaluator-B	0.968	0.087	0.881

Table 3: Baseline Results with different algorithms

RoBERTa (multilingual) and BERT (HAM) models had a nearly equal best performance with an F1-score of 0.725 and 0.706, respectively. Among the machine learning algorithm, logistic regression performed the best with an F1-score of 0.604. We can see that the transformer-based models had better results than machine learning and deep learning models. The relatively lower F1-score of models compared to human evaluators emphasizes the need to develop more advanced and robust algorithms for hate speech detection in contexts like the Indian assembly election campaign.

Conclusion and Future Work

This paper presents the IEHate dataset, which can be a valuable resource for developing and evaluating hate speech detection models in Indian election campaign discourse. The dataset consists of tweets in the Hindi language, which is a language that has not been studied extensively in hate speech detection. Despite the inherent subjectivity of annotations, the high inter-annotator agreement indicates a good level of consistency in labeling hate speech. Developing novel NLP models tailored to detecting hate speech in the context of Indian Election campaigns would be a promising area of exploration. Additionally, exploring hate speech toward detecting targets can be a promising direction. Overall, we believe that the IEHATE dataset will contribute to advancing the development of effective hate speech detection models, promoting a more inclusive and respectful online discourse in India.

References

Barbieri, F.; Anke, L. E.; and Camacho-Collados, J. 2022. XLM-T: Multilingual Language Models in Twitter for Sentiment Analysis and Beyond. arXiv:2104.12250.

Beddiar, D. R.; Jahan, M. S.; and Oussalah, M. 2021. Data expansion using back translation and paraphrasing for hate speech detection. *Online Social Networks and Media*, 24: 100153.

Bohra, A.; Vijay, D.; Singh, V.; Akhtar, S. S.; and Shrivastava, M. 2018. A dataset of Hindi-English code-mixed social media text for hate speech detection. In *Proceedings of the second workshop on computational modeling of people's opinions, personality, and emotions in social media*, 36–41.

Chandramouli, C.; and General, R. 2011. Census of India 2011. *Provisional Population Totals. New Delhi: Government of India*, 409–413.

Cortes, C.; and Vapnik, V. 1995. Support-vector networks. *Machine learning*, 20(3): 273–297.

Das, M.; Banerjee, S.; and Mukherjee, A. 2022. Data Bootstrapping Approaches to Improve Low Resource Abusive Language Detection for Indic Languages. *arXiv preprint arXiv:2204.12543*.

Hochreiter, S.; and Schmidhuber, J. 1997. Long Short-Term Memory. *Neural Computation*, 9(8): 1735–1780.

Kumar, R.; Reganti, A. N.; Bhatia, A.; and Maheshwari, T. 2018. Aggression-annotated Corpus of Hindi-English Code-mixed Data. In *Proceedings of the Eleventh International Conference on Language Resources and Evaluation (LREC 2018)*. Miyazaki, Japan: European Language Resources Association (ELRA).

Mir, A. A.; and Rao, A. N. 2022. The Use Of Social Media In Indian Elections: An Overview. *Webology*, 19(6).

Modha, S.; Majumder, P.; Mandl, T.; and Mandalia, C. 2020. Detecting and visualizing hate speech in social media: A cyber watchdog for surveillance. *Expert Systems with Applications*, 161: 113725.

Mulki, H.; Haddad, H.; Ali, C. B.; and Alshabani, H. 2019. L-hsab: A levantine twitter dataset for hate speech and abusive language. In *Proceedings of the third workshop on abusive language online*, 111–118.

Parihar, A. S.; Thapa, S.; and Mishra, S. 2021. Hate Speech Detection Using Natural Language Processing: Applications and Challenges. In *2021 5th International Conference on Trends in Electronics and Informatics (ICOEI)*, 1302–1308. IEEE.

Parwez, Z. 2022. An Exemplifying Study On Voting Behaviour, Fake News And Associated Laws. *Journal of Positive School Psychology*, 2784–2792.

Rish, I.; et al. 2001. An empirical study of the naive Bayes classifier. In *IJCAI 2001 workshop on empirical methods in artificial intelligence*, volume 3, 41–46.

Rokach, L.; and Maimon, O. 2005. Decision trees. *Data mining and knowledge discovery handbook*, 165–192.

Sreelakshmi, K.; Premjith, B.; and Soman, K. 2020. Detection of hate speech text in Hindi-English code-mixed data. *Procedia Computer Science*, 171: 737–744.

Stoltzfus, J. C. 2011. Logistic Regression: A Brief Primer. *Academic Emergency Medicine*, 18(10): 1099–1104.

Templin, D. 2013. The Devanagari Script. *Hindilangauge. info*.

Thapa, S.; Shah, A.; Jafri, F.; Naseem, U.; and Razzak, I. 2022. A multi-modal dataset for hate speech detection on social media: Case-study of russia-ukraine conflict. In *Proceedings of the 5th Workshop on Challenges and Applications of Automated Extraction of Socio-political Events from Text (CASE)*, 1–6.

Vadesara, A.; and Tanna, P. 2023. Corpus Building for Hate Speech Detection of Gujarati Language. In *Soft Computing and Its Engineering Applications: 4th International Conference, icSoftComp 2022, Changa, Anand, India, December 9–10, 2022, Proceedings*, 382–395. Springer.

Vargas, F.; Carvalho, I.; de Góes, F. R.; Pardo, T.; and Benevenuto, F. 2022. HateBR: A Large Expert Annotated Corpus of Brazilian Instagram Comments for Offensive Language and Hate Speech Detection. In *Proceedings of the Thirteenth Language Resources and Evaluation Conference*, 7174–7183.

Velankar, A.; Patil, H.; Gore, A.; Salunke, S.; and Joshi, R. 2021. Hate and Offensive Speech Detection in Hindi and Marathi. *arXiv preprint arXiv:2110.12200*.

Vidgen, B.; and Yasseri, T. 2020. Detecting weak and strong Islamophobic hate speech on social media. *Journal of Information Technology & Politics*, 17(1): 66–78.

Waseem, Z.; and Hovy, D. 2016. Hateful Symbols or Hateful People? Predictive Features for Hate Speech Detection on Twitter. In *Proceedings of the NAACL Student Research Workshop*, 88–93. San Diego, California: Association for Computational Linguistics.

Zhuravskaya, E.; Petrova, M.; and Enikolopov, R. 2020. Political effects of the internet and social media. *Annual review of economics*, 12: 415–438.